

AD-A055 859

UNIVERSITY COLL LONDON (ENGLAND) DEPT OF MECHANICAL --ETC F/G 13/10  
SYMPOSIUM ON NAVAL HYDRODYNAMICS. UNSTEADY HYDRODYNAMICS OF MAR--ETC(U)  
1978 R E BISHOP, A G PARKINSON, W G PRICE N00014-76-C-0093

UNCLASSIFIED

NL

1 OF 9

AD  
A055859





AD No. \_\_\_\_\_

DDC FILE COPY

A055859

1

DDC  
RECEIVED  
JUN 29 1978  
A

**DISTRIBUTION STATEMENT A**

Approved for public release  
Distribution Unlimited

THIS PAGE IS BEST QUALITY PRACTICABLE  
FROM COPY FURNISHED TO DDC

**THE  
ELEVENTH SYMPOSIUM ON  
NAVAL HYDRODYNAMICS**

APPROVED FOR PUBLIC RELEASE;  
DISTRIBUTION UNLIMITED

1 58 06 08 024

UNCLASSIFIED

SECURITY CLASSIFICATION OF THIS PAGE (When Data Entered)

REPORT DOCUMENTATION PAGE		READ INSTRUCTIONS BEFORE COMPLETING FORM
1. REPORT NUMBER	2. GOVT ACCESSION NO.	3. RECIPIENT'S CATALOG NUMBER
4. TITLE (and Subtitle) The Eleventh Symposium on Naval Hydrodynamics - Unsteady Hydrodynamics of Marine Vehicles		5. TYPE OF REPORT & PERIOD COVERED Final Proceedings Volume
		6. PERFORMING ORG. REPORT NUMBER
7. AUTHOR(s) Editors: R.E.D. Bishop; A.G. Parkinson; and W.G. Price		8. CONTRACT OR GRANT NUMBER(s) N00014-76-C-0093 <i>New</i> NR 062-508
9. PERFORMING ORGANIZATION NAME AND ADDRESS University College London Department of Mechanical Engineering London, England <i>392 016</i>		10. PROGRAM ELEMENT, PROJECT, TASK AREA & WORK UNIT NUMBERS 61153N RR 023-01-01 1-12
11. CONTROLLING OFFICE NAME AND ADDRESS Office of Naval Research Code 438 Arlington, VA 22217		12. REPORT DATE 1978
14. MONITORING AGENCY NAME & ADDRESS (if different from Controlling Office)		13. NUMBER OF PAGES 840
		15. SECURITY CLASS. (of this report)  UNCLASSIFIED
		15a. DECLASSIFICATION/DOWNGRADING SCHEDULE NA
16. DISTRIBUTION STATEMENT (of this Report)  APPROVED FOR PUBLIC RELEASE; DISTRIBUTION UNLIMITED		
17. DISTRIBUTION STATEMENT (of the abstract entered in Block 20, if different from Report)		
18. SUPPLEMENTARY NOTES Published by Mechanical Engineering Publications Limited (LONDON and NEW YORK)		
19. KEY WORDS (Continue on reverse side if necessary and identify by block number) Naval hydrodynamics; Marine vehicles; Unconventional craft; Structural Dynamics; Unsteady Propulsion; Ship hydrodynamics		
20. ABSTRACT (Continue on reverse side if necessary and identify by block number) Continuing the traditional policy of featuring current research results in important problem areas in ship hydrodynamics, "Unsteady Hydrodynamics of Marine Vehicles" was selected as the theme for the Eleventh Symposium. The technical programme covered a broad range of topics under this general theme including several sessions on modern experimental techniques, on the behaviour of marine vehicles in waves and in restricted waters, on related general hydrodynamic problems, on the hydrodynamic loads and structural responses of ships in a seaway, on the hydrodynamic performance of various unconventional		

DD FORM 1 JAN 73 1473

EDITION OF 1 NOV 65 IS OBSOLETE  
S/N 0102-014-6601UNCLASSIFIED  
SECURITY CLASSIFICATION OF THIS PAGE (When Data Entered)

UNCLASSIFIED

SECURITY CLASSIFICATION OF THIS PAGE(When Data Entered)

20. continued

craft, and on unsteady propulsion problems.

UNCLASSIFIED

SECURITY CLASSIFICATION OF THIS PAGE(When Data Entered)



①

# THE ELEVENTH SYMPOSIUM ON NAVAL HYDRODYNAMICS

## UNSTEADY HYDRODYNAMICS OF MARINE VEHICLES

⑥ Symposium on Naval Hydrodynamics •  
Unsteady Hydrodynamics of Marine  
Vehicles (11th) Held at the University  
College, London (England) on  
28 March-2 April 1976.

An International Symposium sponsored jointly by  
the Office of Naval Research and University College London  
with the support of  
Admiralty Experiment Works, Haslar,  
Ship Division, National Physical Laboratory, Feltham,  
and Stone Manganese Marine Ltd, London

DEPARTMENT OF MECHANICAL ENGINEERING  
UNIVERSITY COLLEGE LONDON  
28 March-2 April 1976

⑩ EDITORS: R. E. D./BISHOP, A. G./PARKINSON, W. G./PRICE

⑨ Final rept.

⑪ 1978 ⑫ 856p.

⑮ NP4414-76-C-4493

⑯ RR02301 ⑰ RR0230101

**DISTRIBUTION STATEMENT A**

Approved for public release;  
Distribution Unlimited

DDC  
RECEIVED  
JUN 29 1978  
A

Published by Mechanical Engineering Publications Limited  
LONDON AND NEW YORK

392 016

JOB

This publication is copyright under the Berne Convention and the International Copyright Convention. Apart from any fair dealing for the purpose of private study, research criticism or review as permitted under *The Copyright Act 1956*, no part may be reproduced, stored in a retrieval system or transmitted in any form or by any means without the prior permission of the copyright owners. Inquiries should be addressed to Mechanical Engineering Publications Ltd, PO Box 24, Northgate Avenue, Bury St Edmunds, Suffolk IP32 6BW

© The Institution of Mechanical Engineers 1977

ISBN 0 85298 360 3

Mechanical Engineering Publications Limited  
is the publisher for the Institution  
of Mechanical Engineers

This work relates to Department of the Navy Contract N00014-76-C-0093 issued by the Office of Naval Research under Contract Authority NR 062-508. However, the content does not necessarily reflect the position or the policy of the Department of the Navy or the Government, and no official endorsement should be inferred.

The United States Government has a royalty-free, nonexclusive and irrevocable license throughout the world for Government purposes to publish, translate, reproduce, deliver, perform, dispose of, and to authorize others so to do, all or any portion of this work.

ADDITIONAL	
NTIS	White Section <input checked="" type="checkbox"/>
DOC	Buff Section <input type="checkbox"/>
UNANNOUNCED	<input type="checkbox"/>
JUSTIFICATION	
BY	
DISTRIBUTION/AVAILABILITY CODES	
Dist	AVAIL. and/or SPECIAL
A	



# CONTENTS

Preface	
R. D. Cooper	vii
Introduction	
R. E. D. Bishop, A. G. Parkinson, W. G. Price	ix
Welcoming Address	
<i>The Right Hon. Lord Annan</i>	xi
Welcoming Address	
S. Koslov	xi
Welcoming Address	
R. J. Daniel	xii
Corrigenda	xiv

## SESSION I

### MODERN EXPERIMENTAL TECHNIQUES (1)

Transient-maneuver testing and the equations of maneuvering, by T. Frank, D. J. Loeser, C. A. Scragg, O. J. Sibul, W. C. Webster, and J. V. Wehausen	3
Advanced experimental techniques for testing ship models in transient water waves. Part I The transient test technique on ship motions in waves, by S. Takezawa and M. Takekawa	23
Advanced experimental techniques for testing ship models in transient water waves. Part II The controlled transient water waves for using in ship motion tests, by S. Takezawa and T. Hirayama	37
Experimental techniques and methods of analysis used at Hydronautics for surface-ship manoeuvring predictions, by A. Goodman, M. Gertler, and R. Kohl	55
CPMC—A novel facility for planar motion testing of ship models, by O. Grim, P. Oltmann, S. D. Sharma, and K. Wolff	115
Discussions and Authors' replies	133

## SESSION II

### MODERN EXPERIMENTAL TECHNIQUES (2)

The 'Wavedozer': a travelling beam wavemaker, by N. Hogben	139
An experimental investigation of the three-dimensional turbulent boundary layer on a ship model, by L. Larsson	161
The ultimate half roll before capsize on the analog computer, by K. Kure, H. Ketelsen and V. Jensen	187
The roles of flow transition, laminar separation, and turbulence stimulation in the analysis of axisymmetric body drag, by J. H. McCarthy, J. L. Power, and T. T. Huang	205
Random wave generation for research on immersed marine vehicles, by J. H. van Oorschot and F. Koopmans	233
Discussions and Authors' replies	249

## SESSION III

### MARINE VEHICLES IN WAVES

Some aspects of ship motions and impulsive wave loads on an ore carrier model in two-directional cross waves, by H. Kitagawa	263
Application of the functional polynomial model to the ship added resistance problem, by J. F. Dalzell	279
Numerical solution of unsteady ship wave problems, by R. C-K. Chan and J. H. Stuhmiller	303
Two-dimensional and conditional distribution laws of sea wave components, by I. K. Boroday and Ya. M. Kublanov	315
Three-dimensional calculations of wave forces by a hybrid element method, by D. K. P. Yue, H. S. Chen and C. C. Mei	325
The second-order steady force and moment on a ship moving in an oblique seaway, by Wen-Chin Lin and A. Reed	333
Discussions and Authors' replies	347

## SESSION IV UNCONVENTIONAL CRAFT

Some aspects of sidehull hydrodynamics and maneuvering in the design of surface effect ships, by R. B. Wade and S. Wang	355
The effect of air compressibility on the nonlinear motion of an air-cushion vehicle over waves, by L. J. Doctors	373
Some aspects of hydrofoil motions and their implications for crew performance, by D. Johnson, L. T. Messum, and K. Nicholson	389
Wave impacts on hydrofoil ships and structural implications, by T. G. Drummond, M. Mackay, and R. T. Schmitke	397
An experimental study of a superventilated finite aspect ratio hydrofoil near a free surface, by O. Furuya and A. J. Acosta	415
The results of the experimental investigation on the skirt parameters influence on resistance and stability characteristics of a hovercraft, by E. Brzoska, L. Kobylinski, M. Krezelewski, and K. Paul	441
The use of oscillators to obtain hydrodynamic and structural load data for SES craft, by P. Kaplan, S. Davis, and A. Malakhoff	451
Discussions and Authors' replies	471

## SESSION V GENERAL HYDRODYNAMICS

The interaction of stationary vessels with regular waves, by J. N. Newman	491
A theory for wave power absorption by oscillating bodies, by D. V. Evans	503
Finite-amplitude unsteady slender-body flow theory, by T. Y. Wu and G. T. Yates	517
On the virtual mass, at long wavelengths, of a half-immersed circular cylinder heaving on water of finite depth, by P. Sayer and F. Ursell	529
Prediction of free-surface effects on ship manoeuvring, by R. B. Chapman	533
Velocity potentials of submerged bodies near a free surface-application to wave-excited forces and motions, by M. S. Chang and P. C. Pien	545
Discussions and Authors' replies	555

## SESSION VI STRUCTURAL DYNAMICS

Wave and structural load experiments for elastic ships, by R. Wereldsma and G. Moeyes	567
Theoretical prediction of the vertical dynamic response of ships structures using finite elements and correlation with ship mobility, by D. Catley and C. Norris	587
Low frequency second order wave forces on vessels moored at sea, by J. A. Pinkster	603
Elastic structural response of semisubmersibles in regular waves, by K. Yoshida and K. Ishikawa	617
Discussion and Authors' replies	631

## SESSION VII MARINE VEHICLES IN RESTRICTED WATERS

Ship-ship interaction in shallow water, by I. W. Dand	637
The effects of the restricted waters on the added mass of a rectangular cylinder, by M. Fujino	655
Interaction effects of ships operating in proximity in deep and shallow water, by M. A. Abkowitz, G. M. Ashe, and R. M. Fortson	671
Some characteristics of flow around ships at different drift angles in shallow water, by V. N. Treshchevsky and A. I. Korotkin	693
Discussion and Authors' replies	705

## SESSION VIII UNSTEADY PROPULSION

Low frequency variation of the surface shape of tip region cavitation on marine propeller blades and corresponding disturbances on nearby solid boundaries, by T. Søntvedt and H. Frivold	717
Some ideas about the optimization of unsteady propellers, by J. A. Sparenberg	731
Steady and unsteady loadings and hydrodynamic forces on counterrotating propellers, by S. Tsakonas, W. Jacobs, and M. Ali	745
Vibration excitation forces from a cavitating propeller. Model and full scale tests on a high speed container ship, by C.-A. Johnsson, O. Rutgersson, S. Olsson, and O. Björheden	757
Experimental determination of mean and unsteady loads on a model CP propeller blade for various simulated modes of ship operation, by R. J. Boswell, J. J. Nelka, and S. B. Denny	789
Discussion and Authors' replies	825
List of participants	835

## PREFACE

The Eleventh Symposium on Naval Hydrodynamics was held at the University College London, London, England, on 28 March – 2 April 1976 under the joint sponsorship of the Office of Naval Research and University College London with the support of the Admiralty Experiment Works, Haslar, the Ship Division, National Physical Laboratory, Feltham, and Stone Manganese Marine Ltd, London.

Continuing the traditional policy of featuring current research results in important problem areas in ship hydrodynamics, 'Unsteady Hydrodynamics of Marine Vehicles' was selected as the theme for the Eleventh Symposium. The technical programme covered a broad range of topics under this general theme including several sessions on modern experimental techniques, on the behaviour of marine vehicles in waves and in restricted waters, on related general hydrodynamic problems, on the hydrodynamic loads and structural responses of ships in a seaway, on the hydrodynamic performance of various unconventional craft, and on unsteady propulsion problems.

The Symposium was expertly organized and managed by Professor R. E. D. Bishop of the Department of Mechanical Engineering, University College London, ably assisted by his colleagues, Dr A. G. Parkinson and Dr W. G. Price. The success of this meeting is the direct result of the careful, thoughtful attention given by this triumvirate to the seemingly endless details that must be taken into account in the planning of a symposium of this magnitude. It is also a great pleasure to acknowledge our indebtedness to Shell International Marine Ltd for a delightful reception and film show at the Shell Centre, London, to the Royal Naval College Greenwich, for an interesting tour and lovely reception, to Stone Manganese Marine Ltd, for an entertaining and edifying visit to their propeller works in Birkenhead, and to Lloyd's of London for the elegant symposium banquet held in their Captains' Room. To these and many others who made large and small contributions to the success of this Symposium, my colleague, Mr Stanley Doroff, and myself wish to express our appreciation on behalf of the Office of Naval Research for a job well done.

RALPH D. COOPER  
Fluid Dynamics Program  
Office of Naval Research

## INTRODUCTION

When two of us (R.E.D.B. and A.G.P.) went to Cambridge, Mass. in August 1974 we were attending our first ONR Symposium. And so far as the reading of a paper at one of these meetings goes, we were all entering the ring for the first time. That the very next Symposium of the series would be organized by us on our home ground had not even struck us as a possibility. But so it turned out—and great fun it was.

Truth to tell, it was more than a pleasure to play the host. It was an honour. For 1976 is no ordinary year for the Naval Hydrodynamics Symposia. It is not only 20 years since the first of these gatherings was held, but it is 30 years since their sponsor and instigator, the Office of Naval Research was set up. The enormous prestige, both of the ONR and of its international meetings, needs absolutely no endorsement from beginners like us. But we in UCL can take this chance of offering the ONR the gratitude and congratulations of the whole international community of naval hydrodynamicists.

At the same time, we wonder if we might say a rather more personal word of appreciation. So quietly does Mr Ralph Cooper go about his work, we wonder if any but the actual organizers of the Symposia can have any conception of the enormous contribution that he makes. On the face of it the arrangement of a meeting like an ONR Symposium, in partnership with a huge department of a foreign government, is a pretty daunting undertaking. In practice, thanks to Ralph and his equally self-effacing colleague Stan Doroff, there is never a hitch and business relationships turn into valued friendships.

What about the Symposium itself? With relief we can report nothing untoward. The technical side is, of course, recorded in the pages that follow and it speaks for itself.

As to the social programme, well here we have to acknowledge the generosity of a number of friends. Stone Manganese Marine Ltd invited the delegates to the firm's works in Birkenhead; Shell International Marine Ltd gave a magnificent reception for us at the Shell Centre in London; we were privileged to be allowed to have a reception at the Royal Naval College Greenwich, when both the Commander and the First Lieutenant gave illuminating (and witty) introductions to the lovely old buildings; and the Chairman and Committee of Lloyd's of London permitted us to use the Captains' Room for a Symposium Dinner.

A word must be said about the way the Symposium was run. Early on, an Organizing Committee was empanelled. Its membership was:

- Prof. R. E. D. Bishop (Chairman, UCL)
- Mr T. B. Booth, (AEW)
- Dr R. K. Burcher (MOD)
- Dr G. Gadd (NPL)
- Dr A. G. Parkinson (Secretary, UCL)
- Dr W. G. Price (Secretary, UCL)
- Mr L. Sinclair (Stone Manganese Marine Ltd)
- Prof. F. Ursell (Manchester University)

Once it had been agreed in outline what should be done, that Committee entrusted the actual running of the Symposium to the three of us. Having taken full advantage of this freedom we really must acknowledge the act of faith performed by the Committee.

All in all, our abiding reaction is that the Eleventh Symposium was 'quite a party'. We only hope that the participants enjoyed it as much as we did.

R. E. D. BISHOP  
A. G. PARKINSON  
W. G. PRICE

PRECEDING PAGE BLANK-NOT FILMED



**WELCOMING ADDRESS**  
**THE RIGHT HON. LORD ANNAN**  
PROVOST, UNIVERSITY COLLEGE LONDON

In opening this Symposium and welcoming the delegates, let me say how delighted I am that they have come from all parts of the world to meet here in London. Ever since it was set up, University College has always been a pioneer in research and teaching. It was the first university in England to teach Engineering, Medicine, and Foreign Languages, and it tries to preserve its reputation for originality by developing specialisms within its existing departments. It is very appropriate that the Eleventh Symposium should be meeting here, if only for the fact that our Department of Mechanical Engineering now gives priority to research in Naval Architecture, and has incorporated within it all the advanced teaching for the Royal Corps of Naval Constructors.

**WELCOMING ADDRESS**  
**Dr. S. KOSLOV**

OFFICE OF THE ASSISTANT SECRETARY OF THE NAVY (R & D), USA

I certainly welcome the opportunity to be here today and unfortunately send the regrets of Secretary Marcy and RADM Geiger for their inability to attend. I had the opportunity to attend this Symposium four years ago in Paris and welcome a chance to participate again. This Symposium series, from the beginning, has been designed to be an international forum for exchange of advanced research results in naval hydrodynamics and has been held every two years alternately abroad (from the US viewpoint) and in the United States. This is the twentieth anniversary of this Symposium and also the thirtieth anniversary for ONR. It is fitting indeed to have this special anniversary event here in the United Kingdom in that it is the first held in the United Kingdom. Our British colleagues have continually made major contributions to the success of the Symposia.

We are honored by the participation of the Admiralty Experiment Works and the National Physical Laboratory in sponsoring this symposium. The US Navy and ONR in particular have had a long continuing and fruitful history of collaboration with these establishments. We are deeply grateful to the University College London, particularly to Professor Bishop, Dr Parkinson, and Dr Price for the giant role that they have played in organizing this symposium and for being such gracious and comfortable hosts. Let me also personally note how much work has gone into this symposium by many of the ONR crew, particularly Ralph Cooper. I should add that direct participation includes twelve countries: Australia, Canada, Denmark, Japan, The Netherlands, Norway, Poland, Sweden, UK, US, USSR, West Germany, as well as representatives from many more.

The theme of the symposium 'Unsteady Hydrodynamics of Marine Vehicles' reflects the continuing problem of behaviour of ships in a seaway with its implications for the related aspects of economics and safety and of course for military operations. A wide variety of aspects of the hydrodynamics problem are included in the programme: experimental techniques for laboratory research, wave forces in a seaway, ship motions in a seaway, special attention is given to the unsteady behaviour of unconventional craft—surface effect ships, air cushion vehicles, and hydrofoils, structural responses of ships to wave forces, the special problems of ships operating in shallow water, and, finally, unsteady effects related to propulsion. Change is rapidly evolving in the programme from that of some years ago, both in the form of new concepts in marine vehicles and in the application of modern computer technology to handling the problems of great complexity involved.

Thank you again for the opportunity to meet with you and I look forward to interacting with many of you over the next week.

PRECEDING PAGE BLANK-NOT FILMED

## WELCOMING ADDRESS

MR. R. J. DANIEL

DIRECTOR GENERAL SHIPS, MINISTRY OF DEFENCE, U.K.

In making the opening address to this, the Eleventh Symposium on Naval Hydrodynamics, I am conscious of being in the presence of so many renowned experts in a subject in which we have seen significant developments in the past decade, developments in experimental techniques, in theoretical treatment and in practical application. The papers to be presented at this Symposium reflect this progress.

Over the next five days you are to receive papers on the theme of the Unsteady Hydrodynamics of Marine Vehicles. The sessions are arranged as follows:

- I & II Modern experimental techniques
- III Marine vehicles in waves
- IV Unconventional craft
- V General hydrodynamics
- VI Structural dynamics
- VII Marine vehicles in restricted waters, and
- VIII Unsteady propulsion

The scope of the papers and their authors reflect all that is best in Hydrodynamics and Naval Architecture. I have two general comments. Firstly, I believe that in the next few years we will begin to accept that some of the unconventional craft are numerous enough to be considered conventional for certain services and secondly I am amused that the final session is on unsteady propulsion; I have a vision of the Symposium lurching through its final session like a drunken sea captain.

It is a truism that developments in the Mechanical Sciences and Engineering have depended on the availability of suitable tools and materials as well as an understanding of the problem and its solution—the most obvious example of this is the gas turbine. In hydrodynamics one of the tools that has become available in recent years has been the computer. In the past we understood the problem and suggested means for its analysis but were usually not able to solve the twenty-eight or so simultaneous differential equations that resulted.

Classical hydrodynamics is based upon steady-state models as is the three-dimensional modelling technique pioneered by Froude. It was a criticism of ship hydrodynamic research in the past that there appeared to be an obsession with straight-line motions in calm water to an extent that dynamic qualities, in particular control and behaviour in a seaway were less than adequately studied. This is not so today, and this Symposium reflects the change of attitude, illustrating that there is now an attack on the whole problem on three broad fronts.

Firstly, there is the classical frontal assault by the mathematician supported by his heavy artillery of digital computation. Not only are some complex dynamic problems yielding to this attack, but so also are some of the steady-state subtleties of viscous flow.

Secondly, advances on the flank are achieving success using an approach based upon the measurement of forces required to constrain models along precise and pre-determined paths—a technique pioneered by two of this morning's authors with their development of the submarine planar motion mechanism in the USA.

Finally, there is the assault from the rear, a converse approach where the time history of random or loosely controlled manoeuvres at full size or model scale are dissected and then re-synthesized as cause/effect relationships using systems identification techniques.

Our ability today (or, rather, *your* ability today) to attempt numerate solutions to these more difficult and time-consuming problems and the analysis of experiments has, of course, led to the design and introduction of more complex experimental equipment into hydrodynamic research establishments, together with the instrumentation and people to support them.

Further factors that have fed the awakened interest in theoretical hydrodynamics have been the expansion in seaborne trade, the remarkable increase in the size of large ships and the development of new sorts of ships and marine vehicles. The developments in Naval Architecture in our lifetime have been astonishing; I do not believe that the man in the street understands this; but then, since he or she has been able to sit in his home and watch man-made vehicles land on the moon, what marvels can we present to make him understand the constant battle we wage to extract the last possible percentage of efficiency and safety against that restless and relentless element, the sea?

I have mentioned the new techniques available, the facilities, including analogue and digital computers, which will make solutions possible, and the commercial requirement for better ships and offshore rigs that has fuelled the demand for deeper understanding and, may I say, encouraged a significant increase in the numbers of excellent people working in these fields. These are all significant but to me the most significant development



has been the acceptance that all of the problems of a ship's behaviour at sea are aspects of one set of equations (admittedly a very big set of equations) which represent the dynamic behaviour of a non-rigid body and its propulsor in a non-uniformly disturbed fluid.

In the past we could only provide solutions to dynamic situations by static treatment and, of course, we frequently made a series of static calculations to iterate towards an understanding of the dynamic solution. This is why it was desirable if not essential not to depart too much from previous successful practice. Today we have a greater facility by theory and experimentation to understand the possible consequences of change and the wholeness of a ship's responses to the hydrodynamic forces imposed upon it.

In opening this Symposium may I therefore congratulate the authors on their papers and I am sure on the lively discussions that will ensue, observe the greater understanding that today's problems demand and the measures that you are clearly taking in your daily work to solve them, and finally to remark with pleasure that experts from so many nations can come together to discuss hydrodynamics at this Symposium.

## CORRIGENDA

Pages 145-160

Captions, in full, should read as follows:

Fig. 1(a): Vertical beam tests in No 2 tank. Wave behind carriage

Fig. 1(b): Vertical beam tests in No 2 tank. Waves in test area

Fig. 2: Sketch of experiment in small channel

Fig. 3: Photographs of small channel experiment: (a) view from above; (b) balance arm before installation

Fig. 4: Wave profiles in small channel: (a) 15° incidence; (b) 20° incidence; (c) 25° incidence; (d) 90° incidence

Fig. 5: Results from tests in small channel

Fig. 6: Diagrammatic sketch of prototype installation in No 2 tank

Fig. 7: Photographs of prototype experiment: (a) first crest behind carriage; (b) wave train behind carriage; (c) wave passing test cylinder

Fig. 8: Layout of experiments in No 2 tank

Fig. 9: Results of experiments in No 2 tank: series I, conditions at and behind flap. (a) Sample wave traces; (b) wave height  $H_1$  vs speed; (c) flap drag vs speed; (d) wave steepness  $H_1/\lambda$  vs speed; (e) wetted chord  $L_w$  vs speed

Fig. 10: Results of experiments in No 2 tank: series I, conditions at test cylinders. (a) Sample wave traces; (b) sample wave spectra; (c) wave height  $H_2$  vs speed; (d) wave steepness  $H_2/\lambda$  vs speed

Fig. 11: Results of experiments in No 2 tank: series II, conditions at test cylinders

Fig. 12: Energy convergence

Page 218

Column 1, line 7: Sentence beginning 'It is evident . . . ' should read: 'It is evident that model forebody shape can have a calculable effect on stern boundary-layer development and viscous pressure distribution.'

Page 355

Column 1, line 41 should read:

$x, y$ , Trajectory coordinates of craft C.G.

Page 361

Column 2, first line of eq. (8) should read:

$$m(\dot{u} - rv) = X$$

Page 362

Column 1, first line of eq. (10) should read:

$$m(\dot{u} - rv) = X_{\text{pre}} + X_{\text{drag}} + X_s$$

Page 363

Column 2, line 55, for '26 knots' read '27 knots'

Page 370

Fig. 11, line 2 of caption should read: 'of -2° and an immersion ratio of  $21.2 \times 10^{-3}$ '

Page 512

Column 2, reference 2, for 'J. Fluid Mech. (to be published)' read 'J. Fluid Mech., 1975, 71, 273-282'

Page 513

Fig. 2, line 2 of caption should read 'with  $m = 0.5M$  vs. dimensionless wavenumber  $\nu$  for'

Page 515

Figs. 14 and 15. The diagrams should be interchanged. The captions are correct.

Page 519

Left column, 9 lines below equation (14), replace 'quadrupole' with 'octapole'

Left column, 11-14 lines below equation (14), omit the phrase, 'or equivalently, . . . remains the same.'

Page 520

Equation (28) last term on the middle line should read

$$-\frac{3}{8} \left( \frac{r_1}{a} \right)^2 \left( \log \frac{8a}{r_1} - \cos^2 \psi - \frac{1}{6} \right) \cos \psi$$

Equation at top of right column. The last term should read:

$$+\frac{3}{8} \left( \frac{b}{a} \right)^2 \left( \log \frac{8a}{b} - \cos^2 \psi - \frac{7}{6} \right)$$

Equation (30), last term

$$-\frac{3}{8} \left( \frac{b}{a} \right)^2 \left( \log \frac{8a}{b} - \frac{23}{4} \right)$$

Equation (31) is subject to the above mentioned corrections in equations (28) and (30).

Equation (32), middle line, bracket should read

$$\left[ 1 - \frac{\epsilon}{2} \cos \psi + O \left( \epsilon^2 \log \frac{8}{\epsilon} \right) \right]$$

Page 521

Equation (34), last term should read

$$+ e_r \pi \rho \frac{b^2}{a} V^2 \left[ 1 - \frac{3}{2} \cos^2 \theta \right]$$

Page 523

Equation between equations (58) and (59) should read

$$= U_n^* \cos \psi - U_s \frac{db}{ds}$$

Also add the two relations

$$U_n^* = U_n - \Omega b b' \text{ and } \Omega = -\mathbf{e}_n \cdot \frac{\partial \mathbf{U}}{\partial s}$$

Third equation from bottom in the right column,

$$\beta_n(s, t) = \frac{1}{2} U_n^* b^2,$$

Page 531

Eq. (3.4) should read

$$\begin{aligned} \text{V.M.} = & -\frac{8}{\pi^2} \{ \gamma + \log Ka - G_1(Kh) - \frac{3}{2} + 2 \log 2 \} \\ & + \{ T(Ka, Kh) + A \} \frac{a}{h} + O \left\{ \frac{a}{h} \log \frac{h}{a} \right\}^2, \end{aligned}$$

where

$$T(Ka, Kh) = -\frac{16}{\pi^3} \{ \log Ka - G_1(Kh) \} \{ \log Ka - G_1 \}$$

$$A = -\frac{7}{3\pi} - \frac{16}{\pi^3} \left\{ \gamma - \frac{3}{4} + 2 \log 2 - \frac{1\pi^2}{4} - \frac{7}{8}\zeta(3) + C \right\},$$

$$B = 2\gamma - 3 + 4 \log 2 - \frac{1}{4}\pi^2$$

$$C = \sum_{m=1}^{\infty} \sum_{n=1}^{\infty} \frac{1}{m(4m^2-1)n(2n+1)(2m+2n-1)(2m-2n+1)} \approx 0.0304;$$

whence (3.8) becomes

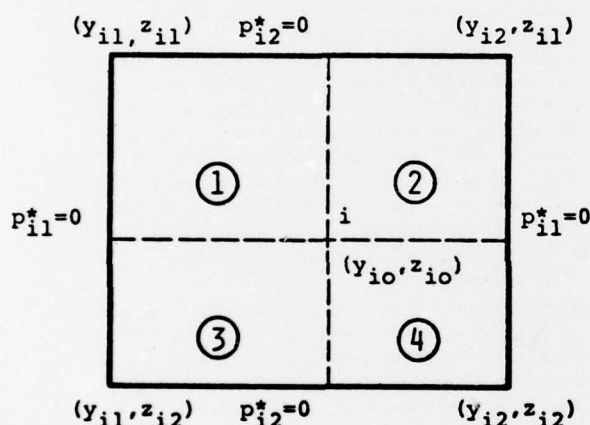
$$\Delta(V.M.) = -\frac{8}{\pi^2} \{ \gamma - \log \pi - G_1(1) \} + O\left\{ \frac{a}{h} \log \frac{h}{a} \right\},$$

$$\rightarrow 0.1166 \text{ as } a/h \rightarrow 0.$$

Therefore the maximum is perceptible for small  $a/h$ .

Page 668

Fig. 2 should be replaced by the following



Page 671

Column 2, line 21 should read: 'scripts—i.e.,  
 $N_{re}^2 = \partial^3 N / \partial r \partial v^2$ '

Page 674

Column 2, last line of eq. (20) should read:

$$\zeta_{62} = \omega \zeta R^2(\xi) \left( 1 + \frac{A_{22}}{\rho V} \right)$$

Page 675

Column 2, third line of eq. (33) should read:

$$+ \zeta_v(\xi) \left\{ \frac{dq_1}{dy} \right\}$$

Page 676

Column 2, line 21 should read:

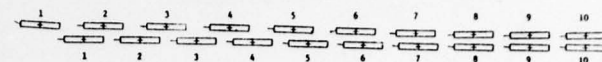
$$Y_{\delta vv} = \left( \frac{\partial^3 Y}{\partial \delta \partial v^2} \right)$$

Page 679

Column 2, line 27 should read: 'Yaw angle  $1.0^\circ$ '

Page 689

Replace upper half of diagram by the following:

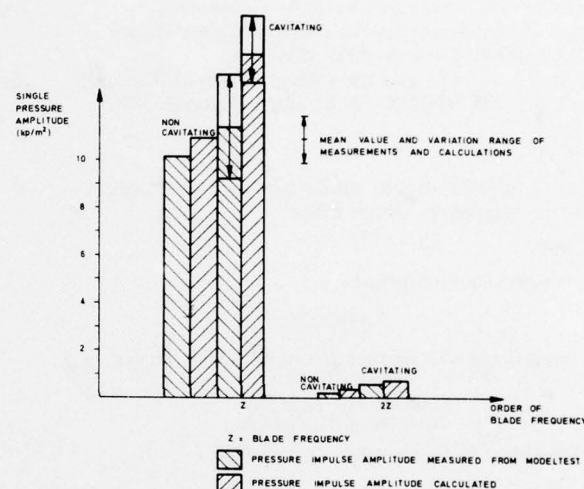


Page 719

Date of reference (1) should read 1976

Page 724

Replace Fig. 8 by:



Pages 731-743

# CORRECTIONS TO THE PAPER SOME IDEAS ABOUT THE OPTIMIZATION OF UNSTEADY PROPELLERS

by J. A. Sparenberg

In section 3 of this paper the incoming velocity  $U$  is defined in the wrong direction. In Fig. 5 this incoming velocity has to be positive in the positive  $x$  direction in order that equation (3.4) will be valid.

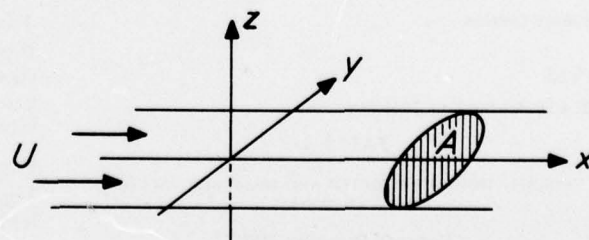


Fig. 5: The plan form A.

The thrust has to be reckoned positive in the negative  $x$  direction, the  $-$  sign before the integrations in (3.7) has to be changed to a  $+$  sign. Also the formulae which follow from (3.7) have to be changed correspondingly. Figure 6 has to be changed as follows.



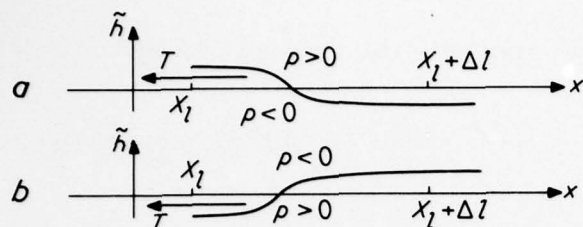


Fig. 6: The kinematic profile: (a) during upward stroke, (b) during downward stroke.

In section 7, fifth paragraph, third line, read:  
—stant vorticity to the whole . . .

Page 745

Insert the following acknowledgement:  
'This study has been conducted under the combined support of the Naval Sea Systems Command General Hydrodynamics Research Program under Contract N00014-67-A-0202-0047 and N00014-75-C-0483 and the Office of Naval Research under Contract N00014-76-M-0023 (NR062-549)'

Page 753

Column 1, line 37 should read: 'any pair of numbers in the two sequences which differ'

Page 754

Table 3 is revised as follows:

TABLE 3

CORRELATION OF PREDICTED AND MEASURED VALUES  
4-0-4 CR SYSTEM

Forward Propeller 3686  
After Propeller 3687-A

Axial Spacing = 0.28 forward propeller radius  $J = 1.1$

$Q = 0$ , Steady State

	THEORY		EXPERIMENT
	Without thickness	With thickness	
Forward $(K_T)_F$	0.126*	0.1639*	0.125
Forward $(K_Q)_F$	0.0295*	0.0373*	0.0315
After $(K_T)_A$	0.145*	0.1335*	0.150
After $(K_Q)_A$	0.0330*	0.0308*	0.0315
$Q = 2N = 8$			
Forward $(K_T)_F$	0.0485	0.0747	0.0285
Forward $(K_Q)_F$	0.0101	0.0154	0.0058
After $(K_T)_A$	0.1156	0.1524	0.0095
After $(K_Q)_A$	0.0242	0.0312	0.0022

\* Including friction

Page 755

Table 4 is revised as follows:

TABLE 4

CORRELATION OF PREDICTED AND MEASURED VALUES  
4-0-5 CR SYSTEM

Forward Propeller 3686  
After Propeller 3849

Axial Spacing = 0.28 forward propeller radius  $J = 1.1$

$Q = 0$ , Steady State

	THEORY		EXPERIMENT
	Without thickness	With thickness	
Forward $(K_T)_F$	0.087*	0.1060*	0.130
Forward $(K_Q)_F$	0.0207*	0.0246*	0.030
After $(K_T)_A$	0.161*	0.1093*	0.130
After $(K_Q)_A$	0.0361*	0.0255*	0.028
$Q_F = 2N_A - 1 = 9$			
Forward $(K_{FH})_F$	0.0079	0.0239	0.0075
After $(K_{FH})_A$	0.0079	0.0239	0.0074
Forward $(K_{QH})_F$	0.0062	0.0053	0.0040
Forward $(K_{QV})_F$	0.0062	0.0053	0.0041
$Q_A = 2N_F + 1 = 9$			
After $(K_{FH})_A$	0.0231	0.0275	0.0057
After $(K_{FV})_A$	0.0231	0.0275	0.0046
After $(K_{QH})_A$	0.0159	0.0181	0.0023
After $(K_{QV})_A$	0.0159	0.0181	0.0023

\* Including friction

Add, at end of 'Conclusions' section:

Some remarks are in order on the discrepancies between theory and experiment.

- (1) A few years ago an attempt was made to calculate unsteady thrust and torque of a counterrotating propeller system by a stripwise method following the Kemp and Sears approach for the mutual interference of blades in cascade due to relative motion of successive blade rows. Results of this study have shown that the unsteady thrust of the after propeller is much higher than that of the forward propeller, when the bound vorticity and the vortex wake shed by the forward propeller are taken into account either with flat plate modes or with an elliptic distribution.
- (2) Furthermore, observation of Dr. Wereldsma's experimental results (although these are for non-uniform inflow conditions), especially of the time records of the horizontal and vertical blade bending moments, show that superimposed on the fluctuations due to the wake at blade frequency, are the fluctuations due to blade interference at blade-blade crossing frequency. It can be seen that these fluctuations due to interference are much larger for the after propeller than for the forward.

The question of the discrepancies thus cannot be considered a closed subject, but requires further investigation both theoretical and experimental.

Page 813

Fig. 9d: Curve labelled 'Without dynamometer boat' should be labelled 'With dynamometer boat'. Curve labelled 'With dynamometer boat' should be labelled 'Without dynamometer boat'

Page 815

Fig. 11a: Curve labelled '+0.6' should be labelled '+1.06'

# SESSION I

## MODERN EXPERIMENTAL TECHNIQUES (I)

Monday, 29 March 1976

10.00—12.30

Chairman: E. P. Lover

Transient-maneuver testing and the equations of maneuvering by T. Frank, D. J.

Loeser, C. A. Scragg, O. J. Sibul, W. C. Webster, and J. V. Wehausen

Advanced experimental techniques for testing ship models in transient water waves.

Part I The transient test technique on ship motions in waves, by S. Takezawa  
and M. Takekawa

Advanced experimental techniques for testing ship models in transient water waves.

Part II The controlled transient water waves for using in ship motion tests, by  
S. Takezawa and T. Hirayama

Experimental techniques and methods of analysis used at Hydronautics for  
surface-ship manoeuvring predictions, by A. Goodman, M. Gertler, and R. Kohl

CPMC—A novel facility for planar motion testing of ship models, by O. Grim,  
P. Oltmann, S. D. Sharma, and K. Wolff

# TRANSIENT-MANEUVER TESTING AND THE EQUATIONS OF MANEUVERING

T. FRANK, D. J. LOESER, C. A. SCRAGG, O. J. SIBUL, W. C. WEBSTER, and J. V. WEHAUSEN  
University of California, Berkeley

This paper discusses the choice of an appropriate set of linearized equations for maneuvering and suggests the use of the planar-motion mechanism and transient maneuvers to determine the coefficients occurring in the selected equations. Details of the necessary analysis and the results of experiments are included. The relation between the selected equations and the classical equations of maneuvering is discussed and it is shown that "quasi-steady" solutions of the former are approximated uniformly by solutions of the latter.

## 1. INTRODUCTION

This paper describes the results obtained so far in trying to apply to the maneuvering of ships ideas introduced by Cummins\* (1962), Newman (1966), and Brard (1964, 1972, 1973). The work of these authors has provided the theoretical framework for the work to be reported here; in particular, they have provided the equations of motion upon which the experimental procedures described later are based.

The difference between the approach of these authors and the customary one lies in the description of the hydrodynamic force and moment acting upon a ship during a maneuver. This difference might be caricatured as follows. Let  $y_1$  represent the lateral displacement of the center of gravity of a ship from a straight course and suppose it to be the only perturbation of the motion. Then in the customary approach the equation of motion for the lateral mode of motion is taken in the form

$$m\ddot{y}_1 = Y(\dot{y}_1, \ddot{y}_1), \quad (1)$$

where the hydrodynamic force is assumed to be expressible as a function of the two functions  $\dot{y}_1$  and  $\ddot{y}_1$ , treated as if they were independent variables. The other (and in our opinion sounder) approach is to start with the equation

$$m\ddot{y}_1 = \int_{\text{hull}} p n_y dS, \quad (2)$$

with the pressure  $p$  to be determined by the equations of hydrodynamics. The difficulty here is, of course, to determine

\* References are identified by author(s) and year and listed in alphabetical order by first author at the end of the text.

the pressure  $p$ . However, there does exist the possibility of formulating a mathematical problem whose solution will provide  $p$ , whereas no such possibility is envisaged for  $Y$ , unless it should turn out that the right-hand side of (2) takes this form.

In either approach one now takes some steps to simplify the problem. In the first approach one assumes that  $Y$  may be expanded in a Taylor series:

$$Y = Y_v \dot{y}_1 + Y_{vv} \ddot{y}_1 + Y_{vvv} \ddot{\ddot{y}}_1 + \dots \quad (3)$$

One may then stop with the linear terms, and having assumed that this provides a satisfactory approximation, proceed to devise an experiment to measure  $Y_v$  and  $Y_{vv}$ . According to the underlying assumption, these coefficients ("derivatives") may depend upon the Froude number but not upon the velocity components associated with a maneuver.

In the second approach one must bring to bear upon the problem some systematic approximation procedure, for the full problem, although it can be formulated, is much too complex to be solved. This is the step that has been taken by Cummins and Brard in the papers cited above. Certain improvements upon Cummins' work were made by Ogilvie (1964) and a foundation within perturbation theory was provided by Lin (1966). The first-order terms then provide an approximation to the right-hand side of (2). This approximate theory also provides a specific form for the right-hand side of (2) in terms of the functions  $\dot{y}_1$  and  $\ddot{y}_1$ , but not the same form as the first two terms of (3) except under special circumstances. The constants and functions associated with this form are in principle computable from the theory, but may also



be determined from experiment. It is this second possibility that we shall exploit here.

There is still another procedure that one may follow in trying to improve upon (1). One aspect of (1) that makes the right-hand side physically unacceptable as a general form for the hydrodynamic force is that the force at time  $t$  depends only upon the velocity and acceleration at that instant and not upon the preceding behavior. This is, of course, demonstrable for the motion of a body in an unbounded fluid if irrotational motion of the fluid is assumed. However, the presence of a free surface obviously provides a means of recording the previous motion in such a way that it can affect the present. In order to meet this objection Bishop, Burcher and Price in a series of papers (1973a,b 1974) have replaced (1) by the equation

$$m\ddot{y}_1 = Y\{y_1(t) | t \leq 0\}, \quad (4)$$

where  $Y$  represents a functional depending upon the whole function  $y_1(t)$  for  $t \leq 0$ . Then as a sort of analog to the Taylor-series expansion in (3), they conjecture that  $Y$  can be expanded in a Volterra series in  $\dot{y}_1(t)$  and  $\ddot{y}_1(t)$ :

$$Y = \int_0^\infty Y_v(\tau) \dot{y}_1(t-\tau) d\tau + \int_0^\infty Y_w(\tau) \ddot{y}_1(t-\tau) d\tau + \\ + \int_0^\infty \int_0^\infty Y_v(\tau_1, \tau_2) \dot{y}_1(t-\tau_1) \dot{y}_1(t-\tau_2) + \dots \quad (5)$$

Here the functions  $Y_v(\tau), \dots$  are weighting functions determining the influence upon the force at time  $t$  of the functions  $\dot{y}_1$  and  $\ddot{y}_1$  at an interval  $\tau$  before  $t$ . They may also depend upon the Froude number. Although this assumed form for  $Y$  is not associated with any hydrodynamic problem, so that there is no way in principle of computing the weighting functions, it is possible to devise ways of measuring them if the series does indeed yield a correct expression for the pressure integral in (2). In fact, it will turn out that the linearized theory based upon this approach is identical with that obtained from an analysis of the hydrodynamic problem insofar as the form of the dependence upon  $\dot{y}_1$  and  $\ddot{y}_1$  is concerned.

The purpose of the present paper is two-fold. After a brief recapitulation of the

linearized theory in a form that seems appropriate to us in the light of the remarks above, we wish to show that in theory the planar-motion mechanism can be used to measure various ship-dependent quantities entering into the equations of motion by a procedure that appears to make a more efficient use of this piece of apparatus than the usual frequency-by-frequency testing. Secondly, we wish to report upon the results of some experiments employing the proposed procedure. The procedure appears to be new in maneuvering experiments, but is well known in pitching and heaving (see, e.g., Smith and Cummins 1964). It is, moreover, closely related to a method of Nomoto and Karasuno (1969) for free models.

Finally, in view of results briefly reported by Fujino and Motora (1975) and by Nomoto (1975) at the 14th International Towing Tank Conference, there may be some question as to whether the direction pursued in this paper is really worth much further effort, for their calculations seem to indicate that for practical ship maneuvers the difference in predicted trajectories using the usual maneuvering equations and the ones used here is miniscule. Even if this turns out to be the case, we believe that the experimental procedure described below may turn out to be an efficient way of using the planar-motion mechanism. Furthermore, as Fujino and Motora point out, steering in waves may require the more accurate equations.

## 2. THE EQUATIONS OF MOTION

We shall take the same coordinate system used by Mandel (1967).  $O_0x_0y_0z_0$  is an inertial coordinate system fixed in the fluid with  $z_0=0$  being the undisturbed water surface;  $O_0z_0$  is downwards.  $Oxy\zeta$  is a coordinate system fixed in the ship. We shall suppose that the  $(x, y)$  plane is its longitudinal plane of symmetry and that the  $(x, y)$  plane coincides with the equilibrium water surface when the ship is at rest. For convenience we may suppose that the  $(y, \zeta)$  plane contains the mid-ship section. In this coordinate system the center of mass of the ship will be supposed to be at  $(x_a, y_a, \zeta_a)$  with  $y_a=0$  in almost all applications. Although it is always easier to express the equations of motion in terms of the motion of the center of mass and rotations about it, the center of mass of a particular ship may vary with the loading, whereas the system  $Oxy\zeta$  will remain the same.

At any instant let  $(x_0(t), y_0(t), \zeta_0(t))$  be the coordinates of  $O$  with respect to  $O_0x_0y_0z_0$ , and let  $\psi(t)$  be the angle between  $O_0x_0$  and  $Ox$ ; the positive direction is from  $Ox$  to  $Oy$  as usual. If  $\vec{r} = (x_0, y_0, 0)$ , then the angle between  $Ox$  and  $\vec{r}$  will be denoted by  $\beta(t)$ . Figure 1 shows the two coordinate systems and the angles  $\psi$  and  $\beta$ .

We now make some assumptions that will simplify our problem, but of course also restrict in principle the applicability of the equations. (1) We suppose the water surface smooth except for the disturbance caused by the ship. (2) Although we do not require that the ship not trim, squat nor heel, we do suppose that if the ship does trim, squat and heel, there is no significant interaction with surge, sway and yaw. As a consequence we may take  $y_0(t) \equiv 0$ . (3) The fluid will be taken to be inviscid and its motion irrotational. Consequently the action of the water on the ship can take place only through normal pressure.

The choice of a model for the flow about the ship remains to be made. We shall suppose that the disturbance of the free surface is small enough that the linearized free-surface boundary condition can be used. When the ship is on a straight course with no side forces, we suppose that the velocity is everywhere continuous as well as irrotational. However, when the ship departs from a straight course, we shall suppose that starting at that instant a discontinuity (vortex sheet) forms at the trailing edge of the rudder and at least that part of the stern that terminates with an edge. Even on a straight course there may be a small rudder angle to compensate for the effect of the ships screw or lack of hull symmetry, and hence a trailing vortex sheet.

A systematically developed perturbation theory based upon such a model does not seem to exist. The work of Cummins (1962) and Lin (1966) assumes only small deviations from a uniform motion and a continuous velocity field everywhere. The work of Brard (e.g., 1972 and 1973) admits trailing vortex sheets, but does not provide a derivation of a set of linearized equations within the framework of a perturbation theory. However, the results of these papers and of other related ones in airfoil theory support the conjecture that the set of equations to be introduced below represent properly the hydrodynamic force and moment within the limitations of linearized theory.

Since  $(x_0, y_0, z_0)$  are not at the center of mass of the ship, the equations of motion in the inertial system take the following form:

$$\begin{aligned} m[\ddot{x}_0 - y_0\ddot{\psi} - x_0\dot{\psi}^2] &= \int p n_{x_0} dS + X_{E0}, \\ m[\ddot{y}_0 + x_0\ddot{\psi} - y_0\dot{\psi}^2] &= \int p n_{y_0} dS + Y_{E0}, \\ I_0\ddot{\psi} + m[-\ddot{x}_0 y_0 + \ddot{y}_0 x_0] &= \\ &= \int p[x_0 n_{y_0} + y_0 n_{x_0}] dS + N_{E0}, \end{aligned} \quad (6)$$

where subscripts  $_0$  on  $X_{E0}$  and  $Y_{E0}$  indicate that the external force has been resolved in the directions  $O_0x_0$  and  $O_0y_0$ , respectively and similarly for  $n_{x_0}, n_{y_0}$ ;  $N_{E0}$  is the moment of the force about  $O_0z_0$ ,  $m$  is the mass of the ship and  $I_0$  its moment of inertia about  $O_0z_0$ . The same equations may be rewritten in the ship coordinate system  $Oxyz$ . If we write

$$u = \dot{x}_0 \cos \psi + \dot{y}_0 \sin \psi,$$

$$v = -\dot{x}_0 \sin \psi + \dot{y}_0 \cos \psi, \quad (7)$$

the equations above become the following:

$$\begin{aligned} m[\dot{u} - v\dot{\psi} - y_0\ddot{\psi} - x_0\dot{\psi}^2] &= \int p n_x dS + X_E, \\ m[\dot{v} + u\dot{\psi} + x_0\ddot{\psi} - y_0\dot{\psi}^2] &= \int p n_y dS + Y_E, \\ I_0\ddot{\psi} + m[x_0(\dot{v} + u\dot{\psi}) - y_0(\dot{u} - v\dot{\psi})] &= \\ &= \int p(x n_y - y n_x) dS + N_{E0}, \end{aligned} \quad (8)$$

where now  $X_E, Y_E, x_0, y_0, n_x$ , and  $n_y$  are referred to  $Oxyz$ .

As has been indicated earlier, the chief difficulty in the theory is in evaluating the pressure integrals. For this purpose we shall suppose that we may write

$$u = u_0 + u_1, \quad v = v_1 \quad (9)$$

and that  $u_1, v_1$  and  $\dot{\psi}$  are "small" in some unspecified sense. It follows that  $\beta$  will also be "small". As a result of this assumption of smallness, one may simplify equations (8) by discarding products of small quantities on the left-hand side; at the same time the right-hand side may be replaced to the same order of approximation by the expressions shown on the right-hand side of (10). This yields the following equations (with  $y_0 = 0$  from symmetry):

$$m\dot{u} = -\mu_{xx}\dot{u}_1 - b_{xx}u_1 - \int_0^t u_1(t-\tau)N_{xx}(\tau)d\tau + X_{E1},$$

$$\begin{aligned}
m[\dot{v}_1 + u_0 \dot{\psi} + x_a \ddot{\psi}] &= -\mu_{yy} \dot{v}_1 - k_{yy} v_1 - \\
&- \int_0^\infty v_1(t-\tau) N_{yy}(\tau) d\tau - \mu_{y\psi} \ddot{\psi} - k_{y\psi} \dot{\psi} - \\
&- \int_0^\infty \dot{\psi}(t-\tau) N_{y\psi}(\tau) d\tau + Y_E, \\
I_0 \ddot{\psi} + m x_a (\dot{v}_1 + u_0 \dot{\psi}) &= -\mu_{\psi\psi} \ddot{\psi} - k_{\psi\psi} \dot{\psi} - \\
&- \int_0^\infty \dot{\psi}(t-\tau) N_{\psi\psi}(\tau) d\tau - \mu_{\psi y} \dot{v}_1 - k_{\psi y} v_1 - \\
&- \int_0^\infty v_1(t-\tau) N_{\psi y}(\tau) d\tau + N_{E0}.
\end{aligned}$$

(10)

The equation associated with  $u_0$  has been omitted, but the subscript on  $X_{E1}$  indicates that we have decomposed  $X_E = X_{E0} + X_{E1}$ . Even if  $u_0 = \text{constant}$ , there will be a  $X_{E0}$  term to balance the wave resistance. The constants  $\mu_{xx}, k_{xx}, \dots$ , and the functions  $N_{xx}, \dots$  are in principle determinable by solving a potential-theory problem (not yet formulated in the most general situation), but we shall follow here a different procedure.

The external force and moment components  $Y_E$  and  $N_{E0}$  can be the result of rudder forces, wind gusts, or any other applied force not included in the pressure integrals. In an application of the equations discussed later they will be the force and moment applied to a model by the Planar-Motion Mechanism (PMM). The integrals in (10) represent the effect of the history of the motion in the interval from  $-\infty$  to  $t$ . If one wishes to discuss an initial-value problem in which  $v_1$  and  $\psi$  are zero before  $t=0$ , the limits of the integrals will be taken from 0 to  $t$ .

We follow custom by defining  $\hat{v} = \dot{\psi}$  and write the last two equations of (10) as follows (dropping the subscript on  $v_1$ ):

$$\begin{aligned}
(m + \mu_{yy}) \dot{v} + \beta_{yy} v + \int_0^\infty v(t-\tau) N_{yy}(\tau) d\tau + \\
+ (\mu_{y\psi} + m x_a) \hat{v} + (\beta_{y\psi} + m u_0) \hat{v} +
\end{aligned}$$

$$\begin{aligned}
+ \int_0^\infty \hat{v}(t-\tau) N_{y\psi}(\tau) d\tau &= Y_E(t), \\
(\mu_{\psi\psi} + m x_a) \hat{v} + \beta_{\psi\psi} v + \int_0^\infty v(t-\tau) N_{\psi y}(\tau) d\tau + \\
+ (I_0 + \mu_{\psi\psi}) \hat{v} + (\beta_{\psi\psi} + m x_a u_0) \hat{v} + \\
+ \int_0^\infty \hat{v}(t-\tau) N_{\psi\psi}(\tau) d\tau &= N_E(t).
\end{aligned}$$

(11)

We have dropped the first (surge) equation of (10), for it is not coupled to the other two and we shall not discuss it further.

It will be convenient to have the Fourier transform of these equations. For absolutely integrable  $f(t)$  define

$$\hat{f}(\omega) = \int_{-\infty}^{\infty} f(t) e^{-i\omega t} dt \quad (12)$$

Since all the functions in our analysis have the property that  $f(t) = 0$  for  $t \leq 0$  we have

$$\hat{f}(\omega) = \int_0^\infty f(t) e^{-i\omega t} dt = \hat{f}_c - i \hat{f}_s. \quad (13)$$

It follows that

$$\hat{f}_c(-\omega) = \hat{f}_c(\omega) \text{ and } \hat{f}_s(-\omega) = -\hat{f}_s(\omega) \quad (14)$$

and also that

$$\begin{aligned}
f(t) &= \frac{1}{2\pi} \int_{-\infty}^{\infty} \hat{f}(\omega) e^{i\omega t} d\omega = \\
&= \frac{1}{\pi} \int_0^\infty [\hat{f}_c(\omega) \cos \omega t + \hat{f}_s(\omega) \sin \omega t] d\omega = \\
&= \frac{2}{\pi} \int_0^\infty \hat{f}_c(\omega) \cos \omega t d\omega = \frac{2}{\pi} \int_0^\infty \hat{f}_s(\omega) \sin \omega t d\omega.
\end{aligned}$$

(15)

Taking the Fourier transform of (11), one finds the following pair of equations:

$$\begin{aligned}
[i\omega(m + \mu_{yy}) + \beta_{yy} + \hat{N}_{yy}(\omega)] \hat{v} + \\
+ [i\omega(\mu_{y\psi} + m x_a) + \beta_{y\psi} + m u_0 + \hat{N}_{y\psi}(\omega)] \hat{v} = \hat{Y}_E,
\end{aligned}$$



$$[i\omega(\mu_{yy} + m\chi_a) + \beta_{yy} + \hat{N}_{yy}] \hat{v} + \\ + [i\omega(I_0 + \mu_{yy}) + \beta_{yy} + m\chi_a u_0 + \hat{N}_{yy}] \hat{u} = \hat{N}_E.$$

Note that the various  $\hat{N}$ 's are complex:

$$\hat{N}_{yy} = \hat{N}_{yy} - i \hat{N}_{yy}, \text{ etc.}$$

### 3. PLANAR-MOTION MECHANISM

A planar-motion mechanism (PMM) is a device that allows a controlled motion of a model in one plane, in our case the  $(x, y)$  plane, while it is moving forward.

The device is attached to the towing carriage, and two rods, separately controllable, are attached to the model at a forward point B and an after point S. At the same time that the motion of the rods is being controlled and recorded, the force components in the rods required to move the model are being measured and recorded. Figure 2 is a schematic drawing of a PMM.

The PMM was introduced originally by M. Gertler and A. Goodman. A detailed description is given in Goodman (1960).

In Figure 2 the points of attachment, B and S, of the rods have been taken equidistant from the coordinate origin O. Although this is convenient, it is not necessary, and the analysis is easily extended to the more general situation. The distances  $y_s$  and  $y_B$  are controllable and may be considered as given functions of time:  $y_s(t)$  and  $y_B(t)$ . Both  $\psi$  and  $\beta$  are then also determined as functions of time as we shall see below. The forces components measured in the longitudinal direction of the bars will be denoted by  $Y_s(t)$  and  $Y_B(t)$ .

Let us now consider the kinematics of the PMM. If the carriage is moving with velocity  $U$  in the direction  $O_0 x_0$ , then the path of the point O is given by

$$x_0 = Ut, \quad y_0(t) = \frac{1}{2}(y_B + y_s). \quad (17)$$

Its slope is given by

$$\frac{dy_0}{dx_0} = \frac{1}{2U}(\dot{y}_B + \dot{y}_s). \quad (18)$$

The velocity of O in the system  $O_0 x_0 y_0$  is given by

$$\vec{v} = (\dot{x}_0, \dot{y}_0) = (U, \frac{1}{2}(\dot{y}_B + \dot{y}_s)). \quad (19)$$

In the system  $Oxy$  it is given by

$$\vec{v} = (u, v) = \sqrt{U^2 + \frac{1}{4}(\dot{y}_B + \dot{y}_s)^2} (\cos \beta, \sin \beta) \quad (20)$$

The angle  $\psi$  is determined by

$$\tan \psi = \frac{y_B - y_s}{2d}, \quad (21)$$

and the angle  $\beta$  by

$$\tan(\psi + \beta) = \frac{1}{2U}(\dot{y}_B + \dot{y}_s). \quad (22)$$

We shall suppose that both  $\psi$  and  $\beta$  are "small", so that

$$\psi \cong \frac{y_B - y_s}{2d}, \quad (23)$$

$$\beta \cong \frac{1}{2U}(\dot{y}_B + \dot{y}_s) - \frac{y_B - y_s}{2d} \cong \sin \beta, \cos \beta \cong 1.$$

We then have the following expressions for  $\vec{v}$  in  $Oxy$ :

$$(u, v) \cong (U, \frac{1}{2}(\dot{y}_B + \dot{y}_s) - U \frac{y_B - y_s}{2d}). \quad (24)$$

Hence, in terms of the measured quantities  $y_B$  and  $y_s$  we have

$$v = \frac{1}{2}(\dot{y}_B + \dot{y}_s) - U \frac{y_B - y_s}{2d},$$

$$\dot{v} = \frac{1}{2}(\ddot{y}_B + \ddot{y}_s) - U \frac{\dot{y}_B - \dot{y}_s}{2d},$$

$$r = \dot{\psi} = \frac{\dot{y}_B - \dot{y}_s}{2d}, \quad \dot{r} = \ddot{\psi} = \frac{\ddot{y}_B - \ddot{y}_s}{2d}. \quad (25)$$

These are the variables appearing on the left-hand side of (11). The force and moment on the right-hand side are given by

$$Y_E(t) = Y_B + Y_s, \quad N_E(t) = d(Y_B - Y_s). \quad (26)$$

If  $y_B(t)$ ,  $y_s(t)$ ,  $Y_B(t)$  and  $Y_s(t)$  have been recorded, it is possible to calculate their Fourier transforms numerically:  $\hat{y}_B(\omega)$ ,  $\hat{y}_s(\omega)$ ,  $\hat{Y}_B(\omega)$ , and  $\hat{Y}_s(\omega)$ . From (25) we find

$$\begin{aligned} \hat{v} &= i \frac{\omega}{2} (\hat{y}_B + \hat{y}_s) - \frac{U}{2d} (\hat{y}_B - \hat{y}_s) = \\ &= \frac{\omega}{2} (\hat{y}_{Bs} + \hat{y}_{ss}) - \frac{U}{2d} (\hat{y}_{Bs} - \hat{y}_{ss}) + \\ &+ i \left[ \frac{\omega}{2} (\hat{y}_{Bs} + \hat{y}_{ss}) + \frac{U}{2d} (\hat{y}_{Bs} - \hat{y}_{ss}) \right], \end{aligned}$$

$$\hat{\kappa} = i \frac{\omega}{2d} (\hat{y}_B - \hat{y}_S) =$$

$$= \frac{\omega}{2d} (\hat{y}_{BS} - \hat{y}_{SS}) + i \frac{\omega}{2d} (\hat{y}_{BC} - \hat{y}_{SC}) . \quad (27)$$

#### 4. ANALYSIS OF PMM DATA

We may now substitute the forms of  $\hat{v}$  and  $\hat{\kappa}$  in (27) into the transformed equations of motion (16):

$$[\beta_{yy} + \hat{N}_{yye} + i\omega(m + \mu_{yy}) - i\hat{N}_{yys}] \cdot$$

$$\cdot \left\{ \frac{\omega}{2} (\hat{y}_{BS} + \hat{y}_{SS}) - \frac{U}{2d} (\hat{y}_{BC} - \hat{y}_{SC}) + i \left[ \frac{\omega}{2} (\hat{y}_{BC} + \hat{y}_{SC}) + \frac{U}{2d} (\hat{y}_{BS} - \hat{y}_{SS}) \right] \right\} +$$

$$+ [\beta_{yy} + mU + \hat{N}_{yye} + i\omega(\mu_{yy} + m\chi_a) - i\hat{N}_{yys}] \cdot$$

$$\cdot \left\{ \frac{\omega}{2d} (\hat{y}_{BS} - \hat{y}_{SS}) + i \frac{\omega}{2d} (\hat{y}_{BC} - \hat{y}_{SC}) \right\} = \hat{Y}_{BC} + \hat{Y}_{SC} - i(\hat{Y}_{BS} + \hat{Y}_{SS}) , \quad (28)$$

$$[\beta_{yy} + \hat{N}_{yye} + i\omega(\mu_{yy} + m\chi_a) - i\hat{N}_{yys}] \cdot$$

$$\cdot \left\{ \frac{\omega}{2} (\hat{y}_{BS} + \hat{y}_{SS}) - \frac{U}{2d} (\hat{y}_{BC} - \hat{y}_{SC}) + i \left[ \frac{\omega}{2} (\hat{y}_{BC} + \hat{y}_{SC}) + \frac{U}{2d} (\hat{y}_{BS} - \hat{y}_{SS}) \right] \right\} +$$

$$+ [\beta_{yy} + m\chi_a U + \hat{N}_{yye} + i\omega(I_0 + \mu_{yy}) - i\hat{N}_{yys}] \cdot$$

$$\cdot \left\{ \frac{\omega}{2d} (\hat{y}_{BS} - \hat{y}_{SS}) + i \frac{\omega}{2d} (\hat{y}_{BC} - \hat{y}_{SC}) \right\} = (\hat{Y}_{BC} - \hat{Y}_{SC})d - i(\hat{Y}_{BS} - \hat{Y}_{SS})d .$$

In these equations one will have measured the functions  $\hat{y}_B(\omega) = \hat{y}_{BC} - i\hat{y}_{BS}$ ,  $\hat{y}_S$ ,  $\hat{Y}_B$ , and  $\hat{Y}_S$ . Hence the equations may be used to determine various clusters of coefficients. We shall assume that experiments have been carried out in which  $y_B = y_S = 0$  for  $t < 0$  and such that  $\hat{y}_B(\omega) \cdot \hat{y}_S(\omega) \neq 0$  for any  $\omega$ .

Although there are infinitely many ways of using the equations (28) to determine the coefficient clusters, we shall consider in detail only the two described below. However, Appendix I describes a different way of using equations (28) and of analyzing the measured quantities.

##### Case A

Let us suppose that the PMM is programmed to move the model in such a way that

$y_B = y_S$ . Then  $\hat{y}_B = \hat{y}_S$  and equations (28) take the following form after separating real and imaginary parts:

$$(\beta_{yy} + \hat{N}_{yye})\omega\hat{y}_{BS} -$$

$$- [\omega(m + \mu_{yy}) - \hat{N}_{yys}]\omega\hat{y}_{BC} = \hat{Y}_{BC} + \hat{Y}_{SC} , \quad (29)$$

$$-(\beta_{yy} + \hat{N}_{yye})\omega\hat{y}_{BC} -$$

$$- [\omega(m + \mu_{yy}) - \hat{N}_{yys}]\omega\hat{y}_{BS} = \hat{Y}_{BS} + \hat{Y}_{SS} ;$$

$$(\beta_{yy} + \hat{N}_{yye})\omega\hat{y}_{BS} -$$

$$- [\omega(\mu_{yy} + m\chi_a) - \hat{N}_{yys}]\omega\hat{y}_{BC} = (\hat{Y}_{BC} - \hat{Y}_{SC})d , \quad (30)$$

$$-(\beta_{yy} + \hat{N}_{yye})\omega\hat{y}_{BC} -$$

$$- [\omega(\mu_{yy} + m\chi_a) - \hat{N}_{yys}]\omega\hat{y}_{BS} = (\hat{Y}_{BS} - \hat{Y}_{SS})d .$$

As long as  $\hat{y}_{BC}^2 + \hat{y}_{BS}^2 \neq 0$ , equations (29) allow in principle determination of  $(\beta_{yy} + \hat{N}_{yye})$  and  $\omega(m + \mu_{yy}) - \hat{N}_{yys}$  and equations (30) of  $(\beta_{yy} + \hat{N}_{yye})$  and  $\omega(\mu_{yy} + m\chi_a) - \hat{N}_{yys}$ .

In matrix and column-vector form the solutions are as follows:

$$\begin{pmatrix} \beta_{yy} + \hat{N}_{yye} \\ \omega(m + \mu_{yy}) - \hat{N}_{yys} \end{pmatrix} = \frac{1}{\omega(\hat{y}_{BC}^2 + \hat{y}_{BS}^2)} \begin{pmatrix} \hat{y}_{BS} & -\hat{y}_{BC} \\ \hat{y}_{BC} & -\hat{y}_{BS} \end{pmatrix} \begin{pmatrix} \hat{Y}_{BC} + \hat{Y}_{SC} \\ \hat{Y}_{BS} + \hat{Y}_{SS} \end{pmatrix} , \quad (31)$$

$$\begin{pmatrix} \beta_{yy} + \hat{N}_{yye} \\ \omega(\mu_{yy} + m\chi_a) - \hat{N}_{yys} \end{pmatrix} = \frac{d}{\omega(\hat{y}_{BC}^2 + \hat{y}_{BS}^2)} \begin{pmatrix} \hat{y}_{BS} & -\hat{y}_{BC} \\ \hat{y}_{BC} & -\hat{y}_{BS} \end{pmatrix} \begin{pmatrix} \hat{Y}_{BC} - \hat{Y}_{SC} \\ \hat{Y}_{BS} - \hat{Y}_{SS} \end{pmatrix} . \quad (32)$$

##### Case B

It is evident that the PMM maneuver of Case A has determined only half the coefficient clusters in (28). For a second maneuver we choose one such that

$y_B = -y_S$ . Then  $\hat{y}_S = -\hat{y}_B$ , and equations

(28) yield the following:

$$\begin{aligned} & (\beta_{yy} + mU + \hat{N}_{yyc}) \frac{\omega}{d} \hat{y}_{bc} - [\omega(\mu_{yy} + m\chi_g) - \hat{N}_{yys}] \frac{\omega}{d} \hat{y}_{bc} = \\ & = \hat{Y}_{bc} + \hat{Y}_{sc} + (\beta_{yy} + \hat{N}_{yyc}) \frac{U}{d} \hat{y}_{bc} + [\omega(m + \mu_{yy}) - \hat{N}_{yys}] \frac{U}{d} \hat{y}_{bc}, \end{aligned} \quad (33)$$

$$\begin{aligned} & -(\beta_{yy} + mU + \hat{N}_{yyc}) \frac{\omega}{d} \hat{y}_{bc} - [\omega(\mu_{yy} + m\chi_g) - \hat{N}_{yys}] \frac{\omega}{d} \hat{y}_{bc} = \\ & = \hat{Y}_{bs} + \hat{Y}_{ss} + (\beta_{yy} + \hat{N}_{yyc}) \frac{U}{d} \hat{y}_{bs} + [\omega(m + \mu_{yy}) - \hat{N}_{yys}] \frac{U}{d} \hat{y}_{bs}; \end{aligned}$$

$$\begin{aligned} & (\beta_{yy} + m\chi_g U + \hat{N}_{yyc}) \frac{\omega}{d} \hat{y}_{bs} - [\omega(I_0 + \mu_{yy}) - \hat{N}_{yys}] \frac{\omega}{d} \hat{y}_{bs} = \\ & = (\hat{Y}_{bc} - \hat{Y}_{sc})d + (\beta_{yy} + \hat{N}_{yyc}) \frac{U}{d} \hat{y}_{bs} + [\omega(\mu_{yy} + m\chi_g) - \hat{N}_{yys}] \frac{U}{d} \hat{y}_{bs}, \end{aligned} \quad (34)$$

$$\begin{aligned} & -(\beta_{yy} + m\chi_g U + \hat{N}_{yyc}) \frac{\omega}{d} \hat{y}_{bs} - [\omega(I_0 + \mu_{yy}) - \hat{N}_{yys}] \frac{\omega}{d} \hat{y}_{bs} = \\ & = (\hat{Y}_{bs} - \hat{Y}_{ss})d + (\beta_{yy} + \hat{N}_{yyc}) \frac{U}{d} \hat{y}_{bs} - [\omega(\mu_{yy} + m\chi_g) - \hat{N}_{yys}] \frac{U}{d} \hat{y}_{bs}. \end{aligned}$$

These equations clearly allow us to determine the remaining coefficient clusters. In a form analogous to (32), they are given as follows:

$$\begin{aligned} & \left( \begin{array}{c} \beta_{yy} + mU + \hat{N}_{yyc} \\ \omega(\mu_{yy} + m\chi_g) - \hat{N}_{yys} \end{array} \right) = \\ & = \frac{d}{\omega(\hat{y}_{bc}^2 + \hat{y}_{bs}^2)} \left( \begin{array}{cc} \hat{y}_{bs} & -\hat{y}_{bc} \\ -\hat{y}_{bc} & -\hat{y}_{bs} \end{array} \right) \left( \begin{array}{c} \hat{Y}_{bc} + \hat{Y}_{sc} \\ \hat{Y}_{bs} + \hat{Y}_{ss} \end{array} \right) + \\ & + \frac{U}{\omega} \left( \begin{array}{c} \omega(m + \mu_{yy}) - \hat{N}_{yys} \\ -\beta_{yy} - \hat{N}_{yyc} \end{array} \right), \end{aligned} \quad (35)$$

$$\left( \begin{array}{c} \beta_{yy} + m\chi_g U + \hat{N}_{yyc} \\ \omega(I_0 + \mu_{yy}) - \hat{N}_{yys} \end{array} \right) =$$

$$\begin{aligned} & = \frac{d^2}{\omega(\hat{y}_{bc}^2 + \hat{y}_{bs}^2)} \left( \begin{array}{cc} \hat{y}_{bs} & -\hat{y}_{bc} \\ -\hat{y}_{bc} & -\hat{y}_{bs} \end{array} \right) \left( \begin{array}{c} \hat{Y}_{bc} - \hat{Y}_{sc} \\ \hat{Y}_{bs} - \hat{Y}_{ss} \end{array} \right) + \\ & + \frac{U}{\omega} \left( \begin{array}{c} \omega(\mu_{yy} + m\chi_g) - \hat{N}_{yys} \\ -\beta_{yy} - \hat{N}_{yyc} \end{array} \right) \end{aligned} \quad (36)$$

It is evident that determination of this last set of four coefficient clusters requires prior determination of the earlier set of four. Although it is possible in principle to program the PMM so that this last set could be determined independently, as is done in the usual frequency-by-frequency procedure, to do so would have complicated the actual experiments considerably. Note that the measured  $Y_b(t)$  and  $Y_s(t)$  used in forming (35) and (36) are not the same as those used in (31) and (32) and that the  $y_b(t)$ 's do not need to be the same.

#### Extended Fourier Transform

Underlying the calculation of the Fourier transforms in the preceding formulas is the assumption that the functions  $y_b(t)$ ,  $y_s$ ,  $Y_b$ , and  $Y_s$  are absolutely integrable. In fact, what we expect practically is that the values return to zero after some time  $t_0 > 0$ . In practice this is hard to realize smoothly. It would be much easier experimentally if it were possible to allow any of the above functions to become a nonvanishing constant for  $t \geq$  some value  $t_0$ . In this case the derivative would be absolutely integrable even though the function is not. A simple extension of the definition of the Fourier transform allows one to include such behavior.

If one takes the derivative with respect to  $t$  of the equations (11), it is evident that the functions  $v, \dot{v}, \ddot{v}, \ddot{v}, \dot{Y}_E$  and  $\dot{N}_E$  all have another dot added on top. If one then refers to (25), one sees that the variables  $\dot{v}, \dot{\dot{v}}, \dot{\ddot{v}}, \dot{\ddot{v}}$  can be expressed in terms of  $\dot{y}_b, \dot{y}_s$  and higher derivatives. Hence, for a forced motion of the desired kind, one can still use the solution (31), (32), (35) and (36) provided one replaces  $\hat{y}_b, \hat{y}_s, \hat{Y}_b$  and  $\hat{Y}_s$  by  $\dot{\hat{y}}_b, \dot{\hat{y}}_s, \dot{\hat{Y}}_b$  and  $\dot{\hat{Y}}_s$ . This would seem to require a preliminary differentiation of the recorded data before making the Fourier transform. To see that this is not the case let  $f(t)$  be any one of these functions and consider



$$\begin{aligned}\hat{f} &= \int_0^{\infty} f(t) e^{-i\omega t} dt = \int_0^{t_0} f(t) e^{-i\omega t} dt = \\ &= f(t_0) e^{-i\omega t_0} + i\omega \int_0^{t_0} f(t) e^{-i\omega t} dt = \\ &= i\omega \left[ \int_0^{t_0} f(t) e^{-i\omega t} dt - i \frac{f(t_0)}{\omega} e^{-i\omega t_0} \right].\end{aligned}$$

If we now define

$$\hat{f} = \int_0^{\infty} f(t) e^{-i\omega t} dt - i \frac{f(t_0)}{\omega} e^{-i\omega t_0}, \quad (37)$$

we see that

$$\hat{f} = i\omega \hat{f}$$

as in the usual Fourier transform. It is then evident from inspection of (31), (32), (35) and (36) that we may continue to use them in their present forms (i.e., without the dots) provided that we interpret the Fourier transform as in (37). This is, of course, equivalent to the well known interpretation of the Fourier transform of a step function at  $t_0$  with jump  $f(t_0)$ . Indeed, in calculating an inverse transform, a term like  $-i\omega^{-1} A e^{-i\omega t_0}$  will transform into a step function of jump  $A$  at  $t = t_0$ . Such a term will show up by calculating  $\lim_{\omega \rightarrow 0} i\omega \hat{f}$ .

#### Effect of Filter

In measuring  $y_B(t)$ ,  $y_s$ ,  $Y_B$  and  $Y_s$  it was convenient to use a filter in order to smooth out noise in the recorded signals. Preliminary tests indicated that the filter was linear. Hence, if  $f(t)$  represents any of the above functions, filtering it through a linear filter is equivalent to replacing  $f(t)$  by

$$\bar{f}(t) = \int_0^{\infty} f(t-\tau) w(\tau) d\tau, \quad \int_0^{\infty} w(\tau) d\tau = 1, \quad (38)$$

where  $w(\tau) = 0$  for  $\tau < 0$  and  $w$  is absolutely integrable. Generally  $w(t)$  has the form shown in Figure 3.

It is easy to verify that the Fourier transform of  $\bar{f}(t)$  is given by

$$\hat{\bar{f}}(\omega) = \hat{f}(\omega) \cdot \hat{w}(\omega), \quad (39)$$

and that this equation is valid also with the extended interpretation (37) of the Fourier transform. However, in applying (37) one should be aware that  $\bar{f}(t)$  does not become constant for  $t \geq t_0$  but rather for  $t \geq t_0 + t_1$ , after which  $\bar{f}(t) = f(t_0)$ .

If one now examines (31), (32), (35) and (36), one sees immediately from (39) that, as long as identical filters are used, the  $\hat{w}$ 's will cancel on the right-hand sides and there will be no loss of accuracy in determining the left-hand sides.

#### 5. TESTING FREQUENCY BY FREQUENCY

In the conventional use of the PMM a separate pair of tests is made for each value of  $\omega$  in which one is interested, the model being forced to make a periodic motion. If the forced motion is determined by

$$y_B = a_0 \sin(\omega t + \alpha_B),$$

$$y_s = a_0 \sin(\omega t + \alpha_s), \quad (40)$$

then the pair of tests correspond to the choices  $\alpha_B = \alpha_s = 0$  and  $\alpha_B = -\alpha_s = \varepsilon$  where  $\tan \varepsilon = \omega d/U$ . These choices may be substituted into (25) and thence into the equations of motion (11). This leads by easy manipulations to well-known formulas determining the same coefficient clusters shown on the left-hand sides of (31), (32), (35) and (36). We omit the derivation of the formulas, which is straightforward. If the forces on the bow and stern rods of the PMM are expressed as follows:

$$Y_B = Y_{Bc} \cos \omega t + Y_{Bs} \sin \omega t,$$

$$Y_s = Y_{sc} \cos \omega t + Y_{ss} \sin \omega t, \quad (41)$$

then the formulas for the coefficient clusters are those shown below:

Pure Sway:  $\alpha_B = \alpha_s = 0$ .

$$\begin{cases} \omega(m + \mu_{yy}) - \hat{N}_{yy} = -\frac{1}{a_0 \omega} (Y_{Bs} + Y_{ss}), \\ \beta_{yy} + \hat{N}_{yy} = \frac{1}{a_0 \omega} (Y_{Bc} + Y_{sc}), \end{cases} \quad (42)$$

$$\begin{cases} \omega(\mu_{yy} + m x_a) - \hat{N}_{yy} = -\frac{d}{a_0 \omega} (Y_{Bs} - Y_{ss}), \\ \beta_{yy} + \hat{N}_{yy} = \frac{d}{a_0 \omega} (Y_{Bs} - Y_{ss}). \end{cases}$$

Pure Yaw:  $\alpha_B = -\alpha_s = \varepsilon$ ,  $\tan \varepsilon = \frac{\omega d}{U}$ .

$$\begin{cases} \omega(\mu_{yy} + m x_a) - \hat{N}_{yy} = -\frac{(U^2 + \omega^2 d^2)^{\frac{1}{2}}}{a_0 \omega^2} (Y_{Bc} + Y_{sc}), \\ \beta_{yy} + m u_0 + \hat{N}_{yy} = -\frac{(U^2 + \omega^2 d^2)^{\frac{1}{2}}}{a_0 \omega^2} (Y_{Bs} + Y_{ss}), \end{cases} \quad (43)$$

(43)

$$\begin{cases} \omega(I_o + \mu_{yy}) - \hat{N}_{yys} = -\frac{d(U^2 + \omega^2 d^2)^{\frac{1}{2}}}{a_o \omega^2} (Y_{Bc} - Y_{Sc}), \\ \beta_{yy} + m x_{y_o} + \hat{N}_{yyc} = -\frac{d(U^2 + \omega^2 d^2)^{\frac{1}{2}}}{a_o \omega^2} (Y_{Bs} - Y_{Ss}). \end{cases}$$

As has been pointed out by Bishop, Burcher and Price (1974), the Kramers-Kronig relations (see, e.g., Kotik and Lurye, 1964) provide equations relating the coefficient clusters in each of the bracketed pairs. They further note that these relations can be used as a test of the acceptability of the linearized equations of motion, or of the accuracy of the experiments. The same test applied to the results of the transient-motion experiments would, of course, be of no significance.

#### RELATION WITH THE CLASSICAL EQUATIONS

The classical linearized equations of motion for ship maneuvering are usually written in the form shown below:

$$\begin{aligned} (m - Y_{\dot{v}})\dot{v} - Y_v v - (Y_{\dot{r}} - m x_{\dot{q}})\dot{r} - (Y_r - m u_o)r &= Y_E, \\ -(N_{\dot{v}} - m x_{\dot{q}})\dot{v} - N_v v + (I_o - N_{\dot{r}})\dot{r} - (N_r - m x_{\dot{q}}u_o)r &= N_E. \end{aligned} \quad (44)$$

In the derivation of these equations it is clear that the various "stability derivatives" are to be considered as constants determined by the shape of the maneuvering body. They may depend upon Froude number but not upon the nature of the motion otherwise, although it is assumed small.

These equations can, of course, also be used in analyzing the transient motions of Cases A and B above or the periodic motions (40). In either case they will provide formulas determining the stability derivatives in terms of the imposed motions and the measured forces in the rods of the PMM. In fact, the following identifications will hold:

$$Y_{\dot{v}} = -\mu_{yy} + \omega^{-1} \hat{N}_{yys},$$

$$Y_v = -\beta_{yy} - \hat{N}_{yyc},$$

$$N_{\dot{v}} = -\mu_{yy} + \omega^{-1} \hat{N}_{yys},$$

$$N_v = -\beta_{yy} - \hat{N}_{yyc},$$

$$Y_{\dot{r}} = -\mu_{yr} + \omega^{-1} \hat{N}_{yrs},$$

$$Y_r = -\beta_{yr} - \hat{N}_{yrc},$$

$$N_{\dot{r}} = \mu_{yr} + \omega^{-1} \hat{N}_{yrs},$$

$$N_r = -\beta_{yr} - \hat{N}_{yrc}.$$

(45)

If the statement above concerning the constancy of the stability derivatives is correct, then measurements with a PMM should show no dependence upon  $\omega$ . Indeed, Gertler in his discussion of Newman (1966, p.231) states that such dependence has been observed only exceptionally among "well over a hundred models of submarines". On the other hand, Paulling and Wood (1962) and vanLeeuwen (1964) had already observed such a dependence in the case of surface ships. This dependence has been found by others since then and is reconfirmed by the experiments reported here.

As is emphasized by Newman (1966, p.223), the presence of "memory effects" in the equations of motion, i.e. of the convolution integrals, is equivalent to a real dependence upon  $\omega$  of at least some of the quantities in (45). Since this dependence has been observed in surface ships, one is forced to conclude that equations (44) are not adequate to describe all situations. On the other hand, it is known that these equations give reasonable predictions for many practical maneuvers, and under certain circumstances must yield a good approximation to (11). Let us turn to this question.

#### 7. QUASI-STEADY MOTION

Because the treatment of the quasi-steady motion approximation of the coupled equations (11) leads to rather complicated inequalities that tend to disguise the fundamental simplicity of the definition of "quasi-steady" motion, we shall treat the question here in the degenerate case of one degree of freedom and relegate the general case to Appendix II. Thus we shall

suppose  $h = \dot{h} = 0$  and consider only the first equation of (11). The question that we shall ask ourselves is the following. Under what conditions can we approximate a solution of

$$(m + \mu_{yy})\dot{v} + \beta_{yy}v + \int_0^\infty v(t-\tau)N_{yy}(\tau)d\tau = Y_E(t) \quad (46)$$

by a solution of

$$(m + \mu_{yy})\dot{v} + [\beta_{yy} + \int_0^\infty N_{yy}(\tau)d\tau]v = Y_E(t) \quad ? \quad (47)$$

We shall suppose that the initial condition is the same for both equations.

Let  $v_1$  be a solution of (46) and  $v_2$  a solution of (47), with  $v_1(0) = v_2(0)$ . If we subtract (47) from (46), we find

$$(m + \mu_{yy})(\dot{v}_1 - \dot{v}_2) + [\beta_{yy} + \int_0^\infty N_{yy}(\tau)d\tau](v_1 - v_2) + \int_0^\infty [v_1(t-\tau) - v_2(t-\tau)]N_{yy}(\tau)d\tau = 0 \quad (48)$$

The definition of quasi-steady motion will be connected with the last term.

We begin by fixing a real number  $\varepsilon > 0$ , to be thought of as small, but the choice is arbitrary. Let

$$\bar{N}_{yy} = \int_0^\infty N_{yy}(\tau)d\tau, \quad V = \sup_t |v_1(t)|. \quad (49)$$

We now define a time constant  $t_c$  by the inequality

$$\frac{1}{\beta_{yy} + \bar{N}_{yy}} \int_{t_c}^\infty |N_{yy}(\tau)|d\tau < \frac{1}{4}\varepsilon. \quad (50)$$

Evidently, the smaller one chooses  $\varepsilon$ , the larger  $t_c$  will be.

We now define the motion  $v_1(t)$  as quasi-steady if

$$\begin{aligned} |v_1(t-\tau) - v_1(t)| &< \\ &< \frac{1}{2}\varepsilon V(\beta_{yy} + \bar{N}_{yy}) / \int_0^\infty |N_{yy}(\tau)|d\tau \end{aligned} \quad (51)$$

for all  $\tau$  such that  $|\tau| \leq t_c$ .

The smaller  $\varepsilon$  is, the smaller the variation in  $v_1$  must be, and that over a longer interval.

Let us now estimate the last integral in (48):

$$\begin{aligned} & \left| \int_0^\infty [v_1(t-\tau) - v_2(t-\tau)]N_{yy}(\tau)d\tau \right| < \\ & < \int_0^{t_c} |v_1(t-\tau) - v_2(t-\tau)| |N_{yy}(\tau)|d\tau + 2V \int_{t_c}^\infty |N_{yy}(\tau)|d\tau < \\ & < \frac{1}{2}\varepsilon V(\beta_{yy} + \bar{N}_{yy}) \frac{\int_0^{t_c} |N_{yy}(\tau)|d\tau}{\int_0^\infty |N_{yy}(\tau)|d\tau} + 2V \frac{1}{4}\varepsilon(\beta_{yy} + \bar{N}_{yy}) < \\ & < \varepsilon V(\beta_{yy} + \bar{N}_{yy}). \end{aligned}$$

In (48) we shall write  $v_1 - v_2 = v$  and denote the last term by  $-\eta(t)$ . Then we have the equation

$$(m + \mu_{yy})\dot{v} + (\beta_{yy} + \bar{N}_{yy})v = \eta(t), \quad (52)$$

where

$$|\eta(t)| < \varepsilon V(\beta_{yy} + \bar{N}_{yy}).$$

The solution of (47) with  $v(0) = 0$  is

$$\begin{aligned} v &= \frac{1}{m + \mu_{yy}} e^{\sigma t} \int_0^t \eta(\tau) e^{-\sigma \tau} d\tau, \\ \sigma &= -\frac{\beta_{yy} + \bar{N}_{yy}}{m + \mu_{yy}} < 0. \end{aligned}$$

From this follows

$$\begin{aligned} |v| = |v_1 - v_2| &\leq \frac{1}{m + \mu_{yy}} e^{\sigma t} \max_{0 \leq \tau \leq t} |\eta(\tau)| \frac{1}{|\sigma|} [e^{-\sigma t} - 1] < \\ &< \frac{1}{\beta_{yy} + \bar{N}_{yy}} \varepsilon V(\beta_{yy} + \bar{N}_{yy}) [1 - e^{\sigma t}] < \varepsilon V. \end{aligned} \quad (53)$$

Evidently by choosing  $\varepsilon$  small enough we can make the difference between  $v_2$  and  $v_1$  as small as we please. However, if we insist upon choosing  $\varepsilon$



very small, then  $t_c$  will be large and the motion, in order to qualify as quasi-steady will be restrained to vary only little over long intervals.

One should note that any steady motion is automatically quasi-steady. Hence in the turning-circle maneuver, both the straight path before the rudder is put over and the steady turning circle will qualify as quasi-steady. The part in between may or may not, depending upon how fast  $v_1$  changes in this interval and upon the standard ( $\epsilon$ ) one has set. A similar remark applies to the spiral maneuver. However, here one might anticipate that most of the trajectory would qualify as quasi-steady since the rudder is changed by relatively small amounts after the initial large deflection. A zig-zag maneuver might very well not qualify as quasi-steady.

Another important conclusion can be drawn from (53). No matter how generously  $\epsilon$  is chosen, the difference between solutions of (46) and (47) is uniformly bounded. Thus one cannot expect important qualitative differences between the two solutions.

Finally we call attention to the fact that quasi-steadiness, called "slow" motion, is also discussed in the cited papers by Bishop, Burcher and Price. However, inasmuch as their definition does not allow quantification, it is at best inadequate and possibly misleading.

## 8. A DIFFICULTY IN TRANSIENT EXPERIMENTS

In carrying out a transient-motion experiment to determine the coefficient clusters by means of formulas (31), (32), (35) and (36), there is a potential difficulty to which one must give attention. In order to see this difficulty let us take  $y_0(t) = 1 - \cos \omega_0 t$ ,  $0 \leq t \leq t_0 = 2\pi/\omega_0$  as a typical transient maneuver. A straightforward calculation yields

$$\hat{y}_B(\omega) = \frac{\omega_0^2}{\omega(\omega^2 - \omega_0^2)} \left( -\sin 2\pi \frac{\omega}{\omega_0} + i 2 \sin^2 \pi \frac{\omega}{\omega_0} \right) \quad (54)$$

$\hat{y}_{Bc}$  has zeros at  $\omega = \frac{1}{2}\omega_0, \frac{3}{2}\omega_0, 2\omega_0, \frac{5}{2}\omega_0, \dots$ , and  $\hat{y}_{Bs}$  has zeros at  $\omega = \omega_0, 2\omega_0, 3\omega_0, \dots$ . The first zero of  $\hat{y}_{Bc}^2 + \hat{y}_{Bs}^2$  is evidently at  $2\omega_0$ ; thereafter they occur at  $n\omega_0, n > 2$ . They are all double zeros, as are also the zeros of  $\hat{y}_{Bs}$  for  $n\omega_0, n > 2$ . Figure 4 shows a graph of  $\hat{y}_{Bc}$ ,  $\hat{y}_{Bs}$  and  $|\hat{y}_B|$ .

Since the combination  $\hat{y}_{Bc}^2 + \hat{y}_{Bs}^2$  occurs in the denominators of all right-hand sides of (31), (32), (35) and (36), there will be a singularity unless the zeros are cancelled out by matching ones in the numerator. The terms in  $\hat{y}_{Bc}$  in the numerator provide only simple zeros, but

one assumes that the transforms of the measured forces will supply additional matching ones. However, even if this is so, one is still in the position of dividing two very small quantities at and in the neighborhood of these zeros and consequently is very vulnerable to small errors in measurement, which may become very large relative to the quantities measured.

One way to try to avoid such measurements is to complete the transient maneuver before the first zero at  $2\omega_0 = 4\pi/t_0$  is reached. Thus, if one wants to measure the coefficients in the interval  $0 \leq \omega \leq \omega_m$ , one should choose  $t_0$  so that  $4\pi/t_0 > \omega_m$  or  $t_0 < 4\pi/\omega_m$ . For example, in the experiments to be reported below where we wished to have  $\omega_m = 4\pi \text{ rad/sec}$ , this required completing the maneuver in less than 1 sec.

There is a better way to avoid this difficulty, although it has the disadvantage of requiring more experiments. Let the same maneuver discussed above be repeated with at least two different values of  $\omega_0$ , say  $\omega_1 < \omega_2 < \omega_3$ . We denote these by  $y_{Bi}(t)$ ,  $i = 1, 2, 3$ , and the corresponding force measurements by  $Y_{Bi}$  and  $Y_{Si}$ ,  $i = 1, 2, 3$ .

We then add all the corresponding functions together, either before or after taking the Fourier transforms, and enter the formulas (31), (32), (35) and (36) with

$$\begin{aligned} \hat{y}_B(\omega) &= \hat{y}_{B1} + \hat{y}_{B2} + \hat{y}_{B3}, \\ \hat{Y}_B(\omega) &= \hat{Y}_{B1} + \hat{Y}_{B2} + \hat{Y}_{B3}, \\ \hat{Y}_S(\omega) &= \hat{Y}_{S1} + \hat{Y}_{S2} + \hat{Y}_{S3}. \end{aligned} \quad (55)$$

We are particularly concerned with the behavior of  $|\hat{y}_B|$ . It is evident from an inspection of Figure 4 that  $\hat{y}_{Bs} > 0$  for  $\omega > \omega_3$ , so that  $|\hat{y}_B|$  is not likely to have any zeros. Figure 5 shows  $|\hat{y}_{B1}|$ ,  $|\hat{y}_{B2}|$ ,  $|\hat{y}_{B3}|$  and  $|\hat{y}_B|$  for  $\omega_1 = 0.8, \omega_2 = 1.0, \omega_3 = 1.3$ .

In any particular experiment  $y_B$  will not have exactly the form chosen above, nor need it. However, varying the time scale of the transient maneuver in several runs and following the above procedure appears to be effective in increasing the accuracy of the results. Figure 6 shows  $Y_{Bc}$  as determined by each of several maneuvers and by their sum. A more elaborate (and statistically correct) way of treating multiple experiments is discussed in Appendix I.

## 9. EXPERIMENTAL TECHNIQUES

The ship model was attached to the same



planar-motion mechanism used by Paulling and Wood (1962), the only alteration being the disconnection of the electric motor so that manual power could be used. The model was attached at two points by means of strain-gauge dynamometers, used to measure the lateral forces. A linear potentiometer connected to the forward scotch yoke measured the lateral displacement.

Since the vibration of the towing carriage produced an unacceptable noise level, it was necessary to pass all three signals through matched, 5Hz, low-pass filters. Although this resulted in a greatly improved signal-to-noise ratio, the noise problem was never totally eliminated. All signals were recorded on a 4 channel FM tape recorder and later digitized at the rate of 250 samples/second.

Operating the planar-motion mechanism manually, the experimenter provided the impetus to initiate the sway or yaw motion and the mechanism was allowed to coast to a smooth stop. The resulting impulses varied considerably between experimental runs, but typically had a duration of about 1 second and maximum energy at 1.25 Hz. It was found that such short pulses had insufficient energy at low frequencies to yield good results in the lowest frequency range. Therefore, a second series of experiments was run with a slower pulse of 4 second duration and maximum energy at 0.25Hz. This was the slowest pulse that would yield forces large enough to be measured with our equipment.

The two models used in our experiments were a light-weight wooden model of a high-speed ship and a fiberglass model of a Mariner. Their dimensions and characteristics are given below.

High-Speed Ship Model		(Bare Hull)
L	1.52	m
B	0.178	m
T	0.0579	m
$C_B$	0.492	
$I_Z$	0.7476	kg·m <sup>2</sup>
M	3.63	kg

Mariner Ship Model		(with Rudder and Propeller)
L	1.68	m
B	0.242	m
T	0.0857	m
$C_B$	0.6125	
$I_Z$	2.861	kg·m <sup>2</sup>
M	10.95	kg

## 10. EXPERIMENTAL RESULTS

The high-speed hull was tested frequency-by-frequency at Froude numbers 0.20, 0.25 and 0.30 and by transient-maneuver tests at 0.20 and 0.30. The Mariner model was tested in both ways at Froude numbers 0.130, 0.194, 0.233 and 0.285. The latter

Froude numbers were chosen because they had been used earlier in the experiments of Paulling and Wood (1962) and thus gave us some values to compare our own with. The data were analyzed by the method described at the end of Section 8. Results will be shown only for  $F_n = 0.30$  for the high-speed hull and for  $F_n = 0.285$  for the Mariner except for two graphs showing Froude number effects upon  $Y_v'$  and  $N_v'$  for the Mariner. At a later time all data will be reanalyzed by the method of Appendix I and presented together.

In order that the results will have a familiar form and to facilitate comparison with other data, the curves are labeled as stability derivatives made dimensionless with  $\frac{1}{2}\rho U^2 L$  and  $u_0$ , i.e. the "prime" system of Mandel's article (1967, p.469) is used. The connection with the variables used otherwise in this paper is given in dimensional form in (45). (That we should have preferred different variables in the body of the paper is made clear, we believe, by the form of equations (11) with which we started.) The frequency  $\omega$  is presented dimensionlessly through the variable  $\tau = \omega u_0 / g$ . Results are displayed only in the range  $0 < \tau \leq 1$ .

Figures 7-14 show the stability derivatives for the high-speed hull. The individual spots are the values obtained by testing at individual frequencies by the conventional method. The continuous curves are obtained from transient-maneuver tests. In the latter the short-duration tests (about 1 sec) and long-duration tests (about 4 sec) are grouped separately. The latter group is useful only in a low-frequency region (roughly,  $\tau < 0.30$  for  $F_n = 0.30$ ).

Figures 15-22 show the stability derivatives for the Mariner hull. Individual spots show our own results in frequency-by-frequency tests. The results obtained by Paulling and Wood (1962) are shown as faired curves and hence suppress any information concerning scatter in the data. Reference to their report shows a scatter of about the same magnitude as ours. The transient-maneuver tests are again divided into those of short and long duration. The little jogs in  $N_v'$  and  $N_h'$  in the long-duration tests are probably of no significance and represent a junction of two sets of data in the addition process described in Section 8. The discrepancy between our frequency-by-frequency measurements and those of Paulling and Wood often seem substantial. We have no explanation of this, but note that our transient-motion tests are generally in fair conformity with individual-frequency tests. Figures 23 and 24 show the effect of Froude number upon  $Y_v'$  and  $N_v'$ .

We have no additional comments upon the experimental results, but believe that they show the usefulness of transient-maneuver testing and anticipate that reanalysis of the data by the methods of Appendix I will improve further the method.

## ACKNOWLEDGEMENT

We are pleased to acknowledge support of the David Taylor Ship Research and Development Center for the work reported in this paper.

## APPENDIX I

The two complex equations (28) decompose into four real equations. These in turn separate into two pairs of equations that do not interact with each other, each pair containing four unknowns. Let us consider just one of these pairs, for the same remarks will apply to the other pair. It is evident that each transient-motion experiment will provide two linear equations in four unknowns, which we shall write as follows:

$$\sum_{j=1}^4 A_{ij} x_j = B_i, \quad i=1,2. \quad (\text{I.1})$$

The motion imposed in Case A is designed to make four of the coefficients  $A_{ij}$  vanish, so that one has two equations in two unknowns and hence can solve for two of the unknowns. The results of a second experiment, Case B, then allows one to solve for the remaining pair. We need not, however, have made the special choice of Case A. Any pair of experiments that yields a nonvanishing determinant of the coefficients for the two pairs taken together allows simultaneous determination of all four unknowns.

Suppose now that one makes  $n$  experiments, each one producing a pair of equations:

$$\sum_{j=1}^4 A_{ij}^{(k)} x_j = B_i^{(k)}, \quad i=1,2, \quad k=1,2,\dots,n. \quad (\text{I.2})$$

What is the best way to use all this information to estimate the unknowns  $x_1, x_2, x_3, x_4$ ? The standard procedure is to use the method of least squares. In the usual formulation this would require minimizing the sum of the squares of the distances from a point  $(x_1^{(0)}, x_2^{(0)}, x_3^{(0)}, x_4^{(0)})$

to each of the linear 2-spaces determined by the intersection of two hyperplanes in 4-space. It is not difficult to work out the appropriate formulas, but they do not take account of an important aspect of the equations.

In Section 8 we have discussed the difficulty of dealing with equations in the neighborhood of values of  $\omega$  where  $|\hat{y}_0| = 0$ . A simple stratagem proposed there was to add together equations corresponding to different experiments with the bothersome zeros occurring at different values of  $\omega$ . Although this device is effective, it is not statistically motivated, for the process of adding equations does not seem to be a step in the

direction of estimating a best value for the variables  $(x_1, x_2, x_3, x_4)$ . It is, in fact, little more than a device for giving small weight to a pair of equations in the neighborhood of a value of  $\omega$  where  $|\hat{y}_0| = 0$ . The same end could be achieved by weighting the distances in the least-squares method by the value  $|\hat{y}_0|$ .

To give formulas for the modified least-squares method, one needs to know the distance from a point  $(x_1^{(0)}, x_2^{(0)}, x_3^{(0)}, x_4^{(0)})$  to the intersection of a pair of hyperplanes in 4-space. If the hyperplanes are given by the equations

$$\sum_{j=1}^4 a_{ij} x_j = b_i, \quad i=1,2, \quad \sum_{j=1}^4 a_{ij}^2 = 1, \quad b_i > 0, \quad (\text{I.3})$$

and if the distance in question is  $D$ , then

$$D^2 = \left\{ [a_{1j} a_{2k} + a_{2j} a_{1k} - (a_{1j} a_{2k} + a_{1k} a_{2j}) a_{1n} a_{2n}] x_j^{(0)} x_k^{(0)} - 2[b_1 a_{1j} + b_2 a_{2j} - (b_1 a_{2j} + b_2 a_{1j}) a_{1n} a_{2n}] x_j^{(0)} + b_1^2 + b_2^2 - 2b_1 b_2 a_{1n} a_{2n} \right\} [1 - (a_{1n} a_{2n})^2]^{-1}, \quad (\text{I.4})$$

where repeated indices are to be summed. For convenience we shall write this in the form

$$D^2 = E_{jk} x_j^{(0)} x_k^{(0)} + F_j x_j^{(0)} + G. \quad (\text{I.5})$$

In order to apply this in the least-squares method, we first introduce the normalized coefficients

$$a_{ij}^{(k)} = A_{ij}^{(k)} / \left[ \sum_{j=1}^4 A_{ij}^{(k)2} \right]^{1/2} \text{sgn } B_i^{(k)}, \quad b_i^{(k)} = |B_i^{(k)}| / \left[ \sum_{j=1}^4 A_{ij}^{(k)2} \right]^{1/2}. \quad (\text{I.6})$$

Let  $D^{(k)}$  be the distance defined above. Then we wish to minimize

$$\Delta = \sum_{k=1}^n D^{(k)2} W^{(k)}, \quad (\text{I.7})$$

where as a weighting function  $W^{(k)}$  we propose the sum of the squares of the absolute values of the coefficients in (28):

$$W^{(k)} = \left( \frac{U^2}{4d^2} + \frac{\omega^2}{2} \left( |\hat{y}_B^{(k)}|^2 + |\hat{y}_S^{(k)}|^2 \right) - \frac{U^2}{2d^2} \operatorname{Re} \hat{y}_B^{(k)} \hat{y}_S^{(k)} + \frac{2U\omega}{d} \operatorname{Im} \hat{y}_B^{(k)} \hat{y}_S^{(k)} \right).$$

This is, in fact, nothing but  $\sum_{j=1}^4 A_{ij}^{(k)}$  (I.8), which is independent of  $i$  in the present case. An easy calculation yields the following set of four linear equations:

$$\begin{aligned} \sum_{j=1}^4 \left( \sum_k W^{(k)} E_{ij}^{(k)} \right) x_j^{(0)} &= \\ &= -\frac{1}{2} \sum_k W^{(k)} F_i^{(k)}, \quad i=1,2,3,4. \end{aligned} \quad (\text{I.9})$$

A further calculation, exploiting the particular choice of  $W^{(k)}$  allows one to omit the step (I.6) and replace (I.9) by

$$\sum_{j=1}^4 \left( \sum_k G_{ij}^{(k)} \right) x_j^{(0)} = \sum_k H_i^{(k)}, \quad i=1,2,3,4, \quad (\text{I.10})$$

where

$$\begin{aligned} G_{ij} &= A_{1i} A_{1j} + A_{2i} A_{2j} - \\ &- (A_{1i} A_{2j} + A_{2i} A_{1j}) A_{3n} A_{2n} / \sum A_{3n}, \\ H_i &= [B_1 A_{1i} + B_2 A_{2i} - \\ &- (B_1 A_{2i} + B_2 A_{1i}) A_{3n} A_{2n} / \sum A_{3n}^2]. \end{aligned} \quad (\text{I.11})$$

## APPENDIX II

In Section 7 we considered the question of when the classical equations of motions provide a good approximation to the equations used here and introduced a definition of "quasi-steady" motion, but only in the degenerate case when one variable was present. We wish now to treat the general case of equations (11). Since the analysis is rather unwieldy, we shall omit most of the details.

Define

$$\bar{N}_{ab} = \int_0^\infty N_{ab}(\tau) d\tau, \quad (\text{II.1})$$

where  $ab$  is any combination of  $y$  and  $\psi$ . The question we ask ourselves is "When can a solution of equations (11) be approximated by a solution of the following pair:

$$\begin{aligned} (m + \mu_{yy}) \dot{v} + (\beta_{yy} + \bar{N}_{yy}) v + \\ + (\mu_{y\psi} + m\chi_g) \dot{\lambda} + (\beta_{y\psi} + m u_0 + \bar{N}_{y\psi}) \lambda = Y_E, \end{aligned} \quad (\text{II.2})$$

$$\begin{aligned} (\mu_{\psi y} + m\chi_g) \dot{v} + (\beta_{\psi y} + \bar{N}_{\psi y}) v + \\ + (I_0 + \mu_{\psi\psi}) \dot{\lambda} + (\beta_{\psi\psi} + m\chi_g u_0 + \bar{N}_{\psi\psi}) \lambda = N_E. \end{aligned}$$

Let  $v_1, \lambda_1$  be a solution of (11) and  $v_2, \lambda_2$  a solution of (II.2), each satisfying the same initial conditions. Then if we let  $v = v_1 - v_2, \lambda = \lambda_1 - \lambda_2$ , it follows that  $v(0) = \lambda(0) = 0$  and that  $v$  and  $\lambda$  satisfy the equations

$$\begin{aligned} (m + \mu_{yy}) \dot{v} + (\beta_{yy} + \bar{N}_{yy}) v + \\ + (\mu_{y\psi} + m\chi_g) \dot{\lambda} + (\beta_{y\psi} + m u_0 + \bar{N}_{y\psi}) \lambda = \eta(t), \end{aligned} \quad (\text{II.3})$$

$$\begin{aligned} (\mu_{\psi y} + m\chi_g) \dot{v} + (\beta_{\psi y} + \bar{N}_{\psi y}) v + \\ + (I_0 + \mu_{\psi\psi}) \dot{\lambda} + (\beta_{\psi\psi} + m\chi_g u_0 + \bar{N}_{\psi\psi}) \lambda = \xi(t). \end{aligned}$$

where  $\eta$  and  $\xi$  are defined as follows:

$$\begin{aligned} \eta(t) &\equiv - \int_0^\infty [v_1(t-\tau) - v_2(t-\tau)] N_{yy}(\tau) d\tau - \\ &- \int_0^\infty [\lambda_1(t-\tau) - \lambda_2(t-\tau)] N_{y\psi}(\tau) d\tau, \\ \xi(t) &\equiv - \int_0^\infty [v_1(t-\tau) - v_2(t-\tau)] N_{\psi y}(\tau) d\tau - \\ &- \int_0^\infty [\lambda_1(t-\tau) - \lambda_2(t-\tau)] N_{\psi\psi}(\tau) d\tau. \end{aligned} \quad (\text{II.4})$$

It will be convenient to write (II.3) in the form

$$A_i \dot{v} + B_i v + C_i \dot{\lambda} + D_i \lambda = \eta_i, \quad i=1,2 \quad (\text{II.5})$$

Let  $\sigma_1$  and  $\sigma_2$  be the roots (supposed distinct) of the equation

$$0 = (A_1 C_2 - A_2 C_1) \sigma^2 +$$

$$+ (B_1 C_2 - B_2 C_1 + A_1 D_2 - A_2 D_1) \sigma + (B_1 D_2 - B_2 D_1)$$

Let  $e_1$  and  $e_2$  be defined by

$$e_i = \frac{A_i \sigma_i + B_i}{C_i \sigma_i + D_i} = \frac{A_2 \sigma_i + B_2}{C_2 \sigma_i + D_2}.$$

(II.6)



The solution of (II.5) is

$$v = (e_1 - e_2)^{-1} (A_1 C_2 - A_2 C_1)^{-1} \cdot \left\{ e^{\sigma_1 t} \int_0^t [(A_2 - C_2 e_2) \eta_1 + (A_1 - C_1 e_2) \eta_2] e^{-\sigma_1 \tau} d\tau + e^{\sigma_2 t} \int_0^t [(A_2 - C_2 e_1) \eta_1 - (A_1 - C_1 e_1) \eta_2] e^{-\sigma_2 \tau} d\tau \right\}, \quad (\text{II.7})$$

$$r = (e_1 - e_2)^{-1} (A_1 C_2 - A_2 C_1)^{-1} \cdot \left\{ e_1 e^{\sigma_1 t} \int_0^t [(A_2 - C_2 e_2) \eta_1 - (A_1 - C_1 e_2) \eta_2] e^{-\sigma_1 \tau} d\tau + e_2 e^{\sigma_2 t} \int_0^t [(A_2 - C_2 e_1) \eta_1 + (A_1 - C_1 e_1) \eta_2] e^{-\sigma_2 \tau} d\tau \right\}.$$

Let us define the following (dimensional) constants:

$$E_i \equiv |e_1 - e_2| |A_1 C_2 - A_2 C_1| \cdot \left[ |A_i - C_i e_2| |\sigma_1|^{-1} + |A_i - C_i e_1| |\sigma_2|^{-1} \right]^{-1},$$

$$F_i \equiv |e_1 - e_2| |A_1 C_2 - A_2 C_1| \cdot \left[ |e_1| |A_i - C_i e_2| |\sigma_1|^{-1} + |e_2| |A_i - C_i e_1| |\sigma_2|^{-1} \right]^{-1}. \quad (\text{II.8})$$

Let  $V = \sup |v_i|$ ,  $R = \sup |r_i|$  and select some small real number  $\varepsilon > 0$ . We then define the time  $t_\varepsilon$  by the following set of eight inequalities:

$$\begin{aligned} \int_{t_\varepsilon}^{\infty} |N_{yy}| d\tau &< \frac{1}{12} \cdot \frac{\varepsilon}{V} (VE_2, RF_2), \\ \int_{t_\varepsilon}^{\infty} |N_{yy}| d\tau &< \frac{1}{12} \cdot \frac{\varepsilon}{R} (VE_2, RF_2), \\ \int_{t_\varepsilon}^{\infty} |N_{yy}| d\tau &< \frac{1}{12} \cdot \frac{\varepsilon}{V} (VE_1, RF_1), \\ \int_{t_\varepsilon}^{\infty} |N_{yy}| d\tau &< \frac{1}{12} \cdot \frac{\varepsilon}{R} (VE_1, RF_1). \end{aligned} \quad (\text{II.9})$$

A solution of (11) is now said to be "quasi-steady" if the following sets of inequalities are satisfied for all  $\tau$  such that  $|\tau| < t_\varepsilon$ :

$$|v_i(t-\tau) - v_i(t)| < \begin{cases} \frac{1}{12} \varepsilon \left[ \int_0^{\infty} |N_{yy}| d\tau \right]^{-1} (VE_2, RF_2), \\ \frac{1}{12} \varepsilon \left[ \int_0^{\infty} |N_{yy}| d\tau \right]^{-1} (VE_1, RF_1), \end{cases} \quad (\text{II.10})$$

$$|r_i(t-\tau) - r_i(t)| < \begin{cases} \frac{1}{12} \varepsilon \left[ \int_0^{\infty} |N_{yy}| d\tau \right]^{-1} (VE_1, RF_1), \\ \frac{1}{12} \varepsilon \left[ \int_0^{\infty} |N_{yy}| d\tau \right]^{-1} (VE_2, RF_2). \end{cases}$$

One may now show that any quasi-steady motion  $v_i, r_i$  may be approximated by a solution  $\bar{v}_i, \bar{r}_i$  of equations (II.2) such that

$$|v_i - \bar{v}_i| < \varepsilon V, \quad |r_i - \bar{r}_i| < \varepsilon R. \quad (\text{II.11})$$

The proof is straightforward and we omit it. The remarks made at the end of Section 7 apply equally well to this more general situation.

#### REFERENCES

- Bishop, R.E.D.; Burcher, R.K.; Price, W.G. The uses of functional analysis in ship dynamics. Proc. Roy. Soc. London. Ser. A. 332 (1973), 23-35.
- Bishop, R.E.D.; Burcher, R.K.; Price, W.G. Application of functional analysis to oscillatory ship model testing. Proc. Roy. Soc. London. Ser. A. 332 (1973) 37-49.
- Bishop, R.E.D.; Burcher, R.K.; Price, W.G. A linear analysis of planar motion mechanism data. J. Ship Res. 18 (1974), 242-251.
- Brard, Roger  
A vortex theory for the maneuvering ship. 5th Symposium on Naval Hydrodynamics, Bergen, 1964, pp. 815-907; disc. 908-911.
- Brard, Roger  
Vortex theory for bodies moving in water. 9th Symposium on Naval Hydrodynamics, Paris, 1972, pp. 1187-1277; disc. 1278-1284.
- Brard, Roger  
A mathematical introduction to ship maneuverability. David W. Taylor Lectures, Sept. 1973, Naval Ship Research and Development Center, Bethesda, Md.
- Cummins, W.E.  
The impulse response function and ship motions. Schiffstechnik 9 (1962), 101-109.

Fujino, Masataka; Matora, Seizo  
On the effect of frequency dependency of the stability derivatives upon steering motions. Proc. 14th Internat. Towing Tank Conf., Ottawa, 1975, vol. 2, pp. 621-630.



Goodman, Alex

Experimental techniques and methods of analysis used in submerged body research. 3rd Symposium on Naval Hydrodynamics, Scheveningen, 1960, pp. 379-445; disc. 446-449.

Kotik, J; Lurye, J.

Some topics in the theory of coupled ship motions. 5th Symposium on Naval Hydrodynamics, Bergen, 1964, pp. 407-424.

van Leeuwen, G.

The lateral damping and added mass of a horizontally oscillating shipmodel. Studiecentrum T.N.O voor Scheepsbouw en Navigatie, Rep. No. 65S (Dec. 1964), 26 pp.

Lin, Wen-Chin

An initial-value problem for the motion of a ship moving with constant mean velocity in an arbitrary seaway. Dissertation, Univ. of Calif., Berkeley, 1966.

Mandel, Philip

Ship maneuvering and control. Chap. 8, pp. 463-606, of Principles of Naval Architecture, J. P. Comstock, ed. Soc. of Naval Arch. Mar. Engrs., New York, 1967.

Newman, J. N.

Some hydrodynamic aspects of ship maneuverability. 6th Symposium on Naval Hydrodynamics, Washington, D.C., 1966, pp. 203-231; comments, pp. 231-237.

Nomoto, K.

Ship response in directional control taking account of frequency dependent hydrodynamic derivatives. Proc. 14th Internat. Towing Tank Conf., Ottawa, 1975, vol. 2, pp. 703-709.

Nomoto, Kensaku; Karasuno, Keiichi

A new procedure of maneuvering model experiment. J. Soc. Naval Arch. Japan 126 (1969), 131-140. Translated in Selected Papers 7, 112-123.

Ogilvie, T. Francis

Recent progress toward the understanding and prediction of ship motions. 5th Symposium on Naval Hydrodynamics, Bergen, 1964, pp. 3-80; discussion, pp. 80-128.

Paulling, J.R.; Wood, Lloyd W.

The dynamic problem of two ships operating on parallel courses in close proximity. Univ. Calif., Berkeley, Inst. Engrg. Res., Rep. Series 189, Issue 1 (July 1962), iii + 26 pp.+15 figs.

Smith, W.E.; Cummins, W.E.

Force pulse testing of ship models. 5th Symposium on Naval Hydrodynamics, Bergen, 1964, pp. 439-457; discussion, 457-459.

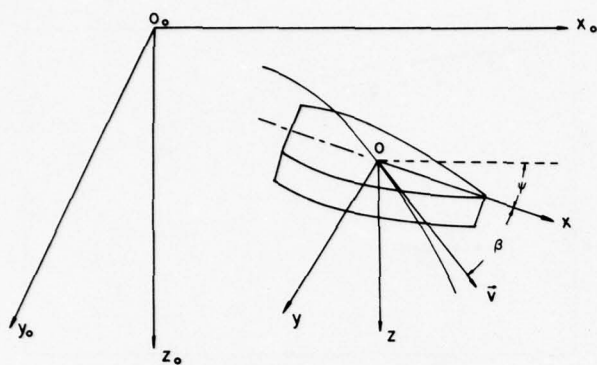


Fig. 1: Sketch defining coordinate systems, heading angle  $\psi$  and drift angle  $\beta$ .

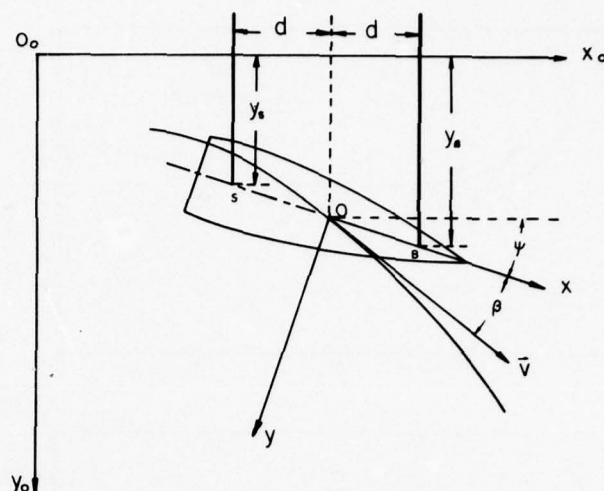


Fig. 2: Sketch defining variables used in PMM analysis.

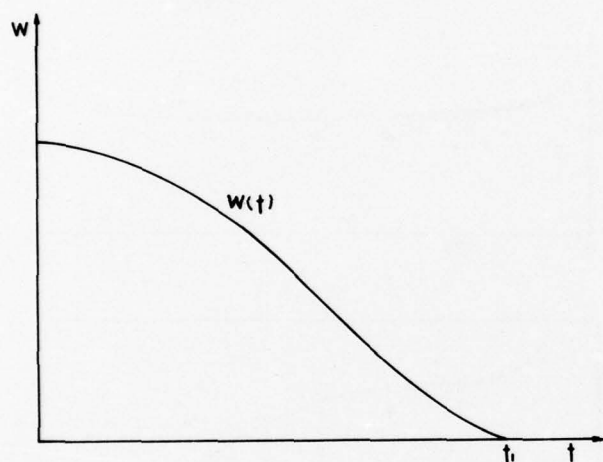


Fig. 3: Typical filter weighting function.

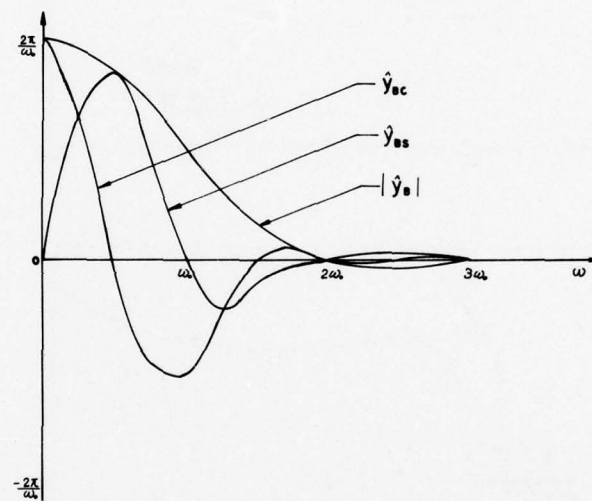


Fig. 4: Graphs of  $\hat{y}_{BC1}\hat{y}_{BS}$  and  $\hat{y}_B$  for  $\hat{y}_B$  given by (54).

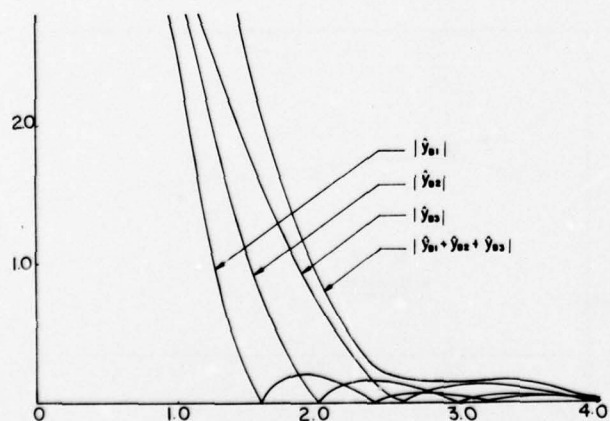


Fig. 5: Mathematical example showing effect of adding data.

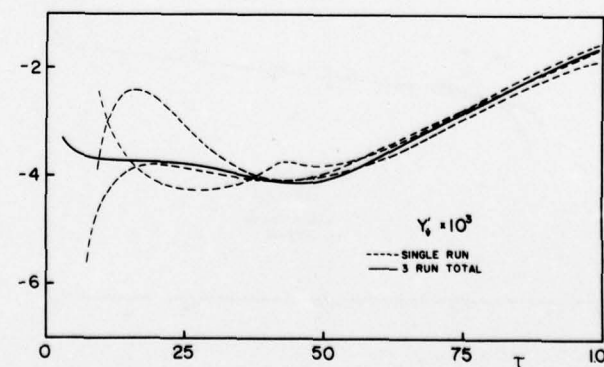
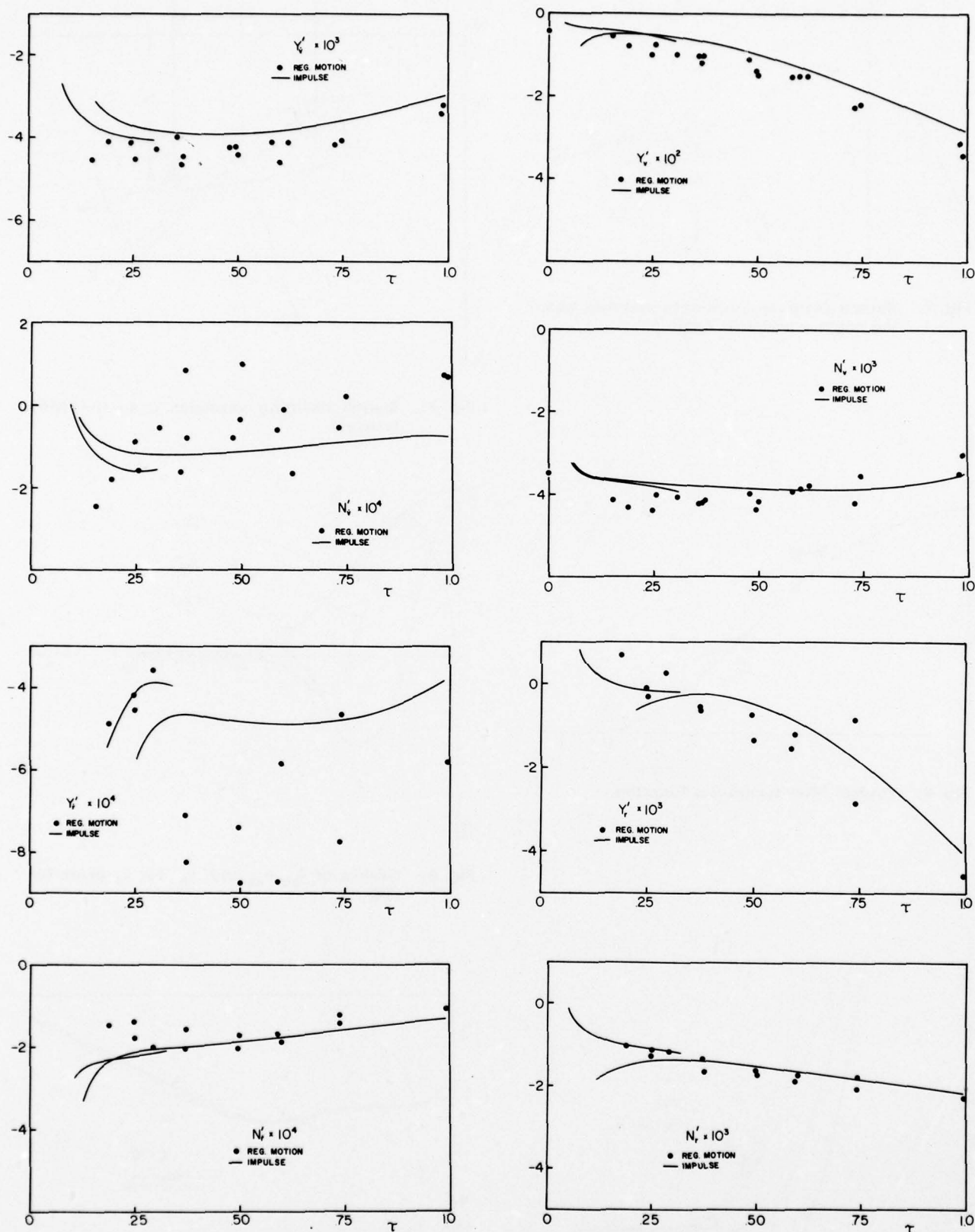


Fig. 6: Illustration of the effect of adding experimental data.



**Figs 7-14: Stability derivatives for a high-speed hull ( $C_B = 0.49$ ) as determined by transient-response tests and individual-frequency tests.**



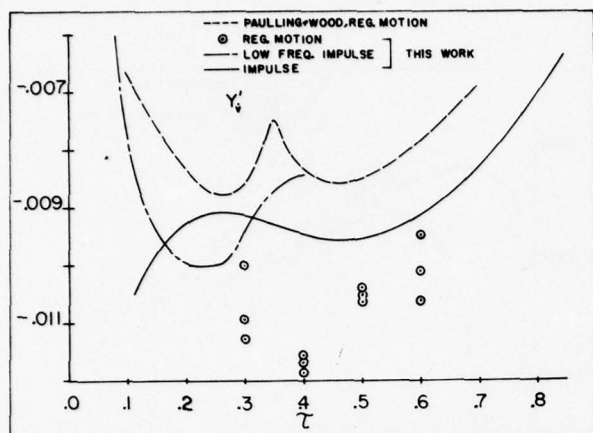


Fig. 15

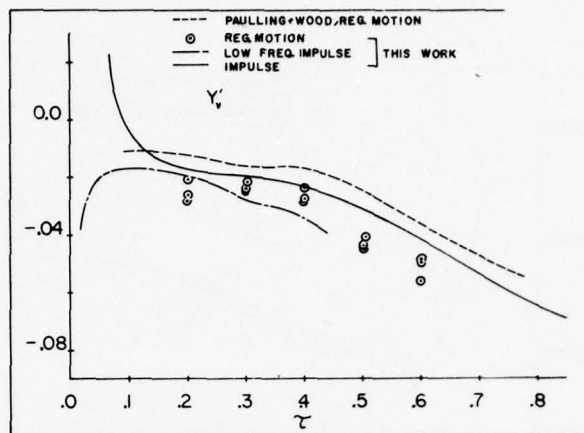


Fig. 16

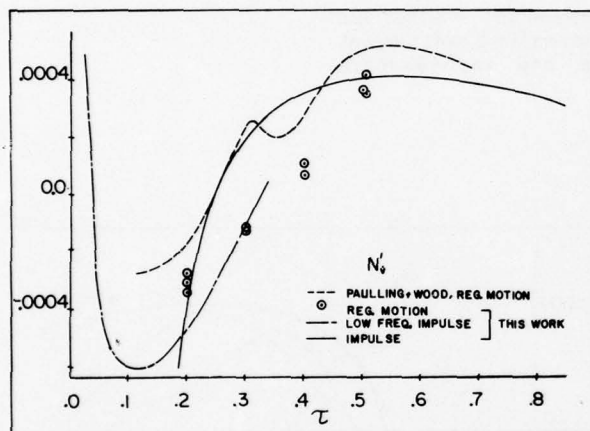


Fig. 17

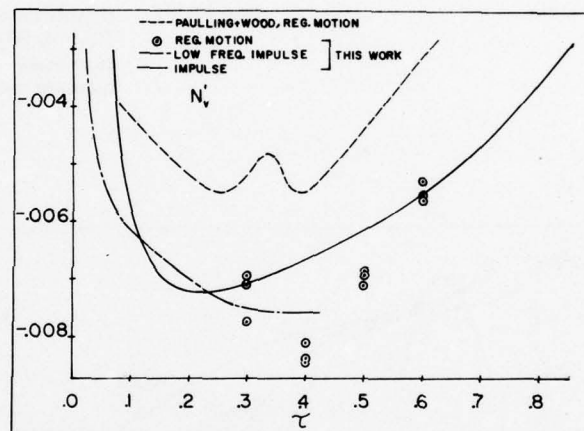


Fig. 18

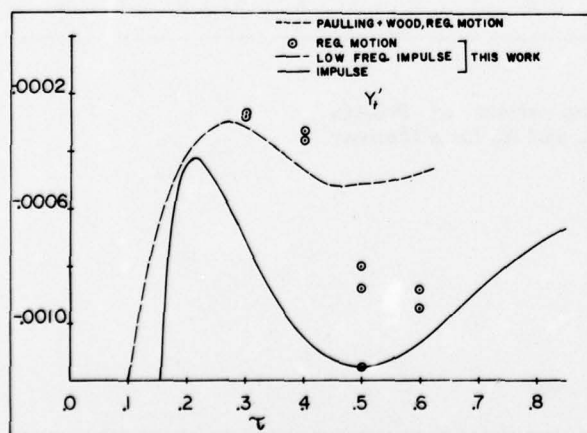


Fig. 19

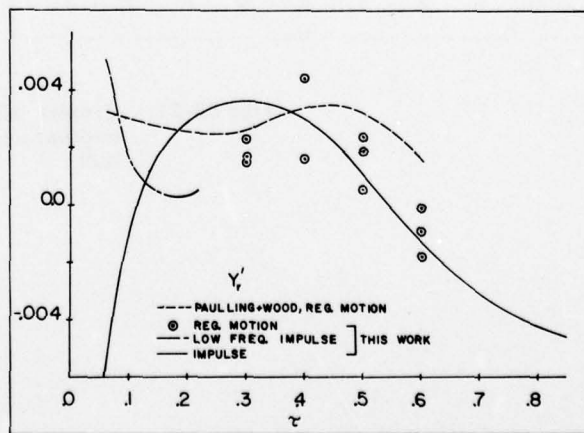


Fig. 20

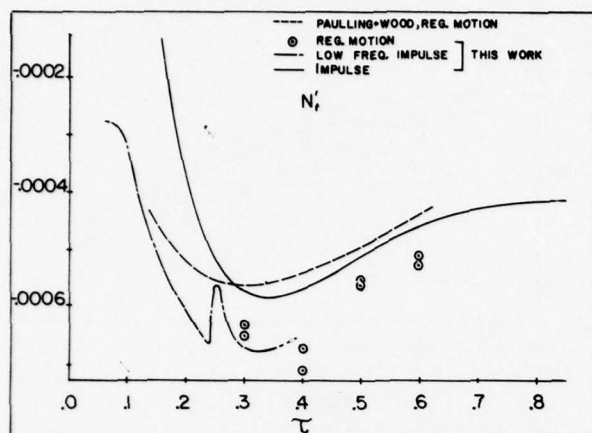


Fig. 21

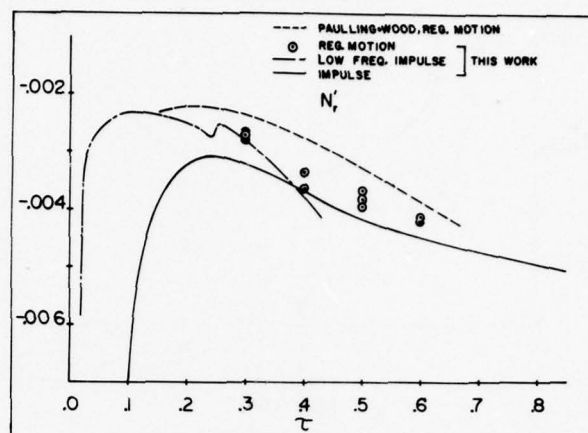
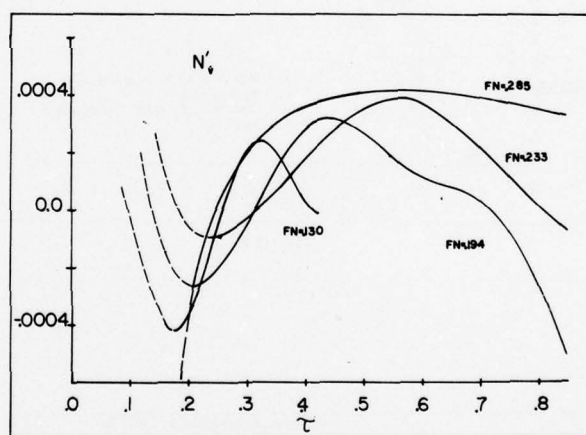
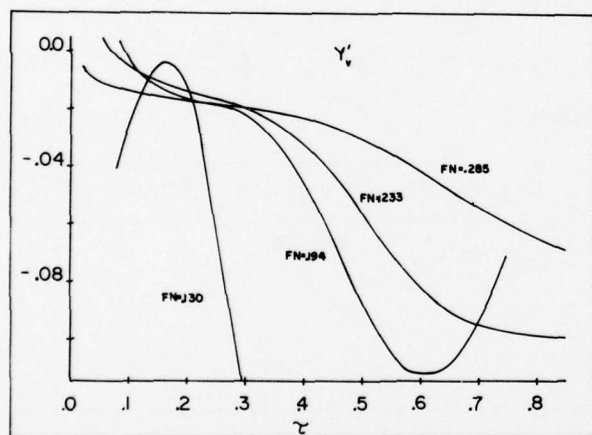


Fig. 22

**Figs 15-22: Stability derivatives for Mariner hull ( $C_B = 0.59$ ) as determined by transient-response tests and individual-frequency tests.**



**Figs 23-24: Graphs showing effect of Froude number upon  $Y'_y$  and  $N'_y$  for a Mariner hull.**

# ADVANCED EXPERIMENTAL TECHNIQUES FOR TESTING SHIP MODELS IN TRANSIENT WATER WAVES

## PART I THE TRANSIENT TEST TECHNIQUE ON SHIP MOTIONS IN WAVES

S. TAKEZAWA

Department of Naval Architecture, Yokohama National University, Yokohama, Japan

M. TAKEKAWA

Sumitomo Shipbuilding & Machinery Co Ltd, Yokosuka, Japan

### SYNOPSIS

In this paper, advanced experimental techniques for using the transient water waves are presented. As the main topic of this paper, ship motions in transient water waves are discussed in detail both in frequency domain and in time domain. Other applications of transient response method are outlined for reference. The experimental values are compared with the test results in regular waves and the theoretical calculations, by which the proposed experimental techniques shall be proved to be practically useful methods. As a conclusion, the proposed methods are useful and effective in the reduction of total testing time and the high accuracy of experiment including the analysis work. The commercial routine work will be considerably shortened by the application of transient response methods.

### 1. INTRODUCTION

The ship motion test in regular waves has been employed in usual to determine the frequency transfer function. However, it takes considerably long time to conduct a series test covering the range of frequency required. Because only one characteristic point can be obtained from one test run with respect to a incident wave at a speed and a heading.

Davis and Zarnick (1) presented an epoch-making experimental technique using Transient Water Wave (T.W.W.) in the fifth O.N.R. Symposium on Naval Hydrodynamics which was based on both the transient response theory and the equations of motion in time domain. According to this method, one continuous characteristic curve can be obtained from one test run. Cummins (2) reported originally that the actual equations in time domain could be transformed into the generally accepted equations in frequency domain. The advanced works were reported by Ogilvie (3), Breslin et al (4) and Yamanouchi (5). These papers assured the validity of the ship motion test in transient water wave.

Then, following these enlightening works, the authors investigated in detail the characteristics of transient water wave and developed the complete generating method of transient water wave with the arbitrary controll of the amplitudes and phases of elementary waves, and established the ship motion testing method in these waves including the practical data analysis procedure (6,7,8,9,10,11). Moreover, the idea of transient response method was applied to the wave exciting forces test with restrained ship model by the authors (12), and the forced oscillation tests which was proposed by Smith and Cummins (13) was carried out by the authors also. In particular, the practical technique of the forced transient oscillation test was investigated in detail so as to be adopted in routine work at ship model basin (12, 14, 15, 16,

17, 18, 19, 20). In another application, we succeeded to measure extremely high wave impact pressure at bow bottom and stem in transient water wave. Such a high pressure has not been measured in regular water waves (21).

As the main topic of this paper, the authors would like to show the test results of ship motions in transient water waves, which was carried out systematically by our ordinary testing method for the presentation of this symposium in last December. Other test results (wave exciting forces test in T.W.W., forced transient oscillation tests, etc.) are mentioned briefly. In part I of this paper, the practical method for testing ship model in T.W.W. is stated, and in Part II, the practical method on generation of T.W.W. in ship model basin and its characteristics are discussed in detail showing many examples. Examples of transient water wave mentioned part II are the same in part I, please refer to both parts alternately.

#### 1.1 Notation

$x(t)$	Arbitrary transient time history
$x_I(t)$	Transient time history of input phenomenon
$x_O(t)$	Transient time history of output phenomenon
$X(i\omega_e)$	Fourier transform of $x(t)$ , Fourier spectrum
$A_x(\omega_e)$	Amplitude of Fourier spectrum $X(i\omega_e)$
$\psi_x(\omega_e)$	Phase of Fourier spectrum $X(i\omega_e)$
$G_{OI}(i\omega_e)$	Frequency transfer function between input and output
$\bar{A}_{OI}(\omega_e)$	Amplitude of frequency transfer function $G_{OI}(i\omega_e)$ , Amplitude ratio
$\phi_{OI}(\omega_e)$	Phase of frequency transfer function $G_{OI}(i\omega_e)$ , Phase difference
$C_{OI}(\omega_e)$	Cosine component of $G_{OI}(i\omega_e)$
$S_{OI}(\omega_e)$	Sine component of $G_{OI}(i\omega_e)$
$W_{OI}(\tau)$	Weighting function calculated by inverse Fourier transformation of $G_{OI}(i\omega_e)$



$\phi'_{OI}(\omega_e)$	Theoretical phase difference against wave crest at the center of gravity of the ship (C.G.)
T	Duration of time history
$\omega$	Circular frequency of wave
$\omega_e$	Circular frequency of encounter wave and ship motions
$\omega_L$	Lower limiting circular frequency of $G_{OI}(\omega_e)$
$\omega_U$	Upper limiting circular frequency of $G_{OI}(\omega_e)$
$[\omega_e]_{s.w.}$	Critical frequency of side walls effect
$[\omega_e]_{cr.}$	Critical frequency corresponding to ship speed
X	Distance between C.G. of model and the forward position where encounter wave probe is installed
$\theta_{L.F.}$	Angle defined in Lewis Form expression of a section
Fn	Froude number
Vs	Ship speed
g	Gravitational acceleration
$\sqrt{L_{pp}/\lambda}$	Non-dimensional wave frequency ( $\lambda$ wave length)
$F_{wo}$	Amplitude of wave exciting force for heave
A	Virtual mass moment of inertia for pitch
Subscripts	
I	Input
O	Output
h	Encounter wave
z	Heave
$\theta$	Pitch
a	Vertical acceleration
P	Hydrodynamic pressure

## 2. EXPERIMENTAL TECHNIQUES AND ANALYSIS OF TRANSIENT PHENOMENA

Considering from the practical aspect of model ship test, it is enough to obtain only the frequency transfer function of ship motion. In this mean, the frequency transfer function obtained by the test in transient water wave has such favorite feature that both the amplitude and the phase are continuous in nature. In this chapter, the authors outline the test techniques and the calculating formula of frequency transfer function.

### 2.1 Experimental techniques

Transient water wave suitable for use in ship model test should be satisfied the following four conditions.

- required wave frequency range is covered.
- water surface is flat initially and is restored in appropriately short time after the disturbance.
- partial wave breaking does not occur during the transition of wave.
- the reflected wave from the end wall of tank does not affect the behavior of ship before a test run ends.

As additive needs for ship motion test, the followings are also to be satisfied;

- amplitudes of elementary waves (in particular shorter waves) are to be appropriately high in linearity, because the accuracy of measured frequency transfer function is greatly dependent on this

requirement. (See Fig. 5 and 7)

- concentration point of transient water wave should not be settled between the encounter wave probe and the model ship, because the dissipation of wave energy occurs in concentration of waves. (See Fig. 6)

The transient water wave that satisfies definitely these conditions is the concentrating wave with moderate and almost constant wave height (i.e. The shorter waves go ahead of the longer waves. See Fig. 2) The wave of this type which called 'Amp. Constant T.W.W.' in this paper, is very suitable for the ship motion test. However it should be noticed that wave crest breaks easily. (Some examples will be shown in Part II.) Even though the same desirable transient water wave is generated, the shape and duration of the measured transient time histories become different according to the position where model ship comes across the wave. This encounter condition that defines recording time can easily be controlled by the time lag necessary to start the towing carriage after beginning of wave generation, but it is not so important if the above mentioned demands (d) and (f) are assured. As shown in Fig. 6, the same characteristics can be obtained from dissimilar records. This is the essence and most interesting point of transient wave method. However, the mechanical parts of the detecting devices to measure ship motions don't respond so quickly that too short time history (one shot impulse) is not adequate. In this mean, desirable recording time should be determined from the response characteristics of the measuring instruments. The measured data of each phenomenon should be recorded on magnetic tape as analog voltage. By using analog data recorder, data processing work can be executed easily and effectively. Ordinary total measuring system adopted in Yokohama National University is shown in Fig. 1.

### 2.2 Analysis of transient time history

The basic tool which is used in numerical analysis of transient time histories is a well known Fourier transformation. When a transient time history  $x(t)$  is measured, it can be transformed into frequency domain as follows.

$$\begin{aligned}
 x(i\omega_e) &= \int_0^T x(t) e^{-i\omega_e t} dt \\
 &= \int_0^T x(t) \cos \omega_e t dt - i \int_0^T x(t) \sin \omega_e t dt \\
 &= A_x(\omega_e) e^{i\psi_x(\omega_e)} \quad (1)
 \end{aligned}$$

where T : Duration of transient time history  
 $A_x$ : Amplitude of Fourier Spectrum  
 $\psi_x$ : Phase of Fourier Spectrum  
 $\omega_e$ : Circular frequency of encounter

In ordinary experiment, encounter wave is usually measured at the moving carriage, so that Fourier transforms of both ship motions and wave are expressed to a base of encounter frequency  $\omega_e$ . If linearity of a system is assumed, a transfer function of the system can be defined by the ratio of input and output.

$$\begin{aligned}
G_{OI}(i\omega_e) &= X_O(i\omega_e)/X_I(i\omega_e) \\
&= [A_O(\omega_e)/A_I(\omega_e)] e^{i\{\psi_O(\omega_e) - \psi_I(\omega_e)\}} \\
&= \bar{A}_{OI}(\omega_e) e^{i\phi_{OI}(\omega_e)} \\
&= C_{OI}(\omega_e) + iS_{OI}(\omega_e) \quad (2)
\end{aligned}$$

where  $\bar{A}_{OI}(\omega_e)$ : Amplitude of frequency transfer function, Amplitude ratio  
 $\phi_{OI}(\omega_e)$ : Phase of frequency transfer function, Phase difference  
 $C_{OI}(\omega_e)$ : Cosine component  
 $S_{OI}(\omega_e)$ : Sine component

In practical procedure of the numerical analysis, the optimum value of sampling frequency (sampling time interval) should be chosen taking account of the computer capacity and the range of frequency expected to be included in a transient time history. The standard sampling frequency is taken as 20Hz in Yokohama National University. The accuracy of the analysis is checked by the following inverse calculation. By using the frequency transfer function obtained by experiment, weighting function is calculated,

$$\begin{aligned}
W_{OI}(\tau) &= \frac{1}{2\pi} \int_{-\infty}^{\infty} G_{OI}(i\omega_e) e^{i\omega_e \tau} d\omega_e \\
&= \frac{1}{\pi} \int_0^{\omega_u} \bar{A}_{OI}(\omega_e) \cos\{\omega_e \tau + \phi_{OI}(\omega_e)\} d\omega_e \\
&= \frac{1}{\pi} \int_{\omega_l}^{\omega_u} \bar{A}_{OI}(\omega_e) \cos\{\omega_e \tau + \phi_{OI}(\omega_e)\} d\omega_e \quad (3)
\end{aligned}$$

where  $\omega_u$ : Upper limiting circular frequency of  $G_{OI}(\omega_e)$   
 $\omega_l$ : Lower limiting circular frequency of  $G_{OI}(\omega_e)$

and then, the response of the system  $x_O(t)$  is calculated by convolution integral.

$$x_O(t) = \int_0^T W_{OI}(t-\tau) x_I(\tau) d\tau \quad (4)$$

If the calculated response time history shows a good agreement with the measured one, we conclude that the assumption of linearity and the accuracy of analysis are held acceptably. In this paper, as the accuracy of data processing work was once checked, eq.(4) is used as a tool of theoretical prediction of time histories.

In Yokohama National University, the above mentioned calculations, graphic display and the hard copy can be completed in almost real time by the fast digital computer applied Fast Fourier Transformation (F.F.T.). Even without such a high quality device, the total execution time including experiment is shortened considerably by the transient response method.

### 3. SHIP MOTIONS IN TRANSIENT WATER WAVE

In this chapter, ship motion in transient water wave are shown in frequency and time domain. Since the reproductivity of transient water wave at ship model basin is sufficiently complete, the ship motions with encounter wave and the wave

itself were measured by the separate test. But the same input voltage signal for wave maker was used to keep the consistency of both experiments. The experimental values obtained by the transient response method are compared with the results in regular waves and the calculations by Ordinary Strip Method (abbreviated here to O.S.M.) (22,23) in detail, by which the proposed experimental technique shall be proved to be a practically useful method.

#### 3.1 Experiment program

The experiments were performed using the 2m long model of ore carrier "KASAGISAN-MARU" in the Experimental Tank of Yokohama National University (50m x 3.6m x 2.3m). The principal particulars and dynamic properties of model ship are given in Table 1. This ship form was chosen in our experiment because series tests of this ship had been conducted by SR-131 Committee of Japan Shipbuilding Research Association, and amount of data had already been obtained.

Table 1. Principal Particulars of Tested Model

Ship Name		KASAGISAN-MARU
Length betw. P.P.,	$L_{pp}$ (m)	2.000
Breadth,	$B$ (m)	0.329
Depth,	$D$ (m)	0.186
Draft,	$d$ (m)	0.130
Displacement, Volume,	$V$ ( $m^3$ )	0.0704
Block Coefficient,	$C_b$	0.8243
Midship Coefficient		0.9975
C.G. from Midship	(m) fore	0.059
C.G. from Keel	(m)	0.099
Longitudinal Gyradius		0.2363 $L_{pp}$
Natural Heave Period	(sec)	0.983
Natural Pitch Period	(sec)	0.880
Scale		1/123.5

Heave, pitch, vertical acceleration at S.S. 8 1/2 section, pressure at bilge ( $\theta_{L.F.} = 50^\circ$  by Lewis Form expression) of S.S. 8 1/2 section and encounter wave at 1.3m forward from C.G. were recorded on a magnetic tape by an analogue data recorder, and these records were simultaneously monitored by the direct recording electromagnetic oscillograph to check success or failure of the experiment.

The following two types of transient water wave were generated.

- T.W.W. with constant wave height in Fourier spectrum (See Fig. 5)
- T.W.W. with constant wave slope in Fourier spectrum (See Fig. 7)

Ship speed was corresponding to Froude number  $F_n = 0.15$ , and ship was mainly tested in the concentrating transient water wave. The situation that ship passes through T.W.W. is schematically illustrated in Fig. 4 of Part II.

The total measuring system and the definition of co-ordinate are shown in Fig. 1.

#### 3.2 Expression of ship motions in frequency domain (frequency transfer function)

Examples of the measured time histories in the

concentrating transient water wave with constant wave height are shown in Fig. 2. Maximum of heave (peak-to-peak value) was 6.5cm (about 0.5d), and of pitch 7.8deg. The duration of time history needed for data analysis is about 12 seconds. It is very interesting that in such a short time history much information is superposed and condensed. Each time history starts from zero level and ends in zero level again. It is assured that experiment carried out successfully. In this case total energy is finite, so that Fourier transformation can be made in the strict sense. Analyzing the time histories by High Speed Analyser with F.F.T. Algorithm, one set of obtained hard copies in which the results are displayed graphically is shown in Fig. 3. Since the arrangement of graphic display and numerical tables can be easily programmed in this analyser, the data analysis work can be conducted smoothly and effectively by using the prepared program. The moderate transient water wave, which is shown in Fig. 2, has been adopted as the standard T.W.W. for ship motion test, but, by amplifying the same wave generation signal, an example of the high transient water wave was generated. In this case, partial breaking of wave crests observed. The time histories of ship motions in this high transient water wave are shown in Fig. 4. Heaving motion of 12.8cm (about 1.0d) and pitching of 14.3deg were measured at the maximum points. Photos, which were taken at intervals of 0.26 second by the motor driven camera, show how severely ship was oscillating among waves. The numbers given on each photo are corresponding to the pulse record shown in Fig. 4. In order to make clear the linearity limit of the ship-wave system, two more experiments carried out at the same condition excepting the amplitude of wave. The results obtained from four different experiments are shown in Fig. 5. The determined frequency transfer functions of pitch coincide with one another excepting the high transient water wave test. It is obvious from this figure that linearity of the system was held in small, moderate and a little high transient water wave. In the later paragraph, mean line of the measured linear responses will be compared with both the experimental values obtained in regular water wave and the calculations by O.S.M.

As mentioned previously, even though the same transient water wave is generated, different time histories are measured according to the position where ship encounters the transient water wave. Typical example of this case is shown in Fig. 6. The towing carriage, in the concentrating transient water wave test (T.W.W.-1), started about 15 seconds after the wave maker had begun to generate waves, but in the diverging transient water wave test (T.W.W.-2) the towing carriage started about 30 seconds later. The time histories are obviously different, but the almost same frequency transfer functions are obtained in this experiment. However, when compared two Fourier spectrum of wave, the decay of the amplitudes is noticed markedly at high frequencies. This implies that the energy of short waves dissipated when all elementary waves concentrated at one point.

The detailed explanation on this characteristic of transient wave will be given in Part II. The authors don't recommend the test in diverging transient water wave because the reflected

waves from the end and side walls of tank affect ship motions.

As another example of ship motions, the test results in the different type of transient water wave (i.e. T.W.W. with constant wave slope) are shown in Fig. 7. It is clear that the amplitude of wave spectrum is smaller in high frequency range. Elementary waves of this transient wave are controlled to have the same slope, so that the amplitude of wave spectrum becomes gradually small in proportion to the increase of the wave frequency. This control brings about slight disadvantage to the determination of frequency transfer function. (See the frequency transfer function shown in Fig. 7.)

Summarizing the above discussion, the authors would like to recommend the ship motion test using the concentrating transient water wave with constant wave height.

On the next stage, let's compare the test results in T.W.W. with the obtained results in regular waves. Generally, the waves generated by an oscillating ship moving in waves at a given speed may be reflected from the walls of the basin will disturb the behavior of ship. This problem is very important for the discussion on the experimental results. Brard (24) and Hanaoka (25) examined the wave sector radiated by the ship theoretically, then, Vossers and Swaan (26) offered a practical chart by which the side walls effect could be taken into account. According to this chart at the experimental tank of Yokohama National University the side walls effect will appear in the frequency range  $\omega_e \leq [\omega_e]_{s.w.} = 0.37 \cdot g/V_s$ . In this case of Froude number  $F_n = 0.15$ , the critical frequency of the side walls effect is 5.46 rad/sec. The side walls effect is noticed considerably in the experimental results in regular water waves as shown in Fig. 8 and 9. On the contrary, this effect isn't observed in the results obtained by the transient water wave test (the mean values of three experiments except the high transient water wave test which were illustrated in Fig. 5). This is probably because the ship moves through the concentrating transient water wave in a short time, so that the reflected waves may not strike the aftbody of the ship. (In (19), the side walls effect which appeared in the transient water wave test and the forced transient oscillation test were investigated in detail.) In the range of frequency higher than the critical frequency, the measured values by two different methods agree satisfactorily, and also coincide well with the theoretical calculations. With respect to the phase difference of frequency transfer functions, the experimental values agree very well with the calculation (See Fig. 8, 9, 10, 11). It is noted that, since the experimental phase difference is defined as the phase difference between input and output (eq. (2)), the phase difference calculated by O.S.M. is corrected as follows for the convenience of the comparison with the experimental value. In the theoretical calculation, as phase difference or motion is usually defined against wave crest at C.G., theoretical phase difference is corrected by the following formula in this paper.



$$\phi_{OI}(\omega_e) = \phi'_{OI}(\omega_e) - \frac{\omega^2}{g} x \quad (5)$$

where  $\phi_{OI}(\omega_e)$ : Corrected phase difference against wave crest at X m forward from the center of gravity of the ship (C.G.)

$\phi'_{OI}(\omega_e)$ : Theoretical phase difference against wave crest at C.G.

x : Distance between C.G. of model and the forward position where wave probe is installed

The theoretical phase differences corrected by eq.(5), which are corresponding to the phase differences obtained by the experiments, are drawn in every figure.

The experimental values of the high transient water wave test, in which the linearity isn't held as mentioned previously, are also plotted on all figures. These values are remarkably smaller in the important frequency range than the calculations. However, the wonder is that the phase differences agree well with those of other experiments and theory.

### 3.2 Expression of ship motions in time domain (prediction of time history)

When ship motions in frequency domain can be described, it is easy to predict them in time domain under the assumption of linear superposition. In the calculation procedure, the weighting function (eq. (3)) is calculated beforehand by using the theoretical frequency transfer function, and then, taking the convolution integral (eq. (4)), ship motions are predicted from the measured time history of encounter wave.

The first example shown in Fig. 12 is the predicted time history of pitch in the moderate transient water wave. The predicted response of pitch in time domain agrees almost precisely with the measured time history. This is the reasonable result which are expected by the agreement of both in frequency domain.

Let's take other examples in which clear differences were observed in frequency transfer functions. In this case, it will be easily expected to get the time history different from the measured one. Pitch and vertical acceleration predicted from the encounter wave of measured high transient water wave and the theoretical weighting functions are shown in Fig. 13. Though the ship-wave system isn't linear, predicted pitch motion doesn't differ so much from the measured time history. About 14 percent difference of amplitude at the maximum point is noticed. As for the vertical acceleration, the remarkable difference of both amplitude and phase is found as expected. From this comparison, it is concluded that ship motions in linear zone can be predicted in time domain if the frequency transfer functions are known.

## 4. APPLICATION OF TRANSIENT RESPONSE METHOD

The idea of transient response method will be applied to various kinds of experiments. The authors would like to introduce three applied experiments here.

### 4.1 The wave exciting forces test with restrained model in transient water wave and the forced transient oscillation test in still water

In order to solve the equations of motion experimentally, the wave exciting forces and the coefficients of equations of motion must be measured. As for the wave exciting forces, the measurement of force and moment with restrained ship model has been conducted in regular wave (27). In the determination of coefficients, the stationary forced oscillation test has been adopted in usual (27, 28). With respect to the time required for testing model, it is the same situation that we met in ship motion test in waves.

The advanced techniques on the basis of transient response method were proposed by the authors as to the wave exciting forces test (12, 17). An example of the measured wave exciting force, which is quoted from (17), is shown in Fig. 14. Analyzing the time histories shown in the left side of Fig. 14, the wave exciting force plotted by the circle was obtained. Experimental values agree well with the calculations by O.S.M.

Smith and Cummins (13) originally proposed the application of transient response technique to the forced oscillation test. Then, the authors investigated in detail the systematic determination of coefficients by means of the forced transient oscillation (12, 14, 15, 17, 18). An example is shown in Fig. 15, as to the forced transient pure pitch oscillation test. The input voltage signal for the electro-hydraulic driving cylinder was made by sweeping from higher frequency to lower one (2.0Hz-0.4Hz) to exclude as possible the side walls effect  $[\omega_e]_{s.w.}$  and the effect of unusual hydrodynamical phenomenon at the critical frequency  $[\omega_e]_{cr.} = g/4V_s$ . The unusual hydrodynamical phenomena occur around the ship when the velocity of waves generated by ship motion becomes the same as the forward speed of ship (19, 24, 25, 26). This effect observed remarkably even in the forced transient oscillation test as shown in Fig. 15. In the quoted case, virtual mass moment of inertia for pitch was obtained from the cosine component of the frequency transfer function between the forced pitch and the measured moment. Both the experimental value and the calculation agree well. It is most important, as to the forced oscillation test, to measure the phase difference accurately, because the accuracy of determination of coefficients depends on the phase difference.

In the experimental determination of coefficients, the authors proposed new forced oscillation method in which transient water waves was used instead of known mechanical forces (20). By this new method coefficients can be obtained without using the ordinary forced oscillation mechanism, and the investigation on coefficients from new aspect is possible, because coefficients are obtainable in waves. The results obtained by applying this technique to longitudinal ship motions almost coincided with ones by conventional forced oscillation method.

### 4.2 The measurement of wave impact pressure in transient water wave

Extremely high wave impact pressures were measured at bow bottom and stem when the ship struck the wave front of concentrating transient water wave (21). The voltage generation signal of transient water wave which was used in this test was made especially so as to be included many high frequency wave components. An example of pressure record is illustrated in Fig. 16. In this case, maximum of impact pressure, measured at the point on stem (corresponding to 20m W.L. of the actual ship) was 148cmAq. As the model ship is 2m long, this impact pressure becomes 183mAq for the actual ship. This type of test, in which only the transient time history changing its profile in time and space domain is important, is one of the special application of transient water wave.

## 5. CONCLUDING REMARKS

From the proceeding discussions, it is certified that in the determination of frequency transfer function the testing ship models by transient response methods excel the former experimental techniques in the reduction of total testing time and the high accuracy of the experiment including the analysis work. The authors hope that the transient response method will be applied to the commercial routine work at large ship model basin in near future.

In addition, the calculations by Ordinary Strip Method are compared with the experimental values in both frequency and time domain. It is concluded that the calculations on longitudinal ship motions is accurate enough for practical usage in linear zone.

As special application of transient water wave from different point of view, it is noteworthy that T.W.W. is effective to realize the extreme condition of ship in model basin, as shown in the measurement of wave impact pressure mentioned in 4.2. Such experiments will have possibility to inquire into non-linear phenomena.

## ACKNOWLEDGEMENTS

The authors would like to express their sincere gratitude to Miss Kazuko Kasahara, Mr. Kiyoshi Miyakawa, Mr. Takehito Takayama and Mr. Yoshiteru Tada, who assisted us in the experiments, the calculations and the drawing of figures, and many students who assisted in the experiments and the data analysis work.

## REFERENCES

- (1) Davis, M. C. and Zarnick, E. E. 'Testing Ship Models in Transient Waves', Proc. 5th Symp. 1964 507-543.
- (2) Cummins, W. E. 'The Impulse Response Function and Ship Motions', Schiffstechnik 1961 9 101-109.
- (3) Ogilvie, T. F. 'Recent Progress toward the Understanding and Prediction of Ship Motions', Proc. 5th Symp. 1964 3-80.
- (4) Breslin, J. P., Savitoky, D., and Tsakonas, S. 'Deterministic Evaluation of Marine Craft in Irregular Seas', Proc. 5th Symp. 1964 461-505.
- (5) Yamanouchi, Y. 'Some Remarks on the Statistical Estimation of Response Functions of a Ship', Proc. 5th Symp. 1964 97-126.
- (6) Takezawa, S., Fukuhara, M., and Yamashita, S. 'On the Properties of the Transient Water Waves in Ship Model Basins', Journal of The Society of Naval Architects of Japan (JSNA Japan) 1968 124.
- (7) Takezawa, S. 'On Testing a Ship Model in Transient Water Waves', JSNA Japan 1970 127.
- (8) Takezawa, S. 'A Practical Method for Testing Ship Models in Transient Water Waves', Selected Papers JSNA Japan (in English) 1972 9.
- (9) Takezawa, S., and Hirayama, T. 'On the Generation of Arbitrary Transient Water Waves', JSNA Japan 1971 129.
- (10) Hirayama, T. 'On Non-linear Characters of Transient Water Waves Used for Ship Response Tests (Part 1)', JSNA Japan 1974 136.
- (11) Hirayama, T. 'On Non-linear Characters of Transient Water Waves Used for Ship Response Tests (Part 2)', JSNA Japan 1975 137.
- (12) Takezawa, S., and Takekawa, M. 'Testing Ship Models on Longitudinal Ship Motions by Transient Response Method', JSNA Japan 1971 130.
- (13) Smith, W. E., and Cummins, W. E. 'Force Pulse Testing of Ship Models', Proc. 5th Symp. 1964 439-459.
- (14) Takezawa, S., and Takekawa, M. 'Testing Ship Models on Longitudinal Ship Motions by Transient Response Method (Part 2 Pure Pitch)', JSNA Japan 1972 131.
- (15) Takezawa, S., and Takekawa, M. 'Testing Ship Models on Longitudinal Ship Motions by Transient Response Method (Part 3 Coupled Motion)', JSNA Japan 1973 133.
- (16) Takezawa, S., 'Testing Ship Models on Longitudinal Ship Motions by Transient Response Method (Part 4 Hydrodynamic Pressure)', JSNA Japan 1973 134.
- (17) Takezawa, S., and Takekawa, M. 'Testing Ship Models on Longitudinal Ship Motions by Transient Response Method', Bulletin F. E. Yokohama National University 1974 23 (in English).
- (18) Takezawa, S., and Takekawa, M. 'Transient Response Method for Testing Ship Models on Longitudinal Ship Motions', 14th ITTC 1975.
- (19) Takezawa, S., and Jungu, N. 'Testing Ship Models on Longitudinal Ship Motions by Transient Response Method (Part 5 Side Wall Effect)', JSNA Japan 1974 136.
- (20) Takezawa, S., Kojima, R., and Takekawa, M. 'New Forced Oscillation Method Using Water Waves as Exciting Forces', JSNA Japan 1974 136.
- (21) Takezawa, S., and Hasegawa, S. 'On the Characteristics of Water Impact Pressures Acting on a Hull Surface Among Waves', JSNA 1974 135.
- (22) Tasai, F. and Takagi, M. 'Theory and Calculation of Ship Response in Regular Waves', Symp. Seaworthiness of Ships, JSNA Japan 1969 1-52.
- (23) Fukuda, J., Nagamoto, R., Konuma, M., and Takahashi, M. 'Theoretical Calculation on the Motions, Hull Surface Pressures and Transverse Strength of a Ship in Waves',

- JSNA Japan 1971 129.
- (24) Brard, R. 'Introduction à l'Étude Théorique du Tangage en Marche', ATMA 1948 47 455-479.
- (25) Hanaoka, T. 'On the Velocity Potential in Michell's System and the Configuration of the Wave Ridges due to a Moving Ship', JSNA Japan 1953 93.
- (26) Vossers, G., and Swaan, W. A. 'Some Seakeeping Tests with a Victory Model', Int. Ship. Prog. 1960 69.
- (27) Gerritsma, J., and Beukelman, W. 'Analysis of the Modified Strip Theory for the Calculation of Ship Motions and Wave Bending Moments', Int. Ship. Prog. 1967 156.
- (28) Glovato, P. 'The Forces and Moments on a Heaving Surface Ship', J. Ship Res. 1957 1.

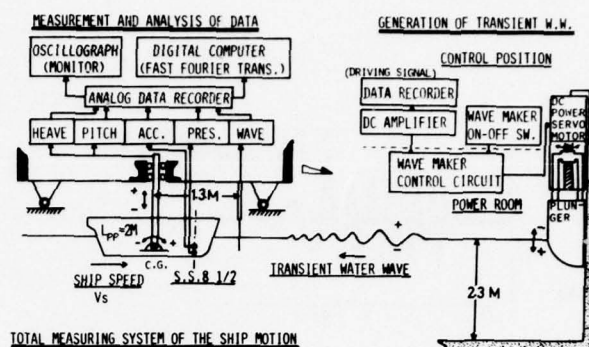


Fig. 1: The total instrumentation installed in Experimental Tank of Yokohama National University.

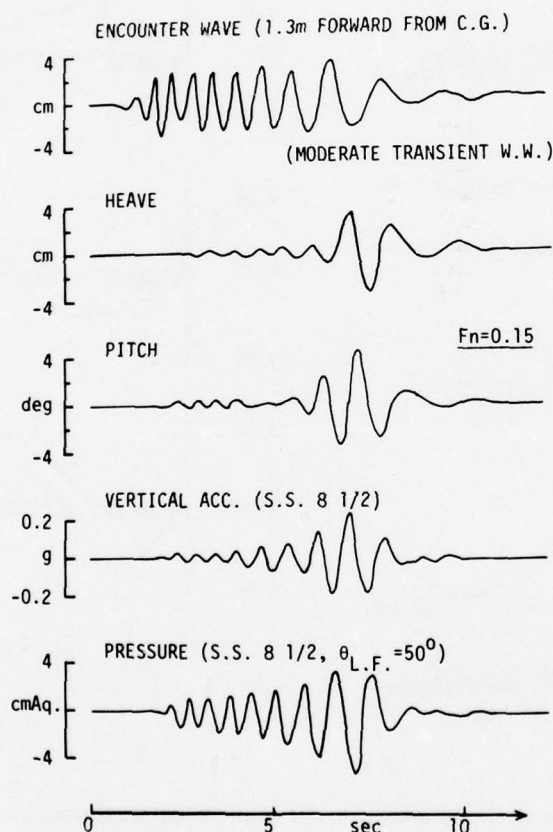


Fig. 2: The measured time histories in the moderate transient water waves (the concentrating T.W.W. with constant wave height in Fourier spectrum; refer to Exp. 111 in Fig. 4, Part II).



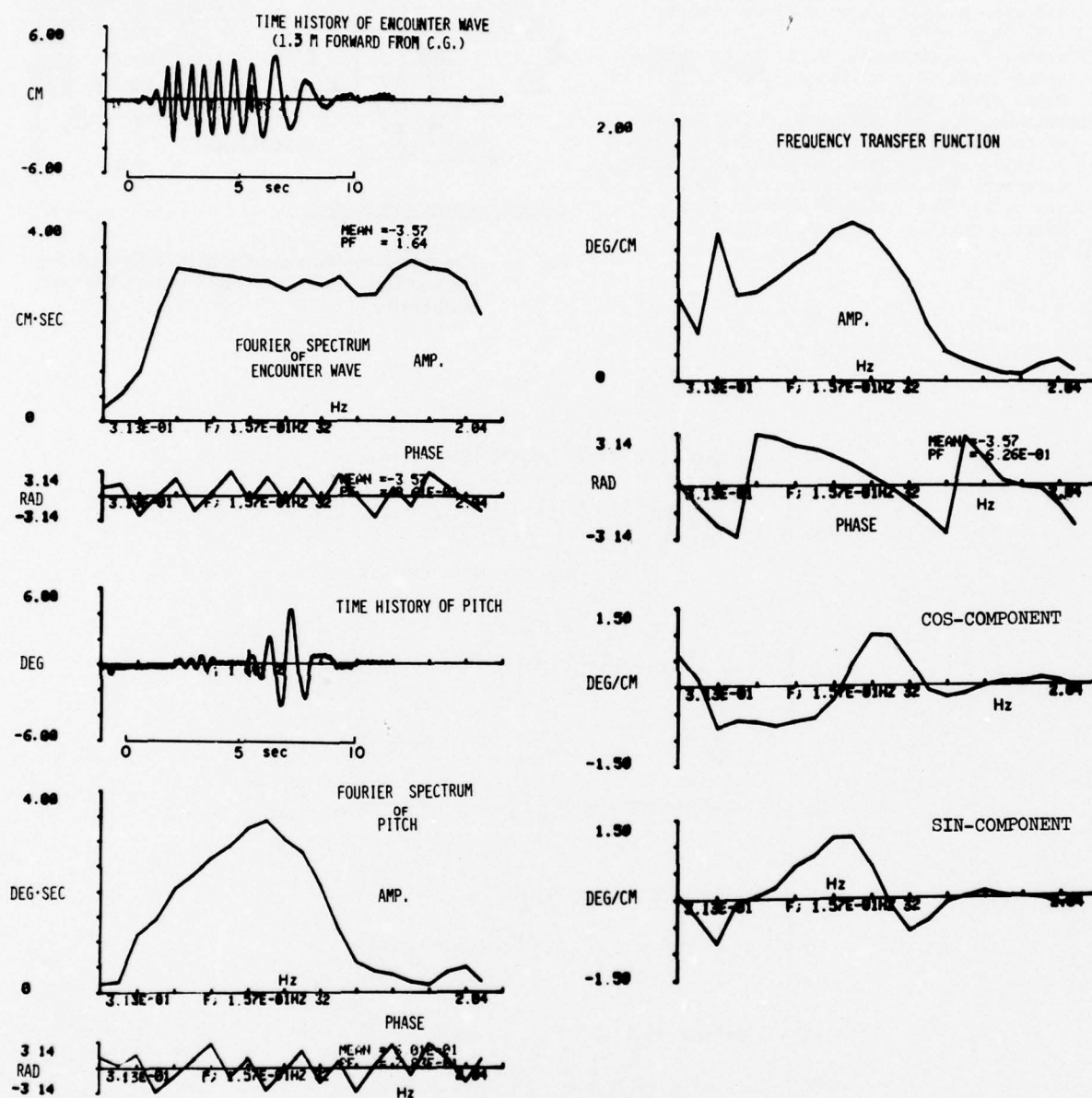
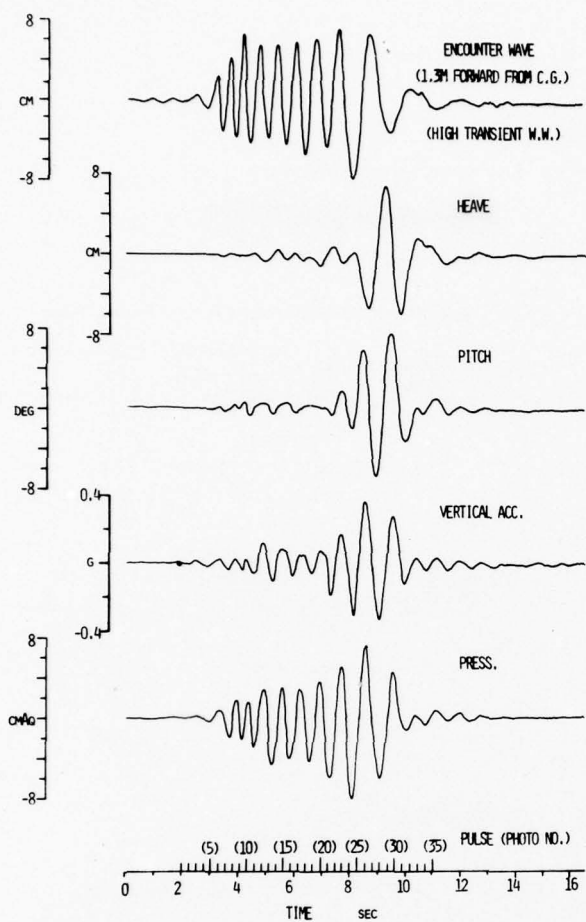
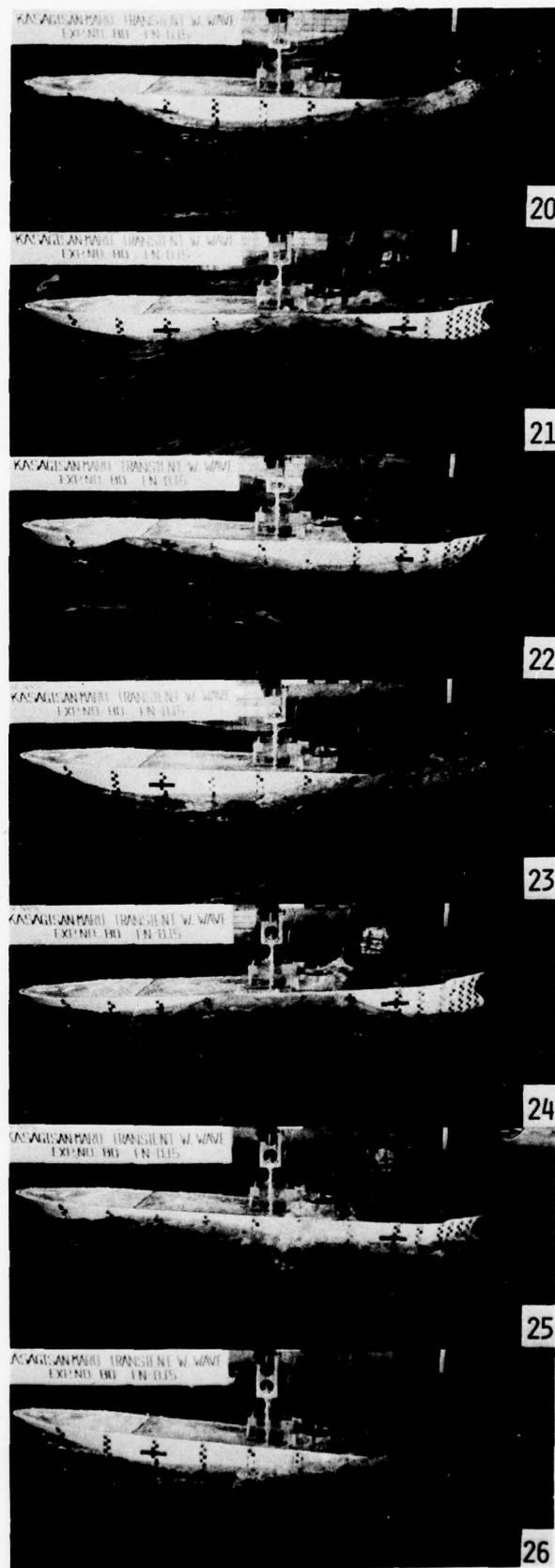


Fig. 3: Examples of hard copies to be obtained by the High Speed Analyser (corresponding to Fig. 2).



**Fig. 4:** The measured time histories in the high transient water waves (the concentrating T.W.W. with constant wave height in Fourier spectrum; refer to Exp. 112 in Fig. 4, Part II).



**Ship motions in the high transient water waves (Numbers correspond to PHOTO No. in Fig. 4).**

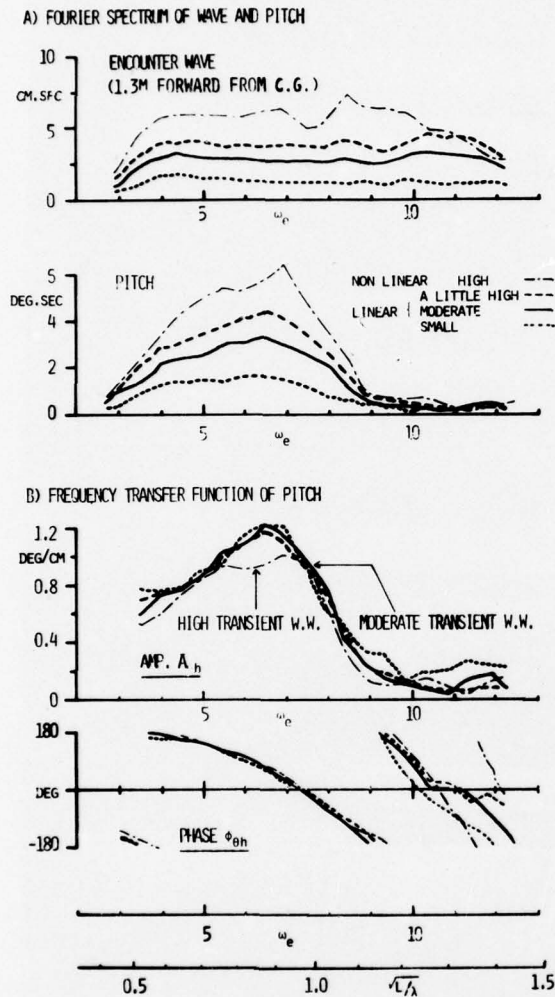


Fig. 5: Linearity and non-linearity of ship motions in various transient water waves.

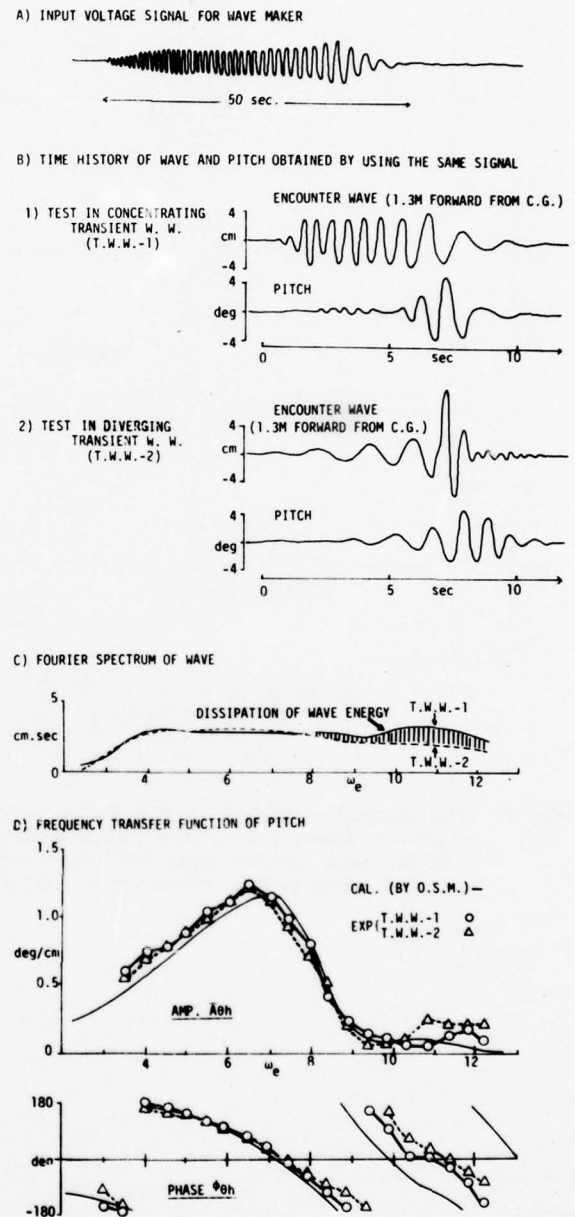
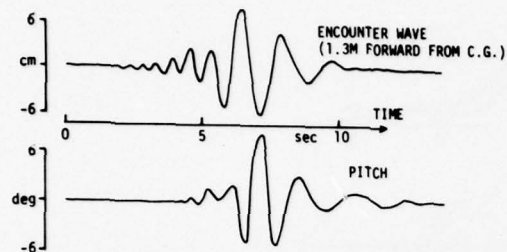


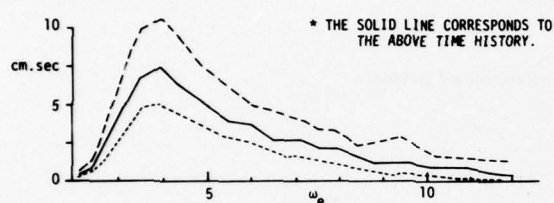
Fig. 6: Comparison between the tests in the concentrating T.W.W. and the diverging T.W.W.



A) TIME HISTORY OF WAVE AND PITCH



B) FOURIER SPECTRUM OF WAVE



C) FREQUENCY TRANSFER FUNCTION OF PITCH

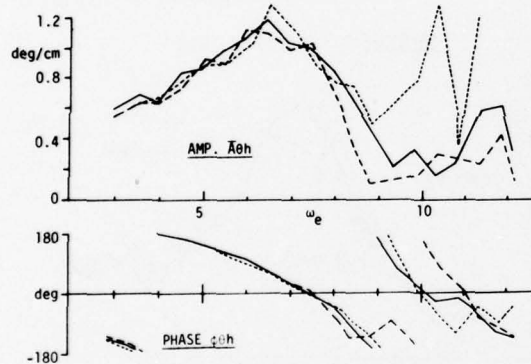


Fig. 7: Test results in the concentrating transient water waves with constant wave slope in Fourier spectrum.

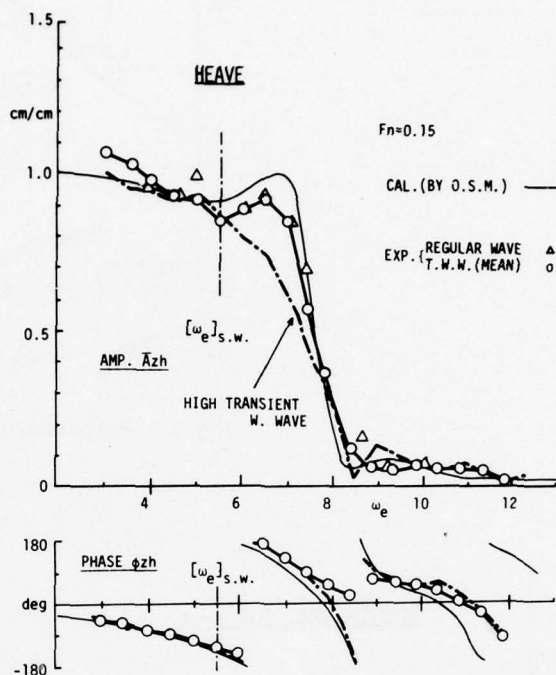


Fig. 8: Frequency transfer functions of heave.

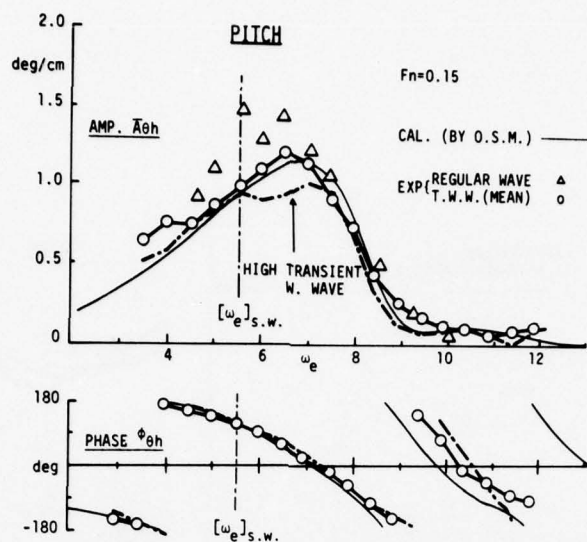


Fig. 9: Frequency transfer functions of pitch.

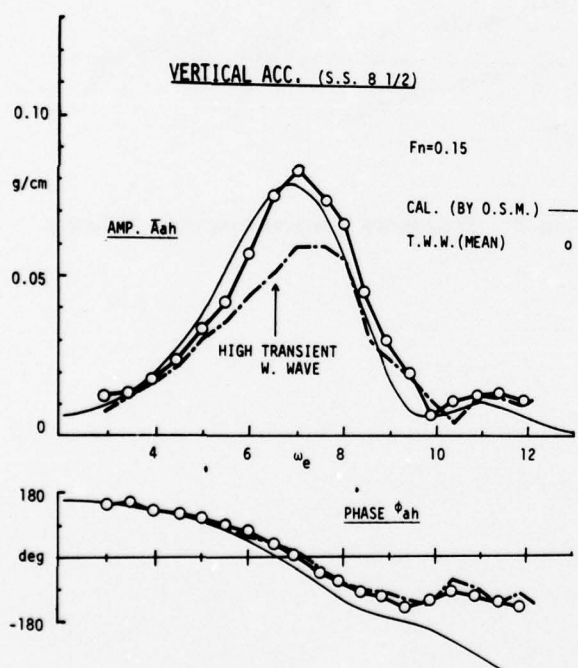


Fig. 10: Frequency transfer functions of vertical acceleration.

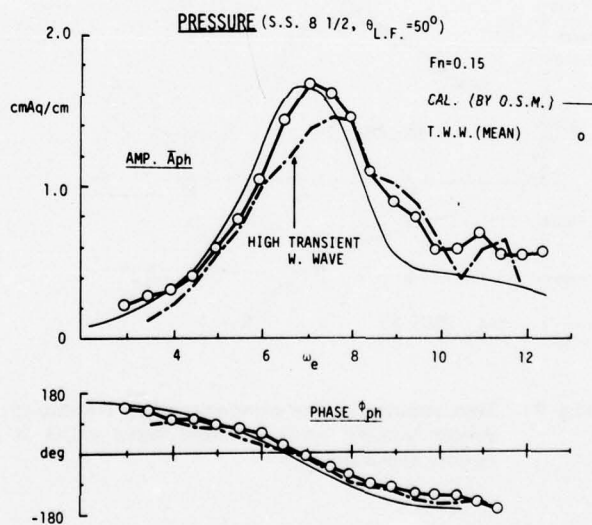


Fig. 11: Frequency transfer functions of hydrodynamic pressure.

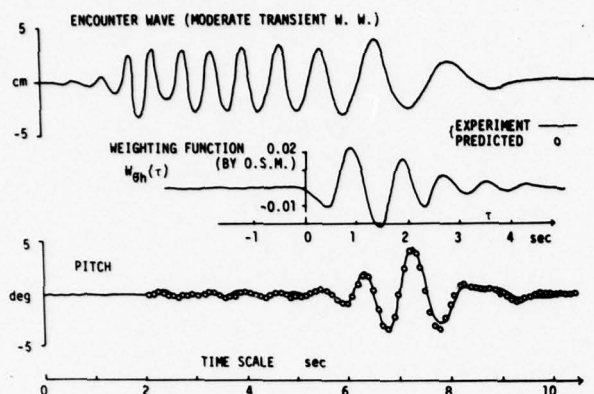


Fig. 12: The predicted time histories of pitch in the moderate T.W.W. (corresponding to Fig. 2).

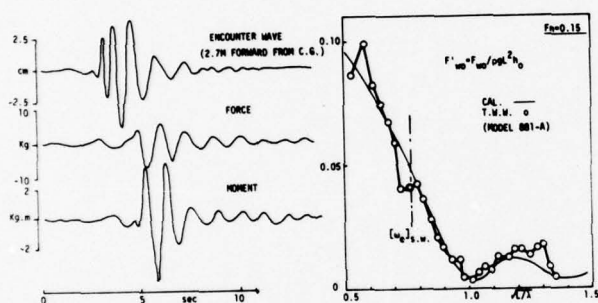


Fig. 14: Wave exciting heave force obtained by the T.W.W. test (from ref. 17).

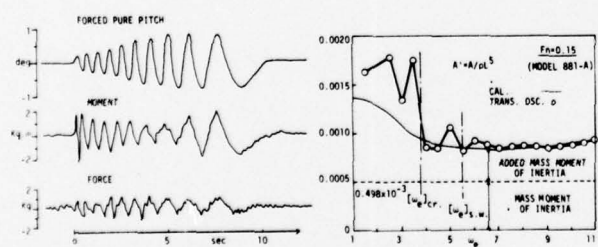


Fig. 15: Vertical mass moment of inertia obtained by the forced transient pure pitch oscillation test (from ref. 17).

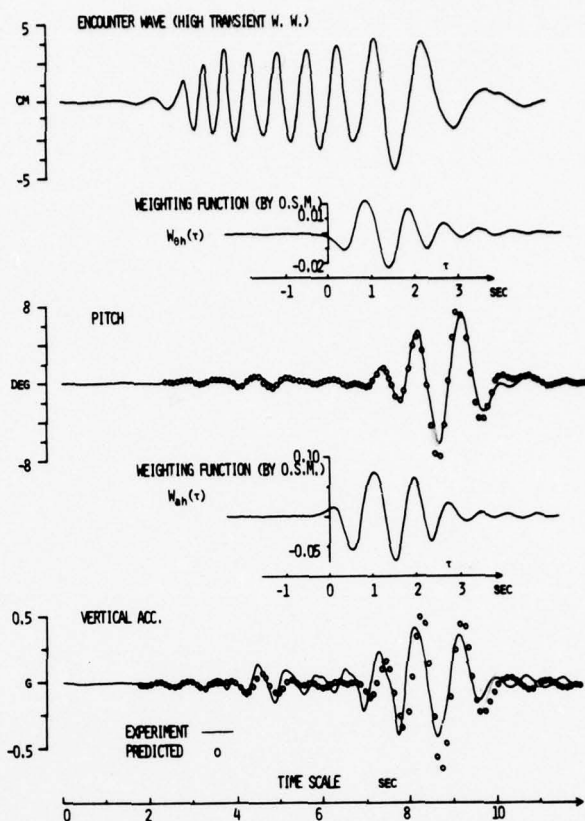


Fig. 13: The predicted time histories of pitch and acceleration in the high T.W.W. (corresponding to Fig. 4).

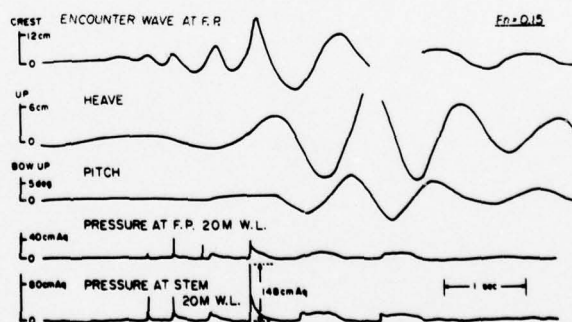


Fig. 16: Wave impact pressures measured by the T.W.W. test (from ref. 21).



# ADVANCED EXPERIMENTAL TECHNIQUES FOR TESTING SHIP MODELS IN TRANSIENT WATER WAVES

## PART II THE CONTROLLED TRANSIENT WATER WAVES FOR USING IN SHIP MOTION TESTS

S. TAKEZAWA and T. HIRAYAMA

Department of Naval Architecture, Faculty of Engineering, Yokohama National University, Yokohama, Japan

### SYNOPSIS

The practical procedure controlling Transient Water Waves (T.W.W.) arbitrarily for using in Ship Motion Tests is presented. Especially, the "Concentration" of T.W.W. is emphasized. Through Part I ("The Transient Test Technique on Ship Motions in Waves") and Part II, experimental data is common, so systematical description is made. For the search of the transfer function of Ship Motion System, the T.W.W. with constant wave height in the domain of Fourier spectrum is suitable, but the nonlinearity of wave itself appears in the region of high frequency especially in the near field of concentration. So, the T.W.W. with constant wave slope is investigated also.

### 1. INTRODUCTION

In Part II, the authors show systematically the concrete methods how the Transient Water Waves (T.W.W.), are controlled and generated, and describe the characteristics of T.W.W. including nonlinearity.

Generally speaking, waves contain two informations-amplitude & phase, and the new method presented by M.C.Davis & E.E.Zarnick (1), was very worthy in the point of view controlling them. Namely, considering the wave dispersion, they had driven the wave maker with sweeping the signal frequency linearly, and the sweep range of frequency was decided to coincide with the frequency of regular wave for using in ship response test.

Following them, the authors (2,3) developed that idea and tried to control T.W.W. exactly, considering the wave maker driving signal as input and the generated wave height as output. In that idea the authors emphasize the importance of the concept of "phase".

Finally it will be noticed that in this paper, the T.W.W. means surface waves with finite duration or finite energy. Then, as mentioned in part I, the representation in frequency domain of T.W.W. is Fourier spectrum.

#### 1.1 Notation

Fundamental notations are common with that of part I.

$h_x(t)$  : Time history of wave height measured at  $x(m)$  away from wave maker.

$H_x(\omega)$  : Fourier spectrum of  $h_x(t)$

$v(t)$  : Time history of driving signal Voltage for wave maker.

$s(t)$  : Time history of motion of wave maker. We use a plunger type wave maker, so  $s(t)$  is the Stroke of vertical motion.

C.W.S.: Transient water waves with Constant Wave

Slope in the domain of Fourier spectrum.

C.W.H.: Transient water waves with Constant Wave Height in the domain of Fourier spectrum

### 2. WAVE MAKING SYSTEM

To control T.W.W., finally we must make a driving signal  $v(t)$ . Our wave maker system is diagramed in Fig. 1 of Part I. The wave maker is one of the plunger type. The plunger is driven through ball screw by electric servo motor. Section of the plunger is shown in Fig. 10.

Now let's the system from the wave maker driving signal to measured wave height be linear. Then we must consider the linear transfer functions between Wave Maker Driving Signal and Wave Maker Stroke, Wave Maker Stroke and Generated Wave, and Wave to Wave. Fourier Spectrum of time history of wave measured at  $x(m)$  from wave maker becomes

$$H_x(\omega) = V(\omega) \cdot G_{h_x v}(\omega) \quad (1)$$

where

$$G_{h_x v}(\omega) = \bar{A}_{sv} \cdot \bar{A}_{h_0 s} \cdot \bar{A}_{h_x h_0} \cdot \exp[i(\phi_{sv} + \phi_{h_0 s} + \phi_{h_x h_0})]$$

so, the Spectrum of driving signal time history in voltage for wave maker  $V(\omega)$  becomes

$$V(\omega) = H_x(\omega) / G_{h_x v}(\omega) \\ = \frac{\bar{A}_{h_x}}{\bar{A}_{sv} \cdot \bar{A}_{h_0 s} \cdot \bar{A}_{h_x h_0}} \cdot \exp[i(\psi_{h_x} - \phi_{sv} - \phi_{h_0 s} - \phi_{h_x h_0})] \quad (2)$$

Frequency transfer characteristics between wave and wave is represented as is shown in Appendix (1), for deep water

$$\bar{A}_{hx}h_0 = 1 \quad (3)$$

$$\phi_{hx}h_0 = -\frac{\omega|\omega|}{g}x \quad (4)$$

Then time history of wave maker driving signal is obtained as

$$v(t) = \frac{1}{\pi} \int_0^\infty \frac{A_{h0}}{A_{sv} \cdot A_{h0s}} \cdot \cos\{\psi_{hx} - \phi_{sv} - \phi_{h0s} + \frac{\omega^2}{g} \cdot x + \omega t\} d\omega \quad (5)$$

For numerical calculations of equation (5), the transfer function  $A_{sv}$ ,  $A_{h0s}$ ,  $\phi_{sv}$ ,  $\phi_{h0s}$  are key points, and practically these values are obtainable from preparatory experiments. In this paper, to make driving signals, we used experimental characteristics with theoretical values as back ground.  $A_{sv}$ ,  $\phi_{sv}$  are decided from mechanical and electrical characteristics of wave maker, and  $A_{h0s}$  is wave height ratio for progressive wave, so it can be calculated theoretically. About the plunger type wave maker with two dimensional ship like section, Ursell & Tasai's Method (7, 8) will be used by introducing Lewis Form approximation.  $\phi_{h0s}$  corresponds to the phase difference between progressive wave and heave at the position of ship center line, and can also be obtained from the theory mentioned above. For this time, we consider the practical control of waves, so we use  $\phi_{h0s}$  as  $\phi_{h0s}$  by making phase difference correction  $(\omega^2/g)x \cdot 5.0$  concerning distance. Results of this correction are shown in Fig. 10.

Fig. 2 illustrates the calculation of  $v(t)$  defined by equation (5).

- (a) is designed Fourier Spectrum of T.W.W.,
- (d) is transfer function of our wave maker.
- So (a)/(d) makes resultant spectrum of signal (e).

By Fourier Transformation of (e) the time history of signal is obtained like (f), (g). It is noticed that they are similar to those by changing frequency linearly.

- (b) is also transformation of (a).

These are characteristic time histories of concentration which will be referred later.

(c) is wave space profiles at concentration. It is noticed that for the lower frequencies than 3.7 rad/s for our experimental tank the finite depth effect results adding correction to  $\psi_v$  as shown in Fig. 2-(e) by dotted line. Because phase speed changes from the value of deep water (2).

The digitized time history from the calculation of eq. 5 with interval  $\Delta t$  sec, is to be punched to paper tape; and by using D-A converter, we obtain time history of analogue voltage for wave maker driving signal. Filtering it by low pass filter about 5Hz and recording on magnetic tape by data recorder, then we can generate the same wave repeatedly. Obtained signal is shown in Fig. 2-(f)(g). This is designed to concentrate at 25m apart from the wave maker, and have time length about 50sec. From linear sweep, this time length is about 41sec. (See Appendix 2)

### 3. UNCONTROLLED TRANSIENT WATER WAVE

First as an example of the T.W.W. which was generated by imposing the only condition of finite duration is shown in Fig. 1. Upper half of Fig. 1 is an example of uncontrolled T.W.W. In spite of short duration of wave maker motion, the time history measured at 20m away from wave maker diverges considerably. In contrast with it, about the controlled one so as to concentrate at  $x = 25m$  measured time history of wave at 20m is 1/4 inspite of duration of wave maker motion is about 4 times longer.

As estimated from this case, if we make no control, component waves with low frequency are generated at the initial stage, and high frequency waves are left behind because of slow speed. Then the measured time history of waves are extended, so the some what control of T.W.W. is desired.

### 4. CONTROLLED TRANSIENT WATER WAVE

Judging from the example of section 3, uncontrolled T.W.W. has following two faults. First, lacking of control on phase results necessarily to make long duration by the reason described in section 3. This means that the during the test in T.W.W. the ship motion is likely affected by the reflected wave from the end of Experimental Tank. Second, at lack of controll for amplitude some times results about zero part of spectrum. This makes the numerical reliability falls down when we calculate the transfer function as waves input. If we introduce the exact control, above two fault immediately dissolved.

About the method of controlling T.W.W., we can classify them in the domain of time history, space profile, and in the domain of frequency and wave number. But considering the transfer functions, the control finally becomes in the domain of frequency i.e. control of Fourier Spectrum. T.W.W. controlled by linear sweep of low frequency signal generator was presented by Davis & Zarnick. But T.W.W. obtained by this signal, had not the complete concentration such the result as obtained by the present method.

### 5. CONCENTRATION OF TRANSIENT WATER WAVE

The duration of T.W.W. which is suitable for ship response test is to be short enough, considering the reflection from the opposite tank wall. As for T.W.W., the concrete meaning of finite length duration is not clear, so we must evaluate by some methods. Here, for example of those, we define the duration of time history by the distribution of energy like value which is calculated from integration of second moment  $M_2$  of square amplitude around  $t=0$ . Now we write  $T_L$  which corresponds to radius of gyration for rigid body as follows.

$$T_L = \sqrt{M_2/M_0} \quad (6)$$

Where from Parseval's theorem

$$M_0 = \int_{-\infty}^{\infty} h^2(t) dt = \frac{1}{2\pi} \int_{-\infty}^{\infty} A^2(\omega) d\omega \quad (7)$$

and

$$M_2 = \int_{-\infty}^{\infty} t^2 h^2(t) dt$$

$$= \frac{1}{2\pi} \int_{-\infty}^{\infty} \left[ \left( \frac{dAh}{d\omega} \right)^2 + A^2 \left( \frac{d\psi}{d\omega} \right)^2 \right] d\omega \quad (8)$$

For the given  $Ah(\omega)$ , the phase  $\psi_h$  which makes  $T_2$  minimum is decided by

$$\frac{d\psi}{d\omega} = 0 \quad (9)$$

it means

$$\psi = \text{const.} \quad (10)$$

We name this as phase part of minimum time history.

Then,  $h(t)$  becomes

$$h(t) = \frac{1}{\pi} \int_0^{\infty} A_h(\omega) \cdot \cos\{\psi_h + \omega t\} d\omega \quad (11)$$

And then, adding further condition that  $h(t)$  realize of it maximum amplitude available, the following equation

$$\psi + \omega t = \pm n\pi \quad (12)$$

must be satisfied independent of  $\omega$ . This means

$$t=0$$

$$\text{and } \psi = \pm n\pi \quad (13)$$

Namely if we planned the phase part as  $\psi = \pm n\pi$ , we can realize maximum amplitude under the condition of given amplitude distribution  $A(\omega)$ . When the condition of eq.(13) is satisfied, we call such state as exact concentration of T.W.W.. Further more, before concentration as concentrating T.W.W., after concentration as diverging T.W.W.. Time history including concentration and, space profile of concentration for designed Fourier spectrum is shown in Fig. 2-(b), (c). Above discussion is made in frequency domain, namely for component wave, so the only phase speed appeared in T.W.W. control. When the wave maker driving signal is made by linear sweep of frequency as was done M.C.Davis & E.E.Zarnick, similar concentration or weak concentration of  $\psi = -\pi/4$  at  $t=0$  is realized (3). For these cases, wave control must be considered in group velocity by phase function. (Appendix 2)

## 6 CONTROL IN FREQUENCY DOMAIN

As far as we control T.W.W. using transfer function, it is clear that we are controlling T.W.W. in frequency domain. As mentioned in part I, when we search transfer function, the very small amplitude of wave spectrum as input is not suitable. So, we consider to generate T.W.W. with "Constant Wave Height", which have constant component wave height to the higher frequency, and then from the point of keeping the linearity, we consider T.W.W. with "Constant Wave Slope", which have component wave of constant slope defined height/length. The concrete example is described in section 9. If the phase is arbitrary, that is no control about phase, the time history becomes considerably long as shown in Fig.1. The control concerning Fourier amplitude only is not good, so we consider the additional control

about phase described previous section.

## 7. CONTROL IN TIME DOMAIN

Control for minimum duration (§5) is of course the one of controls in time domain. When the desired time history of wave is given, we can obtain signal by eq.(5), because from time history its Fourier spectrum is calculated or considering the inverse of convolution, also signal time history is calculated.

## 8. CONTROL IN SPACE DOMAIN

When at  $t=t_0$  the wave space profile  $h(x)$  is given, the corresponding signal time history is realized as following (Appendix 3), first

$$A_h(\omega) = \frac{2\omega}{g} H(k) \exp(-i\omega t_0) \quad (14)$$

where

$$H_k = \int_{-\infty}^{\infty} h(x) \exp(ikx) dx \quad (15)$$

so, from eq.(5) we can calculate the driving signal  $v(t)$ . Of course for the given amplitude of wave spectrum, the maximum wave slope is realized at the concentration and this is suitable for wave impact experiment mentioned part I. If the wave height at the concentration becomes large, the wave slope becomes considerably large by the non linear effect.

## 9. DISCUSSION FOR EXAMPLE OF EXACTLY CONTROLLED TRANSIENT WATER WAVE

In the Fig.3~10 the authors show examples of waves generated by the combination of former controls and also show analyzed results. All of these T.W.W. are used in Part I, but the amplitude of spectrum is chosen only the two of them "High" and "Moderate". First, Fig.3 shows time history of T.W.W. with constant wave slope spectrum. The wave slope " $\beta$ " of component waves are

$$\beta = A(\omega) \cdot k = A(\omega) \frac{\omega^2}{g} \quad (16)$$

so, for  $\beta = \text{const}$ ,  $A(\omega)$  must be proportional to  $1/\omega^2$ .

It must be noticed that the time history of lowest part in Fig.3 are of strokes but not of waves. These are considered as same shape as those of signal. It is clearly shown in the Fig. 3, that the part of T.W.W. progresses by its group velocity defined by local frequencies and concentrating to the designed point of concentration ( $x=25m$ ). The dotted line is as twice stroke amplitude as the solid line, and in spite of large amplitude the linearity of the system is shown because the wave height becomes also about twice in any place before the concentration.

The predicted time history ( $x=30m$ ) is shown in the left region of Fig.3. This prediction is made from the measured time history ( $x=20m$ ) using the linear dispersion relation. In spite of including concentration, the prediction is



considerably good accordance with the measured one for the case of T.W.W. with C.W.S. For the experiments shown by dotted lines, seems also good accordance will be expected from the small deviation of phase lag characteristics shown by the mark  $\square$  in Fig. 9.

Fig. 4 shows the measured time history with Constant wave Height i.e.  $A(\omega)=\text{const.}$  Comparing solidlines (time history) with the dotted straight lines showing the local group velocity defined by local wave frequency of the wave front, it is clearly seen that in the front region of wave train, the group velocity or phase velocity considerably increasing. This phenomenon has contrast comparing the case of C.S.W. And from this reason, the point of concentration is shifted back about 2 m. Time history shown by dotted line is the case of the twice stroke amplitude, so the nonlinearity becomes strong and the wave Breaking occurs at concentration. The prediction of the time history is also shown like Fig.3. Even if in the case of moderate amplitude prediction is not good, especially in the region of high frequencies and this means the loss of linearity assumption.

In this Figure the encountering position of the ship model corresponds to Exp.No.80 (also corresponds to the photo in part I) is drawn. The ship encounterings with T.W.W. looks complicated, but the experimental results confirms the assumption of existing component wave.

The amplitude part of spectrum which corresponds to the series experiment is shown in Fig.5. The left side of the figure is to the C.W.S. and the other the C.W.H. The characteristic differences between the two are clear. These figures are the tracing figure of hard copies obtained by the Analyser with F.F.T mentioned in part I, and the analysis itself finished in very short period. The nonlinear characteristics, described former, also appear in the figures. Namely, the positional change of C.W.S. is small in comparison with that of C.W.H. When we require to search the ship response function from the wave probe in forward position of the ship, no change of spectrum shape is in need of fundamental condition, so in that point, T.W.W. with C.W.H. is not good in exact. But for the transfer function for longitudinal ship motions, the nonlinearity does not appear remarkably, so the T.W.W. with C.W.H. is suitable to avoid null division in high frequency range. This fact is already described in part I.

Next, we discuss the characteristics of generated waves from the view point of frequency transfer function. These are shown in Fig.6, 7. These are also obtained by the analyzer in almost real time. The amplitude ratio of wave to wave should become 1.0. The lowest part of the figure is the transfer function of plunger section which corresponds to so called the amplitude ratio of progressive wave. The right hand side of each Figure expresses the phase difference characteristics. And this must be  $-(\omega^2/g)\cdot\Delta x$  where,  $\Delta x$  is distance between two wave probes ( $\Delta x=x_2-x_1$ ). This phase part is corrected by  $+2n\pi$ , so the resultant line is zig zaged Fig.8. The distance is larger, the inclination becomes larger. The transfer function of Fig. 6, 7 is based on the spectrum measured at  $x=20\text{m}$ , so the phase difference characteristics becomes symme-

tric around  $\phi_{h_2 0 h_2 0}$ .

The phase difference characteristics is not clear from the Fig. 6,7 only. So, in Fig.9 we show the result made by correction  $\omega^2/g\cdot\Delta x$  concerning the distances. This is the deviation from the linear theory, and so if the phenomenon is linear it must be zero. The fact that  $(\phi_{h_1 x_1 h_2 x_2} + \omega^2/g\cdot\Delta x)$  has plus value, means the existence of phase speed increase of component wave. This point is referred in section 10, but generally the case of large amplitude T.W.W. with C.W.H. has large deviation from linear theorem, so attention is required in controlling T.W.W.

## 10. NONLINEARITY. (5,6)

The control of T.W.W. described former section is based on the linearity of the system. But as wave amplitude becomes large, it is clear that the nonlinearity appears. The nonlinearity first appears, as increasing the phase velocity of component waves. This effect results the deviation of phase difference of wave transfer function as shown in Fig. 9. Moreover as the amplitude increase, wave breaking occurs especially at the concentrating point and the energy is lossed. This results the spectrum a great change as shown Fig.12. (Solid and dotted line) From the view point of linearity, T.W.W. with constant wave slope is superior because, as shown in Fig.3, even though there appears wave breaking on the crest at concentration, the concentration position hardly changes for C.W.S.

As for the T.W.W. with constant wave height, at the initial stage of transition, the wave front is unstable and wave breaking appears. From Fig.4 the group velocity of wave front is increased and this also said from the phase characteristics in Fig.8. From this, increase of phase speed seems about 8.1% (See Appendix 4). And by the change of speed, the point of concentration moves back.

When there is a great wave breaking at concentration, about 40% energy loss to the maximum in the frequency domain is reported, and for the case of Fig.12 there was about 41% energy loss. Here the energy loss is evaluated by equation (Ap.4), so it does not shows real energy. Prediction of wave profile from the after concentrated point (37.5m) is shown in Fig.14. Though there was great wave breaking, the prediction describes the tendency of wave profile. Photo.2,3. From this point, the wave system doesn't perfectly break down in spite of the great breaking in deep water and after it the system also recover the linearity.

## 11. CONCLUDING REMARKS AND ACKNOWLEDGEMENT

Evaluating theoretically and experimentally the three transfer function  $G_{sv}$ ,  $G_{hs}$ ,  $G_{hx}$  (driving signal to stroke, stroke to wave height, wave height to wave height), the authors showed the practical procedure controlling the T.W.W. with good accuracy.

By the application of this exact method, we could precisely realize the T.W.W. with C.W.S. and C.W.H. The control of T.W.W. must be performed

by group velocity based on local frequency. When the concentrating point is far away from the wave maker, or the sweep time becomes long enough in the linear sweep method, Fourier spectrum of T.W.W. can be roughly controlled by the linear sweep method.

As this method is based on the assumption of linearity, the limitation to the "exact" control must be recognized. Especially when we realize a large amplitude concentrating T.W.W., non-linearity makes the concentrating position goes back, and in the frequency domain the Fourier spectrum changes in the part of high frequency. So, for the search on the transfer functions of ship, encountering ship and wave at the concentration point must be avoid. As for control of T.W.W. the deviation of concentrating position and Fourier spectrum of the high T.W.W. are estimated approximately except the states forming the large wave breaking and losing the energy of wave.

On the contrary for the severe experiment like a wave impact pressure, the positive use of nonlinear characteristics is possible.

This experiment carried out especially for this symposium at the Experimental Tank of Yokohama National University. Many people joined this work, and without their serious assistant this report could not be accomplished in a very short time. So the authors are gratefully acknowledged to those, K. Miyakawa, T. Takayama, K. Kasahara and others.

#### APPENDIX 1. LINEAR THEORY OF T.W.W.

Under the assumption of incompressible, perfect fluid, the Fourier representation of the solution of Laplace's equation concerning velocity potential  $\phi$  which satisfies free surface condition is

$$\phi(x, z, t) = \frac{1}{\pi} \int_{-\infty}^{\infty} \frac{g}{\omega} A(\omega) \exp\left(\frac{\omega^2}{g} z\right) \sin\left\{\frac{\omega^2}{g} x - \omega t + \delta(\omega)\right\} d\omega \quad (\text{Ap.1})$$

Wave height then becomes

$$h(x, t) = \frac{1}{\pi} \int_0^{\infty} A(\omega) \cos\left\{\frac{\omega^2}{g} x - \omega t + \delta(\omega)\right\} d\omega \\ = \text{Re} \frac{1}{\pi} \int_0^{\infty} A(\omega) \exp\left[i\left\{-\frac{\omega^2}{g} x - \delta(\omega)\right\}\right] \exp(i\omega t) d\omega \quad (\text{Ap.2})$$

and this is the inversed Fourier Transformation of  $A(\omega) \exp[i\{\omega^2/g \cdot x - \delta(\omega)\}]$ . So, the amplitude part  $A(\omega)$  of wave spectrum is independent of  $x$ , and phase part is  $-(\omega^2)/g \cdot x - \delta(\omega)$  or transfer function between  $\Delta x$  is

$$G_{h2h1} = 1 \cdot \exp\left(-i \frac{\omega}{g} \Delta x\right) \quad (\text{Ap.3})$$

Here,  $\omega^2$  is modified to odd function because phase is odd for the real time history.

As for energy, following Parseval theorem, next equation is formed.

$$\tilde{E}_p \equiv \int_{-\infty}^{\infty} h^2 dt = \frac{1}{\pi} \int_0^{\infty} A^2 d\omega \quad (\text{Ap.4})$$

$$E_p \equiv \frac{1}{4g} \int_{-\infty}^{\infty} h^2 dx = \frac{1}{2\pi} \int_0^{\infty} \omega A^2 d\omega \quad (\text{Ap.5})$$

Where  $E_p$  is potential energy and  $\tilde{E}_p$  is potential energy like value defined in the time domain.

Of course

$$\tilde{E}_p \neq \gamma E_p \quad (\text{Ap.6})$$

where  $\gamma$  is constant

Equation (Ap.2) is expanded asymptotically in the field of  $gt^2/4x(\Delta x)$  is large

$$h(x, t) \approx \sqrt{\frac{g}{\pi x}} A\left(\frac{gt}{2x}\right) \cos\left(\frac{gt^2}{4x} - \frac{\pi}{4}\right) + O(\alpha^{-3}) \quad (\text{Ap.7})$$

This shows that the frequency part of  $gt/2x = \tilde{\omega}$  ( $\tilde{\omega} = \text{const.}$ ) moves in group velocity  $(1/2) \cdot \tilde{c}$ , along the line

$$x = \frac{1}{2} \cdot \frac{g}{\tilde{\omega}} t = \frac{1}{2} \tilde{c} t \quad (\text{Ap.8})$$

with amplitude

$$\frac{g}{\sqrt{\pi x}} A(\omega) \quad (\text{Ap.9})$$

And also shows that the amplitude distribution of spectrum corresponds to the envelope of time history. This is clearly seen in Fig.3,4.

We shall discuss equation (Ap.7) further. If we introduce phase function  $\theta(x, t)$  as

$$\theta(x, t) = -\frac{gt^2}{4x} + \frac{\pi}{4} \quad (\text{Ap.10})$$

then we can define local frequency  $\tilde{\omega}$  and wave number  $\tilde{k}$  as follows

$$\tilde{\omega}(x, t) = -\theta_t = \frac{gt}{2x} \quad (\text{Ap.11})$$

$$\tilde{k}(x, t) = \theta_x = \frac{gt^2}{4x^2} \quad (\text{Ap.12})$$

The expression  $h(x, t)$  becomes.

$$h(x, t) = \sqrt{\frac{g}{x}} A(\tilde{\omega}) \cdot \cos(\tilde{k}x - \tilde{\omega}t + \frac{\pi}{4}) \quad (\text{Ap.13})$$

Also, (phase  $+\pi/4$ ) of approximated wave makes  $(\omega^2/g) \cdot x$  in spectrum.

#### APPENDIX 2 RELATION TO LINEAR SWEEP OF FREQUENCY (3)

From the expression equation (Ap.7), if we discuss the time history at the position of wave maker, it becomes,

$$h(0, t) = \sqrt{\frac{g}{\pi x_0}} A(\tilde{\omega}) \cos\left(-\frac{gt^2}{4x_0} + \frac{\pi}{4}\right) \quad (\text{Ap.14})$$

or

$$\theta_0(0, t) = -\frac{gt^2}{4x_0} + \frac{\pi}{4} \quad (\text{Ap.15})$$

then

$$\tilde{\omega} = -\theta_{0t} = \frac{g}{2x_0} t \quad (\text{Ap.16})$$

This means at the point far from the concentration, the positional local frequency  $\tilde{\omega}$ , changes linearly. And this give the base to the construction of wave maker driving signal by linear sweep of frequency.

If we think to cover the frequency range according to local frequencies, frequency sweep time is decided as follows. At  $t=t_L$  the lowest frequency wave with  $\omega_L$  is generated and at  $t=t_H$ , the highest frequency wave with  $\omega_H$ , then sweep time  $T_S$  becomes

$$T_S = t_H - t_L = \frac{2x_0}{g} (\omega_H - \omega_L) \quad (\text{Ap.17})$$

For the case of signal used for the present experiment with  $\omega_H = 10$  rad/s, and  $\omega_L = 2$  rad/s and further the concentration position is designed at 25m. Then sweep time  $T_S = 4$  sec. The other hand, calculated time history has about 50 sec duration.

### APPENDIX 3. WAVE PROFILE PREDICTION

In the linear system, the prediction of wave profile from the measured time history is very simple and the inverse also. As was mentioned in Appendix 1, when the spectrum is known at the given time, the wave profile is

$$h_{t_0}(x) = \frac{1}{\pi} \int_0^\infty A(\omega) \exp(-i \frac{\omega}{g} x) \exp(i \omega t_0) d\omega \quad (\text{Ap.18})$$

Representation in wave number domain is

$$h_{t_0}(x) = \frac{1}{\pi} \int_0^\infty -\frac{g}{2\omega} A(\omega) \exp(i \omega t_0) \exp(ikx) dk \quad (\text{Ap.19})$$

In connection with wave impact experiments (4) we shall refer the surface speed of T.W.W. especially near concentration. From simple analysis, for the  $\alpha/\omega^2$  type spectrum, the horizontal velocity of crest at the concentration is given by

$$c_x = \frac{g}{\omega_L + \omega_H} = \frac{g}{\omega_c} \quad (\text{Ap.20})$$

this means that the speed equals that of phase velocity of mean frequency  $\omega_c = \frac{\omega_L + \omega_H}{2}$ .

For present experiments  $\omega_c = 6$  rad/s, so  $c_x = 1.633$  m/s. Evaluating from the Photo 1,  $\omega_c = 1.35$  m/s. Difference between the two value will be the effect of non-linearity.

### APPENDIX 4. INCREASE OF PHASE VELOCITY OF COMPONENT WAVE IN THE REGION AWAY FROM CONCENTRATION.

In the region away from concentration, locally the T.W.W. will be considered to be simple sine wave. This will be understood in Fig.3 4. So the local characteristics of finite amplitude T.W.W., before concentration, will be estimated adopting the higher order Stokes' Waves. As described before, the phase of local frequency is connected with the phase part of the spectrum, so it is expected by introducing Stokes' effects into local waves, that the nonlinear effect to the phase part deviation will be described.

For example, Constant Wave Height of Fig.(4), the wave front at  $x=15$ m has constant amplitude about  $a=40$ mm. (Corresponds to dotted line) So, if we introduce Stokes' effect as

$$c = c_0 (1 + \frac{1}{2} (k_0 a)^2) = \frac{g}{\omega} (1 + \alpha(\omega)) \quad (\text{Ap.21})$$

in the rough approximation, then

$$\alpha(\omega) = 8.329 \cdot 10^{-6} \cdot \omega^4 \quad (\text{Ap.22})$$

from this, phase difference deviation  $\Delta\phi$  becomes

$$\Delta\phi = \frac{\omega^2}{g} \Delta x \cdot \alpha(\omega) = 4.3 \cdot 10^{-6} \cdot \omega^6 \quad (\text{Ap.23})$$

This curve is drawn in Fig.9 by a dotted line.

For the case of Constant Wave Slope, (Exp. No. 105 in Fig. 3) the wave height is represented approximately as

$$a(\omega) = 0.54/\omega^2 \quad (\text{Ap.24})$$

so,  $\alpha$  becomes,

$$\alpha = \frac{1}{2} \left( \frac{\omega^2}{g} \right)^2 a^2(\omega) = 1.518 \cdot 10^{-3} = \text{const} \quad (\text{Ap.25})$$

then

$$\Delta\phi = \frac{\omega^2}{g} \Delta x \cdot \alpha(\omega) = 7.745 \cdot 10^{-4} \cdot \omega^2 \quad (\text{Ap.26})$$

This curve is also drawn in Fig.(9) by a dotted line. From the comparison of equation (Ap.23), (Ap.26) with the analyzed results, it will be said that the difference of  $\omega^6$  and  $\omega^2$  describes experimental tendency. So we can introduce phase deviation into T.W.W. control.

### REFERENCES

- (1) Davis, M.C. and Zarnick, E.C. 'Testing Ship Models in Transient Waves', Proc. 5th Symp. 1964
- (2) Takezawa, S., Fukuhara, M. and Yamashita, S. 'On the Properties of the Transient Water Waves in Ship Model Basins' Journal of The Society of Naval Architects of Japan (JSNA Japan) 1968 124
- (3) Takezawa, S. and Hirayama, T. 'On the Generation of Arbitrary Transient Water Waves', JSNA Japan 1971 129
- (4) Takezawa, S. and Hasegawa, S. 'On the Characteristics of water Impact Pressures Acting on Hull Surface Among Waves', JSNA 1974 135.
- (5) Hirayama, T. 'On Non-linear Characters of Transient Water Waves Used for Ship Response Tests (Part 1)', JSNA Japan 1974 136.
- (6) Hirayama, T. 'On Non-linear Characters of Transient Water Waves Used for Ship Response Tests (Part 2)', JSNA Japan 1975 137.
- (7) Ursell, F. 'On the heaving Motion of a circular cylinder on the surface of a fluid', Q.J.M and A.M. (1949)
- (8) Tasai, F. 'On the Damping Force and Added Mass of Ships Heaving and Pitching' JSNA JAPAN 1959 105



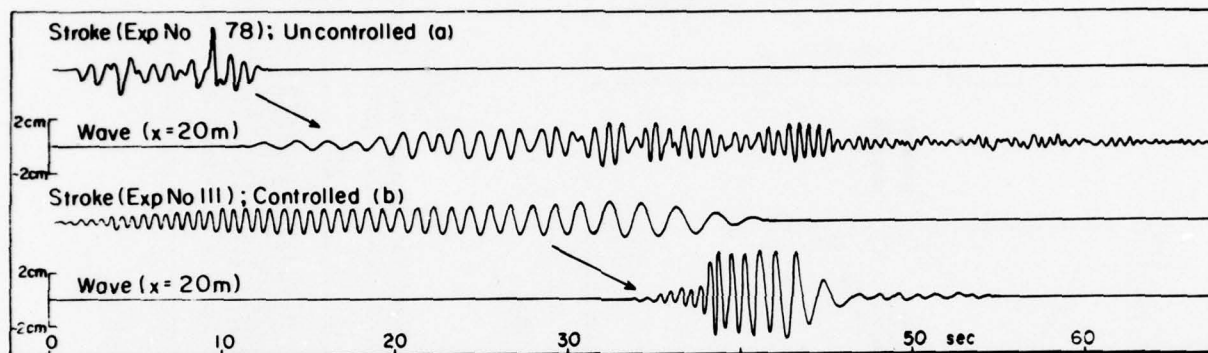


Fig. 1: Comparison of duration between controlled and uncontrolled Transient Water Waves (T.W.W.).

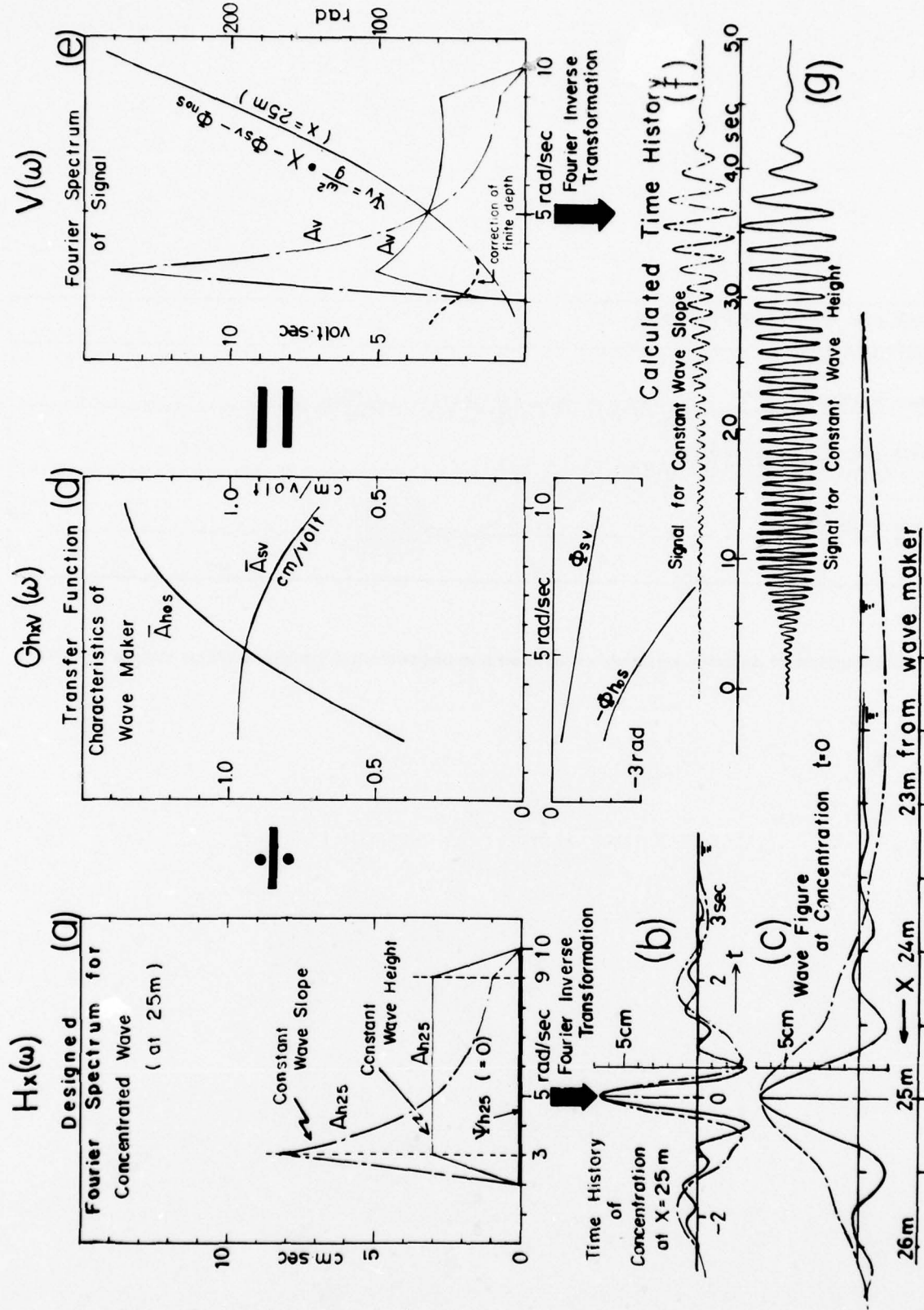


Fig. 2: Calculating procedure for wave maker driving signal.

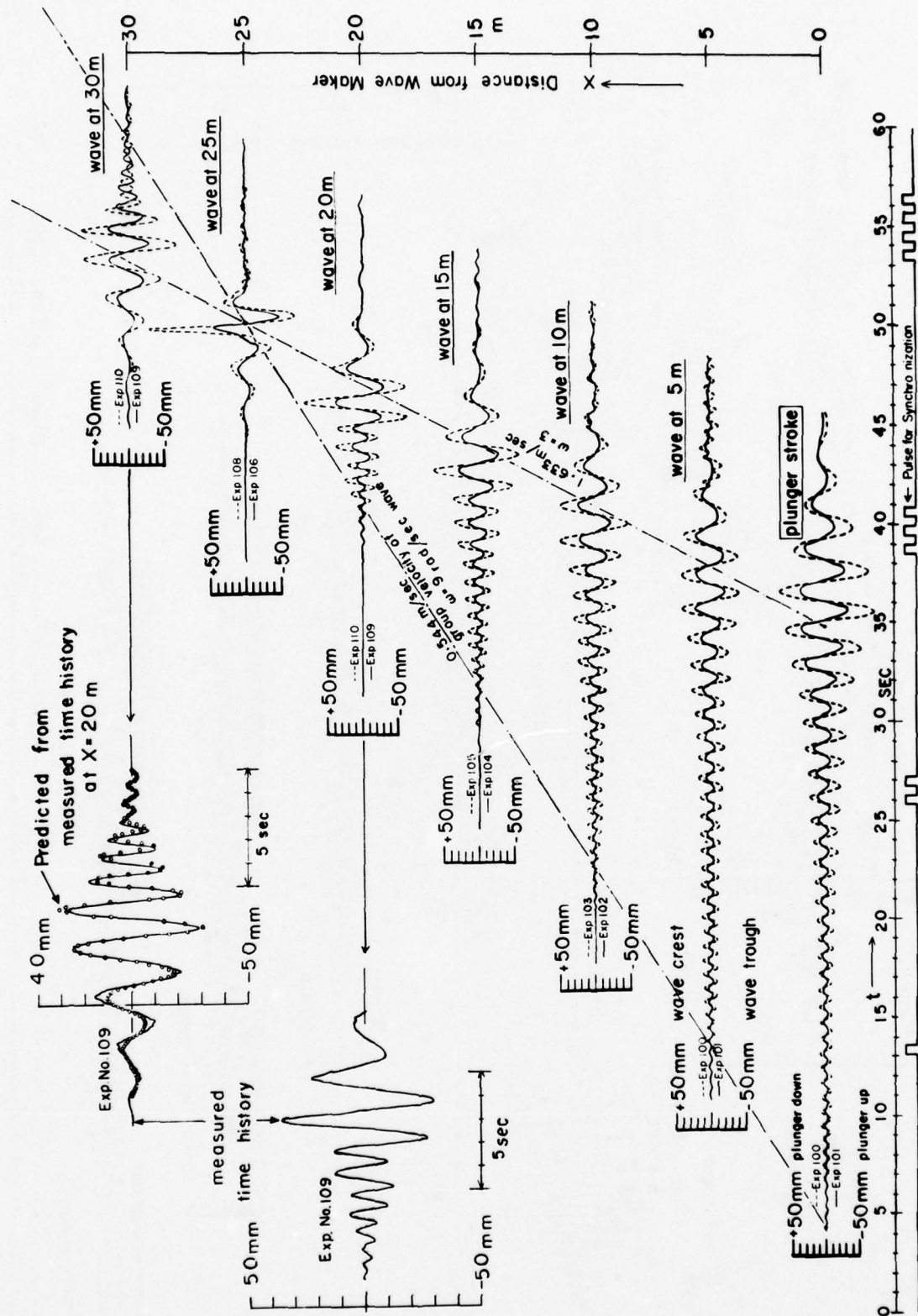


Fig. 3: Concentrating transient water waves with constant wave slope (C.W.S.). These examples are used in part I.



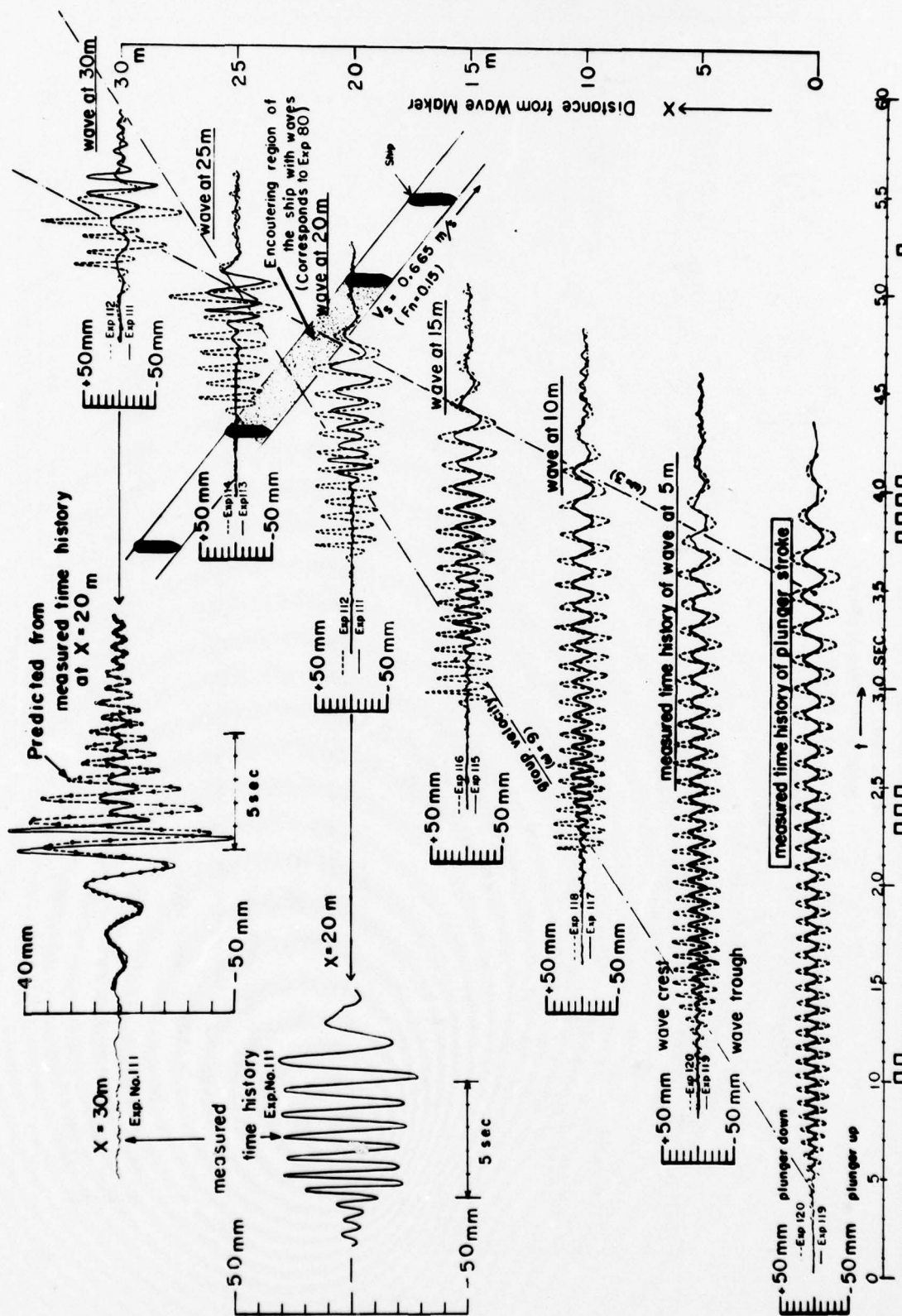


Fig. 4: Concentrating transient water waves with constant wave height (C.W.H.). These examples are used in part I.

# Amplitude Part of Fourier Spectrum by measured time history

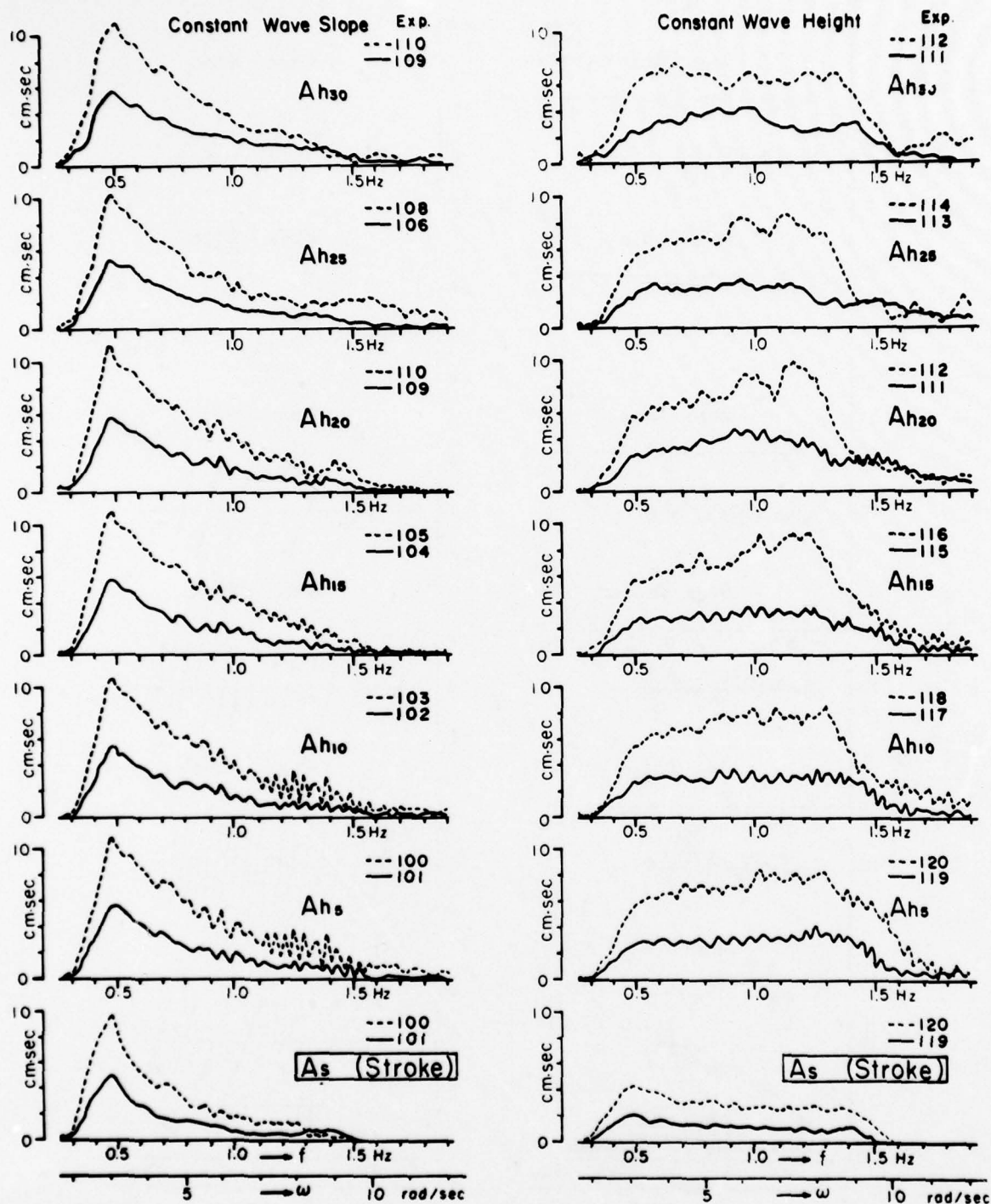


Fig. 5: Amplitude part of Fourier spectrum from measured time history shown in Fig. 3 and 4.

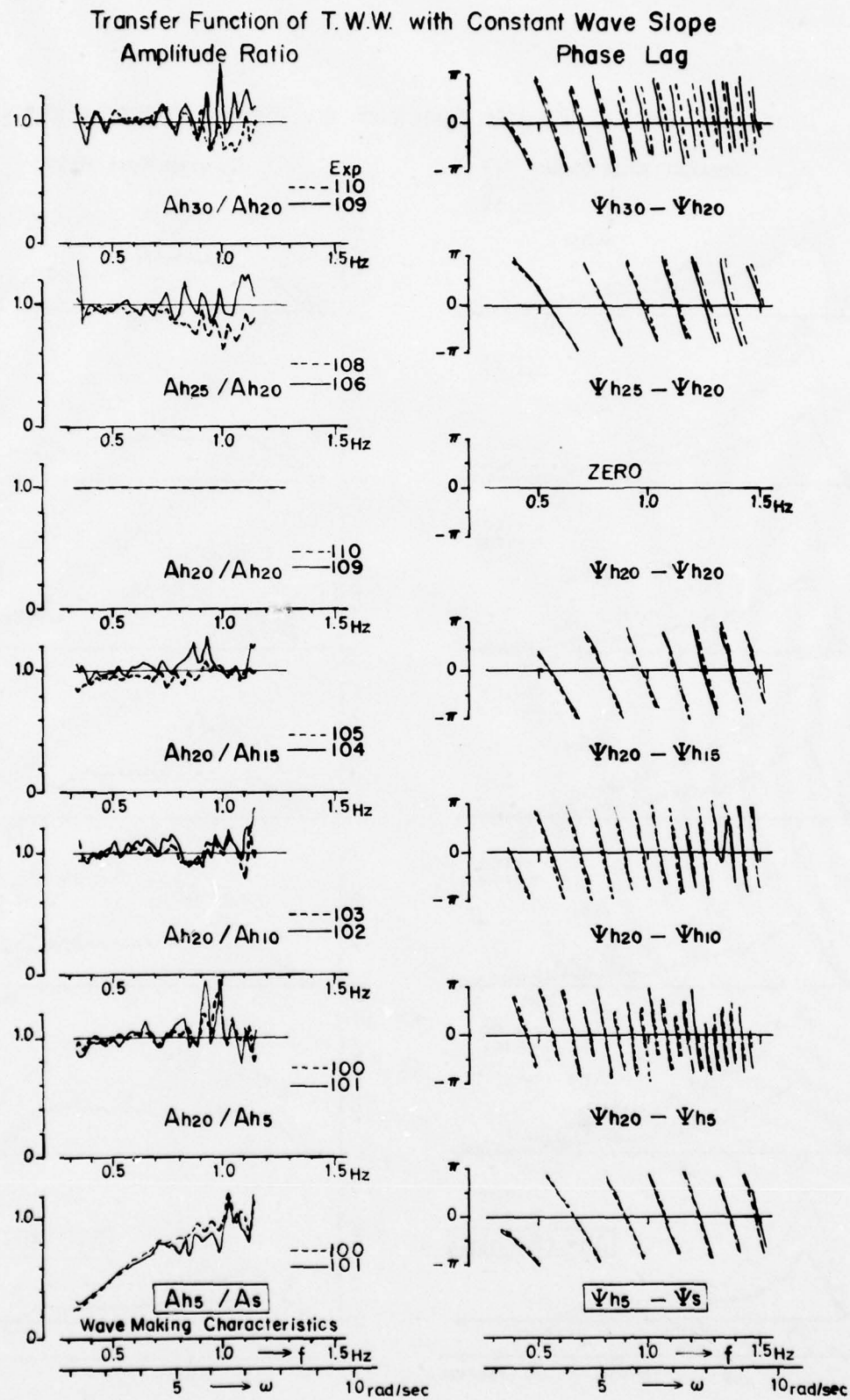


Fig. 6: Transfer function of T.W.W. with constant wave slope corresponds to Fig. 3 and 5 (left).



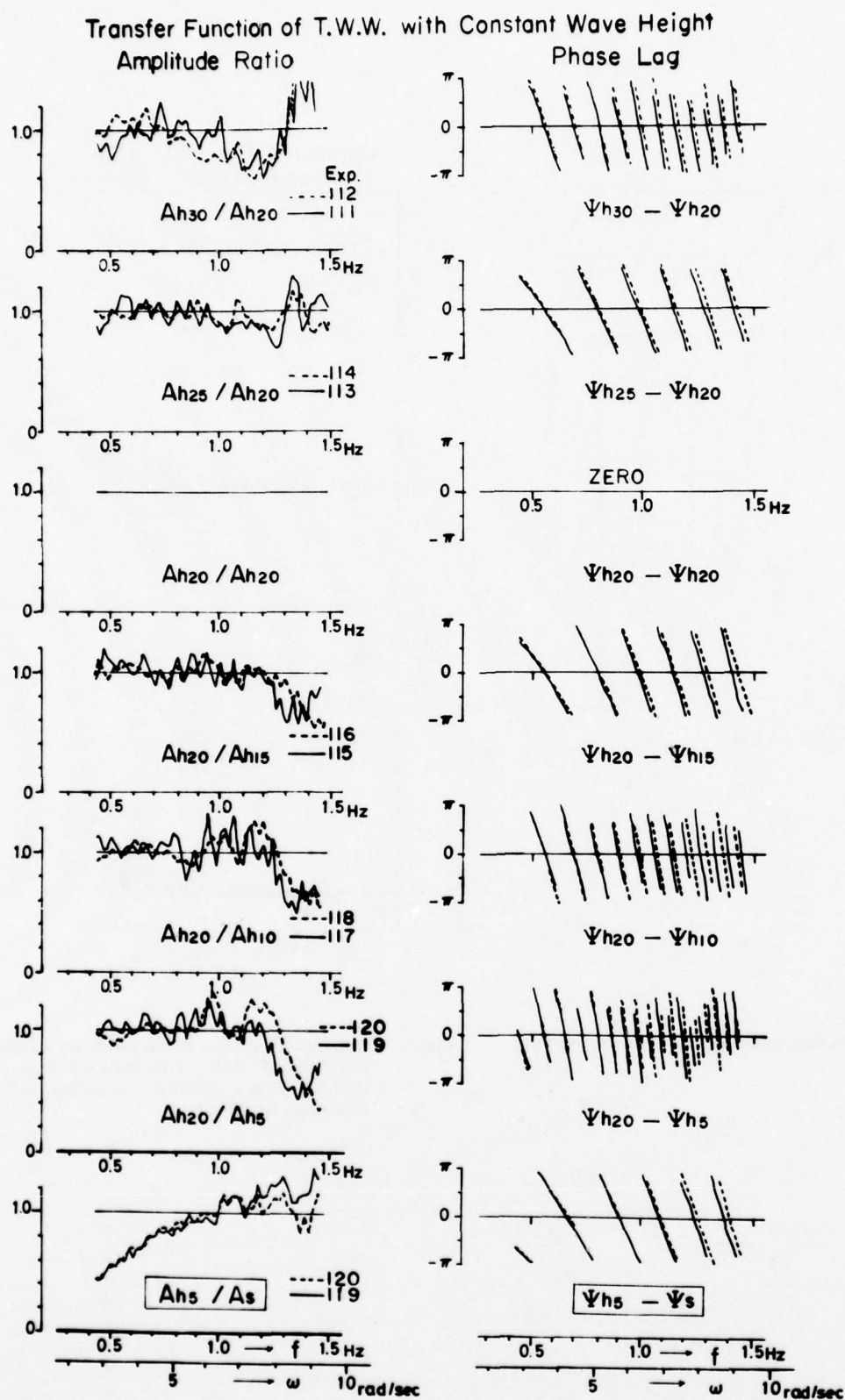


Fig. 7: Transfer function of T.W.W. with constant wave height corresponds to Fig. 4 and 5 (right).

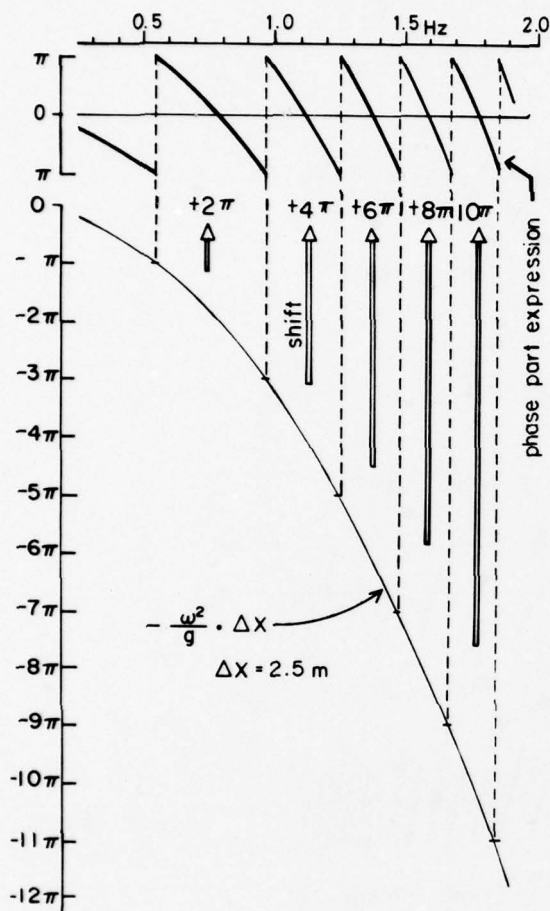


Fig. 8: Phase part expression on Fourier spectrum of T.W.W.

### Corrected Phase Lag by Linear Dispersion Relation

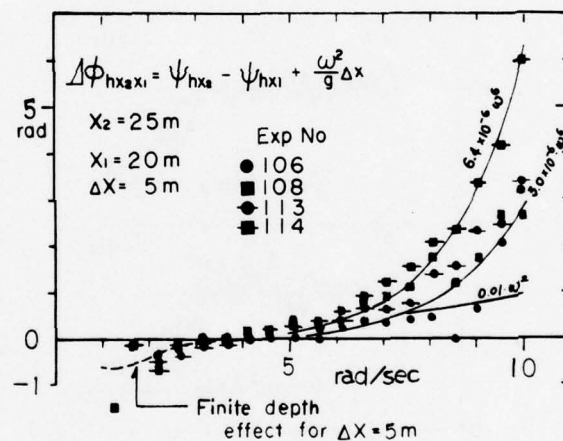
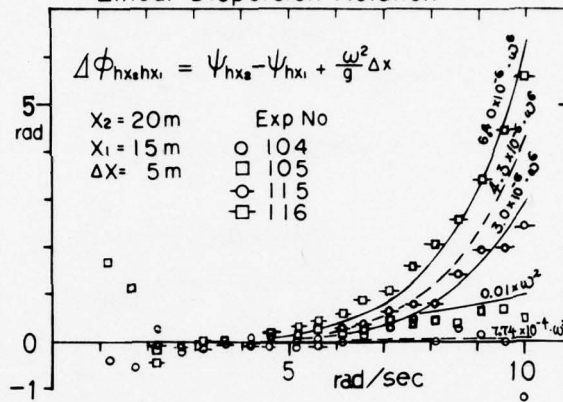


Fig. 9: Corrected phase difference by linear dispersion relation. The measured positions differ in two figures. Lines are reference line (see Appendix 4).

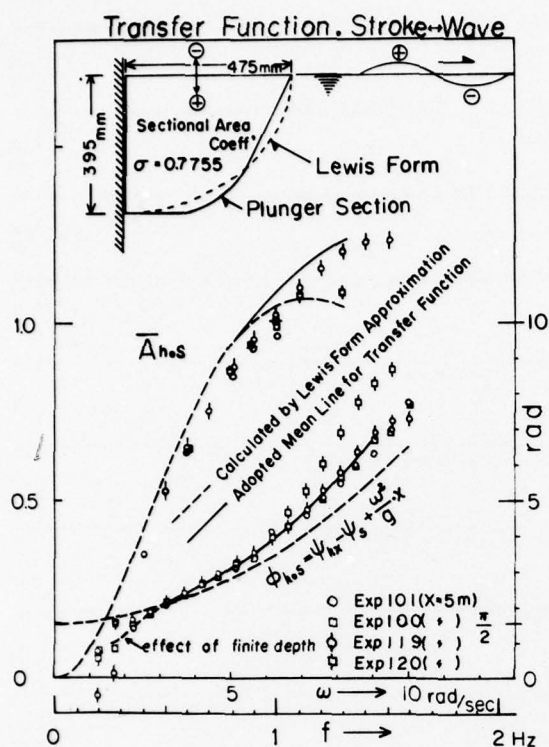


Fig. 10: Transfer function between stroke and generated wave.

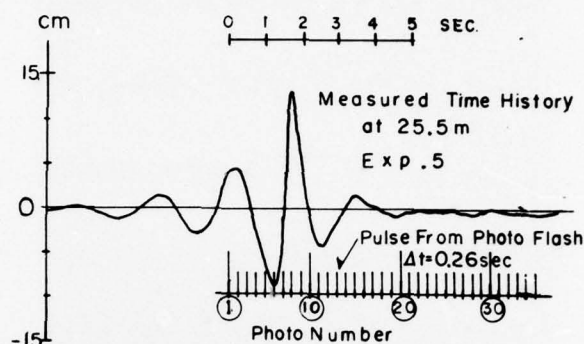


Fig. 11: Measured time history of large amplitude T.W.W. with constant wave slope, which corresponds to Fig. 13.

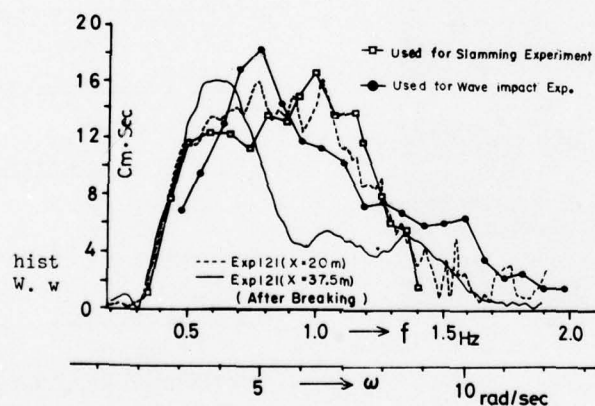


Fig. 12: Fourier spectrum of large amplitude of T.W.W. with constant wave height corresponds to Fig. 14 and 15. The mark  $\square$  and  $\circ$  is from Ref 4 which corresponds to Fig. 16 of part 1.



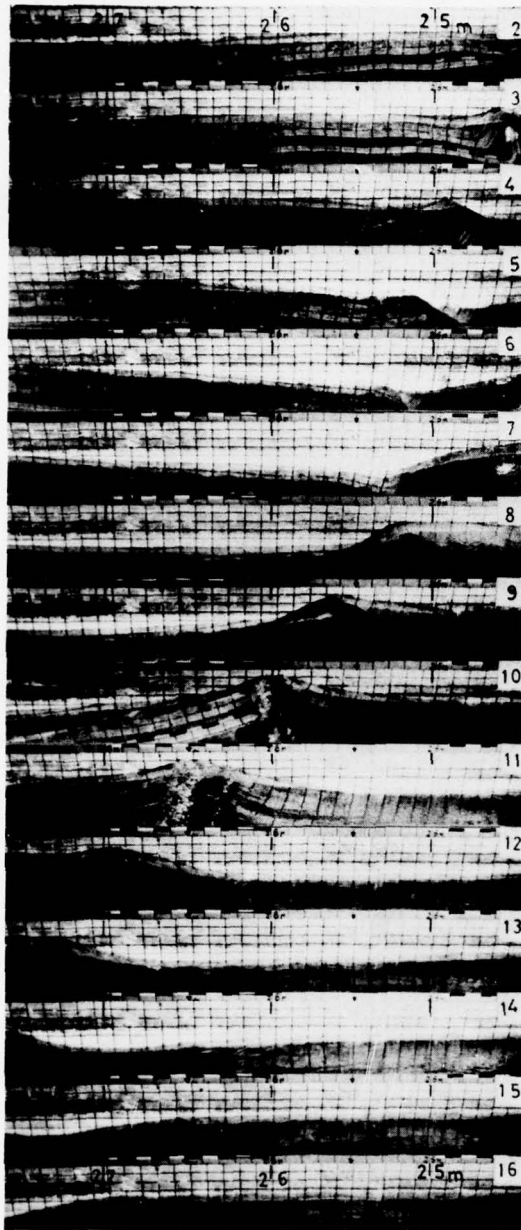


Photo 1: Photograph by motor driven camera. (Exp. No. 5). Concentration of Transient Water Wave (T.W.W.) with constant wave slope (designed position of concentration is 25 m from wave maker). Time history obtained at 25.5 m is shown in Fig. 11.

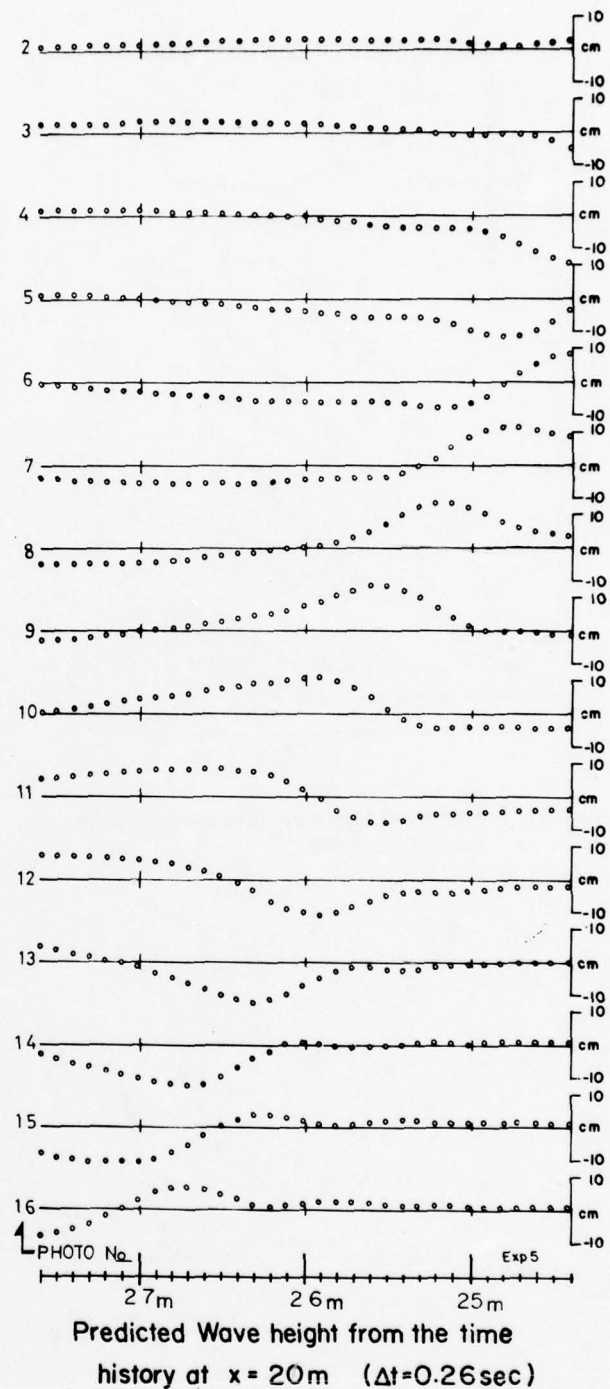


Fig. 13: Predicted wave height from the time history at 20m from wave maker. Corresponds to Photo 1 and Fig. 11.

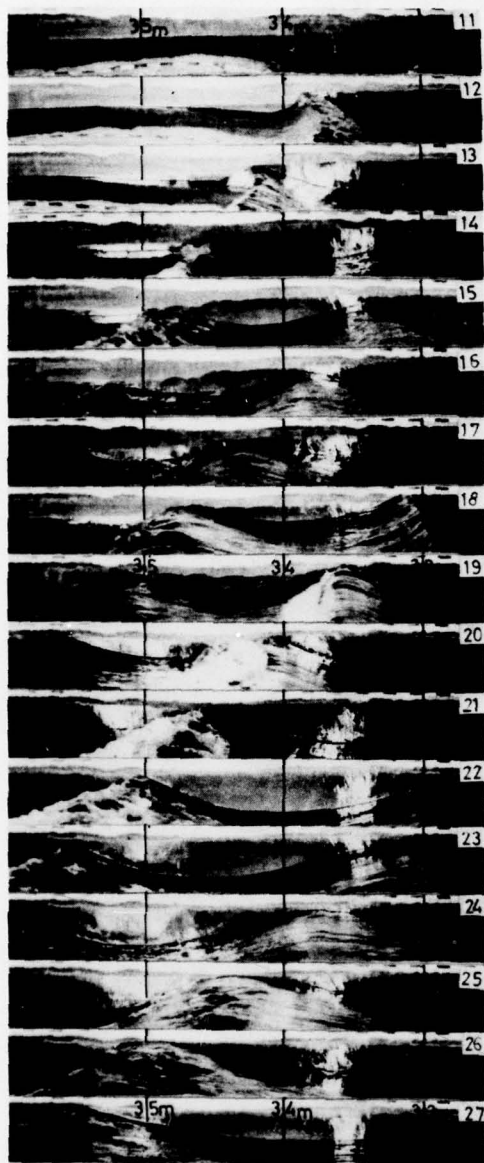


Photo 2: Photograph by motor driven camera. Concentration of Transient Water Wave with constant wave height (Exp. No. 121). Large breaking is observed.

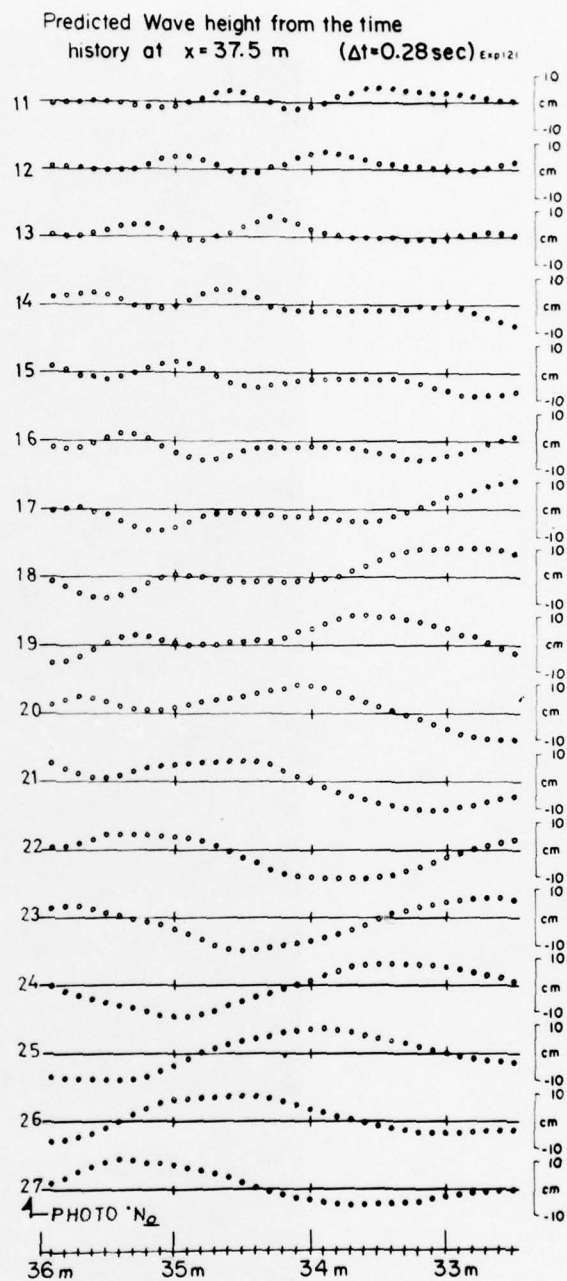


Fig. 14: Predicted wave height from the time history at 37.5 m from wave maker. Corresponds to Photo 2.

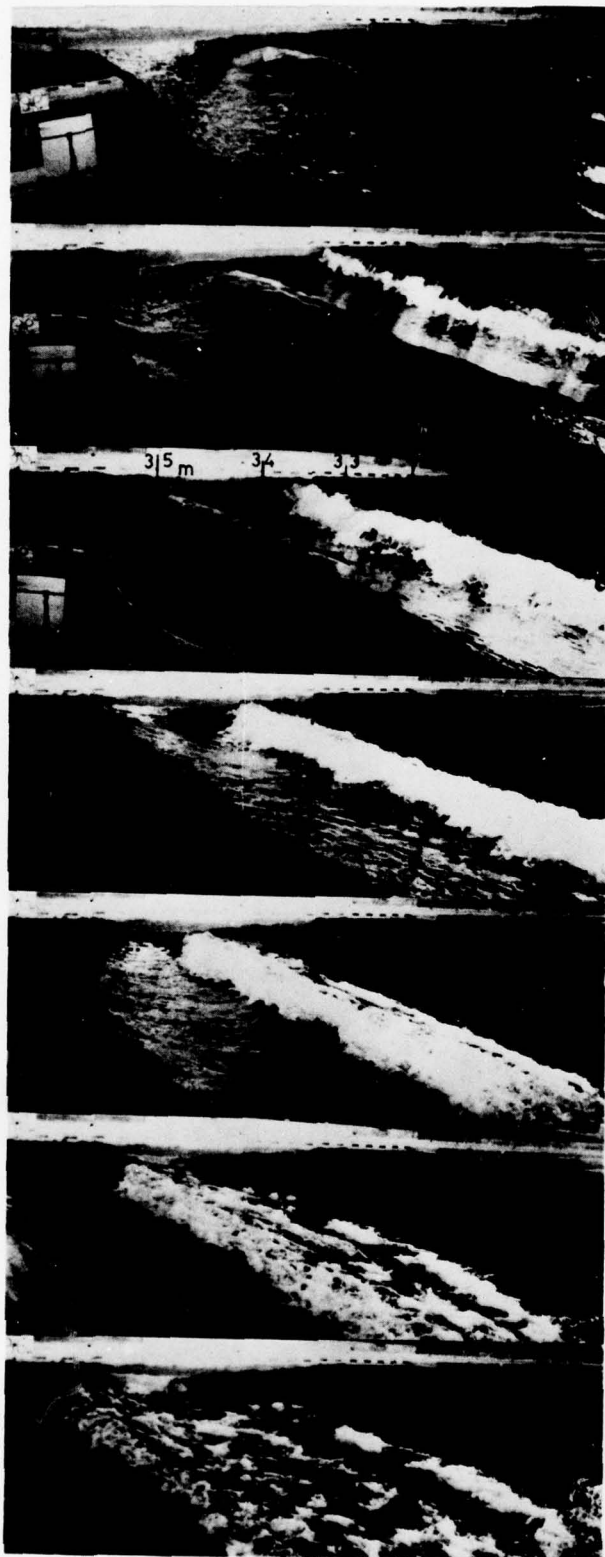


Photo 3: Oblique view of Photo 2.



# EXPERIMENTAL TECHNIQUES AND METHODS OF ANALYSIS USED AT HYDRONAUTICS FOR SURFACE-SHIP MANEUVERING PREDICTIONS

ALEX GOODMAN, MORTON GERTLER and ROBERT KOHL

Hydronautics, Incorporated, Laurel, Maryland.

## ABSTRACT

Standard techniques and analysis methods have been developed at HYDRONAUTICS Ship Model Basin (HSMB) primarily for conducting detailed design and evaluation studies of the directional stability and control characteristics of proposed and existing surface-ship designs. The techniques are based on the use of a new large-amplitude horizontal planar-motion-mechanism system designated as the HSMB LAHPMM System. The new system incorporates several unique features intended to improve efficiency and effect cost savings in the model testing process. Among these is an integrated towing system which permits conduct of all model tests routinely required for specific designs (including calm-water resistance, propulsion, and PMM tests) in uninterrupted sequence without requirement of separate rigging and program. The overall method consists of PMM tests with large surface-ship models (ranging from 18 to 27 feet in length) to determine complete sets of hydrodynamic coefficients including those related to powering; formulation of mathematical models therefrom based on the Standard Equations of Motion; and conduct of maneuvering studies employing the mathematical models in conjunction with computer simulation techniques.

The new HSMB LAHPMM System and associated experimental and analysis techniques are described in detail. The results of a standard program carried out for a MARINER class vessel are presented to illustrate a typical use of the overall system and methodology. Included are: a complete set of hydrodynamic coefficients necessary to formulate the mathematical model; predictions of resistance and propulsion characteristics; and computer simulation predictions involving representative definitive maneuvers. Pursuant to the ITTC Standard Program, the hydrodynamic coefficients obtained for MARINER at HSMB are compared with those derived by other laboratories. The computer simulation predictions based on the HSMB LAHPMM data are compared and show good agreement with corresponding trajectory data measured from full-scale maneuvering trials of the COMPASS ISLAND. For convenient reference, an updated history of the international development and use of PMM and PMM systems is included among the appendixes along with other detailed information related specifically to the HSMB methods.

## INTRODUCTION

One of the most important prerequisites to the successful operation of a naval surface ship is that it possess all of the maneuverability characteristics necessary to carry out its specified mission in an efficient and reliable manner. Accordingly, the U. S. Navy and other navies throughout the world have maintained a continuous interest in the use of various types of model tests and full-scale trials to assure that at least certain tactical requirements are fulfilled (Ref. 1). However, the advent of new merchant ship types, such as the very large crude carrier (VLCC), served to accelerate the development of more advanced experimental and analytical techniques applicable to the field of surface-ship maneuverability because of the major safety, economic, and ecological problems that were generated. Many laboratories throughout the world still use free-running model tests as their primary technique for evaluating the maneuvering characteristics of surface ships. For most practical purposes, such evaluations are limited to those handling qualities associated with inherent or open-loop performance. Fortunately, the modern trend seems to be directed toward the almost exclusive use of captive-model tests and associated computer simulation techniques comparable to those developed earlier by the U. S. Navy for the case of submarines (Ref. 2). Such

techniques provide more fundamental design data as well as the additional means for solving various closed-loop problems, including environmental effects superimposed, which are associated with the control and operation of modern ships. Furthermore, they provide the mathematical model essential to the operation of real-time simulators which now play an important role in the training of both naval and merchant ship personnel.

The main purpose of this paper is to describe the standard techniques developed and currently used at HYDRONAUTICS Ship Model Basin (HSMB) to perform detailed evaluation studies of the maneuvering characteristics for specific designs of displacement type surface ships. The method employs the new HSMB Large-Amplitude Horizontal Planar Motion Mechanism (LAHPMM), which has the capacity for testing surface-ship models ranging from 18 to 27 feet in length, in conjunction with Standard Equations of Motion developed for surface ships. The resulting mathematical models are sufficiently comprehensive to permit computer simulation of trajectories resulting from even the most extreme maneuvers within the capabilities of essentially all modern surface-ship types. A unique feature associated with the HSMB LAHPMM is an integrated towing system which permits the conduct of all required calm-water tests (including resistance, propulsion, and PMM tests) in

an uninterrupted sequence. This feature will improve testing efficiency and effect cost savings particularly in design development investigations of a routine nature since it will eliminate the usual requirement of separate rigging and program.

The intent of this paper is to provide a single-source reference both for laboratory type personnel who must apply the techniques to produce the required data as well as for ship designers, operators, and others who will utilize the end results. It has been deemed necessary, therefore, to include sufficient detail to provide a full understanding of the methodology and equipment involved as well as the range of validity of its use. Specifically, this paper presents the underlying considerations which led to the development of the original PMM System and second generation large amplitude PMM's used for surface-ship model testing; describes in detail the new HSMB LAHPMM System currently in operation including the principal component parts of the hardware in the towing, measurement, data acquisition, and data processing systems; outlines the procedures used for resistance, propulsion, and PMM tests employing the integrated towing system feature; describes the methods used for reduction and analysis of the various test data; explains the methods used to formulate the mathematical models and to conduct the computer simulation studies of ship maneuvers; presents a complete set of hydrodynamic coefficients for a MARINER class vessel derived from tests using the HSMB LAHPMM System pursuant to the ITTC Standard Program and makes comparisons with corresponding values obtained by other laboratories; and compares computer simulation predictions based on the mathematical model obtained from the HSMB LAHPMM tests with corresponding trajectories measured during full-scale trials of the MARINER (COMPASS ISLAND). To augment the text of the paper, other pertinent information is given in Appendixes A through F, respectively, including: a complete notation; a chart outlining the history of the international development and use of PMM and PMM systems; an explanation of the mathematical operations performed during tests with the LAHPMM System; a table of reduction equations and detailed instructions for formulating the mathematical model for computer simulation studies; and step by step procedures for conducting definitive maneuvers used as standard at HSMB for surface-ship maneuvering studies.

#### GENERAL CONSIDERATIONS

It is now generally conceded that captive-model tests of the PMM variety offer the most direct and efficient means available for determining all of the hydrodynamic coefficients required for modern computer simulation studies of ship maneuvering characteristics. This is evidenced by the accelerated development, acquisition, and active use of PMM facilities by laboratories throughout the world, as indicated by the historical chart of Appendix B. Moreover, the PMM technique has been rapidly gaining favor over the free-running model technique for routine design evaluation studies, for reasons given in the next section. The purpose of this section is to outline the basic principles and general philosophy which have governed these PMM developments. Special emphasis is placed on those considerations which have influenced the development and use of large amplitude PMM's, such as the HSMB LAHPMM, for the case of displacement surface ships. The fundamental principles which form the basis of the PMM technique are given in detail for the case

of submarines in References 3, 4, and 5 and for the case of surface ships in References 6 and 7. For those not yet familiar with the technique, these principles are briefly reviewed as follows:

The basic PMM System (Ref. 3) incorporates in one device a means for experimentally determining all of the hydrodynamic coefficients required in the equations of motion of a body moving through a fluid in six degrees of freedom. These coefficients are usually classified into three general categories: static, rotary, and acceleration. The static coefficients are due to the components of linear velocity of the body relative to the fluid; the rotary coefficients are due to components of angular velocity; and the acceleration coefficients are due to either linear or angular acceleration components. Within limited ranges, the coefficients are linear with respect to the appropriate variables, and thus may be utilized as static, rotary, and acceleration derivatives in linearized equations of motion.

The PMM System explicitly determines the numerical values in each of the three foregoing categories by imparting certain hydrodynamically "pure" motions to the body. The primary modes of motion used for this purpose are shown schematically by Figure 1 for the case of horizontal-plane motions of a surface ship (three degrees of freedom). The means for measuring and resolving the force and moment coefficients in each category are described in detail later. Briefly, the static coefficients are obtained directly from measurements of steady force in the static mode; the rotary or damping coefficients are obtained explicitly from measurements of the quadrature components of oscillatory force in the pure yawing mode; and the acceleration coefficients are obtained explicitly from measurements of the in-phase components of oscillatory force in the pure sideswaying and pure yawing modes.

The various modes of motion shown by Figure 1 are imparted to a surface-ship model by means of the forced-motion mechanism of a PMM System in conjunction with a towing carriage operating at a steady speed over a straightline basin. Although the precise methods of generating these motions vary with the particular design of PMM, they can be generally classified into one of two concepts. The so-called conventional PMM, typified by the original HSMB Horizontal PMM described in detail in Reference 5, employs "two-struts" (or pistons) commonly driven through a phase-changer to support the model and to generate the desired oscillatory modes. In essence, pure swaying is obtained by laterally oscillating the two struts (spaced equidistant from the reference point) in phase with each other; pure yawing is obtained by laterally oscillating the two struts with a predetermined phase angle between them based on oscillation frequency, carriage speed and strut spacing. The large amplitude PMM, typified by the SL design (Ref. 8) and the new HSMB LAHPMM, generates the desired oscillatory modes by combined lateral and angular (yawing) motions about a central model support arrangement. The precise methods for generating the pure swaying and pure yawing modes with the HSMB LAHPMM are given later in connection with the description of the test apparatus and procedures.

The general trend for surface ships is toward the use of the large amplitude PMM rather than the conventional PMM. This is particularly true where detailed computer simulation studies involving extreme maneuvers are contemplated, as well as for other reasons discussed in the following paragraphs.



It should be emphasized, however, that the major differences between the conventional and large-amplitude systems are in the methods for generating the oscillatory motions, and the range covered, primarily as applied to the pure yawing mode. Otherwise, the test procedures, instrumentation, and data reduction methods are essentially the same for both types. Therefore, the existing conventional PMM Systems can still provide a valuable service insofar as many naval and merchant surface-ship maneuverability problems are concerned. For example, such PMM Systems can be used very effectively in early design studies and also to provide all of the necessary input for computer simulation studies of a wide variety of maneuvers of interest (see Table 1).

The large amplitude PMM was originally conceived as a means for covering, in a single device, the entire range of kinematic variables necessary to perform computer simulation studies of the most extreme turning maneuvers known to be characteristic of large unstable tanker types (without reliance on supplementary estimates or rotating-arm tests). This, of course, would effect significant savings in model testing and would be especially beneficial to laboratories equipped only with straightline towing tank facilities. Of equal importance, is that the concept offers a means for circumventing certain problems involved in PMM testing of even the standard large surface-ship models used at HSMB. Among these are problems related to the free surface and Froude scaling; matters that were of little concern to PMM testing of submarine models. For example, in PMM tests of a given surface-ship model, the only means of increasing the nondimensional yawing velocity  $r' = rL/U$  are by increasing oscillation frequency or amplitude or a combination of both, since the model speed is fixed by the requirement of Froude law correspondence. Within the capacity of a given PMM system, there is a limit to the extent that frequency alone can be validly increased. This is due to the fact that the oscillating model acts as a wave generator which can lead to towing tank resonance (standing waves) and other unwanted free-surface effects. Furthermore, the use of the lowest practical frequency in conjunction with the largest practical amplitude is desirable since the resulting motion more closely satisfies the quasi steady-state assumption of the basic PMM System as well as being a closer approximation of the corresponding motion obtained on a rotating arm facility. In view of the foregoing, the following have been recommended as a means for avoiding or minimizing unwanted effects associated with PMM testing of surface-ship models (Ref. 9):

1. Tank resonance effects - The oscillation frequency should be appreciably less than 0.30 cps (for tanks with cross-sectional dimensions the same as HSMB).

2. Translatory free-surface wave effects generated by a pulsating source - The value of  $\omega L/U$  should be appreciably less than 1/4.

3. Unsteady lift or memory effects - the value of  $\omega L/U$  should be less than about 3.

Taking the case of a 22-foot model of a VLCC at a speed of 4 feet per second, the limiting upper values for oscillation frequency would be 0.32 and 0.09 cps based on the criteria of Items 2 and 3, respectively. It is felt that the criterion of Item 3 is somewhat unrealistic. This is based on experience with PMM tests of submarine models using considerably higher values of  $\omega L/U$  than 3 without any apparent unsteady lift effects. Aside from satisfying the criteria as to the upper frequency limit, the use of larger amplitudes has the advantage of increasing the forces, and thereby the measurement accuracy, at frequencies corresponding to

the lower values of  $r'$ .

The main philosophy which forms the basis of most of the PMM systems developed to date has been expressed in previous papers by the authors and others. In view of recent developments including the HSMB LAHPMM System, it appears appropriate to repeat some of the basic reasoning here. It should be again emphasized that the original PMM system (Refs. 3,4,5) was conceived and developed as an engineering tool, namely to provide all of the hydrodynamic coefficients required for detailed maneuverability studies of marine vehicles by the most direct and efficient means from a practical standpoint. This philosophy has prevailed among those PMM facilities which have been most successfully applied to the routine solution of maneuverability problems for specific submarine and surface-ship designs. The growing acceptance of such PMM techniques by the industry, as well as the good correlation demonstrated between associated computer simulation predictions and full-scale trial data, both for submarines and surface ships, are strong testimonials to their engineering validity. Further evidence of the correlation that can be expected for surface ships, using data obtained with the HSMB LAHPMM, is presented in a later section.

In recent years, there have been a number of papers authored principally by mathematicians and researchers who have attempted to achieve more scientific rigor in the underlying logic of the PMM system. Also, there has been a tendency on the part of some equipment designers to incorporate more and more eloquence into the hardware aspects of the overall system in an effort to enhance its versatility. Of course, any significant improvements in accuracy and quality of end results arising from either of these two types of activities *must be seriously considered*. However, they must be carefully weighed against the likelihood that the costs of providing equivalent data would be raised excessively due to increases in costs of the initial installation as well as those due to the added complexity in testing, data reduction, and final analysis. This would be unfortunate since one of the greatest selling points of those PMM systems in active service is that the costs to the customer have been reduced to the extent that they are strongly competitive with those of other comparable techniques (see next section).

#### COMPARISON OF EXPERIMENTAL TECHNIQUES

The various approaches to solution of problems in the field of dynamic stability and control used in the past for marine vehicles in general and submerged bodies in particular are outlined in Reference 10. It is of interest herein to review these approaches specifically for the case of displacement-type surface ships taking into account the advances in technology made within the past fifteen years. Figure 2 is a flow diagram which shows those approaches that are still being applied in varying degrees to the study of directional stability and maneuverability of surface ships. As stated earlier, free-running model techniques have become well established over the years since, except as noted later, they provide a direct means for evaluation of performance of specific surface-ship designs. Such techniques range in sophistication from fairly simple tests conducted with cable-controlled models using photographic means for tracking to tests with highly instrumented radio-controlled models using various electronic means for tracking. The PMM technique (with computer simulation), used so successfully for



submarines (Ref. 2), also is now becoming well established for treatment of surface ships and, because of its versatility, has actually supplanted the use of free-running models in some laboratories both abroad (Refs. 9,10) and in the U. S. (Refs. 11, 12). Other captive-model techniques in common usage, but which individually do not supply all of the required hydrodynamic coefficients, include rotating-arm, straightline-yaw or oblique-tow, and oscillator tests (Refs. 9,13,14). Ideally, the use of properly conducted full-scale trials is perhaps the most direct approach toward the final evaluation of the maneuvering characteristics of a specific ship. As a practical matter, however, maneuvering trials required to produce data necessary for detailed analysis are extremely difficult and expensive to conduct and are therefore rarely performed for commercial ships. Nevertheless, it is important to conduct such extensive full-scale trials, at least on several different representative ship types, to fully validate and establish the confidence level that can be placed in the various alternative model prediction techniques. Two of the predictive approaches shown in Figure 2 have not been discussed up to this point since they are not considered to be in an adequate stage of development for routine use for design or evaluation purposes. The development of theoretically based estimation techniques which could be used with confidence to accurately determine a complete set of hydrodynamic coefficients from a set of ship lines and appendage drawings is the ultimate goal for investigators in the field. Obviously, such techniques would effect tremendous savings in both time and money since they would permit design decisions and complete evaluations of performance to be made without resort to model experiments of any kind. Unfortunately, the existing strictly theoretical methods are relatively rudimentary and generally do not take cognizance of practical features of ship design such as size, shape, and location of rudders or skegs as well as propeller slipstream effects, all of which are known to strongly affect maneuvering characteristics of ships. Furthermore, the establishment of the necessary empirical relationships for surface ships has been hampered until recently by the lack of reliable experimental data from PMM tests. A substantial step in this direction was made as the result of the systematic series PMM data of Reference 12, but these data so far are directly applicable only to single-screw merchant ship types of relatively full form. It should be mentioned, however, that the theoretically and empirically based estimation techniques serve a useful purpose in the overall process. This is particularly true in cases where, for some reason, the PMM tests have been conducted over a range insufficient to provide all of the necessary hydrodynamic coefficients. The so-called systems identification technique is another means for generating the values of the necessary hydrodynamic coefficients which has received considerable attention during the past several years. This approach utilizes trajectory measurements made during either free-running model tests or full-scale trials in conjunction with an assumed form of the equations of motion to identify and hopefully quantify both the linear and nonlinear coefficients. The method has been applied to the surface-ship case with a fair amount of success by comparing numerical values of coefficients derived from computer simulated trajectories with those of the input coefficients originally derived from PMM tests. However, error analyses performed to date seem to indicate that, without prior knowledge of any of the coefficient values, the

real full-scale or model trajectories must be measured with much greater accuracy than is obtainable within the foreseeable state of the art in measurement instrumentation. Assuming that these problems eventually can be overcome, the systems identification technique will still require a free-running model test of limited scope, with some of its attendant disadvantages, if it is to be used for prediction purposes in the design stage. The technique applied to proper full-scale trial trajectory data could be useful in a variety of ways including correlation studies based on direct comparisons with the hydrodynamic coefficients obtained from PMM tests. It is doubtful, however, whether full-scale trials of the required caliber, will be performed in the foreseeable future because of the expense involved both with the necessary precision instrumentation and in obtaining the required controlled trial conditions. It should be mentioned, however, that proponents of the technique claim that precision instrumentation requirements can be avoided by the use of special data processing techniques such as that known as Kalman filtering. Table 1 compares the advantages and disadvantages of the two main experimentally based predictive techniques now used regularly by major laboratories to evaluate maneuverability characteristics of specific surface ships for commercial or governmental clients. The comparison assumes that the large model available from propulsion tests is used in both the free-running-model and PMM tests. This is done to put both techniques on even par insofar as model construction costs and certain scale effect problems are concerned. Also, some of the statements made with regard to costs are based on current experience in the U. S., although it is believed that they apply in a relative sense to costs in Europe and Japan as well. It may be noted that the PMM tests are carried out with respect to the ship propulsion point whereas the free-running model tests are conducted at model propulsion point. This is an important technical advantage of the PMM technique since the inherent directional stability and control effectiveness of most commercial ship types are both strongly influenced by the action of the propeller slipstream over the rudder. For example, due mainly to differences in frictional resistance coefficient, the propeller loading coefficient of even a large free-running model may be as much as twice that of its full-scale counterpart in the case of large full-form single-screw merchant ships. Originally the PMM technique was considered to be too expensive to warrant its use for routine evaluation of the maneuvering characteristics of specific surface-ship designs. This is believed to be no longer the case due to recent developments in instrumentation and technology. In fact, for a typical evaluation program based on the use of definitive maneuvers which includes the model tests, data reduction, analysis, and report, the total cost is now nearly the same for either the PMM or free-running model technique. In view of the other benefits shown in Table 1, the PMM technique appears to be more advantageous from the economical as well as the technical standpoint. It may be expected, therefore, that the PMM technique will eventually become the primary methodology used by most laboratories to evaluate the maneuverability characteristics of surface ships.

#### THE HSMB LAHPMM SYSTEM

The HSMB LAHPMM System, like its predecessor PMM Systems at NSRDC and HSMB is a complete system which embraces all mechanical, electrical, and electronic

TABLE 1  
COMPARISON OF EXPERIMENTAL TECHNIQUES FOR SURFACE-SHIP  
MANEUVERABILITY STUDIES

(a) Free-Running Model Technique

Advantages

1. Provides a direct evaluation of inherent directional stability and maneuverability characteristics of specific designs well in advance of construction.
2. Provides a means for investigating the overall consequences of proposed design changes.
3. Can be economical and expedient especially when simple cable-controlled models are used and only one design is evaluated.
4. Can be used for extreme maneuvers to validate computer simulation techniques.

Disadvantages

1. Does not provide data which can be directly related to the separate design of hull and individual appendages.
2. Does not directly provide data to support design changes to effect improvements in performance.
3. Dynamic scaling of model is necessary which may require additional tests when inertial characteristics (mass, moments of inertia, and metacentric heights) are changed.
4. May not accurately simulate maneuvering characteristics of full-scale ship due to differences in propeller loading and failure to account for other possible scale effects.
5. Requires the use of large and expensive maneuvering basin facilities.
6. Can be expensive if tests are conducted with more sophisticated radio-controlled model systems.
7. Can be expensive and/or inefficient for investigating effects of shallow water or other environmental factors on ship maneuverability.

(b) PMM Technique (with Computer Simulation)

1. Provides basic data related to the separate effects of hull and appendages which can be used to study effects of design variations on specific ships and is also a powerful tool for performing research or systematic series investigations.
2. Provides basic data which can be used in conjunction with linearized equations to analyze inherent directional stability and control effectiveness of candidate designs in the early design stage.
3. Provides basic data which can be directly utilized in the design of automatic control systems.
4. Provides the numerical values for the complete set of hydrodynamic coefficients enabling formulation of mathematical model for computer simulation of all types of ship maneuvers.
5. Data are perpetuated since hydrodynamic coefficients are independent of inertial characteristics.
6. Data can be utilized to study effects of design changes without the need for additional model tests.
7. Tests are performed in a conventional straightline towing basin thus eliminating the need for large, expensive maneuvering basins or other special purpose facilities.
8. Tests are relatively economical to conduct since the same large model constructed for propulsion tests can be used and dynamic scaling of model is not necessary.
9. Data are more representative of the full-scale ship since tests are conducted with respect to ship-propulsion point and corrections can be made if required to account for known scale effects.
10. Tests to provide mathematical model representing shallow-water and other environmental effects are relatively economical to conduct.
11. Basic mathematical model can be used in computer simulation studies of definitive maneuvers to evaluate inherent performance and thus provide a basis for establishing handling quality criteria for existing and future ship types.
12. Mathematical model(s) are essential to the operation of research simulators, such as the MARAD CAORF Simulator, and can be used for a wide variety of both open- and closed-loop studies involving manual or automatic control including human engineering studies and studies of overall performance of various combined systems.
13. Mathematical models in conjunction with real time simulation facilities can be used to train operational personnel.
14. Mathematical models can be directly used for ship predictor or other semi-automatic control systems.

Disadvantages

1. Data from tests are one step removed from directly indicating all of the handling qualities.
2. Method may become less economical where a limited evaluation or proof-testing of one specific design is all that is desired.



components necessary to perform all functions associated with PMM testing ranging from model handling to finalized processing of data preparatory to analysis. A schematic of the overall system is given in Figure 3. A unique feature of this system is the integrated towing and instrumentation arrangement which permits the conduct of calm-water resistance, propulsion, and PMM tests in uninterrupted sequence without the requirement of separate rigging and program. This feature should result in improved testing efficiency and substantial cost saving particularly in design development investigations of a routine nature. A detailed description of the HSMB LAHPMM System and its application is given in the following paragraphs.

#### Integrated Towing System

A schematic plan and elevation views are presented in Figure 4 showing the forced-motion mechanism, towing arrangement and dynamometry associated with the overall HSMB Integrated Surface Ship Towing System. As may be seen in Figure 4, the forced motions of the LAHPMM are produced by means of a swaying carriage assembly which incorporates a device for setting drift angles and provides a support for the yawing table and drive system. Photographs of the LAHPMM with the MARINER model attached are given in Figure 5.

Drift Angle Apparatus - The drift-angle-setting arm is fastened directly to the yawing tube as shown in Figures 4a and 4b. The drift angles can be set manually (with model at rest) by means of a spring-loaded locking pin. The settings are in two-degree increments and cover a range of  $\pm 30$  degrees. This method of setting drift angle is used generally for coupling tests which involve pure yawing motion with a constant drift angle superimposed as shown in Figure 1d.

For the static mode (Figure 1a), the drift angle can be set remotely with the model underway by means of the yaw servo motor and use of the drift angle selector switch housed in the LAHPMM Control unit shown in Figure 3 and described in detail in a subsequent section. Increments of two degrees over a range of  $\pm 30$  degrees can be set in the automatic mode.

Swaying Apparatus - The Swaying Carriage is shown in Figures 4b and 5b. The carriage moves horizontally in a direction perpendicular to the basin centerline along a set of four linear-ball-bearing rails mounted on a portable support frame which is rigidly clamped to the towing carriage. A strongback attached to the yawing tube provides the means for connecting the swaying carriage through the bearing and gage assemblies to the model. In this manner, the strongback is always aligned with the centerline of the model in all modes of motion. For the pure swaying mode (Figure 1b), the swaying carriage system is operated with the yawing tube system locked at zero setting. As shown in Figures 4b, 5b, and 6, the swaying carriage is driven laterally by means of a servo-motor-driven-ball-bearing jack screw system. Sinusoidal motions can be produced which cover the following continuous ranges: frequencies of from about 0.01 to 0.30 Hertz and linear (single) amplitudes up to 3.3 feet. These maximum amplitudes and frequencies are defined for the system when used in combination with a model having a mass of 600 slugs.

Yawing Apparatus - The Yawing Apparatus, shown in Figures 4 and 5, consists of a servo-motor, gear reducer, and pinion-bull gear-drive system. The large bull gear is attached to the yawing tube by means of the manual drift angle setting and lockout

unit. The yawing tube is supported by ball bearings in the swaying carriage and the PMM strongback is attached directly to the tube.

For the pure yawing mode, the yawing tube is operated simultaneously at equal frequency with the swaying carriage, but with a 90-degree phase lag; the yawing amplitude setting is determined directly as a function of the swaying amplitude and carriage speed. The net result is to produce a motion whereby the model centerline is always tangent to the path (see Figure 1c). For coupling tests, the system is operated with a constant drift-angle setting superimposed (see Figure 1d).

Sinusoidal motions can be produced with this system which cover the following continuous ranges: frequencies of about 0.01 to 0.30 Hertz; angular (single) amplitudes of up to 30 degrees; and angular amplitudes coupling with drift angles of up to  $\pm 30$  degrees. These maximum amplitudes and frequencies are defined for the system when used in combination with a model having a mass of 600 slugs and a moment of inertia of 20,000 slug-ft<sup>2</sup>.

Servo Motor Control System - The overall control system for the LAHPMM is shown in Figure 3. The sway and yaw d.c. servo motors are controlled by a power amplifier which is a three-phase, half-wave, bi-directional, regenerative SCR amplifier with a current feedback. The two-axis controller is shown in Figure 7. This controller also contains the overload and limit switch protective circuits as well as the control amplifiers which provide the position and rate-feedback loop controls.

The system control center is contained in the LAHPMM Control Unit shown in Figures 3 and 8. The control unit provides the means for setting the yawing and/or swaying amplitudes; the frequency; the drift angle; lateral position of swaying carriage; on-off controls for servo motors; and servo motor brakes. It also provides command and feedback signal amplitude for yawing and swaying; and provides a digital panel meter which selectively displays drift angle, yawing and swaying amplitudes. The servo drive of the function generator and resolver shown in Figures 3 and 9 is also controlled by the LAHPMM Control Unit. The servo motor shown in Figure 7 is connected to a single cup sine-cosine potentiometer which provides the sinusoidal command signals, with the required 90-degree phase relationship, to control the swaying and yawing motions. In addition, the single cup sine-cosine potentiometer is attached to a multi-ganged sine-cosine potentiometer which acts as a force component resolver as described in Ref. (15) and Appendix C. The phase angle of the multi-ganged sine-cosine potentiometer assembly can be set manually with respect to the command sine-cosine potentiometer by means of a precision gear box shown in Figure 9. This capability is necessary to account for the phase lag between the command signals and motions of the system in sway and yaw. The phase lag is determined by processing the LAHPMM feedback signals through the resolver system. The phase lag which varies linearly with frequency, is the same for the yawing and swaying modes (gains of control amplifiers are chosen to satisfy this condition). The phase lag has been calibrated and demonstrated to be independent of inertia and therefore independent of model size within the design range.

Model Attachment System - The towing system, along with all of the rest of the mechanical components of the LAHPMM, is designed to provide a high degree of rigidity in all pertinent directions to accommodate testing of large surface-ship models ranging in length from 15 to 30 feet with weights up to 10,000 pounds. This is accomplished by using a compact but



rugged heave, yaw and pitch bearing assembly to join the strongback to the gage assembly at each of the two locations in the model as shown in Figures 4 and 10. The arrangement allows the model to be free in heave and pitch while providing stiff restraint to lateral force Y, yawing moment N, and longitudinal force X. An added feature is the pneumatically controlled lockout device shown in Figures 11 and 4 which is used to unload the gages while bringing the model up to steady speed, principally in resistance and propulsion tests of very heavy models.

For PMM tests of surface displacement ship models, the towposts are clamped directly to the PMM strongback so that the  $X_1$  (PMM),  $X_2$  (PMM),  $Y_1$ ,  $Y_2$  gages and yaw bearings or gimbals are used in this mode (see Figure 4b). The base plates of the two gage assemblies are mounted in the model so that the gimbal centers are aligned and equidistant from the reference point or longitudinal center of gravity LCG location. In the case of surface-ship models which are buoyant and free to trim, the LCG or reference point is the same for both model and prototype ship. Since the gages move with the model, they measure lateral force Y and longitudinal force X components with respect to a body axis system (origin at model CG), as opposed to the lift-drag components associated with the fixed-axis system. With the LAHPMM gage arrangement shown in Figure 4, the total Y-force exerted on the model is experienced as a pure reaction at each of the gimbal centers; the moment about each of these centers is zero. Thus the total Y-force is equal to the vector sum of the forces measured by the  $Y_1$  and  $Y_2$  gages and, because of symmetry, the yawing moment N is equal to the vector difference between the  $Y_1$ - and  $Y_2$ -forces times the distance from one gimbal center to the CG. Similarly, the vector sum of the pure reaction forces measured by the  $X_1$  (PMM) and  $X_2$  (PMM) gages is equal to the total X-force, but since the reaction X-forces are aligned with the longitudinal axis, there is no contribution to the yawing moment. Also because of the dogleg in the after assembly, the  $X_2$  (PMM) reading is ideally expected to be equal to zero.

For resistance and propulsion tests, the  $X_1$  and  $X_2$  gages shown in the cutout of the strongback in Figure 4b are used for measurement in lieu of those used in the PMM test. With the model set at zero yaw angle, these gages truly measure drag or resistance rather than longitudinal force since the strongback always remains level.

**Dynamometry** - All of the force gages shown by Figures 4 and 10 are the standard 4-inch variable-reluctance block gages used at NSRDC and HSMB in various force measurement systems and described in detail in References (3), (4), (5), and (15). Briefly, the individual block gage is a cube-shaped flexure box machined from a solid block of 17-4pH stainless steel, a material selected for its practically zero mechanical hysteresis as well as its corrosion resistant properties. Each gage is sensitive to only a single component of force exerted in a direction normal to the flexural face of the cube; interaction effects from other force or moment components are practically nil. The relative movement of the flexures between the top and bottom ends of the gage attached to the towing carriage and model, respectively, is sensed by a specially designed variable-reluctance transducer. The measurement range of an individual block gage is governed by its spring constant or thickness of its flexures. For standard LAHPMM tests on large surface-ship models, the Y-gages are usually rated for a range of 250 pounds with a sensitivity of

50 counts per pound, and the X-gages are rated for a range of 50 pounds with a sensitivity of 100 counts per pound. The X-gages used for resistance tests also have a sensitivity of 100 counts per pound.

The propulsion dynamometer shown by Figures 4b and 5a is the variable-reluctance transmission type used at HSMB. The principles of operation of this type of dynamometer are described in detail in Ref. (16). The standard transmission dynamometer used for surface-ship model tests at HSMB has a measurement range of up to 40 pounds thrust and up to 40-inch-pounds torque; it is usually operated at sensitivities of 100 counts per pound and 50 counts per inch-pound, respectively. Since the dynamometer is designed to operate in water, it is installed in a water-filled case. This eliminates the need for shaft seals which tend to increase "no-load" torques and perhaps results in erratic "no-load" thrusts. Although the dynamometer is normally used in propulsion tests, it remains in place and can be used to take measurements of propeller torque and thrust corresponding to the various modes of motion that eventually will be simulated.

#### Shallow Water Apparatus

There is a growing interest regarding the maneuvering characteristics, particularly of large ships, operating in shallow water and restricted channels. Accordingly, the LAHPMM has been provided with additional equipment to facilitate shallow water testing. The arrangement used for these tests is shown in Figure 12. The entire system is attached to the HSMB Carriage vertical rails which allows for vertical adjustment of the system with changes in water depth.

#### Data Acquisition and Processing System

An integral part of the basic system is the means used to process and record the data transmitted from the force gages, dynamometers, and other transducers. The HSMB Data Acquisition System shown in Figures 3 and 13 is described in detail in Refs. (7) and (15). The system is of modular design with each channel being separate and interchangeable in all respects. Each channel is designed to operate in either the static or dynamic modes. In the static mode, the gage signal is processed through a signal conditioner unit (SCU) and the output is fed directly into an integrating digital voltmeter (IDVM) to obtain a single value integrated over a fixed time base. In the dynamic mode, the "sinusoidal" output signal from the SCU is fed across a sin-cos potentiometer into a force component separator (FCS) which resolves the signal into in-phase and quadrature components. The output of the FCS is then fed into the IDVM and integrated over a discrete number of cycles to obtain a single reading for each component (see Appendix C). The output of the IDVMs for all channels are scanned and then transmitted via the digital computer to a printer which records the processed data upon command. The on-site Data General NOVA 2 digital computer (24K capacity) provides the capability for storing data on disc as well as automatically reducing the data to nondimensional form on a run by run basis. In this manner, values of EHP and SHP as well as the dynamic stability indices, which might alter the course of the test program, can be obtained immediately following a given set of related runs. As an optional technique, the computer can be used to resolve the sinusoidal output signals of the force gages, obtained during the LAHPMM tests, into in-phase and quadrature components.

It should be noted, that for the pure-yawing mode shown in Figure 4, the resultant model velocity

varies with yaw angle. The NOVA-2 on-site computer has been programmed to take into account the velocity variation during the data reduction phase. This is the same approach and technique that has been followed successfully by SL in Denmark for the past four years. It is believed that accounting for the model velocity variation by this method produces more accurate and more reliable results than could be obtained by using a " $\Delta x$ " carriage. In addition, it is difficult to justify the additional cost and complexity of a third electro-mechanical-servo-controlled " $\Delta x$ " carriage to account for the one or two percent correction. Also, the addition of a " $\Delta x$ " carriage can reduce system stiffness and introduces the added complexity of requiring that the system motions be controlled entirely by a computer. Such added complexity could introduce errors which exceed the magnitude of the correction.

#### TEST PROCEDURES

As mentioned previously, the integrated towing feature of the HSMB LAHPMM System permits the conduct of calm-water resistance, propulsion, and PMM tests of large surface-ship models in uninterrupted sequence without the requirement of separate rigging. Prior to conducting a formal series of such tests, a deadweight calibration is made on a test stand to establish the sensitivity setting and electrical "cal-step" for each individual block gage and propulsion dynamometer component required to produce the desired measurements. The model (fully equipped as shown in Figure 4) is then carefully ballasted to obtain the predetermined displacement and trim which results in the LCG or reference point for the model being nondimensionally the same as that of the ship. In addition for the PMM tests, the model is either swung in air by means of a bifilar pendulum device or yaw oscillated by means of the PMM to obtain its yaw moment of inertia  $I_z$ . This step can be deferred until after the tests are completed since the model value of  $I_z$  is arbitrary and is taken out as a tare when the data are finally processed. The specific procedures and programs used for each type of test involved in a typical performance evaluation study of a proposed or existing ship design are separately described in the following sections.

#### Resistance and Propulsion Tests

Standard procedures have been developed for conducting resistance and propulsion tests in HSMB on large ship models (18 to 27 feet in length). These procedures are in general accordance with the recommendations of the ITTC (Ref. 17) and are designed to take advantage of improvements in measurement techniques developed specifically for testing of large full-bodied ship models. As a matter of standard practice, all tests are conducted with the model equipped with appropriately located turbulence stimulation studs. Selected resistance tests are also made with studs removed to ascertain whether a correction is necessary to account for parasitic drag of the studs exclusive of their turbulence stimulation effect.

The procedure followed in each resistance-test run using the integrated towing arrangement of Figure 4 is as follows:

1. Set towing carriage jacks to up position to unload pneumatic tires; release pneumatic model lockout device using solenoid operated valve system; initially zero the  $X_1$ - and  $X_2$ -gage readings using 10-second period on the integrating digital voltmeter (IDVM) - in general no further zero adjustment is made throughout a given test condition; and take 30-second integration on IDVM and record

zero reading on typewriter and the carriage digital computer before the start of each run.

2. Lower jacks and accelerate carriage (at a very slow rate for large full-bodied models) with model lockout device engaged. When constant predetermined speed is reached, disengage model lockout device using the solenoid operated valve system; and turn on the IDVM's, timer control unit, and carriage speed unit.

3. After a discrete integration period has elapsed (at least 30-seconds for large full-bodied models), turn to the switch position that stores the readings in the IDVM's, timer control unit, and carriage speed unit and transfer these readings through the typewriter to the carriage digital computer. Engage the model lockout device and decelerate carriage to a stop.

4. Return carriage slowly to starting end of the basin and maintain and monitor a running plot of resistance or resistance coefficient versus speed or Froude number using the data recorded by the line printer (see Figure 3).

5. After a 10-minutes wait between the start of each run, repeat Steps 1 through 4 for the next run.

Two basic methods of conducting propulsion tests are used for each model. The first is the standard method used in the United States for evaluating the propulsion characteristics of specific surface-ship designs. The method consists in propelling the model at full-scale "ship propulsion point" at each of several speeds covering the design range scaled in accordance with the Froude Law of Similitude. Thus two conditions must be satisfied:

1. The model speed in each case must correspond to the speed of the particular full-scale ship of specified dimensions (equal  $F_N$ ).

2. The model propeller rpm at each  $F_N$  value must be adjusted so that the delivered thrust overcomes a model resistance derived from the predicted full-scale resistance, that is  $C_T$  versus  $F_N$  for ship and model are equal.

The current state of the art assumes that the propeller-hull interactions (wake fractions and thrust deductions) for model and full-scale are equal when these two conditions are met. Various procedures have been advocated in an attempt to correct for scale effects on the propeller-hull interactions. In absence of general acceptance, however, none of the proposed corrections are currently incorporated in the HSMB model test and data reduction procedures.

The second method is similar to that recommended by the British Towing Tank Panel. Here the model speed is held constant and the model propeller rpm is varied in discrete increments over a range of overloads and underloads with respect to either the model or ship resistance (loading) coefficients. This method is particularly advantageous in connection with systematic series studies since it produces generalized data which can be used to predict the propulsion characteristics of any sized geometrically similar ship at any service condition that falls within the range of overloads and underloads. Furthermore, by conducting tests in the overload range, better experimental accuracy can be obtained with regard to the propeller-hull interaction coefficients. This is especially true for the case of large bulk carrier type ships since the model resistance at design speed that must be overcome to simulate ship-propulsion point may be only about half the actual model resistance. The procedural steps for conducting the two types of propulsion tests using the integrated towing arrangement of Figure 4 generally parallel those



used for the resistance tests insofar as the X-gage measurements are concerned, and are as follows:

1. If the formal resistance test with fully appended model (dummy hub in place of propeller) was not conducted immediately prior to the propulsion test, repeat runs should be made on the day of the propulsion test particularly at design, maximum, and a few intermediate speeds.

- a. Plot measured model resistance versus measured carriage speed and draw a faired curve as close as possible through the faired data points. The resulting curve of  $R_m$  versus  $v_m$  constitutes the basic reference curve for the propulsion tests and is taken to be the actual resistance of the model on the day of the test (uncorrected for blockage, parasitic drag of turbulence stimulators, or transitional flow effects).

- b. For use in ship-propulsion point type of test ( $F_N$  variation), prepare a curve of model  $\Delta R$  versus speed. This is accomplished by subtracting previously calculated values of model ideal resistance  $R_i$  (see Appendix D) from the measured values of  $R_m$  (Item a.) at about six to eight points covering the model speed range. At any given model speed (carriage speed), the value of  $\Delta R$  is that shown on the X-gages, the difference between  $\Delta R$  and  $-X$  reflects the amount that the model is either under- or over-propelled with respect to the ship-propulsion point at equal  $F_N$ . For large ships,  $R_i$  is always larger than  $R_m$  and therefore  $\Delta R$  shows up as a positive drag at the ship propulsion point.

2. Conduct no-load runs using a dummy hub (of approximately equal weight) in place of the propeller in the following sequence. These runs may be made in conjunction with the reference resistance test of Step 1.

- a. With the propeller shaft rotating at an rps of at least 6.0, establish and record zeros on the torque and thrust units of the transmission dynamometer using an integration time of at least 30 seconds.

- b. Conduct standstill no-load runs at rps values covering the range contemplated for the test and record torque  $Q$ ; thrust  $T$ , and rps  $n$  values using 30-second integration period.

- c. Make 3 or 4 runs covering the important range of speeds to determine whether there is any change in no-load  $Q$  or  $T$  with model speed. There should be little change in propeller no-loads with speed.

- d. Just prior to installing propeller, check zero values of  $Q$  and  $T$  by making a standstill run at the reference  $n$  condition.

3. Install propeller on model immediately following no-load runs and conduct a reference standstill test run as follows:

- a. With propeller stopped, make a zero check on the X-gages (see resistance test procedure). Then with X-gages operative, rotate propeller at a selected reference  $n$  (within test range), record  $T$ ,  $Q$  and  $X$  readings using a 30-second integration period. These runs should be made periodically throughout the regular propulsion tests to provide a time history in the event of instrument drift or other changes.

4. Conduct overload and underload propulsion test at a model (carriage) speed corresponding to design speed for the prototype full-scale ship (or other suitable reference speed) and covering a range of about 0.8 to 2.0 times the  $R_i$  (ship-propulsion point).

- a. Each run is made by setting the propeller rps at a discrete value which, along with

the carriage speed, is maintained constant throughout a given run. About six to eight runs should be made to cover the desired range with the greatest concentration of data points being made toward the overload end of the range. After an integration time of at least 30 seconds for each steady run, record  $v$ ,  $n$ ,  $T$ ,  $Q$ , and  $X$  readings.

- b. Using the measured data from the overload and underload runs (corrected for no-loads and any instrument zero drift, but using the carriage speed uncorrected for blockage), maintain a carriage plot of propeller apparent advance coefficient  $J_a$ , thrust deduction coefficient  $1-t$ , and propulsive coefficient  $PC$  versus resistance loading coefficient  $C_{Ti}$  (see Appendix D). The value of  $J_a$  at  $C_{Ti}$  (ship-propulsion point) can be used as a guide to estimate the values of  $n$  required for ship-propulsion point at other model speeds. The  $J_a$ ,  $1-t$ , and  $PC$  curves should be reasonably fair with acceptable scatter before proceeding with the ship-propulsion-point test. A plot of  $T/Q$  versus  $C_{Ti}$  can be used to reconcile erratic readings if either the thrust or torque readings appear to be inconsistent, as evidenced by the  $1-t$  or  $PC$  data, respectively.

5. Conduct ship-propulsion-point tests over the desired range of model speeds ( $F_N$ ).

- a. Follow the procedures outlined for the individual runs under Step 4a using  $J_a$  to estimate rps as indicated under Step 4b. Step 4a should be used to monitor zero drift. About six additional model speeds or values of  $F_N$  should be adequate for a tanker type ship. Runs should not be made below a  $F_N = 0.10$ . At each  $F_N$ ,  $R_i$  should be within 10 percent of  $R_m$ ; otherwise another run should be made preferably to obtain a value of  $R_i$  to bracket the  $R_i$  sought. The experience gained in each run will be helpful in subsequent runs to obtain closer estimates of the rps required for the ship-propulsion point.

- b. Process the measured data from Step 5a in the same manner as in Step 6c. However,  $J_a$ ,  $1-t$ , and  $PC$  should be plotted against Froude number based on carriage speed in lieu of  $C_{Ti}$ . If  $R_i$  is within 10 percent of  $R_m$ , no correction will be required to  $1-t$  and only a relatively minor correction will be required to  $J_a$  and  $PC$ . Repeat runs can be made at the discretion of the test engineer.

6. At completion of both types of propulsion tests, reinstall dummy hub and check no-loads.

#### PMM Tests

Standard procedures have been developed at HSMB for conducting PMM tests with large surface-ship models using the apparatus shown in Figure 4. These procedures generally follow the ITTC recommendations which were the outgrowth of an international cooperative program to develop standard captive-model test techniques (Refs. 13, 14). Included as standard are:

1. The model has freedom in pitch and heave only for all PMM oscillatory modes of motion; and also freedom in roll in the static mode, if considered significant.

2. All reference tests with the fully appended model are made with the propeller operating at the ship-propulsion point.

3. The force and moment data are taken with respect to a body-axis system with the origin at the ship longitudinal center of gravity. The scope of the PMM test program largely depends upon the stage of development of the design in question and the type of information required. Typically, a fairly complete program intended to provide both design data and the means for fully evaluating the deep-water maneuvering characteristics



of a new surface-ship design would include the following:

1. Resistance and propulsion tests with fully appended model to predict EHP, SHP, and RPM versus speed for prototype full-scale ship.

2. Bare-hull PMM tests to provide a basis for rudder design changes.

3. Reference PMM tests conducted only at ship-propulsion point with fully appended model for analysis of inherent directional stability and control characteristics and for preliminary design of auto-pilot.

4. Standard PMM tests (including overload and underload PMM tests) to provide the complete set of hydrodynamic coefficients (mathematical model) required for computer simulation studies to evaluate the full range of maneuvering characteristics of the specific ship.

For the case of existing ships or where the hydrodynamic design of the ship is essentially fixed, only the reference and standard PMM tests (Items 3 and 4) are conducted.

The reference PMM tests are carried out in all cases as a matter of standard practice. These tests are conducted with model propeller  $n$  corresponding to ship-propulsion point which is determined in advance for existing designs from either model test predictions or full-scale data. For new ship designs, at least abbreviated resistance and propulsion tests may be required to establish the desired model  $n$ . The reference PMM tests for new designs are usually carried out in two steps: first to determine inherent (controls fixed) directional stability and then to determine inherent control effectiveness. If the design proves to be inadequate from a stability standpoint, the tests may be curtailed in favor of an alternative rudder or skeg design. The specific procedures for conducting reference PMM tests using the HSMB LAHPMM System (for each of the three basic modes of motion) are given in the following paragraphs. Unless noted otherwise, the rudder is fixed on center by dowel pins and the model  $n$  is set at ship-propulsion point for zero drift angle ( $\beta = 0$ ) and zero rudder angle ( $\delta_r = 0$ ) throughout the tests.

a. Static stability tests - the model is towed at constant velocity so that its center of gravity moves in a straight path with discrete settings of drift angle held constant for each run. The  $\beta$  values are either manually or remotely set before each run (see Figure 1a) in two-degree increments covering a range of  $-4$  to  $-14$  degrees, or higher depending upon ship type. The  $Y_1$ ,  $Y_2$ ,  $X_1$  (PMM) and  $X_2$  (PMM) force components sensed by the block gages during the steady portion of each run are recorded after a 30-second integration period (static mode on recorder); a waiting period of 10 minutes is usually allowed between each run.

b. Pure sideswaying tests - The model while being towed at constant velocity is oscillated laterally so that its centerline always remains parallel to the direction of motion of the towing carriage while its center of gravity moves in a sinusoidal path (see Figure 1b). The desired forced motion is produced by oscillating the swaying carriage at a prescribed frequency and amplitude by means of its servo-control system with the yawing tube and drift angle setting (Figure 4) both locked at zero. The desired range of values can be obtained by varying amplitude, oscillation frequency, or a combination of both. For surface-ship models tested in HSMB, the range of frequencies should be kept below 0.3 cps to avoid tank resonant standing-wave effects, and preferably below 0.15 cps to avoid other unwanted

frequency effects. Each run is made with carriage speed, oscillation frequency, and oscillation amplitude held constant while measurements are taken. The FCS-resolver system previously described is used to directly resolve the periodic  $Y_1$ -,  $Y_2$ -,  $X_1$  (PMM)-, and  $X_2$  (PMM)-forces sensed by the block gages into in-phase and quadrature force components. Integrations are made over a discrete number of cycles; usually for large surface-ship models, integrations are made for a minimum of two complete cycles at a time. A typical run includes a two-cycle integration in "normal" mode which is recorded, followed by a two-cycle integration in "reverse" mode (gage-signal polarity reversed) which is recorded after the run. The normal and reverse readings are averaged to obtain the desired in-phase and quadrature force components (see Appendix C).

c. Pure yawing tests - The model while being towed at constant velocity is oscillated in the lateral direction so that its longitudinal centerline always remains tangent to the path described by its center of gravity (see Figure 1c). The desired forced motion is produced by oscillating both the swaying carriage and yawing tube (Figure 4), by means of their respective servo control systems, at the same frequency, with a phase difference of 90 degrees, and with amplitudes related as follows:

$$\frac{\psi_{\max}}{\omega} = y_{\max} \frac{\omega}{U_0}$$

where

$\psi_{\max}$  is the yawing amplitude,

$y_{\max}$  is the swaying amplitude,

$\omega$  is the oscillation frequency, and

$U_0$  is the carriage speed.

The remaining procedures for conducting the pure yawing tests are essentially the same as those described for the pure sideswaying tests (Item b.).

d. Control effectiveness tests - For these tests, the rudder dowel pins are removed and the rudder settings are made either manually by means of a split-clamp angle-setting device in the model, or by means of a remotely operated rudder actuator system. Otherwise, the procedures are similar to those for the static stability tests (Item a.) except that discrete rudder angle settings are used with  $\beta$  held on zero; the range covered is usually  $-5$  to  $45$  degrees, depending upon ship type.

The standard PMM tests are performed pursuant to formulation of the complete mathematical model required for computer simulation studies. These tests are usually performed concurrently with, and follow procedures similar to, the reference PMM tests. Typically, they cover a range of kinematic variables broad enough to provide all of the linear, nonlinear, and coupling coefficients required to simulate all calm-water maneuvers within the capability of the given ship. Included as a matter of standard practice is a class of tests called "overload and underload PMM tests" where the model propeller  $n$  (or speed) is varied to produce a wide range of ship-propulsion ratio  $\eta$  values, where  $\eta = 1.0$  corresponds to ship-propulsion point. These tests are required for all ship types for which the rudder characteristics are significantly affected by the relative velocity of the propeller slipstream. They are particularly important for large single-screw full-form ships which are apt to be inherently directionally unstable. For example, it is known that such ships can have a

steady-turning radius as small as one shiplength (nondimensional angular velocity  $r' = 1.0$ ), and experience a loss of speed in the steady turn of as much as 75 percent (corresponding to  $\eta = 4.0$ ). Accordingly, for such ship types, the recommended practice is to cover a range in the static mode which includes discrete variations in  $\alpha_r$  between  $-5$  and  $45$  degrees for each of several  $\beta$  values ranging up to  $25$  degrees, for each of several  $\eta$  values between  $1.0$  and  $4.0$ . Finally, to obtain certain coupling coefficients, tests are made with the yawing mode in combination with the static mode (see Figure 1d). For example, to obtain coupling between linear velocity component,  $v'$  and  $r'$ , pure yawing tests are run with each of several discrete  $\beta$  settings over a range of up to about  $15$  degrees, in addition to the  $\beta = 0$  setting used in the reference PMM tests. For certain naval ship types, such as destroyers which tend to have a high degree of inherent directional stability, the range of  $\beta$ ,  $r'$ , and  $\eta$  covered by the standard PMM tests can be made much smaller.

The data measured during each run of the foregoing types of PMM tests are fed into the HSMB Digital Computer System installed on the towing carriage where they are reduced to the form of nondimensional force and moment coefficients as functions of the appropriate kinematic variables. Running plots are prepared from the resulting data which are used by the test engineer to monitor the quality of the test data as well as to determine the need for additional runs. As each phase of the tests is completed, the plots are used in conjunction with the carriage computer to derive the various coefficients ultimately required for the equations of motion or mathematical model (see Appendix E). In this manner, the values for a complete set of hydrodynamic coefficients are usually available immediately after completion of the last PMM test run.

#### DATA REDUCTION AND ANALYSIS METHODS

The data obtained from the various types of tests conducted with the LAHPMM System are reduced and analyzed in accordance with standard methods which, in some cases, have been adapted to suit the specific needs of HSMB. In general, the data from the resistance and propulsion tests are first reduced to nondimensional coefficient form. These coefficients are then used in conjunction with an appropriate extrapolation formula to make powering predictions for the full-scale ship. The final result usually takes the form of curves of effective horsepower EHP, shaft horsepower SHP, and propeller rpm versus ship speed in knots. However, the powering coefficients are also utilized in computer simulation studies as explained later. The details of the methods used to reduce and analyze the resistance and propulsion test data are given in Appendix D.

The data derived from the various types of PMM tests are reduced to nondimensional form in accordance with the notation given in Appendix A. These coefficients are then plotted as functions of the various nondimensional kinematic variables. The resulting plots form the basis for determination of the values for the derivatives and complete set of hydrodynamic coefficients used for dynamic stability analyses and computer simulation studies, respectively. The specific methods used at HSMB to reduce and analyze the PMM test data are given in detail in Appendix E.

#### METHODS USED FOR COMPUTER SIMULATION OF SHIP MANEUVERS

Computer simulation studies are regularly performed at HSMB for which a complete set of hydrodynamic coefficients resulting from the conduct of standard PMM tests is available. The main objectives of these studies are:

1. To predict and evaluate the overall directional stability and maneuverability characteristics of the specific ship preferably in advance of construction.
  2. To provide a fundamental data base leading to the development of rational handling quality criteria for various ship types.
  3. To provide a basis for planning and implementing a program directed toward establishing correlation between computer simulation predictions and full-scale trial measurements of maneuvering characteristics of various ship types.
  4. To exercise the individual mathematical model as well as to provide a means for setting up and checking out the same mathematical model programmed on training simulators or research simulators, such as the MARAD CAORF Simulator, to perform more detailed maneuvering studies involving the human operator in the control loop.
- The simulation studies are carried out with the HYDRONAUTICS META-4 Digital Computer System using an existing program for the Standard Equations of Motion which has been modified to accommodate the case of large, unstable ships undergoing extreme maneuvers. The Standard Equations of Motion as well as the methods used to perform the simulation studies and evaluate the results therefrom are presented in more detail in the following sections.

#### Standard Equations of Motion

The following equations in three degrees of freedom are referred to a right-hand orthogonal system of moving axes, fixed in the body, with its origin normally located at the center of mass CG of the body. The positive directions of the axes, angles, linear velocity components, angular velocity components, forces and moments are indicated by the sketch accompanying the Notation. Unless otherwise indicated in the Notation, the numerical values for the hydrodynamic coefficients used with the equations are for the ship-propulsion point ( $\eta = 1.0$ ). The equations are written in terms of the complete ship configuration. Thus the values of the coefficients embrace the interaction effects between rudder and hull, propeller and hull, and propeller and rudder, as determined from PMM or other captive-model tests for the completely appended ship in various modes of rigid body motion.

#### AXIAL FORCE

$$\begin{aligned}
 m[\dot{u} - vr - x_G r^2] = & \\
 & + \frac{\rho}{2} L^4 [X_{rr} r^2] \\
 & + \frac{\rho}{2} L^3 [X_{\dot{u}} \dot{u} + X_{vr} vr] \\
 & + \frac{\rho}{2} L^2 [X_{vv} v^2] \\
 & + \frac{\rho}{2} L^2 u^2 [a_1 + b_1 \eta + c_1 \eta^2] \\
 & + \frac{\rho}{2} L^2 u^2 [X_{\delta r \delta r} \delta r^2 + X_{\delta r \delta r \eta} \delta r^2 \eta] \\
 & + \frac{\rho}{2} L^2 [X_{vv \eta} v^2] (\eta - 1)
 \end{aligned}$$



## LATERAL FORCE

$$\begin{aligned}
m(\dot{v} + ur + x_G \dot{r}) = & \\
& + \frac{\rho}{2} L^4 [Y_F \dot{r} + Y_{r|r} |r| r|] \\
& + \frac{\rho}{2} L^3 [Y_{\dot{v}} \dot{v}] \\
& + \frac{\rho}{2} L^3 [Y_{r'} ur + Y_{|r| \delta r} |u| r| \delta r + Y_{v|r} |v| r|] \\
& + \frac{\rho}{2} L^2 [Y_{u'} u^2 + Y_{uv} uv + Y_{v|v} |v| v|] \\
& + \frac{\rho}{2} L^2 [Y_{\delta r} u^2 \delta r] \\
& + \frac{\rho}{2} L^3 Y_{r\eta} ur (\eta - 1) \\
& + \frac{\rho}{2} L^2 [Y_{u\eta} u^2 + Y_{v\eta} uv + Y_{v|v| \eta} |v| v| + Y_{\delta r \eta} u^2 \delta r] (\eta - 1)
\end{aligned}$$

## YAWING MOMENT

$$\begin{aligned}
I_z \dot{r} + m x_G (\dot{v} + ur) = & \\
& + \frac{\rho}{2} L^5 [N_F \dot{r} + N_{r|r} |r| r|] \\
& + \frac{\rho}{2} L^4 [N_{\dot{v}} \dot{v}] \\
& + \frac{\rho}{2} L^4 [N_{r'} ur + N_{|r| \delta r} |u| r| \delta r + N_{v|r} |v| r|] \\
& + \frac{\rho}{2} L^3 [N_{u'} u^2 + N_{uv} uv + N_{v|v} |v| v|] \\
& + \frac{\rho}{2} L^3 [N_{\delta r} u^2 \delta r] \\
& + \frac{\rho}{2} L^4 [N_{r\eta} ur] (\eta - 1) \\
& + \frac{\rho}{2} L^3 [N_{u\eta} u^2 + N_{v\eta} uv + N_{v|v| \eta} |v| v| + N_{\delta r \eta} u^2 \delta r] (\eta - 1)
\end{aligned}$$

The foregoing Standard Equations of Motion for Surface Ships are patterned after the quasi steady-state equations of Ref. (18) which have been used extensively for a number of years in the U. S. to perform simulation studies of submarines undergoing complex maneuvers in six degrees of freedom. As for the submarine case, the nondimensional hydrodynamic coefficients which comprise the basic equations, within current state of the art, are considered to be independent of speed (Froude number). This assumption is reasonably valid particularly when applied to commercial ship types which operate in the low or intermediate speed ranges (Refs. 14, 19, 20). For the surface-ship case involving only three degrees of freedom (surge, sway, and yaw), those coupling terms due to pitching, heaving, and rolling motions are deleted. In addition, some modifications are introduced principally in the axial equation to provide an improved representation of the effects of change in propeller loading on the rudder coefficients. Such effects play an important role in simulating the maneuvers of single-screw merchant ships, particularly the large bulk carrier types which are capable of performing relatively tight turns.

It may be noted that the Standard Equations involve the use of the so-called "square-absolute" method wherein the nonlinear coefficients are represented by least square fits to polynomials carried out only up to the second order. This is in contrast to the "third order Taylor expansion" method commonly used in surface-ship simulation studies (Refs. 6, 14, 21). The square-absolute method now seems preferred by most investigators, even by those who formerly used

the third order Taylor expansion method exclusively (Refs. 19, 20, 21). This is due largely to its convenience for use in computer simulation studies employing analog computers as well as its apparent better foundation in theory. The latter is based on the premise that many of the nonlinearities in the force and moment coefficients are related to cross-flow drag which tends to be a second order function. A case in point is that of the large bulk carriers which often achieve steady-turning diameters of less than 2.0 shiplengths with associated very large drift angles. The coefficients associated with this mode of motion are highly cross-flow drag related. In this respect, cross-flow drag theory, in conjunction with empirical data, has been used successfully to estimate some of the nonlinear coefficients associated with such extreme maneuvers.

With appropriate values for the hydrodynamic coefficients, the Standard Equations as shown are sufficiently comprehensive to enable prediction of trajectories of a ship undergoing a complete range of ahead maneuvers in calm deep water including large amplitude zigzags, tight turns, and other maneuvers involving substantial speed changes. Similarly, by means of other sets of values for the hydrodynamic coefficients, they can also be used to make such predictions for astern maneuvers in deep water as well as ahead or astern maneuvers in shallow-water of constant depth.

For multiple-screw ships, the values of  $\eta$  in the Standard Equations are normally based on the averages of all the propellers operating in unison. For special maneuvers such as low-speed, mooring, and docking maneuvers, it may be desirable to represent separate or differential action of the propellers. This can be readily accomplished by replacing the propeller force term

$$\frac{\rho}{2} L^2 u^2 [a_1 + b_1 \eta + c_1 \eta^2]$$

in the axial equation, for example for the twin-screw case, by

$$\frac{\rho}{2} L^2 u^2 [(a_1 + b_1 \eta + c_1 \eta^2)_p + (a_1 + b_1 \eta + c_1 \eta^2)_s]$$

where the subscripts p and s means the values in the parentheses correspond to the action of the port and starboard propellers, respectively; and by adding appropriate propeller force terms to the yawing-moment and lateral-force equations.

Mathematical Models

The basic mathematical model in each case is defined herein as the Standard Equations of Motion whose various terms are numerically evaluated to represent a specific ship. A complete set of input data for this purpose consists of the numerical values of all of the hydrodynamic coefficients which are predominantly experimentally determined and, in addition, the values of the inertial and pertinent geometrical characteristics which are usually specified. Unless otherwise noted, the basic mathematical models discussed herein are derived from the standard PMM tests and pertain to the case of the designated ship operating in calm water of unrestricted depth and width. A typical set of hydrodynamic coefficients obtained for the MARINER and used to formulate a basic mathematical model for computer simulation studies is presented in Table 2.

For convenience to the users and other interested persons, the procedures used to arrive at the numerical values for the complete set of hydrodynamic



TABLE 2  
 NONDIMENSIONAL HYDRODYNAMIC COEFFICIENTS FOR MARINER  
 (USS COMPASS ISLAND) USED FOR COMPUTER SIMULATION STUDIES

X-Equation		Y-Equation		N-Equation	
Nondimensional Coefficient	Value	Nondimensional Coefficient	Value	Nondimensional Coefficient	Value
$X_u'$	$-36.3 \times 10^{-5}$	$Y_{\star}'$	$3.6 \times 10^{-5}$	$N_{\star}'$	$-1.8 \times 10^{-5}$
$X_{vr}'$	480.0	$Y_v'$	-749.0	$N_v'$	-4.8
$X_{vv}'$	-355.6	$Y_v'$	-1142.6	$N_v'$	-394.1
$X_{\delta r \delta r}'$ ( $\eta=0$ )	-8.0	$Y_{v v} '$	-2380.4	$N_{v v} '$	438.0
$X_{rr}'$	12.5	$Y_r'$	269.6	$N_r'$	-188.7
$X_{vv\eta}'$	0.0	$Y_{r r} '$	207.6	$N_{r r} '$	-47.5
$X_{\delta r \delta r \eta \eta}'$	-10.4	$Y_{v r} '$	-720.0	$N_{v r} '$	-647.0
$a_1$	-34.46	$Y_{r \delta r}'$	0.0	$N_{r \delta r}'$	0.0
$b_1$	-110.02	$Y_{\dot{r}}'$	-12.5	$N_{\dot{r}}'$	-48.2
$c_1$	141.17	$Y_{\delta r}'$	263.6	$N_{\delta r}'$	-128.4
$a_2$	-82.00	$Y_{\delta r \eta}'$	340.0	$N_{\delta r \eta}'$	-162.0
$b_2$	-23.30	$Y_{r \eta}'$	107.0	$N_{r \eta}'$	-51.4
$c_2$	105.30	$Y_{v \eta}'$	-123.6	$N_{v \eta}'$	60.2
$a_3$	-85.40	$Y_{\star \eta}'$	3.6	$N_{\star \eta}'$	-1.8
$b_3$	32.00				
$c_3$	-107.90	$m'$	797.67	$I_z'$	42.8
$a_4$	-84.32				
$b_4$	39.39				
$c_4$	-98.60				

coefficients for the Standard Equations of Motion, such as that given in Table 2 are presented in Appendix E. Because of the nature of the functional relationships involved, the procedures applied to the coefficients for the lateral force and yawing moment equations are discussed separately from those applied to the coefficients for the axial force equations.

In addition to the basic mathematical models, the computer program must also include certain supplementary mathematical models or subroutines in order to perform a complete maneuvering simulation. Typical subroutines used in investigations concerned with simulation of maneuvers of the given ship in calm water of unrestricted depth and width are as follows:

1. Time history of rudder movement in degrees including the scenarios required for the various definitive maneuvers.

2. Time history of change in propeller RPM from full ahead to full astern including appropriate time allowances for lags due to communication, human reaction, and prime-mover response.

3. Autopilot equations for coursekeeping control.

It is anticipated that the basic mathematical models for the deep-water case will be used in conjunction with other PMM test data recently acquired to perform simulation studies of maneuvers in shallow water of varying depth as well as under various environmental conditions. For such studies the following typical subroutines can be added as appropriate data become available:

1. Supplementary mathematical models representing the variation of the static, rotary, and acceleration coefficients with water depth.

2. Forcing functions due to the action of wind and waves.

3. Forcing functions due to asymmetrical forces and moments imposed on the ship due to proximity to a bank in a canal or channel.

#### Evaluations Based on Definitive Maneuvers

The so-called definitive maneuver approach (Refs. 22, 7) is the primary method used in computer simulation studies at HSMB to evaluate the maneuvering characteristics of each specific ship design for which adequate PMM test data are available. This approach was chosen because it provides the most direct means for satisfying all four of the objectives previously stated. For completeness as well as for convenient reference, a detailed account of the logic and procedural steps associated with the use of definitive maneuvers is presented in Appendix F.

#### HYDRODYNAMIC COEFFICIENTS FOR MARINER CLASS VESSEL (ITTC STANDARD PROGRAM)

Pursuant to the ITTC Cooperative Captive-Model-Test Program (Phases 1 and 2), LAHPMM tests were conducted using a 21,841-foot model of the MARINER. The model was borrowed from NSRDC and reconditioned by HYDRONAUTICS. The reconditioned model conformed to the specifications for the ITTC program and therefore differed from the USS COMPASS ISLAND only in that the model bilge keels were longer and the model did not have a sonar dome (see Ref. 23). The model particulars are given in Reference 24.

The hydrodynamic coefficients presented in Table 2 were determined from LAHPMM tests conducted at speed conditions corresponding to 10.5 and 15 knots full-scale. These coefficients in combination with the Standard Equations of Motion were

used for the computer simulation studies discussed in the next section.

Additional LAHPMM tests were conducted with the MARINER model at a speed condition corresponding to 20 knots full-scale for comparison with the published results of Rotating Arm tests from NSRDC and AEW as well as the large-amplitude PMM tests at SL (see Ref. 9). Selected force and moment coefficients derived from HSMB LAHPMM tests are compared in Figure 14 with corresponding data from NSRDC, AEW and SL. For the case of  $Y'$  versus  $r'$ , the HSMB data agree quite well with AEW data. However, the agreement with the SL results when corrected to the CG is fair. For the case of  $N'$  versus  $r'$ , the HSMB data are in excellent agreement with the results from the other laboratories. The values of the hydrodynamic coefficients presented in Table 2 are not directly comparable to those in Reference 9 because of the difference in fitting techniques used, as discussed in the section on Standard Equations of Motion.

#### COMPARISON OF HSMB COMPUTER SIMULATION PREDICTIONS WITH MARINER (COMPASS ISLAND) FULL-SCALE TRIAL RESULTS

A main strength of the computer simulation technique described herein lies in its ability to predict, with reasonable accuracy, the detailed behavior of a specified surface ship undergoing a wide range of maneuvers from moderate to extreme. Furthermore, to derive the maximum benefit, the technique must be able to perform this function well in advance of construction, or at least without involvement of the ship where it already exists. It is apparent, therefore, that an active and vigilant correlation program in the field of ship maneuverability is required to verify the accuracy and continuously upgrade the confidence level associated with the predictions made by various alternative techniques.

The U. S. Navy under the direction of NSRDC has maintained a continuous program of correlation studies primarily in the area of submarines and various naval surface-ship types. The major segment of the submarine program has been devoted to establishing correlation between computer simulation predictions based on PMM tests with large models and data derived from trajectory measurements taken during carefully conducted full-scale trials. Based on the results of such studies on 19 different submarines, it has been concluded that very good correlation can be expected, by the use of this technique, for a wide variety of maneuvers confined either to the vertical or horizontal plane of motion. For the case of naval surface ships, however, essentially all of the correlation studies have been made on basis of data predicted from large free-running model tests. Good correlation has been shown on this basis for the case of 35-degree-rudder steady-turning maneuvers conducted on a fairly large number of different naval ship types. However, predictions of the height and width of loop from spiral maneuvers of unstable ships have not been quite as good (Ref. 22). It should be emphasized that, in contrast to modern bulk carrier ship types, the differences in propeller loading coefficient between the large free-running model and full-scale ship are not very great for the case of most naval surface ships investigated.

Based on the success shown for the case of submarines, it is reasonable to assume that good correlation could also be obtained for merchant ships by means of computer simulation predictions based on properly conducted PMM tests with large models. At least two recent papers (Refs. 9, 20) dealing with

surface ships have contributed to the mounting evidence in support of this contention. Reference 20 presents brief comparisons between computer simulation predictions, based on data from PMM tests performed at SL, Denmark with a large model of a 190,000 DWT tanker, and full-scale trial measurements. Within the limitations of the trial data and the scope of the PMM tests, these comparisons show reasonably good agreement between the simulated and measured values for the cases of a 35-degree-rudder steady-turning maneuver and a 20-20 zigzag. Reference 9 presents a much more extensive correlation study involving a MARINER Class Ship which was performed pursuant to the ITTC Cooperative Captive-Model-Test Program (Phase 2) (Ref. 14). The computer simulation predictions in this case were based on a complete set of tests conducted with a large model on the new large amplitude PMM at SL. Moreover, the full-scale trials (sponsored by the U. S. Navy) were conducted primarily for research purposes and therefore are perhaps the most highly instrumented and carefully controlled maneuvering trials ever conducted on a surface ship (see Ref. 23). This study showed very good agreement between the simulated and measured values resulting from a wide variety of maneuvers including spirals, zigzags and turns, which lends strong credence to the validity of the PMM technique. Computer simulation predictions for the MARINER, using the coefficients for the mathematical model determined by means of the HSMB LAHPMM (Table 2) and the standard equations of motion are compared with full-scale trial results in Figures 15 to 18. The results are presented in the same format as used in Reference 9 to afford easy comparison. As can be seen from Figures 15 to 18, very good agreement is obtained between simulated and measured full-scale values.

#### CONCLUDING REMARKS

Standard techniques and procedures have been developed at HSMB for studying the directional stability and control of displacement type surface ships. These advanced techniques provide a powerful tool in the U. S. for solving a wide variety of problems related to the field of ship maneuverability, including many areas hitherto neglected in the case of surface ships. These techniques should be especially helpful when used to make decisions in the early design stage and to fully evaluate the maneuvering characteristics of specific ships. They should also serve to greatly facilitate studies of international importance related to safety of ships maneuvering in traffic lanes, harbors, and other restricted areas, which are most efficiently treated by simulators requiring the use of mathematical models. Based on information available so far, the combined PMM test and computer-simulation technique described herein can be relied upon to provide reasonably accurate predictions of the various maneuvering capabilities of interest to any given ship type. However, as with most relatively new predictive techniques, an active correlation program should be pursued which involves comparisons with data obtained from properly conducted maneuvering trials on various representative types of ships. Such a program should lead to progressive improvement in the techniques and thus assure that the predictions made are of the highest caliber and can be used by all concerned with fullest confidence. Of particular interest are correlation tests on the new breeds of bulk carrier ship types which tend to be inherently directionally unstable

and, therefore, may need to be investigated more thoroughly in the future. Properly conducted and well instrumented maneuvering trials have been performed in the U. S. on a variety of naval surface-ship types, but unfortunately nearly all of these have not been subjected to the corresponding standard PMM tests. A feasible means to accelerate the overall correlation program, therefore, would be to conduct such PMM tests and associated computer simulation studies on those naval ships for which the standard large models are still in existence.

#### REFERENCES

- 1) "Proceedings of the First Symposium on Ship Maneuverability," David Taylor Model Basin Report 1461, October, 1960.
- 2) Gertler, Morton, "Some Recent Advances in Dynamic Stability and Control of Submerged Vehicles," Proceedings of an International Symposium on Directional Stability and Control of Bodies Moving in Water," The Journal of Mechanical Engineering Science, Vol. 14, No. 7, Supplementary Issue, 1972.
- 3) "Planar-Motion-Mechanism System," U. S. Patent No. 3,052,120 Issued to U. S. Navy, September 4, 1962, (Alex Goodman and Morton Gertler, co-inventors).
- 4) Gertler, Morton, "The DTMB Planar-Motion-Mechanism System," Proceedings of Symposium on Towing Tank Facilities, Instrumentation and Measuring Techniques, Zagreb, Yugoslavia, September, 1959.
- 5) Goodman, Alex, "Experimental Techniques and Methods of Analysis Used in Submerged Body Research," Proceedings of the ONR Third Symposium on Naval Hydrodynamics, 1960.
- 6) Strom-Tejsen, J. and Chislett, M. S., "A Model Testing Technique and Method of Analysis for the Prediction of Steering and Maneuvering Qualities of Surface Vessels," HyA Report Hy-7, September, 1966.
- 7) Goodman, Alex and Gertler, Morton, "Analytical and Experimental Techniques used at HSMB for Surface Ship Directional Stability and Control Studies," Presented before the Chesapeake Chapter of SNAME, 24 April 1975, HYDRONAUTICS, Incorporated Technical Report 7500-1, April, 1975.
- 8) Chislett, M. S. and Smith, L. Wagner, "A Brief Description of the HyA Large Amplitude PMM System," Proceedings of an International Symposium on Directional Stability and Control of Bodies Moving in Water," The Journal of Mechanical Engineering Science, Vol. 14, No. 7, Supplementary Issue, 1972.
- 9) Smith, L. W. and Chislett, M. S., "Large Amplitude PMM Tests and Maneuvering Predictions for a MARINER Class Vessel," Proceedings of Tenth ONR Hydrodynamic Symposium, June, 1974.
- 10) Chislett, M. S. and Strom-Tejsen, "Planar Motion Mechanism Tests and Full-Scale Steering and Maneuvering Predictions for a MARINER Class Vessel," HyA Report Hy-6, April, 1965.
- 11) Gertler, Morton, Kohl, Robert E., and Kirkman, Karl L., "Experimental Investigation of a Systematic Series of Low Length-Beam Ratio, High Block Coefficient Merchant Ship Forms," HYDRONAUTICS, Incorporated Technical Report 7166-1, June, 1973.
- 12) Gertler, Morton and Kohl, Robert E., "Resistance, Propulsion, and Maneuverability Characteristics of MARAD Systematic Series for Large Full-Form Merchant Ships," November, 1974.
- 13) Gertler, M., "The ITTC Standard Captive-Model-Test Program - A Review and Analysis of Data



- Received Prior to May 1966," Appendix II of Maneuverability Report, Proceedings of 11th ITTC, 1966.
- 14) Gertler, Morton, "Final Analysis of First Phase of ITTC Standard Captive-Model-Test Program," Appendix 3, Part 2 of Maneuverability Committee Report, Proceedings of the 12th ITTC, 1969.
- 15) Goodman, Alex, "Description and Operation of Planar-Motion-Mechanism for AEW," HYDRONAUTICS, Incorporated Technical Manual 754-1, April, 1968.
- 16) Altmann, Ronald J., and Goodman, Alex, "Description and Operation of Propeller Dynamometer System for the High Speed Channel of the Bassin D'Essais Des Carenes," HYDRONAUTICS, Incorporated Technical Manual 7026-2, January, 1971.
- 17) "Report of the Propulsion Committee," Proceedings of the Ninth ITTC, Paris, September, 1960.
- 18) Gertler, Morton and Hagen, Grant R., "Standard Equations of Motion for Submarine Simulation," NSRDC Report 2510, June, 1967.
- 19) Norrbin, Nils H., "Theory and Observation on the Use of a Mathematical Model for Ship Maneuvering in Deep and Confined Waters," Swedish State Shipbuilding Experimental Tank Publication No. 68, 1971.
- 20) van Berlekom, Willem B. and Goddard, Thomas A., "Maneuvering of Large Tankers," Transactions SNAME, Vol. 80, 1972.
- 21) Gertler, Morton, "Cooperative Test Program-Review and Status of Second Phase of Standard Captive-Model Test Program," Appendix VI of Maneuverability Committee Report, Proceedings of 13th ITTC, 1972.
- 22) Gertler, Morton and Gover, S. C., "Handling Quality Criteria for Surface Ships," Presented before the Chesapeake Chapter of SNAME, May, 1959, DTMB Report 1514, April, 1961.
- 23) Morse, R. V. and Price, D., "Maneuvering Characteristics of the MARINER Type Ship (USS COMPASS ISLAND) in Calm Seas," Sperry Gyroscope Publication G7-2233-1019, Prepared for David Taylor Model Basin under Contract NONr 3061(00), 1961.
- 24) Gertler, Morton, "Cooperative Rotating-Arm and Straightline Experiments with ITTC Standard Model (MARINER Type Ship), DTMB Report 2221, June, 1966.
- 25) Gertler, M., "The Prediction of the Effective Horsepower of Ships by Methods in Use at the David Taylor Model Basin," DTMB Report 576, Second Edition, December, 1947.
- 26) Hadler, J. B., "Coefficients for International Towing Tank Conference 1957 Model-Ship Correlation Line," DTMB Report 1185, April, 1958.
- 27) Scott, J. R., "On Blockage Correction and Extrapolation to Smooth Ship Resistance," Transactions of SNAME, 1970.
- 28) Gross, A. and Watanabe, K., "On Blockage Correction," Appendix 3, Performance Committee Report, Proceedings of the 13th ITTC, 1972.
- 29) Hughes, G., "Tank Boundary Effects on Model Resistance," Transactions of RINA, Vol. 103, 1961.
- 30) Smitt, L. Wagner, "On Spiral Test Techniques," Report of Maneuverability Committee, Appendix I, Proceedings of the 13th ITTC, 1972.

## HULL GEOMETRY

Symbol	Definition
A	Area of midship section to design full-load waterline
B	Maximum beam at design full-load waterline
L	Characteristic length; length between perpendiculars in this report
$L_E$	Length of entrance measured from forward perpendicular FP
$L_M$	Length of parallel midbody
$L_R$	Length of run measured from after perpendicular AP
LCB	Longitudinal center of buoyancy position
S	Wetted surface area
T	Draft at design full-load condition
V	Volume of displacement at design full-load condition
B/T	Beam-draft ratio
$C_B$	Block coefficient; $V/LBT$
$C_{BE}$	Block coefficient of entrance; $V_E/L_E BT$
$C_{BR}$	Block coefficient of run; $V_R/L_R BT$
$C_M$	Midship section coefficient; $A/BT$
LCB/L	Nondimensional LCB position expressed as percentage of L forward of midships
$L_E/L$	Nondimensional entrance length
$L_M/L$	Nondimensional parallel midbody length
$L_R/L$	Nondimensional run length
$L_R/B$	Length-beam ratio of run
$S/\sqrt[3]{V}$	Wetted-surface coefficient
$C_S$	Wetted-surface coefficient; $S/(\sqrt[3]{VL})^{1/2}$
$C_V$	Volumetric coefficient; $V/L^3$

## RUDDER GEOMETRY

Symbol	Definition
$A_T$	Total planform area
$A_F$	Fixed area
$A_M$	Movable area
$\bar{b}$	Mean span
$c_r$	Root chord
$c_t$	Tip chord
a	Aspect ratio (geometric); $\bar{b}^2/A_T$
$\lambda$	Taper ratio

## PROPELLER GEOMETRY

c	Blade chord at 0.7 radius
D	Diameter
P	Pitch at 0.7 radius
D/T	Diameter-draft ratio
P/D	Pitch-diameter ratio

## RESISTANCE AND PROPULSION

Symbol	Definition
EHP	Effective horsepower
n	Propeller revolutions per unit time
Q	Propeller Torque
$R_A$	Added resistance
$R_F$	Frictional resistance
$R_I$	Ideal resistance; model resistance for ship propulsion point
$R_R$	Residual resistance
$R_T$	Total resistance
T	Propeller thrust
SHP	Shaft horsepower
v	Speed
$v_a$	Propeller speed of advance
$\rho$	Mass density
$\nu$	Kinematic viscosity
$C_A$	Model-ship correlation allowance coefficient; $R_A/\frac{1}{2}\rho Sv^2$
$C_F$	Frictional-resistance coefficient; $R_F/\frac{1}{2}\rho Sv^2$ ; $C_{Fm}$ in model range, $C_{Fs}$ in ship range
$C_R$	Residual-resistance coefficient; $R_R/\frac{1}{2}\rho Sv^2$
$C_T$	Total-resistance coefficient; $R_T/\frac{1}{2}\rho Sv^2$
$C_{T1}'$	Loading coefficient; $C_{T1}' = C_{T1}$ at ship propulsion point
$e_p$	Propeller efficiency
$e_h$	Hull efficiency; $1-t/1-w$
$e_{rr}$	Relative rotative efficiency
$F_N$	Froude number; $v/\sqrt{gL}$
J	Propeller advance coefficient; $v_a/nD$
$J_a$	Apparent advance coefficient
$J_{tQ}$	True advance coefficient-torque identity
$J_{tT}$	True advance coefficient-thrust identity
$K_Q$	Propeller torque coefficient; $Q/\rho n^2 D^5$
$K_T$	Propeller thrust coefficient; $T/\rho n^2 D^4$
PC	Propulsive coefficient; $EHP/SHP = R_I v/2\pi Qn$
$R_N$	Reynolds number; $vL/\nu$
t	Thrust deduction fraction; $1 - \frac{R_1}{T}$
w	Taylor wake fraction; $1 - \frac{v_a}{v}$
$w_Q$	Taylor wake fraction-torque identity; $1 - \frac{J_{tQ}}{J_a}$
$w_T$	Taylor wake fraction-thrust identity; $1 - \frac{J_{tT}}{J_a}$



The following nomenclature conforms to DTMB Report 1319 and NSRDC Report 2510 where applicable. The positive direction of axes, angles, forces, moments, and velocities are shown by the accompanying sketch. (see page 78)

Symbol	Nondimensional Form	Definition
$a_1$		Constant in quadratic fit to axial force equation $X'_{\beta=\delta_r=0} = f(\eta)$ for each of 1 <sup>th</sup> segments where $i = 1, 2, 3, 4$ ; $a_1 = X'_{uu}$ at $\eta = 0$ in appropriate segment
$b_1$		First order coefficient in quadratic fit to axial propeller force equation $X'_{\beta=\delta_r=0} = f(\eta)$ for each of 1 <sup>th</sup> segments where $i = 1, 2, 3, 4$
$c_1$		Second order coefficient in quadratic fit to axial propeller force equation $X'_{\beta=\delta_r=0} = f(\eta)$ for each of 1 <sup>th</sup> segments where $i = 1, 2, 3, 4$
AD	$AD' = \frac{AD}{L}$	Advance
CB		Center of buoyancy
CG		Center of mass of ship
D		Propeller diameter
$D_s$	$D_s' = \frac{D_s}{L}$	Steady-turning diameter
$I_x'$	$I_x' = \frac{I_x}{\frac{1}{2}\rho L^5}$	Moment of inertia of ship about x axis
$I_y'$	$I_y' = \frac{I_y}{\frac{1}{2}\rho L^5}$	Moment of inertia of ship about y axis
$I_z'$	$I_z' = \frac{I_z}{\frac{1}{2}\rho L^5}$	Moment of inertia of ship about z axis
J	$J = \frac{u}{nD}$	Propeller advance coefficient based on ship speed u
$J_c$	$J_c' = \frac{u_c}{n_c D}$	Propeller advance coefficient at steady ship command speed $u_c$
$k_x$	$k_x' = \frac{k_x}{L}$	Radius of gyration of ship about x axis
$k_y$	$k_y' = \frac{k_y}{L}$	Radius of gyration of ship about y axis
$k_z$	$k_z' = \frac{k_z}{L}$	Radius of gyration of ship about z axis
L	$L' = 1$	Characteristic length; length between perpendiculars for commercial ships

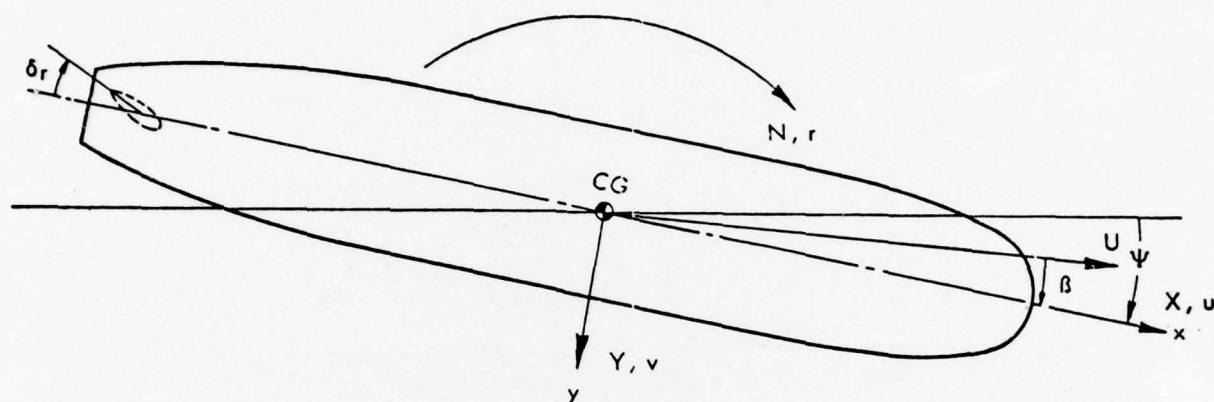
$l_d$	$l_d' = \frac{l_d}{L} = \frac{l_r - l_v}{L}$	Dynamic stability lever
$l_r$	$l_r' = \frac{l_r}{L} = \frac{N_r'}{Y_r' - m'}$	Damping lever
$l_v$	$l_v' = \frac{l_v}{L} = \frac{N_v'}{Y_v'}$	Static stability lever
$m$	$m' = \frac{m}{\frac{1}{2}\rho L^3}$	Mass of ship
$N$	$N' = \frac{N}{\frac{1}{2}\rho L^3 U^2}$	Hydrodynamic moment component about z axis (yawing moment)
$N_*$	$N_*' = \frac{N_*}{\frac{1}{2}\rho L^3 U^2}$	Yawing moment when $\beta = \delta r = 0$
$N_r$	$N_r' = \frac{N_r}{\frac{1}{2}\rho L^4 U}$	First order coefficient used in representing $N$ as a function of $r$
$N_{r\eta}$	$N_{r\eta}' = \frac{N_{r\eta}}{\frac{1}{2}\rho L^4 U}$	First order coefficient used in representing $N_r$ as a function of $(\eta-1)$
$N_{\dot{r}}$	$N_{\dot{r}}' = \frac{N_{\dot{r}}}{\frac{1}{2}\rho L^5}$	Coefficient used in representing $N$ as a function of $\dot{r}$
$N_{r r}$	$N_{r r}' = \frac{N_{r r}}{\frac{1}{2}\rho L^5}$	Second order coefficient used in representing $N$ as a function of $r$
$N_{ r \delta r}$	$N_{ r \delta r}' = \frac{N_{ r \delta r}}{\frac{1}{2}\rho L^4 U}$	Coefficient used in representing $N_{\delta r}$ as a function of $r$
$N_v$	$N_v' = \frac{N_v}{\frac{1}{2}\rho L^3 U}$	First order coefficient used in representing $N$ as a function of $v$
$N_{v\eta}$	$N_{v\eta}' = \frac{N_{v\eta}}{\frac{1}{2}\rho L^3 U}$	First order coefficient used in representing $N_v$ as a function of $(\eta-1)$
$N_{\dot{v}}$	$N_{\dot{v}}' = \frac{N_{\dot{v}}}{\frac{1}{2}\rho L^4}$	Coefficient used in representing $N$ as a function of $\dot{v}$
$N_{ v r}$	$N_{ v r}' = \frac{N_{ v r}}{\frac{1}{2}\rho L^4}$	Coefficient used in representing $N_r$ as a function of $v$
$N_{v v }$	$N_{v v }' = \frac{N_{v v }}{\frac{1}{2}\rho L^3}$	Second order coefficient used in representing $N$ as a function of $v$
$N_{v v \eta}$	$N_{v v \eta}' = \frac{N_{v v \eta}}{\frac{1}{2}\rho L^3}$	First order coefficient used in representing $N_{v v }$ as a function of $(\eta-1)$
$N_{\delta r}$	$N_{\delta r}' = \frac{N_{\delta r}}{\frac{1}{2}\rho L^3 U^2}$	First order coefficient used in representing $N$ as a function of $\delta r$
$N_{\delta r\eta}$	$N_{\delta r\eta}' = \frac{N_{\delta r\eta}}{\frac{1}{2}\rho L^3 U^2}$	First order coefficient used in representing $N_{\delta r}$ as a function of $(\eta-1)$
$n$		Propeller revolution rate
$n_c$		Propeller revolution rate at steady command speed
$n_o$		Ordered propeller revolution rate

$O_y$	$O_y' = \frac{O_y}{L}$	Overshoot width of path
$O_\psi$		Overshoot heading angle; measured from value at second execute
$R$	$R' = \frac{R}{L}$	Steady-turning radius
$r$	$r' = \frac{rL}{U}$	Angular velocity component about z axis relative to fluid (yaw)
$\dot{r}$	$\dot{r}' = \frac{\dot{r}L^2}{U^2}$	Angular acceleration component about z axis relative to fluid
$TD$	$TD' = \frac{TD}{L}$	Tactical diameter
$TR$	$TR' = \frac{TR}{L}$	Transfer
$t$	$t' = \frac{tU}{L}$	Time
$t_1$	$t_1' = \frac{t_1 U}{L}$	Time at 1 <sup>th</sup> execute in an overshoot or zigzag maneuver
$t_o$	$t_o' = \frac{t_o U}{L}$	Time at initiation of a maneuver
$t_{90}$	$t_{90}' = \frac{t_{90} U}{L}$	Time to reach 90-degree change of heading in a turn
$t_{180}$	$t_{180}' = \frac{t_{180} U}{L}$	Time to reach 180-degree change of heading in a turn
$U$	$U' = \frac{U}{U}$	Linear velocity of origin of body axes relative to fluid
$u$	$u' = \frac{u}{U}$	Component of $U$ in direction of the x axis
$\dot{u}$	$\dot{u}' = \frac{\dot{u}L}{U^2}$	Time rate of change of $u$ in direction of the x axis
$u_c$	$u_c' = \frac{u_c}{U}$	Command speed: steady value of ahead speed component $u$ for a given propeller rpm for $\beta = 5r = 0$ ; sign changes with propeller reversal
$V$		Absolute speed in knots
$V_o$		Steady approach speed in knots
$V_{90}$		Speed in knots at 90-degree heading change in a turn
$V_{180}$		Speed in knots at 180-degree heading change in a turn
$v$	$v' = \frac{v}{U}$	Component of $U$ in direction of the y axis
$\dot{v}$	$\dot{v}' = \frac{\dot{v}L}{U^2}$	Time rate of change of $v$ in direction of the y axis
$x$	$x' = \frac{x}{L}$	Longitudinal body axis; also the coordinate of a point relative to the origin of body axes
$x_B$	$x_B' = \frac{x_B}{L}$	The x coordinate of CB
$x_G$	$x_G' = \frac{x_G}{L}$	The x coordinate of CG



$x_o$	$x_o' = \frac{x_o}{L}$	A coordinate of the displacement of CG relative to the origin of a set of fixed axes
$X$	$X' = \frac{X}{\frac{1}{2}\rho L^2 U^2}$	Hydrodynamic force component along x axis (longitudinal, or axial force)
$X_{rr}$	$X_{rr}' = \frac{X_{rr}}{\frac{1}{2}\rho L^4}$	Second order coefficient used in representing $X$ as a function of $r$ . First order coefficient is zero
$X_{\dot{u}}$	$X_{\dot{u}}' = \frac{X_{\dot{u}}}{\frac{1}{2}\rho L^3}$	Coefficient used in representing $X$ as a function of $\dot{u}$
$X_{uu}$	$X_{uu}' = \frac{X_{uu}}{\frac{1}{2}\rho L^2}$	Second order coefficient used in representing $X$ as a function of $u$ in the non-propelled case. First order coefficient is zero
$X_{vr}$	$X_{vr}' = \frac{X_{vr}}{\frac{1}{2}\rho L^3}$	Coefficient used in representing $X$ as a function of the product $vr$
$X_{vv}$	$X_{vv}' = \frac{X_{vv}}{\frac{1}{2}\rho L^2}$	Second order coefficient used in representing $X$ as a function of $v$ . First order coefficient is zero
$X_{vv\eta}$	$X_{vv\eta}' = \frac{X_{vv\eta}}{\frac{1}{2}\rho L^2}$	First order coefficient used in representing $X_{vv}$ as a function of $(\eta-1)$
$X_{\delta r \delta r}$	$X_{\delta r \delta r}' = \frac{X_{\delta r \delta r}}{\frac{1}{2}\rho L^2 U^2}$	Second order coefficient used in representing $X$ as a function of $\delta r$ at $\eta = 0$ . First order coefficient is zero
$X_{\delta r \delta r \eta \eta}$	$X_{\delta r \delta r \eta \eta}' = \frac{X_{\delta r \delta r \eta \eta}}{\frac{1}{2}\rho L^2 U^2}$	Second order coefficient used in representing $X_{\delta r \delta r}$ as a function of $\eta$
$y$	$y' = \frac{y}{L}$	Lateral body axis; also the co-ordinate of a point relative to the origin of body axes
$y_B$	$y_B' = \frac{y_B}{L}$	The y coordinate of CB
$y_G$	$y_G' = \frac{y_G}{L}$	The y coordinate of CG
$y_o$	$y_o' = \frac{y_o}{L}$	A coordinate of the displacement of CG relative to the origin of a set of fixed axes
$Y$	$Y' = \frac{Y}{\frac{1}{2}\rho L^2 U^2}$	Hydrodynamic force component along y axis (lateral force)
$Y_*$	$Y_*' = \frac{Y}{\frac{1}{2}\rho L^2 U^2}$	Lateral force when $\beta = \delta r = 0$
$Y_r$	$Y_r' = \frac{Y_r}{\frac{1}{2}\rho L^3 U}$	First order coefficient used in representing $Y$ as a function of $r$
$Y_{r\eta}$	$Y_{r\eta}' = \frac{Y_{r\eta}}{\frac{1}{2}\rho L^3 U}$	First order coefficient used in representing $Y_r$ as a function of $(\eta-1)$
$Y_{\dot{r}}$	$Y_{\dot{r}}' = \frac{Y_{\dot{r}}}{\frac{1}{2}\rho L^4}$	Coefficient used in representing $Y$ as a function of $\dot{r}$
$Y_{r r}$	$Y_{r r}' = \frac{Y_{r r}}{\frac{1}{2}\rho L^4}$	Second order coefficient in representing $Y$ as a function of $r$

$Y _r \delta r$	$Y _r \delta r' = \frac{Y _r \delta r}{\frac{1}{2}\rho L^3 U}$	Coefficient used in representing $Y_{\delta r}$ as a function of $r$
$Y_v$	$Y_v' = \frac{Y_v}{\frac{1}{2}\rho L^2 U}$	First order coefficient used in representing $Y$ as a function of $v$
$Y_{v\eta}$	$Y_{v\eta}' = \frac{Y_{v\eta}}{\frac{1}{2}\rho L^2 U}$	First order coefficient used in representing $Y_v$ as a function of $(\eta-1)$
$Y_{\dot{v}}$	$Y_{\dot{v}}' = \frac{Y_{\dot{v}}}{\frac{1}{2}\rho L^3}$	Coefficient used in representing $Y$ as a function of $\dot{v}$
$Y_v r $	$Y_v r ' = \frac{Y_v r }{\frac{1}{2}\rho L^3}$	Coefficient used in representing $Y_v$ as a function of $r$
$Y_v v $	$Y_v v ' = \frac{Y_v v }{\frac{1}{2}\rho L^2}$	Second order coefficient used in representing $Y$ as a function of $v$
$Y_v v \eta$	$Y_v v \eta' = \frac{Y_v v \eta}{\frac{1}{2}\rho L^2}$	First order coefficient used in representing $Y_v v $ as a function of $(\eta-1)$
$Y_{\delta r}$	$Y_{\delta r}' = \frac{Y_{\delta r}}{\frac{1}{2}\rho L^2 \eta^2}$	First order coefficient used in representing $Y$ as a function of $\delta r$
$Y_{\delta r\eta}$	$Y_{\delta r\eta}' = \frac{Y_{\delta r\eta}}{\frac{1}{2}\rho L^2 U^2}$	First order coefficient used in representing $Y_{\delta r}$ as a function of $(\eta-1)$
$\beta$		Angle of drift
$\delta r$		Deflection of rudder
$\delta r_1$		Steady rudder angle at 1 <sup>th</sup> execute in an overshoot or zigzag maneuver; $i = 1, 2, 3, \dots$
$\dot{\delta r}$	$\dot{\delta r}' = \frac{\dot{\delta r} L}{U}$	Rudder deflection rate
$\eta$	$\eta = \frac{J_c}{J}$	Ship propulsion ratio; $\frac{u_c}{u}$ or $\frac{n_o}{n}$
$\sigma_{1h}$	$\sigma_{1h}' = \sigma_{1h} \frac{L}{U}$ $\sigma_{1h}'' = \sigma_{1h}' \sqrt{\frac{m}{2}}$	Roots of characteristic stability equation for horizontal plane motions, $i = 1$ or $2$
$\phi$		Roll angle
$\phi_m$		Maximum roll angle in a maneuver
$\psi$		Heading or yaw angle
$\psi_i$		Heading angle at $i^{\text{th}}$ execute in an overshoot or zigzag maneuver, measured from value at first execute; $i = 2, 3, \dots$
$\dot{\psi}$	$\dot{\psi}' = \dot{\psi} \frac{L}{U}$	Rate of change of heading
$\dot{\psi}_h$	$\dot{\psi}_h' = \dot{\psi}_h \frac{L}{U}$	Height of loop at neutral rudder angle from spiral maneuver
$\dot{\psi}_1$	$\dot{\psi}_1' = \dot{\psi}_1 \frac{L}{U}$	Rate of change of heading at $i^{\text{th}}$ execute in an overshoot or zigzag maneuver; $i = 2, 3, \dots$
$\omega$	$\omega' = \frac{\omega L}{U}$	Frequency of oscillation



Sketch showing positive directions of axes, angles, velocities, forces and moments.



## APPENDIX B - HISTORY OF PMM AND PMM SYSTEMS

A chronology of the development and application of the PMM and PMM Systems is presented herein. The chronology is by no means complete. However, it indicates that the PMM System concept has been adopted for marine vehicle testing throughout the world.

DATE	EVENT	LOCATION
July 1952	Concept of PMM first developed by A. Goodman for use in determining lateral stability coefficients of aircraft	NACA Langley Stability Tunnel, Langley Field, Virginia
October 1956- June 1957	DTMB PMM System (MARK I) conceived, developed and placed into service for submarine model testing by A. Goodman and M. Gertler	U.S.A.
May 1959	U. S. patent for PMM System filed	U.S.A.
September 1959	Paper presented by M. Gertler describing PMM System	Zagreb, Yugoslavia
September 1960	Paper presented by A. Goodman describing improved PMM System	Third ONR Symposium Scheveningen, Holland
December 1961	DTMB PMM System MARK II placed into service	U.S.A.
July 1962	PMM built by J. R. Paulling	University of California
September 1962	U. S. Patent 3,052,120 granted	U.S.A.
October 1962	PMM System built by HYDRONAUTICS, Incorporated for use with High-Speed Channel-hydrofoil testing	U.S.A.
1962	PMM built by Delft University for ship model testing	Holland
1963	PMM System supplied by HYDRONAUTICS, Incorporated to Bassin d'Essais des Carenes for submarine model testing	France
1964	PMM System built by Tokyo University for ship model testing	Japan
1964	PMM System built by HyA for ship model testing	Denmark
1965	PMM System built by Nagasaki Technical Institute	Japan
August 1966	Paper presented by J. Strom-Tejsen and M. S. Chislett on HyA PMM System used for ship model testing	Sixth ONR Symposium, Washington, D. C.
May 1968	PMM System supplied by HYDRONAUTICS, Incorporated to AEW for submarine model testing	U.K.
November 1968	PMM Instrumentation System supplied by HYDRONAUTICS, Incorporated to DTMB	U.S.A.
December 1968	PMM System built by HYDRONAUTICS, Incorporated for submarine model testing in HSMB	U.S.A.
1969	PMM System built by NSRDC for ship model testing	U.S.A.
April 1969	Lecture on PMM for ship model testing sponsored by AEW and University College, London	U.K.
December 1970	PMM System supplied by HYDRONAUTICS, Incorporated to Bassin d'Essais des Carenes for use with High-Speed Channel	France
January 1971	PMM adapted by HYDRONAUTICS, Incorporated for ship model testing in HSMB	U.S.A.
1972	Large-amplitude PMM built by HyA for ship model testing	Denmark
1973	Large-amplitude PMM built by AEW for ship model testing	U.K.

DATE	EVENT	LOCATION
1974	Large-amplitude PMM built by NSRDC for SES model testing	U.K.
1974	Various large-amplitude PMM Systems built by University of Tokyo, IHI, and Nagasaki	Japan
1976	CPMC - A naval facility for planar motion testing of ship models	Germany
1976	Large-amplitude horizontal PMM built by HYDRONAUTICS, Incorporated for ship model testing	U.S.A.
1976	Large-amplitude horizontal PMM built by HYDRONAUTICS, Incorporated for U. S. Naval Academy (in process)	U.S.A.

# APPENDIX C - MATHEMATICAL OPERATIONS PERFORMED BY INSTRUMENTATION SYSTEM

The mathematical operations that the instrumentation system performs automatically is described in this section.

To illustrate, assume a pure swaying condition which results in a gage signal of the form

$$Y_R = Y_* + Y_o \sin (\omega t - \phi) \quad (C1)$$

which can be written as

$$Y_R = Y_* + Y_o (\cos \phi) \sin \omega t + [-Y_o (\sin \phi)] \cos \omega t \quad (C2)$$

or

$$Y_R = Y_* + Y_{in} \sin \omega t + Y_{out} \cos \omega t \quad (C3)$$

The gage signal represented by Equation (C3) is impressed across the sin-cos potentiometer which is rotating at the fundamental frequency. The output of the sin-cos pot can be expressed as:

## In-Phase

$$Y_R \sin \omega t = \frac{1}{2} [Y_* \sin \omega t + Y_{in} \sin^2 \omega t + Y_{out} \cos \omega t \sin \omega t] \quad (C4)$$

## Quadrature

$$Y_R \cos \omega t = \frac{1}{2} [Y_* \cos \omega t + Y_{in} \sin \omega t \cos \omega t + Y_{out} \cos^2 \omega t] \quad (C5)$$

## CAL

$$Y_R = \frac{1}{2} [Y_* + Y_{in} \sin \omega t + Y_{out} \cos \omega t] \quad (C6)$$

As shown by Equations (C4), (C5) and (C6), the gage signal is divided by 1/2 due to the fact that the sin-cos potentiometer acts as a voltage divider in this system.

The gage signals represented by Equations (C4), (C5) and (C6) are fed into the integrating digital voltmeter and the following operations are performed:

## In-Phase

$$\begin{aligned} \int_0^{nT} Y_R \sin \omega t d(t) &= \frac{1}{2} \int_0^{nT} Y_* \sin \omega t d(t) \\ &+ \frac{1}{2} \int_0^{nT} Y_{in} \sin^2 \omega t d(t) \\ &+ \frac{1}{2} \int_0^{nT} Y_{out} \cos \omega t \sin \omega t d(t) \quad (C7) \\ &= \frac{nT}{4} Y_{in} \quad (C8) \end{aligned}$$

## Quadrature

$$\int_0^{nT} Y_R \cos \omega t d(t) = \frac{nT}{4} Y_{out} \quad (C9)$$

## CAL

$$\int_0^{nT} Y_R d(t) = \frac{nT}{2} Y_* \quad (C10)$$

Equations (C8), (C9) and (C10) can be expressed in terms of the normal and reverse readings and the calibration constant as follows:

## In-Phase

$$\begin{aligned} Y_{in} &= \frac{4}{nT} \int_0^{nT} Y_R \sin \omega t d(t) = \frac{4}{nT} \frac{N-R}{2} \frac{1}{K_s} \\ &= 2 \left[ \frac{(N-R)}{nT K_s} \right] \quad (C11) \end{aligned}$$

## Quadrature

$$Y_{out} = \frac{4}{nT} \int_0^{nT} Y_R \cos \omega t d(t) = 2 \left[ \frac{(N-R)}{nT K_s} \right] \quad (C12)$$

## CAL

$$\begin{aligned} Y_* &= \frac{2}{nT} \int_0^{nT} Y_R d(t) \\ &= \frac{(N-R)}{nT K_s} \quad (C13) \end{aligned}$$

where

$Y_{in}$  is equal to  $Y_o \cos \phi$ ,

$Y_{out}$  is equal to  $-Y_o \sin \phi$ ,

$T$  is the period of oscillation in seconds,

$n$  is the number of periods over which the signal is integrated,

$K_s = K_{DYN}$  is the static calibration constant for the gage (equal to the dynamic calibration constant)

in  $\frac{\text{counts}}{\text{lb-sec}}$  except as noted,

$N$  is the normal reading in counts, and

$R$  is the reverse reading in counts.

It should be noted that the calibration constant in the DYN-1 mode is 0.1 of the static constant. In the DYN-10 mode the static and dynamic constants are equal. That is,

$$\text{DYN-1} \quad K_{DYN} = 0.1 K_s \quad (C14)$$

$$\text{DYN-10} \quad K_{DYN} = K_s \quad (C15)$$

A similar analysis can be made for the pure yawing case. The operation performed by the electronic system is equivalent to determining the Fourier coefficients of the fundamental of the gage signal. This same type of data analysis can also be performed by the carriagedigital computer.



## APPENDIX D - REDUCTION OF RESISTANCE AND PROPULSION DATA

The procedures for reducing the resistance test data to nondimensional coefficient form and extrapolating the results to obtain values of effective horsepower (EHP) for the prototype full-scale ship are essentially the same as those given in Ref. (25). However, an additional step is taken to account for the tank blockage correction and the ITTC 1957 Line (Ref. 26) is used in lieu of the ATTC 1947 Line for the frictional resistance coefficients both in the model and full-scale ship ranges. The Scott tank blockage correction (Refs. 27, 28) is currently used at HSMB for all specific design test work. For systematic series investigations, the Hughes method (Ref. 29) has been used mainly because it was the most widely used among the modern formulations and it is relatively simple to apply. Comparative results obtained with the various modern blockage correction methods are given by the ITTC Performance Committee in Reference 28. The Scott method as applied at HSMB entails an effective velocity increase based on the following relationship:

$$\frac{\delta v}{v} = k_1 \nabla A_T^{-3/2} + k_2 B L^2 A^{-3/2} \quad (D1)$$

where

$v$  is the towing carriage speed,

$\delta v$  is the effective speed increase of the model,

$\nabla$  is the model displacement volume,

$B$  is the model beam,

$L$  is the model length,

$A_T$  is the cross-sectional area of the towing tank,

$k_1$  is an empirical correction factor which is a function of Reynolds number  $R_N$  and the form factor  $C_{F1}^{1/3} L^{-1}$  obtained from Figure 4 of Reference 28, and

$k_2$  is given in analytical form as

$$k_2 = 2.4(F_N - 0.22)^2 \text{ for } 0.22 < F_N < 0.38$$

$$k_2 = 0 \text{ for } F_N < 0.22.$$

In general, nearly all tests conducted to date at HSMB have been below  $F_N = 0.22$  so therefore the  $k_2$  term is usually neglected. Also, even for the large full-bodies models tested in HSMB, the model speed corrections to account for tank blockage effects rarely exceed two percent. Based on the foregoing, the procedural steps used in the reduction of the resistance test data in the model range are as follows:

1. Multiply towing carriage speed for each run by the calculated value of  $1 + \delta v/v$  to obtain tabulated values of model resistance in pounds versus effective speed based on tank blockage corrections for each model test condition.

2. Using the corrected data, calculate values of the total-resistance coefficient

$$C_{Tm} = \frac{R_T}{\frac{\rho}{2} S v^2} \quad (D2)$$

where  $v$  is the corrected speed.

3. Calculate model Reynolds number  $R_N = vL/v$  using corrected speed and obtain the values of

model frictional-resistance coefficient  $C_{Fm}$  for each of the data points from the tables of Reference 26.

4. Calculate values of residual-resistance coefficient  $C_R$  as follows:

$$C_R = \frac{R}{\frac{\rho}{2} S v^2} = C_{Tm} - C_{Fm} \quad (D3)$$

5. Plot values of  $C_R$  versus Froude number  $F_N = v/\sqrt{gL}$  based on corrected speed and fair the resulting curve.

To obtain EHP values in the prototype ship range proceed as follows:

6. Calculate values of  $F_N$  corresponding to even speeds in knots for the prototype full-scale ship and enter appropriate curve of  $C_R$  versus  $F_N$  to obtain the desired faired values of  $C_R$ .

7. Calculate values of  $R$  for full-scale ship at each selected speed and at standard conditions of salt water of 3.5 percent salinity and 59 deg F, and obtain values of ship frictional-resistance coefficient  $C_{Fs}$  from the tables of Reference 24.

8. Calculate values of total-resistance coefficient for the full-scale ship at each even speed as follows:

$$C_{Ts} = C_{Ti} = C_R + C_{Fs} + C_A = \frac{R_{Ts}}{\frac{\rho}{2} S v^2} \quad (D4)$$

where  $C_A$  is the correlation allowance coefficient and varies with size and type of ship.

9. Convert the values of  $C_{Ts}$  to EHP at each speed using full-scale dimensions and sea conditions as follows:

$$EHP = \frac{R_T v}{550} = C_{Ts} \left( \frac{\frac{\rho}{2} S v_k^3}{550} \right) (1.689)^3 \quad (D5)$$

where  $v_k$  is the ship speed in knots.

The foregoing procedure is programmed on the HYDRONAUTICS META-4 Computer to be carried out in two stages: reduction of test data in model range (Steps 1 through 4 including automatic plotting of data points in Step 5) and extrapolation of faired  $C_R$  versus  $F_N$  values to full-scale EHP (Steps 6 through 9). Steps 1 through 4 and 6 through 9 are also programmed on the HSMB carriage computer with manual plotting for Step 5.

The procedures for reducing and analyzing the data derived from the propulsion tests are divided in three stages. First, the measured test values are processed (including application of no-loads to T and Q) to obtain final model values of  $v$ , T, Q, n, and  $R$ ; where  $v$  is always taken as carriage speed (as opposed to the effective speed used in the final reduction of the resistance test data). These data are then reduced to nondimensional coefficients and cross-faired against related parameters. Finally, discrete values of the faired coefficients are converted to obtain values of SHP and RPM for various even speeds in knots for the prototype full-scale ship of specified dimensions. The procedural steps for reducing the propulsion test data starting with the second stage are as follows:

1. The values of  $F_N$ ,  $J$ ,  $C_{Ti}$ , PC,  $1-t$ ,  $K_T$ , and  $K_Q$  are calculated directly using the final model values from the propulsion tests as follows:

$$J_a = \frac{v}{nD} \quad (D6)$$

AD-A055 859

UNIVERSITY COLL LONDON (ENGLAND) DEPT OF MECHANICAL --ETC F/G 13/10  
SYMPOSIUM ON NAVAL HYDRODYNAMICS. UNSTEADY HYDRODYNAMICS OF MAR--ETC(U)  
1978 R E BISHOP, A G PARKINSON, W G PRICE N00014-76-C-0093

UNCLASSIFIED

NL

2 of 9  
AD  
A055859



$$C_{Ti}' = \frac{R_m - (-X)}{\frac{\rho}{2} S v^2} = \frac{R_i'}{\frac{\rho}{2} S v^2}; \quad (D7)$$

where

$C_{Ti}' = C_{Ti}$  at the ship-propulsion point predicted from the resistance test results (Equation (D4))

$$PC = \frac{R_i' v}{2\pi Q n} \quad (D8)$$

$$1-t = \frac{R_i'}{T} \quad (D9)$$

$$K_T = \frac{T}{\rho n^2 D^4} \quad (D10)$$

$$K_Q = \frac{Q}{\rho n^2 D^5} \quad (D11)$$

2. The values of  $K_T$  and  $K_Q$  are used with the open-water characteristic curves for the same propeller as used in the propulsion tests to obtain the true advance coefficients  $J_{tT}$  and  $J_{tQ}$ . These, in turn, are used to obtain the Taylor wake fractions for thrust and torque identity, respectively, by the following relationships:

$$1 - w_T = \frac{J_{tT}}{J_a} \quad (D12)$$

$$1 - w_Q = \frac{J_{tQ}}{J_a} \quad (D13)$$

3. The values of the propeller open-water efficiency  $e_a$  are also obtained from the propeller characteristic curve at the corresponding values of  $J_{tT}$ . Then the hull efficiency  $e_h$  and relative rotative efficiency  $e_{rr}$  can be obtained from the following relationships:

$$e_h = \frac{1-t}{1-w_T} \quad (D14)$$

$$e_{rr} = \frac{PC}{e_p \times e_h} \quad (D15)$$

4. For the overload and underload type of propulsion test described under test procedures, the coefficient data ( $1-t$ ,  $1-w_T$ ,  $1-w_Q$ ,  $PC$ ,  $e_a$ ,  $e_h$ , and  $e_{rr}$ ) are plotted as functions of  $Q_{C_{Ti}'}^{h_p}$ . The individual coefficient curves are faired and these curves are then cross-faired until the relationship given in Equation (D15) is satisfied over the entire range of  $C_{Ti}'$  values. Where a stock propeller has been used, the curves of  $e_a$  and  $PC$  are arbitrary with respect to the design propeller and are therefore not usually presented along with the final results.

5. For the ship-propulsion point type of test, the data are treated similarly but they are plotted as a function of  $F_N$ . For the case of a specific design propeller, curves of  $J$ ,  $PC$ , and  $e_a$  are given in the final plots. For the case of a stock propeller, curves are usually presented for  $J$ ,  $PC$ , and  $e_a$  which correspond to an optimal propeller of the same diameter as the stock propeller which is obtained from the Troost Series or other propeller series data.

The faired data of Step 5 can be converted to the dimensional values for the corresponding standard-ship prototype as follows:

6. At each value of  $F_N$  corresponding to the same even ship speeds in knots used in Step 9 of the resistance test data reduction procedure, read the faired values of  $PC$  and  $J$ . These faired values should be based on the  $C_{Ti}' = C_{Ti}$  identify using the faired results of the overload and underload tests (Step 4). Then

$$SHP = \frac{EHP}{PC} \quad (D16)$$

and

$$rpm = 101.33 \frac{V_k}{J_a D} \quad (D17)$$

where

$V_k$  is the ship speed in knots and

$D$  is the diameter of the ship propeller in feet.

The foregoing calculation procedure for propulsion test data is programmed on the HYDRONAUTICS META-4 Digital Computer System. Included in the program is automatic plotting of the coefficient data; fairing and cross-fairing are done manually. A similar programming is included in the HSMB Digital Computer System, but data plotting is done manually as the test progresses.



# APPENDIX E - REDUCTION OF DATA AND DETERMINATION OF COMPLETE SETS OF HYDRODYNAMIC COEFFICIENTS FROM TESTS WITH HSMB LAHPMM

In all cases, the data derived from tests performed with the HSMB LAHPMM System are first reduced to nondimensional form in accordance with the notation of Appendix A, and are then plotted as functions of the various kinematic variables investigated. The precise manner in which the data are further processed depends upon the objectives and scope of the test program. Accordingly, the methods used in conjunction with the results of reference PMM tests and standard PMM tests are separately discussed in the following sections. All of the operations described in these sections have been programmed both on the HYDRONAUTICS META-4 and HSMB Carriage Computer Systems.

## Reduction and Analysis of Reference PMM Test Data

As mentioned earlier, it is often desirable as a matter of expediency to conduct only reference PMM tests for a given surface-ship design. This is particularly true in the case of early designs where the hydrodynamic design aspects are not yet firmly established. In such cases, engineering judgments are often made on basis of an analysis of stability and control derivatives in the linearized equations of motion, as explained in the following paragraphs.

The values for the nondimensional static derivatives  $Y_v'$ ,  $N_v'$  and  $Y_r'$ ,  $N_r'$  are taken from the slopes through zero of the  $\delta r'$  appropriate paired curves of  $Y'$ ,  $N'$  versus  $\beta$  and  $\delta r$ , respectively. In general, the derivative is based on the average slope over at least  $\pm 4$  degrees for variation of either  $\beta$  or  $\delta r$ . All angular derivatives are given as per radian. The values of the nondimensional rotary and acceleration derivatives are derived by substituting values from the graphs of the in-phase and quadrature force components obtained as the result of the pure side-swaying and pure yawing tests into the reduction equations in Table E1 which are derived in Reference (15).

TABLE E1

REDUCTION EQUATIONS FOR HORIZONTAL-PLANE  
ROTARY AND ACCELERATION DERIVATIVES

$Y_v' - m'$	$\frac{\partial[(Y_1')_{in} + (Y_2')_{in}]}{\partial \dot{v}_o'}$
$N_v' - x_{CG}' m_m'$	$\frac{x}{L} \frac{\partial[(Y_1')_{in} - (Y_2')_{in}]}{\partial \dot{v}_o'}$
$Y_r' - m_r'$	$\frac{\partial[(Y_1')_{out} + (Y_2')_{out}]}{\partial \dot{r}_o'}$
$N_r' - x_{CG}' m_m'$	$\frac{x}{L} \frac{\partial[(Y_1')_{out} - (Y_2')_{out}]}{\partial \dot{r}_o'}$
$Y_{\dot{r}}' - x_{CG}' m_m'$	$\frac{\partial[(Y_1')_{in} + (Y_2')_{in}]}{\partial \dot{r}_o'}$
$N_{\dot{r}}' - I_{zm}'$	$\frac{x}{L} \frac{\partial[(Y_1')_{in} - (Y_2')_{in}]}{\partial \dot{r}_o'}$

An estimate of the inherent directional stability characteristics of a given surface-ship design can be readily made using dynamic stability indices based on the linearized equations of motion in conjunction with the aforementioned derivatives obtained from PMM tests. The term "inherent directional stability" is applied herein to the case of "controls-fixed" dynamic stability of a surface ship in the horizontal plane of motion. A ship is considered to be inherently directionally stable if, after a disturbance from steady-state motion on straight course, it resumes its steady motion on another straight course (not necessarily in the same direction) with its rudder held fixed at zero or neutral angle. On the other hand, an inherently directionally unstable ship in the same situation can be expected to end up in a turn of stable equilibrium.

The linearized differential equations of motion for the yaw-sway degrees of freedom, referred to a right-hand orthogonal system of moving axes with the origin fixed in the hull (see sketch in Appendix A), are written in nondimensional form as follows:

$$Y_v' v' + (Y_v' - m') \dot{v}' + (Y_r' - m') r' + (Y_r' - m' x_{CG}') \dot{r}' = -Y_{\delta r}' \delta r$$

$$N_v' v' + (N_v' - m' x_{CG}') \dot{v}' + (N_r' - m' x_{CG}') r' + (N_r' - I_z') \dot{r}' = -N_{\delta r}' \delta r \quad (E1)$$

If the origin is taken at the center of gravity of the ship in accordance with the standard practice,  $x_{CG} = 0$  and Equations (E1) reduce to

$$Y_v' v' + (Y_v' - m') \dot{v}' + (Y_r' - m') r' + Y_{\dot{r}}' \dot{r}' = -Y_{\delta r}' \delta r$$

$$N_v' v' + N_v' \dot{v}' + N_r' r' + (N_r' - I_z') \dot{r}' = -N_{\delta r}' \delta r \quad (E1a)$$

If Equations (E1a) are equated to zero, they become the linear equilibrium equations corresponding to the condition of steady straightline motion of the ship with controls fixed at zero or neutral angle which are used as a basis for establishing various dynamic stability indices. The following quadratic equation, based on the equilibrium linearized equations of motion is known as the characteristic stability equation for the yaw-sway mode:

$$A\sigma^2 + B\sigma + C = 0 \quad (E2)$$

where according to common usage,  $\sigma$  in this case denotes the nondimensional quantity  $\sigma' = \sigma(L/U)$  and

$$A = (Y_v' - m') (N_r' - I_z') - Y_{\dot{r}}' N_v'$$

$$B = Y_v' (N_r' - I_z') + N_r' (Y_v' - m') - N_v' (Y_r' - m') - Y_{\dot{r}}' N_v'$$

$$C = Y_v' N_r' - N_v' (Y_r' - m')$$

The two roots of Equation (E2), known as the non-dimensional stability indices, are given by

$$\sigma_{1,2}' = -\frac{B}{2A} \pm \sqrt{\left(\frac{B}{2A}\right)^2 - \frac{C}{A}} \quad (E3)$$

For a ship to be inherently directionally stable (with controls fixed), the values of the roots of

Equation (E2), denoted hereinafter as the stability roots  $\sigma_{1h}'$  and  $\sigma_{2h}'$ , must both be negative. One of the stability roots  $\sigma_{2h}'$  is usually always negative and therefore, the other (least stable root) or  $\sigma_{1h}'$  is often referred to as the stability index.

The nondimensional stability index  $\sigma_{1h}'$ , which is based on derivatives normalized on  $L$ , is quite satisfactory for comparing the effects of different appendages on the same hull. However, for the purpose of comparing directional stability among candidate ships of widely different hull proportions, such as that due to L/B or B/T, a stability index based on equal-volume prototypes perhaps may be more meaningful. Accordingly, a stability index defined as

$$\sigma_{1h}'' = \sigma_{1h}' \sqrt{m'/2} \quad (E4)$$

has been adopted to suit such purposes.

The so-called dynamic stability lever is another criterion suggested for evaluating degree of inherent directional stability which has recently gained favor particularly among the Europeans (Refs. 19, 20). The dynamic stability lever, derived by dividing the C term of the characteristic stability equation (E2) by the product  $Y_v'(Y_r' - m')$ , is defined as

$$\ell_d' = \ell_r' - \ell_v' = \frac{N_r'}{Y_r' - m'} - \frac{N_v'}{Y_v'} \quad (E5)$$

where  $\ell_r'$  and  $\ell_v'$  are the damping lever and static stability lever which, respectively, locate the longitudinal centers of rotary force and static force acting on the ship with respect to the reference point (center of gravity). For dynamically stable ships  $\ell_r' - \ell_v' > 0$  which means that the center of rotary force must lie forward of the center of static force. On the other hand, for dynamically unstable ships  $\ell_r' - \ell_v' < 0$  and the center of static force lies ahead of the center of rotary force. The positive or negative magnitudes of  $\ell_d'$  are considered to provide a measure of the degree of dynamic stability or instability, respectively.

In addition to determining inherent directional stability, it is often desirable in advance of computer simulation studies to have some means for evaluating inherent control effectiveness on which to base judgments in the early design stage. For a given ship design, the nondimensional control derivatives  $Y_{\delta r}'$  and  $N_{\delta r}'$  in themselves can provide some indications of relative changes in rudder effectiveness that can be expected due to changes in size or other parameters affecting rudder performance. Unfortunately, these derivatives do not provide a good measure of the adequacy of the rudder in terms of the hull on which it is installed, a matter of importance particularly when dealing with hulls of widely differing proportions.

A design criterion that has been used primarily for submarines to determine the required degree of control effectiveness is the so-called dimensional angular acceleration parameter  $cp$  (Ref. 2). It has been demonstrated empirically that  $cp$  is related to the time  $t_2$  required to make an initial pitch angle or heading-angle change of 5 degrees. As applied to the case of surface ships, this parameter is defined as follows:

$$cp = \frac{N_{\delta r}' \delta r}{(N_r' - I_z)} \text{ sec}^{-2} \quad (E6)$$

where

$N_{\delta r}' \delta r$  is the dimensional value of the yawing moment imparted to the ship at a given speed for a specified rudder deflection  $\delta r$ , and

$(N_r' - I_z)$  is the dimensional value of the total moment of inertia of the ship including that due to hydrodynamic added mass.

A chart showing the relationship between  $cp$  and  $t_2$  for an execute heading-angle change  $\psi$  of 5 degrees,  $\delta r = 20$  deg, and a rudder deflection rate  $\dot{\delta r}$  of 2.3 deg/sec is presented in Reference 7. The chart was derived from the results of computer simulated 20-20 zigzag maneuvers using the standard techniques described in this paper. The chart was originally prepared for the case of large bulk carrier merchant type ships. However, it should be generally applicable to ships of any type or size for the specified values of  $\psi$ ,  $\delta r$ , and  $\dot{\delta r}$ .

#### Determination of Complete Set of Hydrodynamic Coefficients from Standard PMM Tests

For convenience to the users and other interested persons, the procedures used at HSMB to arrive at the numerical values for the complete set of standard deep-water hydrodynamic coefficients used for computer simulation, such as that given in Table 2, are reviewed in this appendix. Because of the nature of the functional relationships involved, the procedures applied to the coefficients for the lateral force and yawing moment equations are discussed separately from those applied to the coefficients for the axial force equations. In general, most of the operations described herein have been programmed on both the HYDRONAUTICS META-4 Digital Computer System and the HSMB Carriage Computer System.

In the lateral force and yawing moment equations of the Standard Equations of Motion given in this paper, all terms except the " $\eta$ -dependent" terms shown on the last two lines in each case, are considered to constitute the so-called reference equations. As a matter of standard practice, the numerical values of the coefficients for these terms are derived from the reference PMM tests which are always conducted for the case of ship-propulsion point defined as  $\eta = 1.0$ . This approach is particularly advantageous for ship types which might not have the rudder(s) operating in the propeller slipstream, and consequently the values of the  $\eta$ -dependent terms (departure from  $\eta = 1.0$ ) are often small enough to be neglected in most computer simulation studies. Moreover, for simulation of small-scale maneuvers of normal single-screw types, where the changes in speed are small, the  $\eta$ -dependent terms sometimes can be neglected if desired as a matter of simplification.

For the reference equations, the lateral force  $Y$  and yawing moment  $N$  data obtained from the PMM tests conducted at  $\eta = 1.0$  are first reduced to nondimensional form  $Y'$  and  $N'$  in accordance with the normalization formulas given in the notation of Appendix A. The resulting values of  $Y'$  and  $N'$  are then plotted and faired as functions of each of the appropriate nondimensional kinematic variables such as  $v'$ ,  $\dot{v}'$ ,  $r'$ ,  $\dot{r}'$  and  $\delta r$ . Finally, a least square fit is applied to the faired data representing each of the functional relationships to obtain the desired nondimensional coefficients. Certain of these functional relationships are known to be linear from considerations of theory, such as those of the acceleration or "added mass" variety typified by  $Y_v'$ ,  $Y_r'$ ,  $N_r'$ , and  $N_v'$ . In such cases, only a



straightline fit is made, and the resulting numerical values can be used interchangeably as first order coefficients in the Standard Equations of Motion or as derivatives in the linearized equations of motion. A straightline fit is also used in other cases where it is evident from the test data that the functional relationship can be closely approximated by such a fit over the entire range of practical interest. Here again, the resulting values can be treated either as first order coefficients or as derivatives. For nonlinear functional relationships, the least square fits are made to polynomials which are carried up only to second order coefficients. For these cases, the numerical values of the first order coefficients associated with the second order fits are not necessarily equal to those of the corresponding derivatives used for analyses based on the linearized equations. It may be noted that all of the second order coefficients in the reference equations involve the use of absolute values of certain kinematic variables. This is done to assure the proper signs in the computer representations, and is comparable to the use of third order coefficients for odd functions in the Taylor expansion method (Ref. 21). The values of the coupling coefficients in the reference equations, such as  $Y_{|r|}$  and  $N_{|r|}$ , are derived by applying first order least square fits to plots of  $Y'$  and  $N'$  versus the products  $v|r|$  and  $|v|r$ , respectively, using data obtained from PMM tests of the type shown by Figure 1d.

All of the coefficients of the  $\eta$ -dependent terms in the lateral force and yawing moment equations are considered to be of first order. Their values are based on linear fits to the values of the various nondimensional  $Y$ -force and  $N$ -moment derivatives effectively plotted as functions of  $\eta-1$ , which are derived from the aforementioned overload and underload PMM tests. Among these coefficients  $Y_{\delta r \eta}$  and  $N_{\delta r \eta}$  play the most important role particularly for single-screw merchant ship types. This is because of the strong dependence of the rudder force and moment coefficients on the relative velocity of the propeller slipstream as discussed earlier. The values of  $Y_{\delta r \eta}$  and  $N_{\delta r \eta}$  given in Table 2 apply closely to a range of  $\eta$  values between about 0.5 and 4.0. This adequately covers the cases of most types of maneuvers of interest including tight steady-turning maneuvers wherein the loss of speed for essentially constant propeller RPM can amount to as much as 75 percent. The only exception is the stopping maneuver which involves  $\eta$  values below 0.5 and extending well into the negative region. For accurate simulation of the lateral motions in such maneuvers, a supplementary representation or subroutine is used to account for the rudder coefficients affected.

The axial force equation is an essential part of the basic mathematical model and must be properly evaluated to provide an accurate means for simulation of all ship maneuvers involving significant speed changes. This includes simulation of not only acceleration and deceleration maneuvers, but also of large-scale maneuvers initiated from a condition of steady straightline motion with propeller RPM held essentially constant throughout the maneuver. Accordingly, a substantial portion of the standard PMM test program is devoted to mathematically modeling the effects on  $X$ -force of varying each kinematic variable with particular emphasis on the contribution of the  $\eta$  variation. The numerical values for the coefficients  $X'$ ,  $X_{\eta}$ , and  $X_{\eta\eta}$  are associated with a value of  $\eta = 1.0$ . They are generally derived from the reference

PMM tests by a process similar to that for the corresponding lateral force coefficients. The value of  $X_{\eta}$ , which has an important effect on loss of speed particularly in large-scale maneuvers, is also associated in the reference equations with  $\eta = 1.0$ . It is derived by applying a first order fit to a plot of  $X'$  versus the product  $vr$  using data from the PMM coupling tests. The values for  $X_{\eta\eta}$  are obtained experimentally by a process similar to that used for the  $\eta$ -dependent lateral force coefficients. The remaining  $X$ -coefficients are treated somewhat differently and therefore are discussed in more detail in the following paragraphs.

The net or unbalanced force required to change the speed of the ship in straightline motion ( $\beta = \delta r = 0$ ) from one steady value to another is represented in the axial force equation by the expression

$$\frac{\rho}{2} L^2 u^2 [a_1 + b_1 \eta + c_1 \eta^2]$$

which is equivalent to

$$\frac{\rho}{2} L^2 [a_1 u^2 + b_1 u u_c + c_1 u_c^2]$$

given in the Standard Equations of Reference 18. The values of the coefficients,  $a_1$ ,  $b_1$ , and  $c_1$  are obtained by direct experimental means from overload and underload PMM or propulsion tests by the following process: The  $X$  data measured for the case of  $\beta = \delta r = 0$  with model RPM varied to provide a range of  $\eta$  values between -1.0 and 4.0 are first reduced to nondimensional form in accordance with the Notation. The values of  $X'$  so obtained are plotted and faired as a function of  $\eta$ . The resulting curve is then shifted by a constant  $\Delta X'$  so that, at the ship-propulsion point  $\eta = 1.0$ , the value of  $X' = 0$ . The values of  $a_1$ ,  $b_1$ ,  $c_1$  are then obtained by applying quadratic fits to the curve of  $X'$  versus  $\eta$  for the prototype ship. Due to the nature of this curve, the standard practice is to fit the curve in three or four segments depending on the range of  $\eta$  values to be covered in a given problem.

It should be emphasized that the foregoing expression represents the difference between the so-called "delivered propeller force" and the non-propelled resistance of the ship at the given speed. This is in contrast to the propeller thrust used by many investigators (Refs. 15, 20) which requires an adjustment for thrust deduction usually based on estimates. On the other hand, the delivered propeller force is effectively equal to  $T(1-t)$  over the entire range of propeller loadings. Thus at a steady speed corresponding to the condition  $\eta = 1.0$ , the delivered propeller force is equal to the ship resistance and, for the segment fits in Table 2,  $(a_2 + b_2 + c_2) = 0$ . For the case of  $\eta = 0$ ,  $a_2 = a_3 = X_{\eta}$ , and the delivered propeller force is zero. The total-resistance coefficient corresponding to ship-propulsion point at  $\eta = 1.0$  is numerically related to  $X_{uu}$  as follows:

$$X_{uu}' = C_T \frac{S}{L^2} \quad (E7)$$

The  $X$ -forces due to rudder deflection also have a strong influence on speed changes particularly for large-scale maneuvers such as steady-turning maneuvers. The relative magnitudes of these forces become greatly compounded when propeller slipstream effects are superimposed, as is the case with the single-screw ship types covered by this investigation. Accordingly, a somewhat different method is



used herein to represent the rudder-force coefficients in the axial equation than that used in the Standard Equations of Reference 18 which dealt mainly with submarines whose control surfaces were generally located ahead of the propeller. It may be seen that the present method uses the second order coefficient  $X_{\delta r \delta r}$  to represent  $X'$  as a function of  $\delta r$  referred to  $\eta = 0$ , and the second order coefficient  $X_{\delta r \delta r \eta}$  to represent  $X_{\delta r \delta r}$ , as a function of  $\eta$ . This is in contrast to Reference 18 which uses the second order coefficient  $X_{\delta r \delta r}$  to represent  $X'$  as a function of  $\delta r$  referred to  $\eta = 1.0$  and the first order coefficient  $X_{\delta r \delta r \eta}$  to represent  $X_{\delta r \delta r}$  as a function of  $\eta - 1$ .

The numerical values of the rudder-force coefficients in the axial equation are obtained by direct experimental means from the overload and underload PMM tests previously described. This is accomplished as follows: The  $X'$  values for the case of  $\eta = 0$  are first plotted as a function of  $\delta r$  in radians squared. The slope of the resulting straightline fit is then the desired value of  $X_{\delta r \delta r}$  at  $\eta = 0$ . Similar slopes are obtained for other discrete values of  $\eta$  covering a range up to  $\eta = 4.0$  maximum. The resulting values of  $X_{\delta r \delta r}$  including that for  $\eta = 0$  are then plotted against  $\eta^2$ . The slope of the straightline fit through these data is then the desired value of  $X_{\delta r \delta r \eta}$ . It is of interest to note that an excellent fit to the experimental data is obtained by this process over the entire range of  $\eta$  values between 0 and 4.0 whereas the fit using the linear variation with  $\eta - 1$  in accordance with Reference 18 results in values of  $X_{\delta r \delta r}$  which depart significantly from the data particularly at values of  $\eta$  in excess of 2.0.

# APPENDIX F - DEFINITIVE MANEUVERS USED AS STANDARD FOR SURFACE-SHIP MANEUVERING STUDIES

The term definitive maneuvers has been adopted to describe a class of maneuvers designed solely to reveal objective or numerical measures of specific handling qualities of ships or other marine vehicles. Some of these maneuvers may resemble operational maneuvers. It is highly desirable if this is the case since the numerical measures derived from such a definitive maneuver will then have a more direct significance to the operator. There are two general types of definitive maneuvers, those which define inherent qualities of a ship resulting from its hydrodynamic design and are independent of the man or control mechanisms in the loop; and those which define qualities associated with the complete ship-control system and are dependent on the responses of the man, automatic control equipment, and control linkages in the loop.

Maneuvers which define inherent qualities are considered preferable because they directly provide specific numerical measures from a single maneuver of a given type. Also, these measures are indicative of the maximum potentialities of the ship system without qualification as to the efficiency of the operator (or other internal control system components) in executing the maneuver. On the other hand, maneuvers which define qualities associated with the complete system are much more cumbersome and time consuming. Such a maneuver must be repeated many times with several operators, possessing varying degrees of skill, to furnish data which then must be statistically analyzed to obtain the desired figures of merit. Nevertheless, there are cases where the latter type of maneuver must be used if certain handling qualities are to be directly manifested. The following list, by no means all inclusive, are the kinds of handling qualities that operators should reasonably expect from surface ships in general, some of which are not always possible to achieve particularly in the case of large, single-screw bulk carrier ship types:

1. The ability to maintain course with a small amount of heading error, course error, and rudder activity.
2. The ability to initiate a course change rapidly.
3. The ability to check a course change rapidly with small overshoots in heading angle and width of path.
4. The ability to execute an efficient steady-turning maneuver with small tactical diameter, advance, and transfer.
5. The ability to accelerate and decelerate rapidly yet retaining good control.
6. The ability to maneuver in and out of harbors ahead and astern at slow speeds without tug assistance.

A wide variety of definitive maneuvers have been used in the past, and others might conceivably be used in the future, to provide a basis for evaluating handling qualities such as those given on the preceding list. Obviously, many of these maneuvers involve similar modes of performance and to this extent overlap each other in defining certain types of handling qualities. Consequently, in selecting standard definitive maneuvers, one can go from one extreme by considering too few types and perhaps overlooking some important handling qualities to the other extreme by utilizing too many and thus overburden trial schedules and produce excessive amounts of data. To keep the computer simulation program within bounds, as well as to satisfy the four main objectives, the spiral, zigzag, and

steady-turning maneuvers were selected as standard on which to base the evaluation of inherent or open-loop characteristics of the ship.

The following sections describe each type of definitive maneuver in terms of how it would be performed on the actual ship and presents typical results obtained for a representative ship type obtained by means of the computer simulation technique. In keeping with the concept of definitive maneuvers, all derived numerical measures are expressed dimensionally in real time and distance. It is felt that such numbers are more meaningful and within the perspective of the operators. Furthermore, they will ultimately serve as a better basis for handling quality specifications since they can be checked directly in acceptance trials. If it is desired, however, to utilize the data in analyses involving different-sized ships, the dimensional values can be readily converted to nondimensional ones by use of appropriate normalizing factors.

## Spirals

The spiral is a definitive maneuver which is intended to provide quantitative measures of the inherent directional stability characteristics of a ship. These characteristics can be used to impute course-keeping potentialities. The basic spiral maneuver can be conducted on ships without special instrumentation as follows:

1. The propeller speed is adjusted to an rpm corresponding to a predetermined speed (either ahead or astern). Once a steady rpm is achieved, the throttle settings are not changed for the balance of the maneuver.

2. The rudder is manipulated as necessary until a "practically" straight course has been obtained and held for one minute.

3. The rudder is then deflected to about 15 degrees right and held until the rate of change of heading as indicated by the gyro compass and a stopwatch remains constant for one minute (or longer if required in specific cases such as the VLCC's). The rudder angle is then decreased by 5 degrees and held again until the rate of change of heading remains constant for one minute. The procedure is repeated until the rudder has covered a range of from 15 degrees on one side to 15 degrees on the other side and back again to 20 degrees on the first side. For 5 degrees on either side of zero or neutral rudder angle, the intervals are taken in one degree steps. For ships equipped with a rate gyro, each rudder setting in Step 3 is held until the heading-rate reading on the gyro becomes steady. A similar procedure is followed in the computer simulation. The numerical measures associated with the basic spiral maneuver are derived from measured values of the steady rate of change of heading versus rudder angle. A plot of these variables is indicative of the inherent directional stability characteristics of the ship. If the plot is a single continuous curve going from right rudder to left rudder, the ship is said to be inherently directionally stable. On the other hand, if the plot consists of two branches joined together to form a "hysteresis loop", such as is shown for a typical bulk carrier type ship in Figure F1, the ship is said to be inherently directionally unstable. In such case, the size of the loop (height and width), as defined by Figure F1, can be used as a numerical measure of the degree of instability; the larger the loop, the more unstable the ship. The height of the loop is a more direct measure of inherent instability since, for a given rudder planform, it will be the same regardless of whether the rudder is all movable or flapped whereas the width of the loop is affected by the control

effectiveness of the rudder as well. However, the width of the loop is a fairly direct indication of probable coursekeeping ability since it governs the envelope of rudder angles which must be employed to keep the ship from swinging from port to starboard. As is typical of single-screw ships, there is a shift of the loop to starboard. Therefore, the height of the loop is defined herein as that taken at the center of the loop or at neutral rather than zero rudder angle.

In recent years, it has been the tendency in foreign ship trials to employ the "reverse" spiral technique, attributed to Bech, in lieu of the basic spiral, particularly for large bulk-carrier ship types which are apt to be inherently directionally unstable. The advantage of this technique is a substantial saving in time and sea room. To perform such a maneuver, it is necessary that the ship be equipped with a rate gyro and preferably with an autopilot system. The procedure is to actively steer the ship, with as small rudder excursions as possible, to achieve each of a number of constant turning rates. The average rudder angle corresponding to each constant turning rate is then plotted in the same manner as for the basic spiral maneuver. However, instead of the hysteresis loop, the so-called S-curve is obtained from the reverse spiral for the case of unstable ships. From comparisons of full-scale trial data for a number of ships, "it has been concluded that the two techniques, when properly applied will yield identical results apart from points within the instability loop of unstable vessels which can be measured only by means of the reversed technique" (Ref. 30). The reverse spiral technique can be readily applied to computer simulations, as has been demonstrated by other investigators, and the necessary subroutine is now being incorporated in the existing computer program at HSMB.

#### Zigzags

The zigzag is a definitive maneuver which is intended to provide quantitative measures of the inherent effectiveness of the rudder in making changes in heading or width of path. The kinds of handling qualities revealed by this maneuver are typified by the ability to both initiate and check course changes during transient maneuvers. The first half cycle of the zigzag maneuver, known as the overshoot maneuver, provides most of the numerical measures of interest from the standpoint of evaluating handling qualities of merchant ships. A typical procedure for conducting zigzag maneuvers on ships without the use of special instrumentation is as follows:

1. The propeller speed is adjusted to an rpm corresponding to a predetermined speed and when a steady rpm is achieved, the throttle settings are not changed for the balance of the maneuver.
2. The rudder is manipulated as necessary until a "practically" straight course has been obtained and held for one minute.
3. After steady conditions on straight course have been established, the initial heading shown on the ship's gyro compass is noted. The rudder is then deflected at maximum rate to a predetermined angle, say 20 degrees, and held until a predetermined execute change of heading angle, say 20 degrees, is reached.
4. At this point, the rudder is deflected at maximum rate to an opposite (checking) angle of 20 degrees and held until the ship passes through its initial course to complete the overshoot phase of the maneuver.
5. If a zigzag is to be completed, the maneuver is continued until a second execute of 20 degrees

to the other side is reached. Whereupon, the rudder is again deflected rapidly to an angle of 20 degrees in the first direction. This cycle is repeated through 3rd and 4th executes and so on.

In the following paragraphs, a designation such as 20-10 is used to denote a zigzag or overshoot maneuver which is conducted with maximum rudder angles of  $\pm 20$  degrees and the execute heading change is 10 degrees. The standard maneuver usually included in maneuvering trials is the 20-20 zigzag, although other combinations are also used. The 5-5 zigzag has been advocated as a means for evaluating directional stability of full-form ships.

Figure F2 shows the time history of heading-angle and path change obtained from a simulated 20-20 zigzag maneuver with a typical bulk carrier type ship. As shown by the figure, the primary numerical measures obtained from the overshoot maneuver are the time to reach execute change of heading angle, overshoot heading angle, and overshoot width of path. The zigzag maneuver provides the additional measures of reach and period which are perhaps more significant for frequency response analyses than establishment of handling qualities. The time to reach execute is a direct numerical measure of ability to rapidly initiate changes in course. The heading and path-width overshoots are measures of course-checking ability and are indicative of the amounts of anticipation and latitude of error that the helmsman is permitted if he is to remain within tolerable limits of the maneuver. It should be mentioned that, for real ships, path-width data require elaborate instrumentation and therefore are seldom obtained on ship trials, whereas such data are easily acquired in the computer simulation. The ability to initiate and check a course change rapidly is one of the most important handling qualities of a ship. This is particularly true for bulk carrier ship types which operate in restricted areas where there is a risk of collision and major pollution. In such a situation, it is desirable for a ship to have the capability of making a moderate heading change rapidly to avoid an obstacle on the one hand, but then be able to check its swing to avoid another obstacle or grounding the ship on the other hand. The first half cycle of the 20-20 zigzag or the so-called overshoot maneuver, provides an excellent means for objectively evaluating this inherent capability irrespective of questions such as human response and instrumentation. On a comparative basis, the best ship is the one which combines the least time to reach the execute heading change with the smallest overshoot heading angle and width of path. These characteristics are not always compatible since they depend both on the inherent control effectiveness and degree of inherent directional stability or instability. The following trends are expected to apply when comparing numerical measures from 20-20 overshoot maneuvers for ships of equal size having equal control effectiveness but with different degrees of inherent stability or instability:

1. The time to reach the execute heading-angle change should be about the same.
2. The overshoot heading angle should become smaller as the degree of inherent instability is decreased.
3. The overshoot width and total width of path should both be decreased as the degree of inherent instability is decreased.

#### Turning Circles

The turning circle is a definitive maneuver which is intended to provide quantitative measures of the effectiveness of the rudder in producing steady-turning characteristics. It is the oldest, most



familiar, and most widely used of the definitive maneuvers. Certain of the handling qualities defined by this maneuver were generally considered to be more important to naval than to most sea-going merchant ship applications. With the advent of VLCC's, however, these handling qualities have recently received a considerable amount of attention particularly with regard to situations such as turning around in harbors or restricted areas. The standard procedure for the conduct of such maneuvers on an actual ship are as follows:

1. The propeller speed is adjusted to an rpm corresponding to a predetermined speed and when a steady rpm is achieved, the throttle settings are not changed for the balance of the maneuver.
2. The rudder is manipulated as necessary until a "practically" straight course has been obtained and held for one minute.
3. After steady conditions on straight course have been established, the initial heading on the ship's gyro compass is noted. The rudder is then laid to a predetermined angle, say 35 degrees, and held until a change of heading of generally at least 540 degrees has occurred at which point the maneuver is terminated.

Figure F3 shows path data from a simulated 35-degree starboard steady-turning maneuver performed for a typical bulk carrier type ship. The numerical measures of primary interest are the tactical diameter, advance, transfer, and steady-turning diameter, as defined on the figure, and also the times to change heading 90 and 180 degrees, and speed loss in turning. All of these measures should be taken into consideration in defining handling qualities associated with this type of maneuver.

#### Stopping Maneuvers

In addition to the three primary types of definitive maneuvers, simulated stopping maneuvers are regularly performed. To perform such studies, it is necessary to have a time history of the propeller rpm which, for new ship designs, is usually provided by the customer based on the characteristics of other similar ships. The time history of change in propeller rpm simulated for a typical bulk carrier ship type is shown in Figure F4. Typically the following three types of stopping maneuvers are performed in this phase of the evaluation (assuming ideal conditions of calm sea, unrestricted deep-water, and no wind):

1. Uncontrolled - rudder held fixed at zero angle throughout the entire maneuver.
2. Controlled - rudder manipulated during the maneuver by means of a well adjusted autopilot just enough to maintain original course.
3. Fishtailing - rudder is moved back and forth through large right and left rudder angles at maximum deflection rate to aid in slowing the ship. The simulated path for each of these three types of stopping maneuvers is shown by Figure F5 for the same ship whose rpm time history is given by Figure F4. The primary numerical measures obtained from such stopping maneuvers are: head reach, side reach, total heading change from base course, and time to reach zero speed.

Of course, the foregoing types of stopping maneuvers are not too useful for predicting actual ship behavior due to the neglect of important effects such as those due to shallow-water, currents, wind, and waves. Furthermore, for similar reasons, it is more difficult to apply the data to correlation studies. Nevertheless, they do provide guidance in the design stage for evaluating the relative effectiveness of auxiliary stopping devices.

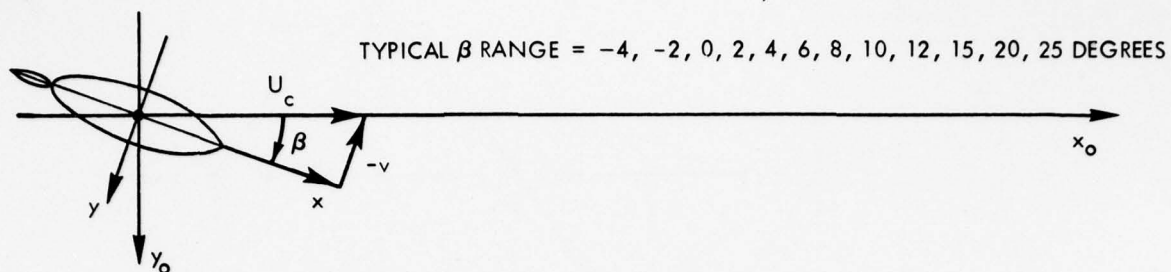
## (a) STATIC DRIFT ANGLE TEST

 $\beta$  Varies $\delta_r = 0$ 

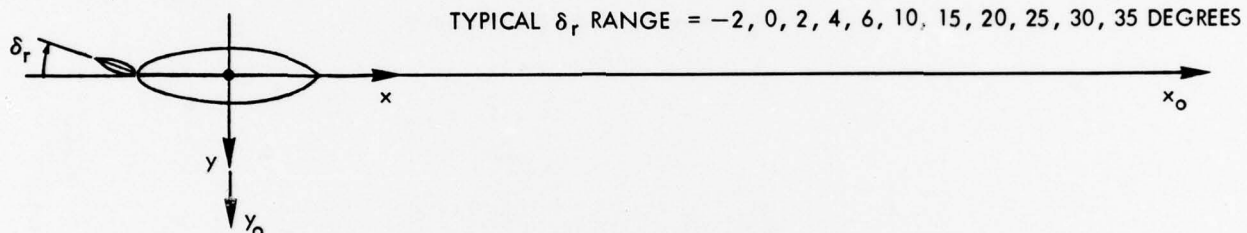
$$\sin \beta = -\frac{v}{U_c}$$

$$\Psi = 0$$

$$y = 0$$



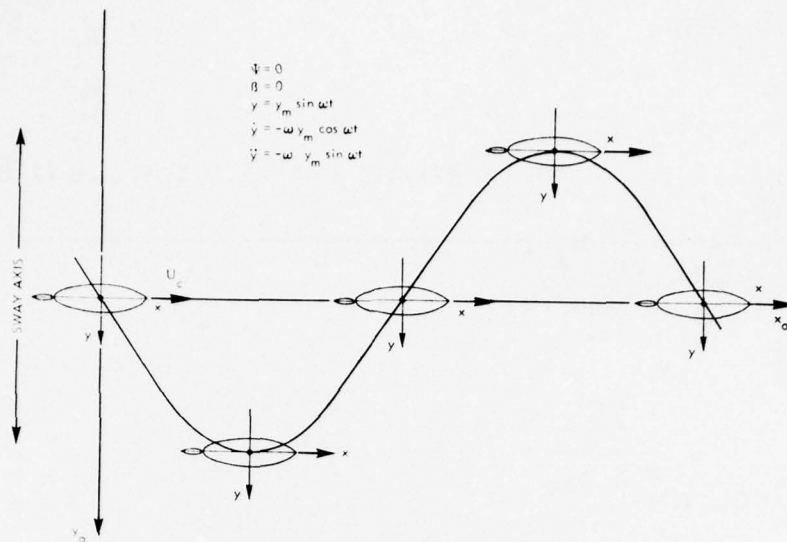
## (b) STATIC RUDDER ANGLE TEST

 $\beta = 0$  $\delta_r$  Varies

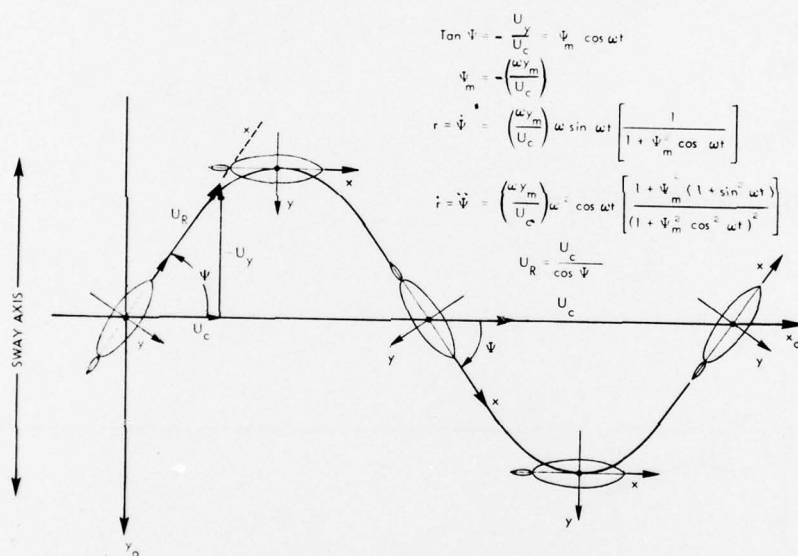
## (c) STATIC DRIFT AND RUDDER ANGLE TEST

 $\beta$  Varies $\delta_r$  Varies

Fig. 1: (a) Static mode test conditions

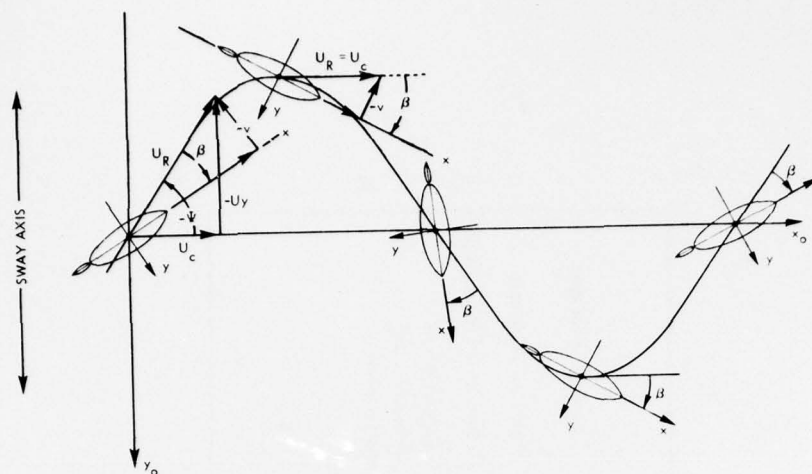


(b) Pure-swaying mode test conditions



(c) Pure swaying mode test conditions with a drift angle  $\beta = 0$  degrees





(d) Pure-yawing mode test conditions with a drift angle  $B < 0$  degrees

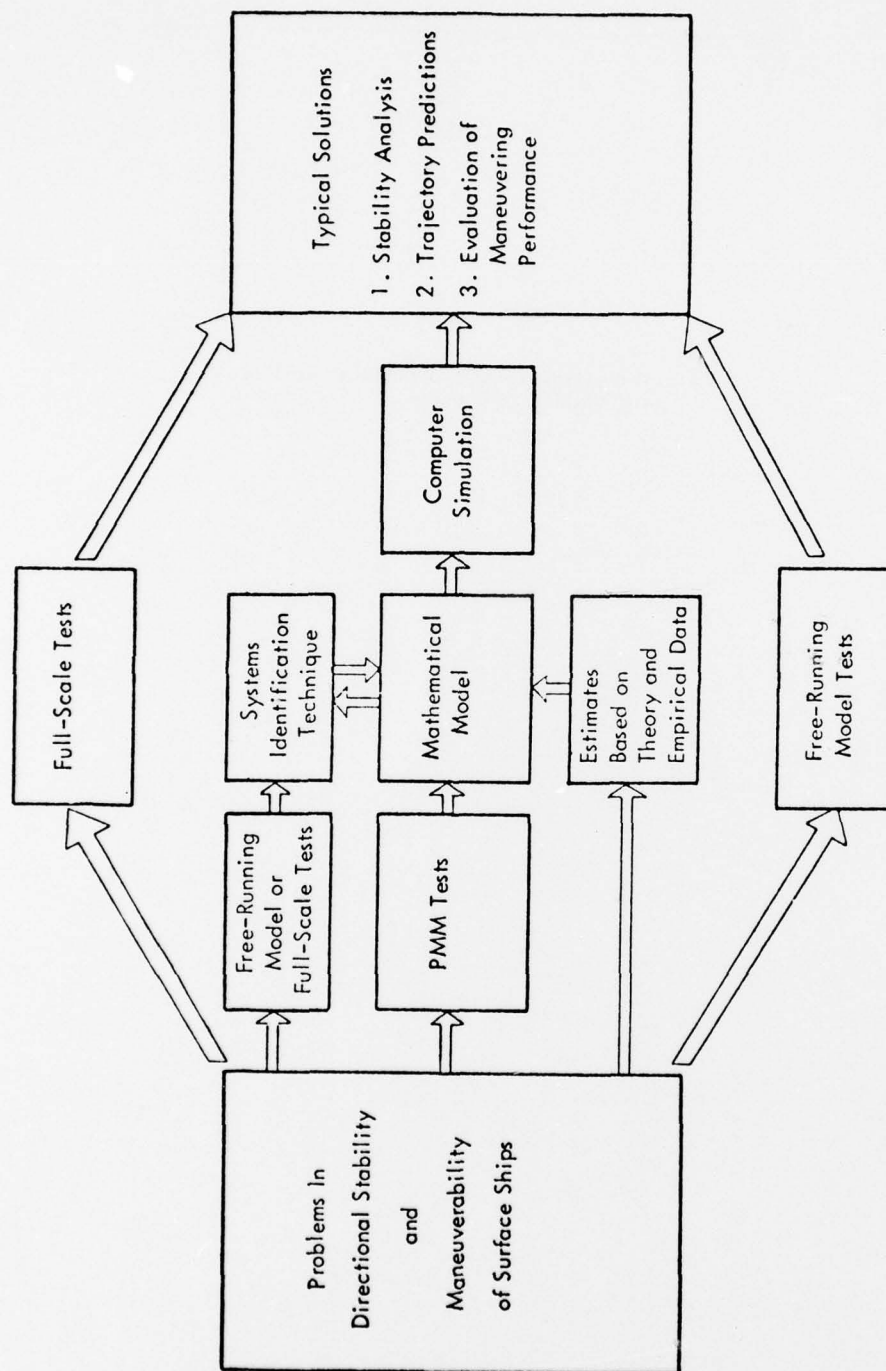


Fig. 2: Approaches to solutions of surface-ship directional stability and maneuverability problems

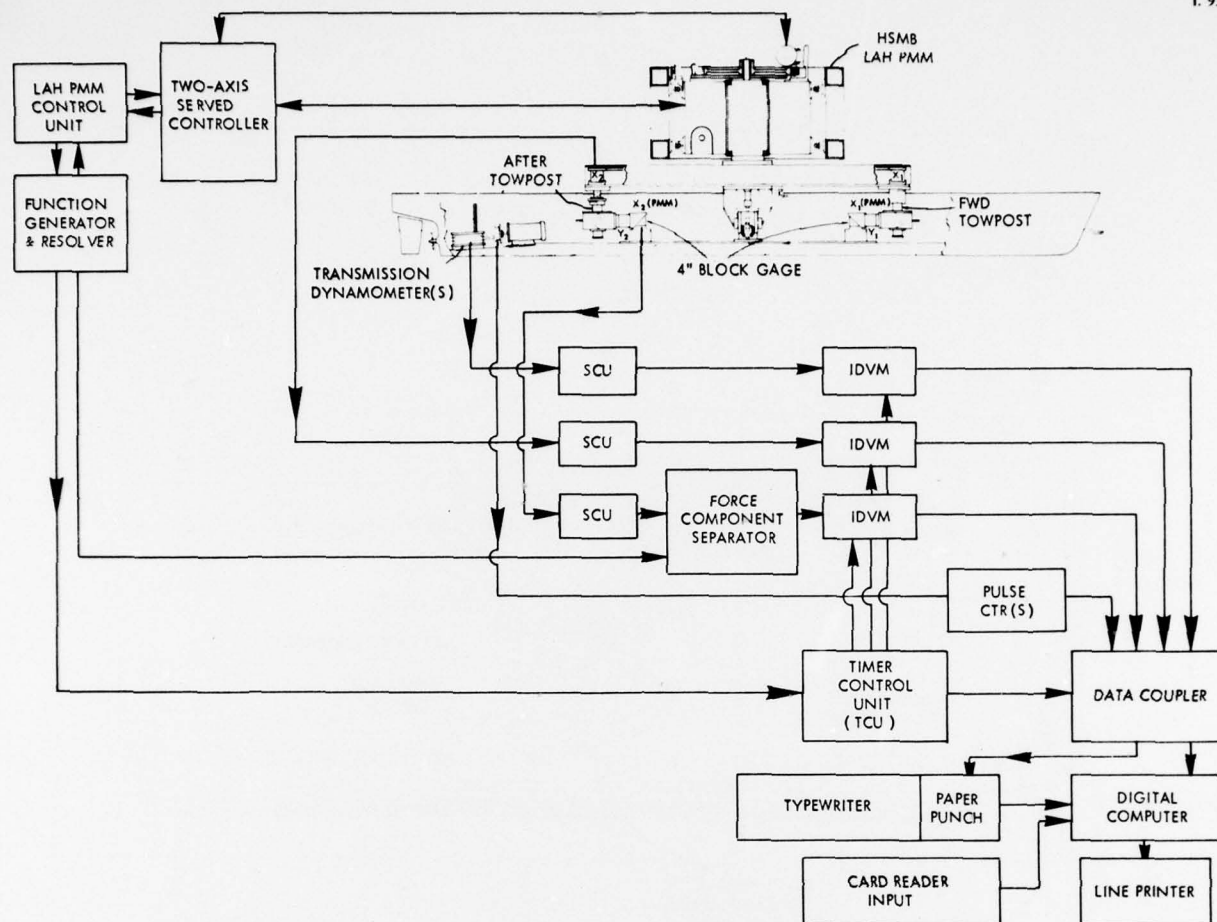


Fig. 3: Schematic of HSMB LAHPMM system



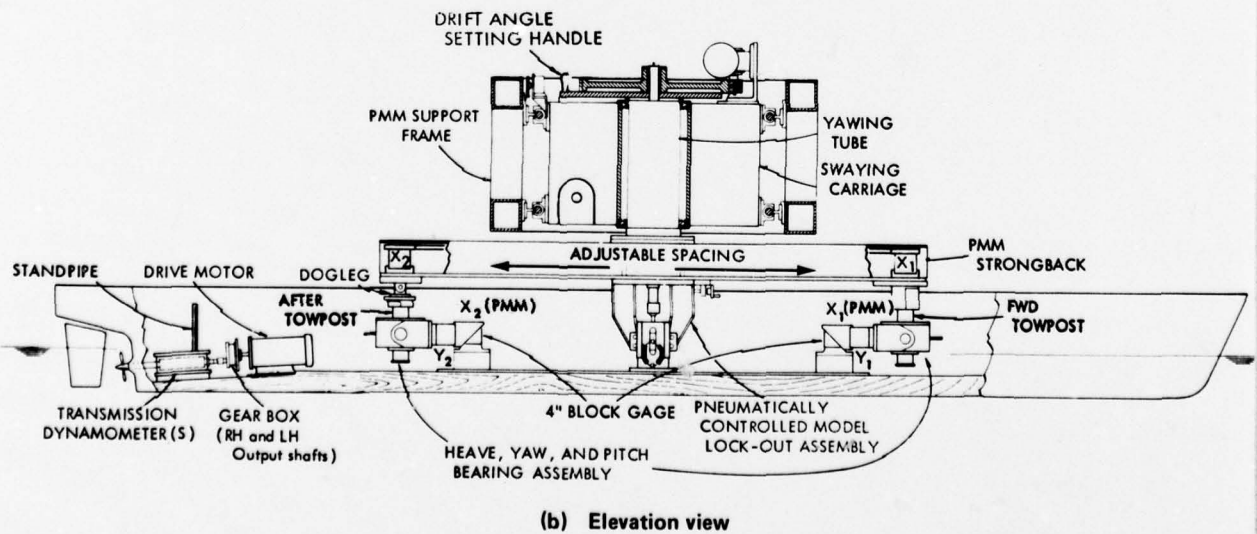
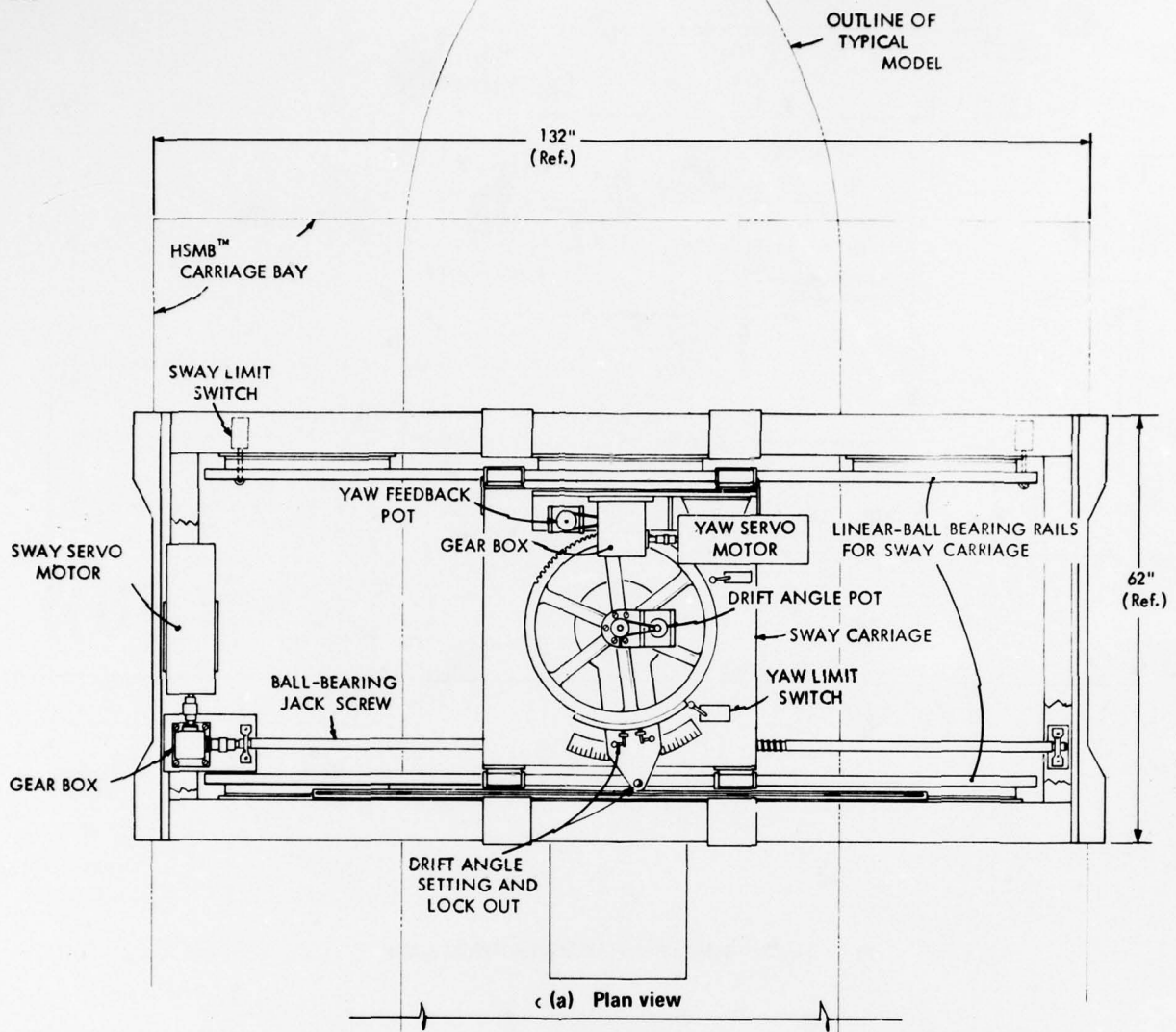


Fig. 4: Integrated surface ship towing system used for resistance, propulsion and LAHPMM tests

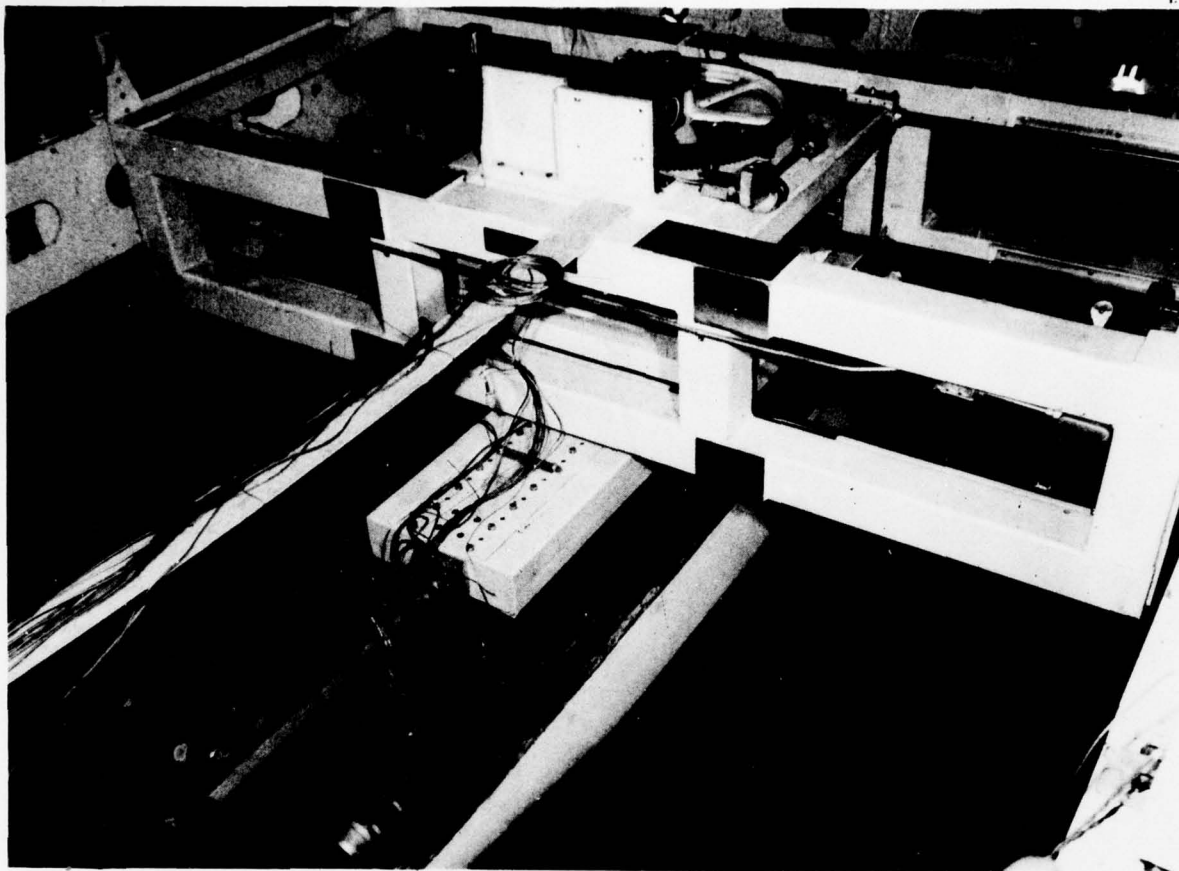


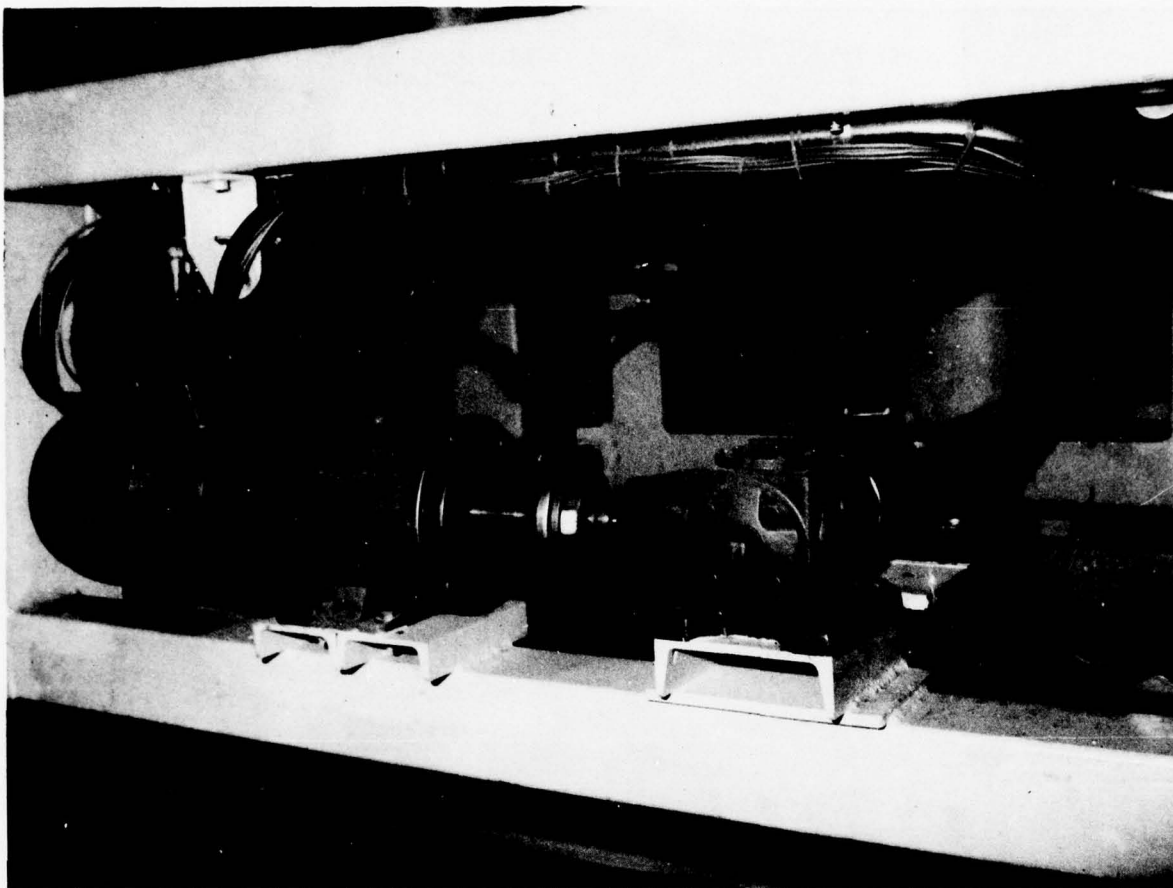
Fig. 5: HSMB LAHPMM with MARINER model attached

(a) View of LAHPMM frame, strongback, model and propulsion system



Fig. 5: (b) Close-up view of swaying carriage, yaw servo and sway servo systems





**Fig. 6:** Swaying carriage servo-ball-bearing jack screw drive system

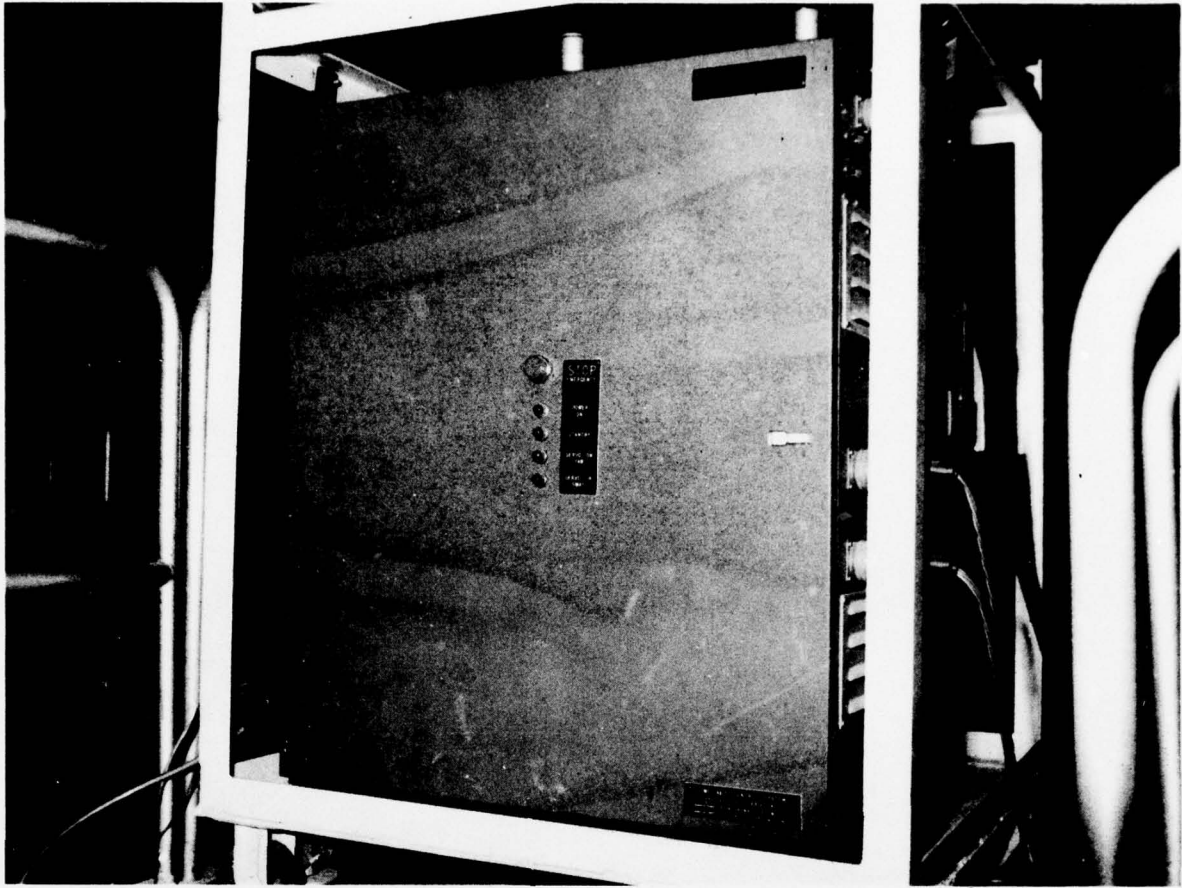


Fig. 7: Two-axis servo controller  
(a) Exterior view

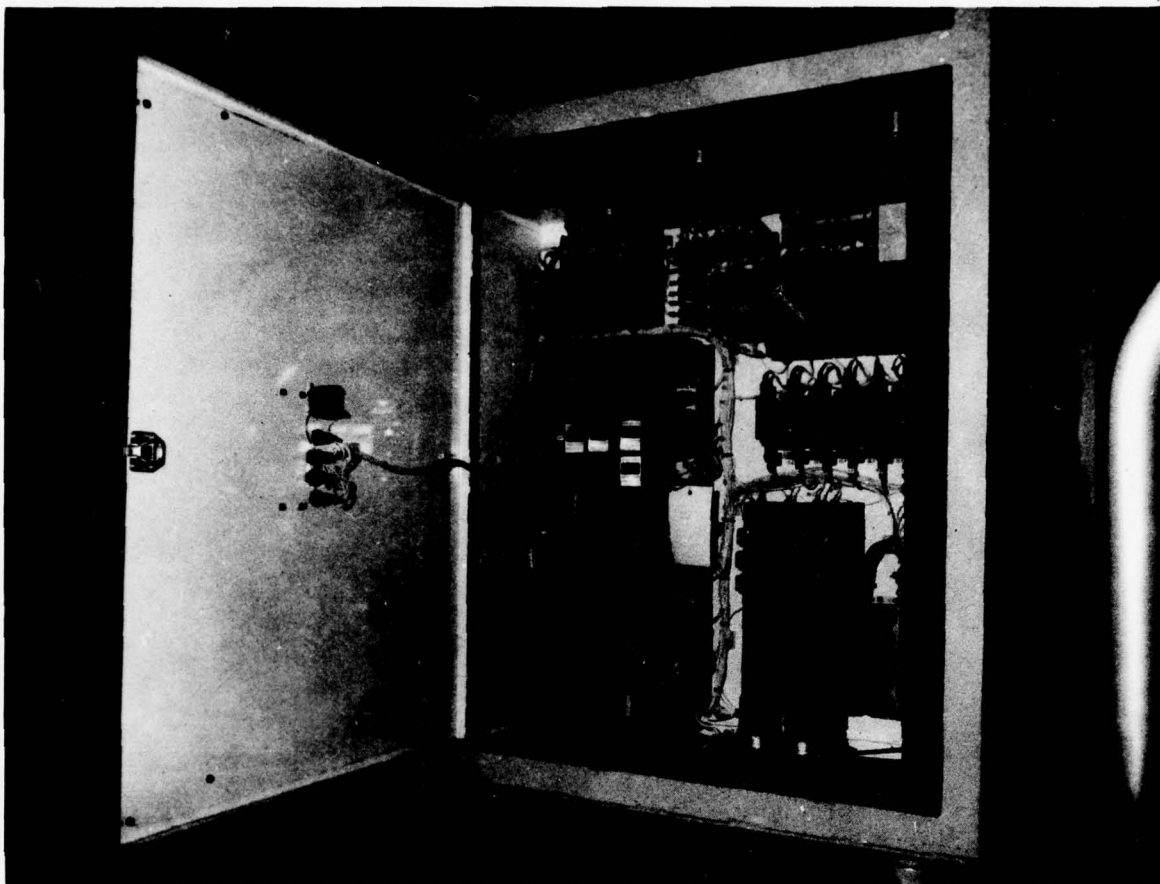


Fig. 7: (b) Interior view



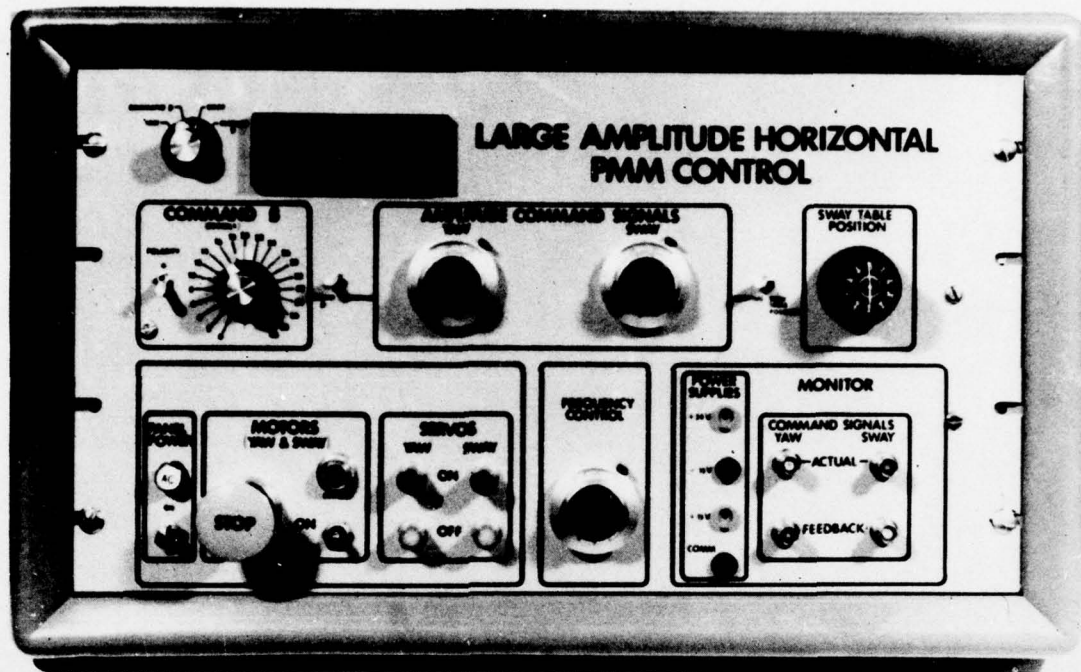


Fig. 8: HSMB LAHPMM control unit

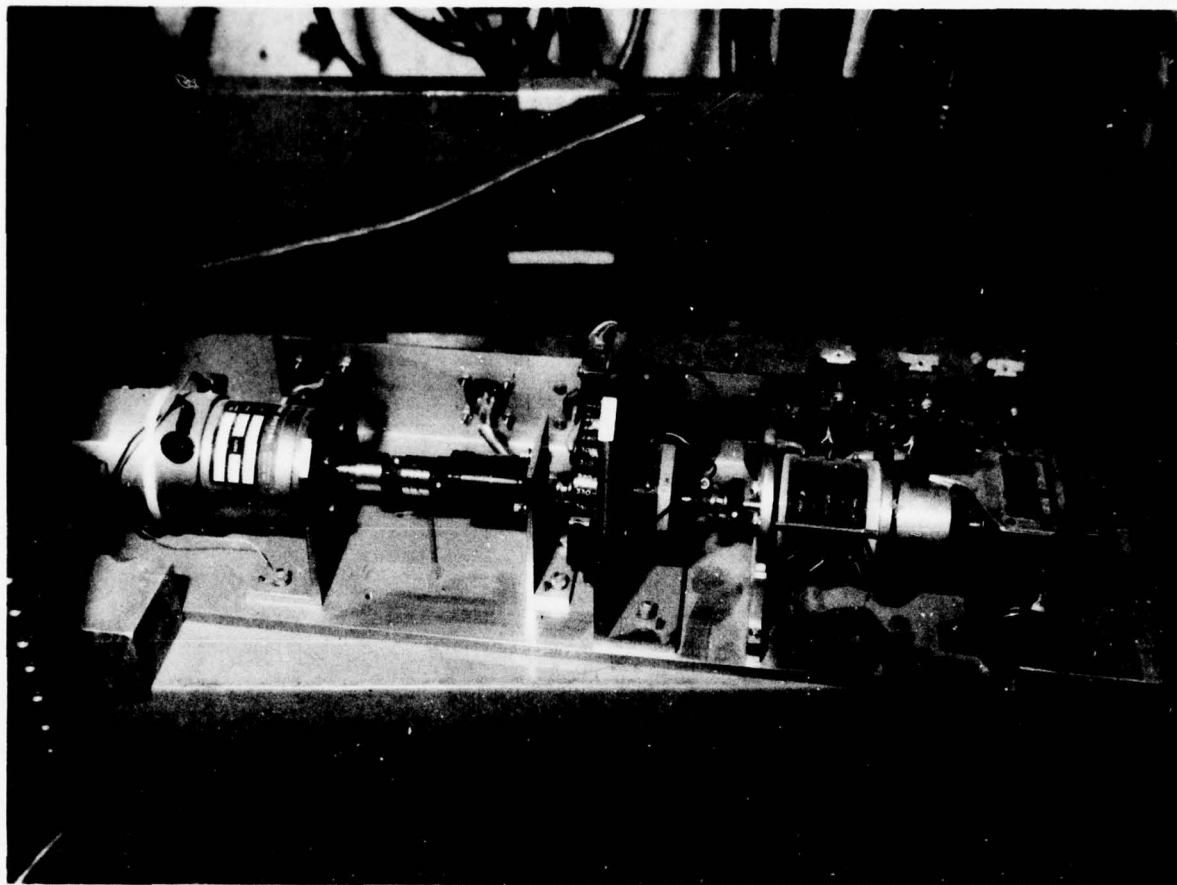
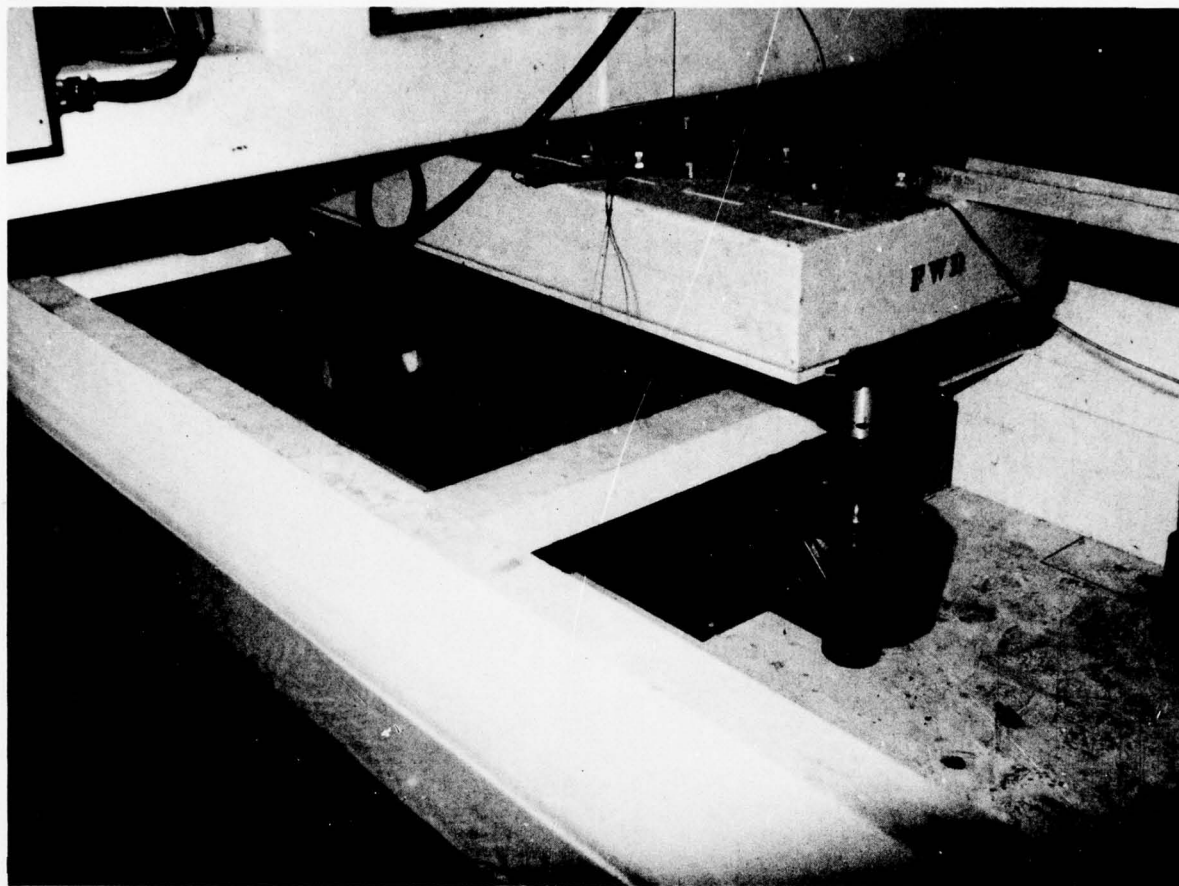


Fig. 9: Function generator and resolver assembly



**Fig. 10: LAHPMM model attachment system**  
**(a) Forward towpost-gage assembly and model lockout**



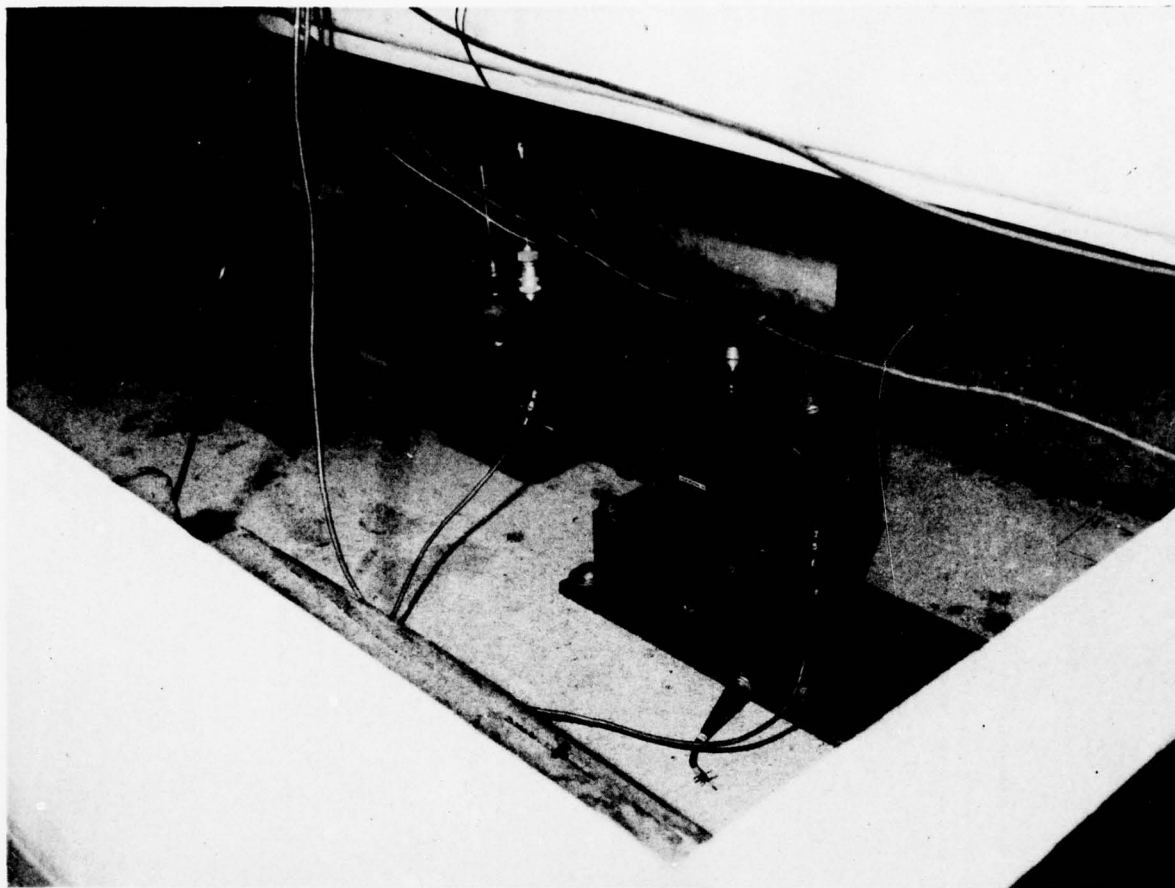
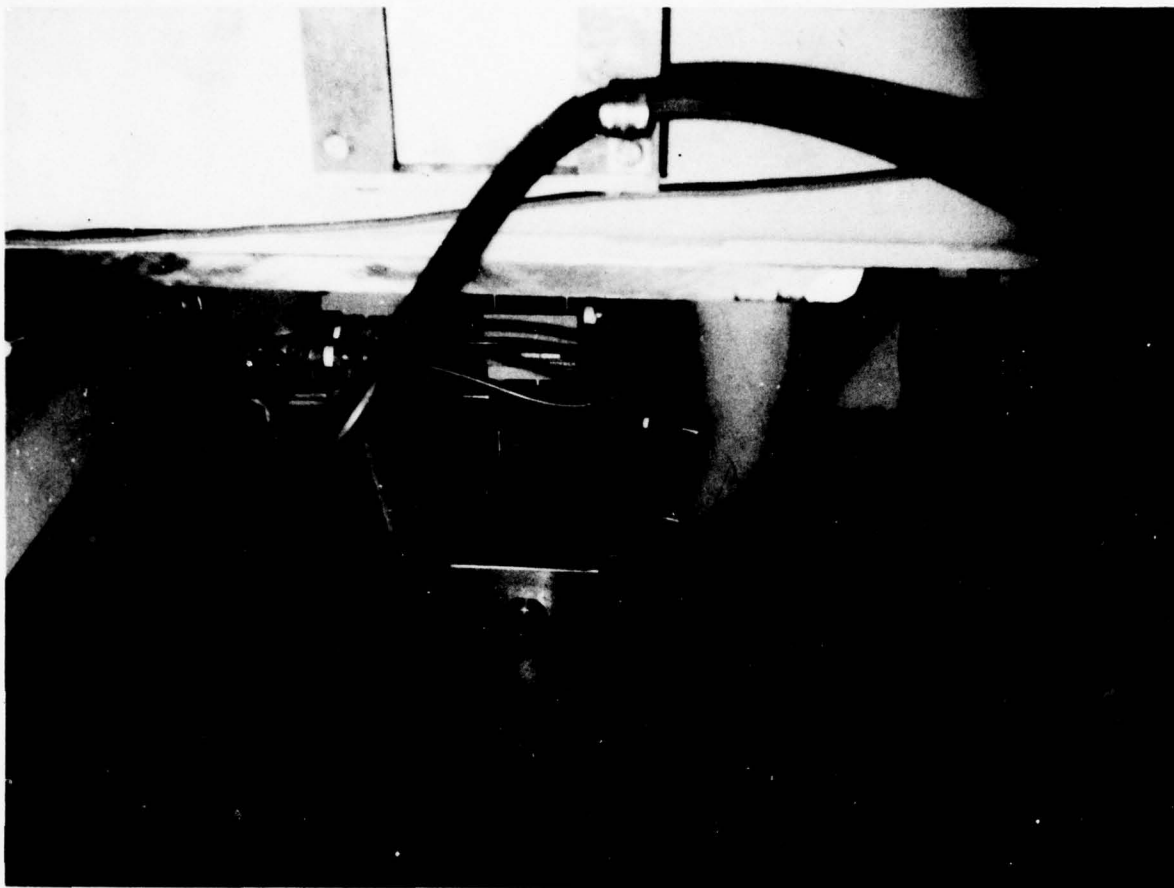


Fig. 10: (b) After towpost-gage assembly



**Fig. 11: Model lockout system**

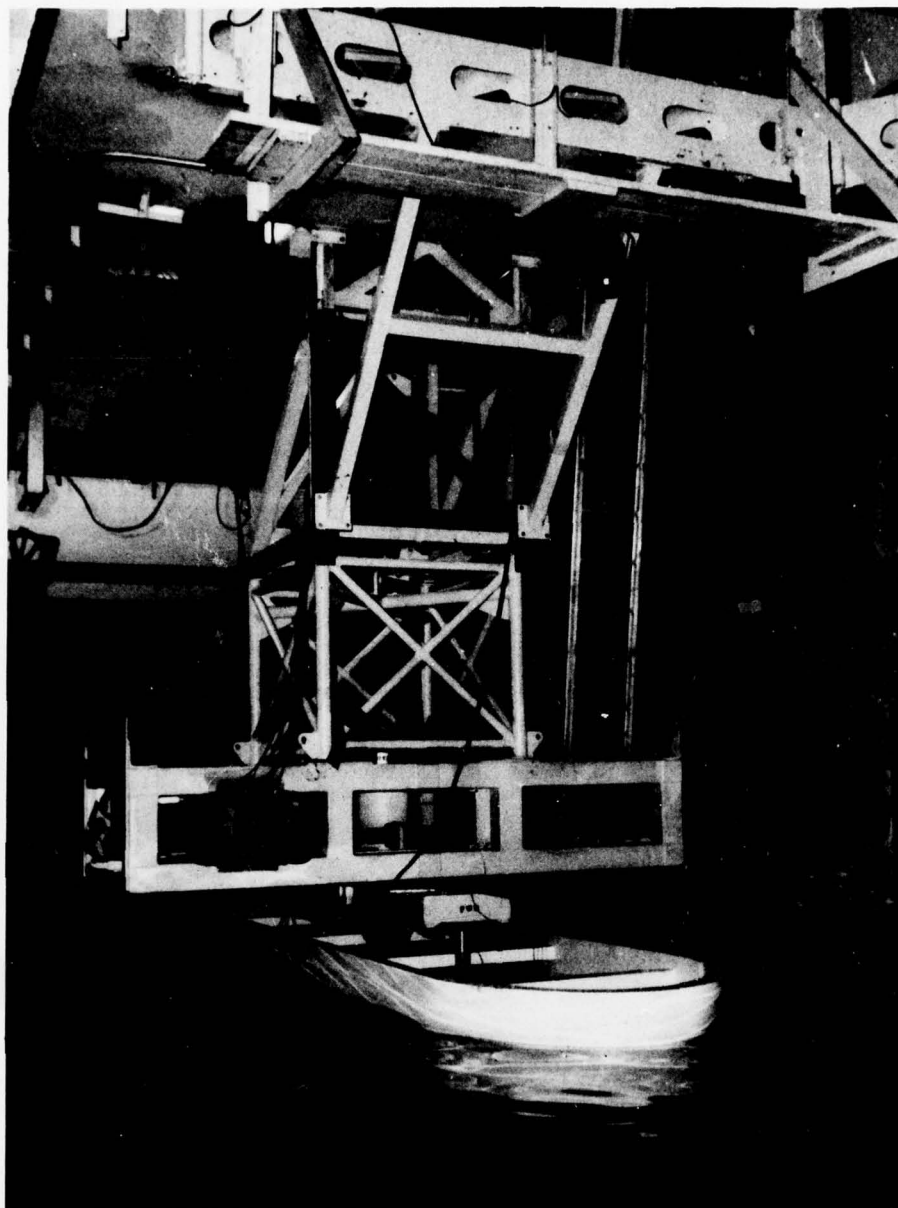


Fig. 12: Arrangement for tests in shallow water using the LAHPMM



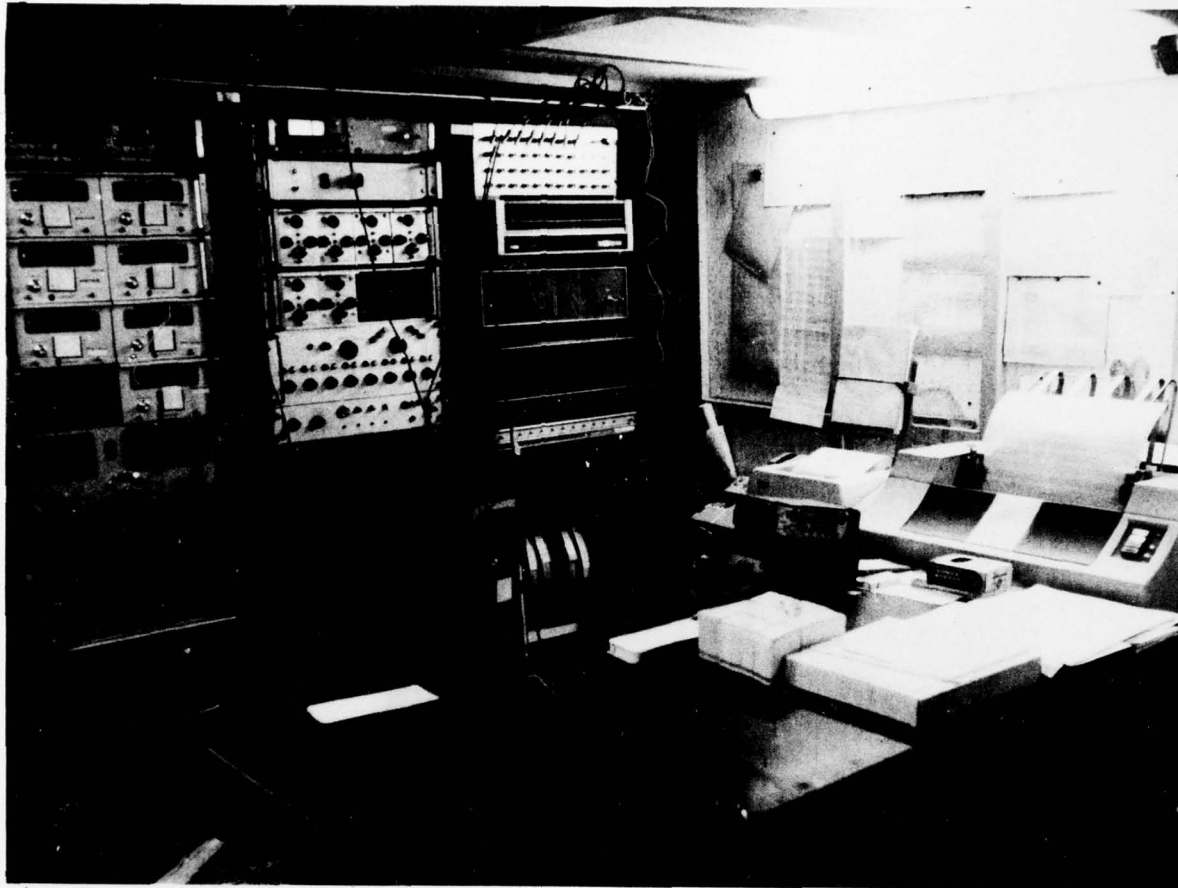


Fig. 13: HSMB data acquisition and data processing systems

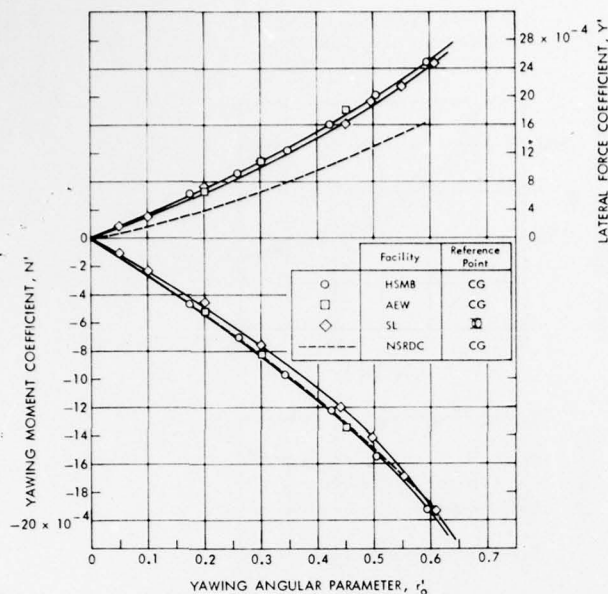


Fig. 14: Comparison between results obtained from LAHPMM yawing mode tests with rotating arm tests for the MARINER.  $\beta = 0$  condition

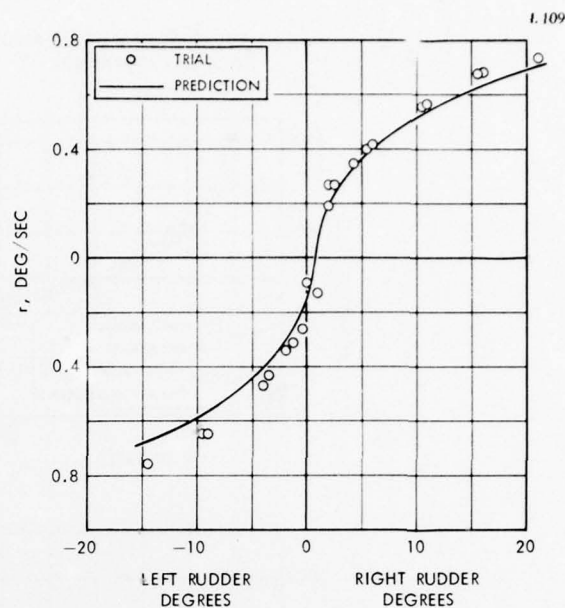
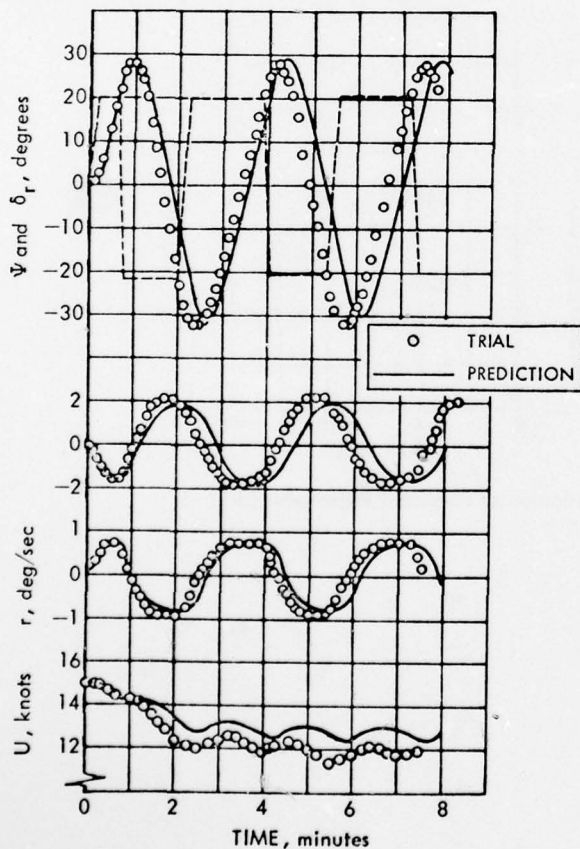


Fig. 15: Comparison between full-scale and computer simulated trajectories for a spiral maneuver at approach speed of 15 knots of the MARINER



Note: 20-20 Z maneuver simulation run with exactly  $\pm 20$  degrees rudder changes.

Fig. 16: Comparison between full-scale and computer simulated trajectories for a 20-20 zigzag maneuver of the MARINER

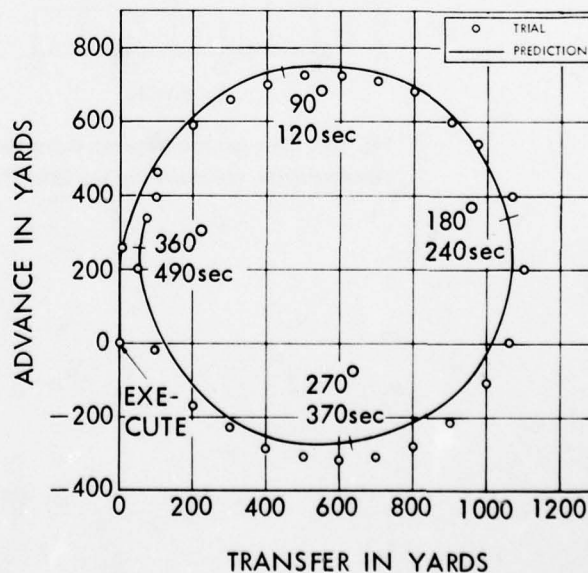
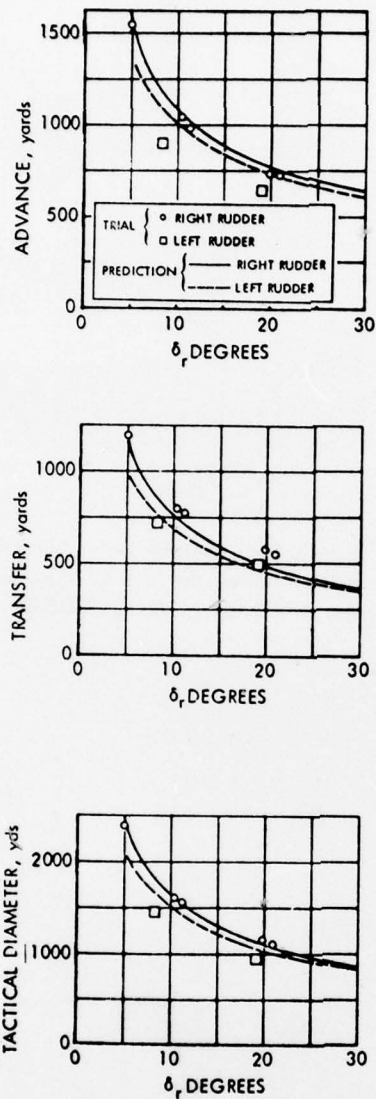


Fig. 17: Comparison between full-scale and computer simulated trajectories for a turn. Approach speed of 15.4 knots; 20.9 degrees right rudder

(A) ADVANCE, TRANSFER AND TACTICAL DIAMETER



(B) FINAL TURNING DIAMETER, DRIFT ANGLE, TURNING RATE AND FINAL SPEED

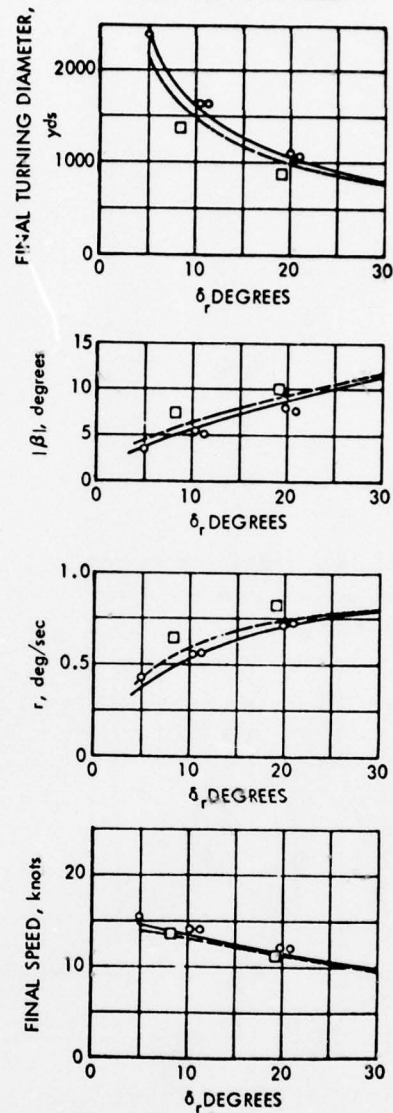


Fig. 18: Comparison between full-scale and computer simulated trajectories for steady-turning maneuvers of the MARINER



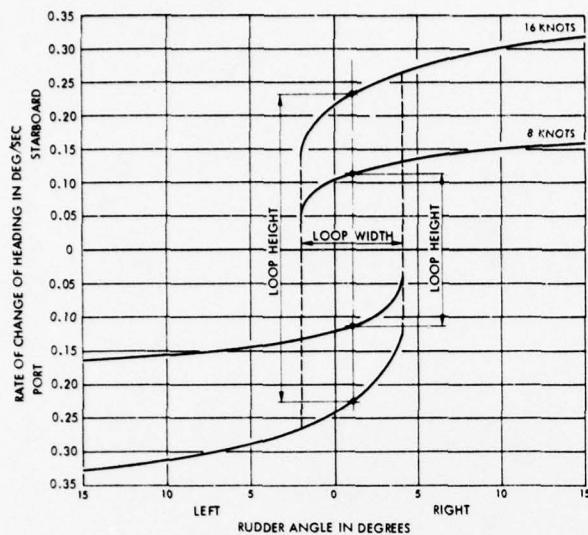


Fig. F1: Results of a simulated spiral maneuver for a typical single-screw bulk carrier type ship.

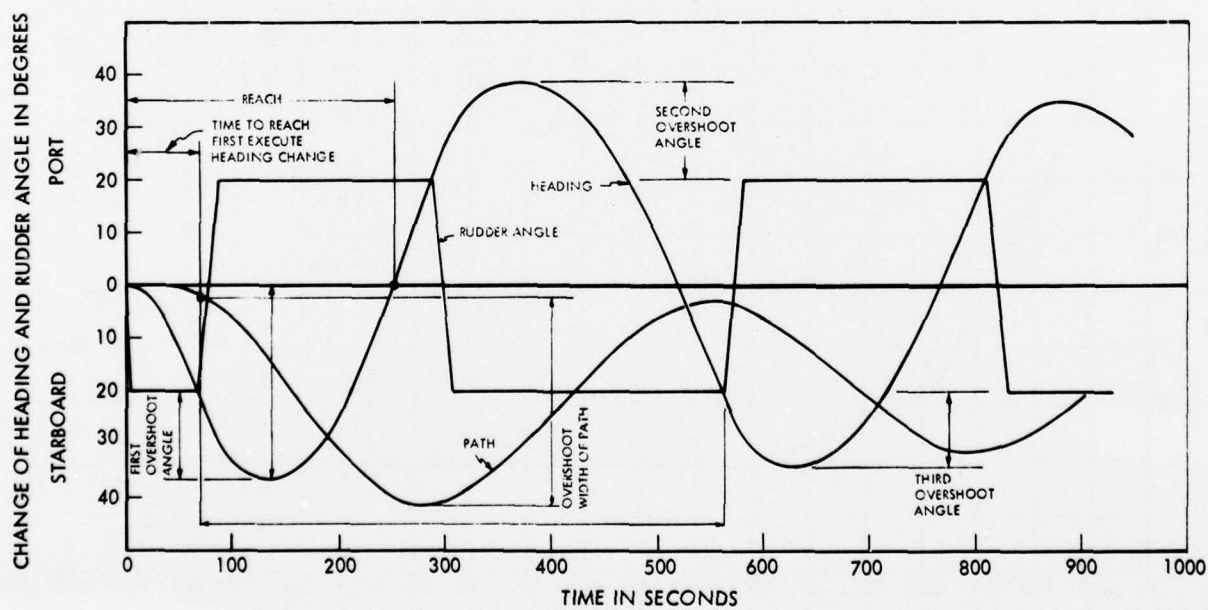
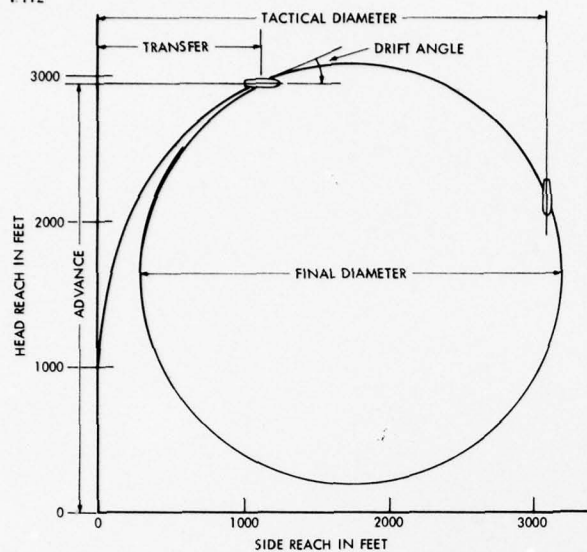
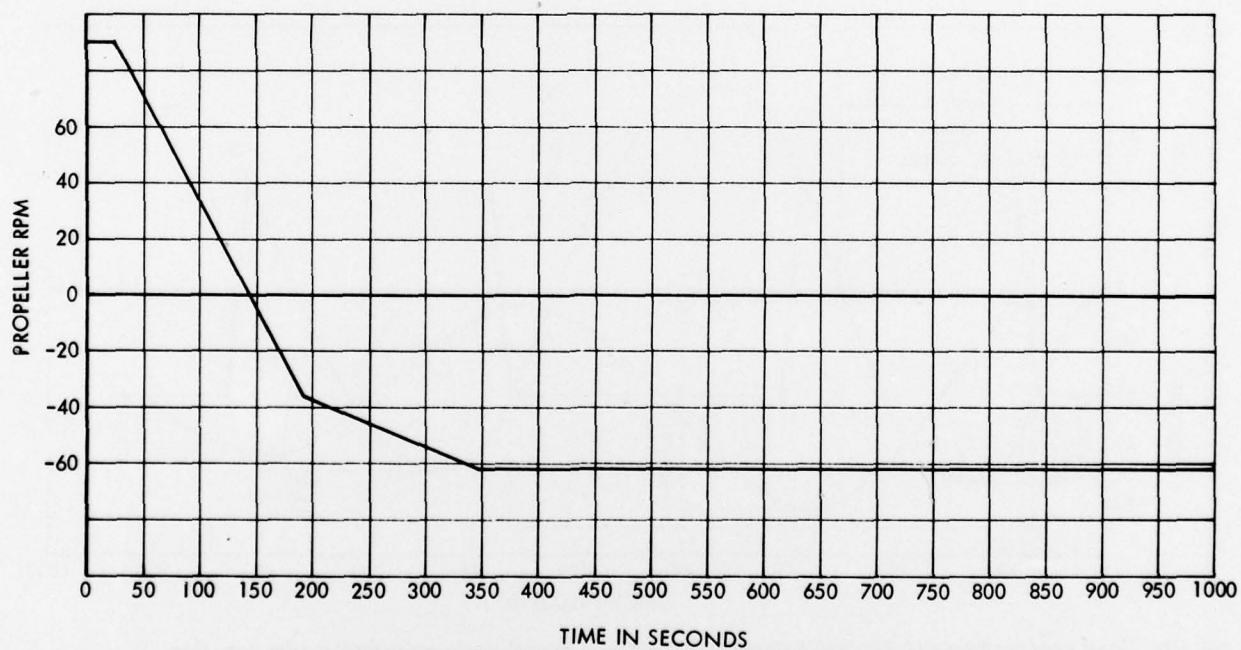


Fig. F2: Time history of a simulated 20-20 zigzag maneuver for a typical single-screw bulk carrier type ship



**Fig. F3: Path during a simulated 35-degree starboard steady-turning maneuver for a typical single-screw bulk carrier type ship**



**Fig. F4: Time history of change in propeller rpm for typical bulk carrier type ship used in simulated stopping maneuvers**

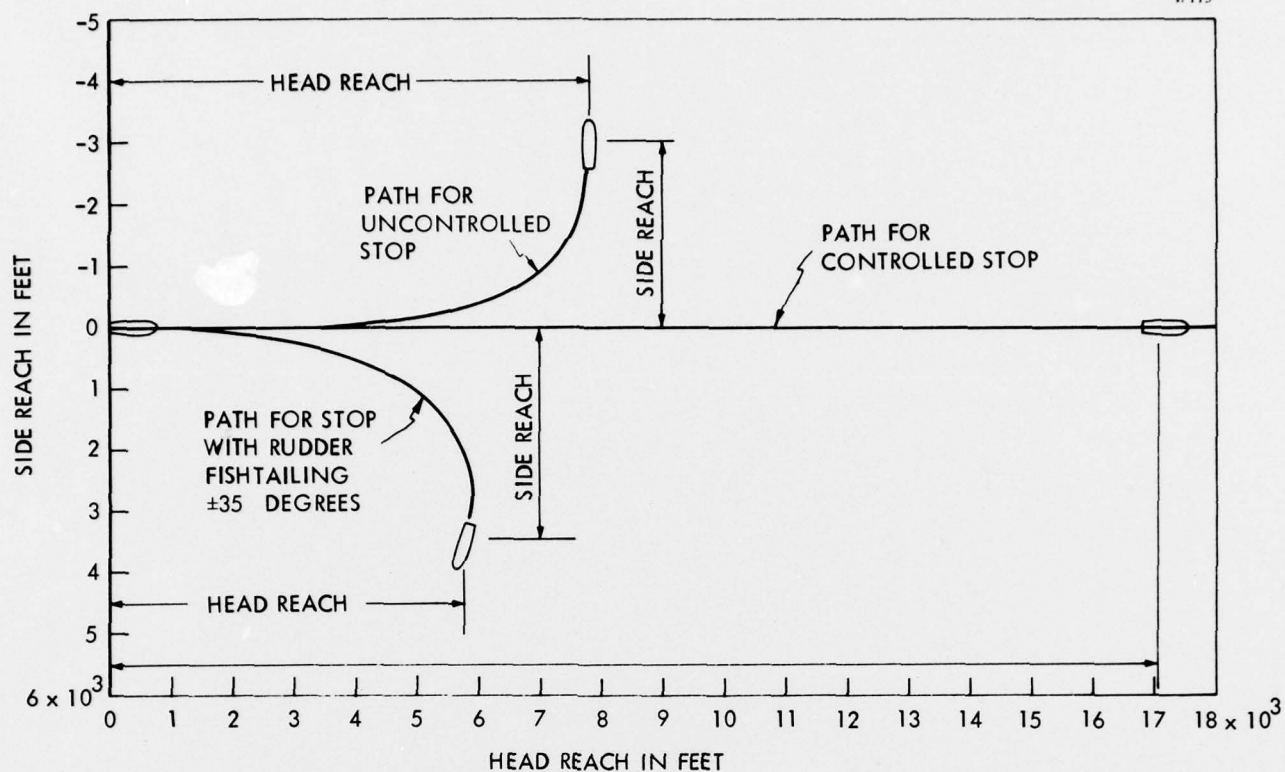


Fig. F5: Path during simulated stopping maneuvers for a typical bulk carrier ship type at an approach speed of 16 knots



# CPMC — A NOVEL FACILITY FOR PLANAR MOTION TESTING OF SHIP MODELS

O. GRIM, P. OLTMANN, S. D. SHARMA and K. WOLFF  
Institut für Schiffbau, Hamburg, Germany.

The Computerized Planar Motion Carriage (CPMC) recently operationalized at Hamburg for better determination of ship maneuverability has several novel features. Carriage controls were specifically designed for generating transient motions. Superposition of four independent drives can generate any realistic horizontal planar motion. A freely programmable, process-control computer executes carriage control, model control, data acquisition and run evaluation. The CPMC can operate either in the towing mode (for measuring hydrodynamic forces on captive models moved along predetermined trajectories) or in the tracking mode (for following and recording trajectories of freely maneuvering models). Sample results of inaugural experiments in each mode are presented.

## INTRODUCTION

### Purpose

The purpose of this paper is to introduce to the international community of naval hydrodynamicists a novel model-testing facility recently operationalized at Hamburg with the aim of determining the maneuvering capabilities of ships more accurately and completely than was previously possible. We have chosen to call it CPMC, an abbreviation for Computerized Planar Motion Carriage. It incorporates the pertinent features of a conventional towing carriage and of special devices for conducting maneuvering experiments such as rotating arms, so-called planar motion mechanisms, and xycarriages. Besides, it has several unique capabilities, not available to our knowledge in any existing single facility, such as independent multiple drives in 3 degrees of freedom, generation of precise transient motions, alternative towing and tracking modes, and flexible computer programming of carriage controls, model controls, data acquisition and run evaluation. The audience will hopefully agree with the organizers that the CPMC is a suitable subject for the opening paper of a Symposium devoted to the "Unsteady Hydrodynamics of Marine Vehicles".

### Brief history of PMMT

In the context of tankery the term planar motion model testing (PMMT) has come to connote in recent years the determination of velocity and acceleration dependent hydrodynamic forces on ocean vehicles by generating idealized planar motions (either horizontal or vertical) of captive models in a tank, recording the resulting forces and finally analysing and synthesizing the data in a manner appropriate to the chosen mathematical form for the equations of motion. Simply steady speed rectilinear oblique towing or even circular rotating arm tests are not considered PMMT. In this particular sense of the term the first published results of PMMT, to the authors' knowledge, were those of Horn and Walinski (1958, 1959).<sup>\*</sup> They used a pair of cranks of 20 cm radius to generate

nearly pure harmonic sway and yaw motions of a captive ship model in the *Versuchsanstalt für Wasserbau und Schiffbau*, Berlin. It is a pity that this pioneering and comprehensive paper, which contains a complete recipe for generating purer yaw motions by means of a pair of Scotch yokes rather than slider cranks and for analysing the recorded forces, has been almost totally ignored in the pertinent literature. The term planar motion mechanism (PMM) was of course coined by Gertler (1959) and Goodman (1960) to denote an ingenious two-point slider-crank oscillator of 1 inch radius designed mainly for testing submarine models at the David Taylor Model Basin (DTMB) near Washington, D.C. This PMM system and subsequent improved versions are reported to have been operating successfully at DTMB for almost two decades now, although nearly all the results seem to be classified. It was followed up by similar devices all over the world: Paulling and Sibul (1962) reported a PMM at the University of California, Berkeley (of 2 inch maximum sway amplitude); Keil and Thiemann (1963) at the *Institut für Schiffbau*, Hamburg (6 cm); Zunderdorp and Buitenhok (1963) at the Technological University, Delft (30 cm); Matora and Fujino (1965) at the University of Tokyo, Tokyo (35 cm); Strøm-Tejsen and Chislett (1966) at the *Hydro- og Aerodynamisk Laboratorium*, Lyngby (10 cm); Fujii (1969) at the Nagasaki Experimental Tank, Nagasaki (47 cm); Chislett and Smitt (1972) again at the *Hydro- og Aerodynamisk Laboratorium*, Lyngby (75 cm), and this list is certainly not complete. The most outstanding published results seem to be firstly by Leeuwen (1964), who thoroughly investigated frequency effects, Froude-number effects and effects of rudder and propeller on a standard Series 60 model, and secondly by Strøm-Tejsen and Chislett (1966) continued in Chislett and Smitt (1974) who demonstrated how to identify well over 50 empirical coefficients in the nonlinear equations of motion in 3 degrees of freedom and to obtain predictions for full scale maneuvers in fair conformity with actual trial trip results.

<sup>\*</sup>References are identified by author(s) and year and listed in alphabetical order by first author, and if necessary in chronological suborder, at the end of the text.

In a series of papers Bishop et al. (1970, 1973, 1973, 1974, 1974) took a critical look at the PMMT technique and pointed up the need for neatly separating formally linear memory (motion history) effects from truly nonlinear effects in modelling hydrodynamic forces as functionals of motions. Using the classical technique of Fourier transforms they also demonstrated, although only within the linear range, the equivalence of representing memory effects either through impulse response or through frequency response functions. This had already been exploited earlier by Cummins (1962) and Kotik and Mangulis (1962), at least for ship motions in the vertical plane. According to Burcher (1975) and Nomoto (1975) the general consensus among maneuvering experimenters now seems to be that memory effects are not a genuine problem of any realistic ship maneuvers but rather an artificial problem of PMMT created by the use of low amplitude, high frequency devices. Leeuwen (1969) had already reached this conclusion several years ago and proposed a horizontal oscillator of extremely large amplitude (about 375 cm) and low frequency in order to simulate ship motions realistically.

#### Motivation for CPMC

When the *Institut für Schiffbau der Universität Hamburg* (IfS) joined hands with the *Hamburgische Schiffbau-Versuchsanstalt* (HSVA) - and with the *Technische Universität, Hanover*, and the *Germanischer Lloyd, Hamburg* - to form a special research pool for shipbuilding designated the *Sonderforschungsbereich Schiffbau* (SFB 98) in 1970, an opportunity arose at least to plan (and partially to build) new ship model testing facilities on a rather grand scale. In particular, one of the projects entitled "Safety of Ships against Collisions" called for a new technique of determining the maneuvering capability of ships more accurately and completely than hitherto considered possible. The team (Keil, Oltmann and Sharma) responsible for planning an experimental device for this purpose was at first considering a PMM of about 80 cm amplitude which would have fitted well into the trend of so-called large amplitude PMM which seemed to be roughly doubling in amplitude every eight years since 1958. However, a chance discussion with Professors Gerritsma, Glansdorp and Meier at Hamburg in early 1971 soon convinced us that such a device, while presumably acceptable for routine tests, would be totally inadequate as a research tool. Only a device of the magnitude proposed by Leeuwen (1969) could be expected to lead to an improved mathematical model for the hydrodynamic forces as functionals of motions, which was needed to calculate radical maneuvers typical of collision avoidance at the last minute. After thorough internal deliberations three firms were invited to submit feasibility studies for various alternatives which were scrutinized by independent reviewers appointed by the *Deutsche Forschungsgemeinschaft*, which was to share the financing with the HSVA. The ultimate product which emerged was CPMC, the subject of this paper. Just to complete the chronology we add that the building contracts were awarded to Messrs. Kempf & Remmers, Hamburg, and to Siemens AG, Erlangen and Hamburg, in 1972; the detailed designs were completed in 1973, and assembly began in 1974. The final adjustments and comprehensive acceptance trials took up the better part of 1975. The CPMC was formally declared operational on 8 October 1975. An advance announcement had been made in a note to the 14th ITTC by Krappinger and Sharma (1975).

#### NOTATION

##### Abbreviations

CPMC	Computerized planar motion carriage
HSVA	<i>Hamburgische Schiffbau-Versuchsanstalt</i>
IfS	<i>Institut für Schiffbau, Hamburg</i>
ITTC	International Towing Tank Conference
K	Amplifier
M	Servomotor
P	Proportional control
PI	Proportional-integral control
PMM	Planar motion mechanism
PMMT	Planar motion model testing
PT	Paper tape
PTI	Paper tape input
PTO	Paper tape output
SFB 98	<i>Sonderforschungsbereich Schiffbau</i>
T	Tachometer
TT	Teletype
TTC	Teletype console

##### Symbols

$B$	Beam of model
$Dt$	Basic control cycle (10 ms)
$Dx_0$ etc.	Increments of $x_0, y_0, \psi$ in time step $Dt$
$f$	Frequency in cycles per second
$F_n$	Froude number
$g$	Acceleration due to gravity
$I_a$	Armature current
$I_{xx}$ etc.	Moment of inertia of model about the $x, y$ or $z$ axes
$K, M, N$	Hydrodynamic moments about the $x, y, z$ axes
$L$	Length of model (between perpendiculars)
$m$	Mass of model
$n$	Rate of revolutions of propeller (motor)
$O$	Coordinate origin defined in the model, usually at midship in the waterplane
$p, q, r$	Rates of turn about the $x, y, z$ axes
$T$	Period of oscillation; also model draft
$t$	Time
$U$	Resultant velocity of $O$ in the horizontal plane
$U_0$	Initial value of $U$ in the approach phase
$u, v, w$	Component of $U$ along $x, y, z$ axes
$X, Y, Z$	Hydrodynamic forces along $x, y, z$ axes
$x, y, z$	Coordinate axes moving with the model
$x_G, y_G, z_G$	Coordinates of model center of gravity
$x_0, y_0, z_0$	Coordinates of $O$ in a tank-fixed system
$\bar{x}_0(t)$	Position of main carriage with respect to tank
$\beta$	Drift angle
$\Delta x_0(t)$	Position of $\Delta x_0$ -subcarriage with respect to its nullpoint
$\Delta \Delta x_0, \Delta y_0$	Tracking lag, i.e. position of $O$ with respect to a reference point of the CPMC
$\delta$	Rudder angle
$\delta x_0$ etc.	Position errors (actual value minus required value) of $x_0, y_0$ and $\psi$
$\rho$	Mass density of water
$\phi, \theta, \psi$	Angles of roll, pitch and yaw
$\omega$	Circular frequency in radians per second

**Note** - ITTC standard symbols have been used as far as possible. A prime denotes that the quantity has been nondimensionalized using as fundamental units  $\rho L^3/2$  for mass,  $L$  for length and  $L/U$  for time. A dot denotes time derivative as usual. A hat is used to denote some constant values of a motion variable, usually the amplitude.



## DESIGN DECISIONS

### General considerations

The basic philosophy leading to the design of the CPMC has already been outlined in the Introduction. The general idea was to build a device capable of generating on the model scale every realistic horizontal motion of which a merchant ship of any type is capable. The purpose of the following remarks is to justify some of the major choices which had to be made at the concept formulation stage and for drafting the technical specifications as a basis for the building contract. Naturally, many of these choices were dictated by the given features of the three main facilities, which were already present and had to be integrated into the total system, viz. the towing tank (280 m x 18 m x 6 m), the main carriage (a relatively soft framework structure of nearly 50 Mg mass), and the general purpose process-control computer (Siemens 301).

At this point it is useful to recall that a typical motion required in PMMT is a harmonic variation of pure yaw at constant forward speed and zero drift angle, e.g.

$$\psi(t) = \hat{\psi} \sin(\omega t), \quad u(t) = \hat{U}, \quad v(t) = 0, \quad (1)$$

alternatively in tank-fixed coordinates:

$$\dot{x}_0 = \hat{U} \cos(\hat{\psi} \sin \omega t), \quad \dot{y}_0 = \hat{U} \sin(\hat{\psi} \sin \omega t), \quad \dot{\psi} = \hat{\psi} \omega \cos(\omega t) \quad (2)$$

Evidently, this involves the perfect combination of a constant speed in the tank longitudinal direction with periodic pure oscillations each in the tank longitudinal direction, the tank transverse direction and about a vertical axis. If maximum realistic yaw rates are to be attained *without* exceeding maximum realistic yaw accelerations, transverse amplitudes on the order of a model length are necessary, cf. Leeuwen (1969). With model lengths typically lying in the range of 6 to 8 m at the HSVA this implied utilizing essentially the entire available tank width for the transverse oscillation and established a rather gigantic magnitude for the projected device!

### Carriage mounting versus trailer

It was decided to mount the oscillating device on an independent trailer rather than on the main towing carriage for the following reasons. Firstly, the carriage was not considered a sufficiently stiff base for measuring forces on captive models in unsteady motion. Due to a steady addition of equipment during the past 20 years it had also already reached its maximum designed weight of about 50 tons. Any permanent structural reinforcement of the carriage to increase its stiffness or carrying capacity would have caused a substantial increase in mass with deterioration of its dynamic performance (and hence a reduction of the useful length of run at high speeds) even for non-oscillatory tests. The trailer, of course, would be hooked to the carriage only for PMMT. Finally, the trailer mounted system would cause during its assembly, testing and servicing a minimum disturbance to the routine operation of the carriage, which is the primary source of income for the HSVA and normally in use 16 hours a day, 5 days a week.

### Single versus multiple drives

It is considered an ingenious feature of existing PMM that fully coordinated transverse and rotary

motions of the model can be derived by means of mechanical linkages from the rotation of a single drive shaft. However, this works well only for small amplitudes. If the concept is extended to amplitudes on the order of a few meters, with the possible additional requirement of a longitudinal oscillation, the size and complexity of the linkages becomes simply ridiculous. Hence we chose mechanically independent drives in 3 degrees of freedom, i.e. 3 independent subcarriages for superimposing arbitrary motions  $\Delta x_0(t)$ ,  $y_0(t)$  and  $\psi(t)$  on the generally uniform motion  $\dot{x}_0(t)$  of the main carriage. The subdivision of the motion  $\dot{x}_0(t)$  in the tank longitudinal direction into an almost steady component  $\dot{x}_0(t)$  and an oscillatory component  $\Delta \dot{x}_0(t)$  served the dual purpose of avoiding having to periodically accelerate the enormous mass of the main carriage and of achieving very accurate motion control using the light subcarriage as a corrective for compensating for unwanted fluctuations of main carriage speed.

### Steady speed versus transient control

In principle any periodic motion can be derived mechanically from the uniform rotation of a drive shaft. Exploiting this fact control units of existing PMM are only required to maintain discrete steady speeds of the drive shaft in face of varying load during the run. Having already dispensed with the mechanical linkages for reasons just explained, we took another bold step and demanded precise transient motion control in face of varying loads. Each subcarriage would run on rails, driven by suitable rack and pinion mechanisms, so that the revolutions of the driving motors must, in general, continuously vary in proportion to the required subcarriage speed. Thus we sacrificed simplicity of controls for the sake of mechanical simplicity and complete flexibility of motion. Perfect phase coordination of the independent drives could now only be achieved by providing an input signal of extremely high temporal and spatial resolution and using a sophisticated hybrid control system. Theoretical calculations and simulation studies revealed that it would suffice to use a basic control cycle of 10 ms and feed in new trajectory coordinates from a process-control computer once in every cycle.

### Additional tracking mode

Having demanded the capability of practically arbitrary horizontal planar motion within the entire tank area, it was a logical next step to introduce an additional operating mode in which the CPMC would physically follow a ship model maneuvering freely in the tank. Here the CPMC would form a base for exchange of energy and information with the model through a loose umbilical cable cord, thus eliminating the nasty problems of energy storage and wireless telemetry. Moreover, the model trajectory could be measured with high precision and resolution built into the control hardware for the towing mode.

### Hydraulic versus electric drives

Careful feasibility studies carried out by the *Ver-einigte Flugzeugbau-Werke*, Bremen, and Siemens AG, Erlangen, in 1971 indicated that the specified dynamic performance of the three subcarriages in both operating modes could be attained by servosystems using either hydraulic or electric motors. We chose electric drives for reasons of economy, compactability, and elimination of the risk of contaminating the tank water by an accidental leakage of oil.

## HARDWARE

General features

The front view photograph (Fig. 1) conveys a general impression of the CPMC relative to the tank cross section. The tank is aligned roughly in the east-west direction and this picture was taken looking west with the trailer in front and the towing carriage in the background. The spine of the trailer is an extremely stiff closed box girder of steel measuring about 20 m in length, 2 m on the side and 1 cm wall thickness reinforced internally by web frames. Its lowest natural frequency in any bending mode is above 6 Hz. At each end are platforms carrying racks of electrical hardware strictly separated into power processing on the north and signal processing on the south. The trailer runs on four wheels of hardened steel with a diameter of 70 cm, base of 4 m and span of over 18 m. It is constrained to the south rail by horizontal guide wheels at the center. When not in use it is parked at the east end of the tank and with its overall length of only 6 m it practically does not affect the routine operation of the 300 m towing tank. For use it can be mechanically hooked to the towing carriage by two tie rods, one on each side, each rod being provided with universal joints at both ends. For power and signal exchange there are multipoint cable connectors on the north and south side respectively. The entire coupling or decoupling operation takes no more than 15 min.

The general arrangement of the various subcarriages is depicted in Fig. 2. The  $y_o$ -carriage runs under the box girder practically over the entire width of the tank and carries two short longitudinal rails over which the  $\Delta x_o$ -carriage runs. The  $\psi$ -carriage, which is actually a turntable capable of rotation about a vertical axis going through the center of the  $\Delta x_o$ -carriage, is suspended from the  $\Delta x_o$ -carriage by a hydraulically operated elevator to accommodate models of different draft and freeboard. The principal particulars of all four carriages are compiled in Table 1. As already stated, the range and dynamics of the CPMC were so dimensioned as to be able to generate (within the constraints of tank size) on model scale every realistic horizontal planar motion of which any merchant ship is capable.

Process control

Fig. 3 is a simplified block diagram showing schematically the flux of information and interaction between essential components of the system. Normally the CPMC is operated under computer control either in Mode A (towing) or in Mode B (tracking). However, for inspection and maintenance as well as for the convenience of model attachment and detachment all carriages can also be moved slowly under manual control (Mode C) from an operating console on the towing carriage. This console contains position and crucial state displays as well as switches for various key functions such as turning power on or off, applying or releasing brakes, starting or stopping a run (under computer control), triggering an emergency halt etc.

The computer, installed in an air-conditioned cabin on the towing carriage, has a cycle time of 1.6  $\mu$ s and a magnetic core storage capacity of 16 k words of 24 bit length. Communication between the human operator and the computer is via teletype, console and paper tape. The CPMC control unit on the trailer, the towing carriage control hardware

and instrumentation in the model interact with the computer via a process control interface currently equipped with eight digital input and output channels of 24 bits each, four analog input channels and two analog output channels. The CPMC control is essentially digital with a basic cycle of 10 ms. In Mode A once every 10 ms the computer reads out a set of trajectory coordinates to the CPMC control unit, reads in (for later inspection) a set of coordinate errors (actual value minus required value), and senses and stores the suitably amplified force signals from the dynamometers in the captive model moving with the CPMC.

The control unit drives each individual carriage independently under digital position control with superimposed speed control as indicated in Fig. 4 for the case of the  $y_o$ -carriage. Digital position feedback is supplied by incremental transducers mounted on carriage wheels while analog speed feedback is supplied by tachometers mounted on drive shafts. Note that each carriage is driven by a symmetrical arrangement of four thyristor-controlled DC servomotors, two driving and two braking with their functions exchanged at each reversal of the sense of rotation, in order to avoid any canting or tooth backlash in the gears, which might affect control accuracy or introduce noise in the force signals.

Towing hardware

The special towing hardware consists of a combined dynamometer and towing guide shown in Fig. 5. It is connected rigidly by four bolts at the top to the center of the  $\psi$ -carriage and by four bolts at the bottom to a metal base frame suitably anchored in the model, see also Fig. 2. The towing guide as shown constrains the model in surge, sway, yaw and roll while leaving it free to heave and pitch during the run, which is the normal mode of operation. However, it can also be rearranged to constrain the model to the CPMC in all six degrees of freedom if desired.\* Moreover, traverse guides with scales at each end can be manually adjusted to constrain the model at any fixed angle of heel between  $-10^\circ$  and  $10^\circ$  for special investigations. The dynamometer is a force balance consisting of two rigid beams, the lower one mounted to the model and the upper one to the carriage via the towing guide. The only mechanical connection between the two beams is by means of six slender tie rods so arranged as to accurately resolve the force and moment acting on the model in the components  $X, Y, Z, K, M$  and  $N$ . Each tie rod has double taper at both ends so that it can transmit only axial forces. At the upper-beam end of each tie rod are built in modular force sensors of the strain gauge type. The entire system is so stiff that the lowest natural frequency with a model of 3.5 Mg mass attached lies at about 5 Hz.

Tracking hardware

In Mode B the model is essentially free in all six degrees of freedom, is necessarily equipped with propulsion and steering gear, and is maneuvered by remote cable control either manually according to will from a command console on the towing carriage or automatically by computer according to a pre-programmed strategy of propeller and rudder com-

\*For instance, this mode was used for a dynamic calibration of the force balance by attaching a steel weight (instead of a model) and swinging it in air at different frequencies by means of the CPMC.



mands. The special tracking hardware consists of electro-mechanical tracking lag transducers in all six degrees of freedom and a model locking device, see Fig. 6. The tracking lag is sensed by relative position transducers of pulse or inductance type mounted on a delicate system of almost frictionless slides and wheels interposed between the  $\Delta x$ -carriage and the model. The three digital transducers measuring the horizontal tracking lag provide the essential control inputs ( $\Delta \Delta x_o$ ,  $\Delta y_o$ ,  $\psi_o - \psi_p$ ) which enable the CPMC to physically follow the model within narrow tolerances, see Fig. 3 and Table 1. The CPMC control unit digitally adds the tracking lag to its own position and transmits to the computer once every 10 ms the tank fixed coordinates of a reference point  $O$  in the model as increments  $\Delta x_o$ ,  $\Delta y_o$ ,  $\Delta \psi$  to economize on channel capacity. The other three tracking lag transducers generate analog signals  $x_o$ ,  $\theta$ ,  $\phi$  also sensed by the computer every 10 ms so that the trajectory of the free-running model can be recorded in six degrees of freedom. The analog channels can, of course, also be used alternatively to record any other quantities of interest, e.g. rudder angle and forces or propeller revolutions and forces.

The model locking device mentioned above consists of two hydraulically operated vertical arms mounted on the  $\psi$ -carriage and corresponding horizontal frames of pentagonal shape mounted in the model. By moving the arms out and in under manual or computer command the model can be engaged or released to serve various purposes. In a typical tracking experiment the model is initially engaged and accelerated from standstill to its approach speed with carriage assistance, then released and allowed to maneuver and finally engaged again and brought to a standstill with carriage assistance in order to make more efficient use of the available tank length. During the freerunning phase the locking device protects the tracking lag transducers and the power and signal exchange cables (hanging as loose umbilical cords from the CPMC into the model) by mechanically bounding the tracking lag despite a possible malfunction of the automatic tracking system. In this case the contact of the vertical arm with the horizontal frame generates a signal which does not automatically abort the run but is recorded by the computer and displayed on the operating console.

#### SOFTWARE

Comprehensive software has been developed by the authors for the freely programmable process control computer Siemens 301 to handle the multifarious tasks of carriage motion control, model motion control, hardware status monitoring, data acquisition and run evaluation. During CPMC experiments typically about 10 k words of core storage are loaded with programs (including the basic operating system) and 6 k words are available for data. As a measured quantity can usually be represented adequately by 12 bits whereas the word length is 24 bits, this means that up to about 12 k independent measurements can be stored in the core during a single run. The current status of the CPMC software has been fully documented in internal reports by Wolff (1974) and Oltmann (1975). For the present purpose it will suffice to give a brief general description of the software for Mode A. The block diagram (Fig. 7) is designed to show that the software is organized in a main program BDIE and five subprograms SWEZ, TEST, VORB, MESS and AUSW, and how these interact with each other and with the in-

put/output and process-control periphery. The functions of the subprograms are best explained by following the chronological sequence of events during a run as illustrated in the logic flow diagram for Mode A (Fig. 8).

The first step is to read appropriate run parameters into the computer, usually from prepared paper tape. These consist mainly of up to 100 Fourier coefficients which define uniquely the functions  $x_o(t)$ ,  $y_o(t)$  and  $\psi(t)$  over a finite interval of time  $T$ . From these the subprogram SWEZ generates the required trajectory coordinates (at 10 ms intervals) in three phases: a periodic phase determined by synthesis of the given Fourier coefficients, a run-in phase calculated to move the subcarriages from their initial resting positions to the synchronous entry points of the periodic phase, and a run-out phase to decelerate the subcarriages from their synchronous exit points of the periodic phase to the final resting positions. The complete trajectory (along with some auxiliary control information) is stored in a highly compact form in the core in a so-called run control list which uniquely determines the course of the run to follow. Now the subprogram TEST checks the run control list by simulating the required run to see for instance whether it is compatible with the available range and dynamics of the four carriages. If no errors are detected the subprogram VORB1 is started to initialize core storage and check the status of the control hardware. After errors, if any, have been corrected a lamp "ready to start" lights up on the console. The human operator may now press the START button. The subprogram VORB2 now accelerates the towing carriage to the desired mean speed  $\bar{x}$  and releases the brakes of the subcarriages. The basic 10 ms control loop MESS now takes over, reading out required coordinates (now calculated in real time from the run control list), reading in path errors and force data, and monitoring control hardware until the predetermined trajectory has been completed. Unless the run has been aborted owing to a bad control state triggering an automatic CPMC-HALT, which immediately brings all carriages to a standstill with the maximum permissible deceleration, the control is gracefully transferred to the subprogram VORB3 which now applies brakes to the subcarriages already at rest and decelerates the towing carriage to a standstill thereby terminating the run. During the return trip of the towing carriage and while waiting for the tank water to calm down for the next run the computer is free to evaluate the stored information and print out the results. This is handled by the subprogram AUSW, the main jobs being a systematic survey of the recorded trajectory errors and a Fourier analysis of the forces recorded during the periodic phase. Although the maximum sampling rate is 100 Hz per channel, it has been found more advantageous to record each error and force at 25 Hz over a correspondingly longer interval of time. Usually the path errors are only documented on teletype whereas the force coefficients (or the entire raw data) are punched out on paper tape for final analysis off site.

We note in passing that for the protection of the CPMC, model and instrumentation against accidental damage following wrong input, improper commands or system component failure an entire hierarchy of sophisticated safety features has been incorporated into the hardware and software, e.g. joint position and speed monitoring for preventing the carriages from transgressing their operating ranges and the model from hitting a tank wall.

## SAMPLE RESULTS IN MODE A

General remarks

The following sample results in Mode A were obtained with a 1:25 scale model of the Mariner class vessel (Table 2) tested in the ITTC standard condition as defined by Gertler (1969). Speed  $U$  corresponded to 20 kn full-scale and propeller revolutions  $n$  were held at the self-propulsion point of the ship. The forces sensed by the dynamometer were corrected for inertial effects arising from the mass and moment of inertia of the model to the extent effective at the transducers, see Equations (5a) in Mandel (1967). The net hydrodynamic forces are plotted in Figs. 9-12 in standard nondimensional form  $X', Y', N'$  as functions of rudder angle  $\delta$ , drift angle  $\beta$  and nondimensional yaw rate  $r'$ , cf. Notation. For further discussion we must distinguish the two types of tests involved.

Steady state tests

In the steady state tests the quantity  $\delta, \beta$  or  $r$  was held constant at selected values for a finite period of time ranging from 5 to 60 s. As the analog force signals were plotted in parallel on a strip-chart recorder it was easy to tell in each case when a nearly steady state had been achieved. Hence the interpretation of measured forces was straightforward. One only had to average the values sampled over the final portion of the steady state run. These results are indicated as discrete points in Figs. 9-12. Of course, the steady state rudder angle and drift angle tests are trivial and might as well have been done using the towing carriage alone. However, the steady state yaw rate tests were accomplished by actually varying the yaw rate periodically as a *trapezoidal* function of time, thus effectively simulating steady state rotating arm tests. This is a benefit accruing from the complete flexibility of motion control in the CPMC. In fact, not only can we simulate rotating arms of any radius from zero to infinity but also realize via input parameters different definitions of pure yaw as illustrated by the circles (zero drift angle at origin  $O$ ) and crosses (zero drift angle at centre of gravity  $x_G$ ) in Fig. 12. As the yaw moment is always taken about the origin  $O$  these two sets of points reflect the genuine hydrodynamic difference in the two definitions of pure yaw! Two other interesting exhibits in our steady state results are the appreciable asymmetry of rudder induced forces (Fig. 9) apparently caused by the single screw, and the significant dependence of  $X$  on  $r$  (Fig. 11). The former effect has been seldom observed as most experimenters were content with tests on one side only, and the latter effect contradicts previous findings of Ström-Tejsen and Chislett (1966) as well as Chislett and Smitt (1974).

Harmonic motion tests

Here the pertinent motion variable  $v$  or  $r$  was varied as a cosinusoidal function of time for several periods  $T = 2\pi/\omega$  of about 20 to 30 s. The measured hydrodynamic forces were analysed into a Fourier series in  $\omega t$ . Assuming quasi-steady flow, the obvious interpretation would be that the first order sine coefficient yields the hydrodynamic mass, while all significant cosine coefficients taken together yield the complete nonlinear damping. (A Fourier analysis in the  $t$ -domain is tantamount to a least squares fit of orthogonal Chebyshev polynomials in the  $v$ - or  $r$ -domain with a natural

weighting function.) This view is substantiated by the results as seen in Figs. 10-11. Each of these six diagrams contains three independent curves, each generated by synthesizing the measured cosine coefficients of the corresponding force from single runs of different amplitudes, viz.  $\beta = 6, 12, 18^\circ$  (Fig. 10) and  $\hat{r}' = 0.3, 0.6, 0.9$  (Fig. 11). The mutual consistency of each triplet of curves and their almost perfect agreement with the discrete points from steady state tests supports the above interpretation and demonstrates how the CPMC yields from each single run an invariant nonlinear force response to velocity for which other techniques require a whole series of runs!

However, one puzzling feature did emerge from these experiments, in that a significant sine coefficient of third order was detected for  $Y$  in the sway tests and  $N$  in the yaw tests. Evidently this coefficient cannot be interpreted as a pure velocity response. Hence the possibility of higher order acceleration or mixed terms had to be examined as shown in Table 3. To date the most plausible explanation seems to be invoking mixed terms of the type  $Y_{v\dot{v}}, v^2\dot{v}$  and  $N_{r\dot{r}}, r^2\dot{r}$ . Contrary to popular belief there is no theoretical difficulty in visualizing such terms as arising from viscous or wave effects. The traditional argument of Abkowitz (1964) that the only force response to acceleration is linear and independent of velocity is theoretically founded only for ideal flow in an unbounded medium. However, further research is warranted before arriving at a definite conclusion.

## SAMPLE RESULTS IN MODE B

The trajectories of two zigzag maneuvers, each constructed from original computer recordings of incremental digital coordinates  $Dx_0, Dy_0, D\psi$  at 100 Hz and samplings of analog signals  $\delta, z, \theta, \phi$  at 20 Hz over a period exceeding 60 s, are reproduced graphically in Figs. 13-16 and numerically in Tables 5 and 6 in order to illustrate the capabilities of the CPMC in the tracking mode. Both runs were part of the comprehensive acceptance trials in Mode B performed with a 1:9 scale model of a twin-screw tug-boat (Table 4) for the compelling reason that it happened to be the most agile model tested at the HSVA during the past 20 years! If the CPMC could cope with a model yawing wildly up to  $\pm 15^\circ/\text{s}$  and zigzagging along the tank at over 1.5 m/s with course angles approaching  $\pm 50^\circ$ , it could easily track any ordinary ship model. Actually the  $y_0$ - and  $\psi$ -carriages had no difficulty in tracking this model with negligible lag! The only serious difficulty was encountered following the first rudder deflection when the model decelerated in the  $x_0$ -direction at over  $0.2 \text{ m/s}^2$  which was almost too much for the limited acceleration of the towing carriage and the limited range of the  $\Delta x$ -subcarriage. The problem was finally mastered by improvements in the hardware and software.

Although originally conceived as an afterthought, the tracking mode is now yielding trajectory data of unprecedented resolution ideally suited for the application of system identification techniques as discussed for example by Oltmann (1973). The task ahead is to find a judicious combination of Modes A and B for identifying a general mathematical model for simulating arbitrary ship maneuvers on the basis of a few runs with a physical model under the CPMC.



## REFERENCES

- Abkowitz, M.A.: Lectures on ship hydrodynamics - Steering and manoeuvrability. Hydro- og Aerodynamisk Laboratorium, Lyngby, Report No. Hy-5 (1964).
- Bishop, R.E.D., and Parkinson, A.G.: On the planar motion mechanism used in ship model testing. *Phil. Trans. R. Soc. Lond. A* **266** (1970) 35-61.
- Bishop, R.E.D.; Burcher, R.K., and Price, W.G.: The uses of functional analysis in ship dynamics; Application of functional analysis in oscillatory ship model testing. *Proc. R. Soc. Lond. A* **332** (1973) 23-35, 37-49.
- Bishop, R.E.D.; Burcher, R.K., and Price, W.G.: On the linear representation of fluid forces and moments in unsteady flow. *Journ. Sound and Vibration* **29** (1973) 113-128.
- Bishop, R.E.D.; Burcher, R.K.; Parkinson, A.G., and Price, W.G.: Oscillatory testing for the assessment of ship manoeuvrability. *Proc. 10th Symp. on Naval Hydrodynamics*, Boston, Mass. (1974).
- Bishop, R.E.D.; Burcher, R.K., and Price, W.G.: A linear analysis of planar motion mechanism data. *Journal of Ship Research*, **18** (1974) 242-251.
- Booth, T.B., and Bishop, R.E.D.: The planar motion mechanism. Admiralty Experiment Works, Haslar (1973).
- Burcher, R.K.: Studies into the validity of quasi steady prediction techniques. *Proc. 14th ITTC*, Ottawa (1975) II 404-407.
- Chislett, M.S., and Smitt, L.W.: A brief description of the HyA large amplitude PMM system. *Journ. of Mechanical Engineering Science, Supplementary Issue* **14** (1972) 80-84.
- Cummins, W.E.: The impulse response function and ship motions. *Schiffstechnik* **9** (1962) 101-109.
- Fujii, H.: Forced oscillation tests on manoeuvrability in Nagasaki Experimental Tank. Mitsubishi Technical Bulletin No. 63 (1969).
- Gertler, M.: The DTMB Planar-Motion-Mechanism system. Symposium on Towing Tank Facilities, Zagreb (1959), also NSRDC, Washington, D.C., Report 2523 (1967).
- Gertler, M.: Final analysis of first phase of ITTC standard captive-model-test program. *Proc. 12th ITTC*, Rome (1969) 601-625.
- Goodman, A.: Experimental techniques and methods of analysis used in submerged body research. *Proc. 3rd Symposium on Naval Hydrodynamics*, Scheveningen (1966) 379-445.
- Horn, F., and Walinski, E.A.: Untersuchung über Drehmanöver und Kursstabilität von Schiffen. *Schiffstechnik* **5** (1958) 173-190 and **6** (1959) 9-33.
- Keil, H., and Thiemann, H.: Ein Oszillator zur Ermittlung hydrodynamischer Massen und Dämpfungswerte. Institut für Schiffbau, Hamburg, Bericht Nr. 120 (1963).
- Krappinger, O., and Sharma, S.D.: Novel planar motion carriage at Hamburg. *Proc. 14th ITTC*, Ottawa (1975) IV 694-697.
- Kotik, J., and Mangulis, V.: On the Kramers-Kronig relations for ship motions. *Intern. Shipbuilding Progress* **9** (1962) 361-368.
- Koyama, T., and Matora, S.: An automatic model tracking system at the Maneuvering Tank of the University of Tokyo, *Proc. 14th ITTC*, Ottawa (1975) II, 615-620.
- Leeuwen, G. van: The lateral damping and added mass of a horizontally oscillating shipmodel. Netherlands Research Center TNO, Delft, Report No. 65 S (1964).
- Leeuwen, G. van: Enkele problemen bij het ontwerpen van een horizontale oscillator. Laboratorium voor Scheepsbouwkunde, Delft, Report No. 225 (1969).
- Mandel, P.: Ship maneuvering and control. Principles of Naval Architecture, SNAME, New York (1967) 463-606.
- Matora, S., and Fujino, M.: On the measurement of the stability derivatives by means of forced yawing technique. *Journal of Zosen Kiokai* **118** (1965) 48-56.
- Newman, J.N.: Some hydrodynamic aspects of ship maneuverability. *Proc. 6th Symp. on Naval Hydrodynamics*, Washington, D.C. (1966) 203-237.
- Nomoto, K.: Ship response in directional control taking account of frequency dependent hydrodynamic derivatives. *Proc. 14th ITTC*, Ottawa (1975) II 408-410.
- Oltmann, P.: Auswertung von Bahnkurven freifahrender Schiffmodelle. Institut für Schiffbau, Hamburg, Bericht Nr. 298 (1973).
- Oltmann, P.: Programmsystem für die Vorbereitung und den Ablauf von Versuchen mit einer rechnergesteuerten Planar-Motion-Modellversuchsanlage (CPMC) bei freimanövrierenden Schiffmodellen (Betriebsart B). Institut für Schiffbau, Hamburg, Schrift Nr. 2243 (1975).
- Oltmann, P.; Wolff, K.; Hoffmann, L., and Kerns, R.: Schwingungsmessungen am großen Schleppwagen und an der Planar-Motion-Modellversuchsanlage (CPMC) der HSVA. Institut für Schiffbau, Hamburg, Schrift Nr. 2244 (1975).
- Paulling, J.R., and Sibul, O.J.: New equipment and techniques for the experimental evaluation of ship's lateral stability. Univ. Calif., Berkeley, Calif., IER Report (1962).
- Smitt, L.W., and Chislett, M.S.: Large amplitude PMM tests and manoeuvring predictions for a MARINER class vessel. 10th Symposium on Naval Hydrodynamics, Boston, Mass. (1974).
- Strøm-Tejsen, J., and Chislett, M.S.: A model testing technique and method of analysis for the prediction of steering and manoeuvring qualities of surface vessels. *Proc. 6th Symposium on Naval Hydrodynamics*, Washington, D.C. (1966) 317-381.
- Wolff, K.: Programmsystem für Vorbereitung, Ablauf und Auswertung von Versuchen mit der Planar-Motion-Modellversuchsanlage in Betriebsart A (gefesselte Schiffmodelle). Institut für Schiffbau, Hamburg, Schrift Nr. 2209 (1974).
- Wolff, K.: Einführungsvortrag zur Besichtigung der PMM-Anlage. Institut für Schiffbau, Hamburg, Schrift Nr. 2234 (1975).
- Zunderdorp, H.J., and Buitenhok, M.: Oscillator techniques at the Shipbuilding Laboratory. Technological University, Delft, Report No. 111 (1963).



Table 1 Principal particulars of computerized planar motion carriage (CPMC)

Drive	Main carriage with trailer	$\Delta x_0$ - subcarriage	$y_0$ - subcarriage	$\psi$ - subcarriage
Empty mass	73000 kg	1370 kg	3250 kg	1500 kg
Mechanical range	280.0 m	$\pm 1.00$ m	$\pm 7.30$ m	$\pm 180.0^\circ$
Operating range	200.0 m	$\pm 0.85$ m	$\pm 6.50$ m	$\pm 150.0^\circ$
Maximum speed	3.0 m/s	0.80 m/s	1.90 m/s	$24.0^\circ/\text{s}$
Maximum acceleration	$0.2 \text{ m/s}^2$	$0.60 \text{ m/s}^2$	$0.90 \text{ m/s}^2$	$12.0^\circ/\text{s}^2$
Trajectory resolution:				
Input every 10 ms	$5 \times 10^{-5}$ m	$5 \times 10^{-5}$ m	$2.5 \times 10^{-5}$ m	$1.25 \times 10^{-6}$ rev
Output every 10 ms	$\leftarrow 10^{-4} \text{ m} \rightarrow$		$10^{-4}$ m	$10^{-5}$ rev
Tolerances:				
Trajectory error (Mode A)	$\leftarrow 0.01 \text{ m} \rightarrow$		0.01 m	$0.1^\circ$
Tracking lag (Mode B)	$\leftarrow 0.20 \text{ m} \rightarrow$		0.20 m	$8.0^\circ$

Table 2 Main dimensions of HSVA Model No. 2654  
Mariner class vessel, Model scale 1:25

Length between perpendiculars	6.437 m
Beam	0.927 m
Draft forward	0.274 m
Draft aft	0.323 m
Displacement	$1.064 \text{ m}^3$
Coordinate origin aft of FP	3.170 m
Center of gravity aft of origin	0.142 m
HSVA Model Propeller No. 1379	
Right-handed single screw	
Diameter	0.268 m
Pitch ratio	0.964
Expanded area ratio	0.660
Number of blades	4

Table 4 Main dimensions of HSVA Model No. 2509  
Twin-screw tug-boat, Model scale 1:9

Length between perpendiculars	3.792 m
Length of waterline	4.113 m
Beam	1.016 m
Draft mean	0.389 m
Displacement	$0.852 \text{ m}^3$
Coordinate origin aft of FP	1.896 m
Center of gravity aft of origin	0.050 m
HSVA Model Propellers No. 1707/1708	
Rotatable Kort nozzle rudders	
Diameter	0.217 m
Pitch ratio	1.260
Expanded area ratio	0.580
Number of blades	4

Table 3 Interpretation of hydrodynamic forces measured in forced harmonic motion

$$U = \text{const}, \quad v = \hat{v} \cos(\omega t), \quad r = 0, \quad n = \text{const}, \quad \delta = 0$$

Possible term	Measured force components			
	$\cos(2k\omega t)$	$\cos \{(2k+1)\omega t\}$	$\sin(2k\omega t)$	$\sin \{(2k+1)\omega t\}$
$v^{2i}$	x			
$v^{2i+1}$		x		
$\dot{v}^{2j}$	x			
$\dot{v}^{2j+1}$				x
$v^{2i} \dot{v}^{2j}$	x			
$v^{2i} \dot{v}^{2j+1}$				x
$v^{2i+1} \dot{v}^{2j}$		x		
$v^{2i+1} \dot{v}^{2j+1}$			x	
Significant $k$ observed in				
$X(t)$	0,2	1		1
$Y(t)$		1,3		1,3
$N(t)$	0	1		1

Table 5 Trajectory of 30°/10° zigzag maneuver

PROGRAM: PD/LSTR3

MSVA=MODEL NO. 2509, RUN NO. 7 (24.10.75)

INITIAL SPEED U0= 2.004 M/S

T	DELTA	U	V	R	PSI	BETA	X0	Y0
S	DEG	M/S	M/S	DEG/S	DEG	DEG	M	M
0	-1.156	2.004	.000	.000	.000	.000	.000	.000
1	-1.133	1.990	-.009	.216	.144	.259	1.999	-.001
2	-1.244	1.991	-.016	.324	.432	.461	3.986	-.002
3	-1.133	1.985	-.014	.468	.792	.417	5.973	.003
4	-11.200	1.970	-.074	3.852	2.520	2.142	7.954	.013
5	-23.933	1.910	-.196	10.332	9.720	5.868	9.983	.075
6	-20.711	1.797	-.284	13.716	22.500	8.993	11.748	.339
7	-8.511	1.749	-.288	10.368	34.884	9.364	13.433	.937
8	3.711	1.738	-.202	3.924	42.084	6.626	14.941	1.839
9	16.133	1.756	-.045	-3.852	41.976	1.478	16.312	2.929
10	26.000	1.755	.139	-11.484	33.948	-4.524	17.660	4.066
11	28.111	1.704	.268	-15.048	20.196	-8.939	19.181	5.047
12	28.889	1.613	.328	-15.804	4.688	-11.481	20.653	5.702
13	28.022	1.516	.348	-15.516	-11.052	-12.931	22.231	5.953
14	20.933	1.454	.343	-14.796	-26.352	-13.275	23.741	5.810
15	8.667	1.457	.312	-11.124	-39.564	-12.107	25.132	5.292
16	-3.178	1.496	.220	-4.644	-47.448	-8.382	26.377	4.462
17	-15.489	1.568	.080	3.096	-48.132	-2.926	27.508	3.417
18	-27.044	1.606	-.098	11.268	-40.644	3.475	28.631	2.283
19	-27.889	1.568	-.236	14.832	-27.036	8.570	29.851	1.247
20	-28.067	1.509	-.302	15.480	-11.736	11.332	31.204	.475
21	-28.178	1.439	-.334	15.408	3.708	13.058	32.648	.052
22	-25.778	1.371	-.345	15.444	19.152	14.121	34.084	-.004
23	-14.778	1.343	-.320	13.104	33.696	13.402	35.436	.298
24	-2.733	1.383	-.258	8.208	44.352	10.577	36.667	.935
25	9.622	1.468	-.165	1.224	49.104	6.411	37.790	1.834
26	21.756	1.538	.085	-6.948	46.044	-.194	38.854	2.903
27	28.533	1.568	.164	-13.212	35.352	-5.971	39.967	3.997
28	28.778	1.531	.272	-15.516	20.592	-10.062	41.229	4.925
29	28.733	1.473	.318	-15.480	4.932	-12.168	42.622	5.548
30	28.956	1.423	.332	-15.372	-10.440	-13.146	44.078	5.805
31	28.022	1.387	.335	-14.616	-25.632	-13.574	45.511	5.692
32	8.622	1.395	.288	-10.620	-38.412	-11.669	46.846	5.217
33	-3.489	1.462	.203	-4.536	-46.008	-7.914	48.058	4.433
34	-15.667	1.544	.067	3.348	-46.548	-2.492	49.190	3.432
35	-27.156	1.575	-.113	11.268	-38.844	4.103	50.313	2.341
36	-27.933	1.545	-.241	14.760	-25.344	8.866	51.535	1.350
37	-28.111	1.481	-.305	15.516	-10.044	11.653	52.890	.622
38	-28.133	1.413	-.328	15.516	5.508	13.076	54.321	.245
39	-24.667	1.347	-.333	15.336	20.952	13.875	55.735	.236
40	-12.578	1.340	-.303	12.384	35.064	12.741	57.062	.585
41	-.489	1.392	-.234	6.876	44.748	9.532	58.273	1.259
42	11.778	1.483	-.125	-.216	48.060	4.805	59.387	2.182
43	24.067	1.544	.043	-8.532	43.452	-1.601	60.465	3.252
44	28.244	1.547	.199	-13.932	31.572	-7.340	61.610	4.306
45	28.733	1.513	.297	-15.372	16.668	-11.094	62.903	5.163
46	28.022	1.458	.327	-15.300	1.296	-12.647	64.320	5.704
47	28.756	1.399	.340	-15.408	-14.040	-13.642	65.773	5.880
48	17.844	1.369	.334	-13.968	-29.052	-13.705	67.176	5.889
49	5.711	1.394	.278	-9.288	-40.768	-11.285	68.474	5.146
50	-6.400	1.471	.186	-2.700	-46.800	-7.194	69.658	4.314
51	-18.733	1.544	.033	5.328	-45.432	-1.219	70.774	3.292
52	-27.378	1.566	-.141	12.492	-35.964	5.143	71.910	2.218
53	-27.489	1.532	-.257	14.940	-21.924	9.516	73.166	1.284
54	-28.222	1.470	-.314	15.488	-6.588	12.042	74.545	.633
55	-28.289	1.398	-.337	15.372	8.820	13.569	75.970	.333
56	-23.600	1.336	-.340	15.156	24.192	14.295	77.380	.395
57	-11.444	1.334	-.301	11.916	37.944	12.714	78.683	.888
58	-.711	1.392	-.231	6.480	47.124	9.439	79.857	1.535
59	13.178	1.482	-.119	-.000	49.932	4.607	80.933	2.502
60	25.489	1.544	.058	-9.148	44.640	-2.144	81.973	3.607

THIS PAGE IS BEST QUALITY PRACTICABLE  
FROM COPY FURNISHED TO DDG

Table 6 Trajectory of 20°/20° zigzag maneuver

PROGRAM: PD/LSTR3

MSVA=MODEL NO. 2589, RUN NO. 15 (24.12.75)

INITIAL SPEED U0= 2.005 M/S

T	DELTA	U	V	R	PSI	BETA	X0	Y0
S	DEG	M/S	M/S	DEG/S	DEG	DEG	M	M
0	-1.133	2.005	-0.001	0.000	0.000	0.029	0.000	0.000
1	-1.156	1.994	-0.009	0.252	0.180	0.266	2.001	-0.001
2	-1.133	1.997	-0.014	0.360	0.468	0.411	3.993	-0.002
3	-1.400	1.991	-0.022	0.396	0.828	0.627	5.987	0.001
4	-13.022	1.978	-0.085	4.320	2.772	2.454	7.976	0.003
5	-16.756	1.926	-0.196	9.792	10.296	9.822	9.931	0.070
6	-18.640	1.855	-0.265	11.628	21.240	8.132	11.813	0.354
7	-18.911	1.804	-0.280	10.656	32.832	8.825	13.565	0.936
8	1.444	1.787	-0.216	5.040	40.824	6.881	15.143	1.818
9	13.889	1.802	-0.074	-2.664	41.940	2.363	16.575	2.907
10	19.111	1.817	0.094	-9.108	35.388	-2.962	17.965	4.062
11	19.178	1.809	0.210	-11.592	24.696	-6.629	19.450	5.112
12	19.244	1.773	0.274	-12.168	12.672	-8.774	21.066	5.918
13	19.222	1.733	0.298	-12.004	0.432	-9.754	22.772	6.484
14	19.267	1.698	0.305	-12.096	-11.700	-10.173	24.504	6.536
15	17.889	1.673	0.309	-12.060	-23.760	-10.476	26.200	6.316
16	7.911	1.666	0.282	-9.684	-35.028	-9.618	27.795	5.757
17	-4.311	1.692	0.197	-3.780	-41.832	-6.632	29.250	4.894
18	-16.911	1.730	0.045	4.032	-41.616	-1.493	30.598	3.833
19	-18.667	1.758	-0.110	9.648	-34.236	3.571	31.947	2.721
20	-18.800	1.746	-0.216	11.916	-23.148	7.046	33.402	1.726
21	-18.844	1.714	-0.268	12.240	-10.944	8.872	34.983	0.982
22	-18.911	1.680	-0.292	12.132	1.260	9.863	36.648	0.560
23	-18.867	1.654	-0.295	11.916	13.320	10.114	38.335	0.481
24	-17.622	1.625	-0.302	12.096	25.308	10.517	39.978	0.739
25	-7.378	1.619	-0.273	9.792	36.648	9.588	41.509	1.325
26	5.222	1.652	-0.190	3.816	43.560	6.556	42.980	2.287
27	18.069	1.701	-0.043	-4.140	43.308	1.454	44.188	3.287
28	19.289	1.733	0.110	-9.828	35.748	-3.644	45.482	4.418
29	19.400	1.735	0.209	-11.844	24.624	-6.874	46.895	5.437
30	19.489	1.721	0.266	-12.132	12.528	-8.791	48.455	6.217
31	19.556	1.692	0.285	-12.024	0.432	-9.569	50.117	6.684
32	19.467	1.668	0.298	-12.024	-11.556	-10.136	51.815	6.812
33	19.533	1.650	0.304	-12.240	-23.088	-10.423	53.484	6.598
34	9.400	1.639	0.276	-10.260	-35.316	-9.539	55.052	6.043
35	-3.067	1.666	0.197	-4.428	-42.768	-6.740	56.476	5.188
36	-15.844	1.707	0.056	3.240	-43.344	-1.881	57.787	4.188
37	-18.756	1.735	-0.097	9.432	-36.396	3.211	59.083	2.971
38	-18.667	1.727	-0.215	11.772	-25.452	7.088	60.483	1.935
39	-18.578	1.703	-0.270	12.132	-13.392	9.810	62.017	1.132
40	-18.609	1.671	-0.287	11.952	-1.332	9.755	63.651	0.638
41	-18.556	1.642	-0.298	11.916	10.584	10.278	65.323	0.480
42	-18.133	1.610	-0.305	11.908	22.572	10.709	66.965	0.654
43	-18.000	1.600	-0.288	10.620	34.236	10.213	68.512	1.153
44	2.156	1.626	-0.220	5.400	42.444	7.703	69.925	1.958
45	14.467	1.672	-0.088	-2.232	43.992	3.014	71.223	2.985
46	18.600	1.712	0.072	-8.748	37.944	-2.393	72.497	4.103
47	18.711	1.729	0.185	-11.268	27.612	-6.106	73.867	5.151
48	19.289	1.715	0.259	-11.952	15.840	-8.582	75.382	5.999
49	19.356	1.689	0.293	-12.060	3.816	-9.848	77.012	6.562
50	19.267	1.662	0.301	-12.096	-8.280	-10.248	78.697	6.794
51	19.289	1.642	0.308	-12.168	-20.448	-10.625	80.370	6.681
52	12.244	1.623	0.292	-11.124	-32.364	-10.202	81.963	6.227
53	0.022	1.644	0.229	-6.156	-41.184	-7.936	83.420	5.453
54	-12.457	1.687	0.102	1.044	-43.704	-3.456	84.751	4.441
55	-18.733	1.722	-0.050	8.244	-38.520	1.937	86.036	3.321
56	-18.800	1.724	-0.183	11.384	-28.404	6.047	87.400	2.258
57	-18.911	1.705	-0.257	12.024	-16.560	8.565	88.900	1.394
58	-18.889	1.676	-0.286	12.024	-4.536	9.682	90.510	0.815
59	-18.933	1.640	-0.297	11.952	7.452	10.274	92.174	0.564
60	-18.933	1.609	-0.302	12.024	19.440	10.625	93.822	0.649



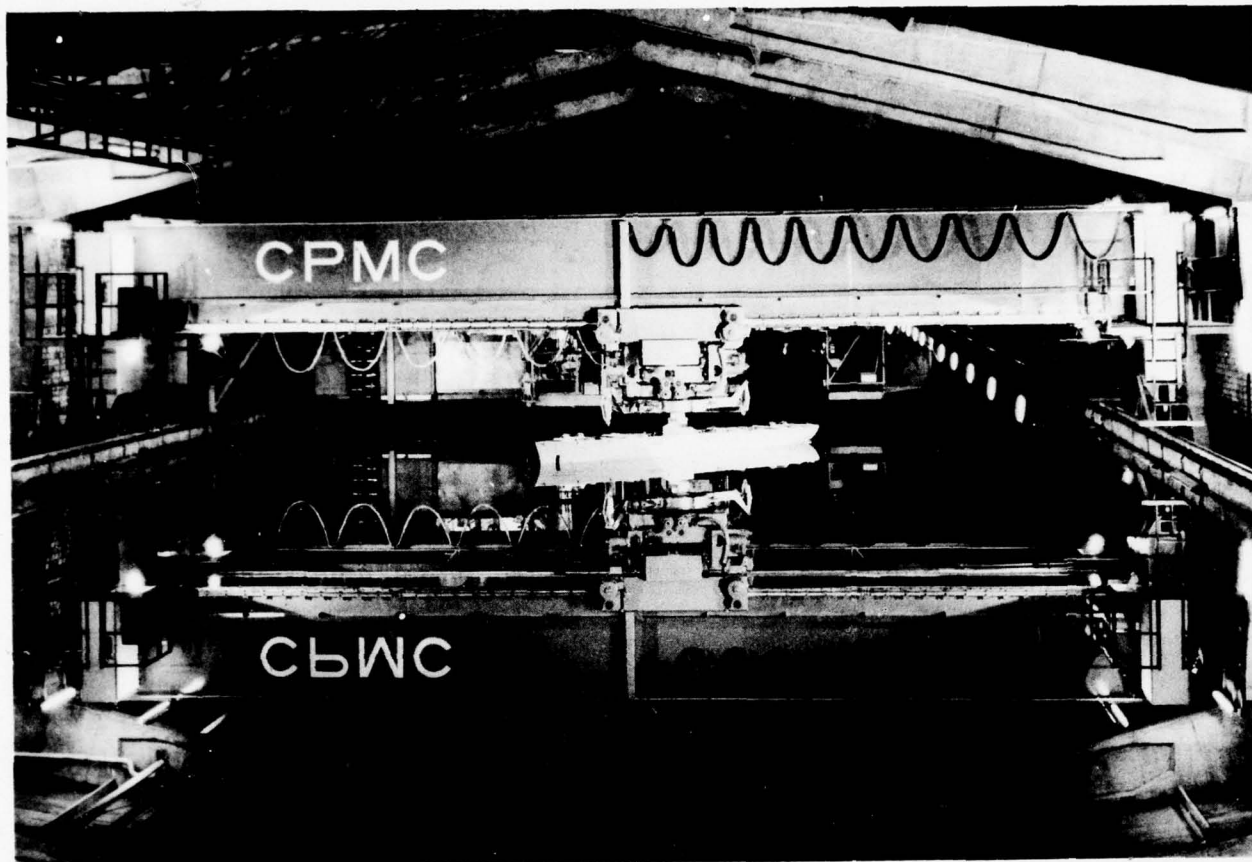


Fig. 1: Front view of CPMC

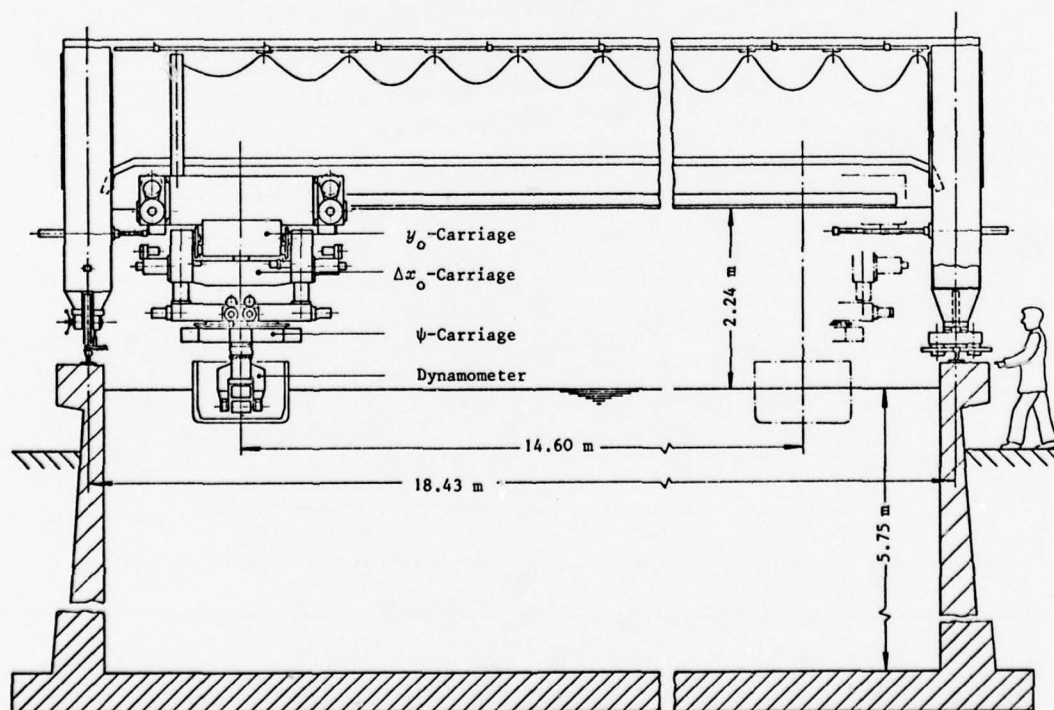
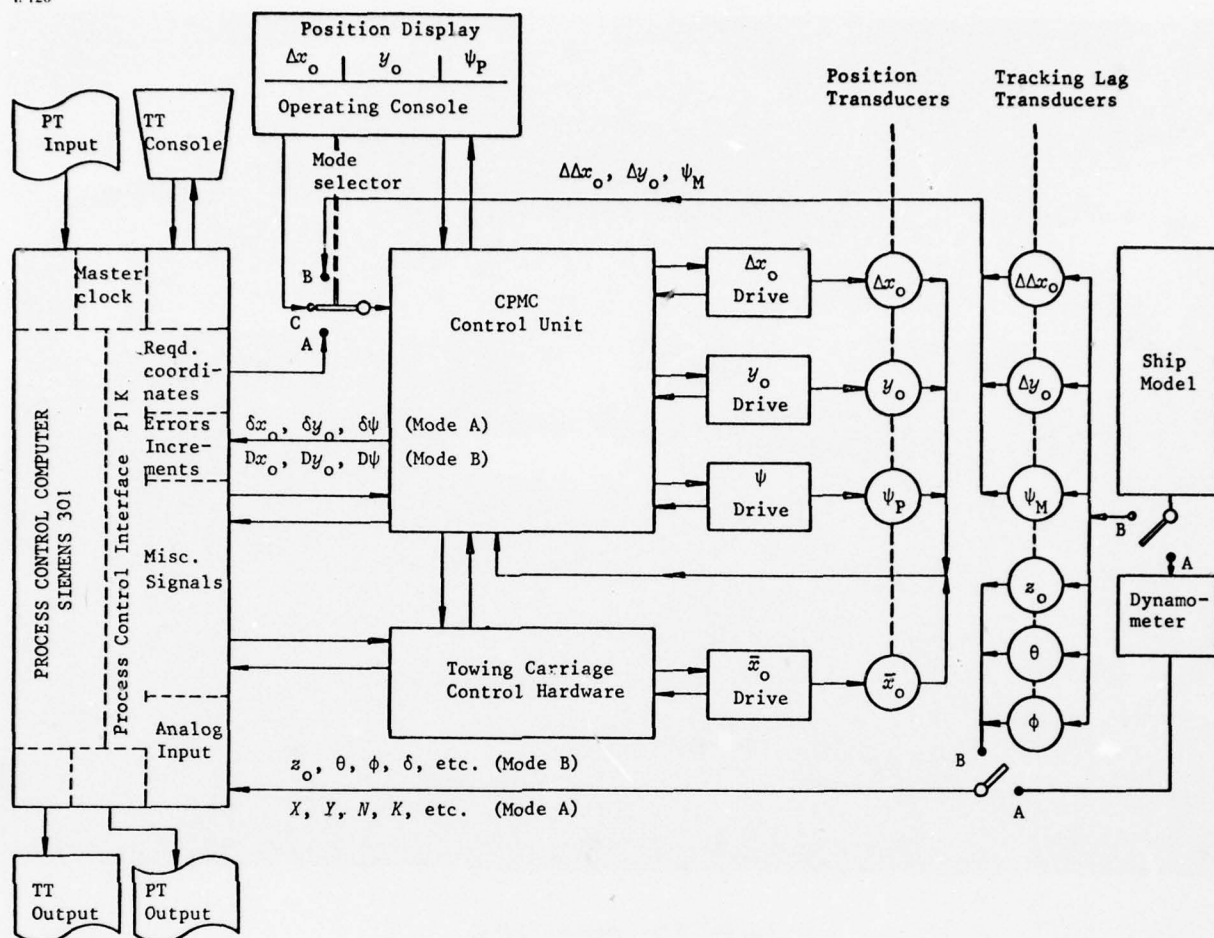
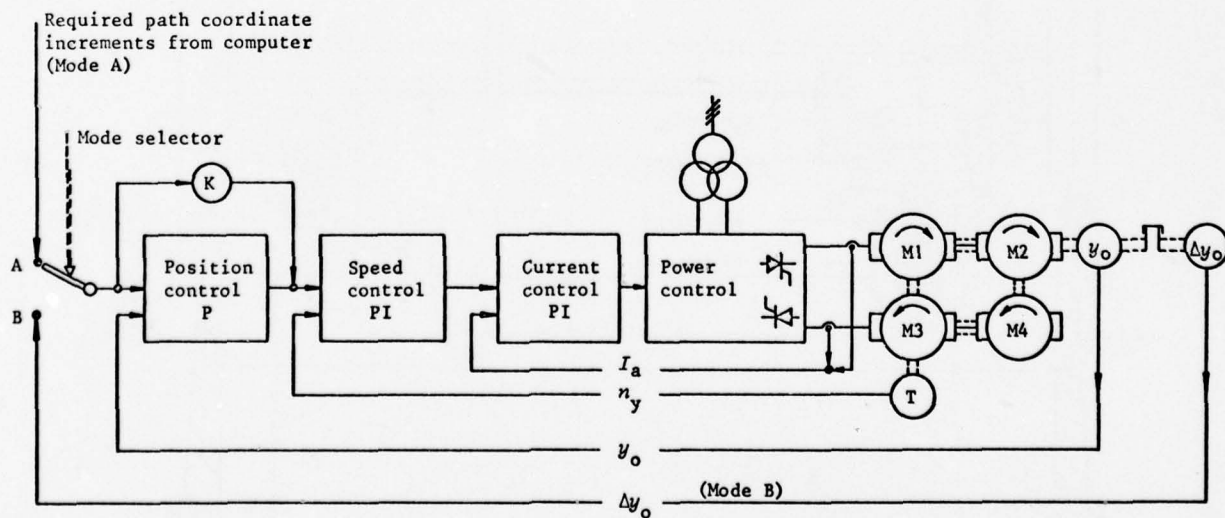


Fig. 2: Schematic of CPMC



**Fig. 3: System flow chart**



**Fig. 4: Schematic of control loop ( $y_0$ — subcarriage)**

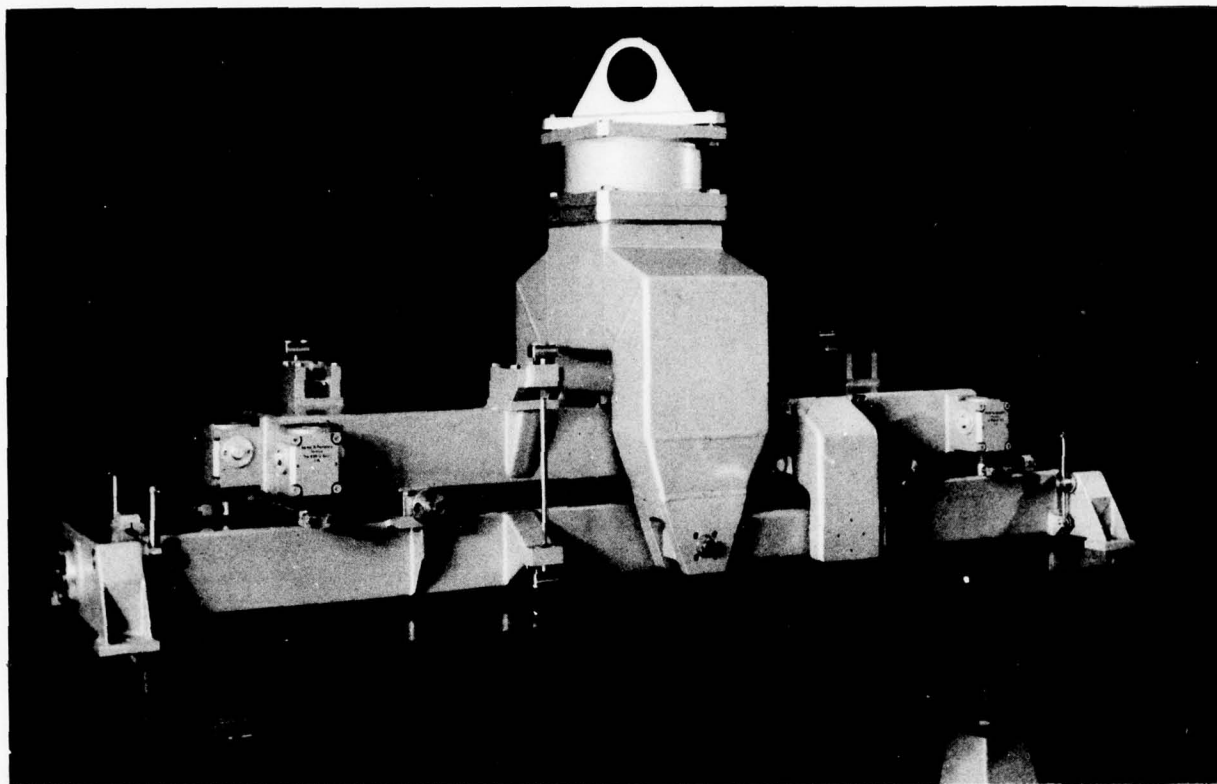


Fig. 5: Dynamometer and guide (Mode A)

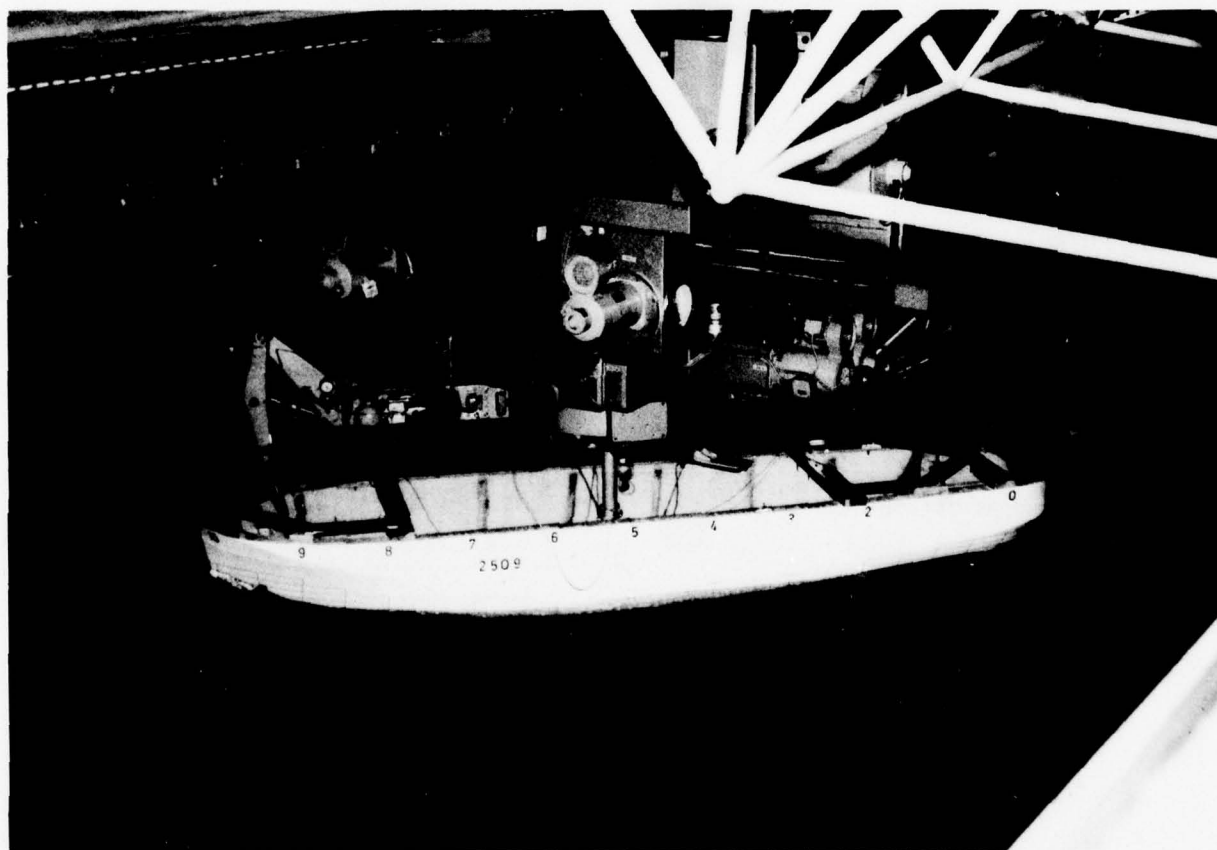


Fig. 6: Typical run in Mode B



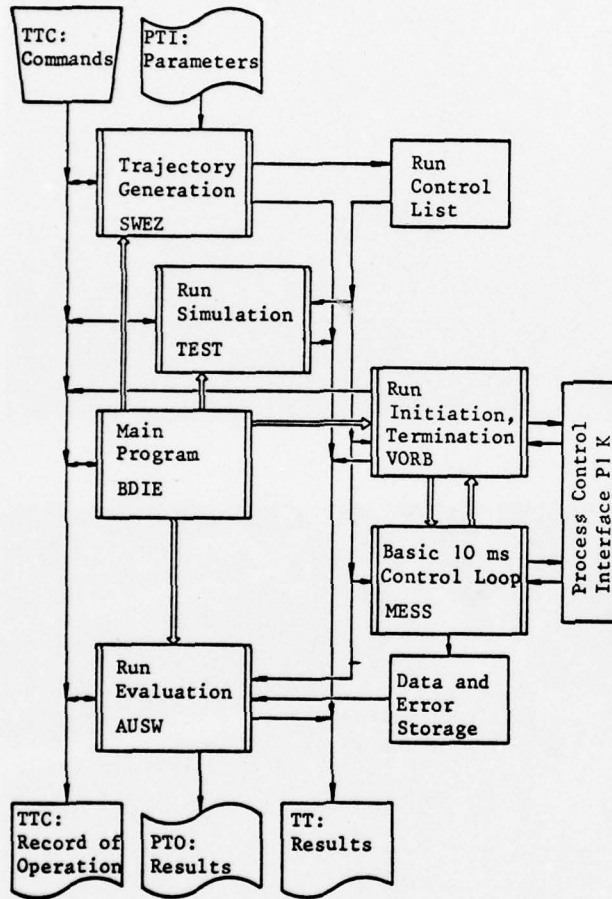


Fig. 7: Organization of soft ware for Mode A

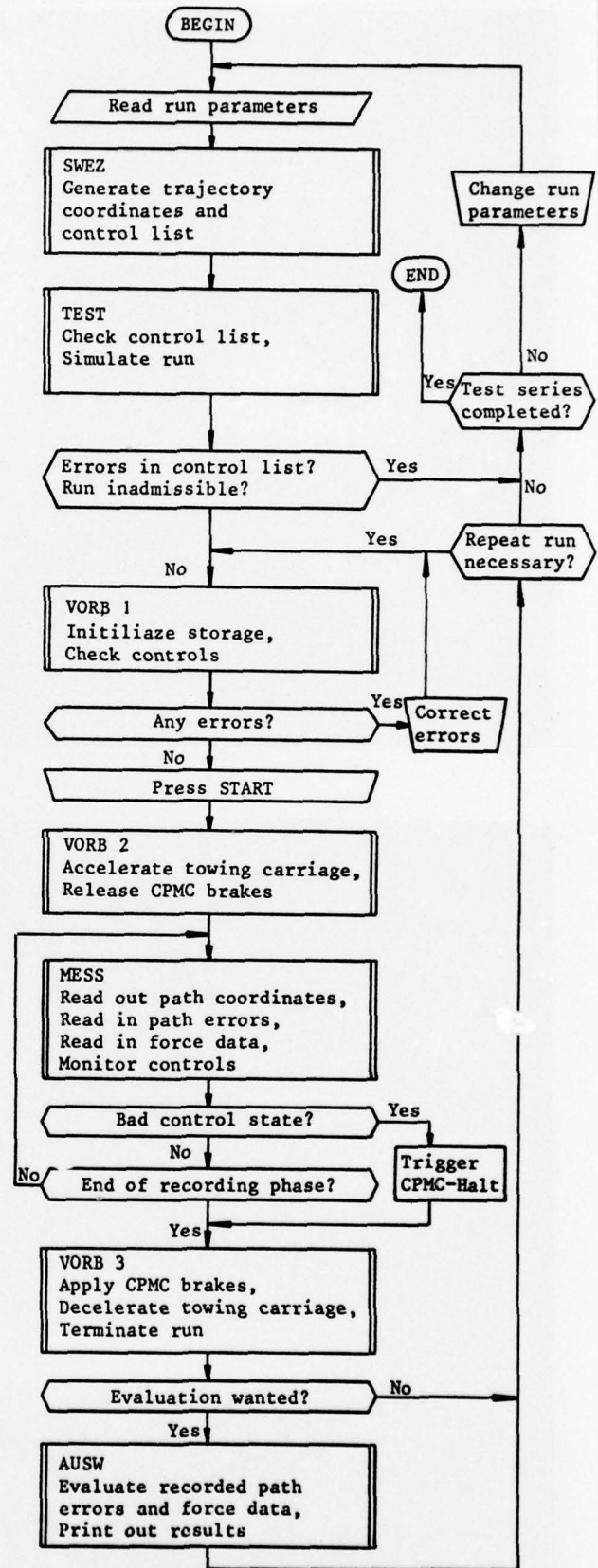


Fig. 8: Logic flow diagram for Mode A

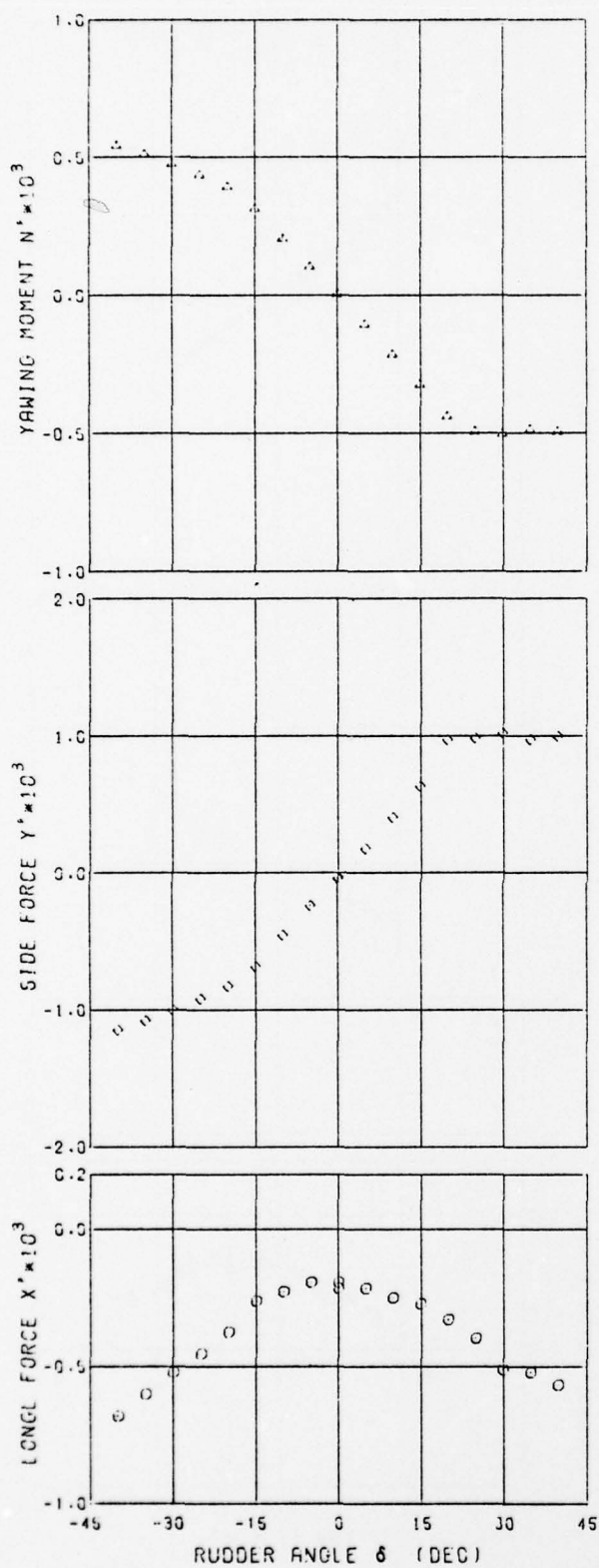


Fig. 9: Results from static rudder angle test, HSVA-Model No. 2654

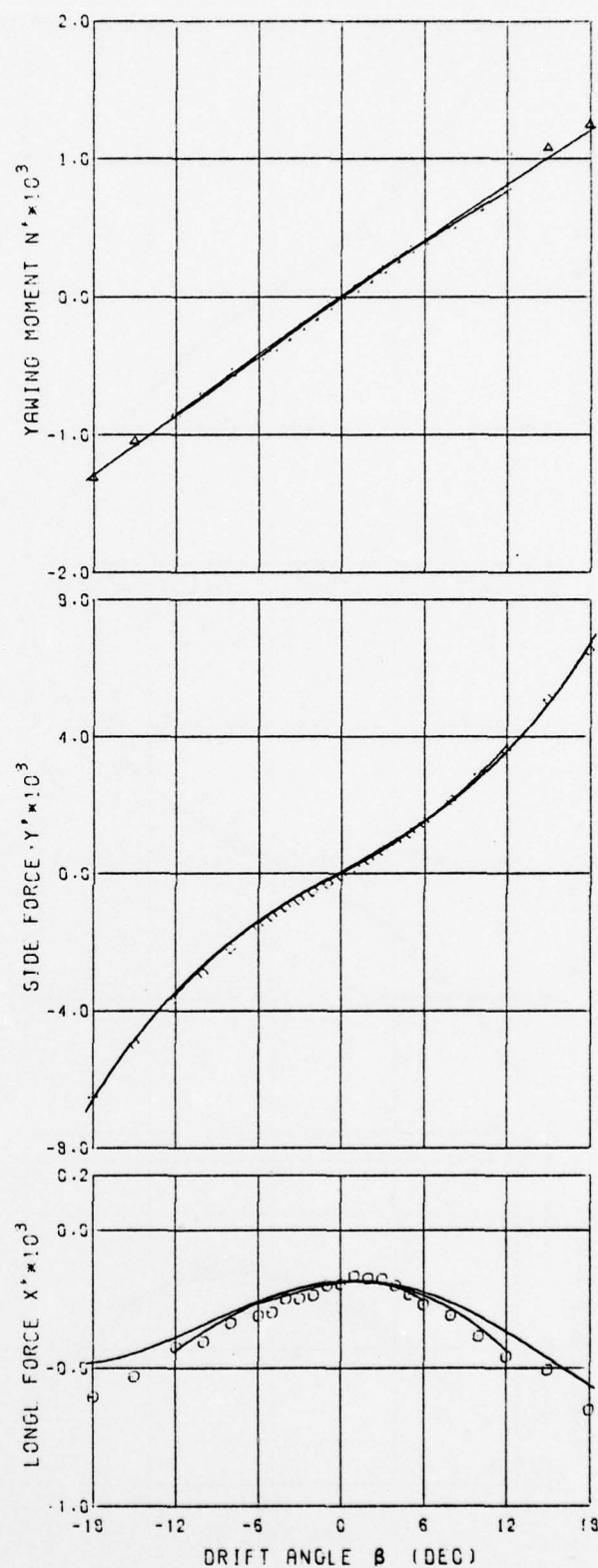


Fig. 10: Results from pure sway test, HSVA-Model No. 2654

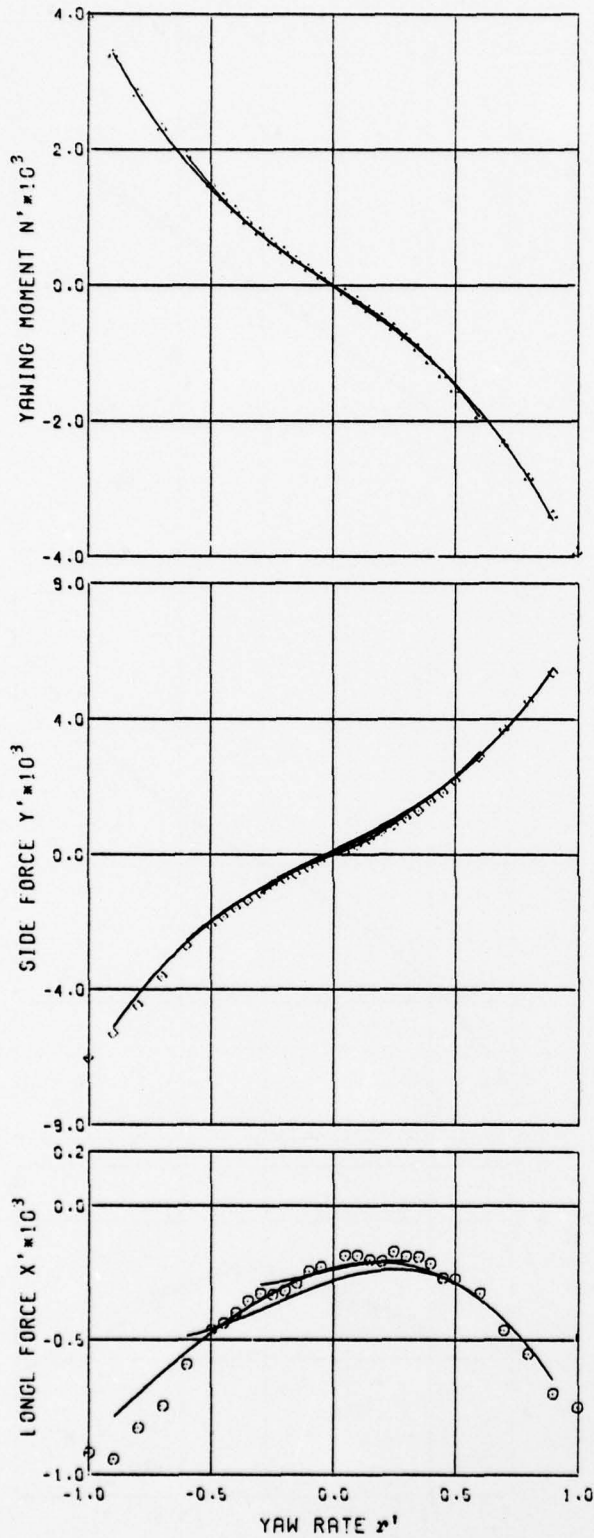


Fig. 11: Results from pure yaw test, HSVA No. 2654

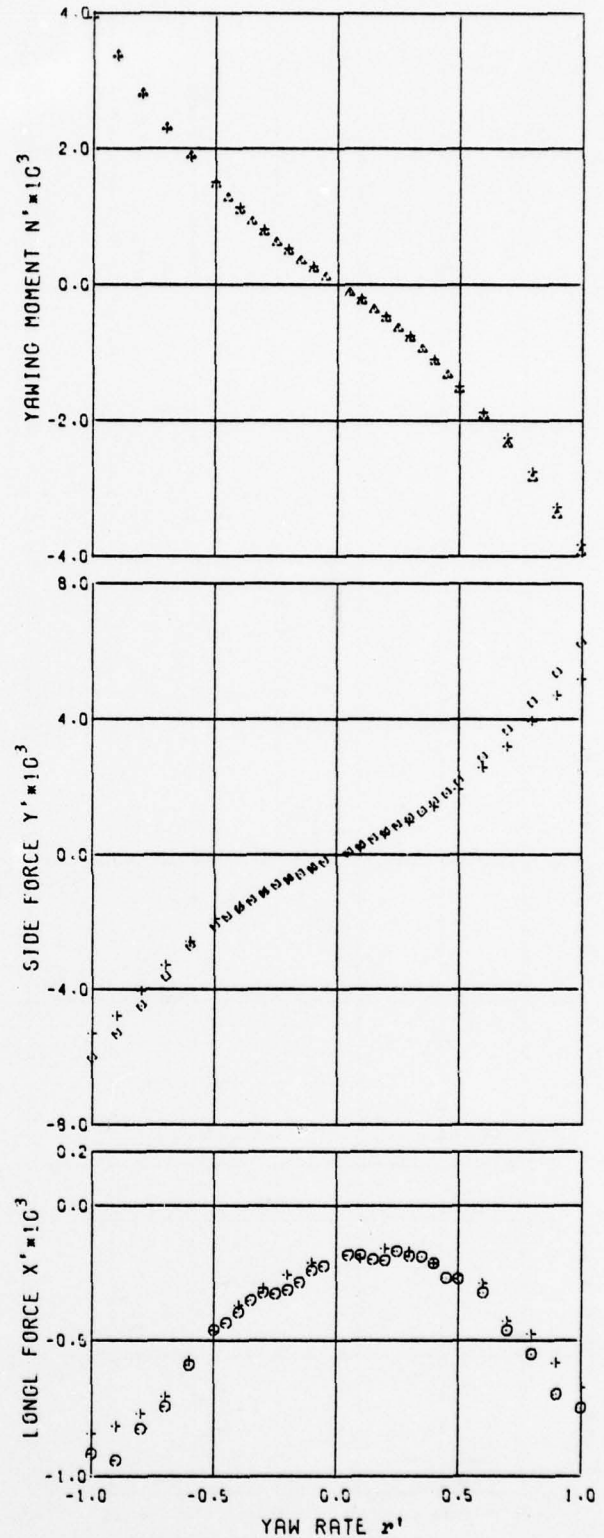


Fig. 12: Results from pure yaw test, HSVA-Model No. 2654



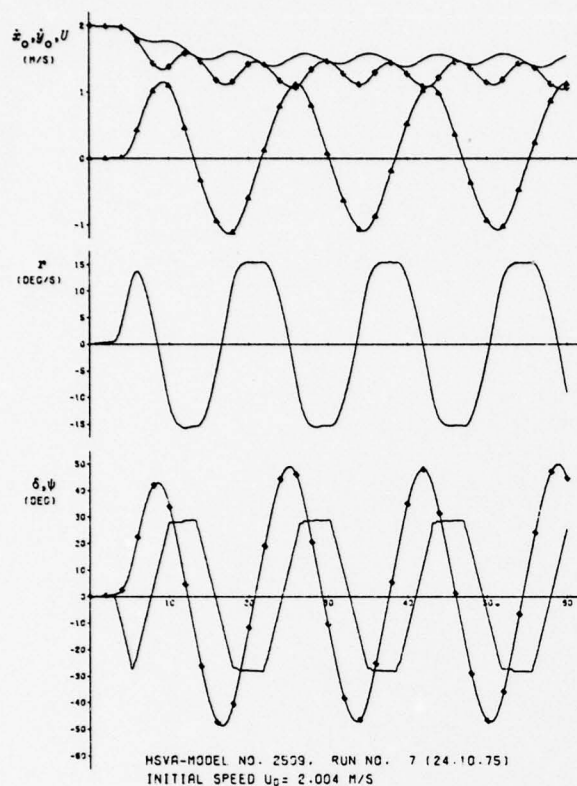


Fig. 13: Trajectory of 30°/10° zigzag maneuver

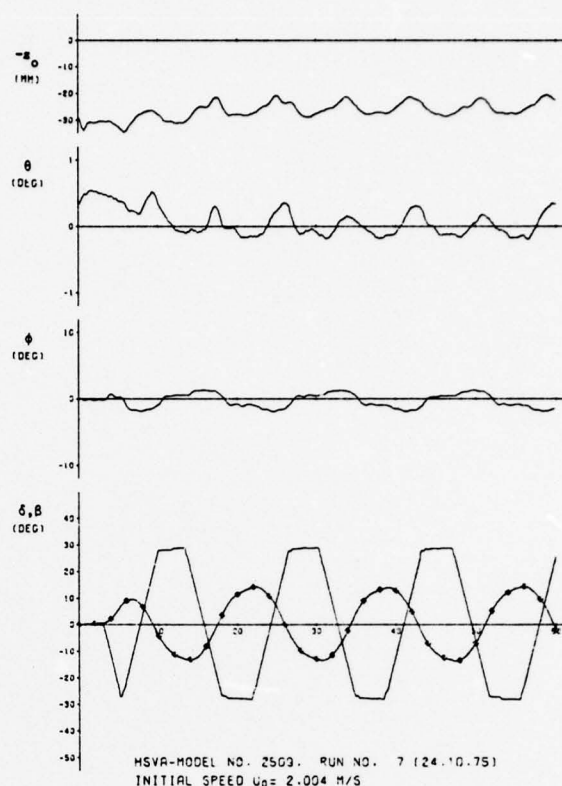


Fig. 14: Trajectory of 30°/10° zigzag maneuver

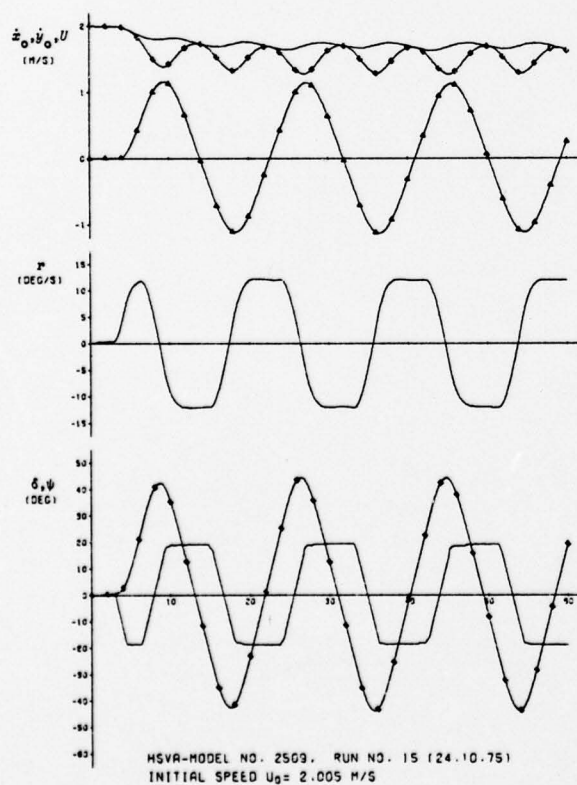


Fig. 15: Trajectory of 20°/20° zigzag maneuver

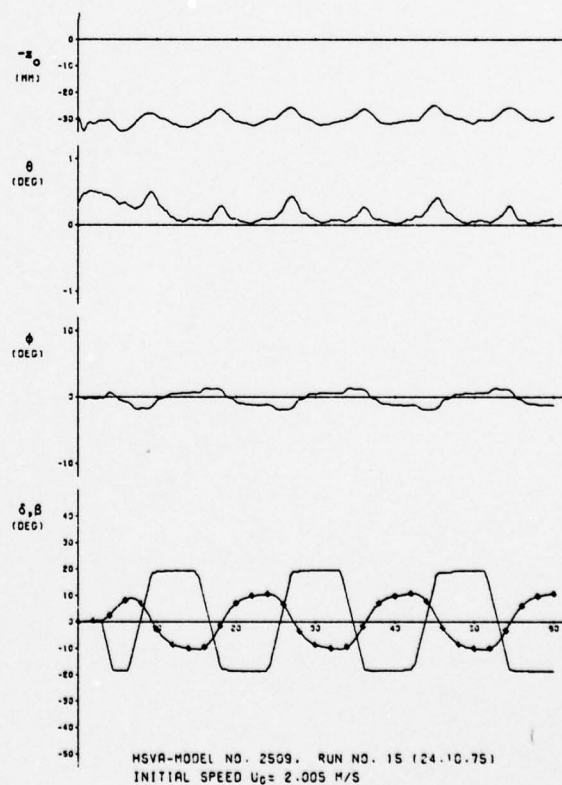


Fig. 16: Trajectory of 20°/20° zigzag maneuver

# Discussion on Paper by T. Frank et al

M. FUJINO

In Section 7, the authors derive a conclusion that the classical equations of manoeuvring motions provide a good approximation to the equations preferred by the authors, i.e. the equations (11). The discussor agrees with this conclusion.

However, he is doubtful that equation (47) stands for the classical equations of manoeuvring motions. It is his understanding that in the conventional description of manoeuvring motion, the stability derivatives of zero frequency are used in the full range of the frequency of motion under the "quasi-steady" assumption, although the stability derivatives should be considered as the functions of frequency.

As the authors show, the stability derivatives  $Y_v(\omega)$  and  $Y_{\dot{v}}(\omega)$  are described as follows:

$$Y_{\dot{v}}(\omega) = -\mu_{yy} + \frac{1}{\omega} \int_0^{\infty} N_{yy}(\tau) \sin \omega \tau d\tau,$$

$$Y_v(\omega) = -\beta_{yy} - \int_0^{\infty} N_{yy}(\tau) \cos \omega \tau d\tau.$$

Since  $N_{yy}(\tau)$  is assumed to be absolutely integrable, the second terms of the above equations diminish to zero as the frequency  $\omega$  tends to infinity, as Riemann-Lebesgue theorem proves. That is to say

$$Y_{\dot{v}}(\infty) = -\mu_{yy},$$

$$Y_v(\infty) = -\beta_{yy}.$$

Hence, the hydrodynamic force arising from the sway motion can be expressed as follows:

$$\begin{aligned} Y(t) &= \mu_{yy} \dot{v}(t) + \beta_{yy} v(t) + \int_0^{\infty} N_{yy}(\tau) v(t - \tau) d\tau \\ &= -Y_{\dot{v}}(\infty) \dot{v}(t) - Y_v(\infty) v(t) + \\ &\quad \int_0^{\infty} N_{yy}(\tau) v(t - \tau) d\tau \end{aligned}$$

Needless to say, the first and the second terms of the right-hand side stand for the hydrodynamic force due to the instantaneous motion of a ship and the last term stands for the effect of the past history of the motion on the hydrodynamic force.

On the other hand, the stability derivatives of zero frequency are

$$Y_{\dot{v}}(0) = -\mu_{yy} + \int_0^{\infty} \tau N_{yy}(\tau) d\tau,$$

$$Y_v(0) = -\beta_{yy} - \int_0^{\infty} N_{yy}(\tau) d\tau.$$

Obviously, the derivatives of zero frequency are different from those of infinite frequency by the second terms of the above equations.

Therefore we should describe the classical equations of motion as follows:

$$\begin{aligned} Y_E(t) &= [m + \mu_{yy} - \int_0^{\infty} \tau N_{yy}(\tau) d\tau] \dot{v}(t) \\ &\quad + [\beta_{yy} + \int_0^{\infty} N_{yy}(\tau) d\tau] v(t) \end{aligned}$$

Namely, equation (47) lacks the underlined term of the above equation.

Consequently, the discussor believes that the authors' reasoning in deducing the conclusion stated at the beginning of this discussion should be revised.

W.G. PRICE

I agree with the authors that the use of adjectives like "slow" in the scientific literature leaves much to be desired. Quantitative expression is needed if sloppiness is to be avoided. Contrary to the remarks in this paper (last paragraph, section 7), Bishop and Price (1974), Bishop, Burcher and Price (1975) have previously defined 'slow motion' in quantitative terms for use in P.M.M. tests and analysis.

In studies of the motion of surface ships, the sway velocity  $v(t)$  can be relied upon to be analytically well behaved and to have derivatives of all orders. In this event, the Taylor series expansion  $v(t - \tau)$  is

$$v(t - \tau) = \sum_{r=0}^{\infty} \frac{(-\tau)^r}{r!} v^{(r)}(t) + R_n$$

where the Lagrange form of the remainder is

$$R_n = \frac{(-\tau)^n}{n!} |v^{(n)}(t - \theta\tau)| \quad 0 < \theta < 1$$

and  $v^{(r)}(t) = d^r v(t)/dt^r$ .

For the typical sway velocity encountered in the manoeuvring of surface ships, it can be shown that

$$\lim_{n \rightarrow \infty} |R_n| = 0.$$

In these circumstances the convolution integral in

equation (46) may be written as

$$v(t) \int_0^{\infty} N_{yy}(\tau) d\tau - \dot{v}(t) \int_0^{\infty} \tau N_{yy}(\tau) d\tau +$$

$$\frac{\ddot{v}(t)}{2!} \int_0^{\infty} \tau^2 N_{yy}(\tau) d\tau \dots$$

It is reasonable to assume that after time  $\tau_s$  (say) the response function  $N_{yy}(\tau)$  decays to zero and we may replace the previous expression by

$$v(t) \int_0^{\infty} N_{yy}(\tau) d\tau - \tau_s \dot{v}(t) \int_0^{\infty} \left(\frac{\tau}{\tau_s}\right) N_{yy}(\tau) d\tau +$$

$$\frac{\tau_s^2 \ddot{v}(t)}{2!} \int_0^{\infty} \left(\frac{\tau}{\tau_s}\right)^2 N_{yy}(\tau) d\tau \dots$$

where the integrals all have finite values because

$$N_{yy}(\tau) = 0 \quad \text{for } \tau > \tau_s$$

## Authors' Reply

M. FUJINO

We are pleased that Professor Fujino has brought up the question of the nature of the quasi-steady approximation, for there does appear to be a discrepancy between equations (45) and the result in section 7 and Appendix II. This discrepancy exists however, only if one admits the premise, often made, that the appropriate quasi-steady equations are (44) with coefficients determined from (45) with  $\omega = 0$ . We believe that we have proved that this is not the case, and that the quasi-steady damping coefficients correspond to  $\omega = 0$  but the added masses to  $\omega = \infty$ . Any disagreement with this conclusion must necessarily be directed at the proof.

The belief that all coefficients should correspond to  $\omega = 0$  may be a result of using the term "slow" motion instead of "quasi-steady" motion, for the word "slow" does seem to be associated with  $\omega = 0$ . However, we recall that the definition of "quasi-steady" in equation (51) does not require  $v_1$  itself be small, but only the variation in  $v_1$  over an interval of time determined by the convolution-integral kernel (i.e., the quality of the "memory" of the system). The smallness of  $v_1$ , according to a different criterion has already been required in assuming the linearised equation (46).

We state once again that the equations (44) have no status as equations of motion except as empirical equations, that the "stability derivatives" cannot depend upon  $\omega$  if even the form (44) is to be correct, and that there is no basis for associating them with a particular value of  $\omega$ . What we have shown in Section 7 and Appendix II is that for quasi-steady motion, solutions of the linearised

and

$$(\tau/\tau_s) < 1 \quad \text{for } N_{yy}(\tau) > 0.$$

The convergence of this series depends on the sway motion and it is seen always to be valid if

$$v(t) > \tau_s \dot{v}(t) > \tau_s^2 \ddot{v}(t) > \dots$$

Thus it will be seen that the assumption of 'slow motion' in P.M.M. tests is only justified if the driving frequency  $\omega$  is less than  $\tau_s^{-1}$ . This may be of the order of 0.05 Hz (i.e.  $\tau_s \sim 3s$ ) in P.M.M. ship model sway experiments.

## REFERENCES

Bishop, R.E.D. and Price, W.G. On the slowness of a small departure from steady flow. Noise, Shock and Vibration Conference, Monash University, Melbourne, 1974.

Bishop, R.E.D., Burcher, R.K. and Price, W.G. The determination of ship manoeuvring characteristics from model tests. Trans.R.I.N.A., 117 (1975), 215-231.

equations of motion can be approximated uniformly by solutions of equations of the form of (44) but with the constant coefficients shown in (II.3).

Finally, we should like to state that we believe that the time has come to abandon the terminology "stability derivatives" and to begin to use one in conformity with that used in other modes of ship motion. (We note that the Russian Spravochnik po Teorii Korablya (Reference Book on Ship Theory, Sudpromgiz, 1960) has already done this long ago.) This will have the advantage of forcing one to consider the hydrodynamic origin of hydrodynamic forces. Although the classical linear equations are evidently satisfactory for quasi-steady motions it is not at all clear that this good fortune will persist in nonlinear theories and especially in situations where the motion is not periodic. We recommend reading the discussion of stability derivatives in A. Robinson and H.A. Laurmann's Wing Theory (Cambridge University Press, 1956, pp. 482-484).

W.G. PRICE

We are sorry if we overlooked in the papers of Bishop, Burcher and Price, a definition of "slow motion" in quantitative terms, as described by Dr. Price. Unfortunately, the cited papers were not available to us when our paper was written, and in fact, are still not. However, the two definitions are clearly related.

There are two aspects to our definition. One, the time constant  $t_c$ , is determined by the 'system' i.e., the ship. The other refers to the motion itself and states that a solution of (46) that also



satisfies (51) can be uniformly approximated by a solution of (47) with the same initial conditions. Dr. Price's time constant  $t_s$  is clearly similar to our  $t_c$  (in fact,  $t_s > t_c$ ), but his later developments do seem to require that  $N_{yy}(\tau) \equiv 0$  for  $\tau > t_s$ . The later statement about convergence of the series seems to presuppose that it is a series with alternating signs, but in fact there is no reason to suppose that  $v, \dot{v}, v, \dots$  are all positive or even all of one sign. The argument can doubtlessly be fixed up, but we note that our own definition handles the question of periodic motion nicely without further assumptions about the existence of higher derivatives or of their boundedness. By the mean-value theorem:

$$|v(t - \tau) - v(t)| = |\tau \dot{v}(t - \alpha\tau)|, \quad 0 < \tau < t_c$$

where  $0 < \alpha(t, \tau) < 1$ , so that our inequality (51) imposes essentially the same requirement upon a periodic motion.

We should like to emphasise a remark already made in the reply to Professor Fujino's discussion. This is that we are not really discussing "slow" motion, but rather quasi-steady motion. Slowness is already involved in the assumption of linearized equations (our (11) or (46)), but not in the present considerations. It has been pointed out by one of us (C.A.S.) that if still a different criterion is introduced, that of 'almost constant acceleration' instead of 'almost constant velocity' then Professor Fujino's proposed equation is obtained as the correct approximating equation. To be specific, define a different time constant  $t_a$  by the inequality

$$\frac{1}{t_a} \int_{t_a}^{\infty} \tau N_{yy}(\tau) d\tau < \frac{1}{4} \epsilon (\bar{\delta}_{yy} + \bar{N}_{yy}).$$

A motion satisfying (46) will be said to be of 'almost constant acceleration' if

$$|\dot{v}_1(t - \tau) - \dot{v}_1(t)| < \frac{1}{2} \epsilon \dot{V}[\bar{\delta} +$$

$$\int_0^{\infty} N_{yy}(\tau) d\tau] / \int_0^{\infty} |N_{yy}(\tau)| d\tau$$

for  $0 < \tau < t_a$ , where  $\dot{V} = \sup |\dot{v}(t)|$ , assumed  $> 0$ . (Here we assume  $\dot{v}$  bounded, whereas in (49) it was  $v$ .) For such a motion it is possible to show that any solution of (46) satisfying the above equality can be uniformly approximated by a solution of Professor Fujino's proposed equation. In particular, if  $v_2(t)$  is a solution of the latter with the same initial conditions, then  $|v_1 - v_2| < t_a \dot{V} \epsilon$ .

The question remains, of course, of deciding which is the more important concept, 'almost constant velocity' (quasi-steadiness) or 'almost constant acceleration'. We believe that the former is more important for most ship manoeuvres, but perhaps there is room for disagreement.

## Discussion on Paper by S. Takezawa et al

A.N. KHOLODILIN

The transient test method is very useful and economical. The work which has been done by the authors of papers, Part I as well as Part II, is very important and interesting. TWW method may be used in many cases for testing ship models.

This method has been used by the Leningrad Shipbuilding Institute towing tank too. The experiments with antipitching fins may be given as example. The results of data received by the test in regular waves and by TWW method were in good agreement. (See A.N. Kholodilin, Ship's Stabilization, in Russian Sudostroenie, Leningrad, 1973.)

## Authors' Reply

The authors are sincerely grateful to Dr. A.N. Kholodilin who introduced the antipitching fin test by TWW method.

As stated in our paper, in the application of transient response method for determining frequency transfer function of a system, the most important point to be considered is that the tested system should be linear in the frequency range of interest. In the case of the antipitching fin test in transient water waves, if fins cause nonlinear effects due to the resultant (effective) attack angle and the aspect ratio of the fin, special treatment may be needed in analysis work. However, pitching motion is small compared with rolling motion, and consequently fin effect may be linear with respect to wave height, and the linear analysis may be allowed.

The authors hope that transient response methods will be applied to various kinds of experiments, and will be developed for the practical methods of testing ship models.

**SESSION II**  
**MODERN EXPERIMENTAL TECHNIQUES (2)**

Monday, 29 March 1976

14.00—17.00

Chairman: J. Gerritsma

The 'Wavedozer': a travelling beam wavemaker, by N. Hogben

An experimental investigation of the three-dimensional turbulent boundary layer on a ship model, by L. Larsson

The ultimate half roll before capsize on the analog computer, by K. Kure, H. Ketelsen, and V. Jensen

The roles of flow transition, laminar separation, and turbulence stimulation in the analysis of axisymmetric body drag, by J. H. McCarthy, J. L. Power, and T. T. Huang

Random wave generation for research on immersed marine vehicles, by J. H. van Oorschot and F. Koopmans



# THE 'WAVEDOZER': A TRAVELLING BEAM WAVEMAKER

N. HOGBEN

National Physical Laboratory, Feltham, UK

## SYNOPSIS

This paper describes the development and operation of a prototype travelling beam wavemaker christened the 'Wavedozer'. It is a simple and relatively cheap device for making large waves in a conventional ship model towing tank. It consists of a transverse flap mounted under the towing carriage and spanning the full tank width which leaves a train of waves in its wake. When the carriage stops these waves continue into the remaining length of tank where the test models are placed.

The paper reports results from systematic proving tests documenting its performance and providing design data.

## 1. INTRODUCTION

The rapid expansion of ocean engineering in recent years has provided a powerful stimulus to the development of new experimental techniques. The 'Wavedozer' is a simple and relatively cheap device for making large waves in a conventional ship model towing tank developed by Ship Division of the National Physical Laboratory mainly for use in testing offshore structure models. It consists of a transverse flap mounted under the towing carriage and spanning the full tank width which leaves a train of waves in its wake when the carriage is running. When it stops these waves continue into the remaining length of tank where the test models are placed.

This paper describes the development and operation of a prototype Wavedozer which at the time of writing is available in the Ship Division No. 2 tank at Teddington and has already been used for several research investigations of considerable practical significance. Brief reference will also be made to the more permanent Wavedozer facility which is in course of development.

## NOMENCLATURE

c	Carriage speed or wave phase speed
c <sub>0</sub>	Value of c during steady run
d	Water depth
D <sub>w</sub>	Flap drag coefficient = $\frac{16 R_w}{\rho g b H^2 (1-2 k d / \sinh 2 k d)}$
F <sub>n</sub>	Froude number = $c / \sqrt{g d}$
g	Acceleration due to gravity
H	Wave height
H <sub>1</sub>	Wave height measured from first crest to second trough behind carriage in metres
H <sub>2</sub>	Height in metres of highest wave from trace recorded at test cylinder
k	Wave number = $2\pi / \lambda$
L, L <sub>1</sub>	Dimensions of flap support arms

L <sub>w</sub>	Wetted chord length
q	Wave group velocity factor
R <sub>w</sub>	Wave resistance
S <sub>1</sub> , S <sub>2</sub> , S <sub>3</sub> and S <sub>4</sub>	Run history parameters (See fig 8)
t, t <sub>1</sub> and t <sub>2</sub>	Time variables (See fig 12)
W	Spring balance reading during steady run
W <sub>0</sub>	Spring balance reading at rest
x, x <sub>1</sub> , x <sub>2</sub>	Distance coordinates (See fig 12)
θ	Flap incidence angle
θ <sub>1</sub>	Incidence of flap support arm
λ	Wavelength according to linear theory
ρ	Density of water

## 2. PRELIMINARY INVESTIGATIONS

Experiments using a vertical beam with a rounded bottom clamped to the back of the No. 2 tank carriage gave a first indication of the possibilities of the technique. The photographs in figure 1 show the waves generated in this case both as formed behind the carriage and as subsequently propagated into the test area beyond the stopping point of the carriage. The No. 2 tank is 6 metres wide and the water depth for these tests was 2.3 m. (This is less than the normal working depth of 2.7 m to allow clearance for the wave crests). The experiments were in fact originally intended merely to study the effect of the slight wall slope in this tank on a train of waves and not as a trial for a new wavemaking device. When it was found however as shown in the figure that waves of the order of  $\frac{1}{2}$  metre high could be generated so simply it was decided to explore the potential of towed beam wavemaking more fully.

With the vertical beam as might be expected there was a high rate of energy loss which was indeed evident from the turbulent appearance of the waves behind the carriage in this case. This involved a correspondingly high drag and in fact the only reason waves higher than half a metre could not be generated was that with the power available the carriage could not be driven faster than about 3 m/s

which is less than half its normal maximum operating speed. Attention was therefore concentrated on seeking a more efficient beam configuration to reduce the losses and hence allow higher carriage speeds to be achieved. Intuitively it was felt that greater efficiency could best be achieved by spreading the load over a wider area of surface. This led to the concept of a planing lamina as a basic model for evaluation and it was decided to undertake some exploratory tests of this idea in a small circulating water channel before trying it on the tank.

## 2.1 Tests in Small Channel

The experiment can be simulated in a small channel with the wavemaking device fixed and the flow speed scaled by Froude's law to correspond to the carriage speed. The tests were in fact conducted at about one tenth of the linear scale of the experiments in the tank, in a channel (see figure 2) 0.36 m wide run at 0.23 m depth. The main purpose was to seek the most efficient configuration and derive data to guide the design of a prototype. The primary design parameters considered were angle of incidence and initial immersion of the lamina and the criterion of efficiency was that the drag should be minimum for a given limiting wave height and that the wetted chord should not be too large. The lamina was mounted on a specially designed pivoted balance arm as shown in figure 3 allowing independent setting of incidence and immersion, the attitude being maintained by weights providing an approximate measure of the lift and drag forces.

A systematic schedule of tests covering a range of incidence angles and immersions was carried out and figure 4 shows some photographs used for measuring the wave heights achieved at various incidence angles. In all cases, the test conditions were adjusted until the flow speed corresponded to a Froude number  $F_n = c/\sqrt{gd} = 0.67$  and the first crest reached the limiting height beyond which it began to break. This was found to be a very clear criterion which could be set with high precision. Figure 4d in which the incidence is  $90^\circ$  is in fact a simulation of the original experiment with the vertical beam in No. 2 tank and indicates the relative inefficiency of this arrangement with high level of turbulence and diminution of the wave height downstream.

Some of the results of the experiments are plotted in figure 5. These broadly confirmed the advantage of the planing lamina concept and showed that the energy loss and associated drag decreased with decreasing incidence but at the cost of increasing wetted chord. Because of the small scale, the difficulty of maintaining steady conditions and certain inherent approximations in the method of measurement, high accuracy cannot be claimed for the results; there is in fact rather a wide scatter although considerable care was taken in the conduct of the tests. Nonetheless the investigation served the purpose of providing a rough experimental basis on which to design a prototype Wavedozer for the No. 2 tank. It also offered the opportunity for comparisons of theoretical methods of estimating the relation of drag and wave height with measurements which yielded some puzzling results.

## 2.2 Comparison of Theory and Experiment

The theory of waves due to travelling disturbances is very extensively documented in the literature

and text book accounts may be found for example in (1) and (2). Linear theory for the present case of a 2-dimensional disturbance leads to the following simple formula relating the drag or 'Wave resistance'  $R_w$ , the wave height (crest to trough)  $H$ , and the water depth  $d$ .

$$\frac{R_w}{b} = \frac{\rho g H^2}{16} (1 - 2 \text{ kd} / \sinh 2 \text{ kd})$$

where  $b$  = Tank width

$$k = \frac{\pi}{c} \tanh kd = 2\pi/\lambda$$

$c$  = Speed of travel

$\lambda$  = Wave length

The same formula applies to the case of an obstacle in a channel with  $c$  being then the speed of flow. It should be noted that at high speeds in water of finite depth, the factor  $(1 - 2 \text{ kd} / \sinh 2 \text{ kd})$  which is unity for deep water decreases and greater wave heights may then be expected for a given drag. When the waves are very steep it must be expected that linear theory will no longer be reliable. Various non-linear theories exist (see for example references (3) to (5)) but they cannot predict the effects of turbulence unless the corresponding energy losses are known.

Comparison of linear theory with experiment is illustrated in figure 5. Figure 5a plots experimental values of the coefficient

$$D_w = \frac{16 R_w}{\rho g b H^2 (1 - 2 \text{ kd} / \sinh 2 \text{ kd})}$$

using the approximation  $R_w = W \sin \theta \cos \theta$  and taking  $H$  to be the height of the 2nd crest as shown in figure 2. Figure 5c shows the corresponding values of wave steepness  $H/\lambda$ . According to linear theory  $D_w = 1$  and the theoretical limit for  $H/\lambda$  is  $1/7 = 0.143$ . Although conditions were in all cases set so that the waves were on the verge of breaking, the measured steepnesses are all somewhat less than half the theoretical limit. The experimental values of  $D_w$  on the other hand range between 3 and 5 times the prediction of linear theory. It was hence found in fact that the measured resistances would be in fair agreement with linear theory if it had been assumed that the first crest of the measured waves had actually reached the theoretical height limit. The full explanation for this finding is not yet known but the defect of wave height is far too great to be attributed to experimental error or to the difference between linear and non-linear theory. Also it may be said that the condition of incipient breaking at the first crest was very clearly defined and easily set. It was decided that substantial energy losses must have been occurring in the neighbourhood of the plate in conditions of incipient wavebreaking and some pitot traverses were made upstream and downstream of the plate to try and identify these. Some losses were detected but they were only enough to account for about a half of the excess wave resistance.

In investigating this anomaly reference was made to a paper by Benjamin (6) which describes an identical experiment. Here it is reported that the resistance, measured in the same way, agreed with the value for a theoretical wave of maximum steepness at the point when the first crest was about to break. It is perhaps significant however that it is not stated whether the wave did in fact reach



the theoretical steepness limit.

Some further light has been shed by the results of the prototype experiments in No 2 tank which displayed similar behaviour as discussed in the next section.

### 3. THE PROTOTYPE IN NO. 2 TANK

The decision to build a prototype Wavedozer happily coincided with a requirement by the Maritime Science Division of NPL to measure loads on vertical cylinders in large waves. The opportunity was thus afforded for proving the technique in application to a practical wave loading experiment. The specification for the prototype was based on the experience gained in the small channel and the design incorporated provision for a similar range of variation of the incidence and immersion and a similar arrangement for approximate measurement of the lift and drag. Unfortunately, time limits and other factors which need not be discussed here, led to compromises in the construction and installation stage which severely limited the scope for variation in incidence and immersion. Figure 6 is a diagrammatic sketch of the prototype arrangement as installed and figure 7 shows some photographs of the waves generated. It may be seen that the waves are now much larger than in the vertical beam tests illustrated in figure 1 because of the higher carriage speed of 4 m/s attainable with the inclined flap.

#### 3.1 Proving Tests

Figure 8 illustrates the experimental layout. Wave profiles were measured by capacitance probes both at the test cylinders and behind the carriage while running. In the latter case the probe was hastily inserted by hand behind the carriage after it had passed and recording was commenced in the neighbourhood of the first trough. A row of small holes was drilled in the flap for observation of the wetted chord length and provision was made for recording a trace of carriage speed for use in studying the effect of variation in the speed history. The flap was loaded with a steel rail weighing about a tonne distributed across most of its width and spring balances fitted to each of 2 supporting cables were used to measure the net weight bearing on the flap during runs as indicated in fig 6.

The proving tests have been conducted partly to document the performance of the prototype and partly to provide basic data for use in design of other similar installations. Two series of tests have been carried out at each of 2 flap angles, namely,  $14^\circ$  and  $17\frac{3}{4}^\circ$ . In the first series, speed was varied over a wide range up to the maximum now attainable of 4 m/s or  $F_n = 0.90$ ; in the second, speed was set always at the maximum and the run history parameters  $S_2$ ,  $S_3$  and  $S_4$  illustrated in fig 8 were varied. Figs 9 to 11 show the results for the tests at  $14^\circ$  flap angle (tests for the  $17\frac{3}{4}^\circ$  angle could not be analysed in time for results to be included in the paper). Fig 9 is concerned with conditions at and behind the flap and fig 10 with conditions at the test cylinders (see fig 8) during the first series of runs in which the speed was varied. Fig 11 is concerned with the waves at the test cylinders during the second series when run history was varied at maximum speed.

#### 3.2 Series I: Speed Variation

**3.2.1 Conditions at and behind Carriage.** Fig 9a presents some sample traces of waves recorded behind the carriage from which the heights  $H_1$  measured in metres from the first crest to the second trough (see fig 6) were derived. The first trough is at the left hand end of each trace. The irregularity developing after the first 3 waves is due to reflection from the flap after the carriage stopped and does not affect the waves in the test area as may be seen from fig 10a. Fig 9b shows that  $H_1$  increases approximately linearly with speed up to a maximum of about 0.7 m ( $H_1/d = 0.3$ ) at  $F_n = 0.9$ . The height from the first crest to the first trough was difficult to measure with confidence but it is estimated that it reached a maximum of about 1 metre at  $F_n = 0.9$ . A photograph of this first trough and crest at the maximum speed is shown in fig 7a. It may be noted in passing that for scaling up to a typical North Sea water depth of say 140 m, the scale factor is 1:60 and an  $H_1$  of 0.7 m corresponds to a wave height full scale of 42 m! It should be added however that in these conditions a very substantial advantage was gained from the effect of the limited depth in increasing the wave height for a given drag as explained in section 2.2. At the maximum carriage speed of 4 m/s in fact, the factor  $(1-2 \text{ kd}/\sinh 2\text{kd})$  in the formula for drag is about a half. This means that the wave height for a given drag according to linear theory is thus about 50% greater than it would be in deep water.

Fig 9c plots measurements of the flap drag coefficient

$$D_w = \frac{16 R_w}{\rho g b H_1^2 (1-2 \text{ kd}/\sinh 2\text{kd})}$$

which should be unity according to linear theory. Here the wave resistance  $R_w$  was derived from measurements of the flap loading read from the spring balances (see fig 6) using the formula

$$R_w = \frac{(W_o - W)(L_1 \cos \theta_1 + L \cos \theta) \sin \theta}{[L + L_1 \cos (\theta - \theta_1)]}$$

where  $W_o$  = Spring balance reading at rest  
 $W$  = Spring balance reading at steady speed  
 $L_1$  = Distance between hinges (See fig 6)  
 $L$  = Distance from lower hinge to trailing edge of flap  
 $\theta$  = Incidence of flap  
 $\theta_1$  = Incidence of flap support arm attached to upper hinge

The relatively large scatter of the spots and absence of results at lower speeds ( $F_n < 0.56$ ) reflects the difficulty of reading the fluctuating spring balances with accuracy. A mean line through the spots indicates however that up to  $F_n = 0.6$ , the experimental drag agrees quite well with linear theory but beyond that speed it rises steeply. This steep rise presumably indicates the development of substantial losses at the higher speeds. It seems significant therefore that the wave steepness plotted in fig 9d rises to a peak at  $F_n = 0.6$  and then declines sharply. It is puzzling however that the peak steepness is less than 0.08 which is little more than half the theoretical maximum and that there was relatively little evidence of wave breaking. Even at the maximum speed the first crest as shown in fig 7b shows only incipient breaking. It must be assumed that the losses are associated with the very strong turbul-



ence in the first trough pictured in fig 7a.

There is some similarity between these results and the corresponding findings in the small channel experiments. Detailed comparison is not possible since here the variable is speed while in the channel it was flap angle. It may be said broadly however that the unexplained losses are relatively much smaller in the tank than in the channel.

The drag data in fig 9c can be used for estimating power requirements for a given wave height. For the prototype run at maximum speed of 4 m/s in water 2.3 m deep when  $H_1$  reached 0.7 m, the drag per metre of tank width was 376 Newtons and the corresponding power per metre was 2 horsepower. Guidance on the size of flap required is given by fig 9d which shows the wetted chord length as a fraction of the wavelength according to linear theory  $\lambda$  computed from the formula

$$\tanh(2\pi d/\lambda)/(2\pi d/\lambda) = F_n^2$$

The larger scatter of spots at the top speed is due to the fact that the water was actually spilling over the leading edge onto the top of the flap in this case. The total chord of the prototype flap was 1.5 m and trailing edge immersion when stationary was 5 cms. It was found to be important to keep this small to minimise drag during acceleration.

**3.2.2 Conditions at Test Cylinders.** Fig 10 gives details of the waves recorded at the test cylinders. Before reaching the test area, the waves must pass the stationary flap and from observation it is clear that there is a significant degree of reflection and energy loss associated with the resulting wave impacts. At the same time the effect of the carriage deceleration is to induce a 'telescoping' of wave energy so that the loss of height due to reflection and impact losses can be recovered as the waves proceed towards the test area, an effect which will be discussed in more detail in section 3.3. It should also be noted that since it is the wave profile and not the actual water which travels along the tank, the surface of the waves reaching the test area is very 'clean' with no trace of the severe turbulence which develops behind the carriage as may be seen in the photograph fig 7c.

Fig 10a shows 2 short sample traces of waves recorded at the test cylinder at 2 different speeds. The number of waves in a train varies with carriage speed but may be estimated by noting that the train of waves generated lengthens at group velocity. At lower speeds therefore when the water is effectively deep and the group velocity is  $\frac{1}{2}c$ , the number of waves should be roughly half the length of steady run divided by the wavelength. For the series I tests the steady run length ranged between about 50 m and 80 m and from fig 9e it may be seen that the wavelength ranged from about 1 m to about 17 m. At the highest speeds the water could not be regarded as deep and the group velocity was therefore greater than  $\frac{1}{2}c$ . The corresponding number of substantial waves in a train was then in fact about 5 or 6.

Fig 10b shows spectra calculated from the 2 sample traces in fig 10a (for these I am indebted to my colleague Mr S J Rowe). As may be expected they are rather narrow banded with energy concentrated in frequencies corresponding to those of the waves generated during steady running. In computing

these spectra care was taken to exclude the very long single hump due to transient components of the disturbance which preceded each wave train as may be seen in fig 10a.

In practice it is often important to know the maximum wave height attainable. Fig 10c shows the variation with speed of  $H_2$  which is the height in meters from crest to trough of the highest individual wave recorded at the test cylinders and fig 10d shows the corresponding wave steepness. It is of interest to note that there is relatively little difference between  $H_2$  and  $H_1$  as may be seen by comparing figs 10c and 9b. In spite of the losses and reflection incurred by impact of the waves passing the stationary flap,  $H_2$  actually reaches higher values at the top speed than  $H_1$ , presumably due to the 'telescoping' or 'energy convergence' effect mentioned above. This is a very favourable result since  $H_2$  is the important height from the model testing point of view. Scaled up by a factor of 60 to typical North Sea depth of 140 m, the maximum  $H_2$  corresponds to a wave height of more than 45 m. It must be remembered of course that as explained when discussing  $H_1$  in section 3.2.1, these waves also owe much of their height to the magnifying effect of limited depth.

### 3.3 Series II: Variation of Run History at Maximum Speed

Because the prototype Wavedozer flap is non retractable it makes waves during all phases of its motion, acceleration, steady running and braking. The propagation speed of the waves generated at any instant will vary with the carriage speed and the waves recorded at the test cylinders will therefore be dependent on the whole speed history and the distance beyond the stopping point at which the waves are measured (referred to in fig 8 as the 'clearance' distance  $S_4$ ). Much of the scatter in the series I tests was in fact probably largely due to the difficulty of accurately controlling the run history. In the series II tests an attempt was made to vary the distances  $S_2$ ,  $S_3$  and  $S_4$  (See fig 8) for 2 main reasons. The steady run length was varied to obtain data on the minimum tank length required for achieving a given wave height. The braking and clearance distances were varied to provide an indication of the optimum siting for a test object to obtain the maximum advantage from the energy convergence effect.

In practice it proved impossible to achieve independent control of the parameters specially in the case of the deceleration distance  $S_3$ . For this reason the plottings in fig 11 do not include any results relating to systematic variation of  $S_3$ . Also the scatter of spots for  $S_2$  and  $S_4$  is very wide and the results must be regarded as rather approximate. Both the heights and the distances have been divided by the wavelength  $\lambda$  to neutralise the effect of speed variations which were significant although all runs in this series were set to the maximum. The value of  $\lambda$  computed from linear theory as explained previously, varied in fact between about 13 m and 17 m with an average of about 15 m or 6.5 d. The dotted lines are rough upper boundaries for the spots.

From fig 11a it may be suggested as a rough guide that for the prototype conditions with water depth of 2.3 m, the steady run length requirement is about  $3\lambda$  for  $H_2 = 0.7$  m and about  $1\lambda$  for  $H_2 = 0.6$  m. When scaled up to typical North Sea water

depth by a factor of 60, 0.7 m becomes 42 m and 0.6 m becomes 36 m both substantially greater than the commonly assumed estimate of 30 m for the highest wave in 50 years.

For practical design purposes it is helpful to be able to estimate the total run length requirement including the acceleration and braking distances  $S_1$  and  $S_3$ . These are of course strongly dependent on the powering and control characteristics of the particular carriage concerned as well as on the drag of the flap. Also it is difficult to be precise in defining the points of transition from acceleration to steady run a fact which explains some of the scatter in fig 11a. Estimates of  $S_1$  and  $S_3$  were made for each run but there was very wide scatter specially in  $S_1$  and the best that can be said is that  $S_1$  lay generally between  $2\lambda$  and  $3\lambda$  and  $S_3$  between  $1\lambda$  and  $2\lambda$ . The total run length requirements were very approximately about 6 $\lambda$  or 90 m for  $H_2 = 0.7$  m and about 4 $\lambda$  or 60 m for  $H_2 = 0.6$  m.

Considering now the clearance distance  $S_4$  for the test object, its effect on wave height is plotted in fig 11b. The scatter of the spots in this case is even greater and only rather tentative comments can be made. The upper boundary indicates a substantial rise of wave steepness attainable as  $S_4$  is reduced towards the minimum value of about 0.8 $\lambda$  possible from the safety point of view. This is consistent with the experimental observation that the waves grew to a peak height about 15 m beyond the stopping point of the carriage as confirmed indeed by the envelope of wetness left on the tank wall. A possible explanation for this as already suggested is that as the carriage begins to brake there is a 'telescoping' or 'convergence' of the wave energy. The effect could also be interpreted as the development of a 'beat' due to the reduction of wave frequency associated with the deceleration. In practice such a mechanism could only have operated in the initial stages of deceleration because the leading wave quite quickly overtook the flap which then lost contact with the water until the impact of the following crest. The beat once established however could be of sufficiently long period to explain the observed peaking of the height envelope.

In principle it seems possible that such an effect could be optimised by suitable control of the deceleration and a tentative theoretical basis for this is outlined in the appendix. The idea is to determine a deceleration history such that all the energy generated while the carriage is slowing down reaches a chosen target point at the same time. It is unlikely to have much relevance to the present experiments since it assumes that the water is sufficiently deep for the group velocity to be  $\frac{1}{2}c$  and also that the flap continues making waves throughout the deceleration. It is included however because there might be cases where the water is sufficiently deep and the slowing down sufficiently gradual for the argument to have some meaning at least during the early stages of deceleration. It leads in fact to the conclusion that the rate of deceleration should be constant and that the target should be at the stopping point.

#### 4. APPLICATIONS

The Wavedozer is seen primarily as a relatively cheap and simple way of generating very large waves in a conventional ship towing tank. In the first

few months of its existence the prototype has already been used for 3 different investigations. The first was a study of wave loading on vertical cylinders with special attention to scale effects and the influence of surface roughness. The ability to make waves high enough to induce large drag forces at reasonably high Reynolds numbers was a crucial factor in this investigation carried out by the NPL Division of Maritime Science. The second was a study of waveloading on horizontal cylinders with special attention to slamming carried out by a team from University College London working under contract to NPL. Here again the large waves were crucial since it was found to be impossible to induce slamming in smaller waves. The third application was a study of the kinematics of plunging breaker waves by Prof. Longuet-Higgins of Cambridge University and the Institute of Oceanographic Sciences. A high speed cine record was made of the profiles of waves breaking on the beach at the far end of the tank for comparison with theoretical computations of the profile history.

The present author was not directly involved in any of these investigations but it is expected that they will be reported in the literature in due course. Meanwhile work is in hand on the development of an improved and more permanent Wavedozer facility with a flap which is retractable to avoid losses and reflection due to impacts by waves passing the stationary carriage.

#### 5. CONCLUSIONS

The paper has described the development and proving of a prototype 'Wavedozer' or travelling beam wavemaker and has referred briefly to practical applications for which it has already been used. It has been shown that it is an effective and relatively cheap and simple way of generating very large waves in a conventional ship towing tank and data defining its performance and providing guidance for design of other installations are presented.

Waves greater than three-quarters of a metre in height in water of 2.3 metres depth have been achieved with the prototype and an improved installation with a retractable flap is being developed which should achieve substantially greater heights by avoiding losses and reflection due to impact of waves passing the stationary carriage. Data on run length requirement for given wave height capability are included in the paper and indicate that when the steady run length is reduced to about one wavelength at maximum speed (about 15 m at 4 m/s for the prototype) wave heights of about 0.6 m could still be attained in the test area. Investigation of the optimum siting of the test object to achieve maximum wave height suggested that this should be within about one wavelength from the stopping point of the carriage.

The paper also includes data on the variation of drag and wetted chord of the flap with speed to assist in design of hardware. The drag data can be used for estimating flap loading and power required and the wetted chord length for deciding the flap size. Data on the effect of varying flap incidence are unfortunately only available from the small scale channel experiments which were not very accurate. These indicate as expected that drag decreases with incidence but wetted chord increases. The 14° angle used for the prototype seemed to strike a reasonable balance between the requirement to minimise drag and the need to avoid



excess flap size and lift forces.

Regarding applications, the Wavedozer is seen primarily as a facility for making very large waves and there are many requirements for such a facility specially in connection with testing of offshore structures where scaling problems and the need to model extreme '50 year wave' conditions are important. The prototype has already been used within the first 4 months of its existence for 3 different practical investigations.

#### ACKNOWLEDGEMENTS

The author wishes to express his appreciation to his many colleagues who participated in the work described specially Mr A Dolman, Mr J D Hannah, Mr J Osborne, Dr R G Standing, Mr A Young and Mr D C Webb.

#### APPENDIX: ENERGY CONVERGENCE

In the case of a conventional wavemaker mounted at the end of a tank, it is known that by suitable variation of frequency a high concentration of wave energy and correspondingly large waves can be made to develop at some chosen distance from the wavemaker. The mechanism involves a steady decrease of frequency so that the flux rate of the wave energy generated at each successive instant increases in such a way that all the energy arrives at the chosen point at the same time. The same basic principle can be applied in the case of the travelling wavemaker the idea now being to control deceleration in such a way that the energy generated at each successive position converges at a chosen target point at the same time.

Fig 12 illustrates the concept and indicates the basis on which the deceleration rate needed to 'hit' a given target can be deduced for the case of deep water in which the group velocity is a constant fraction of the phase velocity. From the figure it may be seen that the condition that all the energy, travelling at group velocity  $c_g = qc$  shall reach the target distant  $x_2$  from the start of deceleration at the same time  $t_2 = \frac{x_2}{qc_0}$  is:

$$x_2 = \int_0^t c \, dt + qc \left( \frac{x_2}{qc_0} - t \right)$$

which on differentiation with respect to  $t$  may be written as

$$\frac{dc}{dt} = c f(t)$$

where  $f(t) = (1-q)/(qt - x_2/c_0)$

It may be shown that this leads to

$$c = c_0 (1-q \frac{c_0}{x_2} t)^{\frac{1}{q} - 1}$$

or

$$\frac{dc}{dt} = \frac{c_0^2}{x_2} (q-1)(1-q \frac{c_0}{x_2} t)^{\frac{1}{q} - 2}$$

#### REFERENCES

- (1) LAMB, H. "Hydrodynamics" Cambridge University Press, 6th Edition 1932.
- (2) WEHAUSEN, J.V. and LAITONE, E.V. "Surface Waves" Encyclopaedia of Physics Vol 9 pp 446-778 Springer, Berlin, 1960.
- (3) BENJAMIN, T.B. and LIGHTHILL, M.J. "On Cnoidal Waves and Bores" Proc. Roy. Soc. A224 pp 448-460 1954.
- (4) DE, S.C. "Contributions to the Theory of Stokes Waves" Proc. Cambridge Phil. Soc. Vol 51 pp 713-736 1955.
- (5) HOGBEN, N. "Wave Resistance of Steep 2-Dimensional Waves" NPL Ship Div. Rep No 72 1966.
- (6) BENJAMIN, T.B. "On the Flow in Channels when Rigid Obstacles are placed in the Stream". J. Fluid Mech. Vol 1 Part 2 pp 227-248 July 1956.

In deep water  $q = \frac{1}{2}$  and these formulae become

$$c = c_0 (1 - \frac{c_0}{2x_2} t)$$

$$\frac{dc}{dt} = - \frac{c_0^2}{2x_2}$$

In water of finite depth  $d$ , the group velocity factor  $q$  is related to the speed  $c$  by

$$q = \frac{1}{2} (1 + 2 kd / \sinh 2kd)$$

$$\text{and } c^2 = \frac{g}{k} \tanh kd$$

This means that when  $c$  is large,  $q$  will vary significantly with speed and the foregoing analysis cannot be applied. It is commonly assumed that water can be regarded as deep when  $\lambda/d < 2$  and this corresponds to  $F_n < \pi^{-2}$ .

The argument also assumes that the flap continues to make waves throughout the deceleration. Unfortunately in the case of the experiments described in the paper the flap only maintained steady contact with the water in the early stages of the deceleration when, at least for the high speed runs, the water could not be regarded as deep. The argument has been included however because there may be situations where the speed is low enough and the deceleration gradual enough for the theory to be relevant. The conclusion to which it leads is that the deceleration should be constant and that the target should be at the stopping point of the carriage.





Fig. 1 (a)

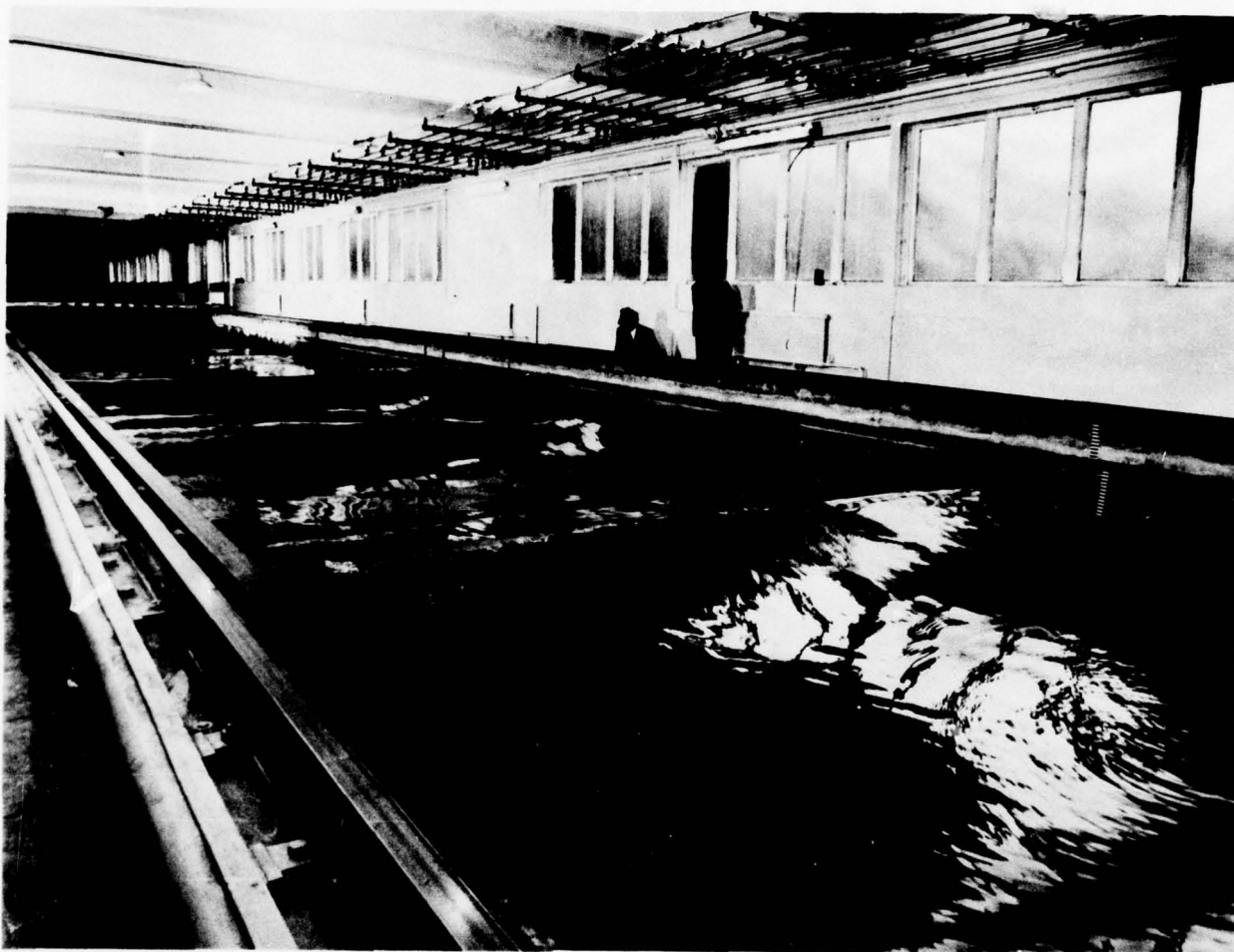


Fig. 1 (b)

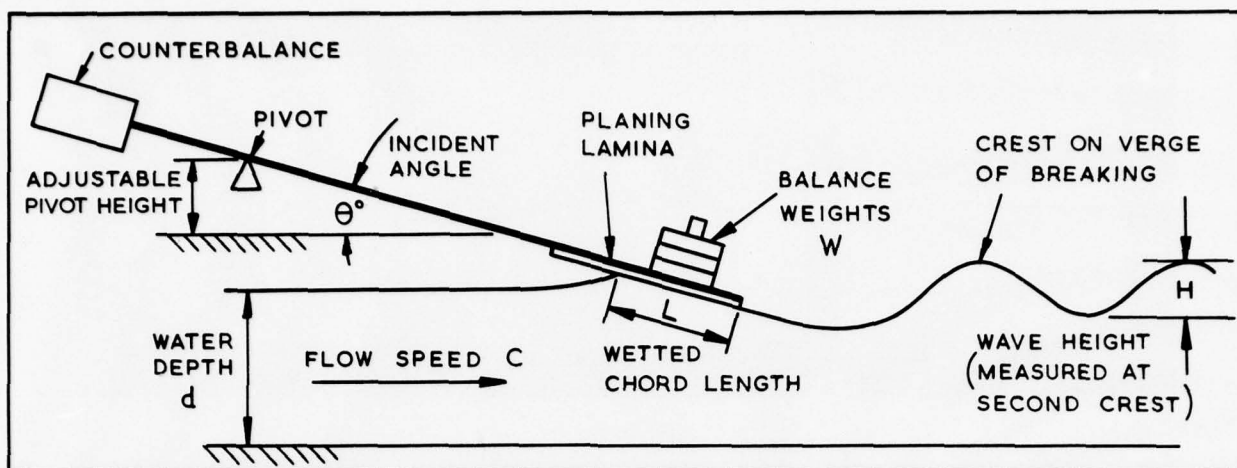


Fig. 2

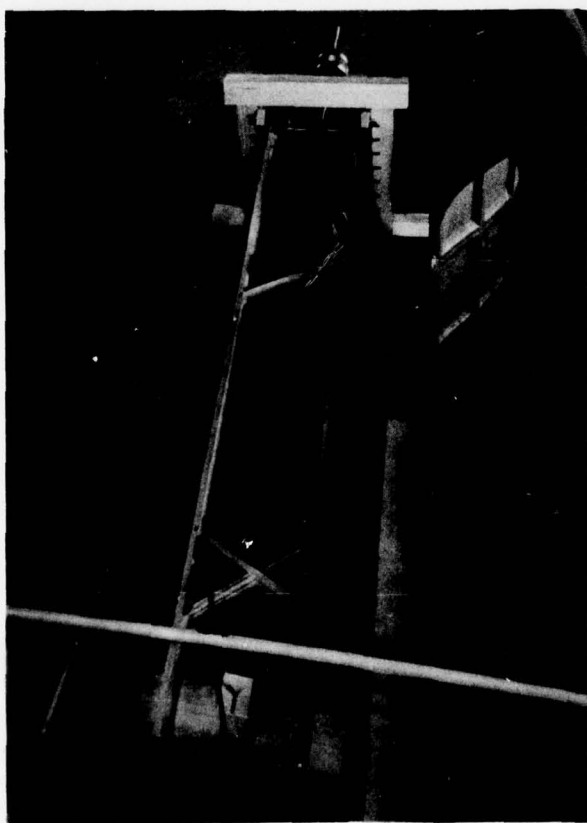


Fig. 3 (a)

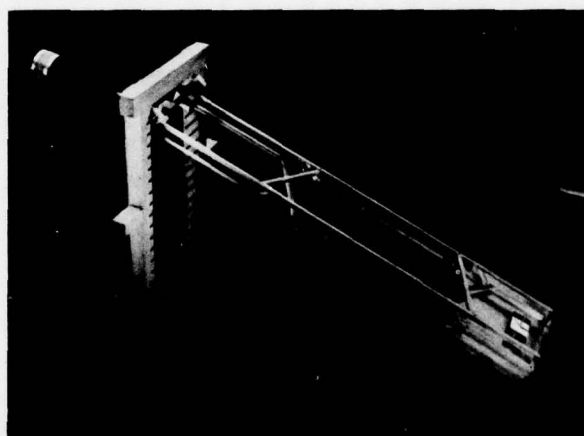


Fig. 3 (b)



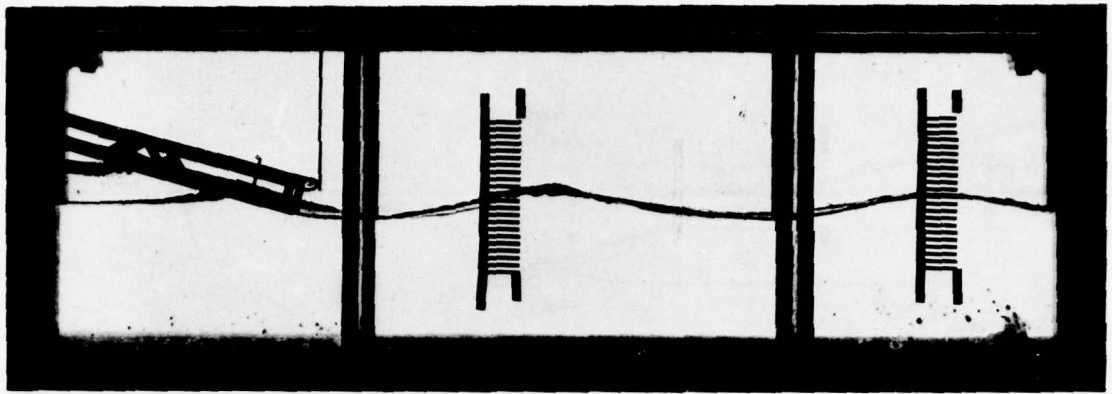


Fig. 4 (a)

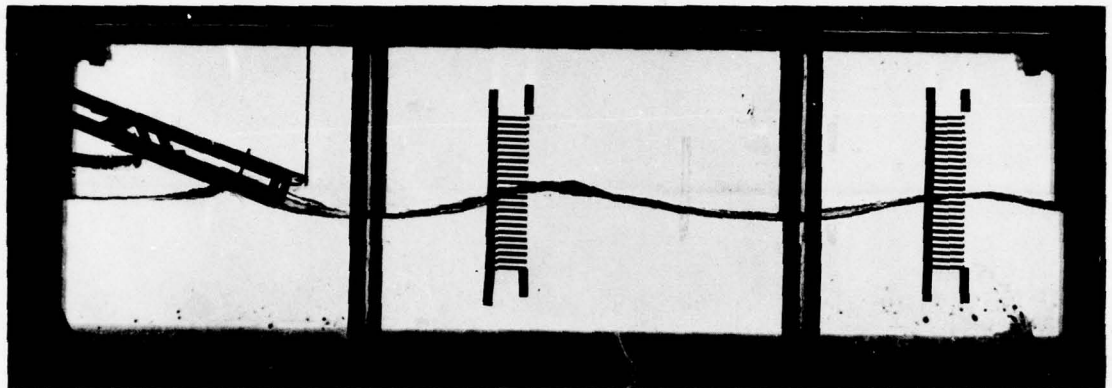


Fig. 4 (b)

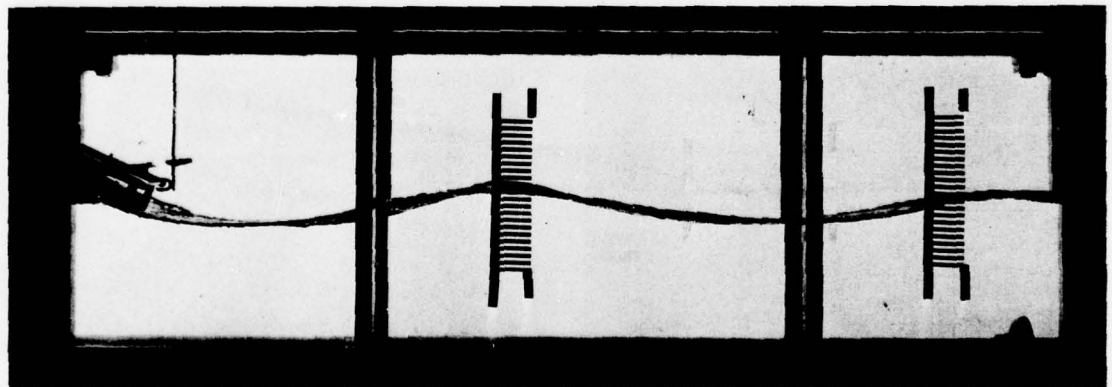


Fig. 4 (c)

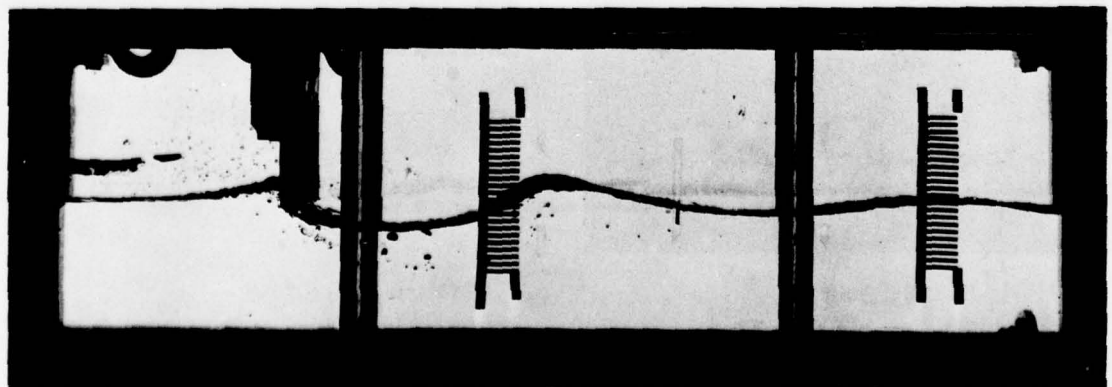


Fig. 4 (d)

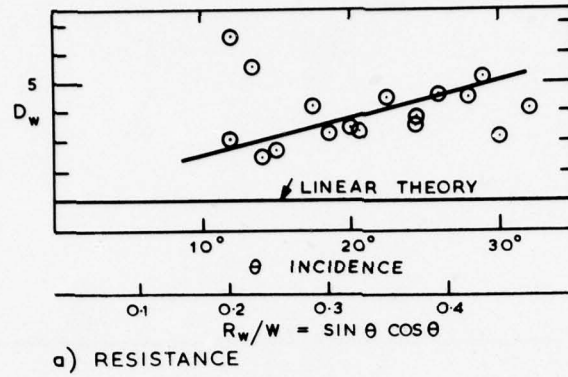


Fig. 5 (a)

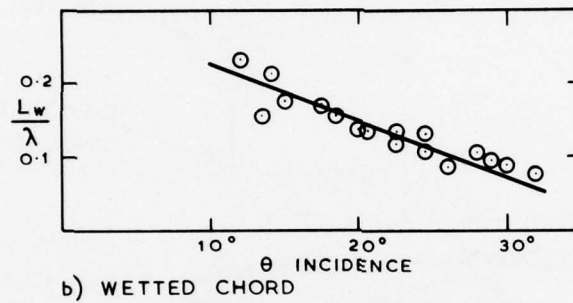


Fig. 5 (b)

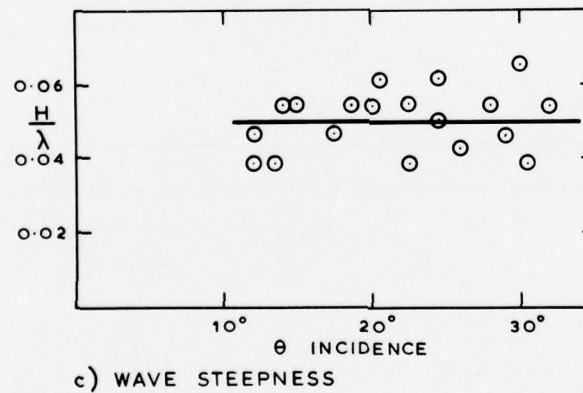


Fig. 5 (c)

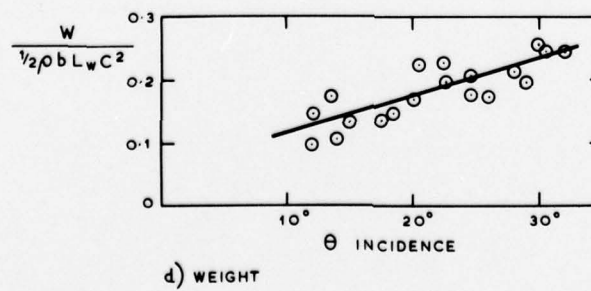


Fig. 5 (d)

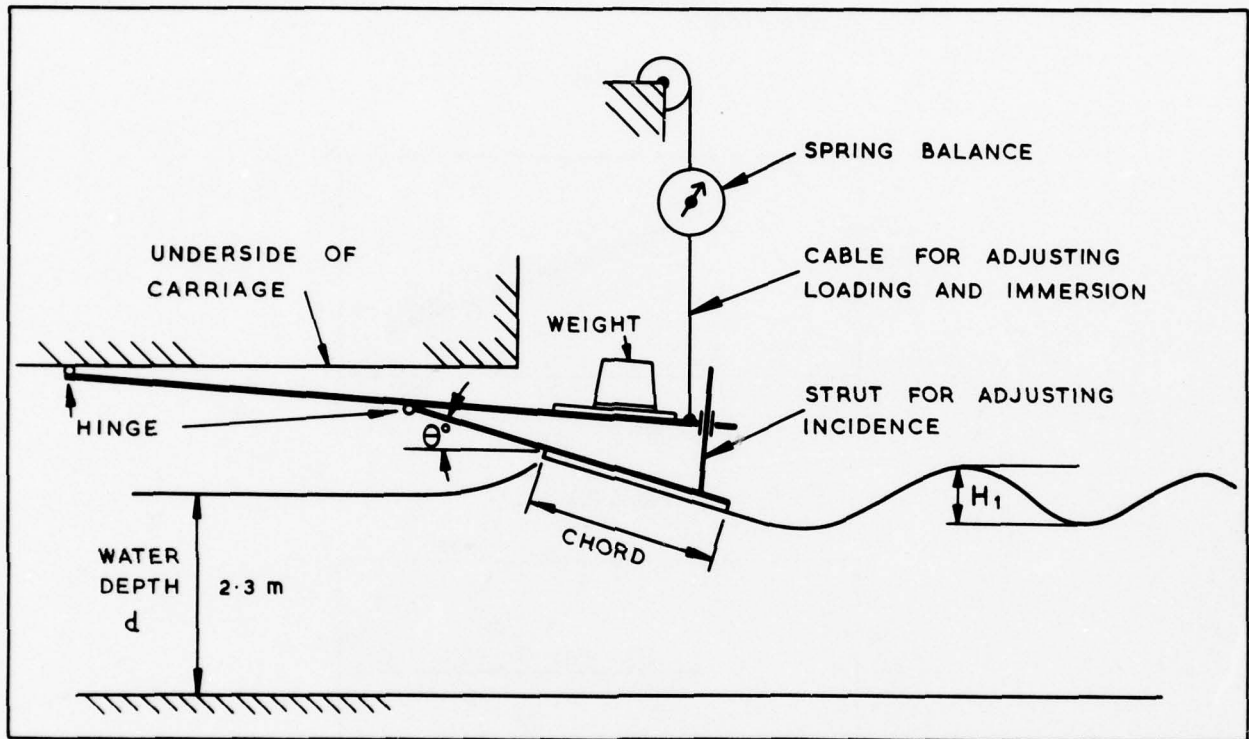


Fig. 6



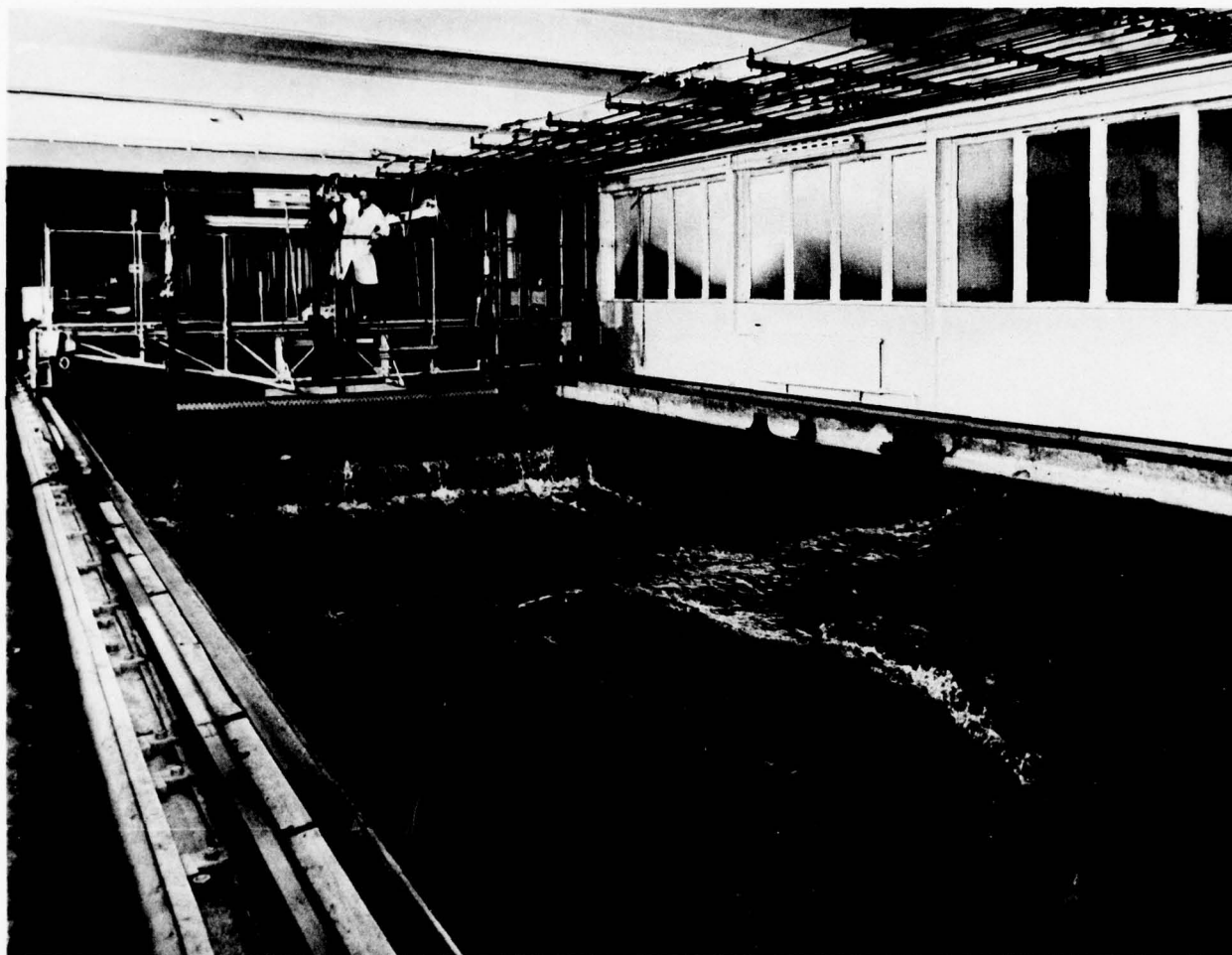


Fig. 7 (a)

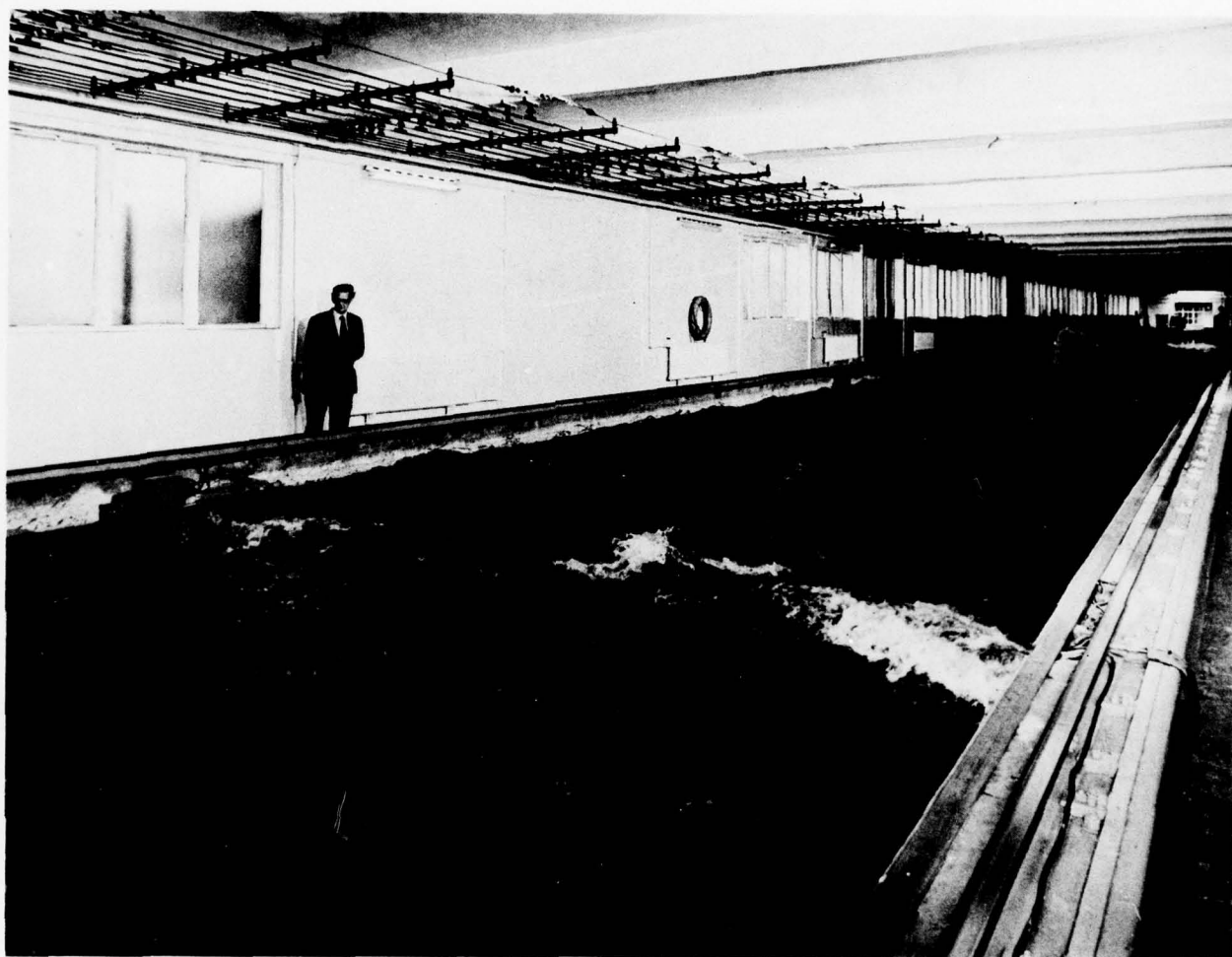


Fig. 7 (b)

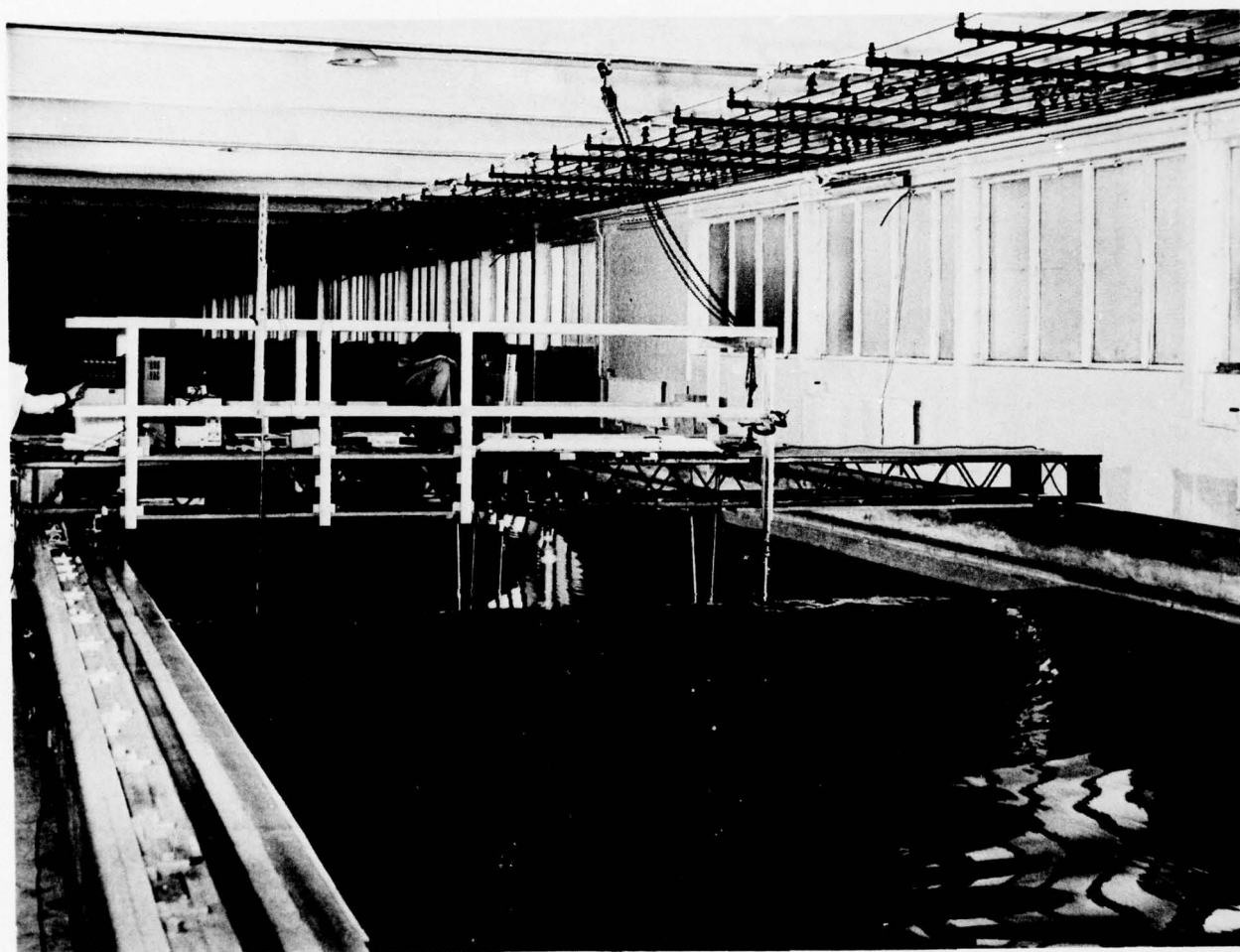


Fig. 7 (c)



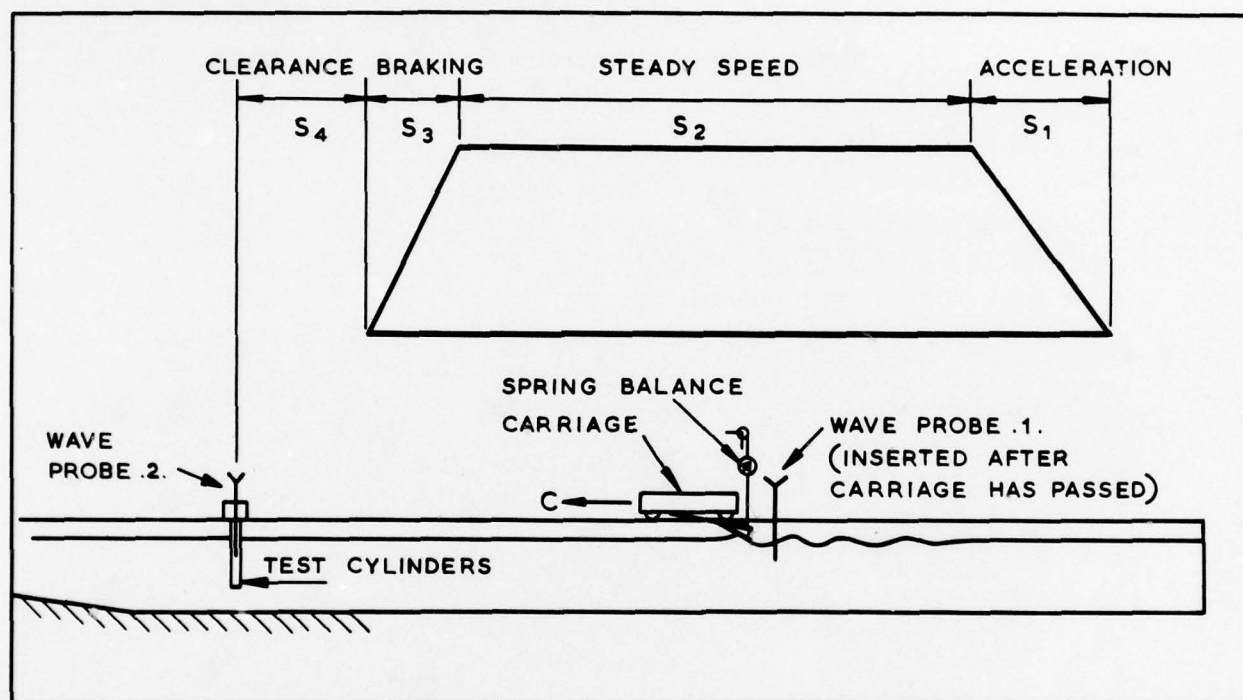


Fig. 8

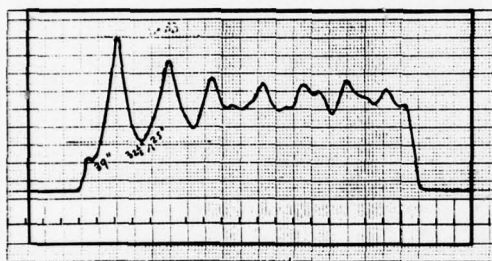
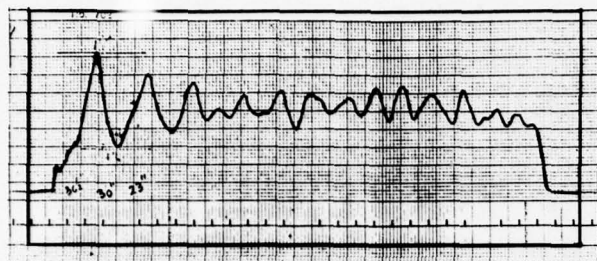


Fig. 9 (a)

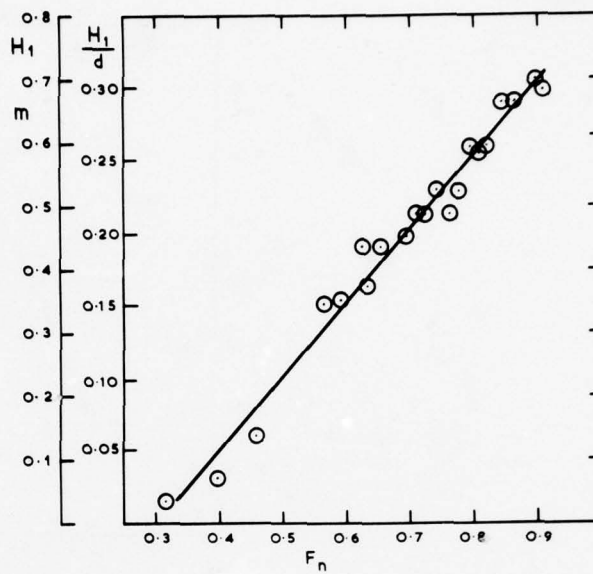


Fig. 9 (b)

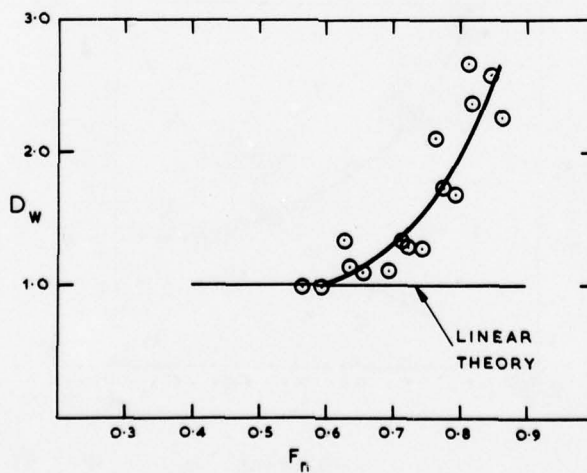


Fig. 9 (c)

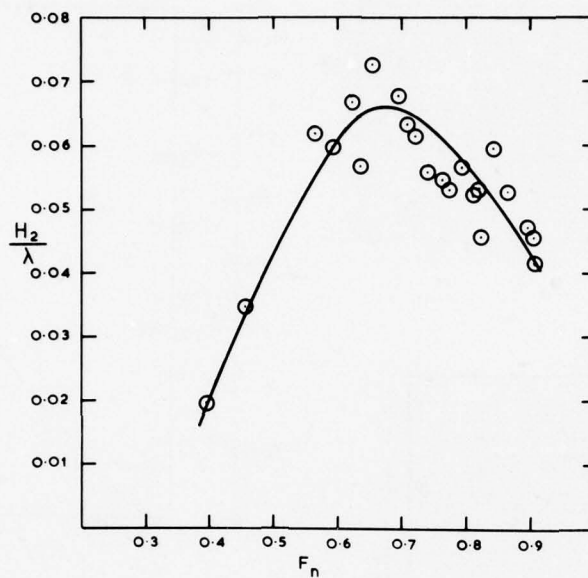


Fig. 9 (d)

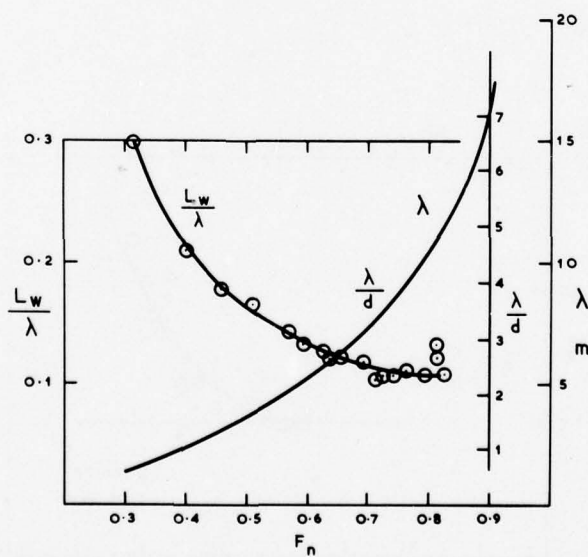


Fig. 9 (e)



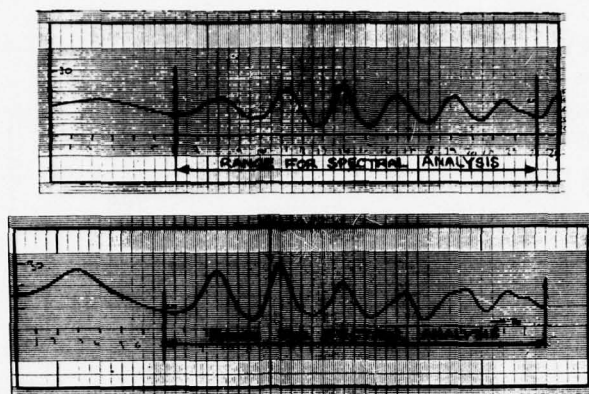


Fig. 10 (a)

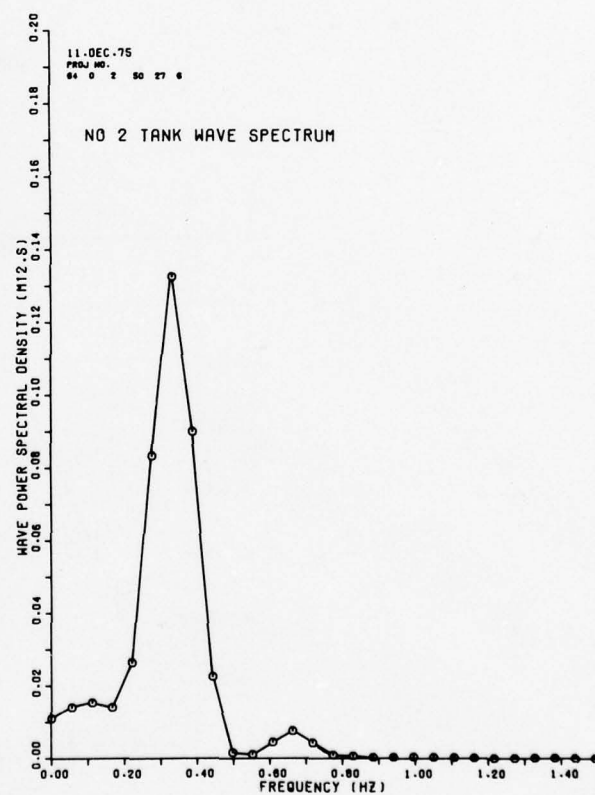
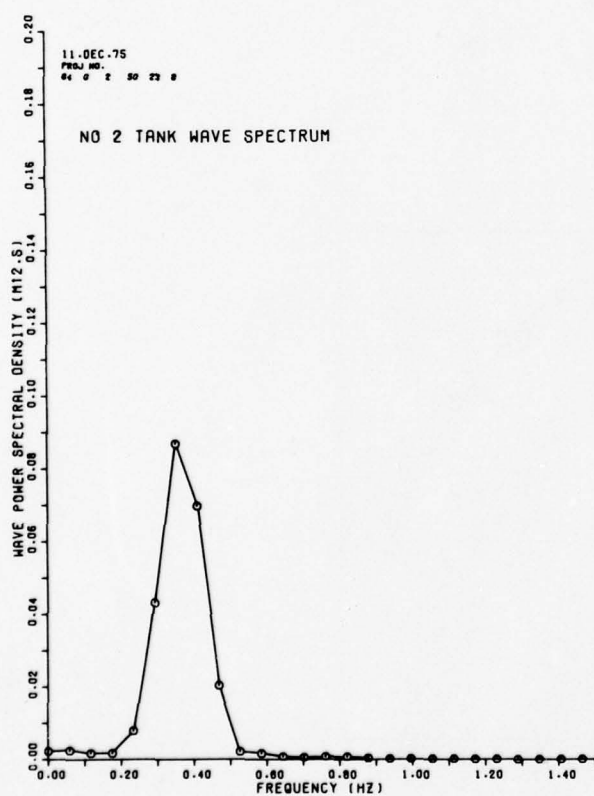


Fig. 10 (b)

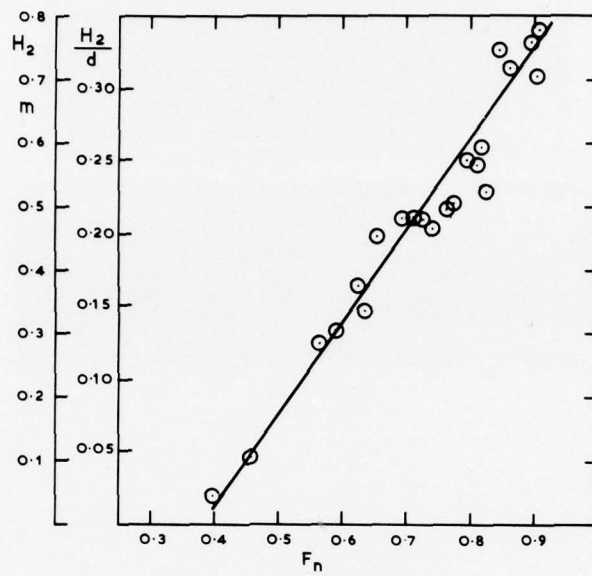


Fig. 10 (c)

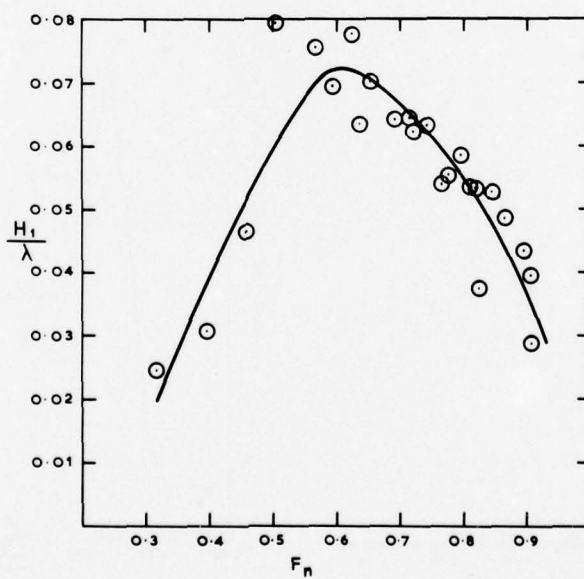


Fig. 10 (d)

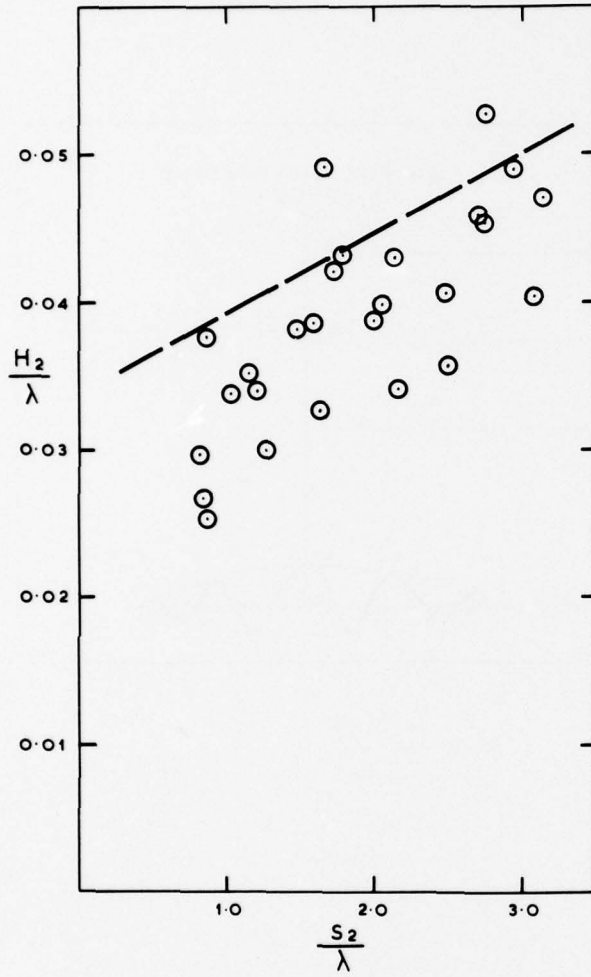


Fig. 11 (a)

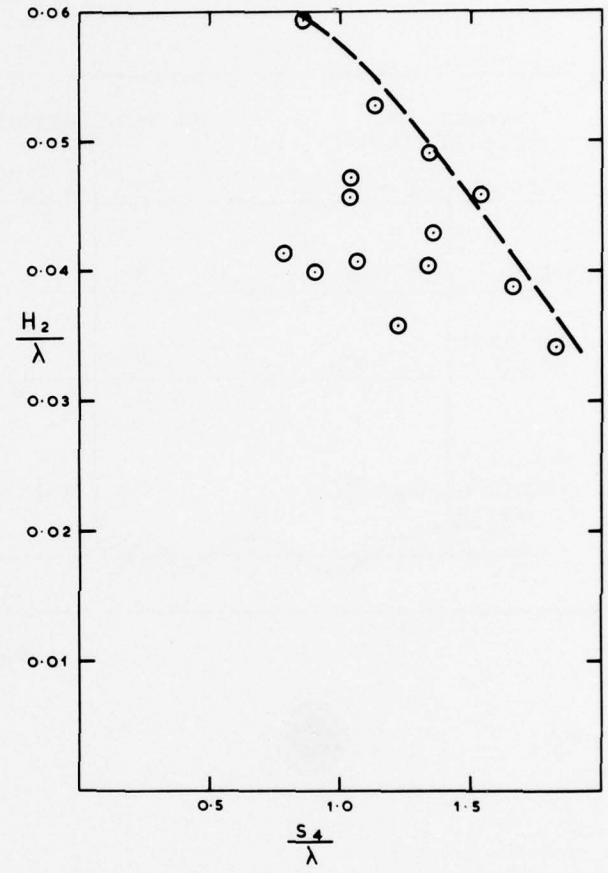


Fig. 11 (b)

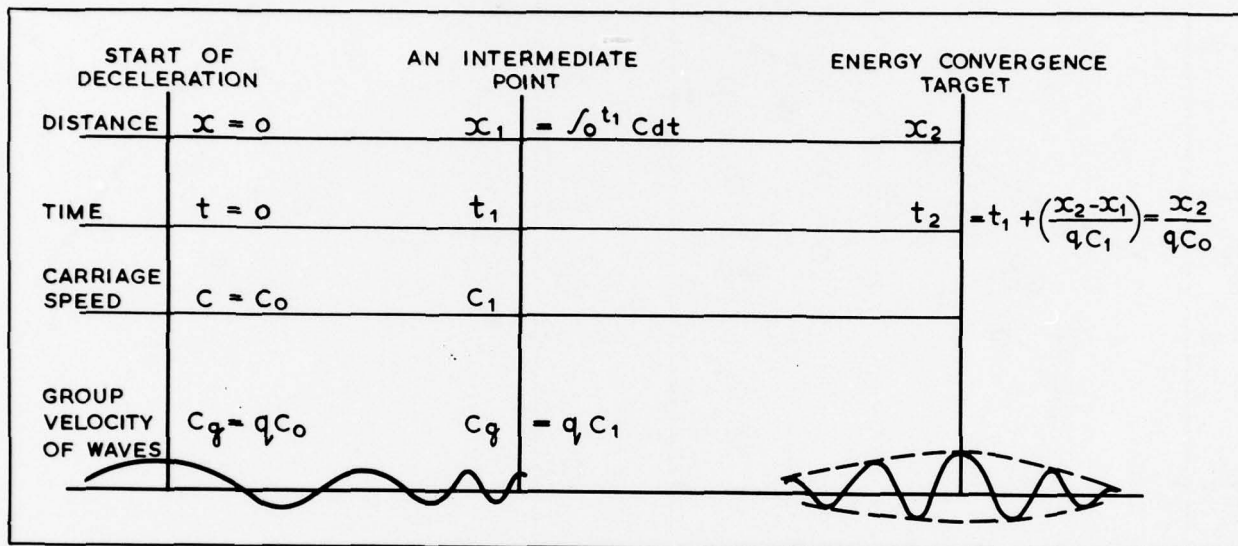


Fig. 12



# AN EXPERIMENTAL INVESTIGATION OF THE THREE-DIMENSIONAL TURBULENT BOUNDARY LAYER ON A SHIP MODEL

L. LARSSON

The Swedish State Shipbuilding Experimental Tank (SSPA) Gothenburg, Sweden

## SYNOPSIS

The purpose of the present investigation has been to produce a test case for boundary layer calculations on ship-like bodies. A 2 m double model of a cargo liner ( $C_B = 0.675$ ) has been investigated in a wind tunnel at  $R_n = 5 \cdot 10^6$ . Boundary layer velocity profiles and static pressure have been measured at a large number of points distributed over the whole surface. An account is given here of the experimental technique, and the results are presented in some detail. First, however, a summary is given of the theory for three-dimensional turbulent boundary layers and of previous work in this area.

## 1. INTRODUCTION

Most work on three-dimensional turbulent boundary layers has been carried out at institutions connected to the aircraft industry. Boundary layers of ships have more seldom been studied, and then quite often in the light of two-dimensional theories. This is a pity since the pressure distribution on ship-like bodies indicates that three-dimensional effects may be significant.

To investigate the state of the art on three-dimensional turbulent boundary layers an extensive literature survey was made by the author /1/. This study was supplemented by a separate survey of the literature on ship boundary layers /2/. It was found that several fairly accurate calculation methods could be used for simple geometries, although little was known about their application to complicated flows, such as the one outside a ship hull. No systematic investigation of the basic assumptions had been carried out for this case and experimental results, which could be compared with complete calculations, were very rare.

Therefore it was considered fruitful to undertake an investigation, in which the basic assumptions could be tested and complete calculations could be compared with measured parameters. This investigation is described here and in more detail in /3/.

## SYMBOLS

A, B, C, D	Constants in the wall law and the law for the blending region
B	Breadth of the model
$C_B$	Block coefficient of the model
$C_f$	Skin friction coefficient along the wall shear stress
$C_p$	Pressure coefficient
G	Form parameter for the velocity profile (Clauser)
$H_1$	Form parameter for the velocity profile (Head)

$H_{12}$	Form parameter for the velocity profile, eq (19)
$H_{23}$	Form parameter for the velocity profile, eq (19)
$K_{12}$	Streamline curvature
$K_{21}$	Potential line curvature
LBP	Length between perpendiculars for the model
$M_1, M_2$	Mean values of differences between assumptions and measurements
$R_\theta$	Reynolds' number based on $\theta_{11}$
T	Depth of the model
$U_e, U_{er}, U_{el}$	Effective velocity measured by the probe turned to the right (r) and to the left (l)
$U_\infty$	Undisturbed velocity
X, Y, Z	Cartesian coordinate system defined in Fig 9
$h_1, h_2, h_3$	Metrics
k	Coefficient in Hinze's law for the directional sensitivity of a hot wire
l	Mixing length
p	Pressure
$p_\infty$	Undisturbed pressure
q	Total velocity
$q_f, q_w$	Law of the wall and law of the wake parts of q
$q_\tau$	Shear velocity (total)
r	Correlation factor
u, v, w	Velocity components in the x, y, z system
$u_e$	Velocity at the edge of the boundary layer
$u_\tau$	Shear velocity along x
v	Half of the probe turning angle

$x, y, z$	Coordinates of a curvilinear system	
$z^*$	Dimensionless distance from the wall ( $= z q_\tau / \nu$ )	
$\beta$	Angle between the velocity vector and the x-axis (crossflow angle)	
$\beta_w$	Wall crossflow angle referred to the x-axis	
$\beta_{z^*} = 30$	Wall crossflow angle measured	
$\gamma$	$(C_f/2)^{1/2}$	
$\delta$	Boundary layer thickness	
$\delta_1, \delta_2$	Integral thicknesses (displacement)	
$\epsilon_1, \epsilon_2$	"-	(energy)
$\theta_{11}, \theta_{12}, \theta_{22}$	"-	(momentum)
$\kappa$	von Karman's constant	
$\nu$	Kinematic viscosity	
$\Pi$	Coles' wake factor	
$\rho$	Density	
$\tau$	Shear stress	
$\tau_t$	Turbulent part of the shear stress	
$\tau_w$	Shear stress at the wall	
$\phi$	Velocity potential	

## 2. THEORY AND PREVIOUS WORK

### 2.1 Governing equations

Three-dimensional boundary layers differ from two-dimensional ones in that pressure derivatives occur in a lateral direction referred to the streamlines at the edge of the boundary layer. These derivatives give rise to velocity components in their own direction and crossflow velocities appear. See Figure 1.

The lateral pressure derivative makes the external streamlines bend in such a way that the centrifugal force acting on each element of fluid is balanced by the lateral pressure force. The problem of calculating the boundary layer may be simplified, if the coordinate system is based on these external streamlines ( $y = \text{const}$ ) and their orthogonal trajectories, i.e. the potential lines ( $x = \text{const}$ ). An orthogonal curvilinear system as in Figure 2 is thus obtained.

Starting from the Navier-Stokes equations, written in curvilinear coordinates, the boundary layer equations may be deduced /1/. The usual assumption that the boundary layer thickness is small compared to relevant dimensions for the body, has influence not only on fluid properties and their derivatives, but also on the coordinate system. Denoting the metric coefficients, representing the linear stretching of the coordinates, by  $h_1, h_2$  and  $h_3$  for the  $x, y$  and  $z$  coordinates respectively, it may be assumed that  $h_1$  and  $h_2$  are functions only of  $x$  and  $y$ , while  $h_3$  is unity. ( $z$  is directed normal to the surface.)

As in two-dimensional flow the equations for the turbulent boundary layer may be shown to differ from the laminar ones only with respect to the expression for the shear stress, and may thus be written

$$\frac{u}{h_1} \frac{\partial u}{\partial x} + \frac{v}{h_2} \frac{\partial u}{\partial y} + w \frac{\partial u}{\partial z} + v(uK_{12} - vK_{21}) = \frac{u_e}{h_1} \frac{\partial u_e}{\partial x} + \frac{1}{\rho} \frac{\partial \tau_x}{\partial z}$$

$$\frac{u}{h_1} \frac{\partial v}{\partial x} + \frac{v}{h_2} \frac{\partial v}{\partial y} + w \frac{\partial v}{\partial z} + uvK_{21} + (u_e^2 - u^2)K_{12} = \frac{1}{\rho} \frac{\partial \tau_y}{\partial z} \quad (1)$$

$$\frac{\partial}{\partial z} \left( \frac{P}{\rho} \right) = 0$$

The continuity equation becomes

$$\frac{\partial}{\partial x}(h_2 u) + \frac{\partial}{\partial y}(h_1 v) + \frac{\partial}{\partial z}(h_1 h_2 w) = 0 \quad (2)$$

In these equations  $u, v, w$  are mean values.  $K_{12}$  and  $K_{21}$  are the curvatures of the stream- and potential lines respectively.  $u_e$  is the velocity at the boundary layer edge, while  $\tau_x$  and  $\tau_y$  are components of the shear stress:

$$\tau_x = \rho \left( \nu \frac{\partial u}{\partial z} - \overline{u'w'} \right)$$

$$\tau_y = \rho \left( \nu \frac{\partial v}{\partial z} - \overline{v'w'} \right) \quad (3)$$

This set of governing equations is the one generally used in three-dimensional turbulent boundary layer theory. It is applicable to very thin layers, "boundary sheets", but cannot be applied to more complex flow regions, such as the flow in a corner or at a ship's stern, /4/, /5/. Spalding et al /6/ have extended the theory to include momentum diffusion in the  $y$ -direction and pressure gradients in the  $z$ -direction. Their theory has been successfully applied to the flow within rectangular ducts /7/. Although the theory looks promising, it has not yet been applied to complex external flows, such as the one at a ship's stern. The present discussion will be restricted to boundary sheets.

The solution of the equations (1)-(2) may proceed along one of two lines. Either the equations may be solved three-dimensionally for the velocity vector ( $u, v, w$ ) and the shear stress vector ( $\tau_x, \tau_y$ ), or two-dimensionally, after integration in the  $z$ -direction, for integral properties.

### 2.2 Partial differential methods

Methods of the first type, the "partial differential methods", require equations for the shear stress vector. In the simplest case this vector is assumed proportional to the velocity gradient vector ( $\partial u/\partial z, \partial v/\partial z$ ). The constant of proportionality, "the eddy viscosity", is usually calculated from Prandtl's mixing length theory, according to which the eddy viscosity is proportional to the magnitude of the velocity gradient vector. The constant of proportionality is in this case  $l^2$  where  $l$  is the mixing length, uniquely defined by the distance from the wall.

For the magnitude of the turbulent part of the shear stress vector the following expression is thus obtained

$$(\tau_{tx}^2 + \tau_{ty}^2)^{1/2} = -\rho(\overline{u'w'^2} + \overline{v'w'^2})^{1/2} =$$

$$= \rho l^2 \left\{ \left( \frac{\partial u}{\partial z} \right)^2 + \left( \frac{\partial v}{\partial z} \right)^2 \right\} \quad (4)$$

The direction of the shear stress is by assumption equal to the direction of the velocity gradient.

To the knowledge of the author there are seven methods based on the mixing length hypothesis\*. Analytical functions for  $l$  are used throughout the boundary layer in the methods by Michel et al /8/, Schreiber /9/, East /10/, Klinksiek & Pierce /11/ and Krause et al /12/, while Cebeci et al /13/ and Fannelöp & Humphreys /14/ use a separate assumption for the eddy viscosity in the outer part of the boundary layer.

A more complicated turbulence model is employed by Bradshaw /15/, Nash /16/ and Wesseling & Lindhout /17/, who calculate the shear stress distribution by solving transport equations for  $\tau_{tx}$  and  $\tau_{ty}$ . The model by Spalding et al /18/ is equally complicated. In their method the turbulent energy and the rate of dissipation are calculated by two separate equations.

### 2.3 Integral methods

Partial differential methods are no doubt more promising than the ones based on the integrated equations. However, for engineering purposes the latter seem a reasonable choice, since the difference in ability to predict three-dimensional turbulent boundary layers is very small. Therefore several assumptions in connection with integral methods have been tested in this investigation.

Six new parameters appear when the governing equations (1) are integrated in the  $z$ -direction.

$$\begin{aligned}\delta_1 &= \int_0^\infty (1 - \frac{u}{u_e}) dz & \delta_2 &= - \int_0^\infty \frac{v}{u_e} dz \\ \theta_{11} &= \int_0^\infty (1 - \frac{u}{u_e}) \frac{u}{u_e} dz & \theta_{12} &= \int_0^\infty (1 - \frac{u}{u_e}) \frac{v}{u_e} dz \\ \theta_{21} &= - \int_0^\infty \frac{uv}{u_e^2} dz & \theta_{22} &= - \int_0^\infty \frac{v^2}{u_e^2} dz\end{aligned}\quad (5)$$

Using the velocity potential  $\phi$  for  $x$ , the momentum integral equations may be written

$$\begin{aligned}u_e \frac{\partial \theta_{11}}{\partial \phi} + \frac{1}{h_2} \frac{\partial \theta_{12}}{\partial y} + \frac{\partial u_e}{\partial \phi} (2\theta_{11} + \delta_1) + \\ + K_{21}(\theta_{11} - \theta_{22}) &= \frac{C_{fx}}{2} \\ u_e \frac{\partial \theta_{21}}{\partial \phi} + \frac{1}{h_2} \frac{\partial \theta_{22}}{\partial y} + 2\theta_{21} \left( \frac{\partial u_e}{\partial \phi} + K_{21} \right) - \\ - K_{12}(\theta_{11} + \theta_{22} + \delta_1) &= \frac{C_{fy}}{2}\end{aligned}\quad (6)$$

Here the right-hand side members are components of a skin friction vector

$$C_f = (C_{fx}, C_{fy}) = \frac{1}{\rho u_e^2} (\tau_{wx}, \tau_{wy}) \quad (7)$$

where  $\tau_w = (\tau_{wx}, \tau_{wy})$  is the wall shear stress vector.

\* There are other methods developed for compressible flows and flows on rotating bodies.

Examining equations (6) it appears that there are seven unknowns: five integral properties and two skin friction components. Since there are only two equations, five further relations must be provided.

As for two-dimensional boundary layers two of these relations are the so called auxiliary equation and the skin friction relation. In this case, however, further relations connecting the integral parameters must be provided. The most common way of doing this is to assume the velocity profile to belong to a family of functions depending on parameters calculable from the unknowns. Separate assumptions for the longitudinal and cross-wise components may be made or the total velocity profile may be considered at once.

Integral calculation methods may thus be classified with respect to

1. The auxiliary equation
2. The skin friction relation
3. The velocity profile family

In the simplest calculation methods the auxiliary equation is replaced by the assumption that the form parameter  $H_{12} = \delta_1/\theta_{11}$  is constant. This has been assumed for instance by Cooke /19/ and Smith /20/. It is, however, more common to use Head's entrainment equation derived for three-dimensional flow by Smith /20/ and Cumpsty & Head /21/. The equation is based on the assumption that the rate of entrainment of "free" fluid into the boundary layer is dependent only on the shape parameter for the velocity profile.

Another way of obtaining an auxiliary relation is to multiply the governing equations either by  $u$  and  $v$  respectively, or by  $z$  before integrating in the  $z$ -direction. In the first case a so called energy equation is obtained. This approach has been used by Eichelbrenner, /22/, /23/ and Cooke /19/. In the second case a moment of momentum equation will be arrived at. Himeno & Tanaka /24/ have developed this procedure for three-dimensional boundary layers. It should be pointed out that new unknowns are introduced when using this type of relation. Separate assumptions must therefore be made to close the system.

Several assumptions for the skin friction have been used in three-dimensional calculations. All of them are originally deduced for two-dimensional flow, and are assumed valid for the longitudinal component of the skin friction. In the most well-known relations, the ones due to Ludwig-Tillmann /25/, Thompson /26/ and Michel et al /27/, the skin friction is a function of a shape parameter ( $H_{12}$  or  $G$ ) for the velocity profile together with a boundary layer thickness ( $\delta_1$  or  $\theta_{11}$ ).

Most work in connection with integral methods has been spent on constructing suitable velocity profile families. In the simplest cases the longitudinal profile is taken from two dimensions, for instance according to the power law /28/ (parameter:  $H_{12}$ ) or to the Thompson profiles /26/ (parameters:  $H_{12}$  and  $\theta_{11}$ ), while the cross-wise component is assumed to follow a simple law by Mager /28/ (parameters:  $H_{12}$  and the wall crossflow angle  $\beta_w$ ).

Another way is to use the above expressions for the longitudinal profile and relate the crossflow to the longitudinal flow in the form of polars  $v =$



$v(u)$ . Parameters are in this case the conditions at the ends of the polar, i.e. at the surface and at the boundary layer edge. These conditions are either calculable from the outer flow, or functions of some other unknowns. Models of this type are described by Johnston /29/, Eichelbrenner /23/ and Shanebrook /30/. The major advantage of this kind of family is that the so called "cross over" profiles (profiles where the crossflow changes sign) may be represented.

A complete profile family has been presented by Coles /31/. The velocity vector is considered as the sum of a wall vector, obeying the well-known law of the wall, and a wake vector, whose magnitude is proportional to the wake function, depending on the relative distance ( $z/\delta$ ) from the wall. The wall components are directed along the wall shear stress, while the wake components, which are also collateral, are directed so as to fulfil the conditions at the outer edge. Parameters are:  $q_r = \tau_w/\rho$ ,  $\delta$ , and  $\Pi$  (the constant of proportionality for the wake function).

The relations due to Michel et al /27/, finally, are not based on velocity profile families, but on connections between the integral properties, which have been obtained from similar solutions to their partial differential method. The parameters are: Clauser's form parameter  $G$ , a Reynolds number based on  $\theta_{11}$ , the skin friction coefficient and a transverse pressure gradient parameter  $T$ .

Introducing the relations between the integral properties into the governing equations it is seen that four unknowns are present. These are: a boundary layer thickness (usually  $\theta_{11}$ ), a crossflow parameter (usually  $\beta$ ), a form factor (usually  $H_{12}$ ) and a longitudinal skin friction coefficient. These properties are calculable from the two equations (6), the auxiliary equation and the skin friction relation.

#### 2.4 Previous experiments

Most experiments on three-dimensional turbulent boundary layers have been carried out on geometries far from a ship-shaped form. As a matter of fact nearly all geometries may be classified in four groups, namely

1. Curved ducts (the boundary layer on the floor bending laterally)
2. Obstacles on plates (the boundary layer on the plate)
3. "Infinite" swept wings
4. Finite wings

The basic requirement is that transverse pressure gradients shall occur, forcing the cross-flow to develop. No further account will be given here of experiments of these kinds.

Instead, interest turns to investigations carried out on ship forms. They are summarized in Table I. Shearer & Steele and Steele & Pearce have only measured skin friction, while in the other experiments velocity profiles are recorded. It is seen that most approaches are two-dimensional, i.e. only the longitudinal component of velocity has been measured. The only extensive three-dimensional measurements were made already in 1933 by Laute. The points were, however, too far from the wall, and too far apart from each other, to allow an analysis based on modern theories to be made.

Author	Year	Scale	Analysis
Laute /32/	1933	M	3-D
Cutland /33/	1958	S	2-D
Hogben /34/	1964	M	2-D
Steele & Pearce /35/	1968	M	only $C_f$
Amamoto et al /36/	1969	S	2-D
Taniguchi & Fujita /37/	1969	S	3-D*
Wiegardt /38/	1970	M	3-D**
Shearer & Steele /39/	1970	M	only $C_f$
Matheson /40/	1971	M	2-D
Vollheim & Nestler /41/	1971	M	2-D
Gadd /42/	1973	M	2-D

S = ship M = model

Table I. Experiments on ship boundary layers

It is also seen from the table that most experiments have been carried out in the model scale, although extensive measurements on ships have been made by Cutland and Amamoto et al. Single two-dimensional velocity profiles have been measured on many ships, but are not reported here.

### 3. EXPERIMENTAL EQUIPMENT

#### 3.1 Model and wind tunnel

The model chosen for the experimental investigation is the parent model (No 720) of the SSPA cargo liner series, Figure 3. Its main dimensions are

LBP = 2.000 m  
B = 0.283 m  
T = 0.118 m  
C<sub>B</sub> = 0.675

Further particulars concerning the geometry may be found in /43/. In order to obtain a plane of symmetry at the load waterline the submerged part of the hull was joined to a model of its image in this plane. Thus the effects of waves were ignored. The model was made of wood. It was painted black and polished until the surface produced clear mirror images. 85 pressure tapings were mounted flush with the surface.

Two thin struts entering the wind tunnel through slits in the floor supported the model firmly during the runs. In Pictures 1 and 2 the setup may be seen. Approximately 0.2 m from the bow there is a row of turbulence studs. Their size and position were calculated according to a thesis by Matheson /40/ so as to produce a virtual origin for the turbulent boundary layer at the bow. In the picture can also be seen eight streamlines along the model. They were traced from a potential flow calculation using the Hess & Smith procedure. Boundary layer traverses were made on these lines at twelve stations.

The experiments were carried out in the low speed wind tunnel L2 of the Department of Applied Thermo and Fluid Dynamics at Chalmers University of Technology. The test section is 1.25 x 1.80 m<sup>2</sup> and has a length of 3.00 m. During the present experiments the tunnel speed was 40 m/s, giving a Reynolds number of  $5 \cdot 10^6$  for the model.

\* Only one profile measured

\*\*Profiles measured at two stations



### 3.2 Measuring equipment

The most important part of the experimental investigation was the measurement of 87 velocity profiles distributed between stations Nos 1 and 16. Both the magnitude and direction of the velocity vector at 15-50 points on the normal to the surface were measured for each profile, using the hot wire technique. Two traverses had to be carried out for each profile, the probe being turned in different directions.

A new traverse gear, having the required flexibility, had to be constructed. The complicated geometry of the model disqualified all constructions previously reported in the literature, so an entirely new solution was worked out. In Pictures 1 and 2 the present construction may be seen. A profiled strut is attached to the tunnel roof and is extended via a ball joint and a shrouded tube to the "head" of the traverse gear. The head is attached to the tube via another ball joint, thus obtaining a wide range of movement. In Figures 4a and b the mode of work for the head is explained. The tube (14) is rotated by the speedometer cable (8) via the worm gear (7). Since the tube (14) is threaded internally and the tube (15) externally the rotation causes a displacement of the tube system (2)-(4)-(12)-(15) and the probe (1). Rotation of the probe  $\pm 45^\circ$  is possible.

The mechanism of the head is shrouded in a NACA profile which is supported by the rod (5) fixed to the model surface. To prevent vibrations sideways two other rods (only one shown in Picture 1) are used. The arrangement obtained in this was found to be very rigid.

The speedometer cable was powered by a stepper motor outside the tunnel. Each step, which corresponded to a displacement of 0.0005 mm for the probe, was counted by an electronic counter. The number of steps between two points could be preset on an external control. In this manner the displacement of the probe was recorded. To obtain the starting position use was made of a measuring microscope. By measuring the distance between the wire and its image on the polished surface the location of the starting point could be obtained, taking the inclination of the microscope into account.

Several checks were made during the runs to get an estimate of the accuracy of the probe positioning. The absolute error was found to increase with distance for small distances. As a result of these checks and of some theoretical speculations (see /3/) it may be established that the maximum relative error was about 5% for the first millimetre from the surface, thereafter decreasing rapidly to a few tenths of a per cent at 10 mm.

The hot-wire probe may be seen in Figure 5. It was manufactured by DISA especially for this investigation. As seen from the figure the probe prongs were bent to the shape of a circular arc. This was done to minimize the influence of the normal velocity gradient (directed along the probe body) at the calibration. The tips of the prongs were thus parallel to the surface.

In Picture 3 the electronic equipment is shown. Its function may be explained by reference to the block diagram in Figure 6. The central unit (1) contains a scanner, a sequencer, an electronic counter and a digital voltmeter. The signals treated are produced by a control unit for the stepper motor (3)

(1 channel), an anemometer (5) (5 channels) and a resistance thermometer (1 channel). From the sequencer the signals are fed into a flexowriter (7) producing a tape and a typewritten record. In the picture is seen an x-y plotter (6). This was used at an early stage to produce calibration curves, but was discarded later on due to the limited accuracy of the method. A mechanical counter (4) was used in connection with the stepper motor control to prescribe the expected number of steps marched by the stepper motor during a displacement of the probe. The oscilloscope (2) could be used to see the turbulence signal.

An RC-filter with a time constant of 0.8 was included in the scanner. In connection with an automatic integration of 0.002 s in the voltmeter the turbulent fluctuations in the mean velocity signals were damped out. Further particulars concerning the electronic equipment are given in the block diagram.

The equipment was tested by measuring the boundary layer on a flat plate. "Cross-flow angles" could be obtained by putting the head at a certain angle to the free stream (which was two-dimensional). A constant angle should thus be registered. It was found that the longitudinal profile could be measured with very good accuracy, while the deviation in the measured angle might amount to about 1°. This was somewhat more than anticipated, although good enough for the purpose.

## 4. DATA EVALUATION

### 4.1 Calculation of the velocity vector

The hot wire was calibrated before and after the measurement of each velocity profile. A Prandtl tube connected to a manometer was used as a reference and the wire voltage could be connected to the air velocity at a given reference temperature. A computer program took care of the tape from the Flexowriter and produced a calibration table and a plot. If the drift during one run (one velocity profile) exceeded 1.5% of the maximum velocity the run was rejected. However, for some profiles a somewhat larger drift was reduced to the tolerable level by a correction for contamination /3/.

The voltages measured during the two traverses for each profile were transformed to (effective) velocities by interpolation in the calibration table, i.e. no functional relationship was used to connect wire voltage and velocity. When interpolating, four points were taken into account in a "least squares" manner.

No correction for heat transfer to the wall was applied in any of the measurements. This is in accordance with the results of Oka & Kostić /44/, who state that this effect is negligible for  $z^* = z_u/\nu > 5$ , a condition, which is fulfilled for all measured points.

To be able to calculate the velocity vector the directional sensitivity of the probe must be known. According to Hinze /45/ the following relation holds for the effective velocity  $U_e(\alpha)$

$$U_e^2(\alpha) = U^2(\cos^2\alpha + k^2 \sin^2\alpha) \quad (8)$$

where  $\alpha$  is the angle between the normal to the wire and the flow direction, and  $k$  is a constant to be determined. In Figure 7 it is shown that the cali-

bration points fall very close to a pure cosine curve, i.e.  $k = 0$ . This conforms with the results of Champagne et al /46/.

Combining the results from corresponding points in the two traverses the flow angle ( $\beta$ ) and the velocity magnitude ( $q$ ) may be calculated as follows:

The two effective velocities are

$$\begin{aligned} U_{el} &= q \cos(v - \beta) \\ U_{er} &= q \cos(v + \beta) \end{aligned} \quad (9)$$

where the indices l and r indicate if the probe is turned to the left or to the right. The angle between the two directions for the probe is  $2v$ .

By expanding the cosines it is easily shown that

$$\tan \beta = \frac{1}{\tan v} \cdot \frac{1 - \frac{U_{er}}{U_{el}}}{1 + \frac{U_{er}}{U_{el}}} \quad (10)$$

and from (9) it follows that

$$q = \frac{U_{el}}{\cos(v - \beta)} \quad (11)$$

#### 4.2 Measured integral parameters

The skin friction coefficient was obtained by means of a so called Clauser plot, based on the law of the wall, which may be written

$$\frac{q}{q_\tau} = A \log \frac{q_\tau z}{v} + B \quad (12)$$

where  $q_\tau$  is the shear velocity defined by the wall shear stress  $\tau_w$

$$q_\tau = \sqrt{\frac{\tau_w}{\rho}} \quad (13)$$

Defining

$$C_f = \frac{\tau_w}{\frac{1}{2} \rho u_e^2} \quad (14)$$

$q_\tau$  may be written as

$$q_\tau = u_e \sqrt{\frac{C_f}{2}} \quad (15)$$

or for  $\sqrt{C_f/2} = \gamma$

$$q_\tau = u_e \gamma \quad (16)$$

Introducing this expression in (12) yields

$$\frac{q}{u_e} = \gamma \left( A \log \frac{u_e z}{v} + A \log \gamma + B \right) \quad (17)$$

i.e. in the region of the law of the wall the graphs

$$\frac{q}{u_e} = f\left(\log \frac{u_e z}{v}\right)$$

will appear as a set of straight lines where  $\gamma$  (or  $C_f$ ) is a parameter. Plotting the measured points in the region of interest the straight line fitting the data will give the value of  $C_f$ . See Figure 8.

Since the velocity profile is twisted in three-dimensional flow the present version of the law of the wall is not indisputable. It might be more consistent to consider the component  $q_\tau$  of  $q$ , in the direction of the wall shear stress. This has been done by Coles /31/ as will be seen below. East & Hoxey /47/ have discussed several ways of obtaining  $C_f$  by a Clauser plot. The present method is recommended.

Having obtained the skin friction coefficient some extra points could be calculated between the first measured point and the wall. (The first point was located at about 0.2 mm from the wall.) This was done to improve the accuracy, when integral parameters according to equations (5) were calculated for the profiles at the most forward stations, where the boundary layer was very thin. Common laws for the viscous sublayer and the blending region were used to obtain these extra "measuring points". All velocity vectors were assumed to be parallel to the wall shear stress in this region.

Using Simpson's rule the integrals according to equations (5) could be obtained. Furthermore two energy thicknesses  $\epsilon_1$  and  $\epsilon_2$  were calculated

$$\epsilon_1 = \delta \int_0^1 \left(1 - \frac{q^2}{u_e^2}\right) \frac{u}{u_e} d\left(\frac{z}{\delta}\right) \quad (18)$$

$$\epsilon_2 = \delta \int_0^1 \left(1 - \frac{q^2}{u_e^2}\right) \frac{v}{u_e} d\left(\frac{z}{\delta}\right)$$

$\delta$  is defined by the point where the velocity  $q = 0.995 u_e$ .

The following form parameters were also obtained

$$\begin{aligned} H_{12} &= \frac{\delta_1}{\theta_{11}} \\ H_{23} &= \frac{\theta_{11}}{\epsilon_1} \\ H_1 &= \frac{\delta - \delta_1}{\theta_{11}} \quad (\text{Head's form parameter}) \\ G &= \frac{H_{12} - 1}{\gamma H_{12}} \quad (\text{Clauser's form parameter}) \end{aligned} \quad (19)$$

As mentioned above, the velocity profile was assumed unskewed within the viscous and blending regions. This is in accordance with Johnston's results /29/, although several authors, for instance Prahlad /48/ have shown that this may not be true. In the present work, however, the wall cross-flow angle  $\beta_w$  is taken as the angle at the edge of the blending region, i.e. at  $z^* = q_\tau z / v = 30$ .

#### 4.3 Test of assumptions

Several assumptions for integral methods according to section 2.3 were tested against the measured parameters. The momentum thickness  $\theta_{11}$ , the form factor  $H_{12}$  and the cross flow angle  $\beta_w$  were then taken from the measurements and put into the expressions (for skin friction or velocity profile) to be tested. New skin friction coefficients or profile parameters could then be obtained and compared with the measured values.

Four skin friction relations were tested. According to Ludwig-Tillmann /25/

$$C_f = 0.246 \cdot 10^{-0.678 H_{12}} \cdot R_\theta^{-0.268} \quad (20)$$

$$\text{where } R_\theta = \frac{u_e \theta_{11}}{v}$$

Thompson /26/ has given graphs for  $C_f$  as a function of  $H_{12}$  and  $R_\theta$ . These graphs have been approximated by Head /49/ as

$$C_f = \exp(0.019521 - 0.386768 X_1 + 0.028345 X_1^2 - 0.000701 X_1^3) H_{12} + 0.191511 - 0.834891 X_1 + 0.062588 X_1^2 - 0.001953 X_1^3 \quad (21)$$

$$\text{where } X_1 = \ln R_\theta$$

The relation due to Michel et al /27/ reads

$$\frac{1}{Y} = A \ln \frac{u_e \delta_1}{v} + D^*(G) \quad (22)$$

$$\text{where } D^*(G) = 2G - 4.25 \sqrt{G} + 2.12$$

These relations were originally deduced for two-dimensional flow. In three dimensions they are supposed to hold for the longitudinal component of the skin friction vector, whose magnitude may be obtained by dividing by  $\cos \beta_w$ .

The fourth relation, finally, for this coefficient comes out as a result of Coles' law for the velocity profile.

The by far most common velocity profile family in three-dimensional calculations is the one by Mager /28/ combined with the power law, i.e.

$$\frac{u}{u_e} = \left(\frac{z}{\delta}\right)^{\frac{H_{12}-1}{2}} \quad (23)$$

and

$$\frac{v}{u_e} = \left(\frac{z}{\delta}\right)^{\frac{H_{12}-1}{2}} (1 - \frac{z}{\delta})^2 \tan \beta_w \quad (24)$$

Since  $\theta_{11}$  and  $H_{12}$  should be used as a basis for the comparisons equation (23) had to be integrated according to equations (5), to obtain  $\theta_{11}$  and  $\delta_1$ . The boundary layer thickness,  $\delta$ , to put into (23) and (24) might then be calculated as

$$\delta = \frac{\theta_{11} H_{12} (H_{12} + 1)}{H_{12} - 1} \quad (25)$$

Thompson's /26/ profiles are given in the form of charts where the ordinates of a profile may be read as soon as  $R_\theta$  and  $H_{12}$  are known. These charts were digitalized for computer application and the profiles obtained were combined with Mager's cross-flow relations (24). Two boundary layer thicknesses were calculated, corresponding to 99.5% and 100% respectively of the maximum velocity.

According to Coles, the total velocity vector is composed of two components. One is parallel to the wall shear stress

$$\frac{q_f}{q_\tau} = A \ln z^* + B \quad (26)$$

$$\text{where } z^* = \frac{q_\tau z}{v}$$

Thus the wall law is supposed to hold in this direction. The other component is directed so as to give a total velocity vector which is parallel to the external flow at the edge of the boundary layer. This component follows the law

$$\frac{q_w}{q_\tau} = \frac{\Pi}{\kappa} W\left(\frac{z}{\delta}\right) \quad (27)$$

where  $W(z/\delta)$  is an empirical "wake function" and  $\Pi$  is a constant to be determined for each profile.

It was assumed by Coles that the wall law (26) is valid all the way down to the surface. This is an approximation which is reasonable for large Reynolds' numbers  $R_\theta$ . However, for the profiles measured at the most forward stations,  $R_\theta$  is quite small, so the thicknesses of the inner parts of the boundary layer are significant. Therefore equation (26) has been employed only for  $z^* > 30$ , while the following relations have been used for the inner parts

$$\frac{q_f}{q_\tau} = z^* \quad z^* < 5 \quad (28)$$

$$\frac{q_f}{q_\tau} = C \ln z^* + D \quad 5 < z^* < 30 \quad (29)$$

The parameters in Coles' law are  $q_\tau (= u_\tau \cos \beta_w)$ ,  $\Pi$  and  $\delta$ . Since the comparison with experiments is to be carried out for constant  $\theta_{11}$ ,  $H_{12}$  and  $\beta_w$  the integrals (5) have been evaluated for  $\theta_{11}$  and  $\delta_1$  by putting in the relations (26)-(29). In reference /3/ the resulting lengthy formulae are given. The equations for  $\theta_{11}$  and  $\delta_1$  (or  $H_{12}$ ) together with the condition at the outer edge of the boundary layer constitute a system from which  $q_\tau$ ,  $\Pi$  and  $\delta$  may be solved. A skin friction coefficient may then be calculated from the formula

$$C_f = 2 \left( \frac{q_\tau}{u_e} \right)^2 \quad (30)$$

As explained in Chapter 2 the profile family by Michel et al /27/ is not given by any analytical relations but the connections between integral parameters are presented direct. The lengthy expressions used here are given in /3/.

Having obtained the parameters of each profile family the integrals (5) could be evaluated for all families. Thus  $\theta_{11}$  and  $\delta_1$  were fixed, while all other boundary layer parameters could be used for comparisons between assumptions and measurements.

Since the material comprises as many as 87 measured profiles a statistical analysis was made for  $C_f$ ,  $\delta$ ,  $\epsilon_1$ ,  $\delta_2$ ,  $\theta_{12}$  and  $\epsilon_2$ . In the case of the first three the percentual difference,  $d$ , between assumptions and measurements was calculated for each profile. Two mean values of  $d$  could then be obtained



$$M1 = \frac{\sum_{k=1}^n d_k}{n} \quad n = \text{number of profiles} \quad (31)$$

and

$$M2 = \frac{\sum_{k=1}^n |d_k|}{n} \quad (32)$$

This method could not be used for the cross-wise parameters  $\delta_2$ ,  $\theta_{12}$  and  $E_2$ , since the deviations were too large. A correlation coefficient was therefore calculated in this case

$$r = \frac{\sum_{k=1}^n (M_k - \bar{M})(A_k - \bar{A})}{\left\{ \sum_{k=1}^n (M_k - \bar{M})^2 \sum_{k=1}^n (A_k - \bar{A})^2 \right\}^{1/2}} \quad (33)$$

where  $M$  is the measured quantity and  $A$  is the assumption. Bars denote mean values.

In Tables IIa, b the results of the statistical evaluation of assumptions are described. They will be discussed in Chapter 5.

#### 4.4 Plots

Automatic plots were produced by the computer for the longitudinal and cross-wise velocity profiles and for the cross-flow angle. More detailed information could thereby be obtained regarding the applicability of the different assumptions which were also plotted. However, in order to get an overall impression of their merits the statistical approach above is more useful. The plots also included a polar diagram of the Johnston type /29/ and a logarithmic plot, which was used to calculate  $C_f$  before the final calculations were made.

Since the amount of plots is very large they can not be included here. They are, however, available for those who are really interested in the detailed nature of the flow.

### 5. RESULTS AND DISCUSSION

#### 5.1 Static pressure

The static pressure was measured at 85appings on one quarter of the model. Results are given in Figure 10 as functions of  $X$  for each streamline.  $X$ ,  $Y$ ,  $Z$  are defined by Figure 9. The measurements are compared with calculations using the Hess & Smith method /50/. 673 elements were used to approximate one fourth of the double model whereas 300 elements approximated the corresponding part of the wind tunnel.

It appears that the agreement between calculations and measurements is quite good except near the stern, where the calculated pressure is too high due to the neglect of viscous effects. Smaller deviations occur near the forward pressure minimum where the  $C_p$ -curves bend sharply, and at the most forward stations, where the calculated pressures are slightly smaller than the measured ones. The latter deviations are unexplained.

#### 5.2 Boundary layer parameters

In Figures 11-14 the measured development along the streamlines of  $\theta_{11}$ ,  $H_{12}$ ,  $C_f$  and  $\beta_{2**} = 30$  is plotted. The angle is measured positive towards the keel. To facilitate the interpretation of the plots, lines have been drawn between the points. It should be noted that these lines do not represent calculations.

Examining the body plan, Figure 3, it appears that most streamlines diverge at the forebody and converge at the afterbody. This, of course, follows from the changes in the wetted perimeter. However, around Streamline No 1 the opposite development is found. Therefore the corresponding distribution of boundary layer parameters may look peculiar. The momentum thickness decreases at the after end and the skin friction increases.

Streamline No 2 is interesting since it turns from the bottom upwards along the skeg rather abruptly. This means that the boundary layer thickness is fairly small over most of the length although far aft it raises steeply. The sharp lateral bend causes large cross flow to occur, so this line may be suitable for testing three-dimensional calculation methods in a thin boundary layer.

The convergence is greatest around Streamline No 5 where the boundary layer becomes very thick. The rate of increase is smooth, however.

$H_{12}$ , the shape parameter is surprisingly constant along all lines, which means that the disposition towards separation is small at the after end, at least as to the two-dimensional type (bubble). Since the cross-flow is small almost everywhere, it seems probable that the same holds for the three-dimensional type (vortex sheet). The wall cross-flow angle should have been zero along Streamline No 1, since it is in a plane of symmetry for the hull. It appears from Figure 14 that the measured angle is of the order of  $0.1^\circ$  up to  $X=400$ , thereafter increasing to about  $1^\circ$ . A slight asymmetry is thus present at the afterbody.

Large fluctuations occur in several curves of Figure 14, so it might possibly be suspected that the accuracy of the measured points is low. However, looking at the Figure it appears that most bends are supported by several points, and in regions where the development should be smooth very little scatter occurs. There is reason to assume that the accuracy of the flow angle measurements is better than  $\pm 1^\circ$ .

#### 5.3 Statistical evaluation of assumptions

Two sets of statistical calculations have been carried out. In Table IIa the results for all profiles have been taken into account, while in Table IIb, the profiles aft of Section  $X=500$  have been excluded. The reason for this is that the conditions at the after end of the model differ considerably from the ones further forward. The flow is much more complicated at the afterbody since the boundary layer thickness increases rapidly, thereby interfering with the potential flow.

The assumptions tested are:

1. Ludwig-Tillmann  $C_f$
2. Mager-power law  $\delta_1, \epsilon_1, \delta_2, \theta_{12}, \epsilon_2$



3. Coles  $C_F, \delta, \epsilon, \delta_2, \theta_{12}, \epsilon_2$   
 4. Thompson-Mager  $C_F, \delta$  (99.5 %, 100 %),  $\epsilon_1, \delta_2, \theta_{12}, \epsilon_2$   
 5. Michel  $C_F, \delta, \delta_2, \theta_{12}$

In Table IIa, b both quantities (M1 and M2) related to the percentual error for each assumption are given for  $C_F, \delta$  and  $\epsilon_1$ , while for  $\delta_2, \theta_{12}$  and  $\epsilon_2$  the correlation coefficient is shown.

As to the skin friction it is seen that Michel's relation is superior when all profiles are taken into account. The  $C_F$ 's predicted by this assumption are consistently the lowest which is an advantage at the afterbody where all calculated  $C_F$ 's are too large. On the other hand, if the after profiles are neglected the results from Michel's relation fit the measured  $C_F$  worse than the others. In this case the results from Coles' and Thompson's laws seem remarkably good.

The properties  $\delta$  and  $\epsilon_1$  may be used to get an impression of the ability to represent the longitudinal velocity profile. ( $\theta_{11}$  and  $H_{12}$  are used as a base for the comparison). As to  $\delta$ , Michel's approach seems to be somewhat better than Coles' and Thompson's, although the differences are small. This holds for Thompson's "99.5 %-thickness"; the "100 %-thickness" is too large. Mager's law (the power law) is obviously inferior, yielding too small values.

The energy thickness  $\epsilon_1$  is very well represented by all the assumptions.

The cross-flow relations work fairly well over the main part of the hull. However, at the afterbody the cross-flow is too complicated, with profiles changing sign ("cross-over profiles") and the results are very poor. The correlation coefficients are remarkably similar for all relations, so it is very difficult to draw any conclusions of their relative merits.

## 6. CONCLUSIONS

The main result of the investigation is the development of boundary layer parameters along eight streamlines on the model. This set of data should be useful when testing calculation methods for boundary layers on ship hulls.

Longitudinal velocity profiles and skin friction are well predicted by several common assumptions, while cross-flow profiles can not be adequately represented at the afterbody by any of the methods tested.

The static pressure on the hull may be calculated with good accuracy using the Hess & Smith method. An exception is the stern region where the thick boundary layer interacts strongly with the potential flow.

## 7. ACKNOWLEDGEMENTS

This work was carried out as a cooperative effort between the Swedish State Shipbuilding Experimental Tank and the Department of Applied Thermo and Fluid Dynamics at Chalmers University of Technology. The author is indebted to both institutions for their raise of funds and for the help received from several members of the staffs.

## 8. REFERENCES

- /1/ Larsson, L: Boundary Layers of Ships. Part I: A Literature Survey on Investigations of Three Dimensional Turbulent Boundary Layers. Swedish State Shipbuilding Experimental Tank (SSPA) Allmän Rapport nr 44, 1974
- /2/ Larsson, L: Boundary Layers of Ships. Part II: A Literature Survey on Investigations of Ship and Model Boundary Layers. SSPA Allmän Rapport nr 45, 1974
- /3/ Larsson, L: Boundary Layers of Ships. Part III: An Experimental Investigation of the Turbulent Boundary Layer on a Ship Model. SSPA Allmän Rapport nr 46, 1974
- /4/ Larsson, L: Boundary Layers of Ships. Part IV: Calculations of the Turbulent Boundary Layer on a Ship Model. SSPA Allmän Rapport nr 47, 1974
- /5/ Spalding, D.B.: Calculation Procedures for 3D Parabolic and Partially - Parabolic Flows. Lecture delivered at the EUROMECH 60, Trondheim, 1975
- /6/ Patankar, S.V. and Spalding, D.B.: A Calculation Procedure for Heat, Mass and Momentum Transfer in Three-Dimensional Parabolic Flows. International Journal of Heat and Mass Transfer Vol 15, 1972
- /7/ Pratap, V.S. and Spalding, D.B.: Numerical Computations of the Flow in Curved Ducts. Imperial College of Science and Technology, Department of Mechanical Engineering, Report HTS/75/3, 1975
- /8/ Michel, R et al: Methode pratique de prévision des couches limites turbulentes bi- et tri-dimensionnelles. La Recherche Aérospatiale No 1, 1972
- /9/ Schreiber: A Finite Difference Method with Mixing Length Hypothesis for the Calculation of Three-Dimensional Incompressible Turbulent Boundary Layers. Lecture delivered at the EUROMECH 60, Trondheim, 1975
- /10/ East, J.L.: An Exact Numerical Solution of the Three Dimensional Incompressible Turbulent Boundary Layer Equations, Ph D thesis, Virginia Polytech Inst, 1971
- /11/ Klinksieck, W.F. and Pierce, F.J.: A Finite Difference Solution of the Two and Three-Dimensional Incompressible Turbulent Boundary Layer Equations. Transactions of the ASME, Journal of Fluids Engineering, September 1973
- /12/ Krause, E: Recent Development of Finite Difference Approximations for Boundary Layer Equations. von Karman Institute for Fluid Dynamics. Lecture Series 63, 1974
- /13/ Cebeci, T et al: A General Method for Calculating Three-Dimensional Incompressible Laminar and Turbulent Boundary Layers. III. Three-Dimensional Flows in Curvilinear Orthogonal Coordinates. Douglas Aircraft Company Report MDC, J6867, 1975

- /14/ Fannelöp, T and Humphreys, D.A.: A Simple Finite Difference Method for Solving the Three-Dimensional Turbulent Boundary Layer Equations. American Institute of Aeronautics and Astronautics 12th Aerospace Sciences Meeting, Washington D C, January 1974
- /15/ Bradshaw, P.: Calculation of Three-Dimensional Turbulent Boundary Layers. JFM Vol 46, Part 3, 1971
- /16/ Nash, J.F.: The Calculation of Three-Dimensional Turbulent Boundary Layers in Incompressible Flow, JFM Vol 37, Part 4, 1969
- /17/ Wesseling, P. and Lindhout, J.P.F.: A Calculation Method for Three-Dimensional Incompressible Turbulent Boundary Layers. Preprint No 93 from the AGARD Conference on Turbulent Shear Flows, 1971
- /18/ Launder, B.E. and Spalding, D.B.: Mathematical Models of Turbulence, Academic Press, London, 1972
- /19/ Cooke, J.C.: A Calculation Method for Three-Dimensional Turbulent Boundary Layers. ARC R and M 3199, Oct 1958
- /20/ Smith, P.D.: Calculation Methods for Three-Dimensional Turbulent Boundary Layers. ARC R and M No 3523, 1966
- /21/ Cumpsty, N.A. and Head, M.R.: The Calculation of Three-Dimensional Turbulent Boundary Layers. Part 1: Flow over the Rear of an Infinite Swept Wing. Aeron Quart Vol XVIII, 1967
- /22/ Eichelbrenner, E.A. and Peube, J.L.: Theoretical and Experimental Investigations on Three-Dimensional (Laminar and Turbulent) Boundary Layers, in Particular on Problems of Transition, Separation and Reattachment. Faculté des Sciences de Poitiers, Laboratoire de Mécanique des Fluides, Sept 1966 (Available as AD 650952)
- /23/ Eichelbrenner, E.A.: La couche limite tridimensionnelle en régime turbulent d'un fluide compressible: Cas de la paroi athermane. Agardograph 97/II, 1965
- /24/ Himeno, Y. and Tanaka, I.: An Integral Method for Predicting Behaviors of Three-Dimensional Turbulent Boundary Layers on Ship Hull Surfaces. Technology Reports of the Osaka University, Vol 23, No 1146, 1973
- /25/ Ludwig, H. and Tillmann, W.: Untersuchungen über die Wandschubspannung in turbulenten Riebungsschichten. Ing Arch, XVII. Band, 1949
- /26/ Thompson, B.G.J.: A New Two-Parameter Family of Mean Velocity Profiles for Incompressible Turbulent Boundary Layers on Smooth Walls. ARC R and M 3643, April 1965
- /27/ Cousteix, J. and Quémar, C.: Velocity Profiles and Wall Shear Stress of Three-Dimensional Turbulent Boundary Layers. Paper presented at the EUROMECH 33, Berlin 1972
- /28/ Mager, A.: Generalization of Boundary Layer Momentum Integral Equations to Three-Dimensional Flows Including Those of a Rotating System. NACA Rpt 1067
- /29/ Johnston, J.P.: On the Three-Dimensional Turbulent Boundary Layer Generated by Secondary Flow. Journ of Basic Eng, March 1960
- /30/ Shanebrook, J.R. and Hatch, D.E.: Discussion to paper /51/
- /31/ Coles, D.: The Law of the Wake in the Turbulent Boundary Layer. JFM Vol 1, Part 2 1956
- /32/ Laute, V.: Untersuchungen über Druck- und Strömungsverlauf an einem Schiffsmodell. Jahrb der Schiffbau Gesellschaft, 34. Band 1933
- /33/ Cutland, R.S.: Velocity Measurements in Close Proximity to a Ship's Hull. Int. Shipb. Progress, Vol 5, No 51, 1958
- /34/ Hogben, N.: Record of a Boundary Layer Exploration on a Mathematical Ship Model. National Physical Laboratory, Ship Rep 52, July 1964
- /35/ Steele, B.N. and Pearce, G.B.: Experimental Determination of the Distribution of Skin Friction on a Model of a High Speed Liner. Trans RINA, Vol 110, January 1968
- /36/ Amamoto, H. et al: Measurements of Boundary Layers of Ships. Executive Committee for the Project, 12th ITTC, Rome 1969
- /37/ Taniguchi, K. and Fujita, T.: Comparison of Velocity Distribution in the Boundary Layer on Ship and Model, 12th ITTC, Rome 1969
- /38/ Wieghardt, K.: Boundary Layer Measurements on a Double Model. 12th ITTC, Rome 1969
- /39/ Shearer, J.R. and Steele, B.N.: Some Aspects of the Resistance of Full Form Ships. Trans RINA, Vol 112, October 1970
- /40/ Matheson, N.: Drag of Ships' Hulls. Ph D Dissertation, University of Melbourne, 1971
- /41/ Vollheim, R. and Nestler, W.: Messung der Wellenentwicklung und der Riebungsverluste bei dem Modell eines Massengutfrachters,  $C_B = 0.80$ , mit Bugwulstvarianten. Teil I. Schiffbau Forschung 10, Jahrgang, Heft 1/2, 1971
- /42/ Gadd, G.E.: A Comparison of Some Model and Full Scale Hull Boundary Layer Measurements. Transactions of the North East-Coast Institution of Engineers and Shipbuilders, Vol 90, 1971
- /43/ Freimanis, E. and Lindgren, H.: Systematic Tests with Ship Models with  $\delta_{pp} = 0.675$ . Part I: Influence of Shape of Sections. Swedish State Shipbuilding Experimental Tank, (SSPA) Publication No 39, 1957
- /44/ Oka, S. and Kostić, Z.: Influence of Wall Proximity on Hot-Wire Velocity Measurements. DISA Information, No 13, May 1972
- /45/ Hinze, J.O.: Turbulence. Mc Graw-Hill Book Company, 1959
- /46/ Champagne, F.H. et al: Turbulence Measurements with Inclined Hot-Wires. Part I. Heat Transfer Experiments with Inclined Hot-Wire. JFM,

Vol. 28, Part 1, April 1967

- /47/ East, L.F. and Hoxey, R.P.: Low Speed Three-Dimensional Turbulent Boundary Layer Data. Parts 1 and 2. ARC R and M 3653, 1969
- /48/ Prahlad, T.S.: Mean Velocity Profiles in Three-Dimensional Incompressible Turbulent Boundary Layers. AIAA Journal Vol 11, No 3, 1973
- /49/ Head, M.R. and Patel, V.C.: Improved Entrainment Method for Calculating Turbulent Boundary Layer Development. ARC R and M 3643, March 1968
- /50/ Hess, J.L. and Smith, A.M.O.: Calculations of Potential Flow about Three-Dimensional Bodies Douglas Aircraft Company, Report No E.S. 40622, 1962
- /51/ Klinksieck, W.F. and Pierce, F.J.: Simultaneous Lateral Skewing in a Three-Dimensional Turbulent Boundary Layer Flow. Journ of Basic Eng, March 1970



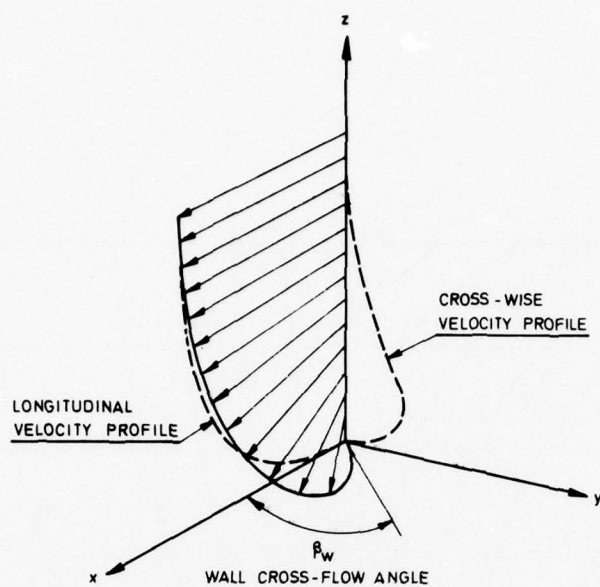
		L-T	Mager	Coles	Thomps.	Michel	Thomps. 100 %
$C_f$	M 1	4.6		4.4	4.7	-0.8	
	M 2	6.9		4.9	5.1	3.4	
$\delta$	M 1		-8.7	-2.3	-3.7	-1.7	12.1
	M 2		10.4	5.2	4.9	7.7	14.0
$\epsilon_1$	M 1		-0.8	-0.7	0.3		
	M 2		0.9	0.8	1.1		
$\delta_2$	r		-0.04	-0.03	-0.04	0.12	
$\theta_{12}$	r		0.61	0.61	0.61	0.68	
$\epsilon_2$	r		0.53	0.53	0.53		

Table IIa. Statistical Evaluation of Assumptions. All Profiles used.

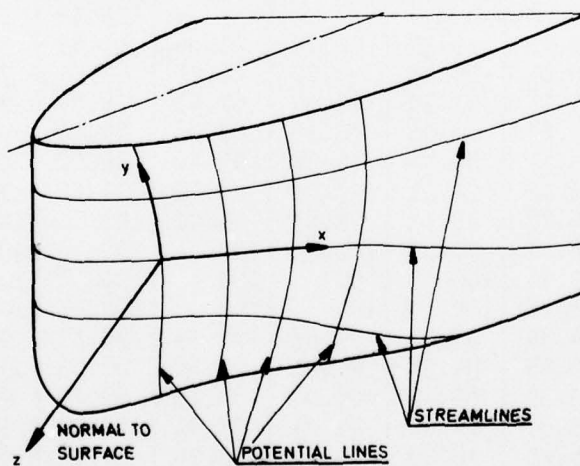
		L - T	Mager	Coles	Thomps.	Michel	Thomps 100 %
$C_f$	M 1	0.6		0.8	1.1	-2.5	
	M 2	3.8		1.4	1.6	3.0	
$\delta$	M 1		-9.9	-1.7	-1.1	-1.9	15.0
	M 2		10.6	4.5	7.7	3.5	15.4
$\epsilon_1$	M 1		-0.9	-0.5	0.7		
	M 2		0.9	0.6	1.0		
$\delta_2$	r		0.86	0.87	0.87	0.81	
$\theta_{12}$	r		0.91	0.89	0.90	0.87	
$\epsilon_2$	r		0.90	0.90	0.90		

Table IIb. Statistical Evaluation of Assumptions. Profiles between  $X = -600$  and  $X = 500$  used.

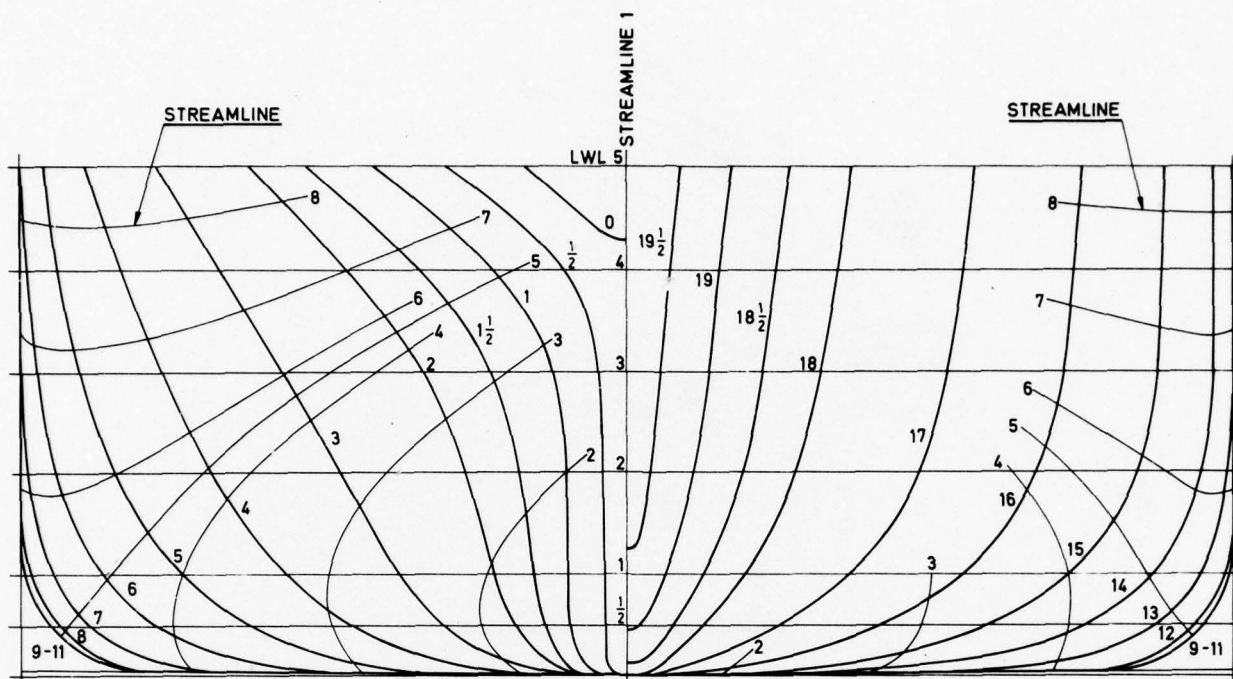




**Fig. 1: A three-dimensional velocity profile**



**Fig. 2: Surface coordinate system**



Stations	Waterline offsets in % of half-breadth								
No	WL 1/2	WL 1	WL 2	WL 3	WL 4	LWL	WL 6	WL 7	WL 8
0 (A. P.)	-	-	-	-	-	16.55	35.60	48.87	56.41
1	9.40	10.13	10.29	12.22	21.86	41.65	59.73	71.00	77.10
2	18.28	22.04	26.48	33.79	46.21	62.51	75.88	84.43	89.20
3	29.97	37.46	47.30	56.94	67.41	78.04	86.81	92.71	95.96
4	44.71	55.64	68.06	76.33	83.16	89.10	93.93	97.24	98.97
5	61.59	73.41	84.03	89.64	93.40	96.08	98.03	99.30	99.88
6	77.40	86.78	94.11	97.08	98.57	99.38	99.73	99.97	100
7	88.31	94.78	98.73	99.65	99.97	100	100	100	100
8	93.83	98.47	99.97	100	100	100	100	100	100
9-11	95.08	99.36	100	100	100	100	100	100	100
12	93.31	98.26	100	100	100	100	100	100	100
13	86.79	94.34	98.98	99.53	99.53	99.53	99.65	99.80	99.92
14	75.15	86.45	94.34	96.21	96.56	96.63	97.04	97.85	98.86
15	58.91	73.30	83.92	87.04	88.13	88.79	90.05	92.19	95.28
16	40.73	55.35	67.61	71.91	73.91	75.30	77.43	81.39	87.18
17	24.60	36.25	48.00	52.70	55.28	57.26	60.10	65.45	73.55
18	12.01	19.31	28.17	32.29	34.89	37.26	40.40	46.35	55.17
19	2.35	6.11	11.01	13.68	15.47	17.58	20.73	25.97	33.67
20 (F. P.)	-	-	-	-	-	1.18	2.85	5.61	10.04

Fig. 3: SSPA model 720

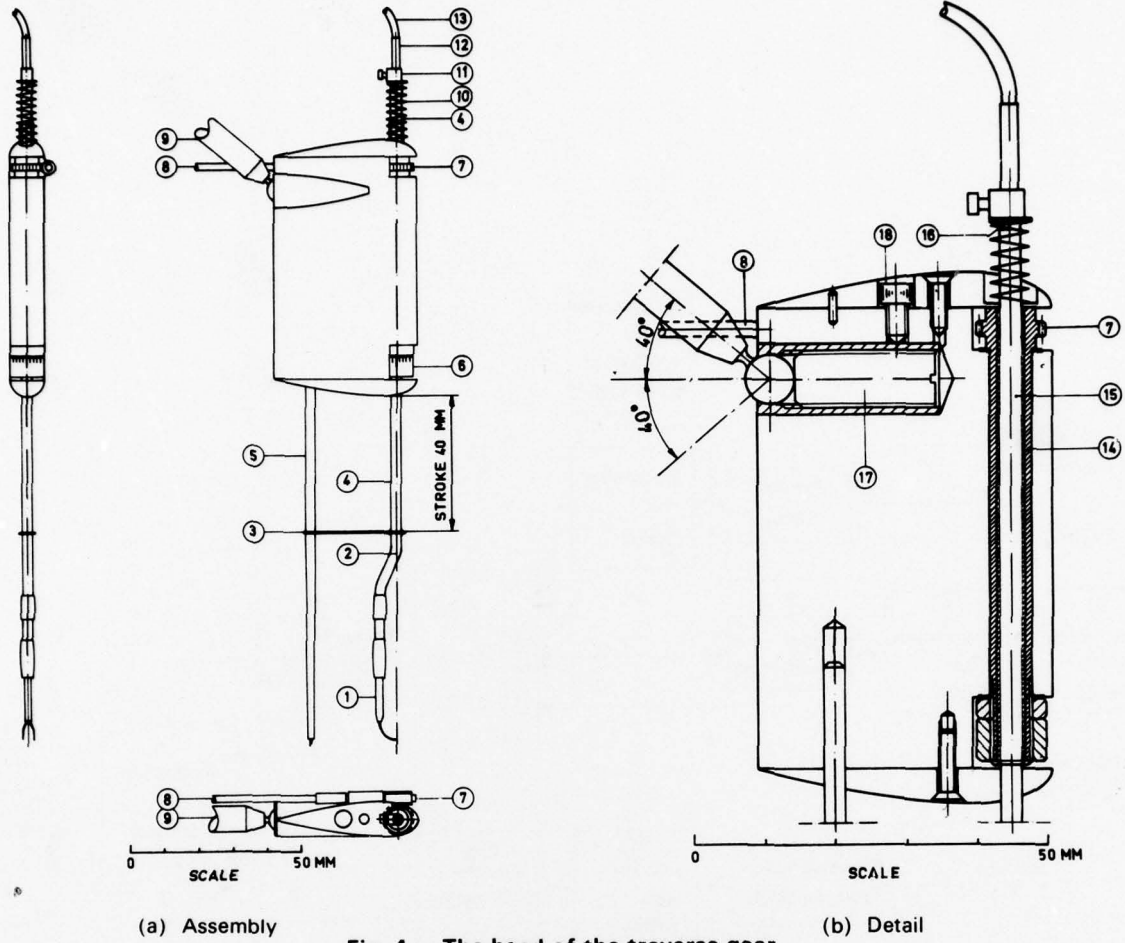


Fig. 4: The head of the traverse gear

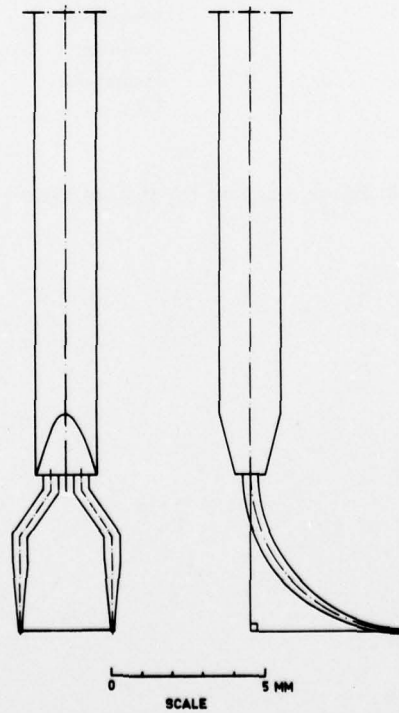


Fig. 5: The probe

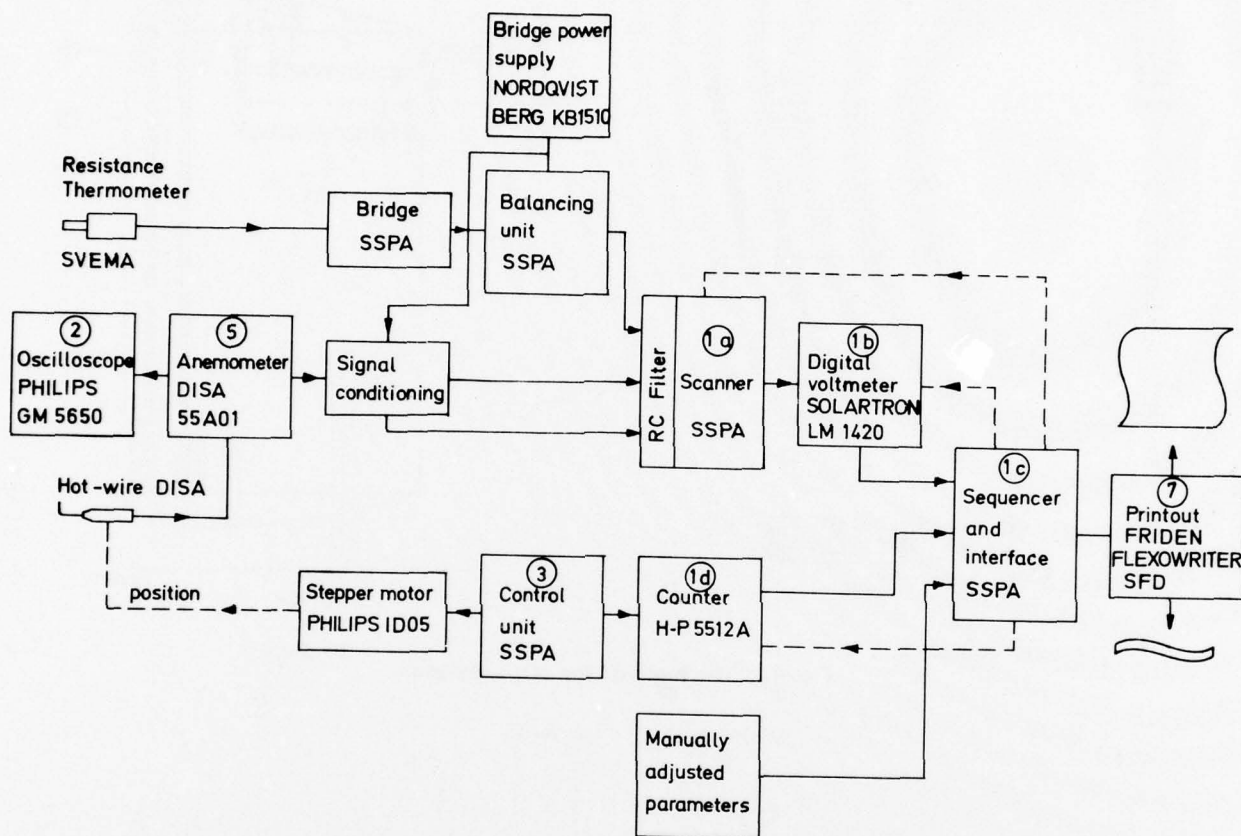


Fig. 6: Block diagram for the electronic equipment



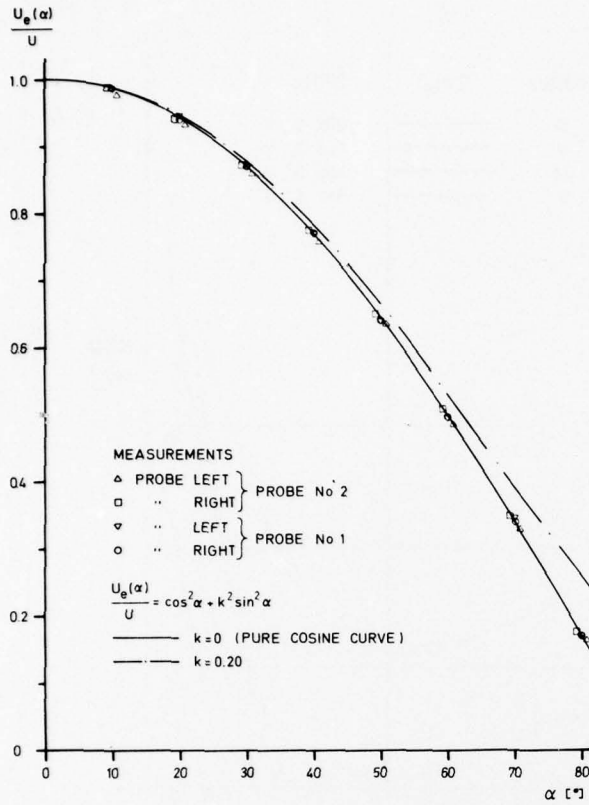


Fig. 7: Directional sensitivity of the probe

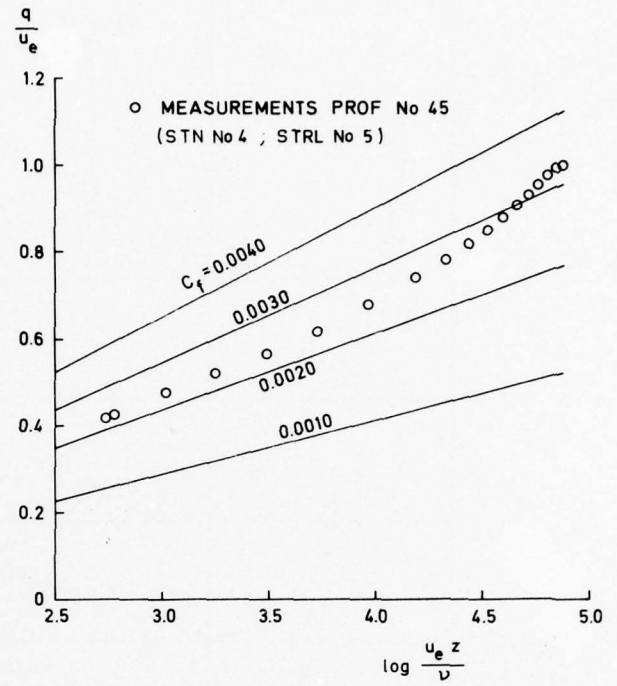


Fig. 8: Clauser plot

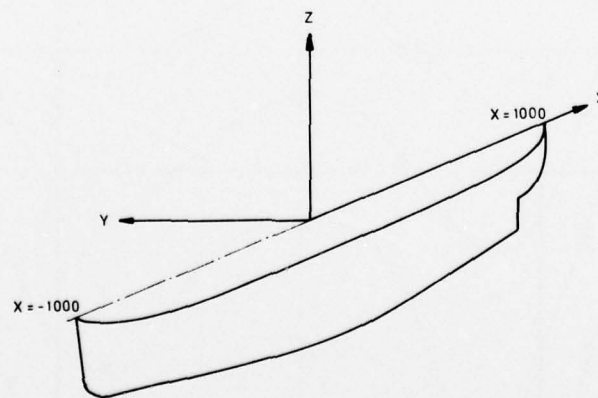


Fig. 9: Space coordinate system

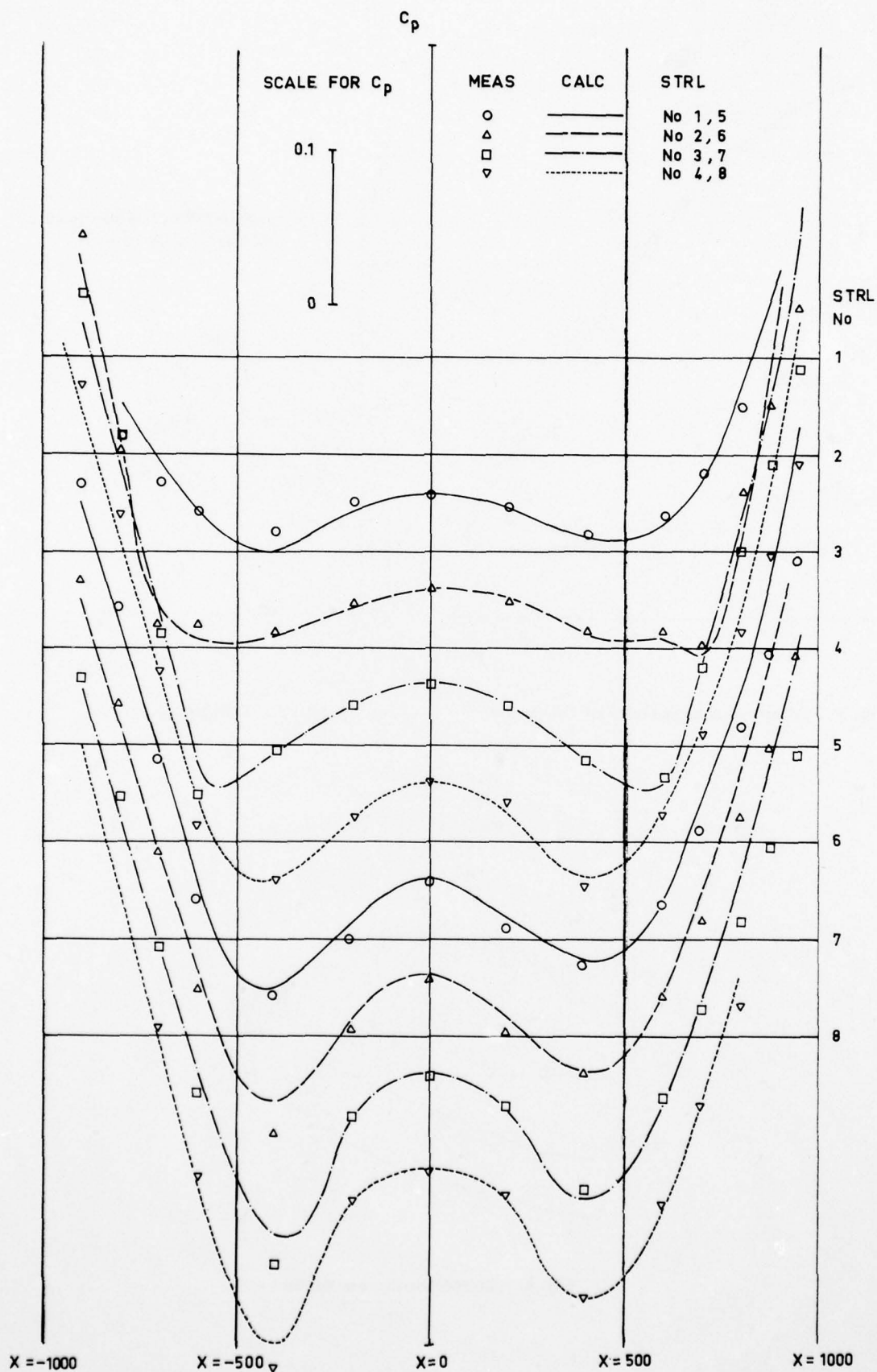
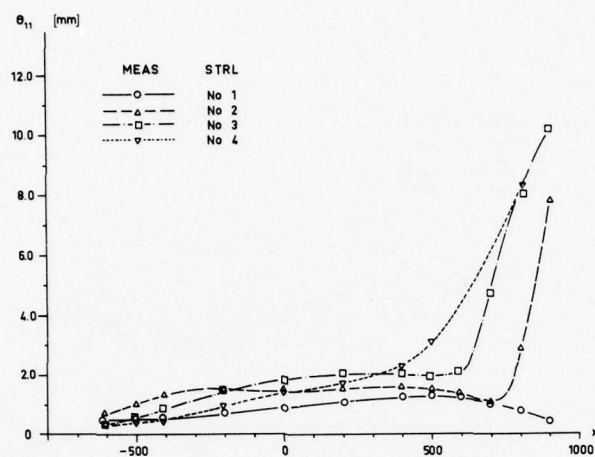
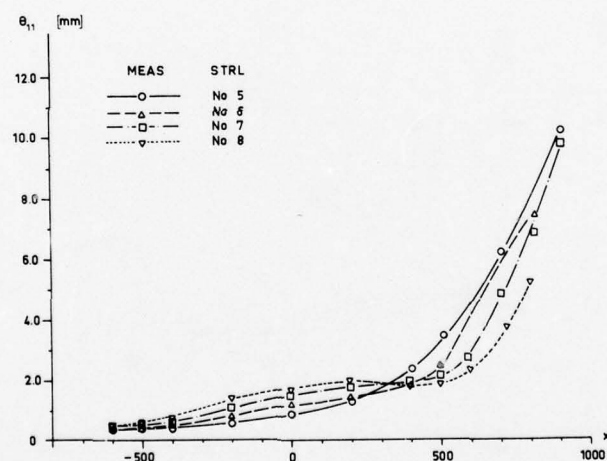


Fig. 10: Comparison between measured and calculated pressure distribution

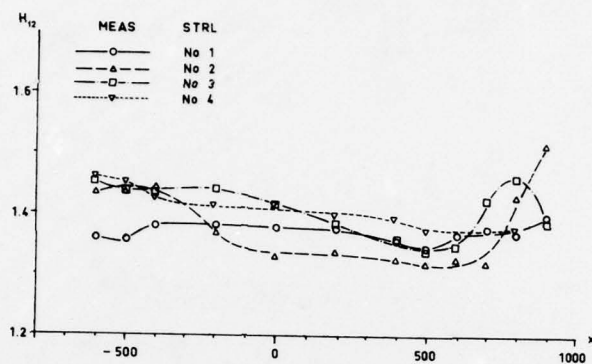


(a) Streamlines 1-4

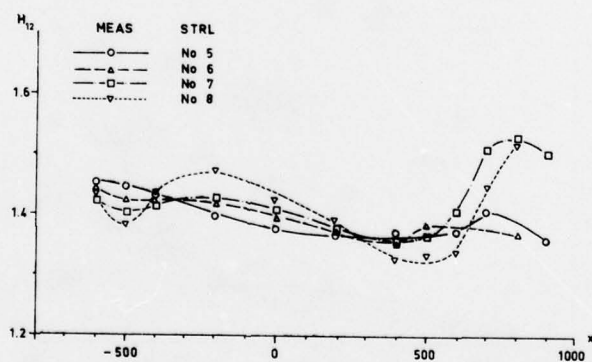


(b) Streamlines 5-8

**Fig. 11: Measured momentum thickness**



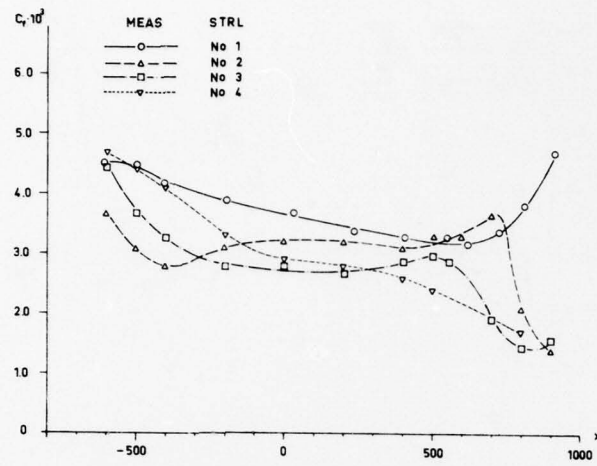
(a) Streamlines 1-4



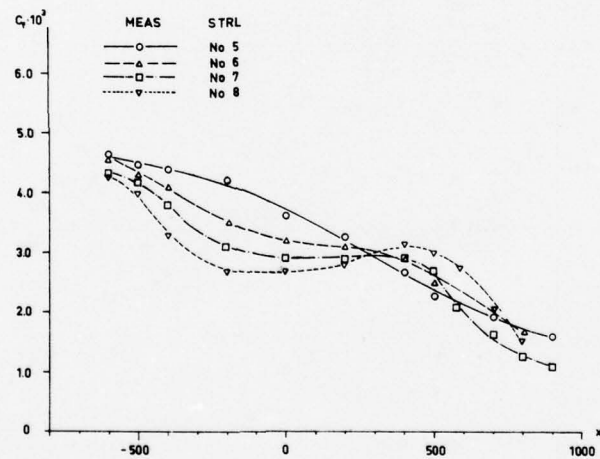
(b) Streamlines 5-8

**Fig. 12: Measured form factor**





(a) Streamlines 1-4



(b) Streamlines 5-8

Fig. 13: Measured skin friction

AD-A055 859

UNIVERSITY COLL LONDON (ENGLAND) DEPT OF MECHANICAL --ETC F/6 13/10  
SYMPOSIUM ON NAVAL HYDRODYNAMICS. UNSTEADY HYDRODYNAMICS OF MAR--ETC(11)  
1978 R E BISHOP, A G PARKINSON, W G PRICE N00014-76-C-0093

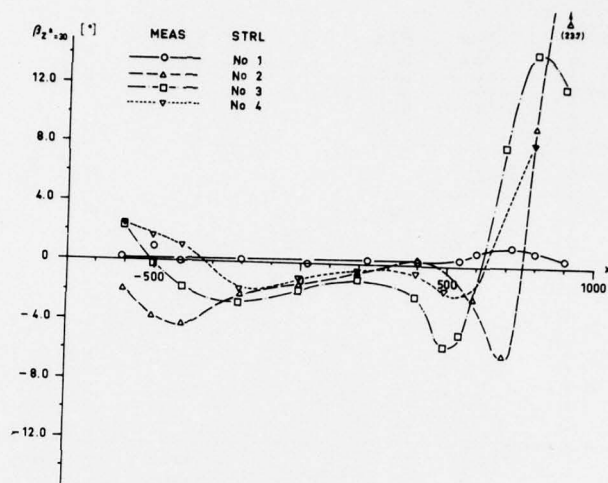
UNCLASSIFIED

NL

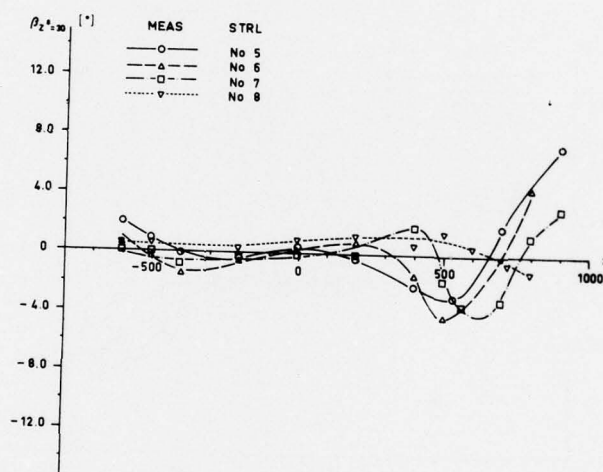
3 OF 9

AD  
A055859



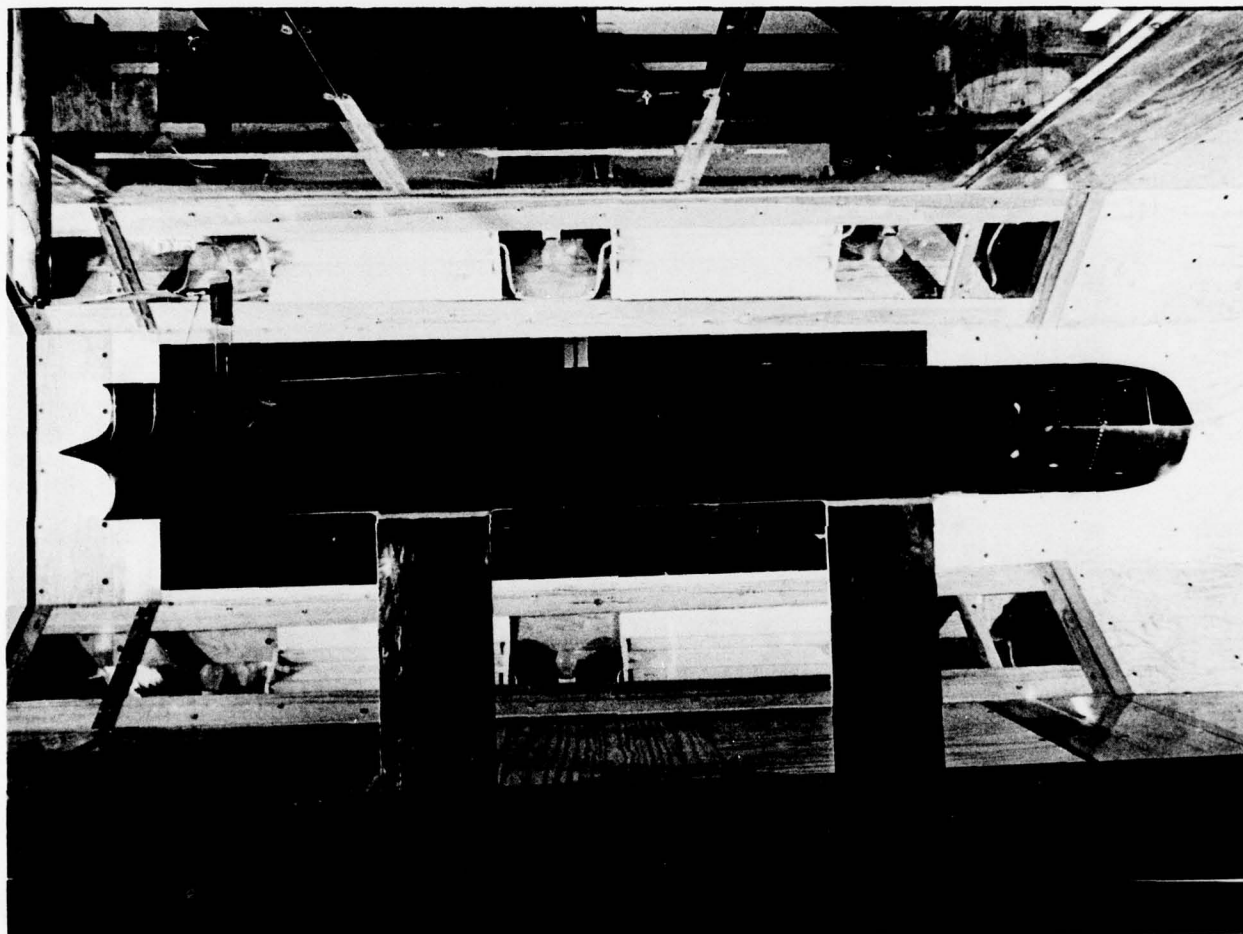


(a) Streamlines 1-4



(b) Streamlines 5-8

**Fig. 14: Measured wall cross-flow angle**

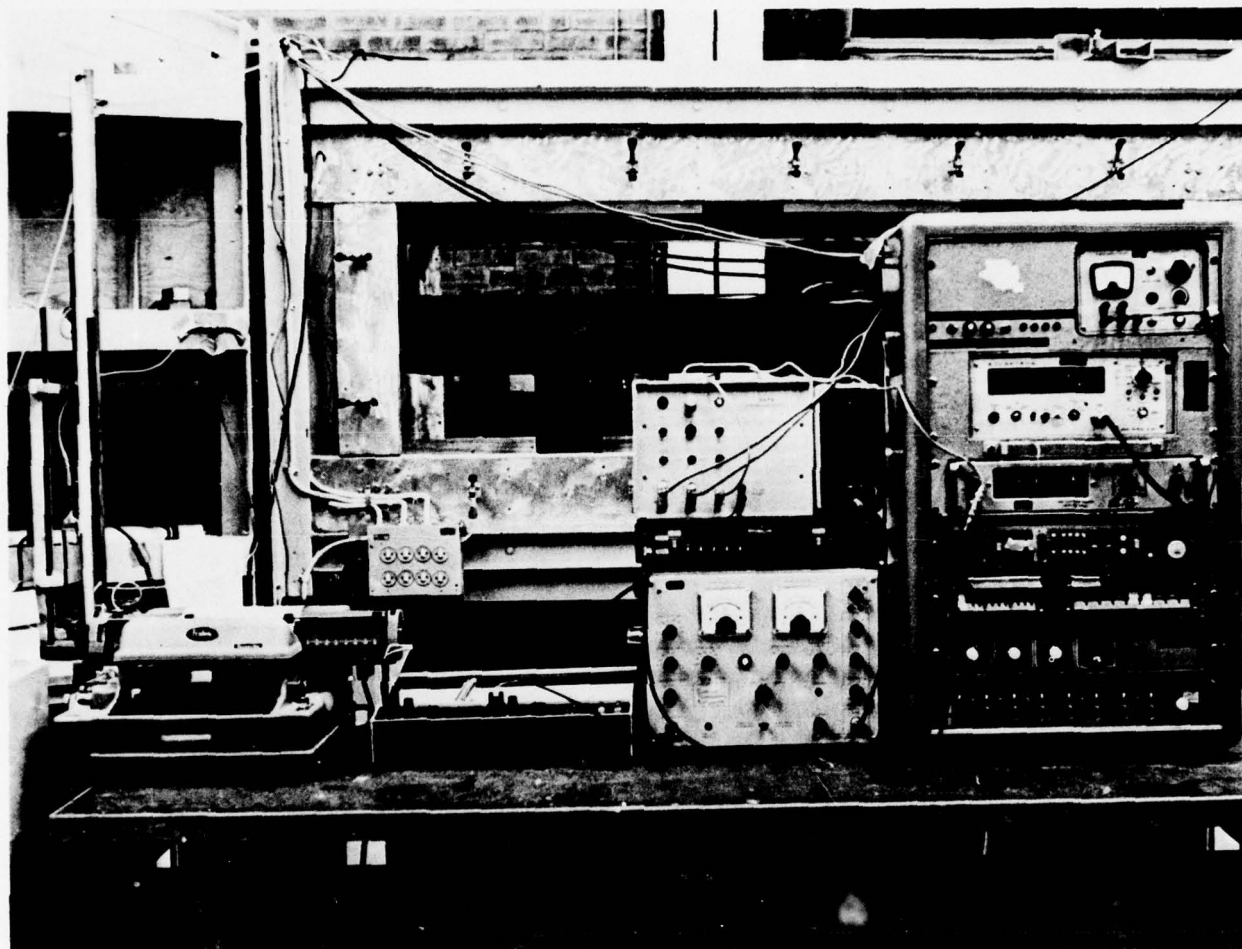


Picture 1: Side view of the model





Picture 2: Front view of the model and the traverse gear



Flexowriter

x-y-plotter

Control  
unitO-  
scopeData aquisition  
systemMechanical  
counter

Anemometer

**Picture 3: The electronic equipment**

# THE ULTIMATE HALF ROLL BEFORE CAPSIZE ON THE ANALOG COMPUTER

K. KURE

Danish Ship Research Laboratory, Lyngby, Denmark

H. KETELSEN and V. JENSEN

Elsinore College of Naval Architecture, Denmark

The present paper deals with the testing of an abstract model regarding an unsteady effect in nonlinear ship motions causing capsize. The testing applies an analog computer and is a continuation of earlier work presented to the International Conference on Stability of Ships and Ocean Vehicles, Glasgow 1975. Principles of testing of abstract models are reviewed and the specific hypothesis is formalized and tested for a set of parameters. The results are used for the evaluation of the hypothesis under test and the implications of the conclusion discussed. Recommendations are given for future work.

## I. INTRODUCTION

The roll motion of ships is steady in a statistical sense as long as the ship does not capsize. The individual roll's are, though, varying much in magnitude within certain bounds, say  $\pm 30$ -40 degrees.

Now and then ships capsize in a dynamical sense rolling over in a random seaway. A particular and well known case has been given considerations in the literature, Bovet et.al. (1). Based on a model scale reconstruction the ultimate half roll was studied in detail by Kure and Bang (2) and a hypothesis was set up to explain that particular case. The hypothesis was based on general ship dynamics and consists of two parts. The first refers to the unsteady effect of the sway motion coupling combined with the strong nonlinearity of the restoring moment. The second is the probably independent effect of the nonharmonic surge motion of the ballasted ship causing long duration of the righting moment reduction on the wave crest which the ship is following in stern quartering seas.

Due to the basic dynamic components the hypothesis might have wider applicability than for the particular case for which it was made. However, strong and/or extensive tests must be made before the reliability is shown. To study the logics of the first part of the hypothesis i.e. the unsteady effect of the coupling term in combination with the nonlinear restoring moment an investigation of the describing equations of motion was decided upon. The investigation was made using a TR 20 analog computer usually applied by Elsinore College of Naval Architecture (founded 1825) in the instruction of students.

The logical tests of the hypothesis described in the present paper are necessary but not sufficient to corroborate the hypothesis in a strict sense. Additional tests against physical reality must be performed based on derived test implications.

## II. PREREQUISITES

### i) Stability Research

In order to relate the present investigation to current research on the subject of ship stability against capsize a short review is given of the two main paths of stability research.

The first may be identified as the equation solving approach and the second as the approach without equation solving. The former is exemplified by the procedures advocated by ISSC for ship structural load and strength analyses. In the ship design process all future time history is principally predicted of motions and loads. Due to the stochastic nature of the loads which can only be described in probabilistic terms the same is necessary for the responses to the future seaways. In terms of demand and capability the risk of failure is finally computed. Alternatively, design loads are determined as the most probable value of the extreme value distribution over some small upper fractile of the long term distribution of events. Dalzell (3) made a study of the roll motion to find the distribution of roll angles. However, in relation to capsize the roll motion needs two variables to specify the instantaneous states and hence a bivariate density distribution to express demand as well as capability. The deterministic variant of the equation solving approach is the studies in time domain of the solutions to the equations excited by selected samples of extreme environments performed by Oakley, Pauling, Wood (4).

The second main road of research does not solve the equations but study stability from the form of the equations and the sign and magnitude of the parameters. This is exemplified by the classical static stability of equilibrium being determined alone by the sign of the slope of the tangent to the righting moment versus heel curve i.e. the metacentric height. In the case the righting moment is linear for all heel angles



and the damping positive then the ship would be asymptotically stable in the large as an input-output system, Willems (5). A more complicated stability condition is needed for the Mathieu type roll motion draining energy from, say, the heave motion. Restrictions to weight distribution and hull waterline belt shape against roll damping must be introduced to ensure stability of the roll motion, i.e. the C.O.G. must nearly coincide with the center of curvature of the envelope of waterlines during heel, Paulling, Rosenberg (6), Leclert (7). Basic principles of the general case along these lines applied for roll motion only are given by Moseley's classical concept of dynamical stability. Quite general principles are embodied in Lyapunov's direct method applied in ship stability by Kuo and Odabasi (8).

The first part of the present investigation as presented in Kure and Bang (2) was in fact a combination of the latter expressed in Moseley terms with the observed extreme environmental load in the analysis of the resulting ultimate half roll. That situation of deterministic analysis of an instrumented case should be distinguished from the probabilistic case of design for stability.

## ii) The Actual Capsize

Some years ago a small Danish Coastal tanker capsized in the Baltic Sea near the Swedish island of Gotland. She was on a ballast journey and steamed south in a stern quartering sea. In between she rolled rather heavily and suddenly she capsized. The weather was a fully developed Beaufort 6 to 7. Only two persons survived. The tanker was the "Edith Terkol". At the instant of capsize she had a GZ-curve a little above the IMCO recommendations. The main particulars appear from chapter II, section ii).

The above and more detailed verbal descriptions are, however, not applicable for analysis or hypothesis testing. For the present purpose the instrumented observations made during the model scale reconstruction are regarded as the basic observations of the phenomena. The model tests have been reported by Kure and Bang (2). The selected case from the model tests had a  $GM = 0.70$  m, a little higher than the case of the full scale case. Figure 1 of the present paper shows the recorded time history of the capsize. The ultimate half roll commences in a 10 degrees roll to port side lasting four or five seconds. The motion progresses to starboard where it reaches a fifty degrees heel about five seconds after upright was passed. A heel of 100 degrees are reached about three seconds later i.e. some eight seconds after upright. If the hypothesis is sound then the analog computer, when properly coded, must be able to generate a time history which resembles the observed one pretty close at least in the main character.

## iii) The Hypothesis

The roll motion of a ship is not a pure roll motion about the longitudinal coordinate axis. Other motion components do also contribute. The contribution from sway is large when the C.O.G. is located high in the ship. For the present case this coupling effect has been computed using linear strip-theory as partly presented in Kure and Bang (2).

The polygon of moment vectors corresponding to the individual terms of the equations of motion is shown in figure 2 of the present paper. Even the roll, sway, yaw motion components in mutual coupling have been computed, the yaw terms have been discarded, as they were found negligible. The linear strip-theory is not valid for the large motions considered, but has been used anyway in lack of better values. It is seen from figure 1 that the direct wave excitation is large, but counteracted heavily by the sway acceleration coupling term to yield a relatively normal wave excitation i.e. effective wave slope. Some of the terms retained are negligible.

The rolling motion is also affected by the periodic variation of the righting moment during wave passage. The ultimate 10 degrees port roll angle is occurring when the ship is in a wave trough causing large values of righting moment and max. obtainable potential roll energy. As the ship rolls over to starboard the wave crest approaches midship and reduces the basic righting moment causing the ship to roll to a large starboard angle.

Like other ship motion components having a righting moment or force, the roll motion is to a large extent governed by the righting moment. The small residuary righting moment at a large angle of heel is not able to accelerate the roll motion to keep pace with the proceeding wave excitation which initially was acting near roll resonance tending to cause large motions. The roll motion is delayed at a large heel. The sway motion on the other hand is not affected by the small righting moment and proceeds with the wave excitation. The coupling moment into roll develops with the motion and attains the large value which would have counteracted the roll motion if it has developed faster. But it did not. The starboard heeling coupling moment capsizes the ship.

## iv) Hypothesis Testing

Hypotheses of the empirical world must be tested to study their validity, they must be tested for their predictive power if they shall be of any use. They are of use if they reflect patterns of the physical world and if they do they will predict phenomena pretty accurately.

In terms of the classical logic such testing of a hypothesis A against the physical world will follow the "modus tollens" of the hypothetical syllogisms

if A then B

not B

Conclude: not A,



meaning that we can refute a hypothesis, not verify it in the strict sense. B is a test implication. Provided our testing had found B to be the case, then we would not have known for sure that A was true. A had only been corroborated as the technical term is. Popper (9)

Hypotheses do not usually lend themselves to direct testing. Test implications must be derived for comparison with observations from the nature we are trying to describe. In the present case the modus tollens would read:

if our hypothesis is true  
then the ship model will capsize.  
The ship model did not capsize

Conclude: The hypothesis is not true.

Conversely, if the ship model capsized as it in fact did, we cannot conclude unambiguously that our hypothesis is true, there might be other reasons. It is also important to note that the physical tests made with the model of the "Edith Terkol" were the origin of the hypothesis and hence cannot be used to supply observation data for a testing unless taking for granted what we were going to prove.

However, the present investigation is not so far ahead as the above discussion indicates. Before we come to that a test of the inherent logic will be needed. The hypothesis deals with several components which are interrelated in a rather complicated manner. The various terms are quite conventional when taken alone and in linear relationship. The hypothesized complex interrelationship is not easy to have a full view of directly. The effect of the coupling moment depends strongly on the lagging behind of the roll motion due to the nonlinear softening of the righting moment and the effect which causes the preliminary large heel, the GM-variation due to the wave passage. So even the hypothesis may seem convincing in its verbal form the inherent logic needs testing. This cannot be accomplished by comparison with physical observations, but must be done in the world of logic. Under the given conditions it was found appropriate to code the describing mathematics on the analog computer.

#### v) The Present Testing

The linear equations of motion for the coupled roll sway yaw case are given in Salvesen, Faltinsen, Tuck (10) and evaluated term by term for the present purpose in Kure, Bang (2). It was concluded that the yaw equation could be left out of consideration as the coupling terms into roll were small. It can be concluded in addition that the sway velocity term in the roll equation can be discarded. The roll damping term is also very small, but has been retained. In the sway equation the sway damping term and the roll velocity coupling term are negligible and have been omitted for simplicity. The resulting linear equations hence read:

for roll,

$$(A44+I44)\ddot{\phi} + B44\dot{\phi} + C44\phi + (A42-Mz_G)\ddot{y} = H(F41+iF42)e^{i\omega t} \quad (1)$$

for sway,

$$(A22+M)\ddot{y} + (A24-Mz_G)\ddot{\phi} = H(F21+iF22)e^{i\omega t} \quad (2)$$

These equations represent a dynamic system which is asymptotically stable in the large for the actual set of parameters. They are not subject to investigation in the present study.

For our purpose the crucial elements of the hypothesis must be introduced. They are the softening nonlinear term in the roll restoring moment and its time variation. The introduction of these terms in the equation is inconsistent with the use of the coefficients from the harmonic motion analysis. However, the resulting discrepancies are believed to cause second order effects only in the present context.

The restoring term in the linear roll equations reads:

$$\Delta GZ = C44\phi$$

It has been converted to:

$$\Delta GZ = C44\phi + D44\phi^3 \quad (3)$$

where D is given a negative value to make  $\Delta GZ = 0$  at a specified angle of heel.

The oscillation due to wave passage is introduced by setting

$$C44 = C440 + C441 \sin(\omega t + \gamma)$$

and taking

$$C441 = f(\text{wave amplitude}) = C442H \quad (4)$$

in a linear representation, where H is the wave amplitude, and C442 has been determined from digital computations of righting levers in the quasi-static case of the ship on a wave-crest, -trough respectively and with the Smith effect included. The final mathematical form on which the hypothesis will be tested then reads:

$$(A44+I44)\ddot{\phi} + B44\dot{\phi} + (C440+C442H \sin(\omega t + \gamma))\phi + D44\phi^3 + (A42-Mz_G)\ddot{y} = H(F41+iF42)e^{i\omega t} \quad (5)$$

for roll,

and for sway:

$$(A22+M)\ddot{y} + (A24-Mz_G)\ddot{\phi} = H(F21+iF22)e^{i\omega t} \quad (6)$$

The solution of these simultaneous, nonlinear equations of motion will reveal the possible virtues of the hypothesis on the unsteady capsizing effect of the large sway, roll coupling moment due to the strongly softening nonlinear roll restoring moment and its variation during wave passage in stern quartering seas.

## III. PREPARATIONS

## i) The Analog Model

The analog computer used is the EAI type TR 20 consisting of several elements capable of performing addition, multiplication, attenuation and integration of the instantaneous electric voltage input which is proportional to each corresponding variable in the physical system simulated.

The basic variables in the present case are the state variables  $\phi$  and  $\dot{\phi}$ . The simulation is performed in such a way that these state variables develop in real time. They are interpreted in the following way:

$$\begin{aligned} \dot{\phi} &= \frac{d\phi}{dt} \\ \text{and} \\ \ddot{\phi} &= \frac{d\dot{\phi}}{dt} \end{aligned} \quad (7)$$

The heart of the analog simulation of eqs. (5) and (6) is the two elements performing the instantaneous integration of  $\ddot{\phi}$  to yield  $\dot{\phi}$  and the integration of  $\dot{\phi}$  to yield  $\phi$ .

The structure of the simulation circuit is made up from a rearranged set of equations of motion (5) and (6).

Expressing explicitly from (5) yields:

$$\begin{aligned} (A44+I44)\ddot{\phi} &= H(F41+iF42)e^{i\omega t} - B44\dot{\phi} \\ &\quad - (C440+C442H \sin(\omega t + \gamma))\phi - D44\phi^3 \\ &\quad - (A24-Mz_G)\ddot{\gamma} \end{aligned} \quad (8)$$

It is seen that after normalization with  $(A44+I44)$  the variable  $\ddot{\phi}$  is made up as the sum using proper signs of the instantaneous values of the individual terms on the right hand side.

The generation of the instantaneous values of the individual terms occupies the bulk of the analog simulator. The primary sub assembly generates the sinusoidal voltage representing the real part of the exponential function  $e^{i\omega t}$  in the external forcing functions. Closely related hereto is the phase-shift circuits causing these external influences to appear in proper phase.

Another sub assembly generates the softening, non-linear restoring moment as a function of the instantaneous value of the  $\phi$  signal and superposes on it the time variation due to wave passage. Finally a sub assembly generates the sway acceleration in its explicit form obtained by normalizing the equation:

$$\begin{aligned} (A22+M)\ddot{\gamma} &= (F21+iF22)e^{i\omega t} \\ &\quad - (A24-Mz_G)\ddot{\phi} \end{aligned} \quad (9)$$

The variable  $\ddot{\gamma}$  is introduced in the roll circuits after being weighted with the proper coefficient.

Adding the instantaneous signals from all the sub generators results in a sum which is proportional to the corresponding value of  $\ddot{\phi}$ .

The sum is used as input to the first integrator in the main roll state circuit. The desired quantities, the state variables  $\phi$ ,  $\dot{\phi}$  appear as output from the two successive integrators as usual. See e.g. Ogata (11). The analog model used is described in some detail in the appendix to the present paper.

## ii) The Model Parameters

The relevant model parameters are the coefficients of the equations of motions inclusive of those of the nonlinear terms. They refer all to the ballasted condition of the "Edith Terkol" as modelled in the wave basin of the Danish Ship Research Laboratory. The metacentric height was a little higher than at the real capsizes. The model did, however, capsize repeatedly in the model basin when in this condition of loading.

The wave basin test conditions corresponded according to Froude's law to a speed of about 10 knots of the real ship in quartering waves about 30 degrees from the stern and of about 100 m in length. Referred to the earth the wave period was about 8 seconds. The Doppler shift towards longer periods in this sailing condition resulted in a period of encounter of about 12 seconds, which was close to the period of resonant roll of the softening ship roll motion having a natural period of roll of 10.6 seconds according to the linear ship characteristics.

Main Particulars of the Model Capsize Condition of the "Edith Terkol".

Table 1.

Displacement	645 m <sup>3</sup>
Length PP	58.6 m
Beam	9.65 m
Depth	4.15 m
Draft at $\Delta$	1.75 m
Trim aft	1.52 m
GM	0.70 m

The coefficients of the linear strip-theory have all been stated in Kure, Bang (2) and have the following values,

Coefficients of the Linear Roll Equations.

Table 2.

Mass terms:

A44	3950 Mgm <sup>2</sup>
I44	- 680 Mgm
A42	7550 Mgm <sup>2</sup>
Mz <sub>G</sub>	1680 Mgm

Damping:

B44	50 kNm.sec.
-----	-------------

Restoring:

C44	4050 kNm
-----	----------

The wave excitation moment components refer to 3.5 m trough to crest wave height due to a specific purpose in the applied strip-theory computer program.

F41 (real part)	98 kNm
F42 (imaginary)	510 kNm

Coefficients of the Linear Sway Equations.

Table 3.

Mass terms:

A22	410 Mg
M	645 Mg
A24	670 Mgm
MzG	1680 Mgm

Wave excitation for 3.5 m wave height:

F21 (real part)	21 kN
F22 (imaginary)	-330 kN

Coefficients of the Non-linear Terms.

Table 4.

3<sup>rd</sup> order restoring:

D44	4050 kNm
-----	----------

Wave passage oscillation:

C442	440 kN
------	--------

The phase of this term has been introduced in the simulation to comply in principle with the minimum value to occur when the wave crest is amidship, at the origin of the strip-theory reference system. This means for the present case that this oscillation leads the wave excitation term in the roll equation abt. 86 degrees. A value of 90 degrees have been used for simplicity.

### iii) Tests of Submodels and Special Cases.

Before the intended use could be made of the simulated system in total, several tests on its subsystems had to be made in order to ensure the reliability of the response of the total system, which will yield the premises for the conclusions.

Such testing took place by decoupling the individual subsystems and exciting them separately. It has been taken for granted that satisfactory testing of the subsystems would ensure correct operation of the total system, provided this is logically structured. An overall test of the linear part of the total system has been made against the strip-theory outprint.

The central integrating circuit for the two state variables of the roll mode is a linear system. It was tested in terms of its analytically predictable response to a step excitation. The test quantities were the period of oscillation which is uniquely determined by the ratio of (A44+I44) to C44 in the equations of motion. The rate of decay of the peak values, i.e. the logarithmic decrement, is determined in addition by the damping coefficient B44.

The prime mover, the sine function generator, was tested simply by recording of period and amplitude of the basic signal of the derived, phase shifted signals. The basic signal is used for the roll excitation and its phase, which lags the angle  $\tan^{-1}(F42 \div F41)$  behind the strip-theory phase reference instant, is taken as reference for phase angles. The sway excitation force, which lags the angle of  $\tan^{-1}(F22 \div F21)$  behind the strip-theory phase reference instant, is thus lagging 168 degrees behind the roll excitation. A time integration was used to produce the 90 degrees phase shift for the signal of the wave passage oscillation of the restoring signal. No check of this angle was hence necessary.

The nonlinear roll restoring moment was tested statically according to definition. The representing signal was plotted versus heel angle signal on an X-Y plotter. See figure 3. The tangent at the origin reflects the coefficient C44 and relates to the zero wave height case. At a distance above and below the still water curve other curves have been drawn by the subsystem generating the oscillation due to wave passage. The amplitude values only have been shown.

A special case of the total system is the subsystem consisting of the central integrators, the excitation generators, the sway coupling generator, i.e. the sway equation circuit, and the linear non-oscillating part of the roll restoring circuit. The response of this linearized simulator circuit should comply with the results from the strip-theory program with smaller deviations due to omission of small terms. The strip-theory results refer to the stationary solution of the equations, obtained when the starting transient has died out. Time had hence to be allowed for this process to finish before readings were taken from the response recorders. About ten minutes were found necessary for this process in the real time simulation. During this period of simultaneous presence of the stationary, forced response and the decaying transient response beats of the two were observed at the theoretically predictable difference frequency between the two which have oscillation period of respectively 11.7 and 10.6 seconds. For trial purposes a much stronger damping were introduced, causing a very fast decay of the starting transient and the beats. A rise time on the excitations were also tried in order to reduce the effect of the starting transient for the comparisons with the strip-theory results. The effect of the rise time was roughly speaking a delay of the initial part of the response time history.

These intermediate tests were, however, of no interest to the intended hypothesis testing. The capsize under study happened in the wave basin amongst the very first waves of a group following almost quiet water and the effect of a rise time could not have been strong. For this case the conditions were not stationary, but included the starting transient.



For a one meter amplitude wave the simulated roll amplitude was found to be 5.3 degrees against the strip-theory value of 5.2 degrees, and the simulated sway acceleration divided by the square of the circular frequency of encounter to yield sway motion amplitude of 0.73 m compared also well to the corresponding strip-theory value of 0.70 m.

#### IV. THE SIMULATION

##### i) General

The purpose of the simulation of the behaviour of the eqs. (5) and (6) was to test the logic of the hypothesis of chapter II section iii). This cannot be done by studying the response of the system with and without the main cause in operation. The main cause was claimed to be the roll moment induced by the sway acceleration obtaining an unsteady effect at large angles of heel where the strongly softening, non-linear restoring moment had become weak. The removal of the coupling moment would disturb the balance of the individual terms of the equations, see figure 2, to an extent which would not permit comparison of the two cases. The physical system under test would need large variations of its describing parameters in order to resemble the equations without the coupling term. That could be physically realized by bringing the centre of gravity 1-2 m down in the ship.


Another way of study has hence been chosen for the present case. The important variables are, besides the roll angle, the wave exciting moment, the sway coupling moment and the righting moment. All four have been recorded continuously on an X-Y recorder draining the signals from the summing device  in the analog circuit. See figure 4 and the appendix. The results from the main case appear as time history in figure 9, which shows the variation of each of these quantities during the oscillations leading to the capsize. The simulation did in fact show capsize after a few waves just as the physical experiments did.

Figure 10 shows the ultimate half roll from this simulation. It has been indicated at its starting peak by a small circle in the time history of roll in figure 9. The diagram in figure 10 shows the individual moments to a base of the instantaneous roll angle and corresponds completely to the ordinary GZ versus heel diagram.

Figures 5 and 6 and figures 7 and 8 are corresponding sets of diagrams referring to four and five meters wave height respectively. Simulation was only performed for the 30 degrees from aft quartering sea case at about 10 knots speed at which the model of the "Edith Terkol" capsized in the wave basin. The wave parameters were as follows:

Wave length:	100 m
Wave period:	8.0 secs.
Period of encounter:	11.7 secs.

##### ii) The Main Simulation Case

The time histories of the individual variables during the simulation of the main case corresponding to the wave basin capsize in 9 m high waves have been reproduced in figure 9. The lower curve shows the instantaneous roll angle beginning from zero through a diminutive heel to, say, port side through a 45 degrees starboard and about 50 degrees port side heel where the ultimate half roll begins. This peak has been encircled.

The second curve from below shows the instantaneous value of the righting moment. The saddles on the peaks reflect the passing of the top of the GZ-curve causing lower values of righting moment than at the top. See also figure 10 showing the ultimate half roll commencing at the circled peak. This angle of heel plots at the utmost left on figure 10 from where it is easily seen that the top of the GZ-curve has been passed. The upper curves are the direct wave exciting moment and the coupling moment from sway. In the first part of the simulation the latter two are seen to almost outweigh each other. This stationary case has been extended into the following time history by the dotted curve to elucidate the actual behaviour of the coupling moment from sway.

It is seen that immediately before the capsize the stationary value of the coupling moment would have had a peak value counteracting the somewhat larger wave moment. See figure 2. In the actual case, however, the coupling moment was reversed to assist the wave moment. This trend is indeed pretty close to the prediction of the hypothesis under test.

##### iii) The Character of the Curves

The regular shape of the time histories of the variables at the beginning of the simulation reproduced in figure 9 is soon lost when approaching the capsize. The similar curves from the simulations for 4 and 5 m wave heights are much more regular over long periods as it could be expected for these cases closer to the initial linear system.

Curves representing wave moment and coupling moment are usually not shown in the  $\phi$ , GZ diagrams as they are in the figures 6, 8 and 10. For the fully linear case these curves would be ellipses having their principal axes inclined in relation to the  $\phi$ , GZ axes. The lengths of the principal axes and their inclination are determined solely by the amplitudes and phases of the roll motion and the individual variables and of course by the units on the coordinate axes. This is best recognized in figure 6 showing the 4 m wave height, almost linear case. Semi-ellipses are seen because only one half roll period is shown. Their principal axes are oppositely inclined towards the  $\phi$  axis because they are of opposite phase, as it appears from the time histories of figure 5. Both elliptically shaped curves are drawn as functions of the instantaneous value of heel on the abscissa axis. Corresponding ordinates will hence represent simultaneous values of the two moments acting in the motion.



#### iv) Other Simulated Cases

The above found preliminary result made it interesting to find the limiting wave height for capsize, all other parameters kept unchanged.

Reducing the wave height in the analog computer was performed by the attenuators 1,6 and 7, see figure 4. The wave height was reduced in steps until so low values that capsize did not occur in the long run. The sets of figures 5, 6 and 7, 8 show the results for 4 m and 5 m wave height respectively. Capsizing occurred in the first case, but not in the second. The time histories of the individual contributions indicate, however, that the unsteady effect from the 9 m case was not present.

In the 5 m wave height case rolling seemed to build up as the wave-train proceeded. When the roll energy was high enough to cope with the diminishing righting moment caused by the strongly negative cubic term the ship capsized, or at least the solution with respect to  $\phi$  of the equations (5) and (6) tended to infinity.

It is seen at the two largest heel angles to each side, before the ultimate half roll begins, that the top of the GZ-curve has been reached. The time history is quite flat meaning that the GZ-curve was constant during this period.

Additional simulations using other wave heights for a fine resolution around the capsize inception value showed this to be in the range of wave heights between 4.4 and 4.8 m.

#### v) Discussion of the Unsteady Effect

The preliminary result of the main simulated case was the occurrence of the inversion of the sway coupling moment during the ultimate half roll. The claim by the hypothesis that this was caused by the strong softening of the restoring moment has been critically examined.

The time history of the coupling moment appears from figure 9 showing the inversion of the peak value from a mode resisting to a mode assisting the wave moment. The corresponding presentation of the instantaneous values versus heel angle in figure 10 reveals some discrepancies from the hypothesis.

Initially it is seen that the effect of the oscillation of GZ during wave passage is such that the GZ-curve has been raised a little in value for both port and starboard heel angles during this half period of roll. A stronger effect was expected by Kure and Bang (2) in setting up the hypothesis. However, phases between the individual contributions must have been different from those presumed and the effect thereby reduced.

Apart from this missing contribution to capsize the unsteady effect looked for was indeed found, but close examination showed the instant of inception to be different from that explained by the hypothesis, and questioned by H. Bird in a written contribution to Kure, Bang (2). The hypothesis claimed that reduction in righting moment would cause the roll motion to lag behind the wave encounter and the sway motion and thus meet the coupling from the latter with the opposite sign of normal. This is not observed in the corresponding simulation. The process there is much more complicated as discussed in the following, centering around figure 10.

The above mentioned slight increase of the righting lever curve is reflected by the shift of the crossing between the curve and the  $\phi$  axis. The curve parameters for still water are chosen to give a crossing at one radian or 57.3 degrees. The crossing at a higher value of  $\phi$  means higher curve ordinates. The wave moment enters the ultimate half roll to the left in the diagram in a semi-ellipse like curve. This is distorted towards the capsize as the abscissa grows indefinitely (in the simulation only).

The stationary counterpart of the sway coupling moment is represented by the dotted curve above the axis. It is also of ellipse like shape at the beginning and distorted at the right hand side approaching capsize. If capsize had not occurred the two moment curves in the diagram would have revealed ellipse like shape at the right hand side also having vertical tangent there at the max. heel angle. The actual time history of the sway coupling moment did not at all follow this form even it approaches it towards the point of no return. This development of the coupling moment does not comply with the hypothesis.

The factual development of the sway coupling moment is to assist the wave moment in the first part of the ultimate half roll where the ship is righting from a heeled state towards upright and to resist it in the ultimate quarter roll. The reasons for this have been sought in the intricate mutual interaction of the individual contributions to the instantaneous total moment. Figure 4 and the modelled equations (5), (6) show the well known fact that not only is the sway coupling into roll, but also vice versa.

Looking at the analog computer diagram figure 4 it is seen that the contributions to  $\dot{\phi}$  are the following:

- The neglected small damping  $B\dot{\phi}$ .
- The righting moment acc. to eq.(4).
- The wave forcing moment ( $F_{41} + iF_{42}$ ).
- The sway coupling moment ( $A_{42} - M_{zG}$ ).

The independent cause, the wave moment, is sinusoidal and do not directly contribute to the unsteady effect. The passage of the top of the righting moment curve does directly affect  $\dot{\phi}$ .

However,  $\dot{\phi}$  is itself affecting the sway acceleration through the coupling term in the sway equation (6). It appears also from the corresponding sway generation circuit of figure 4. The effect on  $\dot{\phi}$  of the saddle in the righting moment curve is thus transferred to the sway motion (and equation) and from there back again to the roll motion in a final effect as seen from figures 9 and 10. The final effect of the sway coupling moment on the ultimate half roll is thus not to reduce the stability work in the second part of this half period, but to increase the heeling work during the first part of it.

## V. CONCLUSIONS AND RECOMMENDATIONS

Capsize of ships is a very serious matter. In the present context it is so because the physics of the dynamic cases are not well understood. This implies a lack of rationality in the rules and regulations and misleading of designers and skippers. The present paper dealt with a hypothesis regarding a mode of dynamic capsize in steady quartering seas, where the inception of an unsteady effect was claimed responsible for the disaster.

In a previous paper on the subject the hypothesis was formulated in verbal terms referring to qualitative aspects. In the present paper it was given a mathematical formulation by introduction of the relevant non-linear terms into the equations of motion and using the original coefficients from harmonic potential flow around each hull section and strip-theory for integration. This is naturally not applicable with great accuracy to the strongly non-linear case of ships' capsize. The intention was to study the general trend.

And the hypothesized inversion of the sway into roll coupling moment was indeed found in the analog computer simulation performed and reported in the paper. A simulation was deemed necessary to study the logic inherent in the hypothesis, but not in itself very clear because of the complexity of the mutual interaction of the terms on the equations of motion.

A critical examination showed that the time history of the coupling moment inversion in certain respects was different from the hypothesized, and it can be discussed if the time history of the roll angle during capsize, as it happened in the wave basin according to figure 1, in one of the first waves in a group, did comply with the analog simulation time history of figure 9. The initial heel angle to the ultimate half roll was about 10 degrees in the wave basin against about 50 degrees in the corresponding simulation.

In spite of the factual occurrence of the coupling moment inversion which in a way corroborated the hypothesis under test it must be concluded that further refinements are necessary.

It is therefore recommended that serious research is promoted within this field of dynamic capsize. A lot has been done already as referred to in the text and directed in a rational way towards single topics. It was not expected that the present small study would reveal the secrets of dynamic capsize. The objective was too specific and the mathematics involved too simple. The added mass and damping concepts referring to the harmonic motion and potentials did not comply good enough with the facts. Other causes such as the surging of the vessel during wave passage and the resulting non-harmonic righting moment variation was not included.

An overall solution will be needed in the time domain treating the flow around the hull together with the hull dynamics to yield a rational approach.

It is hoped, however, that the present very specific investigation has thrown some light on one aspect of the physics of dynamic capsize of ships and thus helped the progress within this field of research.

## VI ACKNOWLEDGEMENT

The authors wish to express their appreciation of the patient, and accurate typing of the camera-ready manuscript done by Mrs. A. Kirketerp of the Danish Ship Research Laboratory. The authors themselves are responsible for the remaining grammatical errors and abuse of the English language.

## LIST OF SYMBOLS

$\Delta$	weight of ship displacement
GM	metacentric height
$\phi$	roll angle
$\dot{\phi}$	roll angular velocity
$\ddot{\phi}$	roll angular acceleration
y	sway motion
$\dot{y}$	sway velocity
$\ddot{y}$	sway acceleration
M	fixed mass of ship
I <sub>44</sub>	fixed mass moment of inertia of ship
G	centre of gravity of ship
z <sub>G</sub>	vertical coordinate of G
C <sub>44</sub>	restoring coefficient
C <sub>440</sub>	$\Delta \cdot GM$
C <sub>441</sub>	amplitude of $\Delta \cdot GM$ oscillation
C <sub>442</sub>	C <sub>441</sub> per meter wave height
D <sub>44</sub>	coefficient of cubic restoring
B <sub>44</sub>	linear damping coefficient
A <sub>44</sub>	hydrodynamic mass moment of inertia in roll
A <sub>22</sub>	hydrodynamic mass in sway
A <sub>42</sub>	hydrodynamic coupling coeff. sway into roll
A <sub>24</sub>	hydrodynamic coupling coeff. roll into sway
H	wave amplitude
F <sub>41</sub>	wave moment, roll. Real part
F <sub>42</sub>	wave moment, sway. Imaginary part
F <sub>21</sub>	wave force, sway. Real part
F <sub>22</sub>	wave force, sway. Imaginary part
i	imaginary unit
e	base of natural logs
$\gamma, \theta$	phase angles

## REFERENCES

- (1) Bovet, D.M. et al, "Recent Coast Guard Research into Vessel Stability",  
Marine Technology, Oct. 1974.
- (2) Kure K, Bang C.J., "The Ultimate Half Roll",  
International Conference on Stability of Ships and Ocean Vehicles, Glasgow 1975.
- (3) Dalzell, J.F., "Distribution of Peaks of a Non-Linear Roll Motion"  
Rep. Davidson Laboratory.
- (4) Oakley, O.G. et al, "Ship Motions and Capsizing in Stern Seas",  
10th Symposium on Naval Hydrodynamics, Boston 1975.
- (5) Willems, J.L., "Stability Theory of Dynamical Systems",  
Nelson Publ., London 1971.
- (6) Paulling, J.R., Rosenberg, R.M., "On the Unstable Ship Motions Resulting from Non-Linear Coupling",  
Journal of Ship Research, Vol.3 No. 1 1959.
- (7) Leclert, E.M., "On Certain Theorems Respecting the Geometry of Ships",  
Transactions I.N.A. 1870.
- (8) Kuo, C, Odabasi, A.Y., "Application of Dynamic Systems Approach to Ship and Ocean Vehicle Stability",  
International Conference on Stability of Ships and Ocean Vehicles, Glasgow 1975.
- (9) Popper, K.R., "The Logic of Scientific Discovery",  
Hutchinson of London, 1968.
- (10) Salvesen et al, "Ship Motions and Sea Loads",  
Transactions of SNAME 1970.
- (11) Ogata, K., "State Space Analysis of Control Systems",  
Prentice Hall 1967.



## APPENDIX

## ANALOG SIMULATION OF THE DYNAMIC SYSTEM

## i) Analog Simulator

Simulation of the dynamic system described by eq. (5) and with model parameters stated in Chapter III section ii) was as previously mentioned executed by means of an Electronic Analog Simulator type EAI TR-20, containing 20 amplifiers with input-output gain of respectively 1 and 10. The amplifiers serve as adding elements, sign converters and by feed-back capacitors as integrators as well. Further the simulator has built-in attenuators, and it has been extended with the necessary number of non-linear elements for generating the non-linear function of  $\Delta GZ$ . These non-linear elements consist of integrated, four-quadrant multiplying circuits of type AD 530 with output functions  $1 \times X \times Y$ .

The variables of the dynamic problem are represented by output voltages from amplifiers and integrators within the range of  $\pm 10$  V in this particular simulator. Other systems are operating with output voltages within the range of  $\pm 100$  V, which gives more space for programming, but not necessarily better reliability and accuracy. The main idea in analog simulation of a dynamic system consists in building an electronic network model with the identical dynamic qualities as the original system, based upon its mathematical model. With this model as initial base the electronic model will be built up step by step, as we shall see next.

## ii) Mathematical Model

The mathematical model for the actual problem is as mentioned in Chapter II section v):

$$(A44+I44)\ddot{\phi} + B44\dot{\phi} + C44\phi + D44\phi^3 + (A42-Mz_G)\ddot{y} = (F41+F42)e^{i\omega t} \quad (1)$$

and

$$(A22+M)\ddot{y} + (A24-Mz_G)\dot{\phi} = (F21+F22)e^{i\omega t} \quad (2)$$

Normalizing by dividing by coefficients to highest derivative of  $\phi$  and  $y$  gives a new set of equations:

$$\begin{aligned} \ddot{\phi} &= \frac{F41+F42}{A44+I44} \cdot e^{i\omega t} - \frac{B44}{A44+I44} \cdot \dot{\phi} \\ &\quad - \frac{C44}{A44+I44} \cdot \phi - \frac{D44}{A44+I44} \cdot \phi^3 \\ &\quad - \frac{A42-Mz_G}{A44+I44} \cdot \ddot{y} \end{aligned} \quad (3)$$

$$\frac{d\dot{\phi}}{dt} = \ddot{\phi} \quad (4)$$

$$\frac{d\phi}{dt} = \dot{\phi} \quad (5)$$

$$\ddot{y} = \frac{F21+F22}{A22+M} \cdot e^{i\omega t} - \frac{A24+Mz_G}{A22+M} \dot{\phi} \quad (6)$$

## iii) Coefficients

In the following metric units for the coefficients will be used, and the simulation model is based on values given below.

The coefficients C44 and D44, used in the model, forming the righting moment, which in turn is a function of heeling angle in a rather complex way, need some further explanation.

The righting moment  $\Delta \cdot GZ = C44 \cdot \phi + D44 \cdot \phi^3$  is simulated by a function with the following structure:

$$\Delta \cdot GZ = (C440 + C442 \cdot H \cdot \sin(\omega t + \gamma)) \cdot \phi + D44 \cdot \phi^3 \quad (7)$$

H is wave amplitude and  $\gamma$  the phase angle between wave-excited moment and oscillating part of righting moment. This phase angle can with more or less approximation be given the value of  $+\frac{\pi}{2}$ .

Further, the value of D44 is established by the assumption that heeling moment takes the value of zero for  $\phi = 1$  radian in calm waters ( $H = 0$ ), which leads to the relation:

$$D44 = -C440 \quad (8)$$

Values of coefficients:

Coeff.	Value	Unit
A44	405	t m s <sup>2</sup>
A42	- 69	t s <sup>2</sup>
A22	42	t s <sup>2</sup> m <sup>-1</sup>
A24	- 69	t s <sup>2</sup>
B44	5	t m s
C440	413	t m
C442	45	t
I44	769	t m s <sup>2</sup>
M	66	t s <sup>2</sup> m <sup>-1</sup>
F41	10	t m
F42	54	t m
F21	2.3	t
F22	- 33	t

Values for forces and moments are given for wave amplitudes of 1 metre.

Forces and moments written as real plus imaginary functions of wave amplitudes in eqs. (1) and (2) above can easily be transformed to trigonometric functions:

$$\begin{aligned} H \cdot (F41+F42) \cdot e^{i\omega t} &= H \cdot |F41+F42| \cdot \sin t \\ &= H \cdot 55 \cdot \sin t \end{aligned} \quad (9)$$

considering that phase angle measuring uses the wave-excited moment as basis.



$$H \cdot (F21 + F22) \cdot e^{i\omega t} = H \cdot [F21 + F22] \cdot \sin(\omega t + \theta) \quad (10)$$

$$H \cdot 18.8 \cdot \sin(\omega t + \theta)$$

where  $\theta$  is the phase angle between wave-excited moment  $F4$  and the moment caused by the sway-force  $F2$ .

Using the values for  $F4$  and  $F2$  this phase angle amounts to  $-164$  deg.

The eqs. (1), (2), (3) and (4) can now be written:

$$\ddot{\phi} = .1 \cdot H \cdot .457 \cdot \sin \omega t - .00425 \dot{\phi} - .325 \phi$$

$$- .1 \cdot H \cdot .0383 (\sin \omega t + 90^\circ) \cdot \phi$$

$$+ .325 \phi^3 + .204 \ddot{y} \quad (11)$$

$$\frac{d\dot{\phi}}{dt} = \ddot{\phi} \quad (12)$$

$$\frac{d\phi}{dt} = \dot{\phi} \quad (13)$$

$$\ddot{y} = 2.22 \ddot{\phi} + .1 \cdot H \cdot 1.75 \cdot \sin(\omega t - 164^\circ) \quad (14)$$

Developing an electronic model with the same dynamic qualities as the math. model, another transformation is necessary. The variables in eqs. (11), (12), (13) and (14) express physical quantities as heeling angle, heeling velocity, heeling acceleration and sway acceleration.

These physical variables are to be represented by voltages, and therefore it is necessary to establish an electronic scale for the variables in such a way that maximum values do not exceed maximum out-put voltage for the amplifiers.

#### Scaling

Phys. vars.	Max value	Scal. fact.	Simul. vars.	Unit
$\ddot{\phi}$	rad. $s^{-2}$	.5	$[10\ddot{\phi}]$	$10V/\text{rad } s^{-2}$
$\dot{\phi}$	rad. $s^{-1}$	1	$[10\dot{\phi}]$	$10V/\text{rad } s^{-1}$
$\phi$	rad	1	$[1\phi]$	$1V/\text{rad}$
$\ddot{y}$	m $s^{-2}$	5	$[1\ddot{y}]$	$1V/m s^{-2}$

Using the variables  $[10\ddot{\phi}]$ ,  $[10\dot{\phi}]$ ,  $[1\phi]$ ,  $[1\ddot{y}]$  eqs. (5), (6), (7) and (8) will appear as:

$$[10\ddot{\phi}] = .1 \cdot H \cdot 4.57 \cdot \sin \omega t - .00425 [10\dot{\phi}]$$

$$- 3.52 [1\phi] - .1 \cdot H \cdot 3.83 \cdot \sin(\omega t + 90^\circ) \cdot [1\phi]$$

$$+ 3.52 [1\phi]^3 + 2.04 [1\ddot{y}] \quad (15)$$

$$\frac{d[10\dot{\phi}]}{dt} = [10\ddot{\phi}] \quad (16)$$

$$\frac{d[1\phi]}{dt} = .1 [10\dot{\phi}] \quad (17)$$

$$[1\ddot{y}] = .222 [10\ddot{\phi}] + .1 \cdot H \cdot 1.75 \cdot \sin(\omega t - 164^\circ) \quad (18)$$

In this form the mathematical model can be translated into a simulator diagram using ordinary symbols for simulator elements.

The simulator diagram figure 4 is divided in sections according to eqs. (15), (16), (17) and (18). The main process is executed in amplifier No. 9, where summing of the right hand terms of eq. (15) takes place. The double integration of  $\ddot{\phi}$  (out put from ampl. No. 9) takes place in amplifiers No. 1 and 2.

The term of eq. (15):

$$-3.52 [1\phi] - 1 \times H \times 3.83 \times \sin(\omega t + 90^\circ) \times [1\phi]$$

is formed by means of multiplier No. 1, potentiometers No. 4, 5 and 6 and amplifier No. 3.

The term  $3.52 \times [1\phi]^3$  is formed by multipliers No. 2 and 3 and necessary potentiometers and amplifiers and it appears as output from potentiometer No. 9. The two mentioned terms are added in amplifier No. 5 and arrives as one single voltage to amplifier No. 9. This voltage represents the righting moment divided by the total moment of inertia of ship and water.

The term  $2.04 [\ddot{y}]$  of eq. (15) appears as output from potentiometer No. 13, the voltage of which represents the moment excited by the translatory movement divided by the total moment of inertia of ship and water.

The remaining two inputs to amplifier No. 9 are wave excited moment and damping moment, which do not need further explanation.

List of potentiometers in Simulator Diagram (Figure 4)

Potm. No.	Value	
1	0 - 1	Wave amplitude
2	.457	Coefficient in eq. (15)
3	.00425	Coefficient in eq. (15)
4	.352	Coefficient in eq. (15)
5	.383	Coefficient in eq. (15)
6	0 - 1	Wave amplitude
7	0 - 1	Wave amplitude
8	.175	Coefficient in eq. (18)
9	.352	Coefficient in eq. (15)
10	.316	Multiplier constant ( $\sqrt{10}$ )
11	.316	Multiplier constant ( $\sqrt{10}$ )
12	.1	Coefficient in eq. (17)
13	.204	Coefficient in eq. (15)
14	.222	Coefficient in eq. (18)
15	-	Driver for plotter
16	.1	Amplitude for $\sin \omega t$
17	-	$\omega$
18	-	$\omega$
19	-	Delay
20	-	Delay

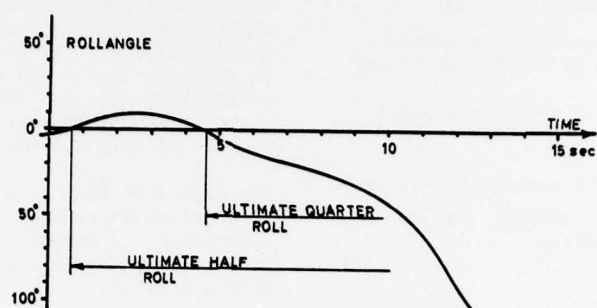


Fig. 1: The capsizing time history from the model of the "Edith Terkol" in the wave basin.

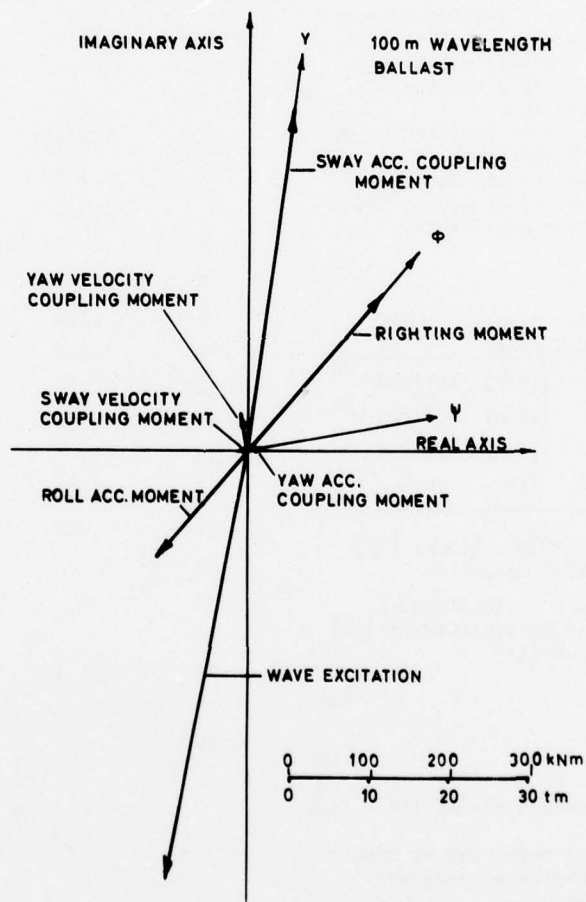


Fig. 2: The individual terms for the roll equation of motion referring to the linear case before capsizing.

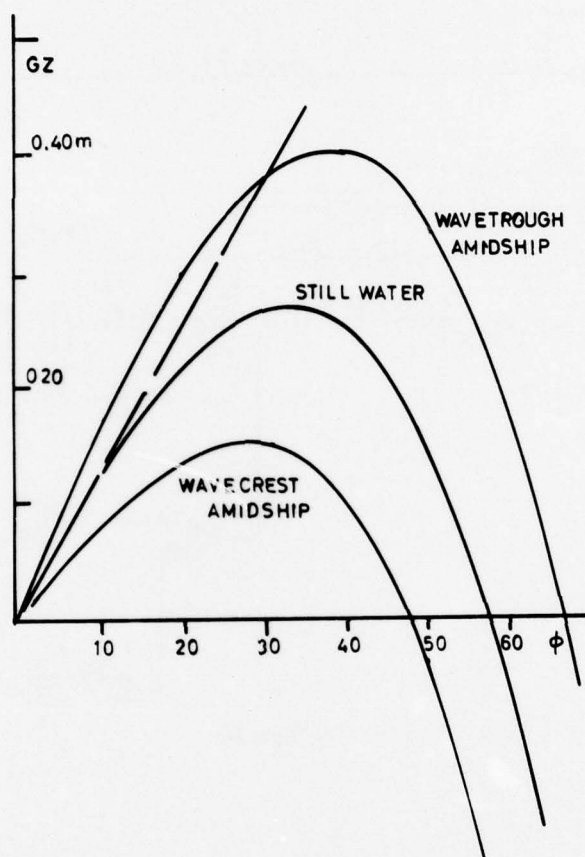


Fig. 3: The bounds within which the righting moment oscillated due to wave passage. A record from the analog computer.





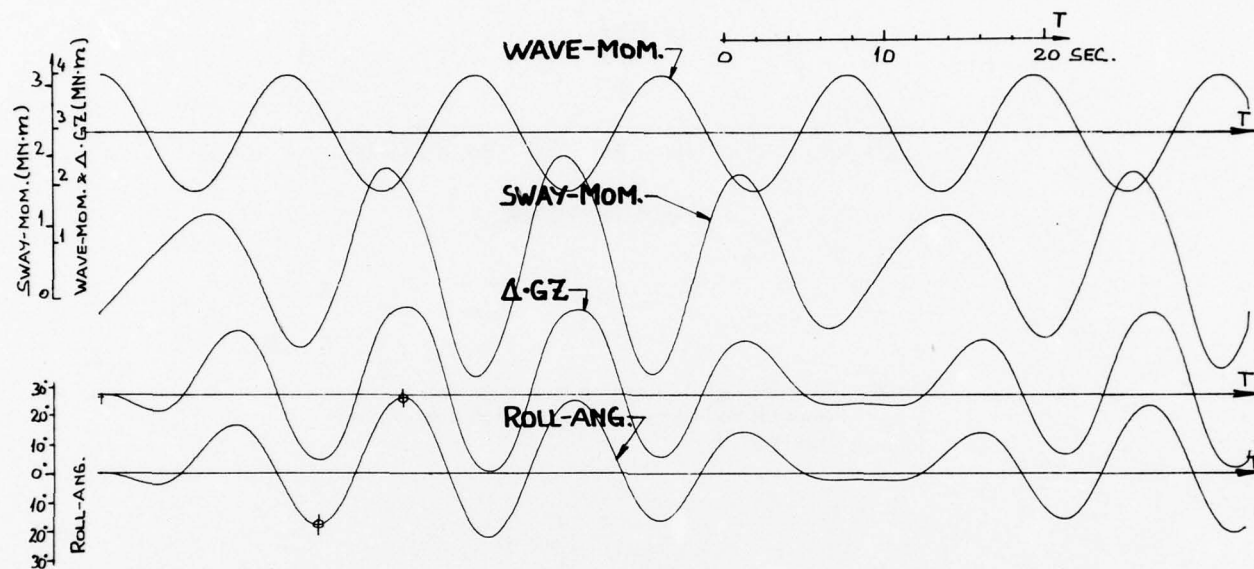


Fig. 5: The time history from the simulation of the behaviour in 4 m high waves

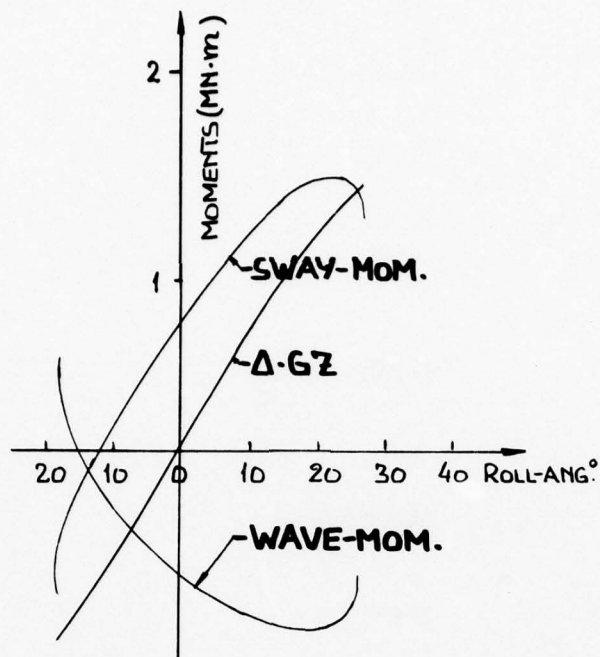


Fig. 6: A usual righting moment diagram showing the half roll between the encircled peaks in figure 5.

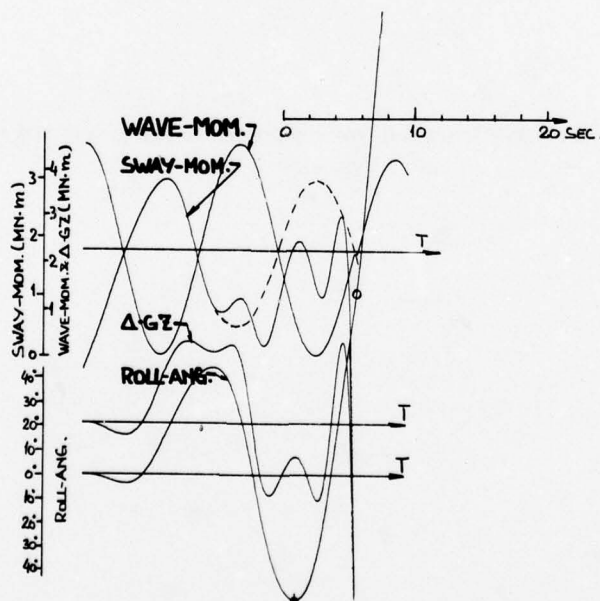


Fig. 7: The time history from the simulation of the behaviour in 5 m high waves.

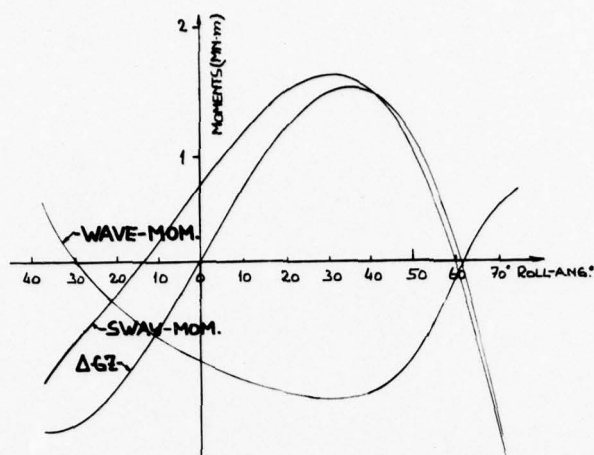


Fig. 8: A usual righting moment diagram showing the half roll to the right of the encircled peak in figure 7.

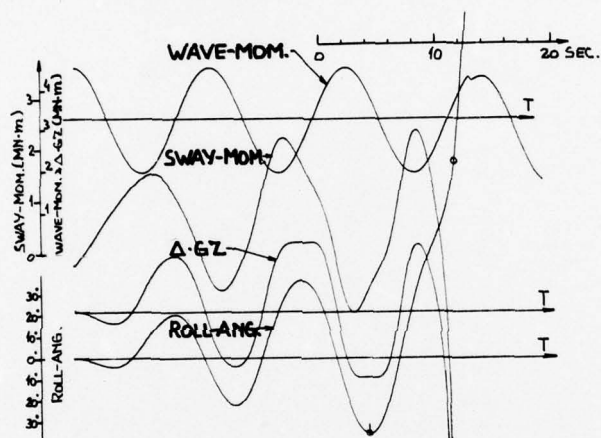


Fig. 9: The time history from the simulation of the behaviour in 9 m high waves.

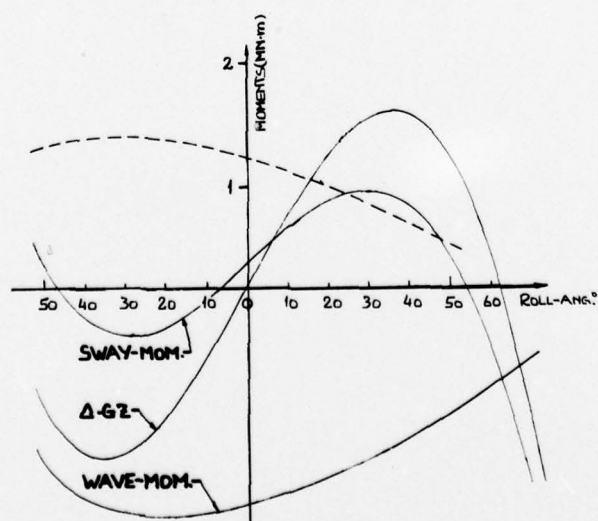


Fig. 10: A usual righting moment diagram showing the half roll to the right of the encircled peak in figure 9.

# THE ROLES OF TRANSITION, LAMINAR SEPARATION, AND TURBULENCE STIMULATION IN THE ANALYSIS OF AXISYMMETRIC BODY DRAG

JUSTIN H. McCARTHY, JOHN L. POWER, and THOMAS T. HUANG  
David W. Taylor Naval Ship Research and Development Center, Bethesda, Md. 20084 USA

## SYNOPSIS

The role of flow transition in model drag analysis is quantitatively investigated. Transition data are given for four submerged axisymmetric bodies having vastly different forebody geometries and pressure distributions. Good correlation is obtained between measured and computed locations of laminar separation and transition. Drag data are presented for each model with and without a variety of turbulence stimulators, and a new method of residual-drag analysis is developed which correctly accounts for the extent of laminar flow. It is concluded that the traditional method of analysis underpredicts residual drag and mispredicts the relative residual drags of models having different forebodies.

## INTRODUCTION

Because ship models are tested in towing tanks at Reynolds' numbers which are typically two orders of magnitude less than those occurring at full scale, laminar flow can be expected to persist over a significantly greater proportion of a smooth model hull than the prototype hull. In order that prototype drag be correctly assessed, particularly when evaluating competing forebodies having different shapes, it is essential that the extent of laminar flow be determined at model scale and/or that model experiments employ turbulence stimulators having known stimulation capabilities and known parasitic drags. The stimulation problems posed by ship models have been recognized for many years, and numerous important aspects of the subject have appeared in the Proceedings of the International Towing Tank Conferences since the early 1930's. Parallel developments can be found in the aerodynamics literature over the same period of time.

In the absence of heating, the location and nature of transition from laminar to turbulent flow on a body are a function of Reynolds' number (1), body shape (2),(3), body surface roughness (4), ambient turbulence levels (5),(6), and possibly other boundary-layer perturbations which may result from vibration or acoustic excitation. Transition is a flow process which does not necessarily occur along a sharply defined line, but over a surface region in which boundary-layer disturbances having critical frequencies grow to create flow instabilities which lead to turbulence. From a theoretical standpoint, for every body, a "neutral-stability" line may be defined downstream of which there exist critical-frequency disturbances whose amplitudes grow in space. Upstream of the "neutral-stability" line, all small disturbances are damped out. The critical frequencies and the extent of the transition region depend on body shape, i.e., pressure distribution and curvature, and Reynolds' number. Physically, transition is usually defined to take place (in a local sense) when intermittent turbulent bursting first occurs in the boundary layer.

Two types of ship-model transition may be distinguished, depending upon whether or not laminar separation occurs prior to transition. If laminar separation occurs, either as a result of body shape or by the use of an artificial "turbulence" stimulator, transition from laminar flow will usually occur immediately downstream of the separated flow region, which is of very small extent provided the Reynolds' number is sufficiently large (6),(7). For a flat plate tested with a variety of turbulence stimulators, Gatzert (8) reports a difference Reynolds' number, based on distance between turbulence stimulator location and measured transition location, of about  $10^4$ . For large ship models tested at Reynolds' numbers of  $10^7$ , the corresponding extent of the transition region is only 0.1 percent of the model's length. When laminar separation is not present, the transition process will usually take place over a larger region, whose inception distance aft of the forward perpendicular and whose extent usually increases with decreasing model Reynolds' number (9). Thus, at full scale, the transition process will occur over a proportionately much shorter distance and much closer to the forward perpendicular than at model scale, in the absence of laminar separation.

In the towing-tank investigation reported here, only the effects on laminar separation, transition and drag, of Reynolds' number, forebody shape, and local roughness, i.e., turbulence stimulators, were examined for four submerged bodies of revolution. Previous, unpublished, work in the David W. Taylor Naval Ship Research and Development Center (DTNSRDC) towing tanks indicates that for large models, and reasonable waiting times between runs, ambient turbulence, carriage vibration, and acoustic noise do not have a measurable effect on model transition. The negligible effect of towing-tank ambient turbulence on large-model transition is also reported by Prischmikhin and Poostoshny (10). The earliest known towing-tank work which clearly shows the importance of turbulence stimulation for a submerged body of revolution was reported by Amsberg in 1937 (11). In this work, model drag



data are given for the bare hull with and without wire trips of 0.2, 0.5, 0.8, and 1.0 mm diameter located at 5-percent of the model length aft of the forward perpendicular. For length Reynolds' numbers of up to  $7 \times 10^6$ , all trip wires larger than 0.2 mm resulted in model drags at least 20-percent greater than the smooth hull drag.

The principal aims of the work reported here are (1) to determine from hot-film data the nature and extent of laminar flow and transitional flow on smooth body-of-revolution models; (2) to explore the efficacy of various types and locations of turbulence stimulators for artificially tripping transition to turbulent flow; and (3) to assess the effect of stimulation technique or the absence thereof, on the analysis of drag data to determine residual (form) drag coefficient. Bodies of revolution were chosen for this investigation because of their geometric simplicity and the availability of well-developed theoretical methods for analyzing axisymmetric boundary layers. However, the results of this work have implications relative to the problem of turbulence stimulation on large surface-ship models if one considers a surface ship in terms of an equivalent body of revolution having the same longitudinal distribution of sectional areas. The end result of the paper is a "new" method for analyzing residual drag.

#### Notation

$C_F$  ... frictional drag coefficient,  $D_F/(1/2)\rho U_0^2 S$   
 $C_{F_L}(S_{x_L})$  ... laminar flow frictional drag coefficient,  $D_{F_L}/(1/2)\rho U_0^2 S_{x_L}$   
 $C_{F_t}(S_{L-x_0})$  ... turbulent flow frictional drag coefficient,  $D_{F_t}/(1/2)\rho U_0^2 S_{L-x_0}$   
 $C_p$  ... pressure coefficient,  $(p-p_0)/(1/2)\rho U_0^2$   
 $C_{PE}$  ... prismatic coefficient of forebody, forebody volume/ $\pi(D/2)^2 L_E$   
 $C_R$  ... residual drag coefficient,  $C_T - (C_F + \Delta C_T)$   
 $C_D$  ... total drag coefficient,  $D_T/(1/2)\rho U_0^2 S$   
 $\Delta C_D$  ... local drag coefficient of trip,  $\Delta D/(1/2)\rho U_0^2 S$   
 $\Delta C_T$  ... drag coefficient of trip,  $\Delta D_T/(1/2)\rho U_0^2 S$   
 $D$  ... maximum diameter of body  
 $D_F$  ... frictional drag of body,  $D_{F_L} + D_{F_t}$   
 $D_{F_L}$  ... laminar flow frictional drag of body  
 $D_{F_t}$  ... turbulent flow frictional drag of body  
 $D_T$  ... total drag of body  
 $\Delta D$  ... local drag of trip,  $\Delta D_T \sec \alpha_k$   
 $\Delta D_T$  ... drag of trip  
 $A$  ... spatial amplification ratio of disturbance  
 $k$  ... roughness or trip height  
 $L$  ... overall body length  
 $L_E$  ... forebody length of entrance  
 $L_M$  ... length of parallel middle body  
 $p$  ... local pressure on body surface  
 $p_0$  ... ambient pressure  
 $r$  ... local body radius (offset)  
 $r_k$  ... local body radius at trip location  
 $RD$  ... Reynolds' number based on diameter,  $U_0 D/\nu$   
 $R_k$  ... Reynolds number based on trip height,  $U_k k/\nu$   
 $RL$  ... Reynolds' number based on total length,  $U_0 L/\nu$   
 $R_{x_2-x_1}$  ... Reynolds' number based on distance  $(x_2-x_1)$ ,  $U_0(x_2-x_1)/\nu$   
 $R_{\theta x}$  ... Reynolds' number based on momentum thickness,  $U_0 \theta_x/\nu$   
 $s$  ... distance along body meridian  
 $S$  ... total surface area of body  
 $S_{x_2-x_1}$  ... body surface area between  $x_2$  and  $x_1$

$U$  ... potential flow velocity on body surface  
 $U_0$  ... body speed  
 $U_k$  ... velocity at distance  $k$  from body surface  
 $x$  ... axial distance from leading edge of body  
 $x_L$  ... axial extent of laminar flow  
 $x_0$  ... virtual origin of turbulence  
 $\alpha$  ... angle between  $x$ -axis and tangent to body meridian  
 $\alpha_k$  ... value of  $\alpha$  at trip location  
 $\beta$  ... ratio,  $(R_{x_L-x_0}/R_L)/(S_{x_L-x_0}/S)$   
 $\delta^*$  ... boundary-layer displacement thickness  
 $\theta$  ... boundary layer momentum thickness  
 $\lambda$  ... pressure-gradient parameter,  $(\theta^2/\nu)dU/ds$   
 $\nu$  ... kinematic viscosity  
 $\rho$  ... mass density of fluid  
 $\tau$  ... surface shear stress  
 $\omega$  ... frequency of disturbance  
 $\omega_{N.S.}$  ... frequency of disturbance at neutral stability

#### BODY OF REVOLUTION MODELS

Following an extensive computer evaluation of the flow characteristics of bodies of revolution, four axisymmetric forebodies, having bow-entrance length/diameter ratios ( $L_E/D$ ) of 0.5, 1.0, 1.82, and 3.0, were selected for experimental investigation (Figure 1 and Table 1). Forebody prismatic ratios ( $C_{PE}$ ) were fixed at a constant value of 0.667. For each forebody, the total hull volume was held constant by varying the length of parallel middle body ( $L_M$ ) which connected each forebody to an existing streamlined afterbody model, having a maximum diameter ( $D$ ) of slightly more than 0.6 meters. Total model lengths ( $L$ ) varied between 6.7 and 7.3 meters, with the bluntest model ( $L_E/D = 0.5$ ) having about 2-percent less wetted surface area ( $S$ ) than the finest model ( $L_E/D = 3.0$ ).

The bluntest forebody ( $L_E/D = 0.5$ ) is hemispherical in shape, with nondimensional offsets,  $\eta = 2r/D$ , given in terms of nondimensional distance  $\xi = x/L_E$ , by:

$$\eta^2 = 1 - (\xi - 1)^2$$

The offsets of the three remaining forebodies are described in terms of Granville's family of polynomials (12) by the expression

$$\eta^2 = 0.833 R(\xi) + 10 \bar{K}_1(\xi) + Q(\xi)$$

where  $R(\xi) = 2\xi(\xi-1)^4$ ,  $\bar{K}_1(\xi) = \frac{1}{3}\xi^2(\xi-1)^3$ ,  
 $Q(\xi) = 1 - (\xi-1)^4(4\xi+1)$ .

The particular choices made for coefficients insure that  $C_{PE} = 0.667$ , and that the slopes and curvatures of the forebody profiles are continuous along their entire lengths including at their points of intersection with the parallel middle body.

The distributions of pressure coefficient,  $C_p = (p-p_0)/(1/2)\rho U_0^2$ , on the four forebodies, calculated by the Hess-Smith potential-flow computer program for an unbounded incompressible fluid (13), are shown in Figure 2. As could be expected, the magnitudes of the suction peaks and the subsequent adverse pressure gradients increase dramatically with increasing forebody fullness, i.e., decreasing  $L_E/D$ . The corresponding distributions of laminar boundary-layer pressure-gradient parameter,  $\lambda = (\theta^2/\nu)(dU/ds)$ , are shown in

Figure 3. Here,  $U$  and  $s$  are respectively the potential flow velocity and distance along a forebody meridian,  $\nu$  is kinematic viscosity and  $\theta$  is the momentum thickness of the axisymmetric laminar boundary layer, which was computed by Granville's integral method for bodies of revolution (14). Making use of Curle and Skan's modified Thwaites' criterion for laminar separation (15), i.e.  $\lambda = -0.09$  at separation, the two fullest forebodies having  $L_E/D = 0.5$  and  $1.0$  are predicted to have laminar separation in the very adverse pressure-gradient regions at short distances aft of their minimum pressure troughs, respectively at locations of  $x/D = 0.47$  and  $0.89$  (Figure 3). The two finer forebodies having  $L_E/D = 1.82$  and  $3.0$  are not predicted to have laminar separation.

Each forebody, together with a portion of its parallel middle body, was constructed of molded fiberglass; specified profile tolerances were held to less than  $\pm 0.4$  millimeters, all imperfections were removed, meridians were faired, and the fiberglass was polished to a  $0.64$  micron rms surface finish. According to Feindt's experimental data (4), uniform sand-grain roughness of height  $k$ , with flow velocity  $U$  at the edge of the boundary layer, will not prematurely trip transition from laminar to turbulent flow if the roughness Reynolds' number  $R_k' = Uk/\nu$  is less than  $120$ . Since a  $0.64$  micron rms surface finish resulted in values of  $R_k'$  two orders of magnitude less than  $120$ , distributed surface roughness should not have been a factor in the forebody transition experiments described here.

#### EXPERIMENTAL TECHNIQUE

For each forebody, towing tank experiments were conducted from Carriage II of the David Taylor Model Basin\* to determine model drag and the extents of the laminar-transitional-turbulent flow regimes, with and without turbulence trips installed. The speed range covered was  $0.5$  to  $5.1$  meters/sec, with most data collected at  $1/4$ -meters/sec intervals proceeding from lower to higher speeds. A wait time of  $5$  minutes between runs was selected because no effects of residual turbulence from preceding runs could be detected after this time. For each model, the centerline submergence depth was fixed at  $2.74$  meters, aligned for zero pitch and zero yaw angle. The models were ballasted for a slight amount of negative buoyancy with zero moment at the towing strut. Throughout the experiments, water temperatures were monitored so that accurate values of kinematic viscosity could be determined.

Total drag was measured by the standard DTNSRDC block-gage-type dynamometer, mounted internal to each model and bolted to a single streamlined strut, located at roughly amidships. This dynamometer has an accuracy of approximately  $1$  percent at its maximum load capability of  $55$  kilograms. At towing speeds above about  $3$  meters/sec, each model began to exhibit some Froude-number dependent, surface wave-making drag. Previous work has shown that the towing-strut, model interference drag coefficient is less than  $0.01 \times 10^{-3}$  for the size of models investigated here.

\* This basin is  $846$  meters long,  $15.5$  meters wide, and  $6.7$  meters deep.

Since this interference drag is within the experimental accuracy of model drag data reported here, no corrections have been made for it.

The extents of the laminar, transitional, and turbulent flow regimes, and the stimulation effectiveness of turbulence trips, were determined in the towing tank by qualitative analysis of the signals from seven to nine constant-temperature hot films flush-mounted on each forebody. Selection of hot film locations, listed in Table 1, was assisted by calculation of transition locations using Granville's method (16) and the Curle-Skan laminar-separation criterion (15) shown in Figure 3. The hot film probes were made by Ling-Tronics Laboratory. The active elements (platinum) were approximately  $1.6$  millimeters long, fixed to one end of a pyrex cylinder  $12.7$  millimeters long and  $2.4$  millimeters in diameter. The cylinders were carefully mounted in pre-drilled holes in the model surfaces and held in place with rubber cement. Any ridge between the model surface and the probe was held to less than  $0.025$  millimeters, and the holes in the model were drilled perpendicular to the surface  $\pm 0.50$  degrees. As a further precaution, each probe was located along a different meridian streamline, to avoid possible spurious signals which might result from tripping of turbulence by probes located at successively further forward positions.

Five channels of instrumentation were available and interchangeable between hot films, allowing the five most significant probes to be activated during a given run. Each channel consisted of an anemometer, linearizer, oscilloscope, and attenuator. For each speed,  $20$ -second samples of hot-film output were recorded on a tape recorder. The output of each channel was kept close to but less than the  $1.4$ -volt overload capacity of the recorder by adjusting the overload ratios of the films, the linearizer amplifiers, and the attenuators. Overheat ratios were kept between  $1.035$  and  $1.050$  for most of the tests but for some of the low-speed runs, slightly higher ratios were needed. Since these adjustments had to be made quickly, as the carriage moved down the basin, no record of amplifications or overheat ratios could be kept. Thus, the information obtained from the hot films was primarily qualitative and was used to determine the nature of the flow at the hot-film locations.

As shown in Figure 4, analysis of the hot-film output signals revealed that four different types of boundary-layer flow could be distinguished: (1) laminar flow, where the hot-film signals were of steady amplitude; (2) a smooth wave-like disturbance of identifiable frequency content, superimposed on a laminar flow, and no doubt associated with Tollmien-Schlichting waves (17); (3) an intermittent turbulent bursting flow of the type reported by Schubauer and Klebanoff (18), preceded and followed in time by periods of type (2) flow; and (4) a fully-turbulent flow of random nature. Under fixed test conditions, probe outputs indicated that types (2) or (3) and types (3) or (4) could alternatively occur on repeat-run tape-recorded time-samples of the signal at a given probe location. This is no doubt a result of the well-known fickle nature of the flow transition process.



In addition to the towing-tank work, oil-film experiments were conducted for two of the axisymmetric bodies (Models 4620-2 and 4620-3) in DTNSRDC's Anechoic Wind Tunnel.\* In these experiments supplemental flow-visualization information was obtained on the transition process and on the longitudinal extent of the laminar-separation region on Model 4620-2. A thin film of SAE-10 oil with phosphorescent additive\*\* was painted on each forebody, and following a constant speed run, photographs were taken to show the relative wiping of oil from the model's surface. As is well-known, separated regions are characterized by large concentrations of oil, and turbulent regions by areas which are wiped clean of oil. Transition regions are characterized by a partial wiping of oil.

#### TRANSITION ON THE SMOOTH FOREBODIES

As shown in Figure 5, for the two fullest forebodies having  $L_E/D = 0.5$  and  $L_E/D = 1.0$ , the hot-film signals indicated that the turbulent flow existed at every probe location downstream of the predicted positions (Figure 3) of laminar separation, over the entire 5.1 meter/sec speed range of the two models. Laminar flow occurred at all probes forward of the predicted positions of laminar separation for all speeds, and the intermediate type (2) or type (3) flows were not observed. Because of the different probe locations on the two forebodies, it is seen from Figure 5 that on one model ( $L_E/D = 0.5$ ) turbulent flow existed immediately aft of the predicted separation location, and on the other model ( $L_E/D = 1.0$ ) laminar flow persisted until immediately forward of the predicted separation location. Wind-tunnel oil-film experiments on the  $L_E/D = 1.0$  forebody verified the predicted location of laminar separation and showed that the length of the separation bubble was about 12 millimeters, or 0.2 percent of the total body length. These findings are consistent with laminar separation data reported by Arakeri (7) for axisymmetric head forms. Thus, for the quite high Reynolds numbers,  $3 \times 10^6 \leq R_L = U_0 L / \nu \leq 4 \times 10^7$ , covered by the present experiments, it may be inferred that laminar separation occurs very close to where predicted, and that the extent of the separated laminar region over which transition from laminar to turbulent flow occurs is exceedingly short. In subsequent analyses of drag, the locations of transition,  $x_t$ , will be taken as the predicted separation locations:  $x_t/L = 0.044$  for the  $L_E/D = 0.5$  forebody, and  $x_t/L = 0.082$  for the  $L_E/D = 1.0$  forebody.

The measured flow regimes on the two finest forebodies,  $L_E/D = 1.82$  and  $L_E/D = 3.0$ , are shown on Figures 6 and 7. For the fuller forebody (Figure 6), laminar flow appears to persist until locations aft of the minimum pressure point over the entire Reynolds' number range. For the finer forebody, laminar flow appears to persist to a still further-aft hull location at least for values of  $R_D$  under about  $2.5 \times 10^6$  (Figure 7); above values of  $R_D$  of about  $1.5 \times 10^6$  laminar flow terminates forward of the finer body's minimum-pressure point. For these two models, which do not have laminar separation, the figures show

well-defined, extended transition regions involving measureable intermediate-flows consisting of wave-like disturbances and intermittent turbulent bursting prior to becoming fully turbulent. At the highest Reynolds numbers at which the two finest models were tested, transition occurs at about 9-percent of model length aft of the forward perpendicular. This is significantly further aft than the typical 5-percent location of turbulence stimulators normally employed on ship models.

While the above facts, together with many more facts derivable from Figures 6 and 7, can be discussed and rationalized by comparing the extents and severities of the favorable and adverse pressure-gradient regions of the two models, arguments are soon lost in a complex sea of words. Because of the resulting confusion, further discussion will be confined to a comparison of the data with predictions of transition calculated by (1) the Smith-Gamberoni method (19)(20), and (2) the Granville method (16):

(1) The Smith-Gamberoni method applies to smooth, convex, two-dimensional or (by Mangler transformation) axisymmetric bodies in low-turbulence onset flows. It proceeds from a detailed numerical solution of the (linear) Orr-Sommerfeld equation for the amplification growth-rate of small, two-dimensional, Tollmein-Schlichting-type disturbance waves in a laminar boundary layer. When the ratio of the amplitude of a disturbance at some frequency to its amplitude at the neutral-stability line exceeds a certain empirically-determined value, transition is assumed to occur, i.e., intermittent turbulent bursting will begin. Smith (20) recommends a spatial amplification ratio of about  $e^9$  to predict the location of transition on two-dimensional bodies.

(2) The Granville method applies to axisymmetric bodies and starts with a theoretically-calculated neutral-stability line. Prediction of the location of transition downstream of this line is based on a simple empirical correlation of the calculated differences between the momentum-thickness Reynolds' numbers at the neutral stability and the measured transition locations, with the local profile slope of the body at transition. The experimental data used in arriving at a correlation line for low-turbulence onset flows are limited to axisymmetric bodies without parallel middle body, and without adverse pressure gradients on their forebodies.

The calculated locations of the neutral-stability curves for the two finest forebodies are shown in Figures 6 and 7; they lie well inside of the laminar flow regions sensed by the hot-film probes. The predicted locations of transition according to Granville's correlation line for low-turbulence onset flows, together with three Smith-Gamberoni predictions, corresponding to spatial amplification ratios of  $e^9$ ,  $e^{11}$ , and  $e^{13}$ , are also shown in Figures 6 and 7. For both forebodies, there is remarkably excellent agreement between the measured inception of intermittent turbulent bursting, i.e. transition, and the  $e^{11}$  Smith-Gamberoni amplification curve. The  $e^9$  curve appears to coincide most closely with the measured inception of type (2) wave-like disturbances; the  $e^{13}$  curve correlates very well with the measured inception of fully-turbulent type (4) flow. As could have been expected, the Granville transition predictions are far better for the  $L_E/D = 3.0$  forebody than for the  $L_E/D = 1.82$  forebody,

\* This tunnel has a 2.4 meter x 2.4 meter rectangular test section, with champhered corners.

\*\* Additive FA-109, American Gas and Chemical, Co.

because transition at values of  $R_D$  above about  $1.2 \times 10^6$  occurs in a favorable pressure gradient or a weak adverse pressure-gradient region well forward of the parallel middle body. For the  $L_E/D = 1.82$  forebody, the prediction is poor because transition takes place in a distinctly adverse pressure-gradient region, for which case the Granville correlation does not apply.

In order to further validate the inherent reliability of the Smith-Gamberoni prediction method, Figure 8 shows a comparison between a narrow-band analysis of the frequency distribution of measured spectral energy at one hot film location and the calculated values of amplification ratios of initial disturbances of arbitrary frequency. The experimental distributions are given at four speeds, as sensed by Probe 6 ( $x/D = 1.58$ ) on the  $L_E/D = 1.82$  forebody. The real-time signals from this probe were previously shown in Figure 4, and cover a range of intermediate type (2) and type (3) flow regimes. In Figure 8, the measured spectral densities have been normalized with respect to the spectral density at the frequency having maximum energy. The calculated energy distributions of disturbance growth are plotted in terms of  $(A/A_{\max})^2$  where  $A$  is the predicted spatial amplification ratio at a given disturbance frequency. The correlation between prediction and experiment is excellent for the speeds shown in Figure 8, and it is noted that there is a relatively narrow frequency-bandwidth for the critical disturbances which have undergone significant amplification at a given speed. Above and below the frequency ranges shown in Figure 8, both experiment and calculation indicated no growth of disturbances. As shown in Figure 9, the frequency  $\omega_{A_{\max}}$  of the disturbance which is most amplified increases linearly with speed. Calculated estimates of the critical  $\omega_{N.S.}$ , at neutral stability, which are also shown on Figure 9, are roughly four times higher than the frequencies of disturbances which grow significantly immediately prior to transition.

As will be discussed below, ship-model experimenters typically require that model transition occur at least as far forward as  $x/L = 0.05$  in order to be able to make meaningful extrapolations of model drag data to full-scale drag predictions. For the bluntest forebody having  $L_E/D = 0.5$ , this requirement is met over the entire speed range as a result of laminar separation which occurs at  $x/L = 0.044$ . For the next bluntest forebody, having  $L_E/D = 1.0$ , transition occurred also as a result of laminar separation, at  $x/L = 0.082$ . To move transition further forward, within the 5 meters/sec model speed range, requires the use of turbulence stimulators. The same is true of the  $L_E/D = 1.82$  forebody, and it is unlikely, given the very steep slope of the  $e^{11}$  transition curve shown in Figure 6, that a reasonable increase in model speed above 5 meters/sec would shift transition to a position as far forward as  $x/L = 0.05$ . In the case of the finest forebody,  $L_E/D = 3.0$ , extrapolation of the  $e^{11}$  transition curve on Figure 7 indicates that the transition location will move to  $x/L = 0.05$  at a model speed of about 6.7 meters/sec.

#### TURBULENCE STIMULATOR EVALUATION

Three types of turbulence stimulators commonly

used in towing-tank work were experimentally evaluated on the  $L_E/D = 1.82$  forebody model. As listed in Table 2, these included 12.7-mm wide sand strips of three coarsenesses, circular wires of three diameters, and studs having a configuration recommended by Hughes and Allen (3). Densely-packed strips of sand-grain roughness were achieved by sprinkling sand on a circumferential strip of wet varnish; local drops of epoxy glue were used to fasten the studs and wires to the model. Drag and hot-film measurements were made over a 0.8-5.1 meters/sec speed range for each stimulator located at  $x/L = 0.05$ ; additional runs were made for the wire trips located further forward at  $x/L = 0.02$ . The hot-film locations in the region of the trips are given by  $x/L = 0.026$ , 0.040, and 0.055 (see Table 1), thus insuring a determination of the flow regimes immediately downstream of the trips.

Except for the finest sand strip and the finest trip wire, the hot-film signals indicated the existence of fully-turbulent flow at all probe locations downstream of the turbulence stimulators for all speeds above about 1.3 meters/sec. For the finest sand strip and the finest wire, speeds in excess of about 2.6 meters/sec were required in order to develop fully-turbulent flow at all probe locations downstream of the trips. At lower speeds type (3) intermittent turbulent bursting was observed at the probe immediately downstream of these trips.

The stimulation ineffectiveness of the finest grit and finest wire at the lower speeds can be explained by reference to the work of Preston (21) on wire trips, and the work of Braslow, Hicks and Harris (22) on sand strips. Here, stimulators are characterized by a roughness Reynolds' number,  $R_k = u_k k / \nu$ , where  $u_k$  is the local boundary-layer velocity at stimulator height  $k$ . In both works a critical  $R_k$  of 600 is recommended to determine the minimum-size trip necessary to cause rapid transition to fully-turbulent flow without incurring significant parasitic trip drag. Preston's recommendation is based on an analysis of experimental data obtained by Dutton (23) for wire trips placed near the leading edge of a flat plate. In the work on sand strips (22), which were tested on several airplane models at subsonic speeds, it was found that  $R_k$ 's of up to about 1200 did not add appreciable parasitic drag, and furthermore could be essential to trip transition at length Reynolds' number (up to the trip location) of less than about  $10^5$ .

Related analyses by Tani (24), (25) of turbulence stimulation data indicate that a critical  $R_k$  of between 600 to 830 is required in order to have transition occur very close to either two- or three-dimensional trips. Tani also found that increased ambient turbulence-levels reduced the critical value of  $R_k$ . In the special case of three-dimensional trips Braslow (26) has concluded that body pressure gradient, i.e. a shape which delays natural transition, does not appear to affect the critical value of  $R_k$ . For two-dimensional trips, having values of  $R_k$  less than 600 body shape can have an effect on turbulence stimulation because body pressure gradient can control the growth of Tollmien-Schlichting waves which have been observed by Klebanoff and Tidstrom (27) downstream of wire trips placed on a flat plate. For effective three-dimensional trips, turbulent bursts appear in the wakes of



the 3-D roughnesses with no opportunity for two-dimensional stability arguments to apply (26). While the precise value of the critical  $R_k$  can be expected to vary somewhat with trip geometry, body shape and ambient free-stream turbulence levels and spectra, a benchmark value of 600 is probably adequate in most cases.

Table 2 lists values of  $R_k$  at two model speeds for all of the stimulators tested on the  $L_F/D = 1.82$  forebody. Values of  $u_k$  for determining  $R_k$  were obtained from Pohlhausen's one-parameter family of velocity profiles (18), using laminar boundary-layer parameters calculated by the method of reference (14). As seen in Table 2, all stimulators but the finest grit and finest wire had  $R_k$ 's greater than the nominal critical value of 600; this correlates well with the hot-film measurements which indicated fully-turbulent flow downstream of the trips. At model speeds of less than 2 meters/sec the finest grit and finest wire had  $R_k$ 's significantly below 600; this correlates well with the hot-film data which indicated intermittent turbulent bursting downstream of these trips at low speeds.

It remains now to evaluate the relative parasitic drags of the various turbulence stimulators. Figures 10 through 13 show plots of the measured total drag coefficients,  $C_T = D_T/(1/2)\rho U_0^2 S$ , versus Reynolds' number,  $R_L = U_0 L/\nu$ , for the  $L_F/D = 1.82$  forebody model with and without the three different types of turbulence stimulators fitted. For comparison purposes, the Schoenherr line of frictional resistance coefficient,  $C_f$ , for turbulent flow over flat plates (28), is also shown on all of these figures. The Schoenherr friction line is described by the expression

$$\sqrt{C_f} \log_{10} (RLCF) = 0.242.$$

For  $R_L < 24 \times 10^6$  the smooth-hull  $C_T$  curve falls below the Schoenherr line because of the previously-discussed extensive region of laminar flow on the forebody. For all turbulence stimulators but the finest sand strip and finest wire, the  $C_T$  curves lie well above the  $C_f$  line because of the increased extent of turbulent flow, and the parasitic drag of the trips. Below a Reynolds' number of about  $18 \times 10^6$ , the tripped and untripped  $C_T$  curves roughly parallel the  $C_f$  line, except for the finest sand and wire trips. At higher Reynolds' numbers, Froude-number-dependent wave-making resistance causes the value of  $C_T$  to increase. The above drag observations are consistent with the hot-film measurements, which as previously noted, indicated turbulent flow immediately downstream of all but the finest sand and wire turbulence stimulators.

Figures 10 and 11, which show  $C_T$  curves for trip wires located at  $x/L$  values of 5 and 2 percent, respectively, indicate that parasitic drag increases substantially with increasing wire thickness. At the 2-percent location differences between the  $C_T$  curves for the three trip wires are not so great as at the 5-percent location because the wires have a smaller circumference and the forebody profile slope is larger at the further forward position. Figure 12, which shows  $C_T$  curves for sand strips located at an  $x/L$  location of 5 percent, indicates that the increase in parasitic drag with increasing sand-grain coarseness is not as great as for a comparable increase in trip-wire thickness. The smaller spread in sand strip drags probably results from their

densely-packed somewhat three-dimensional nature, as opposed to the two-dimensional barrier formed by the trip wires.

Finally, Figure 13 shows, for comparison purposes, the  $C_T$  curves for the stud trips, the medium-coarseness sand strip, and the 0.610-mm trip wire, each at an  $x/L$  location of 5 percent. All of these trips have roughly the same parasitic drag, although at the lower Reynolds' numbers the sand strip and studs appear to give slightly less drag than the wire trip. Thus, for these three particular stimulator geometries and heights which are commonly used in ship-model experiments, no one of them is to be preferred above the others from a parasitic-drag standpoint. This is not to say that the parasitic drag of any of these trips could not be reduced by selectively reducing their heights. As indicated in Table 2, the values of  $R_k$  for each of these trips at model speeds above 2 meters/sec are at least twice the nominal critical  $R_k$  value of 600; thus, some reduction in trip heights could be made without impairing turbulence-stimulation effectiveness. If, from a practical viewpoint, only one size of trip can be installed for turbulence stimulation over a model's entire speed range, then the lower limit on trip height will be determined by its effectiveness at the lower model speeds. At higher model speeds, this trip's parasitic drag will be significant.

For more than two decades, it has been recognized that the ideal stimulator should incur negligible parasitic drag and should trip turbulence as "naturally" as possible. The question of which type of stimulator best satisfies the ideal has been hotly contested for as many years with different laboratories choosing different types of stimulators depending on their unique experiences. The problem of the ideal stimulator has never really been resolved and will not be resolved definitively here.

As far as trip drag is concerned, it is evident from the preceding discussion that all of the effective stimulators investigated here do have measureable parasitic drags which must be accounted for when analyzing body drag. While the investigations of Tani (24), Von Doenhoff and Braslow (29), and Klebanoff, Schubauer and Tidstrom (30) all indicate that two-dimensional trips are more effective in stimulating transition than three-dimensional trips, a smaller-sized two-dimensional trip will result in about the same parasitic drag as an equally-effective larger-sized three-dimensional trip. The latter point concerning parasitic drag is illustrated by comparison of total model drags shown in Figure 13 for both two- and three-dimensional trips.

As far as the "naturalness" of artificial tripping of transition is concerned, the early flat-plate experiments of Klebanoff and Diehl (31) indicate, for trip Reynolds' numbers  $R_k$  in the range of 1000 to 2000, that some distance is required downstream of both two-dimensional wire trips and three-dimensional sand paper trips before the character of the measured mean velocity profiles and spectra of longitudinal velocity fluctuations agree with data obtained for untripped boundary layers which have undergone natural transition. For this range of  $R_k$ 's, similarity velocity profiles were achieved in less distance aft of the two-dimensional trip than for the three-dimensional trip. The distance required for the turbulence

spectra to become similar was about the same for both types of trips. As mentioned earlier, for  $R_k < 600$  two-dimensional trips do give rise to Tollmein-Schlichting waves (28), which are observed to occur during natural transition, whereas three-dimensional trips have not been observed to produce Tollmien-Schlichting waves (26). For values of  $R_k$  above the nominal critical value of 600, when transition occurs very close to the trip, the presence or absence of Tollmein-Schlichting waves is probably not relevant to the choice of turbulence stimulator for model drag experiments. Thus, for  $R_k > 600$ , there does not appear to be much merit in choosing one type of trip over another from the standpoint of "naturalness" of transition.

Because neither two-dimensional or three-dimensional trips are to be distinctly preferred, one over the other, from either a parasitic drag or "naturalness" of transition standpoint, the choice of a two-dimensional trip wire for all of the remaining body-of-revolution experiments reported here was based on other considerations. The reasons for the final choice of a trip wire are as follows:

(1) The geometry of a trip wire is precisely defined and fixed. For sand-grain trips, it is difficult, if not impossible, to reproduce a given geometric arrangement.

(2) Much more parasitic-drag data is available for wire trips than for other types of turbulence stimulators. This is an important point when assessing the various components of model drag.

(3) From a practical standpoint, a trip wire is easier to install and remove from a body-of-revolution model than either the stud or sand-grain type turbulence stimulators. This advantage for the trip wire would apply for other types of two-dimensional trips not investigated in this study.

The 0.610-mm diameter wire trip was chosen for all of the remaining experiments because, of the three wires investigated, this was the smallest wire diameter shown to stimulate turbulence over the entire speed range of the model. While a somewhat smaller diameter probably would have sufficed, experiments were not conducted to determine the minimum diameter required.

The following section presents the method developed for analyzing experimental data to determine body drag components.

#### ANALYSIS OF DRAG COMPONENTS

The total resistance coefficient,  $C_T$ , of a smooth ship model may be divided into three components of drag coefficient:

$$C_T = C_F + C_R + \Delta C_T \quad (1)$$

where,

$$C_T = \frac{D_T}{(1/2)\rho U_0^2 S}, \quad C_F = \frac{D_F}{(1/2)\rho U_0^2 S},$$

$$\Delta C_T = \frac{\Delta D_T}{(1/2)\rho U_0^2 S}, \text{ and } C_R = C_T - (C_F + \Delta C_T).$$

Here,  $C_F$  is the frictional drag coefficient resulting from viscous shear forces applied tangentially to the hull;  $\Delta C_T$  is the coefficient of parasitic drag of a turbulence stimulator; and  $C_R$  is the residual drag coefficient resulting from normal pressure forces acting on the hull.  $C_R$  may be subdivided into components arising from viscous effects (viz. form drag) and free-surface effects (viz. wave-making drag). For deeply-submerged bodies, or bodies operating at sufficiently small Froude numbers,  $C_R$  reduces to a coefficient of form drag. Towing-strut interference drag, which is negligible in the present investigation, can be easily introduced into (1) when it is important to do so.

The entire purpose of conducting model resistance experiments is to determine  $C_R$  from measured values of  $C_T$  and given empirical information on the values of  $C_F$  and  $\Delta C_T$ . Empirical knowledge of  $C_R$  is the baseline for prediction of full-scale ship resistance from model experiments. Starting with Froude in about 1868, it has been traditionally assumed that  $C_F$  can be closely approximated by the frictional resistance of an equivalent flat plate operating at the same length Reynolds' number as the model hull. For many years, the particular semi-empirical formulae which have been used for calculating  $C_F$  have assumed a fully-turbulent, flat-plate boundary-layer flow. For models having significant extents of laminar flow, these formulae will overestimate the value of  $C_F$  and lead to underestimates of the value of  $C_R$ .

For experiments employing turbulence stimulators located near a model's forward perpendicular, the diminution of frictional drag due to laminar flow upstream of the trip has generally been neglected in determining  $C_F$ . As for the determination of  $\Delta C_T$ , it has been commonly assumed that  $\Delta C_T$  can be closely approximated by the difference between the measured values of model  $C_T$ , with and without a trip installed, at the highest model speeds investigated. In order for this method to be valid, natural transition on the untripped model must occur as far forward as on the tripped model, at the highest model speeds. The present work has shown that this requirement is not generally satisfied. The purpose of the following drag analysis is to outline a method which accounts for the extents of laminar flow on model hulls and the effect of stimulation drag on the determination of  $C_T$  and  $C_R$ . The problem of predicting  $C_T$  for a full-scale ship, having determined a model's  $C_R$ , will not be addressed, although the methodology developed here can be adapted to full-scale resistance prediction procedures currently in use.

For analysis purposes, it will be assumed that only two types of flow regimes exist on a model hull: laminar (subscript  $l$ ) and turbulent (subscript  $t$ ). When a significant extent of transitional flow exists on a hull, the longitudinal extent,  $x_l$ , of the laminar flow regime, having wetted area  $S_{x_l}$ , will be assumed to terminate at locations where intermittent turbulent bursting first occurs. When an effective turbulence stimulator is fitted to the model,  $x_l$  will be assumed to coincide with the trip location. For a bare hull, (i.e.  $\Delta D_T = 0$ ) the cumulative frictional drag,  $D_F(x)$ , in moving aft from  $x = 0$  will be



continuous at  $x = x_L$ . When the boundary layer is tripped, a local jump in drag,  $\Delta D_T$ , occurs at  $x = x_L$ . As illustrated in Figure 14, a virtual origin  $x_0 < x_L$  may be defined for the turbulent flow region, such that the sum of the model's total friction drag,  $D_F$ , and the trip's parasitic drag,  $\Delta D_T$ , is given by:

$$D_F + \Delta D_T = D_{F_t}(S_{L-x_0}); \quad (2)$$

here,  $D_{F_t}(S_{L-x_0})$  is the frictional drag due to turbulent flow over the wetted area,  $S_{L-x_0}$ , extending from the virtual origin of turbulence at  $x = x_0$  to the after end of the model at  $x = L$ . Substitution of (2) into (1) yields a formula for  $C_R$  given by:

$$C_R = C_T - C_{F_t}(S_{L-x_0}) \frac{S_{L-x_0}}{S} \quad (3)$$

where

$$C_{F_t}(S_{L-x_0}) \equiv D_{F_t}(S_{L-x_0}) / (1/2) \rho U_0^2 S_{L-x_0}$$

is the coefficient of turbulent frictional drag of the model over the wetted area  $S_{L-x_0}$ . If  $x_0$  can be determined, then  $C_R$  can be computed from measured values of  $C_T$  and calculated values of  $C_{F_t}$ .

To determine  $x_0$ , it is noted (Figure 14) that at the location of transition,  $x_L$ , the sum of the laminar friction drag,  $D_{F_L}(S_{x_L})$ , and the stimulator drag,  $\Delta D_T$ , should equal the turbulent frictional drag,  $D_{F_t}(S_{x_L-x_0})$ , computed over the region from the virtual origin of turbulence,  $x_0$ , to the location of transition,  $x_L$ . Thus

$$D_{F_t}(S_{x_L-x_0}) = D_{F_L}(S_{x_L}) + \Delta D_T,$$

or, in coefficient form,

$$C_{F_t}(S_{x_L-x_0}) \cdot \frac{S_{x_L-x_0}}{S} = C_F(S_{x_L}) \cdot \frac{S_{x_L}}{S} + \Delta C_T, \quad (4)$$

which provides an expression to evaluate  $x_0$ , given explicit expressions for  $C_{F_t}$ ,  $C_{F_L}$ , and  $\Delta C_T$ .

Now, for a body of revolution in axisymmetric flow, the frictional drag,  $D_F(S_{x_2-x_1})$ , over a portion of wetted area  $S_{x_2-x_1}$  extending from  $x = x_1$  to  $x = x_2$ , is given by:

$$D_F(S_{x_2-x_1}) = 2\pi \int_{x_1}^{x_2} r \tau \, dx, \quad (5)$$

where  $r = r(x)$  is the body radius and  $\tau = \tau(x)$  is the shear stress on the body surface. From the momentum equations of boundary-layer theory (17), for either laminar or turbulent flow, the shear stress,  $\tau$ , is given by:

$$\tau = \rho \left[ \frac{1}{r} \frac{d}{dx} (r U^2 \theta) + U \frac{dU}{dx} \delta^* \right] \cos \alpha, \quad (6)$$

where  $\theta$  and  $\delta^*$  are respectively the boundary-layer momentum and displacement thicknesses, and  $\alpha = \alpha(x)$  is the angle between the  $x$ -axis and a line drawn tangent to a meridian of the axisymmetric body. Substitution of (6) into (5), and integration by parts, yields:

$$C_F(S_{x_2-x_1}) = \frac{4\pi}{S_{x_2-x_1}} \left\{ r \left( \frac{U}{U_0} \right)^2 \theta \cos \alpha \right\}_{x_1}^{x_2} - \int_{x_1}^{x_2} r \left[ \theta \left( \frac{U}{U_0} \right)^2 \frac{d}{dx} (\cos \alpha) - \frac{\delta^*}{2} \frac{d}{dx} \left( \frac{U}{U_0} \right)^2 \cos \alpha \right] dx \quad (7)$$

where

$$C_F(S_{x_2-x_1}) \equiv D_F(S_{x_2-x_1}) / (1/2) \rho U_0^2 S_{x_2-x_1}.$$

In the special case of an equivalent flat plate (i.e.  $\cos \alpha = 1$  and  $U = U_0$ ) of constant width  $2\pi r = S_{x_2-x_1} / (x_2-x_1)$ , equation (7) reduces to

$$C_F(S_{x_2-x_1}) = \frac{2(\theta_{x_2} - \theta_{x_1})}{(x_2-x_1)} = \frac{2(R_{\theta_{x_2}} - R_{\theta_{x_1}})}{R_{x_2-x_1}} \quad (8)$$

where  $R_{\theta_x} = U_0 \theta_x / \nu$  and  $R_{x_2-x_1} = U_0 (x_2-x_1) / \nu$  are Reynolds' numbers respectively based on momentum thickness and length.

The following three sections will respectively develop methods for analyzing a model's turbulent-flow friction drag, a model's laminar-flow friction drag, and the parasitic drag of wire trips.

### Turbulent Flow Regions

Following traditional practice, and in order to provide a simple basis for analysis, the frictional drag arising from the turbulent flow region on a model will be considered to be the drag due to the turbulent flow over an equivalent flat plate. The leading edge of the equivalent flat plate will be located at the virtual origin of turbulence,  $x_0$ , on the model hull. Thus, in the flat-plate approximation for the turbulent flow region, the turbulent frictional drag coefficient becomes a function of Reynolds' number alone, i.e.

$C_{F_t}(S_{x_L-x_0}) = C_{F_t}(R_{x_L-x_0})$ . Hence, equations (3) and (4) reduce to the forms:

$$C_R = C_T - C_{F_t}(R_{L-x_0}) \cdot \frac{S_{L-x_0}}{S} \quad (9)$$

and

$$C_{F_t}(R_{x_L-x_0}) \cdot \frac{R_{x_L-x_0}}{R_L} = \beta \left[ C_{F_t}(S_{x_L}) \frac{S_{x_L}}{S} + \Delta C_T \right], \quad (10)$$

where

$$\beta \equiv (R_{x_L-x_0} / R_L) / (S_{x_L-x_0} / S).$$

Making use of equation (8) for flat plates and the fact that  $(R_{\theta_{x_0}})_t = 0$ , we have

$$(R_{\theta_{x_L-x_0}})_t = (1/2) R_{x_L-x_0} C_{F_t}(R_{x_L-x_0}) \quad (11)$$

where from (10) it follows that:

$$(R_{\theta_{x_L-x_0}})_t = \frac{\beta}{2} R_L \left[ C_{F_t}(S_{x_L}) \frac{S_{x_L}}{S} + \Delta C_T \right] \quad (12)$$

The particular formulation of flat-plate turbulent friction drag adopted here is the Schoenherr formula (28), which in the present notation is given by:

$$\sqrt{C_{F_t}(R_{x_L-x_0})} \log_{10} 2(R_{\theta_{x_L-x_0}})_t = 0.242 \quad (13)$$

Substituting for  $C_{F_t}$  in equation (11) yields

$$R_{x_0} = R_{x_L} - 34.151 (R_{\theta_{x_L-x_0}})_t \left[ \log_{10} 2(R_{\theta_{x_L-x_0}})_t \right]^2 \quad (14)$$

where  $(R_{\theta_{x_L-x_0}})_t$  is given by equation (12). For known values of  $C_{F_L}$  and  $\Delta C_T$ , equations (14) and (12) are the expressions to be used to determine the location of the virtual origin of turbulence,  $x_0$ , whence equation (9) can be solved for  $C_R$  using the Schoenherr formulas. In practice, a solution of  $x_0$  is obtained iteratively where the

first iteration assumes  $\beta = 1.0$  in equation (12). It should be noted that the above form of the Schoenherr formula, expression (13), which takes into account a virtual origin of turbulence, was in effect proposed by Landweber in his 1953 paper on the frictional resistance of flat plates (32). Although approached from a somewhat different point of view,  $C$  in Landweber's paper, which appears as a constant of integration, can be considered equivalent to the  $R_{x_0}$  defined here. A least squares fit of Landweber's tabulated "theoretical" values of  $R_{0x_0-x_0}$  and  $(R_{x_0}-R_{x_0})$  for turbulent flow on a flat plate yield the formula

$$R_{0x_0-x_0} = 34.02 (R_{x_0}-R_{x_0})^{0.814}, \quad (15)$$

which is accurate to within  $\pm 3$  percent for the Reynolds' number range:  $1.5 \times 10^5 \leq (R_{x_0}-R_{x_0}) < 2 \times 10^7$ . A form of this equation was proposed by Smith and Walker (33) and used by Joubert and Matheson (34) to determine the locations of the virtual origin of turbulence from measured values of  $R_{0x}$  on a model of LUCY ASHTON.

The Schoenherr formula is employed here because, unlike some other formulations, it may be theoretically derived from the well-established overlapping, inner and outer, logarithmic velocity-similarity laws for turbulent boundary layers. The "overlapping" hypothesis, and hence the Schoenherr formula, can be expected to be valid (32) for naturally-occurring turbulent boundary layers having Reynolds' numbers,  $R_x$ , nominally above  $10^5$ . In cases where turbulence is artificially tripped, some doubt must exist about whether the Schoenherr formula applies, as assumed here, in the region not far downstream of the trip. This is because, as mentioned earlier, Klebanoff and Diehl (31) found that some distance was required downstream of trips before the logarithmic velocity similarity laws are satisfied. To check this point, Figure 15 shows a plot of measured values of  $R_{0x}$  downstream of selected wire and sand-grain trips investigated on flat plates by Klebanoff and Diehl (31) and Dutton (23), together with curves of  $R_{0x-x_0}$  computed from the Schoenherr formula, equation (13), and the Blasius formula (17) for laminar flow over a flat plate. The value of  $R_{x_0}$  for each computed Schoenherr curve was selected to give the best fit to the data for each type of trip; the values of  $R_{x_0}$  correspond to the values of  $R_x$  at the points of intersection of the Schoenherr lines with the line  $R_{0x} = 0$ .

A number of conclusions may be drawn from the comparisons shown in Figure 15. First, negative values of  $R_{x_0}$  can result if trips are located near the leading edge and/or if the trips have large parasitic drags. Second, from an engineering standpoint, the Schoenherr formula appears to give an accurate prediction of the distribution of  $R_{0x-x_0}$  as a function of  $R_x$  for untripped and tripped boundary layers, except in the case of the 1.016-mm diameter wire. For this trip wire, having the greatest diameter of the wires shown in Figure 15, the slope of the  $R_{0x-x_0}$  curve is steeper than the Schoenherr line in the region immediately downstream of the trip. This steeper slope is an indication of increased plate shear stresses in the transition region downstream of the wire, when compared to a fully-developed turbulent flow. Prischemikhin and Poostoshny (10), and Joubert and Matheson (34,35,36) have measured similar increases in shear stresses downstream

of ship-model trip wires having diameters of about 1-mm. The former work shows, however, that the effect of the increased shear stress on drag decreases with increasing values of  $R_{x_0}$ , such that when  $R_{x_0} > 6 \times 10^5$ , the increase in drag coefficient is less than  $0.01 \times 10^{-3}$ , which falls within the normal bounds of experimental error. Similarly the results of Dutton (23) plotted in Figure 15 show that for smaller-diameter trip wires (0.33 mm and 0.56 mm), no measurable increase of shear stress, over that for a fully-turbulent boundary layer, occurs downstream of the stimulator locations. Thus, when model experiments are conducted at high Reynolds' numbers with  $R_{x_0} \geq 6 \times 10^5$  or employ trip wires having diameters less than about 0.6-mm, it can be argued that, to within experimental accuracy, the increased shear stresses in the transition region downstream of the trip can be neglected during drag analysis. Since these conditions are satisfied for the majority of the experimental data presented here, it will be assumed that the increased shear stresses have a negligible effect on the present drag-analysis procedure. This point will be discussed further in subsequent sections.

When a region of markedly-increased shear stress exists over a significant distance downstream of a trip, the drag analysis method presented here (and schematically depicted in Figure 14) will not be correct unless the local frictional drag increase is accounted for in some way. One way would be to lump the increase in as a part of the parasitic drag of the trip. In an entirely experimental approach, Joubert and Matheson (34,35,36) solve this problem by determining the virtual origin of turbulence from a form of equation (15) using experimental values of  $R_0$  obtained some distance downstream of a trip where fully-developed turbulent flow is established. Carrying out the boundary-layer velocity profiles required to determine  $R_0$  is a very tedious process, which hopefully can be avoided when conducting most model drag experiments. For this reason, an analysis method, such as the one presented here, can be of value.

#### Laminar Flow Region

Two representations will be considered here for calculation of the coefficient of drag,  $C_{F_L}(S_{x_0})$ , in equation (12), of the laminar flow region. In the first case, the Blasius flat-plate solution will be used as a simple approximation. In the second case,  $C_{F_L}(S_{x_0})$  will be calculated from boundary-layer theory for axisymmetric bodies. It will be shown that the very simple Blasius solution leads to a high-order approximation of the computed value of  $C_F$ , and is thus quite adequate for analysis of the model resistance experiments described here.

In the flat-plate approximation, the laminar frictional drag coefficient becomes a function of Reynolds' number alone, i.e.  $C_{F_L}(S_{x_0}) = C_{F_L}(R_{x_0})$ . Making use of Blasius' solution (17) and expression (8), the following flat-plate approximation results:

$$R_{0x_0} = \frac{R_{x_0}}{2} C_{F_L}(S_{x_0}) = 0.664 R_{x_0}^{1/2}. \quad (16)$$

In the more accurate calculation of axisymmetric boundary layers, it follows from equation (7) that:



$$\begin{aligned} \overline{R_{\theta x_L}} &= \frac{R_{x_L}}{2} C_{F_L}(S_{x_L}) \\ &= \frac{R_{x_L}}{2} \frac{4\pi}{S_{x_L}} \left\{ r \left( \frac{U}{U_0} \right)^2 e^{-\alpha} \right\}_0^{x_L} \\ &\quad - \int_0^{x_L} r \left[ \left( \frac{U}{U_0} \right)^2 \frac{d}{dx} (\cos \alpha) - \frac{\delta^*}{2} \frac{d}{dx} \left( \frac{U}{U_0} \right)^2 \cos \alpha \right] dx \end{aligned} \quad (17)$$

This expression for  $\overline{R_{\theta x_L}}$ , which is analogous to the  $R_{\theta x_L}$  expression for a flat plate, was evaluated numerically using Pohlhausen's one-parameter family of velocity profiles and laminar boundary-layer parameters calculated by the method of reference (14).

Figure 16 shows the calculated values of  $\overline{R_{\theta x_L}}$  and  $\overline{R_{\theta x_L}}$  (equations (16) and (17)) as a function of experimental values of  $R_{x_L}$ , the length Reynolds' number at transition, for the equivalent flat plate and axisymmetric laminar boundary layers on the four bodies tested without turbulence trips installed. Similar results were obtained when the calculations were performed for the same models fitted with turbulence trips. The maximum deviation of  $\overline{R_{\theta x_L}}$  from  $R_{\theta x_L}$  shown in Figure 17 is 300, and occurs on Model 4620-3 at a model length Reynolds' number,  $R_L$ , of about  $3.8 \times 10^7$ . For  $R_L = 3.8 \times 10^7$  the Schoenherr formula gives a total flat-plate momentum-thickness Reynolds' number  $(R_{\theta L})_t$ , of about 45,000. Since  $(R_{\theta L})_t$  is a direct measure of drag, the drag error introduced by use of the flat-plate approximation for the laminar flow region should be less than 0.7 percent (i.e.  $300/45,000$ ). The resulting error in the value of residual drag coefficient,  $C_R$ , will be less than  $0.017 \times 10^{-3}$ , which falls within the limits of overall experimental accuracy. In fact, direct computations using the flat plate (equation (16)) and body-of-revolution (equation (17)) representations resulted in  $C_R$  differences of less than  $0.01 \times 10^{-3}$  for the four models. Thus, for the range of forebody shapes investigated here, the flat-plate approximation can be adopted in the analysis of drag data when  $R_L$  is sufficiently large, i.e. when the magnitude of the laminar-flow drag is much less than the magnitude of the turbulent-flow drag. Substitution of the Blasius solution, formula (16), into equation (12) yields

$$(R_{\theta x_L - x_0})_t = \beta \frac{R_L}{2} \left[ 1.328 R_{x_L}^{-1/2} \frac{S_{x_L}}{S} + \Delta C_T \right] \quad (18)$$

When a turbulence stimulator is not used,  $\Delta C_T \equiv 0$ , and  $(R_{\theta x_L - x_0})_t$  reduces to a modified Blasius solution.

In the case of forebodies which fall outside of the range of shapes investigated here, where one questions the validity of the flat-plate approximation of the laminar boundary-layer region, substitution of equation (17) into equation (12) yields the more accurate expression:

$$\begin{aligned} (R_{\theta x_L - x_0})_t &= \beta \frac{R_L}{2} \left\{ \frac{4\pi}{S} r \left( \frac{U}{U_0} \right)^2 e^{-\alpha} \right\}_{x_L} \\ &\quad - \int_0^{x_L} r \left[ \left( \frac{U}{U_0} \right)^2 \frac{d}{dx} (\cos \alpha) - \frac{\delta^*}{2} \frac{d}{dx} \left( \frac{U}{U_0} \right)^2 \cos \alpha \right] dx + \Delta C_T \end{aligned} \quad (19)$$

For forebodies which are blunter than a hemisphere, it is recommended that equation (19) be used instead of equation (18). In the case of surface ship models, which generally have bows considerably finer than a hemisphere, the flat-plate approximation, equation (18), of laminar flow on the bow should be quite adequate.

#### Parasitic Drag due to Wire Trips and Laminar Separation

In general, the added drag,  $\Delta D_T$ , in the direction of the free-stream velocity, due to two-dimensional turbulence stimulators, can be written in the form:

$$\Delta D_T = \Delta D \cos \alpha_k - \Delta L \sin \alpha_k \quad (20)$$

Here  $\Delta D$  is the net added-force on the trip-plus-body directed tangent to the body meridian at the trip location;  $\Delta L$  is the net lift force on the trip-plus-body directed normal to the body surface at the trip location; and  $\alpha_k$  is the value of  $\alpha$  at the trip location (Figure 17).

Three fundamental assertions will be made concerning the stimulator experiments reported here. First, "overstimulation" of the turbulence does not occur, i.e. the trip is not so large as to cause excessive thickening of the boundary layer (when compared to naturally-excited transition to turbulence) which results in a more sluggish boundary layer such that an increase in form drag occurs due to premature flow separation on the stern. Second, as discussed earlier, it will be assumed that the increased shear stresses in the transition region immediately downstream of a trip result in a negligible increase of frictional drag, when compared to the frictional drag in a fully-developed turbulent boundary layer. It follows from these two assertions that  $\Delta D$  will be taken to be associated with the parasitic drag of the trip alone. The third fundamental assertion is that the lift force,  $\Delta L$ , on the trip-plus-body is zero. If the trip were on a flat plate, the trip flow could be modeled by the trip together with its mirror image in the wall of the flat plate. Symmetry arguments show that the net lift force resulting from the steady pressure perturbation on the trip-plus-plate is zero. For a curved body surface with a trip whose size is very small compared to the body radius, where the steady pressure perturbations are confined to the immediate neighborhood of the trip, the flat-plate approximation will be locally valid, indicating that  $\Delta L = 0$  is a reasonable approximation.

When transition occurs as a result of laminar separation, the same three assertions as made in the case of trip wires are assumed to be valid in analyzing the present experimental data. For the relatively high Reynolds' numbers of the experiments, wind-tunnel flow-visualization observations on the  $L_E/D = 1.0$  forebody indicated a relatively short separation bubble located just forward of the beginning of the parallel-middle-body. On the basis of Gaster's (37) investigation of mean pressure distributions near separation bubbles, one might expect a small decrease in model pressure drag due to the modified pressure distribution in the vicinity of the short laminar separation bubbles on the two fuller forebodies ( $L_E/D = 0.5$  and  $1.0$ ). While extremely high unsteady pressure

fluctuations have been measured by Huang and Hannan (38) in the transition region immediately downstream of the laminar separation bubble on the  $L_E/D = 1.0$  forebody, the concurrent implied increase in local shear stress will exist over a relatively short extent of the body surface, and tend to be cancelled by the reduction in local pressure drag. Thus, in the absence of detailed measurements of steady pressure distributions and velocity profiles, it will be assumed that  $\Delta D = \Delta L = 0$  when laminar separation occurs on the two fuller forebodies when turbulence trips are not fitted.

From the foregoing, the parasitic drag,  $\Delta D_T$ , of a trip will be simply given by:

$$\Delta D_T = \Delta D \cos \alpha_k, \quad (21)$$

where  $\Delta D$  is represented in terms of a trip drag coefficient,  $\Delta C_D$ , by the formula

$$\Delta D = \Delta C_D \left( \frac{1}{2} \rho u_k^2 \right) \cdot (k \cdot 2\pi r_k),$$

or

$$\Delta C_T = \Delta C_D \left( \frac{u_k}{U_0} \right)^2 \cdot \left( \frac{k \cdot 2\pi r_k}{S} \right) \cdot \cos \alpha_k; \quad (22)$$

here  $u_k$  is the laminar boundary-layer velocity at trip height  $k$ , located at a station having body radius  $r_k$  (Figure 17).

On the basis of unpublished experiments by Sacks (39), Preston (21) recommends a constant value of  $\Delta C_D = 0.75$  for circular wire trips. Other experimental investigations of wire-trip drag coefficients,  $\Delta C_D$ , by Allan and Hughes (2), Prischmikhin and Poostoshny (10), Tagori (40), and Kozlov (41) indicate that  $\Delta C_D$  is a function of trip-wire Reynolds' number,  $R_k \equiv u_k k / \nu$ . Because of the experimental difficulties encountered in making accurate trip-wire drag measurements, there are considerable differences in the results (and trends) reported by the several investigators. In general however, for values of  $R_k$  in the range,  $500 < R_k < 5000$ , values of  $\Delta C_D$  fall in the range,  $0.4 < \Delta C_D < 1.0$ , where  $C_D$  decreases with increasing  $R_k$ . Kozlov recommends the relationship:

$\Delta C_D = 2.6 R_k^{-1/2} + 0.60$ , thereby setting 0.60 as the minimum value of  $\Delta C_D$ . In the present work  $\Delta C_D$  will be chosen at a constant value of 0.75, which appears to represent a reasonable mean value inferred from available data. The reasonableness of this value of  $\Delta C_D$  for analysis of the model drag data and the reasonableness of the fundamental assumptions on trip-plus-body added drag will be demonstrated in the next section.

Substitution of expression (22), with  $\Delta C_D = 0.75$ , into (18) or (19) yields final expressions for  $(R_{\theta_{x_L} - x_0})_t$  when trip wires are employed:

$$(R_{\theta_{x_L} - x_0})_t = \beta \frac{R_L}{2} \left[ 1.328 R_{x_L}^{-1/2} \frac{S_{x_L}}{S} + (0.75) \cdot \left( \frac{u_k}{U_0} \right)^2 \cdot \left( \frac{k \cdot 2\pi r_k}{S} \right) \cdot \cos \alpha_k \right] \quad (23)$$

when the flat-plate laminar boundary-layer approximation is used; and

$$(R_{\theta_{x_L} - x_0})_t = 2\pi \beta \frac{R_L}{S} \left\{ r_k \cos \alpha_k \left( \frac{U_{x_L}}{U_0} \right)^2 \theta_{x_L} + (0.375) k \left( \frac{U_k}{U_{x_L}} \right)^2 - \int_0^{x_L} r \left[ \theta \left( \frac{U}{U_0} \right)^2 \frac{d}{dx} (\cos \alpha) - \frac{\delta^*}{2} \frac{d}{dx} \left( \frac{U}{U_0} \right)^2 \cos \alpha \right] dx \right\} \quad (24)$$

when axisymmetric boundary-layer theory is used for the laminar-flow region.

Substitution of equations (23) or (24) into equation (14) yields expressions which may be solved for the virtual origin of turbulence (i.e.  $R_{x_0}$ ) given the trip location (i.e.  $R_{x_L}$ ), geometric information on the body (i.e.  $L, x_L, S, S_{x_L}, r$ , and  $\alpha$ ), and computed values of the laminar boundary-layer velocities (i.e.  $u_k, U_{x_L}, \theta$ , and  $\delta^*$ ). The value of the residual drag coefficient,  $C_R$ , may then be computed from equation (9), using the Schoenherr formula for  $C_{f_t}(R_L - x_0)$  and measured values of the total drag coefficient,  $C_T$ . A computer code was written for solution of  $C_R$  using the above equations, and data analysis can be carried out either during towing-tank experiments on a carriage-mounted digital computer, or on DTNSRDC's large digital computer following completion of experiments.

#### EXPERIMENTAL RESIDUAL DRAG COEFFICIENTS OF MODELS

Figure 18 shows the measured values of  $C_T$  for all four smooth models, without turbulence trips fitted, together with the Schoenherr  $C_f$  curve for fully-turbulent flow over a flat plate. The relative ordering of the  $C_T$  curves may be largely explained by the previously-discussed relative extents of laminar flow on each forebody. Plots of the measured values of  $C_T$  with turbulence trips fitted to all models are not shown because they give no new information beyond what has already been gained from Figures 10 through 13 for the  $L_E/D = 1.82$  forebody.

The analysis method summarized in the final paragraph of the last section was used to compute the residual drag coefficients,  $C_R$ , of the four forebodies tested both with and without a variety of trip-wire diameters (0.254, 0.610, and 1.016 mm) and locations ( $x_L/L = 1, 2, 3$  and 5 percent). Figures 19a through 19d show the values of  $C_R$ , as a function of model Reynolds' number  $R_L$ , computed from axisymmetric boundary-layer theory for the laminar-flow region (equation (24)). Values of  $C_R$  were also computed from the flat-plate approximation for the laminar-flow region (equation (23)), but are not presented here because they differed from the more accurate calculations of  $C_R$  by less than  $0.01 \times 10^{-3}$ . An expanded ordinate scale is used in Figure 19 in order to magnify the differences in values of  $C_R$  determined from the variety of stimulator sizes and locations tested.

The dotted curves shown in Figures 19a through 19d represent faired mean values of  $C_R$  obtained from all of the experiments with a given model. For



each model the scatter about the mean values of  $C_R$  obtained from the different experiments, with and without trips, is about  $\pm 0.03 \times 10^{-3}$ , which is indicated by the solid lines shown in the figures.\* For each model, the measurement error or bias in experimentally determining  $C_T$  at moderate to high model speeds is on the order of  $\pm$  one-percent; this error will result directly in the observed scatter of about  $\pm 0.03 \times 10^{-3}$  in values of  $C_R$ . At lower model speeds, where the percentage error in drag measurements can be expected to be larger, the scatter of  $C_R$  values will be somewhat greater, as can be seen in Figure 19. No consistent patterns could be discerned in the data scatter and it may be concluded that the scatter is primarily due to dynamometer errors involved in measuring the total drags of the models. Thus, within experimental error, the good correlation of the values of  $C_R$  for each model, with and without a variety of turbulence trip sizes and locations, is an indication of the correctness and reliability of the drag analysis procedure used here to analyze the experimental data. It is concluded that for 7-meter axisymmetric models tested at Reynolds' numbers,  $R_L$ , greater than about  $8 \times 10^6$ , the values of  $C_R$  may be determined to an accuracy of  $\pm 0.03 \times 10^{-3}$  using either of the two drag analysis procedures presented here: (a) From measurements of the total drag of a smooth hull, when the location of flow transition is known as a function of speed, either from direct measurement of transition location or by theoretical prediction; or (b) From measurements of the total drag of a model whose boundary layer is tripped by a turbulence stimulator having calculable parasitic drag. More accurate determination of the values of  $C_R$  requires improved dynamometry and detailed data on the shear stress and pressure distributions both in a body's transition region and elsewhere. The importance of properly taking into account the virtual origin of turbulence when analyzing model drag data has been clearly demonstrated.

It remains now to compare values of  $C_R$  computed from the "new" drag-analysis method with the values computed from the "traditional" method of analysis. As discussed earlier, the "traditional" method requires that a model be tested with and without a turbulence trip (typically located at  $x_t/L = 0.05$ ) and assumes that the trip drag coefficient,  $\Delta C_T$ , is a constant which may be determined from:

$$\Delta C_T = [C_T(\text{tripped}) - C_T(\text{smooth})]_{R_L = \text{max. value}}$$

The value of  $C_R$  is then determined from equation (1), making use of the measured values of  $C_T$  with a turbulence trip installed on the model, the above value of  $\Delta C_T$ , and computed equivalent flat-plate values of  $C_F$  which assume that turbulent flow exists over the entire surface area of the model. Table 3 lists the average value of  $C_R$  for each model as computed by the "new" and "traditional" methods of drag analysis for values of  $R_L$  less than  $2 \times 10^7$ ; at higher values of  $R_L$

\* The very careful wind-tunnel investigation of double-models of LUCY ASHTON by Joubert and Matheson (34), in which the locations of the virtual origin of turbulence were determined directly from detailed velocity-profile measurements downstream of a variety of stud and wire trips, indicate a similar spread in the corrected values of  $C_R$ .

TABLE 3  
Comparison of Computed Values of  $C_R$  by  
Two Methods

Model $L_E/D$	$C_R \times 10^3$ ( $R_L < 2 \times 10^7$ )		$\Delta C_R$
	"TRADITIONAL" METHOD	"NEW" METHOD	
0.5	0.10	0.25	0.15
1.0	0.04	0.24	0.20
1.82	0.01	0.20	0.19
3.0	0.08	0.20	0.12

significant wave-making resistance is encountered. Thus, the values of  $C_R$  shown in Table 3 may be interpreted as coefficients of form drag.

As shown in Table 3 the order of merit of the various forebody shapes, in terms of  $C_R$  values, is different according to the two methods of drag analysis; the "new" method indicates that  $C_R$  increases by  $0.05 \times 10^{-3}$  in going from the finest to the fullest forebody ( $L_E/D = 3.0$  to  $L_E/D = 0.5$ ). A similar result was found by Matheson and Joubert (36), when comparing carefully-analyzed experimental drag data obtained for two axisymmetric bodies, one having a sharp nose and the other having a blunter nose. The reasons for the change in  $C_R$  with forebody fullness will be explored in the next section.

Table 3 also shows that the values of  $C_R$  predicted by the "traditional" analysis method are up to  $0.20 \times 10^{-3}$  smaller than values predicted by the "new" method. This discrepancy results from the failure of the "traditional" method to properly consider the laminar flow regimes and virtual origins of turbulence on the various models. If the classical method of drag extrapolation is used, where  $C_R$  is assumed to be the same at model and full scale, then a significantly smaller correlation allowance is required for the "new" method than for the "traditional" method in order to correlate model and full-scale powering data. Thus, if the "new" model drag-analysis procedure were adopted, previously reported (42) low (or negative) values of correlation allowances for full-form ships would become even smaller, suggesting that the model/full-scale resistance scaling problem is even more severe than previously believed.

#### THEORETICAL COMPUTATION OF RESIDUAL DRAG

In order to provide an independent check of the values of  $C_R$  determined from the above analysis of experimental data, and to provide an explanation for the increase in  $C_R$  with increasing model-forebody fullness, theoretical boundary-layer computations were made for the four axisymmetric bodies (without trips fitted) using a modification of the differential "CS" method of Cebeci and Smith (43). The modified method was used to compute the viscous shear stress and pressure distributions over the laminar and turbulent flow regions on the four smooth bodies, each at a length Reynolds' number of  $1.8 \times 10^7$ . The experimentally determined location of transition was used as the boundary between the laminar and turbulent flow regions for each body.

It will be recalled that the stern was the same for each body; this stern had a streamlined shape and did not separate, except perhaps at a position of less than one-percent of body length upstream of the after perpendicular. Because the "CS" computational method (or any other available method) does not properly assess the effects of the very thick unseparated turbulent boundary layer on the stern and the near-wake region downstream of the stern, the "CS" method was altered according to the following simple scheme developed at DTNSRDC by T.T. Huang and H.T. Wang. A modification was required because the details of the stern boundary-layer/near-wake region have the major effect on stern pressure distribution and form drag. In the modification, the hull boundary-layer calculations are assumed accurate only up to about 95-percent of the body's length; far-field wake characteristics, which depend on total body drag, are marched upstream to about 5-percent of body length downstream of the body. A quintic polynomial is then used to represent the displacement thickness in the stern/near-wake region,  $0.95 < x/L < 1.05$ , and the unknown constants in the polynomial are determined by requiring that the displacement thickness and its slope and curvature be equal to those calculated at  $x/L = 0.95$  and  $1.05$  respectively by turbulent boundary-layer theory and turbulent wake theory. The final viscous stern pressure distribution is iteratively computed starting with the potential-flow pressure distribution and an estimated body drag. Successive iterations on the boundary-layer and wake displacement-thickness distributions indicate convergence of computed stern pressure distributions and body drag. Here, the viscous pressure distribution corresponds to the potential flow pressure distribution computed for the body plus its boundary-layer and wake displacement thicknesses. This basic approach, which has shown good agreement between computed and measured model pressure distributions and drags for a number of body shapes, will be fully reported in a separate publication.

If the coefficient of pressure (or form) drag,  $C_{Dp}$ , is defined by the expression,

$$C_{Dp} = \frac{D_p}{1/2 \rho U_0^2 S} ,$$

it is straightforward to show that it may be computed from the integral:

$$C_{Dp} = \frac{\pi(D/2)^2}{S} \int_0^1 \left( \frac{4L}{D} \cdot \frac{2r}{D} \cdot \Delta C_p \tan \alpha \right) d\left(\frac{x}{L}\right) . \quad (25)$$

Here,  $\Delta C_p$  is a difference pressure coefficient defined by

$$\Delta C_p = (C_p)_{\text{pot}} - (C_p)_{\text{vis}} \quad (26)$$

where  $(C_p)_{\text{pot}}$  is the computed potential-flow pressure coefficient distribution on a body and  $(C_p)_{\text{vis}}$  is the viscous-flow pressure coefficient distribution computed iteratively by the method outlined above. A difference pressure distribution is used in the calculations, because it is numerically very difficult to achieve the theoretically-required zero contribution to pressure drag from the computed potential-flow pressure distribution. Since the computed viscous-flow pressure distribution proceeds from calculation of the potential-flow pressure distribution, any

numerical error in the latter will be directly reflected in the former. It is therefore more accurate to define a difference pressure distribution, as done here, in order to obtain the computed viscous pressure drag. The computed total drag coefficient,  $C_T'$ , is given by

$$C_T' = C_{Dp} + C_F' , \quad (27)$$

where  $C_F'$  is the coefficient of frictional drag obtained by integration of shear stresses computed entirely from axisymmetric boundary-layer theory. The computed equivalent residual-drag coefficient,  $C_R'$ , in order to be comparable to the  $C_R$  values determined from the experimental data, must be analyzed using the flat-plate approximation for the turbulent flow region on a given body. Thus,  $C_R'$  is given by

$$C_R' = C_T' - C_F' , \quad (28)$$

where  $C_F$  is the frictional drag coefficient computed by the Schoenherr flat-plate approximation developed for the "new" method described earlier.

Computations of  $C_{Dp}$ ,  $C_T'$ , and  $C_R'$  were performed for the four smooth models at a length Reynolds' number of  $1.8 \times 10^7$ , making use of equations (25), (27) and (28). The computed values are listed in Table 4 along with values of  $C_R$  determined from the experimental data by the "new" analysis method. Qualitatively the computed values of  $C_R'$  or  $C_{Dp}$  agree trendwise with the values of  $C_R$ : the calculations verify the small but measureable (and calculable) increase in  $C_R$  with increasing forebody fullness. The discrepancy between the computed values of  $C_{Dp}$  and  $C_R'$  are attributable to the differences between the calculated values of frictional drag using an equivalent flat plate and axisymmetric boundary-layer theory, i.e.  $0.08 < (C_F' - C_F) \cdot 10^3 < 0.11$ . If the 1957 ITTC correlation line (44) were used instead of the Schoenherr line when computing equivalent flat-plate frictional-drag coefficients, the differences between  $C_F'$  and  $C_F$  would be roughly halved, thereby resulting in somewhat better agreement between the computed values of  $C_{Dp}$  and  $C_R'$ . There would, however, be no better agreement between  $C_R$  and  $C_R'$ .

TABLE 4  
Comparison of Values of  $C_R$  Determined from  
Experimental Data by the "New" Method  
and from Axisymmetric Boundary-Layer Theory  
at  $R_L = 1.8 \times 10^7$

Model L/D	$C_{Dp} \times 10^3$ (eqn. (25))	$C_T' \times 10^3$ (eqn. (27))	$C_R' \times 10^3$ (eqn. (28))	$C_R \times 10^3$ (Table 3)
0.5	0.11	2.78	0.22	0.25
1.0	0.08	2.70	0.18	0.24
1.82	0.06	2.56	0.14	0.20
3.0	0.05	2.43	0.13	0.20

In order to help explain the differences between values of  $C_{Dp}$  computed for each of the bodies, Figure 20 shows a plot of computed values of the integrand in equation (25) as a function of stern location. At further forward locations the computed values of  $\Delta C_p$  were essentially zero; in addition, because a parallel middle body existed on each model over the majority of the total length, no additional pressure-drag contributions can result from pressures applied further forward on the body surface. Figure 20 clearly shows that



the computed pressure recovery on the stern, in the region  $0.90 < x/L < 0.98$ , is reduced as forebody fullness is increased. The net result for bodies having the same total volume and stern shapes is a computed modest increase in pressure-drag coefficient,  $C_{DP}$ , with increasing forebody fullness. It is evident that forebody shape has an effect on the potential-flow pressure distribution at the stern, which in turn has a calculable effect on the stern boundary-layer development and viscous pressure distribution.

To conclude this section, it can be stated that the modest increase in  $C_D$  with increasing forebody fullness, as determined from the experimental data by the "new" analysis method, is confirmed by the calculations made using a "modified" axisymmetric boundary-layer theory. For a specified volume, selection of the body geometry having minimum total drag will depend on counterbalancing the added pressure-drag against the reduced wetted surface and frictional drag associated with increased forebody fullness. Further, it is an understatement to assert that the axisymmetric boundary-layer computation method very briefly described here appears to be extremely promising.

#### SUMMARY

On the basis of the experimental data and theoretical analyses presented here for four large deeply-submerged bodies of revolution tested at length Reynolds' numbers of up to  $4 \times 10^7$ , the following conclusions may be drawn:

- . The occurrence and location of laminar separation is accurately predicted by the Curle-Skan modified-Thwaites criterion, and the extent of the separation bubble over which transition from laminar to turbulent flow occurs is very short.
- . For forebodies which do not exhibit laminar separation, the location of natural transition, where intermittent turbulent bursting first occurs, correlates well with predictions of the Smith-Gamberoni linear-stability analysis method when the amplitude of boundary-layer disturbances is computed to be a factor of  $e^{11}$  times the amplitude of the initial disturbance assumed at the neutral stability location. The critical frequencies of the most-amplified disturbances at the transition location, which are about a factor of four lower than the critical frequencies at the neutral stability location, are accurately predicted by the Smith-Gamberoni method. The measured locations of the inception of Tollmien-Schlichting waves and fully-developed turbulence respectively correlate well with predicted amplification ratios of  $e^9$  and  $e^{13}$ .
- . Transition data for the three finest forebodies without turbulence trips fitted indicated that transition occurred as far aft as 8 to 10 percent of body length at the highest Reynolds' numbers investigated. The fullest (hemispherical) forebody exhibited laminar separation and transition at 4.4 percent of body length over the entire Reynolds' number range investigated. The former results indicate the incorrectness of the "traditional" method of drag analysis which at the highest Reynolds' numbers assumes that smooth-body transition occurs as far forward as the typical 5-percent location of turbulence stimulators.

For equal turbulence-stimulation effectiveness, experiments conducted with trip wires, sand strips, and studs indicate that there are no compelling reasons to choose one type of turbulence stimulator over another from the standpoint of minimization of stimulator parasitic drag and/or the "naturalness" of turbulence stimulation. In the present work, trips wires were selected because they have precisely defined and fixed geometries, are easy to install and remove, and because much more parasitic-drag data are available for trip wires than for other types of stimulators.

. In determining the residual drag of a model from measurements of total drag, it is essential to carefully evaluate the extent of laminar flow and/or the parasitic drag of the turbulence stimulator employed. A new computational method has been outlined which computes the equivalent flat-plate frictional drag of a body using the concept of a virtual origin of turbulence. The virtual origin of turbulence is determined from calculation of the laminar-flow drag of the body upstream of transition, and in the case of trip wires, computation of their parasitic drags. Within experimental error, the good correlation of the computed values of residual drag coefficient for each model, with and without a variety of trip-wire sizes and locations, is an indication of the correctness and reliability of the analysis procedure.

. When compared to the new method of drag analysis, the traditional method of drag analysis underpredicts residual drag coefficients by up to  $0.20 \times 10^{-3}$  and mispredicts the relative residual drags of the four models investigated. Thus, if the new method were adopted for drag analysis, previously reported low (or negative) values of correlation allowances for full-form ships would become even smaller, suggesting that the model/full-scale resistance scaling problem is even more severe than previously believed.

. The new method for analyzing experimental drag data indicates that for a given stern and total hull volume, an increase in forebody fullness results in a modest increase in residual-drag coefficient. This result is confirmed by detailed computations of the viscous pressure distributions on all four bodies using a "modified" axisymmetric boundary-layer theory. The computed change in pressure drag is the result of changes in the viscous pressure distribution near the stern which are a function of forebody shape.

#### ACKNOWLEDGMENTS

The authors acknowledge with thanks the help given by Messrs. W.G. Day, N. Santelli, D.E. Hannan, E.E. West, and L.B. Crook during the experiments, and the assistance of Dr. H.T. Wang, Ms. N. Groves and Ms. N. White in carrying out some of the theoretical calculations. The work was funded by the DTNSRDC Independent Exploratory Development Program under Element 62152N and by the Naval Sea Systems Command under RDT&E Program Element 62564N.

#### REFERENCES

1. Davidson, K.S.M., "Some Experimental Studies of the Sailing Yacht," Trans. SNAME, Vol. 44 (1936).

2. Allan, J.F. and Conn, J.F.C., "Effect of Laminar Flow on Ship Models," Trans. INA, Vol. 92 (1950).
3. Hughes, G. and Allan, J.F., "Turbulence Stimulation on Ship Models," Trans. SNAME, Vol. 59 (1951).
4. Feindt, E.G., "Untersuchungen über die Abhängigkeit des Umschlages Laminar-Turbulent von der Oberflächenrauigkeit und der Druckverteilung," JSTG, Vol. 50 (1956).
5. Dryden, H.L., Schubauer, G.B., Mock, W.C., and Skramstad, H.K., "Measurements of Intensity and Scale of Wind-Tunnel Turbulence and Their Relation to the Critical Reynolds Number of Spheres," NACA Report No. 581 (1937).
6. Fage, A. and Preston, J.H., "On Transition from Laminar to Turbulent Flow in the Boundary Layer," Proc. Royal Soc. London, Vol. 178, Series A (1941).
7. Arakeri, V.H., "A Note on the Transition Observations on an Axisymmetric Body and Some Related Fluctuating Wall Pressure Measurements," Trans. ASME, (Mar 1975).
8. Gatzert, H., "On the Effect of Turbulence Stimulation on Ship Models and Shiplike Bodies," Proc. Eleventh ITTC, Tokyo (Oct 1966).
9. Breslin, J.P. and Macovsky, M.S., "Effects of Turbulence Stimulators on the Boundary Layer and Resistance of a Ship Model as Detected by Hot Wires," DTMB Report 724 (Aug 1950).
10. Prischmikhin, J.N. and Poostoshny, A.F., "Investigation of Turbulence Stimulation in the Boundary Layer of Ship Models Tested in Towing Tanks," Proc. Ninth ITTC, Paris (Sep 1960).
11. Amsberg, H., "Untersuchungen über die Formabhängigkeit des Reibungswiderstandes," JSTG, Vol. 38 (1937).
12. Granville, P.S., "Geometrical Characteristics of Noses and Tails for Parallel Middle Bodies," NSRDC Report 3763 (Dec 1972).
13. Hess, J.L. and Smith, A.M.O., "Calculation of Potential Flow About Arbitrary Bodies," Progress in Aeronautical Sciences, Vol. 8, Pergamon Press, New York (1966).
14. Granville, P.S., "The Calculation of the Viscous Drag of Bodies of Revolution," DTMB Report 849 (Jul 1953).
15. Curle, N. and Skan, S.W., "Approximate Methods for Predicting Separation Properties of Laminar Boundary Layers," Aero. Quarterly, Vol. 8 (1957).
16. Granville, P.S., "The Prediction of Transition from Laminar to Turbulent Flow in Boundary Layers on Bodies of Revolution," Tenth Naval Hydrodynamics Symposium, Boston (Jun 1974).
17. Schlichting, H., BOUNDARY LAYER THEORY, McGraw Hill, New York, Chapters XII, XVI and XVII (1955).
18. Schubauer, G.B. and Klebanoff, P.S., "Contributions on the Mechanics of Boundary Layer Transition," NACA TN 3849 (1955).
19. Smith, A.M.O. and Gamberoni, N., "Transition, Pressure Gradient and Stability Theory," Douglas Aircraft Report ES 26388 (Aug 1956).
20. Wazzan, A.R., Okamura, T.T., and Smith, A.M.O., "Spatial and Temporal Stability Charts for the Falkner-Skan Boundary-Layer Profiles," Douglas Aircraft Co. Report DAC-67086 (Sep 1968).
21. Preston, J.H., "The Minimum Reynolds Number for a Turbulent Boundary Layer and the Selection of a Transition Device," JFM, Vol. 3, Part 4 (Jan 1958).
22. Braslow, A.L., Hicks, R.M., and Harris, R.V., "Use of Grit-Type Boundary-Layer Transition Trips on Wind-Tunnel Models," NASA TN D-3579 (1966).
23. Dutton, R.A., "The Velocity Distribution in a Turbulent Boundary Layer on a Flat Plate," ARC CP No. 453, London (1959).
24. Tani, I., "Effect of Two-Dimensional and Isolated Roughness on Laminar Flow," Boundary Layer and Flow Control (G.V. Lachmann), Vol. 2, Pergamon Press (1961).
25. Tani, I., "Boundary-Layer Transition," Annual Review of Fluid Mechanics (W.R. Sears and M. Van Dyke), Vol. 1, Palo Alto (1969).
26. Braslow, A.L., "Review of the Effect of Distributed Surface Roughness on Boundary-Layer Transition," NATO AGARD Report 254 (Apr 1960).
27. Klebanoff, P.S. and Tidstrom, K.D., "Mechanism by Which a Two-Dimensional Roughness Element Induces Boundary-Layer Transition," Physics of Fluids, Vol. 7 (Jul 1972).
28. Schoenherr, K.E., "Resistance of Flat Plates Moving Through a Fluid," Trans. SNAME, Vol. 40 (1932).
29. Von Doenhoff, A.E. and Braslow, A.L., "The Effect of Distributed Surface Roughness on Laminar Flow," Boundary Layer and Flow Control (G.V. Lachmann), Vol. 2, Pergamon Press (1961).
30. Klebanoff, P.S., Schubauer, G.B., and Tidstrom, K.D., "Measurements of the Effect of Two-Dimensional and Three-Dimensional Roughness Elements on Boundary-Layer Transition," Jour. Aero. Sci., Vol. 22 (Nov 1955).
31. Klebanoff, P.S. and Diehl, Z.W., "Some Features of Artificially Thickened Fully Developed Turbulent Boundary Layers with Zero Pressure Gradient," NACA Report 1110 (1952).
32. Landweber, L., "The Frictional Resistance of Flat Plates in Zero Pressure Gradient," Trans. SNAME, Vol. 61 (1953).
33. Smith, D.W. and Walker, J.H., "Skin Friction Measurements in Incompressible Flow," NACA TN 4231 (1957).
34. Joubert, P.N. and Matheson, N., "Wind Tunnel Tests of Two LUCY ASHTON Reflex Geosims," JSR, Vol. 14, No. 4 (Dec 1970).
35. Matheson, N. and Joubert, P.N., "Experimental Determination of the Components of Resistance of a Small 0.80 C<sub>B</sub> Tanker Model," JSR, Vol. 17, No. 3 (1973).
36. Matheson, N. and Joubert, P.N., "A Note on the Resistance of Bodies of Revolution and Ship Forms," JSR, Vol. 18, No. 3 (1974).
37. Gaster, M., "The Structure and Behavior of Laminar Separation Bubbles," Part 2 of SEPARATED FLOWS, AGARD Conf. Proc. No. 4, Paris (May 1966).
38. Huang, T.T. and Hannan, D., "Pressure Fluctuations in Regions of Flow Transition," DTNSRDC Report 4723 (1976).

39. Sacks, G.M., M.Sc. Dissertation, University of Cambridge (1956).
40. Tagori, T., "A Study of the Turbulence Stimulation Device in the Model Experiment on Ship Form," Proc. Tenth ITTC, NPL, Teddington (Sep 1963).
41. Kozlov, L.F., "Investigation of the Boundary Layer Turbulence Stimulation of the Ship Models," Proc. Twelfth ITTC, Rome (Sep 1969).
42. McCarthy, J.H., "Ship Resistance due to Surface Irregularities: Waviness, Roughness and Fouling," Proc. Seventeenth ATTC, Pasadena, Calif. (Jun 1974).
43. Cebeci, T. and Smith, A.M.O., ANALYSIS OF TURBULENT BOUNDARY LAYERS, Academic Press, New York (1974).
44. Resistance Committee Report, "Skin Friction and Turbulence Stimulation," Proc. Eighth ITTC, Madrid (Sep 1957).



TABLE 1

Hull Particulars for Axisymmetric Forebodies  
( $C_{pE} = 0.667$ ,  $D = 0.624$  m, Volume =  $1.642$  m<sup>3</sup>)

Model	4620-1	4620-2	4620-3	4620-4
$L_E/D$	0.5	1.0	1.82	3.0
$L_M/D$	5.84	5.50	4.97	4.17
$L/D$	10.73	10.89	11.18	11.56
$S$ (m <sup>2</sup> )	11.486	11.508	11.590	11.738
Hot Film Locations ( $x/D$ )				
1	0.16	0.29	0.29	0.29
2	0.37	0.45	0.45	0.47
3	0.49	0.61	0.61	0.65
4	0.57	0.86	0.81	1.26
5	0.81	0.98	1.02	1.59
6	1.22	1.42	1.58	1.91
7	1.63	2.04	1.71	2.24
8	2.78	2.94	1.87	3.64*
9			2.04	

\*Probe located aft of model joint.

TABLE 2

Turbulence Stimulators Evaluated on Model 4620-3,  $L_E/D = 1.82$

Turbulence Stimulator	Height, $k$ (mm)	Locations, $x_k/L$	$R_k = u_k K/\nu$	
			$U_0 = 2.05$ meters/sec	$U_0 = 5.14$ meters/sec.
Sand Strips (12.7 mm wide)				
Fine - (60 grit)	0.305	0.05	360	1200
Medium (20/30 grit)	$0.660 \leq k \leq 1.092$	0.05	1100 (min)	3500 (min)
Coarse	$1.600 \leq k \leq 3.175$	0.05	5700 (min)	9300 (min)
Circular Wires				
Small	0.254	0.02, 0.05	270 (avg)	800 (avg)
Medium	0.610	0.02, 0.05	1050 (avg)	3150 (avg)
Large	1.016	0.02, 0.05	2150 (avg)	5500 (avg)
Circular Studs (3.175 mm dia)	2.540 (25.4 mm spacing)	0.05	5700	14,300

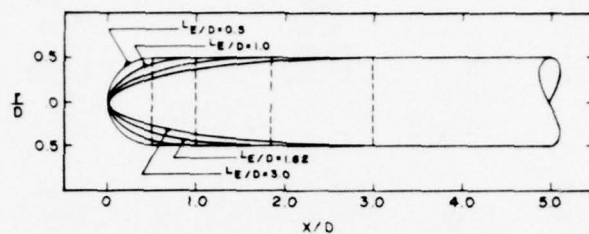


Fig. 1: Drawing of axisymmetric forebodies.

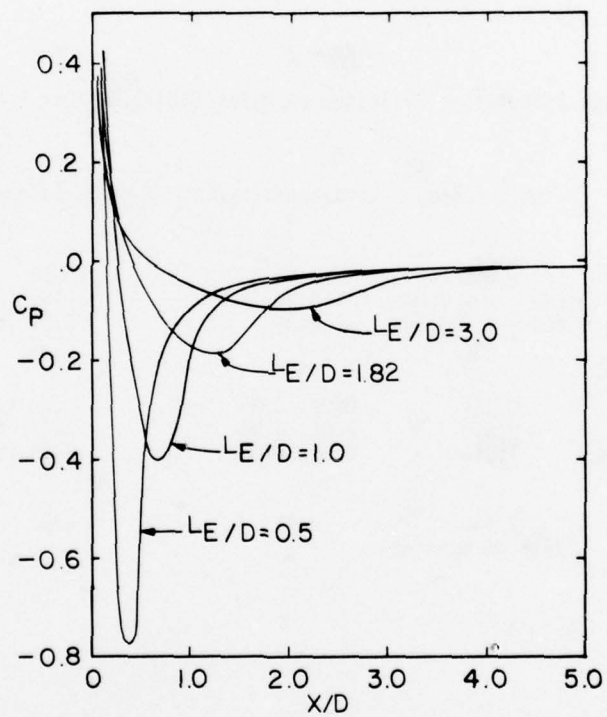


Fig. 2: Computer distributions of pressure coefficient on the axisymmetric forebodies.

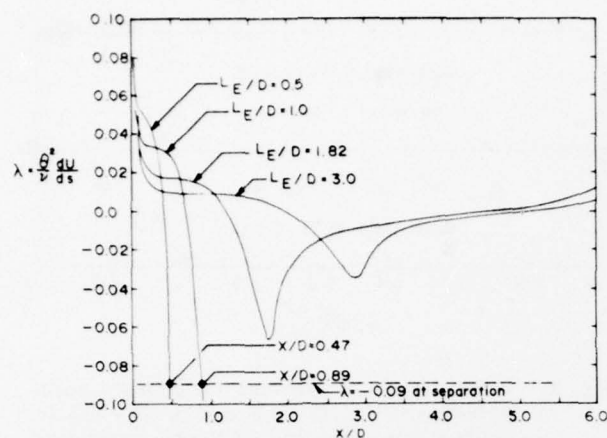


Fig. 3: Computed distributions of pressure gradient parameter on the axisymmetric forebodies.

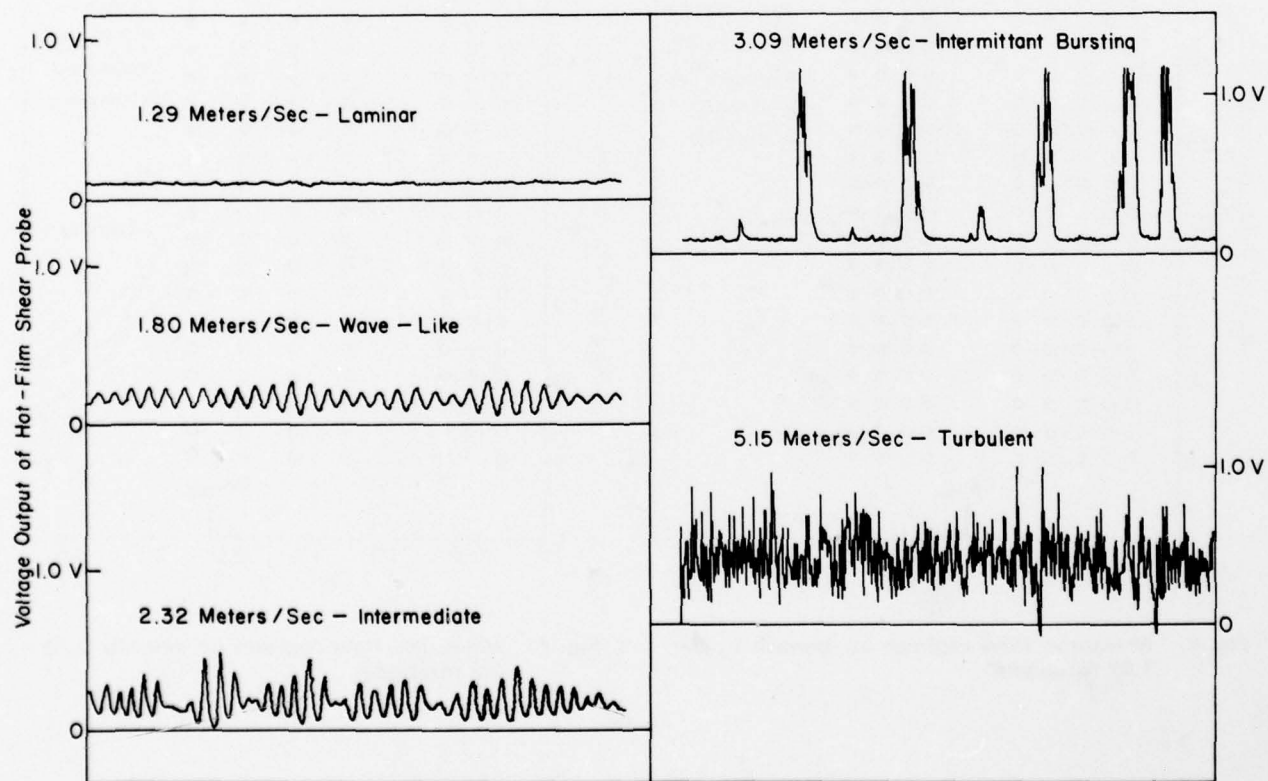


Fig. 4: Representative hot-film signals for various flow regimes (Model 4620-3, Bare Hull).



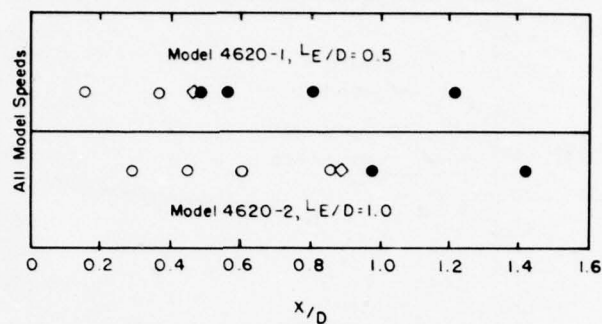


Fig. 5: Measured flow regimes on smooth forebodies with  $L_E/D = 0.5$  and  $L/D = 1.0$  (○ laminar flow, ● turbulent flow, ◇ predicted laminar separation).

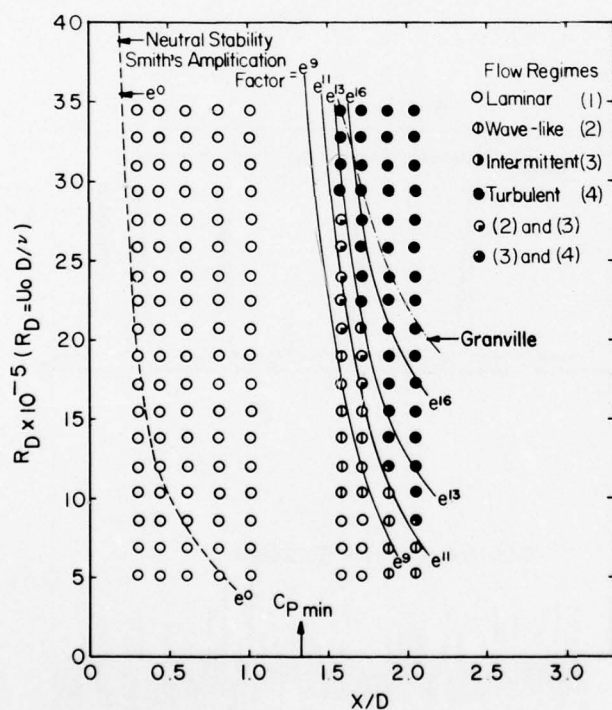


Fig. 6: Measured flow regimes on smooth  $L_E/D = 1.82$  forebody.

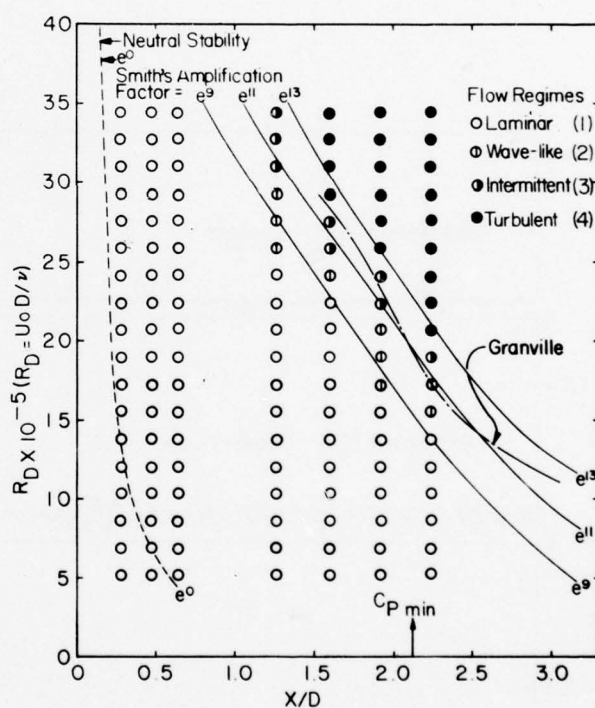


Fig. 7: Measured flow regimes on smooth  $L_E/D = 3.0$  forebody.

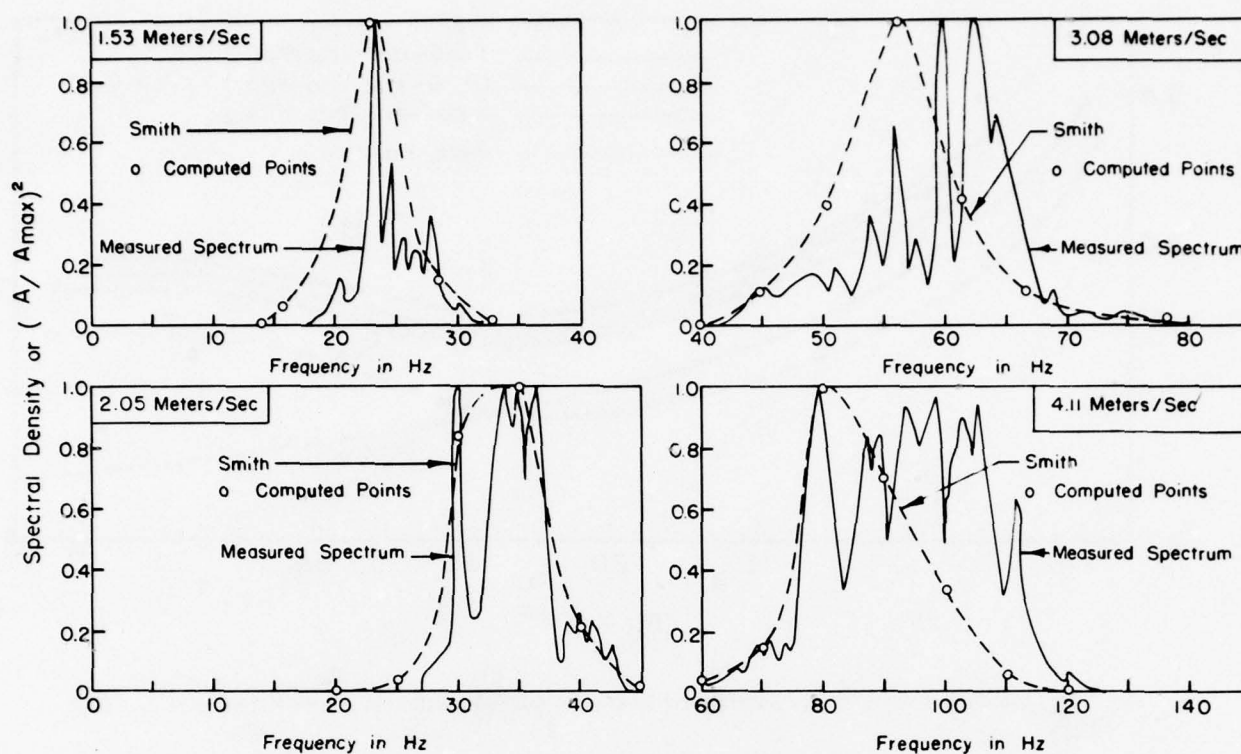


Fig. 8: Comparison of measured critical frequency from spectral density of hot-film shear probe at  $X/D = 1.589$  with computed amplification ratios for model 4620-3, ( $L_E/D = 1.82$ ) at four speeds.

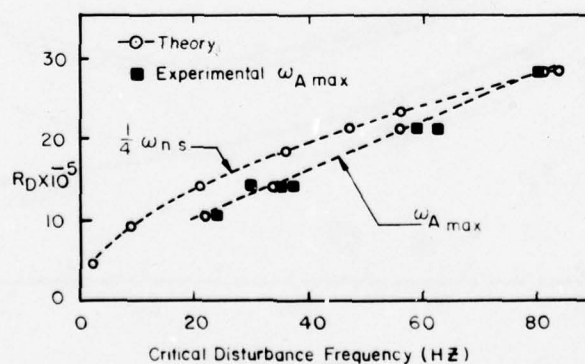


Fig. 9: Frequencies of maximum energy disturbances ( $A_{max}$ ) at  $X/D = 1.589$  and at Neutral stability for the  $L_E/D = 1.82$  forebody as a function of Reynolds number.

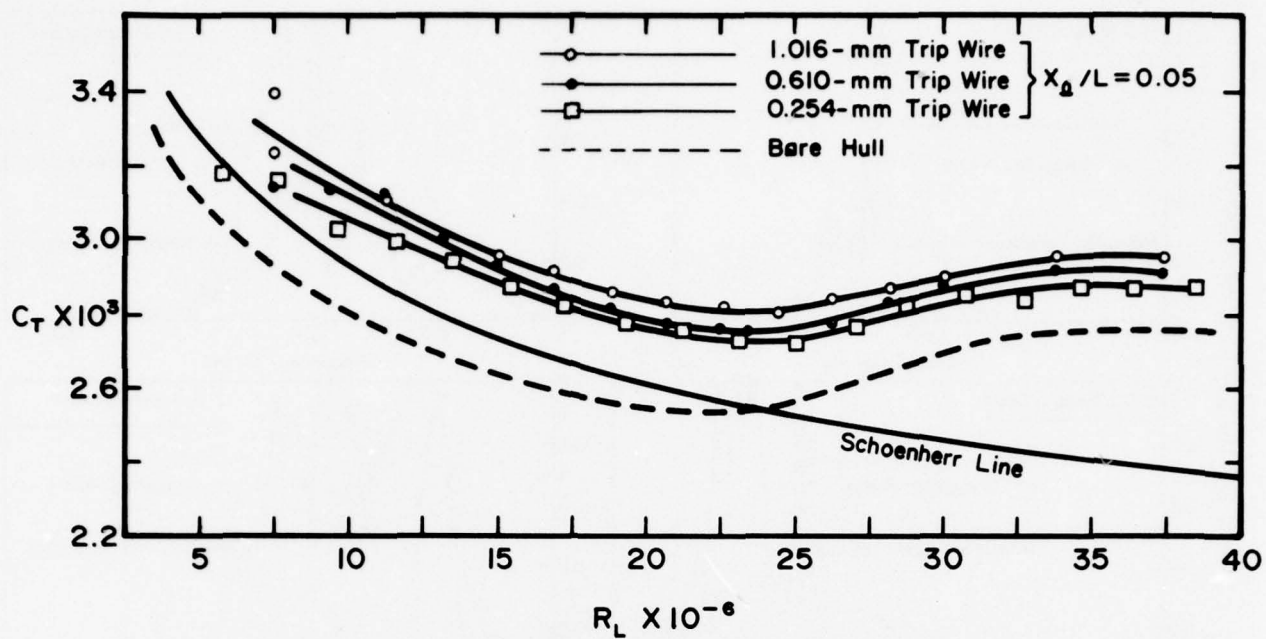


Fig. 10: Measured total drag coefficients of model 4620-3 with trip wires fitted at  $X_d/L = 0.05$ .

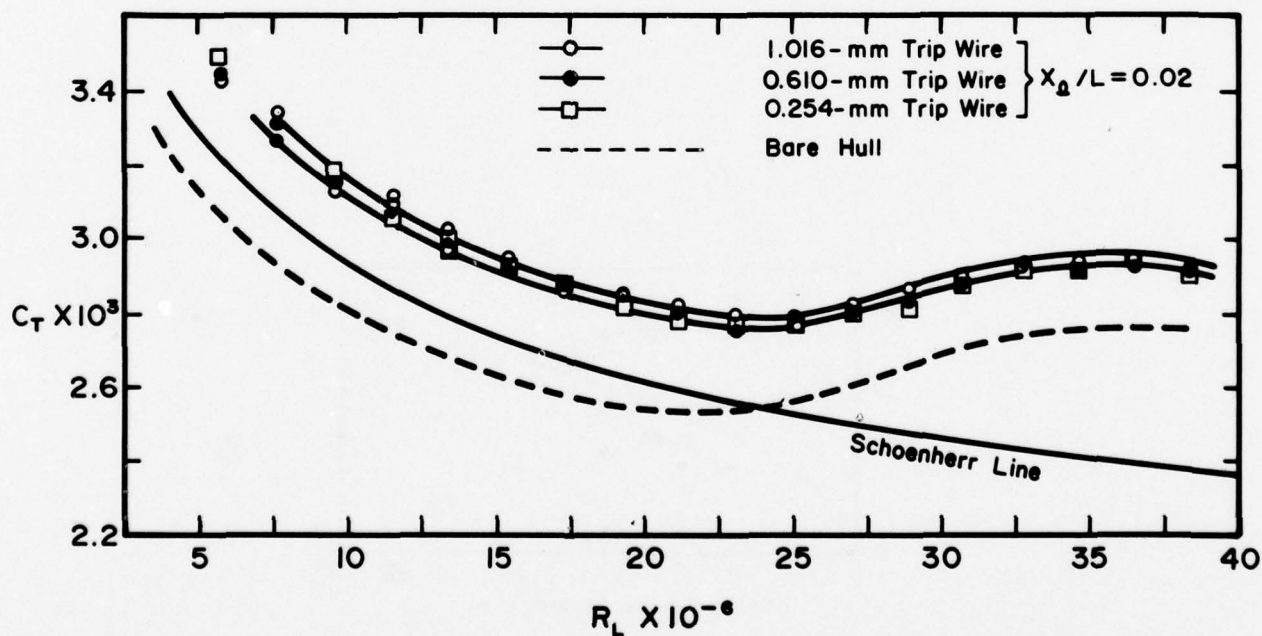


Fig. 11: Measured total drag coefficients of model 4620-3 with trip wires fitted at  $X_d/L = 0.02$ .



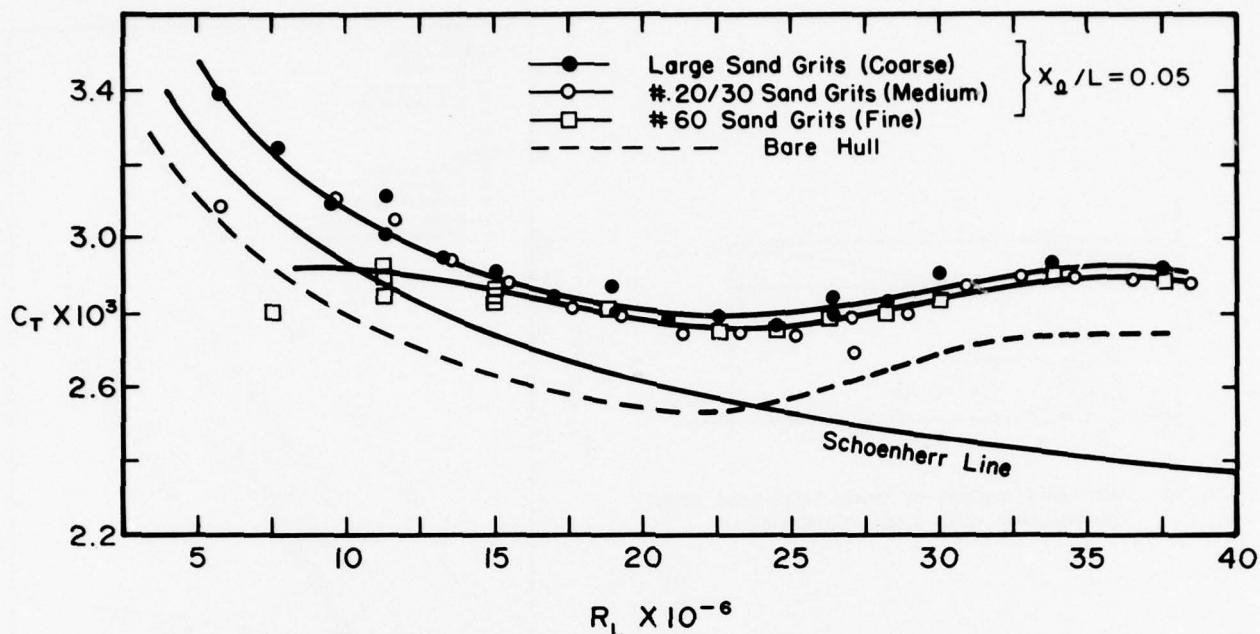


Fig. 12: Measured total drag coefficients of model 4620-3 with sand strips fitted at  $X_d/L = 0.05$ .

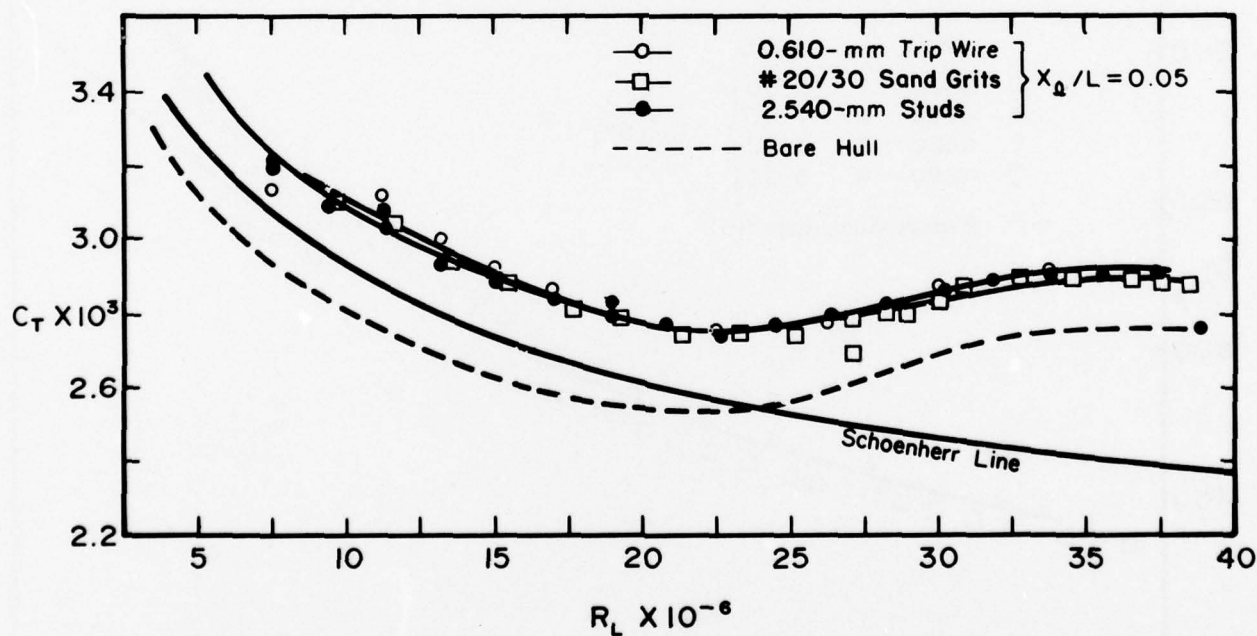


Fig. 13: Measured total drag coefficients of model 4620-3 with wire, sand and stud trips fitted at  $X_d/L = 0.05$ .

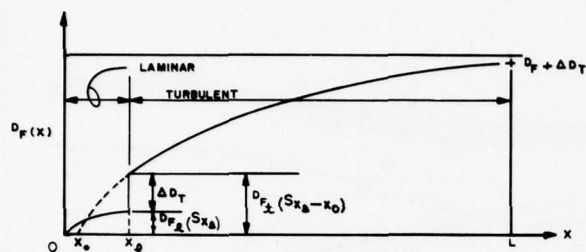


Fig. 14: Idealized sketch of body frictional drag distribution with a turbulence trip.

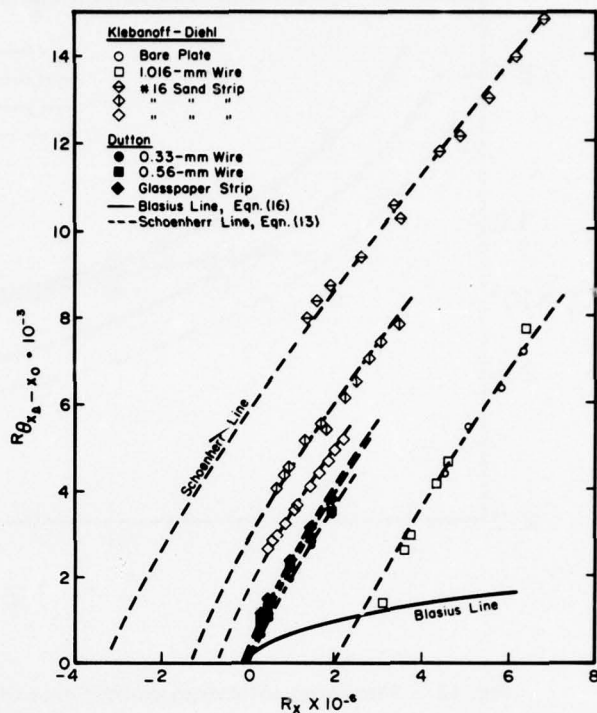


Fig. 15: Distribution of momentum thickness Reynolds number downstream of wire and sand trips on flat plates tested in wind tunnels.

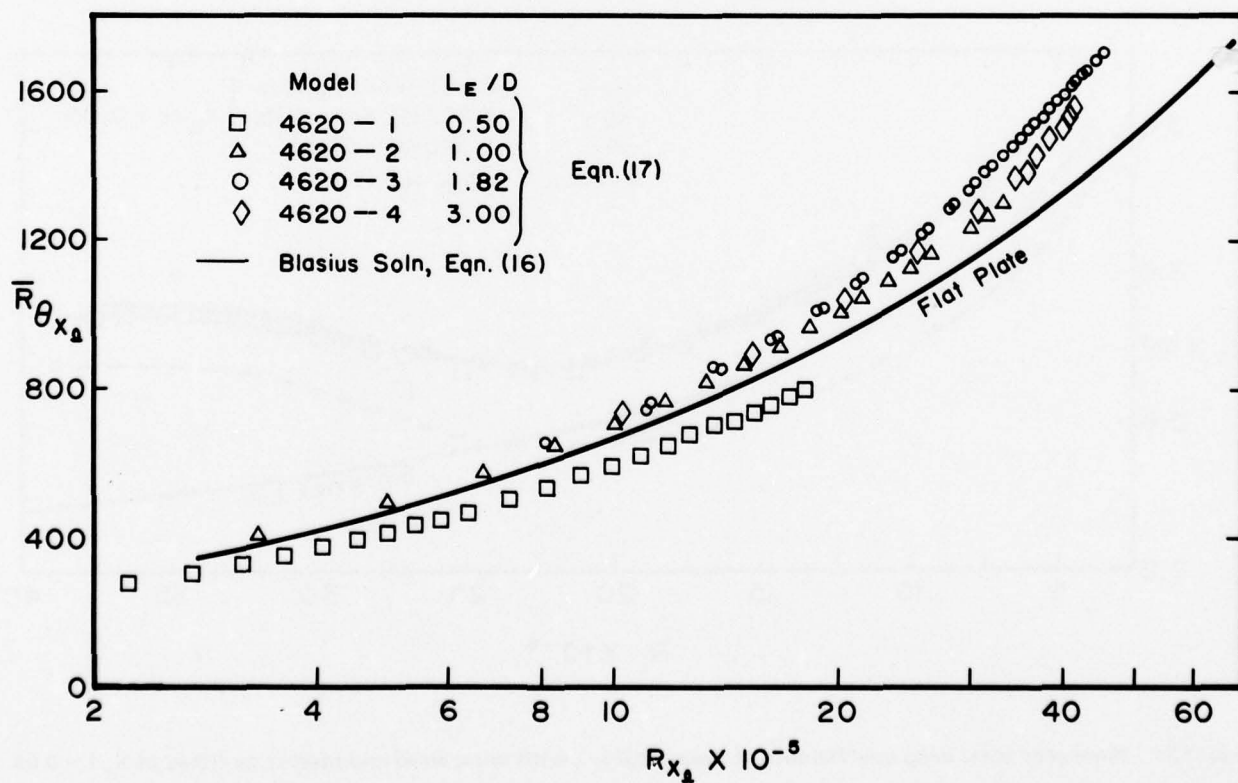


Fig. 16: Comparison between values of laminar-flow momentum thickness Reynolds number computed from flat-plate and axisymmetric boundary-layer theories.

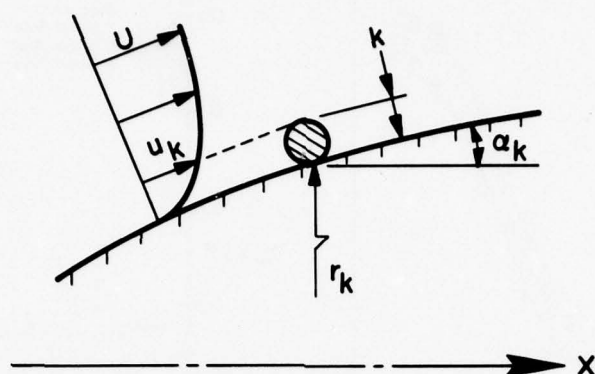


Fig. 17: Sketch of trip wire in boundary layer.

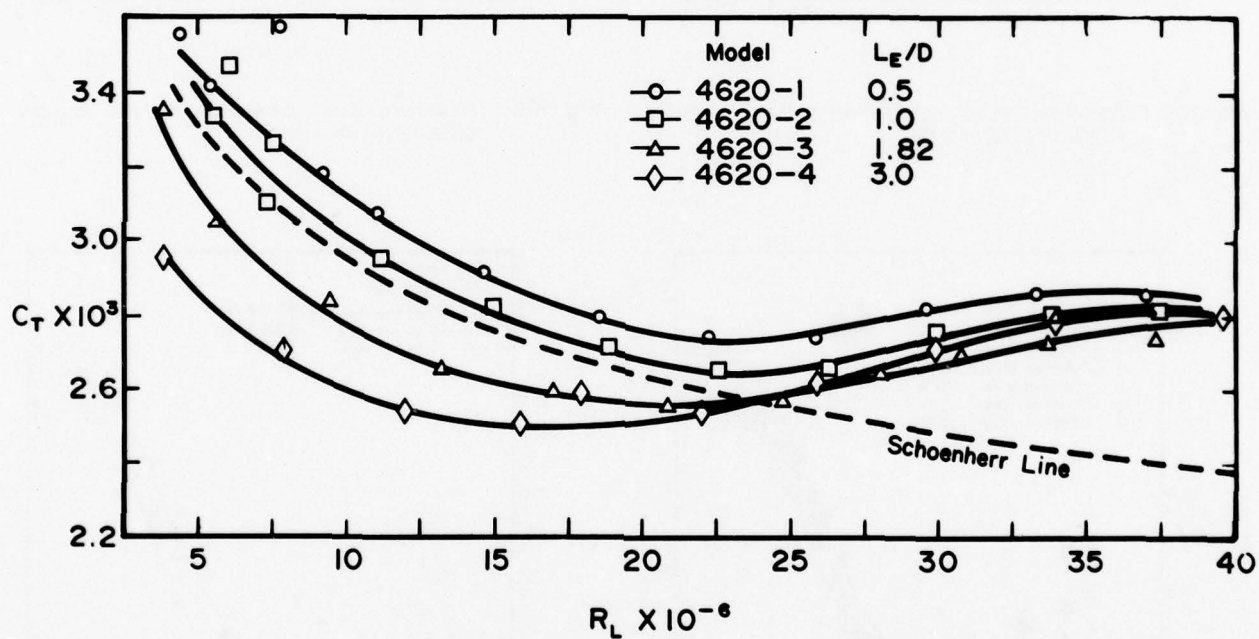


Fig. 18: Measured total drag coefficients of the four smooth models without turbulence trips fitted.



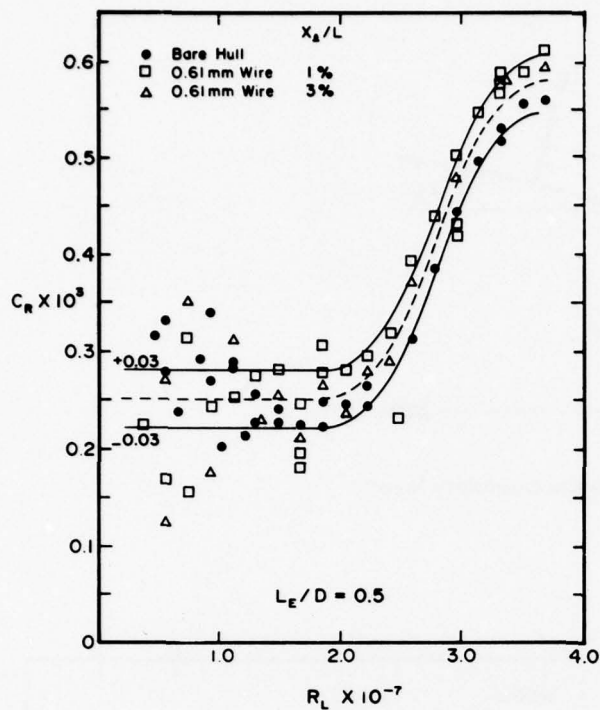


Fig. 19a: Residual drag coefficients for model 4620-1 ( $L_E/D = 0.5$ ).

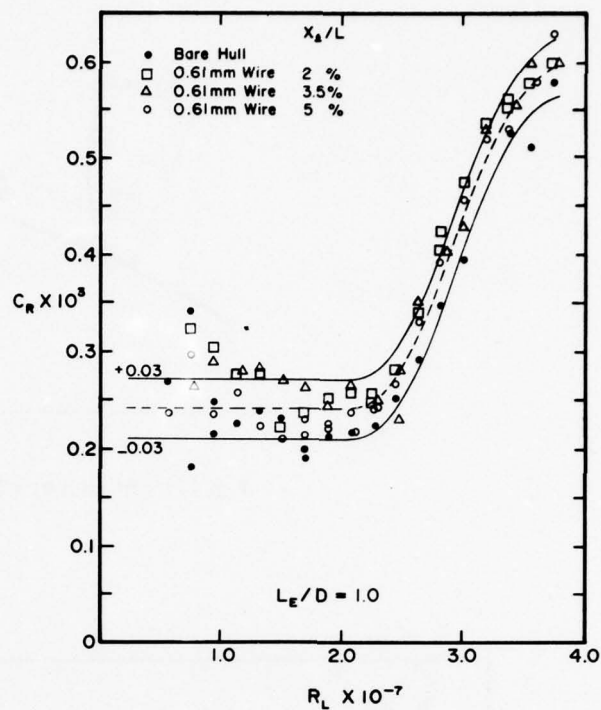


Fig. 19b: Residual drag coefficients for model 4620-2 ( $L_E/D = 1.0$ ).

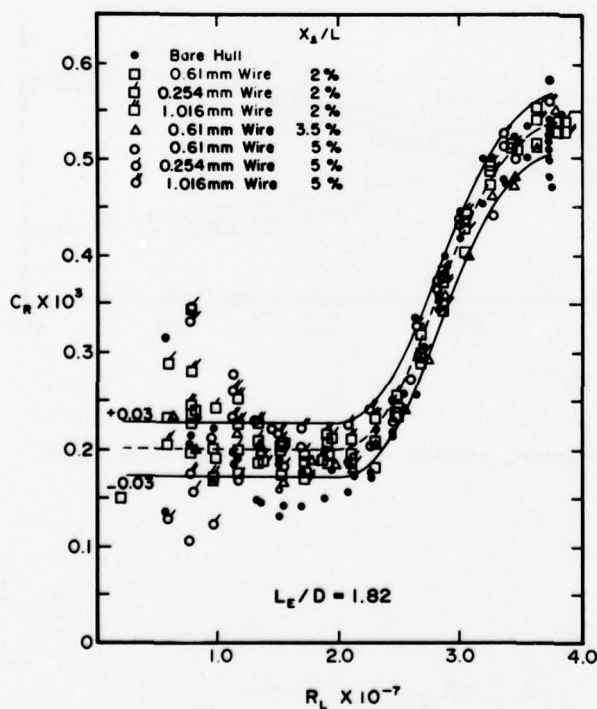


Fig. 19c: Residual drag coefficients for model 4620-3 ( $L_E/D = 1.82$ ).

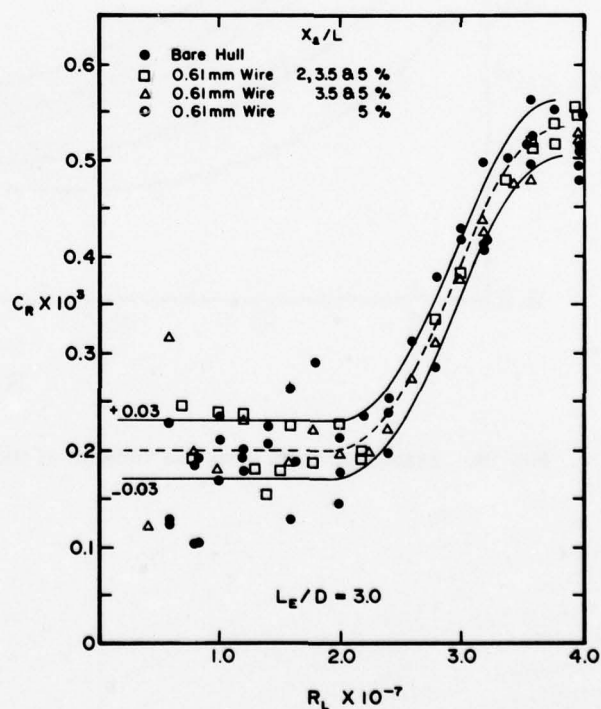


Fig. 19d: Residual drag coefficients for model 4620-4 ( $L_E/D = 3.0$ ).

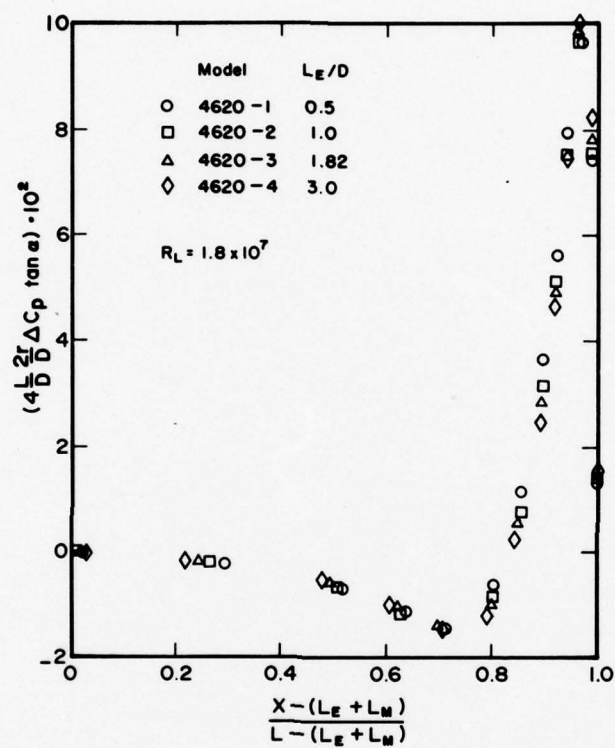


Fig. 20: Computed nondimensional viscous pressure distributions on stern for the four forebodies.

# RANDOM WAVE GENERATION FOR RESEARCH ON IMMERSSED MARINE VEHICLES

J. H. VAN OORSCHOT and F. KOOPMANS  
Delft Hydraulics Laboratory, The Netherlands

## Summary

Facilities for the generation of random waves have been installed at various institutes. For the motion-control of these random wave generators use is made of either an actual recording of a wave motion, or a random analogue or digital signal. Typical features of both systems are discussed, and some general ideas are presented on possible improvements of the system.

The reproduction of natural irregular sea waves is particularly important in those studies where the non-linear aspects are apparent. This is shown to be the case in motions of immersed objects at anchor and of vessels berthed against a jetty, where the non-linear component in the stochastic wave excitation leads to movements and forces that cannot be predicted with the use of harmonic excitation only.

Similarly large surge motions may follow from the grouping and breaking of irregular waves in shallow confined waters, due to the generation of surf beat. However, also in studies on the behaviour of floating objects, responding linearly to the wave amplitude, harmonic wave generation may create problems, particularly in shallow water and at longer wave periods, as a result of the generation of parasitic waves.

## 1 Introduction

For laboratory research on maritime structures in general, use has to be made of facilities to reproduce waves. For some studies it will be sufficient to generate waves with uniform amplitude and uniform frequency (monochromatic waves). This will, for instance, be the case if (a) the behaviour of the structure in one individual wave has to be studied, and there is no interaction from preceding waves; (b) the mean total energy of the wave train only is of importance; (c) the structure responds linearly to the waves. Often, however, a more complex situation exists and a less schematized reproduction of the actual (random) sea waves is required. The possibilities of generating waves in laboratory facilities have been considerably improved in recent years. Facilities for the generation of random waves have now been installed at various research institutes.

As an example, the system set-up of the random wave generators in use at the Delft Hydraulics Laboratory will be discussed hereafter. This system set-up is representative of most of the random wave generators in use at other institutes. In addition it will be shown that in research on immersed marine vehicles the generation of random waves is essential on a number of occasions, as certain phenomena are underestimated, or not observed at all, if regular waves are used.

## 2 Linear model to describe random waves

To describe the natural random sea waves, use is often made of a linear model, in which the wave motion is supposed to be composed of an infinite number of infinitively small frequency components, all at random phase.

$$\eta_t = \lim_{n \rightarrow \infty} \sum a_n \cos(2\pi f_n t + \phi_n) \quad (1)$$

It is to be noted that the term linear model only applies to the description of the waves and has nothing to do with the response of objects to the waves, which still can be decidedly non-linear.

The various components in (1) have phase velocities that follow from the dispersion relationship

$$c_n = \sqrt{g/k_n \tanh k_n d} \quad (2)$$

$$\text{while } c_n = \omega_n/k_n \quad (3)$$

Consequently the wave pattern changes continuously as the various components proceed with different velocity. As the phase differences  $\phi_n$  are random (uniform distribution between 0 and  $2\pi$ ) at the start, they will remain random at any instant and any place. It then follows that it is not necessary and even impossible, to reproduce the exact profile of the natural sea waves. It will be sufficient to reproduce the wave energy spectrum. If this spectrum is a continuous function, the values of  $\eta_t$  will follow a Gaussian distribution. In case of a narrow spectrum, the extreme values of  $\eta_t$  (amplitudes) follow a Rayleigh

distribution.

Statistical analysis of sea waves at completely different locations and generation conditions gives strong support to the hypothesis that the wave motion can indeed be adequately described by the energy spectrum only (Ref. 1, 2, and 3). For the generation of waves in the laboratory this is an important conclusion, as it appears to justify the use of an analogue signal, with the same energy spectrum as the waves to be reproduced, as signal for the motion-control of the wave generator.

Caution is required in cases of apparent non-linear effects in the wave motion (breaking waves, waves in extremely shallow water, etc.). Here the application for wave generation of the linear wave model as described might no longer be justified.

## 3 Waves generated by a mechanical wave generator

The generation of regular waves is relatively simple. Although a large variety of types of wave generators can be found, most of them consist in principle of a flat rigid plate, driven by some mechanical device. The movements of the wave board will preferably be adapted as well as possible to the horizontal component of the orbital velocity. In practice this will not be achieved completely, for two reasons:

- (a) By applying a rigid plate, the velocity reduces linearly with depth, whereas a decrease according to a hyperbolic function is required.
- (b) The motion is generally sinusoidal, whereas the actual variation of the horizontal orbital velocity with time may differ from a sinusoidal one.

Both differences (a) and (b) give rise to the occurrence of parasitic waves with higher frequencies, which will in part damp out quickly, but which partly are persistent and interfere with the basic waves. The most important parasitic wave has a frequency  $2f_0$ , where  $f_0$  is the frequency of the basic wave motion, and is called the secondary wave. The effect mentioned under (a), can fairly well be minimized by letting the wave board oscillate with an optimum ratio between translation and rotation. This ratio depends on the wave frequency and the water depth. The effect mentioned under (b) is harder to avoid, and is generally the main source of the secondary waves.

As opposed to the coupled second harmonic Stokes waves of the trochoidal wave profile, the secondary wave is a free wave that propagates with a velocity that follows from the frequency  $2f_0$ . Consequently the basic wave (and coupled second harmonic Stokes component) will overtake the secondary wave, leading to a continuous changing picture in the space domain (Fig. 2).

The amplitude of the secondary wave to be expected for a sinusoidally moving wave generator can be expressed as a linear function of the Ursell parameter ( $gL^2/d^3$ ). Secondary waves are insignificant for  $U < 10-15$ , but they may be as large as the first harmonic of the basic wave for  $U \approx 80$ .



A considerable reduction of the secondary waves can be obtained, if the motion of the wave generator is composed of more than one frequency component, with optimum mutual amplitude ratios. An example of this is presented in Fig. 3.

In case of random wave generation the situation is much more favourable. The motion of the wave generator follows directly from the surface motion to be reproduced, and is composed of an infinite number of components with proper mutual amplitude ratios. If secondary waves still do occur, the input spectrum can be adapted accordingly, as there is in fact no difference between energy components contained in the command signal and those from free secondary waves.

#### 4 Generation of motion control signal

##### 4.1 Analogue signal generation

As explained in section 3, the wave board should preferably move with a larger amplitude at the surface than at the bottom, that is, it should have a combined translation and rotation. To achieve this, the wave board can be driven by two separate hydraulic actuators, each actuator being controlled by a servo system (Fig. 1). The surface elevation record to be reproduced, however, has to be transferred first into a command signal for the actuators, i.e., the horizontal movement of the wave board. Such a transfer function has been calculated by Biesel (Ref. 4) for monochromatic waves. The transfer function is shown in Fig. 4, and presents the required stroke of the wave board at the water surface and near the bottom as a function of wave height, wave period, and water depth. Though the theory of Biesel has been derived for monochromatic waves only, test results show that the method is also applicable for irregular waves.

In the system in use at the DHL this transfer function has been reproduced with a set of second-order analogue filters, providing the required amplification or damping for translation – and rotation actuator separately. As all analogue filters have a frequency dependent phase shift, the system is also equipped with a phase compensation network. In Fig. 5 a comparison is given between a spectrum and a statistical wave height distribution of an actual North Sea wave record, and the waves reproduced in the laboratory applying the same record as input signal.

Obviously, the most attractive way to obtain the input signal is to apply an actual prototype wave recording. However, prototype recordings are generally only rarely available, while extreme wave conditions, important for testing structures, mostly have not been recorded at all. Even if prototype recordings are available the question remains as to what extent they are representative for the local conditions. As a consequence, use often has to be made of a simulated record, based on the hypothesis of a linear wave model as discussed in section 2.

In the latter case, a wave record can be simulated by using a random-noise generator, the random noise being filtered by a set of analogue second-order filters. As both the resonance frequency and the damping of these filters are variable, the noise can be transformed into a signal having any arbitrary spectrum. The output signal of the filter unit is fed into the transfer network in the same way as in the case of an actual prototype record. An outline of this system is presented in Fig. 1.

As discussed in section 2, the number of components composing the random signal should be infinite, in order to obtain a Gaussian process. In practice every record of a finite length has a finite number of components only, so the wave signal may be approximated by a frequency discrete representation of the wave spectrum. A noise generator that is very suited for this, is a binary waveform generator (Ref. 5). This type of noise generator has  $n$  shift registers. If the system is shifted with a frequency  $F$ , one obtains a line spectrum with equal spaced components at distance  $F/2^n - 1$ , see Figs. 6 and 7. The shape of the spectrum has the form

$$E(f) = \frac{(\sin \pi f/F)^2}{(\pi f/F)^2} \quad (4)$$

so the energy is nearly constant for small values of  $f/F$ . At  $f = 0.45F$  the energy is  $-3$  dB and at  $f = F$  the energy  $E(f) = 0$ .

The sequence will be repeated after  $2^n - 1$  s, and the time series is therefore called pseudo-random noise. For a noise generator with 20 shift registers, driven with a frequency of 100 Hz, components at a distance of  $10^4$  Hz are obtained, whereas the sequence is repeated after  $10^4$  s, or about 3 h.

An example of waves reproduced in this way is shown in Fig. 8, together with data from the original record and of the waves reproduced applying the original recording directly (punch-tape input).

##### 4.2 Digital signal generation

As an alternative to the system described in section 4.1, it is also possible to generate random numbers in a computer. If these random numbers are used as input to a digital filter, which can be programmed in the same computer, the random signal with the required energy spectrum is obtained. The digital filtering can be obtained by the Inverse Fourier Transform of the required spectrum (Ref. 6).

As the waves propagate down the flume, the spectrum tends to change, due to non-linear transfer of energy between adjacent bands of frequency. Description of this phenomenon in terms of a simple multiplication factor is not possible. Additionally some errors may be introduced in the servo dynamics of the wave generator and in the transfer of wave board to wave height. As a result the wave spectrum obtained at some distance from the wave generator may differ from the input spectrum, in spite of the transfer network applied. In practice with an analogue system these differences are compensated by trial and error, changing the setting of the filters.

By using digital signal generation, with Inverse Fourier Transform filtering, an automatic correction system can be built in by using a differencing algorithm, which compares the required spectrum with the measured spectrum (Ref. 6). In this way the often time-consuming phase of selecting the proper filter setting, prior to the actual model testing, might significantly be speeded up.

#### 5 Application of random waves in model testing

In the previous sections, the possibilities and techniques of random wave generation have been discussed. In the following sections some examples of laboratory studies will be discussed, where the application of random waves has proved to be indispensable for a proper reproduction of the natural phenomena.

##### 5.1 Model study on mooring forces

In the response to random waves of floating objects, moored or at anchor, two modes of oscillation can be observed, viz., the harmonic oscillations and the subharmonic oscillations.

The harmonic motion, with periods in the range of the wave periods, is mostly reasonably well linearly related to the wave amplitude. It can therefore generally be determined with sufficient accuracy by model experiments applying monochromatic waves, or by computer simulation, based on linear wave theory. With the use of transfer functions and spectral analysis the six harmonic motion components can subsequently be determined for irregular waves as well.

The subharmonic motion is a mode of oscillation with periods much larger than the range of wave periods. This subharmonic behaviour can partly be caused by the non-linear and asymmetric elastic characteristics of mooring lines and fenders. Another source is to be found in the slowly varying wave drift force. Although several possible causes for the slowly varying drift force can be assigned, none of them is capable of describing correctly the mechanism of the excitation. However, the tendency has been observed that the wave drift force is about proportional to the square of the wave height. As a consequence, in irregular waves the drift force varies in time with the succession of high and low waves. The period of this variation can be, and often is, in the range of the natural period of oscillation of the object in the mooring or anchoring system. As also the damping is relatively small at these extremely low frequencies, resonance might occur, and the subharmonic motions may become predominant, in spite of the fact that the drift force in itself is only a second order effect. See for instance Fig. 11, where the forces in the mooring system of a moored vessel have been presented, together with the wave motion, and the subharmonics appear to be predominant.

Although in special conditions superharmonics (motions with periods smaller than the wave periods) can also be observed, they will not be further discussed here.

Evidently the forces in the mooring or anchoring system will reveal the same type of subharmonic behaviour as the motions. The impact that these subharmonic force fluctuations can have on the design forces will be illustrated with the use of some results of an experimental study, carried out at the DHL, on a 270 000 dwt ore carrier moored against an open jetty (Ref. 7).

**Model set-up:** The data of the ship were:

$\nabla$	= 320 000	m <sup>3</sup>
$L_{oa}$	= 350	m
$L_{pp}$	= 330	m
$B$	= 55	m
$T$	= 20.5	m
$T_\psi$	= about 14	s
$d$	= 24	m
Model scale = 1 to 100.		



The waves applied were regular and irregular long-crested waves, generated as described in sections 3 and 4.1. A variety of wave conditions has been applied. The mooring system used is shown in Fig. 9, depicting a total of 18 mooring lines and 6 fenders. The elastic characteristics are presented in Fig. 10, and are essentially half linear.

**Tests in regular waves:** In regular waves a certain offset occurred due to the drift force. In many cases the ropes became slack and the contact between ship and fenders was lost, but the phenomena remained purely periodical and no subharmonics occurred.

For the wave heights up to 2.5 m that were used the relation between the harmonic force variations and the wave heights was reasonably linear, and so in Fig. 12 the quotient of the force maximum minus pretension and the wave height has been plotted.

The forces that occurred were not extreme. For beam waves they were generally higher than for head waves. This was especially the case for the fender forces. The poorly damped roll resonance apparently increases the forces for beam waves having a period of 14 s.

**Tests in irregular waves:** For irregular waves the subharmonic oscillations take the main part of the total force, see Fig. 11, which holds good for head waves. As a consequence, the statistical distribution of forces that should be about a Rayleigh distribution for a linear system shows progressively increasing forces for decreasing percentages of exceedance, as shown in Fig. 13. To obtain a survey as to how forces varied as a function of wave height, -period, and -direction the statistical distribution of each signal for each test was characterized by the one-percent value, viz. the value that is exceeded by only 1 per cent of all force peaks ( $F_{a1\%}$ ).

**Comparison of test results:** It will now be checked whether the often applied procedure of predicting the behaviour of a system in irregular waves from tests in regular waves leads to correct answers.

Although the restoring forces from ropes and fenders are quite non-linear, the test results in regular waves give the impression that up to wave heights of 2.5 m the system behaves as a linear system. The force fluctuations were quite linear with wave heights and no force fluctuations with frequencies differing from the wave frequency. Thus it could be assumed that for an irregular wave field having a significant wave height of  $H_s = 1.25$ , and consequently a maximum wave height smaller than 2.5 m, the system would behave in a linear way as well.

The output spectrum of a linear system having a transfer function  $T_{\eta F}(\omega)$  from an input wave spectrum  $S_{\eta}(\omega)$  is, according to the spectral analysis theory:

$$S_F(\omega) = [T_{\eta F}(\omega)]^2 \cdot S_{\eta}(\omega) \quad (5)$$

For waves following the Rayleigh distribution (section 2), the significant wave height  $H_s = 4 \sqrt{m_0}$  ( $m_0$  = total area of the wave energy spectrum). Similarly for the force  $F_a$  it follows that  $F_{as} = 2 \sqrt{M_0}$  and  $F_{a1\%} = 3.05 \sqrt{M_0}$  ( $M_0$  being the total area of the force spectrum). So

$$F_{a1\%} = 0.76 \sqrt{\frac{M_0}{m_0}} \cdot H_s$$

If in a simple case the function  $T_{\eta F}$  is more or less constant over the spectrum width, and the value of  $T_{\eta F}$  in the spectrum peak is taken, it follows that

$$F_{a1\%} = 0.76 \cdot \frac{F_a}{\eta_a} \cdot H_s \quad (6)$$

After this the maximum force is obtained by adding the pretension. A few of these calculations for  $H_s = 1.25$  m and  $T_p = 18$  s are given here as an example.

	head waves			beam waves		
	$F_{1\%}(tf)$ computed	$F_{1\%}(tf)$ meas.	ratio	$F_{1\%}(tf)$ computed	$F_{1\%}(tf)$ meas.	ratio
mooring lines:						
F <sub>1</sub> and F <sub>6</sub>	23.5	25-22	1.0	23-27	49-43	1.84
F <sub>3</sub> and F <sub>4</sub>	23	29-28	1.24	18-21	20-24	1.13
fenders:						
F <sub>7</sub> and F <sub>8</sub>	50-45	90-85	1.85	90	260-280	3.0

From these examples it appears that computations on the basis of test results on regular waves may greatly underestimate the one-percent forces: a difference of as much as a factor of 2 or 3 may

even occur. This difference may indeed be even greater if the design load, which will be rather the 0.01-per cent than the one per cent value, is to be calculated. This is due to the fact that the curves for the cumulative frequency distributions in the small percentage range appear to be steeper than those of the Rayleigh distribution which should be assumed for the linear model (see Fig. 13).

It is to be noted that the ratios given in the Table may differ considerably for different ships, mooring arrangements, pretensions, etc.

## 5.2 Ship motions due to harbour basin oscillations

Harbour basin oscillations may easily lead to large forces in the mooring system, as the natural oscillation periods of the moored vessels can be in the range of the oscillation periods of the basin. Harbour basin oscillations may be caused by atmospheric or seismic conditions (seiches and tsunamis), they may also be initiated by the wind waves, as will be explained hereafter.

**Radiation stress:** A phenomenon associated with surface waves (but also with internal waves, electromagnetic- or acoustic waves) is the radiation stress. By definition the radiation stress is the excess flux of momentum due to the presence of the waves (Ref. 8). The principal component of the radiation stress  $S_{xx}$  (in the direction of propagation of the waves) is

$$S_{xx} = \int_{-z}^{\eta} (\rho + \rho u^2) dz - \int_{-z}^0 \rho_0 dz \quad (7)$$

Further elaboration shows that

$$S_{xx} = E \left( \frac{2kd}{\sinh 2kd} + 1/2 \right), \text{ or in shallow water}$$

$$S_{xx} = 3/2 E \quad (8)$$

In a system of wave groups, propagating with the wave group velocity  $C_g$ ,  $S_{xx}$  will in regions of high energy be larger than in regions of low energy. From the equation of conservation of mass and momentum, it follows that

$$\rho z = - \frac{S_{xx}}{gd - C_g^2} + \text{constant} \quad (9)$$

or with  $S_{xx} = 3/2 E = 3/4 \rho g a^2$

$$\bar{z} = - \frac{3 g a^2}{4(gd - C_g^2)} + \text{constant} \quad (10)$$

So the effect is, that water is expelled from under the regions with high energy, towards regions with low energy (Fig. 14). Consequently a surging motion of the mean water level develops, the period of which depends on the group formation and the group velocity of the wave motion. For a harbour basin this surging motion outside may well lead to harbour oscillations, if the dimensions of the basin are such that the natural oscillation period or periods are in the range of periods of the external surging motion.

**Harbour resonance:** As an illustration the effect of the grouping and associated surging motion will be discussed for an existing harbour at the Algerian coast.

The harbour layout is shown in Fig. 15. For this harbour a numerical computation has been carried out at the DHL, to determine the response of the basins to external oscillations. The schematization of the harbour for the computer simulation is shown in Fig. 16, and a few relevant response curves (in the smaller period range) in Fig. 17.

A position of the ship at the point with maximum fluctuations of the slope of the water surface (generally the nodal point) will be most adverse. According to Fig. 17 strong oscillations (transversal oscillations) with a period of 60 s. can occur at the points  $C_1$  and  $C_2$ . At this period of 60 s the (transversal) oscillations at the points  $E_1$  and  $E_2$  are insignificant, so for the berths between the points  $E_2$  and  $C_2$  an amplification factor for the water surface inclination of about 6 can be expected.

Assuming external waves with  $T = 10$  s. and  $a = 1$  m and a water depth of 15 m,  $z$  becomes 0.106 m. So in wave groups with  $0 < a < 1$ , the maximum variation of  $z$  will be 0.1 m. However, the grouping will be random, and consequently also  $z$ . The energy within the frequency band of the resonance peak of Fig. 17 is

estimated to be in the order of 10 per cent of the total energy. Consequently the surges in this frequency band will be in the order of  $\sqrt{(0.1) \times 0.1} = 0.03$  m. Amplification by 6 then leads to differences in surge amplitudes at  $C_2$  and  $E_2$  of about 0.2 m.

**Ship oscillations:** For a ship with a displacement of 40 000 m<sup>3</sup>, at berth between  $C_2$  and  $E_2$ , the exerted force will be about  $(a \cdot 2\pi)/L \cdot 40\,000 = 75$  tonf. The effect of currents can be neglected.

This force will still not directly lead to intolerable conditions, provided no resonance occurs. The natural period of oscillation of the mass-spring system of ship and mooring lines is by approximation

$$\omega = \sqrt{\frac{c}{C_m \cdot m}}$$

for  $\omega = 0.104$  ( $T = 60$  s),  $C_m = 1.1$  and  $m = 40\,000$  tons,  $c$  becomes  $c = 40$  tonf/m. Assuming that the surging forces will be absorbed by the springs, and a length of lines of 40 m, the required elasticity for resonance becomes 40 tonf/2.5% elongation or 16 tonf/% elongation.

The following elasticities can be expected in practice:

steel : 30–50 tonf/% elongation  
 nylon/polypropylene : 1–2 tonf/% elongation  
 Manilla : ~10 tonf/% elongation.

Applying all steel wires the system will be too stiff to create resonance problems. However, applying Manilla ropes, or steel lines with nylon tails, resonance is not excluded.

In the example the direct effects of the waves on the ships was not of importance as appeared from wave penetration tests. Nevertheless the indirect effects can become important, which should be taken into consideration when testing the ship behaviour in a physical model. Clearly, the correct reproduction of the irregular sea waves is essential in that case.

**Surf beat:** A special case of harbour basin oscillations due to external wave conditions is the situation where waves break at or near the harbour entrance. Mass transport in the breaking waves (also arriving in groups) additional to the surging motion described before will be the driving force for the oscillations. This phenomenon has been reported in studies on small ports (Ref. 9), where use was made of random waves in the testing basin. With regard to the limited sizes of the ships, resonance is not likely to occur, and even in resonance conditions the forces in the mooring lines will not directly become excessive.

### 5.3 Motions of freely floating objects

An often applied procedure in assessing the motions of a freely floating object, is to measure the response at a range of discrete wave frequencies, in regular waves. The behaviour in an irregular sea can then subsequently be determined by multiplying the transfer function thus obtained with the wave energy spectrum, which yields the energy spectrum of the motion component concerned. In spite of the fact that the response as such is most often linear, also here problems may be encountered due to non-linearities in the wave motion.

As described in section 3, parasitic- or secondary waves will be generated with a sinusoidally moving wave board and at large values of the parameter  $a \cdot L^2/d^3$ . Although in principle this parameter can be reduced by reducing the wave amplitude  $a$ , measuring accuracy and scale effects set a limit to this. If now the response of an object to the waves is tested at  $a \cdot L^2/d^3 > 10$  (see section 3), the resultant motion will be caused by a wave system of two discrete frequencies,  $f_0$  and  $2f_0$ .

Sometimes use can be made of the length of the wave flume and the fact that the group velocity of the secondary waves is smaller than for the basic waves, so the experiment can be run after the first waves of the train of basic waves have passed, and before the secondary waves (and the reflected basic waves from the end of the flume) arrive. If this is not possible, the experiment can best be carried out in random waves. As the motion-control of the wave board in that case is adjusted so as to arrive at a proper wave spectrum at the site of the model, the occurrence of free secondary waves is no problem. After all there is no difference whether a particular frequency component is the result of the imperfect motion of the wave board, or contained in the input signal from the start. The spectra of the various motion components of the floating object can now be determined from the measurements and together with the wave spectrum transfer functions can be derived, to predict the motions at other than the tested wave spectra.

### List of symbols

$a$	= wave amplitude
$B$	= breadth of ship
$c$	= spring constant
$c$	= phase velocity of the waves
$c_g$	= group velocity of the waves
$C_m$	= added mass coefficient
$d$	= water depth
$E$	= energy
$E(f)$	= energy density at frequency $f$
$F$	= shift frequency
$F_{a1\%}$	= force in component $a$ , exceeded in 1% of the waves
$F_{as}$	= significant force in component $a$
$f$	= frequency
$g$	= acceleration of gravity
$H_s$	= significant wave height
$k$	= wave number, $2\pi/L$
$L$	= wave length
$L_{oa}$	= length overall
$L_{pp}$	= length between perpendiculars
$m$	= mass
$M_0$	= total energy of force spectrum
$m_0$	= total energy of wave spectrum
$p$	= dynamic pressure
$p_0$	= hydrostatic pressure
$S_F(\omega)$	= energy density in force spectrum at frequency $\omega$
$S_\eta(\omega)$	= energy density in wave spectrum at frequency $\omega$
$S_{xx}$	= radiation stress in direction of wave propagation
$T$	= draught
$T$	= wave period
$T_\psi$	= natural period of roll
$T_p$	= period with maximum energy density
$U$	= Ursell parameter
$u$	= orbital velocity
$z$	= vertical coordinate
$\bar{z}$	= variation of mean water level
$\nabla$	= displacement
$\phi$	= phase angle
$\eta$	= surface elevation
$\rho$	= mass density of water
$\omega$	= frequency, $2\pi/T$

### References

- (1) Wilson, J. R. and Baird, W. F. 'A Discussion of some Measured Wave Data', *Proc. 13th Conference on Coastal Engineering*, Vancouver, 1972.
- (2) Patterson, M. M. and Bea, R. G. 'Oceanographic Data from Hurricane Camille', *Proc. Sixth Annual Offshore Technology Conf.*, Houston, 1974.
- (3) Goda, Y. 'Numerical Experiments on Wave Statistics with Spectral Simulation', *Report of the Port and Harbour Research Institute*, Japan Vol. 9, No. 3, 1970.
- (4) Biesel, F. 'Theoretical Study of a Certain Type of Wave Machine', *La Houille Blanche*, Vol. 6, No. 2, 1951.
- (5) Anderson, Fennie and Roberts. 'New Noise Generator Synthesizes Pseudo-Random Gaussian Noise', *Hewlett-Packard Journal*, Sept. 1967.
- (6) Funke, E. R. 'Random Wave Signal Generation by Minicomputer', *Proc. 14th Conference on Coastal Engineering*, Copenhagen, 1974.
- (7) Bunt, J. D. van den. 'Model Study on Mooring Forces due to Regular and Irregular Waves', *Nato A.S.I. Conference*, Wallingford, May 1973.
- (8) Longuet-Higgins, M. S. and Stewart, R. W. 'Radiation Stresses in Water Waves; a Physical Discussion, with Applications', *Deep Sea Research*, Vol. 11, 1964.

- (9) Gravesen, H., J. and Nielsen, A. H. 'Problems of  
Physical Model Harbours', *Proc. Modeling '75*,  
San Francisco, 1975.

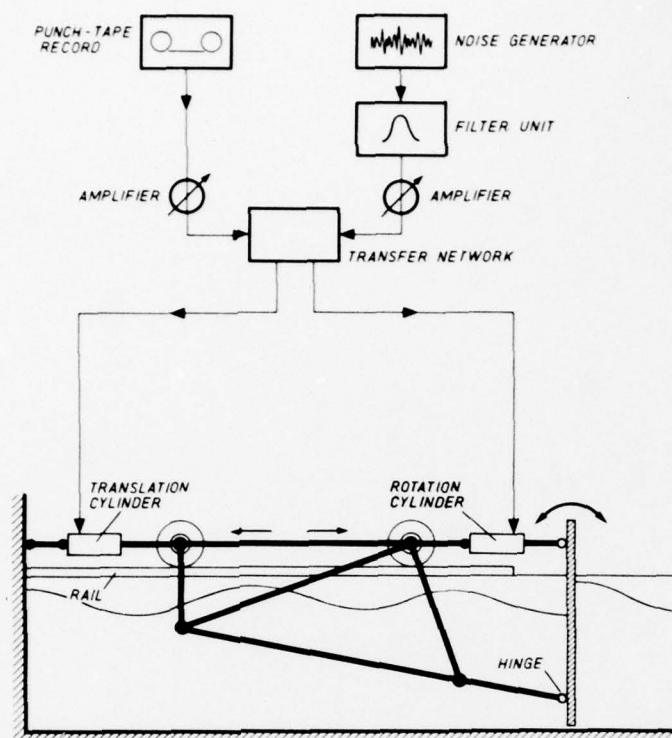


Fig. 1: System set-up wave generator

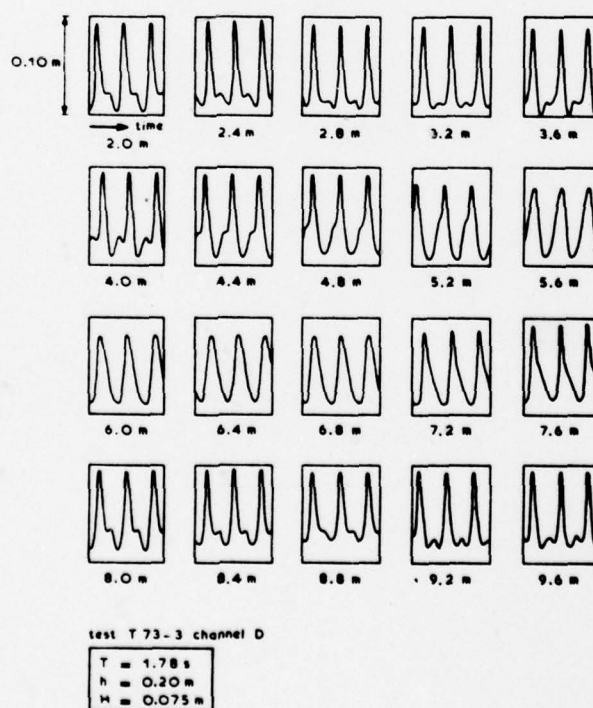


Fig. 2: Typical variation of wave profile with distance to wave generator



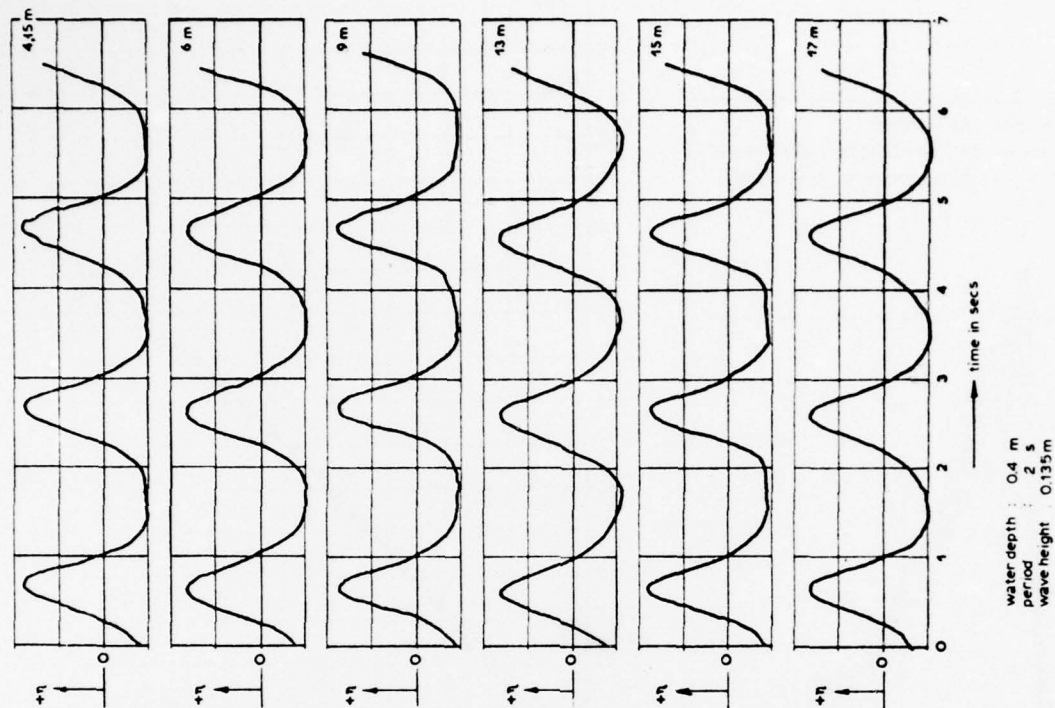


Fig. 3a: Wave profiles at sinusoidal motion of wave board

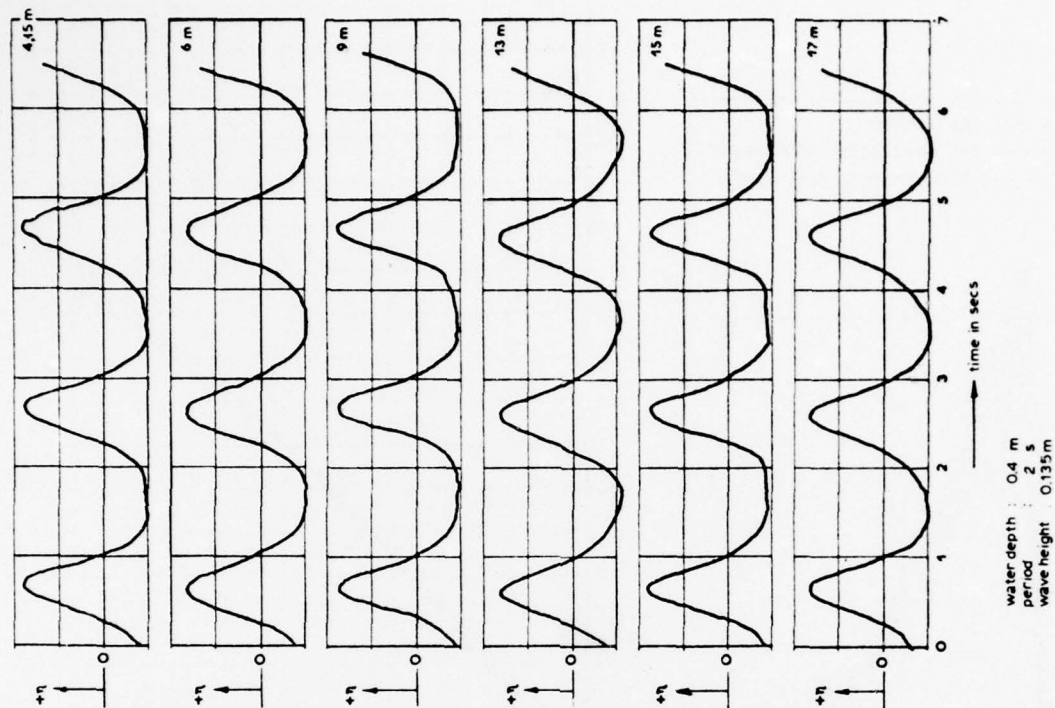


Fig. 3b: Wave profiles at optimal motion of wave board

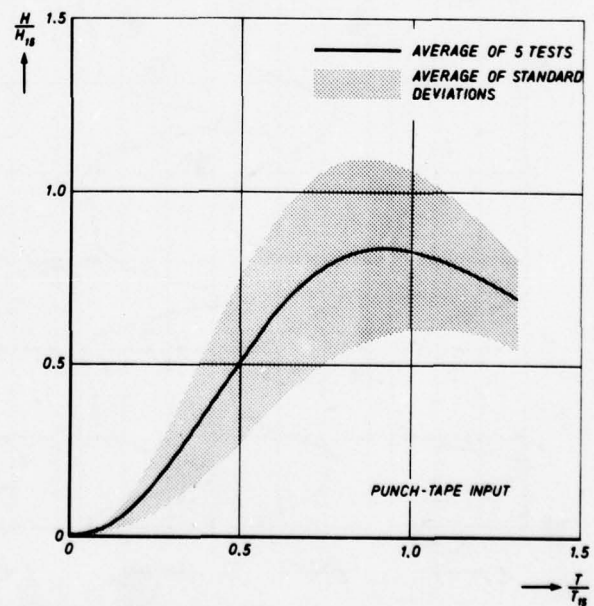
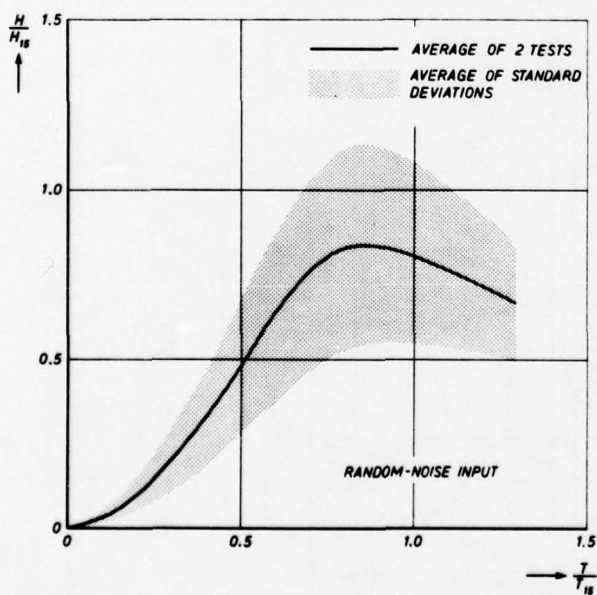
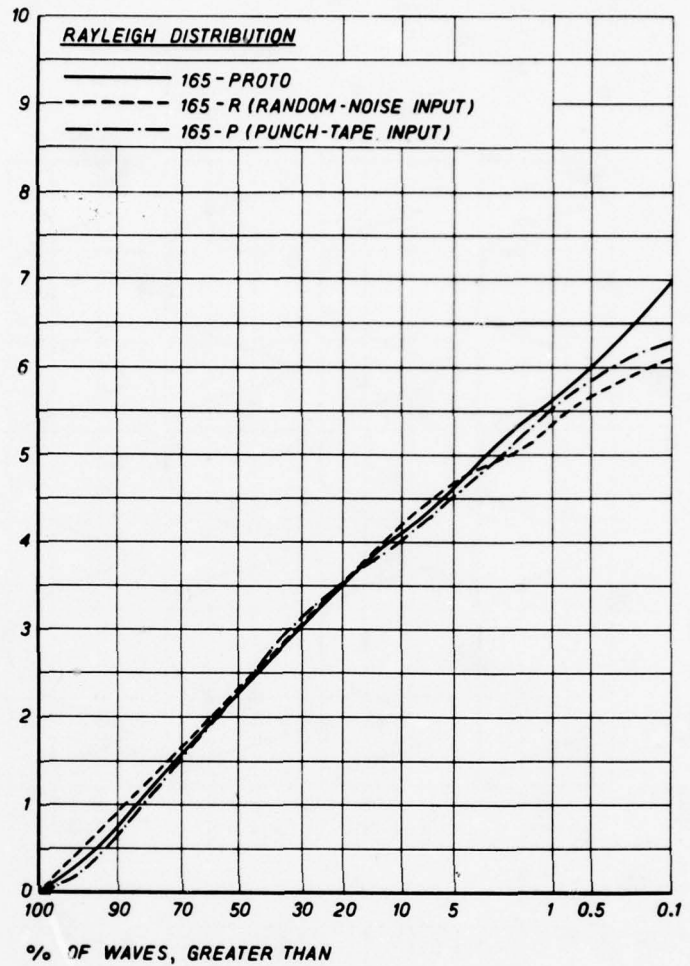
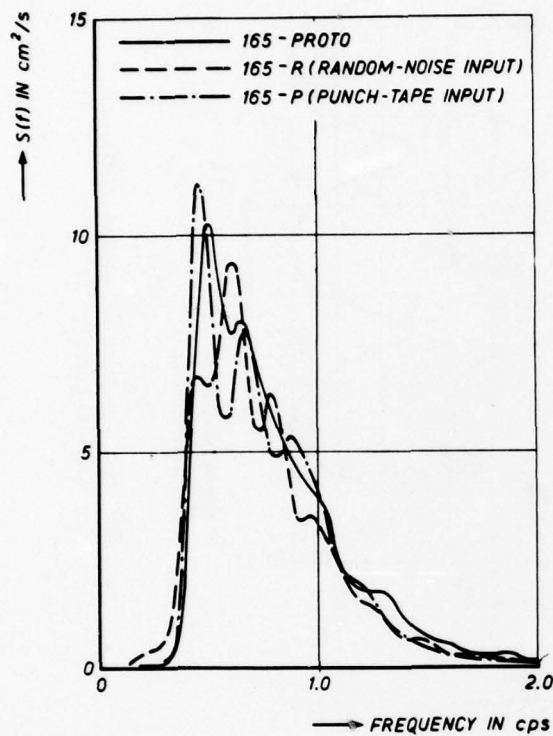
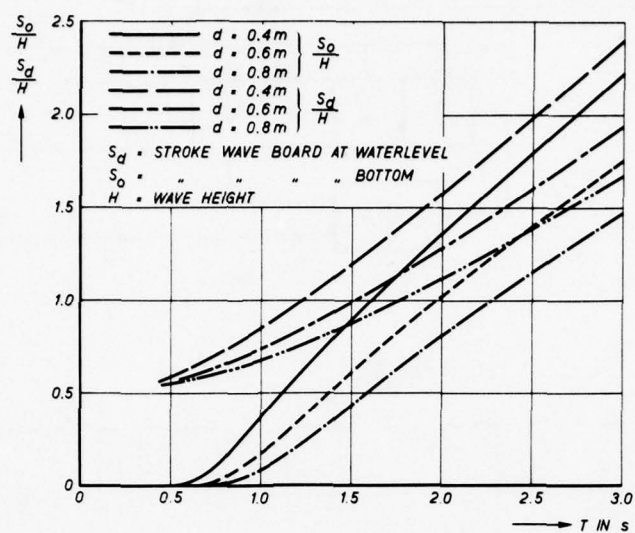
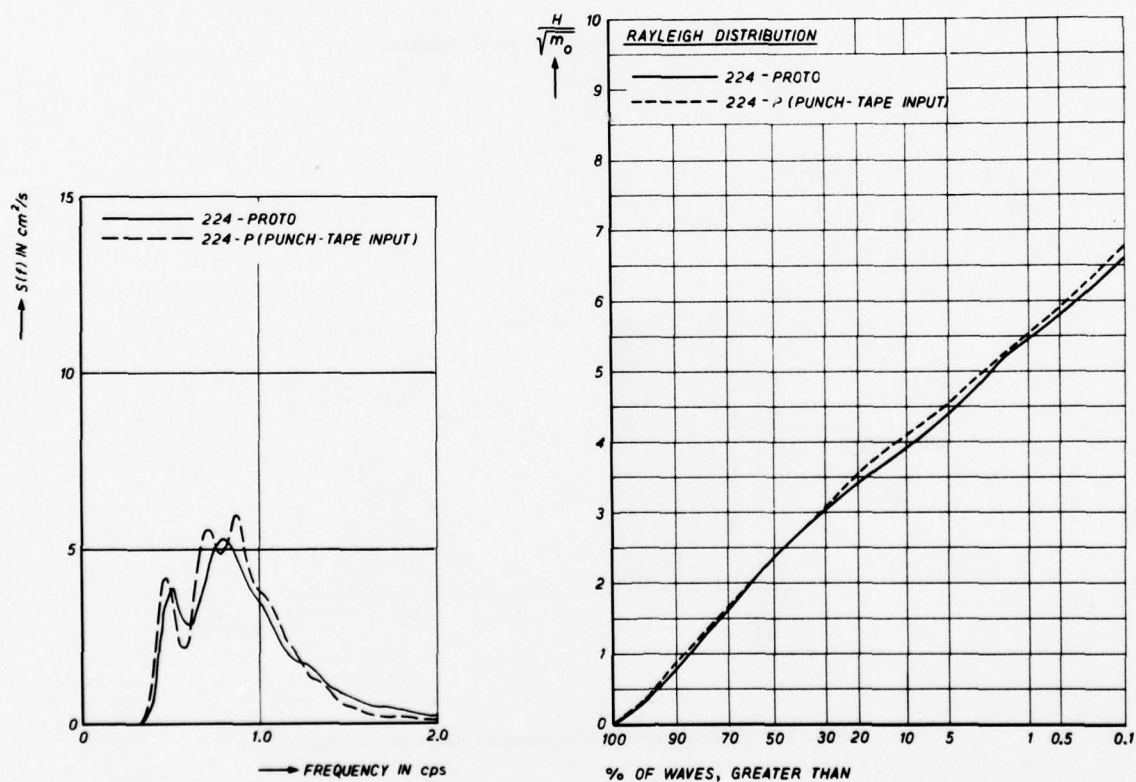


Fig. 8: Comparison of energy spectra, wave height distribution and H-T relation for  
 —prototype record  
 —model waves applying the prototype record as input  
 —model waves applying random noise



**Fig. 4: Transfer function wave height to wave board**



**Fig. 5: Wave spectra and wave height distribution of prototype record, and of model waves applying the prototype record as input**

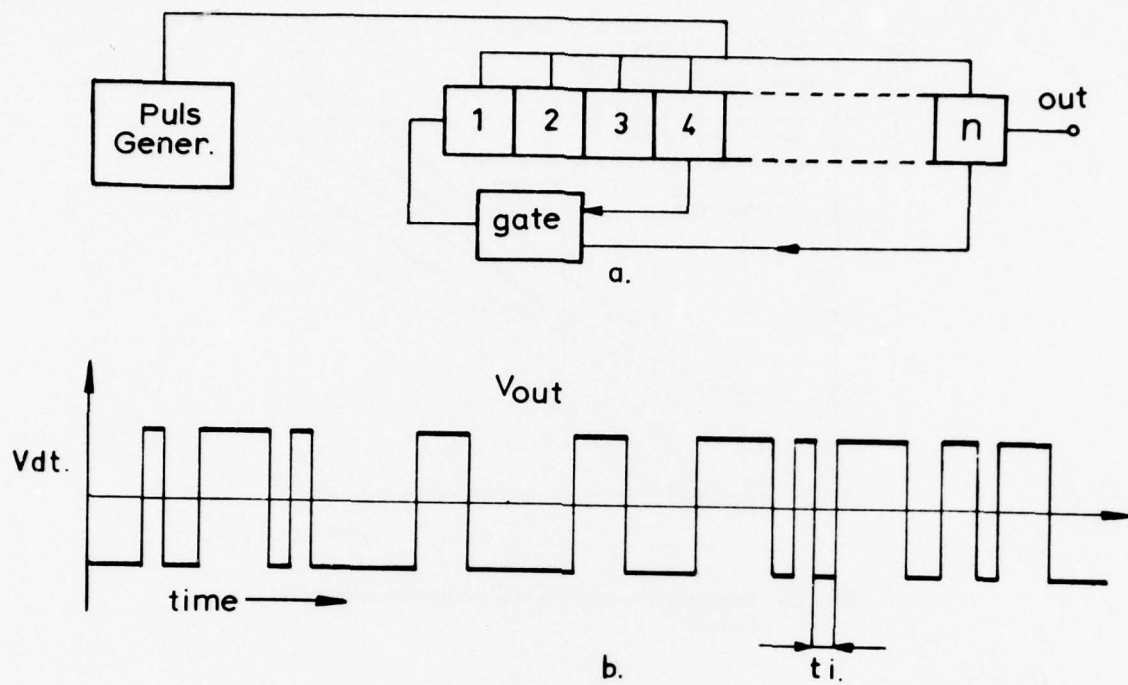


Fig. 6: Output random noise generator

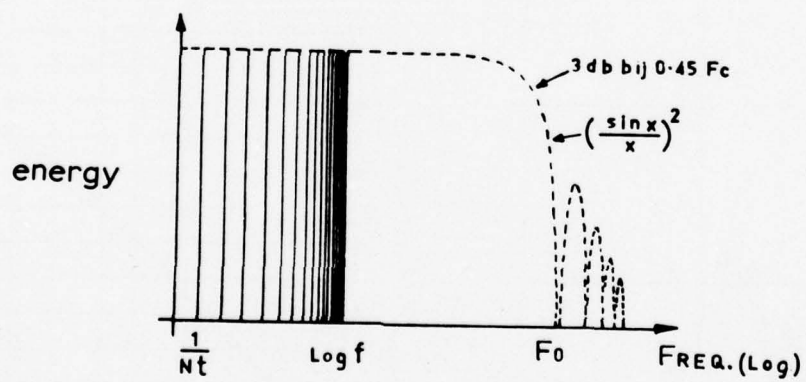


Fig. 7: Energy spectrum pseudo-random noise



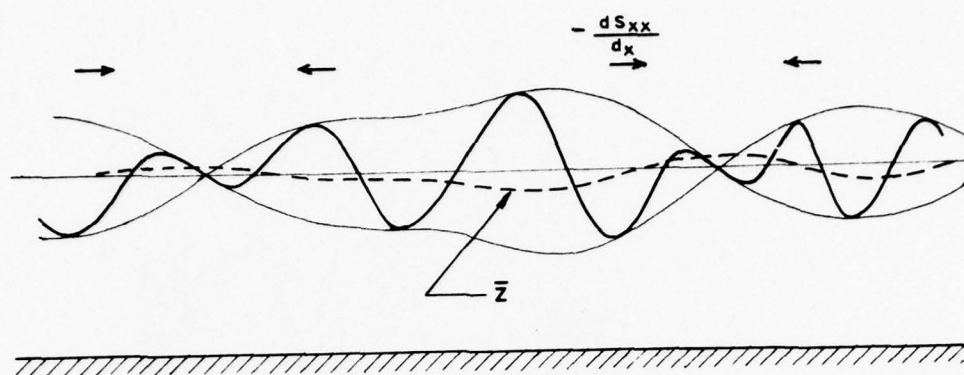


Fig. 14: Variation of mean water level in wave groups

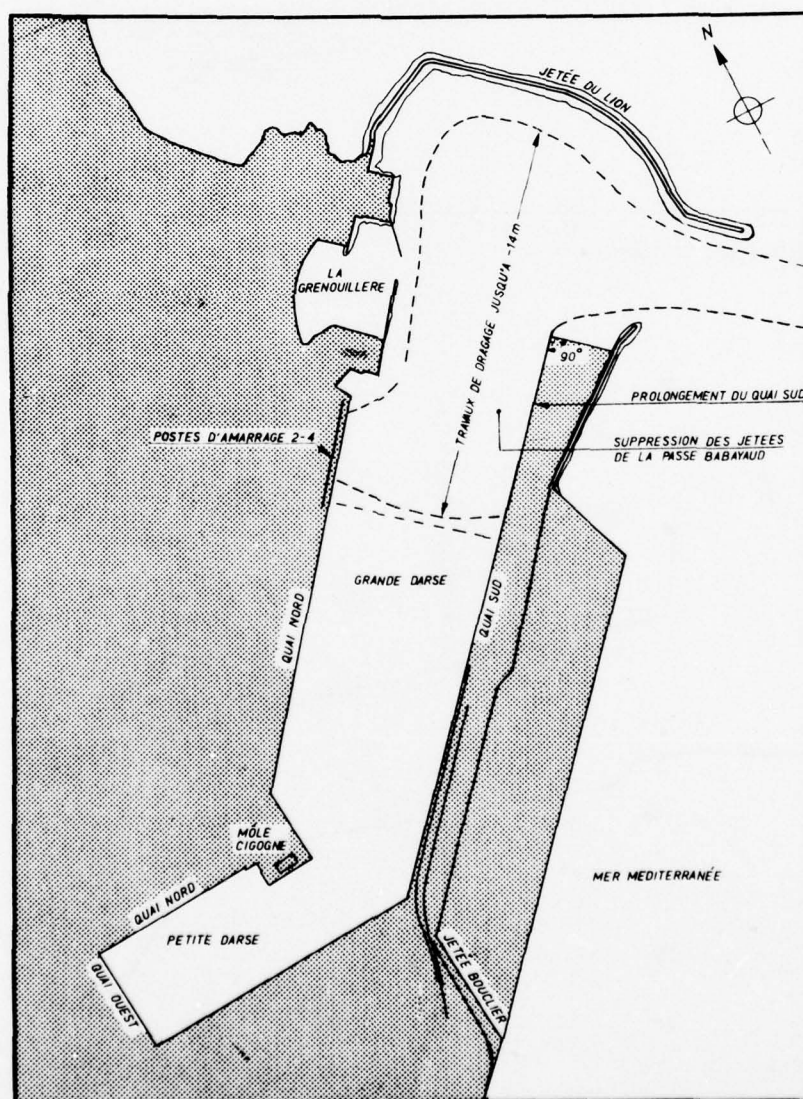


Fig. 15: Port layout

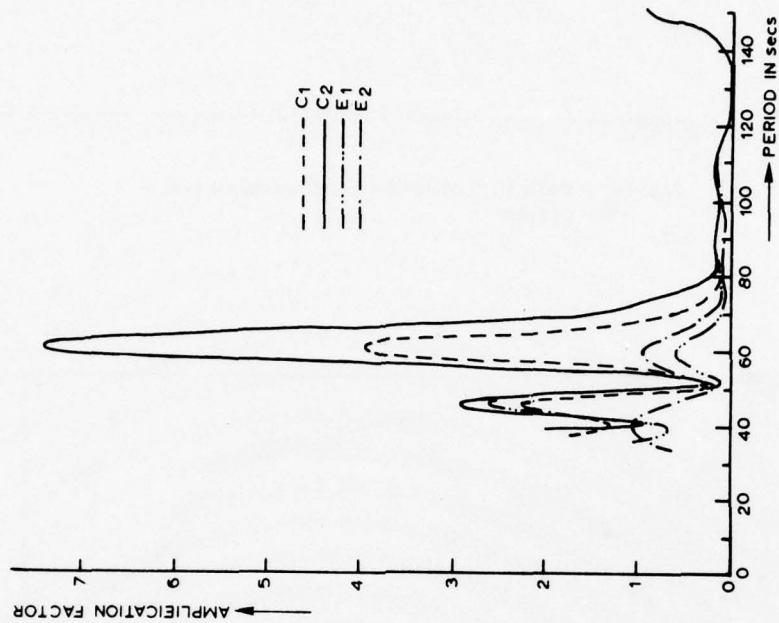


Fig. 17: Response curves

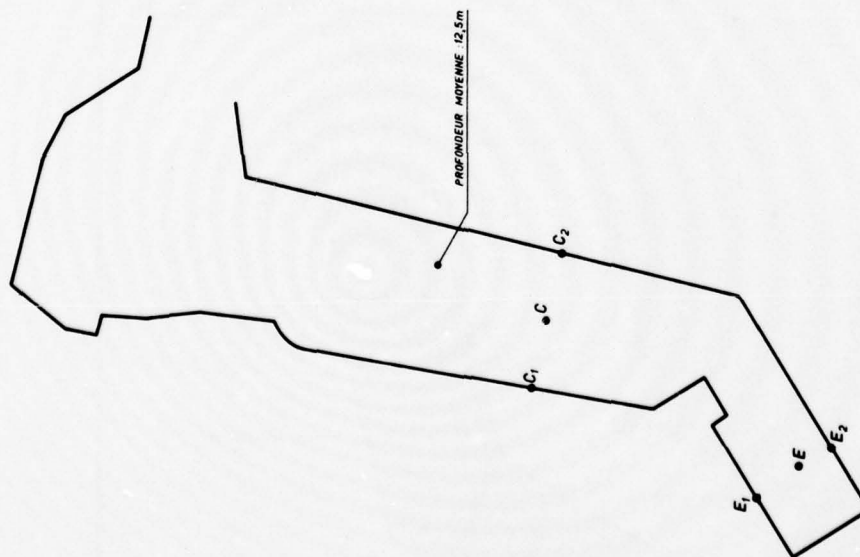


Fig. 16: Schematized port layout for oscillation computation

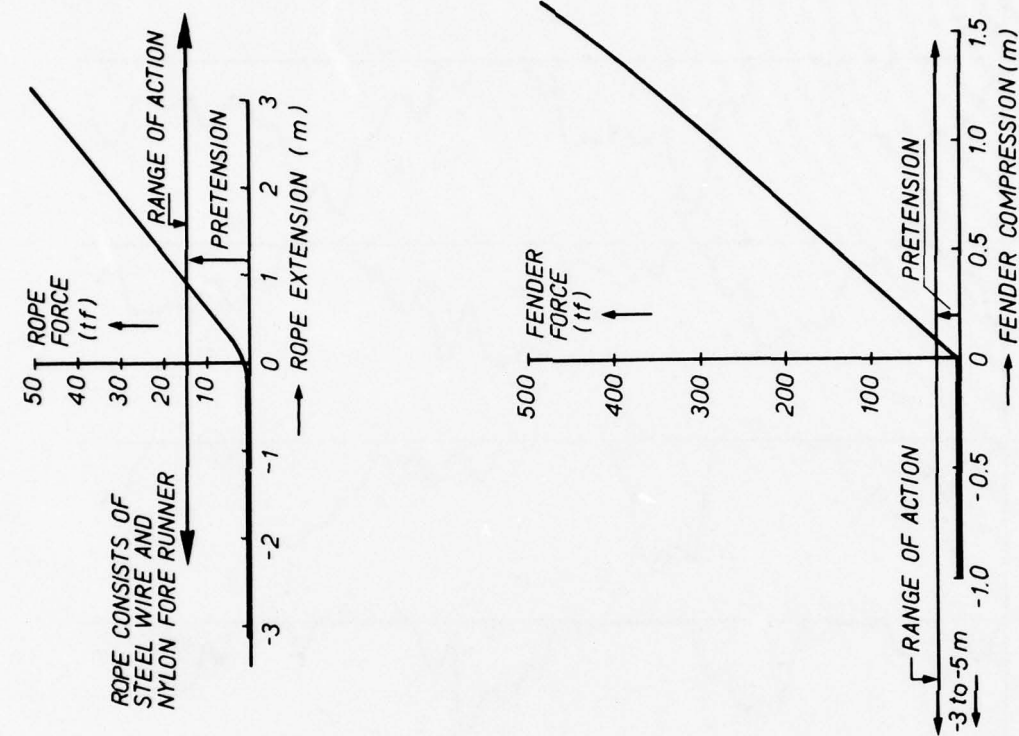


Fig. 10: Stiffness characteristics of ropes and fenders

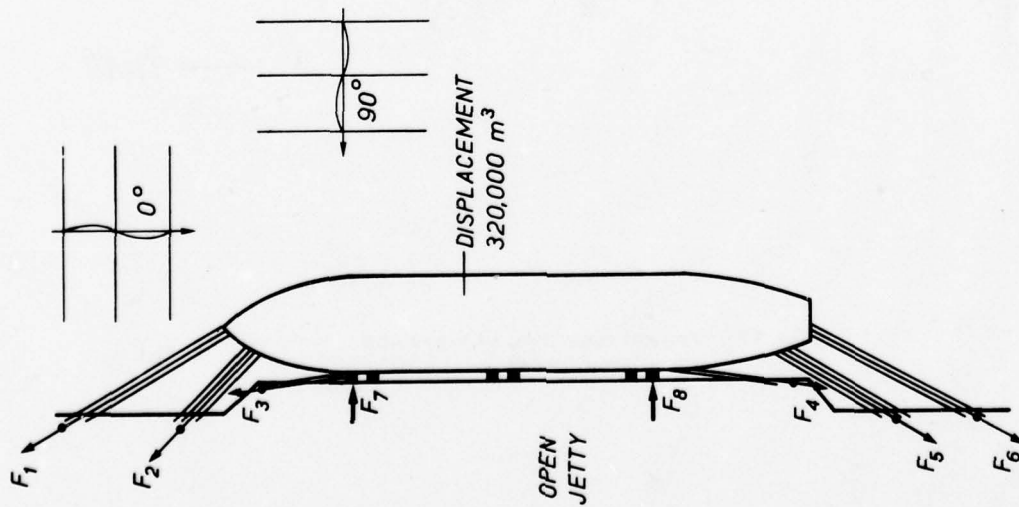


Fig. 9: Mooring arrangement

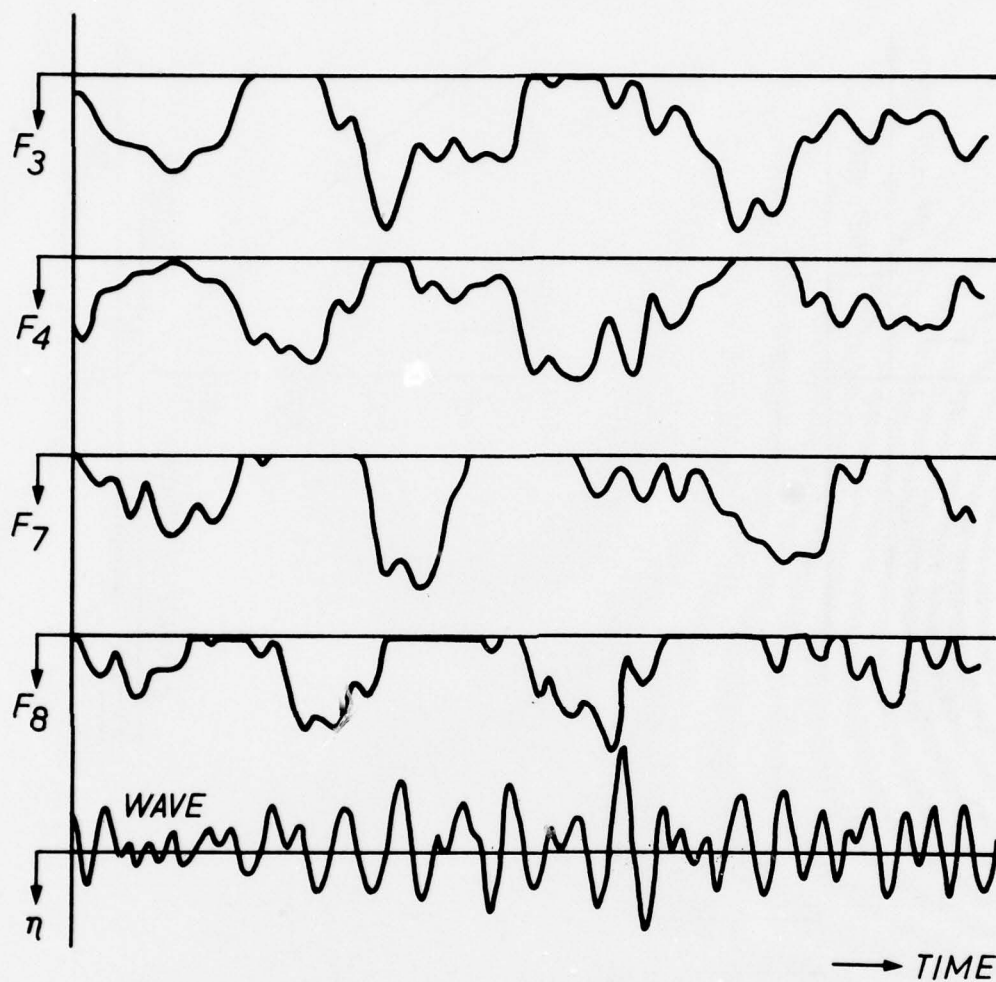


Fig. 11: Typical recording of wave and associated forces



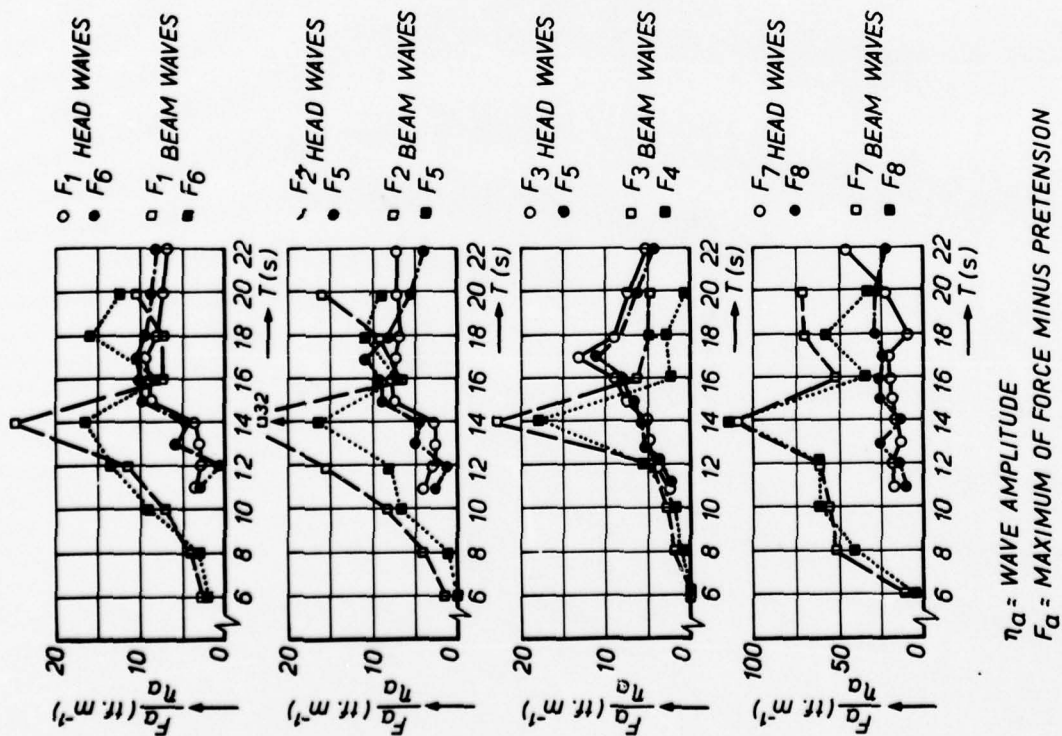


Fig. 12: Ratio between forces and wave amplitudes for regular waves

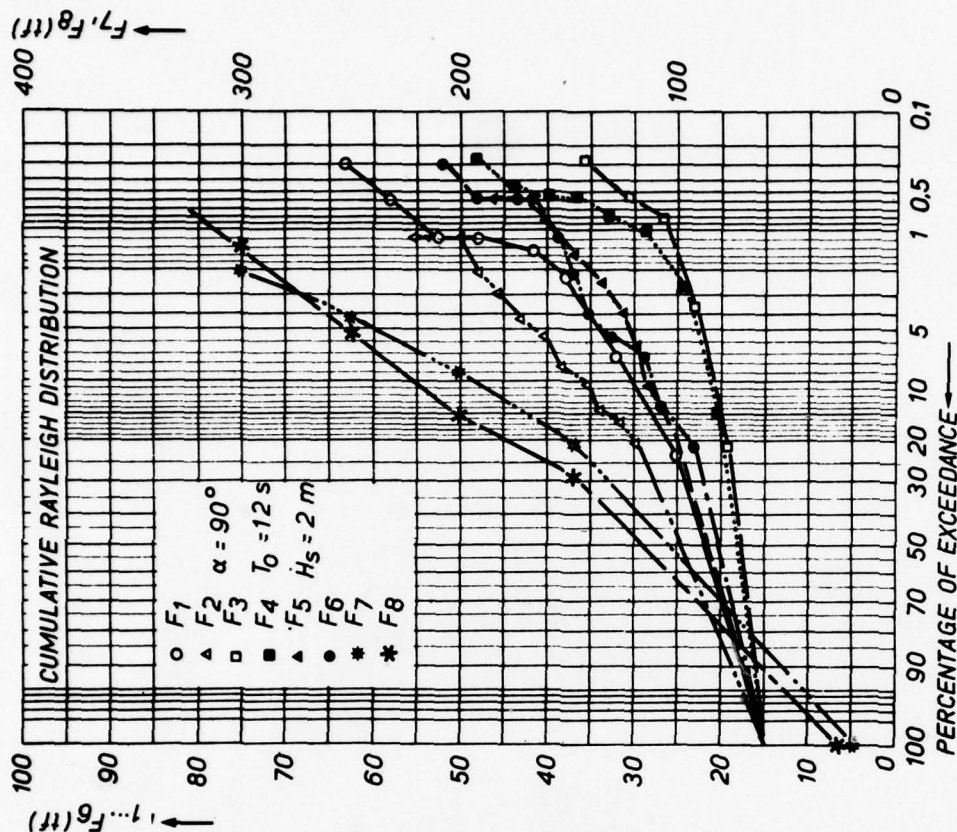


Fig. 13: Typical frequency distribution of forces

# Discussion on Paper by N. Hogben

R.C. Mcgregor

This type of wavemaker for the creation of very large experimental waves is likely to find many uses in towing tanks around the world. The wavemaker as presented is probably the simplest design that could have been envisaged. I wonder, would the author comment on any alternative features that were tried and found to give insufficient return for increased complexity?

Creating waves by towing an angled board is not equivalent simply to a travelling pressure field since there is also a physical water displacement somewhat similar to a progressing sluice gate. This second effect would not seem likely to give velocity distributions in the wave which correspond to those of a normal progressive wave. Would the author comment on whether particle velocities have been measured and whether the velocity induced forces have been in accord with theoretical prediction?

L.J. DOCTORS

The discussor would like to refer to Dr. Hogben's calculations in which he attempted to correlate the drag of the planing-plate wavemaker with the wave resistance determined from the height of the downstream waves.

For example, up to a Froude number (based on water depth) of 0.6, Fig.9(c) shows that the drag tends to agree with linear wave theory based on the height of the wave system actually measured. Above this Froude number, the linear wave theory result is supposedly too low.

It is suggested here that the discrepancy is largely due to the jet drag - resulting from the momentum of the water thrown ahead of the plate. In the experiment, this water would land on the upstream main flow and be a prime cause of the turbulence and aeration which is so evident. For example, Maruo (Ref.7) found approximate formulas for the lift coefficient and the jet-drag coefficient for the planing of a two dimensional flat plate (his equations (31) and (39)). They are:

$$C_L/\alpha = \frac{1}{1/\pi + 1.477 (1/2 F^2)} \quad (i)$$

and

$$C_J/C_L^2 = \frac{1}{\pi} + 0.477 (1/2 F^2) \quad (ii)$$

where F is the Froude number based on wetted plate length, and  $\alpha$  is the angle of attack in radians. Noting that the total-drag coefficient,  $C_D$  is the sum of the wave-resistant coefficient,  $C_W$ , and the jet-drag coefficient, one can combine the above pair of equations to give:

$$C_W/C_D = \frac{1}{2F^2/\pi + 1.477} \quad (iii)$$

Thus, for example, at a Froude number of 2.0, the wave resistance constitutes only about one-quarter of the total drag. (Eqns (i)-(iii) which apply when the Froude number is greater than about 1.0 agree with the finite-element calculations in Ref.8.)

Possibly the author could check to see if this explanation accounts for the "missing" difference. Of course, the skin-friction drag of the plate must be considered too, and the nonlinear effects referred to in the paper are still relevant.

A further point is in regard to the quality of the generated wave. Presumably in most experiments one requires as "clean" a wave as possible. This cannot be achieved by reducing the angle of attack of the plate. Apart from reducing the generated wave height, the energy loss due to the jet would still bear the same relationship to the wave drag - according to linear theory.

A jet-free form can be generated using a parabolic plate with the curvature downwards, as pointed out by the discussor (Ref.8). Unfortunately, the amount of curvature depends on the plate Froude number. Thus, in order to accommodate different carriage speeds one would require an adjustable plate. Alternatively, it should be possible to design a plate of more complicated shape, such that as the Froude number and wetted length varied with carriage speed, so the jet-free condition would be maintained.

The discussor would like to conclude by congratulating Dr. Hogben on a most ingenious invention of great practical application.

## REFERENCES

7. Maruo, H. Twodimensional theory of the hydroplane, Proc. First Japan Nat.Cong. Appl.Mech., Science Council of Japan, Tokyo, (1952), pp. 409-415.
8. Doctors, L.J. Representation of planing surfaces by finite pressure elements. Proc. Fifth Australasian Conference on Hydraulics and Fluid Mechanics, Christchurch, New Zealand, Vol.2 (1974), pp.480-488.

H. RITTER

The development of the beam wavemaker by Dr. Hogben made me wonder whether there might be some advantage in replacing the planing flat plate by a fully submerged hydrofoil at very shallow depth. This should avoid the energy loss associated with the quite considerable turbulent disturbance which occurs under the leading portion of the planing plate. The chord of the foil might

be made smaller than that of the plate and hence the wave should pass it more easily and with less energy loss when the towing carriage stops. Finally, it was hoped that the foil would allow the production of a bigger wave.

A quick and simple investigation was carried out in the same small channel as used by Dr. Hogben for his exploratory tests. First an available length of standard strut, chord 51 mm and thickness = 18 was used and this showed that an incidence of  $15^\circ$ - $25^\circ$  was suitable. This gave a maximum wave steepness of  $H/\lambda$  of about 0.062, the same as the planing plate and also a very similar maximum wave height.

A foil of NACA 0018 section, 100 mm-chord was then made and mounted on an existing strain gauge balance measuring lift and drag. For the depth available in the channel this corresponded to a full size chord in the towing tank of about 1 m. It was found that the foil incidence should be  $15^\circ$ - $28^\circ$ . At the higher of these angles, the height of the first wave crest, but not of the second one, was increased with a steep rise in drag. Submergence was adjusted for best waves and then the depth of flow over the top of the foil was about 0.2 x chord.

Comparative tests of a planing plate were also made on the same rig, repeating the more important conditions given in the present paper. The results confirmed that little or nothing was gained by using the foil rather than the plate. Neither the height nor the steepness of the waves was greater for the foil and the force balance showed that the drag and lift were also of very similar value. If the planing plate is run at an incidence greater than  $15^\circ$  then its wetted length is no more than the chord of the foil giving the same wave height.

The drag ratio  $D_w$  for the hydrofoil was within the scatter of the results in Fig.5 and the height of the second wave crest was practically constant with varying foil incidence.

A quick qualitative look was also taken at the waves generated with negative foil incidence and no advantage was apparent.

Since there is nothing to be gained in performance by using a hydrofoil instead of the planing plate, and there are disadvantages of more complicated construction and added difficulty in providing vertical retraction, the simpler design chosen by Dr. Hogben is to be preferred.

R.G. STANDING

This paper will be of considerable interest to owners of existing towing tanks who wish to test offshore structure models in large waves. I should like to show a few results from further tests on this device.

In Section 3.1, Dr. Hogben refers to a second series of tests carried out in No.2 tank with the flap angle  $\theta$  set at  $17\frac{1}{2}^\circ$ . In fact the angle turned out to be  $19^\circ$ , closer adjustment being difficult. To maintain a constant flap immersion depth the water level was lowered slightly, reducing  $d$  from 2.29 to 2.23 m. These tests have now been analysed and full results will appear shortly in reference (9). Two graphs are of particular interest.

Fig.13 shows wave heights  $H_2/d$  from Fig.10c overlaid with the new values. At high speeds,  $F_n > 0.7$ , the new flap angle caused slightly higher waves at the target point. The maximum height recorded was  $H_2 = 0.89$  m. This additional height was obtained with a reduction in  $D_w$ , shown in Fig.14, and therefore more efficiently; but as before, (Fig.9c), the curve rises steeply at high speeds. The reason for this rise is still not clear, but may be connected with:

- (i) the approach to the critical speed  $F_n = 1$ , where, despite increasing wave steepness  $H_1/\lambda$  (Fig.9d),  $H_1/d$  increases and the waves eventually become non-linear;
- (ii) at moderate speeds, turbulence losses below the flap's leading edge and in the following wave trough;
- (iii) at higher speeds ( $F_n > 0.83$ ), spilling over the top of the flap. This imposed additional fluctuating loads, making lift measurements and their interpretation difficult. Although the wave experienced energy losses tending to increase  $D_w$ , the immediate effect, due to the weight of water on the flap top, was to decrease the lift and apparent drag, and therefore  $D_w$  also.

Section 3.2.1 notes that the steepness limit of  $1/7$  is not achieved. This value applied to free waves, whereas the losses seem to occur in the transient flow below or immediately behind the flap where a different limit may apply. Furthermore, the first wave front is considerably steeper than the following waves where the measurements of  $H_1$  were taken. The leading wave slope may impose an upper limit on the steepness of waves which can be generated in this way. Presumably water depth also limits the steepness of longer waves.

Breaking of the first wave crest was visible at low speeds with the  $19^\circ$  flap angle. This seems to be connected with the lesser efficiency of this angle, the rapid rise in  $D_w$  and the lower wave heights  $H_2/d$  for  $F_n < 0.7$ . The choice of denominator in Fig.14 (which essentially divides drag by  $H_2^2$ ) gives undue prominence to the curve's low speed and to experimental errors therein, but these errors cannot explain the rapid rise entirely. It is also too large to be attributed to skin friction (by a factor of 10, assuming frictional drag per unit tank width =  $\frac{1}{2}C_F \rho L_w c^2$  with  $C_F = 0.004$ ), though the discrepancy in drag does vary roughly with  $c^2$ . There is evidence for a similar rise when  $\theta = 14^\circ$ , but at lower speeds where measurements are unreliable; so these results have been omitted.

Fig.11 has been re-examined. Much of the scatter is caused by speed difference between runs, because  $H_2/\lambda$  varies rapidly with  $F_n$  (Fig.10d). On restricting the speed range to  $F_n = 0.88 \pm 0.03$  and replotting  $H_2/\sqrt{\lambda d}$ , which is less speed-dependent in this range, a more coherent picture emerges. The results, confirmed by more extensive tests with  $\theta = 19^\circ$ , show that  $H_2$  is reduced by about 10% for each wavelength (about 15 m) by which  $x_2$  is shortened or  $x_1$  lengthened. This confirms the curve in Fig.11a, but the curve in Fig.11b is too steep.

The main conclusion of this second series of tests is that the higher flap angle offers some



advantages at high speeds, but is less efficient at the (less important) low speeds.

#### REFERENCE

9. Standing, R.G. Proving trials on the wanedozer, a travelling beam wavemaker. N.P.L. Division report No. 195, (1976).

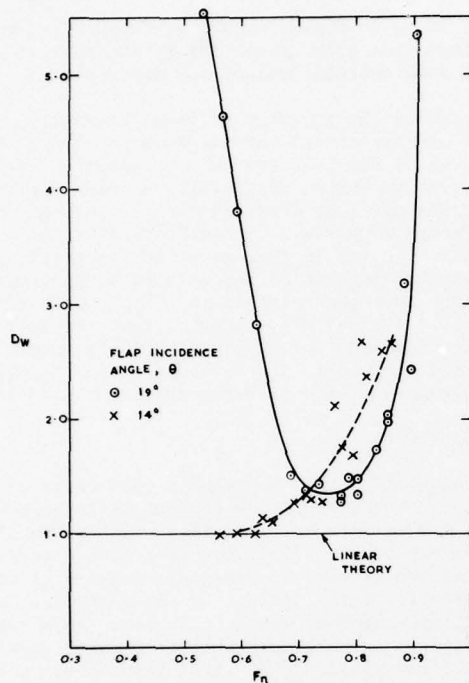


Fig. 13: Variation of wave height  $H_2$  at target point with carriage speed.

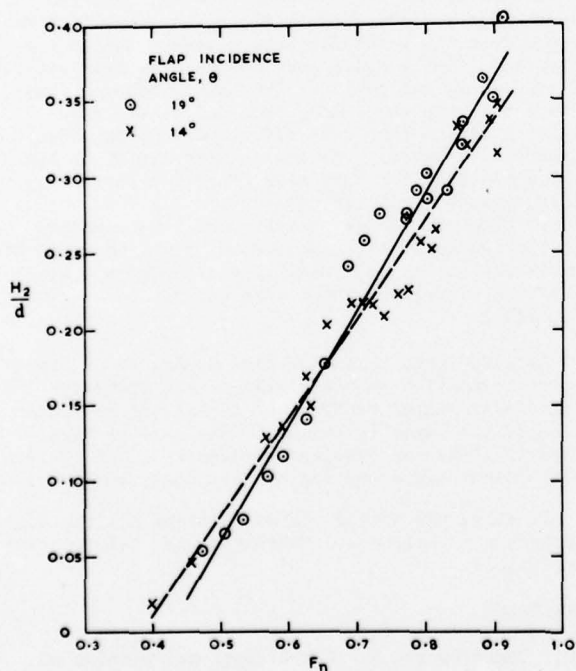


Fig. 14: Variation of flap drag with carriage speed.



# Author's Reply

H. RITTER AND R.G. STANDING

The author is grateful to his colleagues Dr. Ritter and Dr. Standing for supplying some valuable additional material not available at the time of writing the paper. It is gratifying to learn from Dr. Ritter that his investigations of a submerged foil device yielded similar results but led him to the conclusion that the simple planing plate arrangement is to be preferred. It is also reassuring that his experiments using a different method of drag measurements and including repetition of some of the planing plate tests confirmed the results in the paper.

Dr. Standing summarises the salient findings of the prototype test series with a higher flap angle which he has reported more fully in the reference which he cites. These are mentioned in the paper but were not completed in time for the results to be included. The most important finding is that with the higher flap incidence the maximum wave-height achieved is significantly greater and it may be seen in fact that  $H_2$  reaches a value of about 0.86 m. This encourages the author to believe that further increase of the angle would yield even higher waves. It was indeed originally intended in the light of the experiments in the small channel that the prototype should run at an incidence of  $25^\circ$  but unfortunately this proved impossible due to lack of clearance. The more permanent installation which has been designed, however, will have the capability of running with flap angles up to  $30^\circ$ .

L.J. DOCTORS

Dr. Doctors begins his interesting contribution with a discussion of the discrepancy in the energy budget described in Section 2.2 of the paper suggesting that it may be explained in terms of a jet drag effect. The pictures of the channel experiments in Fig.4 show that there was in fact no jet but there was certainly a tumbling disturbance in its place which no doubt involved substantial energy loss and could possibly be regarded as roughly equivalent to the effect of a jet. As noted in Section 2.2 of the paper, however, pitot measurements were made ahead of and behind the plate and though some energy loss was recorded it was only enough to explain about half of the discrepancy indicated by the relation of drag and wave height. A detailed account of these measurements is given by my colleague, Mr. J. Osborne, who carried out the experiments, in an internal memorandum.

The formulae he cites for assessing the significance of jet drag are presumably for deep water since they contain no depth parameter. They should not therefore be expected to apply to the experiments in question for which the Froude number based on depth exceeded 0.8. Nonetheless it may be of interest to note that the corresponding value of the Froude number based on wetted length (see Fig. 9e) was about 1.1. The formula (iii) thus gives  $C_W/C_D = 0.44$ , which means that the experimental

values of  $D_W$  in Fig.5a should be roughly halved for comparison with linear theory and this would indeed substantially reduce the discrepancy.

Regarding the question of wave cleanness, it should be appreciated that the waves arriving in the test area of the tank are free progressive waves and correspondingly very clean even when the waves behind the carriage are very dirty. This is apparent from a comparison in Fig.7c with 7a and 7b. Consideration was in fact given to the possibility of using the concept of the splashless parabola which was described already in 1958 by Cumberbatch, Ref.(10). It was felt, however, that the extra complication and sensitivity of setting required would not be justified specially in view of the poor agreement found between experiment and theory.

R.C. MCGREGOR

Turning now to Mr. McGregor's contribution, his question about alternative designs has been answered in the replies to Dr. Ritter and Dr. Doctors. The comment may be added, however, that a straight flap has two degrees of freedom and there is considerable scope for optimising the incidence and initial immersion at which it is set. As already indicated it seems likely that flap angles greater than  $20^\circ$  may yield higher waves than those so far achieved and the permanent installation which has been designed will allow the angle and immersion to be varied.

Regarding the 'sluice gate' action, this was very small as indicated by Fig.4, but will in theory affect the waves for some distance behind the flap and cause a difference between the mean water levels ahead and behind. The author believes, however, that the waves more than one or two wave lengths behind should be effectively normal free progressive waves. The same remarks apply to the waves reaching the test area after the first very long advance crest has passed (see Fig.10a). Velocities and forces on cylinders were measured in the course of the experiments by the Division of Maritime Science mentioned in the paper, but at the time of writing these have not yet been published.

As a footnote to this reply, it may be of interest to mention that the film of the prototype 'Wavedozer' experiments shown during the presentation of the paper is available for sale or hire from the National Physical Laboratory. (It is 16mm with colour and sound and a six-minute run time.)

Finally, the author wishes to thank all the discussers for their most interesting and helpful contributions.

## REFERENCE

10. Cumberbatch, E. Two-dimensional planing at high Froude number. *J. Fluid. Mech.*, Vol.4, 1958.

## Discussion on Paper by L. Larsson

K. WIEGHARDT

To determine the shear stress velocity  $u_\tau$  from velocity profiles the law of the wall has to be assumed. Yet, near separation its validity seems to be doubtful. H.P. Hoffmann, Hamburg, has measured all three velocity components in the boundary layer of a double-model of a ship in a wind tunnel at  $R_n = 6.8 \times 10^6$ . Fig.15 shows that for the girth at 0.9 length the law of the wall  $|u|/u_\tau = 1/x \ln zu_\tau/\nu + c$  (with  $|u|$  magnitude of velocity at wall distance  $z$ ) is indeed confirmed except at one station (182) where the velocity near the wall is rather small and the cross flow appreciable. Here the measured profile can be approximated by the law of the wall only by assuming the 'constant'  $c$  to be no longer about +5 but -3.8 (say), as with a rough surface.

I wonder if Dr. Larsson has also measured such profiles near separation?

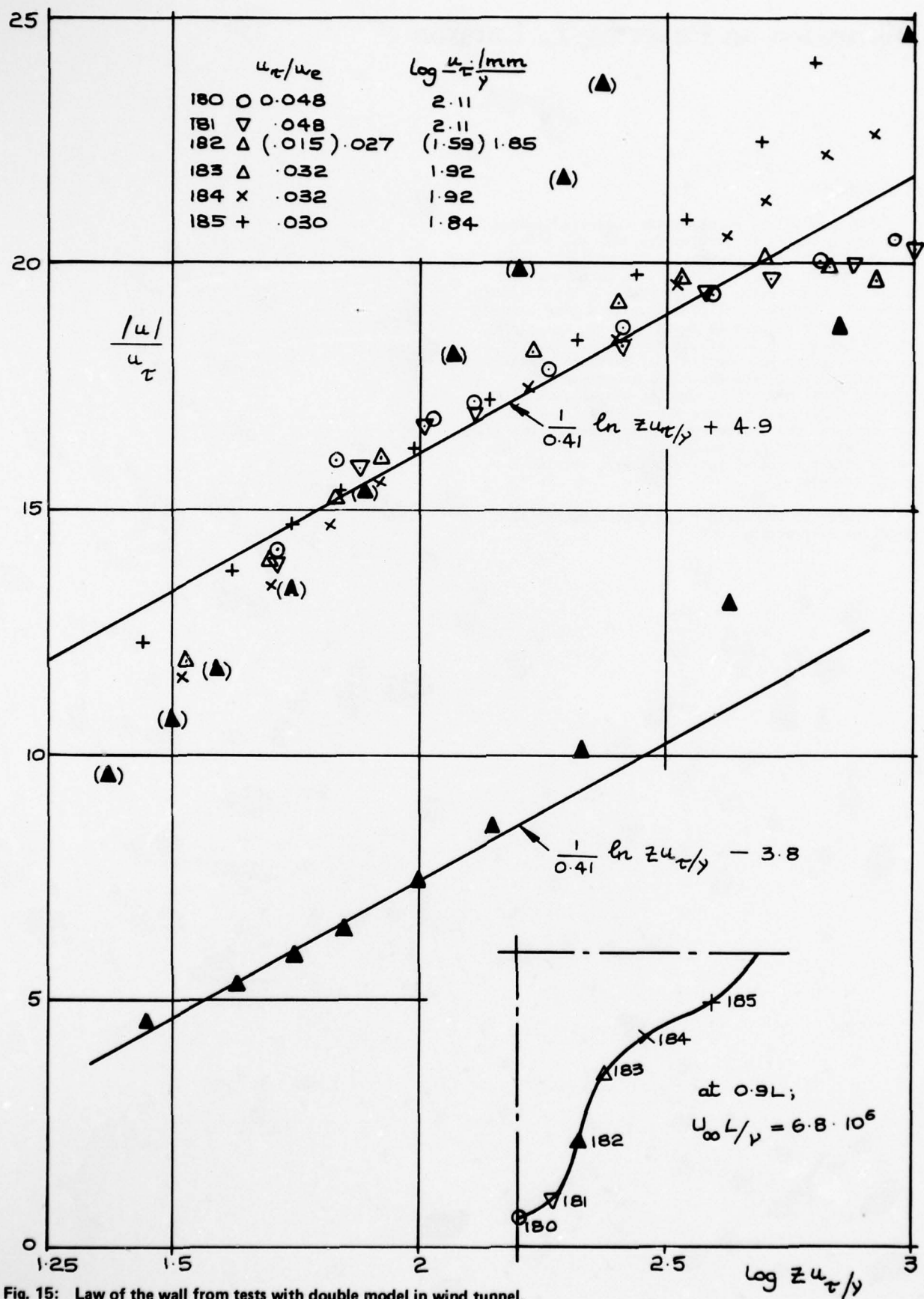


Fig. 15: Law of the wall from tests with double model in wind tunnel, H.P. Hoffmann, 1976.

## Author's Reply

The reason for choosing a model of moderate fullness ( $C_B = 0.675$ ) was to avoid separation. Although this phenomenon is of utmost importance and good data are very rare for three-dimensional cases it was considered too complicated to include this effect in this set of data. As stated in the paper, the purpose of the investigation was to produce a test case for three-dimensional calculation methods. Also without separation this case is more complicated than most other cases due to the rapid thickening of the boundary layer.

In Fig.16 the measured velocity profiles at station 1 (at  $0.95 L$ ) are given. Even though this station is  $0.05 L$  further aft than the one shown by Professor Wieghardt (Fig.15), there is a good fit to the law of the wall for all profiles.

The fact that the law of the wall does not hold close to two-dimensional separation may be seen for instance in the axi-symmetric case by Moses (Case 3, Ref.(52). In three-dimensional flow, where the skin friction may well increase at separation, this may, however, not be true. See for instance the swept wing measurements by van den Berg and Elsenaar, Ref.(53), where the wall law is well confirmed even in the separated region.

### REFERENCES

52. Coles, D.E., Hirst, E.A. Computation of turbulent boundary layers. 1968AFOSR-IFP-Stanford Conference Vol.II, Compiled Data (1968).
53. van den Berg, B., Elsenaar, A. Measurements in a three-dimensional incompressible turbulent boundary layer in an adverse pressure gradient under infinite swept wing conditions. NLR TR 72092U, National Aerospace Laboratory, Amsterdam (1972).



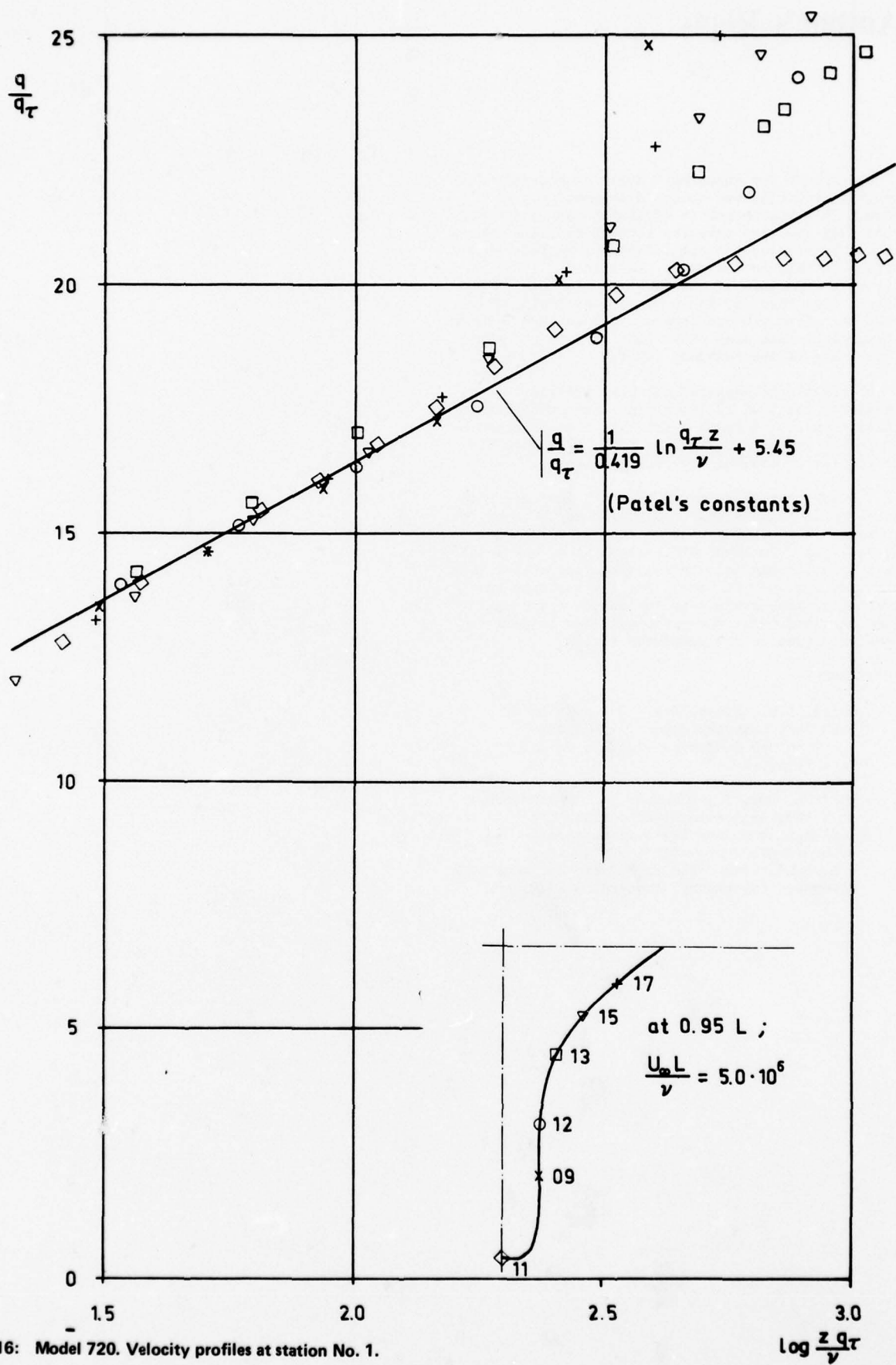


Fig. 16: Model 720. Velocity profiles at station No. 1.

# Discussion on Paper by K. Kure et al

A.N. KHOLODILIN

This work is very important. I am fully in agreement with the authors' remark of the need for theoretical and testing collaboration. An analysis of ship's capsize is at all times very difficult as a result of the influence of many unknown factors. The full analyses can be done only by using both methods, theoretical and experimental.

Of special interest and importance is the behaviour of small vessels under the effect of erupting waves in shallow waters. The results of these analyses have been published. It is shown that only comparison of the kinetic energy of an oscillating ship upon receiving the impulse of an erupting wave with the reserve of dynamical stability, the work of roll-damping forces being taken into account, permits the probability value of inclination to be obtained.

A.Y. ODABASI

I would like to raise some points on the presentation of the results and on the conclusions of the paper. Firstly, although time histories of motion are quite informative in the explanation of the mechanism of capsize, they are inconclusive in so far as the stability of motion is concerned. This is mainly due to two important reasons:

- (1) For nonlinear systems, in general, the solution is not unique and is strongly dependent on the initial conditions. Therefore, if the authors were to use different initial conditions for the same equations of motion they would possibly obtain a completely different time history.
- (2) To have a bounded solution is not an indication of the stability of motion. In this respect it will be useful to redefine the meanings of 'stability' and 'boundedness'. Stability is the property that the motion under consideration will remain within the domain of attraction of the equilibrium position and under the influence of additional perturbations the perturbed and the unperturbed motions will only differ to a small extent. Boundedness, on the other hand, indicates that the solution of the equations of motion, i.e. the motion of the unperturbed system, will have an upper and a lower bound. For example, if we write the equation of motion of a pencil standing on its sharp edge, theoretically the solution is bounded but the motion is unstable. For the oscillatory motion to be stable the boundedness is necessary but not sufficient. These two concepts become equivalent only for linear time-invariant systems.

A more meaningful representation may be either the phase trajectories or the frequency domain plot. Such representations are then evaluated by using either Lyapunov's direct method (Ref.(12)), or

Popov's method (Ref.(13)), respectively.

I too have studied the stability of the "M/T Edith Terkol" by using a newly devised criterion (Ref.(14)) and have found two possible mechanisms of capsize. The first form was of a parametric resonance type for long period waves, while the second form was of an instantaneous capsize type corresponding to conditions almost identical to those identified for the real capsize. In this study no coupling effect was taken into account, yet, distinct from the authors' conclusions this ship was liable to capsize even without any coupling effect.

## REFERENCES

- (12) Malkin, J.G. Theorie der stabilität einer bewegung, R. Oldenburg, Munchen (1959).
- (13) Barbalat, I. and Halanay, A. Nouvelles applications de la méthode fréquentielle dans la théorie des oscillations. Rev. Roumaine des Sciences Techniques, Serie Electrotechnique et Energétique. Tome 16, (1971), 689-702.
- (14) Odabasi, A.Y. Ultimate stability of ships. Paper to be presented at R.I.N.A. (1976).

# Authors' Reply

A.N. KHOLODILIN

The discussion in the paper of scientific method in general reflects the authors' feelings that the subject of ship's capsize mechanics is a very important one. A solution must exist and must be given a form which can be utilized in design and navigation of ships. The must is not merely a matter of scientific progress as such. It is a matter of life and death for men at sea and prevention of ship losses. It is therefore very important to be sure that the particular questions and answers raised in the research on the subject are not given a weight which they cannot sustain. So even the paper's form of abstract theorising must go alongside with the factual theorising and experimentation underlined by A.N. Kholodilin in his written contribution. The published works on capsize in shallow water mentioned by Dr. Kholodilin are not known to the author. The contribution by H.E. Guldhammer to Ref (2) might be one of them. The principle of balancing kinetic energy under load with the instantaneous reserve of dynamic stability is necessarily used both for shallow water and deep water capsize safety studies. All active loads must be included unless they are negligible.

A.Y. ODABASI

The term 'capsize safety' is deliberately used by the authors to avoid confusion between the terms 'stability' and 'boundedness' which Dr. Odabasi brings in from the general stability theory of dynamical systems. The two terms do not comply with the ship capsize safety concept as this is understood in naval architectural circles for their specific application.

The equilibrium stability of the statically floating ship, the ability of the ship to 'stand on its feet' in still water so well expounded in classical naval architecture is basic. The metacentric height is an undisputed determinant here. The capsize safety for a seaworthy ship is a matter of boundedness and not of stability in Dr. Odabasi's terminology. When applied to ships Dr. Odabasi's stability term refers to such phenomena as motion stability studied by Grim (12), Paulling (6), Abicht (13) with discussion and Wellicome (14) and others. Stability in this respect ensures seakindness which is an additional quality to seaworthiness and not necessarily needed for safety. The present work of the authors was not intended to study directly either stability or boundedness. It is a very specific subject studied in continuation of Ref.(2) which deals with capsize safety, meaning boundedness. An ad hoc hypothesis was set forth in Ref.(2) to explain the capsize. The strongly softening righting moment was made responsible for the sign inversion of the strong coupling term from sway into roll. The hypothesis was expressed in verbal form and needed formalisation and testing

Testing the hypothesis for its logical form was intended in the study using the analogue computer.

The formalised mathematical model of the verbally stated hypothesis must yield a response quite similar to the actual, i.e. model basin phenomena.

Regarding the Vessel Edith Terkol, it will be very interesting to learn about Dr. Odabasi's new criterion not involving the coupling term. A corresponding study was presented by H.E. Guldhammer in his discussion to (2). However, the mathematical model of the ship's roll motion involves a large coupling moment and it is difficult to understand how the stability as well as the boundedness criteria can be realistic without its inclusion. The coupling term could, though, be inherent in a mathematical form having another reference frame.

## REFERENCES

- (12) Grim, O. Rollschwingungen, stabilität und sicherheit im seegang. Schiffstechnik, (1952).
- (13) Abicht, W. On capsizing of ships in irregular waves. Proceedings of the Glasgow Stability Conference, (1975).
- (14) Wellicome, J. An analytical study of the mechanism of capsizing. Proceedings of the Glasgow Stability Conference, (1975).

# Discussion on Paper by J. H. McCarthy et al

K. WIEGHARDT

Could you give us more precise information than in Fig.5 about how transition depends on  $R_n$  for various forms? At Admiralty Research Laboratory, Teddington, we had also calculated the laminar boundary layer at various cylindrical heads (Ref. (45)) but, so far, we have not seen experimental verification of what is really happening there.

G.E. GADD

The careful experiments described in this paper give valuable information on the effects of transition-provoking devices on the drag of bodies of revolution. However, it is I think a little misleading to suggest that the 'traditional' method of estimating  $C_R$  is to measure the drag of the body without stimulators, and to subtract the difference of drag at the highest Reynolds numbers from the drag obtained with stimulators at lower Reynolds numbers. Quite obviously in the present instance some of the smooth bodies have a good deal of laminar flow even at the highest Reynolds numbers.

## Authors' Reply

K. WIEGHARDT

Since carrying out the experiments described in the paper, additional wind-tunnel tests have been conducted for the two fuller bodies which experienced laminar separation. Table 5 below shows a small change in the location ( $x_s$  or  $s_s$ ) of the leading edges of the separation bubbles, as determined from oil film experiments for the modest range of Reynolds numbers which was investigated. The agreement between predicted and measured locations of separation was excellent and improved with increasing Reynolds number. For both forebodies hot film measurements indicated that transition occurred immediately forward of the downstream end of the separation bubbles. Information on the length of the separation bubbles on Model 4620-2 ( $L_E/D = 1.0$ ) is given in Ref.(38) of the paper. Additional information will be published in the near future.

G.E. GADD

The 'traditional' method described in the paper is the method which has been traditionally used at D.T.N.S.R.D.C. to determine  $C_R$  for submerged bodies. As correctly pointed out by Dr. Gadd, many commercial tanks conduct drag measurements only with stimulators in place, and in the case of N.P.L. no stimulator-drag corrections are made, apparently

Moreover, in normal commercial tank work there is not time to duplicate the experiments without stimulators. At N.P.L., pin-type stimulators are used and no correction is made for stimulator drag. This may seem a crude procedure, but from Fig.10 it appears that for the 0.6 10 mm trip wire at  $X/L = 0.05$ , for example, the uncorrected total drag measurements would give a value of  $C_R$  for  $R_L$  below  $2 \times 10^7$  of about  $0.19 \times 10^{-3}$ , close to the value  $0.20 \times 10^{-3}$  given in Table 3. Of course an estimate of the pressure drag of the stimulator could be made but it is not always certain that ahead of the stimulator the flow is entirely laminar and to some extent the drag deficit in this region will compensate for the drag excess due to the stimulator pressure drag. Thus the use of uncorrected total drags with stimulators may be quite acceptable, despite its apparent crudity.

### REFERENCE

45. Wieghardt, K.E.G. On a simple method for calculating laminar boundary layers. *Aero. Quart.* 5, 25-38, 1954.

with quite good results. For conventional forebodies which do not deviate greatly from some norm, this can be a reasonable approach when one type and size of stimulator is used over a long period of time, and a backlog of experimental data and correlation allowances are available. Problems arise when one considers different sizes of stimulators or vastly different forebodies, some of which may experience laminar separation and early transition. The paper addresses these problems with an eye to permitting a careful drag evaluation of competing bow shapes for axisymmetric bodies.

TABLE 5  
Measured and Predicted Locations of Laminar Separation

Model 4620-1 ( $L_E/D = 0.5$ )			Model 4620-2 ( $L_E/D = 1.0$ )		
$R_D \times 10^{-6}$	$x_s/D$	$s_s/D$	$R_D \times 10^{-6}$	$x_s/D$	$s_s/D$
0.65	0.438	0.723	0.97	0.853	1.059
0.91	0.458	0.743	1.28	0.885	1.092
1.29	0.460	0.745	1.60	0.890	1.096
1.67	0.467	0.752	1.92	0.890	1.096
1.94	0.467	0.752			
2.58	0.467	0.752	2.20	0.890	1.096
Predicted	0.467	0.752	Predicted	0.889	1.095



### SESSION III

#### MARINE VEHICLES IN WAVES

Tuesday, 30 March 1976

09.00—12.30

Chairman: Y. Yamanouchi

Some aspects of ship motions and impulsive wave loads on an ore carrier model in two-directional cross waves, by H. Kitagawa

Application of the functional polynomial model to the ship added resistance problem, by J. F. Dalzell

Numerical solution of unsteady wave problems, by R. C-K. Chan and J. H. Stuhmiller

Two-dimensional and conditional distribution laws of sea wave components, by I. K. Boroday and Ya. M. Kublanov

Three dimensional calculations of wave forces by a hybrid element method, by D. K. P. Yue, H. S. Chen, and C. C. Mei

The second-order steady force and moment on a ship moving in an oblique seaway, by Wen-Chin Lin and A. Read

PRECEDING PAGE BLANK-NOT FILMED

# SOME ASPECTS OF SHIP MOTIONS AND IMPULSIVE WAVE LOADS ON AN ORE CARRIER MODEL IN TWO-DIRECTIONAL CROSS WAVES

H. KITAGAWA

Ship Research Institute, Tokyo, Japan

## SYNOPSIS

Results of model experiments on an ore carrier are presented to investigate the fundamental behaviour of the ship and impulsive pressures acting on the hull surface in two-directional regular and irregular waves, which are produced by flap and plunger type wavemakers. The superposition principle is examined in relation to roll and pitch motions of the ship at various headings. Effects of ship speed, course angle and sea environment upon impulsive pressures are discussed in cross waves.

## 1. INTRODUCTION

The information of the energy distribution of sea waves with regard to direction of propagation has been not only essential from the point of view of the wave forecaster, but is also of great interest for the naval architect because it is closely associated with the problems of wave loads and optimum routing for the ship. Much work was done on the two-dimensional spectrum of sea waves by Barbar[1] and Longuet-Higgins[2]. The linear properties of surface waves have long been well understood in theory, but the full linear evaluation of the directional wave spectrum has proved difficult in practice. Barbar[3], and Longuet-Higgins, Cartwright and Smith[4] gave an account of a method of measuring the directional spectrum of ocean surface waves by taking records of the elevation and tilt of a free floating buoy.

Waves generated by winds blowing over the water surface are short-crested. The theory of short-crested waves was developed by Jeffrey[5] and extended considerably by Fuchs[6], in its application to the wave field near the shore.

As regards the behaviour of marine vehicles and structures in waves, little attention has been paid to the fundamental responses of them in two- or multi-directional waves. A regrettable lack of the facilities for grappling this subject will certainly have confined researchers' attention to the case of uni-directional waves. Yoshioka et al.[7] carried out some rolling experiments of a small craft model in short-crested waves made by a flap type wavemaker, making use of diffraction plates. Tasai[8] discussed ship motions in short-crested waves generated in a towing tank by a plunger type wavemaker. In this case, short-crested waves were resulted from multiple reflections of the progressive wave systems, which were produced by a linear array of an infinitely long unit of wavemakers. The successive plungers were driven sinusoidally in time, but with a constant phase difference between adjacent plungers. The wave trains, however, necessarily had the same wave length, because they had the same frequency, but their directions of propagation were different, and the composite waves were therefore far from realistic short-crested

seas.

Waves superposed by two long-crested wave trains which cross one another are short-crested. Apart from the wave spectrum, basic properties of two-directional cross waves have never been verified in the actual experiments. Quite recently, the capability of producing realistic short-crested waves of sufficient severity was added to the No.1 Ship Model Basin, which is a 80 m square basin, of the Ship Research Institute. The Square Basin has been equipped with a flap type wavemaker along the southern bank. The second wavemaker of the plunger type was recently fitted up along the eastern bank of the basin for production of short-crested waves.

Model experiments conducted under conditions which are as realistic as possible in simulating a severe rough sea environment will offer one of the best means of gaining full understanding of phenomena associated with the operation of ships in extreme seas. Model experiments in two-directional cross waves, which may be a certain approach to an ideal simulation of realistic seas, will provide a basis of this understanding.

They can undoubtedly serve the primary purpose of the present study to verify the superposition principle of ship responses in two-directional waves. Moreover, two-directional cross waves will offer a favourable sea environment for the purpose of investigating the impulsive hydrodynamic forces acting on the ships, since these forces which cause sometimes serious damage on them will fall into the category of events of rather rare occurrence, in particular, in model experiments in ordinary irregular waves.

Some experiments were performed in two-directional cross waves with a free-running radio-controlled model of an ore carrier. Superposition principle is examined in relation to roll and pitch motions of the ship, and some features of impulsive pressures acting on the ship in cross waves are also discussed[9][10][11].

### III.4

#### 1.1 NOTATION

$C_x, C_y, C_p$	phase velocities of swell, seas and wave pattern
$g$	acceleration due to gravity
$H_w$	wave height
$H_{1/3}^{(1)}, H_{1/3}^{(2)}$	significant wave heights swell and seas
$E[P_{max}]$	short term expected values of impulsive pressure peaks
$k_x, k_y$	wave numbers of swell and seas
$N_I$	total number of impact encountered in waves
$P_I, P_O$	peak values of impulsive and oscillating pressures
$S^{(1)}(\omega), S^{(2)}(\omega), S^{(1+2)}(\omega)$	spectra of swell, seas and cross waves
$T$	mean wave period of irregular waves
$V_o, V_w$	ship speeds in calm water and waves
$x_o, y_o$	coordinates of starting point of the model in the basin
$\epsilon$	phase lag between swell and seas
$\zeta_x, \zeta_y, \zeta_{xy}$	surface profiles of swell, seas and cross waves
$\zeta_{x_o}, \zeta_{y_o}$	wave amplitudes of swell and seas
$\theta_o$	wave pattern angle
$\theta_p$	angle of the direction of wave pattern advance
$\lambda_e, \lambda_x, \lambda_y$	wave lengths of equivalent single wave, swell and seas
$\lambda_m$	mean wave length corresponding to mean wave period of irregular waves
$\sigma_e, \sigma_x, \sigma_y$	circular frequencies of equivalent single wave, swell and seas
$X, X_c, X_d$	heading, course and drift angles

#### 2. TWO-DIRECTIONAL CROSS WAVES

##### 2.1 Production and measurements of cross waves

To enable complex and short-crested wave forms to be generated in the Square Basin, two sets of wavemakers are employed, disposed at right-angles to one another in plan. One of them, which has been installed recently and of the plunger type, is made up of 24 independent units, 2.25 m long which, by operating out of phase, frequency and stroke, will provide such complex systems as may be found necessary for the representation of confused short-crested waves.

In towing tanks, the method of measurement of wave form found to be satisfactory uses the change of capacitance of a plastic coated copper wire, partly suspended in the water at the end of a rigid arm secured to the tank wall. This method, however, cannot be applicable to the case of two-directional waves, since wave records should be taken near the centre of the basin for avoiding erroneous influences due to wave reflection, local disturbance, interaction, edge and corner effects of the wavemakers. The ultra-sonic wave recorder of underwater type has then been utilized, which enables the ship model to run freely in the basin and on the other hand has a disadvantage in accuracy of measurement of considerably steep waves [12]. There should be enough wave detectors, in general, for an array of them to extend from an origin to distance sufficient to include all significant values of the correlogram. The seven detectors were set in the form of a modified Mills cross as shown in Fig.1.

##### 2.2 Two-directional regular cross waves

The system of coordinates is defined as in Fig.1. One of the two regular wave trains which is produced by the flap type wavemaker is supposed to advance in the positive direction of  $x$ . This wave train,  $\zeta_x$ , will correspond to swell, as the characteristics of the wavemaker will certainly be suitable for producing rather long waves. The other is generated by the plunger type wavemaker which is primarily designed to produce comparatively short waves. This wave train, denoted by  $\zeta_y$ , advances in the positive direction of  $y$ , which will naturally correspond to seas. These wave systems will be expressed by the following equations, respectively.

$$\zeta_x = \zeta_{x_o} \sin(k_x x - \sigma_x t) \quad (1)$$

$$\zeta_y = \zeta_{y_o} \sin(k_y y - \sigma_y t + \epsilon) \quad (2)$$

$\zeta_{x_o}$  and  $\zeta_{y_o}$  are wave amplitudes,  $k_x (=2\pi/\lambda_x)$  and  $k_y (=2\pi/\lambda_y)$  are wave numbers,  $\sigma_x$  and  $\sigma_y$  are circular wave frequencies, and  $\epsilon$  is a certain phase lag between these wave systems.

The resultant composite surface profile,  $\zeta_{xy}$ , which is a sum of  $\zeta_x$  and  $\zeta_y$ , can be easily obtained as follows,

$$\begin{aligned} \zeta_{xy} &= \zeta_x + \zeta_y \\ &= (\zeta_{x_o} + \zeta_{y_o}) \left\{ 1 - \frac{4\zeta_{x_o}\zeta_{y_o}}{(\zeta_{x_o} + \zeta_{y_o})^2} \sin^2(p_2 - \sigma_2 t) \right\}^{1/2} \\ &\quad \times \sin\{p_1 - \sigma_1 t + \delta(t)\} \end{aligned} \quad (3)$$

where

$$\begin{aligned} 2p_1 &= k_x x + k_y y + \epsilon \\ 2p_2 &= k_x x - k_y y - \epsilon \\ 2\sigma_1 &= \sigma_x + \sigma_y \\ 2\sigma_2 &= \sigma_x - \sigma_y \\ \delta(t) &= \arctan\left\{ \frac{\zeta_{x_o} - \zeta_{y_o}}{\zeta_{x_o} + \zeta_{y_o}} \tan(p_2 - \sigma_2 t) \right\}. \end{aligned} \quad (4)$$

It is apparent that a wave group or packet is formed by the superposition.

The wave pattern will be observed to advance to the direction of

$$\theta_p = \arctan \frac{C_y}{C_x} = \arctan \left\{ \frac{\lambda_y}{\lambda_x} \right\}^{1/2} \quad (5)$$

as shown in Fig.2, with the velocity of

$$C_p = (C_x^2 + C_y^2)^{1/2} = \{g/2\pi\}^{1/2} (\lambda_x + \lambda_y)^{1/2} \quad (6)$$

so that the wave pattern of short-crested waves travels faster than the component waves, where  $C_x$  and  $C_y$  are phase velocities.

#### 3. MODEL EXPERIMENTS

##### 3.1 The model

For the experiments an ore carrier model was used, the main particulars of which are given in Table 1.

The model was self-propelled, using a d.c.



motor, and radio controlled. The rechargeable battery circuitry was divided to provide power to the instruments and propulsion separately. The autopilot system was designed to simulate a typical full scale system, and the model was mostly able to maintain course.

The model was most fully instrumented; gyroscopes for measurements of ship motions such as roll, pitch, yaw and yaw rate, sub-miniature accelerometers, motor RPM detector, pressure transducers and their amplifiers, amplifiers for measurements of relative water elevations and shipping water on forecastle deck, oscillograph and telemetering unit were installed on board.

Pressure gauges of diaphragm type were fitted on the model for detecting impulsive water pressure acting on the hull surface. The diaphragm which is bounded on ceramics basement is a silicon single-crystal plate of 0.1 - 0.2 mm in thickness, and its surface is coated for protection against erosion and shielding from light. Furthermore, very thin silicon grease film was added to the surface of the diaphragm during the experiment.

A digital memory amplifier (Transient Time Converter) was also used simultaneously to record the signals precisely enough to discuss the wave forms in detail and to examine, in particular, peak values, rise-up time and duration.

Locations of the pressure gauges fitted on the model are illustrated in Fig.3

Details of the experimental procedure were described in refs.[10] and [13].

### 3.2 Test conditions

The model experiments were conducted in regular and irregular cross waves. Wave height of each component regular wave is 1/40 of the ship length, which is equal to 11.25 cm in model scale and 6.2 m in full scale, since it is supposed to be appropriate for the present purpose and of the most frequent use in ordinary model experiments in waves.

The models are usually controlled and run at a constant speed in towing tank experiments. Speed control system could be designed for a free-running model in ordinary waves. It is difficult, however, to utilize such a control unit for a free-running model in two-directional waves, because encounter waves generally form a wave packet. The d.c. motor to drive the propeller of the model was then regulated at a constant voltage that served to sustain the model at the corresponding speed in still water. Consequently, the speed of the model is presumed to fall naturally, as does that of the actual ship in rough seas.

Wave length of each component regular wave was altered over the  $\lambda/L$  range of 0.5 - 1.5, and heading angle of the model was changed to cover the range from  $45^\circ$  to  $270^\circ$  against component waves corresponding to swell. In general, heading angle which is opposite to the direction of wave pattern advance is supposed to give a relatively severe condition to the ship. This heading angle  $\chi = \chi_p$  ( $\chi_p = 180^\circ - \theta_p$ ) is given in Fig.4.

Two-directional waves can bring a realistic and confused sea environment to realization, as noted earlier, which will be more favourable than uni-directional waves for qualitative and quantitative evaluation of impulsive pressure, even if each component wave is regular. Moreover, phase

relation of two-directional regular waves will play an important role in occurrence of impulsive pressures on the hull surface. Two-directional irregular waves will undoubtedly give a more realistic sea environment to the model. Model experiments in irregular cross waves were made mainly for the purpose of evaluation of impulsive pressure. The I.S.S.C. standard spectrum was employed.

A new method using a linear filter was successfully applied to generation of irregular waves by the plunger type wavemaker[14].

## 4. RESULTS

### 4.1 Regular waves

Fig.5 shows an example of wave records. In this case, each of component wave has the same wave height but different wave period, and the expression of the composite wave is simplified as follows,

$$\zeta_{xy} = 2\zeta_0 \cos\left\{\frac{1}{2}(k_x x - k_y y - \varepsilon) - \frac{1}{2}(\sigma_x - \sigma_y)t\right\} \times \sin\left\{\frac{1}{2}(k_x x + k_y y + \varepsilon) - \frac{1}{2}(\sigma_x + \sigma_y)t\right\}. \quad (7)$$

Prediction by this equation is plotted in the figure.

### 4.2 Irregular waves

Wave measurements were monitored with a strip chart recorder during the experiments in irregular waves. Fig.6 shows typical spectra in full scale measured during the model experiments.

The spectrum of two-directional irregular cross waves  $S^{1+2}(\omega)$ , appears to agree reasonably well with a sum of the spectrum of each component irregular wave,  $S^{(1)}(\omega)$  and  $S^{(2)}(\omega)$ , namely,

$$S^{1+2}(\omega) = S^{(1)}(\omega) + S^{(2)}(\omega). \quad (8)$$

Wave reflections from wave absorbers and non-linear mechanics such as breaking of waves and tertiary wave interactions may contribute to some extent to the discrepancy between them.

### 4.3 Speed loss and drift

The model ran through regular and irregular wave systems using an autopilot unit at various angles of encounter, while the propeller power or RPM was substantially held constant, and the resultant speed under these conditions was measured.

Motor RPM was recorded and found to be sufficiently constant except for the extreme case. More strictly speaking, battery voltage of driving motor was held constant at the value corresponding to the ship speed of 14.8 knots or the model speed of 1.028 m/s in still water.

For comparison, the speed loss and drift of the model in oblique regular waves with wave height of  $L/20$  are shown in Figs.7 and 8, respectively[15]. Those in regular cross waves are shown in Figs.9 and 10.

It is a well known fact that slow ships lose more speed in a seaway than fast ships under identical conditions, undoubtedly because of their increased fullness and bluntness, and that the



speed loss increases rapidly for values of  $\lambda/L$  above 0.75, then decreases more slowly at the higher values.

In two-directional waves, the speed loss appears to be affected mainly by the swell component waves and effect of seas seems to be mostly limited in the region of  $\chi \sim \chi_p$ , where severe pitching and marked speed loss are observed. On the contrary, when  $\lambda/L$  of swell component waves is 0.5, the speed loss decreases in this region of the heading. One of the main causes of the speed loss is presumably due to the large rudder deflections required to keep the model on course in waves.

If resistance or thrust increase in waves is proportional to square of wave height as generally assumed, it will be argued that the speed loss is more moderate in two-directional waves than in uni-directional waves under identical conditions.

Drift angle  $\chi_d$  ( $\chi_d = \chi_c - \chi$ ;  $\chi_c$  = course angle) in regular cross waves has quite different features from that in ordinary regular waves. When the heading angle is nearly equal to  $135^\circ$ , drift angles in regular cross waves are found to be rather small, while those in ordinary oblique waves will usually have the highest value. In this region of heading, drifting force due to each component wave will cancel one another, and the drifting forces lose the balance in the slightly higher heading angles. It is found that drift angle in regular cross waves are not always proportional to amplitudes of ship motions and vector summation of the driftings in component waves does not give reasonable prediction of those in cross waves when drift angle is remarkable. Detailed and precise analysis of the phenomenon should require further works on the effects of dynamic characteristics of driving and autopilot systems as well as wave height and ship motions.

#### 4.4 Ship motions

Pitch and roll amplitudes measured in single regular waves are shown in Figs.11 and 12. Computed results are also plotted in the figures using the strip method based on Ursell-Tasai's two-dimensional theory. As the roll damping estimated by the strip theory appears to be too weak and a non-linear effect in it cannot be neglected, roll amplitudes were calculated in another way using the experimental values of damping coefficient including the non-linear term. The total roll damping was computed from the results of roll decay experiments conducted in calm water at both zero and forward speeds. The linear damping term showed slight increase with forward speed. The effect of speed loss in waves was taken into account in the computations.

Fig.13 shows some examples of the records of roll and pitch in regular cross waves. Another examples including relative water elevation, vertical acceleration at midship and shipping water passing through the forecastle deck end are given in Fig.14.

The marked beats are found to appear in pitch and roll motions when the heading angle is nearly equal to  $\chi_p$ . It is also clear that the maxima and the minima within roll and pitch beats have an almost opposite phase relation to one another, and that when the heading angle is  $90^\circ$  or  $180^\circ$ , the model is rolling and pitching with respective encounter periods of swell and seas.

For comparison with those in single regular waves, mean amplitudes of pitch and roll, which were mostly determined through the records of a few beat length, are shown in Figs.15 and 16, respectively.

Maximum amplitudes of them are given in Figs. 17 and 18. They are the mean values of maximum amplitudes within several beats in the records, which appear in considerably regular way. Minimum amplitudes were found to be quite sensitive to slight changes in speed, lateral motions and local sea environment to be encountered, and they are therefore scattered. The maximum amplitudes, as seen from eq.(3), are convenient for verification of the superposition principle.

It should be noted that the model speed was not constant through the experiments and, as mentioned before, it decreased in accordance with the heading and sea environment.

It appears that the maximum pitch amplitudes, which have a similar tendency to that of the mean ones, become minimum at the heading angles of  $\chi = 90^\circ$  and  $180^\circ$  to swell except for the case of small wave to ship length ratio, and have peak values at  $\chi = \chi_p$ . If swell and seas have the same wave length, the maximum pitch amplitudes show nearly symmetrical variation with respect to the heading angle with the centre of symmetry at  $\chi = 135^\circ$ , and asymmetrical appearances gradually turns up with decreasing of wave length of seas, as the effect of responses to seas becomes conspicuous.

As regards roll amplitudes, they have the minimum at  $\chi = \chi_p$  on account of response characteristics in single regular waves. High sensitivity of rolling to encounter angle and period, and predominance in roll motion caused by swell in the vicinity of  $\chi = 90^\circ$  will make the roll response independent of the influence due to seas. The influence due to seas gradually appears with increasing of heading angle.

Composed amplitudes of pitch and roll, which are mere summations of the amplitudes measured in single regular waves, are given by thin lines in Figs.17 and 18. Fairly good agreements are mostly found in the tendency between the measured and the composed amplitudes. Although it will be rather negligible, there is an incorrectness in the compositions which will be suffered from slight differences of the model speed in two sea environments. In short waves, however, it will be added as to the pitch response that the discrepancy between them is attributed to the complicated properties of pitch response in comparatively short waves, wave diffraction due to the model, and phase relation which was not taken into account in the composition procedure.

As for the roll response, a quantitative discrepancy is more remarkable. Drifting, phase relation and effect of the difference in the model speeds in addition to non-linear properties of roll are suggested to be the main causes.

Computations were made using the strip theory. Composed amplitudes obtained by the computation are shown in Figs. 19 and 20, where the model speeds are those measured in regular cross waves. The similar argument noted above can be applied to the computed results.

Predicted amplitudes by an equivalent single wave approximation are also shown by thin lines in Figs.19 and 20, in way of suggestion, where the model is presumed to be a point and two wave systems are replaced by an equivalent single wave

train propagating in the direction of  $\chi_p$  with wave length of

$$\lambda_e = \frac{2\pi g}{\sigma_e^2} \quad (9)$$

The equivalent wave can be expressed by replacing  $x$  and  $y$  in eq.(7) by

$$\begin{aligned} x &= x_o + V_w t \cos \chi \\ y &= y_o - V_w t \sin \chi \end{aligned} \quad (10)$$

and is then given by

$$\begin{aligned} \zeta_{xy} &= 2 \zeta_o \cos \left\{ \frac{1}{2} [k_x x_o - k_y y_o - \epsilon] \right. \\ &\quad + \frac{1}{2} [V_w (k_x \cos \chi + k_y \sin \chi) - (\sigma_x - \sigma_y)] t \} \\ &\quad \times \sin \left\{ \frac{1}{2} [k_x x_o + k_y y_o + \epsilon] \right. \\ &\quad \left. + \frac{1}{2} [V_w (k_x \cos \chi - k_y \sin \chi) - (\sigma_x + \sigma_y)] t \right\}. \end{aligned} \quad (11)$$

It is apparent that such a simple approximation fails unfortunately to give successful results.

There is in general a considerable discrepancy between the composed and the measured amplitudes of the ship motions when the model runs in following seas in relation to the swell component. In the extreme case, an unusual phenomenon was observed, when the model encountered a group of especially steep regular waves. The phenomenon may bear some resemblance to low cycle resonance in rolling. The parametrically induced unstable roll motion is also a well known phenomenon for a ship with low freeboard moving in following seas of considerable steepness. If the ship is running in following seas, the ship will experience periodic variations in its transverse stability, and these variations will naturally affect the roll motion of the ship. A similar phenomenon might be expected if the ship encounters a wave packet of sufficient steepness and regularity, which is a nature of two-directional regular cross waves. In fact, such behaviour has been observed on some occasion in the extreme case.

Much attention should be paid to the behaviour of ships in following and quartering seas, since the ship will run in following or quartering seas at more than half of the headings in two-directional cross waves. Further study will require the information of coupled motions, gyroscopic and non-linear effects, and dynamic properties of driving and steering systems.

#### 4.5 Impulsive pressure

The digital memory amplifier was utilized for precise measurements of peak values, shapes and duration of impulsive pressures. The impulsive pressures were also recorded on an oscillograph simultaneously. Comparison of both records indicated that the shapes of impulsive pressures recorded on each recorder remarkably resemble to one another and the peak values were almost the same. The duration of impact part of the pressure was found to be of order of 10 ms, as far as observations in two-directional waves were concerned.

For convenience of analysis, impulsive pressure records are classified into five categories as shown in Fig.21. The relationships between occur-

rence of impulsive pressure and various parameters such as sea environment, ship speed and heading are illustrated in Fig.22. Histograms of peak values of impulsive pressure are shown in Fig.23. It can be argued that the occurrence of impulsive pressure much depends on wave length of seas rather than that of swell, and that short seas make the occurrence frequent. Complicated interactions between incident and diffraction waves produce steep waves on the weather side of the ship and the local increment of wave steepness will cause the frequent occurrence of impulsive pressure. The ship motions, which are mainly induced by comparatively long component waves, may cause an increase of water particle velocity over the hull surface and sharpening of impact angle. This will certainly aggravate its occurrence. As far as the results of the model experiments are concerned, however, the ship motions seem not to stimulate its occurrence. Free-running ships may have a favourable nature of studious avoidance of a dangerous phase relation to encounter waves.

As shown in Figs.22 and 23, the frequency of occurrence of impulsive pressure, particularly on bow and flare, increases rapidly with ship speed. Naturally the effect of ship speed gradually deteriorates as the location of the occurrence moves towards the midship. Wave height will be closely associated with the phenomenon, and it affects strongly impulsive pressures acting on the hull surface high above the water line, as shown in the figures. However, its effect seems to be little in the vicinity of the water line.

The impulsive pressure happened to exceed 30 mAq. in its peak value in the scale of actual ship when the model encountered fairly short seas and swell.

It will be added that oscillating pressure associated with relative water elevation and impulsive pressure do not exist independently, but that impulsive pressure is superposed upon the oscillating one.

Model experiments were also performed in two-directional irregular cross waves as shown in Fig. 6[11]. Distributions of peak values of oscillating and impulsive pressures are shown in Fig.24. As shown in the figures, short term analysis of peak values of impulsive pressure indicates that the expected peak value distributions of the pressure are supposed to be well approximated by Rayleigh distribution, which will be verified by the chi-square goodness-of-fit test given in Table 2.

Lengthwise distributions of short term expected values of impulsive pressure peaks are given in Fig.25 and the effects of ship speed, mean wave period and heading angle are shown in Figs.26, 27 and 28, respectively. It is well to note that as for the influence of these parameters upon impulsive pressure, the conclusions obtained by the experiments in regular cross waves are generally confirmed by these results as shown in the figures. The details of analysis should be referred to ref. [11].

#### 5. CONCLUSIONS

The model experiments were conducted in two-directional regular and irregular cross waves for the purpose of clarifying the fundamental behaviour of the ship in such waves and evaluating impulsive pressure acting on the hull surface.

As regards pitching, the maximum amplitudes in regular cross waves can generally be predicted by a simple composition of those in single regular waves, and the superposition principle in two-directional cross waves mostly holds with the exception of the case in comparatively short waves. However, only the tendency can be estimated by the composition approximation for roll response in cross waves.

In following and quartering seas with respect to either component wave, the principle fails to hold. Furthermore, drift in cross waves cannot always be well predicted by vector summation of the results obtained in single wave trains.

Two-directional waves can provide a favourable sea environment for an investigation of hydrodynamic impact. The effects of ship speed, course angle and sea environment upon impulsive pressure are clarified in cross waves. The expected peak value distributions of the pressure are supposed to be well approximated by Rayleigh distribution.

Ship capsizing, heavy shipping water and hydrodynamic impact which will cause serious damage to the ship on some occasion will statistically fall into the category of events of rather rare occurrence. The linearized method of waves and ship motion analysis which has received so much attention in recent years with a marked success cannot be applied here with any particular expectation of obtaining directly useable results. Model experiments in waves could then provide an extremely useful information, only if the sea environment is appropriate for the purpose.

Two-directional cross waves can offer a favourable sea environment with sufficient severity, though there are still many points which must be clarified. Unfortunately, it is not such an easy matter as is generally imagined to promote a detailed experimental study on these phenomena in two-directional waves. Effective space in a model basin, in particular, is a vital necessity to a successful experiment in cross waves. There must be a growing need, however, for such a sea environment, because since up to the present both the behaviour of a ship under extreme conditions and sufficient knowledge about the nature of the sea on various ship routes are still lacking.

Also a theoretical investigation of a means to systematize such complicated phenomena is necessarily important.

#### 6. ACKNOWLEDGEMENTS

The present experiments were partially conducted under cooperation with No.131 Committee of Japan Ship Research Association. The author would like to express his gratitude to Prof. Motora, Chairman of the Committee, and the other committee members for their kind guidance and discussions.

He would also like to express his appreciation to Dr. Yamanouchi for his encouragement and giving the motivation for this study.

He is particularly indebted to Dr. Sugai for his helpful advice, encouragement and reviewing the manuscript.

#### REFERENCES

[1] Barbar, N.F., 'Finding the direction of travel of sea waves', *Nature*, 174, 1954.

- [2] Longuet-Higgins, M.S., 'Bounds for the integral of a non-negative function in terms of its Fourier coefficients', *Proc.Camb.Phil.Soc.* 51(4), 1955.
- [3] Barbar, N.F., 'Measurements of sea conditions by the motion of a floating buoy', *Admiralty Research Lab., Note A.R.L./10.3.40/N.2/W.*, 1946.
- [4] Longuet-Higgins, M.S., Cartwright, D.E. and Smith, N.D., 'Observations of the directional spectrum of sea waves using the motions of a floating buoy', *Ocean Wave Spectra*, Englewood Cliffs, Prentice-Hall Inc., 1961.
- [5] Jeffreys, H., 'On water waves near the shore', *Phil.Mag.Ser.6*, 48, 1924.
- [6] Fuchs, R.A., 'On the theory of short-crested oscillatory waves', *Gravity Waves*, National Bureau of Standards Circular No.521, 1952.
- [7] Yoshioka, I., Honma, Y., Uno, S. and Terada, K., 'An experimental result of rolling of ships on the short-crested waves', *J.Soc.Nav.Arch. Japan*, Vol.108, 1960.
- [8] Tasai, F., 'On the sway, yaw and roll motions of a ship in short-crested waves', *J.Seibu Zosen Kai*, No.42, 1971.
- [9] Kitagawa, H. and Ohmatsu, S., 'Some experiments on the behaviour of an ore-carrier model in short-crested regular waves', *J.Soc.Nav.Arch. Japan*, Vol.135, 1974.
- [10] Sugai, K., Goda, K., Kitagawa, H. and others, 'Model tests on impulsive water pressures acting on the hull surface of an ore-carrier in two directional waves', *J.Soc.Nav.Arch. Japan*, Vol.135, 1974.
- [11] Sugai, K., Kitagawa, H., Fuwa, T. and Ohmatsu, S., 'Experimental investigations into impulsive water pressures upon the hull surface in two-directional irregular waves', *J.Soc. Nav.Arch.Japan*, Vol.138, 1975.
- [12] Matsumoto, N., Sugai, K. and Kitagawa, H., 'Some measurements of two-directional cross waves', *Proc.General Meeting of Ship Research Institute*, No.22, 1973.
- [13] Takaishi, Y., Sugai, K. and Ogawa, A., 'The experiment method on the model ship in waves developed in the square tank in recent years', *Bull.Soc.Nav.Arch.Japan*, Nos.525, 526, 1973.
- [14] Kitagawa, H. and Kakugawa, A., 'Generation of irregular waves by a plunger-type wavemaker using a linear filter method', *Proc.General Meeting of S.R.I.*, No.24, 1974.
- [15] Sugai, K., Goda, K., Kitagawa, H. and others, 'Model tests on hydrodynamic pressures acting on the hull of an ore-carrier in oblique waves', *J.Soc.Nav.Arch.Japan*, Vol.133, 1973.



Length between perpendiculars	4.5000 m
Breadth mid.	0.7397 m
Depth mid.	0.4190 m
Draft mid.	0.2915 m
Displacement	0.8013 t
Block coefficient	0.8243
Midship coefficient	0.9975
C.G. from midship	fore 0.1330 m
C.G. from keel	0.239 m
Metacentric radius	0.069 m
Longitudinal gyradius	0.238L
Transverse gyradius	0.360B <sub>pp</sub>
Rolling period	2.01 sec
Rudder area	0.0195 m <sup>2</sup>
Rudder area ratio	0.0149
Bilge keel breadth	0.0077 m
Bilge keel length	1.1353 m
Scale ratio	247.0/4.50

Table 1 Main particulars of the model

SHIP SPEED IN WAVES kts	LOCATION S.S.No.	$\chi^2$	$P=P(\chi^2 \geq \chi_0^2)$		
			k-1	1 %	5 %
9.7	Stem	8.59	9	21.70	16.92
9.7	9 <sup>3</sup> / <sub>4</sub> Up.	3.86	5	15.09	11.07
9.7	9 <sup>3</sup> / <sub>4</sub> Low.	3.73	5	15.09	11.07
11.1	Stem	10.36	8	20.10	15.51
7.6	Stem	4.75	5	15.09	11.07

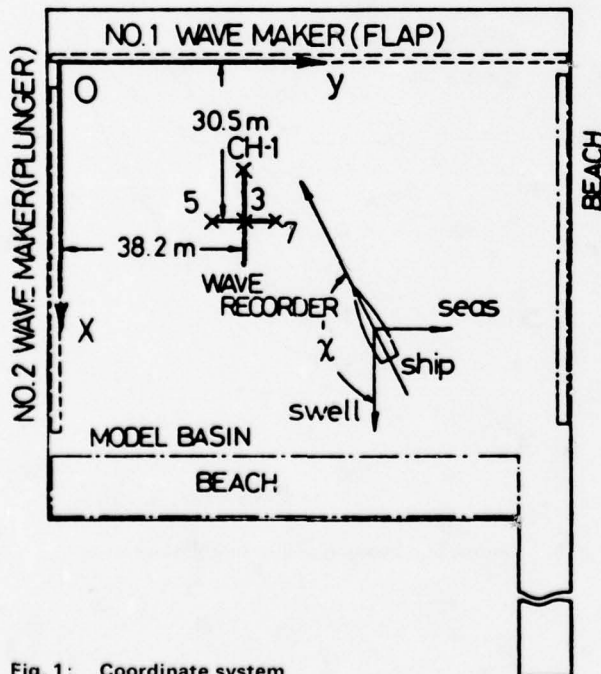
Table 2  $\chi^2$ —confidence

Fig. 1: Coordinate system

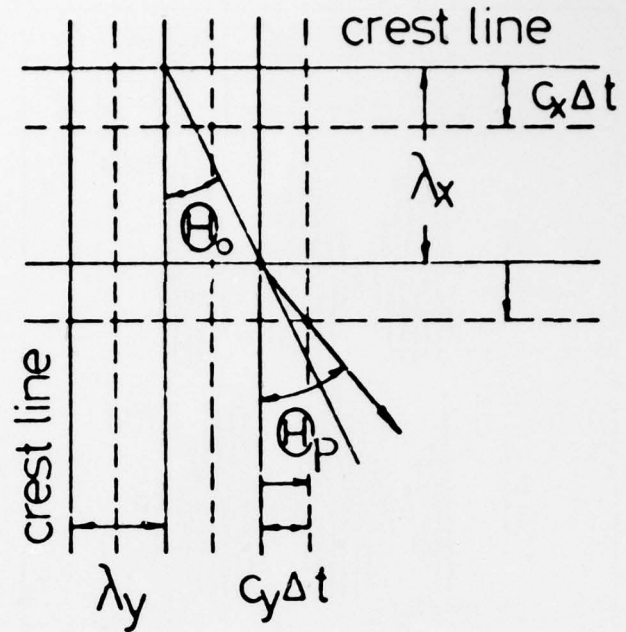


Fig. 2: Wave pattern

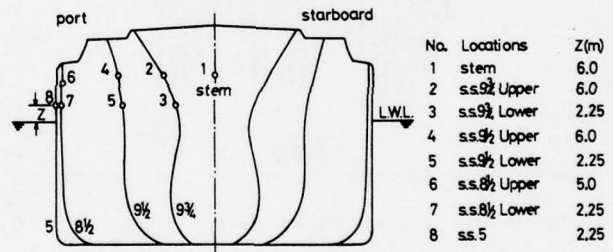


Fig. 3: Locations of pressure gauges

		SWELL					
SEA	KEY	$\lambda / L$	1.50	1.25	1.00	0.75	0.50
	—△—	1.50	135.0°				
	—*—	1.25	137.4°	135.0°			
	—○—	1.00	140.8°	138.2°	135.0°		
	—●—	0.75	144.7°	142.3°	139.1°	135.0°	
	—+—	0.50	150.0°	147.7°	144.7°	140.8°	135.0°

Fig. 4:  $\chi_p$  and marks



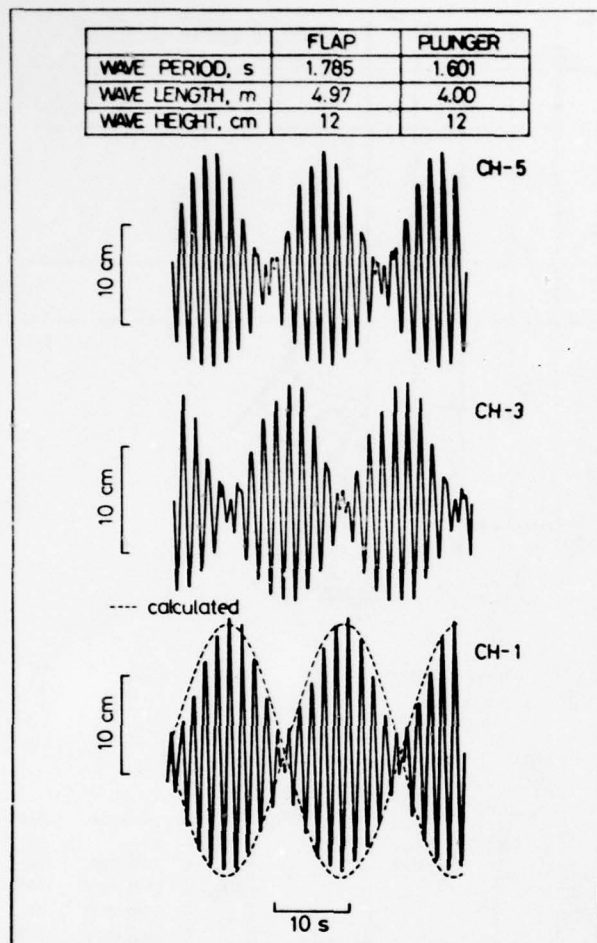


Fig. 5: Records of short-crested waves

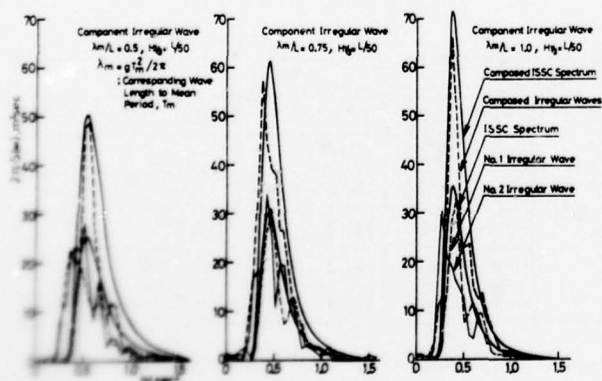


Fig. 6: Wave spectra

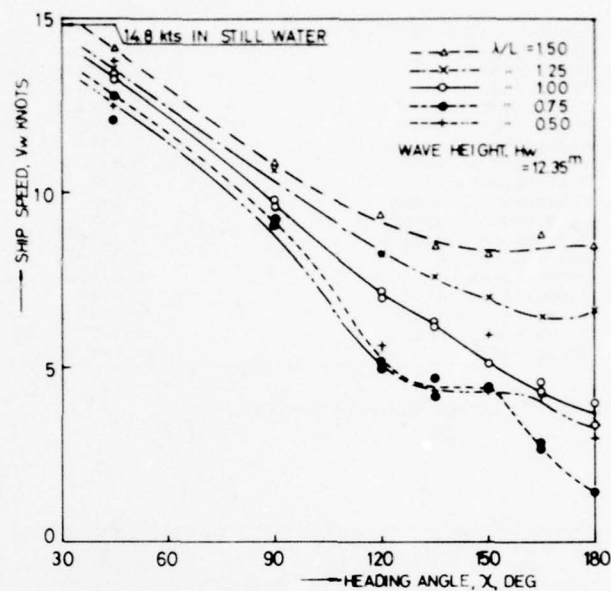


Fig. 7: Speed loss in oblique waves

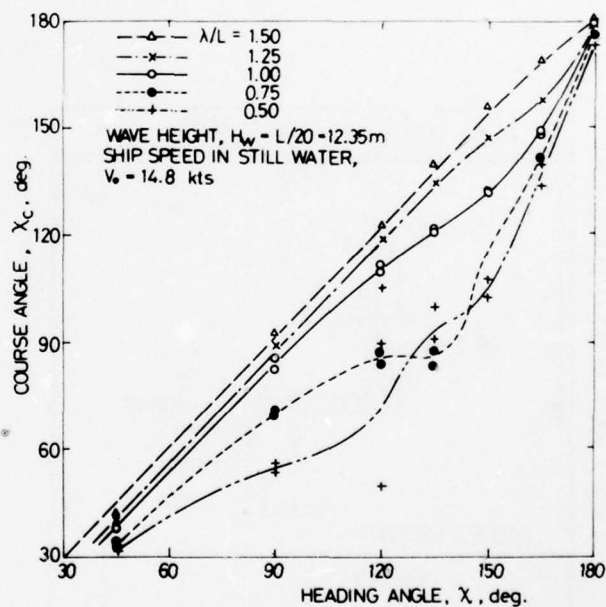


Fig. 8: Course and heading angles in oblique waves

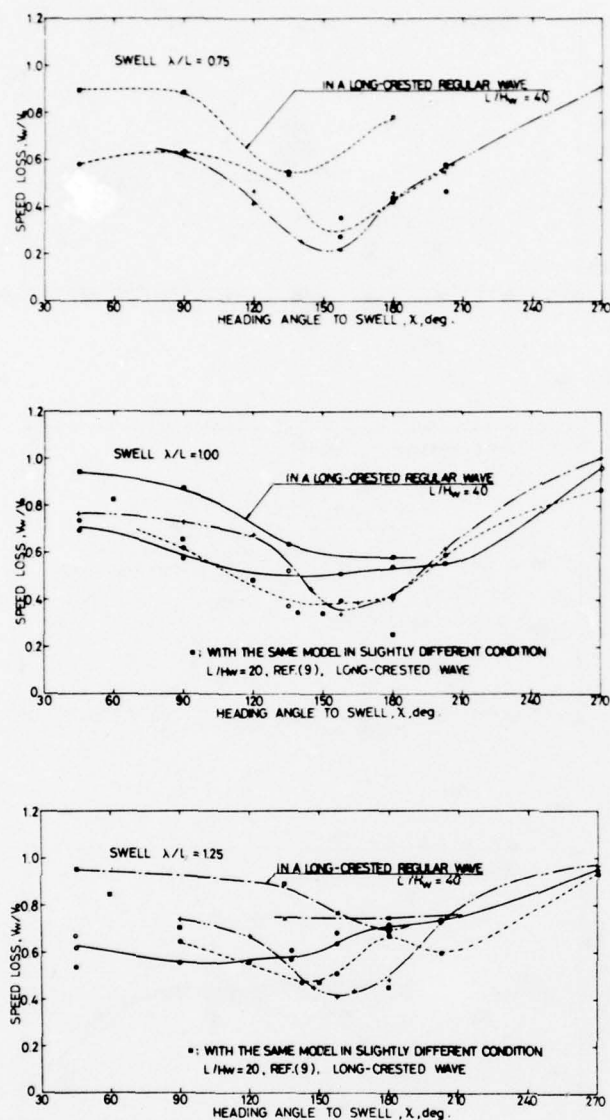


Fig. 9: Speed loss rate in cross waves

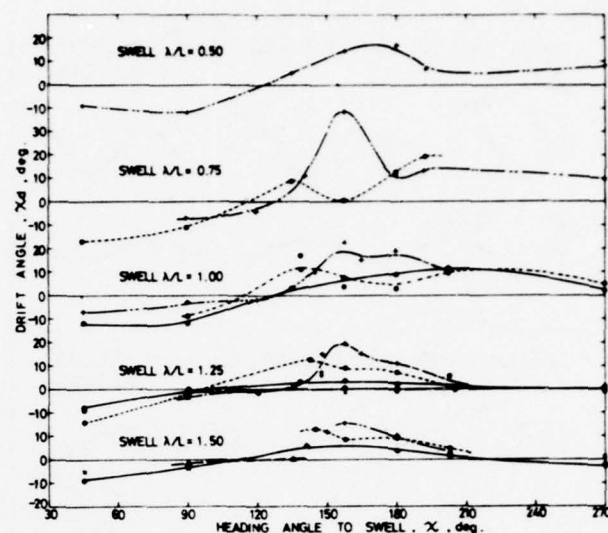


Fig. 10: Drift angle in cross waves

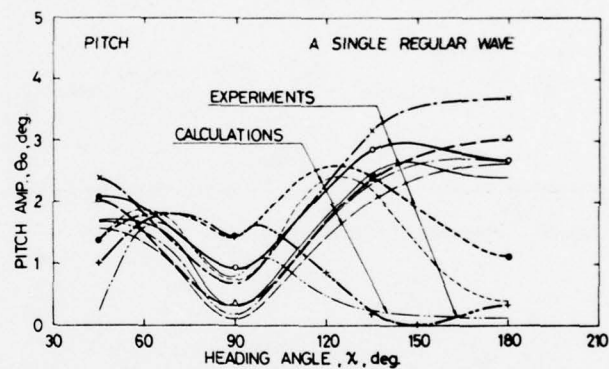


Fig. 11: Pitch response in single regular waves

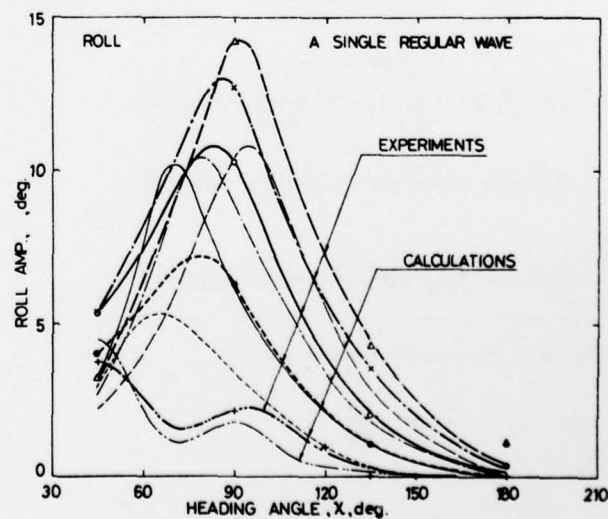


Fig. 12: Roll response in single regular waves

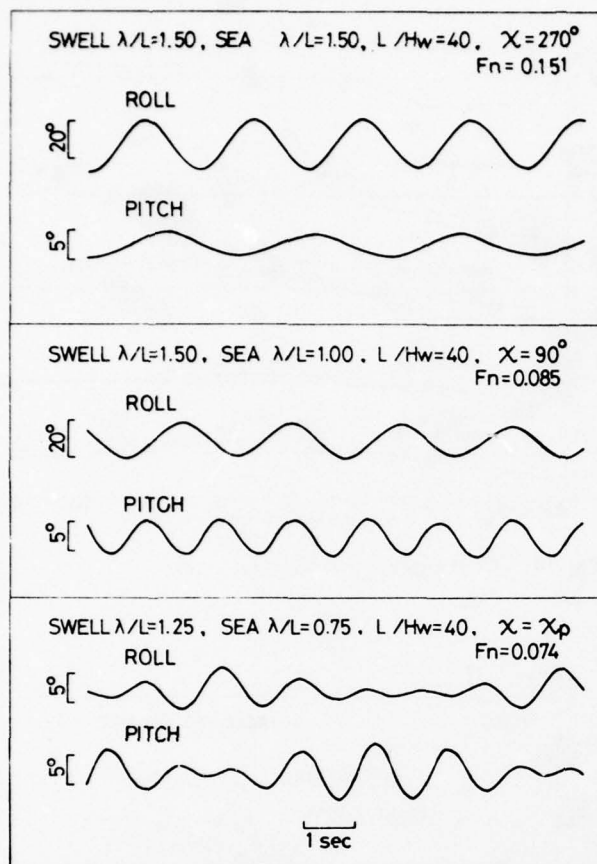


Fig. 13. Records of ship motions

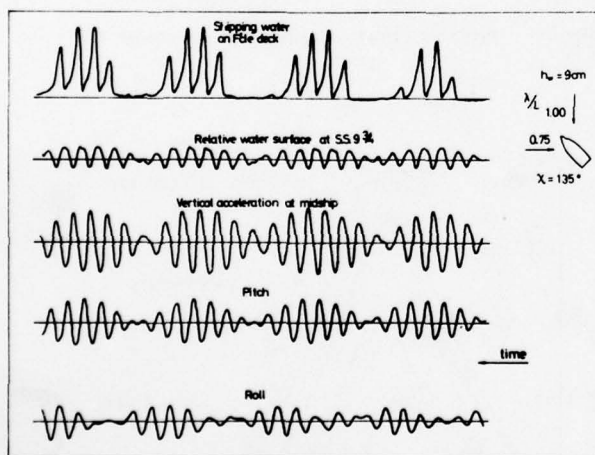


Fig. 14. Records of ship motions

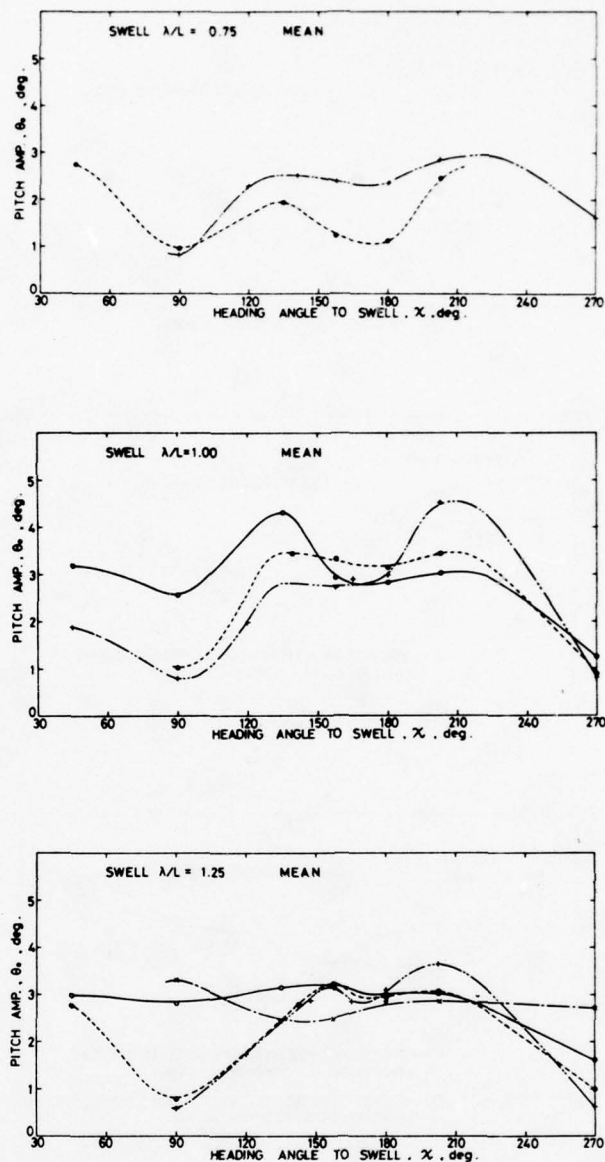


Fig. 15: Mean amplitudes of pitch in cross waves

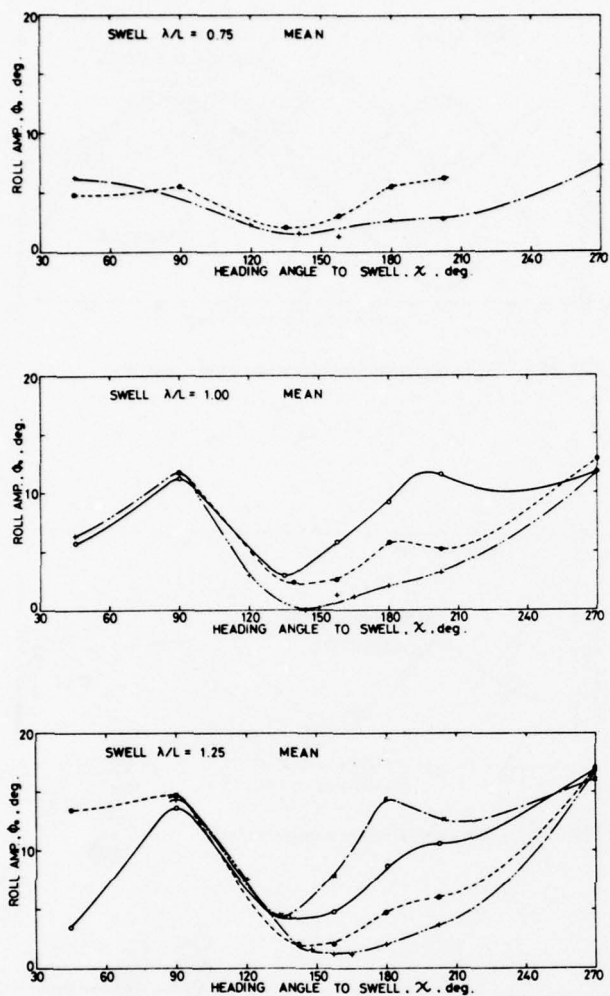


Fig. 16: Mean amplitudes of roll in cross waves

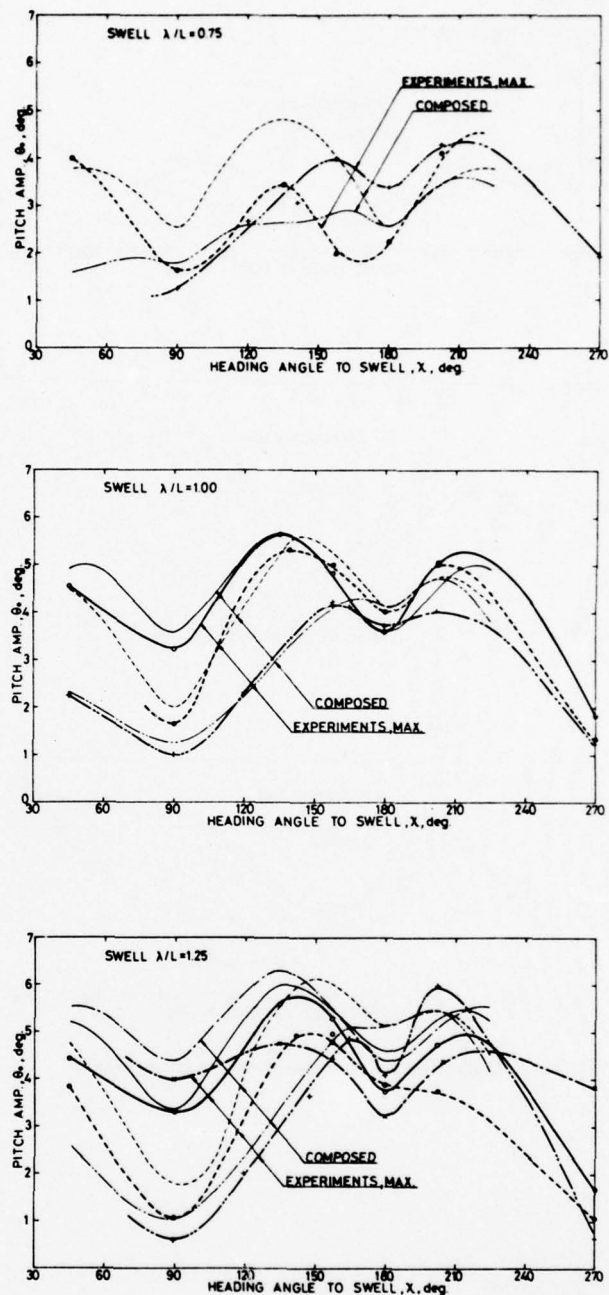


Fig. 17: Maximum amplitudes of pitch in cross waves



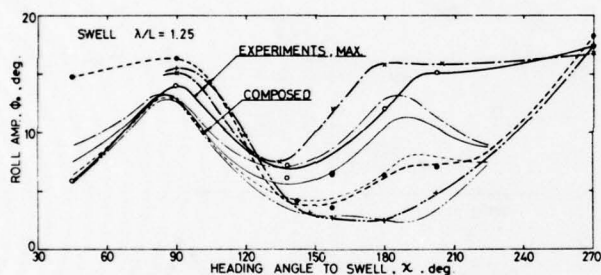
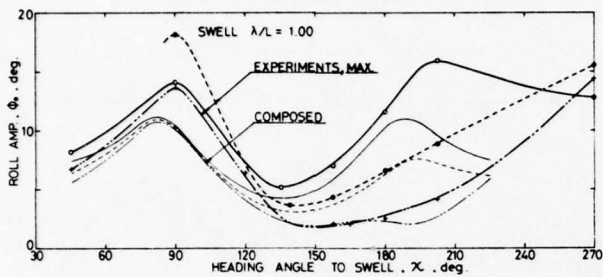
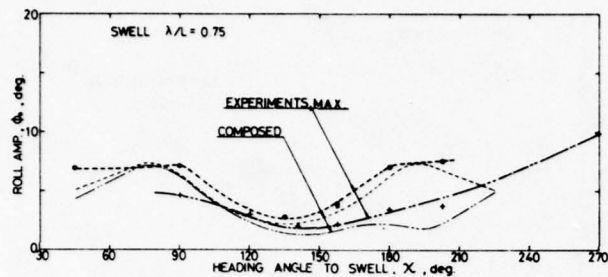


Fig. 18: Maximum amplitudes of roll in cross waves

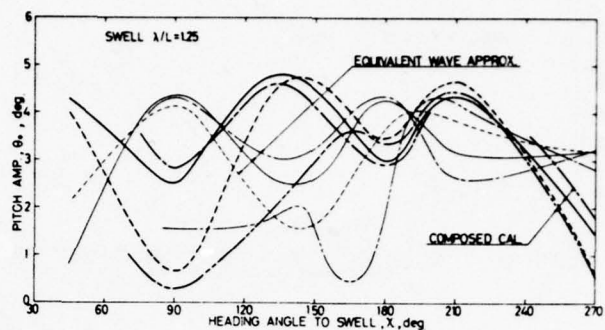


Fig. 19: Equivalent wave approximation (pitch)

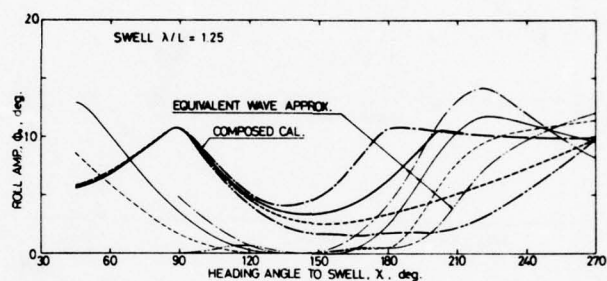


Fig. 20: Equivalent wave approximation (roll)

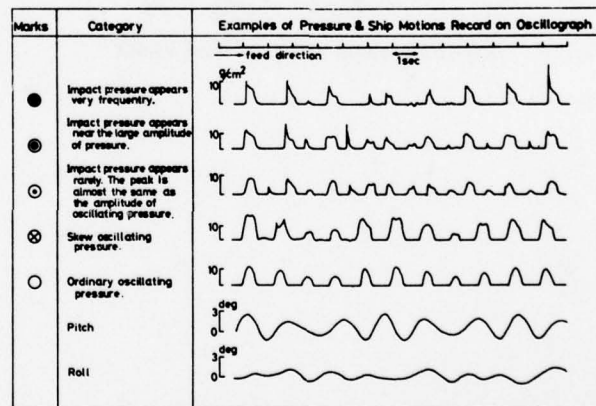


Fig. 21: Classification of impulsive pressure

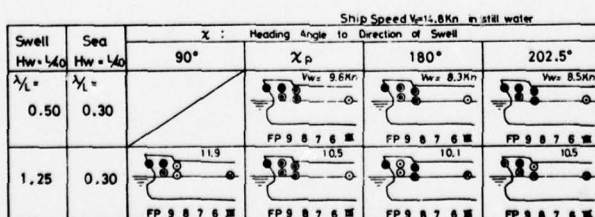
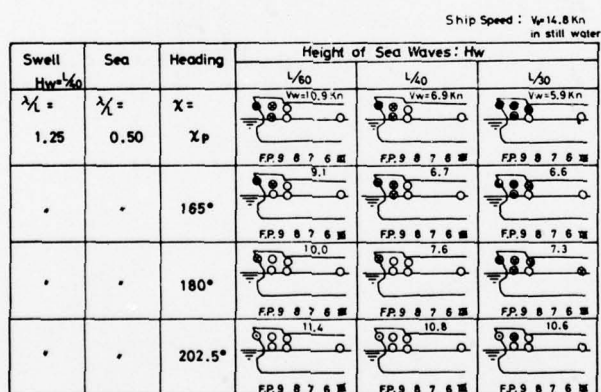
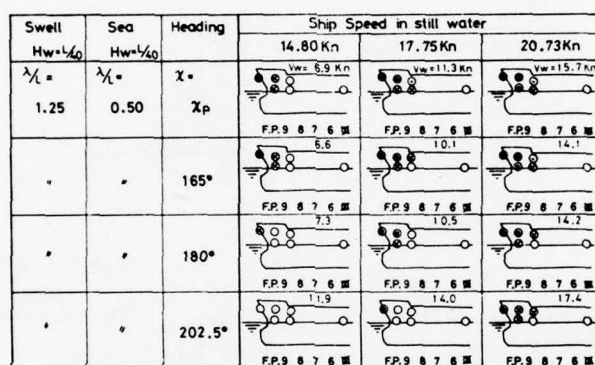
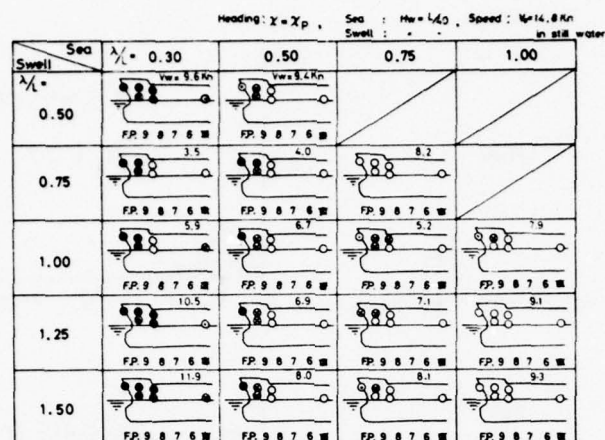


Fig. 22: Diagrams showing occurrence of impact

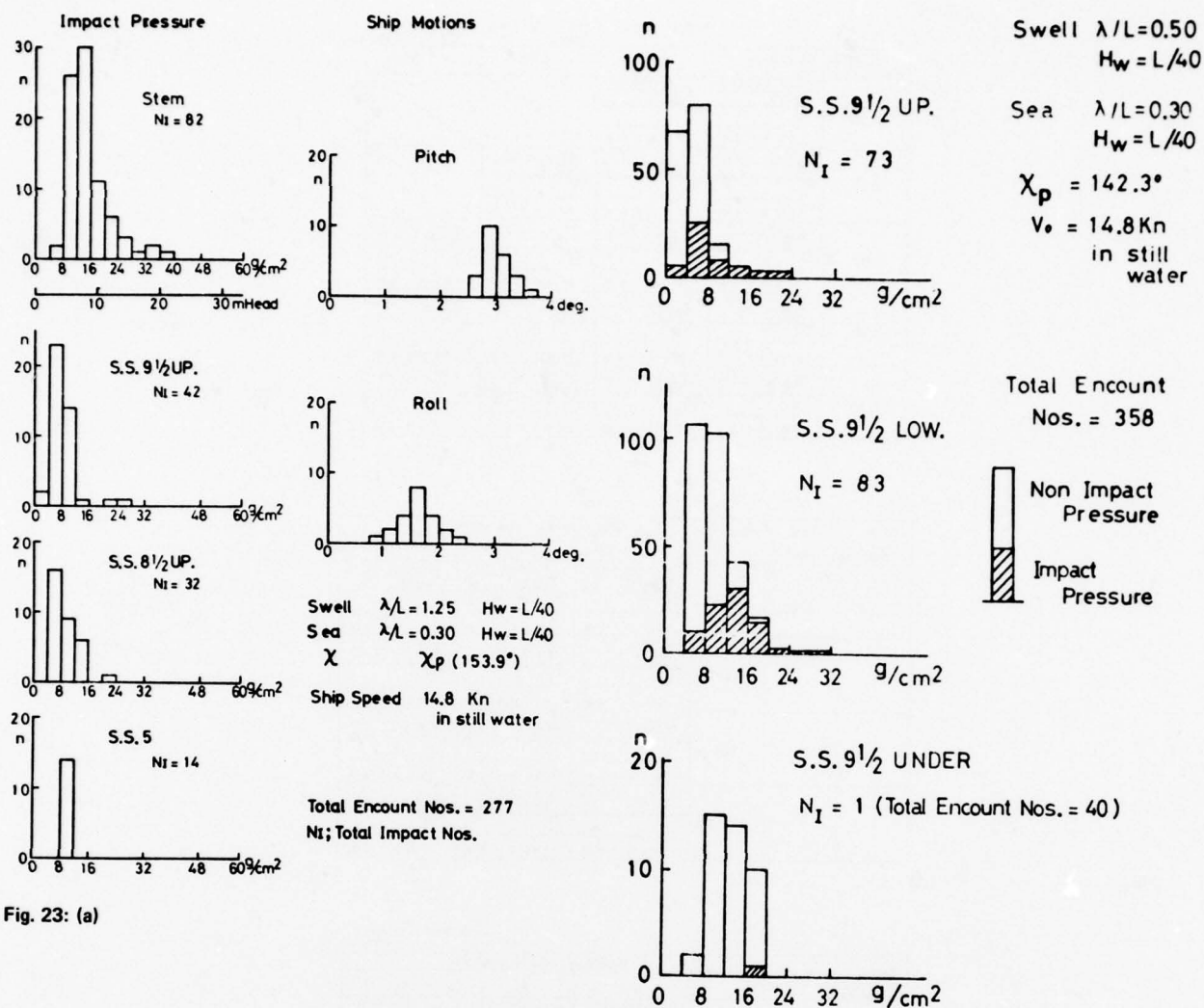
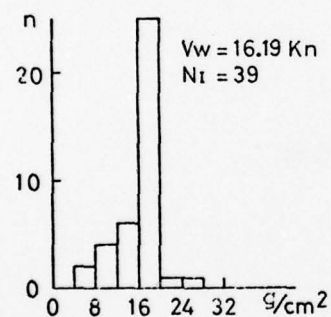
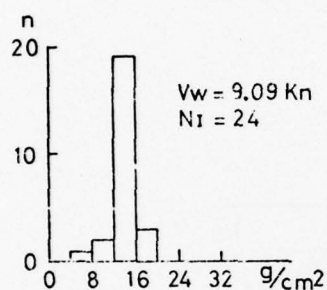
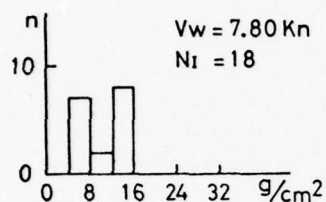
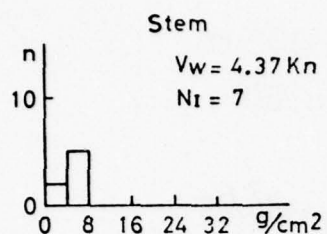


Fig. 23: (a)

Fig. 23: (b)



Swell  $\lambda/L = 1.00$   $H_w = L/40$   
Sea  $\lambda/L = 1.00$   $H_w = L/40$   
 $\chi_p = 135.0^\circ$   
Total Encounter Nos. = 40  
 $N_I$ ; Total Impact Nos.

Fig. 23: (c)

Fig. 23 (a) (b) (c): Histograms of peak values of impulsive pressure

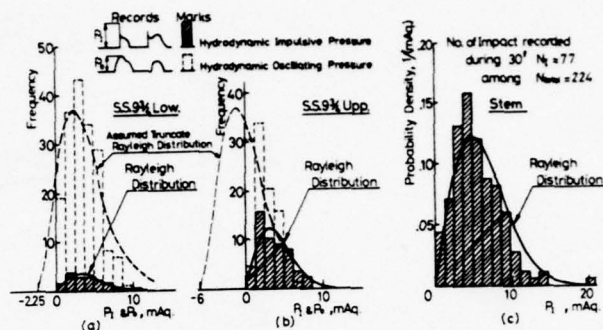


Fig. 24: Distributions of peak values of hydrodynamic oscillating and impulsive pressures

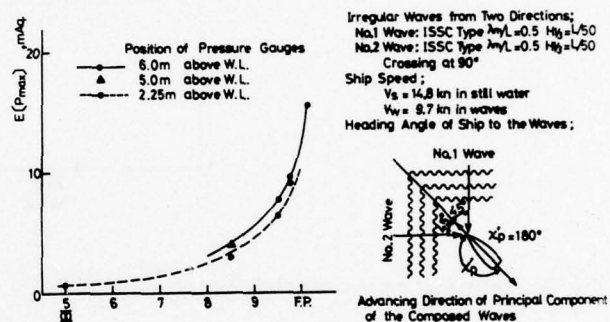


Fig. 25: Lengthwise distributions of short term expected values of impulsive pressure peaks

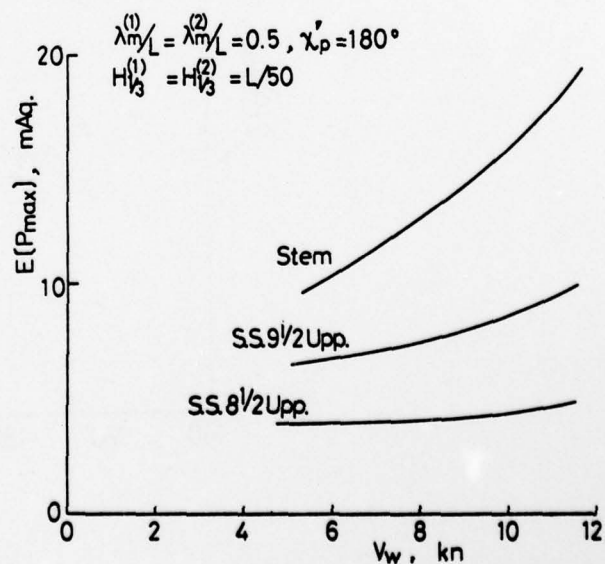


Fig. 26: Effect of ship speed on impulsive pressure



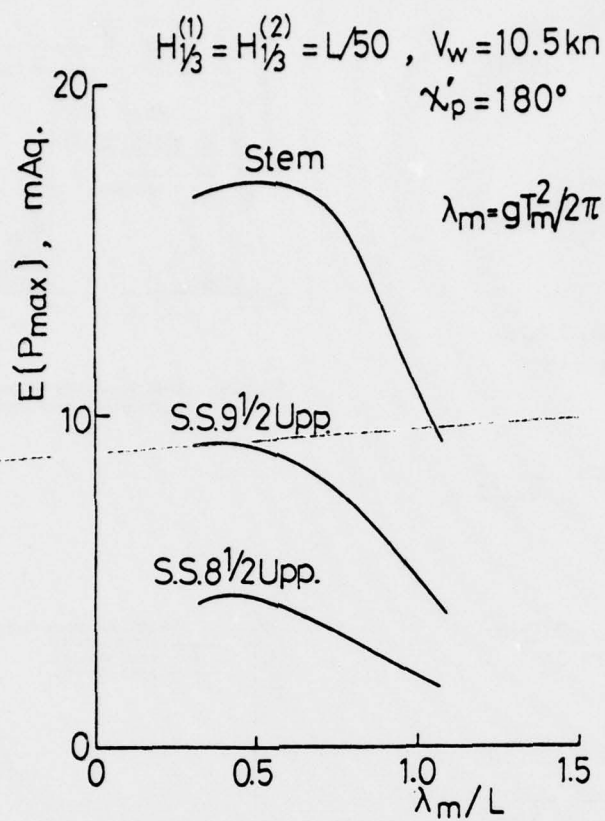


Fig. 27: Effect of mean wave period on impulsive pressure

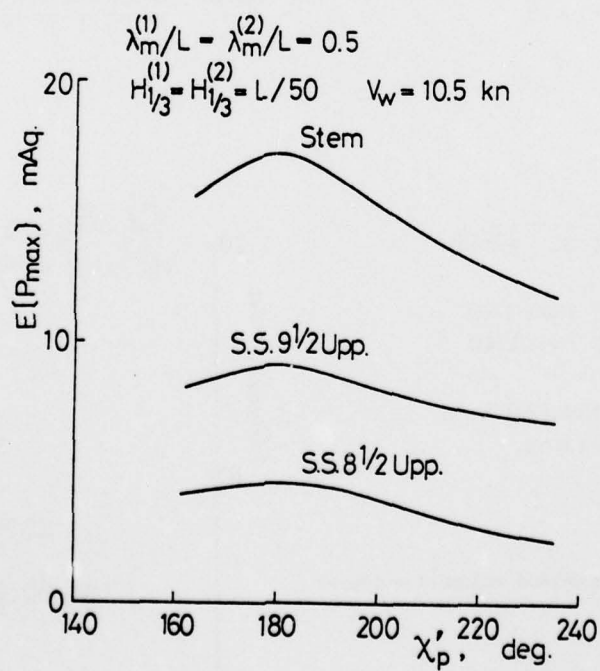


Fig. 28: Effect of heading angle on impulsive pressure

# APPLICATION OF THE FUNCTIONAL POLYNOMIAL MODEL TO THE SHIP ADDED RESISTANCE PROBLEM

J. F. DALZELL

Stevens Institute of Technology, Hoboken, New Jersey, USA

*The objective of the work reviewed herein was to demonstrate by means of analyses of experimental data that a functional polynomial model for added resistance in waves is an adequate engineering approximation. The results obtained indicate that this is so. It is demonstrated that it is possible to identify the quadratic frequency response function for added resistance from experiments in both irregular and periodic waves; and that, given the frequency domain response, it is possible to synthesize at least the nonlinear low frequency resistance components in the time domain.*

## INTRODUCTION

A background motivation for the initiation of the work to be reviewed herein was the lack of general methods for the expeditious practical prediction of the statistics involved in non-linear stochastic seakeeping problems. Given the digital computer and the funds required to exercise it, simulation of solutions in the Monte Carlo sense is often direct and practical, but often not expeditious if the required range of input (sea conditions) is large and the non-linearities are substantial. In many applications, frequency domain prediction methods analogous to the linear-random system outlined by St. Denis and Pierson [1] would be desirable.

It is unrealistic to expect that a universal prediction framework for random non-linear problems can be found. However, it appears that an existing framework, the functional power series, may be applied to restricted classes of seakeeping problems. There are two main attractions in this approach. First, the linear input-output model is a term of the functional power series. Secondly, the model holds for any reasonably well behaved input: periodic, transient, or random. Accordingly, theoretical prediction methods for spectra, etc., may be derived, and it is possible in principle to relate the functions required for these predictions to the results of hydromechanic analyses.

Wiener introduced the functional power series model (also called Volterra Series) into non-linear circuit analysis during World War II, and subsequently published this work and extensions [2]. Over the intervening years the ideas and applications have slowly been amplified and simplified for consumption in the communication and electronics fields. Of the many papers in that literature, those of Barrett [3] and Bedrosian and Rice [4] may be recommended.

Application to seakeeping problems was suggested indirectly by Tick [5] in 1961. Hasselman [6] and Vassilopoulos [7] indicated direct applications to some classes of seakeeping problems about 10 years ago. More recently, the writer [8] and Neal [9] have presented results bearing on the application of the functional series model to what is probably the simplest non-linear seakeeping problem -- the ship resistance added by waves. The

intent in the present paper is to summarize additional results pertaining to the application of the functional series model to added ship resistance.

## PRINCIPAL NOTATION

$C_D(\Omega_1, \Omega_2)$	cross-bi-spectrum (abbreviated C.B.S.), resistance output
$C_\eta(\Omega_1, \Omega_2)$	cross-bi-spectrum, (wave) <sup>2</sup> output
$D_w(t)$	resistance produced by waves
$F_n$	Froude number
$G_1(\omega)$	linear frequency response function
$G_2(\omega_1, \omega_2)$	quadratic frequency response function
$G_2(\omega, -\omega)$	added resistance operator
$g_1(\tau)$	first degree kernel or linear impulse response
$g_2(\tau_1, \tau_2)$	second degree kernel or quadratic impulse response
$h$	regular wave height
$L$	model L.B.P.
$L_j$	coefficients, linear kernel
$Q_{jk}$	coefficients, quadratic kernel
$R_A$	mean added resistance in regular waves
$R_{\eta\eta}(\tau)$	auto-correlation of wave
$S_{\eta\eta}$	wave spectrum, two-sided
$t, t_i$	time
$\Delta$	model displacement
$\Delta t$	sampling interval
$\eta(t)$	wave elevation
$\sigma, \sigma_1, \sigma_2, \sigma_e$	non-dimensional encounter frequency
$\sigma_f$	folding frequency
$\tau$	time (dummy)
$\omega_1$	difference frequency
$\omega_2$	sum frequency
$\omega, \omega_1, \omega_2$	circular frequency

- $\omega_e$  encounter frequency  
 $\omega_{1L}$  frequency of wave of model length

#### THE HYPOTHESIZED ADDED RESISTANCE MODEL AND ITS ORIGIN

For present purposes the ship was assumed to be proceeding at constant forward velocity in a head wave system (the "input") defined in the time domain as the wave elevation  $\eta(t)$  at some point stationary with respect to the mean position of the ship, where  $t$  is time. The wave system may reasonably be assumed to be zero mean whether it is stochastic or deterministic, and in the following this was always assumed to be the case. The resistance to forward motion from all causes (the "output") was denoted  $D(t)$ . The initial assumption was that the resistance,  $D(t)$ , is sufficiently regular so as to at least allow expansion in a functional power series:

$$D(t) = \sum_{n=0}^{\infty} \iint \dots \int [g_n(t_1, t_2, \dots, t_n) \eta(t-t_1) \eta(t-t_2) \dots \eta(t-t_n) dt_1 dt_2 \dots dt_n] \quad (1)$$

(Omission of limits on the integrals signifies limits of  $\pm\infty$ .)

Each term in the above series is a homogeneous functional of degree  $n$ . The kernels,  $g_n(t_1, \dots, t_n)$ , are assumed to be time invariant, smooth, absolutely integrable, and transformable in the multi-dimensional Fourier sense. They are also assumed to be completely symmetrical in their arguments.

Convergence of the series, Eq.(1), is indicated theoretically if the integrals of the absolute value of the kernels are finite -- either for bounded input, or for stochastic input if the input is strictly stationary with bounded moments of all orders.

$D(t)$  may be considered continuous for the present application and is itself a functional. Barrett [3] attributes to Volterra an approximation theorem which says in effect that any continuous functional may be approximated arbitrarily closely by a functional polynomial. (Truncating Eq.(1) at some  $n$  converts the functional series into a functional polynomial.)

Accordingly, the series, Eq.(1) is truncated to form the simple functional polynomial which is the actual model in the present work. By definition, the added resistance due to waves goes to zero when there are no waves. If  $\eta(t)$  is assumed to be zero for all time in Eq.(1), the only term remaining is  $g_0$ , a constant. Accordingly, the term of degree zero in the series may be discarded as far as added resistance is concerned by re-defining the output as only the resistance produced by waves,  $D_w(t)$ .

Vassilopoulos [7] pointed out that the form of the expected mean added resistance predicted by the formula of Maruo [10] was the same as the form for the expected value of the term of the second degree in Eq.(1), and this result is also implicit in the work of Tick [5]. Accordingly, as an hypothesis, the series, Eq.(1) is truncated at  $n=2$ .

The result is the functional polynomial model hypothesized in the present work as representing the resistance added by the wave system:

$$D_w(t) = \int g_1(t_1) \eta(t-t_1) dt_1 + \iint g_2(t_1, t_2) \eta(t-t_1) \eta(t-t_2) dt_1 dt_2 \quad (2)$$

It should be noted again that the wave input,  $\eta(t)$ , in Eqs.(1) and (2) is considered to be as observed in the head sea encounter domain. This is a restriction which is probably removable (see Hasselman [6]) but this was not attempted for the present case because there was a larger conceptual problem.

The transition between Eq.(1) and Eq.(2) was made on the somewhat tenuous grounds that the forms of two theoretical expressions were the same. In practice there has been until recently some argument about the degree to which Maruo's prediction formula [10] represented practical reality -- even in simple head sea towing tank experiments. Clearly, the worth of the functional polynomial model, Eq.(2), for added resistance hinged mostly upon whether or not the series, Eq.(1) had been truncated prematurely; that is, the main problem appeared to be whether the encounter domain model, Eq.(2), would work at all. Accordingly, the approach taken in the present work has been to accept the mathematical model Eq.(2), as a working hypothesis, to study the implications of this model with respect to observable data and to check these implications with experiment.

#### IMPULSE AND FREQUENCY RESPONSE FUNCTIONS

##### Definitions

The first term in Eq.(2) is the ordinary linear convolution of a linear impulse response function  $g_1(t_1)$  with  $\eta(t)$ . The second term is a double convolution, and the second degree kernel  $g_2(t_1, t_2)$  might be called a quadratic impulse response. According to basic assumptions, the two impulse responses are related to the linear and quadratic frequency response functions through the Fourier transform. These two sets of transform pairs may be defined as follows:

$$g_1(\tau) = \frac{1}{2\pi} \int e^{+i\omega\tau} G_1(\omega) d\omega$$

$$G_1(\omega) = \int e^{-i\omega\tau} g_1(\tau) d\tau \quad (3)$$

$$g_2(\tau_1, \tau_2) = \frac{1}{(2\pi)^2} \iint \text{Exp}[+i\omega_1 \tau_1 + i\omega_2 \tau_2] G_2(\omega_1, \omega_2) d\omega_1 d\omega_2$$

$$G_2(\omega_1, \omega_2) = \iint \text{Exp}[-i\omega_1 \tau_1 - i\omega_2 \tau_2] g_2(\tau_1, \tau_2) d\tau_1 d\tau_2 \quad (4)$$

##### Symmetry

The linear frequency response function,  $G_1(\omega)$ , defined by Eq.(3) is absolutely conventional. The quadratic frequency response function,  $G_2(\omega_1, \omega_2)$  is defined in a bi-frequency plane. Because the kernel  $g_2(\tau_1, \tau_2)$  is assumed to be symmetrical in its arguments:

$$g_2(\tau_1, \tau_2) = g_2(\tau_2, \tau_1) \quad (5)$$

and thus:

$$G_2(\omega_1, \omega_2) = G_2(\omega_2, \omega_1) \quad (6)$$

$$G_2^*(\omega_1, \omega_2) = G_2(-\omega_1, -\omega_2) = G_2(-\omega_2, -\omega_1) \quad (7)$$



Figure 1 summarizes the results of applying Eqs.(6) and (7) in the bi-frequency plane for the eight possible coordinate positions of two frequencies whose absolute values are  $a$  and  $b$ . Equation (6) results in a line of symmetry along the line  $\omega_2 = \omega_1$ . Equation (7) results in a line of symmetry of the real part of  $G_2(\omega_1, \omega_2)$  defined by  $\omega_2 = -\omega_1$  (and it may be noted that along this line the imaginary part of the function is zero). These two lines and the  $\omega_1, \omega_2$  axes divide the bi-frequency plane into octants, of which the two on either side of the positive  $\omega_1$  axis may be arbitrarily chosen for reference. The equalities shown in Figure 1 in the remaining six octants are arrived at by applying Eqs.(6) and/or (7). The assumptions of symmetry of the second degree kernel result, with Eq.(4), in a complete definition of  $G_2(\omega_1, \omega_2)$  if the functions are defined in any pair of octants including a semi-axis of either frequency. Thus without loss in generality, further interpretation of the quadratic frequency response needs only to involve the octants on either side of the positive  $\omega_1$  axis. In these octants  $\omega_1$  is positive and  $|\omega_1| \geq |\omega_2|$ .

#### Interpretation of Quadratic Frequency Response Function

The interpretation of the quadratic frequency response function is less direct than for the linear case, but can be approached in a grossly similar manner. If in the linear case the system is considered to be excited by

$$\eta(t) = a \cos \omega t$$

the output is then:

$$\text{Re}\{a G_1(\omega) \exp(i\omega t)\}$$

and  $G_1(\omega)$  is interpreted in terms of normalized amplitude and phase of response. To interpret the quadratic frequency response, dual harmonic excitation is necessary. Accordingly, it is assumed for illustration that:

$$\eta(t) = a_1 \cos \omega_1 t + a_2 \cos \omega_2 t \quad (8)$$

In accordance with the previous discussion of symmetry, both frequencies ( $\omega_1, \omega_2$ ) are considered positive and  $|\omega_1| \geq |\omega_2|$ . The basic model, Eq.(2) is good for any zero-mean excitation. Accordingly, Eq.(8) may be substituted directly in Eq.(2). After considerable algebra and consideration of symmetries, the results appear in the form of single and double Fourier transforms of  $g_1(t_1)$  and  $g_2(t_1, t_2)$ , so that the final result for the response to dual harmonic excitation may be written as follows:

$$\begin{aligned} D_w(t) = & \text{Re}\{a_1 G_1(\omega_1) \exp(i\omega_1 t) + a_2 G_1(\omega_2) \exp(i\omega_2 t)\} \\ & + \frac{1}{2} \{a_1^2 G_2(\omega_1, -\omega_1) + a_2^2 G_2(\omega_2, -\omega_2)\} \\ & + \frac{1}{2} \text{Re}\{a_1^2 G_2(\omega_1, \omega_1) \exp(i2\omega_1 t)\} \\ & + \frac{1}{2} \text{Re}\{a_2^2 G_2(\omega_2, \omega_2) \exp(i2\omega_2 t)\} \\ & + \text{Re}\{a_1 a_2 G_2(\omega_1, \omega_2) \exp[i(\omega_1 + \omega_2)t]\} \\ & + \text{Re}\{a_1 a_2 G_2(\omega_1, -\omega_2) \exp[i(\omega_1 - \omega_2)t]\} \end{aligned} \quad (9)$$

This result shows that the response of the quadratic system, Eq.(2), to dual excitation contains, in general, a shift in the mean and components of six different frequencies [ $\omega_1, \omega_2, 2\omega_1,$

$2\omega_2, (\omega_1 + \omega_2),$  and  $(\omega_1 - \omega_2)$ ]. The first two terms of the result are the superposition of the linear responses at the excitation frequencies. The third and fourth terms of Eq.(9) represent a shift in the mean. These terms allow the identification of the mean added resistance operator as the value of  $G_2(\omega_1, \omega_2)$  along the line  $\omega_2 = -\omega_1$  (or  $G_2(\omega_1, -\omega_1)$ ). The fifth and sixth terms are the second harmonic components ( $2\omega_1, 2\omega_2$ ). Similarly, these terms allow the identification of second harmonic response with the values of  $G_2(\omega_1, \omega_2)$  along the line  $\omega_2 = \omega_1$  (or  $G_2(\omega_1, \omega_1)$ ).

The seventh and eighth terms of Eq.(9) pertain to the bi-frequency plane in general. The seventh term is the response at frequency  $(\omega_1 + \omega_2)$ ; that is,  $G_2(\omega_1, \omega_2)$  expresses the normalized response in the sum frequency due to non-linear interactions. Similarly, the eighth term involves response at frequency  $(\omega_1 - \omega_2)$ ; that is,  $G_2(\omega_1, -\omega_2)$  is the normalized response in the difference frequency. In terms of Figure 1, the octant of the bi-frequency plane above the positive  $\omega_1$  axis corresponds to the portion of the quadratic frequency response function which defines sum-frequency interactions, and the octant below the positive  $\omega_1$  axis corresponds to the portion of the function which defines difference frequency interactions.

Equations (8) and (9) afford a direct way to relate the postulated input-output model to the results of hydromechanic analyses.

#### Cascading with Linear Systems

It is often necessary or advantageous to consider the non-linear model (Eq.2) as being in cascade with various linear systems. The type of cascading of interest is outlined in Figure 2 in block diagram form. Inside the dashed box is the non-linear model, Eq.(2), shown as the summation (D) of the response of a linear and a quadratic term to excitation  $\eta$ . To the right in the diagram a linear filter is shown operating on D, and to the left another linear filter operates on the input  $\zeta$  to produce  $\eta$ . In a physical experiment the left-hand filter may correspond to the transformation of wave elevations measured ahead of a model to the vicinity of the model, and the right-hand filter may correspond to a real instrumentation filter. In practice,  $\zeta$  and E may be observable but not  $\eta$  and D.

The rules of cascading developed by George [11] may be summarized for this case as follows:

$$K_1(\omega) = G_1(\omega) F(\omega) H(\omega) \quad (10)$$

$$K_2(\omega_1, \omega_2) = G_2(\omega_1, \omega_2) F(\omega_1) F(\omega_2) H(\omega_1 + \omega_2) \quad (11)$$

where  $K_1(\omega)$  and  $K_2(\omega_1, \omega_2)$  are the effective linear and quadratic frequency response functions relating E to  $\zeta$ .

The rule for the linear part, Eq.(10), is the same as for normal linear systems. In the quadratic part (Eq.11), the effect of an input modification or filter is felt in both the bi-frequency co-ordinate directions. For example, if  $F(\omega)$  is an ideal low-pass filter with cutoff frequency equal to A, the effective  $K_2(\omega_1, \omega_2)$  will be zero outside the region where  $|\omega_1|$  and  $|\omega_2|$  are less than A.

In describing the effect of output modification or filtering, and for subsequent use, a frequency axis transformation is defined as follows:

$$\begin{aligned} \Omega_1 &= \omega_1 - \omega_2 \\ \Omega_2 &= \omega_1 + \omega_2 \end{aligned} \quad (12)$$



The  $\Omega_1$  and  $\Omega_2$  axes are coincident with the lines of symmetry previously noted in Figure 1. This new axis system is mapped into the  $(\omega_1, \omega_2)$  plane in Figure 3. With respect to Eq.(11) it is seen that the effect of output filtering is the same for constant  $\Omega_2$ . An ideal low-pass output filter with cutoff frequency equal to  $A$  will make the effective quadratic response function zero for  $|\Omega_2| > A$ .

In the case of added resistance, the problems of most practical interest involve fluctuations of very low frequency so that if added resistance is examined through a low-pass filter with very low cutoff frequency, the effective quadratic frequency response function tends to be concentrated along the line  $\omega_2 = -\omega_1$  in the bi-frequency plane ( $\Omega_2 = 0$ ). This line was previously identified as the locus of the added resistance operator. Thus the functional polynomial model for response at very low frequency tends toward the approximate model derived by Newman [12] as the band of frequencies of interest tends toward zero.

#### SUMMARY OF THEORETICAL RESULTS FOR RESPONSE TO RANDOM EXCITATION

Assuming Eq.(2), the essential results for the response to random excitation have been noted elsewhere, [5], [7], [8], [9], [13], [14], and will only be summarized here. It is assumed that the wave system  $\eta(t)$  is a stationary, Gaussian, zero mean process. The auto-correlation of the process will be denoted  $R_{\eta\eta}(\tau)$  and is defined as follows:

$$R_{\eta\eta}(\tau) = \overline{\eta(t)\eta(t-\tau)} \quad (13)$$

where the bar denotes the statistical expectation. The two-sided spectrum of the process is, by definition:

$$S_{\eta\eta}(\omega) = \int R_{\eta\eta}(\tau) e^{-i\omega\tau} d\tau \quad (14)$$

Taking the expected value of Eq.(2), and after some manipulation [5], [7], [13]:

$$\overline{D_w(t)} = \frac{1}{2\pi} \int G_2(\omega, -\omega) S_{\eta\eta}(\omega) d\omega \quad (15)$$

This result is the expected value of resistance added by waves.

The cross spectrum of the resistance and waves may be estimated from observable data with standard techniques. Following Tick [5], it may be noted that the identification of the linear transfer function, Eq.(3), may be carried out with cross-spectral analysis in the same manner as for purely linear systems.

The scalar spectrum of the resistance added by the waves may also be estimated from observable data using standard techniques. Forming the auto-correlation function of  $D_w(t)$ , Eq.(2), and after some manipulation [13], the spectrum of resistance produced by the wave system becomes:

$$S_{DD}(\omega) = |G_1(\omega)|^2 S_{\eta\eta}(\omega) + \frac{1}{\pi} \int |G_2(\omega-\xi, \xi)|^2 S_{\eta\eta}(\omega-\xi) S_{\eta\eta}(\xi) d\xi \quad (16)$$

In order to carry out analyses of observable

data and the identification of the quadratic frequency response function, the cross-bi-spectrum is necessary. The derivation of the cross-bi-spectrum between wave and resistance starts with the definition of a third moment function:

$$M_{\eta\eta D}(\tau_1, \tau_2) = \overline{\eta(t+\tau_1)\eta(t-\tau_1)[D_w(t-\tau_2) - \overline{D_w(t-\tau_2)}]} \quad (17)$$

Combining Eqs.(2) and (15) and after some manipulation [13], in which the properties of Gaussian processes are invoked, and the frequency variables are changed to sum and difference frequencies in accordance with Eq.(12):

$$M_{\eta\eta D}(\tau_1, \tau_2) = \frac{1}{(2\pi)^2} \iint \left\{ G_2^* \left( \frac{\Omega_1 + \Omega_2}{2}, \frac{\Omega_2 - \Omega_1}{2} \right) S_{\eta\eta} \left( \frac{\Omega_1 + \Omega_2}{2} \right) \cdot S_{\eta\eta} \left( \frac{\Omega_2 - \Omega_1}{2} \right) \right\} \text{Exp}[i(\tau_1 \Omega_1 + \tau_2 \Omega_2)] d\Omega_1 d\Omega_2 \quad (18)$$

Then defining the wave, wave, resistance cross-bi-spectrum as  $C_D(\Omega_1, \Omega_2)$ :

$$C_D(\Omega_1, \Omega_2) = \iint M_{\eta\eta D}(\tau_1, \tau_2) \text{Exp}[-i(\tau_1 \Omega_1 + \tau_2 \Omega_2)] d\tau_1 d\tau_2 = G_2^*(\omega_1, \omega_2) S_{\eta\eta}(\omega_1) S_{\eta\eta}(\omega_2) \quad (19)$$

Thus the first basis for an identification procedure for the quadratic frequency response function is:

$$G_2(\omega_1, \omega_2) = \frac{C_D^*(\omega_1 - \omega_2, \omega_1 + \omega_2)}{S_{\eta\eta}(\omega_1) S_{\eta\eta}(\omega_2)} \quad (20)$$

It turns out [14] that in forming a third moment function as in Eq.(17), if the squared input,  $\eta^2(t)$ , is substituted for the output,  $D_w(t)$ , the result may be written:

$$M_{\eta\eta\eta^2}(\tau_1, \tau_2) = \overline{\eta(t+\tau_1)\eta(t-\tau_1)[\eta^2(t-\tau_2) - \overline{\eta^2(t-\tau_2)}]} \quad (21)$$

and a cross bi-spectrum of input, input, input<sup>2</sup> which is defined by an equation of the form of Eq.(19) becomes finally:

$$C_{\eta\eta}(\Omega_1, \Omega_2) = \iint R_{\eta\eta}(\alpha) R_{\eta\eta}(\beta) \text{Exp}[-i(\omega_1 \alpha + \omega_2 \beta)] d\alpha d\beta = S_{\eta\eta}(\omega_1) S_{\eta\eta}(\omega_2) \quad (22)$$

Because the two-sided scalar spectra are even and real,  $C_{\eta\eta}(\Omega_1, \Omega_2)$  is real and has 8-fold symmetry in the bi-frequency  $(\omega_1, \omega_2)$  plane.

Combining Eqs.(20) and (22), a second basis for an identification procedure for the quadratic frequency response function is:

$$G_2(\omega_1, \omega_2) = \frac{C_D^*(\omega_1 - \omega_2, \omega_1 + \omega_2)}{C_{\eta\eta}(\omega_1 - \omega_2, \omega_1 + \omega_2)} \quad (23)$$

Thus this estimate for the quadratic frequency response function is the ratio of cross-bi-spectrum of (input, input, output) to the cross-bi-

spectrum of (input, input, (input)<sup>2</sup>). (In a similar way, the linear frequency response function can be thought of as the ratio of input-output cross spectrum to the input-input cross spectrum.)

#### CROSS-BI-SPECTRAL ANALYSIS

The techniques utilized in the present work for the estimation of cross-bi-spectra from observed data are covered in some detail in References [13] and [14], and are summarized in [8]. These techniques are analogous to the Tukey correlation methods for scalar spectra and cross-spectra. As such they are probably not the most computationally economical, but were straightforward to program and de-bug.

Because the sample is necessarily finite, it is possible only to estimate cross-bi-spectral averages rather than actual densities:

$$\hat{C}(\Omega_1, \Omega_2) = \iint H(\Omega_3, \Omega_4) C(\Omega_1 + \Omega_3, \Omega_2 + \Omega_4) d\Omega_3 d\Omega_4 \quad (24)$$

where the average is weighted by the "cross-bi-spectral window,"  $H(\Omega_3, \Omega_4)$ . The "window" by analogy with scalar spectrum analysis must peak at bi-frequency (0,0), fall off rapidly elsewhere, and remain near zero far away from the peak. As in scalar spectrum analysis, a too-broad window "smudges" the estimates, a too-narrow window in relation to sample length inflates the variance of the estimate, and the optimum choice of window width depends largely upon an advance knowledge of the answer.

The basic cross-bi-spectral estimating formula as derived in Reference [13] is:

$$\begin{aligned} \hat{C}(\Omega_1, \Omega_2) = & \left( \frac{\Delta t}{e_1 + e_2} \right)^2 \sum_{j=-m}^m \sum_{k=-u}^u (e_1 + e_2 \cos \pi j / m) \\ & \cdot (e_1 + e_2 \cos \pi k / u) \exp \left[ i \pi \left( \frac{P_1 j}{m} + \frac{P_2 k}{u} \right) \right] \\ & \cdot \frac{1}{N} \sum_n W(n+j) W(n-j) D(n+k) \end{aligned} \quad (25)$$

This equation is for cross-bi-spectral averages over a bi-spectral window which is essentially a two-dimensional Hamming filter as defined by the product of terms of the form  $(e_1 + e_2 \cos \pi j / m)$  with  $e_1 = 0.54$  and  $e_2 = 0.46$ .

In the equation the several variables are defined as follows:

$\Delta t$  = the sampling interval used to convert the original analog time histories into time series

$m$  = maximum lags in difference frequency ( $\Omega_1$ ) direction

$u$  = maximum lags in sum ( $\Omega_2$ ) frequency direction

As in scalar spectrum analysis, the maximum lag refers both to the maximum time lag used in estimating lagged products and to the number of intervals into which the principal alias of the frequency axis is divided. In the present work there appeared no reason to make the lags different in the different frequency directions and ( $u$ ) was always set equal to ( $m$ ).

Continuing the definitions:

$$\Omega_1 = \frac{\pi P_1}{m \Delta t}$$

$$\Omega_2 = \frac{\pi P_2}{u \Delta t}$$

$N$  = the number of possible products summed

$W(n)$  = the input time series corrected to zero sample mean

$D(n)$  = the output time series corrected to zero sample mean

Equation (25) may be seen to be a discretized version of Eqs. (17) and (19) with two lag window factors added inside the summations. Some studies have been made of the use of cross-bi-spectra estimated via Eq. (25) in the quadratic transfer function identification Eqs. (20) or (23), [13], [14], [15]. These were made with the help of digitally simulated linear plus quadratic processes. The results of the simulation studies may be summarized by noting that the major problems in the cross-bi-spectral identification technique are of the same type as in cross-spectrum identification. In order to produce statistically precise estimates of the quadratic transfer function, sample size needs to be much larger than that required for cross-spectral identification. Estimates via Eqs. (20) or (23) are likely to be highly variable outside the 10% power band of the scalar spectrum of either input or output. Finally any "hump" in the cross-bi-spectrum or the quadratic transfer function should be defined by 4 or 5 estimates in each frequency direction if realistic answers are to be expected.

#### EXPERIMENTAL PROGRAM

The experimental program involved for the present work is detailed in [13]. The main objective of this program was to provide long samples of dynamic ship model resistance in irregular waves. Nominally the conditions on the model were only that it be restrained in surge, move at constant speed, and that resistance measurements include oscillatory components as well as D.C. A five-foot Series 60 model was chosen for the experiments (Parent:  $C_B = 0.60$ ).

The test program involved towing the model at two speeds (Froude Numbers 0.15 and 0.20) in head regular and irregular waves in Davidson Laboratory Tank 3 (300'x12'x6').

In the model experiments in irregular waves, three model sea states were used. Table 1 has been prepared to summarize some of the observations in terms of values for a 500-foot ship. The wave conditions cover a good part of the range of practical interest.

The model was run at both Froude numbers in each of the three seas. For each of the resulting six parameter combinations, enough statistically independent sample was generated so as to result in between 600 and 900 wave encounters (depending upon speed and sea state).

AD-A055 859

UNIVERSITY COLL LONDON (ENGLAND) DEPT OF MECHANICAL --ETC F/G 13/10  
SYMPOSIUM ON NAVAL HYDRODYNAMICS. UNSTEADY HYDRODYNAMICS OF MAR--ETC(U)  
1978 R E BISHOP, A G PARKINSON, W G PRICE N00014-76-C-0093

UNCLASSIFIED

NL

4 OF 9

AD  
A055859





TABLE 1

SUMMARY OF WAVE PARAMETERS  
AND MOTIONS FOR 500-FOOT SHIP

(Beam = 66.7 feet, Draft = 26.7 feet)

Model Sea State	A	B	C
Sea State (U.S. Hydrographic Office)	4/5	6	7
Significant Wave Height, *ft	≈9	≈18	≈33
Significant Pitch, * deg	≈3.5	≈7	≈13.5
Significant Heave, * ft	≈8	≈15	≈28
Largest Wave Crest, ft	≈10	≈18	≈33
Largest Heave Double Amplitude, ft	≈13	≈25	≈46

\* Double Amplitudes

## FIRST ANALYSES OF OBSERVATIONS

The analysis of the experimental irregular wave data was carried through up to a point in [13] and summarized in [8]. The first item of analysis was essentially the same as many other analyses of mean resistance in irregular waves; that is, the comparison of the observed mean added resistance with predictions made from regular wave data and the encountered wave spectrum in accordance with Eq.(15). The observed mean values of added resistance were not in precise agreement with expected values estimated on this basis. The extreme deviations were in fact plus or minus 15% to 30%, about twice what might be expected on the basis of the uncertainty in the regular wave results [13]. Some initial studies on the statistical variability of the means of samples from a simulated quadratic process were carried out in [15]. In this simulation study the total sample was equivalent to about 10 times the total length of the experimental sample (8000 encounters for the simulation). Empirically the variation of the simulation mean appeared to be normally distributed for partitions of this sample into tenths; and the 90% confidence bounds on the mean for 800 encounter samples was estimated at ±14% to 20% according to the normal assumption. The result suggested that the variability of the experimental observations relative to predictions is as seriously affected by sampling variability as it is by inaccuracy in regular wave data. This at present remains an hypothesis.

Estimates made from the data with standard techniques of the scalar spectrum of resistance showed the resistance spectra to have visible content at low frequency which increased relatively with the severity of the sea, as would be expected from the second term in Eq.(16). However the spectra were not obviously richer as expected in the second harmonics of wave frequency. This inconclusiveness was probably because the most significant part of the instantaneous resistance added by waves was essentially at wave encounter frequency -- that is, appeared to be a linear surge exciting force. Standard cross-spectrum analyses were performed upon the experimental wave and resistance time series in [13], and a linear frequency response  $G_1(\omega)$  was identified

for each of the model sea states of the experiment. The estimates from the various sea states collapsed quite well and were in fair agreement with regular wave results, thus demonstrating the validity of the linear term of the basic model, Eq.(2).

The challenging part of the analyses of [13] was to identify the mean added resistance operator from the test results in irregular waves. As a general estimating form, Eq.(25) for the cross-bi-spectrum has the advantage that it can be manipulated to form a reasonably efficient estimator for the cross-bi-spectrum along a line of constant  $\Omega_2$  or  $\Omega_1$  in the bi-frequency plane. This allowed results to be obtained directly for the case of  $\Omega_2=0$  or  $\omega_1 = -\omega_2$ , the line defining the mean added resistance operator,  $G_2(\omega, -\omega)$ . At the time of publication of [8], only the Eq.(20) was known as an identification, and this was employed.

The results given in [8] and [13] showed that the identification of the mean added resistance operator from irregular wave data was possible. The estimates obtained from the data in the various sea states collapsed rather well, scatter from sea state to sea state was of the same magnitude as the estimated uncertainty in the combined results of regular wave experiments, and this was considered a happy result since the model sea states covered much of the range of severity that is important in practice. The results identified from irregular wave data did not agree precisely with those from regular waves. However the simulation studies of [15] indicated the 90% confidence bounds on the estimates of  $G_2(\omega, -\omega)$  for the 800 wave encounter sample size to be in the neighborhood of 0.8 and 1.33. On this basis, the differences between the estimates from regular and irregular wave experiments did not appear to be so significant statistically.

At the conclusion of the work summarized in [8], it was evident from the first results of cross-bi-spectral analysis that the mathematical model Eq.(2) had promise and might be explored further. It was also painfully evident from the results of the simulation analyses that no advance in practical towing tank data reduction technique had been made. In order to achieve accuracy in mean added resistance operator of the order of ±15%, sample sizes were required about an order of magnitude larger than that required for identification of linear operators. In most instances this would represent a decrease rather than an increase in efficiency.

The development in Reference [14] of the identification technique defined by Eq.(23) gave rise to more empirical work with the simulations. The results indicated that Eq.(23) was somewhat superior to Eq.(20) with respect to sampling variability, though the practical conclusions above are not changed. Figure 4 is the result of a re-analysis of experimental data for  $F_n=0.15$ , using Eq.(23) as an identification method.

To summarize the contents and notation of the figure:  $G_2(\sigma_e, -\sigma_e)$  is the mean added resistance operator for encounter frequency  $\sigma_e$ . The operator is non-dimensional; that is, model resistance was divided by model displacement and wave elevation was divided by model length so that in terms of the more familiar mean added resistance ( $R_A$ ) in regular waves of height (h):

$$G_2(\sigma_e, -\sigma_e) = 8 \frac{R_A L^2}{h^2 \Delta}$$

where



$L$  is model length

$\Delta$  is model displacement

The non-dimensional encounter frequency is defined as

$$\sigma_e = \omega_e / \omega_{1L}$$

where

$\omega_e$  = encounter frequency, rad/sec

$\omega_{1L}$  = frequency of a wave of model length  
 $= \sqrt{2\pi g/L}$

Estimates involving cross bi-spectral estimates less than 10% of peak have been omitted. The noted sea states coincide with those of Table 1. Finally, the so-called "regular wave envelope" is an indication of the scatter of the mean added resistance operator obtained from tests in regular waves.

The purpose of this particular presentation is to indicate about how good (or bad) the currently best mean operator identification technique is with respect to regular wave data.

One additional exercise in the identification of the added resistance operator was carried out. The basic reason for the exercise was related to an experimental problem. This was that the experimental wave elevations had been measured a wave length ahead of the model, thus injecting a considerable frequency dependent phase shift between wave and model response. In [13] large phase shifts were found to produce closely packed ripples in both real and imaginary parts of the quadratic frequency response function. This condition produced severe resolution problems in cross-bi-spectral estimates from a finite amount of data because of the previously mentioned necessity of defining any hump by 4 or 5 estimates in each frequency direction. One solution (but not necessarily a best solution) to the problem (input time shifting) was found in [13].

An alternate approach to the problem was as follows: If the conventional assumptions are made that heave is a linear function of wave elevation, and that mean added resistance is importantly related to ship motions, then the hypothesis may be made for analysis (Referring to Figure 2) that the linear heave system acts upon wave input to produce heave, and a non-linear system acts upon heave to produce resistance. Accordingly, if this is true, the result of a cross-bi-spectral identification of mean added resistance operator with respect to heave may be converted to an operator with respect to wave by utilizing the cascade relationship, Eq.(11). In this approach the effects of phase shift between wave and response are concentrated in the linear heave frequency response function.

Some exploratory analyses of data sufficed to show that for present purposes the approach was inferior to the time shifting technique developed in [13]. The residual fluctuations in the quadratic response functions were not significantly different, the extent of coverage of the bi-frequency plane with valid estimates was less because heave is a narrower band process than wave, and, finally, the heave frequency response function as deduced by cross-spectrum analysis from the present experimental data was somewhat non-linear -- thus violating the initial assumption. Figure 5 is an example of the result of the approach as applied to estimation of mean added resistance operator.

Notation and conventions in this figure are identical to that of Figure 4. The range of frequency where the estimates were thought worth plotting is smaller in Figure 5 than that resulting from the original method, Figure 4. The nonlinearities in heave are thought to produce the systematic variation with sea state near the peak. However in the range of frequency between 0.9 and 1.2 or 1.3, the agreement with regular wave results is comparable to that shown in Figure 4.

The fact that this indirect estimating approach works at all suggests that it may be worth exploring in some special applications. For instance, there does not appear to have been any direct correlation between the added thrust observed in model tests and that observed full scale.

It is thought possible that a cross-bi-spectral analysis of observed total full-scale thrust with heave acceleration as "input" could result in estimates of added thrust operators referred to heave acceleration over at least a portion of the encounter frequency scale. These estimates might in turn be directly compared to observations in towing tank experiments in regular waves, or with theory.

#### IDENTIFICATION OF THE COMPLETE QUADRATIC FREQUENCY RESPONSE FUNCTION

##### Cross-Bi-Spectra

The work in [13] and the initial stages in [14] were confined to the exploration of selected bits of the quadratic frequency response function. The initial reluctance to try the identification of the function in general was partially based upon economics (complete implementation of Eq.(25) is expensive) and upon the fact that there were no prior experimental or theoretical results with which to compare answers except along the line defining the mean added resistance operator. (At this writing, this is still the situation.)

Part of the rationalization for trying the general identification was that data were available for three experimental seas covering a good part of the range of practical interest. The identified quadratic frequency response should be invariant with sea state if the basic mathematical model is valid.

The first part of the operation was the computation of cross-bi-spectra of both types, Eqs.(19) and (22). Three sets were estimated from the experimental data obtained at Froude number 0.15, one set for each model sea state, Table 1. The methods, based upon Eq.(25), are detailed in [14].

According to Reference [13] the optimum time shift of the wave data to minimize cross-bi-spectral fluctuations was 18 points for Froude number 0.15. This shift was employed throughout the analysis. The direction of the shift was such that, after shifting, a resistance observed at time  $(n\Delta t)$  was paired with a wave elevation at time  $(n-18)\Delta t$ .

The Nyquist frequency for the data is  $\sigma_f = \pi/\Delta t = 7.49$ . Bi-frequencies outside the principal range  $(-\sigma_f \leq \sigma_1 \leq \sigma_f : -\sigma_f \leq \sigma_2 \leq \sigma_f)$  are aliased with those inside. (For convenience, the "e" in non-dimensional encounter frequency has been dropped; all frequencies under discussion henceforth are encounter frequencies.) The principal alias of the bi-frequency  $(\sigma_1, \sigma_2)$  plane is indicated in Figure 6. In the analysis it has to be insured in some way that the sampling interval is sufficiently short (thus the folding frequency is sufficiently high) so that the cross-bi-

spectrum is negligible outside the principal alias.

A theoretical result due to Brillinger and Rosenblatt [16] is basic to making the foregoing come true. If the scalar spectrum of either input or output is negligible at  $\sigma_0$ , the cross-bi-spectrum must also be negligible at bi-frequencies involving  $\sigma_0$ . For practical purposes, the scalar spectrum analyses of [13] showed that the wave spectra for the cases of interest could be considered negligible beyond  $\sigma = \sigma_f/2$ , and that the resistance spectra were negligible beyond a slightly higher frequency. Accordingly, in the present case, the portion of the bi-frequency plane which needs to be resolved is bounded approximately by  $\sigma_1$  or  $\sigma_2$  equal to  $\pm\sigma_f/2$ . This region is indicated by the dashed line box in Figure 6.

The basic symmetry properties of the cross-bi-spectrum are the same as those of  $G_2(\omega_1, \omega_2)$  noted earlier. Accordingly the quadrant selected for analysis is that including the positive  $\sigma_1$  axis. Since the non-dimensionalization of frequency involves only a scale factor,  $\sigma$  may be substituted for  $\omega$  in all previous equations. In particular Eq.(12) becomes:

$$\begin{aligned}\Omega_1 &= \sigma_1 - \sigma_2 \\ \Omega_2 &= \sigma_1 + \sigma_2\end{aligned}\quad (26)$$

The difference and sum frequency plane is shown mapped into the  $(\sigma_1, \sigma_2)$  plane in Figure 6. The Nyquist frequency ( $\sigma_f$ ) for the  $\Omega_1, \Omega_2$  plane is numerically identical to that for the  $\sigma_1, \sigma_2$  plane. Part of the principal alias of the  $\Omega_1, \Omega_2$  plane is indicated in Figure 6 by the lines  $\Omega_2 = \sigma_f$  and  $\Omega_1 = \sigma_f$ . These lines and the  $\Omega_1, \Omega_2$  axes define the domain of the cross-bi-spectrum computations. This domain was resolved into 50 frequency intervals in both directions so that the real and imaginary parts of the cross-bi-spectra were each represented by  $(51)^2$  estimates of averaged cross-bi-spectral density.

According to the previous considerations, the cross-bi-spectra for the present problem should be negligible far to the right of the line  $\sigma = \sigma_f/2$  in Figure 6, that is, in the region of the  $\Omega_1, \Omega_2$  plane where  $(\Omega_1 + \Omega_2) > \sigma_f$ . In all the computations made, values in this region were typically much less than 1% of the computed peak absolute value of the cross-bi-spectra.

In order to aid in visualization of cross-bi-spectra, some isometric plotting was done. The set of results for sea state B are typical and are shown in Figures 7 and 8. The "view" is toward the origin from the positive  $\sigma_1$  axis (Figure 6). This puts the difference frequency ( $\Omega_1$ ) axis to the left and the sum frequency ( $\Omega_2$ ) axis to the right. The lines are in the nature of section lines, each intersection corresponds to an estimated point. Figure 7 is a sketch of the modulus of the wave, wave, resistance cross-bi-spectrum, and Figure 8 shows the real part of the wave, wave, (wave)<sup>2</sup> cross-bi-spectrum. The vertical scales involve non-dimensional time, length and force (length<sup>2</sup> force sec<sup>2</sup> in Figure 7, and length<sup>4</sup> sec<sup>2</sup> in Figure 8).

There is a pronounced right-to-left symmetry in Figure 8. In theory (Eq.22), the symmetry should be exact. There is also a reasonably triangular domain of significance of each side of the function and this is also to be expected from Reference [16].

Figure 7 shows a much more complicated picture. There is only a vague right-to-left symmetry. There are multiple peaks in general and a

visible "mountain range" corresponding to a sum-frequency ( $\Omega_2$ ) of around unity. Because both the real and imaginary parts of this cross-bi-spectrum contain significant estimates which are not all positive or negative, Figure 7 amounts only to a partial indication of the nature of the result. The detail of the cross-bi-spectral results are given in [14]. The semi-oscillations of these results in the bi-frequency plane were defined by between 3 and 10 estimates, and thus the input time shifting gambit was concluded to be successful enough. As expected, there was a two order of magnitude difference between the results computed from sea state A and those of sea state C.

#### Quadratic Frequency Responses

The identification of the quadratic frequency response function  $G_2(\sigma_1, \sigma_2)$  is given by Eq.(23); that is, the function is the ratio of the complex conjugate of the wave, wave, resistance cross-bi-spectrum to the wave, wave, (wave)<sup>2</sup> cross-bi-spectrum. This operation was carried out for the three sea-states with the convention that no estimate was to be formed if the value of the wave, wave, (wave)<sup>2</sup> C.B.S. was less than 10% of its peak. The results are presented in Figure 9 through 14 (Figures 9 and 10 are real and imaginary parts of  $G_2(\sigma_1, \sigma_2)$  for sea state A; Figures 11 and 12 are those corresponding to sea state B, and Figures 13 and 14 pertain to sea state C). These figures are semi-tabular charts. The convention is that the magnitude of the function is indicated by a number "plotted" at the appropriate position in the bi-frequency plane. The applicable portion of the basic  $(\sigma_1, \sigma_2)$  bi-frequency plane is indicated by the  $\sigma_1, \sigma_2$  axis system. The corresponding portion of the difference/sum frequency plane ( $\Omega_1, \Omega_2$ ) is mapped into the basic bi-frequency plane. The portion of the planes shown corresponds to the left half of the area labeled "domain of cross-bi-spectrum computations," Figure 6. Lines of symmetry are noted. All frequencies are considered to be in the encounter domain. In the figures, blank space indicates either that the magnitude of the estimate is unity or less, or that the wave, wave, (wave)<sup>2</sup> C.B.S. was less than 10% of peak value. Contours are sketched in for the zero level only.

An overview of Figures 9 through 14 indicates that the estimated function  $G_2(\sigma_1, \sigma_2)$  appears to be fairly complicated. There appear humps and hollows, and significant values near the 10% wave, wave, (wave)<sup>2</sup> truncation line. However, in contrast to the cross-bi-spectra, the order of magnitude of estimates at corresponding bi-frequencies is the same for all three sea states. The values along the line  $\sigma_2 = -\sigma_1$  have in fact been compared previously (Figure 4).

#### Discussion of Results

The quadratic frequency response function depicted involves the quadratic relation between resistance and the shifted wave elevation. The first obvious possibility to aid in explaining all the humps and hollows is the correction of wave phase so that the function represents the relation between resistance and the wave at model LCG. The basis for the correction is detailed in Reference [13] and involves applying Eq.(11) with  $H(\omega)=1$  and  $F(\omega)$  equal to the transfer function between shifted wave and wave elevation at LCG. This correction was applied to all the data. The result (not shown) was that the positions of the



zero contours and the relative magnitudes of real and imaginary parts were somewhat changed. The resulting estimates of the function were just as complicated however. For later purposes it was convenient to retain the convention that the input to the system was the shifted wave elevation.

From the discussion of Eq.(9) it may be shown that the absolute values of the  $(\sigma_1, \sigma_2)$  scale frequencies in Figures 9-14 are associated with the two real positive input frequencies in the dual excitation experiment. The  $\Omega_2$  scale, as mapped in Figures 9-14, corresponds to the possible frequencies which can be generated by the quadratic non-linearity.

In general, there are an infinite number of combinations of input frequency components which will yield a given output frequency component. A non-linear output component of frequency 1.5, for example, can be the second harmonic of excitation of 0.75, or the result of interactions between pairs of components; i.e., 1.0, 0.5; 2.0, 0.5; 2.5, 1.0; etc.

In accordance with the above, it is of some advantage to consider the estimates of  $G_2(\sigma_1, \sigma_2)$  for the three sea states for different bands of non-linear output frequency,  $\Omega_2$ .

The first band of frequency to be considered is that above  $\Omega_2 \approx 2.8$ . In this output frequency band the scalar spectra of Reference [13] indicate a quite significant peak centered on a frequency of about 3.2 for sea state A, a less significant peak in sea state B, and a nearly insignificant peak for sea state C. As outlined in Reference [13], this frequency corresponded to a carriage drive induced noise which appeared to be tank position dependent and had no obvious correlation to waves. Longitudinal vibrations of the carriage necessarily accelerated the restrained-in-surge model and thus injected a spurious resistance signal. It may be seen from Figures 9 and 10 that peaks in the estimated values of  $G_2(\sigma_1, \sigma_2)$  near the line  $\Omega_2=3.2$  are more than twice the magnitude of the mean added resistance operator, Figure 4. In the results for sea state B (Figs. 11, 12), the largest peaks are somewhat smaller than the peak mean added resistance operator. No data are shown in Figures 13 and 14 (sea state C) in this region because the excitation was too low. The cross-bi-spectrum of sea state C also has no indication of peaks in this range. On an empirical basis the estimates of  $G_2(\sigma_1, \sigma_2)$  near the line  $\Omega_2=3.2$  appear to behave as the scalar spectra; that is, to be influenced by the spurious noise of this frequency known to be in the observed resistance data. As outlined in Reference [13], the longitudinal vibrations of the carriage were monitored by accelerometer during the experiments and an approximate calibration of the channel was made in terms of apparent resistance. To confirm the above observations, the estimated vibration induced resistance was subtracted from the observed resistance for the sea state A data. The resulting time series was subjected to an exploratory cross-bi-spectrum analysis along a line parallel to the  $\Omega_2$  axis, and the resulting estimates for the quadratic transfer function confirmed that the peaks along the  $\Omega_2 \approx 3.2$  line (Figs. 9, 10) were mostly due to the longitudinal carriage vibration.

Some theoretical consideration was given to the expected influence of noise in the output on cross-bi-spectral estimates. The essence of the results is that: a) if the noise is linearly related to wave, there should be no influence on cross-bi-spectral estimates, b) if the noise is a

quadratic function of wave (in the sense of Eq.2), the estimates of  $G_2(\sigma_1, \sigma_2)$  from cross-bi-spectral analysis should be invariant with wave severity, and c) if the noise is random and statistically uncorrelated with wave, there should be no influence on the estimates. Thus, there should be no carriage vibration induced peaks along the line  $\Omega_2 \approx 3.2$ . The origins of this anomalous result are not clear. The raw longitudinal vibration data appeared to be a randomly modulated sine wave with superimposed effects of occasional rail joint impacts and the subsequent vibratory decay. Perhaps the noise violates the usual random process assumptions, or perhaps the problem is due to too short a sample. In either event, it has to be concluded that the results presented in Figures 9-14 for sum frequency ( $\Omega_2$ ) greater than 2.8 or 3.0 cannot be believed as relating to added resistance.

The next band of output frequency ( $\Omega_2$ ) which can be considered is that between 2 and 3. This is the band where the cross-bi-spectral estimates were most significant. A comparison of the results for the three sea-states between  $\Omega_2 = 2$  and 2.8 indicates some relatively good correlation. The real parts of the function for sea states A and B (Figs. 9, 11) appear to be very much the same, at least within the sort of tolerance indicated for the added resistance operator, Figure 4. The shape of the real part of the function for sea state C (Fig. 13) is correct but the magnitudes are 20% or 30% lower on average. Correlation of the imaginary parts in this frequency band is reasonable throughout.

The correlation across sea state in the last frequency band ( $\Omega_2 < 2$ ) in the upper octant of Figures 9-14 is only fair. The signs and magnitude of the functions are more or less the same near  $\Omega_2=2$  but scatter and inconsistency is shown near the edges of the area shown. Despite the fact that the wave, wave, (wave)<sup>2</sup> cross-bi-spectra are significant in this region, the wave, wave, resistance cross-bi-spectra are generally less than 10% of peak modulus, and on this basis much of the scatter in this region may be ascribed to sampling variability.

Because this may be nearly the first time that a quantification of high frequency added resistance response has been attempted, there exists no independent theoretical or experimental guidance about what the quadratic frequency response function really should look like in the upper octant. However, where the analysis is most reliable, the estimates of the quadratic frequency response function appear more or less invariant with sea state, and the magnitudes are approximately the same as that of the added resistance operator, Figure 4. Intuitively, a sort of symmetry of second harmonic response with the added resistance operator might be expected just from the form of the trigonometric identities for  $\sin^2$  and  $\cos^2$ .

In discussion of the low frequency response represented in the lower octants of Figures 9-14, it is convenient to consider two output frequency bands:  $0 \leq \Omega_2 < 0.5$ , and  $0.5 < \Omega_2 < 1.5$ . The former band is nearly completely below the wave frequency excitation band, and the latter corresponds to the significant band of resistance scalar spectral density.

Taking the lowest band of output frequencies first ( $0 \leq \Omega_2 < 0.5$ ), a comparison of Figures 9, 11 and 13 indicates as good a general correlation over sea state for the real part of the function as is displayed in Figure 4 for the values at  $\Omega_2=0$ . For values in the region  $\Omega_1 = 1$  to 2, the

magnitude is correct and the details are wrong, but, as in the symmetrically located region of the upper octant, the wave, wave, resistance cross-bi-spectra are quite low in this region, and sampling variability problems may be suspected. The 10% truncation point for the wave, wave, (wave)<sup>2</sup> cross-bi-spectrum limits the correlation possibilities for high  $\Omega_1$  (Figs. 9, 11, 13). It is most encouraging to note the magnitude of the values between  $\Omega_1=4$  and 5 in Figure 9 for sea state A. These correspond to added resistance in very short regular waves and compare very well quantitatively with results presented by Strom-Tejsten, et al [17].

The imaginary parts of the function (Figs. 10, 12, 14) do not correlate as well from sea-state to sea state in this low frequency region ( $0 \leq \Omega_2 < 0.5$ ). Most of the values shown are low, often of the order of the differences in real part from sea-state to sea state. The positions of the main zero level contours correlate reasonably however.

The last region of output frequency to be discussed for the lower octant is that from  $\Omega_2=0.5$  to 1.5. Considering the real part first (Figs. 9, 11, 13), it may be seen that there are some significant correlation problems. In Figure 9 (sea state A) there is a negative region centered upon  $\alpha_1=2.2$ ,  $\alpha_2=-1.5$  where the magnitude is 5 times that of the peak added resistance operator. In Figure 11 (sea state B) the corresponding region is only about equal to the added resistance operator. No data are presented in Figure 13 (sea state C) for this region because of lack of excitation. In this region of the bi-frequency plane there is a clear discrepancy. Unfortunately the magnitude of the wave, wave, (wave)<sup>2</sup> cross-bi-spectra is only about 15% of peak in this region and the wave, wave, resistance cross-bi-spectra are either small or involve undulations defined only by about 3 estimates. Accordingly, it is not at all clear if the significant values indicated in Figure 9 are really indicating a strong interaction between input frequencies of 2.2 and 1.5, or whether the result is due to problems of analysis or sample.

Shifting view toward the  $\Omega_2$  axis, there appears a strong positive hump centered approximately on  $\alpha_1=2$ ,  $\alpha_2=-1$ . In this case the results for the real part from sea states A and B agree reasonably well. The imaginary parts do not, but the modulus (not shown) does agree quite closely. Few results for sea state C are presented in this region, those that are were derived from cross-bi-spectral estimates of borderline significance. In this case then, the correlation between the results from two sea-states indicates a significant interaction between input frequencies of 1 and 2. Numerically, the peak near the line  $\Omega_1=3$  raises suspicion. There should be no influence of drive noise, and according to the discussion of Eq.(9) the strong peak in the function at  $\alpha_1=2$ ,  $\alpha_2=-1$  pertains to output at a frequency of 1.0, not the known noise frequency, 3.2. Because the analysis of the upper octant in Figures 9-14 indicated some surprises, similar side investigations were carried out. First, the observed resistance signal for sea state A was corrected for carriage acceleration as was done for the upper octant, and the resulting time series was subjected to exploratory cross-bi-spectral analysis along the line  $\Omega_1=3.14$ . The results were precisely as expected from Eq.(9) and discussion -- the noise had no apparent influence upon the values of estimated  $G_2(\alpha_1, \alpha_2)$  along  $\Omega_1=3.14$ . Secondly, a cross-bi-spectral analysis was carried out for sea state A along the same line but with the carriage

acceleration considered the output. The values of the resulting cross-bi-spectrum (scaled to represent resistance) are a correction to the wave, wave, resistance cross-bi-spectrum if the noise is correlated with wave. The results of this analysis were quite small relative to the wave, wave, resistance cross-bi-spectra, and this investigation too, failed to disqualify the hump under consideration as relevant to added resistance.

The remainder of the values of  $G_2(\alpha_1, \alpha_2)$  shown in the  $\Omega_2$  band from 0.5 to 1.5 were derived from regions of sharply decreasing values of wave, wave, (wave)<sup>2</sup> cross-bi-spectra and/or relatively low values of wave, wave, resistance cross-bi-spectra. The most that can be said about the results in this region ( $0.5 < \Omega_2 < 1.5$ ;  $\Omega_1 < 2.5$ ) is that there is an occasional family resemblance. The correlation across sea state is not really very good.

On the whole, in both octants, correlation between the results for the different sea-states appears reasonably good only where both the cross-bi-spectra involved are quite appreciable, say about 25% of peak. The quadratic transfer function appears to be a fairly complicated affair -- more complicated in fact than can be reliably determined from the present set of data. Despite this, the very fact that empirical collapse was obtained for a number of prominent features of the function adds evidence that Eq.(2) is a valid representation for added resistance.

#### COMPUTATION OF LOW FREQUENCY ADDED RESISTANCE IN THE TIME DOMAIN

The overall plan for the next portion of the work was to reverse the identification process; that is, to use the various estimates for the frequency response functions to estimate the corresponding time domain kernels, and with these to compute added resistance in the time domain for comparison with the experimental data.

Given the results of the last section, some rather arbitrary decisions had to be made about which estimates of  $G_2(\alpha_1, \alpha_2)$  to use. Those from sea state A cover the largest portion of the bi-frequency plane and would be preferred from this point of view. However, the results from sea state A also contain the largest contributions due to noise and the largest unexplained and suspicious hump. The cleanest looking results are from sea state C, but the coverage of the bi-frequency plane is quite restricted. A partial rationalization of which course to take was afforded by considering which portions of the bi-frequency plane are most important to the added resistance problem. The clear answer here is the portion of the plane corresponding to frequencies below the lowest exciting wave frequency. Very low frequency fluctuations in resistance or thrust are observed full scale. What bearing high frequency fluctuations in resistance have on any aspect of the practical problem is not clear.

As noted in the last section, the correlation of estimated quadratic frequency response function (Figs. 9-14) was best below  $\Omega_2=0.5$  and this region of frequency is below the significant range of wave excitation frequency. A systematic way of transforming the estimated quadratic frequency response function is afforded by Eq.(11). If the function is multiplied by a transfer function  $H(\alpha_1 + \alpha_2)$ , this is equivalent to the filtering of the output by a filter with transfer function  $H(\sigma)$ . It is clear then from Figures 9 through 14 that a filter which attenuates output to 1% or 2% above a non-dimensional frequency of unity has the



practical effect of discarding the entire upper octant of the bi-frequency plane, and with it all the high frequency response of any origin. In addition, such a filter, if it is practically realizable, will significantly attenuate frequencies between 0.5 and 1.0, and thus a good deal of the troublesome peak in estimated  $G_2(\sigma_1, \sigma_2)$  ( $\sigma_1 = 2.2$  and  $\sigma_2 = -1.5$ ) would also be eliminated.

In order to proceed along the above lines and yet be able to correlate eventual time domain computations with observations, the filter needed to be digital so that it could also be applied to the observed digitized data. Two digital filters were developed for possible use. The amplitude responses are shown in Figure 15. Both filters are non-realizable in the real-time sense. Their impulse responses are symmetrical so that their transfer functions have no imaginary parts and the real part equals the amplitude response. Filtering in the time domain is done by weighting the digitized data with a discrete approximation to linear convolution.

For the purpose of practical computations in the time domain, the basic time domain model, Eq. (2), must be re-cast into a form suitable for use with digitized time series. This was done in exactly the same way as was done in Reference [13] for a simulated process. The digital model of Eq. (2) becomes:

$$D_w(n) = \sum_{j=-m}^m L_j \eta(n-j) + \sum_{j=-p}^p \sum_{k=-p}^p Q_{jk} \eta(n-j) \eta(n-k) \quad (27)$$

where  $D_w(n)$  = computed added resistance time series

$\eta(n)$  = observed wave time series

and  $L_j$  and  $Q_{jk}$  are weighting coefficients in which the differentials are absorbed.

This model requires discrete approximations to the linear and quadratic impulse responses of the form:

$$\bar{g}_1(\tau) = L_j \delta(\tau - j\Delta t) \quad (28)$$

$$\bar{g}_2(\tau_1, \tau_2) = Q_{jk} \delta(\tau_1 - j\Delta t) \delta(\tau_2 - k\Delta t) \quad (29)$$

(where  $\delta(t)$  is the Dirac delta function)

The Fourier transforms of Eqs. (28) and (29) in accordance with Eqs. (3) and (4) yield continuous (aliased) frequency response functions as follows:

$$\bar{G}_1(\sigma) = \sum_{j=-m}^m L_j [\cos(j\sigma\Delta t) - i \sin(j\sigma\Delta t)] \quad (30)$$

$$\bar{G}_2(\sigma_1, \sigma_2) = \sum_{j=-p}^p \sum_{k=-p}^p Q_{jk} [\cos(j\sigma_1\Delta t + k\sigma_2\Delta t) - i \sin(j\sigma_1\Delta t + k\sigma_2\Delta t)] \quad (31)$$

For practical computing purposes, the process of transforming observed frequency response functions amounts to achieving (with a finite number of coefficients) a reasonable fit of the re-transformed impulse responses (Eqs. 30, 31) to the observed response functions. The general

approach followed was to integrate the first of Eqs. (3) and (4) trapezoidally with observed estimates of the appropriate frequency response function. This is carried out for a sufficient range of time variable(s) so that decisions regarding the truncation limits ( $m$  and  $p$  in Eqs. 27 through 31) can be made. Evaluation of the computed impulse response function is made at integer values of time step  $\Delta t$  and these values are multiplied by  $\Delta t$  or  $\Delta t^2$  as appropriate to result in estimates of the coefficients  $L_j$  and  $Q_{jk}$ . The next step is to adjust the coefficients so that the discrete kernel reflects the correct behavior of the frequency response functions at zero frequency. (If it is assumed that there is no resistance added by an infinitely long wave, the coefficients  $L_j$  and  $Q_{jk}$  should sum to zero.) The final computational step is to insert the coefficients into Eqs. (30) or (31), compute the re-transformed impulse response function and compare the results with the original frequency response estimates. Iteration of the process is sometimes necessary.

For present purposes, it was assumed that the input was the shifted wave and the output was the resistance filtered with Filter No. 1, Figure 15. These conditions on input and output were achievable with the available digitized experimental data and correspond to the conditions underlying the quadratic frequency response function estimates, Figures 9-14.

The estimates of the linear frequency response function obtained by cross-spectral analyses in Reference [13] were used to produce a linear impulse response function. The original estimates were for shifted wave as input and observed resistance as output. These estimates were "filtered" using the response for Filter No. 1, Figure 15. The results are presented as point estimates in Figure 16. Results for all three sea states are indicated in the figure. Estimated coherences were greater than 50% for all results at frequencies in excess of 0.5. The results below a frequency of 0.3 had almost negligible coherencies and were omitted. The average line through the data in Figure 16 is the result of re-transforming (with Eq. 30) the  $L_j$  coefficients which were finally derived. The fit to the data seems quite adequate above a frequency of 0.3 or 0.4. Below these frequencies the fit is speculative. However, in the experimental data there is nearly no wave energy below a frequency of 0.4 and it was thought that whatever low frequency errors which exist would have no practical effect on the time domain calculations. Because the frequency response function in Figure 16 is a band pass filter, the discrete impulse response is quite long -- 161 coefficients were thought necessary. The coefficients of the impulse response are plotted in Figure 17.

It was decided to use the data derived from sea state A in the computations for the quadratic impulse response since the important regions of interacting wave excitation for sea states B and C are roughly sub-sets of the important region of sea state A. The rationalization is the same as that for the low frequency linear response. Errors in quadratic response function for particular combinations of input frequency probably will have no practical effect if the energy of both interacting components is not high. Accordingly, the estimates from the sea state A data (Figs. 9, 10) were "filtered" using the response of Figure 15 and Eq. (11), and the fitting procedure described in conjunction with Eqs. (27) to (31) was carried out

on the result. A truncation parameter ( $p$ ) of 25 was chosen, thus resulting in  $(51)^2 Q_{jk}$  coefficients. Figure 18 is a map of the final result. In order to make it possible to visualize the entire two-dimensional kernel, it was necessary to convert the actual values of  $Q_{jk}$  to single digit magnitudes. This was done arbitrarily by multiplying by 50 and truncating the numerical results to an integer value. The magnitudes noted in Figure 18 range from plus to minus 9. The coefficient matrix is symmetrical about  $j=k$  ( $Q_{jk}=Q_{kj}$ ) as is required by the basic model (Eq.5). In the figure the approximate contours of zero have been drawn, and coefficients with absolute magnitude of 7 and above are circled.

It is clear from Figure 18 that there are a few significant values on the truncation boundary. A truncation limit of 30 or 35 might have been required to make the values at the boundaries insignificant. The truncation limit chosen was a compromise of sorts between a reasonable delineation of the quadratic impulse response and practical considerations of the computing time which would be required for subsequent use. It is clear from the figure, however, that the most significant hills and valleys are contained within the range of  $j$  and  $k = \pm 15$ .

The re-transformation of the final quadratic impulse response function,  $\bar{G}_2(\sigma_1, \sigma_2)$ , according to Eq.(31) is shown in Figures 19 and 20 along with the filtered estimates of  $G_2(\sigma_1, \sigma_2)$  from sea state A. The transformed kernel is much smoother than the original. Considerable smoothing is inevitable since the original  $G_2(\sigma_1, \sigma_2)$  results contain abrupt transitions to zero on the boundaries of the region of significance. Over all, the fit was considered reasonable especially in the region of  $\Omega_1 = 2$  to 3 where the mean added resistance operator is appreciable.

The steps in the computation of the low frequency added resistance were as follows:

- Correct original digitized experimental wave elevations for linear and quadratic trends and to zero sample mean.
  - Using the arrays of coefficients  $L_j$  and  $Q_{jk}$  described above, operate upon the corrected wave time series with Eq.(27) to result in an output time series. This series represents the added resistance which would have been observed through Filter No.1, Figure 15.
  - Filter the result of Step b using the digital Filter No. 2, Figure 15, to result in a time series which should represent the part of the added resistance response which contains only component frequencies below the lowest wave frequency.
- In order to make comparisons with observation, some processing of the resistance observations was also necessary:
- The original digitized experimental resistance was corrected to zero mean and for linear and quadratic trends, and then the corrected mean resistance as determined in the analyses of Reference [13] was added back. This operation was to compensate for a small tank position dependent instrumentation error, noted in [13].
  - The corrected observed resistance (Step d)

was then filtered using coefficients of Filter 1, Figure 15, to result in a time series which should be comparable with the results (Step b) of operating on the wave elevations with Eq.(27).

- The above results (Step e) were filtered using the coefficients of Filter No.2 -- the results to be comparable with the results of Step c.

This process was applied to all the available experimental data obtained at model Froude number 0.15. These data involved 18 experimental runs, 6 runs in each of model sea states A, B and C. The first 1204 points of the set of results for each run were plotted. All the resulting plots (equivalent to about 75% of the total original sample) are included in [14].

Figure 21 is considered typical of all the results which pertain to sea state A. In the figure six time series are plotted on a time base in which the tick marks are equivalent to about  $24\Delta t$ . Each point plotted corresponds to a digitized point of the experimental data or a corresponding point of the computed data. No interpolated points or connecting lines are included. Vertical scales were chosen for each time series to suit the maximum observed or computed for the noted sea state.

The topmost series is the corrected observed wave elevation (non-dimensionalized by model length), and next in order is the corrected observed resistance (non-dimensionalized by model displacement). The wave elevations are shown time-shifted relative to the resistance in accordance with the convention about the input to the estimated linear and quadratic frequency response functions. The differences between the corrected and original raw experimental time series are barely visible at the scales shown.

The third chart down from the top of the figure contains the computed results from Eq.(27), which are plotted with (+), and the results of filtering the observed resistance with Filter No.1 (plotted with a very small "D", on its side). At the bottom of the chart are corresponding results of filtering both the series plotted immediately above with Filter No.2 ("doubly filtered resistance").

The computations shown in Figure 21 are essentially a closing of a circular computing exercise. The observed time domain data were used to compute frequency response functions. These were transformed back into the time domain and used to "re-compute" the low frequency portions of the original data. Considering that the scale of the filtered resistance is blown up by a factor of 5 relative to the original observation, correlation between observation and computation is satisfactory. The differences between observation and computation of the filtered resistance (Figure 21) are fairly typical of all the results obtained for sea state A. These differences involve frequencies of 0.6 or 0.8. Because the linear component of Eq.(27) appears to be pretty solidly estimated for these frequencies (Fig.16), it is suspected that the origin of the errors is one or both of the humps in the quadratic transfer function at  $(\sigma_1, \sigma_2) = (1.5, -0.7)$  and  $(2.2, -1.5)$  as shown in Figures 19 and 20. These are the areas where suspicion of error was previously noted.

The agreement of the observed and computed doubly filtered resistance is quite satisfactory considering that the scale is blown up by a factor of 10 relative to the original resistance time

series. The maximum deviations in Figure 21 and in all the other results for sea state A do not exceed  $1 \times 10^{-3}$  which is about 3% of full scale for the observations. The magnitude of maximum error is approaching the resolution of the original experimental data (which was recorded on standard FM magnetic tape), and is to some extent dependent upon the accuracy of the correction of the mean of the observations for the instrumentation problems noted in Reference [13]. It is clear from the results that the character and frequency content of the very low frequency components of added resistance are very well predicted.

Figure 22 is a typical chart for the results of computing sea state B resistance, essentially by the use of the sea state A data. The agreement between observation and computation is as good or better than that shown for sea state A. There is a little less high frequency excitation, but differences in filtered resistance involve the same frequencies. Differences in doubly filtered resistance appear to be relatively somewhat less than in sea state A, the magnitudes of the low frequency added resistance are larger and the experimental data are probably better resolved.

Finally, Figure 23 contains typical results for the computation of added resistance in sea state C from data in sea state A. The agreement between observation and prediction in this case is just as good as that for the other sea states.

On the whole, if the numbers on the scales and the captions were erased, it would be most difficult to tell the results pertaining to one sea state from another. Considering that the significant heights of the lowest and highest sea state differ by a factor approaching four, the results clearly help substantiate the validity of Eq. (2) as a model for added resistance and indicate that it is feasible to compute added resistance in the time domain.

#### SUMMARY

The overall objective in the present work was to demonstrate that the functional polynomial model for added ship resistance in waves was an adequate engineering approximation, and the results obtained indicate that this is so.

The first three complete cross-bi-spectral analyses of experimental data were used to identify the non-linear responses resulting from the interactions of input frequencies -- in addition to the previously accomplished identification of the direct non-linear mean response function. Empirical collapse of estimates was obtained for some of the prominent features of the quadratic frequency response function over a wide range of sea severity. Some parts of the estimates of the function were unexpectedly influenced by noise, and it appears that not as much is understood about cross-bi-spectral analysis as was thought. The quadratic frequency response function for added resistance appears to be complicated -- more so at least than could be reliably determined from the available experimental data.

In the final part of the work it was shown that at least the very low frequency fluctuations of added resistance can be synthesized in the time domain. Oddly, the success of the synthesis appeared to be better than the success of the identification of the quadratic frequency response function. Of particular note is that fluctuations of resistance observed in a quite severe sea state were reasonably well predicted from analyses of data observed in a sea whose significant height

was  $1/4$  as great.

With this, a demonstration "loop" is closed, in that, following the mathematical properties of the hypothesized model, irregular time domain resistance has been interpreted in the frequency domain, and these results have been used to pass back into the time domain. It appears that a) the (non-linear) added resistance transfer function can be identified from experiments in irregular waves within tolerances inherent in the experiments, b) synthesis of mean added resistance and the resistance spectra can be carried out from the linear and non-linear added resistance transfer functions, and c) time histories of added resistance response can be synthesized from an irregular wave input and the time domain representation of the linear and non-linear operators.

#### ACKNOWLEDGMENT

The present work was carried out under the sponsorship of the Naval Sea Systems Command General Hydromechanics Research Program, administered by the David Taylor Naval Ship Research and Development Center.

#### REFERENCES

1. St. Denis, M. and Pierson, W.J., Jr., "On the Motion of Ships in Confused Seas," *SNAME*, 61, 1953.
2. Wiener, N., "Nonlinear Problems in Random Theory," The Technology Press of MIT and John Wiley and Sons, Inc., 1958.
3. Barrett, J.F., "The Use of Functionals in the Analysis of Non-Linear Physical Systems," *Journal of Electronics and Control*, 15, No. 6, December 1963.
4. Bedrosian, E. and Rice, S.O., "The Output Properties of Volterra Systems (Nonlinear Systems with Memory) Driven by Harmonic and Gaussian Inputs," *Proceedings of the IEEE*, 59, No. 12, December 1971.
5. Tick, L.J., "The Estimation of the 'Transfer Functions' of Quadratic Systems," *Technometrics*, 3, No. 4, 1961.
6. Hasselman, K., "On Non-Linear Ship Motions in Irregular Waves," *Journal of Ship Research*, 10, No. 1, 1966.
7. Vassilopoulos, L.A., "The Application of Statistical Theory of Non-Linear Systems to Ship Motion Performance in Random Seas," *International Shipbuilding Progress*, 14, No. 150, 1967.
8. Dalzell, J.F., "Cross-Bispectral Analysis: Application to Ship Resistance in Waves," *Journal of Ship Research*, 18, No. 1, March 1974, pp. 62-72.
9. Neal, E., "Second-Order Hydrodynamic Forces due to Stochastic Excitation," Tenth ONR Symposium on Naval Hydrodynamics, Massachusetts Institute of Technology, 1974.
10. Maruo, H., "The Excess Resistance of a Ship in Rough Seas," *International Shipbuilding Progress*, 4, 1957.
11. George, D.A., "Continuous Non-Linear Systems," Doctoral Dissertation, Department of Electrical Engineering, M.I.T., July 1959.
12. Newman, J.N., "Second Order, Slowly Varying Forces on Vessels in Irregular Waves," Symposium on Dynamics of Marine Vehicles and Structures in Waves, London, April 1974.
13. Dalzell, J.F., "Application of Cross-Bispectral Analysis to Ship Resistance in Waves," SIT-DL-72-1606, AD749102, Davidson



- Laboratory, Stevens Institute of Technology, May 1972.
14. Dalzell, J.F., "The Applicability of the Functional Polynomial Input-Output Model to Ship Resistance in Waves," SIT-DL-75-1794, Davidson Laboratory, Stevens Institute of Technology, January 1975.
  15. Dalzell, J.F., "Some Additional Studies of the Application of Cross-Bi-Spectral Analysis to Ship Resistance in Waves," SIT-DL-72-1641, AD757363, Davidson Laboratory, Stevens Institute of Technology, December 1972.
  16. Brillinger, D.R. and Rosenblatt, M., Two Papers: "Asymptotic Theory of Estimates of  $k^{\text{th}}$  Order Spectra," and "Computation and Interpretation of  $k^{\text{th}}$  Order Spectra," Proceedings of an Advanced Seminar on Spectral Analysis of Time Series, Edited by B. Harris, October 1966, John Wiley & Sons, New York.
  17. Strom-Tejsen, J., Yeh, H.Y.H., and Moran, D.D., "Added Resistance in Waves," SNAME, 81, pp. 109, 1973.

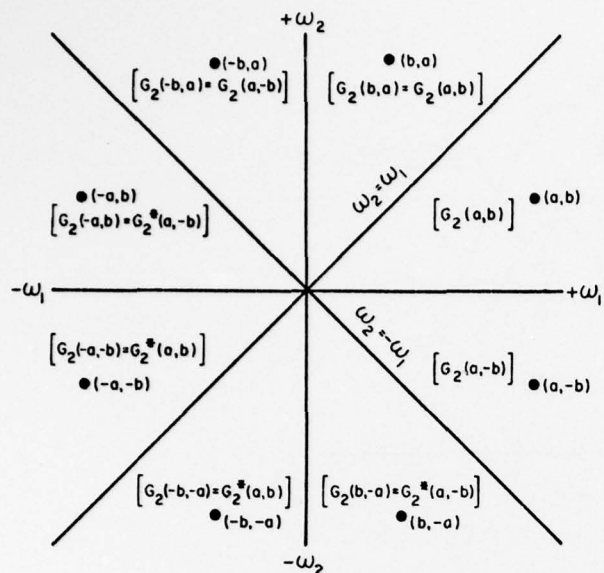


Fig. 1: Symmetry of quadratic frequency response function

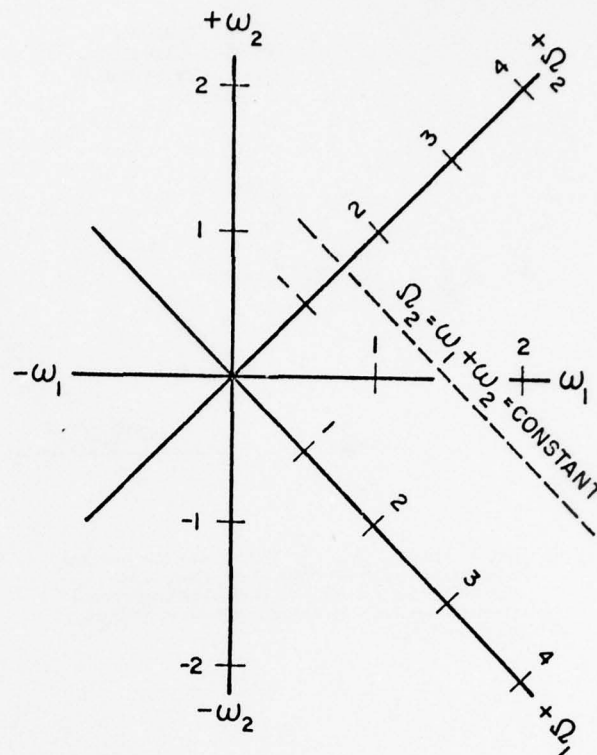


Fig. 3: Mapping of  $\Omega_1, \Omega_2$  plane

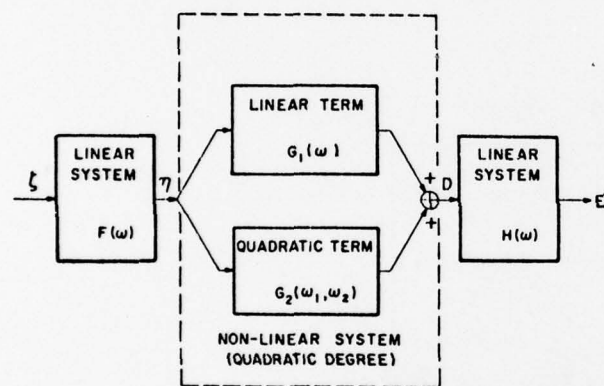


Fig. 2: Block diagram, non-linear system in cascade with linear systems

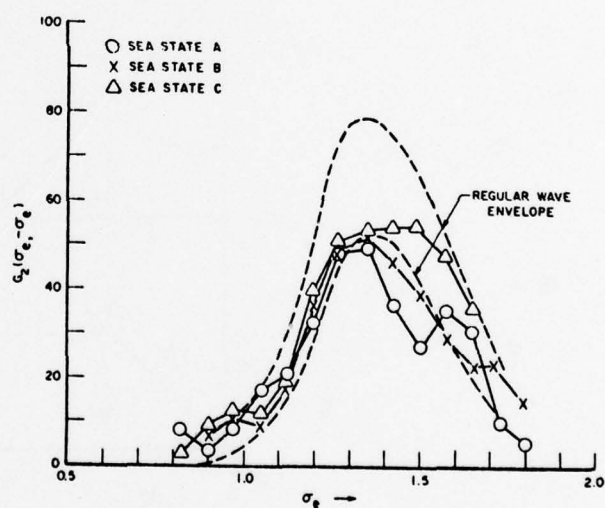


Fig. 4: Revised estimates of  $G_2(\sigma_e, -\sigma_e)$  from cross-bispectral analysis, Froude number 0.15

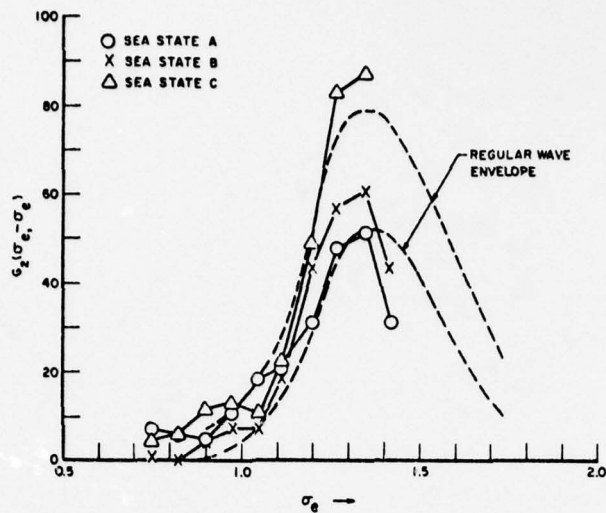


Fig. 5: Estimates of  $G_2(\sigma_e, -\sigma_e)$  from cross-bi-spectral analysis using model heave as input with corrections according to the results of cross-spectral analysis of wave and heave. Froude number 0.15.

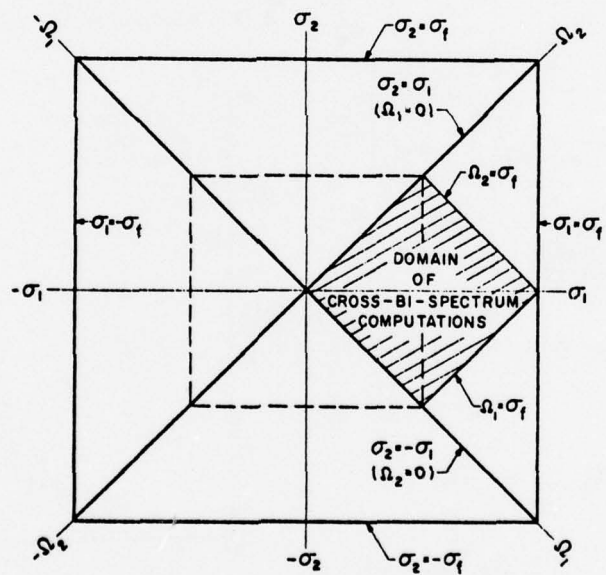


Fig. 6: Principal alias of the bi-frequency plane



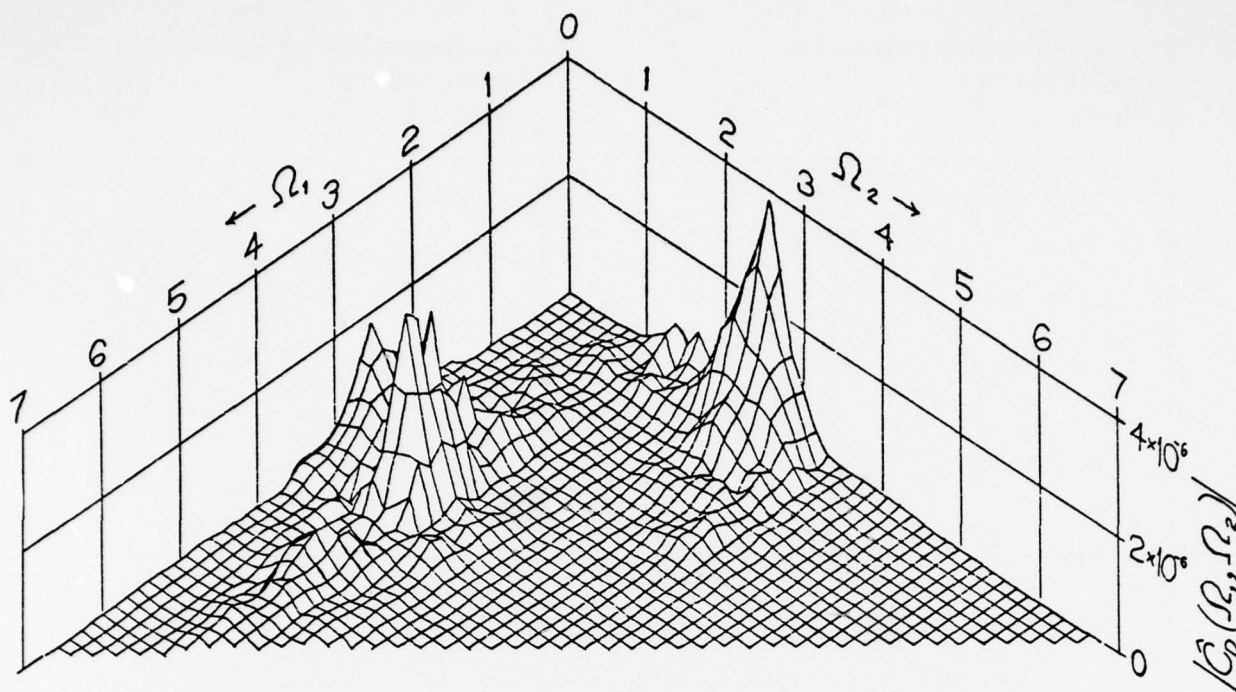


Fig. 7: Isometric sketch of modulus of wave, wave, resistance cross-bi-spectrum sea state b, Froude number 0.15

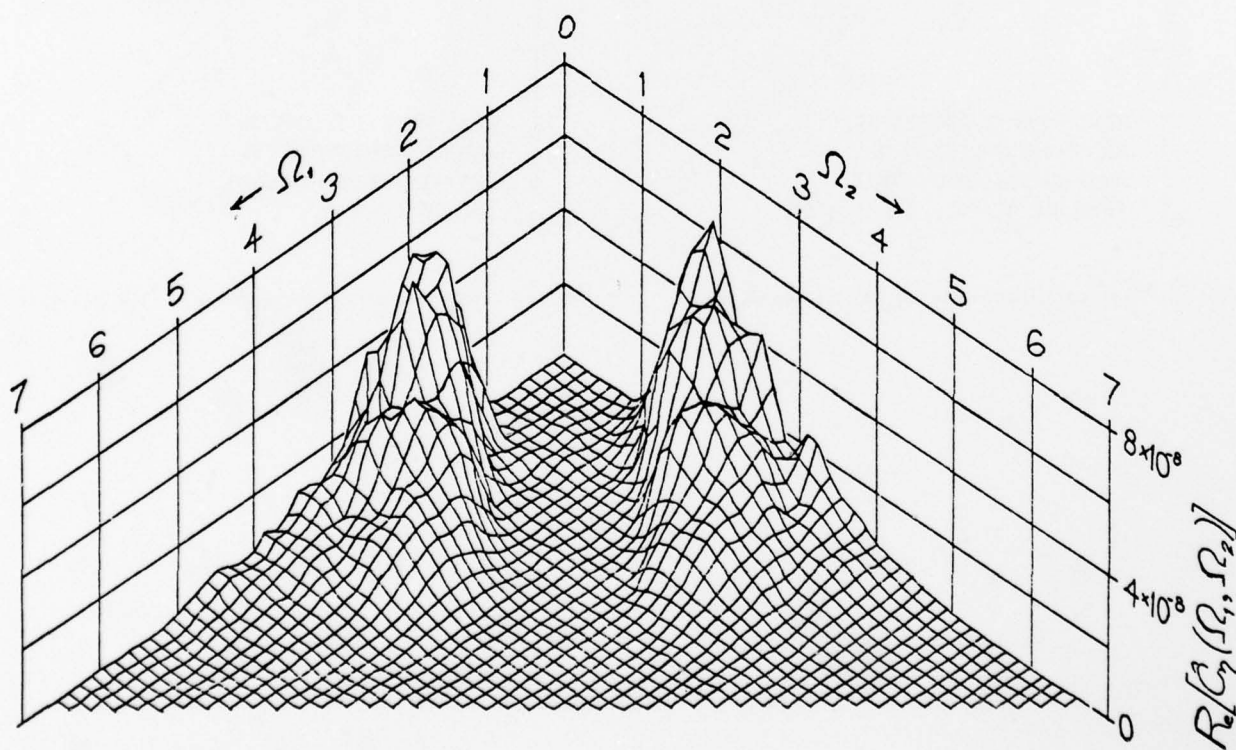


Fig. 8: Isometric sketch of real part of wave, wave,  $(\text{wave})^2$  cross-bi-spectrum sea state b, Froude number 0.15

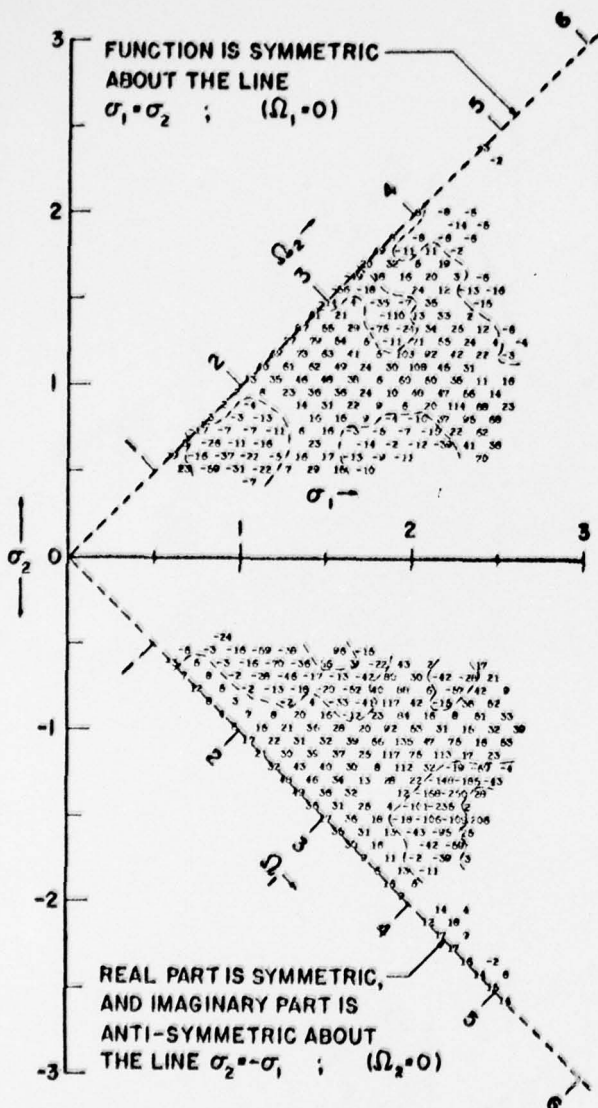


Fig. 9: Real part of estimated  $G_2(\sigma_1, \sigma_2)$ , sea state a,  $F_n = 0.15$

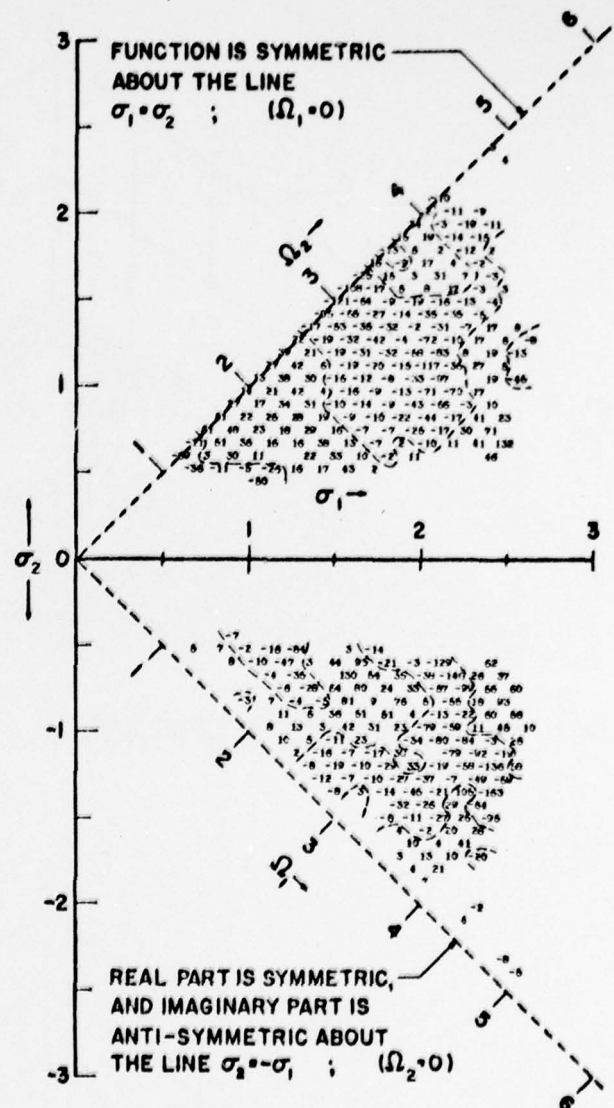


Fig. 10: Imaginary part of estimated  $G_2(\sigma_1, \sigma_2)$ , sea state a,  $F_n = 0.15$

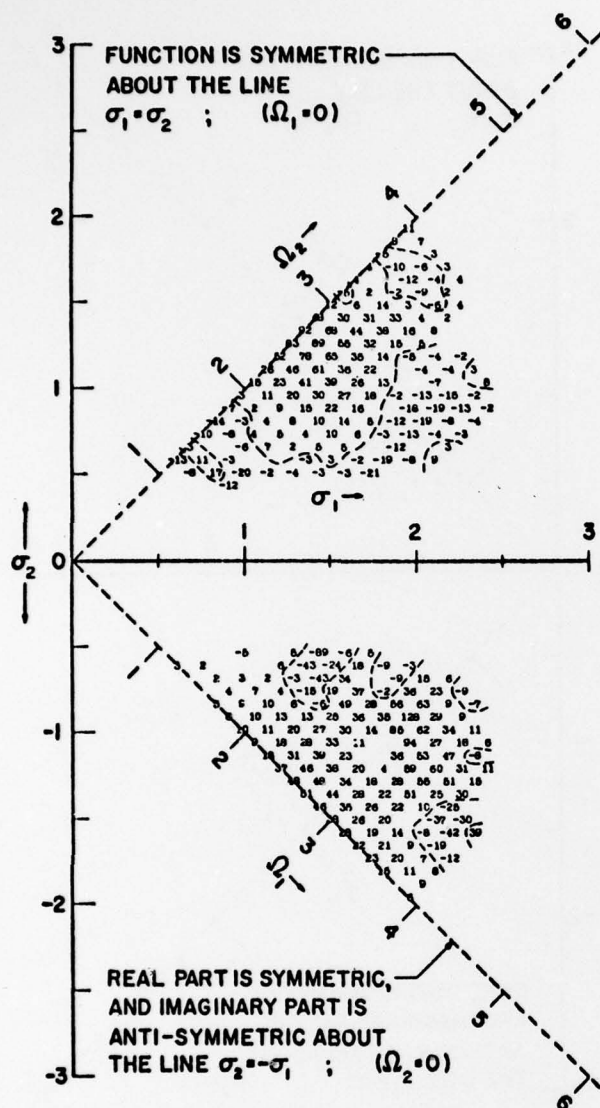


Fig. 11: Real part of estimated  $G_2(\sigma_1, \sigma_2)$ , sea state b,  $F_n = 0.15$

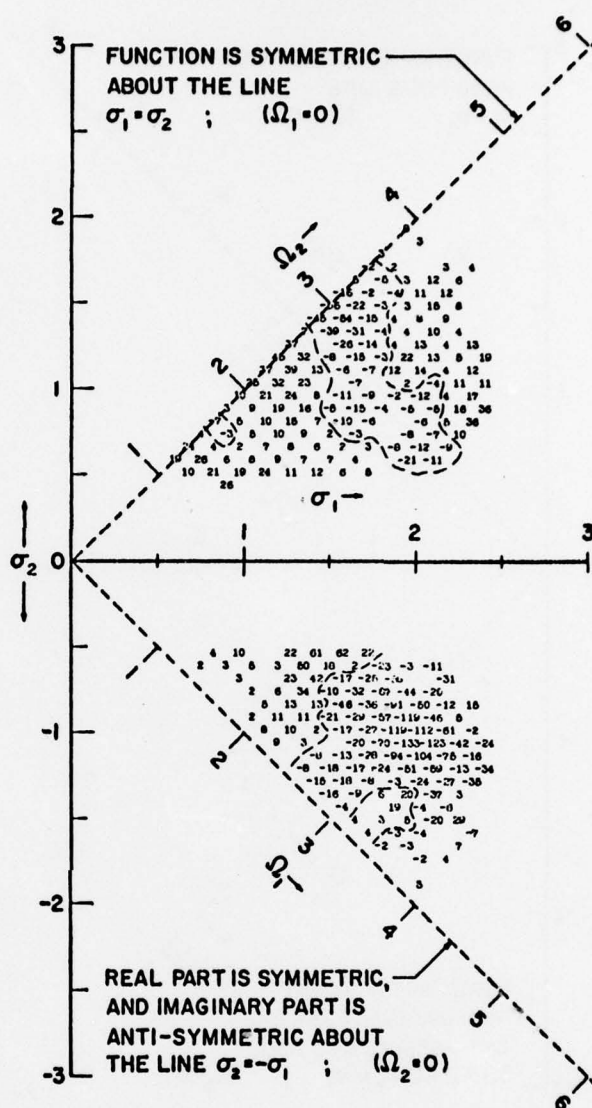


Fig. 12: Imaginary part of estimated  $G_2(\sigma_1, \sigma_2)$ , sea state b,  $F_n = 0.15$



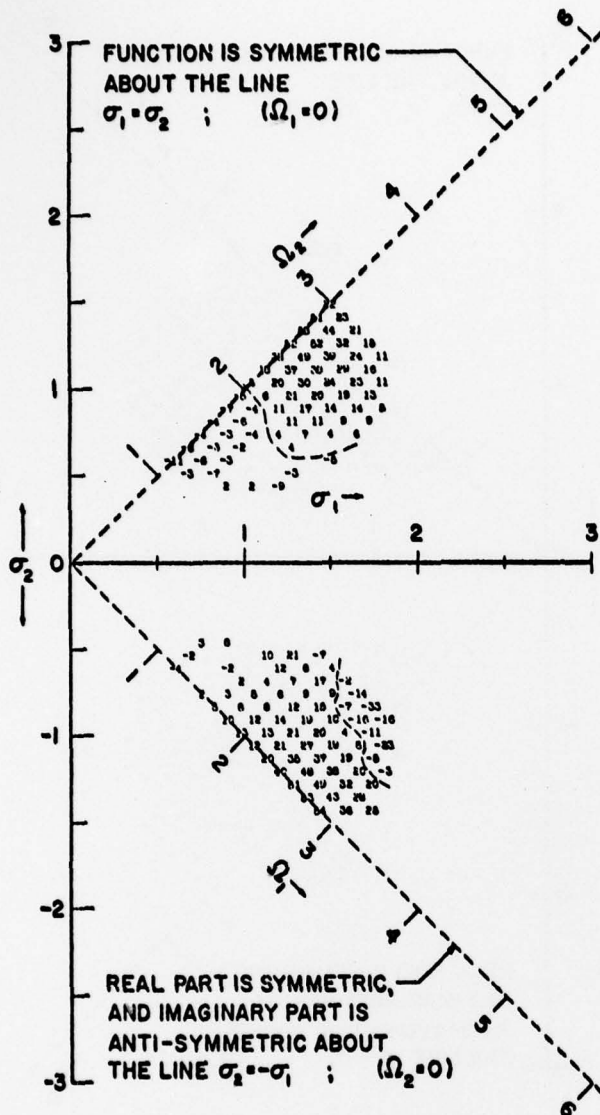


Fig. 13: Real part of estimated  $G_2(\sigma_1, \sigma_2)$ , sea state c,  $F_n = 0.15$

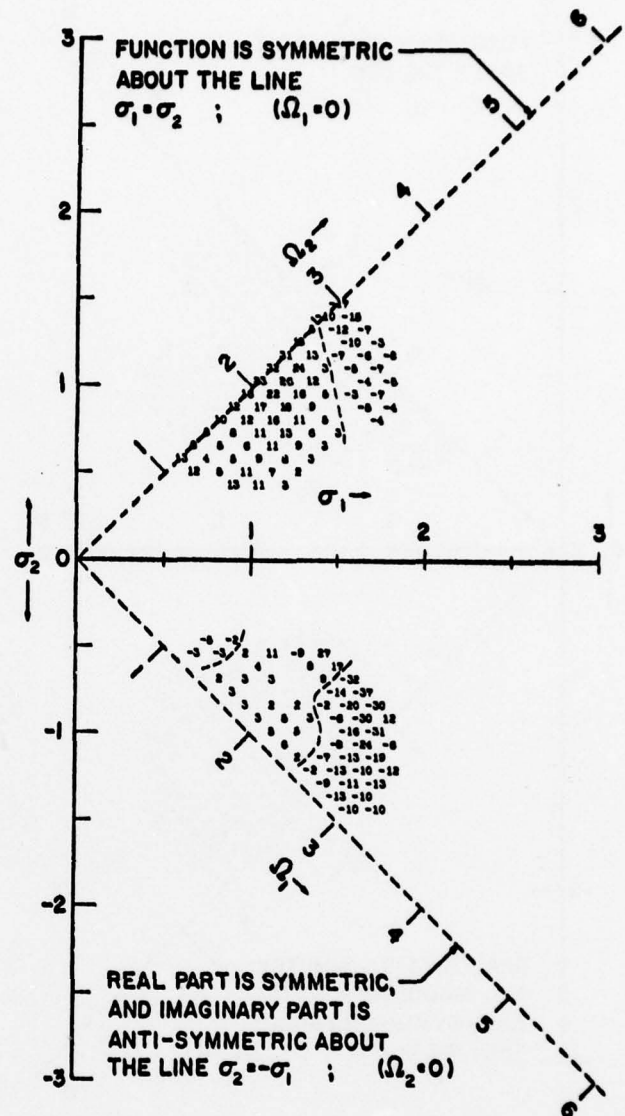


Fig. 14: Imaginary part of estimated  $G_2(\sigma_1, \sigma_2)$ , sea state c,  $F_n = 0.15$

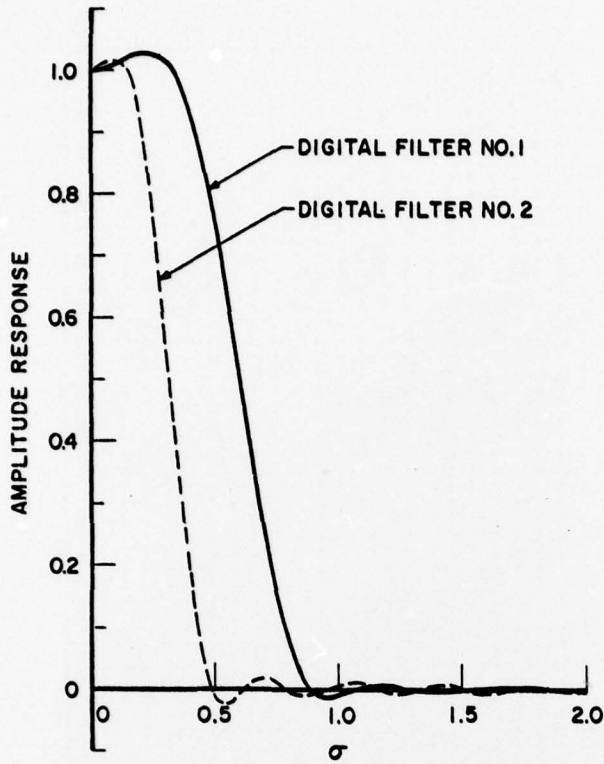


Fig. 15. Amplitude response of two digital filters

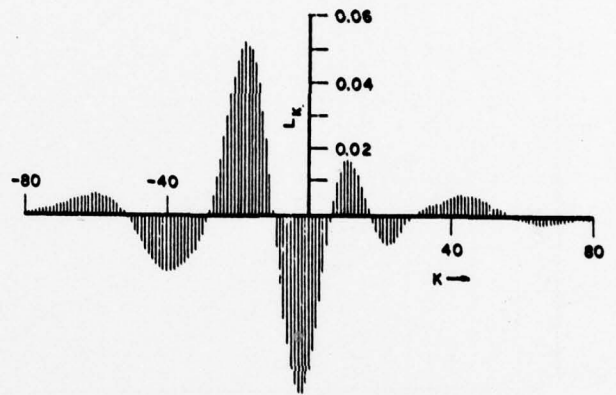


Fig. 17: Coefficients,  $L_k$ , of discrete linear resistance impulse response function

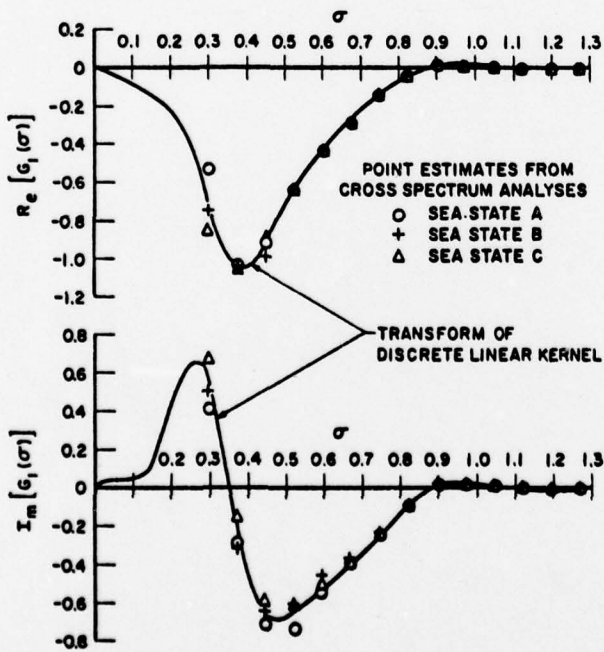


Fig. 16: Filtered linear resistance frequency response function

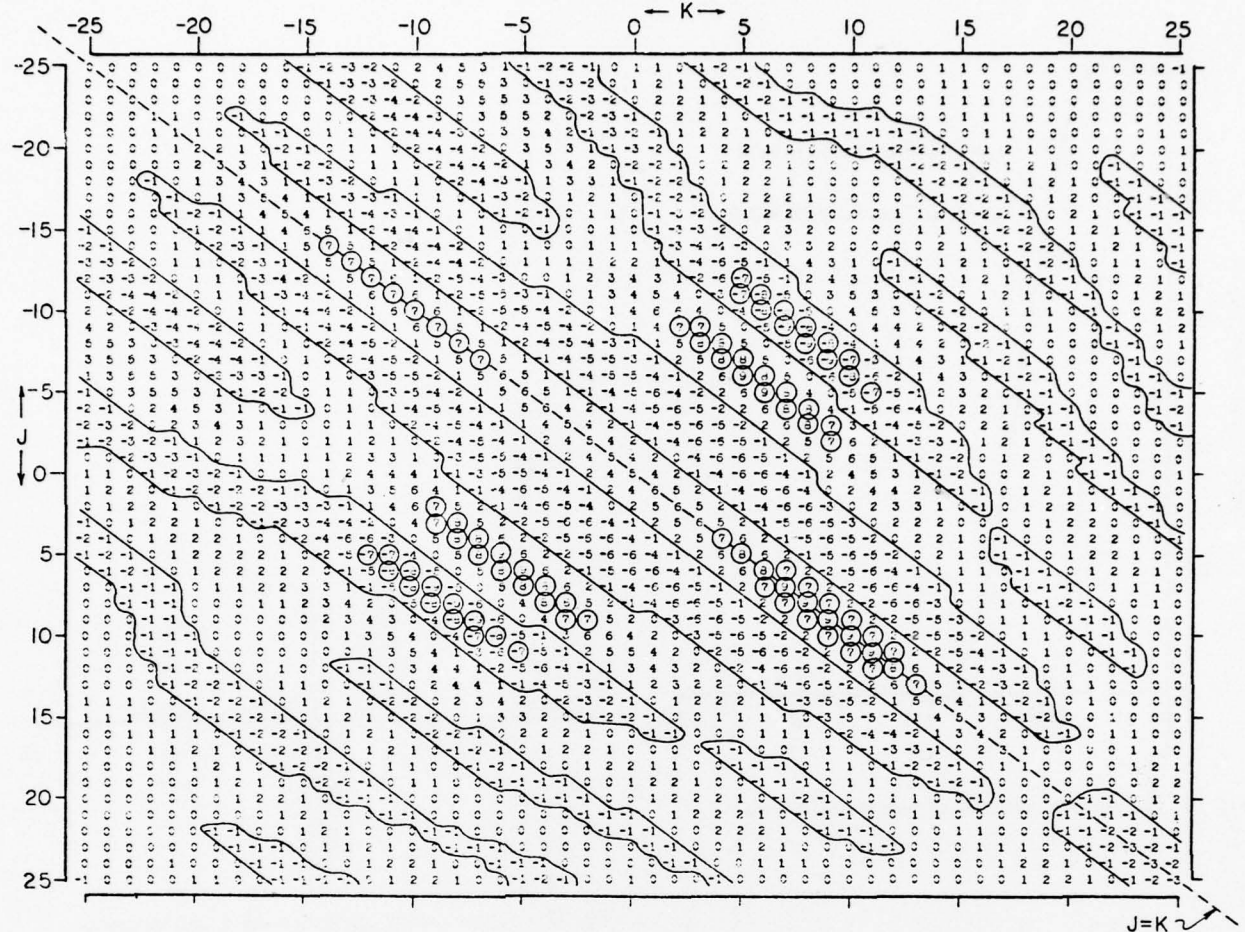
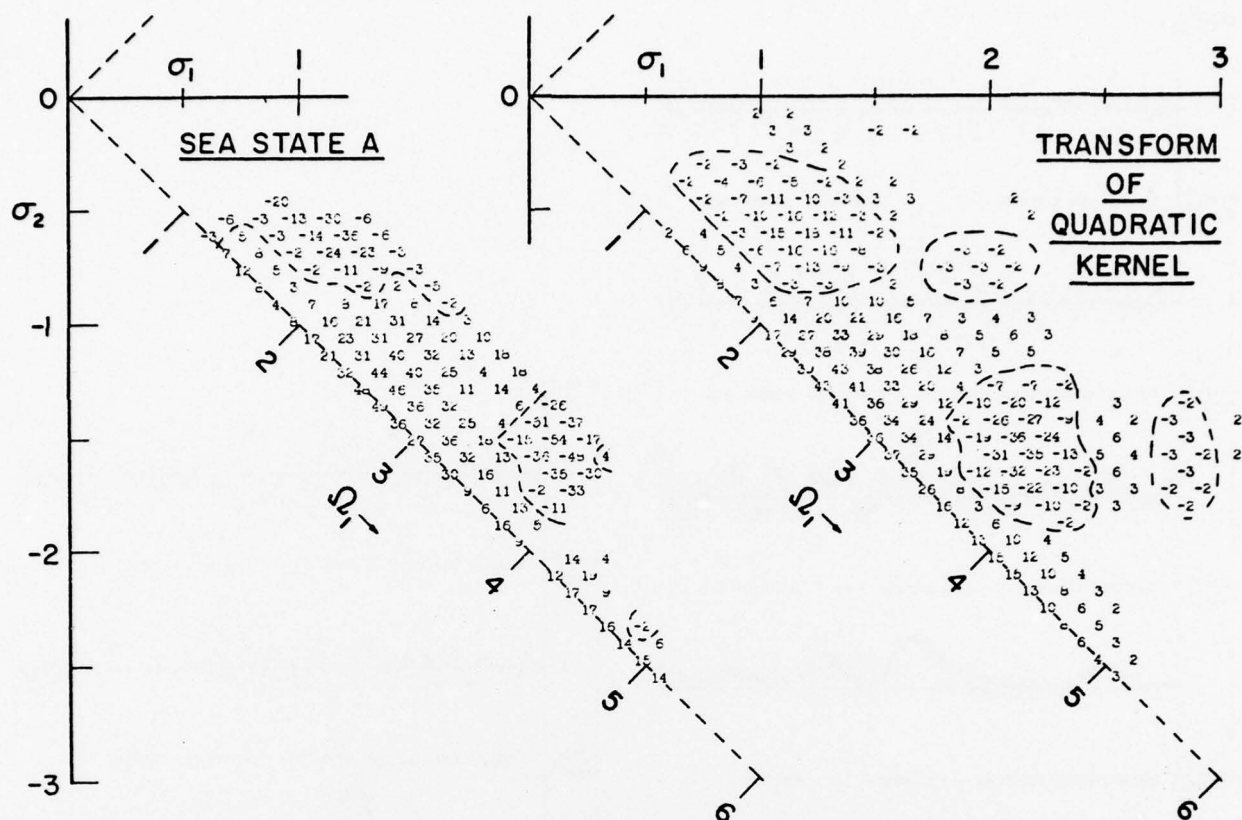
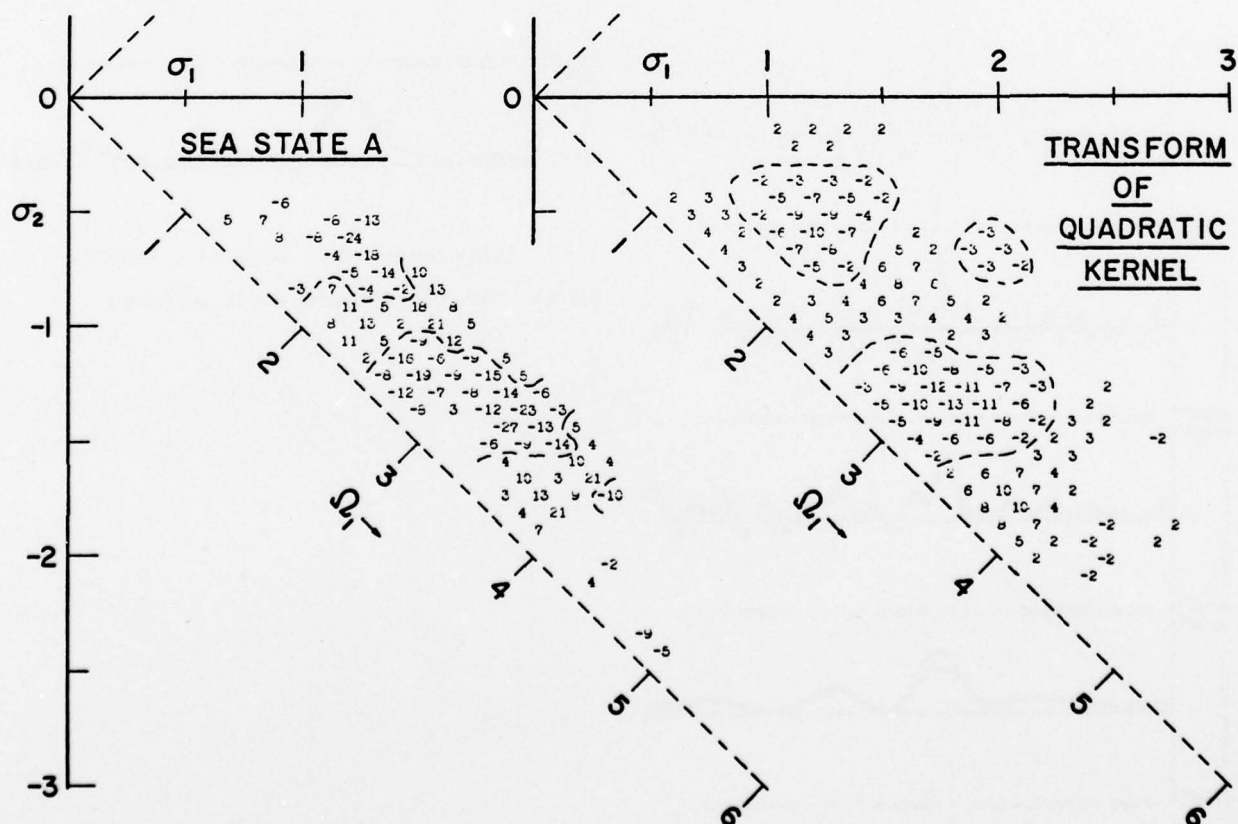


Fig. 18: Magnitudes of coefficients  $Q_{JK}$ , quadratic impulse response, sea state a



Fig. 19: Real part: Filtered estimates of  $G_2(\sigma_1, \sigma_2)$ Fig. 20: Imaginary part: Filtered estimates of  $G_2(\sigma_1, \sigma_2)$

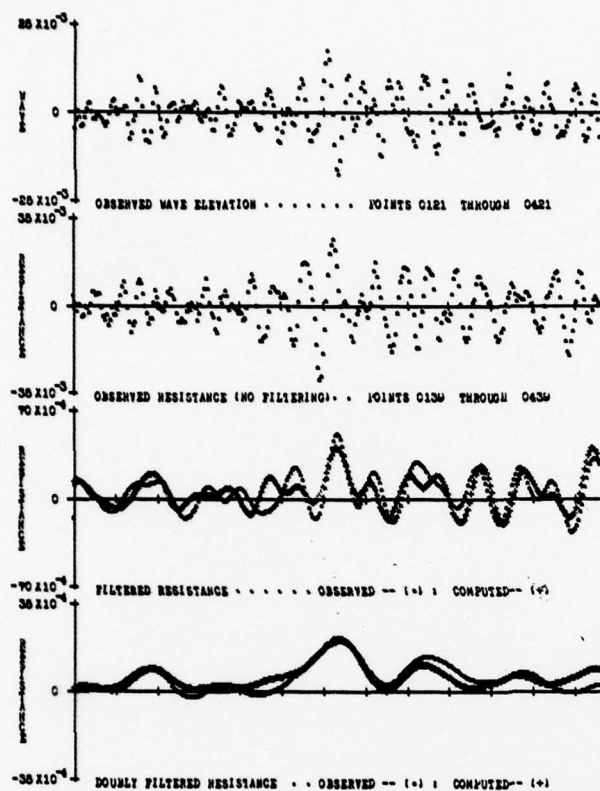


Fig. 21: Time domain results, run 30, sea state a

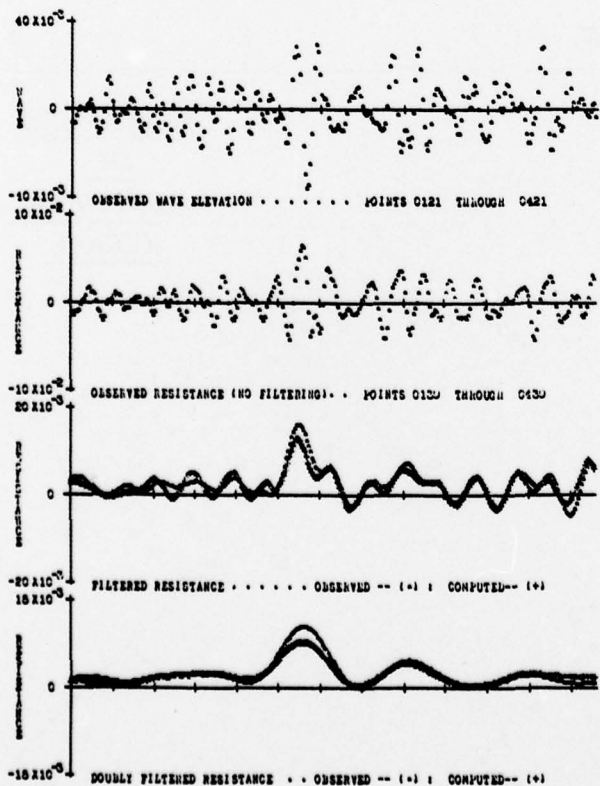


Fig. 22: Time domain results, run 34, sea state b

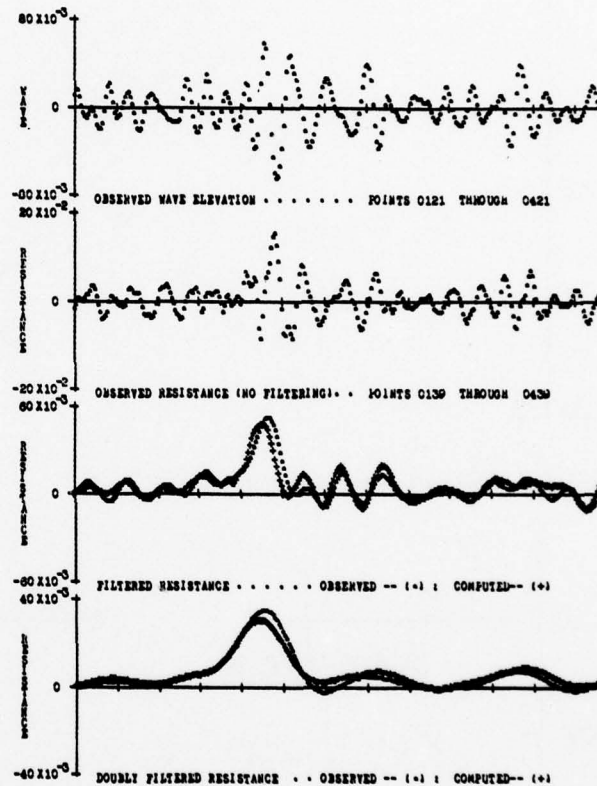


Fig. 23: Time domain results, run 38, sea state c

# NUMERICAL SOLUTION OF UNSTEADY SHIP WAVE PROBLEMS

R. K. C. CHAN and J. H. STUHMILLER  
Jaycor Del Mar, California, USA

A finite-difference numerical technique, employing general curvilinear coordinate systems, has been developed to permit accurate calculation of the unsteady motion of a three-dimensional floating body. The present approach formulates an initial-value problem, so that general transient flows as well as steady-state problems can be treated. Potential flow is assumed, which is separated into a base flow and a perturbation. The base flow is chosen as the flow that would exist if the free surface were replaced by a rigid horizontal plate. Because of the flexibility of this formulation, fairly general body shapes are allowed. In this paper the solution procedure is briefly described, while placing more emphasis on the validation and the results of the unsteady, non-periodic motion of a floating sphere. Results on more complex body shapes will be reported at a later date.

## 1. INTRODUCTION

The major difficulties that arise in studying the flow and the associated wave field about a floating body can be attributed to the complexity of the body geometry on the one hand and to the presence of free surface on the other. Even with the simplest mathematical statement regarding the nature of the flow, i.e., assuming that the flow is inviscid, incompressible, and irrotational so that the Laplace equation  $\nabla^2\phi = 0$  for the velocity potential  $\phi$  governs the entire flow field except at boundaries of the fluid domain, these two difficulties continue to hinder progress in making accurate theoretical predictions.

With the rapid evolution of high-speed, electronic, digital computers and the continual appearance of new numerical techniques, it would seem that both difficulties, i.e. the body geometry and the free surface, can be surmounted by a straightforward application of a simple finite-difference method which solves the complete set of equations of motion. However, before one launches into the study of nonlinear effects and deviations from potential flow, it should be remembered that the linearized potential flow about a ship has not been thoroughly explored. In fact, there is a general feeling among research workers in this area that the use of velocity potential and linearized free-surface boundary conditions may not be responsible for the major deficiencies of the existing analytic models. Rather, more careful treatment of boundary conditions at the ship hull seems to hold promise for improvement.

Most existing analytic models, such as flat-ship, thin ship, or slender-body theories, to mention only a few, are based on perturbation schemes of one kind or another. As the names imply, these methods attempt to take advantage of, and are thus limited to, the special geometric features of the floating body. Furthermore, these approximations are not uniformly valid. In the forward motion, for example, most of the waves may be produced in the bow and stern regions by a ship which, except for the relatively blunt bow and the stern, may qualify as a slender body. For such a problem, the slender-body theory is not valid near the bow and the stern, regions where the most important

physical processes are occurring. Thus, a critical question can be raised: How much progress could one make toward understanding the flow about a floating body if the difficulty associated with the body geometry were completely removed?

In view of the continuing trend toward more rigorous treatment of the body geometry, we present in this paper a numerical technique for computing flow about floating bodies with *no assumptions* about the body shape. As in existing theories, a potential flow satisfying  $\nabla^2\phi = 0$  and linearized free-surface boundary conditions are assumed; what distinguishes the present approach is the choice of the base flow. Obviously, the accuracy and effectiveness of any perturbation scheme is determined by how good an approximation the *base flow* is to the actual flow field. Consider the steady forward motion of a ship, for example. Instead of using a uniform stream with the velocity equal to the speed of the ship, as is usually done in analytic models to render the mathematics tractable, we choose as the base flow the flow about the ship that would exist if the free surface were replaced by a rigid plate. This base flow is preferable because it takes care of the singularities associated with the stagnation points and makes the perturbation field regular; but it is extremely difficult to obtain in a closed form and almost impossible to use in the perturbation equations of a purely analytic approach. As will be shown in Sections 2 and 3, the base flow can be treated quite easily by employing a numerical approach.

For the ease of demonstration and for the purpose of comparing with the results obtained by other investigators, we shall apply the solution technique to the case of a floating sphere, employing the familiar spherical polar coordinates. The use of a general curvilinear coordinate system to study the flow about more complicated three-dimensional floating bodies will be reported at a later date.

## 2. FORMULATION OF THE PROBLEM

Let the undisturbed water surface be the  $x$ - $y$  plane and the  $z$ -axis points vertically upward. Moreover, we adopt a frame of reference fixed at the floating rigid body. The Bernoulli equation



then takes the form<sup>(1)</sup>

$$\frac{\partial \phi}{\partial t} + x \frac{dU_0}{dt} + y \frac{dV_0}{dt} + z \frac{dW_0}{dt} + \frac{1}{2}(\nabla \phi) \cdot (\nabla \phi) + gz + \frac{p}{\rho} = \text{constant} \quad (1)$$

where  $U_0(t)$ ,  $V_0(t)$ , and  $W_0(t)$  are velocity components of the body relative to an inertial frame. In the interior of the flow, Laplace's equation

$$\nabla^2 \phi = 0 \quad (2)$$

is to be satisfied, and the normal derivative  $\partial \phi / \partial n$  should vanish on the body surface. At the free surface, dynamic and kinematic boundary conditions must be satisfied, but their specific forms will be given after we specialize the formulation in spherical polar coordinates.

It is convenient to distinguish two classes of problems:

1. Class A problems—The floating body moves in horizontal directions only, i.e.  $W_0(t) = 0$ , but  $U_0(t)$  and  $V_0(t)$  can be any prescribed function of time.
2. Class B problems—The floating body moves in the vertical direction only, i.e.  $U_0(t) = V_0(t) = 0$ . Examples include heave, pitch, and roll.

We shall elaborate on the formulation of the Class A problems. Formulation for the Class B problems is the more usual one and will be stated at the end of this section.

For Class A problems we separate the flow field into a base flow and the perturbation from it, i.e.

$$\phi = \bar{\phi} + \phi' \quad (3)$$

where an overbar denotes the base flow and the prime the perturbation. The base flow is chosen as that which would exist if the free surface were replaced by a rigid horizontal plate. It is required to satisfy

$$\nabla^2 \bar{\phi} = 0 \quad (4)$$

and

$$\frac{\partial \bar{\phi}}{\partial t} + x \frac{dU_0}{dt} + y \frac{dV_0}{dt} + \frac{1}{2}(\nabla \bar{\phi}) \cdot (\nabla \bar{\phi}) + gz + \frac{\bar{p}}{\rho} = \frac{1}{2}(U_0^2 + V_0^2) \quad (5)$$

subject to the boundary conditions  $\partial \bar{\phi} / \partial z = 0$  at the plate (i.e. mean water level),  $\partial \bar{\phi} / \partial n = 0$  at the surface of the body, and  $\bar{\phi} = -(U_0 x + V_0 y)$  at large distances from the body.

Substituting Eq. (3) into Eq. (1), where the constant on the right-hand side of Eq. (1) is chosen as  $\frac{1}{2}(U_0^2 + V_0^2)$ , and subtracting Eq. (5) from the resulting equation, we obtain the perturbation Bernoulli equation

$$\frac{\partial \phi'}{\partial t} + \frac{1}{2}(\nabla \phi') \cdot (\nabla \phi') + (\nabla \bar{\phi}) \cdot (\nabla \phi') + \frac{p'}{\rho} = 0 \quad (6)$$

Of course, the Laplace equation

$$\nabla^2 \phi' = 0 \quad (7)$$

is to be satisfied throughout the fluid interior. The boundary conditions to be satisfied by  $\phi'$  are the normal derivative  $\partial \phi' / \partial n = 0$  at the body surface and appropriate conditions at the free surface. Since in this paper the technique is applied to the motion of a sphere, it is most convenient to use spherical polar coordinates in subsequent discussions.

In spherical coordinates, Eq. (7) becomes

$$\sin^2 \theta \frac{\partial}{\partial r} \left( r^2 \frac{\partial \phi'}{\partial r} \right) + \sin \theta \frac{\partial}{\partial \theta} \left( \sin \theta \frac{\partial \phi'}{\partial \theta} \right) + \frac{\partial^2 \phi'}{\partial \phi^2} = 0 \quad (8)$$

where  $(r, \theta, \phi)$  are the spherical coordinates. The origin is chosen at the center of the sphere.

To obtain the dynamic free-surface condition in terms of the perturbation potential  $\phi'$ , we use the fact that  $p = \bar{p} + p' = 0$  at  $z = \eta(r, \phi, t)$ , where  $\eta$  is the instantaneous free surface elevation from the undisturbed water surface. Thus, at the free surface, we have

$$\begin{aligned} \frac{p'}{\rho} &= -\frac{\bar{p}}{\rho} \\ &= - \left[ \frac{1}{2}(U_0^2 + V_0^2) - \frac{1}{2}(\nabla \bar{\phi}) \cdot (\nabla \bar{\phi}) - g\eta \right. \\ &\quad \left. - \left( \frac{\partial \phi}{\partial t} + x \frac{dU_0}{dt} + y \frac{dV_0}{dt} \right) \right]_{z=\eta} \end{aligned} \quad (9)$$

The last expression has been obtained by applying Eq. (5) at  $z = \eta$ .

Equations (6) and (9), applied at  $z = \eta(r, \phi, t)$ , supply the dynamic condition at the free surface. Following the treatment in (2), the kinematic free-surface condition can be derived for a general, curvilinear coordinate system. For the present purpose, however, we shall give it in spherical polar coordinates. The kinematic free-surface condition is then

$$\frac{\partial \eta}{\partial t} + \frac{\partial \phi}{\partial r} \left( \frac{\partial \eta}{\partial r} - \cos \theta \right) + \frac{1}{r} \frac{\partial \phi}{\partial \theta} + \frac{1}{r^2 \sin^2 \theta} \frac{\partial \phi}{\partial \phi} \frac{\partial \eta}{\partial \phi} = 0 \quad (10)$$

or

$$\begin{aligned} \frac{\partial \eta}{\partial t} + \left( \frac{\partial \bar{\phi}}{\partial r} + \frac{\partial \phi'}{\partial r} \right) \left( \frac{\partial \eta}{\partial r} - \cos \theta \right) + \frac{1}{r} \left( \frac{\partial \bar{\phi}}{\partial \theta} + \frac{\partial \phi'}{\partial \theta} \right) \\ + \frac{1}{r^2 \sin^2 \theta} \left( \frac{\partial \bar{\phi}}{\partial \phi} + \frac{\partial \phi'}{\partial \phi} \right) \frac{\partial \eta}{\partial \phi} = 0 \end{aligned} \quad (11)$$

to be applied at  $z = \eta(r, \phi, t)$ .

Finally, we linearize the equations by neglecting products of primed quantities and apply the two free-surface conditions at the mean water level  $z = 0$ , i.e.  $\theta = \pi/2$ , to obtain

#### Dynamic Condition

$$\begin{aligned} \frac{\partial \phi'}{\partial t} &= - \left( \frac{\partial \bar{\phi}}{\partial r} \frac{\partial \phi'}{\partial r} + \frac{1}{r^2} \frac{\partial \bar{\phi}}{\partial \theta} \frac{\partial \phi'}{\partial \theta} \right) + \frac{1}{2}(U_0^2 + V_0^2) \\ &\quad - \frac{1}{2} \left[ \left( \frac{\partial \bar{\phi}}{\partial r} \right)^2 + \frac{1}{r^2} \left( \frac{\partial \bar{\phi}}{\partial \theta} \right)^2 \right] - g\eta - \left( \frac{\partial \bar{\phi}}{\partial t} + x \frac{dU_0}{dt} + y \frac{dV_0}{dt} \right) \end{aligned} \quad (12)$$

#### Kinematic Condition

$$\frac{\partial \eta}{\partial t} = - \left( \frac{\partial \bar{\phi}}{\partial r} \frac{\partial \eta}{\partial r} + \frac{1}{r} \frac{\partial \bar{\phi}}{\partial \theta} + \frac{1}{r^2} \frac{\partial \bar{\phi}}{\partial \phi} \frac{\partial \eta}{\partial \phi} \right). \quad (13)$$

In deriving Eqs. (12) and (13) we have used the fact that  $\partial \bar{\phi} / \partial \theta = 0$  at  $z = 0$ .

For a semi-submerged sphere moving arbitrarily in the  $x$ -direction, the base flow that satisfies Eqs. (4), (5) and the attendant boundary conditions is given by

$$\bar{\phi} = -U_0(t) r \sin \theta \cos \phi \left[ 1 + \frac{1}{2} \left( \frac{r_0}{r} \right)^3 \right] \quad (14)$$

where  $r_0$  is the radius of the sphere. Using Eq. (14),  $x = r \sin \theta \cos \phi$ , and  $V_0(t) \equiv 0$ , we can evaluate explicitly, for example, the last term of Eq. (12) as

$$\frac{\partial \bar{\phi}}{\partial t} + x \frac{dU_0}{dt} + y \frac{dV_0}{dt} = - \left( \frac{dU_0}{dt} \right) \cdot \frac{1}{2} r \sin \theta \cos \phi \left( \frac{r_0}{r} \right)^3. \quad (15)$$

Therefore, Eqs. (12) and (13) together with values for the base flow, found analytically as above or numerically, completely determine the solution of the Class A problem.

For Class B problems, we use a frame of reference fixed in the otherwise undisturbed fluid and take the fluid at rest as the base flow. This is just the usual formulation and the linearized free-surface conditions can be written directly as

$$\frac{\partial \phi'}{\partial t} = -g\eta \quad (16)$$

$$\frac{\partial \eta}{\partial t} = -\frac{1}{r} \frac{\partial \phi'}{\partial \theta} \quad (17)$$

Also, the normal derivative condition  $\partial \phi' / \partial n = \vec{V}_B \cdot \vec{n}$  is applied at the mean position of the body surface, where  $\vec{V}_B(t)$  is the velocity of the body and  $\vec{n}$  is the unit normal vector at the body surface.

At large distance from the body, the conditions  $\phi' = 0$  and  $\eta = 0$  are imposed for both Class A and Class B problems.

### 3. NUMERICAL SOLUTION PROCEDURE

The computation domain for the problem of a floating spherical body is bounded by the body surface, the free surface, and the surface of a large outer sphere concentric with the body. The radius of the outer sphere is chosen large enough that no significant amount of disturbance reaches the outer boundary within the problem time of interest.

In general, there are two major phases in the solution procedure: the base flow calculation and the calculation of the perturbation field. When a general curvilinear coordinate system is used, the base flow can be obtained by using the usual finite-difference technique for solving the Laplace equation (4), subject to the conditions discussed in connection with Eq. (5). The only difference is that the Laplacian operator has to be written in the general curvilinear coordinates as do the normal derivatives which appear in the boundary conditions. Detailed discussions on solving this type of problems can be found in Reference 3. For the flow around a sphere, an analytic solution for  $\bar{\phi}$  is available,<sup>(4)</sup> and it is given by Eq. (14). The base flow is computed only once and stored in the computer for later use in calculating the perturbation field. It is interesting to note that, for arbitrary horizontal motions, one only has to compute a base flow,  $\bar{\phi}_1$ , due to  $(U_0, V_0) = (1, 0)$  and another,  $\bar{\phi}_2$ , due to  $(U_0, V_0) = (0, 1)$ . The base flow at any instant is just  $\bar{\phi} = U_0(t)\bar{\phi}_1 + V_0(t)\bar{\phi}_2$ , since the governing equation and boundary conditions are linear.

Having obtained the base flow, the perturbation field can be solved by performing a time integration using a finite difference technique. First, the three-dimensional space occupied by the fluid is subdivided by a finite-difference mesh which, for convenience, is identical with the mesh used in obtaining the base flow. Although the method can handle more general configurations, in what follows we shall consider flows about a semi-submerged sphere only.

For Class A problems, Eqs. (12) and (13) determine the evolution of  $\phi'$  and  $\eta$  at the free surface. Similarly, Eqs. (16) and (17) update  $\phi'$  and  $\eta$  for Class B problems. Equations (12) and (13) can be written in finite difference form as

$$\begin{aligned} & \frac{\zeta_{i,k}^{n+1} - \zeta_{i,k}^n}{\delta t} \\ &= -g\eta_{i,k}^{n+\frac{1}{2}} \left[ A_{i,k}^{n+\frac{1}{2}} \left( \frac{\zeta_{i+1,k}^{n+\frac{1}{2}} - \zeta_{i-1,k}^{n+\frac{1}{2}}}{2\delta r} \right) + \frac{B_{i,k}^{n+\frac{1}{2}}}{r_i^2} \left( \frac{\zeta_{i,k+1}^{n+\frac{1}{2}} - \zeta_{i,k-1}^{n+\frac{1}{2}}}{2\delta \phi} \right) \right] \\ &+ C_{i,k}^{n+\frac{1}{2}} \end{aligned} \quad (18)$$

where

$$\left. \begin{aligned} A_{i,k}^{n+\frac{1}{2}} &= \left( \frac{\partial \bar{\phi}}{\partial r} \right)_{i,k}^{n+\frac{1}{2}} = \frac{\bar{\phi}_{i+1,k}^{n+\frac{1}{2}} - \bar{\phi}_{i-1,k}^{n+\frac{1}{2}}}{2\delta r} \\ B_{i,k}^{n+\frac{1}{2}} &= \left( \frac{\partial \bar{\phi}}{\partial \phi} \right)_{i,k}^{n+\frac{1}{2}} = \frac{\bar{\phi}_{i,k+1}^{n+\frac{1}{2}} - \bar{\phi}_{i,k-1}^{n+\frac{1}{2}}}{2\delta \phi} \end{aligned} \right\} \text{At the mean water level.}$$

$$\begin{aligned} C_{i,k}^{n+\frac{1}{2}} &= \frac{1}{2} (U_0^2 + V_0^2)^{n+\frac{1}{2}} - \frac{1}{2} \left[ \left( \frac{\partial \bar{\phi}}{\partial r} \right)^2 + \frac{1}{r^2} \left( \frac{\partial \bar{\phi}}{\partial \phi} \right)^2 \right]_{i,k}^{n+\frac{1}{2}} \\ &- \left( \frac{\partial \bar{\phi}}{\partial t} + x \frac{dU_0}{dt} + y \frac{dV_0}{dt} \right)_{i,k}^{n+\frac{1}{2}} \quad (\text{at } z=0), \end{aligned}$$

and

$$\begin{aligned} & \frac{\eta_{i,k}^{n+1} - \eta_{i,k}^n}{\delta t} \\ &= \frac{1}{r_i} \left[ \frac{(\phi')_{i,1,k}^{n+\frac{1}{2}} - (\phi')_{i,2,k}^{n+\frac{1}{2}}}{\delta \theta} \right] \\ &- \left[ A_{i,k}^{n+\frac{1}{2}} \left( \frac{\eta_{i+1,k}^{n+\frac{1}{2}} - \eta_{i-1,k}^{n+\frac{1}{2}}}{2\delta r} \right) + \frac{B_{i,k}^{n+\frac{1}{2}}}{r_i^2} \left( \frac{\eta_{i,k+1}^{n+\frac{1}{2}} - \eta_{i,k-1}^{n+\frac{1}{2}}}{2\delta \phi} \right) \right] \end{aligned} \quad (19)$$

We have used the symbol  $\zeta$  to represent  $\phi'$  at the mean water level. The subscripts  $(i, j, k)$  refer to the node points of the computation mesh in the  $(r, \theta, \phi)$  directions, respectively, and  $(\delta r, \delta \theta, \delta \phi)$  refer to the spatial increments in the respective directions. The superscript  $n$  denotes the time level  $t = n\delta t$ , where  $\delta t$  is the temporal increment. For the purpose of this demonstration, we only consider constant temporal and spatial increments. The superscript  $n+\frac{1}{2}$  is defined by

$$F^{n+\frac{1}{2}} = \frac{1}{2} (F^{n+1} + F^n), \quad (20)$$

where  $F$  is any quantity.

The Laplace equation, Eq. (8), is represented by

$$\begin{aligned} & s_j^2 \frac{1}{\delta r} \left[ r_{i+\frac{1}{2}}^2 \left( \frac{\phi'_{i+1,j,k} - \phi'_{i,j,k}}{\delta r} \right) - r_{i-\frac{1}{2}}^2 \left( \frac{\phi'_{i,j,k} - \phi'_{i-1,j,k}}{\delta r} \right) \right] \\ &+ s_j \frac{1}{\delta \theta} \left[ s_{j+\frac{1}{2}} \left( \frac{\phi'_{i,j+1,k} - \phi'_{i,j,k}}{\delta \theta} \right) - s_{j-\frac{1}{2}} \left( \frac{\phi'_{i,j,k} - \phi'_{i,j-1,k}}{\delta \theta} \right) \right] \\ &+ \frac{1}{(\delta \phi)^2} \left[ \phi'_{i,j,k+1} - 2\phi'_{i,j,k} + \phi'_{i,j,k-1} \right] = 0 \end{aligned} \quad (21)$$

in which

$$s_j = \sin \theta_j$$

$$s_{j+\frac{1}{2}} = \sin \left( \frac{\theta_j + \theta_{j+1}}{2} \right); \quad s_{j-\frac{1}{2}} = \sin \left( \frac{\theta_j + \theta_{j-1}}{2} \right)$$

$$r_{i+\frac{1}{2}} = \frac{1}{2}(r_i + r_{i+1}) ; r_{i-\frac{1}{2}} = \frac{1}{2}(r_i + r_{i-1})$$

In Eq. (21), the  $(\phi')$ 's are evaluated at the  $(n+1)$ th level in time.

To begin the numerical integration, we have to specify initial conditions, the simplest being  $\eta = 0$ ,  $\phi' = 0$ ,  $U_0 = V_0 = 0$  at  $t = 0$ . The subsequent fluid motion is due to the prescription of  $U_0(t)$  and  $V_0(t)$ , for  $t > 0$ . The computation for each cycle of time increment consists then of using Eqs. (18) and (19) to obtain the new values  $\zeta_{i,k}^{n+1}$  and  $\eta_{i,k}^{n+1}$ , and solving Eq. (21) by the method of successive over-relaxation (SOR). Since the right-hand sides of Eqs. (18) and (19) contain terms defined at the  $(n+1)$ th level, these equations are solved by a predictor-corrector procedure.

#### 4. RESULTS AND DISCUSSIONS

To validate our numerical model, the flow about and the dynamic forces on a semi-submerged sphere in heave and sway have been calculated. Figure 1 shows the top view (i.e. at mean water surface) of the computational mesh. In actual calculations, a variable mesh spacing  $r$  is used to achieve some economy. In Table 1, the amplitude of the vertical dynamic force in heave is compared with published results,<sup>(5)</sup> and a similar comparison is made for the amplitude of the horizontal dynamic force in sway (Table 2). The agreement is judged to be good. Figure 2 shows the horizontal force experienced by the sphere as a function of time in forced sway at the frequency  $\omega\sqrt{r_0/g} = 0.7071$ . It is seen that at this frequency the base flow, that is, the non-wave part, contributes about 80% to the total dynamic force.

Table 1

Comparison of the Amplitude of the Vertical Dynamic Force in Heave (a is the amplitude of the body displacement)				
$\frac{\omega^2 r_0}{g}$	Yeung	Wang	Bai	$\frac{F_z}{\rho g r_0^2 a}$ Present Result
0.5	0.660	0.763	-	0.580
1.0	0.991	-	0.998	0.950

Table 2

Comparison of the Amplitude of the Horizontal Dynamic Force in Sway (a is the amplitude of the body displacement)			
$\frac{\omega^2 r_0}{g}$	Yeung	Kim	$\frac{F_x}{\rho g r_0^2 a}$ Present Result
0.5	0.602	0.642	0.665
1.0	1.285	1.403	1.370

One of the most valuable features of the present approach is the ability to treat any arbitrary, horizontal motion of the body; that is,  $U_0(t)$  and  $V_0(t)$  can be any continuous, piecewise once-differentiable functions of time. To illustrate this, consider a case of forward acceleration described by

$$U_0(t) = \frac{U_{\max}}{2} \left[ 1 + \tanh(t\sqrt{g/r_0} - 3) \right]$$

$$V_0(t) = 0$$

The body is initially at rest and accelerates to the final speed  $U_{\max}$ . The magnitude of the quantities has been adjusted so that the Froude number  $U_{\max}/\sqrt{gr_0} = 0.1$ . The time increment used is  $\delta t\sqrt{g/r_0} = 0.1$ , which means that the body reaches its peak acceleration at the 30th increment in time. Figure 3 shows the horizontal force experienced by the body. As expected, the contribution from the base flow has its peak coincident with that of  $dU_0/dt$ . During the acceleration most of the horizontal resistance comes from the base flow. The vertical force is shown in Figure 4, where we see that in forward motion the body experiences a downward force. Figure 5 shows the time history of the free surface elevation for a point located at the front surface of the body and for one at the back of the body. During the forward acceleration the water surges up at the front and down at the back. At late times, both surface heights approach the asymptotic limit of  $\frac{1}{2}(U_{\max}^2/gr_0) = 0.5 \times 10^{-2}$ , which is easily deduced from Eq. (12). This does not mean, however, that the pattern of the free surface in front of the body is the same as that behind it. This point will become clear when we look at the contour plots for the surface elevation.

Figures 6(a)-(d) show the time history of free surface elevation as contour plots of  $\eta$ , for the case of forced heave at the frequency  $\omega\sqrt{r_0/g} = 1.0$ . The period of oscillation is  $\tau$ . These plots show the top view of the water surface. As expected, forced heave of a sphere generates waves whose crest and trough lines are concentric with the sphere. A few contour lines in these plots appear to be irregular, i.e. not concentric. These contour lines represent small absolute values in  $\eta$  and are at the noise level of the solution.

Similarly, the time history of  $\eta$  for the case of forced sway is shown in Figures 7(a)-(h).

For the unsteady motion of forward acceleration, the contours of  $\eta$  are shown in Figures 8(a)-(1). In this sequence of plots one can easily see the development of bow and stern waves. A typical calculation requires about 3 minutes of execution time, on a CDC 7600 system, for a computation mesh of  $40 \times 10 \times 40$  cells.

#### 5. CONCLUSIONS

The crux of the approach presented here is the use of a nontrivial base flow, which is amenable to numerical treatment. It is worth recapitulating that this base flow contains the singularities associated with the stagnation points, making the perturbation field regular. Preliminary results have indicated the viability and usefulness of this technique. Extension of the computer program to include general curvilinear coordinates for general body shapes will be the direction of our future work.

#### ACKNOWLEDGEMENT

This work has been supported by the Office of Naval Research under contract N00014-76-C-0455. Computations have been performed using the CDC 7600 computer located at the Lawrence Berkeley Laboratory, Berkeley, California.

#### REFERENCES

1. Lamb, Sir H., *Hydrodynamics*, Dover Publications, 1945.
2. Stoker, J. J., *Water Waves*, Interscience Publishers, Inc., New York, 1957.



3. Thompson, J. F., Thames, F. C., and Mastin, C. W., *Automatic Numerical Generation of Body-Fitted Curvilinear Coordinate System for Field Containing Any Number of Arbitrary Two-Dimensional Bodies*, Journal of Computational Physics, 1974, 15, pp. 299-319.
4. Streeter, V. L., *Fluid Mechanics*, McGraw-Hill, 1962.
5. Yeung, R. W.-C., *A Singularity-Distribution Method for Free-Surface Flow Problems with an Oscillating Body*, Report No. NA 73-6, College of Engineering, University of California, Berkeley, August 1973.

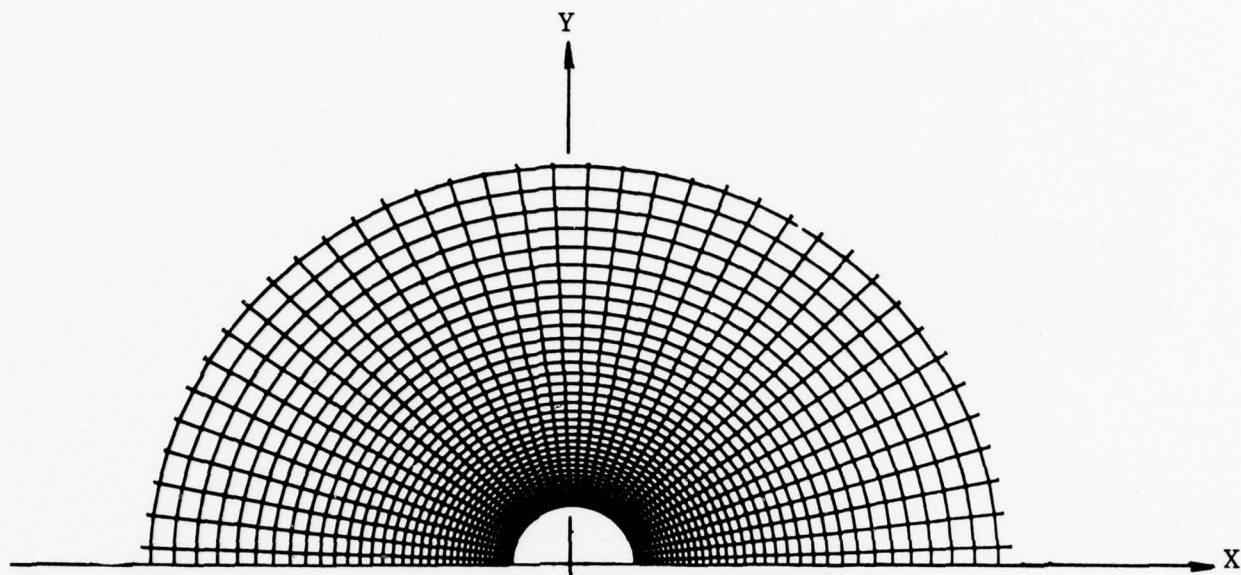


Fig. 1: Top view (i.e. at mean water surface) of the three-dimensional mesh used in the present study.

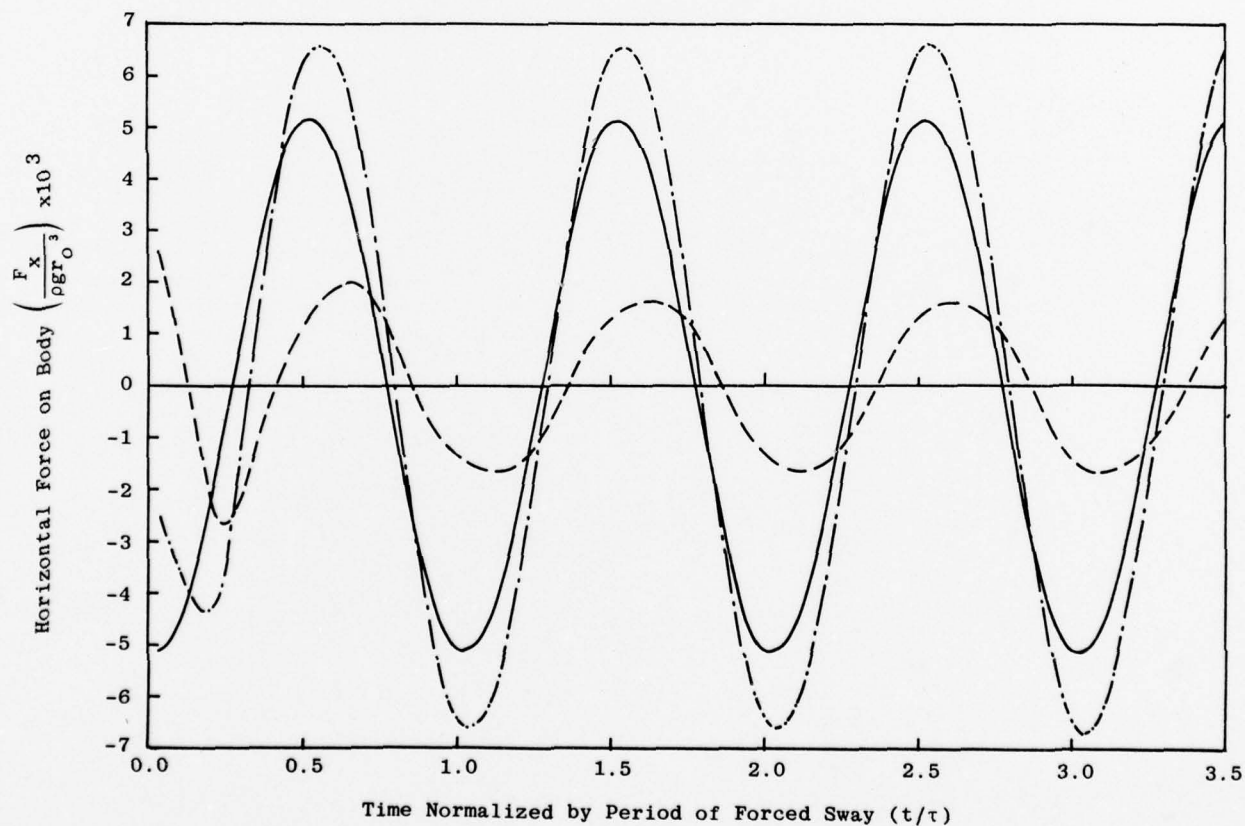


Fig. 2: Horizontal force experienced by the spherical body in forced sway at the frequency  $\omega\sqrt{r_0/g} = 0.7071$ , and the amplitude  $a/r_0 = 0.01$ . The chain line represents the total force, while the solid line is the component force due to the base flow, and the dashed line is that due to the surface waves.

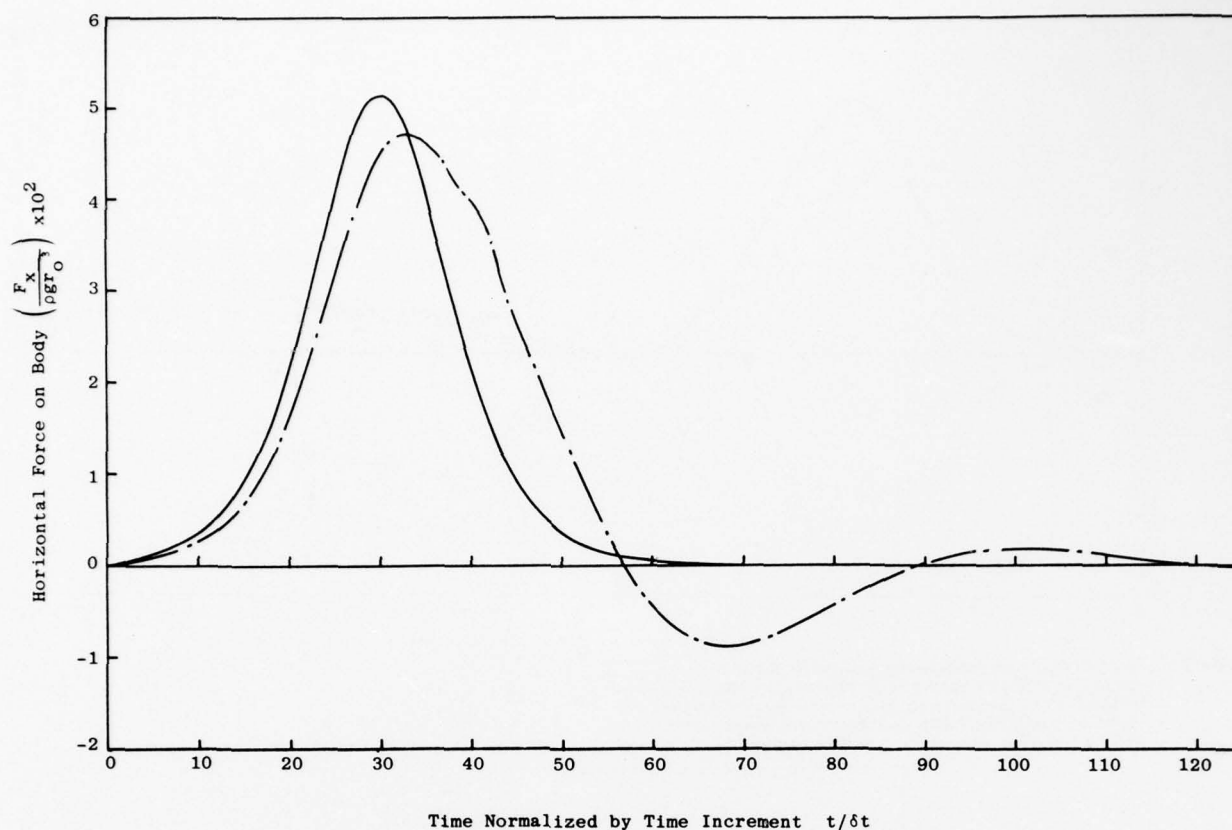


Fig. 3: Horizontal force experienced by the spherical body in forward acceleration. The chain line represents the total force, while the solid line is the contribution of the base flow.

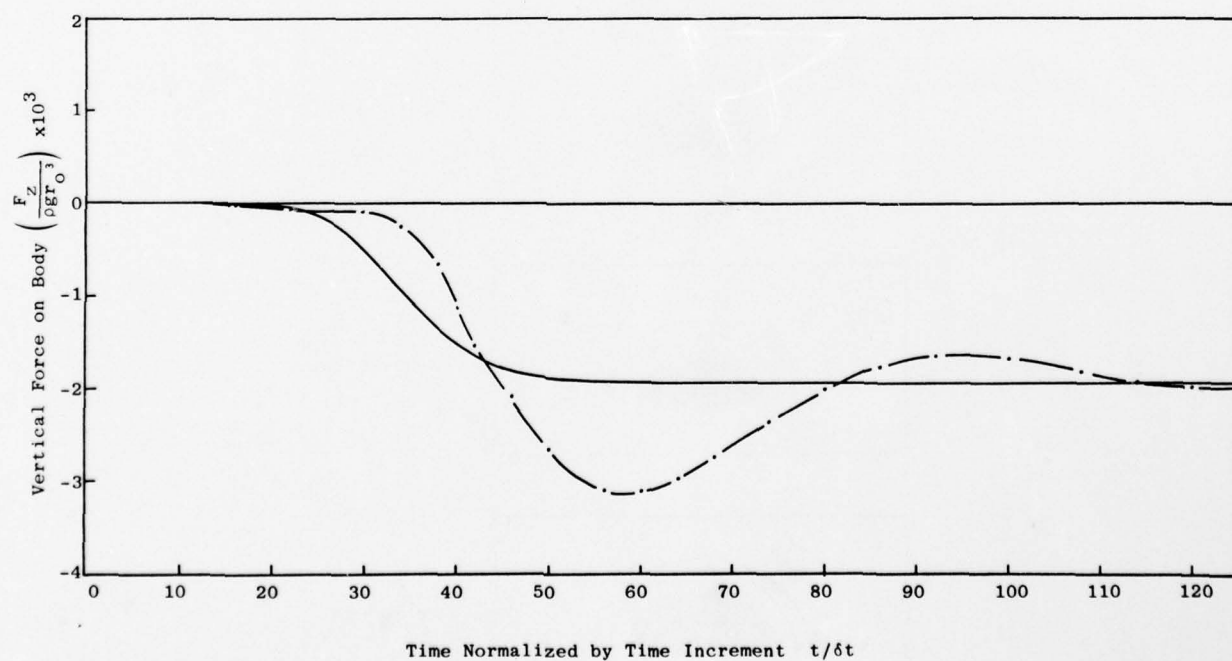


Fig. 4: Vertical force experienced by the spherical body in forward acceleration. The chain line represents the total force, while the solid line is the contribution of the base flow.



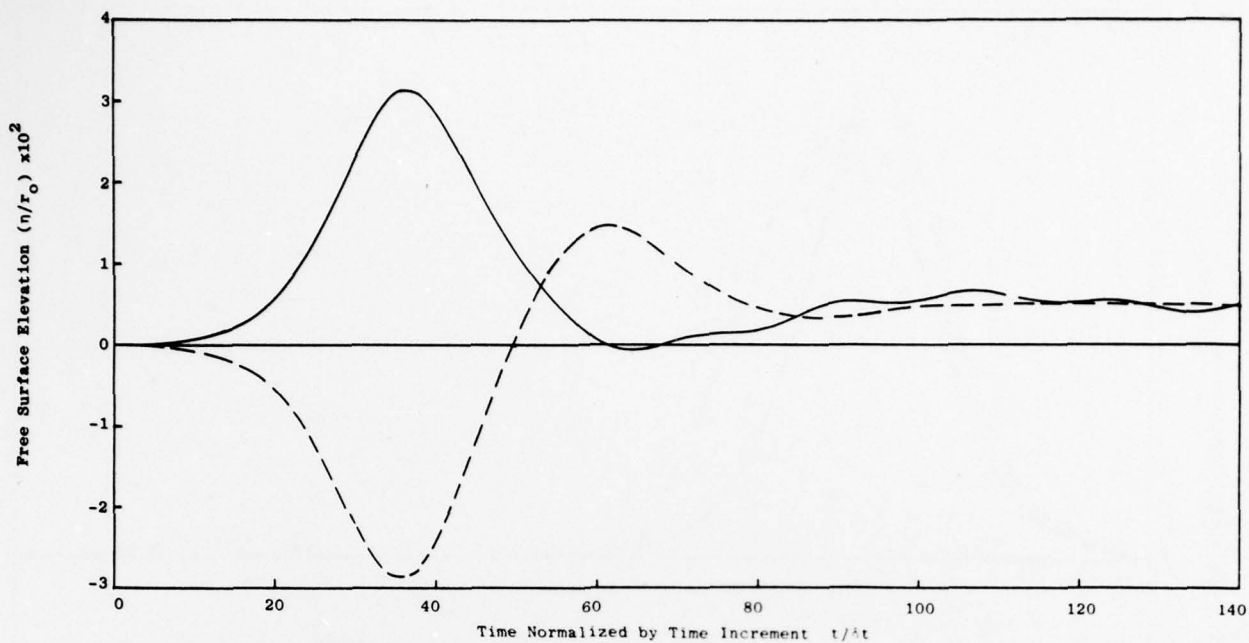


Fig. 5: Time history of free-surface elevation for a spherical body in forward acceleration. The solid line refers to a point located at  $x = r_0$  (i.e. at the front of the body). The dashed line is for a point at  $x = -r_0$  (i.e. at the back of the body).

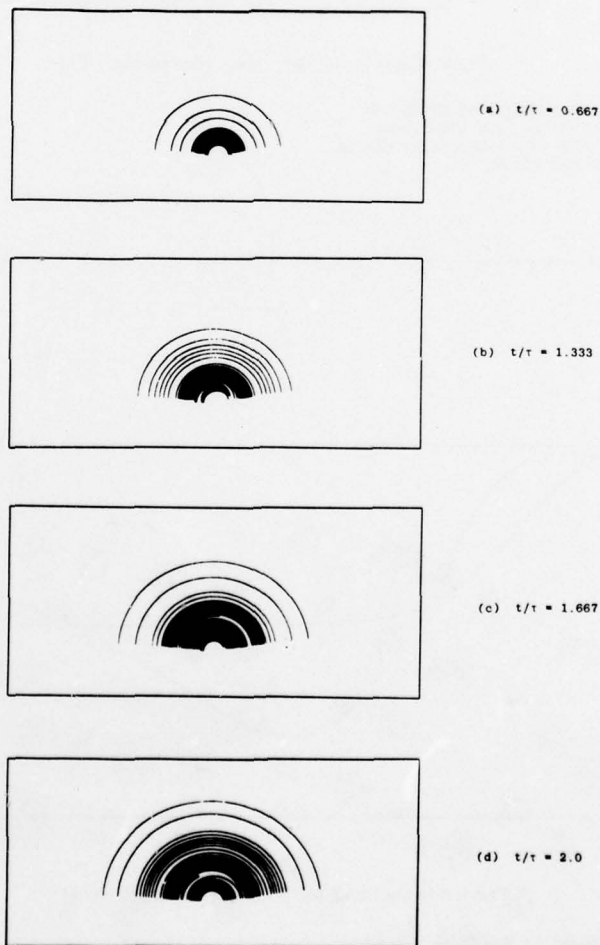


Fig. 6: Contour of free-surface elevation for the case of forced heave ( $\omega\sqrt{r_0/g} = 1.0$ ).

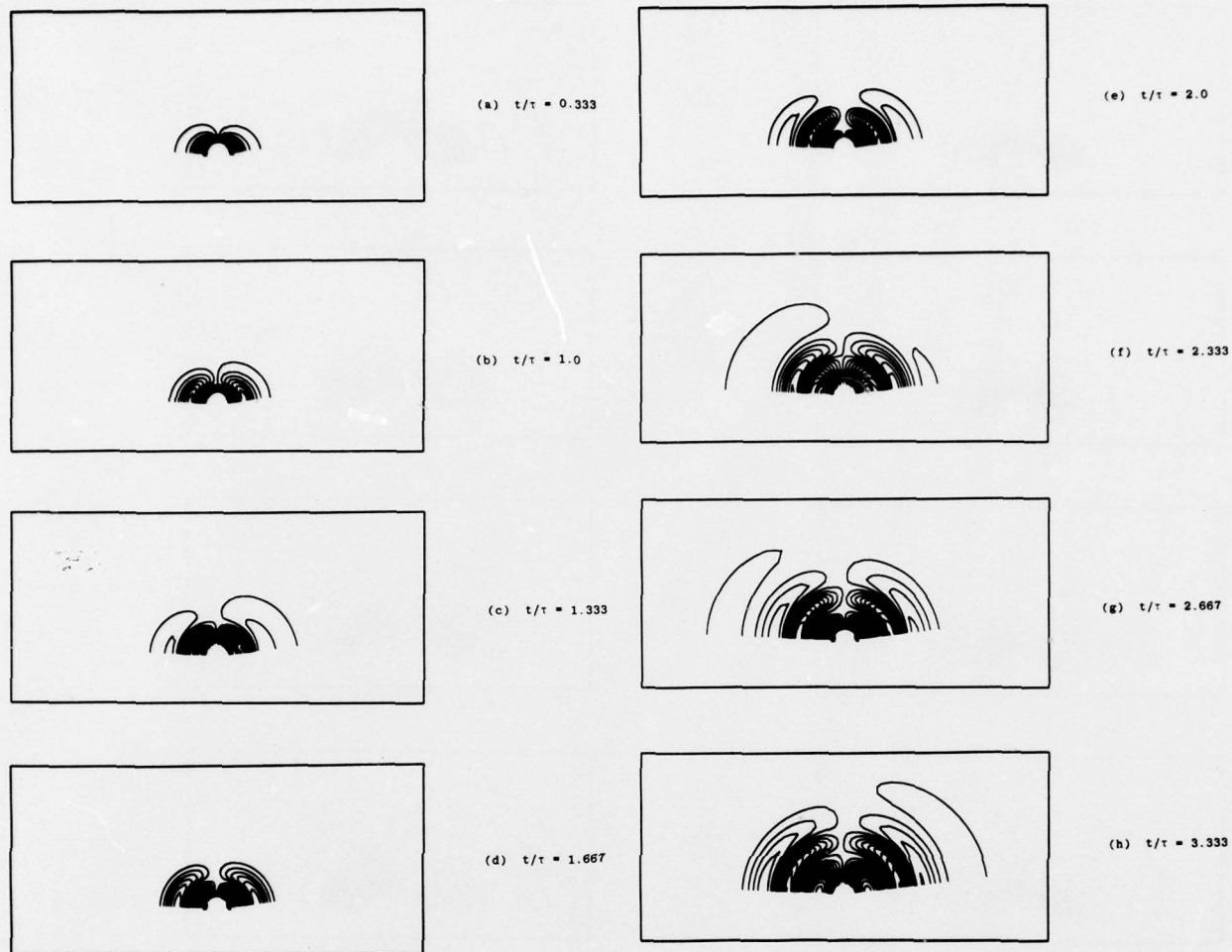


Fig. 7: Contour of free-surface elevation for the case of forced sway ( $\omega\sqrt{r_0/g} = 1.0$ ).



(a)  $\frac{t}{\sqrt{g/\tau_0}} = 3.0$



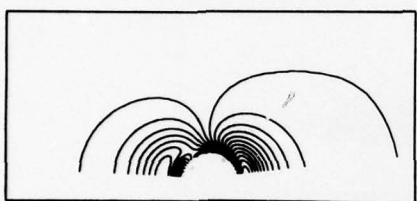
(e)  $\frac{t}{\sqrt{g/\tau_0}} = 7.0$



(b)  $\frac{t}{\sqrt{g/\tau_0}} = 4.0$



(f)  $\frac{t}{\sqrt{g/\tau_0}} = 8.0$



(c)  $\frac{t}{\sqrt{g/\tau_0}} = 5.0$



(g)  $\frac{t}{\sqrt{g/\tau_0}} = 9.0$



(d)  $\frac{t}{\sqrt{g/\tau_0}} = 6.0$



(h)  $\frac{t}{\sqrt{g/\tau_0}} = 10.0$

Fig. 8:

Fig. 8:

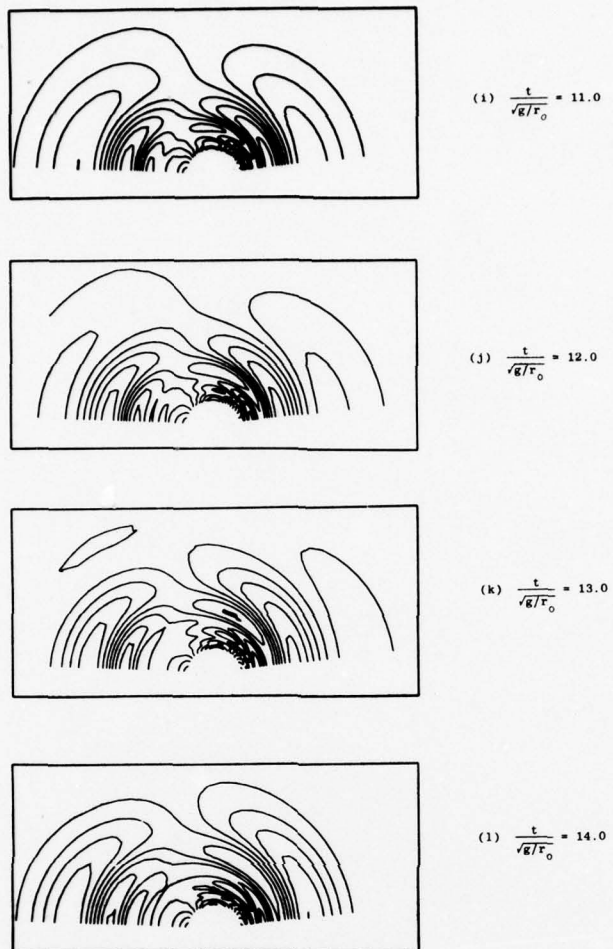


Fig. 8: Contour of free-surface elevation for the case of forward acceleration. The motion of the spherical body is from left to right.



# TWO-DIMENSIONAL AND CONDITIONAL DISTRIBUTION LAWS OF SEA WAVE COMPONENTS

I. K. BORODAY, Ya. M. KUBLANOV  
Krylov Research Institute, USSR

The report describes a theoretical method of plotting two-dimensional distributions of random value systems, viz. the period and the height, as well as the length and the height of irregular wind waves. The method is based on assuming the sea wave process as a narrow-band one with the use of the envelope method which is effective for the descriptions of such processes. Besides, an analysis is made of the regressive relationships between wave periods, lengths and heights, which result from conditional distributions of the wave components under consideration. It is observed that there is a good agreement between the theoretical data and sea wave observations.

## Introduction

The information on multidimensional distribution laws of sea wave components is necessary for the solution of some problems relating to the estimation of seakeeping qualities of ships and determination of wave action upon floating and stationary engineering structures. At the same time two-dimensional and conditional distributions of wave heights, periods and lengths have been investigated so far in much less detail than the one-dimensional ones. A simple way based on the assumption that wave profile components are statistically independent leads to rather a simple result from the analytical point of view [5,8,9], but whether it can be accepted is doubtful, however, which is confirmed by observation data [6,7,14]. The empirical method of approach using experimental data on simultaneous measurements of wave heights, periods and lengths approximated by analytical relationships [7,14] can hardly be considered as a universal one. Aside from the limitations inherent to such a method of approach, the confidence of the approximation as applicable to the wave height and length distributions is not doubtless because of the scarcity of observation data.

In the present paper the required two-dimensional laws are described by the method of envelopes as developed by V.I. Bunimovich [3], and this gives good reasons to consider the obtained relationship between the random values of interest to be following from the properties of the process itself. Taken as basis in this case is the two-dimensional probability density of the amplitude and of the derivative from

the phase of random function

$$u(t) = \tau(t) \cos \varphi(t),$$

obtained in [13]:

$$f(\tau, \dot{\varphi}) = \frac{1}{\sqrt{2\pi} D_u} \frac{\tau^2}{D_u \delta \omega} e^{-\frac{\tau^2}{2D_u} [1 + \frac{(\dot{\varphi} - \omega)^2}{\delta \omega^2}]} \quad (1)$$

In formula (1)

- $D_u$  = variance of  $u$ -value;
- $\tau(t)$  = envelope of the function  $u(t)$ ;
- $\dot{\varphi}(t)$  = phase derivative according to argument  $t$ ;
- $\omega_1$  = first order initial moment of the spectral density  $S_u(\omega)$  of the function  $u(t)$ ,  
 $\delta \omega^2 = \omega_{11}^2 - \omega_1^2$ ,  
 $\omega_{11}^2 = \bar{\omega}^2 = \frac{1}{D_u} \int_0^\infty \omega^2 S_u(\omega) d\omega$   
 square of the mean frequency of the process;
- $t$  = random function argument.

## Two-dimensional distributions

1. Let the disturbed sea surface ordinate be presented as meeting the ergodic requirement in the form of:

$$\zeta(\xi, \eta, t) = \tau(\xi, \eta, t) \cdot \cos[\Omega(t)t - K(\xi) \cdot \xi - K'(\eta) \cdot \eta] \quad (2)$$

The irregular wave process (2) is considered to be narrow banded in the fixed coordinate system  $O\xi\eta$  the axis  $O\xi$  of which coincides with the general direction of the wave propagation.

In relationship (2)

$\Omega(t)$  = frequency of wave ordinate variation at a fixed point slowly changing in comparison with  $\cos[\dots]$

$K(\xi)$  = slowly changing wave form frequency along  $O\xi$  direction;

$K(\eta)$  = slowly changing wave form frequency along  $O\eta$  direction.

In accordance with the envelope method the frequency  $\Omega$  is identified with the absolute derivative  $\dot{\psi}$  value and the function  $\tau(\xi, \eta, t)$  with the random amplitude of wave profile oscillation. In this case the Rayleigh distribution law is true for the ordinates of the envelope.

Following the suggestion of S.M. Travinnin, let us transform expression (1) by changing to a new variable:

$$f(\tau, \Omega) = \frac{1}{\sqrt{2\pi D_\tau}} \cdot \frac{\tau^2}{D_\tau \delta \omega} e^{-\frac{\tau^2}{2D_\tau}} \left[ e^{-\frac{\tau^2(\Omega - \omega_1)^2}{2D_\tau \delta \omega^2}} + e^{-\frac{\tau^2(\Omega + \omega_1)^2}{2D_\tau \delta \omega^2}} \right] \quad (3)$$

It should be noted that using the envelope method apriori eliminates secondary wave profile oscillations from the analysis [1].

Let us introduce into our consideration a relative frequency  $x$  of a random oscillation  $x = \frac{\Omega}{\omega_1}$  and a relative wave height (amplitude)

$$h^* = \frac{h}{\tau} = \frac{\tau}{\tau}$$

where a dash above the letter denotes a symbol of averaging.

From function (3) one can pass to the two-dimensional probability density for relative wave frequencies and heights:

$$f(h^*, x) = 1.563 h^* \frac{1}{\sqrt{2\pi \Delta}} e^{-0.781(h^*)^2} \left[ e^{-\frac{(x-1)^2}{2\Delta}} + e^{-\frac{(x+1)^2}{2\Delta}} \right] \quad (4)$$

where

$$\Delta = \frac{D_\tau \delta \omega^2}{\tau^2 \omega_1^2} = \frac{1}{1.563(h^*)^2} \cdot \frac{\delta \omega^2}{\omega_1^2} \quad (5)$$

The corresponding integral law will be determined by double integration:

$$F(h^*, x_1) = \int_0^{h^*} f(h^*) \cdot F_h(x_1) dh^* \quad (6)$$

where

$$F_h(x_1) = \frac{1}{\sqrt{2\pi \Delta}} \int_0^{x_1} \left[ e^{-\frac{(x-1)^2}{2\Delta}} + e^{-\frac{(x+1)^2}{2\Delta}} \right] dx = \Phi\left(\frac{x-1}{\sqrt{\Delta}}\right) + \Phi\left(\frac{x+1}{\sqrt{\Delta}}\right) \quad (7)$$

= conditional integral distribution law for relative frequencies;

$$\Phi(\xi) = \frac{1}{\sqrt{2\pi}} \int_0^\xi e^{-\frac{y^2}{2}} dy$$

= probability integral;

$$f(h^*) = 1.563 h^* e^{-0.781(h^*)^2} \quad (8)$$

= probability density for wave heights.

Function (6) will be used for plotting a two-dimensional law of distribution of wave heights and periods.

Let  $\tau^* = \tau/\bar{\tau}$  be a relative period of visible waves,  $\tau$  being equal to  $\frac{2\pi}{\omega}$ , and  $\bar{\tau} = \frac{2\pi}{\omega_1}$ .

As from the definition

$$\omega_1 = \frac{1}{D_\tau} \int_0^\infty \omega \cdot S_\tau(\omega) d\omega$$

we have

$$\tau^* = \frac{m}{x} \quad (9)$$

where

$$m = \frac{\bar{\omega}}{\omega_1} \quad (10)$$

The two-dimensional probability density of relative wave heights and periods has the form:

$$f(h^*, \tau^*) = f(h^*) \cdot f_\tau(\tau^*) \quad (11)$$

and the integral law

$$F(h^*, \tau_1^*) = \int_0^{h^*} f(h^*) \cdot F_\tau(\tau_1^*) dh^* \quad (12)$$

$f_\tau(\tau^*)$  being the conditional probability density for  $\tau^*$  values.

Function  $F_\tau(\tau_1^*)$  is expressed using (7) in the following way:

$$F_\tau(\tau_1^*) = 1 - F_h[x_1(\tau_1^*)] \quad (13)$$

after which the integral law of two-dimensional distribution of  $h^*$  and  $\tau^*$

values may be presented as

$$F(h_i^*, T_i^*) = \int_0^{h_i^*} H(h^*, T_i^*) dh^*, \quad (14)$$

where the function

$$H = f(h^*) \cdot \left\{ 1 - \Phi \left[ \frac{x_i(T_i^*) - 1}{\Delta(h^*)} \right] - \Phi \left[ \frac{x_i(T_i^*) + 1}{\sqrt{\Delta(h^*)}} \right] \right\}.$$

To determine the  $Q(h_i^*, T_i^*)$  probability of exceedance of wave heights and periods, let us use the relationship

$$Q(h_i^*, T_i^*) = \int_0^{x_i(T_i^*)} \int_{h_i^*}^{\infty} f[h^*, x(T^*)] dh^* dx, \quad (15)$$

which leads to the following formula:

$$Q(h_i^*, T_i^*) = \int_{h_i^*}^{\infty} H_T(h^*, T_i^*) dh^*, \quad (16)$$

where

$$H_T = f(h^*) - H. \quad (17)$$

As applied to expressions (14) and (16) the following feature should be noted. Relationship (1) serving as a basis for the derivation of these expressions uses the method of envelope according to which the probability density for the relative periods of narrow-band process has the form [1]

$$f(T^*) = \frac{1-a^2}{2} \left[ \frac{T^*}{(1+2T^*a+T^{*2})^{3/2}} + \frac{T^*}{(1-2T^*a+T^{*2})^{3/2}} \right], \quad (18)$$

and, consequently, the probability of exceedance

$$Q(T_i^*) = \frac{1}{2} \left[ \frac{1+aT_i^*}{\sqrt{1+2aT_i^*+T_i^{*2}}} + \frac{1-aT_i^*}{\sqrt{1-2aT_i^*+T_i^{*2}}} \right], \quad (19)$$

where  $a = \frac{1}{m}$ .

Formula (19) is the boundary form of the two-dimensional function of the probability of exceedance  $Q(h_i^*, T_i^*)$  which the latter acquires for  $h_i^* = 0$  and which expresses the probability of exceedance of random values of the periods of sea wave process exactly as with  $T_i^* = 0$  this function degenerates into the Rayleigh law for  $h^*$ . Meanwhile, it is well known that the results of

numerous wave profile measurements in time are well approximated by a one-dimensional function of the probability of exceedance of the form [5,6,9]:

$$Q(T_i^*) = \exp \left[ -\Gamma^4 \left( \frac{5}{4} \right) \cdot (T_i^*)^4 \right], \quad (20)$$

the numerical values of which do not coincide with those of (19).

A prime on the symbol of the probability of exceedance in (20) denotes an empirical character of the formula.

Thus, expressions (14) and (16) which in principle take into account the interrelation between the heights and periods of waves contain the above-mentioned feature in the form of a departure of the theoretical law of period distributions from those observed. This departure manifests itself with the wave height decrease and in the case of  $h_i^* = 0$  leads to the difference in relationships (19) and (20) mentioned above. Let us make a correction of function (16) so as to satisfy the requirement:

$$Q(h_i^*, T_i^*) = Q'(T_i^*) \Big|_{h_i^*=0}. \quad (21)$$

For this we shall introduce the function

$$\psi_T = \frac{Q'(T_i^*)}{Q(T_i^*)}, \quad (22)$$

where the denominator is determined by (19). Following this the final formula for the two-dimensional probability of exceedance of wave heights and periods will be written as

$$Q(h_i^*, T_i^*) = \psi_T(T_i^*) \cdot \int_{h_i^*}^{\infty} H_T(h^*, T_i^*) dh^*. \quad (23)$$

In the limiting cases function (23) transforms into one-dimensional functions of the probability of exceedance, that is condition (21) and the equation following from the Rayleigh law:

$$Q(h_i^*, T_i^*) = Q(h_i^*) = \exp \left[ -\frac{\pi}{4} (h_i^*)^2 \right] \Big|_{T_i^*=0}. \quad (24)$$

are met.

On the basis of formula (23) and using numerical integration, a two-dimensional probability of exceedance of heights and periods was calculated for wind waves determined by the design spectrum of ordinates in the form obtained by Barling [1,4] with



$$\frac{\delta \omega^2}{\omega_1^2} = 0,125, \quad m = \frac{\bar{\omega}}{\omega_1} = 1,051.$$

The results of calculations are given in Fig.1 which also shows the observation data taken from [6]. As is seen, the function of the probability of exceedance  $Q(h_1^*, T_1^*)$  calculated from (23) is in good agreement with the experimentally obtained curves. Estimating the extent to which the theoretical solution agrees with the measured data, it should be borne in mind that, strictly speaking, relation (23) is dependent upon the mean spectrum width determined by the value of  $\frac{\delta \omega^2}{\omega_1^2}$ .

In view of the fact that calculations with expression (23) were performed for the above-mentioned value corresponding to a particular spectrum width, the individual features of the wave process for which the experimental data were obtained might be allowed for incompletely in the calculation as no indication is given in [6] regarding the width of the corresponding spectrum of wave ordinates.

Fig.2 gives the function  $\Psi_T(T_1^*)$ .

2. A section of a disturbed surface cut off by an arbitrarily oriented vertical plane for a given moment of time shows a fixed wave profile in the given direction.

Considering this process in accordance with (2) as a narrow-band one and orienting the said plane in the general direction of wave propagation, let us make up an expression for a two-dimensional function of the probability of exceedance of wave heights and lengths.

By reasoning similar to that given in section 1 a conclusion can be drawn that if relation (1) is taken as a basis and the frequency of wave form  $\kappa$  in the direction of  $O\bar{E}$  axis is identified with the absolute value of the derivative  $\zeta$ , then the two-dimensional density of the values of  $h$  and of the relative frequency of wave form  $\nu = \frac{\kappa}{K}$  will be described by expression (4) with the value of  $x$  substituted by the variable  $\nu$ . In this case the relation  $\frac{\delta \omega^2}{\omega_1^2}$  determining parameter  $\Delta$  should naturally be substituted by a similar relation  $\frac{\delta K^2}{K_1^2}$  representing the mean width of the process of variation in the wave ordinate in the general direction.

Let us express the value  $\frac{\delta K^2}{K_1^2}$  using a known presentation of the spectral density of three-dimensional waves:

$$S_{\zeta}(\omega, \alpha) = \frac{2}{\pi} S_{\omega}(\omega) \cos^2 \alpha, \quad -\frac{\pi}{2} < \alpha < \frac{\pi}{2} \quad (25)$$

where  $S_{\zeta}(\omega)$  = wave spectrum at a point;

$\alpha$  = direction of propagation of wave components in the form of plane irregular waves in relation to the general direction ( $\alpha = 0$ ).

For mean spectral frequency of wave form as obtained along the general direction, the following relationship is true:

$$K_1 = \frac{1}{D} \int_{-\frac{\pi}{2}}^{\frac{\pi}{2}} \int_0^{\infty} \frac{\omega^2}{g} \cos \alpha \cdot S_{\zeta}(\omega, \alpha) d\omega d\alpha. \quad (26)$$

Substituting (25), we shall find

$$K_1 = \frac{8}{3\pi} \cdot \frac{\bar{\omega}^2}{g}. \quad (27)$$

According to the determination we shall have

$$\delta K^2 = K_{11}^2 - K_1^2, \quad (28)$$

where

$$K_{11}^2 = \bar{K}^2 = \frac{1}{D} \int_{-\frac{\pi}{2}}^{\frac{\pi}{2}} \int_0^{\infty} \frac{\omega^4}{g^2} \cos^2 \alpha \cdot S_{\zeta}(\omega, \alpha) d\omega d\alpha. \quad (29)$$

On the basis of (27) and (29) and taking into account (26) we obtain the required characteristics for the mean value of the three-dimensional wave spectrum width which being calculated for the design spectrum used above gives the following result:  $\frac{\delta K^2}{K_1^2} = 1,290$

Let  $\lambda = \frac{2\pi}{K}$  be the wave length in the general direction for a random value of frequency of the form  $K$ . Introducing the relative wave length

$$\lambda^* = \frac{\lambda}{\lambda_1}, \quad (30)$$

we obtain the expression similar to (9)

$$\lambda^* = \frac{m_{\lambda}}{\nu}, \quad (31)$$

where

$$m_{\lambda} = \frac{\bar{K}}{K_1}. \quad (32)$$

For the design spectrum the value of  $m_{\lambda} = 1,513$ .

Therefore the expressions taken for the two-dimensional probability density, the integral law and the function of the probability of exceedance for wave heights and lengths will not differ structurally from relations (11), (12), (14), (16) if the values of  $T^*$ ,  $x$ ,  $m$  in such expressions are substituted by  $\lambda^*$ ,  $\nu$  and  $m_{\lambda}$ , respectively. For instance, formula (16) be replaced by

$$Q(h_1^*, \lambda_1^*) = \int_{h_1^*}^{\infty} H_{\lambda}(h, \lambda_1^*) dh, \quad (33)$$



where

$$H_{\lambda} = f(h^*) \cdot \left\{ \Phi \left[ \frac{\lambda_1(\lambda_1^*) - 1}{\sqrt{\Delta(h^*)}} \right] + \Phi \left[ \frac{\lambda_1(\lambda_1^*) + 1}{\sqrt{\Delta(h^*)}} \right] \right\} \quad (34)$$

Similarly to (16), function (33) should be corrected according to the one-dimensional probability of exceedance of wave lengths. The latter is usually assumed as following from the Rayleigh law [8,9]:

$$Q(\lambda_1^*) = \exp\left[-\frac{\pi}{4}(\lambda_1^*)^2\right]. \quad (35)$$

Fig.3 shows the result of calculation of the correcting function

$$\psi_{\lambda} = \frac{Q(\lambda_1^*)}{Q(\lambda_1^*)}, \quad (36)$$

the denominator of which is determined from the formula similar to (19) with particular reference to the design wave spectrum ( $\alpha = 0,662$ ).

Taking into account function (36), the expression for a two-dimensional probability of exceedance of wave heights and lengths will finally take the form

$$Q(h_1^*, \lambda_1^*) = \psi_{\lambda}(\lambda_1^*) \int_{h_1^*}^{\infty} H_{\lambda}(h^*, \lambda_1^*) dh^*. \quad (37)$$

It should be noted that the mean wave length which appears in (30) can be determined from Fig.4 as a function of the characteristic wave height (in this particular case - the wave height  $h_{0.99}$  with the probability of 3 per cent exceedance). The curves in this figure are calculated from the data on the mean wave periods [1] for three-dimensional waves using the formula

$$\bar{\lambda} = 0.783 \frac{g}{2\pi} (\bar{T})^2,$$

which is true for the design spectrum of wave ordinates. The experimental points shown in Fig.4 are taken from the materials of the LO GOIN (Leningrad Division of the State Oceanographic Institute).

Fig.5 gives the results obtained by formula (37) for the representation of wind wave energy spectrum indicated in section 1. It also shows curves taken from Ref. [7]. These curves are based on the stereophotography data representing a sample of 1000 waves. As the volume of the sample is known, an approximate estimation can be made of the extent to which the theoretical law (37) agrees with the observation for the purposes of such an

estimation let us use A.N.Kolmogorov's criterion developed for the one-dimensional laws. As is seen from Fig.5, the largest discrepancy between the curves is observed in the surface section  $Q(h_1^*, \lambda_1^*)$  cut off by a vertical plane and dividing the angle between the axes  $Oh^*$  and  $O\lambda^*$  in half. Overestimating the number of experimental data used for the establishment of the criterion one can feel that an experimental function of the probability of exceedance in this section is influenced by the adjacent region which contains approximately one third of the whole number of waves forming the sample. Determining the largest discrepancy,  $d$ , between the experimental data and the hypothetical law according to Kolmogorov's criterion we have:  $d \approx 0,06$ , and hence the parameter  $\ell = d\sqrt{n} = 1,10$ . Thus the obtained value of  $\ell$  is in line with the probability  $P(\ell) = 0,18$ . According to recommendations contained in the handbooks dealing with probability calculation, for  $P(\ell) \geq 0,1$  the discrepancy between both the laws is random and the theoretical function is considered to be suitable for the description of one or another distribution. Thus the verification by the criterion of goodness of fit confirms the rightfulness of using relation (37) as a function of two-dimensional probability of exceedance of wave heights and lengths.

### Conditional distributions

Statistical interrelationship of wave heights and periods as also of wave heights and lengths which is determined in the general form by two-dimensional distributions manifests itself in the dependence of conditional mean values of  $T^*$  and  $\lambda^*$  on  $h^*$ . For instance, as stated by the author of Ref. [10], a similar relationship explains in his opinion a decrease in the variance of individual wave periods with increasing wave heights.

Using the probability density (4), S.M.Travinin has defined the following characteristics of relative frequencies:

$$f_{h^*}(x) = \frac{1}{\sqrt{2\pi\Delta}} \left[ e^{-\frac{(x-1)^2}{2\Delta}} + e^{-\frac{(x+1)^2}{2\Delta}} \right] \quad (38)$$

- conditional differential law of frequency  $x$  distribution,

$$\bar{x}(h^*) = 2\Phi\left(\frac{1}{\sqrt{\Delta}}\right) + \sqrt{\frac{2\Delta}{\pi}} e^{-\frac{1}{2\Delta}} \quad (39)$$

- conditional mean value of frequency  $x$ .

$$D_x(h^*) = \Delta + 1 - \bar{x}^2(h^*) \quad (40)$$

- conditional variance of distribution (38).

As the relative frequency and the period are interrelated by expression (9), formula (39) can be used for determining the conditional mean value of  $T^*$

$$\bar{T}^*(h^*) = m \left[ 2\Phi\left(\frac{1}{\sqrt{\Delta}}\right) + \sqrt{\frac{2\Delta}{\pi}} e^{-\frac{1}{2\Delta}} \right]^{-1}, \quad (41)$$

where  $\Delta = \Delta(h^*)$ .

The rightfulness of assuming the relationship between the mean values of  $T^*$  and  $X$  in the form of (9) follows from the nature of the envelope method which implies that the period of each subsequent oscillation in the realization of a random process is very nearly the period of the previous one in magnitude.

Fig. 6 shows the comparison between the regression line  $T^*$  as a function of  $h^*$  calculated from formula (41) for the spectrum in Ref. [4] and the observation data obtained in Ref. [6]. At the wave height values of  $h^* \leq 0.8$  the calculated and the experimental data are in good agreement, although on the average the experimental points are located somewhat higher than the value  $\bar{T}^*(h^*) = 1.051$ . The mean period value according to (41) corresponds to the limiting case of  $h \rightarrow \infty$  ( $\Delta \rightarrow 0$ ), however the period becomes practically constant and independent of the wave heights at  $h^* \approx 0.7+0.9$ .

In Fig. 7 relationship (41) is shown together with the results of wave profile measurements at a fixed point of the sea. The superposed points in the figure refer to sea states 3 to 7.

Using relationship (31) we can obtain an expression for the conditional mean value of  $\lambda^*$

$$\bar{\lambda}^*(h^*) = m_{\lambda} \left[ 2\Phi\left(\frac{1}{\sqrt{\Delta}}\right) + \sqrt{\frac{2\Delta}{\pi}} e^{-\frac{1}{2\Delta}} \right]^{-1}, \quad (42)$$

the value  $\Delta(h^*)$  being dependent upon the width spectrum characteristic  $\frac{\sigma_{\kappa^2}}{\kappa^2}$

Relationship (42) for wind waves obtained with particular reference to the calculated spectrum is shown in Fig. 8. The results of measurements carried out in the LO GOIN by I.N. Davidan, L.I. Lopatukhin and V.A. Rozhkov are also plotted there. When comparing in Fig. 8 the theoretical and experimental data, the earlier remark concerning the impossibility due to lack of required information of taking into account the observed individual features of wave realizations naturally remains valid. At the same time the experimental points lying for the most part somewhat

below the curve showing the analytical relationship between conditional mean wave length and wave height are basically in good agreement with the regularity of variation in function (42).

### Conclusion

The results obtained in this work show the effectiveness of the method of envelope not only for establishing the analytical structure of conditional wave length and wave period densities but also for a more complete characteristic of the set of these values, viz. the two-dimensional distributions. Though the former have certain features which need some additional correction, the integral characteristics, i.e. conditional mean values of the parameters under study determined by these densities, are in good agreement with the observation data.

As to distributions, the following consideration will be true having in any case a direct bearing on the representation of the two-dimensional function of the probability of exceedance of wave heights and lengths. It is known [2], [12] that for irregular seas the steepness of individual waves has a limit which, in accordance with the large wave amplitude theory, can approximately be taken as equal to 0.142. Therefore, the part of the two-dimensional probability of exceedance curve (Fig. 5) for which the combination of  $h$  and  $\lambda$  values results in the steepness value exceeding the limiting one should, strictly speaking, be eliminated from consideration. In relative values the realization area of wave steepness is determined by the following condition:

$$\frac{h^*}{\lambda^*} \cdot \frac{\bar{h}}{\bar{\lambda}} < 0.142.$$

In Fig. 5, for example, the area to the right of the straight line 1 corresponds to the value  $\frac{h}{\lambda} = 0.04$  characteristic, on the average, for sea state 6.

The data on the two-dimensional distributions of wave elements make it possible to determine the probability of ship encounter in a seaway with waves the length and the height of which are unfavourable in terms of the problem under consideration. The problem of determining the R value in the course of estimating the wave induced dynamic loads on the structure may be formulated in a similar probabilistic representation. With such an approach the problem is reduced to calculation of the said probability using the following formula:

$$R = \int_{h_1}^{h_2} \int_{\lambda_1}^{\lambda_2} f(h^*) \cdot f_{\lambda}(\lambda^*) dh^* d\lambda^* = \quad (43)$$

$$= \int_{h_1}^{h_2} f(h^*) \cdot [F_{\lambda}(\lambda_2) - F_{\lambda}(\lambda_1)] dh^*,$$

in which  $\lambda = \lambda(h)$ , function  $F_{\lambda}(\lambda)$  is structurally coincident with expression (7), and parameters  $h_1^*$ ,  $h_2^*$ ,  $\lambda_1^*$ ,  $\lambda_2^*$  are wave height and length values limiting the area of  $h^*$  and  $\lambda^*$  realizations which is chosen for the problem in hand.

### References

1. Boroday, I.K., Netsvetaev, Yu.A.: Ship motions in a seaway, Izd. "Sudostroyenie", 1969.
2. Boroday, I.K.: A method for estimation of maximum wave height and amplitude of ship motions in irregular seas, "Sudostroyenie", N 2, 1971.
3. Bunimovich, V.M.: Fluctuational processes in radioreceiving devices, Izd. "Sovetskoe Radio", 1951.
4. Voznessensky, A.I., Netsvetaev, Yu.A.: Normalized energy spectrum of sea waves, "Okeanologia", t.IV, vyp.6, 1964.
5. Glukhovskiy, B.Kh.: A study of sea wind waves, Gidrometeoizdat, Leningrad, 1966.
6. Davidan, I.N., Rozhkov, V.A., Andreev, B.M., Lopatukhin, L.I., Trapeznikov, Yu.A.: Probabilistic characteristics of waves. Methods for their analysis and calculation, Gidrometeoizdat, Leningrad, 1971.
7. Davidan, I.N., Kublanov, Ya.M., Lopatukhin, L.I., Rozhkov, V.A.: The results of investigations into probabilistic characteristics of wind waves, Report at the International Symposium on the Dynamics of Marine Vehicles and Structures in Waves, London, 1974.
8. Krylov, Yu.M.: Statistical theory and calculation of sea wind waves, ch.I, Trudy GOIN, vyp.33, 1956.
9. Krylov, Yu.M.: Spectral method for investigation and calculation of wind waves, Gidrometeoizdat, Leningrad, 1966.
10. Longuet-Higgins, M.S.: The statistical analysis of a random moving surface, Phil. Trans. Roy. Soc., London, 249, N 966, 1957.
11. Matushevsky, G.V.: On mean wave lengths and crests of irregular three-dimensional sea waves, "Okeanologia", t.V, vyp.6, 1965.
12. Matushevsky, G.V.: Slopes of disturbed sea surface and their connection with orbital velocities and other wind wave characteristics, "Physika atmosfery i okeana", t.IX, N 8, 1973.
13. Sveshnikov, A.A.: Applied methods of the theory of random functions, Moskva, izd. "Nauka", 1968.
14. Wind and waves in oceans and seas (reference data). The Register of Shipping of the USSR, izd. "Transport", 1974.

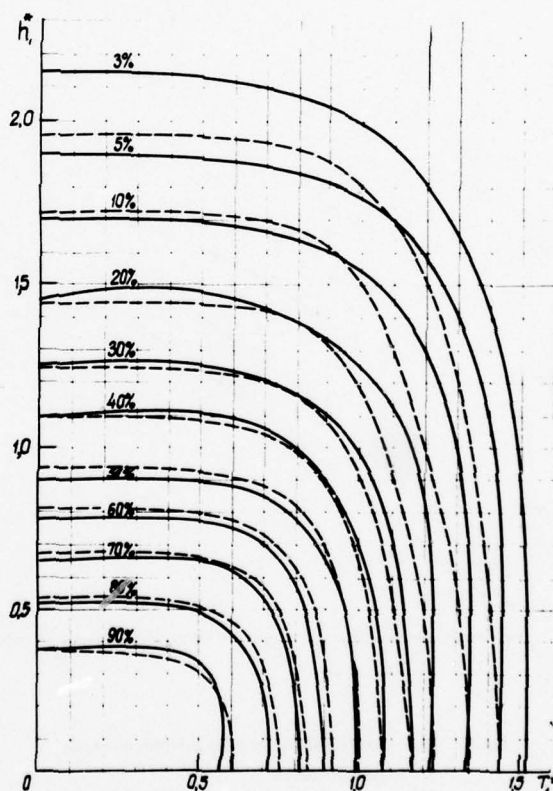


Fig. 1: Two-dimensional probability of exceedance of wave heights and periods (wind waves).  
 — observation data [6]  
 --- calculation by formula (23)



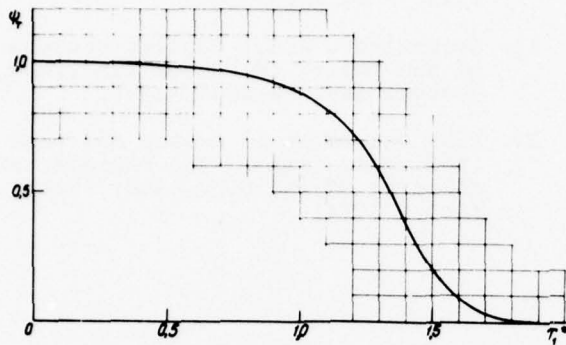


Fig. 2: Function  $\psi_T(T_1^*)$  for the calculated wave spectrum.

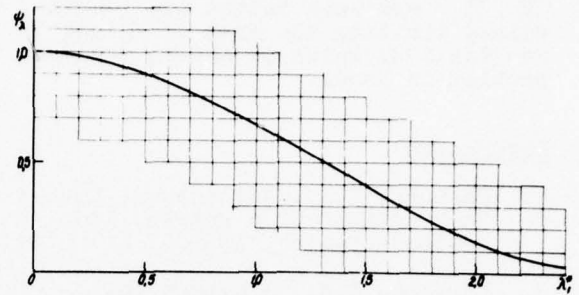


Fig. 3: Function  $\psi_\lambda(\lambda_1^*)$  for the design wave spectrum.

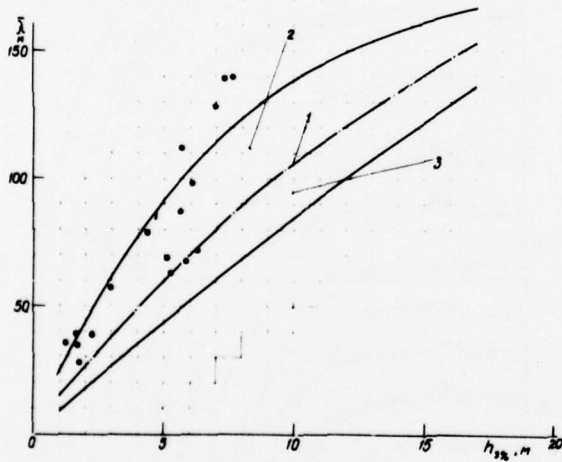


Fig. 4: Mean wavelengths in the general direction versus

- 1 — developed waves;
- 2 — damped waves;
- 3 — developing waves;
- — according to observation data (LO GOIN).

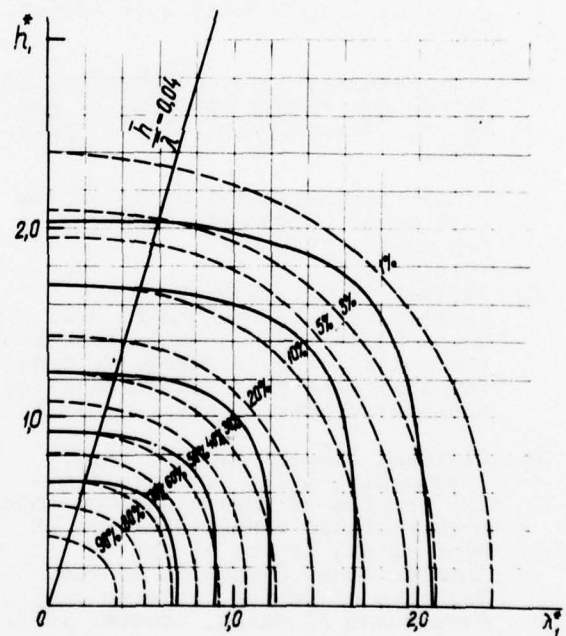


Fig. 5: Two-dimensional probability of exceedance of wave heights and lengths (wind waves).

- observation data [7]
- calculation by formula (37)



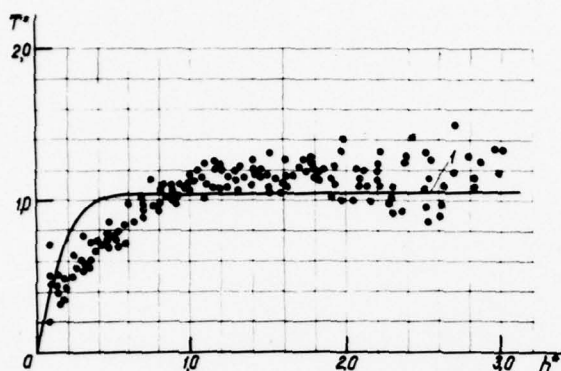


Fig. 6: Conditional mean value of the relative wave period.

• — observation data [6]  
1 — calculation by formula (41)

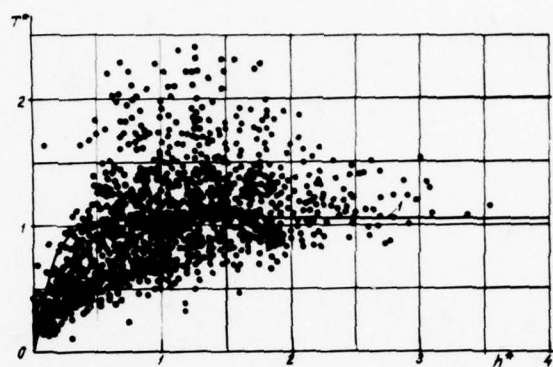


Fig. 7: Relative heights and periods of wave profile. Wave intensity: see states 3 to 7.

• — observation data  
1 — obtained by formula (41)

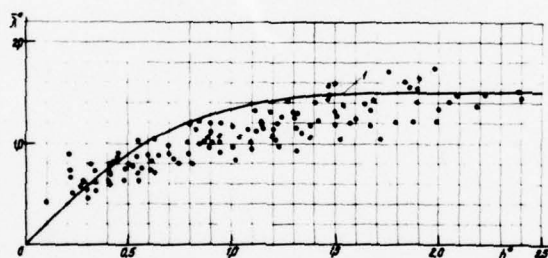


Fig. 8: Conditional mean values of wave length.

• — observation data (LO GOIN)  
1 — calculation by formula (42)

# THREE-DIMENSIONAL CALCULATIONS OF WAVE FORCES BY A HYBRID ELEMENT METHOD

DICK K. P. YUE, HSUAN S. CHEN and CHIANG C. MEI

Department of Civil Engineering  
Massachusetts Institute of Technology

## SYNOPSIS

The hybrid element method, developed previously for two-dimensional water wave problems is extended to three-dimensions. Three-dimensional hexahedral elements are used near the solid body and analytic series solution used in the rest of the fluid. Computed examples are discussed.

## INTRODUCTION

Along with the technological advances in designing and constructing large ships and ocean structures, the need for rational and efficient computation of hydrodynamical effects to supplement laboratory modelling is now widely accepted. As in ship hydrodynamics one usually adopts the linearized approximation which requires the wave amplitudes to be small. In this limited framework many general relationships among the hydrodynamical quantities can be deduced, see for example Wehausen (1) and Newman (2), which can either help to reduce the necessary calculations to a minimum or to provide decisive checks on them. However in practical applications one must eventually face the task of calculating some of these quantities. While for special geometries various *ad hoc* methods are available, for general geometries one must resort to a largely numerical effort. For both two and three dimensional problems the semi-analytical method of Green function has been the most popular. It usually leads to an integral equation along a line for two-dimensional problems or along a surface for three-dimensional problems. The integral equation is then discretized to give an approximate set of algebraic equations. In water waves, the Green function is usually singular and complicated, which implies the same for the kernel of the integral equation. Consequently, one must handle the numerical operations carefully and laboriously; the associated computing cost can often be high. Nevertheless this method has been successfully used by several authors; see for example Garrison (3). There are also situations where the Green functions are either too complicated or cannot be easily constructed; alternative methods are therefore desirable.

In this paper we shall briefly describe a less analytical method involving finite elements. It is in principle an extension of the hybrid element method reported at the Tenth Symposium on Naval Hydrodynamics by Chen and Mei (4) and by Bai and Yeung (5). Briefly the idea is to use simple analytical solutions in the region away from the body and from local depth irregularities, and to use discrete finite elements in the region near them. Similar ideas have been used long ago in conjunction with finite differences where there is a singularity in the region of computation. It is based on the plausible argument that an analytical

solution of reasonably elementary form which satisfies the differential equation and some of the boundary conditions, in particular the singularity condition, must provide a more efficient representation than a simple interpolation function which satisfies few or none of these conditions. Near the body of an arbitrary shape, analytical representations are often too cumbersome or impossible; it is here, however, that the power of finite elements can be most fully utilized. The arrangement of the elements can be very flexible in order to fit the boundary; the resulting stiffness matrix is easier to calculate because of the usually simple interpolation functions. As in classical finite element methods involving a finite domain it is desirable to recast the boundary value problem as a variational principle, so that a certain global quantity is stationary. In a hybrid approach it is computationally desirable to incorporate the continuity requirements as natural boundary conditions at the border of two regions where different representations are used. If this can be done then all the unknowns associated with the finite elements and with the analytical representation can be solved simultaneously after extremization. For scattering and radiation problems in water waves the required variational formulation has been accomplished with a suggestion due to P. Tong. Application to two-dimensional problems is fully explained in (4) and (5) where numerical examples have demonstrated the success of this method.

Although extension of the hybrid method to three-dimensional problems is straightforward in principle, it is valuable to work out a few numerical examples in order to examine its efficacy. Since the increase of one space dimension leads to a significant increase in computer storage and execution time, it is not clear *a priori* whether this method offers a viable alternative to the Green function method. In this paper we report a few test results and the associated computational information. All the results have been found to be very accurate by checking with the *optical theorem* which is an exact conservation relation in scattering theory.

## NOTATION

A	amplitude of the incident wave
A( $\theta$ )	angular distribution of the scattered wave
B	solid boundaries
C <sub>F</sub> <sub>i</sub>	force coefficients $i = x, y, z$ along $x, y, z$ axis
C <sub>M</sub> <sub>i</sub>	moment coefficients $i = x, y, z$ along $x, y, z$ axis
E <sub>opt</sub>	error defined by the optical theorem
E <sub> F </sub>	error in force coefficient magnitude
F	free surface
g	gravitational acceleration
h	sea depth
H <sub>n</sub> <sup>(1)</sup>	Hankel function of the first kind
i	imaginary unit
I <sub>1</sub> ... I <sub>6</sub>	integrals in the functional
J	stationary functional
k <sub>o</sub>	incident wave number
[K], [K <sub>V</sub> ], [K <sub>C</sub> ], [K <sub>F</sub> ], [K <sub>D</sub> ]	stiffness matrices
K <sub>n</sub>	modified Bessel function
N <sub>i</sub> <sup>e</sup>	element interpolation function
{Q <sub>C</sub> }, {Q <sub>P</sub> }	load vectors
r	radial coordinate $r^2 = x^2 + y^2$
S	vertical cylinder bounding the finite element region
t	time
V	fluid volume inside S
V'	fluid volume exterior to S
x, y, z	rectangular coordinates with z vertically upwards
$\alpha_{mn}$ $\beta_{mn}$	expansion coefficients of the solution in V'
$\kappa_m$	imaginary roots of the dispersion relation
$\theta$	polar angle
$\theta_I$	angle of incidence
$\phi$	total wave potential
$\phi_I$	incident wave potential
$\phi_s$	scattered wave potential
$\phi_i^e$	value of potential at node i, element e
{ $\bar{\phi}$ }	nodal potential vector for nodes on the surface S
{ $\mu$ }	unknown coefficients vector consisting of $\alpha_{mn}$ and $\beta_{mn}$
{ $\psi$ }	total unknown vector
$\omega$	wave frequency
{ } <sup>T</sup>	transpose of vector { }
[ ] <sup>T</sup>	transpose of matrix [ ]

## THE BOUNDARY VALUE PROBLEM

The general problem of three-dimensional scattering of water waves in an ocean is formulated under the following usual assumptions:

- (1) potential flow
- (2) small wave amplitude
- (3) simple harmonic incident waves
- (4) constant depth  $h$  away from the floating or the submerged bodies
- (5) rigid and perfectly reflective boundaries

Let the velocity potential be the real part of  $\phi(x, y, z) e^{-i\omega t}$  where  $\omega$  is the angular frequency

of oscillation, then  $\phi$  satisfies

$$\nabla^2 \phi = 0 \quad \text{in fluid} \quad (1)$$

$$\frac{\partial \phi}{\partial z} - \frac{\omega^2}{g} \phi = 0 \quad \text{on the free surface, } F, z = 0 \quad (2)$$

$$\frac{\partial \phi}{\partial n} = 0 \quad \text{on all solid boundaries, } B \quad (3)$$

The incident plane wave

$$\phi_I = \frac{-igA}{\omega} \frac{\cosh k_o(z+h)}{\cosh k_o h} e^{ik_o r \cos(\theta - \theta_I)} \quad (4)$$

is prescribed where  $k_o$  is the positive real root of the dispersion relation

$$\omega^2 = gk \tanh kh \quad (5)$$

At infinity the scattered wave defined as  $\phi_s = \phi - \phi_I$  must be outgoing, i.e.

$$\sqrt{k_o r} \left( \frac{\partial \phi_s}{\partial r} - ik_o \phi_s \right) \rightarrow 0 \quad k_o r \gg 1 \quad (6)$$

The solid boundary B includes all breakwaters, stationary platforms, ships and the sea bottom.

## THE VARIATION PRINCIPLE FOR THE HYBRID ELEMENT METHOD

Referring to Figure 1, we introduce an artificial vertical cylinder S which is just large enough to enclose all solid bodies and depth irregularities, and denote the fluid region inside S by V and outside by V'. Let the wave potential exterior to S be denoted by  $\phi' = \phi_I + \phi_s'$  where the symbol ( )' refers to quantities in V'. We shall require  $\phi_s'$  to satisfy Eq. (1) in V', Eq. (2) on the free surface of V', i.e., on F', Eq. (3) on the sea bottom B' and Eq. (6) at infinity. It is easy to show that  $\phi_s'$  may be represented by

$$\begin{aligned} \phi_s' = & \sum_{n=0}^{\infty} (\alpha_{on} \cos n\theta + \beta_{on} \sin n\theta) \cosh k_o(z+h) \cdot \\ & H_n^{(1)}(k_o r) + \sum_{m=1}^{\infty} \sum_{n=0}^{\infty} (\alpha_{mn} \cos n\theta + \beta_{mn} \sin n\theta) \cdot \\ & \cos \kappa_m(z+h) K_n(\kappa_m r) \end{aligned} \quad (7)$$

where  $\kappa_m$ ,  $m = 1, 2, 3, \dots$  are real and positive

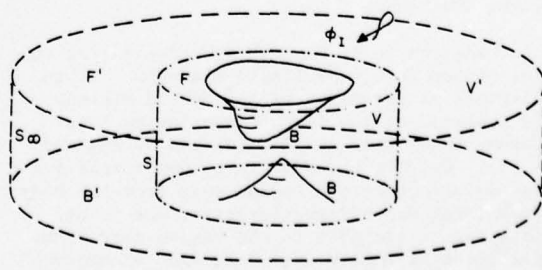


Figure 1 Introduction of an artificial circular cylindrical surface S.



roots of

$$\omega^2 = -g \kappa_m \tan \kappa_m h \quad (8)$$

or equivalently the positive imaginary roots of Eq. (5). The coefficients  $\alpha_{on}$ ,  $\alpha_{mn}$ ,  $\beta_{on}$ , and  $\beta_{mn}$  are to be found. By using the argument in Chen and Mei (4) or its variant by Bai and Yeung (5) it is easy to prove that the following functional,

$$J(\phi, \phi') = \frac{1}{2} \int_V (\nabla \phi)^2 dV - \frac{\omega^2}{2g} \int_F \phi^2 dF + \int_S \left[ \left( \frac{1}{2} \phi'_s - \phi_s \right) \frac{\partial \phi'}{\partial r} - \frac{1}{2} \phi'_s \frac{\partial \phi_I}{\partial r} \right] dS \quad (9)$$

is stationary if and only if  $\phi$  satisfies Eq. (1) in  $V$ , Eq. (2) on the free surface  $F$  in  $V$ , Eq. (3) on the bottom and the solid bodies in  $V$ , and is continuous with  $\phi'$  on the surface  $S$ :

$$\phi = \phi' \quad \text{and} \quad \frac{\partial \phi}{\partial r} = \frac{\partial \phi'}{\partial r} \quad \text{on } S \quad (10, 11)$$

Of particular significance is that Eqs. (10) and (11) are satisfied as natural boundary conditions. This is helpful in computational work since it implies that they will be automatically satisfied in the limit of vanishingly small finite elements and infinitely many terms in Eq. (7).

We comment that the choice of the shape of  $S$  can be quite flexible. For instance, to reduce the number of finite elements, the cylinder  $S$  need not be circular although in practice evaluation of the integral along a circular cylinder is simpler. Secondly, the analytical representation in  $V'$  may also be chosen in a number of ways. One can, for example, employ the Green function representation. However, its use in  $V'$  would lead to an integral equation on  $S$  and therefore much the same tedium as in the direct integral equation approach. The above remarks are intuitive and it would be interesting to check them by numerical experiments. Systematic optimization may be a subject for the future.

#### FINITE ELEMENT APPROXIMATION

The functional is first expressed as a sum of six integrals.

$$J = \int_V \frac{1}{2} (\nabla \phi)^2 dV - \int_F \frac{\omega^2}{2g} \phi^2 dF + \frac{1}{2} \int_S \phi'_s \frac{\partial}{\partial r} \phi'_s dS - \int_S \phi \frac{\partial}{\partial r} \phi'_s dS + \int_S \phi_I \frac{\partial \phi'_s}{\partial r} dS - \int_S \phi \frac{\partial}{\partial r} \phi_I dS \quad (12)$$

$(I_1) \quad (I_2) \quad (I_3)$   
 $(I_4) \quad (I_5) \quad (I_6)$

Each integral is labelled by the symbol beneath.

The first integral over the volume  $V$  is conventional. We choose to divide the interior of  $V$  into a finite number of hexahedral (six-sided block) elements. Correspondingly the boundary

surfaces of  $V$  are divided into quadrilateral area elements. The block elements are isoparametric with 20 exterior nodes and belong to the serendipity family (Zienkiewicz (6), see Figure 2); the interpolation functions are quadratic. The choice is made for convenience of node numbering, ease of checking element arrangement, and for numerical efficiency. The element interpolation functions are expressed in canonical coordinates  $\xi, \eta, \zeta$  which must be mapped to the physical coordinate system  $x, y, z$ . Denoting for each element the potential to be

$$\phi^e(\xi, \eta, \zeta) = \sum_{i=1}^{20} N_i^e \phi_i^e \quad (13)$$

where  $N_i^e = N_i^e(\xi, \eta, \zeta)$ . The global coordinates  $(x^e, y^e, z^e)$  within an element are related to local  $(\xi, \eta, \zeta)$  coordinates by

$$[x^e, y^e, z^e]^T = [N^e]^T [X^e] \quad (14)$$

where  $[N^e]^T = [N_1^e, N_2^e, \dots, N_{20}^e]$  and

$$[X^e] = \begin{bmatrix} x_1^e & y_1^e & z_1^e \\ x_2^e & y_2^e & z_2^e \\ \vdots & \vdots & \vdots \\ x_{20}^e & y_{20}^e & z_{20}^e \end{bmatrix} \quad (15)$$

is the  $3 \times 20$  matrix of (global) coordinate values of the element nodes. We next substitute these into the volume integral to obtain, after assembling

$$I_1 = \int_V \frac{1}{2} (\nabla \phi)^2 dV \approx \frac{1}{2} \{\phi\}^T [K_V] \{\phi\} \quad (16)$$

where  $[K_V] =$  assemblage of  $[K_V^e]$  with

$$[K_V^e] = \left[ \int_{V^e} \nabla \{N^e\} \nabla \{N^e\}^T dV^e \right] \quad 20 \times 20 \quad (17)$$

It should be pointed out that, since  $\{N^e\}$  is expressed in local coordinates,  $dV^e(x, y, z)$  must be expressed as  $J dV^e(\xi, \eta, \zeta)$  where  $J$  is the Jacobian of coordinate transformation. The final integration is carried out numerically by Gauss-Legendre quadrature with 21 integration points in a cubic element.

The integral  $I_2$  on the free surface is a two-dimensional version of  $I_1$  and need not be discussed.

With the circular geometry of  $S$  and the chosen representation for  $\phi'_s$ , the integral  $I_3$  can be integrated directly. Define the vector  $\{\mu\}$  by

$$\{\mu\}^T = \{\alpha_{00}, \alpha_{01}, \beta_{01}, \alpha_{02}, \beta_{02}, \dots, \alpha_{0N_0}, \beta_{0N_0}, \alpha_{10}, \alpha_{11}, \beta_{11}, \dots, \alpha_{M0}, \alpha_{M1}, \beta_{M1}, \dots, \alpha_{MN_M}, \beta_{MN_M}\}^T \quad (18)$$

we obtain for  $I_3$  a quadratic form

$$I_3 = \frac{1}{2} \int_S \phi'_s \frac{\partial}{\partial r} \phi'_s dS \approx \frac{1}{2} \{\mu\}^T [K_D] \{\mu\} \quad (19)$$

where  $[K_D]$  is diagonal. If the  $i$ -th term of  $\{\mu\}$  is either  $\alpha_{mn}$  or  $\beta_{mn}$ , then the corresponding diagonal element of  $[K_D]$  is

$$K_{D_i} = \begin{cases} \frac{\pi r_s}{2\epsilon_n} H_n^{(1)}(k_o r_s) H_n^{(1)*}(k_o r_s) (\sinh 2k_o h + 2k_o h) & m = 0 \\ \frac{\pi r_s}{2\epsilon_n} K_n(\kappa_m r_s) K_n'(\kappa_m r_s) (\sin 2\kappa_m h + 2\kappa_m h) & m = 1, 2, \dots \end{cases} \quad (20)$$

where  $r_s$  is the radius of  $S$  and the Jacobi symbol  $\epsilon_n$  is introduced. We remark that if  $S$  had been non-circular,  $[K_D]$  would be fully populated.

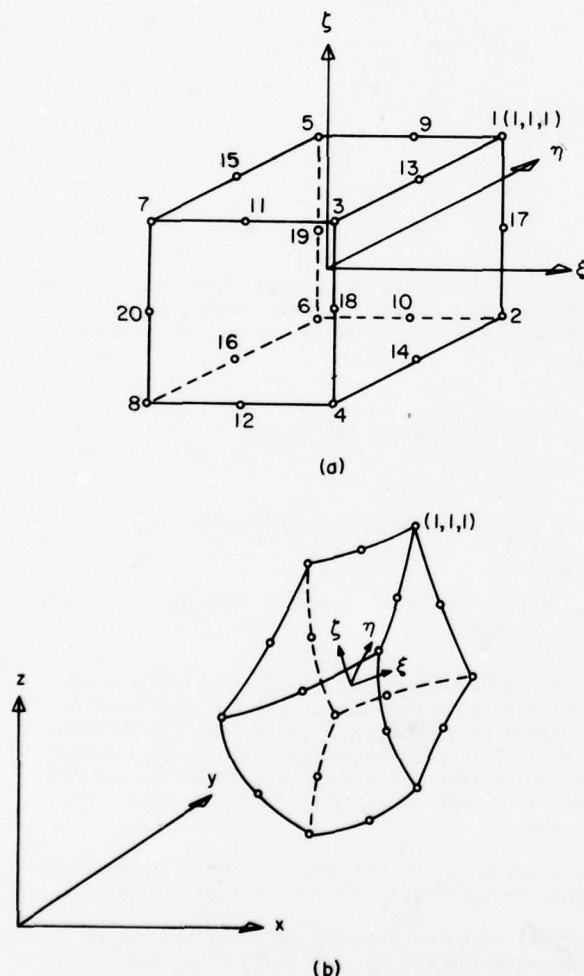


Figure 2 20-node hexahedral element of the serendipity family. (a) in local coordinates. (b) arbitrarily oriented, quadratic-sided daughter element in global coordinates after isoparametric mapping.

Integral  $I_4$  involves the coupling of  $\phi$  and  $\phi'_s$ , along  $S$ . Again numerical quadrature is performed over the isoparametric quadrilateral area elements on  $S$  and

$$I_4 = - \int_S \phi \frac{\partial}{\partial r} \phi'_s dS \approx \sum_{e \in S} \{\mu\}^T [K_C^e] \{\bar{\phi}^e\} = \{\mu\}^T [K_C] \{\bar{\phi}\} \quad (21)$$

where  $\{\bar{\phi}^e\}$ ,  $\{\bar{\phi}\}$  refer to nodal points on  $S$  and are subsets of  $\{\phi^e\}$ ,  $\{\phi\}$ . It is important to rewrite the right hand side of Eq. (21) as

$$I_4 \approx \frac{1}{2} \{\mu\}^T [K_C] \{\bar{\phi}\} + \frac{1}{2} \{\bar{\phi}\}^T [K_C] \{\mu\} \quad (22)$$

This arrangement ensures the symmetry of the global stiffness matrix, although  $[K_C]$  is asymmetric and complex.

$I_5$  and  $I_6$  involve the known potential  $\phi_1$ , hence the integrals may be written as

$$I_5 \approx - \{Q_C\}^T \{\mu\}, \quad I_6 \approx - \{Q_P\}^T \{\bar{\phi}\} \quad (23,24)$$

where the vectors  $\{Q_C\}$  and  $\{Q_P\}$  are known.

Finally, substituting the matrix forms of  $I_1$ - $I_6$  into Eq. (12) and extremizing with respect to  $\{\phi\}$  and  $\{\mu\}$  we obtain

$$([K_V] + [K_F])\{\phi\} + [K_C]\{\mu\} = \{Q_P\} \quad (25)$$

$$[K_D]\{\mu\} + [K_C]^T \{\phi\} = \{Q_C\} \quad (26)$$

which may be combined to give

$$[K]\{\psi\} = \{Q\}$$

with

$$[K] = \begin{bmatrix} \begin{matrix} \xrightarrow{N_V} & \xrightarrow{N_T} \end{matrix} \\ \begin{matrix} \uparrow N_V \\ \downarrow N_T \end{matrix} \begin{bmatrix} [K_V] + [K_F] & 0 \\ 0 & [K_C] \end{bmatrix} \begin{matrix} \uparrow N_S \\ \downarrow N_S \end{matrix} \\ \begin{matrix} \xleftarrow{N_S} \end{matrix} \begin{bmatrix} 0 & [K_C]^T & 0 \end{bmatrix} \end{bmatrix} \quad (27)$$

where  $N_V$ ,  $N_S$  are the number of element nodal points in  $V$  and on  $S$  respectively, and  $N_T$  is the number of entries in  $\{\mu\}$ , and  $\{\psi\}^T$  is the total unknown vector,

$$\{\psi\}^T = [\{\phi\}^T, \{\mu\}^T] \quad (28)$$

with the boundary nodal potentials  $\{\bar{\phi}\}$  assigned to the end of the vector  $\{\phi\}$ .

The final matrix equation which involves complex entries  $[K_C]$ ,  $[K_D]$  is solved by Gaussian elimination. Since the computer programming involved in these steps is lengthy, we have checked the subroutines for the integrals by using simple examples which involve only one of the integrals at a time and which can be evaluated analytically.

#### NUMERICAL EXAMPLES

The following examples were treated by Gaussian elimination in single precision without secondary storage. The total number of unknowns was therefore limited by the available core of the existing IBM 370-168 computer at M.I.T. Our examples were chosen according to these limitations.

As a measure of accuracy, we made use of the *optical theorem* well-known in physics which is a consequence of energy conservation and had been derived for water wave scattering by Maruo (7). It states that the complex angular factor of the scattered wave  $A(\theta)$  in the far field is governed by the following relationship:

$$\int_0^{2\pi} |A(\theta)|^2 d\theta = -\frac{2\pi}{\cosh k_o h} \operatorname{Re}(A(\theta_I)) \quad (29)$$

where  $\theta_I$  is the angle of the incident wave and  $\operatorname{Re}(\cdot)$  denotes the real part of  $(\cdot)$ . For the form of  $\phi'_s$  assumed in Eq. (7), Eq. (29) reduces to

$$\sum_{n=0}^{\infty} \frac{1}{\epsilon_n} (|\bar{\alpha}_{on}|^2 + |\bar{\beta}_{on}|^2) = -\frac{1}{\cosh k_o h} \operatorname{Re} \left( \sum_{n=0}^{\infty} (-1)^n (\bar{\alpha}_{on} \cos n\theta_I + \bar{\beta}_{on} \sin n\theta_I) \right) \quad (30)$$

where  $\bar{\alpha}_{on}$ ,  $\bar{\beta}_{on}$  are dimensions and

$$\begin{Bmatrix} \bar{\alpha}_{on} \\ \bar{\beta}_{on} \end{Bmatrix} = \frac{i\omega}{gA} \begin{Bmatrix} \alpha_{on} \\ \beta_{on} \end{Bmatrix}$$

We shall define a global relative error measure

$$E_{\text{opt}} = \left| \sum_{n=0}^{\infty} \frac{1}{\epsilon_n} (|\bar{\alpha}_{on}|^2 + |\bar{\beta}_{on}|^2) + \frac{1}{\cosh k_o h} \operatorname{Re} \left( \sum_{n=0}^{\infty} (-1)^n (\bar{\alpha}_{on} \cos n\theta_I + \bar{\beta}_{on} \sin n\theta_I) \right) \right| / \sum_{n=0}^{\infty} \frac{1}{\epsilon_n} (|\bar{\alpha}_{on}|^2 + |\bar{\beta}_{on}|^2) \quad (31)$$

We further define dimensionless force and moment coefficients by

$$C_{F_i} = \frac{F_i}{\rho g \pi a H A} \quad i = x, y, z \quad (32.a)$$

and

$$C_{M_i} = \frac{M_i}{\rho g \pi a^2 H A} \quad i = x, y, z \quad (32.b)$$

where  $H$  is the draft and  $a$  is a typical horizontal dimension of the body.  $F_i$  refers to the force component in the  $i$ -th direction and  $M_i$ , the moment component about the  $i$ -axis, i.e.

$$\vec{F} = \{F_i\}^T e^{-i\omega t}, \quad \vec{M} = \{M_i\}^T e^{-i\omega t}$$

As a first check we studied the case of diffraction by a vertical cylinder of circular cross section with radius  $a$ , extending from the sea bottom at depth  $h$  out of the free surface. The exact analytical theory is well-known and affords a check for the correctness and the efficiency of the numerical theory. In the theory  $\alpha_{mn}$ ,  $\beta_{mn}$  all vanish for  $m \geq 1$ , i.e., the double series in Eq. (7) does not appear. In our numerical experiments we took  $m = 0, 1, 2, 3, 4$ , in order to check whether the contribution by terms with  $m \neq 0$  were indeed negligible. The finite element grid consisted of two horizontal rings of 18 elements each, stacked to form a single shell surrounding the cylinder (Figure 3). The numbers of coefficients  $N_m$  chosen for the five eigenvalues were  $N_0 = 12$ ,  $N_1 = N_2 = N_3 = N_4 = 10$ . Excellent results were obtained for

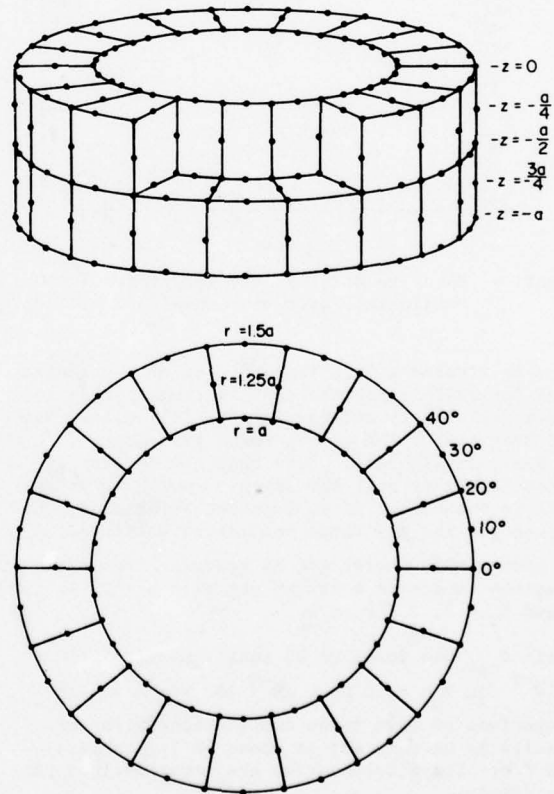


Figure 3 Finite element structure for a complete cylinder radius  $a$ : 36 elements, 342 nodes.



$k_0 a$  up to at least 7 in both the local potential and the horizontal wave force. Furthermore we found that  $\alpha_{mn}$ ,  $\beta_{mn}$ ,  $m \neq 0$  were not always small by themselves but their product with  $K_n(\kappa_m r)$  were always negligible because of the exponential decay of the modified Bessel functions.  $E_{opt}$  ranged from  $\sim 10^{-5}$  for low  $k_0 a$  up to  $\sim 10^{-3}$  for  $k_0 a \sim 7$ . The relative error in the magnitude of the horizontal force

$$E_{|F|} = \frac{|C_{F_x}|_{\text{analytic}} - |C_{F_x}|_{\text{FEM}}|}{|C_{F_x}|_{\text{analytic}}}$$

is presented in Figure 4 as an example.

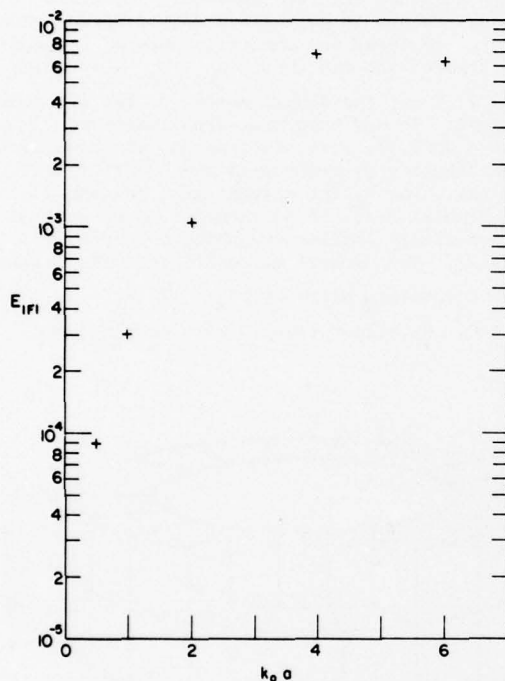


Figure 4 Relative error in the magnitude of the horizontal force on a complete cylinder.

We also treated a less trivial case of a circular dock for which numerical results from a semi-analytical theory exists (Garrett (8), Black, Mei and Bray (9)). The geometry and grid system is shown in Figure 5. Note that the density of nodes is higher near the sharp corners. With regard to the number of coefficient terms used, the result for the  $k_0 a$  range considered was found to be essentially unaffected by reducing from our previous choice to a cruder set with  $m = 0, 1, 2, 3$  and  $N_1 = 9, i = 0$  to 3.

Again  $E_{opt}$  was found to be small, ranging from  $\sim 10^{-5}$  for  $k_0 a = .5$  to  $\sim 10^{-3}$  for  $k_0 a = 6$ . The comparison of wave force coefficients with the results by Garrett (8) is shown in Figures 6.a and 6.b. The discrepancies are imperceptible on the graphs.

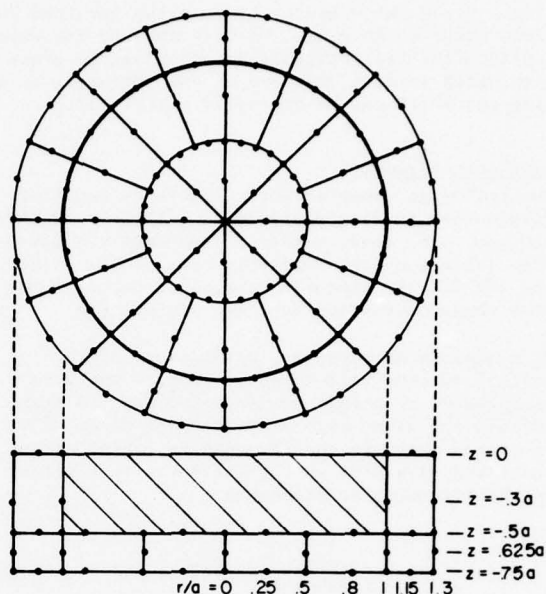


Figure 5 Finite element structure for a floating dock: 56 elements, 435 nodes

As a final example we calculated the wave forces on a square barge. No results for this geometry are known to us. As with the previous cases, no advantage was taken of symmetry in the geometry. A finite element grid with 56 elements and 435 nodes, similar to the one used for the circular dock, was employed here. The complete grid system here, which minimized the bandwidth of the resulting equation matrix, was generated by computer, as in all the examples studied. The corresponding force and moment components for a range of  $k_0 a$  are shown in

Figures 7.a,b,c. The computing time required ranged from about 2.6 to 2.8 minutes per wavelength for all the examples presented. This is already competitive with known Green function methods. Experience indicates that our computing cost is essentially governed by the number of nodes. For finite element method, the number of nodes increases with the fluid volume, while for Green function method, the number of area elements required increases with the total wetted solid surface. Thus as the number and complexity of solid components increase in a given fluid region, we expect the hybrid element method to be less costly while the opposite is true for Green function method.

It is clear that by lifting the restriction on the total number of unknowns, the extension to more complicated structures including depth variations is straightforward. The hybrid element method is therefore, in our opinion, a practical one for industrial applications. It can be easily modified for calculating the added mass and damping coefficients in radiation problems. For practical problems it is desirable to use secondary storage and double precision, the latter is likely necessary to reduce round-off accumulation error.



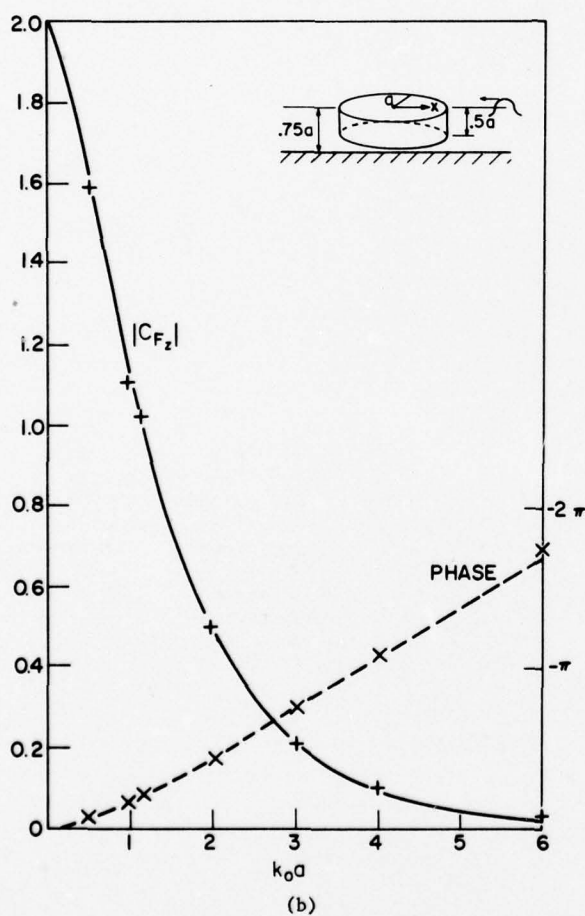
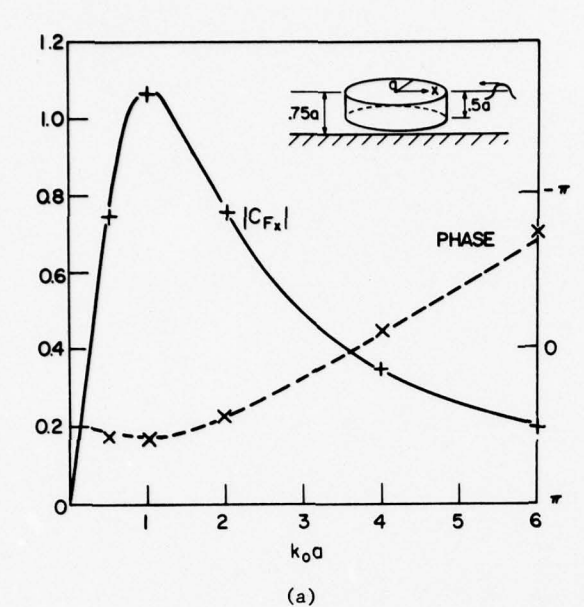


Figure 6 Comparison between finite element solutions +, amplitude; x, phase and Garrett (8) results: —, amplitude; ---, phase; for a circular dock.  
(a) horizontal force coefficient  $C_{Fx}$   
(b) vertical force coefficient  $C_{Fz}$

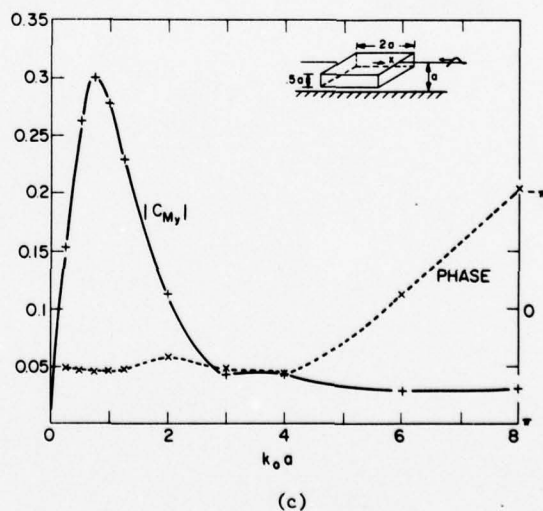
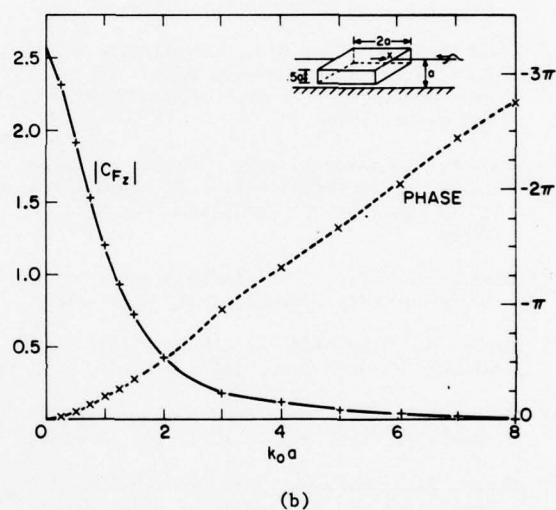
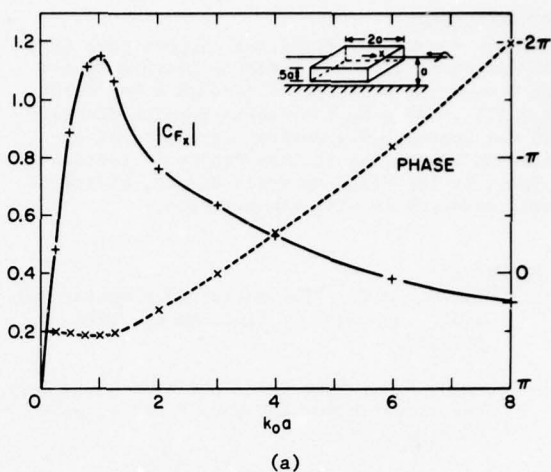


Figure 7 Forces on a square dock: — + —, magnitude; --x--, phase. Wave incident from  $x = +\infty$ .  
(a) horizontal force (b) vertical force  
(c) moment about y-axis.

## ACKNOWLEDGEMENT

The main sources of financial support have been the contracts with the National Administration for Oceans and Atmospheres through a Sea Grant to M.I.T., and with the Public Service Electric and Gas Company, New Jersey, as a part of the Atlantic Generating Station Project. Partial support by the Fluid Dynamics Branch, Office of Naval Research is also acknowledged.

## REFERENCES

- (1) Wehausen, J.V., "The Motion of Floating Bodies", *Ann. Rev. of Fluid Mech.*, 1971, 3, 237-268.
- (2) Newman, J.N., "The Interaction of Stationary Vessels with Regular Waves", these proceedings, 1976.
- (3) Garrison, C.J., "Hydrodynamics of Large Objects in the Sea; Part I: Hydrodynamic Analysis", *J. Hydronautics*, 1974, 8, 5-12.
- (4) Chen, H.S. and Mei, C.C., "Oscillations and Wave Forces in a Man-Made Harbor in the Open Sea", *Proc. 10 Naval Hydrodynamics Symposium*, 1974.
- (5) Bai, K.J. and Yeung, R.W., "Numerical Solutions to Free Surface Flow Problems", *Proc. of 10 Symposium on Naval Hydrodynamics*, 1974.
- (6) Zienkiewicz, O.C., *The Finite Element Method in Engineering Science*, 1971, McGraw-Hill.
- (7) Maruo, H., "The Drift of a Body Floating on Waves", *J. Ship Res.*, 1960, 4, 1-10.
- (8) Garrett, C.J.R., "Wave Forces on a Circular Dock", *J. Fluid Mech.*, 1971, 46, 129-139.
- (9) Black, J.L., Mei, C.C. and Bray, M.C.G., "Radiation and Scattering of Water Waves by Rigid Bodies", *J. Fluid Mech.*, 1971, 46, 151-164.

# THE SECOND ORDER STEADY FORCE AND MOMENT ON A SHIP MOVING IN AN OBLIQUE SEAWAY

WEN-CHIN LIN and ARTHUR M. REED

David Taylor Naval Ship Research and Development Center  
Bethesda, Maryland 20084 U.S.A.

Equations for the second-order steady horizontal force and yawing moment are derived for a ship moving with a constant "mean" forward speed into an oblique plane progressive wave system. The analysis is developed within the context of a linearized ship-motion and infinitesimal waterwave theories for an ideal fluid. General results are obtained from momentum considerations and through use of an asymptotic form of the Green's function valid at a large distance from the ship. The final results are expressed in terms of the Kochin function which requires knowledge of the forced-oscillation and diffraction potentials at the "mean" position of the ship surface. To obtain these velocity potentials a two-dimensional strip method is used. Thus, the free-surface condition is taken into account in determining the appropriate potential on each ship section.

## I. INTRODUCTION

When a ship is exposed to an incoming wave system, in addition to the apparent oscillatory motions, the ship has a tendency to drift away in the direction of the wave propagation. Thus, it seems reasonable to suppose that there exist a net drifting force and moment acting on the ship due to the incoming wave system. This subject was considered by Watanabe (1938) and Havelock (1942), and their analyses confirmed the existence of such a net drifting force by investigating the interaction between the incoming-wave system and the resulting ship motions, even without taking account of wave diffraction. However, the mechanisms of the drifting force and moment involve other aspects of the interaction which were not included in the aforementioned investigations. It appears to be Maruo (1960) who first provided a complete analysis of the drifting force acting on a ship with zero mean forward speed, and clarified the relationship between drifting force and all aspects of wave interaction. Newman (1967) has investigated the problem further and included the drifting-yaw moment and applied a slender-body theory to obtain numerical results for Series 60 ships.

The purpose of the present paper is to extend the analyses of Maruo and Newman to include the effects of constant mean forward speed. To differentiate between the two cases, i.e., with and without a constant mean forward speed, we shall refer to the net drifting force and moment as derived in this paper (i.e., ship with a constant mean forward speed) as the "steady force and moment." Applications of the analytical results of such an investigation are obvious. The longitudinal component of the steady force is applicable to the prediction of the added resistance, while the steady lateral force and yawing moment may be applied to ship's steering and control.

The analytical theory of this paper is developed within the context of the linearized theory of ship motions and the theory of infinitesimal waves in an incompressible inviscid fluid. To describe the fluid motion, the perturbation velocity potential is decomposed into  $\phi_S$ , which describes the fluid disturbance due to a steady forward motion of a ship in calm water, and  $\phi_T$  which describes the remaining time-dependent fluid motions. The time-dependent potential is further decomposed into  $\phi_I$ , which describes the incoming plane progressive wave system, and  $\phi_B$  which accounts for the diffracted waves and waves due to forced ship motions. It is seen that the steady force and moment are obtained as time-averaged quantities contributed by the interactions of  $\phi_I$  and  $\phi_B$ . It is seen further that contributions to the steady force and moment come from two principal mechanisms: the interaction between  $\phi_I$  and  $\phi_B$ , and the action

of  $\phi_B$  upon itself. Using the added resistance as an example, contributions from these two mechanisms are denoted respectively as  $\langle \Delta R_{IB} \rangle$  and  $\langle \Delta R_{BB} \rangle$ . Part of  $\langle \Delta R_{IB} \rangle$  is the component investigated by Havelock (1942) which is associated with the "phase lag" between the incoming-wave exciting force and the resulting ship motions. The remaining part of  $\langle \Delta R_{IB} \rangle$  is due to the interactions between diffracted and incoming waves.

On the other hand,  $\langle \Delta R_{BB} \rangle$  is mainly associated with energy dissipation through out-going ring waves from forced ship motions. As such, it may become more important as the frequency of encounter increases and may become less important, as far as the added resistance is concerned, for a low-speed ship in a head or following sea, especially when the wave length is large. Salvesen (1974) has also investigated the same problem as the present paper by using a somewhat different analytical approach. In his work Salvesen has only included those terms arising from the interaction between the incident waves and the body generated waves. Hence, the results of this paper should complement those of Salvesen by providing the components of the force due to the interaction of the body generated waves with themselves.

In this paper the momentum and moment of momentum equations are used to obtain expressions for the force and moment on a ship in terms of the far-field potential. This far-field potential is expressed in terms of the potential on the mean body surface by means of Green's theorem in conjunction with the proper Green's function. Newman (1959) has obtained an asymptotic form of the Green's function by means of the method of stationary phase. This asymptotic form is further analyzed by means of the method of stationary phase to produce a final form for both the longitudinal force and side force. A similar analysis is carried out for the yawing moment. However, the stationary phase results do not simplify and a final form is not given here.

The final equations for the longitudinal and lateral force components are expressed in terms of the Kochin function. Thus, to obtain numerical results, the final problem becomes that of computing the Kochin function. There are a number of options to this problem: one can use the simpler and more elegant slender-body approximation of Newman (1967), or an elaborate and rigorous method of approximation as did Ogilvie and Tuck (1969). As an initial experiment, we have tried to strike a midground by employing the strip-approximation as developed in the linearized ship-motion theory of Salvesen, Tuck, and Faltinsen (1970). The reason for this choice is that this strip approximation has been shown to give accurate enough predictions of ship motions since, perhaps, it accounts for the free-surface condition as well as the forward-speed effect,



albeit only in an approximate manner.

## NOMENCLATURE

- $(x, y, z) = P = \underline{x}$  - a field point.  
 $(x_0, y_0, z_0) = Q = \underline{x}_0$  - a singularity point, or a point on a surface.  
 $\underline{r}$  - vector  $\overline{OP}$   
 $Oxyz$  - coordinate system translating with constant speed  $U$  in the  $Ox$  direction.  
 $\hat{O}\hat{x}\hat{y}\hat{z}$  - coordinate system fixed to the ship.  
 $\sigma$  - the frequency of oscillation with reference to  $\hat{O}\hat{x}\hat{y}\hat{z}$ , a coordinate system fixed in space.  
 $\omega$  - the frequency of oscillation with respect to the  $Oxyz$  coordinate system (frequency of encounter)  
 $\omega = \sigma - k_0 U \cos \beta$ .  
 $\nu$  - wave number based on frequency of encounter  
 $(\nu = \omega^2/g)$ .  
 $\beta$  - Wave heading:  $\beta = 0 \rightarrow$  following seas,  
 $\beta = \pi/2 \rightarrow$  beam seas,  
 $\beta = \pi \rightarrow$  head seas.  
 $k_0$  - wave number of the progressive wave system  
 $(k_0 = \sigma^2/g)$ .  
 $\tau$  -  $\omega U/g$ .  
 $U$  - mean speed of ship.  
 $\Psi_c$  - the fluid volume.  
 $\partial\Psi_c$  - the boundary of  $\Psi_c$ .  
 $S_B$  - ship's surface.  
 $S_{B0}$  - the mean surface of the ship.  
 $S_F$  - the exact free-surface.  
 $S_F^{(0)}$  - the undisturbed free surface (the plane  $z = 0$ ).  
 $\Sigma_R$  - far field control surface, a cylinder of radius  $R$  extending from  $-\infty$  to the free surface.  
 $\Sigma_R^{(0)}$  - that part of  $\Sigma_R$  extending to  $z = 0$ .  
 $\Sigma_h$  - the bottom control surface, a disk of radius  $R$  at depth  $z = -h$ .  
 $V_n$  - the scalar normal velocity of  $\partial\Psi_c$ .  
 $Z_w$  - the free surface elevation.  
 $g$  - gravitational acceleration.  
 $\rho$  - fluid density.  
 $A$  - incident wave amplitude.  
 $\Phi$  - total velocity potential.  
 $\phi$  - perturbation velocity potential, a real function.  
 $\phi_S$  - steady-state portion of  $\phi$ .  
 $\varphi$  - the complex perturbation potential.  
 $\varphi_T$  - the time varying portion of  $\varphi$ .  
 $\varphi_1$  - the incident wave potential.  
 $\varphi_B$  - the potential of the body generated waves.  
 $\varphi_D$  - the diffraction wave potential.  
 $\varphi_M$  - the forced-oscillation wave potential.  
 $\underline{A} \cdot \underline{B}$  - scalar product of two vectors.  
 $\underline{A} \wedge \underline{B}$  - vector product.  
 $\underline{n}$  - three-dimensional normal vector pointing out of the fluid.  
 $\underline{N}_2 D$  - two-dimensional unit normal vector to a ship cross section.  
 $\underline{F}$  - force due to pressure acting over the actual ship-wetted surface.  
 $\underline{N}_0$  - moment about the origin of the steady-translating coordinate system.

## II. Formulation of the Problem

Consider a ship moving into a plane progressive wave system. As usual, we shall suppose that the fluid is inviscid and incompressible, that the ship is sufficiently "slender", and that the amplitude and slope of the incident waves are small so that the mathematical problem describing the resulting irrotational free-surface flow may be linearized. We shall suppose further that the ship is making small oscillatory motions in a periodic manner about a "mean" position which is translating with a constant forward speed  $U$ . Lastly, we shall suppose that the water is infinitely deep.

Let  $Oxyz$  be a right-hand Cartesian coordinate system translating with the mean position of the ship, with  $Oz$  directed upward (against gravity),  $Ox$  toward the bow,  $Oy$  to port, and the  $Oxy$  plane coinciding with the undisturbed free surface. A similar coordinate system fixed in the ship will be chosen such that when the ship is floating on the undisturbed free surface, the two coordinate systems coincide.

Since the  $Oxyz$  system is translating with a constant velocity, it may be regarded as an inertial reference frame. We shall develop a potential flow with reference to this coordinate system. Let the total velocity potential  $\Phi$  be given by:

$$\Phi(x, y, z, t) = -Ux + \phi, \quad (2.1)$$

so that its gradient gives the total fluid velocity relative to the  $Oxyz$  frame as follows:

$$\underline{q} = \nabla\Phi = -U\underline{e}_1 + \nabla\phi, \quad (2.2)$$

where

$$\nabla\phi = \underline{v} = u\underline{e}_1 + v\underline{e}_2 + w\underline{e}_3 \quad (2.3)$$

represents the perturbation fluid velocity. We shall use  $\underline{e}_1, \underline{e}_2$ , and  $\underline{e}_3$  to represent the three base vectors of the  $Oxyz$  frame. According to linearized theory, the perturbation potential  $\phi$  is required to satisfy the following conditions:

$$\begin{aligned} \Delta\phi &= 0, \quad z < 0, \\ \left[ \left( \frac{\partial}{\partial t} - U \frac{\partial}{\partial x} \right)^2 + g \frac{\partial}{\partial z} \right] \phi &= 0, \quad z = 0, \\ \lim_{t \rightarrow -\infty} |\nabla\phi| &= 0, \quad \left| \frac{\partial\phi}{\partial t} \right| = 0, \quad \text{all } x, y, t. \end{aligned} \quad (2.4)$$

Other conditions which are to be satisfied by  $\phi$  will be specified as needed.

**The Force.** As shown in Appendix A, the force equation may be given by:

$$\begin{aligned} \underline{F} &= \rho \iint_{\Sigma_R} dS \left\{ \underline{n} \left[ \frac{\partial\phi}{\partial t} - U \frac{\partial\phi}{\partial x} + \frac{1}{2} |\nabla\phi|^2 \right] \right. \\ &\quad \left. - \nabla\phi [-U\underline{n}_1 + \nabla\phi \cdot \underline{n}] + g z \underline{n} \right\} \\ &\quad - \rho \underline{e}_3 \iiint_{\Psi_c} d\Psi + \underline{f} - \frac{dQ}{dt}, \end{aligned} \quad (2.5)$$

where  $\Sigma_R$  is a cylindrical control surface with a large radius  $R = \sqrt{x^2 + y^2}$  which extends from  $z = -\infty$  to the actual free surface  $S_F$ .  $Q$ , as given by equation (A.10) is the total fluid momentum (with reference to the  $Oxyz$  system) within the control volume  $\Psi_c$  and  $\underline{f}$ , as given by equation (A.12), is related to the net "flux" of fluid leaving  $\Psi_c$  across the control surface  $\Sigma_R$ .

Since  $\Sigma_R$  is a cylindrical surface, it will be convenient to introduce a cylindrical-polar coordinate system. Let  $(R, \theta, z)$  be the coordinates of such a system. These coordinates are related to the Oxyz system as follows:

$$x = R \cos \theta, y = R \sin \theta, 0 \leq \theta \leq 2\pi, R = \sqrt{x^2 + y^2}. \quad (2.6)$$

Thus, on the cylindrical control surface  $\Sigma_R$ , we have:

$$\begin{aligned} \mathbf{n} \cdot \nabla \phi &= \frac{\partial \phi}{\partial R}, \\ \mathbf{n} &= \frac{\mathbf{R}}{R} = \cos \theta \mathbf{e}_1 + \sin \theta \mathbf{e}_2 \\ dS &= R d\theta dz. \end{aligned} \quad (2.7)$$

Suppose that the force vector, decomposed along the Oxyz system, is:

$$\mathbf{F} = F_1 \mathbf{e}_1 + F_2 \mathbf{e}_2 + F_3 \mathbf{e}_3.$$

In this work, we are only interested in the force components in the horizontal plane,  $F_1$  and  $F_2$ . If we make use of equation (2.7), the following formulas may be obtained from equation (2.5):

$$F_1 = \rho \int_0^{2\pi} d\theta R \int_{-\infty}^{z_w} dz \left\{ -\frac{\partial \phi}{\partial R} \frac{\partial \phi}{\partial x} + \cos \theta \left[ \frac{\partial \phi}{\partial t} + \frac{1}{2} |\nabla \phi|^2 + gz \right] \right\} + \mathbf{e}_1 \cdot \mathbf{f} - \mathbf{e}_1 \cdot \frac{d\mathbf{Q}}{dt}, \quad (2.8)$$

$$F_2 = \rho \int_0^{2\pi} d\theta R \int_{-\infty}^{z_w} dz \left\{ -\frac{\partial \phi}{\partial R} \frac{\partial \phi}{\partial y} + \sin \theta \left[ \frac{1}{2} |\nabla \phi|^2 + \frac{\partial \phi}{\partial t} - U \frac{\partial \phi}{\partial x} + gz \right] + \cos \theta U \frac{\partial \phi}{\partial y} \right\} + \mathbf{e}_2 \cdot \mathbf{f} - \mathbf{e}_2 \cdot \frac{d\mathbf{Q}}{dt}, \quad (2.9)$$

where  $Z_w$  denotes the free-surface elevation. Note that equations (2.8) and (2.9) are still "exact" in that no approximations have been introduced. Thus, the  $z$ -integrations in both equations involve the actual free-surface  $S_F$ ,  $z = Z_w(x, y, t)$ . Since in this work we shall pursue an approximation up to the second order in the perturbation potential, linearization may be introduced to simplify the  $z$ -integrations.

Proceeding with such a linearization, first recall that according to linearized theory the free-surface elevation is given by:

$$z_w = -\frac{1}{g} \left\{ \frac{\partial \phi}{\partial t} - U \frac{\partial \phi}{\partial x} \right\}_{z=0}. \quad (2.10)$$

For example, by making use of the mean-value theorem and a Taylor's series expansion, the  $z$ -integration of a typical term in equation (2.8) may be treated as follows:

$$\begin{aligned} \int_{-\infty}^{z_w} dz \frac{\partial \phi}{\partial t} \cos \theta &= \int_{-\infty}^0 dz \frac{\partial \phi}{\partial t} \cos \theta + z_w \left[ \frac{\partial \phi}{\partial t} \right]_{z=z} \cos \theta \\ &= \int_{-\infty}^0 dz \frac{\partial \phi}{\partial t} \cos \theta + z_w \left\{ \left( \frac{\partial \phi}{\partial t} \right)_{z=0} + \tilde{z} \left( \frac{\partial^2 \phi}{\partial z \partial t} \right)_{z=0} + \dots \right\} \cos \theta \\ &= \int_{-\infty}^0 dz \frac{\partial \phi}{\partial t} \cos \theta - \frac{1}{g} \left[ \left( \frac{\partial \phi}{\partial t} - U \frac{\partial \phi}{\partial x} \right) \left( \frac{\partial \phi}{\partial t} \right) \right]_{z=0} \cos \theta + O(\phi^3). \end{aligned} \quad (2.11)$$

where  $\tilde{z}$  denotes a mean value and  $O(\phi^3)$  indicates that the remainder is of the third order in  $\phi$ . Applying similar approxi-

mations to each of the terms of equations (2.8) and (2.9), the following results are obtained:

$$F_1 = \rho \int_0^{2\pi} d\theta R \int_{-\infty}^0 dz \left\{ -\frac{\partial \phi}{\partial R} \frac{\partial \phi}{\partial x} + \left[ \frac{1}{2} |\nabla \phi|^2 + \frac{\partial \phi}{\partial t} \right] \cos \theta \right\} - \frac{\rho}{2g} \int_0^{2\pi} d\theta \cos \theta R \left\{ \left( \frac{\partial \phi}{\partial t} - U \frac{\partial \phi}{\partial x} \right) \cdot \left( \frac{\partial \phi}{\partial t} + U \frac{\partial \phi}{\partial x} \right) \right\}_{z=0} + \mathbf{e}_1 \cdot \mathbf{f} - \mathbf{e}_1 \cdot \frac{d\mathbf{Q}}{dt}, \quad (2.12)$$

$$F_2 = \rho \int_0^{2\pi} d\theta R \int_{-\infty}^0 dz \left\{ -\frac{\partial \phi}{\partial R} \frac{\partial \phi}{\partial y} + \sin \theta \cdot \left[ \frac{1}{2} |\nabla \phi|^2 + \frac{\partial \phi}{\partial t} - U \frac{\partial \phi}{\partial x} \right] + U \frac{\partial \phi}{\partial y} \cos \theta \right\} - \frac{\rho}{2g} \int_0^{2\pi} d\theta R \left\{ \left( \frac{\partial \phi}{\partial t} - U \frac{\partial \phi}{\partial x} \right) \cdot \left[ \left( \frac{\partial \phi}{\partial t} - U \frac{\partial \phi}{\partial x} \right) \sin \theta + 2 U \frac{\partial \phi}{\partial y} \cos \theta \right] \right\}_{z=0} + \mathbf{e}_2 \cdot \mathbf{f} - \mathbf{e}_2 \cdot \frac{d\mathbf{Q}}{dt}. \quad (2.13)$$

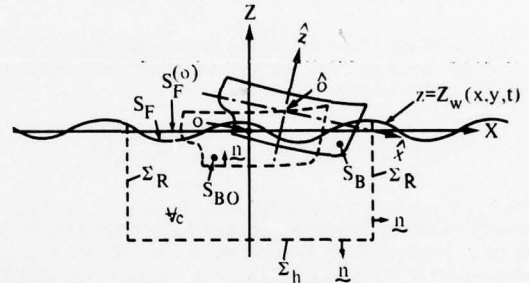


Figure 1 Coordinate System

Note that these two equations are accurate only to the second order in the perturbation potential,  $\phi$ .

We shall now decompose the perturbation potential  $\phi$  into a steady-state part,  $\phi_s$ , and a time-dependent part,  $\phi_T$ , i.e.,

$$\phi = \phi_s(x, y, z) + \phi_T(x, y, z, t), \quad (2.14)$$

where  $\phi_s$  describes the disturbance due to the steady forward motion of the ship in calm water and  $\phi_T$  describes all remaining fluid motions. According to linearized theory,  $\phi_T$  can be further decomposed as:

$$\phi_T = \phi_I + \phi_D + \phi_M = \phi_I + \phi_B, \quad (2.15)$$

where  $\phi_I$  is the potential of the incoming plane progressive wave,  $\phi_D$  the diffracted wave potential, and  $\phi_M$  the forced-oscillation wave potential. Since both  $\phi_D$  and  $\phi_M$  are generated by the ship and satisfy the same radiation condition at infinity, we shall denote their sum as  $\phi_B$ . The function  $\phi_I$  is given by the following equation

$$\phi_I = i \text{Re } \varphi_1(x, y, z) e^{i\omega t}, \quad (2.16)$$

where

$$\varphi_1 = -\frac{Ag}{\sigma} e^{k_0 z} \cdot e^{i[-k_0 x \cos \beta - k_0 y \sin \beta]}. \quad (2.17)$$

In the above equation,  $A$  is the wave amplitude,  $\sigma$  is the wave frequency with reference to a coordinate system fixed in space,  $k_0 = \sigma^2/g$  is the wave number,  $\beta$  is the wave heading angle measured counterclockwise from the positive  $x$ -direction to the direction of wave propagation, and  $\omega$  is the frequency of encounter with reference to the translating coordinate system Oxyz. The wave frequency  $\sigma$  is related to  $\omega$  by:

$$\omega = \sigma - k_0 U \cos \beta. \quad (2.18)$$

Substituting  $k_0 = \sigma^2/g$  into equation (2.18) and solving for  $\sigma$  gives:

$$\sigma = \omega \frac{1 \pm \sqrt{1 - 4\tau \cos \beta}}{2\tau \cos \beta}, \quad (2.19)$$

and

$$k_0 = \frac{\nu [1 - 2\tau \cos \beta - \sqrt{1 - 4\tau \cos \beta}]}{2\tau^2 \cos^2 \beta}, \quad (2.20)$$

where  $\tau = \omega U/g$ , and  $\nu = \omega^2/g$ .

In terms of the complex representation, (2.14) may be written as:

$$\phi = \phi_S(x, y, z) + \text{Re } \varphi_T(x, y, z) e^{i\omega t}, \quad (2.21)$$

and similarly,

$$\phi_B = \text{Re } \varphi_B e^{i\omega t}. \quad (2.22)$$

Recalling that  $\phi$  is required to satisfy the conditions in equation (2.4), the free-surface condition for  $\varphi_T$  becomes:

$$\nu \varphi_T(x, y, 0) + i2\tau \frac{\partial \varphi_T}{\partial x} - \frac{\tau^2}{\nu} \frac{\partial^2 \varphi_T}{\partial x^2} - \frac{\partial \varphi_T}{\partial z} = 0. \quad (2.23)$$

If we next substitute the decomposition equation (2.14) into equations (2.12) and (2.13), we may write the force components,  $F_1$  and  $F_2$  in the following form:

$$F_k = F_{kS} + F_{kST} + F_{kT} + \varepsilon_k \cdot \left( \mathbf{f} - \frac{d\mathbf{Q}}{dt} \right)_{k=1,2} \quad (2.24)$$

where  $F_{kS}$  represents those integrals involving only  $\phi_S$ ,  $F_{kT}$  represents those only involving  $\phi_T$ , and  $F_{kST}$  represents those integrals of cross products between  $\phi_S$  and  $\phi_T$ . Obviously,  $F_{kS}$  is independent of time,  $F_{kST}$  is linear in  $\phi_T$ , and  $F_{kT}$  contains quadratic as well as linear terms in  $\phi_T$ . In order to obtain the steady force and moment we need the time-averaged values of the time-dependent part of the forces and moments.

The time average of a function  $F$  is defined by:

$$\langle F \rangle = \frac{1}{T} \int_{t_0}^{t_0+T} dt F(t), \quad (2.25)$$

where  $T = 2\pi/\omega$  is the period of the oscillation. Suppose that  $A(t) = \text{Re } ae^{i\omega t}$  and  $B(t) = \text{Re } be^{i\omega t}$  are two periodic functions of  $t$ , then the following rules may be easily established:

$$\langle A \rangle = \langle \text{Re } ae^{i\omega t} \rangle = 0, \quad (2.26)$$

$$\begin{aligned} \langle A \cdot B \rangle &= \langle (\text{Re } ae^{i\omega t})(\text{Re } be^{i\omega t}) \rangle \\ &= \frac{1}{2} \text{Re } (ab^*) = \frac{1}{2} \text{Re } (a^*b), \end{aligned} \quad (2.27)$$

where  $a^*$  denotes the complex conjugate of  $a$ .

Applying these rules to the time-averaged force, we have from equation (2.24)

$$\begin{aligned} \langle \Delta F_k \rangle &= \langle F_k - F_{kS} \rangle \\ &= \langle F_{kST} \rangle + \langle F_{kT} \rangle + \left\langle \varepsilon_k \cdot \left( \mathbf{f} - \frac{d\mathbf{Q}}{dt} \right) \right\rangle. \end{aligned} \quad (2.28)$$

From equation (A.10) and (A.12) in Appendix A, it is obvious that the fluid flux  $\mathbf{f}$  and the linear momentum  $\mathbf{Q}$  both are linear in  $\phi_T = \varphi_T e^{i\omega t}$ . Since such a linear dependence is also found in  $F_{kST}$ , by applying equation (2.26) we have:

$$\langle F_{kST} \rangle = 0, \quad (2.29)$$

and

$$\left\langle \varepsilon_k \cdot \left( \mathbf{f} - \frac{d\mathbf{Q}}{dt} \right) \right\rangle = 0. \quad (2.30)$$

Hence, (2.28) yields only:

$$\langle \Delta F_k \rangle = \langle F_{kT} \rangle, \quad k = 1, 2. \quad (2.31)$$

Combining the results obtained in equations (2.28) through (2.31) with equations (2.12) and (2.13), the time-averaged horizontal-force components are respectively:

$$\begin{aligned} \langle \Delta F_1 \rangle &= \rho \int_0^{2\pi} d\theta R \int_{-\infty}^0 dz \left\langle \left( \frac{\partial \phi_T}{\partial R} \frac{\partial \phi_T}{\partial x} + \frac{1}{2} |\nabla \phi_T|^2 \cos \theta \right) \right. \\ &\quad \left. - \frac{\rho}{2g} \int_0^{2\pi} d\theta \cos \theta R \left\langle \left( \frac{\partial \phi_T}{\partial t} - U \frac{\partial \phi_T}{\partial x} \right) \left( \frac{\partial \phi_T}{\partial t} + U \frac{\partial \phi_T}{\partial x} \right) \right\rangle_{z=0} \right. \end{aligned}$$

and

$$\begin{aligned} \langle \Delta F_2 \rangle &= \rho \int_0^{2\pi} d\theta R \int_{-\infty}^0 dz \left\langle \left( -\frac{\partial \phi_T}{\partial R} \frac{\partial \phi_T}{\partial y} + \frac{1}{2} |\nabla \phi_T|^2 \sin \theta \right) \right. \\ &\quad \left. - \frac{\rho}{2g} \int_0^{2\pi} d\theta R \left\langle \left( \frac{\partial \phi_T}{\partial t} - U \frac{\partial \phi_T}{\partial x} \right) \left( \frac{\partial \phi_T}{\partial t} + U \frac{\partial \phi_T}{\partial x} \right) \sin \theta + 2U \frac{\partial \phi_T}{\partial y} \cos \theta \right\rangle_{z=0} \right. \end{aligned} \quad (2.33)$$

where the terms linear in  $\phi_T$  have been dropped.

Next we shall substitute the complex form of the decomposition for  $\phi_T$ , namely:

$$\phi_T = \phi_I + \phi_B = \text{Re } (\varphi_I + \varphi_B) e^{i\omega t}, \quad (2.34)$$

into equations (2.32) and (2.33) respectively. If this is done and the rule of equation (2.27) is applied, we obtain the following results:

$$\langle \Delta F_k \rangle = \langle \Delta F_{kIB} \rangle + \langle \Delta F_{kBB} \rangle, \quad k = 1, 2, \quad (2.35)$$

where

$$\begin{aligned} \langle \Delta F_{1IB} \rangle &= \frac{\rho}{2} \text{Re} \int_0^{2\pi} d\theta R \int_{-\infty}^0 dz \left\{ - \left( \frac{\partial \varphi_B}{\partial R} \frac{\partial \varphi_I^*}{\partial x} + \frac{\partial \varphi_B}{\partial x} \frac{\partial \varphi_I^*}{\partial R} \right) - \nabla \varphi_B \cdot \nabla \varphi_I^* \cos \theta \right\} \\ &\quad - \frac{\rho}{2g} \text{Re} \int_0^{2\pi} d\theta R \cos \theta \left\{ \omega^2 \varphi_B \varphi_I^* - U^2 \frac{\partial \varphi_B}{\partial x} \frac{\partial \varphi_I^*}{\partial x} \right\}_{z=0}, \end{aligned} \quad (2.36)$$

$$\begin{aligned} \langle \Delta F_{1BB} \rangle &= \frac{\rho}{2} \text{Re} \int_0^{2\pi} d\theta R \int_{-\infty}^0 dz \left\{ - \frac{\partial \varphi_B}{\partial R} \frac{\partial \varphi_B^*}{\partial x} + \frac{1}{2} \nabla \varphi_B \cdot \nabla \varphi_B^* \cos \theta \right\} \\ &\quad - \frac{\rho}{4g} \text{Re} \int_0^{2\pi} d\theta R \cos \theta \left\{ \omega^2 \varphi_B \varphi_B^* - \right. \end{aligned}$$



$$-U^2 \frac{\partial \varphi_B}{\partial x} \frac{\partial \varphi_B^*}{\partial x} \Big|_{z=0} \quad (2.37)$$

$$\begin{aligned} \langle \Delta F_{21B} \rangle = & \frac{\rho}{2} \operatorname{Re} \int_0^{2\pi} d\theta \int_{-\infty}^0 dz \left\{ - \left( \frac{\partial \varphi_B}{\partial R} \frac{\partial \varphi_1^*}{\partial y} + \frac{\partial \varphi_B}{\partial y} \frac{\partial \varphi_1^*}{\partial R} \right) + \right. \\ & \left. + \sin \theta (\nabla \varphi_B \cdot \nabla \varphi_1^*) \right\} \\ & - \frac{\rho}{4g} \operatorname{Re} \int_0^{2\pi} d\theta \int_{-\infty}^0 dz \left\{ \sin \theta \left[ \omega^2 \varphi_B \varphi_1^* - i\omega U \cdot \right. \right. \\ & \cdot \left( \varphi_B \frac{\partial \varphi_1^*}{\partial x} + \varphi_1^* \frac{\partial \varphi_B}{\partial x} + U^2 \frac{\partial \varphi_B}{\partial x} \frac{\partial \varphi_1^*}{\partial x} \right) \\ & + \cos \theta \left[ i\omega U \left( \varphi_B \frac{\partial \varphi_1^*}{\partial y} + \varphi_1^* \frac{\partial \varphi_B}{\partial y} \right) - \right. \\ & \left. \left. - U^2 \left( \frac{\partial \varphi_B}{\partial y} \frac{\partial \varphi_1^*}{\partial x} + \frac{\partial \varphi_B}{\partial x} \frac{\partial \varphi_1^*}{\partial y} \right) \right] \right\} \Big|_{z=0} \quad (2.38) \end{aligned}$$

and

$$\begin{aligned} \langle \Delta F_{2BB} \rangle = & \frac{\rho}{2} \operatorname{Re} \int_0^{2\pi} d\theta \int_{-\infty}^0 dz \left\{ - \frac{\partial \varphi_B}{\partial R} \frac{\partial \varphi_B^*}{\partial y} + \frac{1}{2} \sin \theta \cdot \right. \\ & \cdot \left( \nabla \varphi_B \cdot \nabla \varphi_B^* \right) \\ & - \frac{\rho}{4g} \operatorname{Re} \int_0^{2\pi} d\theta \int_{-\infty}^0 dz \left\{ \sin \theta \left[ \omega^2 \varphi_B \varphi_B^* + U^2 \frac{\partial \varphi_B}{\partial x} \frac{\partial \varphi_B^*}{\partial x} \right. \right. \\ & \left. \left. - 2 i\omega U \left( \varphi_B \frac{\partial \varphi_B^*}{\partial x} \right) \right] \right. \\ & \left. + 2 \cos \theta \left[ i\omega U \varphi_B \frac{\partial \varphi_B^*}{\partial y} - U^2 \frac{\partial \varphi_B}{\partial x} \frac{\partial \varphi_B^*}{\partial y} \right] \right\} \Big|_{z=0} \quad (2.39) \end{aligned}$$

Here  $\langle F_{k1B} \rangle$  represents the steady force acting on the ship due to interactions between the incoming wave and the ship-generated waves.  $\langle \Delta F_{kBB} \rangle$  on the other hand represents the steady force due to ship-generated waves, which are respectively described by the diffracted-wave potential  $\varphi_D$  and the forced-oscillation potential  $\varphi_M$  interacting with themselves. In fact  $\langle \Delta F_{1BB} \rangle$  represents the part of the added resistance which is associated with energy dissipation through radiating waves.

Lastly we would like to remark that in deriving (2.35), there is one more part of  $\langle \Delta F_k \rangle$  which should be denoted as  $\langle \Delta F_{k1I} \rangle$ . This is the part which involves terms quadratic in  $\varphi_1$  and therefore the equation for  $\langle \Delta F_{k1I} \rangle$  has the same form as that of  $\langle \Delta F_{kBB} \rangle$  with  $\varphi_B$  replaced by  $\varphi_1$ . However, it is straightforward to verify that  $\langle \Delta F_{k1I} \rangle$  vanishes identically. This fact can also be easily understood physically, since  $\langle \Delta F_{k1I} \rangle$  represents steady force on the ship due to undistorted incoming waves.

**The Moment.** In the following, results similar to those of equation (2.35) through (2.39) for the force will be derived for the yawing moment. The moment equation in vector form is derived in Appendix A as equation (A.9). To obtain the yawing moment we simply take the  $z$ -component of this equation. From equation (A.9) we have, using the cylindrical-polar coordinates in equations (2.6) and (2.7):

$$\begin{aligned} N_{03} = & \mathbf{e}_3 \cdot \iint_{S_B} P [\mathbf{r} \wedge \mathbf{u}] dS \\ = & \rho \int_0^{2\pi} d\theta \int_{-\infty}^0 dz \left\{ - \frac{\partial \phi}{\partial R} \frac{\partial \phi}{\partial \theta} + \right. \\ & \left. + U \cos \theta \frac{\partial \phi}{\partial \theta} \right\} + \mathbf{e}_3 \cdot \left( \mathbf{T} - \frac{d\mathbf{K}_0}{dt} \right) \\ = & \rho \int_0^{2\pi} d\theta \int_{-\infty}^0 dz \left\{ - \frac{1}{R} \frac{\partial \phi}{\partial \theta} \frac{\partial \phi}{\partial R} + \frac{U \cos \theta}{R} \frac{\partial \phi}{\partial \theta} \right\} \\ & - \frac{\rho U}{g} \int_0^{2\pi} d\theta \int_{-\infty}^0 dz \cos \theta \left\{ \frac{1}{R} \frac{\partial \phi}{\partial \theta} \frac{\partial \phi}{\partial t} - \frac{U \cos \theta}{R} \frac{\partial \phi}{\partial \theta} \frac{\partial \phi}{\partial R} \right. \\ & \left. + \frac{U \sin \theta}{R^2} \left( \frac{\partial \phi}{\partial \theta} \right)^2 \right\} \Big|_{z=0} + \\ & + \mathbf{e}_3 \cdot \left( \mathbf{T} - \frac{d\mathbf{K}_0}{dt} \right) + O(\phi^3) \quad (2.40) \end{aligned}$$

where, as defined in equations (A.3) and (A.8) respectively,  $\mathbf{K}_0$  is the moment of fluid momentum about the origin of the translating coordinate system  $Oxyz$ , and  $\mathbf{T}$  is associated with the net flux of fluid across the control surface  $\Sigma_R$ . Here again the equation (2.40) is accurate only up to the second order in the perturbation potential  $\phi$ . Note that equation (2.40) represents the yawing moment about the origin of the  $Oxyz$  reference frame due to pressure integration over the actual wetted surface of the ship. Since the  $Oxyz$  system represents only the mean position of the ship coordinate system  $\hat{O}\hat{x}\hat{y}\hat{z}$ , the moment should be corrected to account for the translation of the ship reference frame from the mean reference frame, if we are interested in the steady yawing moment about the ship reference frame. Such a correction is in general of the second order in magnitude and therefore is neglected in a linearized theory of ship motions.

Next, let us substitute the decomposition of  $\phi$ , namely, equations (2.14) and (2.15), into the expression for the yawing moment, equation (2.40). If we follow similar steps to those which lead to the final expressions for the steady horizontal forces such as equations (2.36) and (2.37), we may obtain the following results for the time-averaged yawing moment:

$$\langle \Delta N_{03} \rangle = \langle \Delta N_{031B} \rangle + \langle \Delta N_{03BB} \rangle \quad (2.41)$$

where

$$\begin{aligned} \langle \Delta N_{031B} \rangle = & \frac{\rho}{2} \operatorname{Re} \int_0^{2\pi} d\theta \int_{-\infty}^0 dz \left\{ - \left( \frac{\partial \varphi_B}{\partial R} \frac{\partial \varphi_1^*}{\partial \theta} + \frac{\partial \varphi_B}{\partial \theta} \frac{\partial \varphi_1^*}{\partial R} \right) \right\} \\ & - \frac{\rho U}{2g} \operatorname{Re} \int_0^{2\pi} d\theta \int_{-\infty}^0 dz \cos \theta \left\{ i\omega \varphi_B \frac{\partial \varphi_1^*}{\partial \theta} - i\omega \varphi_1^* \frac{\partial \varphi_B}{\partial \theta} \right. \\ & \left. - U \cos \theta \left( \frac{\partial \varphi_1^*}{\partial R} \frac{\partial \varphi_B}{\partial \theta} + \frac{\partial \varphi_1^*}{\partial \theta} \frac{\partial \varphi_B}{\partial R} \right) \right. \\ & \left. + 2 \frac{U \sin \theta}{R} \frac{\partial \varphi_B}{\partial \theta} \frac{\partial \varphi_1^*}{\partial \theta} \right\} \Big|_{z=0} \quad (2.42) \end{aligned}$$

and

$$\begin{aligned} \langle \Delta N_{03BB} \rangle = & \frac{\rho}{2} \operatorname{Re} \int_0^{2\pi} d\theta \int_0^\infty dz \left\{ -\frac{\partial \varphi_B}{\partial R} \frac{\partial \varphi_B^*}{\partial \theta} \right\} \\ & - \frac{\rho U}{2g} \operatorname{Re} \int_0^{2\pi} d\theta \int_0^\infty dz \cos \theta \left\{ i\omega \varphi_B \frac{\partial \varphi_B^*}{\partial \theta} - \right. \\ & - U \cos \theta \frac{\partial \varphi_B}{\partial R} \frac{\partial \varphi_B^*}{\partial \theta} \\ & \left. + \frac{U \sin \theta}{R} \frac{\partial \varphi_B}{\partial \theta} \frac{\partial \varphi_B^*}{\partial \theta} \right\} \Big|_{z=0}. \end{aligned} \quad (2.43)$$

This concludes the derivation of the equations for force and moment in terms of the far-field potentials. We shall next develop methods for evaluating these far-field potentials.

### III. EXPRESSION OF THE FORCE EQUATIONS IN TERMS OF THE KOCHIN FUNCTION

Evaluation of the steady force and moment as given by equations (2.36) through (2.39) and equations (2.42) through (2.43) requires knowledge of the ship-generated potential  $\varphi_B$  in the far field. To obtain an appropriate far-field expression for  $\varphi_B$ , we shall first apply Green's formula to obtain an equation for  $\varphi_B$  at a typical point in the fluid. Such a representation in general involves a Green's function suitable for the problem under investigation and the boundary values of  $\varphi_B$ .

The far-field expression of  $\varphi_B$  may be obtained by making use of an asymptotic form of the Green's function. Newman (1959) has obtained such an asymptotic expression. It is shown in Appendix B how Newman's results may be applied to obtain the far-field expression for  $\varphi_B$ .

As given by equations (B.13) through (B.15) the far-field expression of the ship-generated potential  $\varphi_B$  may be written as:

$$\varphi_B(R, \theta, z) \sim \sum_{p,m} f_{Bpm}(R, \theta; \lambda_p, u_m) e^{\lambda_p z}, \quad (3.1)$$

where

$$f_{Bpm} = \left( \frac{1}{2\pi R} \right)^{1/2} (\pm) \left\{ \frac{\lambda_p (u_m) \sin^2 \theta}{\sin^2 u_m \left| \left( \frac{d\theta}{du} \right)_{u=u_m} \cos(u_m - \theta) \right|} \right\}^{1/2} \cdot H(\pi + u_m, \lambda_p) e^{i\lambda_p R \cos(u_m - \theta) + i \frac{\pi}{2} \pm i \frac{\pi}{4}} \quad (3.2)$$

$$H(u, \lambda) = \iint_{S_{B0}} \left\{ \frac{\partial \varphi_B(\mathbf{x}_0)}{\partial n} - \varphi_B(\mathbf{x}_0) \frac{\partial}{\partial n} \right\} e^{\lambda Z_0} \cdot$$

$$e^{i\lambda [x_0 \cos u + y_0 \sin u]} \cdot dS(\mathbf{x}_0) \quad (3.3)$$

and

$$\lambda p = \frac{\nu}{2t^2 \cos^2 u} [1 + 2t \cos u \pm \sqrt{1 + 4t \cos u}], \quad p = 1, 2. \quad (3.4)$$

In equation (3.4) the plus and minus signs are for  $p = 1$  and  $p = 2$ , respectively. The function  $H$  defined by (3.3) is known as the Kochin function which plays an important role in the computation of force and moment.

We shall next substitute equation (3.1) in place  $\varphi_B$  in those equations for the steady forces, namely, equations (2.36) through (2.39). To describe the analysis we shall dwell on the longitudinal component of force,  $\langle \Delta F_1 \rangle$ . If we substitute equation (3.1) into equation (2.37), carry out the  $z$ -integration and compute all the necessary derivatives of  $f_{Bpm}$ , the following result may be obtained:

$$\begin{aligned} \langle \Delta F_1 \rangle = & \frac{\rho}{8\pi} \sum_{p,m} \int_0^{2\pi} d\theta |H(\pi + u_m; \lambda_p)|^2 \cdot \\ & \cdot \frac{\lambda p^2 (u_m) \cdot \cos u_m \operatorname{sign}(\sin u_m \sin \theta)}{\left| \frac{d\theta}{du} \right|_{u=u_m} \sqrt{1 + 4t \cos u_m}} \\ & + \left\{ \text{cross-terms in } p \text{ and } m \right\}, \end{aligned} \quad (3.5)$$

where the cross terms represent cross multiplication between terms of different indices in  $p$  or  $m$ . It can be shown by again applying the method of stationary phase that the cross terms are of order  $1/\sqrt{R}$  and vanish as  $R \rightarrow \infty$ . Further discussion in this regard may be found in Newman (1959). The algebra involved in deducing the final result given in equation (3.5) is somewhat lengthy and will be omitted here. However, the following relationships are rather crucial in making the reduction:

$$\begin{aligned} \text{(i)} \quad & \nu - (1 + 2t \cos u) \lambda p + \frac{t^2 \cos^2 u}{\nu} \lambda^2 p^2 = 0, \\ \text{(ii)} \quad & \frac{d}{d\theta} [\lambda p(u) \cos(u - \theta)] = \lambda p \sin(u - \theta), \\ \text{(iii)} \quad & \cos(u - \theta) = (\mp \sqrt{1 + 4t \cos u}) \frac{\sin \theta}{\sin u}, \\ \text{(iv)} \quad & \cos(u - \theta) + 2t \cos \theta - 2 \frac{t^2 \cos u \cos \theta}{\nu} \lambda p \\ & = \frac{\sin u}{\sin \theta}. \end{aligned} \quad (3.6)$$

The first equation follows from the free-surface condition (2.23) and the remaining equations (ii) through (iv) above may be established by making use of equation (i), equation (3.4), and the stationary-phase relation, equation (B.10):

$$\cot \theta = - \left[ \tan u \pm \frac{\sqrt{1 + 4t \cos u}}{\sin u \cos u} \right]. \quad (3.7)$$

This is the equation which determines the stationary-phase values,  $u_m$ , in equations (3.1) and (3.2), and also is an equation which relates the variable  $u$  to the variable  $\theta$ .

A closer inspection of equation (3.5) tells us that it has a very inconvenient form for further computation since both variables,  $\theta$  and  $u$ , are involved and the values of  $u_m$  cannot be known until we solve equation (3.7). However, in light of equation (3.7), we can make a change of variables and can convert the integration in equation (3.5) into one with respect to  $u$  rather than  $\theta$ . To this end, let us denote symbolically the relationship given in equation (3.6) as  $\theta = \theta(u)$ . Then the  $\theta$  integral in equation (3.5) may be written symbolically in the following form:

$$\begin{aligned} \int_0^{2\pi} \frac{F(u, \theta)}{\left| \frac{d\theta}{du} \right|} d\theta &= \int_a^b \frac{F[u, \theta(u)]}{\left| \frac{d\theta}{du} \right|} \left( \frac{d\theta}{du} \right) du \\ &= \int_a^b F[u, \theta(u)] \operatorname{sign} \left( \frac{d\theta}{du} \right) du, \end{aligned} \quad (3.8)$$

where  $(\alpha, \beta)$  is the range of the variable  $u$  as  $\theta$  varies continuously between 0 and  $2\pi$ . In carrying out the  $u$ -integration in (3.8), one should account for the sign of the derivative  $(d\theta/du)$ .

After carrying out the details of the change of variable, we obtain an expression for  $\langle \Delta F_{1BB} \rangle$  as follows:

$$\begin{aligned} \langle \Delta F_{1BB} \rangle = & -\frac{\rho}{8\pi} \left[ \int_{-\pi/2}^{\pi/2} - \int_{\pi/2}^{\pi+u_0} - \int_{\pi+u_0}^{3\pi/2} \right] \frac{du \lambda_1^2(u) \cos u}{\sqrt{1+4t \cos u}} \\ & \cdot |H(\pi+u, \lambda_1)|^2 \\ & - \frac{\rho}{8\pi} \left[ \int_0^{\pi+u_0} + \int_{\pi+u_0}^{2\pi} \right] \frac{du \lambda_2^2(u) \cos u}{\sqrt{1+4t \cos u}} \\ & \cdot |H(\pi+u, \lambda_2)|^2, \end{aligned} \quad (3.9)$$

where the constant  $u_0$  appearing in the limits of integration is defined by:

$$u_0 = \begin{cases} 0, & t \leq 1/4, \\ \cos^{-1} \left( \frac{1}{4t} \right), & t > 1/4. \end{cases} \quad (3.10)$$

Let us next proceed to investigate  $\langle \Delta F_{11B} \rangle$  as given by equation (2.36). If we substitute equations (2.17) and (3.1) in place of  $\varphi_1$  and  $\varphi_B$ , respectively, perform the necessary computation of the various derivatives, and carry out the  $z$ -integration, the following result is obtained from equation (2.36):

$$\begin{aligned} \langle \Delta F_{11B} \rangle = & \frac{\rho g A}{2\sigma} \operatorname{Re} \sum_{p,m} \int_0^{2\pi} d\theta \frac{k_0 \lambda p}{(k_0 + \lambda p)} \cdot \\ & \cdot \left( \frac{R}{2\pi} \right)^{1/2} (\pm) \left\{ \frac{\lambda p(u_m) \sin^2 \theta}{\sin^2 u_m \left| \frac{d\theta}{du} \right|_{u=u_m} \cos(u_m - \theta)} \right\}^{1/2}, \quad (3.11) \\ & \cdot S_{pm} \cdot H(\pi+u_m, \lambda p) \cdot e^{i\pi/2 \pm i\pi/4} \\ & \cdot e^{iR [\lambda p \cos(u_m - \theta) + k_0 \cos(\theta - \beta)]}, \end{aligned}$$

where

$$\begin{aligned} S_{pm} = & -\cos \beta \cos(u_m - \theta) - \cos u_m \cos(\theta - \beta) \\ & + \cos \theta \cos(u_m - \beta) - \cos \theta \\ & + \frac{1}{2} (k_0 + \lambda p) \cos u_m \cos \beta \cos \theta \\ & + \frac{\nu}{k_0 \lambda p} (k_0 + \lambda p) \cos \theta. \end{aligned} \quad (3.12)$$

The integrand of (3.11) contains the large parameter  $R$  in the complex argument of the exponential function. Therefore, it may be evaluated by the method of stationary phase as given by equation (B.8). Hence, let us put

$$g_{pm}(\theta) = \lambda p(u_m) \cos(u_m - \theta) + k_0 \cos(\theta - \beta). \quad (3.13)$$

By making use of the relationship (ii) in (3.6) and the stationary-phase equation (3.7), we can show that

$$\begin{aligned} g'_{pm} &= \frac{d g_{pm}}{d\theta} = \\ &= \lambda p(u_m) \sin(u_m - \theta) - k_0 \sin(\theta - \beta), \end{aligned} \quad (3.14)$$

and

$$\begin{aligned} g''_{pm} &= \lambda p(u_m) \left[ \sec(u_m - \theta) \frac{du_m}{d\theta} - \cos(u_m - \theta) \right] \\ &- k_0 \cos(\theta - \beta). \end{aligned} \quad (3.15)$$

To find the stationary-phase points of  $\theta$ , say  $\theta_k$ , for the  $\theta$ -integration in equation (3.11), we want to choose  $\theta_k$  such that

$$g'_{pm}(\theta_k) = 0. \quad (3.16)$$

At the same time  $p$ ,  $u_m$ , and  $\theta_k$  must be chosen so that equation (3.7) is simultaneously satisfied. After a complete census of all the stationary-phase points which satisfy these requirements, the only combination which gives a contribution to (3.11) is:

$$u_m = \pi + \beta \quad \text{and} \quad p = 2, \quad (3.17)$$

$$\lambda p(u_m) = \lambda_2(\pi + \beta) = k_0. \quad (3.18)$$

It can be shown that for all other possible roots of equation (3.16), the expression  $S_{pm}$  given by (3.12) vanishes. If we now apply the method of stationary phase with values of the stationary-phase points from (3.17) and (3.18), the following final result may be obtained:

$$\langle \Delta F_{11B} \rangle = \frac{1}{2} \rho \sigma A \cos \beta I_{\epsilon} \{ H(\beta, k_0) \}, \quad (3.19)$$

where  $\operatorname{Im}\{H(\beta, k_0)\}$  denotes the imaginary part of the Kochin function evaluated at  $u = \beta$ , and  $\lambda = k_0$ , according to equation (3.3).

Equations (3.9) and (3.19) are the final results for the longitudinal component of the steady hydrodynamic force acting on the ship. As such, it represents the amount of additional steady thrust necessary in order to maintain the ship moving at a constant mean-forward speed. The added resistance is defined as a quantity opposite to this additional steady thrust. Hence, the added resistance may be given as:

$$\begin{aligned} \langle \Delta R \rangle &= - \langle \Delta F_L \rangle \\ &= \langle \Delta R_{1B} \rangle + \langle \Delta R_{BB} \rangle, \end{aligned} \quad (3.20)$$

where

$$\langle \Delta R_{1B} \rangle = - \langle \Delta F_{11B} \rangle, \quad (3.21)$$

$$\langle \Delta R_{BB} \rangle = - \langle \Delta F_{1BB} \rangle. \quad (3.22)$$



If we proceed further and employ a similar analysis to evaluate the lateral-force component, equations (2.38) and (2.39), the following results are obtained:

$$\begin{aligned} \langle \Delta F_{2BB} \rangle = & -\frac{\rho}{8\pi} \left[ \int_{-\pi/2}^{\pi/2} - \int_{\pi/2}^{\pi+u_0} - \int_{\pi+u_0}^{3\pi/2} \right] \frac{du \lambda_1^2(u) \sin u}{\sqrt{1+4t \cos u}} \\ & \cdot \left| H(\pi+u, \lambda_1) \right|^2 \\ & -\frac{\rho}{8\pi} \left[ \int_0^{\pi-u_0} + \int_{\pi+u_0}^{2\pi} \right] \frac{du \lambda_2^2(u) \sin u}{\sqrt{1+4t \cos u}} \\ & \cdot \left| H(\pi+u, \lambda_2) \right|^2 \end{aligned} \quad (3.23)$$

and

$$\langle \Delta F_{21B} \rangle = \frac{1}{2} \rho u A \sin \beta \operatorname{Im} \left\{ H(\beta, k_0) \right\} \quad (3.24)$$

Thus, the formulas for the longitudinal and lateral force components are essentially similar and only differ by  $\cos u$  or  $\cos \beta$  for the longitudinal component and  $\sin u$  or  $\sin \beta$  for the lateral component.

Note that resemblance between this set of formulas, namely, equations (3.9), (3.19), (3.23) and (3.24), and those obtained by Newman (1967) and Maruo (1960) for the case of zero mean forward speed is remarkable. In particular, the expressions for  $\langle \Delta F_{k1B} \rangle$ ,  $k = 1, 2$ , are essentially identical except for the different forms assumed by the Kochin function for the case with or without a mean forward speed. As seen from equation (3.3), the forward speed effect in the formulas for  $\langle \Delta F_{k1B} \rangle$  can appear only through  $\varphi_B$  and its normal derivative in the definition of the Kochin function.

Thus far, we have completed the derivation of general formulas which express the longitudinal and lateral force components in terms of the Kochin function. In principle, the same method of derivation should apply to the moment, equations (2.42) and (2.43). Unfortunately, the stationary-phase analysis of the moment equations with forward-speed effects is far more involved than that of the force equations, and thus far, we have not succeeded in producing these equations in a form suitable for evaluation.

Our next task is to investigate how the Kochin function may be evaluated. It is appropriate to remark here that one advantage of having the general formulas such as those of (3.9), (3.19), (3.23) and (3.24) is that there are a number of options available for evaluating the Kochin function. In principle one may choose from these available options one specific approximation scheme that appears to give best accuracy for a particular application. For our purpose here, however, we shall make use of the strip approximation developed in the linearized ship-motion theory of Salvesen, Tuck, and Faltinsen (1970).

#### IV. AN APPROXIMATE METHOD FOR EVALUATING THE KOCHIN FUNCTION

The Kochin function, equation (3.3), is defined by an integral over the mean surface of the ship where the integrand is a linear function of the velocity potential,  $\varphi_B$ , on the surface of the ship. Therefore, if we linearly decompose  $\varphi_B$  as follows:

$$\varphi_B = \sum_{j=1}^6 \alpha_j \varphi_j + \varphi_7$$

where the  $\alpha_j$ 's are the amplitude responses in the six modes of motion and  $\varphi_7$  is written instead of  $\varphi_D$ , then we can write:

$$H(u, \lambda p) = \sum_{j=1}^6 \alpha_j H_j(u, \lambda p) + H_7(u, \lambda p),$$

where

$$\begin{aligned} H_j(u, \lambda p) = & \iint_{S_{B0}} dS \left\{ \frac{\partial \varphi_j}{\partial n} - \varphi_j \frac{\partial}{\partial n} \right\} \\ & \cdot e^{\lambda p [z + ix \cos u + iy \sin u]} \end{aligned} \quad j=1, \dots, 7.$$

We shall now approximate the potential functions, the  $\varphi_j$ 's, and the surface integral by means of slender-body theory and the strip method. The most significant approximation which we shall make is the assumption that the component of the normal in the longitudinal direction is much smaller than the components in the transverse plane,  $n_1 \ll n_2, n_3$ . Using this approximation we can now rewrite the surface integral for the Kochin function as follows:

$$\begin{aligned} H_j(u, \lambda p) = & \int_L dx e^{i\lambda p x \cos u} \\ & \cdot \int_{C(x)} dl \left\{ \frac{\partial \varphi_j}{\partial n} - \varphi_j \frac{\partial}{\partial n} \right\} \\ & \cdot e^{\lambda p [z + iy \sin u]} \end{aligned} \quad j=1, \dots, 7, \quad (4.1)$$

or

where  $L$  is the length of the ship and  $C(x)$  is the cross-section of the ship.

For  $j = 1, \dots, 6$ , we can simplify equation (4.1) by making use of the body boundary condition to reduce the first term within the brackets. By employing equation (93) from Salvesen, Tuck, and Faltinsen (1970), equation (STF.93), we can replace  $\partial \varphi_j / \partial n$  by  $i\omega n_j + Um_j$ , where the term  $Um_j$  gives the strip approximation to the correction for forward speed. For a detailed discussion of the boundary value problem for the individual  $\varphi_j$ 's, see Appendix A of Salvesen, Tuck, and Faltinsen (1970). Making the above replacement and substituting  $\partial / \partial n$  for  $\partial / \partial n$ , we obtain:

$$\begin{aligned} H_j(u, \lambda p) = & \int_L dx e^{i\lambda p x \cos u} \\ & \cdot \int_{C(x)} dl \left\{ (i\omega n_j + Um_j) - \varphi_j \frac{\partial}{\partial n} \right\} e^{\lambda p (z + iy \sin u)} \end{aligned} \quad j=1, \dots, 6. \quad (4.2)$$

From the fact that  $n_1$  and  $\varphi_1$  are higher order than the other  $n_j$ 's and  $\varphi_j$ 's we can neglect  $H_1(u, \lambda p)$  with regard to the other  $H_j$ 's. Finally, we may substitute  $\lambda p (n_3 + i n_2 \sin u)$  for  $\partial / \partial n$  and write  $H_j(u, \lambda p)$  in its final form:

$$\begin{aligned} H_j(u, \lambda p) = & \int_L dx e^{i\lambda p x \cos u} \\ & \cdot \int_{C(x)} dl \left\{ (i\omega n_j + Um_j) - \lambda p \varphi_j (n_3 + i n_2 \sin u) \right\} \\ & \cdot e^{\lambda p (z + iy \sin u)} \end{aligned} \quad j=2, \dots, 6. \quad (4.3)$$

Equation (4.3) is ideally suited to numerical integration because all of the quantities within the integrand are known from the solution of the forced oscillation problems.

In order to determine  $H_7(u, \lambda_p)$ , we shall employ a generalization of the treatment developed in Salvesen (1973). First of all, it is easy to show by means of Green's theorem that the first term within the brackets of equation (4.1) is of higher order due to the slenderness of the ship. If we denote the inner integral of the remaining term as  $I_7$ , we have:

$$I_7 = - \int_{c(x)} dl \varphi_7 \frac{\partial}{\partial N} e^{\lambda p(z+iy \sin u)} \quad (4.4)$$

By taking the normal derivative in equation (4.4), and by employing the mean value theorem on the left and right half contours of the integral in equation (4.4), we can simplify  $I_7$  as follows:

$$I_7 = - \lambda p e^{\lambda p \bar{z}} \left\{ e^{-i \lambda p y(\bar{z}) \sin u} \cdot \int_{c(x)} dl \varphi_7 [n_3 + i n_2 \sin u] + e^{i \lambda p y(\bar{z}) \sin u} \int_{c(x)} dl \varphi_7 [n_3 + i n_2 \sin u] \right\} \quad (4.5)$$

where  $\bar{z}$  is the mean value of  $z$ , and  $C(\bar{x})$  and  $C(\bar{x}^+)$  are the left and right half contours respectively. Equation (4.5) can be simplified if we add and subtract the integral over the right half contour,  $C(\bar{x}^+)$ , from the first term. This yields:

$$I_7 = - \lambda p e^{\lambda p \bar{z}} \left\{ e^{i \lambda p y(\bar{z}) \sin u} \cdot \int_{c(x)} dl \varphi_7 [n_3 + i n_2 \sin u] + \sin(\lambda p y(\bar{z}) \sin u) \cdot \int_{c(x)} dl \varphi_7 [n_3 + i n_2 \sin u] \right\} \quad (4.6)$$

By taking advantage of slenderness we can argue that for  $\lambda_p = O(1)$ , the sine term is of higher order than the first term. While for  $\lambda_p$  large, the exponential term in  $\bar{z}$  causes  $I_7$  to vanish. Therefore, we can simplify equation (4.6) as follows:

$$I_7 = - \lambda p e^{\lambda p \bar{z}} \int_{c(x)} dl \varphi_7 [n_3 + i n_2 \sin u] \quad (4.7)$$

If we again take advantage of the body boundary conditions, equation (STF.91), we find that we can replace the normal components,  $n_2$  and  $n_3$ , by their respective body boundary conditions:

$$I_7 = - \frac{\lambda p}{i \omega} e^{\lambda p \bar{z}} \int_{c(x)} dl \varphi_7 \left\{ \frac{\partial \varphi_3}{\partial N} + i \frac{\partial \varphi_2}{\partial N} \sin u \right\} \quad (4.8)$$

Because  $\varphi_2$ ,  $\varphi_3$  and  $\varphi_7$  all satisfy Laplace's equation, the linearized free-surface condition, and the radiation condition, we may apply the two-dimensional Green's theorem to equation (4.8) and write:

$$I_7 = - \frac{\lambda p}{i \omega} e^{\lambda p \bar{z}} \int_{c(x)} dl \frac{\partial \varphi_7}{\partial N} \left\{ \varphi_3 + i \varphi_2 \sin u \right\} \quad (4.9)$$

By substituting the body boundary condition for the diffraction potential, equation (STF.89) into equation (4.9), we find:

$$I_7 = \frac{\lambda p}{i \omega} e^{\lambda p \bar{z}} \int_{c(x)} dl \frac{\partial \varphi_1}{\partial N} \left\{ \varphi_3 + i \varphi_2 \sin u \right\} \quad (4.10)$$

If we now substitute  $\varphi_1$  into equation (4.10) and substitute equation (4.10) back into the equation for  $H_7$  we obtain:

$$H_7(u, \lambda p) = - \frac{i \lambda p k_0 A^2 g}{\omega \sigma} \int_L dx e^{i x [\lambda p \cos u + k_0 \cos \beta]} e^{\lambda p \bar{z}} \cdot \int_{c(x)} dl [\varphi_3 n_3 - \varphi_2 n_2 \sin u \sin \beta] e^{k_0 [z + i y \sin \beta]}$$

Thus, we have obtained an expression for  $H_7(u, \lambda_p)$  in terms of the known potentials resulting from the solution of the forced oscillation problem.

## V. CONCLUDING REMARKS

The general equation for the second-order steady force can be expressed as a sum of two components: one, say  $\langle \Delta L_{IB} \rangle$ , which is due to the interaction between incoming-wave system and ship-generated waves; the other, say  $\langle \Delta L_{BB} \rangle$ , which is strictly due to the interaction of the ship generated waves with themselves. The final equation representing  $\langle \Delta L_{IB} \rangle$  has the same form as that in the case with zero forward speed. On the other hand,  $\langle \Delta L_{BB} \rangle$  with forward-speed effects has a more complicated form but it can be identified as a generalization of the case with zero forward speed.

Since the final equations for the steady force are expressed in terms of the Kochin function, computation of the steady force depends on computation of the Kochin function. Since the Kochin function involves knowledge of the forced-oscillation and diffracted-wave potentials, various approximation techniques developed in linearized theory of ship motion may be utilized to obtain the potential functions. Among these available options we have chosen to experiment with the strip method according to Salvesen, Tuck and Faltinsen (1970). Based on this method, final formulas suitable for numerical evaluation have been obtained. The computational work is currently in progress and the results will be reported in a future paper.

## ACKNOWLEDGMENTS

The authors would like to thank Suzanne Reed and William G. Day for their timely assistance with the preparation of this manuscript. Thanks are also due to Choung Mook Lee and Nils Salvesen for their helpful technical discussions. Finally, we wish to acknowledge the General Hydromechanics Research Program and the High Performance Vehicle Hydromechanics Program for their financial support of this project.

## BIBLIOGRAPHY

- Cummins, W. E. (1957). The force and moment on a body in a time-varying potential flow. *J. Ship Res.*, Vol. 1, No. 1, 7-18 & 54.
- Gerritsma, J.; Beukelman, W. (1972). Analysis of the resistance increase in waves of a fast cargo ship. *Int'l. Shipbldg. Progress*, Vol. 19, No. 217.

- Haskind, M. D. (1946). The hydrodynamic theory of ship oscillations in rolling and pitching. (R) *Prikl. Mat. Mekh.*, Vol. 10, 33-66 (1946). Translated in *Soc. Naval Arch. Marine Engrs. Tech. & Res. Bull.*, No. 1-12, 3-43 (1953).
- Havelock, T. H. (1942). The drifting force on a ship among waves. *Phil. Magazine*, Ser. 7, Vol. 33, 467-475.
- Joosen, W. P. A. (1966). Added resistance of ships in waves. 6th Sym. Nav. Hydrodyn., Washington, D.C.
- Lee, C. M.; Newman, J. N. (1971). The vertical mean force and moment of submerged bodies under waves. *J. Ship Res.*, Vol. 15, No. 3, 231-245.
- Maruo, H. (1957). The excess resistance of a ship in rough seas. *Int'l. Shipbldg. Progress*, Vol. 4, No. 35.
- (1960). The drift of a body floating on waves. *J. Ship Res.*, Vol. 4, No. 1, 1-10.
- (1963). Resistance in waves. "Researches in Seakeeping Qualities of Ships in Japan." Chap. 5, Soc. Nav. Architects Jap. 60th Anniv. Ser., Vol. 8.
- Nakamura, S. (1976). Added resistance and propulsive performance of ships in waves. Int'l. Seminar on Wave Resistance, Tokyo, Japan.
- Newman, J. N. (1959). The damping and wave resistance of a pitching and heaving ship. *J. Ship Res.*, Vol. 3, No. 2, 1-19.
- (1967). The drift force and moment on ships in waves. *J. Ship Res.*, Vol. 11, No. 1, 51-60.
- Ogilvie, T. E.; Tuck, E. O. (1969). A rational strip theory of ship motions: Part I. Dept. of Nav. Arch. and Marine Eng., College of Eng., Univ. Michigan, Report No. 013.
- Salvesen, N. (1974). Second-order steady-state forces and moments on surface ships in oblique regular waves. Int'l. Symp. on the Dynamics of Marine Vehicles and Structures in Waves, Univ. College, London.
- Salvesen, N.; Tuck, E. O.; Faltinsen, O. (1970). Ship motions and sea loads. *Trans. Soc. Naval Arch. Marine Engrs.*, Vol. 78, 250-279; discussion, 279-287.
- Serrin, J. (1959). Mathematical principals of classical fluid mechanics. "Encyclopedia of Physics," Vol. 8/1, 125-263. Springer-Verlage, Berlin.
- Sibul, O. J. (1971). Measurement and calculation of ship resistance in waves. College of Eng., Univ. California, Berkeley, Report No. NA-71-2.
- Stoker, J. J. (1957). *Water waves*. xxviii + 567 pp. Interscience Publishers, New York.
- Strom-Tejsen, J.; Yeh, H. Y. H.; Moran, D. D. (1973). Added resistance in waves. *Trans. Soc. Naval Arch. Marine Engrs.*, Vol. 81.
- Timman, R.; Newman, J. N. (1962). The coupled damping coefficients of a symmetric ship. *J. Ship Res.*, Vol. 5, No. 1-7.
- Watanabe, Y. (1938). Some contribution to the theory of rolling. *Trans. INA*, Vol. 80.

Wehausen, J. V.; Laitone, E. V. (1960). Surface waves. "Encyclopedia of Physics," Vol. 9, 446-778. Springer-Verlage, Berlin.

## APPENDIX A — FORCE AND MOMENT ON THE SHIP FROM MOMENTUM CONSIDERATIONS

In this Appendix, we shall derive general formulas for the force and moment on a ship from momentum considerations. These formulas are developed using the translating coordinate system Oxyz as a frame of reference. As defined in equation (2.1), the total velocity potential and total fluid velocity relative to this reference frame are, respectively:

$$\Phi(x, y, z, t) = -Ux + \phi(x, y, z, t),$$

and

$$\underline{q} = \nabla\Phi = -U\underline{e}_1 + \nabla\phi.$$

With reference to this coordinate system, Bernoulli's equation and Euler's equations of motion may be written, respectively, in the following form:

$$p - p_{\text{ATM}} = -\rho \frac{\partial\phi}{\partial t} - \frac{1}{2} |\underline{q}|^2 - \rho gz + \frac{1}{2} U^2, \quad (\text{A.1})$$

and

$$\frac{\partial \underline{q}}{\partial t} + (\underline{q} \cdot \nabla) \underline{q} = -\frac{1}{\rho} \nabla p - g \underline{e}_3. \quad (\text{A.2})$$

In making use of these equations, we shall follow the usual practice of setting the atmospheric pressure to zero, i.e.,  $p_{\text{atm}} = 0$ .

**The Moment.** Let us now proceed to derive the moment equation. To this end, we shall start by considering the moment of fluid momentum contained in a fluid volume  $V_c$  which is bounded by the free surface,  $S_F$ , the actual wetted surface of the ship,  $S_B$ , a control surface  $\Sigma_R$  (a large vertical cylinder of radius  $R = \sqrt{x^2 + y^2}$ ), and a circular bottom closing  $\Sigma_R$  at a depth  $z = -h$ . We shall take the moment with respect to 0, the origin of the translating coordinate system Oxyz.

Let P be a point in the fluid volume  $V_c$  fixed with reference to the Oxyz frame. Let  $\underline{r} = \underline{OP} = x\underline{e}_1 + y\underline{e}_2 + z\underline{e}_3$  be the position vector of the point P. Then the total moment of fluid momentum with respect to 0 is:

$$\underline{K}_0 = \rho \iiint_{V_c} \underline{r} \wedge \underline{q} \, dV, \quad (\text{A.3})$$

where the fluid volume  $V_c$  is now dependent upon time. If we apply a general formula known as the transport theorem see, for example, Serrin (1959) p. 132, we may compute  $d\underline{K}_0/dt$  as follows:

$$\begin{aligned} \frac{d\underline{K}_0}{dt} &= \rho \iiint_{V_c} \frac{\partial}{\partial t} (\underline{r} \wedge \underline{q}) \, dV \\ &\quad + \rho \iint_{\partial V_c} \underline{r} \wedge \underline{q} \, V_n \, dS \\ &= \rho \iiint_{V_c} \underline{r} \wedge \frac{\partial \underline{q}}{\partial t} \, dV + \rho \iint_{\partial V_c} \underline{r} \wedge \underline{q} \, V_n \, dS, \end{aligned} \quad (\text{A.4})$$



where  $\partial V_c = S_B + S_F + \Sigma_R + \Sigma_h$  is the total boundary surface of  $V_c$  and  $V_n$  is the velocity at any given point of  $V_c$  in the direction of its normal. In this work, the normal vector to  $\partial V_c$  will be chosen as one pointing out the fluid volume  $V_c$ . Hence, at the ship's surface, for example, the normal vector points into the ship. Note that in this equation,  $\partial/\partial t$  denotes differentiation with  $V_c$  fixed and therefore,  $\partial/\partial t = 0$  for a fixed point in the Oxyz coordinate system. Next, we shall make use of the following vector identities:

$$(i) \quad \iiint_{V_c} \mathbf{r} \wedge \nabla \psi \, dV = \iint_{\partial V_c} \psi [\mathbf{r} \wedge \mathbf{n}] \, dS,$$

$$(ii) \quad \iiint_{V_c} \left\{ (\mathbf{r} \wedge \mathbf{A})(\nabla \cdot \mathbf{B}) + \mathbf{r} \wedge [(\mathbf{B} \cdot \nabla) \mathbf{A}] + \mathbf{B} \wedge \mathbf{A} \right\} dV \\ = \iint_{\partial V_c} (\mathbf{r} \wedge \mathbf{A})(\mathbf{B} \cdot \mathbf{n}) \, dS,$$

$$(iii) \quad \iiint_{V_c} \mathbf{r} \wedge [(\nabla \phi \cdot \nabla) \nabla \phi] \, dV = \\ \iint_{\partial V_c} (\mathbf{r} \wedge \nabla \phi)(\nabla \phi \cdot \mathbf{n}) \, dS,$$

where  $\psi$ ,  $\mathbf{A}$  and  $\mathbf{B}$  are differentiable scalar and vector functions defined in  $V_c$ , and (iii) follows immediately from (ii) for the irrotational flow of an incompressible inviscid fluid.

If we now make a substitution from Euler's equation for  $\partial \mathbf{q}/\partial t$  and make use of vector identity (iii), the volume integral in equation (A.4) may be recast as:

$$\rho \iiint_{V_c} \mathbf{r} \wedge \frac{\partial \mathbf{q}}{\partial t} \, dV = - \iint_{\partial V_c} \rho [\mathbf{r} \wedge \mathbf{n}] \, dS - \\ - \rho \iint_{\partial V_c} (\mathbf{r} \wedge \mathbf{q})(\mathbf{q} \cdot \mathbf{n}) \, dS \\ - \rho \iiint_{V_c} \mathbf{r} \wedge \mathbf{g} \, dV. \quad (A.5)$$

Substituting equation (A.5) into equation (A.4), we obtain:

$$\dot{N}_0 \stackrel{\text{Def}}{=} \iint_{S_B} \rho [\mathbf{r} \wedge \mathbf{n}] \, dS \\ = - \frac{d\mathbf{K}_0}{dt} - \iint_{S_F + \Sigma_R + \Sigma_h} \rho [\mathbf{r} \wedge \mathbf{n}] \, dS \\ + \rho \iint_{S_B + S_F + \Sigma_R + \Sigma_h} (\mathbf{r} \wedge \mathbf{q}) [\mathbf{V}_n \cdot \mathbf{q} \cdot \mathbf{n}] \, dS \\ - \rho \iiint_{V_c} \mathbf{r} \wedge \mathbf{g} \, dV, \quad (A.6)$$

where we have made use of the fact that  $\partial V_c = S_B + S_F + \Sigma_R + \Sigma_h$ . Equation (A.6) may be simplified further by observing that  $\mathbf{V}_n \cdot \mathbf{q} \cdot \mathbf{n} = 0$  on  $S_B$  and  $S_F$  due to the kinematic boundary condition,  $p = 0$  on  $S_F$ , and  $\mathbf{V}_n = 0$  on  $\Sigma_R$ , if  $\Sigma_R$  is chosen to be translating with the Oxyz coordinate system. In addition, if we make a substitution from Bernoulli's equation for the pressure  $p$ , and also use the relation  $\mathbf{q} = -\nabla \phi$ , the following final result may be obtained:

$$\dot{N}_0 = \iint_{S_B} \rho [\mathbf{r} \wedge \mathbf{n}] \, dS \\ = - \frac{d\mathbf{K}_0}{dt} + \rho \iint_{\Sigma_R} \left\{ (\mathbf{r} \wedge \mathbf{n}) \cdot \left[ \left( \frac{\partial \phi}{\partial t} - U \frac{\partial \phi}{\partial x} + \frac{1}{2} |\nabla \phi|^2 \right) \right. \right. \\ \left. \left. + (\mathbf{r} \wedge \nabla \phi) [\mathbf{U} \mathbf{n}_1 - \nabla \phi \cdot \mathbf{n}] \right. \right. \\ \left. \left. + \mathbf{g} \mathbf{z} (\mathbf{r} \wedge \mathbf{n}) \right\} \, dS \\ + \rho \iint_{\Sigma_R} \left\{ -U (\mathbf{r} \wedge \mathbf{e}_1) [\mathbf{U} \mathbf{n}_1 - \nabla \phi \cdot \mathbf{n}] \right\} \, dS \\ - \rho \iiint_{V_c} \mathbf{r} \wedge \mathbf{g} \, dV, \quad (A.7)$$

where  $\mathbf{n} = n_1 \mathbf{e}_1 + n_2 \mathbf{e}_2 + n_3 \mathbf{e}_3$ .

In obtaining this final result, we have made use of the fact that  $|\nabla \phi| = 0$  and  $|\frac{\partial \phi}{\partial t}| = 0$  on  $\Sigma_h$  as  $h \rightarrow \infty$ , and also that  $n_1 = 0$  on  $\Sigma_h$ .

Note that the second surface integral over the control surface,  $\Sigma_R$ , in equation (A.7) has a special meaning. It may be written as:

$$\dot{T} = U \iint_{\Sigma_R} (\mathbf{r} \wedge \mathbf{e}_1) [\rho \mathbf{q} \cdot \mathbf{n}] \, dS. \quad (A.8)$$

Since  $\rho \mathbf{q} \cdot \mathbf{n} dS$  represents the rate at which fluid leaves  $V_c$  across a surface element, the surface integral represents the moment of the total rate of fluid flow ("flux") across the control surface  $\Sigma_R$ . Thus, the quantity  $\dot{T}$  as defined in equation (A.8) is strictly a function of time alone. Furthermore, it is linear in the velocity potential. Therefore, if the fluid motion is periodic, then the time average of  $\dot{T}$  is zero. Thus, it would be more convenient for our present application to recast equation (A.7) in the following form:

$$\dot{N}_0 = \iint_{S_B} \rho [\mathbf{r} \wedge \mathbf{n}] \, dS \\ = \rho \iint_{\Sigma_R} \left\{ (\mathbf{r} \wedge \mathbf{n}) \left[ \frac{\partial \phi}{\partial t} - U \frac{\partial \phi}{\partial x} + \frac{1}{2} |\nabla \phi|^2 \right] \right. \\ \left. - (\mathbf{r} \wedge \nabla \phi) [\mathbf{U} \mathbf{n}_1 + \nabla \phi \cdot \mathbf{n}] + \mathbf{g} \mathbf{z} (\mathbf{r} \wedge \mathbf{n}) \right\} \, dS \\ - \rho \iiint_{V_c} \mathbf{r} \wedge \mathbf{g} \, dV + \dot{T}(t) - \frac{d\mathbf{K}_0}{dt}. \quad (A.9)$$

Note that the function  $\phi$  appearing in equation (A.9) is the perturbation potential. Hence, equation (A.9) is now in a form suitable for further decomposition and application.

**The Force.** The force equation is obtained in a manner analogous to that of the moment except that the momentum instead of the moment of momentum is used. The total fluid momentum contained in  $V_c$  is:

$$\mathbf{Q} = \iiint_{V_c} \rho \mathbf{q} \, dV. \quad (A.10)$$

By following a similar analysis to that of the moment and by making use of the following vector identities:

$$\begin{aligned} \text{(i)} \quad & \iiint_V \nabla \psi \, dV = \iint_{\partial V} \psi \underline{n} \, dS, \\ \text{(ii)} \quad & \iiint_V \{ \underline{A}(\nabla \cdot \underline{B}) + (\underline{B} \cdot \nabla) \underline{A} \} \, dV = \iint_{\partial V} \underline{A}(\underline{B} \cdot \underline{n}) \, dS, \\ \text{(iii)} \quad & \iiint_V (\underline{q} \cdot \nabla) \underline{q} \, dV = \iint_{\partial V} \underline{q}(\underline{q} \cdot \underline{n}) \, dS, \end{aligned}$$

the following final formula may be obtained:

$$\begin{aligned} F &= \iint_{S_B} p \underline{n} \, dS \\ &= \rho \iint_{\Sigma_R} \left\{ \underline{n} \left[ \frac{\partial \phi}{\partial t} - U \frac{\partial \phi}{\partial x} + \frac{1}{2} |\nabla \phi|^2 \right] \right. \\ &\quad \left. - \nabla \phi [-U n_1 + \nabla \phi \cdot \underline{n}] + g z \underline{n} \right\} \, dS \\ &\quad - \rho g z_3 \iint_{V_c} dV + \underline{f} - \frac{dQ}{dt}, \end{aligned} \quad (\text{A.11})$$

where

$$\underline{f} = \underline{z}_1 U \iint_{\Sigma_R} \rho \underline{q} \cdot \underline{n} \, dS. \quad (\text{A.12})$$

As in the discussion of the moment, the surface integral over  $\Sigma_R$  in equation (A.12) represents the total flux of fluid leaving the control volume  $V_c$  across the control surface  $\Sigma_R$ . It is clear from the equation that  $\underline{f}$  is linear in the velocity potential. Hence, the time-averaged value of  $\underline{f}$  equals zero if the fluid motion is periodic.

## APPENDIX B - THE FAR-FIELD EXPRESSION OF THE SHIP-GENERATED POTENTIAL

In this appendix we shall derive an asymptotic expression for  $\varphi_B$  valid at a large distance from the ship. As  $\varphi_B$  is supposed to yield the diffracted and forced-oscillation waves, it must meet the radiation condition. In addition it must also satisfy the following conditions: Laplace's equation, the linearized free-surface condition for a disturbance sinusoidal in time moving with constant forward speed, and the condition of boundedness at infinite depth.

$$\begin{aligned} \text{(i)} \quad & \lim_{R \rightarrow \infty} R^{1/2} \left( -\frac{\partial \varphi_B}{\partial R} - i \nu \varphi_B \right) = 0, \quad R = \sqrt{x^2 + y^2}, \\ \text{(ii)} \quad & \Delta \varphi_B = 0, \quad z < 0, \\ \text{(iii)} \quad & \nu \varphi_B(x, y, 0) + i 2 \tau \frac{\partial \varphi_B}{\partial x} - \frac{\tau^2}{\nu} \frac{\partial^2 \varphi_B}{\partial x^2} - \frac{\partial \varphi_B}{\partial z} = 0, \\ & \nu = \frac{\omega^2}{g}, \quad \tau = \frac{\omega U}{g}, \\ \text{(iv)} \quad & \lim_{z \rightarrow -\infty} |\nabla \varphi_B| = 0. \end{aligned} \quad (\text{B.1})$$

Furthermore,  $\varphi_B$  is required to satisfy the linearized kinematic condition on the ship's mean surface,  $S_{BO}$  which is also known as the Timman-Newman condition, [Timman and Newman (1962)]. The explicit expression of this condition will be specified as needed.

To apply Green's formula, let  $V_c^{(0)}$  be a fluid region bounded by the "mean" ship surface  $S_{BO}$ , the undisturbed free surface  $S_F^{(0)}$ , a cylindrical surface  $\Sigma_R^{(0)}$  with a large radius  $R = \sqrt{x^2 + y^2}$ , and a "bottom" disc  $\Sigma_h$  which closes  $\Sigma_R^{(0)}$  at a depth  $z = -h$ . Let  $\underline{x} = (x, y, z)$  be a point  $V_c^{(0)}$ , then Green's formula yields the following representation for  $\varphi_B$ :

$$\varphi_B(\underline{x}) = \frac{1}{4\pi} \iint_{\partial V_c^{(0)}} \left\{ G(\underline{x}; \underline{x}_0) \frac{\partial \varphi_B}{\partial n} - \varphi_B(\underline{x}_0) \frac{\partial G}{\partial n} \right\} dS_{(\underline{x}_0)}, \quad (\text{B.2})$$

where  $\underline{x}_0 = (x_0, y_0, z_0)$  denotes a point on  $\partial V_c^{(0)} = S_{BO} + S_F^{(0)} + \Sigma_R^{(0)} + \Sigma_h$ ,  $\underline{n}$  is the unit normal point out of the fluid volume  $V_c^{(0)}$  (i.e., pointing into the ship at  $S_{BO}$ ), and  $G$  is the Green's function. The appropriate Green's function is required to satisfy all the conditions on  $\varphi_B$  except the kinematic condition at the ship's surface. As such, it represents the velocity potential of a pulsating point source moving under a free surface with a constant speed  $U$  and pulsating with frequency  $\omega$ .

After applying all the boundary conditions, equation (B.2) simplifies to:

$$\varphi_B(\underline{x}) = \frac{1}{4\pi} \iint_{S_{BO}} \left\{ G(\underline{x}; \underline{x}_0) \frac{\partial \varphi_B}{\partial n} - \varphi_B(\underline{x}_0) \frac{\partial G}{\partial n} \right\} dS_{(\underline{x}_0)}. \quad (\text{B.3})$$

It should be noted here that in arriving at equation (B.3), a line integral along the waterline of  $S_{BO}$  which is of higher order has been neglected.

The Green's function for this problem has been constructed by Haskind (1946) and others. The specific form which is convenient for our present application may be found in Newman (1959). By carrying out the complex-contour integrations involved, and by repeated application of the method of stationary phase to the double integrals of this Green's function, Newman (1959) obtained the following intermediate result valid for large  $R = \sqrt{x^2 + y^2}$ :

$$\begin{aligned} G &\sim i 2 \int_{-\pi/2}^{\theta-\pi/2} du \frac{\lambda_1 e^{\lambda_1 [(z+z_0)+iX]}}{\sqrt{1+4\tau \cos u}} \\ &- i 2 \int_{\pi/2}^{\pi/2+\theta} du \frac{\lambda_1 e^{\lambda_1 [(z+z_0)+iX]}}{\sqrt{1+4\tau \cos u}} \\ &- i 2 \int_{\theta+\pi/2}^{\frac{3\pi}{2}} du \frac{\lambda_2 e^{\lambda_2 [(z+z_0)+iX]}}{\sqrt{1+4\tau \cos u}} + O\left(\frac{1}{R}\right), \end{aligned} \quad (\text{B.4})$$

where

$$\begin{aligned} X &= (x - x_0) \cos u + (y - y_0) \sin u \\ &= R \cos(u - \theta) - x_0 \cos u - y_0 \sin u, \end{aligned} \quad (\text{B.5})$$

$$\lambda_{1,2} = \frac{\nu}{2\tau^2 \cos^2 u} [1 + 2\tau \cos u \pm \sqrt{1 + 4\tau \cos u}], \quad (\text{B.6})$$

$$\begin{aligned} u_0 &= \begin{cases} 0, & \tau \leq 1/4 \\ \cos^{-1} \left( \frac{1}{4\tau} \right), & \tau > 1/4 \end{cases} \\ \nu &= \frac{\omega^2}{g}, \quad \tau = \frac{\omega U}{g}. \end{aligned} \quad (\text{B.7})$$

These integrals are valid for  $0 \leq \theta \leq \pi$ . If the value of  $\theta$  lies in  $\pi \leq \theta \leq 2\pi$ , then the ranges of integration for the three integrals must be modified as follows:  $\theta - 3\pi/2 \leq u \leq \pi/2$  for the first integral,  $\theta - \pi/2 \leq u \leq 3\pi/2$  for the second integral, and  $\theta - 3\pi/2 \leq u \leq \theta - \pi/2$  for the third integral. The primed integrals in equation (B.4) denote that the interval  $\pi - u_0 < u < \pi + u_0$  is to be excluded in carrying out the integration.

The specific formula from the method of stationary phase which is used to evaluate these integrals is:

$$\int f(u) e^{iRg(u)} du = \left(\frac{2\pi}{R}\right)^{1/2} \sum_m f(u_m) \cdot \left\{ \left| \frac{\partial^2 g}{\partial u^2} \right|_{u=u_m} \right\}^{-1/2} \cdot e^{iRg(u_m) \pm i\frac{\pi}{4}} + O\left(\frac{1}{R}\right) \quad (B.8)$$

where  $u_m$  is the  $m^{\text{th}}$  root of the equation  $\partial g / \partial u = 0$ , and the sign of  $\partial^2 g / \partial u^2$  determines the plus or minus sign in the exponent.

Note that every integral in equation (B.4) still contains the large parameter  $R$  in the complex arguments of the exponential functions. By applying the method of stationary phase once more to evaluate the integrals in equation (B.4), Newman (1959) obtained the following final result as an asymptotic form of the Green's function:

$$G(R, \theta, z; x_0, y_0, z_0) \sim \left(\frac{8\pi}{R}\right)^{1/2} \sum_{p,m} (\pm) \left\{ \frac{\lambda p(u_m) \sin^2 \theta}{\sin^2 u_m \left| \left( \frac{d\theta}{du} \right)_{u=u_m} \cos(u_m - \theta) \right|} \right\}^{1/2} \cdot e^{\lambda p(u_m)[z+z_0+iR \cos(u_m-\theta)-i x_0 \cos u_m - i y_0 \sin u_m]} \cdot e^{i\frac{\pi}{2} \pm i\frac{\pi}{4}} \quad (B.9)$$

where the  $u_m$ 's are the roots of the equation:

$$\cot \theta = - \left[ \tan u \pm \frac{\sqrt{1+4\tau \cos u}}{\sin u \cos u} \right] \quad (B.10)$$

In applying the method of stationary phase, equation (B.8), to the integrals in equation (B.4) to obtain the result in equation (B.9), the following relationships are used:

$$g_p(u, \theta) = \lambda p(u) \cos(u - \theta) \quad , \quad p = 1, 2 \quad (B.11)$$

$$\left( \frac{\partial^2 g_p}{\partial u^2} \right)_{u=u_m} = - \frac{\lambda p(u_m)}{\cos(u_m - \theta)} \left( \frac{d\theta}{du} \right)_{u=u_m} \quad (B.12)$$

The requirement that  $\partial g_p / \partial u = 0$  and  $v \neq 0$  yields equation (B.10) which relates  $\theta$  to  $u$ . The plus or minus sign after the summation sign,  $\Sigma$ , in equation (B.9) is determined by the sign of the corresponding terms in equation (B.4) while the plus or minus sign in the exponent of equation (B.9) is determined by the sign of  $\partial^2 g_p / \partial u^2$ . For the details of the derivation of these results concerning the asymptotic form of the Green's function, one should consult Newman (1959).

Let us now substitute equation (B.9) in place of  $G$  in equation (B.3). Then  $\varphi_B$  may be written in the following form:

$$\varphi_B(R, \theta, z) \sim \sum_{p,m} f_{Bpm}(R, \theta; \lambda p, u_m) \cdot e^{\lambda p z} \quad (B.13)$$

where

$$f_{Bpm} = \left(\frac{1}{2\pi R}\right)^{1/2} (\pm) \left\{ \frac{\lambda p(u_m) \sin^2 \theta}{\sin^2 u_m \left| \left( \frac{d\theta}{du} \right)_{u=u_m} \cos(u_m - \theta) \right|} \right\}^{1/2} \cdot H(\pi + u_m, \lambda p) \cdot e^{i\lambda p R \cos(u_m - \theta) + i\frac{\pi}{2} \pm i\frac{\pi}{4}} \quad (B.14)$$

The function  $H$  is known as the Kochin function and is defined by:

$$H(u, \lambda) = \iint_{S_{BO}} \left\{ \frac{\partial \varphi_B}{\partial n} - \varphi_B \frac{\partial}{\partial n} \right\} e^{\lambda z_0} \cdot e^{i\lambda [x_0 \cos u + y_0 \sin u]} dS_{(z_0)} \quad (B.15)$$

Equation (B.13) is the far-field expression of  $\varphi_B$  we need for the evaluation of the force and moment equations.



# Discussion on Paper by J. F. Dalzell

A.Y. ODABASI

In this paper the author takes the effect of non-linearity into account by introducing the concepts of bi-spectra and the quadratic frequency response function. When, however, it is considered that the functional series expansion (1) is truncated after the second term, the nonlinearity should be slight, i.e., the system should be almost linear, in order that the procedure explained in the paper should be valid. It is known from practice that for slightly nonlinear systems the method of statistical linearisation works reasonably well. Therefore it is hard to understand the advantages to be gained by employing the proposed approach.

If the system is strongly nonlinear then the proposed method is no longer valid and the available methods for determining the probability density function of phase co-ordinates, such as Kazakov's algorithm, become more attractive.

## Author's Reply

It is certainly true that the two-term functional polynomial model is an approximation which should apply only to weakly non-linear systems. With respect to added resistance, the experimental results indicate that the two-term model does apply. This has been shown for as wide a range of sea severity as has been employed heretofore in demonstrating that the linear model applies to pitch and heave.

Furthermore, the most important practical formula resulting from the approximation of added resistance by the two-term model has been in fairly successful use for about fifteen years (see Eq.15 of the paper). For these reasons it is hard for the author to understand the advantages to be gained in not using the model for added resistance and related problems. For practical purposes all that has been achieved in the present work is to indicate that the model may serve as well for the prediction of low frequency fluctuations in resistance - a subject which it must be admitted is of more immediate concern in offshore platform problems than to ordinary ship design.

The conceptual advantages of the model are that

- (a) any reasonably well behaved wave input (regular, random, transient) may be accommodated;
- (b) the response functions required are not difficult to relate to the results of hydromechanic analyses;
- (c) it appears that the statistics of the process may be approximated.

It is the author's understanding of statistical linearisation that it is necessary first to have a physical (and not too complicated) differential evaluation defining the system. No such equation for added resistance appears in the paper, and the author is not sure if one exists. It is also the author's understanding that the process of statistical linearisation must be carried out over again for each excitation spectrum of interest unless the unrealistic 'white' spectrum is assumed. Once the linear and quadratic response functions required by the functional model are known, there are no restrictions upon the excitation spectrum shape, and no necessity to re-optimize the solution.

PRECEDING PAGE BLANK-NOT FILMED

# Discussion on Paper by D. K. P. Yue et al

A.Y. ODABASI

The authors offer a valuable method for the evaluation of wave forces for three dimensional bodies. Their comparison with the Green's function approach, is, however, unjustified for conventional problems. As is well known, the difficulty in evaluating the Green's function appears when the distance between the source point and the control point is small. In such cases the numerical evaluation of the principal value integral by using Monacella's singularity removal (ref.10) or contour integration (ref.11) methods may become quite time consuming. Recently Mr G.E. Hearn has devised a transformation method (ref.12) by which the computation, is, on average, twelve times faster than the other two methods. Under these circumstances it is hard to believe that the method in this paper can save time in comparison with the Green's function approach.

To make the above statement more clear let us reconsider the formulation and the method of solution in the paper. The convergence of the method can only be guaranteed if the variation of the functional  $J(\phi, \phi')$  defined by equation (9) is zero. Hence when the solution is found by the method described in the paper it should be substituted into the variational equation and the value of the first variation found should be arbitrarily small. To achieve convergence in the first trial is improbable and could only result from a lucky guess. Hence, after the first trial either the number of coefficients have to be increased or the coefficients have to be varied, possibly by means of a gradient method to satisfy the variational equation. This, in turn, involves an iteration process and therefore increases the computation time. Furthermore, if the expression (7) is assumed to be an eigenfunction expansion it would tend to the Green's function (Ref.13) when  $n$  and  $m$  tend to infinity.

This method may have successful application for unconventional problems, such as wave forces in shallow water with a discontinuous bottom for which it is very difficult to derive the Green's function.

## REFERENCES

- (10) Monacella, V.J. (1966). "The disturbance due to a slender ship oscillating in waves in a fluid of finite depth", J. Ship Research, Vol.10, No.4.

- (11) Wehausen, J.V. and Laitone, E.V. (1960). "Surface Waves", Handbuch der Physik, Bd.9, Springer Verlag, Berlin.
- (12) Hearn, G.E. (1976) "Alternative methods of evaluating the Green's function in three dimensional ship-wave problems", to appear in J. Ship Research.
- (13) Morse, P.M. and Feshbach, H. (1953). "Methods of Theoretical Physics", Vol.1, McGraw-Hill Book Co., New York.

R.W. YEUNG

I would like to commend the authors for a very fine paper which treats the water-wave scattering problem in three dimensions using a rational approach of handling the radiation condition. Having actually gone through the process of solving the related forced-motion problem for a body with two planes of symmetry a few years back, I am quite appreciative of the numerical difficulties that the authors must have overcome in work involving three dimensions before fruition is possible.

There are a couple of points that I would like to discuss. The first is that the present treatment of the eigen-function expansion associated with the local disturbance terms may lead to a singular matrix. To see that, we need to refer to Eqn.(27). The coupling submatrix  $[K_c]$  represents the influences on  $\phi$  due to each of the eigenfunctions  $K_n(k_{mr})$ . The diagonal submatrix  $[K_D]$  is also associated with  $K_n(k_{mr})$ ,  $n=m$ . Each combination of  $n$  and  $m$  therefore would correspond to one row of  $[K_c]^T$  or a column of  $[K_c]$ . Each element of these submatrices is thus multiplied by  $K_n(k_{mr})$ . Now, consider a given  $n$ : as we proceed to the higher eigenvalues i.e. as we increase  $m$ , the values of each succeeding row become exponentially smaller and smaller, compared with the rest of the bulk of the stiffness matrix. For a finite precision machine, this would imply that we will have one, or even more than one, row or column of 'zeros'. Hence the present treatment would lead to a more and more singular matrix as one includes more and more eigenfunctions. Of course, in practice, one will not get a zero determinant after the reduction process because of round-off errors. But clearly the system will be more and more unstable. I pointed out in my Gaithersburg paper (Yeung, 1975) that one simple way of over-

coming this is to absorb the  $K_n(\kappa_m r_s)$  factor in the unknown coefficients of the eigenexpansion  $a_{l,m}$ . This is entirely legitimate if one recalls the fact that when one specifies the vertical behavior of a harmonic function, the horizontal behavior is specified implicitly simultaneously. These functions are all harmonic in the fluid domain. The suggestion given here has provided a numerically more stable matrix for the hybrid-integral equation technique I investigated, and should be adaptable in the present formulation. It is worthwhile to note that the problem would occur only if one has more than a few eigenfunctions in the expansion.

The second point concerns the extension of the present method to infinitely deep water, which has traditionally been the easier problem for an analytic approach when compared with finite depth, though quite the contrary for a numerical approach. For shorter waves, one might argue that one can choose a depth such that the waves and the body do not feel the bottom. But for low-frequency waves, the bottom effects can only be eliminated if one uses a very large depth, which would lead to an unacceptably large number of elements. This is of course a problem that all methods such as finite-element, or finite-difference, which require the direct solution of the field equation, must be faced with. In the present case, perhaps the introduction of some sort of super-element below a finite number of dense layers of elements may do the job. However, it is not clear what type of interpolation function would be suitable for such a purpose. Note that any truncation of the fluid domain by a large sphere of radius  $R$  without accounting for contributions outside of the sphere will incur an error of  $O(\frac{1}{R})$  in the functional.

$$\frac{\partial J}{\partial \{\phi\}} = \{0\} \text{ and } \frac{\partial J}{\partial \{\mu\}} = \{0\}$$

which is equivalent to the vanishing of the first variation:  $\delta J = 0$ , hence the substitution he proposes is redundant. Also, our method is a direct one and not an iterative one. The accuracy improves if more and more unknowns are allowed; the idea is similar to approximating an infinite series by a truncated series. Lastly, our Eq(7) is everywhere regular in  $V'$  and does not approach a singular Green's function. The last remark of Dr. Odabasi's second paragraph is incorrect.

R.W. YEUNG

Prof. Yeung has made a valid observation that  $K_n(\kappa_m r)$  decays exponentially as  $m$  (hence  $\kappa_m$ ) increases. In fact  $K_n$  also grows exponentially with the order  $n$ . In our numerical work we normalized all the Bessel functions by their asymptotic formulas for both large order and argument so that the entries in the coefficient matrix are all of order unity in magnitude. This type of care is quite common in any numerical work when one must deal with very large or very small numbers.

For infinite water depth, the simplest thing to do in the finite element region is to use increasingly large elements at great depths without introducing new interpolation functions. This flexibility is not easily available for a numerical scheme such as the finite difference method.

## Authors' Reply

A.Y. ODABASI

Our comments on the merits of the Green's function method are based on experiences which have been described in published literature. We have not seen the unpublished work of G.E. Hearn. It is worth reminding that the choice of a numerical method depends not only on computation time, but also on many other factors such as simplicity of theory, human effort in preparation of computer program, ease of adaptation to more complex geometries etc. The importance of each factor varies with the problem and with the investigator. Judging by information available to us, we feel that the more complicated the geometry, the more advantageous the present method or its modifications.

Dr. Odabasi appears to have missed a fundamental point. Equations (25) and (26) are obtained by requiring that



# Discussion on Paper by Wen-Chin Lin et al

N. SALVESEN

I would like to congratulate the authors on their fine contribution to this difficult problem. They have presented, to my knowledge the most complete derivation of the mean second-order force and moment on a ship advancing in oblique waves. For the prediction of the mean force component in the longitudinal direction of the ship, there exist several other more approximate theories which agree reasonably well with experiments. However, for the mean moment and the side force component, there exists no theory which has any reasonable agreement with experiments for the case with forward speed. It is unfortunate that the theoretical results given in this paper are very difficult to compute numerically and particularly, it is going to be a hard task to compute the term  $\langle F_{1B} \rangle$  in equation (3.9).

The main difference between the present theory and the theory I presented here in London two years ago (Salvesen, 1974) is that I assumed that the body potential,  $\psi_B$ , is much smaller than the incident wave potential,  $\psi_1$ . The second-order mean force may be written as

$$F = F_{1B} + F_{BB}$$

where  $F_{1B}$  is the mean force due to the interaction between  $\psi_1$  and  $\psi_B$  and  $F_{BB}$  is due to  $\psi_B$  interacting with itself. In my work, as a consequence of the assumption that  $\psi_B \ll \psi_1$ , the term  $F_{BB}$  was ignored, whereas in the present paper, expressions have been derived for both of the force components. Recent unpublished work has shown that, at least for the added resistance, there is good agreement between experiments and theory when  $F_{BB}$  is ignored as seen in Figure 2. However, it will be interesting to see numerical results for  $F_{BB}$  so one can better establish the importance of this term.

I would like to point out that the result given for  $F_{1B}$  in this paper

$$F_{1B} = \frac{1}{2} \rho g A \cos \beta \operatorname{Im} \{ H(\beta, k_0) \}$$

is identical to equation (37) in my 1974 paper. Here  $H(\beta, k_0)$  is the Kochin function which can easily be evaluated numerically if it is expressed within the concept of ship theory as shown in this paper and also shown in my 1974 paper. Unfortunately, the Kochin function in the form it appears in the force term  $F_{BB}$  (see equation (3.9)) cannot be expressed within strip theory in the same way as is possible for the interaction term  $F_{1B}$ .

Again, I would like to congratulate the authors for their fine contribution and I am looking forward to seeing numerical results, in particular for the moments for which all other theories seem to give unreasonable results.

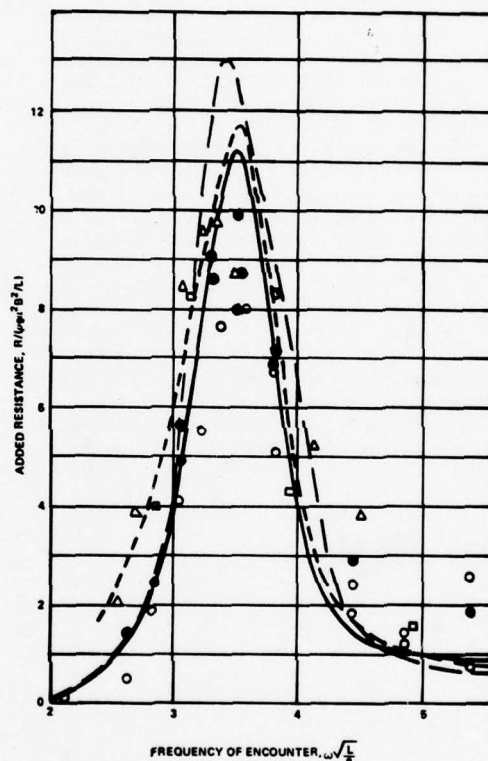


Fig. 2: - Comparison of Experimental and Theoretical Added Resistance for Series 60 Hull with  $C_B = 0.70$  at  $F_n = 0.200$ .

- EXPERIMENTS
  - STROM-TEJSE ET AL. [6], CONST. SPEED
  - GERRITSMAN & BEUKELMAN [12]
  - △ SIBUL [13], CONST. SPEED
  - SIBUL [14], CONST. TOW FORCE
- THEORIES
  - PRESENT THEORY
  - - - GERRITSMAN & BEUKELMAN [5]
  - ... MARUO [3]

## Authors' Reply

We have one remark which we would like to make in response to Dr. Salvesen's discussion.

Newman (1970) has analysed the second order vertical force on a submerged body in incident waves. In his analysis Newman neglected the body potential ( $\phi_B$ ) relative to the incident wave potential ( $\phi_I$ ). He justified this assumption by claiming that his body was a weak scatterer due to its deep submergence.

Salvesen (1974) has performed an analysis, similar to that of Newman, for the added resistance of a ship in a seaway at arbitrary heading. Because of the slender-body approximation which he has used to represent the ship, Salvesen has also assumed that his ship is a weak scatterer, and neglected  $\phi_B$  in relation to  $\phi_I$ . In head seas, this is probably a reasonable assumption, and indeed Salvesen's calculations seem to bear this out. However, in quartering and beam seas the weak scatterer assumption cannot be justified. Witness that  $F_{1IB}$ , the component of added resistance, due to  $\phi_I$ , goes to zero as the ship's heading approaches  $\pi/2$ . It is at this point that it is obviously necessary to include  $\phi_B$  in the analysis. This leads to  $F_{1BB}$  the other component of the added resistance. While we do not have any calculations to show the relative contributions of  $F_{1IB}$  and  $F_{1BB}$  to the added resistance as a function of ship heading; Salvesen's theory for added resistance should be used with great caution for headings away from head seas.

## SESSION IV

### UNCONVENTIONAL CRAFT

Tuesday, 30 March 1976

14.00—18.00

Chairman: J. P. Breslin

Some aspects of sidehull hydrodynamics and maneuvering in the design of surface effect ships, by R. B. Wade and S. Wang

The effect of air compressibility on the nonlinear motion of an air-cushion vehicle over waves, by L. J. Doctors

Some aspects of hydrofoil motions and their implications for crew performance, by D. Johnson, L. T. Messum and K. Nicholson

Wave impacts on hydrofoil ships and structural implications, by T. G. Drummond, M. Mackay and R. T. Schmitke

An experimental study of a superventilated finite aspect ratio hydrofoil near a free surface, by O. Furuya and A. J. Acosta

The results of the experimental investigation on the skirt parameters influence on resistance and stability characteristics of a hovercraft, by E. Brzoska, L. Kobylinski, M. Krezelewski and K. Paul

The use of oscillators to obtain hydrodynamic and structural load data for SES craft, by P. Kaplan, S. Davis and A. Malakhoff

PRECEDING PAGE BLANK-NOT FILMED



# SOME ASPECTS OF SIDEHULL HYDRODYNAMICS AND MANEUVERING IN THE DESIGN OF SURFACE EFFECT SHIPS

R. B. WADE and S. WANG  
Tetra Tech, Inc., Pasadena, California, USA

Free surface water tunnel measurements of the forces and moments on a typical surface effect ship sidehull are presented. These data are used to validate the use of simple classical slender body theory for the prediction of sidehull hydrodynamic characteristics. Generally correlation of the data with the theory is very good. Under certain conditions sidehull ventilation occurs and its significance on performance is discussed. Inclusion of this type of sidehull representation in a four degree of freedom simulation program for the prediction of the turning characteristics of a surface effect ship leads to excellent results.

## NOTATION

$C$	Frictional coefficient
$C_x^f, C_y$	Axial and lateral force coefficients (= Force/ $\frac{1}{2}\rho U^2 l^2$ )
$C_N, C_K$	Yaw and roll moment coefficients (= Moment/ $\frac{1}{2}\rho U^2 l^3$ )
$c$	Characteristic length for spray
$D_m$	Momentum drag
$d$	Sidehull immersion
$Fr$	Froude No.
$f$	Distance of center of fluid pressure on sidehull from craft C.G.
$f_o$	Integrated average of $f(\xi)$
$g$	Acceleration of gravity
$I_x$	Moment of inertia about x-axis
$I_z$	Moment of inertia about z-axis
$i_z$	Index subscript for nozzles
$K$	Roll moment
$k_{yy}$	Lateral added mass coefficient
$l$	Craft length
$m$	Mass
$m_1$	Axial added mass of craft
$N$	Yaw moment
$N_y, N_z$	Unit normal components
$n$	Pump rpm
$p$	Angular velocity about x-axis, roll rate
$q$	Dynamic pressure ( $=\frac{1}{2}\rho U^2$ )
$r$	Angular velocity about z-axis, yaw rate
$S$	Projected area
$T$	Kinetic energy
$T_g$	Gross thrust
$t_g$	Time or maximum thickness of sidehull
$U$	Craft forward speed
$u$	Velocity component along x-axis
$V$	Relative velocity in a cross flow plane
$v_r$	Velocity component along y-axis
$X, Y, Z$	Force components along the body coordinates
$x, y, z$	Coordinate system fixed in the body
$x_o, y_o, z_o$	Initial coordinate system
$x_*, z_*$	Trajectory coordinates of craft C.G. in fixed reference frame
$\alpha$	Nozzle tilt angle of waterjet
$\delta$	Index denotes steering and control, or nozzle deflection angle of waterjet
$\eta$	waterline mean thickness
$\theta$	trim angle
$\mu$ or $\mu_{yy}$	Section added mass in sway
$\mu_{yz}$	Cross coupling of added mass between sway and heave
$\xi$	Station index along the body x-axis

$\rho$	Density of fluid
$\Phi$	Velocity potential
$\phi$	Roll angle
$\psi$	Yaw angle

## 1. INTRODUCTION

With the advent of the development of high performance ocean going craft a great deal of interest has centered on the Surface Effect Ship (SES). This craft, as distinct from its close relative, the air cushion vehicle relies partially on sidehulls to contain the air cushion on which it operates. This feature of the vehicle makes it non amphibious in nature but provides a measure of desirability and ruggedness in an open sea environment and certainly affords the means of considering the design of large size vehicles while keeping the flexible seal design tractable.

Over the last decade considerable attention has been given to this type of craft by the United States Navy. This involvement has seen the development of several craft among which are the XR-1, XR-3 and two 100 ton vehicles, which are currently undergoing test and evaluation operations. As the next generation of such craft the Navy is presently conducting a preliminary design competition for a 2000 ton vehicle. Attendant with this effort has arisen the need to develop a comprehensive technology to aid in the prediction of craft performance, stability, maneuvering and control. These investigations have naturally involved many interesting hydrodynamic problems covering such topics as the development of techniques for the performance prediction of flexible bow and stern seals, appendages, waterjet inlets, supercavitating propellers and sidehulls. The unique characteristics of these craft in operating at the water interface with relatively shallow immersions over a very wide speed range and sea state environment imposes a very challenging and sometimes overwhelming task to the designer. Not only is he confronted with the normal problems of ship-sea-state interaction and its control but he is faced with the added complexities of high speed operation such as cavitation, ventilation and, uniquely to this vehicle, air leakage and broaching phenomena.

In the present paper we address ourselves to only

one facet of the hydrodynamics of SES design - that of the prediction of sidehull performance and its subsequent use in the prediction of maneuvering. The paper presents the results of an experimental investigation conducted in a free surface water tunnel aimed at measuring the forces and moments on a typical SES sidehull. These experiments, conducted some time ago, were motivated by the need to generate much needed data on sidehulls of this type in order to validate the analytic methods being used to predict sidehull performance. These methods, based on classical slender body theory, were adopted for use in the present problem by considering the water surface as an undisturbed constant pressure boundary and considering the body as bounded by the hull lines below the free surface and the free surface itself. The basic requirements for the slender body approximation are well met in this problem as the sidehulls are typically long and slender shapes. This approach was initially formulated for the present application in Reference (1). Whereas, the premise for applying this method to the present problem is intuitively obvious the validity of the assumptions made especially in regard to the free surface requires justification. Additionally, it is necessary to determine whether the appropriate values of added mass coefficient are being applied. Since the sidehulls are typically operated at shallow immersions compared to their lengths, non linear contributions to the forces and moments are accounted for by the use of the cross flow drag concept. Here again the appropriateness of this concept in the present application and the value of the cross flow drag coefficients used require validation.

Another feature of sidehull operation addressed in the present paper is that of drag. At the typical operational speeds of these craft in the 40 to 80 knot range a substantial amount of spray drag can be generated. Assessing the significance of this drag component in relation to the total drag of the sidehull is of importance. An attempt to ascertain and measure this effect is discussed.

It is not the intent of the paper to present a development of the slender body analysis as applied to the SES. This has been treated in some detail in References (1), (2) and (3). Rather a brief synopsis of the basic theory is presented for completeness and certain interesting modifications incorporated into the analysis, in order to enhance correlation with experiment, are discussed.

As most of the testing in this area has been done on complete SES models wherein the interaction of other influences such as seals and the cushion pressure has rendered the interpretation of the sidehull data very difficult, it was considered imperative to conduct these tests on a single sidehull in a free surface water tunnel under controlled conditions, devoid of any influences from attendant seals, appendages and cushion effects. In this manner the forces and moments on the sidehull could be isolated and accurately measured. Furthermore observation of the flow past the sidehull under various orientations could be examined and photographed, thus allowing a qualitative assessment of the flow to be made.

Although all components of force and moment were measured during the tests only the lateral plane forces and moments and the drag will be discussed as it is these components which primarily govern the maneuvering characteristics.

The paper is organized in basically two parts. The first part deals with a description of the sidehull test program and modifications made to the basic slender body theory. Comparisons of lateral plane forces and moments obtained from this modified theory to the experimental results are then presented. As assessment of the spray drag generated by the sidewall is also made. Qualitative aspects of the flow are then discussed supported by photographic coverage. On the basis of the generally excellent results obtained the use of this analytical representation in a four degree of freedom maneuvering program is discussed in the second part of the paper. Justification for the use of this simplified maneuvering representation is given and its use in the prediction of the maneuvering of the XR-1C craft is presented. As will be seen, here again excellent correlation is achieved.

It should be emphasized at this point that the overall objective here, is to present the development of a simple but versatile design tool for the prediction of the maneuvering of a SES. As distinct from a complete six degree of freedom representation, this analytical tool can be used inexpensively to conduct parametric studies of a SES, using a variety of turning schemes or devices, in order to assess the relative merits of each system. It is not intended to imply that a complete dynamical representation of the craft is unnecessary simply that this approach affords a cost effect means of performing screening of conceptual designs prior to a final evaluation using the six degree of freedom simulation.

## 2. EXPERIMENTAL PROGRAMS

**Model Description:** The model of the sidehull was manufactured from aluminium in three sections. The forward section representing approximately the forward third of the model could be interchanged with alternate bow shapes. The center section was of constant deadrise and the aft section included a blister or fairing representing a typical shape for housing a waterjet inlet. The model was hard anodized and lightened by using hollowed sections. Ballast weights were used in order to locate the center of gravity of the model in a desired location so as not to over range the force balance. Horizontal gradation lines, 0.0254 m apart, were painted on the hull to help in the interpretation of water contours obtained from photographs. The model was 1.34 m in overall length with a keel length of 1.2 m. Typical section lines of the model are shown in Figure 1. In this figure station 1 represents the transom and station 16 is located at the intersection of the keel line with the stem. Stations aft of station 16 are 0.079 m apart and in front of it are 0.015 m apart. As will be seen a ramped shaped fairing commences at approximately station 8 which gradually widens and drops below the keel line to a depth of 0.019 m. The fairing is provided with rounded corners to reduce the possibilities of cavitation and flow separation at high speeds under sideslip conditions. The model was mounted to a six component task force balance through a rigid mounting fixture.

**Facility Description:** The tests were conducted in the Free Surface Water Tunnel (FSWT) at the California Institute of Technology. This facility has a working section 2.43 m long by 0.51 m wide with a water depth of 0.51 m. The maximum tunnel speed attainable is 7.32 m/s. Since the critical speed of the tunnel is approximately 2.28 m/s all tests were conducted well above this speed. This necessity is



dictated by the fact that in the neighborhood of this speed it is difficult to maintain an even, undisturbed water surface. Practically, the minimum speed for achieving a relatively uniform surface is approximately 3 m/s. For present purposes a minimum speed of 5.18 m/s was taken for the lateral plane measurements.

The working section is provided with large lucite windows, both at the bottom and sides in order to provide flow visibility and photographic coverage. The model was mounted to a three degree of freedom actuator through a suitable mounting fixture and six component force balance. The actuator was capable of varying the trim, yaw and immersion of the model. Figure 2 illustrates diagrammatically the relationship of the model to the force balance center and the reference point used in calculating all moments.

The strain gauge force balance used, measures the roll moment, axial force, two side forces and two normal forces. From the latter four readings the yaw and pitching moments can be derived. The maximum range of the force elements is  $\pm 178$  N each on the normal forces,  $\pm 62$  N each on the side forces, 111 N in the axial direction and 29 N m in roll. All forces were measured in body coordinates as the force balance was mounted rigidly to the model and rotated with it. The signals from the balance were passed through a balance network and amplifying system before being read out on an integrating digital display.

**Experimental Procedure:** Prior to the tests the force balance was calibrated over the anticipated range of forces and moments. It was found to be linear with a least count of 0.04 N. Great care was taken in aligning the model to the tunnel axis and in zero setting of the angular motion mechanism. The immersion actuator was also calibrated and found accurate to  $0.03 \times 10^{-5}$  m. Since the water surface in the working section is not perfectly horizontal when the tunnel is running the zero trim condition was referenced to the mean water slope as obtained by aligning the keel to the running water surface. This slope being a function of tunnel velocity was determined for each speed. Typically values obtained at 7.01 m/s and 5.18 m/s were -0.28 degrees and -0.16 degrees respectively, where the negative sign signifies a nose down condition.

Typically, the test procedure used was as follows. After setting the tunnel at the desired speed and adjusting the zero trim angle to its running zero position, the keel was set to just clear the water surface and the heave scale adjusted to zero. The yaw was set at zero and with the model clear of the water air tares were recorded. The model was then immersed to the desired value and forces and moments recorded as a function of yaw angle. During the course of this series of runs, photographs of the flow and spray pattern were recorded at selected conditions. Flow phenomena such as the condition of the base ventilation cavity at the sidewall transom, the occurrence of leading edge ventilation or vortex type ventilation were also noted. After each set of runs, which nominally covered approximately 10 data points, an air tare was retaken. Additionally two zero yaw readings were recorded at the beginning and end of each data set to ensure repeatability of the data and to monitor any drifts which might be occurring in the force recording system. This sequence was repeated for varying immersions.

For negative and positive trim angles, the model was lowered until the leading edge of the keel line was just touching the water. Knowing the trim and the length from this point to the reference plane, the model was either raised or lowered to achieve the desired immersion at the reference plane and the procedure described above was repeated.

In addition to the above tests, a series of buoyancy runs was conducted. These tests were taken at zero tunnel speed. This set of runs provided a good check as to the accuracy of the measuring system and data reduction program on comparing to calculated values.

The sign convention used for reducing the forces and moments is shown in Figure 3. As previously mentioned only the roll moment is directly measured. The pitching moment and yaw moment are derived from the two normal forces and two lateral forces, respectively. In reducing the data all moments were calculated about a reference point 0.067 m forward of the transom and 0.024 m above the keel as shown in Figure 2. A computer program was used to reduce all the data and subtract out the appropriate air tares. Hydrostatic tares were also removed in order to obtain the hydrodynamic forces and moments used in the subsequent correlation with theoretical predictions.

### 3. THEORETICAL CONSIDERATIONS

Application of the concepts of slender body theory to the SES sidehull problem has been treated in References (1) and (2). These initial formulations invoked certain basic assumptions regarding the form of lateral and vertical added mass coefficients and the treatment of cross flow drag effects. These assumptions have subsequently undergone a re-evaluation in the light of experimental data as discussed in References (4) and (5). Some of these modifications will be touched upon here in light of the present experimental results.

In addition to the above method of approach, recent work, Reference (6), utilizing the concepts of lifting surface theory has been applied to the problem of low aspect ratio surfaces, such as SES sidehulls in the presence of the free surface. These studies also included the consideration of a fully vented sidehull where one surface is completely ventilated. The method however has limitations in that it considers a flat plate geometry and only addresses the problem of zero trim. As a consequence it fails to account for effects arising from the body geometry and any cross coupling that may exist between vertical and horizontal planes.

For purposes of this discussion the basic slender body formulation as applied to the present problem is given in brief form in Appendix A. The modifications incorporated into the analysis are those originally derived in (5) and are in some instances the same as those obtained independently in (4).

**Lateral Added Mass Properties:** The calculation of the hydrodynamic forces on the sidehull has been based upon the fundamental concept of slender body theory in an infinite fluid. Since we are essentially dealing with a high speed free surface problem, the approximation by neglecting the free surface effect must be justified. For a steady flow of constant speed  $U$  in an inviscid, incompressible fluid the linearized free surface condition is given by:

$$U^2 \frac{\partial^2 \phi}{\partial x^2} + g \frac{\partial \phi}{\partial z} = 0 \quad (1)$$



where  $\Phi$  is a velocity potential. Since the sidewall immersion is small in comparison with the craft length, it is more illustrative to express the above condition with respect to two different length scales as follows:

$$F_r^2 \frac{d}{l} \Phi_{x'x'} + \Phi_{z'z'} = 0 \quad (2)$$

Here  $F_r$  is the Froude number based on craft speed and sidehull length,  $x'$  is the non dimensional axial coordinate referenced to the craft length,  $l$  and  $z'$  is the non dimensional vertical coordinate referenced to craft immersion  $d$ . It will be seen that even though  $F_r$  may be large (typically of the order of 1 to 2 for an SES) the fact that the immersion ratio  $d/l$  is small (of the order of  $10^{-2}$ ) makes the second term dominant. Consequently the free surface can be regarded as a reflection boundary where:

$$\Phi_{z'} = 0 \quad (3)$$

which is, in fact, the usual low speed or low frequency condition. Hence, the added mass coefficient pertaining to low frequency has been selected in the present correlations. Furthermore, in keeping with the practices used in ship theory, this coefficient has been made a function of the local sectional characteristics and is therefore a variable over the length of the sidehull. It has been found that this procedure provides much better correlation for predicting the yawing moments than the use of a constant value for this coefficient.

The added mass may be written in the following form:

$$\mu_{yy}(\xi) = \rho \frac{\pi}{4} k_{yy}(\xi) d(\xi)^2 \quad (4)$$

where  $\rho$  is the density of the fluid,  $d(\xi)$  is the local draft and  $k_{yy}$  is the added mass coefficient. For typical SES sidehull shapes, ranging from triangular to rectangular sections, the value of  $k_{yy}$  lies between 1.6 and 2.8. These values are in conformity with typical low-frequency values used in ship theory (7).

**Camber Effects:** As discussed in Appendix A the slender body forces are supplemented by non linear cross-flow drag terms. These terms depend on the square of the relative cross-flow velocity. In order to account for changes in angle of attack of the flow at sections of the body where there is camber, in particular at the forward sections near the bow and near the fairing where the thickness distribution changes, a term dependent on the local sidehull slope has been added to the cross-flow velocity. In the present case, this cross-flow velocity is represented by the following:

$$V_r = U \psi - U \frac{d\eta}{d\xi} \quad (5)$$

where  $U$  is the tunnel velocity,  $\psi$  is the yaw angle,  $\eta$  is the waterline mean thickness and  $\xi$  is the axial coordinate. This added term has the tendency of localizing an added force at sections where there is a rapid change in body thickness.

The cross-flow drag coefficients used in the present correlation have been taken as 1.0 except in

the trim down cases where, because of the sharpness of the keel and stem line, it was felt more appropriate to use a coefficient of 2.0. This range of values for the cross-flow drag coefficient is within normal expectations.

**Trim Down Conditions:** Application of the slender body concepts to the case when the sidehull is in a trim down condition deserves special attention. As in the case of slender wing theory, the flow over the forward portions of the wing contributes to the lift, whereas flow over the aft sections downstream of the maximum span have little or no lift contribution due to the induced side-wash effects. This concept also carries over to the flow around slender bodies at angles of attack as discussed in (8). As an analogy to this effect, it is postulated that when the craft is in a pitch down condition the flow downstream of the maximum immersion point is influenced by the upstream shed vorticity and consequently generates no side force. This effect leads to a concentration of the side force to forward sections of the sidehull ahead of the maximum immersion point, thus contributing a larger destabilizing moment, a behavior typical of full length SES sidehulls.

Implementation of this concept has been discussed in References (4) and (5) and involves integration of the slender body equations from the bow to the maximum station. It should be noted, in this respect, that when a sidehull having a horizontal keel is in a trim down condition such that the transom is above the water surface, the normal formulation of the slender body equations would give a zero side force, since the force depends on the evaluation of the draft at the transom, which in this instance is zero. Utilization of the above modification however avoids this anomaly.

In the case of the present sidehull where a fairing exists which drops below the keel line, it is most probable that certain sections of the fairing are outside the influence of the wake shed by the forward portions of the sidehull. In this event the above analogy is somewhat obscure and may require further modification. Furthermore due to this fairing, the draft at the transom of the sidehull is no longer zero and the normal slender body approach would give rise to a side force. Since the flow condition is unclear in this case it has been decided in the present work to retain this latter approach.

**Cross Coupling Effects:** Due to the asymmetry of typical SES sidehull shapes as evidenced by the present model it can be expected that, under yawed conditions, vertical forces and moments will be generated. Furthermore, should the sidehull be operated at a trim condition it is expected that side forces and yaw moments will arise. This cross coupling has been included in the theoretical formulation. For the inviscid terms this coupling is representative of a net change in momentum in a particular direction caused by the motion of the body in an orthogonal direction. In the case of the non linear cross-flow drag term the coupling forces occur due to the assumption that the net force on the body is perpendicular to the dead rise surface. In order to estimate the magnitude of this coefficient, the following formula has been used for the inviscid force contributions:

$$\mu_{yz}(x) = \mu_{zz}(x) N_y(x) / N_z(x) \quad (6)$$

where  $N_y(x)$  and  $N_z(x)$  are average values of the horizontal and vertical unit normal components of the hull cross-section at any station. The average is taken with respect to the wetted length of the hull cross sectional area. Note that for a sidehull with axial symmetry  $N_y(x)$  is zero and hence there would be no cross coupling forces or moments. For the case of the non linear cross-flow drag terms, it is assumed that the cross flow force acts normally to the deadrise surface at any given section. The value of the cross-flow drag cross coupling coefficient is therefore equal to the cotangent of the mean deadrise angle at any given section of the sidehull. For the present experiments where the lateral forces and moments were being investigated, cross coupling effects occur when the sidehull is at a trim angle other than zero. In this instance horizontal force and moments arise due to the trim attitude of the sidehull.

**Spray Drag:** In the prediction of sidehull performance one of the most important parameters is that of drag. In addition to the normal components of drag, viz the skin friction drag and the pressure drag, there exists especially at high speed, a significant spray drag. Unfortunately very little information exists regarding this drag component. In an effort to provide some insight into this area, the present tests were used to ascertain the degree of spray generation by utilizing photographs to determine the added wetting caused by spray. On the assumption that the major contribution of spray to drag is due to frictional effects, this information was used to generate a spray drag coefficient. This latter assumption is supported by investigations performed on surface piercing struts in (9). For the sidehull under investigation two components of spray could be identified, one arising at the bow and a second spray sheet emanating from the location of the leading edge of the fairing. In keeping with the findings of Reference (9) the spray drag component was cast in the form:

$$D_{\text{spray}} = f(q, c, t) \quad (7)$$

where  $q$  is the dynamic pressure,  $c$  is the characteristic length from the point of generation of the spray to the maximum thickness point and  $t$  is the maximum thickness of the body.

Based on the results of this analysis the following formulae were obtained for the spray drag caused by the bow section and fairing respectively:

$$D_{\text{spray}} = 0.75 C_f q c t$$

$$D_{\text{spray}} = 5.5 C_f q c t$$

In these formulae the value of  $t$  is taken to be the maximum thickness in the waterline plane and the friction coefficient  $C_f$  is evaluated at the appropriate Reynolds number for the tests. As will be seen in the following section, excellent agreement with the test results is obtained. This correlation is particularly satisfying insofar as the measurements of spray wetted area are difficult at best and quite subjective.

It must be pointed out that the above formulae are dependent on the sidehull geometry and are therefore limited in their application. They do, however, provide some insight into the importance of this drag component in SES sidehull design.

#### 4. EXPERIMENTAL AND THEORETICAL CORRELATION

In this section we present the correlations obtained between experiment and theory. In addition to discussing the quantitative results, some interesting qualitative results will also be presented. The theoretical computations have all been conducted by using the analyses presented in Appendix A, modified according to Section 3. These results have been derived in coefficient form for a single sidehull.

**Forces and Moments:** As was pointed out previously a set of hydrostatic measurements was conducted prior to the tests. These data served a two-fold purpose, first in providing necessary tares for extracting the hydrodynamic forces and moments, and second they were used to check out the validity of the data reduction scheme. Comparison of these data with computed hydrostatic quantities proved to be excellent, thus not only providing a thorough check of the force balance and readout equipment but verifying the location of the force balance electrical centers with respect to the reference point for computing moments.

Figure 4 illustrates a comparison of the drag force as calculated with the experimental data at three tunnel velocities for varying sidehull immersions. Shown in this figure are the computations with and without spray drag effects. Very good agreement is obtained in the former case. The spray drag is seen to contribute about 30% of the sidehull drag. This alarmingly high percentage illustrates the importance of providing adequate spray rails in the design of SES. The sidehull shape in the present investigation was not provided with hard chine lines, thus significant wetting occurred due to the spray. There is no doubt that this drag contribution could have been substantially reduced had either spray rails been provided at the bow and at the commencement of the fairing or alternatively, a chine line had been incorporated in the design to reduce wetting.

Based on geometry of the present sidehull, the spray drag caused by the fairing was found to be approximately four times that of the bow, an important consideration when designing fairings for waterjet inlets.

The behavior of the sidehull with yaw angle at various trim and immersion conditions is shown in Figures 5 through 7. These figures illustrate the behavior of the side force coefficient  $C_y$ , the axial force coefficient  $C_x$ , the yaw moment coefficient  $C_N$  and the roll coefficient with  $C_K$  with yaw angle. Fig. 5 compares the results at zero trim for Froude numbers of 1.51 and 2.04 corresponding to tunnel velocities of 5.12 m/s and 7.10 m/sec respectively. As will be seen, generally excellent correlation is obtained. There is some discrepancy in the roll and yaw moment at larger negative angles of yaw, possibly due to cross coupling effects, as at these conditions the deadrise of the sidehull is presented to the flow. At positive angles of yaw, no such cross coupling occurs as the sidehull force is vertical. The correlations for a positive trim of  $1^\circ$  are shown in Figure 6. Here again, the theoretical projections agree quite well with the data. Again there is evidence of some discrepancy at the larger negative yaw angles, once more possibly due to cross coupling effects. The axial force correlation in this instance is somewhat poorer than in the previous case. This is thought to be due to added



spray drag caused by the inlet fairing at this angle of trim. Figure 7 illustrates the results for a negative trim of  $-1^\circ$ . We see here that whereas good correlation exists in the force coefficients, some discrepancies arise in the moment comparison, especially in the case of the yaw moment. Apart from the cross coupling effects previously mentioned, this particular test condition is subjected to flow anomalies such as leading edge ventilation. This phenomenon was observed in all trim down conditions especially at negative angles of yaw. The qualitative effects of this ventilation will be discussed in a subsequent section.

The behavior of the force and moment coefficients with immersion at a trim of  $0^\circ$  is shown in Figure 8. Here excellent agreement is evidenced in all cases except perhaps for the yaw moment. As in the case for trim down conditions it was observed that at the deeper immersions, the sidehull was more prone to leading edge ventilation. This phenomenon is probably attributable to the thicker section of the bow causing leading edge separation. Nevertheless the correlation is considered to be reasonable.

**Qualitative Results:** As already mentioned in previous sections of this paper, the use of the free surface water tunnel for experiments of this nature is most useful in that it provides an opportunity for detailed flow visualization. Flow phenomena such as ventilation, cavitation, spray, and to some extent separation, can be observed. We shall now discuss some of the phenomena observed during the present test series.

Figure 9 shows a sequence of photographs taken at a tunnel speed of 5.18 m/s at a trim angle of  $+1^\circ$  and an immersion ratio of  $10.6 \times 10^{-3}$ . These photographs are taken through the side window of the tunnel from a point slightly below the free water surface at a slight upward angle. The flow in all instances is from right to left. Figure 9 is illustrative of the flow conditions existing over the full range of yaw angles tested, the top photograph is taken at a yaw angle of  $+4^\circ$ , the center photograph is at  $0^\circ$  and the bottom is at  $-4^\circ$ . Inspection of these figures will show that the water contact surface with the body over this range of yaw angles is little changed. This is of importance when applying slender body theory to the present problem as it validates the use of a constant immersion profile with yaw angle. Close examination of the bottom photograph in this sequence at an angle of  $-4^\circ$  yaw shows a slightly larger spray generation in the vicinity of the fairing near the transom of the sidehull. However, apart from this effect, little difference can be found between the three photographs. It should be noted in this figure that the transom area of the sidehull is fully ventilated and the boundary of the ventilation cavity can be seen emanating from the keel at the transom. Other than the flow characteristics outlined above, little anomalous behavior was seen under conditions of positive and zero trim during the whole test series. At the deeper immersions, however, at a zero angle of trim some evidence was observed of very local flow separation near the leading edge of the sidehull. On occasion this separated region had a tendency to ventilate; however, this ventilation region was confined to very local flow separation near the leading edge. It is considered unlikely that this type of ventilation had any effect on the forces and moments on the sidehull.

Whereas a relatively clean flow condition existed

under the above described conditions, this was not the case at the negative trim angles. In this instance it was noted that ventilation occurred from the leading edge under most conditions of immersion and negative sideslip. Two types of ventilation phenomena can be described: (1) A vortex type ventilation, starting from the intersection of the keel and stem lines and propagating aft under the keel of the sidehull. This type of ventilation occurred at the lower yaw angles and was accompanied by an intermittent region of ventilation attached to the sidehull. (2) At the larger negative yaw angles an attached ventilated cavity was formed at the leading edge of the sidehull. The size of this ventilated cavity was dependent on the yaw angle, trim angle, immersion and speed. In order to illustrate some of these effects Figures 10 and 11 show the sidehull at negative trim angles of  $-1^\circ$  and  $-2^\circ$  respectively. In Figure 10 the leading edge ventilation can be seen starting at the leading edge of the sidehull in the top photograph. A close-up of this area is shown in the center photograph where the outline of the ventilation area can be seen just below the keel. The last photograph is a view taken from underneath the tunnel looking up at the keel line. Here one can clearly see the region of separation from the stem of the sidehull and the wake emanating from the keel on the leeward side. The white striations in the flow are caused by spray and air bubbles in the surface of the water. The outer bright line emanating from the leading edge of the sidehull in the bottom photograph marks the location of the ventilating vortex core. In this particular run the amount of ventilation attached to the sidehull was relatively small and consequently the effect on the overall forces and moments would not be considered high. This situation arises because the immersion is a relatively small one for this trim angle. In contrast to this run, Figure 11 illustrates the flow occurring around the sidehull at a velocity of 5.18 m/s and a trim condition of  $-2^\circ$ . The immersion here is again similar to the previous Figure. As will be seen from the top two photographs, extensive ventilation is occurring from the leading edge of the sidehull. This is evidenced by the outline of the cavity in the top photograph and the separated region from the stem of the sidehull as shown in the center photograph. In order to illustrate more clearly the ventilated area, a photograph was taken from the opposite side of the tunnel. This view is shown in the bottom photograph and it should be noted that here the flow is now from left to right. The ventilated region is clearly evidenced in this latter photograph as the white area attached to the sidehull at the leading edge. As can be seen, this area extends approximately one third of the length of the sidehull. In this circumstance, significant changes would be expected to occur in the lateral forces and moments.

As was pointed out earlier, the negative trim conditions are most prone to this ventilation phenomenon. This is no doubt due to the fact that under these conditions, thicker sections of the sidehull are immersed in the water at the leading edge. Since the onset of ventilation is closely associated with the boundary layer development on the body it is natural to assume that the flow separates more easily under these conditions, thus allowing a path for atmospheric air to feed into the separated region. In light of this evidence therefore, it is not surprising that correlation with theory would break down.



It should be strongly emphasized that the present tests have been conducted under idealized conditions. In the real situation, the influence of the air cushion and the bow seal in the neighborhood of the leading edge of the sidehull would have significant effects on the occurrence of the sidehull ventilation. Furthermore, even in the absence of these influences, the scaling properties of this phenomenon make it difficult to extrapolate the findings from these tests to the full scale. With these factors in mind, it was not the intention of the present test series to conduct an exhaustive investigation into defining the boundaries and flow conditions under which this phenomenon occurs. However, based on the results of this investigation, it is safe to assume that under certain conditions, leading edge ventilation can be expected to occur in the full-scale on this type of sidehull. This condition would not only be of importance from the point of view of its effect on the forces and moments on the craft, but also in its impact on the airflow leakage under the sidehulls and perhaps more importantly, its effect on the performance of the waterjet inlet and directional stabilizers.

## 5. MANEUVERING SIMULATION

In this section we present the development of a four degree of freedom maneuvering program for the prediction of turning characteristics of surface effect ships. The use of a four degree of freedom program was motivated by the desire to develop a design tool in which parametric analyses could be conducted to analyze the various modes of turning such as differential thrust, turning skegs, rudders and thrust vectoring methods. In order to perform these analyses it was felt that the use of a six degree of freedom would be too costly and time consuming. Existing programs of this nature are not well suited to parametric investigations such as these. Computer run times of existing six degree of freedom simulation are several factors longer than real time. Consequently, the use of such programs for these analyses is prohibitively expensive. The present program in contrast can simulate a maneuver such as a full turn, in a typical computer run time of 10 seconds on a CDC 6600 machine.

The four degree of freedom simulation is considered to be an adequate one for representation of turning maneuvers for SES. This conclusion is based on the fact that typically these crafts have a very flat turn with little or no roll angle. As a consequence, the interaction of the bow and stern seals in the turning process is minimal and consequently the leakage patterns during a turn do not significantly affect the vertical dynamics of the craft. In the four degree of freedom simulation the surge, sway, yaw and roll modes only are considered. This design tool has proved most valuable in assessing such diverse turning procedures as thrust vectoring, differential thrust, variation in sidewall immersion and combinations of these procedures.

The motion of the craft will be described in terms of the relationship between a body-fixed reference frame and a coordinate system fixed in space. The inertial coordinates ( $x_0, y_0, z_0$ ) and the body coordinates ( $x, y, z$ ) are both designated according to a right-handed convention with  $z_0$  and  $z$  positive downward. The origin of the body frame is kept fixed at the center of gravity of the craft for all time,  $t$ ; the  $x$ -axis is parallel to the baseline of the craft, positive forward, and positive  $y$  is

therefore pointing to starboard. The two coordinate systems coincide initially at time zero. The subsequent trajectory of the craft can be determined as a function of  $t$  by the position of the craft C.G. and the yaw angle  $\psi$  with respect to the inertial frame.

Confining the craft motion to a horizontal plane with four degrees of freedom, one is concerned with two translatory motion components along  $x$  (surge) and  $y$  (sway), and two angular motions about  $x$  (roll) and  $z$  (yaw). If  $u$  and  $v$  are the linear velocity components of the craft center of gravity along the body axes  $x$  and  $y$ , and  $p$  and  $r$  the angular velocities about the axes  $x$  and  $z$ , respectively, the equations of motion in the body coordinate system are given by: (See Reference 10)

$$\begin{aligned} m(\dot{u} - ru) &= X \\ m(\dot{v} + ru) &= Y \\ I_x \dot{p} &= K \\ I_z \dot{r} &= N \end{aligned} \quad (8)$$

where  $m$  is the mass and  $I_x$  and  $I_z$  are the mass moments of inertia of the body about the  $x$  and  $z$  axes respectively. Terms on the left hand side represent the rigid body inertial reactions and the centrifugal effects acting at the origin with respect to the moving coordinate system. The components  $X, Y, K$  and  $N$  refer to the total forces and moments applied to the craft, including the hydrodynamic effects arising from the overall motions of the craft as well as the results of propulsion and control forces which may affect the craft maneuver. In a functional form, these components can be expressed by:

$$\begin{Bmatrix} X \\ Y \\ K \\ N \end{Bmatrix} = f(u, v, p, r, \dot{u}, \dot{v}, \dot{p}, \dot{r}, \phi, \delta) \quad (9)$$

where  $\delta$  represents a general description of the effect due to various propulsion and control schemes. To reduce the above functional relationship into useful mathematical form, a Taylor expansion is usually used, (References 10 and 11). By keeping a sufficient number of terms for each variable, the forces and moments can be expressed in any desired order of these variables to account for various non linear effects. The solution of these equations generally requires an experimental determination of each of the hydrodynamic coefficients appearing for which a captive model test using either a rotating-arm technique or a planar-motion mechanism technique is necessary.

As already mentioned, the purpose of the present study was aimed at developing a mathematical formulation appropriate for parametric analysis of the maneuver characteristics of an SES in the early design phases. In accordance with normal design procedures, a number of different hull forms are necessarily evolved through the design process. Consequently, it is not always practical nor economical to conduct model tests for parametric investigations. The analysis, therefore, must rely on either the theoretical or empirical procedures. In the present study, the calculation of the hydrodynamic components is based upon physical concepts. These forces are assumed to fall into two major categories arising from viscous and non viscous

interactions. The non viscous components of forces and moments are those directly related with dynamic fluid pressure resulting from the body motion. These forces are intimately associated with the energy exchanges between the fluid and the moving body and can be deduced from the fundamental principals of classical mechanics. Consequently, all nonviscous terms, both linear and non linear, can be analytically identified as functions of the body added inertias. The viscous contributions are drags created through various origins. The major uncertainties with regard to these forces involve the identification of their origins as well as the determination of the functional relationship of these quantities with the body motions. In the present study, all the viscous terms are treated as dependent on velocity-squared and the proportional constants are empirical. While the hydrodynamic characteristics govern the craft stability, the feature of steering and control determines the ability of maneuvering. The steering of an SES can be achieved by various applications of control surfaces or by manipulation of propulsor thrust to produce an appropriate turning moment. The present study considers only the latter option assuming that the steering is controllable through either thrust vectoring or differential thrust. Since the steering control is closely related with the propulsor characteristics in this respect, the effects of propulsion and control are considered as an integral item in the following discussion.

In summary, each component of force or moment is assumed to be expressible by a summation of three independent contributions, the dynamic pressure, the drag and the resulting effect of propulsion and control. In addition, the roll-moment equation must include an extra term due to the effects of changing buoyancy of each sidewall as the craft rolls. Before entering into a brief discussion of each of these items, we write the four component equations in the following form:

$$\begin{aligned} m(\ddot{u}-ru) &= X_{pre} + X_{drag} + X_{\delta} \\ m(\ddot{v}+ru) &= Y_{pre} + Y_{drag} + Y_{\delta} \\ I_x \ddot{p} &= K_{pre} + K_{drag} + K_{buoy} + K_{\delta} \\ I_z \ddot{r} &= N_{pre} + N_{drag} + N_{\delta} \end{aligned} \quad (10)$$

**Hydrodynamic Pressure Effects:** As discussed in the beginning of this section, the effects of cushion pressure and seals are neglected in the present four degree of freedom representation. The pressure forces considered here are thus essentially the contributions attributed from the motion of the two sidehulls in an inviscid fluid. As shown in Reference (12), the hydrodynamic effect on a body moving in an infinite medium is entirely determinable as a function of its added mass along the principal axes of the body. By analogy, the effect on a body floating on a free surface can also be determined provided that both the added mass and damping are known. For the present problem, however, because of the shallow immersion of the sidehull, the free surface effect is negligible and the damping effect can be ignored. Following the procedure of classical mechanics, the effects of the hydrodynamic pressure on the craft are obtained and given by:

$$X_{pre} = X_u \dot{u} + X_{vr} vr + X_{pr} pr + X_{rr} r^2$$

$$\begin{aligned} Y_{pre} &= Y_v \dot{v} + Y_p \dot{p} + Y_r \dot{r} + Y_v v + Y_p p + (Y_r + X_u u) r \\ K_{pre} &= K_v \dot{v} + K_p \dot{p} + K_r \dot{r} + K_v v + K_p p + K_r r \\ N_{pre} &= N_v \dot{v} + N_p \dot{p} + N_r \dot{r} + (N_v - X_u u) v + (N_p + N^*) p + N_r r \end{aligned} \quad (11)$$

in which all the coefficients are a function of the sidehull added mass; the analytical expressions of these coefficients are given in Appendix B.

**Drag Effects:** The calculation of the drag of the craft is subdivided into two parts: the axial drag and the cross-flow drag. The axial drag is further divided into several components according to its source, namely, the sidehull, the cushion, the seal, the appendages and the superstructure. The calculation of the sidehull drag follows the customary practice for surface vessels such that the total drag is regarded as composed of two parts: the frictional and the residual drag. The frictional drag is calculated based upon the sidehull wetted surface and a frictional coefficient varying as a function of Reynolds number. The major part of the residual drag is brought about through wave-making. The wave-making resistance of the sidehulls together with that due to the air cushion pressure is calculated according to Reference (13). Another component of the residual drag is the contribution arising from the pressure difference introduced by the sidehull transom, namely the base pressure drag. Calculation of this component is described in Appendix A. In addition to the frictional and residual drag described above, a contribution due to spray as proposed in the foregoing section is also included in the calculation of the sidehull drag.

The details of the seals are generally not available at the early design stage; the drag of this item is estimated by its frictional contribution only, based upon the instantaneous wetted surface of the seals of an assumed configuration. In regard to the directional stabilizers, the drag is calculated in two parts; the frictional drag and the pressure drag. Whereas the frictional drag is proportional to the fin surface, the pressure drag is essentially a function of the fin thickness to chord ratio. In addition, an induced drag due to the lift generation of the fin is also included. The lift of the directional stabilizers is calculated by the classical methods of low aspect-ratio lifting line theory, Reference (14). As a result of this component, an additional side force, roll moment and yaw moment contribution arises in the equations of motion. Finally, the calculation of the aerodynamic drag of the hull and the superstructure depends upon experimental data. Nevertheless, this component can be approximated with great accuracy through a careful selection of the empirical drag coefficients.

Summing up these components gives the total axial drag of the craft, which must balance the forward thrust, if the craft speed is constant and steady. It is noted that when the immersion of the two sidehulls are not the same due to the roll motion of the craft, an additional yaw moment arises in the yaw equation.

The cross flow drag is the component associated with momentum transfer through the creation of vortices, wakes, and eddies. It is assumed that this component is proportional to the square of the cross flow velocity, but acting in the direction opposite to the velocity. For a craft moving in a



horizontal plane, the sway force, roll and yaw moments due to the effect of viscous cross flow on each sidehull are given in Appendix A.

**Propulsion and Control:** The present study considers the craft to be propelled by means of water jet propulsion. The propulsor nozzles are assumed to be equipped in pairs at the transom, symmetrical with respect to the craft center line. The basic turning scheme considered here is that of thrust vector control which means the side thrust and turning moment are generated by deflecting the nozzles as well as by varying the thrust on different nozzles. A special case of this scheme is known as differential thrust, in which the turning moment is generated by increasing the power on one jet and decreasing it on the other without deflecting the nozzle direction.

Let  $\delta$  be the horizontal deflection angle of the jet nozzle, positive toward portside and  $\alpha$  be the vertical tilt angle, positive upward, then the force and moment contributions for a craft with a trim angle  $\theta$  are given by:

$$\begin{aligned} X_{\delta} &= \sum_{i=1}^n [T_{gi} \cos \delta_i \cos(\alpha_i - \theta) - D_{mi}] \\ Y_{\delta} &= \sum_{i=1}^n T_{gi} \sin \delta_i \cos(\alpha_i - \theta) \\ K_{\delta} &= \sum_{i=1}^n T_{gi} [\sin(\alpha_i - \theta) y_i - \sin \delta_i \cos(\alpha_i - \theta) z_i] \\ N_{\delta} &= \sum_{i=1}^n [T_{gi} \cos(\alpha_i - \theta) (y_i \cos \delta_i - x_i \sin \delta_i) - D_{mi} y_i] \end{aligned} \quad (12)$$

in which  $x_i$ ,  $y_i$  and  $z_i$  are the coordinates of the centerline location of the  $i$ th nozzle,  $T_{gi}$  is the gross thrust at the same nozzle and  $D_{mi}$  the corresponding momentum drag of the waterjet inlet. The propulsor thrust and the momentum drag are exclusive characteristics of an individual propulsion system and depend much upon the inlet configurations. Those quantities can generally be expressed as a function of flow rate, pump rpm and craft speed. The technique of polynomial regression may be used if measured data are available.

The above discussion completes the description of the various forces involved in the craft maneuver. The equations of motion derived above are first order differential equations, with the four velocity components  $u$ ,  $v$ ,  $p$  and  $r$  as the dependent variables. With the initial conditions properly defined, the above equations can be integrated to solve these velocity components as a function of time. As defined earlier, these components are relative to the moving frame. To transform these components into the inertial frame, the following kinematic relations are used:

$$\begin{aligned} \dot{x}_* &= u \cos \psi - v \cos \varphi \sin \psi \\ \dot{y}_* &= u \sin \psi + v \cos \varphi \cos \psi \\ \dot{\varphi} &= p \\ \dot{\psi} &= r / \cos \varphi \end{aligned} \quad (13)$$

in which  $x_*$  and  $y_*$  denote the coordinates of the craft C.G. relative to the fix frame, and  $\varphi$  and  $\psi$  are roll and yaw angles. These variables can be

solved by another integration, and the trajectory and orientation will be completely specified once  $x_*$ ,  $y_*$ ,  $\varphi$  and  $\psi$  are known as a function of time.

**Correlation with Test Data:** Numerical computations to simulate several maneuvers of the U.S. Navy test craft XR-1C have been conducted. Since some tracking data and on-board instrumentation records of this craft are available, comparisons of computed results with measurements are made and presented.

The XR-1C craft is one of the several versions of the test craft developed under the U.S. Navy SES test program. This craft has an overall length of 15.24 m and a nominal weight of 17,200 Kg. The nominal cushion length is 11 m and cushion width is 4.57 m. The maximum sidewall width is 0.61 m at the transom. The body plan of the sidehull bears much similarity to that of a half body of the normal surface vessel, with the inside surface being a vertical plane wall and the outside faired to the bottom, varying from a U shape at the transom to a V at the stem. The wall has a flat keel of 12.2 m long under which at the stern however a 4 m x 0.20 m deep blister is added for housing the waterjet inlet. In addition, for the purpose of improving stability, a 45 degree inboard-canted ventral fin is equipped on each wall under the blister. The fin has a 36 cm span and a 1.6 m mean chord length. Figure 12 is a sketch to show the overall configuration of the craft.

Presented in the following are two sets of numerical simulations for the XR-1C maneuver. The conditions of these simulations are set corresponding to those of the actual test runs in (1) flight #76-37 and (2) flight #85-45. The craft response and its trajectory are then calculated to compare with the measured data. The information with regard to the two test runs as well as some pertinent craft data described in the following are obtained from Reference (15).

**(1) Flight #76-37:** For the purpose of examining the safety and stability of the test craft, an asymmetric propulsor chop during a straight flight was conducted in 1973-4 by Rohr Industries. During the maneuver, the on-board instrumentation recorded the propulsor thrust characteristics as well as the craft responses, such as the yaw-rate, side slip, roll angle and the craft velocity as a function of time. These measured data are shown here by the solid lines in Figure 13. Some useful information with regard to this flight are:

craft C.G. = 6.4 m forward of transom  
= 1.4 m above the keel line  
craft trim = 0.5 degrees  
initial craft speed = 26 knots

To simulate the craft maneuver, the hydrodynamic coefficients must first be calculated. These coefficients as known are dependent upon the immersed geometry of the sidehull. Unfortunately, no sidehull immersion was reported in the test data, except that the trim angle was known to be 0.5 degree. In the calculation, the immersion depth was estimated from the results of the 1/7th scale model tests (Reference 16), in which the immersion and trim were recorded in a series of free-to-trim and heave tests over a range of model speeds. For a craft speed of 27 knots, the immersion at the craft C.G. station was estimated to be 20 cm. Using this immersion and the given trim, the hydrodynamic coefficients were determined. The



calculated results show fairly good agreement with these available data obtained from the model test.

The XR-1C craft was equipped with twin Lycoming T-53 turbines, each driving a Pratt & Whitney Seajet 6-1A pump to provide the propulsion thrust. Available data (Reference 15) show that the gross thrust deliverable from each jet can be related with the pump rpm ( $n$ ) as follows:

$$T_g = 3.149 \times 10^{-3} n^2 \text{ (Newtons)}$$

From the same data source, the drag which accounts for the momentum of the water entering the waterjet inlet is also known and can be approximated as a function of the pump rpm and the craft forward speed  $U$  (in knots):

$$D_m = 9.77 \times 10^{-2} nU \text{ (Newtons)}$$

The pump rpm is known to be 2020 when propelling the craft at a 27-knot steady, forward speed. The above information thus provides sufficient background for determining the thrust characteristics in steady state operation.

The recorded thrust variation after a port throttle chop during the flight 76-37 is shown in Figure 13. It can be seen from the figure that the transition effect during the throttle shut-down is about 12 seconds. Using this transition time as an additional parameter to adjust the thrust of the port jet, the craft responses are calculated and shown in the same figure. The results show that the agreement is excellent in yaw rate and craft velocity. The calculated side slip is slightly larger than recorded. The calculation also shows a very small amplitude roll oscillation, whereas the roll trace shows an inherent list of approximately 0.5 degree to starboard. One possible explanation for this is that the 0.5 degree list may result from a slight built-in tilt angle on the jet nozzles.

**(2) Flight 85-45:** The flight 85-45 of the XR-1C test was aimed at examining the high speed turning response and the turning diameter of the craft as a result of thrust vectoring. The steady speed before the turn was 34.3 knots. The turning was achieved by deflecting both nozzles 26 degrees toward starboard. In the calculation the turning is initiated 7 seconds after the reference time zero. Figure 14 shows a comparison between the calculated craft response and the measured data.

The velocity measurements during the flight were made by two on-board sensors and also determined by the Autotape tracking system. One of the on-board sensor is Signet. The Signet is a magneto tachometer, usable for speed up to 30 knots. The other speed reference is a pitot static pressure probe. This system is reported to be more accurate than the Signet. The Autotape Model DM-40 is an automatic positioning system, with a transponder located on the craft and two responders stationed on shore. The system determines and records the ranges between the transponder and the two fixed responders as a function of time, from which the craft position, velocity and turning rate can be determined. The calculated velocity shows a good agreement with the Autotape tracking results. Beside the tracking system yaw rate information, the craft was also equipped with a rate gyro to monitor the yaw rate. Calculated results of yaw rate show good agreement with both the

measured data and the tracking results.

The calculated trajectory is compared with the tracking data and shown in Figure 15. It is noted that there is a time shift of 13 seconds between Figures 14 and 15, as the tracking system started at a later time as shown in Figure 14. While the calculated trajectory is slightly different from the tracking data, it is believed that the model provides sufficiently accurate prediction of the turning diameter.

## 6. CONCLUSIONS

Based on the results of this study, it is clear that the analysis of SES sidehulls when operating on cushion, can be adequately represented by slender body theory. Certain modifications to this classical theory, however, are needed in order to enhance the correlations with experiment. These modifications stem mainly from the inclusions of non-linear cross-flow drag terms and cross coupling effects into the formulation.

Application of this theory to the prediction of the lateral forces and moments obtained from full SES models have also indicated equally good agreement. These correlations have been extended to include oscillatory tests using planar motion mechanisms. The experience gained in using this approach in the correlation of test data from numerous tests have given confidence that this representation is indeed a valid one. It can be stated without reservation that within normal excursions in pitch, yaw and roll, the sidehull hydrodynamic coefficients are well represented by this approach.

From the experimental results obtained, it has further been shown that spray drag effects are significant in the design of SES sidehulls. This drag contribution can be as much as 30% of the total sidehull drag. It is therefore incumbent on the designer to assure that adequate spray control devices are incorporated in any design.

The occurrence of sidehull ventilation has been shown to occur under certain combinations of sidehull trim, yaw and immersion. This ventilation takes the form of a leading edge cavity either attached to the sidehull or in the form of a ventilated vortex. In either instance this ventilation could give rise to added air leakage or interference effects with the waterjet inlet and directional stabilizers. These findings however, must be tempered by the fact that the present tests were conducted with a single sidehull devoid of the effects of the bow seal and air cushion. In addition, since the scaling of this phenomenon is obscure, the full impact of ventilation on full-scale sidehulls is at best, speculative. It is nevertheless safe to say that under certain circumstances, ventilation will no doubt occur.

The use of a water tunnel test facility for conducting sidehull tests of this nature has been of significance. It has afforded a means of a controlled test environment in which the forces and moments on a typical sidehull design could be measured with great accuracy in order to correlate them with the analytics. Furthermore, the ability for excellent flow visualization and photographic coverage has yielded an insight into some of the flow phenomena that might occur in actual practice. It is felt that these tests have given some confidence in the analytical methods being used to predict SES performance.

This position is further reinforced by the excellent correlations obtained between actual maneuvering and predictions based upon the above methods. This correlation further supports the view that the four degree of freedom simulation for turning is a reasonable approach for analyzing maneuvering and turning characteristics of such craft. The present program is extremely efficient and easy to run and can be used for a variety of analyses such as: acceleration and deceleration maneuvers, turning, collision avoidance, and the performance of alternative turning devices and directional stabilizing systems. It must again be emphasized that this program is in no way intended to take the place of more complete six degree of freedom simulations but rather to supplement them as a realistic design tool for the development of alternate designs and the performance of trade-off studies. The results obtained to date with this program have more than adequately shown that these objectives have been met.

## 7. ACKNOWLEDGEMENTS

We would like to take this opportunity to express our thanks to Aerojet-General Corporation for permission to use some of the data presented in the present report. This work was originally performed under sub-contract to them by Tetra Tech Inc. In addition, our appreciation is expressed to Rohr Industries for the use of the XR-1C data presented.

Finally, we should like to express our thanks to the Surface Effect Ships Program Office, Naval Sea Systems Command, Washington, D.C. for allowing the use of data obtained under their sponsorship.

## REFERENCES

1. Aerojet-General Corp., "Craft Dynamics Program for JSESPO", Report # 9132FR-1, May 1969.
2. "Captive Model Tests with SES Model-Phase I", Hydro-Og Aerodynamisk Laboratorium, Lyngby, Denmark, HYA 7209, Report #1, July 1972.
3. Wade, R., Wang, S. & Wier, T.W., "Sidewall Hydrodynamic Investigation for Surface Effect Ships", Report # TC-295, Tetra Tech, August 1972.
4. Kaplan, P., "An Experimental Study of SES Craft Lateral Hydrodynamic Forces and Moments", Report # 73-97, Oceanics, Inc., May 1973.
5. Wade, R. & Wier, T.W., "SES Sidewall Hydrodynamic Investigations", Report # TC-334, Tetra Tech, June 1973.
6. Bertrand, J., et al, "Low Aspect Ratio Vertical Surface Piercing Hydrofoil Theory", Report # 73-21, Dept. of Ocean Eng., M.I.T., October 1973.
7. Comstock, J.P. (Editor), Principles of Naval Architecture, The Society of Naval Architects and Marine Engineers, New York, 1968.
8. Thwaites, B., Incompressible Aerodynamics Oxford Univ. Printers, 1960.
9. Chapman, R.B., "Spray Drag of Surface-Piercing Struts", NUC TP251, Sept. 1971.
10. Abkowitz, M.A., Stability and Motion Control of Ocean Vehicles, M.I.T., Press 1972.
11. Strom-Tejsen, J., "A Digital Computer Technique for Prediction of Standard Maneuvers of Surface Ships", NSRDC Report 2130, Naval Ship Research and Development Center December 1965.
12. Lamb, H., Hydrodynamics, Sixth Edition, Dover, New York 1932.
13. Yim, B., "On the Wave Resistance of Surface Effect Ships", J.Ship Res. Vol.15, #1, March 1971.
14. Kerr, K.P., "Study of Steering and Control Devices for Surface Effect Ships, Vol. I-Analysis", Report LMSC/D032092, Lockheed Missiles and Space Co., December 1970.
15. Rohr Industries, "R&D Test Craft - XR-1C, Final Report", RHR-74-484A, Prepared for Surface Effect Ship Project Office, Jan. 1975.
16. Wright, R.G., "Performance and Stability Tests of XR-1C SES Model", LMSC/D401600, Lockheed Ocean Laboratory, July 1974.
17. Hoerner, S.F., "Fluid-Dynamic Drag", 1965.

## APPENDIX A: SIDEWALL HYDRODYNAMICS IN A HORIZONTAL PLANE

A simple derivation of the hydrodynamic forces moments on a sidehull is given in this appendix.

Inviscid Hydrodynamic Forces and Moments: Let the body have three-degree of freedom motions in a horizontal plane. If  $v$  is the translatory velocity of the body in sway and  $p$  and  $r$  are the angular velocities in roll and yaw respectively, then the total apparent velocity at a cross flow plane is given by:

$$V_r = v + \xi r - fp \quad (A-1)$$

in which  $f$  is vertical distance of the center of fluid pressure from the body C.G. Assuming the two-dimensional sectional added mass at this plane is known to be  $\mu(\xi)$ , then the kinetic energy of a unit slice of the fluid can be written as:

$$T(\xi, t) = \frac{1}{2} \mu(\xi) V_r^2(\xi) \quad (A-2)$$

Neglecting the second order terms, the hydrodynamic forces and moments acting on a unit axial length at  $\xi$  are given by:

$$\begin{aligned} \frac{dY}{d\xi} &= - \frac{d}{dt} \left( \frac{\partial T}{\partial v} \right) \\ \frac{dK}{d\xi} &= - \frac{d}{dt} \left( f \frac{\partial T}{\partial v} \right) \\ \frac{dN}{d\xi} &= - \frac{d}{dt} \left( \frac{\partial T}{\partial r} \right) - u \left( \frac{\partial T}{\partial v} \right) \end{aligned} \quad (A-3)$$

in which  $u$  is the axial velocity of the body. The kinetic energy  $T$  at a fixed cross flow plane is a

function of  $\xi$  and time  $t$ . The total derivative  $d/dt$  therefore must reflect the changing coordinate of the cross flow plane with time. Thus:

$$\frac{d}{dt} = \frac{\partial}{\partial t} - u \frac{\partial}{\partial \xi}$$

Substituting (A-2) into (A-3), carrying out the differentiation, and then integrating over the side-wall length gives the following expressions for the force and moments:

$$\begin{aligned} Y = & -(\dot{v}-ur) \int \mu(\xi) d\xi \\ & -\dot{r} \int \mu(\xi) \xi d\xi \\ & +\dot{p} \int \mu(\xi) f(\xi) d\xi \\ & +uv \int \mu'(\xi) d\xi \\ & +ur \int \mu'(\xi) \xi d\xi \\ & -up \int [\mu(\xi) f(\xi)]' d\xi \end{aligned} \quad (A-4)$$

$$\begin{aligned} K = & (\dot{v}-ur) \int \mu(\xi) f(\xi) d\xi \\ & +\dot{r} \int \mu(\xi) f(\xi) \xi d\xi \\ & -\dot{p} \int \mu(\xi) f^2(\xi) d\xi \\ & -uv \int [\mu(\xi) f(\xi)]' d\xi \\ & -ur \int [\mu(\xi) f(\xi)]' \xi d\xi \\ & +up \int [\mu(\xi) f^2(\xi)]' d\xi \end{aligned} \quad (A-5)$$

$$\begin{aligned} N = & -(\dot{v}-ur) \int \mu(\xi) \xi d\xi \\ & -\dot{r} \int \mu(\xi) \xi^2 d\xi \\ & +\dot{p} \int \mu(\xi) f(\xi) \xi d\xi \\ & +uv \int \mu'(\xi) \xi d\xi \\ & +ur \int \mu'(\xi) \xi^2 d\xi \\ & -up \int [\mu(\xi) f(\xi)]' \xi d\xi \end{aligned} \quad (A-6)$$

The integrations are taken over the length of both sidehulls to give the total effect on the craft. The derivation of the above equations has assumed that each sidehull is a slender, elongated body such that the interaction between adjacent sections is negligible.

**Cross Flow Drag:** The cross flow drag can be cast into a standard form as:

$$\text{Drag} = \frac{1}{2} \rho C_d S |V_r| V_r$$

where

$C_d$  = Drag coefficient

$S$  = Projected area  
 $V_r$  = Flow Velocity

The coefficient  $C_d$  is a function of geometry and Reynolds number; it can generally be approximated from experimental data on some idealized shapes. Accordingly, the force and moment components due to this effect on a sidehull are:

$$\begin{aligned} Y_{\text{drag}} &= \frac{\rho}{2} C_d \int d(\xi) |V_r| V_r d\xi \\ K_{\text{drag}} &= \frac{\rho}{2} C_d \int d(\xi) |V_r| V_r f(\xi) d\xi \\ N_{\text{drag}} &= \frac{\rho}{2} C_d \int d(\xi) |V_r| V_r \xi d\xi \end{aligned}$$

in which  $d(\xi)$  is the local sidehull immersion at station  $\xi$ .

**Axial Drag:** The axial drag on the sidehull is calculated in two parts, the frictional drag and the pressure drag. The frictional drag can be expressed as follows:

$$\text{Drag}_f = \frac{1}{2} C_f \rho U^2 S_w$$

where

$C_f$  = Frictional coefficient  
 $\rho$  = Fluid density  
 $U$  = Craft velocity  
 $S_w$  = Wetted surface of sidehull

The pressure drag can be expressed by:

$$\text{Drag}_p = \frac{1}{2} C_b \rho U^2 \cdot S_b$$

where

$S_b$  = Immersion area at transom  
 $C_b = 0.029/\sqrt{C_{fb}}$ , and  
 $C_{fb}$  = The equivalent frictional coefficient, based upon the immersed area  $S_b$ , i.e.:

$$C_{fb} = C_f \frac{S_w}{S_b}$$

The above relation holds provided the transom base is not fully ventilated, Reference (17). At high speed and/or shallow immersions the likelihood of ventilation is almost certain, hence the pressure drag coefficient is given by:

$$C_b = 2/F_d^2$$

when  $F_d$  = Froude number based upon the transom immersion =  $U/\sqrt{gd}$

The transition from fully wetted to fully ventilated regime occurs in the neighborhood when  $F_d \geq 3.2$ , based upon experimental evidence as discussed in Reference (17).

#### APPENDIX B: ANALYTICAL EXPRESSIONS OF THE HYDRODYNAMIC COEFFICIENTS IN THE EQUATIONS OF MOTION

$$X_u = -m_1$$



$$X_{vr} = -Y_v$$

$$X_{pr} = -Y_p$$

$$X_{rr} = -Y_r$$

$$Y_v = -\int \mu(\xi) d\xi$$

$$Y_p = \int \mu(\xi) f(\xi) d\xi$$

$$Y_r = -\int \mu(\xi) \xi d\xi$$

$$Y_v = u \int \mu'(\xi) d\xi$$

$$Y_p = -u \int [\mu(\xi) f(\xi)]' d\xi$$

$$Y_r = u \int \mu(\xi) d\xi + u \int \mu'(\xi) \xi d\xi$$

$$K_v = Y_p$$

$$K_p = -\int \mu(\xi) f^2(\xi) d\xi$$

$$K_r = \int \mu(\xi) f(\xi) \xi d\xi$$

$$K_v = Y_p$$

$$K_p = u \int [\mu(\xi) f^2(\xi)]' d\xi$$

$$K_r = -u \int \mu(\xi) f(\xi) d\xi - u \int [\mu(\xi) f(\xi)]' \xi d\xi$$

$$N_v = Y_r$$

$$N_p = K_r$$

$$N_r = -\int \mu(\xi) \xi^2 d\xi$$

$$N_v = u \int \mu'(\xi) \xi d\xi$$

$$N_p = -u \int [\mu(\xi) f(\xi)]' \xi d\xi$$

$$N_p^* = u X_u f_o$$

$$N_r = u \int \mu(\xi) \xi d\xi + u \int \mu'(\xi) \xi^2 d\xi$$

in which

$m_1$  = Added mass of the craft in surge

$\mu(\xi)$  = Section added mass of sidewall in sway, at station  $\xi$

$f(\xi)$  = Vertical distance of the center of fluid pressure, at station  $\xi$ , from the craft center of gravity

$f_o$  = Integrated average of  $f(\xi)$

The integration is taken over the length of both sidehulls. The derivation of the above coefficients has assumed that each sidehull is a slender, elongated body such that the interaction between adjacent sections is negligible. The added inertia in roll for each sidehull about its own axis is neglected, as it is small in comparison with the roll effect about the craft centerline.

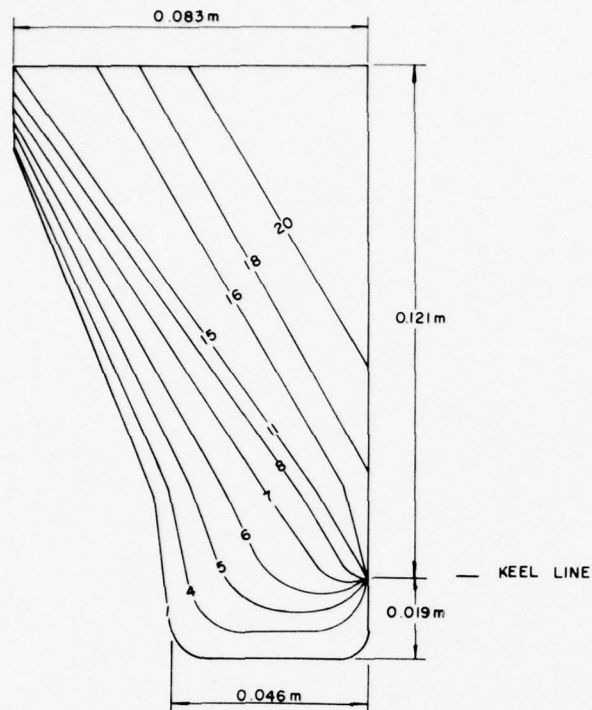


Fig. 1: SES model sidehull section lines.

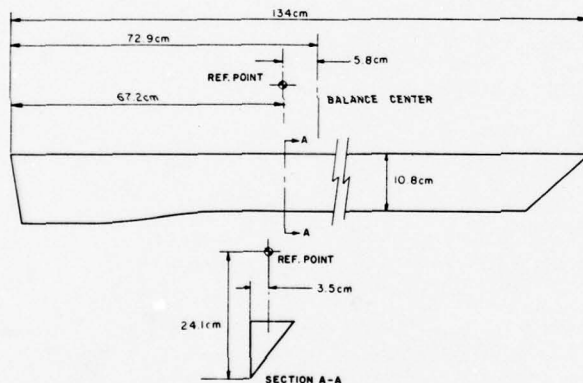


Fig. 2: Diagrammatic sketch of salient dimensions and reference point for reduction of moments.

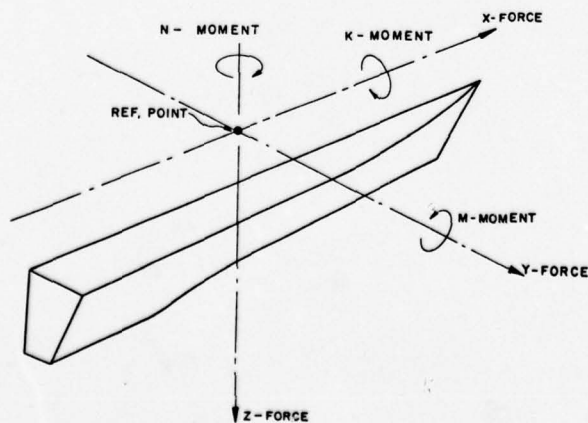
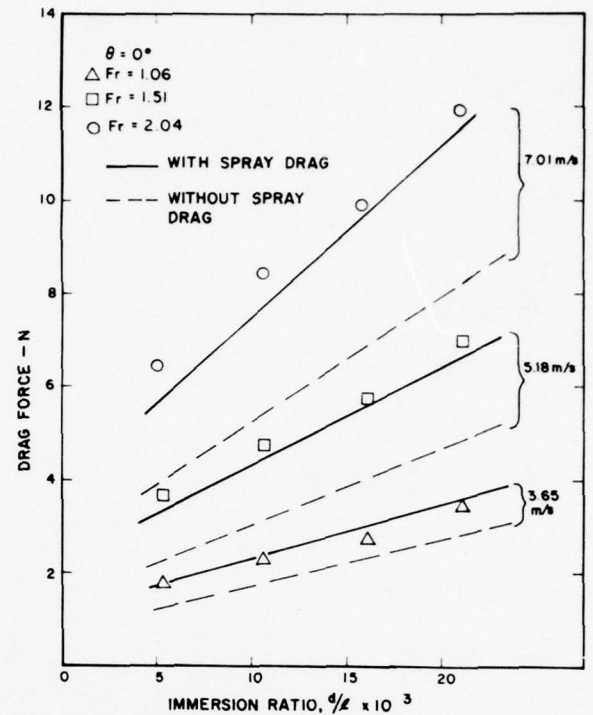
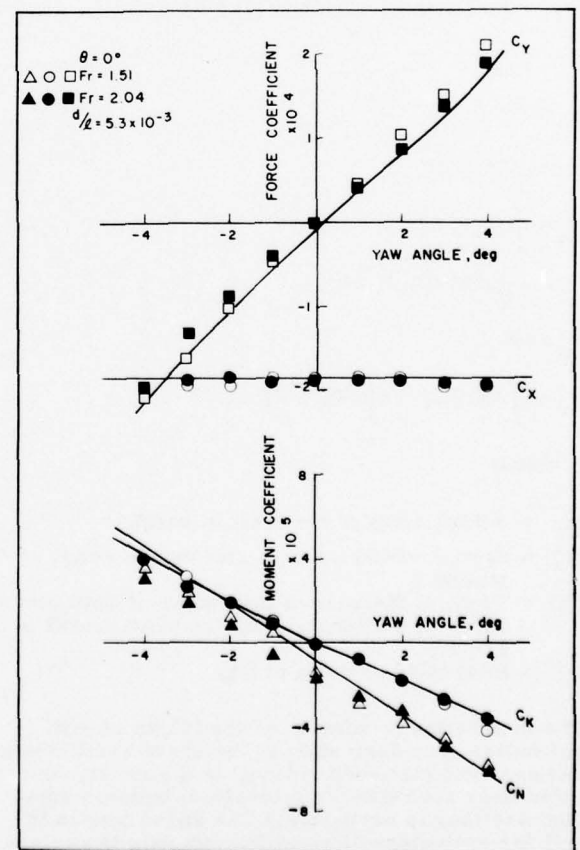


Fig. 3: Notation and sign convention used for forces and moments.

Fig. 4: Analytical predictions of sidehull drag with and without spray as a function of immersion ratio at a trim of  $0^\circ$  for Froude Numbers of 1.06, 1.51 and 2.04.Fig. 5: Variation of force and moment coefficients as a function of yaw angle at a trim of  $0^\circ$  for an immersion ratio of  $5.3 \times 10^{-3}$  at Froude Numbers of 1.51 and 2.04.

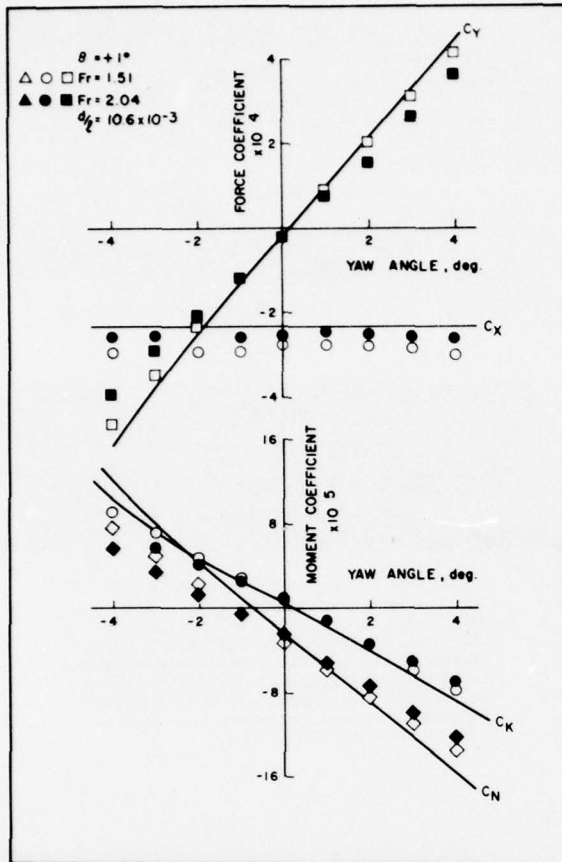


Fig. 6: Variation of force and moment coefficients as a function of yaw angle at a trim of  $+1^\circ$  for an immersion ratio of  $10.6 \times 10^{-3}$  at Froude Numbers of 1.51 and 2.04.

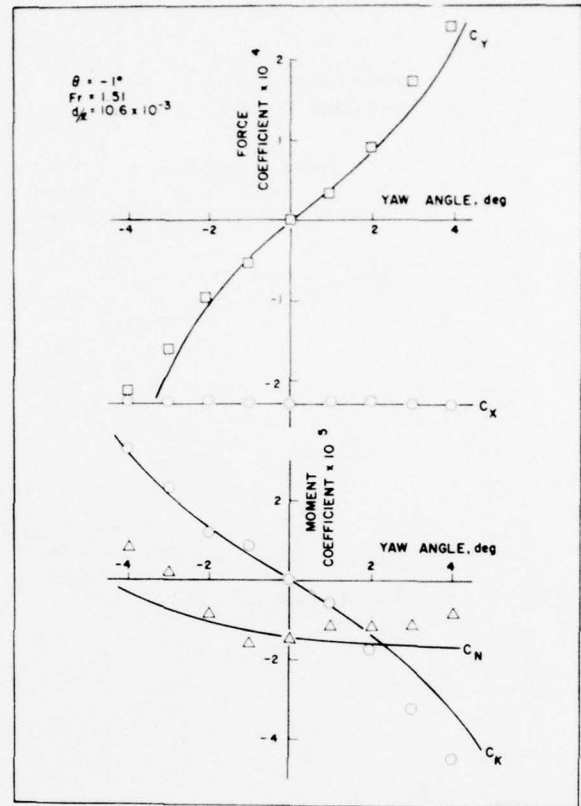


Fig. 7: Variation of force and moment coefficients as a function of yaw angle at a trim of  $-1^\circ$  for an immersion ratio of  $10.6 \times 10^{-3}$  at Froude Numbers of 1.51 and 2.04.



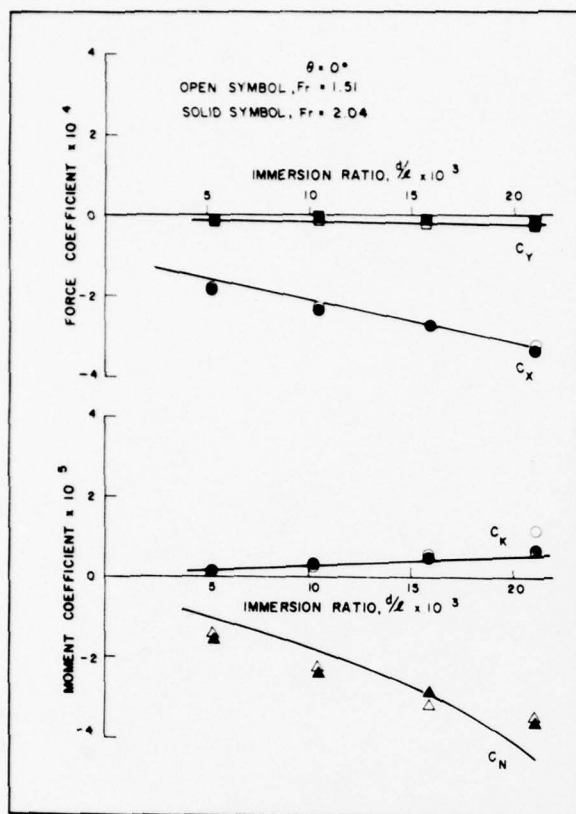


Fig. 8: Variation of force and moment coefficients as a function of immersion ratio at a trim of  $0^\circ$  for Froude Numbers of 1.5 and 2.04.

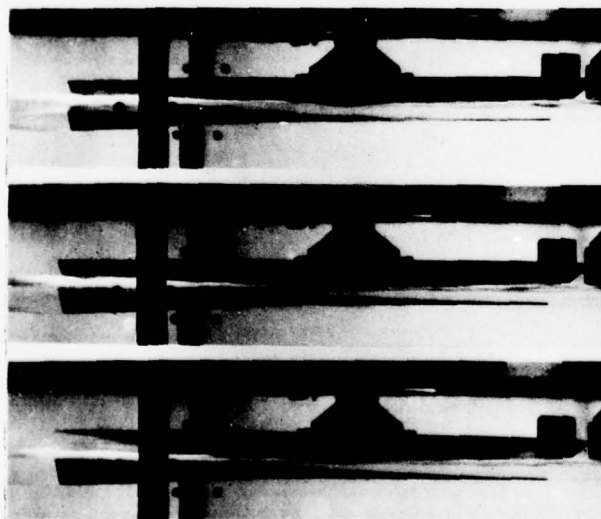


Fig. 9: Photograph illustrating the flow around the sidehull at a trim of  $+1^\circ$  and an immersion ratio of  $10.6 \times 10^{-3}$  for a Froude Number of 1.51. From top to bottom the sequence of photographs shows the flow at yaw angles of  $+4^\circ$ ,  $0^\circ$ ,  $-4^\circ$ , respectively. The flow is from right to left.



Fig. 10: Photographs showing the flow around the sidehull at a trim of  $-1^\circ$  and an immersion ratio of  $10.6 \times 10^{-3}$  for a Froude Number of 1.51 and yaw angle of  $-3^\circ$ . The flow around the sidehull is shown in the top view and a close-up of the leading edge area is shown in the centre photograph. The last photograph is a view looking up at the keel. Leading edge vortex type ventilation is observed just below the keel line in these photographs.



Fig. 11: Photographs of the flow around the sidehull at a trim of  $-2^\circ$  and an immersion ratio of  $21.2 \times 21.2 \times 10^{-3}$  for a Froude Number of 1.51 and yaw angle of  $-3^\circ$ . The top and centre photographs show a side and bottom view of the flow around the sidehull and the bottom photograph is a view looking from the opposite side of the tunnel. The flow in this later case is from left to right. These photographs show an attached ventilation cavity at the leading edge of the sidehull.

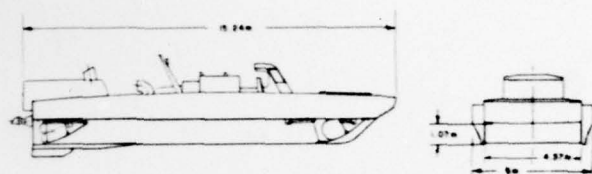


Fig. 12: Diagrammatic sketch of the XR-1C test craft.

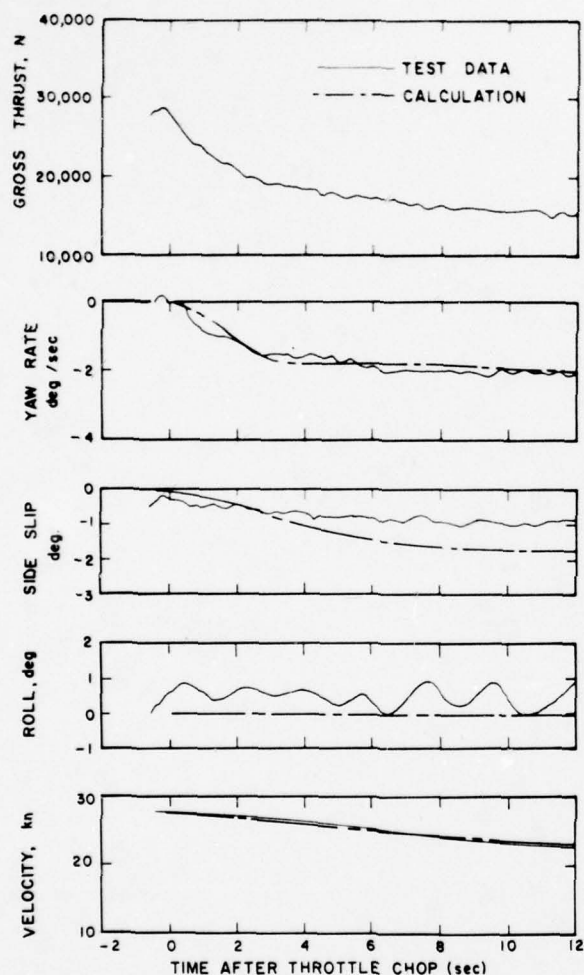


Fig. 13: Comparisons of analytical predictions with test data obtained from Flight 76-37 of the XR-1C.

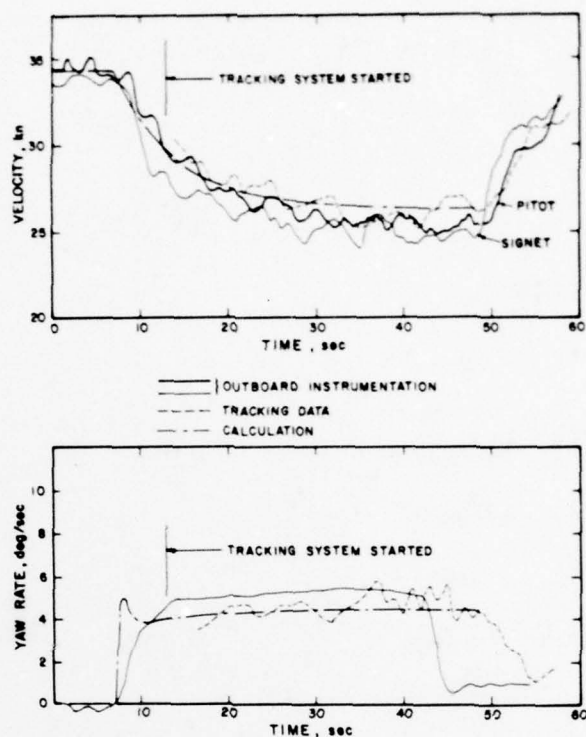


Fig. 14: Comparisons of analytical predictions with test data obtained from Flight 85-45 of the XR-1C.

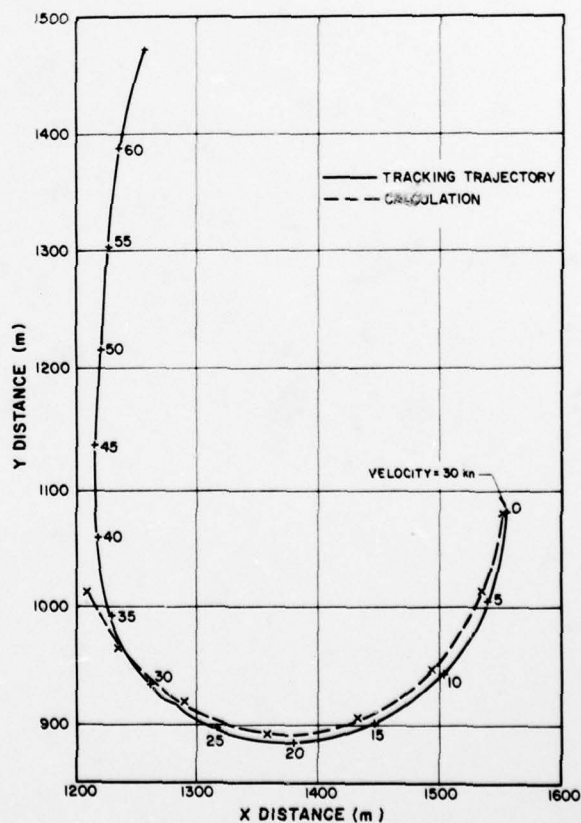


Fig. 15: Comparisons of the calculated trajectory with tracking data from Flight 85-45 of the XR-1C.

# THE EFFECT OF AIR COMPRESSIBILITY ON THE NONLINEAR MOTION OF AN AIR-CUSHION VEHICLE OVER WAVES

L. J. DOCTORS

School of Mechanical and Industrial Engineering,  
University of New South Wales,  
Kensington, NSW, Australia

## SYNOPSIS

The nonlinear behavior of an air-cushion vehicle (ACV) during coupled heave and pitch motion over a sinusoidal water wave is studied. The compressibility of the air flow within the vehicle is considered in addition to the previously-studied effect of the waves generated by the pressure distribution under the craft.

The ACV studied is of the plenum-chamber type with a transverse stability skirt. Linearized potential-flow theory is used to compute the waves generated by the craft. The effect of compressibility is assumed to occur principally in an accumulation of the air within the vehicle compartments.

Numerical computations were made to determine the response of a typical ACV to regular head waves. Non-linearity with respect to wave height is particularly evident at a Froude number of 1.5 and a dimensionless encounter frequency of 9. For the same conditions, the heave and pitch motions were reduced by up to 20% from the hydrodynamic effect. However, the motion could be increased by 50% or more for a craft of length 40 m, when compressibility was accounted for.

## NOMENCLATURE

A = discharge area  
B = craft beam measured at skirt  
c = forward velocity of craft  
C = coefficient  
e = skirt hem clearance  
F = Froude number =  $c/\sqrt{gL}$   
g = acceleration of gravity  
h = height  
I = second moment of craft mass about transverse axis through the center of gravity  
k = wavenumber  
 $k_0$  = fundamental wavenumber =  $g/c^2$   
 $l$  = distance measured around skirt hem  
L = length of craft measured at skirt hem  
m = mass of craft  
M = moment  
N = number of terms in the Fourier series used to represent the cushion pressure  
p = pressure (gauge)  
Q = volume flow  
R = reaction  
S = cushion planform area  
t = time  
V = cushion volume  
w, u = longitudinal and transverse wavenumbers  
x, y = right-handed orthogonal system, with x in the forward direction, and z vertically upwards.  
& z = Craft position relative to datum also given by x and z  
 $\alpha$  = local wave slope, or amplitude of wave slope  
 $\beta$  = angle between skirt hem and x axis, as seen in plan view, i.e.  $\cos \beta = dx/dl$   
 $\epsilon$  = longitudinal position of transverse skirt, ahead of midpoint, as a fraction of L  
 $\zeta$  = free-surface elevation induced by the pressure  
 $\eta$  = skirt-force deflection constant  
 $\theta$  = craft pitch angle, or wave angle

$\lambda$  =  $\lambda_0 \cos \theta$   
 $\lambda_0$  = speed-frequency parameter =  $4\sigma c/g$   
 $\mu$  = coefficient of friction between skirt and the operating surface, or Rayleigh viscosity  
 $\rho$  = density (of water, if unsubscripted)  
 $\sigma$  = radian frequency of pressure distribution  
 $\phi$  = potential function (fluid perturbation velocity being its positive gradient)  
 $\omega$  = wave-encounter radian frequency

## Subscripts

a = air, or atmospheric condition  
c = in-phase (cosine) component  
d = discharge  
e = escape  
f = fan  
g = center of gravity  
h = horizontal  
i = inlet  
k = skirt  
rms = root mean square  
r = craft  
s = out-of-phase (sine) component  
v = vertical  
w = wave  
 $\zeta$  = induced by pressure acting on water surface  
1,2 = forward, aft and stability regions respectively  
3

## Superscripts

- = average  
• =  $\partial/\partial t$   
\* = indicates a variable related to its mean value during the craft motion, divided by  $h_w$ , and nondimensionalized with L, g and  $\rho$ . However, craft pitch angle is divided by  $\alpha_w$  instead.



## INTRODUCTION

Previous Work

Experimental Research. The study of the motion of model air-cushion vehicles (ACVs) has been carried out by many workers. For example, Swaan and Wahab (1) used a peripheral-jet model, and tested it both with, and without, flexible skirts in a towing tank over regular waves travelling in different directions relative to the model. The model exhibited high damping in pitch and also some nonlinearity in that the response was not precisely proportional to the wave height.

Dyne (?) tested a model whose cushion was compartmented into six sections. It was excited on a flat surface and the damping factors in heave and pitch were found to be in agreement with his theory. Predictions were then made for the motion of the model over a regular wave.

Van den Brug and Van Staveren (3 and 4) tested what was essentially a plenum-chamber design. The coefficients in the linearized equations of motion were determined through forced oscillation tests in heave, pitch and roll above ground without forward motion, and above water with forward motion. The above-mentioned coefficients were found to vary with the model speed. Furthermore, the added mass of the water was found to be negative - in contrast with a ship.

The practical operation of ACVs in waves is due entirely to the development of the flexible skirt, and a review of the history of this work was given by Stanton-Jones (5). Some of the results that he quoted indicated a heave damping ratio of about 0.5 and a pitch damping ratio of 0.25. These refer to a skirted annular-jet model of the SRN5. The craft, when fitted with a finger skirt exhibited a damping ratio of about 0.75 - resulting in improved ride characteristics. The model measurements also showed that the response per unit of wave height was less for higher waves, and this would be a measure of the system nonlinearity.

More recently, tests have been carried out on full-size craft, or specially built manned testcraft. For example, Fein, Magnuson and Moran (6) and Magnuson (7) measured the response of a BH.7 hovercraft (whose cushion length is 20.4 m) in head, following and beam seas. The curves of response versus encounter frequency, for heave, pitch and roll, indicated resonances with large amounts of damping. For head seas, the heave resonance occurred at a frequency of about 2.2 rad/s and the pitch resonance at 2.0 rad/s, with the craft travelling at 52 kt.

Tests in twodimensional seas have been carried out by Magnuson and Wolff (8 and 9) on a model surface-effect ship (SES - an ACV with sidewalls). The investigation was performed as part of a program on high length-to-beam ratio craft. The model was 4.22 m long and had a length-to-beam ratio of 6.54. When run in regular head waves, the model exhibited a natural pitching frequency of approximately 5 rad/s for Froude numbers between 0.72 and 1.20. It was found that although the response was nearly linear with respect to wave height, nonlinearity in the heave motion revealed itself near the pitch natural frequency referred to above. The heave acceleration response tended to be more nonlinear still.

Other forms of test - such as finding the response of an amphibious ACV to various types of steps in

the terrain, when travelling over land - have been performed by Moran, Pemberton and Knight (10). For example, the heave and pitch natural frequencies, at zero forward speed, of a 2.03 m model of the JEFF-B amphibious assault landing craft were 24.2 and 11.6 rad/s, respectively, for the loading condition tested.

Theoretical Work. The dynamic heave and pitch motion of an unskirted annular-jet craft fitted with a transverse stability jet was computed by Lin (11). The linearized equations of motion predicted, in particular, the natural frequencies and general magnitudes of the heave and pitch motion quite well. Walker (12) examined the stability of both plenum-chamber and annular-jet ACVs but, also, considered the influence of fan and ducting characteristics. Fan characteristics that produced unstable heave motions were deduced from his theory. Ozawa (13), like Walker, considered simple static and dynamic heaving motion for a peripheral-jet ACV and derived the appropriate spring constants which he then applied to the linear heave motion resulting from a sinusoidal input.

Empirical approaches as well as theoretical ones were described by Hogben (14) for the two types of craft. The heaving response of a plenum-chamber ACV moving over regular waves was studied by Reynolds (15), and later extended to include pitching by Reynolds, West and Brooks (16). The vehicle they considered is shown in Fig. 1. The craft has a fan feeding an intermediate chamber - corresponding to the ducting and flexible supply bag utilized by many ACVs. The cushion is divided into forward and aft compartments by a transverse stability skirt, as shown. The incompressible Bernoulli equation was used and all the equations were linearized about the equilibrium condition.

It is considered that the linearization technique is somewhat invalidated in this case due to the very small daylight clearance under the skirt. Even a very small motion will cause skirt deflection, which is necessarily ignored by the linearization. One must also be concerned about attempting to linearize the equation for the flow under the stability skirt. Due to the usual pressure-versus-flow relationship for an orifice (a square relationship), one cannot linearize this equation unless there is a substantial cross flow in the equilibrium situation - and this is not normally the case.

Compressibility. It has been recognized that the compressibility of the air within the ACV might play a role in determining its motion at high encounter frequencies. Many workers have therefore included this effect but only in terms of the time-rate-of-change of density. Thus accumulation (or depletion) of the actual mass of air in the system, during the motion cycle, was considered. It appears that Mach-number effects have not been considered at all, due to the maximum velocity of the air being less than 80 m/s in most cases.

Linearized treatments of compressibility have been produced by Foss (17), Kaplan and Davis (18) and Lavis, Bartholomew and Jones (19). The latter two papers showed that the effect of compressibility is to increase the craft motion. Thus a model ACV operating in an unscaled atmosphere will give non-conservative motion predictions. Kaplan, Schneider and Goodman (20) have also examined this problem, while Yamamoto (21) restricted his attention to pure nonlinear heaving motion of a plenum-chamber ACV. The act of linearization appears to be justified in

the work of Leatherwood, Dixon and Stephens (22), Guienne (23), Leatherwood (24) and Genin, Ginsberg and Ting (25), since their main interest lies in the application to high-speed tracked ACVs, where no contact with the track will be permitted.

Bickford and Olson (26) analyzed the coupled heave and pitch motion of a multiple-skirt ACV using an analog computer.

**Nonlinearity.** The abovementioned objections to linearized theory were considered by Doctors (27), who used the various nonlinear equations describing the air flow. The effects of skirt contact with the wave surface were also modelled. This was found to be of major importance in terms of affecting the air flow. The forces developed on the skirt itself were shown to be small.

At low encounter frequencies, the predicted motion was almost linear - the pitch and heave amplitudes being proportional to the wave height. At some of the higher frequencies, the heave motion per unit wave height fell with increasing wave height, in confirmation of the previously-mentioned results reported by Stanton-Jones. The pitch motion per unit wave slope was found sometimes to increase and sometimes to decrease with increasing wave height, depending on the encounter frequency and Froude number. At low values of the wave height, the pitch motion was found to be very nonlinear.

The dynamics of the fan, engine and transmission system were incorporated by Schneider and Kaplan (28). The effects they considered were the inertias of the various components as well as the engine response to its load and throttle control.

Other aspects of ACV motion in waves, including the effect of air compressibility, were examined by Breslin (29), Richardson (30) and Trillo (31).

**Hydrodynamic Influence.** The ACV makes its presence felt on the water surface by means of the pressure distribution created by the air cushion. As a start, one can consider periodic coupled heave and pitch motion of angular speed  $\omega$ , over regular waves, and then decompose the pressure into its timewise Fourier series. It is a good approximation to linearize the hydrodynamic problem because of the low typical values of the water depression caused by the cushion compared to, say, the craft length.

Thus one can consider a simple harmonic timewise pressure variation of radian frequency  $\sigma$ , travelling at various speeds of advance  $c$ . The linearized inviscid solution for this problem, or for say an oscillating source (given by Wehausen and Laitone (32), and others), is known to have a singularity when the parameter  $\lambda_0 = 4\sigma c/g = 1$ ,  $g$  being the acceleration due to gravity.

Consequently, the theoretical motion of a ship, computed by Havelock (33), Newman (34) and others is found to be unbounded at this condition.

Returning to the problem of the pressure distribution, this has been examined in two dimensions by Kaplan (35), Wu (36) and Debnath (37) - the latter paper extending the results to finite depth, which alters the critical value of  $\lambda_0$ . Ogilvie (38) included sidewalls to limit physically the pressure and thus modelled a pneumatic wave generator, and also a captured air bubble ACV.

Doctors (39) extended Wu's results to a threedimen-

sional timewise harmonically varying pressure patch travelling at a constant speed over deep water, and applied the results to the periodic motion of an ACV. The hydrodynamic influence is felt through the alteration of the air gap under the skirt due to the water deflection and a change in the effective flux balance of air in the cushion.

His induced free-surface elevation calculations indeed showed the singularity to be expected at the critical value of  $\lambda_0$ , and consequently the ACV motion calculations were centered on a low Froude number,  $F = c/\sqrt{gL}$ , of 0.5, where  $L$  is the craft length. The dimensionless encounter frequency,  $\omega L/g$  should then be equal to 0.5 at the critical condition  $\lambda_0 = 1$ . Surprisingly, no singularity, or even a peak, was exhibited in the craft motion at that frequency.

Nevertheless, at a dimensionless frequency of 3, the heave motion was found to be increased by up to ten percent by the deflection of the water. The pitch motion could be increased by up to one third. A linearized heave analysis was also done and this indicated an effective negative added mass of 44% of the craft mass at  $\omega L/g = 3$ , thus correlating with results of Van den Brug and Van Staveren.

The hydromechanical coupling was also considered by Breslin (40) for a twodimensional craft. Even with the equations of motion linearized, he predicted a large influence from the water.

Measurements of the water surface resulting from a harmonic disturbance have been made by Moran (41 and 42). These showed some interesting trends. Unfortunately, the model tested did not correspond to the theoretical work above, so that a direct comparison cannot be made.

#### Present Work

The object of this paper is to extend the previous work of the writer to higher Froude numbers and encounter frequencies which will therefore be far above the critical value of  $\lambda_0$ . Furthermore, the effect of compressibility of the air within the cushion will be considered. In line with previous workers, a first approximation to this effect will be obtained by including only the accumulation term in the continuity equations of the three volumes seen in Fig. 1.

Although the Mach-number effect will be ignored, it is not entirely obvious that the procedure should be correct in any but a linear theory. The various flow velocities can all typically change in sign.

Considering this and the nature of the balance of the continuity equations, one might indeed have to model more precisely the equations of air flow.

#### HYDRODYNAMIC REPRESENTATION

##### The Velocity Potential

We make use of a coordinate system  $x, y, z$  moving with the pressure, with  $x$  in the direction of motion and  $z$  measured vertically from the undisturbed free surface. Under the usual assumptions of linearized potential flow (see Stoker (43)), the potential,  $\phi$ , satisfies the Laplace equation,

$$\phi_{xx} + \phi_{yy} + \phi_{zz} = 0, \quad (1)$$

the kinematic free-surface condition,

$$\phi_z - \zeta_t + c\zeta_x = 0 \quad \text{on } z = 0, \quad (2)$$

and the dynamic free-surface condition,

$$\phi_t - c\phi_x + \mu\phi + p/\rho + g\zeta = 0 \quad \text{on } z = 0. \quad (3)$$

Here  $\zeta$  is the free-surface elevation and  $\rho$  is the water density. The radiation condition is satisfied by employing the Rayleigh viscosity  $\mu$ , which is made to approach zero from the positive direction at a later stage. Discussion of this technique is given by De Prima and Wu (44), for example. Its purpose is to determine the path of integration which has to be deformed in order to go around the two or four poles that occur in the wavenumber integral. One last condition is obtained by assuming the water to be infinitely deep:

$$\phi_z = 0 \quad \text{on } z = -\infty. \quad (4)$$

Although the solution was previously obtained by setting up an initial value problem, it is in fact easier\* to write the pressure as

$$p(x, y) = \hat{p}(x, y) e^{i\sigma t} \quad (5)$$

and the potential as

$$\phi(x, y, z) = \hat{\phi}(x, y, z) e^{i\sigma t}, \quad (6)$$

where the real parts only are required.

Eqs (2) and (3) are combined in order to eliminate  $\zeta$ :

$$\begin{aligned} \phi_{tt} + c^2\phi_{xx} - 2c\phi_{xt} + g\phi_z + \mu(\phi_t - c\phi_x) = \\ = (c p_x - p_t)/\rho \quad \text{on } z = 0. \end{aligned} \quad (7)$$

To obtain  $\phi$ , we utilize the Fourier transform pair:

$$\hat{\phi}(w, u; z, t) = \frac{1}{2\pi} \int_{-\infty}^{\infty} \int_{-\infty}^{\infty} \phi(x, y, z, t) \exp[-i(wx + uy)] dx dy$$

and

$$\phi(x, y, z, t) = \frac{1}{2\pi} \int_{-\infty}^{\infty} \int_{-\infty}^{\infty} \hat{\phi}(w, u; z, t) \exp[i(wx + uy)] dw du. \quad (8)$$

Here  $w$  and  $u$  are the longitudinal and transverse wavenumbers, respectively, and are related to the (circular) wavenumber  $k$  and the wave angle  $\theta$  by

$$w + iu = k e^{i\theta}. \quad (9)$$

The solution to Eqs (1) and (4) is

$$\hat{\phi} = \hat{A}(w, u; t) e^{kz} \quad (10)$$

which may be substituted into the transformed free-surface condition (7) to give

$$\begin{aligned} \hat{A}[-\sigma^2 - c^2 w^2 + 2c\sigma w + gk + i\mu(\sigma - cw)] = \\ = i(cw - \sigma)\hat{p}/\rho \end{aligned}$$

$$\begin{aligned} \text{or} \quad \hat{A} &= \frac{i(\sigma - cw)\hat{p}}{\rho(cw + \sqrt{gk} - \sigma + i\mu)(cw - \sqrt{gk} - \sigma + i\mu)} \\ &= \frac{\hat{p}}{2i\rho} \left[ \frac{1}{\omega_1} + \frac{1}{\omega_2} \right] \end{aligned} \quad (11)$$

$$\text{where} \quad \omega_{1,2} = cw \pm \sqrt{gk} - \sigma + i\mu \quad (12)$$

and  $\hat{p}$  is the Fourier transform of  $\hat{p}$ .

Now we take the inverse transform:

$$\phi(x, y, z, t) = \text{Real} \frac{1}{8\pi^2 i \rho} \iint \hat{p}' ds' \int_{-\pi}^{\pi} d\theta \int_0^{\infty} dk \quad (13)$$

$$k \left[ \frac{1}{\omega_1} + \frac{1}{\omega_2} \right] \exp[i\{w(x - x') + u(y - y') + kz + \sigma t\}]$$

The problem of taking the real part of this expression can be avoided by simply adding to it the formula when the sign of  $\sigma$  is changed and then halving the sum. This result for  $\phi$  will then be purely real.

#### Free-Surface Elevation

The height of the free surface is given by Eq. (3). We substitute the potential from Eq. (13) and simplify the result using Eq. (12):

$$\begin{aligned} \zeta &= \frac{1}{8\pi^2 \rho c^2} \iint \hat{p}' ds' \int_{-\pi}^{\pi} \sec^2 \theta d\theta \int_0^{\infty} dk \\ &\quad k \cdot \exp[i\{w(x - x') + u(y - y')\}]. \end{aligned} \quad (14)$$

$$\cdot \left[ \frac{e^{i\sigma t}}{k_1 - k_2} \left\{ \frac{k_1}{k - k_1} - \frac{k_2}{k - k_2} \right\} + \frac{e^{-i\sigma t}}{k_3 - k_4} \left\{ \frac{k_3}{k - k_3} - \frac{k_4}{k - k_4} \right\} \right]$$

The four poles in the  $k$  integral are given by

$$\begin{aligned} k_1 &= \frac{1}{4} k_0 \sec^2 \theta (\sqrt{1 + \lambda} + 1)^2 \\ k_2 &= \frac{1}{4} k_0 \sec^2 \theta (\sqrt{1 + \lambda} - 1)^2 \\ k_3 &= \frac{1}{4} k_0 \sec^2 \theta (1 + \sqrt{1 - \lambda})^2, \\ k_4 &= \frac{1}{4} k_0 \sec^2 \theta (1 - \sqrt{1 - \lambda})^2, \end{aligned} \quad (15)$$

where  $k_0 = g/c^2$ ,

$$\text{and} \quad \lambda = \frac{4gc}{g} \cos \theta = \lambda_0 \cos \theta. \quad (16)$$

If  $\lambda_0 > 1$ , then for part of the  $\theta$  integration, namely  $0 < \theta < \theta_1$ , where

$$\cos \theta_1 = 1/\lambda_0, \quad (17)$$

the two poles  $k_3$  and  $k_4$  are complex conjugate and the  $k$  integration can proceed along the real axis. For  $\lambda < 1$ , one must deflect the path below the pole  $k_3$  and above the pole  $k_4$ . (This may be seen by examining the zeroes of Eq. (12) for very small and positive  $\mu$ .) For all values of  $\lambda$ , the path must be deflected above the poles at  $k_1$  and  $k_2$ .

We now reduce the range of the  $\theta$  integration to  $0 < \theta < \pi/2$  making use of the even and odd properties of the trigonometric functions to give

$$\zeta = \zeta_c \cos \sigma t + \zeta_s \sin \sigma t, \quad (18)$$

\* The writer is grateful to Prof. J. N. Newman of Massachusetts Institute of Technology for pointing this out.



where

$$\zeta_c = \frac{-1}{2\pi^2\rho g} \int_0^{\pi/2} d\theta \int_0^\infty dk k U \sum_{j=1}^4 \mu_{1j} \frac{1}{\sqrt{1+\lambda_j}} \frac{k_j}{k-k_j} -$$

$$- \frac{1}{2\pi\rho g} \int_{\theta_j}^{\pi/2} d\theta \sum_{j=1}^4 \mu_{3j} \frac{V_j}{\sqrt{1+\lambda_j}} k_j^2$$
(19)

and

$$\zeta_s = \frac{1}{2\pi^2\rho g} \int_0^{\pi/2} d\theta \int_0^\infty dk k V \sum_{j=1}^4 \mu_{2j} \frac{1}{\sqrt{1+\lambda_j}} \frac{k_j}{k-k_j} -$$

$$- \frac{1}{2\pi\rho g} \int_{\theta_j}^{\pi/2} d\theta \sum_{j=1}^4 \mu_{4j} \frac{U_j}{\sqrt{1+\lambda_j}} k_j^2$$

where  $\mu_{1j} = 1, -1, 1, -1,$

$\mu_{2j} = 1, -1, -1, 1,$

$\mu_{3j} = 1, -1, -1, -1,$

and  $\mu_{4j} = 1, -1, 1, 1$  for  $j = 1$  to 4 respectively,

$$\theta_j = 0 \text{ for } j = 1 \text{ and } 2 \text{ for all } \lambda_0$$

$$= 0 \text{ for } j = 3 \text{ and } 4 \text{ for } \lambda_0 < 1$$
(21)

and  $= \theta_1$  for  $j = 3$  and  $4$  for  $\lambda_0 > 1,$

$$\text{and } \lambda_j = \lambda \text{ for } j = 1 \text{ and } 2$$

$$= -\lambda \text{ for } j = 3 \text{ and } 4,$$
(22)

$$\text{and } U = P_e \cos wx \cos uy + P_o \sin wx \sin uy +$$

$$+ Q_e \sin wx \cos uy + Q_o \cos wx \sin uy,$$
(23)

$$V = P_e \sin wx \cos uy - P_o \cos wx \sin uy -$$

$$- Q_e \cos wx \cos uy + Q_o \sin wx \sin uy,$$

$$P_e = \iint \hat{p}(x,y) \frac{\cos(wx)}{\sin(wx)} \frac{\cos(uy)}{\sin(uy)} dS$$

$$P_o = \iint \hat{p}(x,y) \frac{\cos(wx)}{\sin(wx)} \frac{\sin(uy)}{\sin(uy)} dS$$
(24)

and

$$Q_e = \iint \hat{p}(x,y) \frac{\sin(wx)}{\cos(wx)} \frac{\cos(uy)}{\sin(uy)} dS$$

$$Q_o = \iint \hat{p}(x,y) \frac{\sin(wx)}{\cos(wx)} \frac{\sin(uy)}{\sin(uy)} dS$$

(The subscripts on  $U$  and  $V$  in Eq. (19) refer to the four poles.)

If one considers a pressure of constant value  $P_0$  acting on a rectangular area defined by  $|x| < a$  and  $|y| < b$ , the computation is greatly simplified since

$$P_e = 4 P_0 \frac{\sin aw}{w} \frac{\sin bu}{u}$$
(25)

and  $P_o = Q_e = Q_o = 0$ .

The free-surface response given by Eq. (19) can now be obtained using the rules for combining products of trigonometric functions. The  $k$  integrals are then written in terms of the cosine- and sine- aux-

iliary functions (see Abramowitz and Stegun (45)):

$$g(z) + if(z) = \int_0^\infty \frac{e^{it}}{t+z} dt.$$
(26)

The results for the in-phase and out-of-phase components of the free-surface elevation are

$$\zeta_c = \frac{P_0}{4\pi^2\rho g} \sum_{\ell,m,n=\pm 1} \sum_{j=1}^4 \int_0^{\pi/2} \sec \theta \operatorname{cosec} \theta \cdot$$

$$\cdot \frac{n}{\sqrt{1+\lambda_j}} [\mu_{1j}(g_j - \pi s_j) + \mu_{3j} \ell v \pi s_j] d\theta$$

and

$$\zeta_s = \frac{P_0}{4\pi^2\rho g} \sum_{\ell,m,n=\pm 1} \sum_{j=1}^4 \int_0^{\pi/2} \sec \theta \operatorname{cosec} \theta \cdot$$

$$\cdot \frac{n}{\sqrt{1+\lambda_j}} [\mu_{2j} \ell v (f_j - \pi c_j) + \mu_{4j} \pi c_j] d\theta,$$
(27)

in which the following shorthand notation has been used:

$$f_j = f|rk_j|,$$

$$g_j = g|rk_j|,$$

$$c_j = \cos|rk_j|,$$

$$s_j = \sin|rk_j|,$$
(28)

and  $v = \operatorname{sgn}(r),$

where  $r = (a + \ell x) \cos \theta + n(b + my) \sin \theta.$

The terms with the sign coefficient  $\mu_{33}, \mu_{34}, \mu_{43}$  and  $\mu_{44}$  are all understood to be omitted when  $\theta < \theta_1$ , given by Eq. (17).

By allowing  $\sigma$  to approach zero, one may recover the case of a nonvarying pressure. We use the two limits:

$$f(z) \rightarrow \frac{\pi}{2} \text{ and } g(z) \rightarrow -\gamma - \ln(z) \text{ as } z \rightarrow 0,$$
(29)

$\gamma$  being the Euler constant. The final result is

$$\zeta_c = \frac{P_0}{2\pi^2\rho g} \sum_{\ell,m,n=\pm 1} \sum_{j=1}^4 \int_0^{\pi/2} \sec \theta \operatorname{cosec} \theta \cdot$$
(30)

$$\cdot n[-g_0 + \pi(1-\ell v)s_0 - L_0] d\theta$$

and  $\zeta_s = 0.$

(The zero subscript refers to a function argument with  $k = k_0$  and  $L = \ln|rk|$ ). The logarithm term can be shown to produce the free-surface deformation due to the hydrostatic effect of the pressure alone.

#### Induced Free-Surface Escape Areas and Volumes

The escape areas under the skirt are affected by the water deformation. If one chose to use a linear theory then the induced escape area is required rather than the elevation of the surface itself. The code numbers of the areas are shown in Fig. 2.

Thus the escape areas corresponding to sides 1, 2 and 3 are obtained by an integration of Eq. (27) with respect to  $x$ . This requires the formulas

$$\int \operatorname{sgn}(z) f|z| dz = g|z| + \ln|z| \quad (31)$$

$$\text{and} \quad \int g|z| dz = \operatorname{sgn}(z) \left[ \frac{\pi}{2} - f|z| \right].$$

The result applicable to these three sides is

$$A_{\zeta} = A_{\zeta c} \cos \sigma t + A_{\zeta s} \sin \sigma t, \quad (32)$$

where

$$A_{\zeta c} = \frac{p_0}{2\pi^2 \rho g} \sum_{i,l,n=\pm 1} \sum_{j=1}^4 \int_0^{\pi/2} \sec^2 \theta \operatorname{cosec} \theta \cdot \frac{\ln}{k_j \sqrt{1+\lambda_j}} [\mu_{1j} \lambda v(\pi c_j - f_j - \frac{\pi}{2}) - \mu_{3j} \pi c_j] d\theta$$

and

$$A_{\zeta s} = \frac{p_0}{2\pi^2 \rho g} \sum_{i,l,n=\pm 1} \sum_{j=1}^4 \int_0^{\pi/2} \sec^2 \theta \operatorname{cosec} \theta \cdot \frac{\ln}{k_j \sqrt{1+\lambda_j}} [\mu_{2j}(g_j + L_j - \pi s_j) + \mu_{4j} \lambda v \pi s_j] d\theta. \quad (33)$$

(The changes made in the notation used in Eq. (33) are:

$$my = b, \quad x = x_1,$$

where  $x_1$  and  $x_2$  are the endpoints of the interval under consideration.)

The areas along sides numbered 4 to 7 are obtained by integrating Eq. (27) with respect to  $y$ . The result is the same as that in Eq. (33), but with the "i" summation replaced by an "m" summation, and with an additional factor " $\ln m \cot \theta$ " placed inside the integral. The expression for  $r$  is now given by Eq. (28) with  $x = x_1$  (the longitudinal coordinate of the transverse side) and with  $y = b$ .

The volume above the datum plane and below the free surface results from integrating Eq. (33) with respect to  $y$  over the range  $-b \leq y \leq b$ . We obtain

$$V_{\zeta} = V_{\zeta c} \cos \sigma t + V_{\zeta s} \sin \sigma t \quad (34)$$

where

$$V_{\zeta c} = \frac{p_0}{2\pi^2 \rho g} \sum_{i,l,m,n=\pm 1} \sum_{j=1}^4 \int_0^{\pi/2} \sec^2 \theta \operatorname{cosec}^2 \theta \cdot \frac{i \ln m}{k_j \sqrt{1+\lambda_j}} [\mu_{1j}(\pi s_j - g_j - L_j - \frac{\pi}{2} M_j) - \mu_{3j} \lambda v \pi s_j] d\theta$$

and

$$V_{\zeta s} = \frac{p_0}{2\pi^2 \rho g} \sum_{i,l,m,n=\pm 1} \sum_{j=1}^4 \int_0^{\pi/2} \sec^2 \theta \operatorname{cosec}^2 \theta \cdot \frac{i \ln m}{k_j \sqrt{1+\lambda_j}} [\mu_{2j} \lambda v(\pi c_j - f_j + M_j L_j - \frac{\pi}{2}) - \mu_{4j} \pi c_j] d\theta, \quad (35)$$

in which  $M_j = |rk_j|$  and  $r$  is given by Eq. (28), but with  $y = b$  and  $x = x_1$ . The induced fluxes are

$$Q_{\zeta} = (\sigma V_{\zeta s}) \cos \sigma t + (-\sigma V_{\zeta c}) \sin \sigma t. \quad (36)$$

### Numerical Evaluation

The details of the numerical evaluation of Eqs (27), (30), (33) and (35) are given in Doctors (39). Computations were made for  $\lambda_0 = 0.672$  which, for a Froude number of 1.5, corresponds to  $\sigma L/g = 0.112$ .

The change of variable given by

$$\theta' = \sin \theta / \cos^2 \theta$$

was made as before. For the above range of parameters, it was found suitable to truncate the integral at  $\theta' = 128$  and to use 512 points. Since  $\lambda_0 > 1$  for all but the first case, the terms corresponding to the  $k_3$  and  $k_4$  poles become complex but combine to give a real result which has to be left in the form of the original integral with respect to  $k$ . This integral was truncated at  $ka = 8$ , and 32 points were used in its evaluation. Trial calculations showed that these computing parameters lead to an error of 2 or 3%.

### Results

For brevity, the induced free-surface elevations themselves are not shown here. However, the areas appear in Fig. 3a and 3b, and the volumes in Fig. 4.

Both the in-phase and the out-of-phase components of areas 1, 4 and 5 are somewhat larger than the rest. This is not surprising considering their relative location to the pressure patch (hatched in Fig. 2). It is also not clear that they approach zero with any great rapidity as  $\lambda_0$  becomes large. Thus the water compliance effect appears to be important at higher frequencies - as well as the low ones previously studied.

On the other hand, areas 2, 3, 6 and 7 do in fact seem to show a general decay towards zero at higher frequencies.

The induced volumes in Fig. 4 also indicate values of similar magnitude to those previously computed at a smaller Froude number and lower frequencies. This is particularly so for volume 1, not surprisingly.

### APPLICATION TO ACV MOTION

#### Theoretical Model

The craft considered is shown in Fig. 1. We examine only the heave and pitch motion,  $z$  and  $\theta$ . The air from the lift fan discharges into an intermediate chamber of volume  $V_f$ , and then feeds the two cushions through the inlet areas  $A_{i1}$  and  $A_{i2}$ , respectively.

The characteristic of the fan and the intermediate chamber is represented by

$$P_f = C_{f1} + C_{f2} Q + C_{f3} Q^2, \quad (37)$$

where  $Q$  is the inlet flow and the  $C_f$  are constants which depend on the fan and duct types as well as the speed setting of the fan.

#### Volume Flow Terms

Assuming that the changes in air density are small, then the fan flow is given by

$$Q = Q_{i1} + Q_{i2} + V_f \dot{\rho}_f / \rho_a, \quad (38)$$

where the  $Q_i$  are the two inlet flows to the cushion,  $\rho_f$  is the density of the air in the fan chamber, and  $\rho_a$  is atmospheric density.

The cushion inlet flows, and escape flows are given by the Bernoulli equation:

$$Q_{i1} = \text{sgn}(p_f - p_1) A_{i1} C_{di1} \sqrt{2|p_f - p_1|/\rho_a}, \quad (39)$$

$$Q_{i2} = \text{sgn}(p_f - p_2) A_{i2} C_{di2} \sqrt{2|p_f - p_2|/\rho_a},$$

$$Q_{e1} = \text{sgn}(p_1) A_{e1} C_{de1} \sqrt{2|p_1|/\rho_a},$$

$$Q_{e2} = \text{sgn}(p_2) A_{e2} C_{de2} \sqrt{2|p_2|/\rho_a} \quad \text{and} \quad (40)$$

$$Q_{e3} = \text{sgn}(p_1 - p_2) A_{e3} C_{de3} \sqrt{2|p_1 - p_2|/\rho_a}.$$

The sign function is used since the air flows can reverse their directions.

We now apply continuity to the two air cushions as follows:

$$Q_{i1} = Q_{e1} + Q_{r1} - Q_{w1} + Q_{e3} - Q_{\zeta 1} + V_1 \dot{\rho}_1/\rho_a \quad (41)$$

$$Q_{i2} = Q_{e2} + Q_{r2} - Q_{w2} - Q_{e3} - Q_{\zeta 2} + V_2 \dot{\rho}_2/\rho_a.$$

The flux terms due to craft pumping,  $Q_{r1}$  and  $Q_{r2}$ , are given by

$$Q_r = [\dot{z} + (\bar{x} - x_g)\dot{\theta}] S, \quad (42)$$

$S$  being the area of either compartment,  $\bar{x}$  its centroid and  $x_g$  is the longitudinal position of the craft's center of gravity.

The flux terms due to the compliance of the water surface  $Q_{\zeta}$  can now be obtained if the vehicle motion is taken as periodic (with angular frequency  $\omega$ ) and the Fourier series cosine and sine components ( $a_n$  and  $b_n$ , say) of the two cushion pressures  $p_1$  and  $p_2$  are known. One must also consider the interference between the two cushions. The result for the forward cushion is

$$Q_{\zeta 1} = \sum_{n=1}^{N-1} n\omega \{ [a_{n1} V_{\zeta 2}(n\omega) + b_{n1} V_{\zeta 2}(n\omega) + a_{n2} V_{\zeta 3}(n\omega) + b_{n2} V_{\zeta 3}(n\omega)] \cos(n\omega t) + [b_{n1} V_{\zeta 2}(n\omega) - a_{n1} V_{\zeta 2}(n\omega) + b_{n2} V_{\zeta 3}(n\omega) - a_{n2} V_{\zeta 3}(n\omega)] \sin(n\omega t) \}. \quad (43)$$

The expression for  $Q_{\zeta 2}$  is the same but with the subscripts of  $V_{\zeta C}$  and  $V_{\zeta S}$  reduced by 1. In Eq. (43) we are using the first  $N$  terms in the Fourier series:

$$p = \sum_{n=0}^{\infty} \epsilon_n [a_n \cos(n\omega t) + b_n \sin(n\omega t)], \quad (44)$$

in which  $\epsilon_0 = \frac{1}{2}$  and  $\epsilon_n = 1$  for  $n \neq 0$ . (The first term, that is  $n = 0$ , does not contribute to the fluxes.)

The volume fluxes due to wave pumping are given by

$$Q_w = \int \frac{\partial}{\partial t} (z_w) B(x) dx, \quad (45)$$

in which  $B$  is the local craft beam (constant here)

and  $z_w$  is the forcing wave which is given by

$$z_w = h_w \cos[k_w(x_w - c_w t)],$$

where  $h_w$ ,  $k_w$  and  $c_w$  are respectively the amplitude, wavenumber and velocity of the wave, and  $x_w$  is measured in a stationary reference frame. It is more convenient to use the moving frame:

$$z_w = h_w \cos(k_w x + \omega t), \quad (46)$$

where  $\omega$ , the encounter frequency, is generally positive for a high-speed craft. Substitution of this result in Eq. (45) yields

$$Q_w = \omega [V_{ws} \cos(\omega t) - V_{wc} \sin(\omega t)], \quad (47)$$

$$\text{where } \frac{V_{wc1}}{V_{wc2}} = \frac{h_w B}{k_w} [\sin(\frac{1}{2}k_w L) + \sin(\epsilon k_w L)] \quad (48)$$

$$\text{and } \frac{V_{ws1}}{V_{ws2}} = \frac{h_w B}{k_w} [\cos(\frac{1}{2}k_w L) - \cos(\epsilon k_w L)].$$

In Eq. (41) the last term represents the accumulation effect in each cushion, the volume of each ( $V_1$  and  $V_2$ ) being given, analogous to Eqs. (42) and (47) by

$$V = S[z - z_g + (\bar{x} - x_g)\theta] - [V_{wc} \cos(\omega t) + V_{ws} \sin(\omega t)]. \quad (49)$$

The first term in Eq. (49) shows the influence of craft heave and pitch on the cushion volumes, while the second takes into account the volume occupied by the wave. The effect of the induced volumes  $V_{\zeta}$  is ignored in this equation.

#### The Escape Areas

The clearance under the skirt hem is based on an assumed craft position:

$$e = z - z_g + (x - x_g)\theta - z_w - h_k - z_{\zeta}, \quad (50)$$

where  $h_k$  is the local skirt depth, and  $z_{\zeta}$  is the induced free-surface elevation. The latter may be calculated in a manner similar to the induced fluxes in Eq. (43), using the same Fourier series components of the pressure. For example, the pressure-induced elevation on side 1 is:

$$z_{\zeta 1} = \sum_{n=0}^{N-1} \epsilon_n \{ [a_{n1} \zeta_{c1}(n\omega) - b_{n1} \zeta_{s1}(n\omega) + a_{n2} \zeta_{c2}(n\omega) - b_{n2} \zeta_{s2}(n\omega)] \cos(n\omega t) + [a_{n1} \zeta_{s1}(n\omega) + b_{n1} \zeta_{c1}(n\omega) + a_{n2} \zeta_{s2}(n\omega) + b_{n2} \zeta_{c2}(n\omega)] \sin(n\omega t) \}. \quad (51)$$

The escape area along the various skirt perimeters is obtained by an integration with respect to the distance along the skirt hem,  $l$ :

$$A_e = \int_{l_1}^{l_2} e H(e) dl, \quad (52)$$

where  $H$  is the Heaviside step function.



### Skirt Contact Forces and Moments

Each element of the skirt is considered to act independently. Thus the vertical force on the craft due to skirt deflection is

$$R_v = - \int p \eta e H(-e) d\ell. \quad (53)$$

The local force is thus assumed to be proportional to the cushion pressure. The constant  $\eta$  is essentially the tangent of the angle between the skirt wall (where it meets the water) and the vertical.

The horizontal component of the skirt force can be decomposed into two parts. The first, being frictional, is derived using the result in Eq. (53) together with the usual connection between a horizontal and vertical force moving over a surface:

$$dR_h'/dR_v = (\alpha_w + \mu)/(\mu\alpha_w - 1), \quad (54)$$

where  $\alpha_w$  is the longitudinal slope of the water surface and  $\mu$  is some empirical constant which accounts for the drag due to the water. In fact, calculations have been made which show that the value of  $\mu$  has no significant effect on the craft motion, so that one need not be concerned at this poor model of the mechanics of the skirt interaction with the water. A second part of the horizontal force derives from the pressure acting on the skirt wall. Its component in the  $x$  direction is

$$dR_h'' = p e H(-e) \sin \beta d\ell, \quad (55)$$

$\beta$  being the angle between the skirt and the longitudinal direction.

We now use Eqs (53) to (55) to give the horizontal skirt force on the ACV:

$$\begin{aligned} R_h &= R_h' + R_h'' \\ &= \int p \left[ \sin \beta - \eta \frac{\alpha_w + \mu}{\mu\alpha_w - 1} \right] e H(-e) d\ell, \end{aligned} \quad (56)$$

and the bow-up moment on the craft about its center of gravity:

$$\begin{aligned} M &= \int p \left[ (z_g + h_k + \frac{1}{2}e) \sin \beta - \right. \\ &\quad \left. - \eta \{x - x_g + (z_g + h_k + e) \frac{\alpha_w + \mu}{\mu\alpha_w - 1}\} e H(-e) d\ell. \end{aligned} \quad (57)$$

### Equations of Motion

Newton's laws of motion for heave and pitch about the center of gravity are

$$m(\ddot{z} + g) = p_1 S_1 + p_2 S_2 + R_v \quad (58)$$

$$\begin{aligned} \text{and } I\ddot{\theta} &= p_1 S_1 (\bar{x}_1 - x_g) + p_2 S_2 (\bar{x}_2 - x_g) + M + \\ &\quad + p_1 B(h_{k1} - h_{k3}) [z_g + \frac{1}{2}(h_{k1} + h_{k3})] + \\ &\quad + p_2 B(h_{k3} - h_{k2}) [z_g + \frac{1}{2}(h_{k3} + h_{k2})], \end{aligned} \quad (59)$$

where  $m$  and  $I$  are the mass and its second moment about the transverse axis through the center of gravity, respectively.

### Numerical Solution

The craft motion was numerically solved by starting the vehicle from rest and running it over a number of wave lengths until the behavior became periodic - within the specified criterion.

The details of the procedure are given in Doctors (27 and 39). One feature only will be pointed out here. This refers to the solution of the set of equations (37) to (41). Previously these could be reduced to a pair of nonlinear equations  $f(p_1, p_2) = 0$  and  $g(p_1, p_2) = 0$  which were solved by a two-dimensional Newton-Raphson procedure.

In the present work, it was necessary to consider three functions, namely:

$$\begin{aligned} f &= \frac{2(A_{i1}C_{di1})^2}{\rho_a} (p_f - p_1) - \text{sgn}(Q_1) Q_1^2, \\ g &= \frac{2(A_{i2}C_{di2})^2}{\rho_a} (p_f - p_2) - \text{sgn}(Q_2) Q_2^2 \end{aligned} \quad (60)$$

and

$$h = p_f - (C_{f1} + C_{f2}Q + C_{f3} \text{sgn}(Q) Q^2),$$

whose zeroes are to be found. Thus a three-dimensional Newton-Raphson technique, using analytic expressions for the nine derivatives, was used.

The rate-of-change-of-density terms were computed using the adiabatic isentropic relationship:

$$1 + p/p_a = (\rho/\rho_a)^\gamma, \quad (61)$$

where  $\gamma$  was taken to be 1.4, together with the approximation:

$$\dot{\rho}(t) = [\rho(t) - \rho(t - \Delta t)]/\Delta t. \quad (62)$$

Surprisingly, the convergence rate of this procedure was found to be essentially the same as that for the previously employed simpler equations.

### Encounter Frequency

The wavenumber for the exciting waves may be derived from the relationship

$$k_w = 2\pi/L_w = 1/L \cdot F_w^2, \quad (63)$$

where  $L_w$  is the wavelength and  $F_w = c_w/\sqrt{gL}$ . If one considers the ACV to be moving forward ( $F > 0$ ) in head waves ( $F_w < 0$ ), then there is a unique expression for the wave speed:

$$F_w = [-1 - \sqrt{1 + 4F(\omega\sqrt{L/g})}]/2(\omega\sqrt{L/g}). \quad (64)$$

This is the case of the results in the next section.

### RESULTS

Calculations were carried out for the craft whose particulars appear in Table 1, when travelling at a Froude number of 1.5. The computed points on all the curves plotted in the graphs were at the frequencies  $\omega\sqrt{L/g} = 1(1)12$ . The response of the pressures in the forward cushion, aft cushion, and the fan chamber is shown in Figs 5a, b and c, respec-

tively. The asterisk superscript on the symbol  $p$ , and other parameters occurring later, refers to a division by  $h_w$ , and a nondimensionalization with respect to  $L$ ,  $g$  and  $\rho$ . The subscript "rms" indicates a root-mean-square variation measured from the average value, and multiplied by  $\sqrt{2}$ .

Three types of calculation were considered: (a) the over land case where hydrodynamic and compressibility effects are ignored, (b) the over water case where the first two terms in the Fourier series representation of the pressures are used in calculating the water response (that is,  $N = 2$ ), but compressibility is still ignored, and (c) the over water situation ( $N = 2$ ) and compressibility is considered. In the last case, the dimensionless atmospheric pressure is taken as  $p_a/\rho g L = 0.25$  - relevant to a craft length of about 40.0 m.

It is seen that up to a frequency of  $\omega\sqrt{L/g} = 4$  the pressure variations in the forward and aft cushions (Figs 5a and b) are equal and independent of wave height, thus indicating linearity. The fan pressure variation in Fig. 5c is also independent of wave height in this region, and is of smaller magnitude than the cushion pressure changes themselves. Beyond  $\omega\sqrt{L/g} = 4$ , the process becomes strongly nonlinear and both the hydrodynamic and compressibility effects are increasingly important - particularly at a dimensionless frequency of 8. For the aft cushion, the hydrodynamic effect decreases the pressure changes by up to 20%, but the compressibility increases it by up to 100%.

The heave and pitch motions are shown in Figs 6a and b for the same three cases and two wave heights. The pitch motion is, in contrast to all other quantities, divided by wave-slope amplitude rather than wave amplitude itself. The compliance of the water surface is seen to increase or decrease the heave and pitch, depending on the frequency. The same appears to be true of the compressibility. However, at the resonance frequency - which changes with wave height - this factor always increases the motion.

It is interesting to nondimensionalize the previously mentioned results of Fein, Magnuson and Moran (6) and Magnuson (7). These give dimensionless heave and pitch resonance frequencies of 3.17 and 2.89 for the BH.7 travelling in head seas at a Froude number of 1.70. These are to be compared to our results of between 6 and 8 for heave, and between 5 and 7 for pitch - depending on the wave height. Thus the theoretical frequencies are on the high side - but, of course, the data used in the theory may not be applicable. Magnuson and Wolff (8 and 9) reported a dimensionless pitch frequency in head seas, for an SES, of 3.27, which is again less than the theoretical value in Fig. 6b. Finally, Moran and others (10) measured the zero-speed heave and pitch natural frequencies of a JEFF-B model and found them to be 11.0 and 5.28, respectively, in dimensionless units. In this case, the pitch resonance frequency seems to tally with the calculation here, but the heave frequency is now high compared to the theory.

The craft accelerations are plotted in Fig. 7. It is seen that the hydrodynamic effect can either increase or decrease the accelerations, but the compressibility practically always increases it in the frequency range examined.

The phase angles of the fundamental Fourier component of the heave and pitch motions are shown in Figs 8a and b, respectively. Both the angles are measured ahead of the incident wave, and this ex-

$B/L$	$= 0.5$	$C_{f1}/\rho g L$	$= 0.04$
$\epsilon$	$= 0.0$	$C_{f2}\sqrt{L^3/g\rho^2}$	$= 0.0$
$m/\rho L^3$	$= 0.006$	$C_{f3}L^4/\rho$	$= -30.0$
$I/\rho L^5$	$= 3.25 \times 10^{-4}$	$A_{i1}/L^2$	$= 0.005$
$x_g/L$	$= 0.0$	$A_{i2}/L^2$	$= 0.005$
$z_g/L$	$= 0.1$	$C_{di1}$	$= 1.0$
$h_{k1}/L$	$= 0.08$	$C_{di2}$	$= 1.0$
$h_{k2}/L$	$= 0.08$	$C_{de1}$	$= 0.55$
$h_{k3}/L$	$= 0.08$	$C_{de2}$	$= 0.55$
$\eta_1$	$= 1.0$	$C_{de3}$	$= 0.6$
$\eta_2$	$= 1.0$	$\rho_a/\rho$	$= 0.00125$
$\eta_3$	$= 0.0$	$V_f/L^3$	$= 0.005$
$\mu$	$= 0.0$	$\gamma$	$= 1.4$

Table 1. Craft Particulars

plains why the pitch phase angle is  $90^\circ$  at low frequencies. The general effect of increasing the frequency is to increase the phase lag, but this trend changes at very high encounter frequencies. The strong dependence on wave height is also evident. It should be pointed out that some difficulty was experienced in the convergence of the numerical algorithm for the case of  $h_w/L = 0.03$  at  $\omega\sqrt{L/g} = 9$  and 10. The program generally converged after 3 to 8 cycles, but for these two points, which are indicated on the graphs, it did not converge even after 15 cycles. It is thought that the very strong negative gauge pressures developed in the cushion are related to this problem.

The remaining figures display results plotted as a function of wave height for a dimensionless frequency of 9. Five curves are now shown. These include the previously described three cases. In addition, the incompressible over land case using only one Fourier component for the pressure ( $N = 1$ , equivalent to just the average pressure level in the cushion) is shown. The second additional curve is the compressible over water case with two Fourier components, but with  $p_a/\rho g L = 0.5$ . This corresponds to a craft of length 20.0 m.

Many of the dimensionless heave and pitch curves are seen to become unbounded at low wave heights, in Fig. 9. Of course, the heave and pitch themselves are well defined in the limit. The general effect at this speed and frequency is for the motion to be decreased by water compliance - in contrast to the low speed, low frequency cases studied by Doctors (39). Compressibility uniformly increases the motions.

Fig. 10 displays similar trends for the heave and pitch accelerations. In particular, the strong nonlinearity of the craft response is evident. The last pair of diagrams (Fig. 11) displays the quantity of second harmonic in the craft motion - as a proportion of the fundamental. The harmonic content in the heave and pitch is seen to be occasionally very high, depending on the wave height.

## CONCLUDING REMARKS

Present Work

Referring first to the calculation of the free-surface response due to an oscillating pressure, it is noteworthy that the surface responds almost as much at a Froude number of 1.5 and for  $6 \leq \lambda_0 \leq 72$ , as it does for a Froude number of 0.5 and for  $1 < \lambda_0 \leq 3$  (see results presented in Doctors (39)).

Thus it is not clear at this stage how high the frequency or Froude number must be for one to be able to ignore the compliance of the water. Furthermore, the flux terms are obtained from Fig. 4 by multiplying by  $n\omega$ , the frequency of the  $n$ 'th harmonic - further emphasizing the effect under discussion.

Secondly, it is seen that the influence of the water is not always in the same direction. The craft motion can be increased, or decreased, by the water.

At this stage, it is appropriate to raise the question of the number of terms used in the Fourier series representation of the pressure distributions. For almost all conditions tested, using two terms, rather than one, increased the hydrodynamic influence. That is, the effect continued in the same direction.

Compressibility was found to be an important element of ACV motion at higher frequencies - even more so than the effect of water compliance.

Future Work

At the expense of additional computing effort, one could profitably increase the number of terms in the pressure Fourier series alluded to above. It might well be that taking three or four terms will amplify the hydrodynamic influence.

However, it is felt that more effort should be concentrated on exploring the mechanics of the compressible flows. To this end, the unsteady compressible Bernoulli equations should be utilized. Nevertheless, one must consider the validity of further refining this aspect of the theoretical model in view of the fact that we are only using a simple one-dimensional flow analogy.

An important aspect of this research which has been ignored is the correlation of theoretical work with model and full-size craft. Effort should therefore be directed to theoretically model the actual configurations of existing craft - as well as the conditions under which they operate - so that the assumptions employed can be evaluated.

## ACKNOWLEDGEMENTS

The writer would like to thank Mr R.D. Cooper of the Office of Naval Research (ONR), Washington, for his invitation to present this paper to the Eleventh Symposium on Naval Hydrodynamics. Many benefits have resulted from the research policies of the ONR, and its interest in the writer's work has given him great encouragement.

## BIBLIOGRAPHY

1. Swaan, W.A. and Wahab, R.: "The Behaviour of a Ground Effect Machine over Smooth Water and over Waves", *Hovering Craft and Hydrofoil*, 4, 8, pp 18-24 (1965)

2. Dyne, G.: "An Investigation Concerning the Motions of a Hovercraft in Regular Head Seas", *Trans. Royal Inst. Naval Architects*, 110, 4, pp 465-477, (1968)

3. Van den Brug, J.B.: "The Dynamic Stability of a Ground Effect Machine Model, Determined by Static- and Forced-Oscillation Tests", *Proc. Seventh Symposium on Naval Hydrodynamics*, Office of Naval Research, Washington, 4 pp (1968)

4. Van den Brug, J.B. and Van Staveren, P.: "An Experimental Study on the Dynamic Stability of a Ground Effect Machine Model in Heave, Pitch and Roll", *Int. Shipbuilding Progress*, 16, 181, pp 277-297 (1969)

5. Stanton-Jones, R.: "Hovercraft Skirt Development - an Engineering and Performance Review", *Trans. Royal Inst. Naval Architects*, 110, 4, pp 499 to 524 (1968)

6. Fein, J.A., Magnuson, A.H. and Moran, D.D.: "Dynamic Performance of an Air Cushion Vehicle in a Marine Environment", *American Inst. Aeronautics and Astronautics/Society of Naval Architects and Marine Engineers (AIAA/SNAME) Advanced Marine Vehicles Conference*, 19 pp (1974)

7. Magnuson, A.H.: "Seakeeping Trials of the BH.7 Hovercraft", *Naval Ship Research and Development Center (NSRDC) Rep. SPD-574-01*, 122+vii pp (1975)

8. Magnuson, A.H. and Wolff, K.K.: "Seakeeping Characteristics of the XR-5, A High Length-Beam Ratio Manned Surface Effect Testcraft: Part 1. XR-5 Model Response in Regular Head Seas", *NSRDC Rep. SPD-616-01*, 77+viii pp (1975)

9. Magnuson, A.H. and Wolff, K.K.: *Ibid*, "Part 2. Results of Linearity Investigation, Effects of Changes from Reference Operating Condition and Trim and Draft in Regular Waves", *NSRDC Rep. SPD-616-02*, 44+v pp (1975)

10. Moran, D.D., Pemberton, T.M. and Knight, K.S.: "A Preliminary Experimental Investigation of the Overland Behavior of the JEFF-B Amphibious Assault Landing Craft", *NSRDC Rep. SPD-615-01*, 37+iii pp (1975)

11. Lin, J.D.: "Dynamic Behavior of GEMs in Motion over Waves", *J. Ship Research*, 6, 4, pp 1-10 (1963)

12. Walker, N.K.: "The Influence of Fan and Ducting Characteristics on the Stability of Ground Effect Machines", *J. Aircraft*, 2, 1, pp 25-32 (1965)

13. Ozawa, S.: "Spring Constants of a Peripheral Jet Air Cushion Vehicle in Heaving Motion", *J. Japan Soc. Aeronautical and Space Sciences*, 18, 193, pp 69-73 (in Japanese) (1970)

14. Hogben, N.: "Hovering Craft over Water", *National Physical Laboratory, Ship Division, Tech. Mem. 119*, 78 pp + 29 figs (1966)

15. Reynolds, A.J.: "A Linear Theory for the Heaving Response of a Hovercraft Moving over Waves", *J. Mechanical Engineering Science*, 14, 2, pp 147-150 (1972)

16. Reynolds, A.J., West, R.P. and Brooks, B.E.: "Heaving and Pitching Response of a Hovercraft Moving over Regular Waves", *J. Mechanical Engineering Science*, 14, 5, pp 340-352 (1972)

17. Foss, W.: "The Static and Dynamic Stiffness in Heave of a Simple Plenum Chamber Hovercraft", *Proc. Symposium on Air Cushion Handling*, British Hydromechanics Research Association Fluid Engineering, Cranfield, pp 19-36 (1974)

18. Kaplan, P. and Davis, S.: "A Simplified Representation of the Vertical Plane Dynamics of SES Craft", *AIAA/SNAME Advanced Marine Vehicles Conference*, 25 pp (1974)

19. Lavis, D.R., Bartholomew, R.J. and Jones, J.C.: "Response of Air Cushion Vehicles to Random Seaways and the Inherent Distortion in Scale Models", *J. Hydronautics*, 8, 3, pp 83-94 (1974)

20. Kaplan, P., Schneider, J. and Goodman, T.R.: "Motions of Air Cushion Vehicles (ACV) in Waves",



*Proc. International Symposium on the Dynamics of Marine Vehicles and Structures in Waves*, Office of Naval Research, Washington (Proc. pub. by Institution of Mechanical Engineers, England), pp 227-234 (1975)

21. Yamamoto, A.: "Nonlinear Heaving Motion of Plenum-Chamber-Type Air Cushion Vehicles", *J. Japan Soc. Aeronautical and Space Sciences*, 18, 193, pp 73-78 (in Japanese) (1970)

22. Leatherwood, J.D., Dixon, G.V. and Stephens, D.G.: "Heave Response of a Plenum Air Cushion Including Passive and Active Control Concepts", National Aeronautics and Space Administration, Tech. Note D-5202, 42 pp (1969)

23. Guenne, P.: "Air Cushion Vehicle Suspension", *Aeronautique et l'Astronautique*, 24, pp 17-28 (in French) (1970)

24. Leatherwood, J.D.: "Analog Analysis of the Heave Response and Control of a Plenum-Type Air-Cushion Vehicle", National Aeronautics and Space Administration, Tech. Note D-6257, 30 pp (1971)

25. Genin, J., Ginsberg, J.H. and Ting, E.C.: "Fluid Suspension Model for Air-Cushioned Vehicles", *J. Sound and Vibration*, 25, 1, pp 83-93 (1972)

26. Bickford, L.L. and Olson, G.K.: "Dynamics of a Multiple-Skirt Air-Cushion Vehicle", *J. Aircraft*, 6, 6, pp 564-565 (1969)

27. Doctors, L.J.: "The Nonlinear Motion of an Air-Cushion Vehicle over Waves", *J. Hydronautics*, 9, 2, pp 49-57 (1975)

28. Schneider, J. and Kaplan, P.: "The Incorporation of Fan Dynamics into the Motion Simulation of Surface Effect Ships", *Fourth Ship Control Systems Symposium*, Royal Netherlands Naval College, The Hague, 26 pp (1975)

29. Breslin, J.P.: "The Dependence of SES Heave Response on Model Scaling Parameters as Deduced from a Simplified Linear Approach", Davidson Lab., Stevens Inst. Technology, Tech. Mem. 157, 20 pp (1969)

30. Richardson, J.R.: "A Scaling Technique for Hovercraft Models", National Physical Laboratory, Hovercraft Unit, Rep. 13, 12 pp (1970)

31. Trillo, R.L.: *Marine Hovercraft Technology*, Leonard Hill, London, 245+xxiii pp (1971)

32. Wehausen, J.V. and Laitone, E.V.: "Surface Waves", *Encyclopedia of Physics*, 9, Fluid Dynamics 3, ed. by S. Flügge, Springer-Verlag, Berlin, pp 446 to 815 (1960)

33. Havelock, T.H.: "The Effect of Speed of Advance upon the Damping of Heave and Pitch", *Trans. Inst. Naval Architects*, 100, 2, pp 131-135 (1958)

34. Newman, J.N.: "The Damping and Wave Resistance of a Pitching and Heaving Ship", *J. Ship Research*, 3, 1, pp 1-19 (1959)

35. Kaplan, P.: "The Waves Generated by the Forward Motion of Oscillatory Pressure Distributions", *Proc. Fifth Midwestern Conf. Fluid Mechanics*, Ann Arbor, Michigan, pp 316-329 (1957)

36. Wu, T.Y.: "Water Waves Generated by the Translatory and Oscillatory Surface Disturbance", *Calif. Inst. Tech., Eng. Div., Rep. 85-3*, 36 pp (1957)

37. Debnath, L. and Rosenblat, S.: "The Ultimate Approach to the Steady State in the Generation of Waves on a Running Stream", *Quart. J. Mech. and Appl. Math.*, 22, Part 2, pp 221-233 (1969)

38. Ogilvie, T.F.: "Oscillating Pressure Fields on a Free Surface", Univ. of Michigan, Dept. Naval Architecture and Marine Engineering, Rep. 30, 52 pp (1969)

39. Doctors, L.J.: "The Hydrodynamic Influence on the Nonlinear Motion of an Air-Cushion Vehicle over Waves", *Proc. Tenth Symposium on Naval Hydrodynamics*, Office of Naval Research, Washington, 19 pp (1974)

40. Breslin, J.P.: "Aero-Hydromechanical Coupling in the Heaving, Translating Surface-Effect Ship", Davidson Lab., Stevens Inst. Technology, Rep. P-1752, 20 pp (1975)

41. Moran, D.D.: "The Wave Height under a High Length-to-Beam Ratio Surface-Effect Ship in Regular Waves", NSRDC Rep. SPD-587-01, 43+v pp (1975)

42. Moran, D.D.: "Cushion Pressure Properties of a High Length-to-Beam Ratio Surface-Effect Ship", NSRDC Rep. SPD-600-01, 43+v pp (1975)

43. Stoker, J.J.: *Water Waves*, Pure and Applied Mathematics, 4, ed. by R. Courant and others, Interscience, New York, 567+xxiv pp (1957)

44. De Prima, C.R. and Wu, T.Y.: "On the Theory of Surface Waves in Water Generated by Moving Disturbances", *Calif. Inst. Tech., Eng. Div., Rep. 21-23*, 40 pp (1957)

45. Abramowitz, M. and Stegun, I.A.: *Handbook of Mathematical Functions*, Nat. Bureau of Standards, Applied Mathematics Series - 55, U.S. Govt. Printing Office, Washington, 1046+xiv pp (1965)

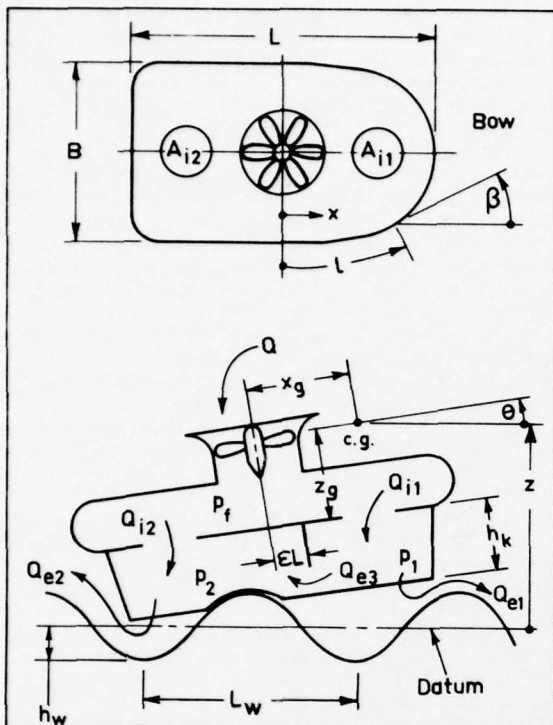


Fig. 1: General layout of craft and notation

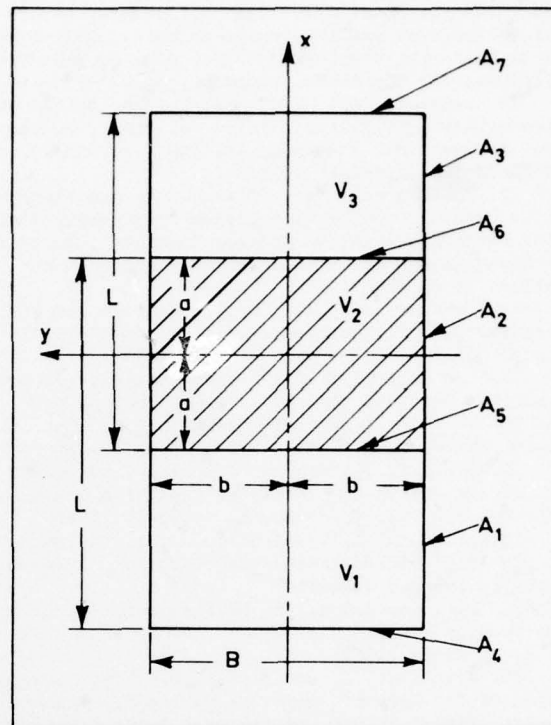
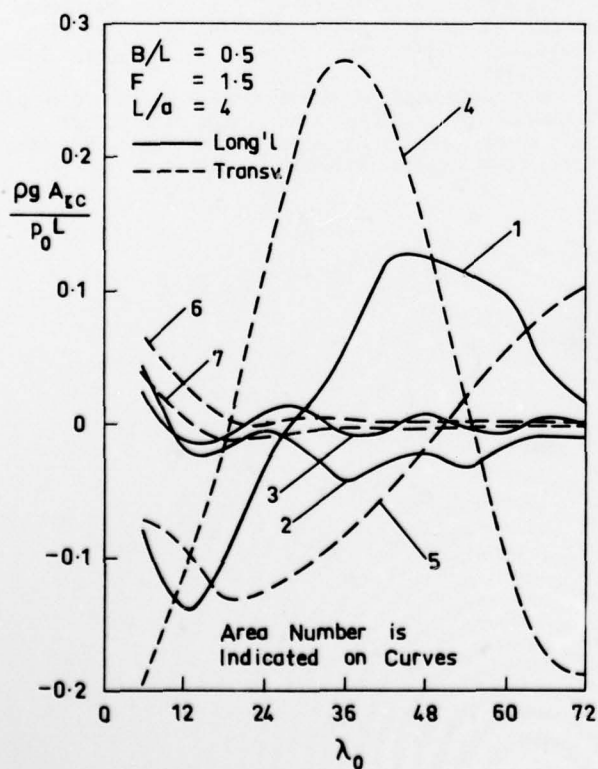
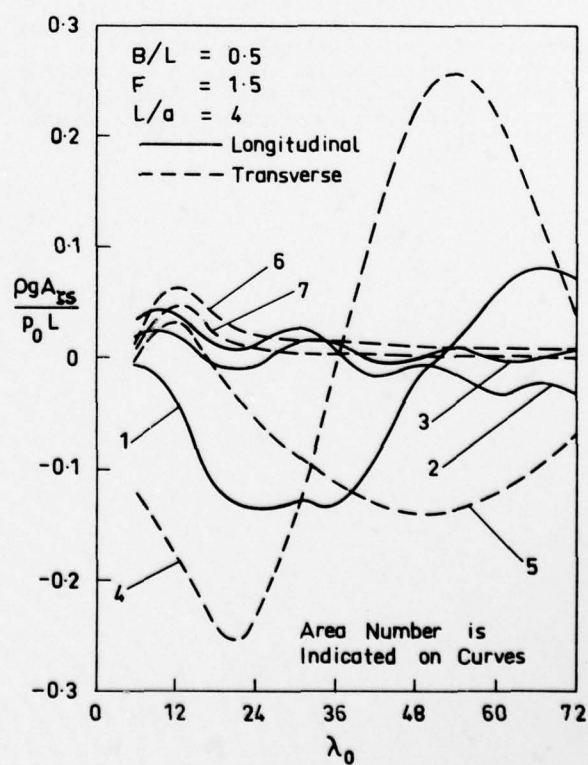


Fig. 2: Notation for escape areas and volumes

Fig. 3: Induced free-surface escape areas  
(a) In-phase componentFig. 3: Induced free-surface escape areas  
(b) Out-of-phase component

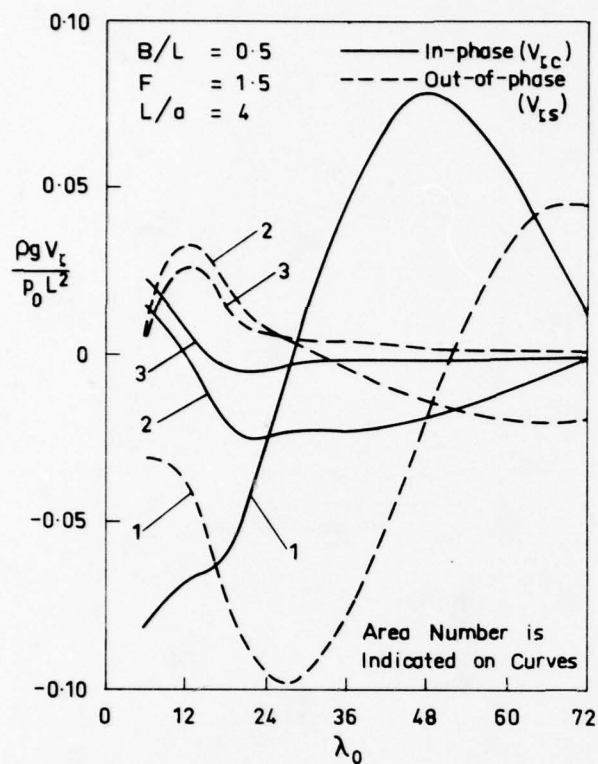
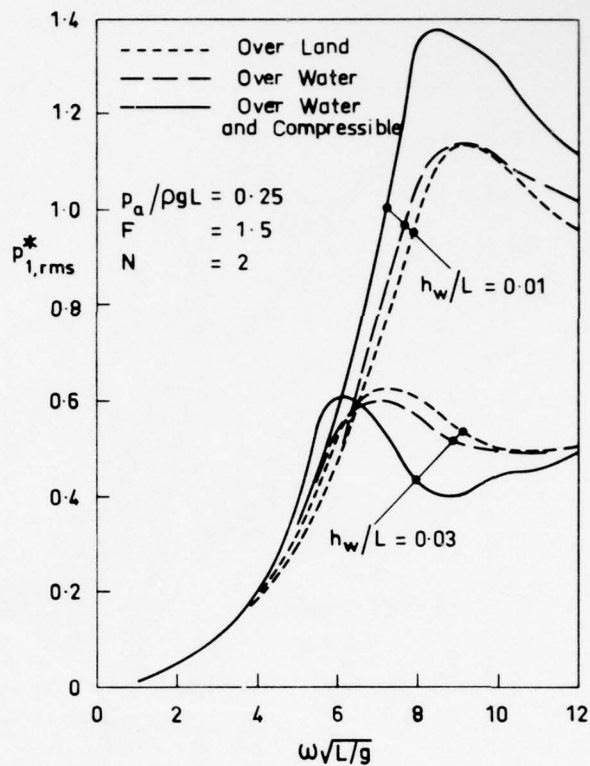
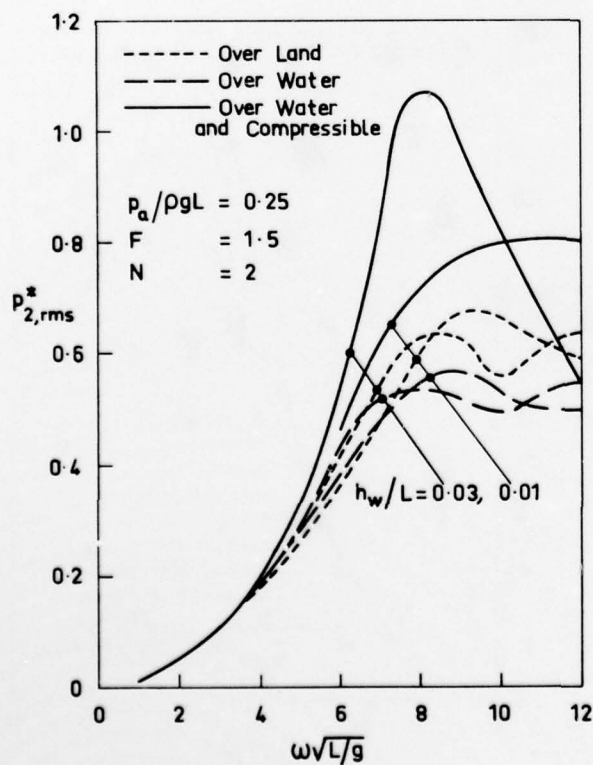
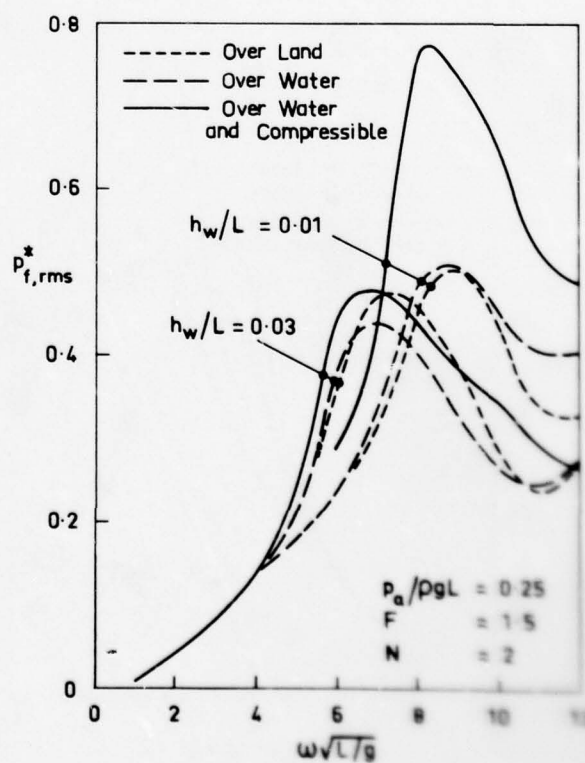


Fig. 4: Induced free-surface volumes

Fig. 5: Craft pressures  
(a) Forward cushionFig. 5: Craft pressures  
(b) Aft cushionFig. 5: Craft pressures  
(c) Fan chamber



AD-A055 859

UNIVERSITY COLL LONDON (ENGLAND) DEPT OF MECHANICAL --ETC F/G 13/10  
SYMPOSIUM ON NAVAL HYDRODYNAMICS. UNSTEADY HYDRODYNAMICS OF MAR--ETC(U)  
1978 R E BISHOP, A G PARKINSON, W G PRICE N00014-76-C-0093

UNCLASSIFIED

NL

5 OF 9

AD  
A055859



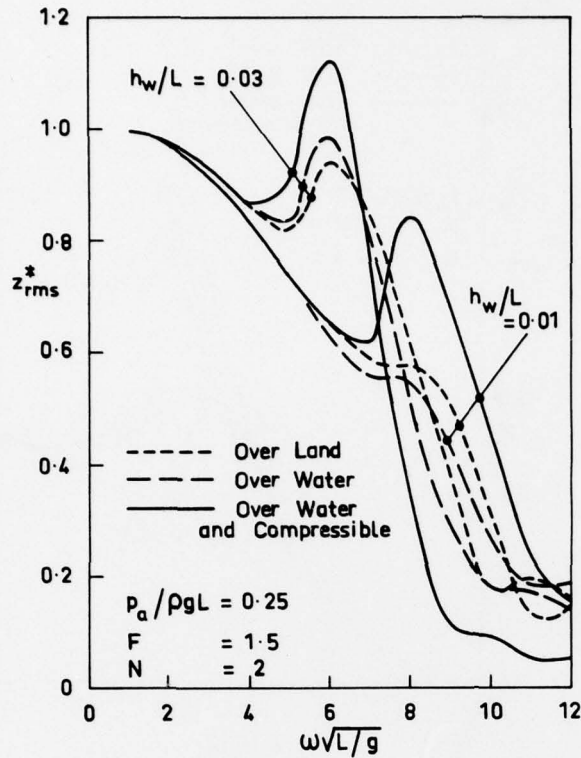


Fig. 6: Craft motion as a function of frequency  
(a) Heave

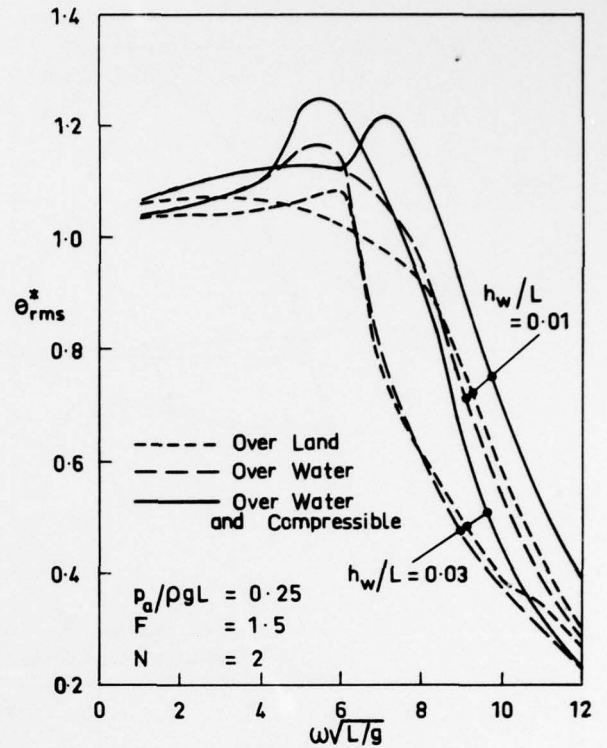


Fig. 6: Craft motion as a function of frequency  
(b) Pitch

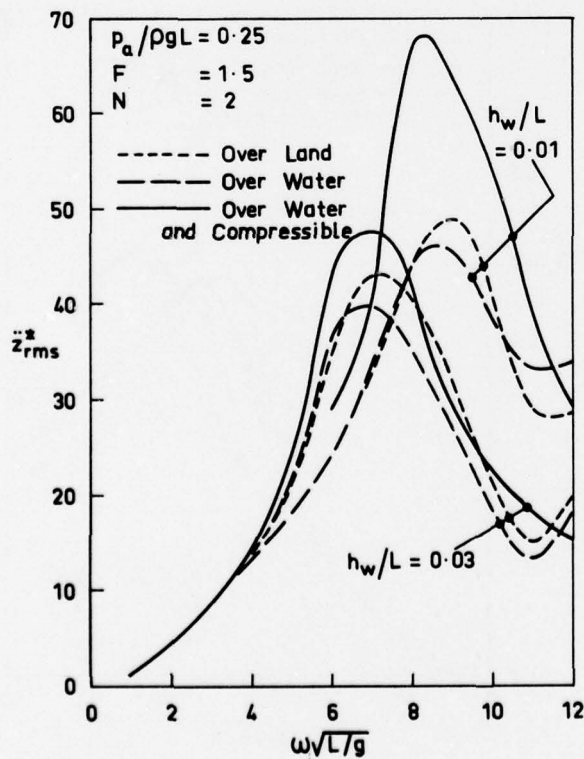


Fig. 7: Craft acceleration as a function of frequency  
(a) Heave

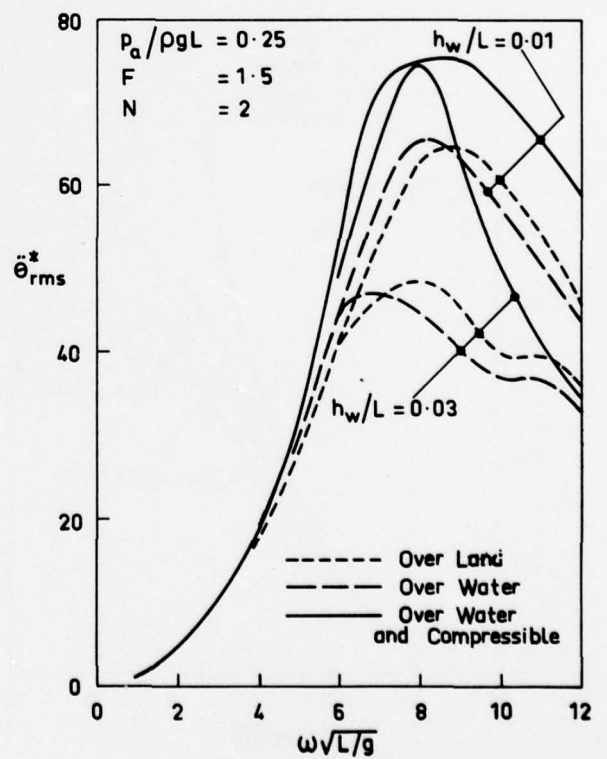


Fig. 7: Craft acceleration as a function of frequency  
(b) Pitch

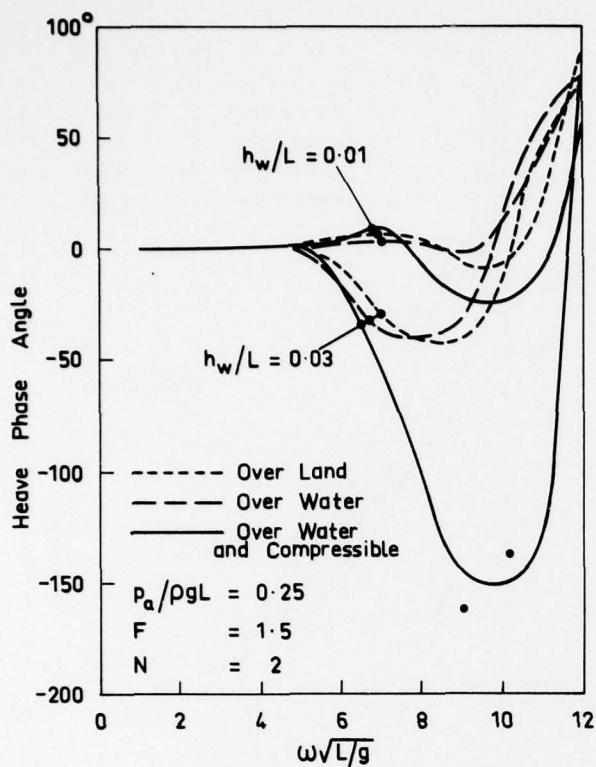


Fig. 8: Phase angle of craft motion  
(a) Heave

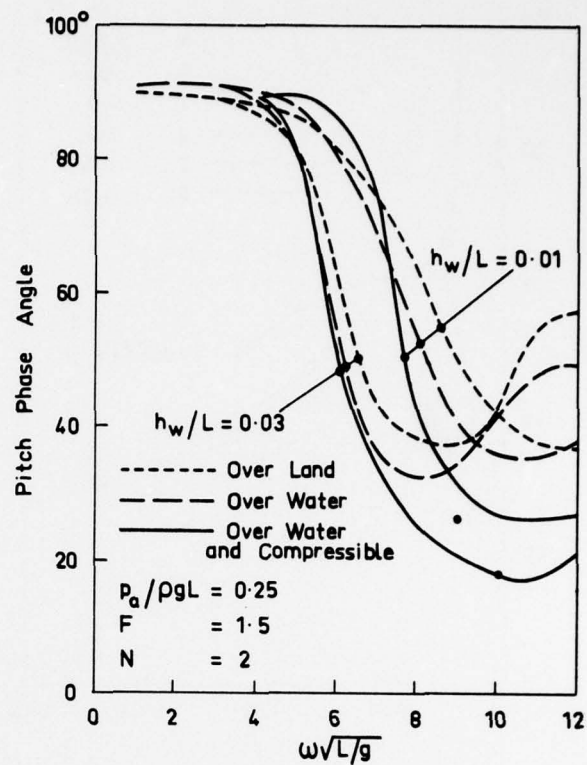


Fig. 8: Phase angle of craft motion  
(b) Pitch

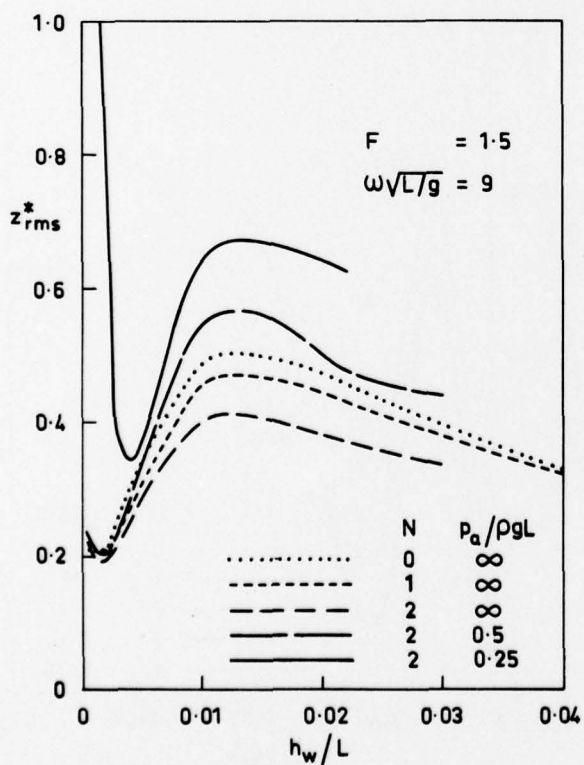


Fig. 9: Craft motion as a function of wave height  
(a) Heave

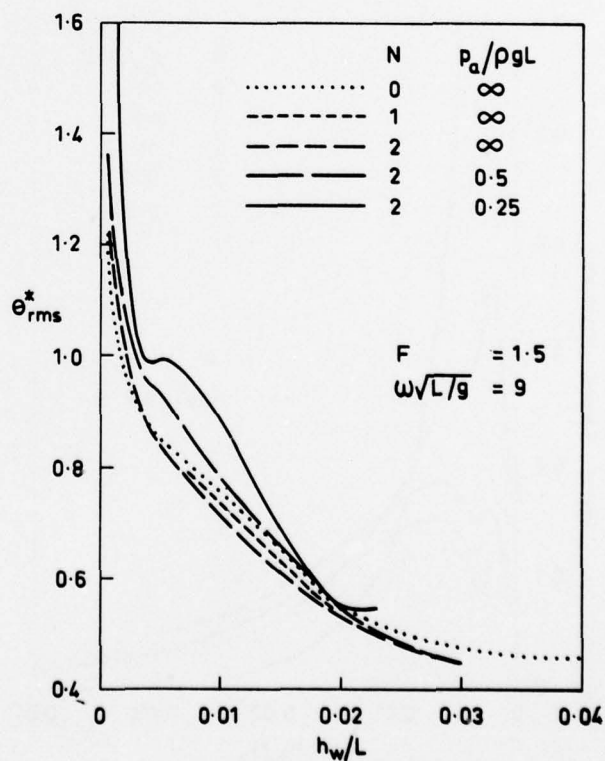
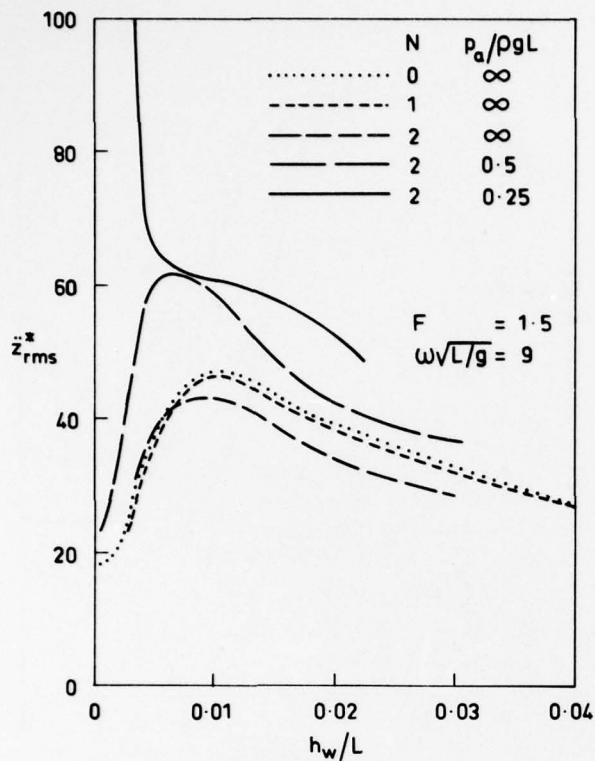
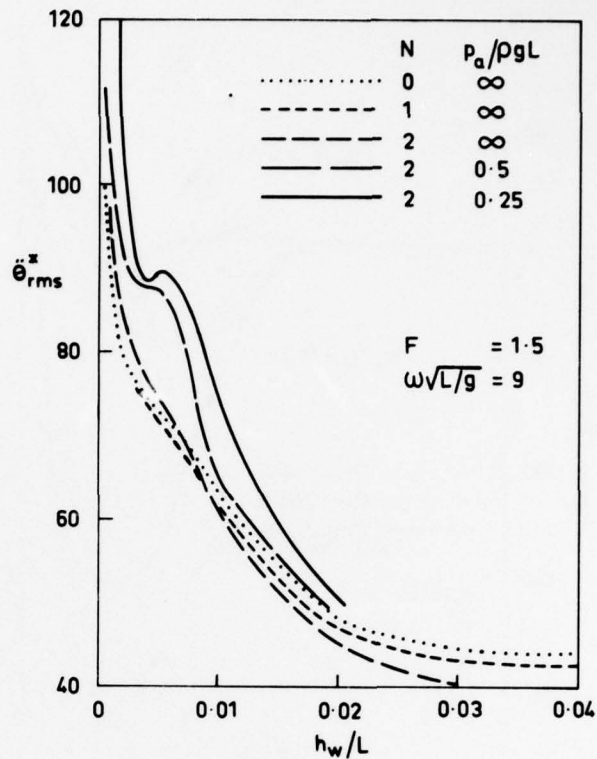
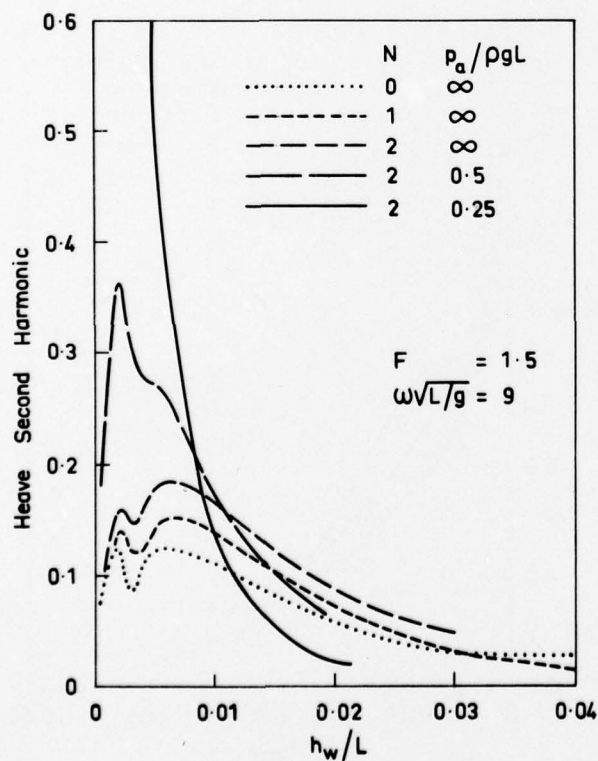
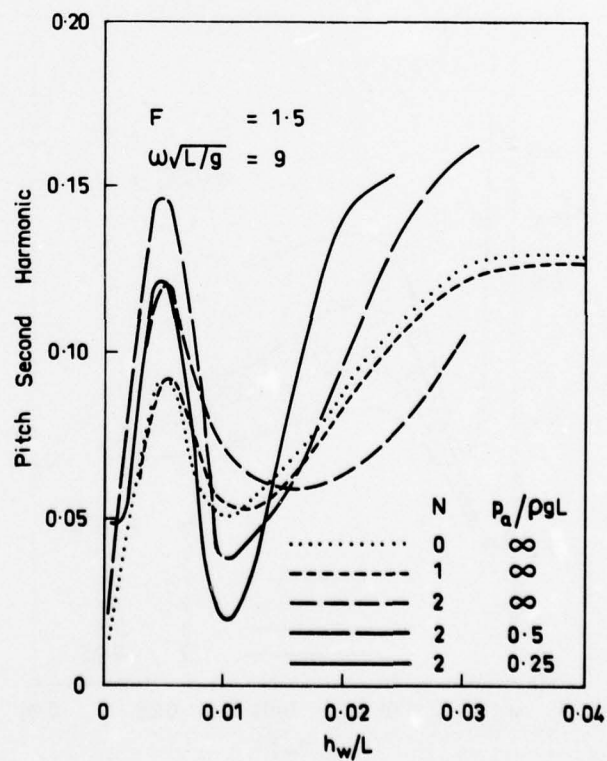


Fig. 9: Craft motion as a function of wave height  
(b) Pitch



Fig. 10: Craft acceleration as a function of wave height  
(a) HeaveFig. 10: Craft acceleration as a function of wave height  
(b) PitchFig. 11: Second harmonic in the craft motion  
(a) HeaveFig. 11: Second harmonic in the craft motion  
(b) Pitch

# SOME ASPECTS OF HYDROFOIL MOTIONS AND THEIR IMPLICATIONS FOR CREW PERFORMANCE

D. JOHNSON and L. T. MESSUM  
Admiralty Research Laboratory, Teddington, UK  
K. NICHOLSON  
Admiralty Experiment Works, Haslar, UK

**SYNOPSIS** Methods for predicting the motions of hydrofoils in a seaway are reviewed and predictions are made for a 450 tonne design over a range of conditions. Spectral distributions of the vertical accelerations show the variation of third octave levels at frequencies between 0.1 and 1 Hz. The predicted motions of the hydrofoil are compared with those of a typical destroyer form and both are related to the limited available criteria for assessing human tolerance to motions. The hydrofoil's ability to remain operational in rough sea conditions is discussed and attention is drawn to areas where further work is thought necessary.

## 1. INTRODUCTION

The rapid increases, over the past 20 years, in the costs of building and manning warships have acted as an incentive for the consideration of vessels which are smaller and cheaper than those of the conventional displacement type. The hydrofoil is amongst the alternatives which have been considered and during this period much research has been aimed at producing craft which are capable of operating outside sheltered coastal waters without the speed limitations experienced by conventional ships. Kehoe (1). Essentially two types of hydrofoil have been built; surface piercing, which rely on variable immersion of the foils to control lift, and the fully submerged foil craft which normally requires an automatic control system and control surfaces to vary lift.

The ability of small hydrofoils of both types to operate foilborne in the higher sea states has been demonstrated by the various craft that have been built in the past 10 years (Jewell (2), Eames and Drummond (3)). This foilborne performance, coupled with the potential of acceptable hullborne seakeeping, has pointed to the possibility of using somewhat larger hydrofoils for open ocean roles in addition to their present off-shore applications. With the advent of more compact weapons it may now be possible to combine, in a vessel of a few hundred tons, the performance and weapon systems formerly only found in ships of many times this size. Good seakeeping will be a primary requirement for such hydrofoils, which would be expected to operate for reasonably long periods in the open ocean. Consequently it is necessary to understand the factors affecting both foilborne and hullborne seakeeping and to establish a method for reliably predicting this facet of performance in any particular design.

In general the motions of any hydrofoil will differ from those of the conventional displacement hull. At typical foilborne speed (35-45 knots) in rough water the hull has little effect on motions, being for the most part clear of the surface, and because of the high speed the hydrofoil struts and foils encounter waves at different frequencies from those experienced by displacement hulls. These differences

may impose operational restraints including those relating to propulsion, machinery and weapons systems and crew performance. The factors which affect crew performance are the subject of this paper, the main objectives of which are:

1. To review the data and methods which can be used to predict hullborne and foilborne motions of hydrofoils in a seaway.
2. To examine the criteria for human tolerance to such motions.
3. To relate the motions predicted for a particular hydrofoil to these criteria.
4. To indicate the limitations of existing methods.
5. To suggest areas for further work if a more complete understanding of hydrofoil prediction methods is to be achieved.

## 2. REQUIREMENTS

Assuming the need for good operational availability, it is necessary to design a craft to operate efficiently in environmental conditions that have a low probability of being exceeded in the area of operations. Taking the Northern North Atlantic as an example of open ocean conditions, Hogben and Lumb (4) show that the probability of sea state 6 being exceeded in any year is only approximately 3% (Fig 1), so that a craft designed to operate foilborne in sea state 6 would have a correspondingly high operational availability. The same sea conditions would also appear to be a reasonable target for maintaining hullborne operations but it is clearly necessary for the hydrofoil to be capable of surviving more severe conditions when hullborne since it would be unable to run for shelter.

Certain constraints, additional to those which would normally apply to a displacement ship, are imposed on the design of a hydrofoil if the requirement to operate foilborne in rough seas with motions and accelerations acceptable to the crew and equipment, is to be met. For example, in a fully submerged foil craft the length of the

struts supporting the foils is affected by the need to minimise the occurrence of broaching (ie the foils emerging through the waves) and hull impacts with waves.

### 3. REVIEW OF AVAILABLE MOTION PREDICTION TECHNIQUES

It may be seen from the preceding section that prediction of the probability that a particular craft will achieve a specified operational requirement depends largely on the calculation of ship motions, at all headings in relevant seas, for comparison with acceptable criteria. The survivability requirement also depends on motion information but additionally involves effects, like the breaking of steep waves over the superstructure, which are not amenable to the usual linear superposition techniques. Both predictions depend on a knowledge of the frequency of occurrence of the various sea states in the envisaged area of operation. The available theoretical, model and trials work applicable to the prediction of foilborne and hullborne motions is reviewed in this section.

#### 3.1. Foilborne Methods

One method of estimating the foilborne motions and accelerations of hydrofoils is to scale up the frequency response functions from those of similar craft or from model tests. To use such a scaling method one must have some confirmed data on the base model, and the relevant published data is limited, in the case of the fully submerged foil hydrofoils, by the very small number of craft examples available for evaluation. The only published data known to the authors on this type of vehicle is that for the US hydrofoil TUCUMCARI given by Jewell (2) which is restricted to vertical motions. The vertical response function in Ref (2) has been used to predict vertical accelerations for hydrofoils in the range 100 to 500 tonnes in sea conditions up to and including sea state 6.

A second and more complex method of evaluating the foilborne seakeeping of hydrofoils is by computer simulation of the craft and the sea environment in which it will operate. This approach, when validated, is a powerful tool with wide application to a range of hydrofoil configurations. The main inputs for this type of simulation include the component geometry of the foil system, the characteristics of the autopilot and the particular lift control system employed, which could be trailing edge flaps, variable incidence or air bleed, and a spectral representation of the sea conditions.

The output from such simulations will normally include frequency response functions of motions, velocities and accelerations in six degrees of freedom. It is also possible using such methods to investigate the effects of problems such as cavitation, ventilation, foil broaching and hull slamming.

Computer simulation of hydrofoils has been used extensively in the USA and Canada (Russ and Ryba (5), Jamieson (6), Schmitke and Jones (7)). In the UK a computer simulation has been developed at Cambridge University and is being implemented at ARL.

#### 3.2. Hullborne Methods

A range of methods similar to those indicated above can be used for predicting hullborne motions. In this mode of operation the hydrofoil may be treated as a conventional ship will allowances made for the additional effects of the foil system.

Most US data on model hullborne seakeeping tests originate from Stevens Institute of Technology (SIT) (8, 9, 10, 11) and deal mainly with PLAINVIEW or a series of hulls based on that form, which includes hulls compatible with tandem and canard foil arrangements, obtained by truncation. No Canadian or UK model work is known other than some tests on a BRAS D'OR model carried out by NPL, and whilst some French work is known to have been performed in the Etang de Bèrre programme no details are known to the authors.

There is also a paucity of relevant quantitative trials data, but Jewell (2) states that both FLAGSTAFF and TUCUMCARI have operated in seas up to state 6. Some information is however available for the Canadian ship BRAS D'OR in sea state 5 and 6, including vertical and lateral accelerations, at various positions in the craft and roll and pitch angles (Ref 3).

Whilst both model and trials data are sparse for hullborne hydrofoils, considerable success has been claimed for a Canadian pitch and heave computer program developed by Schmitke (12). In the program linearised hydrofoil terms are derived by incorporating Theodorsen's unsteadiness effects into a three dimensional quasi-steady formulation. These have been superposed onto the hull exciting forces, added mass and damping terms, computed by the usual strip theory, to predict motions in head seas. There are several assumptions and restrictions in the theory, in addition to those for conventional ship motion programs, but limited comparison made by Schmitke (13) indicate that the method's reliability for hydrofoils is comparable to that of strip theory for purely displacement hulls.

The version of the Canadian program for fully submerged foil craft has been slightly modified and established in the UK by AEW and has subsequently been used to predict the motions of a typical design. The results are presented in the following section.

### 4. PREDICTION OF MOTIONS FOR A 450 TONNE HYDROFOIL

Some of the methods described above have been used to predict the motions of a 450 tonne hydrofoil with a fully submerged foil system. This particular size of vessel was selected on the basis of data given by Eames (3) which indicates that, for over 90% availability in the sea areas under consideration (ie to operate in sea state 6), a craft of about this size is required.

#### 4.1. Foilborne

The computer simulation methods described in section 3.1 are capable of evaluating many more variables than the scaling method, but in the absence of a validated foilborne simulation model, predictions have been based on results scaled from earlier craft. Using the vertical response function given for TUCUMCARI by Jewell (2) the root mean square (rms) heave accelerations on a 450 t hydro-



foil, in head seas at 40 knots, were calculated for a range of seas using the ITTC 1969 single parameter spectral formulation. The results are given in Table 1 which also shows, for comparison, the vertical accelerations at the centre of gravity (cg) of a typical 110 m destroyer form at 20 knots in head seas based on the data given by Conolly (14). Also included in the Table are the vertical accelerations on the destroyer at a point 10% of length abaft the forward perpendicular (ordinate 3).

Table 1

Overall rms vertical accelerations on a 450 t hydrofoil at 40 knots and a 110 m destroyer at 20 knots in head seas.

Signifi- cant Wave Height (metres)	Sea State	Hydrofoil at cg	Destroyer at cg	Destroyer at Ordinate 3
			(rms g)	
1.5	Lower 4	0.017	0.01	0.04
2.9	Lower 5	0.044	0.066	0.174
5.5	Upper 6	0.086	0.114	0.300

The acceleration levels at ordinate 3 have been included because the variation of acceleration along the length of a displacement ship is high and ordinate 3 is a commonly used seakeeping reference point. Jewell (2) stated that pitch angles in foil-borne hydrofoils are extremely small and consequently the variation of vertical acceleration along their length is also small. From the results in Table 1 it can be seen that a 450 tonne hydrofoil at 40 knots in sea state 6 is predicted to experience generally lower accelerations than the destroyer at 20 knots in the same conditions.

#### 4.2. Hullborne

The Canadian pitch and heave program was used to predict rms vertical accelerations at the cg of the hydrofoil at 10 knots in head seas as shown in Table 2. Accelerations for the same hull without foils and those for the 110 m destroyer in the same conditions are also shown.

Table 2

Overall rms vertical accelerations at the centre of gravity of a 450 tonne hydrofoil and a 110 m destroyer both at 10 knots in head seas.

Signifi- cant Wave Height (metres)	Sea State	450 t Hull without Foils	Hydrofoil	Destroyer
			(rms g)	
1.5	Lower 4	0.028	0.024	0.012
2.9	Lower 5	0.064	0.049	0.028
5.5	Upper 6	0.097	0.074	0.052

The Table shows that adding the foils to the hull of the 450 t vessel is predicted to reduce the accelerations experienced by approximately 20%. However, in the highest sea states the accelerations predicted for the hydrofoil are still about 40% higher than those at the cg of the destroyer.

In the hullborne mode the hydrofoil is basically a modified displacement ship and wide variations of accelerations along its length can be expected. To illustrate this point the rms vertical accelerations at ordinate 3 have been calculated and are shown in Table 3.

Table 3

Overall rms vertical acceleration at ordinate 3 of a 450 tonne hydrofoil and a 110 m destroyer both at 10 knots in head seas.

Signifi- cant Wave Height (metres)	Sea State	450 t Hull without Foils	Hydrofoil	Destroyer
			(rms g)	
1.5	Lower 4	0.113	0.067	0.040
2.9	Lower 5	0.193	0.123	0.095
5.5	Upper 6	0.280	0.162	0.150

As before, the effect of the foils is seen to reduce the motions considerably. Also the accelerations at this position are less than 10% greater than those of the much larger displacement ship in the high sea state, whilst at the lowest sea state accelerations on the hydrofoil are about 70% higher.

The fact that accelerations at the worst position, ie near the bow, of the hydrofoil are only slightly greater, in sea state 6, than those at the corresponding position in the destroyer suggests that the operational effectiveness of the hydrofoil may be essentially the same as that of the destroyer. This conclusion is confirmed qualitatively by assessments made by the crew of BRAS D'OR and the Commanding Officer of an escorting destroyer which led to the claim that "the ability of a 200 ton hydrofoil ..... to operate hullborne with the seakeeping qualities of a destroyer-escort has been well demonstrated" (Eames and Drummond (3)).

#### 5. CRITERIA AND COMPARISONS

A new craft can be judged by comparison with other vessels or against specific quantitative criteria. Both these yardsticks have been applied to the hydrofoil since neither gives a complete picture.

##### 5.1. Operability

The overall vertical acceleration predictions described in the preceding section has been used to give a guide to the seakeeping performance of the hydrofoil relative to that of a displacement ship. However, the picture presented by the overall rms acceleration results is incomplete as it does not indicate the frequency at which the vessels respond or the variation of level with frequency. Thus, the single overall figure could mask important differences such as that between a highly tuned response giving large acceleration levels and a much lower response distributed over a wider frequency band. The variation of acceleration with frequency has, therefore, been calculated for both the hydrofoil in its two modes and the destroyer. The results of these calculations are presented in Figs 2, 3 and 4 which show rms acceleration levels in one third octave bands plotted against frequency. The one third octave bandwidth was selected as this is used by the

International Standards Organisation (ISO) when proposing human tolerance levels.

For frequencies above 1 Hz the ISO have proposed limits for human exposure to vertical, lateral and rotational accelerations (15). Examination of Figs 2, 3 and 4 shows, however, that there is no significant response at such frequencies. Below 1 Hz there are at present no internationally accepted levels but the effects on personnel of vibrations at these frequencies have been the subject of a number of recent investigations, since it is known that oscillations at frequencies in this band are the prime cause of motion sickness. In addition to the basic lack of data on human response at frequencies below 1 Hz, even less is known about the effect of excitation at a combination of frequencies along one axis let alone the multi-axis excitations which occur in practice.

Allen (16) has analysed data from various forms of passenger transport and has proposed a "severe discomfort boundary" for 25 minutes exposure to vertical accelerations at frequencies between 0.1 and 1 Hz. The proposed boundary (shown in Figs 2, 3 and 4) is set at 0.051 g rms between 0.1 and 0.3 Hz, rising to 0.71 g at 1 Hz where it coincides with the draft ISO limits for 25 minutes exposure to vertical vibration. The boundary proposed by Allen is supported by the results of some subsequent experiments by O'Hanlon and McCauley (17) in which 300 college students were subjected to a range of accelerations at single frequencies between 0.08 and 0.5 Hz and the incidence of motion sickness was recorded for periods up to 2 hours. It is suggested that, in the present context, this boundary should be regarded as conservative since it makes no allowance for the increased tolerance to motions which is generally believed to occur when personnel are motivated and acclimatised. This view is endorsed by recent work for the Surface Effect Ship (SES) Project (Boyd et al (18)), in which naval personnel have been exposed to higher levels of acceleration for longer periods.

Fig 2 shows the predicted third octave vertical acceleration levels on the hydrofoil at 40 knots in sea states 5 and 6. The levels shown are at the cg but are representative of those for all positions on the craft. The figure shows that the highest level occurs at 0.2 Hz with a value of 0.044 g rms which is just below the severe discomfort boundary. The spectral response at the cg of the destroyer at 20 knots in head seas is also shown and in sea state 6 the maximum levels exceeds the severe discomfort boundary.

Additionally it may be seen that, due to the higher encounter frequency of the hydrofoil travelling at 40 knots, it has some response up to 0.7 Hz whereas that of the destroyer cuts off at about 0.3 Hz. It is seen that the existence of this higher frequency response is unlikely to affect the crew as tolerance is thought to increase in this frequency band. The effects of these higher frequencies on mechanical components have not been assessed but at these low levels they are unlikely to be significant.

Fig 3 shows the spectral response at the cg of the hullborne hydrofoil and the destroyer at 10 knots in head seas. Although the levels on the hydrofoil are higher than those on the destroyer, they are all below the severe discomfort limit and should not therefore impair the effectiveness of

the crew. In order to cover the range of levels encountered on the vessels, the spectral response at ordinate 3 is shown in Figure 4. The critical level is exceeded in sea states 5 and 6 in both cases and the individual spectra confirm the trend of the overall rms predictions showing that the maximum hydrofoil acceleration is only marginally higher than that of the destroyer.

Excessive vertical acceleration is not the only reason for a voluntary reduction in speed in rough weather and two other major reasons in conventional ships are slamming and deck wetness (Nicholson and Price (19)). Both depend on the relative motion of the ship to the waves and this usually increases with speed in any sea state. Table 4 compares the relative bow motion of the hydrofoil with that of the destroyer, and besides showing that the relative motions of the destroyer exceeds that of the hydrofoil in the higher seas, it also demonstrates that there is little speed effect for the hydrofoil in the range of conditions shown.

Table 4

Rms relative bow motions of a 450 t hydrofoil and a 110 m destroyer.

Significant Wave Height	Sea State	450 t Hydrofoil					110 m Destroyer
		0	5	10	15	10	
		knots	knots	knots	knots	knots	
(metres)			(metres)				
1.5	Lower 4	0.73	0.73	0.73	0.59	0.48	
2.9	Lower 5	1.10	1.21	1.21	1.33	1.45	
5.5	Upper 6	1.28	1.45	1.50	1.46	2.3	

These results show a similar trend to those predicted for BRAS D'OR (Schmitke (12)), which confirmed the observations of deck wetness in the sea trials (Eames, Drummond (3)).

Slamming and wetness also depend on the draught and freeboard respectively and the probability of deck wetness is related to both freeboard and the variance of relative motion by an exponential expression (Nicholson and Price (19)), which shows that, if for example the rms relative bow motion of the destroyer is twice that of the hydrofoil, the latter would only need half the freeboard to have an equal expectation of the event occurring. Table 4 shows that ratios of this order can be expected.

Whilst slamming is a more complicated phenomenon, involving not only relative motion but also relative velocity, its frequency of occurrence would be similar for the two vessels if their draughts were scaled in the same ratio as that described above for wetness. Published data (Jane's Surface Skimmers (20)) shows that the draught and freeboard of current hydrofoils is of the order of half that of frigates and destroyers and it seems reasonable to presume therefore that larger ocean going craft should be adequate in this respect, since hydrofoils are generally of deep construction to satisfy foilborne strength requirements.



## 5.2. Survivability

To be a viable open ocean platform a vessel must not only meet operational requirements but must also have a very good chance of surviving those occasions when the sea conditions for which it has been designed to operate are exceeded. In this respect the hydrofoil is no different from any other configuration in the spectrum of choices from surface effect ships to conventional hulls. It is perhaps pertinent to recall that the 450 tonne craft being considered has been chosen to operate in sea state 6 and that even in the severe environment of the Northern North Atlantic that condition is exceeded only about 3% of the time, on average about 10 days a year, whilst sea state 7 is exceeded only about 3 days per year (Fig 1).

Any craft caught in extreme conditions is liable to be uncomfortable and the vertical acceleration predictions in Tables 2 and 3 confirm that the hydrofoil is no exception. However, the calculations used to produce Table 2 have been extended and illustrate that in general acceleration at the cg can generally be reduced in any particular sea condition by a reduction in speed, in a similar manner to the familiar pattern for displacement hulls (viz Conolly (14)). Since the craft would appear from the foregoing to be operable at 10 knots in sea state 6 it should not be too uncomfortable when hove-to in sea state 7 because the overall acceleration levels are similar in the two conditions. It is also likely that the crew would tolerate rare exposure to extreme sea states, which occur for only 3 days a year, as the crews in conventional ships currently do.

An extension of the data in Table 4 to sea state 9 indicates that both slamming and wetness would also be less frequent when hove-to in extreme conditions than when operating at 10 knots in sea state 6. It should be noted, however, that real seas do not necessarily correspond to the spectral formulation on which Table 4 is based, and that steep breaking waves, caused by local wind conditions, could have serious effects on any vessel. No quantitative data are available on this topic, but it would mean that the survival of the crew depends more on the ability of the craft to remain intact and watertight, than on their ability to withstand intermittent exposure to violent motions.

There is little or no hydrofoil experience in extreme conditions but the combined effect of their foils, reducing motions, and their strong construction to satisfy foilborne loading requirements, should ensure that they have at least as good a chance of survival as the numerous open ocean fishing vessels of similar size. Confidence in the ability of the hydrofoil to survive will only really be established by experience of either the actual craft performing its proposed task or smaller vessels of similar type in scaled conditions.

## 6. CONCLUSIONS AND RECOMMENDATIONS

Conventional scaling methods and mathematical simulation techniques can be used to predict the motions of hydrofoils in a sea way. The first approach depends entirely upon the existence of relevant data on the motions of interest for any particular type of craft and so is limited to the small number of concepts evaluated. For the foilborne regime published response information which could be used for direct scaling and for validating

mathematical models is sparse, both at model and full scale. However, it has been possible, for the purpose of this paper, to predict motions in the vertical plane for a 450 t craft from the recorded response of TUCUMCARI. Basing the prediction on this 60 t hydrofoil craft means that the results are unlikely to be optimal for the larger vessel. There is a similar lack of data on hullborne behaviour, especially at full scale, but in this case the availability of a computer simulation for heaving and pitching motions has enabled these to be calculated for the same 450 t craft and the effect of the foils in reducing motions is shown to be significant. No predictions of lateral response were possible for this craft either hull or foilborne.

Human tolerance to oscillatory motions is known to depend on frequency. The vertical motions which have been predicted all occur at less than 1 Hz and are not therefore covered by the draft ISO standard for human tolerance. For the low frequency regime there have been recent attempts to define maximum levels of acceleration which would not cause severe discomfort, ie motion sickness. The reported work is incomplete since the effects of acclimatisation, motivation and simultaneous oscillation at several discrete frequencies and in more than one plane are not taken into account. No proposals have been found for tolerance boundaries to lateral motions in the low frequency band.

The predicted motions for the 450 t hydrofoil craft have been compared with both the tolerance boundary and the motions of a 110 m destroyer, taking into account the different character of the motion of the two types of vessel. The comparison suggests that the operation of the craft by the crew would not be limited by the vertical acceleration levels encountered in sea state 6 either while hull or foilborne. In the more extreme conditions likely to be encountered occasionally it appears from the evidence examined that the risk to survivability would be low. The problem would be little different from that of the numerous vessels of this size which presently operate in open waters.

The prediction methods described in this paper require extension and validation before the motions of hydrofoil craft may be characterised in their entirety. More complete information is required if designs which take account of motions are to be generated. As a first step there is a clear need for the development of a mathematical model for simulating hullborne roll and for data on foilborne lateral motion. The full potential of motion prediction will not be realised unless there is a corresponding level of understanding of the human tolerance aspects; to quote Boyd et al (18) "Although men have been experiencing motion in a wide spectrum of vehicles for many years, there is still a dearth of knowledge as to the quantitative effects of motion exposure." This is especially so for lateral motions. The topic is evidently an area where the proponents of competing vehicles could usefully co-operate.



## 7. REFERENCES

1. KEHOE J W Jr. Destroyer seakeeping: ours and theirs. US Naval Inst Proc 1973, 26-37.
2. JEWELL D A. Hydrofoil Performance in Rough Water. AIAA/SNAME Advanced Marine Vehicles Conference, San Diego, California, Feb 1974, AIAA Paper 74-307.
3. EAMES M C, DRUMMOND T G. HMCS BRAS D'OR - Sea Trials and Future Prospects. Trans RINA, 1972.
4. HOGGEN N, LUMB F E. Ocean wave statistics. 1967 (HMSO London).
5. RUSS J E, RYBA V J. Users guide to NSRDC digital simulation of hydrofoil craft PC(H)-1; revision 0. NSRDC Ship performance technical note 192, Jan 1971.
6. JAMIESON J J. Hydrofoil Simulation Equations study; final report. Hydrofoil simulation equations of motion. Technical report: NAVTRADEVCEM 1630-3 Dec 1966 (AD 649 365).
7. SCHMITKE R T, JONES E A. Hydrodynamics and simulation in the Canadian hydrofoil program. 9th Symposium on Naval hydrodynamics, Paris, Aug 1972.
8. CHEY Y H. Motions and Accelerations of AGEH when hove-to in extreme sea states. Stevens Institute of Technology Report 977. Aug 1963.
9. SAVITSKY D, ROPER J K. Development of an Integrated Program of Research on Hydrofoil hulls. Stevens Institute of Technology Report 1230, July 1967.
10. BROWN P W, CHEY Y H. The effect of length-beam ratio and hydrofoil control on the take-off characteristics of hydrofoil craft in regular head seas. Stevens Institute of Technology Report 1302, May 1968.
11. VAN DYCK R L. Seakeeping Characteristics of Four members of hydrofoil hull series 65. Stevens Institute of Technology Report 1563, April 1973.
12. SCHMITKE R T. Prediction of pitch and heave motions of hullborne hydrofoil vessels. DREA Report 74/2 January 1974.
13. SCHMITKE R T, MACKAY M. The influence of hull form, foil system and pitch-heave control on hydrofoil hullborne seakeeping. Proc 4th Ship Control Systems Symposium, Den Helder, Oct 1975.
14. CONOLLY J E. Standards of good seakeeping for destroyers and frigates in head seas. Proc International Symposium on the Dynamics of Marine Vehicles and Structures in Waves. ONR/RINA London April 1974.
15. BRITISH STANDARDS INSTITUTION. Guide to the evaluation of human exposure to whole-body vibration. DD32:1974. March 1974.
16. ALLEN G R. Proposed limits for exposure to whole body vibration 0.1 to 1.0 Hz. Human Engineering Department RAE Farnborough April 1974.
17. O'HANLON J F, McCAULEY M E. Motion sickness incidence as a function of frequency and acceleration of vertical sinusoidal motion. Human Factors Research Inc, Santa Barbara, Goleta, California. Tech Report 1733-1, Sept 1973.
18. BOYD C J, MALONE W L, VICKERY J M. Simulation as a design aid for ride control systems. Proc 4th Ship Control Systems Symposium, Den Helder, Oct 1975.
19. NICHOLSON K, PRICE W G. Evaluation of the motion and speed characteristics of a ship in irregular waves. British Acoustical Society, Spring Meeting April 1973. Paper No 73VB3.
20. JANES SURFACE SKIMMERS, Jane's Year books (1973-74).

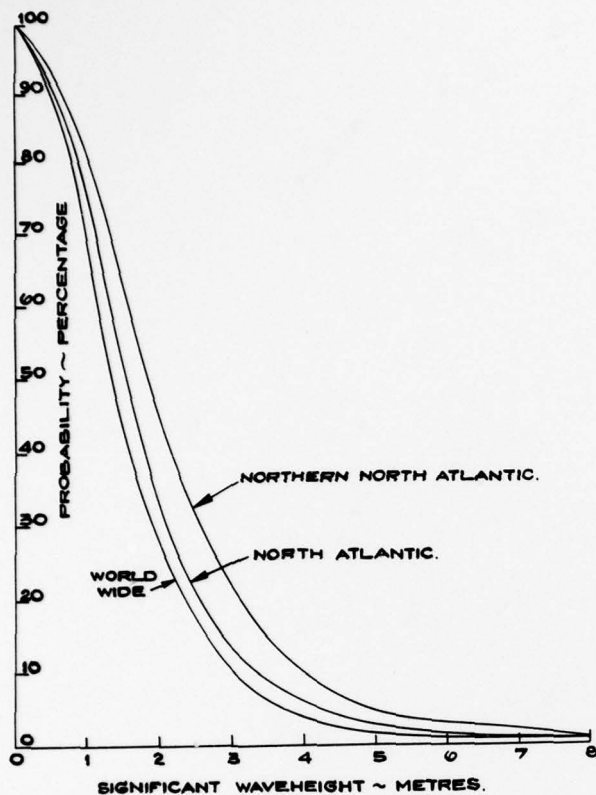


Fig. 1: Probability of exceeding a given significant wave-height

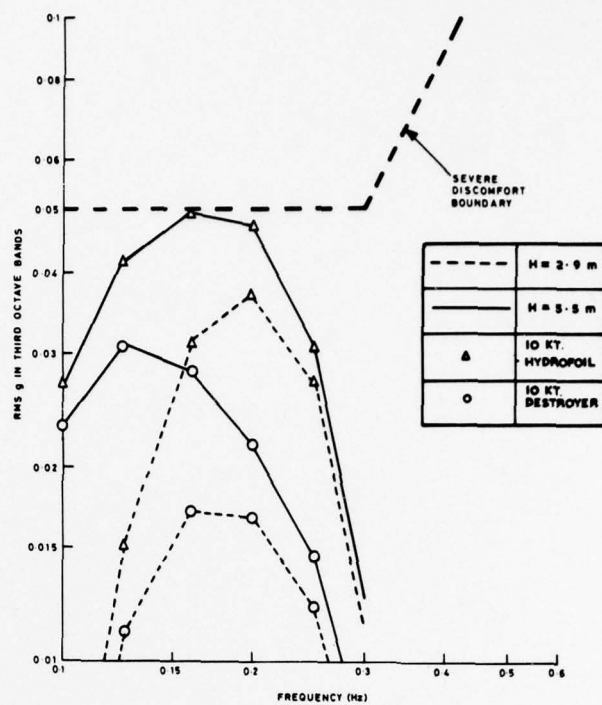


Fig. 3: Third octave acceleration levels at centre of gravity

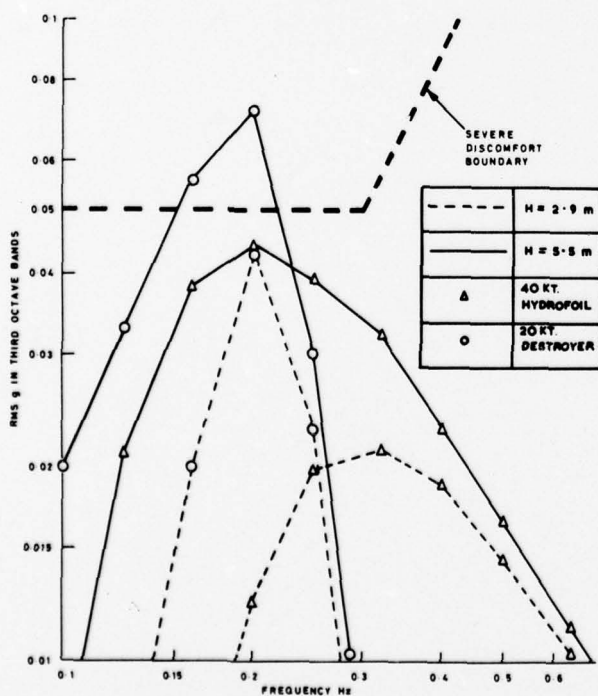


Fig. 2: Third octave acceleration levels at centre of gravity of foilborne hydrofoil at 40 knots and 20 knot destroyer

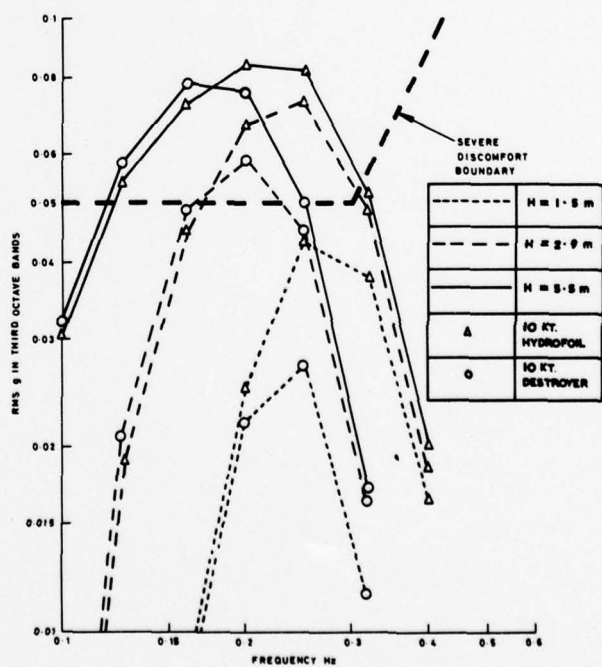


Fig. 4: Third octave acceleration levels at third ordinate

# WAVE IMPACTS ON HYDROFOIL SHIPS AND STRUCTURAL IMPLICATIONS

T. G. DRUMMOND

M. MACKAY

R. T. SCHMITKE

Defence Research Establishment Atlantic, Dartmouth, Canada

## SYNOPSIS

A major consideration in hydrofoil ship design is the structural implications of the impact pressures which arise during foilborne operation in rough water. Many factors influence the magnitude of these pressures. The purpose of the present study is to identify the most significant parameters and to quantify their influences on hull weight. The parameters under study include displacement, foilborne load distribution, design hull clearance, deadrise angle, length-displacement ratio, prismatic coefficient, design speed, and design sea state.

Parameters are varied in a systematic manner and a second-order response surface fitted to the results. This yields quantitative estimates of parameter influences and interactions and establishes the relationship of the various design parameters to hull weight.

## 1. INTRODUCTION

Wave impacts resulting from foilborne operation in rough seas produce impact pressures that influence the design of hydrofoil hull structures. The purpose of this study is to identify the most significant parameters of those considered and to quantify their influence on impact pressures and, consequently, hull weight.

Only ships with automatically controlled fully submerged hydrofoil systems are considered; the control philosophy adopted is to achieve maximum platform stability. Eight parameters have been selected for investigation based on dynamic and naval architectural considerations. These variables are the minimum required to define hull shape and foilborne operating conditions, thus enabling impact pressures and hull weight to be calculated.

$\Delta$	displacement
$(M)$	length-displacement ratio
$C$	prismatic coefficient
$\beta^D$	bottom deadrise angle
$F_M$	fraction of ship weight carried by main foil
$H_w$	significant wave height
$h_x$	design keel clearance
$V_d$	design foilborne speed

A flow chart of the utilization of these variables in the computational process is shown in Figure 1. The major subroutines include calculation of seaway-induced vertical motions, generation of hull lines, calculation of impact pressure distribution, and calculation of the hull weight fraction.

The computation of seaway-induced motions is restricted to long-crested head seas, both for computational simplicity and because these produce the most severe motions in the vertical plane. Only pitch and heave dynamics are considered and, in keeping with conventional ship practice, the problem is linearized. Good precedents exist for

using a linear mathematical model to predict foilborne hydrofoil ship motions; see, for example, Schmitke and Jones (1) and Bender et al (2).

The calculation of pitch-heave frequency response is described in Section 2. These responses are then applied to realistic ocean wave spectra to compute ship motions in irregular seas. Seas with significant wave heights ranging from 5 to 20 feet are considered. The Gospodnetic-Miles quadratic regression spectrum (3) is used to define the seaway.

Definition of hull geometry and calculation of impact pressures are described in Section 3. Generation of the portion of the hull below the design waterline utilizes the mathematical model described by Schmitke and Mackay (4). These underwater lines are extended upward in a simple but realistic manner to define the hull completely. Knowledge of ship motions and hull geometry enables impact pressures to be estimated. This is accomplished by combining results for slamming of wedge-shaped bodies with the statistical approach of Ochi and Motter (5).

Structural aspects of the problem are discussed in Section 4. Hull weight fraction is chosen as the most physically meaningful figure of merit upon which to base comparisons for this study. It is assumed that impact pressures affect only the bottom structure. The remainder of the hull, including sides, decks, and bulkheads, are designed to hydrostatic criteria with the ship in the hullborne mode or flooded condition. This approach of considering the entire hull weight, rather than just the bottom structural weight, tends to put the implications of impact loads into proper perspective.

Each portion of the structure is designed according to estimated loads and to acceptable criteria applicable to that area. The volume of metal so determined for each structural component is then summed over the whole ship to give the total weight



of primary structure. Appropriate weight allowances are added for superstructure, hull fittings, local strengthening, and equipment foundations.

Section 5 describes how the computational process presented in Sections 2 to 4 and illustrated in Figure 1 is used in a parametric study of the wave impact problem. A large data base is generated by systematically varying the eight input variables. A second-order response surface is fitted to the data, and the results are presented in Section 6. These give a quantitative measure of the relative significance of each parameter on both impact pressures and hull weight fraction.

## 2. PITCH AND HEAVE RESPONSE

The pitch and heave response is calculated for a foilborne hydrofoil ship with fully submerged foils travelling along a course directly opposite to the direction of propagation of a train of long-crested regular waves of frequency  $\omega$  (Figure 2). Let  $(x, y, z)$  be a right-handed orthogonal co-ordinate system fixed with respect to the mean position of the ship with origin at the mean position of the centre of gravity. The positive x-axis points forward in the direction of motion and the positive z-axis vertically upward; the pitch angle  $\theta$  is positive for downward rotation of the bow.

Assume that the motions of the ship in response to the encountered waves are both linear and harmonic. Further, assume that the ship is controlled in pitch and heave by trailing edge flaps on both the forward and after foil units. The coupled pitch and heave equations are defined below using the conventional notation that subscript 3 refers to heave and subscript 5 to pitch.

$$(A_{33} + m) \ddot{z} + B_{33} \dot{z} + C_{33} z + A_{35} \ddot{\theta} + B_{35} \dot{\theta} + C_{35} \theta + A_{3M} \ddot{\beta}_M + B_{3M} \dot{\beta}_M + C_{3M} \beta_M + A_{3B} \ddot{\beta}_B + B_{3B} \dot{\beta}_B + C_{3B} \beta_B = F_3 e^{i\omega t} \quad (1)$$

$$A_{53} \ddot{z} + B_{53} \dot{z} + C_{53} z + (A_{55} + I_y) \ddot{\theta} + B_{55} \dot{\theta} + C_{55} \theta + A_{5M} \ddot{\beta}_M + B_{5M} \dot{\beta}_M + C_{5M} \beta_M + A_{5B} \ddot{\beta}_B + B_{5B} \dot{\beta}_B + C_{5B} \beta_B = F_5 e^{i\omega t} \quad (2)$$

where  $z$  is heave,  $m$  is ship mass, and  $I_y$  is pitching moment of inertia.  $\beta_B$  and  $\beta_M$  are flap deflections of the forward (bow) and after (main) foil units, respectively. The subscript convention is the same as in Reference 6. Expressions for the coefficients  $A_{ij}$ , etc., are given in Appendix A.

To complete the mathematical model, the following control system equations are required.

$$-\omega^2 n_M (k_{zM} \ddot{z} + k_{zM} \dot{z} + k_{zM} z + k_{\theta M} \ddot{\theta} + k_{\theta M} \dot{\theta} + k_{\theta M} \theta) + \ddot{\beta}_M + 2\zeta_M \omega n_M \dot{\beta}_M + \omega^2 n_M \beta_M = 0 \quad (3)$$

$$-\omega^2 n_B (k_{zB} \ddot{z} + k_{zB} \dot{z} + k_{zB} z + k_{\theta B} \ddot{\theta} + k_{\theta B} \dot{\theta} + k_{\theta B} \theta) + \ddot{\beta}_B + 2\zeta_B \omega n_B \dot{\beta}_B + \omega^2 n_B \beta_B = 0 \quad (4)$$

where  $\omega_n$  is the undamped natural frequency and  $\zeta$  the damping ratio.  $k_z^*$ ,  $k_\theta^*$ , etc., are the control system gains. In this study, the only gains used are  $k_z^*$  on the bow foil flap and  $k_\theta^*$  on the main foil flap. Large values are chosen in order to represent the stable platform condition for the ship.

Solving the above set of four equations yields the pitch and heave response functions from which the vertical motions are obtained by superposition with the seaway spectrum. The Gospodnetic-Miles quadratic regression spectrum (3) is used to represent the seaway for which the energy-averaged wave period  $T_w$  is obtained from the empirical relationship.

$$T_w = 7.73 + 0.114 H_w \quad (\text{seconds}) \quad (5)$$

where  $H_w$  is the significant wave height in feet. For each value of  $H_w$ , the seaway spectrum is taken to be the average of five spectra with periods of  $0.8 T_w$ ,  $0.9 T_w$ ,  $T_w$ ,  $1.1 T_w$ , and  $1.2 T_w$  seconds.

## 3. HULL DEFINITION AND IMPACT PRESSURES

### 3.1 Hull Definition

The portion of the hull lying below the design waterline is defined using the mathematical model of Schmitke and Mackay (4). Only ten hull variables are required in this formulation: displacement ( $\Delta$ ), length-displacement ratio ( $M$ ), deadrise angle ( $\beta$ ), area coefficient at the section of maximum area ( $C_M$ ), waterplane area coefficient ( $C_w$ ), entrance angle ( $i_e$ ), transom breadth ratio ( $B_T/B$ ), transom area ratio ( $A_T/A$ ), transom sectional area coefficient ( $C_T$ ), forward-most station of maximum area ( $S_M$ ), and after-most station of maximum area ( $S_R$ ).

In order to model the complete hull for the present study, these lines are extended upward to a sheer line obtained by setting the freeboard at the transom equal to the design draft and the freeboard at the stem 1.5 times the draft. The chine line is extended forward and upward to the mid point of the dry portion of the stem. Flare is increased on the forward stations to give a reasonable width of foredeck. The lines produced for the parent model of this study are shown in Figure 3.

Some notable features of the hull are:

- With the exception of the sheer line, the hull is parallel between  $S_M$  and  $S_R$ .
- Deadrise ( $\beta$ ) is constant aft of  $S_M$ .
- Deck width is maximum at  $S_M$ . The deck is approximately parallel between  $S_R$  and station 6 (where station 0 is the FP and station 20 the AP)
- Side flare is constant at  $12^\circ$  aft of  $S_M$ ; it increases forward of  $S_M$ .
- The chine intersects the DWL between station 4 and station 5.

### 3.2 Impact Pressure

Estimation of impact pressures is accomplished by combining the results of Chuang (7) on slamming of wedge-shaped bodies with the statistical approach

of Ochi and Motter (5).

Each hull section is represented by a rigid wedge. Peak impact pressure is given by (7):

$$p_M = \frac{1}{2} \rho k \dot{r}^2 \quad (6)$$

where  $\dot{r}$  is relative velocity,  $\rho$  is fluid density and:

$$k = 1 + \frac{\pi^2}{4\beta^2} \quad (7)$$

In order to account for buttock angle ( $\tau$ ), equivalent to an inclination of the wedge (Figure 4),  $\beta$  in Equation (7) is replaced by  $\beta \cos \tau$ .

Operation in a seaway is approached probabilistically. Let  $c$  be the statistical confidence level that a specified pressure threshold ( $p_o$ ) is not exceeded in a given number of impacts ( $N$ ). Based upon the twin assumptions of linear motion and Rayleigh distributed wave amplitudes, the following relationship between  $p_o$ ,  $c$ ,  $N$ , and  $\sigma_{RV}^2$  is obtained from Ochi and Motter (5):

$$p_o = -\rho k \sigma_{RV}^2 \ln(1 - c^{1/N}) \quad (8)$$

Thus, in  $N$  impacts, the probability of exceeding  $p_o$  is  $(1 - c)$ . For example, if  $c$  is chosen to be 0.99, then the maximum pressure is estimated by (8) with 99% assurance.

Of the independent variables in Equation (8),  $k$  is determined by hull geometry,  $c$  is specified by the designer, and  $\sigma_{RV}^2$  is a function of the foil and control systems, speed, and sea state. Only  $N$  remains to be evaluated.

Let  $z_o$  be an arbitrarily specified waterline between keel and chine. The probability of hull immersion to depth  $z_o$  is

$$p_{z_o} = \exp \left[ -\frac{(h_K + z_o)^2}{2\sigma_{RM}^2} \right] \quad (9)$$

where  $\sigma_{RM}^2$  is the variance of the relative motion and  $h_K$  is the keel clearance. Frequency of immersion to  $z_o$  is given by:

$$n = \frac{1}{2\pi} \left( \frac{\sigma_{RV}}{\sigma_{RM}} \right) p_{z_o} \quad (10)$$

and the number of wave impacts in  $t$  hours of ship operation is

$$N = 3600 n t \quad (11)$$

Besides  $z_o$ , then,  $N$  is a function of keel clearance, ship motion, and period of operation in the given sea condition.

In the following sections, the design impact pressure used to make the structural calculations for the hull bottom will be set equal to  $p_o$  obtained from Equation (8).

The procedure for obtaining a design pressure distribution over the hull bottom is summarized below:

- a) Choose suitable values for confidence level ( $c$ ) and period of operation ( $t$ ).
- b) For each hull station of interest, compute  $N$  for a series of waterlines between keel and chine.
- c) For each waterline  $z_o$  and for all stations, compute the extreme pressure  $p_o$  using Equation (8).

For the present study,  $c = 0.99$  and  $t = 1$  hour. The hull is represented by 20 stations and  $z_o$  is specified in the following manner.

To facilitate the structural calculations, it is desirable to compute the peak impact pressures at equally spaced locations between keel and chine. Therefore, the wedge between keel and chine is divided into five equal intervals. The end points of these intervals are denoted by  $z$ . Then, for the peak impact pressure to occur at  $z$ ,  $z$  and  $z_o$  are related by:

$$\frac{z}{z_o} = (1 - \frac{4\beta^2}{\pi^2})^{1/2} \quad (12)$$

#### 4. HULL WEIGHT CALCULATION

A typical hydrofoil hull section is shown in Figure 5 and consists of thin plating with integral longitudinal stiffeners supported by a system of transverse frames and deck beams and main longitudinal girders. The weight of the primary hull structure is computed by determining the size of each component of the bottom, sides, decks, and bulkheads using the applied loads and suitable structural criteria for the area under consideration.

##### 4.1 Bottom Structure

Bottom structural loading is determined first by dividing the hull into three segments, then subdividing each of these into five longitudinal strakes from keel to chine as shown in Figure 6. The maximum impact pressure ( $p$ ) on each of these fifteen strakes is found using the methods of Section 3. These design pressures are then used as the design loading in the bottom structure.

Bottom plating thickness and stringer geometry are determined by applying the design impact pressure to skin panels bounded by adjacent frames and longitudinal stringers. For this study, a frame spacing of 2.5 feet and a bottom stringer spacing of 7 inches has been used (identical to those of the Canadian hydrofoil HMCS BRAS D'OR).

For panels whose length is greater than three times the width, the end supports at the frames are considered ineffective. Consequently, plate thickness is determined by investigating a thin strip of skin of unit width between the longitudinal stringers and considering this to be a fixed ended beam as shown in Figure 7.

Assuming a factor of safety of 1.5 based on the tensile yield strength ( $\sigma_y$ ) of the material, plate thickness ( $t_p$ ) can be determined from the bending moment and section modulus relationship.

$$t_p = b \sqrt{\frac{1.5 p}{2 \sigma_y}} \quad (13)$$

where  $b$  is the stringer spacing.

The stiffener is designed by assuming the ends are fixed at each frame and the distributed load is equal to the impact pressure acting over the panel area, as shown in Figure 8. Stringer bending moment ( $M_s$ ) and required section modulus ( $Z$ ) for a factor of safety of 1.5 are determined as follows:

$$M_s = \frac{p S_F^2}{12} \quad (14)$$

$$Z = \frac{1.5 M_s}{\sigma_y} \quad (15)$$

where  $S_F$  is the frame spacing.

The plate is assumed to contribute (8) to the longitudinal strength of the section. This contribution is represented by an effective plate breadth ( $b_e$ ) of:

$$b_e = 1.7 t_p \sqrt{\frac{1.5 E}{\sigma_y}} \quad (16)$$

where  $E$  is Young's modulus.

A review of typical hydrofoil plate/stringer sections yields the following stringer proportions for height ( $h_w$ ) and thickness of web ( $t_w$ ), and breadth ( $b_F$ ) and thickness of flange ( $t_F$ ).

$$t_w = h_w/20 \quad (17)$$

$$b_F = h_w/1.5 \quad (18)$$

$$t_F = b_F/11 \quad (19)$$

By assuming a starting value for web height ( $h_w$ ), an iterative solution is found for section geometry. This process is repeated for each of the fifteen bottom strakes, then the weight of the bottom skin and stringers can be determined.

The keel and bottom girders are assumed to be loaded as shown in Figure 9. These main longitudinal members are supported by transverse bulkheads and pillars at intervals of not more than 7 1/2 feet. They are loaded by pressures  $p_K$  and  $p_G$  over a width of one-half the value of the chine offset at station 12. Keel pressure,  $p_K$ , is the average pressure over the two bottom strakes closest to the keel. Similarly, girder pressure,  $p_G$ , is the average pressure over the third and fourth strakes. Bending moment and required section modulus are determined in a similar manner to the longitudinal stringers except that the proportions of these larger sections are as follows:

$$t_w = h_w/25 \quad (20)$$

$$b_F = h_w/2 \quad (21)$$

$$t_F = b_F/11 \quad (22)$$

Again, an iterative solution is used to size each structural member and the section dimensions are constant over their entire length. The keel is

assumed to extend the full (waterline) length of the ship ( $L$ ), whereas each girder has a length of  $0.85 L$  due to tapering of the hull.

Bottom frames are sized separately in the bow, middle body, and stern regions of the ship. Once derived, section shape remains constant in each region. Bottom frames are designed in two sections; from the keel to girder and from girder to chine, as shown in Figure 10. Design pressure on the inboard frame is assumed to be that of the second strake from the keel, while that for the outer section is the average of the third and fourth strake pressure. The average bottom girth ( $G$ ) from keel to chine is determined for each of the three longitudinal sections of the ship and half this value is used as the span of each frame portion.

Section dimensions are derived in a manner similar to that used for the bottom girders and keel, using the same proportions for the web and flange. Knowing the required frame spacing ( $S_F$ ) and the ship geometry, the total length of inboard and outboard frames can be determined in each of the three regions. Therefore, total bottom frame weight can be calculated.

#### 4.2 Side Structure

Side structure loads are determined by calculating a basic pressure ( $p_s$ ) applicable to the side at upper deck level and aft of 1/4 length. This pressure is defined by Cohn et al (9) in terms of significant wave height for hullborne operation ( $H_{wh}$ ) as:

$$p_s = \frac{1}{144} (1600 - 2.5(25 - H_{wh})^2) \quad (23)$$

This pressure is assumed to have a minimum value of 2.5 psi and a maximum value of 11.11. For purposes of this study, the maximum value has been used (equivalent to a hullborne significant wave height of 25 feet). In order to account for increased pressure with depth and greater probability of side impact pressures over the forward part of the ship, a factor of 1.5 is applied to the basic pressure in these areas so that the overall side pressure distribution is as shown in Figure 11.

Side plating and stringers are designed to the larger pressure at the chine and are assumed to have a constant cross section over the whole ship's side. Sectional dimensions are determined in the same way as for the bottom shell except that stringer spacing is increased to 8.5 inches.

Side frames are designed to the pressure distributions shown in Figure 11 and using frame spans (chine to deck edge) in the two regions at stations 5 and 12 respectively. Total side frame length is determined in a manner similar to that use for bottom frames. Having determined sectional properties and total length, side frame weight can now be calculated.

#### 4.3 Decks

The hydrofoil ships considered in this study are assumed to have two decks extending from bow to stern. The upper deck is assumed to be subjected to the same pressure as the ship's side at deck edge level. Plating thickness and stringer dimensions are determined in the same manner as for the bottom shell except that a stringer spacing of



6 inches is used and a minimum plating thickness of 0.1 inches is assumed.

The lower deck is assumed to have the same stringer spacing, a thickness of 0.1 inches and a stringer web height of 1.5 inches. These dimensions result in satisfactory strength to withstand anticipated hydrostatic and personnel loads. For the purposes of determining size of supporting structure, it is assumed to be loaded by a pressure of 2 psi.

Each deck is supported transversely by deck beams and longitudinally by deck girders as shown in Figure 5. The sizes of these components are determined in a manner similar to that for the bottom structure but using the deck pressures stated above.

#### 4.4 Bulkheads and Pillars

Bulkhead sections are designed to withstand hydrostatic flooding pressures and consist of plating with vertically oriented stiffeners spaced 7 inches apart. Maximum stringer span is assumed to be 7.5 feet, essentially the height between decks. The number and location of watertight bulkheads is determined first by calculating a typical watertight compartment spacing ( $l_c$ ) in terms of ship length (L).

$$l_c = 10 + 0.04 L \text{ (feet)} \quad (24)$$

Starting at the bow of the ship, bulkheads are located at stations closest to the above spacing distance. The cross sectional area of the ship is calculated at each bulkhead station. The cross sectional area at the transom is multiplied by a factor of 2.5 to allow for heavier plating and supporting structures in this area. Bulkhead weight can be determined knowing total area and sectional properties.

In addition to bulkheads, pillars are used to support main longitudinal girders and keel. These are assumed to have a cross sectional area of 3 square in. The number of pillars is determined from ship length, bulkhead spacing, and minimum girder spans of 7.5 feet. Pillars are assumed to extend from the upper deck to ship's bottom, the lengths being determined from the hull sectional geometry at station 12. Knowing cross sectional area, length, and number required, pillar weight can be estimated.

#### 4.5 Total Hull Weight

Total hull weight ( $W_H$ ) is assumed to consist of primary structure ( $W_{H1}$ ), secondary structure ( $W_{H2}$ ), and superstructure ( $W_s$ ).

$$W_H = W_{H1} + W_{H2} + W_s \quad (25)$$

The weight of primary structure is obtained by summing those weights previously calculated.

Secondary structure includes engine and equipment foundations, hull fittings, access, attachments, and local strengthening for special purposes. A survey of existing military hydrofoil craft suggest a secondary structure weight of:

$$W_{H2} = 0.19 W_H \quad (26)$$

Also, the average superstructure weight is

$$W_s = 0.075 W_H \quad (27)$$

Total hull weight fraction ( $F_H$ ) may now be calculated.

$$W_H = 1.3605 W_{H1} \quad (28)$$

$$F_H = W_H / \Delta \quad (29)$$

### 5. PARAMETRIC VARIATIONS AND RESPONSE SURFACE

#### 5.1 Parent Configuration and Parametric Variation

The range of values studied for each of the eight input variables shown in Figure 1 is listed below:

Parameter	- levels	Parent	+ levels	Units
$\Delta$	200, 300	400	500	tons
$\textcircled{M}$	6.0	6.5	7.0	
$C_p$	0.641	0.697	0.748	
$\beta$	21	25	28	degrees
$F_M$	0.7	0.8	0.9	
$h_K$	4, 6	8	10, 12	feet
$V_d$	40	45	50	knots
$H_w$	5	10	15, 20	feet

As observed in Section 3,  $C_p$  is not a variable in the hull model used. The variation in  $C_p$  is achieved by a simultaneous variation of the parameters  $C_w$ ,  $C_M$ ,  $i_e$ ,  $(S_M - S_R)$ ,  $C_T$ , and  $A_T/A$  while keeping the LCB as close to 0.6 L as possible.

The parent values define a hull model which is virtually the same as the parent configuration of Reference 4. Increments above and below the parent values are chosen on a rational basis to cover the range of current interest and also to generate a sufficient data base for a second-order response surface.

#### 5.2 Response Surface

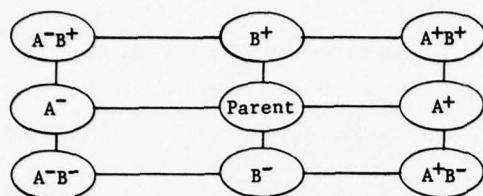
In order to quantify the significance of the parameters under study, a second-order response surface is fitted by the method of least squares to a data base generated from a large number of cases. This response surface consists of an equation of the form:

$$R = a_0 + \sum_{i=1}^n a_i p_i + \sum_{i=1}^n \sum_{j=1}^n a_{ij} p_i p_j \quad (30)$$

where R is the response (either impact pressure or hull weight fraction in the present study),  $p_i$  the  $i$ th parameter,  $a_i$  and  $a_{ij}$  the equation coefficients, and n the number of parameters. We have in the present study eight parameters of which  $p_1 = \Delta$ ,  $p_2 = \textcircled{M}$ , etc., and, consequently, the number of coefficients required for Equation (30) is 45.

To generate the data base, the parameters are varied one or two at a time between levels above and below the parent value. As an example, two parameters (A and B) varied between one level above

(A<sup>+</sup> and B<sup>+</sup>) and below (A<sup>-</sup> and B<sup>-</sup>) the parent values produce eight cases in addition to the parent case.



The cases covered in this study are summarized in the table given in Section 5.1

The relative effectiveness of the terms in the response surface may be deduced from the non-dimensionalized form of Equation (30).

$$\hat{R} = b_0 + \sum_{i=1}^n b_i \hat{p}_i + \sum_{i=1}^n \sum_{j=1}^n b_{ij} \hat{p}_i \hat{p}_j \quad (31)$$

where

$$\hat{R} = \frac{R - R_{\text{parent}}}{R_{\text{parent}}} \quad (32)$$

and

$$\hat{p}_i = \frac{p_i - p_{i \text{ parent}}}{p_{i \text{ parent}}} \quad (33)$$

Using "typical" values for  $p_i$ , namely  $p_i'$ , the relative effectiveness is then given by  $e_i$  and  $e_{ij}$  for the  $i^{\text{th}}$  and  $ij^{\text{th}}$  cross terms, where:

$$e_i = b_i p_i' \quad (34)$$

$$e_{ij} = e_{ij} p_i' p_j' \quad (35)$$

## 6. RESULTS

### 6.1 Summary of Study Limitations

Before discussing the results obtained from this study, it is worth while to summarize the most important limitations involved:

- The motions are calculated for a hydrofoil ship with fully submerged foils in the head sea condition only, using linear motion theory.
- The control system is set to produce a very stable platform. This condition would, in practice, have to be relaxed in extreme sea states. We are, in effect, assessing the penalty to be paid in terms of impact pressure and hull weight for achieving the stable platform.
- The definition of design impact pressure, as used here, depends on the operational requirements of the craft.
- Whereas the parent is believed to represent a realistic configuration, some of the cases in the parametric study depart significantly from usual design practice in that extreme values of one or

two of the parameters are achieved while holding the others constant.

e) In the estimation of hull weights, a factor of safety of 1.5 based on material tensile yield strength has been assumed. This is considered appropriate in view of the criterion of 99% statistical confidence level for the extreme impact pressure.

### 6.2 Discussion of Impact Pressures

Hereafter, "impact pressures" will refer to the maximum impact pressures ( $p$ ) defined in Section 4. These were found to be concentrated in the parallel middle body at the keel, falling off rapidly both fore and aft, and laterally. The peak occurred at the forward end of the middle body (around station 12) on the keel as shown in Figure 12.

The full bottom pressure distribution for the parent is shown in Figure 13. Here, the hull bottom has been projected onto the base plane. The rapid lateral fall-off in impact pressure is typical of the cases run, with the exception of those involving low hull clearance ( $h_K$ ) or high sea state ( $H_w$ ) for which significant values of impact pressure are felt out to the chine.

In Figure 14, the parameters are varied one at a time from the parent. The dominant parameter is  $H_w$ , with significant contributions from  $\beta$ ,  $h_K$ , and  $V_d$ , the rest having a negligible effect. The lack of influence of displacement,  $\Delta$ , and load factor  $F_M$  on impact pressures reflects the use of high control gains.

At large values of hull clearance and small values of wave height, the design impact pressures become uniformly zero and the hull bottom structure dimensions reach a lower limit. This results in discontinuities in the response curves. Consequently, the response surface was fitted omitting the extreme cases of  $h_K$  and  $H_w$ . The resulting coefficients are given in Table I. Table II shows the normalized values for parameter effectiveness calculated by the method outlined in Section 5. In addition to the four first-order terms mentioned above, the second-order terms  $\beta^2$ ,  $\beta h_K$ ,  $\beta H_w$ ,  $V_d H_w$  and  $H_w^2$  make significant contributions to impact pressure. Recomputing the response surface coefficients using just these significant terms provides the following approximation for the peak keel impact pressure:

$$\begin{aligned} p_{KM} = & 4.439 \beta - 38.57 h_K - 5.856 V_d + 44.63 H_w \\ & + 0.193 \beta^2 + 1.023 \beta h_K - 2.6992 \beta H_w \\ & + 0.8336 V_d H_w + 0.4726 H_w^2 \end{aligned} \quad (36)$$

where the units are:  $p$  (psi),  $\beta$  (degrees),  $h_K$  (feet),  $V_d$  (knots), and  $H_w$  (feet).

In cases where Equation (36) gives a negative result, zero must be used. The RMS error over the data base of maximum keel impact pressure using Equation (36) is 6.5% of the mean value. Using the full set of coefficients from Table I in Equation (30) gives an RMS error of 1.87%.

### 6.3 Discussion of Hull Weight

A weight breakdown of the parent hull is given in Table III. To assess the effect of parameter variations, the weights are grouped into the components: bottom, sides, decks (upper and lower), support (bulkheads and pillars), and other structure (secondary structure and superstructure). The first four expressed as a percentage of total hull weight are plotted in Figure 15. The secondary structure and superstructure is a constant 26.5% for all cases.

The dominant parameter in this figure is wave height,  $H_w$ , with significant contributions from  $C_p$ ,  $\beta$ , and  $h_K$ .

As  $C_p$  was not significant for impact pressures, its influence on hull weight derives from hull geometry. The procedures previously described which are used to vary  $C_p$ , produce changes mainly in the hull middle and afterbody where the impact pressure has the greatest effect on bottom weight. Increase of  $C_p$  increases bottom and deck structures at the expense of the side and support structures. The reverse trend has been found for  $\beta$  for which the variation of impact pressure has a strong opposing effect on bottom weight. For the  $h_K$  and  $H_w$  variations, the bottom structure only is affected (the hull geometry and above water loading criteria do not change). A decrease in  $h_K$  or an increase in  $H_w$  result in a higher percentage of bottom weight. The lower limits on bottom structural dimensions are seen to come into effect in the extreme cases.

For hull weight fraction,  $H_w$  is again dominant with  $C_p$ ,  $\beta$ ,  $h_K$  and  $V_d$  as significant parameters as seen in Figure 16. The geometrical changes produced by increasing  $C_p$  are shown to reduce overall hull weight. The trend observed for  $\beta$  is, as previously noted, dominated by the effect of impact pressures.

From Table V, important second-order terms are  $\Delta H_w$ ,  $\beta^2$ ,  $\beta h_K$ ,  $\beta H_w$ , and  $V_d H_w$ . Recomputing the response surface coefficients using just the significant terms, the hull weight fraction is approximated by:

$$\begin{aligned} F_H = & -0.0527 C_p + 0.00851 \beta - 0.0258 h_K \\ & - 0.00105 V_d + 0.0443 H_w - 0.0000041 \Delta H_w \\ & - 0.0000194 \beta^2 + 0.000691 \beta h_K - 0.00151 \beta H_w \\ & + 0.000229 V_d H_w \end{aligned} \quad (37)$$

where  $\Delta$  is in tons and the other units are the same as for Equation (36). The RMS error over the data base using the above equation is 9.76% of the mean value, compared with 0.94% obtained using the full set of coefficients from Table IV in Equation (30).

### 7. CONCLUDING REMARKS

This study has served to quantify the influence of hull, foil, and operational parameters on wave impact pressures and hull weight fraction for foilborne operation of a hydrofoil ship in head seas. Not surprisingly, the most significant parameters are sea state, keel clearance, and deadrise angle.

Of lesser importance are speed and displacement, while prismatic coefficient has little effect on impact pressure but influences hull weight fraction appreciably.

With regard to the significance of wave height and keel clearance, it must be noted that the aim of the present study's control system is minimization of vertical accelerations. Obviously, in rougher seas than the design condition, some compromise is necessary between stabilization and alleviation of wave impacts. Further, a keel clearance margin also appears necessary.

This study can be extended in two ways. First, it would be possible to investigate a range of control system gains and to re-examine the penalty on impact pressure and hull weight. However, acceptance of a greater degree of contouring, while reducing hull weight, increases absolute ship motion. Consequently, an acceptable criterion of weight/motion trade-off would be necessary. The second extension to the study might include investigation of foil system weight in order to account for longer struts at greater keel clearances. Here again, it would be necessary to include another factor in the assessment criterion.

### REFERENCES

- (1) Schmitke, R. T., and Jones, E. A.: "Hydrodynamics and Simulation in the Canadian Hydrofoil Program". Ninth Symposium on Naval Hydrodynamics, Paris, August 1972.
- (2) Bender, E. K., Remington, P. J., and O'Neill, W. C.: "The Minimization of Hydrofoil Ship Control Power". Third Ship Control Symposium, Bath, February 1972.
- (3) Gospodnetic, D., and Miles, M.: "Some Aspects of the Average Shape of Wave Spectra at Station 'India' (59°N, 19°W)". International Symposium on Dynamics of Marine Vehicles and Structures in Waves, London, April 1974.
- (4) Schmitke, R. T., and Mackay, M.: "The Influence of Hull Form, Foil System, and Pitch-Heave Control on Hydrofoil Hullborne Seakeeping". Fourth Ship Control Systems Symposium, The Hague, 1975.
- (5) Ochi, M. K., and Motter, L. E.: "Prediction of Slamming Characteristics and Hull Responses for Ship Design". Transactions SNAME, Vol. 81, 1973.
- (6) Schmitke, R. T.: "Prediction of Pitch and Heave Motions of Hullborne Hydrofoil Vessels". DREA Report 74/2, January 1974.
- (7) Chuang, S-L.: "Experiments on Slamming of Wedge-Shaped Bodies". Journal of Ship Research, September 1967.
- (8) N.S.R.D.C., private communication.
- (9) Cohn, R. A., French, H. R., and Watson, F. B.: "Hydrofoil Craft Structural Criteria," Boeing Co. Report D221-11000-2, April 1972.
- (10) Jones, R. T.: "The Unsteady Lift of a Wing of Finite Aspect Ratio". NACA Report 681, 1940.
- (11) Wright, H. R.: "Optimization of Forward Foil Lift Control for AG(EH) Hydrofoil Craft". Grumman Aerospace Corporation Report HCG-72-1961, December 1972.



## NOTATION

A	immersed maximum sectional area	$P_O$	specified pressure threshold
$A_{jk}$	added mass coefficient	$P_S$	pressure load on ship's side
AP	after perpendicular	R	response surface figure of merit
$A_T$	immersed transom area	$\hat{R}$	non-dimensionalized response surface figure of merit
$a_i, a_{ij}$	response surface coefficients	RMS	root mean square
B	maximum section breadth at waterline	$\dot{r}$	velocity relative to water surface
$B_{jk}$	damping coefficient	$S_F$	frame spacing
$B_T$	transom breadth at waterline	$S_M$	foremost station of maximum area
b	stringer spacing	$S_R$	aftermost station of maximum area
$b_e$	effective plate width	$T_w$	energy-averaged wave period
$b_F$	stiffener flange width	t	time variable
$b_i, b_{ij}$	non-dimensionalized response surface coefficients	$t_F$	stiffener flange thickness
$C_{jk}$	hydrostatic restoring coefficient	$t_p$	plate thickness
$C_M$	midship section coefficient	$t_w$	stiffener web thickness
$C_P$	prismatic coefficient	$V_d$	design foilborne speed
$C_T$	transom sectional area coefficient	$W_H$	total hull weight
$C_w$	waterplane coefficient	$W_{H1}$	primary hull structural weight
c	statistical confidence level	$W_{H2}$	secondary hull structural weight
DWL	design waterline	$W_s$	superstructure weight
E	Young's modulus	w	applied load per unit of length
$e_i, e_{ij}$	relative effectiveness of response surface terms	x	longitudinal co-ordinate
$F_H$	hull weight fraction ( $W_H/\Delta$ )	y	lateral co-ordinate
$F_j$	exciting force	$y_C$	chine offset distance
$F_M$	fraction of ship weight carried by main foil	$y_O$	wedge penetration in y direction
FP	forward perpendicular	Z	section modulus
G	girth (keel to chine)	z	vertical co-ordinate
$H_w$	foilborne significant wave height	$z_O$	waterline associated with wedge penetration $y_O$
$H_{wh}$	hullborne significant wave height	$\beta$	deadrise angle
$h_K$	design keel clearance	$\beta_B$	bow foil flap angle
$h_w$	stiffener web height	$\beta_M$	main foil flap angle
$I_y$	pitching moment of inertia	$\Delta$	ship displacement
$i_e$	bow entrance angle	$\nabla$	displaced volume
k	geometrical factor	$\zeta$	damping ratio
$k_{zB}, k_{\theta B}$	bow foil control system gains	$\theta$	pitch angle
$k_{zM}, k_{\theta M}$	main foil control system gains	$\rho$	fluid density
L	ship waterline length	$\sigma_{RM}$	RMS motion relative to water surface
LCB	longitudinal centre of buoyancy	$\sigma_{RV}$	RMS velocity relative to water surface
$l_c$	watertight compartment spacing	$\tau$	buttock angle
$\bar{M}$	length displacement ratio ( $L/\nabla^{1/3}$ )	$\omega$	frequency of encounter
$M_s$	stiffener bending moment	$\omega_n$	undamped natural frequency
m	ship mass	$\omega_w$	wave frequency
N	number of impacts during time t		
n	frequency of immersion to waterline $z_O$		
$\hat{P}_i, \hat{P}_j$	non-dimensionalized response surface parameters		
$P_{z_O}$	probability of immersion to waterline $z_O$		
$p_O$	design pressure load		
$P_G$	pressure load at bottom girders		
$P_i, P_j$	response surface parameters		
$P_K$	pressure load at keel		
$P_{KM}$	maximum keel impact pressure		
$P_1$	pressure load on 1 <sup>th</sup> strake		
$P_M$	peak impact pressure		

## APPENDIX A

## COEFFICIENTS OF EQUATIONS OF MOTION

A detailed derivation of the pitch, heave, and flap coefficients is given in Reference 6 and will not be repeated here. First, the pitch and heave coefficients are listed using the usual convention that subscript 3 refers to heave and subscript 5 to pitch.

$$A_{33} = \pi \rho \Sigma b \left(\frac{c}{2}\right)^2 \quad (A1)$$

$$B_{33} = \frac{1}{2} \rho U \Sigma SC_{L\alpha} C(k) \quad (A2)$$

$$C_{33} = \Sigma \frac{\partial L}{\partial h} C(k) \quad (A3)$$

$$A_{35} = A_{53} = \pi \rho \Sigma b \left(\frac{c}{2}\right)^2 s \quad (A4)$$

$$B_{53} = -\frac{1}{2} \rho U \Sigma SC_{L\alpha} C(k) x \quad (A5)$$

$$B_{35} = UA_{33} + B_{53} \quad (A6)$$

$$C_{53} = -\Sigma \frac{\partial L}{\partial h} C(k) x \quad (A7)$$

$$C_{35} = UB_{33} + C_{53} \quad (A8)$$

$$A_{55} = \pi \rho \Sigma b \left(\frac{cs}{2}\right)^2 + \frac{\pi \rho}{128} \Sigma bc^4 \quad (A9)$$

$$B_{55} = UA_{35} + \frac{1}{2} \rho U \Sigma SC_{L\alpha} C(k) x \left(s - \frac{c}{4}\right) + \frac{\pi \rho U}{16} \Sigma bc^3 \quad (A10)$$

$$C_{55} = UB_{53} + \Sigma \frac{\partial L}{\partial h} C(k) x^2 \quad (A11)$$

where summation is over all foil elements.  $c$  is mean chord,  $C_{L\alpha}$  lift curve slope,  $b$  and  $S$  horizontally projected span and area,  $x$  and  $s$  the  $x$ -coordinates of quarter and mid chord, respectively.

$$k = \frac{\omega c}{2U} \quad (A12)$$

is the reduced frequency and  $C(k)$  accounts for unsteadiness effects (circulation delay). As regards  $C(k)$ , the following expressions are used rather than the method of Reference 6.

$$C(k) = 1 - \frac{aik}{t + ik} \quad (A13)$$

$$a = 1 - \frac{A + 2}{2AE} \quad (A14)$$

$$t = 2.04(1 - a) - .923 \quad (A15)$$

where  $A$  is aspect ratio and  $E$  the Jones' edge velocity factor (ratio of semi-perimeter to span). This expression for  $C(k)$  is based on the work of R. T. Jones (10).

We next list the control coefficients:

$$A_{3J} = \rho b_{FJ} T_{1J} \left(\frac{c_J}{2}\right)^3 \quad (A16)$$

$$B_{3J} = \frac{1}{4} \rho U b_{FJ} c_J^2 (T_{4J} - \frac{1}{2\pi} C_{L\alpha J} C(k_J) T_{11J}) \quad (A17)$$

$$C_{3J} = -\frac{1}{2} \rho U^2 b_{FJ} c_J C_{L\alpha J} C(k_J) e_{\beta J} \quad (A18)$$

$$A_{5J} = -A_{3J} s_J + \rho b_{FJ} \left(\frac{c_J}{2}\right)^4 (T_{7J} + p_J T_{11J}) \quad (A19)$$

$$B_{5J} = \rho U b_{FJ} \left\{ -T_{4J} \left(\frac{c_J}{2}\right)^2 s_J + \frac{1}{8\pi} C_{L\alpha J} C(k_J) T_{11J} c_J^2 x_J - \left(\frac{c_J}{2}\right)^3 (T_{1J} - T_{8J} - p_J T_{4J} + \frac{1}{2} T_{11J}) \right\} \quad (A20)$$

$$C_{5J} = -C_{3J} x_J - \rho U^2 b_{FJ} \left(\frac{c_J}{2}\right)^2 (T_{4J} + T_{10J}) \quad (A21)$$

where  $J = B$  gives the forward foil coefficients and  $J = M$  the after foil coefficients.  $b_F$  is flap span and  $p$  the distance from the flap hinge line to mid chord, divided by the semi-chord.

$$e_{\beta} = \frac{d\alpha}{d\beta} \quad (A22)$$

is the flap effectiveness parameter and

$$T_1 = -\frac{1}{3}(2 + p^2)\sqrt{1 - p^2} + p \cos^{-1} p \quad (A23)$$

$$T_4 = -\cos^{-1} p + p\sqrt{1 - p^2} \quad (A24)$$

$$T_7 = -\left(\frac{1}{8} + p^2\right) \cos^{-1} p + \frac{1}{8} p(7 + 2p^2)\sqrt{1 - p^2} \quad (A25)$$

$$T_8 = -\frac{1}{3}(1 + 2p^2)\sqrt{1 - p^2} + p \cos^{-1} p \quad (A26)$$

$$T_{10} = \sqrt{1 - p^2} + \cos^{-1} p \quad (A27)$$

$$T_{11} = \cos^{-1} p(1 - 2p) + (2 - p)\sqrt{1 - p^2} \quad (A28)$$

Turning finally to the wave exciting force and moment ( $F_3$  and  $F_5$ ), these are considered in somewhat more detail than in Reference 6. Four foil lift components are distinguished due to wave action. The first is due to wave orbital velocity and is estimated by

$$L_1 = \frac{1}{2} \rho U S C_{L\alpha} G(k) w_{LE} \quad (A29)$$

where  $w_{LE}$  is the vertical component of wave orbital velocity at the leading edge and  $G(k)$  is the gust function, given by

$$G(k) = 1 - \frac{dik}{t + ik} - \frac{(1-d)ik}{3 + ik} \quad (A30)$$

$$d = .641a + .468 \quad (A31)$$

which is also based on the work of R. T. Jones.

Our second component of lift is due to variations in foil operating depth:

$$L_2 = \frac{1}{2} \rho U^2 S \frac{\partial C_L}{\partial h} G(k) \eta_{1/4} \quad (A32)$$

where  $\eta_{1/4}$  is the wave elevation at quarter chord (foil depth is normally referenced to quarter chord).

The last two components of lift are of much less importance. One arises from the variation in dynamic pressure due to the horizontal component of wave orbital velocity,  $u$ , and is approximated by

$$L_3 = \rho U S C_{L_u} u_{1/2} \quad (A33)$$

where the subscript  $1/2$  refers to mid chord.

The final component of the wave forcing function is simply the Froude-Kriloff force, which for thin foils may be approximated by

$$L_4 = i \rho \nabla \omega_w w_{1/2} \quad (A34)$$

where  $\nabla$  is foil displacement and  $\omega_w$  wave frequency.

Gathering terms, we obtain the following expression for lift due to wave action:

$$L_w = \frac{1}{2} \rho U S G(k) \left[ C_{L\alpha} w_{LE} + U \frac{\partial C_L}{\partial h} \eta_{1/4} \right] + \rho U S C_{L_u} u_{1/2} + i \rho \nabla \omega_w w_{1/2} \quad (A35)$$

We shall now use the quarter chord as reference. For gravity waves,

$$w_{LE} = i \omega_w \exp(-k_w h + i k_w c/4) \eta_{1/4} \quad (A36)$$

$$u_{1/2} = \omega_w \exp(-k_w h - i k_w c/4) \eta_{1/4} \quad (A37)$$

$$w_{1/2} = i u_{1/2} \quad (A38)$$

where  $h$  is foil mean depth and

$$k_w = \frac{\omega_w^2}{g} \quad (A39)$$

is wave number.

Substitution for  $w_{LE}$ ,  $u_{1/2}$ , and  $w_{1/2}$  gives

$$L_w = \frac{1}{2} \rho U S \eta_{1/4} \{ G(k) i C_{L\alpha} \omega_w \exp(-k_w h + i k_w c/4) + U \frac{\partial C_L}{\partial h} + 2 \omega_w \exp(-k_w h - i k_w c/4) \cdot (C_L - \omega_w \frac{\nabla}{US}) \} \quad (A40)$$

whence we obtain the following expressions for  $F_3$  and  $F_5$ :

$$F_3 = \sum L_w e^{i k_w x} \quad (A41)$$

$$F_5 = - \sum L_w x e^{i k_w x} \quad (A42)$$

Figure A-1 demonstrates that the above procedures gives a good estimate of the wave forcing function. The experimental data are obtained from Reference 11, and the quantities plotted are defined below:

$$H = \frac{U \Delta C_L}{w C_{L\alpha}} \exp \left[ - \frac{i \pi}{2} \left( \frac{1}{Nc} + 1 \right) \right] \quad (A43)$$

where  $w$  is the amplitude of wave orbital velocity,  $\lambda$  is wave length and

$$\Delta C_L = \frac{L_w}{\frac{1}{2} \rho U^2 S} \quad (A44)$$

Thus, in Figure A-1,

$$\text{ATTENUATION} = |H| \quad (A45)$$

$$\text{PHASE LAG} = \arctan \left[ \frac{\text{Imag}(H)}{\text{Real}(H)} \right] \quad (A46)$$

Note that in Figure A-1, the dynamic pressure term  $L_3$  has been removed from the data.



## RESPONSE SURFACE COEFFICIENTS FOR PEAK KEEL IMPACT PRESSURE

$$a_0 = 372.68$$

	$\Delta$	(M)	$C_p$	$\beta$	$F_M$	$h_K$	$V_d$	$H_w$
i	1	2	3	4	5	6	7	8
$a_1$	$1.14 \times 10^{-2}$	6.03	$-8.22 \times 10^2$	-3.09	$-1.92 \times 10^2$	$-1.45 \times 10^1$	-2.59	$2.80 \times 10^1$
$a_{11}$	$-1.82 \times 10^{-5}$	$8.36 \times 10^{-4}$	$-3.23 \times 10^{-2}$	$-7.11 \times 10^{-4}$	$7.52 \times 10^{-3}$	$-5.07 \times 10^{-4}$	$2.56 \times 10^{-4}$	$3.10 \times 10^{-3}$
$a_{21}$		$-1.77 \times 10^{-1}$	-2.57	$-9.72 \times 10^{-2}$	-2.50	$-4.90 \times 10^{-2}$	$2.46 \times 10^{-2}$	$2.40 \times 10^{-1}$
$a_{31}$			$5.65 \times 10^2$	-1.84	$8.42 \times 10^1$	$-2.60^1$	$4.92 \times 10^{-1}$	6.39
$a_{41}$				$4.83 \times 10^{-1}$	3.00	1.16	$-2.10 \times 10^{-1}$	-2.60
$a_{51}$					$2.87 \times 10^1$	$1.58^1$	$1.51 \times 10^{-1}$	-2.37
$a_{61}$						$-8.84 \times 10^{-1}$	$-3.60 \times 10^{-1}$	$2.43 \times 10^{-1}$
$a_{71}$							$3.40 \times 10^{-2}$	$9.14 \times 10^{-1}$
$a_{81}$								$5.60 \times 10^{-1}$

Table 1

## PARAMETER EFFECTIVENESS FOR PEAK KEEL IMPACT PRESSURES

$$b_0 = -1.233$$

	$\Delta$	(M)	$C_p$	$\beta$	$F_M$	$h_K$	$V_d$	$H_w$
i	1	2	3	4	5	6	7	8
$b_1$	1.331	1.000	2.269	-35.545	-6.287	-60.331	22.696	234.430
$b_{11}$	-0.376	0.088	-0.333	-0.516	0.156	-0.210	0.265	3.207
$b_{21}$		-0.094	-0.134	-0.357	-0.263	-0.103	0.129	1.261
$b_{31}$			2.896	-0.663	0.868	-0.535	0.253	3.295
$b_{41}$				12.271	2.175	16.773	-7.623	-94.209
$b_{51}$					0.595	0.653	0.156	-2.450
$b_{61}$						-7.329	-7.458	5.044
$b_{71}$							1.758	47.330
$b_{81}$								28.990

Table 2

PARENT HULL WEIGHT DISTRIBUTION

	Pounds
Bottom plating and stringers	15,895
Keel	4,232
Bottom girders	5,459
Bottom transverse frames	13,854
Side plating and stringers	12,041
Side frames	19,498
Deck, upper	10,191
lower	5,649
Deck girders, upper	7,173
lower	1,481
Deck beams, upper	12,684
lower	1,522
Bulkheads	17,685
Deck pillars	2,572
Secondary structure	33,588
Superstructure	<u>13,258</u>
	<u>176,782</u>

Total hull weight: 78.92 long tons

Hull weight fraction: 19.73 per cent

Table 3

RESPONSE SURFACE COEFFICIENTS FOR HULL WEIGHT FRACTION

$$a_0 = 0.255$$

	$\Delta$	$\textcircled{M}$	$C_p$	$\beta$	$F_M$	$h_K$	$V_d$	$H_w$
	1	2	3	4	5	6	7	8
$a_1$	$1.84 \times 10^{-4}$	$-1.95 \times 10^{-2}$	$-1.53 \times 10^{-1}$	$-3.49 \times 10^{-3}$	$2.75 \times 10^{-2}$	$-2.77 \times 10^{-2}$	$2.54 \times 10^{-3}$	$2.77 \times 10^{-2}$
$a_{11}$	$1.21 \times 10^{-7}$	$-3.47 \times 10^{-5}$	$-2.12 \times 10^{-4}$	$5.80 \times 10^{-6}$	$1.84 \times 10^{-5}$	$9.15 \times 10^{-6}$	$-1.06 \times 10^{-6}$	$-9.91 \times 10^{-6}$
$a_{21}$		$2.48 \times 10^{-3}$	$2.36 \times 10^{-2}$	$-6.75 \times 10^{-4}$	$-4.58 \times 10^{-3}$	$-9.40 \times 10^{-4}$	$8.28 \times 10^{-5}$	$7.53 \times 10^{-4}$
$a_{31}$			$7.38 \times 10^{-2}$	$-1.28 \times 10^{-2}$	$-9.12 \times 10^{-4}$	$-5.60 \times 10^{-3}$	$6.10 \times 10^{-4}$	$1.14 \times 10^{-2}$
$a_{41}$				$4.29 \times 10^{-4}$	$1.64 \times 10^{-3}$	$1.15 \times 10^{-3}$	$-9.53 \times 10^{-5}$	$-1.45 \times 10^{-3}$
$a_{51}$					$3.41 \times 10^{-2}$	$2.47 \times 10^{-3}$	$8.77 \times 10^{-5}$	$-2.39 \times 10^{-3}$
$a_{61}$						$4.81 \times 10^{-4}$	$-2.99 \times 10^{-4}$	$2.06 \times 10^{-4}$
$a_{71}$							$-1.56 \times 10^{-5}$	$3.78 \times 10^{-4}$
$a_{81}$								$-6.96 \times 10^{-5}$

Table 4

## PARAMETER EFFECTIVENESS FOR HULL WEIGHT FRACTION

$b_o = 2.242$

	$\Delta$	(M)	$C_p$	$\beta$	$F_M$	$h_K$	$V_d$	$H_w$
i	1	2	3	4	5	6	7	8
$b_1$	-1.000	-1.263	-16.448	-6.828	-1.488	-22.327	5.969	126.550
$b_{1i}$	1.939	-2.828	-1.695	3.263	0.296	2.941	-0.853	-7.959
$b_{2i}$		1.022	0.957	-1.925	-0.373	-1.531	-0.337	3.066
$b_{3i}$			0.293	-3.578	-0.007	-0.894	0.244	4.539
$b_{4i}$				8.453	0.923	12.957	-2.679	-40.656
$b_{5i}$					-0.548	0.793	0.070	-1.919
$b_{6i}$						3.092	-4.804	3.310
$b_{7i}$							-0.628	15.161
$b_{8i}$								-2.798

Table 5

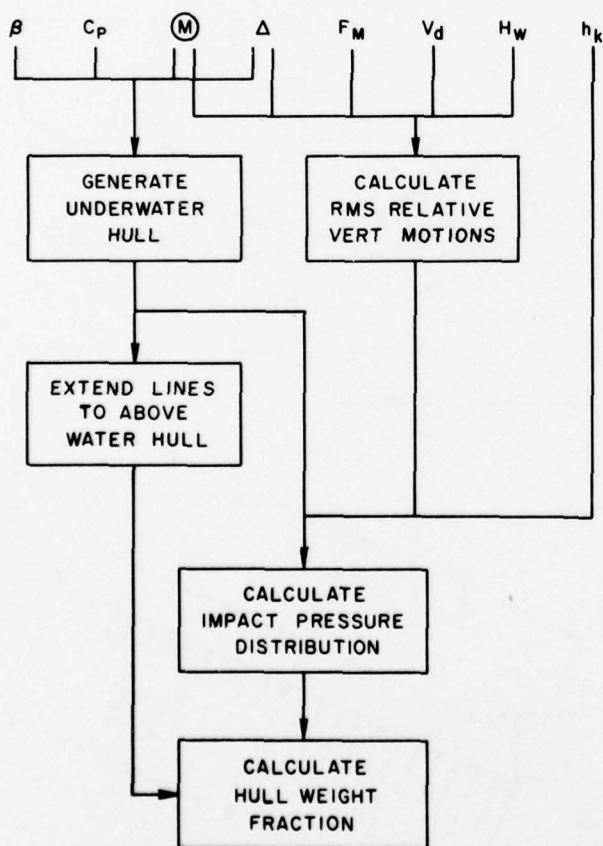


Fig. 1: Computational process

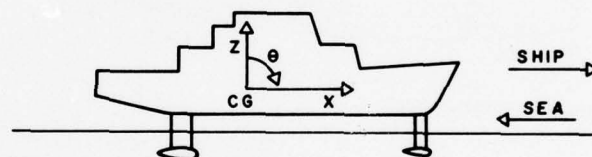


Fig. 2: Axis system

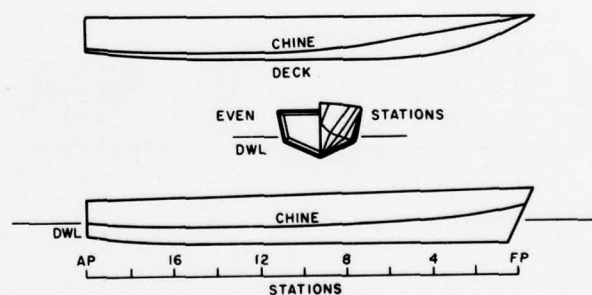


Fig. 3: Hull lines—parent model

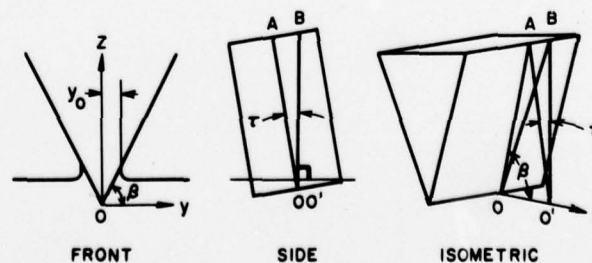


Fig. 4: Geometry of immersed wedge



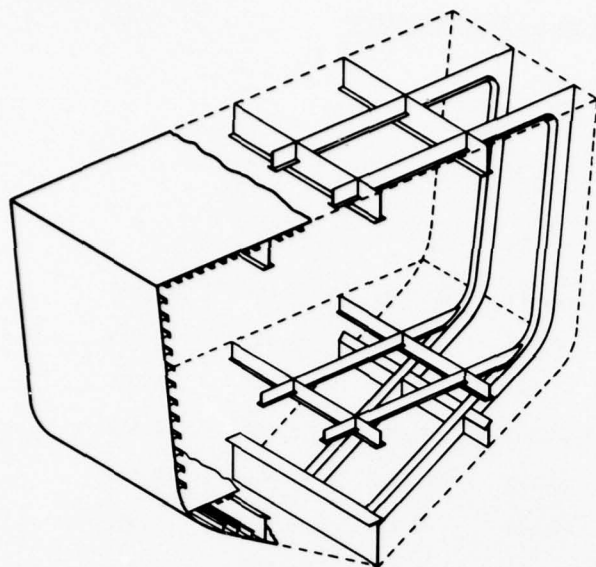


Fig. 5: Typical hydrofoil hull structure

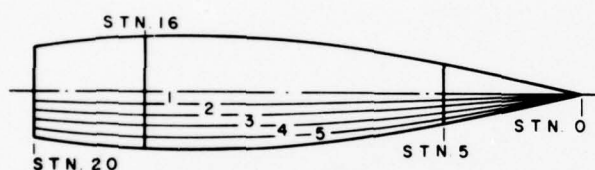


Fig. 6: Bottom strakes

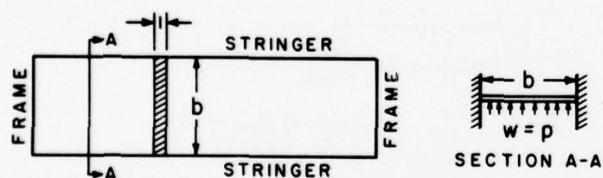


Fig. 7: Skin panel

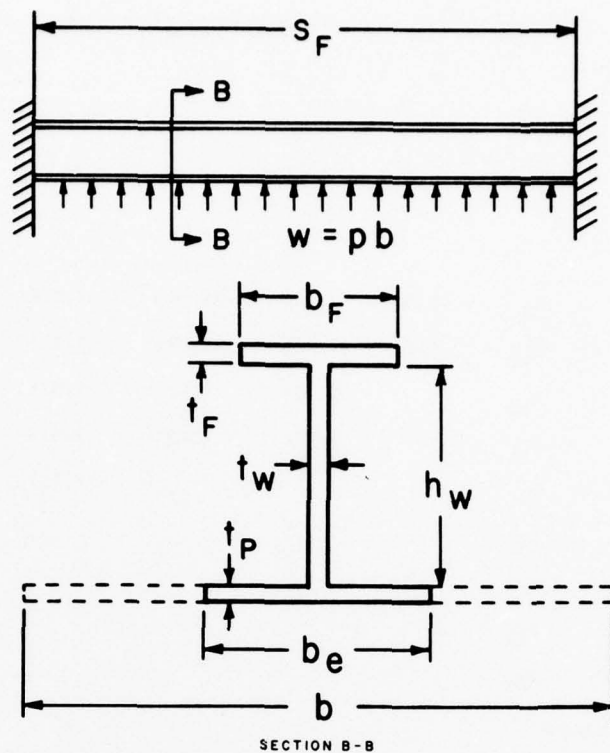


Fig. 8: Typical stiffener

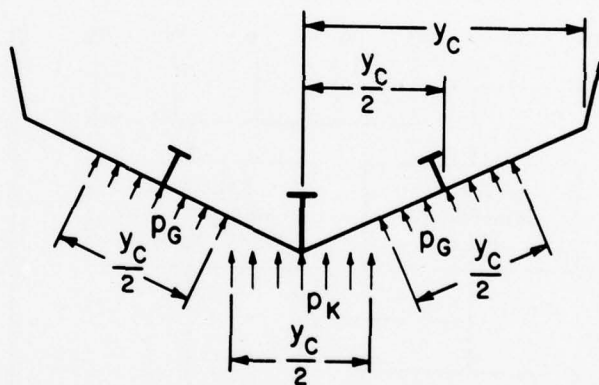


Fig. 9: Keel and bottom girders

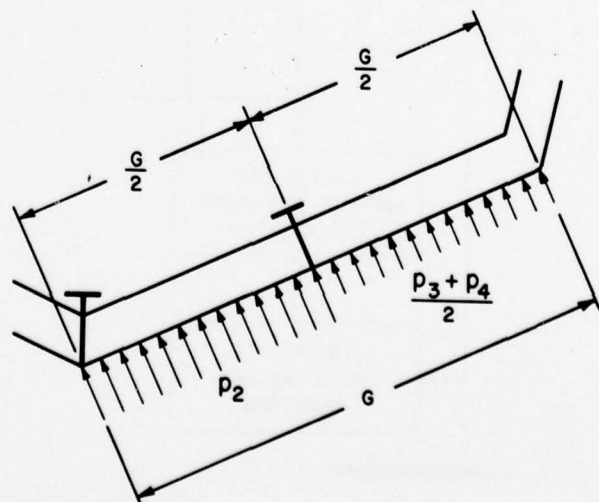


Fig. 10: Bottom frame

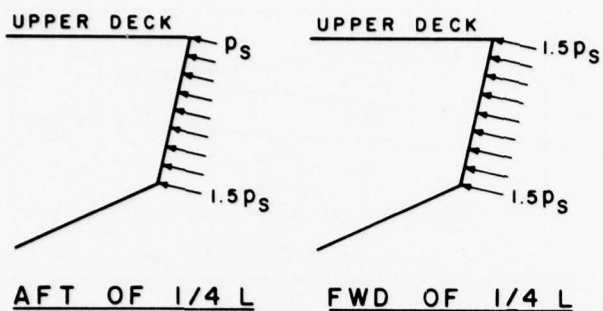


Fig. 11: Side loads

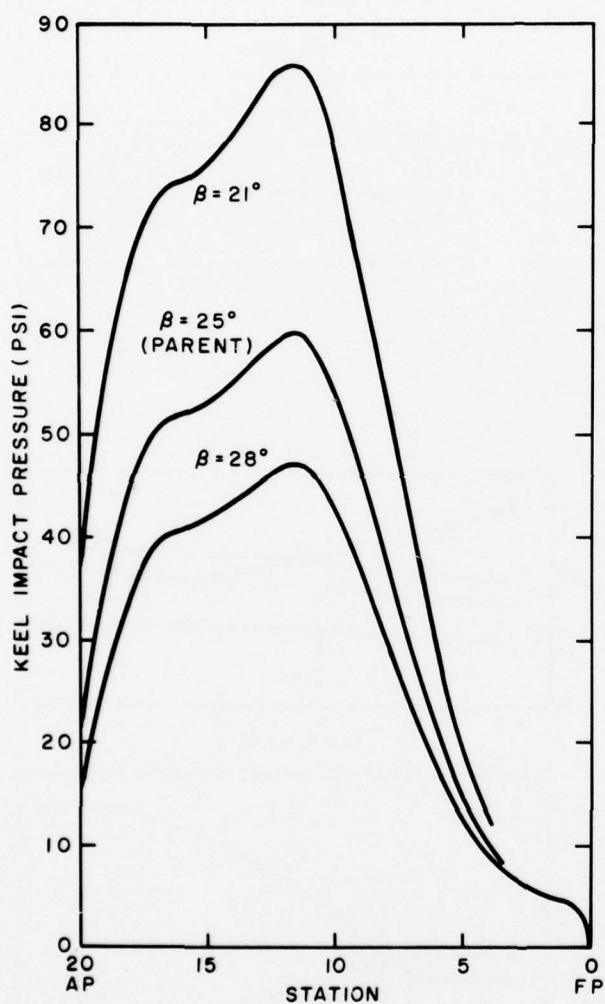


Fig. 12: Keel impact pressure distributions

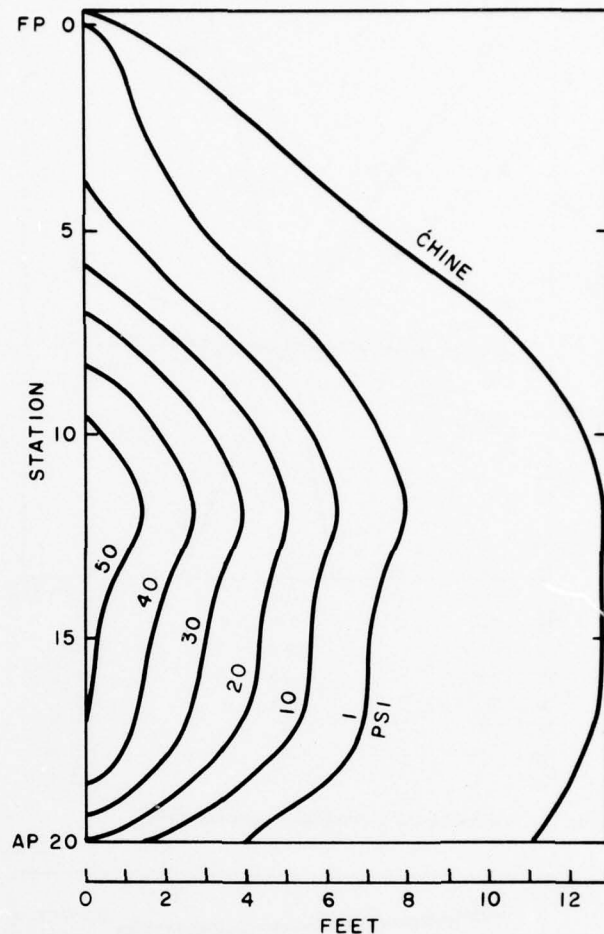


Fig. 13: Bottom impact pressure distribution—parent model

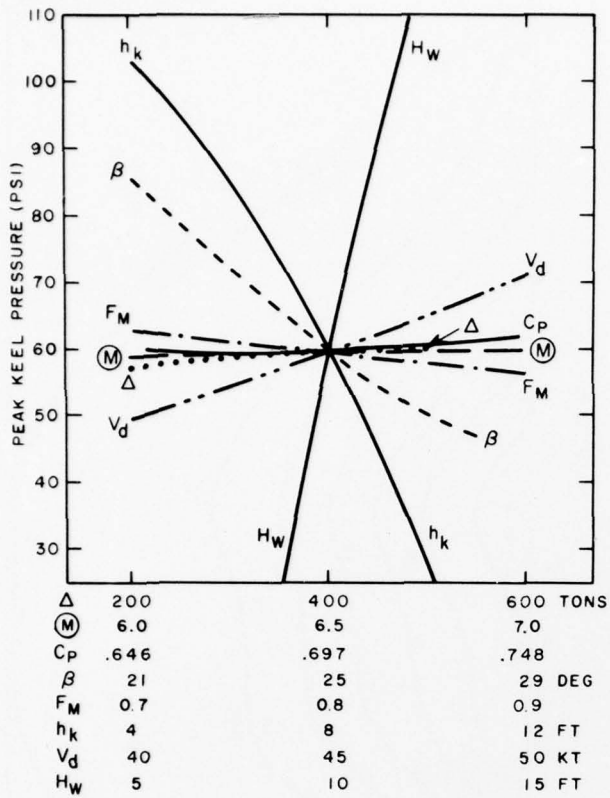


Fig. 14: Peak keel pressure—single parameter variations

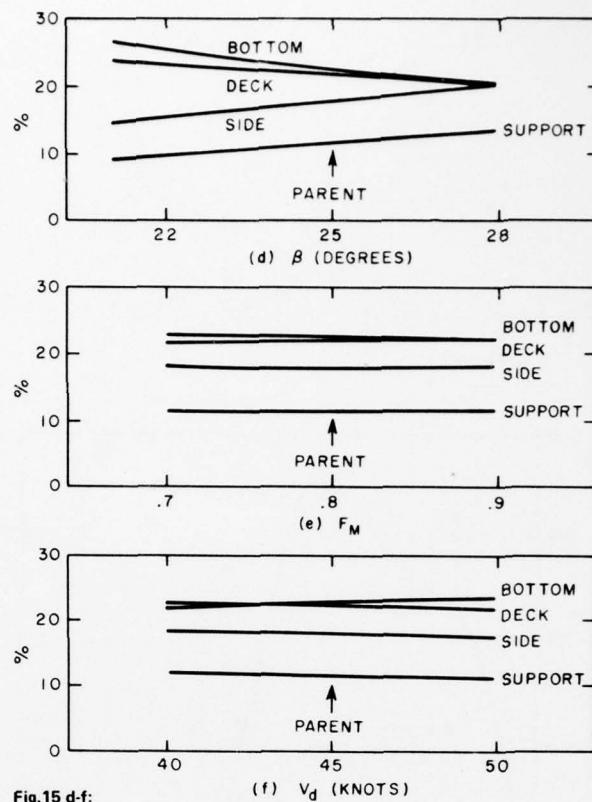


Fig. 15 d-f:

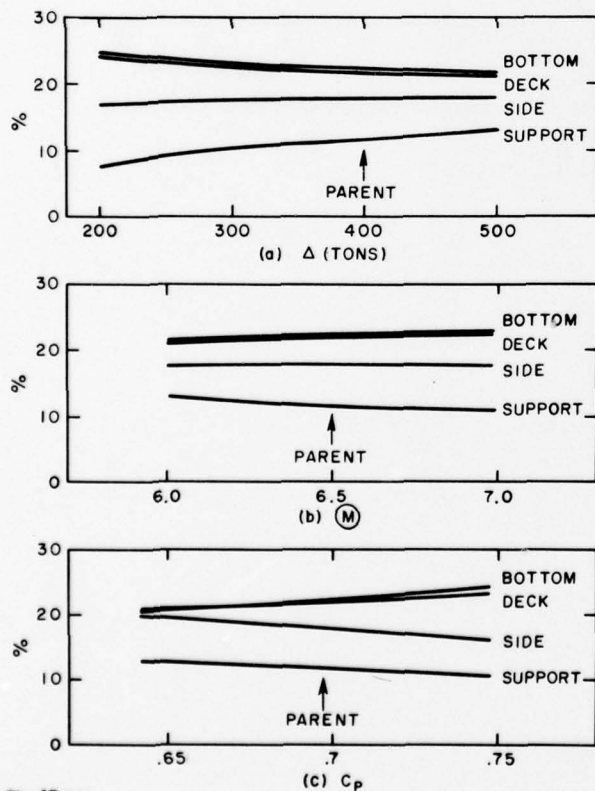


Fig. 15 a-c:

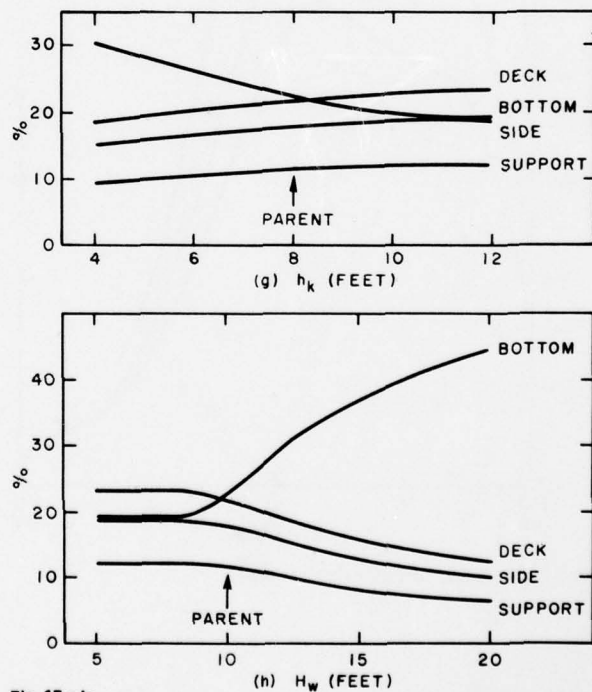


Fig. 15 g-h:

Fig. 15: Hull weight components



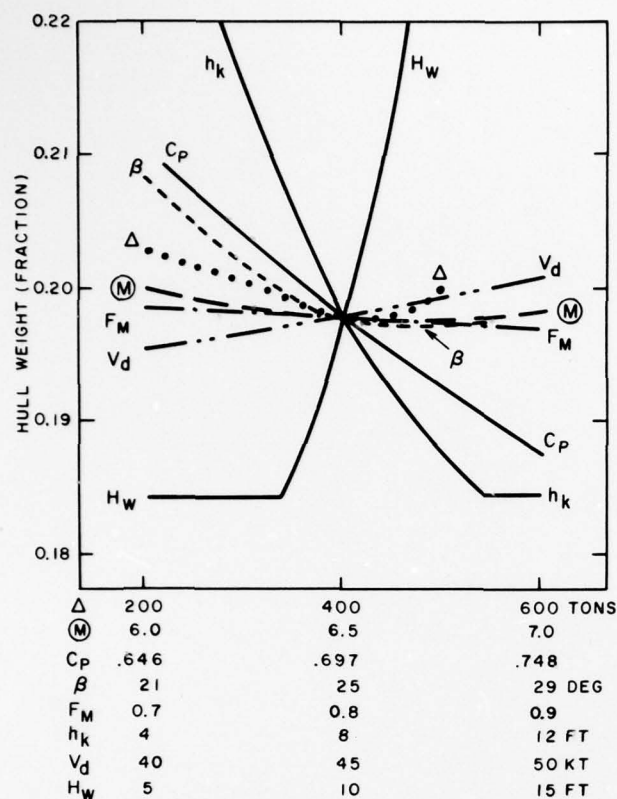


Fig. 16: Hull weight fraction—single parameter variations

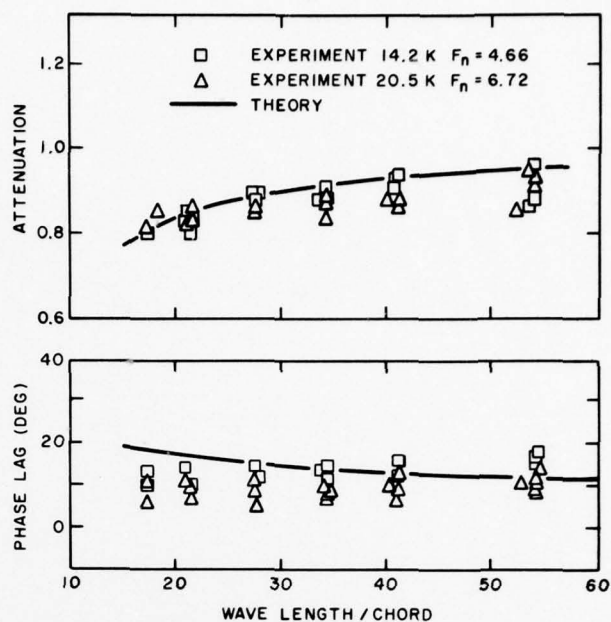


Fig. A1: Attenuation and phase shift of wave forcing function—AG(EH) model

# AN EXPERIMENTAL STUDY OF A SUPERVENTILATED FINITE ASPECT RATIO HYDROFOIL NEAR A FREE SURFACE

O. FURUYA\* and A. J. ACOSTA\*\*

**SYNOPSIS:** Lift and drag measurements on a superventilated flat plate hydrofoil of aspect ratio four operating at various submergences beneath a free surface are presented and compared with a recent three-dimensional non-linear hydrofoil theory. The measurements provide reference data for this type of superventilated flow for angles of attack up to 25 degrees. The effect of gravity is small but not negligible at test Froude numbers of about six; despite this effect the theoretical predictions are quite satisfactory up to angles of attack of about 20 degrees.

## NOTATION:

1.  $\alpha$  Angle of attack
2.  $AR$  Aspect ratio ( $= s^2/S$ )
3.  $C_D$  Drag coefficient ( $= D/(\frac{1}{2}\rho V^2 S)$ )
4.  $C_L$  Lift coefficient ( $= L/(\frac{1}{2}\rho V^2 S)$ )
5.  $D^L$  Drag force parallel to the flow direction
6.  $Fr$  Froude number  $V/\sqrt{gc}$
7.  $L$  Lift force normal to the flow direction
8.  $S$  Area of foil
9.  $V$  Tunnel velocity
10.  $c$  Root chord
11.  $g$  Acceleration of gravity
12.  $p_c$  Pressure inside the cavity
13.  $p_\infty$  Pressure at upstream infinity at the depth of the foil
14.  $s$  Span
15.  $\rho$  Density of water
16.  $\sigma$  Cavitation number ( $=(p_\infty - p_c)/(\frac{1}{2}\rho V^2)$ )

**1. INTRODUCTION.** A great many theories for the calculation of the finite aspect ratio effect on supercavitating wings have appeared within the last fifteen years. For the most part these theories because of the well-known complexities of supercavitating flows have been linearized in the treatment of the free surface portion of the flow. The added complications of the finiteness of the span have been treated in a number of ways by (with an important exception) borrowing aerodynamic procedures. Experiments have also been made to provide a data base for the validation of these theories. Some of these results, theoretical and experimental, are touched upon in recent reviews (Acosta, 1973, Hsu, 1975). Particularly noteworthy for their frequent citations in this experimental literature are the works of Johnson (1957), Kermeen (1961), Schiebe & Wetzel (1961, 1964), Kiceniuk (1964). Based on these earlier experimental results and (essentially) linearized free streamline theory with aeronautical-type corrections supercavitating wing design procedures are described by Altman (1968).

Many of these methods and supercavitating hydrofoil experiments themselves are applied to

\*Tetra Tech, Inc. Pasadena, California 91107

\*\*Division of Engineering & Applied Science, California Institute of Technology, Pasadena, California 91125

conditions where the linear theories are probably not valid. This is often due to the practical difficulty in experimental situations of obtaining a superventilated or supercavitating flow with a sufficiently small camber, angle of attack, lift coefficient, etc., and there is in addition the desire to obtain experimental information at large values of the flow parameters. Thus, much of the experimental findings for hydrofoils having an angle of attack greater than 10 degrees (say) although valid in its own right may not apply for predictions made with linear theories. This is true, for example, of much of the interesting work of Tsen & Guilband (1974).

There is the additional problem of a systematic accounting of the finite aspect ratio itself. These problems have been recently addressed by Ogilvie (1970). Leehey & Stellingner (1975) describe a theory which utilizes linear free streamline section theory and an aspect-ratio effect correct through second order. Their experiments show good correlation for lift down to an aspect ratio of three but drag is not so well predicted.

There is currently, still interest evidenced in the design of practical hydrofoils of finite aspect ratio. Generally, the design features include rounded noses and other geometric features which require for sufficient accuracy the use of a full, non-linear free-streamline analysis. See, e.g., the experiments of Holling (1975), the designs of Baker (1975) and design considerations of Wang & Shen (1975). There is then, ample motivation to increase the available experimental reference base particularly for hydrofoils of finite aspect ratio near free surfaces operating under conditions where these non-linear free-streamline effects are important. Some preliminary steps in this direction have already been taken by Barker & Ward (1975) and some of the configurations studied by Tsen & Guilband. Yet these approaches are primarily experimental because until a comparatively short time ago, a self-consistent, near-surface, non-linear, supercavitating, finite aspect-ratio calculation procedure was not available for test. Very recently however, one such method has become available which does take all these factors into account (Furuya 1975 a, b). With the aid of this work it has been possible to make comparisons with experiments such as those of Schiebe & Wetzel which are well into the non-linear

regime. Calculations of lift coefficient up to 20 degrees angle of attack agreed very well with their findings, for example, even for an aspect ratio of 2.5. There were, however, some discrepancies with drag and it was not known whether these were due to the experiments or to some deficiency of the analysis.

For all of the above reasons it appeared to be very desirable to carry out one or more additional experiments in a supercavitating or superventilating flow whose chief purpose would be to provide accurate forces and geometry of flow to test the non-linear analysis mentioned before. In the following sections the apparatus to do this is described. The measurements of the forces and the tare corrections are then outlined followed by a detailed comparison of experiment with theory. Only one hydrofoil, (flat-plate, tapered of aspect ratio four) is tested in the present work. As will be seen, the analysis provides good estimates of lift, drag, and cavity length well into non-linear regions of angle of attack and cavitation number. It appears therefore that the non-linear analysis mentioned before has some potential as a design technique; for this reason a brief description of it and related work is presented in the next section.

**2. THEORETICAL BACKGROUND.** Analysis of supercavitating flow configurations of interest in naval hydrodynamic applications differ in two important respects from subsonic aerodynamic procedures. The first of course is the unknown shape of the free surface forming the cavity connected with the body. The second is of interest for lifting bodies and it is the establishment of the proper undisturbed reference level for flows (cavitating or not) which take place near a free surface such as that of the ocean or towing tank. Because of the upwash induced by the bound and shed vorticity, the position of the free surface near the body can differ markedly from the undisturbed level far upstream and it too is not known in advance. In fact, as an elementary example will show, in two dimensional unbounded flow the upstream level becomes logarithmically infinite far upstream. But this academic curiosity is removed by the slightest consideration of gravity, the presence of a finite bottom or (even in unbounded flow) finiteness of span. This point was recognized by Johnson (1957) in his early calculations but it was not until the work of Shen and Ogilvie (1972) on planing surfaces that a systematic procedure was developed for the determination of this undisturbed reference level in gravity-free flows with finite aspect ratio. This point is hardly academic because depending upon aspect ratio a planing surface or hydrofoil may ride entirely above the undisturbed upstream level!

Shen and Ogilvie tackled their planing problem by the method of matched asymptotic expansions. In this (briefly) a local two-dimensional flow near the body containing all details of profile shape, cavitation number, etc. is blended systematically to one far from the body. Essentially this far field flow is that of a lifting line. Thus, all local two-dimensional flow details such as the foil profile and the cavity also shrink to a point in the far field. The lifting line is taken to be on the undisturbed water surface. The two regions are scaled by a small parameter, the inverse of the aspect ratio. The extent of the local or inner flow is proportional to this parameter and the extent of the far field or outer flow is inversely proportional to it. Certain parameters in each of the flow fields depend upon conditions in the other

and these are determined together with the matching procedure described at length by Ogilvie (1970). Shen and Ogilvie carried through this process for the planing surface, the local level of the free surface being determined as a part of the solution. Furthermore, their inner solution was the non-linear planing solution for a flat plate of infinite chord. The fact that it was not necessary to linearize the inner two-dimensional flow was also pointed out by Ogilvie (1970).

The same approach was used subsequently by Shen (1973) to formulate the hydrofoil problem although no computations were made. More recently, the whole procedure has been reconsidered by (Furuya, 1975b); the original non-linear two-dimensional theory of Wu and Wang (1964) was modified to incorporate the nearby free surface effect and all aspects of profile camber and leading edge bluntness (Furuya, 1975c). The finite-aspect ratio effect was found to be equivalent to the Prandtl lifting line theory, the submergence of the complete hydrofoil beneath the undisturbed upstream surface being specified in advance. Within the limitation of the aspect ratio correction, all details of cavity shape, pressure distributions, etc. for practical hydrofoils can be determined.

**3. EXPERIMENTAL APPARATUS AND DATA MEASUREMENT.** The test hydrofoil has a flat lower surface with a sharp leading edge and a partially tapered planform (see Figs. 1). The taper was chosen to simulate somewhat an elliptic loading and to avoid the strong tip vortex cavities evident on rectangular planforms. The aspect ratio is four. Particular attention has been paid to the structure of the support system; the foil is supported at the trailing edge by an "annex" which is in turn attached to the support strut (Fig. 1c). The purpose of this arrangement is intended to minimize the strut downwash effect on the foil and to avoid interference of the strut with the cavity surface over the foil. The complete test set-up is shown in Figs. 2; three tubes can be seen in these photographs. Two supply ventilating air to the holes near the leading edge and behind the foil, seen in Fig. 2(1a) and the other is used to measure the pressure within the cavity. The hydrofoil-strut assembly is attached to a six component strain gage balance (see Fig. 2c). This is in turn supported by an elevation and angle of attack adjusting mechanism not shown. The force capability of the balance is 360N in lift and 110N in drag. The strain gage outputs are conditioned and punched onto data cards together with the other experimental parameters for subsequent processing.

The tests themselves were made in the Free Surface Water Tunnel (FSWT) at the Institute. The maximum tunnel speed is about 7.6 m/s and the working section is 0.508 m square by about 2.4 m in length. A vacuum system is available which makes working section pressures down to 0.09 atm possible. But even at the maximum available tunnel speed the minimum cavitation index for vaporous cavitation would be only 0.3. For this reason the forced ventilation technique was adopted to achieve index values near zero. Provided the flow is steady and the cavities are sufficiently longer than the chord the resulting flow closely approximates that of vaporous cavitation. The airflow itself was provided by regulated house air; the volume flow rate was determined by conventional "flow raters". Both tunnel speed and cavity pressure were measured with manometers. Some care was needed to ensure reliable cavity pressure measurement particularly for short cavities.



Then a 'purge' of pressurized air via a two-way valve was found necessary to clear the piezometer and the actual readings were made quickly thereafter.

The FSWT is particularly convenient for experiments of the present type because the hydrofoil and cavity are visible from both the sides and bottom. It was possible therefore to photograph simultaneously side views and bottom views to obtain the conformation of the cavity and the free surface. A light flash of about 10 microsecond duration was used for this purpose. Visual observation of the cavity under strobe illumination was also particularly interesting as it revealed under some conditions a type of resonant cavity.

#### 4. THE EXPERIMENTS.

**Variables:** Measurements of lift and drag forces were made for several tunnel speeds and at nominal submergence depths of 0.5, 1 and 2 chords beneath the undisturbed upstream water surface. The foil was set at angles of attack of 15 degrees to 25 degrees; the lowest value was chosen to ensure that ventilated cavity did not interfere or contact any part of the upper surface of the foil on the air supply and measurement tubes. These values of angle of attack are all rather large from the standpoint of desirable values of lift-drag ratio. As mentioned previously, however, they were chosen deliberately to be well into the non-linear region to provide a better measure of the theory.

It was possible to operate the tunnel up to 7.3 m/s. Because the effect of gravity is neglected in the theory it was desirable to carry out tests at the highest practicable Froude number to reduce this unwanted effect. In the present tests the maximum possible chord Froude number was 9.69 at the top tunnel speed. There were limitations in the supply of ventilating air for some combinations of test parameters and for that reason a lower tunnel speed of 4.6 m/s was used for most tests. For one set of geometric parameters the effect of Froude number on lift and drag was explored from the lowest value of Froude number, 4.04, to the highest, 9.69, but all other measurements were made at the intermediate tunnel speed of 4.6 m/s and Froude number of 6.06.

**Tares and strut interference:** The measured forces include spray and viscous drag on the supporting strut. In addition there is a mutual interference between the strut and the hydrofoil itself. The present work is intended to provide basic data on the hydrofoil only and not the entire assembly. For this reason it is necessary to obtain some estimate of the interference effect as well as the tare forces upon the strut. These tare forces could have been avoided by employing a shielded strut (see e.g., Kiceniuk 1964) but in any case the interference remains. Both of these effects were experimentally determined in the present work by attaching an image strut to the bottom of the tunnel. This image strut was used in two ways; tare forces on the strut were obtained by mounting the hydrofoil on the image strut and measuring the resultant forces on the support strut alone. Care was taken to see that the air supply and measurement tubes which bridge the gap between the supporting strut and the hydrofoil did not exert significant forces. Strut interference measurements were made by bringing up the image strut to penetrate the cavity immediately downstream of the hydrofoil. The cross section of the image strut was the same as that on the supporting strut.

The three kinds of experimental set-ups are shown schematically in Fig. 3 and a photograph of a tare

run is shown in Fig. 4. It was possible in this way to obtain drag and lift tares on the supporting strut over the range of variables. Some of these are shown in Figs. A-1 of the Appendix from which it may be seen that the effect on drag is quite significant as to be expected and the effect on lift is comparatively modest.

The effect of the image strut was always to increase the observed lift; some representative data are included in Figs. A-2, A-3 from which it is seen that the effect is greater at smaller angles of attack and for smaller submergences. These differences are not negligible being up to about ten percent on lift in the worst case. The primary effect of the image strut is to cancel the downwash of the support strut. The present method does not perfectly achieve this cancellation due to the inherent lack of symmetry of the basic flow. However, according to the calculations of Hwang (1965) the downwash effect is a local one. We therefore take the supporting-strut interference to be equal to the measured difference in forces with and without the image strut. There is a curious anomaly in the interference data seen in Fig. A-3; the normally-experienced increase in lift and drag is absent for the large angle of attack, 25 degrees and deepest submergence. Each of the data points of this figure requires a different experimental set-up. This one point is so at variance with the trend that it is tempting to dismiss it. Instead, no strut interference corrections are applied to this one case.

The experimental results which are then to be compared with the theory are first reduced to tunnel axes (from the body axes of the experiment), tare drag and lift are subtracted and the interference strut lift and drag are subtracted. In addition, an assumed laminar drag coefficient on the foil wetted surface is also subtracted; this is actually negligible in the present tests.

No corrections for any tunnel wall effect due to lift or cavity effect were made to the data.

#### 5. DISCUSSION.

**Effect of Froude Number:** The basic influence of gravity was explored only for one flow configuration, a submergence of one chord and angle of attack of 20 degrees. These data-uncorrected for strut interference-are shown in Figs. 5. Perhaps surprisingly there is not a monotone approach of lift or drag to infinite Froude number. The differences in forces observed at the test Froude number (6.06) and the highest one attained are small, about 3 percent for the lowest cavitation index, but rise to about ten percent for large values of the index. The trends of both lift and drag are very similar to the earlier results of Johnson (1957) although his aspect ratio and submergence are both smaller. A similar gravity effect on supercavitating hydrofoils has also been recently observed by Kramer (1975). We do not know the reason for this behavior and consequently have made no attempt to offer experimentally derived Froude number corrections to the present results. It would appear that further effort, experimental and theoretical, would be useful in clarifying this gravity effect in supercavitating flows.

**Lift and Drag:** Corrected lift and drag results for the hydrofoil are shown in Figs. 6-8 for the submergence values of 0.5, 1, 2 chords respectively. (All of the data points recorded are plotted on these figures.) Also shown are the results of computations based upon the recent theory already mentioned\* including an improvement to handle

\* Furuya loc cit.

the case of small cavitation index (Furuya 1975c). There are several interesting trends of these results. Both theory and experiment show the familiar trend to lower lift coefficients as the submergence increases. The theory gives (by construction) a lift-drag ratio of  $\cot \alpha$  for the present flat plate hydrofoil.\* The experimental measurements do not quite agree with this reference value. For the two smaller submergences and angles of attack of 15 and 20 degrees, the experimental results indicate that the resultant hydrodynamic force is within a percent or so of being normal to the wetted surface of the hydrofoil which is considered quite satisfactory. This internal consistency of the experimental results is not so good at the largest angle of attack nor for the deepest submergence of two chords. In this case discrepancies up to 6 percent (with a systematic trend to values of  $L/D$ ) lower than  $\cot \alpha$  are seen in a few cases. The reasons for this behavior are unknown and point out the difficulty of measuring tare forces accurately.

In general the agreement with the prediction method and experiment is quite satisfactory, particularly for a submergence of 0.5 chords (Figs 6a, b). The lift coefficient is seen to be reasonably close but somewhat smaller to that calculated. There appears to be a systematic trend for the lift to increase faster with cavitation number than indicated by the theory. This is more evident at the deeper submergences where it appears that the theory overestimates lift force by about 7 percent at an angle of attack of 25 degrees. Both lift and drag seem very well represented by the theory for an angle of attack of 15 degrees; drag, if anything, seems better predicted than lift although with the present experiment on a flat profile that can only be coincidental.

A similar comparison of theory with the experiments of Schiebe & Wetzel (1961) was carried out by Furuya (1975b). The experimental planform was rectangular in this case; the aspect ratio was varied from 2.5 to 6 and the submergence was varied from 1 to 2 chords. The experimental trends are much the same as in the present work but for smaller values of angle of attack. These trends are well predicted by the computations even for the lowest aspect ratio. But as in the present work there is a tendency for lift to be overestimated somewhat for the largest angles of attack (16.5 and 20 degrees). A strut induced downwash effect was no doubt present in the Schiebe & Wetzel experimental results even with the slender strut used but no direct account of this effect has been made.

It appears from these comparisons of experiment with theory and the present ones of Figs. 6-8 that the non-linear calculation procedure offers a good predictive technique on flat plate foils for angles of attack up to about 20 degrees. There are limitations, however, in both theory and experiment. Gravitational effects on the present type of flow need to be clarified for test Froude numbers less than about ten if experimental results are to be used for comparison to gravity-free computations to within a few percent. The method of computation referred to (Furuya 1975b) assumes the relevant characteristic dimension of importance to be the span; the

submergence and cavity length are therefore, to be scaled to the chord so that a lifting line becomes the correct physical approximation in the outer flow as the aspect ratio becomes large. But in the present experiments the submergence of two chords is one-half the span and for those of Schiebe & Wetzel the submergence and span are nearly equal for the lowest aspect ratio tested. In addition, the length of the experimental cavities for the lower cavitation numbers is also comparable to the span. It is thus seen that the experiments do not closely conform to the requirements needed for the theory to be strictly valid. Perhaps departures from these requirements have only a weak effect on the resulting overall forces. In any case, the prediction method of Furuya should work best for a small submergence and cavitation numbers such that the resultant cavities are shorter than the span. This appears to be the case as can be seen in Fig. 6.

**Cavity Parameters:** The shape and planform of the cavity is shown in Fig. 9 for a submergence of two chords; in the first of these the cavity is quite short and it coincides roughly with the transition to partial cavitation. The re-entrant jet at the terminus of the cavity may occasionally wet the end of the foil. This condition more or less corresponds to peak of the lift coefficient seen in Fig. 8a. The length of the cavity increases with decreasing cavitation number, and in the present experiments, resulted in the unstable pulsating cavity seen in Fig. 9d.

It is always of interest to know the amount of air required to establish the ventilation flow rate. In the present work the required mass flow of gas is normalized by the mass flow of water passing through the projected frontal area of the foil. As can be seen in Fig. 10 this normalizes the data well\*. Also marked on this diagram is the start of resonant cavity pulsations which for the present tests had a frequency of about 45 Hz. This interesting feature of some ventilated tests was first described by Silberman & Song (1959), Song (1961), Hsu & Chen (1962) and more recently by Scheibe & Wetzel (1964).

The cavity length and shape are also of interest. From photographs of the type seen in Fig. 9, the planform of the cavity can be scaled to the chord. Two such examples together with predictions made with the previously mentioned calculation are shown in Fig. 11. The agreement is very good.

**ACKNOWLEDGMENT:** We thank Mr. Tom Ward of the Hydrodynamics Laboratory at the California Institute of Technology for his assistance in running the experiments and Mr. Robert Higley for his help in data reduction and computer plotting. This work was supported by the Naval Ship Systems Command General Hydrodynamics Research Program, technically administered by the Naval Ship Research and Development Center under Contract N00014-75-C-0430.

\* The computations of Furuya show satisfactory agreement in this respect except for the large angle of attack. The lift in this case is a little low indicating incomplete convergence of the iterations. The drag computations are to be preferred in this case.

\* This may be converted to the more usual volumetric flow rate coefficient by multiplying the present results by 832.



## APPENDIX:

**A.1. Tare Force Data.** Typical examples of the tare forces on the supporting strut are shown in Figs. A-1. Measurements were also made for angles of attack of 15 degrees and 25 degrees but are not shown. The submergence depths in these measurements are somewhat different from data runs due to the limitation of adjustment in the image strut height; those are one chord at angle of attack of 15 degrees, 0.46, .077 and 1.63 chords at 20 degrees and 0.78 chords at 25 degrees. For each tare run, measurements were made over a complete range of cavitation numbers (from the shortest cavity before it reaches the end of annex to the longest cavity available with the present air supply system). Linear extrapolation and interpolations were made to obtain tare lift and drag forces  $\Delta C_{LT}$  and  $\Delta C_{DT}$  for general conditions by the formulas

$$\Delta C_{LT} = \Delta C_{LTO} + f_{LT\alpha}(\alpha - \alpha_0) + f_{LT h}(h - h_0) + f_{LT\sigma}(\sigma - \sigma_0)$$

$$\Delta C_{DT} = \Delta C_{DTO} + f_{DT\alpha}(\alpha - \alpha_0) + f_{DT h}(h - h_0) + f_{DT\sigma}(\sigma - \sigma_0)$$

where  $\Delta C_{LTO}$  and  $\Delta C_{DTO}$  are the tare lift and drag at a certain angle of attack, submergence depth and cavitation number,  $\alpha_0$ ,  $h_0$ , and  $\sigma_0$  respectively. In the present corrections 20 degrees, one chord and 0.12 were chosen for  $\alpha_0$ ,  $h_0$  and  $\sigma_0$  respectively.  $f_{LT\alpha}$  in these expressions, for example, is a function obtained by curve fitting of the measured tare lift as a function of angle of attack with the submergence and cavitation number kept constant. It is therefore noted that  $f_{LT\alpha}$ , are zero at  $\alpha_0$ ,  $h_0$  and  $\sigma_0$ . These data are decomposed into those in parallel to and normal to the flow direction and subtracted from also decomposed raw data.

**A.2. Supporting Strut Correction Data.** Fig. A-2 shows a typical example of the lift and drag forces with and without the image strut. It is clearly seen that the flow simulating no strut condition gives higher lift and drag forces than that with the supporting strut.

The effect of the image strut as a function of submergence is shown in Fig. A-3. In most cases the comparison again shows that the data with the image strut gives higher  $C_L$  and  $C_D$  values than those without the image strut except for an angle of attack of 25 degrees and submergence depth of 1.6 chords. This is only one data point which is inconsistent from others in the present experiment. The tare forces on the strut are measured (of necessity) in the presence of the image strut and so are not precisely those of the actual experiment. The difference is believed to be very slight.

It must be mentioned that the data points of the strut correction measurements are also different from those of data run. Particularly, the submergence depths were set at 0.58, 0.9 and 1.76 chords, for angle of attack of 15 degrees, 0.5, 0.76, 1.68 for 20 degrees and 0.41, 0.71, 1.62 for 25 degrees. The correction for the strut was thus made exactly in the same way as done for the tare forces. After decomposition, these data are also subtracted from the raw data.

## REFERENCES

1. Acosta, A. J., 1973, "Hydrofoils and Hydrofoil Craft," *Ann. Rev. Fl. Mech.*, **5**, pp. 161-184.
2. Altmann, R., 1968, "The Design of Supercavitating Hydrofoil Wings," *Hydronautics Inc. Rep. TR-001-14*.
3. Baker, E. S., 1975, "Design of Hydrofoil Model TAP-2," *Nav. Ship Res. and Dev. Ctr.*, Bethesda, Md., Rep. SPD-575-03.
4. Barker, S. J., Ward, T. M., 1975, "Experiments on a Cavitating Hydrofoil Fitted with Flaps in Two and Three Dimensional Flow," *Calif. Inst. Tech.*, Pasadena, Calif., Div. of Eng. and App. Sci., Galtit Rep. 1120.
5. Furuya, O., 1975a, "Non-linear Calculation of Arbitrarily Shaped Supercavitating Hydrofoils near a Free Surface," *J. of Fl. Mech.*, **68**, part 1, pp. 21-40.
6. Furuya, O., 1975b, "Three-Dimensional Theory of Supercavitating Hydrofoils near a Free Surface," *J. of Fl. Mech.*, **71**, part 2, pp. 339-359.
7. Furuya, O., 1975c, "Numerical Procedures for the Solution of Two-Dimensional Supercavitating Flows Near a Free Surface," *Proceedings, First Conference on Numerical Ship Hydrodynamics*, *MD, USA*, October, 1975.
8. Holling, H. D., 1975, "Takeoff Experiments for a Newly Designed High Speed Super Cavitating Hydrofoil (TAP-1) *Nav. Ship and Res. Dev. Ctr.*, Bethesda, Md., Rep. SPD-575-02.
9. Hsu, C. C., 1975, "Some Remarks on the Progress of Cavity Flows," *Parkin, B. R., Morgan, W. B. (eds.) Symp. "Cavity Flows"* *A.S.M.E.*, Minneapolis, Minnesota, pp. 43-56.
10. Hsu, C. C., Chen, C. F., 1962, "On the Pulsation of Finite, Ventilated Cavities," *Hydronautics, Inc.*, Tech. Rep. 115-4.
11. Hwang, T. T., 1965, "Strut Induced Downwash," *Hydronautics, Inc.*, Tech. Rep. 463-7.
12. Johnson, V. E., 1957, "Theoretical and Experimental Investigation of Supercavitating Hydrofoils Operating Near the Free Water Surface," *N.A.S.A. Langley Res. Ctr.*, Tech. Rep. R-93.
13. Kermeen, R. W., 1961, "Experimental Investigations of Three-Dimensional Effects on Cavitating Hydrofoils," *J. Ship Res.*, **5**, 2, pp. 22-43.
14. Kiceinuk, T., 1964, "Superventilated Flow Past Delta Wings," *Calif. Inst. of Tech.*, *Hydrodynamics Lab. Rep. No. E-101.5*.
15. Kramer, R. L., 1975, "Performance of N.S.R.D.C. Tap-1 and Tap-2 Hydrofoil Models," *Lockheed Missiles and Space Div. Tech. Memo 5724-75-46*.
16. Leehey, P., Stelling, T. S., 1975, "Force and Moment Measurements of Supercavitating Hydrofoils of Finite Span with Comparisons to Theory," *Cavity Flows*, *Parkin, B. R., Morgan, W. B. (eds.)*, *A.S.M.E. Symp. May 5-7, Minneapolis, Minnesota*.
17. Ogilvie, T. F., 1970, "Singular Perturbation Problems in Ship Hydrodynamics," in *Eighth Symposium on Naval Hydrodynamics*, *ACR-179 Office of Nav. Res.*, Plesset, M.S., Wu, T. Y., Doroff, S. (eds.), pp. 663-806.
18. Schiebe, F. R., and Wetzel, J. M., 1961, "Ventilated Cavities on Submerged Three-Dimensional Hydrofoils," *University of Minnesota, St. Anthony Falls Hydraulic Lab.*
19. Schiebe, F. R. & Wetzel, J. M., "Further Studies of Ventilated Cavities on Submerged Bodies," *University of Minnesota, St. Anthony Falls Hydraulic Laboratory, Project Report No. 72, 1964*.
20. Shen, Y., 1973, "Non-Linear Theory for Supercavitating Hydrofoil of Finite-Span Near a Free Surface," *Div. of Eng. and Appl. Sci.*, *Calif. Inst. of Tech.* (unpubl.)



21. Shen, Y. T., and Ogilvie, T. F., 1972, "Non-Linear Hydrodynamic Theory for Finite-Space Planning Surfaces," *J. Ship Res.*, 16, 1, pp. 3-21.
22. Silberman, E., and Song, C. S., 1959, "Instability of Ventilated Cavities," University of Minnesota, St. Anthony Falls Hydraulic Lab., Tech. Rep. No. 29, Series B.
23. Song, C. S., 1961, "Pulsation of Ventilated Cavities," University of Minnesota, St. Anthony Falls Hydraulic Lab., Tech. Paper No. 32, Series B.
24. Tsen, L. F., Guilband, M., 1974, "Theoretical and Experimental Study on the Planform of Superventilated Wings," *J. Ship Res.*, 18, 3, pp. 169-184.
25. Wang, D. P., Shen, Y., 1975, "A Validation Study of the Mixed Foil Concept for High Speed Hydrofoils," *J. Ship Res.*, -in press.
26. Wu, T. Y., Wang, D. P., 1964, "A Wake Model for Free-Streamline Flow Theory, Part 2, Cavity Flows Past Obstacles of Arbitrary Profile," *J. of Fl. Mech.*, 18, pp. 65-93.

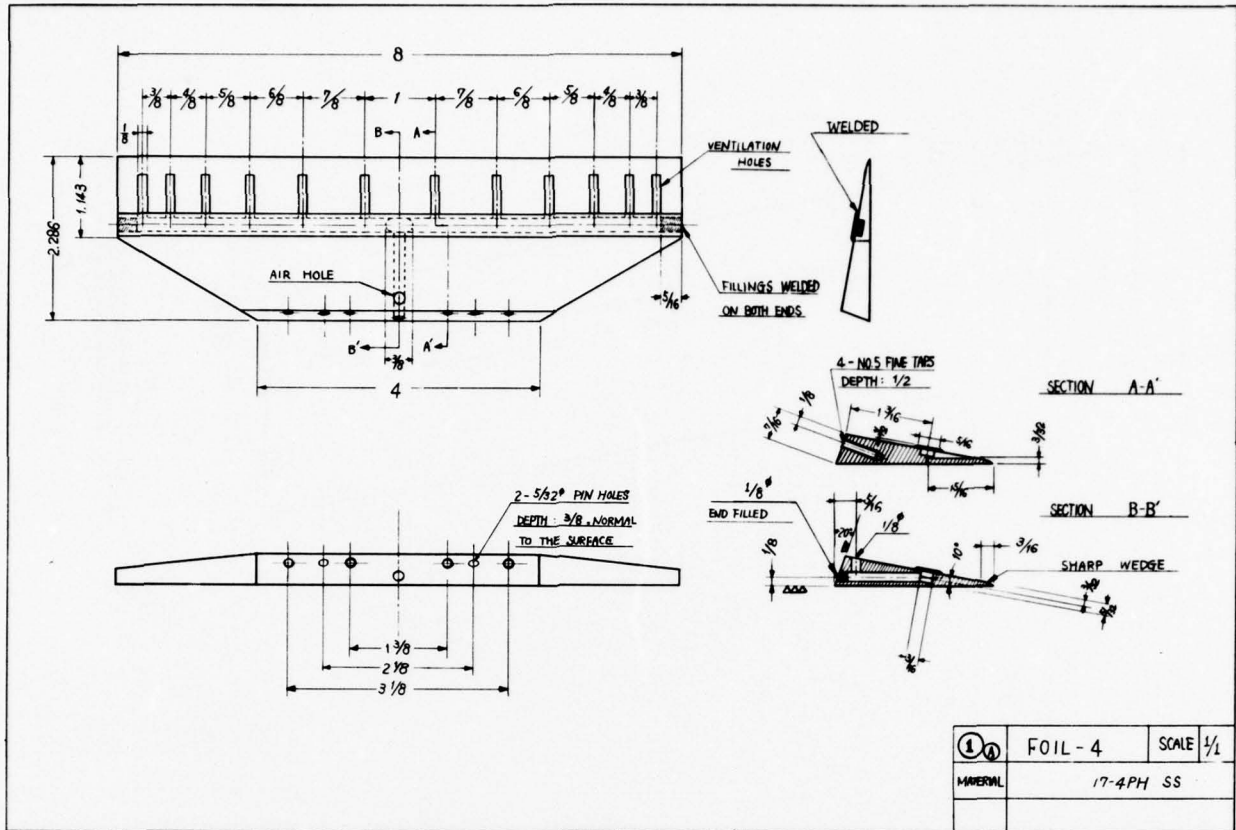


Fig. 1: (a)

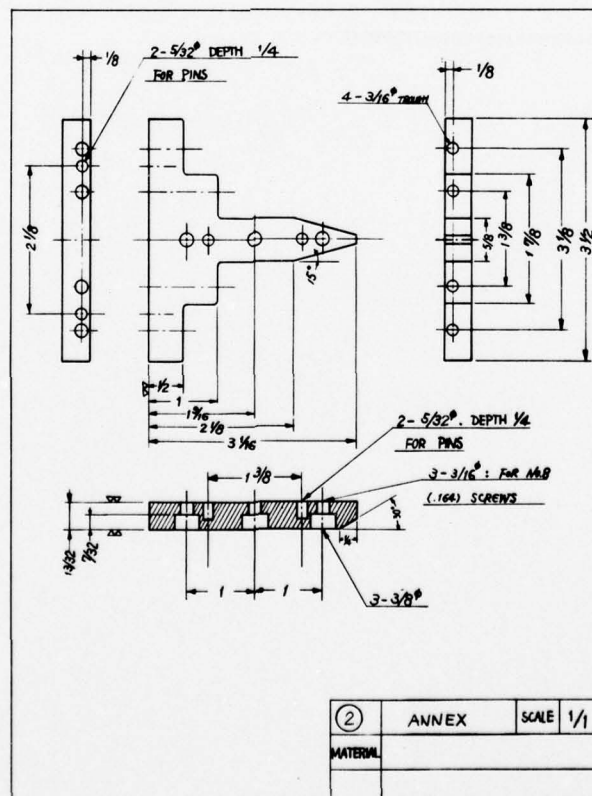


Fig. 1: (b)

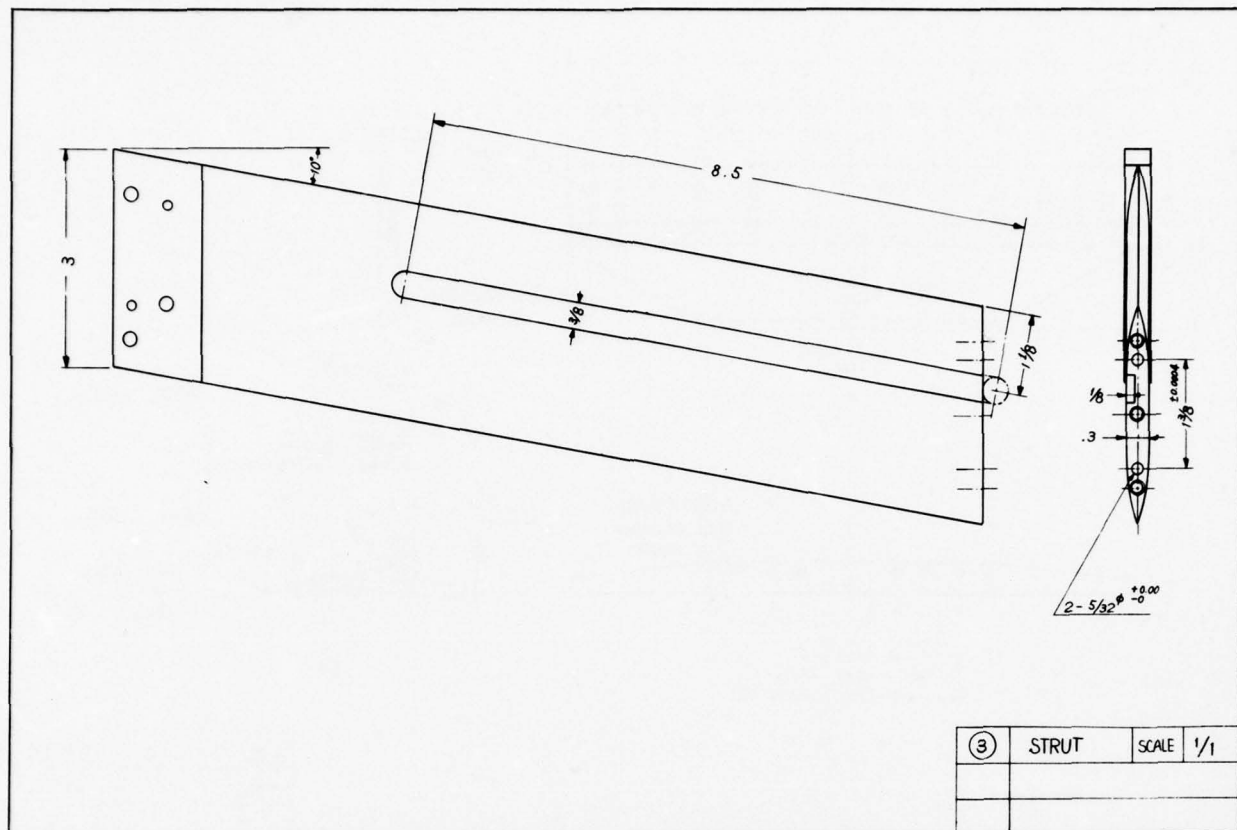


Fig. 1: (c)

Fig. 1: Design details: (a) foil, (b) annex, (c) support strut



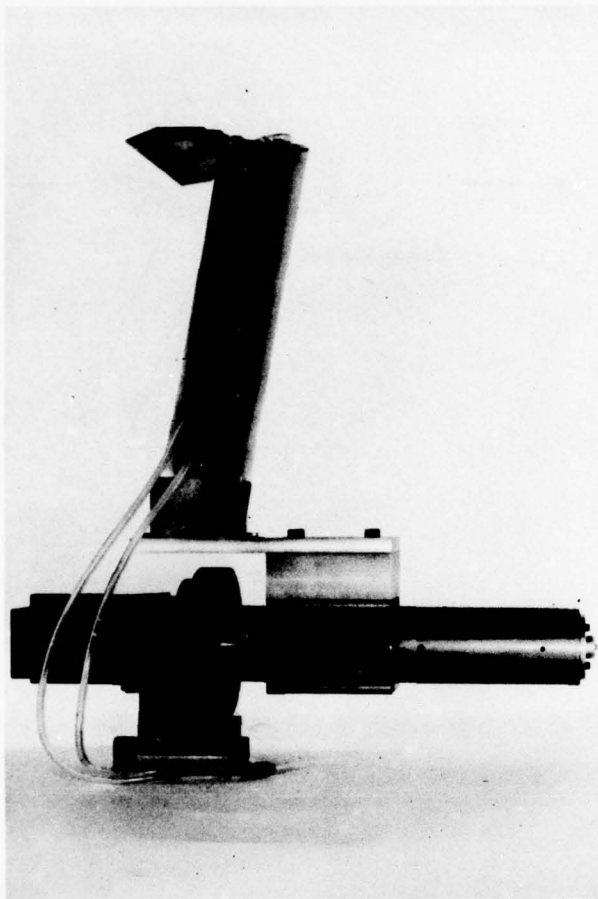


Fig. 2: (a)

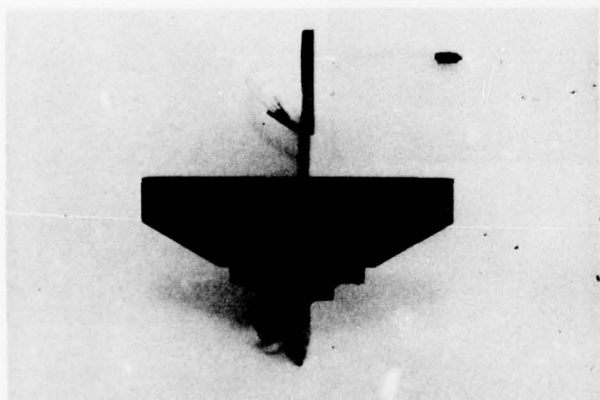


Fig. 2: (b)

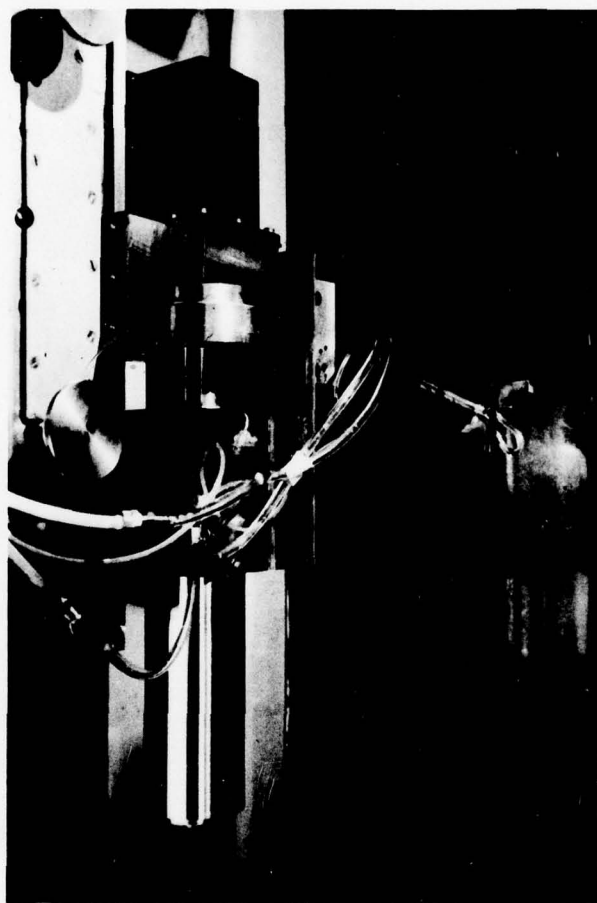


Fig. 2: (c)

Fig. 2: Photographs of the strut-hydrofoil assembly:  
 (a) side view with force balance  
 (b) view showing the lower wetted surface of the foil and  
 (c) photograph from above the strut and force balance assembly mounted in the water tunnel.

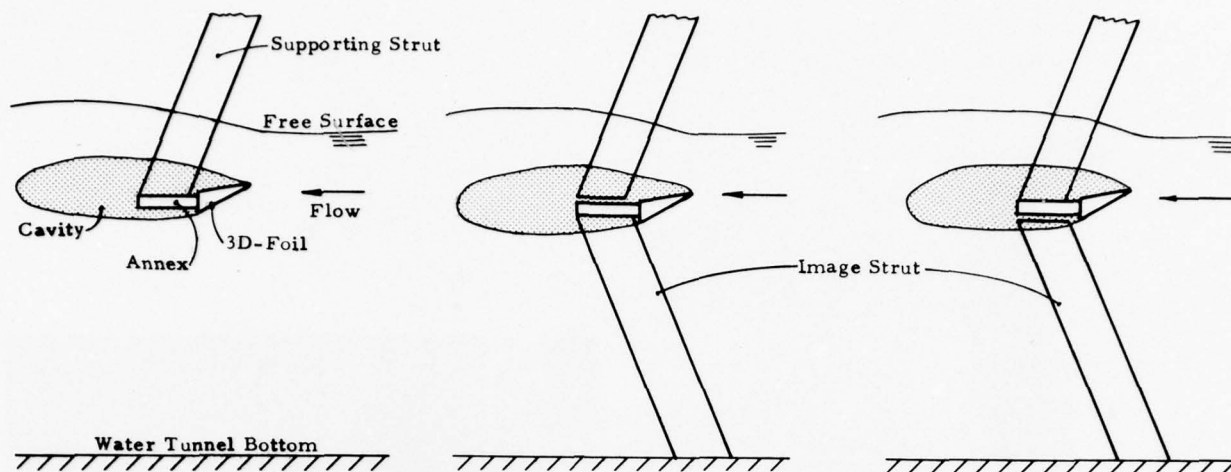


Fig. 3: Schematic diagram showing the experimental set-ups used for  
 (a) data run  
 (b) tare run and  
 (c) strut correction run.

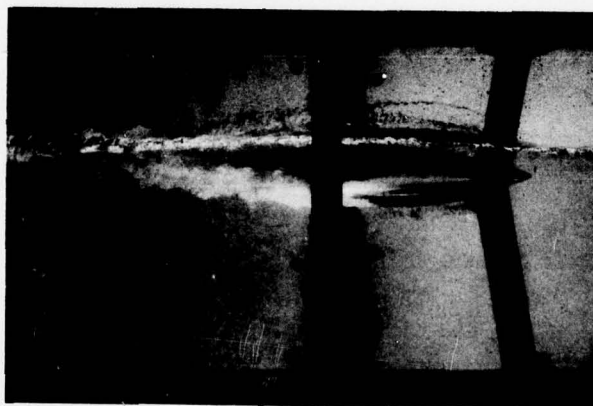


Fig. 4: Photograph showing a tare-run in which the foil is attached to the image strut and tare forces are measured on the supporting strut.

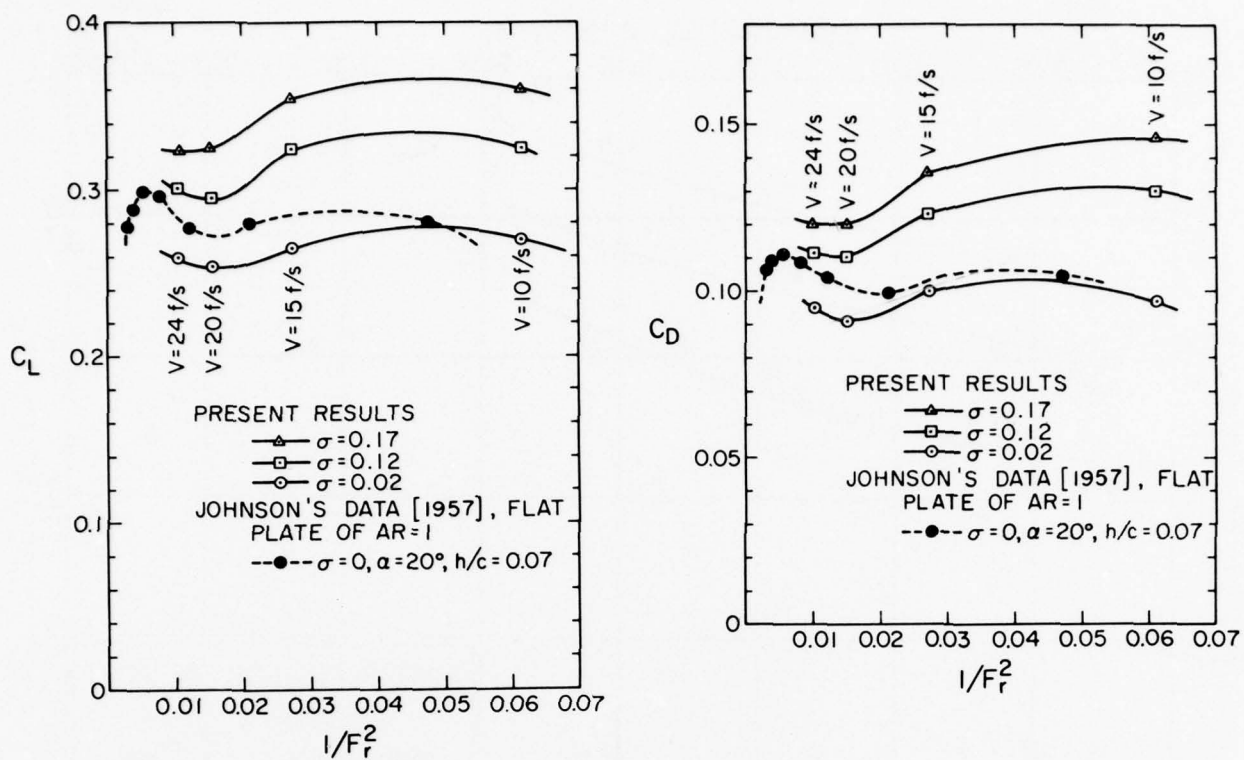


Fig. 5: Effect of the Froude number on  
(a) lift coefficient  $C_L$  and  
(b) drag coefficient  $C_D$  for a submergence depth  
of one chord and an angle of attack of 20 degrees.



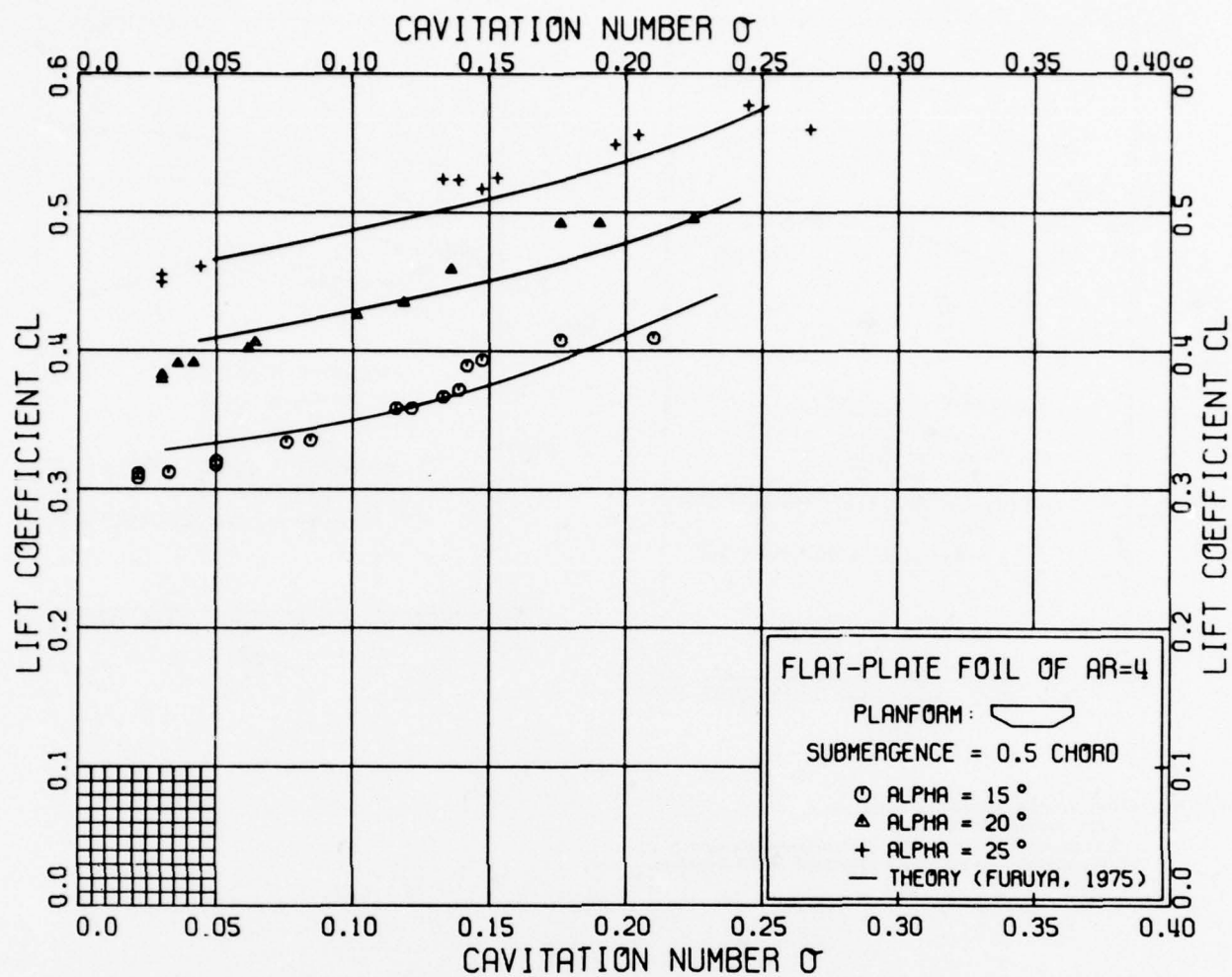


Fig. 6: (a)

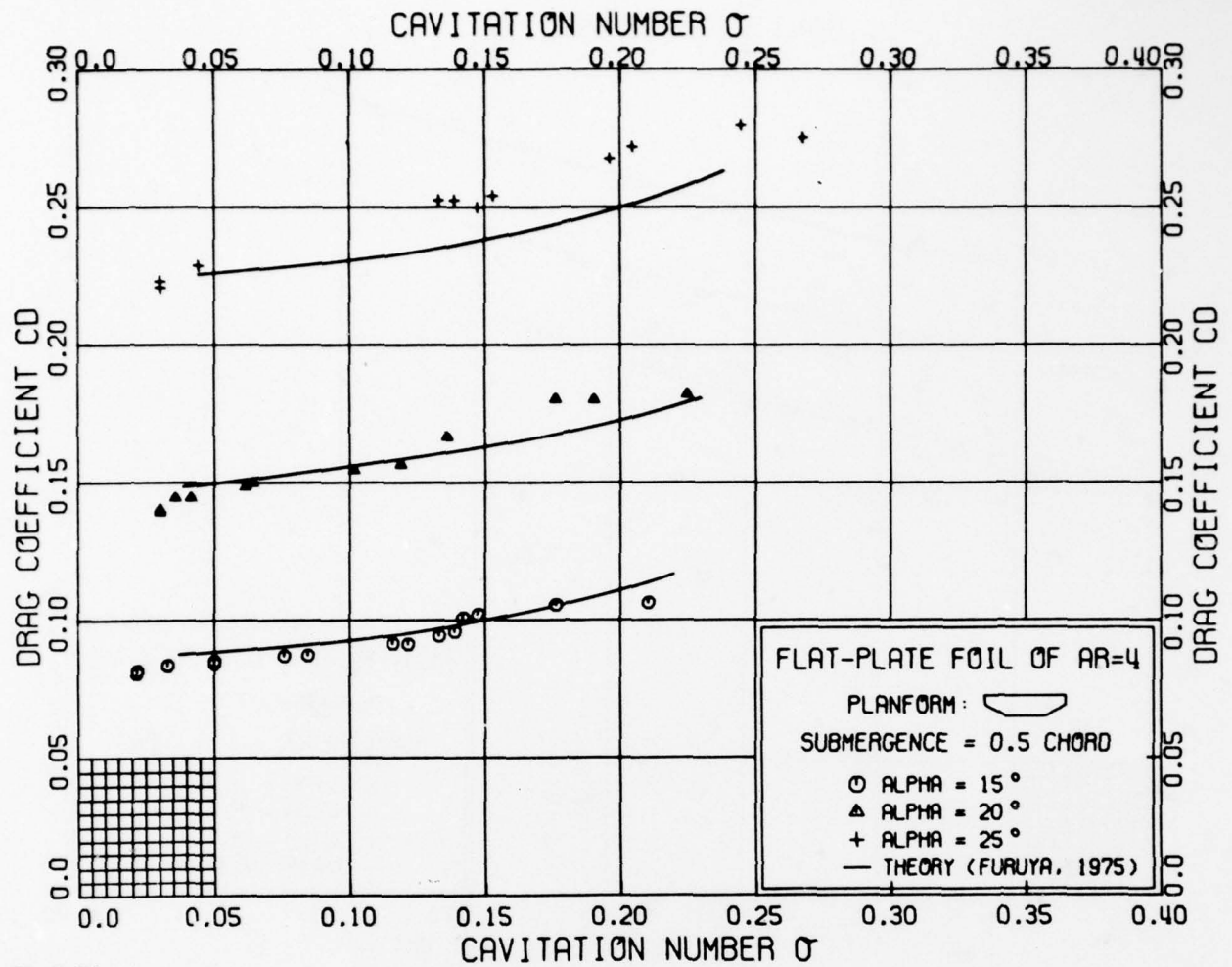


Fig. 6: (b)

Fig. 6: Lift and drag coefficients at a submergence depth of 0.5 chord in comparison with the theory of Furuya (1975b). The chord Froude number is 6.06.

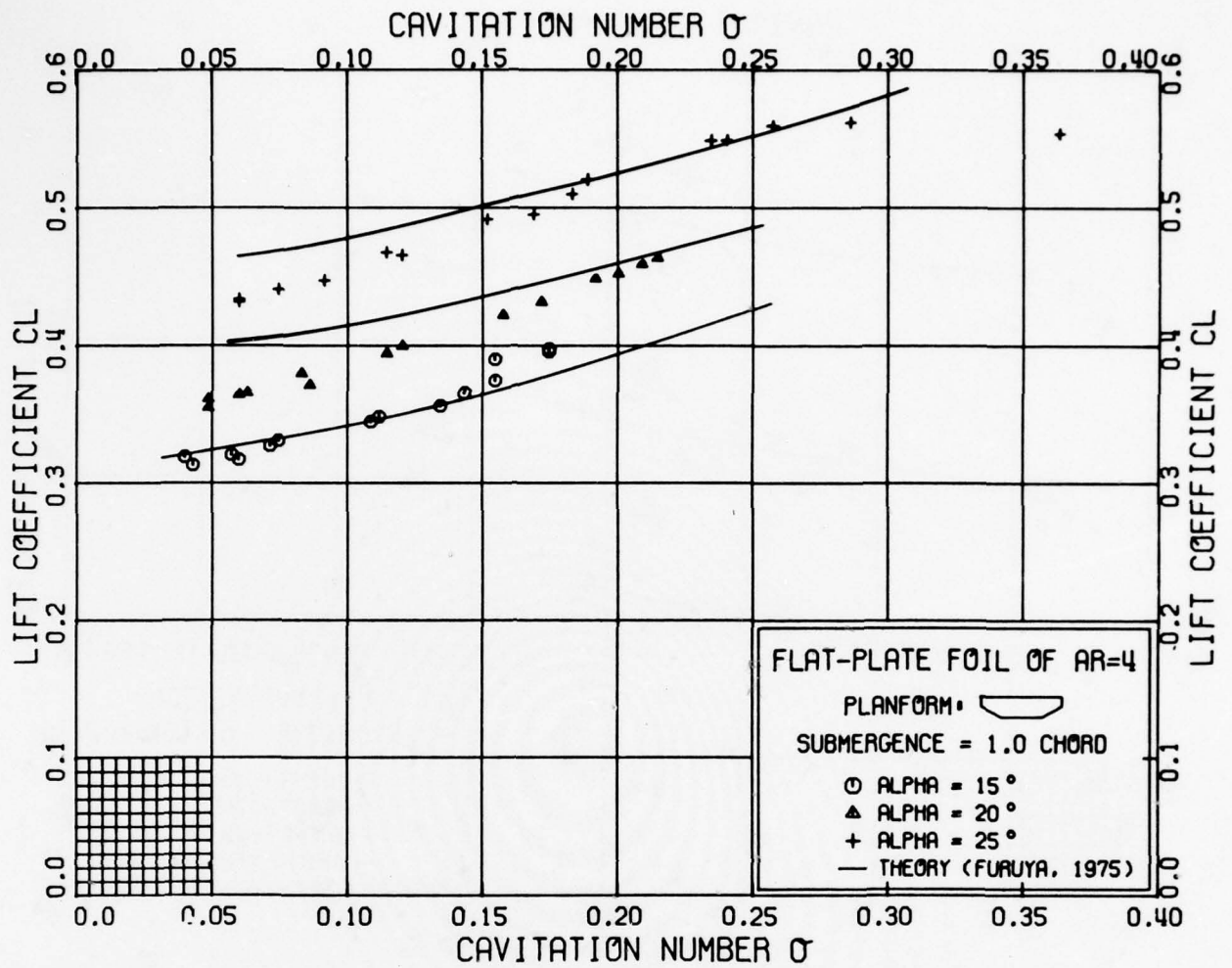


Fig. 7: (a)



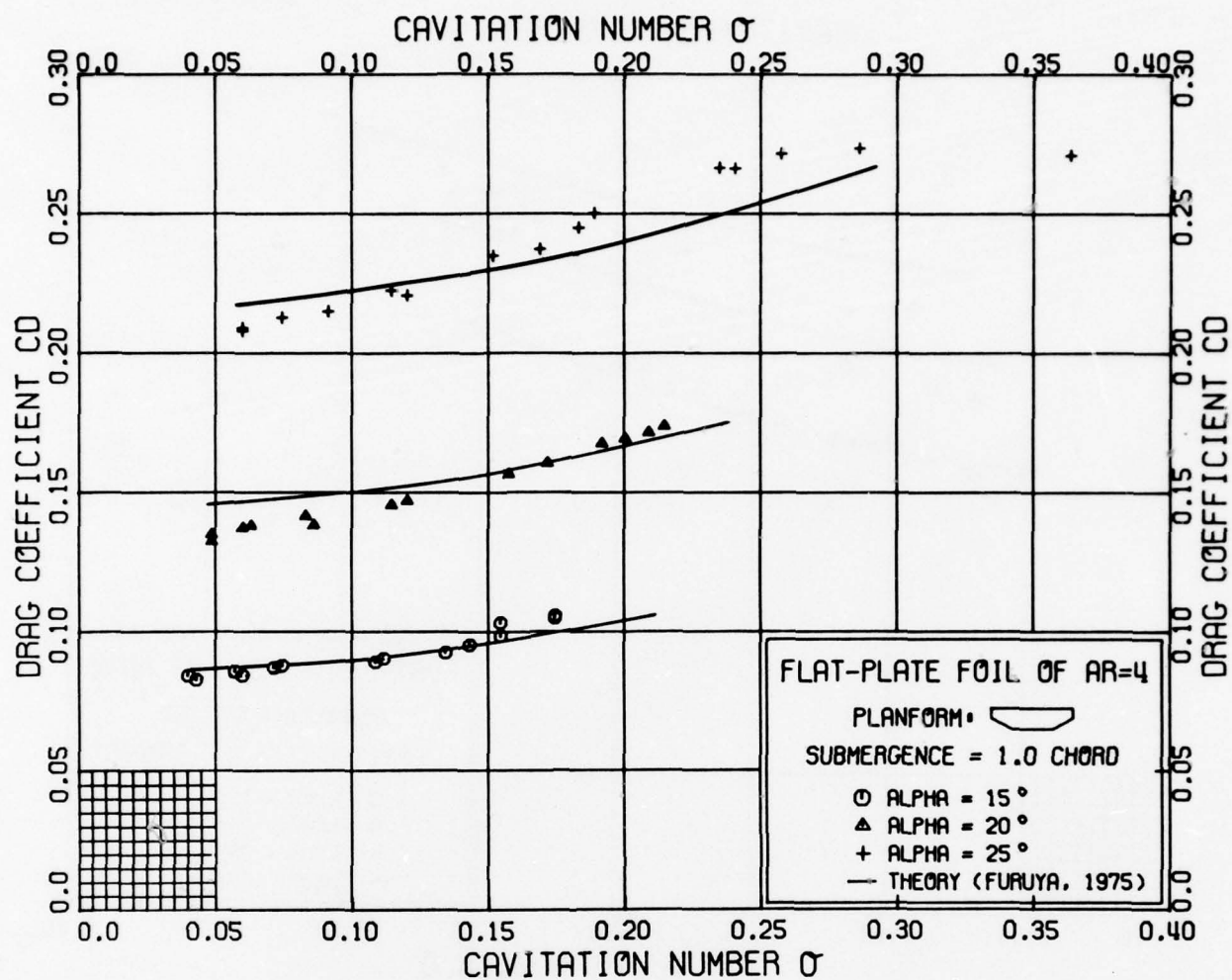


Fig. 7: (b)

Fig. 7: Lift and drag coefficients at submergence depth of one chord in comparison with the theory of Furuya (1975b). The chord Froude number is 6.06.

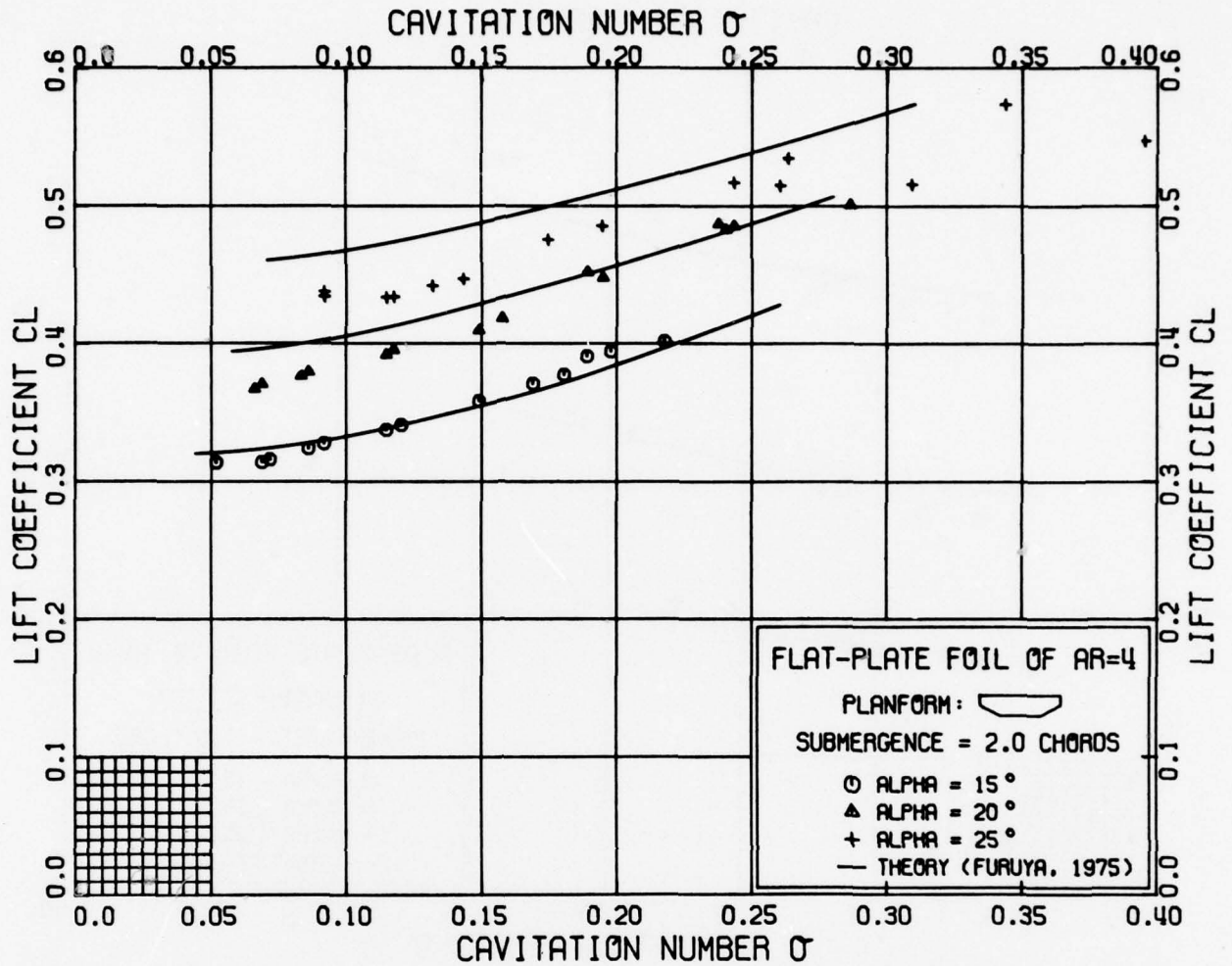


Fig. 8: (a)

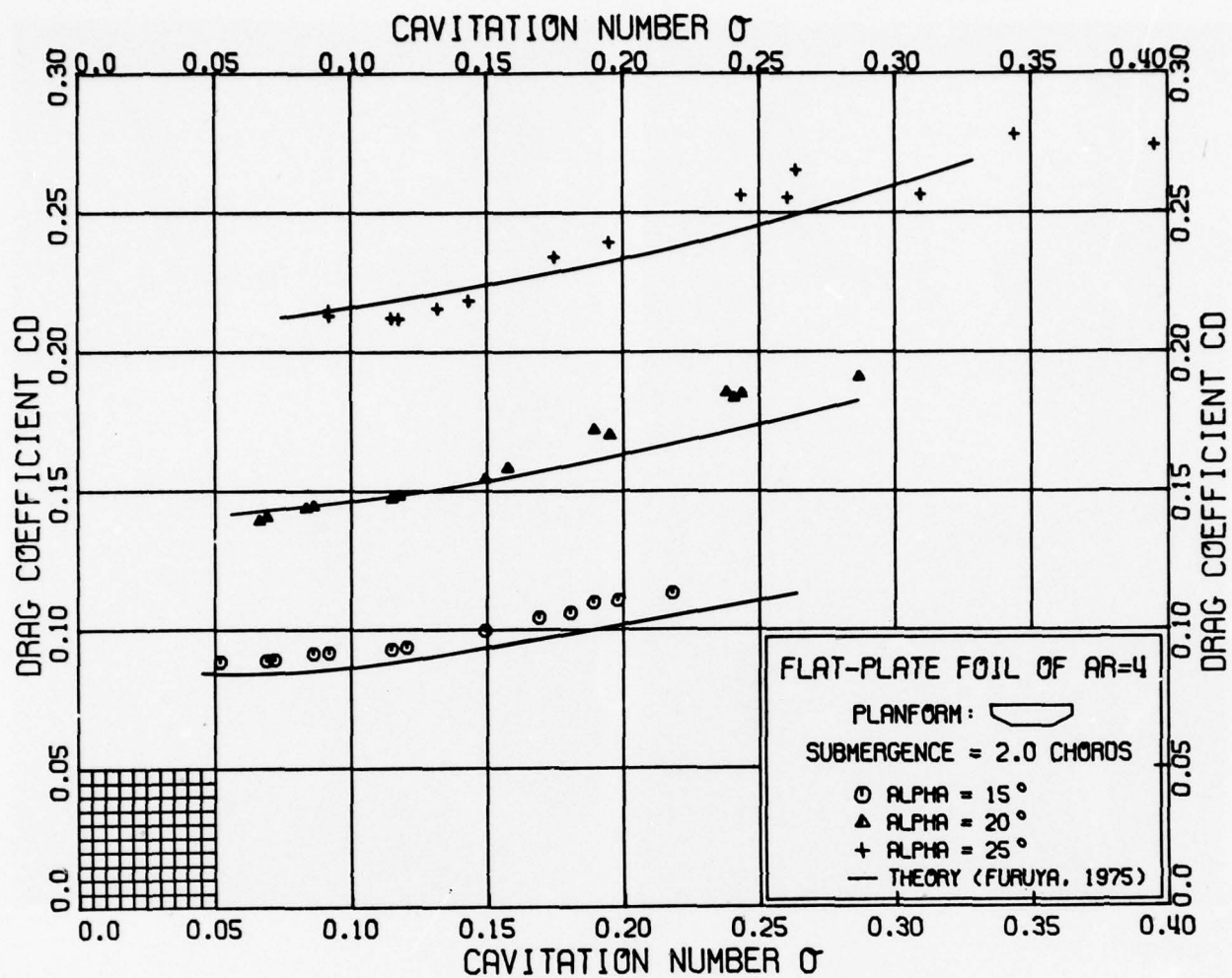


Fig. 8: (b)

Fig. 8: Lift and drag coefficients at submergence depth of two chords in comparison with the theory of Furuya (1975b). The chord Froude number is 6.06.



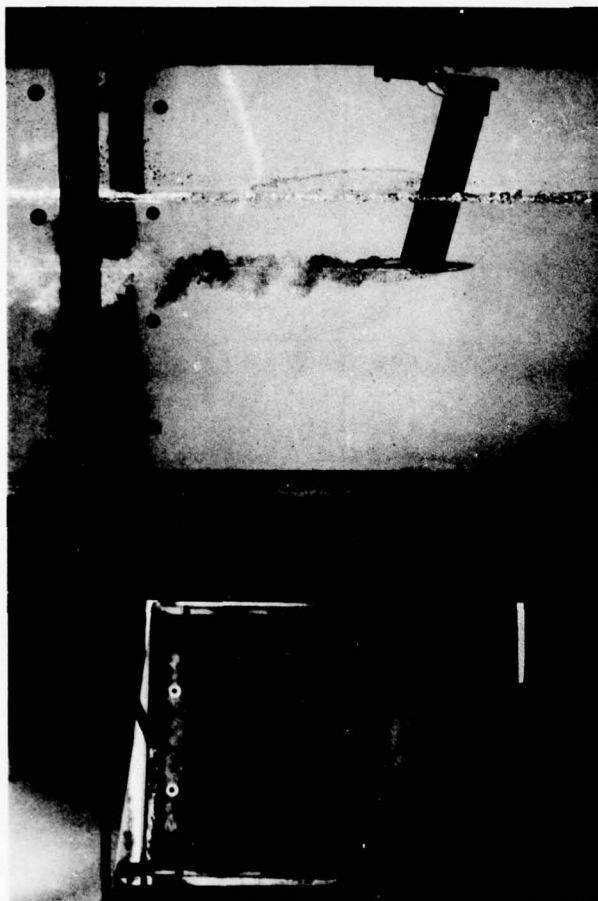


Fig. 9: (a)

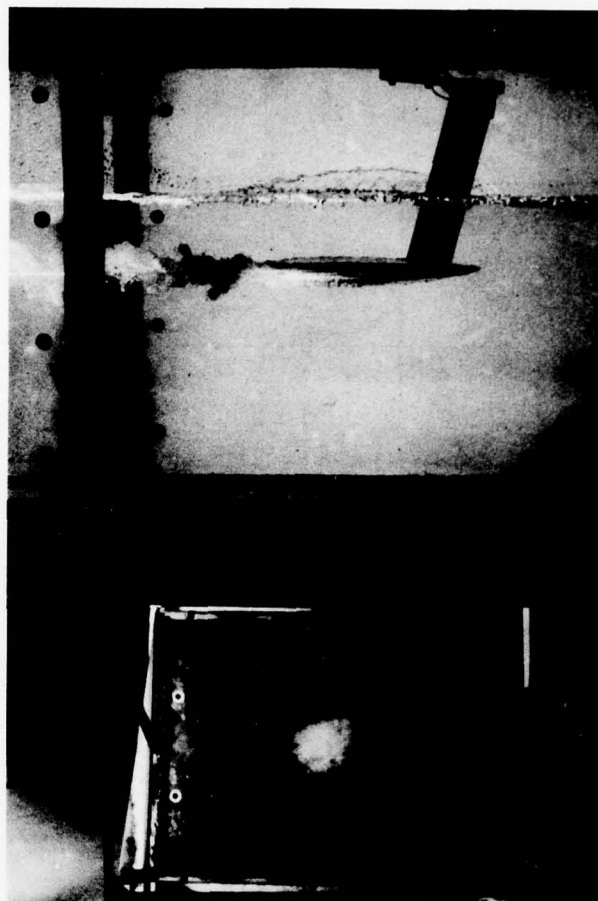


Fig. 9: (b)

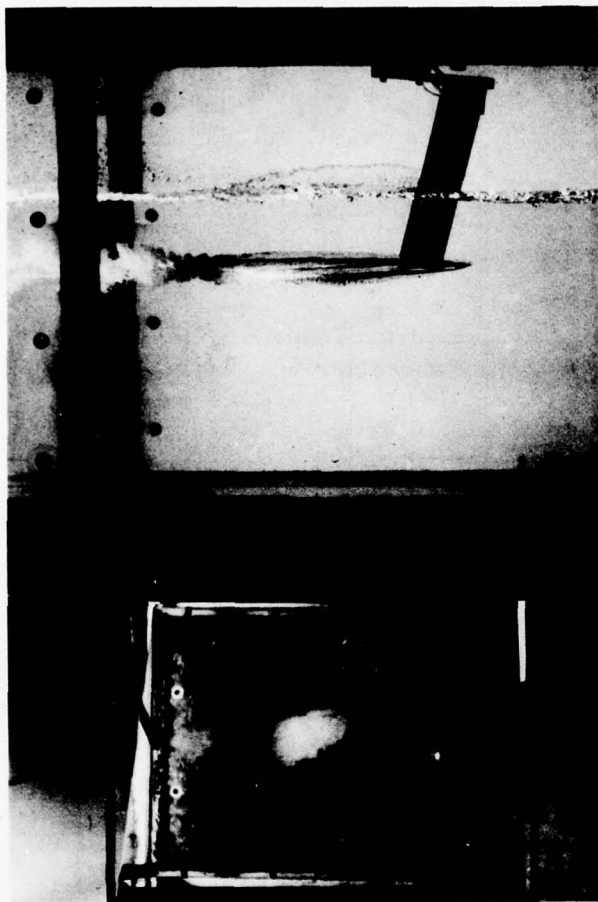


Fig. 9: (c)

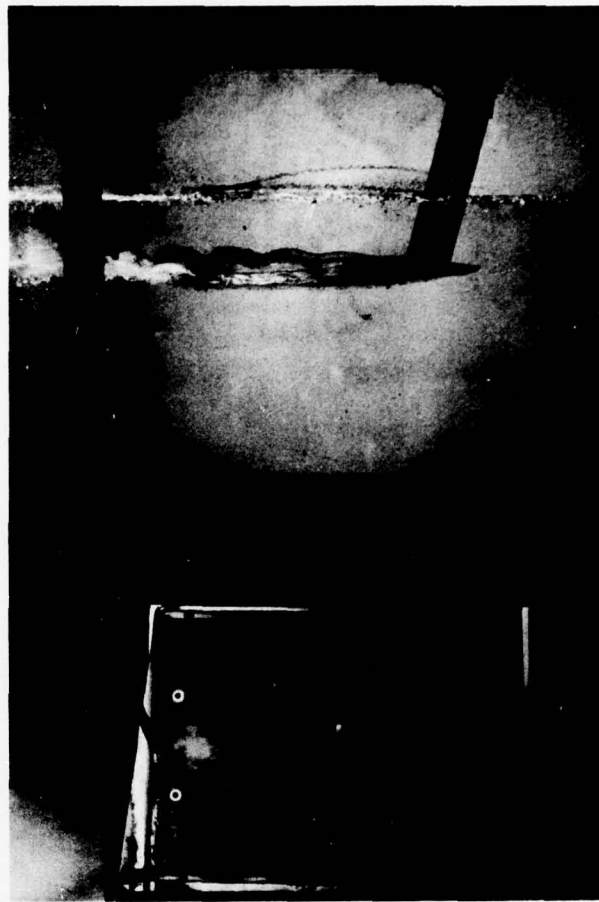


Fig. 9: (d)

Fig. 9: A sequential set of photographs with change of cavitation number sigma for an angle of attack of 15 degrees and submergence depth of two chords at a tunnel velocity of 15 feet per second;  
 (a)  $\sigma = 0.218$ , (b)  $\sigma = 0.115$ , (c)  $\sigma = 0.086$ ,  
 (d)  $\sigma = 0.069$ .

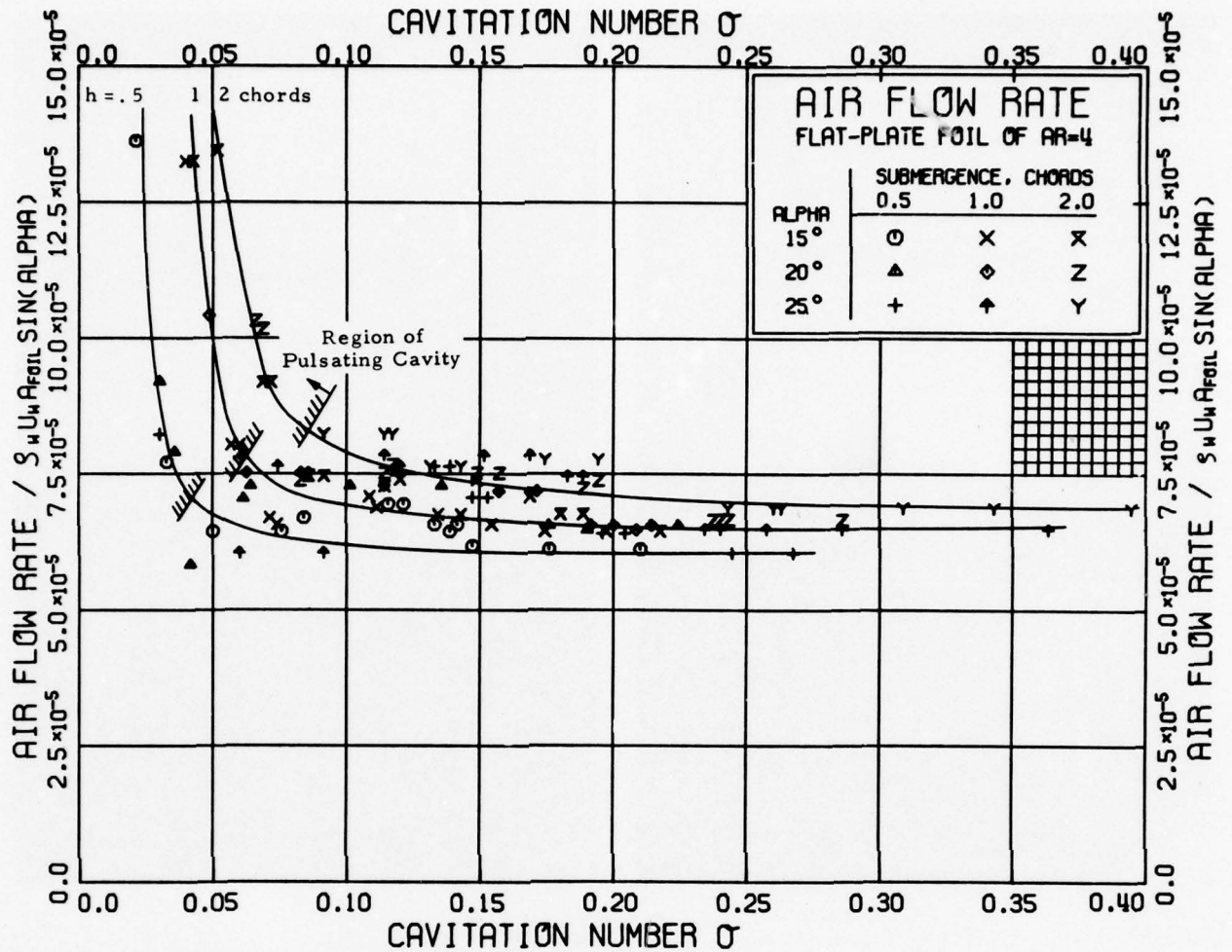


Fig. 10: Normalized air mass flow rate versus cavitation number for a chord Froude number of 6.06. The boundary of the occurrence of cavity pulsation is indicated.

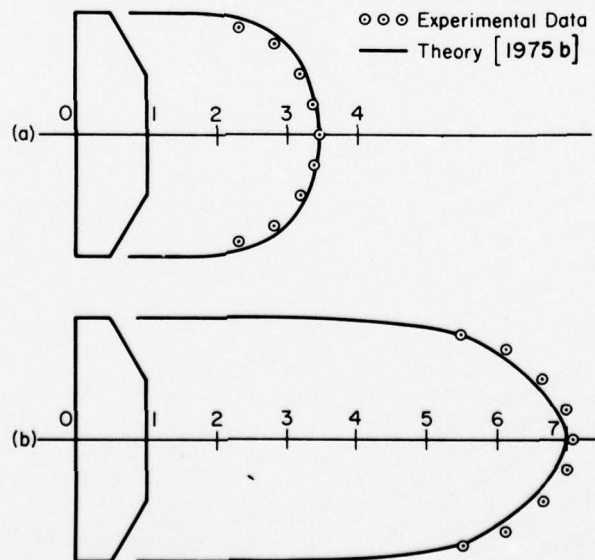


Fig. 11: Spanwise distributions of cavity length at an angle of attack of 15 degrees, one chord submergence and chord Froude number of 6.06. In (a) the cavitation index is 0.13 and in (b) it is 0.072.



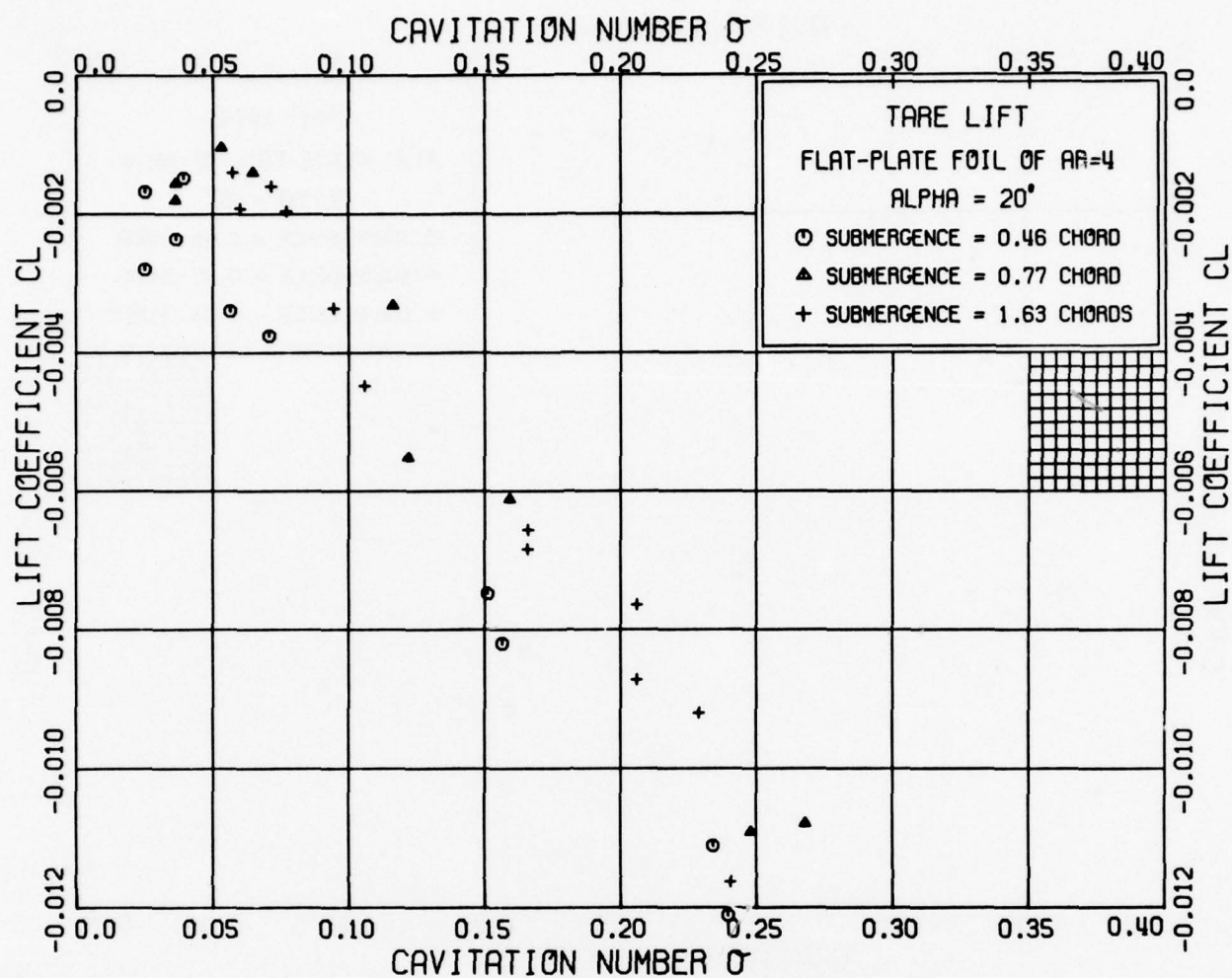


Fig. A-1: (a)

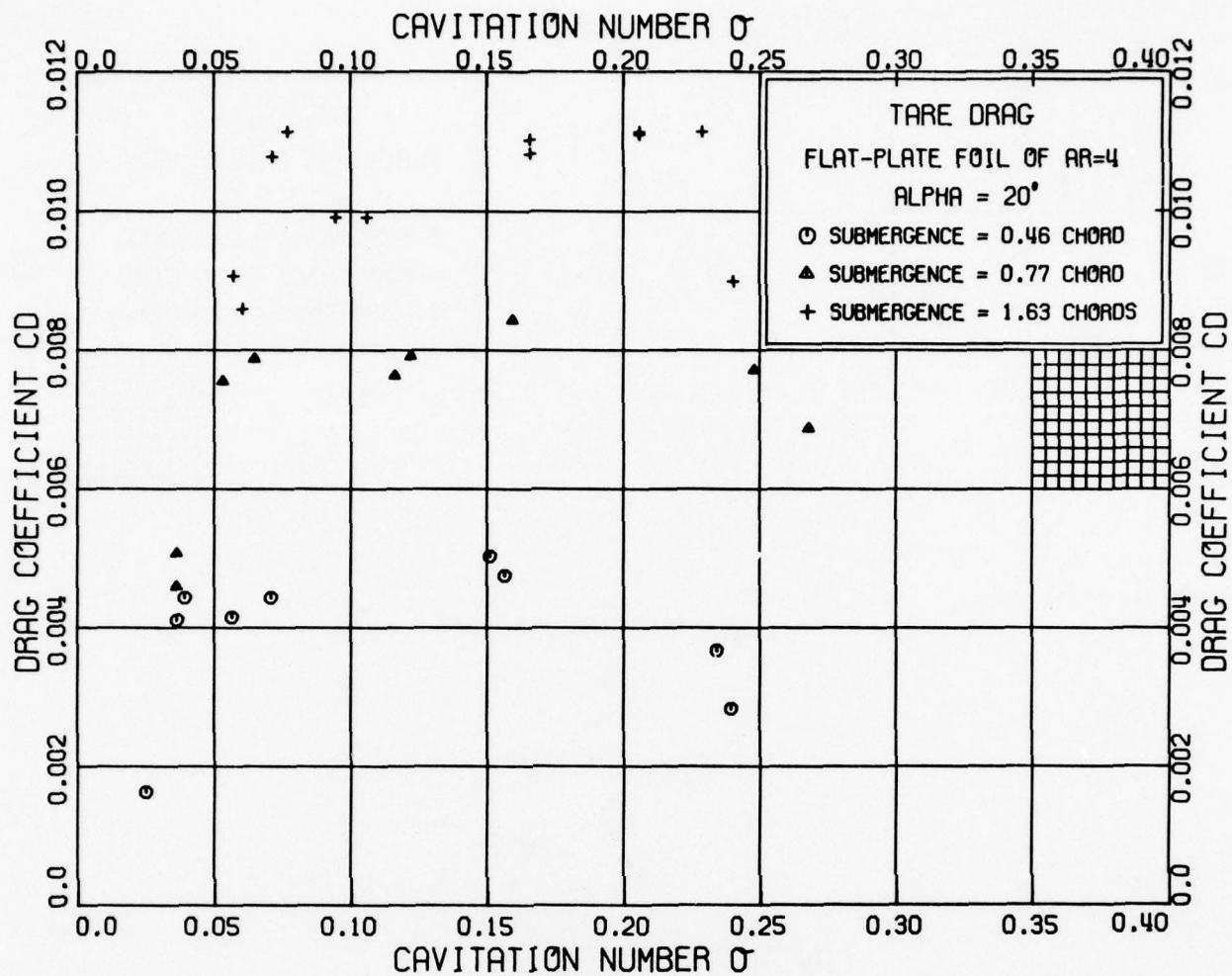


Fig. A-1: (b)

Fig. A-1: Typical tare forces on the supporting strut at an angle of attack of 20 degrees; (a) tare lift coefficient and (b) tare drag coefficient.

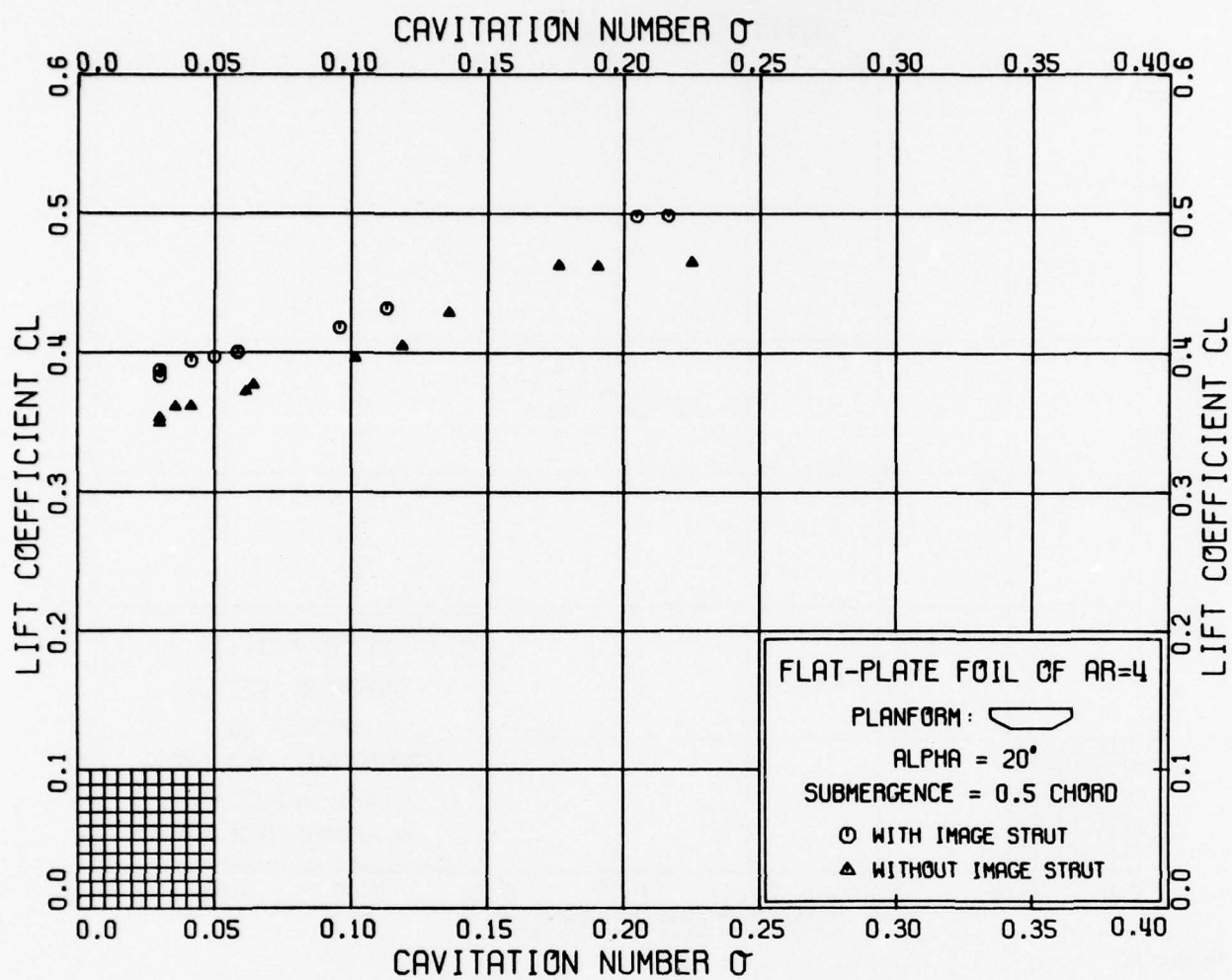


Fig. A-2: (a)



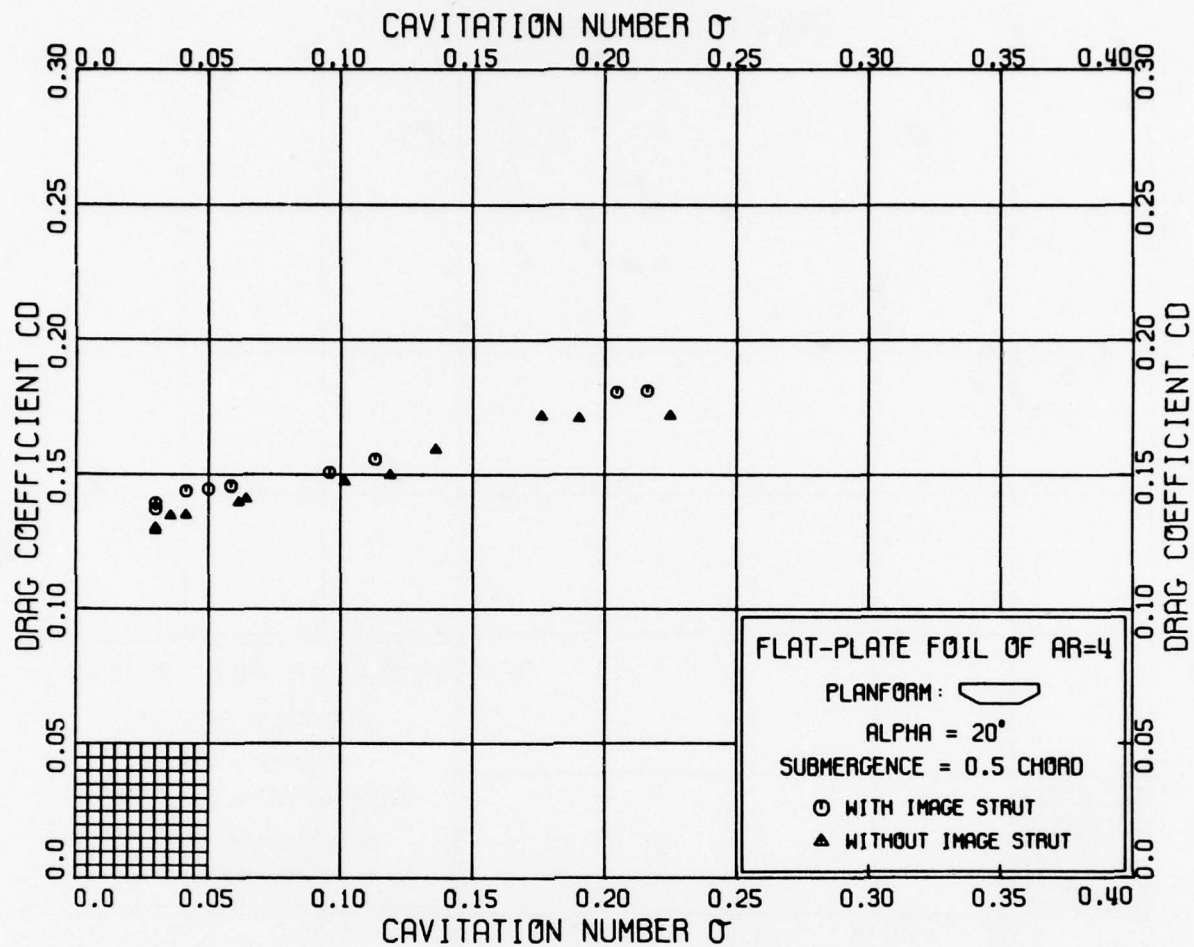


Fig. A-2: (b)

Fig. A-2: Comparison of (a) lift coefficient and (b) drag coefficient with and without the image strut at an angle of attack of 20 degrees and submergence depth of 0.5 chord. These data are corrected strut tare and drag and lift.

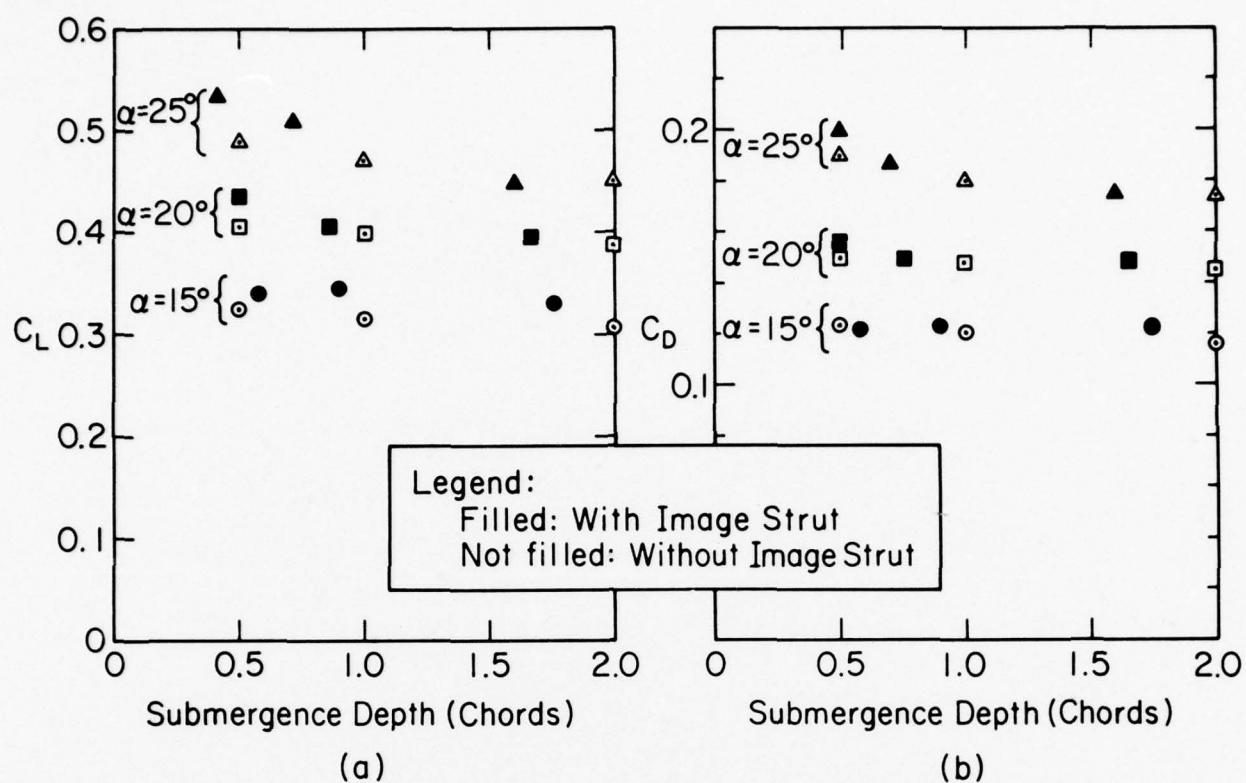


Fig. A-3: Comparison of (a) lift coefficient and (b) drag coefficient with and without the image strut as a function of submergence depth. The cavitation index is 0.12 for all data points.

# THE RESULTS OF THE EXPERIMENTAL INVESTIGATION OF THE SKIRT PARAMETERS INFLUENCE ON RESISTANCE AND STABILITY CHARACTERISTICS OF A HOVERCRAFT

E. BRZOSKA, L. KOBYLINSKI, M. KREZELEWSKI and K. PAUL  
Ship Research Institute, Gdansk Technical University, Poland

During last five years an extensive research programme of particular type of hovercraft has been performed at Ship Research Institute in Gdansk. The programme consisted mainly of extensive experimental investigations in model scale of resistance and stability characteristics of amphibious hovercraft equipped with skirts without compartmentation of cushion. There were tested eight models of the skirts on ground at zero speed and on water in the range of speed from zero to  $2,5 F_n$  / Froude number /. The experiments were conducted by the method elaborated at SRI. In the paper are presented main results of the experimental investigation, namely the influence of main skirt parameters' attitude of the model and its speed on damping coefficients, metacentric height and total resistance. The great influence of skirt parameters on total resistance was observed for the models having the same weight, speed and skirt bag feeding system.

In the paper there are given several useful data on designing of simple hovercraft skirt basing on the results of the experiments.

## INTRODUCTION

The elastic skirt the most important part of the hovercraft, is subject of constant development. Many different variations of the elastic skirt are known at present, some the them of rather complicated configuration. It is well known that the configuration of the skirt has an important influence on hydrodynamic characteristics of the hovercraft. During last few years an extensive research programme has been performed at Ship Research Institute, Technical University of Gdansk the main object of which was finding of the elastic skirt of simple construction leading to low resistance and good stability characteristics.

Taking as the basic design, the segmented elastic skirt being in contact with the water surface at the most part of its length model experiments with systematically varying skirt configurations were arranged. It was assumed at the beginning that:

- i it is possible to find such a configuration of the skirt that satisfactory stability and resistance characteristics could be obtained without additional compartmentation of the cushion,
- ii the increase of the resistance caused by the contact of the skirt with the water will be small in comparison with the decrease of the power necessary to develop the air cushion.

The preliminary model tests confirmed the first assumption. The results of these preliminary model tests together with the description of the experimental method developed at SRI were reported at the 2nd International Hovercraft Conference, 1971 [1].

Encouraging results and usefulness of the open-water experimental method lead to the decision of extension of the research programme with the aim of collecting more informations with regard to the influence of the skirt configuration on stability and resistance characteristics of the hovercraft without skirt compartmentation. The detailed description of models used, skirts tested and results of all experiments together with practical conclusions are contained in unpublished reports of the SRI [2]. In this paper a summary description of the research programme together with some results taken by way of example and main conclusions obtained are given only.

## DESCRIPTION OF MODELS TESTED

Two basic models were used for the tests: CVO4 and CVO6. Main data for both models are as below, where:

- $L$  - length overall
- $L_e$  - effective length of the cushion
- $L_p$  - length of the cushion on ground
- $B$  - breadth overall
- $B_p$  - breadth of the cushion on ground



$S_p$  - area of the cushion on ground  
/all dimensions in millimetres/.

Model	L	B	L/B	$S_p$
CVO4	2250	1670	1,35	2,372
CVO6	2500	1250	2,00	2,040

Model	$L_e$	$L_p$	$B_p$	$L_p/B_p$
CVO4	1855	1910	1280	1,49
CVO6	2060	2125	988	2,15

The drawings of both models are shown in (figs 1) and (3). (Fig. 2) shows the model CVO4 fitted with the skirt No 1 prepared for the stability test at zero speed over the stiff ground, (fig. 4) shows the model CVO6 during the resistance test over the water. Both figures mentioned are good illustration of the experimental method.

#### DATA OF SKIRTS USED

##### Skirts of the model CVO4

The elastic skirts used on the model CVO4 were of the segmented type with open segments, without cushion compartmentation and without design clearance (fig.5). The skirts were attached on the perimeter of the model.

Altogether 8 skirts were tested. All of them have constant angle  $\phi = 45^\circ$  see (fig.5) and constant hover height at zero speed equal to  $h_0 = 160$  mm. All basic dimensions of the skirts are given below:

Skirt number	1	2	3	4
$R_w$	435	435	637	435
$R_z$	100	100	147	100
$h_s$	125	125	95	125
$b_s$	65	65	70	120
$b_s/h_s$	0,52	0,52	0,82	0,96
$h_s/h_k$	0,50	0,50	0,33	0,50
$n_s$	96	96	96	54
sw	70	300	300	140

Skirt number	5	7	8	9
$R_w$	171/435	340	435	435
$R_z$	49/100	78	100	100
$h_s$	180/125	160	125	125
$b_s$	65	65	32	65
$b_s/h_s$	0,36/0,52	0,41	0,26	0,52
$h_s/h_k$	0,75/0,50	0,64	0,50	0,50
$n_s$	100	95	174	96
sw	70	300	140	140

Where:

- $R_w$  - inner radius of the bag curve
- $R_z$  - outer radius of the bag curve
- $h_s$  - height of the segment finger
- $b_s$  - breadth of the segment finger
- $h_k$  - height of the skirt  
/all dimensions in millimetres/
- $n_s$  - number of segments
- sw - specific weight of the fabric  
in  $p/m^2$ .

Where in the table two figures are given, the first one refers to the bow part and the next to side parts of the skirt. Each of the elastic segments is feeded with compressed air from the bag 1 through one circular hole 4 with the diameter equal to 50 mm. Only in skirts No 4 and No 5 feeding holes are in two rows. All skirts were tailored of the fabric used normally for sails (dacron), which does not absorb water during the tests. (Fig. 6) shows the model fitted with the skirt No 8, which has very narrow segments. Their total number is 174 in comparison with the total number 54 used for skirt No 4.

##### Skirts of the model CVO6

Two elastic skirts No 1 and No 2 were used in the model CVO6. The skirt No 1 was basically of the same design as the skirts of the model CVO4. The only difference was that the stern part of the bag was separately feeded and the segments in this part were of the closed type. The lower edge of these segments were raised 45 mm over the lower edge of the side parts of the skirt. The feeding holes in the skirt No 1 were the same as in the model CVO4. In the skirt No 2 feeding holes were rectangular, and feeding holes to the cushion were circular with diameter equal to 25 mm. see (fig.7) Both skirts were tailored of the same fabric - dacron, the specific weight of

which was  $140 \text{ p/m}^2$ .

Geometrical characteristics of these skirts are as follows:

$$\begin{aligned} h_k &= 313; R_w = 540; & h_s/h_k &= 0,465; \\ h_s &= 145; R_z = 125; & h_k/h_c &= 1,82; \\ h_c &= 172; R_w/R_z = 4,32; & \alpha &= 45^\circ \\ b_s &= 65,5; & b_s/h_s &= 0,452; \end{aligned}$$

where:

$h_c$  - height of the cushion  
/dimensions in millimetres/.

The difference in geometry of both skirts lies in that the skirt No 2 is fitted with closed segments on the full perimeter. The number of segments in both cases was the same and equal 94.

### RESULTS OF EXPERIMENTS

During all measuring runs the weight  $\Delta$  of the model CVO4 was kept constant and equal 108 kp for resistance tests, and 135,5 kp for stability tests. For the model CVO6 weight was kept always equal to 110 kp.

Measurements were performed at constant number of revolutions of the fan in all runs.

The shape of the perimeter of the lower edges of the skirt segments was practically the same for all skirts. The difference in static pressure in the cushion in different runs did not exceed 1%.

#### Results of resistance tests

The results of resistance tests for each model and each skirt were presented in the form of diagram of the total resistance  $R$  of the model (this value not contains the momentum drag because of form of general air feeding system) and the running trim of the model  $\psi$ , versus Froude number  $Fn$  for several values of initial trim  $\psi_\Delta$  when floating (plus - trim to the stern, minus - to the bow). The example of diagrams are shown in (figs 8) and (9).

Additional runs were performed with the model CVO6 for several values of initial heeling angle, and values of heel on the cushion were measured respectively. All diagrams obtained are to be found in [2]. The main conclusions obtained from these experiments are:

- i the hump of the measured resistance of the model which occurs at about  $Fn = 0,6$  is always connected with the maximum of the stern trim; the change of trim with regard to the trim at zero speed differs from 1 to 5 degrees, according to the configuration of the skirt and to the initial trim;
- ii minimum of the resistance occurs at  $Fn$  between 1,25 and 1,75 but for greater Froude numbers the resistance again quickly increases, and the slope of the resistance curve is smaller than in the initial part at

$Fn < 0,4$ ;

- iii the resistance of the model strongly depends on initial trim, particularly in the range of  $Fn \approx 0,5$  and  $Fn > 2,0$  - in some cases the difference of the resistance of the skirt No 2 and No 7 model CVO4 was larger than 100 per cent;
- iv the decrease of the resistance of the model in the range of  $Fn > 0,5$  is connected with the decrease of stern trim;
- v the trim of the model at speed depends also on initial trim, the character of the curves of  $\psi$ , for various values of  $\psi_\Delta$  versus  $Fn$  for particular skirt is almost the same in the range of  $Fn < 1,5$ ; however, at larger  $Fn$  the curves of  $\psi$ , for large  $\psi_\Delta$  sharply decline, what is accompanied with sharp increase of resistance caused primarily by the contact of the bow part of the skirt with water; consequently the bow part of the skirt shows a tendency to creep up and then the hovercraft may plough-in or, at wrong conditions, even collapse;
- vi the height of the hump of resistance curve, which occurs at  $Fn \approx 0,5$  depends also on initial trim; as a rule, the resistance at hump increases with increasing stern trim; for some skirts the hump resistance is more than twice as high as the resistance at  $Fn = 1,5$ ; it was observed, that such a high resistance is caused not only by specific maximum of wave resistance, but also by capture of water by the stern part of the skirt.

Resistance curves for the model CVO6 with skirts No 1 and No 2 are shown in the (fig.10). It is seen that minor differences in skirt configuration have strong influence on resistance characteristics of the hovercraft. The comparison of the configuration of both skirts shows that closed segments of the skirt No 2 are more stiff than open segments of the skirt No 1. This may be the cause of difference in contact resistance at Froude numbers over the range  $Fn = 1,0 \div 1,2$  in which wave resistance is rather small.

In the range of small Froude numbers, below  $Fn = 1,0$ , the differences in total resistance must be attributed to differences in wave resistance. The wave resistance of both skirts probably differs because of differences in air flow and formation of vortices (one pair of vortices in skirt No 1 against three pairs of vortices in skirt No 2) and consequently in pressure distributions over the cushion area.

#### Influence of geometry of the skirt on resistance.

From the example (figures 11) and (12) showing curves of resistance versus trim for all 8 skirts tested on the model CVO4 is seen that:



- 1 the total resistance of a hovercraft at the same weight, the same air feeding system, the same cushion area and the same trim may differ widely;
- 11 the lowest resistance of the model CVO4 was observed at about zero running trim;
- 111 at Froude numbers greater than about 0,6 some regularity was observed in relation of the resistance on actual trim; at Froude numbers lower than 0,6 such regularity was not observed - it is also due to capture of water by some skirts.

The influence of geometry of the skirts on resistance may be demonstrated on (figures 13) to (15). (Fig. 13) shows the influence of the height of the segment, (fig. 14) - the influence of the width of the segment and (fig. 15) - the effect of the rigidity of the fabric. It is seen from the (fig. 13) that in the whole range of speed minimum resistance is obtained at  $h_s/h \approx 0,5$  if maximum Froude number is adopted equal to 2,5. If lower Froude number is adopted as the design value, say 2,0, then optimum value of  $h_s/h$  is somewhat lower and equal to about 0,4. From (fig. 14) it is seen that for the design speed corresponding to  $Fn \approx 2,0$  lower resistance is obtained with wide segments ( $b_s/h \approx 1$ ) and for design speed corresponding to  $Fn \approx 2,5$  narrow segments are more appropriate ( $b_s/h \approx 0,5$ ). For very narrow segments ( $b_s/h \approx 0,25$ ) the same resistance is obtained, but it is not practicable to use too many segments.

From (fig. 15) it is seen, that specific weight and consequently rigidity of the fabric has strong influence on resistance of the hovercraft. Within the range of speed which corresponds to  $Fn < 2$ , the resistance increases with increasing rigidity of fabric. However, very small rigidity of fabric involves the necessity of using additional stays, what was the case with the skirt No 1 and what again causes increase of resistance. At the design speed corresponding to  $Fn \approx 2,5$  more rigid fabric leads to lowest resistance.

#### Results of stability tests

Measurements of transverse and longitudinal dynamic and static stability at zero speed over rigid ground and over water were taken for all eight skirts of the model CVO4 and two skirts of the model CVO6. Additionally measurements of transversal dynamic and static stability and longitudinal static stability were taken in function of speed over water. Curves of transverse static stability at zero speed are shown in (figures 16) and (17) over rigid ground and over water respectively. In (figures 18) and (19) curves of longitudinal static stability at zero speed for the model CVO6 with skirt No 1. The character of stability curves for other skirts is similar. The curves of stability over rigid ground show different behaviour when model is heeling to small initial stability of the model and

to the effect of friction between the skirt and ground. When model tested at zero speed over water the hysteresis loop practically vanished. It is seen from the figures that again as in the case of resistance rather small differences in geometry of the skirt lead to large differences in stability characteristics. The stability curves of the hovercraft tested over the rigid ground are strongly non-linear; they are much more linear when measured over water. The linear approximation may be adopted within the range of trim  $\pm 1^\circ$  and heel  $\pm 2^\circ$  for skirts No 7, No 8 and No 9 of the model CVO4 and for the model CVO6. In general, longitudinal stability is approximately twice as high as transversal stability. Change in internal configuration of the skirt has also a considerable effect on stability characteristics. This is seen when comparing stability curves for both skirts No 1 and No 2 of the model CVO6.

More stiff segments and more complicated air flow lead to effect similar as when employing additional stability skirts. The speed has also effect on stability characteristics. This is seen from (fig. 20) showing transverse stability curves versus trim for several values of speed model CVO6, skirt No 1. Generally, stability increases with increasing speed. With regard to the dynamic stability, it may be stated that all models tested were dynamically stable. However, characteristics of dynamical stability expressed in terms of damping coefficients differ widely for different models. This is seen from examples given in (figures 21) to (23). The analysis of the influence of geometry of the skirt on damping coefficients shows that not only absolute values of damping coefficients differ for different models, but also type of curves may be completely different. From the above figures it is seen that with increasing heel the damping coefficient mostly increases; but increasing speed may exert different effect on damping coefficients. They may diminish (fig. 24), increase (fig. 22) or firstly increase, then diminish (fig. 23). From the analysis of measurements it was found that the best results were obtained on model CVO6, skirt No 2 and on model CVO4, skirt No 9. The most unfavourable was skirt No 8 fitted with very narrow segments. The effect of geometry of the skirt and its stiffness on damping coefficients of roll is demonstrated by (figs 23) to (27) taken by way of example. (Figs 23) and (24) show the effect of width of segments, (figs 25) and (26) - the effect of height of segments for Froude numbers equal to  $Fn = 0$  and  $Fn = 2,37$  respectively. From the analysis of all results obtained the conclusions can be drawn:

- i except of very small angles of heel ( $\varphi < 2^\circ$ ) the increase of skirt stiffness caused increased damping coefficients;
- 11 the character of changes of damping coefficient with change of segment



- width differs for different Froude numbers and different heeling angles;
- iii the favourable range of segment width bearing in mind damping coefficients is  $b_s/h_s \in (0,4 ; 0,6)$ ;
  - iv the optimum damping coefficients may be obtained within the segment height  $h_s/h_n \in (0,46 ; 0,53)$  - this ranges corresponds also to low resistance values.

### C O N C L U S I O N S

In the paper are presented partial results of research programme only. The whole programme consisted of more than 400 experiments and few curves obtained from measurements are only shown by way of example in the paper. Experiments were performed from 1970 to 1973. The experimental method was originally developed for the programme and proved to be extremely cheap and useful. Obviously, all results obtained should be treated as comparative and scaling of results to the full scale hovercraft is not directly possible. However, in opinion of the authors it is possible to draw out some very useful conclusions with regard to the designing of a hovercraft.

### ACKNOWLEDGEMENTS

The authors wish to express their gratitude to all members of the staff of the SRI who contributed to the research programme reported and helped greatly in its realisation.

### REFERENCES

- [1] - Kobyliński, L. and Krężelewski, M. - A method of testing models of hovercraft in open waters - Second International Hovercraft Conference - Southampton, England - 1971.
- [2] - SRI reports nos: 41/70, 43/70, 102/72, 133/72, 134/72, 147/72, 148/72, 354/73, 386/74. - Ship Research Institute, Gdańsk, Poland (in polish, unpublished).
- Trans. of the Technical University - No 168 - Gdańsk, Poland - 1971 (in polish).

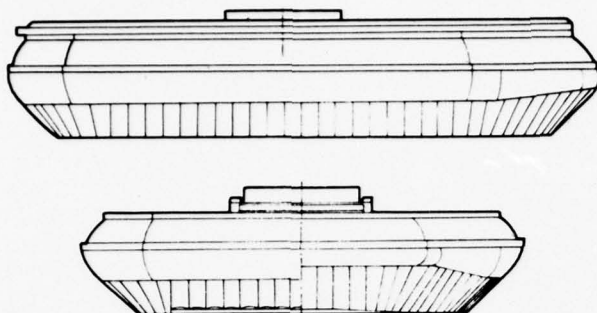


Fig. 1: Model of the CVO4



Fig. 2: The model CVO4 with skirt No. 1 over stiff ground

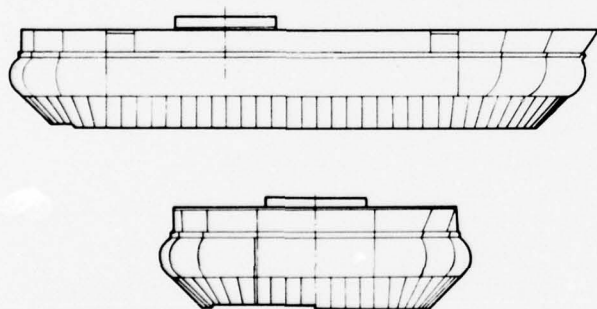


Fig. 3: Model of the CVO6



Fig. 4: The model CVO6 with skirt No. 1 over water

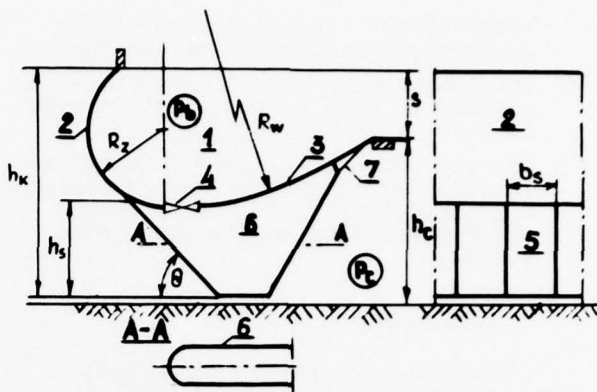


Fig. 5: Main geometrical characteristics of the CVO4 skirts

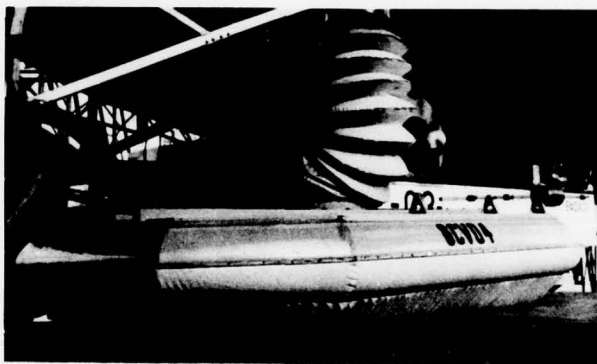


Fig. 6: The model CVO4 with skirt No. 8 over stiff ground

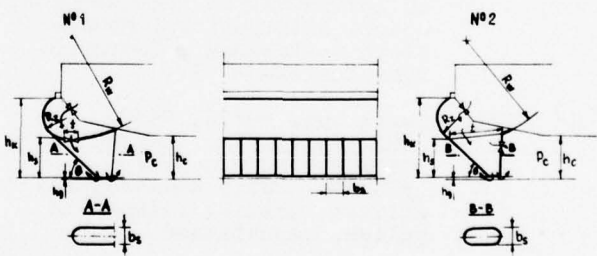


Fig. 7: Main geometrical characteristics of the CVO6 skirts

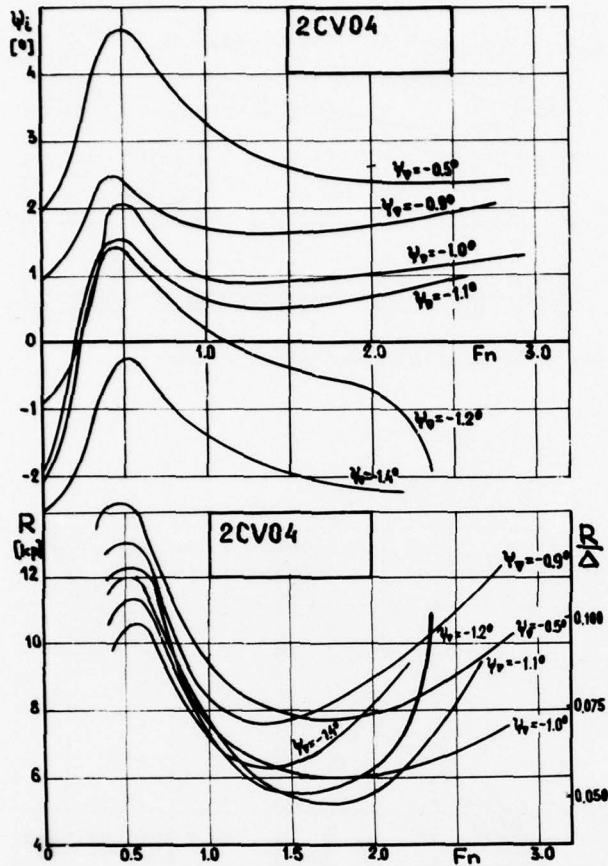


Fig. 8: Resistance and trim results for the CVO4 with skirt No. 2

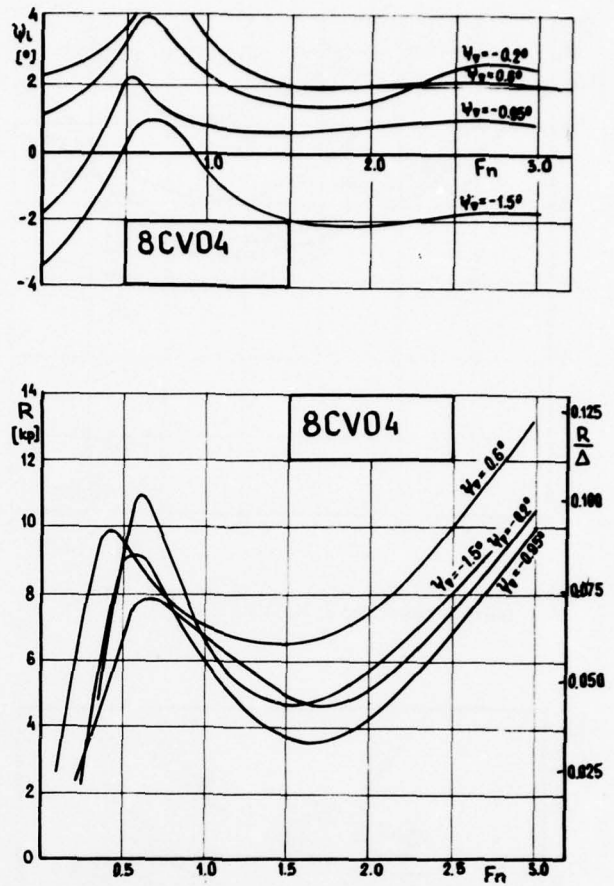


Fig. 9: Resistance and trim results for the CVO4 with skirt No. 8

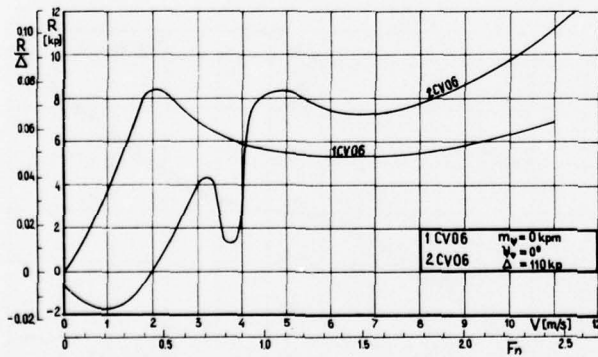


Fig. 10: Resistance results for the CVO6 with skirts No. 1 and No. 2

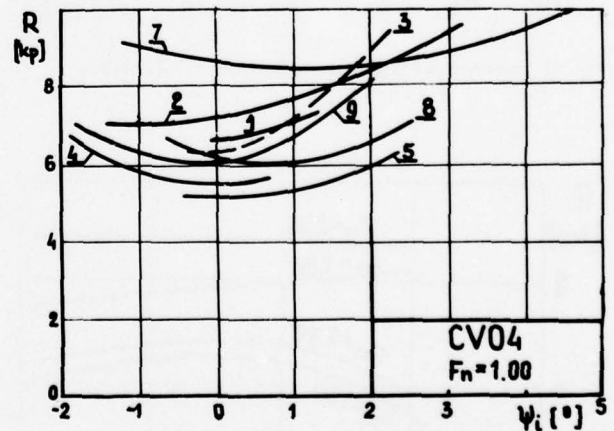


Fig. 11: Resistance versus running trim angle for all eight skirts of the CVO4 at  $F_n = 1$



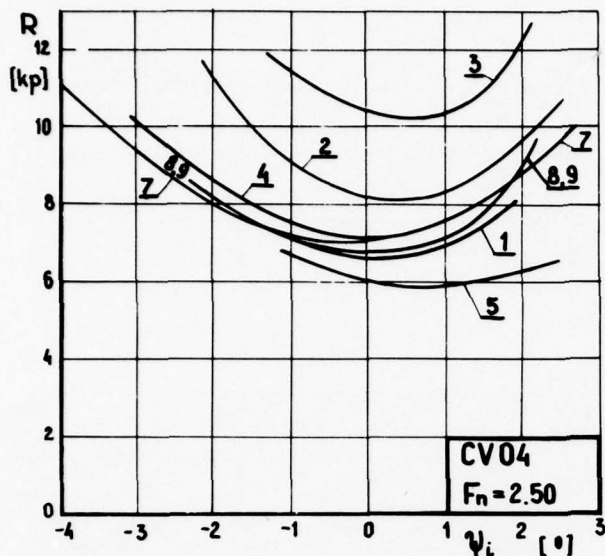


Fig. 12: Resistance versus running trim angle for all eight skirts of the CV04 at  $F_n = 2.5$

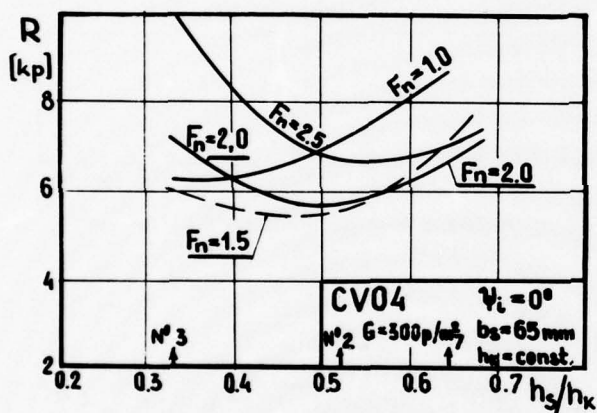


Fig. 13: Influence of segment height ratio on resistance

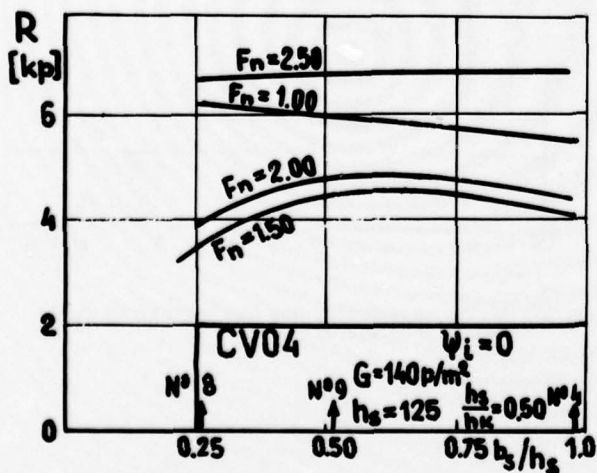


Fig. 14: Influence of segment breadth ratio on resistance

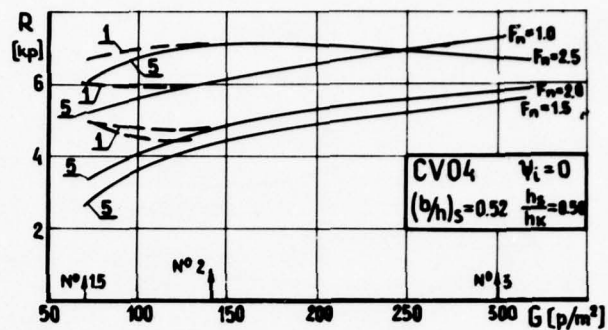


Fig. 15: Effect of fabric's weight on resistance

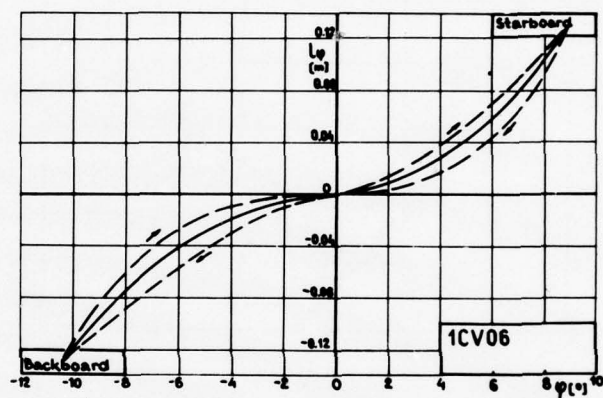


Fig. 16: Transversal righting arm for the CV06 with skirt No. 1 at rigid ground

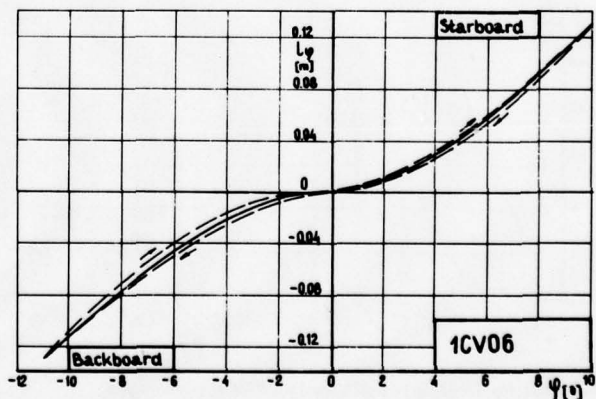


Fig. 17: Transversal righting arm for the CV06 with skirt No. 1 at water

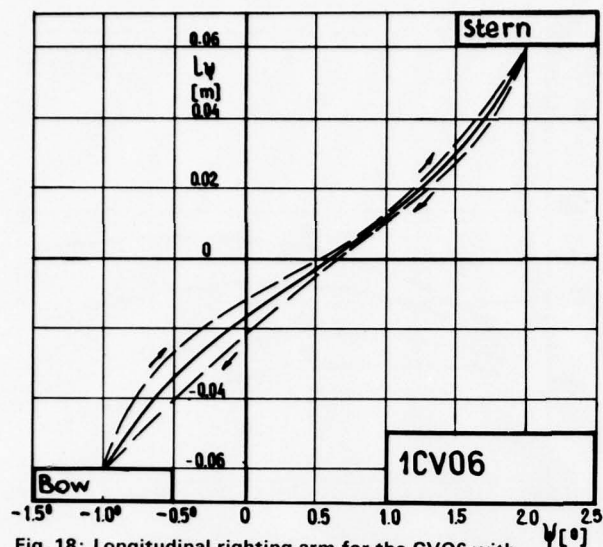


Fig. 18: Longitudinal righting arm for the CVO6 with skirt No. 1 at rigid ground

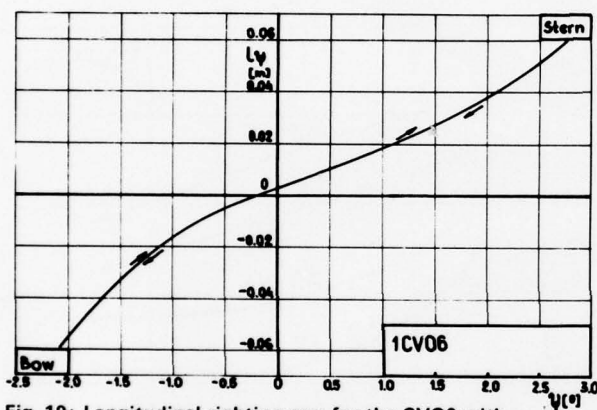


Fig. 19: Longitudinal righting arm for the CVO6 with skirt No. 1 at water

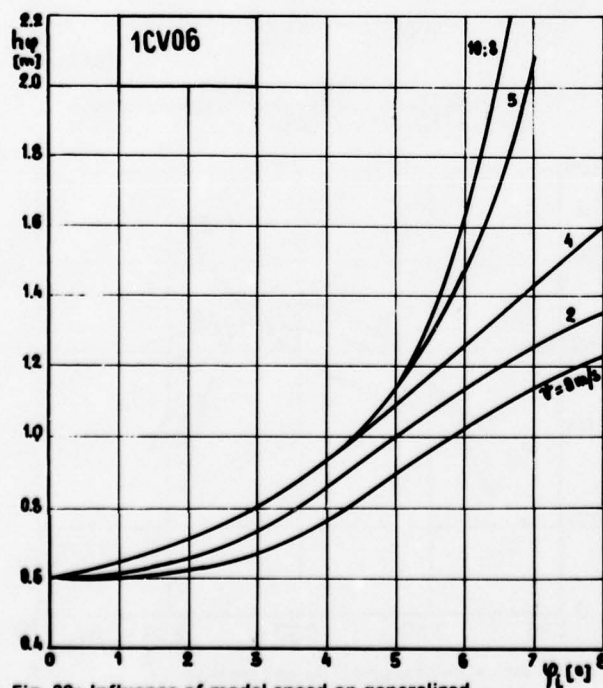


Fig. 20: Influence of model speed on generalized metacentric height

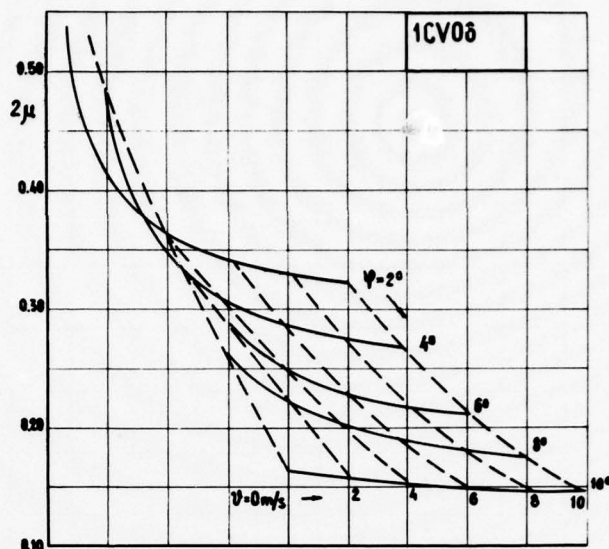


Fig. 21: Influence of speed and heeling angle on nondimensional roll damping coefficient for the CVO6 with skirt No. 1

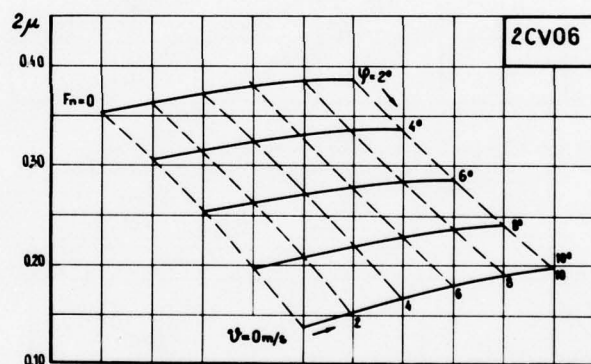


Fig. 22: Influence of speed and heeling angle on nondimensional roll damping coefficient for the CVO6 with skirt No. 2

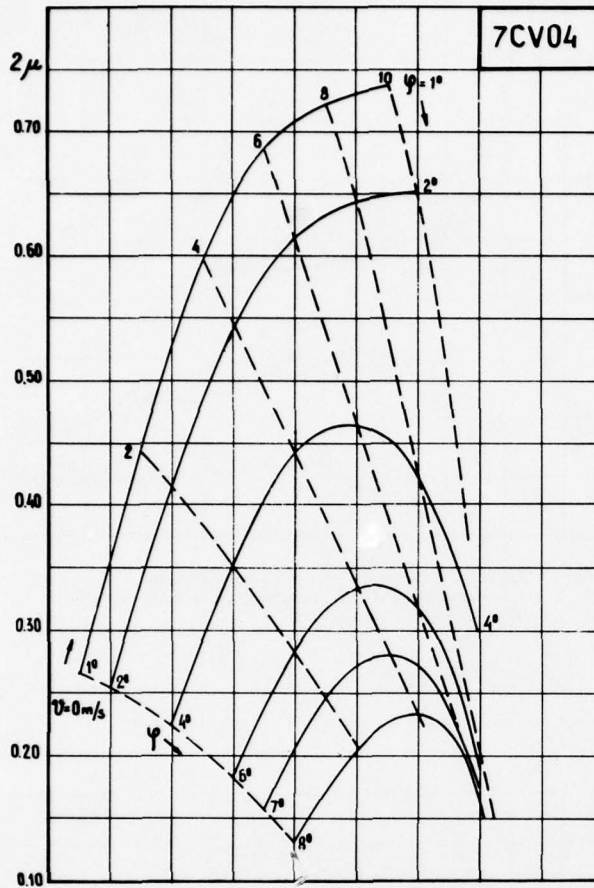


Fig. 23: Influence of speed and heeling angle on nondimensional roll damping coefficient for the CVO4 with skirt No. 7

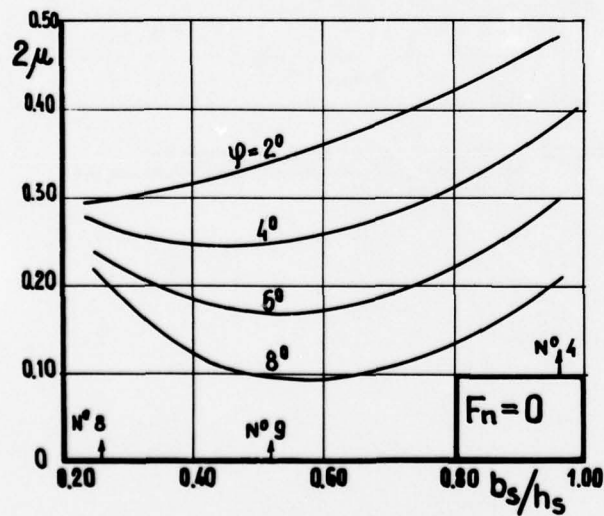


Fig. 24: Influence of segment breadth ratio on nondimensional roll damping coefficient for the CVO4 with indicated skirt Nos. at  $F_n = 0$  over water

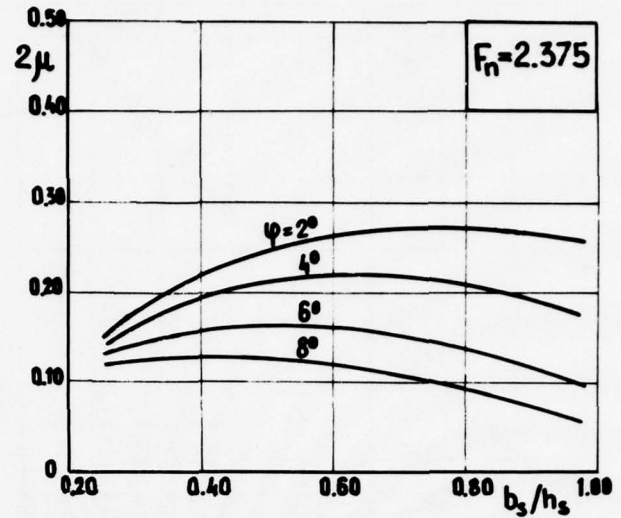


Fig. 25: Influence of segment breadth ratio on nondimensional roll damping coefficient for the CVO4 at high  $F_n$  over water

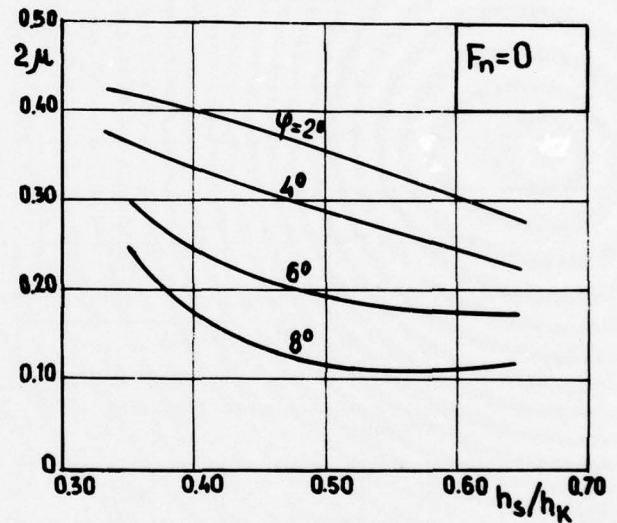


Fig. 26: Influence of segment height ratio on nondimensional roll damping coefficient for the CVO4 at  $F_n = 0$  over water

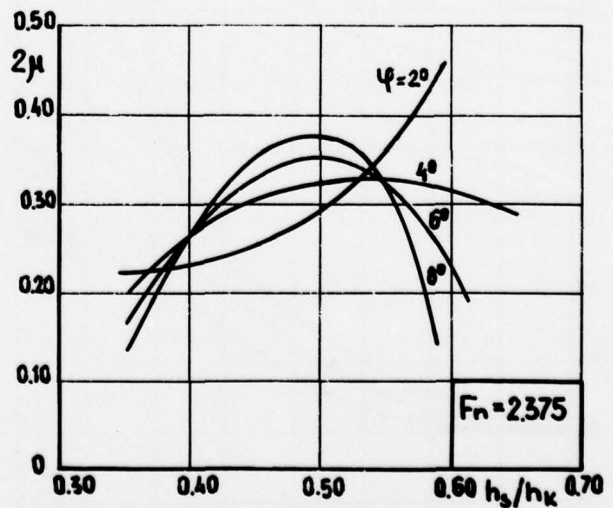


Fig. 27: Influence of segment height ratio on nondimensional roll damping coefficient for the CVO4 at high  $F_n$  over water



# THE USE OF OSCILLATORS TO OBTAIN HYDRODYNAMIC AND STRUCTURAL LOAD DATA FOR SES CRAFT

PAUL KAPLAN, Oceanics, Inc Plainview, N.Y., U.S.A.  
 SYDNEY DAVIS and ALEXANDER MALAKHOFF  
 Nausea, P.M.S. — 304 Bethesda, Md, U.S.A

Alexander Malakhoff  
 Head, Structures Branch,  
 NAVSEA, PMS-304  
 Bethesda, Md., U.S.A.

## SYNOPSIS

A description is given of model test data obtained using oscillators for providing basic data, correlation with theory, etc. for horizontal and vertical plane motions of surface effect ships (SES). In addition results of computations carried out using the verified theory established from the model tests for full scale SES testcraft are also provided, including a comparison with full scale motion trajectories. The use of oscillators for determining the structural loads on SES craft bow structures, which are covered with flexible pressurized seals, is also described. Various aspects of scaling associated with model tests of SES craft are also discussed.

## INTRODUCTION

The surface effect ship (SES) is a relatively recent ship concept that promises high speed and other significant performance characteristics, primarily for naval ship application. An SES has its weight supported primarily by air pressure contained within a cushion region, and it is surrounded by rigid sidewalls that penetrate the water surface as well as fore and aft flexible seals. The presence of the rigid sidewalls distinguishes the SES craft from the more conventional hovercraft that have been successfully operating during the past 15-20 years. Present U.S. Navy development plans envision a 2000 ton craft, with speeds of the order of 80-100 kt., and larger size craft are also being considered.

Since the motion of such craft is quite complicated, and involves consideration of all of the various modes of rigid body motion, computer simulation studies using a six degree of freedom mathematical model serve as the major tool for evaluation of craft performance. It is therefore necessary to determine the nature of the variations of all of the forces and moments with respect to all possible degrees of freedom, in order to provide basic data for a particular design. Similarly, it is also very useful to develop theoretical expressions that can be used for arbitrary craft in order to extend the utility of such simulation studies.

When considering SES craft motions, the initial approach treats the lateral plane forces and moments as functions of lateral plane motion variables primarily, (with appropriate determination of the influence of vertical plane motion variables as well) and similarly for evaluating vertical plane forces and moments in terms of vertical plane motion variables. Conventional towing tank model test procedures for determining force variations primarily involve measurements with varying orientation, such as sideslip (or drift) angle, pitch angle, or draft variations. Such variations are essentially static in nature, and it is important to determine the influence of dynamic motions, such as those due to angular velocities, etc. in order to properly predict

craft stability and motion characteristics.

A method of obtaining such basic data for SES craft is by means of captive model tests, with dynamic variations to represent the different degrees of freedom (in terms of displacements, velocities, and accelerations) in order to determine the necessary form and numerical values of the forces and moments. The test procedures for this purpose involve the use of oscillators to measure the separate lateral and vertical plane forces, in the same general manner that has been used for conventional surface ship dynamic studies, e.g. as described in (1). This data is then compared with theory in order to provide validation of the theoretical models, which are then extended within a computer simulation procedure to predict various motions of SES craft (see (2)). The utility of the simulation procedure then depends upon the basic measured data, which is essential in establishing proper representations of various forces and moments for arbitrary designs under varying operating conditions (which are more extensive than in the case of conventional surface ships).

In addition to that of craft motions another important area of concern for SES craft is that of structural loads, with a major problem associated with slamming of such a high speed craft when operating in waves. Both the local pressures on the bow plating as well as the total impact force, (which determines the bending moment associated with the slam) are significant factors that must be determined for adequate structural design of such. Since SES craft have pressurized flexible bow bag seal elements which impact on the water during slamming, efforts to simulate conditions expected during craft operation require an appropriate model that accounts for the interaction between the bow region and the water during such events. This requires controlled testing wherein the desired measurements are obtained under craft motion conditions, such as vertical velocity, penetration into the water, etc. are continuously known so that relations between instantaneous time histories can be determined. Such information can be obtained by use of a

vertical oscillator that simulates the impact conditions of the bow region, which are primarily due to craft pitch motion, while making simultaneous measurements of pressures, forces, etc. during the various cycles of simulated slamming.

The present paper exhibits the results obtained from experimental studies to measure the hydrodynamic and structural load data for SES craft using oscillators in spectral modes of operation. Comparisons with theory, general conclusions found from the data, and results of full scale craft behavior using this information are also provided. The model tests were carried out on representative SES models at Skibsteknisk Laboratorium (Danish Ship Research Laboratory) in Lyngby, Denmark, using the oscillator equipment at that facility. All of the work reported in this paper was carried out under contracts with the U.S. Navy, NAVSEA Code PMS-304, whose support is sincerely appreciated.

#### NOTATION

$A'_{22}$	= sectional lateral added mass
$A'_{33}$	= sectional vertical added mass
$B^*$	= local beam
$C_{Dc}$	= cross-flow drag coefficient
$C_H$	= lateral added mass coefficient
$\ell$	= characteristic length
$\ell_{ski}$	= stern seal wetted length
$M$	= pitch moment
$N$	= yaw moment
$N'_z$	= sectional vertical damping coefficient
$q=\dot{\theta}$	= pitch angular velocity
$r$	= yaw angular velocity
$r'$	= $r\ell/u$ non-dimensional yaw angular velocity
$u$	= forward speed
$v$	= lateral velocity
$w=z$	= vertical velocity
$X$	= longitudinal force
$Y$	= side force
$Z$	= vertical force
$z$	= heave motion, positive down
$\beta$	= sideslip angle
$\theta$	= pitch angle, positive bow up
$\rho$	= water density
$\sigma$	= $\Delta p / (1/2 \rho u^2)$ cavitation index
$\omega_e$	= encounter frequency, rad./sec.

#### LATERAL PLANE FORCES AND MOMENTS

##### Model Tests

For the lateral plane study, measurements were made of the side force and yaw moment with variations in the drift angle, lateral velocities, and yaw angular velocities. While roll measurements were also obtained, the present paper will be limited to discussing the pure lateral motion variables of yaw and sideslip, for simplicity. The particular apparatus used in these lateral plane tests is the planar motion mechanism (PMM) described in (3), which allows larger displacements, velocities, etc. than the original system in (1), although the actual measurement procedures are essentially the same.

The tests were made with the model restrained at particular trim and draught conditions, in order to have a precise fixed reference for the immersed portions of the craft in the water so that theoretical computations could be carried out

simply. The pressures in the cushion plenum and in the aft seal were also measured during the tests using separate pressure transducers. During the course of the tests, measurements were also made of the towing carriage speed as well as counts of the number of revolutions of the PMM oscillator. All of the measured data in the form of electrical signals were recorded on magnetic tape, and the signals were also sent to an analog processor where they were resolved into in-phase, out-of-phase, and constant components relative to the oscillator input motion of interest. The resulting component terms are digitized, scanned, and recorded on paper tape. The paper tape is then used in data reduction via a digital computer. During the tests the various force component terms obtained from the analog processor are also monitored continuously on an oscillograph pen recorder.

The tests were carried out for a model with a test configuration essentially having a rectangular planform. The basic characteristic dimensions of the model are given by the following:

Table 1 Model Craft Characteristics

Overall length	9.652 ft.
LCG, from transom	45.79 in.
VCG, from keel baseline	10.92 in.
Plenum width	3.0 ft.
Height of wet-deck, from keel	7.7 in.

The model considered in the present paper has sidewalls with a constant 45° angle, with a faired bow region extending approximately 20% over the forward portion. Ventral fins were attached to the model during some of the tests, with the trailing edge located at the craft transom. The fins are rectangular in planform, and tests with fins present on the model were made with the fins canted inboard at 45° as well as with the fins purely vertical. A general layout of the model is given in (Figure 1).

The bow and stern seals used on the model were provided in completely assembled form and bolted to the inside of the centerbody. The bow seal is a simple straight-across finger seal configuration, while the stern seal is a two-lobe membrane system with stiffeners in the lower surface, which is the region in contact with the water surface. Small axial fans were placed in openings in the centerbody plate so that they could feed the main cushion chamber and also the stern seal.

The lateral dynamics test series included tests over a range of sideslip angle orientations; pure sway oscillations; pure yaw oscillations; and oscillations with combined sideslip and yaw. These latter tests of combined motions were made up of "yaw and drift" tests and "drift and yaw" tests, with the (yaw + drift) involving a fixed yaw oscillation over a range of static sideslip angles, while the (drift + yaw) tests involved a fixed static sideslip angle that was combined with a range of yaw oscillations. The oscillations were carried out at the rate of about 15 rpm, which is the highest value possible with the PMM apparatus, in order to obtain the largest possible number of complete oscillation cycles during each run due to the high test speed in the tank. The static sideslip angles tested covered the range of +2° out to -10° or

to an angle condition limit where pressure was reduced significantly due to excessive leakage.

In all of the tests the fans were operating and establishing a particular value of pressure in the main bubble chamber, as well as in the stern seal. Some limited tests were also incorporated into the program to determine the influence of zero bubble pressure by testing with the aft stern seal lifted, as well as other tests with the stern seal trailing in an unpressurized form.

The test conditions are defined by a mean draught value, which was that measured at the assumed model LCG, measured from the baseline; a pitch angle orientation; and a roll angle orientation (all tests were carried out at zero roll angle). A particular forward speed value was also selected, as well as a nominal value of main bubble pressure. The particular conditions for the model are given below:

Table 2 Test Conditions

	Condition No.					
	1	2	3	4	5	6
Mean draft, d, in.	2.4	2.4	3.6	4.6	3.6	2.4
Pitch angle, $\theta$ , deg.	+1	+1	+1	-2	-2	+1
Speed, U, ft./sec.	26.2	26.2	26.2	26.2	26.2	26.2
Nominal main bubble pressure, $P$ , lb/ft <sup>2</sup> m'	9	9	9	9	9	9
Appendages	- ventral fins, 45° cant	-	-	-ventral fins, 45° cant	ventral fins, 45° cant	

The nomenclature used in describing the measurements and their variations with these particular variables is that proposed by SNAME (4). The resulting lateral forces and moments in the present tests are directly applicable to the equations and axis system described in (4).

In the data reduction procedure, the total measured forces are operated upon in the analog processor to determine separate components relative to the imposed oscillatory motion, as described in (1). These analysis procedures determine the force and moment components in phase with the particular aspects of the motion such as velocity, acceleration, etc. Both the linear and nonlinear forces and moment terms, based upon a pre-structured mathematical representation of the total force measurement, are determined from the different components obtained from analysis of the measurements. The static tests involving sideslip angle variations only involve consideration of the constant component terms. Model mass and inertia tares were determined from in-air oscillatory tests, which were then subtracted from the measured values to determine the net hydrodynamic force components. These final values can then be used to compare with theory as well as being in other analyses in the investigation of lateral dynamics of SES craft. Representative results in the test program for the six conditions listed in Table 2 are presented and discussed in later sections of the paper.

#### Comparison With Theory

Theoretical representations of the side force and yaw moment on SES craft are obtained primarily on the basis of slender body theory, modified by semi-empirical means using cross-flow drag. The separate forces and moments acting on a single sidewall are found, and the total value is obtained from the sum of the contribution of each sidewall. This treatment is based upon the assumptions of no interference between the two sidewalls, no influence of the cushion pressure per se on the hydrodynamic forces, and no free surface wave interaction or influence of the difference in water level between the inner wall surfaces and the outer surfaces due to the bubble-generated internal wave surface profile. The theoretical force expressions are evaluated only in terms of craft immersion parameters relative to the undisturbed water surface level in the ambient fluid outside the bubble-craft region. A more exact theory involves nonlinear lifting surface theory in the presence of a free surface for low aspect ratio airfoils. Comparison with theory is therefore limited to the simplified theoretical representation.

The hydrodynamic forces and moments acting on the sidewalls, and also any appendages attached to the sidewalls such as waterjet inlet housing, skegs, fins, etc., are found primarily by application of slender body theory treatments. These methods are linear in nature, with the effect of immersed sectional area, draught, etc., due to orientation changes arising from heave, pitch and roll motions (or fixed positions) reflecting the most significant nonlinear variations for these terms. The sidewall and appendage forces also contain nonlinear terms due to cross-flow drag, which are important for the case of very low aspect ratio lifting surfaces. The sidewall forces are composed of three separate contributions; viz., the terms due to slender body hydrodynamic reactions, the effect of cross-flow drag, and the terms due to various appendages, i.e.

$$F_{\text{sidewalls}} = F_{\text{sw}}^{(1)} + F_{\text{sw}}^{(2)} + F_{\text{sw}}^{(3)} \quad (1)$$

where superscript (1) is the slender body result, superscript (2) is for the cross-flow drag terms, and superscript (3) is the appendage contribution.

The following results are given for the slender body theory forces on a single sidewall (port or starboard, using appropriate values for each):

$$X_{\text{sw}}^{(1)} = -1/2\rho C_{Df} S_w u^2 \quad (2)$$

$$Y_{\text{sw}}^{(1)} = -A'_{22s} u(v+x_s r) \quad (3)$$

$$N_{\text{sw}}^{(1)} = x_s Y_{\text{sw}}^{(1)} - [A'_{22s} + \int_{x_s}^{x_b} A'_{22} dx \cdot r] u \quad (4)$$

where

$\rho$  = water density

$C_{Df}$  = sidewall friction drag coefficient

$S_w$  = wetted area of a sidewall

$A'_{22} = C_H \rho \pi d^2(x)/2$ , lateral added mass of sidewall section, with  $d(x)$  = local wetted draught ( $C_H$  factor is lateral added mass coefficient);  $A'_{22s}$  is value at sidewall stern

$x_s$  = x-coordinate of sidewall stern location ( $x_s < 0$ )



$$x_b = \text{x-coordinate of sidewall bow location}$$

$$A_{22} = \int_{x_s}^{x_b} A'_{22} dx, \text{ total sidewall lateral added mass}$$

The above expressions are given for those quantities that affect the total values of  $Y^{(1)}$  and  $N^{(1)}$  in terms of the particular variables that are present in the model tests.

The total slender body theory forces and moments for both sidewalls are then given by

$$Y^{(1)} = Y_{\text{port}}^{(1)} + Y_{\text{starboard}}^{(1)} \quad (5)$$

$$N^{(1)} = N_{\text{port}}^{(1)} + N_{\text{starboard}}^{(1)} + [X_{\text{port}}^{(1)} - X_{\text{starboard}}^{(1)}]_{\text{sw}} \quad (6)$$

In the calculation of the individual sidewall force terms it is understood that the computation is appropriate to the particular values of the separate elements for the craft in the water, at the orientation condition specified.

In the development of the slender body theory force expressions it has been assumed that all added mass hydrodynamic forces and moments associated with pure acceleration terms ( $\dot{v}$ ,  $\dot{r}$  and  $\dot{p}$ ) are negligible in their influence on the craft motions, since they were expected to be small relative to the craft mass and inertia forces. Thus they were neglected and not included in the present expressions. Although added mass terms are present in the hydrodynamic force expressions given above, they are only used in expressing the "lift" type forces by the formal application of slender body theory.

The cross-flow drag force components that are significant for the lateral force and yaw moment are presented here. The lateral force due to cross-flow drag on a single sidewall is given by

$$Y^{(2)} = \frac{\rho}{2} C_{D_c} \int_{x_s}^{x_b} d(x) v_{\text{rel.}} |v_{\text{rel.}}| dx \quad (7)$$

where

$$v_{\text{rel.}} = v + xr \quad (8)$$

with these expressions appropriate to the particular values associated with either the port or starboard side. The yaw moment due to cross-flow is

$$N^{(2)} = - \frac{\rho}{2} C_{D_c} \int_{x_s}^{x_b} x d(x) v_{\text{rel.}} |v_{\text{rel.}}| dx \quad (9)$$

The total force and moment values due to cross-flow drag are then

$$Y^{(2)} = Y_{\text{port}}^{(2)} + Y_{\text{starboard}}^{(2)} \quad (10)$$

$$N^{(2)} = N_{\text{port}}^{(2)} + N_{\text{starboard}}^{(2)} \quad (11)$$

The appendage force terms for fins or any other appendage attached directly to the sidewall are represented in terms of the lift force behavior of these surfaces together with a cross-flow drag contribution. These appendage forces are determined in the same way as the theoretical expressions for wing-body interaction for low aspect ratio wings. The appropriate component for the lateral force on a fin at a particular fin cant angle is determined geometrically, and the yaw moment is assumed to be that due to the fin force

at a distance from the craft center of gravity measured to the center of area of the fin.

In all of the expressions provided above it is assumed that the craft is oriented at a pitch trim such that the maximum immersion occurs at the stern (i.e. positive trim angle). For cases with negative trim angles the expressions are altered somewhat to refer to conditions applied at the location of the maximum span of the sidewall (when it is pictured as a lifting surface in a lateral direction). The expressions in that case are somewhat more complicated, but are not listed here for purposes of simplicity in the representation of the analytical expressions. Since all of the geometric parameters in the theoretical expressions are precisely known for any particular craft orientation, the main problem is the proper values of the lateral added mass coefficient  $C_H$  and the value of the cross-flow drag coefficient  $C_{D_c}$ .

The results of the tests showed that the variation of side force and yaw moment with lateral velocity, based on the analysis of tests with pure oscillatory sway motion, indicated the same values for variations with lateral velocities as for static variations with sideslip angle. Thus the data from the static tests was sufficient for determining the variation of side force and yaw moment with respect to the lateral velocity variable  $v$ . The variations with sideslip angle obtained statically are presented as functions of the angle  $\beta$ , where the relation

$$\beta = - \frac{v}{u} \quad (12)$$

is used.

Some representative comparisons between theory and experiment in the static tests (variations with sideslip angle) are shown in (Figures 2-4) for the craft in a positive trim orientation. The results in (Figure 2) are for the basic sidewall configuration, while those in (Figures 3 and 4) are for the same craft condition except that ventral fins are present on the craft. It can be seen from these results that both the side force and yaw moment variations are predicted very well by use of the present theory. The theoretical values were determined with the use of the following values of the lateral added mass and cross-flow drag coefficients:  $C_H = 0.8$  and  $C_{D_c} = 2.0$ . A number of separate computations has shown that there is little influence of the cross-flow drag value on the yaw moment since there is no net effect of the cross-flow drag on the yaw moment as it is effectively balanced by the results of the integration over the immersed region. The cross-flow drag has been shown to have the major influence on the side force value. The yaw moment is mainly influenced by the unstable ideal "Munk" moment term. One of the major difficulties in slender body theory is the determination of the location of the point of action of the side force, in regard to its contribution to the yaw moment, which is known to be the major defect in slender body theory, even in infinite fluid aerodynamics. A few other cases (other models) wherein the static variation of yaw moment with sideslip angle has not been adequately predicted by the present theory have been encountered, but the present case illustrated herein represents that where an adequate prediction has been made. As a result of a number of computational experiments the value of the lateral added mass term  $C_H$  has been found to be approximately 1.0. The exact value to be used is

dependent on the actual section shapes and can vary along the craft. The cross-flow drag value  $C_{Dc} = 2.0$  is generally found to be applicable to the present sidewall problem, and it is a value used often for this influence in many aerodynamic and hydrodynamic studies.

Another interesting result obtained in the investigation is also shown on (Figure 2), where data obtained without bubble pressure present are compared with measurements obtained with bubble pressure. It can be seen that there is no significant difference for the side force and yaw moment with or without bubble pressure for this particular case, and similar results have been obtained in a number of other measurements to illustrate the influence of bubble pressure on lateral force and moments.

An illustration of the results obtained for the case where the craft is at a bow-down pitch orientation is shown in (Figure 5). In that case the present theory, when interpreted in terms of the evaluation of slender body theory with reference to the location of the maximum span, shows good agreement with experiment. The results in this figure also indicate the agreement of the experimental data for side force and yaw moment for conditions with and without bubble pressure present.

Illustrations of the comparison between theory and experiment for the case of yawing motion are given in (Figure 6) for the craft with a bow-up pitch orientation. It can be seen that there is extremely good agreement between the theory and experiment for the yaw moment variation with the non-dimensional angular velocity  $r'$ , which is the most significant parameter affecting turning and dynamic stability (i.e. it is the yaw damping term) with only fair agreement shown in the case of the variation of side force with yaw angular velocity. Since the side force magnitude is generally small, and has a relatively small influence on lateral maneuvering characteristics, any small differences has little significance.

An illustration of the variation of yaw moment with yaw angular velocity for the bow-down orientation is shown in (Figure 7). In that case the yaw moment variation with yaw angular velocity is predicted very well by the theory. A number of other cases have also exhibited similar good agreement with theory, with some lesser degree of agreement in regard to the less important side force variation. These results were obtained using the proper lateral added mass coefficient as well as the interpretation of slender body theory that refers the evaluation of the theoretical expressions to the location of the maximum span.

#### Effects of Free Surface, Cavitation, and Frequency

A direct illustration of the effect of the free surface on the lateral forces was obtained from related studies in water tunnels (5). Tests were carried out with models representing the submerged portions of sidewalls previously tested in the Danish tank. Then tests covered a range of sideslip angles, for single sidewalls, with the model attached to the upper wall of the tunnel test section. The measured data was used to establish the results for a two-sidewall craft (using principles of symmetry of forces due to the differing aspect of port and starboard sidewalls) and comparisons were made between the tunnel data and the Danish tank data after scaling the tunnel

results to the Danish model size (since both tests were run at the same Froude number. A representative result of such comparisons is shown in (Figures 8 and 9) where good agreement is exhibited between both sets of data. This result indicates that the free surface, for conditions of static sideslip angle changes, essentially behaves as a rigid wall. Such a result also correlates with the theoretical results given in Equations (3) and (4) since the lateral added mass representation there is based on a "reflected" image model that corresponds to the rigid wall free surface limit behavior.

The investigation in (5) also considered tests wherein cavitation occurred on the model in a closed water tunnel, as well as ventilation in a free surface water tunnel. Since some of the free surface tunnel data was affected by the tunnel wall influence, spray, limited test section dimensions, etc. the result obtained under cavitating conditions in a closed tunnel will be used to illustrate the effects of these related flow phenomena. Illustrations of the effect of cavitation are given in (Figures 10 and 11) where comparison is shown between data obtained at atmospheric pressure and that at reduced pressure corresponding to a cavitation index of  $\sigma = 0.2$ . The data in these figures represents a synthesized two-sidewall hull, as discussed previously, so that comparison can also be made with the towing tank static sideslip test results. It can be seen that there is only little influence of cavitation in these hydrodynamic forces, even for cases with a significant amount of cavitating flow present. Since the water tunnel data at atmospheric pressure compares well with the towing tank data for the same conditions, it can be seen that cavitation effects on the side force and yaw moment characteristics of SES sidewalls are relatively small. Similarly results are also found for the effects of ventilation, as indicated from free surface water tunnel test data in (5).

With regard to frequency dependence of the measured forces, the tests were carried out on single frequency (15 rpm) which was the highest possible for the PMM apparatus used. The non-dimensional frequency  $\omega l/u$  for the model test lies in the range of 0.56 - 0.81, which is a low value that is also associated with the high speed nature of SES craft. For the lateral motions of full scale 100 ton SES testcraft, the maximum frequency affecting the craft yaw and sideslip motions is of the order of the rudder rate during maneuvering, which would be about 0.2 rad./sec. The non-dimensional frequency value for the 100 ton testcraft, with a sidewall length of 60 ft. and a speed in the range of 50 - 80 kt., would be quite low in this case. The largest frequency present during maneuvering of the 100 ton testcraft is about 1.5 rad./sec., which corresponds to the roll motion natural frequency, and that particular mode of motion has been found to have only small influence (during transient maneuvers) on the yaw and sideslip motions. Thus it appears that frequency dependence of the hydrodynamic lateral force and yaw moment is not significant, and that the quasi-steady data obtained from PMM tests can be applied to adequately predict SES craft maneuvering performance. The effectiveness of applying results obtained from the present test data, using the concepts, theory, etc. developed as part of the overall investigation and applied to various craft, is demonstrated by the results exhibited in the following sections.



Comparison With Full Scale Maneuvering Responses  
As a result of the tests reported here, together with the subsequent validation of the theoretical expressions, these expressions were incorporated into the six degree of freedom motions program. Generalized expressions valid for arbitrary sidewall shapes were employed in the computer program, which takes account of the instantaneous position of the craft sidewalls (and other appendages, seals, etc.) relative to the water surface. The program can then be applied to determine craft motions with six degree of freedom, including vertical plane forces associated with the pressurized regions of the craft and hydrodynamic effects (to be discussed in a later section). Comparisons were made with a number of horizontal plane maneuvering trajectories of the U.S. Navy 100 ton SES testcraft that are continually being tested in order to provide basic performance data for SES craft development. Particular illustrations of the results obtained for different operating conditions of the SES 100 B craft, following specified rudder deflections, are shown in (Figures 12 and 13). These figures show the measured craft trajectories (primarily lateral plane responses) which are compared with the predicted motions using the computer program described in (2). As can be seen, there is very good agreement between the computer program and the measurements, with the only significant differences exhibited in the roll responses which can be ascribed to the presence of small ambient waves (the trajectory computations were carried out assuming smooth water conditions). The degree of agreement shown here indicates good correlation between theory (i.e. the computer program) and actual experimental transient maneuvering data, where the basis for the representation of the hydrodynamic forces and moments for this particular testcraft is the mathematical model for lateral hydrodynamic forces that was validated by the extensive PMM test series described here.

#### VERTICAL PLANE FORCES AND MOMENTS

##### Model Tests

The vertical plane motions of SES craft involve different contributions to the vertical force and pitch moment that arise from pressure effects as well as hydrodynamic and hydrostatic terms. In order to determine the hydrodynamic and hydrostatic effects, and to compare the values with available theory, it is necessary to carry out model tests. The method for obtaining such experimental data is by means of captive model tests having static and dynamic variations in the vertical plane variables (heave and pitch and their derivatives), which is similar to the procedure used to determine the lateral plane hydrodynamic forces and moments.

The model tested was essentially similar to that used in the lateral plane investigation. The test apparatus used was an oscillator that had previously been used as the PMM for lateral oscillations of surface ships, described in (1). This particular device was rotated from the horizontal plane to the vertical plane, with new stiffening struts added. The apparatus could then be used to measure vertical force and pitch moment for oscillatory and static displacements of heave and pitch.

The test program involved both static and dynamic tests using the vertical PMM oscillator for imposed displacements in heave and pitch (sepa-

ately). The tests were carried out (with oscillations) for a range of frequencies (24-80 rpm), at a fixed oscillation amplitude. The static tests involved changes (in both directions, i.e. positive and negative) in heave and pitch orientation relative to the initial equilibrium reference condition. All of the tests were carried out for the model oriented at two basic trim reference conditions. These conditions are listed below.

Table 3 Test Conditions

Condition	CG draft, in.	Pitch trim, deg.
1	3.0	+ 0.5
2	4.5	+ 1.0

The tests were carried out for each condition at three different forward speeds. These speeds (in model scale) were 5 kt., 8 kt., and 12 kt., which represented two speeds above the hump speed and one speed for the sub-hump condition for this model. The fan settings were determined (via trial and error) in order to establish representative values of bubble pressure and seal pressure that were considered appropriate to the particular speed, with lower pressures at the lower speed, etc. These nominal pressures were also considered applicable to both geometric conditions given in Table 3.

Since the equations of motion in (2) for vertical plane motions employ a water level coordinate system, the heave motion is purely vertical and the pitch motion is a small angular rotation about the y-axis, which does not require the PMM apparatus to function other than as a pure oscillator in pitch. Corrections to the data to account for model mass and inertia tares are made to account for the forces and moments acting on the model when it is oscillating in air. For the present case of an SES craft, the presence of tare values due to the cushion pressure must also be accounted for, in both the static and dynamic modes of motion, so that the hydrodynamic forces can be obtained after processing the measurements of total craft forces. This procedure allows for determination of the non-pressure effects, which are generally expected to be small for heave motion (since pressure variation is the dominant effect). The pitch moment variations are, however, expected to depend primarily upon the hydrodynamic and hydrostatic effects.

The data reduction and analysis procedure is similar to that employed in the lateral motion tests, after correction for the tare values (including the pressure tare values). Separate identification of the in-phase and out-of-phase components for the oscillation tests allows determination of the variation of any particular force or moment with respect to either displacement, velocity, etc. This procedure is primarily applicable to measurements that are close to harmonic in time history form, and basically accounts for linear terms. The measured data for the static orientation tests are directly obtained after tare corrections, and represent the pure hydrodynamic forces (gage zero reference at zero speed, includes hydrostatic effects). Hydrostatic effects, which are necessary when comparing theory and experiment, are computed for the model craft according to its particular orientation in the water.



### Model Data and Comparison with Theory

The static test data exhibited a variation of vertical force and pitch moment with both heave and pitch orientation that was primarily due to hydrostatic effects, i.e. hydrodynamic effects were generally small. An illustration of the relative values of hydrostatic and hydrodynamic pitch moment variation with pitch angle is shown in (Figure 14) which verifies this result. The hydrodynamic pitch moment exhibited in this figure also includes a small contribution due to pressure forces on the bow seal. The result of this comparison is the lack of influence of the pitch stiffness derivative  $M_{\theta}$  on forward speed, which is also exhibited in data for a range of forward speeds in (6).

Expressions for the vertical force and pitch moment acting on both sidewalls of an SES craft, due to hydrostatic and hydrodynamic effects, were derived on the basis of slender body theory. These relations are given as

$$Z_{sw} = -2\rho g \int_{x_s}^{x_b} S dx - 2A'_{33s} u^2\theta - 2A'_{33s} uw + 2(A'_{33s} x_s - A_{33s}) qu \quad (13)$$

and

$$M_{sw} = -2x_s A'_{33s} qu + 2\rho g \int_{x_s}^{x_b} Sx dx + 2(A'_{33s} x_s + A_{33s}) u (w + u\theta) \quad (14)$$

where

$A'_{33} = \rho \pi B^*(x)^2/8$ , vertical added mass of sidewall section, with  $B^*(x)$  = local sidewall waterline beam;  $A'_{33s}$  is value of sidewall stern

$w$  = vertical velocity

$q = \dot{\theta}$  = pitch angle velocity

$A_{33} = \int_{x_s}^{x_b} A'_{33} dx$ , total sidewall vertical added mass

$S(x)$  = sectional area of sidewall in planes normal to x-axis

In addition there are expressions for the vertical force acting on the bow seal (due to pressure on the wetted "footprint" area of the seal on the water surface) and the stern seal. For the stern seal the vertical force due to craft motions in the vertical plane is given by the quasi-steady representation

$$Z_{stern\ seal} = -\rho \frac{\pi}{4} u b \cdot \ell_{ski} (w - x_{ss} q) \quad (15)$$

where  $\ell_{ski}$  is the wetted length of the seal ( $b \ell_{ski}$  = wetted area of stern seal) and  $x_{ss}$  is the longitudinal coordinate location of the midpoint of stern seal wetted length. The pitch moments of these seal forces are obtained from their geometric moment arms.

In the oscillatory tests the resulting variations of force and moment with vertical velocity showed only small values, and generally no agreement between hydrodynamic theory and the measured values. The only hydrodynamic term of significance, for which some correlation with theory could be obtained, was that of pitch damping,

i.e. the variation of pitch moment with pitch angular velocity  $q$ . In carrying out such a comparison another possible effect is considered, viz. hydrodynamic force associated with wave generation and damping due to the craft sidewalls oscillating in the free surface. The general expressions of the force and moment due to such damping are

$$Z_{damping} = -2 \int_{x_s}^{x_b} N'_z (\dot{z} - x\dot{\theta} + u\theta) dx \quad (16)$$

and

$$M_{damping} = 2 \int_{x_s}^{x_b} N'_z x (\dot{z} - x\dot{\theta} + u\theta) dx \quad (17)$$

using a strip theory representation, with  $N'_z$  the sectional heave damping for the sidewall which can be approximated for low frequencies.

Comparison of the pitch damping variation from experiment with that from the theory is shown in (Figure 15), with the different theoretical contributions shown. It can be seen that the sidewall slender body theory result is relatively small, with the major contributions being that of the stern seal and sidewall wavemaking. Other cases not shown indicate the primary effect to be due to the stern seal. While the stern seal contribution is significant, an accurate evaluation of its effect depends upon the stern seal wetted area which is estimated from static tests for use in this theoretical evaluation. Similarly the validity of the sidewall wave generation representation for high speed conditions, as experienced here, is also open to question, with a more valid demonstration possible if oscillation tests are carried out without a pressurized cushion, seals, etc. in order to isolate pure sidewall effects alone.

### Predicted Vertical Plane Motions

The utility of any theoretical prediction tool, which is based on methods developed in coordination with experimental force measurements as described above, is determined by comparison with a range of test data. A number of operating conditions of full scale 100 ton SES testcraft running in waves (Gulf of Mexico, Chesapeake Bay) have been simulated using the program described in (2). Using the measured wave spectra in the operating area, prediction of vertical plane responses such as CG and bow vertical acceleration, pitch angle, pressure, etc. have been made in the form of mean values, rms and higher order statistical responses (1/3 highest, 1/10 highest, etc.). Comparison with the measurements indicated agreement with 10-15% over the range of operating mission conditions analyzed.

Other comparisons have been made with model test data for responses in regular waves in towing tanks. Since pitch motion is the main response for which the hydrodynamic and hydrostatic effects are important, a representative comparison of predicted pitch motion response with model test data for a model of the same design as those discussed in this paper is shown in (Figure 16). Similar comparisons have been obtained for other model designs, operating over the speed range from 0-20 kt (model scale) which showed good agreement in regard to the important vertical plane responses of pitch, heave, acceleration, etc. The basic formulation in the computer program, when serving as a prediction tool, provide adequate simulation of SES craft responses using the various theoretical expressions that were developed with the aid

of the experimental studies reported here. The effects that are indicated to be dominant are actually so, and those that are small and not significant also behave in that manner (even if the theoretical expressions do not precisely match the force variations that occur with little consequence on craft responses).

#### BOW SLAM PRESSURES AND FORCES

Slamming is an important problem for SES craft since the impact occurs over a large transverse extent of the bow region for such craft. The operating 100 ton testcraft, as well as all of the present designs for large 2000 ton SES craft, incorporate flexible bags as part of the bow seal, which come into contact with the water surface during the impact associated with slamming.

In order to provide some means of simulating the resulting loads that occur during slamming, some form of simulation of slamming should be carried out in order to provide controlled motions that could then be related to the resulting slam pressures and loads of a bow bag seal in time history form. Such a procedure is carried using a vertical oscillation in a towing tank for a model having a bow bag, allowing control of the vertical bow motion as well as the craft forward speed. This technique would then provide information leading to an understanding of the phenomena associated with bow bag slamming, and also to ultimately relate such data to SES design considerations.

#### Test Procedure

Since the purpose of these tests was to study the phenomena associated with bow bag slamming, the pressure and loads acting on the bow are measured continuously with respect to time (and immersion). The PMM oscillator motion is recorded, and together with knowledge of the settings for amplitude, frequency, etc., the instantaneous position and velocity of all craft elements is thereby known at all times. The pressure in the bag is a consequence of the flow into and out of the bag, and also of the state of the bag with respect to its deformation and immersion. The external loads (including moments) are a consequence of the bag deformation and immersion.

In addition to the bag pressure and the loads acting on the bow, the pressures in the cushion and stern seal were also obtained so as to ascertain any influence of bow bag slamming on other aspects of craft performance. Since the loads had to be corrected for acceleration, the vertical bow acceleration was also measured. Table 4 summarizes the measurements made.

The tests are run for various forward speeds, with the oscillator characteristics set to cover a range of vertical velocities that are expected to result in slamming. Time history outputs of all the measured data in Table 4 are then available for comparison of instantaneous values throughout the various cycles, with an expected repetitive characteristic of the measured responses due to the oscillatory motion.

Table 4 Summary of Measurements

Measurement	Location		Type
	Bag	Port and starboard sides	
Pressure	Cushion	Single, at center	
	Stern Seal	Single, at center	
Loads	Bow	Vertical force (port and starboard)	
		Horizontal force (port and starboard)	
		Pitch moment (port and starboard)	
PMM Position	Craft	(i)	Continuous recording
		(ii)	Pulses at min., max. and zero crossings
Acceleration	Bow	Vertical	

#### Data Obtained and Application of Results

Since a theoretical analysis of this problem involves considerations of three distinct physical phenomena, viz.

- i) flow in and out of the bag with volume change
- ii) bag membrane equilibrium
- iii) hydrodynamic flow over the bag - water contact surface

any theoretical analysis would appear to be an extensive and complex study. The measurements obtained, together with motion pictures of the impact process during various oscillation tests, provides insight into the nature of the bag deformation. A representative picture of the possible bag deformation during immersion under slamming conditions is shown in (Figure 17). There are a number of possible shapes during the impact including the possibility of hard structure impact, as illustrated in (Figure 18). The exact nature of the bag shape determines the forces acting on the craft bow, and allows an interpretation that would permit structuring a simplified mathematical analysis. Effective orientation of the bag with respect to the water surface, representing an angle of attack, as well as the deformation of the bag surface being viewed as a continuously changing camber are possible approaches toward this type of representation.

Aside from the visual observations that permit an establishment of a possible analysis based on the bag deformation, the measurements themselves provide useful data for structuring an analysis. The occurrence of the peak pressure relative to the immersion conditions is demonstrated by such data as in (Figure 19). Similar information on the impact forces measured during slamming, in time history form, are also obtained as outputs from this test procedure.

The tests are run over a range of speeds wherein slamming is expected to occur, with the resultant vertical velocity at the bow lying in a range wherein prior investigations have shown slam effects to occur. That data obtained for bow bag pressure and bow loads provides quantitative information on the expected magnitude of such

loads when simulating conditions expected to occur for an SES craft oscillating in waves. Effects of forward speed, vertical velocity, exhaust orifice area, etc. are then determined from a series of runs covering such a range of variables appropriate to various possible craft designs.

In view of the possible sensitivity of slamming responses to the relative angle between the impact region and the water surface, the vertical velocity due to the imposed oscillation may not be a complete simulation of actual SES craft slamming in waves. However the influence of the vertical velocity and the effect of angular orientation, bag deformation, etc. obtained from these tests allows establishment of a mathematical model that will incorporate such effects. This mathematical model could then allow for the presence of the water slope at the bow due to the waves, as well as the wave vertical orbital velocity, in arriving at some means of proper simulation of this complex phenomenon. Work in this area is presently continuing, with further studies planned to allow development of a useful simulation tool that can be incorporated in a computer program in order to predict the range of structural loads that will be experienced by SES craft during slamming in waves.

#### CONCLUDING REMARKS

This paper has shown a number of applications for SES craft development wherein the use of oscillators provides useful data. The application and extension of the measurements obtained for both lateral and vertical hydrodynamic forces and moments allows a theoretical representation of such effects within a computer simulation program, which provides good correlation with experimental data on craft motion response obtained in model tests and for full scale testcraft operating under actual environmental conditions. The test procedures used provide insight into various phenomena, as well as indicate the predominant forces acting on SES craft during the different modes of motion. The important dynamic effects due to angular velocities can only be determined (simply) with oscillator systems, and they are therefore useful devices for SES development just as in the case of conventional surface ship dynamic studies. The utility of the lateral plane PMM system is illustrated by the recent construction and application of such a device in a dedicated towing tank facility at NSRDC for specific use in SES testing and development studies.

The use of a vertical oscillator to simulate slamming effects under controlled conditions is another application for SES craft that represents a method for obtaining insight into different phenomena, as well as providing representative data for the effect of slamming on bow bag seals. Further effects using such a device will ultimately lead to establishing a mathematical model for computer simulation purposes to aid in evaluating slam responses on SES craft. It is a fond hope that the results obtained from such an investigation will provide as useful a model for representation of slam effects as have the oscillators used for determining the hydrodynamic forces that affect the motions of such craft.

#### REFERENCES

1. Strøm-Tejsten, J., and Chislett, M.S., "A Model Testing Technique and Method of Analysis for the Prediction of Steering and Manoeuvring Qualities of Surface Vessels," *Proceedings of the Sixth Symposium on Naval Hydrodynamics*, 1966.
2. Bentson, J., Kaplan, P. and Davis, S., "Simulation of Surface Effect Ship Motions and Loads," Paper to be presented at 1976 Summer Computer Simulation Conf., Washington, D.C., July 12-14, 1976.
3. Chislett, M.S., and Smitt, L.W., "A Brief Description of the Hya Large Amplitude PMM System," *Journal Mechanical Engineering Sci.*, Vol. 14, No. 7, Supplementary Issue, London, 1972, pp. 80.
4. "Nomenclature for Treating the Motions of a Submerged Body Through a Fluid," *SNAME T&R Pub.* No. 1-5, 1952.
5. Lehman, A.F., and Kaplan, P., "Investigation in SES Aero-Hydrodynamic Problem Areas - Part III: Experimental Studies of Free Surface Effect on Hydrodynamic Forces and Pressures of SES Side-walls," *Oceanics, Inc. Rpt. No. 74-108C*, Sept. 1974.
6. Kaplan, P., Silbert, M.N., and Bono, P., "Investigations in SES Aero-Hydrodynamic Problem Areas - Part IV: An Experimental Study of SES Craft Vertical Plane Hydrodynamic Forces and Moments," *Oceanics, Inc. Rpt. No. 74-108D*, Sept. 1974.



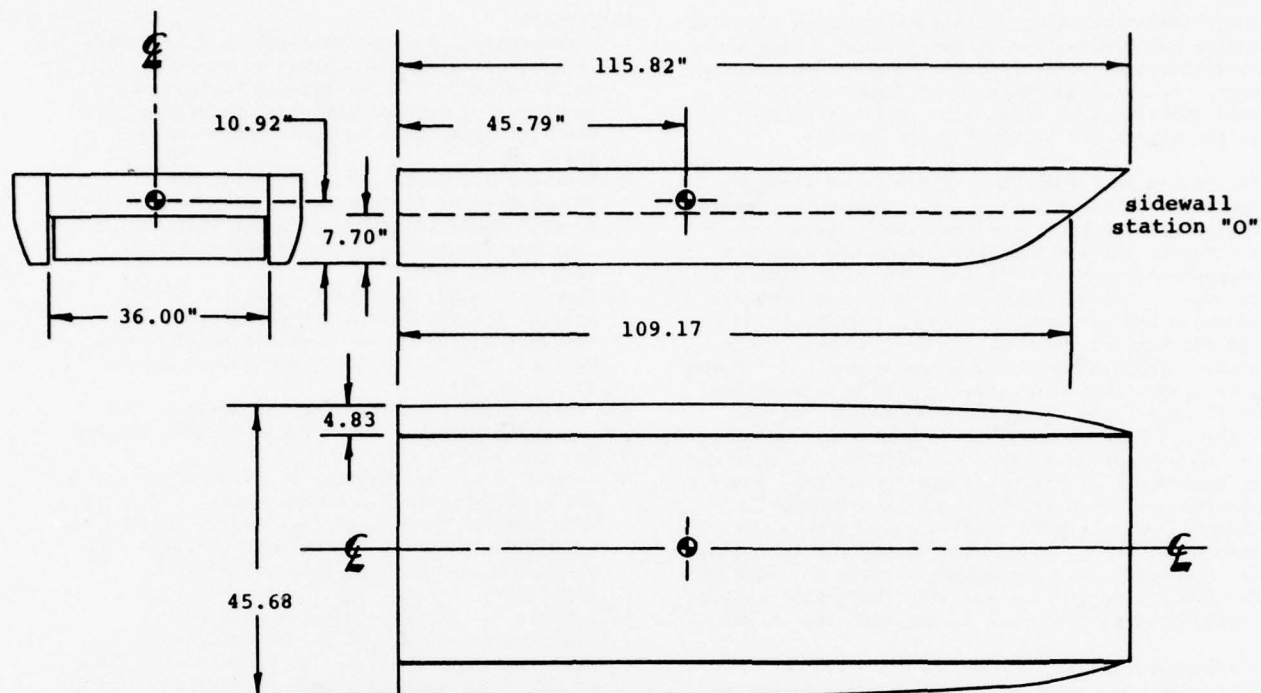
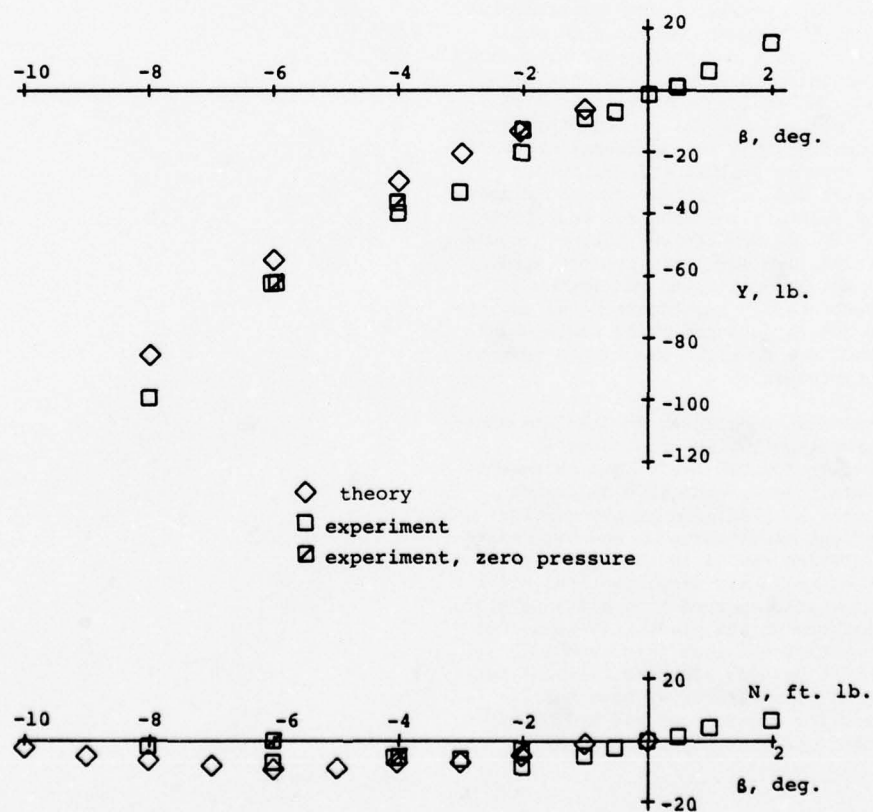


Fig. 1: General arrangement of test model

Fig. 2: Variation of side force and yaw moment with sideslip angle,  $u = 26.2$  ft./sec.

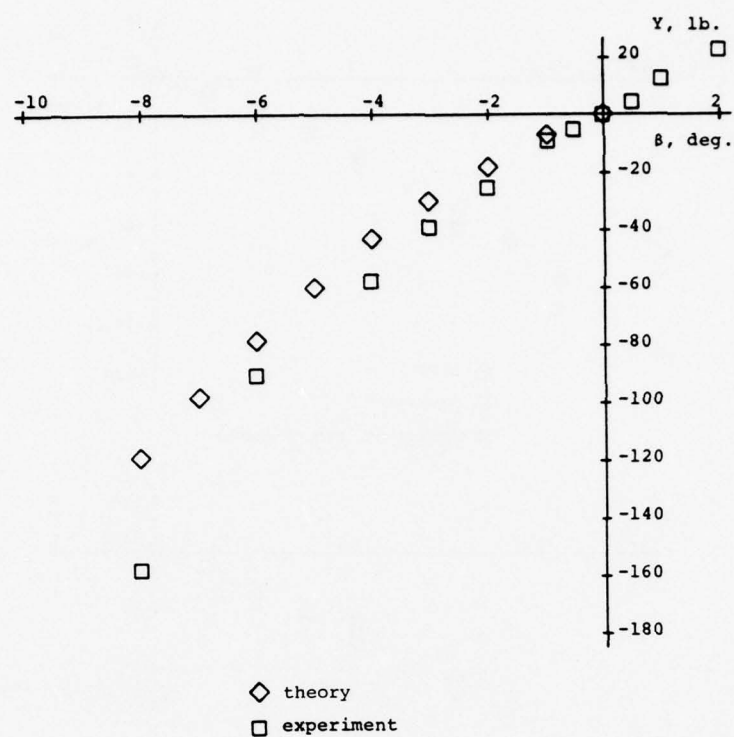


Fig. 3: Variation of side force with sideslip angle, model with ventral fins,  $u = 26.2$  ft./sec.

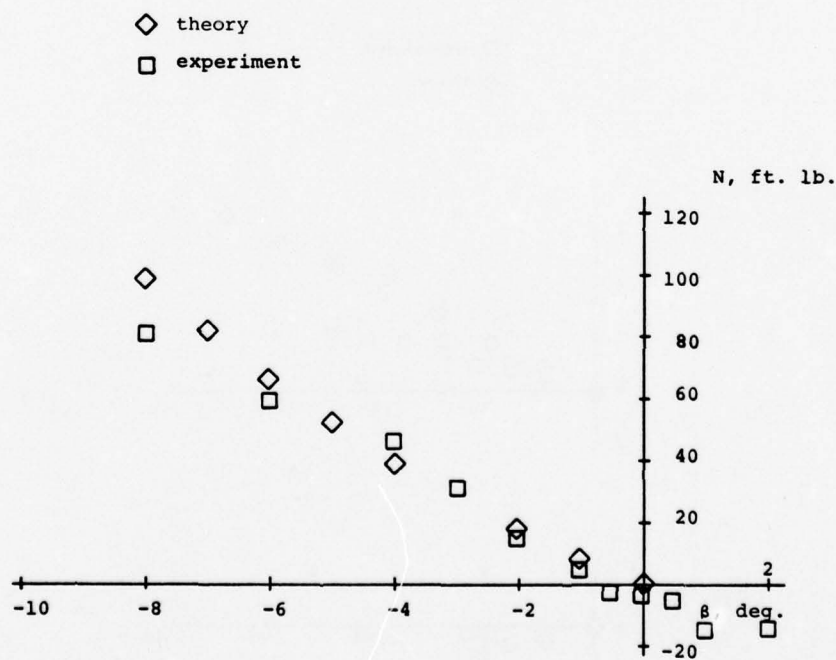


Fig. 4: Variation of yaw moment with sideslip angle, model with ventral fins,  $u = 26.2$  ft./sec.,  $\theta = 1^\circ$ ,  $\beta = 0^\circ$

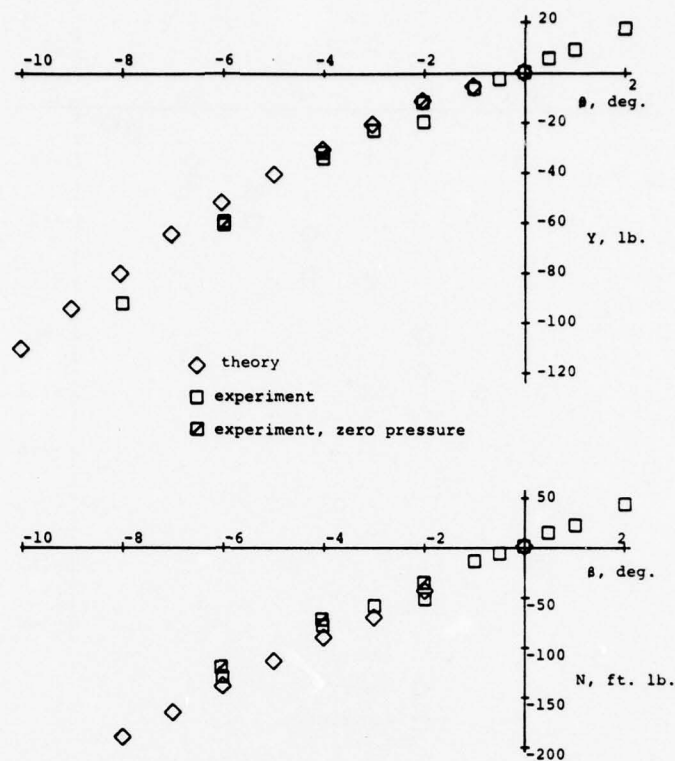


Fig. 5: Variation of side force and yaw moment with sideslip angle,  $u = 18.1$  ft./sec.,  $\theta = -2^\circ$

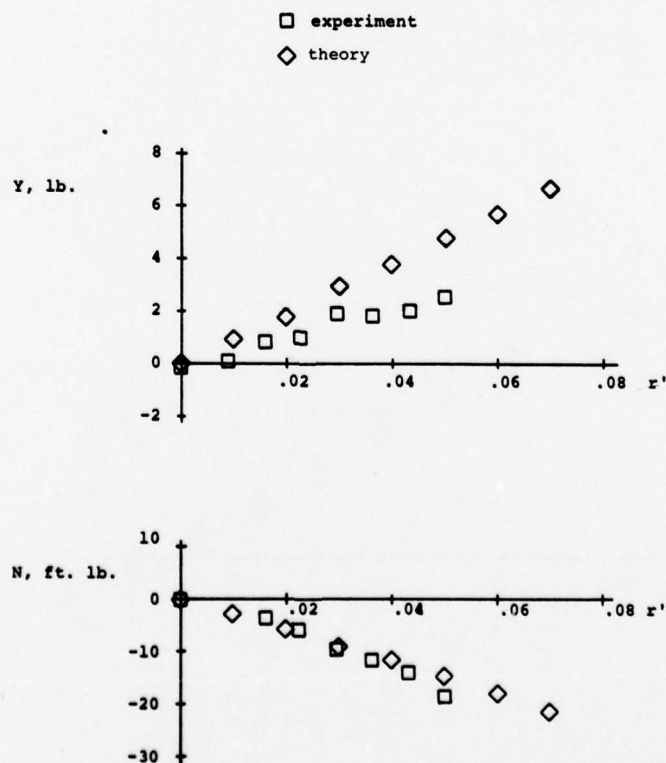


Fig. 6: Variation of side force and yaw moment with yaw angular velocity (nondimensional),  $u = 26.2$  ft./sec.,  $\theta = 1^\circ$ ,  $\beta = 0^\circ$



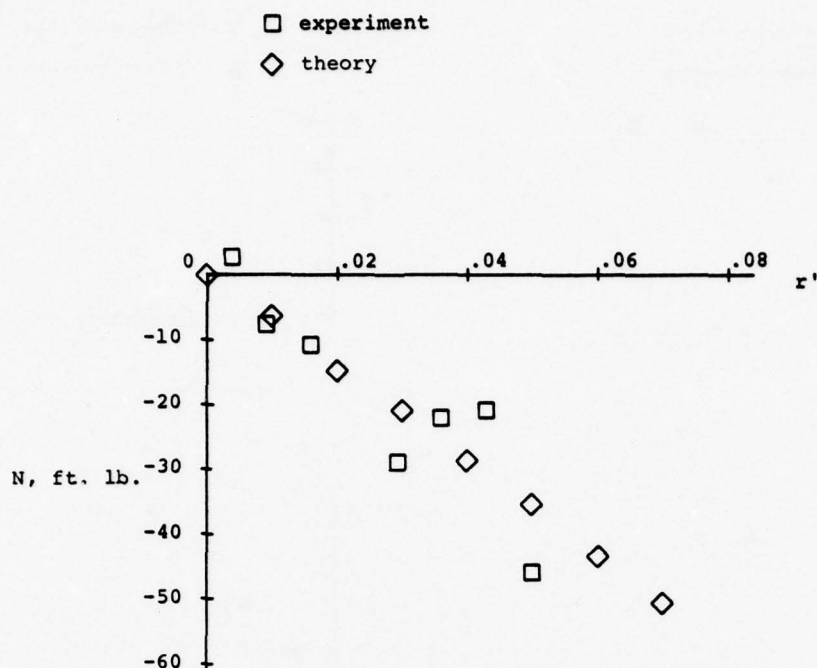


Fig. 7: Variation of yaw moment with yaw angular velocity (nondimensional),  $u = 26.2$  ft./sec.,  $\theta = -2^\circ$ ,  $\beta = 0^\circ$

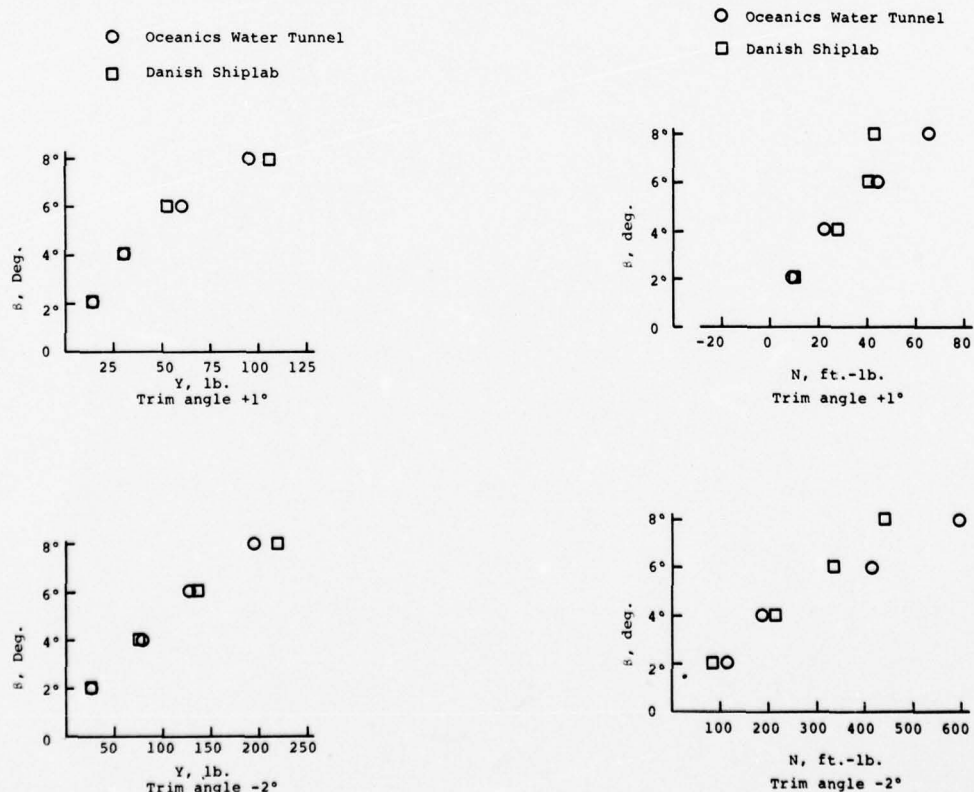


Fig. 8: Side forces obtained at atmospheric pressure data presented in terms of Danish model size at a test velocity of 26.2 ft./sec.

Fig. 9: Yaw moments obtained at atmospheric pressure. Data presented in terms of Danish model size at a test velocity of 26.2 ft./sec.

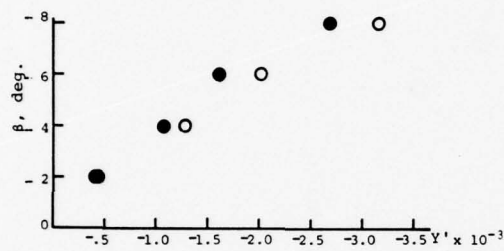
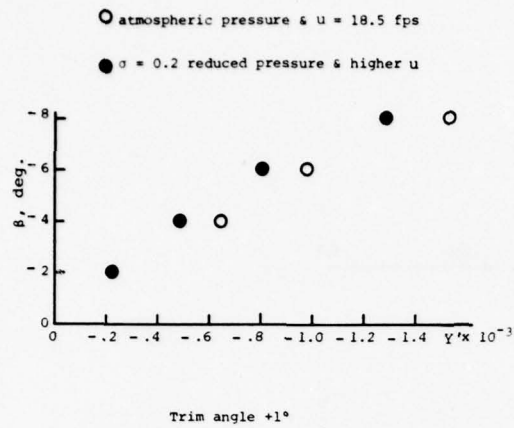


Fig. 10: Side force coefficients for two sidewalls. Oceanics water tunnel data obtained at atmospheric and reduced pressure

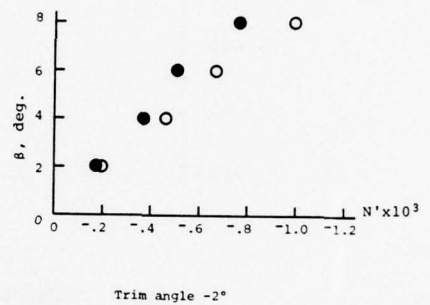
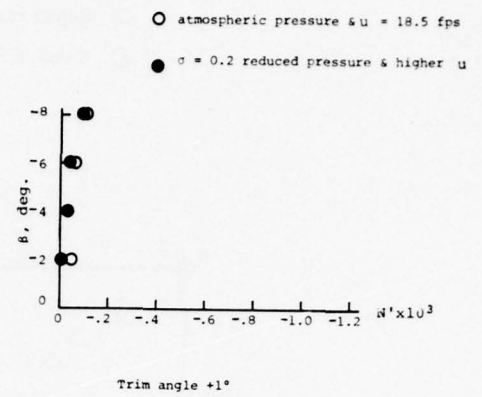


Fig. 11: Yaw moment coefficients for two sidewalls. Oceanics water tunnel data obtained at atmospheric and reduced pressure

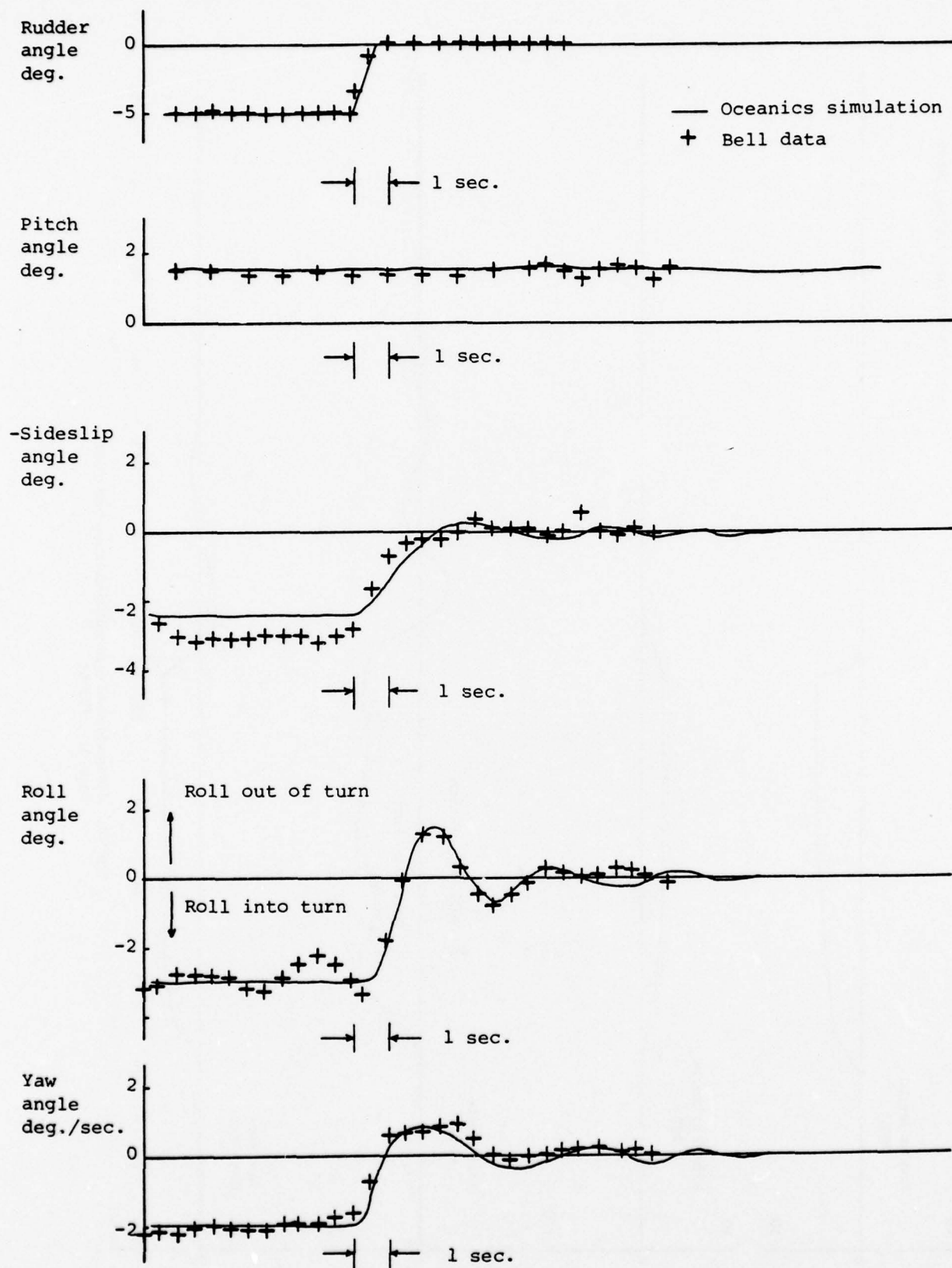


Fig. 12: Comparison of oceanics simulation and craft data, turn exit  $u = 49.5$  Kt



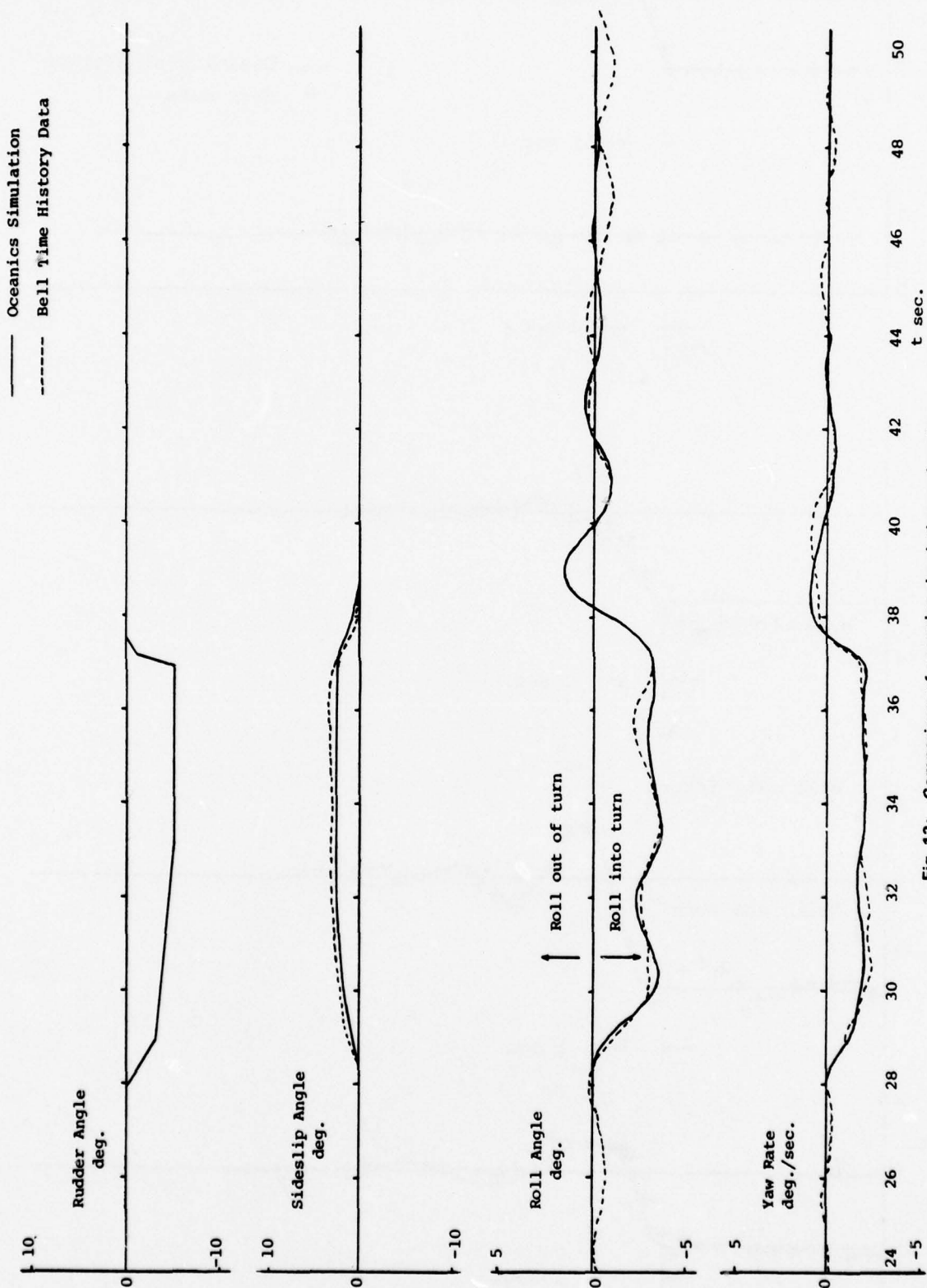


Fig. 13: Comparison of oceanics simulation and craft data  $u = 49.5$  Kt

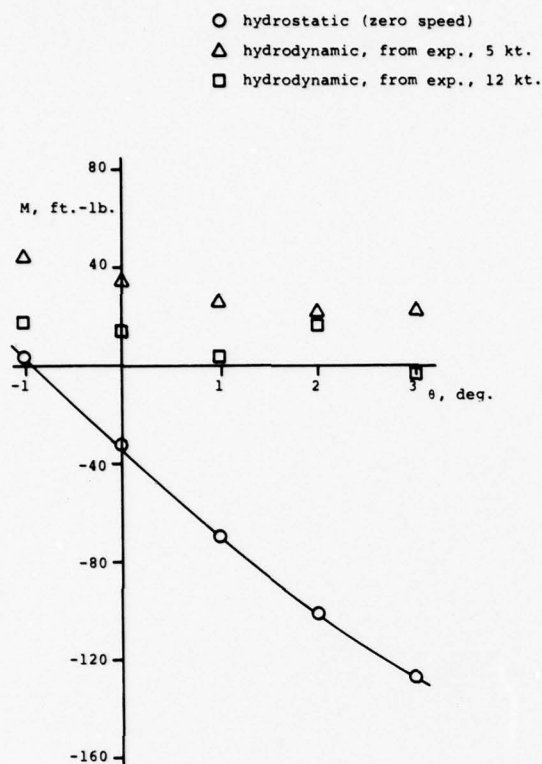


Fig. 14: Variation of pitch moment with pitch angle, illustrating comparison of hydrodynamic moments and hydrostatic valve

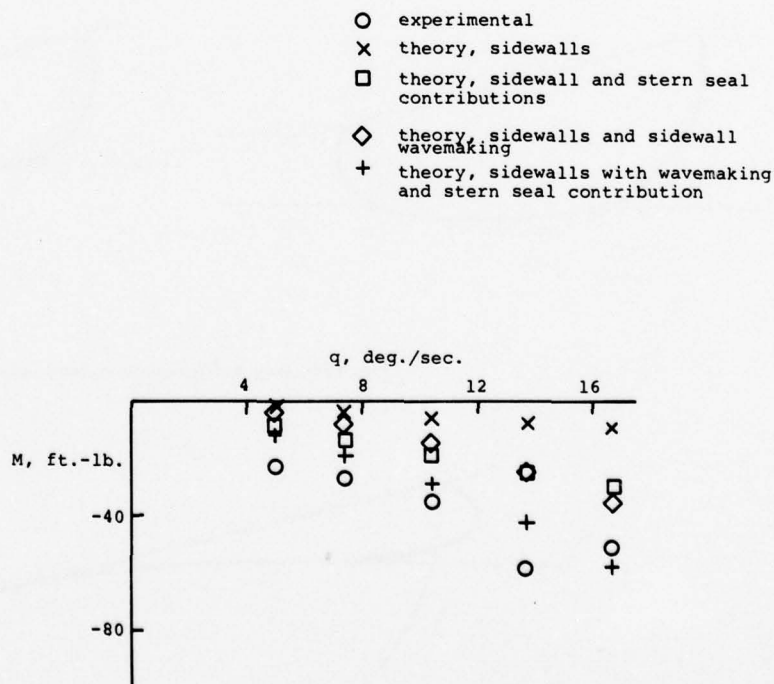


Fig. 15: Variation of pitch moment with angular velocity, condition 1,  $u = 8$  Kt

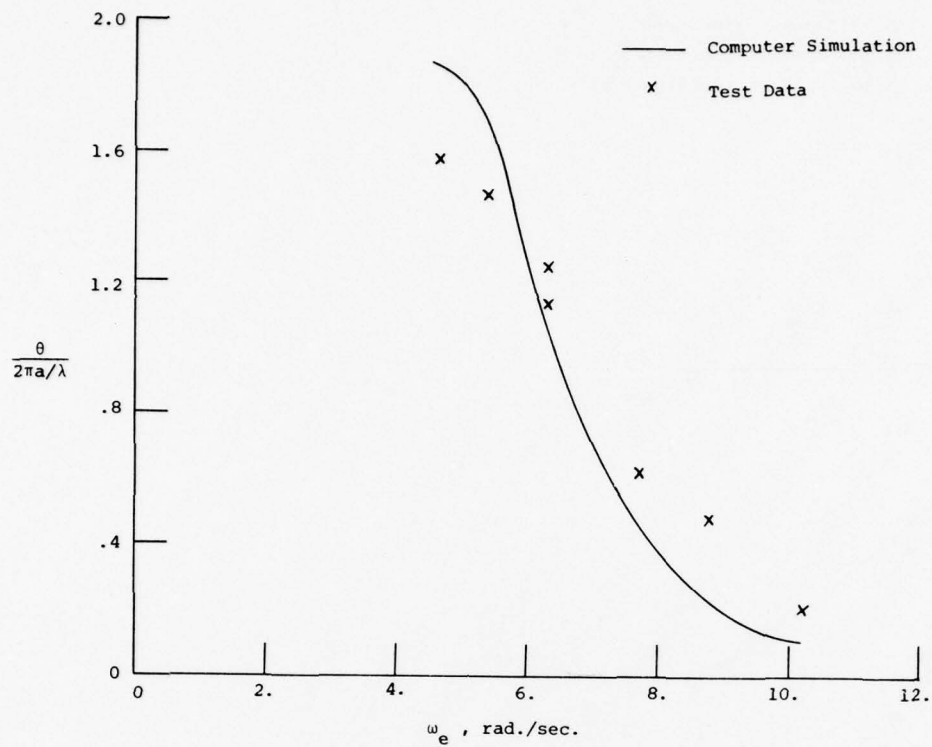


Fig. 16: Comparison between computer simulation and head sea model test data, pitch,  $u = 4 Kt$

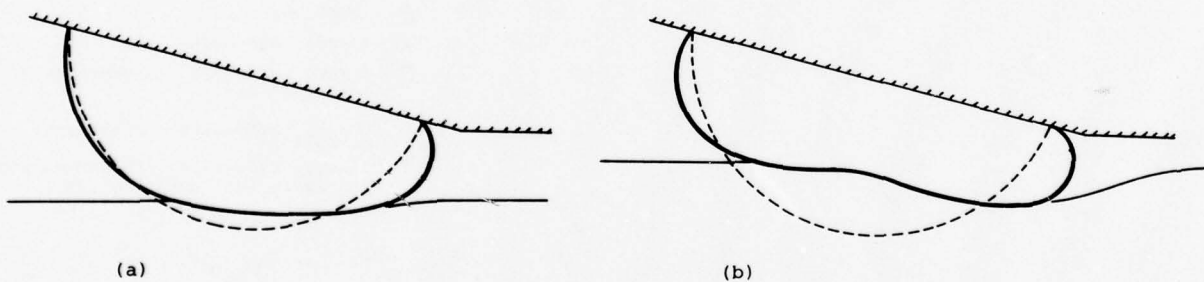


Fig. 17: Bag deformation during immersion

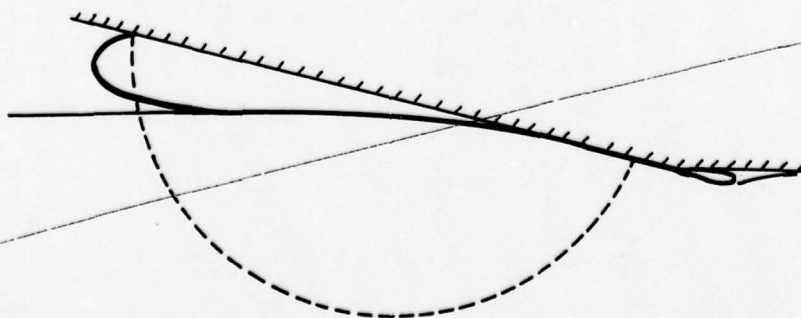


Fig. 18: Head structure impact



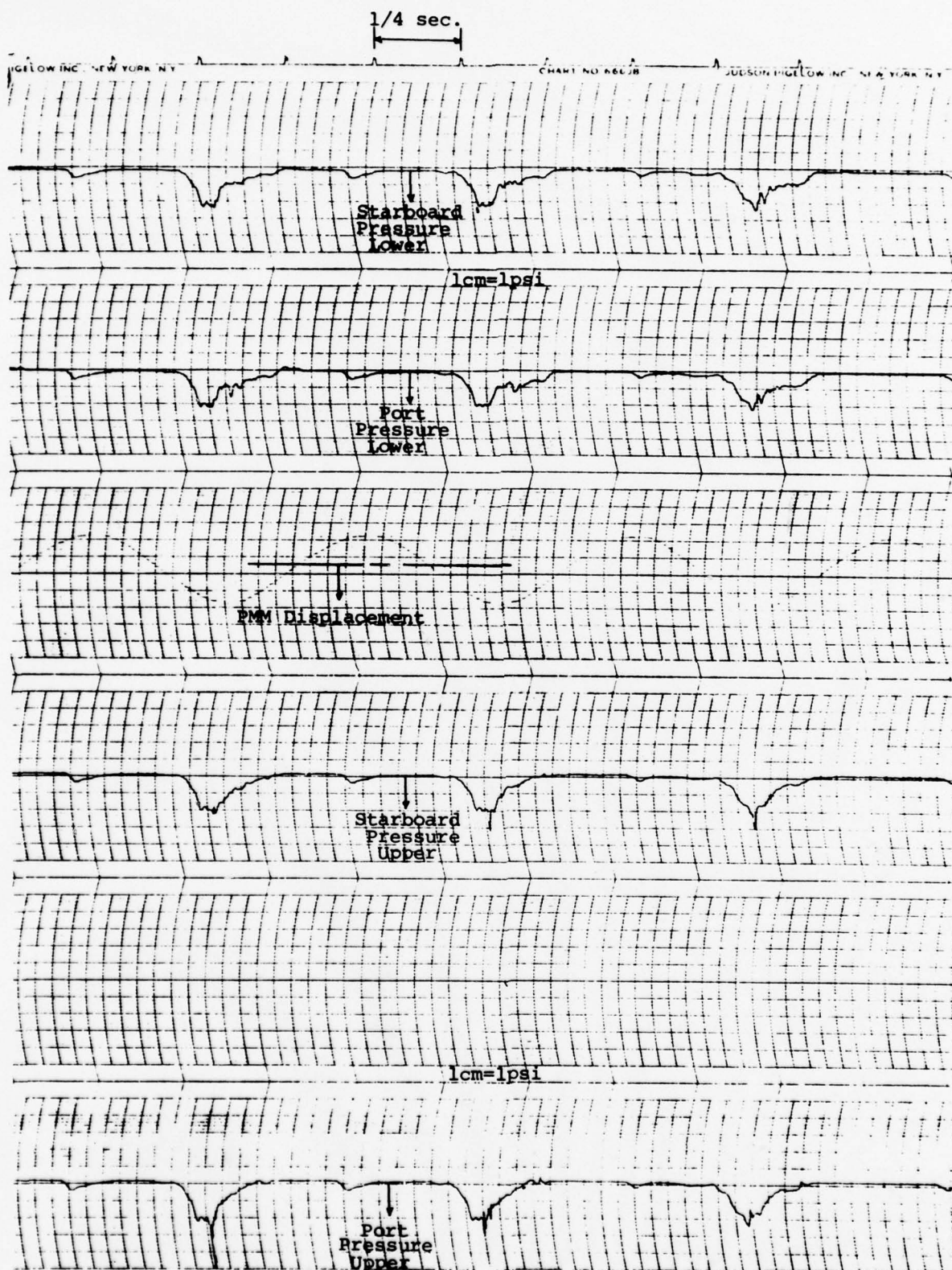


Fig. 19: Bag pressure, run 305, 8 Kt., 76 rpm,  
4° amplitude, 0 heel

# Discussion on Paper by R. Wade et al

L.J. DOCTORS

Could the authors explain the origin of their calculations for the spray drag - in the formulas that follow (7)? The implication of these formulas is that the spray drag is proportional to the strut thickness, presumably for affine shapes. Secondly, the spray drag is shown to be proportional to the cube of the speed, yet surely there are very strong effects of the Reynolds number (based on some measure of the spray thickness), and of the Weber number? A further point here is that the presence of the cushion will reduce the wetted surface in general and this will have a strong influence on the spray drag.

## Authors' Reply

The following comments are offered in response to Dr. Doctor's remarks.

The calculation of the spray drag, as discussed in the paper, was obtained by analysing photographs of the wetted spray areas generated by the spray. Once these wetted areas were obtained, a friction factor  $C_f$  based upon the Reynolds number of the flow was determined and a drag calculated from:

$$D_{\text{spray}} = C_f q A_w$$

where  $A_w$  = wetted spray area;  $q$  = dynamic pressure.

In order to cast this drag formula into the one given in the paper, an equivalence of the wetted spray area  $A_w$  to the characteristic thickness and length of the bow or fairing shape was obtained as

$$A_w = K(tc)$$

where  $K$  = proportionality constant;  $t$  = maximum thickness of the bow or fairing in the waterline plane;  $c$  = characteristic length of the bow or fairing from the point of spray generation to the maximum thickness point.

As seen in the paper, this constant  $K$  was determined to be:

0.75 for the bow section

5.5 for the fairing

It must be reiterated that these formulae form a guide to the estimating of spray drag and are only applicable for the sidehull under consideration. The purpose in developing them was to illustrate the point that spray drag can be of significant impact in the overall drag evaluation of sidehulls

for this type of craft and consequently cannot be ignored unless some adequate spray management system is used, such as spray fences. The use of the above technique for spray evaluation obviously depends on many tacit assumptions concerning the mechanism of spray generation and the origin of the resulting drag. Significant among these are (1) the spray drag is assumed to result from friction effects only and (2) the degree of wetting is a function of the body geometry. These assumptions are open to discussion, insofar as Froude effects and indeed Weber number effects in certain regimes could also be important. However, it was not the intent of the present tests to investigate this aspect of drag, but simply to develop some means of assessing overall sidehull drag for this particular model.

In this regard it should be mentioned that apart from Ref.(9) given in the text, a proposed method of spray evaluation other than that contained in Ref. (17) has been presented by Kaplan (Ref.(18)). This method also based on spray wetted area, develops a method for calculating the wetted area based on the geometric properties of the body.

From the formulae presented in the text the spray drag is not proportional to the cube of the velocity, as suggested by Dr. Doctors. The drag is proportional to the square of the velocity through the dynamic pressure and depends further on the velocity through the Reynolds number-dependent  $C_f$  term. This friction coefficient is a function of the local Reynolds number based on the flow velocity and characteristic length,  $c$ , of the body. This is the only Reynolds number effect used in the present calculations. The Weber number effects mentioned by Dr. Doctors were not considered here as it was felt that the surface tension forces are small compared with the dynamic effects. A more

detailed study of spray sheets of this type, however, would be needed to amplify this point.

It is not necessarily obvious that the cushion effects will reduce wetting on the inside of the sidehulls. It is clear from experiments that the craft tends to trim itself closely to the mean water slope caused by the cushion. Thus, under ideal conditions, (i.e. no seals or sidehull effects in the cushion) a reasonably constant wetting is anticipated in the cushion. Outside the cushion, however, local water deformation and the trim of the craft would cause changes in wetting. The exact determination of the actual wetted surface is indeed a difficult chore depending as it does on the interplay of many factors. The results given in the paper only demonstrate a basis of drag evaluation under rather ideal circumstances and should be interpreted as such.

#### REFERENCE

18. Kaplan, P. et al Advanced loads and motions studies for surface effect ship (SES) craft. Part I Oceanics Report No.73-98A, (June 1973).



# Discussion on Paper by L. J. Doctors

D.D. MORAN

The prediction of the vertical-plane dynamic response of an air-cushion supported vehicle (ACV) travelling over a wave field is of importance to the marine engineering community as the design and operation of commercial and military ACVs continues to increase throughout the world. The author is therefore to be congratulated on this timely update of his 1974 contribution to the symposium.

In this presentation the author has added the effects of cushion fluid compressibility to his previous efforts and has greatly increased his discussion of the nonlinear nature of the ACV dynamics through extended numerical study of the effect of encountered wave height.

The effect of cushion compressibility as embodied in the statement of the adiabatic law (Eq. (61)) and the inclusion of the temporal derivative of cushion-fluid density in all volume flow terms (e.g. Eqs. (38) and (41)) is more significant than indicated by previous investigations. The cushion compressibility is the only mechanism in the present model which can yield this scaling phenomenon and since the scaling distortion is shown by the author to be rather large for realistic values of the scaled atmospheric pressure ratio  $p_a/\rho gL$ , it seems that more effort should be expended to include the various other mechanisms which contribute to dynamic scaling effects. In this regard, this discussor's comments following the author's previous O.N.R. contribution are still valid.

In the present model incorporating cushion compressibility, this discussor would also suggest the use of the presently computed cushion density in place of atmospheric density in the author's discharge equations (39) and (40).

In an unpublished examination of ACV dynamics this discussor has determined that a vertical-seal force model as represented by eq. (53) is valid only for small cushion seal displacements. Through a comparison with experimental data it has been found that a more elaborate nonlinear model for the seal restoring force is required in order to reproduce the dynamic response of an ACV in pitch. Further, this discussor still believes that the horizontal skirt drag given by eq. (54) (and eq. (55)) should include viscous and wavemaking contributions as well as the induced drag included in the author's formulation. If this effect is included then the sides of the ACV support system will also contribute to the longitudinal horizontal skirt forces on the vehicle, perhaps with a magnitude comparable to the transverse sections.

The nonlinear dynamic behaviour of the author's numerical model has been interestingly demonstrated in the curves of heave and pitch root-mean-square response as a function of wave height. The most significant feature of these presentations (Figs. 9 (see Fig. 9a) and 10) is the implication that the inclusion of cushion compressibility results in a

divergent solution for zero wave amplitude. Linear theory must be valid for wave heights approaching zero. This fact requires that the heave response in particular approach a finite limiting value for wave heights equal to zero. Although the author's model behaves properly for stiff cushions, when the cushion fluid is allowed to be compressible the expected limiting value does not occur. In this regard it may be beneficial for the author to re-examine the numerical stability for small excitation.

Finally, this discussor must agree completely with the author's concluding remark concerning the importance of correlation of numerical models with the physical reality of model or full-scale experimental data. It is the discussor's opinion that unverified mathematical models have limited value when placed against the needs of modern naval technology.

M.R. SWIFT

The author has certainly demonstrated the importance of air compressibility effects on the performance of air cushion vehicles in waves. In connection with this type of study, the discussor would like to mention that a related line of research is being conducted at U.N.H. in which numerical models are being developed for ACV with different skirt configurations (This work is being sponsored by the David W. Taylor Naval Ship Research and Development Center.) The purpose of this work is to evaluate and compare the seakeeping of various skirt designs. In particular, numerical models have been developed for peripheral jet type of craft as well as divided cushion vehicles. The models include the effects of compressibility, though the hydrodynamic influence has been neglected corresponding, strictly, to motion over land. The divided skirt model resembles the author's earlier work (27), extended to include the effects of compressibility in a manner similar to that outlined in the author's presentation. In the peripheral jet model, a flow system for the skirt, separate from that of the single cushion and consisting of a loop plenum and skirt pericells, was used. The first harmonic response for the peripheral jet model at a Froude number of 1.66 is shown in Fig. 12. For this model, the nondimensional resonant frequencies were between 7 and 9, which is fairly close to the author's results for divided cushion craft.

The main comment of this discussor, however, concerns our experience with models for divided cushion craft in relation to the numerical approach taken by the author. Since the author refers to his earlier work (27)(39) for details of his numerical procedure, the discussor will assume that this information still applies here unless otherwise noted by the author.

In this presentation and in his earlier work, the author's results indicate that rather large

cushion pressure fluctuations take place. These large pressure fluctuations were also generated by the divided cushion simulations done at U.N.H. In fact, the fluctuations were so large and abrupt that it was suspected that they were induced by the computation scheme. The problem was found to be caused by errors in the extrapolation between time steps due to the very small characteristic times for cross flow adjustment between cushions compared with the time scales associated with the overall motion of the craft. Several extrapolation schemes were tried in addition to the simple Euler extrapolation used by the author. These included Runge-Kutta, multi-step methods, rational function and polynomial extrapolation, as well as special methods developed to handle the so-called 'stiff' problems. These are available in standard texts such as that written by Gear (Ref.(46)). It was found that the polynomial extrapolation yielded reasonable results without extensive use of computer time. Error criteria are also provided which are somewhat more reliable than checking convergence to periodic motion.

While these problems may be peculiar to the simulations used by the discussor, it is suggested that careful attention be given to the method of extrapolation when the model is to include cross flow between cushions.

#### REFERENCE

46. Gear, G.W. Numerical Initial Value Problems in Ordinary Differential Equation. Prentice-Hall, Englewood Cliffs, New Jersey (1971).

A.H. MAGNUSON

The author is to be congratulated upon the presentation of his latest results on the prediction of Air Cushion Vehicle (ACV) motions over waves. The inclusion of compressibility in the latest calculations is undoubtedly an improvement over the author's pioneering work (Ref.(39)). In addition, the development of the hydrodynamic representation was simplified by dropping the initial value problem and assuming a 'steady state' form for the solution and a more typical Froude number of 1.5 was used for the calculations.

The first comment has to do with the hydrodynamic representation. The discussor was intrigued by the author's derivation presented in Ref.(39), which is very similar to the present one. Consequently, in an effort to duplicate these results, a solution was obtained to the two-dimensional (infinite aspect ratio) problem. The results of this investigation appear in reference (47). The two-dimensional formulation is closely related to the three-dimensional one in the sense that the singular  $k$  (wavenumber) integration is virtually identical. The three-dimensional solution requires an additional nonsingular azimuthal ( $\theta$ ) integration.

There is one inconsistency between the discussor's results and the author's which may have introduced an error in the surface elevation calculation. This concerns the location of the  $k_3$  and  $k_4$  poles for the supercritical case ( $\lambda > 1$ ). The discussor feels that the wrong branch was taken in the square root term for  $k_3$  and  $k_4$  in Eq.(15). The correct branch can only be taken by solving the dispersion relation (denominator of the  $k$ -integral) before suppressing the Rayleigh viscosity. The migration of these poles as a function of frequency

(taken from Ref.(47)) is shown in Fig.13. Note that for supercritical frequencies the location of the poles is reversed as compared with Fig.2 of Ref.(39). This reversal of pole locations would cause the wave terms associated with these poles to be complex conjugates of the correct expressions.

Another point is that the singular  $k$ -integration was carried out explicitly in Ref.(47) resulting in an entirely analytical solution in terms of well-known transcendental functions. This solution separates the well-known far-field free waves from the near-field effect characterised by exponential integrals in a very natural way using Cauchy's residue theorem. A similar result can be obtained (at the expense of an increase in algebraic complexity) for the three-dimensional problem. One should be able to perform the  $\theta$  integration explicitly by expanding the exponential integral terms in a power series and integrating term-by-term. This type of approach is more desirable than the author's approach in the discussor's opinion, as one does not have to worry about accuracy of numerical evaluation of principal-value integrals and computer programming errors.

Having dispensed with the criticism, I would now like to make a few observations supporting the author's results. First of all, the relative importance of the water surface compliance on the craft dynamics has been an area of controversy for some time. Doctors has taken the positive approach to the controversy by going ahead and solving the problem analytically, finding that the compliance is indeed a first-order effect. (One would not expect the possible error discussed above to have any effect upon this qualitative conclusion.)

The other school of thought is that, because of the high Froude number regime in which these craft operate, the unsteady component of the surface compliance is small enough to be negligible. This point of view was expressed by Kaplan in his discussion of Doctor's first paper (Ref.(39)). Kaplan was sceptical about the importance of compliance for Froude numbers from 1.0 to 2.0, a range representative of these craft. It appears that Doctors' latest results for a Froude number of 1.5 still show that the compliance is a first order effect.

A more direct assessment of the importance of the surface compliance can be obtained by calculating the power dissipated by the radiated wave train caused by the unsteady component of the cushion pressure. This was not done by Doctors, but results for the two-dimensional case were presented by the discussor in Ref.(47). These are shown in Fig.14. The figure is in agreement with Wu's earlier calculation (Ref.(36)). One has the normalised work rate (power) plotted as a function of the nondimensional frequency  $\alpha$  for a delta function pressure distribution. Note that the work rate increases linearly with frequency  $\alpha$  for supercritical frequencies. A typical value of  $\alpha$  for an ACV or SES at design speed and at the pitch resonance frequency would be about 30. The work rate for this frequency is about four times the quasi-steady ( $\alpha = 0$ ) value. Now, the pressure fluctuations of air cushion supported vehicles in waves are typically of the same order of magnitude as the design cushion pressure, corresponding to an acceleration level of about one  $g$ . In this case the power dissipated by the unsteady wave train is four times the power needed to overcome the steady wavemaking drag. Of course, this

numerical result is based upon a two-dimensional delta function distribution. The qualitative result should not differ for the three-dimensional case. No Froude number effect is evident in the figure, as the delta function distribution has no length scale. The effect of a finite length scale would be to introduce 'humps and hollows' in the curve with the delta function result representing an upper bound.

All this means that one can expect the unsteady radiated wave patterns to dissipate several thousand horsepower for a 100 ton testcraft experiencing a one  $g$  acceleration level. The discussor feels that this is enough horsepower to justify substantial funding for research into the phenomenon.

One possible explanation for the pervasiveness of the controversy regarding the importance of the surface compliance could be the results of some early work done by Kaplan (Ref.(35)). He also analysed the two-dimensional delta function pressure distribution and computed the energy dissipation due to wave radiation. His results indicate that the energy decreases with speed. There must be some mistake in the computation, as the results should depend upon the nondimensional frequency only because the delta function has no length

## Author's Reply

D.D. MORAN

The author would like to thank Dr. Moran for his remarks and will answer the points raised in his discussion in order.

The effect of compressibility, as modelled here, is very great. Indeed, attempts were made to compute the motion of a 100 m long craft - corresponding to  $p_a/\rho g L = 0.1$  - but without success. The calculated motion very quickly diverged, indicating that either a smaller time step was needed or improved extrapolation techniques utilised. It is also thought that including some additional effects such as fan dynamics, might affect this, either favourably or unfavourably.

In a similar connection, Dr. Moran suggests using actual computed values of the density in the discharge equations, Eqs (39) and (40). While this would probably introduce some increase in accuracy, it would then be inconsistent not to proceed further and use the full unsteady incompressible Bernoulli equations. Moreover, one wonders how far the concept of one-dimensional quasi-steady internal aerodynamics can be trusted. Large effects from the three-dimensional unsteady nature of the flow are to be expected. Thus, this aspect of ACV craft motion alone could constitute a major research project.

The author fully agrees with the comments about the vertical seal force, Eq.(53). It would be interesting to examine the wavemaking and viscous contributions of the skirt, although rather severe computational problems would have to be overcome.

scale and therefore there cannot be any speed dependence. The results are clearly in conflict with those of the discussor and Professor Wu.

The author has compared his pitch and heave frequency response functions with experimental ones and found that the natural frequency is overpredicted by about a factor of 2. Fig.15 is a heave frequency response function computed from model data for a vehicle quite similar to the craft used by Doctors. This craft has skirt subdivision and weighs about 150 tons. The Froude number was 1.33. The non-dimensional natural frequency in heave works out to be about 5, which is closer in agreement than the data cited by the author. The predicted change in natural frequency with wave amplitude seems peculiar and has not been seen in the limited experimental data available at this time.

### REFERENCE

47. Magnuson, A.H. The disturbance produced by an oscillatory pressure distribution in uniform translation on the surface of a liquid. *Journal of Engineering Mathematics* (1976) (to be published).

Regarding the strong nonlinearity in the heave-versus-wave-height curves, when compressibility is included (Fig.9a), it was found that for very small wave heights ( $h_w/L = 0.001$ ), the motion converged to a periodic one only after many cycles. This implied the need for a smaller time step, since the pressures within the craft become badly behaved. Of course, the absolute motion approaches zero for small wave heights as required.

The pitch motion was found to be nonlinear at small wave heights, even without compressibility, this being due to the equation for pressure difference across the stability skirt. This point is discussed in the Introduction.

M.R. SWIFT

The author is pleased to learn of progress of work similar to his own - particularly in regard to the fact that there is agreement in the location of the resonant frequencies for a similar craft.

The comments about numerical stability are particularly interesting especially in regard to the predicted fluctuations in the cushion pressures. This problem was also experienced in the work leading to the paper, for three situations. These were: very small wave heights (see discussion of Dr. Moran's comments); lower frequencies ( $\omega\sqrt{L/g} < 4$ ), and occasionally the resonant condition.

It is felt that the difficulty experienced at



very low wave heights is at least partly related to other nonlinear factors at work, while that at low frequencies was due to the larger time step used (the number of time steps per cycle was kept constant for all frequencies, since this choice was found suitable as far as extrapolation of craft motion was concerned). Clearly, in the latter case one needs either a smaller time step due to the numerical instability introduced by compressibility or a more sophisticated extrapolation method, as mentioned by Dr. Swift. In any case, calculations were not performed in the low frequency range, since compressibility then does not play a role. Difficulties at the resonance are not surprising. Those points which are considered to be unreliable are indicated in Fig.8. Again, a better form of extrapolation is needed in this case.

The pressures plotted in Fig.5 are all 'genuine' in the sense that the numerical fluctuations referred to did not occur in these cases. It is interesting to note that the craft motion itself always tends to be better behaved than the pressures, since it is obtained by an integration of the latter.

A.H. MAGNUSON

There appears to be a disagreement regarding the location of the  $k_3$  and  $k_4$  poles for the supercritical case ( $\lambda > 1$ ). One does not need the Rayleigh viscosity here, since these two poles lie off the real axis, and a simple principal-value integral can be taken, without considering the need to deform the contour and the consequent inclusion of contributions from residues. An examination of Eq.(15) when  $\lambda > 1$  shows that the  $k_3$  pole lies below the axis, and the  $k_4$  pole above it.

Incidentally, for  $\lambda < 1$ , when the artificial viscosity is used, the reverse is true, even though the imaginary part is infinitesimal. Thus the transition at  $\lambda = 1$  is indeed undefined.

The locations of the poles are in agreement with Wu (36).

The comments about the  $\theta$  integration are very interesting. In the author's programme, the terms corresponding to  $k_1$  and  $k_2$  for all values of  $\lambda$ , and  $k_3$  and  $k_4$  for  $\lambda < 1$  were represented by the auxiliary functions for the cosine- and sine-integral functions. For  $\lambda > 1$ , the  $k_3$  and  $k_4$  terms had to be performed numerically since the required exponential integrals (with a complex argument) were not available as a computer subprogramme. Finally, the  $\theta$  integral was obtained numerically, since an attempt to produce a simple convergent power series was unsuccessful.

The approach of Dr. Magnuson to compute the actual energy radiated by the waves illustrates the large losses of power by this phenomena. It would be instructive to repeat the analysis for the three-dimensional case under discussion.

The author is grateful to Dr. Magnuson's discussion and hopes to be able to follow some of his suggestions.

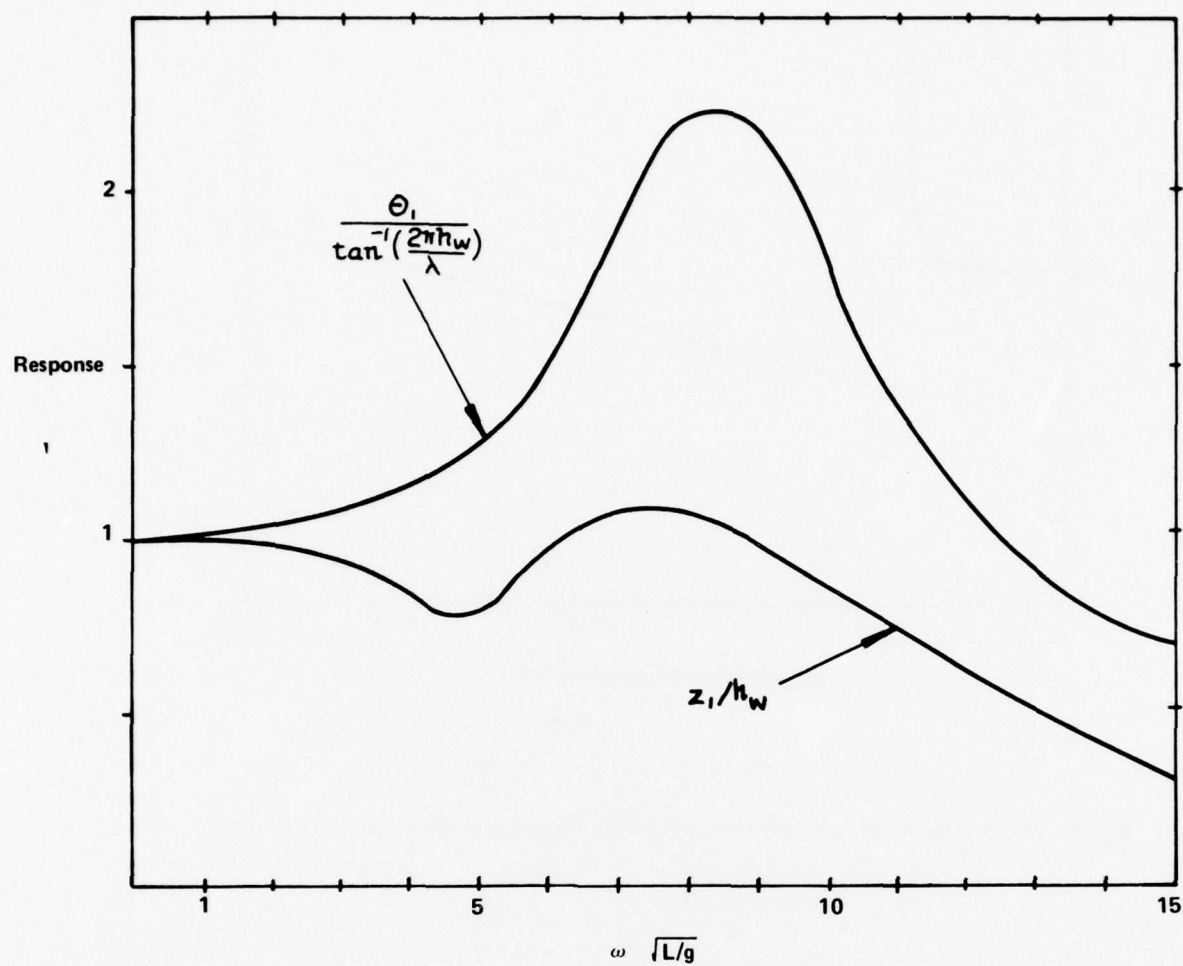


Fig. 12: First Harmonic Response,  $Fr=1.66$

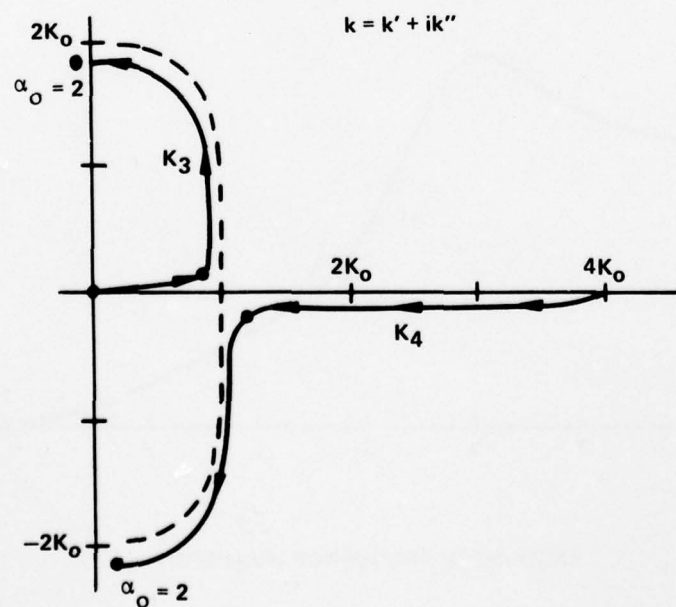


Fig. 13: Migration of  $K_3$  and  $K_4$  poles in complex wavenumber plane as frequency parameter  $\alpha$  increases.

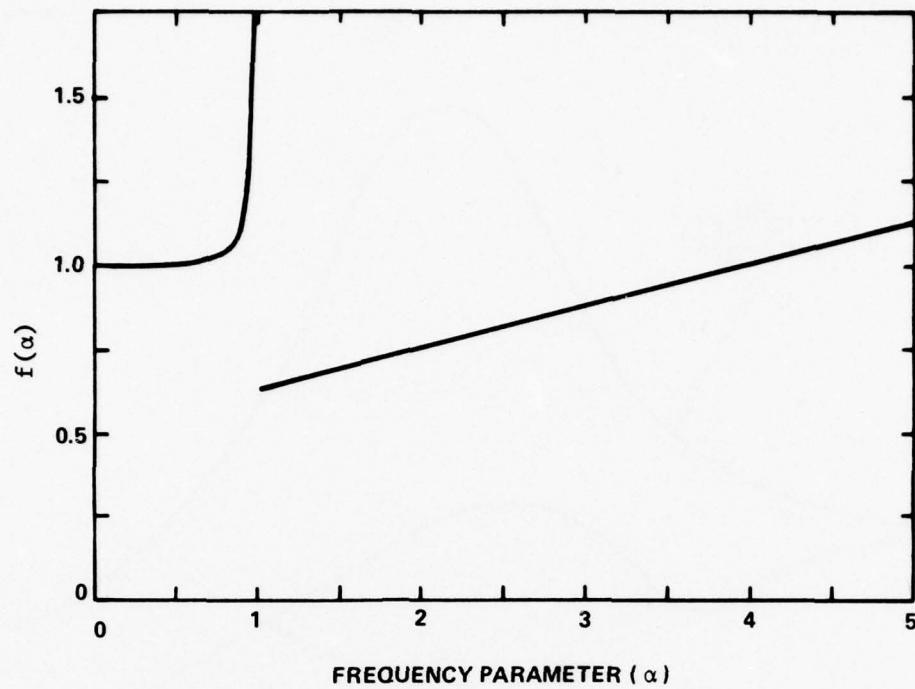


Fig. 14: Normalized mean work rate function  $f(\alpha)$  as a function of the frequency parameter  $\alpha$ .

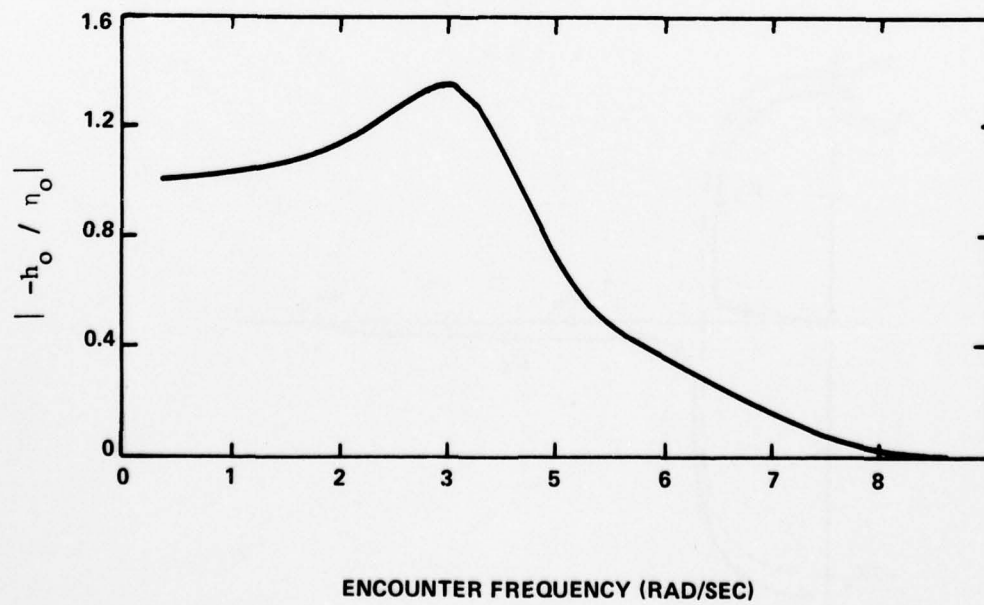


Fig. 15: Heave frequency response function in head waves,  $V_K = 40$



# Discussion on Paper by D. Johnson et al

L.J. DOCTORS

The authors have plotted acceleration levels for various conditions and have related human discomfort to these. The discussor has seen the comfort problem examined by other workers in connection with wheel-supported trains and air-cushion-supported trains. As well as finding acceleration a strong factor in affecting the quality of the ride, it appears that the higher derivatives are also important - such as the time-rate-of-change of acceleration.

Have the authors considered this aspect as well, or do they feel that the acceleration levels alone are sufficient to define ride comfort?

R.C. MCGREGOR

It is a pleasure to see hydrofoil presentations of this nature from 'official' U.K. sources. It is also encouraging to see the predicted performance and operational endurance of the 450 tonne hydrofoil comparing so well with the destroyer.

The choice of both craft for the comparison seems to be strange. Apart from the destroyer's commander's quote in Eames and Drummond (3), comparison with a frigate would seem to be a more obvious step. The choice of 450 tonnes for the hydrofoil (scaling up Tucumcari almost 8 times) without reference to the operational scaled up version Pegasus (4 times) also seems surprising. Is it to be concluded that the rough water performance of craft currently being introduced is not considered adequate for operation in the Royal Navy's main sphere of operations and that a further doubling of size is necessary to achieve this? Generally, information on motions is scarce, imprecise and inconsistently given. From the information of this type which is available it can be argued that the larger hydrofoils could be operated in the North Sea in an oil rig protection role (Ref.(21)). The clarity of the presentation of performance data and the attempt to come to grips with the crucial problem of crew tolerance in this paper is certainly welcome.

## REFERENCE

21. McGregor, R.C. Oil Rig protection: a role for hydrofoils? 2nd Int.Conf.on Hovering Craft, Hydrofoils and Advanced Transit Vehicles, Amsterdam, 1976.

## Authors' Reply

The discussors are thanked for their remarks which we shall answer individually.

L.J. DOCTORS

No, higher derivatives have not been considered, we have merely used the currently accepted techniques. We do not agree with the implication that the situation is an either/or one but think that the question supports one of the points of the paper, namely that the application of human response data to vehicle evaluation is rather poorly understood. More work is needed in the area, not only for application to unconventional naval craft, to quantify the influence of various effects which have hitherto been ignored.

R.C. MCGREGOR

We would agree that the comparisons made in the paper indicate the potential of the 450 tonne hydrofoil relative to the much larger conventional surface vessel, but would emphasise that the particular size is purely illustrative and was selected on the basis of Ref.(3) as indicated in the paper.

It would certainly be wrong to draw any conclusions on the adequacy of current designs for naval roles on the basis of seakeeping alone.

In recent years use of the words 'destroyer' and 'frigate' has become somewhat blurred. In this instance, the choice of label is defended for consistency with the origin of the data, Ref.(14). The response function has, in fact, been scaled to a length of 110 m which corresponds to the length of typical modern frigates.

We do not have the relevant performance data for Pegasus and the available Tucumcari information is adequate for this illustration.

Whilst the authors agree that the larger hydrofoils could be used for North Sea oil rig protection, they would question whether the deployment of such craft would be an optimal solution to that particular problem.

# Discussion on Paper by E. Brzoska et al

L.J. DOCTORS

The discussor would like to refer to Fig. 10 which shows the resistance of the model ACV with two different skirt configurations as a function of the forward speed.

The considerable difference in drag for the two cases is most surprising - particularly in regard to the location of the main hump in the resistance curve. Furthermore, model CVO6 displays a negative drag at zero speed, which could possibly be explained by excess leakage of cushion air out of the stern due to the raised skirt there. However, the resistance is seen to become even more negative at increasing speed indicating one or more of the following: shallow water effects, craft trim changing due to towing point being too high above the model or due to incorrect ballasting, unsteady effects such as the towing boat not travelling at a constant speed.

A further point relates to the external air supply system used, which is inherently different from an on-board fan. One wonders if the flexible pipe cannot apply a longitudinal force when it is buckled (as in Fig. 4) and is also under pressure.

It is therefore felt that further elaboration of the experimental technique is required, plus the supply of additional data, before the graphs will serve a useful purpose.

## Authors' Reply

The authors are grateful to Dr. Doctors for his constructive questions. Before replying to these remarks it must be once more emphasized that:

- a) the presented data are only selected fragments of greater work which has been performed in the Ship Research Institute.
- b) The data was not corrected with regard to accessory factors and also was not presented in nondimensional form mainly to point out the immediate results of experiments.

To return to our reply, it is obvious that the external air supply system is not equivalent to any internal one, for instance to an on-board fan. It is also clear that not all the drag components of a real craft were measured

in these tests. To measure only a part of the total drag is a well known practice in such experiments.

The air supply system used in our tests is one in which air is provided from a fan located on the towing boat and is fed to the model by a tube whose last part is the extension (invisible on fig. 4) of the joint, running straight downward to model. The exhaust plane of this extension lies at the model's deck plane or somewhat higher, when the towing boat is at full speed; in no case can this extension touch the model - in a vertical direction for suitable dimensions and in a horizontal direction because of the nature of the towing system. This one is stiffly constructed with a potentiometric force gauge of lead  $\pm 0.5$  mm fastened between the lever's upper arms; a separate shock-absorber is located at the gauge axis and does not permit any change of distance in quasi-static conditions. The stern guide of the model is measured, so that the distance between it and the model is fixed and it is not possible for the model to contact the tube. The flexible pipe which is seen in fig. 4 and was mentioned by the discussor is only a sealing device between the feeding tube and the model; this flexible element is connected to the edge of a hole in the model's deck and, at its top point, to the feeding tube. At steady conditions pressure in the space between these elements is static only and the force exerted on the model is rather negligible. From another point of view part of the dynamic head pressure (external atmospheric air due to the motion) was registered but it is a small quantity and easy to predict approximately.

The next questions relate to experimental technique, especially to the test conditions. Raised fingers at the stern region of the skirt are a normal practice and must induce a certain consequence, sometimes in the form of negative drag. This phenomenon is well recognized in the experimental works of Everest and Hogben (3) and it is possible to predict it by common sense. Shallow water effects supposedly affecting our results are not easy to believe in, since the water depth of the lake oscillated between 4 and 12 m, which means values of  $d/a$  ( $d$  - water depth and  $a$  - half length of craft) on the same level, while shallow water conditions are studied by Everest and Hogben (3) between 0.10 and 0.43 and by Doctors (4) between 0.25 and 1.00.

With regard to the model's speed, maximal depth influences might be expected between Froude numbers 1.41 and 2.45 respectively to mentioned water depths, but it also must be remembered that the highest cushion pressures used by us were only about 5.5 mbar. The overall length of the lake is about 32 km and so long a running distance gave us a little space to make a

suitable choice. Moreover all ten skirts were tested at the same places and conditions and the influence of water region on experimental results must be similar in all cases.

Longitudinal model trim may be induced by incorrect location of the towing point. This problem was taken into consideration and a suitable position was kept, although it might be in some cases a little too high, when the model was towed without a gyroscope and ballasting plummets (model weight equal to 76 kp), but if there were some differences, they were very small and occurred only at selected speeds. The main reasons for trim changes are, of course, of quite a different nature.

Incorrect ballasting of the model is not possible because initial trim in both cases, namely longitudinal and transversal, were exactly controlled magnitudes and moreover were two of the main parameters in our tests. Both these trims in displacement and "on-cushion" positions are shown in the figures given below. The running trim of the model was also registered in all cases.

With regard to the possibility of unsteady effects, measurements were made at constant speed, the time period for fixing a speed was long enough, and measurements were made for 10 - 15 seconds with continuous speed registration too.

The two principal groups of skirts tested by us contain eight skirts of normal SRN or BHC type used on model CVO4 with one additional 1CVO6 (the general character of results of this series conforms with predictions) and one skirt of another type named 2CVO6. The internal configuration of the fingers, the localization of the feeding holes on skirt 2CVO6 (closed type) was different from normal ones (open type) and for this reason the motion of the air particles in the cushion volume was not quite the same. In quality tests over firm ground (as in fig.6 conducted from a concealed chamber placed under the plate) we detected the presence of three pairs of air vortices (instead of one) in a cross-sectional cut. The kind of motion of the air particles and also other features are probably liable for such unexpected results. This situation is developed by a completely changed flow pattern and thus pressure distribution on the water surface. In our opinion the new pressure distribution modifies the shape of the resistance curves in the speed region where wave drag is a main component of the total drag. The influences of the immersed side skirt edges on the pressure distribution in the craft cushion must be taken into account. We think that the full picture of the flow in the hovercraft cushion is sometimes of a rather delicate nature and may differ with pure theoretical models.

We are pleased to present further data on this theme for skirt numbers 1 or 2 CVO6 with mean cushion static pressures:-

state I 3,8 mbar ( model weight 76 kp)  
state II 5,5 mbar ( model weight 110 kp).

Fig.28 shows that the drag curves agreed with the best trim conditions for both model weight states. The data refers to previous experiments with a model of small weight and  $\psi_{0i}$  is the initial longitudinal trim of model when on-cushion at rest. Figs. 29 to 34 show the results of experiments with both skirts on model CVO6, especially with regard to initial longitudinal and transverse trim. It is interesting to see how the model with skirt No.1 (open type) responds to initial bow trims and, moreover, how different are the reactions of the model with skirt No 2 (closed type) to initial trims (Fig.32 compared with fig.29) and at running conditions (resistance curves on figs.33 and 34), where:

- $m_{\psi}$  - initial longitudinal trimming moment with reference to the model's centre of gravity coordinate system (kpm):
- $m_{\phi}$  - initial transversal trimming moment with reference as above (kpm).

Additionally fig.35 shows how small differences in the skirt geometry (here the introduction of small plates on the edge of the attack of stern's fingers) influence the shape of the drag curves.

#### REFERENCES

- (3) Everest, J.T. and Hogben, N. - Research on hovercraft over calm water - Transactions of the Royal Institution of Naval Architects, vol.109, 1967.
- (4) Doctors, L.J. - The forces on an air cushion vehicle executing an unsteady motion - Ninth Symposium on Naval Hydrodynamics, Paris, France, 1972.



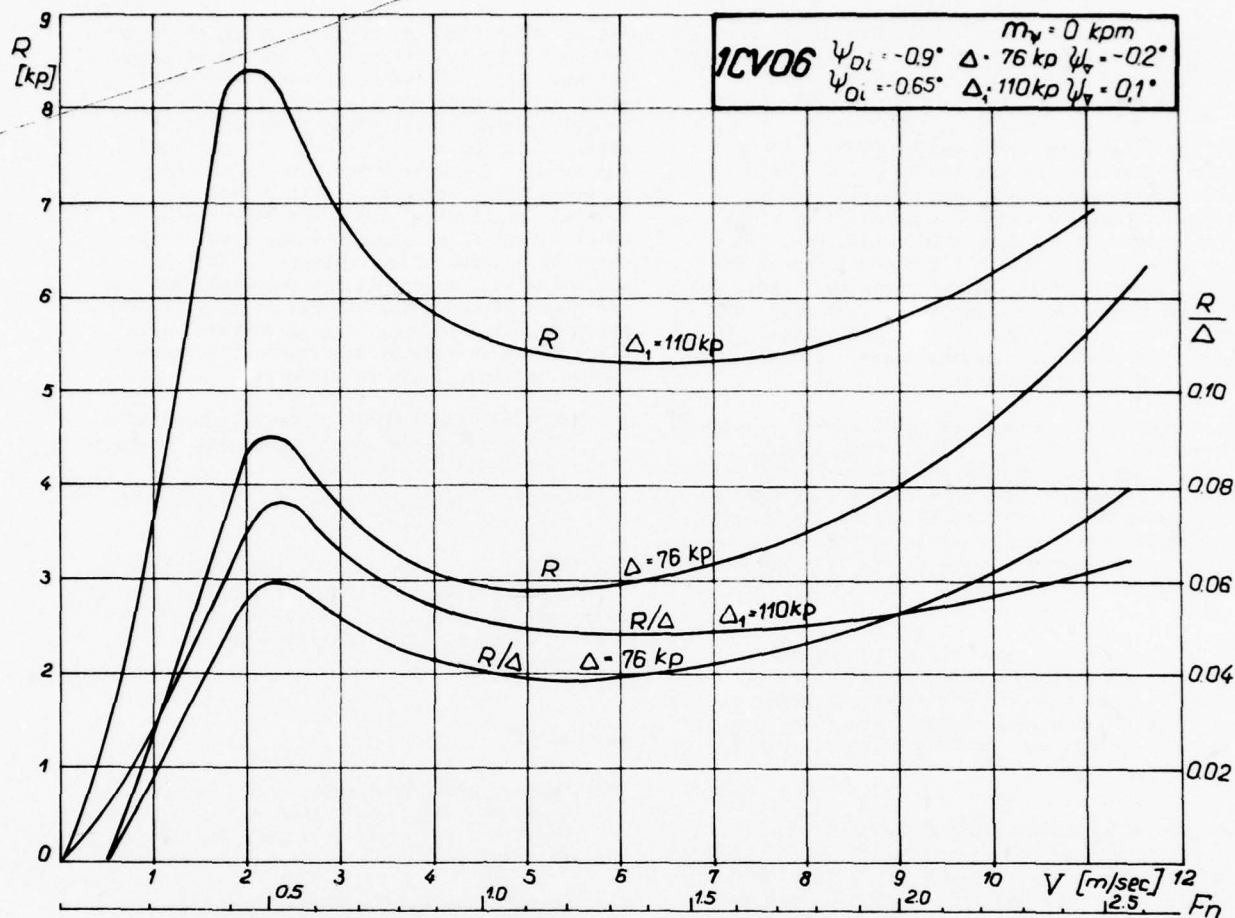


Fig. 28: Influence of models' weights on total measured drag

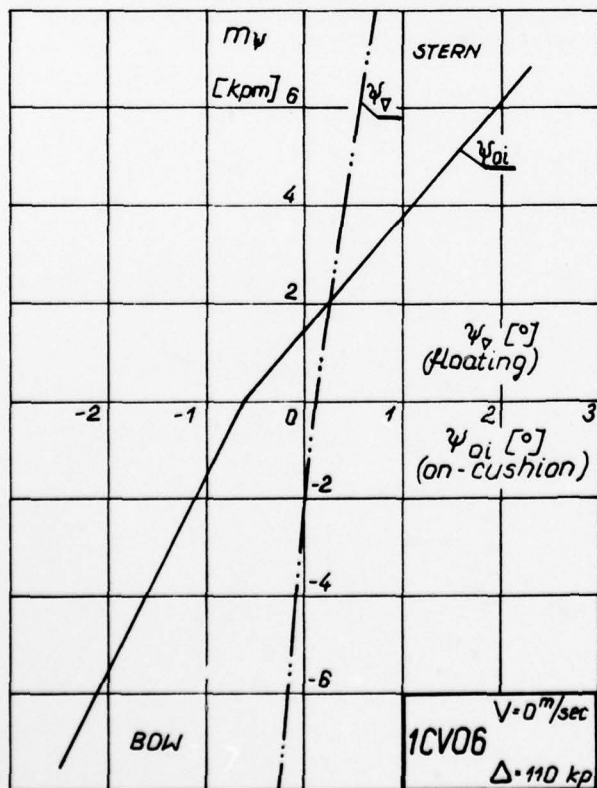


Fig. 29: Band of initial trims for skirt 1 CV06

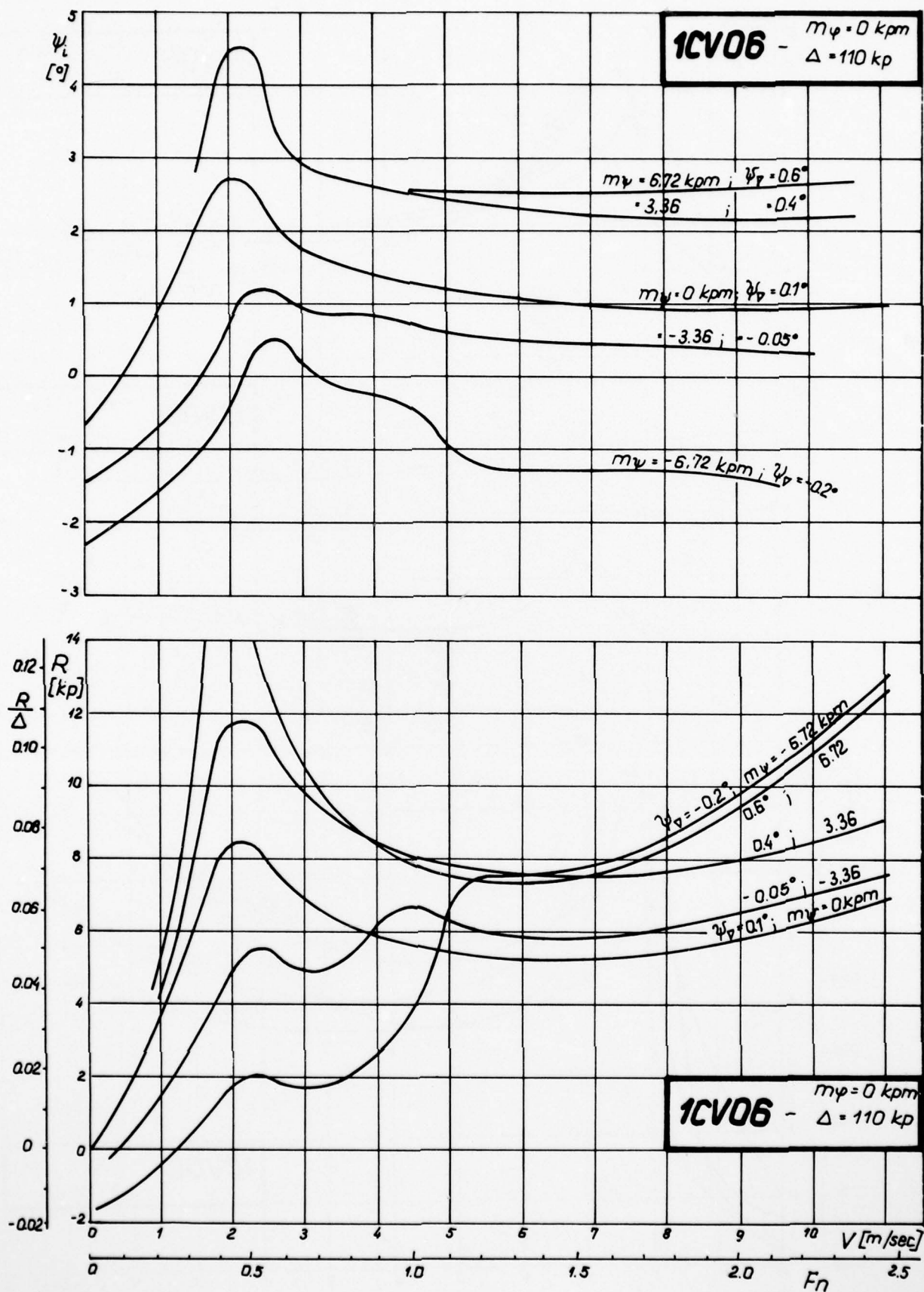


Fig. 30: Measured resistance and running longitudinal trim (without lateral moment) for skirt 1 CV06

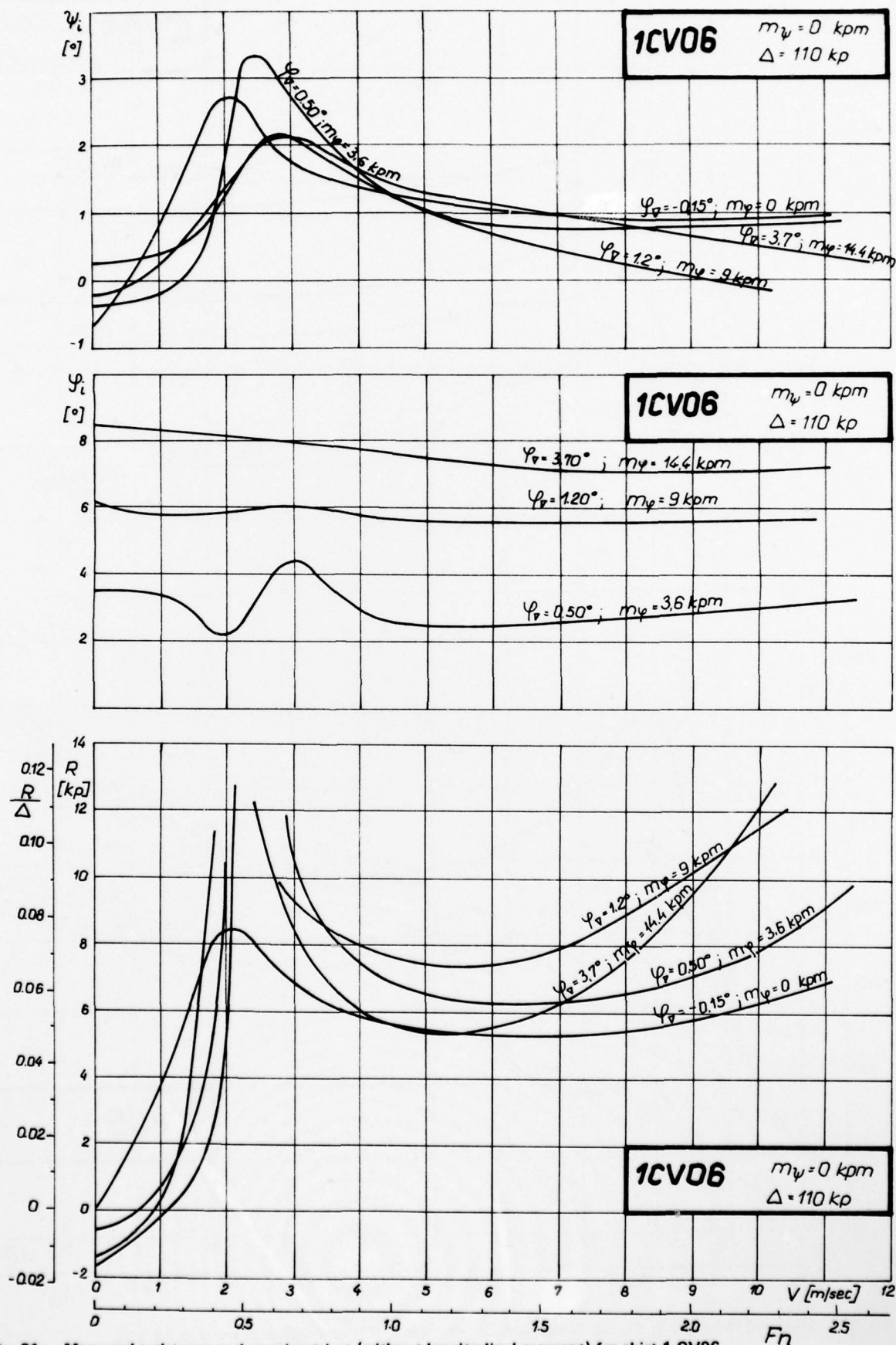


Fig. 31: Measured resistance and running trims (without longitudinal moment) for skirt 1 CV06



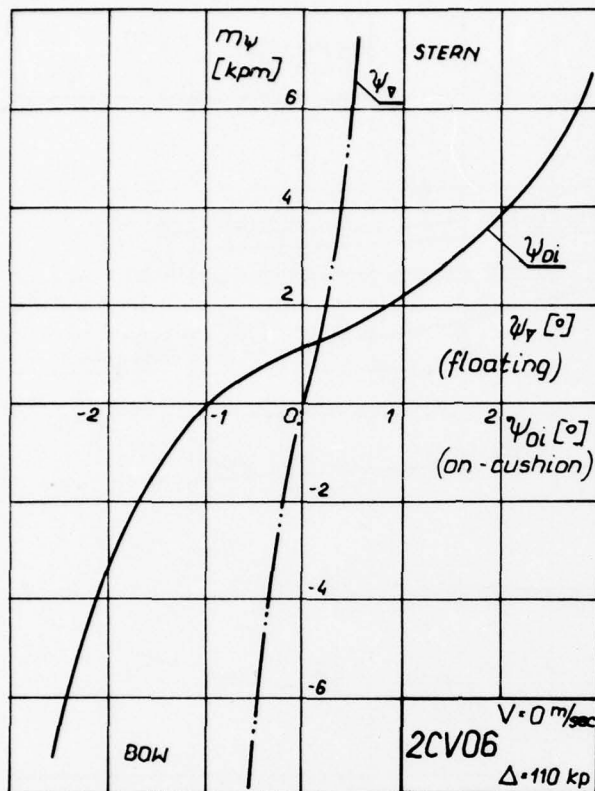


Fig. 32: Band of initial trims for skirt 2 CV06

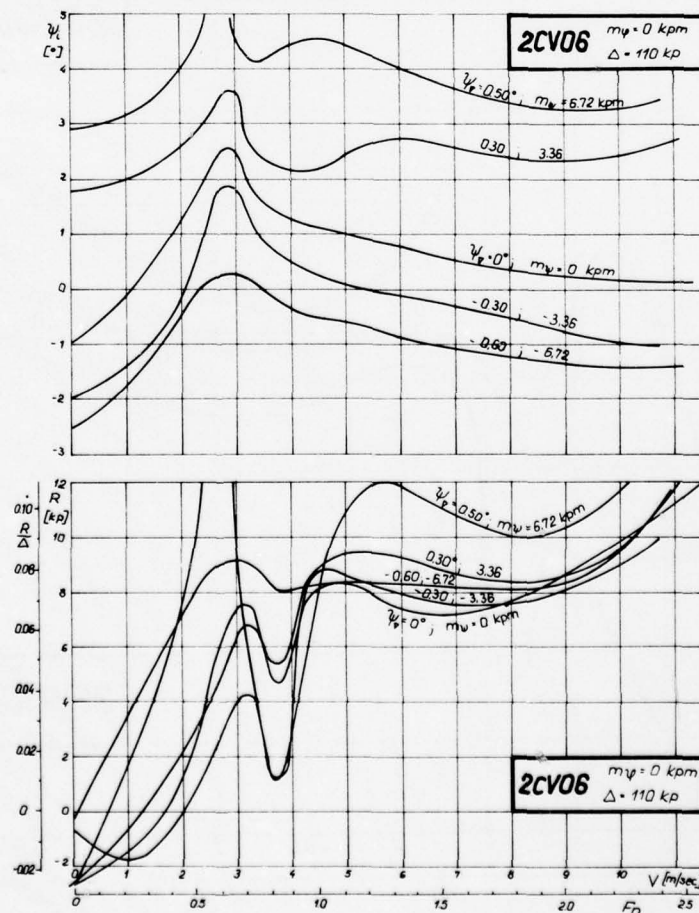


Fig. 33: Measured resistance and running longitudinal trim (without lateral moment) for skirt 2 CV06

AD-A055 859

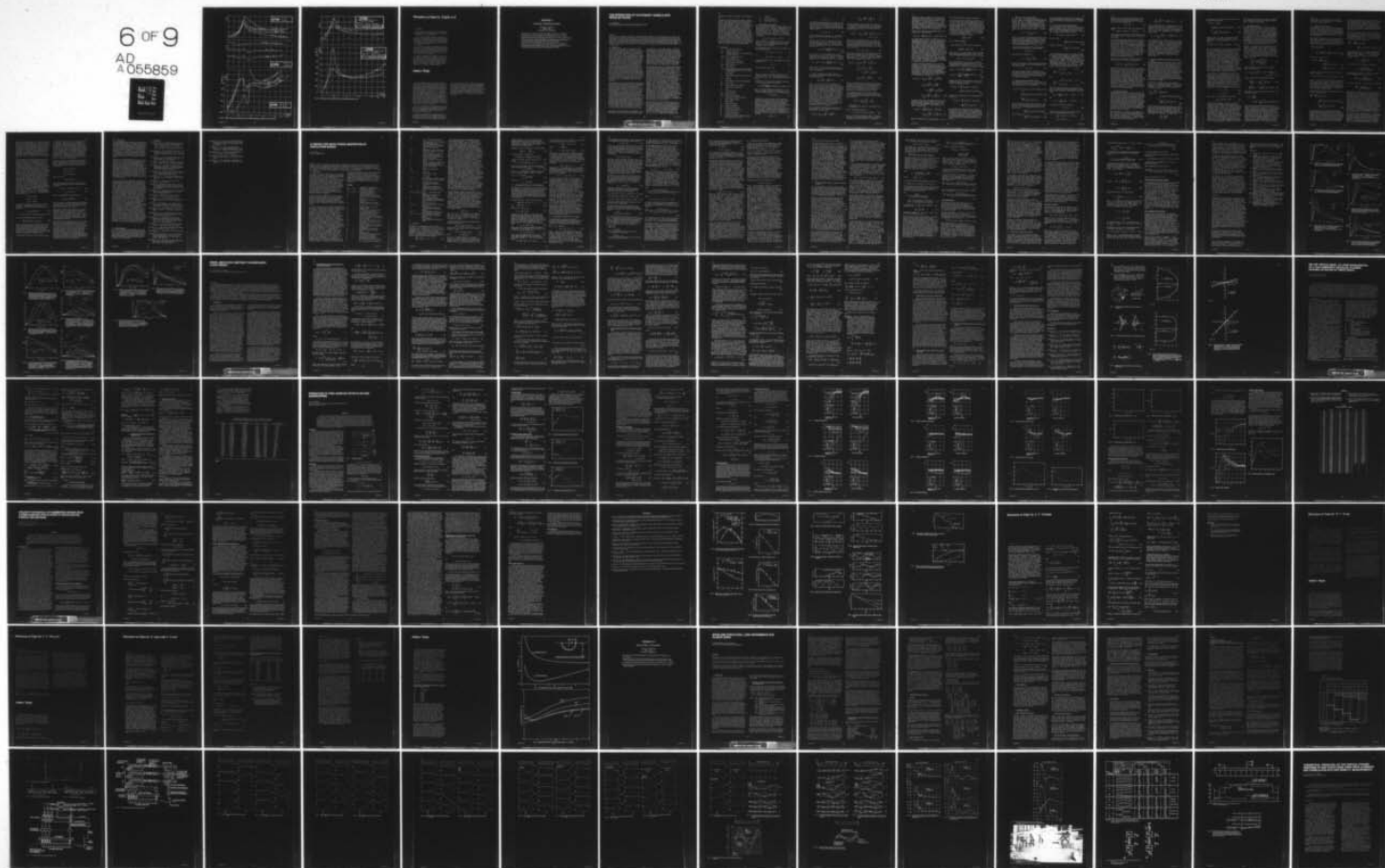
UNIVERSITY COLL LONDON (ENGLAND) DEPT OF MECHANICAL --ETC F/G 13/10  
SYMPOSIUM ON NAVAL HYDRODYNAMICS. UNSTEADY HYDRODYNAMICS OF MAR--ETC (U)  
1978 R E BISHOP, A G PARKINSON, W G PRICE N00014-76-C-0093

UNCLASSIFIED

NL

6 OF 9

AD  
A055859



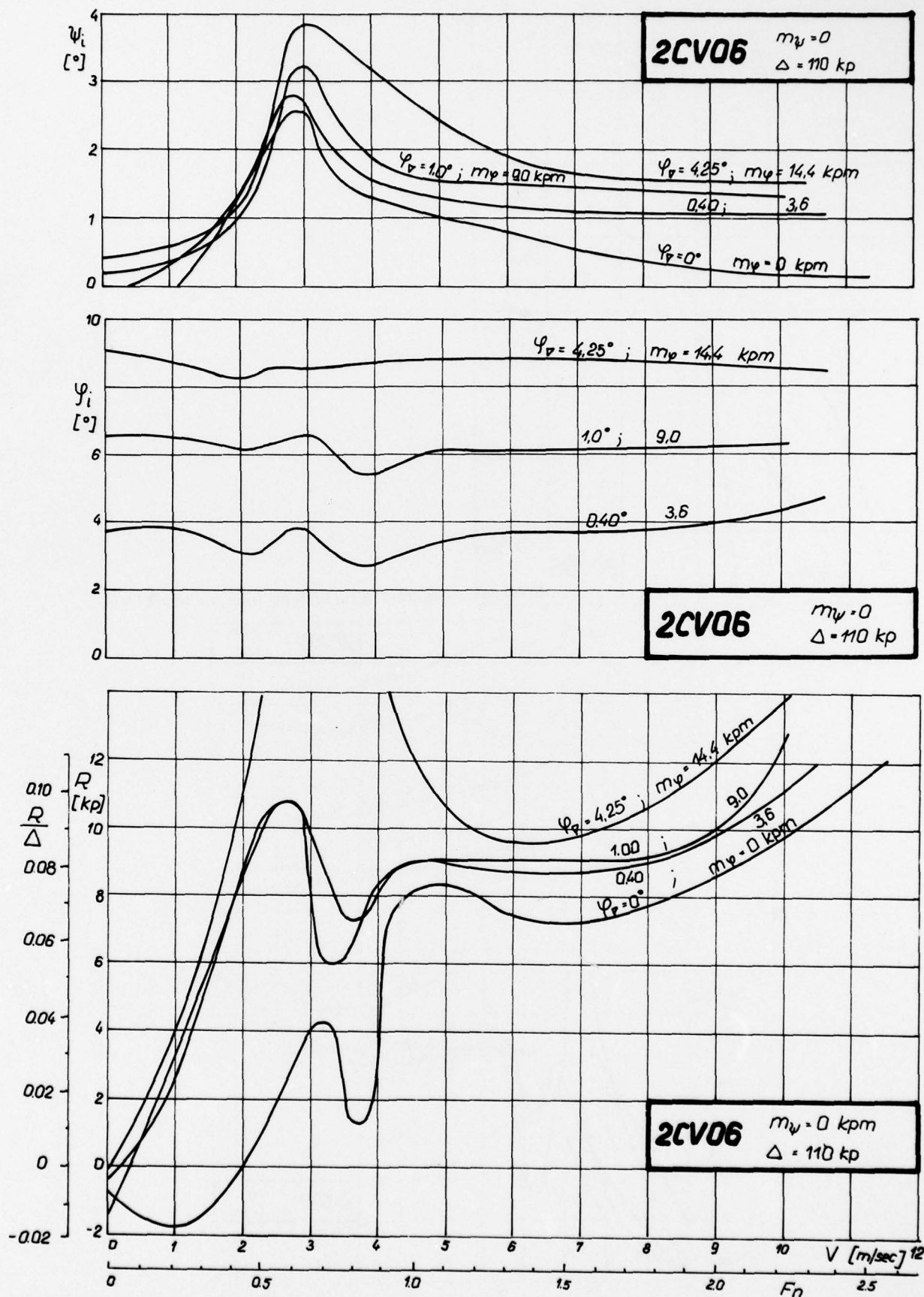


Fig. 34: Measured resistance and running trims (without longitudinal moment) for skirt 2 CV06



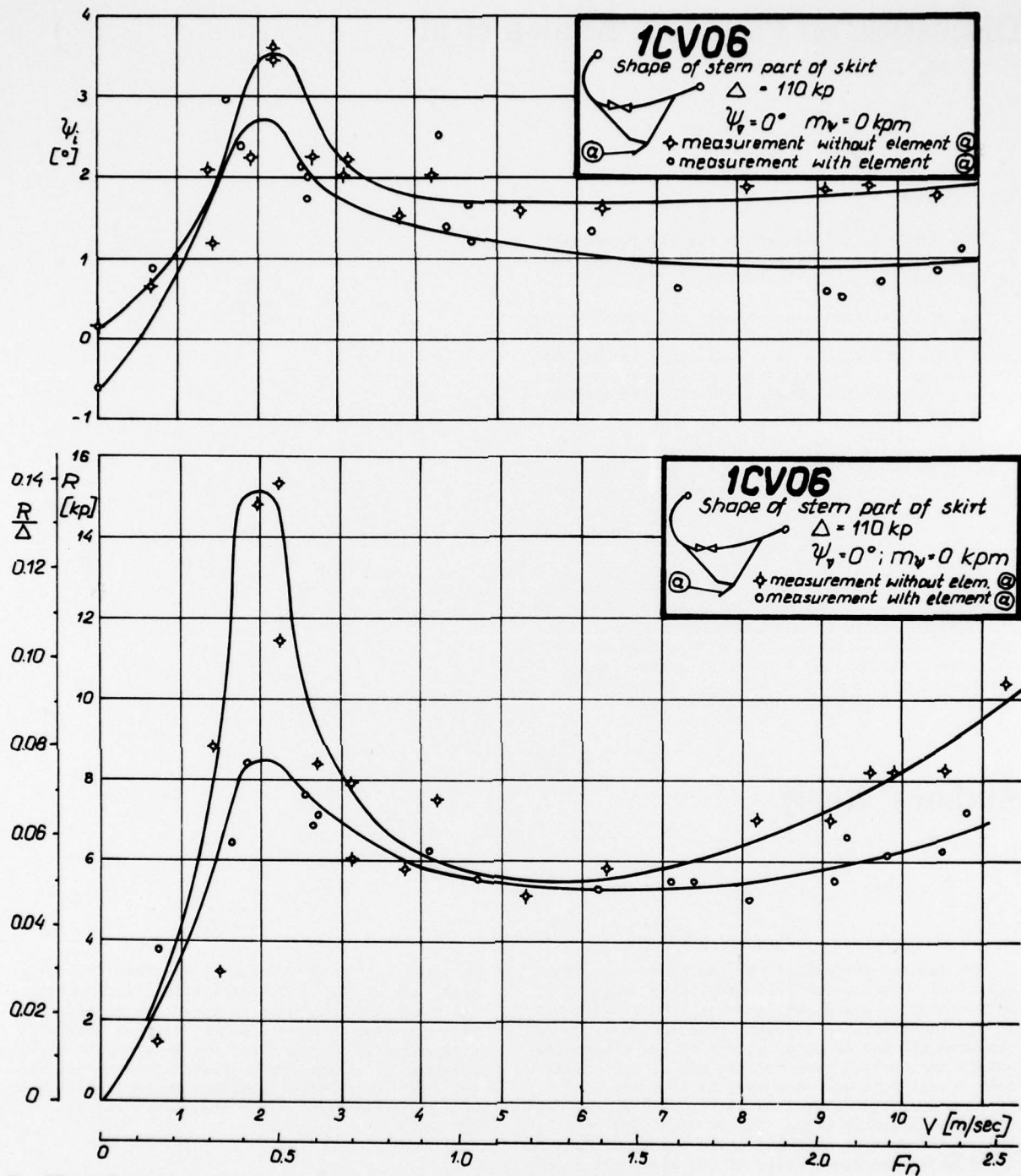


Fig. 35: Influence of stern's fingers plates on total measured drag and trim

# Discussion on Paper by Kaplan et al

L.J. DOCTORS

The discussor is pleased to see the present paper because there is little published information on SES dynamics in the literature.

One of the interesting results indicated by the authors is that the presence of the bubble pressure has little influence on the side force and yaw moment acting on a manoeuvring SES. Could the authors elaborate on this phenomenon and give a physical explanation for it?

The discussor is also concerned about the representation of the vertical force on the stern seal given by (15). This equation represents the force as being proportional to both the craft forward speed and the vertical velocity of the seal. What is the basis for this equation?

Finally, in regard to the impacting of the bow bag with the water surface, which is depicted during various stages of the slamming in Fig.17, do the authors think that this process could be analysed mathematically as a planing surface (whose shape is to be found), either in a quasi-steady manner or in a properly unsteady manner?

## Authors' Reply

The authors appreciate the questions and interest of Dr. Doctors for this particular subject. With regard to his first question, it is difficult to provide a precise physical explanation since no measurements and/or observations of the water flow within the cushion were made in any of our model test investigations. However, it is known that there are certain anomalies in the roll moment behaviour as sideslip angle varies which indicate that there must be alterations in the water elevations along the inner walls of the sidewalls on either side due to the travelling bubble pressure. These varying elevations contribute to the roll moment, but their influence is probably 'balanced' in regard to the side force and yaw moment, leading to little effect on these reactions.

For the second question, concerning the vertical force on the stern seal, the basis for this equation is the mathematical representation of the lift force on a large aspect ratio planing surface according to linear theory.

As far as the question concerning a method of mathematical analysis for the impacting bow bag is concerned, that process can certainly be viewed as a planing surface with varying shape (which is to

be found within the course of any detailed analysis), and is the basis for a simplified mathematical model which we have proposed for representing this process. However, a more precise analysis that properly accounts for the deformation by interrelating the shape, hydrodynamic forces, and the air flow compression equations would certainly be a welcome addition to the analytical literature for SES craft.

**SESSION V**  
**GENERAL HYDRODYNAMICS**

Thursday, 1 April 1976  
09.00—12.30  
Chairman: W. E. Cummins

- The interaction of stationary vessels with regular waves, by J. N. Newman  
A theory for wave power absorption by oscillating bodies, by D. V. Evans  
Finite-amplitude unsteady slender-body flow theory, by T. Y. Wu and G. T. Yates  
On the virtual mass, at long wavelengths, of a half-immersed circular cylinder  
heaving on water of finite depth, by P. Sayer and F. Ursell  
Prediction of free-surface effects on ship manoeuvring, by R. B. Chapman  
Velocity potentials of submerged bodies near a free surface-application to wave-  
excited forces and motions, by M. S. Chang and P. C. Pien



# THE INTERACTION OF STATIONARY VESSELS WITH REGULAR WAVES

J. N. NEWMAN

Massachusetts Institute of Technology, Cambridge, Mass, USA

## SYNOPSIS

A set of unified relations are derived, based upon Green's theorem, for the interactions of vessels with regular waves. Interest is focused on the far-field waves radiated and scattered by the body, and on the first-order forces and moments acting upon it. Derivations are given for the symmetry of the damping and added-mass coefficients, inter-relations between the reflection and transmission coefficients, Haskind's relations for the exciting forces, and a set of new relations between the radiated and scattered waves. The utility of these diverse relationships is illustrated in an analysis of the extraction of wave energy by a floating body.

## 1. INTRODUCTION

The analysis of the effects of water waves upon ships and other vessels was initiated in the last century by William Froude and A. N. Krylov, who neglected hydrodynamic interactions and assumed the fluid pressure to be that of the waves in the absence of the vessel. This assumption is now generally known as the Froude-Krylov hypothesis. Subsequent investigators became progressively more ambitious, particularly in the past two decades when computations have been facilitated by the availability of large digital computers. Various approximate schemes have been set forth for including the effects of the body on the surrounding fluid, and "exact" linearized treatments have been given for some simplified geometries such as circular cylinders and other simple two-dimensional shapes, as well as spheres and spheroids in three dimensions. More general bodies have been analysed by approaches which are inherently numerical. Thus, in the context of stationary bodies (i.e., the case of zero forward velocity) and excluding situations where viscous or nonlinear effects are significant, it can be said that theoretical and numerical methods are well developed.

During recent years, as contributions in this field have become more complete but also more complicated, interest has not diminished in those simple relations and results which add perspicuity to the field and afford opportunities for checking or simplifying the more ambitious calculations. My own personal appetite for simple results of this sort was stimulated fifteen years ago by the discovery of the Haskind relations, wherein the exciting forces in waves could be determined from relatively simple formulae in terms of the properties of the solution for forced oscillations in calm water. At that time there had already been developed several solutions and computations for the forced-motion problem, whereas relatively few direct calculations had been made of the corresponding exciting forces. Thus the Haskind relations extended our knowledge of the exciting forces and permitted a check on the few direct solutions which did in fact exist.

One danger of deriving simple relationships is the possibility that they may seem in retrospect some-

what obvious or, worse, not original. Haskind's relations offer a good example of this, the credit being given on the basis of the paper by Haskind (1), in which he set forth the essential relations based on Green's theorem. Only later did I realize that Hanaoka (2) had derived the same results independently whereas Ogilvie (3) has emphasized that these relations are a consequence of more general reciprocity relations derived by Chertock. To demonstrate the futility of such soul-searching it may be noted that the same reciprocity relations were the subject of an early paper by Lamb (4)!

Reciprocity relations of the type described above, and the Haskind relations in particular, are generally based on Green's theorem. The intent of the present paper is to systematically collect the various relationships which can be derived on this basis, and which pertain to the interaction of vessels with regular waves. Some of these relations are very old, whereas a few are completely new. The motivation for presenting them together is, partially, the efficiency of a unified presentation which may justify the repetition of well-known results. But, more importantly, we derive the complete set of these relations in a systematic manner so as to minimize the chance that some additional relation of practical importance is overlooked. The possibility of this happening may seem remote, in view of the classical nature of this subject, but a counter-example is the fact that the developments to be outlined in §8, relating the far-field waves of the scattering and forced-motion problems are (to the author's knowledge) new within the past year. The two-dimensional analysis of these relations has been presented in a separate paper (5), but the three-dimensional extensions are presented here for the first time.

As an application of the results to be derived in §§2-9, we shall consider in §10 the analysis of wave energy extraction by a floating body. Here it will be seen that our various relations enable us to simplify greatly the formulae for energy extracted by the body, and to draw rather general conclusions regarding optimum body shapes and motions. This application was suggested to the author by Dr. D. V. Evans, and is treated more

completely by Evans in his paper to this Symposium (6).

Throughout the analysis we shall usually consider both two- and three-dimensional problems simultaneously, indicating these by pairs of equations numbered with suffixes a and b respectively. In two dimensions the incident waves are assumed to have crests parallel to the body, but the more general case of oblique incidence can usually be accommodated by straightforward extensions. More significantly our attention is restricted to the case of zero forward speed. Again, in most cases at least, forward speed can be accommodated, but not without considerable complexity and the necessity to introduce additional assumptions. Thus we shall consider here only the "stationary" case which is of limited interest to the classical naval architect, but of much greater importance to the modern ocean engineer concerned with drilling rigs, fixed structures and various types of floating platforms.

### 1.1 Notation

A	incident wave amplitude
$B_{ij}$	damping coefficient
D	parameter defined by (18) proportional to group velocity
$dE/dt$	rate of energy extraction
$F_{ij}$	force coefficients
f	radiating wave amplitude
g	gravitational acceleration
$H(\theta)$	Kochin function
h	fluid depth
(i,j)	indices denoting particular components of potentials, normal vector, or modes of body motion
k	wave number
$\underline{n}$	unit normal (positive into body or out of $S_C$ )
p	pressure
R	polar radius, reflection coefficient
$S_B$	body surface
$S_C$	control surface at infinity
T	transmission coefficient
t	time
v	velocity of body
$v_g$	group velocity
x,y,z	Cartesian coordinates
$\alpha$	phase angle of Kochin function
$\beta$	wave incidence angle
$\theta$	polar angle
$\rho$	density of fluid
$\Phi, \phi$	velocity potentials
$\phi_d$	diffraction potential
$\phi_I$	incident wave potential
$\phi_r$	radiation potential
$\phi_s$	scattering potential
$\psi$	potential satisfying radiation condition (either $\phi_d$ or $\phi_r$ )

$\omega$	frequency
*	complex conjugate
( $\pm$ )	wave amplitude at $\pm\infty$

### 2. THE BOUNDARY-VALUE PROBLEM

We consider an ideal fluid of constant depth h, in which is situated a floating or submerged body with wetted surface  $S_B$ . Cartesian coordinates (x,y,z) are utilized with  $z=0$  the static plane of the free surface and  $z=-h$  the bottom. Assuming oscillatory wave motion of period  $2\pi/\omega$ , and small amplitude, the velocity potential can be expressed in the form

$$\Phi(x,y,z,t) = \text{Re} [\phi(x,y,z) e^{-i\omega t}] , \quad (1)$$

where  $\nabla^2 \phi = \nabla^2 \bar{\phi} = 0$  throughout the fluid. In the special case of two-dimensional motion the dependence on y will be suppressed with the motion confined to the x-z plane.

The linearized boundary condition to be applied on the free surface is

$$\phi_{tt} + g \phi_z = 0 \quad \text{on } z=0, \quad (2)$$

or

$$\omega^2 \phi - g \phi_z = 0 \quad \text{on } z=0. \quad (3)$$

On the fluid bottom  $z=-h$  the appropriate boundary condition is

$$\phi_z = 0 , \quad (4)$$

and on the body surface  $S_B$ ,

$$\phi_n = v_n , \quad (5)$$

where  $v_n$  denotes the complex amplitude of the normal velocity on  $S_B$ . The unit normal vector  $\underline{n}$  is directed out of the fluid domain and into the body.

A solution of all but the last boundary condition is the incident plane-wave potential

$$\phi_I = \frac{gA}{\omega} \frac{\cosh k(z+h)}{\cosh kh} \exp[ik(x \cos \beta + y \sin \beta)] , \quad (6)$$

Here A is the (complex) wave amplitude,  $\beta$  the angle of incidence relative to the x-axis, and k is the wavenumber defined by the dispersion equation

$$\omega^2 = gk \tanh kh . \quad (7)$$

In general we are interested in the interaction between the incident wave (6) and the body, which may be either fixed or moving with oscillatory velocity. This general case may be decomposed linearly into a *scattering problem*, where the body is fixed and subject to incident waves, and a *radiation problem*, where the body is forced to oscillate with appropriate normal velocity in otherwise calm water. Denoting the corresponding velocity potentials by  $\phi_s$  and  $\phi_r$  respectively, the appropriate boundary conditions on the body  $S_B$  are that

$$\partial \phi_s / \partial n = 0 , \quad (8)$$

or

$$\partial \phi_r / \partial n = v_n. \quad (9)$$

The boundary-value problems for  $\phi_s$  and  $\phi_r$  are completed by imposing a radiation condition, that the waves due to the presence of the body are outgoing at infinity. In the scattering problem the incident wave must be excluded from this condition, hence we write

$$\phi_s = \phi_I + \phi_d, \quad (10)$$

where the *diffraction potential*  $\phi_d$  represents the disturbance of the incident wave due to the body.

In their simplest form the radiation conditions applicable to  $\phi_d$  and  $\phi_r$  will differ for two- and three-dimensional motion. In the two-dimensional case outgoing plane waves are prescribed at infinity, hence

$$\phi_j \approx f_j(\pm) \frac{\cosh k(z+h)}{\cosh kh} e^{\pm ikx}, \text{ as } x \rightarrow \pm\infty. \quad (11a)$$

Here ( $j=d, r$ ) is an index denoting the corresponding potential, and  $f_j(\pm)$  denotes the (unknown) amplitude of the radiated wave motion. For three dimensions the corresponding condition is expressed as

$$\phi_j \approx (kR)^{-1/2} f_j(\theta) \frac{\cosh k(z+h)}{\cosh kh} e^{ikR} \text{ as } R \rightarrow \infty, \quad (11b)$$

where ( $R, \theta$ ) are polar coordinates about the  $z$ -axis, and  $f_j(\theta)$  denotes the angular dependence of the outgoing waves.

### 3. GREEN'S THEOREM AND THE KOCHIN FUNCTIONS

For any pair of harmonic functions  $\phi_{i,j}$  Green's theorem states that

$$\iint_S (\phi_i \frac{\partial \phi_j}{\partial n} - \phi_j \frac{\partial \phi_i}{\partial n}) dS = 0, \quad (12)$$

where  $S$  is a closed surface surrounding any region where the two potential functions are harmonic. This theorem is the basis for the relations which we shall develop here, ranging from the classical proof of symmetry of the damping and added-mass matrices to new expressions between the far-field waves. In all cases we take  $S$  to consist of the body surface  $S_B$ , a circular cylindrical control surface  $S_C$  of large radius  $R$  about the vertical  $z$ -axis which extends upwards from the fluid bottom to the free surface, as well as the circumscribed portion of the fluid bottom  $z=-h$  and free surface  $z=0$  exterior to the body. For the two-dimensional case a similar version of Green's theorem holds with  $S$  replaced by a corresponding contour of integration.

From the boundary conditions (3-4) there are no contributions to (12) from the free surface or bottom, hence it follows that

$$I(\phi_i, \phi_j) \equiv \iint_{S_B} (\phi_i \frac{\partial \phi_j}{\partial n} - \phi_j \frac{\partial \phi_i}{\partial n}) dS$$

$$= - \iint_{S_C} (\phi_i \frac{\partial \phi_j}{\partial n} - \phi_j \frac{\partial \phi_i}{\partial n}) dS. \quad (13)$$

If both potentials  $\phi_{i,j}$  satisfy the radiation condition (11), the integral over  $S_C$  will vanish, as is readily confirmed by direct substitution and evaluation of the appropriate normal derivatives. It follows that

$$I(\phi_i, \phi_j) = - \iint_{S_C} (\phi_i \frac{\partial \phi_j}{\partial n} - \phi_j \frac{\partial \phi_i}{\partial n}) dS = 0 \quad (14)$$

( $i=d, r; j=d, r$ ).

There will be contributions from  $S_C$  if one or both of the potentials are of the scattering type (10), since the incident wave potential does not satisfy the radiation condition (11). To be quite general we suppose that both potentials  $\phi_i$  and  $\phi_j$  are of the form

$$\phi_{i,j} = \phi_{Ii,j} + \psi_{i,j}, \quad (15)$$

where  $\phi_{Ii,j}$  are two distinct incident waves with different amplitudes  $A_{i,j}$  and directions  $\beta_{i,j}$ , while  $\psi_{i,j}$  are diffraction or radiation potentials which satisfy (11). The resulting contributions to (13) from the integral over  $S_C$  are

$$\begin{aligned} I(\phi_i, \phi_j) = & - \iint_{S_C} (\phi_{Ii} \frac{\partial \phi_{Ij}}{\partial n} - \phi_{Ij} \frac{\partial \phi_{Ii}}{\partial n}) dS \\ & - \iint_{S_C} (\phi_{Ii} \frac{\partial \psi_j}{\partial n} - \psi_j \frac{\partial \phi_{Ii}}{\partial n} \\ & + \psi_i \frac{\partial \phi_{Ij}}{\partial n} - \phi_{Ij} \frac{\partial \psi_i}{\partial n}) dS \\ & - \iint_{S_C} (\psi_i \frac{\partial \psi_j}{\partial n} - \psi_j \frac{\partial \psi_i}{\partial n}) dS. \end{aligned} \quad (16)$$

The first integral in this equation vanishes identically, since the incident potentials are harmonic throughout the interior of  $S_C$  (including the interior of the body surface  $S_B$ ). The last integral in (16), involving only the radiating wave potentials, also vanishes by virtue of (14).

The remaining integral in (16), which involves cross-terms between the incident and radiated waves, can be evaluated from (6) in terms of the so-called Kochin functions

$$\begin{aligned} H_j(\theta) = & - \frac{k}{D} \iint_{S_B} (\frac{\partial \psi_j}{\partial n} - \psi_j \frac{\partial}{\partial n}) \\ & \cdot \left\{ \frac{\cosh k(z+h)}{\cosh kh} \exp[-ik(x \cos \theta + y \sin \theta)] \right\} dS, \end{aligned} \quad (17)$$

where, following Wehausen (7),

$$D = \tanh kh + kh \operatorname{sech}^2 kh = \frac{2\omega}{g} v_g, \quad (18)$$

and  $v_g$  is the group velocity  $d\omega/dk$ . A separate definition of the two-dimensional Kochin function is customary (7), where the factor  $k$  outside the



integral is deleted. However for convenience we shall extend the definition (17) to hold for two dimensions as well, with the convention that the wave angle  $\theta$  is then equal to 0 or  $\pi$ . The Kochin functions play a fundamental role in wave-body interactions, and will be used extensively hereafter. It may be noted from (13) that they can be expressed alternatively as the negative of the same integral over the control surface  $S_C$ .

Using (17) to evaluate the remaining second integral in (16), it follows that

$$I(\phi_i, \phi_j) = -\frac{gD}{\omega k} \{A_i H_j(\pi + \beta_i) - A_j H_i(\pi + \beta_j)\}. \quad (19)$$

This effectively completes the evaluation of the integrals defined by (13). However, additional and complementary relations can be developed by applying Green's theorem to the complex conjugates  $\phi^*$ . Note that these functions are also harmonic, and satisfy the free-surface and bottom boundary conditions, so that (13) remains valid if either or both of the potentials are replaced by their conjugates. Physically these conjugate potentials are of limited interest; from (1) they are seen to correspond to the solutions for problems with reversed time, and from the radiation conditions (11) it is obvious that the conjugate potentials  $\psi^*$  will have *incoming* waves at infinity. But the consideration of these non-physical solutions is mathematically useful, and enables us to derive conclusions of considerable practical importance.

If Green's theorem is applied to  $\phi_i^*$  and  $\phi_j^*$  together, no new results are obtained since this corresponds to taking the complex conjugate of (13) or (19) directly. But if one of the two original potentials is retained, and the other replaced by its conjugate, then additional and independent relations will follow due to the opposing radiation conditions for the two functions. In particular, the complementary expression to (16) is

$$\begin{aligned} I(\phi_i, \phi_j^*) = & - \iint_{S_C} (\phi_{i1} \frac{\partial \phi_{j1}^*}{\partial n} - \phi_{j1}^* \frac{\partial \phi_{i1}}{\partial n}) dS \\ & - \iint_{S_C} (\phi_{i1} \frac{\partial \psi_{j1}^*}{\partial n} - \psi_{j1}^* \frac{\partial \phi_{i1}}{\partial n} \\ & + \psi_{i1} \frac{\partial \phi_{j1}^*}{\partial n} - \phi_{j1}^* \frac{\partial \psi_{i1}}{\partial n}) dS \\ & - \iint_{S_C} (\psi_{i1} \frac{\partial \psi_{j1}^*}{\partial n} - \psi_{j1}^* \frac{\partial \psi_{i1}}{\partial n}) dS. \quad (20) \end{aligned}$$

Once again there is no contribution from the first integral in this equation, since  $\phi_{i1}$  and  $\phi_{j1}^*$  are both harmonic throughout the interior of  $S_C$ . Using (17) to evaluate the second integral as in (19), it follows that

$$\begin{aligned} I(\phi_i, \phi_j^*) = & -\frac{gD}{\omega k} \{A_i H_j^*(\beta_i) - A_j^* H_i(\beta_j)\} \\ & - \iint_{S_C} (\psi_{i1} \frac{\partial \psi_{j1}^*}{\partial n} - \psi_{j1}^* \frac{\partial \psi_{i1}}{\partial n}) dS, \quad (21) \end{aligned}$$

where the integral must be retained since  $\psi_{i1}$  and

$\psi_{j1}^*$  satisfy different radiation conditions.

In order to evaluate the remaining integral in (21), we now consider the far-field asymptotic behavior of  $\psi_{i,j}$ , specifically the relation which exists between the amplitude of the far-field wave motion and the Kochin functions. After recalling that the control surface  $S_C$  is in the far field, where the radiation conditions (11) are asymptotically valid, we substitute these expressions for the potential in the Kochin-function integrals (17) and perform the vertical integration from  $-h$  to 0, which yields the two-dimensional relation

$$H_j \left( \frac{0}{\pi} \right) = i k f_j \left( \frac{\pm}{\pi} \right) \quad (22a)$$

and, in three dimensions,

$$\begin{aligned} H_j(\theta) = & \frac{1}{2} i(kR)^{1/2} \int_0^{2\pi} d\theta' f_j(\theta') [1 + \cos(\theta - \theta')] \\ & \exp\{ikR[1 - \cos(\theta - \theta')]\}. \quad (22b) \end{aligned}$$

Since  $kR \gg 1$ , the last integral can be evaluated by the method of stationary phase to give the desired three-dimensional analog of (22a) in the form

$$H_j(\theta) = i(2\pi)^{1/2} f_j(\theta) e^{i\pi/4}. \quad (23)$$

Thus, using (22a) and (23) with (11) for the two- and three-dimensional cases respectively, the far-field asymptotic expressions for  $\psi_j$  can be expressed in terms of the Kochin functions as follows:

$$\psi_j(x, z) \approx -(i/k) H_j \left( \frac{0}{\pi} \right) \frac{\cosh k(z+h)}{\cosh kh} e^{\pm i k x}, \quad x \rightarrow \pm \infty, \quad (24a)$$

$$\psi_j(R, \theta, z) \approx \frac{-H_j(\theta)}{\sqrt{2\pi k R}} \frac{\cosh k(z+h)}{\cosh kh} e^{i k R + i\pi/4}, \quad kR \rightarrow \infty. \quad (24b)$$

Substituting (24) in the integral of (21) and performing the vertical integration it follows that, in the two-dimensional case,

$$\begin{aligned} I(\phi_i, \phi_j^*) = & -\frac{gD}{\omega k} [A_i H_j^*(\beta_i) - A_j^* H_i(\beta_j)] \\ & + \frac{iD}{k^2} [H_i(0) H_j^*(0) + H_i(\pi) H_j^*(\pi)], \quad (25a) \end{aligned}$$

whereas in three dimensions the corresponding expression is

$$\begin{aligned} I(\phi_i, \phi_j^*) = & -\frac{gD}{\omega k} [A_i H_j^*(\beta_i) - A_j^* H_i(\beta_j)] \\ & + \frac{iD}{2\pi k} \int_0^{2\pi} H_i(\theta) H_j^*(\theta) d\theta. \quad (25b) \end{aligned}$$

This completes the derivation of the analogous equations to (19) for the case when one potential is replaced by its conjugate. In subsequent sections the relations (19) and (25) will be applied to different situations to obtain a variety of relationships between the physical parameters of practical interest in describing wave-body interactions.

#### 4. SYMMETRY OF THE RADIATION FORCES

As the first, and most familiar application of Green's theorem, we suppress the incident waves and suppose that  $\phi_{1,j}$  correspond to two forced motions of the body in different modes, with unit velocities. Using the linearized Bernoulli equation for the pressure, the hydrodynamic force component  $F_{1j}$  in the direction  $i$  due to a unit velocity of the body in the direction  $j$  is given by

$$F_{1j} = i\omega\rho \iint_{S_B} \phi_j n_i dS, \quad (26)$$

where  $n_i$  denotes the appropriate component of the unit normal vector on the body surface. This expression may be generalized to include the hydrodynamic moment, and higher-order loadings as well, simply by extending the definition of  $n_i$  to be the corresponding component of  $(\underline{r} \times \underline{n})$ , etc.

In view of the definition of  $\phi_i$ , the boundary condition on the body surface takes the form

$$\partial\phi_i/\partial n = n_i. \quad (27)$$

Hence (26) may be expressed as

$$F_{1j} = i\omega\rho \iint_{S_B} \phi_j \frac{\partial\phi_i}{\partial n} dS. \quad (28)$$

Since both potentials in (28) satisfy the radiation condition at infinity, it follows immediately from (13) and (14) that

$$F_{1j} = F_{ji}. \quad (29)$$

This is the classical symmetry relation for the hydrodynamic pressure force. Physically, the force in one mode due to a unit motion in a second mode is equal to the force in the second mode due to unit motion in the first.

#### 5. ENERGY RADIATION AND DAMPING FORCES

Proceeding as in §4 with  $\phi_{1,j}$  the potentials for two forced motions with unit velocities, but using (25) in place of (14), it follows that

$$I(\phi_i, \phi_j^*) = \iint_{S_B} (\phi_i n_j - \phi_j^* n_i) dS = \frac{1}{i\omega\rho} (F_{1j} + F_{ji}^*)$$

$$= \begin{cases} \frac{iD}{k^2} [H_1(0) H_j^*(0) + H_1(\pi) H_j^*(\pi)] & (30a) \\ \frac{iD}{2\pi k} \int_0^{2\pi} H_1(\theta) H_j^*(\theta) d\theta & (30b) \end{cases}$$

Using the symmetry relation (29) to replace  $F_{ji}^*$  by  $F_{ij}^*$ , an expression is obtained for the real part of  $-F_{1j}$ , or the damping coefficient  $B_{1j}$ , in the form

$$B_{1j} \equiv -\text{Re}(F_{1j}) = \begin{cases} \frac{\omega\rho D}{2k^2} [H_1(0) H_j^*(0) + H_1(\pi) H_j^*(\pi)] & (31a) \\ \frac{\omega\rho D}{2\pi k} \int_0^{2\pi} H_1(\theta) H_j^*(\theta) d\theta & (31b) \end{cases}$$

The same expressions can be derived by analysis of the energy radiation at infinity, or alternatively of the work done on the body surface (cf. equation (58)).

#### 6. RELATIONS BETWEEN THE SCATTERED WAVES

Now let us apply (19) and (25) to a pair of scattering potentials  $\phi_1, \phi_2$  of the form (15), both of which satisfy the homogeneous boundary condition (8). In view of this condition, and (13),  $I(\phi_1, \phi_2)$  and  $I(\phi_1, \phi_2^*)$  vanish. Thus, from (19),

$$A_1 H_2(\pi + \beta_1) - A_2 H_1(\pi + \beta_2) = 0 \quad (32)$$

and, from (25),

$$A_1 H_2^*(\beta_1) - A_2^* H_1(\beta_2) = \begin{cases} \frac{i\omega}{gk} [H_1(0) H_2^*(0) + H_1(\pi) H_2^*(\pi)] & (33a) \end{cases}$$

$$\begin{cases} \frac{i\omega}{2\pi g} \int_0^{2\pi} H_1(\theta) H_2^*(\theta) d\theta & (33b) \end{cases}$$

In the two-dimensional case, it is more convenient to define the wave amplitudes at infinity in terms of reflection and transmission coefficients  $R$  and  $T$ . Here one must discriminate between the two cases of waves incident from minus or plus infinity, proportional to  $e^{\pm ikx}$ . We shall denote these two scattering potentials by  $\phi_{1,2}$  respectively, and transmission coefficients  $R_{1,2}$  and  $T_{1,2}$ . These can be defined by the following asymptotic conditions on the free surface  $z=0$  at  $|x|=\infty$ :

$$\frac{\omega}{gA_1} \phi_1 \approx \begin{cases} T_1 e^{ikx}, & x \rightarrow +\infty, \\ e^{ikx} + R_1 e^{-ikx}, & x \rightarrow -\infty, \end{cases} \quad (34)$$

and

$$\frac{\omega}{gA_2} \phi_2 \approx \begin{cases} e^{-ikx} + R_2 e^{ikx}, & x \rightarrow +\infty, \\ T_2 e^{-ikx}, & x \rightarrow -\infty. \end{cases} \quad (35)$$

Comparing these with (24a) and noting that  $\beta_1=0$ ,  $\beta_2=\pi$ , the Kochin functions are related to the reflection and transmission coefficients by the equations

$$R_i = -\frac{i k}{gkA_i} H_i(\pi + \beta_i), \quad (i=1,2), \quad (36)$$

and

$$T_i = 1 - \frac{i\omega}{gkA_i} H_i(\beta_i), \quad (i=1,2). \quad (37)$$

It follows from (32) and (37) that

$$T_1 = T_2 \equiv T. \quad (38)$$

Substitution of (36) and (37) in (33a) gives a total of three additional relations:

$$R_1 R_1^* + T_1 T_1^* = 1, \quad (i=1,2), \quad (39)$$

$$T_1 R_2^* + T_2^* R_1 = 0. \quad (40)$$

Equation (39) is the classical expression of conservation of energy, which holds separately for each of the two scattering problems. In conjunction with (38) it follows that

$$|R_1| = |R_2| \quad (41)$$

Equation (40), with (38), gives the phase-angle relation

$$\arg(R_1) + \arg(R_2) = \pi + 2 \arg(T) \quad (42)$$

The expressions (38-42) have all been derived earlier by Kreisel (8) and Meyer (9) and re-derived by Newman (10).

The corresponding three-dimensional relations will be noted, although these appear to be of somewhat less practical importance. From (32) it follows that incident waves of unit amplitude and arbitrary direction  $\beta_1$  will have a diffracted amplitude, in the direction  $\pi + \beta_2$ , equal to that of unit waves incident in a direction  $\beta_2$  at the angle  $\pi + \beta_1$ . In particular, taking  $\beta_2 = \pi + \beta_1$ , it follows that the three-dimensional "transmission coefficient" is, as in the two-dimensional case, unchanged if the direction of the incident wave is reversed. We emphasize that these conclusions are valid for arbitrary three-dimensional bodies.

When only one incident wave is considered, with  $(A_1, \beta_1) = (A_2, \beta_2)$  in (33b), it follows that

$$\text{Im}(H_d(\beta)) = -\frac{\omega}{4\pi gA} \int_0^{2\pi} |H_d(\theta)|^2 d\theta \quad (43)$$

This equation has been used by Maruo (11) and Newman (12) to calculate the drift force and moment on flowing bodies. A similar result to (43) is well known in other fields of wave propagation, where the integral is proportional to the scattering cross section. One implication of (43) must be borne in mind in studying wave interaction with "weak scatters" or bodies where the Kochin function is small, such as deeply submerged bodies or bodies whose dimensions are small compared to the wavelength; the Kochin function for the diffraction potential is to leading order real, in the direction  $\theta = \beta$ , since from (43) the imaginary part is a second-order quantity. The resulting restrictions are noted by Lee and Newman (13).

#### 7. THE HASKIND RELATIONS

The applications of Green's theorem in §§4-6 seem "natural" in the sense that certain inter-relationships are shown to exist in a single physical problem or pair of closely related problems. But here and in the next section we consider relations between scattering and radiation problems which are not physically related to each other in any obvious manner. However, mathematically, Green's theorem in the forms (19) and (25) can be readily applied to a pair of potentials where one is a scattering potential and the other a radiation potential, for the same body, and the results of this procedure are very useful in practice.

Here we consider the results to be obtained from (19), with  $\phi_1 = \phi_s$  the scattering potential, and  $\phi_j$  a radiation potential for forced motions of unit velocity, as defined in §4. In this instance  $A_j = 0$  and, on the body surface,  $\partial\phi_j/\partial n = 0$ , hence it follows from (13) and (19) that

$$\iint_{S_B} \phi_s \frac{\partial\phi_j}{\partial n} dS = -\frac{gD}{\omega k} A H_j(\pi + \beta) \quad (44)$$

where the subscripts are no longer required for the incident wave amplitude  $A$  and direction  $\beta$ . By analogy to (28), the left side of (44) is proportional to the  $j$ 'th component of the wave exciting force exerted on the fixed body by the incident waves. Thus

$$X_j = i\omega\rho \iint_{S_B} \phi_s \frac{\partial\phi_j}{\partial n} dS = -\frac{i\rho gDA}{k} H_j(\pi + \beta) \quad (45)$$

is a relation for the exciting force  $X_j$  in terms of the Kochin function for the forced-motion problem in the  $j$ -th mode. This equation is generally referred to as "Haskind's relation", having been given for the first time, in this particular context, by Haskind (1). Various extensions and consequences have been observed by Newman (14). As with the symmetry of the radiation forces in §4, the Haskind relations can be applied to higher-order forces and moments, and applications to structural loading in waves have been noted by Ogilvie (15).

#### 8. RELATIONS BETWEEN THE SCATTERED AND RADIATED WAVES

While Haskind relations (45) give a useful relation for the wave exciting forces, they provide no information regarding the corresponding form of the diffracted waves. On the other hand we have at this stage only considered the implications of Green's theorem in the form (19) for the combination of a radiation and scattering potential. The remaining possibility, where (25) is applied to the same combination was surprisingly not exploited until very recently and, even then, was only appreciated after the two-dimensional relations for reflection and transmission coefficients in terms of radiated wave characteristics had been discovered by an indirect argument.

We proceed to consider (25) in the case where  $\phi_1 \equiv \phi_s$  is a scattering potential and  $\phi_j^*$  is the conjugate of a radiation potential. Complementary relations to the Haskind relations are then obtained in the form

$$\iint_{S_B} \phi_s \frac{\partial\phi_j^*}{\partial n} dS = -\frac{gD}{\omega k} A H_j^*(\beta)$$

$$+ \left\{ iD[H_d(0) H_j^*(0) + H_d(\pi) H_j^*(\pi)] \right. \quad (46a)$$

$$\left. + \frac{iD}{2\pi k} \int_0^{2\pi} H_d(\theta) H_j^*(\theta) d\theta \right\} \quad (46b)$$

At first glance these new results seem less useful than (44), since the right-hand-side depends on the solution of the diffraction problem. But if the normal velocity in the forced-motion problem is restricted to be real, as in the case of rigid-body translations and rotations, it follows that

$$\frac{\partial\phi_j}{\partial n} = \frac{\partial\phi_j^*}{\partial n} \quad (47)$$



After using (44) to replace the left side of (46) we obtain the relations

$$H_j(\pi + \beta) - H_j^*(\beta)$$

$$= \begin{cases} \frac{-i\omega}{gkA} [H_d(0) H_j^*(0) + H_d(\pi) H_j^*(\pi)] & (48a) \\ -\frac{i\omega}{2\pi gA} \int_0^{2\pi} H_d(\theta) H_j^*(\theta) d\theta & (48b) \end{cases}$$

Writing (48a) in terms of the reflection and transmission coefficients, using (36) and (37), gives a pair of linear equations for  $R$  and  $T$  in the form

$$R_1 H_j^*(\pi + \beta_1) + T H_j^*(\beta_1) = H_j(\pi + \beta_1), \quad (i=1,2). \quad (49)$$

Here (38) has been used to eliminate the subscripts for the transmission coefficients and, as before,  $\beta_1=0, \beta_2=\pi$ . Since the Kochin function  $H_j$  in this equation can be taken to correspond to any forced mode of the body, subject only to the restriction (47), there is an infinity of simultaneous equations (49) for the three unknowns  $R_1, R_2$  and  $T$ . On the assumption that unique values of these unknowns exist, it follows by considering (49) that there are only two independent values of the ratios  $H_j^*(\pi)/H_j(\pi)$  and  $H_j^*(0)/H_j(0)$ , which uniquely determine  $R_1$  and  $T$ , and two independent values of the ratios  $H_j^*(0)/H_j^*(\pi)$  and  $H_j^*(\pi)/H_j(0)$ , which uniquely determine  $R_2$  and  $T$ . Thus we arrive indirectly at the unexpected conclusion that the phases of outgoing waves in the radiation problems are not completely independent.

This situation is illustrated most easily in the special case of a two-dimensional body which is symmetrical about the vertical axis  $x=0$ . Hence from symmetry  $R_1=R_2=R$  and there must then exist a symmetric forced motion, e.g. vertical oscillations or heave, such that  $H_j(0)=H_j(\pi)$  is an even function, and anti-symmetric motions such as horizontal sway oscillations (or roll) such that  $H_j(0)=-H_j(\pi)$  is odd. If we denote the arguments of these two Kochin functions as  $\alpha_e$  and  $\alpha_o$  respectively, it follows immediately from (49) that

$$R + T = e^{2i\alpha_e}, \quad (50)$$

$$R - T = e^{2i\alpha_o}. \quad (51)$$

Thus  $R$  and  $T$  are given by the relations

$$\begin{Bmatrix} R \\ T \end{Bmatrix} = \frac{1}{2} (e^{2i\alpha_e} \pm e^{2i\alpha_o}). \quad (52)$$

Alternately, as in (5),  $\alpha_e$  and  $\alpha_o$  can be replaced by the phase angle of the radiated wave potentials (24a), in which case the sign of (52) is reversed. Since  $R$  and  $T$  are unique properties of the body shape and wavelength, the same must be true for  $\alpha_e$  and  $\alpha_o$ , hence these phase angles are independent of the precise mode of forced motion and, for example, roll and sway must cause radiated waves of precisely the same phase, modulo 180°. From the Haskind relation (45) the same must apply to the corresponding exciting forces and moments, e.g. the roll moment and sway force must be in phase, with a possible ambiguity of 180 degrees. For two-dimensional symmetric bodies these

properties are discussed in more detail by Newman (5). Extensions to the case of unequal depths at  $x=\pm\infty$  are given by Yeung (16).

## 9. AXI-SYMMETRIC BODIES

The three-dimensional formulae of the preceding sections can be simplified for bodies of rotation about the vertical  $z$ -axis. In terms of polar coordinates  $(r, \theta, z)$  the  $\theta$ -dependence of the potentials can be expressed in terms of Fourier series in  $\sin n\theta$  and  $\cos n\theta$ . The scattering potential  $\phi_s$  will generally contain Fourier components for all values of  $n$ , but the conventional radiation potentials will involve only a single value of  $n$ . For example, the rigid-body mode of heave, being axi-symmetrical, will only involve the term with  $n=0$ , whereas from the boundary condition (5) sway, surge, roll and pitch will involve only  $n=1$ .

Without loss of generality the incident waves are assumed to propagate in the positive  $x$ -direction, and we consider only surge, heave, and pitch motions of the body for which  $j=1, 3, 5$  respectively. The Kochin function  $H_j$  for heave will be independent of  $\theta$ , whereas the Kochin functions  $H_1$  and  $H_3$  for surge and pitch will be proportional to  $\cos \theta$ . Thus the damping coefficients (31b) can be simplified to give

$$\begin{Bmatrix} B_{11} \\ B_{33} \\ B_{55} \end{Bmatrix} = \frac{\omega \rho D}{2k} \begin{Bmatrix} |H_1(0)|^2 \\ 2|H_3(0)|^2 \\ |H_5(0)|^2 \end{Bmatrix}. \quad (53)$$

Using the Haskind relation (45), the exciting forces and moment are

$$X_j = i\omega \rho \iint_{S_B} \phi \frac{\partial \phi_j}{\partial n} dS = (-1)^{(j-1)/2} \frac{gDA}{\omega k} H_j(0), \quad (j=1, 3, 5). \quad (54)$$

Equation (48b) gives the additional relations

$$\frac{H_3(0)}{H_3^*(0)} = 1 - \frac{i\omega}{2\pi gA} \int_0^{2\pi} H_d(\theta) d\theta, \quad (55)$$

$$\frac{H_{1,5}(0)}{H_{1,5}^*(0)} = -1 + \frac{i\omega}{2\pi gA} \int_0^{2\pi} H_d(\theta) \cos \theta d\theta. \quad (56)$$

More generally, for any Kochin function  $H^{(n)}$  proportional to  $\cos n\theta$ ,

$$\begin{aligned} e^{2i\alpha_n} &\equiv \frac{H^{(n)}}{H^{(n)*}} \\ &= (-1)^n \left\{ 1 - \frac{i\omega}{2\pi gA} \int_0^{2\pi} H_d(\theta) \cos n\theta d\theta \right\}. \end{aligned} \quad (57)$$

Since the diffraction Kochin function  $H_d(\theta)$  is uniquely specified for a given body shape and wavelength, the same must be true of  $\alpha_n$ . By analogy to the corresponding two-dimensional situation discussed following (52), the phase of the Kochin function and corresponding radiated waves is therefore unique, for each  $n$ . In particular, the Kochin functions for surge and pitch must be of the same phase (with a possible ambiguity of 180 degrees). From the Haskind relations (54) it then follows that the surge exciting force and pitch exciting moment must be of the same phase (modulo

180 degrees). This conclusion was obtained by Garret (17), for the special case of a floating circular cylinder or "dock".

#### 10. EXTRACTION OF WAVE ENERGY

An engineering problem of increasing importance is the extraction of wave energy by a floating body and the ultimate transfer of this energy into useful power. The relations derived in the preceding sections can be used to study this problem and to draw conclusions regarding the optimum body geometry and motions.

Without loss of generality it may be assumed that the incident waves are moving in the positive  $x$ -direction, hence  $\beta=0$ . From the linearized Bernoulli equation, the time-averaged work done by the pressure forces acting on the body is given by

$$\begin{aligned} \overline{dE/dt} &= \iint_{S_B} p \frac{\partial \Phi}{\partial n} dS \\ &= \frac{1}{4} i\omega\rho \iint (\Phi \frac{\partial \Phi^*}{\partial n} - \Phi^* \frac{\partial \Phi}{\partial n}) dS = \frac{1}{4} i\omega\rho I(\Phi, \Phi^*) \end{aligned} \quad (58)$$

Using (25) it follows that

$$\overline{dE/dt} = - \frac{\rho g A D}{2k} \operatorname{Im}[H(0)] \quad (59a)$$

$$- \left\{ \frac{\omega \rho D}{4k^2} [|H(0)|^2 + |H(\pi)|^2] - \frac{\omega \rho D}{8\pi k} \int_0^{2\pi} |H(\theta)|^2 d\theta \right\} \quad (59b)$$

In general, the Kochin function  $H(\theta)$  may be expanded in the form

$$H(\theta) = H_d(\theta) + H_r(\theta) = H_d(\theta) + \sum_j v_j H_j(\theta), \quad (60)$$

where  $v_j$  is the body velocity in the  $j$ 'th mode of motion, which may be either a rigid-body motion or a generalized mode of motion. In order to utilize the results of §8 we shall assume that each  $v_j$  is of fixed phase on the body surface. (This restriction can always be accommodated by decomposition of a mode with non-constant phase.)

Substituting (60) in (59), and using (43) as well as (48), it follows that

$$\begin{aligned} \overline{dE/dt} &= - \frac{\rho g A D}{2k} \operatorname{Im} \sum_j v_j H_j^*(\pi) \\ &\quad - \left\{ \frac{\omega \rho D}{4k^2} \left[ \left| \sum_j v_j H_j(0) \right|^2 + \left| \sum_j v_j H_j(\pi) \right|^2 \right] \right. \\ &\quad \left. - \frac{\omega \rho D}{8\pi k} \int_0^{2\pi} \left| \sum_j v_j H_j(\theta) \right|^2 d\theta \right\} \end{aligned} \quad (61a)$$

$$(61b)$$

In this form the rate of energy extraction no longer depends on the solution of the diffraction problem, and the optimization problem is therefore simplified in an analogous manner to the use of the Haskind relations. It may be noted that the terms on the second and third lines of (61) are negative definite, and these represent energy radiation in the conventional damping process. Hence energy

extraction is possible only if the first term in (61) is positive, and sufficiently large to offset the remaining terms. Optimum energy extraction will then occur when the phase of each mode is chosen such that  $v_j H_j^*(\pi)$  is negative imaginary, and when the amplitudes of the individual modes are such as to maximize the resulting quadratic equation for  $|v_j|$ .

First let us consider the case of two-dimensional motion with only one degree of freedom. Without specifying the precise mode of motion, we designate the corresponding velocity by  $v_j$  and the associated Kochin function by  $H_j$ . From (61) the rate of energy extraction is given by

$$\begin{aligned} \overline{dE/dt} &= - \frac{\rho g A D}{2k} \operatorname{Im} \{ v_j H_j^*(\pi) \} \\ &\quad - \frac{\omega \rho D}{4k^2} |v_j|^2 \{ |H_j(0)|^2 + |H_j(\pi)|^2 \}. \end{aligned} \quad (62)$$

The optimum phase of  $v_j$  is readily determined by requiring that  $v_j H_j^*(\pi)$  be pure imaginary and negative, and the modulus  $|v_j|$  is determined by finding the stationary point in the remaining equation. Thus

$$v_j = \frac{-i H_j^*(\pi)}{|H_j(\pi)|} |v_j|, \quad (63)$$

and, in order that (62) should be a maximum,

$$|v_j| = \frac{g A k |H_j(\pi)|}{\omega [|H_j(0)|^2 + |H_j(\pi)|^2]}. \quad (64)$$

Substituting (63) and (64) in (62), the optimum rate of energy extraction is given by

$$\overline{dE/dt} = \frac{\rho g^2 A^2 D}{4\omega [1 + |H_j(0)/H_j(\pi)|^2]}. \quad (65)$$

Using (18) to replace  $D$  by the group velocity  $v_g$ ,

$$\overline{dE/dt} = \frac{\frac{1}{2} \rho g A^2 v_g}{[1 + |H_j(0)/H_j(\pi)|^2]}. \quad (66)$$

The numerator of this equation is the rate of energy flux in the incident wave system, hence the inverse of the denominator is the efficiency of the extraction process. Perfect efficiency can be achieved if the body and mode of motion are such that  $H_j(0)=0$ , but for a symmetrical body and motion  $|H_j(0)|=|H_j(\pi)|$  so that the maximum efficiency in this case is only 50%. These conclusions have been independently obtained by Evans (6) and Mei (18), who analyse the problem in terms of the damping and added-mass coefficients of the body, and use the Haskind relations to evaluate the exciting force. Evans (6) has also evaluated the efficiency in non-optimum wavelengths, for specific body geometries and a single degree of freedom.

The desirability of reducing the ratio  $H_j(0)/H_j(\pi)$ , in order to increase the efficiency, is consistent with Salter's (19) "rocking cam" device which is designed to minimize waves generated by the body motion on one side of the body, and has achieved laboratory efficiencies of about 80%. The possibility of achieving 100% efficiency by suitable

choice of the body geometry is of obvious interest. However we note from (49) that if  $H_1(0) = 0$ , and  $H_1(\pi) \neq 0$ , then  $T=0$  which is generally impossible for bodies of finite dimensions relative to the wave length. (Some exceptions, involving resonant situations at certain discrete frequencies, are noted by Evans and Morris, (20), Newman, (21), and Evans, (22). In summary we conclude that for conventional two-dimensional bodies with only one degree of freedom, the maximum efficiency is less than 100%, and for a symmetric body the maximum is 50%.

Next we consider the possible improvement of the above situation, for two-dimensional bodies, if coupled motions in two or more modes occur simultaneously. Indeed it can be anticipated that suitable coupled motions of a symmetric body including both a symmetric mode such as heave, and an anti-symmetric mode such as surge or pitch, will result in complete energy extraction or an efficiency of 100%. Thus there will be no net outgoing waves on either side of the body if the radiated waves due to the body motions are such as to precisely cancel the reflected and transmitted waves due to the scattering problem, and in view of the fact that the symmetric (anti-symmetric) motion will generate even (odd) waves respectively, a suitable linear combination can always be found such that the total radiated waves are equal and opposite to the diffracted waves on both sides of the body. In order to demonstrate this optimum situation in the context of the analysis based on (61a), we consider a two-dimensional symmetric body with coupled rigid-body motions in surge ( $j=1$ ), heave ( $j=3$ ), and pitch ( $j=5$ ), with respective body velocities  $v_1, v_3, v_5$ . Taking advantage of the symmetry conditions for the corresponding Kochin functions,

$$H_1(\pi) = -H_1(0)$$

$$H_3(\pi) = H_3(0)$$

$$H_5(\pi) = -H_5(0)$$

and, from the discussion following (49),  $\arg(H_1) = \arg(H_5)$ . Proceeding as in the case of one degree of freedom, the optimum body motions are given by

$$v_3 = -igkA/2\omega H_3^*(0), \quad (67)$$

$$v_1 H_1(0) + v_5 H_5(0) = igkA H_1(0)/2\omega H_1^*(0), \quad (68)$$

and the corresponding energy-flux rate is

$$\frac{dE}{dt} = \frac{1}{4} \rho g^2 A D / \omega = \frac{1}{2} \rho g A^2 v_g. \quad (69)$$

Thus the efficiency in this case is 100%, or all of the incident wave energy is extracted as anticipated. We note from (68) that the optimum surge and pitch motions are not unique, since both radiate waves of the same phase and thus either one by itself, or a suitable combination of both, will radiate the desired anti-symmetric waves.

A particularly simple case of two coupled motions

with 100% efficiency is that of a submerged circular cylinder, rotating in a circular orbit or, equivalently, with combined heave and sway motions of equal amplitude and one-quarter-period phase difference. As noted by Evans (6), complete energy absorption will result if the amplitude and phase of this orbital motion is suitably chosen, relative to the incident wave. The necessary computations of amplitude and phase can be made readily from Ogilvie's (23) computation of the exciting forces for this body, in conjunction with the Haskind relations (45), from which the Kochin functions  $H_1$  and  $H_3$  in (67-68) can be derived.

Finally we turn to the three-dimensional situation and the corresponding results which follow from (59b), restricting our attention for simplicity to an axi-symmetric body with surge, heave and roll. In this case

$$H_1(\theta) = H_1(0) \cos \theta$$

$$H_3(\theta) = H_3(0)$$

$$H_5(\theta) = H_5(0) \cos \theta$$

and, from (56),

$$H_5/H_5^* = H_1/H_1^*.$$

By a similar procedure as before it then follows that the optimum body motions are defined by the conditions

$$v_1 H_1^*(0) + v_5 H_5^*(0) = 2igA/\omega \quad (70)$$

$$v_3 = -igA/\omega H_3^*(0) \quad (71)$$

and the corresponding energy radiation is

$$\overline{dE/dt} = \frac{3}{2} \frac{\rho g A^2 v_g}{k}. \quad (72)$$

As in the case of two-dimensional symmetric bodies, surge and pitch can occur in arbitrary linear combinations, and either mode by itself will suffice with the other equal to zero in (70).

Comparison of (69) and (72) reveals that the axi-symmetric body is extracting 100% of the incident wave energy over a "cross-section" of width  $3/k \approx \frac{1}{2} \lambda$ . Thus if the body can be made to perform in the optimum manner outlined above, with a diameter of less than half a wavelength, it will be a more economical wave absorbing device than the two-dimensional cylinder.

The optimum rate of energy extraction (72) is independent of the body dimensions and, in principle, the body can be arbitrarily small subject only to the condition that its velocity be given by (70-71). This will generally imply that as the body dimensions become small, relative to the wavelength, the amplitude of motions must increase so that the radiated waves are of constant amplitude. The practical limitations of this are emphasized by Evans (6). Nevertheless, three-dimensional bodies may be more efficient as wave energy absorbers than two-dimensional cylinders, especially when oblique and short-crested waves are considered.



## 11. CONCLUSIONS

In the preceding sections Green's theorem has been applied systematically to a variety of radiation and diffraction problems and combinations thereof. We have been somewhat mundane in this pursuit, so as not to overlook additional new relations that might be obtained, even though the price that has been paid is the rederivation of several well-known results. It cannot be said with certainty that additional and as yet undiscovered relations do not exist, but the approach we have taken has been deliberately chosen to minimize this possibility.

Some of the relations obtained are in fact new or very recent. In particular the relations in Section 8 for the reflection and transmission coefficients, in terms of the radiated-wave phase angles, were developed for the two-dimensional problem only within the past year, and the corresponding three-dimensional results are original with this paper. The application of these relations to the analysis of wave-energy extraction, in §10, is seen to be particularly fruitful, since the latter problem is thereby rendered independent of the properties of the diffraction problem, in an analogous manner that the Haskind relations achieve for the exciting forces.

In §10 we have briefly considered the extraction of wave energy by two-dimensional and three-dimensional axi-symmetric bodies. More detailed analyses are given in the papers of Evans (6) and Mei (18). Much work remains to be done in this potentially important field, notably on the development of suitable electro-mechanical devices which ensure that the body will move with the desired motions and which are capable simultaneously of extracting the wave energy and converting this or storing it in a suitable fashion. These aspects have been considered by Milgram (24) in the development of an active beach for absorbing wave energy. Experimental studies, such as those which have been undertaken by Salter (19), are an obvious parallel here, but it is also clear that the theory has much to offer in the development of optimum configurations. One important theoretical problem which has not been treated here, and which is left for future work, is that of non-axi-symmetric three-dimensional bodies. In particular the case of a long slender configuration of hinged rafts has been advocated in a recent article by Wooley and Platts (25). This type of device has obvious practical advantages, as noted by these authors, and it may be analysed by similar methods to those which have been utilized in §10, possibly incorporating into the analysis the Kochin functions appropriate to snake-like motions of a slender ship in head waves. The latter problem has been studied by Ursell (26) in a more conventional context.

## 12. ACKNOWLEDGEMENT

The author acknowledges support during the preparation of this paper from the Office of Naval Research, Contract N00014-67-A-1204-A-0023, the David Taylor Naval Ship Research and Development Center General Hydromechanics Research Program, Contract N00014-67-A-0204-0081, and the National Science Foundation, Grant GK-43886X.

## 13. REFERENCES

- (1) Haskind, M. D., 'The Exciting Forces and Wet-ting of Ships in Waves', (in Russian) *Izv. Akad. Nauk SSSR, Otd. Tekh. Nauk*, 1957, 7, 65-79. English translation available as *David Taylor Model Basin Translation No. 307*.
- (2) Hanaoka, T., 'On the Reverse Flow Theorem Concerning Wave-making Theory', *Proc. 9th Japan National Congress for Appl. Mech.*, 1959, 223-226.
- (3) Ogilvie, T. F., 'The Chertock Formulas for Computing Unsteady Fluid Dynamic Force on a Body', *ZAMM* 1973, 53, 573-582.
- (4) Lamb, H., 'On Reciprocal Theorems in Dynamics', *Proc. London Math. Soc.*, 1888, 19, 144-151.
- (5) Newman, J. N., 'Interaction of Waves with Two-dimensional Obstacles: A Relation between the Radiation and Scattering Problems', *J. Fluid Mech.*, 1975, 71, 273-282.
- (6) Evans, D. V., 'A Theory for Wave Power Absorption by Oscillating Bodies', *Eleventh Symp. on Naval Hydrodynamics*, 1976, London.
- (7) Wehausen, J. V., 'The Motion of Floating Bodies', *Ann. Rev. of Fluid Mech.*, 1971, 3, 237-268.
- (8) Kreisel, G., 'Surface Waves', *Quart. Appl. Math.*, 1949, 7, 21-44.
- (9) Meyer, R., 'Symétrie du Coefficient (Complexe) de Transmission des Houles à Travers un Obstacle Quelconque', *La Houille Blanche*, 1955, 10, 139-140.
- (10) Newman, J. N., 'Propagation of Water Waves Past Long Two-dimensional Obstacles', *J. Fluid Mech.*, 1965, 23, 23-29.
- (11) Maruo, H., 'The Drift of a Body Floating on Waves', *J. Ship Res.*, 1960, 4, 1-10.
- (12) Newman, J. N., 'The Drift Force and Moment on Ships in Waves', *J. Ship Res.*, 1967, 11, 51-60.
- (13) Lee, C. M. and Newman, J. N., 'The Vertical Mean Force and Moment of Submerged Bodies under Waves', *J. Ship Res.*, 1971, 15, 231-245.
- (14) Newman, J. N., 'The Exciting Forces on Fixed Bodies in Waves', *J. Ship Res.*, 1962, 6, 10-17.
- (15) Ogilvie, T. F., 'On the Computation of Wave-induced Bending and Torsion Moments', *J. Ship Res.*, 1971, 15, 217-220.
- (16) Yeung, R. W., 'A Hybrid Integral-equation Method for Time-harmonic Free-surface Flow', 1975, *Intl. Conf. on Numerical Ship Hydrodynamics*, 1975, Gaithersburg, Md.
- (17) Garrett, C. J. R., 'Wave Forces on a Circular Dock', *J. Fluid Mech.*, 1971, 46, 129-139.
- (18) Mei, C. C., 'Power Extraction from Water Waves', to be published in the *J. Ship Res.*
- (19) Salter, S. H., 'Wave Power', *Nature*, 1974, 249, 720-724.
- (20) Evans, D. V. and Morris, C. A. N., 'Complementary Approximations to the Solution of a Problem in Water Waves', *J. Inst. Math. Applies.*, 1972, 10, 1-9.
- (21) Newman, J. N., 'Interaction of Water Waves with Two Closely Spaced Vertical Obstacles', *J. Fluid Mech.*, 1974, 66, 97-106.

- (22) Evans, D. V., 'A Note on the Total Reflexion or Transmission of Surface Waves in the Presence of Parallel Obstacles', *J. Fluid Mech.*, 1975, 67, 465-472.
- (23) Ogilvie, T. F., 'First- and Second-order Forces on a Cylinder Submerged under a Free Surface', *J. Fluid Mech.*, 1963, 16, 451-472.
- (24) Milgram, J. H., 'Active Water-wave Absorbers', *J. Fluid Mech.*, 1970, 43, 845-859.
- (25) Woolley, M. and Platts, J., 'Energy on the Crest of a Wave', *New Scientist*, May 1, 1975, 241-3.
- (26) Ursell, F., 'The Refraction of Head Seas by a Long Ship', *J. Fluid Mech.*, 1963, 16, 451-472.

# A THEORY FOR WAVE POWER ABSORPTION BY OSCILLATING BODIES

D. V. EVANS  
University of Bristol, UK

**SYNOPSIS** A theory is given for predicting the absorption of the power in an incident sinusoidal wave-train by means of a damped oscillating partly or completely submerged body. General expressions for the efficiency of wave absorption when the body oscillates in one or, in some cases, two modes, are given. It is shown that 100% efficiency is possible in some cases. Curves describing the variation of efficiency and amplitude of the body with wavenumber for various bodies, are presented.

## §1 INTRODUCTION

In a paper in Nature in 1974, Salter (1) described experiments in which he had extracted more than 80% of the wave power from a two-dimensional sinusoidal wave-train using a specially contoured two-dimensional rocking cylinder. The essential features of the Salter cylinder were that it had a circular rear section which did not transmit waves downstream during the motion whilst the front section was contoured so as to reflect as little energy as possible. The efficiency of the device is defined as the proportional of available power per unit crest length of the incident wave, which the cylinder absorbs. This clearly depends on the coupling between the cylinder and the fluid, and will vary with wave frequency.

A complete theory is given here for such devices, based on the usual assumptions of linear water-wave theory, and assuming that the body is suspended relative to some stable reference platform by a system of linear springs and dampers which provide restoring forces in addition to any natural buoyancy forces.

In §3 it is shown how, for a cylinder constrained to oscillate in a single mode, a general expression for the maximum efficiency possible may be obtained without examining the equations of motion of the cylinder. In particular for cylinders which are symmetrical about the axis of oscillation the maximum efficiency turns out to be 50%. Equation (4.8) of §4 shows that knowledge of the solution to the radiation problem, in which the body makes forced oscillations in a given mode, is sufficient to determine a general expression for the efficiency as a function of wavenumber. In §§5-6 the particular cases of a rolling plate and a heaving or swaying half-immersed circular cylinder are considered using known values for the appropriate added mass and damping coefficients which are required for computing the efficiency. §7 describes the corresponding theory for three-dimensional bodies having a vertical axis of symmetry. The remarkable result that the maximum power than can be absorbed by a heaving body of this type is just  $L/2\pi$  times the power per unit crest length in an incident wave of wavelength  $L$  is proved. A comparison between the relative efficiencies of a heaving sphere and a heaving half-immersed circular cylinder is made. In §8 the theory is reworked for

two modes of oscillation and it is shown how 100% efficiency is possible in some cases. This is illustrated by curves for the half-immersed and totally immersed circular cylinder oscillating in a combination of heave and sway motions. In the latter case, wide bandwidths occurred at certain values of the wavenumber to which the cylinder was tuned.

## Notation

$A$	-	amplitude of incident wave
$A_i^+(i = 1, 2, 3)$	-	complex wave amplitude at $x = +\infty$ in radiation problem
$A_i^-(i = 1, 2, 3)$	-	complex wave amplitude at $x = -\infty$ in radiation problem
$a$	-	typical dimension of body
$a_{ii}$	-	added mass coefficient in sway ( $i = 1$ ), heave ( $i = 2$ ) and roll ( $i = 3$ ).
$b$	-	half-width of cylinder at waterline
$b_{ii}$	-	damping coefficient in sway ( $i = 1$ ), heave ( $i = 2$ ) and roll ( $i = 3$ )
$c$	-	depth of point of rotation
$d$	-	dampers constant
$d_i$	-	horizontal ( $i = 1$ ) and vertical ( $i = 2$ ) damper constants
$E$	-	efficiency of power absorption
$F_i$	-	total hydrodynamic force on cylinder in $i$ th direction
$F_{ii}$	-	force on cylinder in $i$ th direction due to oscillation of cylinder in that direction
$F_{ij}$	-	force in the $i$ th direction due to oscillation of cylinder in the $j$ th direction
$F_{is}$	-	force on cylinder in $i$ th direction assuming cylinder held fixed in incident wave
$g$	-	acceleration due to gravity
$h$	-	thickness of vertical plate
$K$	=	$\omega^2/g$
$k$	-	spring constant
$k_i$	-	horizontal ( $i = 1$ ) and vertical ( $i = 2$ ) spring constants
$L$	-	wavelength of incident wave
$\ell$	-	power absorption length
$M$	=	$\frac{\pi}{2} \rho a^2$ (or $\frac{\pi}{4} \rho a^4$ for roll motions) for two dimensional cylinders, or



M	=	$\frac{2}{3} \pi a^3$ for three dimensional symmetric bodies. (M is doubled for submerged bodies.)
m	-	mass (or moment of inertia) of cylinder/unit length or mass of three dimensional body
m'	-	m/M
n <sub>1</sub> , n <sub>2</sub>	-	components of unit normal outwards from cylinder into fluid
n <sub>3</sub>	-	xn <sub>2</sub> - (y + c)n <sub>1</sub>
R	-	complex reflection coefficient for the scattering problem
R <sub>1</sub>	-	complex reflection coefficient for the full problem
s	-	specific gravity of vertical plate
T	-	complex transmission coefficient for the scattering problem
T <sub>1</sub>	-	complex transmission coefficient for the full problem
t	-	time
x, y	-	Cartesian co-ordinates
$\gamma = \gamma_i$	=	$iKA_i^+ \xi_i / A$
$\delta$	=	$ A_i^- ^2 / ( A_i^+ ^2 +  A_i^- ^2)$
$\epsilon$	=	2 (i = 1, 3) 1 (i = 2)
$\zeta_i(t)$	=	displacement of cylinder in sway (i = 1), heave (i = 2) and roll (i = 3)
$\lambda_i$	=	non-dimensional damping coefficient for sway (i = 1)
$\lambda_{i0}$	=	$\lambda_i(v_0)$
$\mu_i$	-	non-dimensional added mass coefficient for sway (i = 1), heave (i = 2) and roll (i = 3)
$\mu_{i0}$	=	$\mu_i(v_0)$
$v = Ka = \omega^2 a/g = 2\pi a/L$	-	dimensionless wave-number
$v_0$	-	dimensionless wavenumber to which body is tuned
$v_1$	-	root of equation (4.14)
$v_i$	-	time-independent displacement in sway (i = 1), heave (i = 2) and roll (i = 3)
$\rho$	-	density of the fluid
$\phi(x, y, t)$	-	velocity potential for the full problem
$\phi_s$	-	time-independent velocity potential for the scattering problem
$\phi(x, y)$	-	time-independent velocity potential for the full problem
$\phi_i (i = 1, 2, 3)$	-	time-independent velocity potential for the radiation problem
$\omega$	-	wave frequency
$\omega_0$	-	wave frequency to which body is tuned

## §2 FORMULATION

The motion is two-dimensional and Cartesian co-ordinates  $x, y$  are chosen so that  $y = 0$  is the undisturbed free surface with  $y$  measured vertically upwards and  $x$  to the right. The usual assumption of the linearised theory of water waves permit the introduction of a velocity potential  $\phi(x, y, t)$  satisfying Laplace's equation in the fluid and the linearised free surface condition

$$\frac{\partial^2 \phi}{\partial t^2} + g \frac{\partial \phi}{\partial y} = 0 \quad \text{on } y = 0. \quad (2.1)$$

It is assumed that a small amplitude sinusoidal wave-train of frequency  $\omega$  is incident from  $x = +\infty$  upon the body, which is a long cylinder having horizontal generators parallel to the wave crests of the incident wave. The cylinder is situated on or beneath the free surface and is constrained to make small amplitude oscillations in response to the incident wave. The oscillations may be of heave, sway, or roll, but not a combination of these. The case of a cylinder oscillating in both heave and sway is considered in §8. In the absence of waves it is assumed that the cylinder is held in equilibrium by a combination of buoyancy forces due to a spring and damper system connected to the cylinder, the latter being capable of extracting energy from the cylinder. In the model chosen by Salter, the cylinder was constrained to make rolling oscillations about a fixed point of itself. The power absorption was measured using an electrical dynamometer consisting of two coils in a magnetic field. Velocity signals from one coil were amplified and sent to the other so as to oppose movement. Velocity and force signals were then multiplied to indicate power absorbed which was then compared with wave height measurements. A possible mechanism for power conversion in full scale models at sea has also been described by Salter. The rotations of the cylinder will produce unidirectional pulses of water through a special pump described in detail in (1). In the theoretical treatment described here, it will be assumed that the mechanism for power absorption can be described by a simple linear damper having a resistance to motion which is proportional to velocity. It is unlikely that an actual pump behaves in so simple a fashion and a more realistic model would have to allow for non-linearities in the pumping mechanism.

On the cylinder we impose the condition that the component of the cylinder velocity normal to itself is equal to the normal velocity of the fluid at that point. Let  $\zeta_i(t)$  describe the displacement of the cylinder from its equilibrium position. Here  $i = 1, 2$  relate to sway and heave motions and  $i = 3$  relates to rolling motions. Then  $\zeta_1, \zeta_2$  describe the horizontal and vertical displacements respectively of the centre of mass of the cylinder, while  $\zeta_3$  describes the angular displacement of the cylinder about its point of rotation. The linearised condition on the equilibrium position of the cylinder is then

$$\frac{\partial \phi}{\partial n} = \dot{\zeta}_i n_i \quad (2.2)$$

for  $(x, y)$  on  $C$  the surface of the cylinder, where  $\underline{n} = (n_1, n_2)$  is the normal vector from the body into the fluid at the point  $(x, y)$  and  $n_3 = n_2 x - (y + c)n_1$ , where  $c$  is the depth of the point of rotation.

It is convenient to eliminate the harmonic time-dependence by writing

$$\phi(x, y, t) = \Re \{ \phi(x, y) e^{i\omega t} \}. \quad (2.3)$$

We next write the complex-valued time-independent potential  $\phi(x, y)$  as

$$\phi(x, y) = \omega^{-1} g A \phi_s + i \omega \xi_i \phi_i \quad (2.4)$$

where

$$\zeta_i = \Re \{ \xi_i e^{i\omega t} \} \quad (2.5)$$

and  $A$  is a complex constant. The complex potential  $\phi_s$  is the solution of the scattering problem in which the cylinder is held fixed in an incident wave of unit amplitude potential. The

complex potential  $\phi_i$  is the solution to the radiation problem in which a normal velocity  $\text{Re}(n_i e^{i\omega t})$  is prescribed on the cylinder surface corresponding to small oscillations of unit amplitude in the three modes.

Condition (2.2) is satisfied if, on the cylinder,

$$\frac{\partial \phi_s}{\partial n} = 0, \quad \frac{\partial \phi_i}{\partial n} = n_i. \quad (2.6)$$

The wave elevation is given by

$$g^{-1} \frac{\partial \phi}{\partial t}(x, 0, t) = \text{Re} \left\{ i\omega g^{-1} \phi(x, 0) e^{i\omega t} \right\}$$

so that the incident wave has amplitude  $|A|$  if we assume

$$\phi_s \sim (e^{iKx} + R e^{-iKx}) e^{Ky} \quad \text{as } x \rightarrow +\infty \quad (2.7)$$

where  $R$  is the complex reflection coefficient for the scattering problem. For  $x \rightarrow -\infty$  we assume

$$\phi_s \sim T e^{iKx+Ky} \quad (2.8)$$

where  $T$  is the complex transmission coefficient for the scattering problem. Here  $K = \omega^2/g$ .

For  $x \rightarrow \infty$  we assume

$$\phi_i \sim A_i^+ e^{-iKx+Ky}, \quad (2.9)$$

and for  $x \rightarrow -\infty$

$$\phi_i \sim A_i^- e^{-iKx+Ky}. \quad (2.10)$$

### §3 THE MAXIMUM EFFICIENCY OF POWER ABSORPTION

The efficiency of the system will be defined as the proportional of available power per unit frontage of the incident wave which is extracted by the body. This will clearly depend on the details of the coupling between the cylinder and the fluid. Some information about the maximum efficiency possible can be gained, however, without knowing the details of the coupling.

We have, from (2.4), (2.7), (2.9) and (2.10),

$$\phi \sim \frac{gA}{\omega} (e^{iKx} + R e^{-iKx}) \quad \text{as } x \rightarrow +\infty \quad (3.1)$$

$$\text{and } \phi \sim \frac{gA}{\omega} T e^{iKx}, \quad x \rightarrow -\infty \quad (3.2)$$

$$\left. \begin{aligned} \text{where } R_1 &= R + iKA_1^+ \xi_1/A \\ T_1 &= T + iKA_1^- \xi_1/A \end{aligned} \right\} \quad (3.3)$$

The power per unit length in a sinusoidal two-dimensional progressive wave is the mean energy flux per unit length crossing a vertical plane normal to the direction of the wave, and it can be shown that  $R_1 \bar{R}_1 (T_1 \bar{T}_1)$  measures the proportion of power in the reflected (transmitted) wave. It follows that  $E$  the efficiency of the system, is just

$$E = 1 - R_1 \bar{R}_1 - T_1 \bar{T}_1 \quad (3.4)$$

(Here a bar over a quantity denotes the complex conjugate). If the cylinder is held fixed so that  $\xi_i = 0$  then from (3.3) and (3.4)

$$E = 1 - R \bar{R} - T \bar{T} = 0 \quad (3.5)$$

showing that wave energy flux is conserved in this case. Recently Newman (2) has demonstrated a relationship between  $R$ ,  $T$  and  $A_i$  which may be written

$$A_i^+ + A_i^- R + A_i^- T = 0 \quad (i = 1, 2, 3). \quad (3.6)$$

If we now use (3.3), (3.5) and (3.6), we can, after some algebra, write (3.4) in the form

$$E = 2 \text{Re} \gamma - |\gamma|^2 (1 - \delta)^{-1} \quad (3.7)$$

$$\text{where } \gamma = iKA_1^+ \xi_1/A$$

$$\text{and } \delta = |A_1^-|^2 / (|A_1^+|^2 + |A_1^-|^2). \quad (3.8)$$

The quantity  $\delta$ , a function of frequency, depends solely on the geometry of the cylinder and cannot be influenced by the particular coupling between fluid and cylinder. The coupling effect occurs in  $\gamma$  through the term  $\xi_1/A$  which must be determined from the equation of motion of the body. If we now maximise the expression (3.7) as a function of  $\gamma$ , we obtain

$$E_{\max} = \gamma_{\max} = 1 - \delta. \quad (3.9)$$

Equation (3.9) is a general result for the maximum efficiency that can be achieved by a given two-dimensional cylinder in a single mode of oscillation. It also follows from (3.3), (3.5), and (3.6) that when (3.9) is satisfied,

$$|R_1| = \delta, \quad |T_1| = \delta^{1/2} (1 - \delta)^{1/2}. \quad (3.10)$$

A highly efficient cylinder is one for which  $\delta$  is as small as possible. That is, the amplitude of the waves produced at  $x = -\infty$  by the forced oscillation of the cylinder in the absence of the incident wave, must be as small as possible compared to the amplitude of the waves produced at  $x = +\infty$ . This is equivalent to the criterion used by Salter in designing an efficient cylinder for which  $T_1$  was as small as possible. The equivalence follows from (3.5) and (3.6) which show that if  $A_i^-$  is small then so is  $T$  and hence  $T_1$  also. Notice from (3.10) that as  $\delta \rightarrow 0$  the reflected wave amplitude tends to zero much faster than the transmitted wave amplitude. For example if  $E_{\max} = 0.9$ , then  $|R_1| = 0.1$  and  $|T_1| = 0.3$  with  $A_1^+ = 9 A_1^-$ . For a body with horizontal symmetry,  $A_i^+ = (-1)^i A_i^-$ , ( $i = 1, 2, 3$ ) so that  $\delta = \frac{1}{4}$  and the maximum possible efficiency is 50%. In this case it follows from (3.10) that  $|R_1|^2 = |T_1|^2 = \frac{1}{4}$ , so that half of the incident wave power is shared equally between the reflected and transmitted waves, the other half being absorbed by the body. This result is consistent with the tests made by Salter (1) on a vertical vane. He obtained an efficiency of 40% with 25% of the incident power being transmitted onwards and 20% being reflected back.

### §4 THE EQUATIONS OF MOTION OF THE CYLINDER

In formulating the equation of motion of the cylinder we shall assume that the cylinder motion is resisted by mechanical forces which can be modelled by a simple spring and damper system.

Thus,  $\zeta_i(t)$  satisfies

$$m \ddot{\zeta}_i = -d \dot{\zeta}_i - k \zeta_i + F_i \quad (4.1)$$

where  $d$  and  $k$  are the damper and spring constants. For heave and roll motions  $k_i$  may also include a buoyancy force. The term  $d \dot{\zeta}_i$  allows a net amount of work to be done on the cylinder over a period, provided  $d \neq 0$ . The term  $F_i$  is the hydrodynamic "force" on the cylinder. For  $i = 1, 2$  the force is horizontal and vertical respectively; for  $i = 3$   $F_3$  is the moment about the point of rotation.

The hydrodynamic forces which do work can conveniently be separated into two parts. Thus we write

$$F_i = F_{is} + F_{ii} \quad (4.2)$$

where  $F_{is}$  is the force acting in the  $i^{\text{th}}$  direction on the cylinder, assumed to be held fixed in the presence of the incident wave and  $F_{ii}$  is the force in the  $i^{\text{th}}$  direction due to the oscillation of the body in that direction, in the absence of the incident wave. This latter force can be expressed in the form

$$F_{ii} = -a_{ii}\ddot{\zeta}_i - b_{ii}\dot{\zeta}_i \quad (4.3)$$

The first term on the right hand side of (4.3) is that part of the force which is exactly out of phase with the acceleration of the cylinder so that  $a_{ii}$  may be interpreted as an added mass term describing the increase in inertia of the cylinder due to the fluid. The second term on the right hand side of (4.3) is that part of the force which is exactly out of phase with the velocity of the cylinder. This term arises because work is done in generating surface waves which radiate away from the cylinder. For motions in an infinite fluid  $b_{ii} = 0$ .

Now Haskind (3) has shown that the exciting force  $F_{is}$  on the fixed cylinder is directly related to the waves generated by the forced oscillation of the cylinder in the  $i^{\text{th}}$  mode. Thus Newman (4), equation (37), updating the work of Haskind, has shown that

$$F_{is} = \rho g A e^{i\omega t} A_i^+ \quad (4.4)$$

Furthermore, (Newman (4) eqn. 38) the damping coefficients are given in terms of the energy radiated to infinity, by the expression

$$b_{ii} = \frac{1}{2} \rho \omega (|A_i^+|^2 + |A_i^-|^2) = \frac{1}{2} \rho \omega |A_i^+|^2 (1 - \delta)^{-1} \quad (4.5)$$

It follows from (2.5) and (4.1) to (4.4), that

$$[k - (m + a_{ii})\omega^2 + i(b_{ii} + d)\omega]\xi_i = \rho g A A_i^+ \quad (4.6)$$

and this equation determines the response of the cylinder to the incident wave.

Now the power per unit length absorbed by the cylinder is the mean rate at which work is being done on the cylinder by the fluid, per unit length. This is

$$\frac{\omega}{2\pi} \int_0^{2\pi} \dot{\zeta}_i F_i dt = \frac{1}{2} \omega^2 d |\xi_i|^2 \quad (4.7)$$

the only contribution coming from the term  $d\dot{\zeta}_i$  in (4.1). The power per unit frontage of the incident wave is obtained by computing the mean energy flux per unit length across a vertical plane normal to the wave direction. This is just  $\frac{1}{2} \rho g^2 |A|^2 / \omega$  so that  $E$ , the proportion of power absorbed, is

$$E = \frac{2\omega^3 d |\xi_i|^2}{\rho g^2 |A|^2} = \frac{2\omega^3 d \rho |A_i^+|^2}{\{k - (m + a_{ii})\omega^2\}^2 + \omega^2 (b_{ii} + d)^2} \quad \text{from (4.6)}$$

$$= \frac{4\omega^2 d b_{ii} (1 - \delta)}{\{k - (m + a_{ii})\omega^2\}^2 + \omega^2 (b_{ii} + d)^2} \dots (4.8) \quad \text{from (4.5)}$$

The same result can be obtained, after some algebra, by substituting for  $\xi_i/A$  from (4.6) into the alternative expression (3.7) for  $E$ , and using (4.5).

We see immediately from (4.8) that for a given cylinder the maximum efficiency occurs when  $k = (m + a_{ii})\omega^2$  and  $d = b_{ii}$  giving  $E_{\text{max}} = 1 - \delta$  in agreement with (3.9). Equation (4.8) can be used to compute the efficiency for different frequencies of the incident wave once the frequency dependent terms  $a_{ii}$ ,  $b_{ii}$  and  $\delta$  are known for the particular cylinder being considered. Notice that for  $d = 0$ , a freely oscillating cylinder, and  $d = \infty$ , a fixed cylinder, then  $E = 0$  as expected. If we assume that the parameters  $k$  and  $d$  can be varied, then for maximum efficiency at a frequency  $\omega_0$ , say, we choose  $k = (m + a_{ii}(\omega_0))\omega_0^2$  and  $d = b_{ii}(\omega_0)$ . Computed values of the added mass and damping terms  $a_{ii}$  and  $b_{ii}$  are typically non-dimensionalised by writing

$$a_{ii} = M \mu_i \quad b_{ii} = M \omega \lambda_i \quad (4.9)$$

where  $M$  is the mass (per unit length) of fluid displaced by a half-immersed circular cylinder having radius  $a$  equal to a typical length of the body. If the body is completely submerged, then  $M$  is taken to be the mass (per unit length) of fluid displaced by a completely submerged circular cylinder. Thus  $M = \frac{1}{2} \pi \rho a^2$  or  $\pi \rho a^2$ . For roll motions the corresponding moments of inertia are taken for  $M$ . We introduce the dimensionless wave-number  $\nu = \omega^2 a / g = 2\pi a / L$  where  $L$  is the wavelength of the incident wave and also  $\nu_0 = \omega_0^2 a / g$ .

Then

$$E = \frac{4\nu(1-\delta)(\nu_0^{\frac{1}{2}}\lambda_i)(\nu_0^{\frac{1}{2}}\lambda_{i0})}{\{(m' + \mu_{i0})\nu_0 - (m' + \mu_i)\nu\}^2 + \nu(\nu_0^{\frac{1}{2}}\lambda_{i0} + \nu_0^{\frac{1}{2}}\lambda_i)^2} \quad (4.10)$$

where

$$\nu_{i0} = \lambda_0(\nu_0), \quad \mu_{i0} = \mu_i(\nu_0), \quad m' = m/M.$$

In a similar manner from (4.6) the expression for the ratio of the amplitude of oscillation of the cylinder to the amplitude of the incident wave, is given by

$$\left| \frac{\xi_i}{A} \right|^2 = \frac{2\rho a^2 M^{-1} (1 - \delta) \lambda_i}{\{[(m' + \mu_{i0})\nu_0 - (m' + \mu_i)\nu]^2 + \nu(\nu_0^{\frac{1}{2}}\lambda_{i0} + \nu_0^{\frac{1}{2}}\lambda_i)^2\}} \quad (4.11)$$

For a symmetric body in heave or sway the numerator in (4.11) is just  $2\lambda_i/\pi$  for partly submerged bodies and  $\lambda_i/\pi$  for completely submerged bodies.

A desirable property of any wave absorbing device is the ability to operate at high efficiency over a wide band-width. In order to test the efficiency for varying  $\nu$  we need to know the variation of  $\mu_i$ ,  $\lambda_i$  and  $\delta$  with wavenumber for the particular body. Unfortunately, to the author's knowledge, no computations exist for these parameters for unsymmetric two dimensional cylinders of the type considered by Salter. There do however exist computations for various two dimensional cylinders having horizontal symmetry as these coefficients are useful in ship hydrodynamics for determining ship motion using strip theory.



Before considering particular cylinders in detail, it is necessary to consider more closely the conditions for maximum efficiency. From (4.8) it is seen that this requires

$$d = b_{ii}(\omega) \quad (4.12)$$

$$k = [m + a_{ii}(\omega)]\omega^2. \quad (4.13)$$

It is assumed that the damping constant  $d$  which models the power absorbing mechanism can be varied so that (4.12) can be satisfied at a given frequency  $\omega_0$ , say. It remains to check whether (4.13) can be satisfied for  $\omega = \omega_0$ .

For partially immersed cylinders in roll this can be achieved by varying the distance of the centre of mass of the cylinder below the metacentre since for cylinders with horizontal symmetry about the roll axis, at least,  $k$  varies as this distance. Generally, for cylinders in roll, the values of  $k$  and  $d$  can be adjusted to satisfy (4.12) and (4.13) with  $i = 3$ , so that the cylinder is "tuned" to any given non-dimensional wavenumber  $\nu_0$ . For cylinders in sway, there is no change in the buoyancy forces so that horizontal springs must be used to provide the restoring force, the stiffness of the springs being chosen to satisfy (4.13) with  $i = 1$ . The situation for partially immersed cylinders in heave is not so straightforward since because of the large buoyancy forces which occur, it is not always possible to satisfy (4.13) over the complete frequency range of interest. Thus in the absence of vertical springs,  $k = 2b\rho g$  for small vertical oscillations, where  $2b$  is the waterline width of the cylinder in equilibrium. Then, in dimensionless form, (4.13) becomes

$$\frac{4}{\pi} \left( \frac{b}{a} \right) = [m' + \mu_2(\nu)]\nu \quad (4.14)$$

where  $m' = m/M$ . In general, the variation of heave added mass coefficient  $\mu_2$  with  $\nu$  is such that (4.14) has one root  $\nu_1$  say, and including vertical springs increases  $k$  and hence increases the left hand side of (4.14). This has the effect of increasing  $\nu_1$  so that by varying the stiffness of the springs it is only possible to tune the system to wavenumbers  $\nu_0 \geq \nu_1$ . This lower bound on  $\nu_0$  may mean that in order to tune the cylinder to the predominant wavelengths an unacceptably large cylinder would be required (since  $\nu = 2\pi a/L$ ). One way round this, is to increase the effective mass of the cylinder thereby reducing  $\nu_1$  in equation (4.14). A method of doing this without affecting the equilibrium position of the floating cylinder is described by Budal and Falnes (5). Alternatively the cylinder in heave can be partially tuned by satisfying (4.12) at any desired frequency and allowing  $k$  its natural value of  $2b\rho g$  so that in general (4.13) is not satisfied.

In the next sections we consider the particular cases of a rolling vertical plate and a half immersed swaying or heaving circular cylinder. In the plate problem we shall be able to tune the plate to any desired wavenumber by varying the position of the centre of mass. The same is true of the swaying circular cylinder by incorporating horizontal springs. For the circular cylinder problem we shall obtain, for different  $m'$ , a lower bound to the wavenumbers to which the cylinder can be tuned. The maximum efficiency attainable in each case is 50%, because of the horizontal symmetry about the axis of oscillation.

## §5 THE ROLLING VERTICAL PLATE

Consider a thin vertical plate submerged to a depth  $a$ , which is constrained to roll about a horizontal axis in the free surface. Since the plate is symmetrical about  $x = 0$ ,  $\delta = \frac{1}{2}$  in (4.10) and (4.11). For rolling motions  $i = 3$  and

$M = \frac{\pi}{4} \rho a^4$  the moment of inertia per unit length of the fluid displaced by a semi-circular cylinder of radius  $a$  around its axis.

The problem of the fluid motion produced by the rolling motion of a thin vertical plate is one of the few water-wave problems which permit an explicit solution. Thus in the Appendix to a paper by Kotik (6) a reviewer has obtained explicit expressions in terms of Bessel and Struve functions for the dependence on  $\nu$  of the added mass coefficient  $\mu_3$  and the damping coefficient  $\lambda_3$ . These were derived from the full solution to the problem given by Ursell (7). Kotik (6) provides numerical values for  $\lambda_3$  and  $\mu_3$  over a wide range of  $\nu$  by making use of the Kramers-Kronig relations. These permit  $\mu_3$  to be computed from a Cauchy-type integral involving  $\lambda_3$ , the latter being relatively easy to find since it is related via the Haskind relations to the exciting force on the fixed plate.

Assuming the plate to be uniform, we have

$$m' = m/M = 4sh/3\pi a$$

where  $s$  is the specific gravity of the plate and  $h$  its (small) thickness. It follows that in general  $m'$  will be small enough for the inertia of the plate to be neglected compared to its added inertia. It is assumed that (4.12) and (4.13) can be satisfied for all frequencies of interest, the latter by varying the position of the centre of mass. In Fig. (1), equation (4.10), with  $\delta = \frac{1}{2}$  and  $m' = 0$ , has been used to plot the power efficiency  $E$  against dimensionless wavenumber  $\nu$  for different values of  $\nu_0$ , the wavenumbers for which maximum efficiency is desired. It can be seen that for  $\nu_0 = 0.3$  the bandwidth is narrow but for  $\nu_0 = 0.5$ ,  $E$  has a second maximum at about  $\nu = 1.8$  where the efficiency reaches almost 50%, the maximum possible in this case since the plate is symmetrical. For  $\nu_0 = 0.5$  then there is a wide bandwidth with the efficiency remaining above 40% for  $\nu = 0.4 - 2.6$ . The same is true for  $\nu_0 = 0.6$  and to a lesser extent for  $\nu_0 = 0.7$  although this is not shown in Fig.(1). For larger values of  $\nu_0$ , the second peak gradually disappears producing narrower bandwidths. It would appear that a vertical plate rolling about an axis in the undisturbed surface operates most efficiently as a wave power absorber when it is tuned to wavenumbers  $\nu_0$  lying between 0.5 and 0.7. For example, a plate of length 20m. tuned for maximum efficiency at  $\nu_0 = 0.5$  would be over 40% efficient in responding to any wave having a wavelength between 50m. and 300m. On a laboratory scale, a similar efficiency is possible with a plate 15 cm. long responding to wavelengths between 40cm. and 160cm.

The effect of increasing the inertia of the plate can be seen in Fig.(2), where  $m' = 0.5$ . For  $\nu_0 = 0.5$  the 40% efficiency bandwidth has been reduced to  $\nu = 0.42 - 1.62$  and the second maximum has disappeared. A better choice of wavenumber at which to tune the system is probably  $\nu_0 = 1.2$  giving  $E > 0.4$  for  $\nu = 0.6 - 1.6$ . In this case our 20m. plate is over 40% efficient for waves with

wavelengths lying between 80m. and 200m.

The roll amplitude of the plate as a function of  $\nu$  is given by (4.11) with  $i = 3$ ,  $\delta = \frac{1}{2}$  and  $M = \frac{1}{2}\pi\rho a^4$ . The complex quantity  $\xi_3$  describes the amplitude and phase of the angular displacement of the plate from the vertical. In Fig.(3) is plotted  $|\xi_3 a/A|$ , the ratio of the maximum displacement of the lower edge of the plate to the incident wave amplitude, against wavenumber  $\nu$ , for different values of the tuned wavenumber  $\nu_0$ . For small values of  $\nu_0$  large resonant plate amplitudes occur near the tuned wavenumber. For instance for  $\nu_0 = 0.3$  the maximum displacement of the lower edge of the plate is 7 times the incident wave amplitude for  $\nu$  close to 0.3. Such large plate displacements are not consistent with a linearised theory and in practice one would expect non-linear effects such as wave breaking to predominate in this case. For larger values of  $\nu_0$ , the peak displacement is much smaller and does not occur near the tuned wavenumber but near to  $\nu = 0.4$ . As  $\nu$  increases the displacement diminishes from its peak to zero monotonically. The effect of plate inertia on the plate displacement is shown in Fig.(4), where it can be seen that for  $m/M = 0.5$ , the plate displacements are diminished and the curves for different values of  $\nu_0$  are compressed, there being little difference between them for  $\nu > 1.4$ .

#### §6 THE HALF-IMMERSED SWAYING OR HEAVING CIRCULAR CYLINDER

As a second example we consider a half-immersed circular cylinder which is constrained to make small horizontal (sway) or vertical (heave) oscillations in response to the incident waves. Values of the sway and heave added mass and damping coefficients were estimated from curves given by Frank (8), for values of dimensionless wavenumber  $\nu$  up to 1.5.

Results for a floating horizontal cylinder constrained to make pure swaying oscillations are shown in Fig.(5). Since there is no buoyancy restoring force in sway, it is assumed that the cylinder is restrained by horizontal springs whose stiffness  $k$  can be varied, along with  $d$  the damping constant, so that both (4.12) and (4.13) can be satisfied for all wavenumbers of interest. Equation (4.10) was computed with  $\delta = \frac{1}{2}$ ,  $i = 1$  and  $m = M$  for different values of  $\nu$  and with  $\nu_0 = .3$ , .5 and 1.0. It can be seen that for  $\nu_0 = .3$  the bandwidth is narrow but that for  $\nu_0 = .5$  and 1.0, it is much wider so that at  $\nu_0 = .5$  for example, over 40% of available power is extracted from waves of wavelength between 5 and 18 times the cylinder radius. When the cylinder is tuned for maximum efficiency at  $\nu_0 = 1.0$  the efficiency is largely insensitive to small variations in wavenumber about  $\nu = 1.0$ . The corresponding sway amplitude of the cylinder compared to the incident wave amplitude is shown in Fig. (6). For both long and short waves the sway amplitude tends to zero so that there is a maximum amplitude for each value of  $\nu_0$ , the maximum decreasing with increasing  $\nu_0$ .

For a floating half-immersed circular cylinder making small vertical oscillations there is a natural buoyancy restoring force and  $k = 2\rho g$  so that with  $m = M$ , equation (4.14) has the root  $\nu_1 = .79$ . At this wavenumber, corresponding to waves of wavelength about 8 times its radius, the heaving cylinder can be tuned to extract 50% of the wave power by choosing  $d$  to satisfy (4.12).

Fig. (7) shows how the efficiency of power extraction computed from (4.10) with  $\delta = \frac{1}{2}$  and  $i = 2$ , varies with  $\nu$ . As for the swaying cylinder,  $E$  decreases monotonically either side of the tuned wavenumber and the cylinder is over 40% efficient to waves of wavelength between about 6 and 11 times the radius of the cylinder. Also shown is the effect of tuning the cylinder to a wavenumber  $\nu_0 = 1.0$ . This is done by choosing  $k$  and  $d$  so that (4.12) and (4.13) are satisfied by  $\nu_0 = 1.0$ , a vertical spring being required to provide the additional restoring force. The two curves are similar, the second curve showing that the cylinder is now 40% efficient in absorbing waves of wavelength between about 5 and 8 times the cylinder radius.

It has already been mentioned that a possible method of producing peak efficiencies at lower wavenumbers is to only partially tune the cylinder. In other words we allow  $k$  its natural value of  $2\rho g$  so that (4.13) is satisfied by  $\nu_1 = .79$  but adjust  $d$  to any desired wavenumber so that (4.12) is satisfied at, say  $\nu = \nu_0$ , but not (4.13). In this case the denominator of the expression (4.10) for  $E$  must be changed to

$$(4\pi^{-1} - (m' + \mu_2)\nu)^2 + \nu(\nu^{\frac{1}{2}}\lambda_2 + \nu_0^{\frac{1}{2}}\lambda_{20})^2 \quad (6.1)$$

and a similar change is required in the expression (4.11) for the heave amplitude ratio. The result is shown by the dashed curve in Fig.(7), where  $\nu_0 = .3$ . It is noticeable how little effect this partial tuning has on shifting the peak efficiency away from  $\nu = .79$ . The efficiency is increased by about 30% for  $\nu = .3$  and reduced by only about 2% for  $\nu = .79$ , suggesting that the restoring force is more important than the damping force in determining the peaks of maximum efficiency.

An alternative method of lowering the wavenumber at which maximum efficiency occurs is to increase the effective mass of the cylinder. Thus Fig.(8) shows the variation of  $E$  with  $\nu$  when  $m/M = 1.5$ . With this value the equation (4.14) has the root  $\nu_1 = .6$ , so that the cylinder can be tuned to 50% efficiency in response to waves of wavelength about 10 times the cylinder radius. Also shown in Fig.(8) is the effect of increasing the "stiffness" of the cylinder by adding vertical springs so that maximum efficiency is achieved at  $\nu_0 = .8$  and  $\nu_0 = 1.0$ . It can be seen that, just as for the rolling vertical plate, the effect of increasing the inertia is to reduce the efficiency bandwidth. Comparing the corresponding curves for  $\nu_0 = 1.0$  and  $m/M = 1$  and 1.5 shows how the 40% efficiency bandwidth is reduced from  $\nu = .77 - 1.24$  to  $\nu = .82 - 1.17$  respectively.

The heave amplitude of the cylinder compared to the incident wave amplitude is shown in Fig. (9). When tuned to the "natural" wavenumber,  $\nu_0 = .79$ , the heave amplitude decreases monotonically with  $\nu$ . The dashed curve shows the heave amplitude for a partially tuned cylinder with  $\nu_0 = .3$ . It is less than the corresponding amplitude for the completely tuned cylinder for all  $\nu$ . The effect of increasing the stiffness of the cylinder so that  $\nu_0 = 1.0$  is to decrease the amplitude for  $\nu < .8$  and to increase it for  $\nu > .8$ , there now being a local maximum at about  $\nu = .7$ . In Fig. (10) is shown the heave amplitude variation with  $\nu$  when the effective mass  $m = 1.5M$ . The curves all show a maximum at a wavenumber  $\nu$  less than the tuned value  $\nu_0$ . In general the effect of increasing the inertia is to decrease the heave amplitude at a

given wavenumber. The values of the amplitudes at  $v = 0$  are obtained from the asymptotic result

$$|\xi_2/A| = 4/\pi(m' + \mu_2)\nu_0 \quad (6.2)$$

which equals 1 for a cylinder with no additional restoring force. Equation (6.2) follows from (4.11) when use is made of the result  $\lambda_2(0) = 8/\pi$  for the heaving half-immersed cylinder given by Kotik and Mangulis (9).

### 57 THREE-DIMENSIONAL WAVE-POWER ABSORBERS

The theory given in §4 can also be applied to three-dimensional bodies having a vertical axis of symmetry. As before it is assumed that the body is constrained to move in a single mode only. The equations of motion are the same as in §4 up to equation (4.4) which must be replaced by the relation between the exciting force  $F_{is}$  and the damping coefficients for such bodies given by Newman (4), equations (31)-(33).

Thus

$$F_{is} = \Re e \left\{ A \left( \frac{2\varepsilon \rho g^3}{\omega^3} b_{ii} \right)^{\frac{1}{2}} e^{i\omega t} \right\} \quad (7.1)$$

where  $\varepsilon = \begin{cases} 2, & i = 1, 3 \\ 1, & i = 2 \end{cases}$ .

It follows that the power absorbed by the body is

$$\varepsilon \omega^{-1} \rho g^3 d b_{ii} \lambda^2 / \{ [k - (m + a_{ii})\omega^2]^2 + \omega^2 (d + b_{ii})^2 \}.$$

The total power in an incident wave of unit frontage is  $\rho g^2 A^2 / 4\omega$ , and the ratio of these quantities provides us with a power absorption length  $\ell$  as defined by Budal and Falnes (5).

Thus

$$\ell = \frac{4\varepsilon g d b_{ii}}{[k - (m + a_{ii})\omega^2]^2 + \omega^2 (d + b_{ii})^2} \cdot \quad (7.2)$$

$$= \frac{\varepsilon g}{\omega^2} \left\{ 1 - \frac{(k - (m + a_{ii})\omega^2)^2 + \omega^2 (d - b_{ii})^2}{(k - (m + a_{ii})\omega^2)^2 + \omega^2 (d + b_{ii})^2} \right\}.$$

It follows that for a given wave frequency  $\omega$ , the maximum value of  $\ell$  is

$$\ell_{\max} = \frac{\varepsilon g}{\omega^2} = \frac{\varepsilon L}{2\pi} \quad (7.3)$$

obtained by choosing  $k = (m + a_{ii})\omega^2$  and  $d = b_{ii}$  as in the two-dimensional case.

The result (7.2) leads to the remarkable conclusion that a correctly tuned floating body of any diameter is capable of absorbing all the power in an incident wave of frontage equal to  $L/2\pi$ , where  $L$  is the wavelength of the incident wave. This result has also been quoted by Budal and Falnes (10) for the case of heave oscillations. It appears, therefore, that in response to long waves, the tuned body may be more efficient than a two-dimensional cylinder which must have  $\ell_{\max}$  less than the cylinder length. However, we find that the response amplitude of the tuned body also increases as  $L$  increases so that the assumptions of small oscillations may be violated by the body when tuned to long waves. In fact, from (7.1) the corresponding expression to (4.6) shows that

$$\left| \frac{\xi_i}{A} \right|^2 = \frac{2\varepsilon \rho g^3 b_{ii} \omega^{-3}}{[k - (m + a_{ii})\omega^2]^2 + \omega^2 (d + b_{ii})^2} \quad (7.4)$$

so that at a given wave frequency,

$$|\xi_i/A|_{\max} = (\varepsilon \rho g^3 / 2b_{ii} \omega^5)^{\frac{1}{2}} = \left( \frac{\varepsilon \rho}{2M\lambda_i} \right)^{\frac{1}{2}} \left( \frac{L}{2\pi} \right)^{\frac{3}{2}}$$

where  $b_{ii} = M\lambda_i \omega$  and it is usual to choose for  $M$  the mass of water displaced by a half-immersed sphere of radius  $a$  equal to a typical radius of the body. Thus  $M = \frac{2}{3} \pi \rho a^3$  (or twice this if the body is completely submerged) and

$$|\xi_i/A|_{\max} = (3\varepsilon / 4\pi \lambda_i \nu^3)^{\frac{1}{2}}. \quad (7.5)$$

We see that this expression may well become large for small values of  $\nu$ , depending on the precise variation of  $\lambda_i$  with  $\nu$ .

If we tune the body to a wavenumber  $\nu_0 = \omega_0^2 a / g$  by choosing  $k = m' + a_{ii}(\omega_0)\omega_0^2$  and  $d = b_{ii}(\omega_0)$  then the full non-dimensional expression for the amplitude of the body compared to the incident wave amplitude is

$$\left| \frac{\xi_i}{A} \right| = \frac{(3\varepsilon \lambda_i \pi^{-1} \nu^{-1})^{\frac{1}{2}}}{\{ [(m' + \mu_i)\nu_0 - (m' + \mu_i)\nu]^2 + \nu(\nu_0^{\frac{1}{2}} \lambda_{i0} + \nu^{\frac{1}{2}} \lambda_i)^2 \}^{\frac{1}{2}}} \quad (7.6)$$

while the non-dimensional power absorption length  $\ell/2a$  is given by

$$\frac{\ell}{2a} = \frac{2\varepsilon (\nu^{\frac{1}{2}} \lambda_i) (\nu_0^{\frac{1}{2}} \lambda_{i0})}{[(m' + \mu_{i0})\nu_0 - (m' + \mu_i)\nu]^2 + \nu(\nu_0^{\frac{1}{2}} \lambda_{i0} + \nu^{\frac{1}{2}} \lambda_i)^2}. \quad (7.7)$$

### The heaving sphere

We consider in detail the particular case of a sphere constrained to make small heaving oscillations in response to the incident waves. This has also been considered by Budal and Falnes (5) but their treatment ignores the effect of the diffracted wave field.

In heave oscillations  $i = 2$  and  $\varepsilon = 1$  in (7.2) and (7.4), and there is a natural buoyancy restoring force such that  $k = \pi \rho a^2$  in (7.4). The non-dimensional form of the optimal tuning condition corresponding to (4.14) is now

$$\frac{3}{2} = (m' + \mu_2(\nu))\nu, \quad \text{where } m' = m/M \quad (7.5)$$

and this has the root  $\nu_1 \doteq 1.045$  for  $m' = 1$ . Thus optimal tuning is only possible for  $\nu = \nu_1$  or, by incorporating additional vertical restoring forces, for  $\nu \geq \nu_1$ . This means that a floating sphere can only be an efficient wave power absorber to waves of wavelength less than about 6 times the sphere radius. If, as in the two-dimensional case we assume that the mass  $m$  can be increased without affecting the buoyancy of the sphere, then  $\nu_1$  can be reduced. Thus for  $m' = 1.5$ , equation (7.5) has the root  $\nu_1 \doteq .75$ .



Curves of  $\ell/2a$  as a function of  $\nu$  are shown in Fig. (11) using values for  $\mu_2$  and  $\lambda_2$  estimated from Havelock (11). A floating sphere with  $m/M = 1.0$ , is tuned to wavenumbers  $\nu_0 \approx 1.045$ . Also shown are the curves obtained when the sphere is tuned to wavenumbers 1.25 and 1.5 by increasing the vertical restoring force by means of springs. The envelope of the peaks in  $\ell/2a$  has the equation  $\ell/2a = (2\nu)^{-1}$ . It can be seen that a heaving sphere can extract all the power in an incident wave of crest length equal to just less than half the diameter of the sphere, and whose wavelength is about 6 times the radius of the sphere. It is of interest to compare this with the heaving circular cylinder (Fig. (7)) which can extract half of the power in an incident wave of crest length equal to the cylinder length and of wavelength about 8 times the cylinder radius. It follows that for a circular cylinder to be as efficient as a sphere of diameter  $2a$  in extracting power from a given incident wave, it must have length  $2a$  and radius  $\frac{1}{2}a$  approximately, with  $6a = L$ , the wavelength of the incident wave. In this case the sphere must be about 1.2 times the mass of the cylinder.

If the sphere is stiffened by increasing the vertical restoring force, the tuned wavenumber increases and the peaks of absorption length ratio decrease. The heave amplitude ratio is also shown in Fig. (11) by the dashed curves. The curves peak at a value of  $\nu$  which is less than the corresponding tuned wavenumber  $\nu_0$ . For long waves, as  $\nu \rightarrow 0$ , the asymptotic value of  $|\xi_2/A|$  is given by

$$|\xi_2/A| \sim 3/[2(m' + \mu_{20})\nu_0]$$

which is derived from (7.6) by using the result  $\lambda_2(\nu) \sim 3\pi\nu/4$  as  $\nu \rightarrow 0$  given in (9) for the heaving sphere. For the unstiffened heaving sphere  $|\xi_2/A| \sim 1$  as  $\nu \rightarrow 0$ . The effect of increasing the restoring force is to decrease the heave amplitude at a given wavenumber.

In Fig. (12) is shown the effect on  $\ell/2a$  of increasing the mass of the sphere so that  $m' = 1.5$ . The natural tuned wavenumber is now  $\nu_0 = .75$  and the peak of  $\ell/2a$  is increased accordingly although the bandwidth is narrower. Also the heave amplitude peak is much larger being over  $1\frac{1}{2}$  times the incident wave amplitude. The curves for  $\nu_0 = 1.0$  and 1.25 show that the same is true for the stiffened sphere. The advantage of increasing the mass of the sphere is that it enables tuning to take place at smaller wavenumbers, which means smaller spheres, and also greater power absorption. This is offset, however, by larger heave amplitudes of the sphere, and narrower bandwidths.

The effect of partially tuning the sphere by satisfying  $d = b_{22}(\omega)$  for any desired  $\omega = \omega_0$  while allowing  $k$  its natural value of  $\pi a^2$  turns out to make little difference to  $\ell/2a$  and is not shown in the Figures. As for the circular cylinder, it appears that the restoring force is more important than the damping force in tuning the sphere for maximum power absorption.

#### §8 OSCILLATIONS IN MORE THAN ONE MODE

It was shown in §3 how the efficiency of power extraction at a given wavenumber can be improved by choosing a cylinder for which  $A_1^-$  is as small as possible. For a cylinder oscillating about an axis of horizontal symmetry it was shown that the maximum efficiency possible at a given wave number was 50%. In this section we consider cylinders with horizon-

tal symmetry about their axis of oscillation which are allowed to oscillate in more than one mode. To be specific, we assume that the cylinder is held in equilibrium by horizontal and vertical springs and dampers so that when excited by an incident wave, the cylinder is constrained to make combinations of small horizontal and vertical oscillations without rotation. (Alternative constraints may also be considered but the present assumptions are chosen for simplicity.) We shall show that at a given frequency, a correctly tuned cylinder, that is, one in which the spring and damper constants have been chosen appropriately, is 100% efficient as a wave absorber.

The motivation for what follows arises from a paper by Ogilvie (12) who considered the effect of waves on a completely submerged circular cylinder. In the course of his work he showed that if the centre of the cylinder described a circle then the waves generated by the cylinder motion travelled away from the cylinder along the free surface, but in one direction only. Recent experiments (13) give a qualitative verification of this result. This phenomenon, while at first appearing remarkable, can be generalised to arbitrary cylinders with horizontal symmetry. Heave oscillations of such a cylinder produce waves of equal amplitude and phase radiating to either infinity whereas sway oscillations produce waves of equal amplitude but exactly out of phase at either infinity. By a suitable combination of the amplitudes and phases of these vertical and horizontal motions it is possible to cancel the wave at one infinity completely thus producing radiation in one direction only. Reversing the sign of the time co-ordinate now shows that there exists a motion of the cylinder which will completely absorb a given incident wave.

Having demonstrated in principle the possibility of a 100% efficient wave absorber, it remains to determine what conditions must be satisfied by the spring and damper constants to ensure that the cylinder will respond in the required fashion and absorb all of the incident wave.

#### Equations of motion

The equations of motion for the cylinder are very similar to those derived in §4. Here we allow  $\zeta_1$  and  $\zeta_2$ , the amplitudes of sway and heave respectively, to occur simultaneously. Thus (4.1) is modified to the two equations

$$m\ddot{\zeta}_i = -d_i\dot{\zeta}_i - k_i\zeta_i + F_i \quad (i = 1, 2) \quad (8.1)$$

where  $d_i$  and  $k_i$  are the dampers and spring constants in the horizontal ( $i = 1$ ) and vertical ( $i = 2$ ) directions. As before  $F_i$  is the total hydrodynamic force in the  $i$ th direction. We may write

$$F_i = F_{is} + \sum_{j=1}^2 F_{ij} \quad (i = 1, 2)$$

where  $F_{is}$  is the force in the  $i$ th direction on the cylinder, assumed to be fixed in the presence of the incident wave, and  $F_{ij}$  is the force in the  $i$ th direction due to the oscillation of the cylinder in the  $j$ th direction. Now for cylinders with horizontal symmetry about their axis of oscillation,  $F_{ij} = 0$  if  $i \neq j$  ( $i, j = 1, 2$ ). Because of this the subsequent development follows closely that leading to equation (4.6). The power per unit length absorbed by the cylinder is modified to

include the work done by both  $F_1$  and  $F_2$ , to give

$$\frac{\omega}{2\pi} \sum_{i=1}^2 \int_0^{2\pi/\omega} \xi_i F_i dt = \frac{1}{2} \omega^2 \sum_{i=1}^2 d_i |\xi_i|^2.$$

The expression for the efficiency, after putting  $\delta = \frac{1}{2}$  because of the symmetry of the cylinder, becomes

$$E = \sum_{i=1}^2 \frac{2\omega^2 b_{ii}}{\{k_i - (m + a_{ii})\omega^2\}^2 + \omega^2 (b_{ii} + d_i)^2} \quad (8.2)$$

An alternative derivation of (8.2) is possible making use of the definition of  $E$  in terms of reflection and transmission coefficients given by (3.4). In this case the time independent potential  $\phi(x, y)$  can be written

$$\phi(x, y) = \frac{gA}{\omega} \phi_s + i\omega \sum_{i=1}^2 \xi_i \phi_i$$

$$\text{so that} \quad R_1 = R + \frac{i\omega^2}{gA} \sum_{i=1}^2 A_i^+ \xi_i \quad (8.3)$$

$$T_1 = T + \frac{i\omega^2}{gA} \sum_{i=1}^2 A_i^- \xi_i \quad (8.4)$$

Equations (3.4) and (3.6) now show that

$$E = 2 \sum_{i=1}^2 \{ \operatorname{Re} \gamma_i - |\gamma_i|^2 \} \quad \dots \quad (8.5)$$

where  $\gamma_i = i\omega^2 A_i^+ \xi_i / gA$  and the fact that  $|A_i^+| = |A_i^-|$  ( $i = 1, 2$ ) has been used. The maximum value of  $E$  occurs when  $\gamma_i = \frac{1}{2}$  ( $i = 1, 2$ ) whence  $E_{\max} = 1$  and the wave is completely absorbed. Substituting  $\gamma_i = \frac{1}{2}$  into (8.3) and (8.4) we obtain

$$R_1 = R + \frac{1}{2} \sum_{i=1}^2 A_i^+ / A_i^+$$

$$T_1 = T + \frac{1}{2} \sum_{i=1}^2 A_i^- / A_i^+$$

It follows that  $R_1 = T_1 = 0$  as expected since  $R + (-1)^1 T = -(A_1^- / A_1^+)$  from (3.6) and  $A_1^+ = (-1)^1 A_1^-$  ( $i = 1, 2$ ).

Returning to (8.2) we see that maximum efficiency is achieved at frequency  $\omega_0$  by choosing

$$k_i = (m + a_{ii})\omega_0^2, \quad d_i = b_{ii}(\omega_0) \quad (i = 1, 2) \quad \dots \quad (8.6)$$

giving  $E = 1$ . If we non-dimensionalise the added mass and damping coefficients in heave and sway by writing  $a_{ii} = M\mu_i$ ,  $b_{ii} = M\omega\lambda_i$  as before, we obtain

$$E = 2\nu \sum_{i=1}^2 \frac{(\nu^{\frac{1}{2}} \lambda_i)(\nu^{\frac{1}{2}} \lambda_{io})}{\{(m' + \mu_{io})\nu_0 - (m' + \mu_i)\nu\}^2 + \nu(\nu^{\frac{1}{2}} \lambda_i + \nu^{\frac{1}{2}} \lambda_{io})^2} \quad \dots \quad (8.7)$$

in the same notation as in (4.10).

Also, the amplitude of oscillation in the  $i^{\text{th}}$  mode is given by

$$\xi_i / A = \rho g A_i^+ / \{k_i - (m + a_{ii})\omega^2 + i\omega(d + b_{ii})\} \quad (8.8)$$

and (8.6) and (4.5) confirm that  $\gamma_i = \frac{1}{2}$  for maximum efficiency.

The non-dimensional form of (8.8) is

$$\left| \frac{\xi_i}{A} \right|^2 = \frac{\rho a^2}{M} \sum_{i=1}^2 \frac{\lambda_i}{\{(m' + \mu_{io})\nu_0 - (m' + \mu_i)\nu\}^2 + \nu(\nu^{\frac{1}{2}} \lambda_i + \nu^{\frac{1}{2}} \lambda_{io})^2} \quad (8.9)$$

similar to (4.11) with  $\delta = \frac{1}{2}$ .

#### The half-immersed circular cylinder

We consider the combined heave and sway oscillations of a half-immersed circular cylinder. As was pointed out in §4 there is a natural buoyancy force in heave and in the expression (8.7) for  $E$ , the term  $(m' + \mu_{20})\nu_0$  must be replaced by  $4\pi^{-1}$  for  $\nu_0 < \nu_1 = .79$  as in (6.1). For  $\nu_0 \geq .79$  (8.7) holds as it stands. In Fig. (13) are drawn curves of  $E$ , modified as described, against  $\nu$  for different values of  $\nu_0$  the tuned wave number. It is assumed that  $m = M$  so that the cylinder is floating. For  $\nu_0 \geq \nu_1$  the horizontal and vertical springs and dampers can be chosen to satisfy (8.6) and 100% absorption occurs at  $\nu = \nu_0$ . This can be seen in the curves for  $\nu_0 = .79$  and  $\nu_0 = 1.0$ . For  $\nu_0 < \nu_1$  only the horizontal part of the motion can be tuned exactly and so the maximum efficiency attainable is somewhat less than 100%. At  $\nu_0 = .3$  it can be seen that the maximum efficiency is about 80% near  $\nu = .7$  and a second smaller peak occurs near  $\nu = .3$ .

#### The submerged circular cylinder

We next consider the problem of the completely submerged circular cylinder held in equilibrium by horizontal and vertical springs and dampers. For this problem the sway and heave added mass and damping coefficients are the same (Ogilvie (12) equation (35)) and values for these coefficients estimated from the results of Frank (8) for a cylinder of radius  $a$  whose centre is submerged is submerged to a depth  $5a/4$  are used. For a completely submerged body no natural buoyancy forces occur during the motion so that  $k_i$  ( $i = 1, 2$ ) can take any desired positive value so that in general (8.6) can be satisfied. (Ogilvie has shown that  $a_{ii}$  can in fact become negative for cylinders close to the surface but this does not occur in the case under consideration.)

Fig. (14) shows curves of  $E$  against  $\nu$  for different values of tuned wavenumber  $\nu_0$ , computed from (8.7) with  $m = M$ . At  $\nu = \nu_0$  the incident wave is completely absorbed by the cylinder whose centre is then moving in a circle. For both very short and very long waves, the efficiency of power absorption tends to zero. In the intermediate

range a cylinder tuned to a wavenumber  $\nu_0 = .5 - .7$  is very efficient in extracting power from waves. Thus for  $\nu_0 = .5$  it can be seen that over 90% of the wave powers is extracted from waves of wavelength between about 7 and 24 times the cylinder radius. It is clear that at this value of  $\nu_0$  the efficiency of the cylinder is remarkably insensitive to changes in the wavelength of the incident wave.

The heave and sway amplitudes compared to the incident wave amplitude are computed from (8.9) with  $M = \pi \rho a^2$ , and shown in Fig. (15) as a function of  $\nu$  for different  $\nu_0$ . At  $\nu = \nu_0$ , the motion of the cylinder is circular but this is not evident from the results as it requires knowledge of the relative phases of the heave and sway motions. For  $\nu_0 = .5$ , when the efficiency bandwidth is widest, the heave or sway amplitude has a maximum of about .8 times the incident wave amplitude at  $\nu = .25$  corresponding to  $E \approx .87$ . At  $\nu = .5$ , when  $E = 1.0$ , the amplitude ratio is .5 so that the cylinder then describes a circle of radius one half the incident wave amplitude.

The variation of  $E$  with depth of submergence of the cylinder can be predicted from (8.7). The damping coefficients for the submerged circular cylinder decay exponentially as the depth of the centre of the cylinder increases relative to the radius of the cylinder. This follows from Ogilvie (12) equation (59). Thus one would expect that for deeply submerged cylinders, the efficiency would drop sharply either side of the  $\nu = \nu_0$  producing a very narrow bandwidth. Also, from (8.9) the amplitude ratio at  $\nu = \nu_0$  is inversely proportional to the damping coefficient and consequently increases exponentially with decreasing depth.

#### CONCLUSION

A simple linearised theory has been presented for the absorption of the power in a sinusoidal wave-train, by an oscillating body. Expressions have been derived for the efficiency of power absorption when the body is a two dimensional cylinder oscillating in either a single mode or in certain combinations of two modes. These expressions show that the efficiency depends solely on the solution to the radiation problem; namely, when the cylinder is forced to oscillate in the particular mode. A special case of a three-dimensional symmetric body was also considered. Curves were presented showing the variation of efficiency with non-dimensional wavenumber, it being assumed that the body was coupled to the fluid using springs and dampers whose constants could be adjusted. Only simple bodies with symmetry whose wave-making properties were known were used in the calculations. The expressions can be applied to more efficient unsymmetric wave-power absorbers such as the Salter cam once the added mass and damping coefficients together with the radiation wave amplitudes are known for such bodies.

Of particular interest in the results was the possibility of 100% efficiency for cylinders oscillating in a combination of modes. The large bandwidth exhibited by the submerged cylinder is encouraging in this respect and may warrant further design studies.

Note: During the preparation of this paper the author was shown a draft copy of the paper to be presented by Professor J.N. Newman of M.I.T. to this Symposium, which contains material which

overlaps with material in the present paper. Thus equations (3.7), (3.9) and (7.3), although derived independently, are also to be found in Newman's paper.

#### REFERENCES

- (1) SALTER, S.H., Wave Power, *Nature*, 1974, **249**, 720-724.
- (2) NEWMAN, J.N., Interaction of waves with two-dimensional obstacles: a relation between the radiation and scattering problems. *J. Fluid Mech.* (to be published).
- (3) HASKIND, M.D., The exciting forces and wetting of ships in waves. *Izv. Akad. Nauk SSSR, Otd. Tekh. Nauk*, 1957, **7**, 65-79. English translation available as David Taylor Model Basin Translation No. 307.
- (4) NEWMAN, J.N., The exciting forces on fixed bodies in waves. *Journ. of Ship Res.*, 1962, **6**, 10-17.
- (5) BUDAL, K., and FALNES, J., A resonant point absorber of ocean-wave power. *Nature*, 1975, **256**, 478-479.
- (6) KOTIK, J., Damping and inertia coefficients for a rolling or swaying vertical strip. *Jour. Ship Res.*, 1963, **7**, 19-23.
- (7) URSELL, F., On the waves due to the rolling of a ship. *Quart. Journ. Mech. Appl.* 1948, **1**, 246-252.
- (8) FRANK, W., Oscillation of cylinders on or below the free surface of deep fluids. *N.S.R.D.C.* 1967, Rep. No. 2375.
- (9) KOTIK, J. and MANGULIS, V., On the Kramers-Kronig relations for ship motions. *Int. Shipbuilding prog.*, 1962, **9**, 3-10.
- (10) BUDAL, K. and FALNES, J., Private communication.
- (11) HAVELOCK, T.H., Waves due to a floating sphere making periodic heaving oscillations. *Proc. Roy. Soc., A*, 1955, **231**, 1-7.
- (12) OGILVIE, T.F., First- and second-order forces on a cylinder submerged under a free surface. *J. Fluid Mech.*, 1963, **16**, 451-472.
- (13) GLENDENNING, E., Private communication, Marchwood Engineering Laboratories, C.E.G.B., Marchwood, Southampton, England.



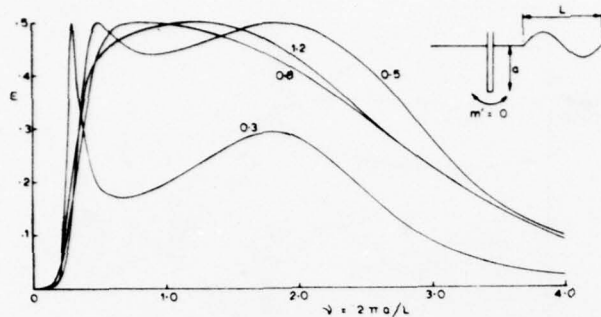


Fig. 1: Efficiency of power absorption  $E$  of a rolling plate with  $m = 0$  vs. dimensionless wavenumber  $\nu$  for different values of the tuned wavenumber  $\nu_0$ .

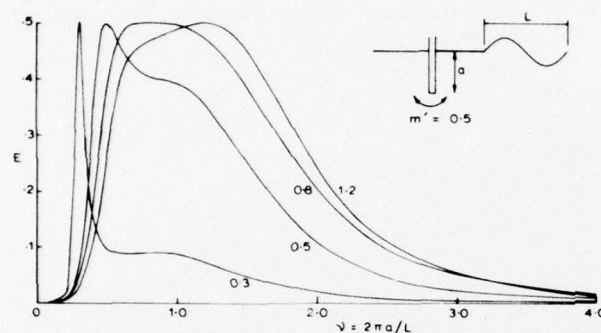


Fig. 2: Efficiency of power absorption  $E$  of a rolling plate  $m = 0.5M$  vs. dimensionless wavenumber  $\nu$  for different values of the tuned wavenumber  $\nu_0$ .

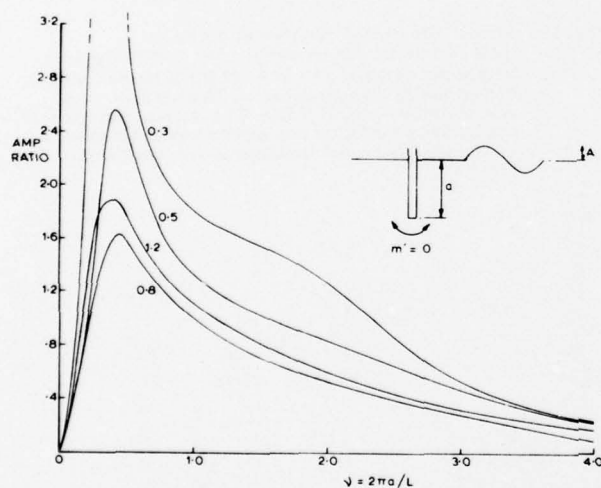


Fig. 3: Ratio of maximum displacement of lower edge of rolling plate with  $m = 0$  to incident wave amplitude,  $|\xi_3 a/A|$ , vs. dimensionless wavenumber  $\nu$  for different values of the tuned wavenumber  $\nu_0$ .

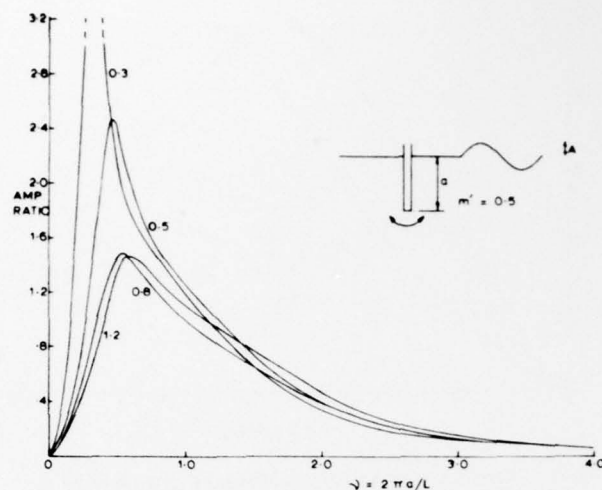


Fig. 4: Ratio of maximum displacement of lower edge of rolling plate with  $m = 0.5M$  to incident wave amplitude,  $|\xi_3 a/A|$ , vs. dimensionless wavenumber  $\nu$  for different values of the tuned wavenumber  $\nu_0$ .

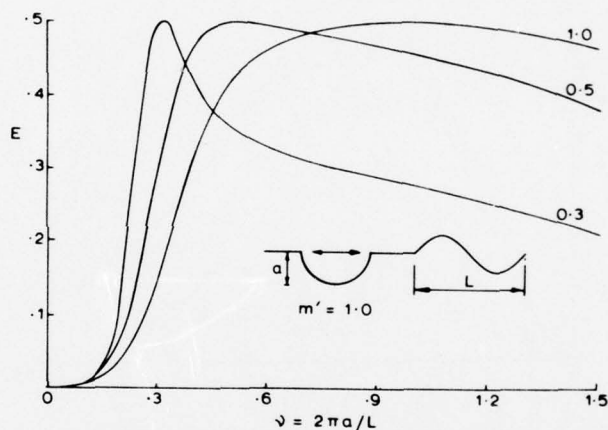


Fig. 5: Efficiency of power absorption  $E$  of a swaying half-immersed circular cylinder with  $m = M$  vs. dimensionless wavenumber  $\nu$  for different values of the tuned wavenumber  $\nu_0$ .

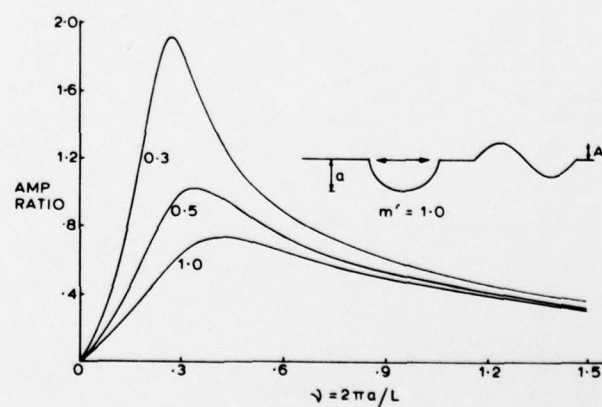


Fig. 6: Ratio of the sway amplitude of the half-immersed circular cylinder to the incident wave amplitude,  $|\xi_1/A|$ , vs. dimensionless wavenumber  $\nu$  for different values of the tuned wavenumber  $\nu_0$ .

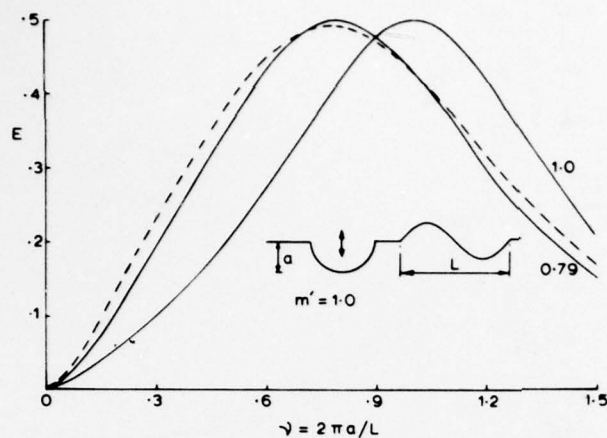


Fig. 7: Efficiency of power absorption  $E$  of a heaving half-immersed circular cylinder with  $m = M$  vs. dimensionless wavenumber  $\nu$  for different values of the tuned wavenumber  $\nu_0$ . The natural tuned wavenumber is  $\nu_0 = 0.79$ . The dashed curve shows the effect of partial tuning at  $\nu_0 = 0.3$ .

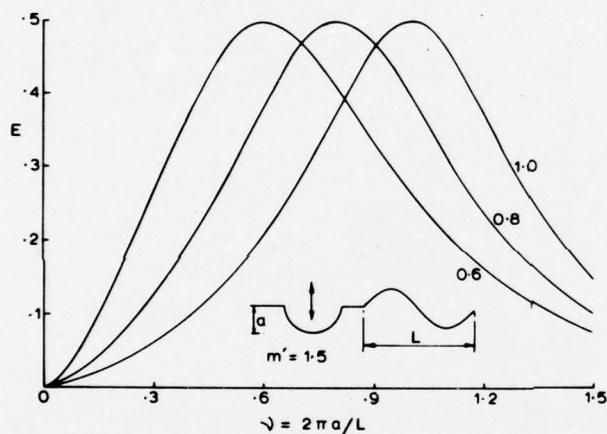


Fig. 8: Efficiency of power absorption  $E$  of a heaving half-immersed circular cylinder with  $m = 1.5M$  vs. dimensionless wavenumber  $\nu$  for different values of the tuned wavenumber  $\nu_0$ . The natural tuned wavenumber is  $\nu_0 = 0.6$ .

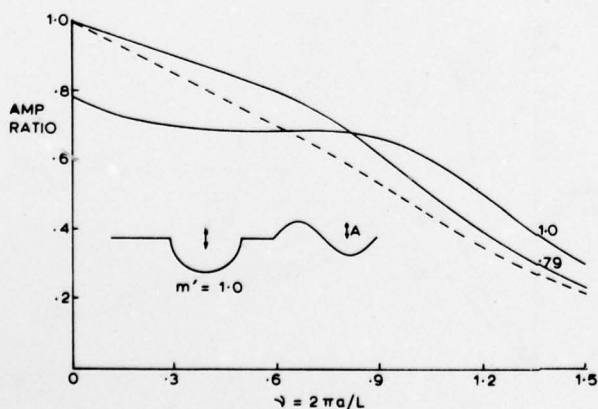


Fig. 9: Ratio of the heave amplitude of the half-immersed circular cylinder with  $m = M$ , to the incident wave amplitude,  $|\xi_2/A|$  vs. dimensionless wavenumber  $\nu$  for different values of the tuned wavenumber  $\nu_0$ . The dashed curve shows the effect of partial tuning at  $\nu_0 = 0.3$ .

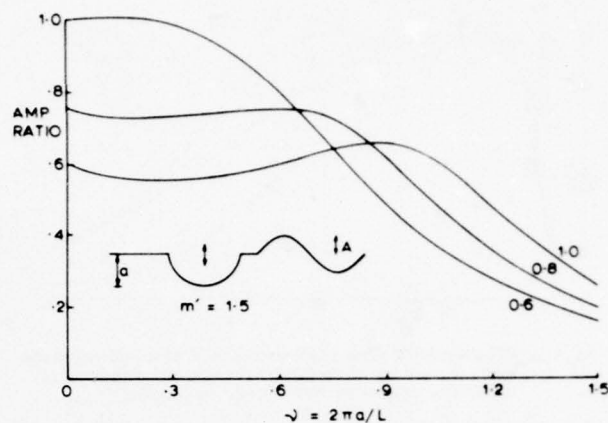


Fig. 10: Ratio of the heave amplitude of the half-immersed circular cylinder with  $m = 1.5M$ , to the incident wave amplitude,  $|\xi_2/A|$  vs. dimensionless wavenumber  $\nu$  for different values of the tuned wavenumber  $\nu_0$ .

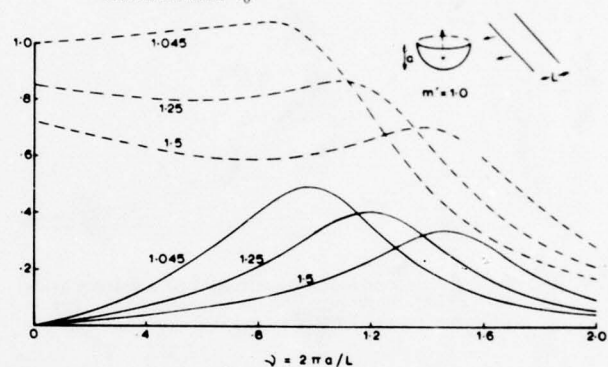


Fig. 11: Power absorption length ratio  $l/2a$  vs. dimensionless wavenumber  $\nu$  for a heaving half-immersed sphere with  $m = M$  for different values of the tuned wavenumber  $\nu_0$ . The natural tuned wavenumber is  $\nu_0 = 1.045$ . The dashed curves are the corresponding ratios of the heave amplitude of the sphere to the incident wave amplitude,  $|\xi_2/A|$ .

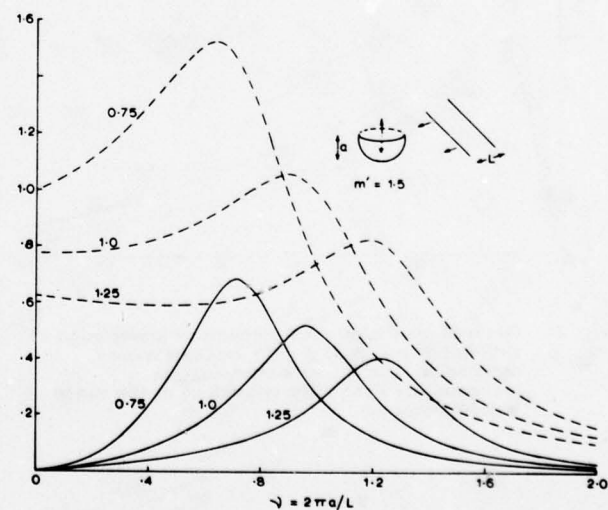


Fig. 12: Power absorption length ratio  $l/2a$  vs. dimensionless wavenumber  $\nu$  for a heaving half-immersed sphere with  $m = 1.5M$  for different values of the tuned wavenumber  $\nu_0$ . The natural tuned wavenumber is  $\nu_0 = 0.75$ . The dashed curves are the corresponding ratios of the heave amplitude of the sphere to the incident wave amplitude,  $|\xi_2/A|$ .

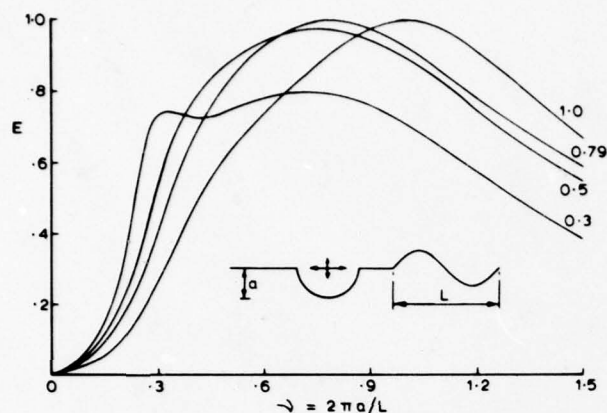


Fig. 13: Efficiency  $E$  of power absorbed of a half-immersed circular cylinder with  $m = M$ , in a combination of heave and sway motions vs. dimensionless wavenumber  $\nu$  for different values of the tuned wavenumber  $\nu_0 \geq 0.79$ . For  $\nu_0 < 0.79$  the effect of partial tuning is shown.

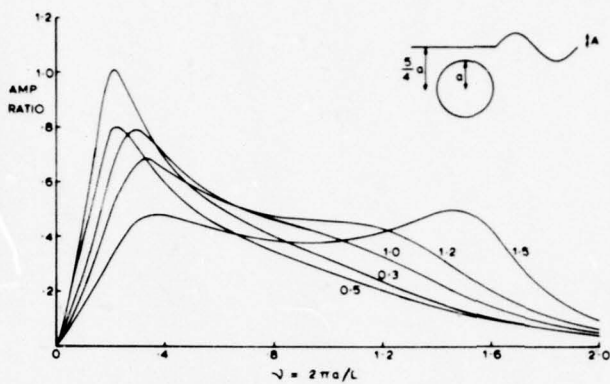


Fig. 14: Efficiency  $E$  of power absorption of a circular cylinder of radius  $a$ , with  $m = M$ , submerged to a depth  $\frac{3}{4}a$  and making a combination of heave and sway motions, vs. dimensionless wavenumber  $\nu$  for different values of the tuned wavenumber  $\nu_0$ .

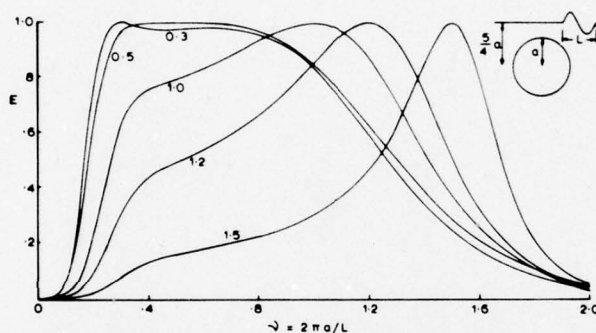


Fig. 15: Ratio of the heave or sway amplitude to the incident wave amplitude,  $|\xi_i/A|$ ,  $i = 1, 2$ , for a cylinder of radius  $a$ , with  $m = M$ , submerged to a depth  $\frac{3}{4}a$ , and making a combination of heave and sway motions, vs. wavenumber  $\nu$  for different values of the tuned wavenumber  $\nu_0$ .



# FINITE-AMPLITUDE UNSTEADY SLENDER-BODY FLOW THEORY

T. Y. WU and G. T. YATES

California Institute of Technology, Pasadena, California, USA

## ABSTRACT

This paper contains two parts. The first is a theoretical study of the potential flow generated by arbitrary finite-amplitude motion of a flexible slender body whose shape is limited, at this stage, to having circular cross sections with continuously varying radius along the body centerline, and without side and tail fins. The velocity potential is represented by a line doublet distributed along the body centerline. Guided by the example of a toroidal ring, of which the relatively simple symmetry in shape has made an accurate solution possible, a general theory is developed for a slender flexible body performing a planar motion of arbitrary amplitude.

The second part is an experimental investigation devoted to an examination of the basic slender-body assumptions underlying various theories. A tri-axial ellipsoid has been selected as a representative case involving all the significant features of interest, for which the exact solution of potential flow and the approximate solution based on slender-body theory are evaluated and compared with the experimental measurements of the pressure distribution obtained by using a set of pressure transducers.

## 1. Introduction

The present study is intended to explore some aspects of unsteady slender-body theory, with special reference to large amplitude motions pertaining to fish locomotion and related problems of hydromechanical interest.

General surveys of the field regarding both historical and current developments have been quite extensively covered in the proceedings of recent symposia devoted to the subject (Proceedings of Symposium on Swimming and Flying in Nature, eds., Wu, Brokaw, & Brennen 1975; International Symposium on Biodynamics of Animal Locomotion held in September 1975 at Cambridge University, Proceedings to be published). In the aspect of unsteady slender-body theory for fish locomotion in particular, the recent development was initiated by Lighthill (1960) who first introduced a perturbation expansion in powers of an amplitude parameter  $\epsilon$  and derived, for the case when no vorticity is shed upstream of the tail section, the thrust and energy loss up to the terms of order  $\epsilon^2$ . Later, Lighthill (1970) considered fins with abrupt trailing edges, in which case the strength of the vortex sheets shed from these edges can be determined at the local body section. The case of longitudinally slanted trailing edges as those occurring in various species of fishes has been discussed by Wu (1971), Wu & Newman (1972). They further investigated the interactions between the outboard vortex sheets and the body of finite thickness (Newman & Wu 1973, Newman 1973), finding that quantitatively, the thickness effect appears to be small. These earlier theories are all based on small-amplitude slender-body approximations.

In order to remove some inadequacy and limitations of small-amplitude theory, Lighthill (1971) developed a large-amplitude elongated-body theory by extending his (1970) physical interpretation of the perturbation-theory results, using the Lagrangian description for the body motion

and considering momentum conservation evaluated with a time-varying control volume whose backward facing surface moves and rotates with the fish tail.

An attempt is made here to provide a mathematical analysis for a direct calculation of the flow quantities by the method of flow singularities. Such a theory involving vortex sheets shed from fins is not easy to develop, so this preliminary study is still limited to bodies of circular cross sections. The first example is a toroidal ring, whose relatively simple symmetry in shape has enabled us to obtain a solution accurate to a high order. Guided by this example, a general theory is developed for a slender flexible body performing a planar motion with arbitrary amplitude. With special reference to large-amplitude motions, it is shown that the effect of body centerline curvature gives rise to a radial force, acting on the body segment in the direction of the local radius of curvature of the body centerline. This 'curved-flow' force is primarily due to a steady Bernoulli effect that has been neglected in the previous theories; it has a magnitude of order  $\epsilon^2$  at finite amplitude and vanishes like  $\epsilon^2\kappa$  with diminishing curvature  $\kappa$  of the body centerline,  $\epsilon$  being the small slenderness parameter. The interaction of this curvature effect with the effect of unsteady motion remains to be further explored.

For the purpose of estimating the validity of various theories as well as their underlying assumptions, a set of experiments has been carried out to measure the pressure distribution over a slender body and to make direct flow visualization over a range of Reynolds numbers. Preliminary results are reported here for the case of a model whose front 70% is nearly the same as a triaxial ellipsoid and compared with theoretical predictions of the exact potential-flow solution and those based on slender-body theory.

## 2. A toroidal ring moving along its axis of rotational symmetry

As we have just noted, the toroidal ring, whose every meridional cross section is a circle like that of a tore, is perhaps the simplest of all body shapes for consideration of potential flow involving finite curvature of the body axis. Its arbitrary motion through an ideal (inviscid and incompressible) fluid consists of three components: a translation along and a translation perpendicular to its axis of rotational symmetry, which will be called the longitudinal axis, and a rotation about an axis perpendicular to the longitudinal axis and lying in a meridional plane. For each of these component flow problems to be discussed presently, the relatively simple symmetry of the ring shape renders the analysis quite readily tractable, and the salient features of the solution will clarify the construction of solution to the general problem of potential flow due to a flexible slender body in arbitrary unsteady motion of finite amplitude. We shall assume that the flow involves no circulation around the ring by going through its aperture.

We first consider the translational motion of a toroidal ring moving with velocity  $U$  (which may depend on time  $t$ ) along its axis of rotational symmetry, which will be taken as the  $x$ -axis of a cartesian coordinate system  $(x, y, z)$ . The meridional cross section of the ring is a circle, of radius  $b$ , with its center located at  $(0, a \cos \theta, a \sin \theta)$ , where  $\theta$  is the meridian angle and  $a$  is the radius of the centroid circle ( $a > b$ , see Fig. 1). We shall confine ourselves to the case in which the torus radius,  $b$ , is small compared to the aperture of the ring, i. e.  $b \ll a$ .

As a first approximation to the velocity potential for the case of  $b \ll a$ , we seek the representation of a line doublet distributed along the centroid circle, with all the doublets pointed in the  $x$ -direction and having a uniform strength as required by the flow symmetry. Such a representation is conveniently derived by differentiation with respect to  $x$  of the velocity potential of a uniform source ring located at the centroid circle, which may be expressed as

$$\varphi_s(\underline{x}) = -m\alpha \int_0^{2\pi} \frac{d\theta'}{R}, \quad (1)$$

where

$$R = \{x^2 + r^2 + a^2 - 2ar \cos(\theta - \theta')\}^{\frac{1}{2}} \quad (2)$$

is the distance between the field point  $\underline{x} = (x, r \cos \theta, r \sin \theta)$  and the source point  $\underline{x}' = (0, a \cos \theta', a \sin \theta')$ , and  $m$  is a constant. If we denote by  $r_1, r_2$  the least and greatest distances, respectively, of the point  $\underline{x}$  from the centroid circle, or

$$r_1^2 = x^2 + (r-a)^2, \quad r_2^2 = x^2 + (r+a)^2, \quad (3)$$

we obtain, after some simple changes of the integration variable,

$$\varphi_s = -4m\alpha \int_0^{\pi/2} \frac{d\theta}{[r_2^2 - 4a^2 \sin^2 \theta]^{\frac{1}{2}}} = -\frac{4m\alpha}{r_2} K(k), \quad (4)$$

where  $K(k)$  denotes the complete elliptic integral of the first kind, with argument  $k$ , and

$$k^2 = \frac{4ar}{r_2^2} = 1 - \left(\frac{r_1}{r_2}\right)^2 = 1 - k'^2, \quad k' = \frac{r_1}{r_2}. \quad (5)$$

The expression (4) is known for the velocity potential of a source ring.

The velocity potential of a doublet ring with a uniform line distribution of doublets oriented in the direction of the  $x$ -axis over the centroid circle has the integral representation

$$\varphi(\underline{x}) = \beta a \frac{\partial}{\partial x} \int_0^{2\pi} \frac{d\theta'}{R},$$

where  $\beta$  is the uniform doublet strength per unit length of the arc. The values of  $\varphi$  can therefore be immediately derived by differentiation of the ring source potential  $\varphi_s$ , giving

$$\varphi = 4\beta a \frac{\partial}{\partial x} \left[ \frac{1}{r_2} K(k) \right] = -\frac{4\beta a x}{r_2^2 r_1} E(k), \quad (6)$$

where  $E(k)$  denotes the complete elliptic integral of the second kind, and in obtaining the last expression in (6) use has been made of the relations given in (5) and the formulas

$$\frac{d}{dk} K(k) = \frac{1}{k} \left[ \frac{E}{k'^2} - K \right], \quad \frac{d}{dk} E(k) = \frac{1}{k} [E - K]. \quad (7)$$

To facilitate our evaluation of the boundary condition we will also use the curvilinear orthogonal coordinate system  $(r_1, \theta, \psi)$  defined by (see Fig. 1)

$$\begin{aligned} x &= r_1 \sin \psi, & y &= (a + r_1 \cos \psi) \cos \theta, \\ z &= (a + r_1 \cos \psi) \sin \theta, \end{aligned} \quad (8)$$

and expand the expression (6) for small values of  $r_1/a$  and  $k' (= r_1/r_2)$ . Thus we obtain in the neighborhood of the toroidal ring,

$$k' = \frac{r_1}{2a} \left( 1 - \frac{r_1}{2a} \cos \psi + \frac{r_1^2}{8a^2} (3 \cos^2 \psi - 1) + O\left(\frac{r_1^3}{a^3}\right) \right), \quad (9)$$

and

$$\begin{aligned} \varphi = -\frac{2\beta \sin \psi}{r_1} \left\{ 1 - \frac{r_1 \cos \psi}{2a} + \frac{r_1^2}{8a^2} \left[ \log \frac{8a}{r_1} + \frac{3}{2} \cos 2\psi \right] \right. \\ \left. + O\left(\frac{r_1^3}{a^3} \log \frac{a}{r_1}\right) \right\}. \end{aligned} \quad (10)$$

If we denote by  $\underline{e}_x$  and  $\underline{e}_{r_1}$  the unit vectors in the directions of increasing  $x$  and  $r_1$ , respectively, the boundary condition requiring the normal component of flow velocity relative to the translating toroidal ring becomes

$$\frac{\partial \varphi}{\partial r_1} = U \underline{e}_x \cdot \underline{e}_{r_1} = U \frac{\partial x}{\partial r_1} = U \sin \psi \quad (r_1 = b). \quad (11)$$

Application of this condition to (10) yields

$$U = \frac{2\beta}{b} \left( 1 - \frac{\epsilon^2}{8} \left( \log \frac{8}{\epsilon} - 1 + \frac{3}{2} \cos 2\psi \right) + O(\epsilon^3 \log \epsilon) \right), \quad (12)$$

where

$$\epsilon = b/a \quad (13)$$

is considered to be small. Since the order  $\epsilon^2$  term in (12) depends on the angle  $\psi$ , which varies from 0 to  $2\pi$  over the ring surface, the doublet strength  $\beta$  is then determined up to this order term as

$$\beta = \frac{1}{8} b^2 \left\{ 1 + \frac{\epsilon^2}{8} \log \frac{8}{\epsilon} + O(\epsilon^2) \right\}. \quad (14)$$

Strictly speaking, the second term in (14) should be combined with the term of order  $\epsilon^2$  to give the error of order  $\epsilon^2 \log \epsilon$  with respect to the leading term  $\beta = \frac{1}{8} U b^2$ , a result which then agrees with the first estimate on local two-dimensional theory (upon substituting this  $\beta$  in the first term of Eq. 10) as would be expected. In order to improve the solution to within order  $\epsilon^2$  one may either superpose on the doublet ring a quadrupole ring, which by implication of (12) will have strength of order  $\epsilon^2$  with respect to  $\beta$ , or equivalently, have the radius of the doublet ring reduced to a smaller radius,  $r = a(1 - 2\epsilon^2)$ , while toroidal ring shape remains the same. We shall not, however, pursue this point any further here.

While the curvature of the ring centerline has little effect on the value of  $\beta$ , for it first appears in the term of  $O(\epsilon^2 \log \epsilon)$ , its effect on the velocity field, however, arises as early as in the term of  $O(\epsilon)$ , as shown by the second term on the right-hand side of (10). Within this order of accuracy the local velocity in the body frame of reference has at the torus surface the value

$$\begin{aligned} u_b &= \underline{e}_\psi \left[ \frac{1}{r_1} \frac{\partial(\varphi - Ux)}{\partial\psi} \right]_{r_1=b} \\ &= \underline{e}_\psi U \left\{ -2 \cos \psi + \frac{\epsilon}{2} \cos 2\psi + O(\epsilon^2 \log \epsilon) \right\}. \end{aligned} \quad (15)$$

The centerline-curvature effect is thus seen to increase on the aperture side and to decrease on the outward side the magnitude of the tangential velocity at the torus surface. This modified velocity field will have such an impact on the pressure distribution and sectional force coefficient as to result in a new feature in force distribution that can be of significance in the general case of unsteady flow involving slender body motions of finite amplitude. In fact, the pressure,  $p$ , is given by the Bernoulli equation

$$\frac{p}{\rho} + \frac{\partial\varphi}{\partial t} + \frac{1}{2} (u_b^2 - U^2) = \frac{p_\infty}{\rho}, \quad (16)$$

where  $p_\infty$  is the pressure at infinity,  $\rho$  the constant fluid density, and the time derivative of  $\varphi$  is evaluated with respect to the body frame of reference. From the above result we obtain the pressure distribution over the toroid surface as

$$\begin{aligned} \frac{p - p_\infty}{\rho} &= \frac{dU}{dt} b \sin \psi \left( 1 - \frac{\epsilon}{2} \cos \psi \right) \\ &+ U^2 \left( \frac{1}{2} - 2 \cos^2 \psi + \epsilon \cos \psi \cos 2\psi \right), \end{aligned} \quad (17)$$

which has an error of  $O(\epsilon^2 \log \epsilon)$ . The contribution of this pressure to the differential force acting on a meridional segment of the toroid subtending a differential angle  $d\theta$  about  $\theta$  is given by

$$d\mathbf{F} = - \int p \underline{n} dS = -b d\theta \int_0^{2\pi} p \underline{e}_{r_1} (a + b \cos \psi) d\psi,$$

since the unit vector normal to the toroid surface is  $\underline{n} = \underline{e}_{r_1}$ , and  $ds_\theta = (a + b \cos \psi) d\theta$  and

$ds_\psi = b d\psi$  are the differential arc lengths in the directions of  $\theta$  and  $\psi$ , respectively, over the toroid surface. The result of integration yields for the differential force per unit arc length of the centroid circle,

$$\frac{d\mathbf{F}}{ds_\theta} = \frac{1}{2} \frac{d\mathbf{F}}{d\theta} = -\underline{e}_x \pi \rho b^2 \frac{dU}{dt} + \underline{e}_r \frac{\pi}{2} \rho \frac{b^2}{a} U^2, \quad (18a)$$

where  $\underline{e}_r$  denotes the unit radial vector parallel to the plane of  $x = 0$ , or

$$\underline{e}_r = \underline{e}_y \cos \theta + \underline{e}_z \sin \theta. \quad (18b)$$

Thus, when the torus accelerates in the  $x$ -direction, every segment of the torus experiences a uniform drag due to the induced mass of the fluid and a uniform outward pull

$$\mathcal{F}_r = \frac{\pi}{2} \rho \frac{b^2}{a} U^2, \quad (18c)$$

which depends on the instantaneous velocity  $U$  and vanishes as the radius of curvature,  $a$ , of the body centerline becomes infinite, though  $\mathcal{F}_r \underline{e}_r$  has no net resultant for the whole ring. The reason for the radial force  $\mathcal{F}_r$  pointing outward, rather than inward, is because the lower (negative) pressure on the aperture side of the ring acts on a much smaller area than that which is exposed to the higher (but still negative) pressure on the outside equatorial belt.

Since the induced mass per unit arc length of the ring is  $\pi \rho b^2$ , the total induced mass of the ring is therefore

$$m_{11} = 2\pi^2 \rho a b^2. \quad (19)$$

By noting that the total doublet strength of the ring is  $\beta_b = \pi a b^2 U$  and the toroidal volume is  $V_b = 2\pi^2 a b^2$ , the above result can also be obtained at once from G. I. Taylor's theorem that relates  $\beta_b$  and  $V_b$  to the flow momentum according to

$$I = 4\pi \rho \beta_b - \rho V_b U = m_{11} U. \quad (20)$$

We note that  $m_{11}$  is equal to the mass of fluid displaced by the toroid.

### 3. Translation of a toroidal ring in its own plane

Now suppose the toroidal ring is moving in the  $y$  direction, with velocity

$$\underline{U} = V(t) \underline{e}_y = V(t) (\underline{e}_r \cos \theta - \underline{e}_\theta \sin \theta), \quad (21)$$

where  $\underline{e}_r$  and  $\underline{e}_\theta$  are unit vectors along the  $r$  and  $\theta$  coordinates, respectively,

$$\underline{e}_r = \underline{e}_y \cos \theta + \underline{e}_z \sin \theta, \quad \underline{e}_\theta = \underline{e}_z \cos \theta - \underline{e}_y \sin \theta. \quad (22)$$

The boundary condition that the velocity has no normal component relative to the moving toroid requires

$$\frac{\partial\varphi}{\partial r_1} = V \underline{e}_y \cdot \underline{e}_{r_1} = V \frac{\partial\varphi}{\partial r_1} = V \cos \psi \cos \theta \quad (r_1 = b). \quad (23)$$

For the solution of  $\varphi$  we seek again the representation of a doublet distribution along the centroid circle at  $r = a$ . Since the undisturbed flow relative to body sections has both normal and tangential components, both of which vary from one body



section to another, we shall assume that the doublet strength (per unit arc length),  $\beta$ , has also both normal and tangential components in order to account for the sectional variations of the flow, that is

$$\beta(\theta) = \underline{e}_r \beta_n(\theta) + \underline{e}_\theta \beta_s(\theta) \quad (0 \leq \theta \leq 2\pi). \quad (24a)$$

In fact, it turns out, as can be verified a posteriori, that  $\partial\varphi/\partial r_1$  will not satisfy at  $r_1 = b$  the specified dependence on  $\psi$  and  $\theta$  as prescribed in (23) unless

$$\beta_n(\theta) = \hat{\beta}_n \cos \theta, \quad \beta_s(\theta) = \hat{\beta}_s \sin \theta, \quad (24b)$$

with  $\hat{\beta}_n$  and  $\hat{\beta}_s$  being two constants, which we now assume.

The velocity potential can then be written as

$$\varphi(\underline{x}) = -a \int_0^{2\pi} \frac{\beta(\theta') \cdot (\underline{x} - \underline{x}')}{R^3} d\theta', \quad (25)$$

where  $R$  is given by (2), and  $\underline{x}, \underline{x}'$  are also there defined. With the above form of  $\beta$ , we have

$$\beta \cdot (\underline{x} - \underline{x}') = \hat{\beta}_n \cos \theta' [r \cos(\theta - \theta') - a] + \hat{\beta}_s r \sin \theta' \sin(\theta - \theta'),$$

and accordingly, after some simplification and integrations by parts,

$$\begin{aligned} \varphi = \frac{2 \cos \theta}{r_2} \{ -(\hat{\beta}_n + 2\hat{\beta}_s) \int_0^{\pi/2} \frac{\cos 2\theta d\theta}{[1 - k^2 \sin^2 \theta]^{\frac{3}{2}}} \\ + \frac{2a\hat{\beta}_n}{r_2} \left( \frac{r_1^2}{2a} + r - a \right) \int_0^{\pi/2} \frac{\cos 2\theta d\theta}{[1 - k^2 \sin^2 \theta]^{\frac{3}{2}}} \}, \end{aligned} \quad (26)$$

where  $r_1, r_2$  are defined by (3) and  $k$  by (5). These integrals can also be expressed in terms of the complete elliptic integrals as

$$\begin{aligned} \varphi = \frac{2 \cos \theta}{r_2} \{ (\hat{\beta}_n + 2\hat{\beta}_s) [ \left( \frac{2}{k^2} - 1 \right) K - \frac{2}{k^2} E ] \\ - \hat{\beta}_n \left( 1 + \frac{2a \cos \psi}{r_1} \right) [ \left( \frac{2}{k^2} - 1 \right) E - 2 \left( \frac{k'}{k} \right)^2 K ] \}, \end{aligned} \quad (27)$$

in which the elliptic integrals  $K$  and  $E$  have the argument  $k$ .

In the vicinity of the toroid surface, where  $r_1/a$  and  $k'$  are small, expansion of (27) together with use of (9) yields

$$\begin{aligned} \varphi = \cos \theta \left\{ -\frac{\hat{\beta}_n + 2\hat{\beta}_s}{a} \left[ \log \frac{8a}{r_1} - 2 + O\left(\frac{r_1}{a} \log \frac{a}{r_1}\right) \right] \right. \\ \left. - \frac{2\hat{\beta}_n}{r_1} \left[ \cos \psi + \frac{r_1}{2a} \sin^2 \psi - \frac{3}{8} \left( \frac{r_1}{a} \right)^2 \left( \log \frac{8a}{r_1} + \frac{5}{6} \right) \cos \psi \right. \right. \\ \left. \left. + O\left(\frac{r_1^3}{a^3} \log \frac{a}{r_1}\right) \right] \right\}. \end{aligned} \quad (28)$$

From this expression we derive at once the normal component of the velocity at the toroidal sur-

$$\begin{aligned} \frac{\partial \varphi}{\partial r_1} = \cos \theta \left\{ -\frac{\hat{\beta}_n + 2\hat{\beta}_s}{ab} [1 + O(\epsilon \log \epsilon)] \right. \\ \left. + \frac{2\hat{\beta}_n}{b^2} \cos \psi \left[ 1 + \frac{3}{8} \left( \frac{b}{a} \right)^2 \left( \log \frac{8a}{b} - \frac{1}{6} \right) + O(\epsilon^3 \log \epsilon) \right] \right\}, \end{aligned}$$

where  $\epsilon = b/a$ . In order that condition (23) is satisfied, we must therefore have

$$\hat{\beta}_s = -\frac{1}{2} \hat{\beta}_n, \quad (29)$$

$$\hat{\beta}_n = \frac{1}{2} V b^2 \left[ 1 - \frac{3}{8} \left( \frac{b}{a} \right)^2 \left( \log \frac{8a}{b} - \frac{1}{6} \right) \right]. \quad (30)$$

From (24b) and (30) we see that the leading term of the normal component of the doublet, namely  $\beta_n = \frac{1}{2} b^2 V \cos \theta$ , would again be as expected from local two-dimensional theory; its actual strength, as indicated by (30), is slightly reduced under the effect of curvature of the centroid line. It is further of interest to observe that a tangential component of doublet distribution, with strength given by (29) and hence being of the same order as  $\beta_n$ , is required so that the local source-like term (the first term on the right-hand side of (28)) can be annihilated. Thus (28) becomes, for  $r_1/a \ll 1$ ,

$$\begin{aligned} \varphi = -V b^2 \frac{\cos \theta}{r_1} \left\{ \cos \psi + \frac{r_1}{2a} \sin^2 \psi \right. \\ \left. - \frac{3}{8} \left( \frac{r_1}{a} \right)^2 \left( \log \frac{8a}{r_1} + \frac{5}{6} \right) \cos \psi \right. \\ \left. - \frac{3}{8} \left( \frac{b}{a} \right)^2 \left( \log \frac{8a}{b} - \frac{1}{6} \right) \cos \psi + O(\epsilon^3 \log \epsilon) \right\}, \end{aligned} \quad (31)$$

where  $\epsilon = b/a$ . It then follows that the flow velocity at the toroid surface has in the body frame of reference the value

$$\underline{u}_b = \underline{e}_\psi \frac{\partial(\varphi - Vy)}{b \partial \psi} + \underline{e}_\theta \frac{1}{(a + b \cos \psi)} \frac{\partial(\varphi - Vy)}{\partial \theta} \quad (r_1 = b)$$

$$\begin{aligned} = 2V \underline{e}_\psi \cos \theta \sin \psi \left[ 1 + \frac{\epsilon}{2} \cos \psi + \frac{3}{8} \epsilon^2 \left( \log \frac{8}{\epsilon} + \frac{1}{3} \right) \right] \\ + V \underline{e}_\theta \sin \theta \left[ 1 + \epsilon \cos \psi + \frac{1}{2} \epsilon^2 (1 - 3 \cos^2 \psi) \right] + O(\epsilon^3 \log \epsilon). \end{aligned} \quad (32)$$

The pressure distribution over the toroid surface can be calculated by using (16) in which  $U$  is to be replaced by  $V$ ,  $u_b^2 = \underline{u}_b \cdot \underline{u}_b$ , with  $\underline{u}_b$  given above, and

$$\frac{\partial \varphi}{\partial t} = \left( \frac{\varphi}{V} \right) \frac{dV}{dt} \quad (r_1 = b), \quad (33)$$

with  $\varphi$  given by (31). Using this pressure we obtain the differential force per unit arc length of the centroid circle as

$$\begin{aligned}\frac{dF}{ds_\theta} &= -\frac{b}{a} \int_0^{2\pi} p \, \underline{e}_r \, (a + b \cos \psi) d\psi \\ &= -\underline{e}_r \pi \rho b^2 \frac{dV}{dt} \cos \theta + \underline{e}_r \pi \rho \frac{b^2}{a} V^2 \left[ 1 - \frac{1}{2} \cos^2 \theta \right],\end{aligned}\quad (34)$$

of which the error is of  $O(\epsilon^2 \log \epsilon)$ . The first term on the right-hand side shows that the sectional induced mass is again  $\pi \rho b^2$  if referred to the normal component of the local acceleration. In addition, the curvature effect again results in an outward traction which now depends on the meridian angle  $\theta$ , but has no net resultant due to the obvious flow symmetry. Finally, upon integration of the differential force we obtain for the total force acting on an accelerating ring the value

$$\underline{F} = \int_0^{2\pi} \frac{dF}{ds_\theta} a d\theta = -\underline{e}_y \pi^2 \rho a b^2 \frac{dV}{dt}, \quad (35)$$

and hence the induced mass of the ring in this case is

$$m_{22} = m_{33} = \pi^2 \rho a b^2 = \frac{1}{2} m_{11}, \quad (36)$$

which is equal to half of the mass of fluid displaced by the toroid. We further note that both  $\underline{\beta}_n$  and  $\underline{\beta}_s$  contribute to the resultant doublet of the body, say  $\underline{\beta}_b$ , since

$$\underline{\beta}_b = a \int_0^{2\pi} \underline{\beta} d\theta = \pi a (\hat{\underline{\beta}}_n - \hat{\underline{\beta}}_s) \underline{e}_y = \frac{3}{4} \pi a b^2 V \underline{e}_y \quad (37)$$

after making use of (29), (30). This resultant doublet of the ring determines the asymptotic flow field at large distances from the ring. With this value of  $\underline{\beta}_b$ ,  $m_{22}$  can also be readily obtained from an equation analogous to (20).

#### 4. Finite-amplitude motion of a flexible slender body

As a typical case of the undulatory motions that most elongated aquatic animals make to propel themselves through water, especially when the viscous effect is unimportant except in drag calculations, we consider the potential flow generated by a flexible slender body moving in an arbitrary manner through an ideal fluid originally at rest. For simplicity we assume that the body has circular cross sections, of local radius  $b(s)$  where  $s$  denotes the arc length along the body centerline and the body may perform a planar, but otherwise arbitrary motion. Thus the present case is more relevant to anguilliform motion, but the method would also be akin, with suitable extensions of the theory, to studies on carangiform propulsion (though such extensions are not included in this paper).

Large-amplitude motions of the slender body in the plane say  $z = 0$  can be generally described in the parametric form

$$x = x(s, t), \quad y = y(s, t) \quad (0 < s < l), \quad (38)$$

which specifies the instantaneous position of a point on the body centerline at an arc length  $s$

from the anterior tip, and  $l$  is the body length. The parametric functions will be assumed twice continuously differentiable in  $s$  and  $t$ . This motion may be either generated by an extraneous agency, or, in self-swimming animals, due to swimming actions and the resultant fluid action, including involuntary recoils. The body centerline will be assumed to be inextensible so that

$$\left(\frac{\partial x}{\partial s}\right)^2 + \left(\frac{\partial y}{\partial s}\right)^2 = 1. \quad (39)$$

Under this condition the unit vectors tangential and normal to the body centerline can be written

$$\underline{e}_s = \left(\frac{\partial x}{\partial s}, \frac{\partial y}{\partial s}, 0\right), \quad \underline{e}_n = \left(\frac{\partial y}{\partial s}, -\frac{\partial x}{\partial s}, 0\right), \quad (40)$$

so that  $(\underline{e}_n, \underline{e}_s, \underline{e}_z)$  form a right-hand system of orthogonal vectors, and the centerline has the instantaneous radius of curvature  $|a|$  where

$$a(s, t) = \left(\frac{\partial^2 y}{\partial s^2} \frac{\partial x}{\partial s} - \frac{\partial^2 x}{\partial s^2} \frac{\partial y}{\partial s}\right)^{-1}. \quad (41)$$

The center of curvature of the line at station  $s$  lies on the positive (or negative) side of the  $n$ -axis if  $a$  is negative (or positive), as shown in Fig. 2. (The present sign convention is adopted in order to make direct comparison with the results of the torus problem.) The velocity of the centerline in planar motion is given by

$$\underline{U}(s, t) = \left(\frac{\partial x}{\partial t}, \frac{\partial y}{\partial t}, 0\right), \quad (42)$$

which can be arbitrarily assigned provided it will always keep the radius of curvature  $|a|$  large compared to the local body radius  $b$  and it satisfies the inextensibility condition (39) for all  $t$ , or  $\underline{e}_s \cdot \partial \underline{e}_s / \partial t = 0$ . As in our discussion on the problem of torus, it is convenient to decompose  $\underline{U}$  into the components normal and tangential to the body centerline,

$$\underline{U}(s, t) = U_s(s, t) \underline{e}_s + U_n(s, t) \underline{e}_n, \quad (43a)$$

where

$$U_s = \frac{\partial x}{\partial t} \frac{\partial x}{\partial s} + \frac{\partial y}{\partial t} \frac{\partial y}{\partial s}, \quad U_n = \frac{\partial x}{\partial t} \frac{\partial y}{\partial s} - \frac{\partial y}{\partial t} \frac{\partial x}{\partial s}. \quad (43b)$$

For the velocity potential we seek again the representation of a line doublet distributed along the body centerline from  $s = 0$  to  $l$  and moving with it for all  $t$ . The unknown doublet strength (per unit length of  $s$ ) will also be decomposed, for the convenience of calculation, into the normal and tangential components

$$\underline{\beta} = \beta_s(s, t) \underline{e}_s + \beta_n(s, t) \underline{e}_n \quad (0 < s < l). \quad (44)$$

In case the body end is blunt, a more accurate account of the local flow requires the doublet line to start from a point ( $s = 0$ ) at a short distance, of the order of the radius of curvature of the body surface at the end, from the body end, but this feature is already known (e.g. Wu & Chwang 1974) to be of secondary importance. There is no need to include in the construction of solution an additional line source since  $\beta_s$ , the tangential

component of the line doublet, is easily seen (by integration of the integral representation (45) by parts) to be equivalent to a line source distribution. The velocity potential can then be expressed as

$$\varphi(\underline{x}, t) = - \int_0^l \frac{\beta(s, t) \cdot (\underline{x} - \underline{x}')}{R^3} ds, \quad (45)$$

where  $\underline{x}'$  is a point on the centerline prescribed by (38) and  $R = |\underline{x} - \underline{x}'|$ . The doublet strength  $\beta$  is to be determined by applying the boundary condition

$$[\nabla\varphi - \underline{U}(s, t)] \cdot \underline{v}(\underline{x}, t) = 0 \quad (\underline{x} \text{ on } S(s, t)), \quad (46)$$

where  $\underline{v}(\underline{x}, t)$  denote the normal vector of the body surface at station  $s$ , at which the body cross section is assumed to remain circular (for every  $s$ ) and its boundary is denoted by  $S(s, t)$ . Since we have assumed that the local radius of curvature of the centerline,  $a(s, t)$  (see Eq. 41), is large compared to the local cross sectional radius,  $b(s)$ , the velocity of the local body surface  $S(s, t)$  is well approximated by the velocity  $\underline{U}(s, t)$  of the body centerline.

To effect our calculation for invoking the required boundary condition, we evaluate the asymptotic representation of  $\varphi(\underline{x}, t)$  for  $\underline{x}$  in the vicinity of  $S(s, t)$  by first decomposing the integral in (45) into three parts

$$\varphi = - \left( \int_0^{s_0-c} + \int_{s_0-c}^{s_0+c} + \int_{s_0+c}^l \right) \frac{\beta \cdot (\underline{x} - \underline{x}')}{R^3} ds \equiv \varphi_1 + \varphi_0 + \varphi_2, \quad (47)$$

where  $s_0$  is the value of  $s$  determined in such a way that the plane containing the vector  $\underline{e}_n(s_0, t)$  and parallel to the  $z$ -axis (hence perpendicular to  $\underline{e}_s(s_0, t)$ ) also contains the specific point  $\underline{x}$  in question, and the range  $2c$  of the integral  $\varphi_0$  will be chosen such that  $b \ll c \ll (a \text{ or } l)$ . This choice implies that within the range of integration for  $\varphi_0$ , the centerline curvature will not have any significant departure from its value at  $s_0$ , and this segment of body would therefore behave like a segment of the torus discussed previously. The location of  $s_0$  is assumed to be sufficiently far from either end, and the end solution is not further pursued here.

Of the three parts of  $\varphi$ ,  $\varphi_0$  is the most important since both  $\varphi_1$  and  $\varphi_2$  cannot make more than a minor contribution to the value of  $\varphi$  on account of the greater distances, from  $s_0$ , of the doublets that represent  $\varphi_1$  and  $\varphi_2$ . To facilitate the calculation of  $\varphi_0$ , we introduce a local system of cartesian coordinates  $(\xi, \eta, \zeta)$ , with the origin at  $s_0$ , the  $\xi$ - and  $\eta$ -axis coinciding with  $\underline{e}_n$  and  $\underline{e}_s$  at  $s_0$ , respectively, and with  $\zeta = z$ . We shall also employ, alternatively for convenience, a system of curvilinear coordinates  $(r_1, \psi, \theta)$  defined by

$$r_1 = (\xi^2 + \zeta^2)^{1/2}, \quad \psi = \tan^{-1}(\zeta/\xi), \quad s - s_0 = a\theta. \quad (48)$$

Note that  $\theta$  is in the same or opposite sense to that of  $s$  according as  $a > 0$  or  $a < 0$ . When expressed in terms of these coordinates, we have

$$\begin{aligned} \underline{x} &= [r_1 \cos \psi, 0, r_1 \sin \psi], \\ \underline{x}' &= [-a(1 - \cos \theta), a \sin \theta, 0], \end{aligned} \quad (49)$$

where the square brackets denote the components of a vector with respect to the system  $[\xi, \eta, \zeta]$ . Also we have

$$\underline{e}_n(\theta) = [\cos \theta, \sin \theta, 0], \quad \underline{e}_s = [-\sin \theta, \cos \theta, 0]. \quad (50)$$

It therefore follows that

$$R = |\underline{x} - \underline{x}'| = [r_1^2 + 2a(a + r_1 \cos \psi)(1 - \cos \theta)]^{1/2}, \quad (51)$$

and

$$\begin{aligned} \beta \cdot (\underline{x} - \underline{x}') &= -\beta_n [(a + r_1 \cos \psi)(1 - \cos \theta) - r_1 \cos \psi] \\ &\quad - \beta_s (a + r_1 \cos \psi) \sin \theta \\ &= -\beta_n \left[ \frac{R^2 - r_1^2}{2a} - r_1 \cos \psi \right] \\ &\quad - \beta_s (a + r_1 \cos \psi) \sin \theta. \end{aligned} \quad (52)$$

Upon substituting (51) and (52) into the integrand of  $\varphi_0$ , we have

$$\begin{aligned} \varphi_0 &= -a \int_{-a}^a \frac{\beta \cdot (\underline{x} - \underline{x}')}{R^3} d\theta \\ &= -(a r_1 \cos \psi + \frac{1}{2} r_1^2) \int_{-a}^a \frac{\beta_n d\theta}{R^3} \\ &\quad + \int_{-a}^a \left( \frac{1}{2} \beta_n + \frac{d\beta_s}{d\theta} \frac{1}{R} - \left[ \frac{\beta_s(\theta)}{R} \right] \right) d\theta, \end{aligned} \quad (53a)$$

in which the integral with  $\beta_s$  has been integrated by parts, and

$$a = c/a \ll 1 \quad (53b)$$

by assumption. Since  $\theta$  is small within the range of integration, we may expand  $(1 - \cos \theta)$ ;  $\beta_n(\theta)$  and  $\beta_s(\theta)$  for small  $\theta$ ,

$$(1 - \cos \theta) = \frac{\theta^2}{2} \left( 1 - \frac{1}{12} \theta^2 + \dots \right),$$

$$\beta_n(\theta) = \beta_n(0) + \theta \beta_n'(0) + \frac{1}{2} \theta^2 \beta_n''(0) + \dots,$$

with a similar equation for  $\beta_s(\theta)$ . Here the primes over  $\beta$  denote differentiation with respect to  $\theta$ . Obviously, the terms  $\theta \beta_n'(0)$  and  $\theta \beta_s'(0)$  in these expansions, being odd in  $\theta$ , have no contribution to the integrals in (53) since  $R$  is even in  $\theta$ . Thus we see that the error committed through neglecting the second and higher terms in the above expansions will introduce a factor  $[1 + O(a^2 \log a)]$  to the final result so obtained (the additional factor



$\log a$  in the order term arises from the integral of  $R^{-1}$ ). Accordingly, we need to be concerned only with the following two integrals

$$I_1 = \int_{-a}^a \frac{d\theta}{R_*}, \quad I_2 = \int_{-a}^a \frac{d\theta}{R_*^3}, \quad (54a)$$

$$\text{where } R_* = [r_1^2 + a^2(1 + \frac{r_1}{a} \cos \psi) \theta^2]^{\frac{1}{2}}. \quad (54b)$$

These elementary integrals can further be expanded for small values of  $r_1/c$  where  $r_1$  is sufficiently close to the body so that  $r_1 = O(b)$ , giving

$$I_1 = \frac{2}{a} (1 + \frac{r_1}{a} \cos \psi)^{-\frac{1}{2}} \{ \log \frac{2c}{r_1} (1 + \frac{r_1}{a} \cos \psi)^{\frac{1}{2}} + O(\frac{r_1^2}{c^2}) \} \\ = \frac{2}{a} \{ \log \frac{2c}{r_1} + O(\frac{r_1}{a} \log \frac{c}{r_1}) \}, \quad (55a)$$

$$I_2 = \frac{2}{ar_1^2} (1 + \frac{r_1}{a} \cos \psi)^{-\frac{1}{2}} \{ 1 + O(\frac{r_1^2}{c^2}) \} \\ = \frac{2}{ar_1^2} \{ 1 - \frac{r_1}{2a} \cos \psi + O(\frac{r_1^2}{c^2}) \}. \quad (55b)$$

The order term in (55b) will hold provided  $(r_1/c)^2$  is of a higher order than  $(r_1/a)$ . By a similar expansion procedure, the last term in (53a) becomes  $-2d\beta/ds$  evaluated at  $s_0$ . We then see that in the leading terms of these expansions, only the first term of  $I_1$  depends on the limits of integration involving  $c$ , whose value is no more precisely prescribed than by its order of magnitude only. This somewhat indefinite (constant) term, namely  $\log c$ , is expected, in principle, to be cancelled out when the asymptotic expansions of  $\varphi_1$  and  $\varphi_2$  are combined with that of  $\varphi_0$  in the final account for  $\varphi$ . Although such expansions of  $\varphi_1$  and  $\varphi_2$  require the prescription of the velocity  $U(s, t)$  of the entire centerline, the fact that both  $\varphi_1$  and  $\varphi_2$  exist at the origin of  $(\xi, \eta, \zeta)$  and are regular in its neighborhood may be used to infer that for small values of  $r_1/c$  and  $|s - s_0|/c$ ,

$$\varphi_1 = \frac{\beta}{c} \{ A_0 + \frac{r_1}{c} (A_1 \cos \psi + A_2 \sin \psi) + O(\frac{r_1^2}{c^2}) \}, \quad (56)$$

and a similar expansion holds for  $\varphi_2$ , where the coefficients  $A_0$ ,  $A_1$ , and  $A_2$  may depend on  $c$ , and are of order  $\log(c/l)$ . Here  $\beta$  represents a bound estimate of  $\beta(s)$  over the centerline; the factor  $(\beta/c)$  and the order estimates of  $A_0$ ,  $A_1$ , and  $A_2$  can be obtained by an approximate evaluation of the lengths involved in the integrand of  $\varphi_1$  and  $\varphi_2$ . The foregoing argument is nevertheless sufficient for the doublet strength to be determined to its leading order.

Compiling the asymptotic expansions for the various terms, we have

$$\varphi = [\frac{1}{a} \beta_n + 2 \frac{\partial}{\partial s} \beta_s(s)] \{ \log \frac{2c}{r_1} + B_0 + O(\frac{r_1}{a} \log \frac{c}{r_1}) \} \\ - 2\beta_n \{ \frac{1}{r_1} \cos \psi + \frac{1}{2a} \sin^2 \psi + B_1 + O(\frac{r_1}{c^2} \log \frac{c}{l}) \}, \quad (57)$$

where  $B_0$  and  $B_1$  may depend on  $c$  and  $s$ , with their magnitude estimated to be of order  $\log(c/l)$ , but are independent of  $r_1$  and  $\psi$ . Here the subscript of  $s_0$  has been dropped as understood. Now, since the body surface at station  $s$ , at which  $r_1 = b(s)$ , has the normal vector given by

$$\mathbf{n} = \mathbf{e}_{r_1} - \mathbf{e}_s db/ds \\ = \mathbf{e}_\xi \cos \psi + \mathbf{e}_\eta \sin \psi - \mathbf{e}_\eta db/ds, \quad (58)$$

the boundary condition (46) becomes

$$\frac{\partial \varphi}{\partial r_1} - \frac{\partial \varphi}{\partial s} \frac{db}{ds} = U_n \cos \psi - U_s \frac{db}{ds} \quad (r_1 = b),$$

which is satisfied by (57) if

$$\beta_n = \frac{1}{2} U_n(s, t) b^2(s), \quad (59)$$

$$\frac{\partial \beta_s}{\partial s} = \frac{1}{2} U_s(s, t) b \frac{db}{ds} - \frac{1}{2a} \beta_n, \quad (60)$$

with a relative error of order  $(b/a) \log(l/b)$ . Thus the local flow field is represented by a normal doublet, of strength  $\frac{1}{2} U b^2$  as predicted on two-dimensional theory, plus a source of strength  $U_s b b'$  as in the small-amplitude slender-body theory, while the centerline-curvature effect remains the same as in the flow past a torus.

In this course we have just proved the following:

**Theorem I.** For an elongated flexible body having circular cross-sections of radius  $b(s)$ , which varies continuously with the arc length  $s$  measured along its inextensible centerline whose motion through an incompressible, inviscid fluid originally at rest, is prescribed over a time range of  $t$  by arbitrary single-valued functions  $\mathbf{x} = \mathbf{x}'(s, t)$ ,  $y = y'(s, t)$ , and  $z = 0$  for every point on the centerline such that its radius of curvature,  $|a|$ , is large compared to maximum  $b$ , the velocity potential of the resulting potential flow is

$$\varphi(\mathbf{x}, t) = \int_0^l \frac{\partial \beta_s}{\partial s} \frac{ds}{R} \\ - \int_0^l [(\mathbf{x} - \mathbf{x}') \frac{\partial y'}{\partial s} - (y - y') \frac{\partial \mathbf{x}'}{\partial s}] \frac{\beta_n}{R^3} ds \quad (I)$$

where

$$R(\mathbf{x}; s, t) = [(\mathbf{x} - \mathbf{x}')^2 + (y - y')^2 + z^2]^{\frac{1}{2}}, \\ \beta_n(s, t) = \frac{1}{2} U_n b^2, \quad \frac{\partial \beta_s}{\partial s} = \frac{1}{2} U_s b \frac{db}{ds} - \frac{1}{2a} \beta_n,$$

$$U_n = \frac{\partial \mathbf{x}'}{\partial t} \frac{\partial y'}{\partial s} - \frac{\partial y'}{\partial t} \frac{\partial \mathbf{x}'}{\partial s},$$

$$U_s = \frac{\partial \mathbf{x}'}{\partial t} \frac{\partial \mathbf{x}'}{\partial s} + \frac{\partial y'}{\partial t} \frac{\partial y'}{\partial s},$$

$$\text{and } a = \left( \frac{\partial^2 y'}{\partial s^2} \frac{\partial x'}{\partial s} - \frac{\partial^2 x'}{\partial s^2} \frac{\partial y'}{\partial s} \right) - 1.$$

**Proof:** The proof is almost immediate upon noting that

$$\beta \cdot (\underline{x} - \underline{x}') = \beta_n [(x - x') \frac{\partial y'}{\partial s} - (y - y') \frac{\partial x'}{\partial s}] - \beta_s \frac{\partial}{\partial s} \left[ \frac{1}{2} R^2 \right],$$

followed by integrating the term with  $\beta_s$  in the integral representation (45) by parts, assuming that the tangential doublet strength  $\beta_s$  vanishes at  $s = 0$  and  $l$ , which is valid for the end with paraboloidal or less blunt shapes (see, e. g. Wu & Chwang, 1974). The conditions  $\beta_s(0) = 0$  and  $\beta_s(l) = 0$  are in fact required by the condition on zero total source strength for closed bodies.

The above solution, (I), of  $\varphi$  is uniformly valid throughout the flow field, and is accurate with a relative error of order  $(b/a) \log(l/b)$ .

## 5. Experiments on flow past slender body

Experimental measurement of the pressure distribution over the surface of a slender body moving through a fluid (at high Reynolds number) is recognized as a difficult task, especially in the case when the body performs an unsteady, undulatory, flexible movement, and when the body is appended with side and tail fins like a fish. As a consequence, there has been no existing experimental results (known to the authors) reporting data on velocity and pressure distributions in unsteady flow past a slender body of this type. Such experimental information is regarded as extremely valuable and necessary for providing a sound basis of estimating the validity of the simplifying assumptions that underlie various theories, as well as a reliable reference against which an error estimate can be obtained for different theoretical predictions.

For these purposes a series of experiments has been started and is being carried out. For the experiments in the first stage, which is devoted to the rigid body case, a model whose front 70% of body is almost the same as a triaxial ellipsoid of axis-ratio 1:0.287:0.179 was (see sketch in Fig. 3) selected as a representative body shape, to which fins of various forms can be appended in a later stage of work. This model thus seems to include most of the important aspects to be investigated, leaving the body flexibility as the only new feature to be included at a later time. In order to make comparison between theories and experiments, the exact solution to the corresponding potential flow problem and the prediction on classical slender-body theory have been obtained, which will be briefly described below.

### 5.1. Exact potential-flow solution for triaxial ellipsoid

The exact solution to the velocity potential of a triaxial ellipsoid in arbitrary translational and rotational motions through an incompressible, inviscid fluid of infinite extent has been known (see e. g. Havelock 1931) and can be expressed in a variety of forms (Wu & Chwang 1974). For the convenience of numerical computation, we adopted the following integral representation of the velocity potential

$$\varphi(\underline{x}) = -2\pi a_1 a_2 a_3 \beta_1 x_1 \int_{\lambda}^{\infty} \frac{du}{(a_1^2 + u)\Delta(u)} \quad (61)$$

for the ellipsoid

$$\sum_{i=1}^3 (x_i/a_i)^2 = 1 \quad (a_1 > a_2 > a_3), \quad (62)$$

where

$$\beta_i = U_i / [2\pi(2 - a_i)] \quad (i = 1, 2, 3), \quad (63)$$

$$a_i = a_1 a_2 a_3 \int_0^{\infty} \frac{du}{(a_i^2 + u)\Delta(u)}, \quad (64)$$

$$\Delta(u) = [(a_1^2 + u)(a_2^2 + u)(a_3^2 + u)]^{\frac{1}{2}}, \quad (65)$$

and  $\lambda$  is the largest root of

$$\sum_{i=1}^3 \frac{x_i^2}{a_i^2 + \lambda} = 1. \quad (66)$$

This representation has been used to calculate the velocity  $\underline{u} = \nabla \varphi$ , and the pressure from the Bernoulli equation. When the flow quantities are evaluated on the body surface there remains only one integral to be calculated, namely  $a_i$ . Though this integral may also be expressed in terms of the incomplete elliptic integrals of the first and second kind, in the calculations made here it was computed numerically on an IBM 370/158 computer, using Simpson's rule.

### 5.2. Pressure distribution based on slender-body theory

We consider a slender fish-shaped body swimming with a mean forward velocity  $U$  in the negative  $x$ -direction. The body has a symmetric thickness function  $g(x, y)$  measured from its centerplane; its transverse undulation from the mean forward direction is prescribed by  $h(x, t)$  (see Fig. 3). The coordinate system is fixed on the stretched-straight body centerline and is moving with the body. According to Lighthill's theory (1960), the velocity potential may be expressed in the body frame of reference as

$$\Phi = Ux + \Phi_0 + \Phi_1 \quad (67)$$

where  $Ux + \Phi_0$  is the solution of the so-called stretched-straight problem (with  $h \equiv 0$ ), and  $\Phi_1$  is the solution to the remaining problem. The stretched-straight problem is now classic and will not be repeated here.

The latter problem for  $\Phi_1$  is a two-dimensional problem in the cross flow plane and can be solved by using the complex potential,  $f(\zeta)$ , where  $\zeta = y + iz$  (Newman & Wu, 1973). For the case of no vortex shedding anterior to the tail,

$$f(\zeta) = iV[(\eta^2 - \beta^2)^{\frac{1}{2}} - \zeta - c_0(x)] \quad (68a)$$

where,

$$V(x, t) = \frac{\partial h}{\partial t} + U \frac{\partial h}{\partial x} \quad (68b)$$

If the body cross section is now assumed to be elliptic,

$$g(x, y) = \frac{A(x)}{B(x)} \sqrt{B^2(x) - y^2} \quad (69)$$

and

$$\beta = A+B, \quad 4c^2 = B^2 - A^2 \quad (70)$$

$$\eta = \frac{\zeta + \sqrt{\zeta^2 - 4c^2}}{2} + \frac{\frac{1}{2}\beta^2}{\zeta + \sqrt{\zeta^2 - 4c^2}} \quad (71)$$

where  $\eta = \eta_r + i\eta_i$  is the complex plane in which the elliptic cross section is mapped conformally into a slit along the  $\eta_r$  axis from  $-\beta$  to  $+\beta$ . The flow velocity and the pressure can be computed from

$$\Phi_1 = \text{Re} \{ f(\zeta) \} \quad (72)$$

Pressures calculated in this way are compared to the pressures computed from exact potential flows over ellipsoids translating at a constant angle of attack (Fig. 4).

### 5.3. Experimentally observed pressures

The fish model was constructed of two fiberglass halves each made from the same mold, and of dimensions taken from a chinook salmon. The resulting rigid model was closely elliptical in body cross section, with major and minor axes given by  $B(x)$  and  $A(x)$  respectively. A least square curve fit was made to these functions, using a fifth order polynomial, for use in calculating the pressures.

The model was towed down a twenty-five foot long towing tank, using a variable-speed central motor to drive an overhead carriage. The carriage accelerated quickly and reached a steady speed within 3 or 4 feet of its starting position and remained constant for the length of a run (10-15 feet). A supporting strut and sting assembly was used to suspend the model from this carriage, and was capable of varying the angle of attack.

Miniature flush mounted pressure transducers were used at the outset of the experimental investigation. In order for the units to be mounted inside the model, water proofing and miniature size (1/8 inch diaphragm) were needed. A high sensitivity of about 20 mm H<sub>2</sub>O full scale was needed and obtained with the aid of high gain carrier amplifiers and piezoresistive (semiconductor strain gage) pressure transducers. The accuracy of these transducers in measuring pressure was found to be greatly influenced by heat-conduction and forced convection effects when the model was towed through water. Since we were already pushing the sensitivity of the units and because of the complex gage geometry, these anomalies were unable to be overcome, and we are now using remote variable reluctance transducers with fluid filled tubes.

The output of these transducers is then monitored on an eight channel thermal writing Sanborn recorder, and a calibration was done at the end of each test. Direct measurements of the pressure difference across the body were made

and thus eliminated the need for a reference pressure.

Some preliminary results of these experiments are shown in Fig. 5 for several different locations on the model. The slight negative pressure at zero angle of attack may be explained by the difference in tank boundaries. The lower side is a solid surface while the upper side is a free surface, and blockage effects indicate an asymmetry in the zero angle of attack case similar to those observed.

For comparison, the pressures calculated from slender body theory (Section 5.2) and from exact potential theory (Section 5.1) are also plotted in Fig. 5. For the exact solution, an ellipsoid was chosen with axes equal to those of the maximum cross section of the model. This resulted in a good fit to the body in the midsection but deviated from the body shape in the nose and tail regions. This body shape is expected to give reasonable results away from the body ends since  $\Delta C_p$  depends only on the local shape of the body.

These preliminary results are all for the steady flow situations. Unsteady flow measurements are more difficult and are currently being considered. Although unsteady motions can be studied with such a rigid model, body curvature effects cannot. A truly flexible model has been made available to us for future investigations in this area.

### Acknowledgments

We are very much indebted to Dr. Allen Chwang for stimulating discussions on this problem. We wish to thank Mr. Glen Bowlus and Mr. Pui Lam for their help in construction of the experimental apparatus and in reduction of the experimental data.

This work was jointly sponsored by the Office of Naval Research and the National Science Foundation.

### References

- Havelock, T. H. 1931 The wave resistance of an ellipsoid. *Proc. Roy. Soc. A* **132**, 480-486.
- Lighthill, M. J. 1960 Note on the swimming of slender fish. *J. Fluid Mech.* **9**, 305-317.
- Lighthill, M. J. 1970 Aquatic animal propulsion of high hydromechanical efficiency. *J. Fluid Mech.* **44**, 265-301.
- Lighthill, M. J. 1971 Large-amplitude elongated-body theory of fish locomotion. *Proc. Roy. Soc. London B* **178**, 125-138.
- Newman, J. N. 1973 The force on a slender fish-like body. *J. Fluid Mech.* **58**, 689-702.
- Newman, J. N. & Wu, T. Y. 1973 A generalized slender-body theory for fish-like forms. *J. Fluid Mech.* **57**, 673-693.
- Wu, T. Y. 1971 Hydromechanics of fish propulsion. Part 3. Swimming of slender fish with side fins and its optimum movements. *J. Fluid Mech.* **46**, 545-568.
- Wu, T. Y., Brokaw, C. J. & Brennen, C. 1975 *Swimming and Flying in Nature*, New York/London: Plenum Press.



Wu, T. Y. & Chwang, A. T. 1974 Double-model flow theory - a new look at the classical problem. Proc. Tenth ONR Symposium on Naval Hydrodynamics, June 24-28, at Massachusetts Institute of Technology.

Wu, T. Y. & Newman, J. N. 1972 Unsteady flow around a slender fish-like body. Proc. Int. Symp. on Directional Stability and Control of Bodies Moving in Water, London, Paper 7, Inst. Mech. Eng. Publ., 33-42.

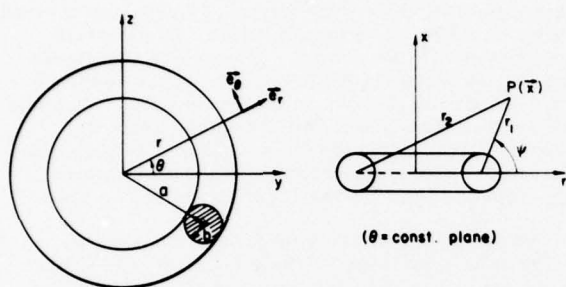


Fig. 1: The coordinate systems for the toroidal ring problem.

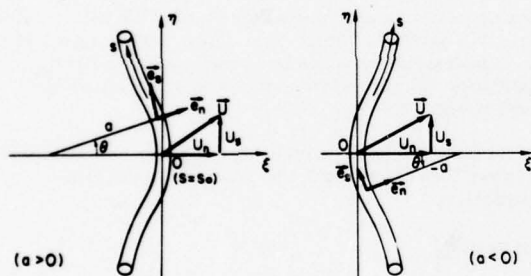


Fig. 2: The coordinate systems for a curved slender body.

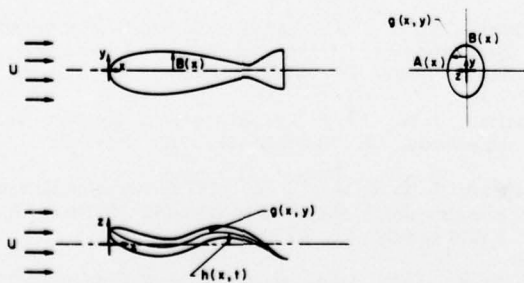


Fig. 3: Illustration of body geometry and coordinate system used.

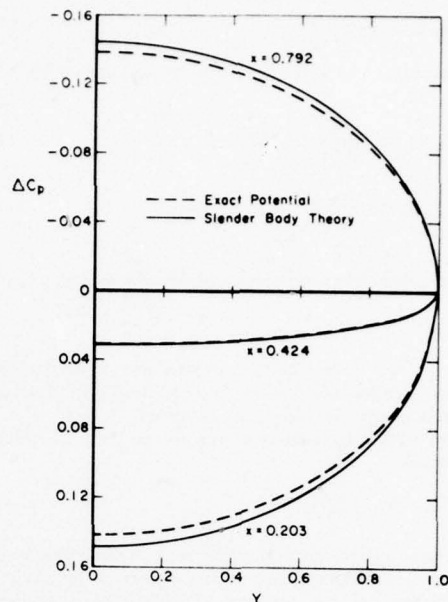


Fig. 4a.

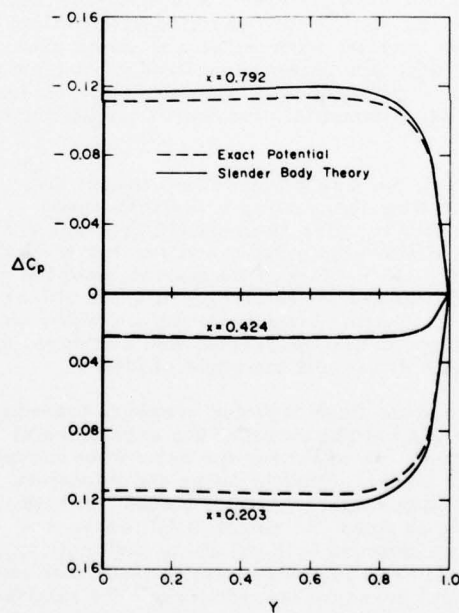


Fig. 4b.

Fig. 4:  $\Delta C_p$  is plotted over a given cross section at several positions along the body, for two different theories. The angle of attack is 5 degrees and the y-axis is scaled by the maximum body extent at that cross section. (a) spheroid,  $a_1 = 1.0$ ,  $a_2 = a_3 = 0.2868$ . (b) ellipsoid,  $a_1 = 1.0$ ,  $a_2 = 0.2868$ , and  $a_3 = 0.1787$ .

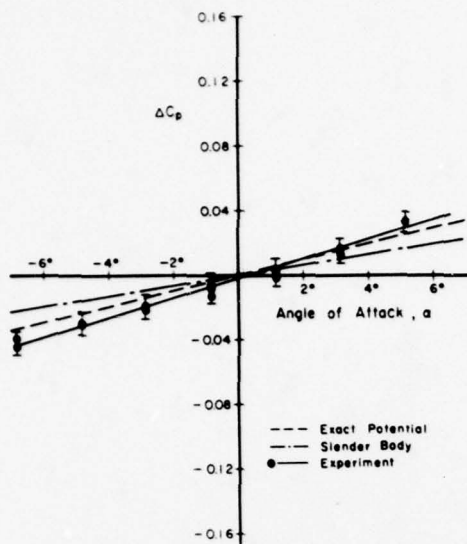


Fig. 5a.

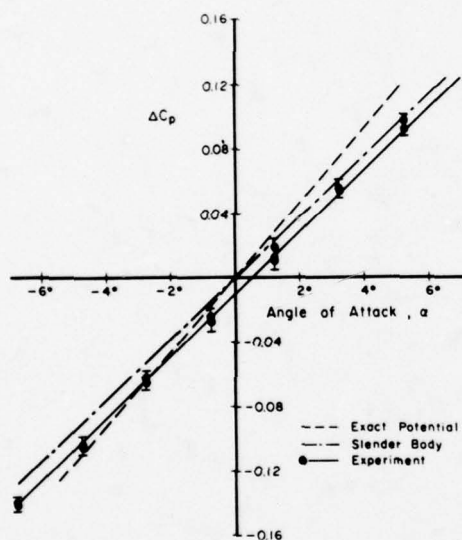


Fig. 5b.

(b)

Fig. 5:  $\Delta C_p$  as a function of angle of attack for model of slenderness ratio  $\epsilon = 0.287$ . (a) a position 7.2 inches from the nose and on the lateral body centerline ( $y = 0$ ). (b) a position 3.45 inches from the nose on the lateral body centerline ( $y = 0$ ).

# ON THE VIRTUAL MASS, AT LONG WAVELENGTHS, OF A HALF-IMMERSED CIRCULAR CYLINDER HEAVING ON WATER OF FINITE DEPTH

P. SAYER and F. URSELL  
University of Manchester, UK

The virtual-mass coefficient (henceforth abbreviated as V.M.) of a heaving circular cylinder describes the force due to the dynamic pressure component in phase with the acceleration. The V.M. of a circular cylinder heaving on water of finite depth is here considered in the long-wave range. Existing computations are in disagreement when  $Ka$  and  $Kh$  are both small. Now it is well-known that, for infinite depth, the V.M. is infinite for  $Ka=0$ , achieves a minimum for  $Ka \approx 0.75$ , and tends to 1 for large  $Ka$ . For finite depth, Ursell has recently confirmed analytically that the V.M. is finite (and thus a function of  $a/h$ ) in the limit  $Ka=Kh=0$ . The present work continues this long-wave investigation by a study of the derivative  $d(V.M.)/d(Ka)$  for small  $Ka$ . It is shown that, for  $a/h$  sufficiently small,  $d(V.M.)/d(Ka) > 0$  in the limit  $Ka=Kh=0$ ; thus the V.M. curve for fixed  $a/h$  has a maximum when  $a/h$  is small and  $Kh$  is near 1. A table of numerical values is given for the V.M. and  $d(V.M.)/d(Ka)$  in the limit  $Ka=Kh=0$ ,  $a/h$  fixed.

## 1. INTRODUCTION

A circular cylinder of radius  $a$  is made to perform a periodic heaving motion in water of finite depth  $h$ . For water of infinite depth it has long been known that the V.M. becomes infinite when the wave number,  $Ka = \sigma^2 a/g$ , tends to 0. More recently it has been established that for finite depth the V.M. remains finite when  $Ka$  tends to 0, with  $a/h$  held fixed. However, recent computations have given inconsistent results in the long-wave range, and the reason for this is now well understood: for small  $Ka$  the resultant force on the cylinder can be calculated without much difficulty and it is found to be nearly in quadrature with the vertical acceleration; the V.M. (which describes the force component in phase with the acceleration) can then be calculated by multiplying the large total-force coefficient by the sine of a small phase angle, a procedure which is likely to involve a loss of accuracy.

Although it is possible to derive an integral equation of the second kind for the velocity potential, it has been found, in the case of a circular cylinder, to be more convenient to expand the potential in terms of a wave-source and an infinite sum of multipole potentials, and thence to derive an infinite system of linear equations for the coefficients. Ursell [1] suggested a rearrangement of the method previously used by Yu and Ursell [2]: the infinite system of linear equations for the complex-valued coefficients was replaced by two associated systems for real-valued coefficients. From these the required real part of the potential on the circle could be found; this process no longer involved the multiplication of a large and a small quantity in order to obtain a quantity of order unity. In this way it was found possible to derive an expression for the limiting value of the V.M. when  $Ka$  tends to 0, keeping  $a/h$  fixed. This involved the limiting potential  $\phi(x,y)$ , which satisfies the limiting boundary condition  $\partial\phi/\partial n = 0$  on the free surface, and is suitably normalized by an additive constant. The normalization is the most difficult part of the calculation.

Thus the numerical results of Yu and Ursell

were shown to be incorrect in the long-wave range. A discussion of more recent work is given in §4 below. In particular there still seems to be some disagreement about the behaviour of the V.M. in the neighbourhood of  $Ka=0$ . By a study of  $d(V.M.)/d(Ka)$  in this long-wave range the present work has found that, for  $a/h$  sufficiently small, this gradient is positive in the limit  $Ka=Kh=0$ . Thus the V.M. curve for fixed  $a/h$  has a maximum when  $Ka$  and  $a/h$  are both small; in this case the maximum is found to lie close to  $Kh=1$ . The present numerical values agree closely with analytical asymptotics for small  $a/h$ .

## NOMENCLATURE

$a$	= radius of cylinder;
$g$	= acceleration of gravity;
$h$	= depth of water;
$\sigma$	= angular frequency;
$K$	= $\sigma^2/g$ ;
$k_0$	= (unique) positive real root of
$K = k_0 \tanh k_0 h$ ;	
$\ell$	= heave amplitude of cylinder;
$U_0$	= vertical velocity of cylinder;
$\rho$	= (constant) density of fluid;
V.M.	= virtual-mass coefficient.

## 2. FORMULATION

A half-immersed circular cylinder of radius  $a$  is made to perform a periodic heaving motion of angular frequency  $\sigma$  in inviscid fluid of constant density  $\rho$  and constant depth  $h$ . The amplitude  $\ell$  of the oscillations is assumed small enough for linearized theory to be applicable. The origin of rectangular Cartesian coordinates is taken in the mean free-surface of the fluid at the mean position of the cylinder,  $x$  measured horizontally,  $y$  vertically (increasing with depth). Let polar coordinates  $r, \theta$ , be defined by the relations  $x=r \sin \theta$ ,  $y=r \cos \theta$ . The velocity potential,  $\phi(x,y) \exp(-i\sigma t)$ , henceforth abbreviated to  $\phi(x,y)$ , satisfies the following boundary-value problem:

$$\left( \frac{\partial^2}{\partial x^2} + \frac{\partial^2}{\partial y^2} \right) \phi(x,y) = 0 \text{ in the fluid, } |x| < \infty, 0 < y < h, r > a \quad (2.1)$$



$$K\phi + \frac{\partial \phi}{\partial y} = 0 \text{ on the free-surface, } y=0, |x|>a. \quad (2.2)$$

$$\frac{\partial \phi}{\partial y} = 0 \text{ on the bottom, } y=h. \quad (2.3)$$

$$\frac{\partial \phi}{\partial r} = U_0 \cos \theta \text{ on the cylinder, } r=a, |\theta| < \frac{1}{2}\pi. \quad (2.4)$$

Here  $U_0 = k\sigma$  and  $K = \sigma^2/g$ .

Uniqueness will be ensured by demanding outgoing waves at infinity:

$$\frac{\partial \phi}{\partial x} \rightarrow ik_0 \phi \operatorname{sgn}(x), \text{ as } |x| \rightarrow \infty, \quad (2.5)$$

$$\text{where } K = k_0 \tanh k_0 h, k_0 \text{ real } > 0. \quad (2.6)$$

Although the potential  $\phi(x,y)$  could in principle be found by solving an integral equation of the second kind, it has been found to be more convenient to adopt the method of Yu and Ursell [2] and to express  $\phi(x,y)$  as the sum of a wave-source potential

$$F + if = \int_0^\infty \frac{\cosh k(h-y) \cos kx}{K \cosh kh - k \sinh kh} dk \quad (2.7)$$

( $\int$  denotes that the path of integration passes below the pole  $k=k_0$  in the complex  $k$ -plane)

and an infinite sum of multipole potentials

$$F_{2m} + if_{2m} = \frac{\cos 2m\theta}{r^{2m}} + \frac{K}{2m-1} \frac{\cos (2m-1)\theta}{r^{2m-1}} + \frac{1}{(2m-1)!} \times \int_0^\infty \frac{e^{-kh} (K+k) (K \sinh ky - k \cosh ky) k^{2m-2} \cos kx}{K \cosh kh - k \sinh kh} dk, \quad (m=1,2,3,\dots); \quad (2.8)$$

viz. to write

$$\frac{\phi}{U_0 a} = -A_0 (F + if) + \sum_1^\infty a^{2m} A_{2m} (F_{2m} + if_{2m}) \quad (2.9)$$

The  $A_0, A_{2m}$ 's are determined from the boundary condition (2.4) on the cylinder:

$$\cos \theta = -A_0 \left\langle a \frac{\partial}{\partial r} (F + if) \right\rangle + \sum_1^\infty a^{2m} A_{2m} \left\langle a \frac{\partial}{\partial r} (F_{2m} + if_{2m}) \right\rangle, \quad (2.10)$$

where angular brackets  $\langle \dots \rangle$  denote that  $r$  is to be put equal to  $a$ . In principle there is no theoretical difficulty in determining these coefficients (see Yu and Ursell, [2], §2.3). However for small  $k_0 h$ , the force is nearly in quadrature with the acceleration. Thus to obtain the V.M. the large total-force coefficient must be multiplied by the sine of a small phase angle, as was stated above. To overcome this difficulty (cf. Ursell [1]) (2.10) is rewritten in the form

$$\cos \theta = -A_0 \left\langle a \frac{\partial F}{\partial r} \right\rangle + \sum_1^\infty a^{2m} A_{2m} \left\langle a \frac{\partial F_{2m}}{\partial r} \right\rangle + i.E.A \left\langle a \frac{\partial}{\partial r} \frac{\cosh k_0(h-y) \cos k_0 x}{(k_0 h)^2} \right\rangle, \quad (2.10a)$$

where

$$A = A_0 + \operatorname{sech}^2 k_0 h \sum_1^\infty \frac{A_{2m} (k_0 a)^{2m}}{(2m-1)!} \quad (2.11)$$

and

$$E = \frac{2\pi \cosh k_0 h}{2k_0 h + \sinh 2k_0 h} (k_0 h)^2 \quad (2.12)$$

Here it has been observed that  $f_{2m}$  is a multiple of

$$f = \frac{-2\pi \cosh k_0 h}{2k_0 h + \sinh 2k_0 h} \cosh k_0(h-y) \cos k_0 x. \quad (2.13)$$

Real quantities  $B_0, B_{2m}, C_0, C_{2m}$ , ( $m=1,2,3,\dots$ ),

are introduced (cf. (2.10a)) as coefficients in the following expansions:

$$\cos \theta = -B_0 \left\langle a \frac{\partial F}{\partial r} \right\rangle + \sum_1^\infty a^{2m} \left\langle a \frac{\partial F_{2m}}{\partial r} \right\rangle, \quad (2.14)$$

$$\left\langle a \frac{\partial}{\partial r} \frac{\cosh k_0(h-y) \cos k_0 x}{(k_0 h)^2} \right\rangle = -C_0 \left\langle a \frac{\partial F}{\partial r} \right\rangle + \sum_1^\infty a^{2m} C_{2m} \left\langle a \frac{\partial F_{2m}}{\partial r} \right\rangle. \quad (2.15)$$

It is readily seen from (2.10a), (2.11), (2.12) that

$$A_{2m} = B_{2m} - i.E.A C_{2m}. \quad (2.16)$$

Thus the  $A_{2m}$ 's can be found when the  $B_{2m}$ 's and  $C_{2m}$ 's are known. By multiplying (2.14), (2.15) by the complete set  $\{\cos 2n\theta\}$ , ( $n=0,1,2,\dots$ ), and integrating from 0 to  $\frac{1}{2}\pi$ , there result two infinite systems of linear equations, the theory of which is analogous to that of integral equations of the second kind.

The virtual-mass coefficient is defined by the following ratio:

$$\text{V.M.} = \frac{(\text{upward force per unit length of cylinder in phase with acceleration})}{(\text{acceleration of cylinder}) \times (\text{mass per unit length of cylinder immersed in fluid})} \quad (2.17)$$

From Bernoulli's equation, the hydrodynamic force is

$$-\rho \partial \phi(x,y,t) / \partial t = \operatorname{Re} \{ i \rho \sigma \phi(x,y) \exp(-i\sigma t) \}. \quad (2.18)$$

Thus the upward force per unit length of cylinder in phase with the acceleration is

$$2 \int_0^{\frac{1}{2}\pi} i \rho \sigma \{ \operatorname{Re} \langle \phi \rangle \} \exp(-i\sigma t) \cos \theta a d\theta, \quad (2.19)$$

whence

$$\text{V.M.} = \frac{2 \int_0^{\frac{1}{2}\pi} i \rho \sigma \{ \operatorname{Re} \langle \phi \rangle \} \exp(-i\sigma t) \cos \theta a d\theta}{(-i\sigma U_0 \exp(-i\sigma t)) (\frac{1}{2}\pi a^2 \rho)} \quad (2.20)$$

If quantities  $\mathcal{B}, \mathcal{L}, \mathcal{D}$  are now defined (cf. (2.11), (2.12)) by the relations

$$\mathcal{B} = B_0 + \operatorname{sech}^2 k_0 h \sum_1^\infty \frac{B_{2m} (k_0 a)^{2m}}{(2m-1)!}, \quad (2.21)$$

$$\mathcal{L} = C_0 + \operatorname{sech}^2 k_0 h \sum_1^\infty \frac{C_{2m} (k_0 a)^{2m}}{(2m-1)!} \quad (2.22)$$

$$\mathcal{D} = 1 + E^2 \mathcal{L}^2, \quad (2.23)$$

then it is found (cf. Ursell [1]) that

$$\frac{\operatorname{Re} \langle \phi \rangle}{U_0 a} = \left\langle -B_0 F + \sum_1^\infty a^{2m} B_{2m} F_{2m} \right\rangle - \frac{\mathcal{B} \mathcal{L} E^2}{\mathcal{D}} \left\langle -C_0 F + \sum_1^\infty a^{2m} C_{2m} F_{2m} \right\rangle - \frac{\mathcal{B} \mathcal{L} E}{\mathcal{D}} \langle f \rangle, \quad (2.24)$$

whence the V.M. quickly follows. We note that  $\mathcal{B} \mathcal{L} E / \mathcal{D} = O(k_0 h)$  and  $\langle f \rangle = O(k_0 h)^{-1}$ .

### 3. RESULTS

#### 1. $Ka = Kh = 0$ , $a/h$ fixed.

Using (2.24) Ursell [1] obtained the following result: for  $a/h$  fixed, the limiting expression for the V.M. in the case  $Ka=Kh=0$  is given by

$$(V.M.)_{Ka=Kh=0} = -\frac{4}{\pi} \int_0^{\pi} \left\{ \langle \hat{B} \rangle - \frac{a}{h} \right\} \cos \theta d\theta, \quad (3.1)$$

where  $\hat{B} = -\hat{B}_0 \hat{F} + \sum_{m=1}^{\infty} a^{2m} \hat{B}_{2m} \hat{F}_{2m}$  is that limiting

potential which satisfies  $\partial \hat{B} / \partial y = 0$  on the free surface and  $\hat{B} = |x|/h \rightarrow 0$  as  $|x| \rightarrow \infty$ . The correct choice of additive constant,  $-a/h$ , is important. ( $\hat{\phantom{x}}$  denotes the limiting value when  $Ka=Kh=0$ ).

Recently both the analytical and the numerical studies have been carried further, and the results will now be described. The details of the calculation will be omitted; it is hoped to publish them elsewhere. Analytical calculations show that for  $a/h \ll 1$ :

$$(V.M.)_{Ka=Kh=0} = \frac{8}{\pi^2} \left\{ \log \frac{\pi a}{h} - \frac{3}{2} + 2 \log 2 \right\} + O\left(\frac{a}{h}\right), \quad (3.2)$$

$$\left( \frac{d(V.M.)}{d(Ka)} \right)_{Ka=Kh=0} = \frac{8}{\pi^2} \left\{ \frac{2}{\pi^2} \zeta(3) \frac{h}{a} + (1 - \frac{2}{\pi}) \log \frac{\pi a}{h} + \frac{1}{2} + \frac{10}{3\pi} + \frac{13}{24}\pi - 3 \log 2 \right\} + O\left(\frac{a}{h} \log \frac{h}{a}\right), \quad (3.3)$$

where  $\zeta(3) = \frac{1}{1^3} + \frac{1}{2^3} + \dots = 1.202057\dots$

is the Riemann zeta function.

It was found that (3.2), (3.3) agreed well with numerical computations, e.g. to 5 significant figures when  $a/h=10^{-5}$ . The numerical computations are presented in the accompanying table 1.

## 2. Qualitative behaviour for small $a/h$ and $Kh \leq O(1)$ .

For  $a/h < 0.02$  the numerical results in table 1 show that, when  $Ka=Kh=0$ , then  $(V.M.) > 2$  and  $(d(V.M.)/d(Ka)) > 0$ ; it is also known that in the short-wave range the V.M.  $= 1 + O(a/h)^2$  for small  $a/h$ . Thus the V.M. necessarily has a turning value (maximum) for some positive  $Ka$ . The following results enable this maximum to be found when  $a/h$  is small.

Let us consider  $a/h$  small, but  $Kh \leq O(1)$ . It can be shown that the analytical expression for the V.M. is given by

$$V.M. = -\frac{8}{\pi^2} \left\{ \gamma + \log Ka - G_1(Kh) - \frac{3}{2} + 2 \log 2 - \frac{2}{3} \left( \frac{a}{h} \right)^2 G_3(Kh) \right\} + O\left(\frac{a}{h}\right)^4, \quad (3.4)$$

where  $\gamma = 0.5772\dots$  is Euler's constant, and

$$G_{2s+1}(Kh) = \int_0^{\infty} \frac{u^{2s+1} e^{-u} du}{(u-Kh)(u \sinh u - Kh \cosh u)}, \quad (s=0,1,2,\dots) \quad (3.5)$$

(the bars through the integral denote that the Cauchy principal value is to be taken at the poles  $u=Kh$  and  $u=k_0 h$ ).

It then follows that

$$\frac{d(V.M.)}{d(Ka)} = -\frac{8}{\pi^2} \left\{ \frac{1}{Kh} - G_1'(Kh) \right\} + O\left(Ka \log \frac{1}{Ka}\right). \quad (3.6)$$

For general values of  $Kh$ ,  $G_1'(Kh)$  has to be evaluated numerically; however it can be shown that  $G_1'(1)=1$  exactly, and thus

$$\frac{d(V.M.)}{d(Ka)} = O\left(\frac{a}{h} \log \frac{h}{a}\right), \quad \text{when } Kh=1. \quad (3.7)$$

If we denote by  $\Delta(V.M.)$  the difference between the values of the V.M. at  $Kh=0$  and near  $Kh=1$  ( $Ka$  being small at both values of  $Kh$ ) then

$$\Delta(V.M.) = \frac{16}{\pi^2} \left( \frac{a}{h} \right)^2 G_3(Kh) + O\left(\frac{a}{h}\right)^4, \quad (3.8)$$

where  $G_3(1) = -0.6528\dots$

Thus the maximum is hardly perceptible for small  $a/h$ .

## 4. DISCUSSION OF RESULTS

Ursell's analytical expression (3.1) for the limiting value of the V.M. when  $Ka=Kh=0$ ,  $a/h$  fixed, shows that the numerical computations of Yu and Ursell [2] are incorrect in the long-wave range, as has already been noted.

The limiting value given by Kim [3], and which we now see is intended to apply to the region  $a/h \ll 1$ ,  $Kh \ll O(1)$ , is

$$\lim_{K \rightarrow 0} V.M. = -\frac{8}{\pi^2} \lim_{K \rightarrow 0} \{ \gamma + \log Ka - G_1(Kh) \}.$$

Since  $\lim_{K \rightarrow 0} G_1(Kh) = \{ \gamma + \log(Kh/\pi) \}$ , we see that Kim's

limiting value for the V.M. should differ from the present one by a constant,  $(8/\pi^2)(3/2 - 2 \log 2) = 0.9224\dots$ . However, comparison with Kim's numerical values for various (fixed) values of  $a/h$  is difficult since his curve for the V.M. shows a very rapid variation for small  $Ka$ , but we understand that these values have recently been revised by him.

Bai [4] uses a variational technique and his results indicate a large negative value for  $d(V.M.)/d(Ka)$  as  $Ka$  tends to 0, when  $a/h=1/4$  and  $2/3$ , contrary to the results of the present work. He observes that, for very small values of  $Ka$ , the real part of the velocity potential remains  $O(1)$  whereas the imaginary part becomes infinite like  $(k_0 h)^{-1}$ . The limiting value of the V.M. involves the imaginary part of the potential multiplied by a term of order  $k_0 h$ , and Bai notes the possibility of numerical errors in his work due to this as  $Ka$  tends to 0.

Keil [5] expresses the potential as the sum of a wave-source and an infinite series of multipoles, as in the present work. His analytical expression for  $G_1(Kh)$ , as  $Kh$  tends to 0, is  $G_1(Kh) = 1 - \gamma - \log Kh$ , compared with the correct value of  $\log \pi - \gamma - \log Kh$ . Thus his limiting value of the V.M. differs from the present one by  $\log \pi - 1 = 0.1447\dots$

Yeung [6] has recently used a 'hybrid' integral equation method, in which the Green's function is the fundamental free-space wave source,  $\log r$ . A discretization scheme is then used to obtain the value of the potential on the circle, whence the V.M. is calculated. His numerical results for the limiting value of the V.M. are in excellent agreement with the values found by the present work, but no analytical results are given.

For  $Ka$  sufficiently far from 0 ( $>0.2$ ) the values of the V.M. given by Kim, Bai, Keil and Yeung are in close agreement. It is hoped that the present results may be of use in checking numerical work at long wavelengths.

## REFERENCES

1. Ursell, F., "On the virtual-mass and damping coefficients in water of finite depth," submitted for publication 1975.
2. Yu, Y.S. and Ursell, F., "Surface waves generated by an oscillating circular cylinder on water of finite depth," *Journal of Fluid Mechanics*, Vol. 11, 1961, pp. 529-551.

3. Kim, C.H., "Hydrodynamic forces and moments for heaving, swaying and rolling cylinders on water of finite depth," *Journal of Ship Research*, Vol. 13, 1969 pp. 137-154.

4. Bai, K.J., "A note on the added-mass coefficients in water of finite depth," June 1974, presented to the 10th O.N.R. Symposium on Naval Hydrodynamics, M.I.T., Cambridge, Mass., U.S.A.

5. Keil, H., "Die hydrodynamischen Kräfte bei der periodischen Bewegung zweidimensionaler Körper an der Oberfläche flacher Gewässer," Report no. 305, February 1974, Institut für Schiffbau der Universität Hamburg.

6. Yeung, R.W., "A hybrid integral equation method for time-harmonic free-surface flow," October 1975, presented to the 1st International Conference on Numerical Ship Hydrodynamics, National Bureau of Standards, Gaithersburg, Maryland, U.S.A.

VIRTUAL-MASS COEFFICIENT OF A CIRCULAR CYLINDER HEAVING ON WATER OF FINITE DEPTH; LIMITING CASE  $Ka=Kh=0$  ( $a/h$  fixed).

$a/h$	V.M.	$d(V.M.)/d(Ka)$	$a/h$	V.M.	$d(V.M.)/d(Ka)$
0.90	1.217	0.7587	0.02	2.361	1.261
0.85	1.018	0.6175	0.01	2.910	7.947
0.80	0.8733	0.5154	0.009	2.994	9.613
0.75	0.7622	0.4372	0.008	3.088	11.75
0.70	0.6756	0.2010	0.007	3.195	14.49
0.65	0.6083	0.1515	0.006	3.319	18.36
0.60	0.5572	0.1108	0.005	3.465	23.91
0.55	0.5208	0.07626	0.004	3.645	32.48
0.50	0.4984	0.04505	0.003	3.877	47.17
0.45	0.4901	0.01432	0.002	4.204	77.44
0.40	0.4969	-0.01931	0.001	4.765	171.3
0.35	0.5208	-0.06002	0.0009	4.850	192.4
0.30	0.5650	-0.6477	0.0008	4.945	218.9
0.25	0.6354	-0.7210	0.0007	5.054	253.2
0.20	0.7418	-0.8243	0.0006	5.178	298.9
0.15	0.9032	-0.9692	0.0005	5.326	363.3
0.10	1.162	-1.149	0.0004	5.507	460.2
0.09	1.234	-1.161	0.0003	5.740	622.2
0.08	1.316	-1.165	0.0002	6.068	947.7
0.07	1.411	-1.152	0.0001	6.630	1928
0.06	1.523	-1.426	0.000075	6.863	2584
0.05	1.657	-1.309	0.00005	7.192	3896
0.04	1.825	-1.044	0.000025	7.754	7837
0.03	2.045	-0.4210	0.00001	8.496	19673

Table 1



# PREDICTION OF FREE-SURFACE EFFECTS ON SHIP MANOEUVRING

R. B. CHAPMAN

David W. Taylor Naval Ship Research and Development Centre,  
Bethesda, Maryland, USA

## ABSTRACT

A numerical method is described for computing the flow induced by lateral motion of a surface-piercing body in a uniform stream. Slender body theory is used to reduce a three-dimensional steady or unsteady flow to a two-dimensional unsteady problem which may be solved numerically. In this way a flat plate at a steady angle of attack was solved with linear and nonlinear boundary conditions. The linearized solution for a truncated cylinder at a constant angle of attack is extended analytically to oscillation in yaw and sway. Hydrodynamic coefficients are computed for a flat plate as a function of Froude number and frequency. Theoretical coefficients are compared with experimental values and are used to predict the maneuvering characteristics of a flat plate and to estimate the propulsive efficiency of a surface piercing plate used as a sculling device.

## Introduction

Maneuvering characteristics of a surface-piercing body such as a ship are most easily estimated from theories which are valid at low and moderate Froude numbers. The free surface may be represented as a rigid plane for steady yaw at low Froude numbers, or strip theory may be applied to unsteady problems if the effects of forward speed are small. Strip theory, however, does not include effects between body sections such as the influence of the free-surface disturbance created by lateral motion of the forward sections of the body on the flow downstream. This particular forward speed effect can greatly influence the hydrodynamic coefficients at high Froude numbers.

This effect is included in the slender body formulation which was applied by the author to a flat plate at a steady angle of attack (Reference [1]). Linear and nonlinear solutions were obtained. Side force and yaw moment coefficients calculated with linearized boundary conditions were in good agreement with values measured at small angles of attack (Reference [2]). In Reference [3] the linear solution was extended to oscillatory yaw and sway.

The present paper contains a review of the flat plate work reported in References [1] and [3] followed by an investigation of related problems; the maneuvering of a plate, the propulsive efficiency of a plate in sculling, and the effect of finite thickness.

## Formulation

The governing equations will be formulated for a surface-piercing body oscillating in yaw and sway. The case of a steady angle of attack corresponds to the sway mode in the zero frequency limit.

A left-handed Cartesian coordinate system  $(x, y, z)$  is fixed in space and another system  $(x', y', z')$  is fixed on the body such that the two systems coincide in the absence of yaw and sway. The  $x$ -coordinate is aligned in the direction of the free-stream velocity  $U$ , that is  $x$  is positive aft. The  $z$ -coordinate is positive upward and  $y$  is positive to port. When the two systems coincide, the common origin is on the longitudinal center-plane of the body at the intersection of the leading edge and the undisturbed free surface. Yawing moment is measured about an axis  $A'$  parallel to the  $z$  axis at the mid-body point ( $x' = \ell/2$ ,  $y' = 0$ ) where  $\ell$  is the body length. Rotation about this axis is positive in the right-hand sense; that is the leading edge moves to port. This geometry is illustrated in Figure 1.

At time  $t$ , the body is displaced distance  $q(t)$  along the  $y$  axis and is rotated  $\alpha(t)$  radians about axis  $A'$  fixed in the body. The surface of the body is described by

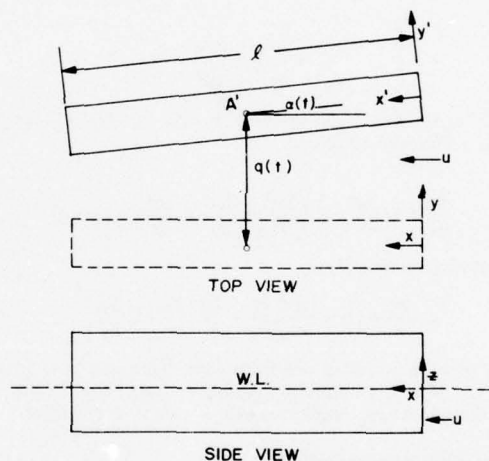


Fig. 1: Coordinate geometry

$$F(x', y', z') = 0, \quad 0 \leq x' \leq \ell'. \quad (1)$$

The function  $F(x', y', z')$  is positive over the exterior of the body and negative in the interior. The length scale of the flow in the transverse plane generated by lateral motion of the body may be characterized by its draft  $a$ . The slender body assumption requires that the ratio of draft to the body length,  $\epsilon = a/\ell$ , remain small. The ratio of the cross velocity to the free-stream velocity is also small. Formally, terms of order  $\epsilon^2$  and higher are neglected and it is assumed that

$$O(a) \leq O(\epsilon), \quad (2)$$

so that terms of order  $a\epsilon$  and  $\epsilon^2$  are neglected as well.

To first order in  $a$ , the space-fixed and body-fixed coordinates are related by

$$\begin{aligned} x' &= x - y' \alpha(t) \\ y' &= y - q(t) - \alpha(t) \left( \frac{1}{2} \ell - x \right) \\ z' &= z \end{aligned} \quad (3)$$

and the velocity components of the two systems are related by

$$\begin{aligned}\dot{x}' &= \dot{x} - y' \dot{a}(t) - \dot{y}' a(t) \\ \dot{y}' &= \dot{y} - \dot{a}(t) - \dot{a}(t) \left( \frac{1}{2} \ell - x' \right) + a(t) \dot{x} \\ \dot{z}' &= \dot{z}.\end{aligned}\quad (4)$$

The flow is assumed to be irrotational and may be described by a velocity potential,

$$\Phi = Ux + \varphi(x, y, z, t). \quad (5)$$

The body boundary condition may be written as

$$\begin{aligned}\dot{x}' \frac{\partial F}{\partial x'} + \dot{y}' \frac{\partial F}{\partial y'} + \dot{z}' \frac{\partial F}{\partial z'} &= 0 \\ \text{on } F(x', y', z') &= 0.\end{aligned}\quad (6)$$

Equations (4), (5), and (6) combine to give,

$$\begin{aligned}\left( \frac{\partial \varphi}{\partial x} + U - y' \dot{a} - \frac{\partial \varphi}{\partial y} a \right) \frac{\partial F}{\partial x'} + \left( \frac{\partial \varphi}{\partial y} - V_B(x', t) + a \frac{\partial \varphi}{\partial x} \right) \frac{\partial F}{\partial y'} \\ + \frac{\partial \varphi}{\partial z} \frac{\partial F}{\partial z'} = 0\end{aligned}\quad (7)$$

where  $V_B(x', t)$  is the cross velocity,

$$\begin{aligned}V_B(x', t) &= V_0(t) + \left( \frac{1}{2} \ell - x' \right) a(t) \\ V_0(t) &= \dot{q}(t) - Ua(t).\end{aligned}\quad (8)$$

The potential,  $\varphi(x, y, z, t)$ , must satisfy Laplace's equation,

$$\frac{\partial^2 \varphi}{\partial x^2} + \frac{\partial^2 \varphi}{\partial y^2} + \frac{\partial^2 \varphi}{\partial z^2} = 0 \quad (9)$$

throughout the flow. On the free surface,  $z = \xi(x, y)$ , the flow satisfies a dynamic condition,

$$\frac{\partial \varphi}{\partial t} + U \frac{\partial \varphi}{\partial x} + \frac{1}{2} \left( \frac{\partial \varphi^2}{\partial x} + \frac{\partial \varphi^2}{\partial y} + \frac{\partial \varphi^2}{\partial z} \right) + g\xi = 0 \quad (10)$$

and a kinematic condition,

$$\frac{\partial \xi}{\partial t} + \left( U + \frac{\partial \varphi}{\partial x} \right) \frac{\partial \xi}{\partial x} + \frac{\partial \xi}{\partial y} \frac{\partial \varphi}{\partial y} = g \frac{\partial \varphi}{\partial z}. \quad (11)$$

Finally there is an initial condition specifying  $\varphi(x, y, z, t_0)$  and  $\xi(x, y, t_0)$ . For the oscillatory problems considered in this paper the initial condition transforms into a radiation condition.

### Slender Body Approximations

The slender body approximation is implemented by assigning orders of magnitude to independent variables,

$$x, x' = O(\ell); y, y', z, z' = O(a); t = O(\ell U^{-1}). \quad (12)$$

Differential operators have consistent orders of magnitude,

$$\frac{\partial}{\partial x} = O(\ell^{-1}), \frac{\partial}{\partial z} = O(a^{-1}), \text{ etc.}, \quad (13)$$

and terms of order  $\epsilon^2 = (a/\ell)^2$  are neglected. Thus, Laplace's equation reduces to a two-dimensional form,

$$\frac{\partial^2 \varphi}{\partial y^2} + \frac{\partial^2 \varphi}{\partial z^2} = 0. \quad (14)$$

Since it has been further assumed that

$$O\left(\frac{V_B}{U}\right) = O(a) \leq O(\epsilon), \quad (15)$$

terms of order  $\epsilon(V_B/U)$  and  $(V_B/U)^2$  are also neglected.

The lateral motion problem become degenerate unless

$$\varphi = O(a V_B) \text{ and } \xi = O(V_B \ell U^{-1}) \quad (16)$$

Application of these assumptions reduces the free-surface conditions to

$$\frac{\partial \varphi}{\partial t} + U \frac{\partial \varphi}{\partial x} + \frac{1}{2} \left( \frac{\partial \varphi^2}{\partial y} + \frac{\partial \varphi^2}{\partial z} \right) + g\xi = 0 \quad (17)$$

and

$$\frac{\partial \xi}{\partial t} + U \frac{\partial \xi}{\partial x} + \frac{\partial \xi}{\partial y} \frac{\partial \varphi}{\partial y} = g \frac{\partial \varphi}{\partial z} \quad (18)$$

with both conditions evaluated on  $z = \xi$ . Although second order terms in  $(V_B/U)$  have been eliminated, nonlinearities remain in the free-surface conditions as a result of the assumption that  $\epsilon = a/\ell$  is also small. The magnitude of these free-surface nonlinearities depends on the relative magnitudes of these two small parameters,  $(V_B/U)$  and  $(a/\ell)$ .

Under the same assumptions, the body boundary condition reduces to

$$\begin{aligned}U \frac{\partial F}{\partial x'} + \left( \frac{\partial \varphi}{\partial y} - V_B(x', t) \right) \frac{\partial F}{\partial y'} + \frac{\partial \varphi}{\partial z} \frac{\partial F}{\partial z'} &= 0 \\ \text{on } F(x', y', z') &= 0.\end{aligned}\quad (19)$$

This condition combined with Laplace's equation (14), the free-surface conditions, (17) and (18), and an appropriate initial or radiation condition will define the flow.

The free-surface conditions have characteristic lines in the  $x$ - $t$  plane defined by

$$\sigma = \frac{1}{2}(t - x U^{-1}) = \text{constant} \quad (20)$$

with the position on the characteristic line specified by the variable

$$s = \frac{1}{2}(t + x U^{-1}) \quad (21)$$

The free-surface conditions on  $z = \xi(s, \sigma, y)$  may be written with independent variables  $(s, \sigma, y, z)$  as

$$\frac{\partial \varphi}{\partial s} + \frac{1}{2} \left( \frac{\partial \varphi^2}{\partial y} + \frac{\partial \varphi^2}{\partial z} \right) + g\xi = 0 \quad (22)$$

and

$$\frac{\partial \xi}{\partial s} + \frac{1}{2} \frac{\partial \xi}{\partial y} \frac{\partial \varphi}{\partial y} = g \frac{\partial \varphi}{\partial z}. \quad (23)$$

If  $s$  is regarded as a time variable, then equations (14), (22), and (23) are equivalent to those governing two-dimensional flow in the  $y$ - $z$  plane. The body boundary condition (19) becomes equivalent to the condition on a body moving in the  $y$ - $z$  plane and distorting with time. In this way the slender body approximation reduces three-dimensional steady or unsteady free-surface flows to two-dimensional unsteady free-surface flows in the  $y$ - $z$  plane. Existing numerical methods for solving this type of two-dimensional problems are applicable.

Several additional features of the solution may be deduced from the characteristics. First, since the solution on any characteristic line is independent of conditions on any other characteristic, the flow in the plane  $x = x_1$  at time  $t = t_1$  is independent of the flow in plane  $x = x_2$  at time  $t = t_2$  unless

$$t_2 - t_1 = (x_2 - x_1) U^{-1} \quad (24)$$

Second, when the solution is constructed for an initial value problem, the solution at any point  $s = s_1$  on a characteristic line depends only on conditions for  $s < s_1$ . Thus, the solution at  $x = x_1$  and  $t = t_1$  is independent of conditions downstream ( $x_2 > x_1$ ) or at a later time in the sense that it is not influenced by the body boundary condition. Finally, it is obvious that an initial condition of identically zero perturbation potential requires the solution to remain zero ahead of the leading edge for all time. These considerations remain applicable to

the oscillatory problem and may be regarded as consequences of a radiation condition.

### Linearized Problem

If the velocity caused by lateral motion of the body is sufficiently small so that it does not interact with itself or with the flow resulting from the body thickness, nonlinear terms in the governing equations may be neglected. In this linearized limit the two free-surface conditions (22) and (23) combine to give

$$\frac{\partial^2 \varphi}{\partial s^2} = -g \frac{\partial \varphi}{\partial z} \quad \text{on } z = 0. \quad (25)$$

The body boundary condition for the linearized problem is specified on the mean (static) position of the body surface,  $F(x, y, z) = 0$ , rather than on the displaced body surface. The body boundary condition is further simplified by eliminating the potential  $\varphi_A(x, y, z)$  which exists in the absence of lateral motion induced by body thickness. This potential satisfies the body boundary condition,

$$U \frac{\partial F}{\partial x} + \frac{\partial \varphi_A}{\partial y} \frac{\partial F}{\partial y} + \frac{\partial \varphi_A}{\partial z} \frac{\partial F}{\partial z} = 0 \quad (26)$$

on  $F(x, y, z) = 0$ .

The body boundary condition for the remaining potential, due to lateral motion alone, is then

$$\left( \frac{\partial \varphi}{\partial y} - V_B(x, t) \right) \frac{\partial F}{\partial y} + \frac{\partial \varphi}{\partial z} \frac{\partial F}{\partial z} = 0 \quad (27)$$

on  $F(x, y, z) = 0$ .

### Flat Plate at Constant Angle of Attack

The most elementary example of the problem just formulated is a flat plate with a constant angle of attack  $\alpha$ . The nonlinear body boundary condition (19) reduces to

$$\frac{\partial \varphi}{\partial y} = -U\alpha \quad (28)$$

on  $y = a \left( \frac{1}{2} \ell - x \right), z > -a$ .

This condition is applied on  $y = 0$  for the linearized problem.

Two parameters characterize this problem;  $(a/\epsilon)$ , a measure of free-surface nonlinearity; and

$$\bar{\ell} = \ell (g/a)^{1/2} U^{-1}, \quad (29)$$

a nondimensional length equivalent to the inverse of the product of the Froude number and the square root of the aspect ratio. The net side force acting on the plate is, for linear case, simply

$$Y(\bar{\ell}) = -2\rho U \int_{-a}^0 dz \varphi(\bar{\ell}, 0+, \bar{z}). \quad (30)$$

The more complex expression for the nonlinear case is given in Reference [1]. Since the flow is independent of conditions downstream, equation (30) also defines  $Y(\bar{x})$ , the net sideforce acting on the portion of the strut forward of  $\bar{x} \leq \bar{\ell}$ . The yaw moment about the strut midchord is

$$N(\bar{\ell}) = \int_0^{\bar{\ell}} d\bar{x} \frac{\partial Y(\bar{x})}{\partial \bar{x}} \left( \frac{\ell}{2} - x \right). \quad (31)$$

Sideforce and moment coefficients are defined as

$$C_Y(\bar{x}) = Y(\bar{x}) \cdot \left( \frac{1}{2} \rho a^2 \alpha U^2 \right)^{-1} \quad (32)$$

$$C_N(\bar{\ell}) = N(\bar{\ell}) \cdot \left( \frac{1}{2} \rho a^2 \ell \alpha U^2 \right)^{-1}$$

In the nonlinear problem, these coefficients depend on  $\alpha$ . The linearized problem represents the limiting case as  $\alpha$  approaches zero. The longitudinal position of the hydrodynamic center is

given by

$$X_f = \ell \left( \frac{1}{2} - C_N(\bar{\ell}) \cdot C_Y^{-1}(\bar{\ell}) \right). \quad (33)$$

Figures (2), (3), and (4) illustrate  $C_Y(\bar{x})$ ,  $C_N(\bar{x})$ , and  $X_f/\ell$  calculated from the linearized formulation compared with experimental values for plates at small angles of attack as reported in Reference [2]. Theory and experiment are in good general agreement for the aspect ratios shown, although the figures do not include measured values for an aspect ratio of 0.04. These values deviate widely with a large amount of scatter caused, possibly, by flow separation.

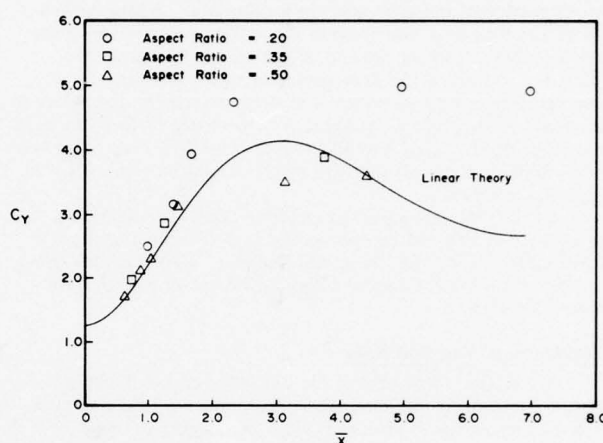


Fig. 2: Theoretical and experimental side force coefficient

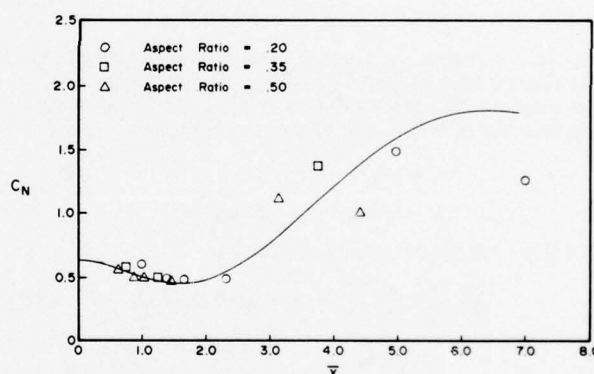


Fig. 3: Theoretical and experimental moment coefficient

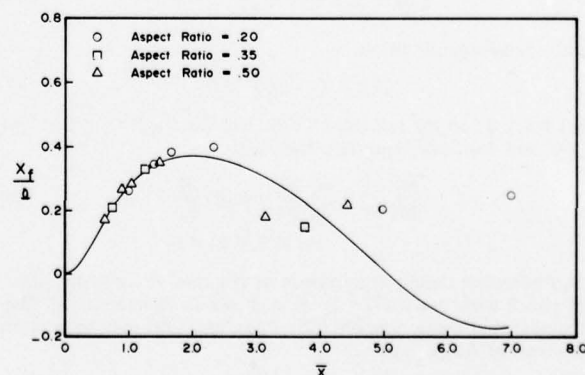


Fig. 4: Theoretical and experimental center of force



It is somewhat surprising to find experimental values in close agreement for aspect ratios as high as 0.50 with a theory based on a low aspect assumption. Without a free-surface experimental values for the center of force are known to move aft of the theoretical position given by low aspect ratio theory as the experimental aspect ratio increases. In the present case, however, no such trend is evident. One possible explanation is that a free-surface effect, not contained in the present formulation, tends to move the experimental hydrodynamic center of high aspect ratio plates forward. Theoretically, the flow is not affected by the plate ahead of the leading edge so that the pressure and potential are both zero on  $z = 0$  at the leading edge. The side force as calculated from (30) therefore receives only a small contribution from the upper portion of the plate near the leading edge. A free-surface disturbance grows downstream of the leading edge increasing the net force on the upper portion of the plate. In reality, the plate does influence the flow upstream of the leading edge so that the free-surface disturbance is already partially developed at the leading edge, which should move the center of force forward. Furthermore, the plate should influence the flow further forward as its draft increases so that this effect should be greatest for high aspect ratios.

The calculations reported in Reference [1] indicate that nonlinearities retained by the slender body formulation have a small effect on the side force and moment. Experimental nonlinearities are much larger and may be caused in part by flow separation effects.

#### Oscillation in Yaw and Sway

Reference [3] illustrates the extension of the linear solution for a truncated cylinder at a steady angle of attack to the case of oscillations in yaw and sway. A cylinder defined by

$$F(y, z) = 0 \quad 0 \leq x \leq L, \quad (34)$$

oscillates with frequency  $\omega$ . The cross velocity is written as

$$V_B(x, t) = b(x) e^{i\omega t} \quad 0 \leq x \leq L. \quad (35)$$

the function  $b(x)$  is a constant for the sway mode and a linear function for the yaw mode. It is convenient to use the non-dimensional length defined in (29) for the longitudinal spatial variables and to define some further nondimensional variables,

$$\begin{aligned} \bar{y} &= y/a, \quad \bar{z} = z/a, \quad \bar{t} = t(g/a)^{1/2} \\ \bar{\omega} &= \omega(a/g)^{1/2}, \quad \bar{s} = s(g/a)^{1/2}. \end{aligned} \quad (36)$$

The linearized body boundary condition is

$$\begin{aligned} \frac{\partial \varphi}{\partial \bar{y}} \frac{\partial F}{\partial \bar{y}} + \frac{\partial \varphi}{\partial \bar{z}} \frac{\partial F}{\partial \bar{z}} &= a b(\bar{x}) e^{i\omega t} H(\bar{x}) \frac{\partial F}{\partial \bar{y}} \\ \text{on } F(\bar{x}, \bar{y}, \bar{z}) &= 0, \end{aligned} \quad (37)$$

where  $H(\bar{x})$  is the step function. The potential must also satisfy the linearized free-surface condition,

$$\left( \frac{\partial}{\partial \bar{t}} + \frac{\partial}{\partial \bar{x}} \right)^2 \varphi = - \frac{\partial \varphi}{\partial \bar{z}}, \quad \bar{z} = 0 \quad (38)$$

and a radiation condition,

$$\varphi(\bar{x}, \bar{y}, \bar{z}) = 0, \quad \bar{x} < 0. \quad (39)$$

Let  $f(\bar{x}, \bar{y}, \bar{z})$  be the potential which satisfies conditions (38) and (39), and the body boundary condition,

$$\begin{aligned} \frac{\partial f}{\partial \bar{y}} \frac{\partial F}{\partial \bar{y}} + \frac{\partial f}{\partial \bar{z}} \frac{\partial F}{\partial \bar{z}} &= H(\bar{x}) \frac{\partial F}{\partial \bar{y}} \\ \text{on } F(\bar{x}, \bar{y}, \bar{z}) &= 0. \end{aligned} \quad (40)$$

This potential clearly corresponds to the case of a steady angle of attack such that  $a\alpha U = 1$ . It is shown in Reference [3] that the potential which satisfies (37), (38), and (39) may be written in terms of  $f(\bar{x}, \bar{y}, \bar{z})$  as

$$\begin{aligned} \varphi(\bar{x}, \bar{y}, \bar{z}, t) &= a e^{i\omega t} \left[ f(\bar{x}, \bar{y}, \bar{z}) b(\bar{x}) e^{-i\bar{\omega}\bar{x}} + \int_0^{\bar{x}} d\bar{q} f(\bar{q}, \bar{y}, \bar{z}) e^{-i\bar{\omega}\bar{q}} \left( i\bar{\omega} b(\bar{x} - \bar{q}) + b'(\bar{x} - \bar{q}) \right) \right], \end{aligned} \quad (41)$$

where  $b'(\bar{x})$  is the derivative of the function  $b(\bar{x})$ . The function  $g(\bar{x})$  is defined as

$$\begin{aligned} g(\bar{x}) &= - \frac{1}{2} \int d\bar{z} f(\bar{x}, \bar{y}, \bar{z}) \\ &= \frac{1}{4} C_Y(\bar{x}) \end{aligned} \quad (42)$$

where the integral in (42) is over the body boundary in the  $y$ - $z$  plane and  $C_Y(\bar{x})$  is the side force coefficient for a steady angle of attack as defined in (32). Then the side force acting on the body forward of  $\bar{x}$  is

$$\begin{aligned} Y(\bar{x}, \bar{t}) &= -2\rho U a^2 e^{i\omega t} (1 + i\bar{\omega} I) \left[ g(\bar{x}) b(\bar{x}) e^{-i\bar{\omega}\bar{x}} + i\bar{\omega} \int_0^{\bar{x}} d\bar{q} g(\bar{q}) e^{-i\bar{\omega}\bar{q}} b(\bar{x} - \bar{q}) + \int_0^{\bar{x}} d\bar{q} g(\bar{q}) e^{-i\bar{\omega}\bar{q}} b'(\bar{x} - \bar{q}) \right] \end{aligned} \quad (43)$$

where  $I$  is an integral operator defined by

$$I \cdot h(\bar{x}, \bar{y}, \bar{z}, \bar{t}) = \int_0^{\bar{x}} d\bar{q} h(\bar{q}, \bar{y}, \bar{z}, \bar{t}). \quad (44)$$

The corresponding moment is

$$N(\bar{x}, \bar{t}) = \int_0^{\bar{x}} \left( \frac{1}{2} L - x \right) \frac{\partial Y(\bar{x}, \bar{t})}{\partial \bar{x}} d\bar{x}. \quad (45)$$

The sway mode may be defined by the condition

$$b(\bar{x}) = 1. \quad (46)$$

The sway velocity and acceleration are

$$V_0(t) = e^{i\omega t} \quad \text{and} \quad \dot{V}_0(t) = i\omega e^{i\omega t} \quad (47)$$

Hydrodynamic derivatives for the sway mode are defined by

$$Y_v(\bar{L}, \bar{\omega}) e^{i\omega t} + Y_v'(\bar{L}, \bar{\omega}) (i\omega e^{i\omega t}) = Y(\bar{L}, \bar{t}) \quad (48)$$

$$N_v(\bar{L}, \bar{\omega}) e^{i\omega t} + N_v'(\bar{L}, \bar{\omega}) (i\omega e^{i\omega t}) = N(\bar{L}, \bar{t}). \quad (49)$$

These derivatives are commonly put into coefficient form,

$$Y_v' = Y_v \left( \frac{1}{2} \rho L^2 a U \right)^{-1}, \quad Y_v'' = Y_v' \left( \frac{1}{2} \rho L^2 a \right)^{-1} \quad (50)$$

$$N_v' = N_v \left( \frac{1}{2} \rho L^2 a U \right)^{-1}, \quad N_v'' = N_v' \left( \frac{1}{2} \rho L^2 a \right)^{-1}$$

Equations (43), (45), and (46) yield the solution,

$$Y_v'(\bar{x}, \bar{\omega}) + i\bar{\omega} \bar{x} Y_v''(\bar{x}, \bar{\omega}) = \epsilon Y^*(\bar{x}, \bar{\omega}) \quad (51)$$

$$N_v'(\bar{x}, \bar{\omega}) + i\bar{\omega} \bar{x} N_v''(\bar{x}, \bar{\omega}) = \epsilon \int_0^{\bar{x}} d\bar{q} \left( \frac{1}{2} - \frac{\bar{x}}{\bar{q}} \right) \frac{\partial Y^*(\bar{x}, \bar{\omega})}{\partial \bar{x}} \quad (52)$$

in terms of  $Y^*(\bar{x}, \bar{\omega})$  defined by

$$\begin{aligned} Y^*(\bar{x}, \bar{\omega}) &= -4 \left[ 1 + i\bar{\omega} I \right] \left( g(\bar{x}) e^{-i\bar{\omega}\bar{x}} + i\bar{\omega} \int_0^{\bar{x}} d\bar{q} g(\bar{q}) e^{-i\bar{\omega}\bar{q}} \right) \\ &= -4 g(\bar{x}) e^{-i\bar{\omega}\bar{x}} - 8i\bar{\omega} \int_0^{\bar{x}} d\bar{q} g(\bar{q}) e^{-i\bar{\omega}\bar{q}} \\ &\quad + 4 \bar{\omega}^2 \int_0^{\bar{x}} (\bar{x} - \bar{q}) g(\bar{q}) e^{-i\bar{\omega}\bar{q}} d\bar{q} \end{aligned} \quad (53)$$

Note that the function  $Y^*(\bar{x}, \bar{\omega})$  is independent of the aspect ratio so that all coefficients defined in (50) are proportional to  $\epsilon$ .

The yaw mode may be similarly analyzed. Let the yaw velocity and acceleration be

$$r(t) = \dot{a}(t) = e^{i\omega t} \quad (54)$$

and

$$\dot{r}(t) = i\omega e^{i\omega t}$$

To fully specify this mode it is necessary to define  $V_0(t)$ . The usual definition for maneuvering is

$$V_0(t) = 0 \quad (55)$$

so that

$$\dot{q}(t) = Ua(t). \quad (56)$$

The function  $b(x)$  for this mode is then

$$b(x) = \left(\frac{1}{2}L - x\right). \quad (57)$$

Hydrodynamic derivatives are defined by

$$\begin{aligned} Y_r(\bar{L}, \bar{\omega}) e^{i\omega t} + Y_{\dot{r}}(\bar{L}, \bar{\omega}) (i\omega e^{i\omega t}) &= Y(\bar{L}, \bar{\omega}) \\ N_r(\bar{L}, \bar{\omega}) e^{i\omega t} + N_{\dot{r}}(\bar{L}, \bar{\omega}) (i\omega e^{i\omega t}) &= N(\bar{L}, \bar{\omega}) \end{aligned} \quad (58)$$

with corresponding coefficients defined by

$$\begin{aligned} Y_r' &= Y_r \left(\frac{1}{2}\rho L^2 a U\right)^{-1}, \quad Y_{\dot{r}}' = Y_{\dot{r}} \left(\frac{1}{2}\rho L^3 a\right)^{-1} \\ N_r' &= N_r \left(\frac{1}{2}\rho L^3 a U\right)^{-1}, \quad N_{\dot{r}}' = N_{\dot{r}} \left(\frac{1}{2}\rho L^4 a\right)^{-1} \end{aligned} \quad (59)$$

These coefficients may be calculated from

$$\begin{aligned} Y_r'(\bar{x}, \bar{\omega}) + i\bar{\omega}\bar{x} Y_{\dot{r}}'(\bar{x}, \bar{\omega}) &= \epsilon Y^{**}(\bar{x}, \bar{\omega}) \\ N_r'(\bar{x}, \bar{\omega}) + i\bar{\omega}\bar{x} N_{\dot{r}}'(\bar{x}, \bar{\omega}) &= \epsilon \int_0^{\bar{L}} d\bar{x} \left(\frac{1}{2} - \frac{\bar{x}}{\bar{L}}\right) \frac{\partial Y^{**}(\bar{x}, \bar{\omega})}{\partial \bar{x}} \end{aligned} \quad (60)$$

The function  $Y^{**}(\bar{x}, \bar{\omega})$  is given by

$$\begin{aligned} Y^{**}(\bar{x}, \bar{\omega}) &= \frac{1}{2} Y^*(\bar{x}, \bar{\omega}) + 4 \left[1 + i\bar{\omega}L\right] \int_0^{\bar{L}} d\bar{q} g(\bar{q}) e^{-i\bar{\omega}\bar{q}} (1 + i\bar{\omega}\bar{L} - i\bar{\omega}\bar{q}) \\ &= \frac{1}{2} Y^*(\bar{x}, \bar{\omega}) + 4 \int_0^{\bar{L}} d\bar{q} g(\bar{q}) e^{-i\bar{\omega}\bar{q}} (1 + 2i\bar{\omega}(\bar{L} - \bar{q}) \\ &\quad - \frac{\bar{\omega}^2}{2} (\bar{L} - \bar{q})^2) \end{aligned} \quad (61)$$

### Flat Plate Oscillations

It has been demonstrated that the unsteady hydrodynamic coefficients for a truncated cylinder in lateral motion can be calculated from the solution for the cylinder at a constant angle of attack within the limits of linearized slender body theory. Coefficients for flat plate oscillations were calculated in this way from the values of  $g(\bar{x})$  for a flat plate as listed in Table 1. Figures (5) through (12) show these coefficients compared with experimental data from Reference [2] for a plate one meter in length at an aspect ratio of 0.20. Results are plotted against a nondimensional frequency,

$$\omega' = \bar{\omega} \epsilon^{1/2}$$

for various Froude numbers,

$$F_n = \bar{x} \epsilon^{-1/2}$$

These coefficients show good overall agreement. In particular the theory predicts Froude number and frequency effects fairly accurately. Strip theory estimates are given in Reference [3]. They are marginally adequate only at the lowest Froude number.

### Maneuvering of a Flat Plate

The results presented in the last section may be used to analyze the maneuvering characteristics of a surface-piercing body represented by a flat plate. The mass and moment of inertia of the plate will be neglected although they may be easily included (see Reference [4]). Consider the plate in a steady turn induced by a force  $F$  acting normal to the plate in the positive  $y'$  direction at the trailing edge. In a steady turn the accelerations,  $\dot{r}$  and  $\dot{v}$ , are both zero and the total force and moment acting on the plate must vanish,

$$\begin{aligned} Y_v v + Y_r r + F &= 0 \\ N_v v + N_r r - \frac{1}{2}LF &= 0. \end{aligned} \quad (64)$$

These conditions are satisfied for

$$r = UF' L^{-1} \left( \frac{N_v' + \frac{1}{2} Y_v'}{Y_v' N_r' - Y_r' N_v'} \right) \quad (65)$$

and

$$v = -UF' \left( \frac{\frac{1}{2} Y_r' + N_r'}{Y_v' N_r' - Y_r' N_v'} \right) \quad (66)$$

where

$$F' = F \cdot \left( \frac{1}{2} \rho L a U^2 \right)^{-1}. \quad (67)$$

A positive control force should turn the plate to starboard. The radius of the turning circle is

$$R = -U/r. \quad (68)$$

The ratio of this radius to the length of the plate is

$$R/L = -\frac{1}{F'} \left( \frac{Y_v' N_r' - Y_r' N_v'}{N_v' + \frac{1}{2} Y_v'} \right) \quad (69)$$

Hydrodynamic coefficients  $Y_v'$ ,  $Y_r'$ , and  $N_r'$  are plotted against Froude number for  $\epsilon = 0.20$  and  $\bar{\omega} = 0$  in Figures (13), (14), and (15). As a result of certain symmetries in the formulation,  $N_v'$  can be determined from the relationship valid for all  $\bar{x}$  and  $\bar{\omega}$ ,

$$N_v' + Y_r' = 0 \quad (70)$$

Figure (16) shows the parameter  $(R/L) F'$  for  $\epsilon = 0.20$  calculated from these coefficients. Note the decrease in turning radius at high Froude numbers.

The theoretical power loss induced by the turn is also of interest. The rate of work done by the plate is

$$\begin{aligned} P &= F \cdot \left( v - \frac{1}{2} L \dot{r} \right) \\ &= -UF' F' \left( \frac{1}{4} Y_v' + N_r' \right) \cdot \left( Y_v' N_r' - Y_r' N_v' \right)^{-1} \end{aligned} \quad (71)$$

The coefficient of power defined as

$$P' = P \cdot \left( \frac{1}{2} \rho L a U^3 \right)^{-1}$$

may be written as

$$P' = (F')^2 \frac{\left( \frac{1}{4} Y_v' + N_r' \right)}{(Y_v' N_r' - Y_r' N_v')} \quad (72)$$

so that

$$P' \cdot (R/L)^2 = (Y_r' N_v' - Y_v' N_r') \cdot \left( \frac{1}{4} Y_v' + N_r' \right) \left( N_v' + \frac{1}{2} Y_v' \right)^{-2} \quad (73)$$

Figure (17) shows  $P'(R/L)^2$  as a function of Froude number ( $\epsilon = 0.20$ ). This parameter also decreases at high Froude numbers.

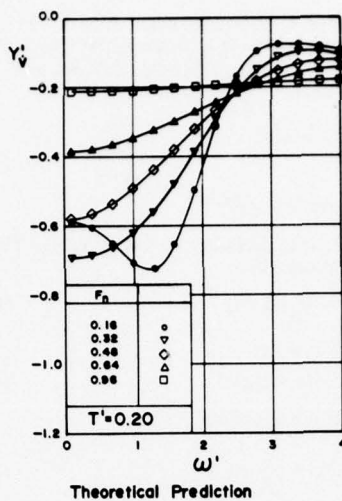
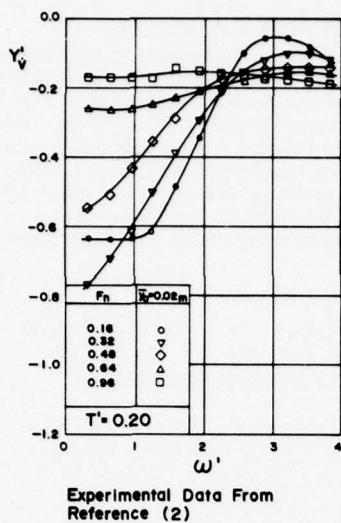


Fig. 5: Flat plate sway added mass

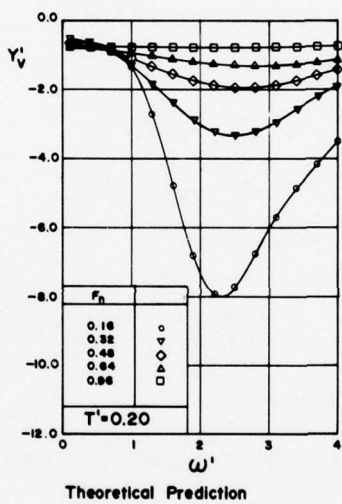
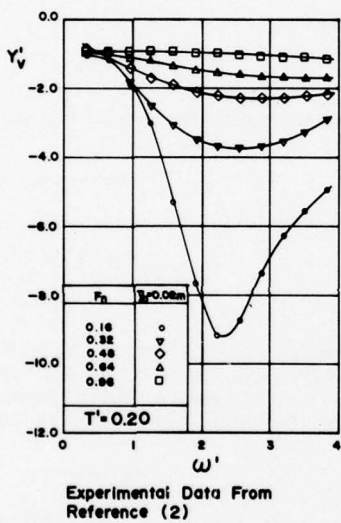


Fig. 6: Flat plate sway damping

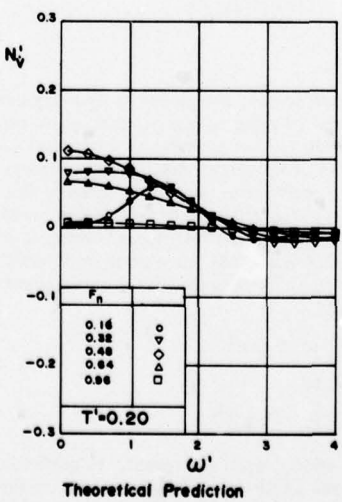
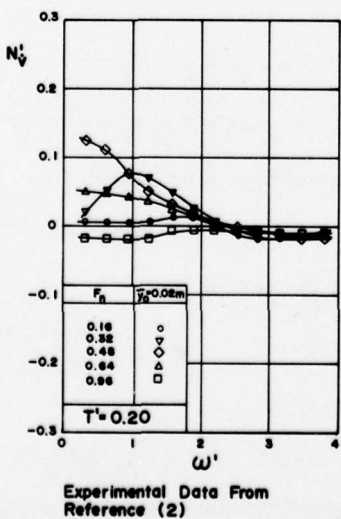


Fig. 7: Flat plate coupling of sway into yaw



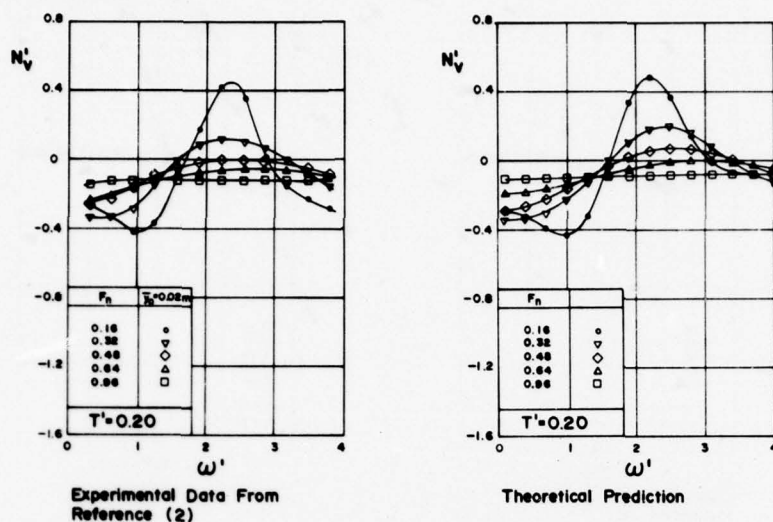


Fig. 8: Flat plate coupling of sway into yaw

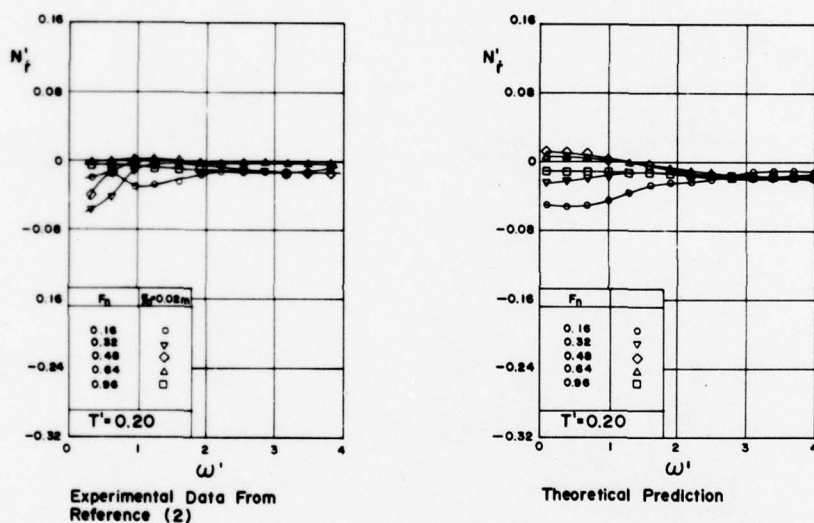


Fig. 9: Flat plate yaw added mass

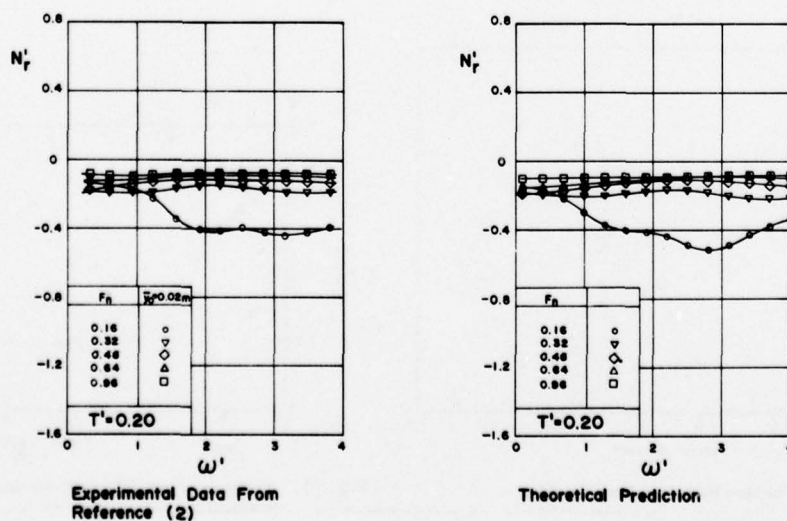


Fig. 10: Flat plate yaw damping

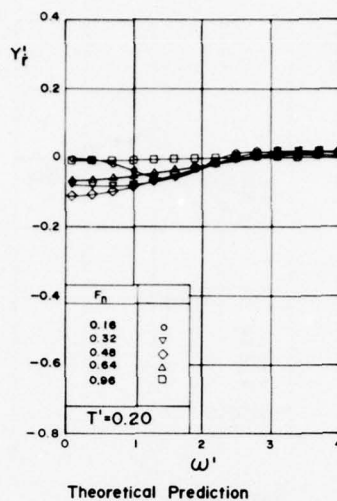
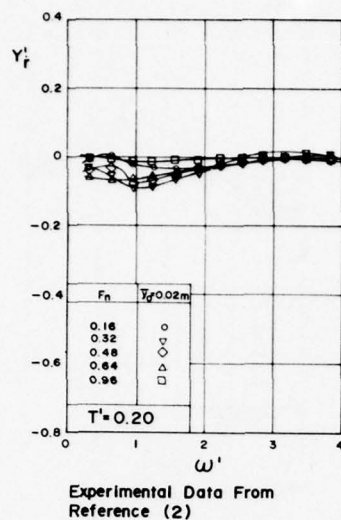


Fig. 11: Flat plate coupling of yaw into sway

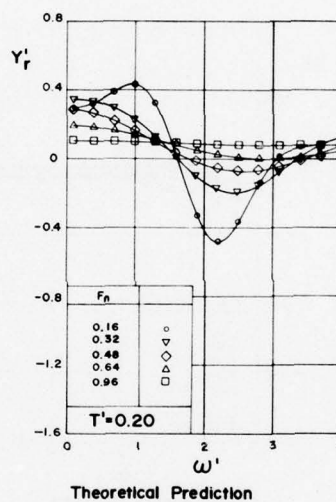
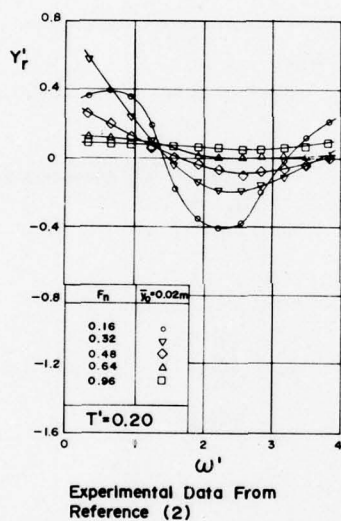
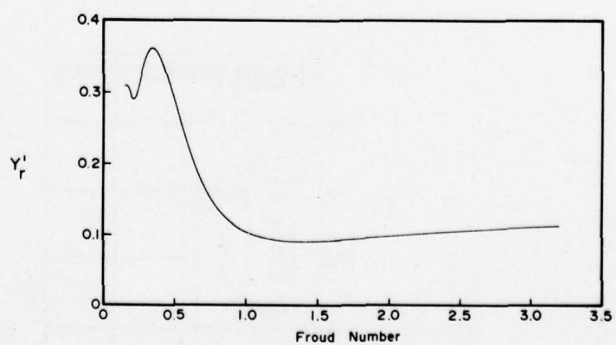
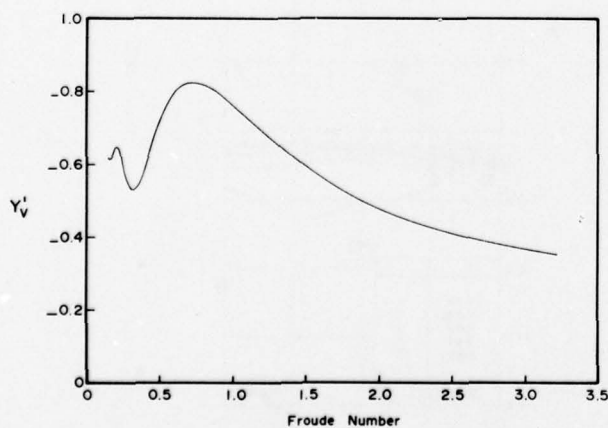
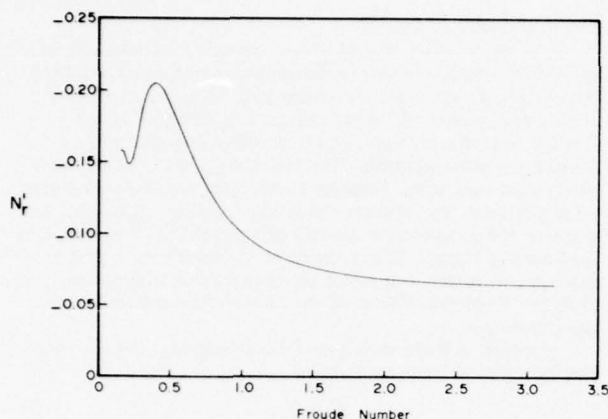
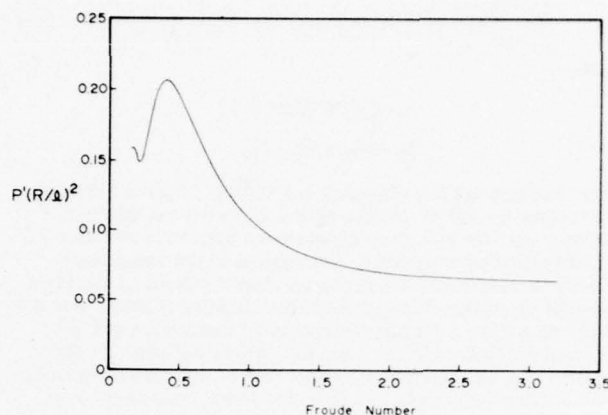
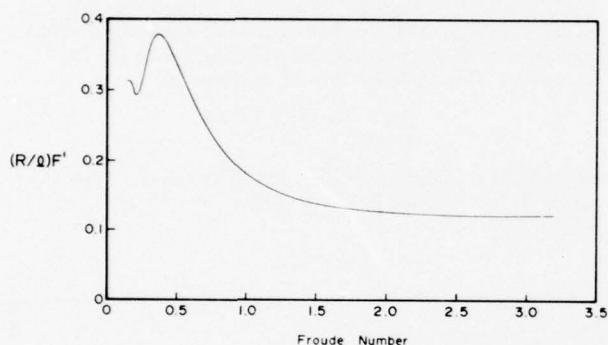


Fig. 12: Flat plate coupling of yaw into sway

Fig. 13: Sway damping for zero frequency limit  $\epsilon = 0.20$ Fig. 14: Coupling of yaw into sway for zero frequency limit  $\epsilon = 0.20$

Fig. 15: Yaw damping in zero frequency limit  $\epsilon = 0.20$ Fig. 17: Power loss in turn versus Froude number  $\epsilon = 0.20$ Fig. 16: Turning radius versus Froude number  $\epsilon = 0.20$ 

These results show moderate Froude number effects on maneuvering for Froude numbers less than  $0.20\epsilon^{1/2}$  followed by large changes in the transitional range  $0.20\epsilon^{1/2} < F_n < 0.60\epsilon^{1/2}$  and nearly constant characteristics at higher Froude numbers. Conventional craft which might be modeled by the plate would normally operate in the low Froude number range. Special craft such as catamarans could operate in the transitional range, however, because of large drafts and high Froude numbers.

#### Sculling by a Surface-Piercing Plate

The flat plate results can also be used to estimate the propulsive efficiency of a surface-piercing plate employed as a sculling device. The motion of such a plate may be described by

$$\begin{aligned} q(t) &= q_0 e^{i\omega t} \\ a(t) &= -a_0 e^{i\omega t} \end{aligned} \quad (74)$$

so that

$$\begin{aligned} r(t) &= -i\omega a_0 e^{i\omega t} \\ V_0(t) &= (i\omega q_0 + U a_0) e^{i\omega t}. \end{aligned} \quad (75)$$

The force normal to the plate is then

$$Y = \frac{1}{2} \rho a^2 U^2 \epsilon^{-1} a_0 \left[ \left( Y'_v - \left( \frac{\omega \ell}{U} \right)^2 \left( \frac{q_0}{\ell a_0} \right) Y'_v - Y'_r \right) \cos(\omega t) - \left( \frac{\omega \ell}{U} \right) \left( \frac{q_0}{\ell a_0} \right) Y'_v - Y'_r + Y'_v \sin(\omega t) \right]. \quad (76)$$

The corresponding moment about the plate midchord is

$$N = \frac{1}{2} \rho a^2 \ell U^2 \epsilon^{-1} a_0 \left[ \left( N'_v - \left( \frac{\omega \ell}{U} \right)^2 \left( \frac{q_0}{\ell a_0} \right) N'_v - N'_r \right) \cos(\omega t) - \left( \frac{\omega \ell}{U} \right) \left( \frac{q_0}{\ell a_0} \right) N'_v - N'_r + N'_v \sin(\omega t) \right]. \quad (77)$$

The thrust  $T(t)$  produced by the motion of the plate is the component of the normal force acting in the negative  $x$  direction

$$T(t) = -Y(t) \sin a(t). \quad (78)$$

For small  $a_0$  this may be approximated as

$$T(t) = a_0 Y(t) \cos(\omega t). \quad (79)$$

The mean thrust over a cycle is then

$$\bar{T} = \frac{1}{4} \rho a^2 U^2 a_0^2 \epsilon^{-1} \left[ Y'_v - \left( \frac{\omega \ell}{U} \right)^2 (\gamma^{-1} Y'_v - Y'_r) \right] \quad (80)$$

where the parameter  $\gamma$  is defined as

$$\gamma = \left( \frac{a_0 \ell}{q_0} \right). \quad (81)$$

This parameter specifies the axis of rotation of the plate. For example, the plate rotates about its leading edge when  $\gamma = 2.0$ . Since  $Y'_v$  is negative, a small, positive  $\gamma$  should produce positive thrust and a small, negative  $\gamma$  should produce negative thrust.

The rate of work done by the plate is

$$\begin{aligned} \dot{W} &= -Y(t) \dot{q}(t) - N(t) \dot{a}(t) \\ &= (q_0 Y(t) - a_0 N(t)) \omega \sin(\omega t). \end{aligned} \quad (82)$$

The mean rate of work is

$$\bar{W} = -\frac{1}{4} \rho a^2 U^3 a_0^2 \gamma^{-1} \epsilon^{-1} \left( \frac{\omega \ell}{U} \right)^2 \left[ Y'_v + \gamma^{-1} Y'_v - \gamma N'_v + \gamma N'_r \right]. \quad (83)$$

The resulting propulsive efficiency in the absence of frictional drag is

$$\eta = \bar{T} U \cdot \bar{W}^{-1}. \quad (84)$$

This efficiency may be expressed as a function of  $\gamma$ ,  $\omega$ , and  $\gamma$ ,

$$\eta(\bar{\ell}, \bar{\omega}, \gamma) = \frac{\gamma Y'_v - \gamma^2 (\bar{\omega} \bar{\ell})^{-2} Y'_v - \gamma^2 Y'_r}{\gamma Y'_v + Y'_v - \gamma^2 N'_v + \gamma^2 N'_r}. \quad (85)$$

Within the limitations of the theory, this efficiency is independent of aspect ratio. The value of  $\gamma$  which maximizes the efficiency, i.e.  $\partial \eta / \partial \gamma = 0$ , is



$$\gamma^* = \left[ (Y_v'^2 k_1^2 + Y_v' Y_v'^2 k_2)^{1/2} - Y_v' k_1 \right] (Y_v' k_2)^{-1} \quad (86)$$

where

$$k_1 = Y_v' + (\bar{\omega} \bar{L})^{-2} Y_v'$$

$$k_2 = k_1 + N_i - N_v$$

The resulting optimal efficiency is  $\eta^*(\bar{L}, \bar{\omega})$ . Figures (18) and (19) show  $\eta^*$  and  $\gamma^*$  plotted against  $\bar{\omega}$  for several values of  $\bar{L}$ . In each case the efficiency approaches a maximum of about 0.5 in the high frequency limit. Frequencies in this range correspond to wavelengths much shorter than the depth of the plate so that the energy lost in free-surface radiation is small. Another local maximum is evident for very small frequencies and low Froude numbers. Here too the free-surface radiation should be small. It is also interesting to note that at the higher frequencies the optimum  $\gamma$  is close to 2.0, which corresponds to rotation about the leading edge.

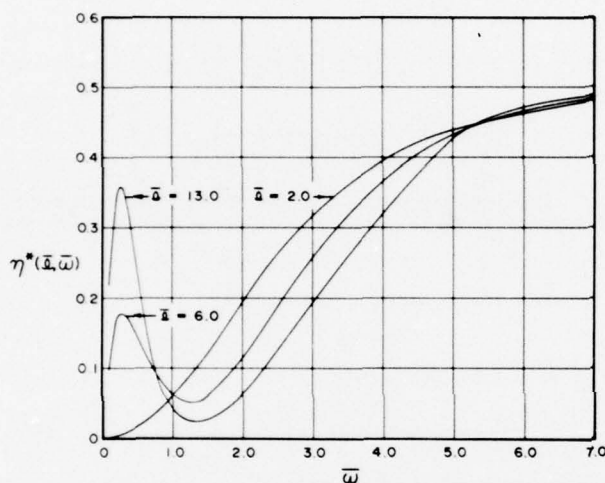


Fig. 18: Propulsive efficiency of flat plate sculling

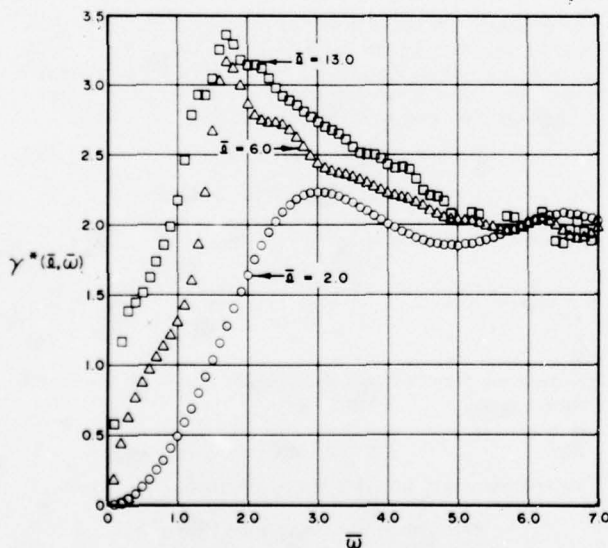


Fig. 19: Optimum value of parameter

### Effect of Finite Thickness

The methods developed in the preceding sections can be applied to a body of uniform cross-section and finite thickness. The thickness can affect the lateral hydrodynamic coefficients in two ways. First, the body creates a disturbance in the absence of lateral motion, which can interact with the flow induced by lateral motion. The free-surface may, for example, be elevated over some portions of the body and depressed over other portions, thus altering the lateral stability. Secondly, the shape of the cross-section directly influences the cross flow and the resulting forces. It was stated in the formulation that the first type of interaction is not accounted for in the present analysis. Thickness effects of the second type are easily calculated, however.

Consider a body with a uniform rectangular cross-section. Let the ratio of beam to draft be

$$B' = B/a \quad (87)$$

The linearized problem has been solved for  $0 \leq \bar{x} \leq 13.0$ , for  $B' = 1.0$  and  $B' = 2.0$  as well as for the flat plate case,  $B' = 0$ . Side force coefficients for these three cases are shown in Figure (20). They illustrate a general increase in the force coefficient with increasing thickness. At large values of  $\bar{x}$ , the coefficient should approach half of the two-dimensional added mass of a  $B \times 2a$  rectangle moving perpendicular to the  $2a$  dimension. This condition may be expressed as

$$\lim_{\bar{x} \rightarrow \infty} C_Y(\bar{x}) = K(b) \pi$$

where  $K(0) = 1.00$ ,  $K(1) = 1.36$ , and  $K(2) = 1.51$ . Numerical values for  $\bar{x} = 13.0$  are  $K(0) = 0.98$ ,  $K(1) = 1.36$ , and  $K(2) = 1.45$ .

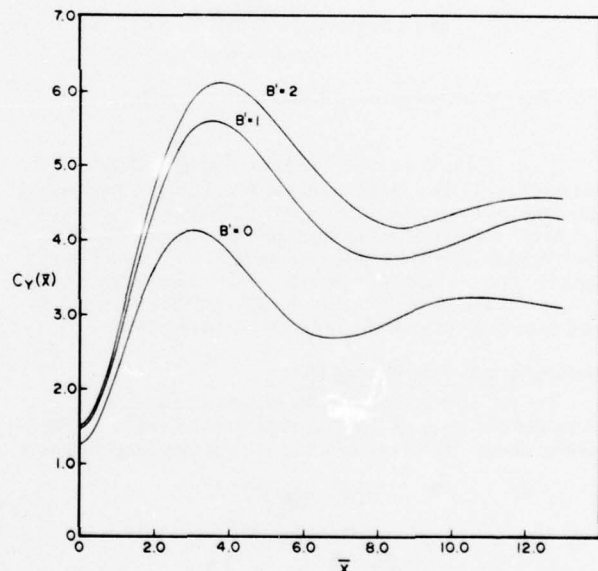


Fig. 20: Side force coefficient for rectangular sections

## References

- [1] Chapman, R.B., "Free-Surface Effects for Yawed Surface-Piercing Plates," to appear in *Journal of Ship Research*.
- [2] Van Den Brug, J.B., W. Beukelman, and G.J. Prins, "Hydrodynamic Forces on a Surface Piercing Flat Plate," Delft University of Technology, 1971.
- [3] Chapman, R.B., "Numerical Solution for Hydrodynamic Forces on A Surface-Piercing Plate Oscillating in Yaw and Sway," First International Conference on Numerical Ship Hydrodynamics, Oct. 1975.
- [4] Mandel, P., "Ship Maneuvering and Control," *Principles of Naval Architecture*, Society of Naval Architects and Marine Engineers, 1967.

TABLE 1  
Flat Plate Side Force Coefficient

x	4g(x)	x	4g(x)	x	4g(x)
0.00	1.2552	4.60	3.4811	9.20	3.0843
0.10	1.2671	4.70	3.4195	9.30	3.1040
0.20	1.3023	4.80	3.3585	9.40	3.1224
0.30	1.3599	4.90	3.2984	9.50	3.1395
0.40	1.4380	5.00	3.2396	9.60	3.1552
0.50	1.5350	5.10	3.1824	9.70	3.1694
0.60	1.6480	5.20	3.1271	9.80	3.1821
0.70	1.7746	5.30	3.0742	9.90	3.1933
0.80	1.9118	5.40	3.0234	10.00	3.2028
0.90	2.0571	5.50	2.9757	10.10	3.2107
1.00	2.2076	5.60	2.9308	10.20	3.2170
1.10	2.3610	5.70	2.8889	10.30	3.2216
1.20	2.5153	5.80	2.8512	10.40	3.2247
1.30	2.6681	5.90	2.8164	10.50	3.2263
1.40	2.8184	6.00	2.7834	10.60	3.2264
1.50	2.9648	6.10	2.7563	10.70	3.2251
1.60	3.1056	6.20	2.7314	10.80	3.2226
1.70	3.2397	6.30	2.7106	10.90	3.2189
1.80	3.3659	6.40	2.6933	11.00	3.2141
1.90	3.4835	6.50	2.6793	11.10	3.2085
2.00	3.5920	6.60	2.6692	11.20	3.2020
2.10	3.6916	6.70	2.6618	11.30	3.1949
2.20	3.7807	6.80	2.6577	11.40	3.1871
2.30	3.8595	6.90	2.6566	11.50	3.1789
2.40	3.9277	7.00	2.6585	11.60	3.1704
2.50	3.9856	7.10	2.6633	11.70	3.1618
2.60	4.0331	7.20	2.6707	11.80	3.1531
2.70	4.0706	7.30	2.6806	11.90	3.1444
2.80	4.0982	7.40	2.6928	12.00	3.1361
2.90	4.1164	7.50	2.7072	12.10	3.1280
3.00	4.1256	7.60	2.7234	12.20	3.1203
3.10	4.1264	7.70	2.7413	12.30	3.1129
3.20	4.1191	7.80	2.7608	12.40	3.1061
3.30	4.1044	7.90	2.7816	12.50	3.0998
3.40	4.0827	8.00	2.8035	12.60	3.0939
3.50	4.0545	8.10	2.8263	12.70	3.0886
3.60	4.0203	8.20	2.8499	12.80	3.0837
3.70	3.9809	8.30	2.8740	12.90	3.0792
3.80	3.9367	8.40	2.8985	13.00	3.0751
3.90	3.8882	8.50	2.9231		
4.00	3.8362	8.60	2.9476		
4.10	3.7812	8.70	2.9720		
4.20	3.7236	8.80	2.9959		
4.30	3.6646	8.90	3.0192		
4.40	3.6041	9.00	3.0419		
4.50	3.5427	9.10	3.0636		

# VELOCITY POTENTIALS OF SUBMERGED BODIES NEAR A FREE SURFACE-APPLICATION TO WAVE-EXCITED FORCES AND MOTIONS

by M. S. Chang and P. C. Pien

David W. Taylor Naval Ship Research and Development Center  
Bethesda, Maryland, USA

## ABSTRACT

An inner-potential doublet-distribution method for calculating the velocity potential around bodies in a uniform flow is extended to the case of bodies in an arbitrary potential flow field. Numerical examples are given for bodies moving beneath surface waves. The wave forces and moments are calculated for bodies in uniform motion and for a body undergoing prescribed maneuvers. The results indicate that the present method can obtain accurate predictions of forces and moments with a small number of control panels. Wave-excited motions are also calculated. The influence of the exciting motions on the exciting forces is discussed and the instabilities of the motions in regular and irregular waves are demonstrated.

## INTRODUCTION

In the calculation of the velocity potential on the surface of a three-dimensional body by an inner potential doublet-distribution method, Pien<sup>1</sup> and Chang and Pien<sup>2</sup> have shown that accurate results can be obtained without dividing the body into very small elements. Both infinite-fluid and free-surface flow problems were considered. For a sphere moving in an infinite fluid Pien showed that the velocity potential could be computed by the inner-potential doublet-distribution method to within a 2-percent error using only 96 panels, while the same accuracy required 1344 panels by the sink-source distribution method.<sup>3</sup> In view of the success<sup>2</sup> of the inner-potential doublet-distribution method in solving problems associated with a body moving under a calm free-surface, the method is extended here to the problem of a submerged body moving under waves on a free-surface. The paper is devoted to the analysis of the exciting forces for both captured and free bodies under arbitrary free-surface waves.

In analyzing the forces on a submerged body moving in a given potential field such as regular waves, the forces are separated into two groups: the exciting forces and the restoring forces. In the linearized theory, the exciting forces have been evaluated with the unsteady motions of the body neglected and the restoring forces have been calculated with the incident waves neglected. Cummins<sup>4</sup> calculated the exciting forces for a slender body of revolution by approximating the body as a system of singularities distributed along its axis. His approximation can be readily evaluated, and can be applied to arbitrary bodies of revolution with large fineness ratios. Havelock<sup>5</sup> has obtained the exciting forces for a spheroid from integration of the pressure over the surface on the spheroid. Extension of Havelock's method to other bodies was considered impractical.<sup>6</sup> Newman<sup>6</sup> generalized the "Haskind relations"<sup>7</sup> for the exciting forces in waves, including the effects of constant forward speed, and applied the results to the case of a submerged ellipsoid. Nevertheless, his analysis can be useful only if the far field asymptotic behavior of the radiation potential due to the oscillatory motion of the body is known. In cases where the far field radiation potentials are not known beforehand, the method of Newman<sup>6</sup> requires extensive computations. The recent development of numerical methods for calculation of potential flows enables one to obtain the velocity potential satisfying the exact body boundary condition. The velocity potential on the body surface can be obtained easily and forces can be obtained from integration of the pressure on the body surface without difficulty.<sup>2</sup> The use of generalized "Haskind relations" has become unnecessary. This paper will present an evaluation of the exciting forces on a submerged body moving under waves from a direct

integration of the body pressure distribution obtained from the inner-potential doublet-distribution method.<sup>2</sup>

In past analyses of the motions of a submerged body near a free-surface, attention has been focused on the restoring force and damping due to the outgoing surface waves created by the oscillatory motion of the body. Considerable work has been done in this area by Ursell,<sup>8</sup> Korvin-Kroukovsky and Jacobs,<sup>9</sup> Hishida,<sup>10</sup> Havelock,<sup>11,12</sup> and Newman.<sup>13</sup> In general, the damping coefficients were derived for either special bodies or approximate body boundary conditions. The present method calculates the damping coefficient for a deeply submerged arbitrary body. Calculations for a spheroid are compared with those of Havelock.<sup>11</sup>

In analyzing the motion of a deeply submerged body the damping forces may be neglected. This paper presents the time series of wave excited motions, neglecting free surface damping and viscous effects.

The next section gives the fundamentals of the method employed. Then, numerical computations of the exciting forces, damping coefficients, and motions of selected bodies, will be presented and compared with the corresponding results of others. Finally, the wave-coupling effect on the motions of a body will be discussed. While for comparison purposes, the results presented are limited to bodies having special geometries, the basic numerical method developed is applicable to arbitrary three-dimensional bodies.

## FORMULATION FOR VELOCITY POTENTIAL

In the analysis of forces on a submerged body in steady motion under a linearized free surface, Chang and Pien<sup>2</sup> have shown that the velocity potential,  $\phi_0$ , on the body surface  $S_B$ , can be expressed simply by

$$\phi_0(P) = D(P) + \phi_i(P) \quad (1)$$

where  $\phi_i$  is the velocity potential defined inside the body surface  $S_B$ , and its normal derivative,  $\partial\phi_i(P)/\partial n$ , is equal to the prescribed normal velocity on the body surface.  $D(P)$  is the normal doublet distribution on the body surface and it is the solution of

$$\phi_i(P) = \frac{1}{4\pi} \iint_{S_B} D(Q) \partial G(P, Q) / \partial n_Q dS, \quad P \text{ on } S_B \quad (2)$$

where  $G(P, Q)$  is the Kelvin singularity for a moving source with  $Q$  denoting the field point and  $P$  denoting the singular point;  $n_Q$  denotes the unit normal vector at  $Q$  on  $S_B$ . It was demonstrated in reference 2 that numerical solutions to equation (2)



can be obtained without extensive computations. Successful applications of this model were made to the calculation of the wave resistance and lift of submerged two and three-dimensional bodies. In the analysis of time-dependent problems, it will be shown in the following that the velocity potential can again be expressed by equation (1) while equation (2) must be modified to reflect the influence of the time dependence of the free surface. In the case of periodic motions, equation (2) does not change form but  $G(P, Q)$  must be replaced by the Kelvin singularity for an oscillatory source. For the problem of a body accelerating from rest, equation (2) will become a convolution integral with respect to time.

Before deriving the velocity potential, we first define the quantities necessary in the derivation. A submerged body is defined by its surface  $S_B$  with unit normal vector  $\hat{n}$  directed into the fluid region;  $(x, y, z)$  and  $(X, Y, Z)$  denote the space coordinates with respect to axes fixed in space and the body, respectively; the  $z$ -axis is taken positive upwards. Initially, the two coordinate systems coincide. The fluid region bounded by  $S_B$ , the free surface,  $S_f$ , and surfaces at infinity,  $S_o$ , is denoted by  $R_o$ .  $R_i$  denotes the space inside surface  $S_B$ ;  $\phi_o$  and  $\phi_i$  are the velocity potentials in  $R_o$  and  $R_i$ , respectively;  $g$  is the acceleration of gravity.

Let  $G_1$  and  $G_2$  be two given harmonic functions defined in both  $R_o$  and  $R_i$ . We let

$$G_1(P, Q) = \frac{1}{r} - \frac{1}{r_1} \quad (3)$$

which is singular at  $P$ , and

$$G_2(P, Q, t, t_1) = \int_0^\infty dk (gk)^{1/2} \sin(gk)^{1/2} (t - t_1) \times \exp \{k[z(t) - z_0(t)]\} J_0(kR(t, t_1)) \quad (4)$$

which has a finite derivative at  $P$ ;  $(x(t), y(t), z(t))$  and  $(x_0(t_1), y_0(t_1), z_0(t_1))$  denote the positions of  $P$  and  $Q$ , respectively;  $t$  and  $t_1$  (with  $t \geq t_1$ ) are the time parameters,  $J_0$  is a Bessel function of the first kind and

$$r^2 = (x(t) - x_0(t_1))^2 + (y(t) - y_0(t_1))^2 + (z(t) - z_0(t_1))^2$$

$$r_1^2 = (x(t) - x_0(t_1))^2 + (y(t) - y_0(t_1))^2 + (z(t) + z_0(t_1))^2$$

and

$$R^2(t, t_1) = (x(t) - x_0(t_1))^2 + (y(t) - y(t_1))^2$$

From Green's theorem one has,

$$-\frac{1}{4\pi} \left\{ \iint_{S_B + S_o + S_f} [G_1(P, Q) \partial \phi_o(Q, t) / \partial n - \phi_o(Q, t) \partial G_1(P, Q) / \partial n] dS \right\} = \begin{cases} \phi_o(P), & P \in R_o \\ 0, & P \in R_i \end{cases} \quad (5)$$

$$\frac{1}{4\pi} \left\{ \iint_{S_B} [G_1(P, Q) \partial \phi_i(Q, t_1) / \partial n - \phi_i(Q, t_1) \partial G_1(P, Q) / \partial n] dS \right\} = \begin{cases} 0, & P \in R_o \\ \phi_i(P), & P \in R_i \end{cases} \quad (6)$$

$$-\frac{1}{4\pi} \left\{ \iint_{S_B + S_o + S_f} [G_2(P, Q, t, t_1) \partial \phi_o(Q, t_1) / \partial n - \phi_o(Q, t_1) \partial G_2(P, Q, t, t_1) / \partial n] dS \right\} = 0, \quad P \in R_o \cup R_i \quad (7)$$

and

$$\frac{1}{4\pi} \left\{ \iint_{S_B} [G_2(P, Q, t, t_1) \partial \phi_i(Q, t_1) / \partial n - \phi_i(Q, t_1) \partial G_2(P, Q, t, t_1) / \partial n] dS \right\} = 0, \quad P \in R_o \cup R_i \quad (8)$$

Addition of (5) and (6) gives

$$\frac{1}{4\pi} \left\{ \iint_{S_B} [\phi_o(Q) - \phi_i(Q)] \partial G_1(P, Q) / \partial n dS - \iint_{S_i + S_o} [G_1(P, Q) \partial \phi_o(Q) / \partial n - \phi_o(Q) \partial G_1(P, Q) / \partial n] dS \right\} = \begin{cases} \phi_o(P), & P \in R_o \\ \phi_i(P), & P \in R_i \end{cases} \quad (9)$$

In obtaining this result, the condition that

$$\partial \phi_o / \partial n = \partial \phi_i / \partial n$$

on the body surface has been used. Addition and integration over time of (7) and (8) give

$$\frac{1}{4\pi} \int_0^t \left\{ \iint_{S_B} [\phi_o(Q, t_1) - \phi_i(Q, t_1)] \partial G_2(P, Q, t, t_1) / \partial n dS - \iint_{S_i + S_o} [G_2(P, Q, t, t_1) \partial \phi_o(Q, t_1) / \partial n - \phi_o(Q, t_1) \partial G_2(P, Q, t, t_1) / \partial n] dS \right\} dt_1 = 0, \quad P \in R_i \cup R_o \quad (10)$$

It can be proved<sup>14</sup> that at any given instant of time  $t$ , the second integrals in (9) and (10) are equal but of opposite sign. Thus, from (9) and (10) one has

$$\frac{1}{4\pi} \left\{ \iint_{S_B} [\phi_o(Q, t) - \phi_i(Q, t)] \partial G_1(P, Q) / \partial n dS + \int_0^t \iint_{S_B} [\phi_o(Q, t_1) - \phi_i(Q, t_1)] \partial G_2(P, Q, t, t_1) / \partial n dS dt_1 \right\} = \begin{cases} \phi_o(P, t), & P \in R_o \\ \phi_i(P, t), & P \in R_i \end{cases} \quad (11)$$

On the free surface  $\phi_o$  satisfies

$$\partial^2 \phi_o / \partial t^2 + g \partial \phi_o / \partial z = 0$$

and

$$\phi_o = \partial \phi_o / \partial t = 0 \quad \text{at } t = 0$$

Equation (11) implies that

$$\phi_o(P, t) = D(P, t) + \phi_i(P, t), \quad P \text{ on } S_B \quad (12)$$

with  $D$  being the solution of

$$\begin{aligned} & \frac{1}{4\pi} \left\{ \iint_{S_B} D(Q, t) \partial G_1(P, Q) / \partial n \, dS \right. \\ & \left. + \int_0^t \iint_{S_B} D(Q(t_1), t_1) \partial G_2(P(t), Q(t_1), t, t_1) / \partial n \, dS \, dt_1 \right\} \\ & = \phi_1(P, t), \quad P \text{ on } S_B \end{aligned} \quad (13)$$

Thus, the velocity potential on the body surface can be obtained from the given inner velocity potential in the same manner as for steady motion. The calculation of forces on the body surface is thus the same as that for steady motion. (For details, see reference 2) However, due to the presence of the time integral in equation (13), the numerical solution for an arbitrary unsteady motion is very difficult even with this representation. In the following sections, we will present the calculation of unsteady forces on an arbitrary body satisfying the exact body boundary condition but with either an approximated free surface condition or special motions wherein the time integration in equation (13) is simplified.

### DEEPLY-SUBMERGED BODY UNDER WAVES

The easiest way out of the complicated time integration in equation (13) is simply to drop it completely. This is physically meaningful when one considers a body moving deeply under waves; in this case the major forces acting on the body are the exciting forces due to the incoming waves. Here, the forces due to body-generated free-surface disturbances are small in comparison to the exciting forces. The approximate wave exciting forces obtained by Cummins<sup>4</sup> employed the same simplification, in addition to the slender body approximation. However, Havelock's analysis satisfied the boundary condition on the spheroid exactly. The results of Newman<sup>6</sup> for ellipsoids were obtained from generalized "Haskind relations" through the use of an approximate radiation potential in the far field. However, it can be shown that the results are equivalent to utilization of a simplified Kernel and an exact boundary condition on the ellipsoids. The following analysis outlines the fundamentals of the present method for evaluating the wave exciting forces on an arbitrary captive body and the motions of a free body under waves, assuming that the time integration in equation (13) may be neglected.

Let  $\phi_1$  be the initial potential field of the fluid in the absence of the body. With  $\phi_i = -\phi_1 + \phi_{iM}$  it follows that

$$\partial \phi_0 / \partial n = \partial \phi_1 / \partial n = -\partial \phi_1 / \partial n + \partial \phi_{iM} / \partial n$$

and

$$\partial(\phi_0 + \phi_1) / \partial n = \partial \phi_{iM} / \partial n$$

on  $S_B$ , where

$$\phi_{iM} = \sum_{N=1}^3 (U_N \phi_N + \Omega_N \chi_N)$$

is the inner velocity potential;  $(U_1, U_2, U_3)$  and  $(\Omega_1, \Omega_2, \Omega_3)$  are the translatory velocity and rotational velocity of the body, respectively, and  $(\phi_1, \phi_2, \phi_3)$  and  $(\chi_1, \chi_2, \chi_3)$  are the corresponding inner velocity potentials for unit body velocities  $U_N$  and  $\Omega_N$ , respectively (for details see reference 2). Hence,  $\phi_0 + \phi_1$  is the velocity potential of the fluid when the body boundary condition is specified by  $\partial \phi_{iM} / \partial n$ . It follows from equation (12) and the definition of  $\phi_1$  that  $\phi_0 + \phi_1$  on the body surface becomes

$$\phi_0 + \phi_1 = D + \phi_i + \phi_1 = D + \phi_{iM} \quad (14)$$

Since  $\phi_{iM}$  and  $G_1$  are known once the body surface  $S_B$  is defined, the numerical solution of  $D$  from equation (13) is straight forward for a simplified Kernel. The numerical solution of  $\phi_0 + \phi_1$  on an arbitrary body moving in a given potential field can be obtained with no complications.

The velocity potential of the wave field is written in the form

$$\phi_1 = \int_0^\infty \int_{-\pi}^\pi S(\omega, \theta) \exp \{ i[k(x \cos \theta + y \sin \theta) - \omega t] + kz \} d\theta d\omega$$

or

$$\phi_1 = \sum_N \sum_M S(\omega_N, \theta_M) \exp \{ i k_N (x \cos \theta_M + y \sin \theta_M) - \omega_N t \} + k_N z \} \Delta \theta_M \Delta \omega_N$$

where  $\omega$  is the wave frequency,  $k = \omega^2/g$  is the wave number,  $\theta$  is the direction of wave propagation, and  $S(\omega, \theta)$  is the complex amplitude of the wave potential. The total velocity potential  $\phi_0 + \phi_1$  on a body moving sufficiently deep under this wave field is given by equation (14), i.e.

$$\phi_0(P, t) + \phi_1(P, t) = D(P, t) + \phi_{iM}(P, t), \quad P \text{ on } S_B$$

where from equation (13),  $D$  is the solution of

$$\begin{aligned} & - \int_0^\infty \int_{-\pi}^\pi S(\omega, \theta) \exp \{ i[kx(P, t) \cos \theta + ky(P, t) \sin \theta - \omega t] \\ & + kz(P, t) \} d\theta d\omega + \phi_{iM}(P, t) \\ & = \frac{1}{4\pi} \iint_{S_B} D(Q, t) \frac{\partial}{\partial n_Q} \left( \frac{1}{r_{PQ}} \right) dS(Q), \quad P \text{ on } S_B \end{aligned} \quad (15)$$

The time derivatives of equations (14) and (15) are, respectively,

$$\frac{\partial}{\partial t} [\phi_0(P, t) + \phi_1(P, t)] = \frac{\partial}{\partial t} [D(P, t) + \phi_{iM}(P, t)], \quad P \text{ on } S_B \quad (16)$$

and

$$\begin{aligned} & - \int_0^\infty \int_{-\pi}^\pi \left\{ i \left[ -\omega + k \cos \theta \frac{\partial x}{\partial t} + k \sin \theta \frac{\partial y}{\partial t} \right] + k \frac{\partial z}{\partial t} \right\} \exp \{ i[kx(P, t) \cos \theta \\ & + y(P, t) \sin \theta] - \omega t \} + kz(P, t) \} d\theta d\omega + \partial \phi_{iM}(P, t) / \partial t \\ & = \frac{1}{4\pi} \iint_{S_B} \partial D(Q, t) / \partial t \frac{\partial}{\partial n_Q} \left( \frac{1}{r_{PQ}} \right) dS(Q), \quad P \text{ on } S_B \end{aligned} \quad (17)$$

It is seen from equations (16) and (17) that the acceleration potential,  $\partial[\phi_0(P, t) + \phi_1(P, t)] / \partial t$  is a function of not only the acceleration potential of the relative field, i.e. the terms associated with  $\omega$  and with the motion  $\partial \phi_{iM} / \partial t$ , but is also a function of the coupling between the motion and the wave field, i.e. the terms associated with the product of  $k$  and  $\partial x / \partial t$ , etc. By examining equation (17) one sees that, for a captive body moving in a wave field (where the positions and motions of the body are specified) the contribution from the waves to the acceleration potential is the linear superposition of contributions from each individual wave. However, for a free body, a coupling effect between the waves is present through both the position of the body and its motions.

In an irrotational field, the pressure,  $p$ , on a body surface can be expressed in terms of the velocity potential through Bernoulli's equation,

$$p = \rho \left[ \partial(\phi_0 + \phi_1) / \partial t - \frac{1}{2} q_r^2 + \frac{1}{2} V^2 + c(t) \right] \quad (18)$$

where  $\rho$  is the density of the fluid,  $q_r$  and  $V$  are the magnitudes of the velocities of the fluid relative to the moving body surface and the velocity of the body surface, respectively, and  $c(t)$  is the Bernoulli constant which contributes no net force to the body. Equation (18) can be expressed in terms of  $D$ , in the same form as for steady translation motions,<sup>2</sup> i.e.

$$p(t) = \rho \left[ \partial(D + \phi_{iM}) / \partial t - \frac{1}{2} | -\nabla_s(D + \phi_{iM}) - \vec{V}_s |^2 + \frac{1}{2} V^2 + c(t) \right] \quad (19)$$

where  $\nabla_s$  is the gradient along the body surface and  $\vec{V}_s$  is the velocity tangent to the body surface. The total force acting on the body can thus be obtained from integration of equation (19) over the body surface after the distribution function  $D$  is obtained from (14) and (15).

## NUMERICAL RESULTS

With the previously discussed formulation, a computer program was developed for calculating both the hydrodynamic forces and the wave-excited motions of a submerged body. Some sample calculations as well as comparisons with the corresponding results of others are given in the following.

### a. Hydrodynamic Forces and Moments

Havelock<sup>5</sup> investigated wave-excitation forces and moments for a spheroid from integration of the pressure on the body surface. To the first order of wave-slope parameter, the forces and moments on a spheroid moving with constant speed under a train of regular waves are given in reference 5. The heaving force,  $F_z$ , pitch moment,  $F_{zz}$ , and yaw moment,  $F_{yy}$ , for a spheroid of fineness ratio 0.3 were calculated according to Havelock.<sup>5</sup> The solid lines in Figure 1 are for the spheroid moving under a wave whose wave length,  $\lambda$ , is twice the length of the spheroid,  $L$ . In the figure the forces and moments are presented as a function of incident wave angle,  $\beta$ , for two Froude numbers  $F = u/\sqrt{gL} = 0$  and 0.5. They are plotted in the non-dimensional form of

$$\begin{aligned} F_z / [\rho g A^2 L (h/\lambda) \exp(-2\pi H/\lambda)], \\ F_{zz} / [\rho g A^2 L^2 (h/\lambda) \exp(-2\pi H/\lambda)], \end{aligned}$$

etc, where  $A^2$  is the cross section area of the spheroid,  $h$  is the wave height, and  $H$  is the submergence depth of the center of the spheroid. The forces and moments on the spheroid have also been calculated from the present computer program. The numerical results, obtained from representing the spheroid by sixty-eight panels, are plotted in Figure 1 as symbols. In comparison with the results calculated by Havelock, the present results are very good at zero Froude number for both force and moments. At a Froude number of 0.5 the comparison between computed heaving forces at larger  $\beta$  is not as good as that at zero Froude number while the comparisons between moments agree quite well.

The present method permits calculation of the pressure with the inclusion of the pressure contributed from the perturbation velocity squared term retained in Bernoulli's equation. The force associated with this pressure is in the form of the square of the wave-slope parameter, i.e.,  $(h/\lambda)^2 \exp(-4\pi H/\lambda)$ . Thus, the second-order contribution to the force is small if the wave-slope parameter is small. However, the ratio of this force to the first-order force may not be small, because at certain wave lengths and Froude numbers, while the first-order force approaches zero, the second-order force does not. The second-order heave force contributes a mean lift. It is called "suction force." We have calculated the heave force with the inclusion of second-order pressure. It is also plotted in Figure 1 for  $F = 0.5$  and  $H/L = 0.3$ . It is seen that the difference between the second-order force and the first-order force ranges from a couple of percent to fifteen percent for the cases calculated. This difference will become smaller when the depth of submergence increases, and become larger when the Froude number increases.

Cummins<sup>4</sup> calculated the hydrodynamic forces on slender bodies of revolution. One of the bodies he used to demonstrate his technique is shown as Figure 2a. This is a slightly non-symmetric body and is generated from Legendre polynomials.<sup>4</sup> Non-dimensional values of surge and heave forces on this body of revolution were calculated by Cummins and are shown as solid lines in Figures 2b and 2c, respectively. Both of the curves shown are independent of Froude number. The corresponding nondimensional forces calculated from the present method with sixty-eight panels are plotted as symbols in the same figures. The present calculations of surge force also show that surge force is independent of Froude number. The surge forces, in

comparison with the slender body approximation of Cummins, are consistently higher. The surge-force discrepancy between the two calculations increases from a few percent at wave lengths larger than the body length to fifteen percent at wave lengths equal to the body length. The discrepancy increases further with decreasing wave length, over the range where the surge forces become small. The present calculations of heave forces do not fall on one single curve as is predicted from the slender-body approximation. The results obtained for Froude numbers -0.5, 0, and 0.5 are plotted in Figure 2c. At first-order, the non-dimensional heave force is weakly dependent on Froude number for long waves. In comparison with the results of the slender-body approximation, the first-order heave forces are a little lower for long waves and higher for short waves. The total second-order heave force in Figure 2c shows strong Froude-number dependence for short wave lengths. This is because of the nondimensional factor  $(1 + U/2c)$  where  $c$  is the phase velocity of the waves. For a given wave, this factor decreases with decreasing speed  $U$ . Thus, the second-order non-dimensional force, which is independent of  $U$ , is amplified for shorter waves (i.e., smaller  $c$ ) at a negative Froude number of -0.5. Experimental values of heave force for a body similar to that shown in Figure 2a were compared to the results of the slender-body approximation.\* It is included in this paper as Figure 2d. The experimental results agree with the slender-body approximation quite well, but do show a tendency of being higher than the theoretical curve for values of  $\pi/L$  larger than 1.5. The comparison of the slender-body approximation to the experimental results, Figure 2d, resembles the comparison with predictions by the present calculation method, Figure 2c. Nevertheless, when considering possible experimental errors, we are not able to draw any definite conclusions.

The previous calculations are for a body moving uniformly under waves. The present method can also calculate the forces and moments on a body moving with time-dependent motions. To demonstrate the capability of calculating the forces on a body during a maneuver, the forces and the moments were evaluated for a spheroid turning with considerable horizontal angular velocity. Figure 3 shows the trajectory and hydrodynamic forces and moments on this spheroid maneuvering under a wave propagating in the x-direction with  $h/\lambda = 0.05$  and  $\lambda/L = \pi$ . The spheroid was located  $0.3L$  beneath the free surface and its fineness ratio was 0.3. The spheroid was turning in the horizontal plane with constant translational velocity of 0.25 at zero pitch angle. The yaw velocity,  $\omega_3$ , of the spheroid was specified by:

$$\Omega_3 = \begin{cases} 0 & (2g/L)^{1/2} t \leq -24 \quad \text{and} \quad (2g/L)^{1/2} t \geq -8 \\ 0.05 \sin [\pi(2g/L)^{1/2} t/8 + \pi], & -24 \leq (2g/L)^{1/2} t \leq -20 \\ -0.05 \sin [\pi(2g/L)^{1/2} t/8 + \pi], & -12 \leq (2g/L)^{1/2} t \leq -8 \\ 0.05, & \text{otherwise} \end{cases}$$

The spheroid, thus, was turned from following the wave to approximately 142.5 degrees to the wave. The time series of the y-component of force and moment clearly reflect this change of headings;  $F_y$  and  $F_{zz}$  are identically zero in the beginning, because the spheroid is following the wave. As the spheroid turns, the amplitudes of  $F_y$  and  $F_{zz}$  increase with decreasing heading angle. The changes in  $F_x$ ,  $F_z$  and  $F_{yy}$  are not significant during this maneuver. This is because these forces and moments vary slowly with heading when a spheroid is under long waves and at large heading angles.

### b. Wave-excited Motions

The presence of wave forces will introduce body motions unless external forces are applied. These wave perturbing motions can be evaluated from the equations of motion once the exciting forces are calculated. The perturbing motions and the wave exciting forces, in general, have to be calculated simultaneously. Since the wave exciting forces depend on the positions and motions of the body relative to the waves, they can only be calculated after one knows the perturbing motions of the body.

The present computer program calculates the wave exciting forces and motions by numerically integrating the equations of

\*The experimental results are from unpublished data of David W. Taylor Naval Ship Research and Development Center.



motion using a two-point Runge-Kutta method. Figures 4a and 4b show the surge and heave motions and surge forces for the body whose profile is given in Figure 2; both figures were calculated for the body submerged at a depth  $0.3L$  and under a wave of wave length  $2\pi L/3$  propagating along the body axis. Figure 4a is the resulting drift of the body when it is only free to have a surge motion. It is seen in the figure that the surge force is periodic and is little influenced by the surge motion. The resulting drift is the sum of a constant drift and a periodic drift. The amplitude of the periodic drift is constant since the body was fixed at a constant depth. The constant drift is the result of the initial condition. By releasing the body at a different time with respect to the wave, one can hold the magnitude of the drift at zero or some other value. Figure 4b is for the same conditions as Figure 4a except that the body is also free to have heave motions. It is seen that the amplitude of the surge force is no longer a constant but decays with time. This is because the heave motion takes the body deeper under the wave and in turn it reduces the amplitude of the surge force and surge motion. The constant drift, in Figure 4b, is negative in contrast to its being positive in Figure 4a. This is because the body was released at a different time as has been discussed previously.

Figures 4a and 4b presented the perturbation motions of a body under a regular wave train. The results show the coupling between the motion and the force; heave perturbations reduce the surge force through the change of depth and in turn reduce the surge motion. When a body is under irregular waves the perturbing motions due to one wave can influence the exciting forces due to the other waves; the perturbation motion of the body generated by one wave changes the positions of the body relative to the other waves. This can, in turn affect the nature of the exciting force on the body caused by other waves. The perturbing motions of the spheroid under one regular wave train and two regular wave trains were calculated. The effect of wave coupling on yaw instability is shown in Figure 5.

In the calculations shown in Figure 5, the first wave train had a wave length of  $\pi L$  propagating in the x-direction (wave I) and the second wave train had a wave length of  $2L$  propagating in a direction at  $70^\circ$  to the x-axis (wave II). The relative phase angle of these two waves was zero at time zero. The spheroid was initially held steady under the waves with body axis parallel to the x-axis. It was then released with freedom to undergo horizontal motions. The broken and dotted lines in Figure 5 are the motions and forces when the spheroid was under each wave alone. The solid lines are for when the spheroid was under the irregular sea of both waves. Since wave I propagated in the direction of the body axis, the perturbations  $U_2$  and  $\Omega_3$ , due to wave I alone are identically zero, while  $U_1$  is the sum of a periodical motion and a constant drift. Wave II was at an angle of  $70^\circ$  to the body axis. With the spheroid under this wave,  $U_1$  is small; because of the incidence angle of wave II, the perturbing motions of  $U_2$  and  $\Omega_3$  were significant. It is seen that for this case the yaw angle of the body was turned approximately  $23^\circ$  at nondimensional time,  $\sqrt{2g/Lt}$ , equal to 28. One can also see in the figure that the periodic part of the yaw motions decreases when the spheroid is turned close to perpendicular to the wave. The effect of wave coupling on the exciting motions of the spheroid can be seen from the comparison of the solid line to the broken and dotted lines in the figure. It is seen that the solid line for  $U_1$ , which is the result for the irregular wave field, is approximately the sum of the other two lines while the solid line for  $U_2$  deviates little from the dotted line at the beginning and becomes smaller as time goes on and the body turns. This is because the surge force is weakly dependent on the relative angle of the body to the waves while the sway force is strongly dependent. The yaw motion of the spheroid under the irregular wave field is significantly different from the sum of the yaw motions under Waves I and II, individually, while the yaw force due to Wave I is no longer identically zero; it was zero initially until the amplitude of the yaw force started to increase when the spheroid was rotated by Wave II. Because these two waves have different frequencies but the same phase angle, the resulting yaw force at the beginning was larger than that under wave II alone and then became smaller as the two waves approached being out of phase. Under irregular waves the yaw angle was only  $11.5^\circ$  at a nondimensional time of 28,

which is only half of the rotation caused by Wave II alone. The presence of wave I acted as a yaw stabilizer for this calculation.

The coupling effect of the waves on the motions of a body depends upon the initial condition of the body as well as the relative phase angle of the waves. If in the above calculations, Wave I is shifted by  $180^\circ$  in phase angle, that is, the two waves are out of phase at the beginning and were in phase when the yaw force from wave I becomes significant, then one can expect that the yaw force will be amplified and the yaw motion will be much larger than that generated by wave II alone. The yaw angle resulting from a  $180^\circ$  phase shift of wave I is given as Figure 6. It is seen that the spheroid was turned to a  $23.0^\circ$  heading sooner. It is also seen that the rotation of the spheroid is due to wave II (low period) at the beginning and due to wave I (longer period) later when the spheroid turns nearly  $90^\circ$  to wave II and  $20^\circ$  to wave I.

#### SUBMERGED BODY MOVING UNDER WAVES WITH FORCED OSCILLATORY MOTION

In the previous section we evaluated the wave exciting forces on a deeply-submerged body when the time integral in equation (13) is negligible. In the case of a body moving under waves near the free surface, the free-surface effects on the scattering potential may still be small but the free-surface effects on the velocity potential associated with the forced motion of the body may not be negligible. For these velocity potentials one has to include the time integral term in calculations. The present method can be used to calculate the forces on a body undergoing forced oscillations in uniform translation under free-surface waves.

Let

$$\phi_o(t) = \phi_{ou}(t) + \phi_{oT}(t) + \phi_{os}(t) + \phi_w(t)$$

and

$$\phi_i(t) = \phi_{iu}(t) + \phi_{iT}(t) - \phi_w(t)$$

where  $\phi_{ou}$  and  $\phi_{iu}$  are the outer and inner velocity potentials due to steady motion, respectively,  $\phi_{oT}$  and  $\phi_{iT}$  are potentials due to forced oscillatory motion,  $\phi_w$  is the known potential, and  $\phi_{os}$  is the scattering potential. Then, to the lowest order of approximation, the linearized free surface condition is given by

$$\partial^2[\phi_{ou}(t) + \phi_{oT}(t)]/\partial t^2 + g\partial[\phi_{ou}(t) + \phi_{oT}(t)]/\partial z = 0 \quad (21)$$

Where the scattering potential  $\phi_{os}$  of a submerged body is considered small and is neglected. It is shown by Havelock<sup>12,15</sup> that, if the perturbation to the body position due to oscillations is neglected, the time integral of equation (13) can be integrated analytically. In the present approach the values of  $\phi_{os}$ ,  $\phi_{ou}$  and  $\phi_{oT}$  on the body are given by

$$\begin{aligned} \phi_{os} &= D_s - \phi_w \\ \phi_{ou} &= D_u + \phi_{iu} \\ \phi_{oT} &= (D_{Tc} \cos \omega t + D_{Ts} \sin \omega t) + \phi_{iT} \end{aligned} \quad (22)$$

where  $\omega$  is the frequency of oscillation, and  $D_s$ ,  $D_u$ ,  $D_{Tc}$  and  $D_{Ts}$  are solutions of the equations

$$\begin{aligned} -\phi_w(P, t) &= \frac{1}{4\pi} \iint_{S_B} D_s(Q, t) \partial \left( \frac{1}{r_{PQ}} \right) / \partial n \, dS(Q), \quad P \text{ on } S_B \\ \phi_{iu}(P, t) &= \frac{1}{4\pi} \iint_{S_B} D_u(Q) \partial G_u / \partial n \, dS(Q), \quad P \text{ on } S_B \end{aligned} \quad (23)$$

and

$$\phi_{iT}(P, t) = \frac{1}{4\pi} \text{Re} \left[ \iint_{S_B} (D_{Tc}(Q) + i D_{Ts}) \partial G_T / \partial n \, dS(Q) \right], \quad P \text{ on } S_B$$

In equations (23),  $G_u$  is the Kelvin singularity for a moving source and  $G_T$  is given by

$$G_T = e^{-i\omega t} \left\{ \left( \frac{1}{r} - \frac{1}{r_1} \right) + \frac{2g}{\pi} \left[ \int_0^\gamma d\theta \int_0^\infty dk F(\theta, k) + \int_\gamma^{\frac{1}{2}\pi} d\theta \int_{L_1} dk F(\theta, k) + \int_{\frac{\pi}{2}}^\pi d\theta \int_{L_2} dk F(\theta, k) \right] \right\} \quad (24)$$

where

$$\gamma = \begin{cases} 0 & \text{if } U\omega < g/4 \\ \arccos(g/4U\omega) & \text{if } U\omega \geq g/4 \end{cases}$$

and

$$F(Q, k) = k \exp[k(z - z_0) + i(x - x_0) \cos \theta + i(y - y_0) \sin \theta] / [gk - (\omega + kU \cos \theta)^2]$$

The calculation of  $\phi_{os}$  was discussed in a previous section and the calculation of  $\phi_{ou}$  has been given in Reference 2. From examination of equation (24) it is seen that the calculation of  $\phi_{oT}$  is not difficult in comparison to the calculation of  $\phi_{ou}$  as long as  $\omega U/g$  is not close to 1/4. The present approach can thus be used to calculate the forces on a body undergoing forced oscillations near a free surface. Figure 7 shows the computed damping coefficients for a spheroid, which agree well with the results of Havelock.<sup>12</sup>

Finally, it should be stated that the calculations presented here were done in the same manner they would be done for bodies of arbitrary shape. A detailed study of wave exciting forces on bodies near a free surface will be the subject of future work.

## CONCLUDING REMARKS

The inner-potential doublet-distribution method proposed by Pien and Chang<sup>15</sup> for steady body motions has been extended in the present paper to unsteady body motions under a free surface with waves. The resulting system of equations to determine the velocity potential for unsteady motion are similar to those for steady motion. Although this approach has advantages over the sink-source distribution method, numerical evaluation of the velocity potential on an arbitrary body with an arbitrary unsteady motion is not easy; the time convolution integral in equation (13) can be very time consuming for an arbitrary motion. Thus, the advantages of the present approach over other non-singularity methods are not obvious. For special cases when the time integration can be evaluated analytically, such as for oscillatory motions, the present approach has proved very useful.

For a body moving in a given potential field, the influence of body-generated free-surface disturbances on the body will in some cases be small in comparison to the influence of the initial potential field. In such cases, the time integral in equation (13) may, thus, be neglected. A method for calculating the wave exciting forces and wave-excited motions of a deeply-submerged body moving under waves has been presented. The wave exciting forces on a body moving steadily under regular waves were calculated and compared with corresponding results of Cummins<sup>4</sup> and Havelock.<sup>5</sup> The numerical calculations indicate that the present method can obtain accurate predictions of forces and moments with a small number of control panels. Also, the calculations show that a slender body approximation is quite good even for body fineness ratios of 0.3.

Wave-excited motions of a body moving under wave trains were calculated for both regular and irregular waves. The wave-coupling effect on the excited motions was discussed. The results for the yaw motions demonstrated the importance of the wave coupling in yaw instability. Figures 5 and 6 show that one is able to turn the motion from stable to unstable by simply changing the relative phase of the waves.

The calculation of wave exciting forces for a body moving near a free surface under a regular wave is not difficult provided

that the body moves at a constant mean horizontal velocity with prescribed small oscillatory motions; the time convolution for this case can be integrated analytically as shown by Havelock.<sup>14</sup> Numerical integration of the Kernel function is not much more complicated than for the case of steady motion. Investigations of wave exciting forces on bodies near a free surface will be the subject of future work.

The motions calculated were due entirely to wave forces without considering viscous effects. These effects can be incorporated into the equations of motion once the functional form of the viscous forces is determined.

## Acknowledgements

This work was performed under the Naval Sea Systems Command General Hydrodynamic Research Program, Task Area SR 023 0101, Program Element 61153N, Work Unit 1521-027.

## REFERENCES

1. Pien, P.C., "Calculation of Non-Lifting Potential Flow About Arbitrary Three-Dimensional Bodies Based on Doublet Distributions," David Taylor Naval Ship Research and Development Center, Departmental Report SPD 601-01, 1975.
2. Chang, M.S. and P.C. Pien, "Hydrodynamic Forces on a Body Moving Beneath a Free Surface," First International Conference on Computational Ship Hydrodynamic, 1975.
3. Hess, J.L. and A.M.O. Smith, "Calculation of Non-Lifting Potential Flow About Arbitrary Three-Dimensional Bodies," Douglass Aircraft Company Report No. E.S. 40622, 1962.
4. Cummins, W.E., "Hydrodynamic Forces and Moments Acting on a Slender Body of Revolution Moving Under a Regular Train of Waves," TMB Report 910, 1954.
5. Havelock, T.H., "The Forces on a Submerged Body Moving Under Waves," Quarterly Transactions, Institution of Naval Architects, Vol. 96, 1954, pp. 74-88.
6. Newman, J.N., "The Exciting Forces on a Moving Body in Waves," Journal of Ship Research, Vol. 9, No. 3, 1965, pp. 190-199.
7. Haskind, M.D., "The Exciting Forces and Wetting of Ships in Waves," Izvestia Akademii Nauk SSSR, Otdelenie Tekhnicheskikh Nauk, No. 7, 1957, pp. 65-79.
8. Ursell, F., "On the Rolling Motion of Cylinders in the Surface of a Fluid," Quarterly Journal of Mechanics and Applied Mathematics, Vol. 2, Part 3, 1949, pp. 335-353.
9. Korvin-Kroukovsky, B.V. and W.R. Jacob, "Pitching and Heaving Motions of a Ship in Regular Waves," Transaction SNAME, Vol. 65, 1975, pp. 590-632.
10. Hishida, T., "Studies on the Wave-Making Resistance for the Rolling of Ships - Part 6," Journal of the Zosen Kiokai, Vol. 87, 1955, pp. 67-78.
11. Havelock, T.H., "The Effect of Speed of Advance Upon the Damping of Heave and Pitch," Transactions of the Institution of Naval Architects, Vol. 100, 1958, pp. 131-135.
12. Havelock, T.H., "The Damping of Heave and Pitch: A Comparison of Two-Dimensional and Three-Dimensional Calculations," Quarterly Transactions of the Institution of Naval Architects, Vol. 98, 1956, pp. 464-469.
13. Newman, J.N., "The Damping of an Oscillating Ellipsoid Near a Free Surface," Journal of Ship Research, Vol. 5, 1961, pp. 44-58.
14. Wehausen, J.V. and E.V. Laitone, "Handbuch der Physik," Vol. 9, Springer Verlag, Berlin, 1960.
15. Pien, P.C. and M.S. Chang, "Potential Flow About a General Three-Dimensional Body," Naval Ship Research and Development Center Report 3608, 1971.



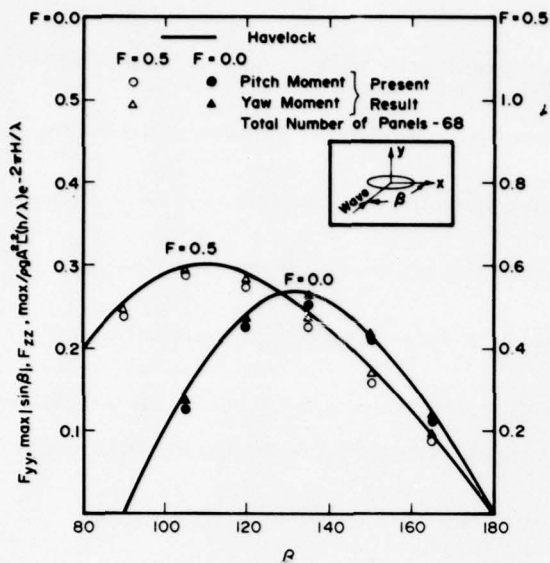


Fig. 1a: Pitch and yaw moments on a spheroid of beam-length ratio 0.3 under regular waves with  $\lambda = 2L$

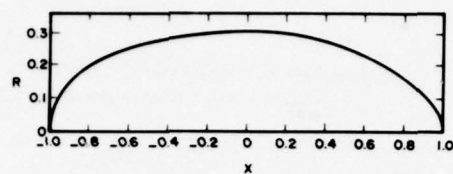


Fig. 2a: A dimensionless profile for a body of revolution

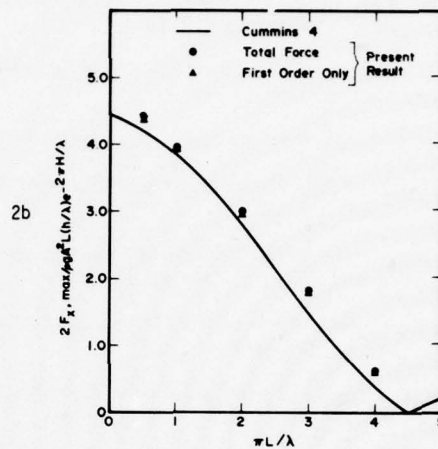


Fig. 2b: Surge-force on a body of revolution in 2a

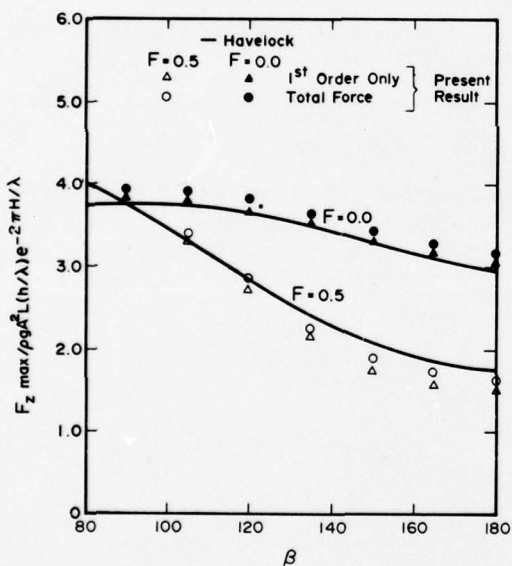


Fig. 1b: Heave-force on a spheroid of beam-length ratio 0.3 under regular waves with  $\lambda = 2L$

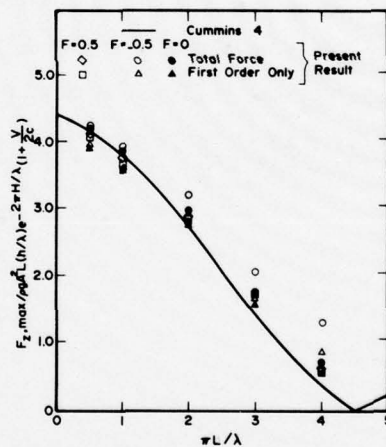


Fig. 2c: Heave-force on a body of revolution in 2a

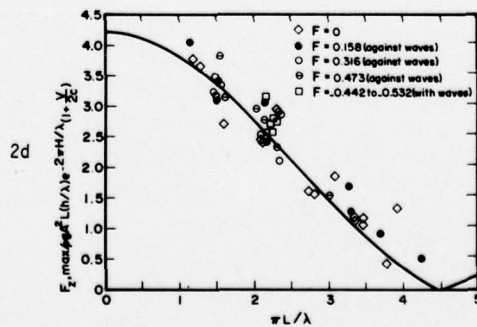


Fig. 2d: Comparison of theoretical heave-force with experimental results of body of 2a

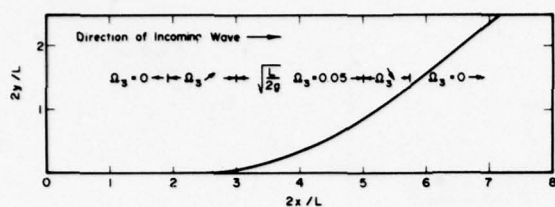


Fig. 3a: Trajectory of a spheroid turning under maneuver

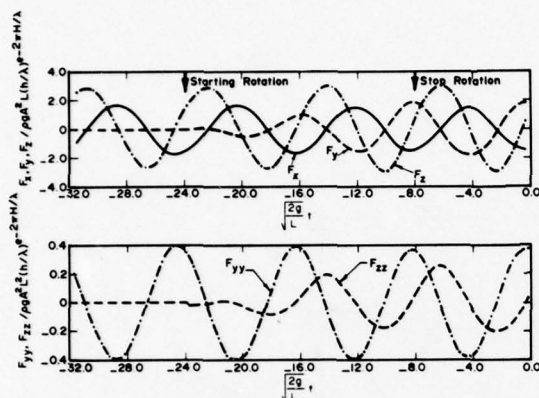


Fig. 3b: Forces and moments on a spheroid turning under maneuver

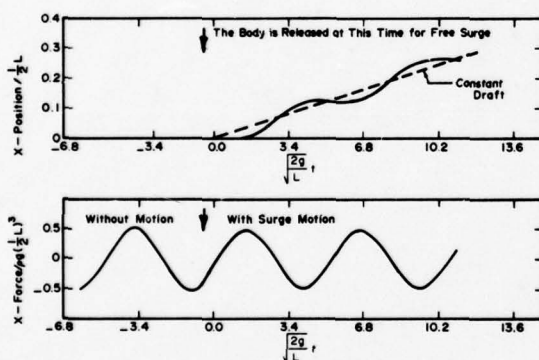


Fig. 4a: Surge motion of a spheroid under a regular wave

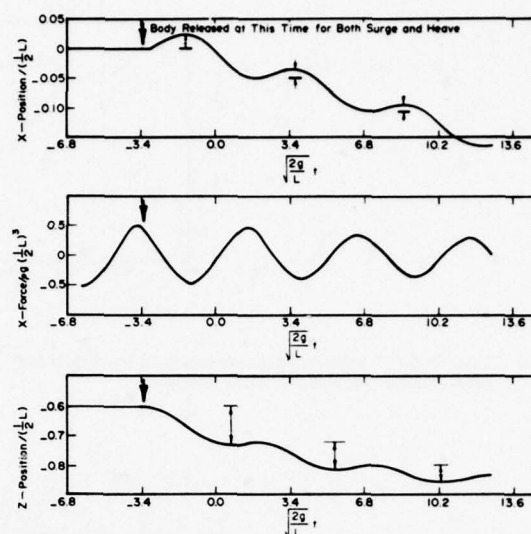


Fig. 4b: Surge and heave motions of a spheroid under a regular wave

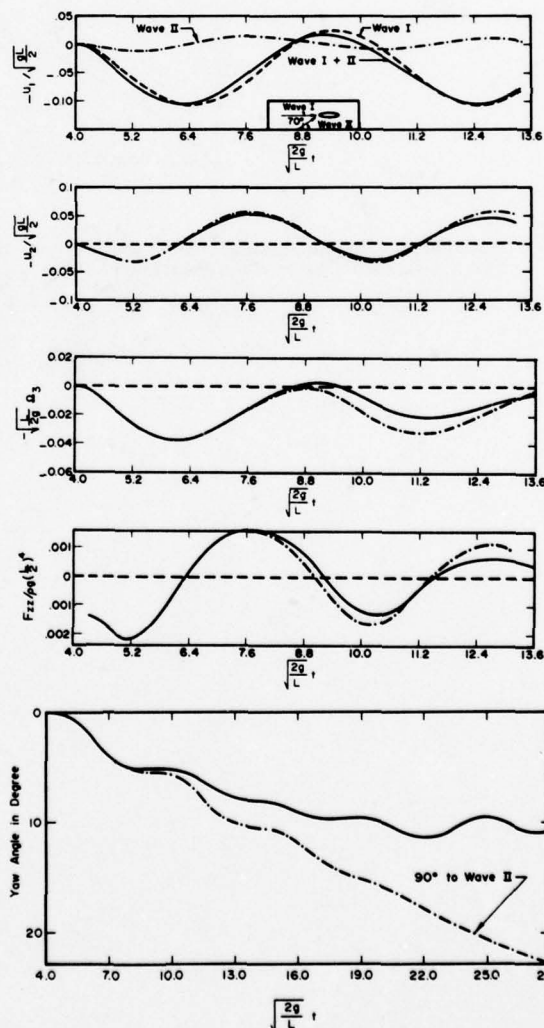


Fig. 5: Horizontal motions of and forces on a spheroid under waves

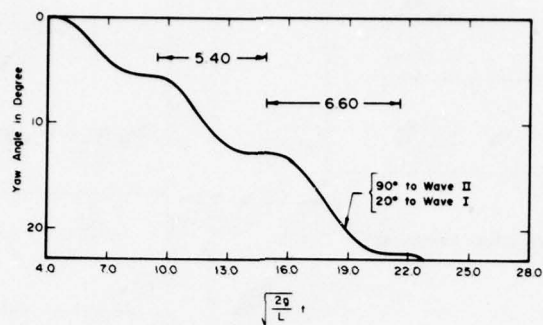


Fig. 6: Yaw angle of a spheroid under waves as for Fig. 5 but with relative wave phase angle changed

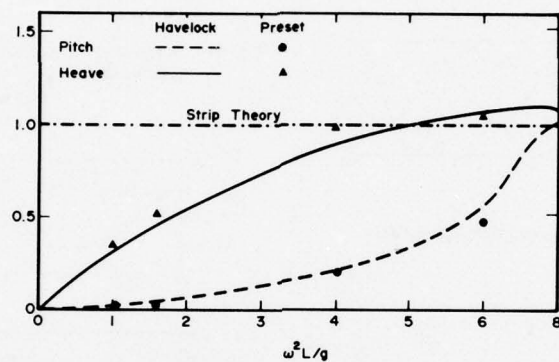


Fig. 7: Ratios of damping coefficients for pitch and heave to that of strip theory for a submerged spheroid of 1:8



# Discussion on Paper by J. N. Newman

G. G. Lei

Professor Newman did an important service in tying together so many general theorems in water waves. Especially interesting is his adroit use of Kochin function which makes it easy to treat two and three-dimensional cases at once.

Although the mathematical elegance is evident, Kochin function is probably not a familiar tool to many workers in the West. From earlier literature it is clear that if one is only interested in two-dimensions the direct use of the asymptotic forms, such as Eqs. (34) and (35) in Newman's paper [1] is more straightforward. For three-dimensions the more universal idea of Green's function can be equally effective, as has already been applied by Maruo (cited in [1]) to deduce Eq. (43) [1] which corresponds to the "optical theorem" in quantum mechanics. It is easy to deduce Eq. (49) [1], the *reciprocity theorem*, in a like manner. For purely pedagogic reasons we shall use Green's function to rederive Eq. (48.b) [1] which relates the scattering and the radiation problems. In addition, an analogous result in *acoustics* will be given.

## ALTERNATIVE DERIVATION OF EQ. (48.b)[1]

Let us define Green's function  $G(\vec{x}|\vec{x}_0)$  by the following conditions:

$$\Delta G = \delta(\vec{x} - \vec{x}_0) \quad -h < z < 0$$

$$\frac{\partial G}{\partial z} - \lambda G = 0 \quad z = 0$$

$$\frac{\partial G}{\partial z} = 0 \quad z = -h$$

$$\sqrt{kr} \left( \frac{\partial G}{\partial r} - ikG \right) \rightarrow 0 \quad kr \gg 1 \quad (1.a, b, c, d)$$

where

$$\lambda = \omega^2/g \quad k \tanh kh = \lambda$$

The solution is well known (see John [2]). We only need the asymptotic expression for large

$kr \gg (1, kr_0)$  where  $r^2 \equiv x^2 + y^2$  and  $r_0^2 \equiv x_0^2 + y_0^2$ . Using the fact that  $[(x-x_0)^2 + (y-y_0)^2]^{1/2}$

$\approx r - r_0 \cos(\theta - \theta_0)$  for  $r_0/r \ll 1$  where  $x = r \cos \theta$ ,  $y = r \sin \theta$ , it is easy to deduce from John [2] that

$$G(\vec{x}|\vec{x}_0) \approx C \cosh k(z_0 + h) \cos k(z + h) \frac{e^{i(kr - \pi/4)}}{\sqrt{kr}} \cdot e^{ikr_0 \cos(\theta - \theta_0)} \quad (2)$$

where

$$C = -\frac{1}{\sqrt{2\pi}} \frac{\lambda^2 - k^2}{(\lambda^2 + k^2)h - \lambda} \quad (3)$$

Let  $\phi_i$  denote the potential of the incident wave with unit amplitude and direction  $\alpha$ :

$$\phi_i = \phi_i(\vec{x}|\alpha) = b \cosh k(z + h) e^{ikr \cos(\theta - \alpha)},$$

$$\text{with } b = \frac{-ig}{\omega \cosh kh} \quad (4)$$

Let  $\phi$  be the total potential for the scattering problem with the special incidence angle  $\alpha = 0$ , and  $\phi_R$  be the radiated wave potential due to forced motion. From Eq. (14)[1] we have

$$\iint_{S_C} \left( \phi \frac{\partial \phi_R}{\partial n_0} - \phi_R \frac{\partial \phi}{\partial n_0} \right) dS_0 + \iint_{S_B} \phi \frac{\partial \phi_R}{\partial n_0} dS_0 = 0 \quad (5)$$

where  $\phi = \phi(\vec{x}_0)$ ,  $\phi_R = \phi_R(\vec{x}_0)$  inside the integrals.

A similar equation holds with  $\phi_R$  being replaced by its complex conjugate  $\phi_R^*$ . Since for a rigid body we may take  $\frac{\partial \phi_R}{\partial n_0} = \frac{\partial \phi_R^*}{\partial n_0}$  = real on  $S_B$ , it follows that

$$\iint_{S_C} \left( \phi \frac{\partial \phi_R}{\partial n_0} - \phi_R \frac{\partial \phi}{\partial n_0} \right) dS_0 = \iint_{S_C} \left( \phi \frac{\partial \phi_R^*}{\partial n_0} - \phi_R^* \frac{\partial \phi}{\partial n_0} \right) dS_0 \quad (6)$$

Now let  $\phi = \phi_i(\vec{x}|0) + \phi_S$  where  $\phi_S$  is the scattered wave potential which satisfies Eq. (1.d). It is

readily shown that

$$\begin{aligned} & \iint_{S_C} [\phi_1(\vec{x}_0|0) \frac{\partial \phi_R}{\partial n_0} - \phi_R \frac{\partial}{\partial n} \phi_1(\vec{x}_0|0)] dS_0 - \\ & - \iint_{S_C} [\phi_1(\vec{x}_0|0) \frac{\partial \phi_R^*}{\partial n_0} - \phi_R^* \frac{\partial}{\partial n} \phi_1(\vec{x}_0|0)] dS_0 \\ & = \iint_{S_C} (\phi_S \frac{\partial \phi_R}{\partial n_0} - \phi_R^* \frac{\partial \phi_S}{\partial n_0}) dS_0 \end{aligned} \quad (7)$$

Define the far field amplitudes by

$$\begin{aligned} \begin{bmatrix} \phi_S \\ \phi_R \end{bmatrix} & \approx \begin{bmatrix} A_S(\theta) \\ A_R(\theta) \end{bmatrix} b \cos hk(z+h)(kr)^{-1/2} \cdot \\ & \cdot \exp(ikr - i\pi/4), \quad kr \gg 1 \end{aligned} \quad (8)$$

The last integral in Eq. (7) is easily seen to be

$$-i|b|^2(h + \frac{1}{\lambda} \sinh^2 kh) \int_0^{2\pi} A_S A_R^* d\theta \quad (9)$$

Applying Green's formula to  $\phi_R$  and  $G$  to the volume bounded by  $S_C$ ,  $S_B$ ,  $S_F$  and the bottom we get

$$\phi_R(\vec{x}) = \iint_{S_B} (\phi_R \frac{\partial G}{\partial n_0} - G \frac{\partial \phi_R}{\partial n_0}) dS_0 \quad (10)$$

In the far field  $kr \gg 1$ , Eq. (2) may be used to give

$$\begin{aligned} \phi_R(\vec{x}) & \approx C \cosh k(z+h) \frac{e^{i(kr-\pi/4)}}{\sqrt{kr}} \cdot \\ & \iint_{S_B} dS_0 \{ \phi_R \frac{\partial}{\partial n_0} [\cos k(z_0+h) \exp(-ikr_0 \cos(\theta_0-\theta))] - \\ & - [\cos k(z_0+h) \exp(-ikr_0 \cos(\theta_0-\theta))] \frac{\partial \phi_R}{\partial n_0} \} \end{aligned} \quad (11)$$

Now  $\{ \}$  in the integrand above can be identified as  $\phi_1^*(\vec{x}_0|\theta)/b^*$ . Hence,  $\phi_R$  may be written as

$$\begin{aligned} \phi_R(\vec{x}) & \approx \frac{Cb}{|b|^2} \cos k(z+h) \frac{e^{i(kr-\pi/4)}}{\sqrt{kr}} \cdot \\ & \iint_{S_B} [\phi_R \frac{\partial}{\partial n_0} \phi_1^*(\vec{x}_0|0) - \phi_1^*(\vec{x}_0|0) \frac{\partial \phi_R}{\partial n_0}] dS_0 \end{aligned} \quad (12)$$

Upon comparing Eqs. (8) and (12) it follows that

$$\begin{aligned} A_R(\theta) & = \frac{C}{|b|^2} \iint_{S_B} \{ \phi_R \frac{\partial}{\partial n_0} \phi_1^*(\vec{x}_0|\theta) - \\ & - \phi_1^*(\vec{x}_0|\theta) \frac{\partial \phi_R}{\partial n_0} \} dS_0 \end{aligned} \quad (13)$$

Taking the complex conjugate of Eq. (13) and let-

ting  $\theta = 0$  we obtain

$$A_R^*(0) = \iint_{S_B} \{ \phi_R^* \frac{\partial}{\partial n_0} \phi_1(\vec{x}_0|0) - \phi_1(\vec{x}_0|0) \frac{\partial \phi_R^*}{\partial n_0} \} dS \quad (14)$$

Since from Eq. (4),  $\phi_1(\vec{x}_0|0) = -\phi_1^*(\vec{x}_0|\pi)$  it follows by letting  $\theta = \pi$  in Eq. (13) that

$$-\frac{|b|^2}{C} A_R(\pi) = \iint_{S_B} \{ \phi_R \frac{\partial}{\partial n_0} \phi_1(\vec{x}_0|0) - \phi_1(\vec{x}_0|0) \frac{\partial \phi_R}{\partial n_0} \} dS_0 \quad (15)$$

Combining Eqs. (9), (14) and (15) in Eq. (7) we finally get

$$A_R(\pi) + A_R^*(0) = -iC(h + \frac{R}{\omega^2} \sinh^2 kh) \int_0^{2\pi} A_S A_R^* d\theta \quad (16)$$

which is equivalent to Eq. (48.b)[1]. As a minor advantage of the present approach, it may be noted that there is no need for a stationary phase calculation as in Eq. (22.b)[1].

#### AN ANALOGOUS RELATION IN ACOUSTICS

Since the idea of Green's functions is quite common in many different physical contexts, one can deduce formulas similar to Eq. (16) for other wave problems. We shall only use acoustic scattering and radiation for illustration.

Consider three-dimensional sound waves in air. The governing equation for the velocity potential is

$$\Delta \phi + k^2 \phi = 0, \quad |\vec{x}| < \infty \quad (17)$$

An incident plane wave in the direction of  $\vec{k}_i$  may be described by

$$\phi_i(\vec{x}|\vec{k}_i) = e^{i\vec{k}_i \cdot \vec{x}} \quad (18)$$

where  $|\vec{k}_i| = k$ . The scattered wave  $\phi_S = \phi - \phi_i$  due to the stationary body, and the radiated wave  $\phi_R$  due to the forced oscillation of the same body, must have the following behavior in the far field

$$\phi_S \approx \frac{e^{ikr}}{kr} f_S(\vec{k}_i|\vec{k}_0) \quad (19.a,b)$$

$$\phi_R \approx \frac{e^{ikr}}{kr} f_R(\vec{k}_0)$$

where  $f_S$  and  $f_R$  represent the angular variations,  $\vec{k}_0 = k \vec{x}/|\vec{x}|$  and  $|\vec{x}| = r$ . Using the ordinary free-space Green function and following the same argument as in the preceding section, we find that

$$\begin{aligned} f_R(-\vec{k}_i) - f_R^*(\vec{k}_i) & = \\ & - \frac{1}{2\pi} \iint d\Omega f_R(\vec{k}_0) f_S(\vec{k}_i|\vec{k}_0) \end{aligned} \quad (20)$$

where  $d\Omega$  refers to the solid angle  $\sin\theta \, d\theta \, d\phi$  for all  $\vec{k}_0$ . This formula has been verified for the special case of a rigid sphere for which  $\phi_S$  and  $\phi_R$  are known exactly, Morse and Ingard (3).

#### REFERENCES:

- (1) Newman, J.N.; "The Interaction of Stationary Vessels with Regular Waves;" these proceedings, 1976.
- (2) John, F.; "On the motion of Floating Bodies, II," Communications of Pure and Applied Mathematics; 1950, pp. 45-101.
- (3) Morse, P.M. and K.U. Ingard; Theoretical Acoustics; McGraw-Hill, 1968.



## Discussion on Paper by D. V. Evans

R.C. McGREGOR

The theory and results presented in this paper will give valuable help to those who like Salter are working towards utilising energy from ocean waves. However efficiency is not necessarily the most important factor in making a wave energy extractor work. In many cases the energy available is far more than the structure can be made capable of coping with and deliberate decisions to go for relatively low efficiencies have to be made. However the choice of a suitable decay of efficiency from the highest levels as the sea state increases may be used to advantage to relieve loads and this may now be predicted.

For the choice between a symmetric body with two degrees of freedom and a non-symmetric body with only one, a major consideration will be the cost and difficulty of converting the power. It will inevitably be cheaper to transform a single motion, especially roll, into a usable form rather than a dual motion. Salter's system does involve motions other than roll when the cams are corded together and he has shown that such motions are not necessarily detrimental. However, he uses the secondary motions primarily to relieve loads on the structure.

Although more than one degree of freedom may have engineering difficulties for wave energy utilisation, as a breakwater there could be appreciable advantages for energy dissipation. In connection with this could the author comment on how permitting the cylinder to roll would be likely to alter the efficiencies of the submerged rotating cylinder, (Ref.(14))?

can be regarded as a linear combination of

- (a) those forces and moments on the cylinder when it is forced to oscillate in each mode separately;
- (b) those forces and moment on the cylinder when it is held fixed in the incident wave.

In (a) there is no motion produced by the rolling motion of the circular cylinder about its mass centre, and hence no moment about the mass centre. Also, in (b) there is no contribution to the moment from the incident wave either, since from the Haskind relations (Eq.(4.4)), the moment on the fixed cylinder is proportional to the wave amplitude produced at large distances from the cylinder due to the corresponding rolling motion of the cylinder, which we have seen is zero.

For non-circular cylinders we would need to know the added moment of inertia and damping coefficients in roll as a function of wave frequency to be able to predict the variation of efficiency with frequency. It will always be possible to achieve a theoretical efficiency of 100% at a particular frequency using any cylinder oscillating in a combination of modes, but whether the large bandwidths obtained with the circular cylinder can be achieved with a non-circular submerged cylinder remains to be seen. It is tempting to surmise that the circular cylinder is the most effective submerged wave absorber, bearing in mind the "irrotational" circular motion of the cylinder when operating at optimum efficiency and the similar behaviour of the water particles in deep water in the absence of the cylinder.

## Author's Reply

It is true that the theoretical advantages of permitting more than one mode of oscillation may well be outweighed by the greater engineering difficulties associated with transforming the dual motion. On the other hand, the large bandwidths which can be achieved, in particular for the submerged circular cylinders, are attractive. In this connection the theory shows that it is quite possible for a wave absorber to be beneath the water and still operate efficiently. This has the advantage of protecting the device from the severest effects of large breaking waves.

As far as permitting the cylinder to roll is concerned, for the submerged circular cylinder suspended on horizontal and vertical springs and dampers, no rolling will occur. This can be seen as follows. The first-order forces and moments on the cylinder

# Discussion on Paper by T. Y. Wu et al

R.C. McGREGOR

Having enjoyed hearing this paper, I would like to ask for the authors' comments on two points.

First, the induced mass for the toroid is calculated in the early parts of the paper. This calculation is not made in the case of the flexible slender body, although it is just as relevant. Lighthill (1975) took the induced mass of such a body to be the same as that of a flat plate of the body's profile in translational motion. This seems to be a major simplification when compared with the thoroughness of the rest of that paper. Have the authors made any estimate of the induced mass of a fishlike body as part of their investigation of fish locomotion?

Secondly, Fig.3(c) shows a fish swimming with three nodal points and in particular  $h(o,t)$  is non-zero at the head indicating a side to side motion there. Conversation with fishing specialists has suggested that fish do not have a lateral head movement and that fish with stiffer bodies than the eel often only have two nodes. The film of the eel did not seem to show any significant head movements other than in the direction of travel, but a frame by frame analysis would clarify this. For mathematical efficiency it is to be hoped that Fig.3(c) is correct but the fish may find it more tiring.

## REFERENCE

Lighthill, M.J. Mathematical Theories of Swimming Fish, IMA Conf. on Fisheries Mathematics, Aberdeen, 1975.

## Authors' Reply

We very much appreciate the questions raised by Dr. McGregor for they give us an opportunity to clarify a few points. Our results for the sectional force on a differential section of a flexible, elongated body, of circular cross section was presented at the meeting, but was not available for inclusion in the preprint. Its expression, to leading order, is

$$\underline{F}(s,t) = \underline{e}_n \left[ -\left(\frac{\partial}{\partial t} - V_s \frac{\partial}{\partial s}\right) (\rho \pi b^2 V_n) - \right.$$

$$\left. \rho \pi b^2 \left( \frac{V_n^2}{2a} - \dot{\Omega} b b' \right) \right] - \underline{e}_s \frac{V_n^2}{2} \frac{\partial}{\partial s} (\rho \pi b^2)$$

where the notation follows the text. The first

term represents the material derivative of the normal component of the flow momentum based on the tangential component,  $V(s,t)$ , of the body velocity rather than on the mean<sup>2</sup> forward velocity,  $U$ , as in the previous theories. The contribution of the centrifugal acceleration,  $V^2/a$ , results in a normal component of force which vanishes for straight bodies. The present result reduces to that of small-amplitude theory, but clearly indicates departure from it due to finite-amplitude and centre-line-curvature effects. As shown in the above result, these effects bring forth new contributions to the sectional forces in addition to the classical concept based on the induced mass of the body.

Fig.3(c) is an artist's representation used only to illustrate a typical fish motion. We agree with Dr. McGregor's observation that fish generally have no significant head movements in steady forward swimming, and that the body wavelength is a good fraction of its body length. Whether there exist such optimum values of these physical factors is being investigated from the standpoint of swimming efficiency and energetics. Furthermore, our theory is intended for arbitrary body movements, including those manifested in nature, such as fish in turning manoeuvres and artificial ones as well.

# Discussion on Paper by P. Sayer and F. Ursell

A.M.J. DAVIS

Discussion of limiting cases is usually justified by the results giving a good approximation to what happens when the parameters are moderately near their respective limits. The displayed graphs indicate that the features discussed in this paper only occur close to the limit  $Ka = 0$  ( $a/h$  fixed), and it is for this reason that I am unhappy about the applicability of the results obtained.

The natural length and time scales of the problem are  $a$  and  $(a/g)^{1/2}$  respectively and it is assumed that  $\sigma^{1/2} \gg (a/g)^{1/2}$ . If  $U$  is the amplitude of the heave velocity, then  $U/\sigma$  is the amplitude of the displacement of the cylinder and is assumed small compared with  $a$  in applying the condition on the boundary of the cylinder at its mean position. Now  $U/\sigma \ll a$  implies

$$\frac{U}{(ga)^{1/2}} \ll \sigma \left(\frac{a}{g}\right)^{1/2} = (Ka)^{1/2} \ll 1$$

and so, measured in terms of the natural velocity scale, the scaling factor  $U$  of all velocities in the fluid motion, is small compared with  $(Ka)^{1/2}$  which tends to zero.

In the low frequency limit, the cylinder heaves either so slowly that the motion is quasi-static or with displacement amplitude too large for the linearisation of the boundary conditions to be valid.

R.W. YEUNG AND J.N. NEWMAN

The authors are to be congratulated on a very interesting contribution which covers the low-frequency behavior of the added-mass coefficient of a circular cylinder in water of finite depth. Their results essentially confirm the earlier findings, presented at the last ONR Symposium, by Bai and Yeung (1974), who have shown, using two different numerical methods, that the added-mass coefficient for a circular and a rectangular section approach finite limits rather than infinite ones as in the case of infinite depth. As pointed out by Professor Ursell in a discussion at that time, the limiting value involves the solution of a limiting (Neumann-type) problem as well as an additive constant whose determination is non-trivial. Namely, if  $\mu$  and  $\lambda$  denote the heave added-mass and damping coefficient respectively,

$$\lim_{ka \rightarrow 0} (\mu + i\lambda/\sigma) = \rho \int_{S_0} (\hat{\phi} + C) n_y ds \quad (1)$$

Here  $n_y$  is the vertical component of an outward normal to the body and  $S_0$  is the body contour. The limiting potential,  $\hat{\phi}$ , is real and satisfies the rigid free-surface condition as well as  $\partial\hat{\phi}/\partial n|_{S_0} = n_y$  (and of course,  $d\hat{\phi}/dn|_y = -n = 0$ ). In addition,  $\hat{\phi}$  satisfies the condition  $\hat{\phi} - x\hat{\phi}_x \rightarrow 0$  as  $|x| \rightarrow \infty$ . The crux of the problem is the determination of  $C$  in (1) which Ursell [1] has shown after some very elaborate analysis, for the case of a circular cylinder, to be

$$C = \frac{-ia}{\sqrt{Kh}} - \frac{a^2}{h} \quad (2)$$

We will show below using matched asymptotics that Equation (2) is valid also for any symmetrical shape.

Let the velocity potential be written  $\phi(x,y).y_0(t)$ ,  $y_0(t)$  being the heave motion of the section. Let  $a$  be waterline half-breadth of the section, the Equations (2.2) to (2.6) of the author's paper apply, except for Equation (2.4), which is to be replaced by  $\partial\phi/\partial n = n_y$  for the general case. If  $a$  and  $h$  are assumed to be  $O(1)$ , and  $k_0 = O(\epsilon)$ , clearly,

$$Kh = (k_0 h)^2, \quad k = \sigma^2/g \quad (3)$$

Now for a sufficiently large distance from the body, the following outer solution must hold

$$\phi(x,y) = A e^{iko|x|} \cosh k_0(y+h) \quad (4)$$

where  $A$  has to be determined by matching. The inner limit (small  $x/h$ ) of this outer solution to order  $O(k_0^2)$  is given by

$$\lim_{x \rightarrow 0} \phi(x,y) = A \left[ 1 + ik_0|x| + \frac{k_0^2}{2} \{(y+h)^2 - x^2\} \right] \quad (5)$$

For the inner problem, we construct the solution as an ordered sequence in the form of:

$$\phi(x,y) = \phi^{(1)} + \phi^{(2)} + \phi^{(3)} + \dots \quad (6)$$

with  $\phi^{n+1} = o(\phi^n)$

Then the lowest two orders of  $\phi$  satisfy

$$\begin{aligned} \nabla^2 \phi^{(1)} &= 0 & \nabla^2 \phi^{(2)} &= 0 \\ \phi_y^{(1)}(x,0) &= 0 & \phi_y^{(2)}(x,0) &= K\phi^{(1)} \\ \phi_y^{(1)}(x,-h) &= 0 & \phi_y^{(2)}(x,-h) &= 0 \\ \phi_n^{(1)}|_{S_0} &= n_y & \phi_n^{(2)}|_{S_0} &= 0 \end{aligned} \quad \begin{aligned} (7a) \\ (7b) \end{aligned}$$



The solution of  $\phi^{(1)}$  is nothing but the solution of the limiting problem  $\hat{\phi}$  defined earlier, with an additive constant to be determined from matching:

$$\phi^{(1)} = \hat{\phi} + C^{(1)} \quad (8)$$

which for large  $x/h$ , behaves like

$$\lim_{x \rightarrow \infty} \phi^{(1)}(x, y) = \frac{a}{h} |x| + C^{(1)} \quad (9)$$

Matching the one term inner expansion of the outer solution with the one-term outer expansion of a one-term inner solution, we thus obtain

$$C^{(1)} = A = \frac{-ia}{k_0 h} \quad (10)$$

Whence, to leading order in  $Kh$ , the wave-amplitude ratio  $|n/y_0|$  due to heave motion is given by

$$\left| \frac{n}{y_0} \right| = \left[ \frac{a}{h} \right]^{1/2} \sqrt{Ka} \quad (11)$$

For the solution of  $\phi^{(2)}$ , we note that the right-hand side of the free-surface condition is given by

$$\phi_y^{(2)} = K\phi^{(1)} \approx KC^{(1)} \quad (12)$$

since  $C^{(1)}$  is lower in order than  $\hat{\phi}$ . The missing portion can always be accounted for by considering  $\phi^{(3)}$  if necessary. The solution for (7b) and (12) can be decomposed as follows:

$$\begin{aligned} \phi^{(2)} &= \psi(x, y) + \chi(x, y) \\ &= \frac{KC^{(1)}}{2h} [(y+h)^2 - x^2] + \chi \end{aligned} \quad (13)$$

where  $\psi$  has been constructed to satisfy (12) and  $\chi$  satisfies the homogeneous boundary conditions on  $y = 0$  and  $y = -h$ , but

$$\frac{\partial \chi}{\partial n} \Big|_{S_0} = - \frac{\partial \psi}{\partial n} \Big|_{S_0} \quad (14)$$

and behaves like

$$\chi(x, y) = \frac{Q}{2h} |x| + C^{(2)}, \quad Q = 2KC^{(1)}a \quad (15)$$

Evidently, it is not necessary to solve for  $\chi$  in detail to determine  $C^{(2)}$ . Thus the one-term outer expansion of a two-term inner solution is given by

$$\begin{aligned} \phi^{(1)} + \phi^{(2)} &= \frac{a}{h} [1 - KC^{(1)}] |x| \\ &\quad + \frac{KC^{(1)}}{2h} [(y+h)^2 - x^2] + C^{(1)} + C^{(2)} \end{aligned} \quad (16)$$

Matching with (5) immediately yields

$$C^{(2)} = - \frac{a^2}{h} \quad (17)$$

Hence (2) is proven for the case of a general cylinder.

The above summarizes the analytical basis used by Yeung (1975) in obtaining the limiting value of a circular cylinder and a rectangular section. A related analysis is also given by Bai (1976) who proceeded further to obtain upper and lower bounds using the dual-extremum principle in conjunction with the finite-element method. The discussers provide below some new results for a triangular section obtained using (2) with the limiting problem  $\hat{\phi}$  solved by the method of Green's function.

Table of Limiting Added-Mass Coefficients for a Triangular Section

$$\bar{u} = u/(\rho \pi a^2/2) \quad \text{Draft/Half-breadth} = 1.7321$$

$h/a$	$\bar{u}$	$h/a$	$\bar{u}$
.55	0.3399	.008	2.901
.50	0.3100	.006	3.132
.45	0.2991	.004	3.458
.40	0.3052	.003	3.690
.35	0.3294	.002	4.017
.3	0.3744	.001	4.577
.2	0.5529	.0008	4.758
.1	0.9748	.0006	4.991
.08	1.129	.0004	5.319
.06	1.335	.0002	5.881
.04	1.638	.0001	6.443
.02	2.174	.00005	7.004
.01	2.723	.00001	8.309

#### REFERENCES

- Bai, K.J. and Yeung, R.W., "Numerical Solutions to Free-Surface Flow Problems", *The 16th Symposium on Naval Hydrodynamics*, Cambridge, Mass., June 1974.
- Bai, K.J. "Added-Mass and Damping Coefficients of Two-Dimensional Cylinders in Water of Finite Depth", DTNSRDC Report, Jan. 1976.
- Yeung, R.W., "A Hybrid Integral-Equation Method for Time-Harmonic Free-Surface Flows", *Proceedings of the 1st International Conference on Numerical Ship Hydrodynamics*, Gaithersburg, Maryland, 1975.

The authors should be congratulated for their efforts to compute the added mass as well as its slope at the zero-frequency limit. Recently I have computed the added mass for the limiting frequencies in water of finite depth. In my work, a simple proof is given which shows that the heave added mass is finite for all frequencies in water of finite depth, by using the complete set of eigenfunctions. Also presented is a reformulation of the problem in the zero frequency limit by using perturbation expansions in a non-dimensional wave number. From this reformulation, I obtained in a simple manner the additive constant  $-a/h$  as well as the asymptotic formula for the damping coefficient  $\lambda$ :

$$\lambda = \rho a \sqrt{g/h} + o(1)$$

I used the finite element method based on the dual extremum principles (also known as dual or complementary principle) and computed the added mass  $\mu_\infty$  for the infinite-frequency limit as well as the added mass  $\mu_0$  for the zero-frequency limit. The added masses  $\mu_0$  and  $\mu_\infty$  of a circular cylinder and three different rectangular sections are presented in reference (7).

I would like to present here some of my results for the circular section. The added masses  $\mu_0$  and  $\mu_\infty$  for several different water depths are given in Table 2 and in Figure 1. There is a good agreement between the results computed by the finite element method and those computed by the present authors. The computations of the added mass  $\mu(\sigma)$  for arbitrary frequency range were also made by the localized finite element method described in Ref (8). These results are plotted in Figure 2, where the results of  $\mu_0$  at the zero-frequency limit were used to connect the  $\mu(\sigma)$ -curve which results in a smooth curve. From the numerical results shown in Figures 1 and 2, it was also concluded that the added mass curve at zero frequency changes its sign at about  $h=2.2a$ . It is very interesting to note that the slope of the added mass curve also changes sign between  $a/h=0.02$  and  $0.03$  which is in a range where we did not make computations; we did not expect that the slope of the added mass changes its sign twice.

Finally I would like to point out that I did not intend that the slope of the added mass curve at zero-frequency should have been computed from the preliminary result which I sent to Prof. Ursell before the 10-th ONR Symposium in 1974 nor did we include this in our paper (Ref (8)). I feel that the statement made by the present authors in this regard is somewhat misleading since our results were not valid at zero frequency. Any computer program would give invalid results if one is dealing with a too small or too large number which is close to the overflow or underflow range of the computer.

## REFERENCES

- (7) Bai, K.J. "Dual extremum Principles for the Added Mass of Two-Dimensional Cylinders Heaving in Water of Finite Depth. (Submitted to the Journal of Fluid Mechanics, 1976).
- (8) Bai, K.J. and Yeung, R.W., 1974, "Numerical Solutions to Free-Surface Flow Problems" The Tenth Symposium on Naval Hydrodynamics, Office of Naval Research held at Massachusetts Institute of Technology, Cambridge, USA.

Table 2 The Upper and lower bounds of  $\mu_0$  and  $\mu_\infty$  for a circular cylinder of radius  $a$  in water of finite depth  $h$ .

h/a	$\mu_0/\rho$ (Submerged Area)		$\mu_\infty/\rho$ (Submerged Area)	
	Lower Bound	Upper Bound	Lower Bound	Upper Bound
1.2	0.9565	0.9577	1.8326	1.8344
1.5	0.6253	0.6263	1.4441	1.4456
2.0	0.4968	0.4976	1.2235	1.2247
2.5	0.4957	0.4967	1.1355	1.1369
3.0	0.5325	0.5326	1.0909	1.0920
4.0	0.6291	0.6370	1.0452	1.0523
5.0	0.7315	0.7438	1.0242	1.0331
6.0	0.8421	0.8512	1.0163	1.0236

# Authors' Reply

In their interesting note Yeung and Newman apply the method of matched asymptotic expansions to obtain the additive constant in the limiting potential, and they achieve this with comparatively little effort. It should be noted however, that in their equation (6) the potential  $\phi^{(n)}$  is of the form  $\phi^{(n)} = \phi^{(n)} + c^{(n)}$  where  $\phi^{(n)}$  is of order  $(k_0 h)^{n-1}$  and the constant  $c^{(n)}$  is of order  $(k_0 h)^{n-2}$ , i.e. of much larger magnitude. Thus the form (6) assumed by Yeung and Newman is not as obvious as a superficial reading might suggest. (Their form is of course consistent with earlier results, including our own). Another simple argument for obtaining the real and imaginary parts of  $C$  can be based on Green's theorem, and is due to appear in our Ref. (1).

Dr. Bai has kindly sent us a preprint of his paper but the detailed study of his arguments requires more time than we have yet been able to give it. His numerical values for the circular section at zero frequency are almost (but not quite) consistent with our own which are given below.

## Virtual Mass coefficient for the half-immersed circle at zero frequency

h/a	(V.M.) Ka=Kh=0
1.2	0.9654
1.5	0.6288
2.0	0.4984
2.5	0.4969
3.0	0.5330
4.0	0.6354
5.0	0.7418
6.0	0.8414

Dr. A.M.J. Davis rightly points out that our asymptotic values apply to physical ranges which are not likely to be realized in practice. A similar objection can be made to the well-known short-wave asymptotics for a heaving circular cylinder on deep water which nevertheless have a practical value because they can be used to provide a check on the computations at moderate wavelengths. If it had been realized in 1961 that in the present problem the virtual mass remains finite this would have served as a warning that the computations in our Ref. (2) were probably incorrect (as we now know they are).

We welcome the application of so many different methods of computation to the present problem. While our own method is particularly suitable for the circular section, other methods will probably turn out to be more suitable for other sections. Our aim in the present work has been the modest one of providing a reliable standard set of values for this one problem and we hope that this will prove useful for checking numerical work in the long-wave range.



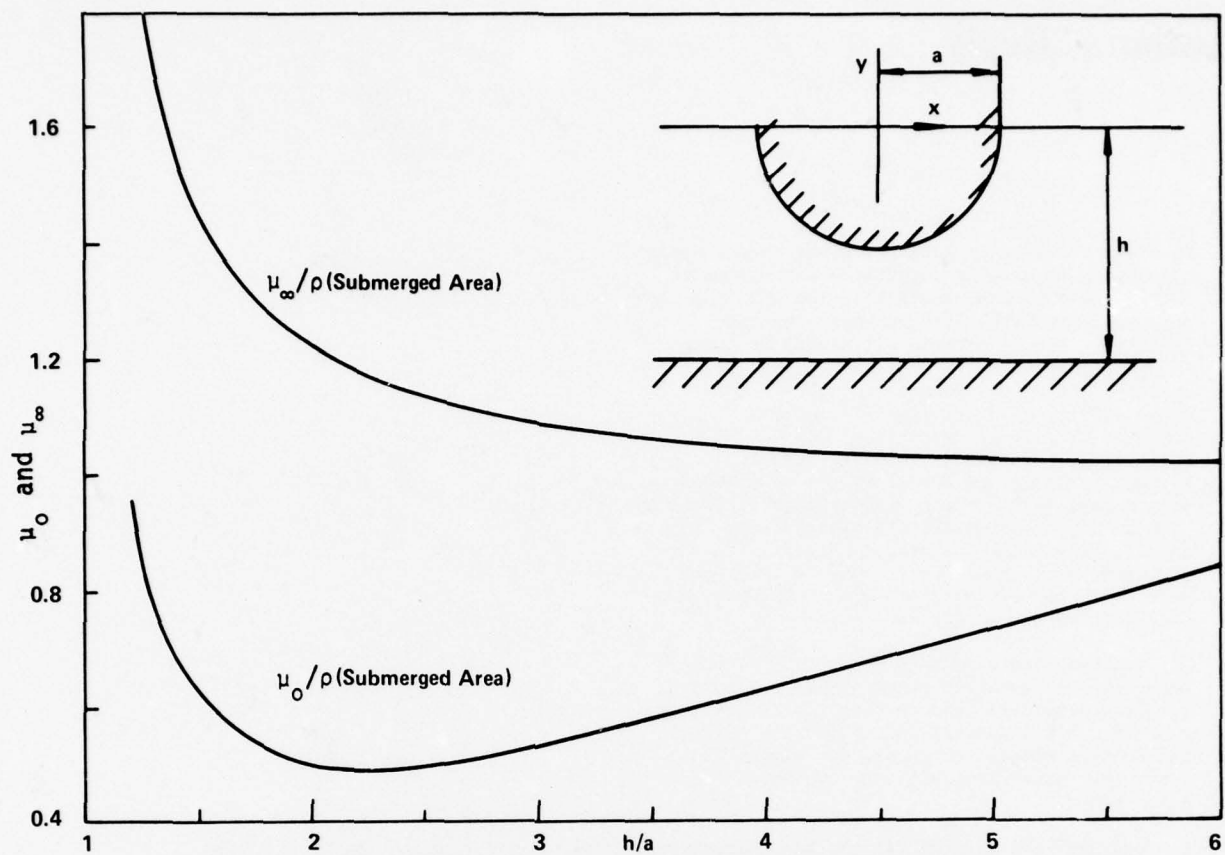


Fig. 1 The added masses of a circular cylinder versus water depth

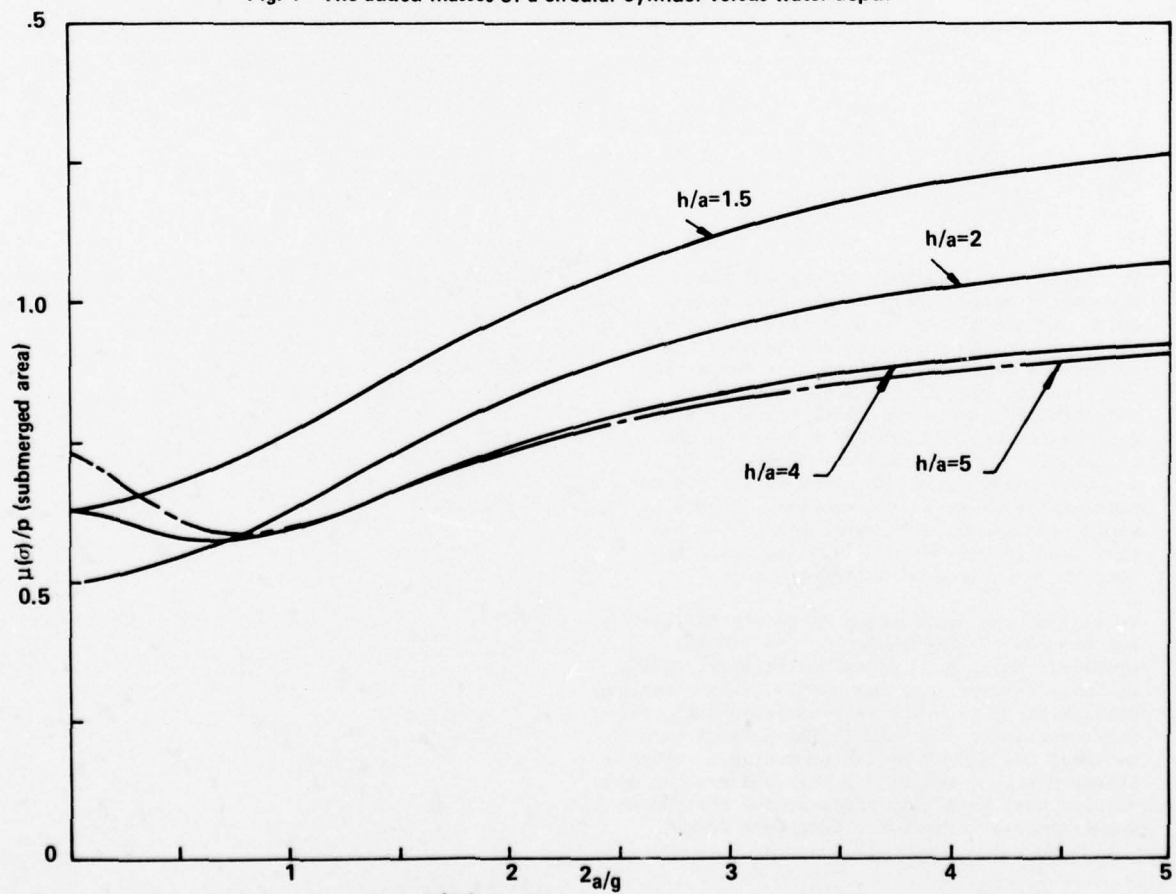


Fig. 2 Added Mass  $\tilde{\mu}(\dot{\sigma})$  of a Circular Cylinder versus  $v$  ( $v = \sigma^2 a/g$ ).

## SESSION VI

### STRUCTURAL DYNAMICS

Thursday, 1 April 1976

14.00—16.30

Chairman: K. Wieghardt

Wave and structural load experiments for elastic ships, by R. Wereldsma and G. Moeyes

Theoretical prediction of the vertical dynamic response of ships structures using finite elements and correlation with ship mobility, by D. Catley and C. Norris

Low frequency second order wave forces on vessels moored at sea, by J. A. Pinkster

Elastic structural response of semisubmersibles in regular waves, by K. Yoshida and K. Ishikawa

# WAVE AND STRUCTURAL LOAD EXPERIMENTS FOR ELASTIC SHIPS

R. WERELDSMA and G. MOEYES  
Delft University of Technology, The Netherlands

## SYNOPSIS

Measurements of wave exciting forces and total girder loadings on a large tanker model in head waves are described, with wave length varying from  $\lambda/L = .085$  to 2.0 and speed ranging from  $F_n = .10$  to .30.

Wave exciting forces may be predicted with strip theory for wave lengths greater than about half the ship length, but could not be calculated accurately for short waves.

The analysis of total girder loading is based on the "Normal Mode Method". Experimentally determined participation factors do qualitatively not agree with predicted curves based on the assumption of a simple sinusoidal longitudinal force distribution.

## 1. INTRODUCTION

The recent growth of maritime activities and its accompanying construction of big tankers, fast container ships, drilling platforms and other units according to new concepts, asks for a rational method of strength analysis. In designing these units experience on equally sized prototypes is not available and extrapolation of standard load calculations is not free from risk. As an example springing of Great Lake carriers, big tankers and long container ships and the resulting higher frequency stress variations and fatigue problems, can be mentioned as a phenomenon which did not occur before. To include frequency and resonance aspects independently in strength analysis the "normal mode technique" might be used to handle any spatial structure, as has been demonstrated by van Gunsteren in ref. (1) for the analysis of springing of a supertanker.

In ref. (2) it is shown how the experiments on models and the construction of models is affected by the application of this "normal mode technique". In this reference a description is given of the possibility to predict the stresses in the structure as a result of the wave loading and of the mass-elastic behaviour of the structure. Also an experimental technique is proposed in ref. (2) in order to arrive at the generalized wave excitation forces.

In this paper the results of preliminary experiments with a captive and a free "rigid back bone" model in the Delft Ship Hydromechanics Laboratory are reported. Tests with the restrained model give the wave exciting forces, whereas the free model tests supply the generalized forces, e.g. the net loading of the ships' girder not affected by the deflection of the girder nor by elastic resonance phenomena.

Due to towing tank and finance limitations only head waves and the resulting vertical loads have

been considered. Measurements are carried out on a large tanker model, which is extremely sensitive to such loads.

## 2. DISCUSSION OF THE OVERALL STRENGTH PROBLEM OF THE SHIPS GIRDER

When the ships girder is discretized in a sufficient number of masses and elasticities and when linearity is assumed, the motions due to heave and pitch and vertical bending can be described by:

$$[\bar{S}] \{x\} + [\bar{C}] \{\dot{x}\} + [\bar{M}] \{\ddot{x}\} = \{F\} - [\bar{M}] \{\ddot{x}\} - [\bar{C}] \{\dot{x}\} - [\bar{S}] \{x\} \quad (1)$$

where:  $\{x\}$  = displacement vector  
 $[\bar{S}]$  = stiffness matrix of the mechanical system  
 $[\bar{C}]$  = damping matrix of the mechanical system  
 $[\bar{M}]$  = mass matrix of the mechanical system  
 $\{F\}$  = wave excitation forces  
 $[\bar{M}]$  = matrix of hydrodynamic added mass, due to relative accelerations of the hull  
 $[\bar{C}]$  = matrix of hydrodynamic damping, due to velocities of the hull  
 $[\bar{S}]$  = matrix of buoyancy forces, due to displacements of the hull.

The right hand side of equation (1) consists of all hydrodynamic forces, both exciting and reaction forces, and is fully determined by the ships' form. The left hand part of equation (1) is closely connected to the ships' structure, which determines mass and stiffness distribution and internal (constructional) damping. Possible vibration dampers must also be included in this part.

During the design process of a ship main dimensions and body form are mostly established in an early stage, before the construction will be determined



and detailed. So the strength analysis method to be applied should preferably contain a one-time determination of the right hand side of equation (1), after which the total problem could be solved in a loop where the left hand constructional side of (1) is evaluated. (See ref. (3)). To facilitate this iteration and to pay full attention to frequencies of elastic motions and their related aspects of fatigue stress, a coordinate transformation of (1) to normal modes of the "dry ship" (i.e. the two rigid body motions heave and pitch and two and more mode vibration modes) will be applied. This results in a diagonalisation of the mechanical mass and stiffness matrix (ref. (4)).

In general the damping matrix can not directly be diagonalized, depending upon the lengthwise damping distribution. However, diagonalization is possible when the damping distribution is supposed to be similar to the distribution of mass or stiffness, which is general practice in ship vibration analysis.

The final result becomes:

$$\begin{aligned} [S] \{\psi\} + [C] \{\dot{\psi}\} + [M] \{\ddot{\psi}\} = \\ = \{\Gamma\} - [M] \{\ddot{\psi}\} - [C] \{\dot{\psi}\} - [S] \{\psi\} \end{aligned} \quad (2)$$

where:  $\{\psi\}$  = vector of normal mode displacements  
 $\{\Gamma\}$  = vector of generalized forces.

The left hand part of equation (2) is now diagonalized and the ship motion problem can be separated from the ship deflection problem. Also the dynamic amplification of one of the modes (e.g. the springing phenomena for the 2-noded deflection) can be dealt with separately. For this purpose it is necessary to diagonalize the entire system. Since this diagonalization requires knowledge of the hydrodynamic effects of the hull and the surrounding water it is proposed to make an approach by two steps.

The expansion of equation (2) for two rigid body modes and one elastic mode reads as follows:

$$\begin{aligned} \begin{bmatrix} M_{11} & 0 & 0 \\ 0 & M_{22} & 0 \\ 0 & 0 & M_{33} \end{bmatrix} \begin{Bmatrix} \ddot{\psi}_1 \\ \ddot{\psi}_2 \\ \ddot{\psi}_3 \end{Bmatrix} + \begin{bmatrix} C_{11} & 0 & 0 \\ 0 & C_{22} & 0 \\ 0 & 0 & C_{33} \end{bmatrix} \begin{Bmatrix} \dot{\psi}_1 \\ \dot{\psi}_2 \\ \dot{\psi}_3 \end{Bmatrix} + \\ + \begin{bmatrix} S_{11} & 0 & 0 \\ 0 & S_{22} & 0 \\ 0 & 0 & S_{33} \end{bmatrix} \begin{Bmatrix} \psi_1 \\ \psi_2 \\ \psi_3 \end{Bmatrix} = \\ = \begin{Bmatrix} \Gamma_1 \\ \Gamma_2 \\ \Gamma_3 \end{Bmatrix} - \begin{bmatrix} M_{11} & M_{12} & M_{13} \\ M_{21} & M_{22} & M_{23} \\ M_{31} & M_{32} & M_{33} \end{bmatrix} \begin{Bmatrix} \ddot{\psi}_1 \\ \ddot{\psi}_2 \\ \ddot{\psi}_3 \end{Bmatrix} - \\ - \begin{bmatrix} C_{11} & C_{12} & C_{13} \\ C_{21} & C_{22} & C_{23} \\ C_{31} & C_{32} & C_{33} \end{bmatrix} \begin{Bmatrix} \dot{\psi}_1 \\ \dot{\psi}_2 \\ \dot{\psi}_3 \end{Bmatrix} - \begin{bmatrix} S_{11} & S_{12} & S_{13} \\ S_{21} & S_{22} & S_{23} \\ S_{31} & S_{32} & S_{33} \end{bmatrix} \begin{Bmatrix} \psi_1 \\ \psi_2 \\ \psi_3 \end{Bmatrix} \end{aligned} \quad (3)$$

If the ship is not restrained by bow hawsers, mooring lines and the like, and if no additional artificial heave or pitch damping devices are fixed, the damping coefficients  $C_{11}$  and  $C_{22}$  are zero. The first step for the solution of the set of equations represented by (3) is to determine the wave exciting forces  $\{\Gamma\}$ , either by calculation or by experiment. The strip-theory (ref. (5), (6)), which is based on a two-dimensional potential calculation combined

with a three-dimensional coordinate transformation, is a proven tool to calculate the forces due to waves which are not too short compared to ship length (e.g.  $\lambda/L > 0.50$ ) (ref. (7)). The experimental determination of wave exciting forces, with a restrained segmented model, is described into more detail in the following paragraphs.

The second step in solving equations (3) is to determine the hydrodynamic coefficients represented by the  $[M]$ ,  $[C]$  and  $[S]$  matrices. These matrices have non-zero elements outside the diagonal, due to hydrodynamic cross-coupling. The coupling coefficients have a significant influence on rigid body motions so analogously their influence on elastic modes can not a priori be neglected. On the other hand rigid body displacements are small at the higher frequencies involved in elastic mode resonance, which does suspect less important influences of heave and pitch motion effects in the elastic modes. Hydrodynamic coupling between elastic modes depends upon the longitudinal distribution of damping and added mass at higher frequencies, about which no accurate results are known for the three-dimensional case.

Calculation of added mass and damping for two-dimensional sections is possible, either including free surface effects for a frequency range where significant rigid body motions occur (see ref. (8)), or in the asymptotic case of very high frequencies where surface waves are neglected.

These two-dimensional values provide a base for a sufficiently accurate prediction of coefficients in  $[M]$  and  $[C]$  which influence rigid body motions, but their applicability in the case of vibration modes becomes questionable because of three-dimensional effects.

The buoyancy matrix  $[S]$  can be calculated for all modes. A direct experimental determination of hydrodynamic reaction forces could be done by means of forced oscillation in one of the modes, with a normal vertical oscillator for rigid body motions and a special sectional oscillator for the elastic motions. Hydrodynamic reaction forces may also be obtained indirectly with the free moving model tests described in the following sections, when exciting forces are known from captive model tests, when the buoyancy matrix  $[S]$  is calculated and when heave and pitch are recorded.

However, these free moving model tests were primarily intended to measure directly the girder loading caused by the waves, including the effect of hull motions, i.e. inertia forces and hydrodynamic reaction forces.

### 3. DESCRIPTION OF THE SHIP AND THE MODEL AND ITS CONSTRUCTION

The particulars of the ship, a tanker, are given in Figure 1 and in Table 1.

Table 1. Particulars of ship.

Length between P.P.	310.0 m
Breadth moulded	46.9 m
Depth moulded	24.5 m
Block coefficient	0.84
Prismatic coefficient	0.85
L.C.B. in percentage of $L_{pp}$	+3.13
Deadweight	215,000.00 tons
Horse power	28,000.00 HP
r.p.m.	80 rpm

The models have been built to a scale 1:200/3 and the test conditions are as follows:

ballast draft (even keel) 12.27 m  
displacement ballasted 146,000 tons.

Ballast condition has been investigated first because loads in short waves are more important in ballast than fully loaded, due to the lower natural frequency of the two-node vertical vibration. It is realized that an even keel ballast condition is not usual for tankers. Even keel, however, has been chosen to ease the comparison with theory.

The captive model consists of a stiff beam and 24 sections connected to the beam. The beam is supported rigidly to the towing carriage of the tank. Each of the 24 connections of the segments to the beam consists of a dynamometer equipped with semi-conductor strain gauges to measure the vertical force exerted on the section. The total rigidity of the system is such that the lowest natural frequency is high in comparison with the frequencies of interest, so that elasto- and hydro-dynamic effects are negligible. (See Figure 2).

The free model consists of a stiff beam, constructed as light as possible. To this beam are connected 12 sections, containing as much of the required weight as possible. The connections of sections to the beam consist of a 3-component balance, in order to sense the vertical loading, the horizontal and the torsional loading (see Figure 3). For the experiments reported in this paper only the vertical loading is measured. The entire stiffness of the model is such that for the wave frequencies of interest no dynamic effects will influence the measurement, except the two possible motions of the model. More details about the weight distribution and the effects of the parasitic mass of the beam are dealt with in the Appendix.

#### 4. MEASUREMENTS AND EVALUATION

##### a. General

A framework of the measured speed and wave length values is presented in Table 2. The design speed of the considered tanker is  $F_n = 0.15$ . Higher speeds are not realistic for the full ship form, but have been included to have a wider range for studying speed effects.

For the free model tests  $F_n = .15$  and  $.25$  have been omitted. The shortest wave length was dictated by the available wave maker and electronic equipment, the longest wave length by model and tank dimensions. For some free model tests additional wave lengths have been investigated, besides those indicated in Table 2, in order to determine the wave length dependency of the measured quantities more accurately.

Some of the low speed, long wave runs suffered from wall influence. Boundaries calculated according to ref. (9) are indicated in Table 2.

The wave height has been chosen so that a reasonable signal could be recorded in connection with the signal-noise ratio, and that linearity was assured ( $\lambda/\zeta_a$  about 60).

##### b. Captive Model Tests

For the measurements in general it can be stated

that the output of the pick-ups coincides with the stiffness matrix multiplied with the displacement vector. Referring to formula (3) it can be stated that due to the stiff structure and the high sensitivity of the pick-ups:

$$\begin{Bmatrix} 0_1 \\ 0_2 \\ 0_3 \end{Bmatrix} = \begin{Bmatrix} S_{11} & \psi_1 \\ S_{22} & \psi_2 \\ S_{33} & \psi_3 \end{Bmatrix} = \begin{Bmatrix} \Gamma_1 \\ \Gamma_2 \\ \Gamma_3 \end{Bmatrix} \quad (4)$$

This is allowed because the mass-elastic and hydro-dynamic effects are negligible and substantial displacements will not take place.

Returning to the original coordinates  $\{x\}$  we find:

$$\begin{Bmatrix} u_1 \\ u_2 \\ \vdots \\ u_{24} \end{Bmatrix} = \begin{Bmatrix} F_1 \\ F_2 \\ \vdots \\ F_{24} \end{Bmatrix} \quad (5)$$

so that for the captive model test each section pick-up has a signal  $u$  equal to the hydrodynamic force exerted on the section, and we obtain 24 concentrated forces representing the wave load.

##### c. Free Model Tests

Referring to formula (3) it can now be stated that  $S_{11}$  and  $S_{22}$  are equal to zero (free model) so that:

$$\begin{aligned} \begin{Bmatrix} 0_1 \\ 0_2 \\ 0_3 \end{Bmatrix} &= \begin{bmatrix} 0 & 0 & 0 \\ 0 & 0 & 0 \\ 0 & 0 & S_{33} \end{bmatrix} \begin{Bmatrix} \psi_1 \\ \psi_2 \\ \psi_3 \end{Bmatrix} = \\ &= \begin{Bmatrix} \Gamma_1 \\ \Gamma_2 \\ \Gamma_3 \end{Bmatrix} - \begin{bmatrix} M_{11} & 0 & 0 \\ 0 & M_{22} & 0 \\ 0 & 0 & M_{33} \end{bmatrix} \begin{Bmatrix} \ddot{\psi}_1 \\ \ddot{\psi}_2 \\ \ddot{\psi}_3 \end{Bmatrix} + \\ &\quad - \begin{bmatrix} M_{11} & M_{12} & M_{13} \\ M_{21} & M_{22} & M_{23} \\ M_{31} & M_{32} & M_{33} \end{bmatrix} \begin{Bmatrix} \ddot{\psi}_1 \\ \ddot{\psi}_2 \\ \ddot{\psi}_3 \end{Bmatrix} - \begin{bmatrix} C_{11} & C_{12} & C_{13} \\ C_{21} & C_{22} & C_{23} \\ C_{31} & C_{32} & C_{33} \end{bmatrix} \begin{Bmatrix} \dot{\psi}_1 \\ \dot{\psi}_2 \\ \dot{\psi}_3 \end{Bmatrix} \\ &\quad - \begin{bmatrix} S_{11} & S_{12} & S_{13} \\ S_{21} & S_{22} & S_{23} \\ S_{31} & S_{32} & S_{33} \end{bmatrix} \begin{Bmatrix} \psi_1 \\ \psi_2 \\ \psi_3 \end{Bmatrix} \quad (6) \end{aligned}$$

From this it follows for the case the model is sufficiently stiff so that deflection modes such as  $\psi_3$  and higher are negligible:

$$\begin{aligned} \begin{Bmatrix} 0_1 \\ 0_2 \\ 0_3 \end{Bmatrix} &= \begin{Bmatrix} 0 & \psi_1 \\ 0 & \psi_2 \\ S_{33} & \psi_3 \end{Bmatrix} = \begin{Bmatrix} \Gamma_1 \\ \Gamma_2 \\ \Gamma_3 \end{Bmatrix} - \begin{bmatrix} M_{11} & 0 \\ 0 & M_{22} \\ 0 & 0 \end{bmatrix} \begin{Bmatrix} \ddot{\psi}_1 \\ \ddot{\psi}_2 \end{Bmatrix} - \\ &\quad + \begin{bmatrix} M_{11} & M_{12} \\ M_{21} & M_{22} \\ M_{31} & M_{32} \end{bmatrix} \begin{Bmatrix} \ddot{\psi}_1 \\ \ddot{\psi}_2 \end{Bmatrix} - \begin{bmatrix} C_{11} & C_{12} \\ C_{21} & C_{22} \\ C_{31} & C_{32} \end{bmatrix} \begin{Bmatrix} \dot{\psi}_1 \\ \dot{\psi}_2 \end{Bmatrix} + \\ &\quad - \begin{bmatrix} S_{11} & S_{12} \\ S_{21} & S_{22} \\ S_{31} & S_{32} \end{bmatrix} \begin{Bmatrix} \psi_1 \\ \psi_2 \end{Bmatrix} \quad (7) \end{aligned}$$

## VI.6

$$O_1 = 0 = \Gamma_1 - M_{11}\ddot{\psi}_1 - M_{12}\ddot{\psi}_2 - C_{11}\dot{\psi}_1 - C_{12}\dot{\psi}_2 - S_{11}\psi_1 - S_{12}\psi_2 \quad (8)$$

$$O_2 = 0 = \Gamma_2 - M_{22}\ddot{\psi}_2 - M_{21}\ddot{\psi}_1 - C_{22}\dot{\psi}_2 - C_{21}\dot{\psi}_1 - C_{22}\dot{\psi}_2 - S_{21}\psi_1 - S_{22}\psi_2 \quad (9)$$

$$O_3 = \Gamma_3 - M_{31}\ddot{\psi}_1 - M_{32}\ddot{\psi}_2 - C_{31}\dot{\psi}_1 - C_{32}\dot{\psi}_2 - S_{31}\psi_1 - S_{32}\psi_2 \quad (10)$$

The outputs  $O_1$  and  $O_2$  are zero, because the generalized wave forces are fully consumed to generate the ship motions. Then, (8) and (9) are the equations of motion describing the rigid body motions heave and pitch.

Output  $O_3$  is the generalized version of the girder loading, composed of the wave excitation  $\Gamma_3$  and corrected for the hydrodynamic reaction forces, added mass, damping and buoyancy, caused by the ship motions  $\psi_1$  and  $\psi_2$ .

Outputs  $O_{4,5,6}$  are similar generalized loads, however now referring to higher node displacement functions (for the sake of simplicity not shown in the formulae), including hydrodynamic effects originating from the rigid body motions  $\psi_1$  and  $\psi_2$  too, but not from other elastic modes.

### d. Instrumentation

Figures 4 and 5 show the instrumentation used for the measurements. The method of signal filtering, based on the frequency of encounter, is for each case (captive versus free model) adapted to the particular requirements. For the captive model tests multiplication is carried out through rotating resolvers, driven by a servo-mechanism following the wave zero-crossings (ref. (10)). For the free model tests the demodulated signals are weighted and summed before being multiplied with the references, i.e. before being Fourier-analyzed on a wave signal base. Multiplication takes place with electronic multipliers. In both cases average values are obtained by integration and time division over a chosen number of wave periods.

## 5. MEASUREMENT RESULTS

### a. Captive Model Test Results

Figures 7 through 16 show amplitude and phase of the sectional wave exciting forces, each for a particular wave length and the whole range of speeds. Amplitudes have been divided by wave amplitude and section length to make them better comparable to each other and to calculations. In this respect it must be realized that most calculations provide a continuous lengthwise distribution of the limit force values on infinitely short sections. The forces on sections with a finite length must be obtained by vectorial integration of the former ones. When the wave length approaches more and more the section length the deviation between the continuous basic force distribution and stepped sectional forces as shown in Figures 7 - 16 grows. Phases have not been determined with respect to the wave at the ships' center of gravity, as is usual, but at the mid-length position of the concerning section, in

order to get a presentation which can physically better be understood.

The distribution of wave exciting forces has also been calculated with the strip-theory as developed by Gerritsma et al. (ref. (5)), however, due to lack of time, without adapting it to the numerical demands put forward by the short waves and without taking into account the finite section length as mentioned above. As an example the results of these preliminary calculations are shown for  $\lambda/L = 0.75$  and 1.0, where the mentioned effects do not yet significantly count, in Figures 13 and 14.

The agreement between measurement and theory is good except for the higher speeds, as could be expected with the excessive wave formation along the full tanker body. Another deviation of theory and measurements is apparent at the parallel mid-body, where strip theory predicts a constant lengthwise distribution, but where experiments show a decay in amplitude due to three-dimensional effects (ref. (11), (12)).

For shorter wave lengths the disagreement between preliminary calculated and experimental results was so large that presentation was not considered useful. The measured forces do not show the considerable decay in amplitude from fore to aft which is sometimes expected in literature. The force peak at the afterbody might cause a significant increase of springing stresses.

An apparent feature of the exciting force distribution at shorter wave lengths and higher speeds is the rapid increase in phases from fore to aft, combined with a fluctuating amplitude. This typical behaviour might result from diffraction terms in the wave force expression, containing wave circular frequency, speed and sectional damping and added mass.

### b. Free Model Test Results

Although the experiments have originally been initiated to investigate the mechanics of springing, i.e. a dynamic phenomenon caused by the time variable short wave loadings, interesting results have been obtained also for larger waves, this because the springing problem can be seen as a special case of the general strength problem of ships. The required method of analysis for springing covers also the regular low frequency analysis in a generalized version. Therefore the experiments are also extended to longer waves and static phenomena.

#### Still Water Test Results

Figure 17 shows for 3 speeds of the model the static load distribution caused by the wave system generated by the model. The model has adjusted itself for heave and pitch so that only higher mode load distributions could be developed.

It can be concluded that for a ship model speed of 1.35 m/sec a static sagging loading is generated which is comparable to the standard wave sagging/hogging loading. From the measurements appears that this static load distribution is not essentially affected by waves, so that the superposition principle may be applied.

#### Wave Test Results in Ship Coordinates

In Figures 18, 19 and 20 the dynamic part of the girder loading due to incoming headwaves is shown



by means of an instantaneous distribution and an estimated envelope of the amplitudes of the variations. For those experiments where the ship motions are not negligible i.e. in the range of about  $0.5 < \lambda/L < 2.0$  a small correction is necessary due to the acceleration forces of the beam. (See Appendix). This correction has not been made, but the general picture will not be affected by this correction.

An example of the total loading in ship coordinates i.e. the static and the dynamic wave loading, is shown in Figure 21. Although it is interesting to have this complete picture of the girder loading for head waves, not very much can be done with it, unless a rational method of analysis is applied. This method is found in the "normal mode method" as described in ref. (2) and a further evaluation of the measurements is made according to this method.

#### Wave Test Results in Generalized Coordinates

As has been outlined in ref. (2) a special modal integration of the 12 section forces results in the participation of the wave excitation in the various elastic modes, or in the excitation forces for the two- and multinode deflection modes, coinciding with the vibration modes.

Together with the mass-spring response function of a particular mode an "Elastic Response Amplitude Operator" can be formulated, similarly as the regular "Response Amplitude Operator" used for ship motions. The modal integration consists of the summation of the mass- and deflection-weighted section forces, measured during the experiments (see Figure 5). Results of the experiments are shown in Figures 22, 23 and 24 for the two-, three- and four-noded deflections for the various ship speeds. These figures show that the systematic pattern, expected when a sinusoidal loading moves along the ship girder, is not realistic. The hydrodynamic loading caused by waves and ship motions obviously disturbs the deterministic picture to be expected.

#### 6. FINAL REMARKS

- a) Further theoretical and experimental study of wave exciting forces in the short wave range is necessary because of the disagreement between results of existing calculation procedures and the experiments described in this paper. This may be greatly influenced by diffraction terms in the wave exciting forces.
- b) Added mass and damping matrices should be investigated more thoroughly, especially in the three-dimensional higher frequency case.
- c) The static girder loading caused by the ship generated wave system amounts to the order of the standard wave sagging-hogging loading.
- d) The originally expected picture (see ref. (2)) of the modal participation of the wave loading as a function of wave length is in strong disagreement with the measured functions. As far as wall effects were not encountered during the experiments, this may be due to the difference between the assumption of simple Froude-Kriloff exciting forces for the prediction (2) and the real forces (see also remark a). It may be concluded that more study is necessary in the range of shorter waves to understand the total physical mechanism.

- e) For a complete picture of the loading on ships it is necessary to investigate oblique waves for the introduction of torsion and horizontal bending, which is essential for the analysis of container and open ships.
- f) A further study is necessary, either theoretical or experimental, to introduce statistics in the girder-load-problem caused by irregular waves.

#### 7. ACKNOWLEDGEMENT

Complicated experiments as have been described in this paper can not be carried out without the support and team-work of many people.

The authors are indebted to the technical and scientific staff of the Delft Ship Hydromechanics Laboratory and Delft Ship Structures Laboratory for their enthusiastic and creative cooperation.

#### 8. REFERENCES

- (1) van Gunsteren, F.F.; Springing; wave induced ship vibrations; Intern. Shipb. Progress; 1970; Vol. 19, No. 195, Nov.
- (2) Wereldsma, R.; Normal mode approach for ship strength experiments, a proposal; Symp. 'The dynamics of marine vehicles and structures in waves'; London, April 1974.
- (3) Wereldsma, R.; Modell-Versuchsprobleme bei elastischen, seegehenden Konstruktionen; Schiffstechnik; 1975; Bd. 22; pp. 29-46.
- (4) Bishop, R.E.D., Eatock Taylor, R. and Jackson, K.L.; On the structural dynamics of ship hulls in waves; Trans. R.I.N.A.; 1973.
- (5) Gerritsma, J. and Beukelman, W.; Analysis of the modified strip theory for the calculation of ship motions and wave bending moments; Neth. Ship Res. Center TNO; 1967; Report No. 96 S, June.
- (6) Salvesen, N., Tuck, E.O. and Faltinsen, O.; Ship motions and sea loads; Trans. S.N.A.M.E.; 1970.
- (7) Wahab, R. and Vink, J.H.; Wave induced motions and loads on ships in oblique waves; Neth. Ship Res. Center TNO; 1974; Report No. 193 S, May.
- (8) Vugts, J.H.; The hydrodynamic forces and ship motions in waves; Doctor's thesis, Delft Univ. of Technology; 1970.
- (9) Hanaoka, T.; On the velocity potential in Michell's system and the configuration of wave ridges due to a moving ship; Japan Soc. of Nav. Architects; 1953.
- (10) Buitenhuis, M.; Phase-locked loop servo-system; Delft Ship Hydromech. Labor.; to be published.
- (11) Grim, O.; Die Deformation eines regelmässigen, in Längsrichtung laufenden Seegang durch ein fahrendes Schiff; Schiffstechnik; 1962; Vol. 9, No. 46.
- (12) Maruo, H.; On the wave pressure acting on the surface of a slender ship fixed in head seas; 14th I.T.T.C., Ottawa; 1975.

## APPENDIX

Construction of ModelMeasurement of Structural LoadingCorrections for Parasitic Mass of the Beam, Idealisation

The ship model for the free model tests is composed of a light stiff beam, representing the bending stiffness of the model. Hooked to the beam are the model sections. These sections represent the shape of the ship, and do contain all the mass of the model (see Figure A-1). The connection of the sections to the beam is equipped with strain gauges so that three force components (i.e. vertical force, horizontal force and torsional moment) can be measured. The stiffness of the entire structure (including beam, pick-ups and sections) is such that the lowest natural frequency is about 23 c.p.s., which is high in comparison with the highest frequency of interest, the frequency of wave encounter, about 5 c.p.s. The sections of the model are as a matter of fact large pressure pick-ups, measuring the integrated pressure over the surface of the section.

The measurements can be analyzed according to a technique of generalized coordinates. Because two rigid body motions are performed during the measurement of this free model it is necessary to analyze the dynamics of the system through normal modes which are in this case assumed. These modes are given in Figure A-2, together with their mass-spring representation.

Originally the break-down in normal modes consists of a regular decomposition of a beam with mixed mass and elasticity into its normal modes. Because the sections are elastically connected to the beam, and this elasticity is applied for the measurement, it is necessary to describe the elastic deflections of the sections relative to the beam in order to analyze the output of the measuring system. Therefore each original mode has been split into two new modes. Besides the rigid body heave- and pitch-motion we have now introduced an elastic motion governing the elastic deformation of the measuring springs in a modal fashion. Each of the elastic modes, i.e. sagging-hogging and the multiple node deflections, are now split into two new modes, composed of "in phase motion distribution" and "opposite motion distributions". Since the model consists of 12 sections we need for a complete description 24 elastic modes and 4 modes related to the rigid body motions, in total 28 degrees of freedom.

For a description of the behaviour of the various modes, in connection with the signal output of the pick-ups, two types of systems as shown in Figure A-3 have to be analyzed. The output of the instrument equals  $x_1 - x_2$ .

In the case of Figure A-3a referring to pitch and heave modes, the transfer of  $\Gamma_1$  to  $C_1 (x_1 - x_2)$  equals:

$$\frac{C_1 (x_1 - x_2)}{\Gamma_1} = \frac{1}{\frac{M_1 + M_2}{M_2} - \omega^2 \frac{M_2}{C_1}} \quad (A1)$$

For the case  $M_2 \rightarrow 0$  (mass of beam of the model tends to zero) the transfer equals:

$$\frac{C_1 (x_1 - x_2)}{\Gamma_1} = 0 \quad (A2)$$

This means that all the excitation  $\Gamma_1$  is used for the acceleration of the mass of the sections.

For the case  $M_2 \neq 0$  but  $C_1$  is sufficiently high (which means a stiff spring, related to a sufficiently high natural frequency, which is indeed the case for our model) the following transfer function is obtained:

$$\frac{C_1 (x_1 - x_2)}{\Gamma_1} = \frac{M_2}{M_1 + M_2} \quad (A3)$$

independent of the frequency,

$$\text{or: } C_1 (x_1 - x_2) = \Gamma_1 \cdot \frac{M_2}{M_1 + M_2} = M_2 \cdot \text{modal acceleration} \quad (A4)$$

This part of  $\Gamma_1$  is an inertia force, that has not been subtracted from the hydrodynamic forces (as should have been the case for  $M_2 = 0$ ). This distributed parasitic force is affecting the output of elastic mode excitation, and, if a substantial error is introduced, corrections need to be applied.

The second system of importance is that of Figure A-3b. This system is involved in all the elastic mode measurements as well as the rigid body modes of the captive model. When the stiffness of the springs involved is sufficiently high (i.e. natural frequencies high in comparison with the maximum frequency of interest) a quasi-static approach can be made and it follows:

$$C_1 (x_1 - x_2) = \Gamma_1 \quad (A5)$$

so that in all cases a measuring output equal to the generalized force is obtained. In general the following conclusions can be made:

a. For the Captive Model

The output of the instruments equals the generalized forces for all the modes, and a reconstruction to the distributed loading results in a proper measurement of the load distribution.

b. For the Free Model

For the case the beam is indeed massless the output of the force pick-ups represents the inertia corrected ships' girder loading, composed of the hydrodynamic wave loading, the hydrodynamic loading due to the ship motions and the inertia forces.

For the practical case that the beam also has a mass, corrections have to be introduced because part of the forces is necessary to accelerate the mass of the beam, and is therefore not included in the correction for the inertia forces.

For the reconstruction of the distributed loading it is in principal necessary to apply an inertia correction, caused by the mass of the beam.

Force Distributions to be Applied for the Correction  
in the Case of the Free Model

The weight distribution of beam, sections and additional equipment, necessary for the guidance of the model under the carriage, is shown in Figure A-4. The correction to be applied is evaluated in Figure A-5. The distributed forces shown in this figure have to be decomposed in generalized forces operating in the applied elastic modes.

The distributed forces are as a matter of fact the result of beam acceleration for the rigid body modes (heave and pitch) and need therefore be applied as corrections. The magnitude of this correction depends on two factors, i.e. the magnitude of the acceleration during the tests and the participation of these force distributions in the modes of interest. Since the area of interest is in the short waves, the ship motions and the accelerations will be small. Also the participation in the 2-noded elastic mode which is the most important for ship strength analysis will be small because of the almost constant distribution. For the evaluation of the measurements it is assumed that, for the time being, the corrections are negligible.


Table 2.

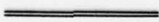
Tested wave lengths and speeds.

$\lambda/L$	$F_n$				
	.10	.15	.20	.25	.30
	$v_m$ in m/sec.				
	0.68	1.01	1.35	1.69	2.03
0.065	C				
0.085	C				
0.120	C F	C	C F	C	C F
0.160	C F	C	C F	C	
0.215	C F	C	C F	C	C F
0.280	C F	C	C F	C	C F
0.375	C F	C	C F	C	C F
0.550	C F	C	C F	C	C F
0.750	C F	C	C F	C	C F
1.00	C F	C	C F	C F	C F
1.25	C	C	C	C	C F
1.50	C	C	C F	C F	C F
2.00			F		F
2.50					F

C = carried out with captive model

F = carried out with free model

 = not tested because of equipment restrictions

 = boundary of region with wall influence, according to ref. (9).



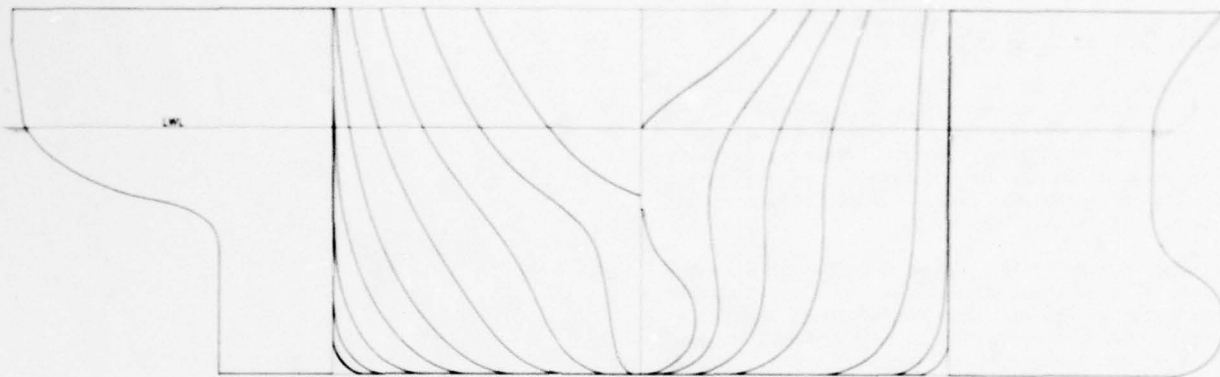


Fig. 1: Body plan of investigated ship.

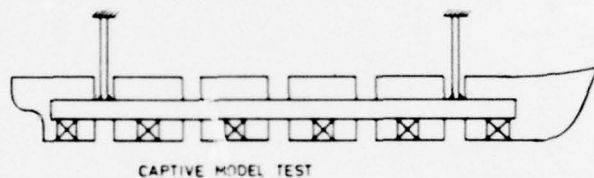


Fig. 2: Captive model test arrangement.

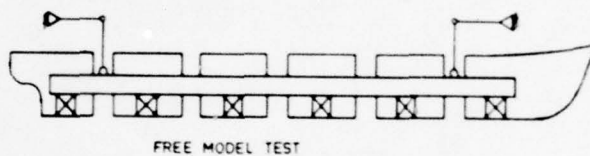


Fig. 3: Free model test arrangement.

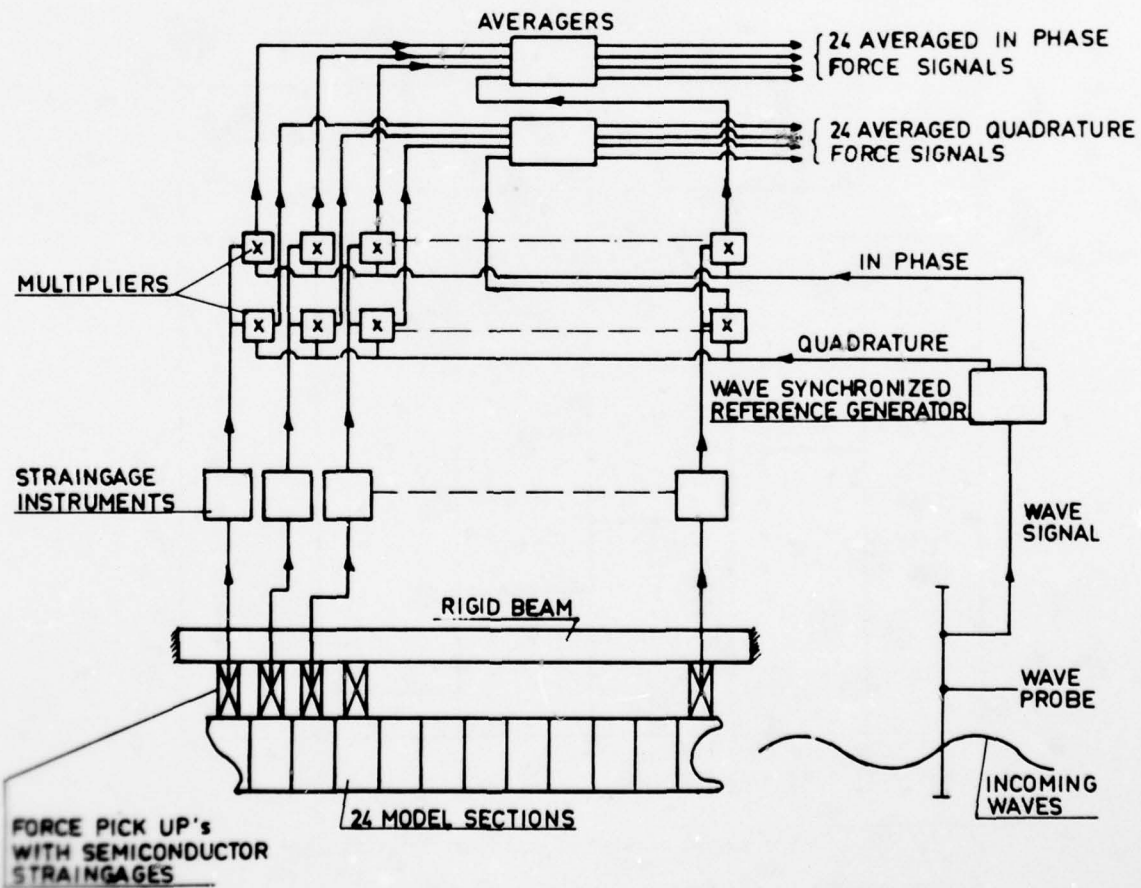


Fig. 4: Instrumentation for the captive model test.

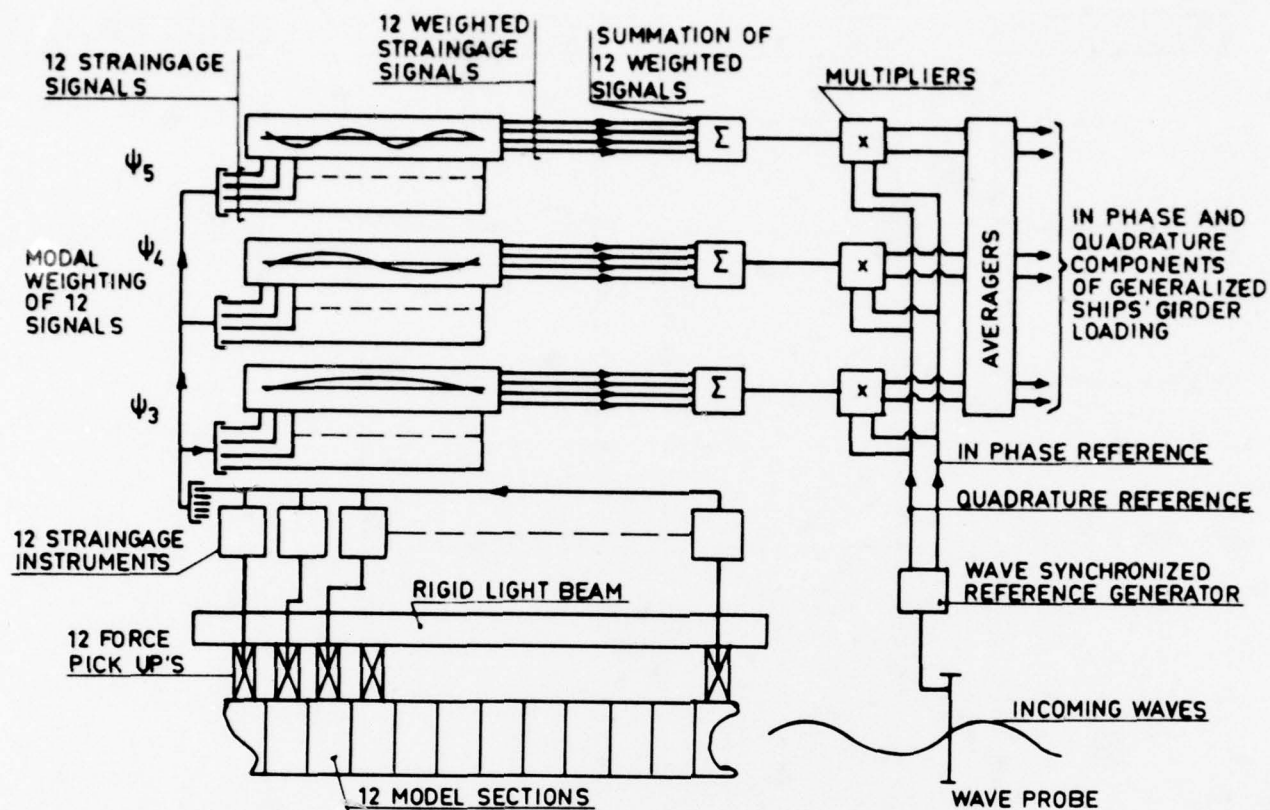


Fig. 5: Instrumentation for the free model test.

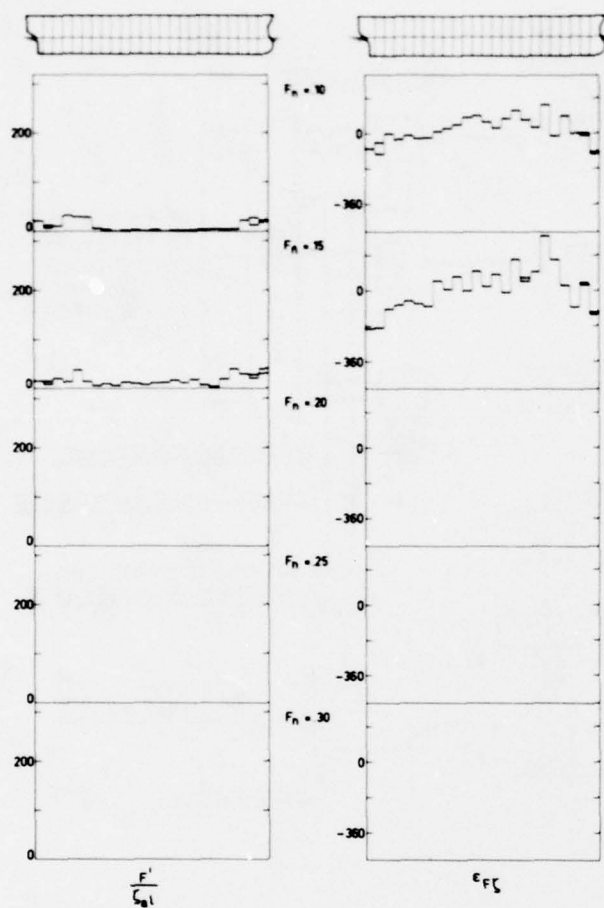


Fig. 6: Sectional wave exciting forces, ballast:  
 $\lambda/L = .085$ .

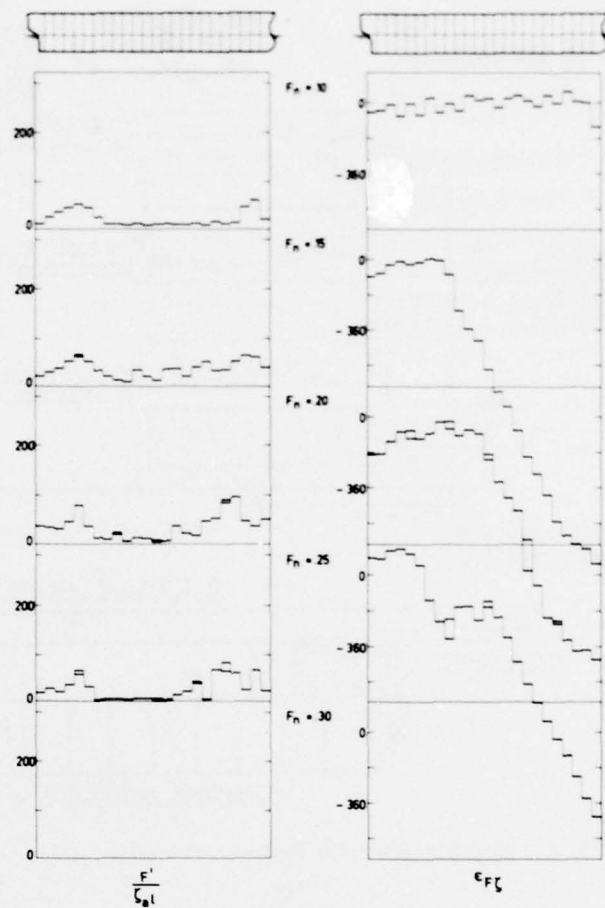


Fig. 7: Sectional wave exciting forces, ballast:  
 $\lambda/L = .120$ .



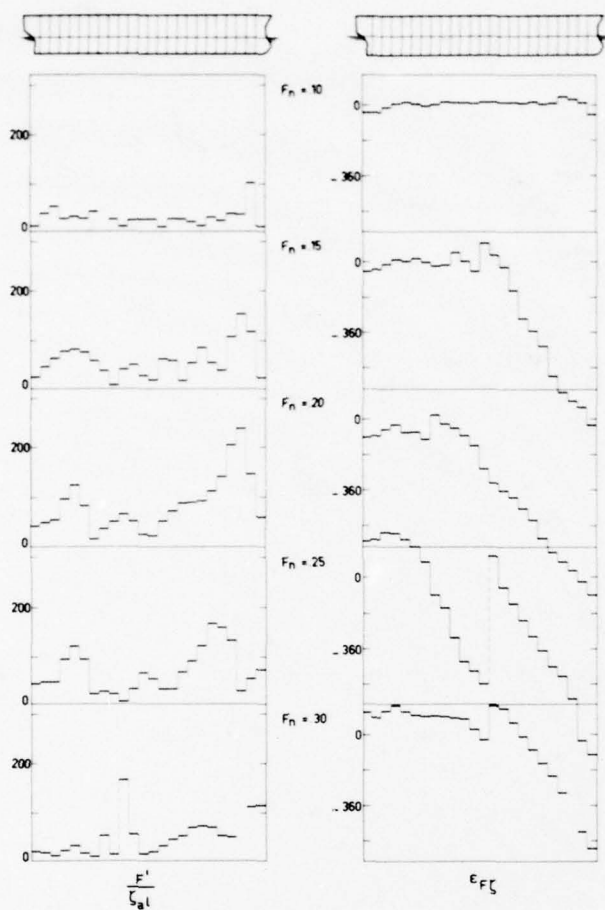


Fig. 8: Sectional wave exciting forces, ballast:  
 $z/L = .160$ .

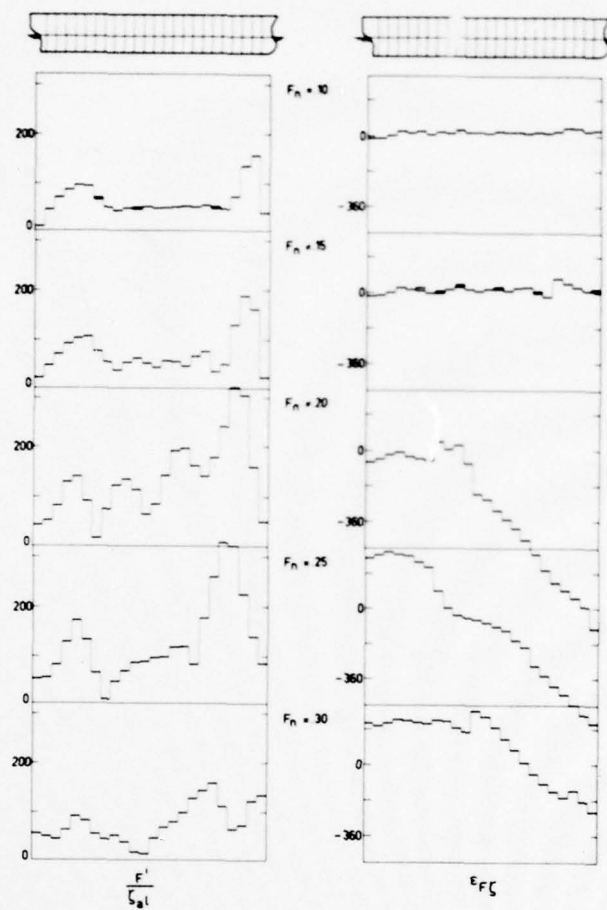


Fig. 9: Sectional wave exciting forces, ballast:  
 $z/L = .215$ .

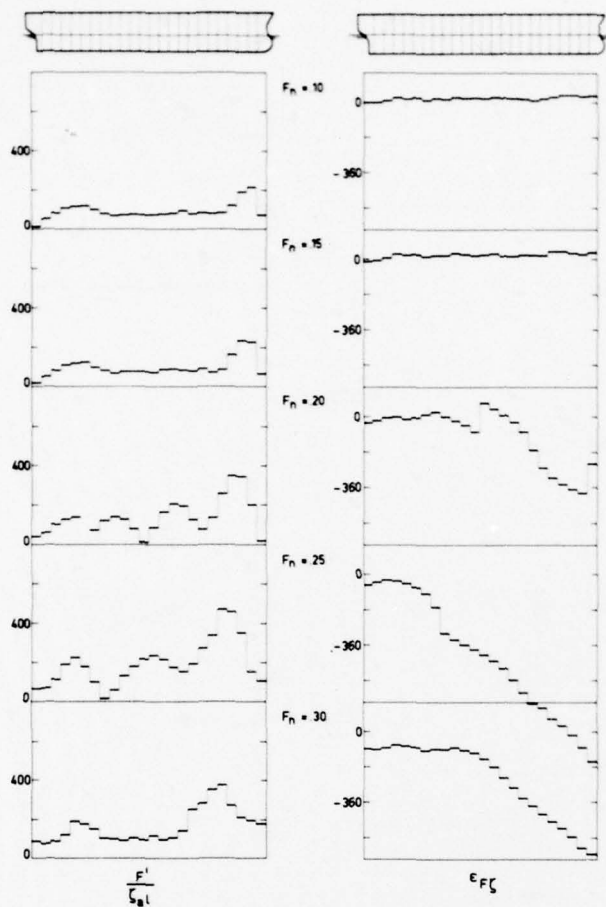


Fig. 10: Sectional wave exciting forces, ballast:  
 $\lambda/L = .280$ .

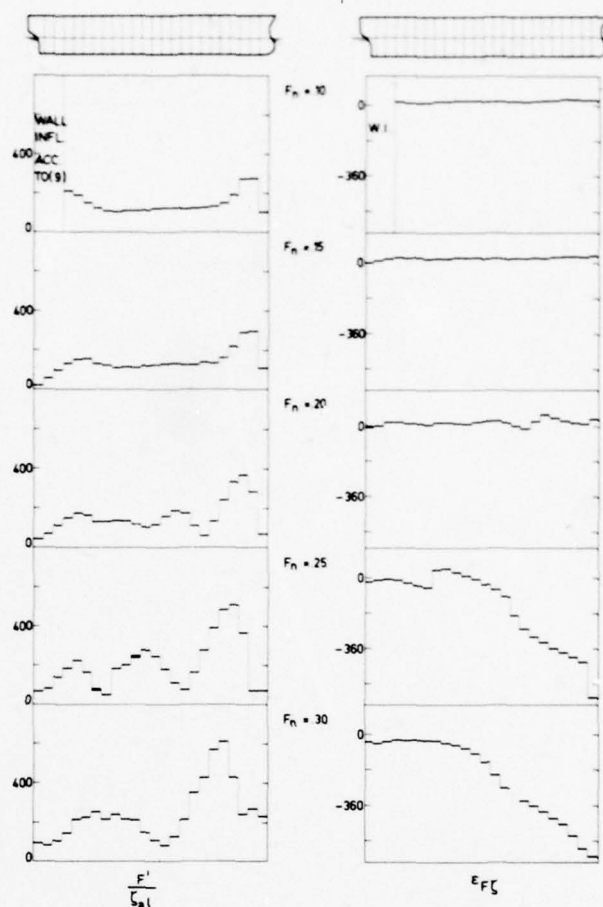


Fig. 11: Sectional wave exciting forces, ballast:  
 $\lambda/L = .375$ .

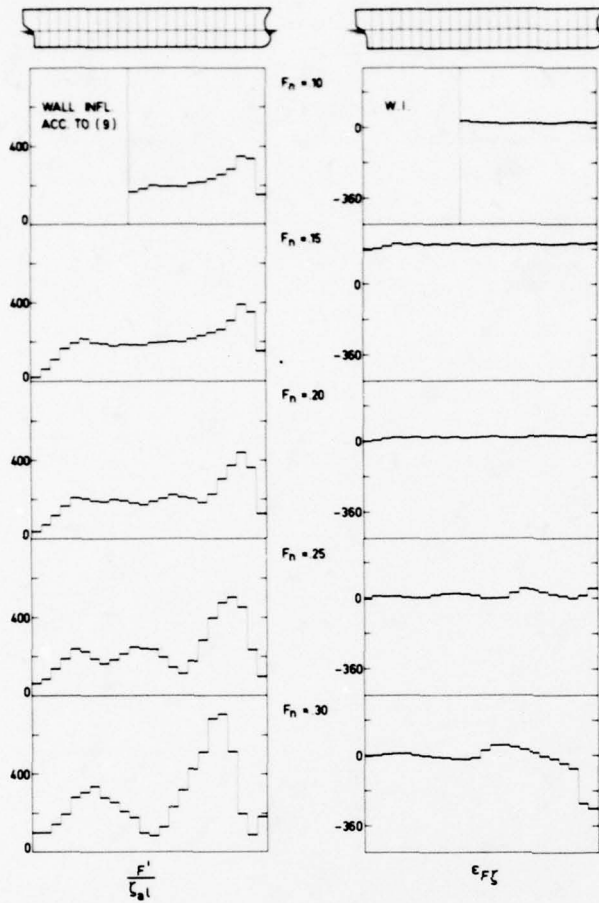


Fig. 12: Sectional wave exciting forces, ballast:  
 $\lambda/L = .550$ .

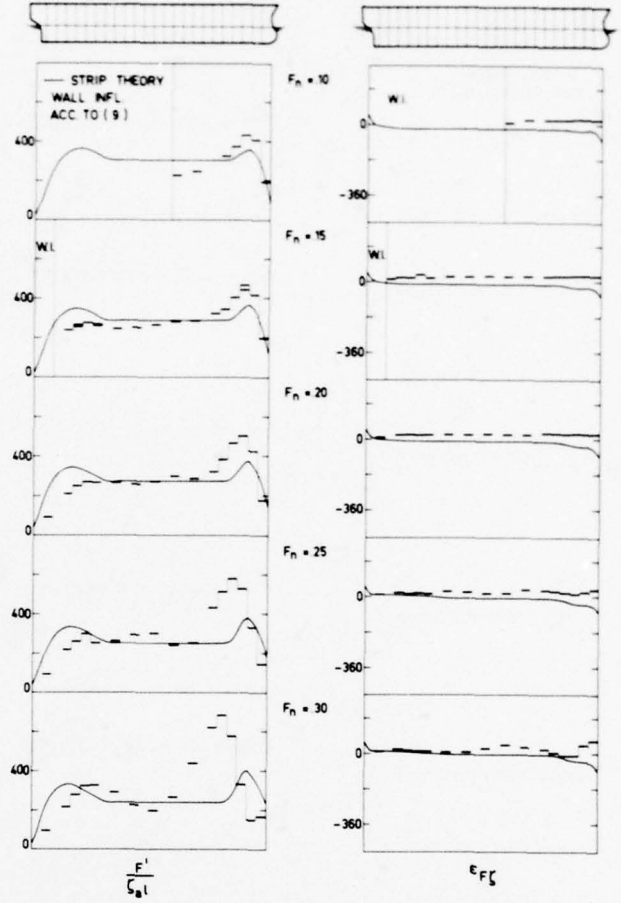


Fig. 13: Sectional wave exciting forces, ballast:  
 $\lambda/L = .750$ .



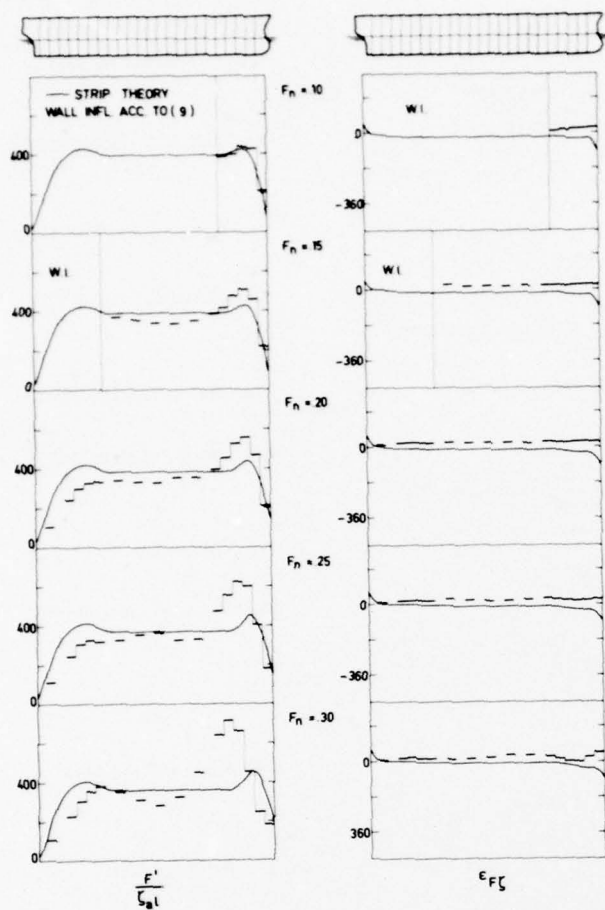


Fig. 14: Sectional wave exciting forces, ballast:  
 $\lambda/L = 1.00$ .

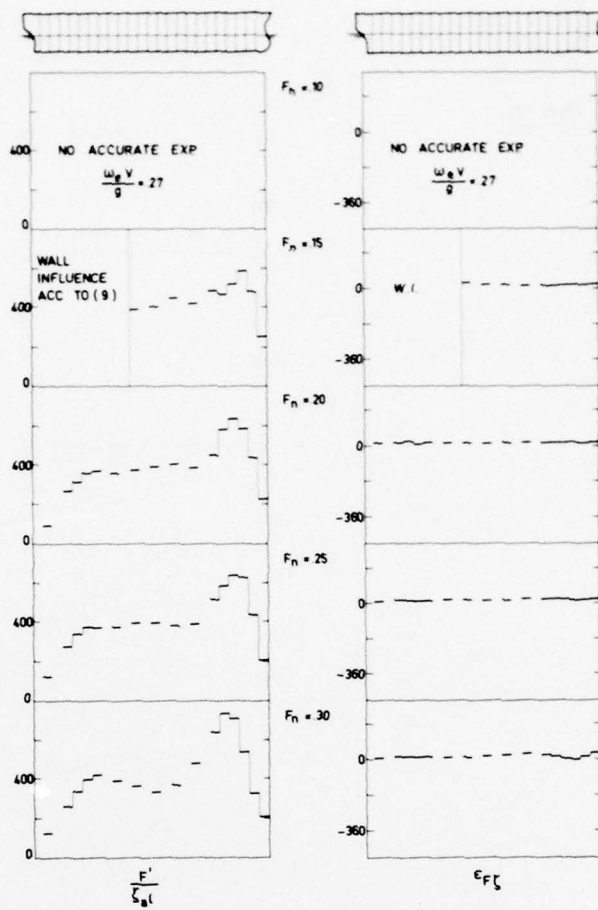
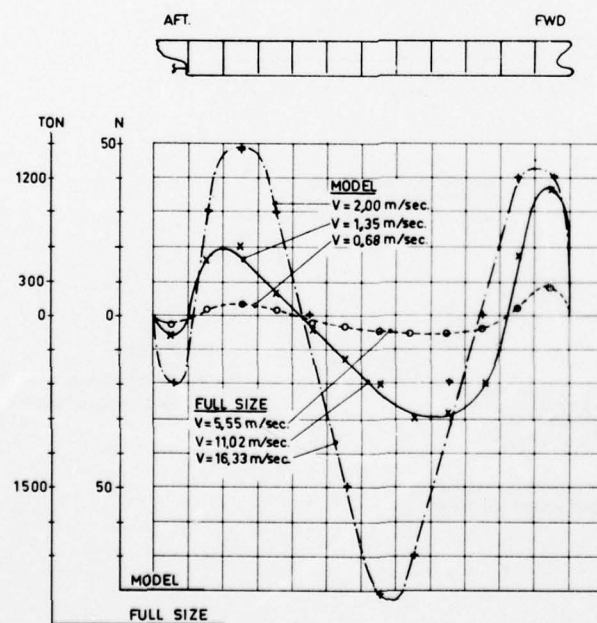
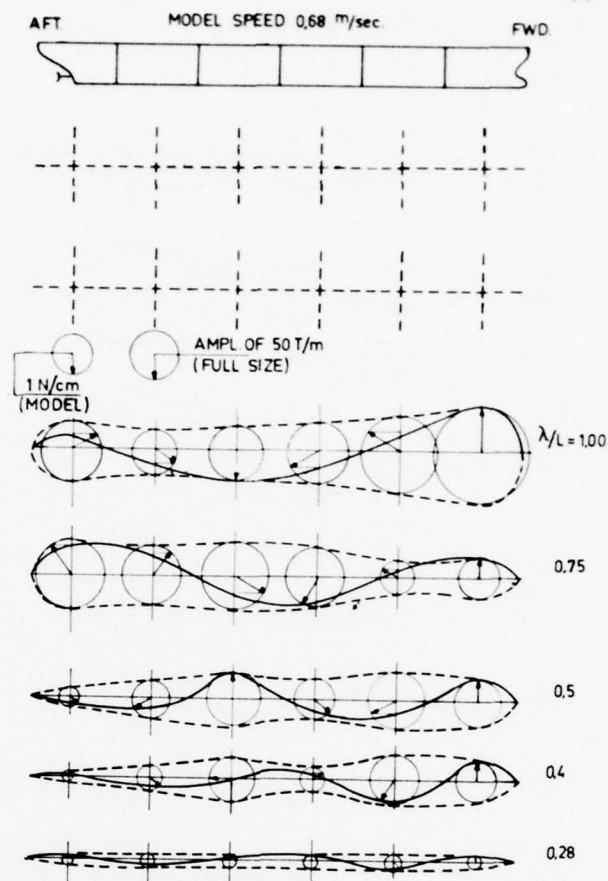
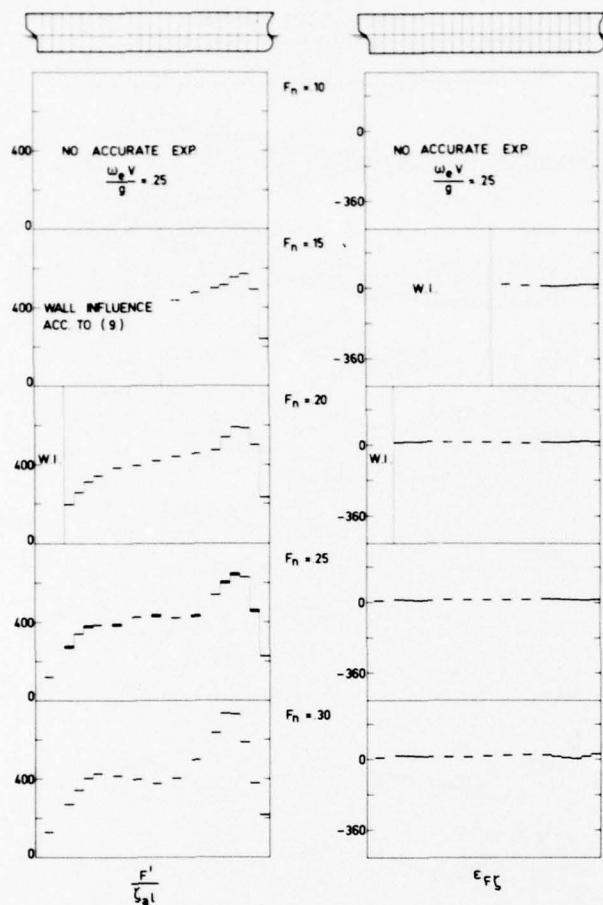


Fig. 15: Sectional wave exciting forces, ballast:  
 $\lambda/L = 1.25$ .



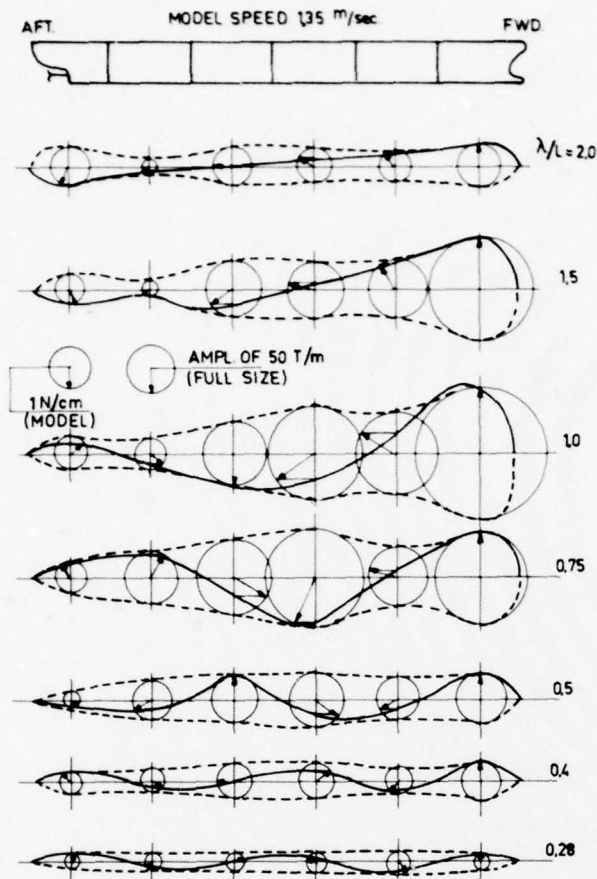


Fig. 19: Sectionalized girder loading per unit wave height at a forward speed of 1.35 m/sec. (force/wave height).

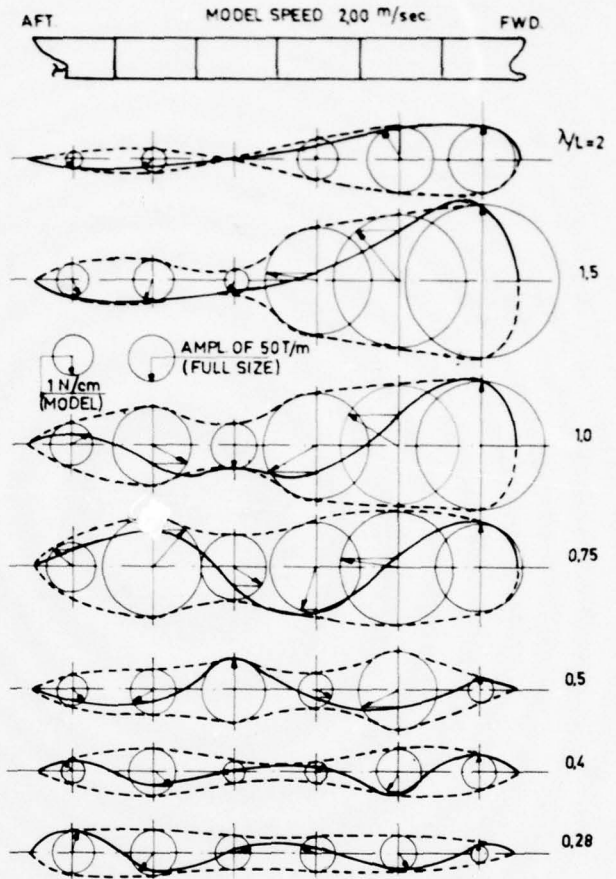


Fig. 20: Sectionalized girder loading per unit wave height at a forward speed of 2.00 m/sec. (force/wave height).

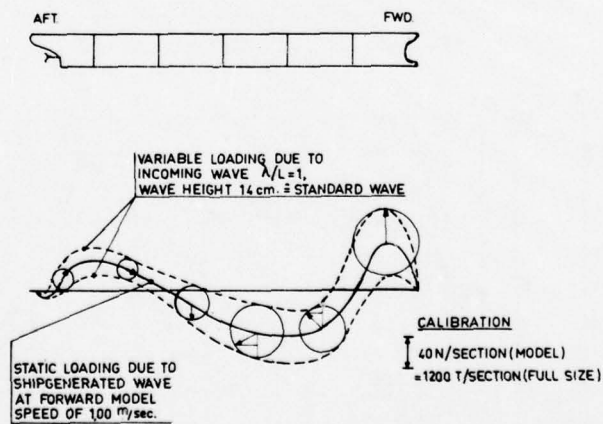


Fig. 21: Combined loading due to the standard wave loading and the ship generated wave loading.



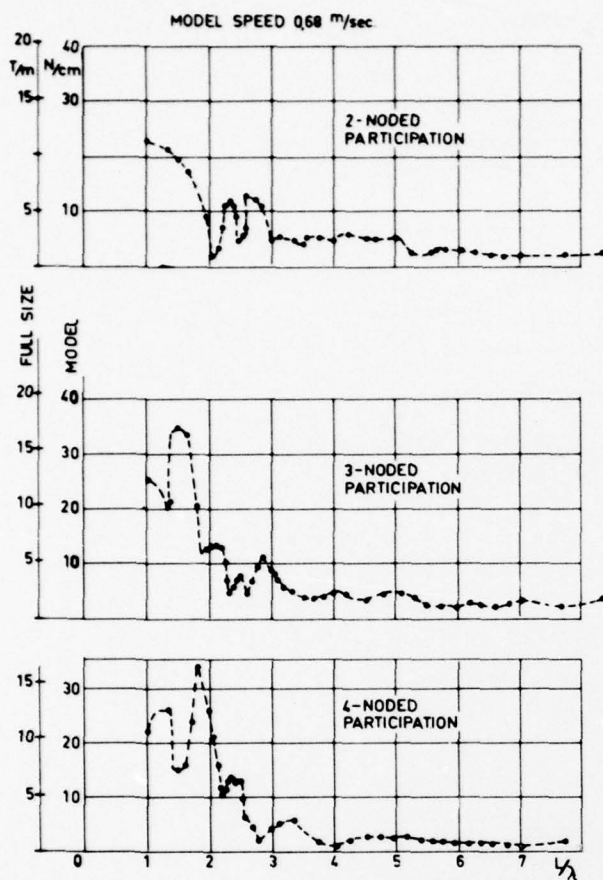


Fig. 22: Generalized forces per unit wave height for various wave lengths at a forward model speed of 0.68 m/sec.

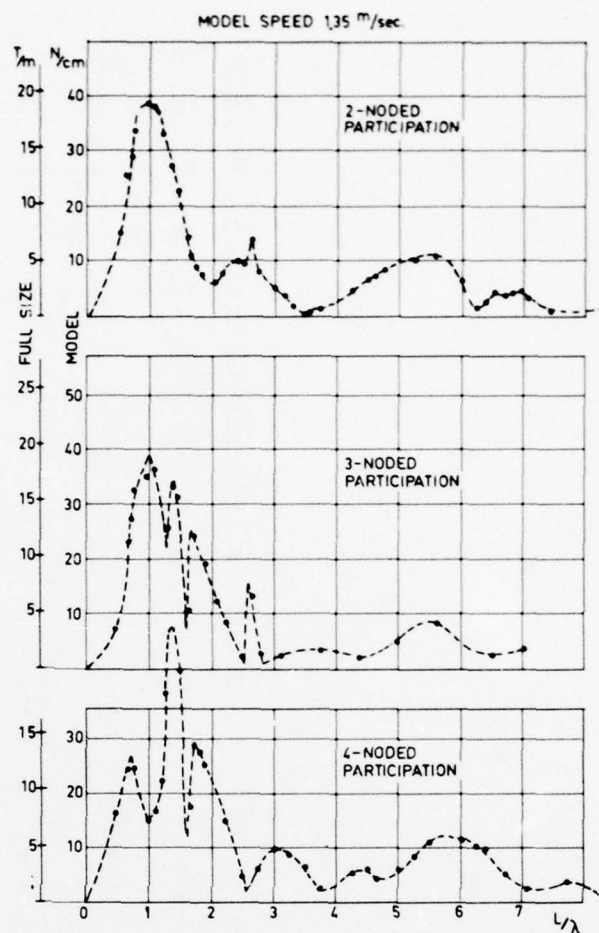


Fig. 23: Generalized forces per unit wave height for various wave lengths at a forward model speed of 1.35 m/sec.

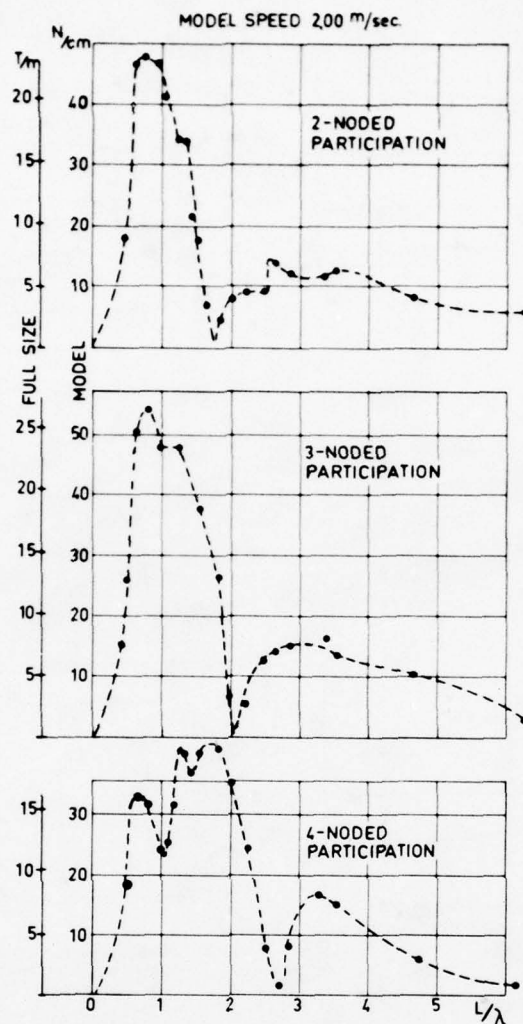


Fig. 24: Generalized forces per unit wave height for various wave lengths at a forward model speed of 2.00 m/sec.

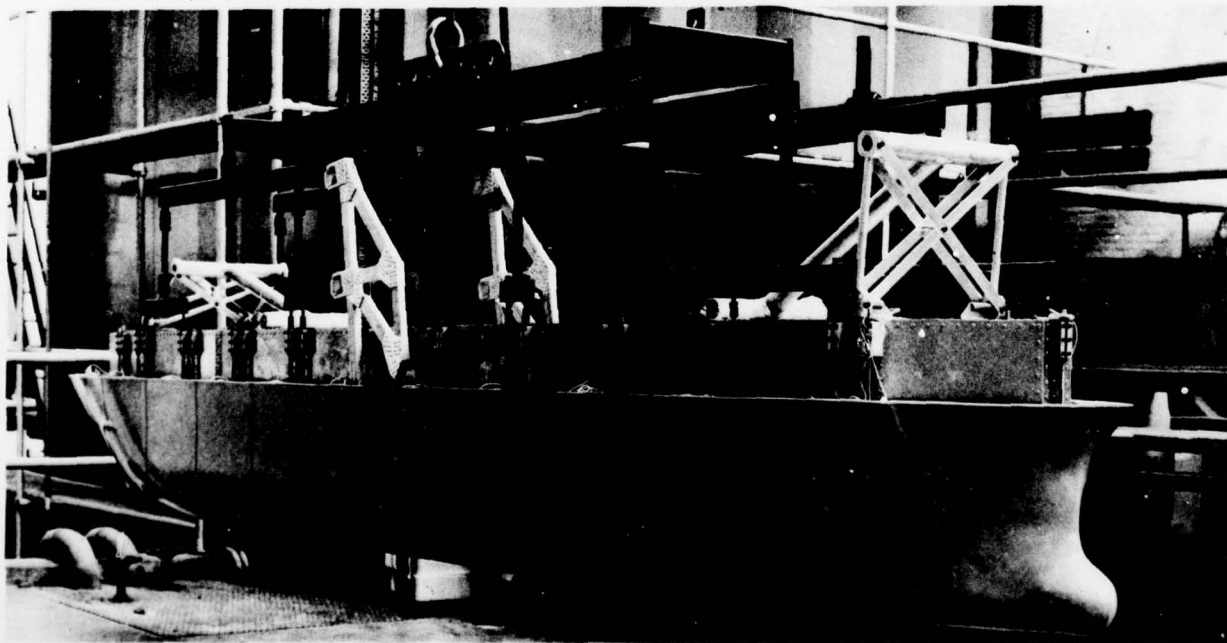


Fig. A1: Photograph of free model with hoisting rig.

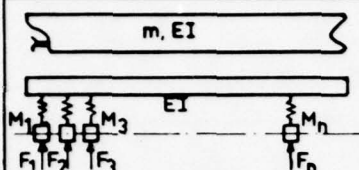
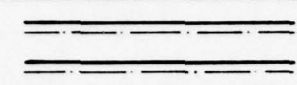


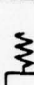

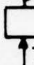


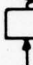
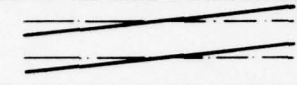


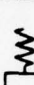



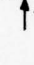



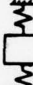














MODE NUMBER	MODE SHAPE	GENERALIZED REPRESENTATION				
		CAPTIVE MODEL		FREE MODEL		
		BEAM WITHOUT MASS	BEAM WITH MASS	BEAM WITHOUT MASS	BEAM WITH MASS	
I						HEAVE  MOTION
I <sub>a</sub>						
II						PITCH  MOTION
II <sub>b</sub>						
III						SAGGING- HOGGING DEFLECTION
III <sub>c</sub>						
R	MULTINODE DEFLECTION					MULTINODE DEFLECTION
R <sub>q</sub>	MULTINODE DEFLECTION					

Fig. A2: Model representation of the sectionalized free model, taking into account the elasticity of the force pick-ups.

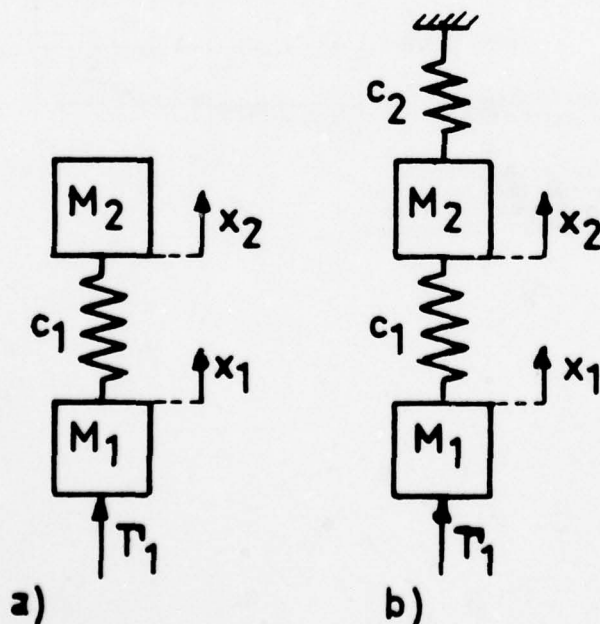


Fig. A3: Generalized representation of the measurement of of:  
a) the rigid body modes, and  
b) the elastic modes.



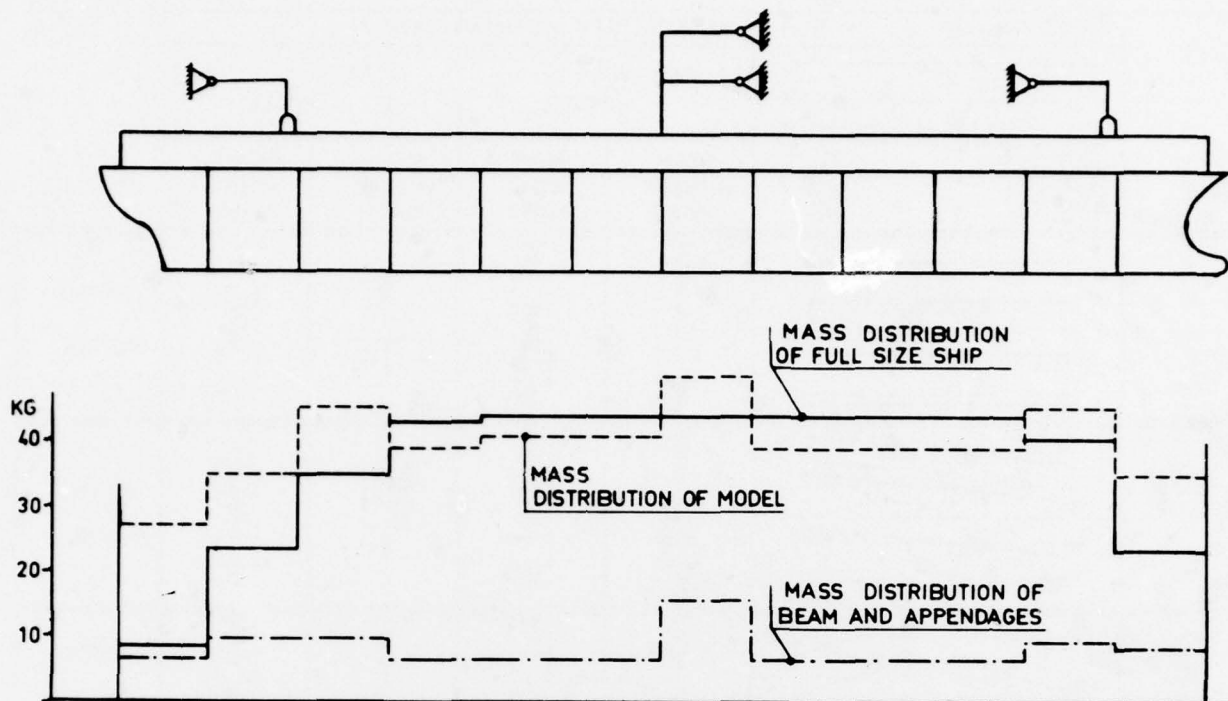


Fig. A4: Mass distribution of the ship, the model, the beam with appendages.

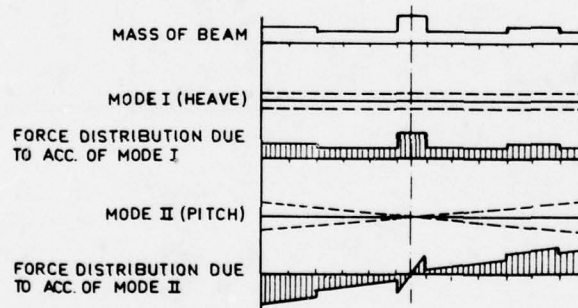


Fig. A5: Distributed forces generated by the parasitic mass of the beam, and the rigid body motions of the free model tests. These distributions are the basis for the corrections to apply on the measured generalized loading.

# THEORETICAL PREDICTION OF THE VERTICAL DYNAMIC RESPONSE OF SHIP STRUCTURES USING FINITE ELEMENTS AND CORRELATION WITH SHIP MOBILITY MEASUREMENTS

D. CATLEY and C. NORRIS  
British Ship Research Association, UK

This paper presents a correlation of theoretical estimates for the vertical vibration response with ship mobility measurements taken aboard a 25 000 tonne dwt Products Tanker. A membrane finite element idealization is the basis of the theoretical model.

The idealization used is shown to be applicable to this ship type, and an improvement on the equivalent beam model.

The mobility technique, which employs a unit, uniaxial force, is illustrated as a means of circumventing the need for estimates of the complex excitation system in determining the dynamic characteristics of the ship structure.

## INTRODUCTION

The vibration of a ship structure is due to a number of different sources of excitation: the two major contributions being forces created by the main propulsion machinery and forces produced by the propeller operating in a non-homogeneous flow field. Vibration caused by the latter source is the subject of an extensive research programme being carried out at B.S.R.A. with the support of the General Council for British Shipping and the Ship and Marine Technology Requirements Board.

The problem of propeller-excited vibration is well established, but in recent years has become more significant due to the increase in power on single screws which have to operate in increasingly severe inflow environments as fuller and beamier hull forms are adopted. Forces are experienced over an area of the hull plating above the propeller and also through the tail shaft support bearings. These forces are extremely complex but in all cases major components corresponding to blade rate (blade passage frequency) and harmonics of blade rate have been found to exist.

Generally the most severe vibration is experienced in the aft end of the ship and therefore the dynamic response of this structural region is of great importance in modern ship types where it is common practice to have fully aft deckhouses and machinery spaces.

Due to the likelihood of a prohibitive cost and/or impracticability of structural modifications that may be recommended by the vibration analyst after the ship has been built, it is essential that the method

adopted to predict the dynamic response of the ship should be available in the early design stages. The method should also be capable of assisting in the design of new ship types. B.S.R.A. has amassed a large amount of empirical data which is suitable for estimating the lower hull mode frequencies from basic ship parameters, and has also produced an empirical relationship for the vertical blade rate vibration at the stern gland, (Ward and Willshare, 1). However, there is a need for a method to calculate the dynamic response at reference locations for frequencies higher than the régime of the lower hull modes, particularly for the large modern tankers for which the blade rate is typically in the 10-20 node main hull mode range.

The complete problem of defining and estimating the dynamic response of a general ship structure is extremely complex. This paper presents an approach which seeks to simplify the theoretical prediction of the dynamic response to the vertical component of the excitation. The general method presented could be adapted in principle to predict the transverse and torsional vibration but would require a more detailed consideration than for the vertical case.

A finite element representation of the ship structure has been adopted for the present theoretical work. The prediction of the dynamic response of complex structures was, in fact, the objective which originally led to the development of the finite element method (Archer, 2). This development has been closely coupled to the advent of the

AD-A055 859

UNIVERSITY COLL LONDON (ENGLAND) DEPT OF MECHANICAL --ETC F/G 13/10  
SYMPOSIUM ON NAVAL HYDRODYNAMICS. UNSTEADY HYDRODYNAMICS OF MAR--ETC(U)  
1978 R E BISHOP, A G PARKINSON, W G PRICE N00014-76-C-0093

UNCLASSIFIED

NL

7 of 9

AD  
A055859





digital computer and rapidly expanding computer facilities. Some 25 years after the original availability of a general purpose machine, we have today a voluminous collection of reports on specialized applications and furtherances of finite element techniques.

A decisive advantage of the finite element method as a design tool is that the idealization is based upon a structural rather than a directly mathematical formulation. Knowledge of the behaviour of individual structural components can be accounted for in the discretization of the real structure into its fundamental components. Thus the idealization is a logical improvement on a simple beam model, enabling a closer modelling of the real structure to be made.

In this study a finite element idealization is employed, using an inhouse computer program, to produce a two-dimensional model of the ship structure by compressing the ship structure into a set of membrane and bar elements along a single vertical plane on the ship's central longitudinal axis. It is known that, although a beam model can be adopted to produce estimates for the lower hull mode frequencies, it is necessary to adopt progressively more detailed idealizations if the higher frequency range is to be investigated. In practice therefore it will be necessary to compromise between coarseness of idealization and the required accuracy of the predictions.

At this time it is hoped that the two-dimensional idealization will prove to be of significant use and it is intended to apply the present system to a range of ship types to determine the degree of applicability in each case. The first ship to be considered is a 25 000 tonne dwt Products Tanker which has been the subject of extensive mechanical exciter tests and sea trials conducted by B.S.R.A. The basic ship parameters are shown in Table 1.

Whilst it is known that other ship research organisations are carrying out similar types of investigations, there is a shortage of published material which correlates directly the calculated and measured responses of the ship. Due to the complexity of the excitation system it is neither practicable nor expedient to compare the actual vibration response levels with calculated response levels. A more satisfactory approach, which circumvents the complication due to the excitation system, is to measure the response per unit force (termed mobility) of the ship using a mechanical exciter as the exciting force, and to compare the measured mobility directly with corresponding calculated mobilities. When suitable estimates of the actual force components are available, it is then a simple task to predict the actual response of the ship.

A problem in the ship response calculation is that reliable damping estimates are difficult to obtain. It is important that

realistic values of damping be included in the theoretical appraisal if the response predictions are to be indicative of the true dynamic characteristics of the ship structure. The approach in this paper has been to assume a level of modal damping, as a factor of the critical value, viscous in nature and with coefficients proportional to the modal stiffness. Values indicated by an empirical approach have been compared in this paper with those values recorded in the exciter tests and subsequently analysed by a polar plotting technique.

Although the authors are aware of several reports containing fluid finite elements and methods of surface singularity distributions, the more traditional treatment of the effects of the entrained water has been adopted in this paper. The added virtual mass obtained from an analysis using the work of Landweber and Macagno (3) for high frequency oscillations has been added to that non-structural mass which is effective along the keel of the Products Tanker. It is considered that this treatment will be reasonable when applied to the present degree of idealization.

#### IDEALIZATION

The finite element method is a process whereby a continuous structure having an infinite number of degrees of freedom can be approximated to by an assemblage of subregions, referred to as elements. Each element has a specified finite number of freedoms at the reference points, i.e. the nodes of the element. Although the choice of elements is often obvious, engineering experience determines the approximations introduced.

Certain basic finite elements are used in this paper in idealizing the ship structure for vertical vibratory response to a given source of excitation. Figure 1 shows the elements used, these being a subset of the elements at present available from the element library at B.S.R.A. Each element is assumed to have uniform thickness or cross-sectional area and to be of elastic, isotropic and homogeneous material, and any non-linearities in the structure are ignored. The two idealizations used in this paper are shown in Figure 2. The beam element used for the simple model, included in this paper for comparison with the accuracy of the membrane - bar idealization, is derived from beam theory (Timoshenko, 4). Shear deflection and rotary inertia effects are included but necessarily the influence of local vibration is neglected.

In the membrane - bar idealization, the 2-noded bar element is merely an axial load bearing member placed along an extremity of a basic membrane element. The constant strain plane stress triangle has been used sparingly, and preference given to the superior linear strain rectangle and a quadrilateral element. Furthermore, it is known that if the number of degrees of freedom associated with an element is increased, while keeping the total

number of structural freedoms the same, then better results are obtained. This improvement is associated with the higher order integration rules employed in the more complex element. For this reason, and also for ease of data preparation, an 8-noded isoparametric quadrilateral element has been used wherever possible and in conjunction with a mid-side node bar element. These elements are very powerful when compared to an equivalent array of basic elements and are ideally suited to the structural geometry in the present idealization of the forward hull.

Compatibility (or conformity) of displacements between adjacent elements is ensured, except in the instances where a higher order element has been connected to basic element types. The extent of the incompatibility in the present modelling is considered to be insignificant. It is then intuitive that the idealization will be to a degree too stiff; corresponding to the monotonic convergence of the total potential energy to a minimum (within the context of a two-dimensional idealization) as the element mesh is refined.

The effective membrane thickness is chosen to represent a summation of the longitudinal shear carrying members of the ship, viz: side-shell and longitudinal bulkheads, although it is suggested by Kline and Daidola (5) that this will give an overestimation of the shear stiffness. Variations in the shear stiffness will clearly be more significant in the higher vibration modes. The longitudinal stiffeners, bottom and deck plating have been included as axial load bearing or "bar" elements of appropriate cross-sectional area. These must be placed carefully so as to maintain a good approximation to the section's second moment of area.

The effect of shear lag in the continuous transverse structure has been ignored in this two-dimensional model. Csupor (6) and Ohtaka, et al (7) give accounts of this effect which is a departure from a uniform stress loading involving shear deformation in the plating: more significant in the higher modes as the distance between nodes decreases: resulting in higher derivatives of the bending displacement.

A lumped mass formulation has been adopted since it is known that a lumped mass model, compared to a distributed mass model, of a compatible system of elements will compensate to some extent for the inherent overestimation of stiffness and give frequencies closer to the frequencies of the real structure. This point was brought out in discussions following the presentation of a paper by Archer (2).

The total structural steel mass may be obtained from the designer in the early stages of the ship. The total mass of the idealized structure is available from the program as an important check on the model. The non-structural mass of the major components, viz: engine, machinery, propeller,

anchor, etc., is suitably lumped to the nearest nodes, before the overall density factor is modified locally to account for fittings, small items and paint etc. Assuming that detailed plans were not available, this process could still be applied with some degree of confidence using preliminary design estimating weights.

The cargo has been lumped at the nodes around each tank so as to retain the correct centre of gravity. Kumai (8) states that liquid cargo has an effectiveness factor of 1.0 for vertical vibration, although the situation is more complex in the case of transverse vibrations.

Treatment of the added mass of the entrained water is described in the next section. For the Products Tanker, the added mass has been suitably lumped at the nodes along the length of the keel.

Structural damping is a very important parameter for the evaluation of the vibratory response and is also considered in a later section. The modal frequencies are assumed to be independent of the damping of the system which is subsequently included as a viscous damping in terms of the modal critical value.

The excitation has been taken as a unit force acting at a single node above the propeller on the steering gear flat. This corresponds to the position of the mechanical exciter during the measurement of mobility. The resulting response at any node of the system is then, by definition, the frequency dependent transfer mobility function to that node. Alternatively, a force vector could be applied to the modal system to represent the fluctuating pressure over the hull plating and the stern bearing forces.

The data for the beam model has been derived directly from the membrane - bar idealization. An assumed flexural axis has been taken for the superstructure. It is realized that this beam model is unsatisfactory and physically unrealistic for the superstructure, but a comparison of natural frequencies and mobilities was sought.

#### THE ADDED MASS

Recent work by Misra (9) includes a collection of references which indicates the volume of research into the added mass problem along traditional lines. Several fluid finite elements are also available, see for example Matsumoto (10), Zienkiewicz (11), and Chowdhury (12), whilst Hess and Smith (13) have employed a surface singularity distribution.

The interaction between the vibrating ship structure and its surrounding fluid is in the form of an induced pressure at the interface. The integration of that part of the pressure which is in phase with acceleration is an additional inertia term whose coefficient is referred to as the added mass of the entrained water. The added mass

is included together with the structural and cargo mass in the equations of motion.

The frequency range of interest for propeller-excited vibration is considered to be above the range for which the added mass is frequency dependent. However, the effect of the mode shape on the value of the added mass to be associated with a particular mode should be considered in a detailed analysis.

In the present paper, a conventional strip theory method has been adopted and the dependence on mode shape ignored. In this approach, due to Landweber and Macagno (3), a basic Lewis form is assumed for the ship section together with a three-dimensional correction factor. Hoffman (14) and others have given a more modern treatment of the added mass by this conformal mapping technique, with extension from the simple two (Macagno, 3) and three (Macagno, 15) parameter families of sectional forms to an  $n$  parameter family. Hoffman does point out, however, that the additional accuracy obtained from the more sophisticated two-dimensional treatment does not necessarily justify the significant increase in computation required.

As the mode of vibration becomes more complex, exact three-dimensional calculations have shown that the added mass decreases. Thus the values of the added mass obtained from the above theory are over-estimated in the higher hull modes. This will have a compensating effect upon the frequencies of the model which is considered to be somewhat too stiff.

#### THE EIGENVALUE PROBLEM

The equations of motion for the structural system can be written as

$$M\ddot{p} + C\dot{p} + Kp = P \quad (1)$$

where  $M$  and  $K$  are respectively the global structural mass and stiffness matrices formed as above and  $C$  is the matrix of viscous damping coefficients as described in a later section.  $\ddot{p}$ ,  $\dot{p}$  and  $p$  are the vectors of nodal acceleration, velocity and displacement respectively.  $P$  is the dynamic load vector. The elements of the coefficient matrices are assumed to be frequency independent and are taken to be linear functions of the nodal parameters.

A second order effect of the damping is to reduce the frequency of the natural oscillations. This effect is neglected in these calculations and the actual natural frequencies are assumed to be the frequencies of free vibration. Thus the procedure employed is to evaluate the normal modes of free vibration and then to include the damping in a generalized form. The equations of free vibration lead to the generalized eigenvalue problem:

$$(M - \lambda K)q = 0 \quad (2)$$

where  $\lambda$  is an eigenvalue solution.

If there are  $n$  degrees of freedom there are  $n$  possible eigenvalues corresponding to the  $n$  natural frequencies,  $\omega = 1/\sqrt{\lambda}$ .

The  $n$  associated eigenvectors,  $q$ , are the corresponding vibration modes. In most dynamic analyses only the lowest  $k$  frequencies are required. These correspond to the  $k$  most dominant eigenvalues of the system.

A suitable method of solution, which has been adopted in this present paper, is due to Jennings and Orr (16) who take advantage of both symmetry and bandform of the mass and stiffness matrices. The problem is reduced to standard form by means of the Choleski factorization of the symmetric, positive definite matrix  $K$  into its upper and lower triangular factors.

$$K = LL' \quad (3)$$

where the prime denotes transposition.  $L$  may overwrite  $K$  in the computer storage.

Equation (2) is then transformed:

$$(L^{-1}ML^{-1} - \lambda I)q_1 = 0 \quad (4)$$

$$\text{where } q_1 = L'q \quad (5)$$

and  $I$  is the unit matrix.

Equation (4) is then the standard form of the eigenvalue problem:

$$(A - \lambda I)q_1 = 0 \quad (6)$$

where  $A$  is a symmetric but full matrix.

Wilkinson (17) in his classic text describes various solutions to this standard equation. The method adopted for this paper is the simultaneous vector iteration method of Jennings. This method enables eigenvectors of close or equal eigenvalues to be resolved.

The method continues with the definition of an orthogonal matrix of starting vectors  $U$ . This matrix may be a matrix of zeros and ones; or may be randomly generated; or reasonable approximations to the true vectors may be available from some previous and similar analysis. These vectors are orthogonalized initially and at each subsequent iteration to maintain linear independence. The results of an interactive analysis are utilized to uncouple the vectors. The matrix  $A$  is never explicitly formed and thus there is no need to work with a full matrix. Convergence of the predominant vectors is rapid for large banded forms.

The present coding is considered to be efficient for small to medium sized dynamic problems. The mass and stiffness matrices are retained in the central core of the computer and three arrays are required for the vectors. For small bandwidths and say 20 modes, the limitation is about 400 freedoms on the B.S.R.A. ICL 1903t which has, at present, 96K words of store available using the operating system GEORGE 3 Mk 8. A variable bandwidth storage scheme is employed for the mass and stiffness matrices. The size of the problem is automatically



increased by 3 modes to accelerate convergence of the highest mode actually required.

The method proceeds by solving:

$$L'X = U \quad (7)$$

for X, where U is the matrix of trial vectors.

The matrix Y is then formed by:

$$Y = MX \quad (8)$$

and the next estimation of the vectors V is found from:

$$LV = Y \quad (9)$$

Equations (7) to (9) define the essential iteration:

$$V = AU = L^{-1} ML^{-1}U$$

The interaction matrix,

$$B = U'V = U'AU$$

is determined, and from B the matrix T is constructed with off-diagonal elements related to those of B, viz.

$$t_{ij} = \frac{-2b_{ij}}{(b_{ii} - b_{jj}) + s\sqrt{(b_{ii} - b_{jj})^2 + 16b_{ij}^2}} \quad (10)$$

where s is the sign of  $b_{ij}$ .

The uncoupled vectors W then follow from

$$W = VT$$

The matrices B and T are not explicitly formed. The diagonal elements  $b_{ii}$  give estimates of the eigenvalues which are used to sort the vectors into their correct order of dominance. The vectors are then orthonormalized. Those vectors which have converged are "locked", and the iteration process continues from the step of equation (7) with U replaced by W until convergence of k vectors is completed.

Having determined the eigenvectors to a required tolerance, the vibration modes, q, may be determined by back-substitution in equation (5). Theoretically the vectors converge half as fast as the eigenvalues. The first few eigenvalues should converge rapidly.

Jennings (16) also gives a modification for treatment of free bodies where the stiffness matrix K is singular and direct decomposition to triangular form not permissible.

Several improvements of the basic algorithm have been suggested but are not included in the present solution technique. Sturm sequences may be incorporated to accelerate convergence by testing for grouping of the eigenvalues. Giurgiutiu and Stafford (18) give several proposed acceleration

routines to be applied to the basic algorithm. The basic method could be adopted for large problems of several thousand degrees of freedom using a modified version of the program which utilizes backing store.

#### DAMPING

The solution to the homogeneous set of linear equations of free vibration, equation (2), as derived in the previous section is never realized in practice due to the presence of damping forces. In the absence of external excitation the damping eventually dissipates the internal energy of the system and the motion ceases.

The actual form of the damping in overall ship vibration is not simple, but to a good approximation may be taken as viscous in nature, i.e. proportional to the velocity of the motion. Kumai (19) states that the external hydrodynamic damping due to water friction, the generation of pressure waves and surface waves may be neglected compared to the damping of the structure itself, especially in the higher modes. In fact its value actually approaches zero.

In the present paper, the total damping is taken to be viscous in nature and is considered in terms of the critical viscous damping value for each natural mode of vibration. Critical damping is that level of modal damping which will just permit free oscillations. In structural systems, the damping is considerably less than the critical value. Archer (2) observes that the only case which leads to simple modal damping in the uncoupled equations is in fact that of proportional viscous damping, in phase with velocity by definition, but with coefficients proportional in magnitude to either the modal mass or the modal stiffness. In general it is to be expected that the damping factor will increase with the frequency of the mode, due to the natural modes increasing in complexity. This was observed by McGoldrick (20) using a vibration generator.

If one considers only the damping values reported by Johnson and Ayling (21) it is soon apparent that there is a wide scatter of measured dampings. As Johnson and Ayling suggest, this scatter is due in part to the inherent inaccuracies in the measurement techniques themselves. It is more difficult to define a measured modal damping for the higher modes due to these modes being more strongly coupled and more difficult to resolve.

The approach of Hylarides (22), who recommends a damping coefficient matrix proportional to the stiffness matrix, has been adopted herein and interpreted in a generalized sense. The constant of proportionality,  $\kappa$ , is dependent to some extent upon the degree of idealization of the ship structure. If  $d_i$  and  $k_i$  are respectively the  $i$ th modal generalized damping and stiffness, then:

$$d_i = \kappa k_i = \xi_i \xi_{CR_i}$$

is suggested, with  $\kappa < 0.002$  for a two-dimensional idealization and  $\kappa$  near to 0.001 for a fully three-dimensional idealization. Here  $\xi_i$  is the modal damping factor and  $\xi_{CR_i}$  is the modal critical value.

Thus, in terms of the damping factor,

$$\kappa = \frac{\xi_i \xi_{CR_i}}{k_i} = \frac{2\xi_i}{\omega_i}$$

and it is seen that the damping factor is proportional to the frequency.

An alternative approach which has been considered by the authors is due to Kumai, whose earlier work (19) includes a modification to an empirical expression due to Lockwood-Taylor. This is based upon a value suggested for the damping factor of the 2-node hull mode as a function of ship length. The values for the higher modes are then defined by

$$\xi_n = \xi_2 (\omega_n / \omega_2)^{\frac{3}{2}}$$

Subsequently, Kumai (23) developed his beam theory to include in some detail the effects on the damping of shear deflection and rotary inertia. Interpreted in terms of the damping factor, Kumai concludes:

$$\xi_n = \pi \mu f_n K_n,$$

where the parameter  $K_n$  is defined by:

$$K_n = \frac{1 + \left(\frac{\nu}{\mu} \alpha + \beta\right) n^2 \pi^2}{1 + (\alpha + \beta) n^2 \pi^2}$$

where  $\mu \approx 2.83 \times 10^{-5}$  min., normal (bending) viscosity coefficient

$\nu \approx 7.50 \times 10^{-6}$  min., tangential (shearing) viscosity coefficient

$\alpha = EI/GA L^2$ , shear deflection factor

$\beta = (r/L)^2$ , rotary inertia factor

$f_n$  = frequency of n-node mode, c/min.

$EI$  = flexural rigidity

$GA$  = shear rigidity

$L$  = overall length of beam

$r$  = radius of gyration of mass moment of inertia of the beam section.

The values suggested by this method rely on estimates for the viscosity coefficients. Assuming the above estimates, the values obtained are some 20% higher than those given by Kumai's empirical formulation when applied to the numerical example of his earlier work (Kumai, 19).

Figure 3 shows the more readily obtained values from a dependence on modal stiffness for consideration of the ballast condition of the Products Tanker. These values are given as a percentage of the modal critical value and compared to the values obtained from Kumai's theoretical formulation. The former model has been used in the present paper for the modes for which measured values are not available.

A survey of damping values in the lower hull modes readily available from the literature, and further values measured by B.S.R.A., suggests that a constant of proportionality,  $\kappa = 0.0014$  is not unreasonable for a typical membrane idealization. Damping values of the lower vertical hull modes quoted by Johnson and Ayling (21) exhibited a wide scatter. From these values, Johnson and Ayling produced a mean frequency dependent line for each n-node mode. These lines have a proportionality factor decreasing in magnitude with increasing number of nodes. Figure 3 shows the range covered by the mean lines for the 2-node through to the 8-node mode. Also included in Figure 3 is the mean damping line from measured values for the 2-node vertical mode on four ships by Aertssen and Lembre (24).

#### THE RESPONSE CALCULATION

The normal modes of free undamped vibration, as obtained above, are used as generalized freedoms to solve equation (1) by the transformation:

$$p = Uq \quad (11)$$

Then (1) may be written:

$$q_i + 2\xi_i \omega_i q_i + \omega_i^2 q_i = \frac{Q_i}{m_i} \sin \omega t, \text{ for}$$

$$i = 1, 2, \dots, n \quad (12)$$

where  $m_i = U_i' M U_i$

$$k_i = U_i' K U_i$$

$$Q_i = U_i' P$$

$$\omega_i = \sqrt{k_i/m_i}$$

Here  $U_i$  is the  $i^{\text{th}}$  normal mode vector;  $m_i$ ,  $k_i$ ,  $Q_i$  are respectively the  $i^{\text{th}}$  mode generalized mass, stiffness and force;  $\omega_i$  is the  $i^{\text{th}}$  natural frequency;  $\omega$  is the forcing frequency;  $\xi_i$  is the  $i^{\text{th}}$  modal damping ratio.

In equation (12) the damping term is included as a factor of the critical value  $2\omega_i$ . Since we are interested in the steady state response of the ship structure, for comparison with mobility measurements, the exciting force is assumed to be a single constant harmonic component. In the propeller-excited vibration case, where the force is periodic, but not simply sinusoidal, it may

be resolved into its Fourier constituents and the following results applied to the harmonics separately - the final solution being obtained by summation.

The general solution to equation (12) is well known:

$$q_i(t) = \frac{Q}{m_i \omega_i^2} \frac{1}{\{(1-r_i^2)^2 + (2\xi_i r_i)^2\}^{1/2}} \sin(\omega t - \theta_i)$$

$$= A_i \sin(\omega t - \theta_i)$$

Here  $r_i = \frac{\omega}{\omega_i}$  and  $\theta_i = \tan^{-1} \frac{(2\xi_i r_i)}{(1-r_i^2)}$  are

respectively the modal frequency ratio and phase, with respect to the excitation.

The absolute nodal displacements are then the vector  $p$  given by

$$p = \left( \sum_{i=1}^n U_i A_i \cos \theta_i \right) \sin \omega t - \left( \sum_{i=1}^n U_i A_i \sin \theta_i \right) \cos \omega t \quad (13)$$

#### MOBILITY THEORY

If an oscillatory force is applied to a continuous mechanical structure, each point of the structure will respond with an oscillatory motion which can be defined in terms of its velocity. If the structure behaves in such a way that the amplitude of the response is directly proportional to the amplitude of the force, then the structure is said to be linear.

The mobility,  $M$ , of a linear system is defined as the ratio of the response velocity,  $V$ , to the ratio of the applied force,  $F$ .

That is:  $M = \frac{V}{F}$

Mobility can be measured either as a point mobility or a transfer mobility. Point mobility is a measurement of velocity divided by force, where both are measured at the point of excitation. Transfer mobility is the measurement of velocity at some other point of the structure divided by the force at the point of excitation.

Since the velocity and force need not be in phase, mobility is a complex quantity and thus the complete equation for mobility is:

$$M = \frac{V}{F} \cos \phi + i \frac{V}{F} \sin \phi$$

where  $i$  is  $\sqrt{-1}$

In order that all the information regarding mobility is available, it is necessary to present both the magnitude of mobility and the phase,  $\phi$ , of the velocity relative to the force as functions of the frequency. This required information could

be presented as two graphs. However, it is possible by using a polar plotting technique to present all the information regarding phase, magnitude and frequency on one graph. This type of presentation is described in detail by Kennedy and Pancu (25). In this technique a resonance is detected not only by a maximum of magnitude, but also by the shape of the curve which is exactly circular for a single uncoupled resonance. Possibly the most useful feature of polar plots is in that they can be used to produce reliable damping values even from data of a moderate quality.

#### INSTRUMENTATION

A schematic representation of the measurement and analysing equipment adopted by B.S.R.A. for the mobility work is shown in Figure 4.

The exciter consists of counter-rotating, out-of-balance weights which are arranged to produce a unidirectional sinusoidal force of 10 kN at 1000 rev/min. The force output is proportional to (speed)<sup>2</sup>. A once per revolution pulse is available for frequency monitoring.

The exciter speed control unit is stabilized by means of a servo loop and has an automatic sweep frequency capability, which produces a linear increase of exciter speed at pre-selected rates of acceleration.

The force is measured using a special force pedestal designed by B.S.R.A. which consists of four steel pillars that are strain gauged, mounted on a rigid base frame. A carrier amplifier system is used to monitor the induced strains. The complete system produces a voltage output which is phase coherent with, and proportional to the amplitude of, the exciting force. The induced velocities are measured using seismic velocity transducers. The test signals are recorded on a 14 channel frequency modulated magnetic tape recorder for subsequent analysis in the laboratory.

The analysis equipment consists basically of an automatic tracking filter wave analyser which produces voltage outputs proportional to mobility,  $|M|$ , phase,  $\phi$ , and frequency,  $\omega$ . The mobility and phase signals can also be transformed to produce  $|M| \sin \phi$  and  $|M| \cos \phi$  values which are the required signals for polar plotting.

#### THE MOBILITY TESTS

Mobility measurements were carried out in two loading conditions, the details of which are shown in Figure 5. The exciter was located close to the propeller arch on the steering gear flat. Previous trials have shown that the response due to excitation at this position correlates well with the propeller excited vibration. Whilst transverse excitation was carried out at other positions, attention in this paper is restricted to vertical excitation.



It is normal B.S.R.A. practice during full scale vibration sea trials to ensure that the ship is in a depth of water not less than five times the mean draught. This condition was satisfied for the ballast condition but may not have been satisfied for the load condition, since the ship was then at anchor in an estuary with a large local variation in depth.

A large number of velocity transducer positions was employed in the vertical direction including the extreme aft end, wheelhouse top, stern gland, extreme fore end and the aft end of the navigating bridge deck. Longitudinal velocity transducers were arranged at a number of locations, including the wheelhouse top. Transverse velocity transducers were also deployed to study the transfer of vibration from the vertical to the transverse direction.

The frequency range investigated with the mechanical exciter was from 150 c/min to 1600 c/min although only results in the range from 150 c/min to 900 c/min are presented in this paper.

Checks for reciprocity and linearity have been carried out by B.S.R.A. which have shown that, within the velocity-force range studied with the exciter, ship structures are both linear and reciprocal.

During the same series of mobility trials the vibration excited by the propeller was also measured. A very good agreement with regard to resonant frequencies in the blade rate frequency range was obtained between the mobility data and the service propeller-excited vibration data. By dividing, for any point, the service vibration velocity by the mobility measured using the exciter, it is possible to derive a total effective force. This derived total effective force is an equivalent point force, acting at the exciter position, which can be used to represent the combined effect of the vertical, transverse and longitudinal stern bearing and pressure force system. Values for the derived blade rate, 2 x blade rate and 3 x blade rate forces have been obtained although they are not presented in this paper.

## RESULTS

Since the internal structure of a ship is, in general, neither homogeneous nor symmetrical about the vertical plane along the major axis of the ship, a vertical exciting force on this axis will produce athwartship vibration in addition to the vertical and fore and aft vibrations. The athwartship transfer mobility at various locations on the ship were measured. These have been found to be typically 6:1 lower than the corresponding vertical mobilities. It is therefore considered that in this case the coupling to the transverse direction can be neglected to a first approximation, and that a two-dimensional idealization is reasonable for vertical response within the frequency range considered for this ship.

Finite element calculations have been carried out for both the load and ballast conditions of the tanker using the membrane-bar idealization and the beam model, shown in Figure 2. The respective loading distributions are shown in Figure 5. The first 20 resonant modes have been calculated for each condition and these are listed in Table 2. For the same mode, the membrane-bar idealization generally produces a lower frequency than does the beam model.

As part of the facilities available at B.S.R.A. it is possible to plot automatically the mode shapes of the various computed normal modes. The mode shapes for the ballast condition membrane-bar idealization are presented in Figures 6, 7, 8, 9. Similar mode shapes, not presented here, were produced for the load condition.

The mode shapes generated by the beam model were similar to those generated by the membrane-bar idealization although the same degree of detail was not available.

From Table 2 it can be seen that 3 axial modes of vibration have been computed in the frequency range considered for both loading conditions by each idealization.

The other modes are predominantly vertical modes. No clear deckhouse mode is computed although many of the modes have large deckhouse components.

It is significant that above 700 c/min there is a group of modes, which are close together in frequency and have high relative aft end displacements. These frequencies are typically in the twice blade rate frequency range for many ships and may well be a reason for severe aft end vibration problems due to the twice blade rate excitation in some ships.

Many of the higher frequency modes show isolated areas of the vertical plating where the lower region is vibrating with a large amplitude relative to the plating above. This is an effect of the added mass of entrained water in these regions.

From the full scale mobility measurements, and also from supporting propeller-excited vibration trials, it has been possible to identify some of the lower hull mode frequencies. The ratios of the computed to the measured values are shown in Table 3, for both loading conditions and the two idealizations. In general the membrane-bar idealization gives a closer estimate of the individual frequencies than the beam model.

Figures 10 and 11 show, for the ballast and load conditions respectively, the computed transfer mobilities from the node on the idealized structure which corresponds to the exciter location to a selection of reference locations for both idealizations. Figure 2 shows the exciter location. The measured transfer mobilities are also presented in Figures 10 and 11.

The computed values were obtained by adopting the damping factors discussed earlier and summing the contributions due to the first 20 modes only. The responses at the higher frequencies should be considered

with caution due to this truncation of the modal model. In fact, the more complex dynamic characteristics suggested by the measured mobilities above about 600 c/min indicate a limitation of the present membrane idealization and the requirement for a more precise treatment of local structural detail for the consideration of the higher frequency range.

For the ballast condition, the membrane-bar idealization produces a better correlation with the measured mobilities than the beam idealization, particularly for the wheelhouse top responses. In all cases the general computed mobility levels follow the same trend lines as the measured values. This is true even for the forward end where there is a rapid decrease in mobility with increasing frequency.

For the load condition the correlation between the measured and computed mobilities is quite reasonable but not as good as for the ballast condition. In this case the beam model produces almost as good a correlation as the membrane-bar idealization.

Clearly the membrane-bar idealization can produce estimates of mobility for locations which can not be considered in the beam model. In general, therefore, it can be seen both from the frequency estimate considerations and from transfer mobility considerations that the membrane-bar idealization is significantly better than the beam model. The membrane-bar idealization has produced fair estimates of the response up to a frequency approaching the twice blade rate frequency.

#### CONCLUSIONS AND FURTHER WORK

This paper has contributed towards a wider programme of research into the problem of propeller-excited vibration which aims to determine the applicability of a range of finite element idealizations, increasing in complexity, and directed primarily at the design stages of a general ship design. It is intended to apply the present system to a range of ship types.

Although improvements on the traditional beam model have been obtained in estimating the dynamic characteristics of a Products Tanker, limitations of various aspects of the present theoretical model have been noted. However, it should be possible to include several minor refinements to lessen these restrictions on the membrane idealization.

Three-dimensional effects on the vertical stiffness representation, such as considerations of shear lag, the lack of detailed continuity locally in the deckhouse, and non-vertical side shell members, still need to be given a satisfactory treatment.

A membrane element which includes in-plane rotation is being included in the element library for use in conjunction with beam rather than bar elements. This should make it possible to model more accurately, but in a similar manner to the basic membrane approach, such regions as the ship's bottom.

A more detailed estimation of the added mass, which is able to account for the dependence on mode shape, should also be considered for subsequent calculations.

There is a need for further information on damping levels, particularly in the higher modes, where it is suggested that the approach adopted in the present paper overestimates the actual damping. It should be possible to obtain this information using the polar plotting technique which has been referred to in this paper.

There is a requirement for a sub-structuring technique which could be used as a design tool to assist in this general programme of work. The main advantages of this technique, which could involve separate consideration of the major structural regions, would be in reducing the maximum core required for a given idealization and in the efficient consideration of varying degrees of idealization for the different regions. Damping could then be treated in a more detailed manner as dependent upon the components of the local vibration modes in the natural mode of vibration.

#### ACKNOWLEDGEMENTS

The authors express their thanks to the Research Council and Director of Research of B.S.R.A. for permission to publish this paper and to the following organizations who have also supported the work financially: the General Council of British Shipping and the Ship and Marine Technology Requirements Board.

#### REFERENCES

- (1) Ward, G. and Willshare, G.T.; "Propeller-Excited Vibration with particular Reference to Full-scale Measurements"; R.I.N.A.; Spring Meeting 1975.
- (2) Archer, J.S.; "Dynamic Analysis"; World Congress on Finite Element Methods in Structural Mechanics; 1975; October.
- (3) Landweber, L. and de Macagno, M.C.; "Added Mass of Two-dimensional Forms Oscillating in a Free Surface"; J. of Ship Research; 1957; Vol. 1, Number 3.
- (4) Timoshenko, S.P.; "Strength of Materials"; Van Nostrand; 1941; Vol. 1.
- (5) Kline, R.G. and Daidola, J.C.; "Ship Vibration Prediction Methods and Evaluation of Influence of Hull Stiffness Variation on Vibratory Response"; Final Report on Project SR-214, "Hull Flexibility Criteria Study"; 1974.
- (6) Von Csopor, D.; "Methoden zur Berechnung der Freien Schwingungen des Schiffskorpers"; Jahrbuch der Schiffbautechnischen Gesellschaft; 1956.
- (7) Ohtaka, K., Takaira, F., Hibino, F., and Ohji, M.; "A Study of Vertical Vibration of Ships"; J. Soc. Naval Arch. Japan; 1966; Vol. 119, June; pp 142-156.
- (8) Kumai, T.; "The Apparent Mass of Cargo Oil in Vibrations of A Tanker"; Report of Research Institute for Applied Mechanics; 1965; Vol. XIII, Number 46.

- (9) Misra, P.N.; "Transverse Vibration of a Ship Hull in Ideal Fluid Determined through Variational Methods"; J. of Ship Research; 1974; Vol. 18, Number 3.
- (10) Matsumoto, K.; "Application of Finite Element Method to Added Virtual Mass of Ship Hull Vibration"; J.S.N.A.J.; 1970; Vol 127.
- (11) Zienkiewicz, O.C. and Newton, R.E.; "Coupled Vibrations of a Structure Submerged in a Compressible Fluid"; Symposium on Finite Element Techniques at I.S.D., Stuttgart; 1969; June.
- (12) Chowdhury, P.C.; "Fluid Finite Elements for Added-mass Calculations"; Int. Shipbuilding Prog.; 1972; Vol. 19.
- (13) Hess, J.L. and Smith, A.M.O.; "Calculation of Non-lifting Potential Flow about Arbitrary Three-dimensional Bodies"; J. of Ship Research; 1964; Vol. 8.
- (14) Hoffman, D.; "Hydrodynamic Pressures on Arbitrary Ship Forms"; Symposium on the Computer in Finite Element Analysis of Ship Structures; University of Arizona; 1972; March.
- (15) Landweber, L. and de Macagno, M.C.; "Added Mass of a Three-parameter Family of Two-dimensional Surfaces Oscillating in a Free Surface"; J. of Ship Research; 1959; Vol. 2, Number 4.
- (16) Jennings, A. and Orr, D.R.L.; "Application of Simultaneous Iteration Method to Undamped Vibration Problems"; Internat. J. Numerical Methods in Engineering; 1971; Vol. 3.
- (17) Wilkinson, J.H.; "The Algebraic Eigenvalue Problem"; Clarendon Press, Oxford; 1965.
- (18) Giurgiutiu, V. and Stafford, R.O.; "An Improvement on Simultaneous Vector Iteration"; 3rd Post Conference on Computational Aspects of the Finite Element Method; 1975; September.
- (19) Kumai, T.; "Damping Factors in the Higher Modes of Ship Vibration"; Reports of Research Institute for Applied Mechanics; 1958; Vol. VI, Number 21.
- (20) McGoldrick, R.T.; "Comparison Between Theoretically and Experimentally Determined Natural Frequencies and Modes of Vibration of Ships"; TMB Report Number 906; 1954.
- (21) Johnson, A.J., Ayling, P.W. and Couchman, A.J.; "The Vibration Amplitudes of Ship's Hulls", Part 1 - General Analysis, Part 2 - Worked Examples; Inst. of Engrs. and Shipbuilders in Scotland; 1962; Paper Number 1271.
- (22) Hylarides, I.S.; "Damping in Propeller-generated Ship Vibrations"; Netherlands Ship Model Basin, Wageningen, Publication Number 468; 1974.
- (23) Kumai, T.; "Effects of Shear Deflection and Rotatory Inertia on the Damping of the Flexural Vibration of a Ship Hull"; Reports of Research Institute for Applied Mechanics; 1965; Vol. XIII, Number 46.
- (24) Aertssen, G. and de Lembre, Ir. R.; "A Survey of Vibration Damping Factors Found from Slamming Expts on Four Ships"; North East Coast Inst. of Engrs and Shpbltrs; 1970-71; Vol. 87.
- (25) Kennedy, C.C. and Pancu, D.P.; "Use of Vectors in Vibration Measurement and Analysis"; J. Aero. Sci.; 1947; Volume 14, Number 11.



MAIN HULL

LENGTH B.P.	161.5 m
BEAM MLD	25.0 m
DEPTH MLD	12.6 m
BLOCK COEFF.	0.8105

DECKHOUSE

POSITION	FULLY AFT
N° OF TIERS	5
MEAN LENGTH	26.8 m
HEIGHT ABOVE MAIN DK.	13.0 m

MIDSHIP SECTIONPROPULSION SYSTEM

PROPELLER rev/min	120
N° OF PROPELLER BLADES	4
BLADE RATE c/min	480

Table 1: Basic ship parameters

FREQUENCY (c/min)				MODE DEFINITION
BALLAST		LOAD		N <sup>o</sup> . OF VERTICAL NODES
BEAM	MEMBRANE - BAR	BEAM	MEMBRANE - BAR	
55.7	54.6	50.9	48.1	2
127	123	114	106	3
199	192	180	170	4
283	273	253	240	5
348	356	298	290	1 <sup>st</sup> AXIAL
353	340	318	307	6
419	409	385	374	7
491	476	454	441	8
540	517	519	496	9
623	619	577	544	2 <sup>nd</sup> AXIAL
663	676	552	564	10
693	687	667	644	11
744	721	695	675	12
803	760	742	701	13
832	790	786	738	14
899	821	809	782	15
920	836	860	800	16
947	853	864	810	17
964	879	846	748	3 <sup>rd</sup> AXIAL
987	913	884	815	18

Table 2: List of calculated frequencies for the two idealizations

MODE	RATIO CALCULATED TO MEASURED FREQUENCY			
	BALLAST		LOAD	
	MEMBRANE -BAR	BEAM	MEMBRANE -BAR	BEAM
2-NODE VERTICAL	—	—	—	—
3- " "	0.99	1.02	0.96	0.99
4- " "	1.02	1.05	0.98	1.04
5- " "	1.09	1.13	1.01	1.06
6- " "	1.03	1.06	0.97	1.00
7- " "	—	—	1.02	1.05

Table 3: Ratios of calculated to measured frequencies

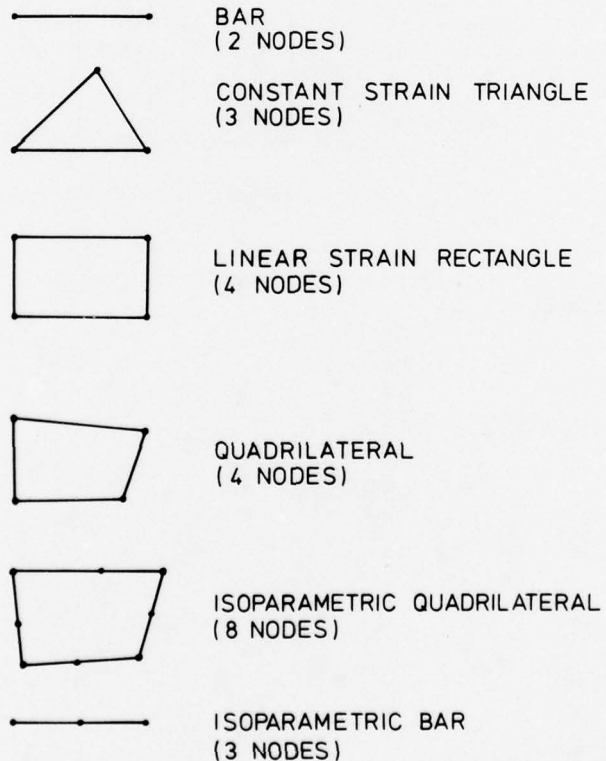
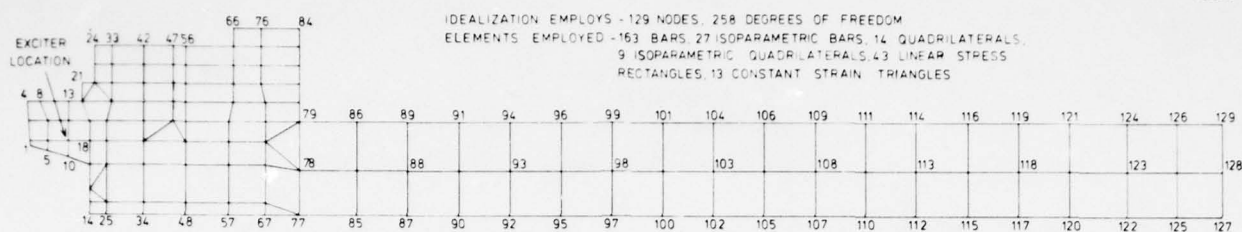
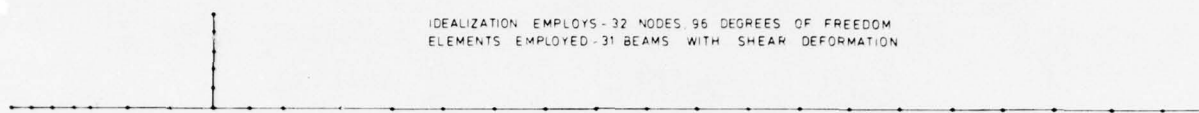


Fig. 1: Element types employed for membrane-bar idealization



(a) MEMBRANE - BAR IDEALIZATION



(b) BEAM IDEALIZATION

Fig. 2: The two idealizations of the structure

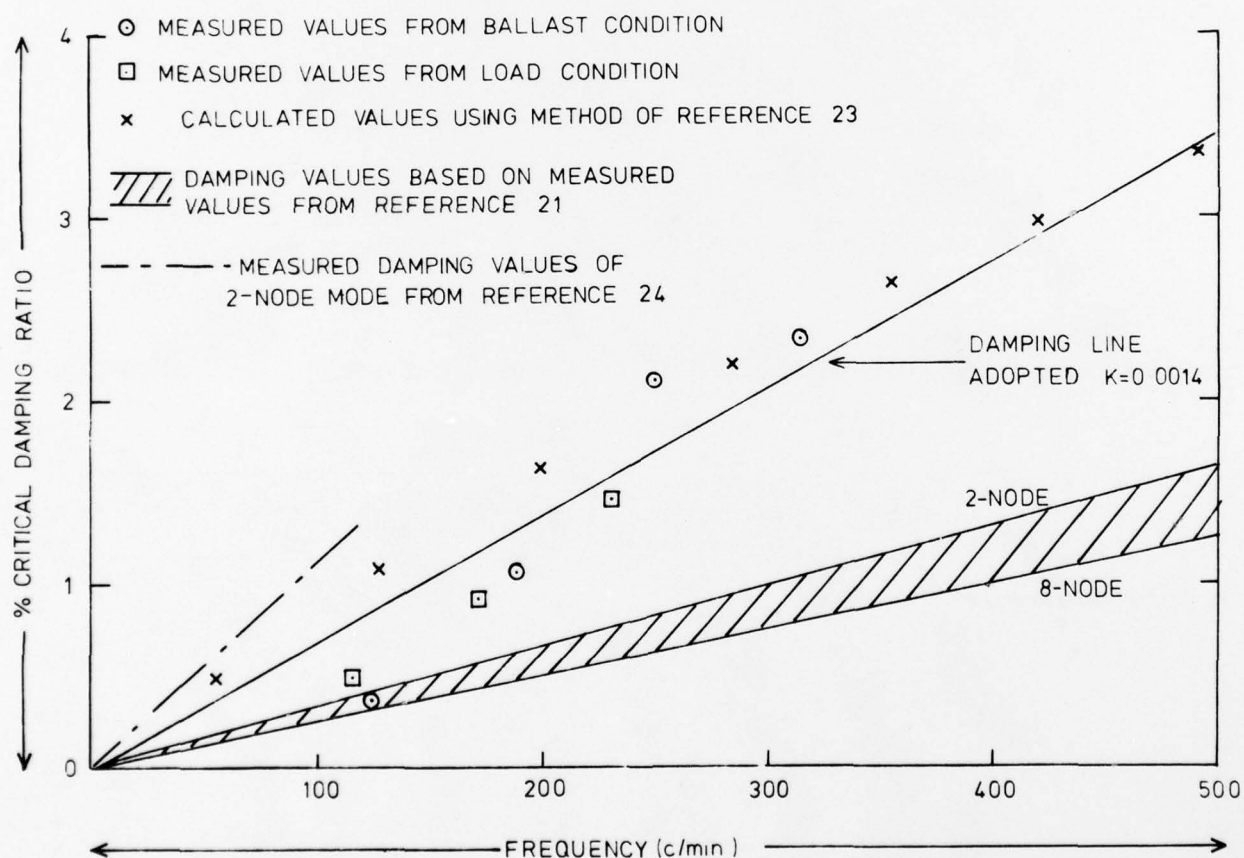


Fig. 3: Damping coefficients of main hull vertical modes



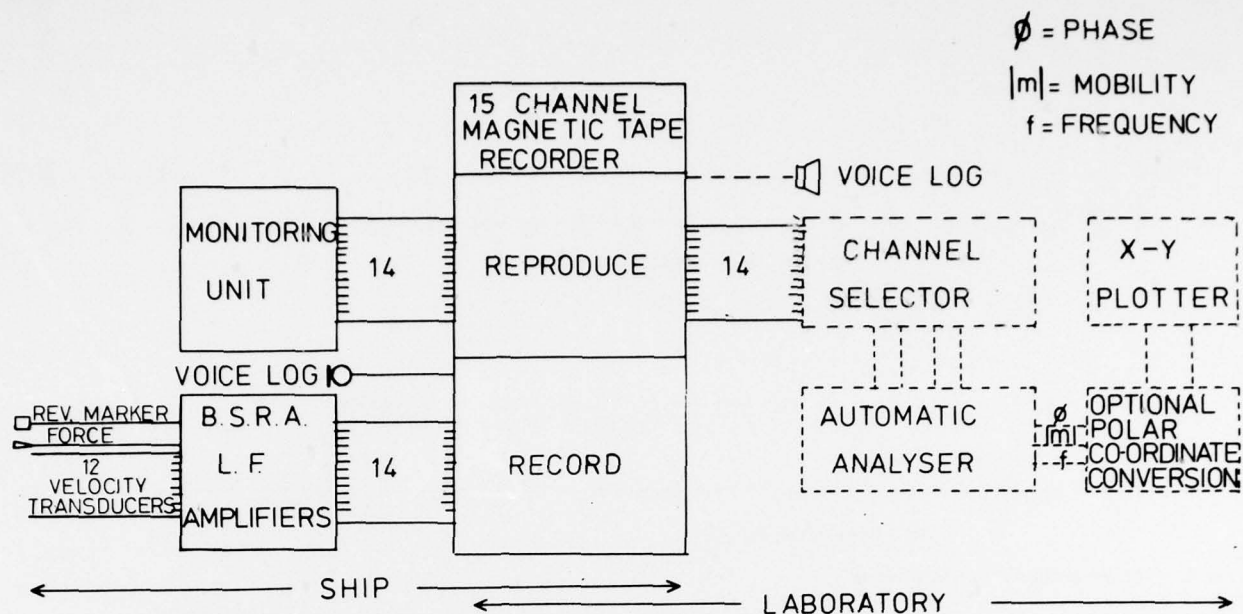


Fig. 4: Schematic arrangement of measurement and analysing equipment

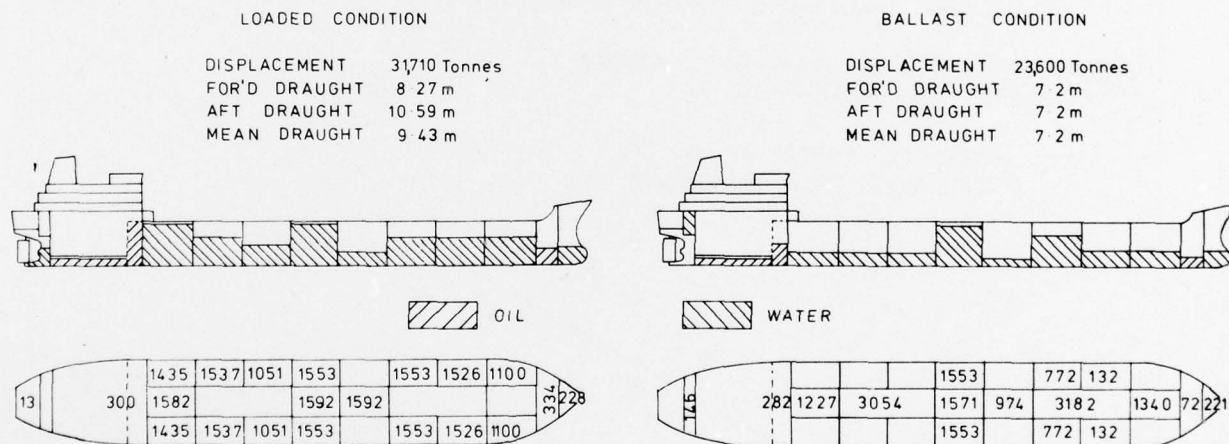
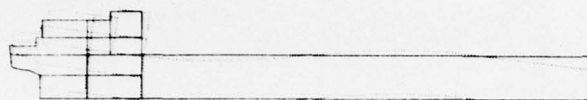


Fig. 5: Test loading conditions



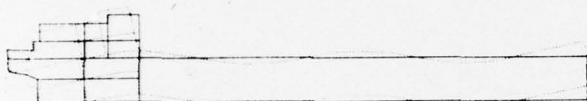
MODE 1 FREQ. 54.6 CPM



MODE 2 FREQ. 122.8 CPM



MODE 3 FREQ. 192.4 CPM

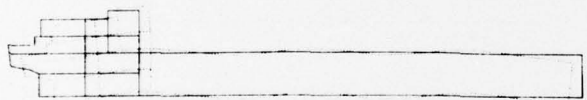


MODE 4 FREQ. 272.8 CPM



MODE 5 FREQ. 349.8 CPM

Fig. 6: Calculated normal mode shapes (modes 1-5) for the ballast condition



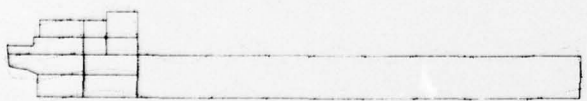
MODE 6 FREQ. 356.8 CPM



MODE 7 FREQ. 488.8 CPM



MODE 8 FREQ. 475.2 CPM



MODE 9 FREQ. 516.8 CPM

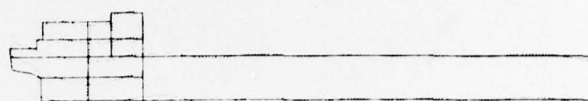


MODE 10 FREQ. 619.4 CPM

Fig. 7: Calculated normal mode shapes (modes 6-10) for the ballast condition



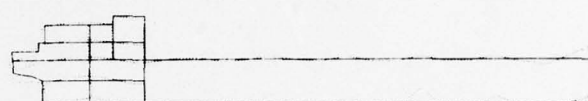
MODE 11 FREQ. 676.8 CPM



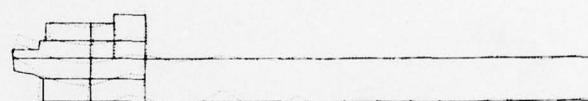
MODE 12 FREQ. 687.4 CPM



MODE 13 FREQ. 720.8 CPM

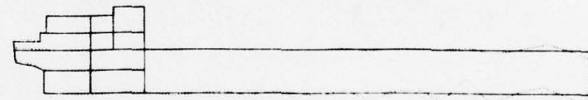


MODE 14 FREQ. 769.2 CPM



MODE 15 FREQ. 789.8 CPM

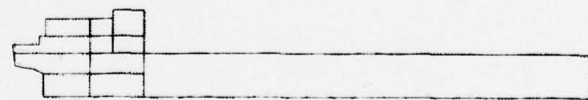
Fig. 8: Calculated normal mode shapes (modes 11-15) for the ballast condition



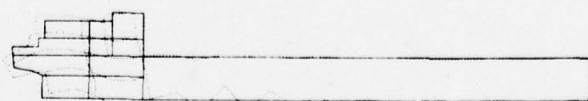
MODE 16 FREQ. 821.8 CPM



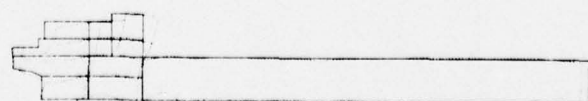
MODE 17 FREQ. 836.8 CPM



MODE 18 FREQ. 852.9 CPM



MODE 19 FREQ. 879.1 CPM



MODE 20 FREQ. 913.8 CPM

Fig. 9: Calculated normal mode shapes (modes 16-20) for the ballast condition

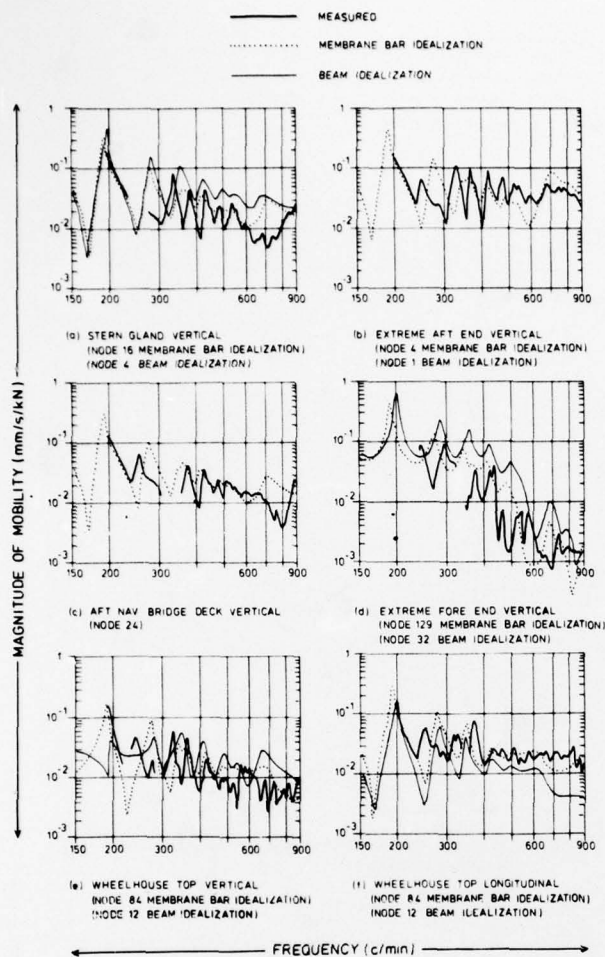


Fig. 10: A comparison of the measured and calculated mobilities (ballast condition)

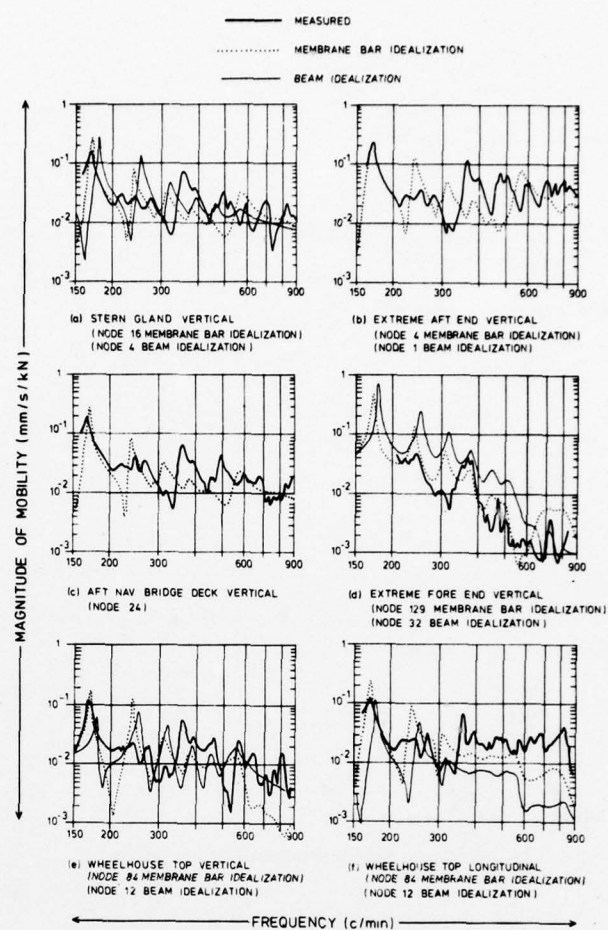


Fig. 11: A comparison of the measured and calculated mobilities (load condition)



# LOW FREQUENCY SECOND ORDER WAVE FORCES ON VESSELS MOORED AT SEA

J. A. PINKSTER

Netherlands Ship Model Basin, Wageningen

## SYNOPSIS

In order to gain more insight in the distribution of the second order force in head waves over the length of a moored vessel, tests were carried out using a three-piece model. The results indicated large asymmetry of the force which is of consequence for the calculation of the low frequency second order force in irregular waves. Expressions are derived based on integration of pressures over the wetted surface of the hull, by means of which the low frequency force in irregular waves may be calculated. An example of the application of these results using input from strip theory ship motion calculations is given

## INTRODUCTION

Low frequency horizontal motions of vessels moored in a sea way are to a large extent attributable to low frequency second order hydrodynamic forces acting on the hull. The necessity to take into account the effects of such low frequency excitations on the horizontal motions and mooring forces has been shown by a number of authors. Generally this has been done on the basis of observations and measurements made from model tests.

In order to determine the effects of low frequency excitation forces on the horizontal motions of moored vessels, it is necessary to determine quantitatively the forces involved. In this paper we will restrict ourselves mainly to the nature of these excitation forces. It should be noted however, that the reactions of the moored vessel to low frequency excitations i.e. the low frequency motions, in themselves form a considerable part of the total problem.

Before entering into more details, we will recall some of the basic properties of the second order wave forces.

In regular waves the second order force on a freely floating vessel or fixed object contains a constant part and a part which oscillates with twice the frequency of the incident waves. Gerritsma (1) has shown experimentally that the constant force is proportional to the square of the wave height.

In irregular waves the second order contains a low frequency part (mean included) with frequencies between zero and the wave frequency and a part with frequencies in the order of twice the frequency of the irregular waves. The quadratic relationship between the low frequency force and the wave height in irregular waves has

been confirmed by tests and calculations carried out by Dalzell (2) and is also inferred by the results of tests carried out at the Netherlands Ship Model Basin with the model of a vessel moored by linear springs in head waves. See Figure 1. This Figure shows a linear relationship between the significant low frequency surge motion and the square of the significant wave height of the irregular head waves, which all had approximately the same mean period. The spectra of some of the waves in which these tests were carried out are shown in Figure 2. Similar results as given here have also been found by Bowers (3).

## NOMENCLATURE

$F_k$	: Force along the axis of fixed system of axes
$S$	: Wetted surface
$S_0$	: Initial wetted surface
$p$	: Pressure
$p^{(0)}$	: Static pressure
$p^{(1)}$	: 1 <sup>st</sup> order pressure linear with wave height
$p^{(2)}$	: 2 <sup>nd</sup> order pressure quadratic with wave height
$n_k$	: Directional cosine of surface element on $S$ along $k$ -axis of fixed system of axes
$dS$	: Surface element on $S$
$\bar{n}_k$	: Directional cosine of surface element on $S$ along $k$ -axis of body axes
$n_k^{(1)}, n_k^{(2)}$	: 1 <sup>st</sup> and 2 <sup>nd</sup> order variation of directional cosine of $dS$ along $k$ -axis of fixed system of axes

$\phi$	: Total velocity potential including all orders
$\phi^{(1)}, \phi^{(2)}$	: 1 <sup>o</sup> and 2 <sup>o</sup> order approximations to $\phi$
$\zeta^{(1)}$	: 1 <sup>o</sup> order incident irregular wave measured in a fixed point
$\zeta_i$	: Amplitude of i <sup>th</sup> component of the irregular wave
$\varepsilon_i$	: Random phase angle
$\zeta_r^{(1)}$	: 1 <sup>o</sup> order relative wave height along the hull
$\zeta_{ri}(X_1), \varepsilon_{ri}(X_1)$	: Amplitude and phase of i <sup>th</sup> component of the relative wave height
$\zeta_{ri}'(X_1), F_{3i}'$	: Relative wave height and vertical force made non-dimensional with amplitude of i <sup>th</sup> component of incident wave
$P_{ij}, Q_{ij}$	: In phase and out of phase components of transfer function of low frequency second order force
$T_{ij}$	: Amplitude of transfer function of second order force
$\varepsilon_{ij}$	: Phase angle of second order force
$\omega, \mu, \omega_i, \omega_j$	: Frequencies in rad./sec.
$\bar{F}_1$	: Mean second order force along $X_1$ axis
$S_\zeta(\omega)$	: Spectral density of irregular waves
$S_F(\mu)$	: Spectral density of low frequency second order force
$A_{WL}$	: Area of water plane
$S_1$	: 1 <sup>o</sup> moment of water plane about the $X_1$ -axis
$S_2$	: 1 <sup>o</sup> moment of water plane about the $X_2$ -axis
$X_{30}^{(1)}$	: 1 <sup>o</sup> order heave motion of origin of body axes in fixed system of axes
$m, b, c$	: Mass, damping and restoring force coefficients of equations of motion
$\bar{x}, \sigma_x$	: Mean and r.m.s. of surge motion
$\zeta_a$	: Amplitude of wave in regular wave tests

#### CALCULATION OF LOW FREQUENCY SECOND ORDER FORCES

Calculation of the low frequency second order force in irregular waves has generally been carried out using the mean second order force in regular waves as a basis (4) (5). Rye (6) has found that the accuracy of the method is increased if tests in regular wave groups are used. Dalzell (2) has demonstrated from analysis of measured low frequency forces in

irregular waves that the relationship between the low frequency second order force and the irregular wave is in reality far more complex than is assumed when use is made of the mean second order force in regular waves. However, Newman (8) has shown that the use of regular wave results is correct as long as only very low frequencies of the second order force are considered. In some cases, a synthesis of the low frequency second order force has been made using the total momentum flux passing through vertical control surfaces situated on either side of the vessel for the beam wave case (7) or at the fore and aft perpendicular when head waves are considered (3). The validity of both these methods has been checked indirectly by comparison of the calculated low frequency horizontal motion and the low frequency motion measured from model tests. In some cases the use of the mean drifting force in regular waves as a basis for calculating the low frequency force appeared to be satisfactory (4) (5), while in other cases (6) considerable discrepancies in calculated and measured motions have occurred. Although the synthesis of the low frequency second order force as used by Bowers (3) is approximative since the actual ship is only roughly incorporated, the results are of interest since the total force is made up of contributions arising at different parts of the vessel, each contribution being related to the pressures at the control surface under consideration.

At the NSMB estimates of the low frequency behaviour of moored vessels have been made using regular wave test results combined with a calculation method outlined in (4) and (5). The degree of success of these estimates was such that the need was felt for more insight in the hydrodynamic phenomena involved. Specifically what was wanted was knowledge of the distribution of the second order force over the length of a vessel moored in head seas. This could be of use to explain some of the discrepancies found between calculated and measured low frequency motions. To this end a series of model tests with a simplified hull form was carried out in head waves.

#### MODEL TESTS

The model chosen for these tests was a three-piece hull consisting of a rectangular mid body with identical pointed bow and stern section (See Figure 3). The three parts were independently connected to a rigid beam running over the length of the vessel. The model was made water tight by means of polythene sheet taped to the seams between mid body and bow and stern section. The connection between the rigid beam and each hull section was such that no relative motions could occur between beam and section. In each section a force transducer was placed by means of which the force parallel to the keel could be measured between the section and the rigid beam. The complete model including rigid beam was free to heave, pitch and surge.

The mooring system, which was linear, consisted of two elastic vertical rods clamped at the upper end to the basin roof construction and connected to the rigid beam on the model via telescopic units by means of ball and socket joint.

Besides the three forces between the rigid beam and the hull sections, the following signals were also measured:

- the relative wave height at 6 positions along the length of the vessel
- the surge motion.

The relative wave heights were measured by means of resistance type wave probes, placed approximately 1 cm away from the side of the hull.

The surge motion was measured by means of a potentiometer.

The model scale was set at 1:50.

The main particulars for full scale were as follows:

Length	230.0 m
Breadth	30.5 m
Draught	7.5 m
Displacement	39262.5 m <sup>3</sup>

The water depth amounted to 50 m in reality.

The test program consisted of tests in regular head waves for a range of wave frequencies followed by a number of tests in irregular head waves using different wave spectra and stiffnesses of the mooring system.

Motion decay tests were carried out to determine the damping and added mass for surge motion.

The main purpose of the tests in regular waves was to measure the contributions of bow, mid body and stern to the overall mean longitudinal force which could be determined from the mean surge and the stiffness of the mooring.

The main purpose of the tests in irregular waves was to supply test results with which later to be calculated results for the surge motion could be compared. During tests in regular waves, analog filtering was applied to the signals of the forces between the rigid beam and the hull sections in order to remove the very large first order force with wave frequency and leave only the constant part of the second order wave force.

The main results of the tests in regular waves are shown in Figure 4 and 5. Figure 4 shows the constant second order forces on each hull section. It is seen that generally the mean force on the bow is directed forward. The force on the unit body may be towards either the bow or the stern.

It should be borne in mind that the forces on each section are not purely hydrodynamic since they were measured in a moving system of axes. This means that also centrifugal forces acting on each element have been measured as well as weight components due to mean shift in the trim of the vessel. These effects have not been corrected for. However, the influence of

these force components does not appear to be excessive if we compare the total mean surge force to the sum of the forces on each element (see Figure 5). Comparison of the forces on each section with the total force on the model shown in Figure 5 shows that the force on bow and stern is considerably larger than the total force for a large range of frequencies.

From the results of these tests it is concluded that the total second order force on the model is not the sum of small contributions with the same sign but rather the difference between large contributions from the fore and aft body each of which may be considerably larger than the total. It can be shown that, if the low frequency second order force was calculated taking the distribution of the force over the hull into account, it is possible to arrive at higher values than would be found using the mean drifting force found for the whole vessel. See ref. (5).

On the basis of the results it was felt that calculation of low frequency second order forces on a vessel should take such effects into account if consistent results are to be expected. This means that the second order force on the vessel should be calculated by integration of individual contributions from each wetted surface element of the hull. This, however, requires that all effects which contribute to the total second order hydrodynamic force on the hull must be known. This can be deduced if we take the general case of a vessel, lying in waves of small amplitude coming from arbitrary directions, carrying out motions in all six degrees of motions and assume that the velocity potential describing the fluid motion and the ship motions are known.

#### DERIVATION OF CONTRIBUTIONS TO SECOND ORDER FORCE

We will first define the systems of co-ordinate axes to be used.

The first system of co-ordinates is a fixed  $O-X_1-X_2-X_3$  system with origin  $O$  in the still water surface and with positive  $X_3$  axis vertically upwards.

The second system of co-ordinates is the  $o-x_1-x_2-x_3$  system of ship bound axes with origin  $o$  in the still water plane of the vessel at half length on the centre line. The positive  $x_3$  axis is vertically upwards, the positive  $x_1$  axis is towards the bow. The positive  $x_2$  axis is to Port. The angular motions of the vessel about the body bound axes are  $x_4$ ,  $x_5$  and  $x_6$  which correspond to roll, pitch and yaw respectively. Positive roll is defined as roll to Starboard, positive pitch; bow down, positive yaw; bow to Port. Both systems of axes are shown in Figure 6. The systems of co-ordinate axes coincide when the ship is at rest and no waves are present. In waves, the ship is assumed to carry out small amplitude motions about the mean position.



Since we are interested mainly in the horizontal low frequency motions of the vessel expressions will be derived for the second order force along the  $X_1$  axis (surge) of the fixed system of axes. The same method may be applied for forces along the  $X_2$  and  $X_3$  axes as well as the angular motions  $x_4$ ,  $x_5$  and  $x_6$ .

In order to determine the hydrodynamic forces acting on a body moving in waves, the following integral must be evaluated:

$$F_k = \iint_S p n_k dS \quad 1.$$

where:

$F_k$  = force along the  $k^{\text{th}}$  axis of the fixed system of co-ordinates

$S$  = total wetted surface of the body

$dS$  = surface element on  $S$

$n_k$  = directional cosine of the surface element  $dS$  along the  $k^{\text{th}}$  axis

$p$  = pressure acting on the surface element  $dS$

The pressure  $p$  can be calculated with the aid of Bernoulli's equation:

$$p = -\rho g X_3 - \rho \phi_t - \frac{1}{2} \rho (\nabla \phi)^2 \quad 2.$$

where  $\phi$  is the velocity potential including all orders and  $X_3$  the vertical motion of the point under consideration.

Since we are only interested in force components of the second order, the potential  $\phi$  may be written as follows:

$$\phi = \epsilon \phi^{(1)} + \epsilon^2 \phi^{(2)} \quad 3.$$

where  $\epsilon$  = a small parameter

$\phi^{(1)}$  = first order approximation which includes the potentials of the undisturbed wave, the diffracted wave and the waves due to motion of the body (see (10))

$\phi^{(2)}$  = second order potential for which the first order potential  $\phi^{(1)}$  forms one of the boundary conditions

The motions of the point under consideration can be regarded as consisting of a mean position  $\bar{X}_k$  and small oscillatory motions about the mean value due to first and second order potential effects:

$$X_k = \bar{X}_k + \epsilon X_k^{(1)} + \epsilon^2 X_k^{(2)} \quad k = 1, 2, 3 \quad 4.$$

In determining the value of  $X_k^{(2)}$ , not only contributions due to second order potential effects, but also contributions due to products of first order angular motions must be taken into account.

Combining the above equation, the pressure  $p$  in the point moving in the vicinity of the mean position yields the following expression for the pressure  $p$  up to and including the second order:

$$p = p^{(0)} + \epsilon p^{(1)} + \epsilon^2 p^{(2)} \quad 5.$$

where:

$$p^{(0)} = -\rho g \bar{X}_3 \quad 6.$$

$$p^{(1)} = -\rho g X_3^{(1)} - \rho \phi_t^{(1)} \quad 7.$$

$$p^{(2)} = -\rho g X_3^{(2)} - \rho \phi_t^{(2)} - \frac{1}{2} \rho (\Delta \phi^{(1)})^2 \quad 8.$$

Similarly the directional cosines  $n_k$  becomes:

$$n_k = \bar{n}_k + \epsilon n_k^{(1)} + \epsilon^2 n_k^{(2)} \quad k = 1, 2, 3 \quad 9.$$

The expressions for  $n_k^{(1)}$  and  $n_k^{(2)}$  are found by projecting the initial directional cosines which move with the vessel on the fixed system of axes. In determining the value of  $n_k^{(2)}$ , not only second order angular motions, but also products of first order angular motions must be taken into account.

Substitution of 9. and 5. in equation 1. results in:

$$F_k = \iint_S \{ p^{(0)} + \epsilon p^{(1)} + \epsilon^2 p^{(2)} \} \{ \bar{n}_k + \epsilon n_k^{(1)} + \epsilon^2 n_k^{(2)} \} dS \quad 10.$$

Using only those terms which give force components up to and including the second order reduces equation 10. to:

$$F_k = \iint_S \{ p^{(0)} + \epsilon p^{(1)} + \epsilon^2 p^{(2)} \} \bar{n}_k dS + \iint_S \{ p^{(0)} + \epsilon p^{(1)} \} \epsilon n_k^{(1)} dS + \iint_S p^{(0)} \epsilon^2 n_k^{(2)} dS \quad 11.$$

The above integrals must be carried out for the complete wetted surface  $S$ . This means that the upper limit of integration is the wave elevation on the hull.

Substitution of the appropriate expressions for the pressures and directional cosines in 11. and working out each individual contribution will give the final expressions for each part. As this is a straight forward procedure, for the sake of brevity this part is left out.

We give here the final expression for the horizontal force in the longitudinal direction ( $k = 1$ ) for the case of arbitrary ship motions:

$$F_1 = \epsilon F_1^{(1)} + \epsilon^2 F_1^{(2)} \quad 12.$$

where:

$$F_1^{(1)} = \iint_{S_0} -\rho \phi_t^{(1)} \bar{n}_1 dS \quad 13.$$

$$F_1^{(2)} = \frac{1}{2} \rho g \int_L \zeta_r^{(1)2} \bar{n}_1 dS - x_6^{(1)} \iint_{S_0} -\rho \phi_t^{(1)} \bar{n}_2 dS + x_5^{(1)} \iint_{S_0} -\rho \phi_t^{(1)} \bar{n}_3 dS + \iint_{S_0} -\frac{1}{2} \rho (\nabla \phi^{(1)})^2 \bar{n}_1 dS + \iint_{S_0} -\rho \phi_t^{(2)} \bar{n}_1 dS - \rho g X_3^{(1)} \cdot x_5^{(1)} A_{WL} + \rho g x_5^{(1)2} S_2 - \rho g x_4^{(1)} x_5^{(1)} S_1 \quad 14.$$

in which:

$\zeta_r^{(1)}$  = first order relative wave height along the initial water line of the vessel

$S_0$  = initial wetted surface

$A_{WL}$  = area of the water plane

- $S_1$  = first moment of the water plane about the  $X_1$ -axis  
 $S_2$  = first moment of the water plane about the  $X_2$ -axis

As can be seen, the first order force  $\epsilon F^{(1)}$  is the integral of the first order pressure  $-\rho\phi^{(1)}$  over the initial wetted surface. The second order force  $\epsilon^2 F^{(2)}$  consists of a number of contributions from products of first order quantities and one contribution from the second order potential pressure  $-\rho\phi^{(2)}$ .

The contributions due to the products of the first order displacements are cancelled by a contribution included in the first integral in 14., so that the sum of the contributions due to displacements remains zero.

We will now take a look at the characteristics of some of the contributions given in equation 14.

The first contribution

$$\frac{1}{2} \rho g \int_L \zeta_n^{(1)} \bar{n}_1 ds \quad 15.$$

is a line integral around the initial water line and represents the force contribution due to the relative first order wave height  $\zeta_1^{(1)}$  along the hull. To show that this integral produces a low frequency longitudinal force, we will write the relative wave height somewhere along the water line as follows:

$$\begin{aligned} \zeta_r^{(1)} &= \zeta_r^{(1)}(X_1, t) = \\ &= \sum_{i=1}^N \zeta_{r_i}(X_1) \cos\{\omega_i t + \epsilon_{r_i}(X_1) + \epsilon_i\} \quad 16. \end{aligned}$$

Squaring  $\zeta_r^{(1)}$  gives:

$$\begin{aligned} \zeta_r^{(1)2} &= \sum_{i=1}^N \sum_{j=1}^N \zeta_{r_i}(X_1) \zeta_{r_j}(X_1) \\ &\quad \cos\{\omega_i t + \epsilon_{r_i}(X_1) + \epsilon_i\} \\ &\quad \cos\{\omega_j t + \epsilon_{r_j}(X_1) + \epsilon_j\} \quad 17. \end{aligned}$$

or

$$\begin{aligned} \zeta_r^{(1)2} &= \sum_{i=1}^N \sum_{j=1}^N \frac{1}{2} \zeta_{r_i}(X_1) \zeta_{r_j}(X_1) \\ &\quad \cos\{(\omega_i - \omega_j)t + (\epsilon_{r_i}(X_1) - \epsilon_{r_j}(X_1)) - \\ &\quad - (\epsilon_i - \epsilon_j)\} + \text{high frequency terms} \quad 18. \end{aligned}$$

This may also be written as:

$$\begin{aligned} \zeta_r^{(1)2} &= \sum_{i=1}^N \sum_{j=1}^N \frac{1}{2} \zeta_{r_i}(X_1) \zeta_{r_j}(X_1) \\ &\quad \cos\{\epsilon_{r_i}(X_1) - \epsilon_{r_j}(X_1)\} \cos\{(\omega_i - \omega_j)t + \\ &\quad (\epsilon_i - \epsilon_j)\} - \sum_{i=1}^N \sum_{j=1}^N \frac{1}{2} \zeta_{r_i}(X_1) \zeta_{r_j}(X_1) \\ &\quad \sin\{\epsilon_{r_i}(X_1) - \epsilon_{r_j}(X_1)\} \sin\{(\omega_i - \omega_j)t + \\ &\quad + (\epsilon_i - \epsilon_j)\} \quad 19. \end{aligned}$$

Substitution in equation 15. gives:

$$\begin{aligned} &\sum_{i=1}^N \sum_{j=1}^N \zeta_i \zeta_j P_{ij} \cos\{(\omega_i - \omega_j)t + (\epsilon_i - \epsilon_j)\} \\ &+ \sum_{i=1}^N \sum_{j=1}^N \zeta_i \zeta_j Q_{ij} \sin\{(\omega_i - \omega_j)t + (\epsilon_i - \epsilon_j)\} \quad 20. \end{aligned}$$

where:

$$P_{ij} = \frac{1}{2} \rho g \int_L \zeta_{r_i}'(X_1) \zeta_{r_j}'(X_1) \cos\{\epsilon_{r_i}(X_1) - \epsilon_{r_j}(X_1)\} \bar{n}_1 ds \quad 21.$$

$$Q_{ij} = -\frac{1}{2} \rho g \int_L \zeta_{r_i}'(X_1) \zeta_{r_j}'(X_1) \sin\{\epsilon_{r_i}(X_1) - \epsilon_{r_j}(X_1)\} \bar{n}_1 ds \quad 22.$$

$\zeta_{r_i}'(X_1), \zeta_{r_j}'(X_1)$  = relative wave height made non-dimensional with the incident waves  
 $\zeta_i, \zeta_j$  =  $i$ th and  $j$ th component of the irregular incident wave

From equation 20. it can be seen that this force component contains both a mean and low frequency component. The mean value is found by putting  $i=j$ .

The undisturbed incident irregular wave is written as follows:

$$\zeta^{(1)} = \sum_{i=1}^N \zeta_i \cos(\omega_i t + \epsilon_i) \quad 23.$$

which, when written as an amplitude modulated signal, becomes:

$$\zeta^{(1)} = A(t) \cos(\omega_0 t + \epsilon(t)) \quad 24.$$

where:

$$\begin{aligned} A(t) &= \left[ \sum_{i=1}^N \sum_{j=1}^N \zeta_i \zeta_j \cos\{(\omega_i - \omega_j)t + (\epsilon_i - \epsilon_j)\} \right]^{\frac{1}{2}} \\ &= \text{wave envelope} \quad 25. \end{aligned}$$

and  $\cos\{\omega_0 t + \epsilon(t)\}$  is a fast oscillating signal below the wave envelope.

Squaring of  $A(t)$  and comparison of the result with 20. shows that the contributions following from the relative wave height represent a part in phase with the square of the wave envelope and a part out of phase with the envelope.

The coefficients  $P_{ij}$  and  $Q_{ij}$  are coefficients

which depend on water line form and the response function for the relative wave height along the water line.  $P_{ij}$  and

$Q_{ij}$  form the in phase and out of phase components of the transfer function by which the low frequency force components are related to the corresponding regular wave group components present in an irregular wave train.

For the contributions

$$\iint_{S_0} -\frac{1}{2}\rho (\nabla \phi^{(1)})^2 \bar{n}_1 dS + \iint_{S_0} -\rho \phi_t^{(2)} \bar{n}_1 dS \quad 26.$$

similar terms as those found for the relative wave height will arise. In that case the  $P_{ij}$  and  $Q_{ij}$  coefficients for these

components also consist of integrals of pressure responses for different combinations of  $i$  and  $j$ . In this case, however, the integrals are over the initial wetted surface of the hull.

The remaining contributions to the longitudinal force are:

$$\begin{aligned} & -x_6^{(1)} \iint_{S_0} -\rho \phi_t^{(1)} \bar{n}_2 dS + x_5^{(1)} \iint_{S_0} -\rho \phi_t^{(1)} \bar{n}_3 dS \\ & + (-\rho g x_{30}^{(1)} A_{WL} + \rho g x_5^{(1)} S_2 - \rho g x_4^{(1)} S_1) x_5^{(1)} \end{aligned} \quad 27.$$

The first two of these are products of the transverse first order wave force times the yaw motion and the vertical first order wave force times the pitch motion respectively.

The remaining three contributions are the total increase in the displacement of the vessel due to the heave ( $x_3^{(1)}$ ), pitch ( $x_5^{(1)}$ ) and roll ( $x_4^{(1)}$ ) times the pitch motion.

All contributions to 27. arise from the fact that a first order force along the ship bound  $x_3$ -axis or  $x_2$ -axis has rotated due to the pitch and yaw motion, about the  $x_2$ -axis and the  $x_3$ -axis respectively, thus producing a second order force component along the fixed  $x_1$ -axis.

Contributions of this type are more straight forward to evaluate as will be shown below.

If, for instance, the total vertical force due to the integral

$$\iint_{S_0} -\rho \phi_t^{(1)} \bar{n}_3 dS \quad 28.$$

is in irregular waves of the form:

$$F_3 = \sum_{i=1}^N \zeta_i F_{3i} \cos(\omega_i t + \epsilon_{3i} + \epsilon_i) \quad 29.$$

and the pitch motion  $x_5^{(1)}$  is of the form:

$$x_5^{(1)} = \sum_{i=1}^N \zeta_i x_{5i} \cos(\omega_i t + \epsilon_{5i} + \epsilon_i) \quad 30.$$

then the low frequency contribution from the product of these two quantities is again of the form:

$$\begin{aligned} & \sum_{i=1}^N \sum_{j=1}^N \zeta_i \zeta_j P_{ij} \cos\{(\omega_i - \omega_j)t + (\epsilon_i - \epsilon_j)\} \\ & + \sum_{i=1}^N \sum_{j=1}^N \zeta_i \zeta_j Q_{ij} \sin\{(\omega_i - \omega_j)t + (\epsilon_i - \epsilon_j)\} \end{aligned} \quad 31.$$

where in this case:

$$P_{ij} = \frac{1}{2} F_{3i}' x_{5j}' \cos(\epsilon_{3i} - \epsilon_{5j}) \quad 32.$$

$$Q_{ij} = -\frac{1}{2} F_{3i}' x_{5j}' \sin(\epsilon_{3i} - \epsilon_{5j}) \quad 33.$$

These are of a more simple form than the previously discussed contributions since the value of  $F_{3i}'$  and  $x_{5j}'$  and their phases

are quantities which need only be known for a range of frequencies and  $P_{ij}$  and  $Q_{ij}$  are

then directly calculable for the  $i$  and  $j$  combinations of interest.

When the coefficients  $P_{ij}$  and  $Q_{ij}$  are known

for all contributions to the second order force given by 19., they are summed to give the total in and out of phase components  $\Sigma P_{ij}$  and  $\Sigma Q_{ij}$  with the square of the wave envelope.

The total second order force may then be written as follows:

$$\begin{aligned} F_1^{(2)} = & \sum_{i=1}^N \sum_{j=1}^N \zeta_i \zeta_j T_{ij} \cos\{(\omega_i - \omega_j)t + \\ & + (\epsilon_i - \epsilon_j) + \epsilon_{ij}\} \end{aligned} \quad 34.$$

where:

$$T_{ij} = \{(\Sigma P_{ij})^2 + (\Sigma Q_{ij})^2\}^{\frac{1}{2}} \quad 35.$$

$$\epsilon_{ij} = \arctan\left(-\frac{\Sigma Q_{ij}}{\Sigma P_{ij}}\right) \quad 36.$$

The mean second order force is found from:

$$\bar{F}_1^{(2)} = \sum_{i=1}^N \zeta_i^2 (\Sigma P_{ij}) \quad 37.$$

In spectral form the expression for the mean force becomes:

$$\bar{F}_1^{(2)} = 2 \int_0^\infty S_\zeta(\omega) \{\Sigma P(\omega, \omega)\} d\omega \quad 38.$$

The spectrum of the oscillating part of the low frequency second order force becomes:

$$S_F(\mu) = 8 \int_0^\infty S_\zeta(\omega) S_\zeta(\omega + \mu) T^2(\omega, \omega + \mu) d\omega \quad 39.$$

in which:

$$T^2(\omega, \omega + \mu) = \{\Sigma P(\omega, \omega + \mu)\}^2 + \{\Sigma Q(\omega, \omega + \mu)\}^2 \quad 40.$$

The results given in equation 38. and 39. are found from equation 37. and 34. respectively using methods described in ref. (5) and ref. (9).

In equations 38., 39. and 41  $\mu$  denotes the frequency difference  $\omega_i - \omega_j$  used in the discrete formulations.

Up to this point it has been assumed that the potential  $\phi$  is known up to the second order. From 14. it was seen that both first and second order contributions are required for complete evaluation of the second order force. It was furthermore assumed that the ship motions were known, also to the second order.



From 14. it appears that only the first order motions need to be known for the force along the  $X_1$ -axis.

With the present state of the art, it is possible to determine, for a freely floating body, in waves coming from arbitrary directions, the contributions due to first order motions and hydrodynamic forces. For a ship shaped vessel this requires the use of numerical methods based on three-dimensional potential theory. Results found by Van Oortmerssen (10) on the motions of ships calculated by this method give confidence in this respect.

Knowledge of the second order potential  $\phi^{(2)}$  is, however, restricted to only the very simplest of cases and since its solution is dependent on non-linear boundary conditions derived from the solution of the first order potential  $\phi^{(1)}$ , which, for a practical case is in itself very complex it is reasonable to suppose that detailed knowledge of  $\phi^{(2)}$  in such cases will not be forthcoming for some time. However, Newman (8) points out, it may be possible to estimate the contribution due to  $\phi^{(2)}$  by means of, for instance, the Froude-Kryloff hypothesis.

#### AN EXAMPLE OF LOW FREQUENCY FORCES CALCULATED FROM INTEGRATION OF PRESSURES

Being engaged in a preliminary survey of equation 14., we have for the present chosen a simple method of approach. This involved calculation of the low frequency second order longitudinal force and surge motion of the previously mentioned barge in head seas. For this case the longitudinal force along the  $X_1$ -axis given by 14. reduces to:

$$F_1^{(2)} = \frac{1}{2} \rho g \int_L \zeta_r^{(1)2} \bar{n}_1 dS + x_5^{(1)} \iint_{S_0} -\rho \phi_t^{(1)} \bar{n}_3 dS \\ + \iint_{S_0} -\frac{1}{2} \rho (\nabla \phi^{(1)})^2 \bar{n}_1 dS + \iint_{S_0} -\rho \phi_t^{(2)} \bar{n}_1 dS \\ - \rho g x_{30}^{(1)} x_5^{(1)} A_{WL} \quad 41.$$

Most of the other terms in 14. are zero since the roll ( $x_4^{(1)}$ ) and the yaw motion ( $x_6^{(1)}$ ) are zero for head seas. The term involving  $S_1$  is zero, since the water plane of the barge is symmetrical about the  $x_2$ -axis when we assume the origin of the  $0-x_1-x_2-x_3$  axis to be midships. Of the five contributions in equation 41. it is possible to estimate three by means of ship motions calculation based on Strip theory. The terms involving the contributions due to the square of the first order velocity  $\nabla \phi^{(1)}$  and the second order potential  $\phi^{(2)}$  were left out. This did not presuppose that these contributions were negligible but rather that, at this stage, it was enough to get an impression of the effectiveness of those contributions which

were readily to be calculated.

Accordingly the hydrodynamic forces and motions of the barge in head waves were calculated for a range of frequencies. The relative wave heights were calculated based on the incident wave without corrections for wave set-up against the hull. The hydrodynamic vertical force along the  $x_3$ -axis given by the integral

$$\iint_{S_0} -\rho \phi_t^{(1)} \bar{n}_3 dS \quad 42.$$

was calculated using the contributions due to the vertical wave exciting force, and the added mass and damping forces arising from the heave and pitch motions.

For the relative wave height contributions the  $P_{ij}$  and  $Q_{ij}$  coefficients were calculated from equations 21. and 22. For contributions due to the vertical hydrodynamic force and hydrostatic force combined with the pitch motion the  $P_{ij}$  and  $Q_{ij}$  coefficients were calculated from equations 32. and 33.

An example of the total  $P_{ij}$  and  $Q_{ij}$  coefficients,  $\Sigma P_{ij}$  and  $\Sigma Q_{ij}$  is given in Figure

7. In Figure 8 the corresponding value of  $T_{ij}^{(2)}$  is given.

The range of  $\omega_i$  and  $\omega_j$  used was sufficiently large to cover the frequency range of the wave spectrum which was used in the subsequent calculation of the low frequency surge motion.

The spectra of irregular waves used for the calculations are shown in Figure 9. These spectra are of the incident waves used for the tests with the barge in irregular waves.

Using these wave spectra and the values of  $\Sigma P_{ii}$  and  $T_{ij}$ , the mean second order wave

force and spectra of the low frequency second order wave force were calculated. The spectra of the low frequency forces are shown in Figure 10.

The low frequency surge motions were calculated using the following equation:

$$S_x(\mu) = S_F(\mu) \cdot \frac{1}{(c - m\mu^2)^2 + b^2 \mu^2} \quad 43.$$

where:

- $S_x(\mu)$  = spectral density of the low frequency motion at frequency  $\mu$
  - $c$  = restoring coefficient for surge motion due to the linear mooring system
  - $b$  = damping coefficient for surge motion determined from surge motion decay tests in still water
  - $m$  = virtual mass for surge motion
- This was also determined from the surge motion decay tests.

Equation 43. is based on the supposition that the equation of motion for the low

frequency surge motion is of the following form:

$$m\ddot{X}_1 + b\dot{X}_1 + cX_1 = F(t) \quad 44.$$

where  $m$ ,  $b$  and  $c$  are constants, determined from static load tests and motion decay tests (see Figure 11 and Figure 12).

From the model tests the following values of the coefficients  $m$  and  $b$  were found:

$$m = 4366 \text{ tf} \cdot \text{sec}^2/\text{m}$$

$$b = 38.59 \text{ tf/m} \cdot \text{sec}.$$

For the calculations two values of  $c$  were used, viz.:

$c = 138.3 \text{ tf/m}$  and  $c = 85.7 \text{ tf/m}$ . The natural surge periods in still water corresponded to 35 and 45 sec. respectively. The highest value of  $c$  was used for tests in all 5 wave spectra, given in Figure 9, while the lower value of  $c$  was only tested in spectrum C given in the same Figure. The low frequency surge motion calculations were carried out for the same cases. Examples of calculated and measured low frequency surge spectra  $S_x(\mu)$  are given in Figure 13. From this Figure it is seen that the calculated spectrum differs considerably from the measured spectrum. This phenomenon is typical for all cases. The reason for this difference in shape of spectrum in our opinion is to be found in the fact that the surge motion damping is very low. With the values of  $b$  and  $c$  and  $m$  used for these calculations magnification factors of around 20 are found for excitations at the natural frequency.

Accurate determination of the spectrum in this type of motion requires very long records since the auto-correlation function shows very little decay. The influence of the test duration on the spectral density found for such a signal is such that the peak value will increase while the spectrum also becomes narrower thus tending towards the calculated surge spectrum. The duration of the model tests which resulted in approximately 170 oscillations in the low frequency surge motions did not permit a more accurate definition of the spectral peak.

Less detailed, but nevertheless important quantities which are much less sensitive to the length of record, are the mean ( $\bar{X}$ ) and r.m.s. ( $\sigma_x$ ) values of the low frequency surge motions. In Figure 14, the calculated  $\sigma_x$  and  $\bar{X}$  values are compared with the measured values for all six cases. From this Figure it is seen that the calculated  $\sigma_x$  values are surprisingly close to the measured values. The mean values  $\bar{X}$  show considerable difference although the trend is the same.

Shown in the same Figure are the mean and r.m.s. values of the surge motions using method of calculation based on the mean total second order force in regular waves. The method is described in detail in ref. (5).

The equations for the mean surge force and the spectral density are in this case as follows:

$$\bar{F} = \rho g \int_0^\infty S_\zeta(\omega) \left\{ \frac{\bar{F}}{\frac{1}{2} \rho g \zeta_a^2}(\omega) d\omega \right. \quad 45.$$

$$S_F(\mu) = 2\rho^2 g^2 \int_0^\infty S_\zeta(\omega) S_\zeta(\omega+\mu) \left\{ \frac{\bar{F}}{\frac{1}{2} \rho g \zeta_a^2}(\omega+\mu/2) \right\}^2 d\omega \quad 46.$$

where:

$$\frac{\bar{F}}{\frac{1}{2} \rho g \zeta_a^2}(\omega) = \text{frequency dependent mean total second order force in regular waves taken from Figure 14.}$$

Comparison with the measured values and those calculated by integration of the pressure components (Figure 14) shows that use of the regular wave coefficient tends to produce a better estimate of the mean surge  $\bar{X}$  while predicting too low a value for the oscillatory part. The fact that the calculation method based on regular wave tests gives a good approximation for the mean surge is in keeping with conclusion reached by other investigations (1) (8). The difference found in the r.m.s. values by both calculation methods are, to some extent, connected with the higher mean values predicted from the method using the integrated pressure. This can be demonstrated by using equation 46. and the coefficients  $\Sigma P(\omega+\mu/2, \omega+\mu/2)$  which are the coefficients corresponding to  $\bar{F}/\frac{1}{2} \rho g \zeta_a^2(\omega+\mu/2)$  from the regular wave tests. The r.m.s. values predicted in this case are also shown in Figure 14. Comparison shows that the motion predicted by the correctly integrated pressure will still give results which are consistently closer to the measured values although the differences between these results and those given by equation 46. using the  $\Sigma P(\omega+\mu/2, \omega+\mu/2)$  coefficients are smaller.

In analysing the relative influence of the two contributions of equation 14., which were used for the calculation, it appears that the major contribution is due to the relative wave height. The term expressing the longitudinal component due to the interaction of the pitch motion and the vertical force accounted for approximately 6% of the oscillatory low frequency motion. A quick analysis of the relative wave heights measured during the regular wave tests revealed that the mean forces on the fore and aft body could also be largely accounted for by the contributions due to the relative wave height.

A more detailed discussion on the differences found here will not be given at this stage since more results need to be obtained for a clearer picture of the phenomena involved. However, in regarding the factors which can introduce errors in the calculation of the low frequency second order force as calculated here by means of the integration of pressures, we can identify the following:

- The contributions of the pressure drop due to  $-\frac{1}{2} \rho (\nabla \phi^{(1)})^2$  and the second order pressure  $-\rho \phi^{(2)}$  have not been included.
- Deformation by the vessel of the incident wave has not been accounted for in the relative wave height.

- Differences in the equation of surge motions used as deduced from motion decay tests (virtual mass and damping) and as it actually is in irregular waves.
- Differences in the actual ship motions with wave frequencies and those calculated by Strip theory.

In the afore going the calculated ship motions have not been compared with measurements because, at the time the model tests were in program, the basic work which resulted in equation 14., had not been completed. As the model test program was purely exploratory and aimed principally at insight into the longitudinal distributions of the second order forces in regular head waves, the pitch and heave motions were not measured. Generally, however, ship motion calculations based on Strip theory produce accurate results for slender ships so that the calculated results given here, may well be indicative for the usefulness of the method for estimation of the low frequency forces in irregular waves.

#### FINAL REMARKS

The method outlined here, has been shown to lead to the calculation of transfer functions  $\Sigma P(\omega, \omega+\mu)$ ,  $\Sigma Q(\omega, \omega+\mu)$  and  $T(\omega, \omega+\mu)$  which give the in phase, out of phase and amplitude relationship respectively between the low frequency part of the square of the incident wave envelope and the low frequency second order wave forces. The results have been obtained based on the supposition of a quadrate relationship between the second order forces and the height of the incident wave. In deducing these results, no restrictions have been placed on the value of the low frequency.

The transfer functions found are in principle equivalent to the quadratic operator which Dalzell (2) extracts from model tests by means of cross bi-spectral methods applied to the incident irregular wave and the low frequency second order part of the total longitudinal force on a ship travelling into head waves. If it is possible to augment the quantitative accuracy of a synthetic quadratic operator, it will be possible to calculate correctly, for instance, in the time domain the first and second order forces acting on floating bodies. See (2). This allows analysis of practical, non-linear, mooring systems requiring calculations in the time domain.

#### REFERENCES

1. Gerritsma, J. and Beukelman, W.:  
"Analysis of the resistance in waves of a fast cargo ship"  
Report No. 334, Laboratorium voor Scheepsbouwkunde, Technical University Delft, 1971.
2. Dalzell, J.F.:  
"Cross-Bi-spectral Analysis: Application to ship resistance in waves"  
Journal of Ship Research, Vol 18, No.1,

March 1974.

3. Bowers, E.C.:  
"Long period oscillations of moored ships in short wave seas"  
Paper presented before the Royal Institute of Naval Architects, August 1975.
4. Remery, G.F.M. and Hermans, A.J.:  
"The slow drift oscillations of a moored object in random seas"  
Paper (SPE 3423, OTC 1500) Offshore Technology Conference, Houston 1971.
5. Pinkster, J.A.:  
"Low frequency phenomena associated with vessels moored at sea"  
Paper SPE 4837, Society of Petroleum Engineers of AIME, 1974, Spring Meeting, Amsterdam.
6. Rye, H. et al.:  
"On the slow drift oscillation of moored structures"  
Paper OTC 2366, Offshore Technology Conference, Houston 1975.
7. Hsu, F.A. and Blenkarn, K.A.:  
"Analysis of peak mooring forces caused by slow vessel drift oscillations in random seas"  
Paper OTC 1159, Offshore Technology Conference, Houston 1970.
8. Newnan, J.N.:  
"Second order, slowly varying forces on vessels in irregular waves"  
International Symposium on the Dynamics of Marine vehicles and structures in waves"  
University College, London, 1974.
9. Rice, S.O.:  
"Mathematical Analysis of Random Noise"  
Bell system Technical Journal, Vols 23 and 24.
10. Van Oortmerssen, G.:  
"The motions of a ship in shallow water"  
Paper presented before the Chesapeake Section of SNAME, November 1975.



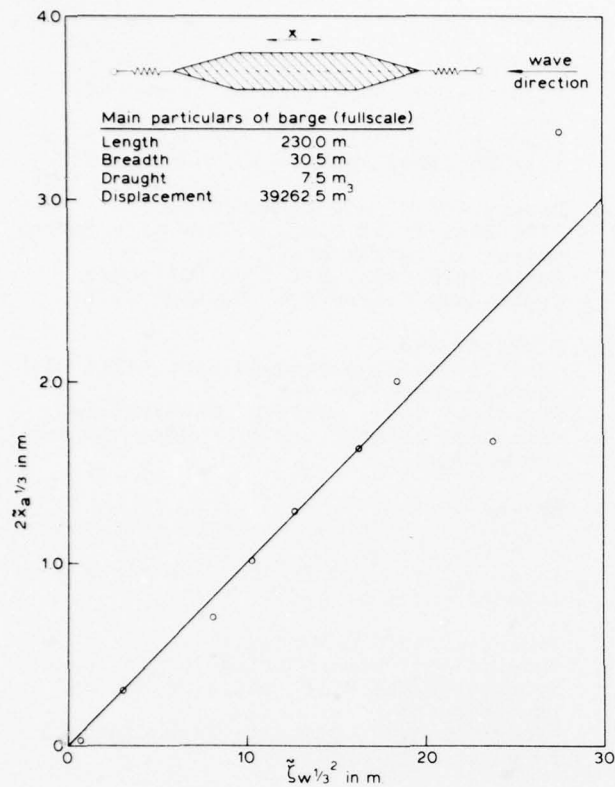


Fig. 1: Low frequency oscillatory surge motions of a barge in irregular head waves

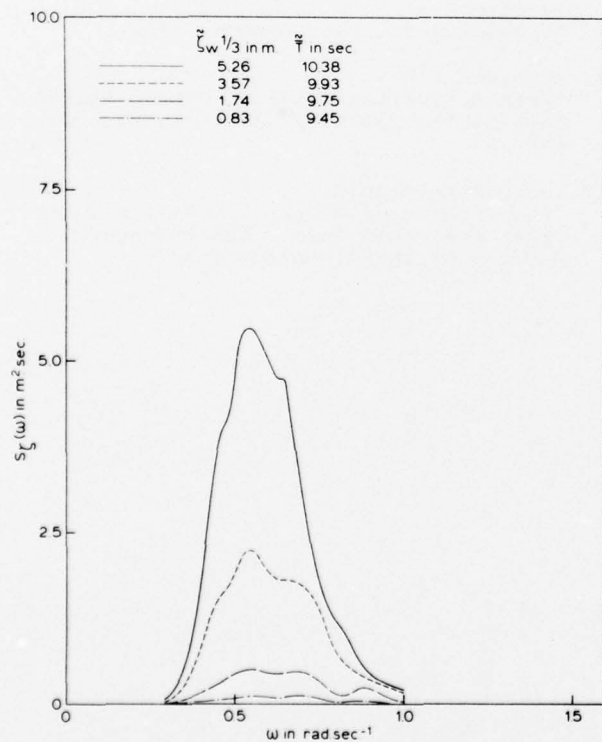


Fig. 2: Spectra of irregular waves

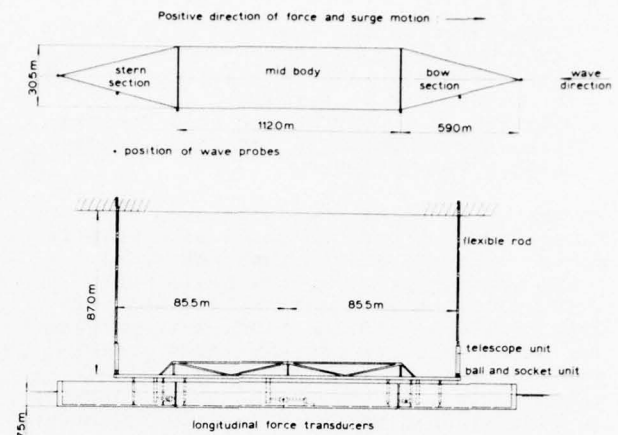


Fig. 3: Mooring system and construction of 3-piece barge model

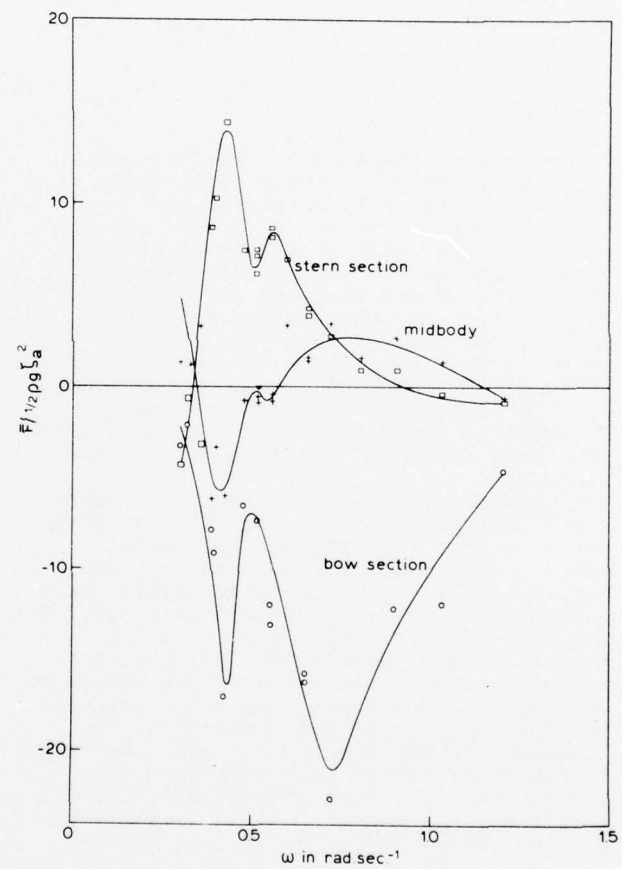


Fig. 4: Constant second order wave force on hull elements

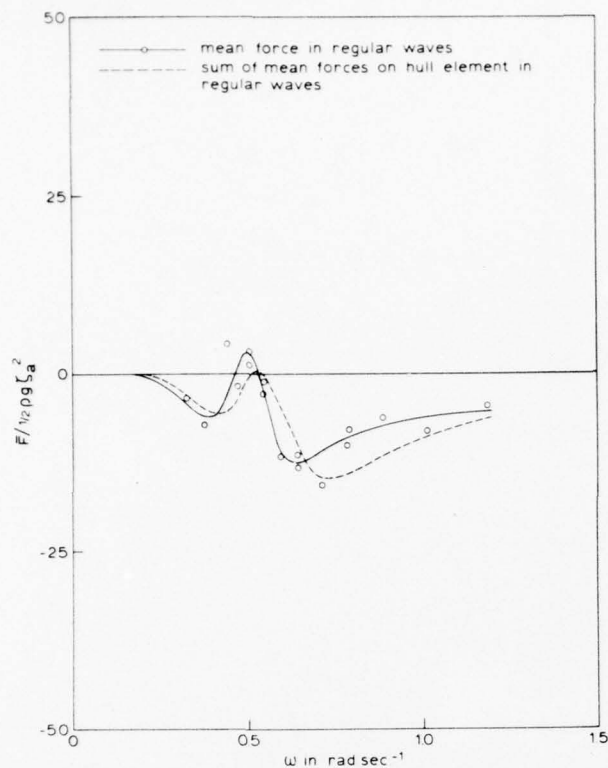


Fig. 5: Total constant second order force on hull and sum of contributions from hull elements

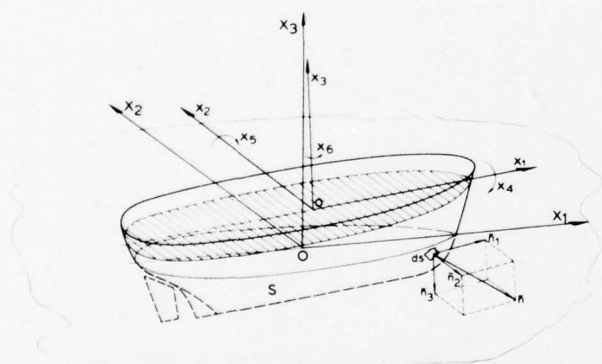


Fig. 6: Systems of co-ordinate axes

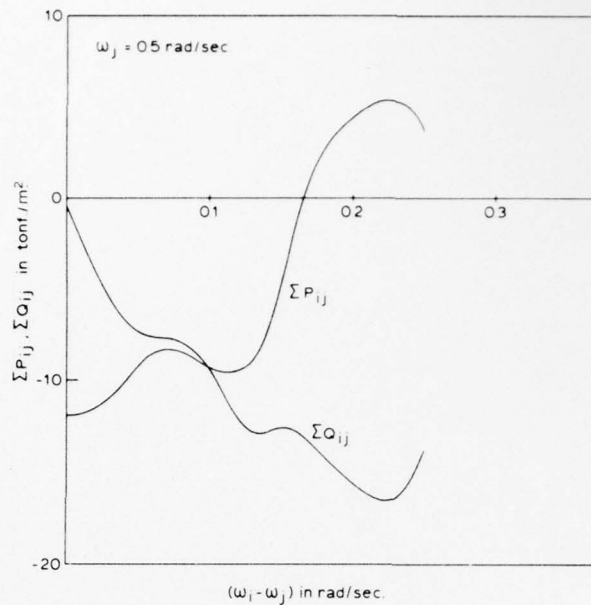


Fig. 7: The coefficients  $\Sigma P_{ij}$  and  $\Sigma Q_{ij}$

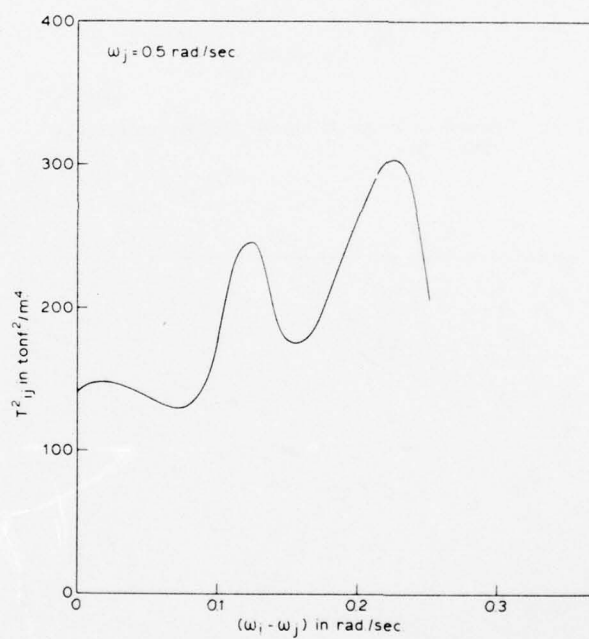


Fig. 8: The coefficient  $T_{ij}^2$

V1.50

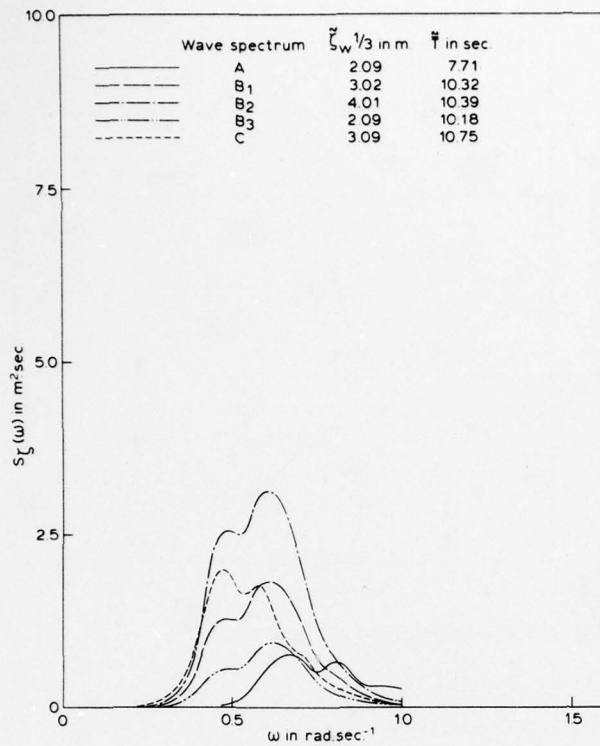


Fig. 9: Spectra of irregular waves used for tests and calculations

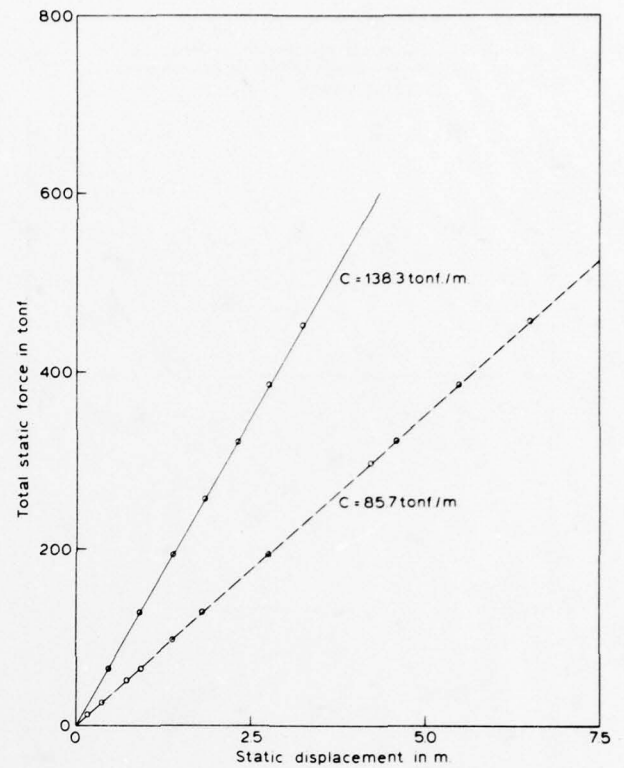


Fig. 11: Static load tests for surge ( $X_1$ ) direction

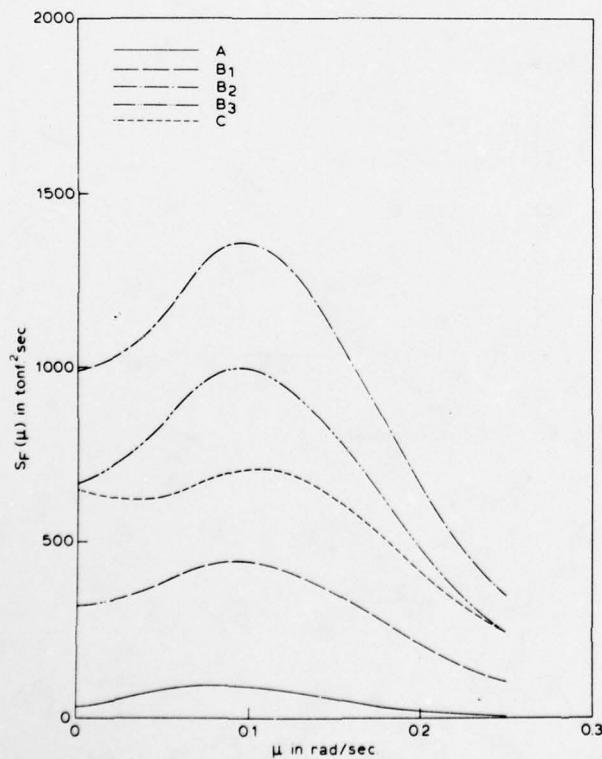


Fig. 10: Spectra of low frequency second order force in head waves for different wave spectra

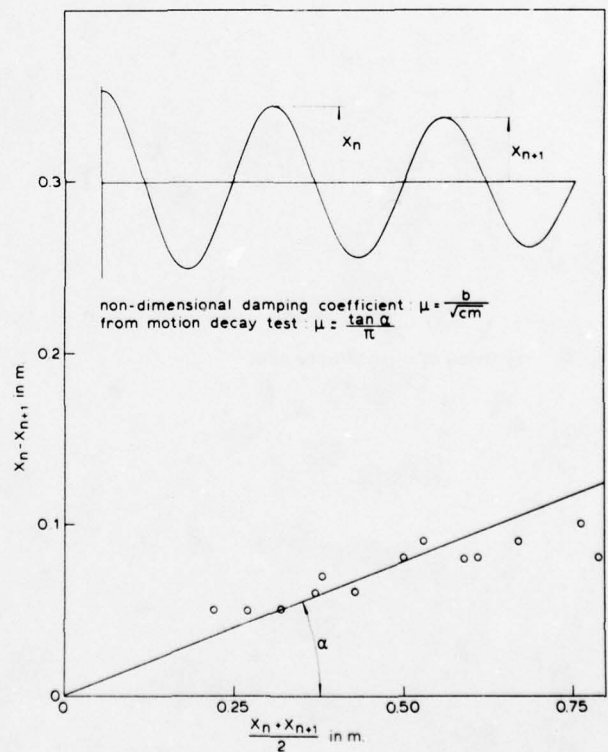


Fig. 12: Surge motion decay test in still water



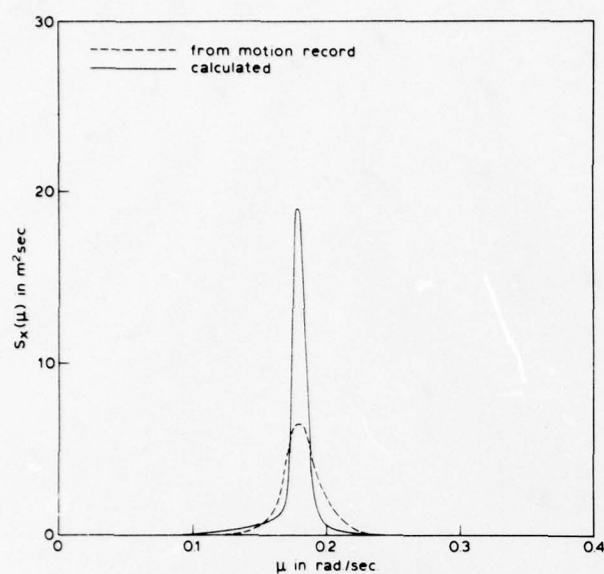


Fig. 13: Example of measured and calculated low frequency surge motion spectra

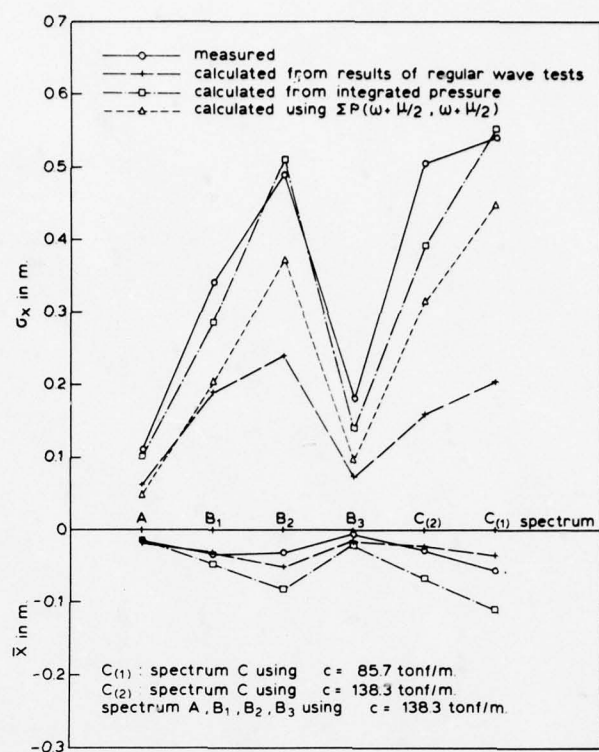


Fig. 14: Mean and r.m.s. values of low frequency surge motion in irregular head waves

# ELASTIC STRUCTURAL RESPONSE OF SEMISUBMERSIBLES IN REGULAR WAVES

K. YOSHIDA and K. ISHIKAWA  
University of Tokyo, Tokyo, Japan

In this paper, a method analyzing the response of floating framed ocean structures subjected to periodic waves is presented, where stiffness of structural members is contained in equations of motion and internal forces are calculated simultaneously with the motion. Therefore, the influence of stiffness of members on the motion may be taken account of and high accuracy in the estimation of internal forces may be expected. The equations of motion based on the analytical model was introduced in the matrix form and the computer program was made. The calculations were compared with experiments on fundamental semisubmersible models.

## INTRODUCTION

Periodic response analysis of ship hulls is usually divided into two groups. One is quasi-static analysis, which consists of two steps; motion is analyzed as a rigid body by strip theory [1],[2] and after that, internal forces are analyzed [3]. The other is further subdivided into two categories. One is periodic ship hull vibration induced by machinery or propellers and the other is springing excited by waves [4],[5],[6]. Against the conventional separation, Bishop [7],[8] emphasized the necessity of a unified analysis in order to study the probability of coupling of ship motion and ship hull vibration. Another example is the case of floating ocean structures, to which the relationship between motion and internal force is significant.

A semisubmersible unit is one of the fundamental types of floating ocean structures, which usually consist of several cylindrical floating bodies and connecting members. This type has been adopted as basic structures for many kinds of floating ocean structures because this is not subjected to so big wave exciting forces as a ship for sparseness of the structure at the level of sea surface and also desirable abilities on seakeeping can be attained by using hydrodynamical characteristics [9],[10] particular to immersed body.

The modern studies on the over-all structural response of semisubmersible units started from the design of a drilling rig in the Mohole Project [11]. In recent years, several papers [12],[13],[14],[15] were published on the semisubmersible units for offshore mining. The analytical method adopted in these papers fundamentally belongs to the first group mentioned at the top of this introduction. On the other hand, Taylor [16] studied the dynamic response of floating structures by the modal analysis and this qualitative conclusions on the estimation of internal forces are as follows; internal forces of the stiff floating structures can be approximately estimated by the quasi-static analysis, whereas internal forces of not sufficiently stiff floating structures should be estimated by the analysis based on the motion involving the elastic deformation.

This paper presents a method analyzing the response of the semisubmersible type of floating structures [17],[18], where both motions and internal forces are analyzed simultaneously, from the following points of view.

(1) The relationship between motions and internal forces of the semisubmersible type of floating structures should be clarified qualitatively and also quantitatively for making rational design possible.

(2) High accuracy of internal forces obtained in the analysis of over-all structures is necessary for the detailed analysis of local structures, for example, the junctions of members.

(3) Studies on the phenomenon similar to springing of ships may be important because this type of structures may become much larger in future.

## NOTATIONS

$x, z$	: Global co-ordinates fixed in plane
$x_i, z_i$	: Local co-ordinates of element
$u, \dot{u}, \ddot{u}$	: x-directional displacement, velocity and acceleration
$w, \dot{w}, \ddot{w}$	: z-directional displacement, velocity and acceleration
$\theta, \dot{\theta}, \ddot{\theta}$	: Rotation angle, angular velocity and angular acceleration
$\eta$	: Elevation of wave surface
$a$	: Amplitude of wave
$\lambda$	: Wave length
$\kappa$	: Circular wave number
$c$	: Phase velocity of wave
$\omega$	: Circular frequency of wave
$\phi$	: Velocity potential of wave
$\rho$	: Density of water
$g$	: Acceleration of gravity
$p$	: Pressure
$M$	: Mass of element
$A$	: Sectional area of element
$V_w$	: Displacement volume of element
$I_\theta$	: Moment of inertia of element
$M_{ax}, M_{az}$	: Added mass for x- and z-directional motion
$N_x, N_z$	: Damping coefficient for x- and z-directional motions
$F_x, F_z, F_\theta$	: External force in x-, z- and rotational directions

- $f_x, f_z, f_\theta$ : Wave exciting force in x-, z- and rotational directions  
 $E$ : Young's modulus  
 $I$ : Second moment of area of element  
 $l, \bar{z}$ : Length of element, span length

Other notations and abbreviations are defined at the locations of first appearance in paragraphs, figures and tables.

## 1. FUNDAMENTAL ASSUMPTIONS

The following fundamental assumptions are made in the analysis.

- (1) Fluid is incompressible, inviscid and irrotational.
- (2) Comparing with the incoming wave length, the sectional dimensions of members are small.
- (3) Airy wave theory is adopted and the response is a harmonic one around the equilibrium.
- (4) The whole phenomena in both hydrodynamics and structural dynamics is linear and elastic.
- (5) Hydrodynamical interactions due to existence of multi-members can be neglected.
- (6) Structural members are slender and structures can be analyzed as frames.
- (7) Structures are plane frames which exist in the plane defined by directions of wave propagation and of sea depth.

Members of plane frames are divided into three groups; vertical, horizontal and diagonal members. The diagonal members are here assumed not subjected to hydrodynamic forces because their sectional dimensions are small. Each member is subdivided into elements in order to make it possible a simple and unified estimation of hydrodynamic and structural characteristics of it. As for an element, the following assumptions are made.

- (1) Corresponding to hydrodynamical and structural functions of a member, two kinds of element are considered. One is named as hull element which is a rigid body with the same mass, shape and sizes as the subdivided portion of the member. The other is named as beam element which has concentrated elastic rigidity of the subdivided portion of the member at the location of a line connecting the center of gravity of adjacent two hull elements. (Fig.1)
- (2) Hull element is rigidly connected to the beam element only at the position of the center of gravity of the hull element and compatibilities of displacements of these two kinds of elements and dynamic equilibriums of forces are satisfied at this position. (nodal point of an elastic frame)

## 2. EXTERNAL FORCES

The forces to which the hull element is subjected are usually composed of gravity force, hydrostatic pressure, wind force, current force, wave force, inertia force, restoring force by mooring and so on. The subject of this paper is the analysis of dynamic response of structures in waves and it is assumed that the effects due to the forces except the forces related to the dynamic response in the waves are analyzed separately and superposed linearly. As to the restoring force by mooring, however, it can be treated as one part of structural system when this force can be assumed to be proportional to the displacement.

The forces to which hull element is subjected are

assumed as the following five kinds and treated as concentrated external forces at the nodal points of the frame by D'Alembert's principle.

- (1) inertia force; mass of hull element (mass moment) multiplied by acceleration (angular acceleration) of it
- (2) pressure; pressure due to linearized Bernoulli's theorem
- (3) force due to relative displacement; estimation of complementary buoyancy due to the difference between surface elevation and the rise of the center of gravity of partially immersed vertical element (Table 1)
- (4) force due to relative velocity; damping coefficient multiplied by relative velocity where relative velocity means the difference between the fluid particle velocity estimated at the appropriate representative point in the hull element and the velocity of the hull element itself
- (5) force due to relative acceleration; added mass (added mass moment) multiplied by relative acceleration (relative angular acceleration) where 'relative' has the same meaning as above

As the kind and expression of forces to which the hull element is subjected depend on the location and attitude of it, hull element is classified into following 7 kinds for convenience.

- (1) Vertical non-immersed element
  - (2) Vertical partially-immersed element with end
  - (3) Vertical partially-immersed element without end
  - (4) Vertical fully-immersed element with end
  - (5) Vertical fully-immersed element without end
  - (6) Horizontal non-immersed element
  - (7) Horizontal fully-immersed element
- (Table 1 and 2)

In the fixed co-ordinate system in plane (x-z axes, Fig. 2), the surface elevation and velocity potential can be written as

$$\eta = a \cos(\kappa x - \omega t) \quad (1)$$

$$\phi = cae^{\kappa z} \sin(\kappa x - \omega t) \quad (2)$$

where  $a$ ,  $\kappa$ ,  $c$  and  $\omega$  are the amplitude of wave, the circular wave number, the phase velocity and the circular frequency, respectively. From the velocity potential  $\phi$ , the particle velocity of fluid is induced.

$$\dot{u} = \frac{\partial \phi}{\partial x} = a\omega e^{\kappa z} \cos(\kappa x - \omega t) \quad (3)$$

$$\dot{w} = \frac{\partial \phi}{\partial z} = a\omega e^{\kappa z} \sin(\kappa x - \omega t) = e^{\kappa z} \dot{\eta} \quad (4)$$

the particle acceleration of fluid is

$$\ddot{u} = \frac{\partial^2 \phi}{\partial x \partial t} = a\omega^2 e^{\kappa z} \sin(\kappa x - \omega t) \quad (5)$$

$$\ddot{w} = \frac{\partial^2 \phi}{\partial z \partial t} = -a\omega^2 e^{\kappa z} \cos(\kappa x - \omega t) = e^{\kappa z} \ddot{\eta} \quad (6)$$

pressure is

$$p = -\rho \frac{\partial \phi}{\partial t} - \rho g z \quad (7)$$

By using these expressions, five kinds of external forces are formulated. For example, the forces for the vertical partially-immersed element with end (left hand side of Fig. 2) are arranged in the following form.

$$F = -K_a \ddot{U} - K_v \dot{U} - K_d U + F \quad (8)$$

where  $F$  and  $U$  are nodal external force vector and



nodal displacement vector and have the following component, respectively.

$$\mathbf{F} = \begin{Bmatrix} F_x \\ F_z \\ F_\theta \end{Bmatrix}, \quad \mathbf{U} = \begin{Bmatrix} u \\ w \\ \theta \end{Bmatrix} \quad (9)$$

$K_a$ ,  $K_v$  and  $K_d$  are virtual mass matrix, damping coefficient matrix and restoring coefficient matrix and are concretely expressed as follows, respectively.

$$K_a = \begin{bmatrix} M+M_{ax} & 0 & M_{ax}L_1 \\ 0 & M+M_{az} & 0 \\ M_{ax}L_1 & 0 & I_0+M_{ax}L_2 \end{bmatrix} \quad (10)$$

$$K_v = \begin{bmatrix} N_x & 0 & N_xL_1 \\ 0 & N_z & 0 \\ N_xL_1 & 0 & N_xL_2 \end{bmatrix} \quad (11)$$

$$K_d = \begin{bmatrix} 0 & 0 & 0 \\ 0 & \rho g A & 0 \\ 0 & 0 & \rho g V_w L_1 \end{bmatrix} \quad (12)$$

Wave exciting force is

$$\mathbf{f} = \begin{Bmatrix} f_x \\ f_z \\ f_\theta \end{Bmatrix} = \begin{Bmatrix} a\sqrt{\alpha_x^2 + \beta_x^2} \cos(\kappa x - \omega t + \gamma_x) \\ a\sqrt{\alpha_z^2 + \beta_z^2} \cos(\kappa x - \omega t + \gamma_z) \\ a\sqrt{\alpha_\theta^2 + \beta_\theta^2} \cos(\kappa x - \omega t + \gamma_\theta) \end{Bmatrix} \quad (13)$$

where  $\alpha$ ,  $\beta$  and  $\gamma$  have the following components, respectively.

$$\begin{Bmatrix} \alpha_x \\ \alpha_z \\ \alpha_\theta \end{Bmatrix} = \begin{Bmatrix} N_x \omega \varepsilon_1 \\ \rho g A - (\rho V_w + M_{ax}) \omega^2 \varepsilon_1 \\ N_x \omega \varepsilon_2 \end{Bmatrix} \quad (14)$$

$$\begin{Bmatrix} \beta_x \\ \beta_z \\ \beta_\theta \end{Bmatrix} = \begin{Bmatrix} (\rho V_w + M_{ax}) \omega^2 \varepsilon_1 \\ N_z \omega \varepsilon_1 \\ (\rho V_w + M_{ax}) \omega^2 \varepsilon_2 \end{Bmatrix} \quad (15)$$

$$\begin{Bmatrix} \gamma_x \\ \gamma_z \\ \gamma_\theta \end{Bmatrix} = \begin{Bmatrix} \tan^{-1}(-\beta_x/\alpha_x) \\ \tan^{-1}(-\beta_z/\alpha_z) \\ \tan^{-1}(-\beta_\theta/\alpha_\theta) \end{Bmatrix} \quad (16)$$

The external forces of other kind of hull element can be arranged in the same form as eq.(8) and the results are tabulated in the matrix and vector forms in (Table 1) and (Table 2). The notations used to formulate the external forces are given in the last column of (Table 2).

As mentioned in the description on the kinds of the external forces to which hull element is subjected, only linear term with respect to the velocity is adopted here under the assumption of ideal fluid and non linear term due to existence of viscosity is neglected. This comes from several reasons that as columns have the comparatively large diameters, inertia force is predominant and also axial forces which are considered to be most important in the internal forces of connecting members are almost determined by the forces to which columns are subjected and moreover it becomes easy to get the global appearance of behaviours by the linearization of the whole phenomena.

### 3. EQUATIONS OF MOTION

Let us set a local co-ordinates ( $x_1$ - $z_1$  axes, see Fig. 3) for the beam element  $ij$ . By the bending rigidity  $EI$ , the axial rigidity  $EA$  and the length  $l$  of the beam element, the element stiffness matrix  $\bar{\mathbf{R}}$  (local co-ordinates) is given as

$$\bar{\mathbf{R}} = \begin{bmatrix} EA/l & 0 & 0 & -EA/l & 0 & 0 \\ 0 & 12EI/l^3 & 6EI/l^2 & 0 & -12EI/l^3 & 6EI/l^2 \\ 0 & 6EI/l^2 & 4EI/l & 0 & -6EI/l^2 & 2EI/l \\ -EA/l & 0 & 0 & EA/l & 0 & 0 \\ 0 & -12EI/l^3 & -6EI/l^2 & 0 & 12EI/l^3 & -6EI/l^2 \\ 0 & 6EI/l^2 & 2EI/l & 0 & -6EI/l^2 & 4EI/l \end{bmatrix} \quad (17)$$

By transforming each element stiffness matrix into the stiffness matrix with respect to the global co-ordinates and assembling them, global stiffness matrix  $\mathbf{K}$  can be obtained

$$\mathbf{K}\mathbf{U} = \mathbf{F} \quad (18)$$

As the force vector  $\mathbf{F}$  of the left hand side of eq.(8) is essentially the force vector with respect to hull element  $i$ ,  $\mathbf{F}$  should be written as  $\mathbf{F}_i$ . In eq.(8), these subscripts were abbreviated for simplicity. Similarly,  $K_a$ ,  $K_v$ ,  $K_d$  and  $\mathbf{f}$  should be written as  $K_{ai}$ ,  $K_{vi}$ ,  $K_{di}$  and  $\mathbf{f}_i$ , respectively.

Substituting the external forces given in eq.(8) into the righthand side of eq.(18) and defining the replacements shown below, equations of motion can be written as eq.(19) where the unknowns are the displacements  $\mathbf{U}$  of the center of gravity of each hull element.

$$K_a \ddot{\mathbf{U}} + K_v \dot{\mathbf{U}} + (K_d + \mathbf{K}) \mathbf{U} = \mathbf{F} \quad (19)$$

where

$$K_a = \sum K_{ai}, K_v = \sum K_{vi}, K_d = \sum K_{di}, \mathbf{F} = \sum \mathbf{F}_i \quad (20)$$

When the restoring force by mooring can be assumed as proportional to the displacements, the coefficients have only to be added to the third term of eq.(19). As it is assumed that the wave exciting force is periodic and the system is linear,  $\mathbf{U}$  is solved as the harmonic response with the same circular frequency as the wave exciting force.

The floating framed structures like semisubmersible units have usually several members whose sectional dimensions are considerably bigger than other members', for example, columns of semisubmersible units. These members are suitable and sometimes needed to be treated as rigid bodies and some devices to do so are mentioned hereafter.

Let us define  $\mathbf{T}_i$  as a matrix which connects the displacement  $\mathbf{U}_i$  of the center of gravity of the element  $i$  in the rigid body with the displacement  $\mathbf{U}_g$  of the center of gravity of the rigid body by the assumption of the rigid motion.

$$\mathbf{U}_i = \mathbf{T}_i \mathbf{U}_g \quad (21)$$

The contribution of the external force  $\mathbf{F}_i$  of the element  $i$  to the center of gravity of the rigid body is expressed as  $\mathbf{T}_i^t \mathbf{F}_i$ . Therefore, if the summation of the external forces of every element included in the rigid body is written as  $\mathbf{F}_g$ , it is

$$\mathbf{F}_g = -(\sum \mathbf{T}_i^t K_{ai} \mathbf{T}_i) \mathbf{U}_g - (\sum \mathbf{T}_i^t K_{vi} \mathbf{T}_i) \dot{\mathbf{U}}_g - (\sum \mathbf{T}_i^t K_{di} \mathbf{T}_i) \ddot{\mathbf{U}}_g + (\sum \mathbf{T}_i^t \mathbf{f}_i) \quad (22)$$

When the vertical member is treated as a rigid body, it is needed that the term (the displacement weight of the element multiplied by the distance between the center of gravity of the element and

the center of gravity of the rigid body [the sign must be considered in the distance]] should be added to the (3,3) element of the matrix  $K_{di}$ . The reason why this term is not included in the original restoring force due to rotation is that the matrix  $T_i$  introduced above is defined not at the inclining position but at the up-right position. Any point other than the center of gravity of the rigid body can be, of course, selected as the representative point for the summation and the same procedure as above can be applied. On the other hand, the element stiffness matrix  $K$  (global co-ordinates) of the beam element whose both nodal points are included in the rigid body is transformed to the stiffness matrix corresponding to the center of the rigid body as

$$T_i^t K_{ii} T_i + T_j^t K_{ji} T_i + T_i^t K_{ij} T_j + T_j^t K_{jj} T_j \quad (23)$$

However, this expression is naturally equal to zero because no elastic deformation is permitted in the rigid body and eq.(23) does not have any essential meaning. Next, let us consider the case where one end (nodal point  $i$ ) of the beam element is connected to the rigid body and the other (nodal point  $j$ ) is connected to other beam element. The transformation of the element stiffness matrix  $K$  (global co-ordinates) in this case is

$$\begin{pmatrix} U_i & U_j \\ T_i^t K_{ij} T_i & T_i^t K_{ij} T_j \\ K_{ji} T_i & K_{jj} \end{pmatrix} \quad (24)$$

In this way, elimination of the nodal points included in the rigid body is attained and the equations of motion is contracted, whose number of freedom is less than the original one.

In the analysis by the matrix method developed in this paper, frames with pin or roller joint at an arbitrary position can be treated without so complicated procedure. The relationship between nodal force  $\bar{F}$  and nodal displacement  $\bar{U}$  of beam element is written by the element stiffness matrix eq.(17) (local co-ordinates).

$$\bar{F} = \bar{K} \bar{U} \quad (25)$$

This equation is expressed alternatively.

$$\bar{F}_i = \sum_{j=1}^6 \bar{K}_{ij} \bar{U}_j \quad (i = 1, 2, \dots, 6) \quad (26)$$

When a beam element has a pin or roller joint at the either nodal point, such a procedure is adopted here that the nodal force corresponding to the pin or roller action is released. If  $\bar{F}_k$  is the nodal force to be released, it can be written.

$$\bar{F}_k = 0 = \sum_{j=1}^6 \bar{K}_{kj} \bar{U}_j \quad (27)$$

$\bar{U}_k$  is eliminated by using  $\bar{K}_{kk} \neq 0$

$$\begin{aligned} \bar{F}_i &= \sum_{j=1}^6 (\bar{K}_{ij} - \bar{K}_{ik} \bar{K}_{kj} / \bar{K}_{kk}) \bar{U}_j \\ &= \sum_{j=1}^6 \bar{K}'_{ij} \bar{U}_j \quad (i = 1, 2, \dots, 6) \end{aligned} \quad (28)$$

where

$$\bar{K}'_{ij} = \bar{K}_{ij} - \bar{K}_{ik} \bar{K}_{kj} / \bar{K}_{kk} \quad (29)$$

If  $\bar{K}'$  is defined as the modified element stiffness matrix whose  $ij$  element is  $\bar{K}'_{ij}$  of eq.(29), the re-

lationship between the nodal force  $\bar{F}$  and the nodal displacement  $\bar{U}$  is written as the same form as eq. (25)

$$\bar{F} = \bar{K}' \bar{U} \quad (30)$$

In the procedure mentioned here, it is needed in the element subdivision to pay such an attention that the external force with the same component as the force released should be made as small as possible by the fine element subdivision.

Now, the response is a harmonic one with the same circular frequency as the incoming wave and the amplitudes and the phases of the displacements of the free nodal points are solutions wanted. By using the usual manner to introduce the complex number, the simultaneous linear equations with the real coefficients whose number of unknowns is twice as many as the original ones are obtained and these solved by Gauss elimination method.

#### 4. MODELS FOR CALCULATIONS AND EXPERIMENTS

The computer program based on the theory mentioned up to the preceding section was made and several kinds of models of semisubmersible units, which basically consisted of several cylindrical columns with footing and connecting members, were analyzed and some of them were checked by the comparison with the experiments. The shapes, dimensions and materials of the models are shown in (Fig.4) and (Table 3).

The added mass and the damping coefficient used in the calculations were obtained from the experiments. As for the  $z$ -directional added mass and damping coefficient of the cylindrical column with footing, they were obtained from the amplitude and the phase lag of the force measured in the forced heaving tests and the dependence of them on the frequency was taken account of in the calculations by the piece wise linear approximation, whereas, other directional added masses and damping coefficients were obtained from the free oscillation tests with the same draft kept as wave exciting tests.

In the wave exciting tests of the models shown in (Fig.4), the displacements and the strains of the models subjected to regular waves were measured by a motor-drive camera and strain gauges, respectively.

In such a case of a cylindrical column with footing, it is a questionable point how to distribute the hydrodynamical force coefficients measured for the column as a whole to the subdivided elements. In this paper, as for the  $z$ -directional added mass, all of it was distributed to the lowest element and as for the  $x$ -directional added mass and the damping coefficients, they were distributed in proportion to the volume to the elements composing the immersed part of the column.

#### 5. CALCULATIONS AND EXPERIMENTS

##### 5.1 Model R10, R1P, R1R

In all the cases shown in the following figures, the models are subjected to the incoming wave with unit amplitude ( $H_w/2 = 1$  cm) proceeding from the left to the right and columns are treated as rigid

bodies in calculations.

According to the calculated rotation angle at the top of the left hand side column of R10, R1P and R1R (Fig.5), at  $\omega \approx 5.1$ , a resonance exists in common with three models and the calculated mode of motion at the vicinity of the resonance is the rigid-bodylike mode. On the other hand, the resonance containing remarkable elastic deformation of the upper beam exists at  $\omega \approx 6.6$  for R10 and the resonance containing kink of the upper beam at the pin joint exists at  $\omega \approx 1.6$  for R1P. As for R10, the amplitudes of three internal forces at the resonance containing the elastic deformation are naturally much bigger than ones at the resonance with the rigid-bodylike mode, as illustrated in (Fig.6).

As the rigid-bodylike mode is, of course, not a complete rigid-body mode but contains small elastic deformation of the upper beam, this is considered to be what is called the pseudo rigid mode [8] and this term is used in the following description.

The resonance containing remarkable elastic deformation of the upper beam can be considered to be a phenomenon similar to springing of ships because both have a common feature of the resonance due to stiffness and buoyancy of members.

## 5.2 Model SP

The agreement of calculations and experiments with respect to the motions of SP is fairly good, as shown in (Fig.7) and (Fig.8).

The resonance of z-directional displacement of the column exists at  $\omega \approx 3.7$  which coincides with the frequency of the resonance in heaving of the column. The appearance of the response function of rotation angle differs from a usual one of a floating body because of the existence of the fixed end.

## 5.3 Model F1M

The calculated response functions and the experiments of F1M are given in (Fig.9), (Fig.10) and (Fig.11). The ordinate of (Fig.11) is the amplitude of the axial normal surface strain at the point shown in the figure.

The two peaks at  $\omega \approx 3.7$  and  $\omega \approx 4.6$  are the resonance with the pseudo rigid mode and with the mode containing the elastic deformation, respectively.

To study the variation of the resonance frequency due to the variation of the stiffness of the upper beam of this model, the Young's modulus of the upper beam was made smaller and smaller, whereas its dimensions were kept constant. According to the calculated results shown in (Fig.12), the frequency of the resonance with the pseudo rigid mode is almost constant, irrespective of the stiffness of upper beam because this resonance is based predominantly on buoyancy of floating bodies.

## 5.4 Model F1K

As an example, the element subdivision of F1K is shown in (Fig.13). Being different from the flexible models mentioned above, F1K behaves in the pseudo rigid mode in the whole frequency range because combination of the upper beam and the K-brace is stiff enough. In the range of higher frequency than the resonance at  $\omega \approx 3.7$ , the displacements are very small with the repetition of zero ampli-

tude at some particular frequencies.

Let us take the axial forces of connecting members as the representatives of the internal forces. Several maxima and minima of the amplitude of the axial forces exist, as illustrated in (Fig.15). These behaviours can be roughly interpreted by the reciprocal occurrence of the elastic deformation pattern A and B shown in (Fig.18) which are contained in the pseudo rigid mode. In the pattern A, the relation between wave length  $\lambda$  and the span length  $l$  is  $\lambda = 2l, 2l/3, 2l/5 \dots$  and in the pattern B, it is  $\lambda = l, l/2, l/3 \dots$ , which correspond to  $\omega \approx 6.64, 11.49, 14.24, \dots$  and  $\omega \approx 9.38, 13.27, 16.25, \dots$  in the case of  $l = 70\text{cm}$ , respectively. (Fig.16) shows the comparison of the calculated axial strain converted from the axial force of (Fig.15) with experiments. The calculated relative phase lag of the axial strain at the three points 6, 20 and 21 with respect to the point 7 in the K-brace are compared with the experiments in (Fig.17).

## 5.5 Model F3K

The calculated response functions for the motion are similar to the case of F1K as shown in (Fig.19) and (Fig.20) and the mode is a pseudo rigid mode only.

As an example of the internal forces, the amplitude of the axial force of the upper beam at the mid-point of the over-all length is given in (Fig.21), where a number of minima ( $=0$ ) exist at  $\omega = 6.64, 9.38, 11.49 \dots$ , which correspond to  $\lambda = 2l, l, 2l/3 \dots$ , respectively and at the frequency between adjacent two minima, a maximum exists.

## 5.6 Model F5K

(Fig.22) and (Fig.23) show the calculated response functions and the experiments.

In (Fig.24), the calculated amplitude of the axial force of the upper beam at the mid-point of over-all length is shown. In this case, the minima ( $=0$ ) exist at  $\omega \approx 5.42, 7.66, 9.38, 10.83 \dots$  which correspond to  $\lambda = 3l, 3l/2, l, 3l/4 \dots$ , respectively and at the frequencies between the adjacent two minima, one or two maxima exist.

In the case of F1K, F3K and F5K, the response functions of axial forces of the connecting members have a number of maxima and minima at the frequencies determined by some particular relationship between the wave length and the length of the structure or the span length in these cases. This situation can be considered to be analogous to "ship/wave matching" [8] for the quasi-static bending of ships.

## 6. CONCLUSION

- (1) A method for the periodic response analysis of floating framed structures was presented and its applicability was confirmed by the comparison with the experiments.
- (2) Such a frequency range exists that the elastic deformation of members affect the motion in the case of flexible floating framed structures.
- (3) The frequency characteristics of internal forces can be roughly interpreted by some relationship between the wave length and the length of the structure in the case of stiff floating framed



structures.

(4) The proposed method is effective for the analysis of the floating framed structures with pin or roller joint.

#### 7. ACKNOWLEDGEMENT

The authors wish to express their appreciation to Prof. K. Iida, who encouraged them continuously and to Mr. H. Nagai and others who helped them with tests and drawings of figures and tables.

#### REFERENCES

1. Kroukovsky, K & Jacobs, W. R. ; Pitching and Heaving Motions of a Ship in Regular Waves ; Trans. SNAME ; 1957 ; Vol. 65 ; pp. 590-632.
2. Tasai, F. & Takagi, M. ; Theory of Response and Method of Estimation in Regular Waves ; Proc. Symp. of Seakeeping, Soc. Nav. Archit. Japan ; 1969 ; pp. 1-52.
3. Akita, Y. et al. ; Total System of Analysis on the Longitudinal Strength of Ships -on the Longitudinal Strength of Oil Tankers- ; J. Soc. Nav. Archit. Japan ; 1974 ; Vol.135, June ; pp. 229-238.
4. Goodman, R. A. ; Wave-Excited Main Hull Vibration in Large Tankers and Bulk Carriers ; Nav. Archit. ( J.RINA ) ; 1971, April ; pp. 167-184.
5. Gunsteren, F. F. V. ; Springing. Wave Induced Ship Vibrations ; Int. Shipbldg. Prog. ; 1970 ; Vol. 17, No. 195 ; pp. 333-347.
6. Kumai, T. ; On the Exciting Force and Response of the Springing of Ships ; Bull. Res. Inst. App. Mech., Kyushu Univ. ; 1973 ; No.40, Nov.; pp. 1-8.
7. Bishop, R. E. D. ; On the Strength of Large Ships in Heavy Seas ; South African Mech. Engr. ; 1971 ; Dec.
8. Bishop, R. E. D., Taylor, R. E. & Jackson, K. L. ; On the Structural Dynamics of Ship Hulls in Waves ; Nav. Archit. ( J.RINA ) ; 1973 ; No.4, Oct.; pp. 257-274.
9. Matora, S. & Koyama, T. ; On Wave-Excitation Free Ship Forms ; J. Soc. Nav. Archit. ; 1965 ; Vol. 117, June ; pp. 115-126.
10. Sao, K., Maeda, H. & Hwang, J.H. ; On the Heaving Oscillation of a Circular Dock ; J. Soc. Nav. Archit. Japan ; 1971 ; Vol. 130, Dec.; pp. 121-130.
11. McClure, A. C. ; Development of the Project Mohole Drilling Platform ; Trans. SNAME ; 1965 ; Vol. 73 ; pp. 50-98.
12. Pedersen, B., Egeland, O. & Langfelt, J. N. ; Calculation of Long Term Values for Motions and Structural Response of Mobile Drilling Rigs ; Offshore Tech. Conf. ; 1973 ; No. OTC 1881.
13. Opstal, G. H. C. et al. ; MOSAS: A Motion and Strength Analysis System for Semisubmersible Units and Floating Structures ; Offshore Tech. Conf. ; 1974 ; No. OTC 2105.
14. Pincemin, M. et al. ; An Integrated Program for the Dynamic Structural Calculation of Mobile Offshore Units ; Offshore Tech. Conf. ; 1974 ; No. OTC 2052.
15. Paulling, J. R. ; Elastic Response of Stable Platform Structures to Wave Loading; Proc. Int. Symp. Dynam. Marine Vech. Struct. Waves ; 1974 ; Paper 25 ; pp. 263-272.
16. Taylor, R. E. ; Elastic Response of Stable Platform Structures to Wave Loading ; Proc. Int. Symp. Dynam. Marine Vech. Struct. Waves ; 1974 ; Paper 24 ; pp. 249-261.
17. Yoshida, K., Ishikawa, K. & Iida, K. ; Periodic Response Analysis of Floating Framed Structures ; J. Soc. Nav. Archit. Japan ; 1974 ; Vol. 136, Dec. ; pp. 355-363.
18. Yoshida, K. & Ishikawa, K. ; Periodic Response Analysis of Floating Framed Structures (continued) ; J. Soc. Nav. Archit. Japan ; 1975 ; Vol. 138, Dec. ; pp. 297-306

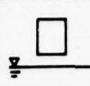

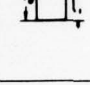
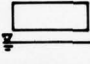
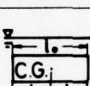
	Virtual Inertia Matrix			Damping Coefficient Matrix			Restoring Coefficient Matrix			Notation
	$\ddot{u}$	$\ddot{w}$	$\ddot{\theta}$	$\dot{u}$	$\dot{w}$	$\dot{\theta}$	$u$	$w$	$\theta$	
Vertical Non-immersed Element	M	0	0	0	0	0	0	0	0	 $L_1 = \frac{l_2 - l_1}{2}$ $L_2 = \frac{l_2^2 - l_2 l_1 + l_1^2}{3}$ $L_3 = \frac{l_2 - 2l_1}{2}$ $L_4 = \frac{3l_1^2 - 3l_1 l_2 + l_2^2}{3}$
Vertical Partially-immersed Element with End	M+Max	0	MaxL1	Nx	0	NxL1	0	0	0	
	0	M+Max	0	0	Nz	0	0	$\rho g A$	0	
	MaxL1	0	$I_0 + \text{Max}L_2$	NxL1	0	NxL2	0	0	$\rho g V w L_1$	
Vertical Partially-immersed Element without End	M+Max	0	MaxL1	Nx	0	NxL1	0	0	0	
	0	M	0	0	Nz	0	0	$\rho g A$	0	
	MaxL1	0	$I_0 + \text{Max}L_2$	NxL1	0	NxL2	0	0	$\rho g V w L_1$	
Vertical Fully-immersed Element with End	M+Max	0	MaxL3	Nx	0	NxL3	0	0	0	
	0	M+Max	0	0	Nz	0	0	0	0	
	MaxL3	0	$I_0 + \text{Max}L_4$	NxL3	0	NxL4	0	0	$\rho g V w L_3$	
Vertical Fully-immersed Element without End	M+Max	0	MaxL3	Nx	0	NxL3	0	0	0	
	0	M	0	0	Nz	0	0	0	0	
	MaxL3	0	$I_0 + \text{Max}L_4$	NxL3	0	NxL4	0	0	$\rho g V w L_3$	
Horizontal Non-immersed Element	M	0	0	0	0	0	0	0	0	
	0	M	0	0	0	0	0	0	0	
	0	0	$I_0$	0	0	0	0	0	0	
Horizontal Fully-immersed Element	M	0	0	0	0	0	0	0	0	
	0	M+Max	-MaxL1	0	Nz	-NzL1	0	0	0	
	0	-MaxL1	$I_0 + \text{Max}L_2$	0	-NzL1	NzL2	0	0	0	

Table 1: Hydrodynamic forces due to motion

		Force = $a \sqrt{\alpha^2 + \beta^2} \cos(Kx - \omega t + r)$		Notation
		$\alpha$	$\beta$	
Vertical Non-immersed Element	x	0	0	<p>a: amplitude K: circular wave number  <math>\omega</math>: circular wave frequency <math>r: \tan^{-1}(-\beta/\alpha)</math>  <math>\alpha</math>: coefficient to the term <math>\cos(Kx - \omega t)</math>  <math>\beta</math>: coefficient to the term <math>\sin(Kx - \omega t)</math>  A: sectional area Vw: displacement volume  <math>\rho</math>: density of water  <math>E_1 = \frac{1 - e^{-(l_1 + l_2)K}}{l_0 K}</math> <math>E_2 = \frac{(l_2 K - 1) + (l_1 K + 1)e^{-(l_1 + l_2)K}}{l_0 K^2}</math>  <math>E_3 = \frac{e^{l_0(l_1 + l_2)K} - e^{-(l_1 + l_2)K}}{l_0 K}</math>  <math>E_4 = \frac{(l_0 K - l_1 K - 1)e^{l_0(l_1 + l_2)K} + (l_1 K + 1)e^{-(l_1 + l_2)K}}{l_0 K^2}</math>  <math>E_5 = \frac{2e^{Kx_1}}{l_0 K} \sin \frac{(l_1 + l_2)K}{2} \sin \frac{(l_2 - l_1)K}{2}</math>  <math>E_6 = \frac{2e^{Kx_2}}{l_0 K} \sin \frac{(l_1 + l_2)K}{2} \cos \frac{(l_2 - l_1)K}{2}</math>  <math>E_7 = \frac{e^{Kx_1}}{l_0 K} ((\cos K l_2 + K l_2 \sin K l_2) - (\cos K l_1 + K l_1 \sin K l_1))</math>  <math>E_8 = \frac{e^{Kx_2}}{l_0 K} ((\sin K l_2 - K l_2 \cos K l_2) + (\sin K l_1 - K l_1 \cos K l_1))</math>  M<sub>ai</sub>: added mass for i directional motion  N<sub>i</sub>: damping coefficient for i directional motion  M: mass <math>I_0</math>: moment of inertia  g: acceleration due to gravity</p>
	z	0	0	
	$\theta$	0	0	
Vertical Partially-immersed Element with End	x	$N_x \omega E_1$	$(\rho V w + \text{Max}) \omega^2 E_1$	
	z	$\rho g A - (\rho V w + \text{Max}) \omega^2 E_1$	$N_z \omega E_1$	
	$\theta$	$N_x \omega E_2$	$(\rho V w + \text{Max}) \omega^2 E_2$	
Vertical Partially-immersed Element without End	x	$N_x \omega E_1$	$(\rho V w + \text{Max}) \omega^2 E_1$	
	z	$\rho g A - \rho V w \omega^2 E_1$	$N_z \omega E_1$	
	$\theta$	$N_x \omega E_2$	$(\rho V w + \text{Max}) \omega^2 E_2$	
Vertical Fully-immersed Element with End	x	$N_x \omega E_3$	$(\rho V w + \text{Max}) \omega^2 E_3$	
	z	$-(\rho V w + \text{Max}) \omega^2 E_3$	$N_z \omega E_3$	
	$\theta$	$N_x \omega E_4$	$(\rho V w + \text{Max}) \omega^2 E_4$	
Vertical Fully-immersed Element without End	x	$N_x \omega E_3$	$(\rho V w + \text{Max}) \omega^2 E_3$	
	z	$-\rho V w \omega^2 E_3$	$N_z \omega E_3$	
	$\theta$	$N_x \omega E_4$	$(\rho V w + \text{Max}) \omega^2 E_4$	
Horizontal Non-immersed Element	x	0	0	
	z	0	0	
	$\theta$	0	0	
Horizontal Fully-immersed Element	x	$\rho V w \omega^2 E_5$	$\rho V w \omega^2 E_6$	
	z	$-(\rho V w + \text{Max}) \omega^2 E_5 + N_z \omega E_5$	$(\rho V w + \text{Max}) \omega^2 E_5 + N_z \omega E_5$	
	$\theta$	$(\rho V w + \text{Max}) \omega^2 E_7 - N_z \omega E_8$	$(\rho V w + \text{Max}) \omega^2 E_8 - N_z \omega E_7$	

Table 2: Wave exciting forces

MODEL	TYPE (FIG.4)	UPPER BEAM*1				K-BRACE*2			EXPERI- MENT	REMARKS
		$l(\text{mm})^4$	$b(\text{mm})$	$t(\text{mm})$	MATERIAL*3	$d(\text{mm})$	$t(\text{mm})$	MATERIAL*3		
R10	A	928.0	22.0	4.0	STEEL	—	—	—		
R1P	A	928.0	22.0	4.0	STEEL	—	—	—		PIN JOINT
R1R	A	928.0	22.0	4.0	STEEL	—	—	—		ROLLER JOINT
S P	B	700.0	28.0	10.0	ACRYL	—	—	—	✓	TWO PIN JOINTS & FIXED END
F1M	C	700.0	28.0	10.0	ACRYL	—	—	—	✓	
F1K	D	700.0	28.0	10.0	ACRYL	7.0	—	ACRYL	✓	SECTION OF K-BRACE IS PRISMATIC
F3K	E	700.0	28.0	10.0	ACRYL	20.0	2.0	ACRYL		SECTION OF K-BRACE IS HOLLOW
F5K	F	700.0	28.0	10.0	ACRYL	20.0	2.0	ACRYL	✓	SECTION OF K-BRACE IS HOLLOW

\*1 RECTANGULAR SECTION

\*2 LOWER BEAMS AND BRACES

\*3 (YOUNG'S MODULUS) = 21000 (kgf/mm<sup>2</sup>) FOR STEEL AND 336.7 (kgf/mm<sup>2</sup>) FOR ACRYL -

\*4 ONE SPAN LENGTH

Table 3: Dimensions of upper beams and K-braces of models

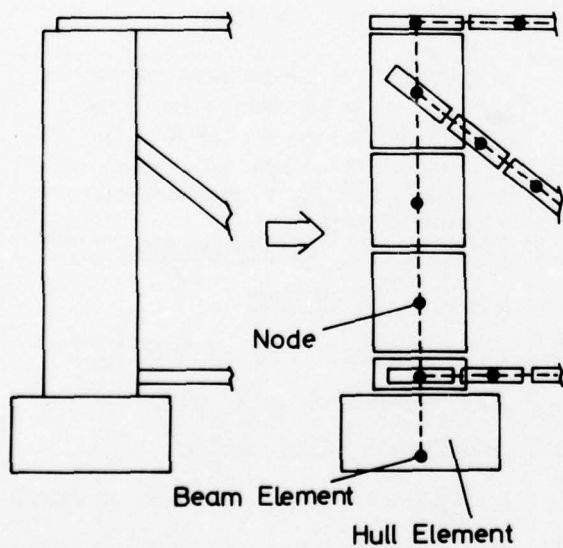


Fig. 1: Hull element and beam element

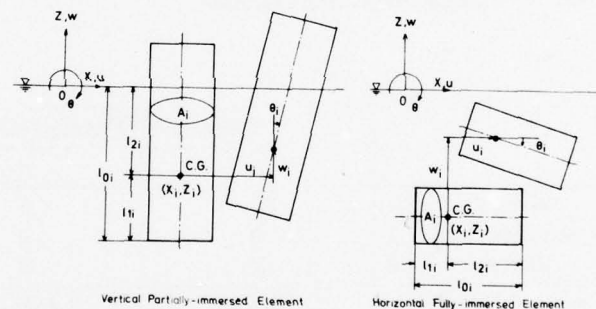


Fig. 2: Examples of hull elements

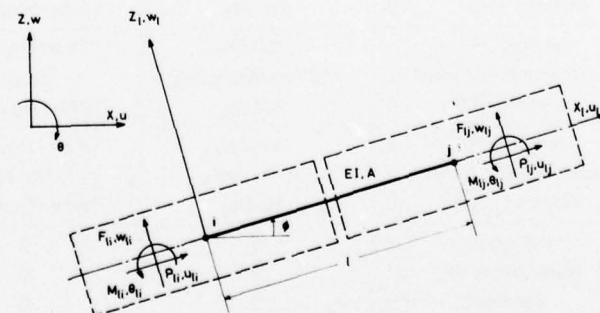


Fig. 3: Local co-ordinate of beam element



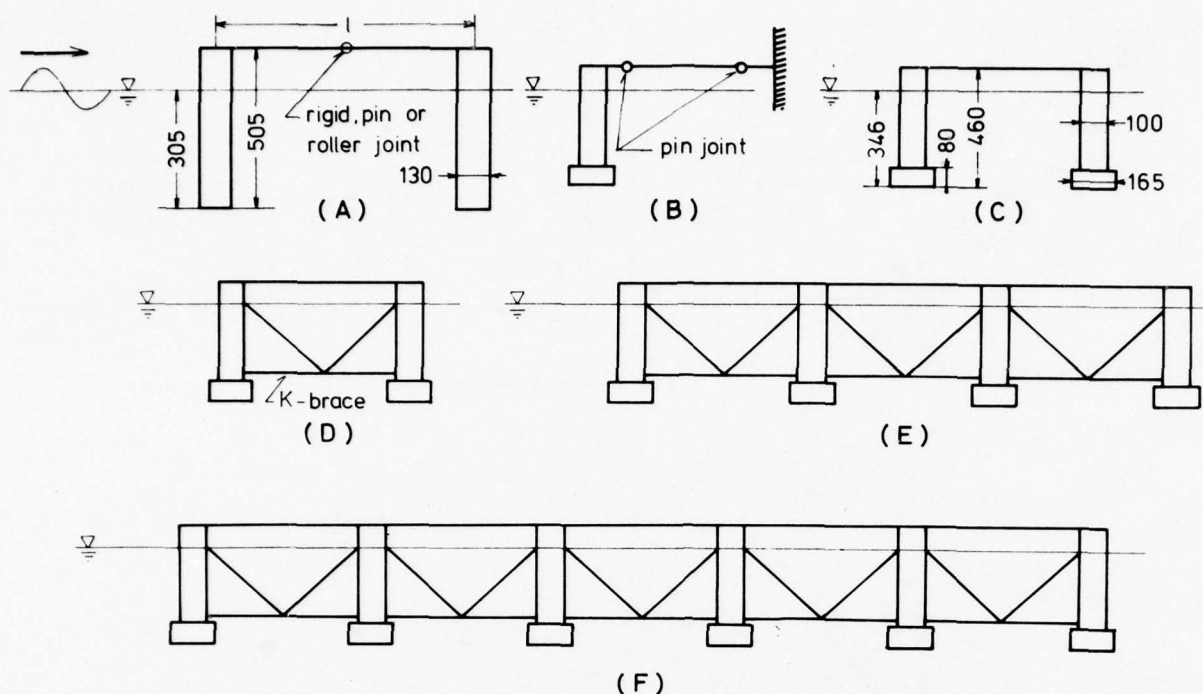


Fig. 4: Types of models

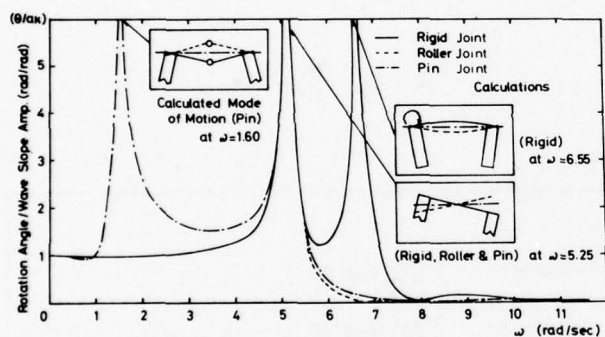


Fig. 5: Rotation angle of R10, R1P and R1R

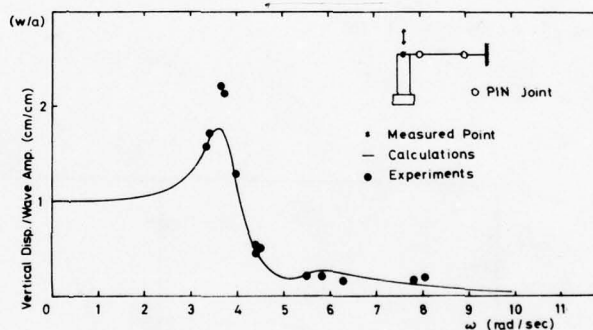


Fig. 7: Vertical displacement of SP

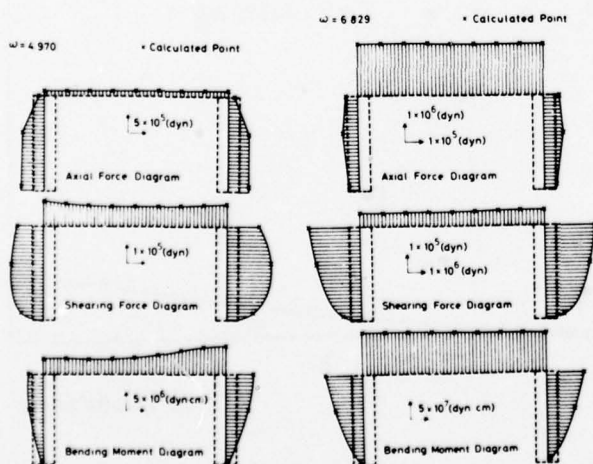


Fig. 6: Sectional force amplitude of R10

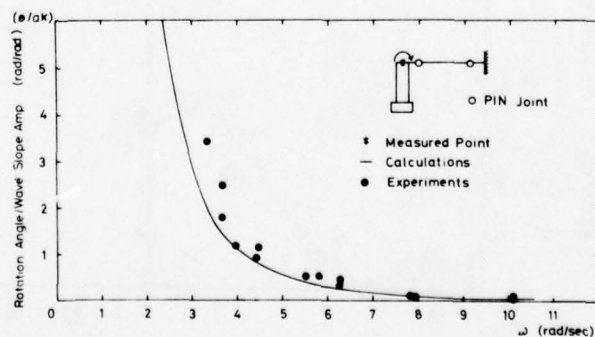


Fig. 8: Rotation angle of SP

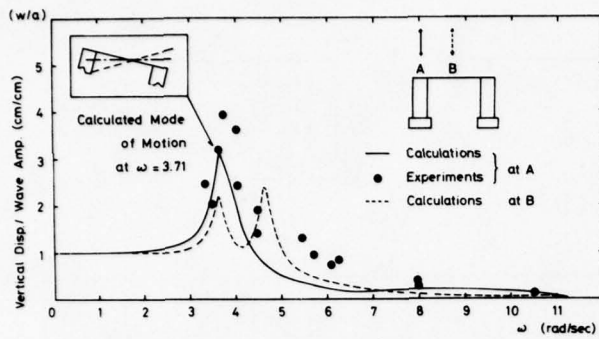


Fig. 9: Vertical displacement of F1M

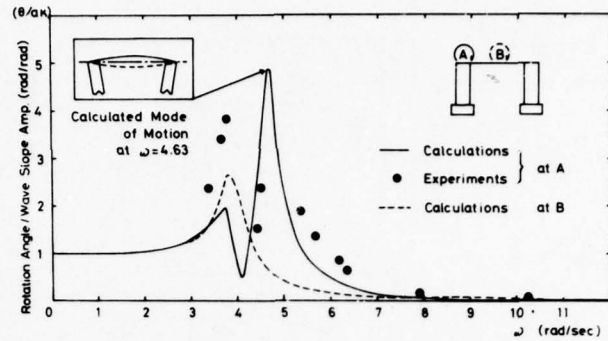


Fig. 10: Rotation angle of F1M

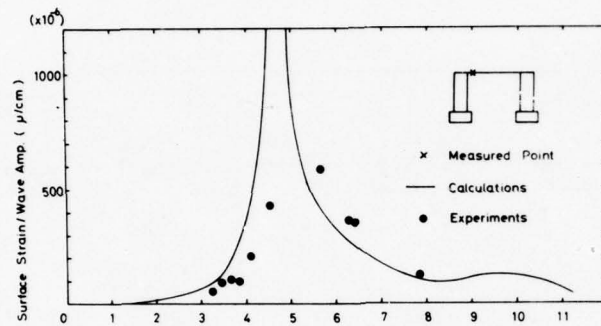


Fig. 11: Surface strain of F1M

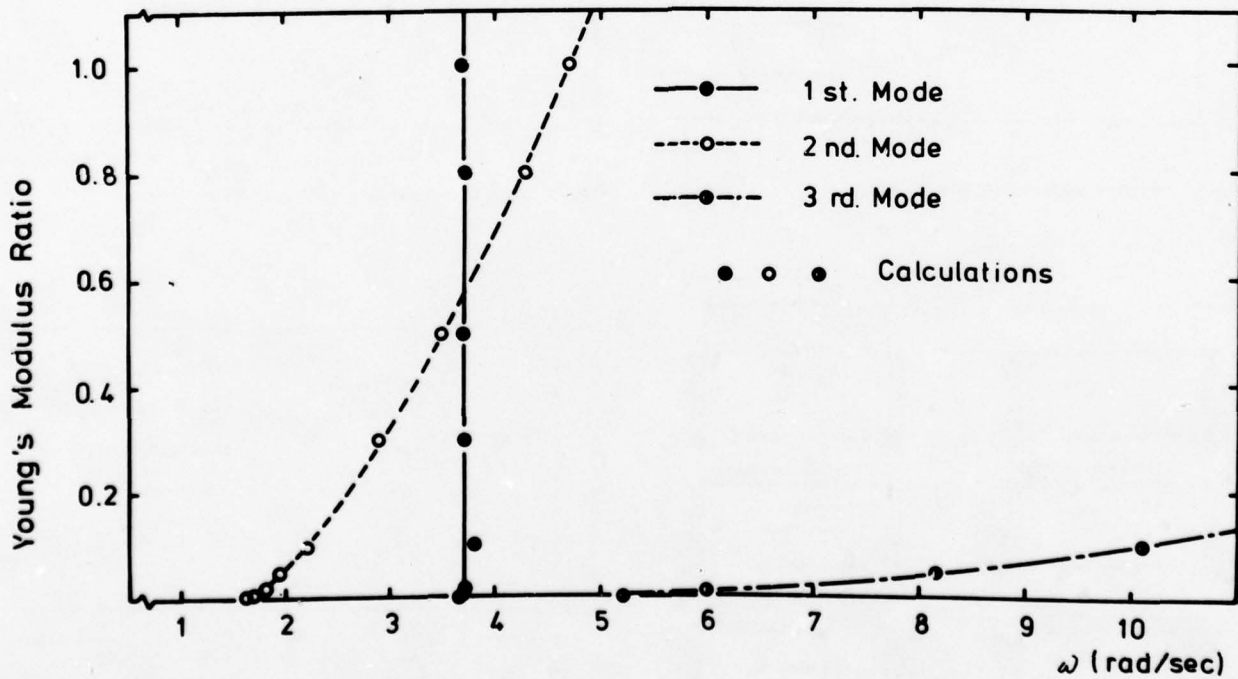


Fig. 12: Variation of resonance frequency of F1M

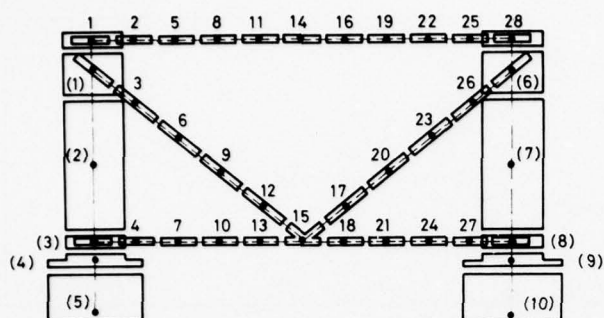


Fig. 13: Elements subdivision of F1K

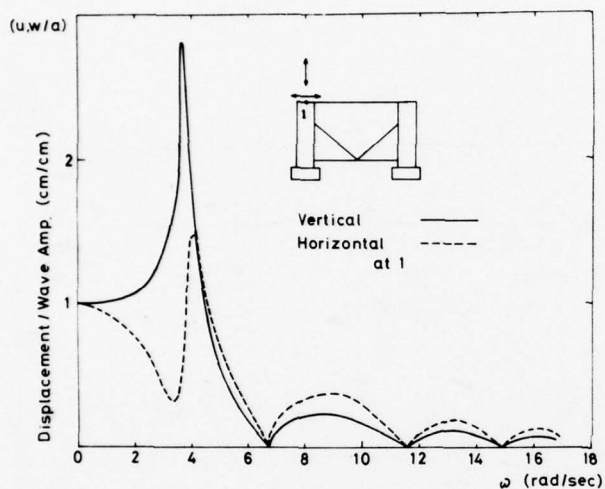


Fig. 14: Vertical and horizontal displacement of F1K

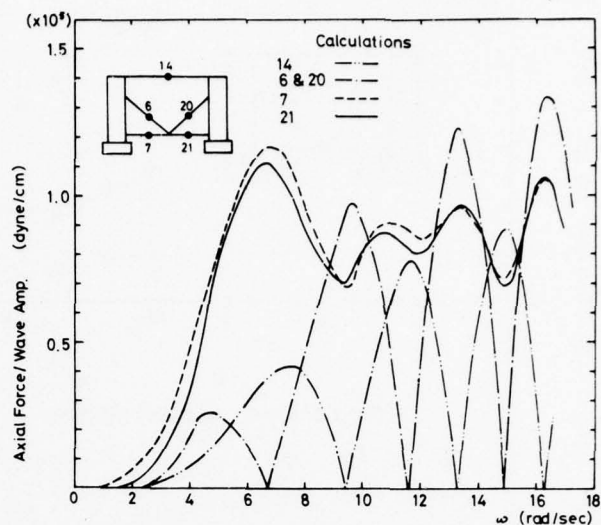


Fig. 15: Axial strain of F1K

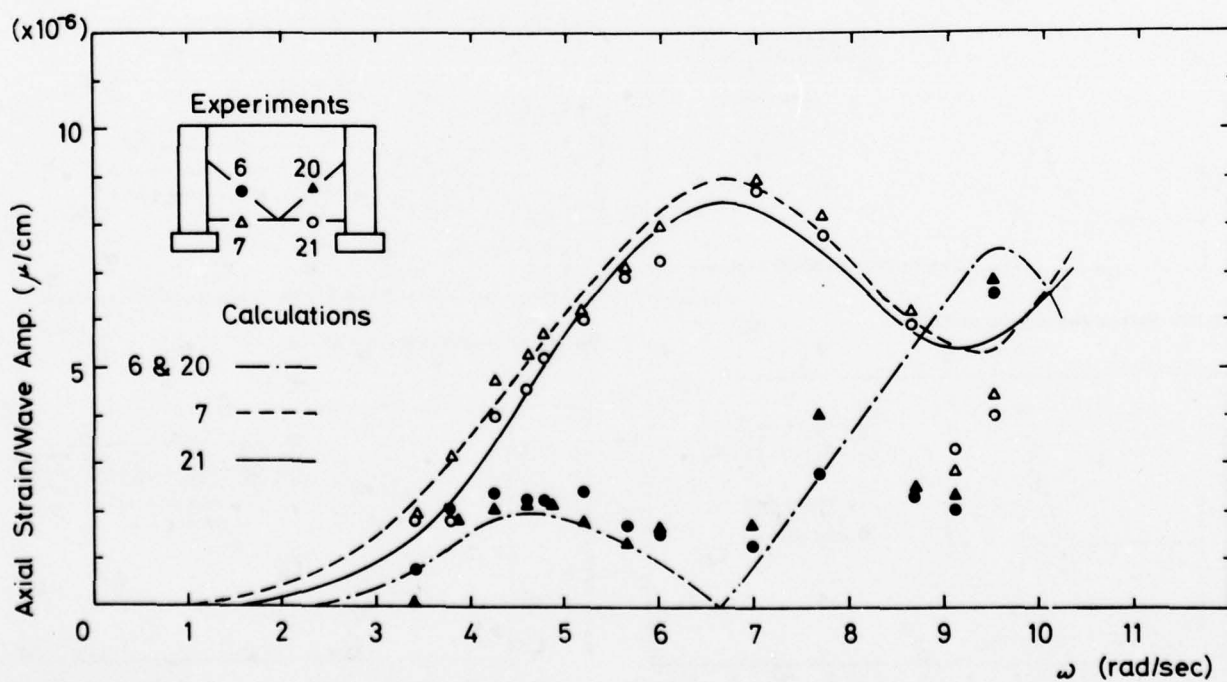


Fig. 16: Axial force of F1K



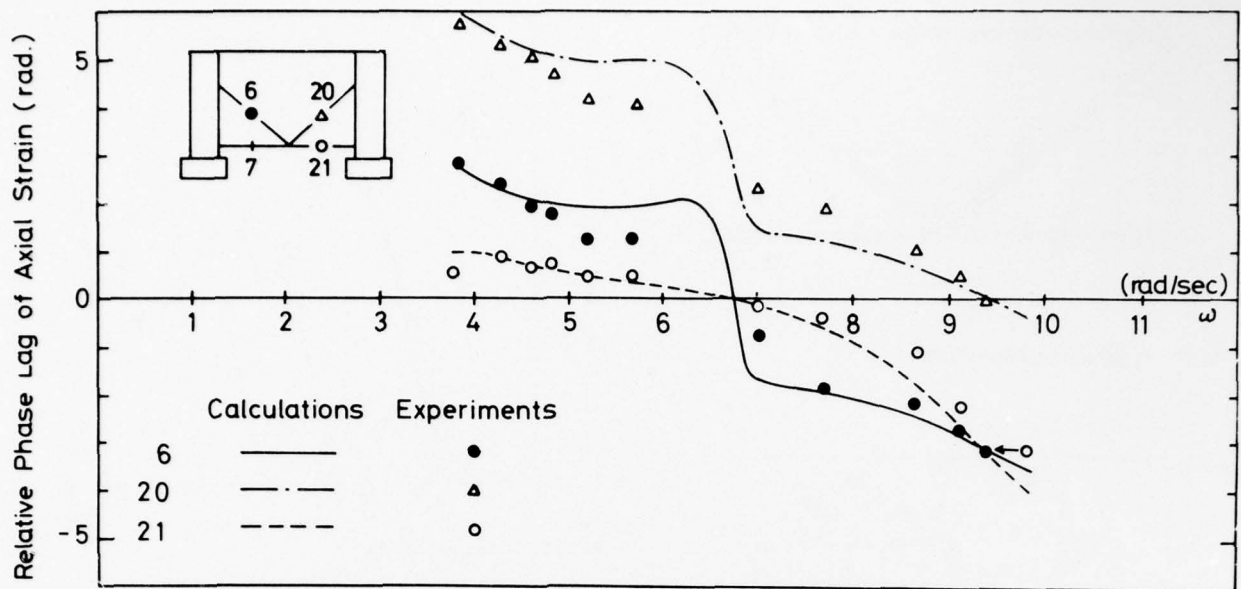


Fig. 17: Relative phase lag of axial strain of F1K

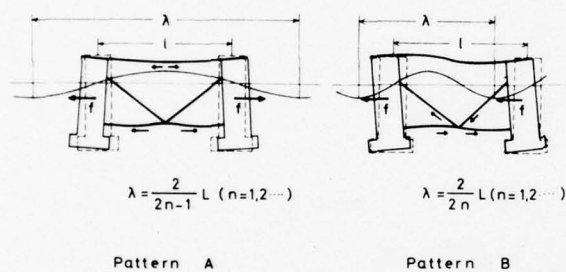


Fig. 18: Elastic deformation pattern of F1K

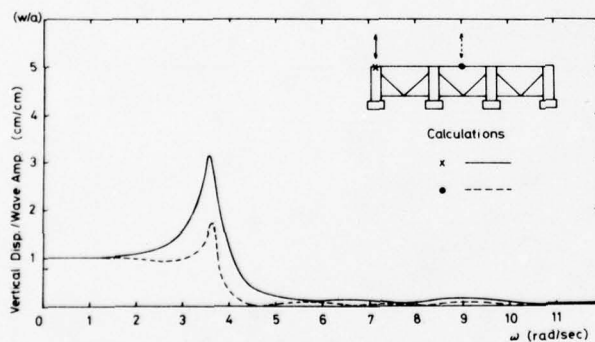


Fig. 19: Vertical displacement of F3K

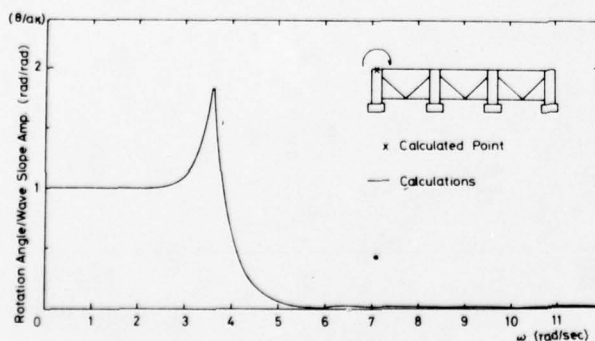


Fig. 20: Rotation angle of F3K

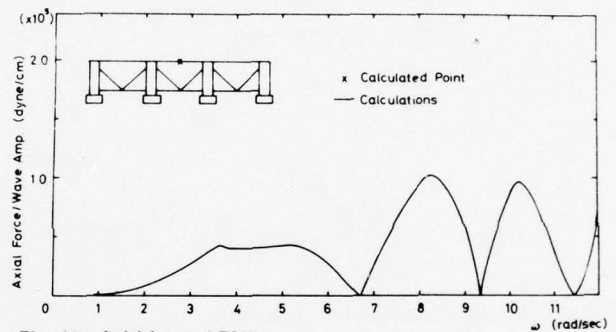


Fig. 21: Axial force of F3K

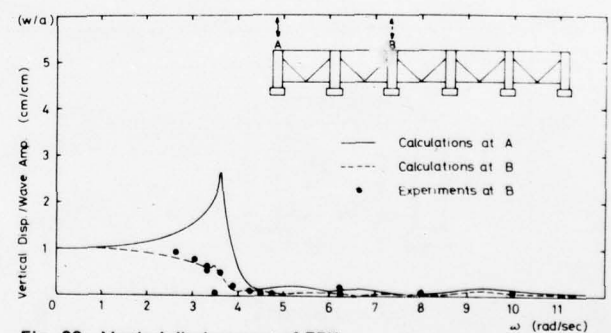


Fig. 22: Vertical displacement of F5K

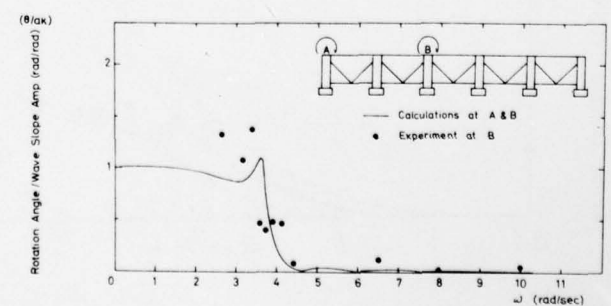


Fig. 23: Rotation angle of F5K

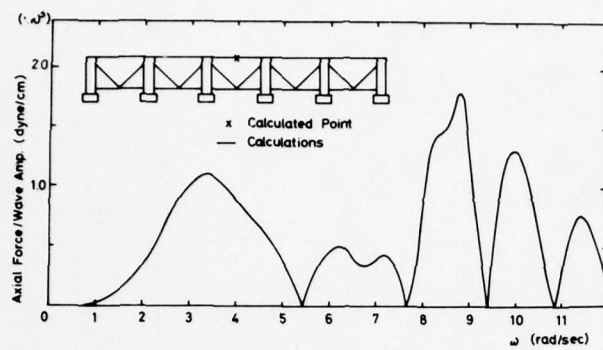


Fig. 24: Axial force of F5K

# Discussion on Paper by D. Catley and C. Norris

C.A. CARLSEN, H. FRIVOLD and H. JOHANNESSEN

The extensive work undertaken by BSRA to investigate ship vibration both by measurements and theoretical investigations and the publishing of this material are much appreciated by all concerned within this field.

The problem of dynamic analysis of ship structures may be roughly divided into problems of structural modelling and evaluation of forces and damping.

When applying the Finite Element Method in ship vibration, modelling accuracy is primarily a question of computer cost. The Timoshenko beam modelling, however, seems in general to have lost its confidence except for analysing the 2-5 lowest hull modes, depending on the hull slenderness. Beam model analysis carried out by Det Norske Veritas and others shows that the ratio of theoretical to measured natural frequency increases uniformly for increasing order of hull modes. This despite the fact that mode-dependent added mass and shear lag effects are accounted for. Reasons for deviations may be that the Navier hypothesis for beam deflection is not valid for the higher modes and that pure higher order hull beam modes as calculated by simple models do not exist in practice. Thus, measurements and three-dimensional Finite Element calculation have shown that for tankers of medium size, the longitudinal bulkheads and sides vibrate as separate systems at higher vertical hull modes, the bulkhead usually being the most beamlike structure. For bulk carriers, the double bottom, carrying the majority of the cargo, vibrates as a subsystem, significantly affecting the hull vibrations.

Referring to Table 3, we would like to ask the authors what in their opinion could be the reason for the very good agreement for the simple Timoshenko beam model at higher hull modes, and why the deviations to measured values were not systematically increasing?

Regarding the exciter test, we would like to ask the authors if any of the calculated axial hull modes were verified by measurements, and whether the found 5- and 6-noded vertical hull modes were verified along the whole hull girder?

For the membrane Finite Element model some of the excessive stiffness of a coarse mesh may be compensated by using non-conforming elements, for example the Quadrilateral Paulling element. A different approach is to use the Master-Slave technique.

The authors emphasise the need of a substructure technique. It would be of interest to get more details of this approach, specifically with regard to damping.

In Det Norske Veritas the superelement technique of the SESAM-69 system is used to make more refined models while keeping down the dynamic

degrees of freedom by specifying a number of super-nodes. Thereby it is possible to model smaller parts as separate superelements and perform local vibration analyses before reducing the element and adding them to the global ship model. Local elements which are subject to resonance may also be added to the ship model without reduction to analyse the forced local vibration excited by the global hull vibration.

Together with a three-dimensional afterbody model the added mass can be included as fluid elements with moderate costs, using the superelement technique, with the water as one single "boundary" superelement.

Judging from Figs. 10 and 11, the membrane - bar idealisation seems to fit the measured values better than the beam model. Although giving a correct mobility trend for the various measuring positions and load conditions, we still would reckon that the discrepancies are rather big for the peak frequencies and also mobility level in most of the frequency range. A closer study of the graphs reveals that except for a general shift in peak frequencies the calculated response in ballasted and loaded condition are very alike, while the measured response differs significantly for the two conditions.

We would appreciate the authors' comments on what could be the reasons for the deficiency of their model to reproduce the different response pictures for the two load conditions in spite of the detailed load representation.

Analytical parameter studies and full-scale measurements carried out by Det Norske Veritas has shown that the afterbody vibration is primarily affected by the mass and stiffness representation in this area, and much less by variations of mass and stiffness in the rest of the ship. In many cases, due to a high degree of interaction between the superstructure and the afterbody, the superstructure natural frequency may be sensitive to the amount of added mass applied.

To get satisfactory accuracy of mass discretisation it is our experience that as a guide rule at least 2-3 mass points should lie within each half wavelength of a vibration mode. Furthermore, only two elements over the depth of the ship are likely to produce artificial higher order beam modes.

While a two-dimensional model may be appropriate in many cases, as in the present one with a very long superstructure, where the natural frequency is well above the exciting frequencies of interest, analysis of afterbody vibration of modern ships often requires a three-dimensional modelling to account for transverse effects and to simulate the support of the superstructure appropriately.

The authors have derived a single total effective force vector from the mobility tests and service vibration measurements. The response calculation is dependent on the force applied to the Finite Element



model and must be of comparable accuracy to the model itself and the anticipated response, both with respect to magnitude, geometrical distribution and frequency range. With this in mind, some opinions concerning propeller induced pressure forces based on some recent extensive measurements of pressure may be of interest.

The area of influence of the blade rate component of hull pressure force is considered to depend on ship type. Referring to the paper given by Sontvedt and Frivold at this Symposium (Session VIII), their Fig.1 shows the propeller induced hull pressure as measured in service for one ship. The pressure forces are shown to be significant on a large part of the afterbody hull. This is also confirmed by a later measurement on a similar ship. On the other hand, another extensive pressure measurement on a different and much smaller ship type the pressure distribution extended only half the distance of the former. The phase of blade rate pressure is in all cases nearly constant. Based on this experience, we think that an equivalent point force of blade rate may be applied when only global response is required, but allowance should be made for the ship type in question.

What is said about blade rate force is even more significant for 2 x blade rate. For this component however, the phase will not be constant, but will decrease with distance at a rate comparable with the effect of sound velocity. Applied to a finite element response calculation, this phase shift has shown to have great influence on, for example, superstructure response.

Concerning 3 x blade rate, our experience is that only local vibrations are excited. The relevance of applying 3 x blade rate forces on a global finite element model of ships with normal shaft speed seems therefore questionable. Another point is the great difficulties in obtaining a reliable theoretical prediction of the 3 x blade rate pressure for design calculation purposes.

As an important parameter in ship vibration the propeller induced pressure distribution and phase are subject to continuous research in Det Norske Veritas.

Knowledge of damping is indeed the weakest link in forced ship vibration analysis today. Det Norske Veritas has also put great efforts into finding global ship damping values by using response data from our own exciter tests. Our results so far are in accordance with the hypothesis of Hylarides (Ref.(22)). We strongly agree with the authors that there is a need for further knowledge about damping. Future work by Det Norske Veritas in this field will be concentrated on substructure damping values, especially for superstructures.

## Authors' Reply

The constructive comments of Messrs. Carlsen, Frivold and Johannessen are welcomed, and the contributors are to be thanked for raising several interesting and important points.

The paper considers the mobility technique and concentrates upon the structural modelling aspects of the problem of ship vibration and has generally avoided details of the propeller forces, but the contributors comments on these are a welcome addition to the discussion.

Referring to the specific points raised in discussion on the paper, it is agreed that the structure of a bulk carrier is more difficult to idealise, compared with the products carrier which was the subject of the paper. Indeed this point was made in the presentation. A further requirement here as regards the vertical vibration of the double bottom as a subsystem, is the accurate distribution of the added mass in the structural idealisation employed. The added mass, together with the mass of cargo which is carried by the bottom further reduces the frequency of such a local distortion mode.

A bulk carrier has a cross-section which experiences significant shear distortion in the higher hull modes. This compares with the products tanker whose vertical modes of the service blade rate range exhibit only a limited shear distortion effect on the modal frequencies. See, for example, Ref.(6) of the paper. BSRA are currently investigating possible methods for simulating the complex effects of shear whilst retaining a two-dimensional model. A degree of success is being achieved.

Simple membrane elements are being used to obtain a reasonable representation of the cross-section of a bulk carrier. The higher order elements which proved to be very powerful for the products tanker do not readily lend themselves to the cross-section of the bulk carrier.

Considering now the natural frequencies of the products tanker, the presence of an axial mode complicates the situation as regards the general trend of increasing frequency and percentage error of the calculated values. The calculations for both the load and ballast conditions show two 6-node vertical modes coupled to the axial freedom in the frequency range considered.

In the exciter tests, there is some verification of these axial modes, although the axial vibration was only recorded at the stern and the wheelhouse top. These levels are low. However, from the sea trials that were also carried out, it is possible to confirm axial frequencies of 295 and 540 c/min for the ballast condition and 262 and 520 c/min for the loaded condition. The higher modes were determined from an analysis of the 3 x blade rate component in the loaded case.

The measured 5- and 6-node vertical hull modes were verified over regions of the ship only, viz at

the ends of the hull girder and in the deckhouse region. Agreement with the sea trial results is excellent.

As regards the finite elements, it is considered that the mesh used is sufficiently fine for a two-dimensional analysis and indeed there would be no real benefit in a further refined and necessarily more costly idealisation in two dimensions. With the present degree of idealisation, the overall modes of vibration are sufficiently well defined for the purposes of predicting the response levels of interest and a significant improvement would only be achieved by using a truly three-dimensional approach.

It is considered preferable to use compatible elements and to realise that the structure is inherently too stiff. The 'master-slave' technique lends itself to the full three-dimensional calculation, but effective application in two dimensions is questionable.

With regard to three-dimensional calculations, an attractive substructure technique is one which considers the characteristics of branches of the structure separately and then represents them by generalised freedoms. Refs.(26) and (27) outline such an approach which is distinct from the super-element technique of SESAM - 69. Using such an approach, damping levels could then be dependent upon the dampings in those branch modes constituting the normal mode of the whole structure. This would be a first step away from a global damping value, at present taken by BSRA as being dependent only on the frequency of the normal mode.

As mentioned in the paper, there is some doubt as to the depth of water at the time the exciter tests were conducted for the load condition. The ship was then also at anchor. Comparison with results obtained in a similar load condition but in deep water, comparable with the conditions for the ballast case, indicates that the modal peaks in the mobility plots presented in Fig.11 could be more pronounced in ideal test conditions. This point is supported by exciter results obtained from a third, intermediate, loading condition of 27,500 tonnes displacement. The exciter results for the intermediate load condition and the ballast condition do show similar characteristics.

For the loaded condition, a well defined peak at 318 c/min corresponding to the 6-node mode was obtained from the sea trials data. This particular mode is not well defined in the response obtained using the exciter whilst anchored in the estuary. However, apart from this one anomaly, the load and ballast measurements are not too dissimilar when one allows for the correspondingly higher frequencies of the ballast case. The mobility levels are, in fact, consistently higher in the ballast case for both the calculations and measurements.

Experience has shown that damping levels can vary with loading and draft, but for this ship it

is apparent that loading with a water 'cargo' other than by proportion to the frequency of the corresponding modes, does not affect the damping levels as compared with the ballast case.

Returning to the question of the finite elements the powerful nature of the higher order elements used for the analysis of this particular ship should be emphasised. The nine, eight-noded membrane elements and associated bar elements were found to give exactly the same first ten frequencies of the forward hull branch, cantilevered at the forward end of the deckhouse, compared with an equivalent grid of 4 x 52 simple elements.

The importance of superstructure vibration and its dependence on the possible coupling effect with the main hull modes is realised. The deckhouse root fixity and this interdependence of the two branches of the structure is a particular problem area which is difficult to simulate efficiently with a simple mathematical model. Accurate modelling of this problem area is required and further full-scale verification of any calculated results essential.

The response of the deckhouse region is very sensitive, near the frequency of a deck house resonance, to the modal damping of that resonance. Work is required to establish such damping levels.

It is of interest to note that Dn N are also allocating some effort to the use of mechanical exciters and the measurement of damping values and it is felt that when these are published they will be of interest to all concerned in ship vibration work. It is important, for any theoretical prediction of vibration, that detailed correlation with full-scale measurements are carried out.

#### REFERENCES

26. Hurty, W.C. Dynamic Analysis of Structural Systems using Component Modes, AIAA Journal, Vol.3, No.4, 1965.
27. Rubin, S. Improved Component-Mode Representation for Structural Dynamic Analysis, AIAA Journal, Vol.13, No.8, 1975.



## SESSION VII

### MARINE VEHICLES IN RESTRICTED WATERS

Friday, 2 April 1976

09.00—11.30

Chairman: E. V. Lewis

Ship-ship interaction in shallow water, by I. W. Dand

The effects of the restricted waters on the added mass of a rectangular cylinder, by  
M. Fujino

Interaction effects of ships operating in proximity in deep and shallow water, by  
M. A. Abkowitz, G. M. Ashe, and R. M. Fortson

Ship flow features at different drift angles in shallow water, by V. N. Treshchevsky  
and A. I. Korotkin

# SHIP-SHIP INTERACTION IN SHALLOW WATER

I. W. DAND

Ship Division, National Physical Laboratory, Feltham, UK

## SYNOPSIS

As a result of a research programme in progress at Ship Division, National Physical Laboratory into the behaviour of ships in shallow water, experiments have been carried out to measure the interaction forces between various models. Results of these experiments are presented and compared with computed predictions made using a two-dimensional theory.

This comparison enables conclusions to be drawn as to the short-comings of the theory and suggests areas where it might be improved, notably by the inclusion of free-surface effects.

Some experiments designed to relate certain features of hull design to lift-induced interaction forces are presented and it is shown that lift-induced crossflow on the skeg and rudder significantly affects the sense and magnitude of the interaction forces and moments at certain overlaps.

As the experiments were conducted in the large circulating water channel at Ship Division, experimental technique and accuracy is discussed in some detail. This is important as experiments carried out in this facility are subject to constraints which are different from those encountered in a towing tank and the results should be interpreted accordingly.

## 1. INTRODUCTION

At the Tenth ONR Naval Hydrodynamics Symposium papers were presented which considered the subject of hydrodynamic interaction between ships. (References 1 and 2) By this is meant the longitudinal and lateral forces and moments exerted on one ship by the other when both are in close proximity. These papers relied heavily on theoretical treatments of the subject as few quantitative experimental results were available in the literature allowing verification of the theory.

Moreover, it was shown in reference 1 that interaction between ships would be more pronounced in shallow rather than deep water due to the more two-dimensional nature of the flow around the vessels. Recent studies at Ship Division NPL of the behaviour of ships in shallow and confined waters have incorporated some experimental measurements of interaction forces and moments between ship models. These, although confined to the steady state case, have been used in conjunction with the theory of reference 3 to illuminate certain hydrodynamic features of interaction which might not be readily apparent from theory alone.

Some of these results are presented in this paper and are discussed from a hydrodynamic viewpoint. They may be further interpreted from the point of view of ship behaviour in collision situations and the handling of craft such as tugs whose work of necessity brings them into close proximity with other ships. These aspects are discussed further in references 3 and 4.

## 2. NOMENCLATURE

B	maximum beam
C <sub>N</sub>	turning moment coefficient $N/\frac{1}{2}\rho B^2TV^2$
C <sub>X</sub>	longitudinal force coefficient $X/\frac{1}{2}\rho BT^2V^2$
C <sub>Y</sub>	sideforce coefficient $Y/\frac{1}{2}\rho BT^2V^2$
F <sub>nh</sub>	Froude depth number $V/\sqrt{gh}$
g	gravitational acceleration
h	water depth
L <sub>A,B,C,D,E</sub>	length of model between perpendiculars. Subscript gives model identification letter
m	number of source panels used to represent one hull
n	shaft revolutions
N	turning moment
R <sub>x</sub>	local Reynolds Number $Vx/\nu$
T	at-rest draught
V	steady velocity
x	distance from leading edge of false floor of circulating water channel
X	longitudinal force
X <sub>0</sub>	overlap parameter
Y	sideforce
Y <sub>0</sub>	transverse separation of centreplanes of models
δ	boundary layer thickness
δ*	boundary layer displacement thickness
ν	kinematic viscosity
ρ	density

## 3. THEORETICAL CONSIDERATIONS

In reference 2 a numerical method for calculating

interaction forces and moments between two-dimensional bodies was presented, based on the theoretical work of Collatz (reference 5). In reference 1 however, the inclusion of vorticity in such a theory was shown to be essential to satisfy the Kutta condition at the stern of each ship.

The NPL computer program was therefore modified as described in reference 3 so that both the ordinary and extended Kutta conditions could be included in the computation. The inclusion of the extended Kutta condition allowed an approximate representation of the effects of ships' wakes in the solution should this appear to be necessary. In the event, although some calculations have been made incorporating wakes, their effect has been shown to be small and they do not significantly improve agreement between theory and measurement.

It is not intended to consider theoretical aspects in detail in this paper as these may be found in the references. The hulls are represented by a series of source panels and the strengths of the surface singularities are found by a numerical solution of 2 m simultaneous equations where m is the number of source panels used to represent each hull. The equations arise from satisfying the linearised condition that no flow exists normal to the body on its boundary. Using a method similar to that of reference 6, a point vortex is placed at the centre of each hull and singularity distributions are calculated which cancel normal components of flow at each hull panel arising from the onset flow and each vortex. The strengths of the vortices are then chosen so that the Kutta condition is satisfied at the stern of each ship. This enables linearised pressures to be computed on the source panels which, after summation and resolution, give a longitudinal force X, a sideforce Y and a turning moment about amidships N. These are then non-dimensionalised according to the scheme.

$$C_X = X / \frac{1}{2} \rho B V^2 \quad C_Y = Y / \frac{1}{2} \rho B V^2 \quad C_N = N / \frac{1}{2} \rho B^2 V^2$$

where B is the maximum beam of the ship and V is its steady velocity.

In all the calculated results shown in the paper a value of m equal to 60 and constant panel length were used. Steady state conditions were assumed throughout.

It is of some interest to note that longitudinal interaction forces are calculated. Due to the assumption of a perfect fluid made in the potential theory these cannot represent the total longitudinal forces acting in a real fluid; viscous forces do not exist in perfect fluid and, as it is further assumed that the free surface remains flat, wave-making forces are also absent. The computed longitudinal forces therefore represent the 'inertia drag' experienced by one ship as it moves in flow which has been accelerated or decelerated by the presence of other ship, and it is a force whose consideration is of some importance when studying the behaviour of ships in interaction situations.

#### 4. EXPERIMENTAL DETAILS

Experiments to measure interaction forces between various ship models were carried out in the large circulating water channel at Ship Division NPL which allows one or more models to be held stationary while the flow streams past. Provision of

a false floor in the working section whose vertical height is easily adjusted allows the channel to be run in a shallow water mode.

This facility is ideally suited to the measurement of interaction forces because it may be run continuously while the longitudinal and lateral separations of the models are varied. Water depth can also be changed with ease so that results from a wide variety of experimental conditions may be obtained rapidly and conveniently.

There are some disadvantages in using this facility when compared to a conventional towing tank, and these are discussed below. However, for the investigations carried out so far it has been found that the limitations of the facility, once recognised, have not unduly impeded the experiments.

##### 4.1 Model Details

The models used in the interaction experiments were as detailed below.

###### Model A

A single screw closed-stern cargo-liner form with a block coefficient of 0.701. It was fitted with propeller and rudder.

###### Model B

A single screw closed-stern tanker form with a block coefficient of 0.761. It was fitted with propeller and rudder and, with model A, comprised a pair of geosims of the free-running models A and B of reference 2. The ratio  $L_{pp}(\text{model A})/L_{pp}(\text{model B})$  was 0.839; the free-running geosims of reference 2 had a scale ratio of 0.459 to the larger pair used in the water channel experiments.

###### Model C

A single screw conventional tug, fully described in reference 4. For these experiments it was fitted with a detachable rudder, but no propeller.

###### Model D

This was a tug-like form designed at NPL for the reasons given in section 5.2 below. It was not fitted with propeller or rudder, but had a large detachable skeg aft as shown in Figure 1.

###### Model E

A single screw tanker form with a cylindrical ram bow and a block coefficient of 0.838. It was characterised by a bluff forebody but a reasonably easy run in the aft-body. This gave rise to pronounced shoulders forward with somewhat less pronounced shoulders aft. It was run without propeller or rudder and the ratio  $L_{pp}(\text{tug})/L_{pp}(\text{model E})$  was 0.212 for both tug models C and D.

#### 4.2 Experimental Methods and Instrumentation

##### 4.2.1 The Experiments

The experiments were carried out with one model fixed to the carriage on the centreline of the working section, while the other model was rigidly moored independently of the carriage and to one side. The model attached to the carriage was instrumented while the other was not, so to measure



interaction forces on the other model, their positions were interchanged. As forces were only measured on the model on the channel centreline, lateral forces arising from wall interference were eliminated so that only the pure interaction forces between the models remained.

The experiments were run in general at a constant depth and various overlaps although one series of measurements was made for various water depths at one overlap.

The effect of speed was investigated by repeating the measurements at two speeds and constant depth and, for models A and B the effect of self-propelling the models was studied. Finally for models A, B and C the part played by flow past the rudder on interaction forces was investigated.

For the particular experiments described in this paper, transverse separation between the models was not varied although this has been studied in previous experiments involving models C and E.

#### 4.2.2 Instrumentation

Measurement of the interaction forces was straightforward although operating features of the circulating water channel had to be borne in mind when designing equipment. When the channel is at rest, the static water level above the false door is considerably less than the operating level and for models A and B was also considerably less than the draughts of the models. This meant not only that one or both of the models were aground when at rest but also that when starting and stopping the channel the measuring equipment had to cater for vertical changes in operating level of up to 200 mm.

The fact that the model could be aground when at rest meant also that some means of completely disconnecting the measurement system from the model had to be devised so that true 'no-load' zero readings could be taken. It was found that unless the instrumentation was so designed, large non-repeatable loads were imposed on it when the model grounded. The presence of these forces during starting and stopping also meant that suitable stops had to be provided to prevent overload damage to the transducers.

#### Measuring System

The system finally adopted for use with models A and B was similar to that of reference 7 and is shown diagrammatically in Figure 2 which also incorporates a block diagram of the data acquisition system.

Lateral forces were measured at bow and stern by two 200 N modular force gauges manufactured from EN24 steel and incorporating linear displacement transducers with a range of  $\pm 0.127$  mm. These were attached to vertical legs which in turn were firmly clamped to a longitudinal box-section steel strong-back mounted on the carriage.

On the bottom of each block gauge was mounted a vertical roller which engaged in horizontal rollers fitted in the model on its waterplane. The clearance between vertical and horizontal rollers was 0.381 mm and this arrangement allowed the force gauges to be completely disconnected from the model by raising the carriage which caused the vertical rollers to disengage from the horizontal rollers.

Longitudinal force was measured using a 50 N force gauge mounted in the model and connected to a towing strut by a rigid towing hook. This hook was not engaged until a steady-state condition had been reached after the start of a run and was similarly disengaged before shutting down at the end of a run; the large transient forces during starting and stopping were taken on a towing chain permanently attached to the model but which was slack during normal running.

Suitable stops were provided in each force gauge to prevent overload in the direction of the measured force and further stops prevented large vertical buckling loads being applied to the lateral force gauges during starting and stopping. Clearances at these vertical stops was continually monitored by means of closed-circuit television.

The measuring system employed for models C and D was altogether simpler as the small size of these models allowed them to be placed in position by hand once the channel was running at steady speed. Side-forces at bow and stern were measured using two lateral spring balances. The vertical arms from these balances fitted in cups mounted in the models, the side-forces acting on the model causing the vertical arm to move against a calibrated spring. Balance was restored by extension of the spring with, if necessary, the addition of dead-weights.

For all experiments water speed in the channel was measured using a small propeller-type current meter with a 10 mm rotor. This was mounted ahead of the model under the carriage at a depth of 100 mm and approximately half way between the centreline and the wall of the working section on the side opposite to the moored model.

#### Data Handling

For the measuring system used with models A and B, voltages from each of the three force gauges together with pulses from the propeller shaft rev. counter and the current meter were interfaced to the data logging system of Figure 2 and integrated for 60 seconds. Integrated results were then printed out on a Teletype and punched on paper tape. By using the editing facilities of the Teletype complete data tapes were prepared which were analysed by computer to produce non-dimensionalised force and moment coefficients and other relevant information.

The same computer program was also used to process data collected from models C and D although in this case readings were written down and data tapes prepared after the experiments.

Measured forces and moments were non-dimensionalised according to the scheme

$$C_X = \frac{X}{\frac{1}{2}\rho BTV^2} \quad C_Y = \frac{Y}{\frac{1}{2}\rho BTV^2} \quad C_N = \frac{N}{\frac{1}{2}\rho B^2TV^2}$$

where  $T$  is the draught of the model and these were then directly compared with the force and moment coefficients obtained from the two-dimensional theory. A longitudinal overlap  $X_0$  was defined as

$$X_0 = x_{\text{bow}} (\text{model E or model B}) - x_{\text{bow}} (\text{tug or model A})$$

and this was non-dimensionalised with respect to the length of model B or model E, the distinction being made clear on the appropriate plottings. The lateral separation  $Y_0$  of the centrelines of the models was also non-dimensionalised with respect to the length of model B or E as appropriate.

The axis system used is indicated on the plottings of results with the x-axis in the direction of motion and the y-axis to one side.

#### 4.3 Errors

Apart from the sources of error which occur in most tank experiments arising from limitations of transducers, balances, amplifiers etc. additional sources of error arise in experiments in the circulating water channel which originate in the limitations of the facility itself.

##### 4.3.1 Channel Flow Characteristics

###### Unsteadiness

The channel does not have the same inherent accuracy as a towing tank because the fluid moves past the model and does so with a certain degree of unsteadiness and a higher turbulence level than in a towing tank. Moreover certain structural features of the channel (such as the false floor) can cause extra disturbances in the flow which make accurate measurement difficult. The unsteadiness in the flow was minimised by using an integration time of 60 seconds for the experiments involving models A and B and waiting a similar length of time to estimate a mean value for the experiments with models C and D. Repeat values were obtained for all runs. Furthermore a rotary damper was provided on the balances used with models C and D.

###### Boundary Layer Growth

The main feature of flow in a water channel is the growth of a boundary layer over the floor and sides. This gives rise to a flow which accelerates from one end of the working section to the other and has a major effect on longitudinal steady state (drag) force measurements. The accelerating flow in conjunction with the high blockage ratios obtained in the channel also appears to have an effect on the transverse crest positioning of the model wave train so that measured values of squat may be seriously in error. As an example of this model B was known to squat by the bow in a towing tank at a given speed and water depth but was observed to squat by the stern at the same speed in the same depth of water in the water channel whose width is 0.6 that of the towing tank.

The longitudinal flow acceleration was measured in the channel at two speeds with either model A or model B fixed to the carriage but with the other model absent. Velocities were measured with the current meter at approximately 20 positions along the working section. Boundary layer displacement thickness  $\delta^*$  on the false floor was calculated using the flat plate value of (reference 8)

$$\delta^* = \frac{\delta}{8} \quad \text{where} \quad \delta = 0.37 R_x^{-0.2}$$

and assuming turbulent flow. Results of these investigations are given in Table 1.

In table 1 the calculated displacement thickness

$\delta^*$  is related to the at-rest underkeel clearance ( $h-T$ ) and a range of values is given corresponding to the growth of the boundary layer from one end of the false floor to the other. From this it is seen that the models are likely to experience the greatest local interference from the channel boundary layer when they are at longitudinal positions remote from the leading edge of the false floor. As it was not possible to accommodate the whole range of overlaps in the available length of the working section it was necessary to re-moor the 'dumb' model so that overlaps which had been remote from the leading edge of the false floor (where  $\delta^*$  was large) were moved close to the leading edge of the false floor (where  $\delta$  was small). By repeating certain critical overlap positions in this way it was possible to minimise errors arising from the channel boundary layer over most of the overlap positions.

Although the growth of the channel boundary layer will undoubtedly quantitatively affect longitudinal forces and squat, it was assumed that it had a negligible effect on lateral forces; further it was assumed that the general character of the longitudinal forces were not significantly affected and squat was not measured.

###### Crossflow

The water channel comprises a horizontal hydraulic circuit around which water is pumped in an anti-clockwise direction. During the experiments it was found that a sideforce and moment were induced on the model under test when the moored model was absent. These appeared to be due to crossflow in the working section and they were measured and subsequently used to correct the interaction force measurements.

###### Water depth

Both water depth and speed in the working section are related to the hydraulic characteristics of the water channel. Therefore, just as unsteadiness in water speed occurs so does some unsteadiness in the water depth, which was seen to vary slightly throughout the day. This variation was not thought to affect the results unduly as the interaction forces were varying slowly with depth for all the models. Some idea of the variation with water depth is given in table 2 derived from measurements made with model A.

	For 1% change in $h/T$	
	$\delta C_Y$	$\delta C_N$
mean $h/T$ 1.68	0.01	0.03
1.38	0.03	0.10

TABLE 2

The variation in  $h/T$  was generally  $\leq 1.0\%$  during the experiments.

###### Blockage

Blockage in the working section was high with blockage ratios of the order of 0.10. No corrections were made for blockage, but this is not

expected to affect the general conclusions about the nature of the interaction forces. As stated above the effects of the channel walls on sideforces were eliminated by taking measurements only from the model on the centreline of the channel.

#### 4.3.2 Force and Velocity Measurements

The resolutions of the modular force gauges and sideforce balances are shown in Table 3 together with the resolution of the current meter which had a threshold velocity of 0.042 m/s. Also shown in Table 3 are overall values of repeatability at constant overlap derived from several pairs of repeat values. These are given as mean values of repeatability of the force and moment coefficients and combine both velocity and force measurement errors. They are therefore used to indicate the overall accuracy of the experimental measurements bearing in mind the characteristics of the channel flow mentioned above.

Sources of error in the experiments have been considered in some detail because the results are used to compare both theoretical predictions and the effect of changes in operating conditions of the models; clearly any comparison of differences between results must take account of the accuracy with which the results have been obtained.

#### 5. Tug-Ship Interaction

The subject of tug-ship interaction has been discussed at some length in references 3 and 4. A few results are included here however to illustrate certain hydrodynamic features relevant to the general topic of interaction.

##### 5.1 Conventional Tug

Results obtained with models C and E are shown in Figure 3. Neither model was propelled for these experiments and model C was tested with and without its rudder. Also shown, to a different scale, are calculated values of interaction sideforce and moment induced on model C by model E.

The depth/draught ratio for model C was 3.26 whereas that for model E was 1.15.

Features of these sideforce and moment curves are discussed in reference 4 but the main item of interest here is the measured bow-in turning moment which occurs in the range  $-0.3 \leq X_0/L_E \leq -0.1$ . It is seen that this potentially dangerous turning moment is not predicted qualitatively by theory even though other features of the force and moment curves show reasonable qualitative agreement.

It was agreed in reference 4 that this turning moment did not arise from the bow wave of model E pushing aside the stern of model C - a conventional explanation of the phenomenon - but rather it originated from crossflow over the rudder of the tug causing the rudder to be at an effective angle of attack and so turning the tug. This crossflow arose from the flow accelerating past the bluff forebody of model E and crossflow angles at the rudder of up to  $20^\circ$  were observed.

Removal of the rudder of model C significantly reduced this turning moment as is seen from Figure 3 and lent support to the argument that wave interference had little to do with the phenomenon.

It seemed in fact that the computed bow-out turning moment in this region was not unreasonable as one might expect the constricted flow between the aft-body of the tug and the forebody of the ship to cause the stern of the tug to be sucked toward the ship. That this did not happen was clearly due in part to the lift induced on the rudder in this region of strong crossflow. However some 'bow-in' turning moment remained with the rudder removed as is seen from Figure 3 and this was thought to arise predominantly from crossflow impinging on the skeg incorporated in the aft-body lines of model C.

##### 5.2 Design Exercise

To test the arguments advanced in section 5.1 and to investigate the part which lift-producing features of hull design could play in interaction crossflows, a tug hull was designed with the following aims:-

- i) To have the lift-inducing features of the hull concentrated aft and incorporated in a separate, removable entity so that the effect of these features in a crossflow could be identified.
- ii) To reduce the number of lift-inducing features of the rest of the hull to a minimum.
- iii) To make the length and sectional area curve as close as possible to those of model C.
- iv) The hull should have a shallow draught so that, if wave effects were a significant cause of certain features of interaction, they would be readily observed on the model.

Model D which resulted from this exercise is shown in Figure 1 and is seen to bear more than a passing resemblance to a modern 'water tractor' hull form. The lift-producing feature of the hull is the large removable flat plate skeg aft and it is seen that the hull form is both shallow and rounded so that little effect of crossflow would be expected on the hull without its skeg.

Results obtained with models D and E are shown in Figure 4 where measured sideforces and moments are shown with and without the skeg fitted and with a 'clear water' separation between the sides of models D and E the same as that between models C and E at  $X_0/L_E = 0.5$ .

The effect of the skeg is seen to be dramatic. The bow-in turning moment when model D was in the range  $-0.3 \leq X_0/L_E \leq -0.08$  is seen to be entirely due to the skeg, the 'hull alone' moment curve having the same qualitative trend as the calculation shown in Figure 3. No 'pushing' was observed from the bow-wave of model E and this is confirmed by the results.

The crossflow in the range  $-0.3 \leq X_0/L_E \leq 0.0$  which causes the lift on the skeg is seen to be a major contributor to the repulsion sideforce the tug experiences in this region, although some sideforce is evident with the 'hull alone' due perhaps to some lift being developed in a manner similar to that discussed in reference 9, page 405-418.

Similar effects are found when model D is near the



aft-body of model E, the crossflow now being directed inward and so causing an inward-directed lift force or the skeg of model D. Other features of the interaction curves in the region  $0 \leq X_0/L_B \leq 0.4$  where crossflow is small are seen to be similar to those occurring in Figure 3, the causes of these features being discussed in reference 4.

One observation made of model D was that, when the skeg was added and the model was run in a region of strong crossflow, the lift generated by the skeg acting at a point low on the skeg/hull combination, caused a pronounced heel on the model. This was not observed when the skeg was removed, and suggests another result of interaction which could prove hazardous for a tug.

These model experiments emphasise the part that lift forces play in interaction, bearing out the conclusions of reference 1. They also show the part hull design plays in features of the interaction curves; for example it might be expected that a ship ahead of another with a bluff bow might experience a tendency to turn across the other's bows due to the strong crossflow induced near the bow of the bluff vessel. Such a tendency might be expected to occur to a much lesser extent ahead of a ship with a fine forebody.

## 6. Ship-Ship Interaction

Interaction between models of similar size, moving at the same speed on parallel courses was investigated with models A and B. The depth of water was such that for most of the experiments, except those exploring the variation of interaction forces with water depth, the at-rest water depth/draught ratios were 1.67 for model A and 1.30 for model B. For all experiments a constant value  $Y_0/L_B$  of 0.252 was maintained and the rudders, where fitted, were fixed amidships.

### 6.1 Basic Interaction Forces and Moments

The basic interaction forces and moments i.e. those measured on each model with the propellers stationary, are shown in Figure 5 together with the experimental results from which the continuous fair curves are derived. Experiment points are omitted in subsequent Figures for clarity. Repeatability figures from Table 3 are also shown on this Figure.

Figure 6 shows calculated results obtained using the two-dimensional theory alluded to in section 2 above. Results obtained with and without the inclusion of circulation in the computation are shown and the models were assumed to be represented by two-dimensional struts having waterplanes of the same shape as the load waterplanes of the models.

The three components of interaction shown on these Figures are discussed separately.

#### Longitudinal Force $C_x$

It is clear that both models experienced increases or decreases in steady-state drag depending on overlap. It is also clear that when one model experienced a decrease in drag, the other experienced an increase. These features are reproduced qualitatively by the calculations, the effect of circulation being most pronounced on the model that

is ahead and therefore having to contend with the effect of large streamline curvatures induced near its stern by the bow of the following model as suggested in reference 1.

It is seen that the computed results oscillate about a mean 'open sea' drag of zero which is to be expected from a perfect fluid theory and that the phasing of the curves from the two models does not agree with the measurements of Figure 5. For example model A experienced a minimum drag value at  $X_0/L_B = 0.6$  in the experiments and at about  $X_0/L_B = 0.5$  in the calculations whereas model B reaches a maximum drag at  $X_0/L_B = 0.4$  in the experiments and at about  $X_0/L_B = 0.8$  in the calculations. It is probable that the neglect of free surface effects in the theory is responsible in part for this discrepancy.

#### Sideforce $C_y$

It is in the computation of sideforce that the importance of including circulation is seen, again bearing out the conclusions of reference 1. The character of the sideforce curves in Figure 6 is quite different when circulation is included and the effect of satisfying the Kutta condition on the ahead model is clear.

The measurements of Figure 5 bear out qualitatively the results of the computations although quantitatively the measured  $C_y$  values are very much less than their computed counterparts, emphasising the crudity of the two-dimensional mathematical model. It is again possible that the neglect of free-surface effects in the computations is responsible for the phasing discrepancies between calculation and measurement; this may be especially true when the models are side-by-side ( $-0.2 \leq X_0/L_B \leq 0.4$ ) in which condition large free-surface changes in the gap between the models were observed.

#### Turning Moment $C_N$

It is in the comparison of computed and measured turning moment that discrepancies are of most interest not only from an academic but from a practical point of view. When on a ship in an interaction situation it is the effect of the turning moment on the ship which will be perceived first; moreover it is the interaction feature which the ship is best able to counter by means of its rudder.

It appears from a comparison of Figures 5 and 6 that the measured results are qualitatively reasonably well predicted by the calculations. However the phase differences between measurement and calculation are crucial to any analysis of the interaction experienced by two ships on parallel courses. At an overlap of  $X_0/L_B = 0.3$  it is seen from Figure 5 that model B experienced a large 'bow-out' turning moment while model A experienced a very small moment toward model B. At an overlap of  $X_0/L_B = 0.1$  both models are experiencing moments tending to turn them away from each other. If the results of Figure 5 are assumed to apply approximately to the case of two models in an overtaking situation, it might be expected that when the models are side-by-side they would be subjected to moments which would turn them away from each other with some violence. Such behaviour was in fact observed in free-running model tests at NPL and is discussed in references 2 and 3.

The calculated  $C_N$  values of Figure 6 however, although in better quantitative agreement with measurement than the  $C_y$  values show a phasing discrepancy compared to measured values in the range  $-0.1 \leq X_0/L_B \leq 0.3$ . This has the effect of almost completely suppressing the tendency of the models to turn away from each other; the calculations suggest in fact that the models turn more or less together.

The other main area of disagreement between theory and experiment occurs when one model is ahead of the other in the region  $|X_0/L_B| \geq 0.8$ . It is seen from Figure 5 that when model A is ahead of model B the turning moment curve becomes negative for  $-1.1 \leq X_0/L_B \leq -0.7$ , a feature not predicted by the calculations of Figure 6. The reason for this is presumably due to crossflow at the stern of model A as the streamlines curve to pass the bows of the fuller formed model B, this crossflow inducing a lift on the aft-body and rudder of model A in a manner analogous to that discussed in section 5 above. It is noteworthy that when model B is ahead of model A it appears that the crossflow induced on the stern of model B by the bows of the fine-formed model A is not quite large enough to produce a positive turning moment in the range  $0.9 \leq X_0/L_B \leq 1.2$ . Although these turning moments induced by crossflow may appear to be small, they cause the ahead model to turn across the bows of the other in a manner which in a practical situation could cause a hazardous situation to arise almost imperceptibly (see references 2 and 3).

During the model experiments it was noted that the squat of each model varied with overlap as they 'rode' on each other's wave system. When both models were side-by-side, the squat of both models was enhanced due no doubt to the low pressure fields around the models.

## 6.2 Effect of Speed

Measurements of interaction forces were made for each model at two speeds corresponding to 9.1 knots and 7.1 knots full scale. The effect of this can be seen in Figure 5 where as might be expected the longitudinal forces do not appear to follow a  $V^2$  law as discrete curves of  $C_x$  are produced at each speed; this would not be the case if a  $V^2$  law were followed as the longitudinal force has been non-dimensionalised with respect to  $V^2$ .

It is clear that the sideforce is nearly proportional to  $V^2$  but the turning moment is not. As the longitudinal force and turning moment are perhaps more likely to be affected by free-surface effects than the sideforce, this could be the cause of the non- $V^2$  relationship. Some experiments with tug models, described in references 3 and 4 showed that there were certain features of the interaction curves when the tug was alongside the ship model which were associated strongly with free-surface effects - wave patterns, reflections etc. - and it was these features which did not follow a  $V^2$  law. With models A and B, wavemaking effects might be expected to be greatest when the ships are alongside and maximum distortion of the wave systems of each model occurs.

## 6.3 Effect of Self-Propulsion

Both models A and B were self-propelled for a further series of experiments at constant revolutions to give 'open sea' propeller loadings approximating

to those obtained full-scale. Results are shown in Figure 7 for a full-scale speed of 9.1 knots and several interesting points emerge.

It is clear that propelling the models has an effect on all measured interaction components. The reduction in drag on model A in the region  $0.4 \leq X_0/L_B \leq 0.8$  is such as to suggest that a ship would experience a marked acceleration at this overlap if approaching at constant revolutions. At the same time the other ship would experience an increased drag and would be caused to slow down so that a dangerous situation could arise suddenly and with increased severity.

It appears that the effect of self-propulsion on  $C_y$  and  $C_N$  depends, for a single-screw form, on whether the ship is to port or starboard of the other. Both models A and B had single right-handed propellers and for all experiments model A was to starboard of model B. It is clear that in the range  $0 \leq X_0/L_B \leq 0.3$  the effect of propulsion is to increase the bow-out turning moment of models A and B and to increase the attraction between them. For  $0.3 \leq X_0/L_B \leq 0.8$  the effect of propulsion is to increase the bow-in turning moment of model A and to increase the bow-out turning moment of model B.

Also shown on Figure 7 are the initial turning moment coefficients produced by the rudders of both models at the 'hard over' position of  $\pm 35^\circ$  when the models were propelled. It is clear from this that at certain overlaps the turning moments induced by interaction in shallow water are considerably in excess of any correcting moment that could be applied by the ship's rudder. This differs from the deep water case where model tests can be used to predict rudder angles to counteract interaction (reference 10). This illustrates the magnification of interaction forces by shallow water which is discussed further in section 6.5 below.

## 6.4 Effect of Rudder

The effect of removing the rudders of both models is shown in Figure 8. It is apparent that the effect of the rudder in the interaction-induced crossflows is much less than that of model C as shown in Figure 3. The effect on  $C_x$  and  $C_y$  is barely perceptible but there is some change in  $C_N$ , generally on the 'ahead' model where crossflow is greatest; it is clear that, as suggested by the results of models C and D, the interaction effects on the rudder and the aft-body cause the ahead model to show a tendency to turn across the bows of the overtaking model.

Neither model was propelled while the results shown in Figure 8 were obtained but the propellers were fitted and their presence ahead of the rudders may have reduced the lift generated by the rudders in crossflow. Furthermore, both models had fairly substantial skegs incorporated in the aft-bodies and, as shown in section 5.2 these, as well as the rudders may have developed a large proportion of the sideforces and turning moments induced by lift.

## 6.5 Effect of Water Depth

To study the effect of water depth on interaction, models A and B were held at a constant overlap  $X_0/L_B = 0.635$  and forces were measured on model A while its  $h/T$  value was varied from 1.375 to



2.150 by increasing the water depth. Neither model was propelled for this experiment although rudders and propellers were fitted.

Results are shown in Figure 9 and it is clear that an increase of  $h/T$  has the effect of reducing the size of both the sideforce and turning moment rather in the manner suggested in reference 1.

The behaviour of the longitudinal force is interesting however; it is seen to increase with increasing  $h/T$  from a value which is at the 'minimum drag' value shown for model A on Figure 5. This is presumably due to the fact that the drag reduction at this overlap is due, in part at least, to the presence of an accelerated flow between the forebody of model A and the aft-body of model B. This might be expected to reduce the pressures over the forebody of model A and the aft-body of model B resulting in a drag reduction for model A and an increase for model B. In very shallow water where the flow is more two-dimensional, this increased velocity of flow might be expected to be greater than in deeper water where the flow has more room to 'escape' underneath as well as round the sides of the models.

Thus for drag at least, a complex interplay of forces takes place, the interaction force tending to depart less from the 'open sea' value with increasing  $h/T$  (and thus appearing to increase) while the 'open sea' drag value might be expected to decrease with increasing  $h/T$ .

It should be noted that the longitudinal forces shown in Figure 9 have not been corrected for longitudinal flow accelerations in the water channel discussed in section 4.3.1.

#### 7. General Discussion

The results obtained with models A and B in shallow water have been compared with calculation and it has been shown that a comparatively crude two-dimensional theory shows the main qualitative features of the interaction forces and moments. The results obtained with model D however show that certain aspects of hull design can drastically alter the forces and moments obtained and this suggests that a more comprehensive theory would be required to show these changes adequately. Furthermore, it appears from the results from models A and B that the forces do not simply vary as the square of the speed and it is suggested that wavemaking effects may well be the cause of this and the cause of phase errors with overlap noted between theory and experiment.

A complete three-dimensional theory including the effects of shallow water and wavemaking would be complex although some progress has been made, notably in reference 1. However, only steady state situations have been discussed in this paper and Norrbin has shown (references 11, 12) the importance of unsteady effects. Further extension of the theory to include unsteady effects, and thus to model the more usual real-life interaction situations where ships pass each other, would add further complication (reference 1).

It would seem therefore that a combination of a simpler theory in conjunction with model experiment results could profitably be used to study interaction for, as shown in section 5 above the areas

of disagreement between circulation and measurement are as important as the areas of agreement.

Although the model measurements were made in a steady-state situation, results from models A and B have appeared to confirm deductions made from free-running geosims of the same models in overtaking situations mentioned in reference 2. However, the results did differ in some important details, notably in the tendency of model B to turn across the bows of model A when free running which was more pronounced than measurements from the captive models suggested.

The effects of shallow water have been shown to be pronounced and Figure 9 suggests that they become important at depth/draught ratios less than about 2.0. It is worth noting that from Figure 9 it appears that, at an overlap  $X_0/L_B$  of 0.635, the interaction turning moment exceeds the maximum initial turning moment which can be developed by the rudder at a depth/draught ratio of about 1.9. At depth/draught ratios less than this it seems that situations could arise in which control might be lost.

#### 8. Conclusions

Several conclusions emerge from the experiments in shallow water described above and comparison of the results obtained with a two-dimensional theory. These are:-

- i) Calculation and measurement show reasonable qualitative agreement if circulation-induced effects (i.e. lift) are included in the calculation.
- ii) For similar-sized models, experimental and calculated results are out-of-phase on overlap possibly due to the neglect of free-surface effects in the theory.
- iii) For similar-sized models in steady-state conditions, the longitudinal forces and turning moments induced by interaction are not proportional to  $V^2$  at all overlaps. This suggests again that free-surface effects are important over the range of Froude Depth Numbers encountered in practice.
- iv) The interaction force and moment acting on a model are strongly affected by the crossflow-induced lift on certain appendages of the hull. This is particularly true of the bow-in turning moment felt by the 'ahead' ship in an overtaking situation.
- v) Whether free surface or lift effects predominate in the interaction forces acting on a model depend on its overlap with the other model.
- vi) Self-propelling a model has an effect on interaction. For single screw forms, the effect depends on whether the model is to port or starboard of the other.
- vii) Interaction can cause significant drag reductions to occur at certain overlaps.
- viii) Measured interaction forces decrease in magnitude with increasing water depth.



The longitudinal force in particular tends to show smaller excursions from the 'open sea' drag value.

- ix) In shallow water the turning moments induced by interaction may be several times greater than the maximum initial turning moment which can be applied by the rudder to counteract them.
- x) Interaction produces forces in the lateral plane which can cause a model to heel if the point of application of the force is sufficiently far beneath the free surface.

#### 9. References

1. TUCK, E.O. and NEWMAN, J.N. 'Hydrodynamic Interactions between Ships' Tenth ONR Naval Hydrodynamics Symposium, M.I.T., Boston, June 1974.
2. DAND, I.W. 'Some Aspects of Manoeuvring in Collision Situations in Shallow Water' Tenth ONR Naval Hydrodynamics Symposium, M.I.T. Boston, June 1974.
3. DAND, I.W. 'Hydrodynamic Aspects of Shallow Water Collisions' paper submitted to RINA Spring Meetings, 1976.
4. DAND, I.W. 'Some Aspects of Tug-Ship Interaction' Fourth International Tug Convention, New Orleans, October 1975. Thos. Reed Publications.
5. COLLATZ, G. 'Potentialtheoretische Untersuchung der Hydrodynamischen Wechselwirkung zweier Schiffskorper' Jahrb. der STG, Band 57, 1963, p.281.
6. GEISING, J.P. and SMITH, A.M.O. 'Potential Flow about Two-Dimensional Hydrofoils' Journal of Fluid Mechanics, vol. 28, part 1, 1967, p.113-129.
7. MOODY, C.G. 'The Handling of Super Ships Through a Widened and Asymmetrically Deepened Section of Gaillard Cut in the Panama Canal'. NSRDC (formerly DTMB) report 1705, 1964.
8. DUNCAN, W.J., THOM, A.S. and YOUNG, A.D. 'Mechanics of Fluids' Edward Arnold Limited, 1960.
9. THWAITES, B. 'Incompressible Aerodynamics' Oxford University Press, 1960.
10. NEWTON, R.N. 'Some Notes on Interaction Effects Between Ships Close Aboard in Deep Water' NSRDC (formerly DTMB) report 1461, 1960.
11. NORRBIN, N.H. 'Manoeuvring in Confined Waters: Interaction Phenomena due to Side Banks or Other Ships'. Report of the Manoeuvring Committee Appendix VIII, 14th ITTC, Ottawa, September 1975.
12. NORRBIN, N.H. 'Bank Effects on a Ship Moving through a Short Dredged Channel' Tenth ONR Naval Hydrodynamics Symposium, M.I.T., Boston, June 1974.

#### 10. ACKNOWLEDGEMENTS

This paper is published with the permission of the Director of the National Physical Laboratory. The author is particularly grateful to his colleagues Miss A Plumley and Mr G L Taylor for help with the experiments and the design of model D.

	$F_{nh}$	$\partial v / \partial x \text{ sec}^{-1}$	$\delta^* / (h-T) \text{ range}$	$h/T$
MODEL A	0.364 0.459	- $0.012 \pm 0.001$	0.10 - 0.20 0.09 - 0.19	1.669
MODEL B	0.364 0.467	$0.006 \pm 0.001$ $0.011 \pm 0.003$	0.17 - 0.34 0.16 - 0.33	1.300

Table 1

RESOLUTION				REPEATABILITY		
Velocity	Force gauge	Y force gauges	Spring balances	$C_X$	$C_Y$	$C_N$
/s	0.005N	0.009N	-	0.024	0.004	0.011
m/s	-	-	0.009N	-	0.015	0.017

Note

Repeatability figure defined as  $|C_{X,Y,N}(\text{run 1}) - C_{X,Y,N}(\text{run 2})|_{X_0/L_B} = \text{const}$   
 measured over several pairs of runs.

Table 2

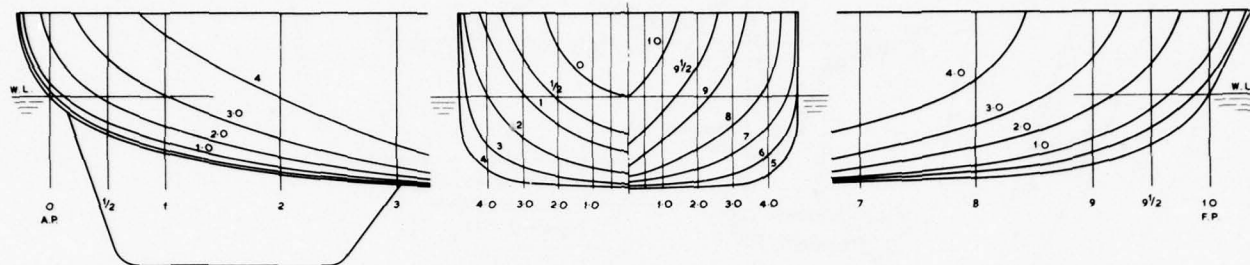


Fig. 1: Body plan and buttock lines for model D

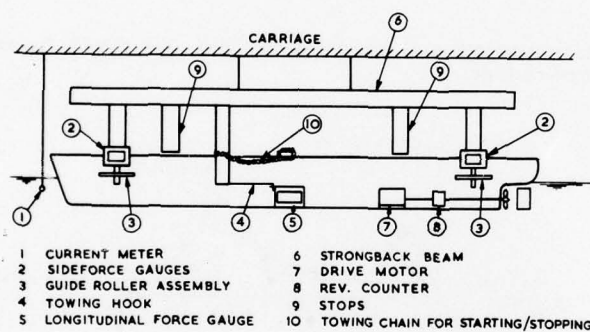


Fig. 2: Model set-up and data acquisition system used with models A and B



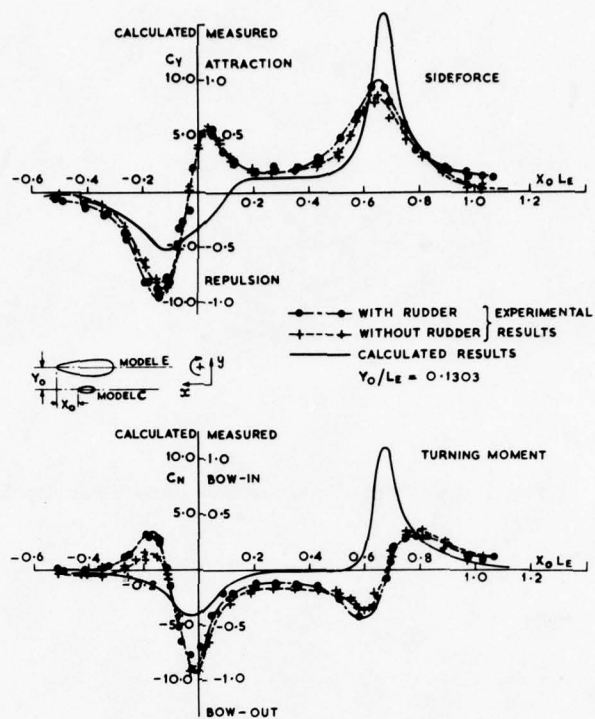


Fig. 3: Interaction forces and moments induced on model C by model E – effect of rudder.

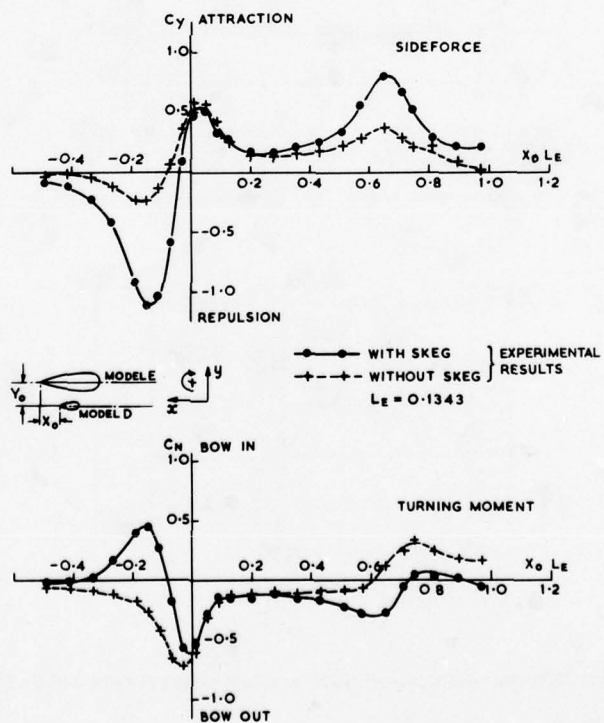


Fig. 4: Interaction forces and moments induced on model D by model E – effect of skeg.

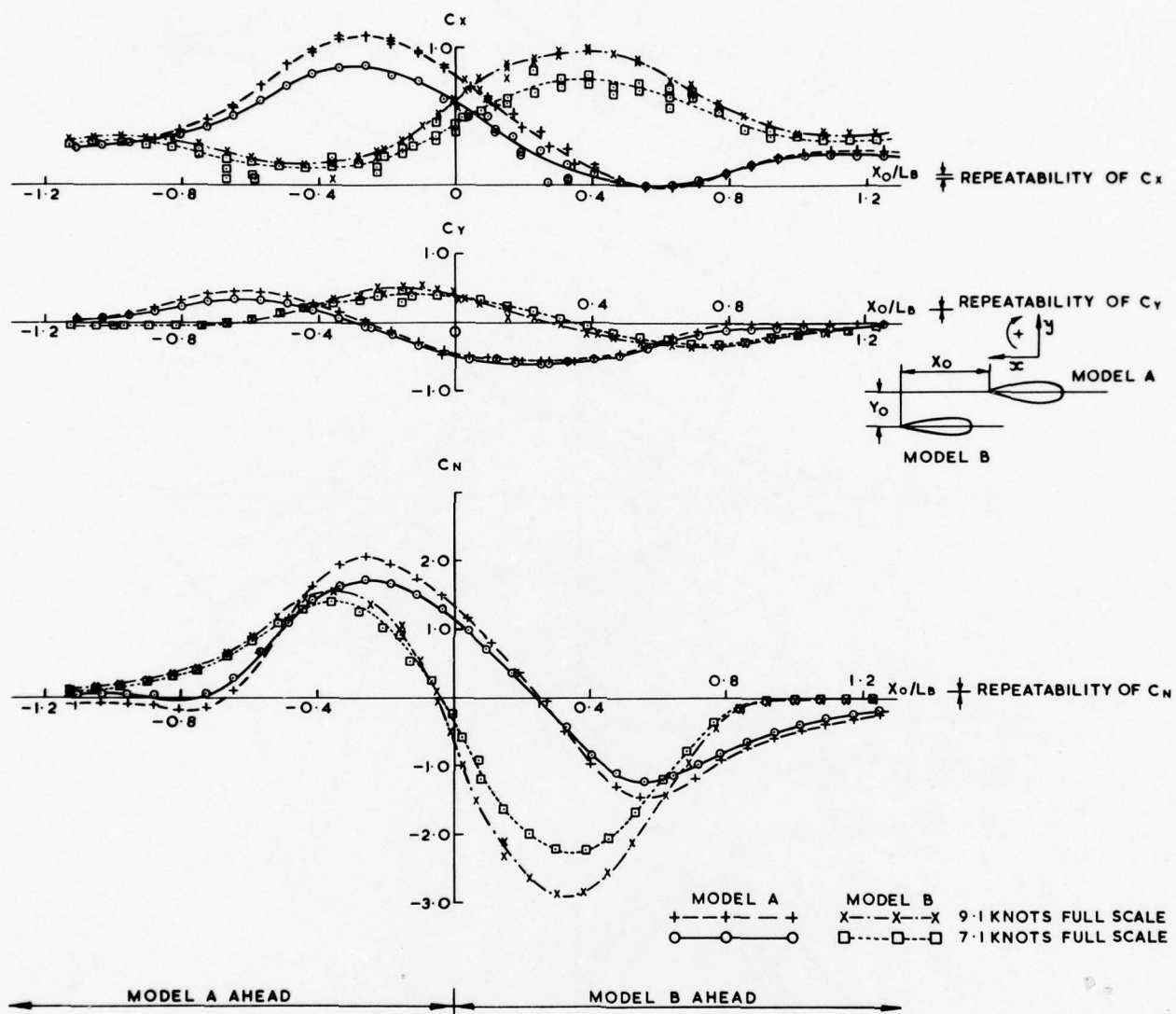


Fig. 5: Measured interaction forces and moments on models A and B - effect of speed. Not self-propelled;  $Y_0/L_B = 0.252$ .

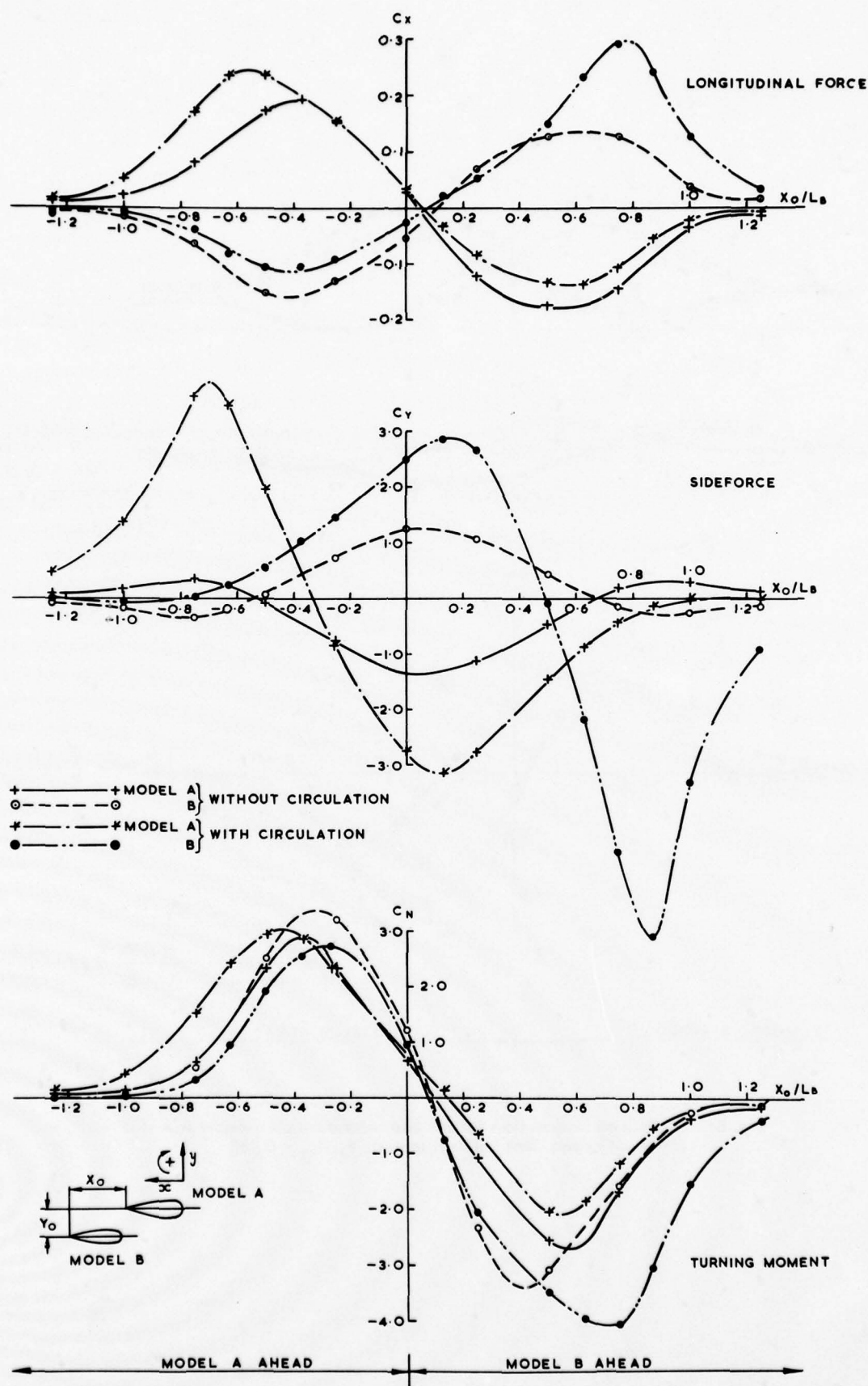


Fig. 6: Calculated interaction forces and moments on models



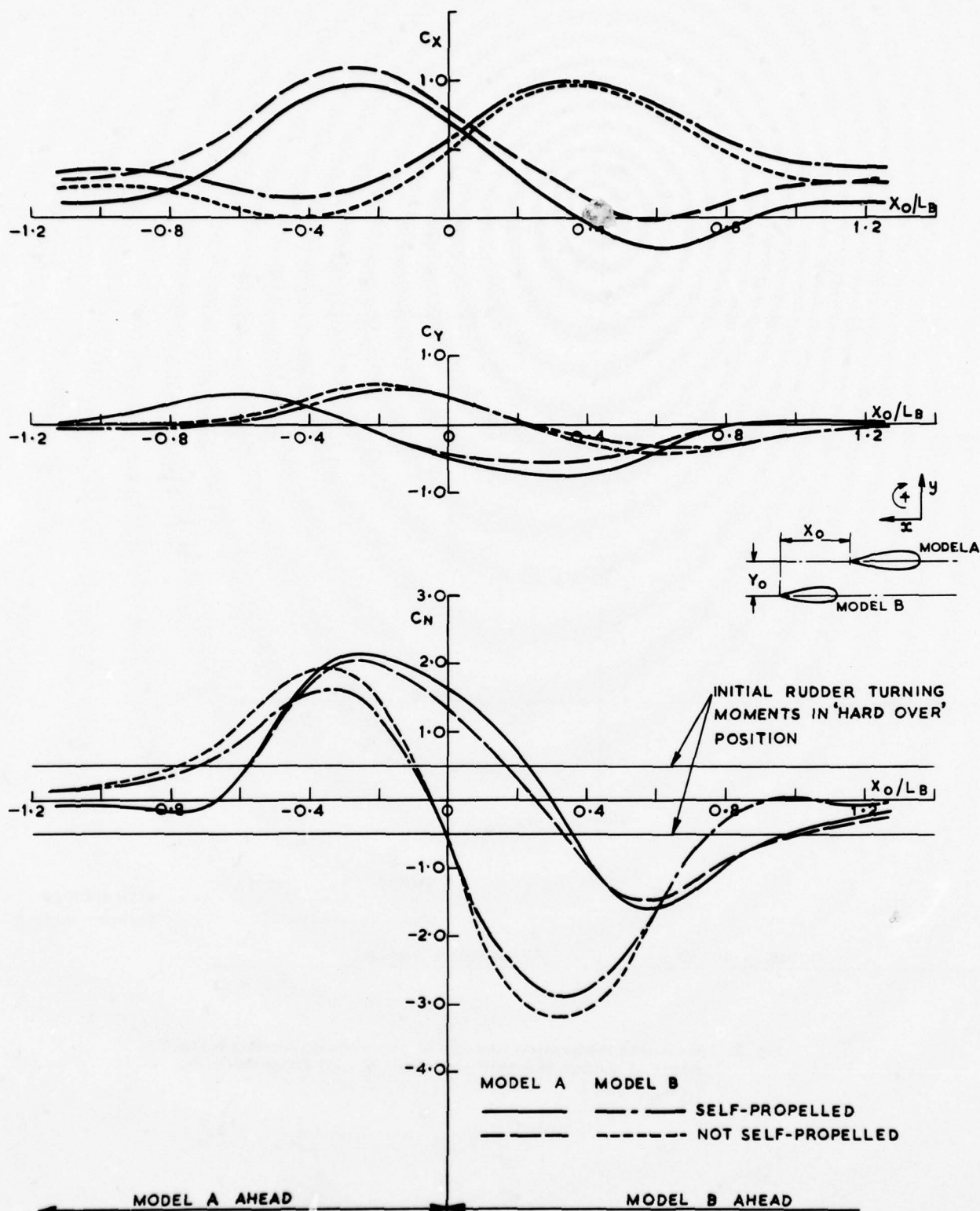


Fig. 7: Measured interaction forces and moments on models A and B, effect of self-propulsion. Steady velocity  $V = 9.1$  knots full'  $Y_0/L_B = 0.252$ .

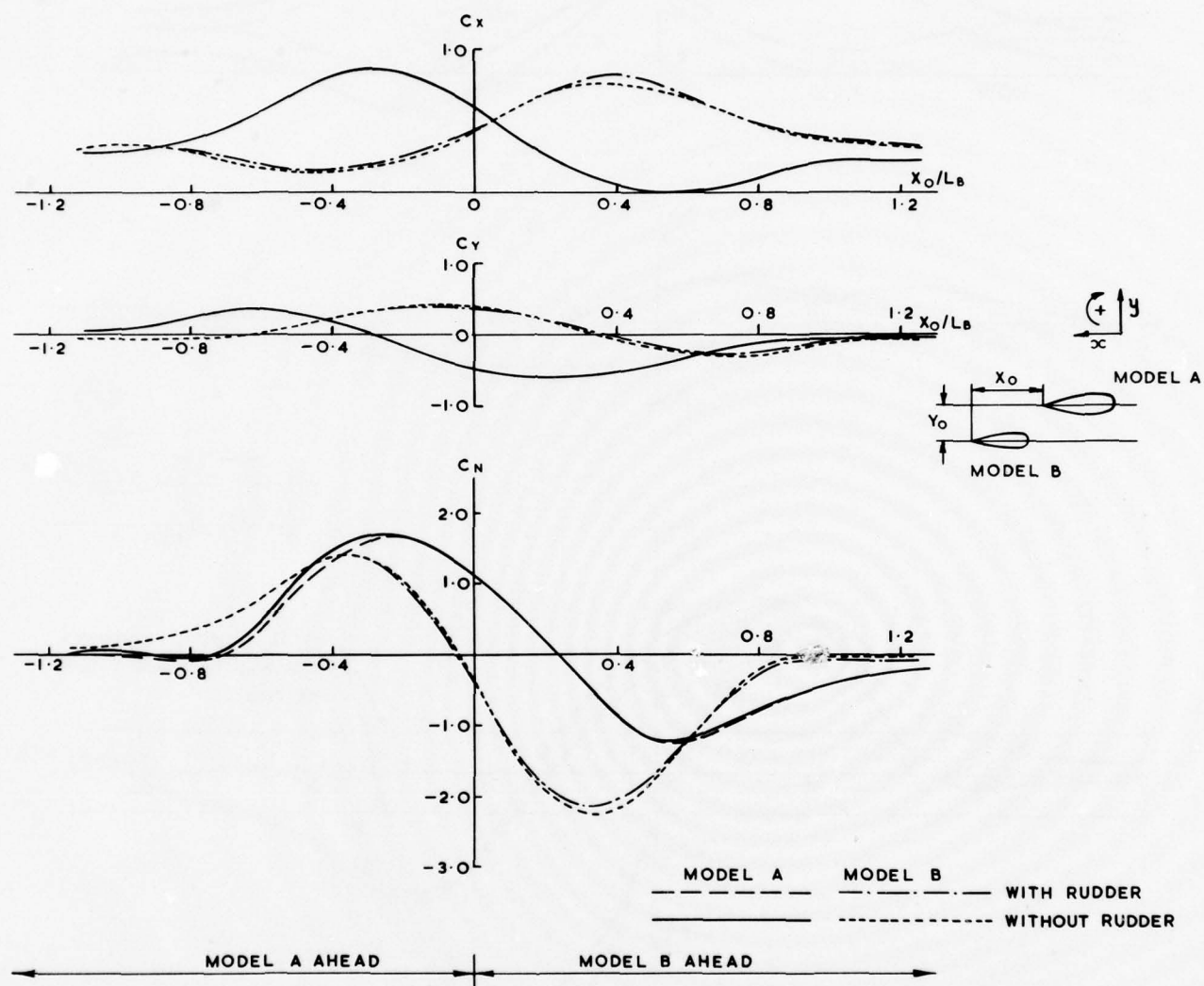


Fig. 8: Measured interaction forces and moments on models A and B — effect of rudder. Not self-propelled;  $V = 7.1$  knots full size;  $Y_0/L_B = 0.252$ .

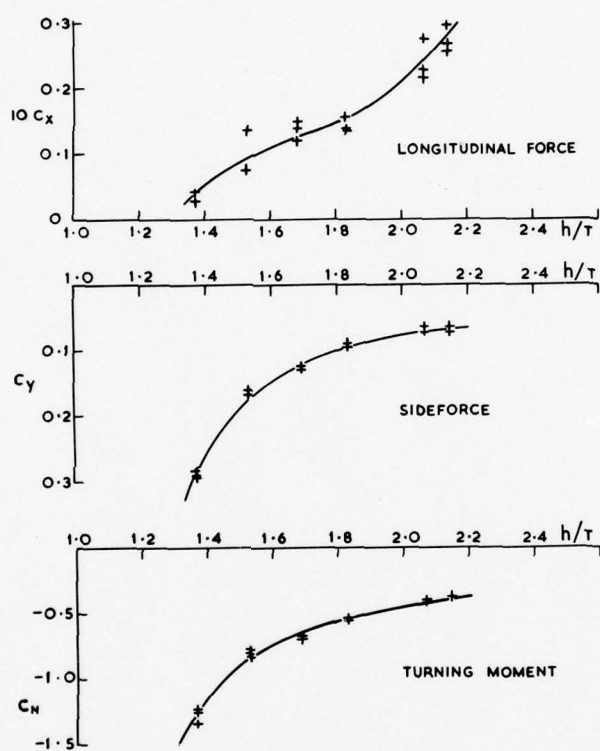


Fig. 9: Measured interaction forces and moments on model A – effect of depth/draught ratio. Not self-propelled;  $V = 8.3$  knots full size;  $Y_O/L_B = 0.252$ ;  $X_O/L_B = +0.635$ .



# THE EFFECTS OF THE RESTRICTED WATERS ON THE ADDED MASS OF A RECTANGULAR CYLINDER

M. FUJINO

University of Tokyo, Bunkyo-Ku, Tokyo, Japan

The upper and the lower bounds of the sway added mass of a rectangular cylinder translating at the center of a rectangular channel are calculated by the hypercircle method for various cases which are presented and compared with sway added mass values calculated by using other numerical methods. The lower bounds are calculated from the hypercircle method in order to discuss the effects of restricted water on the sway added mass of a rectangular cylinder. The cylinder is considered as translating at various off-center positions in a rectangular channel and also vibrating on the free surface of a restricted waterway.

## INTRODUCTION

It is well known that the added mass of a ship travelling on the free surface of the restricted channel is strongly affected not only by the finite depth of the waterway but also by the finite width of the waterway. By means of the strip theory synthesis, it is possible to estimate the effect of the restricted water on the added mass of a three-dimensional body through considerations of two-dimensional sections. In general, however, the strip theory synthesis overestimates the added mass of a three-dimensional body, because the actual fluid flows around both ends of the three dimensional body.

The three-dimensional nature of the flow around an actual ship becomes more noticeable in shallow water compared with deep water. As a result, the strip theory synthesis gives an overestimation of the effect of the shallow water on the added mass. Consequently, it is necessary to correct the result of the strip theory synthesis by taking account of the three-dimensional nature of the flow [1].

Needless to say, it is possible to calculate directly the added mass of a three-dimensional body by means of an adequate three-dimensional method. In particular, when we want to obtain an accurate estimate of the added mass of a three-dimensional body, we must use a three-dimensional calculation. However, the two-dimensional calculation can reveal the effect of the restricted water on the added mass without losing the essential nature of the effects.

Therefore, in what follows, the effect of the restricted waters on the added mass will be discussed on the basis of the numerical values of the added mass obtained by a two-dimensional calculation method which is called the hypercircle method. To be more precise, the aim of this paper is to investigate the applicability of the hypercircle method to computation of the added mass of a two-dimensional body moving in a restricted channel and to compare the numerical values of the added mass obtained by the hypercircle method with those obtained by other methods.

At present, there exist some numerical methods which are preferably used to solve the boundary

value problem related to the fluid motion. For example, the representation of the velocity potential function through distribution of singularities as source and sink is one of the orthodox methods. Also, a purely numerical method, the finite element method, has been highly developed with appearance of large and high speed digital computers. By means of those methods, we can easily calculate the added mass of a body having an arbitrary shape. However, it must be noted that most of the numerical methods give only an approximate estimate of the added mass. In most cases, we cannot know to what extent the approximate value obtained represents the exact value, or in other words, whether the approximate value is larger or smaller than the exact value. This is an inevitable question which hangs over most of the existing numerical solutions.

On the other hand, relying on the hypercircle method, it is possible to fix the limits of the exact value by obtaining both an upper bound and a lower bound. In this sense, the hypercircle method does not give the exact solution itself.

However, if we can make both bounds approach closely one another, either the upper bound or the lower bound can be considered as an approximate value of the exact solution. Furthermore, the nature of such an approximate solution is definite, because the approximate solution will always be larger or smaller than the exact solution, depending upon whether the approximate solution is an upper bound or a lower bound.

This fact is the biggest advantage that the hypercircle method has over most of the other numerical methods.

This paper deals with the effect of the restricted waters on the added mass of a "rectangular" cylinder moving on a free surface of a "rectangular" channel, partly because the rectangular body-form is regarded as representative of the main part of an actual ship hull and partly because it is easy to obtain the analytical representation for the various kinds of the scalar products. In principle, the hypercircle method is applicable for any arbitrary geometrical form. The frequency of motion of the cylinder is either zero or infinite. That is to say, the former is concerned with the manoeuvring motion and the lat-

ter is concerned with the ship's hull vibration. As well known, in both cases, the added mass of the body can be obtained by determining the kinetic energy of the fluid surrounding the body.

The mathematical background of the hypercircle method is fully treated in Synge's textbook [2], but has not been widely adopted by naval architects. Therefore, the author 'dares' to describe the mathematical background at the beginning of the next section.

Finally, it should be pointed out that this paper is based on the author's previously published papers [3], [4] and [5].

#### CALCULATION OF THE SWAY ADDED MASS OF A RECTANGULAR CYLINDER TRANSLATING IN A RECTANGULAR CHANNEL

##### Mathematical Background of the Hypercircle Method

On the assumption that the frequency of motion has a value equal to either zero or infinity, the free surface is considered as a rigid surface or an equipotential surface. In these cases, the velocity potential function is given as a solution of a boundary value problem formulated as follows:

$$\frac{\partial^2 \phi}{\partial y^2} + \frac{\partial^2 \phi}{\partial z^2} = 0 \quad \text{in the fluid domain } S \quad (1)$$

$$\frac{\partial \phi}{\partial n} = g(s) \quad \text{on a part of the boundary } \Gamma_1 \quad (2)$$

$$\phi = f(s) \quad \text{on the remaining part of the boundary } \Gamma_2 \quad (3)$$

where  $g(s)$  and  $f(s)$  are known functions, whose values are fixed on the boundary of the fluid. Now, we introduce two vector spaces as follows:

(I) complementary vector space  $\Pi(p_1, p_2)$ : This is a vector space of which any vector has two components  $p_1$  and  $p_2$  defined by the equations (4) and (5).

$$\frac{\partial p_1}{\partial y} + \frac{\partial p_2}{\partial z} = 0 \quad \text{in the domain } S \quad (4)$$

$$p_1 \frac{\partial y}{\partial n} + p_2 \frac{\partial z}{\partial n} = g(s) \quad \text{on the boundary } \Gamma_1 \quad (5)$$

(II) associated vector space  $\Omega(q_1, q_2)$ : This is a vector space, of which any vector has two components,  $q_1$  and  $q_2$ , defined as the first partial derivatives of an arbitrary function  $\phi$  which satisfies the boundary condition  $\phi=f(s)$  on the boundary  $\Gamma_2$ ;

$$q_1 = \frac{\partial \phi}{\partial y}, q_2 = \frac{\partial \phi}{\partial z} \quad (6)$$

where  $\phi=f(s)$  on the boundary  $\Gamma_2$ .

From the definition of these two spaces, it is self-evident that the common vector,  $R=(r_1, r_2)$ , of two spaces defined above, if obtained, is the exact solution of the boundary value problem at hand, formulated by the equations (1) to (3). It is not so easy to obtain the common vector, or in other words, the exact solution of the boundary value problem. Hence, instead of the exact solution, we shall obtain an approximate solution as follows: To begin with, we introduce two homogeneous vector spaces by replacing the non-homogeneous boundary conditions on  $\Gamma_1$  and  $\Gamma_2$  with the homogeneous ones.

(III) homogeneous complementary vector space  $\Pi^*(p^*_1, p^*_2)$ : Two components,  $p^*_1$  and  $p^*_2$ , of a vector belonging to this space satisfy the following equations:

$$\frac{\partial p^*_1}{\partial y} + \frac{\partial p^*_2}{\partial z} = 0 \quad \text{in the domain } S \quad (7)$$

$$p^*_1 \frac{\partial y}{\partial n} + p^*_2 \frac{\partial z}{\partial n} = 0 \quad \text{on the boundary } \Gamma_1 \quad (8)$$

In what follows, we describe a vector of this space as  $I_i$  vector with the variable subscript  $i$ , i.e.,  $I_i=(p^*_{i1}, p^*_{i2})$ . Needless to say, two components,  $p^*_{i1}$  and  $p^*_{i2}$ , must satisfy the equations (7) and (8).

(IV) homogeneous associated vector space  $\Omega^*(q^*_1, q^*_2)$ : Two components,  $q^*_{k1}$  and  $q^*_{k2}$ , of a vector belonging to this space which is denoted as  $J_k$ , i.e.,  $J_k=(q^*_{k1}, q^*_{k2})$  with the subscript  $k$  being varied, are defined as follows:

$$q^*_{k1} = \frac{\partial \phi^*_k}{\partial y}, q^*_{k2} = \frac{\partial \phi^*_k}{\partial z} \quad (9)$$

where an arbitrary function  $\phi^*_k$  should be zero on the boundary  $\Gamma_2$ .

##### NOMENCLATURE

$a, b, c, d$  : size parameters of a rectangular cylinder and a rectangular channel (see Figure 1)  
 $a_1, a_2$  : parameters to fix an off-center position of a cylinder (see Figure 5)  
 $a_1, b_k$  : constant coefficients  
 $B$  : breadth of a cylinder  
 $I_i$  : homogeneous complementary vector,  $I_i=(p^*_{i1}, p^*_{i2})$   
 $J_k$  : homogeneous associated vector,  $J_k=(q^*_{k1}, q^*_{k2})$   
 $m$  : mass of a cylinder with the same density as that of the surrounding fluid  
 $m_y$  : added mass in y-axis  
 $m_z$  : added mass in z-axis

$m(m'), n(n')$  : integers to define the subscript  $k(k')$  or  $i(i')$  of vectors  
 $n$  : unit inner normal  
 $p$  : complementary vector,  $p=(p_1, p_2)$   
 $\bar{p}$  : a vector of complementary space,  $\bar{p}=(\bar{p}_1, \bar{p}_2)$   
 $q$  : associated vector,  $q=(q_1, q_2)$   
 $\bar{q}$  : a vector of associated space,  $\bar{q}=(\bar{q}_1, \bar{q}_2)$   
 $R$  : common vector of complementary space and associated space,  $R=(r_1, r_2)$   
 $R_{\Pi}, R_{\Omega}$  : arbitrary vectors of complementary space and associated space respectively  
 $W$  : channel width

[To be continued to the bottom of the next page.]

Then, we define  $p$  vector as the linear combination of  $\bar{p}$  vector and  $I_i$ 's vectors as follows:

$$p = \bar{p} + \sum_{i=1}^N a_i I_i \quad (10)$$

where  $\bar{p}$  vector is an arbitrary vector of the  $\Pi$  space.

Similarly,  $q$  vector is defined as follows:

$$q = \bar{q} + \sum_{k=1}^M b_k J_k \quad (11)$$

where  $\bar{q}$  vector is an arbitrary vector of the  $\Omega$  space.

Here, it should be noted that the coefficients  $a_i$ 's and  $b_k$ 's are constant but are still unknown. It

is obvious from the above-stated definitions that  $p$  and  $q$  belong to the  $\Pi$  and  $\Omega$  spaces respectively.

Now, we introduce the so-called Dirichlet scalar product into the vector spaces defined above. The scalar product of two vectors, of which each is lying in  $\Pi$  and  $\Omega$  spaces respectively, that is to say, the scalar product of two vectors  $I_i$  and  $J_k$  of the  $\Pi^*$  and  $\Omega^*$  spaces respectively, is

$$(I_i, J_k) = \iint_S (p_{i1}^* q_{k1}^* + p_{i2}^* q_{k2}^*) dS \\ = \iint_S (p_{i1}^* \frac{\partial \phi_k^*}{\partial y} + p_{i2}^* \frac{\partial \phi_k^*}{\partial z}) dS \quad (12)$$

Assuming that both  $p_{i1}^* \phi_k^*$  and  $p_{i2}^* \phi_k^*$  are continuously differentiable in the domain  $S$ , we can transform the above surface integral into a line integral along the whole boundary of the domain and another surface integral as follows:

$$(I_i, J_k) = - \iint_S (\frac{\partial p_{i1}^*}{\partial y} + \frac{\partial p_{i2}^*}{\partial z}) \phi_k^* dS \\ - \int_{\Gamma_1 + \Gamma_2} (p_{i1}^* \frac{\partial \phi_k^*}{\partial n} + p_{i2}^* \frac{\partial \phi_k^*}{\partial n}) \phi_k^* ds = 0 \quad (13)$$

This equation says that two spaces,  $\Pi$  and  $\Omega$ , are orthogonal to one another. Furthermore, it is clear from the previous definitions that they are linear subspaces. It is useful to recall that two orthogonal linear subspaces cannot intersect in more than one point [2]. On the basis of this fact, we can obtain some important inequalities with respect to the squared scalar product.

Let  $R_\Pi$  and  $R_\Omega$  be arbitrary vectors in  $\Pi$  and  $\Omega$  spaces respectively, then

$$(R_\Pi - R_\Omega)^2 = (R_\Pi - R)^2 + (R - R_\Omega)^2 \quad (14)$$

since the scalar product,  $(R_\Pi - R, R - R_\Omega)$  vanishes because of the orthogonality of  $\Pi$  and  $\Omega$  spaces. From the equation (14), we immediately obtain the following inequalities;

$$(R_\Pi - R_\Omega)^2 \geq (R_\Pi - R)^2 \quad (15)$$

$$(R_\Pi - R_\Omega)^2 \geq (R_\Omega - R)^2 \quad (16)$$

These inequalities imply that if we want to let  $R_\Pi$  or  $R_\Omega$  approach the exact solution  $R$  of our problem, we have to minimize the squared distance  $(R_\Pi - R_\Omega)^2$ .

Applying this minimum principle to the  $p$  and  $q$  vectors, it is possible to determine the unknown coefficients  $a_i$ 's and  $b_k$ 's so that the  $p$  and  $q$  vectors may approach the exact solution;

$$(p-q)^2 = (\bar{p}-\bar{q})^2 + (\sum_{i=1}^N a_i I_i - \sum_{k=1}^M b_k J_k)^2 \\ + 2(\bar{p}-\bar{q}, \sum_{i=1}^N a_i I_i - \sum_{k=1}^M b_k J_k) \\ = (\bar{p}-\bar{q} + \sum_{i=1}^N a_i I_i)^2 + (\bar{p}-\bar{q} - \sum_{k=1}^M b_k J_k)^2 - (\bar{p}-\bar{q})^2 \quad (17)$$

Since the last term of the right-hand side has a fixed value, it is sufficient to minimize the first and the second terms. Differentiating partially the first and the second terms with respect to the unknown coefficients  $a_i$ 's and  $b_k$ 's, and then equating them to zero, the conditions necessary to minimize these terms are as follows:

$$(\bar{p}-\bar{q} + \sum_{i=1}^N a_i I_i, I_j) = 0 \quad (j=1, 2, \dots, N) \quad (18)$$

$$(-\bar{p}-\bar{q} + \sum_{k=1}^M b_k J_k, J_l) = 0 \quad (l=1, 2, \dots, M) \quad (19)$$

These equations infer that we can determine the unknown coefficients  $a_i$ 's and  $b_k$ 's independently on one another by solving the linear algebraic equations (18) and (19).

From now on, we assume that the  $p$  and  $q$  vectors have the coefficients  $a_i$ 's and  $b_k$ 's satisfying the equations (18) and (19).

Then,

$$(R-\bar{p})^2 = (R-p+p-\bar{p})^2 \\ = (R-p)^2 + (p-\bar{p})^2 + 2(R-p, p-\bar{p}) \quad (20)$$

On the other hand,

$$0 = (R-q, I_1) = (R-p+p-q, I_1) = (R-p, I_1) + (p-q, I_1) \\ = (R-p, I_1) \quad (21)$$

Therefore, the equation (20) becomes

#### NOMENCLATURE (Continued from Page 2)

$y, z$	: coordinate axes
$y_{10}, y_{11}, y_{12}$	: coordinates of the four corners and a grid-point of $i$ -th basic unit (see Figure 2)
$z_{10}, z_{11}, z_{12}$	: constant coefficients in the linear representation of homogeneous complementary vector
$\alpha_{10}, \alpha_{11}, \alpha_{12}$	: clearance between the channel wall and the moving body.
$\beta_{10}, \beta_{11}, \beta_{12}$	: distance between the body-center and the channel-

$\Pi$	: center
$\Pi^*$	: complementary vector space
$\phi$	: homogeneous complementary vector space
$\phi^*$	: velocity potential function
$\psi$	: arbitrary function satisfying $\phi^*=0$ on the given boundary
$\psi^*$	: stream function
$\omega$	: arbitrary function satisfying $\psi^*=0$ on the given boundary
$\Omega$	: frequency of the motion
$\Omega^*$	: associated vector space
	: homogeneous associated vector space



$(\bar{p}-\bar{p})^2 = (R-\bar{p})^2 + (\bar{p}-\bar{p})^2$  (22)  
Combining this equation with the inequality (15), we obtain

$$(\bar{p}-\bar{p})^2 \leq (R-\bar{p})^2 \leq (\bar{p}-\bar{p})^2 + (\bar{p}-q)^2$$
 (23)  
Similarly, we obtain

$(q-\bar{q})^2 \leq (R-\bar{q})^2 \leq (q-\bar{q})^2 + (\bar{p}-q)^2$  (24)  
Furthermore, if we can select the zero-vector as an arbitrary  $\bar{p}$  vector, the inequality (23) becomes simplified. In this case, the right-hand side of the equation (23) reduces to

$$p^2 + (p-q)^2 = (p+q-p)^2 - 2(p, q-p) = q^2$$
 (25)  
Consequently, we finally obtain the simple relationship between the squared vectors, namely,  $R^2$ ,  $p^2$  and  $q^2$ ;

$p^2 \leq R^2 \leq q^2$  (26)  
On the other hand, if we can select the zero-vector as an arbitrary  $\bar{q}$  vector, the inequality (24) reduces to

$$q^2 \leq R^2 \leq p^2$$
 (27)

Here, the squared exact vector,  $R^2$ , of the relevant problem is

$$R^2 = \iint_S (\text{grad} \phi)^2 dS$$
 (28)

Therefore, the inequalities (26) and (27) represent both the upper and the lower bounds of the added mass of a two-dimensional body moving in a restricted channel, assuming that the fluid density is equal to 1.0.

#### The Added Mass of a Rectangular Cylinder Translating in Parallel to the Free Surface in a Rectangular Channel

##### 1. Translation at the Center of the Channel

For simplicity, we shall consider the added mass of a rectangular cylinder translating at unit velocity parallel to the free surface of a rectangular channel and at the center of the channel.

However, as shown in Figure 1 the right-half of the whole domain will be considered. That is to say, the rectangle AGCO is the right-half of the rectangular body, and the rectangle BEDO is the right-half of the rectangular channel. The boundary  $\Gamma_1$  stands for the free surface, which here will be treated as a rigid wall.

The problem to determine the velocity potential function  $\phi$  for this case is formulated as follows:

$$\frac{\partial^2 \phi}{\partial y^2} + \frac{\partial^2 \phi}{\partial z^2} = 0 \quad \text{in the fluid domain } S$$
 (29)

$$\frac{\partial \phi}{\partial n} = \begin{cases} 0 & \text{on the boundaries } \Gamma_1, \Gamma_3, \Gamma_5, \Gamma_6 \\ 1 & \text{on the boundary } \Gamma_2 \end{cases}$$
 (30)

$$\phi = 0 \quad \text{on the boundary } \Gamma_4$$
 (32)

Corresponding to this formulation, we can define the vector spaces  $\Pi$ ,  $\Omega$ ,  $\Pi^*$  and  $\Omega^*$  as follows:

(I)  $\Pi$  space :  $p = (p_1, p_2)$

$$\frac{\partial p_1}{\partial y} + \frac{\partial p_2}{\partial z} = 0 \quad \text{in } S$$
 (33)

$$p \frac{\partial y}{\partial n} + p \frac{\partial z}{\partial n} = \begin{cases} 0 & \text{on } \Gamma_1, \Gamma_3, \Gamma_5, \Gamma_6 \\ 1 & \text{on } \Gamma_2 \end{cases}$$
 (34)

(II)  $\Omega$  space :  $q = (q_1, q_2)$

$$q_1 = \frac{\partial \phi}{\partial y}, q_2 = \frac{\partial \phi}{\partial z}$$
 (36)

where  $\phi$  is an arbitrary function which satisfies

$\phi = 0$  on the boundary  $\Gamma_4$ .

(III)  $\Pi^*$  space :  $I_i = (p^*_{i1}, p^*_{i2}) \quad i=1, 2, \dots$

$$\frac{\partial p^*_{i1}}{\partial y} + \frac{\partial p^*_{i2}}{\partial z} = 0 \quad \text{in } S$$
 (37)

$$p^*_{i1} \frac{\partial y}{\partial n} + p^*_{i2} \frac{\partial z}{\partial n} = 0 \quad \text{on } \Gamma_1, \Gamma_2, \Gamma_3, \Gamma_5, \Gamma_6$$
 (38)

(IV)  $\Omega^*$  space :  $J_k = (q^*_{k1}, q^*_{k2}) \quad k=1, 2, \dots$

$$q^*_{k1} = \frac{\partial \phi^*_k}{\partial y}, q^*_{k2} = \frac{\partial \phi^*_k}{\partial z}$$

where  $\phi^*_k$  is arbitrary except for the restriction that  $\phi^*_k$  must vanish on the boundary  $\Gamma_4$ .

From the above formulation, it is evident that we can select the zero-vector, i.e.,  $0 = (0, 0)$  as an arbitrary  $\bar{q}$  vector of  $\Omega$  space. Consequently, in this problem, a squared  $q$  vector represents a lower bound of the added mass and a squared  $p$  vector represents an upper bound.

First, we will consider the upper bound of the added mass. For this purpose, it is necessary to devise the  $I_i$ 's vector of  $\Pi^*$  space. When we verified the orthogonal character of the linear subspaces  $\Pi$  and  $\Omega$ , we assumed the continuous differentiability of the functions  $p^*_{i1}$  and  $p^*_{i2}$  in the whole fluid domain. However, we can relax this restriction, because the orthogonal character of  $\Pi$  and  $\Omega$  spaces, which is all that we need when constructing the hypercircle method, is satisfied under a weaker restriction of the continuous differentiability (for detail, refer to Synge's textbook [2], pp. 136~137), which here will be called the "permissible discontinuity".

Now, we devise the  $I_i$ 's vectors concretely. To begin with, we divide the whole fluid domain  $S$  of Figure 1 into a net of rectangular meshes as shown in Figure 1. Considering any four meshes which possess one grid-point in common as a basic unit (Figure 2), we define the  $I_i$  vector as follows: the subscript  $i$  stands for the  $i$ -th grid-point, and the  $I_i$  vector vanishes outside the  $i$ -th basic unit which consists of four rectangular meshes possessing the  $i$ -th grid-point in common. In order to solve a system of linear algebraic equations, for instance the equation (18), we need to know the values of the scalar products  $(p, I_i)$  and  $(I_i, I_j)$  in advance.

For this purpose, it is better to define the  $I_i$ 's vectors in as simple a form as possible to easily compute those scalar products. Here, we adopt the following linear representations;

$$p^*_{i1} = \alpha_{i1} y + \alpha_{i2} z + \alpha_{i0}$$
 (39)

$$p^*_{i2} = \beta_{i1} y + \beta_{i2} z + \beta_{i0}$$
 (40)

where  $\alpha_{i0}$ ,  $\alpha_{i1}$ ,  $\alpha_{i2}$ ,  $\beta_{i0}$ ,  $\beta_{i1}$  and  $\beta_{i2}$  are constant but are not yet known.

Taking account of the permissible discontinuity, these constants are uniquely determined. The vector components  $p^*_{i1}$  and  $p^*_{i2}$  which are defined below, are obtained by normalizing the equations (39) and (40) by dividing them with the factor  $(y_{i1} - y_{i0})$  (refer to Figure 2) [3];

$$a) \text{ mesh } \textcircled{1} \quad p^*_{i1} = \frac{y - y_{i1}}{y_{i0} - y_{i1}}, p^*_{i2} = \frac{-(z - z_{i1})}{y_{i0} - y_{i1}}$$
 (41)

$$b) \text{ mesh } \textcircled{2} \quad p^*_{i1} = \frac{-(y - y_{i2})}{y_{i2} - y_{i0}}, p^*_{i2} = \frac{z - z_{i1}}{y_{i2} - y_{i0}}$$
 (42)

$$c) \text{ mesh } \textcircled{3} \quad p^*_{i1} = \frac{(z_{i0} - z_{i1})(y - y_{i1})}{(y_{i0} - y_{i1})(z_{i0} - z_{i2})}$$

$$p^*_{12} = \frac{-(z_{10}-z_{11})(z-z_{12})}{(y_{10}-y_{11})(z_{10}-z_{12})} \quad (43)$$

$$\text{d) mesh } \textcircled{4} \quad p^*_{11} = \frac{(z_{10}-z_{11})(y-y_{12})}{(y_{10}-y_{12})(z_{10}-z_{12})} \\ p^*_{12} = \frac{-(z_{10}-z_{11})(z-z_{12})}{(y_{10}-y_{12})(z_{10}-z_{12})} \quad (44)$$

where  $y_{10}$ ,  $y_{11}$ ,  $y_{12}$ ,  $z_{10}$ ,  $z_{11}$  and  $z_{12}$  are the coordinates of the four corners and the grid-point of the  $i$ -th basic unit.

Next, we select a  $\bar{p}$  vector which is an arbitrary vector of  $\Pi$  space as follows (refer to Figure 1):

$$\text{a) domain AGFB } \bar{p}_1 = \frac{b-y}{b-a}, \bar{p}_2 = \frac{z}{b-a} \quad (45)$$

$$\text{b) domain GHEF } \bar{p}_1 = \frac{c(b-y)}{(b-a)(c-d)}, \bar{p}_2 = \frac{c(z-d)}{(b-a)(c-d)} \quad (46)$$

$$\text{c) domain CDHG } \bar{p}_1 = \frac{c}{c-d}, \bar{p}_2 = 0 \quad (47)$$

where  $a$ ,  $b$ ,  $c$  and  $d$  are the abscissas or the ordinates of the points A, B, C and D, representing the half-width of the body, the half-width of the channel, the depth of the body and the depth of the channel respectively.

From the above definitions of the  $I_i$ 's vectors, it is easily understood that most of the scalar products  $(I_i, I_j)$  ( $i, j=1, 2, \dots, N$ ) vanish. For example, for the basic unit with the subscript  $i$  equal to 10, are zero the scalar products except for  $(I_2, I_{10})$ ,  $(I_3, I_{10})$ ,  $(I_4, I_{10})$ ,  $(I_9, I_{10})$ ,  $(I_{10}, I_{10})$ ,  $(I_{10}, I_{11})$ ,  $(I_{10}, I_{18})$ ,  $(I_{10}, I_{19})$  and  $(I_{10}, I_{20})$ . The non-zero values of the other scalar products can be computed by either of the following formulas (see Figure 3).

a) in case where the meshes  $\textcircled{2}$  and  $\textcircled{4}$  of the  $i$ -th basic unit overlap the meshes  $\textcircled{1}$  and  $\textcircled{3}$  of the  $j$ -th basic unit respectively;

$$(I_i, I_j) = \frac{(z_{11}-z_{10})(z_{11}-z_{12})}{6(z_{10}-z_{12})(y_{12}-y_{10})} \times \\ [(y_{12}-y_{10})^2 - 2(z_{11}-z_{10})(z_{10}-z_{12})] \quad (48)$$

b) in case where the mesh  $\textcircled{4}$  of the  $i$ -th basic unit overlaps the mesh  $\textcircled{1}$  of the  $j$ -th basic unit;

$$(I_i, I_j) = \frac{(z_{10}-z_{11})}{6(y_{12}-y_{10})} [(y_{12}-y_{10})^2 + (z_{10}-z_{12})^2] \quad (49)$$

c) in case where the meshes  $\textcircled{3}$  and  $\textcircled{4}$  of the  $i$ -th basic unit overlap the meshes  $\textcircled{1}$  and  $\textcircled{2}$  of the  $j$ -th basic unit respectively;

$$(I_i, I_j) = \frac{(z_{11}-z_{10})(y_{12}-y_{11})}{6(y_{10}-y_{11})(y_{12}-y_{10})} \times \\ [(z_{10}-z_{12})^2 - 2(y_{10}-y_{11})(y_{12}-y_{10})] \quad (50)$$

d) in case where the mesh  $\textcircled{3}$  of the  $i$ -th basic unit overlaps the mesh  $\textcircled{2}$  of the  $j$ -th basic unit;

$$(I_i, I_j) = \frac{z_{10}-z_{11}}{6(y_{10}-y_{11})} [(y_{10}-y_{11})^2 + (z_{10}-z_{12})^2] \quad (51)$$

e) the scalar product of the  $i$ -th basic unit itself;

$$(I_i, I_i) = \frac{(z_{11}-z_{10})(z_{11}-z_{12})(y_{12}-y_{11})}{3(z_{10}-z_{12})(y_{10}-y_{11})(y_{12}-y_{10})} \times$$

$$[(y_{10}-y_{11})(y_{12}-y_{10}) + (z_{11}-z_{10})(z_{10}-z_{12})] \quad (52)$$

Then, the scalar product  $(\bar{p}, I_i)$  is computed as follows: If the  $i$ -th basic unit is included entirely inside the domain AGFB or the domain GHEF or the domain CDHG, the scalar product  $(\bar{p}, I_i)$  vanishes, being proved directly through a manipulation of integration. For instance, the scalar products,  $(\bar{p}, I_1)$ ,  $(\bar{p}, I_{15})$  and  $(\bar{p}, I_{17})$  in Figure 1 vanish. The non-zero value of the scalar product  $(\bar{p}, I_i)$  occurs in case where the grid-point is located just on the line GF or GH. In case of Figure 1, for example, the scalar product  $(\bar{p}, I_i)$  provides a non-zero value for  $i=8, 9, 10, 11, 12, 13, 14, 16, 25$  and 34.

a) in case where the grid-point of the  $i$ -th basic unit is located on the line GF;

$$(\bar{p}, I_i) = \frac{d(z_{11}-z_{10})(y_{12}-y_{11})(y_{10}+y_{11}+y_{12}-3b)}{6(b-a)(c-d)} \quad (53)$$

b) in case where the grid-point of the  $i$ -th basic unit is located on the line GH;

$$(\bar{p}, I_i) = \frac{-c(z_{11}-z_{10})(z_{11}-z_{12})(z_{10}+z_{11}+z_{12}-3d)}{6(b-a)(c-d)} \quad (54)$$

From the formulas (48) to (54), we can compute immediately the scalar products which are necessary to solve a set of the simultaneous linear algebraic equations of the unknown coefficients  $a_i$ 's, if only the geometrical sizes of the rectangular body and the rectangular channel are given. Once the simultaneous equations (18) are solved, the upper bound of the added mass  $p^2$  can be computed easily.

Next, we consider the lower bound of the added mass. We have devised the  $I_i$ 's vectors by taking account of the permissible discontinuity. In fact, the component tangential to a boundary between two adjacent meshes is discontinuous, while the other component, namely the component normal to a boundary is continuous across the boundary. In this circumstance, the function  $\phi_k^*$  must be continuous in the whole domain in order to keep the orthogonality of  $\Pi$  and  $\Omega$  spaces. Needless to say, the function  $\phi_k^*$  must satisfy the condition that  $\phi_k^*$  vanishes on the boundary  $\Gamma_4$ . Except for these restrictions, the function  $\phi_k^*$  may be arbitrary. In what follows, we use a  $\phi_k^*$  function defined as follows:

$$\phi_k^* = 2b \sin \frac{(2n+1)\pi y}{2b} \cos \frac{m\pi z}{d} \quad n, m=0, 1, 2, \dots \quad (55)$$

where the subscript  $k$  is defined by

$$k = \frac{n(n+1)}{2} + n \cdot m + \frac{m(m+3)}{2} + 1 \quad (56)$$

The equation (56) infers that if the integers,  $n$  and  $m$ , are varied in such a manner as shown in Table 1, the subscript  $k$  increases one by one. From the function  $\phi_k^*$  of the equation (55), two components of the  $J_k$  vector are defined as follows:

$$q^*_{k1} = (2n+1)\pi \cos \frac{(2n+1)\pi y}{2b} \cos \frac{m\pi z}{d} \quad (57)$$

$$q^*_{k2} = -\frac{2bm\pi}{d} \sin \frac{(2n+1)\pi y}{2b} \sin \frac{m\pi z}{d} \quad (58)$$

In order to determine the coefficients  $b_i$ 's of the equation (11), we need the numerical values of the scalar products  $(J_k, J_l)$  and  $(\bar{p}, J_l)$  for  $k, l=1, 2, \dots, M$ . The  $J_l$  vector is also devised in the same way as the  $J_k$  vector has been obtained;

$$q^*_{l1} = (2n'+1)\pi \cos \frac{(2n'+1)\pi y}{2b} \cos \frac{m'\pi z}{d} \quad (59)$$

$$q^*_{l2} = -\frac{2bm'\pi}{d} \sin \frac{(2n'+1)\pi y}{2b} \sin \frac{m'\pi z}{d} \quad (60)$$

where the subscript  $\ell$  is defined by

$$\ell = \frac{n'(n'+1)}{2} + n'm' + \frac{m'(m'+3)}{2} + 1 \quad (61)$$

Table 1. Variation of the Subscript  $k$  by a Systematic Change of the Integers  $n$  and  $m$ .

$m \backslash n$	0	1	2	3	4	5
0	1	2	4	7	11	16
1	3	5	8	12	17	
2	6	9	13			
3	10	14				
4	15					

After manipulation of integration, we obtain the analytical formulas of the scalar products  $(J_k, J_\ell)$  and  $(\bar{p}, J_\ell)$  for the various cases of the integer  $n$ ,  $n'$ ,  $m$  and  $m'$ , which are tabulated in Table 2.

Table 2. The Scalar Products  $(J_k, J_\ell)$  and  $(\bar{p}, J_\ell)$  for the Lateral Translation of a Rectangular Cylinder at the Center of a Channel

a)  $n \neq n', m \neq m'$ :

$$(J_k, J_\ell) = \frac{(2n+1)(2n'+1)bd}{4} \left[ \frac{1}{n-n'} \sin \frac{(n-n')\pi a}{b} + \frac{1}{n+n'+1} \sin \frac{(n+n'+1)\pi a}{b} \right] \left[ \frac{1}{m-m'} \sin \frac{(m-m')\pi c}{d} + \frac{1}{m+m'} \sin \frac{(m+m')\pi c}{d} \right] + \frac{m m' b^3}{d} \left[ \frac{1}{n-n'} \sin \frac{(n-n')\pi a}{b} - \frac{1}{n+n'+1} \sin \frac{(n+n'+1)\pi a}{b} \right] \left[ \frac{1}{m-m'} \sin \frac{(m-m')\pi c}{d} - \frac{1}{m+m'} \sin \frac{(m+m')\pi c}{d} \right]$$

b)  $n \neq n', m = m' \neq 0$ :

$$(J_k, J_\ell) = \frac{(2n+1)(2n'+1)bd}{4} \left[ \frac{1}{n-n'} \sin \frac{(n-n')\pi a}{b} + \frac{1}{n+n'+1} \sin \frac{(n+n'+1)\pi a}{b} \right] \left[ \frac{c\pi}{d} + \frac{1}{2m} \sin \frac{2m\pi c}{d} \right] + \frac{m^2 b^3}{d} \left[ \frac{1}{n-n'} \sin \frac{(n-n')\pi a}{b} - \frac{1}{n+n'+1} \sin \frac{(n+n'+1)\pi a}{b} \right] \left[ \frac{c\pi}{d} - \frac{1}{2m} \sin \frac{2m\pi c}{d} \right]$$

c)  $n \neq n', m = m' = 0$ :

$$(J_k, J_\ell) = \frac{(2n+1)(2n'+1)bc\pi}{2} \left[ \frac{1}{n-n'} \sin \frac{(n-n')\pi a}{b} + \frac{1}{n+n'+1} \sin \frac{(n+n'+1)\pi a}{b} \right]$$

d)  $n = n', m \neq m'$ :

$$(J_k, J_\ell) = \frac{(2n+1)^2 bd}{4} \left[ \frac{a\pi}{b} + \frac{1}{2n+1} \sin \frac{(2n+1)\pi a}{b} \right] \left[ \frac{1}{m-m'} \sin \frac{(m-m')\pi c}{d} + \frac{1}{m+m'} \sin \frac{(m+m')\pi c}{d} \right] + \frac{m m' b^3}{d} \left[ \frac{a\pi}{b} - \frac{1}{2n+1} \sin \frac{(2n+1)\pi a}{b} \right] \left[ \frac{1}{m-m'} \sin \frac{(m-m')\pi c}{d} - \frac{1}{m+m'} \sin \frac{(m+m')\pi c}{d} \right]$$

e)  $n = n', m = m' \neq 0$ :

$$(J_k, J_\ell) = -\frac{(2n+1)^2 \pi^2 bd}{4} + \frac{(2n+1)^2 bd}{4} \left[ \frac{a\pi}{b} + \frac{1}{2n+1} \sin \frac{(2n+1)\pi a}{b} \right] \left[ \frac{c\pi}{d} + \frac{1}{2m} \sin \frac{2m\pi c}{d} \right] - \frac{m^2 \pi^2 b^3}{d} + \frac{m^2 b^3}{d} \left[ \frac{a\pi}{b} - \frac{1}{2n+1} \sin \frac{(2n+1)\pi a}{b} \right] \left[ \frac{c\pi}{d} - \frac{1}{2m} \sin \frac{2m\pi c}{d} \right]$$

f)  $n = n', m = m' = 0$ :

$$(J_k, J_\ell) = -\frac{(2n+1)^2 \pi^2 bd}{2} + \frac{(2n+1)^2 \pi bc}{2} \left[ \frac{a\pi}{b} + \frac{1}{2n+1} \sin \frac{(2n+1)\pi a}{b} \right]$$

a)  $m' \neq 0$

$$(\bar{p}, J_\ell) = \frac{bd^2}{(b-a)(c-d)m'\pi} \sin \frac{m'\pi c}{d} \left[ -2(b-a) \sin \frac{(2n'+1)\pi a}{2b} + \frac{4b}{(2n'+1)\pi} \cos \frac{(2n'+1)\pi a}{2b} \right] + \frac{2bcd}{m'\pi(c-d)} \sin \frac{(2n'+1)\pi a}{2b} \sin \frac{m'\pi c}{d} - \frac{4b^2 d^2}{(2n'+1)m'\pi^2(b-a)(c-d)} \cos \frac{(2n'+1)\pi a}{2b} \sin \frac{m'\pi c}{d}$$

b)  $m' = 0$

$$(\bar{p}, J_\ell) = 2bc \sin \frac{(2n'+1)\pi a}{2b}$$

From those formulas, we can compute all the scalar products required to solve a system of simultaneous algebraic equations (19). Once the unknown coefficients  $b_k q^2$  are solved, the lower bound of the added mass  $q^2$  can be computed immediately.

In Table 3 are shown some numerical examples of the upper and the lower bounds of the sway added mass of a rectangular cylinder whose width/draft ratio is equal to 2, translating at the center of a

channel. The upper bounds shown in this table were obtained by dividing the whole fluid domain as follows: The vertical intervals between the water surface and the bottom of the body, and between the bottom of the body and the bottom of the channel were divided into  $m_1$  and  $m_2$  pieces of equal parts respectively. Furthermore, the lateral intervals between the center of the body and the side of the body, and between the side of the body and the wall of the channel were divided into  $n_1$  and  $n_2$  pieces of equal parts respectively.

For instance, in case of Figure 1,  $m_1=2$ ,  $m_2=4$ ,  $n_1=2$  and  $n_2=8$ . The total number of the grid-points used at the computation of which the results are shown in Table 3, are about 190. However, in case where the fluid domain is narrow, we can considerably reduce the total number of the grid-points. For instance, in case of  $a=2.0$ ,  $b=2.2$ ,  $c=-2.0$  and  $d=-2.2$ , the upper bound obtained by using only 18 grid-points is 55.96, compared with 55.80 in Table

3.

On the other hand, the lower bounds were obtained as follows: the lower bound  $q^2$  was calculated for every value of the parameter  $k$  defined by the equation (56). When the difference between the  $k$ -th lower bound and the  $(k+1)$ -th lower bound became small enough, the process of increasing the parameter  $k$  was stopped, and the  $(k+1)$ -th lower bound was adopted as the expected lower bound. At the



calculation, of which the results are shown in Table 3, the final value of the parameter  $k$  was at most 80 to 100.

From Table 3, it can be understood that the accuracy of the upper bounds becomes less as the fluid domain becomes larger. Also, the accuracy of the lower bounds becomes less with the expansion of the fluid domain, although it is not as bad as the accuracy of the upper bounds. In the same table are also tabulated a few numerical examples of the

On the other hand, Lewis [8] and Wendel [9] computed the vertical added mass of a rectangular cylinder oscillating with infinite frequency and in the perpendicular direction to the free surface of infinite fluid. This kind of added mass can be considered as the sway added mass of the cylinder translating horizontally along the free surface of infinite fluid, if the roles of the side wall and the bottom surface of the rectangular cylinder are interchanged into one another. According to Lewis and Wendel, the sway added mass coefficient of a rectan-

Table 3. Added Mass Coefficients  $m_y/m$  of a Rectangular Cylinder (breadth/draft=2) Moving in a Rectangular Channel

a	b	c	d	horizontal translation		horizontal oscillation	
				upper bound	lower bound	lower bound	
2.0	2.1	-2.0	-2.1	27.27	26.68	4.191	(4.095)
.	2.2	.	-2.2	13.95	13.64	2.133	
.	2.4	.	-2.4	7.290	7.203	1.121	
.	2.6	.	-2.6	5.085	4.920	0.7985	
.	3.0	.	-3.0	3.342	3.253	0.5613	(0.5513)
.	3.6	.	-3.6	2.397	2.303	—	
.	5.0	.	-5.0	1.719	1.565	0.3845	(0.3858)
.	7.0	.	-7.0	1.472	1.294	0.3701	
.	10.0	.	-10.0	1.402	1.152	0.3512	(0.3620)
2.0	2.1	-2.0	-3.0	10.09	9.580	2.318	(1.871)
.	2.2	.	.	6.370	6.075	1.401	
.	2.4	.	.	4.440	4.248	0.8955	
.	2.6	.	.	3.805	3.675	0.7128	
.	3.0	.	.	3.342	3.253	0.5613	
.	3.6	.	.	3.160	3.060	—	
.	5.0	.	.	3.105	2.973	0.4209	(2.98)
.	7.0	.	.	3.112	2.935	0.4102	
.	10.0	.	.	3.137	2.895	0.4046	(2.95)
2.0	2.2	-2.0	-2.1	24.04	23.46	2.535	
.	.	.	-2.2	13.95	13.64	2.133	
.	.	.	-2.4	9.030	8.845	1.743	
.	.	.	-2.6	7.488	7.233	1.564	
.	.	.	-3.0	6.372	6.078	1.402	
.	.	.	-3.6	5.870	5.410	—	
.	.	.	-5.0	5.690	5.190	1.273	
.	.	.	-7.0	5.847	4.898	1.250	
.	.	.	-10.0	6.285	4.880	1.228	

\* Number in the parentheses is obtained by the finite element method.

sway added mass computed by the finite element method, which are very close to the lower bounds obtained by the hypercircle method. This matter can be inferred from the fact that the finite element method tends to provide an approximate value lower than the exact value [6], though this is not always true. Furthermore, the numerical examples listed in the second and the third groups of the table indicate that if the channel width and the water depth are about five times as large as the width and the draft of a body respectively, the effects of the restricted waters on the sway added mass become so small that they can be neglected from the practical point of view (see also Figure 4). Considering the added mass of two-dimensional cylinders vibrating on a free surface, a similar conclusion has been obtained by Matsuura and Kawakami, who examined the propriety of replacing infinite fluid domain with a finite fluid domain bounded by some artificial boundaries when computing the added mass of vibrating cylinders using the finite element method [7]. Therefore, we can consider the lower bound 1.152 in the last line of the first group in Table 3 as an approximate value of the sway added mass coefficient of the rectangular cylinder in infinite water.

gular cylinder with the width/draft ratio being equal to 2, is 1.186 on the assumption that the density of the cylinder is the same as that of surrounding fluid, while the present method provides 1.152 as the lower bound of the sway added mass coefficient.

From these facts, we can conclude that the lower bound obtained by the present method can be considered as a good approximate value of the added mass. Hence, in the following sections, we shall compute only the lower bounds and use them to discuss the effects of the restricted waters on the added mass.

In Figure 4 is shown the sway added mass coefficient of a rectangular cylinder which translates horizontally at the center of the various rectangular channels. The dotted lines drawn in this figure represent Newman's formula

$$\frac{m+m_y}{(m+m_y)_H} = 1 + \left\{ 3 \sum_{n=1}^{\infty} \operatorname{cosech}^2 \frac{\pi}{H} \left( \xi + \frac{W}{2} + nW \right) - 6 \sum_{n=1}^{\infty} \operatorname{cosech}^2 \frac{n\pi W}{H} \right\} \times \left\{ 1 - \frac{(m+m_y)_{\infty}}{(m+m_y)_H} \right\} \quad (62)$$

where the subscripts H and  $\infty$  stand for a finite water depth H and infinite water depth respectively [10]. The virtual mass  $(m+my)_H$  in a finite water depth H has been computed by using the numerical data reported in Flagg and Newman's paper [11]. Comparing the solid lines with the dotted lines, it can be concluded that the present method provides larger values for the wall effect on the sway added mass than the formula (62) does.

In particular, the difference between both lines is remarkable in relatively deeper water. For instance, in case where the water-depth/draft ratio and the channel-width/body-width ratio are 1.50 and 1.05 respectively, the sway added mass coefficient obtained by the present method is 9.43, where formula (62) gives a value of 3.66.

On the other hand, in relatively wider channels, the present method gives a smaller added mass value than formula (62).

At any rate, it can be concluded that the wall effects or the finite width effects on the sway added mass are remarkably small except for extremely narrow channels. Therefore, it is anticipated that the wall effect on the sway added mass of a body translating at an off-center position of a channel will be also small except for an extreme deviation from the centre of the channel.

## 2. Translation at the Off-Center Position of the Channel

In this case, we have to take the whole fluid domain into consideration (see Figure 5). This problem is formulated as follows:

$$\frac{\partial^2 \phi}{\partial y^2} + \frac{\partial^2 \phi}{\partial z^2} = 0 \quad \text{in the fluid domain S} \quad (63)$$

$$\frac{\partial \phi}{\partial n} = \begin{cases} 0 & \text{on the boundaries } \Gamma_1, \Gamma_3, \Gamma_5, \\ & \Gamma_6, \Gamma_7, \Gamma_8 \\ 1 & \text{on the boundary } \Gamma_2 \\ -1 & \text{on the boundary } \Gamma_4 \end{cases} \quad \begin{matrix} (64) \\ (65) \\ (66) \end{matrix}$$

This is the so-called Neumann boundary value problem. However, it is convenient to convert this problem into an equivalent Dirichlet problem. Substituting the velocity potential function  $\phi$  with the stream function  $\psi$ , the equivalent Dirichlet problem is described as follows:

$$\frac{\partial^2 \psi}{\partial y^2} + \frac{\partial^2 \psi}{\partial z^2} = 0 \quad \text{in S} \quad (67)$$

$$\psi = \begin{cases} 0 & \text{on } \Gamma_1, \Gamma_5, \Gamma_6, \Gamma_7, \Gamma_8 \\ z & \text{on } \Gamma_2, \Gamma_4 \\ c & \text{on } \Gamma_3 \end{cases} \quad \begin{matrix} (68) \\ (69) \\ (70) \end{matrix}$$

Since the kinetic energy of the fluid is still expressed by the equation (28), in which the velocity potential function  $\phi$  should be replaced by the stream function  $\psi$ , the inequalities (23), (24), (26) and (27) provide the upper and the lower bounds of the sway added mass. Similarly to the preceding section, we can define  $\Pi$ ,  $\Omega$ ,  $\Pi^*$  and  $\Omega^*$  spaces as follows:

(I)  $\Pi$  space :  $p = (p_1, p_2)$

$$\frac{\partial p_1}{\partial y} + \frac{\partial p_2}{\partial z} = 0 \quad \text{in S} \quad (71)$$

(II)  $\Omega$  space :  $q = (q_1, q_2)$

$$q_1 = \frac{\partial \psi}{\partial y}, \quad q_2 = \frac{\partial \psi}{\partial z} \quad (72)$$

$$\text{where } \psi = \begin{cases} 0 & \text{on } \Gamma_1, \Gamma_5, \Gamma_6, \Gamma_7, \Gamma_8 \\ z & \text{on } \Gamma_2, \Gamma_4 \\ c & \text{on } \Gamma_3 \end{cases} \quad \begin{matrix} (73) \\ (74) \\ (75) \end{matrix}$$

(III)  $\Pi^*$  space :  $I_i = (p_{i1}^*, p_{i2}^*) \quad i=1, 2, \dots$

$$\frac{\partial p_{i1}^*}{\partial y} + \frac{\partial p_{i2}^*}{\partial z} = 0 \quad \text{in S} \quad (76)$$

(IV)  $\Omega^*$  space :  $J_k = (q_{k1}^*, q_{k2}^*) \quad k=1, 2, \dots$

$$q_{k1}^* = \frac{\partial \psi_k^*}{\partial y}, \quad q_{k2}^* = \frac{\partial \psi_k^*}{\partial z}$$

where  $\psi_k^*$  vanishes on the boundaries  $\Gamma_\ell$  ( $\ell = 1, 2, \dots, 8$ ).

In this problem, it is possible to choose the zero-vector as an arbitrary vector of  $\Pi$  space, that is to say,  $p=0=(0,0)$ . Consequently, the added mass can be evaluated by the inequality (26). However, as stated in the preceding section, only the lower bounds will be calculated and used as the approximate values of the sway added mass for discussion of the effect of the restricted waters on the added mass. Hence, it is sufficient to consider the  $\bar{q}$  vector and the  $I_i$ 's vectors.

First of all, we introduce  $\bar{q}$  vector of  $\Omega$  space as follows:

$$\text{a) domain ABIH: } \bar{q}_1 = \frac{z}{a_1-b}, \quad \bar{q}_2 = \frac{y-b}{a_1-b} \quad (77)$$

$$\begin{aligned} \text{b) domain BJGI: } \bar{q}_1 &= \frac{c(z-d)}{(a_1-b)(c-d)} \\ \bar{q}_2 &= \frac{c(y-b)}{(a_1-b)(c-d)} \end{aligned} \quad (78)$$

$$\text{c) domain BCKJ: } \bar{q}_1 = 0, \quad \bar{q}_2 = \frac{c}{c-d} \quad (79)$$

$$\begin{aligned} \text{d) domain CLFK: } \bar{q}_1 &= \frac{c(z-d)}{(a_2+b)(c-d)} \\ \bar{q}_2 &= \frac{c(y+b)}{(a_2+b)(c-d)} \end{aligned} \quad (80)$$

$$\text{e) domain CDEL: } \bar{q}_1 = \frac{z}{a_2+b}, \quad \bar{q}_2 = \frac{y+b}{a_2+b} \quad (81)$$

It must be noted that two components,  $\bar{q}_1$  and  $\bar{q}_2$ , of  $\bar{q}$  vector defined above are not always continuous across the boundary between two adjacent domains. However, this discontinuity is permissible because of the permissible discontinuity which infers that there may exist discontinuity in the normal derivative  $\partial \psi / \partial n$  across any curve drawn in the domain S, if  $\psi$  function satisfying the conditions (73) to (75) is continuous in the domain S [2]. Taking account of this permissible discontinuity, we have defined the above-stated  $\bar{q}$  vector as the first partial derivatives of  $\psi$  functions which are continuous in the whole fluid domain S;

$$\text{a) domain ABIH: } \psi = \frac{z(y-b)}{a_1-b} \quad (82)$$

$$\text{b) domain BJGI: } \psi = \frac{c(y-b)(z-d)}{(a_1-b)(c-d)} \quad (83)$$

$$\text{c) domain BCKJ: } \psi = \frac{c(z-d)}{c-d} \quad (84)$$

$$\text{d) domain CLFK: } \psi = \frac{c(y+b)(z-d)}{(a_2+b)(c-d)} \quad (85)$$

$$\text{e) domain CDEL: } \psi = \frac{z(y+b)}{a_2+b} \quad (86)$$

Next, we shall devise the  $I_1$ 's vectors satisfying the equation (76), which must be continuous in the whole domain  $S$  because the permissible discontinuity is already used to devise  $\bar{q}$  vector. Here, we use the  $I_1$ 's vectors defined as follows:

$$p_{i1}^* = n \sin \frac{n\pi z}{d} \cos \frac{m\pi(y+b)}{2b} \quad (87)$$

$$p_{i2}^* = -\frac{md}{2b} \cos \frac{n\pi z}{d} \sin \frac{m\pi(y+b)}{2b} \quad (88)$$

where the subscript  $i$  is determined through the next relationship in terms of the integers  $n$  and  $m$ ;

$$i = \frac{n(n+1)}{2} + nm + \frac{m(m+3)}{2} \quad n, m = 0, 1, 2, \dots \quad (89)$$

The integers  $n$  and  $m$  are varied in the same way as the subscript  $k$  defined by the equation (56) is increased one by one. However, it must be noted that in the present case, the integers  $n$  and  $m$  do not become zero at the same time. When it is necessary to distinguish between  $I_1$  vector and  $I_j$  vector, the subscript  $j$  of the  $I_1$  vector is expressed by an equation similar to the equation (89). Namely,

$$j = \frac{n'(n'+1)}{2} + n'm' + \frac{m'(m'+3)}{2} \quad n', m' = 0, 1, 2, \dots \quad (90)$$

The scalar products  $(\bar{q}, I_1)$  and  $(I_1, I_j)$  which are necessary to compute the lower bound  $J^2$ , can be easily obtained by the formulas tabulated in

Table 4. For the sake of convenience, the scalar product  $(I_1, I_j)$  is split into two parts,  $S_1$  and  $S_2$ , defined as follows:

$$(I_1, I_j) = S_1 + S_2$$

$$S_1 = \left[ \int_{-b}^b \int_{-d}^0 - \int_{a_2}^1 \int_c^0 \right] n n' \cos \frac{m\pi(y+b)}{2b} \cos \frac{m'\pi(y+b)}{2b} \times$$

$$\sin \frac{n\pi z}{d} \sin \frac{n'\pi z}{d} dy dz \quad (91)$$

$$S_2 = \left[ \int_{-b}^b \int_{-d}^0 - \int_{a_2}^1 \int_c^0 \right] \frac{mm'd^2}{4b^2} \sin \frac{m\pi(y+b)}{2b} \sin \frac{m'\pi(y+b)}{2b} \times$$

$$\cos \frac{n\pi z}{d} \cos \frac{n'\pi z}{d} dy dz \quad (92)$$

As numerical examples of computation, the sway added mass of a rectangular cylinder (width/draft=2) which translates horizontally at the various off-center positions are shown in Figure 6 in two cases where the channel width is 1.5 and 2.5 times as wide as the breadth of the rectangular cylinder. In this figure, Newman's formula (62) is also drawn with dotted lines for the sake of comparison. As

Table 4. The Scalar Products  $(\bar{q}, I_1)$  and  $(I_1, I_j)$  for the Off-Center Translation of a Rectangular Cylinder

a)  $n \neq 0, m \neq 0$ :

$$(\bar{q}, I_1) = \frac{d^2}{n\pi^2} \sin \frac{n\pi c}{d} \left[ \cos \frac{m\pi(a_1+b)}{2b} - \cos \frac{m\pi(a_2+b)}{2b} \right]$$

b)  $n \neq 0, m = 0$ :

$$(\bar{q}, I_1) = 0$$

c)  $n = 0, m \neq 0$ :

$$(\bar{q}, I_1) = \frac{cd}{\pi} \left[ \cos \frac{m\pi(a_1+b)}{2b} - \cos \frac{m\pi(a_2+b)}{2b} \right]$$

a)  $n \neq n', m \neq m'$ :

$$S_1 = \frac{n n' b d}{2\pi^2} \left[ \frac{1}{n-n'} \sin \frac{(n-n')\pi c}{d} - \frac{1}{n+n'} \sin \frac{(n+n')\pi c}{d} \right] \times$$

$$\left[ \frac{1}{m+m'} \left\{ \sin \frac{(m+m')\pi(a_1+b)}{2b} - \sin \frac{(m+m')\pi(a_2+b)}{2b} \right\} + \frac{1}{m-m'} \left\{ \sin \frac{(m-m')\pi(a_1+b)}{2b} - \sin \frac{(m-m')\pi(a_2+b)}{2b} \right\} \right]$$

$$S_2 = \frac{m m' d^3}{8\pi^2 b} \left[ \frac{1}{n+n'} \sin \frac{(n+n')\pi c}{d} + \frac{1}{n-n'} \sin \frac{(n-n')\pi c}{d} \right] \times$$

$$\left[ \frac{1}{m-m'} \left\{ \sin \frac{(m-m')\pi(a_1+b)}{2b} - \sin \frac{(m-m')\pi(a_2+b)}{2b} \right\} - \frac{1}{m+m'} \left\{ \sin \frac{(m+m')\pi(a_1+b)}{2b} - \sin \frac{(m+m')\pi(a_2+b)}{2b} \right\} \right]$$

b)  $n \neq n', m = m' \neq 0$ :

$$S_1 = \frac{n n' d}{4\pi} \left[ \frac{1}{n-n'} \sin \frac{(n-n')\pi c}{d} - \frac{1}{n+n'} \sin \frac{(n+n')\pi c}{d} \right] \left[ a_1 - a_2 + \frac{b}{m\pi} \left\{ \sin \frac{m\pi(a_1+b)}{b} - \sin \frac{m\pi(a_2+b)}{b} \right\} \right]$$

$$S_2 = \frac{m^2 d^3}{16\pi b^2} \left[ \frac{1}{n+n'} \sin \frac{(n+n')\pi c}{d} + \frac{1}{n-n'} \sin \frac{(n-n')\pi c}{d} \right] \left[ a_1 - a_2 - \frac{b}{m\pi} \left\{ \sin \frac{m\pi(a_1+b)}{b} - \sin \frac{m\pi(a_2+b)}{b} \right\} \right]$$

c)  $n = n', m = m' = 0$ :



$$S_1 = \frac{n n' (a_1 - a_2) d}{2\pi} \left[ \frac{1}{n-n'} \sin \frac{(n-n')\pi c}{d} - \frac{1}{n+n'} \sin \frac{(n+n')\pi c}{d} \right]$$

$$S_2 = 0$$

d)  $n=n' \neq 0, m \neq m'$  :

$$S_1 = \frac{n^2 b}{2\pi} \left[ c - \frac{d}{2n\pi} \sin \frac{2n\pi c}{d} \right] \left[ \frac{1}{m+m'} \left\{ \sin \frac{(m+m')\pi(a_1+b)}{2b} - \sin \frac{(m+m')\pi(a_2+b)}{2b} \right\} + \frac{1}{m-m'} \left\{ \sin \frac{(m-m')\pi(a_1+b)}{2b} - \sin \frac{(m-m')\pi(a_2+b)}{2b} \right\} \right]$$

$$S_2 = \frac{m m' d^2}{8\pi b} \left[ c + \frac{d}{2n\pi} \sin \frac{2n\pi c}{d} \right] \left[ \frac{1}{m-m'} \left\{ \sin \frac{(m-m')\pi(a_1+b)}{2b} - \sin \frac{(m-m')\pi(a_2+b)}{2b} \right\} - \frac{1}{m+m'} \left\{ \sin \frac{(m+m')\pi(a_1+b)}{2b} - \sin \frac{(m+m')\pi(a_2+b)}{2b} \right\} \right]$$

e)  $n=n' \neq 0, m=m' \neq 0$  :

$$S_1 = -\frac{n^2 b d}{2} + \frac{n^2}{4} \left[ c - \frac{d}{2n\pi} \sin \frac{2n\pi c}{d} \right] \left[ a_1 - a_2 + \frac{b}{m\pi} \left\{ \sin \frac{m\pi(a_1+b)}{b} - \sin \frac{m\pi(a_2+b)}{b} \right\} \right]$$

$$S_2 = -\frac{m^2 d^3}{8b} + \frac{m^2 d^2}{16b^2} \left[ c + \frac{d}{2n\pi} \sin \frac{2n\pi c}{d} \right] \left[ a_1 - a_2 - \frac{b}{m\pi} \left\{ \sin \frac{m\pi(a_1+b)}{b} - \sin \frac{m\pi(a_2+b)}{b} \right\} \right]$$

f)  $n=n' \neq 0, m=m'=0$  :

$$S_1 = -n^2 b d + \frac{n^2 (a_1 - a_2)}{2} \left[ c - \frac{d}{2n\pi} \sin \frac{2n\pi c}{d} \right]$$

$$S_2 = 0$$

g)  $n=n'=0, m \neq m'$  :

$$S_1 = 0$$

$$S_2 = \frac{m m' c d^2}{4\pi b} \left[ \frac{1}{m-m'} \left\{ \sin \frac{(m-m')\pi(a_1+b)}{2b} - \sin \frac{(m-m')\pi(a_2+b)}{2b} \right\} - \frac{1}{m+m'} \left\{ \sin \frac{(m+m')\pi(a_1+b)}{2b} - \sin \frac{(m+m')\pi(a_2+b)}{2b} \right\} \right]$$

h)  $n=n'=0, m=m' \neq 0$  :

$$S_1 = 0$$

$$S_2 = -\frac{m^2 d^3}{4b} + \frac{m^2 c d^2}{8b^2} \left[ a_1 - a_2 - \frac{b}{m\pi} \left\{ \sin \frac{m\pi(a_1+b)}{b} - \sin \frac{m\pi(a_2+b)}{b} \right\} \right]$$

has been anticipated from the numerical examples which are obtained in the previous section, the lateral position of a cylinder in a channel does not greatly affect the sway added mass except for the case of extreme deviation of the body from the center of the channel.

#### ADDED MASS OF A RECTANGULAR CYLINDER OSCILLATING HORIZONTALLY AND VERTICALLY IN A RECTANGULAR CHANNEL

##### Mathematical Formulation

In this section, we consider the added mass of a rectangular cylinder oscillating at infinite frequency and parallel to a free surface, that is to say,  $\Gamma_1$  and  $\Gamma_5$ , or in the perpendicular direction (see Figure 5). In what follows, the oscillation in parallel to the free surface will be called the horizontal oscillation, with the other one called the vertical oscillation. In case of infinite frequency, as well known, the free surface can be considered as an equipotential surface  $\phi=0$ .

The difference between the horizontal and the vertical oscillations is only the boundary condition on the body surface. Therefore, these two problems can be described simultaneously.

##### I) horizontal oscillation

$$\frac{\partial^2 \phi}{\partial y^2} + \frac{\partial^2 \phi}{\partial z^2} = 0 \text{ in the fluid domain } S \quad (93)$$

$$\frac{\partial \phi}{\partial n} = \begin{cases} 0 & \text{on the boundaries } \Gamma_3, \Gamma_6, \Gamma_7, \Gamma_8 \end{cases} \quad (94)$$

$$1 \quad \text{on the boundary } \Gamma_2 \quad (95)$$

$$-1 \quad \text{on the boundary } \Gamma_4 \quad (96)$$

$$\phi = 0 \quad \text{on the boundaries } \Gamma_1, \Gamma_5 \quad (97)$$

##### II) vertical oscillation

$$\frac{\partial^2 \phi}{\partial y^2} + \frac{\partial^2 \phi}{\partial z^2} = 0 \text{ in } S \quad (98)$$

$$\frac{\partial \phi}{\partial n} = \begin{cases} 0 & \text{on } \Gamma_2, \Gamma_4, \Gamma_6, \Gamma_7, \Gamma_8 \end{cases} \quad (99)$$

$$1 \quad \text{on } \Gamma_3 \quad (100)$$

$$\phi = 0 \quad \text{on } \Gamma_1, \Gamma_5 \quad (101)$$

From the above formulation, it is evident that as an arbitrary  $\bar{q}$  vector of  $\bar{\Omega}$  space, we can select the zero vector, namely,  $\bar{q}=0=(0, 0)$  and that homogeneous associated spaces are the same for both cases of the horizontal and the vertical oscillations. Therefore, the added mass can be evaluated by the inequality (27), and moreover it is possible to use the same  $J_k$ 's vectors for the vectors of  $\Omega^*$  space for both oscillations. We decide to use what is defined by the equation (102) as an arbitrary function  $\phi^*_k$  which must satisfy the boundary condition  $\phi^*_k=0$  on the boundaries  $\Gamma_1$  and  $\Gamma_5$ :

$$\phi^*_k = 2b \cos \frac{m\pi(y-b)}{2b} \sin \frac{(2n+1)\pi z}{2d} \quad (102)$$

where the subscript  $k$  is

$$k = \frac{n(n+1)}{2} + nm + \frac{m(m+1)}{2} + 1 \quad n, m=0, 1, 2, \dots$$

From this definition of  $\phi^*_k$ , the  $J_k$  vector can be immediately defined as follows:

$$q^*_{k1} = -m\pi \sin \frac{m\pi(y-b)}{2b} \sin \frac{(2n+1)\pi z}{2d} \quad (103)$$

$$q^*_{k2} = \frac{(2n+1)\pi b}{d} \cos \frac{m\pi(y-b)}{2b} \cos \frac{(2n+1)\pi z}{2d} \quad (104)$$

When it is necessary to distinguish between  $J_k$  vector and  $J_\ell$  vector,  $J_\ell$  vector will be defined by substituting the integers  $n$  and  $m$  of the above definitions (103) and (104) with the integers  $n'$  and  $m'$ .

On the other hand, the complementary space  $\Pi$  is different according to the direction of oscillation.

I) complementary space for the horizontal oscillation

$$\frac{\partial p_1}{\partial y} + \frac{\partial p_2}{\partial z} = 0 \quad \text{in } S \quad (105)$$

$$p_1 \frac{\partial y}{\partial n} + p_2 \frac{\partial z}{\partial n} = \begin{cases} 0 & \text{on } \Gamma_3, \Gamma_6, \Gamma_7, \Gamma_8 \\ 1 & \text{on } \Gamma_2 \\ -1 & \text{on } \Gamma_4 \end{cases} \quad (106)$$

$$(107)$$

$$(108)$$

II) complementary space for the vertical oscillation

$$\frac{\partial p_1}{\partial y} + \frac{\partial p_2}{\partial z} = 0 \quad \text{in } S \quad (109)$$

$$p_1 \frac{\partial y}{\partial n} + p_2 \frac{\partial z}{\partial n} = \begin{cases} 0 & \text{on } \Gamma_2, \Gamma_4, \Gamma_6, \Gamma_7, \Gamma_8 \\ 1 & \text{on } \Gamma_3 \end{cases} \quad (110)$$

$$(111)$$

Thus, as an arbitrary  $\bar{p}$  vector, two different vectors are defined by taking account of the permissible discontinuity:

I)  $\bar{p}$  vector for the horizontal oscillation

$$a) \text{ domain ABIH : } \bar{p}_1 = \frac{b-y}{b-a_1}, \bar{p}_2 = \frac{z-c}{b-a_1} \quad (112)$$

$$b) \text{ domain CDEL : } \bar{p}_1 = \frac{y+b}{a_2+b}, \bar{p}_2 = \frac{c-z}{a_2+b} \quad (113)$$

$$c) \text{ other domains : } \bar{p}_1=0, \bar{p}_2=0 \quad (114)$$

II)  $\bar{p}$  vector for the vertical oscillation

$$a) \text{ domain ABIH : } \bar{p}_1=0, \bar{p}_2 = \frac{a_1-a_2}{2(b-a_1)} \quad (115)$$

$$b) \text{ domain BJGI : } \bar{p}_1 = \frac{-(a_1-a_2)(y-b)}{2(c-d)(b-a_1)}$$

$$\bar{p}_2 = \frac{(a_1-a_2)(z-d)}{2(c-d)(b-a_1)} \quad (116)$$

$$c) \text{ domain BCKJ : } \bar{p}_1 = \frac{2y-a_1-a_2}{2(c-d)}, \bar{p}_2 = \frac{d-z}{c-d} \quad (117)$$

$$d) \text{ domain CLFK : } \bar{p}_1 = \frac{-(a_1-a_2)(y+b)}{2(c-d)(b+a_2)}$$

$$\bar{p}_2 = \frac{(a_1-a_2)(z-d)}{2(c-d)(b+a_2)} \quad (118)$$

Table 5. The Scalar Product ( $J_k, J_\ell$ ) for the Horizontal and the Vertical Oscillations at Off-Center Positions

a)  $n \neq n', m \neq m'$  :

$$(J_k, J_\ell) = -\frac{mm'bd}{2} \left[ -\frac{1}{n-n'} \sin \frac{(n-n')\pi c}{d} + \frac{1}{n+n'+1} \sin \frac{(n+n'+1)\pi c}{d} \right] \times \\ \left[ \frac{1}{m-m'} \left\{ \sin \frac{(m-m')\pi(a_1-b)}{2b} - \sin \frac{(m-m')\pi(a_2-b)}{2b} \right\} - \frac{1}{m+m'} \left\{ \sin \frac{(m+m')\pi(a_1-b)}{2b} - \sin \frac{(m+m')\pi(a_2-b)}{2b} \right\} \right] \\ - \frac{(2n+1)(2n'+1)b^3}{2d} \left[ -\frac{1}{n-n'} \sin \frac{(n-n')\pi c}{d} - \frac{1}{n+n'+1} \sin \frac{(n+n'+1)\pi c}{d} \right] \times \\ \left[ \frac{1}{m-m'} \left\{ \sin \frac{(m-m')\pi(a_1-b)}{2b} - \sin \frac{(m-m')\pi(a_2-b)}{2b} \right\} + \frac{1}{m+m'} \left\{ \sin \frac{(m+m')\pi(a_1-b)}{2b} - \sin \frac{(m+m')\pi(a_2-b)}{2b} \right\} \right]$$

b)  $n \neq n', m=m'=0$  :

$$(J_k, J_\ell) = -\frac{m^2\pi d}{4} \left[ -\frac{1}{n-n'} \sin \frac{(n-n')\pi c}{d} + \frac{1}{n+n'+1} \sin \frac{(n+n'+1)\pi c}{d} \right] \left[ a_1-a_2 - \frac{b}{m\pi} \left\{ \sin \frac{m\pi(a_1-b)}{b} - \sin \frac{m\pi(a_2-b)}{b} \right\} \right] \\ - \frac{(2n+1)(2n'+1)\pi b^2}{4d} \left[ -\frac{1}{n-n'} \sin \frac{(n-n')\pi c}{d} - \frac{1}{n+n'+1} \sin \frac{(n+n'+1)\pi c}{d} \right] \times \\ \left[ a_1-a_2 + \frac{b}{m\pi} \left\{ \sin \frac{m\pi(a_1-b)}{b} - \sin \frac{m\pi(a_2-b)}{b} \right\} \right]$$

c)  $n \neq n', m=m'=0$  :

$$(J_k, J_\ell) = \frac{(2n+1)(2n'+1)\pi b^2(a_1-a_2)}{2d} \left[ \frac{1}{n-n'} \sin \frac{(n-n')\pi c}{d} + \frac{1}{n+n'+1} \sin \frac{(n+n'+1)\pi c}{d} \right]$$

d)  $n=n', m \neq m'$  :

$$(J_k, J_l) = -\frac{mm'\pi b}{2} \left[ -c + \frac{d}{(2n+1)\pi} \sin \frac{(2n+1)\pi c}{d} \right] \times \\ \left[ \frac{1}{m-m'} \left\{ \sin \frac{(m-m')\pi(a_1-b)}{2b} - \sin \frac{(m-m')\pi(a_2-b)}{2b} \right\} - \frac{1}{m+m'} \left\{ \sin \frac{(m+m')\pi(a_1-b)}{2b} - \sin \frac{(m+m')\pi(a_2-b)}{2b} \right\} \right] \\ - \frac{(2n+1)^2 \pi b^3}{2d^2} \left[ -c - \frac{d}{(2n+1)\pi} \sin \frac{(2n+1)\pi c}{d} \right] \times \\ \left[ \frac{1}{m-m'} \left\{ \sin \frac{(m-m')\pi(a_1-b)}{2b} - \sin \frac{(m-m')\pi(a_2-b)}{2b} \right\} + \frac{1}{m+m'} \left\{ \sin \frac{(m+m')\pi(a_1-b)}{2b} - \sin \frac{(m+m')\pi(a_2-b)}{2b} \right\} \right]$$

e)  $n=n', m=m' \neq 0$  :

$$(J_k, J_l) = -\frac{m^2 \pi^2 b d}{2} - \frac{m^2 \pi^2}{4} \left[ -c + \frac{d}{(2n+1)\pi} \sin \frac{(2n+1)\pi c}{d} \right] \left[ a_1 - a_2 - \frac{b}{m\pi} \left\{ \sin \frac{m\pi(a_1-b)}{b} - \sin \frac{m\pi(a_2-b)}{b} \right\} \right] \\ - \frac{(2n+1)^2 \pi^2 b^3}{2d} - \frac{(2n+1)^2 \pi^2 b^2}{4d^2} \left[ -c - \frac{d}{(2n+1)\pi} \sin \frac{(2n+1)\pi c}{d} \right] \times \\ \left[ a_1 - a_2 + \frac{b}{m\pi} \left\{ \sin \frac{m\pi(a_1-b)}{b} - \sin \frac{m\pi(a_2-b)}{b} \right\} \right]$$

f)  $n=n', m=m'=0$  :

$$(J_k, J_l) = -\frac{(2n+1)^2 \pi^2 b^3}{d} - \frac{(2n+1)^2 \pi^2 b^2 (a_1 - a_2)}{2d^2} \left[ -c - \frac{d}{(2n+1)\pi} \sin \frac{(2n+1)\pi c}{d} \right]$$

e) domain CDEL :  $\bar{p}_1=0, \bar{p}_2=\frac{a_1-a_2}{2(b+a_2)}$  (119)

From the above definitions of  $J_k$  and  $J_l$  vectors, we can get the analytical expressions of the scalar product  $(J_k, J_l)$ , which are shown in Table 5. On the other hand, the scalar product  $(\bar{p}, J_k)$  is different for the horizontal and vertical oscillations.

I) horizontal oscillation

$$(\bar{p}, J_k) = \frac{4bd}{(2n+1)\pi} \left[ 1 - \cos \frac{(2n+1)\pi c}{2d} \right] \times \\ \left[ \cos \frac{m\pi(a_1-b)}{2b} - \cos \frac{m\pi(a_2-b)}{2b} \right] \quad (120)$$

II) vertical oscillation

a)  $m \neq 0$ ,

$$(\bar{p}, J_k) = -\frac{4b^2}{m\pi} \sin \frac{(2n+1)\pi c}{2d} \times \\ \left[ \sin \frac{m\pi(a_1-b)}{2b} - \sin \frac{m\pi(a_2-b)}{2b} \right] \quad (121)$$

b)  $m=0$ ,

$$(\bar{p}, J_k) = -2b(a_1 - a_2) \sin \frac{(2n+1)\pi c}{2d} \quad (122)$$

Using these formulas, the scalar products  $(J_k, J_l)$  and  $(\bar{p}, J_k)$  necessary to solve the unknown  $b_k$ 's are determined immediately, if the geometrical sizes of a rectangular cylinder and a rectangular channel are designated.

### Numerical Examples

The vertical oscillation ( $\omega=\infty$ ) at the center of a rectangular channel is equivalent to the horizontal translation ( $\omega=0$ ) at the center of the channel, if the roles of the channel-bottom and the channel-wall are interchanged with one another. Hence, the added mass coefficients for the horizontal translation shown in Table 3, can be regarded as those for the vertical oscillation. Also,

in the same table, are tabulated the added mass coefficients for the horizontal oscillation at the center of a channel. Here, it must be noted that those numerical values are computed not by using the  $\bar{p}$  and  $J_k$  vectors stated above, but by only considering half of the fluid domain because of symmetry of the fluid motion with respect to the center of the total domain. That is to say, the boundary conditions (94), (95), (96) and (97) are replaced by the following conditions (see Figure 1):

$$\frac{\partial \phi}{\partial n} = \begin{cases} 0 & \text{on } \Gamma_3, \Gamma_5, \Gamma_6 \end{cases} \quad (123)$$

$$= \begin{cases} 1 & \text{on } \Gamma_2 \end{cases} \quad (124)$$

$$\phi = 0 \quad \text{on } \Gamma_1, \Gamma_4 \quad (125)$$

The  $J_k$ 's vectors and  $\bar{p}$  vector are devised as follows:

 $J_k$  vectors:

$$q_{k1}^* = (2n+1)\pi \cos \frac{(2n+1)\pi y}{2b} \sin \frac{(2m+1)\pi z}{2d} \quad (126)$$

$$q_{k2}^* = \frac{(2m+1)\pi b}{d} \sin \frac{(2n+1)\pi y}{2b} \cos \frac{(2m+1)\pi z}{2d} \quad (127)$$

where the subscript  $k$  is defined by

$$k = \frac{n(n+1)}{2} + nm + \frac{m(m+3)}{2} + 1 \quad n, m = 0, 1, 2, \dots$$

 $\bar{p}$  vector:

$$\text{a) domain AGFB : } \bar{p}_1 = \frac{b-y}{b-a}, \bar{p}_2 = \frac{z-c}{b-a} \quad (128)$$

$$\text{b) other domain : } \bar{p}_1=0, \bar{p}_2=0 \quad (129)$$

The analytical formulas of the scalar products,  $(J_k, J_l)$  and  $(\bar{p}, J_k)$ , are obtained easily, and they are summarized in Table 6.

Besides the numerical examples obtained by the present method, a few numerical values of the added mass obtained by the finite element method shown in parentheses are also included in Table 3.

In the first group of the numerical examples, the added mass coefficients obtained by the present method and by the finite element method agree well



Table 6. The Scalar Products ( $J_k, J_l$ ) and ( $\bar{P}, J_k$ ) for the Horizontal Oscillation at the Center of a Channela)  $n \neq n', m \neq m'$ :

$$(J_k, J_l) = -\frac{(2n+1)(2n'+1)bd}{4} \left[ \frac{1}{n-n'} \sin \frac{(n-n')\pi a}{b} + \frac{1}{n+n'+1} \sin \frac{(n+n'+1)\pi a}{b} \right] \left[ -\frac{1}{m-m'} \sin \frac{(m-m')\pi c}{d} + \frac{1}{m+m'+1} \sin \frac{(m+m'+1)\pi c}{d} \right] \\ - \frac{(2m+1)(2m'+1)b^3}{4d} \left[ \frac{1}{n-n'} \sin \frac{(n-n')\pi a}{b} - \frac{1}{n+n'+1} \sin \frac{(n+n'+1)\pi a}{b} \right] \left[ -\frac{1}{m-m'} \sin \frac{(m-m')\pi c}{d} - \frac{1}{m+m'+1} \sin \frac{(m+m'+1)\pi c}{d} \right]$$

b)  $n \neq n', m = m'$ :

$$(J_k, J_l) = -\frac{(2n+1)(2n'+1)bd}{4} \left[ \frac{1}{n-n'} \sin \frac{(n-n')\pi a}{b} + \frac{1}{n+n'+1} \sin \frac{(n+n'+1)\pi a}{b} \right] \left[ -\frac{\pi c}{d} + \frac{1}{2m+1} \sin \frac{(2m+1)\pi c}{d} \right] \\ - \frac{(2m+1)^2 b^3}{4d} \left[ \frac{1}{n-n'} \sin \frac{(n-n')\pi a}{b} - \frac{1}{n+n'+1} \sin \frac{(n+n'+1)\pi a}{b} \right] \left[ -\frac{\pi c}{d} - \frac{1}{2m+1} \sin \frac{(2m+1)\pi c}{d} \right]$$

c)  $n = n', m \neq m'$ :

$$(J_k, J_l) = -\frac{(2n+1)^2 bd}{4} \left[ \frac{\pi a}{b} + \frac{1}{2n+1} \sin \frac{(2n+1)\pi a}{b} \right] \left[ -\frac{1}{m-m'} \sin \frac{(m-m')\pi c}{d} + \frac{1}{m+m'+1} \sin \frac{(m+m'+1)\pi c}{d} \right] \\ - \frac{(2m+1)(2m'+1)b^3}{4d} \left[ \frac{\pi a}{b} - \frac{1}{2n+1} \sin \frac{(2n+1)\pi a}{b} \right] \left[ -\frac{1}{m-m'} \sin \frac{(m-m')\pi c}{d} - \frac{1}{m+m'+1} \sin \frac{(m+m'+1)\pi c}{d} \right]$$

d)  $n = n', m = m'$ :

$$(J_k, J_l) = -(2n+1)^2 \frac{2bd}{4} - \frac{(2n+1)^2 bd}{4} \left[ \frac{\pi a}{b} + \frac{1}{2n+1} \sin \frac{(2n+1)\pi a}{b} \right] \left[ -\frac{\pi c}{d} + \frac{1}{2m+1} \sin \frac{(2m+1)\pi c}{d} \right] - \frac{(2m+1)^2 \pi^2 b^3}{4d} \\ - \frac{(2m+1)^2 b^3}{4d} \left[ \frac{\pi a}{b} - \frac{1}{2n+1} \sin \frac{(2n+1)\pi a}{b} \right] \left[ -\frac{\pi c}{d} - \frac{1}{2m+1} \sin \frac{(2m+1)\pi c}{d} \right]$$

$$(\bar{P}, J_k) = \frac{4bd}{(2m+1)\pi} \sin \frac{(2n+1)\pi a}{2b} \left[ 1 - \frac{\cos(2m+1)\pi c}{2d} \right]$$

with each other. However, for the cases where the fluid domain is extremely narrow, for example the first case of the second group, the finite element method tends to provide a remarkably smaller value than the present method, although the total number of the nodal points was increased in order to improve the accuracy of the finite element method. Therefore, this discrepancy between the numerical values which are obtained by the present method and by the finite element method, for example, in case of  $a=2.0, b=-2.1, c=-2.0$  and  $d=-3.0$  means that the present method is better as far as this case is concerned, because the exact value must be greater than that obtained by the present method.

With respect to the effect of the restricted waters on the added mass of rectangular cylinders oscillating in a free surface, Matsuura and Kawakami have published a paper on the basis of the numerical calculations by the finite element method [7].

Hence, in the remaining part of this section, the effect of a single-wall on the added mass of a rectangular cylinder oscillating near the wall will be discussed on the basis of the numerical values obtained by the present method.

For this purpose, it is necessary to place another wall on the opposite side of the cylinder as well as adequately far from the cylinder in order to substitute a finite domain of the fluid for the infinite fluid. To decide where the additional wall should be placed, the added mass was computed for the various distances between the cylinder and this additional wall. As a result, it was clarified that the additional wall which was placed at the distance of five times of the half-breadth of a cylinder, did not affect the added mass from the practical point of view.

The numerical examples representing the effect of a single-wall on the added mass of a rectangular cylinder (breadth/draft=2) are shown in Figures

7 and 8, in which the former is for the horizontal oscillation and the latter is for the vertical oscillation. In both figures, the experimental data by Koch in shallow water (exactly speaking, the clearance/body's breadth ratio,  $\eta/B$ , is equal to 7) are plotted for the sake of comparison [12]. In each case, the numerical values obtained by Koch are larger than those by the present method. However, it was also pointed out by Wendel [9] and Matsuura and Kawakami [7] that the experimental data by Koch are larger than their numerical values. Therefore, the discrepancy between Koch's data and the numerical values by the present method does not imply that the accuracy of the present method is poor. In Figure 8 are drawn the curves representing the single-wall effect for a semi-submerged circular cylinder, which are quoted from the paper of Yoshiki and others [13]. The large discrepancy between the results by the present method and by Yoshiki and others is partly because of the difference between the geometrical forms of the oscillating body and partly because of inaccuracy of Yoshiki and others' approximate analysis in case of a small clearance between the body and the side-wall of the waterway.

Comparing the results by the present method, which are shown in Figures 7 and 8, with each other, it is possible to say that in case of the horizontal oscillation, the clearance between the cylinder and the wall has the primary effect on the added mass, while the added mass of the vertical oscillation is affected to almost the same extent by the wall clearance and by the bottom clearance. Furthermore, the value of the added mass coefficient may become larger in the vertical oscillation than in the horizontal oscillation.

#### ACKNOWLEDGEMENT

In completing this paper, the author received in-

valuable help and advice from many persons. Prof. S. Motora and Prof. F. Tasai gave helpful advice for computing the added mass for the oscillation. The numerical results of the added mass by the finite element method were provided by Mr. J. Takashina and Mr. S. Yamamoto, and Mr. T. Ida executed a part of computation by the hypercircle method. To these persons, the author wishes to express his gratitude.

## REFERENCES

- 1) Fujino, M., Takashina, J. and Yamamoto, S.: "On the Three-Dimensional Correction Factors for the Added Mass and the Added Mass Moment of Inertia Related to Manoeuvrability in Shallow Water", Jour. Soc. Nav. Archit. Japan, Vol. 135, 1974, pp. 121-128 (in Japanese)
- 2) Synge, J.L.: "The Hypercircle in Mathematical Physics", Cambridge Univ. Press, 1957
- 3) Fujino, M.: "Application of the Hypercircle Methods to Estimating the Transverse Added Mass of Two-Dimensional Bodies in Restricted Waters", Jour. Soc. Nav. Archit. Japan, Vol. 134, 1973, pp. 165-172 (in Japanese)
- 4) Fujino, M. and Sugita, M.: "On the Added Mass of a Two-Dimensional Rectangular Cylinder Vibrating in Parallel to the Free Surface and in a Perpendicular Direction in Restricted Waters", Jour. Soc. Nav. Archit. Japan, Vol. 136, 1974, pp. 129-140 (in Japanese)
- 5) Fujino, M.: "On the Added Mass of a Rectangular Cylinder Moving in a Rectangular Channel", International Shipbuilding Progress, Vol. 22, No. 248, 1975, pp. 115-131
- 6) Zienkiewicz, O.C. and Cheung, Y.K.: "The Finite Element Method in Structural and Continuum Mechanics", McGraw-Hill, 1967
- 7) Matsuura, Y. and Kawakami, H.: "Calculation of Added Virtual Mass and Added Virtual Mass Moment of Inertia of Ship Hull Vibration by the Finite Element Method", Jour. Soc. Nav. Archit. Japan, Vol. 124, 1968, pp. 281-292 (in Japanese)
- 8) Lewis, F.M.: "The Inertia of the Water Surrounding in a Vibrating Ship", Trans. S.N.A.M.E., Vol. 37, 1929
- 9) Wendel, K.: "Hydrodynamische Massen und Hydrodynamische Massenträgheitsmomente". Jahrb. d. STG, Vol. 44, 1950
- 10) Newman, J.N.: "Some Theories for Ship Manoeuvring", Jour. Mechanical Engineering Science, Vol. 14, No. 7, 1972
- 11) Flagg, C.N. and Newman, J.N.: "Sway Added-Mass Coefficient for Rectangular Profiles in Shallow Water", Jour. Ship Res., Vol. 15, 1971
- 12) Koch, J.J.: "Eine Experimentelle Methode zur der Reduzierten Mass des Mitschwingenden Wässers bei Schiffschwingungen", Ingenieur-Archiv, IV Band, 2 Heft, 1933
- 13) Yoshiki, M., Yamamoto, Y., Sakuma, T. and Nagamoto, Y.: "A Contribution to the Virtual Mass of a Vibrating Ship", Jour. Soc. Nav. Archit. Japan, Vol. 84, 1952 (in Japanese)

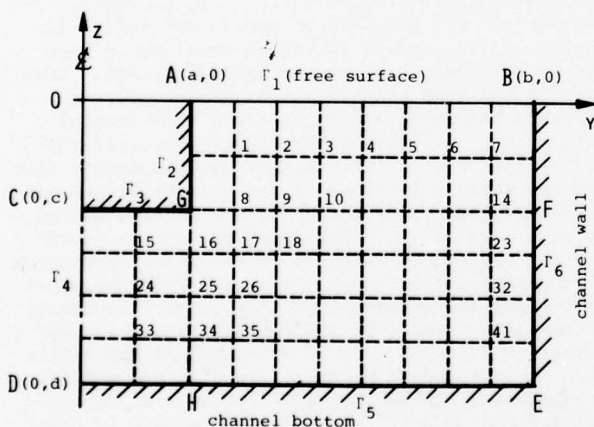


Fig. 1: Division of the fluid domain bounded by a rectangular cylinder and a rectangular channel into a net of rectangular meshes. Note: only the right-half of the whole domain is shown.

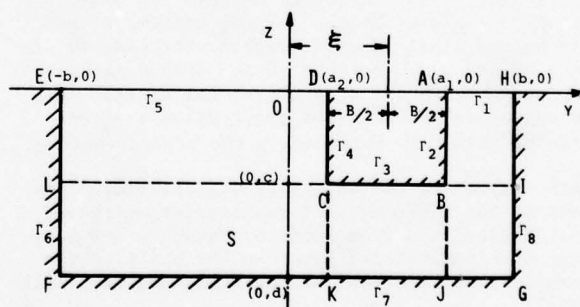


Fig. 2: Basic unit consisting of four rectangular meshes which possess the  $i$ -th grid-point in common.

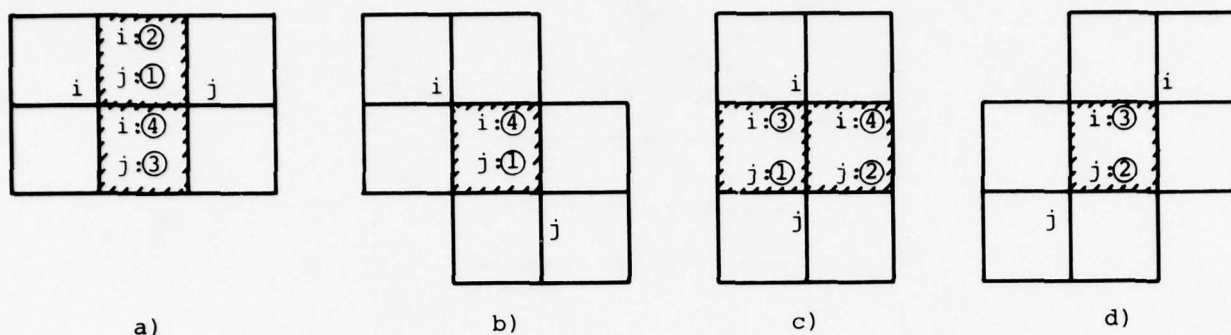


Fig. 3: Canonical configuration of two basic units which provides the non-zero value of the scalar product  $(l_i, l_j)$ .

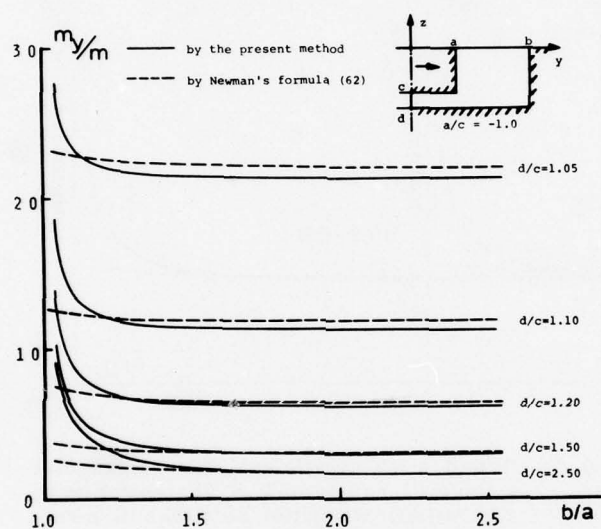


Fig. 4: Added mass coefficient of a rectangular cylinder (breadth/draft = 2) translating horizontally at the center of a rectangular channel.

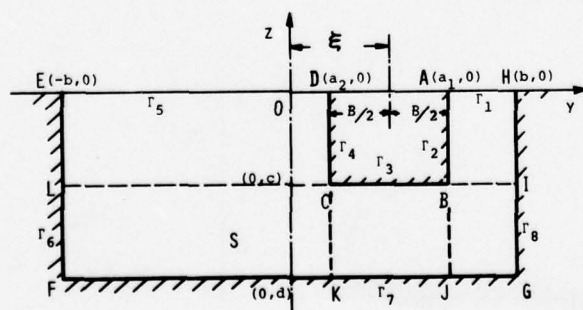


Fig. 5: Coordinate system for describing an off-center translation of a rectangular cylinder.



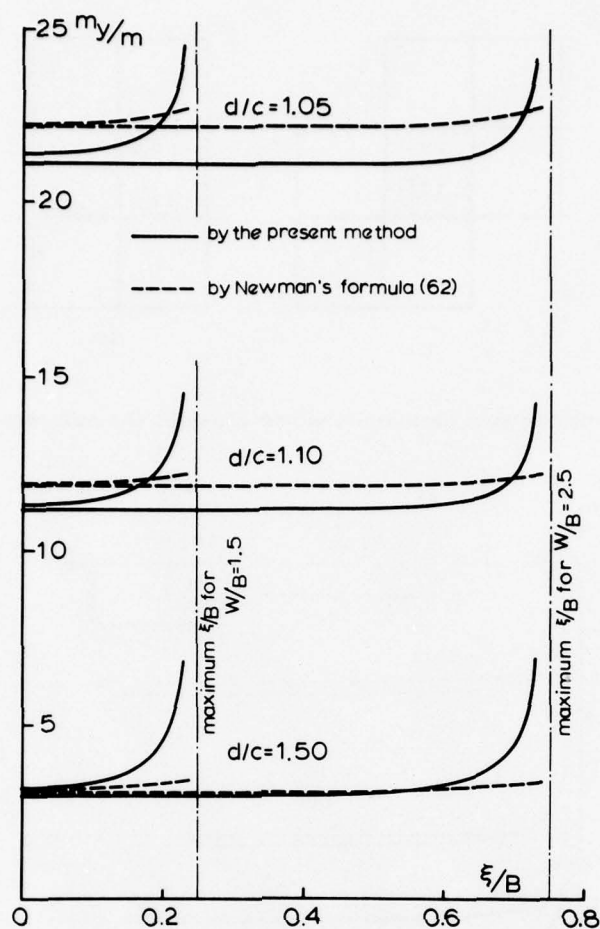


Fig. 6: Added mass coefficient of a rectangular cylinder (breadth/draft = 2) translating at the various off-center positions of a rectangular channel.

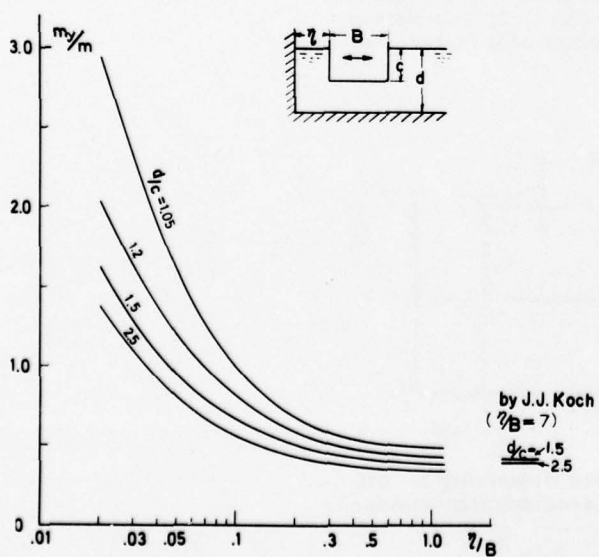


Fig. 7: Single-wall effect on the added mass of a rectangular cylinder (breadth/draft = 2) in the horizontal oscillation.

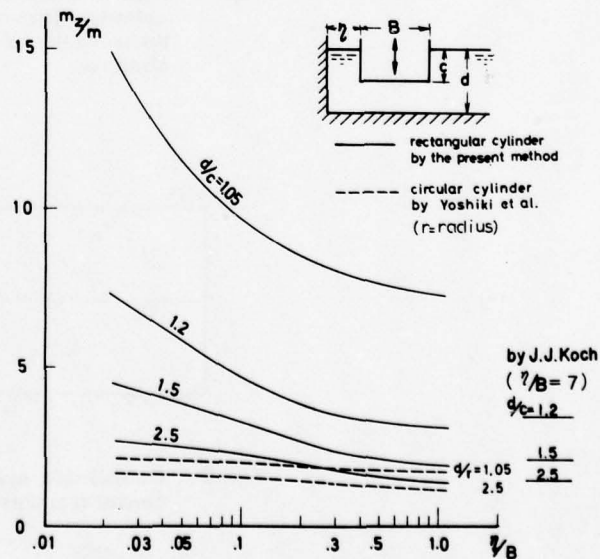


Fig. 8: Single-wall effect on the added mass of a rectangular cylinder (breadth/draft = 2) in the vertical oscillation.

# INTERACTION EFFECTS OF SHIPS OPERATING IN PROXIMITY IN DEEP AND SHALLOW WATER

M. A. ABKOWITZ

Massachusetts Institute of Technology, Cambridge, Mass., USA

G. M. ASHE

Naval Ship Engineering Center, Washington, DC, USA

R. M. FORTSON

United States Navy

## ABSTRACT

Mathematical models and associated computer programs are developed in order to calculate the steady and unsteady interaction forces between ships operating close to one another in deep and shallow water. The potential description of the flow about the body by means of a line distribution of singularities consisting of sources and doublets (horizontally and vertically oriented) and the use of Lagally's theorem provide a relatively inexpensive, not too complicated, and yet rather accurate method of calculating the interaction forces and moments. Good agreement is obtained between the results of model tests in the towing tank and those calculated for several diverse ship types.

Since the overall dynamics of the ships must be considered in the evaluation of any operational or special maneuver, the interaction force model was combined with the ordinary maneuvering mathematical model to provide a trajectory model and computer program for use in the simulation of ships maneuvering in proximity. Examples are given of the use of the trajectory model in the simulation of ship replenishment operations at sea.

## NOMENCLATURE

$A_{i,j}$  added (hydrodynamic) inertia,  $i$  defines the force component and  $j$  the motion component from which the force arises  
 $A_{22}$  lateral added mass  
 $A_{66}$  added inertia in yaw  
 $a, b$  end points of body  
 $BMLD$  molded beam of ship  
 $CLAG$  rudder control system time lag  
 $DLAG$  propeller control system time lag  
 $DR$  rudder deflection angle  
 $\vec{F}$  vector force acting on body  
 $f$  functional relationship  
 $I_z$  yaw moment of inertia  
 $K_{i,j}$  control coefficients,  $i$  refers to ship,  $j$  refers to motion parameter sensitivity  
 $\vec{M}$  vector moment acting on body  
 $m$  source (singularity) strength  
 $m$  mass of body  
 $N$  yaw moment  
 $n$  rotational speed of propeller  
 $q$  velocity component  
 $q'_n$  cross flow normal velocity component  
 $R$  radius of body section  
 $r$  yaw angular velocity  
 $r$  radial distance  
 $SUPLY$  desired lateral ship separation  
 $t$  time  
 $U$  free stream velocity  
 $u$  forward component of velocity  
 $\vec{u}_0, u$  translational velocity of body  
 $u_0$  initial forward speed  
 $V$  volume of displacement of body  
 $v$  transverse component of velocity  
 $X, Y$  longitudinal and lateral force components respectively  
 $x$  distance from origin along the longitudinal axis of body

$x_G$  longitudinal position of center of gravity from origin  
 $y$  distance along the transverse axis of body  
 $x_0, y_0$  positional coordinates in space  
 $\Delta$  increment  
 $\nabla$  vector gradient  
 $\delta$  rudder deflection  
 $\zeta$  doublet (singularity) strength  
 $\xi$  longitudinal positional coordinate on body  
 $\rho$  mass density of fluid  
 $\phi$  potential function  
 $\psi$  yaw angle (orientation)  
 $\omega, \vec{\omega}$  rotational velocity  
 $\cdot$  dot - derivative with respect to time

## Subscripts:

int interaction  
 $p$  refers to perturbation  
 $ss$  steady state  
 $tr$  transient  
 $u, v, r, \delta$  partial derivative with respect to subscripts - i.e.,  $N_{rv^2} = \partial^3 N / \partial r \partial^2 v$   
 $x, y$   $x$  and  $y$  components  
 $\alpha$  degrees of freedom 1 to 6  
 $\gamma$  due to body alone  
 $\eta$  due to the presence of other bodies

## INTRODUCTION

The ability of a ship to maneuver properly is, in many cases, a critical item in the effective operations of the ship and in certain circumstances, is critical even to its survivability. Maneuverability is to be understood in its broadest sense; that is, the ability for the skipper to make the ship go where he wants it to go safely, efficiently, and with confidence under the existing environmental constraints such as high seas, shallow waters, can-

als, restricted waterways, or in close proximity with other ships. This definition of maneuverability goes beyond the mechanical ability of a ship and its control system to respond to a call of rudder action and must include the ability of the helmsman to avoid entering into any situation wherein, even if the maneuverability capabilities of the ship are employed in optimum fashion, a collision, grounding, damage, or breakup becomes unavoidable. Obviously the best level of maneuverability is obtained when (a) the ship and its control system are effectively designed, (b) the skipper is familiar with the ship's capabilities and understands how to bring the control system into most effective use, and (c) the skipper knows what situations may be beyond recovery capability and therefore tries to avoid getting into such situations.

The proper development of each of the maneuvering capabilities mentioned above (a, b, c) requires an ability to predict the motion response of the ship to a call for rudder action. When this prediction procedure takes the form of a mathematical model which simulates the ship dynamics and predicts the ship's trajectory, analysis of simulated maneuvers can ultimately produce the proper design of the ship's hull, rudder, and control system for the mission assigned. The simulation can be used to have the operator become familiar with ship capabilities either directly through results of the simulated runs or by incorporation of the mathematical model into a real time "pilot trainer". Also, the analysis can be used to establish under what situations collision is unavoidable and thereby provide information to the skipper as to what situations to avoid during various operations, or furnish necessary information on which to develop "rules of the road" for ship operation during certain missions at sea or in harbor traffic. Mathematical trajectory models have been developed and used for such purposes for the case where the forces acting on the ship are based on the ship operating by itself without the effect of other ships or flow boundaries nearby. This model is inadequate for simulating the motion during those missions which require ships to operate in close proximity to one another because there may exist strong interaction forces between the ships which can result in collisions.

The development of a mathematical model which predicts the forces and moments acting on ships operating on parallel courses at various speeds with a given longitudinal and lateral relative positioning is only the first step in obtaining the complete model for the simulation of the maneuvering of ships in proximity. The model must include difference in headings, unsteady effects such as interaction forces resulting from velocities and accelerations (as well as position), and the total dynamics of the situation which includes the effects of the previous history of the trajectory on the state of the motion at a given time. In order to demonstrate this latter "dynamics" effect, the case of a small ship overtaking a larger ship close abeam in a harbor is chosen as an example. Figure 1 shows the typical moment acting on a 300-foot ship (A) while it is overtaking a 900-foot tanker (B) 100 feet abeam. As Ship A moves along the forward portion of Ship B, Ship A experiences a sizeable "bow out" moment tending to move Ship A away from Ship B. That is what the "statics" of the situation indicates. However, the "dynamics" of the situation will indicate just the opposite; it will indicate Ship A tending to cross over the bow of Ship B. Let us assume for the sake of simplicity that

the moment acting on Ship A is of similar order of magnitude as that shown in Figure 1, even though there will be a heading and separation distance change as Ship A moves up on Ship B. When Ship A is at the stern of Ship B there is a "bow in" moment tending to head Ship A towards Ship B. Since impulse equals the momentum change, the following relationship holds,

$$\int N dt = I_z \int d\omega$$

where  $N$  is the yaw moment,  $I_z$  the mass moment of inertia in yaw,  $\omega$  the angular velocity in yaw, and  $t$  is time. This gives

$$\omega = \frac{\int N dt}{I_z} = \frac{\int N dx}{I_z (u_A - u_B)}$$

where  $x$  is the relative longitudinal distance travelled and  $u_A - u_B$  is the relative speed. The yaw angle  $\psi$  is given by  $\int \omega dt$  and the transverse distance moved (due to heading angle) can be approximated as  $\int u_A \psi dt$ . Figure 1 shows  $\omega$ ,  $\psi$ , and  $y$  as they vary with relative position for this fictitious case. We find that when Ship A is at the bow of Ship B, Ship A has its largest bow in heading at approximately the position where it experiences its maximum bow out moment and Ship A continues to close on Ship B even well beyond this point.

The authors are familiar with an actual collision which occurred in a harbor when a small fishing trawler was overtaking a tanker close by. The trawler swung across the bow of the tanker, was rammed, and sank. When the trawler was retrieved, it was noted that the rudder was hard over to avoid the collision but to no avail. Also, there have been several collisions at sea wherein an overtaking vessel has moved across the bow of the overtaken vessel.

This paper describes the development of a mathematical model for use in the effective simulation of ship motions when ships operate in close proximity to one another or in a canal. The model calculates the longitudinal and lateral interaction forces and the interaction yaw moment arising from both steady effects (due to relative longitudinal, lateral, and heading orientation) and unsteady effects (due to ships' velocities and accelerations, both linear and angular) and includes the effects of shallow water. It combines these proximity forces with those obtained for the ship in the unrestricted condition to form a complete trajectory model. The skipper's call for rudder action as he senses the various ship motions (such as heading, closing rate, ship swinging, etc.) and the resulting rudder response is also incorporated into the model in the form of control coefficients (which can be adjusted for those motion responses sensed by the skipper). The output of the associated computer program is the total dynamics of the ships involved plus a plotted schematic of the ships' positions and orientation. In order for the mathematical model and associated program to be a useful "tool", the calculation of the forces must give results which are of acceptable accuracy, must involve efficient computational methods, and be relatively inexpensive to use. The model and computer programs described herein have these properties and present an effective device by which ship maneuvers can be simulated and analyzed for the purpose of improving ship design and operations.



# DEVELOPMENT OF THE MATHEMATICAL MODELS AND COMPUTATIONAL PROCEDURES

## Description of the potential function

The model developed herein for predicting ship interaction forces uses as a basis the hypothesis proposed by Havelock that the potential field describing the flow situation without free surface effects is sufficient to explain the interaction phenomenon. This approach seems reasonable in light of certain justifiable assumptions. The first is that the forces sought arise only from a pressure disturbance quantified in terms of a potential description, an assumption justified by the dominance of these forces over other components which might arise from wave pattern interaction near the vessel. Acceptance of this assumption further allows the postulation of a rigid free surface and, thus, makes possible the use of "double-body" models for the vessels under consideration. These simplifications seem valid in light of minimal wave and wake disturbances created by vessels maneuvering at relatively slow speeds in close-proximity operations or in restricted waters.

If the fluid is taken to be ideal, then the flow with a rigid free surface can be modelled using bodies of revolution moving horizontally as there will exist no flow component normal to the waterline plane. The body of revolution model for a vessel can be produced using only a single axial distribution of singularities and, thus, the expensive computation process of surface singularity distributions is avoided. If the additional assumption is now made that the bodies are very slender, or, in other words, the lateral dimensions are small compared to the length of the bodies, the boundary condition may be evaluated on the body axis with the normal assumed in the radial direction without the introduction of noticeable error.

A continuous axial distribution of singularities which represents a body moving in a uniform stream may be represented by the following expression:

$$\Phi(x) = -U(x) + \int_a^b \frac{m(\xi)}{\sqrt{(x-\xi)^2 + y^2 + z^2}} d\xi \quad (1)$$

where  $\Phi(x)$  is the potential description of the body;  $U(x)$  is the free stream velocity;  $a, b$  are end points of the body;  $x, y, z$  are body oriented orthogonal axes; and  $m(\xi)$  is the singularity strength.

With the above assumption, the boundary condition reduces to satisfaction of the condition:

$$q_{\text{radial}}(x) = 0 \quad \text{on the body surface} \quad (2)$$

where  $q_{\text{radial}}(x)$  is the radial velocity with respect to the body oriented axis. Then,

$$-\frac{\partial \Phi(x)}{\partial r} \bigg|_{r=R} = \frac{1}{R} \int_a^b \frac{m(\xi)}{[(\frac{\xi-x}{R})^2 + 1]^{3/2}} d(\frac{\xi-x}{R}) \quad (3)$$

where  $R(x)$  is the radius of the body. This, then, reduces to

$$q_{\text{radial}} \bigg|_{\text{body}} = U \frac{dR}{dx} = \frac{2m(x)}{R} \quad (4)$$

and

$$m(x) = \frac{UR(x)}{2} \frac{dR(x)}{dx} \quad (5)$$

Thus, we may model each of the vessels under consideration as a continuous line source with strengths determined by the expression above. Now, it is apparent that when two or more of these source distributions are brought into proximity, each will induce velocities at points along the other, and thereby will disturb any satisfaction of the body surface boundary conditions established in the earlier approach. However, if we assume that at any discrete point on the surface, this induced cross flow is uniform, an axial distribution of doublets may be sized which will exactly counter this cross flow velocity, and thus restore satisfaction of the boundary condition. The axial perturbations are also accounted for by revising the source strengths.

The potential model for an infinite cylinder in a uniform cross flow may be represented by:

$$\Phi(x) = \int_{-\infty}^{\infty} \frac{\zeta(\xi)y}{r^3} \quad (6)$$

where  $\zeta(\xi)$  is the strength of the axial distribution of doublets;  $y$  is the transverse distance from the axis; and  $r$  is the radial distance from the axis.

This approach is shown by Streeter [1] to yield, under the assumptions made above, the following expression for the strength of the dipole distribution:

$$\zeta(\xi) = \frac{q'_n(\xi)}{4} \left(1 + \frac{A_{22}}{\rho V}\right) R^2(\xi) \quad (7)$$

where  $\zeta(\xi)$  is the dipole distribution strength;  $q'_n(\xi)$  is the cross flow velocity component induced normal to the body on the surface;  $A_{22}$  is the lateral "added mass" of the body; and  $\rho V$  is the mass displacement of the body.

Upon further consideration, it is seen that this may still not be satisfactory as the newly introduced singularities will, in turn, disturb the boundary conditions again. However, by iterating the procedure and resizing the singularity strengths on each body, convergence is obtained and the boundary conditions ultimately satisfied. It has been found that in the situations studied thus far, as few as three iterations are sufficient to insure convergence. Figure 2 gives a graphical representation of the singularity distribution for a typical proximity situation.

Applications of this model in an overall trajectory prediction program will also necessitate consideration of both rotational and lateral body motions. Lateral motion is modelled just as in the procedure above with the added axial dipole distribution possessing a strength derived by the familiar expression:

$$\zeta_v(\xi) = \frac{v}{4} \left(1 + \frac{A_{22}}{\rho V}\right) R^2(\xi) \quad (8)$$

where  $v$  is the lateral velocity of the body and the dipoles are oriented so as to oppose the oncoming flow. Rotational motion can be handled in an analogous manner with the strength of the distribution being:

$$\zeta_\omega(\xi) = \omega \xi R^2(\xi) \left(1 + \frac{A_{22}}{\rho V}\right) \quad (9)$$

where  $\omega$  is the angular velocity and the dipoles are again oriented so as to oppose the oncoming flow.

This, then, forms the core of the interaction model. A conceptualization with appropriate delineation of the axis systems and the orientation to be used in this study is pictured in Figure 3.

It should be noted that this development has proceeded under the assumption of an infinitely deep fluid. The effects of introducing bottom interactions will be explored in a later section.

#### Computation of the Interaction Forces and Moments

Having the potential description for each body, Bernoulli's equation could be used to obtain pressure distributions and, by further integration, forces and moments acting over the body. However, by noting that since the potential description consists of some particular combinations of singularities, be they sources, sinks or dipoles, the integration can be carried out as a first step and, as it were, the force treated as a summation of all differential forces arising from singularity pair interaction. This was first reasoned in 1922 by Lagally and he was able to derive simple expressions relating the force acting on a body to the singularity distribution used to describe it. Lagally's expressions were restricted to steady flow problems but, in 1953, Cummins [2] was able to expand this technique to include unsteady motion. As Cummins showed, if we consider  $\rho$  to be the fluid density;  $m$  to be the source strength in the velocity potential considered with respect to a coordinate system fixed in the body;  $\vec{q}'$  to be the flow induced at the singularity in question from all singularities external to the body;  $\vec{r}$  to be the position vector from the body origin to the singularity in question ( $\vec{r}_g$  being the centroid);  $\vec{\zeta}$  to be the dipole strength;  $\vec{u}_0$  to be the translational velocity of the body;  $\vec{\omega}$  to be the rotational velocity of the body; and if the velocity potential can be expressed as:

$$\Phi = u_\alpha \phi_\alpha + \phi_0 \quad (10)$$

where the  $\phi_\alpha$ 's are the unit potentials for the six possible body motions assuming all other boundaries are at rest; and  $\phi_0$  is the potential representing the motion of all external boundaries assuming the body is at rest (letting  $\phi'_0$  be that arising from singularities which are all external to the body and  $\phi''_0$  be from all internal singularities); then the simplified expressions for the total force and moment acting on the body are as follows:

$$\vec{F} = 4\pi[\rho \frac{d\vec{u}_0}{dt} + \vec{F}_1 + \vec{F}_2 + \vec{F}_3] \quad (11)$$

$$\vec{M} = 4\pi[\rho \vec{r}_g \times \frac{d\vec{u}_0}{dt} + \vec{M}_1 + \vec{M}_2 + \vec{M}_3] \quad (12)$$

$\vec{F}_3$  and  $\vec{M}_3$  are shown to be zero for both sources and doublets and the other terms are:

$$\vec{F}_1 = -\rho[m\vec{q}' + (\vec{\zeta} \cdot \nabla)\vec{q}'] \quad (13)$$

$$\vec{F}_2 = -\rho \frac{d}{dt}[\vec{r}_m + \vec{\zeta}] \quad (14)$$

$$\vec{M}_1 = (\vec{r} \times \vec{F}_1) + \rho(\vec{q}' \times \vec{\zeta}) \quad (15)$$

$$M_{2i} = \frac{d}{dt}(\omega_j A_{3+j,\beta}) - \frac{d}{dt} \rho \int [m_\beta (\phi'_0 + u_j x_j) - m_0 \phi'_\beta - \zeta_{\beta j} (q'_{0j} - u_j) - \zeta_{0j} q'_{\beta j}] \quad (16)$$

$\beta = i + 3$

where  $i$  represents the component under considera-

tion ( $i = 1, 2, 3$ ). This last term was not due to Cummins but Landweber and Yih [3].

It is a straightforward matter to integrate the expression for  $\vec{F}_1$  and  $\vec{M}_1$  into a computer program in order to arrive at expressions for ships on steady courses at constant speeds. In considering this work for inclusion in the overall trajectory model, it was decided that an investigation should be made into the impact of the unsteady terms. Thus, it was necessary to incorporate  $\vec{F}_2$  into the numerical calculation, and also interpret and incorporate the term  $M_{23}$  (unsteady yaw moment).

Zucker [4] points out that the origin of the body must be chosen at a point of zero acceleration or, as is done here, at the centroid, or at a point whose acceleration vector passes through the centroid in order for his expression of Landweber and Yih's results to be applicable. Since the interest here is in the yaw moment,  $i = 3$ , the expression reduces to:

$$M_{23} = \frac{d}{dt}(\omega_j A_{3+j,6}) - \rho \frac{d}{dt} \int [m_6 (\phi'_0 + u_j x_j) - m_0 \phi'_6 - \zeta_{6j} (q'_{0j} - u_j) - \zeta_{0j} q'_{\beta j}] \quad (17)$$

$j = 1, 2, 3$

Now, as was seen in the model description:

$$u_6 \phi_6 = \phi''_6 \quad (18)$$

and, as has been seen,  $\phi''_6$  can be described entirely by a doublet distribution of strength equal to:

$$\omega[\xi R^2(\xi)(1 + \frac{A_{22}}{\rho V})] \quad (19)$$

oriented in the positive and negative  $y$ -directions. Thus,

$$\begin{aligned} m_6 &= 0 \\ \phi'_6 &= 0 \\ \zeta_{6j} (j \neq 2) &= 0 \\ q'_{62} &= 0 \\ \zeta_{02} &= \omega \xi R^2(\xi) (1 + \frac{A_{22}}{\rho V}) \quad \text{where} \end{aligned} \quad (20)$$

$q'_{02}$  is the flow in the  $y$ -direction with respect to body-fixed coordinates induced by external singularities as if the body in question were completely at rest; and  $u_2$  is the translational velocity of the body in the  $y$ -direction. The "virtual" moment term for this particular problem then becomes:

$$M_{23} = \frac{d}{dt}(\omega_3 A_{66}) + \rho \frac{d}{dt} \int [\zeta_{62} (q'_{02} - u_2)] \quad (21)$$

Now, what is really desired are those portions of the expressions above which arise due to the interaction of the bodies which have been modelled. From D'Alembert's paradox, it is seen that the steady-state force, in its entirety, must arise from interaction effects. Thus,

$$(F_x)_{ss} = -4\pi\rho[m \cdot q'_x + \zeta \frac{d}{dy} q'_x] \quad (22)$$

$$\text{and } (F_y)_{ss} = -4\pi\rho[m \cdot q'_y + \zeta \frac{d}{dy} q'_y] \quad (23)$$

Now, there could exist a transient force without the presence of a second body, thus it becomes necessary to separate the transient force terms ( $F_{xtr}$  and  $F_{ytr}$ ) as follows:

$$F_{xtr} = (F_{xtr})_{int} + (F_{xtr})_o = -4\pi\rho \cdot \xi \cdot \frac{d}{dt} \{m_Y(\xi) + m_\eta(\xi)\} \quad (24)$$

$$F_{ytr} = (F_{ytr})_{int} + (F_{ytr})_o = -4\pi\rho \cdot \frac{d}{dt} \{\zeta_Y(\xi) + \zeta_\eta(\xi)\} \quad (25)$$

where  $m_Y$  and  $\zeta_Y$  are due to the presence of the body alone and  $m_\eta$  and  $\zeta_\eta$  are due to the presence of the other body. Thus, the forces sought become:

$$(F_{xtr})_{int} = -4\pi\rho \cdot \xi \cdot \frac{d}{dt} m_\eta(\xi) \quad (26)$$

$$(F_{ytr})_{int} = -4\pi\rho \cdot \frac{d}{dt} \zeta_\eta(\xi) \quad (27)$$

As before, there could exist a steady-state moment without the presence of the other body, so therefore, insurance must be made that the terms included are due only to the presence of the second ship. Thus, terms in the steady-state moment expression which include elements arising entirely from the body under consideration should not be included. Thus, this becomes:

$$M_{ss} = \xi \cdot F_{yss} + 4\pi\rho [q'_{xp} \cdot (\zeta_\omega + \zeta_v) + q'_x \cdot \zeta] \quad (28)$$

where  $q'_{xp}$  is the axial perturbation velocity arising from the presence of the second body;  $q'_x$  is the total axial velocity; and  $\zeta_\omega$ ,  $\zeta_v$ ,  $\zeta$  are as defined previously.

The virtual moment term can be expanded as follows:

$$M_{23tr} = \frac{d}{dt} (\omega_3 A_{66}) + 4\pi\rho [\zeta_{62} \frac{d}{dt} q'_{02} + q'_{02} \frac{d}{dt} \zeta_{62} - u_2 \frac{d}{dt} \zeta_{62} - \zeta_{62} \frac{d}{dt} u_2] \quad (29)$$

Now the terms  $\zeta_{62}$  and  $u_2$  are in no way related to the presence of the second ship as is the first term, thus the virtual interaction moment becomes:

$$(M_{23tr})_{int} = 4\pi\rho [\zeta_{62} \frac{d}{dt} q'_{02} + q'_{02} \frac{d}{dt} \zeta_{62}] \quad (30)$$

In summary, then, the expressions needed for the interaction forces to be included in the trajectory program in terms of their components are as follows:

$$(F_{xss})_{int}(\xi) = -4\pi\rho [m(\xi) \cdot (q'_x - u_{ox}) + (\zeta(\xi) + \zeta_\omega(\xi) + \zeta_v(\xi)) \cdot \frac{dq'_x}{dy}] \quad (31)$$

(since  $\int_{-l/2}^{l/2} m(\xi) u_{ox} d\xi = 0$  is a result of no cross flow on the body surface restriction)

$$(F_{xtr})_{int}(\xi) = -4\pi\rho \cdot \xi \cdot \frac{dm_\eta(\xi)}{dt} \quad (32)$$

$$(F_{yss})_{int}(\xi) = -4\pi\rho [m(\xi) \cdot q'_y + (\zeta(\xi) + \zeta_\omega(\xi) + \zeta_v(\xi)) \cdot \frac{dq'_y}{dy}] \quad (33)$$

$$(F_{ytr})_{int}(\xi) = -4\pi\rho \cdot \frac{d\zeta_\eta(\xi)}{dt} \quad (34)$$

$$(M_{ss})_{int}(\xi) = \xi \cdot F_{yss} + 4\pi\rho [(q'_x - u_{ox}) \cdot (\zeta_\omega + \zeta_v) + q'_x \cdot \zeta] \quad (35)$$

$$(M_{tr})_{int}(\xi) = 4\pi\rho [\zeta_{62} \frac{dq'_{02}}{dt} + q'_{02} \frac{d\zeta_{62}}{dt}] \quad (36)$$

Then the total forces and moments acting on the body are:

$$F_x \text{ int} = \int_{-l/2}^{l/2} [(F_{xss})_{int}(\xi) + (F_{xtr})_{int}(\xi)] d\xi \quad (37)$$

$$F_y \text{ int} = \int_{-l/2}^{l/2} [(F_{yss})_{int}(\xi) + (F_{ytr})_{int}(\xi)] d\xi \quad (38)$$

$$M_{int} = \int_{-l/2}^{l/2} [(M_{ss})_{int}(\xi) + (M_{tr})_{int}(\xi)] d\xi \quad (39)$$

#### The Trajectory Model

The development of a mathematical model and associated computer program with the capability of calculating the interaction forces, both steady and unsteady, on ships in proximity situations provides the remaining necessary information to compute the general trajectories of ships moving close to other ships or canal walls. In the previous section, care was taken to calculate only those forces due to proximity of another body as a function of relative positional coordinates ( $x_o$ ,  $y_o$ , and  $\psi$ ) and the velocity and acceleration components of the ships. The interaction forces as calculated have purposely excluded the forces on the bodies due to the velocities and accelerations of the bodies in open water. Hence, it is only necessary to add to the proximity forces (and moments), those forces on the body which result from the body motions ( $u$ ,  $v$ ,  $r$ ,  $\dot{u}$ ,  $\dot{v}$ ,  $\dot{r}$ ,  $\delta$ ) in unrestricted waters. Mathematical models and computer programs exist and have been readily used for calculating the trajectory of ships in open water using hydrodynamic coefficients theoretically calculated and measured by scaled model tests. Such a mathematical model was introduced by Abkowitz [5], and used by Strom-Tejsten [6] and Calvano [7]. Within the model the forces and moments in the equations of motion are expressed in the form of a Taylor expansion in the body velocity and acceleration components and the rudder deflection.

If the ship is restricted to motion in the horizontal plane without roll, then the general assumption that the forces and moments must depend on ship orientation, velocity, acceleration, and control surface deflection gives the following functional form:



$$\begin{aligned} X &= f_x \\ Y &= f_y(x_0, y_0, \psi, u, v, r, \dot{u}, \dot{v}, \dot{r}, \delta, \dot{\delta}, \dot{n}, \dot{n}) \\ N &= f_n \end{aligned}$$

where  $X$  is the component of force along the ship's longitudinal axis (forward positive);  $Y$  is the component of force along the transverse axis (positive to starboard);  $N$  is the yaw moment (positive bow to starboard);  $f$  represents a functional relationship;  $x_0$  is the longitudinal positional coordinate;  $y_0$  is the lateral positional coordinate;  $\psi$  is the heading angle relative to some given direction;  $u$  is the component of ship's velocity along the longitudinal ship's axis ( $x$ -axis);  $v$  is the component of velocity along the ship's transverse axis ( $y$ -axis);  $r$  is the component of angular velocity about the ship's vertical axis ( $z$ -axis) - i.e., yaw velocity;  $\delta$  is the rudder (control surface) deflection;  $n$  is the rotational speed of the ship's propeller;  $\dot{\cdot}$  a dot above a quantity indicates the derivative of that quantity with respect to time.

It is further assumed that, (i) the forces on the ship due to rudder rate ( $\dot{\delta}$ ) and rudder acceleration ( $\ddot{\delta}$ ) are negligible in comparison to other forces, (ii) the propeller speed ( $n$ ) remains constant during the maneuver, (iii) the forces are linear with respect to the apparent acceleration components  $\dot{u}$ ,  $\dot{v}$ , and  $\dot{r}$ , and (iv) that the non-linear forces on the ship due to  $u$ ,  $v$ ,  $r$  and  $\delta$  of the ship can be adequately expressed through the cubic term of a Taylor expansion. These assumptions have been shown to be valid for the types of trajectory under consideration in this study.

The equations of motion then take the form of:

$$\begin{aligned} (m - X_u)\dot{u} &= f_1(u, v, r, \delta, X_{int}) \\ (m - Y_v)\dot{v} + (mx_G - Y_r)\dot{r} &= f_2(u, v, r, \delta, Y_{int}) \\ (mx_G - N_v)\dot{v} + (I_z - N_r)\dot{r} &= f_3(u, v, r, \delta, N_{int}) \end{aligned}$$

where

$$\begin{aligned} f_1 &= X_* + X_u(\Delta u) + \frac{1}{2}[X_{uu}(\Delta u)^2 + X_{vv}v^2 \\ &+ (X_{rr} + 2mx_G)r^2 + X_{\delta\delta}\delta^2] + (X_{vr} + m)vr \\ &+ X_{r\delta}r\delta + X_{v\delta}v\delta + \frac{1}{6}X_{uuu}(\Delta u)^3 + \frac{1}{2}[X_{vvu}v^2(\Delta u) \\ &+ X_{rru}r^2(\Delta u) + X_{\delta\delta u}\delta^2(\Delta u)] + X_{vru}vr(\Delta u) \\ &+ X_{v\delta u}v\delta(\Delta u) + X_{r\delta u}r\delta(\Delta u) + X_{int} \end{aligned}$$

$$\begin{aligned} f_2 &= Y_* + Y_u(\Delta u) + Y_{uu}(\Delta u)^2 + Y_vv + Y_{\delta\delta}\delta^2 \\ &+ Y_{vu}v(\Delta u) + (Y_r - mu)r + Y_{ru}r(\Delta u) \\ &+ Y_{\delta u}\delta(\Delta u) + \frac{1}{6}[Y_{vvv}v^3 + Y_{rrr}r^3 + Y_{\delta\delta\delta}\delta^3] \\ &+ \frac{1}{2}[Y_{vrr}vr^2 + Y_{v\delta\delta}v\delta^2 + Y_{vu}v(\Delta u)^2 \\ &+ Y_{rvv}rv^2 + Y_{r\delta\delta}r\delta^2 + Y_{ruu}r(\Delta u)^2 + Y_{\delta vv}\delta v^2 \end{aligned}$$

$$+ Y_{\delta rr}\delta r^2 + Y_{\delta uu}\delta(\Delta u)^2] + Y_{vr\delta}vr\delta + Y_{int}$$

$$\begin{aligned} f_3 &= N_* + N_{*u}(\Delta u) + N_{*uu}(\Delta u)^2 + N_vv \\ &+ (N_r - mx_Gu)r + N_{\delta\delta}\delta + N_{vu}v(\Delta u) + N_{ru}r(\Delta u) \\ &+ N_{\delta u}\delta(\Delta u) + \frac{1}{6}[N_{vvv}v^3 + N_{rrr}r^3 + N_{\delta\delta\delta}\delta^3] \\ &+ \frac{1}{2}[N_{vrr}vr^2 + N_{v\delta\delta}v\delta^2 + N_{vu}v(\Delta u)^2 \\ &+ N_{rvv}rv^2 + N_{r\delta\delta}r\delta^2 + N_{ruu}r(\Delta u)^2 + N_{\delta vv}\delta v^2 \\ &+ N_{\delta rr}\delta r^2 + N_{\delta uu}\delta(\Delta u)^2] + N_{vr\delta}vr\delta + N_{int} \end{aligned}$$

where  $m$  is the mass of the ship;  $I_z$  is the moment of inertia in yaw;  $x_G$  is the longitudinal distance from the origin (usually amidships) to the center of gravity, positive forward;  $Y_*$  and  $N_*$  are the initial values of transverse force and yaw moment in straight ahead motion due to asymmetrical effects (single screw with a preferred direction of rotation);  $X_{\text{subscript}}$ ,  $Y_{\text{subscript}}$  and  $N_{\text{subscript}}$  are the partial derivatives of the  $X$ ,  $Y$  and  $N$  hydrodynamic functions respectively, with respect to the subscript, taken at the equilibrium condition of straight ahead motion, i.e.,

$$N_v = \left(\frac{\partial N}{\partial v}\right)$$

$$Y_{\delta vv} = \left(\frac{\partial^3 Y}{\partial \delta \partial v^2}\right);$$

$\Delta u$  is the change in speed during the maneuver; and  $X_{int}$ ,  $Y_{int}$ , and  $N_{int}$  are interaction forces and

moments.

The interaction forces and moments are functions of  $u$ ,  $v$ ,  $r$ ,  $\dot{u}$ ,  $\dot{v}$ ,  $\dot{r}$ ,  $x_{oi}$ ,  $y_{oi}$ ,  $\psi_i$ ,  $u_i$ ,  $v_i$ ,  $r_i$ ,  $\dot{u}_i$ ,  $\dot{v}_i$ , and  $\dot{r}_i$  where the subscript  $i$  refers to other ships in proximity ( $i = 1, 2, \dots$ ) and  $x_{oi}$ ,  $y_{oi}$ ,

and  $\psi_i$  refer to the positional orientation of the ship under consideration with respect to the ship  $i$  nearby.

The solution of the equations for the acceleration components gives

$$\begin{aligned} \dot{u} &= \frac{f_1}{m - X_u} \\ \dot{v} &= \frac{(I_z - N_r)f_2 - (mx_G - Y_r)f_3}{f_4} \\ \dot{r} &= \frac{(m - Y_v)f_3 - (mx_G - N_v)f_2}{f_4} \end{aligned}$$

where

$$f_4 = (m - Y_v)(I_z - N_r) - (mx_G - Y_r)(mx_G - N_v)$$

Since  $u(t) = u_0 + \int \dot{u} dt$  and similarly for  $v(t)$

and  $r(t)$ , the computer can integrate the non-linear functions by step-by-step integration in short increments of time  $\Delta t$  so that

$$u(t + \Delta t) = u(t) + \Delta t \cdot \dot{u}(t)$$

$$v(t + \Delta t) = v(t) + \Delta t \cdot \dot{v}(t)$$

$$r(t + \Delta t) = r(t) + \Delta t \cdot \dot{r}(t)$$

The trajectory of each ship,  $x_0$ ,  $y_0$ , and  $\psi$ , can similarly be calculated by this same step-by-step progress in accordance with the following relationships,

$$x_0(t) = \int (u \cos \psi + v \sin \psi) dt$$

$$y_0(t) = \int (u \sin \psi + v \cos \psi) dt$$

$$\psi(t) = \int r dt$$

With the positional orientation in space of each ship now calculated the relative orientation between two ships can be obtained through subtraction and  $x_{0i}$ ,  $y_{0i}$ , and  $\psi_{0i}$  obtained, and these values along with other variables are then put into the force functions  $f_1$ ,  $f_2$ , and  $f_3$  to determine the trajectory over the next increment of time,  $\Delta t$ .

We now have a trajectory mathematical model and associated computer program for calculation of the absolute and relative motion of several ships operating close to one another.

As mentioned in the introduction, the overall maneuverability of the ship depends on the ship and control system design and how well the skipper shows skill and caution in the handling of the rudder action, including the knowledge of what situations to avoid. Hence, there is the human element in the exercise of critical maneuvers in certain ship operations. The trajectory model includes the effects of a rudder deflection,  $\delta(t)$ , but it is expected that decisions as to what rudder action should be called for will be outside the trajectory model. The next section deals with the simulation of skipper action during an operational maneuver.

#### Applications to Operational Procedures

With these three tools: a potential description model, a force computation model; and a trajectory model, it becomes possible to derive time histories for vessels operating in close proximity.

In order to allow the model to operate in a realistic manner, it was necessary to somehow arrive at a method for determining helm and lee helm orders that the steersmen of the vessels would be receiving during the course of the simulation. That is to provide values of indicated rudder angle and desired speed to the equations of motion during each time interval. There were two approaches to this problem, the first being to allow computer-individual interaction and actually have two people sit and review their specific situations at each time interval and return to the computer, as continuing input, values of rudder angle and desired speed. The other was to develop some sort of automatic control routine, inherent in the model, that

would furnish these values after operating in some manner on the variables of significance.

Upon initial consideration, it would seem that the most desirable of these options would be the first, in that the human element in the real time situation is exactly accounted for as long as individuals interacting with the model are cautioned to react in a manner appropriate to the developing situation. In addition, with human interaction, actual situations involving disasters or near-disasters can be simulated as long as rudder traces and bell-books for the vessels involved are obtainable. Unfortunately, this is much more expensive than inherent control techniques, and it was decided that subroutines should be developed which would provide values for these control variables so that model development cost could be minimized. In hindsight, it seems this was a beneficial choice in that the computational model may now be modified to allow interaction if that is desired, and an inherent control option exists and thus, is available to investigate differing types of automatic control systems.

Individuals on the bridge of a ship underway as well as most commercially available control sensors are sensitive only to the following variables:

- 1) absolute position;
- 2) position relative to another body;
- 3) absolute velocities (linear and angular);
- 4) relative velocities (with respect to another body);
- 5) absolute orientation (heading angle); and
- 6) relative orientation (with respect to another body).

Thus, the control operators chosen should be functions of these variables, and it was decided to use operators which were linear functions of these variables with different sets of control coefficients representing different "personalities" in control of the vessels. Now it was further decided that in the simulations to be run as demonstrations of this system, the situation to be modelled would be the underway replenishment evolution. In this process one ship, known as the guide, usually the replenishment ship, endeavors to maintain a constant heading and constant speed while the other moves slowly into replenishment station from aft of the guide. Upon reaching station, this vessel attempts to parallel the guide's course and match his speed until the replenishment transfers are completed, whereupon he increases his speed and turns away in what is termed the "breakaway". As such it was recognized that in the control expressions, the guide would be sensitive to absolute position, heading angle, yaw rate, and absolute velocity, while the approaching ship should be sensitive to relative position, relative heading, relative yaw rate and relative velocity. Upon further consideration it was felt to initially consider the guide's sensitivity to absolute position as negligible in that most replenishment operations occur in the open sea and it is both unnecessary and impossible for the replenishment ship to pinpoint his location with any accuracy. Thus, the control equations for the guide are as follows:

$$\begin{aligned} DR_1 = & K_{11}(\psi_1 - r \cdot CLAG_1) + K_{12}(r - CLAG_1 \cdot \dot{r}) \\ & + K_{13}(y_0 - v \cdot CLAG_1) + K_{14}(v - \dot{v} \cdot CLAG_1) \end{aligned}$$

where  $DR$  is the rudder angle;  $\psi$  is the heading angle;  $r$  is the angular velocity;  $y_0$  is the absolute lateral distance from the origin;  $v$  is the linear velocity parallel to  $y_0$ -axis;  $CLAG$  is the time delay in control system response (rudder system);  $K_{1j}$  are

control coefficients ( $j = 1, 2, 3, 4$ ).

With the assumptions above,  $K_{13}$  and  $K_{14}$  were set equal to zero, and in order to rid the initial simulation of as many variables as possible, CLAG was also considered as negligible. Thus, the equation reduced to:

$$DR_1 = K_{11}\psi_1 + K_{12}r$$

The speed equation was as follows:

$$u_1 = u_1 + K_{15}(u_{01} - u_1 + u_1 \cdot DLAG_1)$$

where  $u_1$  is the actual velocity of the vessel;  $u_{01}$  is the desired velocity; DLAG is the time delay in control system response (propeller system); and  $K_{15}$  is the control coefficient. In the same manner as before, this equation was initially reduced to:

$$u_1 = u_1 + K_{15}(u_{01} - u_1)$$

It should be pointed out here that if it is so desired, CLAG, DLAG,  $K_{13}$  and  $K_{14}$  values can be inserted in the simulation as this option has been provided in the input subroutine. Thus, no generality has been sacrificed.

As could be expected, the control provisions for the ship to be replenished are somewhat more complex. First, three separate time intervals must be considered: the approach, the replenishment evolution, and the breakaway.

During the approach, the ship to be replenished would begin at some distance aft and to the beam of the guide and would slowly approach his replenishment station directly abeam of the guide. When there, he would then attempt to maintain this station, deviating only at the completion of the evolution when he would slowly increase his speed and then turn away when assured that his stern was clear of the guide's bow. In the simulation, these differing situations are accounted for by various routines which analyze the ship's relative position and the time and operate accordingly. Until the approaching ship is within a lateral distance of twice the desired supply interval, he will continue his approach at the initial approach angle and speed. Upon entering this envelope, a switch is made so that the ship comes under the control of an operator similar to that of the guide but now sensitive to relative position and velocities. The control equation for the rudder angle is as follows:

$$\begin{aligned} DR_2 = & K_{21}[\psi_2 - \psi_1 - (r_2 - r_1)CLAG_2] \\ & + K_{22}[r_2 - r_1 - (\dot{r}_2 - \dot{r}_1)CLAG_2] \\ & + K_{23}\{(Y_2 - Y_1)\cos\psi_1 - (x_2 - x_1)\sin\psi_1 \\ & - (SUPPLY + \frac{BMLD_1}{2} + \frac{BMLD_2}{2\cos(\psi_2 - \psi_1)})SIDE \\ & + [(v_2 - v_1)\cos\psi_1 - (u_2 - u_1)\sin\psi_1]CLAG_2\} \\ & + K_{24}\{(v_2 - v_1)\cos\psi_1 - (u_2 - u_1)\sin\psi_1 \\ & - [(\dot{v}_2 - \dot{v}_1)\cos\psi_1 - (\dot{u}_2 - \dot{u}_1)\sin\psi_1]CLAG_2\} \end{aligned}$$

where SUPPLY is the desired lateral separation; BMLD is the molded beam of the vessel; and SIDE is a multiplier which controls the sign depending on which side of the guide the approaching vessel is on.

As before, in the initial simulations, CLAG<sub>2</sub> will be taken as negligible and the equation becomes:

$$\begin{aligned} DR_2 = & K_{21}(\psi_2 - \psi_1) + K_{22}(r_2 - r_1) \\ & + K_{23}\{(Y_2 - Y_1)\cos\psi_1 - (x_2 - x_1)\sin\psi_1 \\ & - (SUPPLY + \frac{BMLD_1}{2} + \frac{BMLD_2}{2\cos(\psi_2 - \psi_1)})SIDE\} \\ & + K_{24}\{(v_2 - v_1)\cos\psi_1 - (u_2 - u_1)\sin\psi_1\} \end{aligned}$$

The speed control for the ship to be replenished while in the replenishment envelope was also more involved. A routine was developed which controls the speed of the vessel sensitive to relative position and one control coefficient which allows the "personality" of the bridge to be varied from slow and cautious to quick and daring. This is accomplished by determining at what longitudinal separation the approaching ship will begin to slow. Knowing that he desires to be at zero relative speed when abeam, it is then assumed that the relative speed versus longitudinal separation curve will vary as the square of the relative velocity. This allows a desired speed to be determined. This is compared to the actual velocity and speed change which are made realizing that increments must be restricted to practical values to allow for acceleration and deceleration. During research, it was found that the maximum deceleration possible in most vessels was approximately 0.14 feet per second per second while acceleration was limited to a value of about 0.18 feet per second per second. As an example, suppose it is desired to begin deceleration at a longitudinal separation of 200 feet and that at this point there will be a relative speed of the approaching vessel of 2 knots. Thus,

$$\text{Longitudinal Separation} = (\text{Control Coefficient}) \times (\text{Relative Velocity})^2$$

or

$$\begin{aligned} XREL2 &= (PERS)(VELOC)^2 \\ 200 &= (PERS)(2 \cdot 1.6889)^2 \\ PERS &= 17.53 \end{aligned}$$

and the desired relative velocity (DES) will be determined by

$$DES = \frac{XREL2}{17.53}$$

Now, at the point in time at which it has been determined that breakaway should begin, a switch is again made which speeds the replenished ship to a relative velocity of five knots and holds him on a parallel course until his stern is clear of the guide's bow at which time he is turned away until clear of the envelope. This completes the range of desired options which could be called in the simulation as far as control is concerned. The only remaining step was to determine values for the



control coefficients which would provide stabilizing influence on the ships just as human operators on the bridges would. The results of various choices will be shown in a later section.

## COMPUTED RESULTS AND DISCUSSION

### Steady State Force and Moment Computations

The first calculations made and results obtained were used to check the validity of the interaction force and moment model. Sizing the singularities by matching sectional areas of the vessels under consideration with those of the derived bodies of revolution yielded results which compared with experimental results as shown in Figure 4 for the Taylor Models [8]. It was felt that the large discrepancy was the result of the fact that this sectional area modelling severely oversized the beam of the vessel at the bow and stern areas as is shown in Figure 5. The first correction procedure attempted was to size the body of revolution by taking the average of the real beam and the radius determined by the sectional area curve alone. The reasoning behind this choice was the search for some compromise between accounting for the proper underwater volume disturbance creating the pressure and the correct distance over which it was to react to the presence of the other disturbance. The graphical results for this averaging technique are shown in Figure 6. Of the other methods of correction attempted, none yielded results comparable to these and, thus, it was decided to use this method for the model.

Comparisons between theoretical results derived from the model and experimental data from both the Admiralty Experimental Works in Haslar [9] and the David W. Taylor Naval Ship Research and Development Center [10] are pictured in Figures 7 through 10. Agreement is quite good with the most obvious discrepancy appearing as a phase difference in the moment curve. It is felt that this discrepancy arises due to the departure of the experimental flow from that modelled in the theoretical approach as a result of separation and wake formation. This, in effect, "lengthens" the vessel defined by streamlines and would cause a slight increase in the interaction force and a shift in the point of zero moment which would more closely correlate with the experimental curves. The fact that the Taylor models did not possess transom sterns probably accounts for the better phase correlation in that case. As the correlation was still quite good and with no sound theoretical approach to accounting for this effective increase in ship length, it was decided to accept this discrepancy as it was felt it would not significantly alter the conclusions which could be drawn from exercising the trajectory model.

### Effects of Unsteady Forces and Moments

In order to include unsteady force and moment components in the trajectory prediction model, the interaction force model had to be used at every time interval. If unsteady terms could be ignored, it would be possible to arrive at cross-faired sets of curves for the forces and moments and place the data in memory storage for later retrieval, thus saving the expense of continually calling a subroutine involving large numbers of calculations. Therefore, a comparison was made in a representative case both including and excluding unsteady effects. The results are shown in Figure 11. It is seen that unsteady effects, while relatively insignifi-

cant in the case of the interaction force, can significantly affect the interaction moment. Thus, it was decided to include unsteady terms in the total model.

### Replenishment at Sea Operation

With the above determined, it was then possible to run the entire model. The control coefficients were varied in order to find a set which yielded a stable situation with the vessels alongside. One of these early attempts is shown in Figure 12 for the case of a simulated replenishment operation between two Mariner ships where the controller of the tracking vessel was not given adequate sensitivity to lateral separation and thereby allowed his vessel to collide with the guide after approximately 5 minutes.

The results of a proper selection are shown in Figure 13 where the vessels stabilize in an along-side position with approximately 70 feet lateral separation. As has been found in actual practice, in order to counteract the interaction forces and moments it is seen that steady state values of yaw angle and rudder angle must be maintained by each vessel. In the case pictured, these values are:

#### Ship One (Guide):

Rudder Angle  $5^\circ$   
Yaw Angle  $10^\circ$

#### Ship Two (Tracking Vessel):

Rudder Angle  $-3^\circ$   
Yaw Angle  $-1.4^\circ$

### The Overtaking Maneuver

Ship collisions have occurred in harbors when a small vessel overtakes a larger vessel at small relative speeds but at moderate ship speeds. The smaller ship seems to swing across the bow of the larger ship. If the passing is attempted at too small a distance abeam, then there is a possibility that even with optimum rudder action on the part of the helmsman, a collision is unavoidable. Figure 14 shows the interaction force and moment on the smaller vessel as calculated for a 300-foot ship (of Mariner geometry) overtaking a 900-foot tanker with 100 feet between hull sides (about 2.5 times the beam of the smaller ship). Also shown in Figure 14 is the required rudder angle to counteract the interaction moment. If the maximum available rudder deflection is 35 degrees, then if the helmsman had supernatural powers and immediately sensed the interaction moment and the ship had super controls without time lags, the interaction moment would just be able to be counteracted by rudder moment. However, the skipper does not sense the moment as it occurs but some time later after the ship has picked up an angular velocity and heading change and the control system has definite time lags.

The overtaking maneuver model can be effectively used in determining rules of the road for overtaking maneuvers in harbors to assure the proper safety in harbor traffic control.

### Shallow Water Effects

During the development of the interaction force and moment model described earlier, it was realized that an obvious extension to the approach would be the inclusion of a method to account for finite water depth so that bottom proximity effects on

these forces could be investigated. In addition, it was realized that a useful byproduct of such an extension would be the calculation of vertical forces and moments acting on the ships due to the proximity of the bottom. Yeung [11], using the equations obtained by Wehausen based on Lagrangian formulation, has developed a computer program which yields values for sinkage and trim for a ship operating in very deep water. Thus, to a first approximation, by adding these values and those resulting from shallow water interaction, total sinkage and trim could be evaluated and used to predict such things as maximum safe speeds in shallow harbors and channels.

In order to represent the presence of a finite depth, a reflection of the potential model as derived earlier is introduced in the plane wherein it is desired to place the bottom. Thus, the boundary condition at the bottom is immediately satisfied, but the question arises as to the perturbation effect this will have on the satisfaction of the body surface boundary conditions. It is true that these will be disturbed; however, by introducing a vertical dipole distribution to correct for the normal cross flow at the keel and iterating between both vessels and their images, convergence to a correct solution is possible. Figure 15 shows the arrangement of the vessels and images. This arrangement also represents the effect of a near canal wall placed midway between the two hulls. It should be noted that in this case of the vertical dipoles, their strengths are sized in relation to actual draft at the keel at each station. Again, making use of Lagally's Theorem as extended by Cummins, Landweber and Yih, the forces acting on each vessel are obtainable. The method for perturbation velocities at a point on one body in terms of that body's axis system due to a singularity at another point on the other body is shown in Appendix I.

With the model thus established, plots of force and moment as caused by changes in water depth may be investigated. These are presented in Figures 16 and 17. The first interesting fact to notice is that even in water of such a depth as to be ordinarily considered infinite, the satisfaction of the additional keel boundary condition has caused approximately a 10% increase in force and moment which represents a better fit to the station shape than the original semi-circular approximation. It is also immediately apparent that decreasing water depth greatly increases the interaction forces and moments and thus could play a major role in the possibility of collision between vessels operating in close proximity. In addition, as shown by experimental results, there exists a sinkage and trim effect on vessels operating in shallow water. Finally, it appears that all these effects seem to begin to become significant in a relatively narrow depth/draft ratio range for a ship operating at a specific Froude number.

#### CONCLUDING REMARKS

The availability of a complete trajectory model and associated computer program provides a valuable and relatively inexpensive tool for the design of ships' control systems and the development of ship operational procedures with the view of obtaining acceptable if not optimum performance of the ship in pursuing its mission requirements. The technique of simulating the ship with a relatively uncomplicated distribution of singularities has kept down the computer time and costs required to calculate the proximity forces, yet gives computed values for these forces which agree with towed model test results as well as, and probably better

than those obtained by other methods.

Analysis of the results of simulated maneuvers such as ships passing in a canal, overtaking one another in a harbor, in replenishment operations, or in convoy formation can provide information on the desired level of dynamical stability required, the proper size and design of rudders, and the necessary items for proper control system design such as rudder rate, control gains, and motion parameter sensitivity.

For a given ship, analysis of simulated maneuvers can provide optimization of operational performance of a given mission, can provide advance information of what situations to avoid, can provide sort of training experience to skippers, and can help develop acceptable harbor traffic routing patterns and rules of the road.

It is planned to make significant use of the trajectory model and program in the near future in the relevant areas of ship design and operation.

#### ACKNOWLEDGEMENT

The authors wish to acknowledge the support of and assistance to this project given by the U.S. Navy and the staff of the Department of Ocean Engineering at MIT.

#### REFERENCES

1. Streeter, V.L., Handbook of Fluid Dynamics, McGraw-Hill Book Company, Inc., New York, New York, 1961.
2. Cummins, W.E., "The Forces and Moments Acting on a Body Moving in an Arbitrary Potential Stream", David Taylor Model Basin Report No. 780, Washington, D.C., June, 1953.
3. Landweber, L. and C.S. Yih, "Forces, Moments and Added Masses for Rankine Bodies", Journal of Fluid Mechanics, Vol. 1, September, 1956, pp. 319-336.
4. Zucker, R.D., "Lagally's Theorem and the Lifting Body Problem", Journal of Ship Research, Vol. 14, June, 1970, pp. 135-141.
5. Abkowitz, M.A., Stability and Motion Control of Ocean Vehicles, MIT Press, Cambridge, Mass., 1969.
6. Strom-Tejsten, J., "A Digital Computer Technique for Prediction of Standard Maneuvers of Surface Ships", David Taylor Model Basin Report No. 2130, December, 1965.
7. Calvano, C.N., "An Investigation of the Stability of a System of Two Ships Employing Automatic Control While on Parallel Courses in Close Proximity", MIT Thesis, Ocean Engineering, 1970.
8. Fortson, R.M., "Interaction Forces Between Ships", MIT Thesis, Ocean Engineering, 1974.
9. Newton, R.N., "Some Notes on Interaction Effects Between Ships Close Aboard in Deep Water", First Symposium on Ship Maneuverability, David Taylor Model Basin Report No. 1461, Washington, D.C., October, 1960, pp. 1-24.
10. Layne, D.E., "Interaction Effect of a Large Aircraft Carrier (CVA) on a Fast Combat Support Ship (AOE) When in Close Proximity to One Another", DTNSRDC Report in Preparation.
11. Yeung, R.W., "Sinkage and Trim in First Order Thin Ship Theory", Journal of Ship Research, March, 1972, pp. 47-53.

#### APPENDIX I

A necessary step in the derivation of the model presented in the body of this paper was the determination of the expressions for the velocities and velocity gradients induced by a singularity at one

point on the body at another point on another body. That is, consider a singularity triplet consisting of a source strength  $m$  and two dipoles of strength  $\zeta_z$  and  $\zeta_y$  at point 1 on body K. It is necessary to find the velocities and velocity gradients induced at point 2 on body 1 in terms of the variables describing the axis system of ship 1. The potential strength induced by these singularities at point 2 in terms of the axis system of Ship K is then  $\phi_K(2)$  where

$$\phi_K(2) = \frac{m}{r_{12}} + \frac{\zeta_y \cos \theta_{12} y}{r_{12}^2} + \frac{\zeta_z \cos \theta_{12} z}{r_{12}^2}$$

Note that in the problem addressed by this paper, singularity contributions at two other points in space will have to be considered, but the method is analogous and for the sake of simplicity, they will not be included here.

Now it can be seen from Figure 18 that

$$r_{12} = \sqrt{x^2 + y^2 + z^2}$$

$$\text{and } \cos \theta_{k,y} = y_k / r_{12} \quad \cos \theta_{k,z} = z_k / r_{12}$$

Thus,

$$\begin{aligned} \phi_K(2) = & \frac{m}{(x_k^2 + y_k^2 + z_k^2)^{1/2}} + \frac{\zeta_y y_k}{(x_k^2 + y_k^2 + z_k^2)^{3/2}} \\ & + \frac{\zeta_z z_k}{(x_k^2 + y_k^2 + z_k^2)^{3/2}} \end{aligned}$$

If we neglect roll and let  $V_0$  be a vector measure in a fixed reference frame, and  $V_{I,k}$  be vector measures in the reference frame moving with ships I and K respectively, Then,

$$V = T(\theta, \psi) V_0$$

where  $\theta$  is the trim angle and  $\psi$  is the yaw angle.

$$T(\theta, \psi) = \begin{vmatrix} \cos \theta \cos \psi & \cos \theta \sin \psi & -\sin \theta \\ -\sin \psi & \cos \psi & 0 \\ \cos \psi \sin \theta & \sin \psi \sin \theta & \cos \theta \end{vmatrix}$$

then  $V_0 = T^{-1}(\theta, \psi)$  where:

$$T^{-1}(\theta, \psi) = \begin{vmatrix} \cos \psi \cos \theta & -\sin \psi & \sin \theta \cos \psi \\ \sin \psi \cos \theta & \cos \psi & \sin \theta \sin \psi \\ \sin \theta & 0 & \cos \theta \end{vmatrix}$$

Then to change a vector measure in terms of Ship K's moving axis system to one in terms of Ship I's moving axis system, all that is necessary is the following:

$$\begin{vmatrix} x_k \\ y_k \\ z_k \end{vmatrix} = T_k T_I^{-1} \begin{vmatrix} x_I \\ y_I \\ z_I \end{vmatrix}$$

and, after reduction:

$$T_k T_I^{-1} = \begin{vmatrix} \cos(\psi_k - \psi_I) \cos \theta_k \cos \theta_I + \sin \theta_k \sin \theta_I \\ \cos \theta_I \sin(\psi_I - \psi_k) \\ \cos(\psi_k - \psi_I) \sin \theta_k \cos \theta_I - \sin \theta_I \cos \theta_k \\ \cos \theta_k \sin(\psi_k - \psi_I) \\ \cos(\psi_k - \psi_I) \\ \sin \theta_k \sin(\psi_k - \psi_I) \end{vmatrix}$$

$$\begin{vmatrix} \cos \theta_k \sin \theta_I \cos(\psi_k - \psi_I) - \sin \theta_k \cos \theta_I \\ \sin \theta_I \sin(\psi_I - \psi_k) \\ \sin \theta_k \sin \theta_I \cos(\psi_k - \psi_I) + \cos \theta_k \cos \theta_I \end{vmatrix}$$

Now, the vector  $r_{12}$  = Position 2 - Position 1

$$\vec{r}_{12} = \begin{bmatrix} x_1(I) \\ y_0(I) \\ z_0(I) \end{bmatrix} + T_I^{-1} \begin{bmatrix} x_1(2) \\ 0 \\ 0 \end{bmatrix} - \begin{bmatrix} x_0(k) \\ y_0(k) \\ z_0(k) \end{bmatrix} - T_k^{-1} \begin{bmatrix} x_k(1) \\ 0 \\ 0 \end{bmatrix}$$

After reduction this becomes in terms of Ship I's reference system:

$$\begin{aligned} x_I = & [x_0(I) - x_0(k)] \cos \theta_I \cos \psi_I + [y_0(I) - y_0(k)] \cos \theta_I \sin \psi_I \\ & - [z_0(I) - z_0(k)] \sin \theta_I + x_k(2) - x_k(1) [\cos \theta_k \cos \theta_I (\psi_k \\ & - \psi_I) + \sin \theta_k \sin \theta_I] \end{aligned}$$

$$\begin{aligned} y_I = & -[x_0(I) - x_0(k)] \sin \psi_I + [y_0(I) - y_0(k)] \cos \psi_I \\ & + x_k(1) \cos \theta_k \sin(\psi_I - \psi_k) \end{aligned}$$

$$\begin{aligned} z_I = & [x_0(I) - x_0(k)] \cos \psi_I \sin \theta_I + [y_0(I) - y_0(k)] \sin \theta_I \sin \psi_I \\ & + [z_0(I) - z_0(k)] \cos \theta_I - x_k(1) [\sin \theta_I \cos \theta_k \cos(\psi_I - \psi_k) \\ & - \cos \theta_I \sin \theta_k] \end{aligned}$$

and if we let

$$A = \cos \theta_I \sin(\psi_I - \psi_k)$$

$$B = \cos(\psi_I - \psi_k)$$

$$C = \sin \theta_I \sin(\psi_I - \psi_k)$$

$$D = \cos(\psi_I - \psi_k) \sin \theta_k \cos \theta_I - \sin \theta_I \cos \theta_k$$

$$E = -\sin \psi_k \sin(\psi_I - \psi_k)$$

$$F = \cos(\psi_I - \psi_k) \sin \theta_k \sin \theta_I + \cos \theta_k \cos \theta_I$$

$$G = \cos(\psi_I - \psi_k) \cos \theta_k \cos \theta_I + \sin \theta_k \sin \theta_I$$

$$H = -\cos \theta_k \sin(\psi_I - \psi_k)$$



$$Q = \cos(\psi_I - \psi_K) \cos \theta_K \sin \theta_I - \sin \theta_I \sin \theta_K \cos \theta_I$$

then

$$\vec{x}_K = \vec{x}_I G + \vec{y}_I H + \vec{z}_I Q$$

$$\vec{y}_K = \vec{x}_I A + \vec{y}_I B + \vec{z}_I C$$

$$\vec{z}_K = \vec{x}_I D + \vec{y}_I E + \vec{z}_I F$$

and

$$\phi \left| \begin{array}{l} \text{at pt. on Ship I} \\ \text{due to sings. on} \\ \text{Ship K, in terms} \\ \text{of Ship I} \end{array} \right. = \frac{m}{[x_K^2 + y_K^2 + z_K^2]^{1/2}} + \frac{\zeta_y [Ax_I + By_I + Cz_I]}{[x_K^2 + y_K^2 + z_K^2]^{3/2}} + \frac{\zeta_z [Dx_I + Ey_I + Fz_I]}{[x_K^2 + y_K^2 + z_K^2]^{3/2}}$$

It can be shown that  $[x_K^2 + y_K^2 + z_K^2] = [x_I^2 + y_I^2 + z_I^2]$

therefore:

$$\phi \left| \begin{array}{l} \text{at pt. on Ship I} \\ \text{due to sings. on} \\ \text{Ship K, in terms} \\ \text{of Ship I} \end{array} \right. = \frac{m}{[x_I^2 + y_I^2 + z_I^2]^{1/2}} + \frac{\zeta_y [Ax_I + By_I + Cz_I]}{[x_I^2 + y_I^2 + z_I^2]^{3/2}} + \frac{\zeta_z [Dx_I + Ey_I + Fz_I]}{[x_I^2 + y_I^2 + z_I^2]^{3/2}}$$

It is a simple but tedious matter to now differentiate to obtain:

$$\frac{\partial \phi}{\partial x}, \frac{\partial^2 \phi}{\partial x \partial y}, \frac{\partial^2 \phi}{\partial x \partial z}, \frac{\partial \phi}{\partial y}, \frac{\partial^2 \phi}{\partial y^2}, \frac{\partial^2 \phi}{\partial y \partial z}, \frac{\partial \phi}{\partial z}, \frac{\partial^2 \phi}{\partial z \partial y},$$

and  $\frac{\partial^2 \phi}{\partial z^2}$  in order to use them in the force and moment expressions.

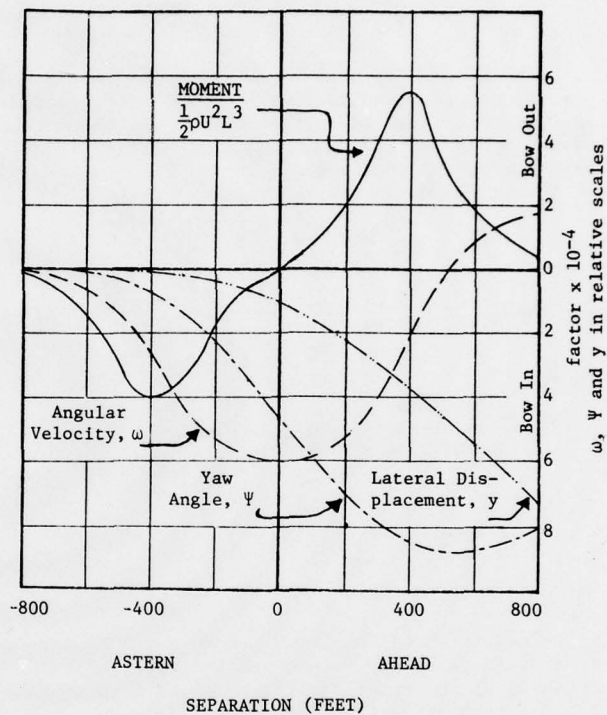
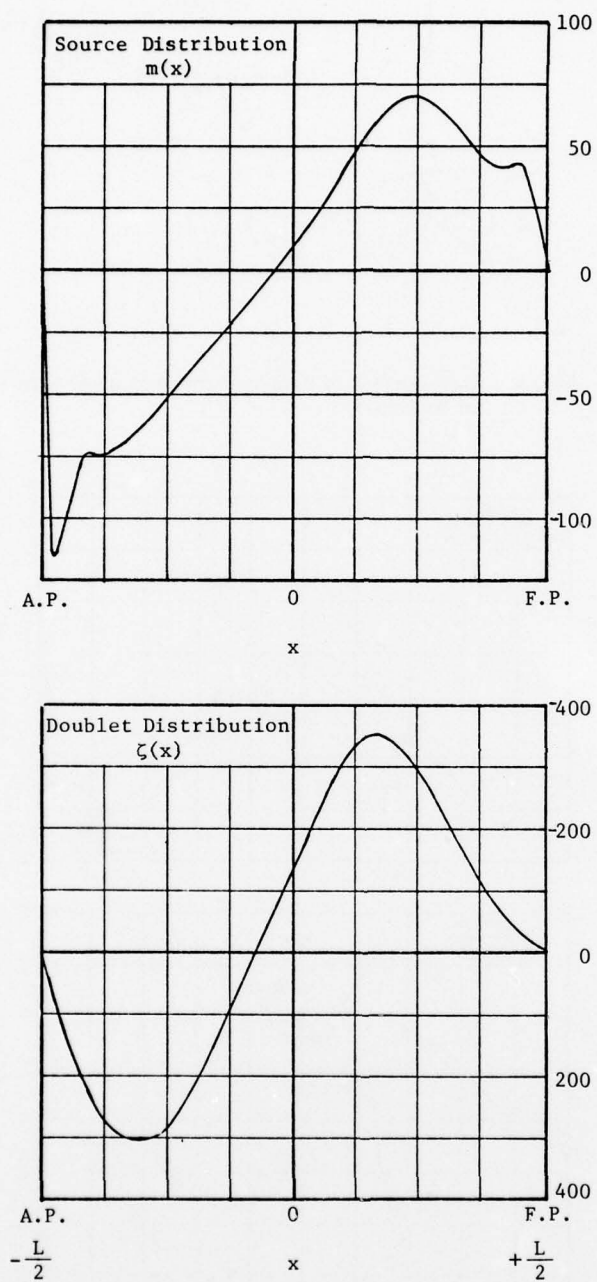


Fig. 1: Comparison of "Static" and "Dynamic" effects in an overtaking maneuver.



**Fig. 2: Singularity distribution approximating the flow about a ship for a typical proximity situation.**

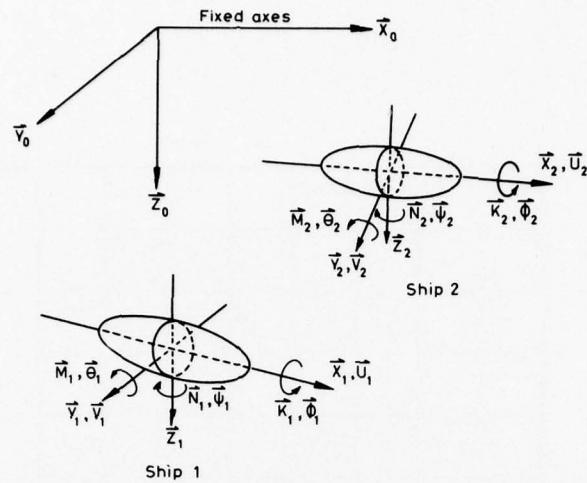


Fig. 3: Delineation of axis systems and orientation of bodies.

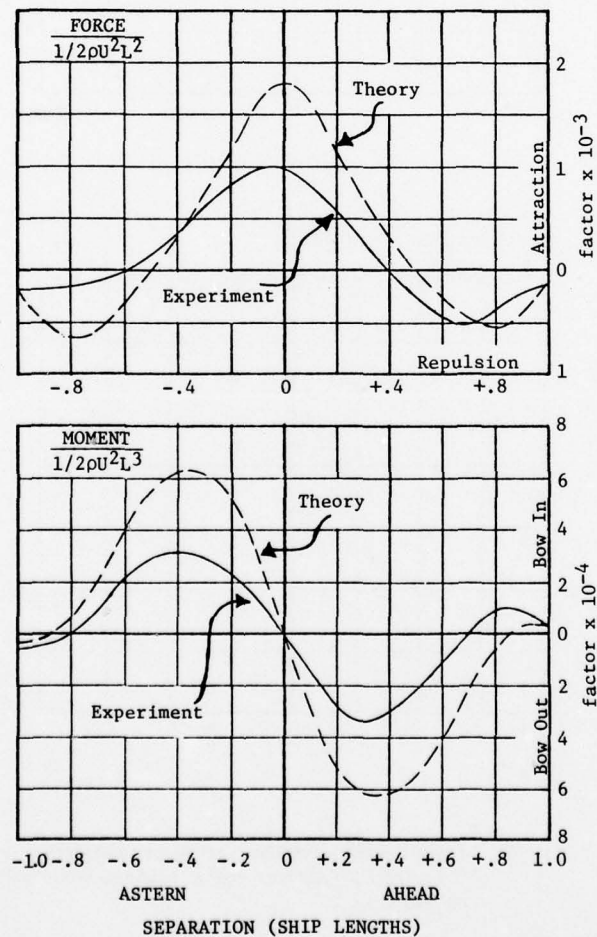


Fig. 4: Comparison between theoretical calculations and model tests for the interaction forces on a Taylor model (beam based on sectional area).



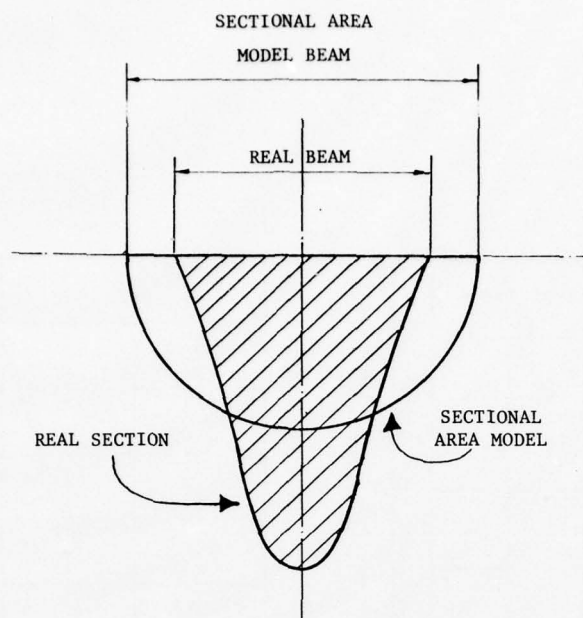


Fig. 5: Sectional beam based on sectional area.

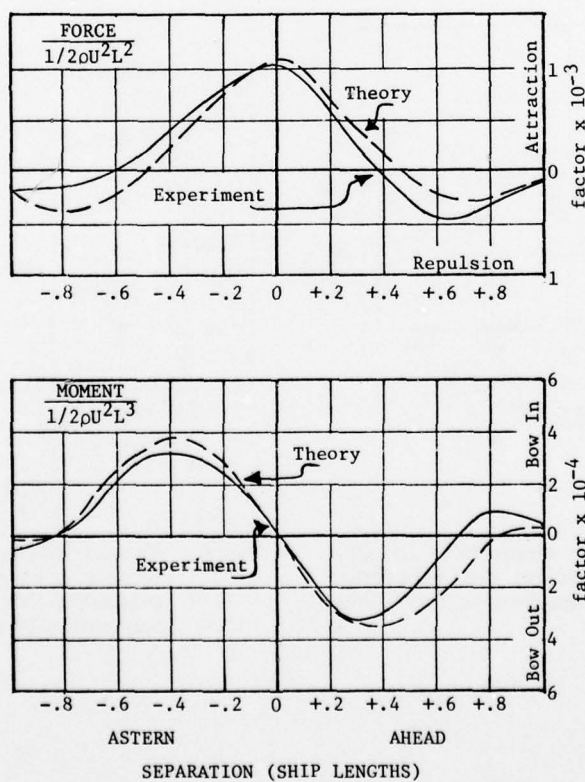


Fig. 6: Comparison between theoretical calculations and model tests for the interaction forces on a Taylor model (beam sized as average of actual beam and sectional area beam).

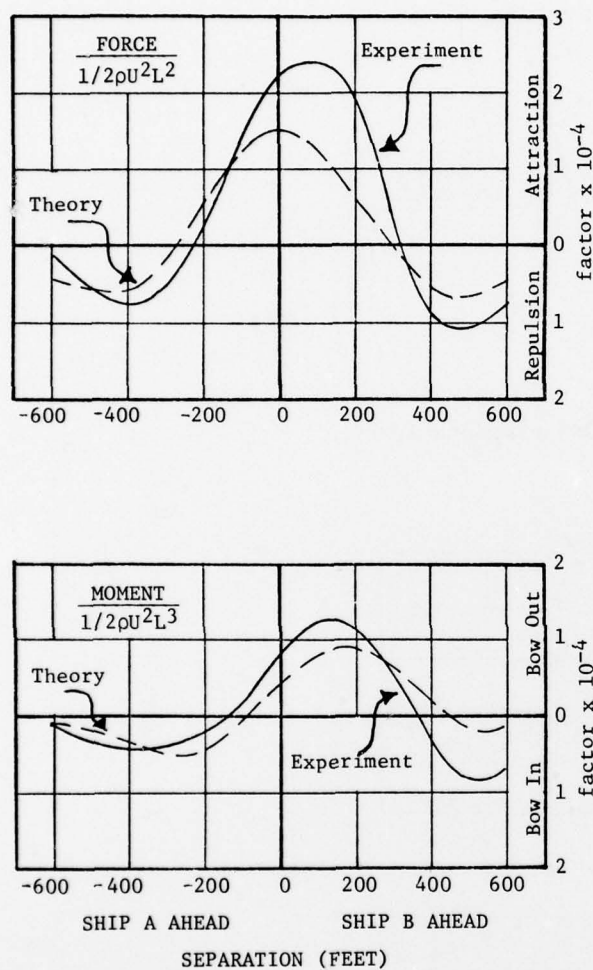


Fig. 7: Comparison between theoretical calculations and model tests for the interaction forces on ship A "King George V" (lateral separation 100 ft.)

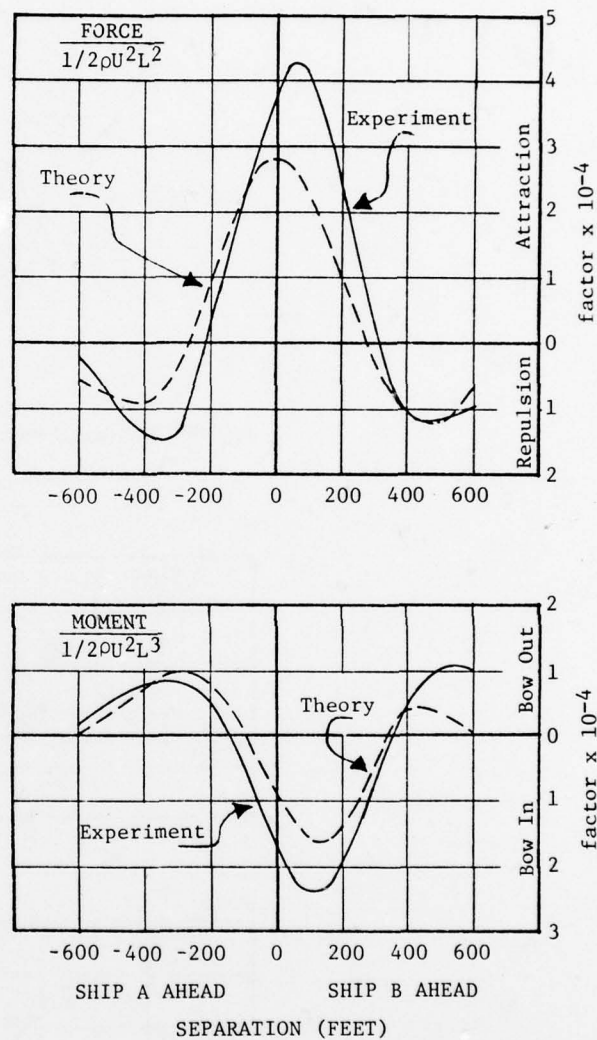


Fig. 8: Comparison between theoretical calculations and model tests for the interaction forces on ship A "King George V" (lateral separation 50 ft.)

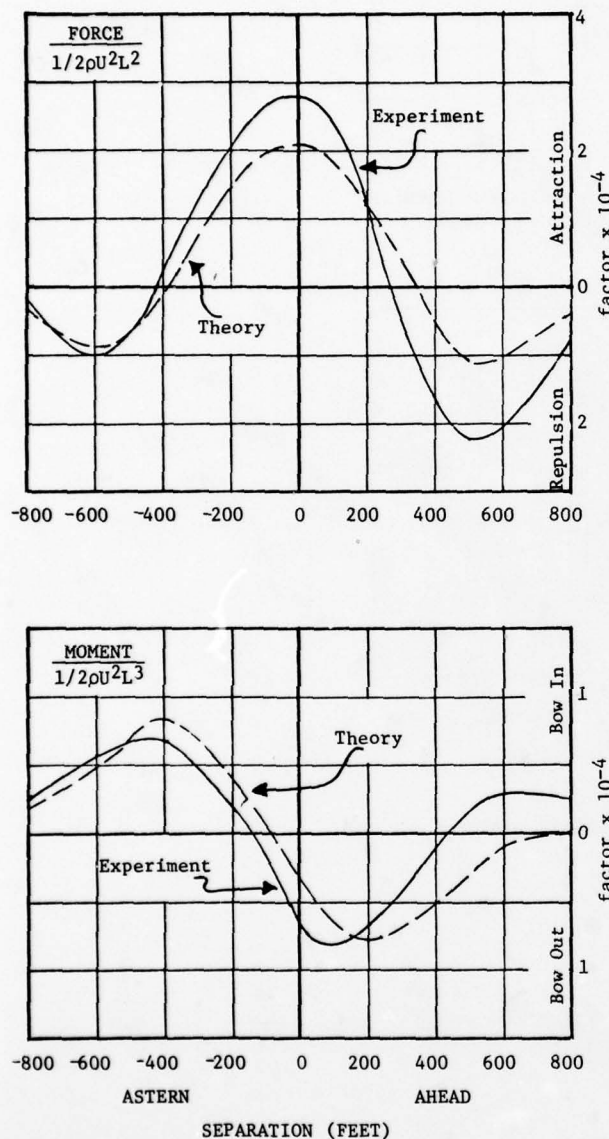


Fig. 9: Comparison between theoretical calculations and model tests for the interaction forces on a navy oiler in proximity with a large aircraft carrier (lateral separation 150 ft.—speed 15 knots).

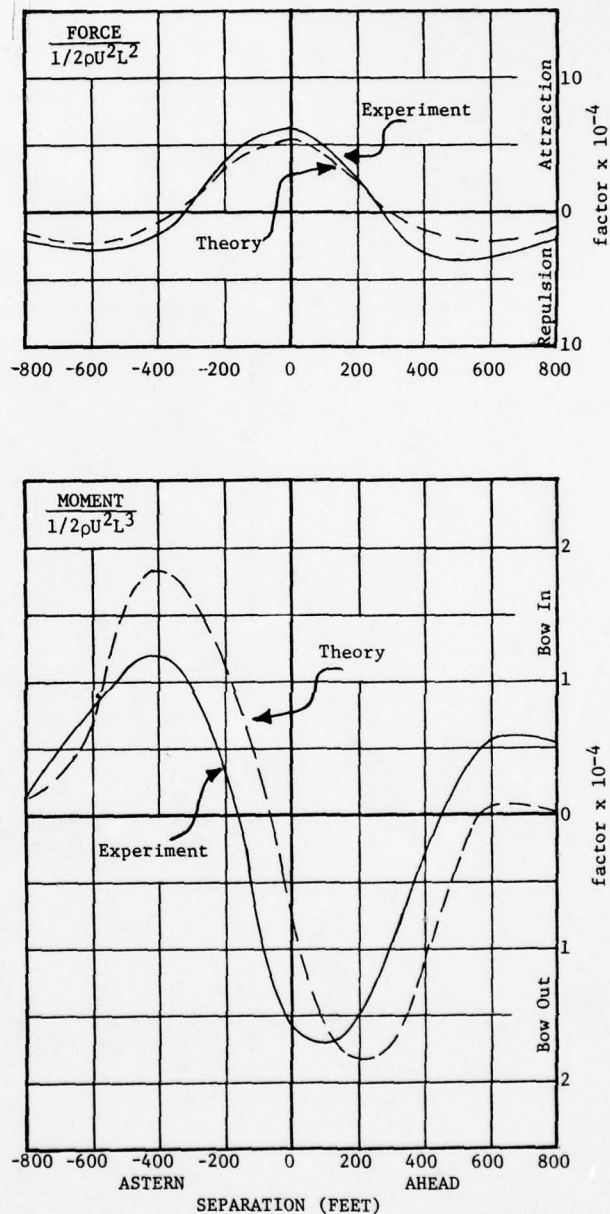


Fig. 10: Comparison between theoretical calculations and model tests for the interaction forces on a navy oiler in proximity with a large aircraft carrier (lateral separation 50 ft.—speed 15 knots).



AD-A055 859

UNIVERSITY COLL LONDON (ENGLAND) DEPT OF MECHANICAL --ETC F/G 13/10  
SYMPOSIUM ON NAVAL HYDRODYNAMICS. UNSTEADY HYDRODYNAMICS OF MAR--ETC (1)  
1978 R E BISHOP, A G PARKINSON, W G PRICE N00014-76-C-0093

UNCLASSIFIED

NL

8 OF 9

AD  
A055859



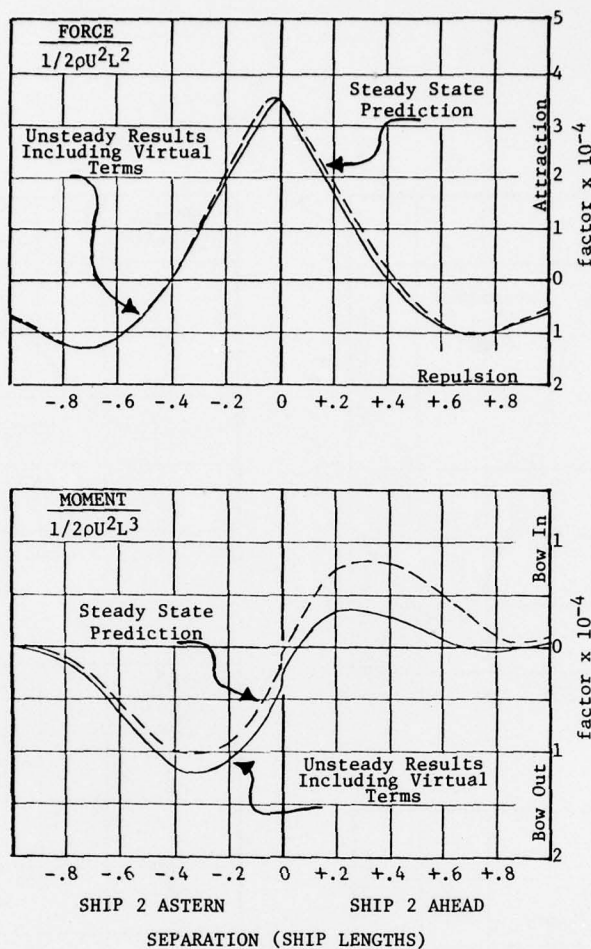


Fig. 11: The effect of unsteady motions on the interaction forces.

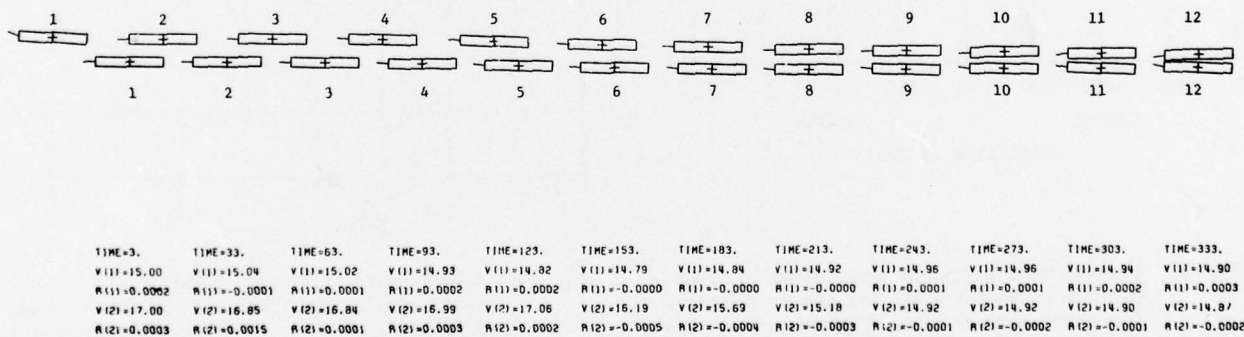


Fig. 12: Ship trajectories during a simulation of replenishment operations (time in seconds, ship speed V in knots, yaw velocity R in radians/sec.)

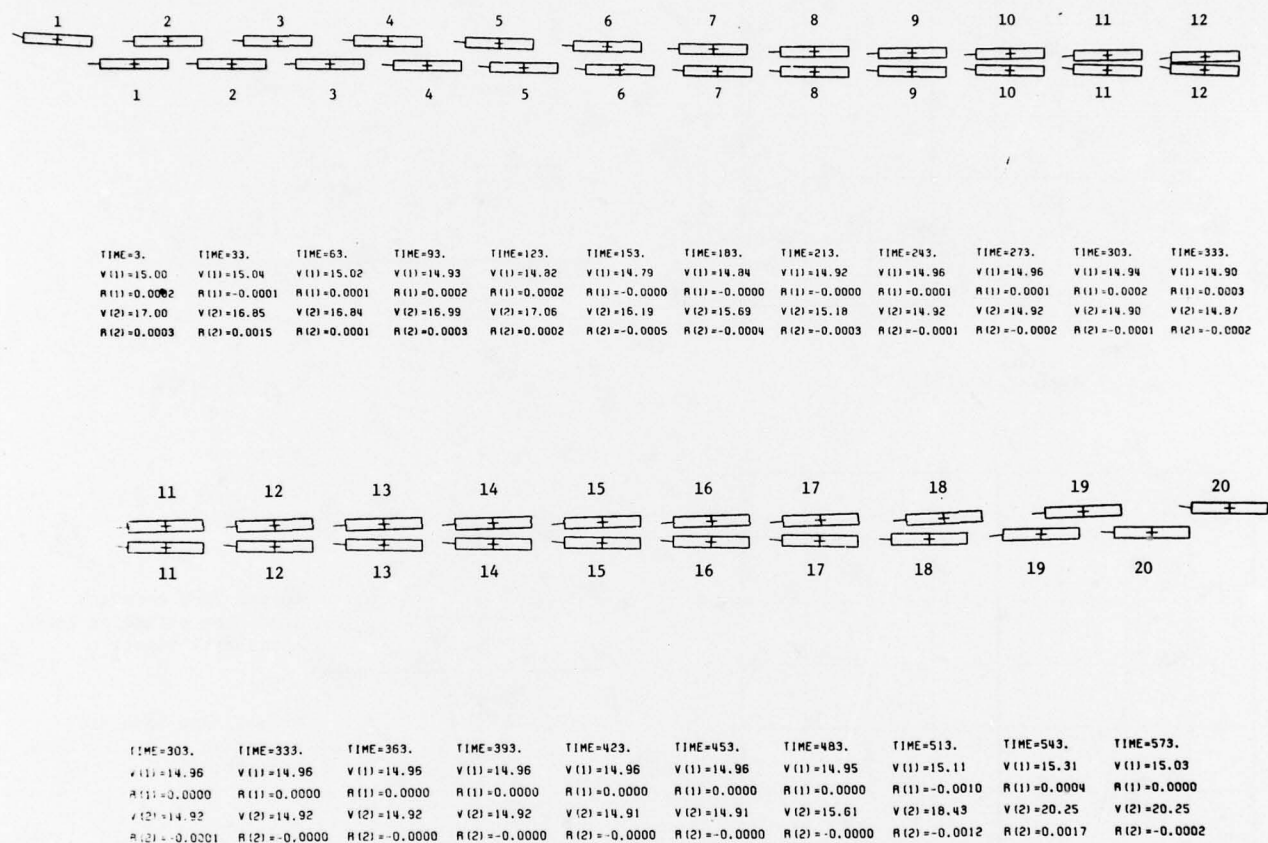


Fig. 13: Ship trajectories during a simulation of replenishment operations (time in seconds, ship speed  $V$  in knots, yaw velocity  $R$  in radians/sec.)



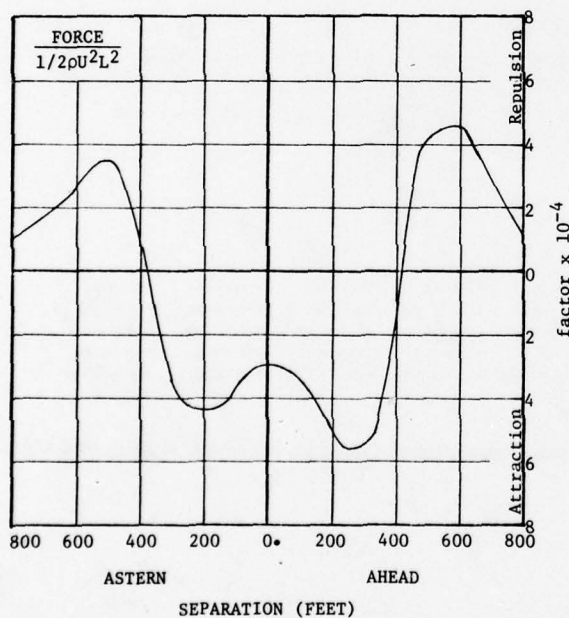
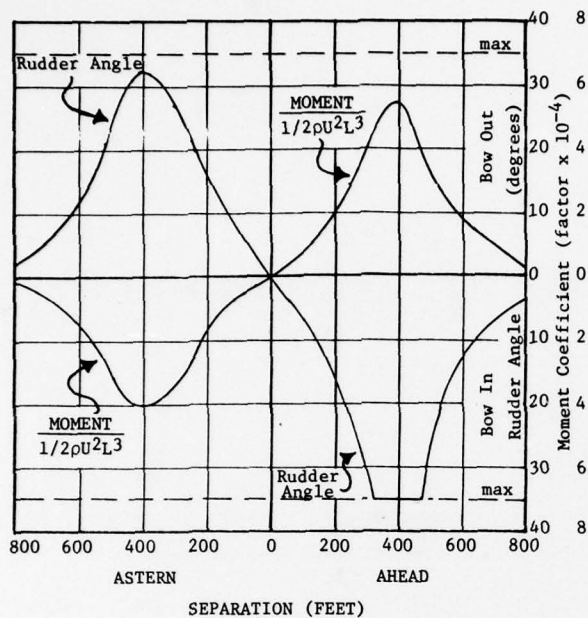


Fig. 14: Interaction forces on a 300 ft. ship overtaking a 900 ft. tanker with lateral separation of 100 ft.

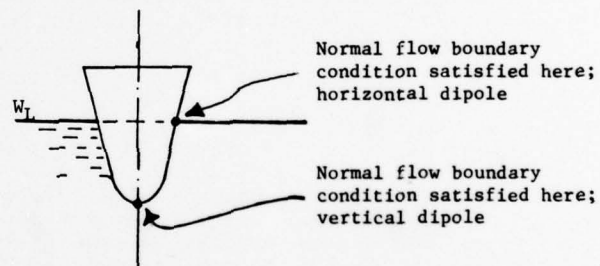
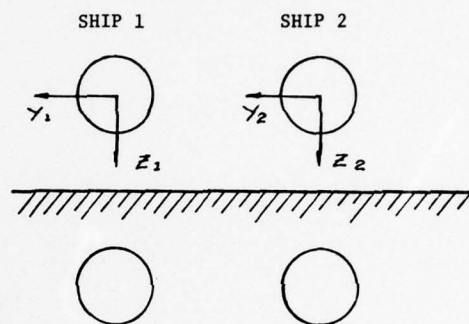


Fig. 15: Vessel arrangement and images for approximating shallow water effects on proximity forces.

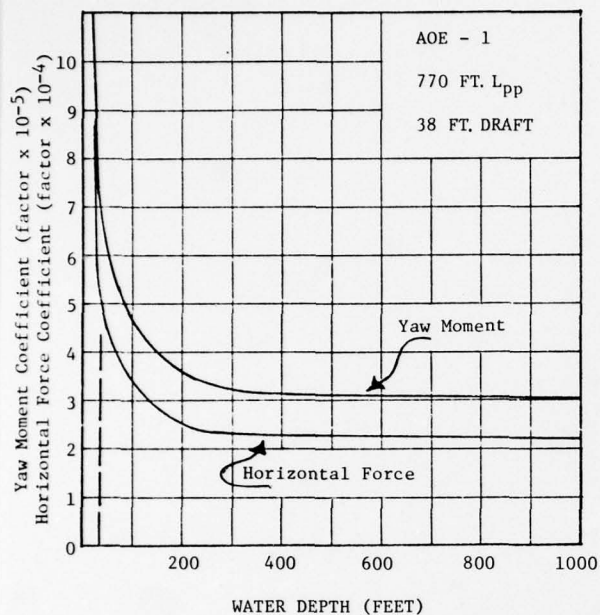


Fig. 16: Effect of shallow water on the interaction forces for a navy oiler.

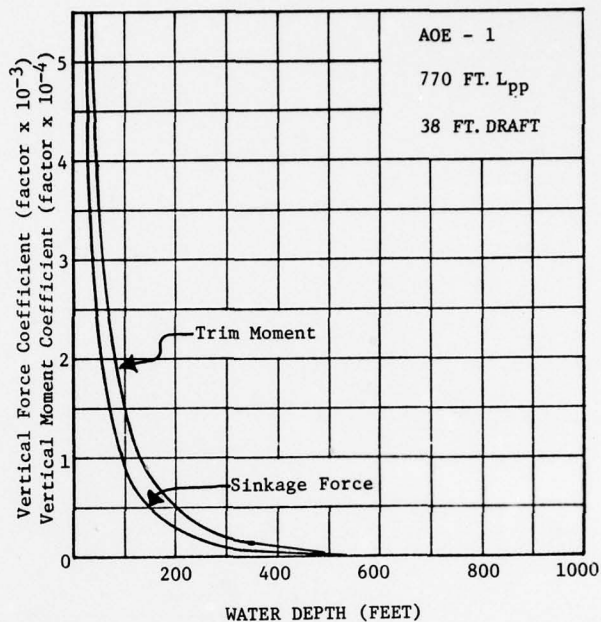


Fig. 17: Vertical forces and moments on a navy oiler in shallow water.

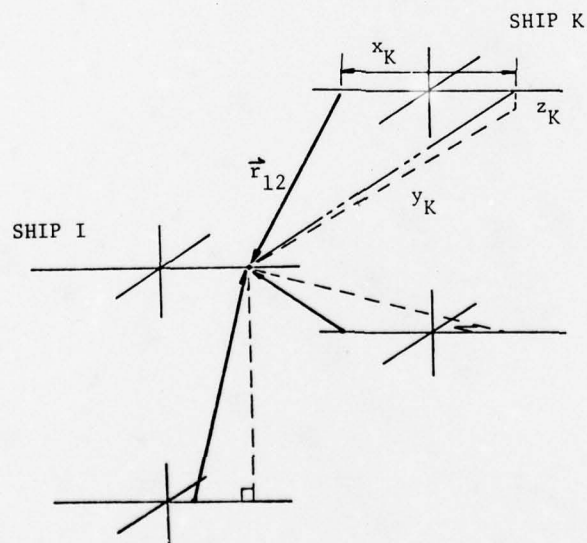


Fig. 18: Orientation of two ships in proximity and their images.

# SOME CHARACTERISTICS OF FLOW AROUND SHIPS AT DIFFERENT DRIFT ANGLES IN SHALLOW WATER

V. N. TRESHCHEVSKY, A. I. KOROTKIN  
Krylov Ship Research Institute, USSR

The paper considers the subject of flow around the ship simulation in an aerodynamic tunnel at various angles of drift in shallow water. In particular such features are discussed as: taking into account the boundary layer formed at the water basin bottom; the three-dimensional ship flow pattern at large angles of drift; taking into account the effects of Reynolds number upon the ship hydrodynamic characteristics in all the range of drift angles.

The hydrodynamic static-flow characteristics of most displacement ships of inland navigation can be predicted in aerodynamic tunnels by making use of the double-model method. This is accounted for by the fact that the effect of wave-making upon the values of these characteristic is insignificant at Froude numbers below 0,2 [1]. In simulating flow around the ship in shallow water, there exist some hydro-mechanical peculiarities which should be taken into account for proper model - ship correlation.

## 1. Small drift angles

It is convenient to consider the peculiarities of defining hydrodynamic characteristics of ship in shallow water by using some particular example. When simulating in an aerodynamic tunnel the ship motion in shallow water, it is necessary to make an infinite grid of double models. In practice, however, one usually limits himself to using a three-element grid. For the experiments in the aerodynamic tunnel three double models of the underwater hull were manufactured, the lines drawing of the ship being shown in Fig.1a. The principal dimensions of the model are given in the drawing. The models were positioned in the working section of the tunnel in such a way as is shown in Fig.1b. Measurements of forces and moments were taken on the mean model in a fixed coordinate system  $XOZ$  (Fig.1c). The amount of the double-model wetted surface  $S = 1,48 \text{ m}^2$  was taken as being characteristic, and the model length  $L$  was taken for a characteristic linear dimension. The ratio  $H/T$  (where  $H$  is the water basin depth and  $T$  is ship's draught) was varied by changing the distance between the models.

When setting the angle of drift all the models turned in relation to the free stream velocity vector  $V$ . The experiments were carried out at Reynolds number  $Re = 5,9 \times 10^6$ . The hydrodynamic coefficient values  $C_x, C_y, M_x$  are represented in Fig.2(a,b,c). Let us now direct our attention to the following. Using three models makes it possible to satisfy approximately the boundary condition at two surfaces characteristic for ship motion in shallow water. With this method of simulation, however, it is quite impossible to measure the forces and the moments in the plane  $XOY$ . In order to estimate forces and moments in this plane one can make measurements of the pressure distributions over the bottom of the mean model. The measurements of pressures in the centerline plane within the ratio range of  $2,5 > H/T > 1,5$  (Fig.2d) showed that the rarefaction under the ship bottom increased with decrease in water depth  $H$ , which in real motion conditions should lead to an increase in the ship's draught even though the propeller may not be working. The character of changes in  $C_x, C_y, M_x$  with the decrease in  $H/T$  is quite natural and agrees with the well-known data [1] obtained for  $H/T > 1,5$ .

When considering the method of double models, it is necessary to note the following peculiarity of flow conditions, which distinguishes this method from the one for full-scale conditions.

When the ship is moving near the bottom, a boundary layer is formed on the latter where the ship motion-induced velocities drop to zero in the fixed system of coordinates (Fig.3a) and change to  $V$  in the ship-bound system of coordinates. No boundary layer of that kind is formed when the method of double



models is used (Fig.3b). If two stationary screens are used (Fig.3c) instead of two auxiliary models, then the velocity in the bound system of coordinates at the boundary characterizing the bottom of the water basin is reduced to zero. The presence of the boundary layer at the bottom of the water basin leads to additional consumptions of power due to the fact that additional friction forces have to be overcome. This latter circumstance results in an additional resistance acting upon the hull in real conditions of ship's motion in shallow water. The mechanism of transmitting additional resistance to the hull at not very small values of  $\frac{H}{T}$  consists in the following. Due to the presence of the boundary layer at the wall, the streamlines of the fluid near the hull deviate causing the pressure redistribution which leads to an increase in hull resistance. For qualitative estimation of the phenomenon, a two-dimensional case of motion was used.

An extension of the existing methods of boundary layer calculations [2] to the case of fluid motion in the vicinity of the water basin bottom made it possible to obtain quite simple relationships for calculation purposes.

The estimated data of additional resistance for the turbulent boundary layer in two-dimensional flow are presented in Fig.3d where the relative increase in the frictional resistance coefficient is expressed as a function of the maximum induced velocity at the water basin bottom.

In connection with the discussion of additional resistance associated with the occurrence of boundary layer at the water basin bottom, it is interesting to compare the relative increase in the viscous resistance

$$\frac{C_x(H/T) - C_x(2.5)}{C_x(2.5)},$$

obtained by the double-model method described above with the one gained during ship model tests [3] in the shallow water basin (Fig.3e). From the Figure it is obvious that there is a noted increase in resistance obtained during the tests in the basin as compared to the double-model tests.

Thus when estimating the ship viscous resistance in shallow water using the double-model method, it is necessary to take into account the additional resistance associated with the occurrence of the boundary layer at the water basin bottom.

## 2. Large angles of drift

Ship hulls being streamlined bodies at small angles of drift become bluff at large angles of drift. Among other features associated with the hydrodynamics of bluff bodies (by a bluff body usually is meant one which has a developed flow separation at the after-end), let us note the cellular pattern of the velocity and pressure distributions in the boundary layer separation zone and a significant change in the resistance coefficient with the increase of Reynolds number in the critical and supercritical regions of flow. As these phenomena are from the qualitative point of view only slightly dependent on the shape of ship frames, they can be considered with a circular cylinder taken as an example.

### 2.1. The three-dimensional flow pattern in the separation area

The measurements of pressure distribution along the generatrix of the circular cylinder in the case of transverse flow (Fig.4a) enable one to note the following interesting fact: in the front part of the cylinder ( $0 \leq \theta \leq 70^\circ$ ) and in the stagnation region ( $140^\circ \leq \theta \leq 180^\circ$ ) the pressure along the generatrix remains practically constant, while the pre-separation area and the area of separation ( $90^\circ \leq \theta \leq 130^\circ$ ) are characterized by a considerable regular non-uniformity of pressure along the generatrix. For some values of  $\theta$  the amplitude of pressure variation reaches the value of velocity-head.

The visualization of flow lines in the separation area (Fig.4b) on the cylinder using dyes also shows a prominent periodicity of flow along the span.

The periodicity of flow remains in the presence of boundary (Fig.4c). With a decrease in the angle of drift from  $\beta = 90^\circ$  to  $\beta = 50^\circ$  the non-uniformity gradually vanishes. Due to the non-uniformity in pressure distribution along the generatrix of the cylinder in case of the transverse flow, the method of experimental evaluation of its resistance coefficient using the pressure distribution across a single, usually middle section seems to be unsubstantiated. As the experimental data processing shows, the local resistance coefficient  $C_{x0}$  varies on the cylinder, for  $Re = 10^6$ , in the range of  $0.28 \leq C_{x0} \leq 0.55$ .

In order to explain the phenomenon under consideration a hypothesis was set up in Ref.[4] that the non-uniformity in the separation area is associated with the non-uniformity of the boundary-layer transition to turbulence. To verify this assumption experiments were carried out with

tufts [5] for flow visualization in the area of separation on the cylinder under subcritical flow conditions when the boundary layer was fully laminar down to the point of separation. The subcritical flow pattern was checked by measuring pressure across several transverse sections along the cylinder length. A well pronounced cellular pattern for  $\lambda/D = (\frac{2}{3} + \frac{1}{3}) \cdot 10^5$  in the subcritical flow conditions (the crisis would begin at  $Re = 3.3 \times 10^5$ ,  $D$  - diameter of cylinder) indicates that the hypothesis suggested in Ref. [4] is invalid.

To find out the physical mechanism of the initiation of three-dimensional flow in the separation area let us consider the fluid streamlines in the vicinity of the point of flow separation (Fig. 5). At the point of boundary layer separation the dividing streamline AB forms an angle  $\psi$  with the plane. The amount of this angle is determined by the expression [6]

$$\tan \psi = -3 \frac{\partial \tau_w}{\partial x} / \frac{\partial p}{\partial x}.$$

Therefore, the flow lines in the region of the boundary layer separation will always be concave even for a convex streamlined contour (because the angle  $\psi$  is taken from the tangential plane). This leads to a situation in the separation area which is favourable for the development of nonsteady flow of the Görtler vortex type.

On the basis of the well-known expressions for the Görtler number, Ref. [7], we obtain for long-wave disturbances ( $\lambda - \frac{1}{Re} \ll 1$ , where  $\lambda$  - wave length of disturbances and  $\delta$  - thickness of boundary layer) the following formula

$$\frac{\lambda}{D} = \frac{500 Re^{1/4}}{(31 + Re)^{1/4}}, \quad (1)$$

where the constant coefficient is taken on the assumption that the left side coincides with the experimental data at  $Re = 10^4$ .

The calculations made by using formula (1) are represented by curve I in Fig. 5b. The same Figure shows the test data on  $\lambda/D$  taken from Refs. [4], [10], [11], [12], as well as the experimental points plotted on the basis of the results of tests carried out at the KSRI aerodynamic tunnel. It should be noted that there is a satisfactory qualitative agreement between the relation (1) and the experimental data. This latter circumstance confirms in our opinion the validity of the proposed physical interpretation of the three-dimensionality of flow in the separation area. Owing to an ambiguous dependence of the Görtler parameter  $G$  (Fig. 5c) on wave number  $\lambda$ , in addition

to long-wave disturbances ( $\lambda \ll 1$ ) for a given value of  $G$  there must also be short-wave disturbances at large values of  $\lambda$ . Using the same quantities as for the calculation of long-wave disturbances, we can obtain similarly to formula (1)

$$\frac{\lambda}{D} = 3.03 Re^{-1/4} (1 + \frac{31}{Re})^{1/4}. \quad (2)$$

The comparison between the results calculated by formula (2) and the experimental data represented in Fig. 5d shows a qualitative agreement existing between the character of variations in short-wave disturbances upon the increase in Reynolds number. The quantitative agreement between the theory and the experiment will be much better if in the cause of calculations the values  $U$ ,  $\delta$  characteristic of the mean flow in the separation area are based on the experimental rather than calculated data of the boundary layer on the cylinder with a potential pressure distribution along its surface.

## 2.2. Reynolds number effect on ship hydrodynamic characteristics at large angles of drift

When the ship model is streamlined at large angles of drift some critical phenomena are observed in the behaviour of hydrodynamic coefficients. These phenomena are well known for a circular cylinder in the case of a transverse flow (Fig. 6a). They are common to various bodies both in unlimited fluid flow and close to the solid-liquid interface (Fig. 6b).

The displacement of the lines of the boundary layer separation is responsible for a scale effect associated with sharp variations in the hydrodynamic coefficients at large angles of drift within the critical zone. If using one or another method one manages to dispose the lines of flow separation at test conditions in aerodynamic tunnel in the same manner as they are disposed at full-scale test, the total hydrodynamic characteristics will give a closer approximation to the real ones.

The boundary layer separations can be controlled by different methods [7]: varying the turbulence of the external flow; changing the roughness of the model surfaces; blowing in/out the liquid at the walls; heating or cooling surfaces.

A most simple and effective mode of controlling the separation is, in our opinion, a procedure which uses models having a roughness produced deliberately and requires neither additional arrangements nor reconstructions of the aerodynamic tunnel. One can have an idea about the effectiveness of this method starting from the data given in Fig. 7a



where pressure distributions are shown along a smooth cylinder at  $Re = 8,5 \cdot 10^5$  and  $Re = 3,6 \cdot 10^6$  and along a rough one at  $Re = 1,10^5$  ( $K_s/D = 4,5 \cdot 10^{-3}$ ). It is seen that the coincidence of the flow separation points obtained by making the surface rougher results practically in a full identity of pressure diagrams. Naturally the roughness of the surface causes considerable changes in the distribution of friction along the body. However, as the experiments showed [14], even being the roughness very marked ( $K_s/D = 9 \cdot 10^{-3}$ ), the portion of the surface-friction resistance does not surpass 3% of the total resistance at  $Re = 10^7$ .

The main problem arising when the method of a roughness produced deliberately is used consists in selecting ratios of  $K_s/D$  for given conditions of model testing. Strictly speaking, for each model and each angle of drift a selection of  $K_s$  may be realized only when the hydrodynamic characteristics of a full-scale ship and of a model are known at different values of  $K_s$ . Naturally, the validity of such a labour-consuming accurate selection of  $K_s$  from data of the experiment is minimal. That is why an approximate experimental method of selecting values of the roughness  $K_s$  was proposed based on the known experimental data for rough circular cylinders.

The systematic trials [14], [15], [16] as well as experiments carried out at the Krylov Ship Research Institute made it possible to formulate the relation  $C_{xi} = C_{xi}(Re, K_s/D)$  for circular cylinders shown in Fig. 7b.

The trend of curves  $C_{xi} = C_{xi}(Re)$  at the fixed value of  $K_s/D$  evidences the possibility of selecting such a ratio of  $Re$  at a given number  $K_s/D$ , which will give a necessary value  $C_{xi}$  corresponding to a smooth circular cylinder resistance in the transcritical area ( $C_{xi} = 0,6+0,7$ ).

The ambiguous dependence  $Re = Re(C_{xi})$  taken into account, the use of the right branches of curves  $C_{xi} = C_{xi}(Re)$  should be recommended, because the flow regime in the separation area is kept more persistent in the region of the ascent  $C_{xi}$  than in the region of the descent  $C_{xi}$  of the curve.

Disposing of the information given above one can formulate a relation  $K_s/D = f(Re)$  which makes it possible to define a desired value of the relative roughness  $K_s/D$  (Fig. 8). This relation gives a resistance coefficient value corresponding to the transcritical value of the full-scale ship at Reynolds number we dispose (the number  $Re$  which may be obtained at a given experimental plant).

In connection with the above-proposed method using a value of the roughness

produced deliberately with a view to simulate transverse flows for cylindrical bodies at transcritical Reynolds numbers it is appropriate to mention the work published recently [17].

A comparison between hydrodynamic characteristics of a full-scale river-service ship (the lines drawing of which is given at Fig. 9a) and the characteristics of its smooth- and rough-surface models obtained in aerodynamic tunnel is presented at Fig. 9b.

The procedure of the full-scale testing can be seen at Fig. 9c. By increasing the length of the principal towline it was possible to avoid any influence the presence of the tow exerted upon the flow nearby the ship on a line. By varying the towline lengths "a" and "b" different angles of drift relative to the ingoing flow were obtained. The angles of drift and velocities of the flow were recorded by devices fixed on a bar put forward on the bow of the towed ship. The tension of the towline was measured by a dynamometer located at a tow and recorded on a magnetic tape. The heel of the towed ship was balanced with the help of weights transported in a special carriage moved along the deck. Given the geometrical parameters of the towing system, the towline tension and the velocity of the flow  $V = 2$  m/sec, it is not difficult to estimate the components of the hydrodynamic forces  $X$  and  $Y$ . When calculating the coefficient  $C_y$  (Fig. 9b), the area of the submerged part of the center plane was chosen as a representative one.

The data given at Fig. 9b indicate that the test results for a rough-surface model correlate fairly well with the results of the full-scale ship experiment.

## References

1. Goffman, A.D., "The theory and calculation of turning of ships for inland navigation", Izd. "Sudostroyeniye", 1971, L., 265 s.
2. Loitsyansky, L.G., "Fluid and gas mechanics", GITTL, 1957, M., 784 s.
3. Voitskunsy, Ya.I., "Water resistance to ship motion", Izd. "Sudostroyeniye", 1964, L., 412 s.
4. Humphreys, J.S., "On a circular cylinder in a steady wind at transition Reynolds numbers", J. Fluid Mech., v.9, N 4, 1960.
5. Korotkin, A.I., "On the three-dimensional character of transverse flow around circular cylinders", Uchonye zapiski TSAGI, 1973, t.IV, N 5, s.26-33.



6. Oswatitsch, K., "Die Ablösungsbedingung von Grenzschichten. Grenzschichtforschung, Symposium, Freiburg, 1957/1958, s.357-367.
7. Basin, A.M., Korotkin, A.I., Kozlov, L.F., "Ship Boundary Layer Control", Izd. "Sudostroyeniye", L., 1968, 491 s.
8. Schlichting, G., "Boundary Layer Theory", Izd. "Nauka", 1969, M., 742 s.
9. Achenbach, E., "Distribution of local pressure and skin friction around a circular cylinder in cross-flow up to  $Re = 5 \cdot 10^6$ ", J. Fluid Mech., 1968, v.34, N 4.
10. Phillips, O.M., "The intensity of aeolian tones", J. Fluid Mech., 1956, v.1.
11. Ukhanova, L.N., "The statistical characteristics of two-dimensional turbulent wake at a small distance from the cylinder", Zb. "Promyshlennaya aerodinamika", 1966, vyp.27, Izd. "Machinostroyeniye", M.
12. Marris, A.W., "A Review on Vortex Streets, Periodic Wakes, and Induced Vibration Phenomena", Journal of Basic Engineering Transactions of the ASME, Series D, Volume 86, Number 2, 1964 (In Russian translation).
13. Kestin, J., Wood, R.T., "On the stability of two-dimensional stagnation flow", J. Fluid Mech., v.44, N 3, 461-479, 1970.
14. Achenbach, E., "Influence of surface roughness on the cross-flow around a circular cylinder", J. Fluid Mech., 1971, v.46, N 2.
15. Fage, A., Warsap, J., "The effects of turbulence and surface roughness on the cross-flow around a circular cylinder", ARC R. and M., 1930, N 1283.
16. Gorlin, S.M., Sterenlicht, D.V., Romanenko, G.A., "Aerodynamic characteristics of rough cylinders", Zb. "Gidraerodinamika", KhGU, 1966, Vyp.4.
17. Szechenyi, E., "Supercritical Reynolds number simulation for two-dimensional flow over circular cylinders", J. Fluid Mech., 1975, v.70, N 3, pp.529-542.

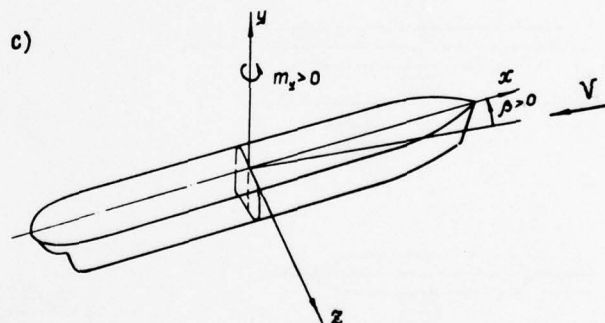
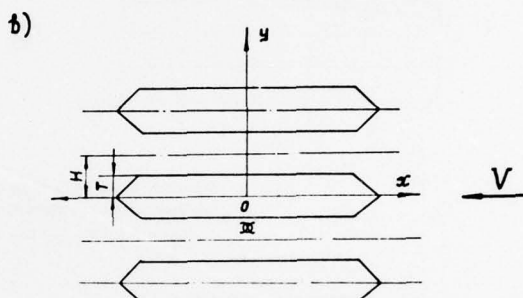


Fig. 1: (a) Lines drawing of the model

$L_u = 2.21 \text{ m}$   
 $B = 0.26 \text{ m}$   
 $T = 0.07 \text{ m}$

(b) Test model procedure in the aerodynamic tunnel

(c) Coordinate system

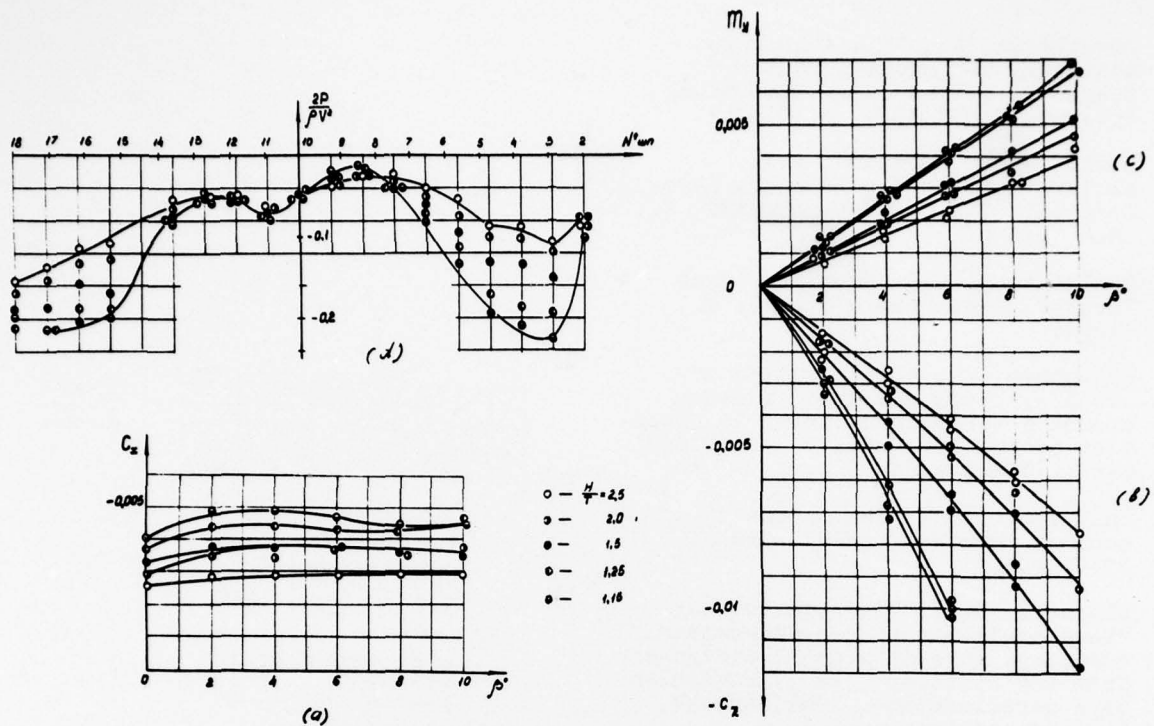


Fig. 2: Pressure distribution along the bottom of the model and the hydrodynamic coefficients of its submerged hull.  
 $\circ - \frac{H}{T} = 2.5$ ;  $\bullet - 2$ ;  $\bullet - 1.5$ ;  $\bullet - 1.25$ ;  $\bullet - 1.15$ .

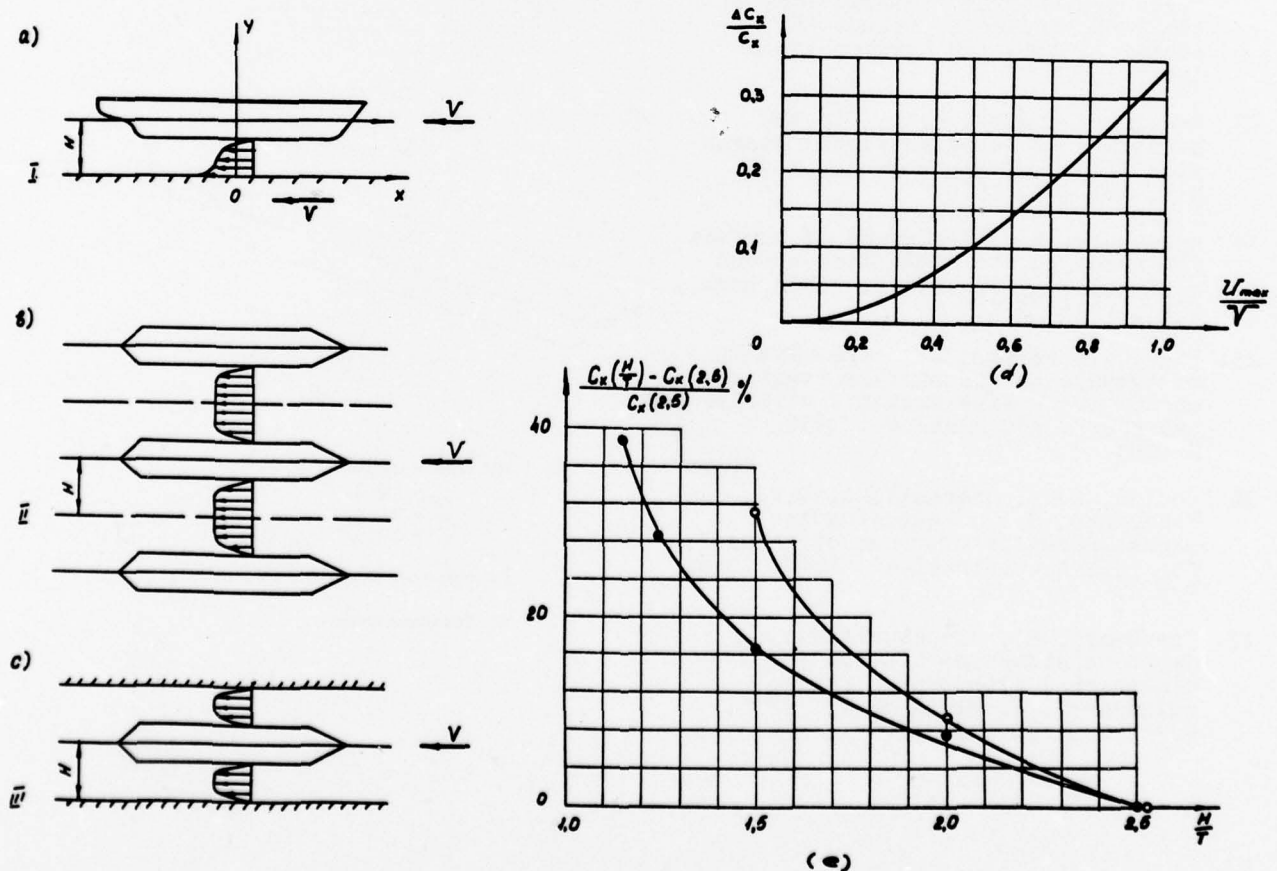
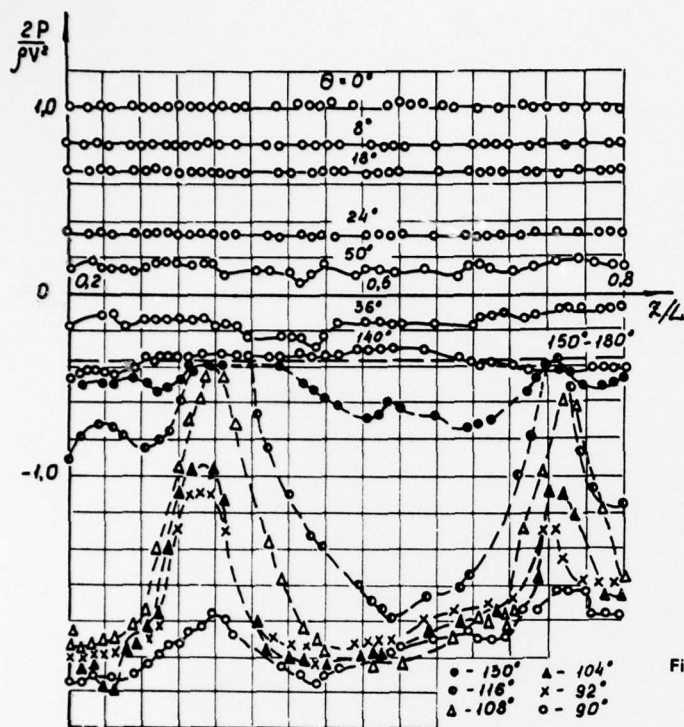
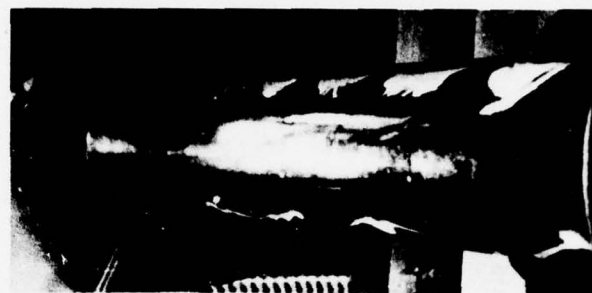


Fig. 3: Procedures of the model tests near the solid-liquid interface (a, b, c). Increase in the model resistance due to the presence of the boundary layer at the tunnel wall (d, e);  $B = 0$ ;  $\bullet$  - test data (aerodynamic tunnel);  $\circ$  - data from [3].

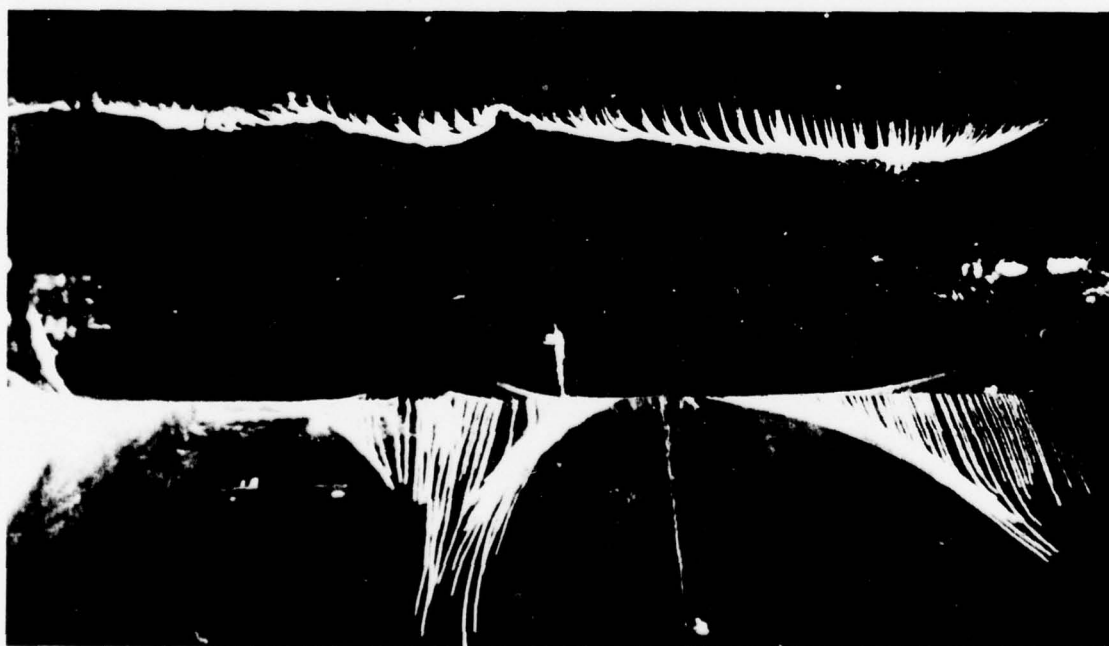


(a)



(b)

Fig. 4: Pressure distribution along the circular cylinder span (a). Visualization of the separation area on the cylinder in the infinite flow at  $Re = 1.66 \times 10^6$  (b) and near the wall at  $Re = 1.66 \times 10^6$ ;  $\frac{h}{D} = 0.02$  (c).



(c)



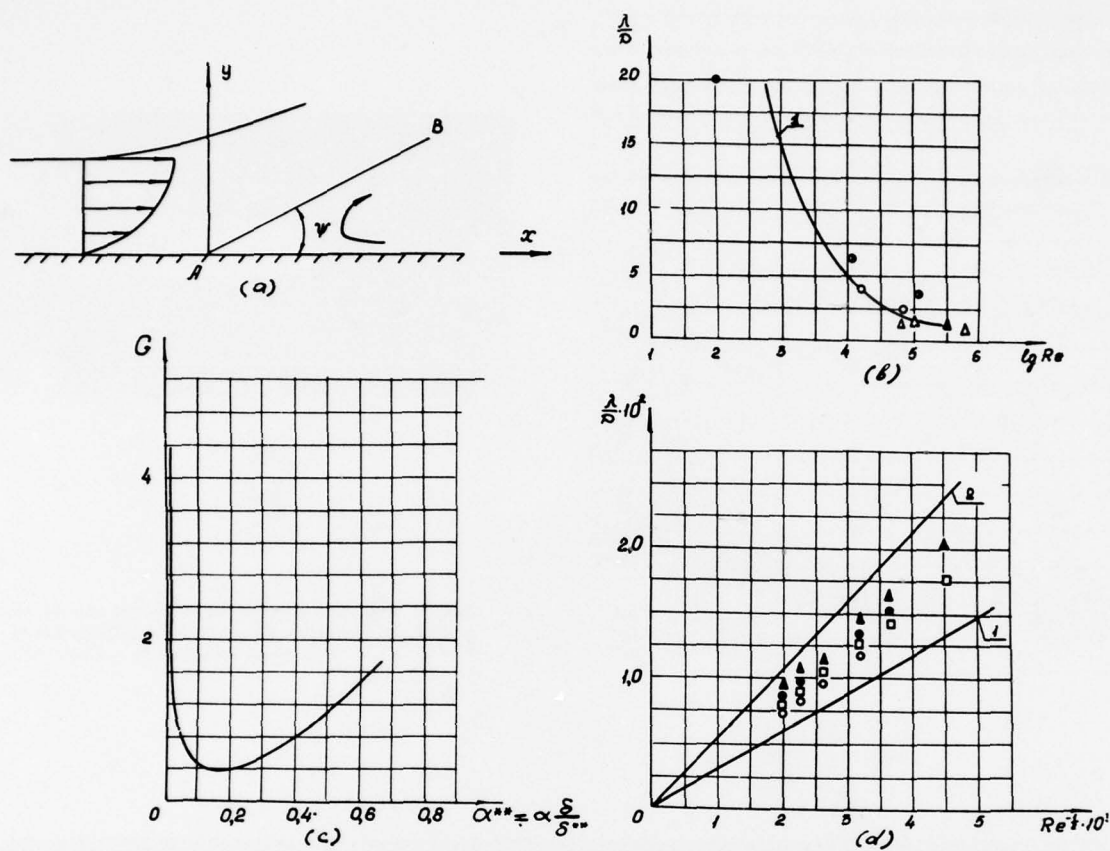


Fig. 5: (a) Flow pattern in the separation area;

(b) The relation  $\frac{\lambda}{D} = f(Re)$ :

1 — calculations using formula (1);  
 1 — calculations using formula (1); ● — data from [10]; ○ — data from [12]; ▲ — data from [4]; □ — data from [11]; △ — test data obtained at the KSRI aerodynamic tunnel;

(c) Neutral stability curve for eddy disturbances;

(d) The relation  $\frac{\lambda}{D} = f(Re)$  for small-scale disturbances; experiment [13] ▲ —  $\epsilon = 0.2\%$ ; ● —  $1.0\%$ ; □ —  $2\%$ ; ○ —  $4.0\%$ ; calculations: 1 — from formula (2); 2 — data from [13].

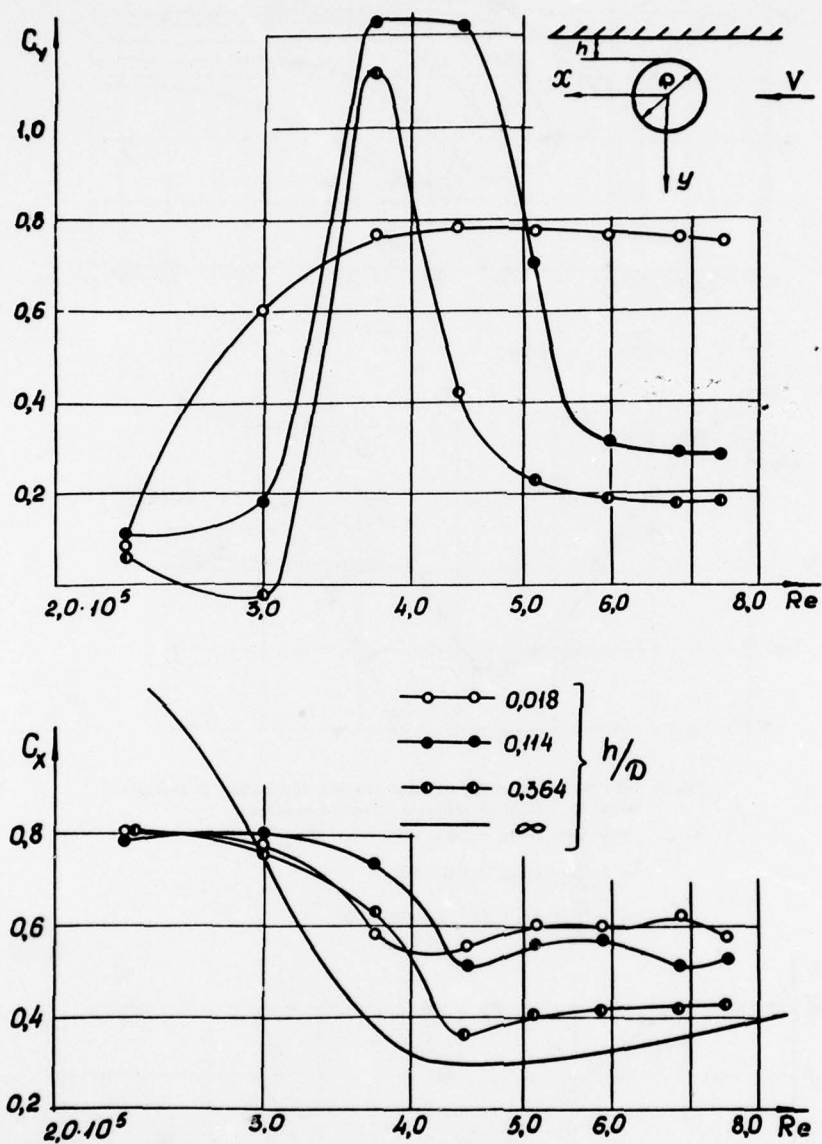


Fig. 6: The hydrodynamic coefficients of the circular cylinder located near the wall:  
 $\circ - \frac{h}{D} = 0.018$ ;  $\bullet - 0.114$ ;  $\circ - 0.364$ ;  $- \frac{h}{D} = \infty$

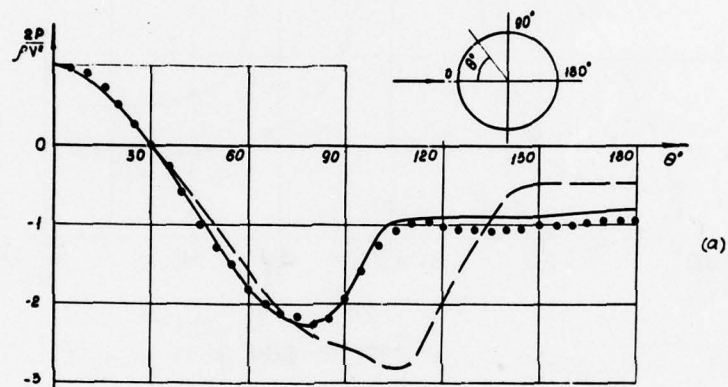
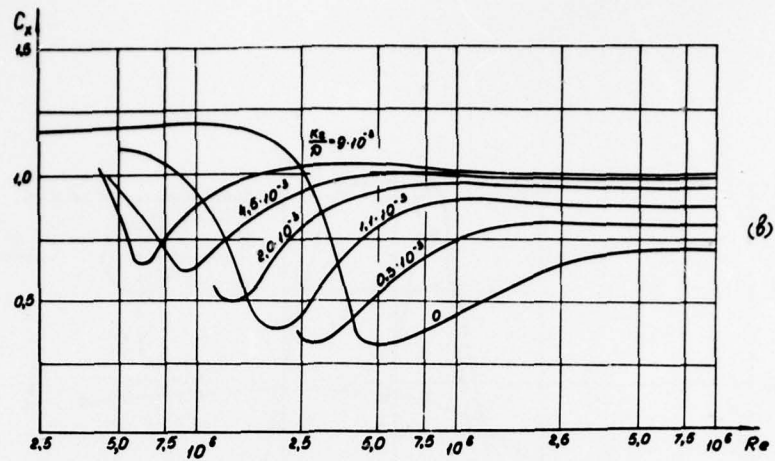


Fig. 7: The resistance of the cylinder and the distribution of pressures along its surface of different values of roughness:

- $\frac{K_s}{D} = 0$ ,  $Re = 3.6 \times 10^5$ ;
- $\frac{K_s}{D} = 0$ ,  $Re = 8.5 \times 10^5$ ;
- $\frac{K_s}{D} = 4.5 \times 10^{-3}$ ,  $Re = 1 \times 10^6$ .

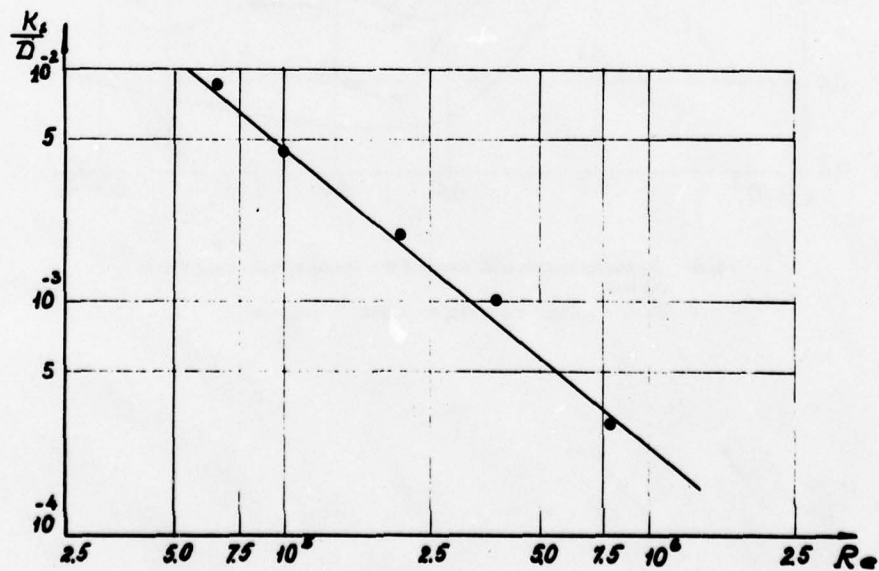


Fig. 8: The relation  $\frac{K_s}{D} = f(Re)$  obtained from experiments with circular cylinders.



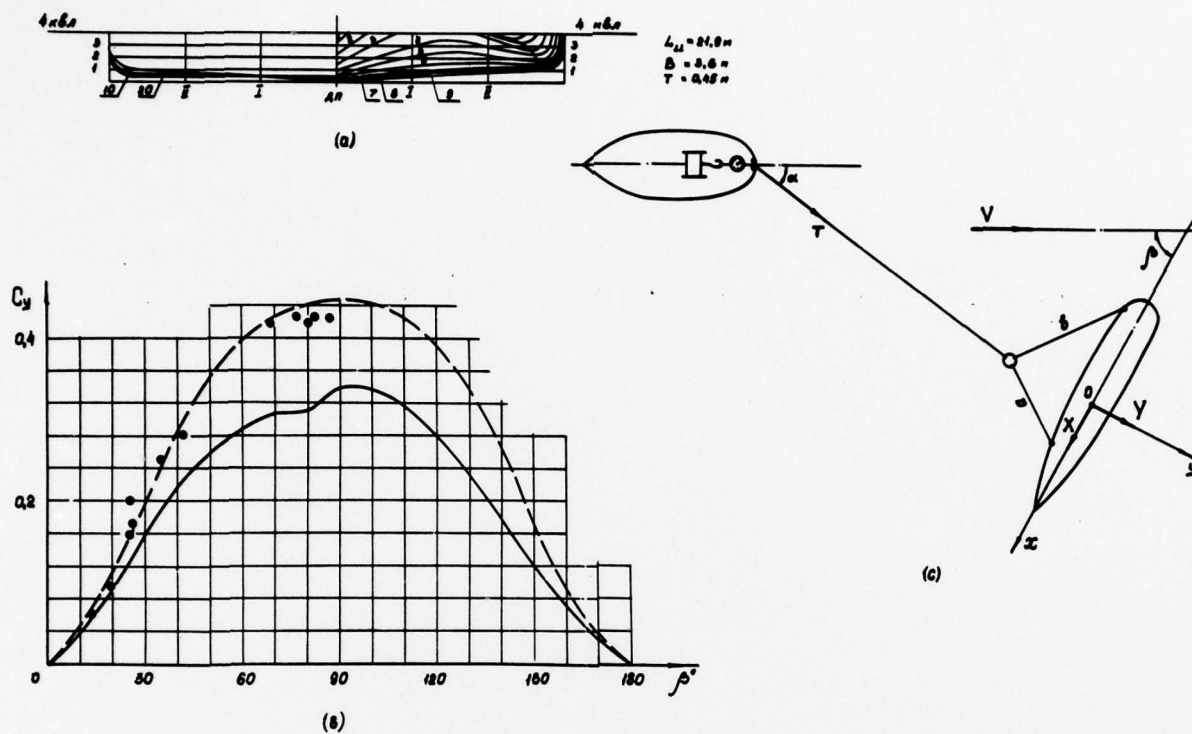


Fig. 9: (a) Ship lines drawing:

$$\begin{aligned} L_H &= 21.9 \text{ m}, \\ B &= 3.6 \text{ m}, \\ T &= 0.45 \text{ m}. \end{aligned}$$

(b) Model test results

$$\frac{K_s}{T} = 0, \text{Re} = \frac{2VT}{\nu} = 2.4 \times 10^5;$$

$$\frac{K_s}{T} = 10^{-2}, \text{Re} = 2.4 \times 10^5;$$

and full-scale ship test results  $\bullet$  —  $\text{Re} = 2.7 \times 10^5$ .

(c) The sketch of towing.

# Discussion on Paper by I. W. Dand

R.W. YEUNG

I wish to congratulate Dr. Dand for presenting to us such an extensive series of experimental results related to the interaction of vessels in each other's proximity. These experiments, the need for which is long overdue, will provide us with important information for correlating or validating the various models in theoretical work, as well as shed a substantial amount of light on hydrodynamics of the subject matter.

I have the following comments to offer concerning the two-dimensional model used by the author. At the onset, one can perhaps suspect the following deficiencies will occur: Since the mathematical model consists essentially of a vertical strut for the representation of the hull, it will overpredict the interaction forces, for most ships are far from being wall sided. The fact that there is a bottom clearance, suggests these bodies should be treated as porous bodies rather than as impenetrable objects. Otherwise, the prediction will be off quantitatively by one order of magnitude. Furthermore, the introduction of a two-dimensional model as such will lead to two degrees of indeterminacies in the problem. These being that to render the solution unique, one must now apply two Kutta conditions at the trailing edges of these bodies. However, it is by no means obvious that these conditions are valid, since the hull behaves more like a low aspect-ratio lifting surface than a wing. A strong Kutta condition is far from being the ideal condition.

It appears to this discussor that any reasonable quantitative prediction requires the solution of the hydrodynamic problem of the flowfield that takes into account the sectional characteristics of the hull.

At MIT, we have been working on a slender-body model for shallow-water interaction. In this model one sees at a typical section both hulls and their interaction in the cross-flow plane can be properly accounted for. This straightly potential-flow model does not include free-surface effects nor any separation drag. It yields reasonably good quantitative agreement with experimental data obtained by Dr. Dand for a tug-cargo ship combination. The discussor concurs with Dr. Dand's conclusions that the effects of free surface are important, particularly in very shallow water, and that the appendages play an important role in the interaction. It is because of this latter physical phenomenon that one should try to account for the hull geometry in a more detailed fashion.

## Author's Reply

The author thanks Professor Yeung for his kind remarks and is glad to hear that the results presented in the paper are of use in verifying existing and future theoretical work.

Professor Yeung's points about the deficiencies of the two-dimensional theory mentioned in the paper are well-made, but it must be emphasised that the theory was used principally to guide the experiments and therefore served to highlight those aspects of the study which deserved closer study. It is perhaps worth mentioning in passing however that for the Tug/Ship case, inclusion of circulation in the theory has proved to be essential whereas for models A and B the effect of its inclusion is less spectacular - in fact the sideforce measurement and theory show rather poorer quantitative agreement with measurement when circulation is included than when it is not.

But it seems to the author that it is of great importance to be able to predict turning moment accurately in shallow water rather more than sideforce. For this it is apparent that the inclusion of circulation does little to improve agreement between theory and measurement; one solution may be to include a more detailed analysis of the effects of hull geometry and for this reason the results of the MIT calculations, mentioned by Professor Yeung, are eagerly awaited.

PRECEDING PAGE BLANK-NOT FILMED

# Discussion on Paper by M. Fujino

A.M.J. DAVIS

When the rectangular cylinder heaves at high frequency, it has, to first order, no wave-making effect, a fact which can be exploited to show analytically that the term of order 1 in the potential is wave-free. It is, of course, the limit potential obtained by letting  $K \rightarrow \infty$  in the free surface boundary condition, as the author does for his infinite frequency calculations. It should be pointed out that there is at least one geometry, of comparable interest in ship design, for which this limit potential and hence the added mass can be calculated explicitly.

Suppose the cylinder and channel have circular boundaries which are such that they have vertical tangents at the free surface. Then, in agreement with Fujino, it is found (Ref 14) that the addition to the virtual mass coefficient due to the restricted water, i.e. its difference from 1, is small except for extreme deviation of the cylinder from the centre of the channel. For this asymptotic result, it has to be assumed that the forced (high) frequency is not close to one of resonance of the water on either side of the cylinder. Analogous results can be obtained for two circular cylinders in infinite fluid.

Preparation of similar work on the corresponding axisymmetric problems - sphere in hemispherical lake, sphere near a wall or two spheres in infinite fluid - is now complete.

## REFERENCES

- 14) A.M.J. Davis, 1976. Quart. J.L. Mech. Appl. Math. Vol.29, Part III.

J.N. NEWMAN

Professor Fujino's numerical solution, for the added-mass coefficients of a rectangular cylinder in a canal, provides a welcome opportunity to test some of our analytical approximations for the same problem. Our theory shown by the dashed lines in Figures 4 and 6 is based on a simple image-dipole representation of the canal walls, and this approximation is expected to break down as the horizontal clearance between the body and the nearest wall becomes small. On the other hand, this theory should be correct asymptotically for large  $b/a$ , in Figure 4, as well as for small  $\xi/B$  and large  $w/B$  in Figure 6. The differences which are shown in these limits, especially for small  $d/c$ , appear to be larger than between Professor Fujino's upper and lower bounds, although this domain is not explicitly included in Table 3.

Is it possible that the upper and lower bounds are effected by the discretization, and as such are not strict bounds?

Turning to the opposite limit, where the horizontal clearance is small, we have recently developed a first-order theory for this case, based on the method of matched asymptotic expansions. This theory includes the linearized free-surface effects, and follows a similar analysis carried out for the resonant motion between two closely-spaced surface-piercing obstacles (J. Fluid Mechanics, 66, pp.97-106). For the zero-frequency limit, corresponding to Professor Fujino's Figure 4, the new result is expressed by the simple formula

$$\frac{m_y}{m} = \frac{d^3}{3ac(b-a)} + \frac{d^2}{c(d-c)}$$

This is valid to leading order in the small parameters  $(b-a)$  and  $(d-c)$ . Similar expressions can be given for the problems shown in Figures 6, 7, and 8. In all cases the accuracy appears satisfactory for  $d/c$  equal to 1.05 or 1.1, but the error in our approximation appears to be significant for deeper water. We anticipate that a second-order theory will improve this situation.

KWANG JUNE BAI

The author should be congratulated for his continuing effort on the application of the hypercircle method in obtaining the upper and lower bounds of the added mass for a two-dimensional body in a canal. Recently, I have made a similar investigation by the finite-element method based on the dual extremum principles (also known as dual or complimentary variational principles). I have computed the lower and upper bounds of the heave added mass for the zero and infinite frequency limits in water of finite depth (Ref.15). Some of these results are given in my discussion of the paper by Sayer and Ursell in this Proceedings.

I have applied this method to the restricted-water problem which is considerably simpler than the unbounded-water problem (Ref.16). Some of my numerical results for the restricted-water problem will be presented here and compared with the author's results. I have found, contrary to the author, that the upper and lower bounds can be obtained more easily and with better accuracy by the finite-element method than by the hyper-circle method.



In this discussion  $\mu_1$  denotes the sway added mass in the zero-frequency limit, or that of the zero Froude number limit for horizontal translation motion. This can also be interpreted as the heaving added mass of the infinite frequency limit by rotating all of the boundary configurations by 90 degrees when the geometry is symmetric with respect to the y-axis. However, the zero limiting frequency problem is ill-posed when the floating body is heaving in restricted water.  $\mu_2$  denotes the sway added mass in the infinite frequency limit, or the added mass of a floating cylinder translating in the horizontal direction at an infinite Froude limit. In this numerical method, there is no restriction on the body or the canal geometries.

I have computed the upper and lower bounds of  $\mu_1$  and  $\mu_2$  for four different body geometries; a rectangular section, a triangular section, a circular section, and a Lewis form (nearly rectangular) section, all in a rectangular canal, with half-width  $b$  and depth  $d$ . The nomenclature for the body and geometry is the same as used by the author. The eight-node isoparametric quadrilateral element was used, and the entire fluid domain was subdivided into from 18 nodes to approximately 400 nodes depending on the specific problem. The relative error here is defined as the difference of the upper and lower bounds divided by their sum, since the solution may be best approximated as the mean value of the upper and lower bounds.

Table 1 shows the convergence of the numerical results by testing several different numbers of total nodes in the entire fluid for a rectangular section at the centre of the canal. In this specific case, Table 1 shows that a good approximate solution for  $\mu_1$  and  $\mu_2$  can be obtained within 1 percent error relative to the true solutions, even by taking only three elements (18 nodes). When 20 elements (25 nodes) are taken, the relative errors in  $\mu_1$  and  $\mu_2$  are less than 0.4 and 0.3 percent, respectively.

Table 2 shows the added masses  $\mu_1$  and  $\mu_2$  of a triangular section (half beam  $a$  and draft  $c$ ) at the centre of the canal. Our results are compared with the results obtained in a previous paper by the author (Ref.3). As shown in Table 2, the results by the finite-element method are far more accurate than those obtained by the hypercircle method.

Table 3 shows the added masses  $\mu_1$  and  $\mu_2$  of a rectangular section at the centre of the canal. Our results are compared with those obtained by the author. It is seen that the results by the finite-element method are more accurate than those of the author. The relative errors in our results are one order of magnitude less than those in the author's results. It is of particular interest to note that the lower bound of  $\mu_1$  for  $b/a = 5$ ,  $d/c = 5$ , in our results is 1.28362 with an error of 0.1 percent whereas that in the author's results is 1.152 with an error of 10 percent. Our numerical results seem to indicate that his lower bound of  $\mu_1$ , 1.152 is less accurate than the lower bound value obtained by the finite-element method.

However, the author made some misleading remarks, based on the comparison between his lower bound value of 1.152 and the exact added mass coefficient of 1.186 obtained by Lewis for an infinite fluid. It is not obvious to me that the lower bound value of the added mass in a canal with  $b/a = 5$  and  $d/c = 5$ , should be the same as the lower bound value in an infinite fluid. The author also concluded from this comparison that the lower bound in his method is a good approximate value of the true solution and hence he computed only the lower bound for  $\mu_2$ . I do not understand how the author can make such a conclusion, since it is not known whether the true solution is closer to the lower bound or the upper bound. However, the author states that the greatest advantage of the hypercircle method over other methods is to obtain the upper and lower bounds.

The author has not given any results for curved bodies so I have included in Tables 4 and 5 the results for both a circular section (with radius  $a$ ) and a Lewis form. For these results, it is seen that the relative errors are also small.

Table 6 shows the added masses of a rectangular section at different off-center locations in a canal. The author made comparisons between his results and Newman's analytic result for the off-centre case showing that there is a considerable discrepancy even in the range of  $\xi/B$  from 0 to 0.7. Our results reveal that the author's results are less accurate than the results by Newman's formula in the range of  $\xi/B$  from 0 to 0.7 as also shown in Figure 9. In view of the accuracy of our results for the case of  $d/c = 1.05$  and  $W/B = 2.5$ , where relative errors are approximately 1 percent, it is apparent that the author's results are considerably lower than the true value.

Table 7 shows results for a rectangular section in a canal with only a single wall. The added mass  $\mu_2$  for  $d/c = 1.05$  and for  $\eta/B = 0.3$  is accurate within 0.6 percent in our results. It is also found that the results of the author are slightly lower than the lower bound of our results. In concluding, I would like to raise these two questions:

- (1) The author states that his method is in principle equally applicable to any body geometry. However, it seems to me that this approach is more difficult for non-rectangular shapes than for a rectangular section due to the difficulty involved in representing the analytic trial functions in the global coordinate system. In the finite-element method, any complex body and canal geometry can be accommodated as easily as a rectangular geometry. I would like to ask the author if he has any thoughts with regard to the application of his method to non-rectangular geometry, for instance, a circular section.
- (2) I would also like to know how the upper bound for  $\mu_2$  can be computed by the hypercircle method.

#### REFERENCES

- 15) Bai, K.J. "Dual Extremum Principles of the Added Mass of Two-Dimensional Cylinders Heaving in Water of Finite Depth," (submitted to the Journal of Fluid Mechanics, 1976).
- 16) Bai, K.J. "Dual Extremum Principles of the Added Mass of the Two-Dimensional Cylinders in Restricted Waters," (in preparation for publication).

# Author's Reply

A.M.J. DAVIS

I am very glad to hear from Dr. Davis that in agreement with me, he gets a similar conclusion regarding the effects of the restricted water on the added mass of a two-dimensional body oscillating normally to the free surface; the added mass of a heaving cylinder in the channel is not so much affected except for extreme deviation of the cylinder from the center of the channel. I look forward to hearing more of new analytical work on this subject in the near future, which Dr. Davis has completed.

J.N. NEWMAN

I am very grateful for the interesting discussion of Prof. Newman who has suggested a simple formula by which the effects of restricted waters on the added mass of a rectangular cylinder can be evaluated.

Concerning the differences between the added mass coefficients obtained by Prof. Newman's formula (62) and those by my calculation, which are shown in Figures 4 and 6, I agree with Prof. Newman's opinion that his formula is correct asymptotically for large  $b/a$ , in Figure 4, as well as for small  $\xi/B$  and large  $W/B$  in Figure 6. Because the accuracy of lower bounds, which are plotted in Figures 4, 6, 7 and 8, becomes poorer as the fluid domain increases remarkably, although the accuracy of lower bounds is far better than that of upper bounds.

Here, it must be pointed out that it is possible to bring the upper bound as close to the exact value of the added mass as we want by increasing the total number of grid-points to divide the fluid domain into a net of rectangular meshes, and it is also possible to bring the lower bound as close to the exact value as we want by increasing the  $k$ -parameter of  $J_k$ -vectors in case of canal center translation. However, it is impossible to increase the number of grid-points and the  $k$ -parameter infinitely, since the accuracy of solutions of the simultaneous linear equations (18) and (19) breaks down because the matrix of coefficients of the unknowns  $a_i$ 's and  $b_k$ 's becomes nearly singular. Furthermore, another remark should be added: In this paper, the lower bounds have been exclusively used to demonstrate the effects of restricted waters on the added mass because of less accuracy of the upper bound. But this is not an essential nature of the hypercircle method. Less accuracy of the upper bound is due to my inappropriate choice of  $I_i$ -vectors. Namely, the  $I_i$ -vector used in this

paper is just one of infinite candidates of  $I_i$ -vectors. Therefore, it is possible to improve the accuracy of upper bounds by selecting another adequate form of the  $I_i$ -vector.

In Figure 10, which is a duplicate of Figure 4 and will be shown below, is plotted Prof. Newman's new formula which provides numerical values of the lateral added mass for canal center translation. The chain lines connecting the circular points represent the new formula. For the convenience of comparison, besides the numerical values obtained by the new formula, the upper and the lower bounds which are shown in Table 3, are written in for some of the circular points.

From comparing the numerical values obtained by the new formula, which are underlined, with the corresponding upper and lower bounds, it can be said that Prof. Newman's new formula overestimates the effects of restricted waters especially for large  $d/c$ .

KWANG JUNE BAI

I express my gratitude to Dr. Bai for letting me know his fine numerical results of the upper and lower bounds of the added mass, which are computed by the finite element method based on the dual extremum principles.

Concerning the discrepancy between the sway added mass coefficients obtained by Prof. Newman's analytical formula and by my method, which is shown again by Dr. Bai in Figure 9, I think that my calculation is less accurate for small  $\xi/B$  in Figure 6, as I have replied to Prof. Newman's discussion. Besides, I agree with Dr. Bai's opinion that the finite element method is easier to be applied for non-rectangular geometry.

In case of canal center-line oscillation, I have tried to compute the upper bound for sway added mass in the infinite frequency limit by using the same  $I_i$  vectors as those used for sway added mass in zero frequency limit, that is to say, the  $I_i$  vectors defined by the equations (41) to (44). Needless to say, an arbitrary vector of  $\pi$  space, that is to say,  $\bar{p}$  vector should be different from that for the zero frequency limit. As a result of a few numerical calculations, it is proved that the accuracy of the upper bounds for  $\mu_2$  obtained thus is not so good. However, it is possible to improve the accuracy of the upper bounds if we replace  $I_i$  vectors and  $\bar{p}$  vector with different ones chosen adequately.



Node Number	$\mu_1/2\rho ac$			$\mu_2/2\rho ac$		
	Lower Bound	Upper Bound	Error	Lower Bound	Upper Bound	Error
18	26.83240	27.34294	0.00939	4.18542	4.22368	0.00455
28	26.93745	27.33688	0.00734	4.19420	4.22339	0.00347
48	27.04602	27.32708	0.00517	4.20218	4.22267	0.00243
85	27.07043	27.30346	0.00428	4.20404	4.22097	0.00201

Table 1: The numerical test on the convergence of  $\mu_1$  and  $\mu_2$  of a rectangular cylinder in a canal ( $a/c = 1$ ,  $b/a = 1.05$ ,  $d/c = 1.05$ )

b/a	$\mu_1/\rho ac$			$\mu_2/\rho ac$		
	Lower Bound	Upper Bound	Error	Lower Bound	Upper Bound	Error
1.05	2.214296 (2.185)	2.240591 (2.4345)	0.0059 (0.054)	1.141291	1.186527	0.0194
1.1	2.165025 (2.139)	2.191148 (2.3795)	0.0060 (0.0532)	1.029996	1.062103	0.0154
1.2	2.099719 (2.0765)	2.125655 (2.308)	0.0062 (0.0528)	0.921227	0.947102	0.0139
1.3	2.060161 (2.038)	2.085992 (2.265)	0.0062 (0.0528)	0.864646	0.888730	0.0137
1.5	2.019459 (1.999)	2.045191 (2.2215)	0.0063 (0.05248)	0.804854	0.828339	0.0144
2.0	1.993443 (1.960)	2.019169 (2.205)	0.0064 (0.0588)	0.748060	0.773977	0.0170
2.5	1.990240 (1.952)	2.016105 (2.209)	0.0065 (0.06176)	0.729279	0.759396	0.0202

Table 2: The added masses of a triangular cylinder ( $a/c = 1$ ,  $d/c = 1.5$ ) in a canal. (The values in the parenthesis are obtained by Fujino (3))

b/a	d/c	$\mu_1/2\rho ac$			$\mu_2/2\rho ac$			Method
		Lower Bound	Upper Bound	Error	Lower Bound	Upper Bound	Error	
1.05	1.5	9.82949	10.09428	0.0133	2.35926	2.41145	0.0109	B
		9.580	10.09	0.0259	2.318	/	/	F
1.1	1.5	6.24970	6.37091	0.0096	1.42032	1.44254	0.0078	B
		6.075	6.370	0.0237	1.401	/	/	F
1.2	1.5	4.38057	4.44000	0.0067	0.90486	0.91581	0.0060	B
		4.248	4.440	0.0221	0.8955	/	/	F
1.3	1.5	3.75839	3.80126	0.0057	0.71980	0.72807	0.0057	B
		3.675	3.805	0.0174	0.7128	/	/	F
1.5	1.5	3.30581	3.33932	0.0050	0.56769	0.57461	0.0061	B
		3.253	3.342	0.0135	0.5613	/	/	F
2.5	1.5	3.05503	3.09371	0.0063	0.42908	0.43789	0.0102	B
		2.973	3.105	0.0217	0.4209	/	/	F
3.5	1.5	3.04699	3.09793	0.0083	0.41469	0.42719	0.0148	B
		2.935	3.112	0.0293	0.4102	/	/	F
5.0	1.5	3.03374	3.11142	0.0117	0.41044	0.42945	0.0226	B
		2.895	3.137	0.0401	0.4046	/	/	F
5.0	5.0	1.28362	1.31182	0.0011	0.38000	0.39571	0.0203	B
		1.152	1.402	0.0979	0.3512	/	/	F

Table 3: The added masses of a rectangular cylinder at the center of a rectangular canal ( $a/c = 1$ ). (B denotes the results by Bai and F by Fujino)

b/a	$\mu_1 / \frac{1}{2} \rho \pi a^2$			$\mu_2 / \frac{1}{2} \rho \pi a^2$		
	Lower Bound	Upper Bound	Error	Lower Bound	Upper Bound	Error
1.5	3.825745	3.829186	0.00045	0.672034	0.675308	0.00243
2.0	3.790567	3.793783	0.00042	0.560933	0.563956	0.00269
2.5	3.788085	3.791289	0.00042	0.535095	0.538067	0.00277
3.0	3.787902	3.791170	0.00042	0.528340	0.531301	0.00279
4.0	3.787878	3.791104	0.00043	0.526035	0.529008	0.00565
5.0	3.787856	3.791126	0.00043	0.525848	0.528859	0.00285
10.	3.787229	3.791760	0.00060	0.525401	0.529282	0.00368

Table 4: The added masses of a circular cylinder at the centre of a rectangular canal. ( $d/a = 1.2$ ,  $a = c$ )

b/a	$\mu_1/2\rho ac$			$\mu_2/2\rho ac$		
	Lower Bound	Upper Bound	Error	Lower Bound	Upper Bound	Error
1.5	2.576920	2.580815	0.00076	0.498735	0.501801	0.00307
2.0	2.448349	2.451861	0.00072	0.411363	0.414284	0.00354
2.5	2.433891	2.437395	0.00072	0.387188	0.390105	0.00380
3.0	2.432081	2.435680	0.00074	0.379073	0.382056	0.00392
4.0	2.431524	2.435748	0.00087	0.375091	0.378482	0.00450
5.0	2.430754	2.436514	0.00118	0.374204	0.378450	0.00564

Table 5: The added masses of a Lewis form (nearly rectangular) section at the center of a rectangular canal. ( $a/c = 1$ ,  $d/c = 1.5$ , the area coefficient = 0.941)

d/c	$\xi/B$	$\mu_1/\rho Bc$			$\mu_2/\rho Bc$		
		Lower Bound	Upper Bound	Error	Lower Bound	Upper Bound	Error
1.05	0.40	21.613239	22.166780	0.0126	0.566988	0.574093	0.0062
	0.60	21.789459	22.223882	0.0099	0.801438	0.807948	0.0040
	0.65	21.991502	22.403572	0.0093	1.020049	1.027327	0.0036
	0.70	22.713380	23.111889	0.0087	1.639717	1.650404	0.0033
	0.72	23.774386	24.179225	0.0085	2.367068	2.383094	0.0034
	0.74	29.304004	29.848698	0.0092	5.044749	5.094342	0.0049
1.5	0.40	3.091651	3.156993	0.0105	0.461233	0.476091	0.0159
	0.60	3.393256	3.463925	0.0103	0.590998	0.607153	0.0135
	0.65	3.703790	3.784876	0.0108	0.703193	0.721585	0.0129
	0.70	4.634910	4.757809	0.0131	1.003221	1.029781	0.0131
	0.72	5.829749	6.020889	0.0162	1.352111	1.392232	0.0146
	0.74	11.521012	12.094877	0.0243	2.861330	2.986958	0.0215

Table 6: The added masses of a rectangular cylinder at the off-center location in a canal ( $a/c = 1$ )

$\eta/B$	$\mu_1/\rho Bc$			$\mu_2/\rho Bc$		
	Lower Bound	Upper Bound	Error	Lower Bound	Upper Bound	Error
1.0	21.456842	22.745617	0.0292	0.501996	0.520908	0.0185
0.3	21.616915	22.183099	0.0129	0.592008	0.599457	0.0063
0.1	21.986840	22.414629	0.0097	1.019841	1.027451	0.0037
0.05	22.711055	23.117480	0.0089	1.639575	1.650512	0.0033
0.03	23.772989	24.182598	0.0085	2.366953	2.383200	0.0034

Table 7: The added masses of a rectangular cylinder in a canal with a single wall ( $a/c = 1$ )



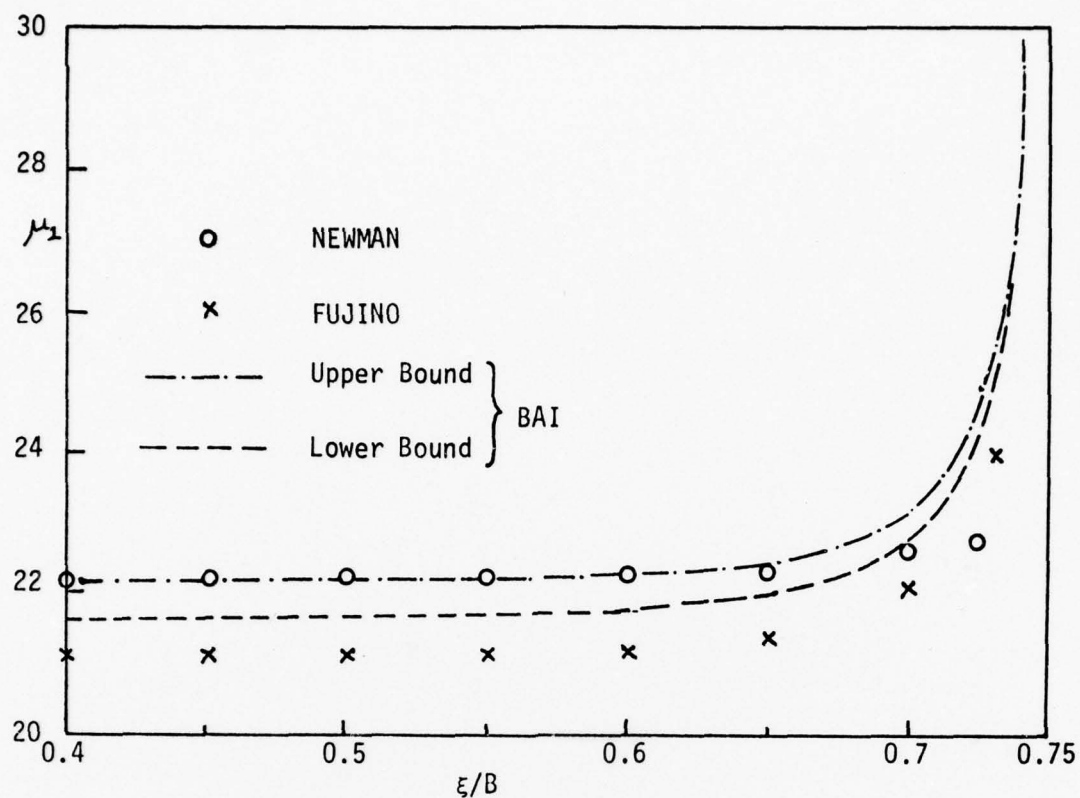


Fig. 9: Comparison of the added mass  $\mu$  of a rectangular cylinder at the off-center location in a rectangular canal

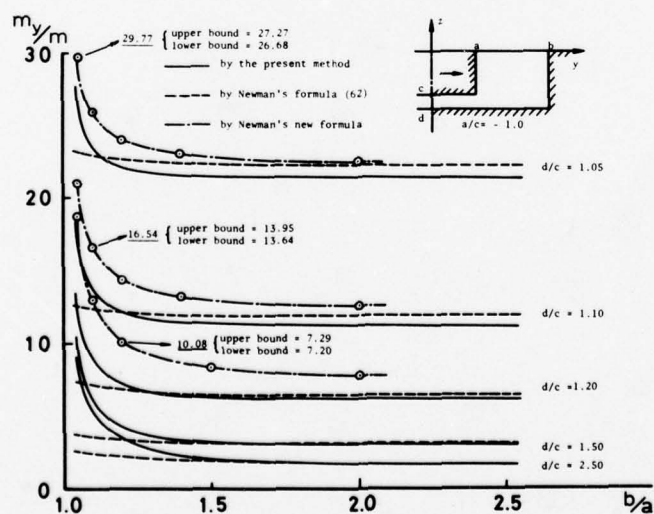


Fig. 10:

## SESSION VIII

### UNSTEADY PROPULSION

Friday, 2 April 1976

11.30—12.30

14.00—15.30

Chairman: J. A. H. Paffett

Low frequency variation of the surface shape of tip region cavitation on marine propeller blades and corresponding disturbances on nearby solid boundaries, by T. Søntvedt and H. Frivold

Some ideas about the optimization of unsteady propellers, by J. A. Sparenberg

Steady and unsteady loadings and hydrodynamic forces on counterrotating propellers, by S. Tsakonas, W. Jacobs, and M. Ali

Vibration excitation forces from a cavitating propeller. Model and full scale tests on a high speed container ship, by C.-A. Johnsson, O. Rutgersson, S. Olsson, and O. Björheden

Experimental determination of mean and unsteady loads on a model CP propeller blade for various simulated modes of ship operation, by R. J. Boswell, J. J. Nelka, and S. B. Denny

PRECEDING PAGE BLANK-NOT FILMED

# LOW FREQUENCY VARIATION OF THE SURFACE SHAPE OF TIP REGION CAVITATION ON MARINE PROPELLER BLADES AND CORRESPONDING DISTURBANCES ON NEARBY SOLID BOUNDARIES

T. SØNTVEDT and H. FRIVOLD

Det Norske Veritas, Division for Marine Technology, Oslo, Norway

## SYNOPSIS

Two features are considered in this paper:

The effectiveness of the apparent volumes of water/cavitation-bubble mixture on and near to heavily loaded blades in inducing fluctuating pressure on near field solid boundaries.

Cavitating bubbles may travel from the tip region of heavily loaded blades to near by solid boundaries causing severe erosion and excitation of vibrations.

## 1. INTRODUCTION

The main purpose of this paper is to throw more light on the following two important features, both related to cavitating marine propellers:

(I) The effectiveness of the apparent volume of water/cavitation-bubble mixture on and near to heavily loaded blades in inducing fluctuating pressure on near field solid boundaries. (Fig. 1 - Frivold /1/).

(II) Cavitating bubbles may travel from the tip region of heavily loaded blades to near by solid boundaries causing severe erosion and excitation of vibrations.

Various types of merchant ships have been equipped with high speed cameras providing valuable basis for study of somewhat more real time characteristics of the process giving rise to (I) and (II), /2/.

Further, TV-equipment has allowed study of 1st order and blade frequency variations of blade cavitation /2/.

Finally, photogrammetry has been employed to estimate real thickness of water-bubble mixture on ship propellers for propeller hull configuration given in Table I, /2/ and /3/.

The data collected by methods described above then serve as basis for identification of basic mechanisms involved in (I) and (II), and subsequently development of more advanced theoretical methods and model test procedures. Such methods will be reported elsewhere in the near future.

## 2. FLUCTUATING PRESSURE FIELD

### 2.1 Analysis of Data from Twin-screw Tanker

The object of this section is to investigate how much of the apparent volume of water/cavitation bubble-mixture on and off the blades is involved in instantaneous displacement of water and corresponding induction of pressure impulses.

The net volume of water/cavitation bubble mixture within the control-volume, exhibited by the observed cavity-mixture surface and the blade surface extrapolated to a particular section behind the trailing edge, is plotted against angular position of blade generatrix (Fig. 3). The standard deviation for the found thickness of mixture is for the example 0,7 cm. Fortunately, observations on various propellers from above have revealed a lower "surface" of travelling cavities, similar in shape to the extrapolated surface/2/. As such, the apparent volume of the cavity-mixture and its time derivative seems to be fairly correct. The volume is computed from stereo-diagrams of the type shown in Fig. 4.

Different effects may affect the ability of the apparent cavity volume to induce pressure impulses. The observed volume surface is cloudy and may consist of a diffusive water/cavity-mixture which affects the displacement of water and correspondingly the pressure impulses. Separation of the cavitation from the blade may occur, leaving a cloud of cavitation bubble-mixture behind the blade possibly not very effective. It is further known that a "re-entrant jet" may penetrate all the way forward to the leading edge /7/ and /8/. If this jet pulsation occurs with suitable frequency, it will make its own contribution to the pressure impulses.

The method of calculation is described in the APPENDIX.

Assuming solid boundary factors in accordance with Frivold/1/, comparison

PRECEDING PAGE BLANK-NOT FILMED



between the calculated low frequency pressure signal with the recorded pressure impulse amplitude spectra, reveals that calculated figures are of the same magnitude. - (Fig. 5). The "solid boundary factor" is in this case in the 1,9 - 2,1 range. It should be mentioned that the stereophotos of the type given in Fig. 4 represent random shots within boundaries of maximum and minimum extent of cavity mixture. Rough extrapolation of thickness to said boundaries was used in computation of the extreme magnitude of pressure signals (Fig. 5). The second propeller of this twin-screw ship will of course affect the recordings of pressure, but at the chosen point of comparison these contributions are not significant.

Non-cavitating magnitudes of pressure impulses included in computations-known to correlate well with several model tests on flat plates on model hulls (at low RPM)- are included in Fig. 5. For the twin-screw full scale propellers in question their magnitudes are small.

Further, the inclusion of the apparent volume of cavity/water-mixture in the same diagram serves to illustrate parts of this volume of particular importance for the pressure signal.

With the different transfer functions, derived in the APPENDIX and integrated across the apparent cavitating area, we observe the relative importance of the terms in producing the net pressure signal (Fig. 6).

In our theoretical model the term  $\frac{1}{d} U_x \frac{\partial^2 \tau}{\partial t \partial x}$  (See APPENDIX) constitutes the main contribution to the net pressure signal.

## 2.2 Analysis of Data from Model Tests-Homogeneous Flow

The model propeller described in /4/ was tested with a horizontal flat plate mounted above the propeller, containing differential pressure transducers. Stereodiagrams were obtained for blade cavitation for the range of cavitation numbers (shaft center) and advance ratios presented in Table II.

From the stereodiagrams of the type shown in Fig. 7, the effect of cavitation on the pressure signals were computed (see APPENDIX). The term  $e U_x \frac{\partial^2 \tau}{\partial t \partial x}$  and the experiments both produced results as illustrated (Fig. 8). The accuracy of recorded stereodiagrams is known to range from approximately 30% (of maximum thickness) at maximum  $\sigma$ ,  $J$ , to more favourable values, at lower values of  $\sigma$  in particular. This inaccuracy does not alter the above-stated observations with regard to "mixture effectiveness".

Also as expected, calculated non-cavitating magnitudes closely resemble experimental figures.

## 2.3 Analysis of Data from Model Tests-

### Propeller in Wake

Working behind a dummy model, the volume (of mixture)-change with angular position is included in Fig. 9 together with our computation of corresponding pressure signal- all based on

stereodiagrams made for various angular positions in the wake peak. The discrepancy may have been caused by the inaccuracy of model propeller stereodiagrams (ranging from 30% to 100% error, dependent on thickness during the blade sweep). The main reason for this inaccuracy is the difficulty in obtaining sharp pictures of model propeller cavitation with the given radial/tangential motion of mixture surface /3/, and possibly window configurations employed.

## 3. STRUCTURE OF STREAM OF CAVITATING BUBBLES LEAVING THE BLADE

### 3.1 Analysis of Data from Twin screw Tanker

Cross sections a) and b) in the bubble/water-mixture (see Fig. 4) are plotted for two angular positions in Fig. 10. For all other angular positions, the contour obtained is more or less similar to those exhibited in Fig. 10. The equivalent radius  $R_c$  at each angular position for section a) is included in Fig. 11. The  $R_c$  distribution is found for random "shots" in each position. Consequently the variation of  $R_c$  (constant angular position) with time should be subject to study. By combination of the linear nature of the plot  $R_c$  against  $B$  (breadth of "vortex" at section a), (Fig. 12), and blade frequency variation of  $B$  with time (Fig. 13), we observe that the instability of  $R_c$  increases with increased shaft horse-power. This feature (observed by TV-equipment) can also be caused by slight change of sea-state, or even the random choice of  $t = 0$  on the videotape. Proper investigation of instability of cavitation requires an extensive data material analysed by statistical methods. Corresponding high speed movies indicate that the "visible" mechanisms of tip vortex roll-up is modified when leaving the wake peak caused by feeding of blade cavitation into the vortex. Thus  $R_c$ , when entering the wake peak, is significantly smaller than when leaving the wake peak- the overall blade loading being fairly similar during "enter" and "leave".

At present semi-empirical methods are developed to predict the growth and decline of the characteristic parameter  $R_c$  (Søntvedt et al. /6/).

### 3.2 Model Propeller in Homogeneous Flow

Cavitation patterns included in Fig. 14 serve as identification of  $\sigma, J$  combinations, used during model tests (propeller P-832, Huse & Børresen /4/). The cross-section a) downstream of trailing edge appears somewhat similar to those experienced on board the ship in question (Fig. 15). The relative importance of propeller load and cavitation number on equivalent "tip vortex" radius  $R_c$  and the breadth  $B$  is found in Fig. 16. The breadth of mixture  $B$  appears to follow the trend exhibited by  $R_c$ . A regression equation is therefore fitted to the data for  $R_c \sim B$ , giving a slope similar to that found for the corresponding data on board the twin-screw tanker (Fig. 17). Except for  $J = 0$ , cavitation patterns are stable, thus no  $R_c \sim$  time analysis is required.

### 3.3 Model Propeller in Wake

Plots of  $B$  and  $R_c$  against angular position (Fig. 18) with included for one position variation in load (constant  $\sigma$ ), and variation in  $\sigma$  (constant load) indicate that  $B$  and  $R_c$  are more sensitive to  $\sigma$  than to load. Observations in the cavitation tunnel reveal that the "tip vortex" downstream of trailing edge is stable in  $B$ (breadth) at each angular position, while some instability is noticed on the blade. Again high speed movies illustrate the "feeding" of the tip vortex with cavitating bubble sheets originally on the blade, when leaving the wake peak.

#### 4. CONCLUDING REMARKS

Fortunately, scatter in cavitation pattern at each angular position on board the ship in question was limited. Thus we may study the transfer function stereodiagram/hull pressure fluctuations for this propeller/hull configuration.

The time-dependent displacement of flow along the propeller blade by water/cavity mixture seems to be reasonably well approximated by a solid equivalent surface. At least the simple discrete element representation of the average shape of cavity surface led to displacement of water as experienced by the pressure transducers mounted on the ship.- The cross-sectional area of this stream of cavitating bubbles leaving the blade in the roll-up region downstream the propeller blade, varies in a regular fashion with both blade loading, cavitation number, and with "enter" and "leave" of the wake peak. The regularity presented has already been employed in semi-empirical methods now in development /6/.

Both high speed cameras, TV-equipment and stereotechnique applied to still pictures, constitute valuable tools in studying phenomena discussed on board the ship. Improvement of accuracy in construction of stereodiagrams is required for model tests in the type of cavitation tunnel employed for experiments presented. This statement applies in particular to tests simulating behind conditions and load actually experienced on modern merchant-ship propellers.

#### 5. REFERENCES:

- /1/ H. Frivold "Solid Boundary Factor for the Aftbody of a LNG Carrier"  
-Norw. Maritime Research-  
No 1, 1975
- /2/ K. Holden "Propeller Cavitation as a Source of Vibration"  
-NTNF Project SKB0930365  
(Classified)
- /3/ K. Holden "On Stability and Volume of Marine Propeller Cavitation and Corresponding Spectral Distribution in Hull Pressure Fields"  
-Symposium on "High Powered Propulsion of Large Ships"  
-NSMB, Dec. 1975

- /4/ R. Børresen & E. Huse "Stereophotography applied to Cavitating Model Propeller in Homogeneous- and Uneven Wake, with Corresponding Measurements of Pressure Fields on a Flat Plate and a Hull Model"  
-Report No. 834.4639,  
Ship Research Institute of Norway-  
(Classified)
- /5/ C.A. Johnsson & T. Sønftvedt "Propeller Excitation and Response of 230 000 t.d.w. Tankers"  
-DnV Publ. No. 79, Nov. 1972-  
Read at Ninth Symposium on Naval Hydr.,  
Paris, August 1972
- /6/ T. Sønftvedt, O. Frydenlund & T. Jenssen "Tip Region Cavitation on Marine Propellers"  
-DnV Report No. 74-53-M-  
(Classified)
- /7/ P. Leehey & T. S. Stellinger "Force and Moment Measurements of Supercavitating Hydrofoils of Finite Span with Comparisons to Theory"  
-MIT Dept. of Ocean Eng., -75-
- /8/ R. W. Kermeeen "Experimental Investigations of 3-dimensional Effects on Cavitating Hydrofoils"  
-California Inst. of Techn.  
Report No. 47-14, Sept. 1960-
- /9/ J. L. Hess & A. M. O. Smith "Calculation of Non-lifting Potential Flow about arbitrary Three-dimensional Bodies"  
- J. Ship Res., 1964, 8

#### NOMENCLATURE

- $B$  : Breadth of cross-section of cavitating mixture (ln extrapolated blade surface)
- $b$  : Distance in  $B$  direction
- $C$  : Speed of sound in water
- $C_p$  : Non-dimensional pressure
- $D$  : Dia. of propeller
- $d$  : Distance from source to field point
- $f$  : Field point
- $J$  : Advance ratio
- $n$  : RPS (and unit normal vector)
- $t$  : Time
- $R_c$  : Equivalent radius of mixture downstream trailing edge
- $r$  : Radial direction co-ordinate

- P : Pressure of field point  
 p : Point on surface  
 S : Surface area  
 s : Integration point on surface  
 x : Chordwise direction co-ordinate  
 U<sub>x</sub> : Velocity of advance  
 Z : Number of blades  
 U : Fluid velocity vector  
 σ : Cavitation number referred to shaft center  
 (and source distribution)  
 τ : Thickness of cavity/water mixture relative to blade surface  
 ρ : Density of fluid  
 φ : Velocity potential

## APPENDIX

## Pressure Fluctuations induced by Cavitation Volumes in Translatory Motion

For calculating the low frequency pressure field, the fluid is regarded as ideal and irrotational. The fluid velocity potential φ may then be constructed by a source distribution σ (s):

$$\phi(f) = \iint_S \frac{\sigma(s)}{d(f,s)} dS \dots\dots\dots(1)$$

d is the distance from the integration point s on the surface S to the field point f, where the potential is being evaluated. S is the propeller blade surface, where cavitation is present, and the observed cavitation surface.

By the boundary condition (zero normal velocity on S), a two-dimensional integral equation for σ on S may be obtained:

$$2\pi\sigma(p) - \iint_S \sigma(s) \frac{\partial}{\partial n} \frac{1}{d(p,s)} dS = -\vec{n}(p) \cdot \vec{U}(p) \quad (2)$$

Here p is the point on the surface S, where σ is to be evaluated,  $\vec{n}(p)$  is the unit normal vector on that point, and  $\vec{U}(p)$  is the relative fluid velocity vector as without cavitation. To solve equation (2), for each time instant, the surface may be divided into surface elements with specified source properties and (2) replaced by a set of linear algebraic equations like the Hess and Smith Method /9/. This procedure will imply extensive calculations and seems too elaborate compared to the accuracy of measurements. Instead, the time dependent cavitation volume element is replaced by a source producing the equivalent volume.

At a field-point f the velocity potential φ due to one blade will be:

$$\phi(f,t) = \frac{1}{4\pi} \iint_S U_x \frac{\partial \tau}{\partial x} + \frac{1}{d} \frac{\partial \tau}{\partial t} \Delta x \Delta r \dots\dots (3)$$

where:

- S : Area of integration equal to extent of cavitation projected to the propeller blade  
 U<sub>x</sub> : Velocity of advance of volume source  
 τ : Thickness of cavitation perpendicular to blade surface

- x : Chordwise dimension  
 r : Radial dimension  
 t : Time

For unsteady potential flow, the linearized pressure, p, at the field-point with no solid boundaries present is:

$$p(f,t) = \rho \sum_{l=1}^Z \frac{\partial \phi}{\partial t} = \frac{\rho}{4\pi} \sum_{l=1}^Z \iint_S U_x e^{\frac{\partial \tau}{\partial x} + U_x \frac{1}{d} \frac{\partial^2 \tau}{\partial r \partial x} + e^{\frac{\partial \tau}{\partial t} + \frac{1}{d} \frac{\partial^2 \tau}{\partial t^2}} \Delta x \Delta r \quad (4)$$

where:

- ρ : Density of water  
 Z : Number of propeller blades  
 e :  $\frac{\partial}{\partial t} \left( \frac{1}{d} \right)$

The pressure fluctuations are computed by equation (4). For ease of comparison, the pressure is made non-dimensional:

$$C_p = \frac{p}{\rho n^2 D^2} \dots\dots\dots(5)$$

where:

- n : RPS  
 D : Diameter of propeller

This procedure has proved to be sufficiently accurate for non-cavitating and stationary cavitating propellers, when the element mesh is relatively coarse. It is assumed to be valid for estimates of Z·n and 2·Z·n frequencies. Then the effect of compressibility can be neglected, since the Mach number

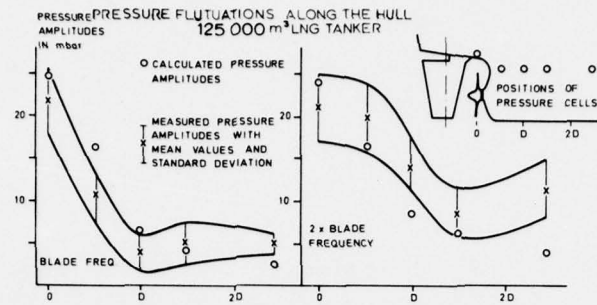
$$\frac{D\pi \cdot 2 \cdot n \cdot Z}{C}^2 < < 1 \dots\dots\dots(6)$$

C : Speed of sound in water



Type of Ship	SHP	$V_s$	Diam.	Z	Vibration recorded	Wake recorded
		Knots	mm			
OBO Motor Tanker	26100	16.5	7000	4	Yes	No
Turbin Tanker	34500	15.9	9000	6	Yes	No
LNG Turbin Tanker	30500	20.5	7750	4	Yes	No
Turbin Tanker	31500	15.8	8900	5	YES	Yes
Motor Tanker	6000	15.98	3250	4	Yes	No
Motor Tanker	31800	16.5	6650	5	Yes	No
Turbin Tanker	39600	16.0	9100	5	Yes	Yes
Coast Ship	990	9.0	1780	3	Yes	No
Motor Tanker	34200	17.4	7300	5	Yes	No
LNG	45000	21.8	7700	5	Yes	No
LPG	20500	17.5	6400	4	Yes	No
LPG	20500	17.5	6400	4	Yes	No
LNG	40000	20.5	7650	5	Yes	Yes
Turbin Tanker	30000	18.0	7800	5	Yes	No
Chem. Tanker	17300	17.25	6000	6	Yes.	No

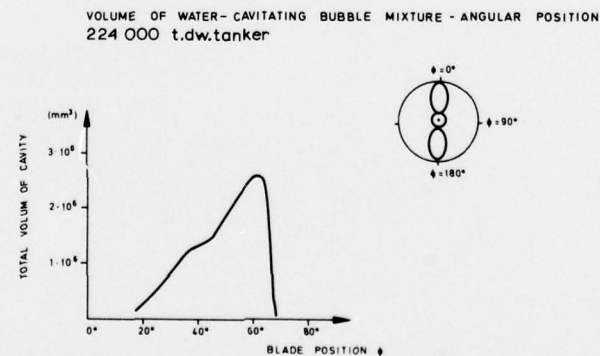
TABLE 1



**Fig. 1: Pressure fluctuations along the hull 125 000 M<sup>3</sup> LNG tanker.**



**Fig. 2: Travelling cavitation giving erosion on a large duct.**



**Fig. 3: Volume of water-cavating bubble mixture versus angular position. 224 000 t.d.w. tanker.**

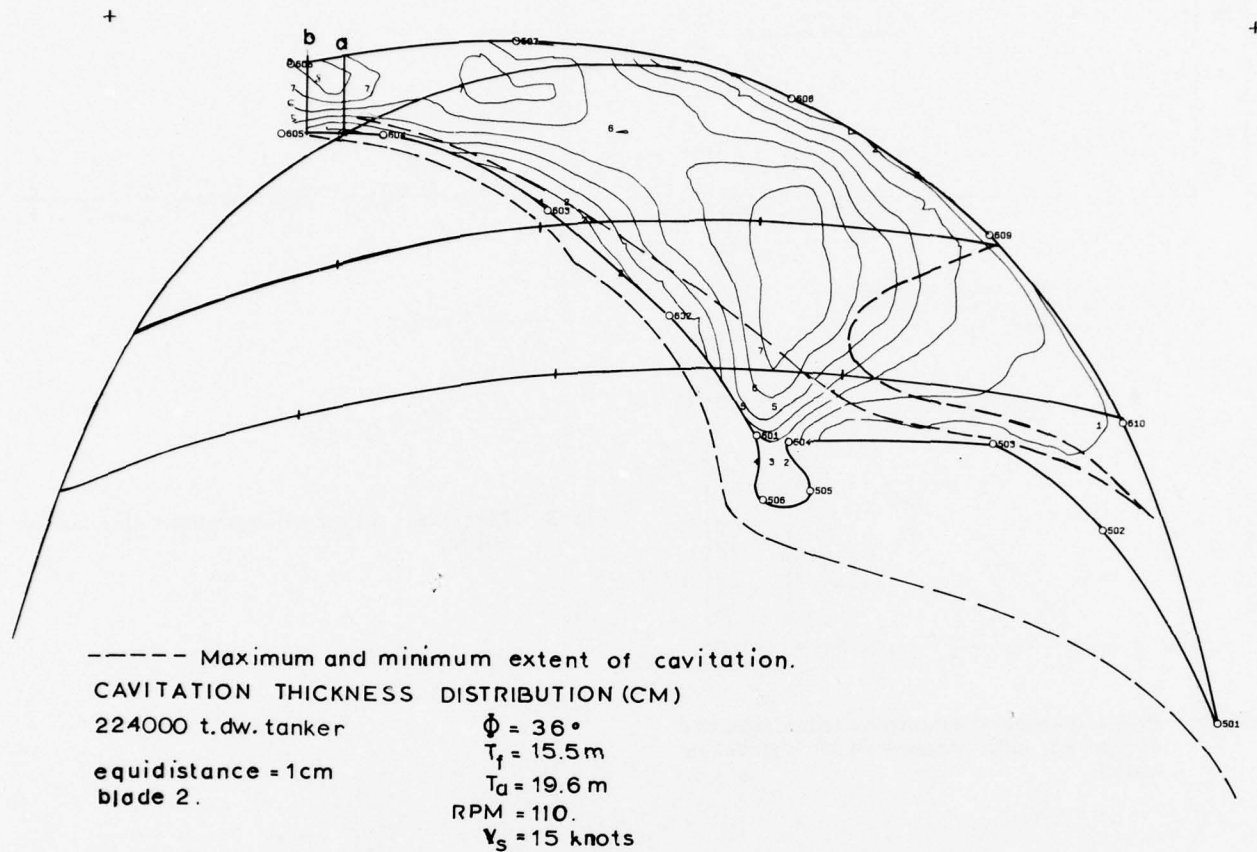


Fig. 4: Cavitation thickness distribution—224 000 t.d.w. tanker.



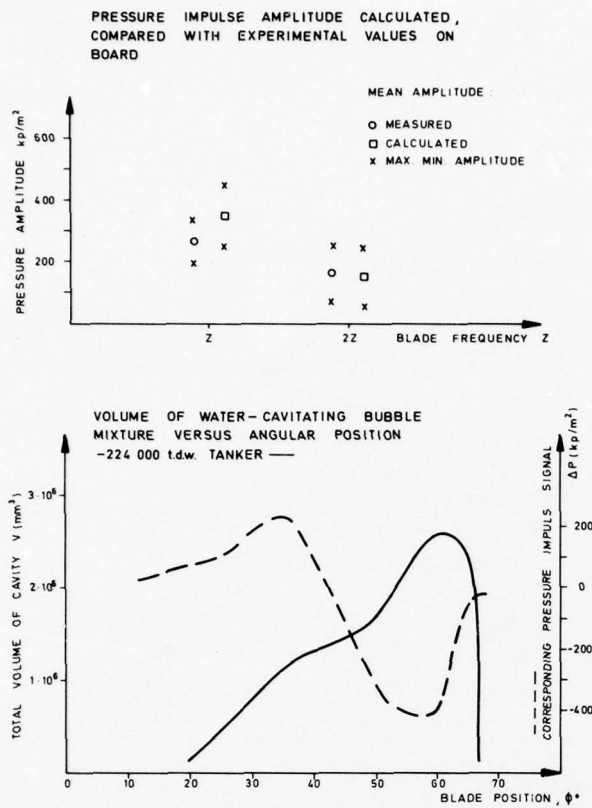


Fig. 5: Pressure impulse amplitude calculated and compared with experimental values on board.

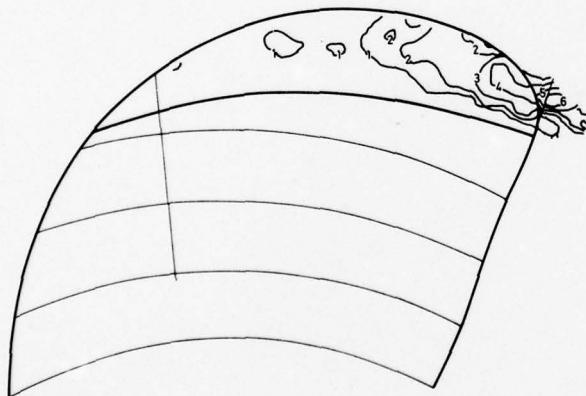


Fig. 7: Model test/Homogeneous flow. Type of stereodiagram used.

#### ELEMENTS OF MATHEMATICAL SIMULATION MODEL

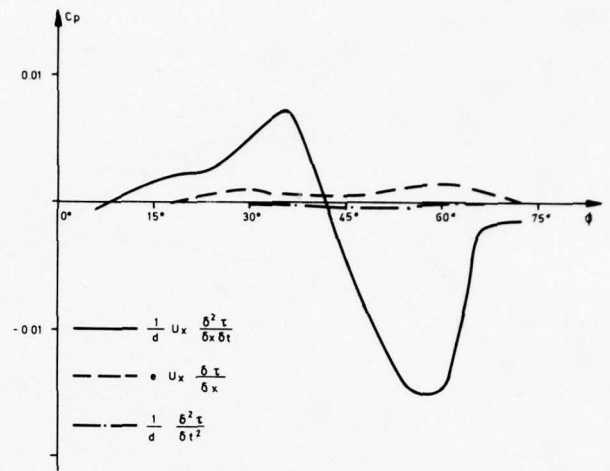


Fig. 6: Elements of mathematical simulation model.

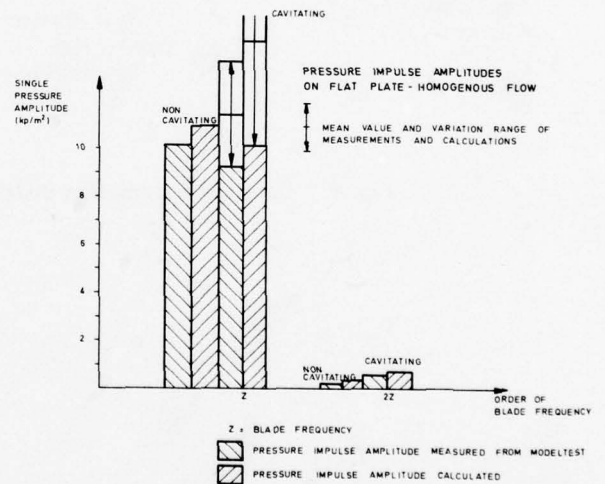


Fig. 8: Pressure impulse amplitude on flat plate/Homogeneous flow.

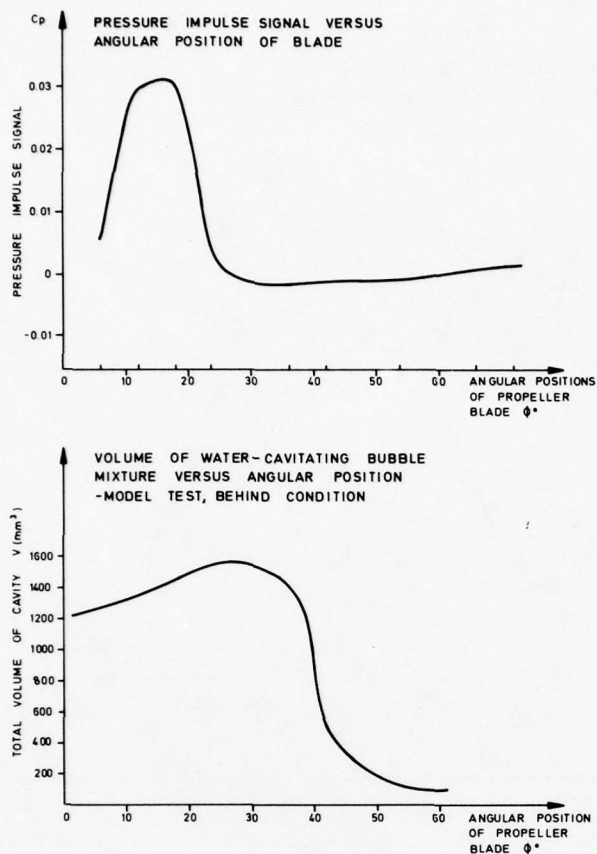


Fig. 9: Volume of water-cavitating bubble mixture versus angular position—Model test, behind condition—Corresponding pressure impulse signal.

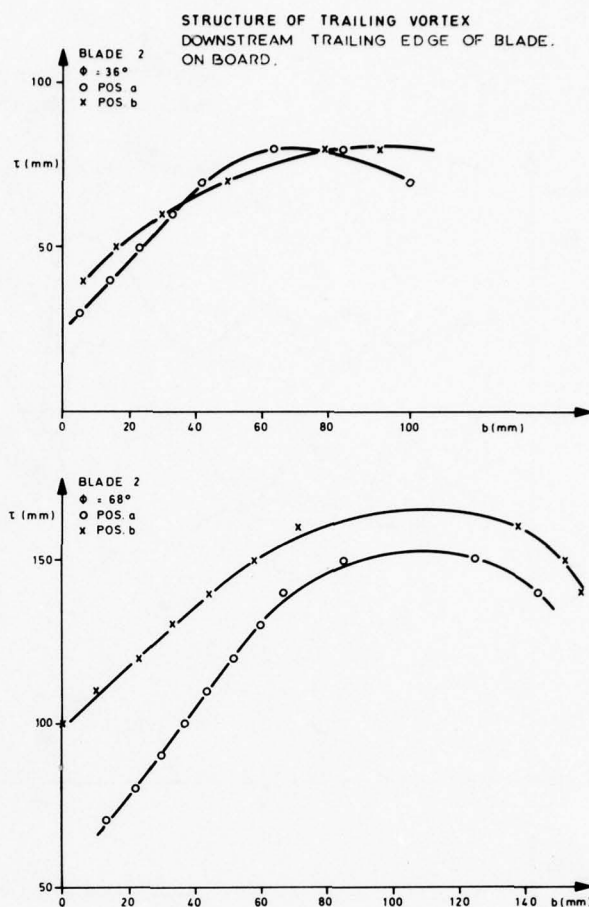


Fig. 10: Structure of trailing vortex. Downstream trailing edge of blade—on board.

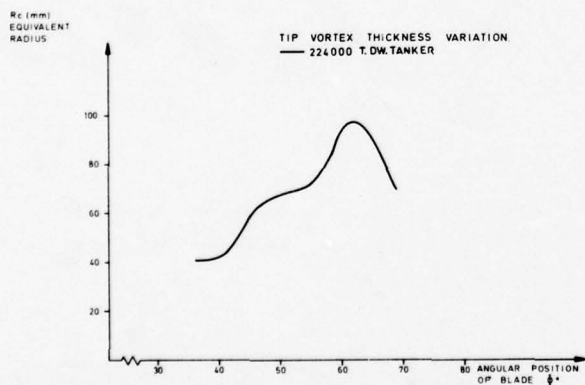


Fig. 11: Tip vortex thickness variation 224 000 t.d.w. tanker.

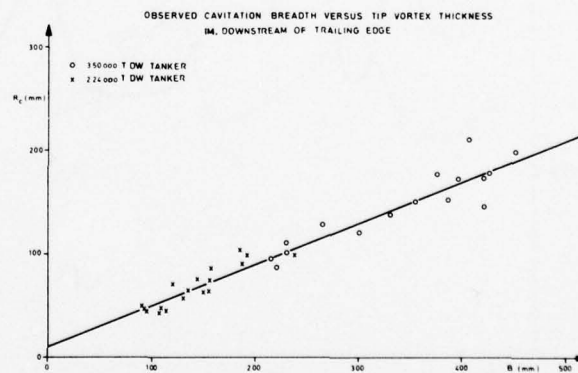


Fig. 12: Observed cavitation breadth versus tip vortex thickness (Imm. downstream of tip edge).

CAVITATION BREADTH VARIATIONS WITH TIME  
FULL LOAD CONDITION (im. downstream of t. edge)

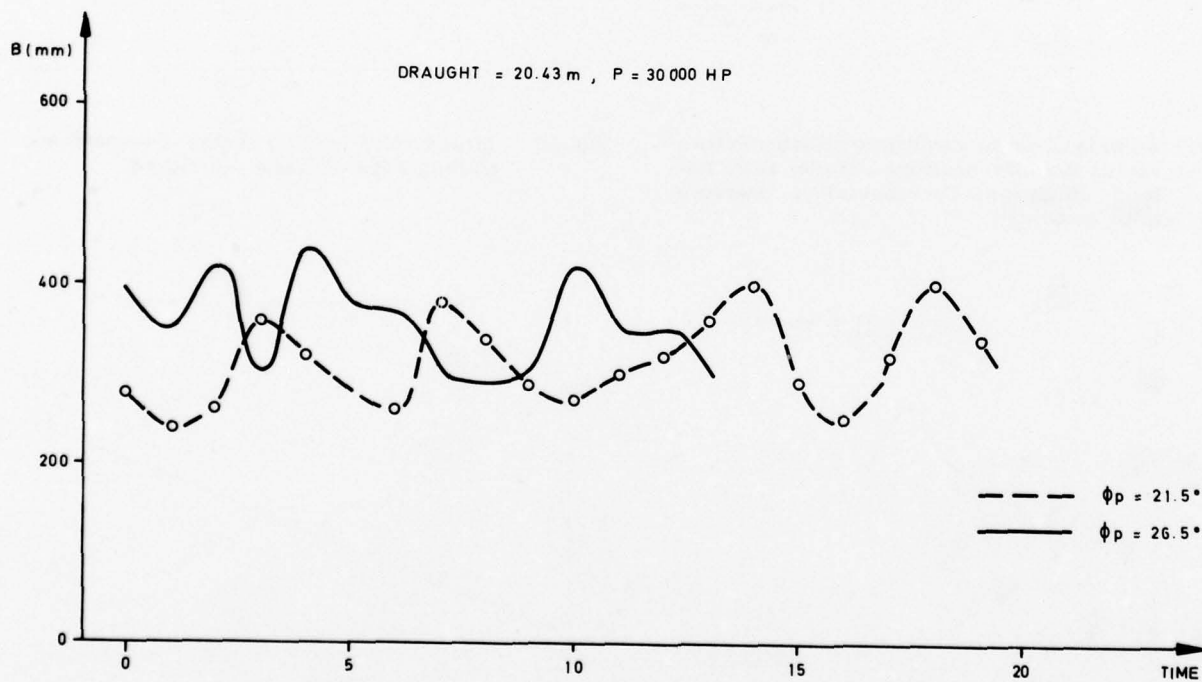
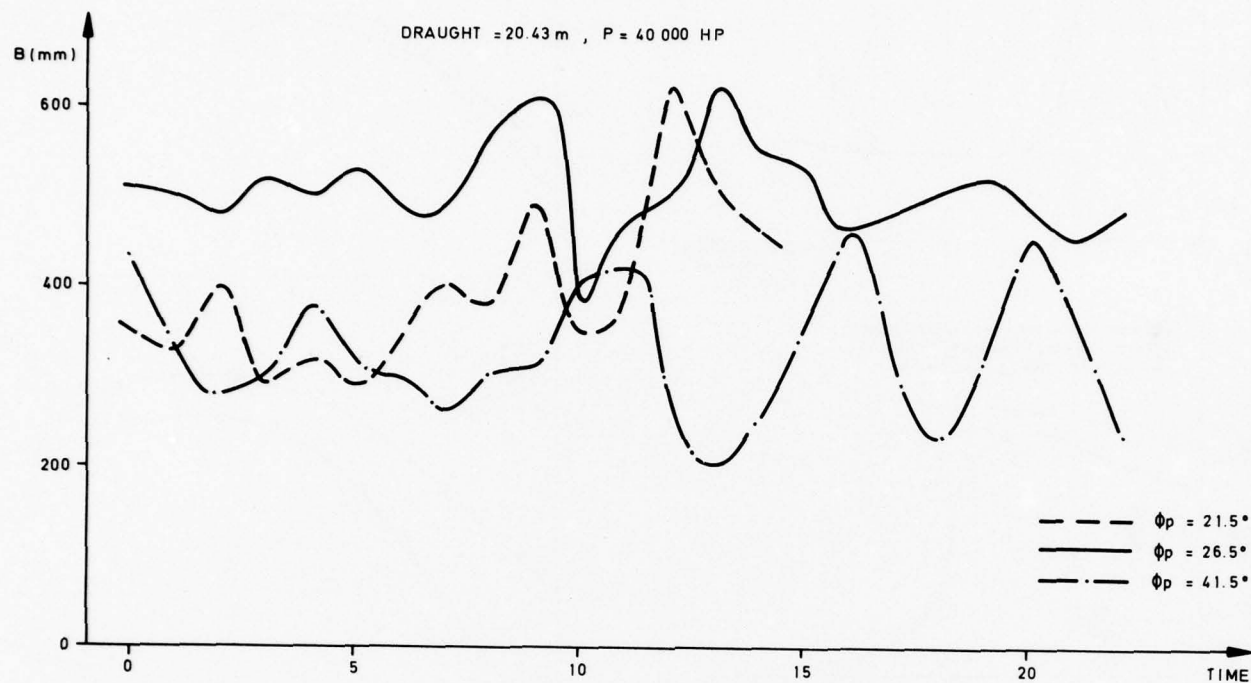


Fig. 13: Cavitation breadth variations with time, full load condition (Imm. downstream of tip edge).



CAVITATION PATTERNS  
HOMOGENEOUS FLOW  
PROPELLER MODEL P-832

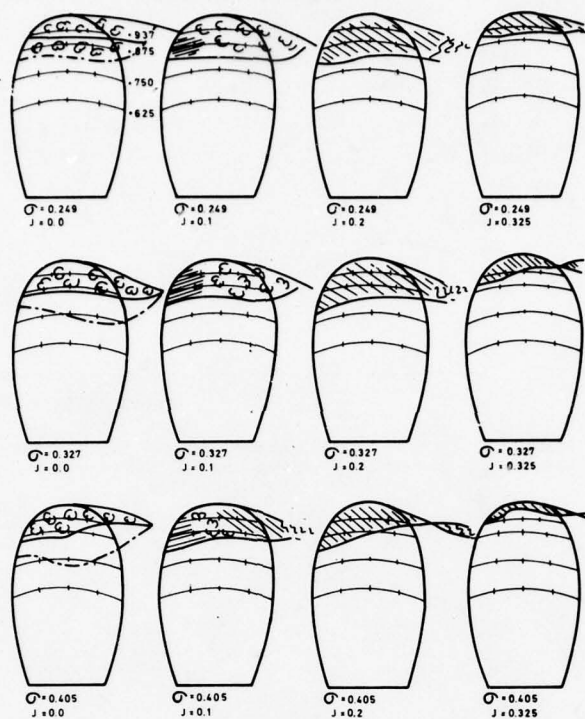


Fig. 14: Cavitation patterns in homogeneous flow.

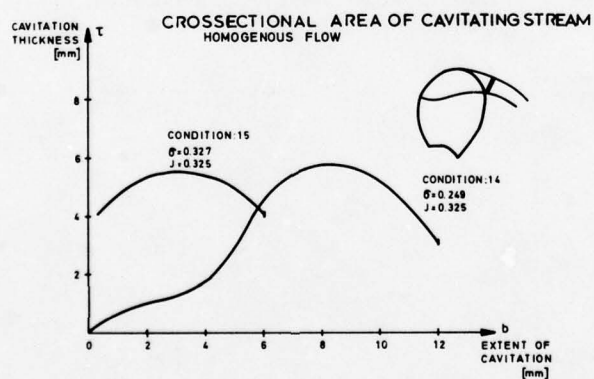


Fig. 15: Cross-sectional area of cavitating stream—Homogeneous flow.

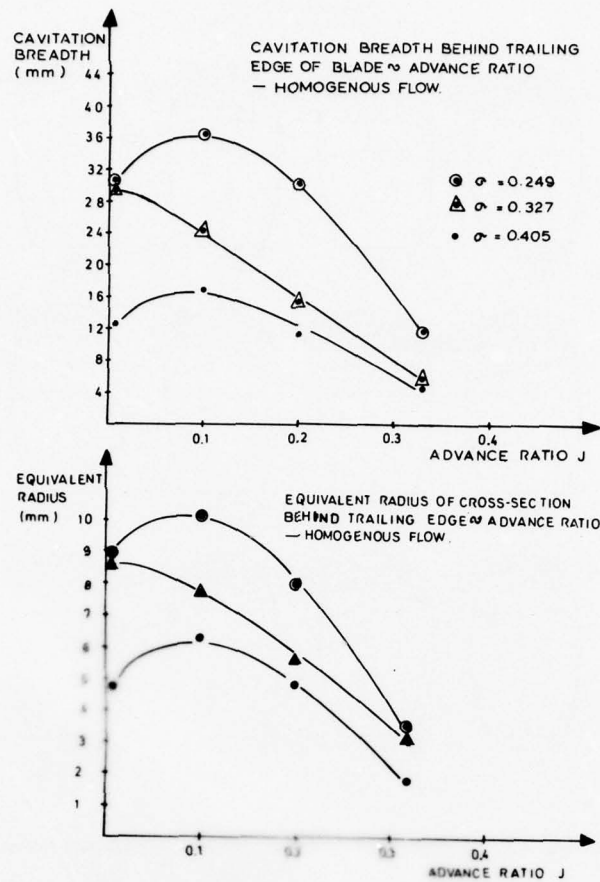


Fig. 16: Cavitation breadth behind trailing edge of blade versus advance ratio,  $J$ —Homogeneous flow.

Equivalent radius of cross-section behind trailing edge versus advance ratio,  $J$ —Homogeneous flow.

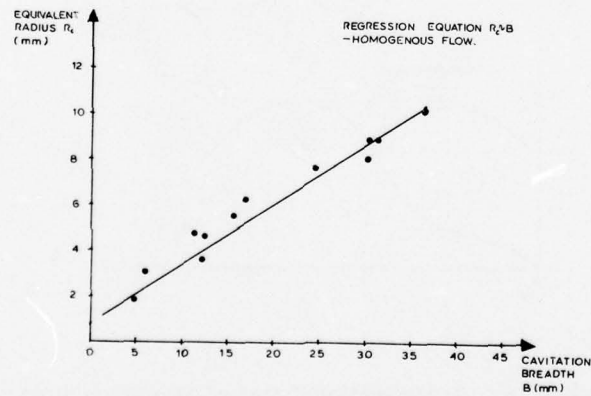
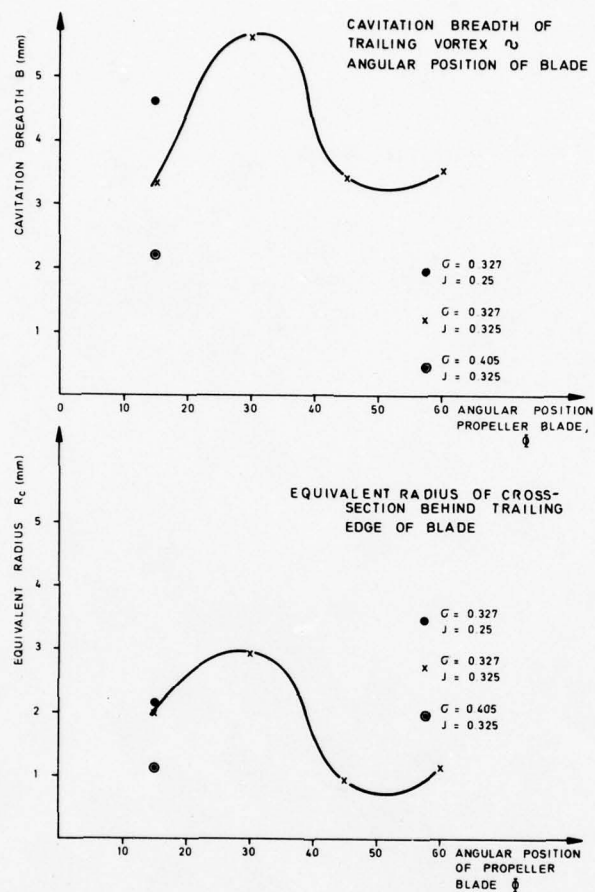


Fig. 17: Regression equation  $R_c \sim B$ —Homogeneous flow.



**Fig. 18: Cavitation breadth of trailing vortex versus angular position of blade.**

**Equivalent radius of cross-section behind trailing edge of blade.**



# SOME IDEAS ABOUT THE OPTIMIZATION OF UNSTEADY PROPELLERS

J. A. SPARENBERG

University of Groningen, The Netherlands

The unsteady propulsion by thrust producing lifting surfaces is discussed. Three regimes of working are distinguished. A rather general necessary condition for optimality of one of the regimes is derived. Questions about existence or non-existence of optimum propellers are considered. A qualitative method for the comparison by inspection of optimum propulsion systems is discussed.

## 1. Introduction

The intention of this paper is to discuss some aspects of the efficiency and optimization of a type of unsteady propulsion. First we have to give a meaning to the expression "unsteady propeller". The most simple one seems to be; a propeller is unsteady when no inertial reference system exists with respect to which the induced fluid flow is time independent. This however is not appropriate, we probably exclude from the conceivable propulsion systems only the sails of a yacht in steady motion, even the free running screw propeller becomes unsteady. A better definition seems; a propeller is unsteady when the relative fluid flow is time dependent while this time dependency is essential for its functioning. The second part of this definition is vague in some degree, it is intended to exclude for instance the screw propeller in a wake. Essential unsteady propulsion occurs in the case of Voith-Schneider propellers, contra rotating propellers, the propulsion wheels of a paddle boat, the fish tail, the flagella of some bacteria, etc.

The type of unsteady propulsion we will consider here belongs to a more restricted class. We assume that the fluid is incompressible and inviscid and that propulsion occurs by lift only. The last two assumptions exclude the flagella of bacteria and the paddle wheel. We agree that viscosity is very important in optimization, because it restricts in a natural way diameters of propulsion systems which in potential theory have to be bounded by artificial constraints. However in order to avoid mixing difficulties we first consider an inviscid fluid. We also demand that the propulsion device will be lightly loaded, hence its shed free vorticity is small, say of  $O(\epsilon)$  where  $\epsilon$  is a small parameter. Then we assume that this free vorticity is not transported by its own induced velocities.

What is left now are propulsion systems consisting of possibly flexible lifting surfaces making flapping motions which are assumed to be periodic and which are still allowed to have a "small or a large" amplitude of  $O(\epsilon)$  or of  $O(\epsilon^0)$  respectively. For the propellers in this class we admit three different regimes of working which will be characterized in the following section. These regimes have different ranges of application and different properties with respect to optimization, so it

seems worth while to give a short account of these properties and to discuss consistently the order of magnitude of their relevant quantities.

In this paper from a certain point of view, a number of aspects of "inviscid unsteady propulsion by lift" are considered, of course many more aspects exist, we mention accelerated swimming [1], applications of slender body theory for instance [1], [2]. One of our intentions is to stimulate interest in questions on the existence or non-existence of optimum propulsion and on the kind of constraints which have to be imposed in order that we can be sure that an optimum exists. For the two dimensional small amplitude motion results with respect to this are given in [3].

## 2. Three regimes of working

In this section we discuss three regimes, numbered i, ii and iii, of unsteady propulsion already announced in the introduction and we will state some of their similarities and differences with respect to optimization.

Regime i, small amplitude propulsion, including propulsion of fishes by tail and fins. For a survey we refer to the article of Wu [4] and for instance for later work we mention [5].

We consider first one lifting surface  $W$  which moves in an  $\epsilon$  neighbourhood, where  $\epsilon$  is a small parameter, of a flat reference strip  $H$  while also the local angles of incidence of  $W$  are assumed to be of  $O(\epsilon)$ . The strip is part of the plane  $z = 0$  (Fig.1) and stretches along the  $x$  axis.  $W$  moves in the positive  $x$  direction with a velocity  $U$  of  $O(\epsilon)$ . When  $W$  moves exactly along  $H$  it does not disturb the fluid at all and does not shed free vorticity. This motion we call the base motion. The small deviations of this base motion which are of  $O(\epsilon)$  and by which a thrust can be generated, will be called the added motion. The boundary conditions related to this lifting surface as well as its bound and free vorticity of  $O(\epsilon)$  are assumed to be at the reference strip  $H$ . This usual assumption facilitates the calculations and introduces inaccuracies of  $O(\epsilon^2)$  for the induced velocities.

The mean value with respect to time, or what is here the same with respect to  $x$ , of the thrust  $T$

will be of  $O(\epsilon^2)$ . Such a small thrust can be described by writing  $T = \epsilon^2$ , which defines the small parameter. The kinetic energy  $E$  left behind per period of time  $\tau$  of the motion is also  $O(\epsilon^2)$  and will be written as  $E = b C_E \epsilon^2$ , where  $b = U\tau$  is the length of a period in the  $x$  direction. Hence  $C_E \epsilon^2$  is the mean value of the kinetic energy left behind per unit of length. The general formula for the efficiency  $\eta$  is

$$\eta = \frac{\tau TU}{\tau TU + E} \quad (2.1)$$

In this theory the efficiency becomes, by substituting the above mentioned expressions for  $T$  and  $E$ ,

$$\eta = \frac{1}{1 + \frac{E}{\tau TU}} \stackrel{\text{def}}{=} 1 - C_\eta = 1 - O(\epsilon^0) \quad (2.2)$$

where the constant  $C_\eta$  is independent of  $\epsilon$ . Hence when  $\epsilon \rightarrow 0$ , the efficiency will not tend to one.

The following optimization problem can be posed. How to choose (by prescribed mean value of the thrust  $T = \epsilon^2$ ) the added motion of the wing so that the energy coefficient  $C_E$  or the efficiency coefficient  $C_\eta$  are as small as possible. In this general form the problem will have no solution within the realm of this type of theory. This is proved in section 3 of this paper. In order to have a well posed problem we need constraints on the added motion of  $W$ .

When in this small amplitude case two lifting surfaces are moving one behind the other, with the same span, the second one can in the linear theory annihilate the free vorticity of the first one, while the thrust of both together has a non zero mean value of  $O(\epsilon^2)$ . Hence at first sight we would predict an efficiency  $\eta = 1$ , because in (2.1)  $E = 0$ . This clearly is against first principles of fluid mechanics. A more close examination [6] shows that there are two free vortex sheets of strength  $O(\epsilon)$  behind the two lifting surface, which are of opposite strength, and at a small distance of  $O(\epsilon)$  apart. Hence in this linearized theory, they cannot be observed separately and they annihilate each other. However, it is not difficult to calculate their distance up to and including  $O(\epsilon)$ . In between these sheets is a fluid flow in agreement with the impulse theorem, which causes energy losses per period  $E = b C_E \epsilon^3$  where  $C_E$  can be calculated. The efficiency in this case becomes

$$\eta = \frac{1}{1 + \frac{E}{\tau TU}} \stackrel{\text{def}}{=} 1 - C_\eta \epsilon = 1 - O(\epsilon) \quad (2.3)$$

Hence in this situation when  $\epsilon \rightarrow 0$  then  $\eta \rightarrow 1$ . Also here it is necessary to impose constraints on the added motions of the two lifting surfaces in order to obtain a well posed optimization problem.

Regime ii, finite amplitude motion, the flexible wing  $W$  moves in an  $\epsilon$  neighbourhood of a periodic curved reference strip  $H$  (Figure 2). Again when  $W$  moves exactly along  $H$  it does not disturb the fluid at all, this is the base motion. Small deviations of  $O(\epsilon)$  of this base motion, which induce velocities and vorticity, will be called the added motion. The boundary conditions related to  $W$  as well as its bound and free vorticity of  $O(\epsilon)$  are assumed to be at  $H$ . The mean value with respect to time of the thrust produced by such a wing is  $O(\epsilon)$ , say  $T = \epsilon$ . The kinetic energy  $E = b C_E \epsilon^2$ , hence the efficiency  $\eta$  has the form (2.3).

We remark that due to the linearization procedure there is an inaccuracy in  $T$  of  $O(\epsilon^2)$ , in fact

$$T = \epsilon + a \epsilon^2, \quad (2.4)$$

with some unknown factor  $a$ . However, this factor does not enter into the efficiency because it appears both in the numerator and in the denominator of (2.1) and up to and including the desired accuracy with respect to  $\epsilon$  it cancels in the expression (2.3) for  $\eta$ .

Again we can ask for the added motion of the wing which minimizes the coefficient  $C_E$  or the coefficient  $C_\eta$  for given mean value of thrust  $T = \epsilon$ . In this case the free vorticity shed by the optimum added wing motion is uniquely determined by  $H$  alone, see [7] or section 4 of this paper. The added motion of the wing is not uniquely determined, although it is not difficult to find added motions which leave behind the desired free vorticity. Hence as contrasted with the small amplitude motion, regime i, we can find now optimum added motions in the realm of this linearized theory, while no constraints on the added motion are needed.

Here it makes no sense to let move a second wing behind  $W$ , which annihilates the free vorticity of  $W$  because then we would reduce the mean value  $T$  with respect to time of the thrust to a quantity of  $O(\epsilon^2)$ , which makes no sense in connection with the inaccuracy of the finite amplitude motion, as indicated by the factor  $a$  in (2.4).

Having optimized the motion of  $W$  for a fixed  $H$ , we can ask for an optimum reference strip  $H$ . This was not possible for regime i, because there this strip was by definition flat. Here some constraints on  $H$  have to be posed otherwise no extremum exists. For instance by making the amplitude of  $H$  larger and larger for fixed  $T = \epsilon$  then  $C_E \rightarrow 0$  or  $\eta \rightarrow 1$ . However we can demand that  $H$  has to remain within a cylinder with generators parallel to the  $x$  axis of cross section area  $S$ , then there is an optimum value of  $\eta$  [7]. This is the efficiency of an actuator disk with a constant load  $\sigma = T/S$  (pressure jump), of which the area is the cross section of the aforementioned cylinder

$$\eta = \left(1 + \frac{\sigma}{2\rho U^2}\right)^{-1}, \quad (2.5)$$

where  $\rho$  is the density of the fluid and  $U$  the mean velocity of advance in the  $x$  direction. The surface  $H$  which yields this optimum is not uniquely determined, however, it has to be rather complicated and will be discussed in sections (5) and (6).

Regime iii, finite amplitude motion of a wing which induces finite disturbance velocities, however, which sheds free vorticity of  $O(\epsilon)$ . We restrict ourselves to the two dimensional case in which the phenomenae are independent of the  $y$  coordinate (Figure 3). The profile of this wing of infinite span will be specialized to a rigid flat plate moving with its three-quarter chord point  $Q$  along a periodic line  $\ell$  while remaining tangent to it. The quantities mentioned below are per unit of span. When we assume that the Kutta condition is satisfied at the trailing edge, the circulation of this profile is always zero hence it does not shed free vorticity [8]. This motion, although it induces disturbance velocities of  $O(\epsilon^0)$ , will be called the base motion. Hence for all three regimes, the base motions do

not shed free vorticity. As in the two previous cases we allow the profile to deviate slightly of  $O(\epsilon)$  from its base motion by means of the added motion. Then it will shed free vorticity of  $O(\epsilon)$  and it will be possible to have a mean value with respect to time of the thrust  $T = \epsilon$ . The energy left behind per period is written as  $E = b C_E \epsilon^2$  and the efficiency  $\eta$  has again the form (2.3).

One difference with the previous two cases is that although the free vorticity is  $O(\epsilon)$  and within the accuracy of the theory is not transported by its own induced velocities, it is transported by the velocities induced by the base motion. Hence its final position and strength has to be calculated. A well posed problem is then to ask for those added motions for which  $T = \epsilon$  and  $C_E$  is a minimum or  $\eta$  a maximum. Then as is discussed in [8], the shed free vorticity is uniquely determined while the optimum added motion is not uniquely determined. However, some choice can be made for an added motion, which sheds this free vorticity. From this point of view regime ii and regime iii behave analogously.

When next we want to optimize also the line  $\ell$  it is again necessary as for regime ii, to impose constraints on  $\ell$  in order that an optimum  $\ell$  exists. The constraints in this case have to be more severe. For instance when we only ask that  $\ell$  has to stay within a strip  $|z| \leq \text{const.}$  no optimum exists. As is shown in [8] it is possible by curving  $\ell$  sufficiently "wild" to transport by the base motion the free vorticity as far away from the  $x$  axis as is desired, by which  $\eta \rightarrow 1$  for given  $T = \epsilon$ . However when sufficient smoothness conditions are given for  $\ell$ , such as bounds for its steepness and for its curvature, it becomes acceptable that optimum lines  $\ell$  do exist.

-----  
A propulsion system operates in general in the neighbourhood of a hull which causes, among others by friction effects, an inhomogeneous flow in the propeller region. In order to simulate this to a certain extent we can allow that in the fluid before the propeller passes, is present a velocity field  $(u_0, v_0, w_0)$  of  $O(\epsilon)$ , periodic in the mean direction of motion and which will be assumed to be independent of time with respect to a reference system coupled to the undisturbed fluid at large values of  $z$ . Problems of this kind are for instance discussed by Wu and Coene [5] where it was, however, allowed that the velocity field  $(u_0, v_0, w_0)$  was time dependent, in fact these velocities were induced by surface waves which were assumed to remain unchanged.

In our case, time independent velocity field  $(u_0, v_0, w_0)$ , there is a simple trick to estimate the maximum amount of energy which can be extracted by the propulsion system out of this inhomogeneity. The only possibility in a linear theory (regimes i and ii), for a propulsion system to sense the inhomogeneity of  $O(\epsilon)$  is by its velocity components perpendicular to the reference strips  $\Pi$  along which the lifting surfaces  $W$  have to move. Hence we can replace the inhomogeneity by another one consisting of a free vorticity layer  $\tilde{\gamma}_0$  on  $H$ , of which the total circulation around  $H$  equals zero and which reproduces these normal velocity components. The energy  $E_0$  of  $O(\epsilon^2)$  per period of this vorticity  $\tilde{\gamma}_0$  can be recovered by the wings by shedding free vorticity  $-\tilde{\gamma}_0$ . Hence  $E_0$  is the desired maximum amount of energy the wings can extract per period. This will be discussed further in section 4.

With respect to the definition of efficiency some ambiguity occurs. In (Figure 4) a scheme is given of the energy balance of a propulsion system P.S.. The symbol  $\tilde{E}$  represents the energy fed into the system by the machinery,  $E_0$  is the maximum energy which can be recovered by the blade  $W$  from the energy in the fluid as discussed above and  $E$  is the energy left behind in the wake, all these energies are per period of time of the motion. Then we have the relation

$$\tilde{E} + E_0 = TU + E \quad (2.6)$$

where  $U$  is the constant velocity of the propelled body. Now we can define two efficiencies. First the "economical efficiency",  $\eta_e$  which is the quotient of the useful work and the energy fed into the system by the machinery

$$\eta_e = \frac{TU}{\tilde{E}} = \frac{TU}{TU + E - E_0} \quad (2.7)$$

Second, the "physical efficiency"  $\eta_p$  which can be defined as the quotient of the useful work and energy totally supplied to the propeller

$$\eta_p = \frac{TU}{\tilde{E} + E_0} = \frac{TU}{TU + E} \quad (2.8)$$

The "economical efficiency"  $\eta_e$  can assume all values  $-\infty < \eta_e < +\infty$  while the "physical efficiency"  $\eta_p$  behaves better  $0 \leq \eta_p \leq 1$ .

We remark that the vorticity  $\gamma_0$  can have at most a contribution to the mean value with respect to time  $T$  of the thrust of  $O(\epsilon^2)$ . Hence, it can have a substantial influence on  $T$  only for regime i.

In the next section we prove that without constraints there exists no optimum motion for regime i, in the case of a "simple wing". This type of wing will be defined later on. In the remaining part of the paper we direct our attention to propulsion systems belonging to regime ii. In section 4 a necessary condition for optimum motion is derived when the surface  $H$  is given. This has been done also in [7] by means of a more mechanical reasoning which puts small amounts of the bound vorticity of the wing to places far down stream. Here analogous results are derived by means of a simple application of ideas of the calculus of variations. Also in the present derivation still another type of constraints is admitted and it is allowed that in the fluid is already a disturbance velocity field  $(u_0, v_0, w_0)$  of  $O(\epsilon)$ . In section 5 some considerations are given about the existence of optimum reference surfaces  $H$  which are sufficiently smooth. In section 6 it is discussed how the efficiency of two propulsion systems can be compared by visual inspection of their surface  $H$ . Finally, in section 7 some results obtained from experiments with respect to Voith-Schneider propellers, are explained by means of the developed theory.



### 3. Non existence of an optimum simple wing, regime i

In this section we restrict ourselves to regime i and consider a flexible wing  $W$  of finite span, with a velocity  $U$  moving in an  $\epsilon$  neighbourhood of the flat reference strip  $H$ , (Figure 1). As the planform  $A$  of this wing we define as usual the projection of  $W$  at the strip  $H$ . Wings of which the boundary of the planform is cut only twice by lines parallel to the  $x$  axis are called simple wings.

We will show that no optimum motion exists for a simple wing  $W$  when  $T = \epsilon^2$ ,  $A$ ,  $U$  and  $b$  or  $\tau$  are prescribed, which minimizes the kinetic energy  $E = bC_E \epsilon^2$  which is left behind. The reason that such a proof can be of value is that in the past efforts have been made to find such optimum wings. We refer to [3] where for the two dimensional case the optimum motion under suitable constraints is discussed. *Our proof shows clearly the difference of a wing with a gap filled with non zero free vorticity and a simple wing.* The proof will have the following steps.

a) First we show that when a simple wing does not leave behind free vorticity it cannot have a mean value of thrust.

b) Hence when an optimum simple wing with a mean value of thrust  $T = \epsilon^2$ , does exist it has to leave behind kinetic energy  $E = bC_E \epsilon^2$  for some non zero  $C_E$ , and has an efficiency  $\eta = 1 - O(\epsilon^0) \neq 1$ .

c) Next we show that we can construct a sequence of wing motions, while  $T = \epsilon^2$ ,  $A$ ,  $U$  and  $b$  or  $\tau$  are prescribed, for which  $\eta \rightarrow 1$ . This contradicts by b) the existence of an optimum motion.

a) Although this is clear in the exact non linear theory, it is not clear at all in a linearized theory, in fact it even is not true in general for non simple wings.

We use for convenience a coordinate system in which the fluid flows with a velocity  $U$  in the negative  $x$  direction (Figure 5). The vorticity of the wing is assumed to be at  $A$  and has the two components

$$\begin{aligned}\Gamma_x(x, y, t) &= \Gamma_x(x, y, t + \tau), \\ \Gamma_y(x, y, t) &= \Gamma_y(x, y, t + \tau)\end{aligned}\quad (3.1)$$

reckoned positive with a right hand screw in the positive  $x$  and  $y$  direction respectively. The vorticity components satisfy

$$\frac{\partial \Gamma_x}{\partial x}(x, y, t) + \frac{\partial \Gamma_y}{\partial y}(x, y, t) = 0. \quad (3.2)$$

The condition that no free vorticity is shed can be written as

$$\int_{x_l(y)}^{x_t(y)} \Gamma_y(x, y, t) dx \equiv 0, \quad (3.3)$$

where  $x_l(y)$  and  $x_t(y)$  represent the leading and the trailing edge respectively.

When we assume the vorticity to be given the camber  $h = h(x, y, t)$  of the wing satisfies

$$U \frac{\partial h}{\partial x} + \frac{\partial h}{\partial t} =$$

$$\begin{aligned}&= \iint_A \{ \Gamma_x(\xi, \eta, t) K_x(x - \xi, y - \eta) + \\ &+ \Gamma_y(\xi, \eta, t) K_y(x - \xi, y - \eta) \} d\xi d\eta\end{aligned}\quad (3.4)$$

where by Biot and Savart's law we have

$$\begin{aligned}K_x(x, y) &= \frac{1}{4\pi} \frac{y}{(x^2 + y^2)^{3/2}}, \\ K_y(x, y) &= -\frac{1}{4\pi} \frac{x}{(x^2 + y^2)^{3/2}}.\end{aligned}\quad (3.5)$$

From (3.4) we obtain

$$h(x, y, t) = \tilde{h}(x - Ut, y) + \frac{1}{U} \int_{x_l}^x L(\sigma, y, t + \frac{\sigma - x}{U}) d\sigma; \quad (3.6)$$

where  $L(x, y, t)$  represents the right hand side of (3.4) and  $\tilde{h}(x, y)$  is an arbitrary function of its arguments. By choosing  $\tilde{h}(x, y)$  periodic with respect to  $x$  with period  $U\tau$ ,  $h(x, y, t)$  will be a periodic function of time with period  $\tau$ .

The mean value of the thrust, reckoned positive in the positive  $x$  direction can be written as

$$\begin{aligned}T(\epsilon^2) &= -\frac{\rho}{\tau} \int_0^\tau \iint_A \{ U \Gamma_y(x, y, t) + \\ &+ \frac{\partial}{\partial t} \int_{x_l}^x \Gamma_y(\xi, y, t) d\xi \} \frac{\partial h}{\partial x}(x, y, t) dx dy dt = \\ &= -\frac{\rho}{\tau} \int_0^\tau \iint_A \{ U \Gamma_y(x, y, t) \frac{\partial}{\partial x} h(x, y, t) + \\ &- \frac{\partial}{\partial t} \Gamma_y(x, y, t) h(x, y, t) \} dx dy dt,\end{aligned}\quad (3.7)$$

where we used (3.3). In this equation we do not consider a contribution of the suction force at the leading edge which can arise from a square root singularity of the pressure distribution. This however is not really a restriction of generality. We can always introduce a slight change of the vorticity so that it becomes a smooth function which is zero at the leading edge. Then the surface  $h(x, y, t)$  becomes heavily curved so that "so to speak" the contribution of the suction force is brought to the inner part of  $A$  and contributes correctly to (3.7) within any desired degree of accuracy. In fact we have only to consider  $\Gamma_x(x, y, t)$  and  $\Gamma_y(x, y, t)$  which are for instance zero and sufficiently smooth at the edge of the wing.

It is crucial for our considerations that the ranges of integration for  $(\xi, \eta)$  in (3.4) and  $(x, y)$  in (3.7) are equal, namely  $A$ , with other words that the wing is simple and does not shed free vorticity. When the planform  $A$  had a gap at which  $\Gamma_x(x, y, t)$  and  $\Gamma_y(x, y, t)$  were not zero then these ranges of integration would be different.

By partial integration with respect to time we can write (3.7) in the form

$$\begin{aligned}T(\epsilon^2) &= -\frac{\rho}{\tau} \int_0^\tau \iint_A \Gamma_y^*(x, y, t) \{ U \frac{\partial h}{\partial x}(x, y, t) + \\ &+ \frac{\partial h}{\partial t}(x, y, t) \} dx dy dt\end{aligned}\quad (3.8)$$

Substitution of (3.4) in (3.8) yields

$$\begin{aligned} T(\epsilon^2) &= -\frac{\rho}{\tau} \int_0^\tau \iint_B \iint_B \Gamma_y(x, y, t) \cdot \\ &\quad \{ \Gamma_x(\xi, \eta, t) K_x(x-\xi, y-\eta) + \\ &\quad + \Gamma_y(\xi, \eta, t) K_y(x-\xi, y-\eta) \} d\xi d\eta dx dy dt = \\ &= -\rho \int_0^\tau \iint_B \iint_B \Gamma_y(x, y, t) \\ &\quad \Gamma_x(\xi, \eta, t) K_x(x-\xi, y-\eta) d\xi d\eta dx dy dt \end{aligned} \quad (3.9)$$

The part of the integrand which has disappeared has zero contribution, because of the antisymmetry of  $K_x$  with respect to its arguments (3.5) and by the equal regions of integration for  $(x, y)$  and  $(\xi, \eta)$ .

By integrating (3.9) twice partially, first with respect to  $y$  and second with respect to  $x$ , while using (3.2) we find

$$\begin{aligned} T(\epsilon^2) &= \frac{\rho}{\tau} \int_0^\tau \iint_B \iint_B \Gamma_x(\xi, \eta, t) \cdot \\ &\quad \Gamma_x(x, y, t) \left\{ \frac{\partial}{\partial x} \int_y^\infty K_x(x-\xi, \tilde{y}-\eta) d\tilde{y} \right\} dx dy d\xi d\eta dt \end{aligned} \quad (3.10)$$

Again by the antisymmetry properties with respect to its arguments of

$$\frac{\partial}{\partial x} \int_y^\infty K_x(x-\xi, \tilde{y}-\eta) d\tilde{y} = \frac{1}{4\eta} \frac{(x-\xi)}{\{(x-\xi)^2 + (y-\eta)^2\}^{3/2}}, \quad (3.11)$$

and by the equality of the regions of integrations for  $(x, y)$  and  $(\xi, \eta)$  we find

$$T(\epsilon^2) = 0. \quad (3.12)$$

Herewith we have settled part a) of the proof. Part b) is the statement which connects a) and c), so we come to part c).

We will construct for a given planform  $A$ , a sequence of wings with increasing efficiency. Consider a sufficiently narrow region  $\Delta W$  of width  $\Delta l$  along the leading edge. This will be the active part of the wing and will be given a purely heaving motion

$$\begin{aligned} h^*(x, y, t) &= \epsilon a \sin \omega t, \\ x(y) - \Delta l &\leq x \leq x(y), \end{aligned} \quad (3.13)$$

where  $\omega = 2\pi/\tau$  and  $a = O(\epsilon^0)$  is some factor. The remaining part of the wing will be a membrane without mass, stiffness or tension, hence with no pressure jump across it. Together these parts form the profile  $h^*(x, y, t)$ . It is then clear by the narrowness of the active parts  $\Delta W$  that during a relatively large part of the upstroke the pressure at the upper side of  $\Delta W$  is positive and negative at the bottom side and inversely for the downward stroke.

Now we superimpose on  $h^*(x, y, t)$  a motion which belongs to the homogeneous part of

equation (3.4) namely  $\tilde{h}(x-Ut, y)$  as denoted in (3.6). The addition of this "kinematic" profile changes neither the induced velocities nor the vorticity, however it can add to the thrust by giving it the shape of suitable step like functions, as is drawn in (Figure 6). We now take in the general formula for the mean value of the thrust (first part of (3.7)), the sequence of motions

$$\begin{aligned} h_n(x, y, t) &= \tilde{h}_n(x-Ut, y) + \\ &+ h^*(x, y, t), \quad n = 1, 2, 3, \dots, \end{aligned} \quad (3.14)$$

where the profiles  $\tilde{h}(x-Ut, y)$  are of the shape of figure (3.2) with increasing magnitude of their steps for larger values of  $n$ . These profiles have to be "pushed" along the original profile  $h^*(x, y, t)$ , with velocity  $U$  in the negative  $x$  direction, against the pressure jump across the region  $\Delta W$ . In this way thrust is created without further disturbing the fluid. When the magnitude of the steps increases without bounds, also the mean values  $T_n$  belonging to  $h_n(x, y, t)$  increase without bounds. Because no extra vorticity is shed the lost energy  $E(\epsilon^2)$  remains constant. Hence for the efficiency we find

$$\lim_{n \rightarrow \infty} \eta_n = \lim_{n \rightarrow \infty} \frac{T_n U}{T_n U + E} = 1. \quad (3.15)$$

Otherwise by decreasing the factor  $a$  of  $h^*(x, y, t)$  it is possible by choosing sufficiently steep  $\tilde{h}_n(x-Ut, y)$  to keep  $T_n \approx E$  while  $E_n \rightarrow 0$ , hence also  $\eta_n \rightarrow 1$  (3.14). This means in connection with b) that no optimum motion exists in the linearized theory.

The objection can be made that by taking steeper and steeper profiles  $\tilde{h}_n(x-Ut, y)$ , the linear theory will no longer be valid. Of course this is true, however our statement only says that without constraints it is not possible to find by mathematical methods an optimum simple wing motion by using the formulae of the linearized theory of regime i.

This proof remains valid in the two dimensional case, then we have to put  $\Gamma_y(x, y, t) \equiv 0$  and  $\Gamma_x(x, y, t) = \Gamma(x, t)$ .

When the wing is not simple we have for instance a situation as is described in section 2 at the end of the discussion of regime i. Here, without leaving behind free vorticity within the realm of the linearized theory, thrust can be delivered and the proof is invalidated.

#### 4. Optimum vorticity for prescribed reference surfaces $H$ , regime ii.

We consider an unbounded, incompressible and inviscid fluid of density  $\rho$ , in which we have a Cartesian inertial reference frame  $(x, y, z)$ . The fluid will have a time independent velocity field  $(\tilde{u}, \tilde{v}, \tilde{w})$  of  $O(\epsilon)$  periodic in the  $x$  direction with period  $b$ . In this fluid we have a reference surface  $H$  periodic in the  $x$  direction also with period  $b$ . We remark that just as has been done in [7], the whole derivation is equally well possible for any finite number of surfaces  $H$ . For a schematic picture we refer to (Figure 2). As has been discussed in the last part of section 2 we replace the velocity field  $(\tilde{u}, \tilde{v}, \tilde{w})$  by another one  $(u_o, v_o, w_o)$  caused by a vorticity layer  $\gamma_o$  of  $O(\epsilon)$  at  $H_o$  of total circulation zero around  $H$ , which has the same normal component as  $(\tilde{u}, \tilde{v}, \tilde{w})$ . Then for a wing  $W$  moving in an  $\epsilon$  neighbourhood of  $H$  nothing has changed.

When the wing  $W$  has passed along, it has left behind free vorticity  $\vec{\gamma}$  at  $H$  by which it alters the kinetic energy which before passing belonged to  $\vec{\gamma}_0$  only. The resulting kinetic energy due to  $\vec{\gamma}_0$  and  $\vec{\gamma}$  together, being lost, should be made as small as possible. We introduce the velocity potential  $\varphi_0(x, y, z)$  which belongs to the velocity induced by  $\vec{\gamma}_0$  and the potential  $\varphi(x, y, z)$  which belongs to  $\vec{\gamma}$ . Then the kinetic energy left behind per period can be written as

$$E = \frac{1}{2} \rho \iiint_{-\infty}^{+\infty} \int_0^b \left\{ \left( \frac{\partial}{\partial x} \varphi_0 + \frac{\partial}{\partial x} \varphi \right)^2 + \left( \frac{\partial}{\partial y} \varphi_0 + \frac{\partial}{\partial y} \varphi \right)^2 + \left( \frac{\partial}{\partial z} \varphi_0 + \frac{\partial}{\partial z} \varphi \right)^2 \right\} dx dy dz \quad (4.1)$$

A theoretical advantage of this formulation by means of  $(u_0, v_0, w_0)$  or  $\varphi_0$  instead of the original field  $(\vec{u}, \vec{v}, \vec{w})$  is that now the kinetic energy of the infinite slab of integration (4.1) is finite, which need not to be the case for the original field  $(\vec{u}, \vec{v}, \vec{w})$ . That the kinetic energy is indeed finite follows from the fact that the total circulation around  $H$  is zero.

The quantity  $E$  of (4.1) has to be minimized under some constraints, for instance the mean value with respect to time  $T$  of thrust must have some prescribed value. When we use constraints which bear on such mean values we can without restricting generality replace the lifting surface by a lifting line which leaves behind the same free vorticity. For this lifting line we can choose the intersection of a flat plane; perpendicular to the  $x$  axis, with  $H$ . When the flat plane moves with the velocity  $U$  along the  $x$  axis the lifting line moves along  $H$  with a velocity which depends on the local "slope" of  $H$  with respect to the  $x$  axis. This is again no restriction of generality. It will be shown that, in order to have the optimum case, it is only necessary to leave behind free vorticity of some strength distribution which is independent of the special velocity distribution with which the wing moves in the period of time  $\tau$  over a distance  $b = U\tau$  in the  $x$  direction.

Along the lifting line we introduce a length parameter  $s$  with  $0 \leq s \leq \ell(t)$ . The spanwise circulation distribution of the lifting line will be denoted by  $\Gamma(s, t)$  and its velocity, which is tangent to  $H$ , will have a component normal to the lifting line of magnitude  $V(s, t)$ . We can write the mean value  $T$  with respect to time of the thrust in the  $x$  direction as

$$T = \rho \frac{U}{b} \int_0^\tau \int_0^{\ell(t)} \Gamma(s, t) V(s, t) \cos(n, x) ds dt = O(\epsilon), \quad (4.2)$$

where  $U$  is again the mean velocity of advance, or which is the same the constant velocity of the propelled body, the normal  $\vec{n}$  is denoted in (Figure 2). Changing the time integration variable into a length parameter along  $H$  and locally perpendicular to  $s$ , we can write (4.2) in the form

$$T = \rho \frac{U}{b} \iint_{H_b} [\varphi(P)]_+^+ \cos(n, x) d\sigma \quad (4.3)$$

where the domain of integration  $H_b$  is one period of the surface  $H$ ,  $P$  is some point on  $H_b$ ,  $[\varphi(P)]_+^+$  is the jump of  $\varphi$  across  $H$  at the point  $P$  and  $d\sigma$

represents an element of area. In (Figure 2) a possible choice for the  $+$  and  $-$  side of  $H$  is denoted. Remark that in this constraint the velocity  $V(s, t)$  has disappeared.

More general it can be assumed that the constraints on  $\varphi$  have the following form, of which (4.3) is a special case.

$$\iint_{H_b} g_i(P) [\varphi(P)]_+^+ d\sigma - G_i = 0, \quad i = 1, \dots, M, \quad (4.4)$$

where the  $g_i$  are given periodic functions of position and the  $G_i$  are given numbers. By (4.4) it is possible to impose concurrently a number of constraints for instance mean values with respect to time of thrust, lift forces, moments and so on.

Another type of constraints appear when at each moment of time or at each place a hydrodynamical force action is prescribed. Suppose for simplicity, that our real wing is slender so that it can be represented with sufficient accuracy by a lifting line, again we choose the intersection of a flat plane  $x = f(t)$  moving in the positive  $x$  direction, and  $H$ . For  $H$  we choose to fix attention, a cylindrical strip with generators parallel to the  $z$  axis. We remark that here the assumption of a lifting line is a restriction of generality, so that opposite to the previous case, the necessary conditions which we will find for these constraints, are valid only for slender wings. It seems not to be difficult to set up a theory for non slender wings and non cylindrical reference surfaces  $H$ , however, this would complicate the analysis. Suppose for instance that the central chord of the wing moves in the  $y = 0$  plane and that we will prescribe the bending moment  $\tilde{M}(t)$  around the central chord as a function of time, or because in this case the velocities of the wing have to be known, as a function of  $x$ ,  $M(x)$ . Then such a constraint reads,

$$M(x) = \rho V(x) \int_0^h y \Gamma(x, y) dy \quad (4.5)$$

where the span of the lifting line is  $2h$  and  $V(x)$  the given velocity of the wing along  $H$ . This type of constraint can be written, more generally as

$$\int_0^h g_i(P) [\varphi(P)]_+^+ dy + G_i(x) = 0, \quad i = M+1, \dots, N, \quad (4.6)$$

where the functions  $G_i(x)$  are prescribed and should be chosen in such a way that no contradictions arise with constraints of type (4.4). The points  $P$  in (4.6) lie on the lifting line.

A variation of  $\varphi(x, y, z)$  in (4.1) can be effected only by periodic changes of the free vorticity at  $H$ , hence by changing the jump  $[\varphi]_+^+$  at  $H$ . Suppose that now  $\varphi$  represents the optimum potential then we replace  $\varphi$  by  $\varphi + \delta\varphi$ , where  $\delta\varphi$  is a periodic potential function. Then the first variation of  $E$  (4.1) becomes

$$\delta E = \rho \int \int_{-\infty}^{+\infty} \int_0^b \left\{ \frac{\partial}{\partial x} (\varphi_0 + \varphi) \cdot \frac{\partial}{\partial x} \delta\varphi + \frac{\partial}{\partial y} (\varphi_0 + \varphi) \cdot \frac{\partial}{\partial y} \delta\varphi + \frac{\partial}{\partial z} (\varphi_0 + \varphi) \cdot \frac{\partial}{\partial z} \delta\varphi \right\} dx dy dz \quad (4.7)$$



By partial integration of the three terms of the integrand in (4.7), with respect to  $x, y$  and  $z$  respectively, we find

$$\delta E = -\rho \iint_{H_b} \frac{\partial}{\partial n} (\varphi_0 + \varphi) \cdot [\delta\varphi]_n^+ d\sigma \quad (4.8)$$

where we used the fact that  $\varphi_0$  and  $\varphi$  are potential functions.

The jump  $[\delta\varphi]_n^+$  in the disturbance potential can be chosen zero everywhere at  $H_b$  with the exception of the neighbourhood of some point  $P$ . This is most easily effectuated by placing around that point a "slightly distributed" closed vortex ring. Then  $[\delta\varphi]_n^+$  is zero outside this ring and has a nearly constant value "inside" it. However, we have to satisfy  $M$  constraints of type (4.4) and  $N - M$  constraints of type (4.6). In order to handle these we consider a disturbance  $[\delta\varphi]_n^+$  which is nonzero in the neighbourhood of  $N + 1$  points  $P_1, \dots, P_{N+1}$  at  $H_b$ . The integral over the disturbance  $[\delta\varphi]_n^+$  at point  $P_\ell$  over the small region where it is nonzero will be denoted by  $\delta\varphi_\ell$ . Then (4.8) becomes

$$\begin{aligned} \frac{1}{\rho} \delta E = & -\sum_{\ell=1}^N \frac{\partial}{\partial n} (\varphi_0(P_\ell) + \varphi(P_\ell)) \delta\varphi_\ell + \\ & -\frac{\partial}{\partial n} (\varphi_0(P_{N+1}) + \varphi(P_{N+1})) \delta\varphi_{N+1}. \end{aligned} \quad (4.9)$$

For these disturbances the constraints of type (4.4) can be written as

$$\sum_{\ell=1}^N g_i(P_\ell) \delta\varphi_\ell = -g_i(P_{N+1}) \delta\varphi_{N+1}, \quad i=1, \dots, M. \quad (4.10)$$

The constraints of type (4.6) have to be handled more carefully. Because they are local we assume that the points  $P_{M+1}, \dots, P_{N+1}$  have the same  $x$  coordinate ( $x=\xi$ ) while the disturbances around them satisfy for each  $x$  coordinate where they do not vanish, the homogeneous part of (4.6). Now integrating over a sufficiently narrow strip of  $H_b$  around  $x=\xi$ , we find that these constraints assume the form

$$\sum_{\ell=M+1}^N g_i(P_\ell) \delta\varphi_\ell = -g_i(P_{N+1}) \delta\varphi_{N+1}, \quad i=M+1, \dots, N, \quad (4.11)$$

where because the strip of integration is sufficiently small, for almost all values of  $\xi$  no contribution arises from the disturbances around the points  $P_1, \dots, P_M$ . By equations (4.10) and (4.11) we can express the values of  $\delta\varphi_1, \dots, \delta\varphi_N$  into  $\delta\varphi_{N+1}$ . The coefficient matrix of these  $N$  linear equations for  $\delta\varphi_\ell, \ell=1, \dots, N$  has the form

$$\begin{pmatrix} g_1(P_1) \dots g_1(P_M) & g_1(P_{M+1}) \dots g_1(P_N) \\ \vdots & \vdots \\ g_M(P_1) \dots g_M(P_M) & \vdots \\ \vdots & \vdots \\ 0 \dots \dots \dots 0 & \vdots \\ \vdots & \vdots \\ 0 \dots \dots \dots 0 & g_N(P_{M+1}) \dots g_N(P_N) \end{pmatrix}, \quad (4.12)$$

where the elements of the left lower rectangle ( $(N-M)$  rows,  $M$  columns) are zero. Then the inverse of this matrix has the same property, we assume that this inverse exists which in general will

be true when the points  $P_1, \dots, P_N$  are not chosen pathologically. Solving the equations (4.10) and (4.11) we find by Cramer's rule

$$\delta\varphi_\ell = -D^{-1} \sum_{j=1}^N D_{\ell j} g_j(P_{N+1}) \delta\varphi_{N+1}, \quad (4.13)$$

where  $D$  is the determinant of (4.12) and  $D_{\ell j}$  is the minor of the element  $g_\ell(P_\ell)$ . By the occurrence of the zero elements in (4.12) and in its inverse it can be seen that the factors

$$D^{-1} D_{\ell j}, \quad \ell=1, \dots, N; \quad j=1, \dots, M; \quad (4.14)$$

are independent of

$$g_\ell(P_j), \quad \ell=1, \dots, N; \quad j=M+1, \dots, N, \quad (4.15)$$

and are zero for  $M < \ell \leq N$ . This is important for the difference of the influence of the two types of constraints. Indeed the necessary condition of optimality  $\delta E = 0$ , by using (4.9), (4.13) and the just mentioned properties of (4.14), becomes

$$\begin{aligned} \frac{\partial}{\partial n} \{ \varphi_0(P_{N+1}) + \varphi(P_{N+1}) \} = \\ \sum_{j=1}^M \{ \sum_{\ell=1}^M \left( \frac{\partial \varphi_0}{\partial n}(P_\ell) + \frac{\partial \varphi}{\partial n}(P_\ell) \right) \frac{D_{\ell j}}{D} \} g_j(P_{N+1}) + \\ \sum_{\ell=M+1}^N \{ \sum_{j=1}^N \left( \frac{\partial \varphi_0}{\partial n}(P_\ell) + \frac{\partial \varphi}{\partial n}(P_\ell) \right) \frac{D_{\ell j}}{D} \} g_j(P_{N+1}). \end{aligned} \quad (4.16)$$

Now we consider the points  $P_1, \dots, P_M$  to be chosen at fixed places at  $H_b$ , the point  $P_{N+1}$  is allowed to move freely around taking with it the points  $P_{M+1}, \dots, P_N$  at the same value of the  $x$  coordinate. Then the factor of  $g_j(P_{N+1}), j=1, \dots, M$  is a fixed still unknown constant denoted by  $\lambda_j$ . The factor of  $g_j(P_{N+1}), j=M+1, \dots, N$ , contains the unknown functions  $\frac{\partial \varphi}{\partial n}(P_\ell)$ , because the  $P_\ell, \ell=M+1, \dots, N$ , move around with  $P_{N+1}$ . The unknown functions are denoted by  $\mu_j(x)$ . Dropping the index  $N+1$  of  $P_{N+1}$ , we find for the general point  $P \in H_b$ , as a necessary condition for optimality

$$\begin{aligned} \frac{\partial \varphi}{\partial n}(P) = & -\frac{\partial \varphi_0}{\partial n}(P) + \sum_{j=1}^M \lambda_j g_j(P) + \\ & \sum_{j=M+1}^N \mu_j(x) g_j(P), \end{aligned} \quad (4.17)$$

where the  $x$  occurring in the functions  $\mu_j(x)$  is the  $x$  coordinate of  $P$ .

This is a Neumann problem for the potential  $\varphi(x, y, z)$  which has to be solved while the  $\lambda_j$  and  $\mu_j(x)$  are still unknown and have to be determined afterwards by the constraints (4.4) and (4.6). Ofcourse we still need the condition that the total circulation around  $H$  belonging to this potential is zero, with other words the potential has to be one valued outside  $H$ . In principle this problem can be treated as follows. Suppose

$$\mu_j(x) = \sum_{i=1}^{\infty} v_{ij} f_i(x), \quad (4.18)$$

where the  $f_i(x)$  are a complete system of coordinate functions and the  $v_{ij}$  are still unknown. Then the following Neumann problems have to be solved numerically

$$\frac{\partial \varphi}{\partial n}(P) = g_j(P), \quad j=1, \dots, M, \quad (4.19)$$

$$\frac{\partial \varphi_{ij}}{\partial n}(P) = f_i(x) g_j(P), \quad i=M+1, \dots, N; j=1, 2, \dots \quad (4.20)$$

where again the  $x$  coordinate in the functions  $f_i(x)$  is the  $x$  coordinate of  $P$ . Then consider the potential

$$\varphi = -\varphi_0 + \sum_{j=1}^M \lambda_j \varphi_j + \sum_{j=1}^{\infty} \sum_{i=M+1}^N v_{ij} \varphi_{ij} \quad (4.21)$$

Substitution of this  $\varphi$  into (4.4) and (4.6) yields linear algebraic equations for the  $\lambda_i$  and  $v_{ij}$  which have to be solved approximately.

In condition (4.17) unknown constants occur in connection with the global constraints (4.4) and unknown functions in connection with the local constraints (4.6). The reason is that, loosely said, constraint (4.6) is equivalent to infinitely many constraints (4.4). Indeed when in (4.4) the functions  $g_j(P)$  are zero at  $H$  except in the neighbourhood of the intersection of  $H$  with a plane  $x = \text{const.}$ , then a local condition arises. Hence to (4.6) belongs an infinite number of constraints  $\lambda$  which are represented by the unknown values of  $\mu_i(x)$ .

When in this way the optimum potential  $\varphi(x, y, z)$  belonging to the shed free vorticity is found it is not difficult in principle to calculate bound vorticity of  $W$  which leaves behind this free vorticity.

At last we make a remark about the case that is not possible to represent the extractable kinetic energy  $F_0$ , already present in the fluid by a sheet of vorticity  $\gamma_0$  and hence by a potential  $\varphi_0$ . This happens when there are infinitely many surfaces  $H$  which fill a three dimensional cylinder, as in the case for a simple model of the Voith-Schneider propeller (section 7). Then it is more appropriate to use in the given derivations the original velocity field  $(\vec{u}, \vec{v}, \vec{w})$ . For instance, in the principal result (4.17) the expression  $\frac{\partial \varphi_0}{\partial n}(P)$  has to be replaced by

$$(\vec{u}, \vec{v}, \vec{w}) \cdot \vec{n}|_P, \quad (4.22)$$

which, by definition of  $\varphi_0$  is exactly the same.

##### 5. On optimization of the reference surface $H$ , regime ii

In section 4 we discussed the optimization problems with respect to lost kinetic energy when the reference surface  $H$  of the wing was prescribed. In this section we will give some considerations on the possibility to optimize also  $H$  itself, hence to compare different propulsion systems. We limit ourselves to the case that only the mean value  $T$  with respect to time of the thrust is prescribed (4.3). In the following we assume that the constant velocity  $U$  of the propelled body, which is the mean velocity of advance of the propeller is the same for the different propellers we compare.

When we do not limit the dimensions of the propulsion system it will grow without bounds in an optimization process when, as is the case here, viscosity is neglected. So we introduce a cylinder  $C$  with generators parallel to the  $x$  axis within which the blades or wings are allowed to move in the positive  $x$  direction. Hence in this linear theory the shed free vorticity will be within  $C$ .

First we show that it cannot be expected that technically realizable reference surfaces  $H$  will appear when the only constraint on the motion of the flexible wings is that they have to stay within  $C$ . We consider one flexible wing  $W$  moving along  $H$ . Because only  $T$  is prescribed it follows from (4.17) with (4.3), when there is no disturbance potential  $\varphi_0$ , that

$$\frac{\partial \varphi}{\partial n}(P) = \lambda \cos(n, x), \quad (5.1)$$

where  $P \in H$ ,  $(n, x)$  is the angle between the normal at  $H$  at the point  $P$  and the  $x$  axis, while  $\lambda$  is the unknown constant which is determined by the prescribed  $T$  by means of (4.3). From (5.1) it follows that the optimum free vorticity left behind at  $H$  by the wing is the same as the vorticity which is needed at  $H$  when it is placed as a rigid impermeable surface in a flow with velocity  $\lambda$ , parallel to the  $x$  axis. From [7] however it follows that the optimum reference surface  $H$  has to be such that it shields the entire interior of  $C$  from the outside and divides periodically this interior in finite disconnected regions. Hence  $H$  has to be such that it hampers as much as possible the flow in  $C$ , when  $H$  is placed in the above mentioned parallel flow. In fact in the optimum case no flow occurs in  $C$  in this situation. Then the vorticity on  $H$  becomes concentrated on the boundary  $\partial C$  of  $C$ , is constant of strength and perpendicular to the  $x$  axis. Inversely, when at  $H$  we have this vorticity left behind by  $W$ , then far behind  $W$  the shed vorticity creates inside  $C$  a homogeneous flow opposite to the direction of the mean thrust, while outside  $C$  the fluid is in rest. This flow which is needed for the balance of momentum, belongs to an actuator disk (linearized theory), with, for instance as area the perpendicular cross section of  $C$  and with a constant normal load with resultant strength  $T$ .

We remark that in the just mentioned case, in essence there is no difference between a finite number of wings  $W$ , with reference surfaces  $H$ , or one wing  $W$  with one  $H$ . This follows from the fact that within a period one wing  $W$  can follow the surfaces  $H$ , by "jumping" from one to another without shedding vorticity. Then  $H$  consists of the  $H_i$  connected by strips where  $W$  is inactive.

Now it is clear that we cannot expect, under the only condition that  $H$  has to stay within  $C$ , that by an optimization process a sufficiently smooth optimum  $H$  for one  $W$ , comes out. This because as has been said,  $H$  has to include  $\partial C$  and to cut the interior of  $C$  in finite disconnected parts. The question arises which extra constraints can be imposed on  $H$  such that a smooth optimum  $H$  exists, which of course does not yield results as good as the  $H$  which only has to stay within  $C$ .

In the following we neglect the condition that  $H$  has to stay within  $C$ , because by adjusting some constants this can be achieved easily. Suppose that the admissible reference surfaces  $H$  have the representation (Figure 2).

$$z = g(x, y), \quad h_1 \leq y \leq h_2, \quad (5.2)$$

where the continuous functions  $g$  are "one valued", periodic with period  $b$  in the  $x$  direction and have continuous first and second order partial derivatives. The space of all such functions will be denoted by  $G$ . As a norm we introduce

$$\|g\| = \max_{\substack{0 \leq x \leq b \\ h_1 \leq y \leq h_2}} (|g|, |g_x|, |g_y|, |g_{xx}|, |g_{xy}|, |g_{yy}|) \quad (5.3)$$

This space is complete which means that for each Cauchy sequence  $g_m \in G$  there exists a  $g \in G$  with

$$\lim_{m \rightarrow \infty} \|g_m - g\| \rightarrow 0 \quad (5.4)$$

Next consider the subset  $F \subset G$  consisting of elements  $g \in G$  which have continuous third order partial derivatives with

$$|g| \leq A_1, |g_x| \leq A_2, |g_y| \leq A_3, \dots, |g_{xyy}| \leq A_9, |g_{yyy}| \leq A_{10}. \quad (5.5)$$

Then it can be shown that  $F$  is relatively compact, by which is meant that the closure  $\bar{F}$  of  $F$  is compact.

On  $F$  we define the functional  $E$  which is the kinetic energy which remains behind per period  $b$  in the  $x$  direction when the lifting surface  $W$  moves along  $H(z=g(x,y))$  in an optimum way and delivering a mean thrust  $T$ . This functional can be expressed as followed.

Denote by  $\phi = \phi(x,y,z)$  the velocity potential which belongs to the Neumann problem (compare (5.1))

$$\frac{\partial \phi}{\partial n}(P) = \cos(n,x), \quad P \in H, \quad (5.6)$$

where  $H$  is represented by  $z = g(x,y)$ ,  $g \in G$ , while  $\phi$  is one valued outside  $H$ . Suppose  $\phi(x,y,z) = \lambda \phi(x,y,z)$  belongs to the optimum shed vorticity when  $W$  delivers the mean value  $T$  with respect to time of the thrust. Hence when  $H_b$  denotes again one period of  $H$ ,  $\lambda$  follows from

$$T = \frac{\rho U \lambda}{b} \iint_{H_b} [\phi]_-^+ \cos(n,x) dx. \quad (5.7)$$

The kinetic energy  $E$  which remains behind can then be written as

$$E = \rho \lambda^2 \iint_{H_b} [\phi]_-^+ \frac{\partial \phi}{\partial n} d\sigma = \frac{b^2 T^2}{\rho U^2 \iint_{H_b} [\phi]_-^+ \cos(n,x) d\sigma} \quad (5.8)$$

From the point of view of applied mathematics there seems to be little doubt that the integral in the denominator of the right hand side of (5.8) is a continuous functional for the norm (5.3) on  $G$ . In fact consider two surfaces  $H_1$  and  $H_2$  represented by two equations  $y=g_1(x,z)$  and  $y=g_2(x,z)$ , then to each of these surfaces belongs lost kinetic energy  $E_1$  and  $E_2$  in the optimum case for the same  $T$  and  $U$ . Then it is acceptable that for a fixed  $g_1(x,z)$  and variable  $g_2(x,z)$  for each  $\epsilon$  a  $\delta(\epsilon)$  exists such that when

$$\|g_1(x,z) - g_2(x,z)\| \leq \delta(\epsilon) \quad (5.9)$$

then

$$|E_1 - E_2| < \epsilon. \quad (5.10)$$

A rigorous proof of such a statement is rather complicated, and should be given in the future for a good foundation of the theory.

Assuming this for granted we have a continuous functional  $E$  on a relatively compact subset  $F \in G$ . Such a functional assumes its extremes hence also its minimum at the closure  $\bar{F}$  of  $F$ . Hence  $G$  being complete this minimum is assumed for some  $z=g(x,y) \in G$ . This means there exists an optimum  $H$  with continuous and bounded slopes and curvatures which satisfy (5.5) upto and including  $A_6$ .

Analogous considerations can be given for regimes i and iii, all be it that for the latter type the reasoning will be essentially more difficult. In this case it must be proved also that the place where the free vorticity is deposited by the base motion, depends sufficiently smooth on the line  $\ell$  of (Figure 3).

## 6. Comparison of the efficiency of optimum propulsion systems by inspection, regime ii

In this section we compare optimum propulsion systems and show that some times it is predictable by simple inspection of the shape of their reference surfaces  $H$ , which one will be the best. We start from the verbal characterization in italics of section 5 of the optimum reference surface  $H$  within a prescribed cylinder  $C$ . However, in order to adapt it to our problem of comparing propellers we will change it slightly.

*Given two propulsion devices each working in a cylinder  $C$  which has the same dimensions for both and for the same values of  $T$ ,  $U$  and  $\tau$  or  $b$ . Then the propeller of which the surfaces  $H$ , "hamper most" the flow in  $C$  will have the highest efficiency.*

Of course this is not a rigorous quantitative statement. However we will show its applicability by means of a numerical example, given in [9] some years ago, but not published before in current literature.

The given examples are two dimensional so that in (Figure 2) the surfaces  $H$  extend infinitely far in the direction of the positive and negative  $y$  axis. Hence our problem is independent of the  $y$  coordinate. The propulsion device consists of two infinitely long wings  $W_1$  and  $W_2$  moving along the surfaces  $H_1$  and  $H_2$  respectively of which the projection on the  $(x,z)$  plane are given by

$$\begin{aligned} H_1: z_1(x) &= b_1 - b_2 + \delta + b_1 \cos 2\pi x + b_2 \cos 4\pi x, \\ H_2: z_2(x) &= -z_1(x), \end{aligned} \quad (6.1)$$

which are drawn schematically in (Figure 7) for specific choices of the numbers  $b_1$  and  $b_2$ . The parameter  $\delta$  is still variable. The two cases I) and II) of (Figure 7), are clearly related. The surface  $H_1$  of case II) originates from  $H_1$  of case I) by a simple reflection and translation. Hence the only difference of case I) and II) is the different interaction of their wings  $W_1$  and  $W_2$  while moving along  $H_1$  and  $H_2$ , in the optimum case.

The numerical results are given by means of a number  $q$  belonging to a propeller, which characterizes its quality. This quality factor is defined as follows. We prescribe the cylinder  $C$  in which the wings of the propeller are allowed to move periodically, hence again the shed free vorticity remains in  $C$ . Consider the kinetic energy  $E$  per period  $b$  in the  $x$  direction left behind by the optimum wings  $W_1$  for some  $T$  and  $U$ . Next consider an actuator disk with constant normal load and total thrust  $T$ , which leaves behind the ki-



netic energy  $E_D$  per length  $b$  in the  $x$  direction

$$E_D = \frac{b T^2}{2\rho S U}, \quad (6.2)$$

where  $S$  is the area of the disk which equals the area of the cross section of  $C$  and  $U$  is its velocity. Remember that  $T$  was the mean value with respect to time of the thrust and  $U$  is the mean velocity of the propeller. Then we define the quality factor  $q$ , which by the foregoing has to be less or equal to one, by

$$q = \frac{E_D}{E} \leq 1. \quad (6.3)$$

For  $S$  we can take in our two dimensional example the cross section per unit length of span in the  $y$  direction. This cross section consists of two parts separated by a gap of width  $2\delta$  and has a total area  $S = 4b_1$  as follows from figure 6.1.

We remark that the quality factor  $q$  is independent of  $T$ ,  $U$  and  $\rho$ , which occur in both  $E$  and  $E_D$  in the same way. It depends only on the shape of the  $H_1$ . We can write the efficiency  $\eta$  of any propulsion system of regime ii, by means of its quality factor as,

$$\eta = \frac{TUb}{TUb+E} = \left(1 + \frac{T}{2\rho q S U^2}\right)^{-1} = 1 - O(\epsilon), \quad (6.4)$$

which for  $q=1$  is the efficiency of the actuator disk (2.5). From this it follows that the quality factor is a measure for the possible performance of the "system", which characterizes it better than for instance its efficiency. A "system" with a given  $q$  can have a large or a small efficiency by choosing a small or a large thrust  $T$ ; a large or a small velocity  $U$ . However a system with a larger  $q$  will perform better under the same demands than a system with a smaller  $q$ .

In (Figure 8) the quality factor is given as a function of the distance  $\delta$  between the two surfaces  $H_1$  and  $H_2$  for the two cases of (Figure 7) and also for the case III of pure cosines, hence  $b_2=0$  in (6.1). First we discuss the cases I and II with  $b_2=0,0375$  and  $b_2=-0,0375$  respectively and try to predict their relative efficiency. It is clear that for large values of  $\delta$  there is no interaction between the free vortex sheets at  $H_1$  and  $H_2$  (and hence of the wings) in both cases I and II. Further the geometry of the surfaces  $H_1$  and  $H_2$  in both cases is the same, hence there will be no difference in their quality  $q$  for  $\delta \rightarrow \infty$ . When  $\delta$  becomes smaller interaction will occur. Then the flow inside one of the two parts of  $C$  is hampered by the reference surface  $H$  in the other part and reversely. Hence it is clear that for smaller  $\delta$  in the optimum case  $q$  increases for each of the cases I and II. The question arises for which of these  $q$  increases most. Looking at  $H_1$  and  $H_2$  it is clear that in case II the region  $C$  is more blocked than in case I. The surfaces  $H$  in case II are indented more sharply and "enclose" more fluid. Hence for small values of  $\delta$  the quality factor  $q$  of case II will be larger than the one of case I. All these conclusions are confirmed by (Figure 8).

Next we consider case III ( $b_2=0$ ), with respect to case I and II. For large values of  $\delta$  it is conceivable that the more sharply indented  $H_1$  and  $H_2$  with  $b_2=0,0375$  (cases I and II) hamper the fluid more than the gently waving pure cosine, although all have the same total amplitude. This is in agreement with (Figure 8), where for large  $\delta$  the quality factor of the cosine is less than the quality factor of cases I and II. When  $\delta$  becomes small however the

two pure cosines of case III "enclose" more fluid than the surfaces  $H_1$  and  $H_2$  of case I and less than those of case II. So it seems predictable that for small  $\delta$  the quality factor of case III is in between the quality factors of case I and case II. By (Figure 8) also this happens to be true.

#### 7. On the quickly rotating Voith-Schneider propeller.

We shall discuss here shortly a simplified picture of the quickly rotating vertical axis propeller. Theoretically the performance of such a propeller is discussed in a large number of papers for instance, [10], [11] and [12]. In [12] the case of an inviscid fluid was considered and part of it was the base of an experimental investigation [13]. In this part it was assumed first that there are an infinite number of "elemental" blades, distributed continuously over the blade circle and second that the blades were infinitely long. The second assumption means that no tip vorticity is included in the consideration. This however causes an indeterminacy of the bound vorticity of the blades in the optimum case. A constant circulation could be added to the optimum time-dependent vorticity of each elemental blade, which by the infinite length of the blades does not shed free vorticity, the tip vortices of this constant vorticity being at infinity. Hence by this addition the theoretical efficiency has not changed. This constant vorticity however makes that we can choose at will whether the blades are contributing effectively to the thrust for instance only in their front position, only in their aft position or equally at both. In [13] these three possibilities have been tested. The experiments indicated that the last mentioned type of equally distributed thrust was relatively the best one.

This can be predicted by using the previously discussed concepts for optimization. In order to simulate the bottom of the ship under which the propeller operates, we mirror the blades with respect to this bottom and consider a vertical axis propeller of which the blades are twice as long as the real ones. Because we have infinitely many "elemental" blades, the cylinder  $C$  (Figure 9) in which the free vorticity is allowed to be is "filled" with surfaces  $H$  behind these blades. Placing this mass of surfaces  $H$  in a stream parallel to  $C$  it follows that in the optimum case no free vorticity is inside  $C$  and all free vorticity is at the boundary  $\delta C$ . This is drawn in (Figure 9), where the arrows are connected with a right hand screw to the vorticity. In this figure is also drawn the propeller region, which moves in the positive  $x$  direction with the velocity  $U$ .

Suppose that the bound vorticity per unit of length of blade circle is  $\Gamma$  in front and  $-\Gamma$  at the aft position of the blades. When this bound vorticity passes the line  $a-a$  it changes from  $\Gamma$  to  $-\Gamma$  hence leaves behind free vorticity at the vertical wall of strength.

$$2\Gamma\omega R/U, \quad (7.1)$$

where  $R$  is the radius of the blade circle and  $\omega$  the rotational velocity of the blades. The inverse happens at the line  $b-b$ .

The vorticity shed by the continuously distributed tips of the blades is drawn also in (Figure 9). The free vorticity shed by the front tips lies along cycloidal lines. It is a question of simple algebra

to find that the tip vorticity of the front and aft tips combine behind the latter ones to vorticity of strength (7.1) at the lower and upper boundaries of C and is perpendicular to the x axis. By this the optimum free vorticity demanded by the theory is created.

We now can explain easily the already mentioned results of the experiments [13]. When we add a constant velocity to the whole blade ring, the free vorticity behind the propeller at the upper and lower parts of the boundary  $\delta C$ , will have components in the direction of the x axis. This is clearly in conflict with the necessary optimum free vorticity condition. Hence theory and experiment both come to the result that the thrust has to be delivered equally by the front and the aft part of the ring of blades.

From this picture of the free vorticity we find that the wake behind an optimum propeller of this type equals the wake of an actuator disk with a rectangular plan form and a constant normal load. This means that the quality factor q has the highest possible value

$$q=1. \quad (7.2)$$

Although an ordinary vertical axis propeller has a finite number of blades (4-6) in general its rotational velocity or better its advance ratio, is such that its wake is rather crowded by surfaces H. Hence it can be expected that its quality coefficient q is large  $q \approx 1$ .

We remark that with respect to reality there are besides other shortcomings of this picture, two difficulties which, be it qualitatively, can be discussed by an inviscid theory. First, the propeller is working under a ship hence in the "boundary layer", or approximated by potential theory, in layers of inviscid fluid with different velocities in the x direction. This means that the propeller encounters plane free vorticity sheets of approximately constant strength. The sheets are perpendicular to the z axis and their vorticity is in the y direction. Now the bound vorticity  $\Gamma$  of the blades has to be a function of z such that their shed free vorticity annihilates the incoming free vorticity inside C. In this way it is not difficult to calculate  $\Gamma(z)$ .

The second difficulty is, can we realize by using rigid blades the prescribed circulation distribution of the blades, or to which extent is this possible. Such a problem would occur also by the optimization of contra rotating tandem propellers.

#### References

- [1] Wu T.Y., Hydromechanics of swimming propulsion J. Fluid Mech. 1971, vol. 46, pp.337-355.
- [2] Lighthill M.J., Note on the swimming of slender fishes J. Fluid Mech. 1960, vol. 9, pp. 305 - 317.
- [3] Wu T.Y., A.T.Chwang and P.K.C. Wang Optimization problems in hydrofoil propulsion, Lecture Notes in Physics, 21, Optimization and Stability Problems in Continuum Mechanics, Springer-Verlag, 1973, pp. 38-62.
- [4] Wu T.Y., Advances in Applied Mechanics, Vol. 11, 1971, pp. 1-63.
- [5] Proceedings Symposium Swimming and Flying in Nature, California Institute of Technology, 1974.
- [6] Sparenberg J.A. and A.K. Wiersma, On the efficiency increasing interaction of thrust producing lifting surfaces, Proc. Symp. Swimming and Flying in Nature, California Institute of Technology, 1974.
- [7] Sparenberg J.A., A linear theory for optimum lifting surface systems, Journal of Ship Research, 1970, vol. 14, pp. 15-22.
- [8] Sparenberg J.A. and F. Takens, On the optimum finite amplitude motion of a thrust producing profile, Journal of Ship Research, 1975, vol. 19, pp. 93-98.
- [9] Graaf R.de, On optimum fish tail propellers with two blades, Thesis University of Groningen, Netherlands, 1970.
- [10] James E.C., A small perturbation theory for cycloidal propellers, Thesis California Institute of Technology, USA, 1971.
- [11] Isay W.H., Moderne Probleme der Propellertheorie, Springer Verlag, 1970.
- [12] Sparenberg J.A., On the efficiency of a vertical axis propeller, Proceedings Third Symposium on Naval Hydrodynamics, 1960, pp. 45-66.
- [13] Manen J.D. van Ergebnisse systematischer Versuche mit Propellern mit Annäherend senkrecht stehender Achse, Jahrbuch der Schiffbautechnische Gesellschaft, Band 57, 1963, pp. 377-397.

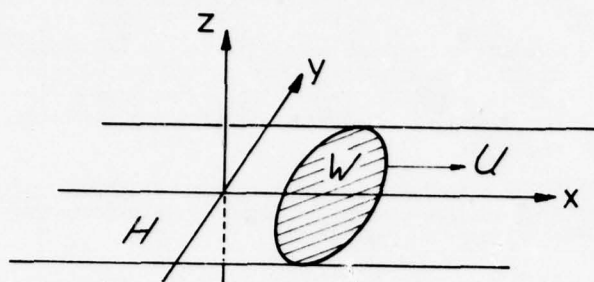


Fig. 1: Small amplitude flexible wing, regime i.

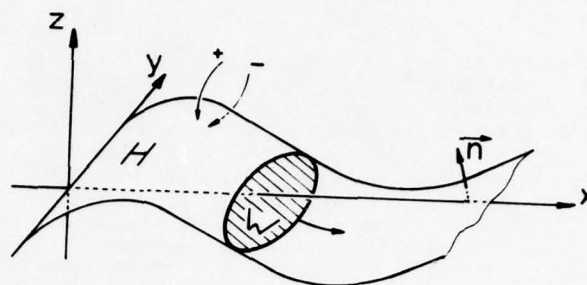


Fig. 2: Large amplitude flexible wing, regime ii.

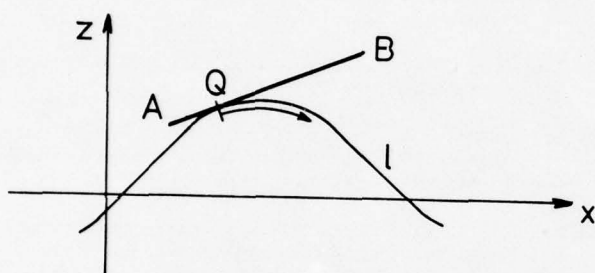


Fig. 3: Flat rigid profile A-B moving along l, regime iii.

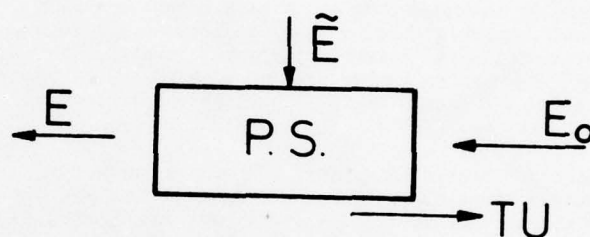


Fig. 4: Scheme of energy balance of a propulsion system P.S.

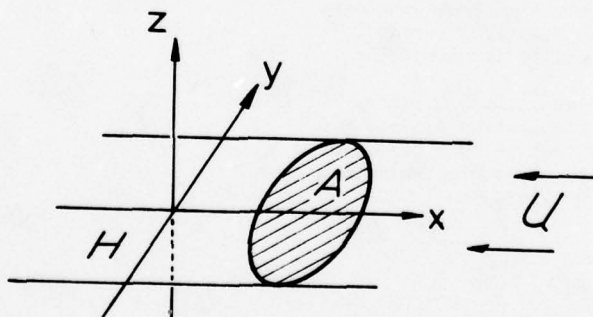


Fig. 5: The plan form A.



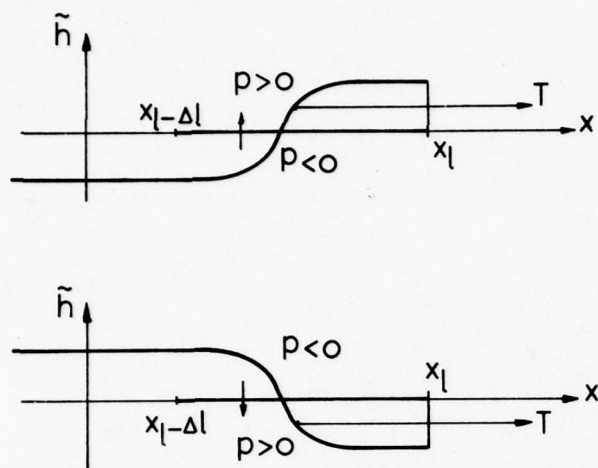


Fig. 6: The "kinematic" profile  $\tilde{h}$ , a) during upward stroke, b) during downward stroke.

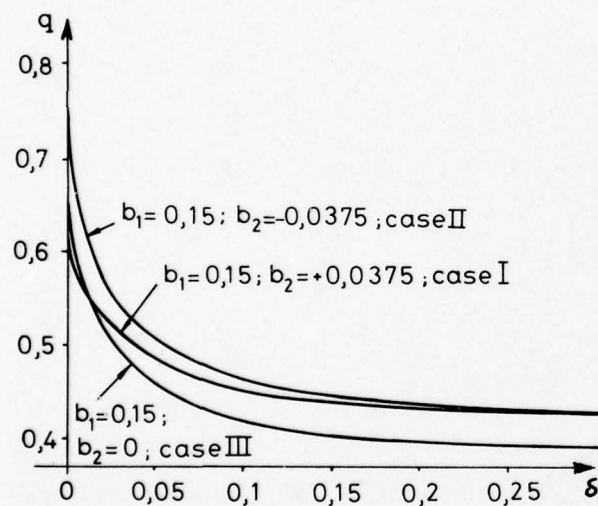


Fig. 8: The quality factor  $q$  as a function of the minimum distance of the two wings, for three different sets of  $H_1$  and  $H_2$ .

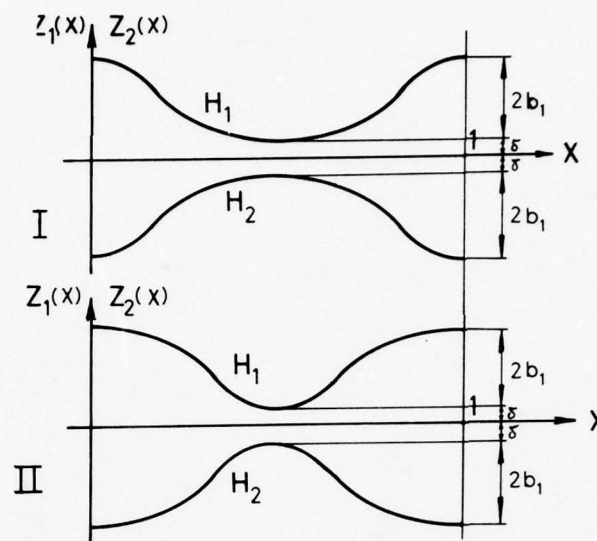


Fig. 7: Two different arrangements of geometrical congruent shapes of the reference surfaces  $H_1$  and  $H_2$ , I)  $b_1 = 0.15$ ;  $b_2 = 0.0375$ , II)  $b_1 = 0.15$ ;  $b_2 = -0.0375$ .

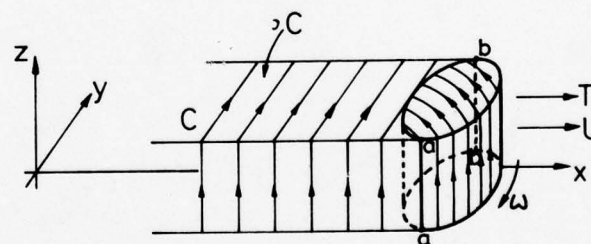


Fig. 9: The vorticity of an optimum vertical axis propeller with "many" blades.

# STEADY AND UNSTEADY LOADINGS AND HYDRODYNAMIC FORCES ON COUNTERROTATING PROPELLERS

S. TSAKONAS, W. JACOBS and M. ALI  
Stevens Institute of Technology, Hoboken, New Jersey, USA

*The linearized lifting surface theory has been applied to the evaluation of blade loadings and resultant hydrodynamic forces and moments (thrust, torque, bearing forces and bending moments) of counter-rotating propeller systems with equal and unequal number of blades operating in uniform and nonuniform inflow fields, both units rotating with the same RPM. The mathematical model takes into account as realistically as possible the geometry of the propulsive device, the mutual interaction of both units and the three-dimensional spatially varying inflow field. A computer program has been developed adaptable to high-speed digital computers (CDC 6600-7600) for counterrotating propulsion systems of equal and unequal blade number in uniform inflow for comparison with experimental results if available.*

## 1. INTRODUCTION

The combination of two counterrotating propellers on fast ships has been shown to offer considerable improvement in propulsive efficiency when compared with a single screw [1]. Furthermore, since the total required power is divided between two propellers, this results in a reduction of blade loadings and hence the inception of cavitation is delayed. These are the main advantages of this propulsive system; its principal disadvantage lies in the mechanical complications in transmitting power through a coaxial counter-rotating shaft.

The CR (counterrotating) propulsive system is also expected to have more favorable vibrational behavior. From tests of a 4-0-5 CR system (4-bladed forward and 5-bladed after propeller) in the wake of a model of a fast cargo liner [2], it appears that the ratios of amplitudes of excitation to mean thrust are comparable to those of a single screw providing the same power. However in these tests the nonuniform wake is by far the dominating cause of vibration. The effects of the interaction of both propellers are small in comparison and the higher frequency excitations cannot be determined at all accurately.

A better understanding of the mechanism of the interaction can be obtained by considering the CR system under open-water conditions (uniform inflow field) so that wake harmonics are not present to mask the interaction phenomenon.

The calculation procedure is based on the analysis of Reference 3 for the cases of CR systems of equal and unequal blade number, operating at equal or unequal RPM in uniform and nonuniform inflow fields. In that reference the true geometry of the helicoidal blades was taken into account with the exception that blade thickness was assumed negligible.

In the present paper, CR systems of equal and unequal number of blades will be considered operating at equal RPM in a uniform inflow field. The blade thickness effects will also be considered, as additional velocity perturbations on the LH (left-hand) sides of the two surface integral equations which state the kinematic conditions on both units

of the CR system.

The development of this pair of surface integral equations is based on a linearized unsteady lifting surface theory as adapted to the marine propeller case. Their kernel functions are derived by means of the acceleration potential method and the surface integrals are reduced to line integrals by employing the mode approach in conjunction with the "generalized lift operator" technique [4]. Then by the collocation method the line integral equations are reduced to two simultaneous sets of algebraic equations. Finally, the solution of these is obtained by an iterative procedure, assuming at first that the effect of the after propeller on the forward propeller, except for the velocity field due to the thickness of its blades, may be neglected.

The computation procedure adapted to a high-speed digital computer (CDC-6600 or 7600) will be utilized if experimental information will be available.

## NOMENCLATURE

A	subscript index of after propeller
a	$\Omega r_0/U$
F	subscript index of forward propeller
$F_{x,y,z}$	forces in axial, horizontal and vertical directions
$I(\bar{m})(x)$	defined in Equation (7a)
$I_m(v)$	modified Bessel function of order m
i	subscript index of control point
j	subscript index of loading point
$K_m(v)$	modified Bessel function of order m
$K_{ji}$	kernel function of integral equation
$\bar{K}_{ji}, \bar{K}_{ji}^*$	modified kernels, after chordwise-integrations
$L(r)$	spanwise loading distribution, lb/ft
$L(\bar{n})(p)$	spanwise loading components (coefficients of chordwise distribution), lb/ft
$\ell_k$	integer multiple

$\bar{m}$	order of lift operator
$m_k$	index of summation
$N_F, N_A$	number of blades of forward and after propellers
$\bar{n}$	order of chordwise mode
$n$	blade index
$P$	perturbation pressure
$Q_{x,y,z}$	moments about x-, y- and z-axes
$q_i$	order of blade harmonic
$r$	radial coordinate of control point
$r$	superscript index of control point
$r_{Ao}$	after propeller radius
$r_{Fo}$	forward propeller radius
$S_j$	lifting surface
$t$	time
$U$	uniform velocity
$u$	variable of integration
$V_i(r)$	Fourier coefficients of velocity normal to the blade
$W_i(x, r, \varphi; t)$	induced velocity at control point
$x, x'$	longitudinal coordinate of control point
$x(\xi'), r, \varphi$	cylindrical coordinate system of control points
$y$	horizontal Cartesian coordinate
$z$	vertical Cartesian coordinate
$\beta$	hydrodynamic pitch angle
$\epsilon$	distance between the two propeller planes
$\Theta(\bar{n})$	chordwise mode
$\theta_j$	angular coordinate of loading point
$\theta_\alpha$	angular chordwise location of loading point
$\theta_{bF}, \theta_{bA}$	projected semichord length, in radians, of forward and after propellers
$\bar{\theta}_{jn}$	$\frac{2\pi}{N_j}(n-1), n=1, \dots, N_j$
$\theta_p(r)$	geometric pitch angle
$\Lambda(\bar{n})(x)$	defined in Equation (7b)
$\lambda_k$	positive integer multiple
$\xi, \xi'$	longitudinal coordinate of loading point
$\xi(\xi'), \rho, \theta$	cylindrical coordinate system of loading points
$\rho$	radial coordinate of loading point
$\rho$	superscript index of loading point
$\rho_f$	mass density of fluid
$\sigma$	angular measure of skewness
$\hat{\Phi}(\bar{m})$	generalized lift operator
$\varphi_i$	angular coordinate of control point
$\varphi_\alpha$	angular chordwise location of control point
$\Omega$	angular velocity of propeller (absolute value)

## 11. LINEARIZED UNSTEADY LIFTING SURFACE THEORY

Two counterrotating propellers are operating in the flow of an ideal incompressible fluid. The propeller arrangement and the coordinate system are shown in Figure 1.

The basic relation of the interaction phenomenon is that the negative velocities induced by the propulsion system on each propeller lifting surface should be balanced by the downwash velocity distribution at that surface, thus expressing the requirement of an impermeable boundary. The kinematic boundary conditions on both lifting surfaces are expressed as two simultaneous surface integral equations:

$$W_F(x_F, r_F, \varphi_F; t) = \iint_{S_F} \Delta P_F(\xi_F, \rho_F, \theta_F; t) \cdot K_{FF}(x_F, r_F, \varphi_F; \xi_F, \rho_F, \theta_F; t) dS_F + \iint_{S_A} \Delta P_A(\xi_A, \rho_A, \theta_A; t) \cdot K_{AF}(x_F, r_F, \varphi_F; \xi_A, \rho_A, \theta_A; t) dS_A \quad (1)$$

$$W_A(x_A, r_A, \varphi_A; t) = \iint_{S_F} \Delta P_F(\xi_F, \rho_F, \theta_F; t) \cdot K_{FA}(x_A, r_A, \varphi_A; \xi_F, \rho_F, \theta_F; t) dS_F + \iint_{S_A} \Delta P_A(\xi_A, \rho_A, \theta_A; t) \cdot K_{AA}(x_A, r_A, \varphi_A; \xi_A, \rho_A, \theta_A; t) dS_A \quad (2)$$

where

$x(x'), r, \varphi$  and  $\xi(\xi'), \rho, \theta$ : cylindrical coordinates of control and loading points, respectively

F and A: subscripts indicating forward and after propeller

t: time, sec

$S_F, S_A$ : forward and after propeller surfaces, ft<sup>2</sup>

$W_F, W_A$ : velocity distributions normal to forward and after propellers, ft/sec

$\Delta P_F, \Delta P_A$ : unknown loadings; pressure jumps across the lifting surfaces, lb/ft<sup>2</sup>, i.e.,  $\Delta P = P_u - P_d$ , pressure difference between back (suction side) and face (pressure side)

$K_{ji}$ : kernel function representing the induced velocity on an element  $i$  of a blade due to unit amplitude load located at each and every element  $j$ , ft/lb-sec

The second term on the RH (right-hand side) of Eq.(1) and the first term on the RH of Eq.(2) are the interaction effects. The remaining terms are the self-induced velocities by the individual propellers.

The unknown loadings and the onset velocity distributions are cyclic in nature. Then for a CR system with right-hand aft propeller and left-hand forward propeller rotating at equal RPM



$$\begin{aligned}\Delta P_F(\xi_F, \rho_F, \theta_F; t) &= \operatorname{Re} \sum_{\lambda_k=0}^{\infty} \bar{\Delta P}_F^{(\lambda_k)}(\xi_F, \rho_F, \theta_F) e^{-i\lambda_k \Omega t} \\ \Delta P_A(\xi_A, \rho_A, \theta_A; t) &= \operatorname{Re} \sum_{\lambda_k=0}^{\infty} \bar{\Delta P}_A^{(\lambda_k)}(\xi_A, \rho_A, \theta_A) e^{i\lambda_k \Omega t} \\ W_F(x_F, r_F, \varphi_F; t) &= \operatorname{Re} \sum_{q_F=0}^{\infty} \bar{W}_F^{(q_F)}(x_F, r_F, \varphi_F) e^{-iq_F \Omega t} \\ W_A(x_A, r_A, \varphi_A; t) &= \operatorname{Re} \sum_{q_A=0}^{\infty} \bar{W}_A^{(q_A)}(x_A, r_A, \varphi_A) e^{iq_A \Omega t}\end{aligned}\quad (3)$$

$$(4)$$

where  $q_i$  designates the order of shaft frequency or order of harmonic of the inflow field,  $\lambda_k$  that of the loading distribution to be determined by the analysis, and  $\Omega$  is the absolute value of the angular velocity of each propeller. ( $q_i$  and  $\lambda_k$  are both positive integers.) The known downwash velocities and the unknown loadings are expressed in complex conjugate form in (3) and (4), where finally the real part is taken.

The velocities  $W_i$  are caused by flow disturbances such as those due 1) to wake, 2) to incident flow angle which is the difference between the geometric pitch angle  $\theta_p$  of the propeller blade and the hydrodynamic pitch angle  $\beta = \tan^{-1} W/U$  where  $U$  is forward speed and  $r$  is the radial location of the corresponding helix, 3) to blade camber, 4) to "non-planar" blade thickness, and 5) to the effects of the thickness of the blades of each propeller on the velocity field of the other. Within the limits of the linear theory, the effects of the flow disturbances can be obtained separately and then simply added together.

Although the analysis applies to both non-uniform and uniform inflow, as mentioned earlier, the solution by an iterative procedure will be restricted to the uniform inflow case (no wake). Furthermore, the disturbance due to the so-called "non-planar" thickness (since a propeller blade lies on a helicoidal surface of variable pitch, its thickness affects its own velocity field) will be ignored as negligibly small [5].

After the chordwise integrations are performed by means of the mode approach and the generalized lift operator technique, the pair of surface integral equations (1) and (2) are reduced to the following set of line integral equations for given  $q_i$ , order of shaft frequency, given  $\bar{m}$ , order of lift operator, and  $\bar{n}$ , order of chordwise mode shapes, for the case of equal RPM:

$$\begin{aligned}\frac{\bar{W}_F(q_F, \bar{m})}{U}(r_F) &= \int_{\rho_F} L_F^{(q_F, \bar{n})}(\rho_F) \sum_{m_1=-\infty}^{\infty} \bar{K}_{FF}^{(\bar{m}, \bar{n})}(m_1=q_F+\ell_1 N_F) d\rho_F \\ &+ \int_{\rho_F} \sum_{\lambda_2=0}^{\infty} \sum_{m_2=0}^{\infty} L_A^{(\lambda_2=q_F-2\ell_2 N_A, \bar{n})}(\rho_A) \\ &\cdot \bar{K}_{AF}^{(\bar{m}, \bar{n})}(m_2=q_F-\ell_2 N_A) d\rho_A\end{aligned}\quad (5)$$

$$\begin{aligned}\frac{\bar{W}_A(q_A, \bar{m})}{U}(r_A) &= \int_{\rho_F} \sum_{\lambda_3=0}^{\infty} \sum_{m_3=0}^{\infty} L_F^{(\lambda_3=q_A+2\ell_3 N_F, \bar{n})}(\rho_F) \\ &\cdot \bar{K}_{FA}^{(\bar{m}, \bar{n})}(m_3=q_A+\ell_3 N_F) d\rho_F \\ &+ \int_{\rho_A} L_A^{(q_A, \bar{n})}(\rho_A) \sum_{m_4=-\infty}^{\infty} \bar{K}_{AA}^{(\bar{m}, \bar{n})}(m_4=q_A+\ell_4 N_A) d\rho_A\end{aligned}\quad (6)$$

Here  $L^{(\bar{n})}(\rho_F)$  and  $L^{(\bar{n})}(\rho_A)$  are the unknown normal loading components of the  $\bar{n}$  chordwise mode for each blade in lb/ft of span,  $N_F$  and  $N_A$  are the blade number of forward and after propellers, and  $\ell_k$  is integer. The bars and superscripts  $\bar{m}$  and  $\bar{n}$  indicate that the quantities have been integrated along the chord.

The values of  $\lambda_k$  and  $m_k$  shown in (5) and (6) are arrived at by equating the time-dependence on LH and RH sides so that

$$\begin{aligned}e^{-iq_F \Omega t} &= e^{-i\lambda_1 \Omega t} && \text{for the first term of the first integral equation} \\ e^{-iq_F \Omega t} &= e^{i(\lambda_2-2m_2)\Omega t} && \text{for the second term of that equation} \\ e^{iq_A \Omega t} &= e^{-i(\lambda_3-2m_3)\Omega t} && \text{for the first term of the second integral equation} \\ e^{iq_A \Omega t} &= e^{i\lambda_4 \Omega t} && \text{for the second term of that equation}\end{aligned}$$

and from the summation over all blades of a propeller which is represented by

$$\sum_{n=1}^N e^{i(m_k-\lambda_k)\bar{\theta}_n} = \begin{cases} N & \text{for } m_k-\lambda_k=\ell_k N, \ell_k=0, \pm 1, \dots \\ 0 & \text{otherwise} \end{cases}$$

$$\text{where } \bar{\theta}_n = 2\pi(n-1)/N$$

The respective kernels are derived in Reference 3 for RH forward propeller and LH after-propeller. For LH forward and RH after propeller, they are given in the following section in final form.

### III. THE KERNEL FUNCTIONS

The kernels  $\bar{K}_{FF}$  and  $\bar{K}_{AA}$

These functions describe the self-induced velocity at a point on a propeller blade due to unit amplitude load at various locations on all the blades of the same propeller. The development for a right-hand propeller is given in Reference 6 and yields

$$\sum_{m=-\infty}^{\infty} \bar{K}^{(m, n)}(m=q+\ell N) = \left\{ \frac{-N}{4\pi\rho_F U^2 r_0} \right\} \frac{r e^{-iq\Delta\sigma}}{a\sqrt{1+a^2}r^2} \sum_{m=q+\ell N}^{\infty} \left\{ g(0) - \frac{i}{\pi} \int_0^{\infty} \frac{g(u)-g(-u)}{u} du \right\} \quad (7)$$

where

$$g(u) = (IK)_m B'(u) e^{i\frac{u}{a}\Delta\sigma}$$

$$(IK)_m = \begin{cases} I_m(1+u+a\ell N\rho) K_m(1+u+a\ell N r) & \text{for } \rho < r \\ I_m(1+u+a\ell N r) K_m(1+u+a\ell N \rho) & \text{for } r < \rho \end{cases}$$

$$B'(u) = \left( au + a^2 \ell N + \frac{m}{\rho^2} \right) \cdot \left( au + a^2 \ell N + \frac{m}{\rho^2} \right)^{(\bar{m})} \left( \left( q - \frac{u}{a} \right) \theta_b^r \right)^{(\bar{n})} \left( \left( q - \frac{u}{a} \right) \theta_b^p \right)$$

$\rho_F$  = fluid mass density, slugs/ft<sup>3</sup>

$r_0$  = propeller radius, ft

$\Delta\sigma = \sigma^r - \sigma^p$  = difference between skewness of the blade at the control point  $r$  and skewness at a loading point  $\rho$ , radians

$a = \Omega r_0/U$  and  $\rho$  and  $r$  are also non-dimensionalized by  $r_0$

$\theta_b^r, \theta_b^p$  = subtended angle of projected semichord of blade at  $r$ , at  $\rho$ , radians

$I_m(\ )$  = modified Bessel function of first kind

$K_m(\ )$  = modified Bessel function of second kind

$l = 0, \pm 1, \pm 2, \dots$

In this equation the chordwise integration is represented by

$$I(\bar{m})(x) = \frac{1}{\pi} \int_0^\pi \hat{\Phi}(\bar{m}) e^{ix \cos \varphi_\alpha} d\varphi_\alpha \quad (7a)$$

where  $\hat{\Phi}(\bar{m})$  is the lift operator function and

$$\Lambda(\bar{n})(y) = \frac{1}{\pi} \int_0^\pi \Theta(\bar{n}) e^{-iy \cos \varphi_\alpha} \sin \varphi_\alpha d\varphi_\alpha \quad (7b)$$

where  $\Theta(\bar{n})$  is the chordwise mode shape selected. (See References 3,4,5,6.)

In Eq.(6) the kernel function

$$\sum_{m_4=-\infty}^{\infty} \bar{K}_{AA}(\bar{m}, \bar{n}) (m_4 = q_A + l_4 N_A)$$

is given by Eq.(7) with  $q=q_A$ ,  $N=N_A$ ,  $r=r_A$  and  $\rho=\rho_A$ . However,  $r_0=r_{F0}$  the radius of the forward propeller.

In Eq.(5) the kernel function

$$\sum_{m_1=-\infty}^{\infty} \bar{K}_{FF}(\bar{m}, \bar{n}) (m_1 = -q_F + l_1 N_F)$$

is also given by Eq.(7) but with  $q=q_F$ ,  $N=N_F$ ,  $r=r_F$  and  $\rho=\rho_F$ . In both Eqs.(5) and (6), the radial positions  $r$  and  $\rho$  and the inverse advance ratio  $a$  are non-dimensionalized by forward propeller radius  $r_{F0}$ .

#### The kernels $\bar{K}_{AF}$ and $\bar{K}_{FA}$

These are the kernels of the cross-coupling terms of Eqs.(5) and (6). Let the distance between the propeller planes of the two units of the CR system be  $\epsilon$  (in terms of  $r_{F0}$ ). Then for a RH after propeller at a distance  $\epsilon$  from a LH forward propeller operating at the same RPM, the derivations of Reference 3 can be reduced to the following final forms:

$$\begin{aligned} \bar{K}_{AF}(\bar{m}, \bar{n}) (m_2 = q_F + l_2 N_A \geq 0) &= \left\{ \frac{-N_A}{4\pi\rho_F U^2 r_{F0}} \right\} \frac{r_F}{a \sqrt{1+a^2 r_F^2}} e^{im_2(2\sigma_4 + a\epsilon)} \\ &\cdot e^{iq_F(\sigma_F - \sigma_A - a\epsilon)} \left\{ A(0)B(0) - \frac{i}{\pi} \int_0^\infty [A(u)B(u) - A(-u)B(-u)] \frac{du}{u} \right\} \end{aligned} \quad (8)$$

where

$$A(u) = \begin{cases} I_{m_2}(1u - a(m_2 - q_F)l_2) K_{m_2}(1u - a(m_2 - q_F)l_2) & \text{for } \rho_A \leq r_F \\ I_{m_2}(1u - a(m_2 - q_F)l_2) K_{m_2}(1u - a(m_2 - q_F)l_2) & \text{for } r_F < \rho_A \end{cases}$$

$$B(u) = \left[ au - a^2(m_2 - q_F) - \frac{m_2}{r_F^2} \right] \left[ au - a^2(m_2 - q_F) + \frac{m_2}{\rho_A^2} \right]$$

$$\cdot e^{iu(\sigma_F - \sigma_A - a\epsilon)/a} I_l(\bar{m}) \left( (-q_F - \frac{u}{a}) \vartheta_{bF} \right)$$

$$\cdot \Lambda(\bar{n}) \left( (2m_2 - q_F - \frac{u}{a}) \vartheta_{bA} \right)$$

and

$$\bar{K}_{FA}(\bar{m}, \bar{n}) (m_3 = q_A + l_3 N_F \geq 0) = \left\{ \frac{-N_F}{4\pi\rho_F U^2 r_{F0}} \right\} \frac{r_A}{a \sqrt{1+a^2 r_A^2}} e^{-im_3(2\sigma_F - a\epsilon)}$$

$$\cdot e^{-iq_A(\sigma_F - \sigma_A - a\epsilon)} \left\{ C(0)D(0) - \frac{i}{\pi} \int_0^\infty [C(u)D(u) - C(-u)D(-u)] \frac{du}{u} \right\} \quad (9)$$

where

$$C(u) = \begin{cases} I_{m_3}(1u + a(m_3 - q_A)l_3) K_{m_3}(1u + a(m_3 - q_A)l_3) & \text{for } \rho_F \leq r_A \\ I_{m_3}(1u + a(m_3 - q_A)l_3) K_{m_3}(1u + a(m_3 - q_A)l_3) & \text{for } r_A < \rho_F \end{cases}$$

$$D(u) = \left[ au + a^2(m_3 - q_A) + \frac{m_3}{r_A^2} \right] \left[ au + a^2(m_3 - q_A) - \frac{m_3}{\rho_F^2} \right]$$

$$\cdot e^{-iu(\sigma_F - \sigma_A - a\epsilon)/a} I_l(\bar{m}) \left( (q_A - \frac{u}{a}) \vartheta_{bA} \right)$$

$$\cdot \Lambda(\bar{n}) \left( (-2m_3 + q_A - \frac{u}{a}) \vartheta_{bF} \right)$$

The kernels have been programmed with proper consideration being given to evaluating the finite contributions of the Cauchy-type singularities in the  $u$ -integrations at  $u=0$  and of the Hadamard-type higher order singularities in the  $\rho$ -integrations when  $\rho=r$ .

#### IV. THE NORMAL VELOCITIES

The LH sides of the integral equations represent the normal components of the velocity perturbations above that producing zero loading (lift) which corresponds to a rotating thin plate lying on the helicoidal surface of pitch angle (i.e., hydrodynamic pitch angle)

$$\beta = \tan^{-1} \frac{U}{\Omega r}$$

where  $U$  = forward speed,  $r$  = radial location of the corresponding helix. The perturbations considered are those due to hull wake (non-uniform inflow field), blade camber, incident flow angle, and also due to the thickness of the blades which mainly affect the velocity field around both propellers of the CR system. The effect of "nonplanar" thickness which contributes to the loading of both units is neglected as being small [5]. The effects of each of these imposed flows on the blade are calculated separately and simply added together as allowed by the linearity of the theory.

The left-hand sides of the integral equations due to the wake contribution can be harmonically analyzed and written in the form

$$W(r, \vartheta) = \sum_{q=0}^{\infty} V_n(r) e^{-iq\vartheta}$$

where  $\vartheta$  can be expressed in terms of the moving coordinator system attached to each propeller by  $\vartheta_F = \vartheta_{0F} - \Omega_F t$  and  $\vartheta_A = -\vartheta_{0A} + \Omega_A t$  for the case of the forward and after propeller, respectively, as shown in Figure 1. The normal wake velocities  $V_n(r)$  can be determined from the harmonic analysis of the wake measurements, as shown in Reference 5. After the trigonometric transformation

$$\vartheta_0 = \sigma - \vartheta_b \cos \vartheta_\alpha$$

and application of the "lift operator" of order  $\bar{m}$

$$\frac{1}{\pi} \int_0^\pi \hat{\Phi}(\bar{m}) W(r, \vartheta) d\vartheta_\alpha$$

the following expressions result for the left-hand sides of the pair of integral equations relating the unknown loadings with the given "downwash" at each propeller:

$$\frac{\bar{w}_A^{(q_A, \bar{m})}(r_A)}{U} = \frac{v_A^{(q_A)}(r_A)}{U} e^{-iq_A \sigma_A I(\bar{m})} (q_A \theta_{bA})$$

for the after propeller, and

$$\frac{\bar{w}_F^{(q_F, \bar{m})}(r_F)}{U} = \text{conj} \left[ \frac{v_F^{(q_F)}(r_F)}{U} e^{-iq_F \sigma_F I(\bar{m})} (q_F \theta_{bF}) \right]$$

for the forward propeller. It should be noted that the factor  $\exp i q \Omega t$  has been omitted from the above expressions.

The velocities induced by the incident flow angle and camber effects are independent of time because the blades are considered rigid so that only the steady-state loadings will be affected.

For the flow angle ( $f$ ) effects, the dimensionless perturbation velocities after the application of the lift operator become:

$$\left( \frac{\bar{w}_F^{(0, \bar{m})}(r_F)}{U} \right)_f = -\sqrt{1+a^2 r_F^2} \left[ \theta_{pF}(r_F) - \beta_F(r_F) \right] I(\bar{m}) \quad (0)$$

and

$$\left( \frac{\bar{w}_A^{(0, \bar{m})}(r_A)}{U} \right)_f = -\sqrt{1+a^2 r_A^2} \left[ \theta_{pA}(r_A) - \beta_A(r_A) \right] I(\bar{m}) \quad (0)$$

for the forward and after propellers, respectively, where  $\theta_p$  is the blade pitch angle and  $\beta$  is the hydrodynamic pitch angle of the reference helicoidal surface (i.e., of zero loading).

For the camber ( $c$ ) effect of the forward propeller, the dimensionless velocity ratio after the application of the lift operator becomes

$$\left( \frac{\bar{w}_F^{(0, \bar{m})}(r_F)}{U} \right)_c = \frac{\sqrt{1+a^2 r_F^2}}{\pi} \int_0^\pi \hat{\phi}(\bar{m}) \frac{\partial f(r_F, s_F)}{\partial s_F} d\varphi_\alpha \quad (12)$$

where

$f(r_F, s_F)$  = camberline ordinates as fraction of expanded chord length, measured from the face pitch line

$s_F = (1 - \cos \varphi_\alpha)/2$ , chordwise location non-dimensionalized on the basis of chord length

For the after propeller, the same expression is valid and only the subscript  $F$  must be replaced by  $A$ .

The evaluation of the integral of (12) is given in Reference 7 for arbitrary camber shape.

## V. THE EFFECTS OF BLADE THICKNESS OF EACH PROPELLER ON THE VELOCITY FIELD OF THE OTHER

In addition to the disturbances of the velocity field about each propeller due to wake, its flow angle and camber, the disturbances considered are those due to the effects of the thickness of the blades of one propeller on the velocity incident on the other. These normal velocities on the LH side of the integral equations have been developed on the basis of "thin" body approximations [8]. Furthermore, it is assumed that the thickness distribution is approximated by a lenticular cross-section, an assumption which has

been shown to be a good approximation for determining velocity and pressure [8,9] on a point in the neighborhood of an operating propeller as long as it is not a point on its blade and particularly near the leading edge. It should also be recalled that the velocity and pressure fields generated by an operating propeller even in a uniform inflow yields steady and unsteady components of the respective field. Thus although it is independent of time, the blade thickness produces both steady and unsteady components of the velocity field.

Following the same procedure as in Reference 8, it can be shown that the dimensionless velocity normal to the blades of the forward propeller induced by the after propeller thickness, with maximum thickness-chord ratio  $t_0/c$ , is given for  $q_F = 0$  by

$$\left( \frac{\bar{w}_F^{(0, \bar{m})}(r_F)}{U} \right)_{tA} = -\frac{4a^3 r_F N_A}{\pi^2 \sqrt{1+a^2 r_F^2}} \int_{\rho_A}^{\rho_A} \frac{\rho_A}{\theta_{bA}} \sqrt{1+a^2 \rho_A^2} \frac{t_0}{c} (\rho_A) \cdot \int_0^\infty u(IK)_0 F(u, \rho_A) R.P. \left[ e^{iu(\sigma_A - \sigma_F + a\epsilon)/a} I(\bar{m}) \left( \frac{u}{a} \theta_{bF} \right) \right] du d\rho_A \quad (13)$$

where

$$(IK)_0 = \begin{cases} I_0(u\rho_A) K_0(ur_F) & \text{for } \rho_A < r_F \\ I_0(ur_F) K_0(u\rho_A) & \text{for } r_F < \rho_A \end{cases}$$

$$F(u, \rho_A) = \frac{\sin \frac{u\theta_{bA}}{a} - \frac{u\theta_{bA}}{a} \cos \left( \frac{u\theta_{bA}}{a} \right)}{u}$$

$I_0()$  and  $K_0()$  are modified Bessel functions of first and second kind of order zero

and for  $q_F = 2\ell N_A$  where  $\ell = 1, 2, \dots$ , by

$$\left( \frac{\bar{w}_F^{(2\ell N_A, \bar{m})}(r_F)}{U} \right)_{tA} = -\frac{4a^2 r_F N_A}{\pi^2 \sqrt{1+a^2 r_F^2}} e^{-i\ell N_A (2\sigma_F - a\epsilon)} \cdot \int_{\rho_A}^{\rho_A} \frac{\rho_A}{\theta_{bA}} \sqrt{1+a^2 \rho_A^2} \frac{t_0}{c} (\rho_A) \cdot \int_0^\infty F(u, \rho_A) [G(u) - G(-u)] du d\rho_A \quad (14)$$

where

$$G(u) = \left[ au + \ell N_A \left( a^2 - \frac{1}{r_F^2} \right) \right] I_{\ell N_A} (|u + a\ell N_A| \rho_A) K_{\ell N_A} (|u + a\ell N_A| r_F) \cdot e^{iu(\sigma_A - \sigma_F + a\epsilon)/a} I(\bar{m}) \left( (2\ell N_A + \frac{u}{a}) \theta_{bF} \right)$$

for  $\rho_A < r_F$ . If  $\rho_A > r_F$ , these factors are interchanged in the modified Bessel functions.

The velocity normal to the blades of the after propeller induced by the forward propeller thickness is for  $q_A = 0$

$$\left( \frac{\bar{w}_A^{(0, \bar{m})}(r_A)}{U} \right)_{tF} = \frac{-4a^3 r_A N_F}{\pi^2 \sqrt{1+a^2 r_A^2}} \int_{\rho_F}^{\rho_F} \frac{\rho_F}{\theta_{bF}} \sqrt{1+a^2 \rho_F^2} \frac{t_0}{c} (\rho_F) \quad (15)$$

[Cont'd]



$$\int_0^{\infty} u(IK)_0 F(u, \rho_F) R.P. \left[ e^{-iu(\sigma_A - \sigma_F + a\epsilon)/a} I_{\bar{m}} \left( \frac{u\theta_{bA}}{a} \right) \right] du d\rho_F \quad (15)$$

where

$$(IK)_0 = \begin{cases} I_0(u\rho_F) K_0(ur_A) & \text{for } \rho_F < r_A \\ I_0(ur_A) K_0(u\rho_F) & \text{for } r_A < \rho_F \end{cases}$$

$$F(u, \rho_F) = \frac{\sin \frac{u\theta_{bF}}{a} - \frac{u\theta_{bF}}{a} \cos \frac{u\theta_{bF}}{a}}{u^2}$$

and for  $q_A = 2\ell N_F$ ,  $\ell=1, 2, \dots$

$$\begin{aligned} \left( \frac{\bar{w}_A^{(2\ell N_F, \bar{m})}(r_A)}{U} \right)_{tF} &= \frac{-4a^2 r_A N_F}{\pi^2 \sqrt{1+a^2 r_A^2}} e^{-i\ell N_F(2\sigma_F + a\epsilon)} \\ &\cdot \int_{\rho_F}^{\rho_F} \frac{\rho_F}{\theta_{bF}} \sqrt{1+a^2 \rho_F^2} \frac{t_0}{c}(\rho_F) \\ &\cdot \int_0^{\infty} F(u, \rho_F) [N(u) - N(-u)] du d\rho_F \quad (16) \end{aligned}$$

where

$$N(u) = \left[ au + \ell N_F \left( a^2 - \frac{1}{2} \right) \right] I_{\ell N_F}(1u + a\ell N_F | \rho_F) K_{\ell N_F}(1u + a\ell N_F | r_A) \cdot e^{-iu(\sigma_A - \sigma_F + a\epsilon)/a} I_{\bar{m}} \left( (2\ell N_F + \frac{u}{a}) \theta_{bA} \right)$$

for  $\rho_F < r_A$ . If  $\rho_F > r_A$ , these factors are interchanged in the modified Bessel functions.

## VI. SOLUTION OF THE PAIR OF INTEGRAL EQUATIONS

It is seen from Eqs.(5) and (6) that the loading on each propeller of the CR system is affected by all the harmonics of the inflow field. Here, however, the solution will be limited to the uniform inflow case, i.e., to the steady-state normal velocities due to camber (c) and to incident flow angle (f), and to the steady and unsteady effects of the interaction (i.e., cross-coupling terms) between the propellers and to their respective thicknesses.

Equation (5) becomes for each  $\bar{m}$  and  $\bar{n}$ , for  $q_F = 0$

$$\begin{aligned} \left[ \frac{\bar{w}_F^{(0)}(r_F)}{U} \right]_{c+f+tA} &= \int_{\rho_F} L_F^{(0)}(\rho_F) \bar{K}_{FF}'(q_F=0) d\rho_F \\ &+ \int_{\rho_A} \left\{ L_A^{(0)}(\rho_A) \bar{K}_{AF}(m_2=0) + L_A^{(2N_A)}(\rho_A) \bar{K}_{AF}(m_2=N_A) + \dots \right\} d\rho_A \quad (17a) \end{aligned}$$

and for  $q_F = 2N_A$

$$\begin{aligned} \left[ \frac{\bar{w}_F^{(2N_A)}(r_F)}{U} \right]_{tA} &= \int_{\rho_F} L_F^{(2N_A)}(\rho_F) \bar{K}_{FF}'(q_F=2N_A) d\rho_F \\ &+ \int_{\rho_A} \left\{ L_A^{(0)}(\rho_A) \bar{K}_{AF}(m_2=N_A) + L_A^{(2N_A)}(\rho_A) \bar{K}_{AF}(m_2=2N_A) + \dots \right\} d\rho_A \quad (17b) \end{aligned}$$

Equation (6) becomes for each  $\bar{m}$  and  $\bar{n}$ ,

for  $q_A = 0$

$$\begin{aligned} \left[ \frac{\bar{w}_A^{(0)}(r_A)}{U} \right]_{c+f+tF} &= \int_{\rho_F} \left\{ L_F^{(0)}(\rho_F) \bar{K}_{FA}(m_3=0) \right. \\ &\quad \left. + L_F^{(2N_F)}(\rho_F) \bar{K}_{FA}(m_3=N_F) + \dots \right\} d\rho_F \\ &+ \int_{\rho_A} L_A^{(0)}(\rho_A) \bar{K}_{AA}'(q_A=0) d\rho_A \quad (18a) \end{aligned}$$

and for  $q_A = 2N_F$

$$\begin{aligned} \left[ \frac{\bar{w}_A^{(2N_F)}(r_A)}{U} \right]_{tF} &= \int_{\rho_F} \left\{ L_F^{(0)}(\rho_F) \bar{K}_{FA}(m_3=N_F) \right. \\ &\quad \left. + L_F^{(2N_F)}(\rho_F) \bar{K}_{FA}(m_3=2N_F) + \dots \right\} d\rho_F \\ &+ \int_{\rho_A} L_A^{(2N_F)}(\rho_A) \bar{K}_{AA}'(q_A=2N_F) d\rho_A \quad (18b) \end{aligned}$$

where

$$\bar{K}_{FF}' = \sum_{m_1=-\infty}^{\infty} \bar{K}_{FF}$$

$$\bar{K}_{AA}' = \sum_{m_4=-\infty}^{\infty} \bar{K}_{AA}$$

(The higher frequencies are assumed negligible.)

Even in this simplified problem, a direct solution of the equations is impracticable; therefore an iteration procedure must be devised. It is assumed at first that the effect of the after propeller on the forward propeller (except for the thickness effect) is small and hence the second terms on the RH of Eqs.(17a) and (17b) may be omitted.

The iteration procedure is given below for two cases: for a CR system with equal number of blades (i.e.,  $N_F = N_A = N$ ) and for one with unequal number (i.e.,  $N_F \neq N_A$ ), and neither one is an integer multiple of the other.

Case #1:  $N_F = N_A = N$

0-iteration (first)

$$1) L_{FO}^{(0)}(\rho_F) = [\bar{K}_{FF}'(q_F=0)]^{-1} \cdot \left\{ \left( \frac{\bar{w}_F^{(0)}(r_F)}{U} \right)_{c+f} + \left( \frac{\bar{w}_F^{(0)}(r_A)}{U} \right)_{tA} \right\}$$

$$2) L_{FO}^{(2N, \bar{n})}(\rho_F) = [\bar{K}_{FF}'(q_F=2N)]^{-1} \cdot \left\{ \left( \frac{\bar{w}_F^{(2N, \bar{n})}(r_F)}{U} \right)_{tA} \right\}$$

$$\text{where } \bar{K}_{FF}'(q_F) = \sum_{m_1=-\infty}^{\infty} \bar{K}_{FF}^{(\bar{m}, \bar{n})}(m_1)$$

$$\begin{aligned} 3) L_{A1}^{(0, \bar{n})}(\rho_A) &= [\bar{K}_{AA}'(q_A=0)]^{-1} \cdot \left\{ \left( \frac{\bar{w}_A^{(0, \bar{n})}(r_A)}{U} \right)_{c+f} + \left( \frac{\bar{w}_A^{(0, \bar{n})}(r_F)}{U} \right)_{tF} \right. \\ &\quad \left. - \sum_{\rho_F} \left[ L_{FO}^{(0, \bar{n})}(\rho_F) \bar{K}_{FA}^{(\bar{m}, \bar{n})}(m_3=0, q_A=0) \right. \right. \\ &\quad \left. \left. + L_{FO}^{(2N, \bar{n})}(\rho_F) \bar{K}_{FA}^{(\bar{m}, \bar{n})}(m_3=N, q_A=0) \right] \right\} \end{aligned}$$

$$4) L_{A1}^{(2N, \bar{n})}(\rho_A) = [\bar{K}_{AA}'(q_A=2N)]^{-1} \cdot \left\{ \left( \frac{\bar{W}_A^{(2N, \bar{m})}(r_A)}{U} \right)_{tF} - \sum_{\rho_F} \left[ L_{F0}^{(0, \bar{n})} \cdot \bar{K}_{FA}^{(\bar{m}, \bar{n})}(m_3=N, q_A=2N) + L_{F0}^{(2N, \bar{n})} \cdot \bar{K}_{FA}^{(\bar{m}, \bar{n})}(m_3=2N, q_A=2N) \right] \right\}$$

$$\text{where } \bar{K}_{AA}'(q_A) = \sum_{m_4=-\infty}^{\infty} \bar{K}_{AA}^{(\bar{m}, \bar{n})}(m_4)$$

1-iteration (second iteration)

$$1) L_{F1}^{(0, \bar{n})}(\rho_F) = [\bar{K}_{FF}'(q_F=0)]^{-1} \cdot \left\{ \left( \frac{\bar{W}_F^{(0, \bar{m})}(r_F)}{U} \right)_{c+f} + \left( \frac{\bar{W}_F^{(0, \bar{m})}(r_F)}{U} \right)_{tA} - \sum_{\rho_A} \left[ L_{A1}^{(0, \bar{n})} \cdot \bar{K}_{AF}^{(\bar{m}, \bar{n})}(m_2=0, q_F=0) + L_{A1}^{(2N, \bar{n})} \cdot \bar{K}_{AF}^{(\bar{m}, \bar{n})}(m_2=N, q_F=0) \right] \right\}$$

$$2) L_{F1}^{(2N, \bar{n})}(\rho_F) = [\bar{K}_{FF}'(q_F=-2N)]^{-1} \cdot \left\{ \left( \frac{\bar{W}_F^{(2N, \bar{m})}(r_F)}{U} \right)_{tA} - \sum_{\rho_A} \left[ L_{A1}^{(0, \bar{n})} \cdot \bar{K}_{AF}^{(\bar{m}, \bar{n})}(m_2=N, q_F=2N) + L_{A1}^{(2N, \bar{n})} \cdot \bar{K}_{AF}^{(\bar{m}, \bar{n})}(m_2=2N, q_F=2N) \right] \right\}$$

$$3) L_{A2}^{(0, \bar{n})}(\rho_A) = [\bar{K}_{AA}'(q_A=0)]^{-1} \cdot \left\{ \left( \frac{\bar{W}_A^{(0, \bar{m})}(r_A)}{U} \right)_{c+f} + \left( \frac{\bar{W}_A^{(0, \bar{m})}(r_A)}{U} \right)_{tF} - \sum_{\rho_F} \left[ L_{F1}^{(0, \bar{n})} \cdot \bar{K}_{FA}^{(\bar{m}, \bar{n})}(m_3=0, q_A=0) + L_{F1}^{(2N, \bar{n})} \cdot \bar{K}_{FA}^{(\bar{m}, \bar{n})}(m_3=N, q_A=0) \right] \right\}$$

$$4) L_{A2}^{(2N, \bar{n})}(\rho_A) = [\bar{K}_{AA}'(q_A=2N)]^{-1} \cdot \left\{ \left( \frac{\bar{W}_A^{(2N, \bar{m})}(r_A)}{U} \right)_{tF} - \sum_{\rho_F} \left[ L_{F1}^{(0, \bar{n})} \cdot \bar{K}_{FA}^{(\bar{m}, \bar{n})}(m_3=N, q_A=2N) + L_{F1}^{(2N, \bar{n})} \cdot \bar{K}_{FA}^{(\bar{m}, \bar{n})}(m_3=2N, q_A=2N) \right] \right\}$$

and so on, until values of loadings are stabilized.

Case #2:  $N_A \neq N_F$

0-iteration (first)

$$1) L_{F0}^{(0, \bar{n})}(\rho_F) = [\bar{K}_{FF}'(q_F=0)]^{-1} \cdot \left\{ \left( \frac{\bar{W}_F^{(0, \bar{m})}(r_F)}{U} \right)_{c+f+tA} \right\}$$

$$2) L_{F0}^{(2N_A, \bar{n})}(\rho_F) = [\bar{K}_{FF}'(q_F=-2N_A)]^{-1} \cdot \left\{ \left( \frac{\bar{W}_F^{(2N_A, \bar{m})}(r_F)}{U} \right)_{tA} \right\}$$

$$3) L_{A1}^{(0, \bar{n})}(\rho_A) = [\bar{K}_{AA}'(q_A=0)]^{-1} \cdot \left\{ \left( \frac{\bar{W}_A^{(0, \bar{m})}(r_A)}{U} \right)_{c+f+tF} - \sum_{\rho_F} L_{F0}^{(0, \bar{n})} \cdot \bar{K}_{FA}^{(\bar{m}, \bar{n})}(m_3=0, q_A=0) \right\}$$

$$4) L_{A1}^{(2N_F, \bar{n})}(\rho_A) = [\bar{K}_{AA}'(q_A=2N_F)]^{-1} \cdot \left\{ \left( \frac{\bar{W}_A^{(2N_F, \bar{m})}(r_A)}{U} \right)_{tF} - \sum_{\rho_F} L_{F0}^{(0, \bar{n})} \cdot \bar{K}_{FA}^{(\bar{m}, \bar{n})}(m_3=N_F, q_A=2N_F) \right\}$$

$$\text{where } \bar{K}_{FF}'(q_F) = \sum_{m_1=-\infty}^{\infty} \bar{K}_{FF}^{(\bar{m}, \bar{n})}(m_1)$$

$$\text{and } \bar{K}_{AA}'(q_A) = \sum_{m_4=-\infty}^{\infty} \bar{K}_{AA}^{(\bar{m}, \bar{n})}(m_4)$$

1-iteration (second)

$$1) L_{F1}^{(0, \bar{n})}(\rho_F) = [\bar{K}_{FF}'(q_F=0)]^{-1} \cdot \left\{ \left( \frac{\bar{W}_F^{(0, \bar{m})}(r_F)}{U} \right)_{c+f+tA} - \sum_{\rho_A} \left[ L_{A1}^{(0, \bar{n})} \cdot \bar{K}_{AF}^{(\bar{m}, \bar{n})}(m_2=0, q_F=0) \right] \right\}$$

$$2) L_{F1}^{(2N_A, \bar{n})}(\rho_F) = [\bar{K}_{FF}'(q_F=-2N_A)]^{-1} \cdot \left\{ \left( \frac{\bar{W}_F^{(2N_A, \bar{m})}(r_F)}{U} \right)_{tA} - \sum_{\rho_A} \left[ L_{A1}^{(0, \bar{n})} \cdot \bar{K}_{AF}^{(\bar{m}, \bar{n})}(m_2=N_A, q_F=2N_A) \right] \right\}$$

$$3) L_{A2}^{(0, \bar{n})}(\rho_A) = [\bar{K}_{AA}'(q_A=0)]^{-1} \cdot \left\{ \left( \frac{\bar{W}_A^{(0, \bar{m})}(r_A)}{U} \right)_{c+f+tF} - \sum_{\rho_F} \left[ L_{F1}^{(0, \bar{n})} \cdot \bar{K}_{FA}^{(\bar{m}, \bar{n})}(m_3=0, q_A=0) \right] \right\}$$

$$4) L_{A2}^{(2N_F, \bar{n})}(\rho_A) = [\bar{K}_{AA}'(q_A=2N_F)]^{-1} \cdot \left\{ \left( \frac{\bar{W}_A^{(2N_F, \bar{m})}(r_A)}{U} \right)_{tF} - \sum_{\rho_F} \left[ L_{F1}^{(0, \bar{n})} \cdot \bar{K}_{FA}^{(\bar{m}, \bar{n})}(m_3=N_F, q_A=2N_F) \right] \right\}$$

and so on, until values of loadings are stabilized.

It is to be noted that, in contrast to the case of equal number of blades for the two propellers of the CR system, when the propellers have an unequal number of blades,  $N_A \neq N_F$ , the series representing the cross-coupling terms due to the interaction effects are more limited. As will be shown later, for this case there is no unsteady loading  $L_F$  on the forward propeller at frequency  $2N_F$  and no unsteady loading  $L_A$  on the after propeller at frequency  $2N_A$ . It should be kept in mind that the iteration scheme has been restricted to the lowest possible frequencies of the interacting CR system. It will be easily generalized by means of Eqs.(5) and (6) by varying parameters  $\ell_1, \ell_2, \ell_3, \ell_4$  (all integers) to other values than those already used (0,  $\pm 1$ ).

## VII. PROPELLER LOADING AND RESULTING HYDRODYNAMIC FORCES AND MOMENTS

### Propeller Loading

Once the values of  $L^{(q, \vec{n})}(r)$ , the spanwise loading components, or coefficients of the chordwise distribution, are obtained, the spanwise load distribution  $L^{(q)}(r)$  is determined as [5,6]:

$$L^{(q)}(r) = \sum_{\vec{n}=1}^{\vec{n}_{\max}} L^{(q, \vec{n})}(r) \Theta(\vec{n}) \sin \theta_{\alpha} d\theta_{\alpha} \quad (19)$$

where  $\Theta(\vec{n})$  = chordwise modes. Because the interaction phenomenon introduces an angle of attack even in the steady-state case  $\Theta(\vec{n})$  is taken as the complete Bimbaum series which has the proper leading edge singularity and satisfies the Kutta condition at the trailing edge. In this case it can be shown that

$$L^{(q)}(r) = L^{(q, 1)}(r) + \frac{1}{2} L^{(q, 2)}(r) \quad (19a)$$

### Hydrodynamic Forces and Moments

The principal components of these forces and moments which are evaluated for each member of the CR system are listed below and shown in Figure 2 for a RH propeller with the sign convention adopted.

Forces:  $F_x$ =thrust (x-direction)  
 $F_y$  and  $F_z$ =horizontal and vertical components, respectively, of the bearing forces

Moments:  $Q_x$ =torque about the x-axis  
 $Q_y$  and  $Q_z$ =bending moments about the y- and z-axis, respectively  
 (Subscripts F and A added to these symbols will designate forward and after propeller cases.)

The elementary forces and moments can be determined by resolving the chordwise loadings, acting on an elementary radial strip, normal to the strip and taking the corresponding moments about any axis as in Reference 5. However, for simplification of the discussion which follows, the assumption will be made, as in Reference 10, that the spanwise loading  $L^{(q)}(r)$  acts at the mid-chord. This is exactly the case as far as thrust and torque are concerned and a good approximation for the transverse bearing forces and bending moments if the blades are not wide, which is the case with counterrotating propellers.

Thus the elementary forces acting at radius  $r$  of an  $N$ -bladed propeller will be given by

$$\Delta F_x = \sum_{n=1}^N L^{(q)}(r) e^{iq(\Omega t + \bar{\theta}_n)} \cos \theta_p(r) \Delta r$$

$$\Delta F_y = \sum_{n=1}^N L^{(q)}(r) e^{iq(\Omega t + \bar{\theta}_n)} \sin \theta_p(r) \cos(\Omega t + \bar{\theta}_n) \Delta r$$

$$\Delta F_z = - \sum_{n=1}^N L^{(q)}(r) e^{iq(\Omega t + \bar{\theta}_n)} \sin \theta_p(r) \sin(\Omega t + \bar{\theta}_n) \Delta r \quad (20)$$

where  $\theta_p(r)$  is the geometric pitch angle at radius  $r$  and  $\bar{\theta}_n = 2\pi(n-1)/N, n=1, 2, \dots, N$ . The elementary moments will be given by

$$\Delta Q_x = - \sum_{n=1}^N r L^{(q)}(r) e^{iq(\Omega t + \bar{\theta}_n)} \sin \theta_p(r) \Delta r$$

$$\Delta Q_y = \sum_{n=1}^N r L^{(q)}(r) e^{iq(\Omega t + \bar{\theta}_n)} \cos \theta_p(r) \cos(\Omega t + \bar{\theta}_n) \Delta r$$

$$\Delta Q_z = - \sum_{n=1}^N r L^{(q)}(r) e^{iq(\Omega t + \bar{\theta}_n)} \cos \theta_p(r) \sin(\Omega t + \bar{\theta}_n) \Delta r \quad (21)$$

The summation over all the blades of a propeller involves

1) for thrust and torque

$$\sum_{n=1}^N e^{iq\bar{\theta}_n} = \begin{cases} N & \text{when } q=nN, n=0, 1, 2, \dots \\ 0 & \text{for all other } q \end{cases} \quad (22)$$

2) for transverse forces and bending moments

$$\sum_{n=1}^N e^{i(q \pm 1)\bar{\theta}_n} = \begin{cases} N & \text{when } q=nN \pm 1, n=0, 1, 2, \dots \\ 0 & \text{for all other } q \end{cases} \quad (23)$$

It is thus evident that in the steady-state case ( $q=0$ ) thrust and torque from each propeller will be present (see Eq.22), whereas, since the condition under consideration is that of uniform inflow into the forward propeller, there will be no transverse forces and bending moments (see Eq.23). This will be so whether the propellers are of equal or unequal number of blades.

As has been shown the interaction phenomenon induces unsteady loadings on both units of the CR system. In the case of equal blade number, those on the forward propeller are  $L_F^{(2\ell N)}(r_F)$ , on the after propeller,  $L_A^{(2\ell N)}(r_A)$ . As seen from Eqs.(22) and (23) both propellers generate thrust and torque at frequencies  $q = 2\ell N, \ell=1, 2, \dots$ , which corresponds to blade-blade crossing frequency for such propellers, and no unsteady transverse bearing forces and moments, since no combination of integers  $\ell$  and  $n$  can satisfy the relation  $(2\ell - n)N = \pm 1$ .

In the case of unequal blade number,  $N_A \neq N_F$ , the unsteady loadings on the forward propeller are at frequencies  $q_F = 2\ell_1 N_A$  and  $2\ell_2 N_F$  and on the after propeller at  $q_A = 2\ell_3 N_F$  and  $2\ell_4 N_A$ . The criterion for thrust and torque, Eq.(22), yields

$$\begin{aligned} q_F &= 2\ell_1 N_A = n_1 N_F \\ q_F &= 2\ell_2 N_F = n_2 N_F \\ q_A &= 2\ell_3 N_F = n_3 N_A \\ q_A &= 2\ell_4 N_A = n_4 N_A \end{aligned} \quad (22a)$$

and the criterion for transverse forces and bending moments, Eq.(23), yields



$$\begin{aligned}
 q_F &= 2\ell_1 N_A = n_1 N_F \mp 1 \\
 q_F &= 2\ell_2 N_F = n_2 N_F \mp 1 \\
 q_A &= 2\ell_3 N_F = n_3 N_A \mp 1 \\
 q_A &= 2\ell_4 N_A = n_4 N_A \mp 1
 \end{aligned} \quad (23a)$$

The conditions of (22a) for thrust and torque are always satisfied for frequency  $q=q_F=q_A$  by choosing  $\ell_1 = \ell_4 = mN_F$ ,  $\ell_2 = \ell_3 = mN_A$ ,  $m=1,2,\dots$ , so that  $q = 2mN_A N_F$ , i.e., the so-called blade-blade crossing frequency and multiples thereof. Equation (22a) can also be satisfied at lower frequencies (1) if  $N_A = kN_F$ ,  $k$  being an integer, in which case choosing  $\ell_1 k = \ell_2 = \ell_3 = \ell_4 k$  yields  $q = 2mkN_F$ , and (2) if  $N_A$  and  $N_F$  are both even numbers, in which case  $q = mN_A N_F$ . In the latter two cases the conditions of (23a) for transverse forces and bending moments are obviously not satisfied.

When  $N_A \neq kN_F$  and  $N_A$  and  $N_F$  are not both even numbers, the CR system generates thrust and torque only at  $q = 2mN_A N_F$  (blade-blade crossing frequencies).

The conditions of (23a) are satisfied for

$$\begin{aligned}
 q &= q_F \mp 1 = 2\ell_1 N_A \mp 1 = n_1 N_F \\
 q &= q_A \pm 1 = 2\ell_3 N_F \pm 1 = n_3 N_A
 \end{aligned}$$

since  $2\ell_1 N_A + 2\ell_3 N_F = n_3 N_A + n_1 N_F$  is possible. The frequencies at which side forces and bending moments of the CR system occur are

$$q = 2\ell_1 N_A \mp 1 = 2\ell_3 N_F \pm 1$$

from which  $2\ell_1 N_A = 2\ell_3 N_F \pm 2$ .

An easy way of determining the frequencies for alternating forces and moments is to write out the sequence of numbers which are integer multiples of twice the blade number. For example, for 3 and 5 blades

$$\begin{array}{ccccccc}
 3: & 6 & 12 & 18 & 24 & 30 & \dots \\
 5: & & 10 & 20 & & 30 & \dots
 \end{array}$$

The frequencies for side forces will be the mean of any pair of numbers in the two squares which differ by 2, in this case 11, 19... The frequencies for thrust and torque will be the mean of any pair of numbers which are alike, in this case 30, 60... For 6 and 4 blades, the two lowest frequencies will be 24 and 48 for thrust and torque. (There is no side force in this case.)

Another derivation of the frequencies of the alternating forces developed by interactions between a pair of counterrotating propellers in a uniform inflow is given by Reference 11, with the same results.

On the basis of the preceding discussion, the total forces and moments are obtained from (20) and (21) as:

1) for thrust and torque

$$\begin{aligned}
 (F_x)_F &= N_F r_o e^{iq\Omega t} \int_0^1 L_F^{(q)}(r_F) \cos\theta_P(r_F) dr_F \\
 (F_x)_A &= N_A r_o e^{iq\Omega t} \int_0^1 L_A^{(q)}(r_A) \cos\theta_P(r_A) dr_A
 \end{aligned} \quad (24a)$$

$$\begin{aligned}
 (Q_x)_F &= -N_F r_o e^{iq\Omega t} \int_0^1 L_F^{(q)}(r_F) \sin\theta_P(r_F) r_F dr_F \\
 (Q_x)_A &= -N_A r_o e^{iq\Omega t} \int_0^1 L_A^{(q)}(r_A) \sin\theta_P(r_A) r_A dr_A
 \end{aligned} \quad (24b)$$

where  $q=0$  for steady state, and the lowest frequency of the alternating thrust and torque is

$$q = 2kN_F \text{ when } N_A = kN_F, k=1,2,\dots$$

$$q = N_A N_F \text{ when } N_A \neq kN_F \text{ and both are even numbers}$$

$$q = 2N_A N_F \text{ for all other } N_A \neq N_F$$

2) for transverse bearing forces and bending moments, when  $N_A \neq kN_F$  and  $N_A$  and  $N_F$  are not both even numbers,

$$\begin{aligned}
 (F_y)_F &= \frac{N_F}{2} r_o e^{i(q_F \mp 1)\Omega t} \int_0^1 L_F^{(q_F)}(r_F) \sin\theta_P(r_F) dr_F \\
 (F_z)_F &= \mp i(F_y)_F \\
 (F_y)_A &= \frac{N_A}{2} r_o e^{i(q_A \pm 1)\Omega t} \int_0^1 L_A^{(q_A)}(r_A) \sin\theta_P(r_A) dr_A \\
 (F_z)_A &= \pm i(F_y)_A
 \end{aligned} \quad (25a)$$

$$\begin{aligned}
 (Q_y)_F &= \frac{N_F}{2} r_o e^{i(q_F \mp 1)\Omega t} \int_0^1 L_F^{(q_F)}(r_F) \cos\theta_P(r_F) r_F dr_F \\
 (Q_z)_F &= \mp i(Q_y)_F \\
 (Q_y)_A &= \frac{N_A}{2} r_o e^{i(q_A \pm 1)\Omega t} \int_0^1 L_A^{(q_A)}(r_A) \cos\theta_P(r_A) r_A dr_A \\
 (Q_z)_A &= \pm i(Q_y)_A
 \end{aligned} \quad (25b)$$

where the upper signs (at  $q=q_F-1=q_A+1$ ) are used when  $N_A > N_F$  and the lower signs (at  $q=q_F+1=q_A-1$ ) are used when  $N_A < N_F$ , and  $q_F=2\ell_1 N_A$  and  $q_A=2\ell_3 N_F$  where  $\ell_1$  and  $\ell_3$  must satisfy the condition  $2\ell_1 N_A = 2\ell_3 N_F \pm 2$ .

It is to be noted that  $r_o = r_{Fo}$  = forward propeller radius and  $r_A$  and  $r_o$  are fractions of  $r_{Fo}$ , and that finally the real parts of the forces and moments are to be taken.

#### Blade Bending Moment

Following Reference 6, the blade bending moment about the face pitch line at any radius  $r_j$  of a blade of the forward or after propeller is calculated from the spanwise loading  $L^{(q)}(r)$  at any shaft frequency  $q$  as

$$M_b^{(q)} = r_o e^{iq\Omega t} \int_{r_j}^1 L^{(q)}(r) \cos[\theta_P(r) - \theta_P(r_j)] (r - r_j) dr \quad (26)$$

The instantaneous blade bending moment distribution

as the blades swing around the shaft is

$$M_b = \operatorname{Re} \sum_q M_b(q) e^{iq\Omega t} \quad (27)$$

Here  $q=q_F$  for the forward propeller and  $q=q_A$  for the after propeller.

### VIII. NUMERICAL RESULTS

On the basis of the theoretical procedures outlined in the preceding sections, a numerical approach has been established and adapted to the CDC-6600 or 7600 high-speed digital computer. The program furnishes in the case of uniform inflow to the forward propeller, a) the steady and time-dependent blade loadings, b) the corresponding hydrodynamic forces and moments, and c) the blade bending moment about the face-pitch line at any radius.

The expressions for the kernel functions given by Eqs. (7-9), those for the normal velocities on the left-hand sides of the integral equations given by Eqs. (11-16), and the pair of integral equations (17a,b and 18a,b), constitute the desired working forms. The computer program prepares all the necessary information for the execution of the suggested iteration procedure. It is a lengthy program, the duration depending on the number of blades of each component of the CR system, on the number of selected chordwise modes, and the number of frequencies for which information will be desired.

To establish the accuracy and usefulness of the computational procedure, a correlation with existing experimental results must be made. Calculations have been performed for two CR configurations for which data are available from tests at David Taylor NSRDC [12,13]. The data are for the two lowest frequencies,  $\ell_i=0$  and  $\ell_i=1$ , and the computations have been limited to these frequencies.

The iterative procedure starts after all the required information has been computed and stored properly. The necessary kernel functions and inverse kernel functions are calculated for both a 4-0-4 and a 4-0-5 CR system for values of  $m$  and  $q$  as indicated in the table below.

TABLE 1

4-0-4 CR System				4-0-5 CR System			
Matrix	Inverse Matrix	m	q	Matrix	Inverse Matrix	m	q
$K_{AF}$		0	0	$K_{AF}$		0	0
$K_{AF}$		4	0				
	$K_{FF}$		0	$K_{FF}$		0	
$K_{AF}$		4	8	$K_{AF}$		5	10
$K_{AF}$		8	8				
	$K_{FF}$		-8	$K_{FF}$		-10	
$K_{FA}$		0	0	$K_{FA}$		0	0
$K_{FA}$		4	0				
	$K_{AA}$		0	$K_{AA}$		0	
$K_{FA}$		4	8	$K_{FA}$		4	8
$K_{FA}$		8	8				
	$K_{AA}$		8	$K_{AA}$		8	

A workable program has been established which

indicates that the number of iterations need not be greater than 10, although the execution time of an additional iteration is minimal.

The 4-0-4 CR system is composed of the David Taylor NSRDC propeller 3686 forward and propeller 3687-A aft, and the 4-0-5 set of propeller 3686 forward and propeller 3849 aft [13]. Propeller characteristics and flow conditions are given in the following table.

TABLE 2

	Propeller 3686	Propeller 3687-A	Propeller 3849
Number of Blades, N	4	4	5
EAR	0.303	0.322	0.379
P/D at 0.7R	1.291	1.320	1.287
Diameter, D, in	12.017	11.776	11.785
Rotation	L.H.*	R.H.*	R.H.*
n, rps	12	12	12
Speed, ft/sec	13.22	13.22	13.22
Advance rate, J	1.1**	1.1**	1.1**

\*L.H. rotation is ccw looking forward

R.H. rotation is cw looking forward

\*\*J based on diameter of forward propeller 3686

The theoretical predictions with and without thickness effects and the experimental results are summarized in the following table.

TABLE 3

### CORRELATION OF PREDICTED AND MEASURED VALUES 4-0-4 CR SYSTEM

Forward Propeller 3686

After Propeller 3687-A

Axial Spacing = 0.28 forward propeller radius  
J=1.1

Q = 0, Steady State

		THEORY		EXPERIMENT
		Without Thickness	With Thickness	
Forward	$(\bar{K}_T)_F$	0.126*		0.125
Forward	$(\bar{K}_Q)_F$	0.0295*		0.0315
After	$(\bar{K}_T)_A$	0.145*		0.150
After	$(\bar{K}_Q)_A$	0.0330*		0.0315
<u>Q = 2N = 8</u>				
Forward	$(\bar{K}_T)_F$	0.0485		0.0285
Forward	$(\bar{K}_Q)_F$	0.0101		0.0058
After	$(\bar{K}_T)_A$	0.1156		0.0095
After	$(\bar{K}_Q)_A$	0.0242		0.0022

\*including friction

TABLE 4

CORRELATION OF PREDICTED AND MEASURED VALUES  
4-0-5 CR SYSTEM

Forward Propeller 3686

After Propeller 3849

Axial Spacing = 0.28 forward propeller radius  
 $J=1.1$  $Q = 0$ , Steady State

	THEORY		EXPERIMENT
	Without Thickness	With Thickness	
Forward $(\bar{K}_T)_F$	0.087*		0.130
Forward $(\bar{K}_Q)_F$	0.0207*		0.030
After $(\bar{K}_T)_A$	0.161*		0.130
After $(\bar{K}_Q)_A$	0.0361*		0.028
<u><math>Q_F = 2N_A - 1 = 9</math></u>			
Forward $(\bar{K}_{FH})_F$	0.0079		0.0075
Forward $(\bar{K}_{FV})_F$	0.0079		0.0074
Forward $(\bar{K}_{QH})_F$	0.0062		0.0040
Forward $(\bar{K}_{QV})_F$	0.0062		0.0041
<u><math>Q_A = 2N_F + 1 = 9</math></u>			
After $(\bar{K}_{FH})_A$	0.0231		0.0057
After $(\bar{K}_{FV})_A$	0.0231		0.0046
After $(\bar{K}_{QH})_A$	0.0159		0.0023
After $(\bar{K}_{QV})_A$	0.0159		0.0023

\*including friction

## IX. CONCLUSIONS

Linearized unsteady lifting-surface theory has been applied in the study of two interacting propellers of a counterrotating system, when both units operate in a spatially non-uniform inflow. A mathematical model is introduced taking into account the exact geometry of the propulsive system as well as the three-dimensional spatially varying inflow. The propeller blades are considered to be of finite thickness and lying on a helicoidal surface of varying pitch. The blades have arbitrary planform, camber and sweep angle.

The computational procedure, however, has been developed and adapted to the CDC 6600 and 7600 high-speed digital computer, for the case where both units operate with the same RPM in a uniform inflow field.

The uniformity of the inflow field provides for a better understanding of the mechanism of interaction of the CR system, since the presence of wake harmonics would have such a dominant effect as to mask the interaction phenomenon.

The study provides information about the steady and unsteady blade loading distributions and the corresponding hydrodynamic forces and moments on both components of the propulsive device.

Rules have been established for the presence or absence of the steady and unsteady hydrodynamic

forces and moments when the CR system is made up of equal and unequal numbers of blades. In fact, when the propellers of the CR system have equal number of blades, only the steady and unsteady thrust and torque will be generated on each propeller of the CR system, at zero and blade-blade crossing frequencies or multiples thereof ( $q=2\&N$ ,  $\&=1,2,3 \dots$  and  $N$ =common number of blades). When the CR system is made up of propellers with unequal number of blades, i.e.,  $N_F \neq N_A$ , there is an easy way of determining the frequencies of alternating (unsteady) forces and moments.

The numerical work has been limited. The calculations without thickness effect have shown a reverse trend to that of experiment for the unsteady forces and moments generated on the after propeller. The numerical calculations have shown much higher values for the forces and moments exerted on the after propeller than those on the forward propeller. It is difficult to explain the discrepancy until more detailed and exhaustive numerical calculations are performed (including thickness effect). Furthermore, additional experimental work should also be conducted.

## REFERENCES

1. Hadler, J.B., Morgan, W.B. and Meyers, K.A., "Advanced Propeller Propulsion for High-Powered Single-Screw Ships," Transactions SNAME, Vol.72, 1964.
2. Wereldsma, R., "Investigations on the Vibratory Output of Contrarotating Screw Propellers," 7th Symposium on Naval Hydrodynamics, Rome, August 25-30, 1968.
3. Tsakonas, S. and Jacobs, W.R., "Counterrotating and Tandem Propellers Operating in Spatially Varying, Three-Dimensional Flow Fields, Part 1 - Analysis," DL Report 1335, Stevens Institute of Technology, September 1968.
4. Jacobs, W.R. and Tsakonas, "A New Procedure for the Solution of Lifting Surface Problems," J. Hydronautics, Vol.3, No.1, January 1969.
5. Tsakonas, S., Jacobs, W.R. and Ali, M.R., "Propeller Blade Pressure Distribution Due to Loading and Thickness Effects," DL Report 1869, Stevens Institute of Technology, in preparation.
6. Tsakonas, S., Jacobs, W.R. and Ali, M.R., "An Exact Linear Lifting-Surface Theory for a Marine Propeller in a Non-Uniform Flow Field," DL Report 1509, Stevens Institute of Technology, February 1972; J. Ship Research, Vol.17, No.4, December 1973.
7. Tsakonas, S. and Jacobs, W.R., "Propeller Loading Distributions," DL Report 1319, Stevens Institute of Technology, August 1968; J. Ship Research, Vol.13, No.4, December 1969.
8. Jacobs, W.R. and Tsakonas, S., "Propeller-Induced Velocity Field Due to Thickness and Loading Effects; Report SIT-DL-73-1681, Stevens Institute of Technology, July 1973; J. Ship Research, Vol.19, No.1, March 1975.



9. Jacobs, W.R., Mercier, J. and Tsakonas, S., "Theory and Measurements of the Propeller-Induced Vibratory Pressure Field," Report SIT-DL-70-1485, Stevens Institute of Technology, December 1970; *J. Ship Research*, Vol.16, No.2, June 1972.
10. Tsakonas, S., Breslin, J.P. and Miller, M., "Correlation and Application of an Unsteady Flow Theory for Propeller Forces," *Transactions, SNAME*, Vol.75, 1967.
11. Strasberg, M. and Breslin, J.P., "The Frequencies of the Alternating Forces Due to Interactions of Contrarotating Propellers," to be published in *J. Hydronautics*, April 1976.
12. Hecker, R. and McDonald, N.A., "The Effect of Axial Spacing and Diameter on the Powering Performance of Contrarotating Propellers," David Taylor Model Basin Report 1342, February 1960.
13. Miller, M.L., "Experimental Determination of Unsteady Forces on Contrarotating Propellers in Uniform Flow," David W. Taylor Naval Ship Research and Development Center Report SPD-659-01, May 1976.

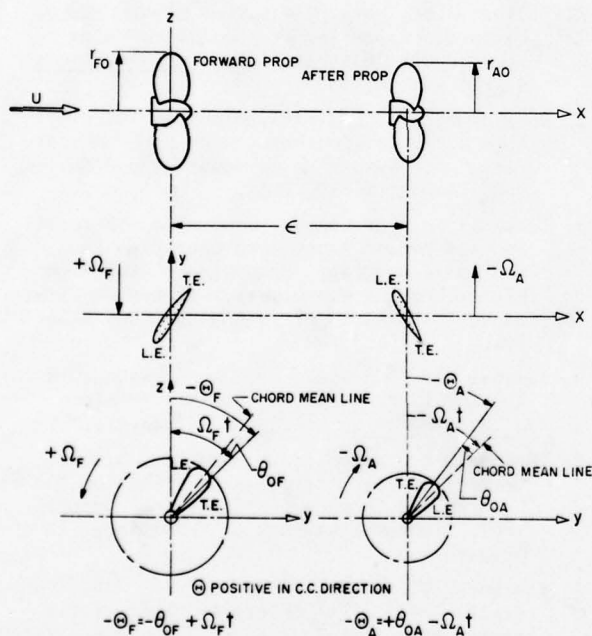


Fig. 1: Counterrotating propeller arrangement - angular coordinates.

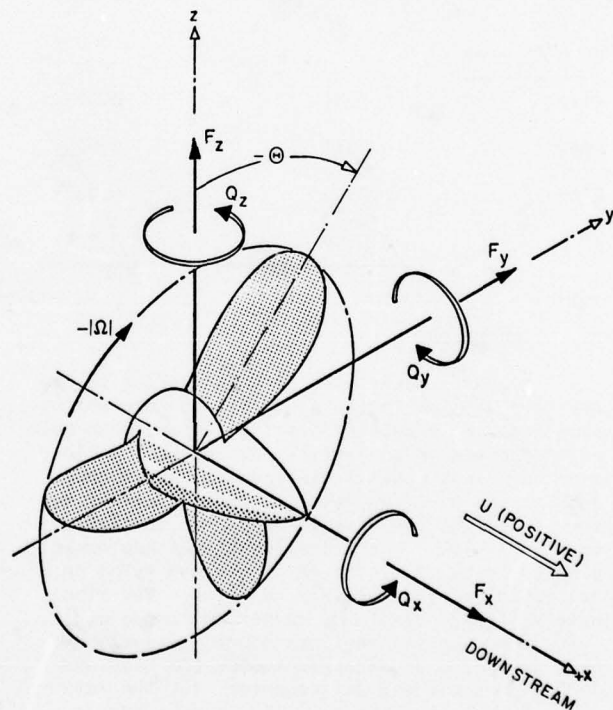


Fig. 2: Resolution of forces and moments.

# VIBRATION EXCITATION FORCES FROM A CAVITATING PROPELLER. MODEL AND FULL SCALE TESTS ON A HIGH SPEED CONTAINER SHIP

C.-A. JOHNSON and O. RUTGERSSON

The Swedish State Shipbuilding Experimental Tank, Göteborg, Sweden

S. OLSSON

AB Götaverken, Göteborg, Sweden

O. BJÖRHEDEN

AB Karlstads Mek Werkstad, Kristinehamn, Sweden

## SYNOPSIS

In connection with the technical trials with the triple screw container ship M/S Nihon measurements of pressure fluctuations and observations of propeller cavitation were carried out. In the present report the results thus obtained are compared with the corresponding results from tests in cavitation tunnel. The comparison also includes some results of theoretical calculations.

The measurements of full scale vibration are analysed and compared with criteria of comfort.

The results of the investigation are summarised at the end of the report.

In an Appendix the different methods used for analysing the measurements of pressure fluctuations are described and compared.

## 1. INTRODUCTION

When planning the technical trials with the triple screw container ship M/S Nihon the idea was raised by the technical staff of the shipowners, the Broström Group, that, as the ship could be regarded as extreme in several respects, it would be of great value to carry out special measurements and registrations with the emphasis on vibration and cavitation. Accordingly the Swedish Ship Research Foundation (SSF) was contacted and an advisory group formed.

It was decided that the following kinds of measurements should be carried out in connection with the technical trials:

Observations of the cavitation patterns on the back side of the center propeller through windows in the stern, including sketching, photographing and high speed filming (to be carried out by AB Karlstads Mekaniska Werkstad (KMW), the manufacturer of the center propeller).

Measurement of the pressure fluctuations caused by the propellers, by fitting transducers in different places of the stern, close to the center propeller (to be carried out by AB Götaverken, builder of the ship through their affiliate company, Öresundsvärvet AB).

Measurement of the vibrations in one point on the 2nd deck at the aft end of the ship and in one point close to one of the pressure transducers (to be carried out by AB Götaverken).

A preliminary analysis of these measurements and observations indicated that the material could be valuable for research purposes and a special project was started for further analysis work, including the following items:

New model tests at the Swedish State Shipbuilding

Experimental Tank (SSPA) in order to get a good basis for correlation studies on cavitation patterns and pressure fluctuations, induced by propellers.

Correlation between model tests, theoretical calculations and full scale measurements as regards cavitation extension and pressure fluctuations on the hull, induced by propellers.

Theoretical response calculations based on finite element technique (to be carried out by Det norske Veritas).

A summary of the most important results of the complete investigation was given in /1/.

In the present report emphasis will be put on the correlation between model tests, theoretical calculations and full scale results as regards cavitation on the center propeller, in particular the influence of cavitation on the pressure fluctuations on the hull, emanating from the propeller. The separation of the influence of the three propellers on the pressure fluctuations is facilitated by the fact that the number of blades is different for the center and wing propellers. As the interest during the tests was concentrated on the center propeller the ship is looked upon, in the present report, as a single screw ship.

The measurements of the pressure fluctuations in the cavitation tunnel were carried out using water of different gas content ratios, resulting in different cavitation patterns. The influence of these differences on the signals obtained on the pressure transducers are discussed in some detail in the present report.

## 2. NOTATION

$C_{nz}$  = single amplitude of pressure fluctuations,  $nz$ th harmonic  
 $D$  = propeller diameter  
 $J$  =  $V_A/nD$  = advance ratio for propeller  
 $J^1$  =  $V_S/nD$  " " " "  
 $K_{pnz}$ ,  $K_p$  =  $2C_{nz}/\rho D^2 n^2$  = non-dimensional amplitude for pressure fluctuations  
 $K_Q$  =  $Q/\rho D^5 n^2$  = torque coefficient  
 $K_T$  =  $T/\rho D^4 n^2$  = thrust coefficient  
 $l$  = profile length  
 $n$  = number of revs  
 $n, j$  = order of harmonics relative to blade frequency  
 $P$  = propeller pitch  
 $P$  = power  
 $p$  = pressure  
 $p_O$  = static pressure in ambient flow  
 $p_v$  = vapor pressure  
 $Q$  = torque  
 $q$  =  $\frac{1}{2} \rho V^2$   
 $R$  =  $D/2$   
 $r$  = radius of propeller section  
 $T$  = thrust  
 $T_A$  = draught of ship, aft  
 $T_F$  = draught of ship, forward  
 $V_A$  = advance velocity of propeller  
 $V_S$  = ship speed  
 $V_{0.7R}$  = inflow velocity to propeller blade section at 0.7R  
 $w$  = local wake  
 $w_Q$  = effective wake from torque identity  
 $w_T$  = effective wake from thrust identity  
 $x$  =  $r/R$   
 $x$  = chordwise coordinate, measured from leading edge of profile  
 $z$  = number of blades  
 $\alpha$  = gas content of water (volume under standard conditions)  
 $\alpha_s$  = gas content of saturated water at atmospheric pressure and a certain temperature (volume under standard conditions)

$\alpha_s^1$  = gas content of saturated water at a certain pressure and temperature (volume under standard conditions)  
 $\rho$  = density of water  
 $\sigma_{VA}$  =  $(p_O - p_v)/\frac{1}{2} \rho V_A^2$  = cavitation number for propeller  
 $\sigma_n$  =  $(p_O - p_v)/\frac{1}{2} \rho D^2 n^2$  = cavitation number for propeller  
 $\sigma_{0.7}$  =  $(p_O - p_v)/\frac{1}{2} \rho V_{0.7}^2$  = cavitation number of propeller  
 $\sigma_i$  =  $(p_O - p_v)/\frac{1}{2} \rho V_A^2$  = inception cavitation number for propeller blade section  
 $\phi_{nz}$  = phase angle of  $nz$ th harmonic  
 $\phi$  = blade position angle

## 3. SHIP AND PROPELLERS

The main dimensions of the ship are

Length between perpendiculars	Lpp=257.60 m
Breadth	B = 32.21 m
Draught fully loaded condition	T = 11.607 m
Deadweight, " " "	34450 tons
Displacement, " " "	57525 m <sup>3</sup>
Depth, moulded to upper deck	23.90 m
" , " " 2nd "	20.96 m

Engines, 3 low speed diesels:

Power, center propeller	28200 BHP
" , wing propellers	2 x 23400 BHP
Nominal No of revs	115 r/m
Design speed, fully loaded	28 knots

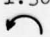

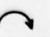
Body plan and contour for the ship are given in Fig 1.

Model scale 1:32.3.

The main data of propellers are given in Table 1.

Table 1

## Main data for propellers

Propeller	Center	Wing
Manufact	KMW	Stone Mang
Type	Control pitch	Fixed pitch
Diameter, m	6.25	5.85
No of blades	5	6
Blade area ratio	0.65	0.70
Pitch ratio, $P/D^x$ )		
0.31 R (hub)	1.10	
0.7 R	1.33	1.42
1.0 R	1.30	
Dir of rotation		 

x) Normal values when 3-props driving



Note. At the model tests a right-handed center propeller was used. As this is the most common arrangement, it will be assumed, when discussing relations between results of measurements obtained on starboard and port side, that a right-handed center propeller was fitted.

#### 4. FULL SCALE TESTS. EQUIPMENT AND TEST CONDITIONS.

Most of the measurements and observations were carried out in connection with the speed trials but not at the runs on the measured mile. The values of the ship speed referred to below were recorded by the log of the ship, which is not a very accurate method. Accurate registration of the number of revs was however carried out in connection with all the measurements. Most of the results in this paper are therefore related to number of revs instead of speed. The weather conditions were good during the trials, the wind speed being 2-8 meters/sec and the sea state 1-3 according to the Douglas scale.

##### 4.1 Observation of cavitation

The windows for observing and photographing the cavitation extension were placed in accordance with Fig 1. The observations were made mainly through the forward window, on which a waterfilled prism was mounted in order to obtain viewing angles suitable for the observation of the back of the blades when in and around top position. For illumination of the propellers two stroboscopes General Radio 1540 were placed in the aft windows. These stroboscopes develop 40 joules at a flash duration of 17  $\mu$ s and at a frequency of 10 Hz. When taking photographs a capacitor circuit was added which amplified the light intensity about three times. For synchronising the stroboscope with the shaft a microswitch was working against cams on the propeller shaft, making it possible to observe or photograph any blade in a position desired.

The photographs were taken by the use of a Hasselblad camera equipped with a wide angle lens. Black and white film was used (Kodak 3X).

##### 4.2 Measurement of pressure fluctuations and vibrations

For the measurement of pressure fluctuations three pressure transducers, Endevco 8503 were used, being connected to three Sanborn carrier frequency amplifiers.

Measurement of vibration was carried out using two vibration transducers CEC4-102-0001 connected to two preamplifiers.

The signals were recorded on a 7 channel magnetic tape recorder, Philips Analog 7 together with a signal for synchronising the stroboscopes. The location of the different transducers is shown in Fig 1.

#### 5. MODEL TESTS. TEST ARRANGEMENTS AND FACILITIES.

##### 5.1 Cavitation tunnel

The cavitation tests were carried out in the large cavitation tunnel of SSPA making it possible to use complete ship models for creating the wake field for the propeller. This tunnel, see /2/, is powered by a 1000 Hp motor and has two interchangeable test sections, one being circular, as the remaining part

of the circuit. The other test section, which is of interest in this connection, is of rectangular shape with a breadth of 2.6 m, a height of 1.5 m and a length of about 10 m. The section is covered by a recess in which the ship model is placed. This model is the one used in the towing tank for the self propulsion tests and it is normally made of paraffin wax.

The vertical position of the model is adjusted in such a way that the waterline, corresponding to the level of the free water surface in the towing tank, is flush with the top of the test section. Individually cut wooden plates are then fitted to simulate the free surface, and the test section and the recess are filled completely with water. So far flat plates have been used and no attempts have been made to simulate the wave system around the hull. The maximum water speed is 6.8 m/sec. An electric motor and a strain gauge dynamometer for measuring thrust and torque for the propeller are placed in a watertight cylinder in the model. In the present case all three propellers were driven by the same motor over a gear. The arrangement made measurement of the thrust on the center propeller possible.

##### 5.2 Measurement of pressure fluctuations on the hull

For the measurements of the pressure fluctuations differential transducers were used, being of the strain gauge type, manufactured by Statham. The maximum range for the transducers, used at the tests in the cavitation tunnel is  $\pm 25$  psi, the natural frequency being about 9 kHz in air. The diameter of the membrane is 1/4" (6.35 mm). One end of the transducer was connected to the atmospheric pressure. Carrier frequency amplifiers, Philips PT 1200, were used, permitting signal frequencies up to 1250 Hz. The signals were recorded on a 14 channel magnetic tape recorder (Honeywell, 5600 C) together with two reference signals, one giving one pulse when Blade 1 is in upright position and one giving 100 pulses on each revolution.

##### 5.3 Model tests. Determination of loading cases for the center propeller

At the speed trials speed was measured using a log as well as Decca registrations. After the sea trials the log was adjusted and the speed values obtained are used without further corrections. However the number of revs is used as reference when determining the loading cases.

The loading cases for the model tests were determined in the way outlined in Table 2 (at the end of the paper), the values of number of revs, power etc referring to the center propeller.

At the speed trials the draught was  $T_F = 7.30$  m,  $T_A = 8.90$  m giving a mean draught of 8.1 m but at the tests referred to in this report  $T_F = 6.65$  m,  $T_A = 10.05$  m giving a mean draught of 8.35 m. According to the model tests this difference in draught and trim should not affect the wake distribution and mean wake very much. Accordingly the values of  $w_{0.5}$  are very similar for the two cases, which in turn indicates that the speed registrations on the calibrated log are reasonably accurate.

On the basis of Table 2 it was decided to use the following values of pitch ratio, advance ratio and effective wake for the center propeller throughout

the model tests:

$$(P/D)_{0.7} = 1.31$$

$$J = 0.96$$

$$w_{QS} = w_{TS} = 0.22$$

Due to the arrangement in the tunnel all three propellers had to have the same number of revs at the model tests. As the difference in number of revs between center and wing propellers was rather small in full scale (see Table 2) and the interference between the propellers is small anyhow (see Fig 3) this was considered to be a reasonable approximation.

Using the value  $H = 5.714$  m,  $H$  being the depth of the centerline of the shaft below the undisturbed water surface, the values of cavitation numbers shown in Table 3 are obtained.

Table 3

Cavitation numbers at model tests

1	2	3	4	5
No revs	Cavitation number			
full scale	$V_A$	$\sigma_{VA}$	$\sigma_n$	$\sigma_{0.7R}$
r/m	m/s			
86	8.60	4.19	3.86	0.671
99	9.90	3.16	2.91	0.506
109	10.90	2.61	2.41	0.418
117	11.70	2.27	2.09	0.363

When setting the water speed and number of revs of the propeller at the cavitation tests thrust identity between results of atmospheric tests in the tunnel and open water tests with the propeller in the towing tank is normally used. All three propellers being driven by the same motor in the present case the accuracy of the thrust measurements could be expected to be lower than usual. Accordingly the value  $w_T = 0.26$  obtained in this way was not used. Instead the relation  $w_w/w_T$  from the corresponding tests in the towing tank was used, giving  $w_T = 0.22$ . The undisturbed water speed was set to 5.5 m/s giving  $V_A = 4.29$  m/s.

#### 5.4 Gas content ratio

It has been found that, in the tunnel configuration used, gas content ratio related to the pressure in the test section  $\alpha/\alpha_s \approx 1$  is suitable for this kind of tests, i.e. the water should be close to saturation. Within the range of static pressures used to set the different cavitation numbers of Table 3 this corresponds to values  $0.25 < \alpha/\alpha_s < 0.4$ . It was therefore decided to use  $\alpha/\alpha_s = 0.25$  as a nominal value but to make investigations also at one higher and one lower gas content,  $\alpha/\alpha_s = 0.40$  and  $\alpha/\alpha_s = 0.07$  respectively.

#### 6. MODEL TESTS. RESULTS OF WAKE MEASUREMENTS.

Results of the wake measurements are given in Figs 2-5. In Fig 2 the results obtained in the cavitation tunnel at two different water speeds (2 and 6 meters/sec) are compared with the corresponding results from the towing tank, obtained at the speed 2.65 meters/sec, the latter corresponding to Froude

similarity. This comparison shows that the agreement between cavitation tunnel and towing tank is good and that the influence of water speed on the results from the tunnel is small.

Some of the results obtained in the cavitation tunnel are shown in Figs 3-5.

Fig 3 shows the results obtained at three different radii with and without driving wing propellers. It is evident from these results that the induced flow from the wing propellers do not disturb the flow to the center propeller.

In Fig 4 some results of the measurements with five-hole pitot tubes are given. They show that the tangential component of the wake is very similar for the two radii investigated.

Fig 5 shows the wake distribution in the plane of the center propeller, measured with driving wing propellers.

#### 7. CAVITATION PATTERNS ON THE CENTER PROPELLER. COMPARISON BETWEEN OBSERVATIONS IN CAVITATION TUNNEL AND ON FULL SCALE SHIP.

In Figs 6-7 the cavitation patterns observed on the full scale propeller at sea and the model propeller in the cavitation tunnel are compared, the latter case being represented by values obtained at a gas content ratio  $\alpha/\alpha_s = 0.26$ . In the model case the maximum as well as the mean (steady) extension of cavitation is marked in the diagrams.

In Fig 8 the radial extension of cavitation (leading edge) is shown for different blade positions and number of revs. Only in the model case a complete picture is shown, as the full scale observations could only be carried out over a limited number of angles.

If the maximum extension of cavitation on the propeller in a certain blade position is used as representative for the model case, the comparison in Figs 6-8 shows that the chordwise extension was somewhat larger in the model case than in full scale. For the radial extension the difference is the other way about. These differences will be further discussed in connection with the results of the theoretical calculations of cavitation extension, see Paragraph 9.1.

A significant difference between model and full scale was however that the extension was more steady in the full scale case i.e. more similar from one revolution to another. This could be concluded from direct observations as well as from the high speed films taken in the two cases. A difference of this kind can be expected to affect the signals of the pressure transducers mounted in the stern above the propeller on the model and ship. This problem will be discussed in some detail in Section 11.

#### 8. PRESSURE FLUCTUATIONS ON THE HULL. COMPARISON BETWEEN MEASUREMENTS IN CAVITATION TUNNEL AND ON FULL SCALE SHIP.

##### 8.1 Position of transducers

The pressure fluctuations were measured in three points located in the same positions on the model and ship, see Fig 1.

## 8.2 Gas content ratio at model tests

In the comparison presented in Figs 9-11 the model results obtained at the gas content ratio  $\alpha_g = 0.26$  in the tunnel, are used. Results from measurements at other gas contents are discussed in Section 11.

## 8.3 Analysis of the signals from the transducers

The results used for the comparison in Figs 9-11 were evaluated by converting the analog tape recordings from the tests to digital form and carrying out harmonic analysis. (see Appendix, Method 1). By doing so also the phase angles between blade position and amplitude maximum could be obtained, as defined by Eq (1).

$$p_{nz} = C_{nz} \cos(nz\omega t - \phi_{nz}) \quad (1)$$

where

$p_{nz}$  = instantaneous value of the  $n$ th harmonic of the pressure signal

$C_{nz}$  = suction peak of the  $n$ th harmonic of the pressure signal

$\phi_{nz}$  = phase angle

$z$  = number of blades

$n$  = integer ( $n = 1, 2$  and  $3$  in the present report).

Thus a value of  $\phi_{nz} = 0$  means that the suction peak occurs when one blade is in upright position. Positive values of  $\phi_{nz}$  mean that the suction peak occurs after one blade has passed the upright position.

## 8.4 Results of the comparison

In Figs 9-11 the amplitudes and phase angles of the first and second harmonics of the pressure fluctuations are shown at different number of revs for the three different transducer positions of Fig 1.

As regards the amplitude of the first harmonic the agreement between model and full scale can be regarded as very good for all transducers. It may be noticed that, at higher speeds, when cavitation is important, the amplitudes are larger for the transducer on the starboard side than for the corresponding transducer on the port side, and that this difference is larger in the model case than in full scale. The main reason for this is probably that most of the volume change of the cavity occurs on the starboard side which is evident from Fig 8. Thus the distance between the dynamic parts of the cavity and the transducer on the port side is larger than the corresponding distance on the starboard side. Further the hull might have a shielding effect on the port transducer.

The amplitudes of the second harmonic were, in general, smaller at the model tests than in full scale, when evaluated in this way. One of the main reasons for this seems to be that the variation of the phase angles around their mean values was considerably larger at the model tests than in full scale. It is well known that such a modulation mainly affects the higher harmonics. This argument is further discussed in Section 11, where it is also shown that the difference between model and full scale can be reduced, if the signals are analysed in another way.

Regarding the phase angles it has to be emphasised that the comparison is only relative, as the exact position of the pulse for measuring the number of revs was not known in the full scale case. As values of the phase angles are necessary for the discussion in Section 11, it was decided to put, arbitrarily,  $\phi_{nz, \text{full}} = \phi_{nz, \text{model}}$  for the starboard transducer at 100 rpm, the gas content ratio being  $\alpha_g = 0.26$  in the model case, see Fig 11. By doing so the change in difference between model and full scale when changing number of revs, order of harmonics, transducer position and gas content ratio at the model tests could be determined. It is evident from the diagrams of Figs 9-11 that the change of the phase angle when changing number of revs, transducer position and order of harmonics is very similar in model and full scale.

## 9. CAVITATION PATTERNS AND PRESSURE FLUCTUATIONS. COMPARISON BETWEEN THEORETICAL CALCULATIONS AND EXPERIMENT.

### 9.1 Cavitation patterns

Using a method which is a development of the one described in /3/ the extension of sheet cavitation over the blades in different blade positions was calculated for the highest number of revs run i.e. 117 r/m. As shown in Fig 12 the character of the patterns thus obtained for different blade positions is similar to that of the patterns observed at the model tests. The patterns observed in full scale have a somewhat different appearance, being characterised by larger radial and smaller chordwise extension than in the model case. Differences in this direction were found in two of the three cases for which model-full scale comparisons were carried out and published earlier by SSPA, i.e. those published in /4/. In the third case /5-6/ no such tendency could be found, the reason probably being that, in that case, the leading edge radii of the model propeller were larger relative to the length of the blade sections than those of the full scale propeller, which may compensate a tendency of this kind.

The two main reasons why differences between cavitation patterns in model and full scale could be expected are

- a) The wake distributions are different
- b) Also if the pressure distribution along a blade section is assumed to be the same in model and full scale, the pressure-time relation is different.

Results of investigations on the influence of the wake distribution have been published e.g. in /7-8/ but no definite answer can yet be given on the magnitude of this influence on the cavitation patterns and pressure fluctuations.

The method used in the present paper for calculating the inception and extension of cavitation includes a hypothesis on how the pressure-time relation influences the inception of cavitation /3/. The following equation is used for the calculation of the radial extension of cavitation

$$T \cdot \sqrt{(p_v - p_{x \min})} = C_i \quad (2)$$



which, for a certain blade section, corresponds to

$$\frac{1 \cdot (x/l)_n \cdot \sqrt{-(\sigma_i + C_{pmin})q}}{V} = C_i \quad (3)$$

where

$l$  = profile length

$T$  = time that the pressure is below vapor pressure

$(x/l)_n$  = part of profile where the pressure is below vapor pressure

$V$  = inflow velocity to profile

$\sigma_i = (p_o - p_v)/q$  = inception cavitation number based on velocity  $V$

$C_{pmin} = -(p_o - p_{xmin})/q$

$p_{xmin}$  = minimum pressure at cavitation inception

$C_i$  = empirical constant

Using Eq(3) the inception cavitation number can be calculated for the different blade sections, giving curves of the kind shown in Figs 16 and 17 for determination of the radial extension of cavitation for a certain experimental cavitation number.

Using the same constant  $C_i$  as for the model case the values of the radial extension of cavitation (leading edge) for the full scale case were calculated and compared with those observed on the ship, see Fig 13. The results shown in Fig 13 indicate that very nearly the same difference between model and full scale is obtained by the calculation as that observed at the tests, indicating that the pressure-time relation is an important scale effect factor.

Using an analogous formula for calculating the chordwise extension of cavitation /3/ the differences shown in Fig 14 are calculated for the blade positions, 15 and 45 degrees. Also in this case the calculated difference between model and full scale is of about the same magnitude as that observed at the experiments.

## 9.2 Pressure fluctuations on the hull

Based on the calculated extension of cavitation, shown in Figs 12-14, the amplitudes and phase angles of the pressure fluctuations of blade frequency and twice blade frequency were calculated by the use of SSPA program 159, see /6/. The calculations were carried out for the three points shown in Fig 1, for which results are available from measurements in full scale and in cavitation tunnel.

The results of the comparison between calculation and experiment are shown in Fig 15. The results indicate good agreement between calculated and measured amplitudes for the points B (starboard) and D (centerline).

For point C (port) the calculations give too high values, compared to experiment. Thus the difference between starboard and port sides seems to be underestimated by the calculations. A possible explanation of this result might be the following:

When carrying out the calculations, the presence of the hull is represented by the wake distribution only. The amplitudes calculated apply to a field-point in free flow. To obtain the corresponding values in a point of the stern these values are multiplied by a "solid boundary factor"  $s$ . The normal value (applying rigorously only to a flat plate having infinite extension), which was used at these calculations, is  $s = 2$ . Probably this value applies only to the side of the ship where the main part of the blowing up and collapse of the cavity occurs (starboard side for a right-handed propeller). For the port side the hull may have a shielding effect on the amplitudes (most likely manifested as a circulation around the stern), giving lower values for the factor  $s$ . These phenomena which, at present, limit the range of application of the theoretical methods, have to be further investigated.

A further feature of interest in this connection is illustrated by the diagrams in Fig 16 and 17, showing values of the cavitation number of inception for different blade positions calculated for the present case and for a tanker propeller /9/.

As mentioned above the cavitation extension observed in the cavitation tunnel is very unstable in the present case, see Fig 8, while in the tanker case the extension was very stable, characterised by very little variation between the extension from one revolution to another.

A possible explanation for this difference between the behaviour of the cavitation patterns in the two cases is that, as is evident from Fig 16, the cavitation number for inception is, in the present case, very nearly the same for the blade sections  $0.6R - 0.8R$  at the blade positions  $0^\circ - 30^\circ$ . Thus a relatively small change of the inflow velocity will cause rather large changes of the cavitation number of inception within this region. As it is known that the instantaneous flow velocities in a wake can vary appreciably with time this offers a plausible explanation for the variations of the cavitation extension shown in Fig 8. In the tanker case the corresponding variations of the inflow velocities cause only relatively small variations of the extension of cavitation. Thus the degree of instability of the signals can be expected to vary from one propeller to another, important factors being radial pitch distribution /9, 10/, blade form, pitch ratio etc.

What remains to be explained is why the cavitation extension is more stable in full scale than in model scale. One circumstance to be mentioned is that the wake is narrower in full scale due to thinner boundary layer on the ship. As the significant velocity variations are related to the boundary layer thickness, this should mean smaller variations in full scale. Further the relation between the blade frequency and the frequency of the predominant velocity variations should be different in model and full scale. This problem can be further investigated by making registrations of the instantaneous velocities in the wake in model and full scale.

## 10. MEASUREMENTS OF VIBRATION ON THE SHIP

Measurement of vibration of the ship was carried out in several points in the deck house aft in a way which is standard for the ships delivered by Götaverken. For two points the values were however registered on a tape recorder, one of the points being close to one of the transducers used for measurement of pressure fluctuations (the one on the

port side) and one being located on upper deck, extreme aft, see Fig 1.

On both transducers small vibrations were recorded, indicating that the recordings of the pressure fluctuations can be used without corrections.

The recordings of the transducer located on the upper deck were analysed in a way similar to the recordings of the pressure fluctuations. Some results thus obtained are given in Fig 18 and they will be discussed somewhat in detail below.

Two kinds of amplitudes are given in Fig 18.

- a) Mean values of the amplitudes of blade frequency, twice, three times and four times blade frequency harmonics.
- b) Mean and maximum values of the raw signals or (peak to peak values)  $\cdot 0.5$ . The mean values are taken over about ten revs and the maximum value is occurring once during this time.

The results are compared to some of the limits proposed by ISO /11/. It should be noted that the ISO limits are given as accelerations in /11/. However when transformed into vibration velocities, as in Fig 18, they give values independent of frequency for frequencies above 8 Hz for vertical vibrations and 2 Hz for horizontal vibrations.

The following comments can be made to the results presented in Fig 18.

The difference between the mean values of the first harmonic and the mean values of the raw signal is rather large compared to what is the case for the pressure fluctuations. Further the relative magnitude of the higher harmonics compared to the first harmonic is larger than for the pressure fluctuations.

The main reason for this difference is most likely that the vibration is caused by the total force on the stern, integrated from local pressures having different phase angles relative to the blades. Because of this the signals can be expected to contain more higher harmonics and thus the difference between the largest harmonics and the peak to peak values is rather large.

It is evident from the diagram in Fig 18 that the degree of unpleasantness indicated by a comparison of the vibration levels with the different limits proposed by ISO is highly dependent on how the vibration signals are analysed.

It is pointed out in the ISO recommendations that the limits proposed apply strictly to sinusoidal vibrations of one frequency only. The results should be obtained from 1/3 octave band analysis, the center frequency being used as reference. This corresponds closely to the harmonics given in Fig 18, at least for blade frequency. For non-sinusoidal vibration, random or broad band, it is assumed that, in respect of human tolerance, no significant interactions occur between vibration effects at different frequencies. This view is in contrast to /12/ in which it is recommended, in principle, that the different harmonics should be added together. In this particular case this gives a result which very closely corresponds to the peak to peak values, see Fig 18.

The peak to peak values are very often used as reference when vibration levels are discussed for ships delivered by the Swedish shipyards.

Thus two ways of comparing results of vibration measurements with the ISO limits exist, which are not in agreement with what is proposed in the ISO draft recommendations /11/. This may create confusion when different ships, delivered by different shipyards, are compared from vibration point of view.

## 11. FURTHER COMPARISONS BETWEEN RESULTS OBTAINED AT SEA AND IN CAVITATION TUNNEL

### 11.1 General

In Section 8 a comparison was made between pressure fluctuations in three different points of the hull, registered in cavitation tunnel and at sea. The comparison was based on the mean values of the blade frequency and twice blade frequency harmonics over a large number of revolutions, the model case being represented by results obtained at the gas content  $\alpha/\alpha_s = 0.26$  of the tunnel water. It was commented that the agreement between model and full scale is very good for the blade frequency harmonics but that the model tests give too low amplitudes for the twice blade frequency harmonics.

In connection with the discussion of the results of the theoretical calculations of the cavitation extension in Paragraph 9.1, it was shown that the time variations of the inflow velocity to the propeller known to exist in a wake of this kind can be expected to cause variations of the cavitation extension from one revolution to another, which are rather large in the present case, compared to many other cases. As a plausible explanation why the cavitation extension is more stable in the full scale case than at the cavitation tunnel tests was mentioned that the time variations of the velocities in the wake can be expected to be smaller in full scale and the relation between the characteristic frequency of the variations and the blade frequency different in the two cases.

The instabilities mentioned above are most likely one of the main reasons for the instabilities of the signals of the pressure transducers. The latter disturbances can be of two kinds:

- a) The fact that the cavitation inception starts at different blade positions for different revolutions can be expected mainly to cause a phase angle modulation.
- b) The fact that the growth and disappearance of the cavity for some revolutions is completed faster than for others causes mainly a modulation of the amplitudes of the signal.

Another factor which can be expected to influence the degree of instability of the cavitation patterns at the cavitation tunnel tests is the gas content of the water. To try to clarify how such instabilities affect the comparison with full scale it was decided to vary the gas content within rather wide limits at the model tests included in the present investigation. Accordingly tests were carried out at three gas content ratios  $\alpha/\alpha_s = 0.07, 0.26$  and  $0.40$ .

When being used for the present purpose it is

important that the signals are properly analysed. To try to accomplish this several methods have been tried at SSPA over the years and the results compared. A description of these methods and some comparative results when applying them in the present case are given in the Appendix and in Fig 25.

It was found that, for the purpose of the discussion below, the best method is the one referred to as No 1 in the Appendix.

When using this method the analog signals are digitised and both maximum and mean values determined for the different harmonics, as well as for the unfiltered signals.

Some results obtained when applying this method to the signals obtained from the transducer located in the centerline of the ship and model are shown in Figs 19-24.

In Figs 19-21 the signals registered by the centerline transducer on the ship at three different number of revs and in the cavitation tunnel at the corresponding cavitation numbers are shown. The model tests are represented by results obtained at three different gas content ratios of the water i.e.  $\alpha/\alpha_s = 0.07, 0.26$  and  $0.40$ . The signals shown can be characterised as trains of pulses, the periodicity being 5 pulses per revolution. The shape of the pulses is rather similar but variations in amplitudes and phase angles occur from one revolution to another.

In Figs 19-21 also the amplitude spectra, obtained by the analog analysis method, Method 4 (see Appendix) are shown.

The results of an analysis of the signals by the use of the digital "harmonic sampling" technique (Method 1) appear from the diagrams in Figs 22-24. Two investigations are covered by the diagrams, which will be discussed separately, i.e. the influence of gas content at the model tests and the comparison between signals obtained in cavitation tunnel and on the full scale ship.

#### 11.2 Influence of the gas content of the water at the model tests

The variation of the gas content at the cavitation tunnel tests covered the rather wide range  $0.07 < \alpha/\alpha_s < 0.40$ , the higher value being the practical limit at these low cavitation numbers when considering visibility of the water and possibilities of maintaining constant pressure in the test section. In spite of this the maximum extension of cavitation on the propeller blades at different blade positions was very nearly the same for all three air contents used, the main difference between the different tests being that, the lower the gas content, the more unstable the extension of cavitation. Accordingly the pressure signals obtained at different air contents are of different character, see Figs 19-21. There are however in no case any abrupt changes of the amplitude level from one revolution to another of the kind reported in /10/ for propellers having unloaded blade tips.

The following effects of gas content can be detected in the diagrams in Figs 22-24.

The amplitudes of the unfiltered signals show very little variation with gas content. Only for the lowest propeller speed and the lowest gas content

the amplitudes are reduced considerably. It is interesting to note that the unfiltered signal registered in the cavitation tunnel is rather insensitive not only to changes of the gas content but also to changes of the cavitation number.

The amplitudes of the blade frequency harmonic increase considerably with increasing gas content, except for  $\alpha/\alpha_s = 0.4$  and the lowest cavitation number, (Fig 24) where a slight reduction of the amplitude occurs. The latter may be caused by a damping effect of the free bubbles in the test section.

The influence of gas content on the magnitude and modulations of the phase angle is rather small.

For the second and third harmonics applies that the mean values of the amplitudes as well as the phase angles are rather similar for different gas contents.

The phase angle modulations, which are much larger for the higher harmonics than at blade frequency, are however somewhat reduced when the gas content is increased. Further the modulations are reduced when the cavitation number is reduced.

It is known that phase angle modulation reduces the mean value of the amplitude /13/. This can be observed if the mean values for the "demodulated" and the original signals are compared ("demodulated" means in this case that the effect of the phase angle modulation has been eliminated in the way outlined in the Appendix). For the first harmonic this effect is very small. For the second and third harmonics the mean values of the "demodulated" signal are however considerably larger than the mean values of the original signal. For the lowest gas content this difference is most pronounced, see Figs 22 and 23.

Summarising, the influence of gas content on the phase angle modulation is not very large. For extremely low gas content the amplitudes of the first harmonic are however considerably smaller than at the higher gas content ratios.

#### 11.3 Comparison between full scale and cavitation tunnel

When making this comparison the model case is represented by the values obtained at the gas content  $\alpha/\alpha_s = 0.26$ .

As pointed out above the mean values and modulation of the unfiltered signal from the cavitation tunnel changes very little with cavitation number, while in full scale they are both increased considerably when the propeller speed is increased. This makes the unfiltered signal rather unsuitable for full scale - cavitation tunnel comparisons.

The mean values of the amplitudes of the first harmonic measured in full scale and in the cavitation tunnel agree well for all propeller speeds. The modulations and mean values of the 5 largest pulses are however somewhat higher in the cavitation tunnel. As mentioned in Paragraph 8.4, no direct comparison can be made between the phase angles in model and full scale. It may however be noticed that the change of the mean value with propeller speed is very similar in model and full scale. The phase angle modulations are somewhat higher in the model case.



The mean values of the amplitudes of the second and third harmonics are appreciably smaller in the model case than in full scale. The main reason for this is that the phase angle modulations are much larger in the cavitation tunnel than in full scale. This effect can be illustrated in three ways:

- a) the standard deviation for the phase angles is much larger in the cavitation tunnel than in full scale.
- b) the difference between the mean values of the original signal and the "demodulated" signal is larger in the cavitation tunnel.
- c) in the spectra of Figs 19-21 the phase angle modulations cause a transport of energy from the harmonics to adjacent frequencies. This effect is small in full scale but in the cavitation tunnel case it is very difficult to detect the second and third harmonics due to this effect.

The amplitude modulation is slightly larger in the cavitation tunnel than in full scale.

An interesting difference between cavitation tunnel and full scale is that, in the latter case, the maximum values of the first, second and third harmonics occur at the same revolution, which is not the case in the cavitation tunnel, where high values of the first harmonic correspond to low values of the higher harmonics, see Figs 22-24.

Summarising, the results of Figs 22-24 indicate that, when taking mean values in a conventional way, good agreement between model and full scale is obtained for the amplitudes of the first harmonic in the present case, while too low values are obtained for the higher harmonics in the cavitation tunnel.

For the higher harmonics better agreement is obtained if the values of the "demodulated" signal are used, but the 5 of 100 largest values will probably give even better agreement in the present case. This discrepancy is primarily due to the effect of the phase angle modulation, which is mainly affecting higher harmonics. The phase angle modulation can be expected to be smaller in cases with more stable cavitation (like the one discussed in Paragraph 9.2). Thus, before making any proposals on the best way of comparing the amplitudes of higher harmonics an investigation of the kind discussed here has to be carried out for such a case.

## 12 SUMMARY AND CONCLUSIONS

The results of the investigations reported in the present paper can be summarised as follows:

The observations of the cavitation patterns carried out on the center propeller show that the maximum extension is rather similar in model and full scale, the radial extension being somewhat larger in full scale and the chordwise extension somewhat larger in the model case, see Figs 6-8. A significant difference was however that the extension was more steady in the full scale case.

Results of theoretical calculations of the cavitation extension show good agreement with experiment for the model case, see Fig 12. When making the corresponding calculations for the full scale case, using the unchanged wake distribution as a basis,

similar differences in extension relative to model scale are obtained as those observed at the experiments, see Figs 13-14. This indicates that the different time-pressure relation is an important factor for explaining the differences in extension between model and full scale mentioned above.

The results of the theoretical calculations further indicate that one reason why the cavitation patterns are unstable in the present case, in contrast to many other cases, is that the cavitation number of inception is very nearly the same for several blade sections around the upright position, see Figs 16-17. Thus fluctuations of the inflow velocity with time will cause unusually large fluctuations of the cavitation extension in the present case. The main reason why the fluctuations of extension are considerably larger in the model case than in full scale is most likely that the fluctuations of inflow velocity can be expected to be smaller in the latter case because of smaller boundary layer thickness. This factor should be further investigated by comparative measurements of the instantaneous velocities in model and full scale wakes of ships of different types.

Regarding experimental values of the pressure fluctuations emanating from the propeller good agreement is obtained between model and full scale for the mean values of the amplitudes of the blade frequency harmonics, see Figs 9-11. For the higher harmonics and the raw (unfiltered) signal lower values are however obtained in model than in full scale.

The fluctuations of the phase angles around their mean values are considerably larger in the model than in the full scale case, the main reason most likely being the corresponding fluctuations of the cavitation extension discussed above, see Figs 22-24. The magnitude of these fluctuations is very little dependent on gas content ratio.

The differences between the amplitudes obtained in model and full scale for the higher harmonics are most likely caused by the large fluctuations of the phase angle at the model tests. Accordingly better agreement is obtained in the present case, if the higher harmonics are represented by amplitudes for a "demodulated" signal and probably even better agreement achieved if the 5 of 100 largest values are used (regarding the procedure used for calculating the "demodulated" signal see the Appendix). The fluctuations of the phase angles can be expected to be smaller in cases having more stable cavitation. Thus, before making any proposals on the best way of comparing the amplitudes of higher harmonics an investigation of the kind discussed in the present report has to be carried out for such a case.

Results of theoretical calculations of the amplitudes of the pressure fluctuations show good agreement with experiment for two of the three points investigated, see Fig 15. The reason for the discrepancy obtained in the third point is most likely a lack of generality of the "solid boundary factor" used at the calculations.

It is evident from the diagram in Fig 18 that the degree of unpleasantness obtained when comparing the vibration levels with the different limits proposed by ISO is highly dependent on how the vibration signals are analysed. Several ways of carrying out this comparison exist, which may create confu-

sion when different ships are compared from vibration point of view.

A comparison between five different methods of analysing the signals of the transducers for measuring pressure fluctuations shows that the mean values of the amplitudes obtained are very similar, see Fig 25. The amount of other important information obtained differs however from one method to another.

### 13. ACKNOWLEDGEMENTS

The investigation was carried out in close cooperation between the initiator Broströms Tekniska AB, the Swedish State Shipbuilding Experimental Tank, AB Götaverken, AB Karlstads Mek Werkstad, Det norske Veritas and the Swedish Ship Research Foundation.

The work was financed by Broström's Technical Company, the Defence Material Administration, Det norske Veritas, Eriksbergs Mekaniska Verkstad, Götaverken, Karlstads Mekaniska Verkstad, Kockums Mekaniska Verkstad, Salénrederierna, Uddevallavarvet, the Swedish Ship Research Foundation and by a contribution from the Swedish Board for Technical Development. Further the comparative tests in the cavitation tunnel at different gas contents were carried out and analysed within the current research program of the Swedish State Shipbuilding Experimental Tank.

The project was made possible by the kind permission of the shipowners, the Swedish East Asia Company, to use their ship for the investigation.

The authors would like to express their sincere thanks to all those members of the staffs of the above-mentioned establishments and companies who have taken part in the investigation and contributed to the analysis of the material.

### 14. REFERENCES

- /1/ Ekholm, S, Björheden, O, Johnsson, C-A, Olsson, S, Mugaas, B: "Cavitation Studies in Full Scale, Model Tests and Calculation Correlation". Swedish Ship Research Foundation. Report No 113, 1975.
- /2/ Edstrand, H: "The Cavitation Laboratory of the Swedish State Shipbuilding Experimental Tank". SSPA Circular No 32, June 1974.
- /3/ Johnsson, C-A: "Correlation of Predictions and Full Scale Observations of Propeller Cavitation". International Shipbuilding Progress, Vol 20, No 226, June 1973.
- /4/ Lindgren, H, Johnsson, C-A: "Studies of Cavitation Patterns on Tanker Ship Propellers". Symposium on Testing Techniques in Ship Cavitation Research May-June 1967. Skipsmodelltanken. Publ No 99, Trondheim December 1967.
- /5/ Lindgren, H, Johnsson, C-A, Simonsson, E: "Propulsion and Cavitation Investigation on 230 000 tons dwt Tankers - Full Scale and Model Experiments". Trans Royal Institution of Naval Architects, Vol 114, 1972, pp 449-464.
- /6/ Johnsson, C-A, Söntvedt, T: "Propeller Excitation and Response of 230 000 tdw Tankers". Proc 9th ONR Symposium on Naval Hydrodynamics Paris,

August 1972. See also SSPA Publ No 70 and Report No 79 from Det norske Veritas.

- /7/ Dyne, G: "A Study of the Scale Effect on Wake, Propeller Cavitation and Vibratory Pressure at Hull of Two Tanker Models". Trans Soc Nav Arch and Marine Eng Vol 82, 1974.
- /8/ Huse, E: "Cavitation Induced Hull Pressures, Some Recent Developments of Model Testing Techniques". Norwegian Maritime Research Vol 3, No 2, 1975.
- /9/ Johnsson, C-A: "Propeller Design Aspects of High Powered Ships". Symposium on High Powered Propulsion of Large Ships, Wageningen Dec 1974.
- /10/ Oosterveld, M W C, Verdonk, J, van der Kooij, J, van Oossanen, P: "Some Propeller Cavitation and Excitation Considerations for Large Tankers". West European Conference on Marine Technology, The Hague 14-17 May 1974.
- /11/ "Guide for the Evaluation of Human Exposure to Whole-Body Vibrations". Draft International Standard ISO/DIS 2631, 1972.
- /12/ Proceedings of the 1967 International Ship Structures Congress, Oslo, Sept 1967.
- /13/ Bark, G: "Introductory Remarks on Modulation in Propeller Cavitation". SSPA Memorandum, Dec 1975.
- /14/ Beauchamp, K G: "Signal Processing Using Analog and Digital Techniques". George Allen and Unwin Ltd, London 1973.
- /15/ Burgess, J C: "On Digital Spectrum Analysis of Periodic Signals". Journal of Acoust Soc America, Vol 58, No 3, Sept 1975.
- /16/ Cooley, J W, Lewis, P A W, Welch, P D: "The Fast Fourier Transform Algorithm and its Applications". IBM Research Paper R C 1743, February 9, 1967.
- /17/ "Real Time Signal Processing in the Frequency Domain". Federal Scientific Corp Monograph No 3, March 1973.
- /18/ Olsson, S, Gustavsson, L: "Measurement and Evaluation of Propeller Induced Pressure Excitations on the Hull Plating and Vibration on the Same Plating and the Aft Ship". The Swedish Ship Research Foundation Report 5513:3, 1974.

### APPENDIX

#### PRESSURE FLUCTUATIONS AND VIBRATIONS MEASURING TECHNIQUE AND SIGNAL PROCESSING

##### Control signals

When registering the signals at the model tests three different control signals were recorded on separate channels of the tape recorder to make it possible to determine the phase angles of the pressure fluctuations relative to the blade position accurately. Together with the pressure signals two trains of pulses were recorded, one train containing one pulse per revolution for the indication of the position of blade No 1 and another contain-

ing 100 pulses per revolution. Finally a starting pulse was recorded on a third channel to ensure that the analysis always starts at the same station on the tape.

At the full scale tests only one pulse was used, which, due to practical difficulties, had to be taken from the motor and not from the propeller. Thus it was only possible to evaluate relative values of the phase angles in full scale.

#### Analysis method No 1. Digital harmonic analysis

This method involves analog to digital conversion and harmonic analysis for determining the amplitudes and phase angles of the different harmonics. Further the peak to peak values are determined. Maximum and mean values and deviation is determined for all variables.

#### Analog to digital conversion

The analog to digital conversion is carried out in a computer and monitored by the control signals described above. The digital signal thus obtained is related to the angular position of blade No 1 instead of being based on time as the analog signal. The digitising process starts at the first upright position of blade No 1 (after the start pulse has passed) and is continued for every 3.6th degree of rotation until 100 revolutions has passed (10 000 digital values). By the digitising program it is also checked that there will always be 100 digital values between two successive revolution pulses. In this way no extra values will disturb the analysis and no values will be dropped.

The propeller speed is usually about 20-30 r/s giving a sampling frequency of about 2-3 kHz. Since the carrier frequency bridge is cutting off the frequency range at about 1250 Hz aliasing is avoided without lowpass filtering at the analog to digital conversion /14/.

#### "Harmonic sampling"

When developing an analysing method a choice has to be made between high resolution and increased information about the modulation of the signal. If high resolution is desired it is necessary to analyse rather long sequences and the information about the modulation is lost but if the modulation is important, it is necessary to analyse short sequences with a low resolution as a result. Since the modulation is regarded to be an important parameter in this analysis the shortest possible sequence is chosen, i.e. the analysis is carried out for each pressure pulse in the signal. This implies however that:

- the signal is nearly periodic. Otherwise a "leakage" effect will move energy from the first harmonic to the higher harmonics /15/.
- the background noise level is not too high and disturbances from gears etc can be neglected. Otherwise the harmonics will be changed when the frequencies of the disturbances fall within the bandwidth for respective harmonic.

In most cases when a pressure fluctuation originating from a cavitating propeller is analysed the conditions a and b are however fulfilled.

In the procedure used by SSPA the frequency ana-

lysis is carried out pulse by pulse using an ordinary Fourier series transform. For a pulse, index  $i$  ( $i = 1...z$ ) of the revolution, index  $k$  ( $k = 1...100$ ) the following formulas apply:

$$A_{kij} = \frac{1}{\pi} \int_0^{2\pi} P_{ki}(z \cdot \phi) \cos(j \cdot z \cdot \phi) d\phi$$

$$B_{kij} = \frac{1}{\pi} \int_0^{2\pi} P_{ki}(z \cdot \phi) \sin(j \cdot z \cdot \phi) d\phi$$

where  $j = 1...5$  (first to fifth harmonics)

The integrals are evaluated by Simpson's formula using the digitised values of the pressure signal.

The A and B values are stored in the line, index  $j$  and the column, index  $k$  in the matrix, index  $i$ , meaning that the pulses originating from the different blades are kept separate in the analysis. Thus if there are differences between the blades they can be traced in the analysis.

Next the order of the columns are changed with respect to  $C_{kil} = \sqrt{A_{kil}^2 + B_{kil}^2}$ , so that the pulses with the highest first order amplitudes are moved to the left in the matrices and the pulses with the lowest values of  $C_{kil}$  are moved to the right.

Finally the mean values of the amplitudes

$$C_{Nij} = \sqrt{\left(\frac{\sum_{k=1}^N A_{kij}}{N}\right)^2 + \left(\frac{\sum_{k=1}^N B_{kij}}{N}\right)^2}, j = 1...5$$

and the phase angles

$$\phi_{Nij} = \arctan \left( \frac{\sum_{k=1}^N B_{kij}}{\sum_{k=1}^N A_{kij}} \right), j = 1...5$$

are calculated for the first 5, 10, 25, 50, 75 and 100 columns of each matrix. Also the maximum and minimum values of the amplitudes are given together with the standard deviation for each harmonic:

$$\sigma_{ij} = \sqrt{\frac{1}{99} \sum_{k=1}^{100} (C_{kij} - C_{100ij})^2}$$

$C_{100ij}$  being the mean value of all the 100 columns.

In the normal case, in which all blades of the propeller cavitate, the final mean values  $C_{Ni}$  and  $\phi_{Ni}$  can be calculated by summation over  $i$  ( $1...z$ ).

It is interesting to note that the mean values  $C_{100ij}$ , as calculated above, are identically the same as those obtained by the widely used technique of periodic sampling where a mean signal is calculated from the digitised signal and the frequency analysis carried out at the end of the processing /16/. The main disadvantage when using the latter technique is of course that no information is obtained on the dispersion of the amplitudes and



phase angles around the mean values. This is a serious limitation as the dispersion of the phase angles affects the mean values of the amplitudes in the direction that too low values of the mean amplitudes are obtained compared with the amplitudes of the individual pulses. The larger the dispersion, the larger this effect and to investigate its magnitude in different cases also a mean value of the amplitudes of a "demodulated" signal is calculated by the program. This means that the mean value of the 100 columns is calculated without considering the modulations of the phase angles, i.e.

$$C_{Dij} = \frac{1}{100} \sum_{k=1}^{100} \sqrt{A^2_{kij} + B^2_{kij}} ; 1 \dots 5$$

The difference between  $C_{100ij}$  and  $C_{Dij}$  is a measure of the phase angle modulation of the harmonic  $j$  in the signal.

Peak to peak values

Sometimes it is interesting to know not only the amplitudes of the different harmonics but also the peak to peak value of the unfiltered signal. When using the procedure discussed here, these values are obtained from the digitised signal in the way outlined below.

First the suction and pressure peaks are located by comparing successive digital values. Since the peak values should be calculated for the pulses and not for possible disturbances the program has to check the distance between the suction and pressure peaks.

If the angular distance between a suction and pressure peak is larger than  $\frac{\pi}{2z}$  and the angle between two successive pressure peaks larger than  $\frac{\pi}{2}$  then the pressure difference between the suction and pressure peak is accepted as a peak to peak value. When the whole signal has been traversed, the peak to peak values are sorted and presented in a similar way as the results from the "harmonic sampling".

#### Analysis Method No 2. Analog harmonic analysis

Information about the amplitude modulation can also be obtained by the use of analog equipment. At SSPA standard instruments manufactured by Brüel & Kjaer are used for this purpose. By a slave filter (type 2020) combined with a control-unit (type 1901) monitored by the signal "one pulse per revolution" mentioned above the different harmonics (one at a time) of the pressure fluctuations are followed by the filter frequency. By an amplifier (type 2607) the maximum and minimum values are then estimated and also the mean values for different integration intervals. Corresponding values can also be estimated for the unfiltered signal.

#### Analysis Method No 3. Loop Oscilloscope

This simple method was the first one used when evaluating the results of measurements of pressure fluctuations in the large cavitation tunnel at SSPA. When using this method the signal is registered by a loop oscilloscope on self developing photographic paper and mean and maximum values of the unfiltered signal can be directly estimated and the first harmonic obtained by passing the signal through a bandpass filter tuned on the blade fre-

quency and the filtered signal too is registered on the paper. In the present comparison only the unfiltered signal has been considered. The galvanometer for this signal has a natural frequency of 1650 Hz and a damping factor of 0.7.

#### Analysis Method No 4. Real-time spectrum analysis

Such an analysis is carried out at SSPA using a timecompression analyser. Federal Scientific Corp UA-500, see /17/. This analyser gives the complete amplitude spectrum over the whole frequency range in contrast to methods 1-3 which focus on multiples of the blade frequency.

Using this method the analog input signal is digitised by the analyser and stored in a memory. While the memory is being updated with new data, its content is read out repeatedly at a very high rate and converted back into an analog signal. The speeded-up high frequency replica of the input signal is then analysed, using a wide filter which is being rapidly stepped 500 times for each spectrum. This transformation of the signal to a much higher frequency range gives an amplitude spectrum with high resolution in a much shorter time than when using a conventional sweeping analyser. With this analyser it is also possible to get a mean spectrum averaged from up to 1024 spectra.

The spectra shown in Figs 19-21 are averaged from 8 spectra which give about the same length (100 propeller revolutions) of the analysed signal as is obtained by the digital SSPA method. The resolution for these spectra is about 0.1 Hz for the full scale cases and about 1 Hz for the spectra from the cavitation tunnel.

#### Analysis Method No 5. FFT spectrum analysis

This procedure /18/ has been developed at the Götaverken shipyard and is normally used when analysing results of measurements of pressure fluctuations on technical trials with new built ships. Like Method No 4 it gives the power or amplitude spectrum for the whole frequency range. This method is however digital, and the calculations are carried out using the fast-Fourier-transform algorithm /16/. The method is very general and frequency range, sampling rate and cut off frequencies can be chosen in a rather arbitrary way. To reduce the "leakage" a cosine taper weighting function is used.

In this special case the frequency range 0 to 50 Hz was used, the sampling rate was 200 Hz and the low-pass filter cut off frequency about 100 Hz. This gave a power spectrum which represents the mean values of 12 spectra calculated for totally 61 seconds measuring time (about 100 revolutions) with a resolution of 0.098 Hz. The amplitude spectrum was then accomplished by successively calculating the area below the power spectrum within a 0.39 Hz wide band sweeping over the frequency range.

#### Comparison of the methods

The methods described above have been applied to the pressure signals shown in Fig 21. The estimated amplitudes for the signals measured in full scale and at a gas content of 0.26 in the cavitation tunnel are compared in Fig 25. The procedures are summarized in Table 4.

Table 4.

Method No	Specification
1 "Digital harmonic analysis"	Mean values, standard deviations and maximum values calculated for the first to third harmonics and for the unfiltered signal.  Analysed sequence 100 revolutions for cavitation tunnel and 10 revolutions for full scale. The bandwidth for each analysis about 7 Hz for full scale signal and about 100 Hz for signal from cavitation tunnel. Estimate of mean values means reduction of the bandwidth to 0.7 Hz resp 1 Hz.
2 "Analog harmonic analysis"	Mean values of first to third harmonics and unfiltered signal estimated with 10 s integration time. Variations of harmonics measured with instrument set at 0.1 s integration time and 10 Hz bandwidth. For unfiltered signals also maximum values given.
3 "Loop oscilloscope"	Mean and maximum values estimated for unfiltered signals. About 10 revolutions analysed.
4 "Real time spectrum analysis"	Mean values of 8 spectra estimated both in full scale and cavitation tunnel. The analysed signal length corresponds to about 100 revolutions. Bandwidth about 0.1 Hz in full scale and 1 Hz in cavitation tunnel.
5 "FFT spectrum analysis"	Mean values of 12 spectra of full scale signal. Analysed signal length of about 1 minute corresponds to about 100 revolutions. Bandwidth about 0.4 Hz.

Similar comparisons as in Fig 25 have been made for all the signals in Figs 19-21 and the results shown in Fig 25 are typical.

Unfiltered signal. The agreement between Methods 1 and 3 is rather good for the signal measured in full scale as well as for the cavitation tunnel signal. By Method 2 the same mean value as the other methods is estimated for the cavitation tunnel signal. Otherwise Method 2 seems however to give lower values than Methods 1 and 3 for the unfiltered signal.

First to third harmonics. The methods compared seem to give about the same values for the mean values of all three harmonics.

Methods 4 and 5 give almost exactly the same values. As a matter of fact, the whole spectra of the two methods are almost identical.

It is interesting to note that by Method 2 a deviation is estimated that agrees rather well with the standard deviation. For the signal measured in the cavitation tunnel the deviations are however unsymmetrical with respect to the mean values. This

means that the amplitudes of this signal are not distributed in a Gaussian way. For the full scale signal the deviations are more symmetrical. As pointed out earlier the background noise will disturb the estimation of the modulations. Because of this it is important to estimate the whole spectrum as in Figs 19-21. In a cavitation tunnel it is also advisable to estimate the background noise by running the propeller shaft without propeller. In this investigation the level of the noise is well below the signal level for the frequencies of interest. The "noise" between the harmonics in the spectra of Figs 19-21 is believed to originate mainly from the amplitude and phase angle modulations of the signals.

The discussions above show that the digital Method No 1 seems to give realistic estimates of mean values, standard deviations and maximum values for the amplitudes of the harmonics and the peak to peak values of the pressure fluctuations. Only the results of Method 1 have been used in the discussions in the present paper.

Table 2

Propeller loadings, center propeller

1	2	3	4	5	6	7	8	9
No of revs N	Power P	(P/D) <sub>0.7</sub>	K <sub>Q</sub>	J <sub>QS</sub>	Speed V <sub>s</sub>	J'	w <sub>QS</sub>	No of revs wing props
r/m	hp				knots			r/m
Speed trials								
94.1	13780	1.264	0.0418	0.949	23.88 <sup>*)</sup>	1.253	0.243	95.7
94.2	"	"	0.0427	"	23.22 <sup>*)</sup>	1.217	0.220	95.7
119.1	29077	1.31	0.0442	0.978	30.26 <sup>*)</sup>	1.255	0.221	121.8
119.0	28811	1.325	0.0443	0.996	29.14 <sup>*)</sup>	1.209	0.176	122.0
Photographing								
117	28565	1.31	0.0461	0.959	29.3 <sup>**)</sup>	1.237	0.225	120
109	23148	"	0.0462	0.958	27.0 <sup>**)</sup>	1.223	0.217	112
99	17435	"	0.0465	0.956	24.7 <sup>**)</sup>	1.232	0.224	103
86	11623	"	0.0473	0.946	20.9 <sup>**)</sup>	1.200	0.212	88

$$\textcircled{2} P = 0.985 \cdot P_{\text{meas}}$$

$$\textcircled{4} K_Q = \frac{11.937 \cdot P}{\rho D^5 (n/60)^3}$$

$$\textcircled{5} \text{ From open water curve}$$

$$\textcircled{6} \text{ *) Decca registrations } \text{ **) Adjusted log } \textcircled{7} J' = V_s / nD$$

$$\textcircled{8} w_{QS} = 1 - J_{QS} / J'$$

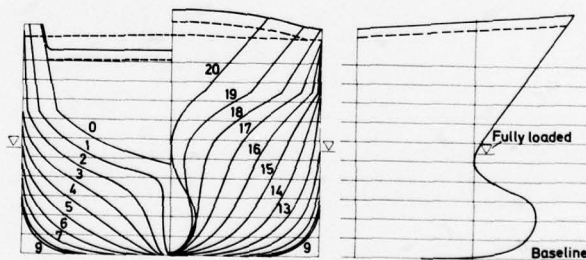
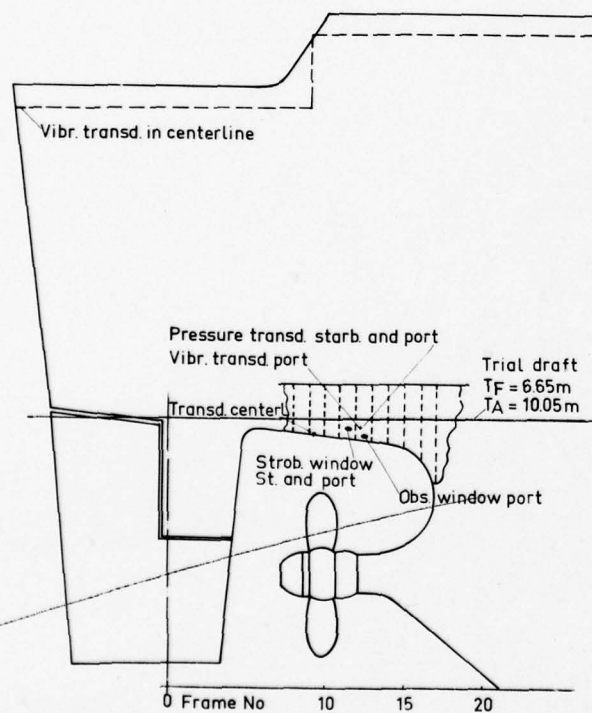


Fig. 1: Body plan and contour of ship. Location of observation windows and transducers for measurement of pressure fluctuations and vibration.



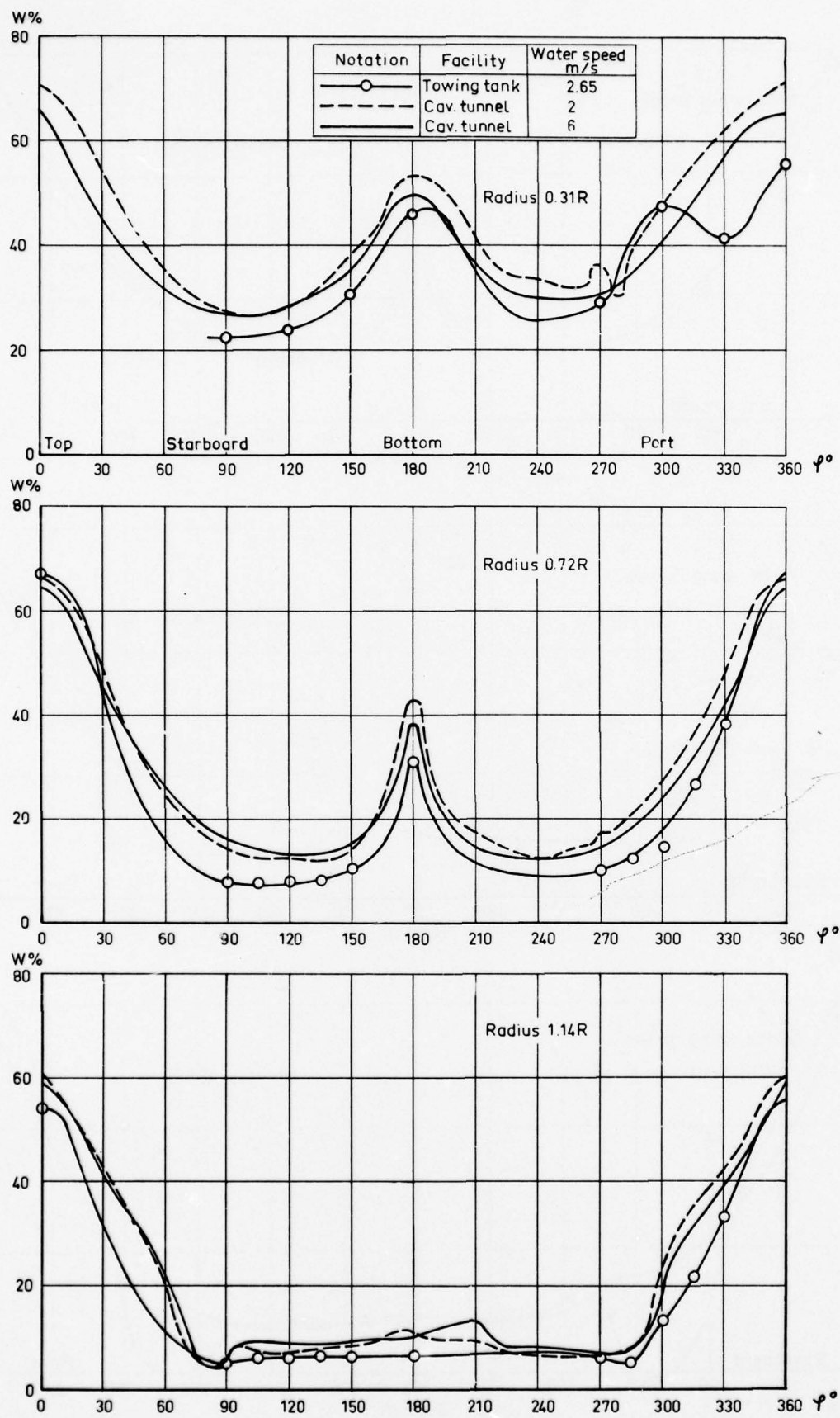


Fig. 2: Peripheral wake distribution for the centre propeller on the radii 0.31 R, 0.72 R and 1.14 R. Rotating wing propellers.

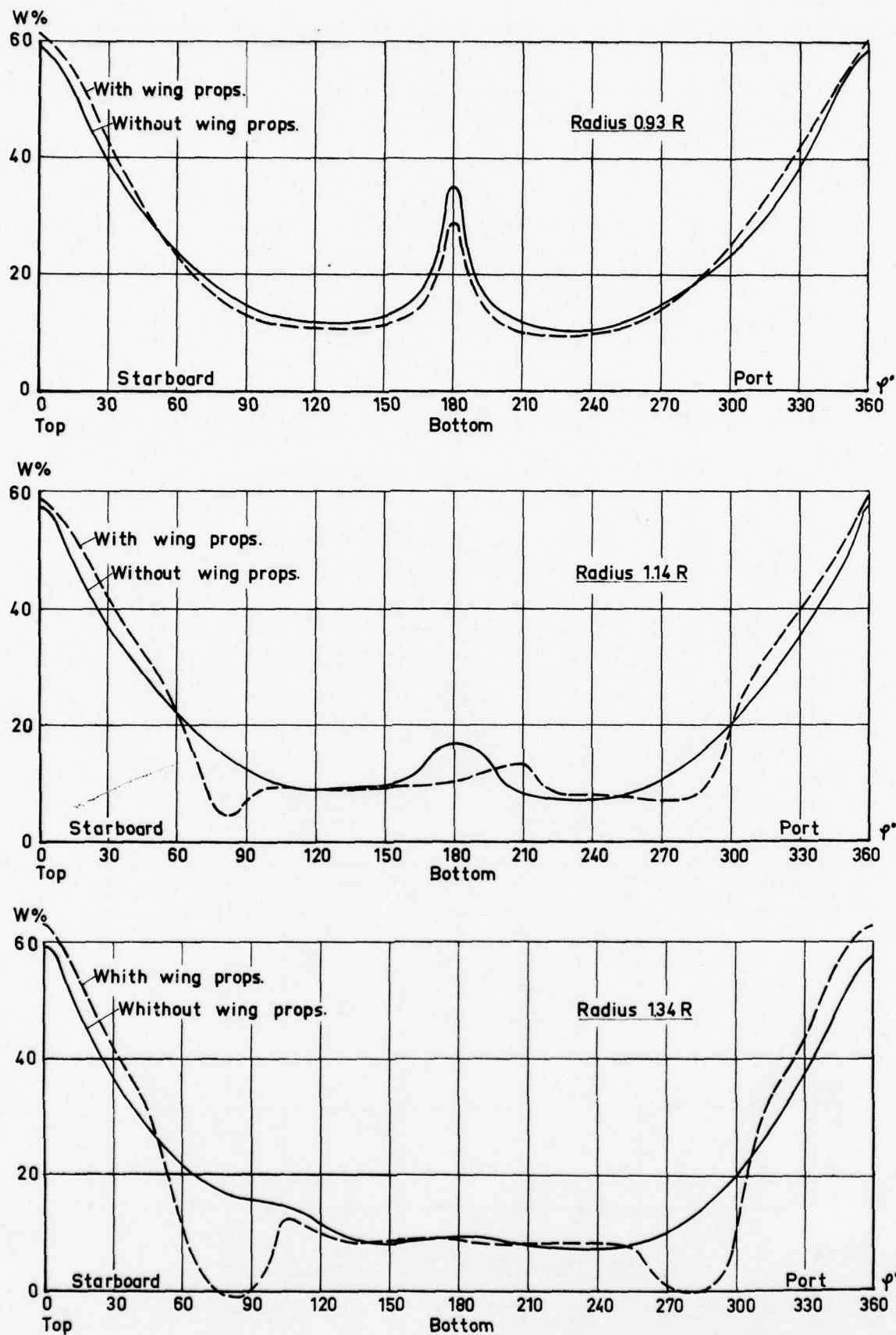


Fig. 3: Influence of wing propellers on wake distribution for centre propeller. Cavitation tunnel. Water speed, 6 metres/sec.

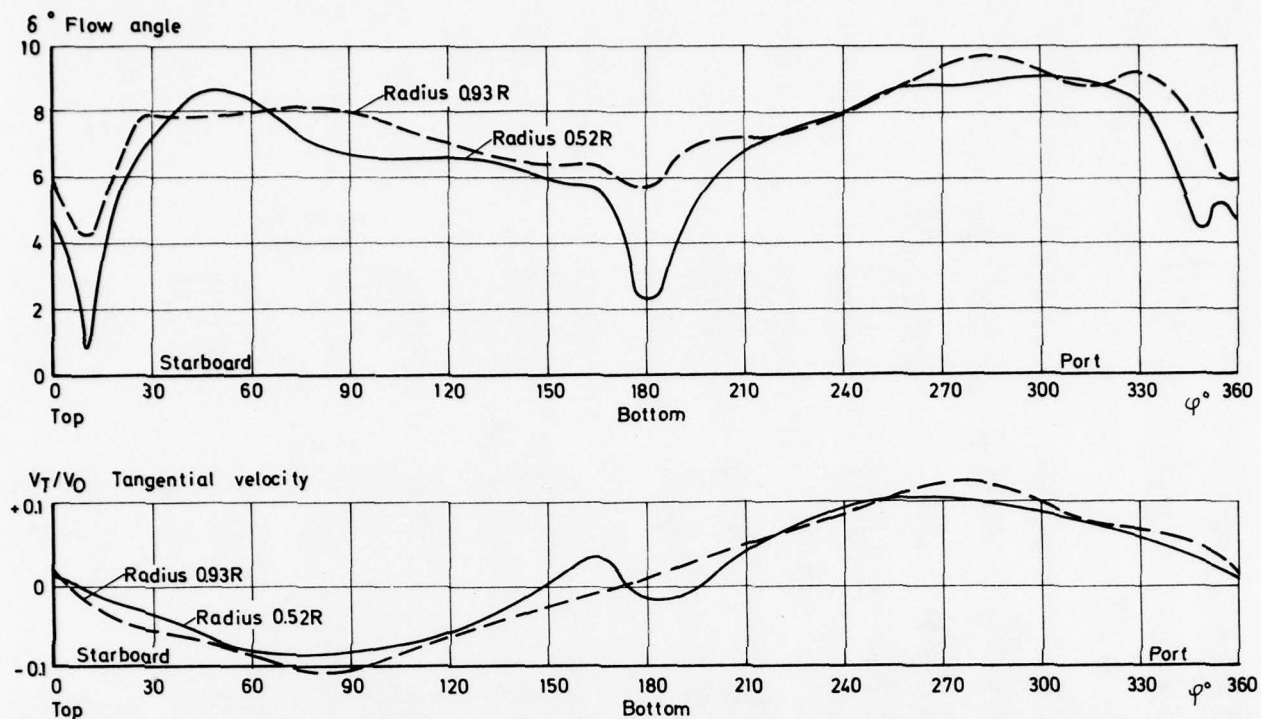


Fig. 4: Results of measurements with five-hole pitot tubes in cavitation tunnel. Water speed, 6 metres/sec.

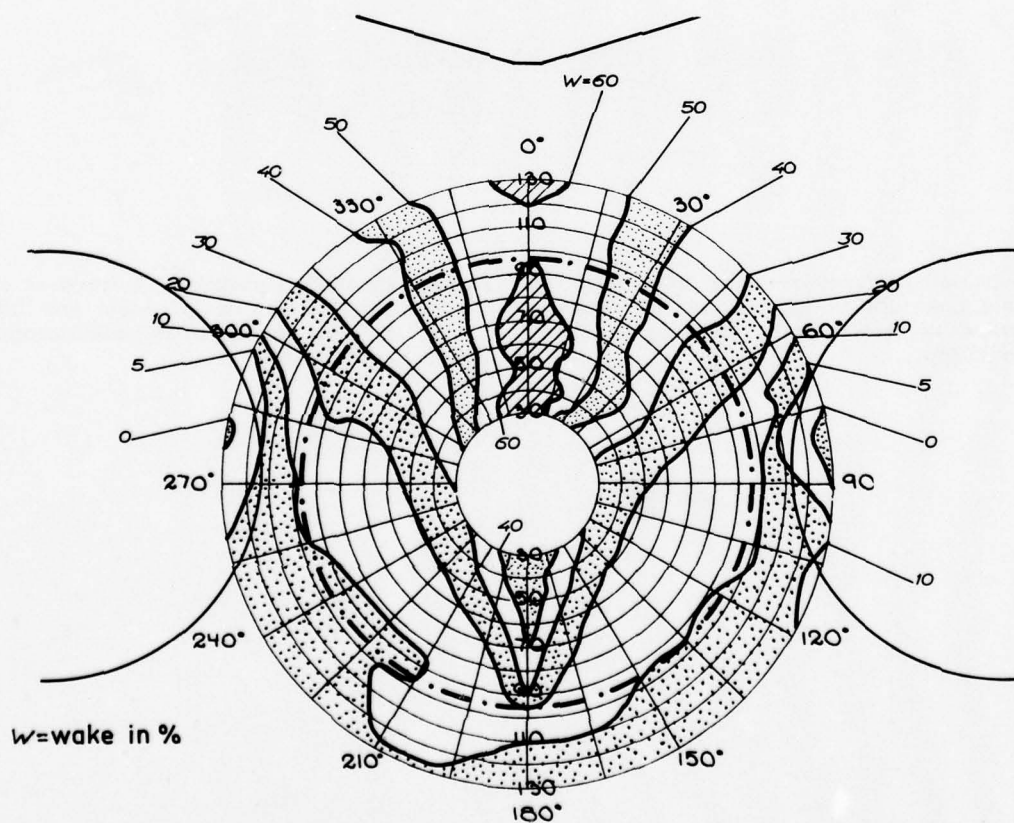
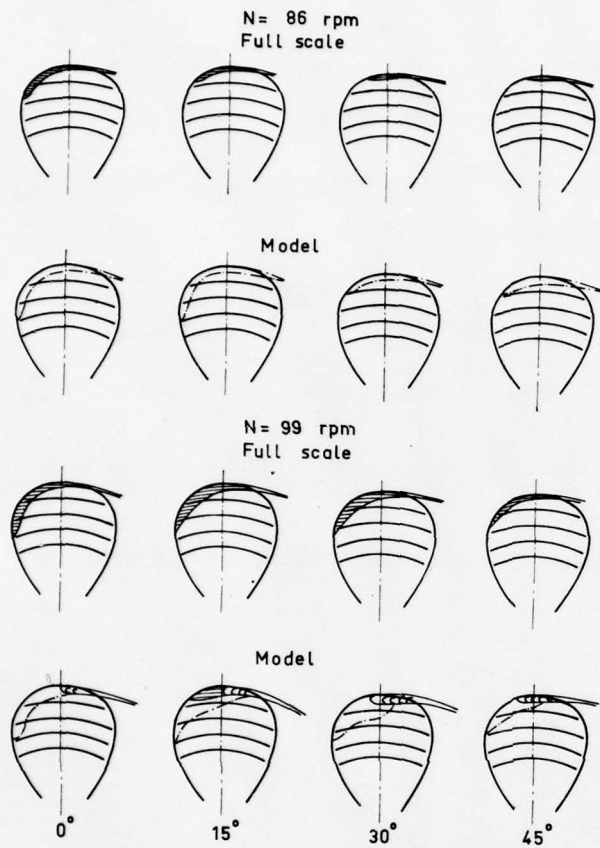
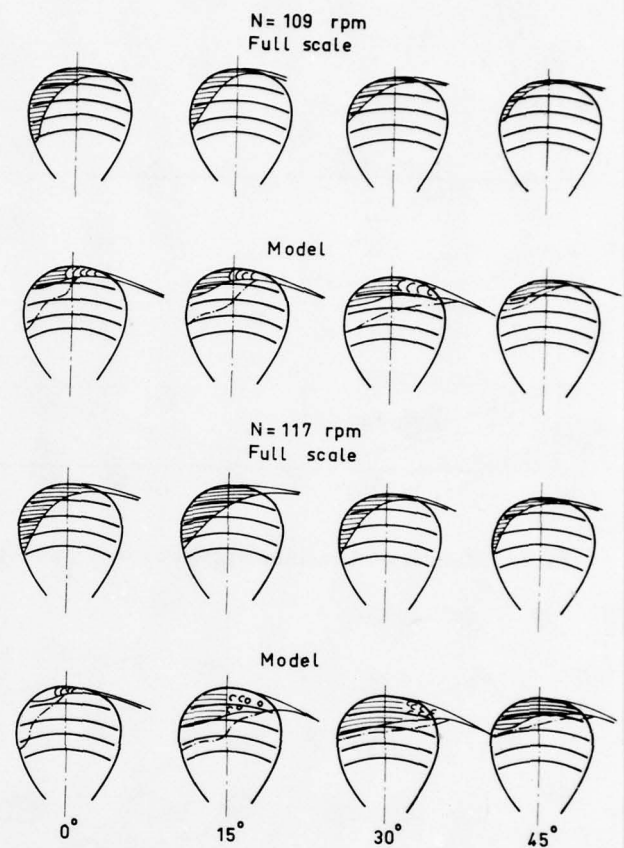


Fig. 5: Wake distribution in the plane of centre propeller measured in cavitation tunnel with working wing propellers. Water speed, 6 metres/sec.

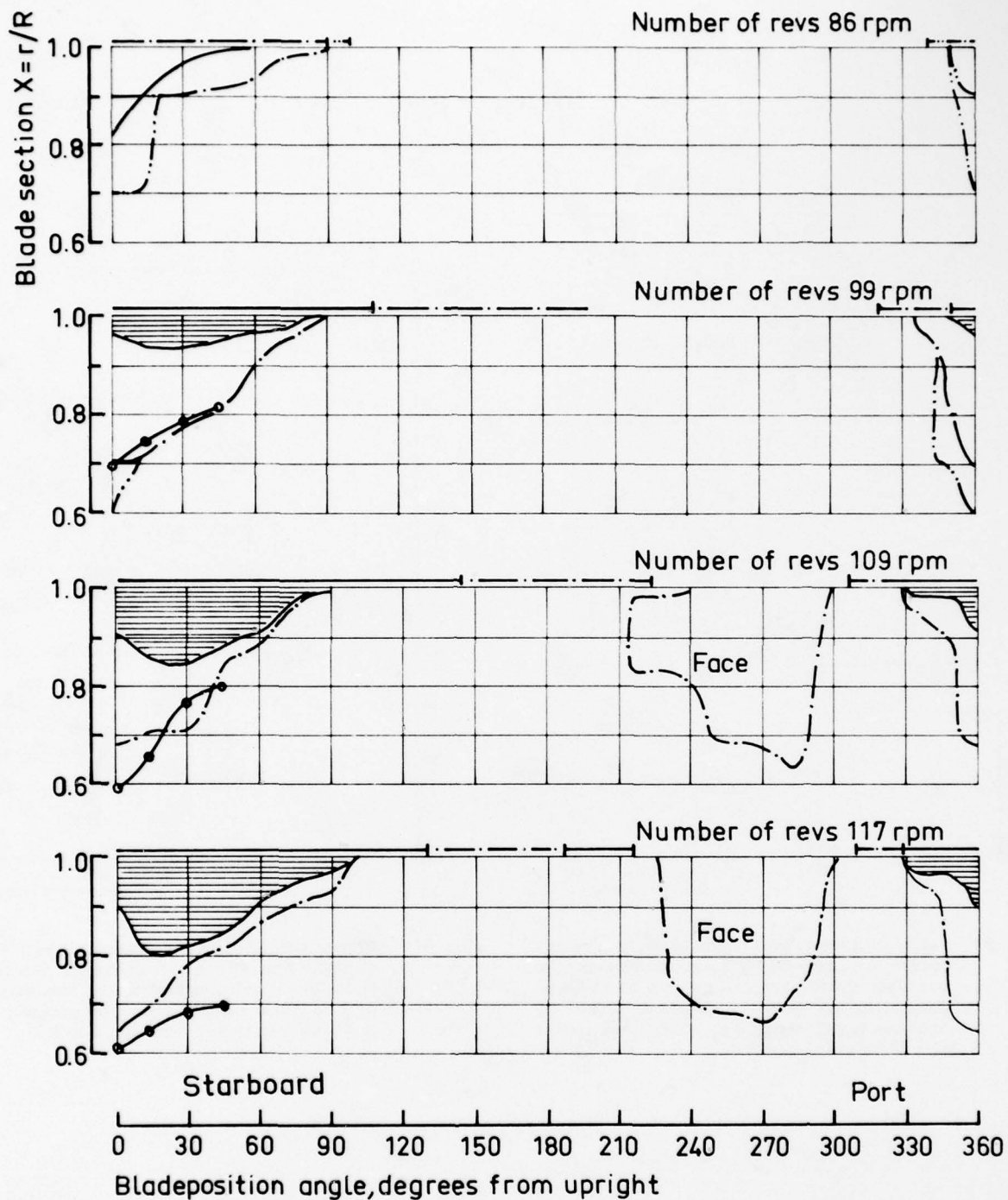




**Fig. 6:** Cavitation patterns observed at different blade positions in model and full scale. Number of revs of full scale propeller 86 and 99 rpm.



**Fig. 7:** Cavitation patterns observed at different blade positions in model and full scale. Number of revs of full scale propeller 109 and 117 rpm.



- Model tests, tip vortex, continuous
- - - Model tests, tip vortex, intermittent
- Model tests sheet cavitation, steady extension
- Model tests sheet cavitation, max extension
- Full scale, sheet cavitation

Fig. 8: Radial extension of cavitation in model and full scale. Different number of revs.

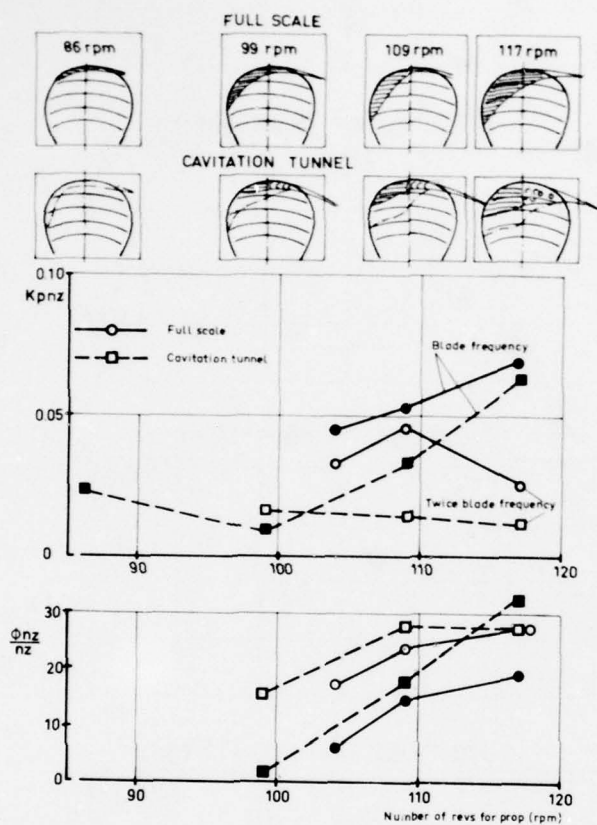


Fig. 9: Blade frequency and twice blade frequency harmonics of pressure fluctuations in model and full scale. Transducer on port side. Cavitation patterns in blade position 15 degrees. Note, comparison for phase angles is only relative, see 8.4.

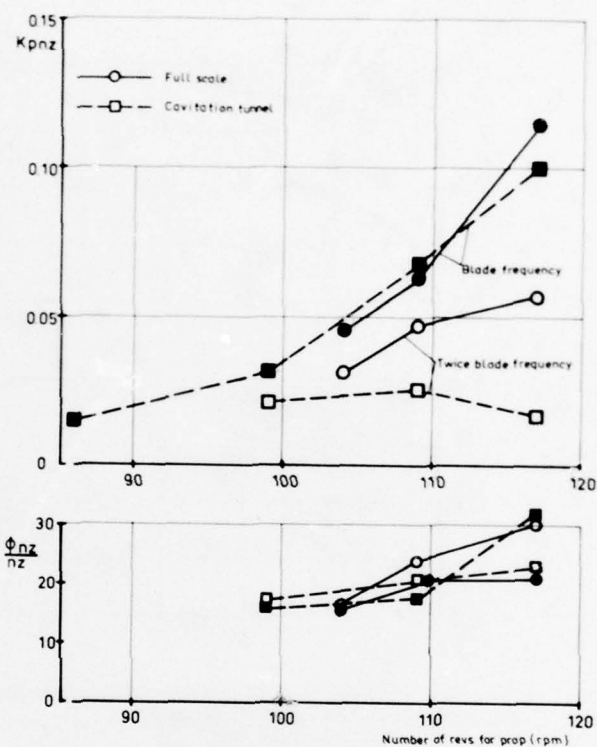


Fig. 10: Blade frequency and twice blade frequency harmonics of pressure fluctuations in model and full scale. Transducer in ship centre line. Note, comparison for phase angles is only relative, see 8.4.



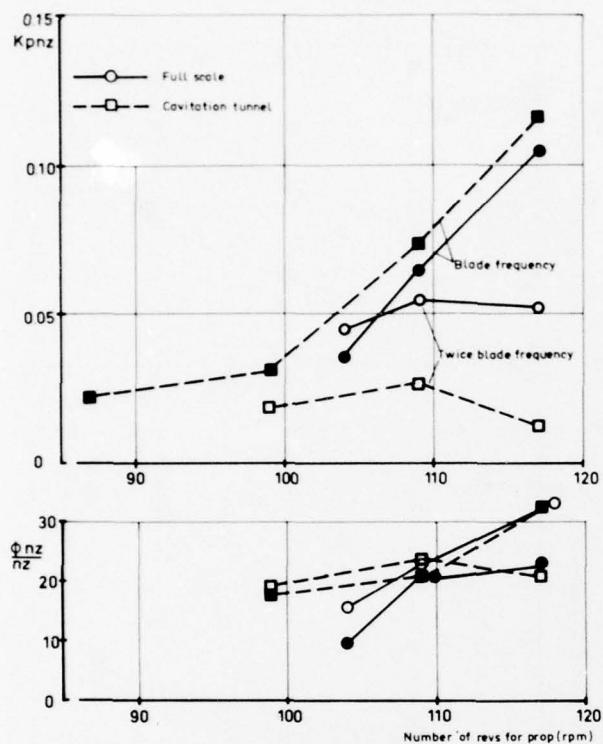


Fig. 11: Blade frequency and twice blade frequency harmonics of pressure fluctuations in model and full scale. Transducer on starboard side. Note, comparison for phase angles is only relative, see 8.4.

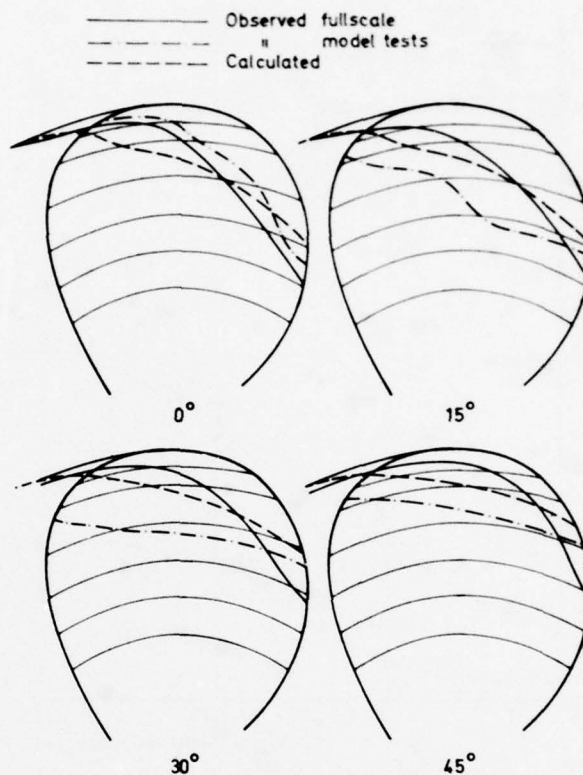


Fig. 12: Extension of sheet cavitation (back side) at different blade positions. Comparison between theoretical calculations and experiment. Number of revs, 117 rpm. Starboard side.

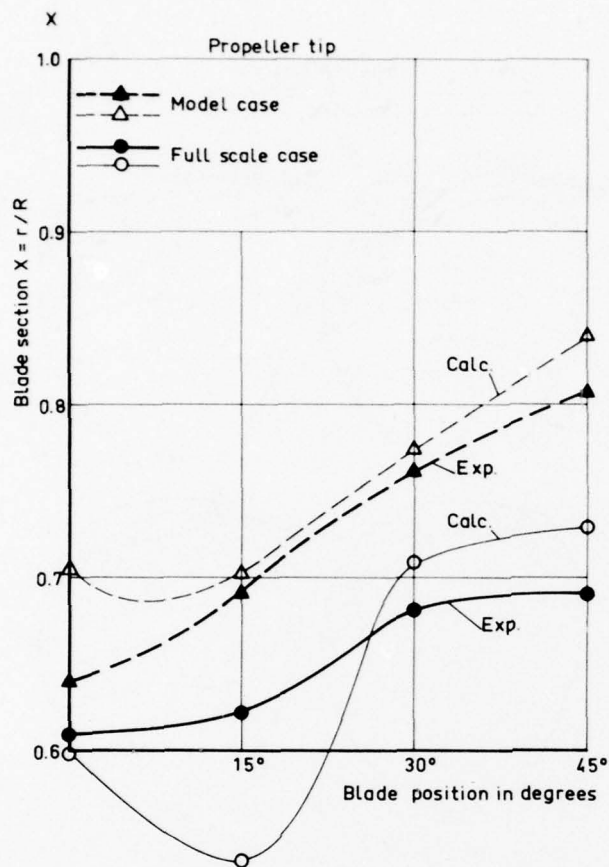


Fig. 13: Comparison between calculated and observed radial extensions of sheet cavitation in model and full scale case. Number of revs, 117 rpm. Starboard side.

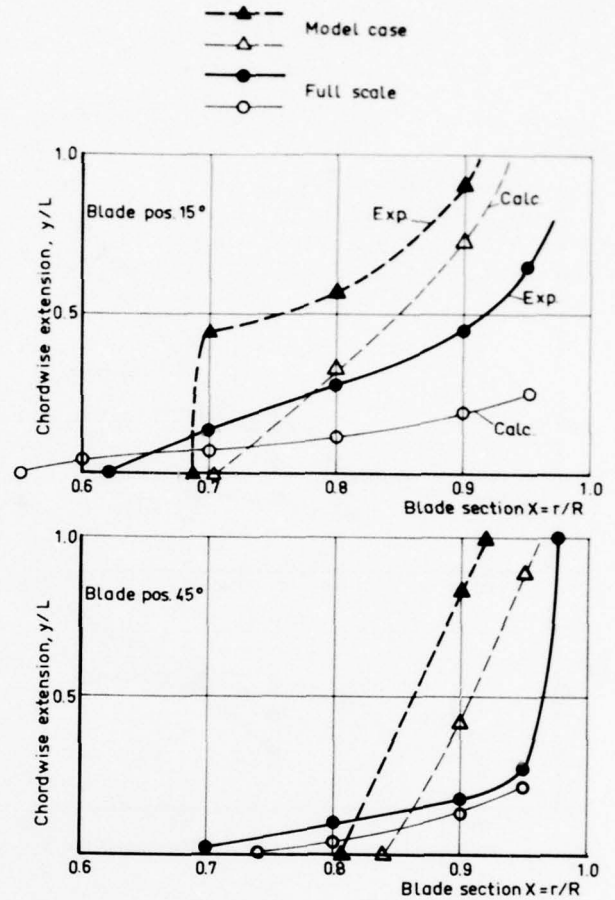
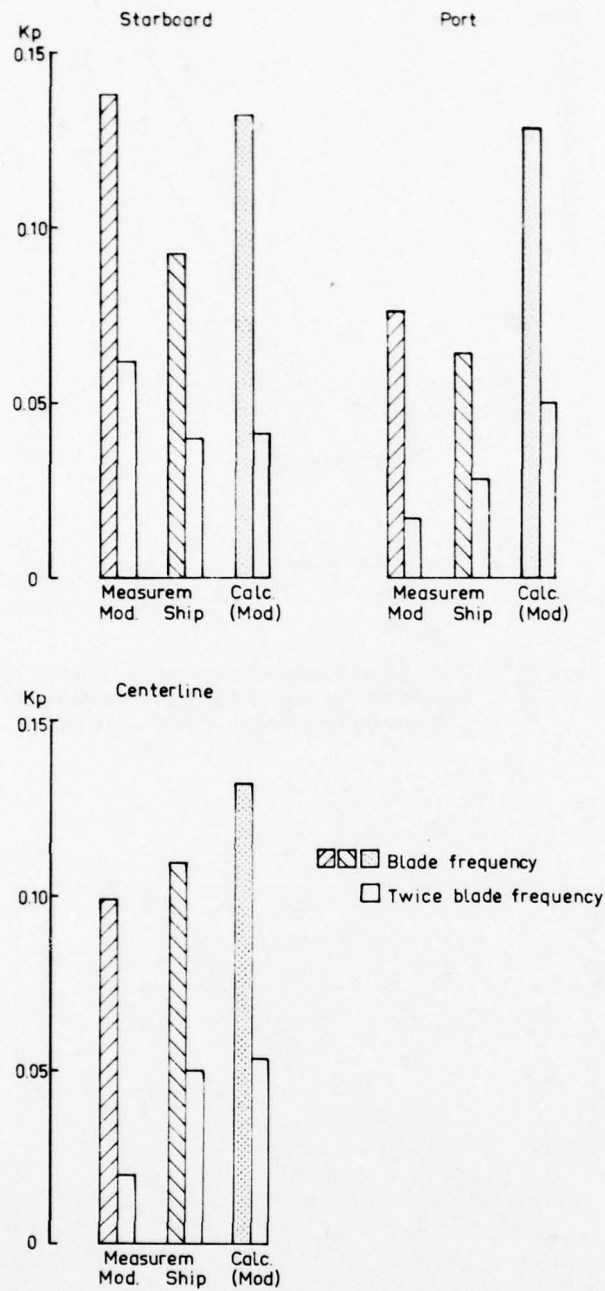


Fig. 14: Comparison between calculated and observed chordwise extensions of sheet cavitation in model and full scale case. Number of revs, 117 rpm. Starboard side.



**Fig. 15: Amplitudes of pressure fluctuations at 117 rpm. Comparison between theoretical calculations and experiment.**



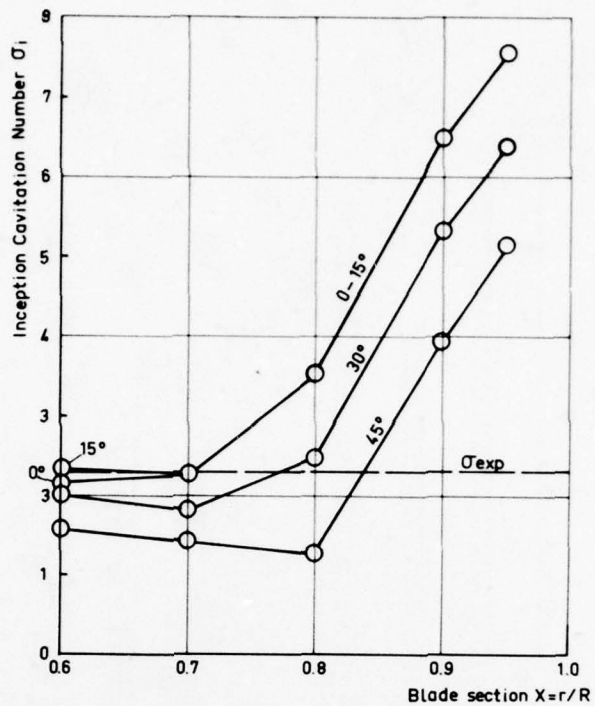


Fig. 16: Calculated values of cavitation number of inception for container ship propeller of present investigation. Starboard side.

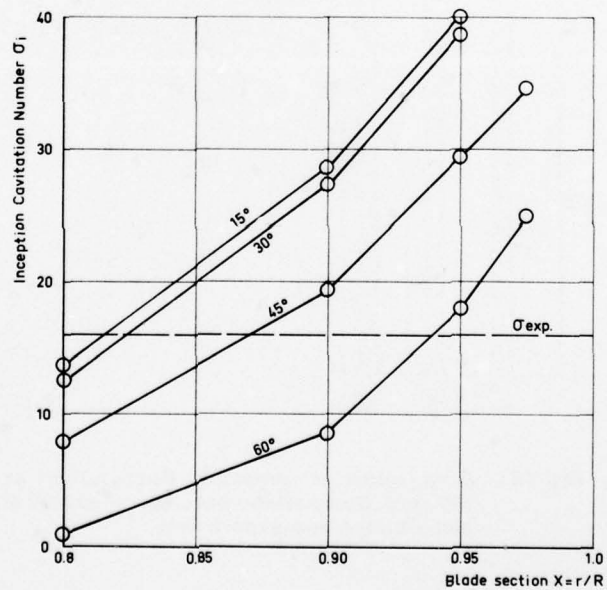


Fig. 17: Calculated values of cavitation number of inception for tanker ship propeller, see /9/. Starboard side.

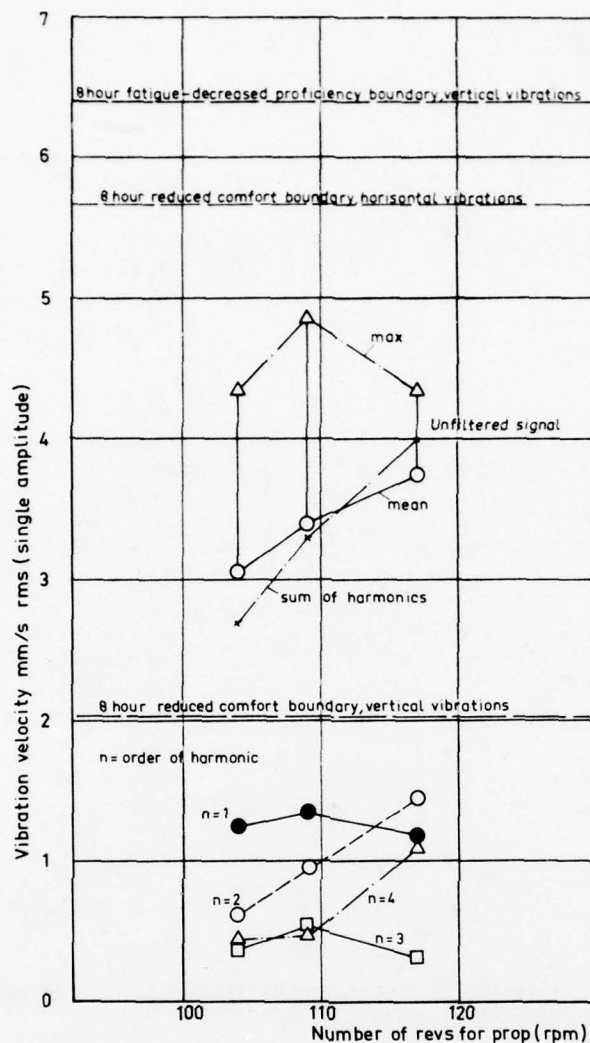
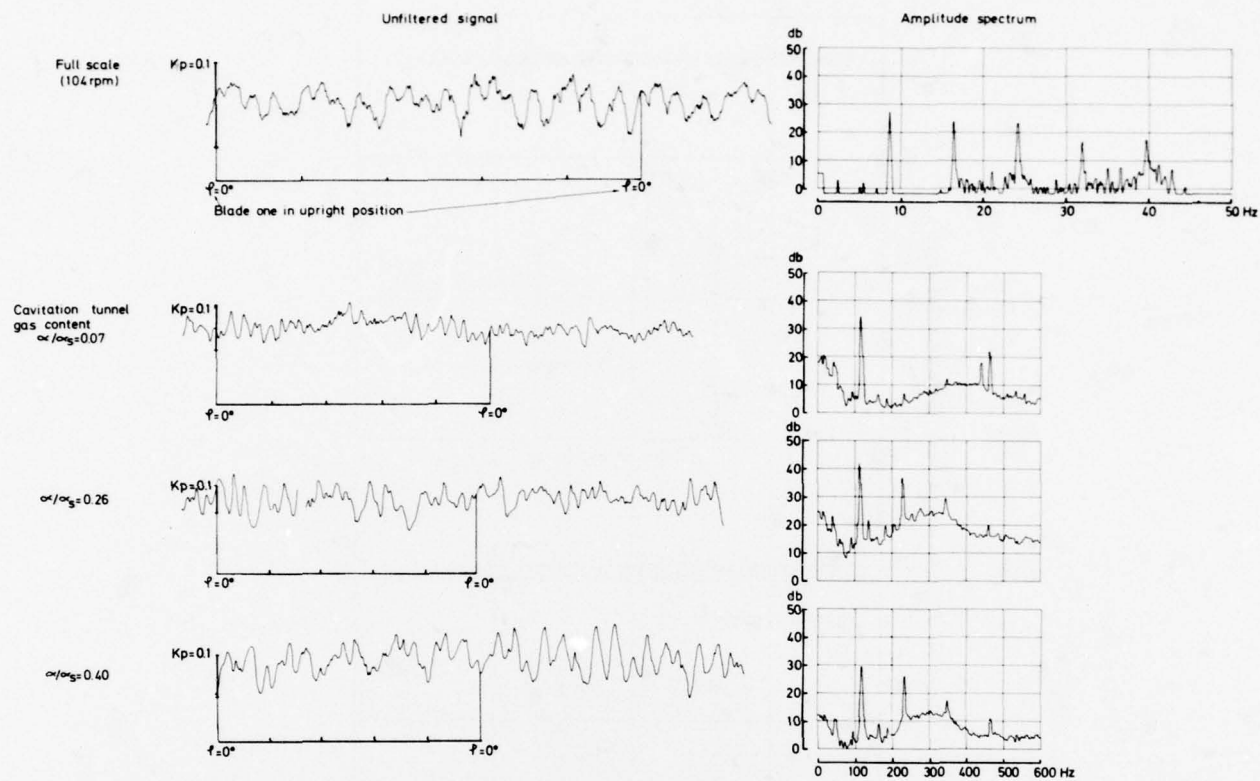
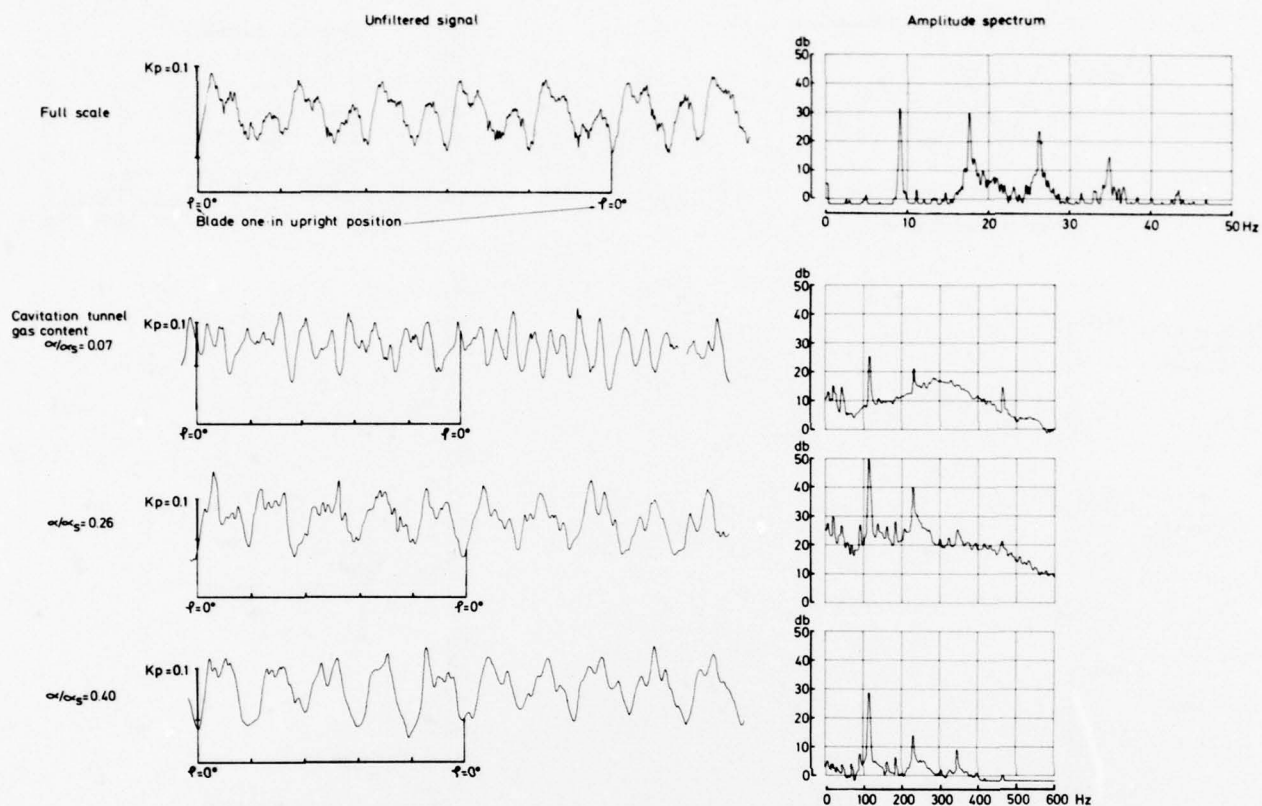


Fig. 18: Measurements of vertical vibration on upper deck, extreme aft (for location of transducer, see Fig. 1).



**Fig. 19: Pressure fluctuations measured in the centreline transducer in full scale and cavitation tunnel. Unfiltered signals and amplitude spectra. Number of revs, 99 rpm.**





**Fig. 20: Pressure fluctuations measured in the centreline transducer in full scale and cavitation tunnel. Unfiltered signals and amplitude spectra. Number of revs, 109 rpm.**

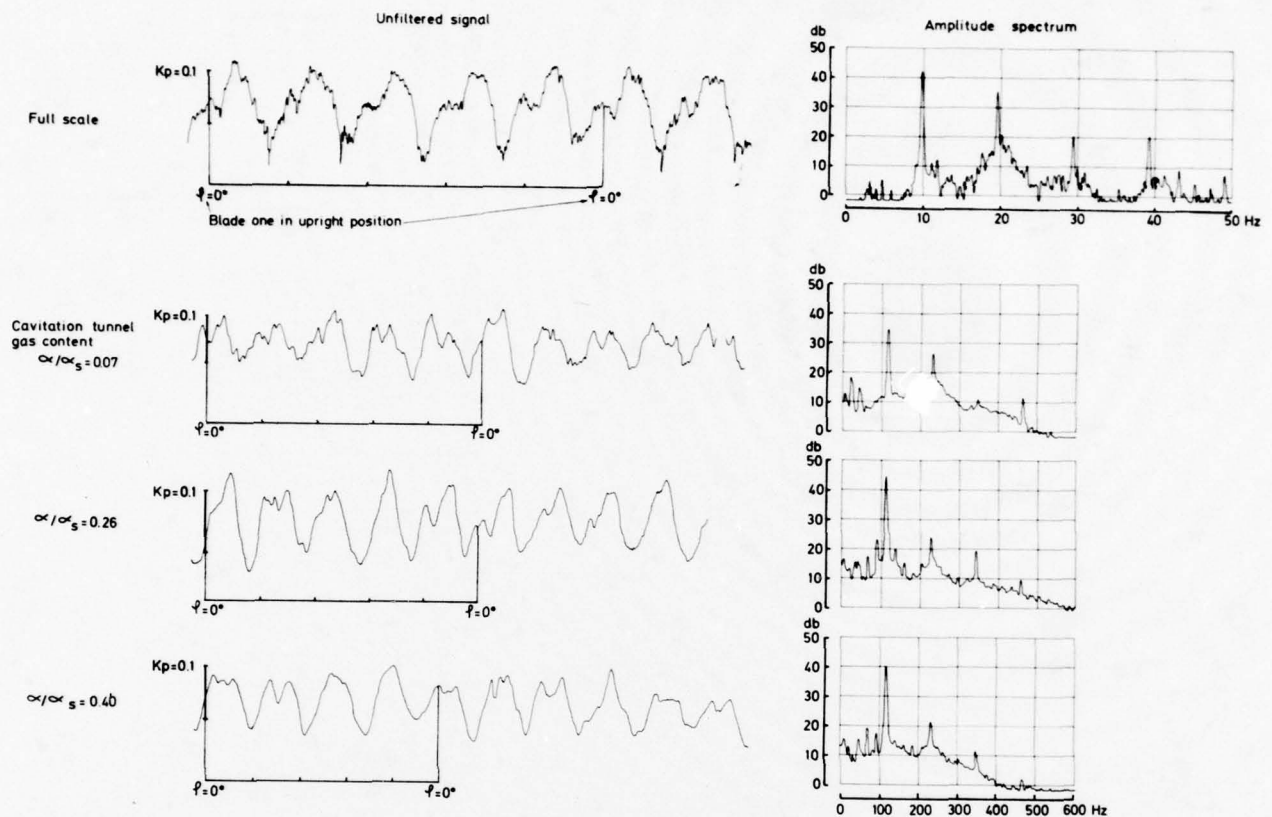
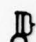






Fig. 21: Pressure fluctuations measured in the centreline transducer in full scale and cavitation tunnel. Unfiltered signals and amplitude spectra. Number of revs, 117 rpm.

 Standard deviation  
 Mean value

-  Mean value for the "demodulated signal"  
 Mean value for the 5(of 100) pulses with the highest blade frequency amplitudes  
 Maximum value

Filled points mean full scale signal  
 Unfilled points mean cavitation tunnel signal

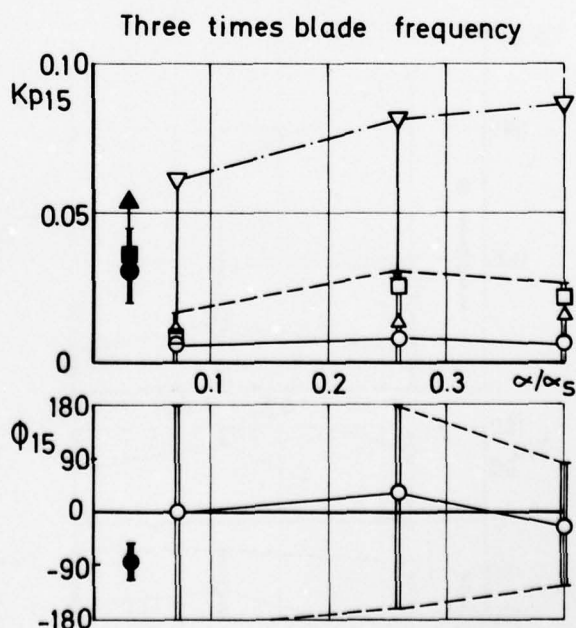
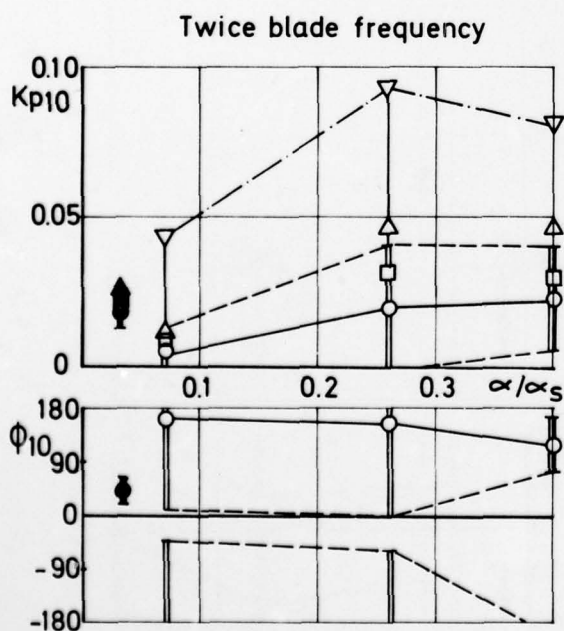
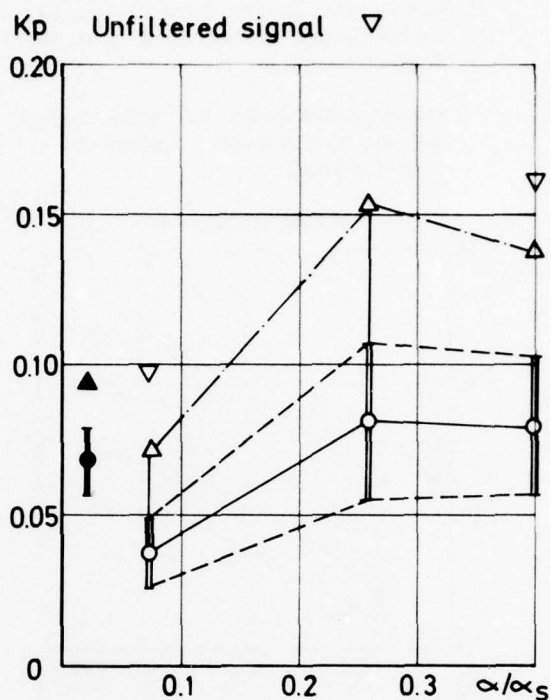
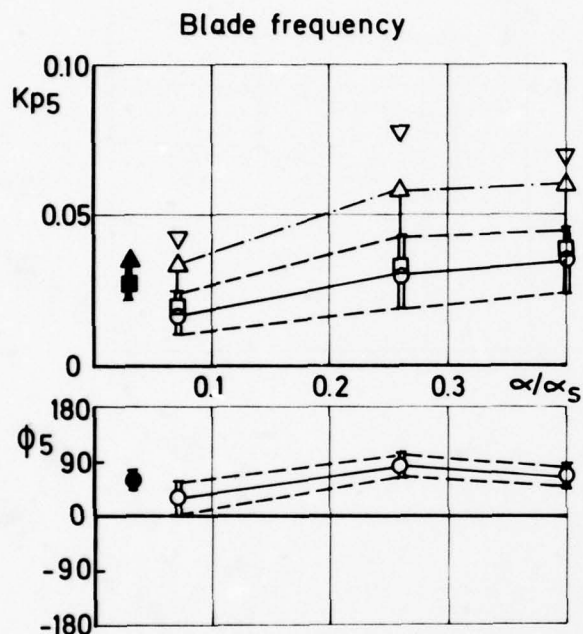


Fig. 22: Comparison of pressure fluctuations in full scale and cavitation tunnel. Amplitudes and phase angles for different harmonics and peak to peak values. Number of revs, 99 rpm.



- ▮ Standard deviation  
 ○ Mean value  
 □ Mean value for the "demodulated signal"  
 △ Mean value for the 5 (of 100) pulses with the highest blade frequency amplitudes  
 ▽ Maximum value

Filled points mean full scale signal  
 Unfilled points mean cavitation tunnel signal.

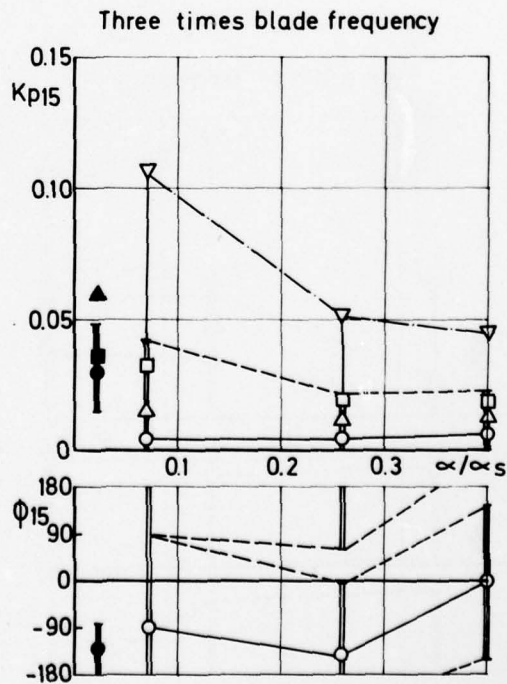
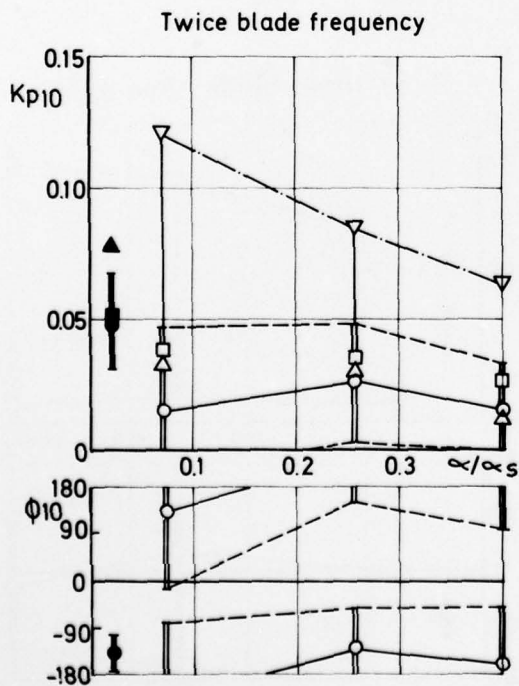
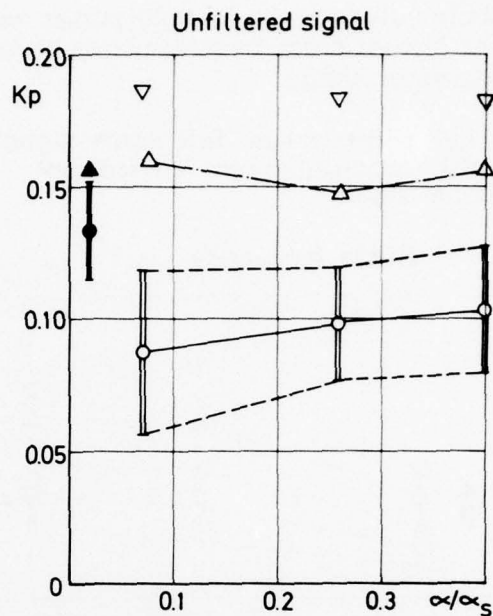
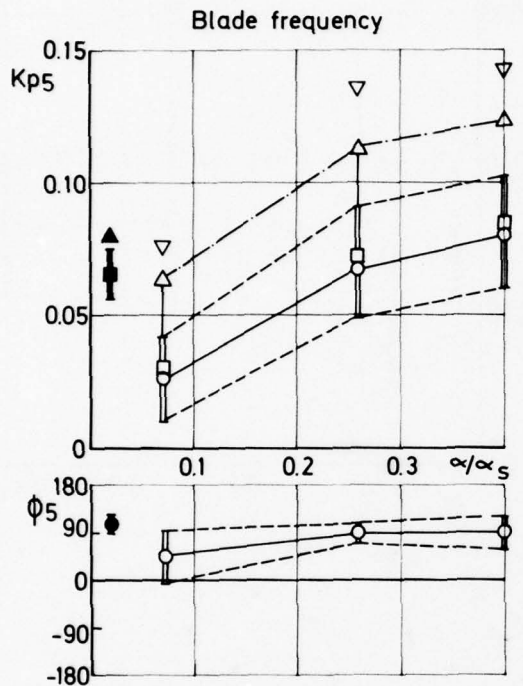


Fig. 23: Comparison of pressure fluctuations in full scale and cavitation tunnel. Amplitudes and phase angles for different harmonics and peak to peak values. Number of revs, 109 rpm.

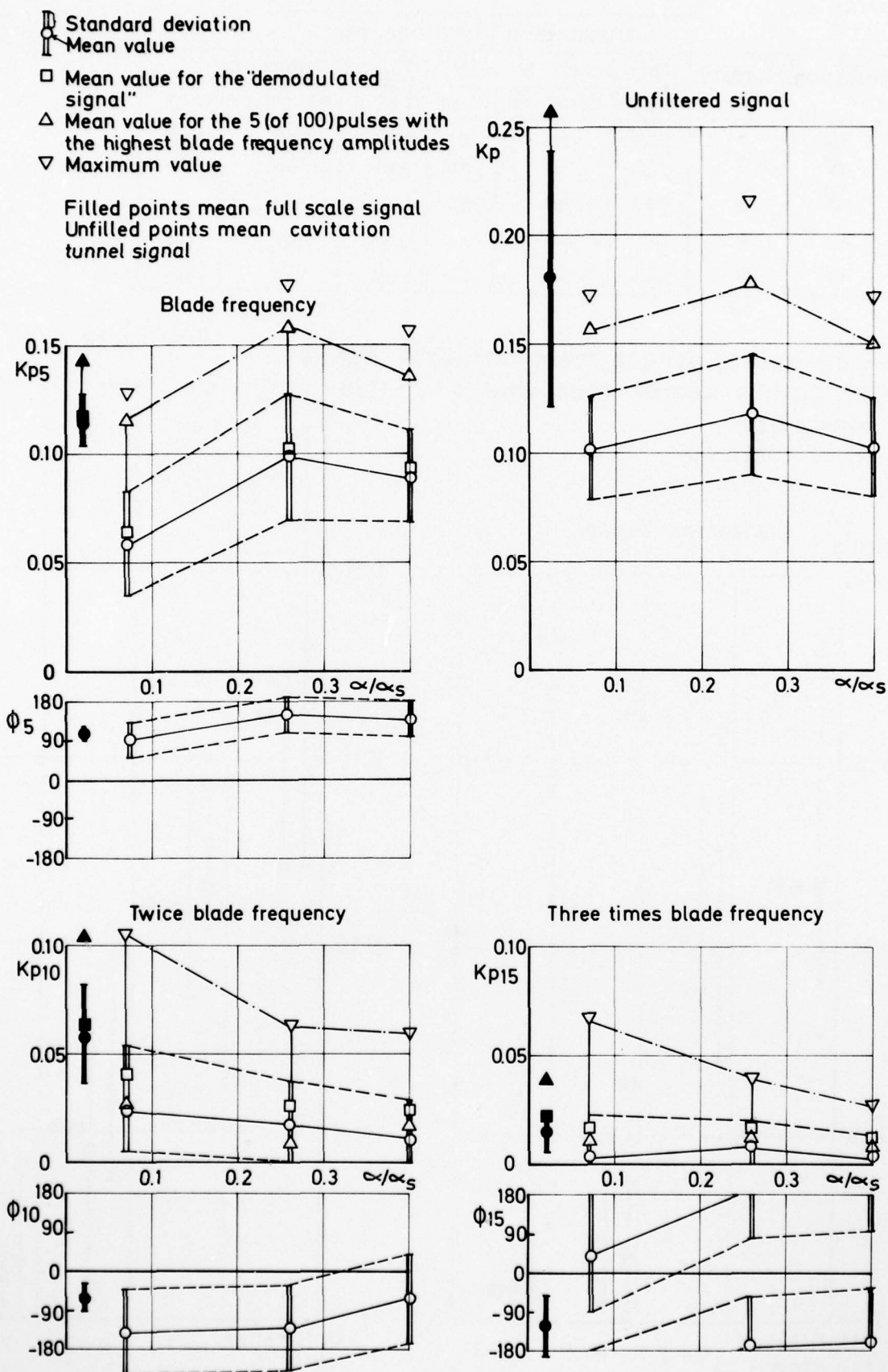


Fig. 24: Comparison of pressure fluctuations in full scale and cavitation tunnel. Amplitudes and phase angles for different harmonics and peak to peak values. Number of revs, 117 rpm.

Notation	Method no	Comparison is made for:					
		Unfiltered signal			Signal harmonics		
		mean	deviation	max	mean	deviation	max
○	1	yes	yes	yes	yes	yes	yes
△	2	yes	no	yes	yes	yes	no
▽	3	yes	no	yes	—	—	—
□	4	—	—	—	yes	no	no
◇	5	—	—	—	yes	no	no

Filled points denote mean values  
 Open points denote max values  
 I deviation  
 (See table 4)

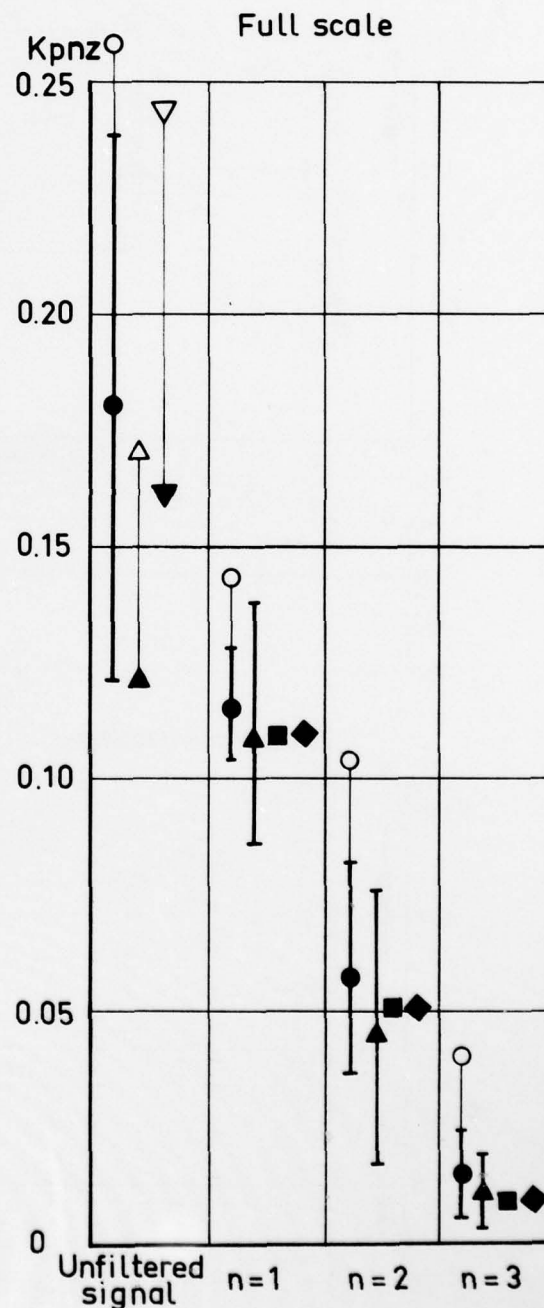
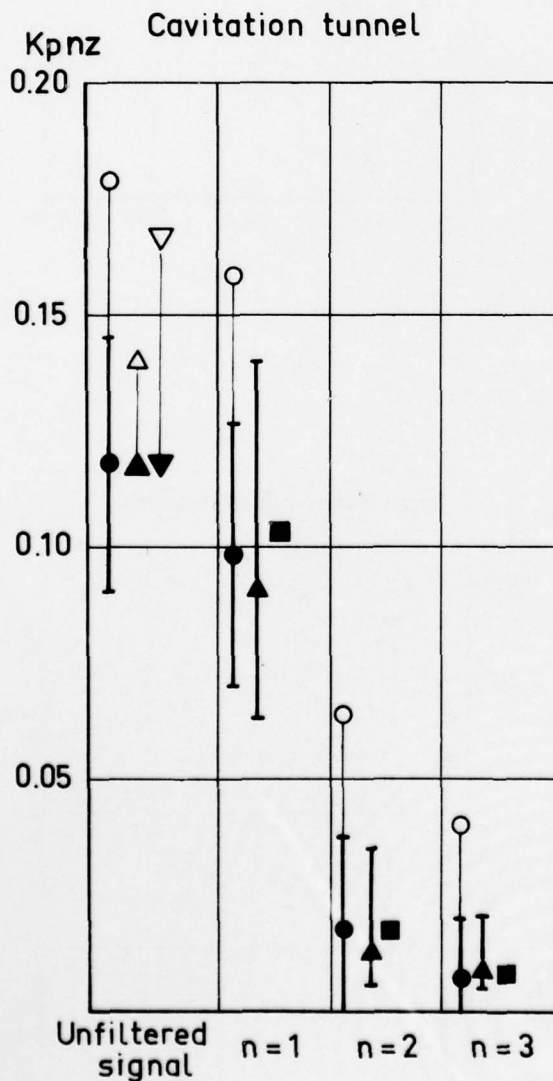


Fig. 25: Pressure fluctuations. Comparison of results from different analysing methods. Number of revs, 117 rpm.



# EXPERIMENTAL DETERMINATION OF MEAN AND UNSTEADY LOADS ON A MODEL CP PROPELLER BLADE FOR VARIOUS SIMULATED MODES OF SHIP OPERATION

R. J. BOSWELL, J. J. NELKA and S. B. DENNY

David W. Taylor Naval Ship Research and Development Center, Bethesda, Maryland, USA

## SYNOPSIS

The mean and unsteady loads were measured on a single blade of a controllable pitch propeller behind a model hull under steady ahead operation, hull pitching motions, simulated crash ahead maneuvers, and simulated crash astern maneuvers. The experimental techniques are described including a description of the dynamometer and data analysis system.

The results show that the unsteady loads are increased substantially by dynamic pitching of the model hull. For simulated crash ahead or crash astern maneuvers the circumferential variation of the loads are smaller than for steady ahead operation.

For steady ahead operation, circumferential variation of loading determined from the model experiments agrees reasonably well with full scale data, but is larger than the theoretically calculated values.

## NOTATION

$A_E$ .....Expanded area, $Z_{rh}^R$ cdr	$M_{x,y,z}$ .....Moment components about x,y,z axes from loading on one blade
$A_0$ .....Propeller disc area, $\pi D^2/4$	$(M)_n$ .....nth harmonic amplitude of M
$C_{i,j}$ .....Elements of calibration matrix	$n$ .....Propeller revolutions per unit time
$C_{Th}$ .....Thrust loading coefficient, $T/[(\rho/2)VA^2A_0]$	$P$ .....Propeller blade section pitch
$c$ .....Blade section chord length	$Q$ .....Time average propeller torque arising from loading on all blades, $-ZM_x$
$D$ .....Propeller diameter	$R$ .....Radius of propeller
$(F)_n$ .....nth harmonic amplitude of F	$R_n$ .....Reynolds number, $c_{0.7}V_R^*/\nu$
$F_{x,y,z}$ .....Force components on blade in x, y, z directions	$r$ .....Radial coordinate from propeller axis
$f_M$ .....Camber of propeller blade section	$S$ .....Skew back of propeller blade section, measured from the spindle axis to the midchord point of the blade section, positive towards trailing edge
$J$ .....Advance coefficient, $J=VA/nD$	$T$ .....Time average thrust of propeller, positive forward, $ZF_x$
$J_T$ .....Effective advance coefficient based on thrust identity	$t$ .....Maximum thickness of propeller blade section
$J_Q$ .....Effective advance coefficient based on torque identity	$V$ .....Model speed
$J_V$ .....Ship speed advance coefficient, $J=V/nD$	$V_A$ .....Propeller speed of advance
$K_{F_{x,y,z}}$ .....Force coefficient, $F_{x,y,z}/(\rho n^2 D^4)$	$V_t(r, \theta_W)$ .....Tangential component of wake velocity, positive counterclockwise looking upstream
$K_{M_{x,y,z}}$ .....Moment coefficient, $M_{x,y,z}/(\rho n^2 D^5)$	$V_x(r, \theta_W)$ .....Longitudinal component of wake velocity, positive forward
$K_Q$ .....Torque coefficient, $Q/(\rho n^2 D^5)$	$V_r(r, \theta_W)$ .....Radial component of wake velocity, positive toward hub
$K_{SC}$ .....Centrifugal blade spindle torque coefficient, $M_{ZC}/(\rho n^2 D^5)$	
$K_T$ .....Thrust coefficient, $T/(\rho n^2 D^4)$	

AD-A055 859

UNIVERSITY COLL LONDON (ENGLAND) DEPT OF MECHANICAL --ETC F/G 13/10  
SYMPOSIUM ON NAVAL HYDRODYNAMICS. UNSTEADY HYDRODYNAMICS OF MAR--ETC(U)  
1978 R E BISHOP, A G PARKINSON, W G PRICE N00014-76-C-0093

UNCLASSIFIED

NL

9 of 9

AD  
A055859



END  
DATE  
FILMED

8 -78

DOC

$V_R^*$ .....Vector sum of speed of advance and rotational velocity at the 0.7 radius,  $[V_A^2 + (0.7\pi nD)^2]^{1/2}$   
 $w_Q$ .....Taylor wake fraction determined from torque identity  
 $w_T$ .....Taylor wake fraction determined from thrust identity  
 $x,y,z$ .....Coordinate axes  
 $Z$ .....Number of blades  
 $Z_R$ .....Rake of propeller blade section measured from the propeller plane to the generator line, positive aft  
 $\theta$ .....Angular coordinate used to define location of blade and variation of loads, from vertical upward positive clockwise looking upstream,  $\theta = -\theta_w$   
 $\theta_s$ .....Skew angle measured from spindle axis to projection of blade section mid-chord into propeller plane, positive toward trailing edge  
 $\theta_w$ .....Angular coordinate of wake velocity, from upward vertical positive counterclockwise looking upstream,  $\theta_w = -\theta$   
 $\lambda$ .....Ship to model linear scale ratio  
 $\nu$ .....Kinematic viscosity of water  
 $\rho$ .....Mass density of water  
 $\rho_p$ .....Mass density of propeller blade  
 $\phi$ .....Pitch angle of propeller blade section,  $\tan^{-1}[P/(\pi x D)]$   
 $(\phi_{F,M})_n$ .....nth harmonic phase angles of F,M based on a cosine series,  $(F,M) = (F,M) + \sum_{n=1}^{\infty} (F,M)_n \cos(n\theta - (\phi_{F,M})_n)$   
 $\psi$ .....Pitch angle of hull  
**Subscripts**  
 $A$ .....Applied values of loads  
 $C$ .....Arising from centrifugal loading  
 $CW$ .....Value in calm water  
 $h$ .....Value at hub radius  
 $I$ .....Indicated values of loads before calibration matrix is applied  
 $M$ .....Model value  
 $MAX$ .....Maximum value at any blade angular position  
 $MES$ .....Value at model conditions derived from measurements on full scale ship  
 $n$ .....Value of nth harmonic  
 $S$ .....Ship value

$SP$ .....Value at self propulsion point  
 $x,y,z$ .....Component in x,y,z direction  
 $0.4$ .....Value at  $r=0.4R$   
 $0.7$ .....Value at  $r=0.7R$

#### Superscripts

$-$ .....Time average value per revolution  
 $\sim$ .....Unsteady value  
 $\dot{\phantom{x}}$ .....Rate of change with time

#### INTRODUCTION

With the increasing use of marine gas turbines as the prime mover, controllable-pitch (CP) propellers are being applied to ships of increasing speed and power. For high power CP propellers extreme care must be taken to design the blades and pitch-changing mechanisms so that they possess adequate strength including consideration of yield and fatigue stresses. This requires an accurate estimate of the maximum time average and alternating loads under all operating conditions. High time-average and alternating loads occur at steady full-power ahead conditions and during high speed maneuvers including full-power crash astern, full-power crash ahead, and full-power turns. In addition, the influence of the seaway may substantially increase the time average and alternating loads. At present there appears to be no confirmed technique whereby the pertinent loads can be predicted to the desired accuracy. Schwanecke and Wereldsma (1) give a review of the factors affecting blade loading for propellers in general, and Rusetskiy (2) and Hawdon, et al (3) discuss some of the factors peculiar to blade loading of CP propellers.

Near the self propulsion point in calm water the time-average loads can probably be calculated with reasonable accuracy. However, even at these conditions, the variation of loads with blade angular position apparently cannot be calculated with high accuracy. Various techniques, including quasi-steady procedures, stripwise unsteady procedures, and methods based on unsteady lifting surface theory, have been proposed for calculating the unsteady loading arising from the circumferential variation in the inflow velocity (4,5,6). However, all of these procedures require knowledge of the flow patterns (wake profile) in the propeller disc. In current practice, the wake profile is measured in the plane of the propeller behind the model hull with the propeller removed. For high-speed displacement ships of the type under consideration in this paper results are usually extrapolated to full scale without making allowance for (1) the change in Reynolds number, and the corresponding reduction in relative boundary layer thickness; and (2) the effect of the propeller suction on the boundary layer and thereby the wake pattern in the propeller disc.

Existing measurements which give information on unsteady blade loading include:

(1) Measurements of strain on the blades of the model propellers or full scale propellers. However, some calculations and assumptions are



required to convert measured strains into loads. A summary of published data of this type is given by Meyne (7).

(2) Measurement of bearing (shaft) forces and moments on model propellers operating in wakes generated by model hulls or wire grid screens. However, this gives information on only some components of blade loading and on only those harmonics of shaft rotational speed corresponding to  $nZ-1$ ,  $nZ$  and  $nZ+1$ , where  $n$  is an integer and  $Z$  is the number of blades. Measurements of this nature have been conducted by many investigators (5,8).

(3) Measurements of forces and moments on individual blades of model propellers operating in wakes generated by model hulls or wire grid screens. Measurements behind model hulls have been made by Huse (9) and Blaurock (10), measurements behind screens have been made by Hawdon, et al (3), and measurements on partially submerged propellers have been made by Dobay (11).

Experiments in wakes generated by screens are advantageous for evaluating the ability of a procedure to calculate the loading for a given wake since for this case the propeller apparently does not influence the wake pattern. Although some good correlation has apparently been obtained between analytical predictions and unsteady bearing forces measured behind wire grid screens (6) correlation between analytically predicted unsteady blade loads, or resulting strains, and measured blade loads, or strains, has been rather inconsistent (8,12).

The mechanism by which the seaway influences the mean and unsteady blade loads is complex. The factors include increased mean propeller loading due to increased hull resistance, and increased unsteady loading resulting from influence of the free surface and modification of the flow patterns into the propeller disc. This flow pattern is influenced by (1) direct trochoidal velocities from the ocean waves, (2) relative velocities of the propeller due to ship motions, and (3) modification of the hull wake pattern due to the seaway and ship motions. Procedures for calculating the loads in a seaway are much less refined than they are for steady operation in calm water. Tasaki (13) gives a good review of the mechanisms and procedures for predicting the effect of the seaway on bearing forces, which in principle also applies to unsteady loading on an individual blade.

There are apparently no rational analytical procedures whereby the time-average loads per revolution or the unsteady loads including variation with blade angular position during crash ahead, or crash astern maneuvers can be accurately calculated. These loads may depend on many factors including the time rate of change of propeller pitch  $P$  (for CP propellers), time rate of change of rotational speed  $\dot{n}$ , time rate of change of ship speed  $\dot{V}$ , propeller blade section stall, cavitation, ventilation, flow separation from the hull, and large interactions between the propeller and the hull. Some of these factors are discussed and considered by Hawdon, et al (3). For crash astern maneuvers a CP propeller has negative pitch  $P$  and develops negative thrust for forward speed; i.e., it decelerates the flow into the propeller, which may tend to increase the

time average and time dependent interaction between the propeller and the hull.

For turns, the factors affecting the time-average loads per revolution and the unsteady loads are somewhat the same as those affecting the loads under crash ahead and crash astern conditions, except for turns there is a relatively large drift angle of the flow into the propeller. This drift angle tends to increase the circumferential nonuniformity of the flow into the propeller and thereby increase the unsteady loading. However, this circumferential nonuniformity of the inflow tends to be offset somewhat by the lower values of ship speed and propeller rotational speed in turns compared to steady ahead operation.

There are no experimental measurements known to the authors of time-average loads and circumferential variation of loads with blade angular position on CP propellers behind a hull under a wide range of operating conditions. Therefore, an experimental program was undertaken to measure the six components of loading (Figure 1) on a model CP propeller operating behind a model hull. The experimental conditions include: (1) steady ahead operation near the self propulsion point, (2) steady ahead operation near the self propulsion point with forced dynamic pitching of the model hull, (3) simulated crash ahead operation, and (4) simulated crash astern operation. For the steady ahead operation the results were correlated with predictions based on unsteady lifting surface theory as developed by Tsakonas, et al (14), with the quasi-steady method of McCarthy (15) and with strains measured on the corresponding full scale propeller at sea.

The propeller used in these experiments is shown in Figure 2 and the geometry is given in Table 1. The model hull used in these experiments is shown in Figure 3. This model is similar to DTNSRDC Model 4954, which is described by Hadler and Cheng (16).

## EXPERIMENTAL TECHNIQUE

### Facility And Dynamometry

All experiments were conducted on Carriage I of the David Taylor Model Basin. The propeller was located in its proper position relative to the model hull but was isolated from the model hull and driven from downstream (see Figure 3).

This downstream drive system was necessary in order to obtain the required characteristics of the system for measuring unsteady loading. The general criteria for the design of an unsteady force measuring system are:

- A. The support structure of the force measuring system should be soft mounted and possess a large mass to eliminate transmission of extraneous vibration to the system.
- B. The natural frequency of the system should be well above the highest frequency of the quantities to be measured (to avoid phase-shift and amplification of the signal).
- C. The system response should be sufficiently large in the force magnitude range to be measured (sensitivity).

D. The system should be free of interaction, that is, each measuring element should respond to only that force or moment which it is intended to measure.

These four major aims are not complementary. The high natural frequency requires a stiff, rigid system while high sensitivity requires an elastic, soft system. The necessary compromise between these two requirements results in some interaction between the force-measuring elements.

Criteria A dictates that a massive flywheel be used, and criteria B dictates that this flywheel be connected to the sensing elements (located inside the propeller hub) by a short thick shaft. Therefore, due to the geometry of the hull and shafting of the configuration under evaluation, it was not feasible to achieve criteria A and B with an upstream drive system from inside the model hull. Criteria A and B controlled the minimum allowable beam and draft of the downstream body, and the maximum allowable clearance from the bow of the downstream body to the propeller. Although the downstream body may exert some influence on the flow into the propeller, this was considered necessary in order to meet the measuring criteria A and B. The influence of the downstream body on the flow into the propeller is discussed in the Experimental Results section.

The drive and mounting system is basically the same as that used in the DTNSRDC BASS dynamometer which has been described by Brandau (17). Utilized from this dynamometer were the propeller (tail) shaft, drive shaft with flywheel, belt-type (quiet) transmission, and slip rings. Power to rotate the propeller was supplied by a DC permanent-magnet, servo motor capable of delivering up to 45 N-m of torque. This motor was selected for its ability to control and hold the shaft revolution rate over a wide range of propeller torque loadings which is required for some of the experimental conditions. A digital encoder is mounted on the propeller shaft. This is used for generating electrical pulses as a function of shaft angular position. Two types of pulses are generated: a single pulse per revolution and a multi-pulse per revolution (90 equally spaced pulses for the current experiment). The single pulse is synchronized with the reference line of the instrumented propeller blade. The pulses generated by this encoder are accurate to within 0.01 degrees.

The downstream body which houses the drive system is a modification of that used by Dobay (11). This body was modified to allow deeper submergence and an inclined shaft angle. Both the body housing the drive system (the drive system is soft mounted to this body) and the model hull was rigidly attached to a pitch-heave oscillator which is rigidly mounted on the towing carriage. With this arrangement the model hull and the drive system can be dynamically pitched together while maintaining independent support from one another.

The sensing elements are flexures to which are bonded high sensitivity semiconductor strain gage bridges. The design of these flexures has been described by Dobay (11). There are three flexures, each of which measures two components of blade loading. Flexure No. 1 measures components  $F_x$  and  $M_y$ , flexure No. 2 measures components  $F_y$  and  $M_x$ , and flexure No. 3 measures

components  $F_z$  and  $M_z$  (Figures 1 and 4). This arrangement using three separate flexures was adopted, rather than using one flexure to measure all components of blade loading, because it appears to result in higher natural frequencies (criteria A), higher sensitivities (criteria C) and lower interactions (criteria D) than would have resulted if a single flexure had been used.

The flexures are mounted inside a propeller hub which are specifically designed for these experiments (Figure 5). Due to space limitations, only one flexure could be mounted at a time. This necessitated duplicate runs with the different flexures, as discussed in the Experimental Conditions and Procedure section.

The strain gage bridges are excited by a common DC voltage source, transmitted through the slip rings on the propeller shaft. The constant-current excitation used by Dobay (11) was not used in the present experiment because it appeared to be too sensitive to temperature.

The voltage output from the flexures (due to blade loading) is transmitted through the slip-rings to individual NEFF 119-121 amplifiers. These amplifiers utilize field effect transistors to produce an extremely high input-impedance (100 megohms, minimum). This high impedance essentially eliminates the slirpring noise to the amplifier. The voltage signals are transferred across the slirprings in the presence of only small amount of noise-producing current. The amplifiers used here have zero-phase shift qualities in the DC - 20 KHz range. They are chopper-stabilized in order to record both the steady and unsteady signals simultaneously. This signal-conditioning system is essentially the same as that used by Dobay (11).

The signals are then digitized and analyzed using a Model 70 Interdata Digital Computer, and stored in digital form on a 9-track magnetic tape. The on-line analysis of the data is discussed in the Data Acquisition and Analysis section.

#### Calibration

Prior to the experiment each flexure was statically calibrated in air to establish the flexure sensitivities, interactions, and linearity over the loading range of interest. These calibrations were conducted with the flexures mounted in the propeller hub which was connected to the flywheel and drive assembly as is the situation during the experiment. Each flexure was subjected to independently controlled forces in the axial, transverse, and radial directions; i.e.,  $F_x$ ,  $F_y$ , and  $F_z$ , respectively, and to independently controlled moments about the axial, transverse, and radial directions; i.e.,  $M_x$ ,  $M_y$ , and  $M_z$ , respectively (Figure 1).

The static calibration showed that all flexures had a linear response over the load range of interest. Table 2 shows the interaction matrix. These calibrations show that all flexures had good sensitivity except  $F_z$  which had lower sensitivity than desirable. The interactions are small except the effect of  $M_z$  on  $F_z$ . The rather poor characteristics of the  $F_z$  flexure is not considered to be a serious shortcoming since  $F_z$  arises primarily from centrifugal loading and can be analytically calculated. In addition, no significant variation of  $F_z$  with blade angular position



is anticipated. Flexure No. 3, which measures  $F_z$  and  $M_z$  was further evaluated by correlation of air-spin experiments with analytically calculated results, as discussed in the Experimental Procedure and Experimental Results sections. The interactions are taken into consideration in the data analysis as discussed in the Data Acquisition and Analysis section.

A dynamic calibration of the flexures used in this experiment was performed by Dobay (11). The purpose of the dynamic calibration was to determine the frequency range over which unsteady forces and moments could be reliably measured.

The dynamic calibration of the flexures consisted of applying a relatively constant maximum amplitude, variable frequency force or moment-excitation in all six component directions to all six flexure-elements, using an electromagnetic shaker in air. The force or moment-amplitude imposed by the shaker was monitored through an extremely light-weight, strain-gaged single flexure-element. The measured lowest natural frequencies of the three flexures in air are as follows:

Flexure Number	1	2	3
Lowest Natural Frequency in air ( $H_z$ )	550	450	282
Mode	$M_x$	$M_y$	$M_z$

The measured amplification factor (ratio of output amplitude to input amplitude) and phase shift for all three flexures is as follows:

Frequency range ( $H_z$ )	0 to 60	60 to 120
Phase shift (degrees)	0 to 0.05	0.05 to 0.15
Amplification factor	1.00	1.00 to 1.05

A check of the effect of submergence in water on the lowest natural frequency was made after the experimental apparatus was completely assembled with propeller blades and attached in place under the towing carriage. The blade was struck with a sharp light blow and the response of flexure number 1 (the  $F_x$ ,  $M_y$  flexure) was recorded. The measured response indicated that the lowest natural frequency of the flexure was approximately 250 Hz or approximately 0.45 times its value in air. Similar measurements were not made with the other two flexures but it is assumed that the natural frequencies of these flexures in water are approximately 0.45 times the measured values in air. With this assumption, the natural frequencies in water are:

Flexure Number	1	2	3
Lowest Natural Frequency in Water ( $H_z$ )	250	202	127

During the experiment the highest propeller rotational speed was 17.65 rps. Thus, the flexures have a "true" dynamic response (determined in air) up to at least the third harmonic of shaft rotation, and have no greater than five percent amplification up to the sixth harmonic of shaft rotation. Assuming the lowest natural frequency of each flexure in water is 0.45 times its measured value in air, the lowest natural frequency of flexures 1, 2, and 3 are greater than 14, 11, and 7, respectively, times the highest propeller rotational speed used during the experiments. As discussed in the Experimental Results section, extraneous signals appeared in the unfiltered experimental data at frequencies close to the deduced natural frequency of each flexure in water.

The propeller shaft drive and soft-mount support system were dynamically loaded in the vertical, longitudinal, and transverse directions to obtain the system lowest natural frequencies. The natural frequencies of the system in air were found to be:

Mode	Natural Frequency ( $H_z$ )
Vertical bending	12.25
Horizontal bending	6.0
Axial	4.6

The support system has a low resonant range; however, the soft mount system was specifically designed to prevent the towing-carriage oscillation (with the resonance at 100 to 200 Hz) from being transmitted to the blade flexures. Based on the measured resonances, it is concluded that the soft mount system should successfully meet this objective. Although some of the resonances are close to the propeller rotational speed for some experimental conditions, it is considered more desirable to isolate the system from the towing carriage vibration. Therefore, the soft mount system is considered to be satisfactory.

### Experimental Conditions and Procedures

Experiments were conducted at several conditions including steady ahead operation, simulated pitching of the hull, simulated crash ahead (acceleration), and simulated crash astern (deceleration). All conditions were run with the model hull rigidly attached to its support with no freedom to sink or trim.

The steady ahead condition, which corresponds to a self propulsion point, is defined in Table 3. The trim and draft at this speed was determined by setting the specified still water trim and draft, attaching the model to the carriage so that it is free to trim and sink, running at the specified speed, and locking the model at this equilibrium trim and draft.

Runs simulating hull pitching were conducted at the same conditions as the steady ahead run, except that the hull pitch was varied. Two types of runs were conducted: (a) quasi-steady simulation in which the hull pitch angle  $\psi$  was set at various fixed positions, and (b) unsteady simulation in which  $\psi$  was varied sinusoidally with time. For the quasi-steady simulation, runs were conducted at five different values of  $\psi$ , from two degrees bow up from the calm water equilibrium  $\psi$  ( $\psi = \psi_{CW}$ ) to two degrees bow down from  $\psi_{CW}$  (Table 3). For the unsteady pitch simulation the value of  $\psi$  was varied sinusoidally about  $\psi_{CW}$  with an amplitude of two degrees and a frequency of 0.8 Hz. All runs were conducted in calm water; therefore, the response of the hull to the seaway was simulated but the seaway was not simulated.

Crash ahead runs were conducted using the still-in-the-water point as the initial condition. Trim and displacement were fixed at the values corresponding to the self propulsion condition (Condition 1 of Table 3). Two types of runs were conducted: (a) quasi-steady runs in which all quantities including model speed  $V$ , rotational speed  $n$ , and propeller pitch  $P$  were held constant ( $\dot{V} = \dot{n} = \dot{P} = 0$ ), and (b) unsteady runs in which  $V$  was varied with time but  $n$  and  $P$  were held constant ( $\dot{V} > 0$ ,  $\dot{n} = \dot{P} = 0$ ). For the quasi-steady simulation,



runs were conducted at five different combinations of  $V$ ,  $n$ , and  $P$ . The conditions for each run represent the conditions at one instant of time during a "true" crash ahead in which  $V$ ,  $n$ , and  $P$  vary with time. Thus, one "true" crash ahead run is represented by five steady runs which do not simulate the time rate of change of  $V$ ,  $n$ , and  $P$ . For the unsteady simulation, runs were conducted at the same five combinations of fixed  $n$  and  $P$  as used for the quasi-steady simulation, and  $V$  was varied with time (the same variation was used for each run) representing an acceleration of the model hull (Figure 6). For each of these runs, data are of interest only near the value of  $V$  which occurs concurrently with the fixed values of  $n$  and  $P$  during the "true" crash ahead ( $\dot{V} \neq 0$ ,  $\dot{n} \neq 0$ ,  $\dot{P} \neq 0$ ). Thus, one "true" crash ahead run is represented by five runs which simulate the proper time rate of change of  $V$  but not the proper time rate of change of  $n$  and  $P$ . The quasi-steady and unsteady crash ahead simulations are for the same conditions, the only difference being that for the quasi-steady simulation  $\dot{V}=0$  whereas for the unsteady simulation  $\dot{V}>0$ . In general  $P$  varies with time during a "true" crash ahead run; however, for the crash ahead run under simulation here  $P$  is constant throughout the portion of the run simulated.

Crash astern runs were conducted using the self propulsion condition (condition 1 in Table 3) as the initial condition. Both quasi-steady ( $\dot{V}=\dot{n}=\dot{P}=0$ ) and unsteady ( $\dot{V}<0$ ,  $\dot{n}=\dot{P}=0$ ) runs were conducted (Table 3 and Figure 6) to simulate one "true" crash astern ( $\dot{V} \neq 0$ ,  $\dot{n} \neq 0$ ,  $\dot{P} \neq 0$ ) condition by procedures similar to those described for the crash ahead condition. Unlike the crash ahead simulation, the value of propeller pitch  $P$  varies through the portion of the "true" crash astern under simulation.

For the unsteady crash ahead and crash astern runs the carriage speed was manually varied with time in a carefully controlled manner. This was achieved with the aid of an inked pen on a two-dimensional Cartesian plotter. In one direction the pen is controlled so that it moves linearly with time, and in the orthogonal direction it is controlled so that it varies with the instantaneous carriage speed. When a crash ahead or crash astern maneuver is to be executed the switch moving the pen with time is turned on, and the carriage operator manually varies the carriage speed so that the inked pen follows a prescribed velocity versus time curve.

As discussed in the Facility and Dynamometry section, each of the three load sensing flexures measures only two components of blade loading. Therefore, each of the experimental conditions described in Table 3 was run with each of the three blade-loading flexures.

The blade pitch was set using a template. In order to change either the blade pitch or the flexure the propeller had to be removed from the drive system.

Supplemental experiments were conducted to assess the influence of the downstream dynamometer boat on the flow in the propeller plane. These supplemental experiments consisted of (1) wake surveys in the propeller plane at the self propulsion point (condition 1 in Table 3) with and without the downstream body, (2) measurement of time average thrust and torque using a transmission

dynamometer in the model hull near the self propulsion point with and without the downstream body, and (3) measurement of the six components of blade loading at  $P/D=1.06$  over a range of advance coefficient  $J$  with the downstream body at zero shaft angle but without the upstream ship model. The supplemental experiment (1) (wake surveys) yields a direct measure of the change in volume mean velocity through the propeller disc due to the downstream body. The change in effective velocity through the propeller disc is deduced from supplemental experiments 2 and 3 by thrust and torque identity between similar conditions with and without the downstream body.

Some air spin experiments were conducted with the  $F_z$ ,  $M_z$  flexure over a range of pitch settings. The objective of these experiments was to isolate the centrifugal loading in the  $F_z$  and  $M_z$  directions, and to evaluate the reliability of the results with this flexure by correlation with analytically calculated centrifugal loading.

#### Data Acquisition and Analysis

Data were collected, stored, and analyzed on-line using a Model 70 Interdata Digital Computer. A special-purpose computer program was written with options for analyzing each of the three basic types of runs: (1) steady ahead, (2) dynamic hull pitching, and (3) unsteady crash-ahead or crash-astern. The types of runs are discussed in more detail in the Experimental Conditions and Procedures section.

The program allows the propeller blade force and moment data to be sampled and stored on magnetic tape as a function of shaft position. Sampling is triggered by external pulses generated by a digital encoder mounted on the propeller shaft, as discussed in the Facility and Dynamometry section. Pulses are generated as a function of shaft angular position; hence, the sampling of blade force and moment data is related to the shaft position. There are two outputs from the shaft encoder; a single pulse per revolution and multi-pulse (90 pulses per revolution for the current experiments).

When the experimental condition is achieved, the computer operator initiates the data collection cycle. The program "waits" until the single pulse occurs. When the single pulse occurs, the computer again "waits" for the occurrence of the first following pulse of the 90 pulses; data are then sampled for all channels through an analog-to-digital converter and stored in computer memory. This process is repeated for 180 pulses, or two shaft revolutions. At the same time the program "reads" two frequency counters into core memory which measure model velocity  $V$  and propeller rotational speed  $n$ .  $V$  and  $n$  are measured by counting the pulses from geared wheels attached to the towing carriage drive system and to the propeller shaft, respectively. The  $V$  and  $n$  are averaged over two shaft revolutions. Thus, there is an average  $V$  and  $n$  corresponding to each pair of two consecutive revolutions.

After two revolutions of data have been sampled and stored in core memory, the data are transferred from core to a 9-track digital tape recorder. The transfer time is small and no pulses are missed during the transfer. The data collect cycle proceeds continuously

until the operator disengages the computer. The sampling procedure is the same for all types of experimental conditions. Therefore, at the completion of an experimental run all data are stored on magnetic tape. The data can then be analyzed immediately or at any later time. For analysis, the computer operator selects the appropriate option of the program depending on the type of run; i.e., (1) steady ahead, (2) dynamic hull pitching, or (3) unsteady crash ahead or crash astern.

The appropriate calibration factors are stored in the computer and are considered in the analysis. However, since only two of the six components of blade loading are measured during a given run, the interactions between the various loading components cannot be considered during the on-line analysis. The interactions are taken into account later after measurements are completed with all three flexures for a given condition.

For the steady ahead condition, blade force and moment data at each 4-degree increment of blade angular position are averaged over the number of cycles recorded (usually over more than 200 cycles). Spurious data not related to shaft position is averaged out by this method. A harmonic analysis is then performed on the average wave forms of the blade loading components. This gives the amplitude and phase of the first 16 harmonics.

For the dynamic pitch runs the hull pitch angle  $\psi$  varies sinusoidally with a frequency of 0.8Hz. A position potentiometer translates bow vertical displacement into hull pitch angle which is read into the computer in the same manner as blade loading components. During dynamic pitching the shaft rotates independent of the pitch oscillator. During a single propeller revolution 90 pitch positions are measured. Thus, to correlate pitch angle position and revolution an average pitch must be taken over each revolution.

Sixteen dynamic pitch angle positions are selected for analysis. These are characterized by pitch angle  $\psi$  and the sign of the time rate of change of pitch angle  $\dot{\psi}$ . The computer calculates an average  $\psi$  and sign of  $\dot{\psi}$  corresponding to each propeller revolution. Based on these calculated average values of  $\psi$  and sign of  $\dot{\psi}$ , each propeller revolution is placed in a suitable hull pitch angle category, or is discarded if its average  $\psi$  falls outside the tolerance band of all the 16 specified values of  $\psi$ . Several passes down the towing tank are required in order to obtain a sufficient number of samples. After all the data have been sorted based on ( $\psi$ , sign of  $\dot{\psi}$ ), and tolerance, the cycles for each combination of ( $\psi$ , sign of  $\dot{\psi}$ ) are analyzed in exactly the same manner as the data for the steady ahead condition at fixed  $\psi$ .

For unsteady crash ahead and crash astern runs the model speed  $V$  varies with time  $t$ . During a crash ahead or crash astern run, data, including a measure of  $V$ , are sampled and stored in the same manner as for the steady ahead runs.

Five values of  $V$  are specified for analysis. For each crash ahead or crash astern run and for each specified  $V$  the computer selects the propeller revolution which has the average value of measured  $V$  nearest to the specified  $V$ . However,

for a single crash ahead or crash astern run only one revolution at each specified velocity is obtained. Therefore, each crash ahead or crash astern run is repeated from 3 to 5 times. This yields from 3 to 5 revolutions at each specified velocity. All the cycles for each specified  $V$  are then analyzed in exactly the same manner as the data for the steady ahead conditions.

Therefore, the on-line analysis system yields average wave forms and harmonic analysis of the average wave forms for steady ahead conditions, for specified conditions of ( $\psi$ , sign of  $\dot{\psi}$ ) during the dynamic pitch cycle, and for specified velocities  $V$  during the crash ahead or crash astern operation. However, these on-line results are preliminary because:

(1) They do not consider the interactions between the various loading components. These interactions were determined during the static calibration of the flexures.

(2) They include the complete measured signals with no filtering. As discussed in the Experimental Results section, there appeared to be some extraneous signals near the natural frequency of the flexure being used superimposed on the signals generated by blade loading.

Final analyses were conducted after completion of the experiment to consider interactions and to filter out extraneous high frequency noise. These analyses were conducted using a CDC 6700 computer. For each condition, the average wave form for each of the 6 loading components were multiplied by the inverse of the calibration matrix given in Table 2.

$$\begin{bmatrix} F_{xA} \\ F_{yA} \\ F_{zA} \\ M_{xA} \\ M_{yA} \\ M_{zA} \end{bmatrix} = \begin{bmatrix} F_{xI} \\ F_{yI} \\ F_{zI} \\ M_{xI} \\ M_{yI} \\ M_{zI} \end{bmatrix} \cdot [C_{i,j}]^{-1}$$

This matrix multiplication was performed at 4-degree increments of blade angular position. A harmonic analysis was then performed on the signals corrected for the interactions.

Based on a harmonic analysis of the wake in the propeller plane it was judged that there should be no significant loading of hydrodynamic origin at frequencies above 10 times shaft frequency. Therefore, the wave form was then reconstructed using the first 10 harmonics of shaft frequency, except for the spindle torque  $M_z$  which used the first 5 harmonics of shaft frequency. This reconstruction using only the first 10 (or 5) harmonics had the same effect as filtering out all frequencies above 10 (or 5) times shaft frequency.

From the known values of  $F_x$ ,  $F_y$ ,  $M_x$ , and  $M_y$ , the values of the bending moment normal to the nose-tail line at the blade root (the 0.289 radius) and at the 0.4 radius were calculated. For the calculation about the 0.4 radius it was assumed



that the loading between the blade root and the 0.4 radius accounted for 3 percent of the moments about the shaft centerline. These bending moments were calculated at every 4 degrees of blade angular position, harmonically analyzed, and the wave form reconstructed using the first 10 harmonics of blade angular position in exactly the same manner as was used for the other components of blade loading.

Plots of the data were generated by the CDC computer system using a Calcomp Plotter.

### Accuracy

During the experiments, for steady ahead operation  $\dot{V}=0$ , the model speed  $V$  and rotational speed  $n$  could be controlled to within accuracies of  $\pm 0.005$  M/sec and  $\pm 0.01$  rev/sec, respectively. For the unsteady crash astern and crash ahead maneuvers ( $\dot{V} \neq 0$ ), the average of the three to five values of  $V$  and  $n$  during the unsteady runs for which data are presented was generally within  $\pm 0.01$  M/sec and  $\pm 0.05$  rev/sec, respectively, of the target values.

For runs with fixed hull pitch angle  $\psi$ , ( $\dot{\psi}=0$ ) the value of  $\psi$  can be controlled to within 0.005 degrees. For dynamic pitch runs,  $\dot{\psi} \neq 0$ , the selection of a propeller revolution at a specified  $\psi$  necessitates a tolerance of 0.1 degree to  $\psi$ ; however, the average value of  $\psi$  during the unsteady runs for which data are presented is generally within 0.02 degree of the target  $\psi$ .

The forces  $F_x$  and  $F_y$  and moments  $M_x$ ,  $M_y$ , and  $M_z$  are accurate to within plus or minus the following variations:

	$F$ [N]	$F_{MAX}$ [N]	$M$ [N-m]	$M_{MAX}$ [N-m]
Steady ahead, $\dot{V}=0, \dot{\psi}=0$	1.0	1.5	0.04	0.06
Dynamic pitch, $\dot{V}=0, \dot{\psi} \neq 0$	1.5	2.0	0.06	0.08
Crash ahead, $\dot{V} > 0, \dot{\psi}=0$	2.0	2.5	0.08	0.10
Crash astern, $\dot{V} < 0, \dot{\psi}=0$	2.0	2.5	0.08	0.10

The values are somewhat more accurate for the steady ahead runs than for the time-dependent runs, because the experimental conditions could be controlled more precisely for the steady runs and the measured forces and moments were averaged over many more revolutions of the propeller. The time-average values per revolution are slightly more accurate than the maximum values considering variation with blade angular position because the time-average values are based on 90 samples per revolution whereas the maximum values are based on one sample per revolution. Further, the peak values may be slightly influenced by the dynamic response of the flexures as discussed in the Calibration section.

The measured values of  $F_z$  are substantially less accurate than the other components of blade loading. Therefore, results for  $F_z$  are not presented, as discussed in the Experimental Results section.

## EXPERIMENTAL RESULTS

### Centrifugal Loads

The results of the air-spin experiments with the  $F_z$ ,  $M_z$  flexure were compared with calculated values of  $F_z$  and  $M_z$  using the method of

Boswell(18). Previous measurements of spindle torque by Boswell, et al(19) and by Hawdon, et al(3) have correlated well with values calculated by this procedure. Figures 7 and 8 show the correlation for  $M_z$  and  $F_z$ , respectively.  $M_z$  correlates fairly well except at  $P/D=-0.67$  and the correlation for  $F_z$  is rather poor. This poor correlation for  $F_z$ , combined with the large interaction effect of  $M_z$  on  $F_z$  and the low natural frequency of this flexure casts doubt on the reliability of the measured values of  $F_z$ . In addition, the experimental values of  $F_z$  in water were rather inconsistent. Since  $F_z$  arises primarily from centrifugal loading, no experimental results for  $F_z$  in water are presented.

### Influence of Dynamometer Boat

The results of the wake surveys with and without the downstream body (dynamometer boat) are presented in Figures 9 and 10. These data indicate that the downstream body has only a small effect on the circumferential and radial variation in the flow, and only a small effect on the harmonic content of the flow. However, these data indicate that the downstream body reduces the volume mean velocity through the propeller disc by approximately 12 percent. This reduction in mean flow due to the downstream body was confirmed by values deduced from thrust and torque identity between model experimental values with and without the downstream body in place. The values of reduction in effective velocity deduced in this manner are as follows:

(1) From measurement of mean thrust and torque using a transmission dynamometer inside the model hull at the self propulsion point (condition 1 in Table 3) with and without the downstream body in place: 10 to 14 percent.

(2) From mean thrust and torque deduced from the blade loading experiments at the self propulsion point (condition 1 in Table 3) and thrust and torque measured during a previous self propulsion model experiment: 10 to 14 percent.

(3) From mean thrust and torque coefficients deduced from blade loading experiments at  $P/D=1.06$  over a range of advance coefficient  $J$  with the downstream body at zero shaft angle with no upstream hull, and thrust and torque coefficient determined by previous open water experiments (Figure 11): 9 to 12 percent.

Based on these results it was concluded that the downstream body reduced the mean velocity into the propeller by 12 percent at the self propulsion condition. It was assumed that this 12 percent reduction occurred at all conditions at which experiments were conducted. Therefore, the time average value per revolution of each loading component was corrected for the effect of the downstream body as follows: From the measured blade thrust ( $F_x$ ) and blade torque ( $M_x$ ) an effective advance coefficient  $J$  based on thrust identity,  $J_T$ , and torque identity,  $J_Q$ , were deduced from the open water data (Figure 11). These were multiplied by (1/0.88) to obtain corrected values of  $J_T$  and  $J_Q$ , i.e., without the downstream body. The corrected values of  $F_x$  and  $M_x$  are obtained from the open water data at the corrected advance coefficients  $J_T$  and  $J_Q$ , respectively. It is assumed that the downstream body does not affect the radial center of thrust  $F_x$  and tangential force  $F_y$ . Therefore,



$$M_{y\text{corrected}} = \left( \frac{F_{x\text{corrected}}}{F_{x\text{measured}}} \right) M_{y\text{measured}}$$

$$F_{y\text{corrected}} = \left( \frac{M_{x\text{corrected}}}{M_{x\text{measured}}} \right) F_{y\text{measured}}$$

The spindle torque ( $M_z$ ) was corrected by the same procedure as used for  $F_x$  and  $M_x$ , except that the centrifugal and hydrodynamic components of spindle torque were separated so that the correction was applied to the hydrodynamic component only. Centrifugal spindle torque was determined by air spin experiments as discussed previously. The open water hydrodynamic spindle torque data used for these corrections was that reported by Denny and Stevens(20). These data were presented over a range of pitch ratio  $P/D$  and advance coefficient  $J$  for a propeller which was very similar to that used in the present investigation (the number of blades, blade outline shape, and spindle axis location are the same for these two propellers).

In addition to the correction to hydrodynamic spindle torque for mean advance coefficient, the centrifugal spindle torque was corrected for the difference in density between the aluminum model propeller and a nickel-aluminum-bronze full scale propeller. Since centrifugal spindle torque is directly proportional to the density of the material, this correction factor is simply  $(\rho_{\text{NI-AL-BR}})/(\rho_{\text{AL}})$ . The time-average spindle torque per revolution presented in this paper is the sum of the hydrodynamic spindle torque corrected for the downstream body and the centrifugal spindle torque which corresponds to nickel-aluminum-bronze propeller blades.

No correction for the effect of the downstream dynamometer boat was made to the measured circumferential variation of the loading components. Calculations using the methods of Tsakonas, et al(14) and McCarthy(15) indicate that the influence of the downstream body may reduce the peak to peak circumferential variation of the loads by approximately 10 percent of the uncorrected unsteady loading. However, these methods did not agree well with the experimental results, as discussed in the Correlation with Full Scale Data and Theory section.

#### Steady Ahead

For operation near the self propulsion point (condition 1 in Table 3), Figure 12 presents the variation of  $F_x$  with blade angular position, and Figure 13 presents the amplitude of the first 25 harmonics of  $F_x$ . For the harmonic amplitudes and phases, the variation with blade angular position is represented as:

$$F_x(\theta) = F_x + \sum_{n=1}^N (F_x)_n \cos(n\theta - (\phi_{F_x})_n)$$

where  $F_x$  = circumferential average value of  $F_x$ ,  
 $(F_x)_n$  = amplitude of the  $n$ th harmonic of  $F_x$ ,  
 $\theta$  = angular position in disc, positive clockwise from the vertical upward looking upstream. The reference line on the blade is the radial line through midchord at the hub radius.  
 $(\phi_{F_x})_n$  = phase angle of  $n$ th harmonic of  $F_x$ .

A similar representation is used for all components of blade loading.

Based on the dynamic calibration, as discussed in the section Calibration, it was judged that for all loading components the data are valid for the first 10 harmonics, except  $M_z$  which was judged to be valid for the first 5 harmonics. Therefore, all data and analyses except Figures 12 and 13, are based on reconstructed signals using 5 harmonics for  $M_z$  and 10 harmonics for other loading components. The spots shown on Figure 12 are the unfiltered values determined from the experiment, each spot representing the average value at the indicated blade angular position for over 200 propeller revolutions. The lines are the signals reconstructed from the first 10 harmonics. Figure 12 indicates that the variation of the signal with blade angular position is adequately represented by the number of harmonics retained. Figures 12 and 13 show that there is a resonance in the  $F_x$  signal near the 14th harmonic. This corresponds to  $(14)(17.65\text{Hz}) = 247\text{Hz}$  which is near the natural frequency of this flexure in water as discussed in the Calibration section. The characteristics of the data for  $F_x$ , as illustrated in Figures 12 and 13 is typical of the data for all components of blade loading.

The variation of all measured loading components with blade angular position for condition 1 in Table 3 is shown in Figure 14. Figure 15 presents the amplitude and phases of the harmonics of these loading components. The values for each loading component are presented as decimal fractions of the time average value of the corresponding loading component. These time average values are presented in Table 4. These data indicate that for all loading components the extreme values occur near  $\theta = 90$  degrees and  $\theta = 270$  degrees and the variation is predominately a once per revolution variation. This suggests that the tangential component of the wake is the primary driving force.

For  $F_x$  and  $M_y$ , which are the largest measured force and moment components, the maximum values are approximately 1.38 times the time average values; and the range of values with blade angular position, i.e., the maximum value minus the minimum value (double amplitude) are approximately 0.80 times the time-average value. For  $F_y$  and  $M_x$  the maximum values and range of values with blade angular position are somewhat smaller fractions of the respective time-average values. For  $M_z$  the maximum value and range of values with blade angular position are much greater fraction of its time average. This large fractional variation in  $M_z$  occurs because  $M_z$  is very small at the self propulsion point. This small value of  $M_z$  occurs because the blade is designed with its area balanced forward and aft the spindle axis at the self propulsion point.

#### Hull Pitch

Figure 16 presents the variation of the peak values and time average values per revolution of  $F_x$  with hull pitch angle  $\psi$  for both quasi-steady simulation, (time rate of change of hull pitch angle  $\dot{\psi} = 0$ ) and unsteady simulation ( $\dot{\psi} \neq 0$ ). The data for other components of blade loading show similar trends. These data show that, except for spindle torque,  $M_z$ , the time average value per revolution of each loading component remains

within 4 percent of its value corresponding to self propulsion in calm water. This holds true for both quasi-steady simulation,  $\psi=0$ , and unsteady,  $\psi \neq 0$ . The time-average spindle torque per revolution,  $M_z$ , varies by up to 20 percent from its value at  $\psi=\psi_{CW}$ , where  $\psi_{CW}$  is the value of  $\psi$  in calm water. This large percentage variation occurs because  $M_z$  is very small at  $\psi=\psi_{CW}$  as discussed previously.

For the quasi-steady runs, data at each specified value of hull pitch angle  $\psi$  were recorded and averaged for a minimum of 200 propeller revolutions, whereas for the dynamic pitching runs data at each specified  $\psi$  represented an average of from 10 to 35 propeller revolutions. As discussed in the Data Acquisition and Analysis section, the selection of a propeller revolution at a specified  $\psi$  during the dynamic pitch runs necessitates a tolerance of 0.1 degree to  $\psi$ ; however, the average value of  $\psi$  during steady runs for which data are presented is generally within 0.02 degree of the target  $\psi$ . Therefore, the differences between the results for the quasi-steady and unsteady simulations, including the time average values per revolution, is significantly larger than any errors which may arise from inaccuracies in setting the experimental conditions.

For both quasi-steady and unsteady simulation, the absolute value of the time-average value per revolution of all loading components, except spindle torque  $M_z$ , decreases slightly for bow up and increases slightly for bow down. This suggests that the effective speed of advance of the propeller increases slightly for the bow up condition and decreases slightly for the bow down condition. This appears reasonable since for bow down the propeller tends to be further into the boundary layer of the hull.

For the peak values, there is a significant difference between the results for the quasi-steady simulation and the unsteady simulation. For the quasi-steady simulation the variation of the peak values with hull pitch angle  $\psi$  follows the same trend as the variation of the time average values per revolution. These quasi-steady results indicate that for  $\psi$  up to two degrees the maximum increase in the peak value of any loading component above the corresponding value for  $\psi=\psi_{CW}$  is four percent. By contrast, the dynamic simulation shows that the maximum value of the peak loads may increase by up to 20 percent above the corresponding value for steady ahead at a fixed hull pitch,  $\psi=\psi_{CW}$ .

The dynamic simulation shows a dramatically different trend of peak load with  $\psi$  than indicated by the quasi-steady simulation. For the dynamic simulation the largest values of the peak loading components occur near  $\psi=\psi_{CW}$  as the hull passes from the bow up to the bow down position of the cycle, and the smallest value of peak loading components occurs near  $\psi=\psi_{CW}$  as the hull passes from the bow down to the bow up position of the cycle. Apparently, the time dependent motion of the hull has an adverse effect on the wake pattern into the propeller disc, i.e., it appears to cause the circumferential variation of the wake to increase. Comparison of the time, or location during the cycle of hull pitch angle  $\psi$  at which the largest peak loads occur for quasi-steady and unsteady simulations, shows a lag of approximately 0.95 seconds, or 0.75 cycles,

between the motion of the hull and the flow pattern into the propeller resulting from this motion. It is reasonable to expect that this time lag is approximately the time that it takes for a particle of fluid to move from the longitudinal center of the ship to the propeller. This time is approximately

$$(L/2V)=(6.49M)/[(2)(3.33)M/sec]=0.975 \text{ seconds}$$

and the corresponding fraction of the cycle is

$$(\text{time})(\text{frequency})=(0.975)(0.8)=0.78$$

These values agree with the observed lag of the maximum values of the peak loading components for the dynamic simulation as compared to the quasi-steady simulation.

The unsteady loading is important from consideration of fatigue of the propeller blades and hub mechanism. Since a ship may operate for an extended period in a seaway, the effect of the ship motions, such as dynamic hull pitching, on unsteady blade loads is of significance. The difference between the peak load and the time-average load per revolution is a measure of the unsteady loading. Using this difference as a measure of the unsteady loading, the quasi-steady simulation indicates that for hull pitch angles  $\psi$  up to two degrees, each unsteady loading component is increased by not more than 5 percent above its corresponding value for  $\psi=\psi_{CW}$ . By contrast, the dynamic simulation shows that the unsteady loading components are increased by over 50 percent above their corresponding values for  $\psi=\psi_{CW}$ . This indicates that the quasi-steady simulation is completely inadequate for estimating the effect of the seaway on unsteady loading. This also shows that the effect of the ship motions can dramatically increase the unsteady loading on the blades. Therefore, the effect of the ship motions due to operation in a seaway should be considered in any analysis of blade loading, and in any fatigue analysis of the propeller blades or hub mechanism.

#### Crash Ahead and Crash Astern

Figures 17 and 18 present the variation of components of blade loading with blade angular position, and the amplitude and phase of the harmonics of  $F_x$ , respectively, for the quasi-steady simulated crash-ahead condition,  $V=\dot{\psi}=\dot{\eta}=0$ . Figures 19 and 20 present similar results for the quasi-steady simulated crash-astern conditions,  $V=\dot{\eta}=\dot{\psi}=0$ . The values for each loading component are presented as decimal fractions of the time-average value of the corresponding loading component at the self propulsion condition (condition 1 of Table 3). These time-average values are presented in Table 4.

Taylor wake fraction based on thrust,  $1-w_T$ , and Taylor wake fraction based on torque,  $1-w_Q$ , derived from the measured values of  $F_x$  and  $M_x$  and the open-water characteristics of the propeller (Figure 11) are presented in Figure 21. These data indicate a substantial variation in  $1-w_T$  and  $1-w_Q$  during the simulated crash ahead and crash astern maneuvers. During the crash-ahead maneuver  $1-w_T$  is larger than its value near the self-propulsion point and  $1-w_Q$  is smaller than its value near the self-propulsion point. For the crash astern maneuver both  $1-w_T$  and  $1-w_Q$  initially



decrease with decreasing speed, and then increase dramatically as speed is further reduced. At the lowest experimental speed during simulated crash-astern ( $V=0.17M/sec$ ) both  $l-w_T$  and  $l-w_Q$  are greater than 2.5.

These indicated values of  $l-w_T$  and  $l-w_Q$  are subject to significant inaccuracies in the initial portion of the simulated crash forward, and in the final portion of the crash astern (shown dotted in Figure 21). These inaccuracies arise because the thrust and torque, which are measured on only one blade, are small in these regions

$$(F_X \leq 15N, \bar{M}_X \leq 0.5N\cdot m).$$

In addition, for  $P/D \leq 0.4$ ,  $K_Q$  is not sensitive to  $J$  in the region of interest during the simulated crash astern. This introduces significant inaccuracies in  $l-w_Q$  in this region.

Figures 17 and 19 show that for almost all measured loading components the maximum time average values per revolution and the peak values, including variation with blade angular position, occur at the third experimental condition ( $V=1.46M/sec$ ,  $n=11.19rev/sec$ ,  $P/D=1.39$ ) during the crash-ahead maneuver. For  $M_y$ , which is the largest moment component, the peak value and the maximum time average value per revolution are 1.51 and 1.35, respectively, times the time average value at the self propulsion point. For the other loading components, except spindle torque  $M_z$ , the peak value and the maximum time average value per revolution are in the range 1.35 to 1.60, and 1.20 to 1.45, respectively, times the corresponding time average value at the self propulsion point. For spindle torque  $M_z$  the peak value and the maximum time average value per revolution are 5.6 and 4.8, respectively, times the time average value at the self propulsion point. These large increases occur for  $M_z$  because  $\bar{M}_z$  is quite small at the self propulsion point as discussed in the Steady Ahead subsection.

For the crash astern maneuver, these results show that, except for spindle torque, the maximum time average load per revolution and the peak load, including variation with blade angular position, occurs at the initial (steady ahead) condition.

Higher loads than those shown in Figures 17 and 19 could, of course, be developed during crash-ahead or crash-astern maneuvers, depending upon values of  $\dot{V}$ ,  $\dot{n}$ , and  $\dot{P}$ .

For all loading components the variation with blade angular position tends to be dominated by the first harmonic for all conditions throughout the simulated crash-ahead and crash-astern maneuvers. For all conditions at which there is significant variation in loading with blade angular position  $\theta$  the maximum and minimum values occur near  $\theta=90$  degrees or  $\theta=270$  degrees. This suggests that the variation in loading with blade angular position is produced primarily by the circumferential variation of the tangential velocity in the propeller plane (see Figures 9 and 10). For the crash-ahead simulation, in which pitch  $P$  is constant throughout, the angular variation of each loading component retains basically the same shape independent of speed and advance coefficient. By contrast, for the crash-astern simulation, in which  $P/D$  changes from +1.06 to -0.67 for the different simulated conditions,

the circumferential variation of each loading component changes shape substantially with the different simulated combinations of speed, advance coefficient, and pitch ratio.

For both crash-ahead and crash-astern simulations, there is a dramatic reduction in the circumferential variation of all measured loading components with decreasing speed  $V$  and decreasing rotational speed  $n$ . Previous data have shown that for a given propeller in a given flow field the circumferential variation in the loading varies approximately as the product of ship speed  $V$  and rotational speed  $n$ ; see Wereldsma(21). Figure 22 presents some "typical" results in a form which allows evaluation of how closely measured unsteady loading varies with  $nV$ . The ordinate is  $(F_X)_1 \sin \phi$  which is the portion of the first harmonic in phase with the tangential velocity. This measure of the unsteady loading was selected because it may be positive or negative depending on  $\phi$ . The abscissa is  $nV \sin \phi_{0.7}$ . The term  $\sin \phi_{0.7}$  is intended to correct for the difference in pitch for the various runs, since the tangential component of the first harmonic of the wake  $(V_T)_1$  is the primary forcing function, and the component of  $(V_T)_1$  normal to the blade is  $(V_T)_1 \sin \phi_{0.7}$ ; see Wereldsma(21).

The data shown in Figure 22 indicate that the unsteady loading  $(F_X)_1 \sin \phi$  is approximately proportional to  $nV \sin \phi_{0.7}$ . The results for the crash-ahead simulation, with  $P/D=1.39$ , are consistently somewhat higher than those for the crash-astern simulation, and follow a linear variation with  $nV \sin \phi_{0.7}$  somewhat more closely than the results for the crash-astern simulation.

The reason for the systematic difference between the crash-ahead data and crash-astern data in Figure 22 is not clear; however, it may result from one or more of the following:

- (1) the difference in the time-average loading between the crash-ahead and crash-astern conditions. Thrust loading coefficient  $\bar{C}_{Th}$  is a measure of this time-average loading. For crash-ahead simulation the algebraic value of  $\bar{C}_{Th}$  is much larger than it is for crash-astern. This tends to increase the axial induced velocities and increase the spacing of the downstream vortex sheets for a given value of  $nV \sin \phi_{0.7}$ . This would tend to reduce the influence of the shed vorticity and thereby increase the net unsteady loading.
- (2) The effect of the action of the propeller on the wake pattern in the propeller disc. During a portion of the crash-astern maneuver the propeller generates negative thrust so that the time-average induced-velocity is upstream. This may interact with the flow over the hull and thereby influence the circumferential mean and circumferential variation of the flow pattern. As discussed previously the time average loading indicates that  $l-w_T$  and  $l-w_Q$  vary substantially over the simulated crash-ahead and crash-astern maneuvers (see Figure 21). However, using  $V(l-w_T)$  rather than  $V$  as the reference velocity in Figure 22 would not substantially change the trends shown.
- (3) Failure of the factor  $\sin \phi_{0.7}$  to properly account for the difference in propeller pitch over the range of  $(P/D)_{0.7}$  from +1.39 to -0.67. As



nominal pitch is changed over this range, the radial distribution of pitch changes dramatically.

(4) Experimental accuracy. For  $nV \sin \phi_0 < 2.0M/sec^2$  the measured unsteady loading is quite small; therefore, these results are not nearly as accurate as the results for higher values of  $nV \sin \phi_0$ .

The trends shown in Figure 22 for  $(F_x)_1$  are typical of the trends of all measured loading components when plotted versus  $nV$  times the appropriate function of pitch as presented by Wereldsma(21). Even though there is some scatter, the data follow the  $nV$  law quite well considering the wide range of advance coefficient  $J$  and pitch ratio  $P/D$  covered by these data.

Figure 23 presents the variation of the time average values per revolution and peak values of  $F_x$  for both the quasi-steady simulated crash-ahead ( $\dot{V}=n=P=0$ ) and the unsteady simulated crash-ahead ( $\dot{V}>0, n=P=0$ ). Figure 24 presents similar data for quasi-steady and unsteady simulated crash-astern runs. The difference in experimental results between the two types of crash ahead and crash astern simulations shown for  $F_x$  are typical of the differences for all measured loading components.

The variation in the measured loading components between the quasi-steady simulated crash-ahead and the unsteady simulated crash-ahead is not large. Except for spindle torque, the largest variation between the results from two types of simulation expressed on a decimal fraction of the corresponding time-average value at the self-propulsion point are 0.05 for the peak values and 0.03 for the time-average value per revolution. For most cases the variation is much smaller than these largest variations. The variation in the results between the two types of simulation appears to be almost random. This suggests that these deviations are some measure of the experimental accuracy, and do not represent any systematic trends arising from the difference in  $\dot{V}$  between the two types of simulation.

For the crash-astern, the variation in loads between the quasi-steady simulation and the unsteady simulation is not great but is somewhat larger than the variation for the crash-ahead simulations. Except for spindle torque, the largest variation between the results for the two types of simulation is approximately 0.20 times the time-average steady-ahead value for the peak load and 0.15 times the time-average steady-ahead value for the mean load. For most cases the variation is much smaller than these largest variations. The magnitude of most loading components is larger for the unsteady simulation for time

$t > 13.6 \text{ sec } (V < 1.67M/sec)$

and larger for the quasi-steady simulation for

$t > 9.05 \text{ sec } (V = 2.57M/sec)$ .

For the quasi-steady simulation, data were recorded and averaged for a minimum of 200 propeller revolutions, whereas for the unsteady runs the data presented represents an average of only three revolutions for crash-ahead simulation and five revolutions for crash-astern simulation. Further, the steady experimental conditions which were set during the quasi-steady simulation allow the values of  $V$  and  $n$  to be controlled more precisely than during the unsteady runs; however, the average of the three to five values of  $V$  and  $n$

during the unsteady runs for which data are presented is generally within one percent of the target values.

Therefore, for crash-astern the differences between the results for the quasi-steady simulation and the unsteady simulation is significantly greater than the errors arising from inaccuracies in setting the experimental results. It is concluded that there is a small influence of  $\dot{V}$  on the measured loads at a given combination of  $V, n$ , and  $P$ . However, this difference does not affect the peak loads that occur during a crash-astern maneuver.

#### CORRELATION WITH FULL SCALE DATA AND THEORY

For operation near the self propulsion point (condition 1 in Table 3) correlation was made between the model experimental results obtained in the present investigation, bending moments deduced from strains measured on the corresponding full scale propeller, and analytical calculations.

From the experimental values of  $F_x, F_y, M_x$ , and  $M_y$ , the bending moment can be calculated about any radial station  $r < r_h$  and about any axis normal to the radial direction. However, for calculating bending moments about  $r_0 > r_h$  an adjustment must be made for the contribution of the loading in the region  $r_0 > r > r_h$ . In calculating the bending moment about the 0.4 radius,  $M_{0.4}$ , from experimental values of  $F_x, F_y, M_x$ , and  $M_y$ , it was estimated that for all harmonics including the time-average values 3 percent of  $M_x$  and  $M_y$  was contributed by the loading in the region  $0.4R > r > r_h$ .

The full scale strains used for correlation were measured\* at the mid-chord position of the 40 percent radius on the face of the propeller under steady ahead operation. The full scale operating condition corresponds approximately, but not precisely, to the Froude scaled steady ahead condition on the model (condition 1 in Table 3).

The correlation is based on the bending moment vector parallel to the nose-tail line at the 40 percent radius at conditions corresponding to condition 1 in Table 3. For the trial data, radial stresses are deducted from strains using the appropriate values of Young's Modulus and Poisson's Ratio. The bending moment vector parallel to the nose-tail line is deduced from the stress assuming the blade behaves structurally as a cantilever beam.

The time-average bending moment deduced from the full-scale data was corrected for the difference between the scaled thrust and torque measured during the full-scale trial and the thrust and torque measured on the model. With this correction, the time-average bending moment determined from the full-scale data is 1.02 times the value determined from the model experiment.

The unsteady bending moment determined from the full-scale data was adjusted to the model conditions using the following:

$$M_{MES} = (M_S / \lambda^4) [(V_M n_M \rho_M) / (V_S n_S \rho_S)]$$

\*The full-scale measurements were conducted by C.J. Noonan and G.P. Antonides of DTNSRDC.

where subscript M refers to model values, subscript S refers to ship values,  $M_{ES}$  is the equivalent bending moment at the model conditions as deduced from the ship data, and  $\lambda$  is the linear scale ratio,  $LS/LM$ . This adjustment assumes that the unsteady loading varies linearly with  $nV$ ; see Wereldsma(21). Since the ship conditions are near the Froude scaled model conditions this adjustment is small except for the factor  $\lambda^4$ .

Figures 25 and 26 present the variation with blade angular position and the first ten harmonics, respectively, of  $M_{0.4}$  from the model data and from the full scale ship data. All data are nondimensionalized on the same quantity; i.e., the time average bending moment determined from the model experiments. This comparison indicates that for peak to peak values and for the first harmonic the experimental results obtained from the model and from full scale ship agree reasonably well with one another.

Theoretical calculations were made using the method of Tsakonas et al(14) which is based on unsteady lifting surface theory; and using the method of McCarthy(15) which is a quasi-steady technique utilizing the open-water characteristics of the propeller. These calculations were made for condition 1 in Table 3 using the wake measured in the plane of the propeller both with and without the downstream dynamometer boat in place (Figures 9 and 10). The difference in the calculated results with and without the dynamometer boat is a measure of the effect of the dynamometer boat on the circumferential variation of the unsteady loads.

For the method of Tsakonas, et al, calculations were conducted for the first ten harmonics of the wake. These calculations were made using the computer program developed at Davidson Laboratory including refinements made in December 1975. The "normal" components of wake harmonics as required by this method were defined as the wake harmonics normal to the chord line of the blade section at the local radius rather than normal to the advance angle at the local radius as recommended by Tsakonas, et al(22). With the wake harmonics resolved normal to the blade chord, this method apparently considers both the unsteady flow parallel to the resultant inflow and the unsteady flow normal to the resultant inflow.

The quasi-steady calculations are based on the circumferential variation of the wakes measured at the 0.71 radial station, except the narrow velocity defects behind the struts at approximately  $\theta_w=25$  degrees and  $\theta_w=335$  degrees are not considered. Since these defects are narrow relative to the blade width, it is judged that these should have only slight influence on the circumferential variation of blade loading. It is assumed that the radial centers of the unsteady thrust and tangential force are the same as the radial centers of the respective mean values.

Figures 26 through 28 present the variation with blade angular position and the first ten harmonics of  $M_{0.4}$  from the model experiment and analytical calculations. All data are nondimensionalized on the same quantity; i.e., the time average bending moment determined from the model experiments. This comparison indicates that the experimental results are considerably higher than

the calculated results. For other components of blade loading,  $F_x$ ,  $F_y$ ,  $M_x$ , and  $M_y$ , the circumferential variation in the model experimental results is larger than the values calculated by the two indicated procedures by approximately the same ratio as shown for  $M_{0.4}$ . These comparisons are not shown.

The reason for the large discrepancy between the experimental results and the calculated results is not clear. Some possibilities are as follows:

- (1) Interaction between the propeller and the hull may increase the circumferential nonuniformity of the flow into the propeller from the values measured without the propeller in place. (Both sets of calculations are based on the wake measured in the plane of the propeller with the propeller removed.) The experimental data show that the maximum and minimum loading occurs near  $\theta=90$  degrees and near  $\theta=270$  degrees. This implies that the dominant influence of the wake is the tangential velocity. Therefore, if the effect of the propeller on the wake pattern is the reason for the large discrepancy between theory and experiment, the propeller must increase the upsweep angle between the flow and the propeller shaft from approximately 10 degrees without the propeller to approximately 20 degrees with the propeller.
- (2) Other interactions between the propeller and the nearby surfaces which are not considered in the calculations based on the measured wake distribution.
- (3) Inaccuracies in the measured wake. This is unlikely since the tangential component of the wake indicates that the flow is approximately parallel to the stern.
- (4) Error in the experimental results. This appears unlikely since the model experiments and full scale experiments, which were conducted entirely independently, are in reasonably good agreement.
- (5) Inaccuracies in theoretical results. The unsteady lifting surface procedure of Tsakonas, et al(14) is based on linearized theory which considers the harmonic content of the longitudinal and tangential components of the wake. It is possible that nonlinear effects or the significant radial component of the wake may influence the circumferential variation of the loading. In addition, there may be inaccuracies in the numerical evaluation of the theory. The quasi-steady procedure of McCarthy(15) is exceedingly simple and should give reasonable results, especially for the first harmonic which has a low reduced frequency. However, this method does not consider any possible effects of the circumferential variation of the radial component of inflow velocity.

#### SUMMARY AND CONCLUSIONS

Experiments were described in which the mean and unsteady loads were measured on a single blade of a model controllable-pitch propeller. The experiments were conducted behind a model hull under steady ahead operation, hull pitching motions, simulated crash ahead maneuvers, and simulated crash astern maneuvers. The experimental techniques were described including a description of the dynamometer and data analysis system.



The results are summarized as follows:

(1) The circumferential variation of all measured components of blade loading is primarily a first harmonic, with maximum and minimum values occurring near the blade angular position at which the blade spindle axis is horizontal.

(2) For steady ahead:

(a) For measured forces and bending moments the maximum values are up to approximately 1.38 the time-average values and the peak to peak circumferential variations are up to approximately 0.80 the time-average values.

(b) For circumferential variation of bending moments about the nose-tail line of the 0.4 radius, the model experimental results agree fairly well with loads deduced from strain measurements on the full scale propeller, but are larger than theoretically calculated values.

(3) For simulated hull pitch (maximum pitch angle is 2 degrees).

(a) The maximum value of measured forces and bending moments increase over the corresponding values without hull pitch by 4 percent for quasi-steady simulation and by 20 percent for unsteady simulation with pitching frequency equal to 0.8Hz.

(b) The peak to peak circumferential variation of the measured forces and bending moments increase over the corresponding values without hull pitch by approximately 5 percent for quasi-steady simulation and by 50 percent or more for unsteady simulation with pitching frequency equal to 0.8Hz. Therefore, any quasi-steady simulation of ship motions is completely inadequate for estimating the effect of ship motions on unsteady propeller blade loading.

(4) For simulated crash forward:

(a) The dominant first harmonic of the measured forces and bending moments varies in a nearly linear manner with the product of ship speed and propeller rotational speed.

(b) The acceleration of the hull does not have a significant effect on the measured loads. Therefore, propeller blade loading during a crash ahead maneuver can be adequately estimated by quasi-steady experiments.

(c) The maximum time average values of measured forces and bending moments per revolution during the simulated crash forward maneuvers are in the range of 1.20 to 1.45 the time-average values at the self propulsion point.

(d) The peak values of measured forces and bending moments during the simulated crash forward maneuvers are in the range of 1.35 to 1.60 the time-average values at the self propulsion point.

(e) The Taylor wake fractions deduced from the time-average thrust and torque per revolution vary substantially from the values at the self propulsion point.

(5) For simulated crash astern:

(a) The first harmonic of the measured forces and bending moments varies approximately linearly

with the product of ship speed and propeller rotational speed, and is a function of propeller pitch.

(b) The deceleration of the hull alters the peak value of a given component of loading at a given condition by up to 20 percent of the time-average value at the self propulsion point; however, this does not alter the peak load occurring at any time during the simulated crash astern maneuver. Therefore, propeller blade loading during a crash astern maneuver can be adequately estimated by quasi-steady experiments.

(c) The largest time-average loads per revolution and the peak loads including circumferential variation occur at the initiation of the simulated crash astern maneuver; i.e., loads during the crash astern maneuver did not exceed the loads at the self-propulsion point.

(d) The Taylor wake fractions deduced from the time-average thrust and torque per revolution vary substantially from the values at the self propulsion point.

#### ACKNOWLEDGMENTS

The authors are indebted to members of the staff of the David W. Taylor Naval Ship Research and Development Center; especially to Mr. Stephen E. Callanen for adaptation and design of the experimental apparatus, to Mr. Arthur W. Block for development of the on-line data analysis system, to Mr. John J. Gordon for development of electronic and mechanical systems for the experiment, to Mr. Richard D. Kader for assistance in conducting the experiments and data analysis, to Messrs. Charles R. Crockett and Jack A. Diskin for assistance in data analysis and analytical calculations, to Dr. William B. Morgan and Mr. Richard A. Cumming for overall guidance and review of the manuscript, and to Ms. Kelice K. McCabe for preparation of the manuscript.

#### REFERENCES

- (1) Schwanecke, H. and Wereldsma, R., "Strength of Propellers Considering Steady and Unsteady Shaft and Blade Forces, Stationary and Nonstationary Environmental Conditions," Proceedings of the Thirteenth International Towing Tank Conference, Report of the Propeller Committee, Appendix 2b, Vol. 2, 1972
- (2) Rusetskiy, A.A., "Hydrodynamics of Controllable Pitch Propellers," Shipbuilding Publishing House, Leningrad, 1968
- (3) Hawdon, L., Carlton, J.S., and Leathard, F.I., "The Analysis of Controllable Pitch Propeller Characteristics at Off-Design Conditions," Transactions of the Institute of Marine Engineers, Vol. 88, 1976
- (4) Schwanecke, H., "Comparative Calculations on Unsteady Propeller Blade Forces," Proceedings of the Fourteenth International Towing Tank Conference, Vol. 3, 1975, p 357-397
- (5) Breslin, J.P., "Propeller Excitation Theory," Proceedings of the Fourteenth International Towing Tank Conference, Report of the Propeller Committee, Appendix 2c, Vol. 2, 1972



- (6) Boswell, R.J. and Miller, M.L., "Unsteady Propeller Loading-Measurement, Correlation with Theory, and Parametric Study," Naval Ship Research and Development Center Report 2625, October 1968
- (7) Meyne, K., "Propeller Manufacture - Propeller Materials - Propeller Strength," International Shipbuilding Progress, Vol. 22, No. 247, March 1975, p 77-102
- (8) Wereldsma, R., "Comparative Tests on Vibratory Propeller Forces," Proceedings of the Thirteenth International Towing Tank Conference, Report of the Propeller Committee, Appendix 2a, Vol. 2, 1972
- (9) Huse, E., "An Experimental Investigation of the Dynamic Forces and Moments on One Blade of a Ship Propeller," Proceedings of the Symposium on Testing Techniques on Ship Cavitation Research, The Norwegian Ship Model Experimental Tank, Trondheim, Norway, May-June 1967
- (10) Blaurock, J., "Propeller Blade Loading in Nonuniform Flow," The Society of Naval Architects and Marine Engineers, Propellers 75 Symposium, July 1975
- (11) Dobay, G.F., "Time-Dependent Blade-Load Measurements on a Screw-Propeller," Presented to the Sixteenth American Towing Tank Conference, August 1971
- (12) Wereldsma, R., "Last Remarks on the Comparative Model Tests on Vibratory Propeller Forces," Proceedings of the Fourteenth International Towing Tank Conference, Vol. 3, 1975, p 421-426
- (13) Tasaki, R., "Propulsion Factors and Fluctuating Propeller Load in Waves," Proceedings of the Fourteenth International Towing Tank Conference, Vol. 4, 1975, p 224-236
- (14) Tsakonas, S., Jacobs, W.R., and Ali, M.R., "An Exact Linear Lifting Surface Theory for Marine Propeller in a Nonuniform Flow Field," Journal of Ship Research, Vol. 17, No. 4, December 1974
- (15) McCarthy, J.H., "On The Calculation of Thrust and Torque Fluctuations of Propellers in Nonuniform Wake Flow," David W. Taylor Model Basin Report 1533, October 1961
- (16) Hadler, J.B. and Cheng, H.M., "Analysis of Experimental Wake Data in Way of Propeller Plane of Single and Twin-Screw Ship Models," Transactions of the Society of Naval Architects and Marine Engineers, Vol. 73, 1965, p 287-414
- (17) Brandau, J.H., "Static and Dynamic Calibration of Propeller Model Fluctuating Force Balances," David Taylor Model Basin Report 2350, March 1967; also Technologia Naval, Vol. 1, January 1968, p 48-74
- (18) Boswell, R.J., "A Method of Calculating the Spindle Torque of a Controllable-Pitch Propeller at Design Conditions," Naval Ship Research and Development Center Report 1529, August 1961
- (19) Boswell, R.J., Nelka, J.J., and Kader, R.D., "Experimental Spindle Torque and Open-Water Performance of Two Skewed Controllable-Pitch Propellers," David W. Taylor Naval Ship Research and Development Center Report 4753, December 1975
- (20) Denny, S.B. and Stephens, H.G., "Blade Spindle Moment on Controllable-Pitch Propellers," Naval Ship Research and Development Center Report SPD-011-14, July 1974
- (21) Wereldsma, R., "Tendencies of Marine Propeller Shaft Excitations," International Shipbuilding Progress, Vol. 19, No. 218, October 1972
- (22) Tsakonas, S., Breslin, J., and Miller, M., "Correlation and Application of an Unsteady Flow Theory for Propeller Forces," Transactions of the Society of Naval Architects and Marine Engineers, Vol. 75, 1967, p 158-193

TABLE 1

## Characteristics of Model Propeller

Diameter,  $D$ : 0.2343 meters

Rotation: Right Hand

Number of Blades,  $Z$ : 5Expanded Area Ratio,  $A_E/A_0$ : 0.83

Section Meanline: NACA 65

Section Thickness Distribution: NACA 16 (Modified)

Design Advance Coefficient,  $J$ : 0.767Design Advance Angle,  $\beta^*$ : 19.23 degreesDesign Thrust Loading Coefficient,  $C_{Th}$ : 0.706

$r/R$	$c/D$	$P/D$	$S/D^*$	$\theta_s$	$Z_R/D$	$t/D$	$f_M/c$
0.30	0.1853	1.008	0.0185	4.826	0	0.0437	0.0243
0.40	0.2482	1.044	0.0248	5.465	0	0.0328	0.0302
0.50	0.3111	1.067	0.0311	5.896	0	0.0250	0.0280
0.60	0.3740	1.072	0.0374	6.209	0	0.0187	0.0240
0.70	0.4369	1.061	0.0437	6.443	0	0.0131	0.0191
0.80	0.4760	1.025	0.0476	6.313	0	0.0089	0.0140
0.90	0.4600	0.964	0.0460	5.544	0	0.0061	0.0082
0.95	0.4587	0.922	0.0459	4.750	0	0.0051	0.0042
1.00	0.3400	0.878	0.0340	2.272	0	0.0040	0.0000

\*Measured from the propeller reference line, which coincides with the spindle axis, to the section mid-chord position.

TABLE 2  
Calibration Matrix

$$\text{Calibration Matrix} = [C_{i,j}] = \begin{bmatrix} 0.0652 & 0.0017 & -0.0003 & 0.0292 & -0.0531 & -0.0212 \\ -0.0025 & 0.0680 & -0.0001 & 0.0398 & 0.0434 & 0.0363 \\ 0.0002 & 0.0018 & 0.0203 & 0.0319 & -0.0027 & -0.3363 \\ 0.0005 & 0.0009 & 0.0004 & 1.6853 & -0.0080 & 0.0920 \\ -0.0018 & -0.0026 & 0.0013 & -0.0460 & 1.6605 & 0.0478 \\ -0.0002 & 0.0002 & 0.0000 & 0.0035 & 0.0035 & 1.1666 \end{bmatrix}$$

where

$$\begin{bmatrix} F_{x_I} \\ F_{y_I} \\ F_{z_I} \\ M_{x_I} \\ M_{y_I} \\ M_{z_I} \end{bmatrix} = \begin{bmatrix} F_{x_A} \\ F_{y_A} \\ F_{z_A} \\ M_{x_A} \\ M_{y_A} \\ M_{z_A} \end{bmatrix} \cdot [C_{i,j}]$$

$F_{x_I}, F_{y_I}, F_{z_I}$  are indicated forces in volts.

$M_{x_I}, M_{y_I}, M_{z_I}$  are indicated moments in volts.

$F_{x_A}, F_{y_A}, F_{z_A}$  are applied forces in Newtons.

$M_{x_A}, M_{y_A}, M_{z_A}$  are applied moments in Newton-meters.

$C_{i,j}$  for  $j=1,2,3$  are in volts/Newton.

$C_{i,j}$  for  $j=4,5,6$  are in volts/Newton-meters.



TABLE 3  
Experimental Conditions

	Condi- tion No.	V (M/sec)	n (rev/sec)	$J_V$	P/D	$(\psi - \psi_{cw})$ degrees	$\dot{V}$ (M/sec <sup>2</sup> )
Self Propulsion	1	3.33	17.65	0.80	1.06	0	0
Quasi-steady Hull Pitch	2	3.33	17.65	0.80	1.06	-2	0
	3	3.33	17.65	0.80	1.06	-1	0
	4	3.33	17.65	0.80	1.06	+1	0
	5	3.33	17.65	0.80	1.06	+2	0
Unsteady Hull Pitch	6	3.33	17.65	0.80	1.06	variable <sup>2</sup>	0
Quasi-steady Crash Forward	7	0.33	6.26	0.22	1.39	0	0
	8	0.81	9.35	0.37	1.39	0	0
	9	1.46	11.19	0.56	1.39	0	0
	10	2.26	12.07	0.80	1.39	0	0
	11	3.10	13.40	0.99	1.39	0	0
Unsteady Crash Forward	12	0.33 <sup>1</sup>	6.26	0.22	1.39	0	+0.19 <sup>1</sup>
	13	0.81 <sup>1</sup>	9.35	0.37	1.39	0	+0.23 <sup>1</sup>
	14	1.46 <sup>1</sup>	11.19	0.56	1.39	0	+0.33 <sup>1</sup>
	15	2.26 <sup>1</sup>	12.07	0.80	1.39	0	+0.33 <sup>1</sup>
	16	3.10 <sup>1</sup>	13.40	0.99	1.39	0	+0.01 <sup>1</sup>
Quasi-steady Crash Astern	17	3.33	17.65	0.80	1.06	0	0
	18	2.57	17.43	0.63	0.61	0	0
	19	1.67	16.59	0.43	0.14	0	0
	20	0.74	6.77	0.46	-0.67	0	0
	21	0.17	7.64	0.10	-0.67	0	0
Unsteady Crash Astern	22	3.33 <sup>1</sup>	17.65	0.80	1.06	0	0.00 <sup>1</sup>
	23	2.57 <sup>1</sup>	17.43	0.63	0.61	0	-0.32 <sup>1</sup>
	24	1.67 <sup>1</sup>	16.59	0.43	0.14	0	-0.43 <sup>1</sup>
	25	0.74 <sup>1</sup>	6.77	0.46	-0.67	0	-0.32 <sup>1</sup>
	26	0.17 <sup>1</sup>	7.64	0.10	-0.67	0	-0.18 <sup>1</sup>

<sup>1</sup>Varies with time (Figure 6), value shown is at time of interest.

<sup>2</sup>Sinusoidal with amplitude equal to 2.0 degrees, frequency equal to 0.8Hz.

TABLE 4  
TIME AVERAGE LOADS FOR STEADY AHEAD OPERATION NEAR  
THE SELF-PROPULSION POINT

$V = 3.33 \text{ M/sec}$   
 $n = 17.65 \text{ rev/sec}$   
 $J_V = 0.80$   
 $P/D = 1.06$

$\bar{K}_{F_x} = 0.0321$	$\bar{F}_x = 30.0 \text{ N}$
$\bar{K}_{F_y} = 0.0213$	$\bar{F}_y = 19.9 \text{ N}$
$\bar{K}_{M_x} = -0.0059$	$\bar{M}_x = -1.29 \text{ N-m}$
$\bar{K}_{M_y} = 0.0118$	$\bar{M}_y = 2.59 \text{ N-m}$
$\bar{K}_{M_z} = -0.0006$	$\bar{M}_z = -0.13 \text{ N-m}$
$\bar{K}_{M_h} = 0.0069$	$\bar{M}_h = 1.51 \text{ N-m}$
$\bar{K}_{M_{0.4}} = 0.0050$	$\bar{M}_{0.4} = 1.10 \text{ N-m}$

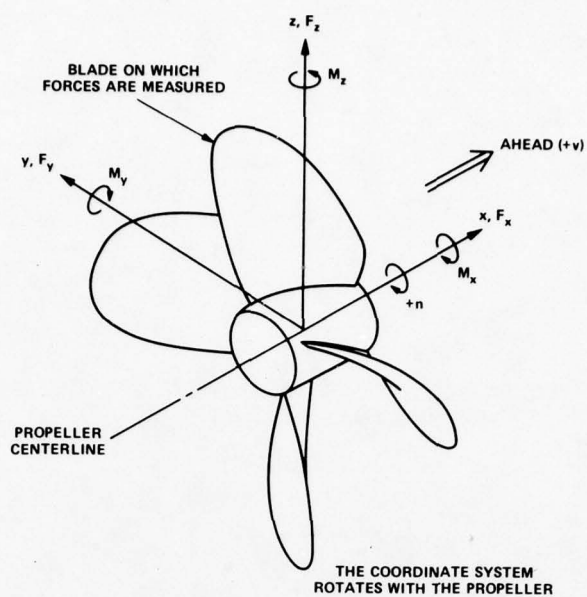


Fig. 1: Components of blade loading

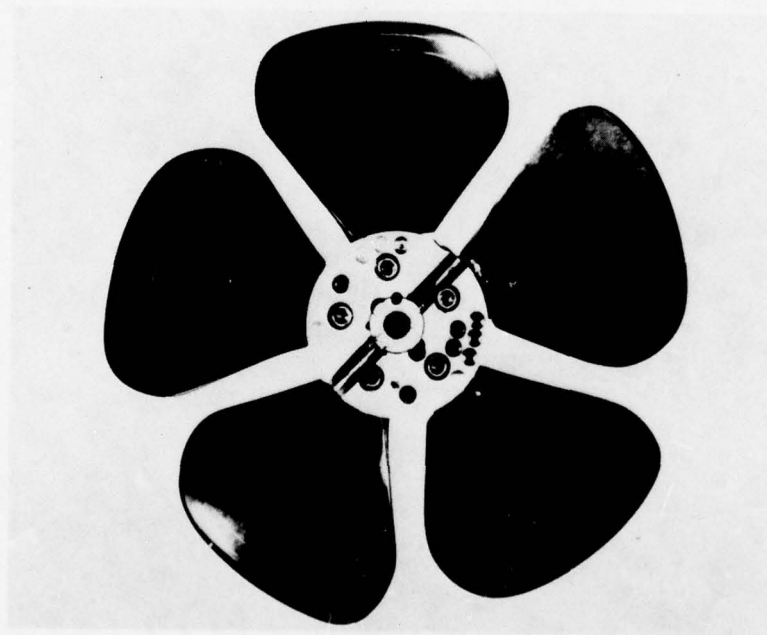


Fig. 2: Model propeller



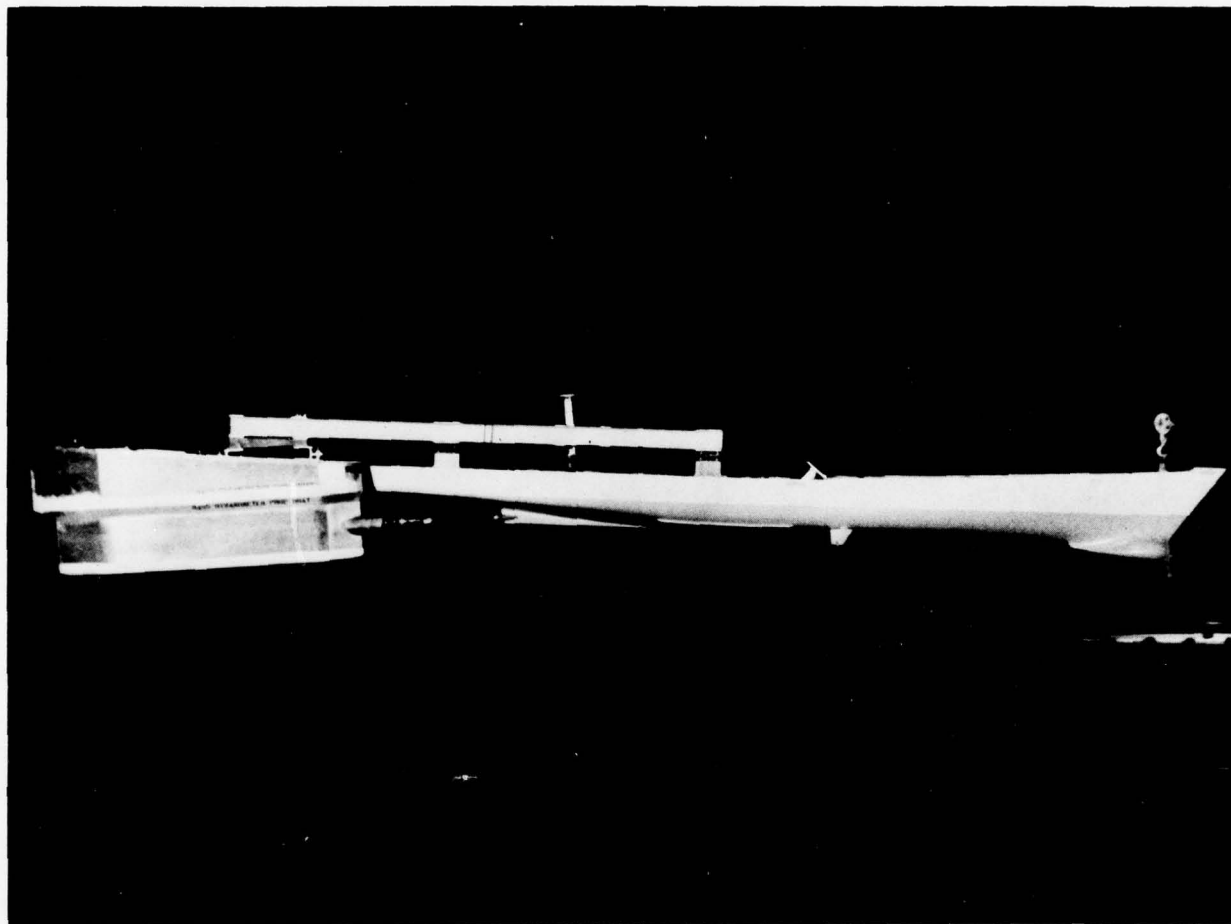


Fig. 3a: Overall view

Fig. 3: Hull and dynamometer boat

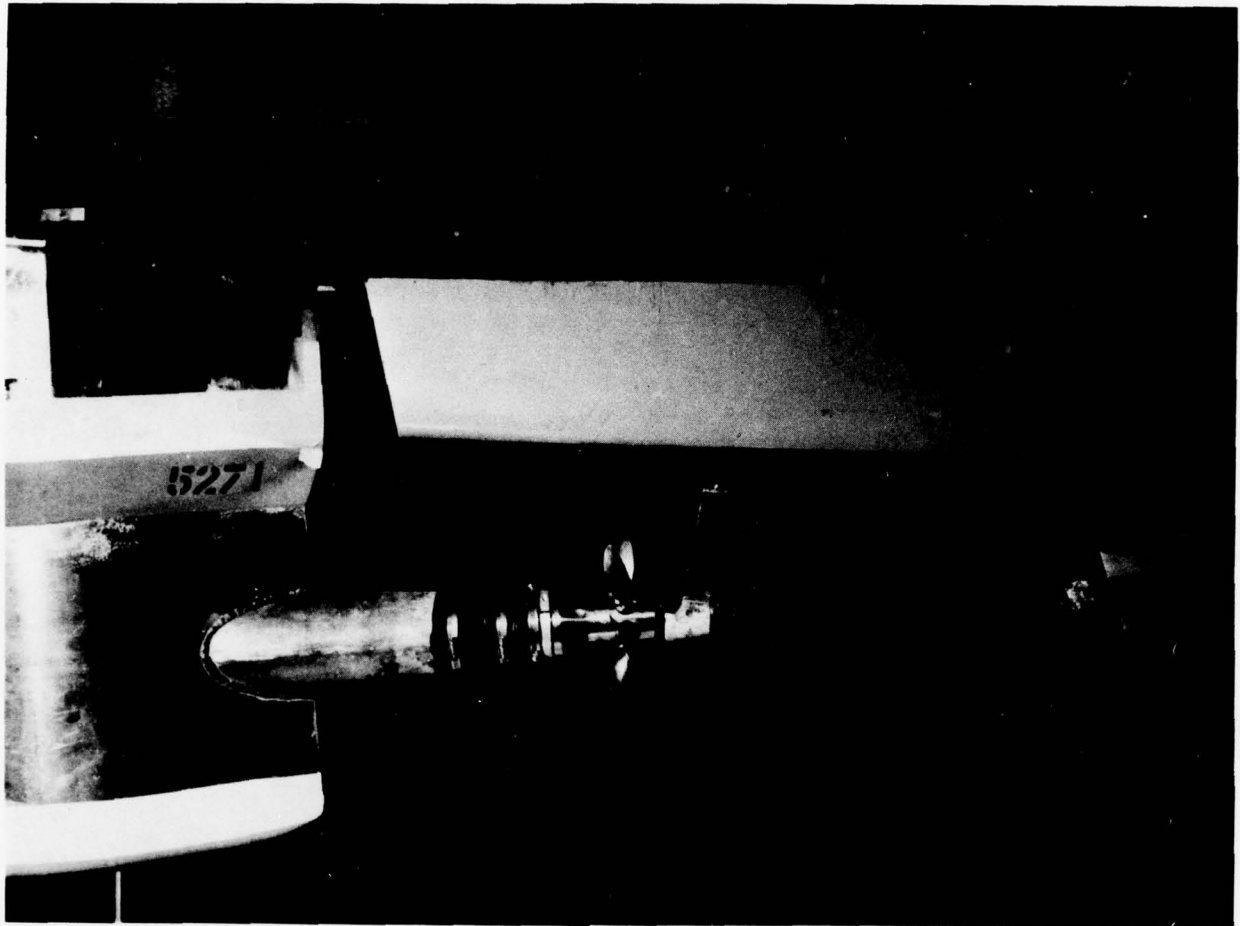
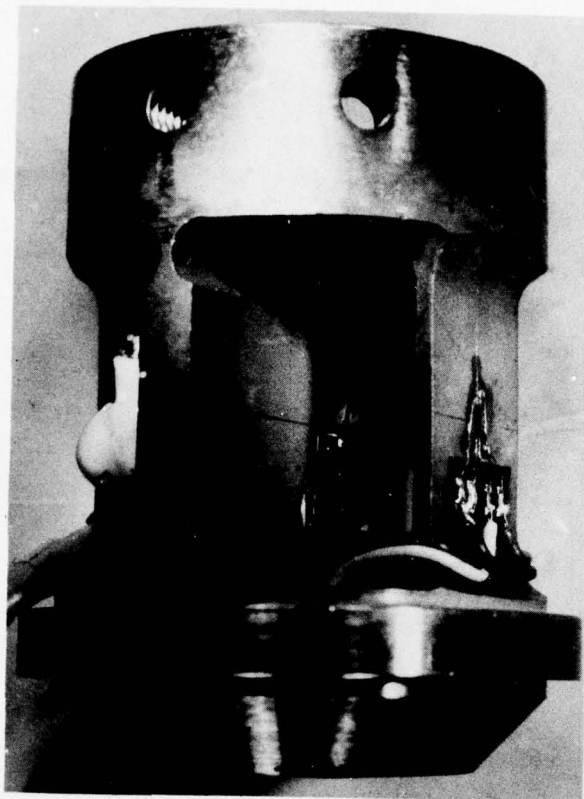


Fig. 3b: Closeup of propeller



**Fig. 4: Strain gaged blade flexure**



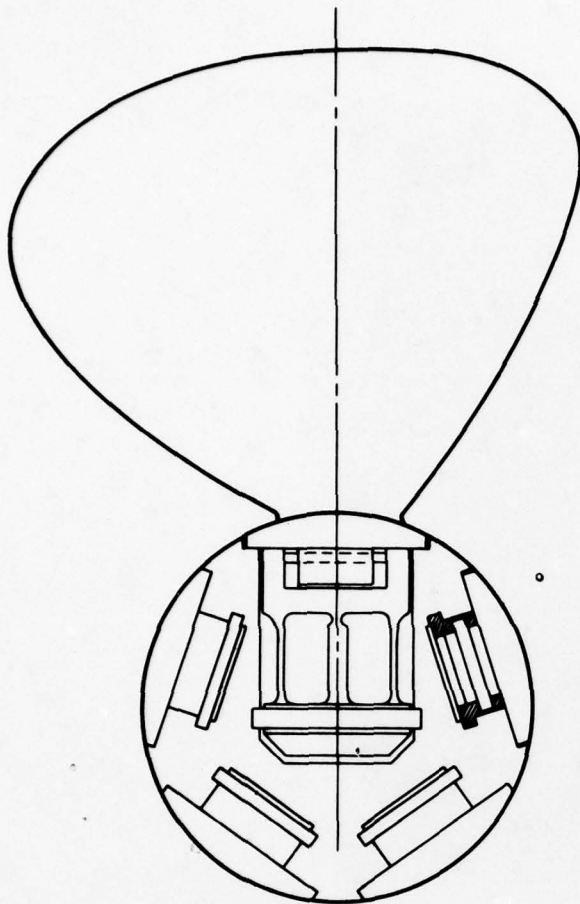


Fig. 5: Arrangement of flexures in hub

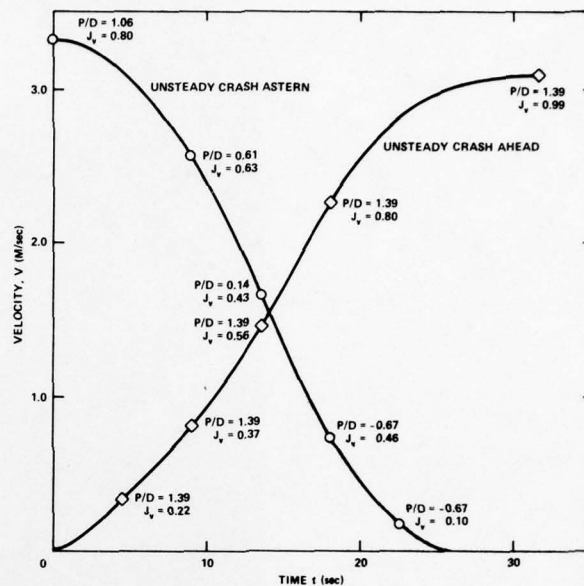


Fig. 6: Experimental deceleration and acceleration conditions

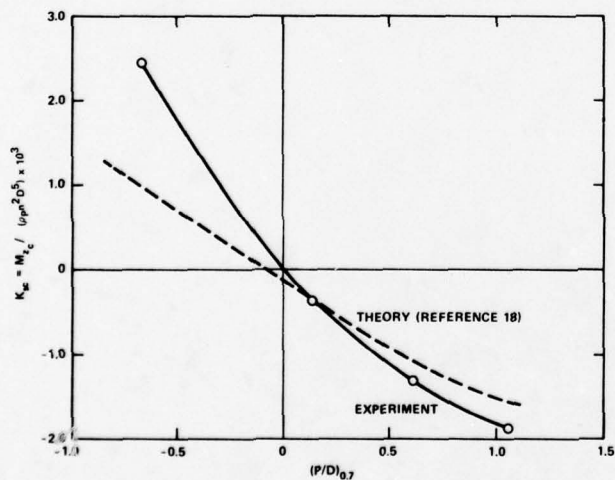


Fig. 7: Correlation of theory and experiment for centrifugal spindle torque

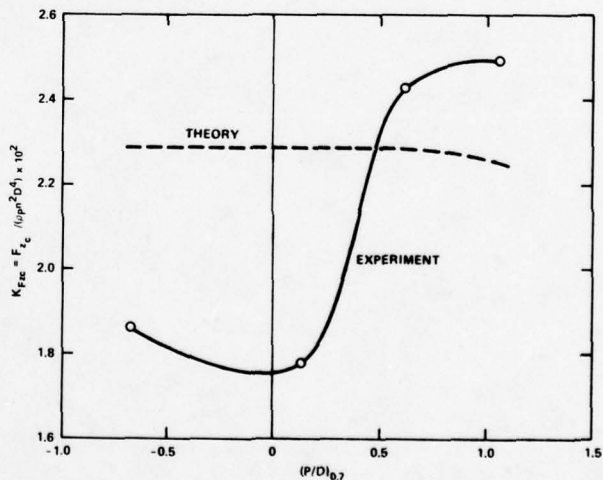


Fig. 8: Correlation of theory and experiment for centrifugal force

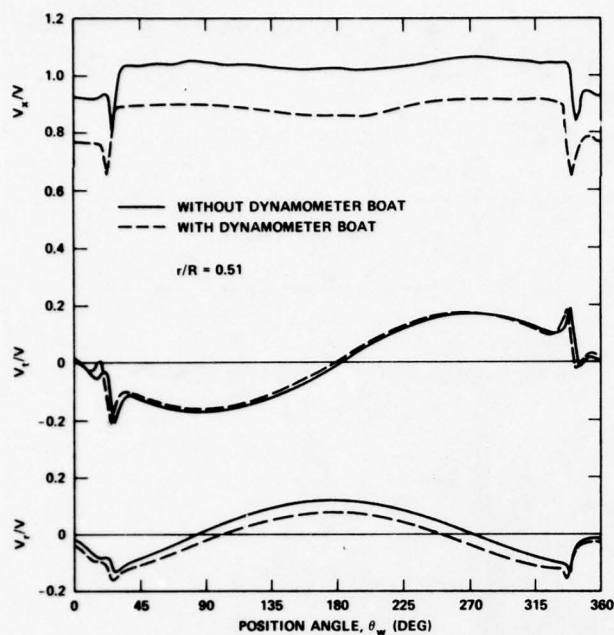


Fig. 9a: 51 percent radius

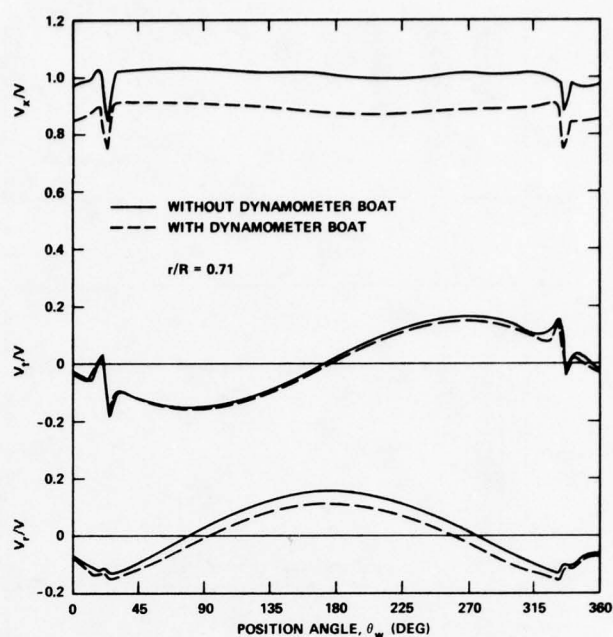


Fig. 9b: 71 percent radius

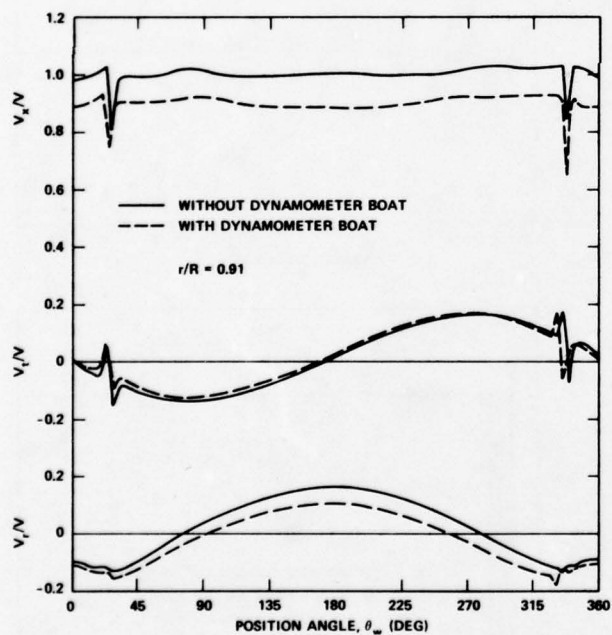


Fig. 9c: 91 percent radius

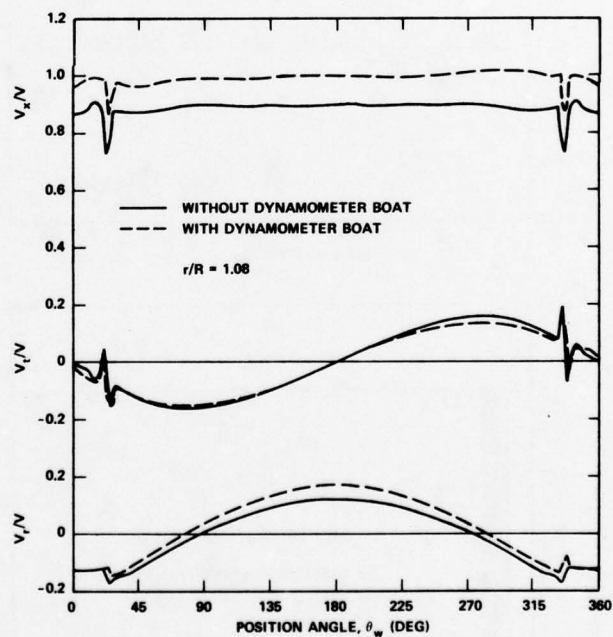


Fig. 9d: 108 percent radius

Fig. 9: Circumferential distribution of wake in propeller disc

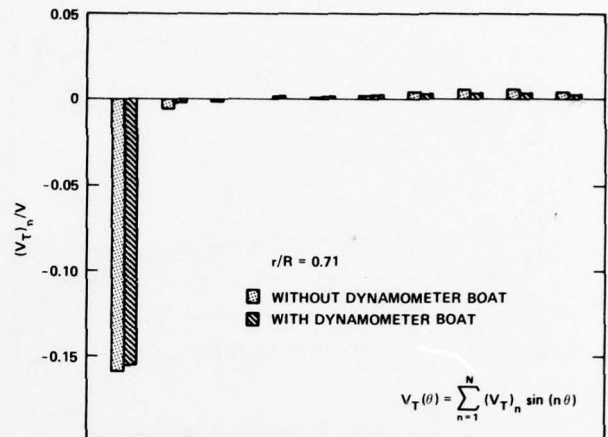
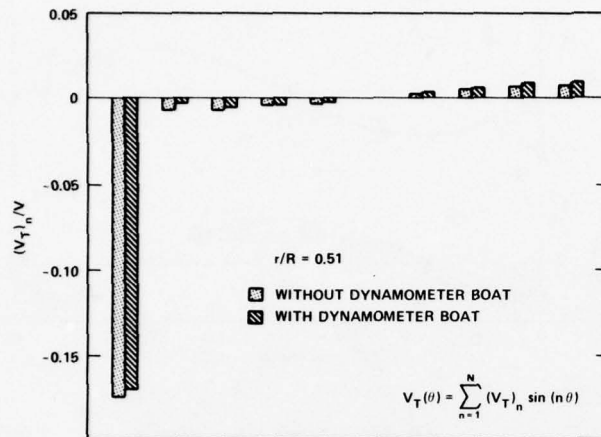
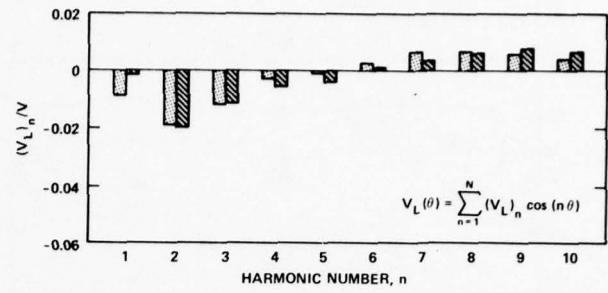
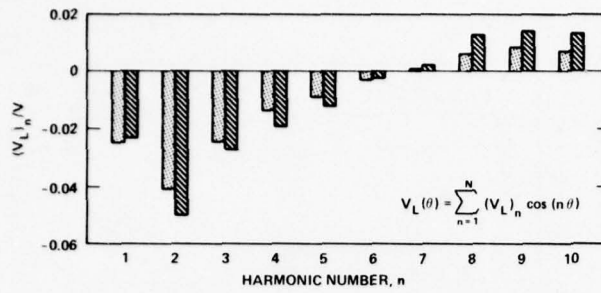


Fig. 10a: 51 percent radius

Fig. 10b: 71 percent radius

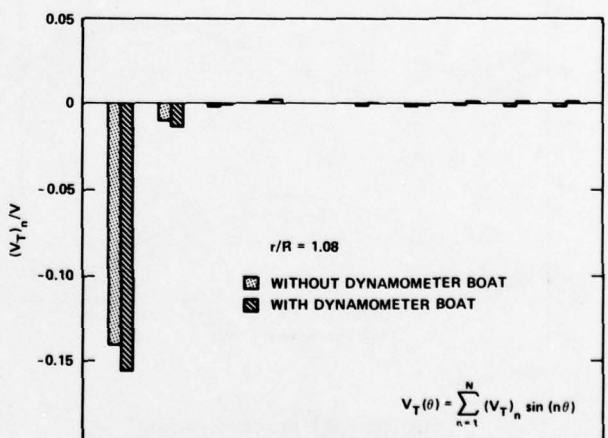
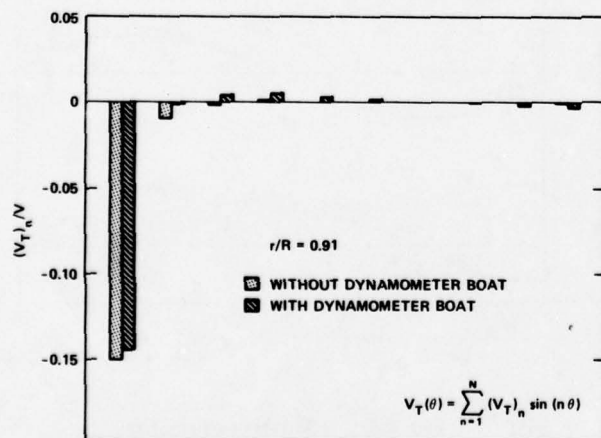
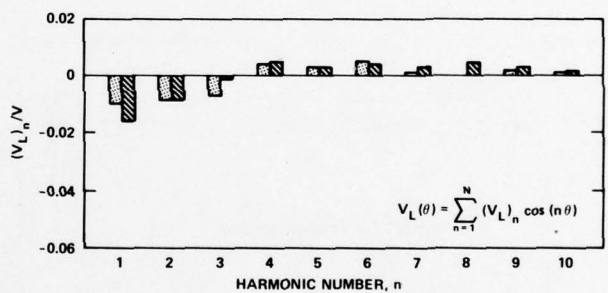
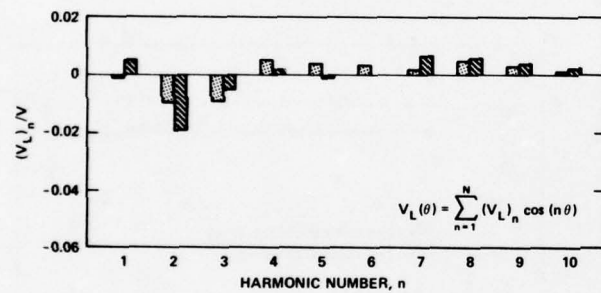


Fig. 10c: 91 percent radius

Fig. 10d: 108 percent radius

Fig. 10: Harmonic amplitudes of wake velocities



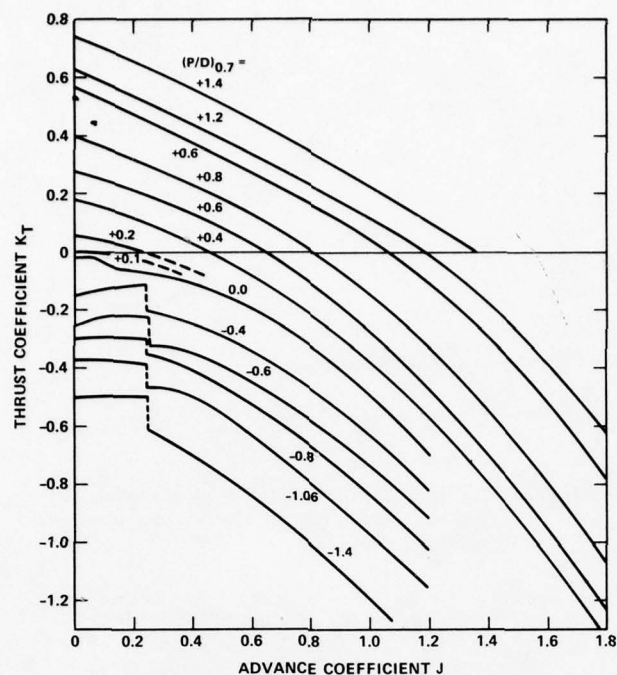


Fig. 11a: Thrust coefficient

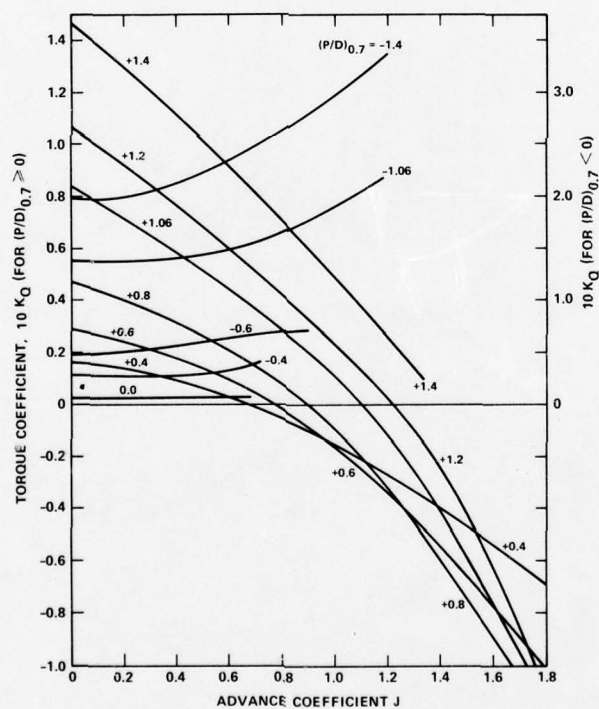


Fig. 11b: Torque coefficient

Fig. 11: Open water characteristics of propeller

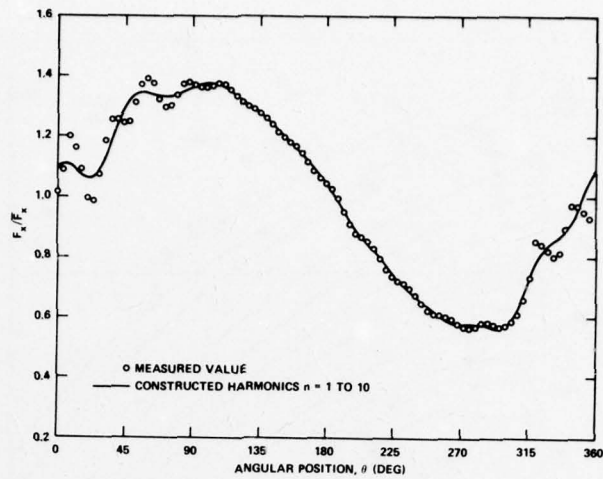


Fig. 12: Sample experimental data showing influence of extraneous signals on measured loads

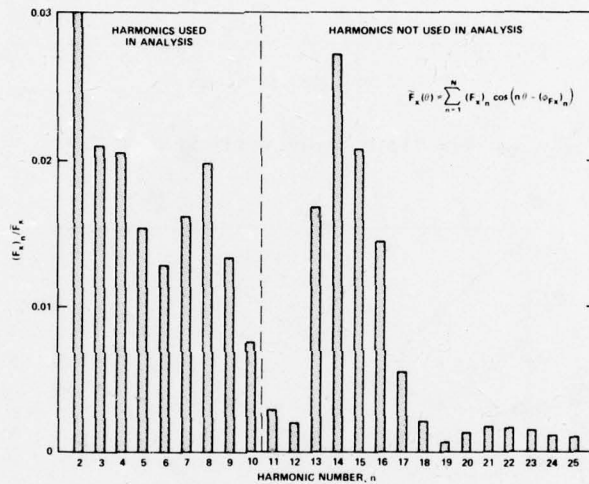


Fig. 13: Sample experimental data showing extraneous higher harmonics

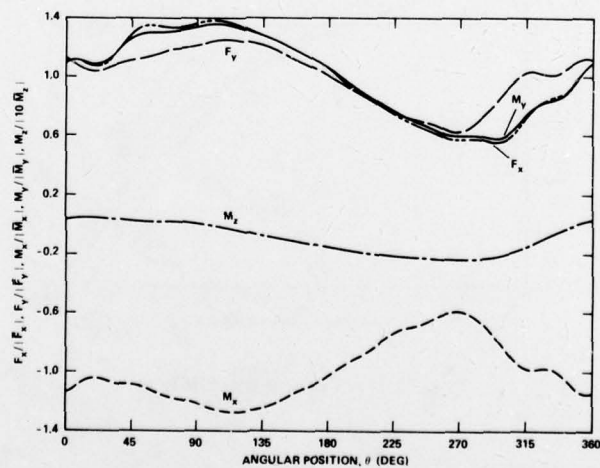


Fig. 14: Variation of experimental loads with angular position for steady ahead operation

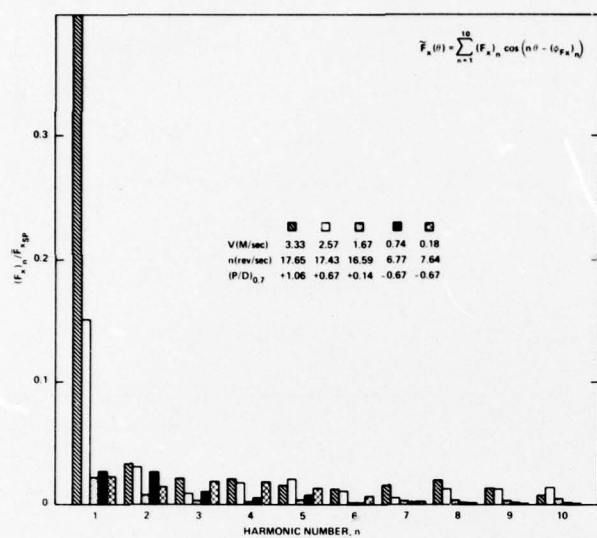


Fig. 15a: Amplitudes

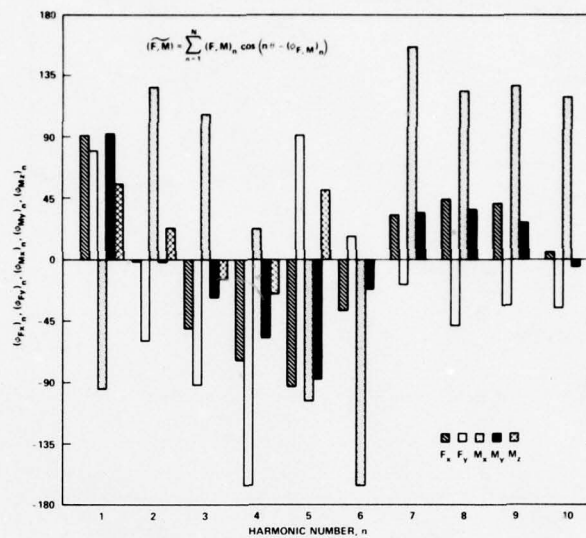
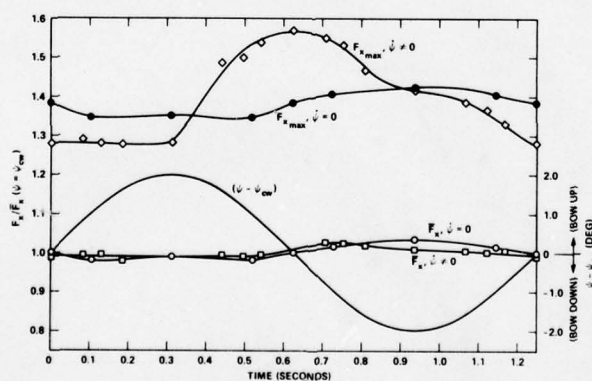


Fig. 15b: Phases

Fig. 15: Harmonic content of experimental loads for steady ahead operation

Fig. 16: Variation of  $F_x$  with hull pitch angle  $\psi$



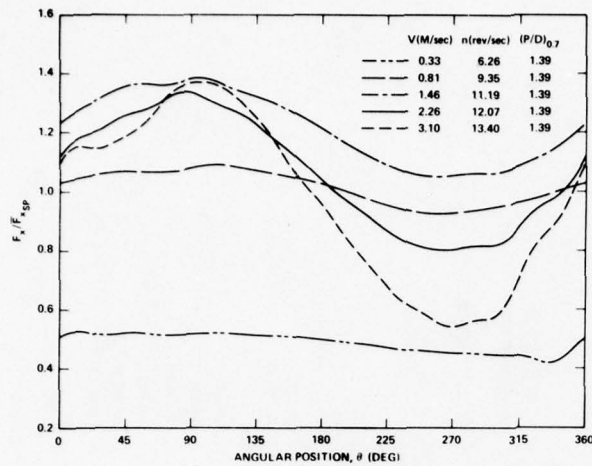
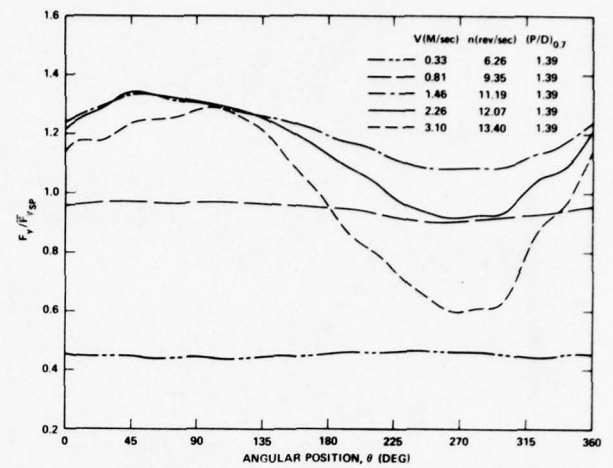
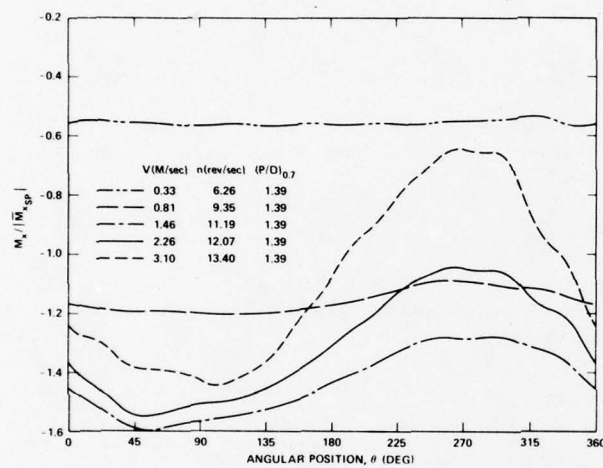
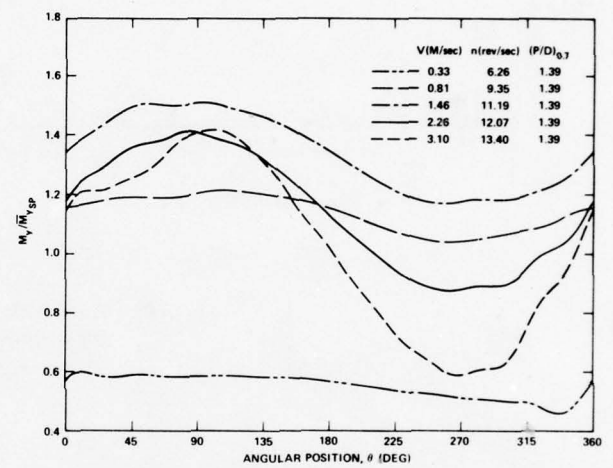
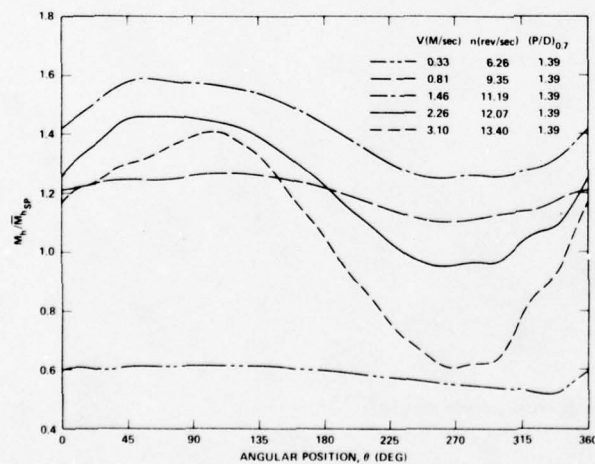
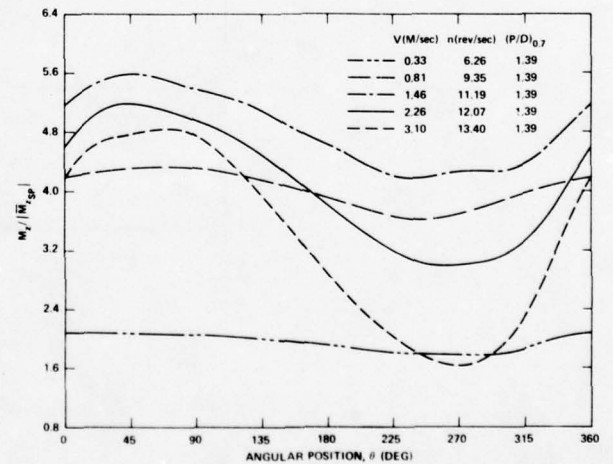
Fig. 17a:  $F_x$ Fig. 17b:  $F_y$ Fig. 17c:  $M_x$ Fig. 17d:  $M_y$ Fig. 17e:  $M_h$ Fig. 17f:  $M_z$ 

Fig. 17: Variation of loads with angular position for quasi-steady crash ahead

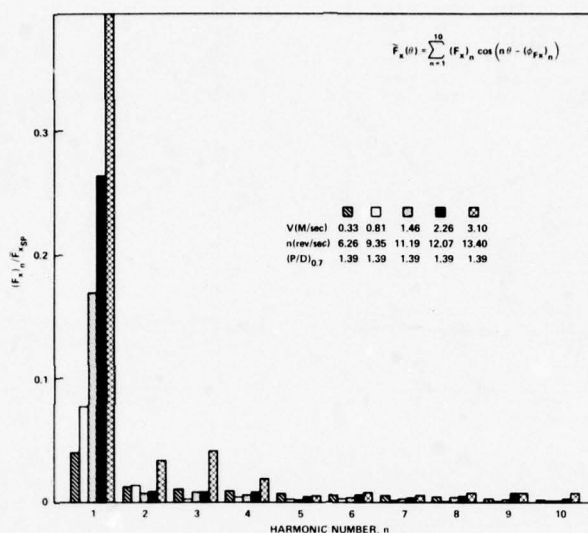


Fig. 18a: Amplitudes

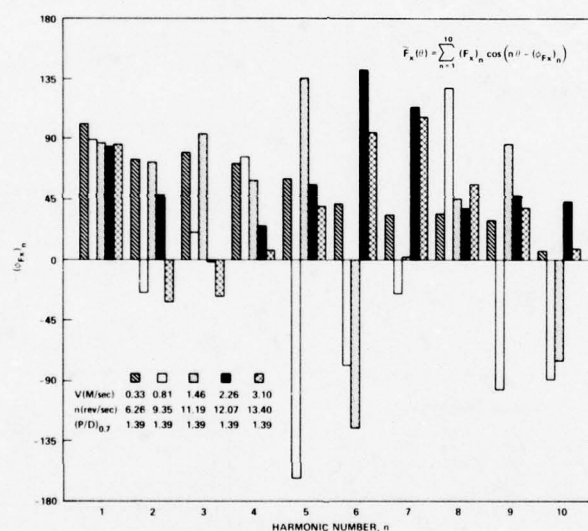


Fig. 18b: Phases

Fig. 18: Harmonic content of  $F_x$  for quasi-steady crash ahead

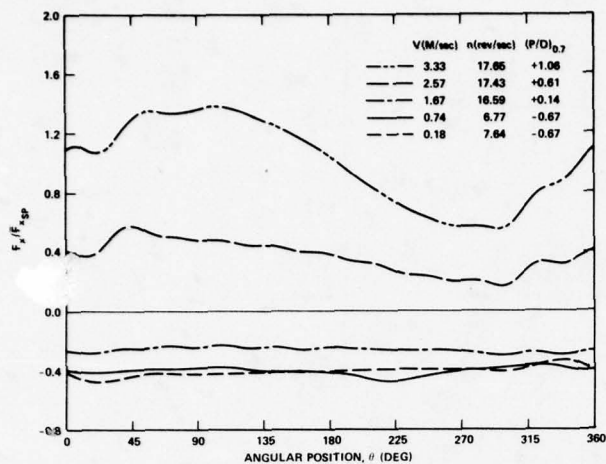
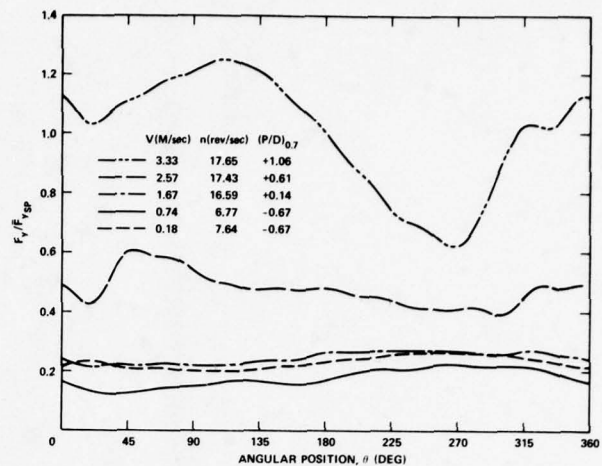
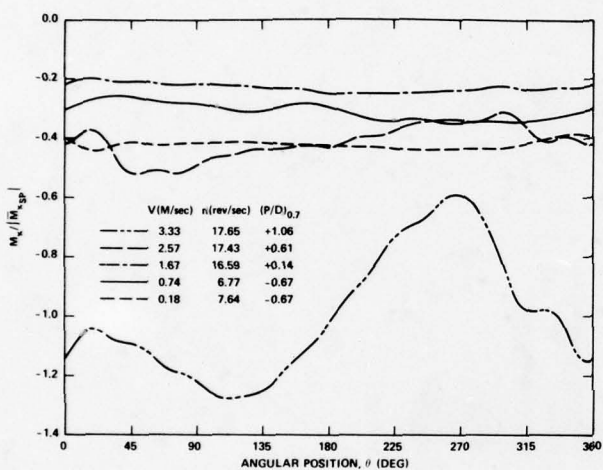
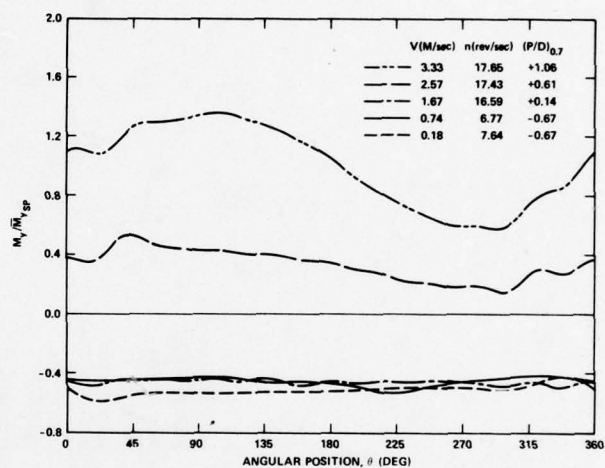
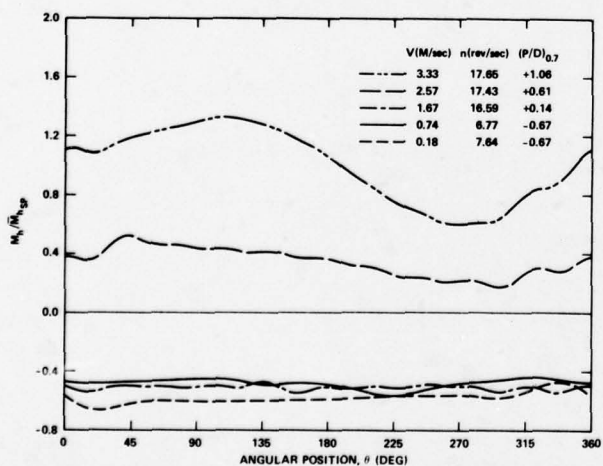
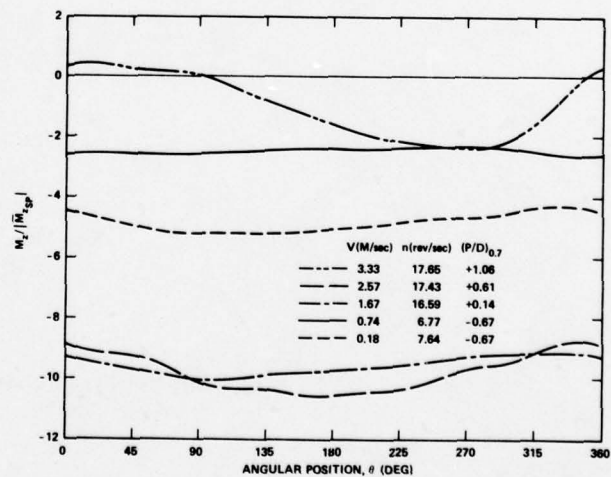
Fig. 19a:  $F_x$ Fig. 19b:  $F_y$ Fig. 19c:  $M_x$ Fig. 19d:  $M_y$ Fig. 19e:  $M_h$ Fig. 19f:  $M_z$ 

Fig. 19: Variation of loads with angular position for quasi-steady crash astern



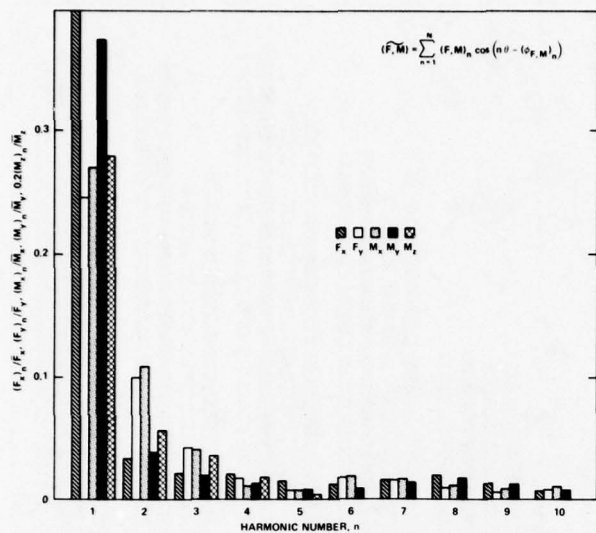


Fig. 20a: Amplitudes

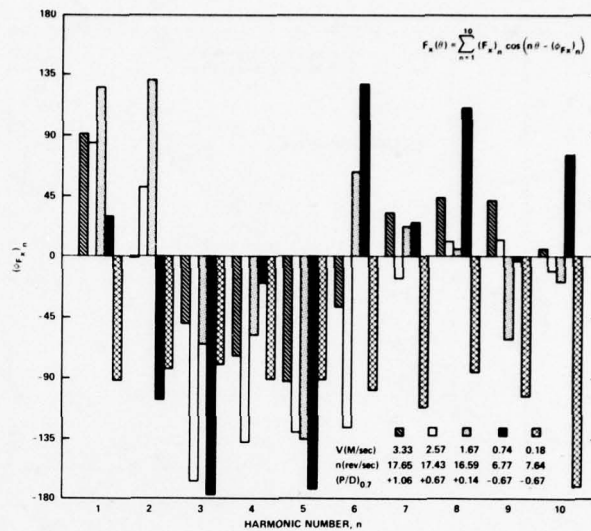


Fig. 20b: Phases

Fig. 20: Harmonic content of F. for quasi-steady crash astern

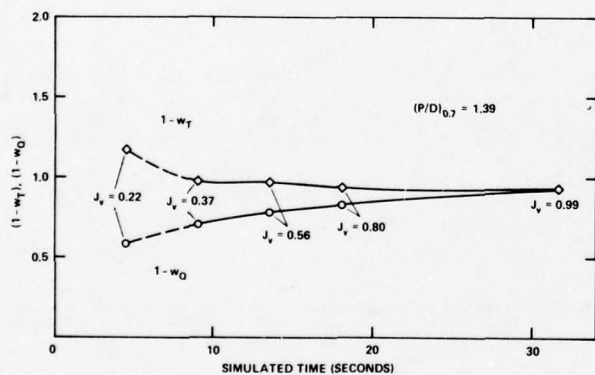


Fig. 21a: Crash ahead

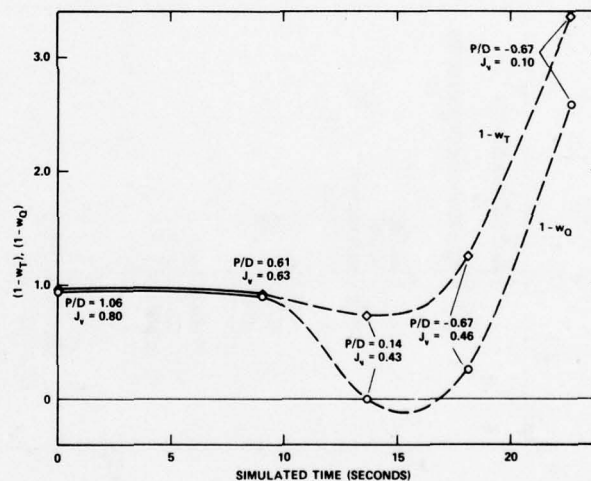


Fig. 21b: Crash astern

Fig. 21: Taylor wake fraction during simulated crash ahead and crash astern maneuvers

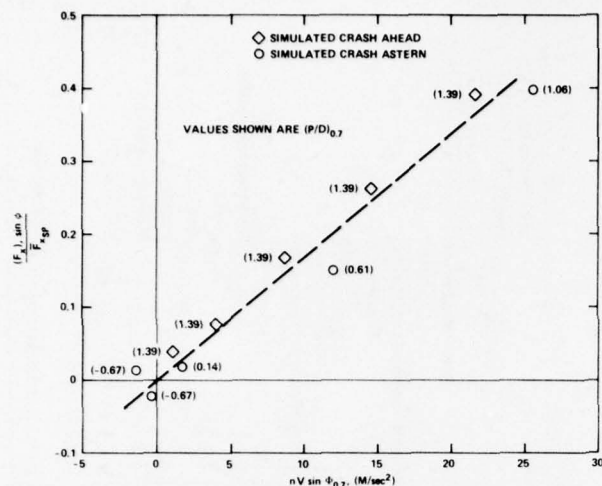


Fig. 22: Variation of  $(F_x)_1 \sin \phi / \bar{F}_{xSP}$  with  $nV \sin \phi$  for quasi-steady crash ahead and crash astern

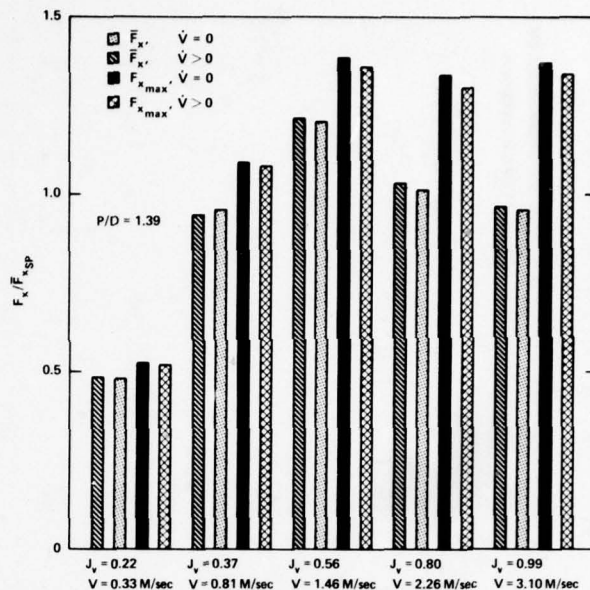


Fig. 23: Comparison of time average values per revolution and peak values of  $F_x$  for quasi-steady and unsteady simulated crash ahead

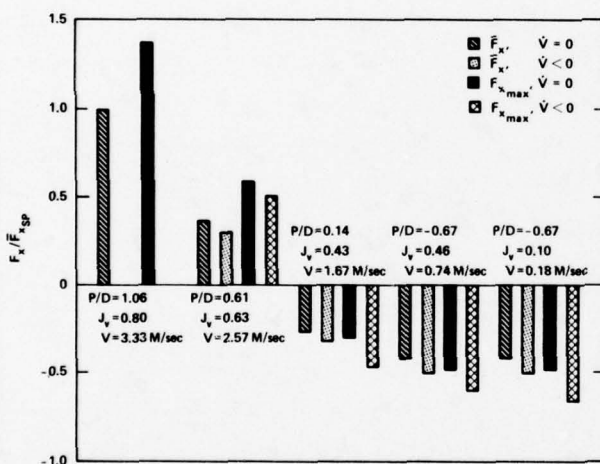


Fig. 24: Comparison of time average values per revolution and peak values of  $F_x$  for quasi-steady and unsteady simulated crash astern

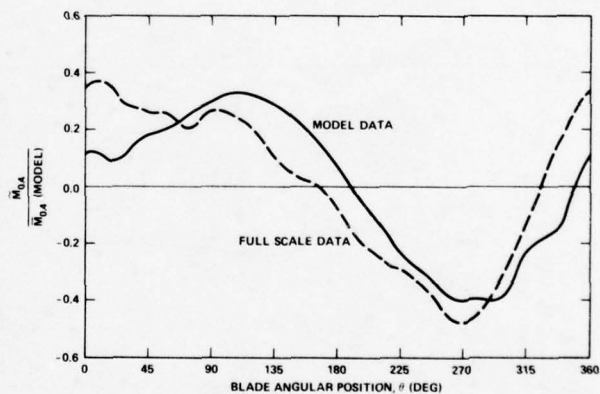


Fig. 25: Variation of bending moment at 40 percent radius with blade angular position, comparison of model data and full scale data

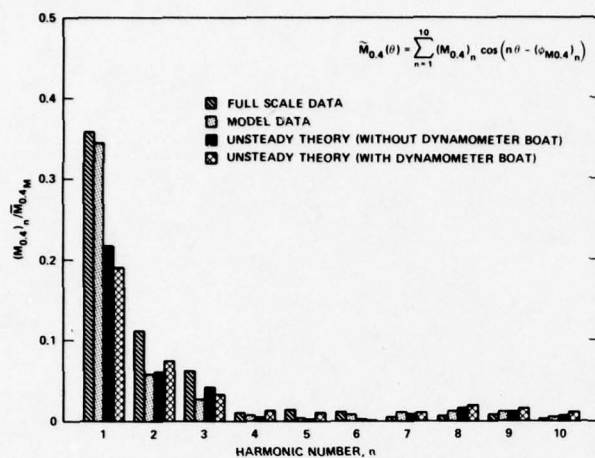


Fig. 26a: Amplitudes

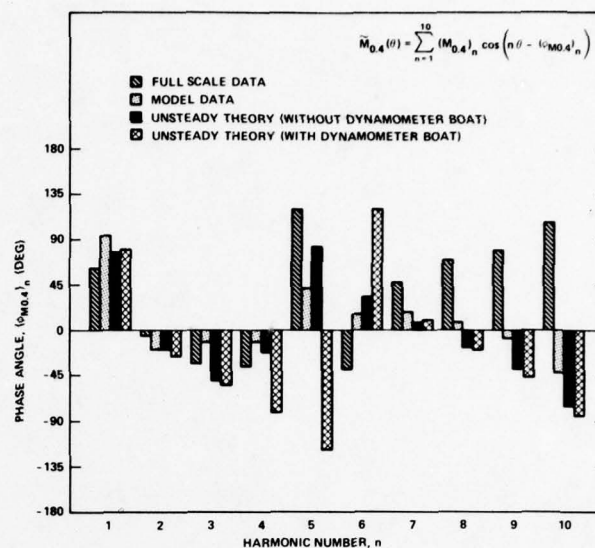


Fig. 26b: Phases

Fig. 26: Harmonic content of bending moment at 40 percent radius—comparison of model data, full scale data and theory

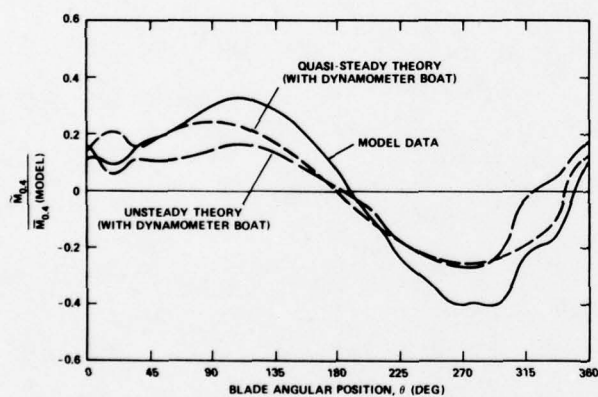


Fig. 27: Variation of bending moment at 40 percent radius with blade angular position—comparison of model data with theory

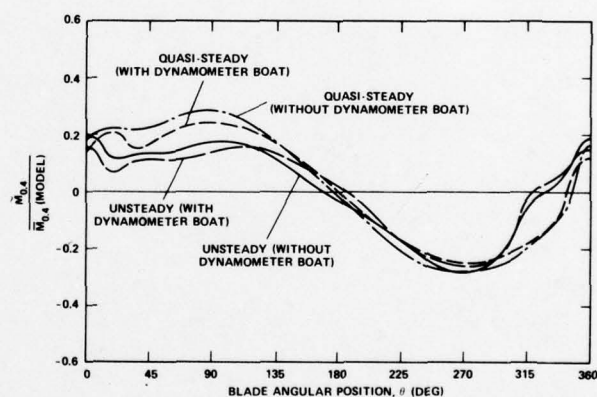


Fig. 28: Variation of bending moment at 40 percent radius with blade angular position—theoretical prediction with and without downstream body



# Discussion on Paper by Søntvedt and Frivold

A.Y. ODABASI

I would like to commence by congratulating the authors for presenting to us the results of their valuable full-scale measurements on cavitating propellers. Further information on these experiments will, no doubt, receive a warm welcome from everyone working in this field. My comments on the paper will be concerned with the method of analysis presented in the Appendix of the paper and with some of the interpretations concerning the effects of a water-cavitation bubble mixture.

Firstly, since the method used (Ref 10) is a linear treatment and since the velocity potential satisfies Laplace's equation, to obtain pressures with the twice blade-rate frequency the input, i.e. the incident flow and/or the rate of change of the cavity thickness, must have the same frequency. In the latter case the thickness  $\tau(x,t)$  must have an expression

$$\tau(x,t) = e^{i\omega t} \tau_1(x) + e^{i2\omega t} \tau_2(x) \quad (7)$$

where  $\omega$  is the blade-rate frequency. However, it is a known fact that both the thickness variation and the cavity pulsation period heavily depend on the wake flow structure and consequently it will be quite restrictive to assume that the thickness variation has the expression given by equation (7). If the twice blade-rate component of pressure is obtained independently of the input information the method will be violating the basic principles of field theory and the asymptotic paradox (Ref.11).

Another important feature is the definition of the cavity. In the paper only a part of the cavity, that part on the blade, is defined as the cavity and the entire calculations are based on this assumption, whilst both the demonstration film and Figures 2 and 4 indicate that the cavity extends beyond the propeller blade. Since the ratio  $V_{max}/V_{min}$  plays an important role in the pressure waves created by the pulsations of a cavity (Ref.12), suppression of the additional cavity volume may have a strong influence on the computed results ( $V_{max}$  and  $V_{min}$  are, respectively, the maximum and the minimum volume of the cavity). Although the authors attempt to include this effect by means of an additional pulsating bubble, this may add further complexity, because in theory, a pulsating bubble in an incompressible fluid produces unrealistic extremely high pressures (Ref.13).

Finally, the water-bubble mixture trailing the cavity forms the wake of the cavitating blade and behaves quite differently compared with a single bubble. Firstly, the water-bubble mixture transmits the pressure waves, rather than creating them, hence their pulsation is an effect rather than a cause, and secondly, in a water-bubble mixture, different from a single bubble, the pressure waves decay exponentially with time and are propagated with variable velocity (Ref.14).

## REFERENCES

- (10) Huse, E. (1972) "Pressure Fluctuations on the Hull Induced by Cavitating Propellers", Norwegian Ship Model Experiment Tank, Publ. No.111.
- (11) Birkhoff, G. (1950) "Hydrodynamics, A Study in Logic, Fact and Similitude", Princeton.
- (12) G  th, G. (1956) "Zur Entstehung der Stosswellen bei der Cavitation", *Acustica*, Vol. 6, No.6.
- (13) Flynn, H.G. (1971) "Dynamics of Cavitation Bubbles Set into Large Amplitude Motion by Acoustic Pressure Field", in "Proc. JUTAM Sym. on Non-Steady Flow of Water at High Speed", Leningrad.
- (14) Iordanskii, S.V. (1960) "Equations of Motion for a Liquid Containing Gas Bubbles", (in Russian), *P.M.T.F.* Vol.1, No.3.

PRECEDING PAGE BLANK-NOT FILMED

## Authors' Reply

We will first thank those who contributed to the informal discussion and the written contribution of Dr. Odabasi.

Dr. Odabasi's questions gives us the opportunity to clarify some parts of the numerical procedure underlying the calculation of the pressure impulses. In the case of the twin-screw tanker stereophotos were obtained for 6 different blade positions with blade cavitation present ( $18^\circ$ ,  $25^\circ$ ,  $36^\circ$ ,  $42^\circ$ ,  $62^\circ$ ,  $68^\circ$ ). The thicknesses were then interpolated by cubic interpolation to every  $6^\circ$ . The equivalent source strength at each mesh point on the blade was then calculated and the pressure at a field point was obtained by integration and summation (eq. (4) in the Appendix) as a function of angular position. This function is periodic in time and the period is the angle between the blade generatrices divided by the velocity of rotation. A simple Fourier analysis of this function gives us the components of first and second order of blade frequency. Thus, performing all calculations in timespace, no basic principles are neglected.

Concerning the definition of cavitation extent and amount of cavity mixture volume included in the analyses, the volume of the cavity-mixture is defined by two surfaces. The upper one is obtained from the stereophotos and will usually extend outside the blade, as demonstrated in fig.4. The lower surface consists of the blade surface and, outside this, the extrapolated blade surface. Where tip vortex cavitation is present (as in fig.4), the volume is not closed. Observations (both model and full scale) have shown that the tip vortex becomes stable immediately behind the trailing edge, following the slipstream passively. This is accounted for in the calculations by truncating the tip vortex volume at a particular section well behind the trailing edge where the thickness is assumed constant (in space). In the case of the twin-screw tanker this distance is approximately 0.75 m. The passive tip vortex "elements" (outside truncation limit), are assumed to make little contribution to the pressure. The integration area  $S$  (in the Appendix) should therefore be stated as: "the extent of cavitation projected to the extended blade surface" (truncated as said).

The cavity-mixture volume is now treated as a solid volume changing with time and the pressure is calculated accordingly, as shown in the Appendix. No additional pulsating bubble exists therefore in our analysis.

# Discussion on Paper by C.-A. Johnson

P.A. FITZSIMMONS

I should like to congratulate the authors on presenting a very concise account of their extensive model and full-scale cavitation experiments. The model/ship comparisons, however, appear to raise more questions than they answer, and point to a need to know more about the differing structures of ship and model wakes and blade cavities.

I should like to ask the authors whether in setting up their experiments they considered applying a scale correction to the measured model wake, and if so why they opted for the model wake. Part of the B.S.R.A. research effort in propeller excited vibration has involved extensive cavitation tunnel tests on a single screw, container ship model for which scale corrected wakes (fig.26) have been simulated both at the National Physical Laboratories and the Ship Research Institute, Norway. Pressure records (fig. 27) from these tests (Refs 8,19) show that only the N.P.L. wake (which was a first attempt at scale correction) gives agreement with the blade rate and twice blade rate components of pressure measured on the ship.

On the comparisons between ship and model cavity extent and pressure shown in figures 6 to 11 I am surprised that good agreement is obtained (even for blade rate pressure). The different character and extent of the ship and model cavity patterns should (considering equation 4 (ref.20)) result in different pressures.

## REFERENCES

19. J.W. English, "Experimental Results on a Wake Generator Rig in No.2 Water Tunnel, Ship Division, N.P.L." Confidential.
20. T. Sontvedt and H. Frivold, "Low Frequency Variation of the Surface Shape of Tip Region Cavitation on Marine Propeller Blades and Corresponding Disturbances on near by solid boundaries". 1976, 11th Symposium on Naval Hydrodynamics Paper VIII.2.

L. NOORDZIJ

We want to congratulate the authors with this paper. The paper covers a considerable part of the field connected with difficult problems such as propeller induced vibrations. Some interesting results are obtained on cavitation patterns and pressure fluctuations. The way in which the pressure signals are processed yields important additional information.

In this discussion we like to focus attention to problems related with gas content and cavitation inception. As mentioned by the authors, the gas content can play a striking role in cavitation inception phenomena and consequently in the pressure fluctuations on the hull. It is our opinion that mainly the free or undissolved gas content contributes in the inception phenomena. This is illustrated by a paper of Albrecht and Bjorheden, (Ref.21). In this paper the tremendous effect of air nuclei on inception and extension of cavitation, in particular bubble cavitation, is shown. However, only a few experimental results were presented. In order to proceed in finding more experimental evidence of the effect of free stream nuclei on type and extent of propeller cavitation some preliminary tests are conducted in the NSMB Depressurized Towing Tank. Towing tests with two ship models, with operating propellers, are performed. Cavitation patterns are observed and the pressure on the hull of the ship models is registered. Details of these tests will be presented in a forthcoming paper by Noordzij (Ref 22). It is thought, however, that it would be interesting to present some first results in the course of this discussion. During the above mentioned towing tests the number of free stream nuclei (tiny gas bubbles) in the propeller plane is varied. The additional nuclei are created by electrolysis of the tankwater in front of the propeller plane. The electrolysis configuration is fitted on the hull of the ship model (Ref.22). For two conditions, with and without additional nuclei, the cavitation pattern on the propeller blades was registered for a certain blade position at different instants in order to find out about the effect of nuclei on inception. It was established that for an additional amount of nuclei, the cavitation pattern changed considerably. The cavitation pattern was found to become periodic, whereas in the other case the pattern was aperiodic. It was noticed that without additional nuclei the extent of the sheet cavities varied between zero and a maximum equal to the extent as found in the situation with additional nuclei. This is illustrated in figure 28.

In figure 28 the effect of additional nuclei is shown. On the left side are the pictures obtained without electrolysis, on the right the pictures are shown for the situation with electrolysis. These pictures are taken with a remote controlled camera in the ship model. For each situation a sequence of photographs is shown. As mentioned, these are obtained at different instants. This was done to emphasize the stabilizing action of nuclei. It is clearly shown that the additional nuclei make the inception periodic and stabilize sheet cavitation. It will be shown by Noordzij (Ref.22) that electrolysis also stabilizes tip



vortex cavitation. In order to increase insight into this inception problem the number of nuclei must be determined. Another matter of investigation is if there exists a critical number of nuclei. These questions must be answered in order to find out if the situation with additional nuclei is realistic or not. In this respect we like to repeat the statement of Acosta given in the discussion on the paper of Albrecht and Bjorheden (Ref.21): "This bubble seeding method has real merit when the (natural) bubble distribution of the prototype flow as well as that of the laboratory flow is known".

#### REFERENCES

21. Albrecht, K., Bjorheden, O., "Cavitation testing of propellers in a free stream tunnel utilizing micro air bubble control", Journal of Fluids Engineering, Dec.1975.
22. Noordzij, L., Some experiments on cavitation inception with propellers in the NSMB Depressurized Towing Tank, 1976 (to be published).

# Authors' Reply

First we want to thank the two discussers for their contributions which both illustrate the difficulties in applying experiences from one type of facility to another. Both discussers refer to important factors which have been investigated also in our laboratory. In both cases, however, our experiences do not agree with those of the discussers.

L. NOORDZIJ

Turning first to Dr Noordzij he describes how the stability of the cavities and the pressure fluctuations was improved in the depressurized towing tank at NSMB when introducing artificially produced nuclei ahead of the propeller. Although an interesting point, it has to be emphasised that these problems are much more pronounced for a free surface facility than for a closed jet tunnel like the one at SSPA. Accordingly the instabilities discussed in our paper are, in our opinion, mainly due to time variations in local velocity and static pressure, as is explained in the paper. This opinion is based on the following observations:

a) From recordings of pressure fluctuations published earlier by NSMB, see for instance Ref.10, it is evident that the instabilities occurring in the depressurized towing tank result in amplitude modulations which indicate that nuclei are present in insufficiently small numbers. These modulations affect all harmonics including that of blade frequency. In our case phase angle modulations occur, indicating variations in velocity, as mentioned before. These modulations affect only higher harmonics.

b) For a closed jet tunnel like the one at SSPA an increase of the total air content means a corresponding increase of the number and content of free nuclei which could be observed visually at the tests at different air content ratios referred to in the paper and which was confirmed by recent measurements in different tunnels using laser technique (Refs.23,24). Accordingly, at the tests referred to in our paper, amplitude modulations affecting the blade frequency harmonic, were noticed only at the extremely low air content  $\alpha/\alpha_s \approx 0.07$ .

In a depressurized towing tank on the other hand the presence of a very large free surface may well explain why the number of nuclei is small and largely independent of pressure, as is stated in Ref.23, which refers to measurements in the vacuum tank at NSMB.

P.A. FITZSIMMONS

Also the problem of wake distribution in model and full scale, referred to by Mr Fitzsimmons, has been investigated at SSPA and some of the results published (Ref.7). The published results refer to an investigation including a change of the wake distribution towards the one in full scale, accomplished by taking away the parallel middlebody, thereby increasing the effective Reynolds number. Two tanker models having different afterbody shape were used for this investigation. Important results of this investigation are:

a) The change of the wake pattern had no dramatic effect on the levels of the pressure fluctuations.

b) Extrapolation of the wake distributions to full scale Reynolds number indicated that the Sasajima method for calculating the full scale wake can in some cases give misleading results.

Bearing these facts in mind and considering that we have carried out several successful correlations between model and full scale pressure fluctuations we are very reluctant to introduce more or less hypothetical full scale wake distributions at the cavitation tunnel tests. It must however be pointed out that the scale effect in the mean wake is considered by running the tests at values of advance ratio and cavitation number calculated to correspond as closely as possible to those of the full scale ship. In reality this means also a correction of the wake distribution, the magnitude of which is illustrated for one case in Ref.25.

An explanation why the change of wake distribution had such a dramatic influence on the pressure fluctuations in the cases referred to by Mr Fitzsimmons may be that this change was accomplished (by taking away nets or similar) in such a way that the interference between hull and propeller was effected.

## REFERENCES

23. Arndt, R.E.A. Keller, A.P: "Free Gas Content Effects on Cavitation Inception and Noise in a Free Shear Flow". IAHR Symposium on Two Phase Flow and Cavitation, Grenoble 1976, proceedings, pp 3-16.
24. Keller, A.P, Weitendorf, E.A: "Influence of Undissolved Air Content on Cavitation Phenomena at the Propeller Blades and on Induced Hull Pressure Amplitudes". *ibid* pp 65-76.
25. Dyne, G, Hoekstra, M: "Propulsion, Cavitation and Propeller-induced Pressure Fluctuations of a Tanker (Comparative Tests in SSPA Cavitation tunnel No2 and NSMB Depressurized Towing Tank)". Paper presented at Spring Meeting of Soc of Naval Arch & Marine Eng, June 76.

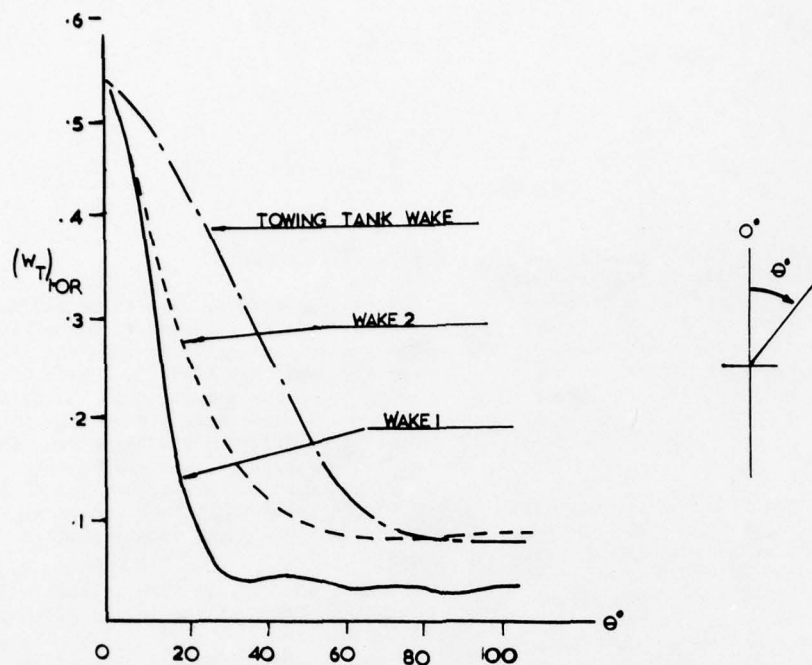


Fig. 26: Wake fraction at angular position  $\theta$  in propeller plane

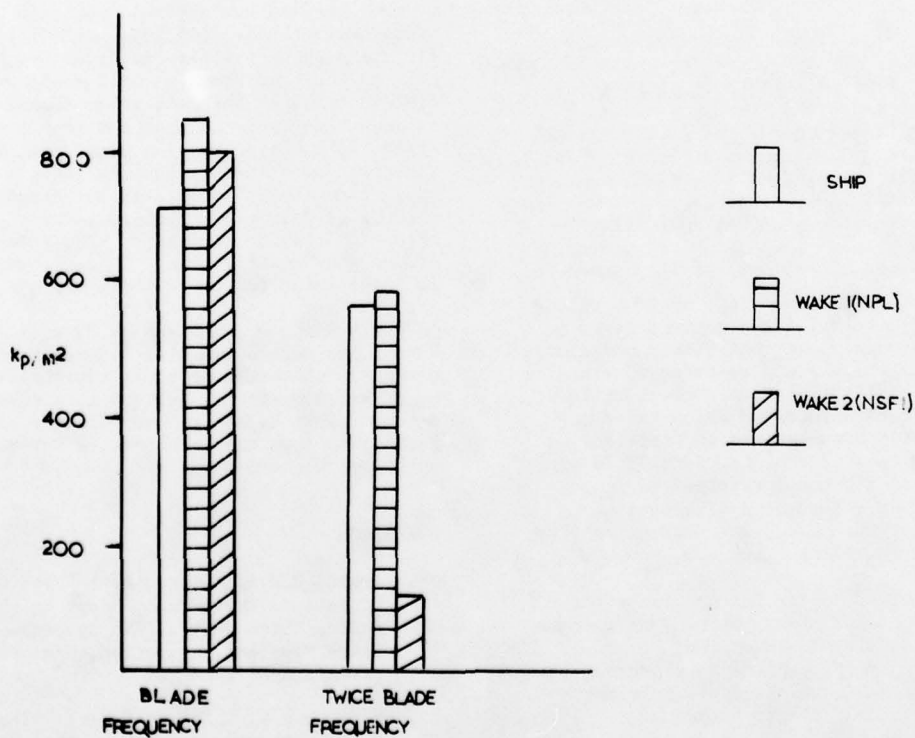
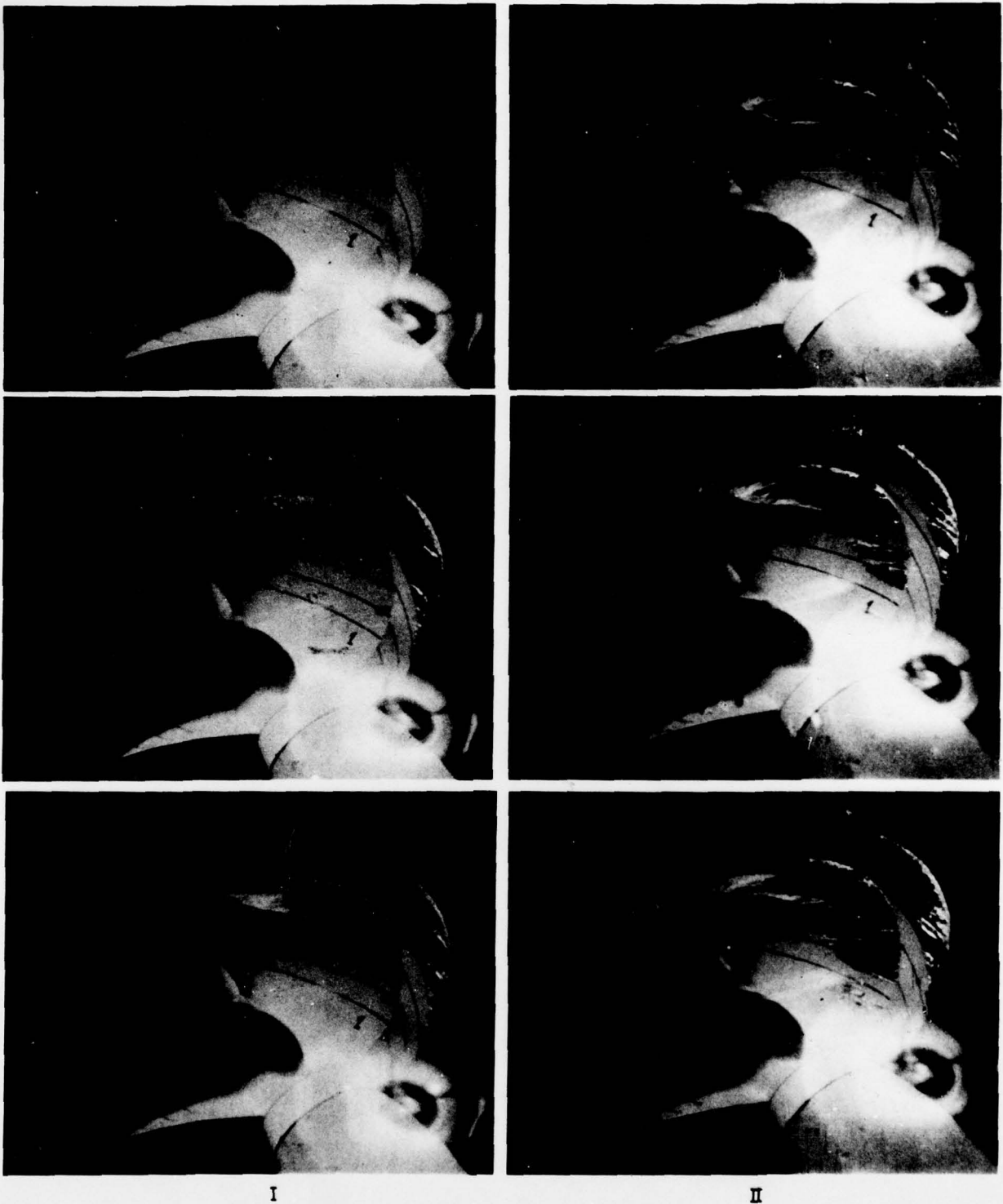


Fig. 27: Components of pressure on ship centreline above propeller tips



WITHOUT ELECTROLYSIS

WITH ELECTROLYSIS



**Fig. 28:** In this figure the effect of additional nuclei on cavitation is illustrated. To the left a sequence of photographs without additional nuclei is shown for one condition at different instants. The three photographs on the right show the patterns with additional nuclei. The stabilizing effect of additional nuclei is clearly demonstrated.

# Discussion on Paper by R. J. Boswell

J.P. BRESLIN

Mr Boswell and his colleagues have indicated in this highly comprehensive study that the vibratory bending moments on this D.E. propeller are not as well predicted by the unsteady lifting surface theory as we would like. Since the theory has been successfully correlated with other data, some in which screen-generated wakes were not used (not subject to propeller-induced alteration of the wake) and other cases in which measurements were made on full-scale ships, the lack of better correlation here is somewhat surprising.

As a check, we have made two sets of calculations one with the wake harmonics used by Boswell, et al and the other for a D.E. wake which might be considered as typical of this class of vessel as may be seen by referring to the summary of wakes provided by Cheng and Hadler in the SNAME Transactions.

First, let us look at the variation of the perturbation velocity imposed by these wakes *normal* to the blade section at 0.71 radius as shown in Figure 29. Here the sum of the first three harmonics (the remaining being very small) shows that this total normal velocity is not perfectly symmetrical with respect to  $180^\circ$  (as would be the case for the first tangential harmonic) and this explains why the bending moment data shows larger values in the vicinity of 9 o'clock than near 3 o'clock ( $90^\circ$ ). This is due to the constructive contribution of the axial second harmonic at  $270^\circ$  and the opposing contribution at  $90^\circ$ . Since the axial harmonics were much smaller for the wake measured for this hull as compared to all others summarized by Cheng and Hadler, we selected that for Model 4881 shown as the dashed curve of Figure 29. This proved to be fruitless as the tangential components were weaker. The results of the calculations are shown in Figure 30 where the *circles* are the theory with Boswell's wake with the dynamometer boat present and the *pluses* for the wake of Model 4881.

As might have been anticipated, we get no help from this latter wake. Our curve for the *circles* agrees with those calculated by Boswell from our program, but by eye this disagreement with the model data is not as great as alluded to by Mr Boswell in his oral presentation.

The trace of the full-scale data which departs strongly from the model data in the neighbourhood of 12- and 6-o'clock suggests that the full-scale wake has much stronger axial or cosine content than that of the model. This is in keeping with the trend of the viscous flow with Reynolds number, the full-scale being sharper and, hence, having larger harmonic content. It is puzzling that the model

measurements are well below the full-scale values at 12 o'clock ( $0^\circ$ ) whereas they are substantially above those at 6 o'clock ( $180^\circ$ ). Perhaps the lack of scaling of the model wake in the shadow of the inclined shaft is to be suspected. It is understood that the temporal variations in the measurements were pronounced in the 12 o'clock region.

We have looked at the effect of mean propeller induction which causes the blades to see a contracted distribution of harmonics but, as the disc loading coefficient is only of the order of 0.7, nothing significant could be extracted by this alteration of the radial distribution of harmonics - in fact a slight reduction in the bending moment could be anticipated. For an inclined propeller, the mean-induction flow-tube will be bent around and induction of fluid nearer the hull forward of the propeller may be expected to have reduced axial velocities and, hence, a larger axial harmonic than is reflected in the nominal wake (measured without the propeller operating).

I do not agree with Mr. Boswell's conjecture that the theory is inaccurate because of the omission of non-linear effects. The requirements for linearization are well met here; besides, non-linear effects can only give rise to mean and second harmonic effects which would not at all seem to be the missing effects here. I am more inclined to believe that the distortion of the inflow due to the non-angular-dependent image of the propeller in the hull may be significant since it is the first few harmonics of the inflow which are important here.

# Authors' Reply

The authors wish to thank Dr. Breslin for his discussion to the paper. The following closure will attempt to clarify some of the points raised.

Dr. Breslin made several comments regarding the poor correlation between the experimental results and calculated results based on the method of Tsakonas, et al (Ref.14), for unsteady blade loading under steady ahead operation. Our experience with the method of Tsakonas, et al has been that correlation with experimental results has been rather inconsistent, except for some data obtained in wakes generated by screens at DTNSRDC, Ref.6. However, these data obtained behind wake screens differ from the data in the present paper in three important aspects. For the data obtained behind screens, Ref.6:

1. There is no nearby upstream boundary as there is in the present study, therefore, it is less likely that the propeller alters the wake pattern.
2. The wakes contain only an axial component whereas in the present study the wake contains axial, tangential, and radial components with the first harmonic of the tangential wake being dominant.
3. Forces and moments were measured only at multiples of blade frequency whereas in the present study forces and moments were measured at all harmonics of shaft frequency.

Therefore, it is not necessarily inconsistent that good correlation was obtained in Reference 6 and poor correlation obtained in the present study.

Future systematic blade loading experiments are planned to determine whether correlation between theory and experiment depends on the presence of a nearby boundary, or if it depends on whether the wake is axial or tangential.

Previous investigations (Ref.23,24,25), which were inadvertently omitted from the references to the present paper, compared experimentally determined unsteady forces and moments on a single blade of various propellers in inclined flow with forces and moments calculated by a quasi-steady procedure similar to that described by McCarthy (Ref.15). These experimental loads were obtained either by direct measurement of unsteady forces and moments on a single blade (Ref.23,24) or were deduced from measured steady transverse forces and moments along axes fixed relative to the flow, i.e. not rotating with the propeller. References 23 to 25 show that for non-cavitating conditions the experimental unsteady blade

loading was from 1.7 to 2.0 times as large as the values calculated by the quasi-steady method. This agrees with the results of the present investigation; see Figure 27. Although no correlations were made with the method of Tsakonas, et al, it is expected that predictions by this procedure would be even smaller than the quasi-steady prediction.

Dr. Breslin presented calculations using the method of Tsakonas, et al, based on the wake of a model used in the present paper. The purpose of these calculations is not clear; however, they demonstrate the sensitivity of calculated unsteady loads to changes in the wake patterns. Dr. Breslin is correct that the larger unsteady loading at  $\theta_w = 270$  degrees than at  $\theta_w = 90$  degrees arises from the reinforcing effect of the longitudinal and tangential wake components at  $\theta_w = 270$  degrees, and the cancelling effect at  $\theta_w = 90$  degrees.

We generally agree with Dr. Breslin's comments regarding the difference between model and full-scale results for the blade nearly vertical upward. However, the full-scale data represent an average of only six revolutions and there was significant variation between the various revolutions in this region. This variation may have resulted from effects of the seaway, such as ship motions or time-dependent free surface effects.

We do not follow Dr. Breslin's contention that in the method of Tsakonas, et al, "non-linear effects can only give rise to mean and second harmonic effects". This computation scheme is based on calculating the loading response to one harmonic of the wake at a time independent of all other harmonics. Therefore, it appears that any linearization must apply to all harmonics of the loading.

Again, the authors wish to thank Dr. Breslin for his discussion.

## REFERENCES

23. Albrecht, K., and Suhrbier, K.R. "Investigation of the Fluctuating Blade Forces of a Cavitating Propeller in Oblique Flow" International Shipbuilding Progress, Vol.22, No.248 April 1975, p 132-147.
24. Bednarzik, R. "Untersuchung uber die Belastungs-schwankungen am Elinselflugel schrag angestromter Propeller," Schiffbauforschung, Vol.8, No.1/2, 1969, p 57-80.
25. Gutsche, F. "Untersuchung von Schiffsschrauben in schrager Anstromung," Schiffbauforschung, Vol 3, No.3/4, 1964.



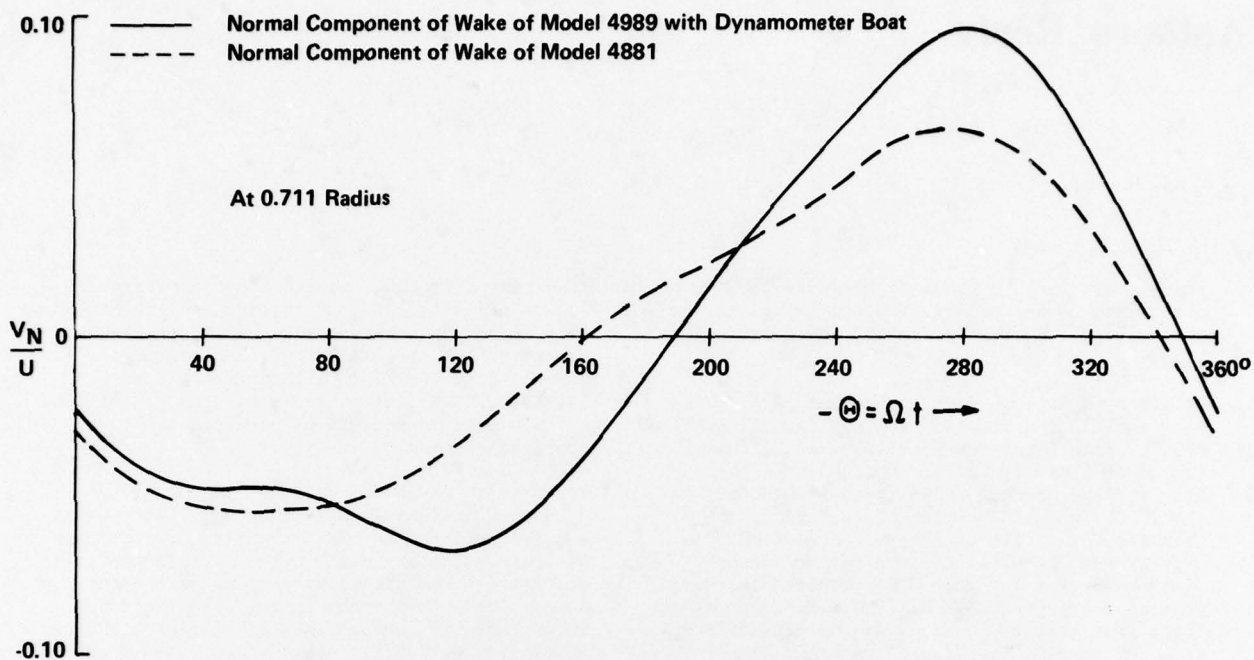


Fig. 29: Normal Components of Wake (1st, 2nd and 3rd Harmonics)

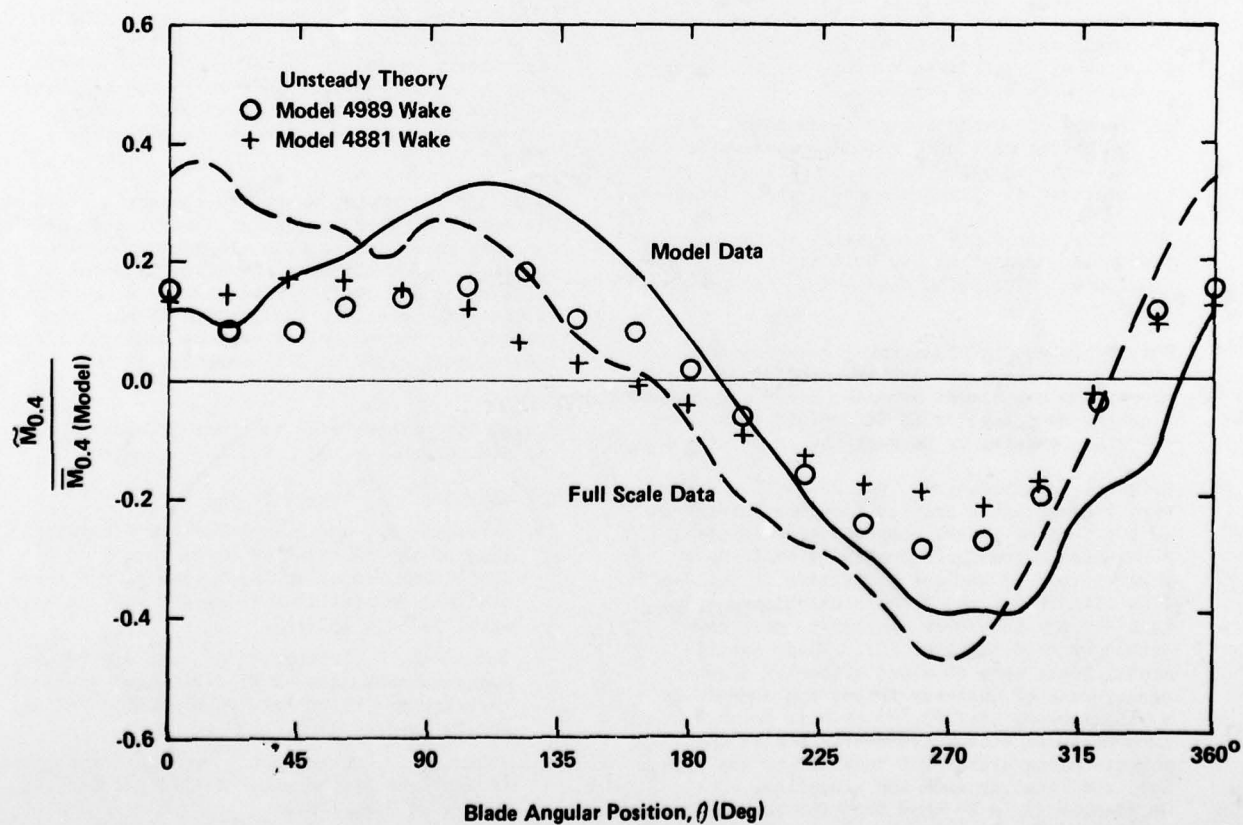


Fig. 30: Variation of Bending Moment at 40 Percent Radius with Blade Angular Position, Comparison of Model Data, Full-Scale Data and Theoretical Calculations

# LIST OF PARTICIPANTS

(\*indicates contributed by written discussion only)

Abkowitz, M. A.	Massachusetts Institute of Technology, Cambridge, USA.	Chaszeyka, M. A.	Office of Naval Research, Chicago, USA.
Acosta, A. J.	California Institute of Technology, Pasadena, USA.	Cheng, H. M.	Office of the Chief of Naval Operations, Washington, DC, USA.
Alaez, J. A.	Canal de Experiencias Hidrodinamicas, El Pardo, Madrid, Spain.	Coene, R.	Technische Hogeschool Delft, The Netherlands.
Alvarez-Canovas, C.	Canal de Experiencias Hidrodinamicas, El Pardo, Madrid, Spain.	Cooper, R. D.	Office of Naval Research, Arlington, USA.
Andersson, B. J.	The Royal Institute of Technology, Stockholm, Sweden.	Coppola, C.	INSEAN. (Rome Tank), Rome, Italy.
Ashe, G. M.	Naval Ship Engineering Centre, Hyattsville, USA.	Crago, W. A.	EEL. British Hovercraft Corporation Ltd, East Cowes, England.
Astorquiza, G. V.	Armada de Chile, Valparaiso, Chile.	Cummins, W. E.	David Taylor Naval Ship R & D Center, Bethesda, USA.
Bailhache, J.	Chantier Naval, Saint-Nazaire, France.	Dalzell, J. F.	Stevens Institute of Technology, Hoboken, USA.
Bakenhus, J.	BWB, Koblenz, Germany.	Dand, I. W.	National Physical Laboratory, Feltham, England.
Baù, F. C.	Cantieri Navali Riunti, Genova, Italy.	Daniel, R. J.	Ministry of Defence (PE), Bath, England.
Bishop, R. E. D.	University College London, London, England.	*Davis, A. M. J.	University College London, London, England.
Bogdanov, P. A.	Shipbuilding Research Institute, Varna, Bulgaria.	Davis, M. D.	David Taylor Naval Ship R & D Center, Bethesda, USA.
Booth, T. B.	Admiralty Experiment Works, Haslar, England.	De Loof, J. P.	Ste Bertin et Cie, Plaisir, France.
Børresen, R.	The Ship Research Institute of Norway, Trondheim, Norway.	Demanche, J. F.	Bassin d'Essais des Carènes, Paris, France.
Boswell, R. J.	David Taylor Naval Ship R & D Center, Bethesda, USA.	Demoulins, J. F.	Bureau Veritas, Paris, France.
Brard, R.	Bassin d'Essais des Carènes, Paris, France.	Dern, J. C.	Bassin d'Essai des Carènes, Paris, France.
Bratu, Ch.	Institute Français du Pétrole, Rueil Malmaison, France.	Dirkzwager, J. M.	Ministry of Defence Netherlands, The Hague, The Netherlands.
Breslin, J. P.	Stevens Institute of Technology, Hoboken, USA.	Doctors, L. J.	University of New South Wales, Kensington, Australia.
Bria, M. G.	Cetena, Genova, Italy.	Doroff, S. W.	Office of Naval Research, Arlington, USA.
Brix, J.	Hamburgische Schiffbau-Versuchsanstalt, G.m.b.H., Hamburg, Germany.	Drummond, T. G.	Defence Research Establishment Atlantic, Dartmouth, Canada.
Bussemaker, O.	Schottel Nederland B.V., Den Haag, Nederland.	Eames, M. C.	Defence Research Establishment Atlantic, Dartmouth, Canada.
Butler, C.	Hawker Siddeley Dynamics Ltd, Stevenage, England.	Eatock Taylor, R.	University College London, London, England.
Cagle, B.	Office of Naval Research, Pasadena, USA.	Eda, H.	Stevens Institute of Technology, Hoboken, USA.
*Carlsen, C. A.	Det Norske Veritas, Oslo, Norway.	Evans, D.	University of Bristol, Bristol, England.
Catley, D.	British Ship Research Association, Wallsend, England.	Fabris, F.	Australian Naval Construction Liaison Officer, MOD (Navy), Bath, England.
Chan, R. K-C.	Jaycor, Del Mar, USA.	Falkemo, C.	Chalmers Tekniska Hogskola, Göteborg, Sweden.
Chang, Ming S.	David Taylor Naval R & D Center, Bethesda, USA.	Falls, R.	Maritime Administration, Washington DC, USA.
Chapman, R. B.	David Taylor Naval Ship R & D Center, Bethesda, USA.	Ferdinande, V.	Dienst Voor Scheepsbouwkunde, Gent, Belgium.

- Fink, P. T. University of New South Wales, Kensington, Australia.
- Fitzpatrick, H. M. Office of Naval Research, Chevy Chase, USA.
- \*Fitzsimmons, P. A. British Ship Research Association, Wallsend, England.
- Flokstra, C. Delft Hydraulics Laboratory, Delft, The Netherlands.
- Frederiks, W. G. Mathematisch Institute, Groningen, The Netherlands.
- Frivold, H. Det Norske Veritas, Oslo, Norway.
- Fruman, D. H. Laboratoire D'Aerodynamique, Orsay, France.
- Fujii, H. Nagasaki Technical Institute, Nagasaki, Japan.
- Fujino, M. University of Tokyo, Tokyo, Japan.
- Fureya, Okitsugu Tetra Tech. Inc., Pasadena, USA.
- Gadd, G. E. National Physical Laboratory, Feltham, England.
- Garcia, A. Canal de Experiencias Hidrodinamicas, El Pardo, Madrid, Spain.
- Garrett, D. P&O SN Co, London, England.
- Gerritsma, J. Technische Hogeschool Delft, Delft, The Netherlands.
- Gill, A. D. National Physical Laboratory, Feltham, England.
- Glen, I. F. Canadian Dept of National Defence, Ottawa, Canada.
- Gomez, M. P. Buenos Aires, Argentina.
- Goodman, A. Hydronautics Incorporated, Laurel, USA.
- Guilloud, J. Alsthom—TDF, Grenoble, Cedex, France.
- Hadjimihalev, P. H. Shipbuilding Research Institute, Varna, Bulgaria.
- Hagen, G. R. David Taylor Naval Ship R & D Center, Carderock, USA.
- Harvald, Sv. Aa. Inst. for Skibs- og Havteknik, Lyngby, Denmark.
- Haynes, F. Vickers Ltd, Barrow-in-Furness, England.
- Heradstveit, B. O. Royal Norwegian Naval Academy, Ytre Laksevåg, Norway.
- Hermans, A. J. Technische Hogeschool Delft, Delft, The Netherlands.
- Hirata, K. Kawasaki Heavy Industries Ltd., London, England.
- Hirayama, T. Yokohama National University, Yokohama, Japan.
- Hogben, N. National Physical Laboratory, Feltham, England.
- Honkanen, M. Helsinki University of Technology, Espoo, Finland.
- Hooft, J. P. Netherlands Ship Model Basin, Wageningen, The Netherlands.
- Hunley, W. H. Naval Ship Engineering Center, Hyattsville, USA.
- Jami, A. ENSTA, Paris, France.
- Jens, J. L. E. IMCO, London, England.
- Jensen, J. V. Helsingør Teknikum, Helsingør, Denmark.
- Johnsson, C. A. Statens Skeppsprovsningsanstalt, Göteborg, Sweden.
- Johnson, B. US Naval Academy, Annapolis, USA.
- Johnson, D. Admiralty Research Laboratory, Teddington, England.
- Jorde, J. H. Royal Norwegian Material Command/Bureau of Ships, Haakonvern, Norway.
- Jouaillec, M. F. Ecole Nationale Supérieure de Techniques Avancées, Paris, France.
- Jovev, J. K. Shipbuilding Research Institute, Varna, Bulgaria.
- Kaplan, P. Oceanics Inc., Plainview, USA.
- Keil, H. Institut für Schiffbau, Hamburg, Germany.
- Kennel, C. Naval Ship Engineering Center, Hyattsville, USA.
- Ketelsen, H. Helsingør Teknikum, Helsingør, Denmark.
- Kholodilin, A. N. UNESCO.
- Kim, M. W. D. Washington Navy Yard, Washington, USA.
- Kitagawa, H. Ship Research Institute, Tokyo, Japan.
- Kobylnski, L. Technical University Gdansk, Gdansk, Poland.
- Koeman, J. W. Delft Hydraulics Laboratory, Delft, The Netherlands.
- Kokkinowrachos, K., Technical University Aachen, Aachen, Germany.
- Koopmans, F. Delft Hydraulics Laboratory, Delft, The Netherlands.
- Koslov, S. Office of the Assistant Secretary of the Navy (R & D), Washington, DC, USA.
- Kowalski, T. The University, Glasgow, Scotland.
- Krezelewski, M. Gdansk Technical University, Gdansk, Poland.
- Kuo, C. University of Strathclyde, Glasgow, Scotland.
- Kure, K. Danish Ship Research Laboratory, Lyngby, Denmark.
- \*Kwang June Bai David Taylor Naval Ship R & D Center, Bethesda, USA.
- Lackenby, H. British Ship Research Association, Wallsend, England.
- Lambert, T. H. University College London, London, England.
- Langfeldt, J. N. Chr. Michelsen Inst., Bergen, Norway.
- Lap, A. J. W. Royal Netherlands Naval Academy, Den Helder, The Netherlands.
- Larsson, L. Swedish State Shipbuilding Experimental Tank, Göteborg, Sweden.
- Lazarov, G. M. Shipbuilding Research Institute, Varna, Bulgaria.
- Leone, P. C. Instituto de Pesquisas, Sao Paulo, Brazil.
- Lewis, E. V. Webb Institute of Naval Architecture, Glen Cove, USA.
- Lin, Wen-Chin. David Taylor Naval Ship R & D Center, Bethesda, USA.
- Lloyd, A. R. J. Admiralty Experiment Works, Haslar, England.
- Loukakis, T. National Technical University of Athens, Athens, Greece.
- Lover, E. P. Admiralty Experiment Works, Haslar, England.
- Low, D. J. Ministry of Defence (PE), Bath, England.
- Lyons, R. A. Atkins Research and Development, Epsom, England.
- McCarthy, J. H. David Taylor Naval Ship R & D Center, Bethesda, USA.
- McGregor, R. C. The University of Glasgow, Glasgow, Scotland.
- \*Magnuson, A. H. David Taylor Naval Ship R & D Center, Bethesda, USA.



- Martinussen, K. The Ship Research Institute of Norway, Trondheim, Norway.
- Mazarredo, L. Ciudad Universitaria, Madrid, Spain.
- Mei, C. C. Massachusetts Institute of Technology, Cambridge, USA.
- Melson, L. B. US Navy Sci. & Tech. Gr. Europe, Munich, Germany.
- Merbt, H. Fraunhofer-Gesellschaft zur Förderung der angewandten Forschung e.V. Forschungsgruppe Hydroakustik, Ottobrunn bei München, Germany.
- Messum, L. T. Admiralty Research Laboratory, Teddington, England.
- Meyerhoff, K. Planungsgesellschaft mbH, Hamburg, Germany.
- Miles, M. D. National Research Council, Ottawa, Canada.
- Millward, A. University of Liverpool, Liverpool, England.
- Moeyes, G. Technische Hogeschool Delft, Delft, The Netherlands.
- Moor, D. I. Ship Model Experiment Tank, St. Albans, England.
- \*Moran, D. D. David Taylor Naval Ship R & D Center, Bethesda, USA.
- Morgan, W. B. David Taylor Naval Ship R & D Center, Bethesda, USA.
- Morsi, S. A. University College London, London, England.
- Müller, E. Versuchsanstalt für Binnenschiffbau, Duisburg, Germany.
- Newman, J. N. Massachusetts Institute of Technology, Cambridge, USA.
- Nicholson, K. Admiralty Experiment Works, Haslar, England.
- Nienartowicz, K. Centrum Techniki Orkgtowej, Gdansk, Poland.
- \*Noordzij, L. Netherlands Ship Model Basin, Wageningen, The Netherlands.
- Norris, C. British Ship Research Association, Wallsend, England.
- Nowacki, H. Technische Universität Berlin, Berlin, Germany.
- Nuñez, J. F. Canal de Experiencias Hidrodinámicas, El Pardo, Madrid, Spain.
- Oda, T. Mitsui Shipbuilding & Engineering Co Ltd, Tokyo, Japan.
- \*Odabasi, A. Y. The British Ship Research Association, Wallsend, England.
- Oltmann, P. Institut für Schiffbau, Hamburg, Germany.
- Oosterveld, M. W. C. Netherlands Ship Model Basin, Wageningen, The Netherlands.
- Osborn, R. J. Ministry of Defence (PE), Bath, England.
- Paffett, J. A. H. National Physical Laboratory, Feltham, England.
- Parkinson, A. G. University College London, London, England.
- Paul, K. Technical University Gdansk, Gdansk, Poland.
- Pérez-Sobrino, M. Canal de Experiencias Hidrodinámicas, El Pardo, Madrid, Spain.
- Piantini, E. Mariconavarmi, c/o Italian Embassy, London, England.
- Pinkster, J. A. Netherlands Ship Model Basin, Wageningen, The Netherlands.
- Powell, A. David Taylor Naval Ship R & D Center, Bethesda, USA.
- Price, W. G. University College London, London, England.
- Pronk, C. Drunen, The Netherlands.
- Prytz, K. Chantiers Navals de La Ciotat, France.
- Pylkkänen, J. Helsinki University of Technology, Espoo, Finland.
- Rainey, R. C. T. Y-ARD, Glasgow, Scotland.
- Rawson, K. J. University College London, London, England.
- Remmers, K. Kempf and Remmers, Hamburg, Germany.
- Ritter, H. National Physical Laboratory, Feltham, England.
- Roberts, G. O. Science Applications Inc., McLean, USA.
- Robins, A. J. Admiralty Research Laboratory, Teddington, England.
- Roucous, R. Centre Universitaire, Orsay, France.
- Roy, S. University College London, London, England.
- Rutgersson, O. Statens Skeppsprovvningsanstalt, Göteborg, Sweden.
- Rynning, S. River & Harbour Laboratory, Trondheim, Norway.
- Sabuncu, T. Technical University of Istanbul, Istanbul, Turkey.
- Salaün, P. Office National D'Etudes et de Recherches Aérospatiales, Châtillon-Sous Bagneux, France.
- \*Salvesen, N. David Taylor Naval Ship R & D Center, Bethesda, USA.
- Sani, G. Cetena, Genova, Italy.
- Sayer, P. University of Manchester, Manchester, England.
- Schenzle, P. Hamburg University, Hamburg, Germany.
- Schmiechen, M. Für Wasserbau und Schiffbau, Berlin, Germany.
- Schmitke, R. T. Defence Research Establishment Atlantic, Dartmouth, Canada.
- Schwanecke, H. Technische Universität Wien, Wien, Austria.
- Sharma, S. D. Institut für Schiffbau der Universität Hamburg, Hamburg, Germany.
- Simmonds, M. H. Hawker Siddeley Dynamics Ltd, Stevenage, England.
- Sinclair, L. Stone Manganese Marine Ltd, London, England.
- Slaattelid, O. H. A/S Strømmen Staal, Strømmen, Norway.
- Smitt, L. W. Skibsteknisk Laboratorium, Lyngby, Denmark.
- Søntvedt, T. Det Norske Veritas, Oslo, Norway.
- Sparenberg, J. A. University of Groningen, Groningen, The Netherlands.
- Spencer, J. B. Ministry of Defence (PE), Bath, England.
- \*Standing, R. G. National Physical Laboratory, Feltham, England.
- Steele, B. N. Admiralty Experiment Works, Haslar, England.
- Strasser, G. Technische Universität Wien, Wien, Austria.
- Stuhmiller, J. H. Jaycor, Del Mar, USA.
- Stuurman, A. M. Ministerie Van Defensie Marine, The Hague, Netherlands.
- Suhrbier, K. R. Vosper Thornycroft Ltd, Portsmouth, England.

Sukselainen, I. J.	Technical Research Centre of Finland, Espoo, Finland.	Vermeer, H.	Netherlands Directorate General of Shipping and Navigation, The Hague, The Netherlands.
Sulmont, P.	Ecole Nationale Supérieure de Mécanique, Nantes, France.	Visconti, M.	Alsthom—TDF, Grenoble Cedex, France.
*Swift, M. R.	University of New Hampshire, Durham, USA.	Vytlačil, N.	Westinghouse Electric Corp., Annapolis, USA.
Swift, P. M.	Shell International Marine Ltd, London, England.	Wade, R. B.	Tetra Tech Inc, Pasadena, USA.
Takekawa, M.	Sumitomo Shipbuilding and Machinery Co Ltd, Yokosuka, Japan.	Walderhaug, H.	Kockums Mek Verkstads AB, Malmö, Sweden.
Takezawa, S.	Yokohama National University, Yokohama, Japan.	Wang, S.	Tetra Tech Inc, Pasadena, USA.
Tam, P.	University College London, London, England.	Watson, T.	Panama City, Florida, USA.
Tasaki, R.	Ishikawajima—Harima Heavy Industries Co Ltd, Yokohama, Japan.	Webster, W. C.	Hamburg, Rothenbaumchaussee 34, Germany.
Tattersall, E.	Hovermarine Transport, Southampton, England.	Wehausen, J. V.	University of California, Berkeley, USA.
Thomas, P. V.	Admiralty Experiment Works, Haslar, England.	Wellicome, J.	University of Southampton, Southampton, England.
Tran-Van-Nhieu, M.	Ecole Nationale Supérieure de Techniques Avancées, Paris, France.	Wereldsma, R.	Technical University Delft, Delft, The Netherlands.
Treshchevsky, V. N.	Krylov Ship Research Institute, Leningrad, USSR.	Wermter, R.	David Taylor Naval Ship R & D Center, Bethesda, USA.
Tsakonas, S.	Stevens Institute of Technology, Hoboken, USA.	Wieghardt, K.	Institut für Schiffbau, Hamburg, Germany.
Tupper, E. C.	Admiralty Experiment Works, Haslar, England.	Wiersma, A. K.	Mathematisch Instituut, Groningen, The Netherlands.
Uhlen, R. C.	Exxon International Co, New York, USA.	Williams, N. R.	AERE, Harwell, England.
Ursell, F.	University of Manchester, Manchester, England.	Williams, S.	University of Newcastle upon Tyne, Newcastle upon Tyne, England.
van de Voorde, C. B.	TNO—IWECO, Delft, The Netherlands.	Wolff, K.	Institut für Schiffbau, Hamburg, Germany.
van Gent, W.	Netherlands Ship Model Basin, Wageningen, The Netherlands.	Wood, A. D.	Office of Naval Research, Boston, USA.
van Oorschot, J. H.	Delft Hydraulics Laboratory, Delft, The Netherlands.	Wu, T. Y.	California Institute of Technology, Pasadena, USA.
van Oortmerssen, G.	Netherlands Ship Model Basin, Wageningen, The Netherlands.	Yamanouchi, Y.	Mitsui Shipbuilding & Engineering Co Ltd, Tokyo, Japan.
		Yeung, R. W.	Massachusetts Institute of Technology, Cambridge, USA.
		Yoshida, K.	University of Tokyo, Tokyo, Japan.
		Yue, D.	Massachusetts Institute of Technology, Cambridge, USA.

## PREVIOUS BOOKS IN THE NAVAL HYDRODYNAMICS SERIES

"First Symposium on Naval Hydrodynamics," National Academy of Science—National Research Council, Publication 515, 1957, Washington, D.C.; PB133732, paper copy \$11.25, 16-mm microfilm \$2.25.

"Second Symposium on Naval Hydrodynamics: Hydrodynamic Noise and Cavity Flow," Office of Naval Research, Department of the Navy, ACR-38, 1958; PB157668, paper copy \$13.25, 16-mm microfilm \$2.25.

"Third Symposium on Naval Hydrodynamics: High-Performance Ships," Office of Naval Research, Department of the Navy, ACR-65, 1960; AD430729, paper copy \$15.25, 16-mm microfilm \$2.25.

"Fourth Symposium on Naval Hydrodynamics: Propulsion and Hydroelasticity," Office of Naval Research, Department of the Navy, ACR-92, 1962; AD447732, paper copy \$29.25, 16-mm microfilm \$2.25.

"The Collected Papers of Sir Thomas Havelock on Hydrodynamics," Office of Naval Research, Department of the Navy, ACR-103, 1963; AD623589, paper copy \$15.25, microfiche \$2.25.

"Fifth Symposium on Naval Hydrodynamics: Ship Motions and Drag Reduction," Office of Naval Research, Department of the Navy, ACR-112, 1964; AD640539, paper copy \$29.25, microfiche \$2.25.

"Sixth Symposium on Naval Hydrodynamics: Physics of Fluids, Maneuverability and Ocean Platforms, Ocean Waves, and Ship-Generated Waves and Wave Resistance," Office of Naval Research, Department of the Navy, ACR-136, 1966; AD676079, paper copy \$17.25, microfiche \$2.25.

"Seventh Symposium on Naval Hydrodynamics: Unsteady Propeller Forces, Fundamental Hydrodynamics, Unconventional Propulsion," Office of Naval Research, Department of the Navy, DR-148, 1968; AD721180, paper copy \$49.25, microfiche \$2.25.

"Eighth Symposium on Naval Hydrodynamics: Hydrodynamics in the Ocean Environment," Office of Naval Research, Department of the Navy, ACR-179, 1970; AD748721; Available from Superintendent of Documents, U.S. Government Printing Office, Washington, D.C., 20404, Clothbound, 1185 pages, illustrated (Catalog No. D 210.15: ACR-179; Stock No. 0851-0056), \$11.75, microfiche \$2.25.

"Ninth Symposium on Naval Hydrodynamics: Unconventional Ships, Ocean Engineering, Frontier Problems," Office of Naval Research, Department of the Navy, ACR-203, 1972; Two Volumes; Vol. 1, ADA010505; Vol. 2, ADA010506; Available from Superintendent of Documents, U.S. Government Printing Office, Washington, D.C., 20404, Clothbound, 1108 pages, Vol. 1, 903 pages, Vol. 2, illustrated (Catalog Nos. D210.15:ACR-203/V1; D210.15:ACR-203/V2; Stock Nos. 0851-00062, 0851-00063); Vol. 1, \$15.55, Vol. 2, \$13.55; microfiche \$2.25.

"Tenth Symposium on Naval Hydrodynamics: Hydrodynamics for Safety, Fundamental Hydrodynamics," Office of Naval Research, Department of the Navy, ACR-204, 1974.

*NOTE: The above books are available on microfilm and microfiche from the National Technical Information Service, US Department of Commerce, Springfield, Virginia 22151. The first six books are also available from NTIS in paper copies. The catalog numbers and the prices for paper, clothbound, and microfilm copies are shown for each book.*